Coupled Problems in Science and Engineering VII

12 – 14 June 2017, Rhodes Island, Greece

Manolis Papadrakakis, Eugenio Oñate and Bernhard Schrefler (Eds.)

Coupled Problems in Science and Engineering VII

COUPLED PROBLEMS 2017

Proceedings of the VII International Conference on
Coupled Problems in Science and Engineering
Rhodes Islad, Greece
June 12 – 14, 2017

Edited by:

Manolis Papadrakakis
Institute of Structural Analysis & Antiseismic Research
National Technical University of Athens, Greece

Eugenio Oñate
International Center for Numerical Methods in Engineering (CIMNE), Spain
Universitat Politècnica de Catalunya (UPC)

Bernhard A. Schrefler
Department of Civil, Environmental and Architectural Engineering
Università degli Studi di Padova, Italy

A publication of:
International Center for Numerical Methods in Engineering (CIMNE)
Barcelona, Spain

International Center for Numerical Methods in Engineering (CIMNE)
Gran Capitán s/n, 08034 Barcelona, Spain

COUPLED PROBLEMS 2017
M. Papadrakakis, E. Oñate and B. Schrefler (Eds.)

First Edition: May 2017

Printed by: Artes Gráficas Torres S.L., Huelva 9, 08940 Cornellà de Llobregat, Spain

ISBN: 978-84-946909-2-1

TABLE OF CONTENTS

PREFACE

This volume contains the Technical Programme of the papers accepted for presentation at the **VII International Conference on Computational Methods for Coupled Problems in Science and Engineering, *COUPLED PROBLEMS 2017 (*12 - 14 June 2017, Rhodes Island, Greece).**

The previous five editions of this conference were held on the islands of *Santorini (Greece) on 25-28 May 2005, Ibiza (Spain) on 21-23 May 2007, Ischia (Italy) on 8-11 June 2009, Kos (Greece) on 20-22 June 2011, Ibiza (Spain) on June 17 – 19 June 2013 and on San Servolo, Venice, Italy on May 18 - 20 2015.*

The objectives of **COUPLED PROBLEMS 2017** are to present and discuss state of the art, mathematical models, numerical methods and computational techniques for solving coupling problems of multidisciplinary character in science and engineering. The conference goal is to make a step forward in the formulation and solution of real life problems with a multidisciplinary vision, accounting for all the complex couplings involved in the physical description of the problem.

The conference is one of the Thematic Conferences of the European Community on Computational Methods in Applied Sciences (**ECCOMAS**) and a Special Interest Conference of the International Association for Computational Mechanics (**IACM**).

The conference is jointly organized by the National Technical University of Athens (Greece), the International Centre for Numerical Methods in Engineering (CIMNE) of the Technical University of Catalonia (UPC) and the Department of Civil, Environmental and Architectural Engineering (DICEA), of the University of Padova (Italy).

The organizers would like to thank the authors for submitting their contributions and for their respect of the deadlines. Special thanks go to the colleagues who contributed to the organization of the **26 Invited Sessions** in the fields of the Conference, and to the colleagues of international prestige that accepted the invitation to address a **Plenary Lecture**.

Manolis Papadrakakis	**Eugenio Oñate**	**Bernhard A. Schrefler**
Institute of Structural Analysis & Antiseismic Research National Technical University Athens, Greece	*International Center for Numerical Methods in Engineering (CIMNE) Univ. Politècnica de Catalunya (UPC), Barcelona, Spain*	*Department of Civil, Environmental and Architectural Engineering (DICEA) Università di Padova Padova, Italy*

SUPPORTING ORGANIZATIONS

National Technical University of Athens (NTUA), Greece

International Center for Numerical Methods in Engineering (CIMNE), Spain

UNIVERSITÀ DEGLI STUDI DI PADOVA

Department of Civil, Environmental and Architectural Engineering (DICEA)

of the University of Padova, Italy

European Community on Computational Methods in Applied Sciences (ECCOMAS)

International Association for Computational Mechanics (IACM)

Technical University of Catalonia (UPC), Spain

ACKNOWLEDGEMENTS

The conference organizers acknowledge the support towards the organization of the COUPLED PROBLEMS 2017 Conference to the following **organizations**:

- National Technical University of Athens, Greece
- International Center for Numerical Methods in Engineering (CIMNE), Barcelona, Spain
- Universitat Politècnica de Catalunya, Spain
- Department of Civil, Environmental and Architectural Engineering (DICEA), Università di Padova, Italy
- European Community on Computational Methods in Applied Sciences (ECCOMAS)
- International Association for Computational Mechanics (IACM)

PLENARY SPEAKERS AND INVITED SESSION ORGANIZERS

We would also like to thank the Plenary Speakers and the Invited Session Organizers for their help in the setting up of a high standard Scientific Programme.

Plenary Speakers: *Ferdinando Auricchio, Thierry Coupez, Antonio Huerta, Antonia Larese, Bernd Markert, Miriam Mehl, Alfio Quarteroni, Harald van Brummelen and Wolfgang Wall.*

Invited Session Organizers: *Giuseppe Abbiati, Gernot Beer, Marek Behr, Pavel B. Bochev, Oreste S. Bursi, Hugo Casquero Penelas, Luis Chacon, Francisco Chinesta, Elías Cueto, Eric C. Cyr, Suvranu De, Laura De Lorenzis, Paolo Decuzzi, Dieter Dinkler, John A. Evans, Carlos Felippa, C. Alberto Figueroa, Felix Fritzen, Michael W. Gee, Antonio J. Gil, Hector Gomez, Massimo Guarnieri, Sergio Idelsohn, A.V. Karapetyan, Alexey Kireenkov, Manfred Krafczyk, Paul Ledger, Bernd Markert, Hermann G. Matthies, Kurt Maute, Matthias Mayr, Federico Moro, Ralf Müller, Roger Ohayon, Eugenio Oñate, K.C. Park, Roger P. Pawlowski, Jacques Periaux. Simona Perotto, Kara Peterson, Annalisa Quaini, Gianluigi Rozza, David Ryckelynck, Pavel Ryzhakov, Lorenzo Sanavia, Bozidar Šarler, Guglielmo Scovazzi, John N. Shadid, Ole Sigmund, Claudio Tamagnini, Nicola Tondini, Haim Waisman, Wolfgang A. Wall, Peter Wriggers, Zohar Yosibash, Yue Yu and Yonggjie (Jessica) Zhang*

SUMMARY

CONTENTS

INVITED SESSIONS

IS - Advanced Models and Methods in CFD

IS - Advances in Heterogeneous Numerical Methods

IS - Computational Models and Methods for Multiphysics Processes in Multiphase Porous Media

IS - Control, Uncertainty Quantification, and ROMs in Coupled Problems

IS - Coupled Problems in Advanced Energy Research

IS - Coupled Problems in Liquid-Solid Systems

IS - Coupled Problems in the Biomechanics of Bones and Arteries

IS - Coupled Problems of the Dynamics of the Solid Systems with Friction

IS - Coupled Problems with Numerical and Physical Subdomain Interactions

IS - Coupling of different numerical methods and to CAD

IS - Isogeometric Methods for Coupled Problems on Complex Geometries

IS - Model Order Reduction for Coupled Problems

IS - Multi-physics Modeling and Multi-Scale Simulation of Aging and Deteriorating Materials I

IS - Optimization in Coupled Problems

IS - Particle-Based Methods in Coupled Problems

CONTRIBUTED SESSIONS

Applications of Coupled Problems

Coupled Problems in Bio-Medicine

Coupled Problems in Electro-Magnetics

Coupled Problems in Fluid-Structure Interaction

Coupled Problems in Geomechanics

Coupled Problems in Thermo-Mechanics

Coupled Solution Strategies

Design Optimization and Control

High Performance Computing

Mathematical Formulation of Coupled Problems

Multiphysics Problems

Multiscale Problems

Numerical Methods in Coupled Problems: Finite Difference, Particle Methods, Meshless Methods, etc.

INVITED SESSIONS

VII International Conference on Computational Methods for Coupled Problems in Science and Engineering
COUPLED PROBLEMS 2017
M. Papadrakakis, E. Oñate and B. Schrefler (Eds)

NOVEL KINETIC CONSISTENT ALGORITHM FOR THE MODELING OF INCOMPRESSIBLE CONDUCTING FLOWS

B. CHETVERUSHKIN[*], N. D'ASCENZO[†] , A.SAVELIEV[**††] AND V. SAVELIEV[**†]**

[*] Keldysh Institute of Applied Mathematics
Russian Academy of Science (KIAM RAS)
4 Miusskaya sq, 125047 Moscow, Russia
e-mail: chetver@imamod.ru, web page: http://www.kiam.ru

[†]Deutsches Elektronen Synchrotron (DESY)
85 Notkestrasse, 22607 Hamburg, Germany
e-mail: ndasc@mail.desy.de - Web page: http://www.desy.de

[††]Hamburg University
85 Notkestrasse, 22607 Hamburg, Germany
e-mail: Andrey.Saveliev@desy.de - Web page: http://www.desy.de

[**] Immanuel Kant Baltic Federal University
14 Alexandr Nevsky str., 236016, Kaliningrad, Russia
e-mail: saveliev@mail.desy.de - Web page http://www.kantiana.ru

Key words: MGD pump, numerical methods, kinetic consistent algorithms

Abstract. In this study we aim at demonstrating that kinetic consistent magneto gas dynamic algorithms are a valid for the computation of the dynamics of incompressible conductive flows. We obtain numerical solutions for the test problems, namely the laminar flow inside a wall-driven cavity and a magnetic driven pump. We show that kinetic consistent algorithms have a high stability in the solution of convection-dominated flows, due to a correct physical modeling of the fluid viscosity and to the possibility of tuning appropriate regularization terms on the basis of the physical properties of the fluid. We show that the kinetic consistent approach offers a stable basis for a correct physical description of the shear viscosity, thermal conduction and electric resistivity effects in incompressible magneto hydrodynamics flows.

1 INTRODUCTION

Recently many important critical technical applications are based on the magnetohydrodynamic principles. The magnetohydrodynamic pumping (MHP) of electrically con-

ductive fluid is of growing interest for many industrial applications requiring precise flow control, especially in the critical conditions, enabling to break the flow or reverse flow direction without any moving parts or mechanical devices. Today, different MHD pump systems are widely used in many metal melting environments such as, among others, extrusion billet casting, metal refinery for transporting molten metals, liquid metal circulation for alloys production. These pumps have many advantages over the mechanical pumps including precise flow control, reduced energy consumption and less dross formation.

In the recent publications of the authors [1, 2], using a complex statistical distribution function and kinetic consistent scheme, it was investigated the effective numerical algorithm for the parallel high performance computing systems for the solution of the magneto gas dynamic problems. In [2] the results were presented of the mathematical modeling of the accretion processes of interstellar matter on the compact massive astrophysical object. We investigated the three dimensional system of differential equations including he three dimensional equation of the magnetic induction with the magnetic viscosity.

The goal of the present study is the extension of the proposed kinetic consistent magneto gas dynamic algorithms, efficient with numerical computations on the detailed space mesh, more than 10^9 cells, for the mathematical modeling of the conducting incompressible liquid flows.

In common approaches the algorithms of mathematical modeling of incompressible liquids are dramatically different from viscous heat conductive magneto gas dynamics algorithms. The present study, based on the "equivalence" of the gases with Mach numbers less then 0.1, investigated the possibility of using the method of magneto gas dynamics with minimal changes for the mathematical modeling of the incompressible conductive liquid flow.

2 Mathematical Model

The sound speed in liquids is significantly higher then in gases. Taking into account that in technological systems the characteristic velocities is of the order of few meters per second the condition

$$U \leq 0.1M \tag{1}$$

is fully satisfied.

The state equation (artificial) can be formulated as

$$P = P_0 + \beta(\rho - \rho_0) \tag{2}$$

where the parameter β should define the condition of strong changes of the pressure with smallest changes in density.

In this conditions the kinetic consistent system of equations is :

$$\frac{\partial \rho}{\partial t} + \frac{\tau}{2}\frac{\partial^2 \rho}{\partial t^2} + \frac{\partial}{\partial x_i}\rho u_i = \frac{\partial}{\partial x_i}\left(\frac{\tau}{2}\frac{\partial}{\partial x_k}\Pi_{ik}\right) \tag{3}$$

$$\frac{\partial \rho u_i}{\partial} + \frac{\tau}{2}\frac{\partial^2}{\partial t^2}\rho u_i + \frac{\partial}{\partial x_k}\Pi_{ik} = \frac{\partial}{\partial x_k}\Pi^D_{ik} + \frac{\partial}{\partial x_k}\left[\left(\frac{\tau}{2}\frac{\partial}{\partial x_k}\Pi_{ik}\right)u_k\right] \tag{4}$$

$$\begin{aligned}\frac{\partial E}{\partial t} + \frac{\tau}{2}\frac{\partial^2 E}{\partial t^2} + \frac{\partial F_i}{\partial x_i} &= \frac{\partial Q_i}{\partial x_i} + \frac{\partial}{\partial x_i}\Pi^D_{ik}u_k - B_k\Pi^{DB}_{ik} \\ &+ \frac{\partial}{\partial x_i}\left[\frac{1}{\rho}\left(E + p + \frac{B^2}{8\pi}\right)\left(\frac{\tau}{2}\frac{\partial}{\partial x_k}\Pi_{ik}\right)\right]\end{aligned} \tag{5}$$

$$\frac{\partial B_i}{\partial t} + \frac{\tau_M}{2}\frac{\partial^2 B_i}{\partial t^2} + \frac{\partial}{\partial x_k}M^B_{ik} = \frac{\partial}{\partial x_k}\Pi^{DB}_{ik} \tag{6}$$

where the fluxes are:

$$\Pi_{ik} = \left(p + \frac{B^2}{8\pi}\right)\delta_{ik} + \rho u_i u_k - \frac{B_i B_k}{4\pi} \tag{7}$$

$$F_i = \left[\left(E + p + \frac{B^2}{8\pi}\right)u_i - \frac{B_i u_k B_k}{4\pi}\right] \tag{8}$$

$$M^B_{ik} = u_k B_i - u_i B_k \tag{9}$$

$$\Pi^D_{ik} = \frac{\tau}{2}\left[p\frac{\partial u_i}{\partial x_k} + p\frac{\partial u_k}{\partial x_i} - \frac{2}{3}p\frac{\partial u_m}{\partial x_m}\delta_{ik}\right] + O\left(Ma^2\right) \tag{10}$$

$$Q^D_i = \frac{\tau}{2}\left[\frac{5}{2}p\frac{\partial}{\partial x_i}\frac{p}{\rho}\right] + O\left(Ma^2\right) \tag{11}$$

$$\Pi^{DB}_{ik} = \frac{\tau_M}{2}\left[\frac{1}{\rho}\left(p + \frac{B^2}{8\pi}\right)\left(\frac{\partial B_i}{\partial x_k} - \frac{\partial B_k}{\partial x_i}\right)\right] + O\left(Ma^2\right) \tag{12}$$

On the left-hand side of the system of Eqs. 3-6 we retrieve the ideal magneto gas dynamics fluxes, which are extensively expressed in the first three terms of Eq. 12. The respective fluxes are the momentum, heat and magnetic field flux of the ideal magneto gas dynamics.

On the right-hand side of the system of Eqs. 3-6 we obtain additional dissipative terms. We have shown in [2] that the leading dissipative terms correspond to the Navier-Stokes and the physical resistivity, the additional dissipative terms being a smaller order computational stabiliser. The respective fluxes are extensively expressed in the last three terms of Eq. 12. They are the Navier-Stokes momentum and thermal flux and the additional magnetic flux due to the finite resistivity. We note here that, in comparison with the dissipative fluxes proposed in [2], the correction of $O(Ma^2)$ are neglected, as we deal with low Mach number Ma problems in this study.

3 NUMERICAL EXAMPLES

3.1 Lid driven cavity

This test is presented in [4, 5]. Here we use the same normalized units thereby defined for a better comparison of the results. A cavity filled in with fluid is defined on the two-dimensional domain $[0,1] \times [0,1]$. At the initial time the fluid is at rest, its density is constant and equal to $\rho_0 = 1$, its pressure is constant and equal to $p_0 = \gamma^{-1} Ma^{-2}$. The Mach number $Ma = 0.15$ and the adiabatic constant $\gamma = 1.4$ are used. The magnetic field is absent. The simulation is performed with different numbers of the Reynolds number $Re = 400, 1000, 3400$. The chosen set of parameters defines the fluid viscosity and the thermal conductivity:

$$\mu = \frac{Ma \cdot c}{Re} \qquad k = \frac{\mu}{\gamma - 1} \tag{13}$$

where c is the thermal velocity of the fluid $c = \sqrt{\gamma p/\rho}$. The value of τ in the kinetic algorithm is:

$$\tau = \frac{\mu}{p} + \alpha \frac{h}{c} \tag{14}$$

where h is the mesh size. The computational domain is divided into a mesh of 128×128 cells in order to provide a direct comparison with [4]. The boundary conditions are open for all variables, except for the velocity, which is set to 0 on the $x = 0, x = 1, z = 0$ borders and to 1 on the $z = 1$ border.

Although this numerical example does not include the magnetic field, it provides a solid and well-established test for the gas dynamic components of the kinetic algorithm. The solution presents in fact a regular turbulent structure, with vortexes at a position and size confirmed by a large number of theoretical and experimental studies. In comparison with the traditional approaches [4], the set of kinetic consistent equations used in this study includes the density continuity equation and the energy dissipation. We like to show that the incompressibility of the fluid follows from the physical property of the fluid at a low Mach number.

The simulation is run until the steady state is reached, a time at which the density and the streamlines of the velocity field are calculated and the results are shown on Fig. 1–Fig. 3.

In the three cases under examination, the density keeps its initial constant value within a 5% tolerance, which defines a small level of compressibility due to the set of equations used. The velocity streamlines are consistent with the expectations in []. The central vortex is moving closer to the center with increasing Reynold number. At $Re = 400$, besides the central vortex, two additional vortexes on the lower corners appear. Their size increases with higher Reynold number. In addition the appearance of a vortex on the top left corner for the higher Reynold number $Re = 3200$ guarantees the correctness of the kinetic consistent equations used in this study.

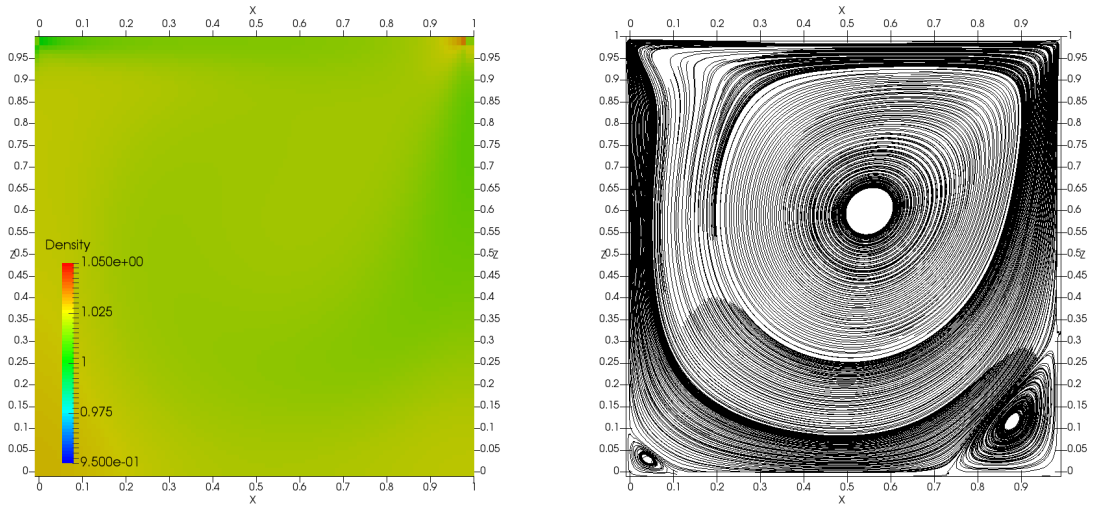

Figure 1: Density (left) and streamlines of the velocity field (right) of the lid driven cavity problem with $Re = 400$.

3.2 Lid driven cavity with liquid sodium

As a second test we repeat the lid-driven cavity test proposed in the previous section using the physical parameters and units for the description of the behavior of liquid sodium. A cavity of size 0.3 m×0.3 m is filled in with liquid sodium. At the initial time the liquid metal is at rest, with initial density $\rho_0 = 874$ Kg/m^3 and temperature T = 600° K. The magnetic field is absent.

The upper lid is moving with a velocity of 2 m/s, which defines a Mach number of 0.005. This is a typical value of the stream velocity of liquid metal systems.

The liquid sodium viscosity and thermal conductivity are calculated with the empirical formulation from tabulated data [6]:

$$\mu = \exp\left(-6.4406 - 0.3958 \log T + \frac{556.835}{T}\right) \tag{15}$$

$$k = -124.67 - 0.11381T + 5.5226 \times 10^{-5}T^2 - 1.1842 \times 10^{-8}T^3 \tag{16}$$

The value of τ in the kinetic algorithm is calculated as in Eq. 14.

The computational domain is decomposed into 128×128 cells, the mesh size being then $h = 2.34375$ mm. As above the boundary conditions are open for all variables, except for the velocity, which is set to 0 on the $x = 0, x = 1, z = 0$ borders and to 2 m/s on the $z = 1$ border.

Although also this test does not include the magnetic field, it is a necessary step for the evaluation of the modeling performance. We aim at showing that, using a more realistic set of parameters for the description of the liquid sodium, the structure of the streamlines of the velocity field assumes specific features, which can not be easily included

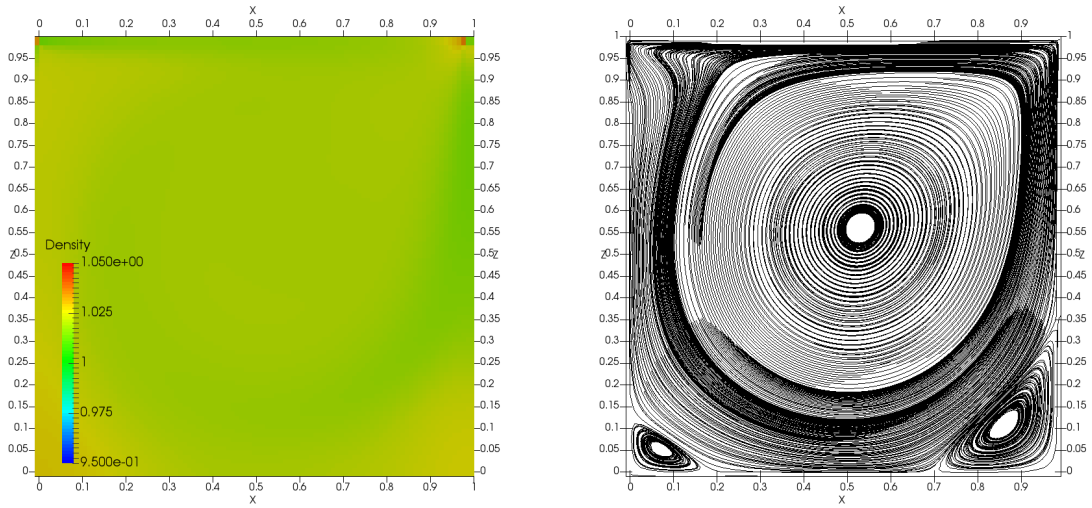

Figure 2: Density (left) and streamlines of the velocity field (right) of the lid driven cavity problem with $Re = 1000$.

in the previous lid-driven cavity normalized problem. Moreover as before the set of kinetic consistent equations used in this study includes the density continuity equation and the energy dissipation. We like to show that the non compressibility of the liquid sodium follows from the physical property of the fluid at a low Mach number.

In Fig. 4 we show the solution at time $t = 1s$. Although it is far from the steady state, the vortex structure inset is clearly visible. We plan to extend the simulation to further time, in order to study the vortex structure at the steady state. The density is constant, with the exception of the points at the edges of the lid, which are well-known as discontinuity points in this test. Thus also the compressible-fluid approximation of the solution is preserved at initial times by the kinetic consistent set of equations used in the calculation.

3.3 Liquid sodium flow in pipe with magnetohydrodynamic pump

In this third numerical test we include the magnetic field for the simulation of a prototype of a liquid sodium magnetic pump pipe. This problem arises in the cooling systems of high-density thermal power, which require fluids with high thermal conductivity, such as liquid metals. Electromagnetic pumps are used in liquid metal flow control in cooling systems. The operation of the electromagnetic pump used for the flow control is based on the Faraday principle, where the electric current and the magnetic field interaction generates the magnetic driving force which produces the metallic fluid flow [7]. This type of equipment can control a high conductivity liquid metal flow in a close circuit and facilitates natural circulation in the event of failures or accidents, which is highly convenient for the safety of nuclear reactors.

In this simulation a 2-dimensional pipe with dimensions 0.3 m×0.1 m is filled with liquid

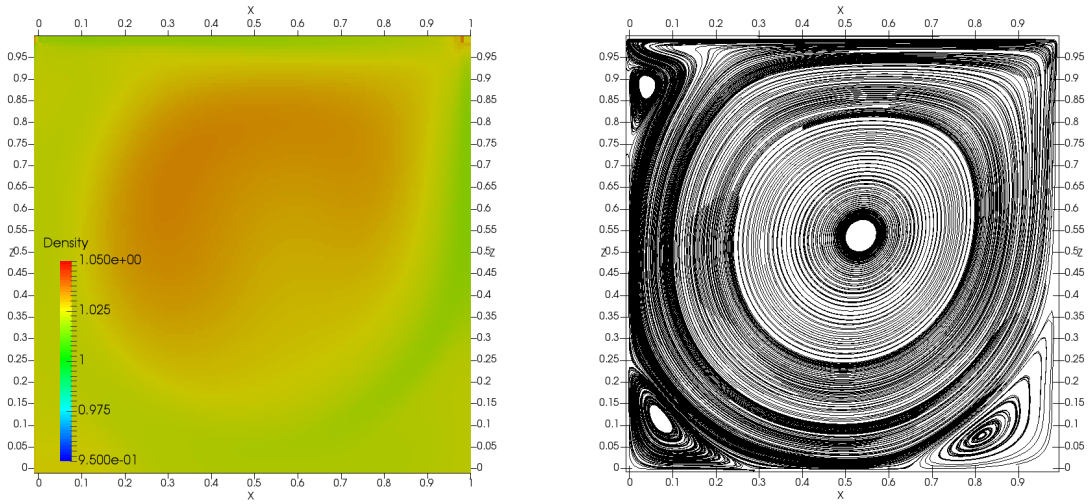

Figure 3: Density (left) and streamlines of the velocity field (right) of the lid driven cavity problem with $Re = 3400$.

sodium. At the initial time the liquid metal is at rest, with initial density $\rho_0 = 878$ Kg/m^3 and temperature T = 600° K. In the first portion of the pipe, at $x < 0.1$ m, an external current is placed, with direction perpendicular to the pipe and strength $I = 800$ A. In the same portion of the pipe and initial magnetic field directed along the y-axis is placed, with strength $B = 0.05$ T. These magnetic field and current provide the driving force of the liquid meal flow.

Border conditions are open for all variables at all boundaries, with the exception of the velocity, which is set to 0 at the upper and lower boundaries. The liquid sodium viscosity and thermal conductivity are calculated with the empirical formulation from tabulated data [6] as in Eq. 15 and Eq. 16. The resistivity is calculated also from tabulated data:

$$\mu_b = \big(-9.9141 + 8.2022 \times 10^{-2} T - 1.3215 \times 10^{-4} T^2 + 1.7272 \times 10^{-7} T^3 \\ -9.0265 \times 10^{-11} T^4 + 1.9553 \times 10^{-14} T^5\big) \times 10^{-8} \qquad (17)$$

The results of the numerical modeling are shown on Fig. 5 at a time $t = 10$ ms. Following the magnetic force induced by the magnetic field and he current, a flow is organized in the pipe. The profile of the velocity flow is shown on Fig. 6 and is in agreement with a laminar flow hypothesis. The velocity flow has a maximum strength of 2.5 m/s in the center of the pipe. The density is uniform within a tolerance of 3%, which provides also the magnitude of the compressible liquid approximation in the kinetic consistent equations used in this study. The magnetic field lines are distorted and smoothed, as as result of the interaction with the produced flow and of the liquid sodium resistivity.

This test is the first successful step for the demonstration of the use of the kinetic consistent magneto gas dynamics equations in the modeling of the magnetic pump flow for liquid metals.

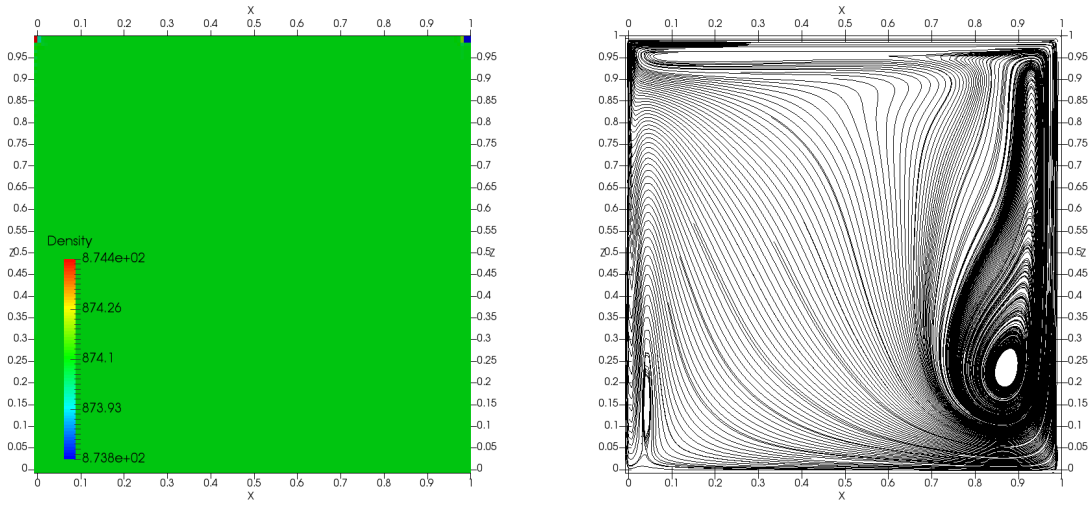

Figure 4: Density (left) and streamlines of the velocity field (right) of the lid driven cavity problem for liquid sodium at time t=1s .

4 CONCLUSIONS

Kinetic consistent model previously is used for the mathematical modeling of the ionized gases, can be successfully used for the mathematical modelling of the incompressive conducting liquid flow (magnetohydrodynamic problems). Proposed algorithm is inportant for mathematical modelling of the processes in number of the inportant technological systems at parallel high performance computing systems.

ACNOWLEDGEMENT

This study was supported by Russian Science Foundation grant 14-11-00170

REFERENCES

[1] B.N. Chetverushkin, N. DAscenzo, V.I. Saveliev, Kinetically Consistent Magnetogasdynamic Equations and Their Use in Supercomputer Computations, *Dokl. Math, RAS.* (2014) **90**:495-498.

[2] B.N. Chetverushkin, N. DAscenzo, V.I. Saveliev, Kinetically Consistent Magnetogasdynamic Equations and Their Use in Supercomputer Computations, *Dokl. Math, RAS.* (2014) **90**:495-498.

[3] B.N. Chetverushkin, N. DAscenzo, V.I. Saveliev, Hyperbolic type explicit kinetic scheme of magneto gas dynamics for high performance computing systems,*Russ. J. Num. Anal. Math. Model.* (2015) **30** 27-36.

[4] Chia U., Chia K.N., Shin C.T. High Re Solutions for Incompressible Flow Using the Navier-Stokes Equations and a Multigrid Method. *J. of Computational Physics* (1982) **48**:384–411.

[5] J.L.Sohn Evaluation of Fidap on some Classical Laminar and Turbulent Benchmarks *Int. J. for Num. Meth. in Fluids* (1998) **8**:1469–1490.

[6] J.K. Fink and L. Leibowitz, *Thermodynamic and transport properties of sodium liquid and vapor*, ANL/RE-95/2, 1995.

[7] E. M. Borges, F.A. Braz Filbo, L. N. F. Guimaraes, *Liquid metal flow control by DC electromagnetic pump*, Thermal Engineering, (2010) **9** 47-54.

[8] U.Chia, K.N.Chia and C.T.Shin, *Thermodynamic and transport properties of sodium liquid and vapor*, ANL/RE-95/2, 1995.

[9] J.K. Fink and L. Leibowitz, *Thermodynamic and transport properties of sodium liquid and vapor*, ANL/RE-95/2, 1995.

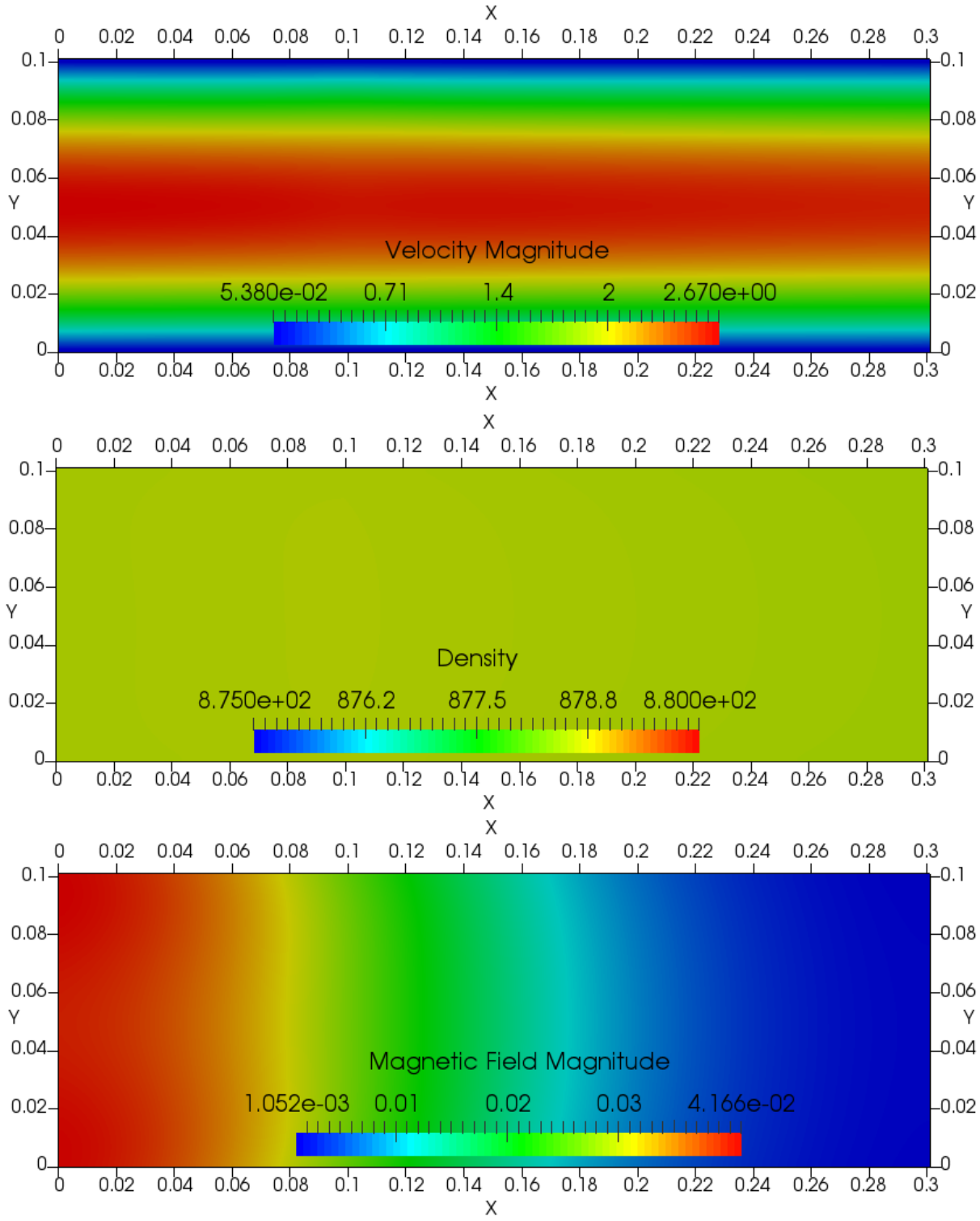

Figure 5: Density, magnetic field and velocity of the liquid sodium magnetic pump pipe problem at t=10 ms.

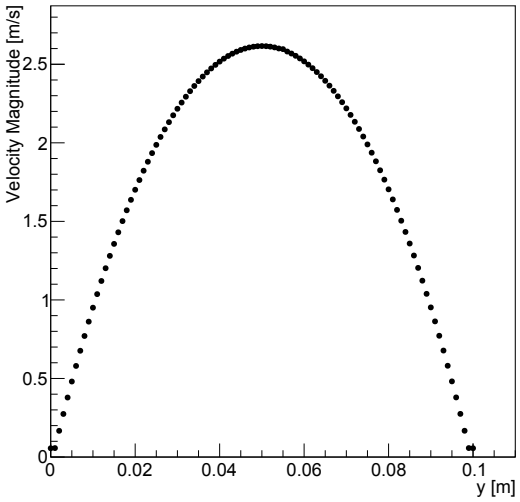

Figure 6: Profile of the velocity magnitude along a line parallel to the y-axis for the liquid sodium magnetic pump pipe problem at t=10 ms.

VII International Conference on Computational Methods for Coupled Problems in Science and Engineering
COUPLED PROBLEMS 2017
M. Papadrakakis, E. Oñate and B. Schrefler (Eds)

A THEORETICAL STUDY OF A SIMPLIFIED AIR-SEA COUPLING PROBLEM INCLUDING TURBULENT PARAMETERIZATIONS

C. PELLETIER*, F. LEMARIÉ† AND E. BLAYO*

†Corresponding author : Inria, Univ. Grenoble-Alpes, CNRS, LJK
F-38000, Grenoble, France
e-mail: florian.lemarie@inria.fr - Web page: https://team.inria.fr/airsea/en/

* Univ. Grenoble-Alpes, CNRS, LJK, Inria
F-38000, Grenoble, France
e-mail: charles.pelletier@univ-grenoble-alpes.fr, eric.blayo@univ-grenoble-alpes.fr

Key words: Multiphysics coupling, Air-sea interface, Subgrid scales parameterizations, Ekman boundary layers

Abstract. In this paper we study a simplified mathematical model representative of air-sea coupling. This model incorporates parameterizations of the turbulent boundary layers as used in realistic models. We show that even if simple equations like the one-dimensional stationary heat equation are considered the presence of parameterizations renders the problem extremly complex to study and the unicity of solutions is no longer guaranteed. We motivate and describe a coupling algorithm which ensures that a unique physically sound solution is obtained.

1 INTRODUCTION

The use of fully coupled ocean-atmosphere models has become widespread in recent years. Historically limited to global climate studies, such models are now routinely used for regional and coastal applications. There is yet no systematic studies carefully investigating the formulation of atmospheric and oceanic coupled models including the interplay between numerical and physical aspects. Proper representation of air-sea interactions in such models cover a large range of issues: parameterization of atmospheric and oceanic boundary layers, estimation of air-sea fluxes, time-space numerical schemes, non conforming grids, coupling algorithms... Several coupling methods, whose precise contents, theoretical justification and stability properties are often somewhat difficult to compare precisely, are presently used in actual applications [1, 2]. In this context, our objective is to study more systematically the numerical properties of coupling algorithms used for practical applications to clarify their merits and flaws and establish more robust methods.

The oceanic and atmospheric models must rely on parameterization schemes to account for unresolved scales. Those parameterizations are essential to maintain a reasonable level of plausibility of the numerical solutions, but their mathematical formulation is often devised empirically and can impair the regularity of the associated solutions (e.g. [3]). Moreover, sub-grid scales parameterization schemes used for representing the oceanic and atmospheric boundary layers and for computing the turbulent components of air-sea fluxes are generally developed independently, without any guarantee regarding the well-posedness of the overall coupled problem. This latter aspect will be specifically addressed in this paper using a simplified mathematical model representative of most of the delicacies arising in air-sea coupling problems. We propose to analyze the so-called coupled Ekman boundary layer problem. Several aspects of this problem have already been studied in [4, 5]. In the present study we extend these works by incorporating parameterizations of the turbulent boundary layers as used in realistic models.

The paper is organized as follows. Section 2 motivates and introduces the coupled problem under insterest. Theoretical mathematical results are presented in Section 3 to emphasize how the parameterization schemes could alter the well-posedness of the coupled problem. Finally, Section 4 describes a consistent coupling algorithm and numerical results are shown to illustrate some of the aspects previously discussed.

2 THE MATHEMATICAL MODEL

Most state-of-the-art atmospheric and oceanic models solve the stratified Reynolds-averaged Navier-Stokes equations (in the following we will note $\langle\cdot\rangle$ the Reynolds averaging operator) with possibly additional simplifying assumptions like the hydrostatic, Boussinesq or so-called traditional assumptions. Due to the complexity of those equations, it is customary to work with simplified equations sets to focus on specific problems. In particular, studies of turbulent mixing traditionally rely on the horizontal homogeneity assumption (i.e. $\partial_x = \partial_y = 0$) and neglect vertical advection which is considered a small effect compared to vertical mixing in the vicinity of the air-sea interface [6, 7]. For this preliminary study, we also assume the absence of stratification (i.e. potential temperature, seawater salinity and air humidity are held constant).

2.1 The coupled Ekman layer problem

We define two subdomains $\Omega_a =]z_a^1; z_a^\infty[$ and $\Omega_o =]z_o^\infty; z_o^1[$ with $0 < z_a^1 < z_a^\infty$ and $z_o^\infty < z_o^1 < 0$ as well as a time interval $[0,T]$. Under the various assumptions presented so far, the problem of interest reads, for a given initial condition,

$$\left\{\begin{array}{rcll} \partial_t \mathbf{u}_a - f\mathbf{k}\times(\mathbf{u}_a - \mathbf{u}_a^g) + \partial_z \langle w_a' \mathbf{u}_a' \rangle &=& 0, & \text{in } \Omega_a \times [0,T] \\ \mathbf{u}_a(z = z_a^\infty, t) &=& \mathbf{u}_a^g, & \text{in } [0,T] \\ \rho_a \langle w_a' \mathbf{u}_a' \rangle (z = z_a^1, t) &=& \rho_o \langle w_o' \mathbf{u}_o' \rangle (z = z_o^1, t), & \text{in } [0,T] \end{array}\right. \tag{2.1}$$

$$\left\{\begin{array}{rcll} \partial_t \mathbf{u}_o - f\mathbf{k}\times(\mathbf{u}_o-\mathbf{u}_o^g) + \partial_z\left\langle w_o'\mathbf{u}_o'\right\rangle &=& 0, & \text{in } \Omega_o\times[0,T] \\ \mathbf{u}_o(z=z_o^\infty,t) &=& \mathbf{u}_o^g, & \text{in } [0,T] \\ \rho_o\left\langle w_o'\mathbf{u}_o'\right\rangle(z=z_o^1,t) &=& \rho_a\left\langle w_a'\mathbf{u}_a'\right\rangle(z=z_a^1,t), & \text{in } [0,T] \end{array}\right. \tag{2.2}$$

where $\mathbf{u}_\alpha = (u_{\alpha,x}, u_{\alpha,y})$, $(\alpha = o, a)$ is the horizontal velocity vector in the fluid of density ρ_α, $\mathbf{u}_\alpha^g$ corresponds to a prescribed large-scale geostrophic forcing, w_α' is the vertical velocity fluctuation, f represents the Coriolis frequency associated to earth rotation and $\mathbf{k}$ is a unit vector in the vertical direction. In (2.1) and (2.2) the terms in the form $\langle w_\alpha'\mathbf{u}_\alpha'\rangle$ are the vertical components of the Reynolds stress tensor associated to turbulent subgrid scales fluctuations. Coupled problem (2.1-2.2) corresponds to the so-called Ekman equations which are for instance often used to study the wind-driven motions in the ocean. To fully define the problem under investigation, additional closure assumptions need to be made to express the $\langle w_\alpha'\mathbf{u}_\alpha'\rangle$ terms.

2.2 Closure assumptions

This section introduces parameterizations to express $\langle w_a'\mathbf{u}_a'\rangle(z,t)$ in the atmospheric boundary layer, $\langle w_o'\mathbf{u}_o'\rangle(z,t)$ in the oceanic boundary layer and $\langle w_\alpha'\mathbf{u}_\alpha'\rangle$ in the surface layer (i.e. in $\Omega_\Gamma =]z_o^1, z_a^1[$).

2.2.1 Surface layer parameterization

In the absence of stratification the turbulent flow in the vicinity of the air-sea interface is given by a classical law of the wall which stipulates that the velocity is proportional to the logarithm of the distance from the interface :

$$\mathbf{u}_a(z) = \mathbf{u}_a(z_a^r) + \frac{u_a^*}{\kappa}\ln(z/z_a^r)\,\mathbf{e}_\tau, \qquad \text{for } z\in]z_a^r, z_a^1[\tag{2.3}$$

$$\mathbf{u}_o(z) = \mathbf{u}_o(z_o^r) - \frac{u_o^*}{\kappa}\ln(z/z_o^r)\,\mathbf{e}_\tau, \qquad \text{for } z\in]z_o^1, z_o^r[\tag{2.4}$$

with u_α^* a friction velocity, κ the von Karman constant, $z_{r,\alpha}$ the roughness lengths to be defined delimiting a viscous sublayer, and $\mathbf{e}_\tau$ a unit vector in the direction of $[\![\mathbf{u}]\!]_0^{z_a^1} = \mathbf{u}_a(z_a^1) - \mathbf{u}_a(0)$ $(= \mathbf{u}_a(z_a^1) - \mathbf{u}_o(0))$. The Reynolds stress component in the surface layer is given by

$$\langle w_\alpha'\mathbf{u}_\alpha'\rangle = -(u_\alpha^*)^2\mathbf{e}_\tau$$

where u_α^* is computed thanks to (2.3) and (2.4) using atmospheric and oceanic inputs at $z = z_a^1$ and $z = z_o^1$. The roughness lengths are

$$z_a^r(u_a^*) = a\frac{u_a^{*2}}{g} + b\frac{\nu_a}{u_a^*}, \qquad z_o^r = -\frac{u_o^*}{u_a^*}z_a^r \tag{2.5}$$

which is derived from [8], where a, b, g and ν_a are all known constants. The condition on z_o^r ensures the $\mathcal{C}^1$ character of the solution profiles at the crossing of the interface $z = 0$, assuming the wind stress $\boldsymbol{\tau} = \rho_a(u_\alpha^*)^2\mathbf{e}_\tau$ is constant in the surface layer, and that the solution has constant vertical gradient in $]z_o^r, z_a^r[$.

2.2.2 Boundary layer parameterization

Considering that turbulence acts as mixing, the usual closure assumption used in the overwhelming majority of numerical models is

$$\langle w'_\alpha \mathbf{u}'_\alpha \rangle (z) = -\nu_\alpha \partial_z \mathbf{u}_\alpha$$

where ν_α is a flow-dependent turbulent viscosity. In the absence of stratification, a typical way of computing ν_α, based on the so-called K-profile parameterization (KPP), is given in [7] :

$$\nu_\alpha(u^*_\alpha, z) = \frac{c\kappa {u^*_\alpha}^2}{|f|} G(\sigma)\, H(1-\sigma) + \nu^m_\alpha \qquad \text{where} \begin{cases} c := 0.7,\ \kappa := 0.41,\ \sigma := \dfrac{|z|}{h^\alpha_{pbl}(u^*_\alpha)} \\ h^\alpha_{pbl}(u^*_\alpha) := \dfrac{c u^*_\alpha}{|f|},\ \text{PBL height} \\ G(\sigma) := \sigma(1-\sigma)^2 \\ H \text{ Heaviside} \end{cases} \tag{2.6}$$

where ν^m_α is a background value to ensure that ν_α will remain strictly positive. In each medium, the KPP scheme predicts a parabolic profile of ν_α between the air-sea interface and the PBL (Planetary Boundary Layer) height h^α_{pbl} whereas ν_α is constant outside the PBL i.e. between h^α_{pbl} and z^∞_α.

2.3 The coupled Ekman layer problem including turbulent parametrizations

Putting all the different pieces together, we end up with the following coupled problem

$$\begin{cases} \partial_t \mathbf{u}_a - f\mathbf{k}\times(\mathbf{u}_a - \mathbf{u}^g_a) - \partial_z\left(\nu_a(u^*_a, f, z)\partial_z \mathbf{u}_a\right) &=& 0, & \text{in } \Omega_a \times [0,T] \\ \mathbf{u}_a(z = z^\infty_a, t) &=& \mathbf{u}^g_a, & \text{in } [0,T] \\ \rho_a \nu_a \partial_z \mathbf{u}_a(z = z^1_a, t) &=& \rho_a (u^*_a(t))^2 \mathbf{e}_\tau & \end{cases} \tag{2.7}$$

$$\begin{cases} \partial_t \mathbf{u}_o - f\mathbf{k}\times(\mathbf{u}_o - \mathbf{u}^g_o) + \partial_z\left(\nu_o(u^*_o, f, z)\partial_z \mathbf{u}_o\right) &=& 0, & \text{in } \Omega_o \times [0,T] \\ \mathbf{u}_o(z = z^\infty_o, t) &=& \mathbf{u}^g_o, & \text{in } [0,T] \\ \rho_o \nu_o \partial_z \mathbf{u}_o(z = z^1_o, t) &=& \rho_o (u^*_o(t))^2 \mathbf{e}_\tau & \end{cases} \tag{2.8}$$

where the way to evaluate u^*_α is given in §2.2.1. Note that existing studies of this problem often consider simplified physics where the turbulent viscosities are held constant. Here, we aim at studying the mathematical properties of this coupled problem to assess the impact of taking into account all the complexity of the turbulent parameterizations.

3 SOME MATHEMATICAL RESULTS

From (2.7)-(2.8) we expect that the main difficulties in the mathematical analysis will be related to the 'mixing' term $\partial_z\left(\nu_\alpha \partial_z \mathbf{u}_\alpha\right)$. We, thus, focus our theoretical work on this particular term assuming stationarity and absence of rotation (i.e. $f = 0$) to make an analytical study tractable.

3.1 Analytic determination of the coupled solution

Thanks to § 2.2.1 and § 2.2.2, we can clearly subdivide our problem into different layers reflecting different behaviors of the solution (see also Fig. 1) :

- Outside the PBL (i.e. for $z > h^a_{pbl}$) the viscosity is constant meaning that the flow is not affected by the presence of the air-sea interface (this is the so-called "free atmosphere"). The solution thus behaves as

$$\partial^2_{zz}\mathbf{u}_a = 0, \qquad z \in]h^a_{pbl}(u^*); z^\infty_a[$$

- In the PBL (i.e. for $z^1_a < z < h^a_{pbl}$) we define the KPP-A region where the solution satisfies

$$\left\{ \begin{array}{rcll} \partial_z \left(\nu_a(u^*_a, z)\partial_z \mathbf{u}_a\right) & = & 0, & z \in]z^1_a, h^a_{pbl}[\\ \nu_a \partial_z \mathbf{u}_a(z = z^1_a) & = & (u^*_a)^2 \mathbf{e}_\tau & \end{array} \right. \tag{3.1}$$

- In the surface log-layer (i.e. for $z^r_a < z < z^1_a$) named LL-A region, the vertical gradients are constant and given by (the solution is thus controlled by the jump $[\![\mathbf{u}_a]\!]^{z^1_a}_{z^r_a} = \mathbf{u}_a(z^1_a) - \mathbf{u}_a(z^r_a)$)

$$\partial_z \mathbf{u}_a = \frac{u^*_a}{\kappa z}\mathbf{e}_\tau, \qquad z \in]z^r_a, z^1_a[$$

  which is equivalent to having $\nu_a = \kappa u^*_a z$.

- In the viscous sublayer, referred to as VSL-A region (i.e. for $0 < z < z^r_a$), we assume a linear evolution of the solution since

$$\partial_z \mathbf{u}_a = \frac{u^*_a}{\kappa z^r_a}\mathbf{e}_\tau, \qquad z \in]0, z^r_a[$$

Same applies on the oceanic side by replacing u^*_a by u^*_o as illustrated by figure 1. Note that the continuity of the momentum flux at the interface implies that $u^*_o = \sqrt{\rho_a/\rho_o}u^*_a = \lambda u^*_a$ with $\lambda \approx 3/100$. The stationary solution is thus function of the value of u^*_a (which is a function of $\mathbf{u}_s = \mathbf{u}_a(z = 0)$ and $\mathbf{u}_1 = \mathbf{u}_a(z = z^1_a)$) which itself depends on the external boundary conditions ($\mathbf{u}^\infty_\alpha = \mathbf{u}_\alpha(z = z^\infty_\alpha)$). To reflect this dependency, we define the *Ekman planetary boundary function* $\mathcal{F}_E$ as such:

$$\begin{array}{rccc} \mathcal{F}_E : & \mathbb{R}_+ & \to & \mathbb{R}^2 \\ & u^*_a & \mapsto & \mathbf{u}^\infty_a - \mathbf{u}^\infty_o \end{array}$$

where u^*_a is directly linked to $\mathbf{u}_1$ and $\mathbf{u}_s$ by the following relation

$$(u^*_a)^2 = C_D\|\mathbf{u}_1 - \mathbf{u}_s\|^2 = \left(\frac{\kappa}{\ln(z^1_a/z^r_a)}\right)^2 \|\mathbf{u}_1 - \mathbf{u}_s\|^2 \tag{3.2}$$

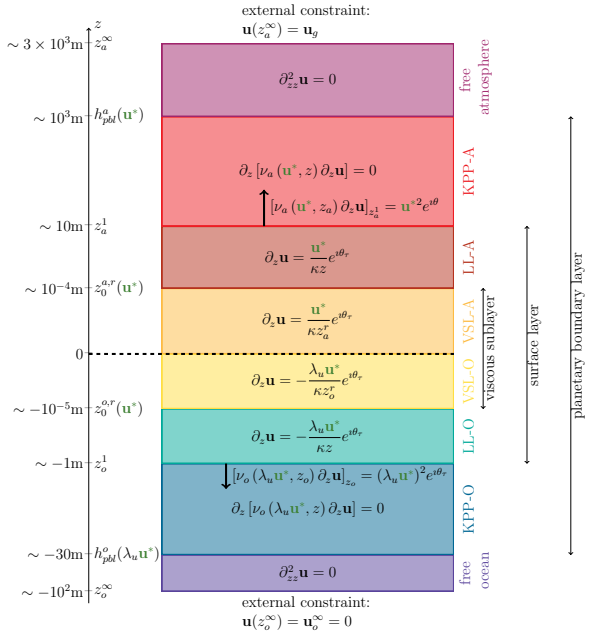

Figure 1: Sublayers for the Ekman problem, illustrating the dependencies on the u^* scale.

with C_D a drag coefficient and z_a^r is the roughness length defined in (2.5). Expression (3.2) directly arises from the application of the law of the wall (2.3)-(2.4) in the surface layer.

Since we do not consider the Coriolis term, in the remaining we decide for simplicity to align our local plane in the direction of $\mathbf{e}_\tau$ so that we only have to consider one component of the velocity vector ($\mathbf{u}_\alpha = (u_\alpha, 0)$) instead of two. Next step is to find an explicit expression for the function $\mathcal{F}_E$. Knowing that on each subdomain the solution satisfies $\nu_\alpha(z, u^*_\alpha)\partial_z u_\alpha = (u^*_\alpha)^2$ we easily find that on the atmospheric side

$$\int_0^{z_a^\infty}(\partial_z u_a)dz = u_a(z_a^\infty) - u_s = (u_a^*)^2\left\{\int_0^{z_a^r}\frac{dz}{\kappa z_a^r u_a^*} + \int_{z_a^r}^{z_a^1}\frac{dz}{\kappa z u_a^*} + \int_{z_a^1}^{h^a_{\rm pbl}}\frac{dz}{\nu_a(z, u_a^*)} + \int_{h^a_{\rm pbl}}^{z_a^\infty}\frac{dz}{\nu_a^m}\right\},$$

same rationale applies on the oceanic side to determine analytically $u_s - u_o(z_o^\infty)$. Taking the sum of the atmospheric and oceanic solutions and explicitly computing the integrals

on the right hand side, we end up with an expression for the operator $\mathcal{F}_E$

$$\mathcal{F}_E(u_a^*) = u_a(z_a^\infty) - u_o(z_o^\infty) = \frac{u_a^*}{\kappa}\left[\overbrace{1+\lambda}^{\mathcal{F}_{E,VSL}} + \overbrace{\ln\left(\frac{z_a^1}{z_a^r(u_a^*)}\right) + \lambda\ln\left(\frac{z_o^1}{-\lambda z_a^r(u_a^*)}\right)}^{\mathcal{F}_{E,LL}} + \underbrace{\mathcal{I}_{KPP}^a(u_a^*) + \mathcal{I}_{KPP}^o(\lambda u_a^*)}_{\mathcal{F}_{E,KPP}} + \underbrace{\frac{z_a^\infty - h_{pbl}(u_a^*)}{\nu_a^m} - \frac{h_{pbl}(\lambda u_a^*) + z_o^\infty}{\nu_o^m}}_{\mathcal{F}_{E,\text{free}}}\right] \tag{3.3}$$

where the terms $\mathcal{I}_{KPP}^\alpha$, corresponding to the integral of the inverse of the parabolic KPP viscosity profiles are explicit and analytical functions of (u_α^*) not given here for simplicity. The different terms in the right hand side are arranged to respectively match the viscous sublayer (VSL), the surface log-layer (LL), the PBL viscosity given by the K-profile parameterization (KPP) and the free atmosphere/ocean where the viscosity corresponds to the molecular viscosity and is thus independent of the state of the air-sea interface.

Our objective is now to determine whether (3.3) is invertible, i.e. given $[\![u]\!]_{z_o^\infty}^{z_a^\infty} = u_a(z_a^\infty) - u_o(z_o^\infty) \in \mathbb{R}_+$, is there a scale u^* such that (3.3) is satisfied? Is this scale unique?

3.2 Unicity of the solution

We start by imposing a simple constraint on the value of z_α^∞ to ensure that these values are larger than the planetary boundary layer thickness (i.e. $z_a^\infty > cu_a^*/|f|$, $z_o^\infty < -\lambda c u_a^*/|f|$, with c introduced in (2.6)) which is always the case in numerical codes where the the PBL thickness is systematically limited respectively by the total depth of the ocean and the maximum height in the atmospheric model. In an equivalent way, for given values z_α^∞, this contraint is satisfied as long as the friction velocity u_a^* is bounded by $u_m^* = \min\{z_a^\infty|f|/c, (-z_o^\infty)|f|/c\}$. For properly chosen values of z_α^∞, Figure 2a shows the contributions from the various vertical layers to the final value of $\mathcal{F}_E$ as a function of u_a^*. It is not surprising to see that the main contribution comes from the layer with small background viscosity since the inverse of the viscosity appears directly in the right-hand-side of (3.3). More importantly, the dashed black line in figure 2b shows that the function $\mathcal{F}_E$ is not injective since two distinct values u_1^* and u_2^* of u_a^* can lead to the same value of $\mathcal{F}_E$; $\mathcal{F}_E(u_1^*) = \mathcal{F}_E(u_2^*) = u_a^\infty - u_o^\infty$. This lack of invertibility is due to the contribution of the free ocean/atmosphere which is the only contribution that is not monotonically increasing with increasing u_a^* (Fig. 2b). Indeed, using the notations introduced in (3.3) we can easily show that

$$\begin{array}{ll} \partial_{u_a^*}\mathcal{F}_{E,VL} = 2/\kappa > 0, & \forall u_a^* \in \mathbb{R}_+ \\ \partial_{u_a^*}\mathcal{F}_{E,LL} > 0 & \forall u_a^* \in]0; u_{\max}^*[, u_{\max}^* \approx 30\text{m}\,\text{s}^{-1} \\ \partial_{u_a^*}\mathcal{F}_{E,KPP} > 0 & \forall u_a^* \in \mathbb{R}_+ \end{array} \tag{3.4}$$

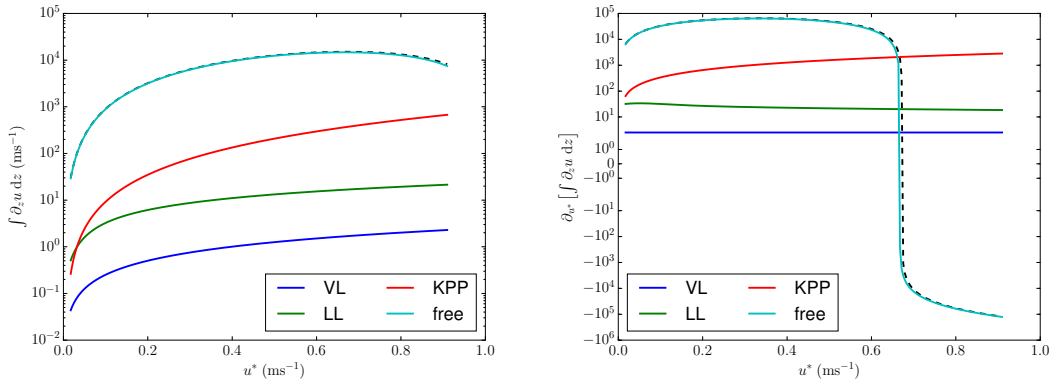

(a) $\mathcal{F}_E$ (b) $\partial_{u^*}[\mathcal{F}_E]$

Figure 2: Different contributions in the $\mathcal{F}_E$ operator (a) and $\partial_{u^*}[\mathcal{F}_E]$ (b), using the subdivision described in (3.3). Here, the maximum value for $[\![u]\!]_0^{z_a^1}$ is 20 m s^{-1}, leading to $u_m^* \sim 0.7\text{ms}^{-1}$, through equation (3.2). The colored lines represent the different contributions from all four types of sublayers; the dashed black line being their sum, which are respectively $|u_a^\infty|$ and $\partial_{u^*}|u_a^\infty|$. Here, $z_a^1 = 10\text{m}$, $z_o^1 = -3\text{m}$, $\nu_m^o = 10^{-4}\text{m}^2\text{s}^{-1}$, $\nu_m^a = \nu_m^o/\lambda^2$, $z_a^\infty = 1.1 \times h_{pbl}(u_a^*([\![u]\!]_0^{z_a^1} = 20\text{m s}^{-1}))$ and $z_o^\infty = -\lambda z_a^\infty$.

which means that $\forall u_a^* \leq u_{\max}^*$ we will systematically get that $\partial_{u^*}\mathcal{F}_E \geq \partial_{u^*}\mathcal{F}_{E,\text{free}}$. Note that the value of $u_{\max}^*$ is unrealistically large, such large values of u_a^* are not expected to occur in realistic simulations even in the case of extreme events like tropical cyclones meaning that the special case $u_a^* \geq u_{\max}^*$ does not have to be considered here. If we now note u_b^* (resp. $u_{b,\text{free}}^*$) the only nonzero root of $\partial_{u_a^*}\mathcal{F}_E$ (resp. $\partial_{u_a^*}\mathcal{F}_{E,\text{free}}$) we get from (3.4) that $u_b^* \geq u_{b,\text{free}}^*$. Moreover, we can analytically find

$$u_{b,\text{free}}^* = \frac{2|f|}{3c}\left[\frac{z_a^\infty}{\nu_a^m} - \lambda^2\frac{z_o^\infty}{\nu_o^m}\right]. \tag{3.5}$$

As a consequence, as long as u^* stays within the bounds $]0, u_{b,\text{free}}^*[$ invertibility of the function $\mathcal{F}_E$ is guaranteed and the solution of the associated coupled problem is unique. The strategy is then to choose (z_a^∞, z_o^∞) so that u_a^* is guaranteed to be in $]0;\ u_{b,\text{free}}^*[$. We introduce in the following section a coupling algorithm specifically built to enforce this constraint.

4 THE COUPLING ALGORITHM

This section will first describe the algorithm used for the coupling of the Ekman layers, before presenting numerical results. The objective of this algorithm is to properly select the altitude z_a^∞ and the depth z_o^∞ at which the external data are provided to ensure a physically sound solution. In practice z_a^∞ and z_o^∞ can indeed be considered as degrees

of freedom as soon as they are located outside the boundary layers i.e. far from the influence of the interface. Once z_a^∞ and z_o^∞ are chosen we can then extract the boundary conditions $u_a(z_a^\infty)$ and $u_o(z_o^\infty)$ from a three-dimensional simulation before starting the coupling process for the planetary boundary layers. With this methodology we avoid coupling the entire atmospheric and oceanic model by only modifying the region of the solution that it is influenced by the coupling and leaving unchanged the solution in the free ocean and free atmosphere. This approach is expected to enable a substantial gain in efficiency while ensuring unicity of the solution.

4.1 Description

The objective of the algorithm is basically to invert the $\mathcal{F}_E$ operator, as described in (3.3), avoiding convergence toward a non-physically acceptable solution. We suggest here simple fixed point iterations.

Initialization step :

1. Select a maximum allowed value $u^*_{\max}$ such that the expected solution $u^*_a \in [0, u^*_{\max}]$.
2. From $u^*_{\max}$, compute z_a^∞ and z_o^∞ to ensure unicity of the solution. Using (3.5), the idea is to choose z_a^∞ and z_o^∞ such that $u^*_{\max} = u^*_{b,\text{free}}$ and $z_o^\infty = -\lambda z_a^\infty$.
3. Select the values $u_a(z_a^\infty)$ et $u_o(z_o^\infty)$ for the external boundary conditions.

Fixed point iterations :

The purpose is to create a sequence $(u^*_k)_{k\in\mathbb{N}}$ such that $u^*_k \longrightarrow u^*_{sol}$, with u^*_{sol} the unique fixed point, only using u_a^∞ and u_o^∞ as inputs. $u^*_{k=0}$ can be taken arbitrarily as long as $u^*_{k=0} \leq u^*_{max}$ is satisfied. Then, an iterative loop begins

(i) From the u^*_k scale, compute all the integrals in the $\mathcal{F}_E$ function (3.3). Also compute its gradient with regard to u^*_k, $\partial_{u^*}\left[\mathcal{F}_E\right]_{u^*_k}$. Compute $z^r_{a,k}$ from u^*_k via (2.5) and $z^r_{o,k} = -\lambda z^r_{a,k}$.

(ii) Compute

$$[\![u]\!]^{z^1_a}_{0,k} = [\![u]\!]^{z^\infty_a}_{z^\infty_o} - \mathcal{F}_E(u^*_k) + \frac{u^*_k}{\kappa}\left[1 + \ln\left(\frac{z^1_a}{z^r_{a,k}}\right)\right] \tag{4.1}$$

(iii) Assess

$$C_{D,k} = \left(\frac{\kappa}{\ln\left(z^1_a / z^r_{a,k}\right)}\right)^2 \tag{4.2}$$

(iv) Convergence is supposed to be reached when (4.1) and (4.2) satisfy:

$$u^{*2}_k \approx C_{D,k} \times \left|[\![u]\!]^{z^1_a}_{0,k}\right|^2 \tag{4.3}$$

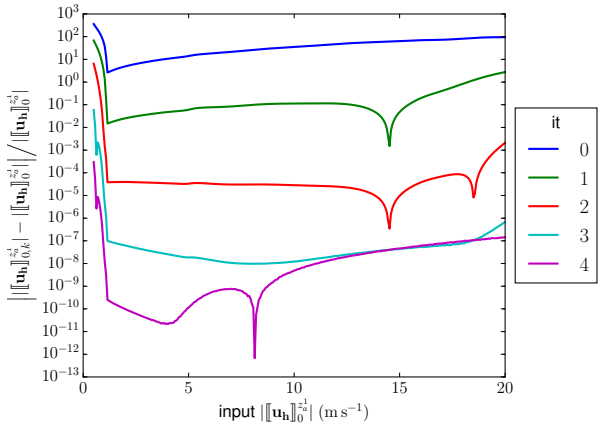

Figure 3: Results obtained with the algorithm described in Section 4.1. This figure shows the relative error between the input $|\,[\![u]\!]_0^{z_a^1}\,|$ and the iterated values $|\,[\![u]\!]_{0,k}^{z_a^1}\,|$, computed through (4.1). Each line represents a different iteration. Here, $z_o^1 = -3$ m, $z_a^1 = 10$ m.

up to an arbitrary numerical precision. If (4.3) is not satisfied, then go back to (i) with

$$u_{k+1}^* = u_k^* + \frac{|\,[\![u]\!]_{0,k}^{z_a^1}\,| - u_k^*/\sqrt{C_{D,k}}}{\partial_{u^*}\left[\mathcal{F}_E^0\right]_{u_k^*}} \tag{4.4}$$

4.2 Numerical results

Figure 3 illustrates that following the procedure described above, convergence toward a physically acceptable solution is obtained in a few iterations. Generally speaking a fast convergence is expected for air-sea coupling problems because of the large jump in densities between the ocean and the atmosphere. Indeed one component (the atmosphere) is very fast and adjusts itself quickly to the slow component (the ocean).

5 CONCLUSION AND PERSPECTIVES

In this paper we have introduced a coupled Ekman layer problem, emphasizing the influence of the underlying turbulent parameterizations and closure assumptions on the unicity of the solutions. Thanks to a thorough mathematical analysis of the coupled problem we have been able to propose a simple procedure which guarantees that a unique physically sound solution is obtained. The work presented here should be interpreted as a first step toward building satisfactory coupling algorithms for Ekman layers (and possibly stratified Ekman layers). Using the formalism introduced here, our objective is to progressively discard restrictive hypotheses, namely:

1. Incorporating effects due of the Coriolis force. This would change the mathematical structure of the problem, as the solution profiles in the KPP-layers could not simply

be expressed thanks to an invariant gradient, as in (3.1). Incorporating Coriolis effects would mean solving a Sturm-Liouville problem with complex coefficients, for which there are mathematical results of existence and unicity [9]; however, obtaining analytical results at a continuous level is expected to become much more tedious.

2. Taking fluid stratification into account, ie. considering a non-constant temperature T as a prognostic variable. A consequence is that the parameterizations of the boundary layers and of air-sea fluxes will become much more complicated to analyze since they greatly depend on the stability of the air/water column (i.e. if the temperature is decreasing or increasing with altitude/depth).

3. Further investigating the impact of the viscous sublayer parameterization. State of art surface layer parameterizations typically assume that given the thinness of viscous sublayers, $\mathbf{u}_\alpha$ can be considered as constant in this region. While this is numerically accurate, we believe that including the viscous layer influence in the air-sea flux parameterizations should systematically be done within the log-layer, for ensuring the self-consistency of the coupling problem at a continuous level. Indeed, not including the viscous sublayer leads to a friction velocity of the form (3.2), i.e. $u_a^{*2} = C_D \times \left\| [\![\mathbf{u_a}]\!]_{z_a^r}^{z_a^1} \right\|$, while, following pioneering mathematical results [10], the jump in wind speed should be taken from $z = 0$ and not from $z = z_a^r$. The drag coefficient C_D in (3.2) can be rewritten as:

$$\frac{\kappa}{\sqrt{C_D}} = \ln\left(z_a^1 / z_a^r\right) + \gamma_{VL} \tag{5.1}$$

where γ_{VL} should incorporate viscous layer parameterization effects. Our choice of assuming constant vertical gradient in the viscous layer leads to $\gamma_{VL} = 1$.

4. Study the time-dependent problem, ie. reintroduce the $\partial_t u$ term to the equations of the Ekman layer problem.

Acknowledgements

The authors acknowledge the support of the French national research agency (ANR) through contract ANR-16-CE01-0007.

REFERENCES

[1] F. Lemarié, E. Blayo, and L. Debreu. Analysis of ocean-atmosphere coupling algorithms: Consistency and stability. *Procedia Computer Science*, 51(0):2066 – 2075, 2015.

[2] A. Beljaars, E. Dutra, G. Balsamo, and F. Lemarié. On the numerical stability of surface–atmosphere coupling in weather and climate models. *Geoscientific Model Development*, 10(2):977–989, 2017.

[3] C. Pelletier, F. Lemarié, and E. Blayo. Sensitivity analysis and metamodels for the bulk parameterization of turbulent air-sea fluxes. *Q. J. R. Meteorol. Soc.*, 2017. submitted.

[4] D.M. Lewis and S.E. Belcher. Time-dependent, coupled, Ekman boundary layer solutions incorporating Stokes drift. *Dynamics of Atmospheres and Oceans*, 37(4):313–351, 2004.

[5] J.A. Bye. Inertially coupled Ekman layers. *Dynamics of atmospheres and oceans*, 35(1):27–39, 2002.

[6] W. G. Large, J. C. McWilliams, and S. C. Doney. Oceanic vertical mixing: A review and a model with a nonlocal boundary layer parameterization. *Reviews of geophysics*, 32(4):363–403, 1994.

[7] J. C. McWilliams and E. Huckle. Ekman layer rectification. *Journal of Physical Oceanography*, 36:1646–1659, 2005.

[8] S. D. Smith. Coefficients for sea surface wind stress, heat flux, and wind profiles as a function of wind speed and temperature. *Journal Of Geophysical Research*, 93(C12):15467–15472, 1988.

[9] B. M. Brown, D. K. R. McCormack, W. D. Evans, and M. Plum. On the spectrum of second-order differential operators with complex coefficients. *Proceedings of the Royal Society of London A: Mathematical, Physical and Engineering Sciences*, 455(1984):1235–1257, 1999.

[10] J.L. Lions, R. Temam, and S. Wang. Mathematical theory for the coupled atmosphere-ocean models (CAO III). *Journal de Mathématiques Pures et Appliquées*, 74:105–163, 1995.

VII International Conference on Computational Methods for Coupled Problems in Science and Engineering
COUPLED PROBLEMS 2017
M. Papadrakakis, E. Oñate and B. Schrefler (Eds)

RADIAL BASIS FUNCTION INTERPOLATION FOR BLACK-BOX MULTI-PHYSICS SIMULATIONS

FLORIAN LINDNER*, MIRIAM MEHL* AND BENJAMIN UEKERMANN†

*Institute for Parallel and Distributed Systemes
University of Stuttgart
Universitätsstraße 38, 70569 Stuttgart, Germany
e-mail: {florian.lindner, miriam.mehl}@ipvs.uni-stuttgart.de, web page:
https://www.ipvs.uni-stuttgart.de

† Scientific Computing in Computer Science, Technical University of Munich
Boltzmannstraße 3, 85748 Garching b. München, Germany
e-mail: uekerman@in.tum.de, web page: http://www5.in.tum.de

Key words: Interpolation, Coupled Problems, Multiphysics Problems, Applications, Computing Methods, Radial Basis Functions

Abstract. Interpolation based on radial basis functions (RBF) is a standard data mapping method used in multi-physics coupling. It works on scattered data without requiring additional mesh topology or neighborhood information of support points. However, system matrices of the equations for the coefficients tend to be ill-conditioned. In this work, we illustrate the problem by a simple example and discuss possible remedies. Furthermore, we investigate the numerical performance of this method on uniform and non-uniform meshes with a particular focus on the coupling of black-box components where typically no information about the underlying discretization can be extracted. Radial basis function interpolation usually uses an enhancement of the radial basis functions by a global polynomial in order to properly capture constant components and linear trends in the given data. We present a method that determines this polynomial independent from the radial basis function ansatz, which substantially improves the condition number of the remaining RBF system. Furthermore, we show that a rescaling approach can be used to either increase the accuracy or improve the condition number even further by choosing radial basis functions with a smaller support radius. The results represent an intermediate state with the aim to be integrated into the multi-physics coupling library preCICE.

1 INTRODUCTION

While multi-physics simulations are an emerging field in science and industry, most groups concentrate their work on a single aspect of the simulation. Adding additional physical aspects to their simulation requires work on additional solvers, which hinders fast prototyping of coupled simulation environments.

preCICE[1] [3, 9] is a black-box, partitioned coupling library. It is developed to foster quick integration of new codes into the overall coupled model. The black-box approach enables integration of solvers with only minimal knowledge about the numerical details of the coupled codes. The software is free and open source under the LGPL 3 license. One of the crucial parts of a partitioned multi-physics coupling is data interpolation between non-matching meshes. Due to the the black-box approach, the mesh is represented as a point cloud. While solvers can optionally provide topological information using basic primitives such as edges, triangles and quads, the coupling library cannot rely on it. Also the missing information about the solvers discretization approach and mesh topology restricts the choice of applicable data mapping algorithms or the use of adaptive methods.

Several interpolation methods that work on point cloud data exist, of which interpolation by radial basis functions is among the most used. Radial basis function interpolation is well known to produce ill-conditioned systems, which harms the solution accuracy and the time-to-solution, in particular for large systems. Methods to cope with this are reviewed in this work. These methods include preconditioning [6], rescaling of the interpolant [4] and a different numerical treatment of the additional polynomial that is used to properly capture global constant or linear components of the data.

2 DATA MAPPING USING RADIAL-BASIS FUNCTIONS

Consider a function $f : \mathbb{R}^d \to \mathbb{R}$ of d variables, that is to be approximated by $S : \mathbb{R}^d \to \mathbb{R}$ based on the given values $\{f(x_i) : i = 1, \dots, n\}$. Using radial basis function interpolation, the resulting interpolant S of the function f reads

$$S(x) = \sum_{i=1}^{n} \gamma_i \, \varphi(||x - x_i||) + \beta_0 + \beta^T x, \tag{1}$$

where $\varphi : \mathbb{R}_+ \to \mathbb{R}$ is a radial basis function, $\beta \in \mathbb{R}^d$ and $|| \cdot ||$ denotes the Euclidean norm.

The interpolation conditions are $S(x_k) = f(x_k), k = 1, \dots, n$. To guarantee that the interpolation problem has a unique solution [10], we enhance the interpolation conditions with $d + 1$ equations for the polynomial:

$$\sum_{i=1}^{n} \gamma_i = 0 \text{ and } \sum_{i=1}^{n} \gamma_i \, x_i^{(j)} = 0 \quad \forall j = 1, \dots, d \tag{2}$$

[1] `www.precice.org`

One of the most common choices for the basis function φ are Gaussians

$$\varphi(x) = \exp\left(-\left(s||x||\right)^2\right) \tag{3}$$

We restrict to this basis function type in the remainder of this paper. Other common choices include Thin Plate Splines and Multi Quadrics, of which the latter two were also investigated, but not further detailed in this paper.

The interpolant S can yield a matrix $\bar{S}$ defining a linear mapping of the input values $f(x_k)$ from the input mesh to a vector δ of values in the output mesh:

$$\delta = \bar{S}\,\omega \;\text{ with }\; \omega = \begin{pmatrix} f(x_1) \\ f(x_2) \\ \vdots \\ f(x_n) \end{pmatrix} \tag{4}$$

When the row-sum of $\bar{S}$ is equal to one, the interpolation is consistent, which means that constant values are interpolated exactly. On the other hand, when the column-sum of $\bar{S}$ equals to one, the interpolation is conservative [1]. The operator can be changed from consistent to conservative and vice versa by transposing it. While obviously this operator can be both consistent and conservative, ensuring this requires acccess to the underlying solver's basis functions and is thus not suited for black-box coupling [7]. Conservative mapping preserves integral values and is, therefore, usually applied to integral quantities such as forces. Consistent mapping is usually applied to point values such as velocities or displacements. Equations (1) and (2) define the consistent formulation of the radial basis function interpolation. We do not further consider the conservative variant throughout this paper, though both variants are implemented in `preCICE`.

In order to ensure that $\bar{S}$ is a sparse matrix, we use a cut-off radius r for the basis functions φ and shift them to achieve continuous functions:

$$\varphi_{\text{local}}(x) = \begin{cases} \varphi_{\text{global}}(x) - \varphi_{\text{global}}(r) & \text{for } x < r, \\ 0 & \text{for } x \geq r. \end{cases} \tag{5}$$

2.1 Numerical Challenges & Solution Approaches

It is well known that radial basis function interpolation suffers from ill-conditioning of the resulting linear system [6]. This conditioning can be controlled by the shape parameter s of φ, i.e., by controlling the width of the basis functions. This results in a trade-off between accuracy and conditioning of the interpolation which is illustrated in Sect. 3.

A suitable choice for the shape parameter s is therefore of tremendous importance for the resulting approximation quality and convergence properties. This can be illustrated by $s \to 0$, an infinitely flat basis function. The resulting matrix would only consist of ones and thus be singular, which corresponds to condition number ∞. On the other

hand, $s \to \infty$ yields singular peaks as basis functions resulting a diagonal system matrix but very poor interpolation accuracy. In our approach, we use a cut-off value of 10^{-9}, i.e., choose the radius r such that $\varphi(r) = 10^{-9}$. Together with the definition of a basis function, a shape parameter, resulting in a carrier that includes exactly a given number of vertices m based on the maximal mesh width of the discretization can be determined. If $h_{\max}$ is the maximum mesh width of the input mesh, the corresponding shape parameter s for Gaussian basis functions is given by

$$s = \frac{\sqrt{-\ln 10^{-9}}}{m \cdot h_{\max}} \tag{6}$$

This ensures that the basis function decays to 10^{-9} within the m neighboring vertices from its center if the distance between data points is $h_{\max}$. It is common practice to include at least the nearest neighbor [4] in both the input and the output mesh [2]. For a non-uniform mesh, the largest distance should be considered [1]. While these statements are based on experiences, [5] gives a systematic approach to this issue, based on *leave-one-out cross validation* (LOOCV). Whereas naive LOOCV requires to create one interpolant for each vertex followed by an optimization step, [8] was able to simplify the algorithm such that the interpolant needs to be created only once for all vertices. Because it is still followed by the optimization step and needs to explicitely create the inverse of the interpolation matrix, it significantly increases the computational cost. The algorithm also optimises only with respect to accuracy and does not take the harming effect of the ill-conditioning into account. We, therefore, use a heuristic approach to determine the best value for m.

The ill-conditioning of the interpolation problem is aggravated by non-uniform meshes, which are used, e.g., in discontinous-Galerkin based solvers. A common representation uses a Gauss-Chebyshev distribution of nodes, which is defined by

$$x_k = \cos\left(\frac{2k-1}{2n}\pi\right), \quad k = 1, \ldots, n \tag{7}$$

for polynomial degree n in the one-dimensional interval $(-1, 1)$. Non-uniform point distribution greatly complicates finding an appropriate shape parameter and thus to control accuracy and conditioning.

An obvious remedy to the problem of the fixed shape parameter of the basis function on non-uniform meshes are adaptive methods. Techniques that use basis functions with a variable shape parameter, computed based on the local mesh density are known to reduce the condition number by four orders of magnitude, see section 3. More sophisticated methods also include adaptive refinement of the input mesh. This can result in a reduced problem size given the input data are sufficiently smooth. [10] uses a local error indicator on a coarse mesh to determine areas to refine. Both methods, however, require a definition of mesh density, e.g., based on the distance to the nearest neighbor for each data point, which would potentially compromise one of the main features of RBFs to work on scattered data.

The problem of the conditioning can also be tackled by preconditioning techniques, such as preconditioning by accelerated iterated approximate moving least squares as presented in [6]. The technique has shown good first results reducing the condition number on uniform meshes. However, achieving stability on non-uniform meshes remains problematic, as the method requires control of the distance of the interpolation system matrix to the identity matrix. If this distance is not bounded by one, convergence can not be reached. Thus, the method is not fully applicable to coupled problems with black-box solvers where the eigenvalues of the interpolation matrix are unknown.

The rescaling procedure proposed in [4] does not try to address the ill-conditioning by using a preconditioner, but improves interpolation quality, thus making it possible to use skinnier smaller basis functions, i.e., smaller values for m which, in turn, improves the condition number of the interpolation problem. The method showed very promising results during first investigations. Basically, it works by constructing a rescaled interpolant $\bar{S}$ by

$$S_r(x) = \frac{S_f(x)}{S_1(x)} \tag{8}$$

where $S_f(x)$ denotes the interpolant constructed from the given values as shown in Eq. (1) and $S_1(x)$ is the interpolant of the constant function $g(x) = 1$. Substantial improvements can be observed in particular for small m without negatively affecting the conditoning. The additional computational cost remains moderate as it only involves the computation of one additional interpolant for each set of data positions to be mapped. We present results in Sect. 3.

2.2 Our Algorithm

In this section, we show the structure of the matrices and describe the algorithm we use to compute the interpolation result. We present two variants to treat the polynomial with the second variant leading to a significant improvement in conditioning and equal accuracy.

Integrated Polynomial We construct the system matrix C that defines the linear system for the coefficients $\gamma_i, i = 1, \ldots, n$ and $\beta_i, i = 0, \ldots, d$ of interpolant S from Eq. (1) including the polynomial equations:

$$\underbrace{\begin{pmatrix} 0 & Q^T \\ Q & P \end{pmatrix}}_{C} \underbrace{\begin{pmatrix} \beta \\ \gamma \end{pmatrix}}_{p} = \begin{pmatrix} 0 \\ \omega \end{pmatrix} \tag{9}$$

where $P \in \mathbb{R}^{n \times n}, P_{i,j} = \varphi\left(||x_i - x_j||_2\right), i, j = 1, \ldots, n$ and where the i th row of $Q \in \mathbb{R}^{n \times d+1}$ is $(1\, x_i^{(1)} \ldots x_i^{(d)})$, i.e., holding the coordinates of the input data.

The evaluation matrix A is smiliarly constructed:

$$A = \left(\begin{array}{c|c} V & P' \end{array} \right) \tag{10}$$

with $P'_{i,j} = \varphi\left(||y_i - x_j||_2\right)$, $i = 1, \ldots, \tilde{n}$, $j = 1, \ldots, n$ and $V_{i,\cdot} = (1\, y_i^{(1)} \ldots y_i^{(d)})$. y_i, $i = 1, \ldots, \tilde{n}$ are the evaluation points in the output mesh. While P and P' account for the basis functions evaluated at the input resp. output mesh, Q and V hold the coordinates of the input or output vertices and account for the polynomial part of Eq. (1).

The output values δ are now computed by

$$\delta = A \cdot C^{-1} \omega \tag{11}$$

Separated Polynomial In the formulation above, the polynomial is embedded into the system and solved together with it. Another approach is to treat the polynomial coefficients separately by first solving a least squares problem

$$\begin{bmatrix} \\ Q \\ \\ \end{bmatrix} \cdot \begin{bmatrix} \beta \end{bmatrix} \approx \begin{bmatrix} \\ \omega \\ \\ \end{bmatrix} \quad \Rightarrow \quad \beta = Q^{\dagger} \cdot \omega \tag{12}$$

for polynomial coefficients β by QR-decomposition. $Q^{\dagger}$ denotes the pseudo-inverse of Q. In the next step, the polynomial values have to be subtracted from the input values ω before the basis function coefficients γ can be computed from

$$P \cdot \gamma = \omega - Q \cdot \beta \quad \Rightarrow \quad \gamma = P^{-1}\left(\omega - Q \cdot \beta\right) \tag{13}$$

Evaluation involves adding the polynomial values computed at the output positions V:

$$\delta = P' \cdot \gamma + V \cdot \beta = P'\, P^{-1}\left(\omega - Q\, Q^{\dagger} \cdot \omega\right) + V\, Q^{\dagger} \cdot \omega. \tag{14}$$

Parallelization Using basis functions with a compact support yields sparse matrices P and P'. However, Q and V that represent the polynomial are dense. Using the integrated polynomial therefore adds global communication overhead in the process of solving the ill-conditinoned system. The separated polynomial, on the other hand, solves a smaller, better conditioned system, resulting in less global communication.

As an effect of the black-box approach to coupling, we reuse the surface partitioning of the respective solver and therefore cannot guarantee optimal load balancing. In practice, however, the partitioning already provides a good clustering of the vertices. As a result, the matrix P and P' have are band-matrices and, thus, the corresponding systems are easy to solve in parallel.

3 RESULTS

In the remainder of this work, we present results that illustrate the trade-off between conditioning and accuracy for uniform and non-uniform meshes. We compare techniques such as adaptive basis functions and rescaled interpolants as well as integrated and separated computation of the polynomial.

The test function to be interpolated is a rescaled Gaussian

$$f(x) = \exp(-|x - 3|^2) + 2 \tag{15}$$

Albeit this test function appears simplicistic, it is able to reproduce properties of the interpolation we experienced on real-world FSI simulations.

Figs. 1 and 2 show the resulting root mean squared error (RMSE) and the condition of the interpolation matrix C or P, respectively, using a Gaussian basis function. The shape parameter is set according to Eq. (6). While the interpolation using uniform meshes has a condition number of 8.50×10^{15} when reaching an error of 10×10^{-6} ($m = 17.71$), the non-uniform mesh results in a condition number of 2.57×10^{18} reaching the same error ($m = 13.73$). Using an adaptive basis function, the condition number is significantly lower, resulting in 7×10^{14} for the same level of accuracy as illustrated in Fig. 3.

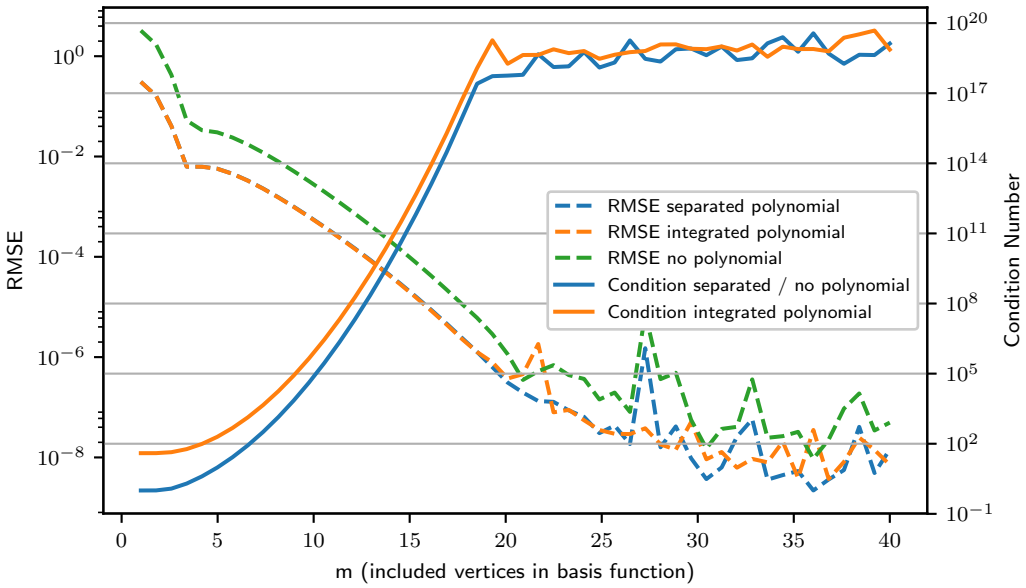

Figure 1: Condition number and root mean square error (RSME) for a uniform point distribution with 192 points.

Figs. 4 and 5 show accuracy and condition number for increasing mesh sizes. Since the shape parameter is computed based on the maximum mesh width, in most parts

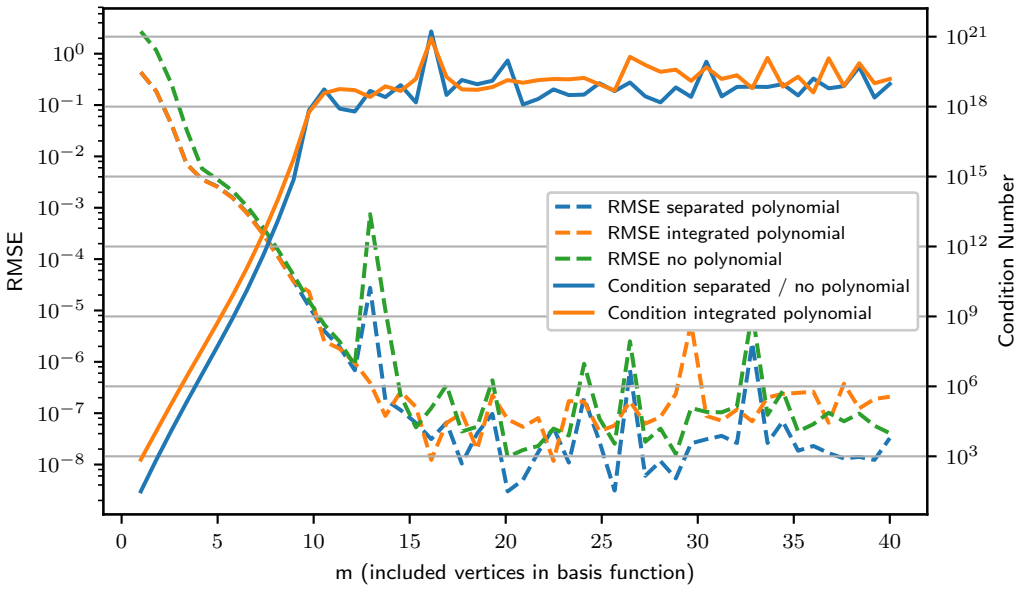

Figure 2: Condition number and root mean square error (RSME) for a Gauss-Chebyshev non-uniform point distribution, using 16 elements of 12th order, resulting in 192 points.

of the interval, the actual m is larger than the prescribed one for the Gauss-Chebyshev distribution, which explains the better accuracy. The Gauss-Chebyshev mesh yields a condition of 1.3×10^{18} to reach an error below 1×10^{-4} on a mesh of size 848. The uniform mesh, on the other hand, requires a higher value for m to reach a comparable accuracy, but the condition remained below 5×10^{9}. In contrast to the non-uniform mesh, condition number and accuracy curves flatten out, making m a suitable parameter to control accuracy and condition for uniform meshes of different sizes. Non-uniform meshes show an unstable behavior for larger mesh sizes, resulting in an smaller, but heavily oscillating error.

The rescaled basis functions method does not change the interpolation matrices themselves and, therefore, obviously results in identical condition numbers. With regard to accuracy, it performs about two orders of magnitude better. This gain in accuracy makes it possible to use a smaller value for m, which in turn improves the conditioning. Whereas, without rescaling, the interpolant supplemented by the polynomial performed much better than without polynomial, both methods are comparable when combined with rescaling.

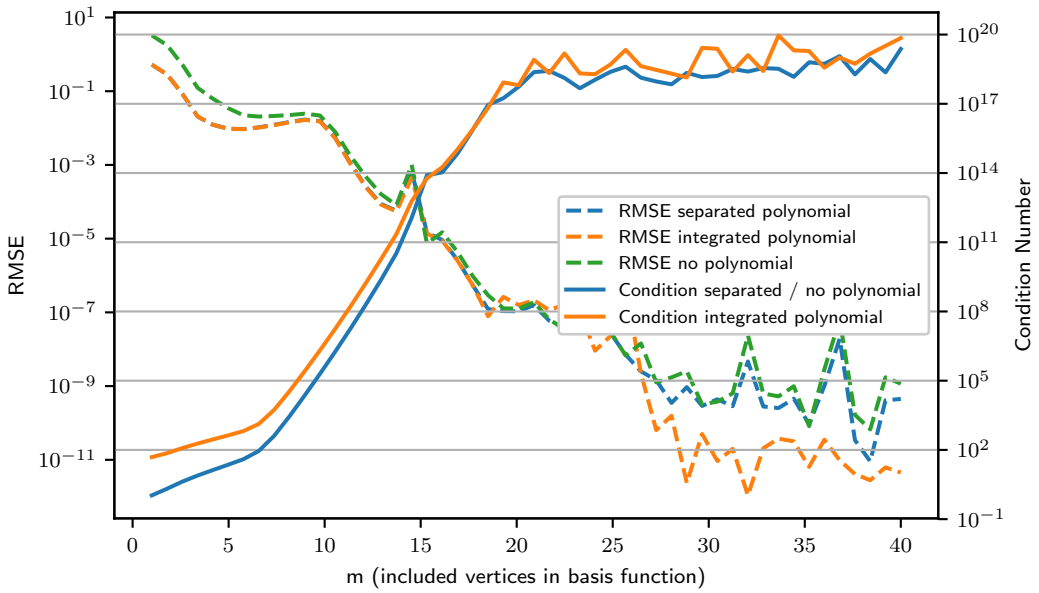

Figure 3: Condition number and root mean square error (RSME) for Gauss-Chebyshev non-uniform point distribution, using 16 elements of 12th order, resulting in 192 points using shape parameters adapted to the local mesh width.

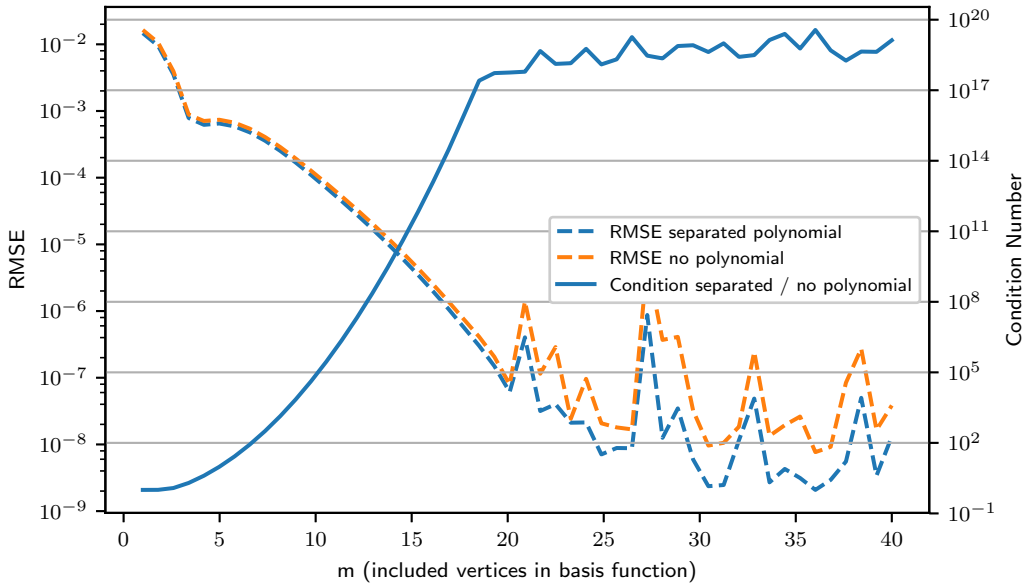

Figure 6: Condition number and root mean square error (RSME) for the rescaled interpolator and uniform point distribution using 192 points.

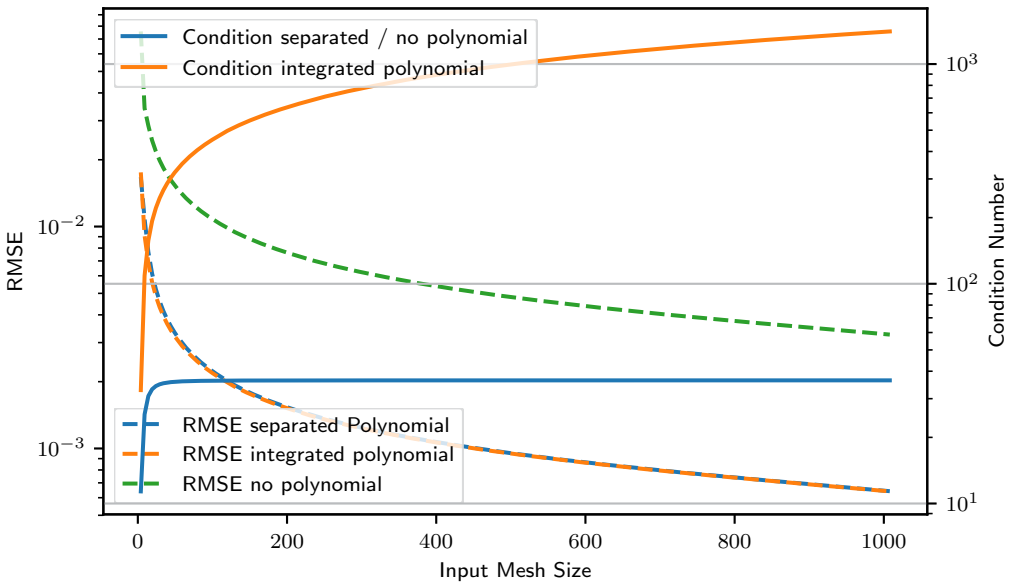

Figure 4: Condition number and root mean square error (RSME) for uniform point distribution, using Gaussian basis functions with width $m = 6$.

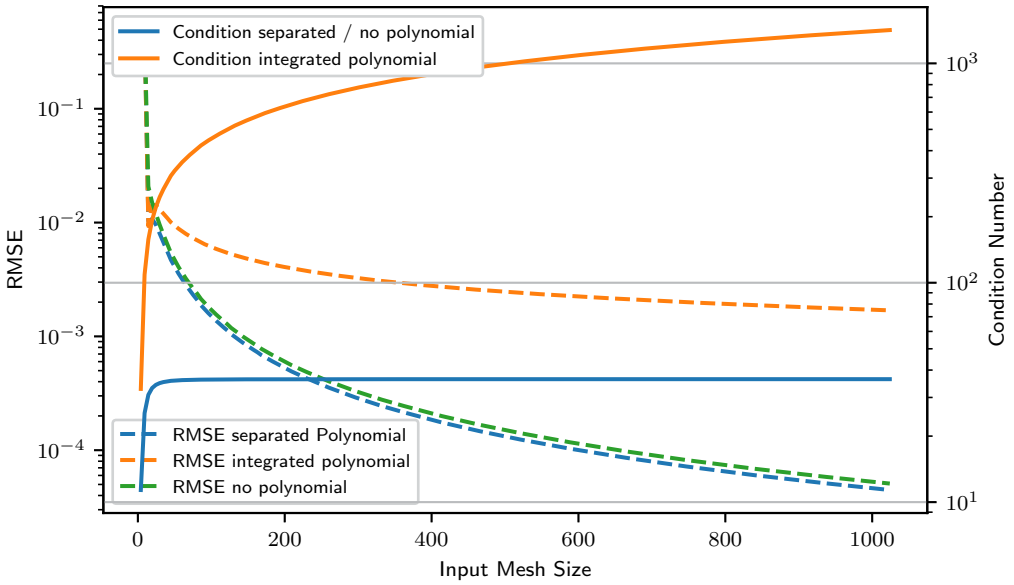

Figure 7: Condition number and root mean square error (RSME) for the rescaled interpolator and uniform point distribution, using a Gaussian basis function whith $m = 6$.

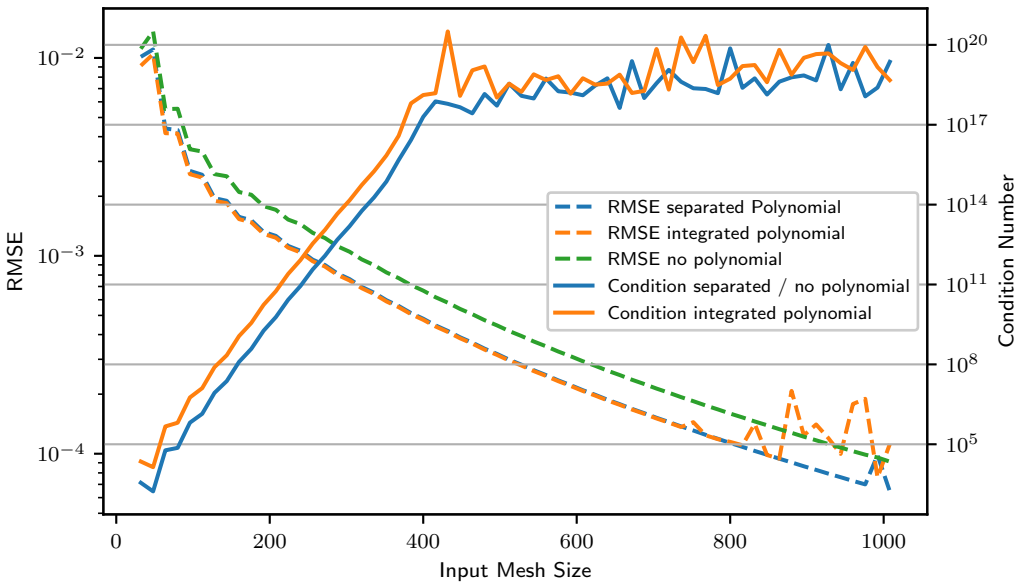

Figure 5: Condition number and root mean square error (RSME) for Gauss-Chebyshey non-uniform point distribution, using a fixed element size of 0.25 with varying degrees from 2 to 64 for basis functions with width $m = 6$ neighboring vertices (based on maximum mesh width).

4 CONCLUSIONS

We evaluated the conditioning of the interpolation system matrix, as well as the accuracy of the interpolation using radial basis functions on uniform and non-uniform meshes. For this paper, we focused on consistent interpolation using a Gaussian basis function. Multi Quadrics and Thin Plate Splines are other often mentioned basis function for FSI, but require a global support and therefore are detrimental to parallelization. Results show that interpolation by RBF is powerful, easy to implement and works well on uniformely scattered data. On uniform meshes, the width m of the basis functions is an effective parameter to control the accuracy-condition trade-off and is applicable to meshes of different sizes. This trade-off also appears when other basis functions, such as Multi-Quadrics or Thin Plate Splines are used. However, the interpolation performs less well on non-uniform meshes. The parameter m needs to be reduced on larger meshes to keep the condition reasonably low and to produce reliable numerical results. Adaptivity can ease the bad conditioning but requires the knowledge of local mesh density, which needs to be either supplied by the solver providing the mesh or computed by the interpolation algorithm. In addition to the computational overhead, this would require significant changes to the software stack to efficiently provide and use this information. Another problematic feature of RBF interpolation is oszillations at the edges of the interpolation interval, similiar to Runge's phenomenon for polynomial interpolation. This can in particular harm solvers

that - following the black-box coupling - rely on the interpolation results close to the edge of the mesh or even outside the source mesh (extrapolation). The rescaling approach also solves this issue in large parts.

The investigation in this paper were performed on one-dimensional data sets. Though experiences show similiar behavior for three-dimensional sets, it warrants further investigation with particular focus on the rescaled interpolation approach. At the current state of RBF interpolation, preCICE provides a powerful and efficient implementation, which still needs significant user experience to control the results. Future work will introduce automated methods to remove this burden from the user. Next steps include the implementation of the rescaling into the coupling software preCICE and tests on real-world multi-physics problem as well as performance optimization.

References

[1] Aukje de Boer, Alexander van Zuijlen, and Hester Bijl. "Comparison of conservative and consistent approaches for the coupling of non-matching meshes". In: *Computer Methods in Applied Mechanics and Engineering* 197.49-50 (Sept. 2008), pp. 4284–4297.

[2] Aukje de Boer, Alexander van Zuijlen, and Hester Bijl. "Review of coupling methods for non-matching meshes". In: *Computer Methods in Applied Mechanics and Engineering* 196.8 (Jan. 2007), pp. 1515–1525.

[3] Hans-Joachim Bungartz et al. "preCICE - A Fully Parallel Library for Multi-Physics Surface Coupling". In: *Computers and Fluids* (2016), pp. 1–9.

[4] Simone Deparis, Davide Forti, and Alfio Quarteroni. "A Rescaled Localized Radial Basis Function Interpolation on Non-Cartesian and Nonconforming Grids". In: *SIAM J. Sci. Comput.* 36.6 (2014), A2745–A2762.

[5] Gregory E. Fasshauer and Jack G. Zhang. "On choosing "optimal" shape parameters for RBF approximation". In: *Numerical Algorithms* 45.1-4 (2007), pp. 345–368.

[6] Gregory E. Fasshauer and Jack G. Zhang. "Preconditioning of Radial Basis Function Interpolation Systems via Accelerated Iterated Approximate Moving Least Squares Approximation". In: *Progress on Meshless Methods*. Ed. by A. J. M. Ferreira et al. Dordrecht: Springer Netherlands, 2009, pp. 57–75.

[7] Bernhard Gatzhammer. "Efficient and Flexible Partitioned Simulation of Fluid-Structure Interactions". PhD Thesis. Technische Universität München, 2014, p. 261.

[8] Shmuel Rippa. "An algorithm for selecting a good value for the parameter c in radial basis function interpolation". In: *Advances in Computational Mathematics* 11 (1999), pp. 193–210.

[9] Benjamin Uekermann. "Partitioned Fluid-Structure Interaction on Massively Parallel Systems". PhD thesis. Technical University of Munich, 2016.

[10] Qi Zhang, Yangzhang Zhao, and Jeremy Levesley. "Adaptive radial basis function interpolation using an error indicator". In: *Numerical Algorithms* (Jan. 2017).

VII International Conference on Computational Methods for Coupled Problems in Science and Engineering
COUPLED PROBLEMS 2017
M. Papadrakakis, E. Oñate and B. Schrefler (Eds)

REDUCED-ORDER HYBRID MULTISCALE METHOD COMBINING THE MOLECULAR DYNAMICS AND THE DISCONTINUOUS-GALERKIN METHOD

N. Emamy[†], M. Lukáčová-Medvid'ová[†], S. Stalter[‡], P. Virnau[‡], L. Yelash[*†]

[†] Institute of Mathematics, Johannes Gutenberg-Universität,
Staudingerweg 9, 55128 Mainz, Germany
emamy@mathematik.uni-mainz.de, lukacova@uni-mainz.de, yelash@uni-mainz.de

[‡] Institute of Physics, Johannes Gutenberg-Universität,
Staudingerweg 9, 55128 Mainz, Germany
ststalte@uni-mainz.de, virnau@uni-mainz.de

Key words: Numerical Methods, Multi-Scale, discontinuous Galerkin, HMM, CFD, Molecular Dynamics

Abstract. We present a new reduced-order hybrid multiscale method to simulate complex fluids. The method combines the continuum and molecular descriptions. We follow the framework of the heterogeneous multi-scale method (HMM) that makes use of the scale separation into macro- and micro-levels. On the macro-level, the governing equations of the incompressible flow are the continuity and momentum equations. The equations are solved using a high-order accurate discontinuous Galerkin Finite Element Method (dG) and implemented in the BoSSS code. The missing information on the macro-level is represented by the unknown stress tensor evaluated by means of the molecular dynamics (MD) simulations on the micro-level. We shear the microscopic system by applying Lees-Edwards boundary conditions and either an isokinetic or Lowe-Andersen thermostat. The data obtained from the MD simulations underlie large stochastic errors that can be controlled by means of the least-square approximation. In order to reduce a large number of computationally expensive MD runs, we apply the reduced order approach. Numerical experiments confirm the robustness of our newly developed hybrid MD-dG method.

1 Introduction

The most accurate description of complex fluids can be obtained by the molecular dynamics. However, such microscale description is computationally inefficient if large scale regions in space and time need to be simulated. To overcome this restriction and to obtain practically tractable simulation techniques suitable combinations of macroscopic and microscopic models have been proposed in the literature. A hybrid molecular-continuum

approach aims in combining the best attributes of both parts: it combines molecular accuracy with the computational efficiency of continuum models. In the case when processes occurring on a small scale are only loosely coupled with the behavior on a much larger scale and the so-called *scale separation* occurs, the hybrid schemes known in the literature as the *Heterogeneous Multiscale Methods* (HMM) have been successfully used, see, e.g., [1, 2, 3, 4, 5] and the references therein.

In this paper we present a novel hybrid multiscale method that is based on the combination of the discontinuous Galerkin (dG) method and molecular dynamics (MD) in order to simulate complex fluids, such as colloids in a Newtonian solvent. The main aim of the present study is two-fold: we use (i) modern numerical method for macroscopic flow equations which allows more flexible discretization including per-cell momentum conservation as well as (ii) the reduced order techniques in order to control the number of needed but computationally expensive MD simulations. As far as we know this is *the first study* implementing techniques (i) and (ii) within the HMM framework. Consequently, our main goal is to increase the accuracy as well as efficiency of this very attractive multiscale simulation framework.

2 Particle model

To simulate colloids, we use non-equilibrium Molecular Dynamics (MD) [6]. The colloids are treated as hard spheres with the interaction modelled using a Weeks-Chandler-Andersen (WCA) potential, which corresponds to the repulsive part of a cut and shifted Lennard-Jones potential

$$V_{WCA} = 4\varepsilon \left[\left(\frac{\sigma}{r}\right)^{12} - \left(\frac{\sigma}{r}\right)^{6} + \frac{1}{4} \right] \ , \quad r < r_c = \sqrt[6]{2}\sigma \ , \text{ else } V_{WCA} = 0 \ , \tag{1}$$

where r is the distance between two particles, r_c the cut-off distance, ϵ the well depth of the Lennard-Jones potential (in our case, $\epsilon = kT$), σ the typical radius of a colloid used as the length scale of the MD simulations.

The MD simulations are performed using the velocity Verlet time integration, which yields a Hamiltonian preserving second order approximation, with the standard Lees-Edwards periodic boundary conditions [7] for an one-dimensional shear flow, see Figure 1a. The temperature is preserved by using a thermostat. We employed the momentum conserving, Galilean invariant, Lowe-Andersen thermostat (LAT) [8]. For high shear rates, this thermostat needs a long relaxation time, therefore we also employed the isokinetic thermostat (ISO) with the SLLOD method [9], see Figure 1b.

The important quantity we obtain from the particle based model is the stress tensor calculated via the Irving-Kirkwood formula [10] using peculiar velocities of particles $\mathbf{v}_i = \tilde{\mathbf{v}}_i - \mathbf{v}_{i,s}$, where $\tilde{\mathbf{v}}_i$ is the total and $\mathbf{v}_{i,s}$ the streaming velocity of particle i, respectively,

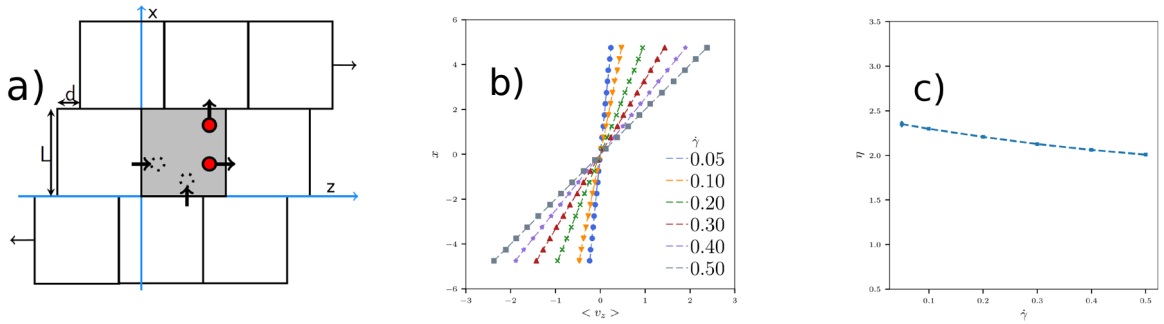

Figure 1: a) Lees-Edwards boundary conditions; b) Shear profiles for different shear rates with the isokinetic thermostat and the SLLOD algorithm for a density of $\rho = 0.8442$ after 1 000 MD-times; c) The viscosity of the system with density $\rho = 0.8442$.

$$\sigma_{\alpha\beta}(t) = -\frac{1}{V}\left(\sum_{i}^{N}(m_i v_{i,\alpha} v_{i,\beta}) + \sum_{i}^{N}\sum_{j>i}^{N} r_{ij,\alpha} F_{ij,\beta}\right). \tag{2}$$

The mean stress is $\pi = Tr(\sigma)/n$ with $n = \{2, 3\}$ the number of space dimensions. From the stresses we calculate the fluid pressure as $p = -\pi_{\dot{\gamma}=0}$ and the dynamic viscosity $\eta = |\sigma_{xz}/\dot{\gamma}|$. As indicated by Figure 1c, the simulated fluid is weakly non-Newtonian.

3 Continuum model

3.1 Governing equations

At the macroscopic level, the motion of the incompressible fluid flow is governed by the continuity and momentum equations,

$$\nabla \cdot \mathbf{u} = 0, \qquad \text{in } \Omega \times [0, t_F] \tag{3a}$$

$$\rho\left(\frac{\partial \mathbf{u}}{\partial t} + \mathbf{u} \cdot \nabla \mathbf{u}\right) = \frac{1}{Re}\nabla \cdot \boldsymbol{\sigma} + \mathbf{g}, \qquad \text{in } \Omega \times [0, t_F] \tag{3b}$$

$$\mathbf{u} = \mathbf{u}_D, \qquad \text{on} \quad \partial\Omega_D \tag{3c}$$

$$\mathbf{u}(t = 0) = \mathbf{u}^{(0)} \qquad \text{in } \Omega, \tag{3d}$$

where $\mathbf{u}$ is the velocity vector, $\boldsymbol{\sigma}$ the Cauchy stress tensor, $\mathbf{g}$ an external body force, ρ the density and Re the Reynolds number. The computational domain Ω is surrounded by the boundary $\partial\Omega = \partial\Omega_D \cup \partial\Omega_P$, where the Dirichlet and periodic boundaries are considered, respectively. In case of the Navier-Stokes equations for Newtonian fluids, $\boldsymbol{\sigma} = -p\mathbf{I} + \boldsymbol{\tau}$, where $\boldsymbol{\tau} = \mu(\nabla \mathbf{u} + \nabla \mathbf{u}^T)$, the above momentum equations reduce to

$$\rho\left(\frac{\partial \mathbf{u}}{\partial t} + \mathbf{u} \cdot \nabla \mathbf{u}\right) = -\nabla p + \frac{1}{Re}(\mu \Delta \mathbf{u}) + \mathbf{g} \quad \text{in } \Omega. \tag{4}$$

3.2 Time integration

For the time integration of the continuity equation (3a) and momentum equations (3b) we apply the following multi-step projection method. Using the first-order Euler method we have

$$\text{I} \quad \tilde{\mathbf{u}} = \Delta t\Big(- \mathbf{u}^{(n)} \cdot \nabla \mathbf{u}^{(n)} + \frac{1}{Re}\nabla \cdot (\boldsymbol{\sigma}^{(n)}/\rho) + \mathbf{g}^{(n)}/\rho\Big), \quad \text{in } \Omega \tag{5a}$$

$$\text{II} \quad \Delta \bar{p}^{(n+1)} = \nabla \cdot \Big(\tilde{\mathbf{u}}/\Delta t\Big), \qquad \text{in } \Omega \tag{5b}$$

$$\frac{\partial \bar{p}}{\partial \mathbf{n}}^{(n+1)} = \mathbf{n} \cdot \Big(\tilde{\mathbf{u}}/\Delta t\Big), \qquad \text{on } \partial\Omega \tag{5c}$$

$$\tilde{\tilde{\mathbf{u}}} = \tilde{\mathbf{u}} - \Delta t \nabla \bar{p}^{(n+1)}, \qquad \text{in } \Omega \tag{5d}$$

$$\text{III} \quad \mathbf{u}^{(n+1)} = \mathbf{u}^{(n)} + \tilde{\tilde{\mathbf{u}}}, \qquad \text{in } \Omega. \tag{5e}$$

Here we define the average pressure $\bar{p}^{(n+1)} = 1/\Delta t \int_{t^n}^{t^{n+1}} p'/\rho \, dt$ with the normal derivative $\partial \bar{p}^{(n+1)}/\partial \mathbf{n} = \mathbf{n} \cdot \nabla \bar{p}^{(n+1)}$. To obtain a unique solution for (5b)-(5c), we require $\int_\Omega \bar{p}^{(n+1)} = 0$. Note that p' is a correction to the pressure to ensure the divergence-free constraint. As one notices, the pressure is already present in the stress tensor in equation (3b). For the second-order time integration of the velocity, we use the Adams-Bashforth method in the first step I,

$$\tilde{\mathbf{u}}_{AB} = \Delta t \sum_{j=0}^{J-1} \beta_j \Big(- \mathbf{u}^{(n-j)} \cdot \nabla \mathbf{u}^{(n-j)} + \frac{1}{Re}\nabla \cdot (\boldsymbol{\sigma}^{(n-j)}/\rho) + \mathbf{g}^{(n-j)}/\rho\Big),$$

with the coefficients $\beta_0 = 3/2$ and $\beta_1 = -1/2$. However, the effective pressure, $\bar{p}^{(n+1)}$, is first-order accurate in time. If required, one can reconstruct the pressure for higher-order accuracy, see [11, 12]. In the above Chorin projection scheme, we use by construction $\nabla \cdot \mathbf{u}^{(n-j)} = 0$, for all $j \geq 0$, which is suggested in [13]. Therefore, we can integrate the unsteady terms in the third step III. In this way, by replacing the intermediate velocity from the first step, the right-hand side of the Poisson equation in the second step II is independent of the time step. This prevents the numerical instability observed in [14, 15, 16] using the dG method.

3.3 Spatial discretization

Following the notations and definitions in [17], we use a matching simplicial geometry-conforming mesh $\mathcal{T}_h$ with mesh size h on the domain Ω. For a mesh element T, $\mathbf{n}_T$ is the unit outward normal to T on the boundary ∂T. Mesh faces $\mathcal{F}_h$ can be either the inner interfaces between adjacent elements $\mathcal{F}_h^i$ or boundary faces $\mathcal{F}_h^b$. The face normal $\mathbf{n}_\mathcal{F}$ points from an arbitrarily chosen (but fixed) element T_1 towards T_2. Therefore, $\mathbf{n}_\mathcal{F} = \mathbf{n}_{T_1} = -\mathbf{n}_{T_2}$ on face $\mathcal{F} \in \mathcal{F}_h^i$. The face normal points outward of Ω on boundary faces. We consider

a broken polynomial space V_h, which consists of piecewise polynomial functions of d variables (spatial dimension) with the maximum total degree k, $V_h := \mathcal{P}_d^k(\mathcal{T}_h)$, $N_d^k = \dim(\mathcal{P}_d^k(T)) = \frac{(k+d)!}{k!d!}$, $\mathcal{P}_d^k(\mathcal{T}_h) := \{v \in L^2(\Omega) | \, \forall T \in \mathcal{T}_h, v|_T \text{ is polynomial}, \deg(v|_T) \leq k\}$. The usual average and jump operators of a scalar-valued function f_h on interfaces between adjacent elements T_1 and T_2 are defined as $\{\!\{f_h\}\!\} = 0.5(f|_{T_1} + f|_{T_2})$ and $[\![f_h]\!] = f|_{T_1} - f|_{T_2}$. Vector-valued functions are treated component-wise. For boundary faces, we have $\{\!\{f_h\}\!\} = [\![f_h]\!] = f|_T$, when not mentioned otherwise. In the following, first we define the forms a, b, b_{st}, b_{gr} and t, which are used in the weak formulation of the governing equations below. The notation $(\cdot\,,\cdot)$ is used for the $L^2(\Omega)$ inner product of scalar- and vector-valued functions. The Einstein summation convention is considered throughout the paper.

Discrete form of the convective terms

To discretize the convective terms we consider the conservative form with the Lax-Friedrich flux

$$t(\mathbf{u}_h, \mathbf{w}_h, \boldsymbol{\varphi}_h) = -\int_\Omega (\mathbf{u}_h \otimes \mathbf{w}_h) : \nabla \boldsymbol{\varphi}_h + \int_{\mathcal{F}_h} \Big(\{\!\{\mathbf{u}_h \otimes \mathbf{w}_h\}\!\} \cdot \mathbf{n}_\mathcal{F} + \frac{1}{2}\Lambda [\![\mathbf{u}_h]\!] \Big) \cdot [\![\boldsymbol{\varphi}_h]\!],$$

where $\Lambda = \max(\lambda|_{T_1}, \lambda|_{T_2})$ and λ is the absolute eigenvalue of the Jacobian matrix $\Big(\partial[(\mathbf{u} \otimes \mathbf{w}) \cdot \mathbf{n}_\mathcal{F}]/\partial \mathbf{u}\Big)|_{\bar{\mathbf{u}},\bar{\mathbf{w}}}$. The average and jump operators on the Dirichlet boundaries are defined as $\{\!\{\mathbf{u}_h \otimes \mathbf{w}_h\}\!\} = 0.5\Big((\mathbf{u}_h \otimes \mathbf{w}_h)|_T + (\mathbf{u}_D \otimes \mathbf{w}_D)\Big)$, $[\![\mathbf{u}_h]\!] = (\mathbf{u}_h|_T - \mathbf{u}_D)$, $[\![\boldsymbol{\varphi}_h]\!] = \boldsymbol{\varphi}_h|_T$.

Discrete form of the Laplacian of the pressure

To discretize the Laplacian of the pressure we take the following general form using the Symmetric Interior Penalty (SIP) flux

$$a(p_h, q_h) = -\int_\Omega \nabla p_h \cdot \nabla q_h + \int_{\mathcal{F}_h} \Big(\{\!\{\nabla p_h\}\!\} \, [\![q_h]\!] + \{\!\{\nabla q_h\}\!\} \, [\![p_h]\!] \Big) \cdot \mathbf{n}_\mathcal{F} - \int_{\mathcal{F}_h} \mu_p \, [\![p_h]\!] \, [\![q_h]\!] \, .$$

On the Dirichlet boundaries $\mathcal{F} \subset \partial\Omega_D$ we have the boundary condition (5c) $\{\!\{\nabla p_h\}\!\} \cdot \mathbf{n}_\mathcal{F} = \mathbf{n}_\mathcal{F} \cdot \Big(\tilde{\mathbf{u}}_h^{(n)}/\Delta t\Big)$, $[\![p_h]\!] = 0$, $\{\!\{\nabla q_h\}\!\} = \nabla q_h|_T$. In the above discretizations, μ_P is a penalty parameter. The minimal values suggested for the penalty parameter for triangular and tetrahedral meshes can be found in [18, 19] for generic types of elements including hybrid grids. For quadrilateral elements we set

$$\mu_p = \alpha_P c = \begin{cases} \alpha_P \max(c|_{T_1}, c|_{T_2}) & \mathcal{F} \in \mathcal{F}_h^i \\ \alpha_P \, c|_T, & \mathcal{F} \in \mathcal{F}_h^b \end{cases}, \quad c|_T = (k+1)^2 \, \frac{A(\partial T \backslash \mathcal{F}_h^b)/2 + A(\partial T \cap \mathcal{F}_h^b)}{V(T)},$$

where $\alpha_P \geq 1$ is a user defined coefficient to ensure the stability. Area and volume are denoted by A and V, respectively.

Discrete divergence and gradient operators

The divergence of the intermediate velocity $\tilde{\mathbf{u}}_h$ is approximated in the following way

$$b(\tilde{\mathbf{u}}_h/\Delta t, q_h) = -\int_\Omega \tilde{\mathbf{u}}_h/\Delta t \cdot \nabla q_h + \int_{\mathcal{F}_h} \{\tilde{\mathbf{u}}_h/\Delta t\} \cdot \mathbf{n}_\mathcal{F} [\![q_h]\!].$$

We treat the discrete gradient of the pressure component-wise and use the form $b(.,.)$ to define the form $b_{gr}(.,.)$ as follows

$$b_{gr}(p_h, \boldsymbol{\varphi}) = b(p_h \mathbf{e}_i, \varphi_{h,i}) = -\int_\Omega p_h \mathbf{e}_i \cdot \nabla \varphi_{h,i} + \int_{\mathcal{F}_h} \{\!\{p_h\}\!\}\, \mathbf{e}_i \cdot \mathbf{n}_{\mathcal{F}} [\![\varphi_{h,i}]\!].$$

Discrete form for the viscous terms

The discrete form for the viscous term (divergence of the stress tensor), $b_{st}(.,.)$, is defined component-wise using the form $b(.,.)$ by adding a penalty term

$$\begin{aligned} b_{st}(\boldsymbol{\sigma}_h/\rho, \boldsymbol{\varphi}_h) =& b(\sigma_{h,ij}/\rho \mathbf{e}_j, \varphi_{h,i}) - \int_{\mathcal{F}_h} \mu_v \mu_p [\![u_{h,i}]\!]\, [\![\varphi_{h,i}]\!] \\ =& -\int_\Omega \sigma_{h,ij}/\rho \mathbf{e}_j \cdot \nabla \varphi_{h,i} + \int_{\mathcal{F}_h} \{\!\{\sigma_{h,ij}/\rho\}\!\}\, \mathbf{e}_j \cdot \mathbf{n}_{\mathcal{F}} [\![\varphi_{h,i}]\!] - \int_{\mathcal{F}_h} \mu_v \mu_p [\![u_{h,i}]\!]\, [\![\varphi_{h,i}]\!]\,. \end{aligned}$$

On the Dirichlet boundaries $\mathcal{F} \subset \partial\Omega_D$ we have $\{\!\{\sigma_{h,ij}/\rho\}\!\} = (\sigma_{h,ij}/\rho)|_T$, $[\![u_{h,i}]\!] = (u_{h,i}|_T - u_{D,i})$, $[\![\varphi_{h,i}]\!] = \varphi_{h,i}|_T$. Realizing that the stress is a function of the strain, its divergence depends on the second derivatives of the velocity. Therefore, the same penalty term as for the SIP method above is considered here for stability. On the other hand, by adding this penalty term, the no-slip boundary condition is implemented. The penalty parameter μ_p is the same as defined above for the Laplacian of the pressure. The additional penalty parameter μ_v can be set to μ/ρ, where μ is the dynamic viscosity of an equivalent Newtonian fluid.

dG weak formulation of the governing equations

In order to discretize equations (5a)-(5e) in space, we set $\mathbf{u}_h = u_{h,i}\mathbf{e}_i$, $\boldsymbol{\varphi}_h = \varphi_{h,i}\mathbf{e}_i$, where $u_{h,i}$, $\phi_{h,i} \in V_h$, $\mathbf{e}_i$ is the unit vector in direction i, $\boldsymbol{\sigma}_h = \sigma_{h,ij}\mathbf{e}_i\mathbf{e}_j$ and $p_h, q_h \in V_h$,

$$(\widetilde{\mathbf{u}}_h, \boldsymbol{\varphi}_h) = \Delta t\Big(- t(\mathbf{u}_h^{(n)}, \mathbf{u}_h^{(n)}, \boldsymbol{\varphi}_h) + \frac{1}{Re} b_{st}(\boldsymbol{\sigma}_h^{(n)}/\rho, \boldsymbol{\varphi}_h) + (\mathbf{g}_h^{(n)}/\rho, \boldsymbol{\varphi}_h)\Big), \tag{6}$$

$$a(\bar{p}_h^{(n+1)}, q_h) = b(\widetilde{\mathbf{u}}_h/\Delta t, q_h), \tag{7}$$

$$(\widetilde{\widetilde{\mathbf{u}}}_h, \boldsymbol{\varphi}_h) = (\widetilde{\mathbf{u}}_h, \boldsymbol{\varphi}_h) - \Delta t\, b_{gr}(\bar{p}_h^{(n+1)}, \boldsymbol{\varphi}_h), \tag{8}$$

$$(\mathbf{u}_h^{(n+1)}, \boldsymbol{\varphi}_h) = (\mathbf{u}_h^{(n)}, \boldsymbol{\varphi}_h) + (\widetilde{\widetilde{\mathbf{u}}}_h, \boldsymbol{\varphi}_h). \tag{9}$$

4 Hybrid multiscale method (HMM)

To compute the solution of the macroscopic problem, the stress tensor is required at each quadrature point. These data are provided by MD simulations, however, the continuum assumption must still be valid. In dense liquids, MD simulations confirm the continuum assumption up to $2-3\,\mathrm{nm}$ channels [20]. Because of different characteristic values of the microscopic and macroscopic models, adjustments are required for the data transfer between the macroscopic and microscopic simulations. The macroscopic non-dimensional strain $\mathbf{S}$ and stress $\boldsymbol{\sigma}$ tensors are related to the non-dimensional strain $\mathbf{S}_a$

and stress $\boldsymbol{\sigma}_a$ in reduced atomic units in the following way, $\mathbf{S}(u_b/l_b) = \mathbf{S}_a(u_r/l_r)$ and $\boldsymbol{\sigma}(\mu_b u_b/l_b) = \boldsymbol{\sigma}_a(\mu_r u_r/l_r)$. Subscripts b and r correspond to the characteristic values of the box and the reduced atomic units in the particle simulations, respectively. We define $l_a = l_b/l_r$, $u_a = u_b/u_r$, and $\mu_a = \mu_b/\mu_r$ to be the length, velocity, and viscosity of the MD box in the reduced atomic units. For simplicity, we consider $u_a = 1$ and $\mu_a = 1$, and choose $l_a = 10$ for the MD box length. In order to obtain an one-dimensional strain field for the particle simulations we rotate the MD boxes [3]. The following relations apply for the data transfer in 2D hybrid simulations

$$\begin{aligned}\mathbf{S}_a &= \Theta(\mathbf{S}/l_a)\Theta^T \\ &= \frac{1}{l_a}\begin{bmatrix} 0 & \sin(2\theta)(S_{22}-S_{11})/2 + S_{12}\cos(2\theta) \\ \sin(2\theta)(S_{22}-S_{11})/2 + S_{12}\cos(2\theta) & 0 \end{bmatrix},\end{aligned} \tag{10}$$

$$\boldsymbol{\sigma} = \Theta^T(l_a\boldsymbol{\sigma}_a)\Theta, \tag{11}$$

$$\Theta = \begin{bmatrix} \cos(\theta) & \sin(\theta) \\ -\sin(\theta) & \cos(\theta) \end{bmatrix}, \qquad \theta = \frac{1}{2}\tan^{-1}\left(\frac{(S_{22}-S_{11})/2}{S_{12}}\right),$$

4.1 Reduced-order approach

Unknown nonlinear function for stress $\boldsymbol{\sigma}^* = F(\mathbf{S}^*)$ is approximated in the following way

$$\boldsymbol{\sigma}_i^* \approx \widetilde{F}_i(\dot{\gamma}) = \sum_{j=0}^{k} \alpha_{ij}\dot{\gamma}^j, i = \begin{cases} 1,2,3 & \text{2D} \\ 1,..,6 & \text{3D} \end{cases}. \tag{12}$$

Here $\dot{\gamma}$ represents $2S_{12}^*$ for 2D and $2S_{13}^*$ for $3D$ simulations, k is the degree of the approximating polynomial. To reduce a large number of particle simulations we use an offline training phase and an online phase of fast multiple queries. For this training, we solve a least-square problem with the Tikhonov regularization for each component i of the stress tensor

$$\arg\min_x \left(\|Ax-b\|_2^2 + \lambda_1^2\|x\|_2^2 + \lambda_2^2\|Dx\|_2^2\right). \tag{13}$$

Here b is the vector of n ($n \geq k+1$) data points of the corresponding component of the stress tensor obtained by the particle simulations, x is the vector of unknown coefficients. The penalty term Dx is added to damp the oscillations in the derivative function $\partial A/\partial\dot{\gamma}\, x = ADx$. λ_1 and λ_2 are the regularization parameters. The equivalent problem $(A^TA + \lambda_1^2 I + \lambda_2^2 D^TD)x = A^Tb$ is solved by the LU factorization using the LAPACK library [1].

[1] http://www.netlib.org/lapack

Test case 1. We take $\rho = 0.8$ and consider $n = 35$ data points for $\dot{\gamma} \in [0, 1.5]$ to approximate σ_{12}^* for 2D simulations. Least-square problems are solved for λ_1 and λ_2 between 10^{-15} and 10^{-1} and $k = 0, .., 8$. As one can see in Figure 2, we find the optimized solution using the L-curve [21] approach employing a minimum-product corner criterion. The corner of the plot at approximately $(0.005, 3.6)$ represents the optimized solution. The L^2-norm and root-mean-square of the residual of the optimized solution are shown in Table 1 for different degrees k.

Table 1: Numerical convergence of the L^2-norm of the residual for the optimized solution (shown in Figure 2) with respect to the polynomial degree.

k	$\|Ax-b\|_2$	$\|x\|_2$	$\sqrt{(\|Ax-b\|_2^2)/n}$
0	8.029124	0.392878	1.357170
1	0.596365	1.862069	0.100804
2	0.059931	2.655598	0.010130
3	0.033173	2.845212	0.005607
4	0.011536	3.246203	0.001950
5	0.005229	3.838724	0.000884
6	0.005343	3.608710	0.000903
7	0.004903	3.658437	0.000829
8	0.004816	3.467192	0.000814

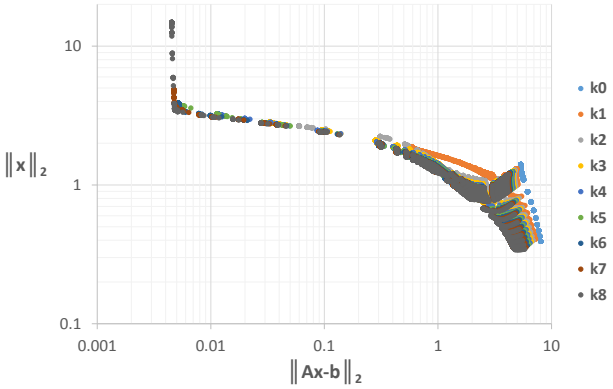

Figure 2: L-curve method to determine the optimized coefficients. L^2-norm of the solution is plotted vs. L^2-norm of the residual for different values of regularization parameters λ_1 and λ_2.

4.1.1 Data refinement strategy

In order to find a proper approximation of the stress tensor with fewer number of particle simulations, we solve the optimization problem above with a relatively small number of samples. Then we use the greedy algorithm (worst scenario search), see e.g. [22], for the data refinement to suggest the shear rate(s) for new particle simulations. If one plots the residual $(Ax - b)$ versus $\dot{\gamma}$, the proposed shear rate for a new simulation $\dot{\gamma}_{new} = 0.5(\dot{\gamma}_M + \dot{\gamma}_N)$, is found in the neighborhood of $\dot{\gamma}_M = \arg\max_{\dot{\gamma}}(Ax - b)$, where $\dot{\gamma}_N$ is the left or right neighbor of $\dot{\gamma}_M$ which corresponds to the larger residual.

4.2 Extension of the approximation

In some cases, the density of the polymers may play a magnificent role. Thus, in order to find the corresponding stress for different densities, we use the extended approximation

$$\boldsymbol{\sigma}_i^* \approx \widetilde{F}_i(\dot{\gamma}, \rho) = \sum_{j_1=0}^{k_1} \sum_{j_2=0}^{k_2} \alpha_{ij_1j_2} \dot{\gamma}^{j_1} \rho^{j_2}, i = \begin{cases} 1,2,3 & \text{2D} \\ 1,..,6 & \text{3D} \end{cases}, \tag{14}$$

where we consider m different density values ρ_l, $l = 1, .., m$ and n_l different shear rates, $l = 1, .., m$. Therefore, the corresponding approximation matrix A has the size $(\sum_{l=1}^{m} n_l) \times \Big((k_1+1)(k_2+1)\Big)$. In order to find the appropriate degrees k_1 and k_2 efficiently, for each density we first find the corresponding approximation as described in Section 4.1. Then, for all densities, k_1 would be the maximum of the degrees of approximation. Now, we start from $k_2 = 0$ and solve for the above approximation in the same way as for approximation (12). We increase k_2 until the residual converges.

4.3 Algorithm for the optimization problem

The following algorithm holds for the case (12) and is applicable to (14), if k_1 is fixed as described in Section 4.2, k_2 is considered as k, and m corresponds to n. Also, extended matrices A, b, and *stderr* (for the standard error of the data) must be used. Depicting $3 \times stderr$, 99% of the samples, which deviate from the (averaged) data points, are taken into account. $k_{\max}$, δ, and ϵ are user-defined parameters.

- Step 1: Set $k = \text{degree}_{\min} = 0$ and $n_{\min} = (\text{degree}_{\min} + 1)$. Consider $n = \max(n_{\min}, N)$, where N is the number of available samples of the parameter, for which the refinement applies. At least $n_{\min}$ samples are required to start the optimization. Set $\text{degree}_{\max} = \min(n, k_{\max})$.

- Step 2: Considering degree k, assemble the corresponding matrix A and solve the least-square problem 13. Set $x_{\text{old}} = x$, $res_{\text{old}} = \text{A}x - b$ and $res_{L^2,\text{old}} = \|x_{\text{old}}\|_2^2$.

- Step 3: Compute $\text{diff} = \|\text{A}x - b\|_2^2 - res_{L^2,\text{old}}$ and $\text{diff}_{\text{rel}} = \text{diff}/\|x_{\text{old}}\|_2^2$. If $\text{diff} < \|stderr\|_2^2$ or $\text{diff}_{\text{rel}} < \delta$ the solution is converged with respect to k. Therefore, set $x = x_{\text{old}}$, $res = res_{\text{old}}$, $res_{L^2} = res_{L^2,\text{old}}$, and $k = k - 1$.

- Step 4: If $res \leq 3 \times stderr$ for each data point, the solution is optimized.

- Step 5: If the solution does not converge or is not optimized, $k = k+1$, assemble A, set $x_{\text{old}} = x$, $res_{\text{old}} = res$, $res_{L^2,\text{old}} = res_{L^2}$ and solve the least-square problem 13.

- Step 6: If $k < \text{degree}_{\max}$ and the solution does not converge and is not optimized, go to Step 3. Otherwise, x is the vector of coefficients and k is the degree of approximation.

- Step 7: Compute $res_{\text{RMS}} = \sqrt{res/n}$. If $res_{\text{RMS}} > \epsilon$ find the new sample for refinement by the worst scenario search (Greedy algorithm), perform the required MD simulations, $N = N + 1$ and go to Step 1. Otherwise, the optimization procedure stops.

Test Case 2. We apply optimization procedure 4.3 to a set of 2D MD data consisting of shear rates $\dot{\gamma} = 0.00, 0.01, ..., 1.00$ to find approximation (12) considering each density

$\rho = 0.1, 0.2, ..., 0.8$. Parameters λ_1 and λ_2 are between 10^{-15} and 10^{-2}, and $\delta = 0.05$. The refinement Step 7 of the algorithm is excluded. The coefficients are shown in Table 2 for $\rho = 0.5$ as an example. The coefficient α_1 can be considered as the viscosity of an equivalent Newtonian fluid. The coefficients α_0 of the normal components of the stress are used to compute the pressure as one half of the trace of the stress tensor. The fluid pressures calculated in this way for different densities are compared with the Henderson equation of state for hard disks in Figure 3.

Table 2: Coefficients of approximation (12) using 2D MD data at density $\rho = 0.5$.

	σ_{11}	σ_{12}	σ_{22}
α_0	-1.559856	0.019031	-1.524225
α_1		0.516020	
$\text{Residual}_{\text{rms}}$	0.044120	0.008918	0.016566

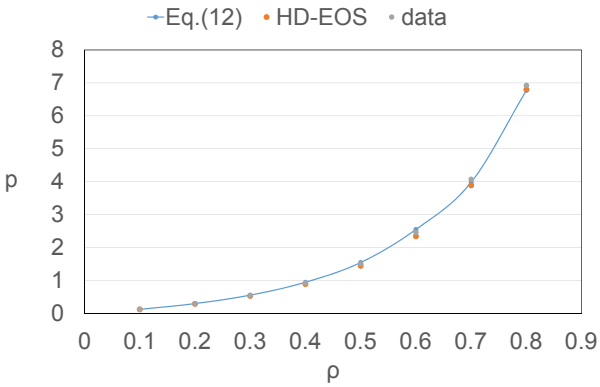

Figure 3: Pressure from the mean stress in 2D MD in comparison with the Henderson equation of state for hard-disks and approximation (12).

Test Case 3. We apply optimization procedure 4.3 to a set of 3D MD data to find approximations (12) and (14). The data set consists of 48 data points of 12 shear rates $\dot{\gamma} = 0.0, 0.001, 0.005, 0.01, 0.025, 0.033, 0.05, 0.066, 0.075, 0.1, 0.5, 1.0$ and densities $\rho = 0.4, 0.5, 0.6, 0.8$. The same numerical settings as in Test case 2 are used, parameters λ_1 and λ_2 are between 10^{-15} and 10^{-2} and $\delta = 0.05$. The refinement Step 7 of the algorithm is excluded. The coefficients of approximation (12) are shown in Tables 3 for $\rho = 0.5$. The coefficients of approximation (14) are shown in Table 4. The pressures as one third of the trace of the stress tensor found from approximations (12) and (14) are compared with the Carnahan-Starling equation of state for hard spheres in Figure 4.

Table 3: Coefficients of approximation (12) using 3D MD data for $\rho = 0.5$.

	σ_{11}	σ_{12}	σ_{13}	σ_{22}	σ_{23}	σ_{33}
α_0	-1.702695	-0.000039	0.002679	-1.698915	-0.000216	-1.739654
α_1			0.438956			
$\text{Residual}_{\text{rms}}$	0.038215	0.000160	0.002336	0.030139	0.000498	0.030025

Table 4: Coefficients of approximation (14) using 3D MD data.

	σ_{11}	σ_{12}	σ_{13}	σ_{22}	σ_{23}	σ_{33}
α_{00}	-3.543503	-0.0000013	0.007578	-3.767376	-0.000019	-3.746758
α_{10}			0.519910			
α_{01}	16.503534		0.042466	17.262241		16.961379
α_{11}			-1.421053			
α_{02}	-25.455935		-0.196039	-26.026600		-25.708823
α_{12}			1.0097451			
α_{03}			0.179535			
α_{13}			2.939758			
$\text{Residual}_{\text{rms}}$	0.090635	0.000001	0.006968	0.060957	0.000394	0.084390

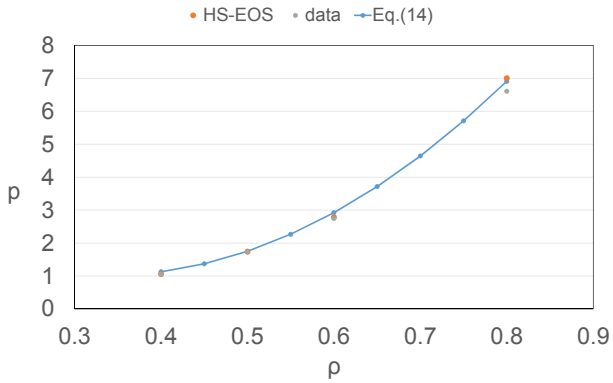

Figure 4: Pressure from the mean stress in 3D MD in comparison with the Carnahan-Starling equation of state for hard-spheres and approximation (14).

5 Reduced-order hybrid simulations

Two-dimensional hybrid simulations of the Couette flow are performed using the 2D MD data for $\rho = 0.5$ from Test case 2. Here we apply the optimization algorithm including the refinement Step 7 according to Section 4.1.1 to find approximation (12) with the greedy refinement strategy. The levels of refinement are shown in Figure 5. We start with 4 data points, which are shown in Table 5. The refinement procedure terminates after 10 levels including 23 data points out of 101 total data points. The best approximation for σ_{12} is found after 3 levels of refinement including 10 data points. However, if one considers all components of the stress, the best approximation would be the one from the first level with 6 data points. Note that one should stop the refinement algorithm at this level in order to avoid considering data points with higher statistical errors. The coefficients using 6 and 10 data points are shown in Table 5, which are similar to the coefficients in Table 2 using all data points. Therefore, we choose $\alpha_1 = 0.516$ as the viscosity of the equivalent

Table 5: Coefficients of approximation (12) for 2D MD data at $\rho = 0.5$ applying the refinement shown in Figure 5.

Starting values, $\dot{\gamma} = \{0.0, 0.25, 0.75, 1.0\}$

	α_0	α_1	$\text{Residual}_{\text{rms}}$
σ_{11}	-1.566603		0.057684
σ_{12}	0.011217	0.515426	0.010882
σ_{22}	-1.528000		0.022316

6 values, $\dot{\gamma} = \{0.0, 0.25, 0.75, 0.87, 0.88, 1.0\}$

	α_0	α_1	$\text{Residual}_{\text{rms}}$
σ_{11}	-1.582399		0.053632
σ_{12}	0.011120	0.516600	0.008897
σ_{22}	-1.534684		0.020448

10 values, $\dot{\gamma} = \{0.0, 0.06, 0.12, 0.13, 0.5, 0.6, 0.65, 0.75, 0.94, 1.0\}$

	α_0	α_1	$\text{Residual}_{\text{rms}}$
σ_{11}	-1.564935		0.058747
σ_{12}	0.010471	0.516323	0.007196
σ_{22}	-1.528257		0.022103

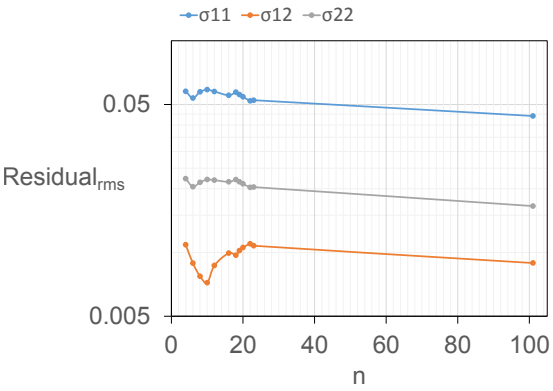

Figure 5: Optimization algorithm including the greedy data refinement strategy.

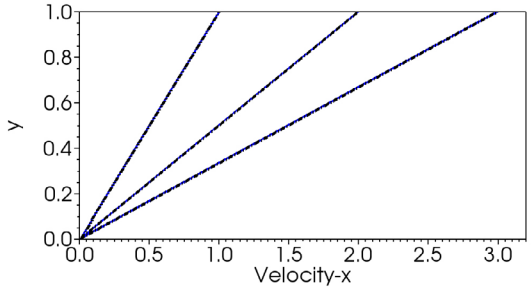

Figure 6: Velocity profiles in the streamwise direction for shear velocities $U = 1, 2, 3$. Blue solid lines: hybrid simulations, black dash-dot lines: analytic solutions $u_x = yU$.

Newtonian fluid with the same density $\rho = 0.5$ for comparison.

The macroscopic hybrid simulations of the Couette flow are performed on the domain $[-1, 1] \times [0, 1]$. The flow is periodic in the streamwise x-direction. The no-slip boundary condition is applied at the walls. At the lower wall $y = 0$, the velocity is zero. At the upper wall $y = 1$, the velocity in x-direction is equal to U and the velocity in y-direction is zero. A grid of 3×3 cells is employed. A polynomial degree $k = 1$ is assigned in the dG method, $Re = 1$. The velocity profiles presented in Figure 6 overlap with the analytical solution $u_x = yU$ for the equivalent Newtonian fluid with density $\rho = 0.5$ and viscosity $\mu = 0.516$.

Three-dimensional hybrid simulations of the Poiseuille flow are performed using approximation (14) to the 3D MD data in Test case 3. The approximation coefficients are shown in Table 4. We take the corresponding coefficients of σ_{13} to estimate the viscosity of the equivalent Newtonian fluid using relation $\mu = \alpha_{10} + \alpha_{11}\rho + \alpha_{12}\rho^2 + \alpha_{13}\rho^3$. The viscosities for different densities are listed in Table 6 and plotted in Figure 7. The viscosi-

Table 6: Estimates of the Newtonian fluid viscosity $\mu = \lim_{\dot{\gamma}\to 0} |\sigma_{13}/\dot{\gamma}|$ using approximations (12) and (14) with 3D MD data.

	Eq.(12)	Eq.(14)
0.4	0.301957	0.301193
0.45	0.352795	
0.5	0.438956	0.429290
0.55		0.532881
0.6	0.649864	0.665775
0.65		0.830174
0.7		1.028285
0.75		1.262313
0.8	1.537902	1.534461

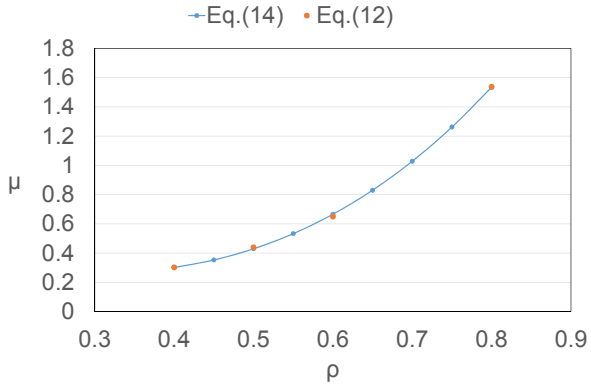

Figure 7: Estimated Newtonian fluid viscosity vs. density in 3D MD.

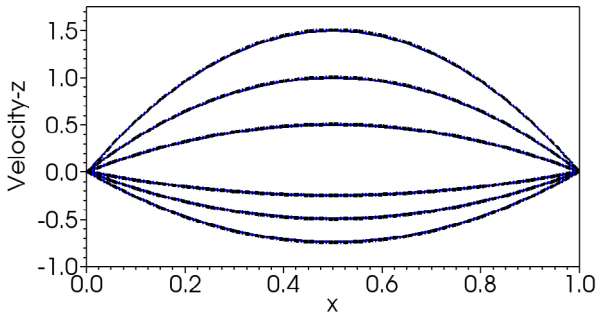

Figure 8: Velocity profiles in the streamwise direction for pressure gradient parameter $P = -3, -2, -1, 2, 4, 6$. Blue solid lines: hybrid simulations, black dash-dot lines: analytic solutions $u_z = x(1-x)P$.

ties obtained from approximations (12) and (14) match very well. The hybrid simulations are performed for $\rho = 0.55$, for which we do not have the MD data. The computational domain is taken as $[0,1]\times[-1,1]\times[-1,1]$. The flow is periodic in y- and z-directions. The no-slip boundary condition is applied at the walls $x = 0$ and $x = 1$, where the velocity is zero. The pressure gradient $f_z = -2\mu\, P/Re$ is applied in the streamwise z-direction with $Re = 1$. We estimate the viscosity of the equivalent Newtonian fluid $\mu = 0.53$. A grid of $3\times 3\times 3$ cells is employed. The polynomial degree is $k = 2$ in the dG method. Velocity profiles in z-direction are plotted for different values of the pressure gradient parameter P in Figure 8.

6 Acknowledgments

The present work is supported by German Science Foundation (DFG) under the grant TRR 146. We would like to thank M. Oberlack, F. Kummer and B. Müller for providing their code BoSSS. The authors gratefully acknowledge the computing time granted on the HPC cluster Mogon at Johannes Gutenberg-University Mainz.

REFERENCES

[1] W. E and B. Enquist. The heterogeneous multiscale methods. *Commun. Math. Sci.*, 1(1):87–132, 2003.

[2] W. Ren and W. E. Heterogenous multiscale method for the modeling of complex fluids and micro-fluidics. *J. Comput. Phys.*, 204:1–26, 2005.

[3] Sh. Yasuda and R. Yamamoto. A model for hybrid simulations of molecular dynamics and computational fluid dynamics. *Phys. Fluids*, 20(11):113101, 2008.

[4] W. E, W. Ren, and E. Vanden-Eijnden. A general strategy for designing seamless multiscale methods. *J. Comput. Phys.*, 228(15):5437–5453, 2009.

[5] M.K. Borg, Lockerby D.A., and J.M. Reese. A hybrid molecular–continuum method for unsteady compressible multiscale flows. *J. Fluid Mech.*, 768:388–414, 2015.

[6] D. Frenkel and B. Smit. *Understanding Molecular Simulations.* Academic Press, 1996.

[7] A. W. Lees and S. F. Edwards. The computer study of transport processes under extreme conditions. *J. Phys. C.*, 5:1921–1929, 1972.

[8] C. P. Lowe. An alternative approach to dissipative particle dynamics. *Europhys. Lett.*, 47:145–151, 1999.

[9] P. J. Daivis and B. D. Todd. A simple, direct derivation and proof of the validity of the SLLOD equations of motion for generalized homogeneous flows. *J. Chem. Phys.*, 124:194103, 2006.

[10] J. H. Irving and J. G. Kirkwood. The statistical mechanical theory of transport processes. iv. the equations of hydrodynamics. *J. Chem. Phys.*, 18:817, 1950.

[11] B. Sanderse and B. Koren. Accuracy analysis of explicit Runge-Kutta methods applied to the incompressible Navier-Stokes equations. *J. Comput. Phys.*, 231(8):3041–3063, 2012.

[12] G. A. Reis, I. V. M. Tasso, L. F. Souza, and J. A. Cuminato. A compact finite differences exact projection method for the Navier-Stokes equations on a staggered grid with fourth-order spatial precision. *Comput. Fluids*, 118:19–31, 2015.

[13] S. A. Orszag, M. Israeli, and M. O. Deville. Boundary conditions for incompressible flows. *J. Sci. Comput.*, 1:75–111, 1986.

[14] E. Ferrer, D. Moxey, R. H. J. Willden, and S. J. Sherwin. Stability of projection methods for incompressible flows using high order pressure-velocity pairs of same degree: continuous and discontinuous Galerkin formulations. *Commun. Comput. Phys.*, 16(3):817–840, 2014.

[15] D. T. Steinmoeller, M. Stastna, and K. G. Lamb. A short note on the discontinuous Galerkin discretization of the pressure projection operator in incompressible flow. *J. Comput. Phys.*, 251:480–486, 2013.

[16] N. Emamy. *Numerical simulation of deformation of a droplet in a stationary electric field using DG*. PhD thesis, TU Darmstadt, Darmstadt, 2014.

[17] D. A. Di Pietro and A. Ern. *Mathematical Aspects of Discontinuous Galerkin Methods*. Springer-Verlag Berlin Heidelberg, 2012.

[18] K. Shahbazi. An explicit expression for the penalty parameter of the interior penalty method. *J. Comput. Phys.*, 205(2):401–407, 2005.

[19] K. Hillewaert. *Development of the discontinuous Galerkin method for high-resolution, large scale CFD and acoustics in industrial geometries*. Ph.D. thesis, Université catholique de Louvain, 2013.

[20] D. M. Holland, M. K. Borg, D. A. Lockerby, and J. M. Reese. Enhancing nano-scale computational fluid dynamics with molecular pre-simulations: Unsteady problems and design optimisation. *Comput. Fluids*, 115:46–53, 2015.

[21] P. Ch. Hansen and D. P. O'Leary. The use of the L-curve in the regularization of discrete ill-posed problems. *SIAM J. Sci. Comput.*, 14(6):1487–1503, 1993.

[22] V. N. Temlyakov. Greedy approximation. *Acta Numer.*, 17:235–409, 2008.

VII International Conference on Computational Methods for Coupled Problems in Science and Engineering
COUPLED PROBLEMS 2017
M. Papadrakakis, E. Oñate and B. Schrefler (Eds)

SIMULATING THE INTERACTION OF ELECTROSTATICALLY CHARGED PARTICLES IN THE INFLOW AREA OF CABIN AIR FILTERS USING A FULLY COUPLED SYSTEM

CAROLIN SCHOBER*, DAVID KEERL†, MARTIN LEHMANN° AND MIRIAM MEHL#

*Graduate School of Excellence advanced Manufacturing Engineering (GSaME)
University of Stuttgart
Nobelstraße 12, 70569 Stuttgart, Germany
e-mail: carolin.schober@gsame.uni-stuttgart.de, web page:
http://www.gsame.uni-stuttgart.de/

†MANN+HUMMEL Innenraumfilter GmbH & Co. KG
Kulmbacher Straße 12, 95502 Himmelkron, Germany
e-mail: david.keerl@mann-hummel.com - Web page: http://www.mann-hummel.com/

°MANN+HUMMEL GmbH
Grönerstraße 50, 71636 Ludwigsburg, Germany
e-mail: martin.lehmann@mann-hummel.com - Web page: http://www.mann-hummel.com/

#Institute of Parallel and Distributed Systems (IPVS)
University of Stuttgart
Universitätsstraße 38, 70569 Stuttgart, Germany
e-mail: miriam.mehl@ipvs.uni-stuttgart.de, web page: http://www.ipvs.uni-stuttgart.de/

Key words: Molecular Dynamics, Four-way Coupling, Continuum Mechanics, Air Filtration, Electrostatics

Abstract. Precise simulations of particulate flow through fibrous filters are essential in order to predict and enhance filtration performances. To run the computation in reasonable time, a continuum approach is commonly used to emulate the air flow. The software GeoDict [1] allows for the simulation of the complete process, ranging from calculating a flow field, tracking particles inside that field to finding collisions with porous filter media. However, this approach completely neglects particle-particle interactions although particles often carry electrostatic charges [2]. Comparing the results of GeoDict to a fully coupled system shows the influence of this simplification. The software ESPResSo [3, 4] uses such a four-way coupling combining a molecular-dynamics-like approach for partricle simulation with an integrated Lattice-Boltzmann fluid dynamics solver. Already

for a simple scenario, which represents the filter media as a mesh consisting of cylindrical fibers, significant influences of the full coupling on the particle trajectories and even the collection efficiency can be observed. We decribe the modeling and setup for both approaches and present numerical results for simplified yet meaningful test cases.

1 INTRODUCTION

Cabin air filters are applied to prevent small particles such as pollen, fine dust and soot amongst others from being transferred through the HVAC system into the interior (cabin) of a vehicle. Further enhancement of the fibrous filters with regard to filtration efficiency, pressure drop and dust holding capacity is essential due to steadily increasing requirements on air quality in car cabins as well as increasing exposure to pollutants at the same time – especially in fast-growing markets like China. One promising approach to achieve improved filtration performances maintaining a decent differential pressure level is the electrostatic charging of the fibrous media. Thus, electrostatic filtration effects supplement the well-known mechanical collection mechanisms (such as inertia, diffusion, etc.). However, the lack of long-time stability of the charges is a major problem. As traditional development methods are no longer sufficient at this point because they reach their limits of feasability and, moreover, are too expensive virtually prototyping filter media has been an ongoing research subject for years [5]. Regarding the simulation of electrostatic separation mechanisms the fundamentals are still missing. Besides the interference of several fiber-particle interactions (i.e. Coulombic attraction/repulsion, induced dipolar forces, image charge effects) particle-particle interactions potentially play an important role. However, this effect is completely neglected in previous research studies due to the high degree of complexity [2]. In this work, we introduce a new and basic approach to simulate filtration performances using a fully-coupled system. Similarities and differences to the standard one-way coupling approach are presented in detail.

2 ONE-WAY COUPLING APPROACH

In the one-way coupling approach, the fluid is treated as a continuum, i.e., the values for density, temperature and velocity in three spatial dimensions can be calculated at any point in time.

2.1 The One-Way Coupled Model

The underlying mathematical model consists of a system of partial differential equations (PDEs) based on physical conserved quantities. In order to model the behaviour of fluids, mass conversation

$$\nabla u = 0, \tag{1}$$

and momentum conservation

$$\rho(\frac{du}{dt} + (u \cdot \nabla)u) = -\nabla p + \mu \Delta u + f \tag{2}$$

must be ensured. In the equations (1) and (2) u denotes the fluid velocity. The left hand side of the momentum equation with ρ being the density, describes the inertial fluid transport along the flow. The first term on the right hand side describes the acceleration due to a gradient in the pressure p. The diffuse movement resulting from the fluid viscocity μ is considered in the second term. Furthermore, external forces f such as gravitational forces are considered in the momentum equation. The combination of both conservation laws together is well-known as the Navier-Stokes equations. For small Reynolds numbers implying laminar fluid flows the inertial term can be neglected yielding the Stokes equations

$$0 = -\nabla p + \mu \Delta u + f, \quad \nabla u = 0. \tag{3}$$

The disperse multiphase flow is subsequently simulated based on the Euler-Lagrange model, i.e., particle tracking is calculated based on a steady-state flow field by solving the ordinary differential equation

$$\frac{dv}{dt} = \underbrace{\gamma\,(u(x) - v(x))}_{friction} + \underbrace{\frac{QE(x)}{m}}_{electrostatics} + \underbrace{B(t)}_{Brownian\ motion} + \underbrace{f}_{external\ forces}. \tag{4}$$

In the equation of motion, v denotes the particle velocity. The friction γ between particles and fluid flow is modeled in the first term. The subsequent term takes into account the electrostatic interaction of the particle charges Q among the electric field E generated by the filter fibers. The influence of elctrostatic attraction or repulsion respectively depends on the particle mass m. The term $B(t)$ corresponds to the diffusive (Brownian) motion and f again models additional external forces.

In this approach, the particle motion is influenced by the flow field, but there is no interaction between severeral particles and no dependency of the flow field from the particle motion.

2.2 GeoDict

The CFD software GeoDict offers modular tools for the simulation of materials and fluid flows in diverse applications. It was mainly developed for modeling porous media and composite materials. For this purpose, GeoDict offers the possiblity to virtually generate structures as well as to simulate multiphase flow physics in porous media. Thus GeoDict is well suited for filtration procedures, oil and gas transport through digital rocks and electrochemical processes in fuel cell and battery media. In this work, GeoDict is used to calculate the particulate air flow through simplified filter media structures with the

FilterDict [2, 6] module.

Flow Field Calculation. In order to solve the flow equations before, after and inside filter media, GeoDict uses an equidistant voxel mesh discretization. The following three PDE solvers are available to solve the (Navier-) Stokes equations.

- The Explicit Jump (EJ) immersed boundary method can only be used to solve the steady Stokes equation on a regular grid.
- The SIMPLE-FFT is an enhancement of the semi implicit methods for pressure linked equations (SIMPLE) which uses a Fast Fourier transformation (FFT) as a fast solver for the pressure Poisson equation. The solver can be used to aquire a solution of the Stokes as well as the Navier-Stokes equations.
- The LIR (Left Identity Right) solver uses a simplified LIR-tree for spatial partitioning. Thus, it is possible to coarsen the voxel geometry in areas where the velocity or pressure gradient are small. [7]

Due to its short computational runtime and at the same time low memory requirements for porous media only the LIR solver is deployed in this work. After the solver converges the flow field is kept fix and particles are added to the inflow area.

Particle Tracking. During particle tracking, GeoDict permanently searches for collisions of particles with the filter medium. Particles which are captured by the fibers become part of the solid filter structure.

Batch-Wise Geometry Updates. GeoDict uses a batch-wise approach to take into account changes of the filter medium structure due to deposited particles. This means, that we track a batch of (independent) particles along the flow through the filter medium and determine as described above whether or not each particle is captured by a fiber. The batch contains a certain number of particles. After finishing the calculations for the whole batch, the fiber structre is updated, i.e., enhanced by the captured particles. Subsequently, a new flow field is calculated and the next batch of particles is tracked and so forth.

3 FULLY COUPLED APPROACH

The fully coupled approach models interactions between single molecules or particles based on a molecular dynamics like method (MD) and includes the full transient interaction between flow and particles. Therefore, the approach allows for more precise simulations of particle trajectories and becomes suitable for the simulation of particle dynamics in porous filter media.

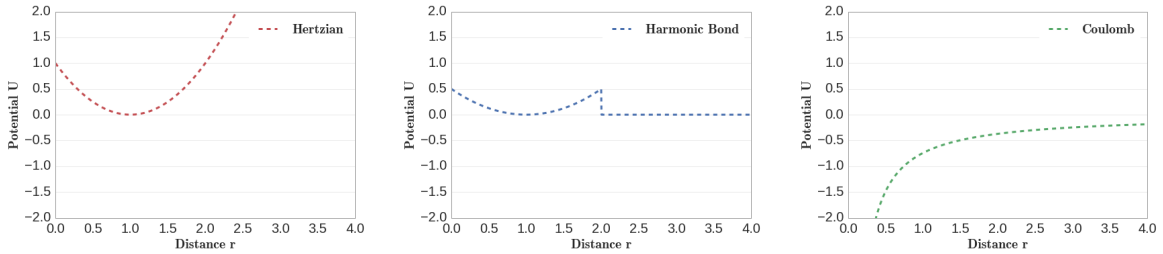

Figure 1: Most important potentials (Hertzian, harmonic bond and Coulomb) regarding interactions in cabin air filtration as a function of the distance between two particles.

3.1 The Fully Coupled Model

The basic component of each particle interaction is the the potential energy $U(|\mathbf{r}|)$ induced by each pair of particles. $U(|\mathbf{r}|)$ depends on the distance $\mathbf{r}$ between two interacting molecules, is described with simple mathematical equations and allows for the calculation of the force $\mathbf{F}(|\mathbf{r}|)$ according to

$$\mathbf{F}(\mathbf{r}) = -\nabla U(|\mathbf{r}|) \quad \text{with} \quad U(|\mathbf{r}|) = U_{Hz}\left(|\mathbf{r}|\right) + U_{hb}\left(|\mathbf{r}|\right) + U_{C}\left(|\mathbf{r}|\right). \tag{5}$$

The equation of motion

$$\ddot{\mathbf{r}} = \frac{\mathbf{F}(\mathbf{r})}{m} \tag{6}$$

describes the resulting particle transport.

For dust particles, we use the Hertzian potential U_{Hz} in combination with two other potentials. The Hertzian potential

$$U_{Hz}\left(|\mathbf{r}|\right) = \epsilon \left(1 - \frac{|\mathbf{r}|}{\sigma}\right)^{\frac{5}{2}}, \tag{7}$$

which is plotted in Fig. 3.1 models collisions of deforming particles [14]. The loss of energy due to deformation ought to be more realistic for the collision of dust particles than the Lennard-Jones potential which is usually used in molecular dynamics for gaseous transport.

The second potential plotted in Fig. 3.1 is implementing dynamic bonding mechanisms. These bond potentials are switched 'on' during the simulation whereever particles collide, thereby friction between the touching particles is assumed. In the simulations of this work a harmonic bond potential

$$U_{hb}\left(|\mathbf{r}|\right) = \frac{1}{2}k\left(|\mathbf{r}| - R\right)^2 \tag{8}$$

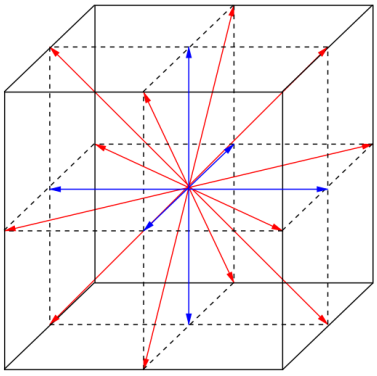

Figure 2: The 19 velocity vectors $\mathbf{c}_i$ for a D3Q19 lattice. From the central grid point, the velocity vectors point towards all 6 nearest neighbours marked in blue and towards 12 next-to-nearest neighbours shown in red. The 19th velocity vector is the rest mode (zero velocity). [15]

is used. The potential is minimal at the distance R and the prefactor is given by k. The described collision detection is especially important when particles carry electrostatic charges. They result in attractive forces which are modeled by the long-ranged electrostatic Coulomb potential

$$U_C\left(|\mathbf{r}|\right) = l_B k_B T \frac{q_1 q_2}{|\mathbf{r}|} \tag{9}$$

that is effective even for large distances. Besides the slow decay for large distances, the Coulomb potential further is singular at $r = 0$.

In addition to the interaction between particles, the fully coupled approach takes into consideration the bi-directional interaction between particles an the backgroud air flow, modeled by the Lattice-Boltzmann method (LBM) approximating the Navier-Stokes equations. LBM is based on mesoscopic kinetic equations. The main idea is that gases or fluids consist of a large number of microscopic particles. During their movement the particles exchange momentum and energy through streaming and particle collision. This particle transport can be modeled with the Boltzmann equation given by

$$\frac{df\left(\mathbf{x}, \mathbf{p}, t\right)}{dt} = \Omega\left(f\right), \tag{10}$$

where $f(\mathbf{x}, \mathbf{p}, t)$ denotes the particle distribution depending on position $\mathbf{x}$, momentum $\mathbf{p}$ and time t. The collison operator (modeling firiction/diffusion) is Ω. To make the equations solvable, LBM discretises the velocity space with a finite number of discrete velocities $\mathbf{c}_i$ and finite differences on a cubic grid in the three-dimensional coordinate space. Fig. 2 shows the widely used D3Q19 discretisation for velocities with 19 velocity components associated to the center of a three-dimensional cubic grid cell. The two algorothmic step of LBM, the streaming (modeling convection) and collision steps can be

calculated according to

$$\underbrace{f_i\left(\mathbf{x}+\mathbf{c_i}dt, t+dt\right) - f_i\left(\mathbf{x},t\right)}_{streaming} = \underbrace{-\frac{dt}{\tau}\left(f_i\left(\mathbf{x},t\right) - f_i^{eq}\left(\mathbf{x},t\right)\right)}_{collision} = \Omega_i. \tag{11}$$

The bi-directional interactions between particles and background flow are considered by the point-coupling between MD and LBM described in [13].

3.2 ESPResSo

The software package ESPResSo (Extensible Simulation Package for RESearch on SOft matter), is based on a molecular dynamics approach for soft matter simulations. Classical examples for soft matter systems are polymers, colloids, liquid crystals or glasses [3]. Besides these applications ESPResSo was originally developed for, the sofware package meanwhile also comprises efficient algorithms for electrostatics [8, 9, 10, 11, 12], dielectrics, magnetostatics and hydrodynamics. By means of coarse-graining ESPResSo enables simulations with diverse length scales on a mesoscopic level. That also allows for yoking molecules together to dust particles in the size of one µm as they occur in real aerosols. Furthermore, the molecular dynamics simulation allows to be coupled to a Lattice-Boltzmann fluid dynamics solver in order to simulate background fluid flows [13]. Therefore, ESPResSo provides a new and basic approach for the simulation of cabin air filtration.

MD in ESPResSo. ESPResSo provides a wide range of interaction potentials [3], among them all potentials required in this work. Regarding the implemented algorithms, a distinction is made between short- and long-ranged interactions. The p3m algorithm of ESPResSo separates the two classes, tackling the short-ranged potential in real space based on cut-off and a linked-cell algorithm, and handling the (smooth) long-range potentials in Fourier space [3].

Lattice-Boltzmann in ESPResSo. In ESPResSo, the fluid particle densities are located on the nodes of the lattice and a linear relaxation towards the equilibrium distribution f_i^{eq} is assumed. Besides the MPI parallized CPU version ESPResSo can also employ GPU acceleration for hydrodynamics [15] which is exploited in this work.

Coupled Simulation in ESPResSo. The fully-coupled model realizes a four-way coupling for simulations of particulate flow through a porous medium. Due to the high degree of complexity, the computational effort is very high, but ESPResSo delivers very precise results for the simulation of particle trajectories.

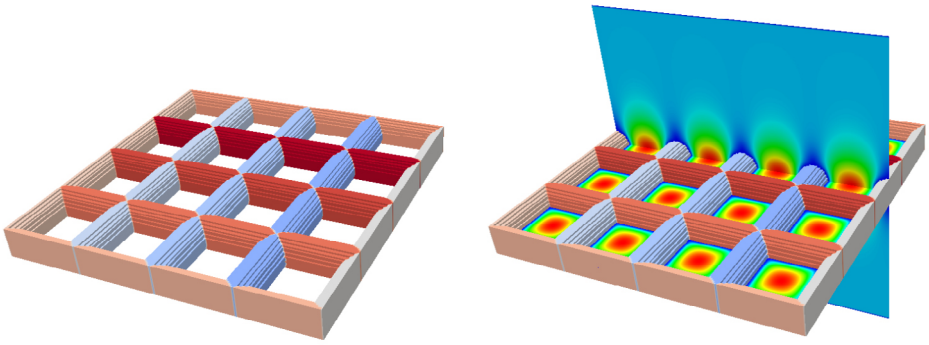

Figure 3: The simulation setup consists of uniformly aligned cylindrical fibers creating a mesh. On the right hand side scliced plots of the magnitude velocity are shown.

4 EXPERIMENTAL SETUP

Since the computational effort becomes immense when considering the fully coupled approach, the experimental setup is chosen as a simple scenario. Fig. 3 shows the used fiber network consisting of uniformly aligned cylindrical constraints. The particulate flow through this mesh is simulated with both software approaches, GeoDict and ESPResSo. The cubic simulation domain has a size of $(200 \times 200 \times 200)\,\mu m^3$ and is assumed to be periodic in each direction for the flow field as well as for the particles. After the flow field has converged, spherical monodisperse particles of the size of two µm are added at the top of the simulation domain. At this point, two different experiments are performed. In a first step, 20 uncharged particles are distributed statistically and added to the flow fields with the same starting positions for each approach. Thereby, the difference in applying uni- and bi-directional interactions between particles and the background flow field is analyzed. As the simulation domain is relativly small, the particle concentration $c_P = 2.8 \cdot 10^{-2}\,{}^{kg}/_{m^3}$ is chosen excessively high in order to have a reasonable number of particles in the simulation domain. In the second experiment, the focus is on the influence of particle-particle interaction during particle motion. For this scenario only two particles are considered, but they carry electrostatic charges q_1 and q_2 that are multiples of the elementary charge $e = 1.602 \cdot 10^{-19}\,C$ ($q_1 = 0.04\,e$ and $q_2 = -0.01\,e$). q_1 and q_2 are unirealisticaly low but allow for stable simulation without further nmerical measures such as time-step restrictions. Important simulation parameters for both experiments are listed in Tab. 1.

5 RESULTS

Flow field simulation. The stand-alone flow field for the used mesh is plotted in Fig. 3. At this point, ESPResSo and GeoDict provide no visible differences regardless of the used solver.

Flow with neutral particles. The particle trajectories of 20 neutral particles in a

Table 1: Simulation parameters for particles, fibers and air flow

fiber diameter	d_F	20	µm
particle diameter	d_P	2	µm
particle density	ρ_P	2650	$^{kg}/_{m^3}$
mean velocity	u_f	0.2	$^{m}/_{s}$
fluid density	ρ_f	1.204	$^{kg}/_{m^3}$
fluid viscosity	η_f	$1.834 \cdot 10^{-5}$	$^{kg}/_{ms}$

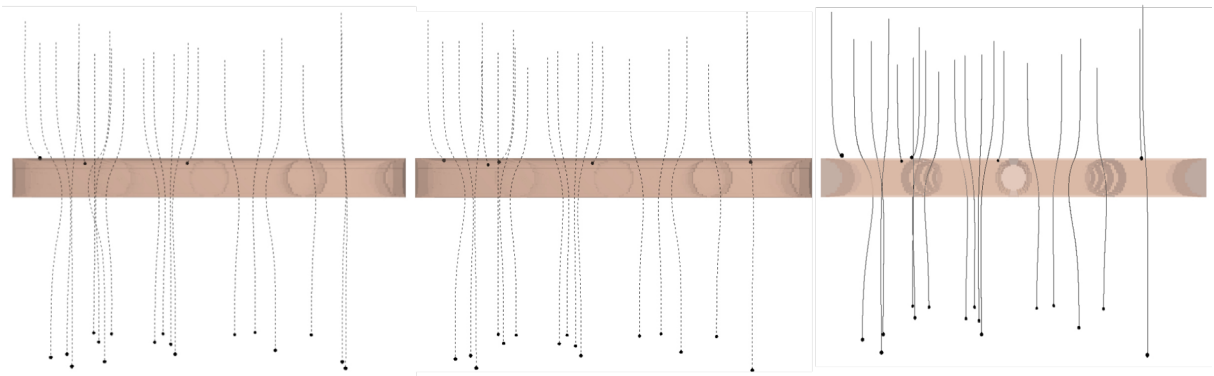

Figure 4: Particle trajectories of 20 particles using the GeoDict Stokes solver, GeoDict Navier-Stokes solver and the ESPResSo LBM for calculating the background air flow.

background flow are plotted in Fig. 4. The two pictures on the left side are both achieved with the LIR solver of GeoDict. The background flow field on the left side is calculated with the Stokes equations whereas the middle one uses the more complex Navier-Stokes equations. The comparison of both GeoDict plots shows minimal deviations in the particle trajectories. However, these deviations result in different collision efficiencies with the fibers. Based on the Stokes flow field, only three particles are captured whereas with the Navier-Stokes version, two more particles stick to the fibers. Already for the small total amount of 20 particles, differences in the collection efficiency can be observed at this point. Tracking the particles with the ESPResSo software package results in the third plot of Fig. 4. Using LBM for the background flow also leads to the deposition of five out of 20 particles. The simulation results point out that for the given flow parameters we are not in the Stokes regime anymore but have to use the Navier-Stokes equations. The comparison between the one-way coupling and the fully coupled approach does not show any effects for this simple scenario.

Flow with charged particles. The simulation results for the two opposite charged particles are displayed in the picture series in Fig. 5. For better viewing, the particles are magnified and their trajectories are additionally plotted again. Although the parti-

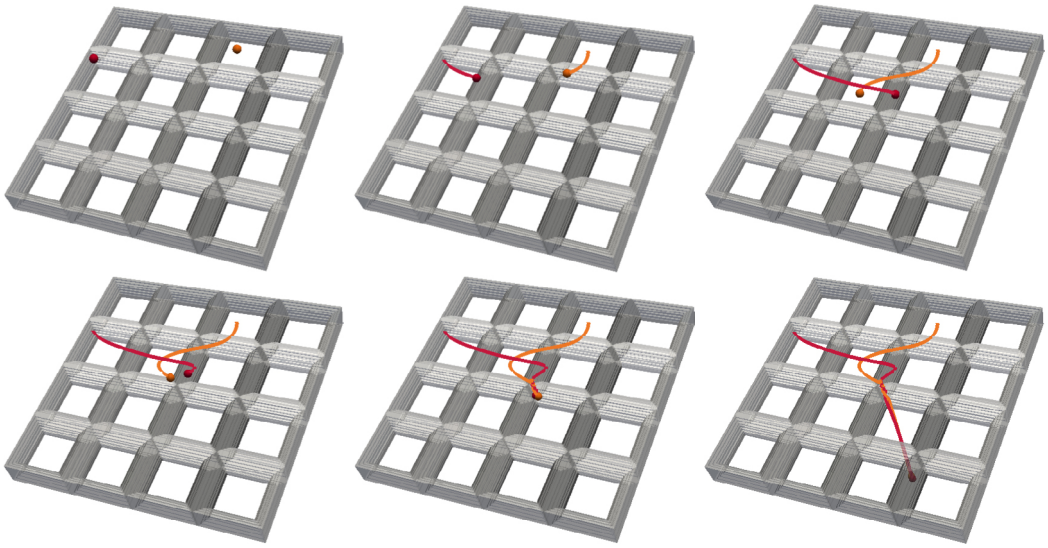

Figure 5: Particle trajectories of two charged particles ($q_1 = 0.04\,e$ and $q_2 = -0.01\,e$) at different times simulated with ESPResSo.

cles only carry extremely low electrostatic charges, we observe a strong attraction and even a collision. The particles already stick together before they reach the fiber network. Subsequently, the particles pass through one of the pores as a kind of agglomerate. The simulation with the same particle starting points is executed without electrostatic interactions. Again a picture series is recorded and plotted in Fig. 6. Omitting the Coulomb potential results in totally different particle trajectories, one particle even collides with the mesh. This points out that particle-particle interactions definitely need to be considered for charged particles.

6 CONCLUSIONS AND OUTLOOK

The preliminary results presented in this paper for particulate air flow through a simple fiber mesh support the assumption that a simple and computationally efficient one-way coupled approach leads to acceptable results as long as we simulate the filtration of uncharged particles in uncharged filter media, only. However, the influence of particles which are added one after the other on the flow field might be more pronounced. Particles thus influence the following particles in the slipstream. As soon as we consider charged particles, already a simulation with only two particles with the fully coupled model shows that particle trajectories change dramatically if particle-particle interactions are properly modeled. The resulting agglomeration of particles into larger clusters is assumed to have an essential effect on filtration efficiency and should therefore not be neglected upon designing filter media exploiting electrostatic effects.

Next steps towards more realistic and application-relevant simulations would be the continous addition of particles (at randomly chose times) instead of at a single point in

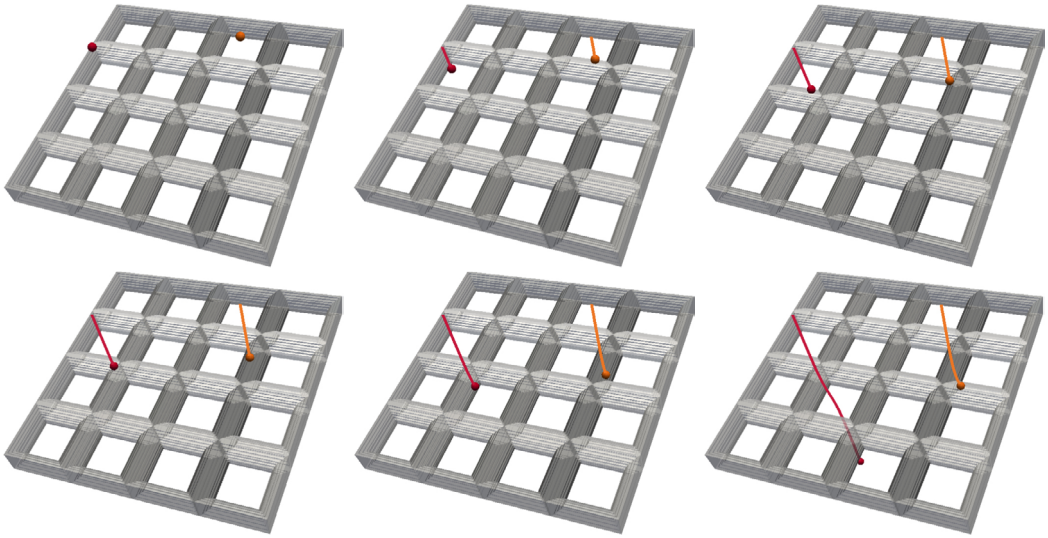

Figure 6: Particke trajectories of two neutral particles at different times simulated with ESPResSo.

time. A new version of the Lattice-Boltzmann solver in ESPResSo working on adaptively refined grids [16] will further allow to simulate more complex filter media structures, larger domain sizes, and longer physical time spans. This enables us to achieve significant simulation results also for lower, more realistic, particle concentrations. Further steps will be the modeling of more realistic charge and particle size distributions and simulations with charged filter media instead of charged particles only.

REFERENCES

[1] *GeoDict. The virtual material laboratory.* © 2001-2011 Fraunhofer ITWM, © 2012-2017 Math2Market GmbH, www.geodict.com

[2] Rief, S., Latz, A. and Wiegmann, A. *Computer simulation of air filtration including electric surface charges in three-dimensional fibrous microstructures.* Filtration, volume 6, no.2, 169-172, (2006).

[3] Limbach, H.J., Arnold, A., Mann, B.A. and Holm, C. *ESPResSo - an extensible simulation package for research on soft matter systems.* Computer Physics Communications, 174(9):704-727, (2006).

[4] Arnold, A., Lenz, O., Kesselheim, S., Weeber, R., Fahrenberger, F., Roehm, D., Kosovan, P. and Holm, C. *ESPResSo 3.1 - molecular dynamics software for coarse-grained models.* In M. Griebel and M.A. Schweitzer, editors, Meshfree Methods for Partial Differential Equations VI, volume 89 of Lecture Notes in Computational Science and Engineering, pages 1-23. Springer Berlin Heidelberg, (2013).

[5] Lehmann, M.J., Weber, J., Kilian, A. and Heim, M. *Microstructure Simulation as Part of Fibrous Filter Media Development Processes – From Real to Virtual Media.* Chemical Engineering & Technology 39.3: 403-408, (2016).

[6] Wiegmann, A., Iliev, O. and Schindelin, A. *Computer aided engineering of filter materials and pleated filters.* Global Guide of the Filtration and Separation Industry, pp. 191-198, (2010).

[7] Linden, S., Wiegmann, A. and Hagen, H. *The LIR space partitioning system applied to the Stokes equations.* Graphical Models 82, 58-66, (2015).

[8] Arnold, A., Breitsprecher, K., Fahrenberger, F., Kesselheim, S., Lenz, O. and Holm, C. *Efficient algorithms for electrostatic interactions including dielectric contrasts.* Entropy, 15(11):4569-4588, (2013).

[9] Desemo, M. and Holm, C. *How to mesh up Ewald sums. I. A theoretical and numerical comparison of various particle mesh routines.* Journal of Chemical Physics, 109:7678, (1998).

[10] Arnold, A. and Holm, C. *A novel method for calculating electrostatic interactions in 2D periodic slab geometries* . Chemical Physics Letters, 354:324-330, (2002).

[11] Arnold, A., de Joannis, J. and Holm, C. *Electrostatics in periodic slab geometries II.* Journal of Chemical Physics, 117:2503-2512, (2002).

[12] Arnold, A. and Holm, C. *MMM1D: A method for calculating electrostatic interactions in 1D periodic geometries.* Journal of Chemical Physics, 123(12):144103, (2005).

[13] Dünweg, B. and Ladd, A.J.C. *Lattice boltzmann simulations of soft matter systems.* In Advanced Computer Simulation Approaches for Soft Matter Sciences III, volume 221 of Advances in Polymer Science, pages 89-166. Springer-Verlag Berlin, Berlin, Germany, (2009).

[14] Machado, M. et al. *Compliant contact force models in multibody dynamics: Evolution of the Hertz contact theory.* Mechanism and Machine Theory, 53:99-121, (2012).

[15] Röhm, D. and Arnold, A. *Lattice Boltzmann simulations on GPU with ESPResSo.* The European Physical Journal Special Topics 210.1, 89-100, (2012).

[16] Lahnert, M., Burstedde, C., Holm, C., Mehl, M., Rempfer, G. and Weik, F. *Towards Lattice-Boltzmann on Dynamically Adaptive Grids – Minimally-Invasive Grid Exchange in ESPResSo.* In: Papadrakakis, M.m Papadopoulos, V., Stefanou, G., Plevris, V. (Hrsg): ECCOMAS Congress 2016, VII European Congress on Computational Methods in Applied Sciences and Engineering.

VII International Conference on Computational Methods for Coupled Problems in Science and Engineering
COUPLED PROBLEMS 2017
M. Papadrakakis, E. Oñate and B. Schrefler (Eds)

INFLUENCE OF MECHANICAL YIELDING ON PREDICTIONS OF SATURATION: THE SATURATION LINE

MARTÍ LLORET-CABOT* AND SIMON J. WHEELER *

* University of Glasgow (UofG)
Rankine Building, G12 8LT Glasgow, UK
e-mail: marti.lloret-cabot@ glasgow.ac.uk,

Key words: unsaturated soils, saturated soils, mechanical behaviour, water retention, suction, saturation, de-saturation, retention hysteresis.

Abstract. It is now well accepted that the mechanical and the water retention behaviour of a soil under unsaturated conditions are coupled and, that such coupling, should be incorporated into a constitutive model for a realistic representation of soil's response. In existing models, the influence of the mechanical behaviour on the water retention is often represented by a shift of the main wetting retention curve to higher values of matric suction (the difference between pore air and pore water pressures) when the specific volume decreases. This means that any variation of total volumetric strains of compression (whether these are elastic or elasto-plastic) will result in a shift of the main wetting and drying curves to the right, when these curves are represented in the water retention plane. This shift of the main water retention curves, however, should not only influence the unsaturated stress states as often described in the literature, it should also have some impact on the saturated stress states and, more specifically, on the predictions of de-saturation (air-entry point) and saturation (air-exclusion point). From a modelling point of view, it is advantageous to represent this influence through the plastic component of volumetric strain of compression only because, in this way, a consistent representation of the mechanical behaviour for both unsaturated and saturated states can be naturally achieved. This and other advantages resulting from this singular approach are demonstrated in the paper in the context of the Glasgow Coupled Model (GCM).

1 INTRODUCTION

A major challenge of existing constitutive models for soils is the proper representation of transitions between unsaturated and saturated conditions. This challenge is intimately linked to: the incorporation of hysteresis in the water retention behaviour, the consideration of the influences between mechanical and water retention behaviour and the choice of stress state variables. As discussed in Gens [1], proper representation of these transitions is likely to be difficult in models that use net stress (excess of total stress over pore air pressure) and matric suction (difference between pore air pressure and pore water pressure) as stress state variables. This is because de-saturation during drying will not necessarily occur at zero suction and subsequent re-saturation on wetting will neither occur always at zero suction

(Lloret-Cabot, Wheeler and Sánchez [2]). The consequence of having saturated states at non-zero values of suction makes especially complicated the unification of the mechanical behaviour for unsaturated and saturated states when using net stress and matric suction as stress state variables, because net stress only reverts to the saturated effective stress tensor (the conventional stress state variable for the representation of the mechanical behaviour for saturated soils, Terzaghi [3]) when suction equals zero. This situation worsens when using a critical state framework (Roscoe and Burland [4]) as underlying formulation for the saturated conditions, because representations of elastic and plastic volumetric straining for unsaturated states will only converge to the saturated case for the single case of zero suction. These challenges are discussed in the paper in the context of the Glasgow Coupled Model, showing how to resolve them through the use of non-conventional stress state variables, proper consideration of water retention hysteresis and appropriate representation of the influences between mechanical and water retention behaviour.

2 THE GLASGOW COUPLED MODEL (GCM)

The Glasgow Coupled Model (GCM) is an elasto-plastic constitutive model to represent the mechanical and water retention behaviour in unsaturated soils. It was first presented for isotropic stress conditions by Wheeler et al. [5] and has been later extended to general stress states ([6]-[7]). The analysis presented in this paper is based on how this model represents unsaturated soil behaviour, with particular emphasis on the way the influence of mechanical behaviour on water retention is formulated within the model. It has been then considered convenient to discuss first its basic features. As the discussion is only a summary (limited to isotropic stress conditions) interested readers are referred to other publications of the authors ([8]-[10]).

2.1 State or constitutive stress variables

For the restricted range of stress states that apply in tests under isotropic stress conditions, it is sufficient to consider only the mean Bishop's stress p^* (sometimes called *average skeleton stress*, Jommi [11]) and the modified suction s^* defined as:

$$p^* = p - S_r u_w - (1 - S_r) u_a = \bar{p} + S_r s \tag{1}$$

$$s^* = n(u_a - u_w) = ns \tag{2}$$

where p is mean total stress, $\bar{p}$ is mean net stress, s is matric suction, u_a and u_w are the pore fluid pressures for air and water respectively, S_r is degree of saturation and n is porosity. The stress variables p^* and s^* are work-conjugate with volumetric strain increment $d\varepsilon_v$ and decrement of degree of saturation $-dS_r$ respectively [12]. As first suggested by Schrefler [13], Equation 1 has replaced the weighting factor χ proposed in the original Bishop's expression [14] by the degree of saturation.

2.2 Elastic behaviour

Elastic components of $d\varepsilon_v$ and $-dS_r$ are:

$$d\varepsilon_{\mathrm{v}}^{\mathrm{e}} = \frac{\kappa dp^*}{vp^*} \tag{3}$$

$$-dS_{\mathrm{r}}^{\mathrm{e}} = \frac{\kappa_{\mathrm{s}} ds^*}{s^*} \tag{4}$$

where κ is the gradient of elastic swelling lines in the v: $\ln p^*$ plane (mechanical behaviour) and κ_{s} is the gradient of elastic scanning curves in the S_{r}: $\ln s^*$ plane (water retention behaviour).

2.3 Yield curves

To model isotropic stress conditions, the GCM includes three yield curves in the s^*:p^* plane (see Figure 1). A Mechanical yield curve (M) to represent mechanical behaviour and a Wetting Retention (WR) and Drying Retention (DR) yield curves to represent water retention behaviour. Plastic volumetric strains occur during yielding on M curve, whereas plastic variations of S_{r} occur during yielding on WR or DR curves. The M curve is the only one of the three describing mechanical yielding and this can occur during loading, wetting or drying as demonstrated in [8]. The other two (WR and DR) represent retention behaviour. Their respective equations are given by:

$$p_0^* - p^* = 0 \tag{5}$$

$$s_1^* - s^* = 0 \tag{6}$$

$$s^* - s_2^* = 0 \tag{7}$$

where $p_0{}^*$, $s_1{}^*$ and $s_2{}^*$ are hardening parameters defining the current positions of the M, WR and DR yield curves respectively (Figure 1).

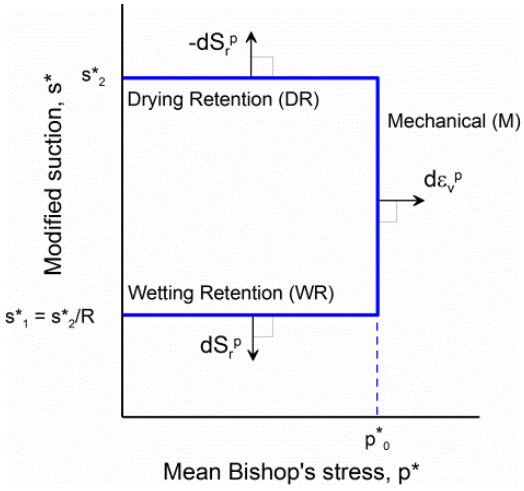

Figure 1: Yield curves for isotropic stress states (after [5])

2.4 Flow rules

Associated flow rules are assumed on all three yield curves. This means that yielding on the M curve alone corresponds to:

$$d S_r^p = 0 \qquad \text{and} \qquad d\varepsilon_v^p > 0 \tag{8}$$

Yielding on the WR curve alone corresponds to:

$$d\varepsilon_v^p = 0 \qquad \text{and} \qquad d S_r^p > 0 \tag{9}$$

and yielding on DR alone corresponds to:

$$d\varepsilon_v^p = 0 \qquad \text{and} \qquad d S_r^p < 0 \tag{10}$$

2.5 Hardening laws

The mechanical hardening law gives movements of the M curve and includes a direct component of movement caused by plastic volumetric strain (due to yielding on the M curve) and also a second (coupled) component of movement caused by any plastic changes of S_r due to yielding on WR or DR curves:

$$\frac{dp_0^*}{p_0^*} = \frac{v d\varepsilon_v^p}{\lambda - \kappa} - k_1 \frac{d S_r^p}{\lambda_s - \kappa_s} \tag{11}$$

where λ and κ are the gradients of normal compression and swelling lines respectively in the v: $\ln p^*$ plane for isotropic loading and unloading tests involving no plastic changes of S_r (such as the saturated tests), λ_s and κ_s are the gradients of main wetting/drying curves and scanning curves respectively in the plane S_r: $\ln s^*$ (see Figure 2a) for retention tests involving no plastic volumetric strains, and k_1 is a coupling parameter.

The hardening law for the water retention gives movements of the WR or DR yield curves and includes a direct component movement caused by plastic change of S_r (due to yielding on the WR or DR curve) and a second (coupled) component of movement caused by any plastic volumetric strains due to yielding on the M curve:

$$\frac{ds_1^*}{s_1^*} = \frac{ds_2^*}{s_2^*} = -\frac{d S_r^p}{\lambda_s - \kappa_s} + k_2 \frac{v d\varepsilon_v^p}{\lambda - \kappa} \tag{12}$$

where k_2 is a second coupling parameter. Equation 12 ensures that the movements of the DR and WR yield curves are such that the ratio of s_2^* to s_1^* remains constant and equal to a soil constant R:

$$\frac{s_2^*}{s_1^*} = \mathrm{R} \tag{13}$$

The special cases of the hardening laws during yielding on only a single yield curve (M, WR or DR) are given by inserting the relevant condition from Equation 8, 9 or 10 ($d S_r^p = 0$ or $d\varepsilon_v^p = 0$) into Equations 11 and 12 [2].

Figure 2 illustrates how the GCM treats the saturated conditions. When the soil reaches

$S_r = 1$, further elastic increases of degree of saturation are prevented (Equation 4 no longer applies for decreases of s^*) and further plastic increases of degree of saturation are prevented ($d\varepsilon_v^p = dS_r^p = 0$ replaces Equation 9 for states on the WR yield curve alone). In addition, the consistency condition on the WR yield curve is removed, so that the stress state can pass beyond the WR curve [2]. Figure 2a shows water retention behaviour (with $d\varepsilon_v^p = 0$), including a saturated stress state X. Figure 2b shows the corresponding positions of the yield curves when the stresses are at X. While the soil remains saturated, the M yield curve is still operative, and Equation 11 (with $dS_r^p = 0$) reverts to the conventional Modified Cam Clay (MCC) hardening law [4], because $p^* = p'$, where p' is the saturated mean effective stress [3]. Also, while the soil remains saturated, Equation 12 (with $dS_r^p = 0$) is still used to determine coupled movements of the WR and DR curves caused by plastic (not total) volumetric strain [9]. As explained in further detail in [2], this represents changes of air-entry value caused by plastic volumetric strain.

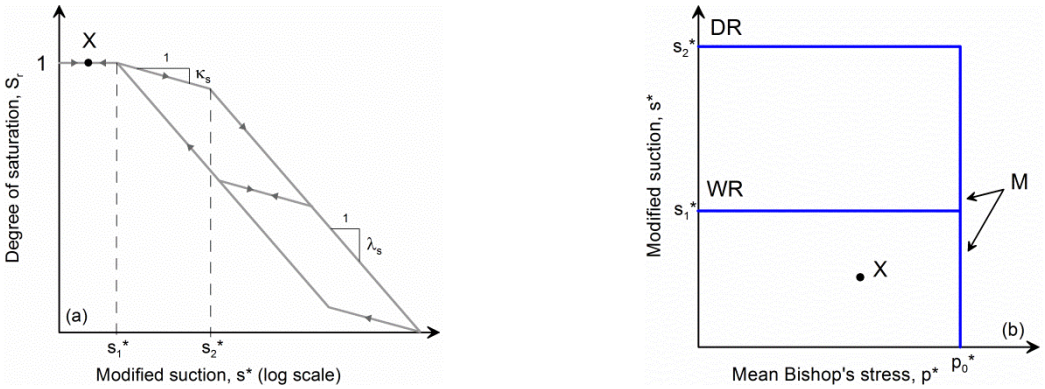

Figure 2: Modelling retention behaviour and treatment of saturated conditions [2]

3 MODELLING TRANSITIONS BETWEEN UNSATURATED AND SATURATED CONDITIONS

The GCM represents soil behaviour under both unsaturated ($S_r < 1$) and saturated conditions ($S_r = 1$). For $S_r = 1$, the GCM converges to the mechanical relationships of the MCC model for saturated soils because, in contrast to mean net stress, mean Bishop's stress p^* reverts to the saturated mean effective stress p' every time $S_r = 1$, even if $s \neq 0$.

Furthermore, under isotropic compression states on the M curve, as saturation progresses further, approaching S_r to 1, the GCM response for v should converge to the conventional Normal Compression Line, NCL:

$$v = N - \lambda \ln p' \tag{14}$$

where λ and N are, respectively, the gradient and intercept of the saturated NCL in the v: $\ln p'$ plane. To satisfy this requirement with the formulation of the GCM it is necessary that $\kappa_s = 0$ [2]. This restriction on the value of κ_s is due to a small inconsistency in the model highlighted by Ravendiraraj [16] and is discussed in the following.

Figure 3 shows a wetting stress path ABC, followed by a loading-unloading cycle CDE (not plotted in the figure) while the soil is saturated and then a drying path EFG. If yielding on the M curve occurs during the loading-unloading cycle CDE, this will cause plastic volumetric strains while the soil is saturated (for simplicity, no plastic volumetric strains occur during either AB or FG, while the soil is unsaturated). Consequently, coupled movements of the WR and DR yield curves occur resulting in a translation of the water retention curves from the positions shown by fine continuous lines to those shown by the fine dashed lines. This means that, whereas the soil reaches a saturated state at a value of modified suction s_B^* during wetting, de-saturation occurs at a higher value of modified suction s_F^* during subsequent drying. Thus, elastic increases of S_r occur over the range of modified suction s_F^* to s_B^* during the wetting path (plastic changes of S_r also occur) but no elastic decreases of S_r occur between s_B^* and s_F^* during the drying path, which means that elastic changes of S_r have not been reversible over the range of modified suction s_B^* to s_F^*, and this contravenes a basic tenet of elastic behaviour [2]. A simple way to overcome this problem is by assuming $\kappa_s = 0$ and this is the assumption adopted for the remainder of the paper.

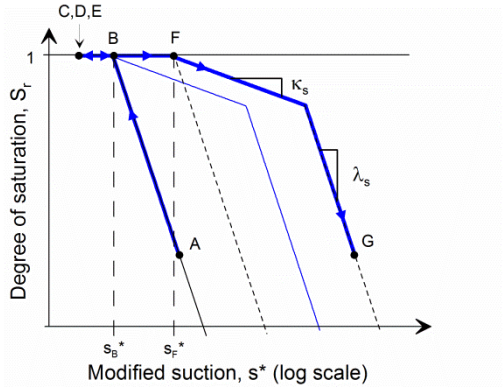

Figure 3: Demonstration of irreversible elastic changes of S_r if $\kappa_s > 0$ [2]

3.1 Isotropic normal compression planar surfaces for v and S_r

To show how the GCM handles the transition from unsaturated to saturated states, it is convenient to introduce first the work of Lloret [15] on the model predictions for isotropic stress states at the intersection of the mechanical (M) and wetting retention (WR) yield curves. This work shows that any stress paths involving mechanical yielding (occurrence of plastic compression) and wetting retention yielding (occurrence of plastic increases of S_r) correspond to this intersection of M and WR curves; and that, for these isotropic normal compression (NC) states at the intersection of M and WR curves, the GCM predicts unique expressions for specific volume v and degree of saturation S_r. The form of these unique expressions corresponds to two planar surfaces when plotted, respectively, in the v: $\ln p^*$: $\ln s^*$ and S_r: $\ln p^*$: $\ln s^*$ spaces. Their respective expressions are given by:

$$v = N^* - \lambda^* \ln p^* + k_1^* \ln s^* \tag{15}$$

$$S_r = \Omega^* - \lambda_s^* \ln s^* + k_2^* \ln p^* \tag{16}$$

where λ^*, k_1^*, λ_s^*, k_2^*, N^* and Ω^* are soil constants (see Appendix).

Lloret-Cabot, Wheeler and Sánchez [2] show that for the unsaturated NC planar surfaces for v (Equation 15) to converge to the saturated NCL (Equation 14) at $S_r = 1$, it is necessary that $\kappa_s = 0$.

3.2 Transitions from unsaturated to saturated conditions: the saturation line

With $\kappa_s = 0$, Figure 4a shows a three-dimensional view (in v: $\ln p^*$: $\ln s^*$ space) of the unsaturated isotropic NC planar surface for v (Equation 15) and the saturated isotropic NCL. The intersection of the two surfaces defines a "saturation line" (Figure 4a) corresponding to the transition from unsaturated to saturated conditions. Equivalent surfaces for S_r are illustrated in Figure 4b (in S_r: $\ln p^*$: $\ln s^*$ space), where the same saturation line is observed.

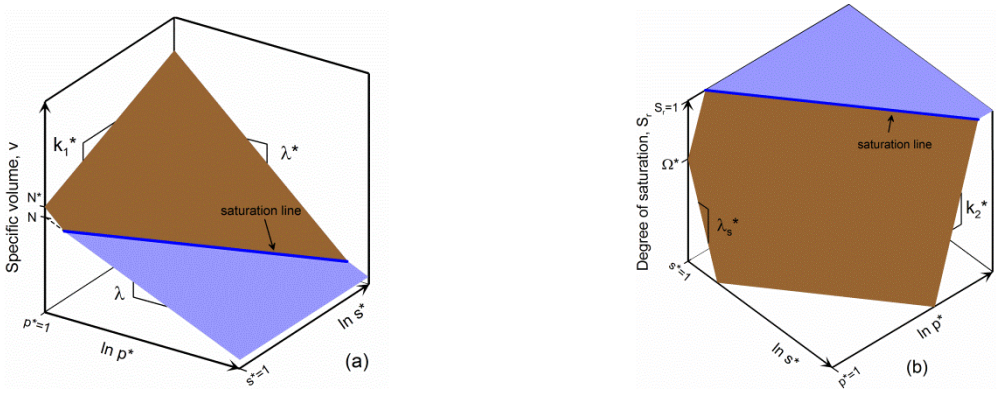

Figure 4: Isotropic NC planar surfaces for unsaturated and saturated conditions: (a) for v; (b) for S_r [2]

Lloret-Cabot et al. [2] demonstrate that the following expression for the saturation line shown in Figures 4a and 4b is obtained by using Equation 16 with $S_r = 1$ (and assuming $\kappa_s = 0$):

$$\ln s^* = \frac{\Omega^* - 1}{\lambda_s^*} + k_2 \ln p^* \tag{17}$$

Equation 17 represents the pairs of s^* and p^* at which transitions from unsaturated to saturated conditions will occur if the stress state is isotropic and at the intersection between M and WR yield curves. According to [2], with $\kappa_s = 0$, transitions from unsaturated to saturated conditions can only occur whilst on the WR yield curve, but it is not necessary for the stress state to be on the M yield curve or for the stress state to be isotropic at the point of transition from unsaturated to saturated conditions. Given that changes of p^* do not produce elastic changes of S_r, it is straightforward to derive a more general expression for transition from unsaturated to saturated conditions, applicable to any isotropic, including those not on the M yield curve:

$$s^* = \exp\left(\frac{\Omega^* - 1}{\lambda_s^*}\right)\left(p_0^*\right)^{k_2} \tag{18}$$

Equation 18 defines the expression for the saturation line, corresponding to transition from unsaturated to saturated conditions (sometimes known as the air-exclusion point), and is illustrated in Figure 5 (in both a log-log plot and a linear plot). Equation 18 and Figure 5 show that the saturation value of s^* is uniquely dependent on the position of the M yield surface (i.e. the value of p_0^*) [2].

3.3 Transitions from saturated to unsaturated conditions: the de-saturation line

Lloret-Cabot, Wheeler and Sánchez [2] demonstrate that transitions in the reverse direction, from saturated to unsaturated conditions, must occur on the DR yield surface if $\kappa_s = 0$, but it is not necessary for the stress state at the point of de-saturation to be on the M surface. This transition from saturated to unsaturated conditions occurs on a "de-saturation line" defined by:

$$s^* = \mathrm{R}\exp\left(\frac{\Omega^* - 1}{\lambda_s^*}\right)\left(p_0^*\right)^{k_2} \tag{19}$$

Figure 5 illustrates that the GCM includes the influences of both water retention hysteresis and plastic volumetric straining on transitions between saturated and unsaturated conditions. The difference between the saturation and de-saturation values of s^* (at the same value of p_0^*) shows the influence of retention hysteresis, whereas the variation of both saturation and de-saturation values of s^* with p_0^* shows the influence of plastic (not total) volumetric strains on air-exclusion and air-entry points [2].

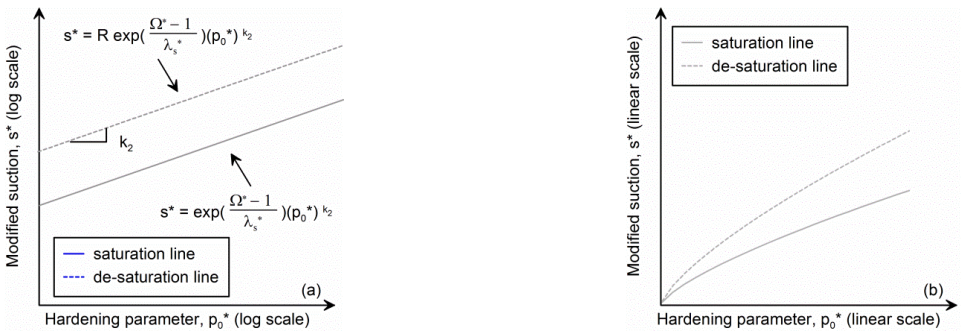

Figure 5: Predicted saturation and de-saturation lines [2]

4 CONCLUSIONS

- The Glasgow Coupled Model (GCM) predicts that isotropic normal compression states in isotropic stress paths involving plastic volumetric strains and plastic increases of S_r correspond to points at the intersection of M and WR yield curves. For these states, the model predicts unique unsaturated isotropic normal compression planar surfaces for v and for S_r (in $v{:}\ln p^*{:}\ln s^*$ and $S_r{:}\ln p^*{:}\ln s^*$ spaces, respectively).
- The GCM represents consistently the transitions between saturated and unsaturated states, including the influence of retention hysteresis and the effect of plastic

volumetric strains on water retention behaviour. The GCM gives unique expressions to predict saturation and de-saturation conditions (air-exclusion and air-entry points respectively), in the form of two unique straight lines in the $\ln s^* : \ln p_0^*$ plane.

APPENDIX

For cases with $\kappa_s = 0$, the gradients of the isotropic normal compression surface for v are given by:

$$\lambda^* = \frac{\lambda - k_1 k_2 \kappa}{1 - k_1 k_2} \tag{A1}$$

$$k_1^* = k_1 \frac{(\lambda - \kappa)}{(1 - k_1 k_2)} \tag{A2}$$

Similarly, the gradients for the isotropic normal compression surface for S_r are given by:

$$\lambda_s^* = \frac{\lambda_s}{1 - k_1 k_2} \tag{A3}$$

$$k_2^* = k_2 \frac{\lambda_s}{(1 - k_1 k_2)} \tag{A4}$$

ACKNOWLEDGEMENTS

This research is funded by the Marie-Skłodowska Curie project "COUPLED-706712" (https://twitter.com/Coupled_UofG). The support from the EU project "TERRE" (ETN-GA-2015-675762) is also acknowledged.

REFERENCES

[1] Gens, A. "Constitutive modelling: application to compacted soils." *Unsaturated soils* (eds E. Alonso & P. Delage), Vol. 3, pp. 1179–1200. Rotterdam: Balkema (1996).

[2] Lloret-Cabot, M., Wheeler, S.J. and Sánchez, M. "A unified mechanical and retention model for saturated and unsaturated soil behaviour." *Acta Geotechnica* (2017) **12**(1):1–21.

[3] Terzaghi, K. "The shearing resistance of saturated soils and the angle between the planes of shear." *Proc. 1st Int. Conf. Soil Mech. Found. Engng*, pp. 54–56, Cambridge, MA 1 (1936).

[4] Roscoe, K.H. and Burland, J.B. "On the generalised stress-strain behavior of 'wet' clay". *Engineering Plasticity* (eds J. Heyman & F.A. Leckie), pp. 535–609, Cambridge University Press (2013).

[5] Wheeler, S.J., Sharma, R.S. and Buisson, M.S.R. "Coupling of hydraulic hysteresis and stress–strain behaviour in unsaturated soils." *Géotechnique* (2003) **53**(1):41–54.

[6] Lloret, M., Sánchez, M. and Wheeler, S.J. "Generalised elasto-plastic stress-strain and modified suction-degree of saturation relations of a fully coupled model." *Proc. 4th Asia-Pacific Conf. Unsat. Soils* (eds O. Buzzi, S. Fityus, & D. Sheng), pp. 667-672, CRC press (2010).

[7] Lloret-Cabot, M., Sánchez, M. and Wheeler, S.J. "Formulation of a three-dimensional constitutive model for unsaturated soils incorporating mechanical-water retention couplings." *Int. J. Numer. Anal. Methods Geomech.* (2013) **37**:3008–3035.

[8] Lloret-Cabot, M., Wheeler, S.J. and Sánchez, M. "Unification of plastic compression in a coupled mechanical and water retention model for unsaturated soils." *Can. Geotech. J.* (2014a) **51**(12):1488–1493.

[9] Lloret-Cabot, M., Wheeler, S.J., Pineda, J.A., Sheng, D. and Gens, A. "Relative performance of two unsaturated soil models using different constitutive variables." *Can. Geotech. J.* (2014b) **51**(12):1423–1437.

[10] Lloret-Cabot, M., Pineda, J.A., Cordão Neto, M.P. and Sheng, D. "Some remarks on the mechanical yielding of unsaturated soils". *Proc. 6th Asia-Pacific Conf. Unsat. Soils* (eds Z. Chen, C.Wei, D. Sun & Y. Xu), pp. 197–203, CRC press (2016).

[11] Jommi, C. "Remarks on the constitutive modelling of unsaturated soils." *Experimental evidence and theoretical approaches in unsaturated soils* (eds A. Tarantino & C. Mancuso), pp. 139–153, Rotterdam: Balkema (2000).

[12] Houlsby, G.T. "The work input to an unsaturated granular material." *Géotechnique* (1997) **47**(1):193–196.

[13] Schrefler, B.A. *The finite element method in soil consolidation (with applications to surface subsidence)*. PhD Thesis, University College of Swansea, UK (1984).

[14] Bishop, A.W. "The principle of effective stress." *Teknisk Ukeblad*, (1959) **39**:859–863.

[15] Lloret, M. *Numerical modelling of coupled behaviour in unsaturated soils*. PhD Thesis, University of Strathclyde and University of Glasgow (2011).

[16] Raveendiraraj. A. *Coupling of mechanical behaviour and water retention behaviour in unsaturated soils*. PhD Thesis, University of Glasgow (2009).

VII International Conference on Computational Methods for Coupled Problems in Science and Engineering
COUPLED PROBLEMS 2017
M. Papadrakakis, E. Oñate and B. Schrefler (Eds)

UNCERTAINTY QUANTIFICATION OF COUPLED ODES WITH STOCHASTIC GALERKIN METHODS USING ADAPTIVE HIGHER ORDER RUNGE–KUTTA METHODS

JOACHIM RANG*

*Institute of Scientific Computing
TU Braunschweig
Mühlenpfordtstrasse 23, 38106 Braunschweig, Germany
e-mail: j.rang@tu-bs, web page: http://www.wire.tu-bs.de

Key words: Time integration, Runge–Kutta methods, stochastic collocation, uncertainty

Abstract. Many real world problems are so complex that simplifications of these problems are needed. Otherwise the computing costs would be so high that specific problems, for example uncertainty quantification, could not be solved.

In this paper we consider a system of coupled ODEs and discretise the subsystems in time with adaptive high order Runge–Kutta methods. This approach is called "partitioned method", and we use a Block Gauss-Seidel method for solving the final linear or non-linear systems. The motivation for using high order methods is the computation of very accurate numerical results. Moreover, these time integration methods are more effective than lower order methods, and in the case of the partitioned approach they need less iterations than lower order methods.

For the stochastic discretisation we use a stochastic Galerkin method which only needs a few solutions of the deterministic ODE system. We show that using higher order methods in time leads to a better and more accurate quantification of uncertainties because we can expect a higher accuracy and a faster convergence for the deterministic problem. Numerical results show the advantages of the novel approach.

1 INTRODUCTION

Many physical or engineering problems can be described with differential equations, such as the simulation of time–dependent laminar or turbulent flows. As input quantities of such models we have, for example, boundary and initial conditions, geometries, and coefficients, which are in general not exactly known since they may be the result of measurements.

There are two kinds of uncertainties. First there are the so-called aleatoric uncertainties. Here the uncertainties are described as inherent randomness inside the phenomenon.

Then there are epistemic uncertainties which are related to our incomplete knowledge [17, 13, 29]. The uncertainties considered here are more or less epistemic uncertainties. Aleatoric uncertainties are nearly always described probabilistically [17, 13, 29, 9]. For epistemic uncertainties different ansatzes are used: Fuzzy systems, convex sets, intervals [22, 8, 29], as well as Bayesian probabilistic models [17, 13, 29, 6, 14].

The identified uncertainties should not only be indicated and verbally described by modelling and simulation, they should also be quantified (see for example [17]). The quantification of uncertainties plays an important role in the determination of optimal processes and to find feedback control which are robust with respect to perturbations and uncertainties. There are different possibilities to describe and quantify uncertainties. In this article uncertainties are described with probabilistic or stochastic models since this approach is based on a deep mathematical structure [17].

A good probabilistic description can be achieved, for example, with Gaussian random variables if the random variables are continuous. As Wiener suggests [32] every random variable $\mathsf{r}(\omega) \in L_2(\Omega)$ can be represented with polynomials, which depend on uncorrelated and independent Gauß variables [12, 16, 19, 20, 18]. This leads to functional approximations such as the polynomial chaos expansion (PCE), which delivers a suitable representation of the stochastic process and of the random variable in independent identically distributed (**iid**) standard-Gauß variables.

In this paper we consider linear coupled ODEs, where we assume that the initial conditions are uncertain. For the solution of this system of ODEs we need a temporal discretisation. Therefore we will concentrate on implicit schemes such as implicit Runge–Kutta methods, since a high order of convergence can be achieved (see [24]). Often an order reduction phenomenon can be observed if stiff problems or DAEs are solved (see [15] and [10]). Moreover, the costs for the linear algebra are very high. Therefore often diagonally implicit Runge-Kutta (DIRK) methods or Rosenbrock–Wanner (ROW) methods are used. But in this case the order reduction is much stronger. Many papers study the order reduction phenomena and derive further order conditions to reduce this effect. One possibility is the consideration of the Prothero–Robinson example [27]. In [23] and [26] better ROW methods are developed, and numerical studies show that full order can be achieved for the Prothero–Robinson example. Similar results for SDIRK and ESDIRK methods are presented in [23] and [25].

Here we want to use very accurate methods, i.e. methods which have a high order of convergence. Therefore fully implicit Runge–Kutta methods may be a good choice. But these methods need a high computational effort, since in every timestep a nonlinear system of dimension ns has to be solved, where n is the dimension of the problem and s is the number of internal stages of the Runge–Kutta method. In the last decades several papers have discussed the efficient solution of the nonlinear or linear equations. Here we use a transformation from Butcher [4] and Bickart [2] of the coefficient matrix of the Runge–Kutta method. If a simplified Newton method is applied this splitting leads to s complex valued systems of dimension n. An application of this technique for Radau

methods can be found in [11] and [28]. These nonlinear systems can be solved directly with the help of LU-decompositions and back- and forward substitutions.

For coupled ODEs such a discrete system can be very large, and a monolithic method may be not a good choice since the computations of the matrix-vector products need a lot of time and a lot of memory. A partitioned method may be a better choice. In this case we split the huge nonlinear system into smaller ones. This approach is known, for example, from the numerical solution of multi-field problems like fluid–structure interaction (see [21]).

This paper is structured as follows: First we discuss implicit Runge–Kutta methods and apply them on a coupled system of ODEs. Then stochastic Galerkin methods are presented, and finlly a numerical example shows the benefit of using higher order time integration methods.

2 TIME DISCRETISATION METHODS

We start our considerations with the initial value problem

$$\dot{\mathbf{u}} = \mathbf{f}(t, \mathbf{u}), \quad \mathbf{u}(t_0) = \mathbf{u}_0. \tag{1}$$

A Runge-Kutta (RK) method for the implicit ODE (1) is given by

$$\mathbf{k}_i = \mathbf{f}\left(t_m + c_i\tau, \mathbf{u}_m + \tau_m \sum_{j=1}^{s} a_{ij}\mathbf{k}_j\right), \quad i = 1, \dots, s, \tag{2}$$

$$\mathbf{u}_{m+1} = \mathbf{u}_m + \tau_m \sum_{i=1}^{s} b_i \mathbf{k}_i, \tag{3}$$

where τ is a given timestep size, s is the number of internal stages and a_{ij}, b_i, and c_i are the coefficients of the RK-method, which should be determined in such a way that the method has a sufficiently high order convergence [5, 10, 30]. The order of the RK-method can be determined with the so-called simplifying conditions from Butcher [3], which are defined as follows.

Definition 2.1 *(see [3]). An s-stage RK-method satisfies the simplifying conditions if the conditions*

$$\begin{aligned}
B(p): &\quad \sum_{i=1}^{s} b_i c_i^{k-1} &&= 1/k, && k = 1, \dots, p,\\
C(q): &\quad \sum_{j=1}^{s} a_{ij} c_j^{k-1} &&= c_i^k/k, && i = 1, \dots, s, k = 1, \dots, q,\\
D(r): &\quad \sum_{i=1}^{s} b_i c_i^{k-1} a_{ij} &&= b_j(1 - c_j^k)/k, && j = 1, \dots, s, k = 1, \dots, r
\end{aligned}$$

are fulfilled.

The condition $B(p)$ is equivalent to a quadrature rule with nodes c_i and weights b_i, which integrates polynomials of degree $p-1$ exactly. The conditions $C(q)$ have the following meaning: The intermediate values $\mathbf{k}_i$ are integrated exactly by a quadrature rule with weights a_{ij} and nodes c_i, which integrates polynomials of degree q exactly.

Theorem 2.2 *(see [5, 30]) An RK-method with s internal stages has the convergence order p if the simplifying conditions $B(p)$, $C(l)$, and $D(m)$ with*

$$p \leq \min\{l+m+1, 2l+2\}$$

are satisfied.

For the proof we refer to the book of Butcher [5]. Next we derive the coefficients of Radau-IIA methods, which need the roots of the shifted Legendre polynomial of degree s, i.e.

$$P_s(2t-1) = \frac{1}{s!}\frac{d^s}{dt^s}[t^s(t-1)^s].$$

With respect to the $L^2(0,1)$-scalar product the polynomial $P_s(2t-1)$ is orthogonal to all polynomials of degree $< s$. The roots of the Legrendre polynomials P_s can be found in the book of Abramowitz and Stegun [1] or can be computed with a computer algebra tool. It can be proven that the roots are pairwise distinct. From this fact it follows that the Vandermonde matrix

$$V_s = (V_{ij}) := (c_i^{j-1}) = \begin{pmatrix} 1 & c_1 & c_1^2 & \dots & c_1^{s-1} \\ \vdots & \vdots & \vdots & & \vdots \\ 1 & c_s & c_s^2 & \dots & c_s^{s-1} \end{pmatrix}, \qquad i,j = 1,\dots,s$$

is regular. In the case of the Radau methods we need the following theorem.

Theorem 2.3 *Let be given a Runge–Kutta method with $p = 2s-1$. Then the nodes c_i of the RK method are given by the roots of the polynomial*

$$P_{s,\xi}(2x-1) = P_s(2x-1) + \xi P_{s-1}(2x-1), \quad \xi \in \mathbb{R}.$$

For the proof we refer to the book of Strehmel and Weiner (see [31]). Here we are intested in the case $\xi = -1$, which leads to the Radau-IIA methods with $c_s = 1$ (see [7]). The condition $B(p)$ reads as $\mathbf{b}^\top \mathbf{c}^k = 1/k$, where the vector $\mathbf{c}^k$ is defined as $\mathbf{c}^k = (c_1^k, \dots, c_s^k)^\top$. The condition $C(q)$ can be written as $A\mathbf{c}^{k-1} = \mathbf{c}^k/k$, where $A = (a_{ij})_{i,j=1}^s$. The nodes b_i are then uniquely determined by the conditions $B(1)$, ..., $B(s)$, i. e. by

$$\mathbf{b}^\top \mathbf{e} = 1, \mathbf{b}^\top \mathbf{c} = 1/2, \dots, \mathbf{b}^\top \mathbf{c}^{s-1} = 1/s.$$

This system can be written in matrix-vector notation as

$$\mathbf{b}^\top V_s = \mathbf{e}_H^\top := \left(1, \frac{1}{2}, \dots, \frac{1}{s}\right).$$

Multiplying from the right with the inverse of V_s generates our nodes b_i, i.e. $\mathbf{b}^\top = \mathbf{e}_H^\top V_s^{-1}$. Next we determine the matrix A with the help of conditions $C(1), \ldots, C(s)$, which can be written as

$$A\mathbf{e} = \mathbf{c}, A\mathbf{c} = \mathbf{c^2}/2, \ldots, A\mathbf{c}^{s-1} = \mathbf{c^s}/s,$$

or in matrix notation by $AV_s = C$, where

$$C := (c_{ij}) = \frac{1}{j} c_i^j, \qquad i, j = 1, \ldots, s.$$

As it is shown in [24] the method can be equipped with an embedded method. Therefore we set

$$\tilde{\mathbf{e}}_H^\top := \left(1, \frac{1}{2}, \ldots, \frac{1}{s-1}, 0\right).$$

Then the nodes $\tilde{b}_i$ are given simply by

$$\tilde{\mathbf{b}}^\top = \tilde{\mathbf{e}}_H^\top V_s^{-1}$$

and the embedded method is of order $s-1$. Finally, the Butcher table is given by

$\mathbf{c}$	CV_s^{-1}
	$\mathbf{e}_H^\top V_s^{-1}$
	$\tilde{\mathbf{e}}_H^\top V_s^{-1}$

and the Radau-IIA methods with 2 and 3 internal stages are given by

$\frac{1}{3}$	$\frac{5}{12}$	$-\frac{1}{12}$
1	$\frac{3}{4}$	$\frac{1}{4}$
	$\frac{3}{4}$	$\frac{1}{4}$
	1	0

$\frac{4-\sqrt{6}}{10}$	$\frac{88-7\sqrt{6}}{360}$	$\frac{296-169\sqrt{6}}{1800}$	$\frac{-2+3\sqrt{6}}{225}$
$\frac{4+\sqrt{6}}{10}$	$\frac{296+169\sqrt{6}}{1800}$	$\frac{88+7\sqrt{6}}{360}$	$\frac{-2+3\sqrt{6}}{225}$
1	$\frac{16-6\sqrt{6}}{36}$	$\frac{16+6\sqrt{6}}{36}$	$\frac{1}{9}$
	$\frac{16-6\sqrt{6}}{36}$	$\frac{16+6\sqrt{6}}{36}$	$\frac{1}{9}$
	-1	$1-\frac{7}{12}\sqrt{6}$	$1+\frac{7}{12}\sqrt{6}$

.

3 APPLICATION TO COUPLED ODEs

Let us consider a simple coupled ODE given by

$$\dot{\mathbf{u}} = \begin{pmatrix} a & b \\ -b & a \end{pmatrix} \mathbf{u}, \qquad \mathbf{u}(0) = \mathbf{u}_0. \tag{4}$$

In the following we solve the ODE (4) with a partitioned approach, where we use a Block Jacobi and a Block Gauss–Seidel method. The convergence of these partitioned methods

depends strongly on the spectral radius of the iteration matrix which depends on the Runge–Kutta method and on the chosen stepsize. The variables a and b in ODE (4) are set as follows: $a = -1/10$ and $b = 24$. As stepsizes we use $\tau = 1/10$ and $\tau = 1/100$. Note, that for $\tau = 1/10$ the implicit Euler and the trapezoidual rule do not converge if they are applied with a Block Jaboci or Block Gauss–Seidel method. In Figure 1 we show the results for Radau-IIA methods with $2, \ldots, 30$ internal stages. It can observed that

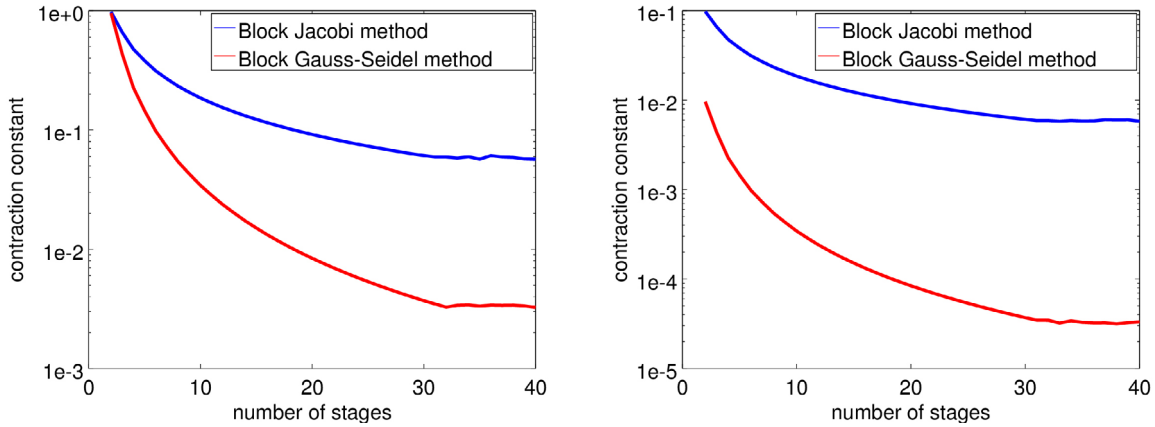

Figure 1: spectral radii in dependency of the internal stages with $\tau = 1/10$ (left) and $\tau = 1/100$ (right)

increasing the number of stages decreases the spectral radius, i.e. the numerical results are getting better and we need less iterations of our partitioned methods. Moreover, the spectral radius for the Block Gauss-Seidel method is lower than for the Block Jacobi method. The spectral radius can be reduced if the stepsize τ is reduced, because τ acts as a damping parameter.

In our next experiment we want to show that higher order methods need less iterations for the partitioned methods and that the numerical error decreases if the number of stages increases. Again we chose $a = -1/10$ and $b = 24$. For the stepsize we take $\tau = 1/10$. The numerical results are shown in Figure 2. In the left we plot the number of iterations for the partitioned methods in dependency of the number of internal stages. It can be observed that the lower order methods need much more iterations than the methods with 10 or more internal stages. A similar observation can be made if the numerical error is considered (left part of Figure 2). Again, methods with 10 or more stages have a smaller numerical error than lower order methods.

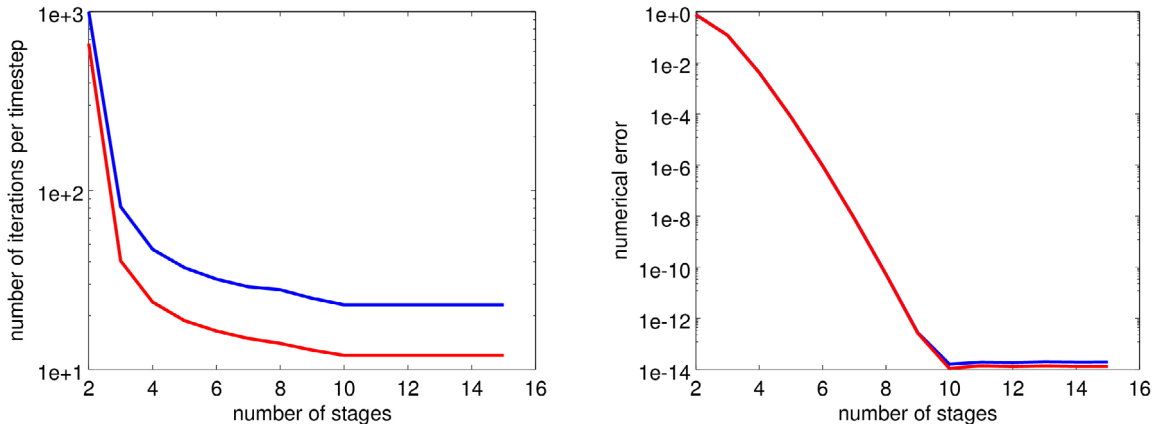

Figure 2: Iterations per timestep (left) and numerical error (right)

4 STOCHASTIC GALERKIN METHOD

In the next step we assume that the initial conditions of the ODE (4) are uncertain, i.e. we have a stochastic ODE given by

$$\dot{\mathbf{u}}(t,\omega) = \begin{pmatrix} a & b \\ -b & a \end{pmatrix} \mathbf{u}(t,\omega), \qquad \mathbf{u}(0,\omega) = \mathbf{u}_0(\omega), \tag{5}$$

where ω is an elementary event (of a realisation) in a probability space $(\Omega, \mathcal{A}, \mathbb{P})$ of random events. For the stochastic discretisation we use a Galerkin approach, i.e. we look for a variational formulation. Therefore we multiply equation (5) with a testfunction H_γ and integrate over the stochastic domain Ω. We receive

$$\int_\Omega \dot{u}(t,\omega) H_\gamma(\omega) \mathbb{P}(d\omega) = \int_\Omega \left[a u(t,\omega) + b v(t,\omega) \right] H_\gamma(\omega) \mathbb{P}(d\omega), \tag{6}$$

$$\int_\Omega \dot{v}(t,\omega) H_\gamma(\omega) \mathbb{P}(d\omega) = \int_\Omega \left[a v(t,\omega) - b u(t,\omega) \right] H_\gamma(\omega) \mathbb{P}(d\omega) \tag{7}$$

Any random variable $r(\omega) \in L_2(\Omega)$ can be represented as a series of polynomials in uncorrelated and independent Gaussian variables $\theta = (\theta_1, \dots)$ (see [32]). This idea is called *polynomial chaos expansion* (PCE). We set

$$u(t,\omega) = \sum_\alpha u_\alpha(t) H_\alpha(\theta(\omega)),$$

$$v(t,\omega) = \sum_\alpha v_\alpha(t) H_\alpha(\theta(\omega)).$$

For more details about we PCE we refer to [17]. Inserting these formulas into our variational formulation leads to the following system

$$\sum_\alpha \dot{u}_\alpha(t) \int_\Omega H_\alpha((\theta(\omega))H_\gamma(\omega)\mathbb{P}(d\omega) = \sum_\alpha u_\alpha(t)a \int_\Omega H_\alpha((\theta(\omega))H_\gamma(\omega)\mathbb{P}(d\omega) + \sum_\alpha v_\alpha(t)b \int_\Omega H_\alpha((\theta(\omega))H_\gamma(\omega)\mathbb{P}(d\omega), \tag{8}$$

$$\sum_\alpha \dot{v}_\alpha(t) \int_\Omega H_\alpha((\theta(\omega))H_\gamma(\omega)\mathbb{P}(d\omega) = \sum_\alpha v_\alpha(t)a \int_\Omega H_\alpha((\theta(\omega))H_\gamma(\omega)\mathbb{P}(d\omega) - \sum_\alpha u_\alpha(t)b \int_\Omega H_\alpha((\theta(\omega))H_\gamma(\omega)\mathbb{P}(d\omega). \tag{9}$$

The polynomials H_α are chosen in such a way that the integrals can be solved analytically. One choice are multivariate Hermite polynomials which can be defined with a recursion formula given by $h_{k+1}(t) = th_k(t) - kh_{k-1}$, $k \in \mathbb{N}$. The Hermite polynomials are orthogonal polynomials w.r.t. the standard Gaussian probability measure Γ, where $\Gamma(dt) = (2\pi)^{-1/2}e^{-t^2/2}$. The set $\{h_k(t)/\sqrt{k!} \mid k \in \mathbb{N}_0\}$ forms a complete orthonormal system in $L_2(\mathbb{R}, \Gamma)$, since the Hermite polynomials satisfy

$$\int_{-\infty}^{\infty} h_m(t)h_n(t)\Gamma(dt) = n!\delta_{nm}.$$

A multivariate Hermite polynomial is defined by

$$H_\alpha(\mathbf{t}) := \prod_{j=1}^{d} h_{\alpha_j}(t_j), \qquad \forall \mathbf{t} \in \mathbb{R}^d,$$

where α is a multi-index. In Figures 3 and 4 we have visualised the Hermite polynomials H_{23}, H_{33}, H_{35}, and H_{55}.

We can write each polynomial as a linear combination of Hermite polynomials. A product of two Hermite polynomials is again a polynomial which can be represented by Hermite polynomials, i. e.

$$h_k(t)h_l(t) = \sum_{n=|k-l|}^{k+l} c_{kl}^{(n)} h_n(t).$$

The coefficients $c_{kl}^{(n)}$ are only non-zero if $g := (k + l + n)/2 \in \mathbb{N}$ and if $g \geq k$, $g \geq l$ and $g \geq n$ (see [16]).

These properties of the Hermite algebra can be used to simplify equations (8)–(9). First of all we note that

$$\int_\Omega H_\alpha H_\gamma \mathbb{P}(d\omega) = \alpha!\delta_{\alpha\gamma}, \qquad \forall \alpha, \gamma$$

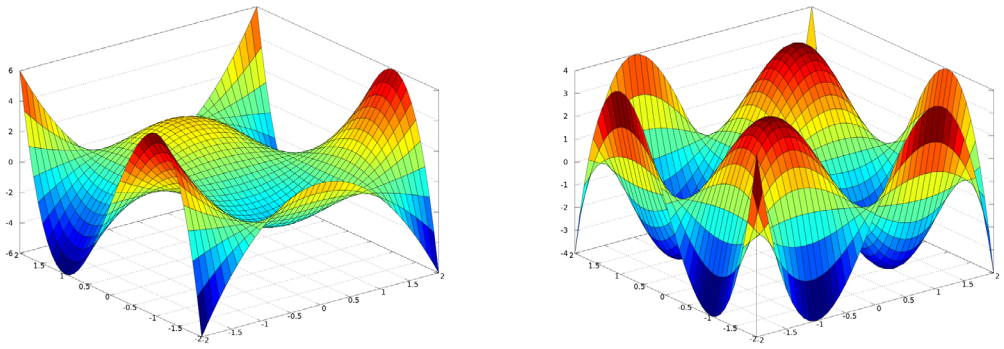

Figure 3: Hermite polynomials H_{23} and H_{33}

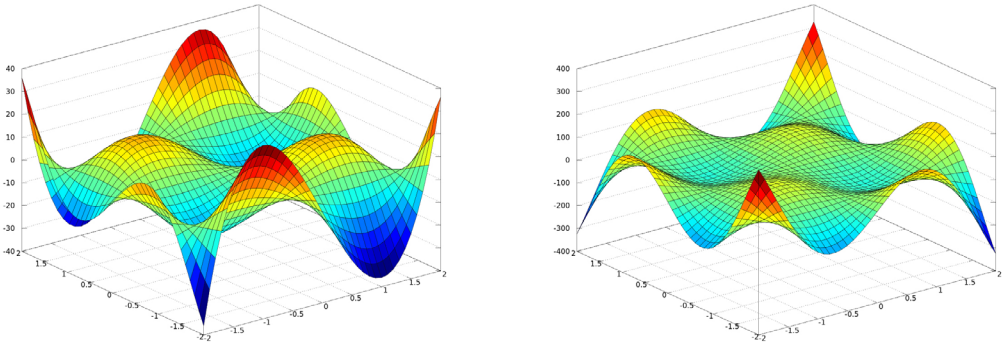

Figure 4: Hermite polynomials H_{35} and H_{55}

holds. If we use this result our stochastic ODE system simplifies to

$$\dot{u}_\alpha(t) = au_\alpha(t) + bv_\alpha(t), \tag{10}$$
$$\dot{v}_\alpha(t) = av_\alpha(t) - bu_\alpha(t). \tag{11}$$

This is a similar system as our deterministic system, i.e. we have to solve the original one with different initial values to compute the PCE.

5 NUMERICAL RESULTS

In our numerical example we consider the stochastic ODE (5). We solve this equation in the time interval $[0, 1]$ with Radau-IIA methods, where $s = 2, \ldots, 6$. From 1000 Monte Carlo runs the mean value and the variance is computed for the stochastic Galerkin method and the Monte Carlo method. The results are displayed in Figure 5. It can be observed that the results are more accurate if $s \geq 4$, i.e. if we use a Radau-IIA method of order 7. This observation holds for the stochastic Galerkin and the Monte Carlo method.

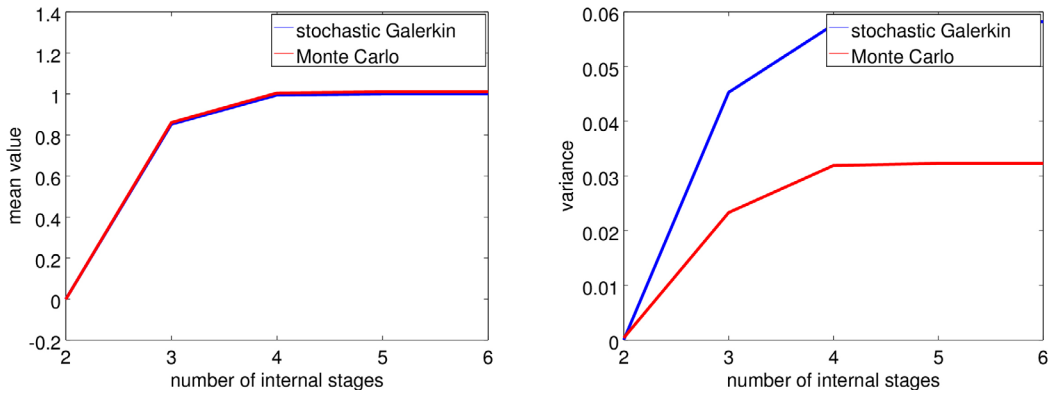

Figure 5: Results for the mean value (left) and the variance (right)

6 CONCLUSION

In this paper we have considered implicit Runge–Kutta methods of higher order and applied them on stochastic coupled ODEs. We have seen that in the case of deterministic problems a higher order leads to a smaller numerical error and higher order of convergence. Moreover a partitioned approach such as the Block Jacobi or the Block Gauss–Seidel method needs less iterations if the number of stages increases. This properties can be used for solving stochastic ODEs, too. We discretised our stochastic ODE with a stochastic Galerkin method, which in the case of stochastic initial conditions leads to a Block diagonal linear system, which can be easily solved.

In future work this approach should be applied on the model problem, where the matrix entries are uncertain, too. Moreover, a comparison with stochastic collocation methods should be carried out.

REFERENCES

[1] I.A. Abramowitz, M.; Stegun. *Handbook of Mathematical Functions.* John Wiley & Sons, 1984.

[2] Theodore A. Bickart. An efficient solution process for implicit Runge-Kutta methods. *SIAM J. Numer. Anal.*, 14:1022–1027, 1977.

[3] J.C. Butcher. On Runge–Kutta processes of high order. *J. Austral. Math. Soc.*, 4:179–194, 1964.

[4] J.C. Butcher. On the implementation of implicit Runge-Kutta methods. *BIT*, 16:237–240, 1976.

[5] J.C. Butcher. *The numerical analysis of ordinary differential equations. Runge-Kutta and general linear methods.* John Wiley & Sons, Chichester, 1987.

[6] George Christakos. *Random field models in earth sciences*. Academic Press, San Diego, CA, 1992.

[7] B.L. Ehle. High order A-stable methods for the numerical solution of systems of D.E.'s. *BIT*, 8:276–278, 1968.

[8] I. Elishakoff. *Whys and Hows in Uncertainty Modelling-Probability, Fuzziness, and Anti-Optimization*. Springer-Verlag, Berlin, 1999.

[9] M. Grigoriu. *Stochastic Calculus—Applications in Science and Engineering*. Birkhäuser Verlag, Basel, 2002.

[10] E. Hairer and G. Wanner. *Solving ordinary differential equations. II: Stiff and differential-algebraic problems*, volume 14 of *Springer Series in Computational Mathematics*. Springer-Verlag, Berlin, 1996.

[11] Ernst Hairer and Gerhard Wanner. Stiff differential equations solved by Radau methods. *J. Comput. Appl. Math.*, 111(1-2):93–111, 1999.

[12] Helge Holden, Bernt Øksendal, Jan Ubøe, and Tu-Sheng Zhang. *Stochastic Partial Differential Equations*. Birkhäuser Verlag, Basel, 1996.

[13] E.T. Jaynes. *Probability Theory, the Logic of Science*. Cambridge University Press, Cambridge, 2003.

[14] M. Kennedy and A. O'Hagan. Bayesian calibration of computer models. *Journal of the Royal Statistical Society, Series B*, 63:425–464, 2001.

[15] J. Lang. *Adaptive Multilevel Solution of Nonlinear Parabolic PDE Systems*, volume 16 of *Lecture Notes in Computational Science and Engineering*. Springer-Verlag, Berlin, 2001.

[16] Paul Malliavin. *Stochastic Analysis*. Springer-Verlag, Berlin, 1997.

[17] H. G. Matthies. Uncertainty quantification with stochastic finite elements. In E. Stein, R. de Borst, and T. R. J. Hughes, editors, *Encyclopedia of Computational Mechanics*. John Wiley & Sons, Chichester, 2007.

[18] H. G. Matthies and A. Keese. Galerkin methods for linear and nonlinear elliptic stochastic partial differential equations. *Comp. Meth. Appl. Mech. Engrg.*, 194:1295–1331, 2005.

[19] Hermann G. Matthies, Christoph E. Brenner, Christoph G. Bucher, and Carlos Guedes Soares. Uncertainties in probabilistic numerical analysis of structures and solids—stochastic finite elements. *Structural Safety*, 19(3):283–336, 1997.

[20] Hermann G. Matthies and Christian G. Bucher. Finite elements for stochastic media problems. *Comp. Meth. Appl. Mech. Engrg.*, 168:3–17, 1999.

[21] Hermann G. Matthies, Rainer Niekamp, and Jan Steindorf. Algorithms for strong coupling procedures. *Comput. Methods Appl. Mech. Eng.*, 195(17-18):2028–2049, 2006.

[22] H.G. Natke and Y. Ben-Haim, editors. *Uncertainty: Models and Measures*. Akademie-Verlag, Berlin, 1997.

[23] J. Rang. An analysis of the Prothero-Robinson example for constructing new DIRK and ROW methods. *Journal of Computational and Applied Mathematics*, 262:105–114, 2014.

[24] Joachim Rang. Apdative timestep control for fully implicit Runge–Kutta methods of higher order. Informatik-Bericht 2014-03, TU Braunschweig, Braunschweig, 2014.

[25] Joachim Rang. An analysis of the Prothero–Robinson example for constructing new adaptive ESDIRK methods of order 3 and 4. *Applied Numerical Mathematics*, 94:75–87, 2015.

[26] Joachim Rang. Improved traditional Rosenbrock–Wanner methods for stiff ODEs and DAEs. *Journal of Computational and Applied Mathematics*, 286:128–144, 2015.

[27] Joachim Rang. The Prothero and Robinson example: Convergence studies for Runge–Kutta and Rosenbrock–Wanner methods. *Applied Numerical Mathematics*, 108:37–56, 2016.

[28] Joachim Rang and Rainer Niekamp. A component framework for the parallel solution of the incompressible Navier-Stokes equations with Radau-IIA methods. *Int. J. Numer. Meth. Fluids*, 78(5):304–318, 2015.

[29] C. J. Roy and W. L. Oberkampf. A complete framework for verification, validation and uncertainty quantification in scientific computing. *AIAA-Paper*, 2010-124, 2010.

[30] K. Strehmel and R. Weiner. *Linear-implizite Runge–Kutta-Methoden und ihre Anwendung*, volume 127 of *Teubner-Texte zur Mathematik*. Teubner, Stuttgart, 1992.

[31] K. Strehmel and R. Weiner. *Numerik gewöhnlicher Differentialgleichungen*. Teubner, Stuttgart, 1995.

[32] Norbert Wiener. The homogeneous chaos. *American Journal of Mathematics*, 60:897–936, 1938.

VII International Conference on Computational Methods for Coupled Problems in Science and Engineering
COUPLED PROBLEMS 2017
M. Papadrakakis, E. Oñate and B. Schrefler (Eds)

MODELLING PIEZOELECTRIC ENERGY HARVESTERS BY A FINITE INTEGRATION TECHNIQUE FORMULATION FOR ELECTROMECHANICAL COUPLED PROBLEMS

F. MORO[*], D. DESIDERI[*], A. DORIA[*], A. MASCHIO[*], C. MEDÉ[*], AND

L. CODECASA[†]

[*] Dipartimento di Ingegneria Industriale
Università di Padova
Via Gradenigo 6/A, 35131 Padova, Italy
e-mail: federico.moro@unipd.it

[†] Dipartimento di Elettronica, Informazione e Bioingegneria
Politecnico di Milano
Via Ponzio 34/5, 20133 Milano.Italy

Key words: Coupled Problems, Multiphysics, Piezoelectric, Energy Harvesting, Finite Integration Technique, Cell Method.

Abstract. A detailed analysis and optimization of piezoelectric devices, which nowadays are of widespread use in electronic applications, requires numerical analysis. Numerical models based on the Finite Element Method (FEM) have already been proposed in literature. The Finite Integration Technique (FIT) provides stable and consistent discretization schemes for coupled multiphysics problems. A FIT formulation with unstructured meshes, for 2-D/3-D coupled electromechanical static or dynamic problems, is presented. Piezoelectric bimorph cantilevers, with a realistic multilayered geometry, can be analyzed. Comparisons with FEM show the validity and the accuracy of the method.

1 INTRODUCTION

Piezoelectric materials are nowadays of widespread use for producing actuators, sensors, and energy harvesters for feeding ultra-low power electronics [1]. Analytical models are well-assessed and important tools for designing and optimizing piezoelectric devices [2]. Lumped circuit models are derived for instance in control applications [3]. Non ideal conditions like clamping setup, local variations in geometry and material properties, and residual stress may significantly affect the device performance, and in particular its resonance frequency. Accurate numerical electromechanical 3-D coupled models are thus required. The FEM analysis of piezoelectric structures is thoroughly documented in the literature [4]. In particular, thin-plate finite elements were proposed to limit the amount of problem unknowns [5].

The Finite Integration Technique or, equivalently, the Cell Method (CM) are numerical techniques, which provide field equations directly in algebraic form, thus suitable for computer

coding [6,7]. These are alternative to FEM because the field problem is formulated in a circuit-like manner in terms of degrees of freedom (DoFs), i.e. volume and surface integrals of vector fields and scalar potentials. This feature is suitable for modelling multiphysics problems, where different types of couplings occur. A coupling between different physics is provided in [8] by solving an electro-thermal problem with CM. In [9] different computational domains, which can be discretized independently, are matched by a CM formulation. An example of coupling between different numerical methods, e.g. the CM and the Boundary Element Method (BEM), is finally provided in [10]. The extension of FIT and CM to elastic problems has been more complex due to mathematical structure of elasticity, inherently different from electromagnetic problems. A first attempt of CM elastic formulation was proposed by Tonti in [11]. The role of topological operators in elasticity was evidenced in [12]. Finally, CM formulations for multiphysics problems including elasticity were proposed in [6,7,13].

The basic idea here is to extend this algebraic approach for analysing piezoelectric coupled problems, where the elastic problem is coupled to the electrostatic problem via constitutive relationships.

2 FIT PIEZOELECTRIC FORMULATION

Let $\Omega \in \mathbb{R}^d$ $(d = 2, 3)$ be a piezoelectric body with boundary $\Gamma = \partial\Omega$. The response to external body-surface forces is ruled by dynamic equilibrium and compatibility equations, which exhibit a more simple representation when the small displacement assumption holds true. This condition is well verified in typical piezo-mechanical applications like energy harvesters, actuators, and sensors. Similarly, electrostatics is governed by curl-free constraint and charge conservation. These equations are complemented by local piezoelectric relationships:

$$\mathrm{T_{ij}} = \mathrm{c^{E}_{ijkh}}\,\mathrm{S^{kh}} - \mathrm{e_{kij}}\mathrm{E^{k}}, \tag{1}$$

$$\mathrm{D_{i}} = \mathrm{e_{ikh}}\mathrm{S^{kh}} + \varepsilon^{\mathrm{S}}_{\mathrm{ik}}\mathrm{E^{k}}, \tag{2}$$

where $\mathrm{T_{ij}}$, $\mathrm{S^{kh}}$ are the stress and the strain tensors, $\mathrm{D_i}$, $\mathrm{E^k}$ are the electric displacement and electric fields, and $\mathrm{c^{E}_{ijkh}}$, $\mathrm{e_{ikh}}$, $\varepsilon^{\mathrm{S}}_{\mathrm{ik}}$ are the elastic, piezoelectric, and dielectric tensors. In (1) and (2) the Einstein summation convention is implicitly assumed.

In FIT formulations problem variables are DoFs defined on geometric entities like points, lines, surfaces, and volumes. The computational domain is first meshed into tetrahedrons so that a primal grid $\mathcal{G}_\Omega$ with N nodes and E edges is built. Dual grids $\tilde{\mathcal{G}}_\Omega$ and $\tilde{\mathcal{G}}_\Gamma$ are defined on Ω and Γ by taking the barycentric subdivisions of primal grids $\mathcal{G}_\Omega$ and $\mathcal{G}_\Gamma$ (the restriction of $\mathcal{G}_\Omega$ to Γ). The *augmented dual grid* is built by joining volume and boundary grids as $\tilde{\mathcal{G}}_{\Omega\Gamma} = \tilde{\mathcal{G}}_\Omega \cup \tilde{\mathcal{G}}_\Gamma$ [14]. The following incidence matrices are defined for discretization on dual grids: $\mathbf{G}_\Omega$ (edges to nodes on $\mathcal{G}_\Omega$), $\widetilde{\mathbf{D}}_\Omega = -\mathbf{G}_\Omega^{\mathrm{T}}$ (volumes to faces on $\tilde{\mathcal{G}}_\Omega$), $\widetilde{\mathbf{D}}_{\Omega\Gamma}$ (volumes on $\tilde{\mathcal{G}}$ to faces on on $\tilde{\mathcal{G}}_\Gamma$).

For the mechanical problem the following arrays of DoFs are defined for any i–th spatial component (with $i = 1 \ldots d$): displacements on primal nodes n, $\mathbf{s}^i = (s^i_n)$; line integrals of the displacement gradient $x^{kh} = s^{k,h}$ along primal edges e, $\mathbf{x}^i = (x^i_e)$, where $x^i_e = \int_e \mathrm{x^{ij}t_j}\, d\gamma$ and $\mathrm{t_j}$ is unit tangent vector along e; fluxes of the stress tensor on dual faces $\tilde{f}$, $\tilde{\mathbf{t}}_i = (\tilde{t}_{i\tilde{f}})$, where

$\tilde{t}_{i\tilde{f}} = \int_{\tilde{f}} \mathrm{T}_{ij}\, \mathrm{n}^{\mathrm{j}}\, d\sigma$ and n^{j} unit normal vector to face $\tilde{f}$. For the electrostatic problem, arrays of DoFs are: electric potentials at primal nodes $\mathbf{\Phi} = (\varphi_n)$; electric voltages along primal edges, $\mathbf{u} = (u_e)$, where $u_e = \int_e \mathrm{E}^j\, \mathrm{t}_{\mathrm{j}}\, d\gamma$ is the line integral of the electric field E^j; fluxes of electric displacement D_j on dual faces $\tilde{\mathbf{d}} = (\tilde{d}_{\tilde{f}})$, where $\tilde{d}_{\tilde{f}} = \int_{\tilde{f}} \mathrm{D}_j\, \mathrm{n}^{\mathrm{j}}\, d\sigma$.

3.1 Static coupled problem

In a FIT scheme, similar to a circuit-like electric problem formulation, topological and constitutive relationships have to be constructed in order to fully constrain arrays of DoFs. Topological relations on the primal grid for the mechanical and electrical variables are:

$$\mathbf{x}^i = \mathbf{G}_\Omega\, \mathbf{s}^i, \tag{3}$$

$$\mathbf{e} = -\mathbf{G}_\Omega\, \mathbf{\Phi}, \tag{4}$$

The topological relationships for the dual grid are the equilibrium equations for electrostatics and mechanics:

$$\widetilde{\mathbf{D}}_\Omega\, \tilde{\mathbf{t}}_i + \widetilde{\mathbf{D}}_{\Omega\Gamma}\, \tilde{\mathbf{t}}_{\Gamma,i} = \tilde{\mathbf{f}}_i, \tag{5}$$

$$\widetilde{\mathbf{D}}_\Omega\, \tilde{\mathbf{d}} + \widetilde{\mathbf{D}}_{\Omega\Gamma}\, \tilde{\mathbf{d}}_\Gamma = \tilde{\mathbf{q}}, \tag{6}$$

where $\tilde{\mathbf{t}}_{\Gamma,i}$, $\tilde{\mathbf{d}}_\Gamma$ are stress tensor and dielectric displacement fluxes on the boundary dual faces, $\tilde{\mathbf{f}}_i = (\tilde{f}_i)$ is the array of external body forces.

By integrating on dual faces strain tensor and electric displacement in (1) and (2), the following discrete relationships are obtained:

$$\tilde{\mathbf{t}}_i = \mathbf{C}_{ij}\, \mathbf{x}^j - \mathbf{E}_i\, \mathbf{e}, \tag{7}$$

$$\tilde{\mathbf{d}} = \mathbf{E}_j^{\mathrm{T}} \mathbf{x}^j + \boldsymbol{\varepsilon}\, \mathbf{e}, \tag{8}$$

where $\mathbf{C}_{ij} = (c_{ij,ee\prime})$, $\mathbf{E}_i = (E_{i,ee\prime})$, $\boldsymbol{\varepsilon} = (\varepsilon_{ee\prime})$ are respectively the elastic, piezoelectric, dielectric constitutive matrices, all of size $E \times E$. These matrices are assembled from local matrices constructed as described in [6].

For instance, the elastic matrix is obtained as follows. For a given tetrahedron τ, edge vectors and dual face vectors (within the tetrahedron), depicted in Fig. 1, are computed for any primal edge. By assuming an affine displacement distribution within any tetrahedron τ, the displacement gradient is uniform within τ. For any edge $e_{(\tau)}$ of τ, this becomes $x^i_{e_{(\tau)}} = \int_{e_{(\tau)}} \mathrm{x}^{ij} \mathrm{t}_{\mathrm{j}}\, d\gamma = \mathrm{x}^{ij} \mathrm{L}_{e_{(\tau)},\mathrm{j}}$, where $\mathrm{L}_{e(\tau),\mathrm{j}}$ is the edge vector related to $e_{(\tau)}$. In the same way, the stress flux for any dual face portion within τ, $\tilde{f}_{(\tau)}$, becomes $\tilde{t}_{i\tilde{f}_{(\tau)}} = \int_{\tilde{f}_{(\tau)}} \mathrm{T}_{ij}\, \mathrm{n}^{\mathrm{j}}\, d\sigma = \mathrm{T}_{ij}\, \widetilde{\mathrm{A}}^{\mathrm{j}}_{(\tau)}$, where $\widetilde{\mathrm{A}}^{\mathrm{j}}_{(\tau)}$ is the area vector related to $\tilde{f}_{(\tau)}$. By noting that for a single tetrahedron three DoFs (displacement gradients) are independent only, previous relationships can be cast in matrix form, that is: $\mathbf{S}_{(\tau)} = \mathbf{P}_{(\tau)}\, \mathbf{x}_{(\tau)}$, where $\mathbf{S}_{(\tau)}$ is the vector (written in Voigt notation) of strain tensor components, $\mathbf{P}_{(\tau)}$ is a (6 x 18) linear mapping constructed as described in (4), and $\mathbf{x}_{(\tau)}$ is the

(18 x 1) vector of displacement gradient line integrals; $\tilde{\mathbf{t}}_{(\tau)} = \widetilde{\mathbf{A}}_{(\tau)}\, \mathbf{T}_{(\tau)}$, where $\tilde{\mathbf{t}}_{(\tau)}$ is the (18 x 1) stress flux local vector, $\widetilde{\mathbf{A}}_{(\tau)}$ is the (18 x 6) area matrix, and $\mathbf{T}_{(\tau)}$ is the vector (written in Voigt notation) of stress tensor components. Similarly, local constitutive equation $T_{ij} = c^{E}_{ijkh}\, S^{kh}$ becomes $\mathbf{T}_{(\tau)} = \mathbf{C}^{\mathbf{E}}_{(\tau)}\, \mathbf{S}_{(\tau)}$ in matrix form. By combining previous relationships, the discretized local constitutive matrices $\mathbf{C}_{(\tau)} = \widetilde{\mathbf{A}}_{(\tau)} \mathbf{C}^{\mathbf{E}}_{(\tau)} \mathbf{P}_{(\tau)}$ are obtained. The global constitutive matrix $\mathbf{C}_{ij}$ is finally derived by assembling local matrices over the whole mesh.

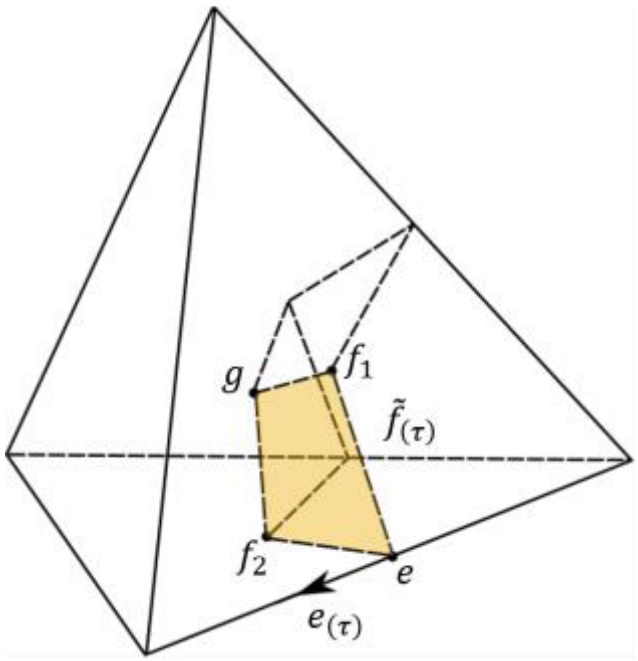

Figure 1: Primal edge $e_{(\tau)}$ within a tetrahedron τ and its corresponding dual face $\tilde{f}_{(\tau)}$ (shaded in color). The dual face vertices are the cell centroid g, the face centroids f_1, f_2, and the edge centroid e.

By inserting (7) and (8) in (5) and (6), respectively, and by using displacement and potentials as unknown variables by means of (3) and (4), a coupled linear system is obtained:

$$\begin{pmatrix} \mathbf{K_{11}} & \cdots & \mathbf{K}_{1d} & \mathbf{K}_{1\Phi} \\ \vdots & \ddots & \cdots & \vdots \\ \mathbf{K}^{\mathbf{T}}_{1d} & \cdots & \mathbf{K}_{dd} & \mathbf{K}_{d\Phi} \\ \mathbf{K}^{\mathbf{T}}_{1\Phi} & \cdots & \mathbf{K}^{\mathbf{T}}_{d\Phi} & \mathbf{K}_{\Phi\Phi} \end{pmatrix} \begin{pmatrix} \mathbf{s}^{1} \\ \vdots \\ \mathbf{s}^{d} \\ \mathbf{\Phi} \end{pmatrix} = \begin{pmatrix} -\tilde{\mathbf{f}}_{\Omega,1} + \widetilde{\mathbf{D}}_{\Omega\Gamma}\, \tilde{\mathbf{t}}_{\Gamma,1} \\ \vdots \\ -\tilde{\mathbf{f}}_{\Omega,d} + \widetilde{\mathbf{D}}_{\Omega\Gamma}\, \tilde{\mathbf{t}}_{\Gamma,d} \\ -\tilde{\mathbf{q}} + \widetilde{\mathbf{D}}_{\Omega\Gamma}\, \tilde{\mathbf{d}}_{\Gamma} \end{pmatrix}, \tag{9}$$

where $\mathbf{K}_{ij} = \mathbf{G}^{\mathrm{T}} \mathbf{C}_{ij} \mathbf{G}$ is the mechanical stiffness matrix, $\mathbf{K}_{i\Phi} = -\mathbf{G}^{\mathrm{T}} \mathbf{E}_i\, \mathbf{G}$ is the the electro-mechanical stiffness matrix, and $\mathbf{K}_{\Phi\Phi} = -\mathbf{G}^{\mathrm{T}} \boldsymbol{\varepsilon}\, \mathbf{G}$ is the the electrostatic stiffness matrix. The final coupled matrix system (9) can be written in compact form as $\mathbf{K}\,\mathbf{x} = \mathbf{f}$, where the solution vector is $\mathbf{x} = \left(\mathbf{s}^{1}, \ldots, \mathbf{s}^{\mathrm{d}}, \mathbf{\Phi}\right)^{\mathbf{T}}$. A direct solver is applied to (9) after imposing Dirichlet (displacements) and Neumann (tractions) boundary conditions.

3.1 Dynamic coupled problem

Steady state FIT formulation can be extended to dynamic coupled piezoelectric problems adding inertia forces and dumping.

The inertia force on the *i*-th dual volume $\tilde{\tau}_j$ is given by $\tilde{f}_i = \int_{\tilde{\tau}_j} \rho\, g_i(x)\, d\tau$, where g_i the *i*-th component of the acceleration and ρ the mass density. The mass matrix $\mathbf{M}_\rho = (\int_{\tilde{\tau}_j} \rho\, d\tau)$, of size $N \times N$, is diagonal in FIT. According to Rayleigh's theory, damping matrices (for mechanical problem only) are defined as a linear combination of mass and stiffness matrices, that is $\mathbf{D}_{v,ij} = \alpha\, \mathbf{M}_\rho + \beta\, \mathbf{K}_{ij}$ where α and β are damping coefficients defined experimentally.

The dynamic behaviour of the coupled piezoelectric problem in discrete form is then described by the following second order ordinary differential equation (ODE) system:

$$\mathbf{M}\,\ddot{\mathbf{x}} + \mathbf{D}\,\dot{\mathbf{x}} + \mathbf{K}\,\mathbf{x} = \mathbf{f}, \tag{10}$$

where:

$$\mathbf{M} = \begin{pmatrix} \mathbf{M}_\rho & \cdots & \mathbf{0} & \mathbf{0} \\ \vdots & \ddots & \vdots & \vdots \\ \mathbf{0} & \cdots & \mathbf{M}_\rho & \mathbf{0} \\ \mathbf{0} & \cdots & \mathbf{0} & \mathbf{0} \end{pmatrix}, \quad \mathbf{D} = \begin{pmatrix} \mathbf{D}_{v,11} & \cdots & \mathbf{D}_{v,1d} & \mathbf{0} \\ \vdots & \ddots & \vdots & \mathbf{0} \\ \mathbf{D}_{v,1d}^{\mathrm{T}} & \cdots & \mathbf{D}_{v,dd} & \mathbf{0} \\ \mathbf{0} & \mathbf{0} & \mathbf{0} & \mathbf{0} \end{pmatrix},$$

and matrix **K** is defined in (9). The ODE system (10) is solved by the Newmark-β integration scheme, that is the responses after time Δt, i.e. $\mathbf{x}_{n+1}, \dot{\mathbf{x}}_{n+1}, \ddot{\mathbf{x}}_{n+1}$, are calculated from those at the previous time step, i.e. $\mathbf{x}_n, \dot{\mathbf{x}}_n, \ddot{\mathbf{x}}_n$ and from the rhs $\mathbf{f}_{n+1}$, as

$$\begin{aligned} \boldsymbol{A}_{n+1}\, \ddot{\mathbf{x}}_{n+1} &= \mathbf{b}_{n+1}, \\ \dot{\mathbf{x}}_{n+1} &= \dot{\mathbf{x}}_n + (1-\gamma)\Delta t\, \ddot{\mathbf{x}}_n + \gamma \Delta t\, \ddot{\mathbf{x}}_{n+1}, \\ \mathbf{x}_{n+1} &= \mathbf{x}_n + \Delta t\, \dot{\mathbf{x}}_{\boldsymbol{n}} + \Delta t^2 \left[\left(\tfrac{1}{2} - \beta\right) \ddot{\mathbf{x}}_n + \beta\, \ddot{\mathbf{x}}_{n+1}\right], \end{aligned} \tag{11}$$

where:

$$\begin{aligned} \boldsymbol{A}_{n+1} &= \mathbf{M} + \gamma \Delta t\, \mathbf{D} + \beta \Delta t^2 \mathbf{K}, \\ \mathbf{b}_{n+1} &= \mathbf{f}_{n+1} - \mathbf{K}\,\mathbf{x}_n - (\mathbf{D} + \Delta t\, \mathbf{K})\, \dot{\mathbf{x}}_{\boldsymbol{n}} - \left[(1-\gamma)\Delta \mathrm{t}\, \mathbf{D} + \Delta \mathrm{t}^2 \left(\tfrac{1}{2} - \beta\right) \mathbf{K}\right] \ddot{\mathbf{x}}_n. \end{aligned}$$

The iterative time-stepping integration algorithm is proved to be unconditionally stable and convergent for a proper choice of parameters γ and β such that $4\beta \geq 2\gamma \geq 1$ [15].

3 NUMERICAL RESULTS

The static FIT model is validated by FEM results (COMSOL Multiphysics®) on a 2-D test case consisting in a multilayered PVDF bimorph beam used as an actuator, under an external voltage excitation. The dynamic FIT model is validated on a 3-D test case consisting in a

multilayered PZT bimorph cantilever harvester excited by a force impulse (e.g. which is typical for devices mounted within tires) and in electrical open circuit conditions.

3.1 PVDF bimorph beam

The piezoelectric actuator presented in [16] is considered for validating the 2-D FIT static model ($d = 2$). The plane stress assumption holds in fact with thin structures. The bimorph beam (size $20\times5\times1$ mm) consists of two piezo PVDF layers (0.5 mm thick each) with opposite polarity. A constant potential is applied to top and bottom sides of the cantilever (the bottom side is the mass electrode). Clamping BCs are applied to one end and deflection due to external voltage is then computed.

The bimorph beam model is discretized by FIT into 20,116 triangles. The assembly time for the discretized FIT model (30,982 unknowns) is 1.46 s. The system solution with direct solver requires 0.46 s on a Intel Core i7 processor (2.70 GHz).

Fig. 2 shows the tip displacement for applied voltages varying from 0 V up to 200 V. FIT results are compared with data provided in [16], showing a very good agreement. The FEM model proposed by Park is fully 3-D, being based on plate bending elements. Other data used for comparison are obtained from experimental measurements and 1-D analytical modelling.

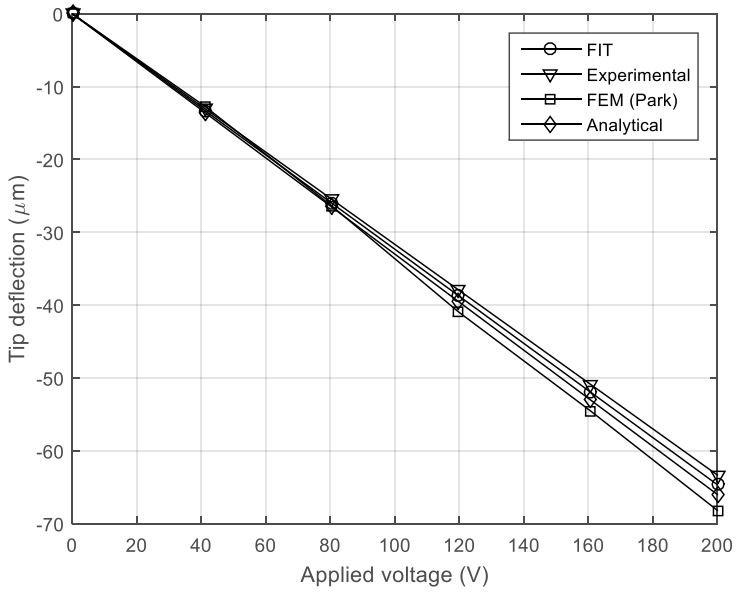

Figure 2: Tip displacement along the z-axis vs. applied voltage (experimental, FEM, and analytical data are provided in [16] for the actuator test case; FIT data are computed by a 2D FIT in-house code).

3.2 PZT bimorph cantilever

In order to validate the 3-D FIT dynamic model ($d = 3$) a commercial piezo energy harvester for feeding ultra-low power electronic devices is considered. This can be used e.g. for supplying wireless sensors used in tire pressure monitoring systems [17]. The bimorph beam, with size

25.4 x 3.81 x 0.72 mm, has a complex multi-layered structure: two inner piezo layers (0.18 mm thick each) with opposite polarization, made of lead zirconate titanate (PZT-5A), are used for charge generation, and two external layers of FR4 composite material (epoxy) are used to provide structure stiffness. The intermediate layer of Espanex® (copper conductor) is not included in the CAD geometry and is modelled simply by assuming a circuit terminal condition. The cantilever is excited by a vertical inertia force impulse, of sinusoidal waveform, to simulate the typical excitation experienced by the harvester mounted inside a rotating tire [18]:

$$g_z(x,t) = -\rho\, P\, \mathrm{rect}\left(\frac{t}{\delta}\right) \sin\left(\pi \frac{t}{\delta}\right), \tag{12}$$

where ρ is the mass density, P the pulse amplitude, rect is the unit rectangular function, and δ is the pulse width. Constant (unknown) potentials are imposed at top and bottom sides of the piezo structure. Clamping boundary conditions are applied to one end of the cantilever.

The displacement and voltage system responses are simulated by 3-D FEM and the 3-D FIT dynamic model illustrated in Section 2. FIT formulation is coded in Matlab® in a vectorized language style to speed-up computations. The model geometry is meshed into 160,948 tetrahedrons, 203,882 edges, and 32,369 nodes. First order elements are used for mechanics and electrostatics coupled physics with FEM, whereas affined basis functions are used with FIT. Note that a transient 3-D FEM model with second order elements, for the test case considered, is computationally unfeasible due to the huge number of DoFs. The assembly time for the discretized FIT model (106,639 unknowns) is 30.02 s. The system solution at each time step requires 7.29 s on the same machine as above. To finely resolve the electromechanical transient, a sufficiently small time step $\Delta t = 0.005\ \delta$ is set for both FEM and FIT, with $t_{max} = 10\ \delta$ analysis time. Different integration schemes are used: BDF (5th order backward differentiation, to get an accurate integration) for COMSOL® and Newmark-β for FIT. The simulation time of transient analysis is 4 h 23 min for the COMSOL® solver and 4 h 28 min for the FIT code. Electromechanical constitutive tensors for FR4 and PZT-5A are taken from the COMSOL® material library. Other relevant parameters for simulations are P = –9.81 m/s^2, δ = 1.5 ms for the force impulse, and $\alpha = 0$ s^{-1}, $\beta = 4 \cdot 10^{-6}$ s for damping.

In order to compare FEM and FIT analyses the open circuit voltage and the displacement at the center of the cantilever are computed. Fig. 3 and 4 show that FIT time responses agree very well with FEM, even though different time integrators have been used. Maximum discrepancy values between FEM-FIT distributions are 0.21 % for voltage and 0.20 % for displacement.

Finally, spatial solutions at the last time step are compared to estimate overall accuracy of the FIT model. A horizontal line of coordinates x = [0, 25.4] mm, y = 1.905 mm, z = 0.36 mm, placed along the cantilever horizontal axis, is considered (Fig. 5). Fig. 6 and 7 show that profiles of the z–axis displacement component, computed along the beam axis for the most significant time steps $t = t_{max}/2$ and $t = t_{max}$, agree very well with FEM. Maximum discrepancy values between FEM-FIT distributions are 0.05 % ($t = t_{max}/2$) and 0.02 % ($t = t_{max}$), respectively.

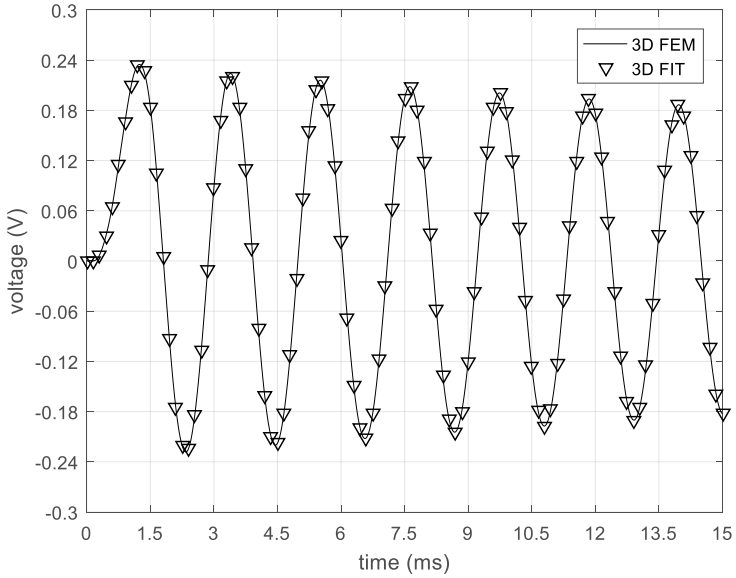

Figure 3: Open circuit voltage response for 1g acceleration pulse (3-D FEM: straight line, 3-D FIT: markers).

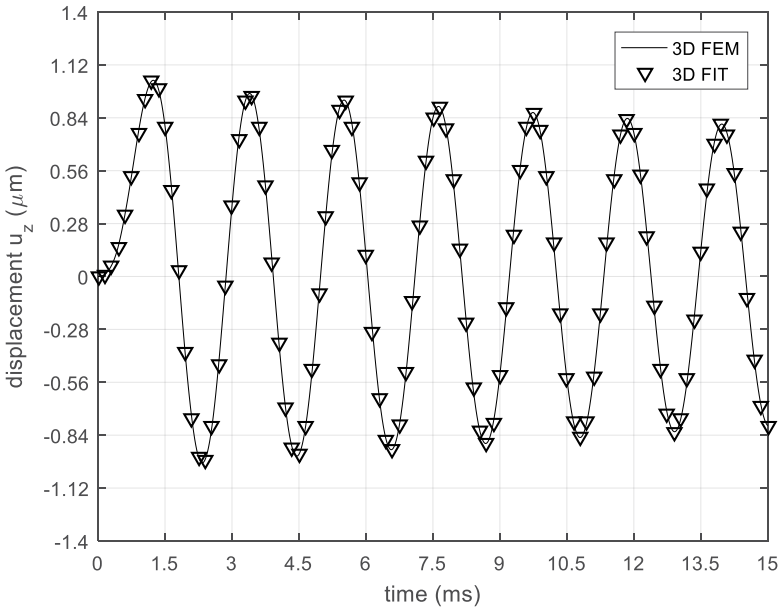

Figure 4: z–axis displacement component at the center of the cantilever for 1g acceleration pulse (3-D FEM: straight line, 3-D FIT: markers).

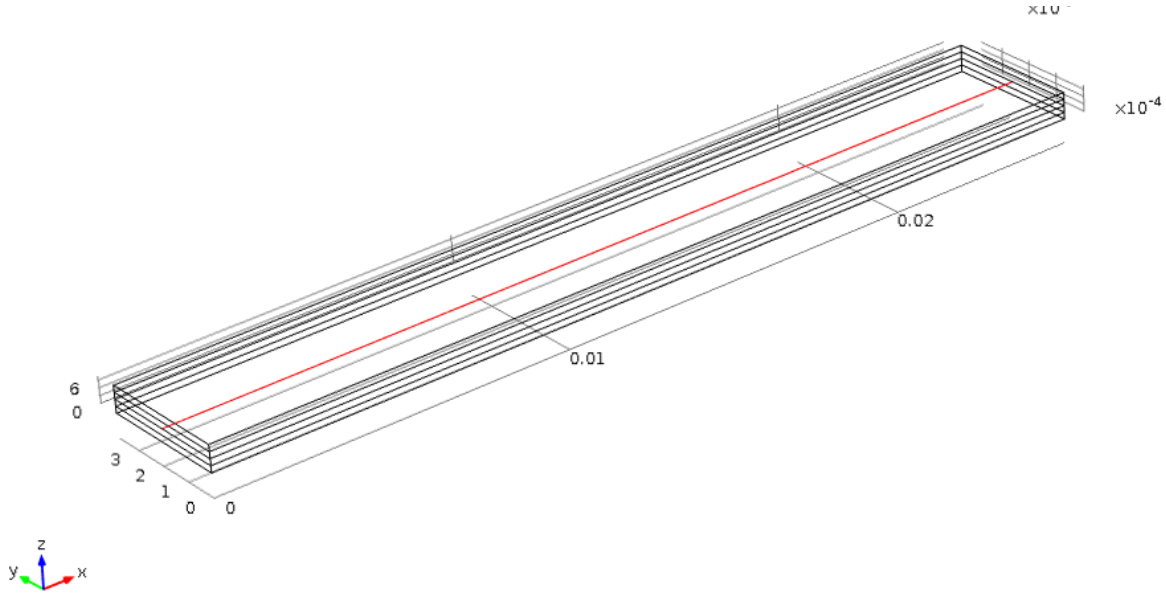

Figure 5: Horizontal line along the beam axis (x = [0, 25.4] mm, y = 1.905 mm, z = 0.36 mm; red color).

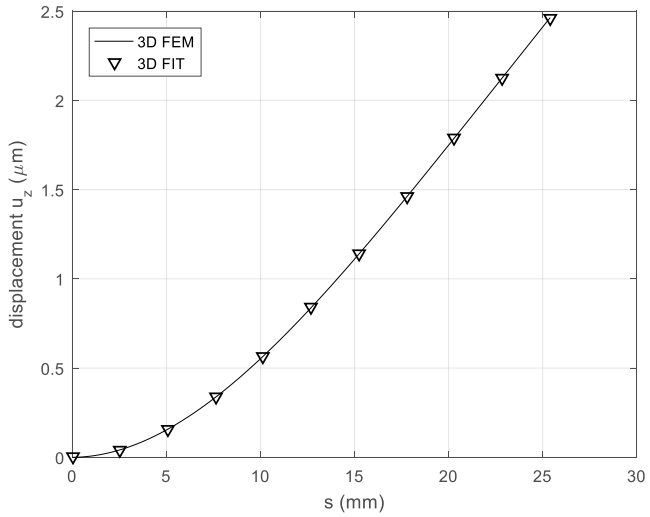

Figure 6: z–axis displacement component along the beam axis at the time step $t = t_{max}/2$ (evaluated at points on x = [0, 25.4] mm, y = 1.905 mm, z = 0.36 mm; 3-D FEM: straight line, 3-D FIT: markers).

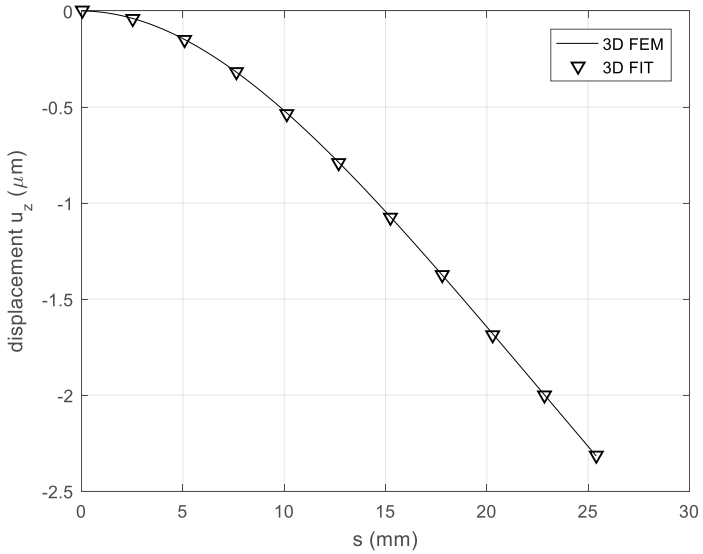

Figure 7: z–axis displacement component along the beam axis at the last time step $t = t_{max}$ (evaluated at points on x = [0, 25.4] mm, y = 1.905 mm, z = 0.36 mm; 3-D FEM: straight line, 3-D FIT: markers).

11 ACKNOWLEDGMENT

This work was supported by the Università di Padova under the Grant CPDA142798 (project PRAT14 “Piezoelectric Micro-Electro-Mechanical Power Supply for Automotive Wireless Sensors”).

12 CONCLUSIONS

This work demonstrates that FIT, for tetrahedral meshes, also extends to piezoelectric problems by assuming a local affine displacement vector field. The building strategy for local constitutive matrices is similar to that one used for elastic problems. In such a way, topological and constitutive relationships are split and the construction of the final coupled system becomes simpler and can be solved in a matrix-oriented numerical environment such as Matlab®. Test cases show that FIT code is accurate and reliable even with 3-D numerical models of commercial cantilevers, exhibiting a complex multilayered and multi-material structure.

REFERENCES

[1] Rincón-Mora, G. A. and Yang, S. Tiny Piezoelectric Harvesters: Principles, Constraints, and Power Conversion. *IEEE Trans. on Circuits and Systems I: Regular Papers* (2016) **63**: 639–649.

[2] Priya, S., and Inman, D.J. *Energy Harvesting Technologies*. Springer-Verlag (2009).

[3] Kázmierski, T.J., and Beeby, S. *Energy Harvesting Systems: Principles, Modelling, and Applications*. Springer-Verlag (2011).

[4] De Marqui, C., Erturk, A, and Inman, D.J. An electromechanical finite element model for piezoelectric energy harvester plates. *Journal of Sound and Vibration* (2009) **327**: 9-25.

[5] Lam, K.Y., Peng, X.Q., Liu, G.R., and Reddy, J.N. Finite element model for composite laminates. *Smart Materials & Structures* (1997) **6**: 583–591.

[6] Alotto, P., Freschi, F., Repetto, M., and Rosso, C. *The Cell Method for Electrical Engineering and Multiphysics problems. An Introduction*. Lecture Notes in Electrical Engineering 230, Springer (2013).

[7] Alotto, P., Freschi, F., and Repetto, M. Multiphysics problems via the cell method: The role of Tonti diagrams. *IEEE Trans. Magn.* (2010) **46**: 2959–2962.

[8] Alotto, P., Bullo, M., Guarnieri, M., and Moro, F. A Coupled Thermo–Electromagnetic Formulation Based on the Cell Method. *IEEE Trans. Magn*. (2008) **44**: 702–705.

[9] Alotto, P., Guarnieri, M., Moro, F. A mortar cell method for electro-thermal contact problems. *IEEE Trans. Magn.* (2013), **49**: 795–798.

[10] Moro, F., and Codecasa, L. Indirect Coupling of the Cell Method and BEM for Solving 3–D Unbounded Magnetostatic Problems. *IEEE Trans. Magn.* (2016) **52**: Art. ID 7200604.

[11] Tonti, E., and Zarantonello, F. Algebraic formulation of elastostatics: The Cell Method. *Comput. Modeling Eng. Sci.* (2009) **39**: 201–236.

[12] Bossavit, A. Discrete magneto-elasticity: A geometrical approach. *IEEE Trans. Magn.* (2010) **46**: 3485–3491.

[13] Moro, F., Alotto, P., Freschi, F., and Guarnieri, M. A Cell Method Formulation of 3-D Electrothermomechanical Contact Problems With Mortar Discretization. *IEEE Trans. Magn.* (2012) **48**: 503–506.

[14] Codecasa, L. Refoundation of the Cell Method Using Augmented Dual Grids. *IEEE Trans. Magn*. (2014) **50**: pp. 497–500.

[15] Kagawa, Y., et al. Finite Element Simulation of Dynamic Responses of Piezoelectric Actuators. *Journal of Sound and Vibration* (1996) **191**: 519-538.

[16] Hwang, W.S., and Park, H.C. Finite Element Modelling of Piezoelectric Sensors and Actuators. *AIAA Journal* (1993) **31**: 930–937.

[17] Mak, K.H., McWilliam, S., and Popov, A. Piezoelectric energy harvesting for tire pressure measurement applications. *Proc. Mech. E Part D: J Automobile Engineering* (2013) **227**: 842–852.

[18] Doria, A., Moro, F., Desideri, D., Maschio, A., and Zhang, Z. An impulsive method for the analysis of piezoelectric energy harvesters for intelligent tires. *Proc. ASME Int. Design Engineering Technical Conference IDETC 2016, Charlotte, USA (August 21-24, 2016).*

VII International Conference on Computational Methods for Coupled Problems in Science and Engineering
COUPLED PROBLEMS 2017
M. Papadrakakis, E. Oñate and B. Schrefler (Eds)

ON FORWARD AND REVERSE COUPLING OF VIBRATING PIEZOELECTRIC ENERGY HARVESTERS

ELVIO BONISOLI*, NICOLÓ MANCA+ AND MAURIZIO REPETTO†

*Department of Mechanical and Aerospace Engineering (DIMEAS)
e-mail: elvio.bonisoli@polito.it - Web page: http://www.dimeas.polito.it/en/
+Department of Management and Production Engineering (DIGEP)
e-mail: nicolo.manca@polito.it - Web page: http://www.digep.polito.it/en/
†Department of Energy ≪Galileo Ferraris≫ (DENERG)
Politecnico di Torino, Corso Duca degli Abruzzi, 24, 10129 Torino, Italy
e-mail: maurizio.repetto@polito.it - Web page: http://www.cadema.polito.it

Key words: Piezoelectric materials, Energy harvesters, Vibrations

Abstract. This document provides information about the analysis of effects coupling the mechanical and the electrical phenomena going on inside a piezoelectric energy harvester. Two characteristics are exploited in energy harvesting: direct piezoelectric effect where stress is resulting by the application of an electric field and reverse effect showing an electric field resulting by stress application. Piezoelectric patches, bonded on beams free to vibrate under a mechanical stimulus, can be used as active elements. Point-wise material characteristics are described by symmetric matrices coupling together stress and electric field to the strain and the electric polarisation leading to reciprocal direct and reverse effects. Under operating conditions, the stress and electric field values applied to the material patch are not uniform and do not have the same spatial pattern resulting in a non reciprocal interaction. An explanation of this phenomenon is attempted by applying the Euler-Bernoulli beam theory model that allows the computation of two geometrical coefficients for direct and inverse interactions under uniform stress distribution. Comparisons versus experiments carried out on a Macro Fiber Composite piezoelectric patch show that the model is able to estimate the effect.

1 INTRODUCTION

PiezoElectricity (PE) phenomenon can be used as sensor if the stress applied to a sample can be measured by a voltage appearing on the material, or as actuator if the material changes its shape due to the application of a electric field. In energy harvesting applications both effects have to be exploited since power is converted from the mechanical action, as for instance mechanical vibrations, to the electrical domain when power is transferred to an external electric circuit. These effects are well known and have been

used to recover part of the vibration energy applied to the material in an external electrical circuit [1].

In all harvesting applications the estimation of the maximum power that can be extracted by some kind of excitation is of fundamental importance for the evaluation of potential applications. In this respect the accurate simulation of all the components present in the energy conversion chains is fundamental [2].

The energy conversion chain is composed by a direct effect where an elastic beam is set in motion by a vibrating source. This primary action creates stresses on the PE material and, in consequence, a voltage is generated. If an external circuit is connected to the voltage a power is drained and dynamic of the system is modified by the appearance of a force that is responsible for the power transferred from the mechanical to the electrical domain. These effects are called *direct effect* for the actions going from the mechanical to the electrical domain and *reverse effect* for the opposite.

If the vibrating beam is described by one degree of freedom, for instance the displacement of the free end from its equilibrium position, these two phenomena can be modelled by lumped parameters approach of the electromechanical model. Experimentally a non reciprocity of the energies exchanged by the two domains, mechanic and electric, is measured. To explain this fact an analysis of the actual stresses acting on the structure must be carried out and the model must be validated by experiments.

This paper is structured as: in the following chapter the analysis of the PE electromagnetic conversion is described while the following one deals with the experimental setup used to validate the model. Eventually a discussion of the obtained results is performed and the comparison with experiments is carried out.

2 PIEZOELECTRIC MATERIAL MODELLING

In energy harvesting applications, the piezoelectric effect can be described by using the linear constitutive equations of the piezoelectric materials [3]:

$$\begin{aligned} \boldsymbol{\delta_p} &= \boldsymbol{s^E} \cdot \boldsymbol{\sigma} + \boldsymbol{d}^T \cdot \boldsymbol{E} \\ \boldsymbol{D} &= \boldsymbol{d} \cdot \boldsymbol{\sigma} + \boldsymbol{\varepsilon^\sigma} \cdot \boldsymbol{E} \end{aligned} \tag{1}$$

where $\boldsymbol{\delta_p}$ is the mechanical strain, $\boldsymbol{\sigma}$ is the mechanical stress, $\boldsymbol{D}$ is the electrical displacement (charge density), $\boldsymbol{E}$ is the electric field, $\boldsymbol{s^E}$ is the compliance under a zero or constant electrical field (indicated by the superscript E) and $\boldsymbol{\varepsilon^\sigma}$ is the dielectric permittivity under a zero or constant stress (indicated by the superscript σ). $\boldsymbol{d}$ and $\boldsymbol{d}^T$ are the matrices for the direct and the reverse piezoelectric effect, where the superscript T means the transposed matrix. All matrices are (3×3) and express the anisotropy of the problem.

In the present application the PE material is exploited by applying a single axis stress, like in figure 1. As a result the constitutive equation (1) can be simplified in one dimension as:

$$\begin{aligned} \delta_1 &= s_{11}^E \cdot \sigma_1 + d_{31} \cdot E_3 \\ D_3 &= d_{31} \cdot \sigma_1 + \varepsilon_{33}^\sigma \cdot E_3 \end{aligned} \tag{2}$$

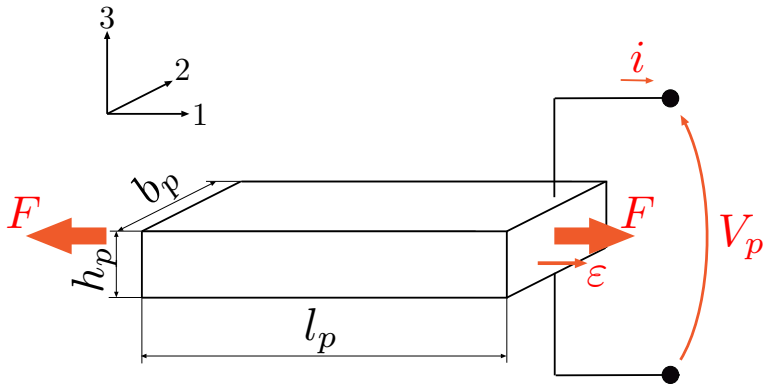

Figure 1: Layout of the PE harvester.

When a force F is applied along the 1 direction, it causes the elongation ϵ along the same direction. Due to the piezoelectric effect, a voltage V_p is generated in the 3 direction and, if a circuit is connected, a current i is created.

A lumped parameter model of the structure can be defined if, instead of considering equation (2), macroscopic variables F, ϵ, V_p and i are used. By taking into account geometric dimensions defined in figure 1, and considering that all quantities are uniform on the patch, the following relations can be written:

$$E_3 = -\frac{V_p}{h_p}\,; \qquad q = D_3 b_p l_p\,; \qquad \sigma_1 = \frac{F}{b_p h_p}\,; \qquad \delta_1 = \frac{\varepsilon}{l_p}\,; \qquad i = \frac{dq}{dt} \tag{3}$$

and, by substitution in eq. (2), the following dynamic equations are obtained:

$$\begin{cases} F = k_p \varepsilon + \Gamma V_p \\ i = \Gamma \dot{\varepsilon} - C_p \dot{V}_p - \frac{V_p}{R} \end{cases} \tag{4}$$

where:

$$k_p = \frac{b_p h_p}{l_p\, s_{11}^E}\,; \qquad C_p = \left(\varepsilon_{33}^\sigma - \frac{d_{31}^2}{s_{11}^E}\right)\frac{b_p l_p}{h_p}\,; \qquad \Gamma = \frac{d_{31} b_p}{s_{11}^E}$$

Eq. (4) has been derived from the constitutive equations of the piezoelectric material in static condition so that no mechanical dissipative effects are present. Even if, in the majority of cases, this effects are negligible at least in the modelling of the system it has to be considered. Thus, in dynamic conditions, the term $c_p\dot{\varepsilon}$ is added to the expression of F, where c_p is the mechanical damping of the piezoelectric patch.

3 BONDED PATCH DYNAMICS

The relations obtained in the previous section are the PE constitutive equations, that is they are relevant to the material characteristics. Being the PE patch bonded to an elastic beam the actual stress conditions applied to the material must be related to the macroscopic variables of the beam and to the average non-uniform stress conditions.

3.1 Relation between beam and PE variables

The clamped beam is free to move on one end and the relative vertical position z_r of the beam tip with respect to the clamped end is a quantity that can be measured. At the same time, due to the deformation of the beam, the PE patch is subject to an elongation ϵ that appears in the equation (4). In order to relate the two variables, the analysis of the one dimensional dynamic of the structure must be performed. As a result, the $1d$ model of the mechanical part will be defined in terms of the macroscopic variables $\dot{z}_r$ and F_T.

In a cantilever beam EH system, the piezoelectric force F acting on the patch along the 1 direction, due to the characteristics of the system, produces a force F_T applied to the free-end of the cantilever beam along the z axis. In the same way, the displacement of the free-end along the z axis, due to the characteristics of the system, induces elongation along the 1 direction of the piezoelectric patch.

3.1.1 direct effect: A coefficient

When voltage is applied at the piezoelectric patch along the 3 direction, a force F is produced along the 1 direction due to piezoelectric 31 effect. Being the patch neutral surface at a distance Δh along the 3 direction from the neutral surface of the support beam, the piezoelectric layer imposes a moment M to the support beam. The equilibrium of the system is achieved applying a force F_T at the free-end of the support beam creating a moment M_T that balances M, Fig. 2a.

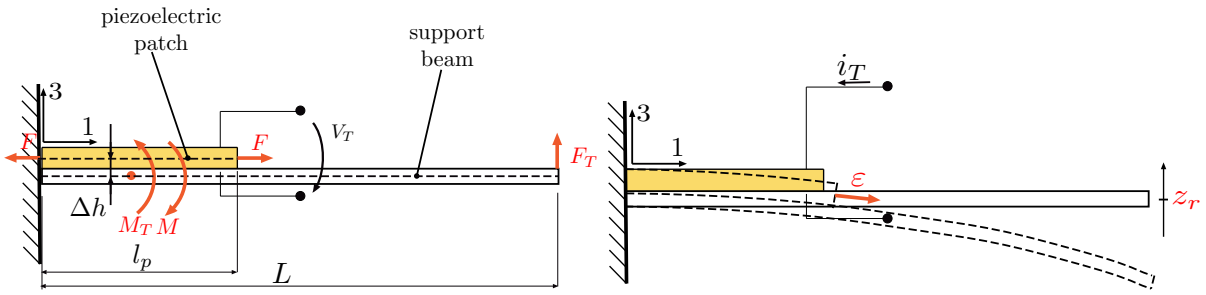

(a) (b)

Figure 2: Piezoelectric cantilever beam schemes for a) the calculation of A and b) B coefficients.

The coefficient that relates F and F_T is derived as follows.

$$M_T + M = 0 \tag{5}$$

$$F_T\big(L - \frac{l_p}{2}\big) + F\Delta h = 0 \tag{6}$$

$$F_T + \frac{\Delta h}{\big(L - \frac{l_p}{2}\big)}F = 0 \tag{7}$$

$$F_T = -\frac{\Delta h}{\big(L - \frac{l_p}{2}\big)}F = -AF \tag{8}$$

$$\Rightarrow A = \frac{\Delta h}{\big(L - \frac{l_p}{2}\big)} \tag{9}$$

where geometric variables are highlighted in figure 2a.

3.1.2 inverse effect: B coefficient

A displacement z imposed to the free-end of the piezoelectric beam induces a curvature to the neutral surface, see figure 2b. In the hypothesis that the mechanical properties of the piezoelectric material are negligible with respect to that of the support beam material, the neutral surface of the support beam is not shifted, the curvature $\frac{d^2 z_r}{dx^2}$ of the neutral surface of the cantilever beam loaded at the free end and its displacement are:

$$\frac{d^2 z_r}{dx^2} = \frac{F_T}{E_s I_s}(L - x) \tag{10}$$

$$z_r = \frac{L^3}{3E_s I_s}F_T \tag{11}$$

$$\Rightarrow \frac{d^2 z_r}{dx^2} = \frac{3}{L^3}z_r(L - x) \tag{12}$$

Being the patch at a distance Δh from the neutral surface of the support beam, strain is induced along the 1 direction. The average strain is obtained by integrating $\delta_1(x)$ along the PE patch:

$$\delta_1(x) = -\Delta h\frac{d^2 z_r}{dx^2} = -\Delta h\frac{3}{L^3}z_r(L - x) \tag{13}$$

$$\delta_1 = -\frac{3\Delta h\, z_r}{L^3}\frac{1}{l_p}\int_0^{l_p}(L - x)dx = -\frac{3\Delta h}{L^3}z_r\big(L - \frac{l_p}{2}\big) \tag{14}$$

The piezoelectric patch elongation is:

$$\varepsilon = l_p \delta_1 = -l_p \frac{3\Delta h}{L^3}\big(L - \frac{l_p}{2}\big) z_r = -B z_r \tag{15}$$

$$\Rightarrow B = l_p \frac{3\Delta h}{L^3}\big(L - \frac{l_p}{2}\big) \tag{16}$$

$$\tag{17}$$

3.2 Electromechanical PE equations in terms of beam variables

By the computation of the geometrical coefficients A and B it is now possible to relate the beam and the patch quantities as:

$$F_T = -AF \tag{18}$$

$$\dot{\epsilon} = -B\dot{z}_r \tag{19}$$

The coupling equations of the piezoelectric patch used in 31 mode, eq.(4), become the equations of the piezoelectric transducer consisting of a the patch bonded on a cantilever beam:

$$\begin{cases} F_T &= -A\,F = -A(c_p\dot{\varepsilon} + k_p\varepsilon + \Gamma V_T) = c_{p\_eq}\,\dot{z}_r + k_{p\_eq}\,z_r - \alpha V_T \\ i_T &= \Gamma\dot{\varepsilon} - C_p\dot{V}_T - \frac{V_T}{R} = -\beta\dot{z}_r - C_p\dot{V}_T - \frac{V_T}{R} \end{cases} \tag{20}$$

where coefficients are relevant to patch behaviour when it is referred to the relative displacement of the tip mass and are:

- F_T is the force acting on the tip mass along z direction due to the piezoelectric patch;
- $k_{p\_eq} = ABk_p$ is the equivalent mechanical stiffness;
- $c_{p\_eq} = ABc_p$ is the equivalent damping;
- i_T and V_T are the output current and voltage of the transducer;
- $\alpha = A\Gamma$ and $\beta = B\Gamma$ are the electromechanical coupling coefficients of the transducer respectively for the reverse and forward piezoelectric effect;
- C_p and R are the clamped capacitance and the dielectric loss respectively.

4 GOVERNING EQUATIONS OF THE SYSTEM

Equations (20) describe dynamics of the patch but are not taking into account the presence of the beam, whose mechanical characteristics must be considered in the overall behaviour of the system. The mass, damping and elastic parameters of the two bonded systems will be merged by considering that they are both contributing to the model simulations formulated in terms of z_r.

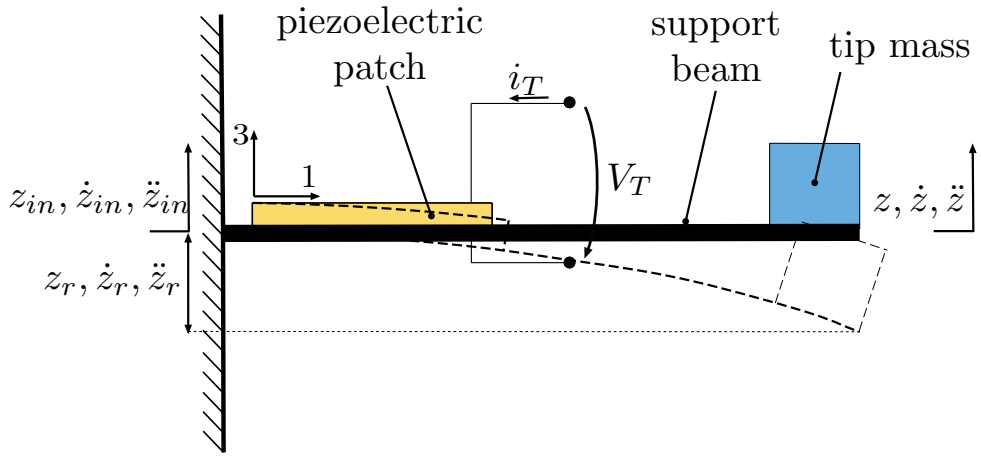

Figure 3: Structure of the vibrating harvester.

The complete simulated structure is outlined in figure 3 where a tip mass is added to enhance harvesting capabilities.

The parameters that must be combined together are:

- *system mass*: the overall mass is given by the combination of the mass m_p of the patch, m_s of the supporting beam and m_t of the tip mass. Since the position of the beam and patch are not coincident with that of the tip, a geometric coefficient θ is used to add them up correctly.

$$m = m_t + \theta(m_s + m_p) \tag{21}$$

- *system stiffness*: the overall stiffness of the mechanical system k_m is given by the contribution due to the bending stiffness k_s of the cantilever beam and the contribution due to the bonded piezoelectric patch k_p:

$$\begin{aligned} k_m &= k_s + k_{p\_eq} \\ k_s &= \tfrac{3E_sI_s}{L^3} \\ k_{p\_eq} &= A\,B\,k_p \end{aligned} \tag{22}$$

  where E_s is the elastic modulus of the cantilever beam and $I_s = \frac{b_s h_s^3}{12}$ is its second moment of inertia.

- *system damping*: the overall damping of the mechanical system c_m is given by the sum of the contribution of the cantilever beam c_s and the one of the piezoelectric patch c_p.

- *coupling electromechanical coefficients*: the two physical domains are coupled by the force due to the *electrical* effects $F_{el} = A\Gamma V_T = \alpha V_T$. Physical dimensions of α are N/V. The current generated by patch deformation along 1 direction is $i_p = B\Gamma\dot{z}_r = \beta\dot{z}_r$. Physical dimensions of β are As/m;

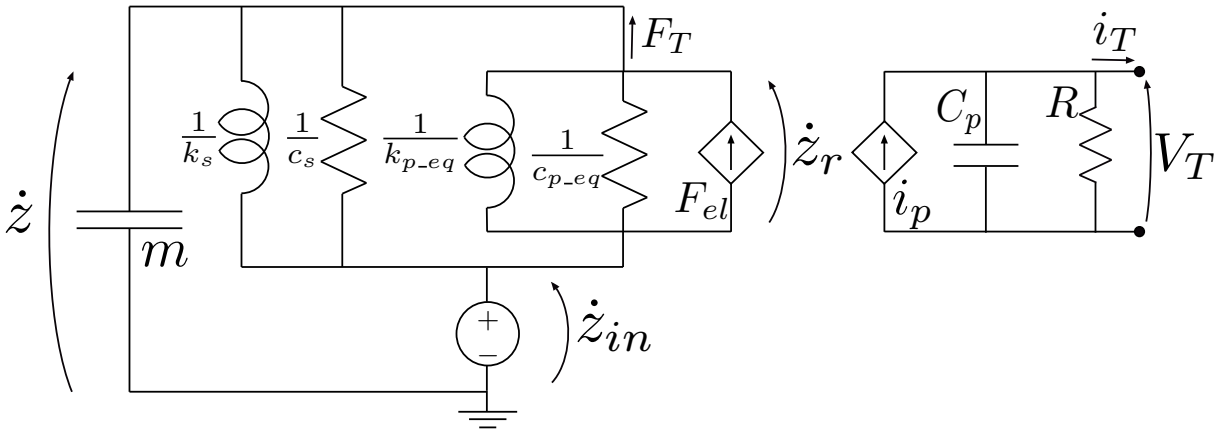

Figure 4: Equivalent circuit of the electromechanical conversion.

- *system excitation*: the system is free to vibrate when a displacement z_{in} is applied to the clamped end of the beam. The mass dynamic is written in terms of the relative position $z = z_r + z_{in} \Rightarrow m\ddot{z} = m\ddot{z}_r + m\ddot{z}_{in}$. The last term is known and can be considered as the forcing term of the equation [4].

The governing equations of the system can thus be written as

$$\begin{cases} m\ddot{z}_r + c_m\dot{z}_r + k_m z_r + F_{el} = -m\ddot{z}_{in} \\ i_T = i_p - C_p\dot{V}_T - \frac{V_T}{R} \end{cases} \tag{23}$$

4.1 Electromechanical circuit model

Using these assumptions the system dynamics can be described by the electromechanical circuit outlined in figure 4.

The dynamic of the mechanical part of the model is described in terms of the concept of *across* or *effort* variables and of *through* or *flow* variables. An across/effort variable is a variable determined by measuring the difference of values acting at the two extreme points of an element or in a specific point. A through/flow variable is a variable transmitted through an element without modification. The product of the two must be a power. By using the Firestones analogy, the mass m is substituted by a grounded capacitor $C = m$, and the spring k_m by an inductor $L = 1/k_m$. The inertial force imposed by the kinematics is substituted by a current source and the electric force by the transducer terminals [5].

The network is shown in open circuit conditions but a R_L load resistor can be connected at the terminals so that it is subject to the electric variables V_T and i_T.

4.2 Power considerations

By multiplying the first of eq. (23) by $\dot{z}_r$ and the second by V_T, the power balance of the mechanical part and of the electrical side is derived:

$$\begin{aligned} \underbrace{-m\ddot{z}_{in}\dot{z}_r}_{input} &= \underbrace{m\ddot{z}_r\dot{z}_r}_{kinetic} + \underbrace{c_m\dot{z}_r^2}_{damping} + \underbrace{k_m\dot{z}_r z_r}_{elastic} + \underbrace{(-\alpha V_T\dot{z}_r)}_{piezoelectric} \\ \underbrace{V_T i_T}_{output} &= \underbrace{(-\beta\dot{z}_r V_T)}_{converted} - \underbrace{C_p\dot{V}_T V_T}_{capacitance} - \underbrace{\frac{V_T^2}{R}}_{piezo\,losses} \end{aligned} \tag{24}$$

The input power of the system, namely the power extracted from the mechanical source and injected in the harvester, consists of the kinetic power of the floating mass, the elastic power stored in the mechanical spring, the power wasted through the mechanical damper and the overall power delivered to the the electric part of the system through the piezoelectric element. The output power, namely the electric power provided to the electrical part of the system, consists of the converted power from the mechanical domain minus the power stored in the clamped capacitance of the piezoelectric patch and that lost by the dielectric.

It is worth noting that the input power of the electrical part, the converted power, is different from the power outgoing the mechanical system due to the piezoelectric coupling. As $\alpha > \beta$, the input power in the electrical part, namely the maximum recoverable, is lower than the power outgoing the mechanical part.

The electromechanical coupling coefficients β and α describe how the transducer relates the mechanical variable $\dot{z}_r$ to the electrical variable i and how the electrical variable V_T is related to the mechanical variable F_{el}. β and α extend the meaning of Γ when a mechanical transformer is interposed between the vibrating system and the transducer piezoelectric patch. In this case the mechanical transformer is represented by the cantilever beam that relates the 1 direction of the piezoelectric patch to the 3 or z direction of the vibrating system through the coefficients A and B.

4.3 Behaviour in short and open circuit conditions

The behaviour of the system can be highlighted in two extreme operating conditions: if output terminals are short circuited the voltage V_T is null and so are the converted power and the direct effect. On the other hand if output terminals are left open all the power is transferred to the conservative element C_p and resulting in an increase system stiffness.

Considering open and short-circuit condition of the electric terminals of the transducer, Fig. 4, two different resonance frequencies exist.
In short circuit, V_T is null, thus no energy is transferred to the electric load and no electrical feedback force acts to the mechanical part. The resonance frequency of the

system depends only on its mechanical properties:

$$k_{SC} = k_m \omega_{SC} = \sqrt{\frac{k_{SC}}{m}} \tag{25}$$

In open circuit, i_T is null and V_T is in phase with z_r. Thus, the controlled force generator acts as a spring k_{el} or, according to the mobility analogy, it can be replaced with an inductor $\frac{C_p}{\alpha\beta}$. It follows a stiffer mechanical system:

$$k_{OC} = \frac{1}{L_{OC}} = k_{SC} + \frac{\alpha\beta}{C_p} > k \tag{26}$$

where an electric stiffness is defined as:

$$k_{el} = \frac{\alpha\beta}{C_p} \tag{27}$$

Higher resonance frequency results:

$$\omega_{OC} = \sqrt{\frac{k_{OC}}{m}} = \omega_{SC} \sqrt{1 + \frac{\alpha\beta}{k_{SC} C_p}} \tag{28}$$

It is worth noting that, in both open and short circuit conditions, the damping effect due to the electric load ($R_L = \infty$ and $R_L = 0$ respectively) is null.

5 EXPERIMENTAL VALIDATION

The model developed in the previous sections has been validated on an experimental setup and evaluation of the accuracy of direct and inverse coefficients has been checked.

5.1 Experimental setup

The support cantilever beam is a stainless steel beam which geometrical features are summarised in figure 5. The patch is 28 mm long and beam is 100 mm long, 25 mm wide, 0.5 mm tick, and consists of two parts: a clamped portion of 40 mm that is locked in the shaker fixture and a free portion of 60 mm that represents the effective oscillating elements. Considering standard stainless steel, $E_s = 180$ GPa, the first flexural mode occurs at 109 Hz.

The tip-mass is obtained clamping the free-end of the beam with two $\varnothing 15 \times 3$ mm magnets in attraction. It results a cylindrical shape mass of $7.95 \cdot 10^{-3}$ kg whose application point on the support beam, with respect to the free-end, is shifted half of the diameters toward the joint. It follows a shorter effective oscillating length of the support beam.
The first flexural mode of the system is at 56 Hz, that falls in the frequency range of interest.

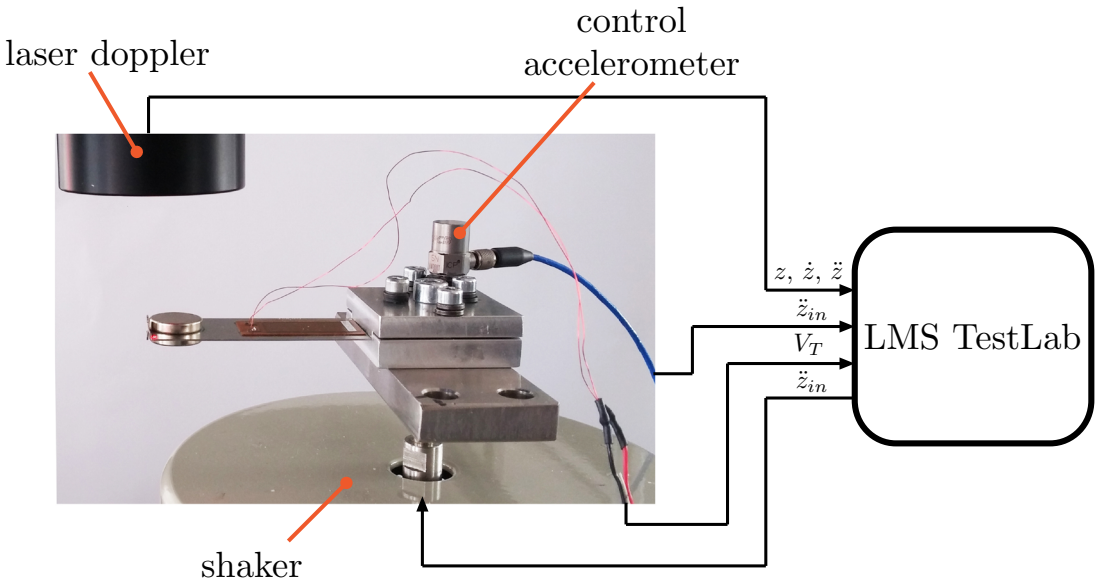

Figure 5: Experimental setup and measurement points connected to the external software *LMS TestLab*.

5.2 Experimental validation of the coupling coefficients

In order to assess experimentally the two coefficients of direct and inverse coupling, the structure is stressed in two extreme conditions: short and open circuit. These two operating conditions allow to highlight the power transfer between the two domains of the energy conversion.

The direct coupling coefficient β has been evaluated in steady state condition following the procedure proposed in [6]. A short circuit configuration is emulated by connecting the piezoelectric patch terminals to a low resistor, $R_L = 110.5\ \Omega$. The electrical feedback on the mechanical part αV_T is almost cancelled. The load resistor impedance is, in fact, at least two orders of magnitude lower than that of the clamped capacitance at the involved frequencies and, thus, the current through C_p is negligible. The induced current $\beta \dot{z}_r$ flows almost entirely through the load resistor so that:

$$i_T = \frac{V_T}{R_L} \cong \beta \dot{z}_r \ \Rightarrow \ \beta = \frac{V_T}{\dot{z}_r R_L} \tag{29}$$

Measuring the amplitude of the output voltage V_T and of the mass relative velocity $\dot{z}_r$, the direct coupling coefficient β is derived. Vibrating mechanical input is applied at the short circuit resonance frequency ω_{SC} considering two acceleration amplitude levels, 0.5 and 0.8 m/s^2. Two slightly different values derive for the direct coupling coefficient, but with relative difference lower than 3%. The mean value is considered and $\beta = 7.993\,10^{-4}$ As/m results.

The reverse coupling coefficient α has been evaluated considering the definition of k_{el},

eq. (27):

$$\alpha = \frac{C_p k_{el}}{\beta} \tag{30}$$

$\alpha = 8.353\,10^{-4}$ N/V results. A second evaluation of α has been performed considering static condition in order to cancel the direct piezoelectric effect. Constant voltage is applied to the transducer terminals. The first of eq. (23) becomes:

$$kz_r + \alpha V_T = 0 \;\Rightarrow\; \alpha = \frac{kz_r}{V_T} \tag{31}$$

and by measuring the mass displacement z_r at equilibrium, α is derived. When $V_T = 15$ V is applied, $z_r = 9.4447\,10^{-6}$ m is measured and $\alpha = 8.418\,10^{-4}$ N/V follows. The difference between the two values obtained for α results lower than 1%. The mean value $\alpha = 8.386\,10^{-4}$ N/V is considered. The ratio between the two values is:

$$\frac{\alpha}{\beta} = 1.049 \tag{32}$$

the ratio between α and β is a pure number.

By computing the geometrical coefficients A and B it is possible to evaluate the same ratio that turns out to be:

$$\frac{A}{B} = 1.162 \tag{33}$$

6 DISCUSSION

The evaluation of the direct and inverse effect of the piezoelectric energy conversion is important to evaluate the potential of energy harvesting. The asymmetry between direct and inverse effect is experimentally observed and its explanation is attempted by addressing the different stress conditions created by electric potential and strain. The direct effect, that is the strain created by the application of electric field, is in fact applying a distributed load on the beam, while the vibration is loading the beam at its tip. Different strain patterns arise and this is explained in terms of the Euler-Bernoulli beam theory. The model obtained is one dimensional as the only geometric variable is the relative tip elongation with respect to the clamped end z_r.

The theoretical model is evaluated versus a experimental mock-up and ratios between the computed and experimental direct and inverse coefficients are evaluated. The theoretical model is able to point out a difference between the α and β values but its estimate is larger than the one obtained experimentally.

This effect can be attributed to some restrictive hypotheses that have been adopted in the theoretical treatment. In particular the uniformity of stresses and properties within the PE patch are to be investigated in deeper details. Also boundary conditions of the bonded patch on the beam could be not ideal as supposed. These aspects will be investigated in future researches.

Acknowledgents

Authors would like to thank the help of the team of Prof. Lauric Garbuio of the Grenoble Institute of Technology (G2Elab) for the experimental activity on the piezoelectric arrangement.

References

[1] Thomas Daue and Jan Kunzmann. Energy harvesting systems using piezo-electric mfcs. In *2008 17th IEEE International Symposium on the Applications of Ferroelectrics*, volume 1, pages 1–1. IEEE, 2008.

[2] Elvio Bonisoli, Maurizio Repetto, Nicolo Manca, and Alessandro Gasparini. Electromechanical and electronic integrated harvester for shoes application. *IEEE/ASME Transactions on Mechatronics*, ¡not found¿(¡not found¿):1–12, 2017.

[3] Thorsten Hehn and Yiannos Manoli. *Piezoelectricity and Energy Harvester Modelling*, pages 21–40. Springer Netherlands, Dordrecht, 2015.

[4] Elvio Bonisoli, Nicoló Manca, and Maurizio Repetto. Multi-physics optimisation of energy harvesters. *COMPEL: The International Journal for Computation and Mathematics in Electrical and Electronic Engineering*, 34(5):1392–1403, 2015.

[5] P Gardonio and MJ Brennan. *Mobility and impedance methods in structural dynamics*, volume 9. chapter, 2004.

[6] Aldo Romani, Rudi Paolo Paganelli, Enrico Sangiorgi, and Marco Tartagni. Joint modeling of piezoelectric transducers and power conversion circuits for energy harvesting applications. *IEEE Sensors Journal*, 13(3):916–925, 2013.

VII International Conference on Computational Methods for Coupled Problems in Science and Engineering
COUPLED PROBLEMS 2017
M. Papadrakakis, E. Oñate and B. Schrefler (Eds)

APPLICATION OF LOCAL RBF COLLOCATION METHOD TO PREDICTION OF MECHANICS-RELATED PHENOMENA DURING DC CASTING OF ALUMINIUM ALLOYS

BOŠTJAN MAVRIČ* and BOŽIDAR ŠARLER*,†

*Institute of Metals and Technology
Lepi pot 11, SI-1000 Ljubljana, Slovenia
e-mail: bostjan.mavric@imt.si, web page: http://www.imt.si

†Faculty of Mechanical Engineering, University of Ljubljana
Aškerčeva 6, SI-1000 Ljubljana, Slovenia
e-mail: bozidar.sarler@fs.uni-lj.si, web page: http://www.fs.uni-lj.si

Key words: coupled fluid flow and solid mechanics, DC casting, Radial Basis Functions, Viscoplasticity, Solidification, Local Radial Basis Function Collocation Method

Abstract. A meshless local collocation method using radial basis functions (LRBFCM) has been developed to model the thermomechanical phenomena during the process of DC casting. The model uses elastic-viscoplastic constitutive relations to describe the inhomogeneous material below the coherency isotherm. It is coupled with the results of the fluid flow model, which is used to determine the computational domain and to calculate the thermal strain.

1 INTRODUCTION

Direct chill casting is a widespread technology for casting of aluminium billets and slabs, which are further used for extrusion. The achievement of high quality of the product is difficult since the thermomechanical phenomena that occur during DC casting of aluminium billets can have a significant impact on the quality of the ingot. The main defects caused by thermomechanics are hot tearing and cracking which can occur under specific stress conditions [1].

Because of the widespread use of the process in industry, a significant effort was dedicated to the development of numerical models of the process with the aim of improving the quality of the billet at optimal productivity. This resulted in many numerical models of the process, which consider several aspects of the physical problem and are stated either with the finite-element or the finite-volume method.

In recent years, a new class of methods has emerged and has started to compete with the classic discretization methods. Various meshless methods were successfully used to solve a wide spectrum of scientific and engineering problems. In contrast to the established numerical methods, the meshless methods aim to reduce the complexity of the structure associated with the node arrangement, removing the need for polygonization of the computational domain.

The LRBFCM, which is used in the present paper, has been already successfully applied to several coupled transport problems in solidification. The first were models of continuous casting of steel [2] including the influence of electromagnetic braking [3, 4]. Later on, the method was improved with a sophisticated adaptive algorithm allowing for the design of high-accuracy macrosegregation models [5].

Although the first implementations of the method dealt with solid mechanics problems [6], a lot of effort was invested into development of the method before the application of the method to the mechanical problems in metal processing. The first use was in a model of hot-rolling process, coupling the thermal transport with the large plastic deformations [7].

In this contribution we expand the mentioned efforts by developing a meshless model of thermomechancis during DC casting of aluminium alloys. The model describes the behavior of the non-homogeneous, viscoplastic material in steady state conditions. The model is one-way coupled to the results of the associated meshless heat and momentum transfer model [13]. This model supplies the thermomechanical model with the steady state values of liquid fraction, pressure, temperature and electromagnetic force. The supplied fields are used by the thermomechanical model to determine the geometry of the computational domain and the thermal strain, which is the driving term.

2 GOVERNING EQUATIONS

The thermomechanical model is stated in small-strain approximation and considers three contributions to the total strain: the elastic strain $\boldsymbol{\varepsilon}^e$, the viscoplastic strain $\boldsymbol{\varepsilon}^p$ and the thermal strain $\boldsymbol{\varepsilon}^t$. The thermal strain is the driving term of the model and is given by

$$\boldsymbol{\varepsilon}^t(T) = \boldsymbol{I} \int_{T_s}^{T} \alpha(T) \mathrm{d}T = \boldsymbol{I}\varepsilon^t, \tag{1}$$

where T_s is the solidus temperature and $\alpha(T)$ is the temperature dependent coefficient of thermal expansion. The viscoplastic strain rate

$$\dot{\boldsymbol{\varepsilon}}^p = -\boldsymbol{v}_{cast}\nabla\boldsymbol{\varepsilon}^p + \frac{3\boldsymbol{\tau}}{2\sigma_e}\dot{\varepsilon}_0(T, \boldsymbol{\sigma}). \tag{2}$$

is determined by two terms. The first term is the advection term, which is the result of the Eulerian description of the material moving with the casting velocity $\boldsymbol{v}_{cast}$ through

the computational domain. The second term describes the contribution of the viscoplastic deformation, caused by the stresses in the billet. In the expression, the stress is present in the octahedral stress tensor $\boldsymbol{\tau} = \boldsymbol{\sigma} - \boldsymbol{I}\mathrm{tr}\boldsymbol{\sigma}/3$ and the effective stress $\sigma_e = \sqrt{2\boldsymbol{\tau} : \boldsymbol{\tau}/3}$. The effective strain rate $\dot{\varepsilon}_0(T, \boldsymbol{\sigma})$ is given by

$$\dot{\varepsilon}_0(T, \boldsymbol{\sigma}) = \begin{cases} A \exp\left(-\dfrac{Q}{RT}\right)\left(\dfrac{\sigma_e}{\sigma_0}\right)^n, & \text{if } T < T_s \\ A'\left(\dfrac{\sigma_e}{\sigma_0'}\right)^{n'}, & \text{otherwise.} \end{cases} \tag{3}$$

Two variations of the Norton-Hoff's law are used to describe the behavior of the material in the mushy zone ($T_s < T < T_{coh}$) and in the solid material ($T < T_s$) as proposed in [8]. By expressing the total strain with displacement vector $\boldsymbol{u}$, the following equilibrium equation is obtained

$$\begin{aligned} 0 = & G\nabla^2\boldsymbol{u} + (G+\lambda)\nabla(\nabla\cdot\boldsymbol{u}) \\ & + \nabla\lambda(\nabla\cdot\boldsymbol{u}) + \nabla G\big(\nabla\boldsymbol{u} + (\nabla\boldsymbol{u})^T\big) \\ & - \nabla\cdot(2G\boldsymbol{\varepsilon}^p) - \nabla\big((3\lambda+2G)\varepsilon^t\big) \\ & + \boldsymbol{f}_g. \end{aligned} \tag{4}$$

The equation accounts for inhomogeneous material properties and coupling of deformation field with thermal and plastic strain. The dependence of Lame parameters λ and G on temperature is obtained from JMatPro database for the considered alloy [14]. The body force $\boldsymbol{f}_g$ is the gravitational body force.

2.1 Boundary conditions

The boundary conditions of the problem and the computational domain are illustrated in Figure 1. The problem is axisymmetric, so the cylindrical coordinate system with the coordinates (r, z) is used. The computational domain is determined by the extent of the computational domain of the heat and mass transfer model. At the top, the computational domain is limited by the position of the isoline at coherency temperature T_{coh}, above which the material cannot transfer stress and is governed by the equations of fluid dynamics.

At the coherency isoline, the material has to support the metalostatic pressure of the liquid $\boldsymbol{t} = -p\boldsymbol{n}$, where p is the pressure of the liquid calculated by the heat and momentum transfer model. The center of the billet coincides with the symmetry axis, where $u_r = 0$ and $\frac{\partial u_z}{\partial r} = 0$. At the bottom of the computational domain we set $u_z = 0$ and $t_r = 0$. The outer surface is traction free $\boldsymbol{t} = 0$ except at the top, where the contact with the mold is possible. In that area, an iterative method is used to satisfy the boundary conditions $u_r \leq 0$ and $t_r \leq 0$.

There are no specific boundary conditions for the viscoplastic strain for the most of the boundary and the rate equation is used to calculate the values on the boundary also. The

only exception to this is the top boundary, where the material is solidifying. We assume that the freshly solidified material does not accumulate any plastic strain by setting $\boldsymbol{\varepsilon}^p = 0$ at the top boundary.

3 NUMERICAL METHOD

3.1 Spatial discretization

The spatial discretization is in this contribution achieved by the LRBFCM. Elaboration of the method for linear thermoelasticity is given in [9, 10].

To formulate the method, a node arrangement is constructed with points positioned in the domain Ω and on boundary Γ. For each point in the computational domain $\boldsymbol{r}_l$ a set of nearby points, called local subdomain, is selected. The points in the subdomain are used to construct the local interpolation of the solution. The selection of the subdomain induces mapping ${}_ls(k)$, which maps the local index $k = 1, \ldots, {}_lN$ in the subdomain l to the global index in the range $1, \ldots, N$, where N is the total number of points in the node arrangement.

On each subdomain an interpolation of the unknown solution $\boldsymbol{y}$ is constructed by using multiquadrics (MQ). A MQ centered at node l is given by

$$\Phi_l(\boldsymbol{r}) = \sqrt{\frac{\epsilon^2}{h_l^2}|\boldsymbol{r} - \boldsymbol{r}_l|^2 + 1}. \tag{5}$$

Here ϵ is the shape parameter and h_i is the size of the subdomain on which the interpolation is being constructed. It is defined as

$$h_l = \sqrt{\sum_{j=1}^{{}_lN} \frac{|\boldsymbol{r}_{{}_ls(j)} - \boldsymbol{r}_l|^2}{{}_lN - 1}}. \tag{6}$$

Since MQs are only conditionally positively definite, the interpolation problem formulated solely by MQs might be ill-conditioned. The remedy is to augment the interpolation problem with m monomials $p_i(r)$, $i = 1, \ldots, m$, which constitute a basis for the polynomials of certain order. The approximation of an arbitrary field $\boldsymbol{y}$ is then given by

$$y_\xi(\boldsymbol{r}) \approx \sum_{i=1}^{{}_lN} {}_l\alpha_{i,\xi}\Phi_{{}_ls(i)}(\boldsymbol{r}) + \sum_{i=1}^{m} {}_l\alpha_{({}_lN+i),\xi}p_i(\boldsymbol{r}) = \sum_{i=1}^{{}_lN+m} {}_l\alpha_{i,\xi}\Psi_i(\boldsymbol{r}). \tag{7}$$

Here l is the index of the subdomain centered on the node closest to the evaluation point $\boldsymbol{r}$. The index $\xi = 1, \ldots, n_d$ is running over the components of the physical field that is being interpolated. In this equation the basis function $\Psi_i(\boldsymbol{r})$ is implicitly defined. It is either MQ or a monomial, depending on the value of i.

The values of the coefficients ${}_l\alpha_{i,\xi}$ are determined by solving an linear system $A\alpha = \gamma$, where the components of A are

$${}_lA_{ji,\xi\chi} = \begin{cases} \Psi_i(\boldsymbol{r}_{{}_ls(j)})\delta_{\xi\chi} & \text{if} \quad \boldsymbol{r}_{{}_ls(j)} \in \Omega \\ \mathcal{B}_{\xi\chi}(\boldsymbol{r}_{{}_ls(j)})\Psi_i(\boldsymbol{r}_{{}_ls(j)}) & \text{if} \quad \boldsymbol{r}_{{}_ls(j)} \in \Gamma \\ p_j(\boldsymbol{r}_{{}_ls(i)})\delta_{\xi\chi} & \text{if} \quad j \geq {}_lN \quad \text{and} \quad i \leq {}_lN \\ 0 & \text{otherwise} \end{cases} \tag{8}$$

and the elements of the right-hand side vector γ by

$${}_l\gamma_{j,\xi} = \begin{cases} y_\xi(\boldsymbol{r}_{{}_ls(j)}) & \text{if} \quad \boldsymbol{r}_{{}_ls(j)} \in \Omega \\ b_\xi(\boldsymbol{r}_{{}_ls(j)}) & \text{if} \quad \boldsymbol{r}_{{}_ls(j)} \in \Gamma \\ 0 & \text{if} \quad j \geq {}_lN \end{cases}. \tag{9}$$

If a point in a subdomain lies on the boundary, linear boundary conditions of the form $\sum_\xi \mathcal{B}_{\chi\xi}(\boldsymbol{r})y_\xi(\boldsymbol{r}) = b_\chi(\boldsymbol{r})$ are included in the local interpolation, forcing the local interpolation to analytically satisfy the boundary conditions.

From this construction, the result of applying a linear differential operator $\mathcal{D}$ to the local interpolation is

$$\sum_{\chi=1}^{n_d} \mathcal{D}_{\xi\chi}(\boldsymbol{r}_l)y_\chi(\boldsymbol{r}_l) \approx \sum_{k=1}^{{}_lN+m} \sum_{\chi=1}^{n_d} {}_l\gamma_{k,\chi} \sum_{i=1}^{{}_lN+m} \sum_{\zeta=1}^{n_d} {}_lA^{-1}_{ik,\zeta\chi}\mathcal{D}_{\xi\zeta}\Psi_i(\boldsymbol{r}_l). \tag{10}$$

By introducing discretization coefficients ${}_lw_{k,\xi\chi}$ given by

$${}_lw_{k,\xi\chi} = \sum_{i=1}^{{}_lN+m} \sum_{\zeta=1}^{n_d} {}_lA^{-1}_{ik,\zeta\chi}\mathcal{D}_{\xi\zeta}\Psi_i(\boldsymbol{r}_l). \tag{11}$$

this gives

$$\mathcal{D}\boldsymbol{y}(\boldsymbol{r})_\xi = \sum_{k=1}^{{}_lN+m} \sum_{\chi=1}^{n_d} {}_l\gamma_{k,\chi l}w_{k,\xi\chi}, \tag{12}$$

an expression similar to the finite-difference type of methods.

3.2 Time discretization

The viscoplastic strain rate equation causes the problem to be time-dependent and requires use of a time discretization scheme. In this paper, the implicit Euler method is used. The resulting system of nonlinear equations is solved simultaneously with the stress equilibrium equations. The unknowns are u_r, u_z, ε^p_{rr}, ε^p_{rz}, ε^p_{zz} and $\varepsilon^p_{\phi\phi}$.

To obtain the solution, Bouaricha tensor method is used. The linear solves required by the method are performed by FGMRES preconditioned by PARDISO solves with Jacobian that is evaluated at the start of each time step.

Casting parameter	Value
Melt temperature	730 °C
Casting speed	80 mm/min
DC water temperature	20 °C
DC water flux	7 m^3/h

Table 1: Casting parameters used in HMTM of DC casting of Al-Cu alloys.

Law parameter	Value
A	$9 \cdot 10^5\,s^{-1}$
Q	$145\,kJ/kg$
n	3.8
σ_0	4 MPa
A'	$10^{-6}\,s^{-1}$
n'	4
σ_0'	1 MPa

Table 2: Parameters of the viscoplastic constitutive law given by equation (3).

4 RESULTS

The unknown displacement vector and viscoplastic strain are the primary results of the model. They are illustrated in figures 2 and 3 for the Al 4% Cu alloy. The material properties and process parameters are given in tables 2 and 1, respectively. The plots in the figures demonstrate the typical results of the model.

Because of the thermal contraction, the component u_r is negative throughout the billet, except for a thin strip at the top of the mushy zone. The component negative values of u_z are caused by thermal contraction and the gravitational force, combined with the fact that the z coordinate of the bottom boundary is kept fixed.

The components of the plastic strain have a more complicated spatial dependence. Most of the changes occur in the mushy zone or immediately below it. No changes of the plastic strain components outside this area are the result of the exponential damping of the viscoplastic strain rate as temperature decreases. Below this area, the r profiles of the stress components dependence remain constant.

The impact of the mold contact can be seen in the plots of components ε^p_{rr} and ε^p_{zz} in figures 3a and 3b, respectively. The thin strip of high plastic strain at the top of the mushy zone near the outer surface of the billet is caused by the compressive forces caused by the melt pressure. They result in compressive strain in the r direction and extension in the z direction because of the volume-preserving nature of the plastic flow.

By studying the profile of ε^p_{rz} shown in Figure 3d, we can gain insight on the conditions that are experienced by the material as it travels through the computational domain. Lets track a thin ring of material with radius $r = 0.1$ m. The material in the ring becomes coherent at $z = -0.10$m. and starts to move downwards with the casting velocity. As it solidifies, it is positioned on the innermost part of the solid shell. The outer surface of the shell is cooled as it moves downwards, causing it to contract. This contraction puts the observed ring under compressive stress in circumferential direction, forcing it to contract. As enough material is accumulated on the inside of the shell, the observed ring changes its role. It starts to cool faster that the newly accumulated solid on the interior, which

results in it being subjected to tensile stress conditions. This results in the increase in the plastic strain, which can only go on while the ring is at high enough temperature in the area above $z = -0.25$ m. Below this position, the strain remains constant, since the stresses there are too small to cause the plastic deformation.

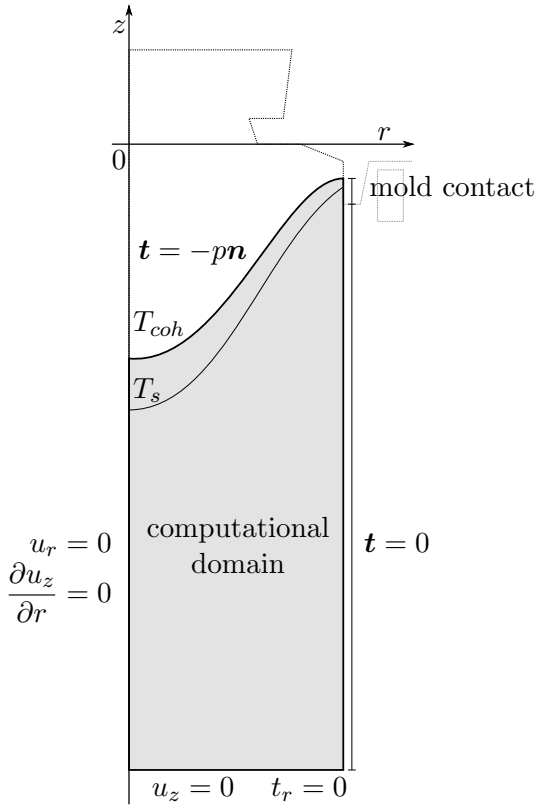

Figure 1: Geometry of the DC casting model and the boundary conditions.

5 CONCLUSIONS

The model presented in this paper is capable of modeling the viscoplastic stress and strain during the process of DC casting. The model couples the thermomechanical model of a viscoplastic solid with the steady state results from the model of heat and mass transfer. The results given in terms of displacement and viscoplastic strain show the behavior expected from the casting practice.

In the future, the model will be used to analyze the effect of casting parameters on hot-tearing susceptibility and on formation of porosity.

ACKNOWLEDGMENTS

The research presented in this paper was funded by the Young Researcher program by Slovenian Ministry of Higher Education, Science and Sport and by companies Impol,

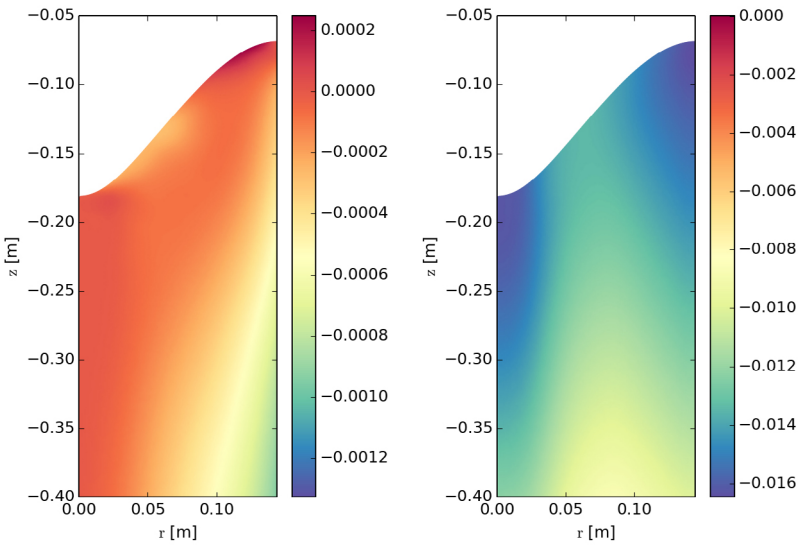

(a) u_r **(b)** u_z

Figure 2: Displacement field.

Slovenska Bistrica and Štore Steel.

REFERENCES

[1] Eskin, D.G. *Physical Metallurgy of Direct Chill Casting of Aluminum Alloys*. Taylor & Francis, (2008).

[2] Vertnik, R. and Šarler, B. Simulation of continuous casting of steel by a meshless technique *International Journal of Cast Metals Research* (2009) **22**:311–313.

[3] Mramor, K. and Šarler, B. A meshless model of electromagnetic braking for the continuous casting of steel *Materials and Technologies* (2015) **49**:961–967.

[4] Mramor, K., Vertnik, R. and Šarler, B. Low and intermediate Re solution of lid driven cavity problem by local radial basis function collocation method *CMES: Computer Modeling in Engineering & Sciences* (2013) **92**:327–352.

[5] Kosec, G., Založnik, M., Šarler, B. and Combeau, H. A meshless approach towards solution of macrosegregation phenomena *Computers, Materials and Continua* (2011) **22**:169–195.

[6] Lee, C. K., Liu, X. and Fan, S. C. Local multiquadric approximation for solving boundary value problems *Computational Mechanics* (2003) **30**:396–409.

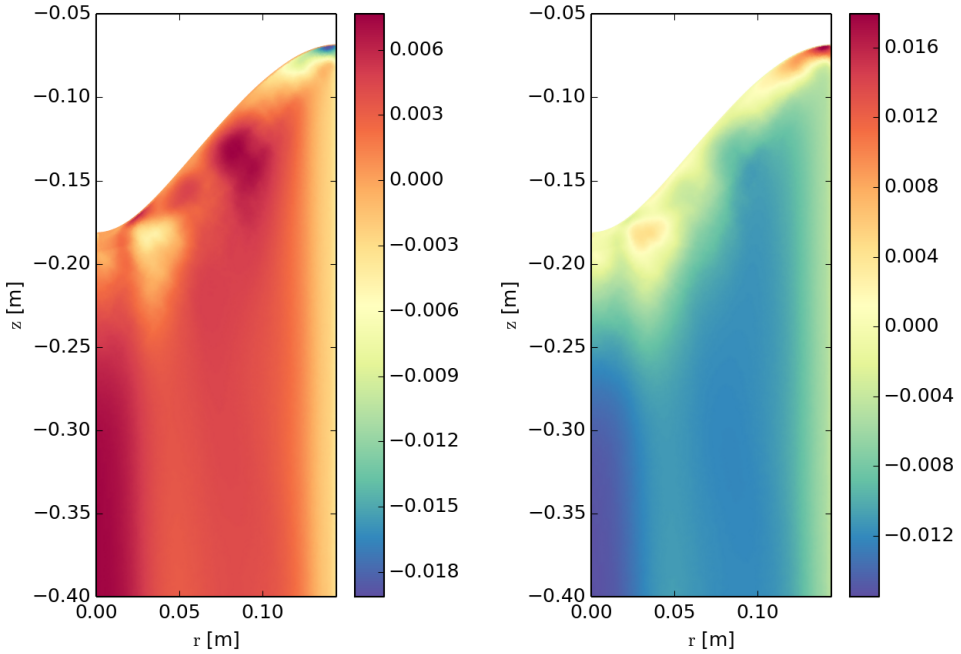

(a) ε^p_{rr} **(b)** ε^p_{zz}

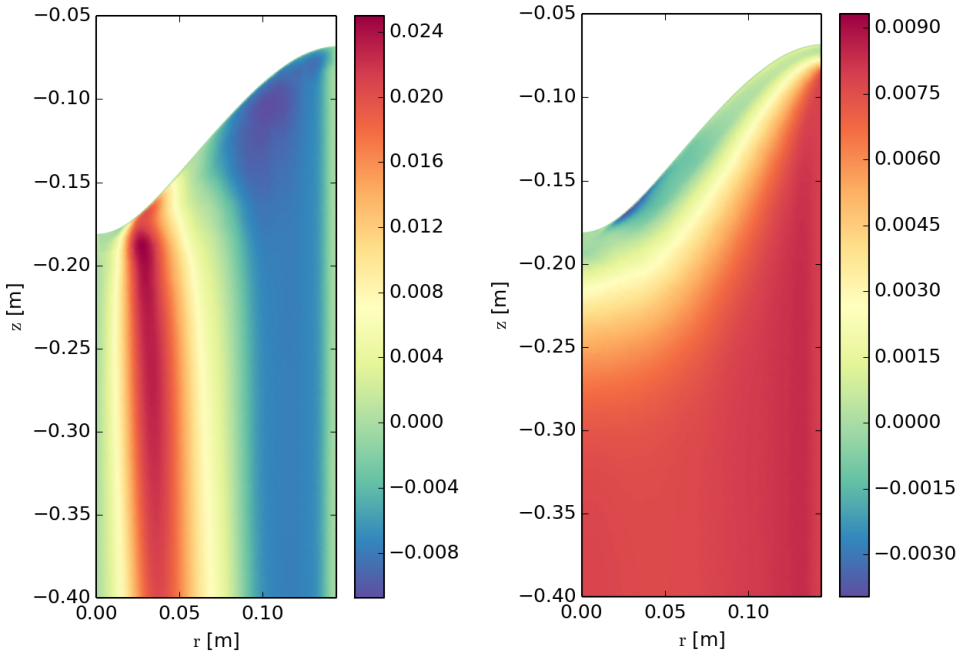

(c) ε^p_{rz} **(d)** $\varepsilon^p_{\phi\phi}$

Figure 3: Viscoplastic strain.

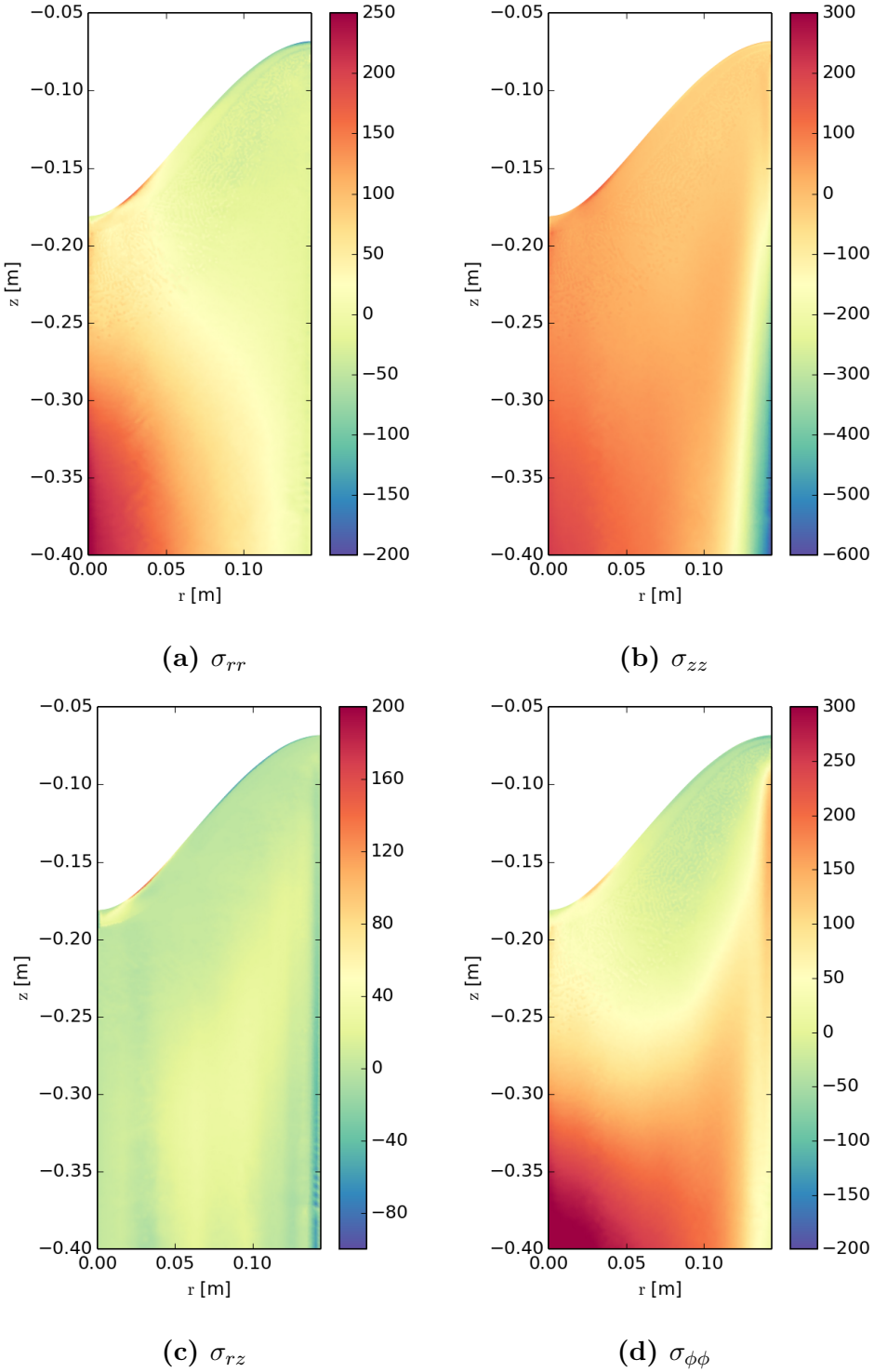

(a) σ_{rr} **(b)** σ_{zz}

(c) σ_{rz} **(d)** $\sigma_{\phi\phi}$

Figure 4: Stress tensor components in MPa.

[7] Hanoglu, U. and Šarler, B. Simulation of Hot Shape Rolling of Steel in Continuous Rolling Mill by Local Radial Basis Function Collocation Method *CMES: Computer Modeling in Engineering & Sciences* (2015) **109**:447–479.

[8] Nallathambi, A. K., Tyagi, M., Specht, E. and Bertram, A. Thermomechanical simulation of direct chill casting *Transactions of The Indian Institute of Metals* (2011) **64**:13–19.

[9] Mavrič, B. and Šarler, B. Local radial basis function collocation method for linear thermoelasticity in two dimensions *International Journal of Numerical Methods for Heat & Fluid Flow* (2015) **25**:1488–1510.

[10] Mavrič, B. and Šarler, B. Application of the RBF collocation method to transient coupled thermoelasticity *International Journal of Numerical Methods for Heat & Fluid Flow* (2017) **27**(5).

[11] Ludwig, O., Drezet, J. M., Martin, C. L. and Suery, M. Rheological behavior of Al-Cu alloys during solidification constitutive modeling, experimental identification, and numerical study *Metallurgical and Materials Transactions A* (2005) **36**:1525–1535.

[12] Suyitno, O., Kool, W. H. and Katgerman, L. Integrated Approach for Prediction of Hot Tearing *Metallurgical and Materials Transactions A* (2009) **40**:2388–2400.

[13] Hatić, V., Mavrič, B., Košnik, N., and Šarler, B. Simulation of direct chill casting under the influence of a low-frequency electromagnetic field *Applied Mathematical Modelling* (2017) (accepted).

[14] Saunders, N., Guo, U. K. Z., Li, X., Miodownik, A. P. and Schillé, J.-Ph. Integrated Approach for Prediction of Hot Tearing *JOM* (2003) **55**:60–65.

VII International Conference on Computational Methods for Coupled Problems in Science and Engineering
COUPLED PROBLEMS 2017
M. Papadrakakis, E. Oñate and B. Schrefler (Eds)

INFLUENCE OF CURRENT AND FREQUENCY ON ELECTROMAGNETIC STIRRING IN CONTINUOUS CASTING OF STEEL

MARJAN MAČEK*, ROBERT VERTNIK*† AND BOŽIDAR ŠARLER*‡

* Laboratory for Simulation of Materials and Processes
Institute of Metals and Technology (IMT)
Lepi pot 11, SI-1000 Ljubljana, Slovenia
e-mail: marjan.macek@imt.si, web page: http:// http://www.imt.si/

† Štore Steel d.o.o., Quality and Development
Železarska cesta 3, SI-3220 Štore, Slovenia
e-mail: robert.vertnik@store-steel.si, web page: http://www.store-steel.si/

‡ Laboratory for Fluid Dynamics and Thermodynamics
Faculty of Mechanical Engineering, University of Ljubljana
Aškerčeva 6, SI-1000 Ljubljana, Slovenia
e-mail: bozidar.sarler@fs.ung-lj.si, web page: http://www.fs.uni-lj.si/

Keywords: Continuous casting, Electromagnetic stirring, Steel, Meshless methods.

Abstract.
The purpose of this paper is a multiphysics simulation of 3D temperature and velocity fields in continuous casting of steel under the influence of electromagnetic stirring by a combined meshless - finite element method approach. The transport phenomena are calculated by a meshless local radial basis function collocation technique and the magnetic force by the finite element method solver Elmer. The electromagnetic stirring increases the mixing in the molten steel. The thermal gradient is sharper and solidification is faster along the strand. The results are similar to other publications in the field. The local radial basis function collocation method is for the first time applied to 3D continuous casting problem with mold electromagnetic stirring.

1 INTRODUCTION

In continuous casting (CC) of steel, the molten metal is poured into the water-cooled mold, where it partially solidifies. Solidified shell is strong enough to withstand the ferrostatic pressure when it is pulled out from the mold. The mechanical properties of the product depend on many different variables ranging from billet chemical composition and size to process parameters such as cooling rate, casting speed, submerged entry nozzle (SEN) position and details of the fluid flow of the molten steel [1].

Many defects can occur in CC, such as surface defects, inclusions, and segregation, and may lead to unacceptable quality. In addition to the proper tuning of the casting parameters (temperature, velocity, primary and secondary cooling rate) electromagnetic stirring (EMS) is another instrument to achieve an enhanced quality. EMS promotes the columnar to equiaxed

transition, reduces segregation and improves the surface quality. Different positions of stirrer are possible, but most widely used is the mold electromagnetic stirring (M-EMS) since mechanical properties are mostly determined in the mold region [1, 2]. Since the optimal stirrer parameters are different for each plant, each casting machine has to be calibrated separately [3].

The fluid flow in CC was studied experimentally with water instead of steel, since it has a similar kinematic viscosity as molten steel, but is not suitable for electromagnetic stirring (EMS), since it is not conductive. There are some experiments with mercury but are not practical on an industrial scale. The experiments are usually used only to test new ideas and phenomena and not for parameter optimization [4]. Further, measurements during casting are not practical, if even possible, hence numerical models are of great necessity [1].

The first models for EMS were analytical or semi-analytical [4]. The first pure numerical models were made by Fujisaki [5]. Similar studies of modeling more complex geometries, closer to the industrial setting were made [6]. In recent years the discussed multiphysics field expanded drastically, which reflects in a vast number of publications regarding different stirrers, strand shapes and alloys [3, 7–9].

The majority of the mentioned works uses the finite element method for magnetic field calculation and the finite volume method for fluid flow, mainly with commercial software packages such as ANSYS Fluent. Another, a novel class of numerical methods are meshless methods, where the computational domain is discretized into nodes and a further topological connection between them, such as polygonization, is not needed. Local radial basis function collocation method (LRBFCM) [10], a class of meshless methods, was persistently developed for even more complex and realistic problems, eventually modeling macrosegregation and electromagnetic braking during CC of steel [11, 12]. Despite that one of the main advantages of the meshless methods are their simple implementation, irrespective of the number of dimensions, the first LRBFCM 3D calculation of CC is achieved only in 2016 [1]. There exists also other meshless methods (e.g. finite point method, diffuse approximate method, element free Galerkin method), but the present work model only 2D phenomena in CC [13, 14].

In this work, a 3D continuous casting model for finding a steady-state solution is presented for 18 cm×18 cm billet casting machine (Figure 1), installed in Štore-Steel plant. Because it incorporates the electromagnetic stirring and the strand curvature, the model has to incorporate the whole domain, in contrast to the previous 3D study, where due to the symmetry and lack of EM stirring, only one quarter can be modeled [1]. However, in this study, macrosegregation is not modeled.

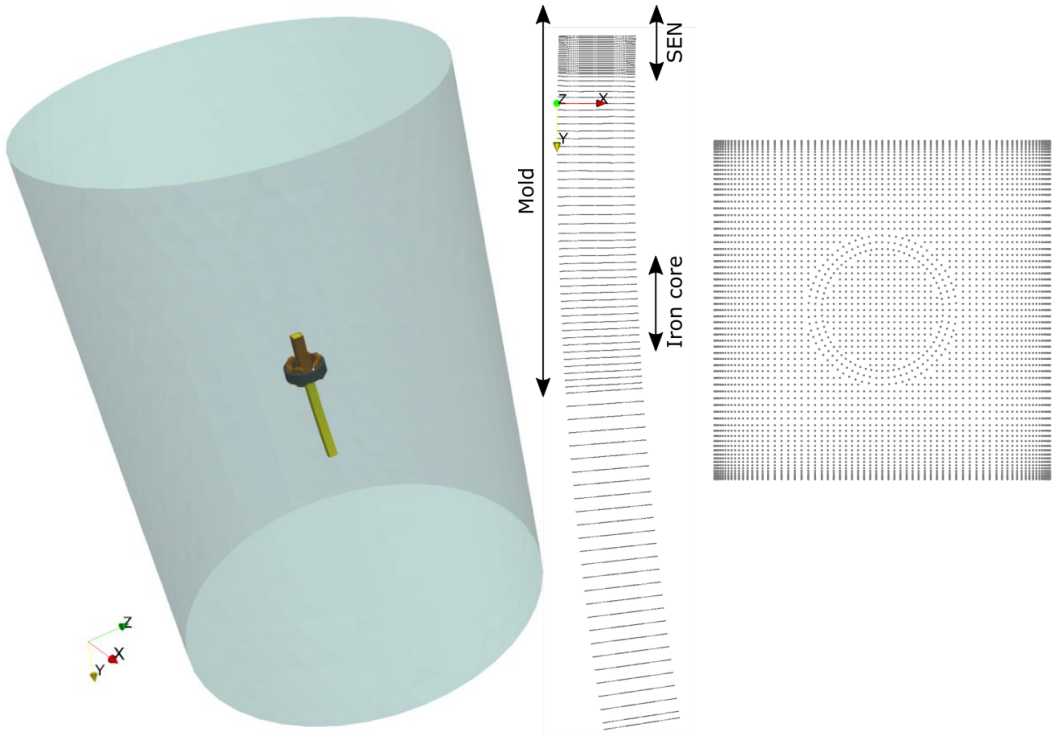

a) b) c)

Figure 1: Geometry used in the magnetic field calculation with the bounding air cylinder (a) and node distribution for casting calculation, where only the strand is modeled (b and c).

2 MAGNETIC STIRRING FORCE

The governing equations for electromagnetic field are

$$\nabla \times \mathbf{E} = -\frac{\partial \mathbf{B}}{\partial t} \tag{1}$$

$$\nabla \times \mathbf{B} = \mu_0 \mathbf{j} \tag{2}$$

$$\nabla \cdot \mathbf{B} = 0. \tag{3}$$

They are in the present work solved primarily with an open source finite element solver Elmer in **A**–V potential form, where the vector potential **A** is discretized into edge elements [15]. The equations (1)–(3) are solved in a frequency domain. Afterward, Lorentz force $\mathbf{f} = \mathbf{j} \times \mathbf{B}$ is calculated. The following assumptions are made [9]:

a) magnetic Reynolds number is small $R_\mathrm{m} = vL/\eta \ll 1$;
b) steel temperature is always above the Curie temperature;
c) the electrical conductance of solidified and molten steel is equal and constant;
d) characteristic time of magnetic force is much shorter than the fluid flow;
e) Joule heating $P = \int |j|^2 / \sigma \mathrm{d}V < 1\ \mathrm{kW}$ is ignored.

The magnetic Reynolds number stands for a ratio of magnetic advection and diffusion, where the magnetic diffusivity is $\eta = 1/\sigma\mu_0$. By inserting material properties of CC shows that the effect of conducting fluid flow is negligible, so a) is true. Because Curie temperature, below which the steel is ferromagnetic, is only about 750 °C (compared to casting temperature 1534 °C), almost no effect is expected since the calculations show that approximately only 0.2 % of the steel in the mold region is bellow Curie temperature. Nevertheless, the temperature profile in the strand has a strong effect on electrical conductivity σ. From the center of the strand to the mold, steel cools for about 700 °C with increasing σ for more than a factor of two. Because the temperature gradient is concentrated in the solidified zone, where the electric current $\mathbf{j}$ is the largest, it is questionable, if c) holds and has to be checked in future works. On the contrary, the temperature effect on the skin depth $\delta = (1/\sigma\omega\mu)^{1/2} \approx 0.3$ m in the strand is insignificant.

The characteristic time of the magnetic force is $1/2f < 0.3$ s, where f is current frequency, and characteristic time of the fluid flow is $L/u > 5$ s. The force has double the frequency of the electric current, since $|\mathbf{f}| \propto fB^2 \propto fI^2$. The assumption d) therefore allows a time-averaging of the Lorentz force to [4, 9]

$$\mathbf{f}_\mathrm{m} = (\mathbf{f}_\mathrm{Re} + \mathbf{f}_\mathrm{Im})/2. \tag{4}$$

Together with the first three assumptions this completely decouples the calculation of the magnetic force from the thermo-fluid calculations.

Consequently, we can have two separate geometries and node arrangements (Figure 1). The first one is used for magnetic force calculation and models the strand, the mold, the stirrer and also the bounding cylinder of air in which $\mathbf{A}$ and V drop to zero, which is also the only boundary condition necessary for EM field calculation. The second node arrangement (only nodes) used for casting simulation contains only the strand.

3 FLUID FLOW

The governing equations for turbulent incompressible fluid flow and heat transport with solidification are [1]

$$\nabla \cdot \mathbf{u} = 0 \tag{5}$$

$$\rho\frac{\partial \mathbf{u}}{\partial t} + \rho\nabla\cdot(\mathbf{uu}) = -\nabla P + \nabla\cdot[2(\mu_\mathrm{L}+\mu_\mathrm{t})\mathbf{S}] - \frac{2}{3}\rho\nabla k - \mu_L K_0 \frac{(1-f_\mathrm{L}^2)}{f_\mathrm{L}^3}(\mathbf{u}-\mathbf{u}_\mathrm{S}) + \mathbf{f}_\mathrm{b} + \mathbf{f}_\mathrm{m} \tag{6}$$

$$\rho\frac{\partial h}{\partial t} + \rho\nabla\cdot(\mathbf{u}h) = \nabla\cdot(\lambda\nabla T) + \rho\nabla\cdot[f_\mathrm{S}(h_\mathrm{L}-h_\mathrm{S})(\mathbf{u}-\mathbf{u}_\mathrm{S})] + \nabla\cdot(f_\mathrm{L}\frac{\mu_\mathrm{t}}{\sigma_\mathrm{T}}\nabla h_\mathrm{L}), \tag{7}$$

which represent mass, momentum and energy conservation, respectively. In the equations u, P, h and T stand for velocity, pressure, enthalpy and temperature. $\mathbf{S}$ is the strain rate tensor. Boussinesq buoyancy force is $\mathbf{f}_\mathrm{b} = \rho[\beta_T \mathbf{g}(T - T_\mathrm{ref})]$, where β_T stands for the thermal expansion coefficient. The magnetic force $\mathbf{f}_\mathrm{m}$ is inserted from (4). Density ρ, morphology constant K_0 in the Darcy term and dynamic viscosity μ are considered constant, but the thermal conductivity $\lambda(T)$ has temperature dependence.

The turbulence is modeled with $k-\epsilon$ turbulence model by using Abe-Kondoh-Nagano (AKN)[16] closure coefficients and put into effect with the third term on RMS in (6) and (7) with effective viscosity $\mu+\mu_\mathrm{t}$, where the turbulent dynamic viscosity is

$$\mu_\mathrm{t}=\rho c_\mu f_\mu \frac{k^2}{\epsilon}. \tag{8}$$

The turbulent kinetic energy k and the dissipation rate ϵ are determined from equations

$$\rho\frac{\partial k}{\partial t}+\rho\nabla\cdot(\mathbf{u}k)=\nabla\cdot\left[\left(\mu_\mathrm{L}+\frac{\mu_\mathrm{t}}{\sigma_k}\right)\nabla k\right]+P_k-\rho\epsilon+\rho D+\mu_\mathrm{L}K_0\frac{(1-f_\mathrm{L}^2)}{f_\mathrm{L}^3}k, \tag{9}$$

$$\rho\frac{\partial \epsilon}{\partial t}+\rho\nabla\cdot(\mathbf{u}\epsilon)=\nabla\cdot\left[\left(\mu_\mathrm{L}+\frac{\mu_\mathrm{t}}{\sigma_\epsilon}\right)\nabla\epsilon\right]+\rho\left(c_{1\epsilon}f_1-c_{2\epsilon}f_2\epsilon\right)\frac{\epsilon}{k}+\rho E+\mu_\mathrm{L}K_0\frac{(1-f_\mathrm{L}^2)}{f_\mathrm{L}^3}\epsilon, \tag{10}$$

where $c_\mu, f_\mu, c_{1\epsilon}, f_1, c_{2\epsilon}, f_2, \sigma_T, \sigma_k,$ and σ_ϵ are the closure coefficients. D and E are additional source terms of the low-Reynolds number turbulent model [17].

Solidification is modeled with lever rule liquid/solid fraction

$$f_\mathrm{L}=1-\frac{1}{1-k_\mathrm{p}}\frac{T-T_\mathrm{L}}{T-T_\mathrm{m}},\quad f_\mathrm{S}=1-f_\mathrm{L}, \tag{11}$$

where k_p is partition coefficient, T_L is liquidus temperature and T_m is melting temperature. Temperature is calculated from enthalpy $h(T)$ [1]

$$h_\mathrm{S}(T)=\int_{T_\mathrm{ref}}^{T}c_{p\mathrm{S}}\mathrm{d}T,\quad h_\mathrm{L}=h_\mathrm{S}(T)+\int_{T_\mathrm{S}}^{T}(c_{p\mathrm{L}}-c_{p\mathrm{S}})\mathrm{d}T+h_\mathrm{m}. \tag{12}$$

First, the equations (5) and (6) are solved by using Chorin fractional step method [14]. Then, h, k and ϵ are updated (7)–(10) with explicit time stepping. Finally, the new values of T, f_L and μ_t are calculated for each node. The steps are repeated until a steady-state is reached [1].

The meshless local radial basis function collocation method (LRBFCM) is employed for the numerical solution procedure. In each (overlapping) subdomain, the involved field Φ (e.g. temperature, pressure, velocity component, turbulent kinetic energy, turbulent dissipation rate) is represented by a set of radial basis function (RBF) $\psi(\mathbf{p})$, over K nodes positioned at nodes $\mathbf{p}_k$ in the subdomain

$$\Phi(\mathbf{p})=\sum_{k=1}^{K}\psi_k(\mathbf{p})\alpha_k. \tag{13}$$

The derivatives are considered with corresponding derivatives of $\psi_k(\mathbf{p})$. RBFs used in the present work are multiquadrics $\psi_k(\mathbf{p})=\sqrt{|\mathbf{p}-\mathbf{p}_k|^2+c^2}$, where c is the shape parameter. The elaboration of the method can be found in [18].

The boundary conditions at the inlet (i.e. SEN) are

$$u_{\text{inlet},x} = 0\frac{\text{m}}{\text{s}}, u_{\text{inlet},z} = 0\frac{\text{m}}{\text{s}}, u_{\text{inlet},y} = u_{\text{cast}}(a_b/d_2)^2, T_{inlet} = T_0, \frac{\partial P}{\partial y} = 0\frac{\text{N}}{\text{m}^2} \tag{14}$$

$$k_{inlet} = 1.5(I_t u_{\text{inlet},y})^2, \epsilon_{\text{inlet}} = \frac{c_\mu^{0.75} k_{\text{inlet}}^{1.5}}{0.07 d_2} \tag{15}$$

where I_t is the turbulent intensity

$$I_t = 0.16\text{Re}^{-1/8}, \quad \text{Re} = \rho u_{\text{inlet},y} d_2/\mu. \tag{16}$$

Pressure outlet with $P = 0\,N/\text{m}^2$ is prescribed at the outlet. Other variables are set to zero gradients in the vertical direction. On the top surface (i.e. meniscus), the free surface flow is prescribed with $u_y = 0\,\text{m/s}$.

On the side walls the boundary conditions for velocity are of the no-slip type if there is a liquid phase, or $u = u_{\text{cast}}$ is prescribed if the steel has solidified. For the heat transfer, Robin boundary conditions are used in the mold, where the heat transfer coefficient equals to $2000\ \text{Wm}^{-2}\text{K}^{-1}$. In the secondary cooling region, below the mold, the heat transfer coefficient equals to $800\ \text{Wm}^{-2}\text{K}^{-1}$.

4 RESULTS

The correctness of Elmer solver and the problem setup is verified on an analytical case (magnetic field of coils without the iron core) and on an axisymmetric case of DC aluminium casting, where the results are compared to those obtained from another open source finite element solver FEMM, which is intended for 2D electromagnetic problems [19]. The latter is also compared to our own meshless calculation too.

The vertical and the horizontal profiles for different frequencies and currents can be seen in Figure 2 and

Figure **3**. They roughly obey the dependency $|\mathbf{f}| \propto f I^2$, although they reach maximum intensity between 3 Hz and 5 Hz, after which the skin effect in the mold dominates over the frequency factor in $|\mathbf{f}|$. A strong spike is seen right at the bottom of the mold. This is because the stirrer is mounted right above the bottom of the mold (Figure 1), where the magnetic field should be still strong, but is shielded by the mold. The effect becomes stronger with higher frequencies, which further confirms the argument. This does not influence the stirring effect, because the force is in the vertical direction [8].

EMS has a dramatic effect on solidification shell and the effect on fluid flow is rotational, as expected (Figure 4). However, as noted in previous publications, the main effect is not due to swirling flow, but due to better mixing and thermal transport, resulting in a sharper temperature gradient along the strand [3]. It is clear that because of this, a particular cross section in the strand solidifies faster than without the stirring (a blunt solidification front in Figure 4 for EMS case).

The settings shown in the present paper are not optimal. As we can see in Figure 5 the rotational flow distorts the solidification front and makes the solidification non-symmetric. A

similar effect was found in literature [20]. It is expected, that this problem can be overcome by stronger stirring.

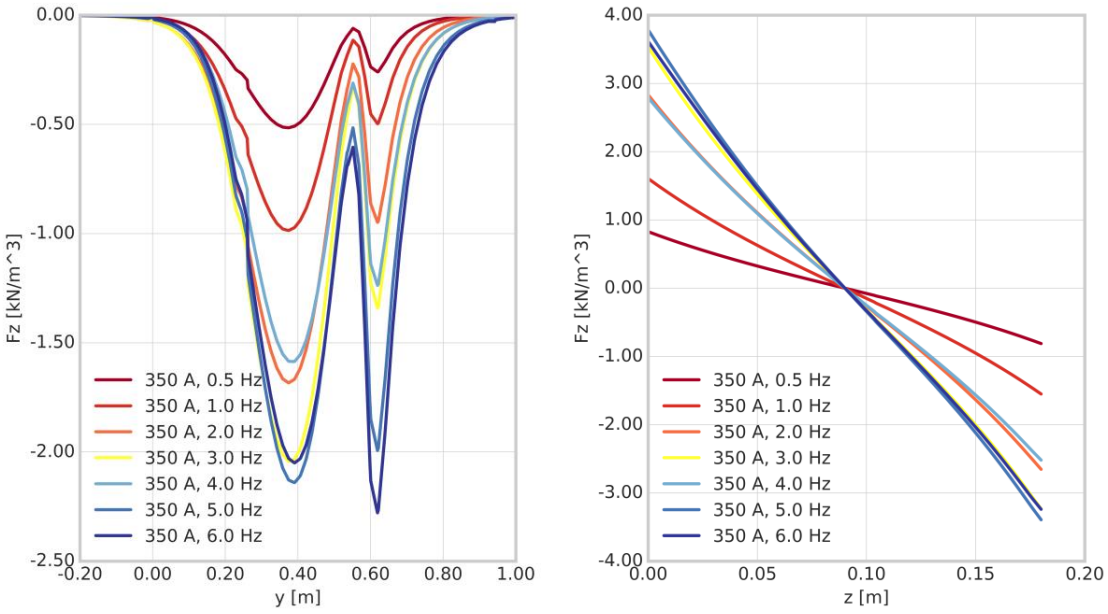

Figure 2: The magnetic force horizontal component z for different frequencies for vertical cross-section in the middle of the strand and 3 cm from the side (a) and in the horizontal cross section in the center of the EMS (b).

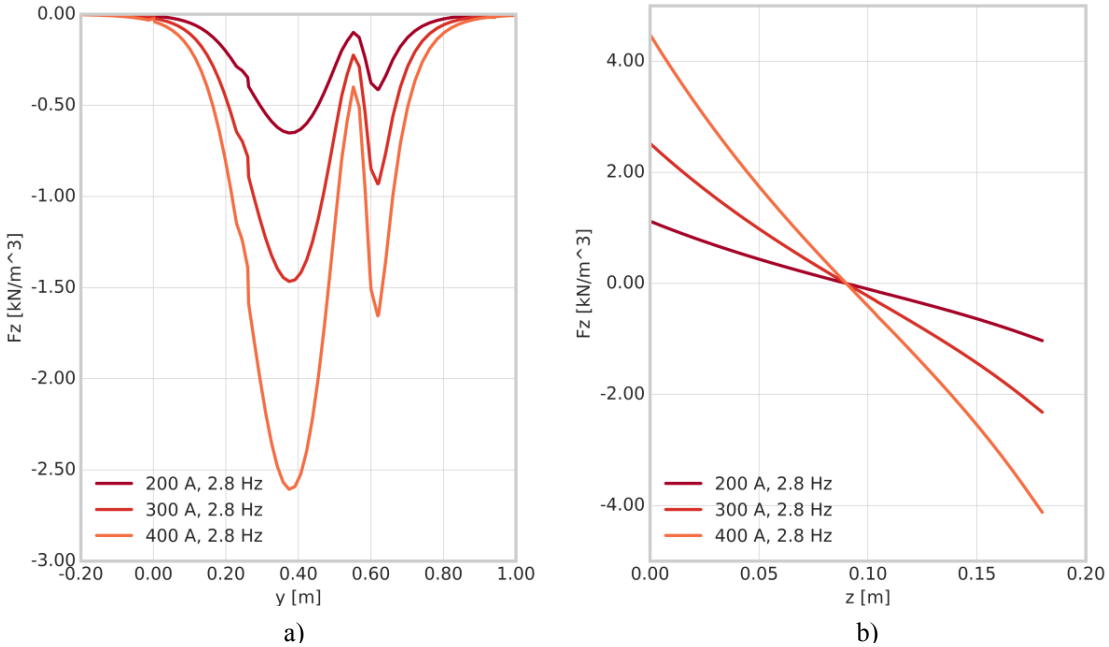

Figure 3: The magnetic force horizontal component z for different currents for vertical cross-section in the middle of the strand and 3 cm from the side (a) and in the horizontal cross section in the center of the M-EMS (b).

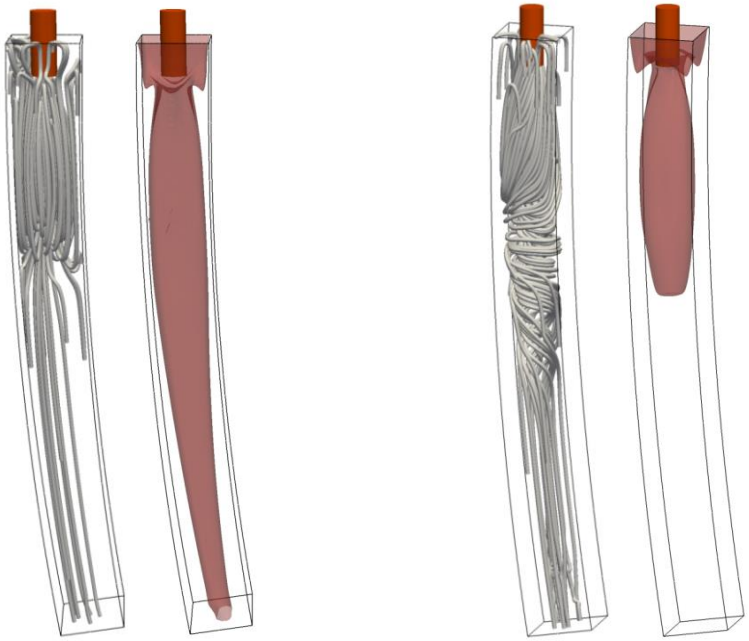

No EMS 300 A; 2.8 Hz

Figure 4: Streamlines and solidification front without and with EMS.

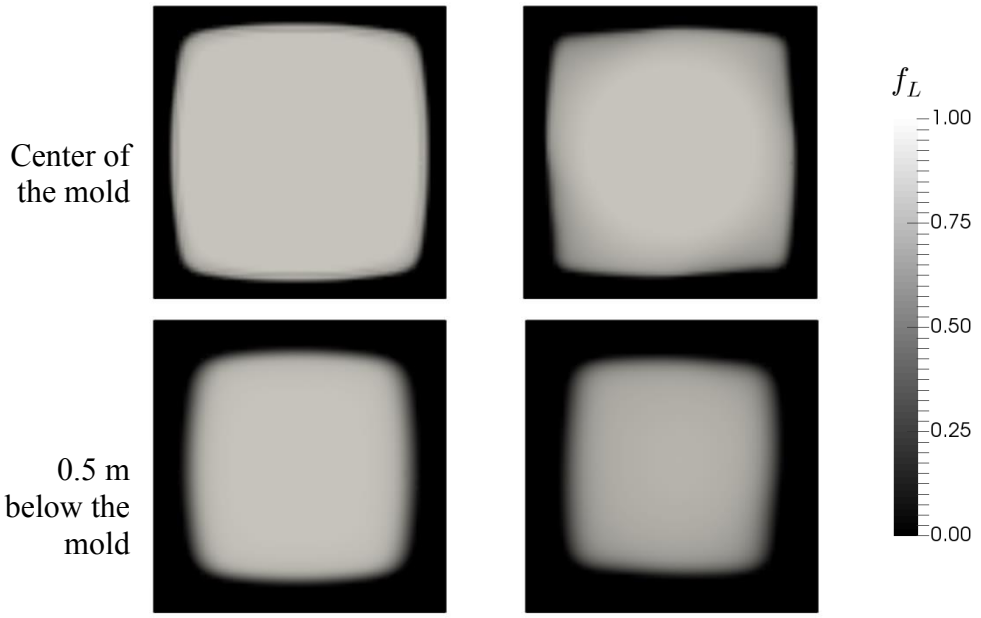

Figure 5: Liquid fraction without and with EMS for cross sections at the center of the stirrer and 0.5 m below it.

5 CONCLUSIONS

Lorentz force is successfully incorporated into the existing 3D meshless model of turbulent strand solidification and solved with LRBFCM in 3D. Due to the loss of symmetry the whole strand has to be considered and not only one quarter [1]. The obtained results are in accordance with those found in literature [7, 8, 20].

The calculation of the EM force with the use of a combination of our own meshes and open source finite element software is proven practical. Despite that, the challenge remains in efficiently connecting solvers for fully coupled problems. This is necessary, if one wants to study for example the effect of temperature dependence of electrical conductivity.

Challenges also remain in finding optimal stirring parameters for steel production and including macrosegregation and inclusion transport.

ACKNOWLEDGEMENTS

This work was funded by the Slovenian Grant Agency (ARRS) in the framework of applied research project L2-6775, co-sponsored by companies IMPOL and Štore-Steel.

REFERENCES

[1] Vertnik, R. and Šarler, B. Three dimensional simulation of macrosegregation in steel billets by a meshless method. *IOP Conf. Ser. Mater. Sci. Eng.* (2016) **117:**012069.
[2] Kunstreich, S. Electromagnetic stirring for continuous casting. *Rev. Métallurgie* (2003) **100:**395–408.
[3] Guo, Q., *et al*. Effect of Final EMS on Shrinkage Cavity of Bloom. *J. Iron Steel Res. Int.* (2015) **22:**93–97.
[4] Spitzer, K.-H., Dubke, M. and Schwerdtfeger, K. Rotational electromagnetic stirring in continuous casting of round strands. *Metall. Trans. B* (1986) **17:**119–131.
[5] Fujisaki, K. In-mold electromagnetic stirring in continuous casting. *IEEE Trans. Ind. Appl.* (2001) **37:**1098–1104.
[6] Trindade, L.B., *et al*., and Soares, R.B. Numerical model of electromagnetic stirring for continuous casting billets. *IEEE Trans. Magn.* (2002) **38:**3658–3660.
[7] Liu, H., *et al*. Numerical Simulation of Fluid Flow in a Round Bloom Mold with In-Mold Rotary Electromagnetic Stirring. *Metall. Mater. Trans. B* (2012) **43:**1657–1675.
[8] Geng, X., *et al*. Optimisation of electromagnetic field and flow field in round billet continuous casting mould with electromagnetic stirring. *Ironmak. Steelmak.* (2015) **42:** 675–682.
[9] Ren, B.-Z., *et al*. Numerical simulation of fluid flow and solidification in bloom continuous casting mould with electromagnetic stirring. *Ironmak. Steelmak.* (2015) **42:**401–408.
[10] Vertnik, R. and Šarler, B. Simulation of continuous casting of steel by a meshless technique. *Int. J. Cast Met. Res.* (2009) **22:**311–313.
[11] Vertnik, R., Šarler, B., and Senčič, B. Solution of Macrosegregation in Continuously Cast Billets by a Meshless Method. *IOP Conf. Ser. Mater. Sci. Eng.* (2012) **27:**012058.

[12] Mramor, K., Vertnik, R., and Šarler, B. A meshless model of electromagnetic braking for the continuous casting of steel. *Mater. Tehnol.* (2015) **49:**961–967.
[13] Košnik, N., *et al*. A multiphysics and multiscale model for low frequency electromagnetic direct-chill casting. *IOP Conf. Ser. Mater. Sci. Eng.* (2016) **117:**012052.
[14] Alizadeh, M., Jahromi, S. A. J., and Nasihatkon, S. B. Applying finite point method in solidification modeling during continuous casting process. *ISIJ Int.* (2010) **50:**411–417.
[15] 'Elmer 8.2'. [Online]. Available: https://csc.fi/web/elmer/elmer. [Accessed: 30-Mar-2017].
[16] Abe, K., Kondoh, T., and Nagano, Y. A new turbulence model for predicting fluid flow and heat transfer in separating and reattaching flows—I. Flow field calculations. *Int. J. Heat Mass Transf.* (1994) **37:**139–151.
[17] Wilcox, D. C., *Turbulence modeling for CFD*, 3rd ed. La Cãnada, Calif: DCW Industries, (2006).
[18] Šarler, B. and Vertnik, R. Meshfree explicit local radial basis function collocation method for diffusion problems. *Comput. Math. Appl.* (2006) **51:**1269–1282.
[19] Meeker, D. Finite element method magnetics (FEMM). 16-Oct-2010. [Online]. Available: http://www.femm.info/wiki/HomePage. [Accessed: 30-Mar-2017].
[20] Wang, B., *et al*. Analysis of the effects of electromagnetic stirring on solidification structure of bearing steel. *Metalurgija*, (2015) **54:**327–330.

VII International Conference on Computational Methods for Coupled Problems in Science and Engineering
COUPLED PROBLEMS 2017
M. Papadrakakis, E. Oñate and B. Schrefler (Eds)

MESHLESS MODELLING OF MICROSTRUCTURE EVOLUTION IN THE CONTINUOUS CASTING OF STEEL

TADEJ DOBRAVEC[*], BOŠTJAN MAVRIČ[*], ROBERT VERTNIK[*,†] AND BOŽIDAR ŠARLER[*,††]

[*] Laboratory for Simulation of Materials and Processes
Institute of Metals and Technology
Lepi pot 11, SI-1000 Ljubljana, Slovenia
e-mail: tadej.dobravec@imt.si, web page: http://www.imt.si

[†] Quality and Development
Štore Steel, d.o.o.
Železarska 3, SI-3220 Štore, Slovenia
e-mail: robert.vertnik@imt.si, web page: http://www.store-steel.si

[††] Laboratory for Fluid Dynamics and Thermodynamics
Faculty of Mechanical Engineering, University of Ljubljana
Aškerčeva 6, SI-1000 Ljubljana, Slovenia
e-mail: bozidar.sarler@fs.uni-lj.si, web page: https://www.fs.uni-lj.si

Key words: Continuous Casting, Steel, Microstructure Evolution, Slice Model, Two-Scale Model, Meshless Methods.

Abstract. A two-dimensional two-scale slice model has been developed to predict the microstructure evolution in the solidifying strand with an arbitrary cross section geometry during continuous casting of steel. The enthalpy equation is solved at the macro level by using meshless local radial basis function collocation method (LRBFCM) based on multiquadrics for spatial discretization and explicit Euler scheme for temporal discretization. The temperature and the solid fraction in computational nodes are calculated by using a continuum model formulation while the lever rule is used as the supplementary microsegregation relation. The temperature field is interpolated to the micro level by using LRBFCM. At the micro level, the normal distribution and Kurz-Giovanola-Trivedi model are proposed to determine temperature dependent nucleation rate and grain growth velocity, respectively. Meshless point-automata algorithm is applied to implement nucleation and grain growth equations. Several examples of computations of the strand with different cross-sections are shown.

1 INTRODUCTION

The continuous casting (CC) is the most widely used technique in the mass steel production since its introduction in the 1950s [1]. The numerical models for simulation of CC of steel represent powerful tools for in-depth understanding and optimization of the casting

process [2, 3]. The development of the numerical models is a very challenging process due to a highly complex nature of the coupled physical phenomena such as fluid flow, heat, mass and solute transport of solidification. These phenomena affect microstructure evolution, having a decisive impact on the material properties of the final product.

The comprehensive three-dimensional numerical models are time consuming, hence alternative approaches are derived for simulation of solidification in the CC. One of the most popular alternative approaches is the so called slice model approximation, where the three-dimensional strand is approximated by a traveling two-dimensional Lagrangian slice, moving with casting velocity in the axial direction. Such simplification is justified, since the conduction is less important than the advection in the axial direction [4]. The constant velocity in the strand has only z-coordinate in this approximation, hence the fluid flow could not be simulated, however the solidification phenomena can still be observed due to the heat and solute transfer in the radial direction [5]. The numerical models for the heat and solute transfer are coupled to the models for the simulation of the microstructure evolution, i.e., nucleation and grain growth. Since the simulation of the microstructure evolution is required on a micrometer scale, the simple grain growth algorithms like the Cellular Automata (CA) [6, 7] are more suitable than the time consuming algorithms like the Phase Field [8, 9, 10]. CA was first used in the CAFE [11] model for the simulation of the nucleation and grain growth along with finite element method that was used to determine the temperature field. A similar approach was used in the two-scale model [12] as the Local Radial Basis Function Collocation Method (LRBFCM) [2] was used for the simulation of the heat transport at the macro level and CA for the nucleation and grain growth at the micro level.

In the present paper, two-scale slice model for the simulation of the microstructure evolution in the continuous casting of steel is presented. Similarly as in the model from [12], the LRBFCM is used for simulation of the temperature field evolution at the macro level. At the micro level, the Point Automata (PA) [13] is used instead of CA, since PA reduces the anisotropy caused by the mesh [14]. The main novelity of this paper is a computationally effective simulation of the microstructure evolution in the continuous casting of steel with arbitrary cross section geometry of the strand. The results of the simulations provide useful qualitative information about the microstructure evolution to engineers in the steel production companies; for example, the dependence of the positions of Equiaxed to Columnar Transitions (ECT) and Columnar to Equaixed Transitions (CET) [4] on the caster geometry and the process parameters.

2 GOVERNING EQUATIONS

The two-scale model describes the heat transfer and the solidification at the macro level and the nucleation and the grain growth at the micro level. The equations are at both scales solved in a transverse Lagrangian slice moving in the axial direction with the casting speed v_{cast}. The temperature field in each slice depends only on its history and on the axial z-coordinate dependent boundary conditions that are determined by the caster geometry and the process parameters. The axial z-coordinate of the slice is determined as

$$z(t) = \int_{t_{start}}^{t} v_{cast}(t')dt' + z_{start}, \tag{1}$$

where t_{start} and z_{start} stand for the initial time and the initial axial coordinate of the slice, respectively.

2.1 Macroscopic model

The heat transfer is described by the heat diffusion equation

$$\frac{\partial(\rho h)}{\partial t} = \nabla \cdot (k \nabla T), \tag{2}$$

where ρ, h, k and T stand for density, enthalpy, thermal conductivity and temperature, respectively. Robin boundary condition is incorporated

$$-k \frac{\partial T}{\partial \hat{n}} = h_0 (T - T_0), \tag{3}$$

where $\hat{n}$, h_0 and T_0 stand for the unit normal vector on the boundary, the effective heat transfer coefficient and the effective surrounding temperature, respectively. The initial temperature in the domain is set to the supercooling ΔT_0 above the liquidus temperature. A linearized eutectic phase diagram is proposed, hence the liquidus and the solidus temperatures T_{liq} and T_{sol} are calculated as

$$T_{liq} = T_m + mC_0, \qquad T_{sol} = T_m + mC_0 / k_p \tag{4}$$

where m, C_0 and k_p stand for the liquidus slope, the concentration of the carbon and the partition coefficient, respectively. The mixture formulation [15] is used to define the enthalpy and the thermal conductivity in the computational domain, containing liquid and solid phase

$$h = f_\ell (c_\ell T + h_\ell^0) + f_s c_s T, \qquad h_\ell^0 = (c_s - c_\ell) T_{sol} + h_f, \tag{5}$$

where f and c stand for mass fraction and specific heat, respectively. The subscripts s and ℓ denote solid and liquid phase. h_f stands for the latent heat of the phase change. The mixture thermal conductivity is defined as

$$k = f_s k_s + f_\ell k_\ell, \tag{6}$$

where k_s and k_ℓ stand for the conductivities in the solid and the liquid phase, respectively. In the present paper the lever rule [4] is used as the supplementary microsegregation relation needed to calculate the enthalpy inverse $T=T(h)$. The use of the lever rule yields the following relation between the solid fraction and the temperature

$$f_s = \frac{1}{1 - k_p} \left[\frac{T - T_{liq}}{T - T_m} \right], \tag{7}$$

where T_m stands for the melting temperature of pure iron.

2.2 Microscopic model

Microscopic model describes nucleation and grain growth as a function of the temperature calculated at the macro level. The nucleation density change dn, induced by the change of the

undercooling $d\Delta T$ is described by the normal distribution

$$\frac{dn}{d\Delta T} = \frac{n_{\max}}{\sqrt{2\pi}\Delta T_\sigma} \exp\left[-\frac{1}{2}\left(\frac{\Delta T - \Delta T_\mu}{\Delta T_\sigma} \right)^2 \right]; \qquad \Delta T = T_{liq} - T, \tag{8}$$

where n_{max}, ΔT_σ and ΔT_μ stand for the maximal nucleation density, the standard deviation and the mean of the undercooling, respectively. Grain growth is in analytical studies described as a growth of a paraboloid with a tip radius R_{tip} and velocity V [4]. In the present model, the Kurz-Giovanola-Trivedi (KGT) model [16] is proposed to determine the relation $V(\Delta T)$. The KGT model consists of two non-linear equations which relate the material properites, C_0, ΔT, V and R_{tip}. In the KGT equations, the non-dimensional Péclet number Pe is introduced

$$\mathrm{Pe} = \frac{R_{tip} V}{2 D_\ell}, \tag{9}$$

where D_ℓ is the solutal diffusion coefficient in the liquid phase. The first KGT equation relates R_{tip} to the material properties, C_0 and Pe

$$R_{tip} = \sqrt{\frac{\Gamma D_\ell \left[1 - (1-k_p) Iv(Pe) \right]}{-mV(1-k_p)C_0}}; \qquad V = -\frac{mC_0(1-k_p)PeD_\ell}{k_p \left[1 - (1-k_p) Iv(Pe) \right] \Gamma}, \tag{10}$$

where $Iv(Pe)$ and Γ stand for the Ivantsov function and the Gibbs-Thompson coefficient, respectively. The second KGT equation relates ΔT to the material properties, C_0 and R_{tip}

$$\Delta T = m\left(C_0 - \frac{C_0}{1-(1-k_p)Iv(Pe)} \right) + \frac{2\Gamma}{R_{tip}}. \tag{11}$$

3 SOLUTION PROCEDURES

3.1 The distribution of the computational nodes

The computational nodes with typical Euclidian inter-nodal distances l_{macro} and l_{micro} are distributed at the macro and at the micro level, respectively, as shown in Figure 1. First, the temperature field at the computational points at the macro level is calculated, followed by the interpolation of the macroscopic temperature field to the computational points at the micro level, where the microscopic governing equations are solved.

3.2 Solution of the macroscopic model

At the macro level, the explicit Euler scheme is used for temporal discretization of the governing equation

$$\frac{\partial(\rho h)}{\partial t} \approx \frac{\rho h - \rho_0 h_0}{\Delta t_{macro}}, \tag{12}$$

where Δt_{macro} stands for the time step at the macro level. The LRBFCM is used for the spatial

discretization of the enthalpy equation. The computational nodes are grouped into overlapping local domains. A general quantity ϕ in the point $\boldsymbol{p}$ is approximated as

$$\phi(\mathbf{p}) \approx \sum_{k=1}^{{}_lK} {}_l\psi_k(\mathbf{p})\,{}_l\alpha_k, \tag{13}$$

where ${}_l\alpha_k$ and ${}_lK$ stand for the interpolation coefficients of the k-th node in the l-th local domain and the number of nodes in the l-th local domain, respectively. ${}_l\psi_k$ is the multiquadric radial basis function

$${}_l\psi_k(\mathbf{p}) = \sqrt{c\left(\frac{{}_lr_k}{l_{macro}}\right)^2 + 1}, \tag{14}$$

where ${}_lr_k$ and c stand for the distance between the point $\boldsymbol{p}$ and k-th node in the l-th local domain and the shape parameter, respectively. Shape parameter in each local domain is chosen according to the targeted condition number 10^{20} of the interpolation matrix.

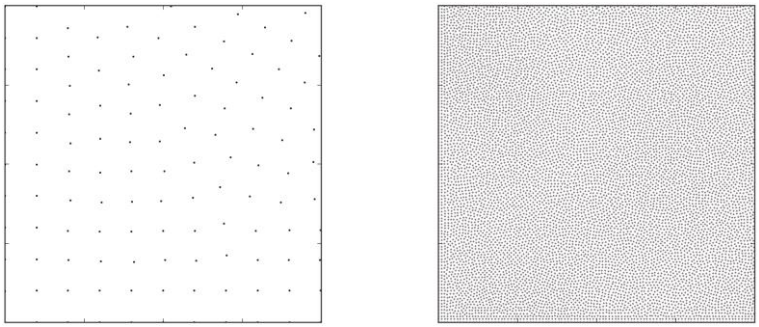

Figure 1: A section of the computational domain illustrating the distribution of the computational points at the macro (left) and at the micro (right) level.

3.3 Macro-micro interpolation

The temperature field is interpolated from the nodes at the macro level to the nodes at the micro level by using LRBFCM with multiquadric basis functions. The time step at the macro level Δt_{macro} is larger than time step at the micro level Δt_{micro}, hence a linear interpolation is used to determine the temperature in-between the interpolated temperatures T_i at two sequential macro times t^n_{macro} and t^{n+1}_{macro}

$$T(t) = T_i(t^n_{macro}) + \frac{T_i(t^{n+1}_{macro}) - T_i(t^n_{macro})}{\Delta t_{macro}}(t - t^n_{macro}); \qquad t^n_{macro} \le t \le t^{n+1}_{macro}. \tag{15}$$

3.4 Solution of the microscopic model - nucleation

At the micro level, the PA method is used to solve the nucleation and the grain growth equations. To each point (node) at the micro level an unsigned integer $\mathcal{S}$ is assigned. $\mathcal{S}$=0 represents the liquid phase and $\mathcal{S}$>0 the solid phase. Different non-zero values of $\mathcal{S}$ denote different grains. As the molten steel is poured into the mold, the whole system is in liquid

phase, hence $\mathcal{S}$=0 is assigned to each point in the computational domain at the beginning of the simulation. At every time step at the micro level, all the points with $\mathcal{S}$=0 are considered and different random numbers $r \in [0,1)$ are assigned to each of them. The nucleation at a point occurs, i.e., the point changes its $\mathcal{S}$ from $\mathcal{S}$=0 to $\mathcal{S}$>0, if [17]

$$r < V_{PA} \int_{\Delta T}^{\Delta T+\delta(\Delta T)} \frac{dn}{d(\Delta T')} d(\Delta T'), \tag{16}$$

where V_{PA} is the volume represented by the point and $\delta(\Delta T)$ is the change of the undercooling during one time-step. The assigned value $\mathcal{S}_r$ is a random non-zero unsigned integer calculated from r.

3.5 Solution of the microscopic model - growth velocity

The grain growth velocity as a function of undercooling is calculated by evaluating equations (10) and (11) for the equidistant values $\{Pe_1, Pe_2, ..., Pe_n\}$ with $Pe_1 = 4.0\,10^{-3}$, $Pe_n = 10.0$ and $n = 5000$. As the values $\{V(Pe_1), V(Pe_2), ..., V(Pe_n)\}$ and $\{\Delta T(Pe_1), \Delta T(Pe_2), ..., \Delta T(Pe_n)\}$ are calculated, least squares interpolation is performed to obtain

$$V(\Delta T) = a_1 \Delta T^3 + a_2 \Delta T^2 + a_3 \Delta T, \tag{17}$$

where $a_i, i = 1,2,3$ are the interpolation coefficients.

3.6 Solution of the microscopic model - grain growth

The PA method is also used for the solution of the grain growth equations. Each point with $\mathcal{S}$>0 has a neighbourhood defined with radius R as shown in Figure 2. Grain growth is represented as a growth of a circle with radius

$$l(t) = \int_{t_0}^{t} V(\Delta T) dt, \tag{18}$$

where t_0 is the time when the point was nucleated. Considering a solid point with $\mathcal{S}=\mathcal{S}_r>0$ and $l(t)<R$, the distances to its liquid neigbours are compared to $l(t)$. The liquid neighbouring point changes its index from $\mathcal{S}$=0 to $\mathcal{S}=\mathcal{S}_r$ if

$$l(t) \geq d, \tag{19}$$

where d is the distance between the solid and its neighbouring liquid point.

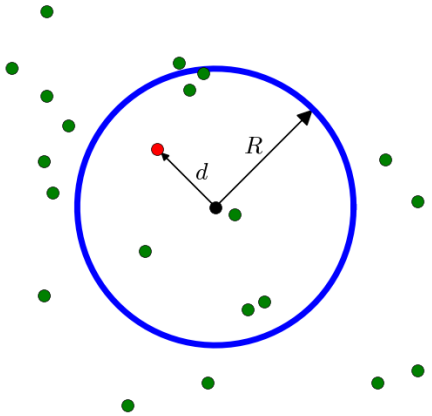

Figure 2: The neighbourhood of a point with $\mathcal{S} > 0$ defined by the radius R.

4 SIMULATION RESULTS

Simulation of the microstructure evolution is tested for the continuous casting of binary Fe-0.51wt%C steel. Square, H-profile and circular cross section geometries of the strand are used. For the heat transfer coefficient in equation (3), two different values are used

$$h_0 = \begin{cases} h_{mold}, & z < z_{mold} \\ h_{spray}, & \text{elsewhere} \end{cases}, \tag{20}$$

where h_{mold} and h_{spray} stand for the heat-transfer coefficients in the mold and in the spray section, respectively, and z_{mold} for the length of the mold. For the parameters of the normal distribution in equation (8) two different values are used

$$\Delta T_\sigma = \begin{cases} \Delta T_\sigma^{surface}, & d < d_{surface} \\ \Delta T_\sigma^{bulk}, & \text{elsewhere} \end{cases}, \quad \Delta T_\mu = \begin{cases} \Delta T_\mu^{surface}, & d < d_{surface} \\ \Delta T_\mu^{bulk}, & \text{elsewhere} \end{cases}, \tag{21}$$

where d and $d_{surface}$ stand for the distance between a computational node and the boundary and the thickness of the surface nucleation area, respectively. The final microstructures in the continuous casting of steel with square, H-profile and circular cross section geometry are shown in Figures 3, 4 and 5, respectively. The material properties, the continuous casting parameters and the numerical model parametes used are listed in Tables 1, 2 and 3, respectively. ECT and CET are observed in all three final microstructures.

Table 1: Material properties of the Fe0.51wt%C.

Property	Symbol	Unit	Value
Specific heat capacity in the liquid phase	c_ℓ	J/kg/K	1395.8
Specific heat capacity in the solid phase	c_s	J/kg/K	824.92
Thermal conductivity in the	k_ℓ	W/m/K	39.3

liquid phase			
Thermal conductivity in the solid phase	k_s	W/m/K	25.0
Density	ρ	kg/m^3	7430.0
Solute diffusion coefficient	D_ℓ	m^2/s	1.36 10^{-9}
Melting temperature of pure Fe	T_m	°C	1562.0
Partition coeffcient	k_p	-	0.37
Latent heat of fusion	h_f	J/kg	2.71 10^5
Liquidus line slope	m	°C/wt.%C	-30.0
Composition	C_0	wt.%C	0.51
Gibbs-Thompson coefficient	Γ	Km	1.9 10^{-7}

Table 2: Continuous casting parameters.

Parameter	Symbol	Unit	Value
Casting velocity	v_{cast}	m/min	1.0
Billet length	L_{billet}	m	25.0
Mould length	z_{mold}	m	0.8
Heat transfer coefficient in the mould area	h_{mold}	W/m^2/K	200.0
Heat transfer coefficient in the spray area	h_{spray}	W/m^2/K	80.0
Temperature of the cooling water	T_0	°C	30.0
Initial supercooling	ΔT_0	°C	25.0

Table 3: Numerical model parameters.

Parameter	Symbol	Unit	Value
Inter-nodal distance at the macro level	l_{macro}	m	2.0 10^{-3}
Inter-nodal distance at the micro level	l_{micro}	m	2.0 10^{-4}
Time step at the macro level	Δt_{macro}	s	1.0 10^{-2}
Time step at the micro level	Δt_{micro}	s	1.0 10^{-3}
Number of points in the collocation	${}_lK$	-	8
Thickness of the surface nucleation regime	$d_{surface}$	m	5.0 10^{-3}
Mean of the normal	$\Delta T_\mu^{surface}$	°C	0.6

distribution in the surface area			
Standard deviation of the normal distribution in the surface area	$\Delta T_{\sigma}^{surface}$	°C	0.2
Mean of the normal distribution in the bulk area	ΔT_{μ}^{bulk}	°C	7.0
Standard deviation of the normal distribution in the bulk area	ΔT_{σ}^{bulk}	°C	1.75
Neighbourhood radius in PA	R	m	$3.0\ 10^{-4}$
Growth velocity interpolation coefficient	a_1	$m/s/K^3$	$4.01\ 10^{-3}$
Growth velocity interpolation coefficient	a_2	$m/s/K^2$	$4.37\ 10^{-3}$
Growth velocity interpolation coefficient	a_3	m/s/K	$2.02\ 10^{-4}$

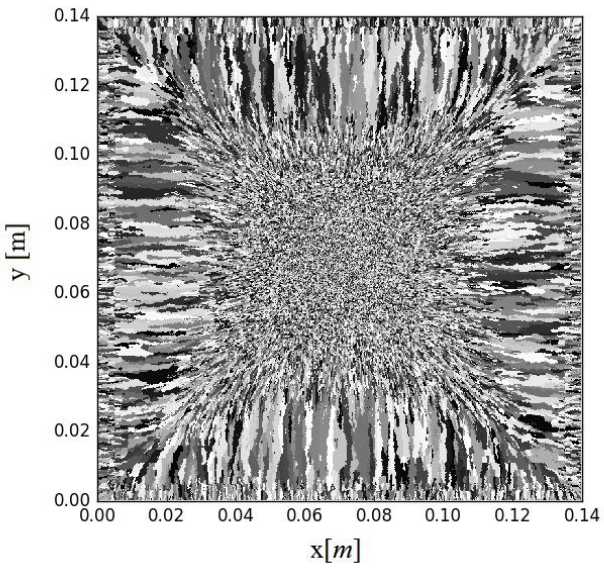

Figure 3: Final microstructure for the square cross section geometry of the strand.

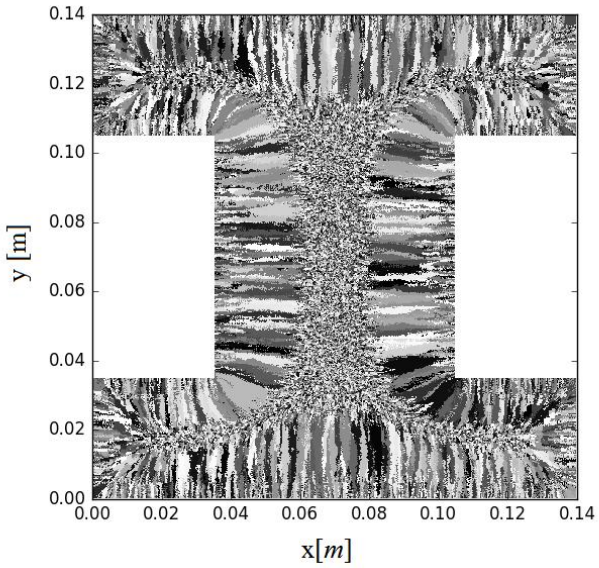

Figure 4: Final microstructure for the H-profile cross section geometry of the strand.

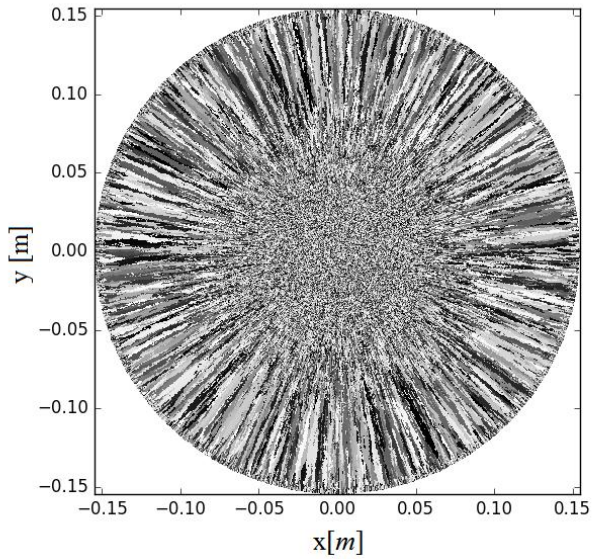

Figure 5: Final microstructure for the circular cross section geometry of the strand.

5 CONCLUSIONS

In the present paper, a two-scale slice model for simulation of microstructure evolution in the continuous casting of steel with arbitrary cross section geometry of the strand is presented. Meshfree LRBFCM and PA algorithms are used for the spatial discretization of the enthalpy equation and the solution of the microstructure evolution equations, respectively. The model

can be used for qualitative prediction of the microstructure evolution, e.g., for the determination of the ECT and CET positions in the continuous casting of steel. The material properties of the binary Fe-0.51wt%C steel that are used in the simulations can be replaced by material properites of multicomponent steels, obtained by JMatPro [18] database. Grain growth KGT equations become more complex in the case of multicomponent steels, since the concentrations and the partition coefficients of all alloyed elements have to be accounted for [19].

ACKNOWLEDGEMENTS

This work was funded by the Slovenian Grant Agency (ARRS) in the framework of applied research project L2-6775, co-sponsored by the companies IMPOL and Štore Steel.

REFERENCES

[1] Irving, W. R. *Continuous Casting of Steel*. Institute of Materials, (1993).
[2] Vertnik, R. and Šarler B. Solution of a continuous casting of steel benchmark test by a meshless method. *Eng. Anal. Bound. Elem.* (2014) **45**:45–61.
[3] Maurya, A. and Jha, P. K. Influence of electromagnetic stirrer position on fluid flow and solidification in continuous casting mold. *Appl. Math. Model.* (2017) In press, Corrected Proof.
[4] Dantzig, J. A. and Rappaz, M. *Solidification*. EFPL Press, (2009).
[5] Vušanović, I., Vertnik, R. and Šarler, B. A simple slice model for prediction of macrosegregation in continuously cast billets. *IOP Conf. Ser. Mater. Sci. Eng.* (2012) **27:**12056.
[6] Zhu, M. F. and Hong, C. P. A Modified Cellular Automaton Model for the Simulation of Dendritic Growth in Solidification of Alloys. *ISIJ Int.* (2011) **41**:436–445.
[7] Krane, M. J. M., Johnson, D. R. and Raghavan, S. The development of a cellular automaton-finite volume model for dendritic growth. *Appl. Math. Model.* (2009) **33**:2234–2247.
[8] Kobayashi, R. Modeling and numerical simulations of dendritic crystal growth. *Phys. Nonlinear Phenom.* (1993) **63**:410–423.
[9] Karma, A. and Rappel, W.-J. Quantitative phase-field modeling of dendritic growth in two and three dimensions. *Phys. Rev. E* (1998) **57**:4323.
[10] Boettinger, W. J., Warren, J. A., Beckermann, C. and Karma, A. Phase-Field Simulation of Solidification. *Annu. Rev. Mater. Res.*(2002) **32**:163–194.
[11] Gandin, C.-A. and Rappaz, M. A coupled finite element-cellular automaton model for the prediction of dendritic grain structures in solidification processes. *Acta Metall. Mater.*(1994) **42**:2233–2246.
[12] Lorbiecka, A. Z., Vertnik, R., Gjerkeš, H., Manojlovič, G., Senčič, B., Cesar, J. and Šarler, B. Numerical Modeling of Grain Structure in Continuous Casting of Steel. *Comput. Mater. Contin.* (2009) **8**:195–208.
[13] Lorbiecka, A. Z. and Šarler, B. Simulation of Dendritic Growth with Different Orientation by Using the Point Automata Method. *Comput. Mater. Contin.* (2010) **18**:69–104.
[14] Reuther, K. and Rettenmayr, M. Perspectives for cellular automata for the simulation of dendritic solidification–A review. *Comput. Mater. Sci.* (2014) **95**:213–220.
[15] Bennon, W. D. and Incropera, F. P. A continuum model for momentum, heat and species transport in binary solid-liquid phase change systems—I. Model formulation. *Int. J. Heat Mass Transf.* (1987) **30**:2161–2170.
[16] Kurz, W., Giovanola, B. and Trivedi R. Theory of microstructural development during rapid solidification. *Acta Metall.* (1986) **34**:823–830.
[17] Luo, S. and Zhu, M. Y. A two-dimensional model for the quantitative simulation of the dendritic growth with cellular automaton method. *Comput. Mater. Sci.* (2013) **71**:10–18.
[18] Saunders, N., Guo, U. K. Z., Li, X., Miodownik, A. P., Schilé, J. -Ph. Using JMatPro to model materials properties and behavior. *JOM* (2003) **55**:60–65.
[19] Šarler, B.,Vertnik, R., Lorbiecka, A. Z., Vušanović, I. and Senčič, B. A multiscale slice model for continuous casting of steel. *IOP Conf. Ser. Mater. Sci. Eng.* (2012) **33**:12021.

VII International Conference on Computational Methods for Coupled Problems in Science and Engineering
COUPLED PROBLEMS 2017
M. Papadrakakis, E. Oñate and B. Schrefler (Eds)

RESIDUAL STRESSES RESULTING FROM GROWTH AND REMODELING IN ARTERIAL WALLS

DANIEL BALZANI[†*] AND ANNA ZAHN[†]

[†]Institute of Mechanics and Shell Structures, Department of Civil Engineering
Technische Universität Dresden
01062 Dresden, Germany
Web page: https://imf.tu-dresden.de

[*]Dresden Center for Computational Materials Science (DCMS)
01062 Dresden, Germany
e-mail: daniel.balzani@tu-dresden.de

Key words: Biomechanics, Multiplicative Growth, Fiber Remodeling, Residual Stresses

Abstract. A model for multiplicative anisotropic growth in soft biological tissues, which relates the growth tensor to the fibrous tissue structure, is combined with a fiber remodeling framework. Both adaptation mechanisms are supposed to be governed by the intensity and the directions of the tensile principal stresses. Numerical examples on idealized arterial segments, illustrating stress and fiber angle distributions as well as resulting residual stresses in cases with and without fiber remodeling, are presented. It turns out that all processes including growth and remodeling are necessary to obtain qualitatively realistic distributions of fiber orientations, residual stresses, and stresses under loading.

1 INTRODUCTION

Being exposed to changes in its mechanobiological environment, arterial tissue continously strives to optimize its load-bearing capacities by adapting to altering conditions, for example to a sustained elevation of the blood pressure. This optimization procedure is characterized by growth and remodeling processes and is supposed to be the source of residual stresses which are typically existent in externally load-free states. Since these residual stresses are held responsible to reduce stress magnitudes and gradients in loaded states, they have to be accounted for in numerical simulations, see e. g. [4, 14, 18]. Constitutive equations for soft biological tissues commonly describe the anisotropic material behavior by modeling the tissue as an isotropic matrix material with embedded fibers. Based thereon, the reorientation of fibers and the addition of supplementary material can be considered to model adaptation processes and to quantify the associated residual

stresses. For both mechanisms, the intensity and the direction of principal stresses are assumed to be of particular importance.

Starting with the modeling of growth processes, an anisotropic growth model based on the multiplicative decomposition of the deformation gradient into a growth tensor and a remaining elastic part [15] is presented. In existing approaches based on this decomposition, e. g. in [8, 16], structural directions are used to incorporate growth in specific directions, for instance the radial direction in an artery. Here, a general local formulation is proposed, where the growth tensor is related to the fibrous tissue structure, which again is supposed to be directly linked to the directions of the highest (tensile) principal stresses. Establishing such a relation between the orientation of the fibers and the growth directions, the consequential extension of the model is to take remodeling of the fibers into account. A reorientation of the fibers ending up in a realistic arrangement, as for example discussed in [9, 7], is then expected to have twofold effects: an advantageous redistribution of the stresses and a direct influence on the growth directions, which are automatically adapted such that a reduction of high principal stresses is promoted. The basic assumption motivating both aspects of the combined framework is a symmetric alignment of the two fiber families in arteries with respect to the tensile principal stresses, which are supposed to be mainly located in the plane of the vessel wall. Following this assumption, a growth tensor designed to reduce the tensile principal stresses and an algorithm for the rearrangement of the fibers is proposed here.

2 BASICS OF THE COMPUTATIONAL MODEL

2.1 Growth model

A multiplicative decomposition of the deformation gradient $\boldsymbol{F} = \boldsymbol{F}_\mathrm{e}\boldsymbol{F}_\mathrm{g}$ is one of two methods frequently adopted to describe growth in soft biological tissues [1, 6]. The growth deformation arising from the growth part $\boldsymbol{F}_\mathrm{g}$ is characterized by a stress-free volume change increasing the reference volume with a factor $J_\mathrm{g} = \det[\boldsymbol{F}_\mathrm{g}]$. The second part of the deformation gradient, the elastic part $\boldsymbol{F}_\mathrm{e} = \boldsymbol{F}\boldsymbol{F}_\mathrm{g}^{-1}$ is linked with the deformation from the intermediate, grown state to the actual configuration, which is accompanied by the emergence of stresses. A polyconvex hyperelastic formulation for fiber-reinforced soft biological tissues of Balzani et al. [3] is applied, where the stresses are computed by differentiating a polyconvex strain energy function with respect to the deformation tensor. The 2nd Piola-Kirchhoff stress tensor in the intermediate configuration is obtained by $\boldsymbol{S}_\mathrm{e} = 2\,\partial\psi/\partial\boldsymbol{C}_\mathrm{e}$ with the elastic part of the deformation tensor $\boldsymbol{C}_\mathrm{e} = \boldsymbol{F}_\mathrm{g}^{-T}\boldsymbol{C}\boldsymbol{F}_\mathrm{g}^{-1}$. The growth tensor $\boldsymbol{F}_\mathrm{g}$ can not be determined from equilibrium conditions [1] and thus has to be postulated by means of assumptions regarding growth directions and evolution equations. In the simplest case of isotropic growth with $\boldsymbol{F}_\mathrm{g} = \vartheta\boldsymbol{I}$ for instance, a single growth factor ϑ is involved. Based on an evolution equation $\dot{\vartheta} = k_\vartheta(\vartheta)\,\phi(\boldsymbol{Z})$, which is formulated in terms of the growth-driving quantity $\phi(\boldsymbol{Z})$, and the growth function k_ϑ, which includes time-dependency and prevents unlimited growth, the growth factor ϑ can

be identified [11]. Due to their material composition including a multitude of fiber-reinforced layers, the material behavior of soft biological tissues is highly non-linear and anisotropic. From the mechanical point of view, the complex tissue structure can be idealized by an isotropic ground matrix with embedded fibers, which are mainly arranged in two directions. Based on this idealization, the stress-strain-relation of soft biological tissues can be approximated by constitutive equations. Adaptation processes aim at reducing strains or stresses or their gradients within the loaded tissue state, which are thus governed by the microstructure, i. e. by the fiber reinforcement. It is therefore reasonable to assume that the tissue composition plays an important role in the context of adaptation processes as well, which leads to the conclusion that purely isotropic growth as mentioned above may not be sufficient.

Focusing on the reduction of principal stresses, an increase of the cross-section perpendicular to the direction of the principal stress appears reasonable. Such a growth process can be described by a growth tensor $\boldsymbol{F}_{\mathrm{g}} = \vartheta \boldsymbol{I} + (1-\vartheta)\, \boldsymbol{A} \otimes \boldsymbol{A}$, where $\boldsymbol{A}$ is the direction of the principal stress. Arteries are thick-walled and tube-like structures which transform the internal pressure to tensile loads in the circumferential/axial plane of the wall. This is the reason why in arteries mainly two collagen fiber families are found within this plane. The particular orientation adapts to the stress state such that an improved load-bearing behavior is obtained. It is assumed that the orientations of the two fiber families are therefore defined symmetrically to the directions of the two highest principal stresses. With these two positive principal stresses (denoted by index I and II) which are sought to be reduced by growth, there are two directions which have to be taken into account for an appropriate definition of the growth tensor. To realize this, the growth tensor is multiplicatively decomposed into two parts $\boldsymbol{F}_{\mathrm{g}} = \boldsymbol{F}_{\mathrm{g}}^{(\mathrm{II})} \boldsymbol{F}_{\mathrm{g}}^{(\mathrm{I})}$ related to the first and second principal stress directions $\boldsymbol{A}_{\mathrm{g}}^{(\mathrm{I})}$ and $\boldsymbol{A}_{\mathrm{g}}^{(\mathrm{II})}$, where each part is defined as

$$\boldsymbol{F}_{\mathrm{g}}^{(a)} = \vartheta^{(a)} \boldsymbol{I} + \left(1 - \vartheta^{(a)}\right) \boldsymbol{A}_{\mathrm{g}}^{(a)} \otimes \boldsymbol{A}_{\mathrm{g}}^{(a)} \qquad \text{with} \qquad a = \mathrm{I}, \mathrm{II}. \tag{1}$$

The simple case of isotropic growth can casually be enclosed in the framework by setting the multiplicative parts of the growth tensor to $\boldsymbol{F}_{\mathrm{g}}^{(a)} = \vartheta^{(a)} \boldsymbol{I}$ with $a = \mathrm{I}, \mathrm{II}$, which allows a comparison of both approachs. Due to the split of the growth tensor into two parts, two independent growth factors $\vartheta^{(\mathrm{I})}$ and $\vartheta^{(\mathrm{II})}$ have to be derived from the two evolution equations

$$\dot{\vartheta}^{(a)} = k_{\vartheta}(\vartheta^{(a)})\, \phi^{(a)}(\boldsymbol{Z}^{(a)}), \qquad a = \mathrm{I}, \mathrm{II}. \tag{2}$$

The growth function k_{ϑ} is identically adopted from [12] for both growth factors. The growth-driving quantities $\phi^{(a)}$ are chosen such that those stress components are included, which are intended to be reduced, i. e. the principal stresses in the direction of the vectors $\boldsymbol{A}_{\mathrm{g}}^{(a)}$. Based on the isotropic driving force $\phi(\boldsymbol{C}_{\mathrm{e}}\boldsymbol{S}_{\mathrm{e}}) = \boldsymbol{C}_{\mathrm{e}}\boldsymbol{S}_{\mathrm{e}} : \boldsymbol{I}$ proposed in e. g. [11, 8, 16], the projections

$$\phi^{(a)}(\boldsymbol{C}_{\mathrm{e}}\boldsymbol{S}_{\mathrm{e}}) = \boldsymbol{C}_{\mathrm{e}}\boldsymbol{S}_{\mathrm{e}} : \boldsymbol{M}_{\mathrm{e}}^{(a)} \qquad \text{with} \qquad \boldsymbol{M}_{\mathrm{e}}^{(a)} = \boldsymbol{A}_{\mathrm{g}}^{(a)} \otimes \boldsymbol{A}_{\mathrm{g}}^{(a)}, \quad a = \mathrm{I}, \mathrm{II} \tag{3}$$

of the elastic part of the Mandel stress into the directions of the vectors $\boldsymbol{A}_{\mathrm{g}}^{(a)}$ are presumed in the context of anisotropic growth with the multiplicative parts of the growth tensor given by eq. (1). In case of isotropic growth, the isotropic measure $\phi^{(a)}(\boldsymbol{C}_{\mathrm{e}}\boldsymbol{S}_{\mathrm{e}}) = \boldsymbol{C}_{\mathrm{e}}\boldsymbol{S}_{\mathrm{e}} : \boldsymbol{I}$ ($a = \mathrm{I}, \mathrm{II}$) is used. In both cases, each evolution equation depends on both growth factors $\vartheta^{(\mathrm{I})}$ and $\vartheta^{(\mathrm{II})}$ because strain and stress quantities in the intermediate configuration are involved which depend on the overall growth tensor $\boldsymbol{F}_{\mathrm{g}}$. For the numerical treatment of this coupled set of evolution equations see [21], where the procedure of computing the growth factors is described for the case of anisotropic growth. Once the growth factors $\vartheta^{(a)}$ have been identified, strains $\boldsymbol{C}_{\mathrm{e}}$ and stresses $\boldsymbol{S}_{\mathrm{e}}$ are known and the 2$^{\mathrm{nd}}$ Piola-Kirchhoff stress tensor $\boldsymbol{S} = \boldsymbol{F}_{\mathrm{g}}^{-1}\boldsymbol{S}_{\mathrm{e}}\boldsymbol{F}_{\mathrm{g}}^{-T}$ can be computed. Here, the tangent moduli $\mathbb{C} = 2\partial\boldsymbol{S}/\partial\boldsymbol{C}$ are computed numerically using a complex-step derivative approximation scheme [19]. Note that alternatively such schemes can also be applied to the implementation of the global tangent stiffness matrix [2].

2.2 Fiber remodeling

As another important mechanism in arterial tissue besides growth, fiber remodeling is part of the adaptation processes which optimize the load-bearing behavior. The combination of growth and fiber remodeling thus might result in stress distributions which are still more advantageous for the tissue.

In previous numerical examples, as e. g. in [21], the angles $\beta^{(1)}$ and $\beta^{(2)}$ between the fiber vectors and the direction of the first principal stress have been defined as constant over the wall thickness. This is however unrealistic since experimental observations show that the fiber angle is rather distributed through the thickness in healthy arteries. For atherosclerotic arteries, where a complex geometry of the artery is present and the idealization as a cylindrical tube is not applicable anymore, it becomes even more complex. Then, the circumferential, axial and radial directions, and thus the plane in which the fiber families are situated, are difficult to be defined. Therefore, an automated procedure to calculate realistic fiber directions is required, in particular for patient-specific analysis. For the calculation of the fiber orientation vectors subjected to stress-driven remodeling, the definition of the plane of the fiber families as the plane of the first two principal stresses is not sufficient, since it does not allow the determination of the orientation within the plane and thus, the fiber angles $\beta^{(a)}$. Therefore, an additional hypothesis postulated by Hariton et al. [9] is accounted for. Their fiber remodeling mechanism is based on the assumption that the fiber angles with respect to the principal directions are regulated by the ratio of the tensile principal stresses. Then, the target orientation of the fiber vectors in the actual configuration can be expressed by

$$\boldsymbol{a}_{\mathrm{targ}}^{(1)} = \langle\sigma_{\mathrm{I}}\rangle\,\boldsymbol{e}_{\mathrm{I}} + \langle\sigma_{\mathrm{II}}\rangle\,\boldsymbol{e}_{\mathrm{II}} \qquad \text{and} \qquad \boldsymbol{a}_{\mathrm{targ}}^{(2)} = \langle\sigma_{\mathrm{I}}\rangle\,\boldsymbol{e}_{\mathrm{I}} - \langle\sigma_{\mathrm{II}}\rangle\,\boldsymbol{e}_{\mathrm{II}}, \tag{4}$$

where $\boldsymbol{e}_{\mathrm{I}}$ and $\boldsymbol{e}_{\mathrm{II}}$ are unit vectors in the directions associated with the first and second principal stresses σ_{I} and σ_{II}. These are in turn determined by solving the characteristic equation $\det[\boldsymbol{\sigma} - \sigma\boldsymbol{I}] = 0$ of the eigenvalue problem. The use of the Macaulay brackets

$\langle\bullet\rangle = \frac{1}{2}\left(||\bullet|| + \bullet\right)$ guarantees that only positive principal stresses are taken into account. It hence embeds the case of only one tensile principal stress, which may occur in arteries growing strongly in axial direction. Then, both fiber families will arrange in circumferential direction, cf. the numerical examples. The formulation of the constitutive equations often requires knowledge of normalized fiber orientation vectors in the reference configuration, which are given by

$$\boldsymbol{A}^{(a)}_{\text{targ}} = \frac{\boldsymbol{F}^{-1}\boldsymbol{a}^{(a)}_{\text{targ}}}{||\boldsymbol{F}^{-1}\boldsymbol{a}^{(a)}_{\text{targ}}||}\,, \qquad a = 1, 2. \tag{5}$$

The algorithmic treatment of the fiber remodeling model within the framework of finite elements is implemented as proposed by Fausten et al. [7]. There, at first an initial boundary value problem is solved where the external loads and an initial fiber orientation is prescribed. Then, the target fiber vectors are computed based on the assumptions given above. Setting the fiber orientations to the target orientations will influence the stress and strain distribution and thus, again equilibrium has to be accomodated by solving for the resulting displacements. In the context of a nonlinear Finite Element implementation this means that for large changes in the fiber orientation vectors the initial values for the Newton iterations will not be suitable. For this reason, the fiber orientation vectors are updated incrementally, applying only fractions of the whole difference vectors $\boldsymbol{A}^{(a)}_{\text{targ},0} - \boldsymbol{A}^{(a)}$ in such a way, that the change in the fiber angle does not exceed a predefined value. Further details concerning the fiber remodeling approach can be found in [7].

2.3 Combined approach

The presented framework for anisotropic growth in arterial walls relies on the assumption that growth can effectively reduce stresses if it occurs in the planes whose normal vectors are the directions $\boldsymbol{e}_{\text{I}}$ and $\boldsymbol{e}_{\text{II}}$ of the tensile principal stresses. Combining the growth model with the fiber remodeling framework, it is ensured that the two included families of collagen fibers are always arranged symmetrically with respect to the principal stress directions. This allows an identification of the principal stress directions from the fiber orientations, i. e.

$$\boldsymbol{e}_{\text{I}} = \frac{\boldsymbol{A}^{(1)} + \boldsymbol{A}^{(2)}}{||\boldsymbol{A}^{(1)} + \boldsymbol{A}^{(2)}||} \qquad \text{and} \qquad \boldsymbol{e}_{\text{II}} = \frac{\boldsymbol{A}^{(1)} - \boldsymbol{A}^{(2)}}{||\boldsymbol{A}^{(1)} - \boldsymbol{A}^{(2)}||}\,. \tag{6}$$

The vectors $\boldsymbol{A}^{(a)}_{\text{g}}$ in eq. (1) are then trivially given by

$$\boldsymbol{A}^{(\text{I})}_{\text{g}} = \boldsymbol{e}_{\text{I}} \qquad \text{and} \qquad \boldsymbol{A}^{(\text{II})}_{\text{g}} = \boldsymbol{e}_{\text{II}}. \tag{7}$$

With this relations at hand, it is possible to define an anisotropic growth tensor based on the local tissue microstructure, and there is no need of computing structural, geometric directions like the radial, circumferential or axial direction which do in general not coincide with the global coordinate system in patient-specific geometries. In this contribution we

propose to include a growth evolution as soon as the boundary value problem changes, i. e. not only if time proceeds or the loading conditions change, but also if a new fiber orientation is computed. However, we are rather interested in the final saturated state of fiber orientation and stress distribution than in the time-evolution of this process and thus, the growth velocities can be set rather arbitrarily. They will however, influence to some extent the results since faster/slower growth would change the stresses within each remodeling step. Therefore, these velocities can be considered as parameters to the algorithm, which require further analysis. On the other hand, if one was interested in the evolution of growth and remodeling instead of the final saturated state the values of the growth velocities would rather be physical parameters.

2.4 Residual stresses

Residual stresses in arterial walls and the related deformations are three-dimensional and thus strongly dependent on the radial and on the axial position within the vessel. A single parameter is therefore not suitable to entirely characterize the residual stress state [10]. However, since the early attempts of quantifying the magnitude of residual stresses, see e. g. [20], the opening angle experiment is often picked up to explain and to visualize the existence of residual stresses in arterial segments. It is therefore desirable to provide the possibility of simulating such experiments numerically. In this context, axial and radial cuts through the arterial wall have to be simulated in order to permit the expected deformations, namely a contraction in axial direction and an opening of the segment to a certain degree referred to as opening angle. Obviously, such a sudden change of the boundary conditions of a residually stressed body is followed by large deformations which can not be computed in a single step within a non-linear Finite Element framework. Therefore, an alternative procedure, which enables a stepwise identification of the final deformed state, has to be applied. This procedure, see [21] for details, is based on the definition of a secondary boundary value problem using the grown and deformed geometry of the residually stressed arterial segment with altered boundary conditions. In absence of any external load, the stress tensor is updated internally in several steps, such that the related deformation steps are small enough.

It is worth mentioning that the proposed method is also applicable to compute layer-specific opening angles in multilayered arterial segments. The numerical examples in the following section are nonetheless restricted to idealized, one-layered arterial segments and focus on the effect of adding a fiber remodeling formulation to the preexistent growth model, which has also an effect on the residual stresses and deformations. The mentioned opening angle is defined to be the angle between one of the cut edges and the symmetry axis which divides the opened segment into two equal halves. Axial strain in the opened segments is computed with respect to the residually stressed geometry before applying the cuts. It is dependent on the radial position and therefore averaged over the wall thickness.

3 NUMERICAL EXAMPLES OF IDEALIZED ARTERIAL SEGMENTS

For the evaluation of the combined approach for growth and remodeling, idealized arterial segments with material and growth parameters according to Tab. 1 are loaded by an internal pressure of 16 kPa (120 mmHg) and by axial displacements of 8 % or 10 % of the initial length. Five different arterial segments are considered for each load case: a reference segment without growth and remodeling as well as an isotropically and an anisotropically growing segment, each of them with and without remodeling. The initial fiber orientation vectors of two reinforcing fiber families are defined such that they enclose $\pm 30°$ with the circumferential direction. Within the first second of the simulation time, the loads are simultaneously applied and afterwards held constant until $t = 20\,\mathrm{s}$. During the entire time period, depending on the considered case, growth is enabled and remodeling is performed in each time step.

An overview of the resulting stress distributions at $t = 20\,\mathrm{s}$ is given in Fig. 1 (a) for isotropic and Fig. 1 (b) for anisotropic growth. The dashed lines refer to the non-adapting reference segments, whereas solid lines are used for the growing segments (luscious colors) and for the segments where growth and remodeling is taken into account (light colors). Several observations concerning remodeling can be noted. Remodeling strongly reduces

Table 1: Material parameters for arterial tissue [5] and (dimensionless) parameters of the function k_ϑ from [12] used in the numerical examples.

c_1 [kPa]	ϵ_1 [kPa]	ϵ_2 [-]	α_1 [kPa]	α_2 [-]	ϑ^+	k_ϑ^+	m_ϑ^+	ϑ^-	k_ϑ^-	m_ϑ^-
17.5	499.8	2.4	30 001.9	5.1	1.1	1.0	3.0	0.9	1.0	3.0

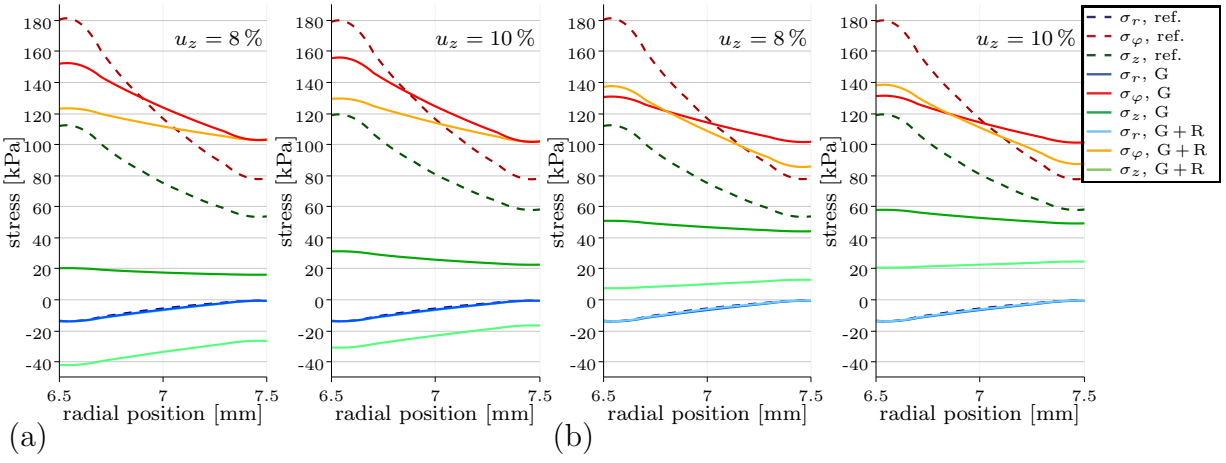

Figure 1: Radial, circumferential and axial stresses in the arterial segments at $t = 20\,\mathrm{s}$ for (a) isotropic and (b) anisotropic growth with and without remodeling at different levels of axial displacement. In each diagram, the reference stresses of the non-growing and non-remodeling artery are given as dashed lines.

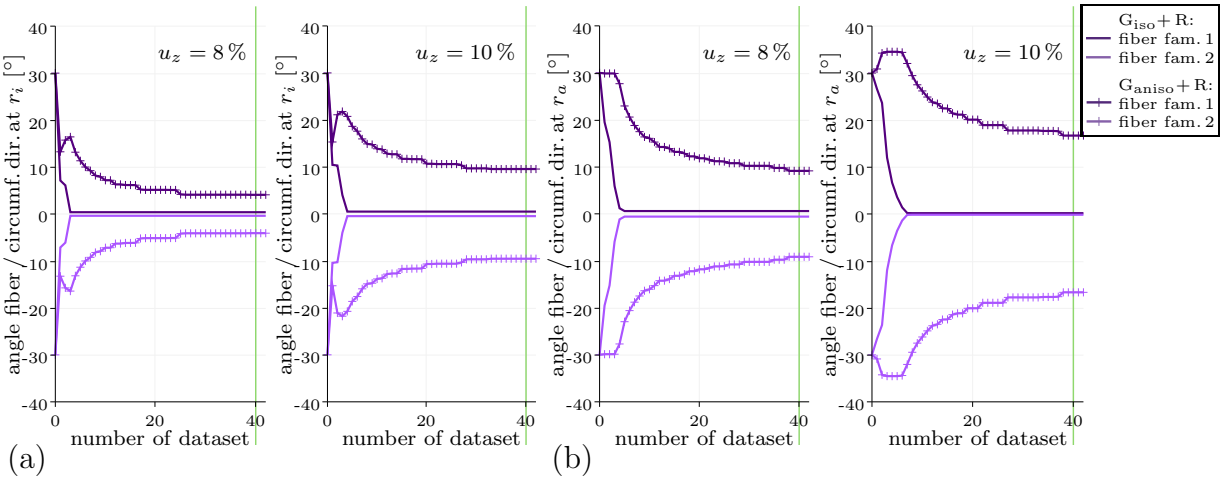

Figure 2: Development of the fiber orientation angles over time at (a) the inner surface and (b) the outer surface of the arterial segment for axial displacements of 8 % and 10 % and for isotropic (solid lines) and anisotropic growth (solid lines with markers). The number of dataset divided by 2 corresponds to time in s. At $t = 20\,\mathrm{s}$, remodeling is deactivated and no more change of the fiber angles takes place.

the axial stresses, especially if isotropic growth is active. This implies that the axial stresses, which are already strongly reduced by growth alone, may fall below zero and become compressive depending on the growth model and the value of the axial displacement. The impact of remodeling on the circumferential stresses varies from case to case. In combination with anisotropic growth, remodeling induces a slight increase of the circumferential stress peak and gradient, the differences between arterial segments with 8 % and 10 % axial displacement are marginal. In contrast to that, positive effects of remodeling on the circumferential stress distributions can be stated in combination with isotropic growth. The circumferential stress peaks are even lower than in the corresponding anisotropically growing segments without remodeling. Moreover, the dependence of the circumferential stresses on the axial displacement is more pronounced if isotropic instead of anisotropic growth is considered.

In Fig. 2 (a) and (b), the development of the angles over the remodeling process between the fiber orientation vectors and the circumferential direction at the inner and at the outer surface of the remodeling arterial segments is shown. Significant differences indicate that the remodeling results are fairly sensitive with respect to the chosen growth model and/or the height of the axial displacement. In isotropically growing segments, where the axial component of growth is larger than in anisotropically growing ones, compressive axial stresses result in an alignment of both fiber families in circumferential direction over the whole wall thickness. For the anisotropically growing segments, the level of axial strain is high enough to obtain two tensile principal stresses. Then, the fibers arrange with angles that are distributed over the wall thickness and lie between 4° and 9° or 9.5° and 16.5° for axial displacements of 8 % or 10 % at the end of the simulated time period, which is rather in line with experimental observations [13, 17].

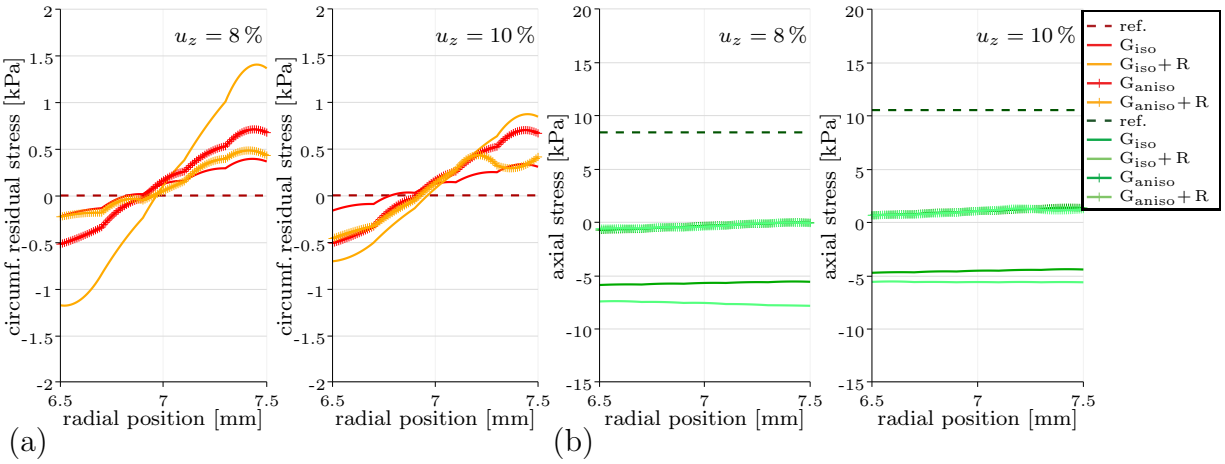

Figure 3: (a) Circumferential residual stresses and (b) axial stresses arterial segments subjected to isotropic or anisotropic growth with and without remodeling at $t = 20\,\mathrm{s}$ after removal of the internal pressure while retaining the axial displacement.

The effect of remodeling on the residual stresses is illustrated in Fig. 3, where the circumferential and the axial stress distributions after the removal of the internal pressure are given. The axial displacement is retained in order to be able to simulate radial and axial cuts in the segments afterwards. Therefore, the axial stresses in Fig. 3 (b) are no residual stresses in the classical meaning since axial loading is still present. Without remodeling, the circumferential residual stresses are almost independent on the two different axial displacements, which can also be seen at the corresponding opening angles given in Tab. 2. This changes drastically if remodeling is included. In combination with isotropic growth, remodeling increases residual stresses and opening angles. In contrast to that, the opposite happens in combination with anisotropic growth. For the considered axial displacements, axial stresses are influenced by remodeling only in case of isotropic growth. Contradicting experimental observations, most of the arterial segments extend after release of the axial boundary, see Tab. 2. However, this could be resolved by applying larger

Table 2: Opening angles and mean axial strain in (residually) stressed arterial segments after simulation of radial and axial cuts.

axial displacement	reference case	isotropic growth	isotropic growth + rem.	anisotropic growth	anisotropic growth + rem.
8 %	0.18°	6.94°	32.59°	11.54°	6.15°
10 %	0.45°	5.09°	21.28°	11.12°	8.68°
8 %	−7.8 %	5.5 %	7.3 %	0.5 %	0.5 %
10 %	−9.9 %	4.5 %	5.4 %	−0.9 %	−0.9 %

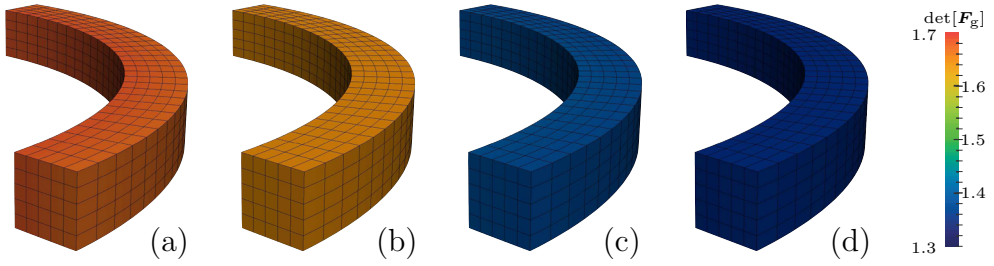

Figure 4: Comparison of the growth deformation of (a) isotropically growing, (b) isotropically growing and remodeling, (c) anisotropically growing and (d) anisotropically growing and remodeling arterial segments subjected to an internal pressure of 16 kPa and an axial displacement of 8 %.

axial displacements which indicates that there may be rather large axial average loads in arteries. In Fig. 4, the determinant J_g of the growth tensor is illustrated to clarify the effect of remodeling on the growth deformation. Arterial segments with activated fiber remodeling manifest lower volume increases than the corresponding segments with fixed fiber orientation vectors. This also holds for axial displacements of 10 %.

4 CONCLUSIONS

A combined approach for growth and remodeling was proposed. Besides the enclosed possibility of simulating isotropic growth, anisotropic growth relating the growth tensor to the local fiber orientation vectors is the main feature of the growth model. In this regard, an automated computation of reasonable fiber distributions is an important enhancement of the model, which has been designed based on the assumption that the two dominating fiber families in arterial tissue arrange symmetrically with respect to the directions of the local tensile principal stresses.

The effects of remodeling on the stress and fiber angle distributions in simulated growing arterial segments were dependent on the chosen growth model and on the ratio between radial and axial loadings. It can be stated that circumferential stress peaks and gradients were reduced for the considered examples of isotropic growth and slightly increased if growth is anisotropic. In each example, remodeling provoked a reduction of axial stresses. As apparent here and also in [21], circumferential residual stresses resulting from isotropic or anisotropic growth were comparatively insensitive with respect to the intensity of the axial displacement. If remodeling was included, the sensitivity of the circumferential residual stresses and opening angles with respect to the axial displacement increased, which was probably caused by the fiber angle distribution with its dependence on the ratio between pressure and axial loading. Summarizing, qualitatively reasonable distributions of residual stresses and fiber orientations were obtained for the anisotropic growth model. Furthermore, it appears that this model does require less growth to enable these stress-regularizing distributions. The knowledge of the obtained fiber orientation vectors was the only necessity for the definition of the anisotropic growth tensor, which

is therefore a local property of the material point and does not depend on external geometric parameters which are difficult to obtain for patient-specific diseased arteries. The effect of the parameters of the growth model, which have been set rather intuitively and identically for each variation of the simulations so far, should be analyzed.

5 ACKNOWLEDGEMENT

The authors greatly appreciate funding from the German Science Foundation (Deutsche Forschungsgemeinschaft DFG) through the institutional strategy "The Synergetic University" at TU Dresden and in the project BA2823/13-2.

REFERENCES

[1] Ambrosi, D.; Ateshian, G. A.; Arruda, E. M.; Cowin, S. C.; Dumais, J.; Goriely, A.; Holzapfel, G. A.; Humphrey, J. D.; Kemkemer, R.; Kuhl, E.; Olberding, J. E.; Taber, L. A.; Garikipati, K. Perspectives on biological growth and remodeling. *J. Mech. Phys. Solids* (2011) **59**:863–883.

[2] Balzani, D.; Gandhi, A.; Tanaka, M.; Schröder, J. Numerical calculation of thermo-mechanical problems at large strains based on a robust approximation scheme for tangent stiffness matrices. *Comput. Mech.* (2015) **55**:861–871.

[3] Balzani, D.; Neff, P.; Schröder, J.; Holzapfel, G. A. A polyconvex framework for soft biological tissues. Adjustment to experimental data. *Int. J. Solids Struct.* (2006) **43**:6052–6070.

[4] Balzani, D.; Schröder, J.; Gross, D. Simulation of discontinuous damage incorporating residual stresses in circumferentially overstretched atherosclerotic arteries. *Acta Biomater.* (2006) **2**:609–618.

[5] Brands, D.; Klawonn, A.; Rheinbach, O.; Schröder, J. Modelling and convergence in arterial wall simulations using a parallel FETI solution strategy. *Comput. Methods Biomech. Biomed. Engin.* (2008) **11**:569–583.

[6] Cyron, C. J.; Humphrey, J. D. Growth and remodeling of load-bearing biological soft tissues. *Meccanica* (2017) **52**:645–664.

[7] Fausten, S.; Balzani, D.; Schröder, J. An algorithmic scheme for the automated calculation of fiber orientations in arterial walls. *Comput. Mech.* (2016). **58**:861–878.

[8] Göktepe, S.; Abilez, O. J.; Kuhl, E. A generic approach towards finite growth with examples of athlete's heart, cardiac dilation, and cardiac wall thickening. *J. Mech. Phys. Solids* (2010) **58**:1661–1680.

[9] Hariton, I.; deBotton, G.; Gasser, T. C.; Holzapfel, G. A. Stress-driven collagen fiber remodeling in arterial walls. *Biomech. Model. Mechan.* (2007) **6**:163–175.

[10] Holzapfel, G. A.; Sommer, G.; Auer, M.; Regitnig, P.; Ogden, R. W. Layer-Specific 3D Residual Deformations of Human Aortas with Non-Atherosclerotic Intimal Thickening. *Ann. Biomed. Eng.* (2007) **35**:530–545.

[11] Kuhl, E.; Maas, R.; Himpel, G.; Menzel, A. Computational modeling of arterial wall growth. Attempts towards patient-specific simulations based on computer tomography. *Biomech. Model. Mechan.* (2007) **6**:321–331.

[12] Lubarda, V. A.; Hoger, A. On the mechanics of solids with a growing mass. *Int. J. Solids Struct.* (2002) **39**:4627–4664.

[13] O'Connell, M.K.; Murthy, S.; Phan, S.; Xu, C.; Buchanan, J.; Spilker, R.; Dalman, R.L.; Zarins, C.K.; Denk, W.; Taylor, C.A. The three-dimensional micro- and nanostructure of the aortic medial lamellar unit measured using 3D confocal and electron microscopy imaging. *Matrix Biology* (2008) **27**:171–181.

[14] Pierce, D. M.; Fastl, T. E.; Rodriguez-Vila, B.; Verbrugghe, P.; Fourneau, I.; Maleux, G.; Herijgers, P.; Gomez, E. J.; Holzapfel, G. A. A method for incorporating three-dimensional residual stretches/stresses into patient-specific finite element simulations of arteries. *J. Mech. Behav. Biomed. Mater.* (2015) **47**:147–164.

[15] Rodriguez, E. K.; Hoger, A.; McCulloch, A. D. Stress-dependent finite growth in soft elastic tissues. *J. Biomech.* (1994) **27**:455–467.

[16] Sáez, P.; Peña, E.; Martínez, M. A.; Kuhl, E. Computational modeling of hypertensive growth in the human carotid artery. *Comput. Mech.* (2014) **53**:1183–1196.

[17] Schriefl, A.J.; Zeindlinger, G.; Pierce, D.M.; Regitnig, P.; Holzapfel, G.A. Determination of the layer-specific distributed collagen fibre orientations in human thoracic and abdominal aortas and common iliac arteries. *J. Roy. Soc. Interface* (2012) **9**, doi = 10.1098/rsif.2011.0727.

[18] Schröder, J.; Brinkhues, S. A novel scheme for the approximation of residual stresses in arterial walls. *Arch. Appl. Mech.* (2014) **84**:881–898.

[19] Tanaka, M.; Fujikawa, M.; Balzani, D.; Schröder, J. Robust numerical calculation of tangent moduli at finite strains based on complex-step derivative approximation and its application to localization analysis. *Comput. Methods Appl. Mech. Engrg.* (2014) **269**:454–470.

[20] Vaishnav, R. N.; Vossoughi, J. Residual stress and strain in aortic segments. *J. Biomech.* (1987), **20**:235–239.

[21] Zahn, A.; Balzani, D. Modeling of Anisotropic Growth and Residual Stresses in Arterial Walls. *Acta Polytechnica CTU Proceedings* (2017) **7**:85–90.

VII International Conference on Computational Methods for Coupled Problems in Science and Engineering
COUPLED PROBLEMS 2017
M. Papadrakakis, E. Oñate and B. Schrefler (Eds)

CONTROLLABILITY OF A RIGID BODY IN A PERFECT FLUID IN THE PRESENCE OF FRICTION

SERGEY M. RAMODANOV[*], ALEXEY A. KIREENKOV[†◊]

[*] A.Blagonravov Institute of Machines Science of the Russian Academy of Sciences
Maly Kharitonievskiy Pereulok 4, Moscow, 101990, Russia
e-mail: ramodanov@mail.ru

[†] Institute for Problems in Mechanics of Russian Academy of Sciences,
Prospekt Vernadskogo 101, korp.1, 119526 Moscow, Russia
[◊] Moscow Institute of Physics and Technology (State University),
Institutskiy per. 9, Dolgoprudny, Moscow Region, 141701, Russia
e-mail: kireenk@ipmnet.ru, kireenk@mail.ru

Key words: Controllability of a rigid body, perfect fluid, viscous friction

Abstract. We study a mechanical system that consists of a 2D rigid body immersed in an unbounded volume of perfect fluid. The body is controlled by two internal point masses. The fluid's influence manifests itself through the added mass effect and dissipation (whose magnitude is small) described by the Rayleigh dissipation function. These assumptions allow for an analytical study of the problem using the small parameter method. Indeed, the unperturbed system (no dissipation) has, according to the Noether's theorem, a complete set of integrals of motion. For a fixed value of the integrals, the equations of motion reduce to a non-autonomous system of ordinary differential equations. The controllability of the system is then studied. In the presence of small dissipative friction these linear in velocities integrals (given their evolution is slow and can therefore be determined via a standard averaging procedure) can still be used to adopt non-dissipative strategies for the dissipative case.

1 INTRODUCTION

A body can propel itself through a liquid provided there is a mechanism of energy transfer between the body and the liquid. In the case of a viscous liquid the mechanism (of course, apart from jet propulsion and its kind) is well known - superficial friction and vortex shedding (e.g. from the tip of a fish's fin). In spite of the obvious importance, there are quite a few mathematically rigorous results (most results in the field have been obtained via computer simulations). In this connection a mention should be made of the famous paper [1], the classical texts of Taylor [2,3] and the book [4].

It is well known that in a perfect liquid the equations governing the motion of the immersed body decouple from the equations of motion of the liquid. This decoupled system of ODEs (Kirchhoff equations) looks more preferable and attractive for mathematical

treatment (since there is no need in solving the Navier-Stokes equations etc.). However, in this perfect realm there is no friction and no vortex shedding meaning that any body-liquid energy transfer (at least at the first glance) is hardly feasible. Many researches overcome this difficulty by *postulating* the vortex shedding [5,6]. Here a question arises: Is vorticity absolutely necessary for a body to be able to propel itself through a *perfect fluid*? The answer is no as it was shown in [7], where a deformable sphere was proved to be able to travel a considerable distance by suitably varying its radii. Moreover [8], thanks to the added-mass effect a body *even with rigid surface* and no moving external parts can take itself as far from its original location as one wishes by redistributing masses inside the body. In this paper we extend the results of [8,10] and offer a control strategy for a body immersed in a resistive medium.

2 PROBLEM STATEMENT

Consider a 2D rigid body moving in an infinite immense of incompressible perfect fluid resting at infinity. There are no other external forces and torques acting on the body except for the hydrodynamic reactions, which manifest themselves through the added-mass effect and small dissipative force described by the Rayleigh dissipation function εR (ε is a small parameter). The body is controlled by two internal masses that move along circles. Their rates of rotation $\Omega_1(t)$ and $\Omega_2(t)$ are the control inputs for the system. The governing equations read:

$$\left(\frac{\partial T}{\partial u}\right)^{\cdot} - \omega\frac{\partial T}{\partial v} = -\varepsilon\frac{\partial R}{\partial u}, \quad \left(\frac{\partial T}{\partial v}\right)^{\cdot} + \omega\frac{\partial T}{\partial u} = -\varepsilon\frac{\partial R}{\partial v}, \quad \left(\frac{\partial T}{\partial \omega}\right)^{\cdot} + u\frac{\partial T}{\partial v} - v\frac{\partial T}{\partial u} = -\varepsilon\frac{\partial R}{\partial \omega} \tag{1}$$

where T is the kinetic energy of the system, u, v and ω are the components of the absolute velocity of the body's center and the angular velocity of the body (Fig. 1a). Both T and R are quadratic forms in u, v and ω, that is,

$$T_{bf} = \frac{a_1 u^2}{2} + \frac{a_2 v^2}{2} + \frac{b\omega^2}{2},$$

$$T = T_{bf} + \frac{m}{2}[(v + \dot{\xi}_1 - \omega\eta_1)^2 + (v + \dot{\eta}_1 + \omega\xi_1)^2 + (u + \dot{\xi}_2 - \omega\eta_2)^2 + (v + \dot{\eta}_2 - \omega\xi_2)^2],$$

$$R = \frac{c_1 u^2}{2} + \frac{c_2 v^2}{2} + \frac{c_3 \omega^2}{2}.$$

Here (ξ_i, η_i) are the coordinates of an i-th point and

$$\xi_1 = r\cos\beta_1 + R, \quad \xi_2 = r\cos\beta_2 - R, \quad \eta_i = r\sin\beta_i$$

$$\dot{\xi}_i = -\Omega_i r\sin\beta_i, \quad \dot{\eta}_i = \Omega_i r\cos\beta_i.$$

The constant coefficients a_1, a_2 and b include the mass (and the added massses) of the body and its moment of inertia (and the added moment of inertia). We assume that $a_2 > a_1$ and $c_2 > c_1$.

The system of equations (1) should be augmented with trivial kinematics

$$\dot{x} = u\cos\alpha - v\sin\alpha, \quad \dot{y} = u\sin\alpha + v\cos\alpha, \quad \dot{\alpha} = \omega,$$

which together with (1) constitute a complete set of equations governing the body+masses+fluid system. Our goal is to design an effective way for steering the body through an appropriate choice of the control inputs $\Omega_1(t)$ and $\Omega_2(t)$.

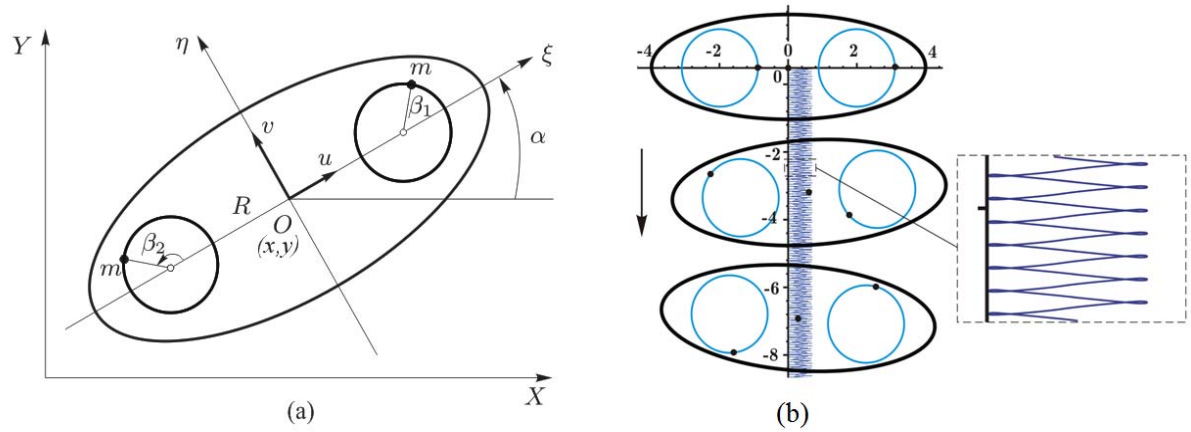

Figure 1. a) 2D body with two internal masses, b) almost rectilinear path of the body's center as the masses uniformly rotate in the opposite directions ($\dot{\beta}_1(t) = -\dot{\beta}_2(t) = \Omega$, $\beta_1(0) = \beta_2(0) = 0$).

3 NO-FRICTION CASE ($\varepsilon = 0$).

In this case, assuming the body to be initially at rest, equation (1), admit three Noether integrals of motion:

$$P_1 = \frac{\partial T}{\partial \dot{x}} = \frac{\partial T}{\partial u}\cos\alpha - \frac{\partial T}{\partial v}\sin\alpha = f_1, \quad P_2 = \frac{\partial T}{\partial \dot{y}} = \frac{\partial T}{\partial u}\sin\alpha + \frac{\partial T}{\partial v}\cos\alpha = f_2 \tag{2}$$

$$P_3 = x\frac{\partial T}{\partial \dot{y}} - y\frac{\partial T}{\partial \dot{x}} + \frac{\partial T}{\partial \omega} = f_3.$$

Assuming the system to be initially at rest leads to $f_i = 0,$ which in its turn gives

$$\frac{\partial T}{\partial u} = \frac{\partial T}{\partial v} = 0, \quad \frac{\partial T}{\partial \omega} = 0.$$

Solving these equations for u, v and ω and substituting the result into the kinematic equations yield what is known as a control-affine system:

$$(\dot{x}, \dot{y}, \dot{\alpha}, \dot{\beta}_1, \dot{\beta}_2)^T = \Omega_1 \mathbf{V}_1 + \Omega_2 \mathbf{V}_2 \tag{3}$$

$$\mathbf{V}_1^T = (X_1(\alpha, \beta_1, \beta_2), Y_1(\alpha, \beta_1, \beta_2), \Phi_1(\beta_1, \beta_2), 1, 0),$$

$$\mathbf{V}_2^T = (X_2(\alpha, \beta_1, \beta_2), Y_2(\alpha, \beta_1, \beta_2), \Phi_2(\beta_1, \beta_2), 0, 1)$$

Here, for example,

$$A_i = a_i + 2m, \quad S = \sin\beta_1 + \sin\beta_2, \quad C = \cos\beta_1 + \cos\beta_2$$

$$\Phi_i = \frac{-A_1A_2mr((-1)^{i+1}R\cos\beta_i + r) + A_1m^2r^2C\cos\beta_i + A_2m^2r^2S\sin\beta_i}{A_1A_2(b + 2m(r^2+R^2) + (-1)^{i+1}2rR(\cos\beta_i - \cos\beta_{i+1})) - A_2m^2S^2 - A_1m^2C^2}.$$

Provided that the body is hydrodynamically non-symmetric (meaning that the body is essentially prolate, i.e. $a_1 \neq a_2$), the system satisfies the conditions of the Rashevsky-Chow [9] theorem and thus is fully controllable [10]. Some effective gaits can be found to prove that the body can be driven to any desired position. For example, when the masses go synchronously in opposite directions the motion of the body's center is practically rectilinear (Fig.1b).

4 DISSIPATIVE CASE ($\varepsilon \neq 0$)

This case presents an intriguing interplay between the viscous friction and the friction proportional to the acceleration (added-mass effect). Now the body can obviously propel itself even with its added masses being equal [11]. In particular, moving the masses synchronously in the opposite directions $\left(\dot\beta_1(t) = -\dot\beta_2(t) = \Omega,\ \beta_1(0) = \beta_2(0) = 0\right)$ no longer produces the path depicted in Fig. 1b – the actual path will gradually deflect to the right as shown in Fig.2. Next we evaluate necessary corrections to the functions $\beta_1(t)$ and $\beta_2(t)$ for the path to remain almost rectilinear.

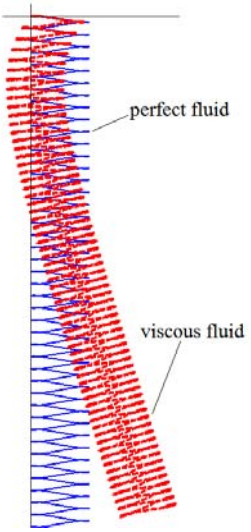

Figure 2: The path of the center of the body generated by the input $\beta_1(t) = -\beta_2(t) = \Omega t$ in the dissipative and non-dissipative cases.

Suppose that for $\varepsilon = 0$ periodic inputs $\beta_1^{(0)}(t)$ and $\beta_2^{(0)}(t)$ (e.g. $\beta_1^{(0)}(t) = -\beta_2^{(0)}(t) = \Omega t$) generated a path $x^{(0)}(t), y^{(0)}(t), \alpha^{(0)}(t), u^{(0)}(t), v^{(0)}(t), \omega^{(0)}(t)$. For $\varepsilon > 0$ the functions P_1 and P_2 from (2) are no longer conserved, that is,

$$\dot{P}_1(t) = -\varepsilon\left(uc_1\cos\alpha - vc_2\sin\alpha\right), \quad \dot{P}_2(t) = -\varepsilon\left(uc_1\sin\alpha + vc_2\cos\alpha\right) \tag{4}$$

Now we plug our unperturbed ($\varepsilon = 0$) path into these equations but leaving $\beta_i(t)$ unchanged. Note that, by virtue of (3) and the kinematic relations, the functions $\cos(\sin)\alpha^{(0)}(t), u^{(0)}(t), v^{(0)}(t), \omega^{(0)}(t)$ are periodic and the period is that of $\beta_i^{(0)}(t)$. Averaging the right-hand sides of (4) gives $P_1(t) = p_1 t,\ P_2(t) = p_2 t,$ where the constants p_i are the corresponding mean values. Solving the two last equations for $\dot{\beta}_1(t)$ and $\dot{\beta}_2(t)$ yield a bulk but structurally simple system of equations

$$\dot{\beta} = F\left(\beta, t, \varepsilon\right),\ \beta = \left(\beta_1, \beta_2\right) \tag{5}$$

The solution to this system can be found in the form $\beta_i(t) = \beta^{(0)}(t) + \varepsilon\beta^{(1)}(t),$ where $\varepsilon\beta^{(1)}(t)$ is the first approximation to the sought-for corrections. For the rectilinear motion in Fig. 2 the corrected inputs generate a path (not depicted in the Figure) which is somewhat intermediate between the viscous and the perfect paths.

Thus, path-planning control in the presence of small dissipation can be implemented as follows: 1) obtain the zeroth approximation $\beta_i^{(0)}(t)$ by solving the problem for $\varepsilon = 0,$ 2) then insert the result into slowly evolving functions $P_i(t)$, which, on averaging, produce the system (5), which can then be solved to obtain the necessary corrections $\varepsilon\beta_i^{(1)}(t)$ to the zeroth inputs $\beta_i^{(0)}(t)$.

ACKNOWLEDGEMENTS

This research was financially supported by the Russian Foundation for Basic Researches under grants No. 16-01-00809-a and No.17-01-00902-a.

REFERENCES

[1] Purcell, E.M. Life at low Reynolds number // Am. J. Phys. 1977. V. 45. № 1. P. 3–11.
[2] Taylor G. I. Analysis of the swimming of long and narrow animals // Proc. Roy. Soc. London.1952. V. 214. P. 158–183.
[3] Taylor G. I. The action of waving cylindrical tails in propelling microscopic organisms // Proc. Roy. Soc. London. Sec. A. 1952. V. 211. P. 225–239.
[4] Childress S. Mechanics of Swimming and Flying. Cambridge University Press. 1981.
[5] Michelin S., Smith S. G. L. Falling cards and flapping flags: understanding fluid-solid interactions using an unsteady point vortex model // Theor. Comput. Fluid Dyn. 2010.V.24. № 1–4. P.195–200.
[6] Wu T. Y. Swimming of a waving plate // J. Fluid. Mech. 1961. V. 10. P. 321–344.
[7] Benjamin T. B., Ellis A. T. The collapse of cavitation bubbles and the pressure thereby produced against solid boundaries // Phil. Trans. Roy. Soc. London. Sec. A. 1966. V. 260. № 1110. P. 221–240.

[8] Kozlov V.V., Ramodanov S.M. The motion of a variable body in an ideal fluid. JAMM 2001; 65(4): 579-88.
[9] Sussmann, H.J. Orbits of families of vector fields and integrability of distributions. *Trans. Amer. Math. Soc* **(**1973) **180**: 171–188.
[10] Ramodanov, S.M., Tenenev, V.A. The motion of a two-dimensional body, controlled by two moving internal masses, in an ideal fluid. *JAMM* (2015) **79(4)**: 325–33.
[11] Chernous'ko, F.L. Optimal control of the motion of a multilink system in a resistive medium. *JAMM* (2012) **76(3)**: 255-67.

VII International Conference on Computational Methods for Coupled Problems in Science and Engineering
COUPLED PROBLEMS 2017
M. Papadrakakis, E. Oñate and B. Schrefler (Eds)

COUPLED DYNAMICS OF SOLID SYSTEM WITH SLIDER-CRANK MECHANISMS AS INTERNAL MOVERS ON ROUGH SURFACE WITH FRICTION

SERGEY V. SEMENDYAEV

Moscow Institute of Physics and Technology (MIPT)
9 Institutskiy per., Dolgoprudny, Moscow Region, 141700, Russian Federation
e-mail: semendyaevsergey@gmail.com, web page: https://mipt.ru/english/

Key words: Coupled Dynamics, Solid System, Internal Movers, Slider-Crank Mechanisms, Dry Friction, Mathematical Modeling.

Abstract. Equations of coupled dynamics of the solid system with slider-crank mechanisms as internal movers are obtained on rough surface with friction for cases of translational and rotational movement by the methods of mathematical modeling. Such class mechanism driven by inner movements of masses being isolated from surrounding space in shell can be used in conditions where traditional movers (wheels, tracks, legs) for some reasons are not applicable.

1 INTRODUCTION

An interest in solid systems driven by inner movements of masses without outer movers, such as wheels, chain tracks, or legs, arises in the last decade [1-4]. A new class of mechanisms (robots), able to move in a resisting medium without external movers due to movement of internal bodies, attracts attention and is studied. At constant outer shell by changing internal geometry of mass the movement of solid system can be carried out in an arbitrary point.

A solid system moving on three points of support is also very attractive for researchers [5-7]. They investigate: dynamics of a body sliding on a rough plane and supported at three points; exact normal forces and trajectories for a rotating tripod sliding on a smooth surface; problems on the motion of a disc with three supports on a rough plane.

This work is devoted to the same class mechanism. Studied solid system consists of main frame (supporting structure) that has three points of contact with rough surface and moves coplanar; and two nesting slider-crank mechanisms that move respectively two internal masses (sliders) relatively to the frame. The crank is rotated by direct-current motor, so in mathematical modelling it moves under assumption of a decreasing linear relationship between torque of motor and angular velocity of its shaft. In dry friction between frame and surface the local Amontons–Coulomb law is used. The movement of the system is studied with the help of mathematical modelling.

The equations of motion of the system with movable masses are obtained. Two types of the frame movement are considered: translational (sliding) and rotational (spinning). Preliminary experimental observations make it possible to assert that approximately periodic movement

can be achieved in sliding or spinning of supporting frame on rough surface.

The movement can be explained qualitatively as follows. Slider-crank mechanism approximately periodically moves masses with different accelerations in different directions. Unequal pulses of the masses are converted into a non-uniform translational/rotational movement of the supporting frame, and hence there are unequal frame pulses differently compensated by friction forces between points of contact and rough surface.

Such class mechanism being isolated from surrounding space in shell can be used in conditions where traditional movers (wheels, tracks, legs) for some reasons are not applicable: corrosive environments or limited in size, on the outside plating of a spaceship or pipeline, in conditions of different planets, etc.

2 MECHANICAL MODEL

3D-concept of the mechanism is shown in Figure 1. As you can see, the solid system has three points of contact with the horizontal surface.

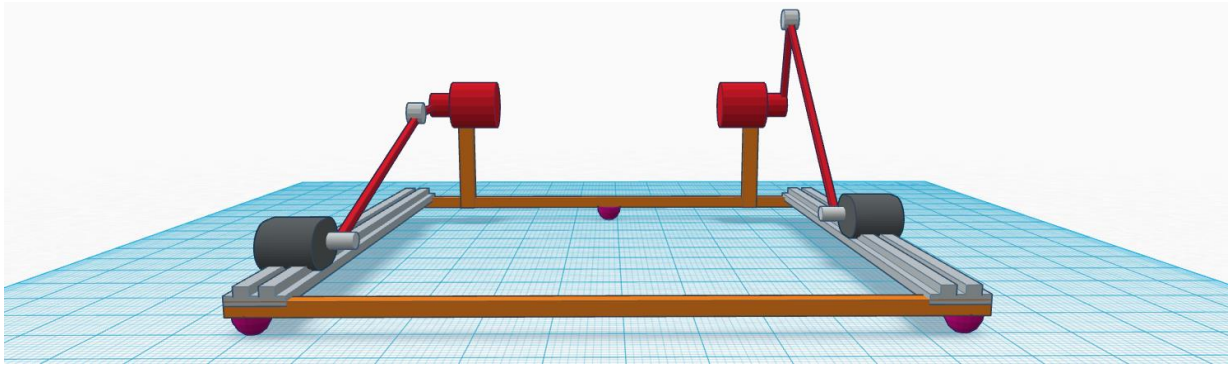

Figure 1: 3D-concept of the model

Two heavy sliders move along the guide rails on the supporting structure. Two motors transmit mechanical power through cranks and links to the sliders. When moving, mechanism does not bounce as well as sliders. It remains in full contact with the surface.

3 MATHEMATICAL MODEL

For motion control on a predictable trajectory let's divide the movement into two basic types. The first – sliding or moving forward in a straight line; and the second – spinning or rotation around a fixed point. In this section we obtain the equations of motion for these cases.

3.1 Underlying assumptions

No friction is inside construction. Friction is only between points of contact and horizontal surface. The friction is described by Amonton-Coulombs law, we use dry friction model. Direct current motor is described by linear dependence between torque and angular velocity of shaft. Supporting structure movement occurs without jumping, as well as sliders. We lay in the model that the contact points do not lose contact with the surface, and the reaction forces

are always opposite to direction of free fall acceleration.

3.2 Translational case (sliding)

Illustration for the translational case of mathematical model is presented in Figure 2.

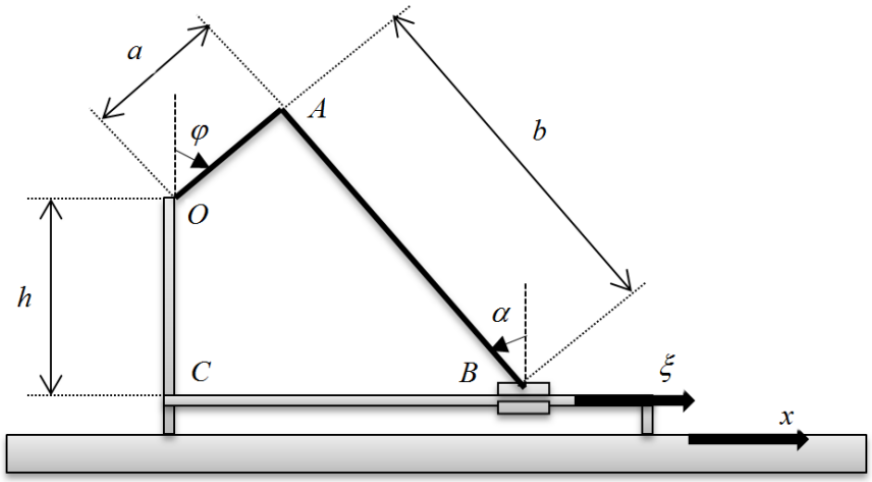

Figure 2: Mathematical model of the translational case (side view)

Mechanical coupling equation for slider-crank mechanism:

$$h + a\cos\varphi = b\cos\alpha \tag{1}$$

Kinetic energy of the system:

$$T = \frac{M\dot{x}_C^2}{2} + \frac{m\dot{x}_B^2}{2} \tag{2}$$

For absolute and relative coordinates we have:

$$x_B = x_C + \xi_B,\ \ \dot{x}_B = \dot{x}_C + \dot{\xi}_B \tag{3}$$

where:

$$\xi_B = a\sin\varphi + b\sin\alpha,\ \ \dot{\xi}_B = a\cos\varphi\dot{\varphi} + b\cos\alpha\dot{\alpha} \tag{4}$$

Taking into account the relation of the equation (1), we have:

$$a\sin\varphi\dot{\varphi} = b\sin\alpha\dot{\alpha} \tag{5}$$

Consequently:

$$\dot{\alpha} = \frac{a\sin\varphi}{b\sin\alpha}\dot{\varphi} \tag{6}$$

So for the relative velocity of slider B:

$$\dot{\xi}_B = a\cos\varphi\dot{\varphi} + \left(h + a\cos\varphi\right)\frac{a\sin\varphi}{b\sin\alpha}\dot{\varphi} \tag{7}$$

In our model $\sin\alpha > 0$, hence we obtain:

$$\sin\alpha = \left(1-\cos^2\alpha\right)^{1/2} = \left(1-\left(\frac{h+a\cos\varphi}{b}\right)^2\right)^{1/2} = \frac{1}{b}\left(b^2-\left(h+a\cos\varphi\right)^2\right)^{1/2} \tag{8}$$

With regard to the latter, we can write for (7):

$$\dot{\xi}_B = a\dot{\varphi}\left(\cos\varphi + \frac{\left(h+a\cos\varphi\right)\sin\varphi}{\left(b^2-\left(h+a\cos\varphi\right)^2\right)^{1/2}}\right) \tag{9}$$

For simplicity, we omit the index:

$$x_C \equiv x \tag{10}$$

Then finally for kinetic energy:

$$T = \frac{M\dot{x}^2}{2} + \frac{m}{2}\left(\dot{x} + a\dot{\varphi}\left(\cos\varphi + \frac{\left(h+a\cos\varphi\right)\sin\varphi}{\left(b^2-\left(h+a\cos\varphi\right)^2\right)^{1/2}}\right)\right)^2 \tag{11}$$

In our model, the potential energy is constant, so we assume it to be zero. The Lagrangian is equal to the kinetic energy.

Generalized force, taking into account the friction forces with the local Amontons–Coulomb law, will be equal to:

$$Q_x = \begin{cases} -\mu N, if\ \dot{x} > 0 \\ 0, if\ \dot{x} = 0 \\ +\mu N, if\ \dot{x} < 0 \end{cases} \equiv -\mu N \operatorname{sgn}\dot{x} \tag{12}$$

And for the generalized force applied to the crank we consider direct-current motor, so in mathematical modelling it moves under assumption of a decreasing linear relationship between torque of motor and its shaft angular velocity:

$$Q_\varphi = \mathrm{A} - \mathrm{B}\dot{\varphi};\quad \dot{\varphi}, \mathrm{A}, \mathrm{B} > 0 \tag{13}$$

The first equation of motion in the Lagrangian form is:

$$\frac{d}{dt}\frac{\partial T}{\partial \dot{x}} - \frac{\partial T}{\partial x} = Q_x \tag{14}$$

Let's denote the following functions:

$$f \equiv \left(h+a\cos\varphi\right)\sin\varphi \tag{15}$$

$$g \equiv \left(b^2-\left(h+a\cos\varphi\right)^2\right)^{1/2} \tag{16}$$

Then rewrite the expression for the kinetic energy in the form:

$$T = \frac{M\dot{x}^2}{2} + \frac{m}{2}\left(\dot{x} + a\dot{\varphi}\left(\cos\varphi + \frac{f}{g}\right)\right)^2 \tag{17}$$

So:

$$\frac{\partial T}{\partial \dot{x}} = M\dot{x} + m\left(\dot{x} + a\dot{\varphi}\left(\cos\varphi + \frac{f}{g}\right)\right); \quad \frac{\partial T}{\partial x} = 0 \tag{18}$$

$$\frac{d}{dt}\frac{\partial T}{\partial \dot{x}} = M\ddot{x} + m\left(\ddot{x} + a\ddot{\varphi}\left(\cos\varphi + \frac{f}{g}\right) + a\dot{\varphi}\left(-\sin\varphi\dot{\varphi} + \left(\frac{f}{g}\right)'\right)\right) \tag{19}$$

It is well known that:

$$\left(\frac{f}{g}\right)' = \frac{f'g - g'f}{g^2} \tag{20}$$

We calculate the derivatives:

$$f' = \left[\left(h + a\cos\varphi\right)\sin\varphi\right]' = -a\sin^2\varphi\dot{\varphi} + \left(h + a\cos\varphi\right)\cos\varphi\dot{\varphi} = \tag{21}$$

$$= \dot{\varphi}\left(a\cos 2\varphi + h\cos\varphi\right)$$

$$g' = \left[\left(b^2 - \left(h + a\cos\varphi\right)^2\right)^{1/2}\right]' = \frac{1}{2g}\left(b^2 - \left(h + a\cos\varphi\right)^2\right)' = \tag{22}$$

$$= \frac{1}{2g}2\left(h + a\cos\varphi\right)a\sin\varphi\dot{\varphi} = \frac{f}{g}a\dot{\varphi}$$

So, for (20) we have:

$$\left(\frac{f}{g}\right)' = \frac{\dot{\varphi}\left(a\cos 2\varphi + h\cos\varphi\right)g - \frac{f}{g}a\dot{\varphi}f}{g^2} = \tag{23}$$

$$= \frac{\dot{\varphi}}{g^3}\left(\left(a\cos 2\varphi + h\cos\varphi\right)g^2 - af^2\right)$$

In this way for (19) we obtain:

$$\frac{d}{dt}\frac{\partial T}{\partial \dot{x}} = \left(M + m\right)\ddot{x} + ma\left(\ddot{\varphi}\left(\cos\varphi + \frac{f}{g}\right) + \dot{\varphi}^2\left(-\sin\varphi + \frac{1}{g^3}\left(\left(a\cos 2\varphi + h\cos\varphi\right)g^2 - af^2\right)\right)\right) \tag{24}$$

Consequently for (14) we have equation:

$$\left(M + m\right)\ddot{x} + ma\left(\ddot{\varphi}\left(\cos\varphi + \frac{f}{g}\right) + \dot{\varphi}^2\left(-\sin\varphi + q\right)\right) = -\mu N\operatorname{sgn}\dot{x} \tag{25}$$

where:

$$q \equiv \frac{1}{g^3}\left(\left(a\cos 2\varphi + h\cos\varphi\right)g^2 - af^2\right) \tag{26}$$

As for normal reaction N, we can find it from projection of Newton's law on the vertical direction (opposite to the free fall acceleration g_{FF}), taking into account that the common center of mass does not move vertically:

$$\left(\left(M+m\right)\vec{a},\vec{n}\right) = \left(\vec{R}^{ext},\vec{n}\right) \;\Rightarrow\; 0 = -\left(M+m\right)g_{FF} + N \tag{27}$$

$$N = \left(M+m\right)g_{FF} \tag{28}$$

Finally the first equation of motion:

$$\left(M+m\right)\ddot{x} + ma\left(\ddot{\varphi}\left(\cos\varphi + \frac{f}{g}\right) + \dot{\varphi}^2\left(-\sin\varphi + q\right)\right) = -\mu\left(M+m\right)g_{FF}\,\mathrm{sgn}\,\dot{x} \tag{29}$$

Now let's consider the second equation of motion in the Lagrangian form:

$$\frac{d}{dt}\frac{\partial T}{\partial\dot{\varphi}} - \frac{\partial T}{\partial\varphi} = Q_\varphi \tag{30}$$

Calculation of derivative gives us:

$$\frac{\partial T}{\partial\dot{\varphi}} = ma\left(\dot{x} + a\dot{\varphi}\left(\cos\varphi + \frac{f}{g}\right)\right)\left(\cos\varphi + \frac{f}{g}\right) \equiv ma\left(\dot{x} + a\dot{\varphi}u\right)u \tag{31}$$

where:

$$u \equiv \cos\varphi + \frac{f}{g} \tag{32}$$

We continue calculation:

$$\frac{d}{dt}\frac{\partial T}{\partial\dot{\varphi}} = \left[ma\left(\dot{x} + a\dot{\varphi}u\right)u\right]' = ma\left(\left(\ddot{x} + a\ddot{\varphi}u + a\dot{\varphi}u'\right)u + \left(\dot{x} + a\dot{\varphi}u\right)u'\right) = \tag{33}$$

$$= ma\left(\left(\ddot{x} + a\ddot{\varphi}u\right)u + \left(\dot{x} + 2a\dot{\varphi}u\right)u'\right)$$

where, taking into account also (23) and (26):

$$u' = \left[\cos\varphi + \frac{f}{g}\right]' = \dot{\varphi}\left(-\sin\varphi + q\right) \tag{34}$$

For simplicity we may assign:

$$w \equiv -\sin\varphi + q \tag{35}$$

Then:

$$\frac{d}{dt}\frac{\partial T}{\partial\dot{\varphi}} = ma\left(\left(\ddot{x} + a\ddot{\varphi}u\right)u + \left(\dot{x} + 2a\dot{\varphi}u\right)\dot{\varphi}w\right) \tag{36}$$

$$\frac{\partial T}{\partial \varphi}=\left[\frac{M\dot{x}^2}{2}+\frac{m}{2}\left(\dot{x}+a\dot{\varphi}u\right)^2\right]'_{\varphi}=m\left(\dot{x}+a\dot{\varphi}u\right)a\dot{\varphi}u'_{\varphi}=m\left(\dot{x}+a\dot{\varphi}u\right)a\dot{\varphi}w \tag{37}$$

Finally the second equation of motion:

$$ma\left\{\left(\ddot{x}+a\ddot{\varphi}u\right)u+auw\dot{\varphi}^2\right\}=\mathrm{A}-\mathrm{B}\dot{\varphi} \tag{38}$$

In (29) and (38) let's express higher derivatives through the lower order:

$$\begin{cases}\left(M+m\right)\ddot{x}+mau\ddot{\varphi}=-\mu\left(M+m\right)g_{FF}\operatorname{sgn}\dot{x}-maw\dot{\varphi}^2\\ u\ddot{x}+au^2\ddot{\varphi}=\dfrac{\mathrm{A}-\mathrm{B}\dot{\varphi}}{ma}-auw\dot{\varphi}^2\end{cases} \tag{39}$$

Or in vector-matrix form:

$$\begin{pmatrix}\beta_{11} & \beta_{12}\\ \beta_{21} & \beta_{22}\end{pmatrix}\begin{pmatrix}\ddot{x}\\ \ddot{\varphi}\end{pmatrix}=\begin{pmatrix}\gamma_1\\ \gamma_2\end{pmatrix} \tag{40}$$

where for coefficients:

$$\begin{aligned}&\beta_{11}=M+m,\quad \beta_{12}=mau,\quad \beta_{21}=u,\quad \beta_{22}=au^2\\ &\gamma_1=-\mu\left(M+m\right)g_{FF}\operatorname{sgn}\dot{x}-maw\dot{\varphi}^2\\ &\gamma_2=\frac{\mathrm{A}-\mathrm{B}\dot{\varphi}}{ma}-auw\dot{\varphi}^2\end{aligned} \tag{41}$$

We can solve the system (40) using Cramer's rule:

$$\begin{pmatrix}\ddot{x}\\ \ddot{\varphi}\end{pmatrix}=\frac{1}{\begin{vmatrix}\beta_{11} & \beta_{12}\\ \beta_{21} & \beta_{22}\end{vmatrix}}\begin{pmatrix}\begin{vmatrix}\gamma_1 & \beta_{12}\\ \gamma_2 & \beta_{22}\end{vmatrix}\\ \begin{vmatrix}\beta_{11} & \gamma_1\\ \beta_{21} & \gamma_2\end{vmatrix}\end{pmatrix}=\frac{1}{\beta_{11}\beta_{22}-\beta_{12}\beta_{21}}\begin{pmatrix}\gamma_1\beta_{22}-\gamma_2\beta_{12}\\ \gamma_2\beta_{11}-\gamma_1\beta_{21}\end{pmatrix} \tag{42}$$

Then we reduce the problem to the Cauchy problem with variables:

$$\begin{pmatrix}\dot{x}\\ \dot{\varphi}\end{pmatrix}=\begin{pmatrix}v\\ \omega\end{pmatrix} \tag{43}$$

$$\begin{pmatrix}\dot{v}\\ \dot{\omega}\end{pmatrix}=\frac{1}{Mau^2}\begin{pmatrix}-\mu\left(M+m\right)g_{FF}au\operatorname{sgn}v-\left(\mathrm{A}-\mathrm{B}\omega\right)u\\ \left(M+m\right)\left(\dfrac{\mathrm{A}-\mathrm{B}\omega}{ma}+\mu g_{FF}u\operatorname{sgn}v\right)-Mauw\omega^2\end{pmatrix}$$

where, taking into account (32) and (35):

$$u=\cos\varphi+\frac{\left(h+a\cos\varphi\right)\sin\varphi}{\left(b^2-\left(h+a\cos\varphi\right)^2\right)^{1/2}} \tag{44}$$

$$w = -\sin\varphi + \frac{\left(a\cos 2\varphi + h\cos\varphi\right)\left(b^2 - \left(h + a\cos\varphi\right)^2\right) - a\left(h + a\cos\varphi\right)^2 \sin^2\varphi}{\left(b^2 - \left(h + a\cos\varphi\right)^2\right)^{3/2}} \tag{45}$$

As we can see the system (43) is valid when $u \neq 0$, but in case of $u = 0$ we should return to the main system of motion (39). This case of $u = 0$ corresponds to the extreme points that the slider may occupy in relative motion on guide rail. It is at these points (or near) that a pulse is transmitted from the slider to the carrier platform. As a result, the platform is moving. Let us assume in equation (39) that $u = 0$, so we obtain the angle corresponding to this value from equation (44):

$$\cos\varphi = \left\{-\frac{h}{a+b}, \frac{h}{b-a}\right\} \tag{46}$$

and substitute in the system (39):

$$\begin{cases} \ddot{x} = -\mu g_{FF}\,\operatorname{sgn}\dot{x} - \dfrac{ma}{M+m} w\left(\dfrac{\mathrm{A}}{\mathrm{B}}\right)^2 \\ \dot{\varphi} = \dfrac{\mathrm{A}}{\mathrm{B}} \end{cases} \tag{47}$$

The latter relations determine the conditions for the onset of motion (note that $\dot{x} = \ddot{x} = 0$ in state of rest), in view of the overcoming of frictional forces.

3.3 Rotational case (spinning)

Illustration for the rotational case of mathematical model is presented in Figure 3.

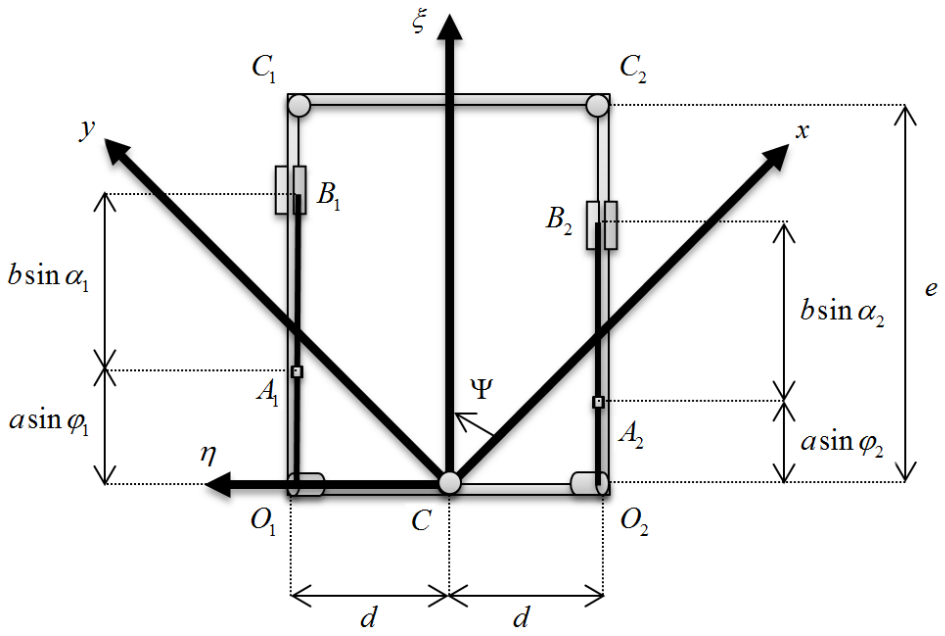

Figure 3: Mathematical model of the rotational case (view from above)

While in the case of the translational motion the sliders moved synchronously, in the case of rotational motion of supporting structure we must consider the movement of the sliders separately. This means that it has to be written for each slider mechanical coupling equation for slider-crank mechanism:

$$h + a\cos\varphi_i = b\cos\alpha_i, \quad i = 1,2 \tag{48}$$

Here, since point C is fixed (center of mass of the support structure coincides with the middle point of contact in the projection onto a plane), the kinetic energy of the system can be written as:

$$T = \sum_{i=1}^{2} \frac{m}{2}\left(\dot{x}_i^2 + \dot{y}_i^2\right) \tag{49}$$

The absolute coordinates of each slider:

$$\vec{r}_{B_i} = \begin{pmatrix} x_i \\ y_i \end{pmatrix} \tag{50}$$

We can link the absolute and relative coordinates through rotation matrix:

$$\vec{r}_{B_i} = A_\Psi \vec{\rho}_{B_i} \tag{51}$$

where:

$$A_\Psi = \begin{pmatrix} \cos\Psi & -\sin\Psi \\ \sin\Psi & \cos\Psi \end{pmatrix} \tag{52}$$

And for relative coordinates of the sliders:

$$\vec{\rho}_{B_1} = \begin{pmatrix} \xi_1 \\ \eta_1 \end{pmatrix} = \begin{pmatrix} a\sin\varphi_1 + b\sin\alpha_1 \\ d \end{pmatrix} \equiv \begin{pmatrix} a\sin\varphi_1 + g_1 \\ d \end{pmatrix}$$
$$\vec{\rho}_{B_2} = \begin{pmatrix} \xi_2 \\ \eta_2 \end{pmatrix} = \begin{pmatrix} a\sin\varphi_2 + b\sin\alpha_2 \\ -d \end{pmatrix} \equiv \begin{pmatrix} a\sin\varphi_2 + g_2 \\ -d \end{pmatrix} \tag{53}$$

where:

$$g_i \equiv \left(b^2 - \left(h + a\cos\varphi_i\right)^2\right)^{1/2} \tag{54}$$

Hence, considering (51) and (52):

$$\vec{r}_{B_i} = \begin{pmatrix} \xi_i\cos\Psi - \eta_i\sin\Psi \\ \xi_i\sin\Psi + \eta_i\cos\Psi \end{pmatrix} \tag{55}$$

For the absolute velocities of the sliders:

$$\vec{v}_{B_i} = \frac{d}{dt}\vec{r}_{B_i} = \begin{pmatrix} \dot{\xi}_i\cos\Psi - \xi_i\sin\Psi\dot{\Psi} - \eta_i\cos\Psi\dot{\Psi} \\ \dot{\xi}_i\sin\Psi + \xi_i\cos\Psi\dot{\Psi} - \eta_i\sin\Psi\dot{\Psi} \end{pmatrix} \tag{56}$$

In (55) we take into account that for the relative coordinates:

$$\eta_i = const \tag{57}$$

By analogy with the translational case (9) for the sliders it can be written:

$$\dot{\xi}_i = a\dot{\varphi}_i\left(\cos\varphi_i + \frac{\left(h + a\cos\varphi_i\right)\sin\varphi_i}{\left(b^2 - \left(h + a\cos\varphi_i\right)^2\right)^{1/2}}\right) = a\dot{\varphi}_i\left(\cos\varphi_i + \frac{f_i}{g_i}\right) \tag{58}$$

where:

$$f_i \equiv \left(h + a\cos\varphi_i\right)\sin\varphi_i \tag{59}$$

On this basis of (56) – (59), we find for kinetic energy:

$$T = \frac{1}{2}\sum_{i=1}^{2}\left(\vec{v}_{B_i}\right)^2 = \frac{1}{2}\sum_{i=1}^{2}\left(\left(a\dot{\varphi}_i\left(\cos\varphi_i + \frac{f_i}{g_i}\right) - \dot{\Psi}\eta_i\right)^2 + \left(\dot{\Psi}\xi_i\right)^2\right) \tag{60}$$

As in the previous case, the potential energy is constant, so we assume it to be zero. The Lagrangian is equal to the kinetic energy.

And for the generalized forces applied to the cranks we consider direct-current motors, so in mathematical modelling they move under assumption of a decreasing linear relationship between torque of motor and its angular velocity:

$$Q_{\varphi i} = \mathrm{A} - \mathrm{B}\dot{\varphi}_i; \quad \dot{\varphi}_i, \mathrm{A}, \mathrm{B} > 0; \quad i = 1,2 \tag{61}$$

For the generalized force of friction we have:

$$Q_\Psi = -\mu\left(e^2 + d^2\right)^{1/2}\left(N_1 + N_2\right)\operatorname{sgn}\dot{\Psi} \tag{62}$$

Since the center of mass does not move relative to the vertical:

$$\left((M + m + m)\vec{a}, \vec{n}\right) = \left(\vec{R}^{ext}, \vec{n}\right) \;\Rightarrow\; 0 = -\left(M + m + m\right)g_{FF} + N + N_1 + N_2 \tag{63}$$

Since the structure does not rotate relatively around its longitudinal axis passing through the point C:

$$\left(\vec{M}_C, \vec{e}_\xi\right) = 0 \quad \Rightarrow \quad N_1 = N_2 \tag{64}$$

And because the structure does not rotate relatively around its transverse axis passing through the point C:

$$\left(\vec{M}_C, \vec{e}_\eta\right) = 0 \quad \Rightarrow \quad -e\left(N_1 + N_2\right) + mg_{FF}\left(\xi_1 + \xi_2\right) = 0 \tag{65}$$

Considering (53), (64) – (65) we obtain:

$$N_1 = N_2 = \frac{mg_{FF}}{2e}\sum_{i=1}^{2}\left(a\sin\varphi_i + \left(b^2 - \left(h + a\cos\varphi_i\right)^2\right)^{1/2}\right) \tag{66}$$

So finally we get for (62):

$$Q_\Psi = -\mu\left(e^2+d^2\right)^{1/2}\frac{mg_{FF}}{e}\sum_{i=1}^{2}\left(a\sin\varphi_i+\left(b^2-\left(h+a\cos\varphi_i\right)^2\right)^{1/2}\right)\operatorname{sgn}\dot{\Psi} \tag{67}$$

The equations of motion in the Lagrangian form are:

$$\frac{d}{dt}\frac{\partial T}{\partial\dot{q}_i}-\frac{\partial T}{\partial q_i}=Q_i,\qquad \vec{q}=\left(\varphi_1,\varphi_2,\Psi\right)^T,\qquad \vec{Q}=\left(Q_{\varphi 1},Q_{\varphi 2},Q_\Psi\right)^T \tag{68}$$

Omitting details of derivatives calculation, we get after reduction to a first-order system:

$$\dot{\omega}_1=\frac{\Delta_1}{\Delta},\qquad \dot{\omega}_2=\frac{\Delta_2}{\Delta},\qquad \dot{\Omega}=\frac{\Delta_3}{\Delta} \tag{69}$$

where we have:

$$\omega_1\equiv\dot{\varphi}_1,\quad \omega_2\equiv\dot{\varphi}_2,\quad \Omega\equiv\dot{\Psi} \tag{70}$$

and where for determinants:

$$\Delta=\begin{vmatrix}\beta_{11}&\beta_{12}&\beta_{13}\\ \beta_{21}&\beta_{22}&\beta_{23}\\ \beta_{31}&\beta_{32}&\beta_{33}\end{vmatrix},\quad \Delta_1=\begin{vmatrix}\gamma_1&\beta_{12}&\beta_{13}\\ \gamma_2&\beta_{22}&\beta_{23}\\ \gamma_3&\beta_{32}&\beta_{33}\end{vmatrix},\quad \Delta_2=\begin{vmatrix}\beta_{11}&\gamma_1&\beta_{13}\\ \beta_{21}&\gamma_2&\beta_{23}\\ \beta_{31}&\gamma_3&\beta_{33}\end{vmatrix},\quad \Delta_3=\begin{vmatrix}\beta_{11}&\beta_{12}&\gamma_1\\ \beta_{21}&\beta_{22}&\gamma_2\\ \beta_{31}&\beta_{32}&\gamma_3\end{vmatrix} \tag{71}$$

for the coefficients in these determinants:

$$\begin{aligned}&\beta_{11}=au_1^2,\quad \beta_{12}=0,\quad \beta_{13}=-u_1d,\quad \beta_{21}=0,\quad \beta_{22}=au_2^2,\quad \beta_{23}=u_2d,\\ &\beta_{31}=-au_1d,\quad \beta_{32}=au_2d,\quad \beta_{33}=\xi_1^2+\xi_2^2+2d^2\\ &\gamma_1=\frac{\mathrm{A}-\mathrm{B}\omega_1}{ma}+\xi_1u_1\Omega-au_1w_1\omega_1^2,\quad \gamma_2=\frac{\mathrm{A}-\mathrm{B}\omega_2}{ma}+\xi_2u_2\Omega-au_2w_2\omega_2^2\\ &\gamma_3=ad\left(w_2\omega_2^2-w_1\omega_1^2\right)-2\Omega a\left(u_1\omega_1+u_2\omega_2\right)-\mu\left(e^2+d^2\right)^{1/2}\frac{g_{FF}}{e}\left(\xi_1+\xi_2\right)\operatorname{sgn}\Omega\end{aligned} \tag{72}$$

with the functions:

$$u_i=\cos\varphi_i+\frac{f_i}{g_i},\quad w_i=-\sin\varphi_i+\frac{1}{g_i^3}\left(\left(a\cos 2\varphi_i+h\cos\varphi_i\right)g_i^2-af_i^2\right) \tag{73}$$

Just as in the case of sliding in the case of spinning there is a division by 0 in the system (69) in some conditions (extreme relative positions of the sliders on guide rails) when $\Delta=a^2u_1^2u_2^2\left(\xi_1^2+\xi_2^2\right)=0$, and we must return to the main (nondeterminant form) system for the case of rotation. If $\Delta\to 0$ then a sharp increase in value of the angular acceleration of supporting structure is observed. If $\Delta=0$ we have:

$$\begin{cases}\ddot{\Psi}=\dfrac{ad\left(\dfrac{A}{B}\right)^2\left(w_1-w_2\right)-\mu\left(e^2+d^2\right)^{1/2}\dfrac{g_{FF}}{e}\left(\xi_1+\xi_2\right)\operatorname{sgn}\dot{\Psi}}{\xi_1^2+\xi_2^2+2d^2}\\ \dot{\varphi}_i=\dfrac{\mathrm{A}}{\mathrm{B}},\quad i=1,2\end{cases} \tag{74}$$

The latter relations determine the conditions for the onset of spinning (note that $\ddot{\Psi}=\dot{\Psi}=0$

at a rest), in view of the overcoming of frictional forces.

4 DISCUSSION

In the equations of translational/rotational motion (43)/(69) under certain conditions $(\Delta = 0 \ \Rightarrow \ u = 0 / u_i = 0)$, corresponding to the extreme position of the sliders on rail guides, certain functions tend to zero, which gives a sharp increase in the values of the accelerations/angular accelerations. When these functions are equal to zero, it is necessary to go to the basic equations of motion, where there is no division by zero and where we can obtain the conditions for the beginning of the movement, meaning the overcoming of frictional forces. The system has periodic functions with respect to the shaft's angle of rotation. In the case of steady motion, this suggests a periodic character of the motion.

5 CONCLUSIONS

- Equations for coupled dynamics of the solid system with slider-crank mechanisms as internal movers are obtained on rough surface with friction for cases of translational and rotational movement.
- Such class mechanism driven by inner movements of masses being isolated from surrounding space in shell can be used in conditions where traditional movers (wheels, tracks, legs) for some reasons are not applicable.

ACKNOWLEDGEMENTS

I would like to thank my colleagues encouraged me to explore new ways of movement.

REFERENCES

[1] Chernous'ko, F.L. and Bolotnik, N.N. and Figurina, T.Yu. Optimal control of vibrationally excited locomotion systems. *Reg. and Chaotic Dynam*. (2013) **18**(1–2):85–99.

[2] Ivanov, A.P. and Sakharov, A.V. Dynamics of rigid body, carrying moving masses and rotor, on a rough plane. *Nelin. Dinam*. (2012) **8**(4):763–772 (Russian).

[3] Volkova, L.Yu. and Jatsun, S.F. Control of the three-mass robot moving in the liquid environment. *Nelin. Dinam.* (2011) **7**(4):845–857 (Russian).

[4] Sakharov, A.V. Rotation of the body with movable internal masses around the center of mass on a rough plane. *Reg. and Chaotic Dynam*. (2015) **20**(4):428-440.

[5] Borisov, A.V. and Mamaev, I.S. and Erdakova, N.N. Dynamics of a body sliding on a rough plane and supported at three points. *Theor. and Appl. Mechanics.* (2016) **43**(2):169-190.

[6] Field, P. On the motion of a disc with three supports on a rough plane. *Phys. Rev. (Series I)*. (1912) **35**:177.

[7] Shegelski, M.R.A. and Goodvin, G.L. and Booth, R. and Bagnall, P. and Reid, M. Exact normal forces and trajectories for a rotating tripod sliding on a smooth surface. *Canad. J. of Physics*. (2004) **82**(11):875-890.

VII International Conference on Computational Methods for Coupled Problems in Science and Engineering
COUPLED PROBLEMS 2017
M. Papadrakakis, E. Oñate and B. Schrefler (Eds)

HOW ONE CAN INTRODUCE COMPLIANCE INTO COMPUTER MODELS OF THE MULTIBODY DYNAMICS USING FEATURES OF OBJECT-ORIENTED MODELING

IVAN I. KOSENKO[*] AND MIKHAIL E. STAVROVSKIY[†]

[*] Moscow Aviation Institute (National Research University)
Volokolamskoe shosse 4, 125993, Moscow, Russia
e-mail: kosenko@ccas.ru
http://www.ccas.ru/depart/mechanics/TUMUS/Kosenko/Kosenko.html

[†] Research Center on Problems for Management of Resource Saving and Waste
Olympic avenue 42, 141006, Mytishi, Moscow region, Russia
e-mail: stavrov@mail.ru

Key words: object-oriented modeling, bond graphs, mechanical constraint, the Hertz contact model, ball bearing model, contact tracking algorithm.

Summary. *Dynamics of a multibody system is simulated in a most universal way in case of contacts having a compliance property. This latter case is implemented usually by elasticity / viscosity along the direction normal to the rigid body outer / inner surface and by friction along its tangent direction. The Hertz model is one of the most popular elastic contact models for engineering applications. Object-oriented approach for building up the multibody dynamics model simulating compliant contacts is under development in this paper. A technology for constructing classes-templates is applied to build up contact objects in the dynamical model. The Hertz contact model is under consideration as a simplest example.*

1 INTRODUCTION

A lot of methods for describing a structure of the multibody system using different graph approaches are known. See for instance [1, 2, 3], and further references one can find there. Usually multibody system is assumed to consist of rigid bodies. Note that in frame of the bond graph approach a background of energy exchanges is used [4].

Either directed or undirected graphs are used depending on the problems to be resolved for implementing the multibody structural analysis based on the force interactions. Using known Newton's laws [5] one can approach the dynamics from so called Newton's viewpoint. In such a way the translational-rotational motion of each body is described by the system of Newton – Euler's ODEs. The multibody system graph structure is constructed using an analysis for mutual interactions of bodies the system composed from. Such interactions are caused mainly by mechanical constraints. In general, Newton's third law of dynamics implies a mutual nature of interactions between the bodies thus causing the system graph to be undirected.

In some particular cases the graph can have a special structure, like it takes place for

holonomic constraints composing the system of tree structure. Such a situation occurs for instance in robotics where the tree structure is used to reduce the source Newton – Euler system of ODEs with an attached subsystem of algebraic equations to some special kind of dynamical equations, like ones of Lagrange of the second kind.

In general case the situation is more complicated, especially if non-holonomic constraints are used. In any way one has to take into account equations of constraints being attached to dynamical ODEs. One can mention that there exists a background for building up models of a type mentioned above using: algorithms [6], modeling languages [7], and compilers [8]. To describe the model of the multibody system under consideration one starts from: (a) an object-oriented paradigm [9] on one hand, and (b) so called physical principles of modeling [10] on the other one.

2 DESCRIPTION USING UNDIRECTED GRAPH

Thus assume the multibody system consists of $m + 1$ bodies $B_0, \ldots, B_m$, see Figure 1. Represent them as composing a finite set $\mathcal{B} = \{B_0,\ldots, B_m\}$. Here B_0 is assumed to be a base body. The body B_0 is assumed to be connected with an inertial frame of reference, or to have a known motion with respect to the inertial frame of reference. One can represent the base body, for example, as a rotating platform, or as a vehicle performing known predefined motion.

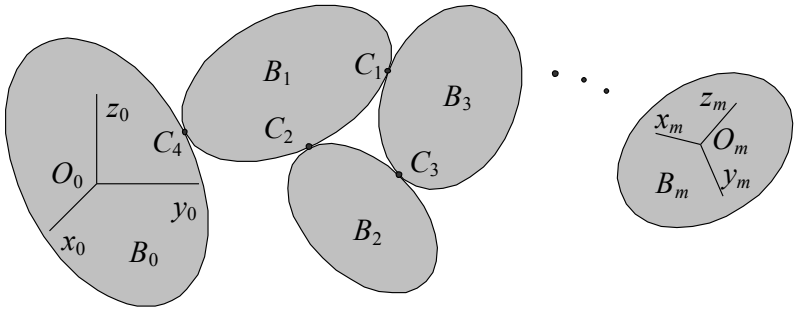

Figure 1: Multibody system

Some bodies are possible to be interconnected mechanically by constraints. Assume that all constraints compose the set $\mathcal{C} = \{C_1,\ldots, C_n\}$. We include in our considerations constraints of the following types: holonomic / nonholonomic, scleronomic / rheonomic, and, what essential, mechanical contacts with compliances.

As a result one can uniquely represent a structure of the multibody system by an undirected graph $G = (\mathcal{B}, \mathcal{C}, \mathcal{I})$. Here $\mathcal{I} \subset \mathcal{C} \times \mathcal{B}$ is an incidence relation setting in a correspondence for every edge $C_i \in \mathcal{C}$ of the graph the vertex $B_k \in \mathcal{B}$ incident to it. According to physical reasons it is easy to see that for any mechanical constraint C_i there exist exactly two bodies / vertices $B_k, B_l \in \mathcal{B}$ being connected by this constraint.

The incidence relation generates an adjacency relation $\mathcal{S} \subset \mathcal{B} \times \mathcal{B}$ on the set of vertices. In our case this relation has the properties: (a) antireflexiveness, a body cannot be connected with itself; (b) symmetry, because of the graph is undirected: if $(B_k, B_l) \in \mathcal{S}$, then $(B_l, B_k) \in \mathcal{S}$.

3 DESCRIPTION USING COMMUNICATION NETWORK

Evidently, one has insufficient structural information derived from graph G for describing the multibody system dynamics. Indeed, in addition to the force interaction which is represented usually by wrenches between bodies B_k, B_l via the constraint C_i one has also a kinematical conditions specific for constraints of different kind. Wrenches acting between interconnected bodies themselves are mutually interconnected by virtue of Newton's third law of dynamics because one can represent these wrenches in turn by constraint forces, and constraint couples.

Thus if one can associate the system of ODEs for translational-rotational motion with the object of a model corresponding to the rigid body, then one can in a natural way associate the system of algebraic equations with the object of a model corresponding to constraint. Note that according to consideration has been done above the set of an algebraic equations is composed of equations for constraint forces (reactions), torques of couples (also reactions), and kinematical equations attached depending on a type of the constraint. So in a way outlined above the differential and algebraic equations are said encapsulated in behavioral sections of objects representing rigid bodies and constraints respectively.

Furthermore, one can reduce any multibody system dynamical model to two subsets of objects: subset of rigid body models (objects $B_0,\ldots, B_m$), and subset of models for constraints (objects $C_1,\ldots, C_n$). According to such an approach simulation of the whole system behavior is reduced to the permanent information interchange between objects of these two types have been enumerated above. Based on Newton's laws of dynamics one can build up the communication network implementing such an interchange.

Information channels connecting objects of two classes from above can also be classified into two types of ports: (a) class for the wrench transportation consisting of the force, torque, and point of the force application; (b) class for the twist transportation consisting of the mass center velocity, rigid body angular velocity plus additional auxiliary kinematical data. In our idealized model force interaction between bodies is performed at a geometric point. Its coordinates are exported to communicative network through the wrench port mentioned permanently in time.

Metaphorically an object of the rigid body class works as follow: it accepts data of wrenches acting to the rigid body and exports kinematical data of this body. At the same time and permanently the constraint object imports kinematical data of two interconnected rigid bodies and exports data of wrenches acting in directions of these two rigid bodies under constraint mentioned and being assumed to be generated by the constraint of specific type. As a result all these objects interact like total communication network permanently in time. The library of classes performing functionality under description here is implemented in frame of Modelica language [7].

One must consider all connections used as bidirected ones. This property corresponds to the undirectional case for the multibody graph edge. Real direction of the causality „flow" is usually defined by the compiler. Such style of the model development is called an acausal modeling [8].

4 DESCRIPTION USING MULTIBOND GRAPH

Let us trace now the similarities between the bond graphs [4] and our models of the

multibody systems. Power is a fundamental property of any (multi) bond graph. To be exact power is associated with or is conducted by the particular multibond at any current instant. Regarding our case consider the power of the forces acting upon the rigid body. Let the rigid body kinematics be defined by the twist (**v**, **ω**), where **v** is the mass center velocity, and **ω** is the rigid body angular velocity. Further let all the forces acting upon the body be reduced to the wrench (**F**, **M**) with the total force **F** and the total torque **M** being reduced to the mass center. Thus the total power of all the forces acting on the body is computed by the known formula: $W = (\mathbf{v}, \mathbf{F}) + (\boldsymbol{\omega}, \mathbf{M})$. This is exactly the same formula using for representing a multibond in the bond graph simulating the multibody system dynamics. We have thus an evident canonical duality between twists and wrenches.

Further, the pair of classes simulating twist and wrench plays a role of the multiport notion, and corresponding pairs of connections in visual model represent a notion of the multibond. One can associate in this way an object of the rigid body class with 1-junction, while 0-junction is associated with the object of a constraint class. The relevant general multibond graph representation of a constraint implementing compliant contact in any multibody system may be depicted as shown in Figure 2.

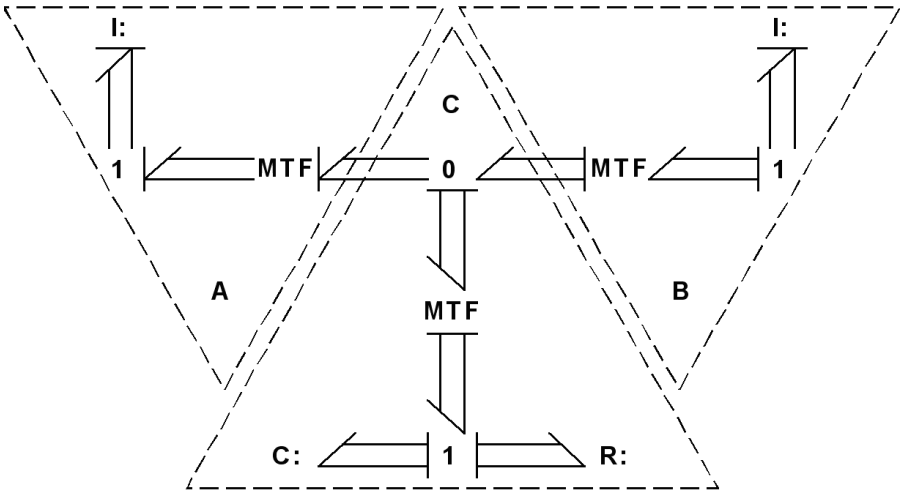

Figure 2: Multibond graph of constraint with compliance

Each multibond here consists of the twist (**v**, **ω**) signals representing the flow component and the wrench (**F**, **M**) signals as an effort. Causality of the inertance element arranges according to the Newton – Euler system of ODEs. Left and right transformers are to shift the twist from the mass center to the contact point according to the known Euler formula: (**v**, **ω**) $\mapsto$ (**v** + [**ω**, **r**], **ω**) where the vector **r** begins at the corresponding mass-center and ends at the point of contact. Reciprocally the wrenches shift to the body mass center from point of the contact in a following way: (**F**, **M**) $\mapsto$ (**F**, **M** + [**r**, **F**]). As one can see easily transformers conserve power.

Central transformer in Figure 2 is responsible for the transfer to orthonormal base at the contact point with the common normal unit vector and two other base unit vectors being tangent ones to both contacting bodies' surfaces. These surfaces supposed regular enough. For

certainty we interpret here the case of usual contact interconnection between the bodies by their outer / inner surfaces. If the inertial coordinates of these vectors compose columns of the orthogonal matrix of rotation Q then for shift from bottom to top across the transformer in Figure 2 one has the relation for the flow signals: $(\mathbf{v}, \boldsymbol{\omega}) \mapsto (Q\mathbf{v}, Q\boldsymbol{\omega})$. Likewise when shifting in a reverse direction one has a transformation of the efforts: $(\mathbf{F}, \mathbf{M}) \mapsto (Q^{-1}\mathbf{F}, Q^{-1}\mathbf{M})$ also conserving the power. Organization of the 0-junction depicted in Figure 2 provides a possibility for computing exactly the relative velocities at the constraint contact point.

Note that usually inertance elements are attached just to 1-junctions of bond graphs. This is because of causality issues in the models. Note also that Figure 2 can remind us in some degree an element of the lumped model for the flexible beam dynamics. On the other hand if we will act in a manner close to the real cases of constraints with the compliance then one has to use a compliant element with the explicit causality thus uniquely determined, see Figure 2, instead of the usual constraint elements. For details see the paper [11].

5 IMPLEMENTATION OF THE MECHANICAL CONTACT GENERAL MODEL

An experience of developing the models for elastic contacting of rigid bodies interactions in the multibody dynamics shows that an object-oriented facility, namely class templates, see Figure 3, provided by Modelica can be used to utilize a wide variety of different properties concerning a contact of solids. The properties are mainly from the following list: 1) geometric properties for surfaces in vicinity of the contact patch: (a) equations defining surfaces, (b) their gradients, (c) the Hesse matrices; 2) a model for computing the contact area dimensions and normal elastic force; 3) model for the normal viscous force of resistance; 4) model for the tangent forces along the tangent plane normal to elastic force.

A submodel of the geometry properties is to describe analytically algebraic surfaces of the structure complex enough [12]. For implementing the normal force computation one can choose now from at least two approaches: the Hertz model, or its volumetric modification [12]. Force of viscous resistance can also be modeled in several different ways: linear, non-linear, one proposed by Lankarani and Nikravesh [13], etc. In the models for tangent forces one can adopt either “simplest” approaches based on the Coulomb friction or more complex ones represented by the Contensou–Erismann [14, 15] model, or other models.

Class parameterization implemented in Modelica is the facility in line to apply to the problem under description. In our case we have four class parameters corresponding to the submodel categories enumerated above. An example to construct specific contact interaction model see in Figure 3. The example includes two stages of inheritance:

1) to derive a template with the force models, namely: the Hertz model for normal force, non-linear viscous force, the Contensou–Erismann model for the tangent dry friction forces;

2) to complete the whole construct one should define a specific geometry submodel for surfaces in contact.

6 CONCLUSIONS

For ellipsoid over the horizontal surface the Hertz model and the volumetric one were compared thoroughly in frame of wide range for different regimes of the ellipsoid motion. Ball bearing model has been verified for different models of elastic contact. The Contensou – Erismann model has been verified using known dynamics of the Tippe-Top.

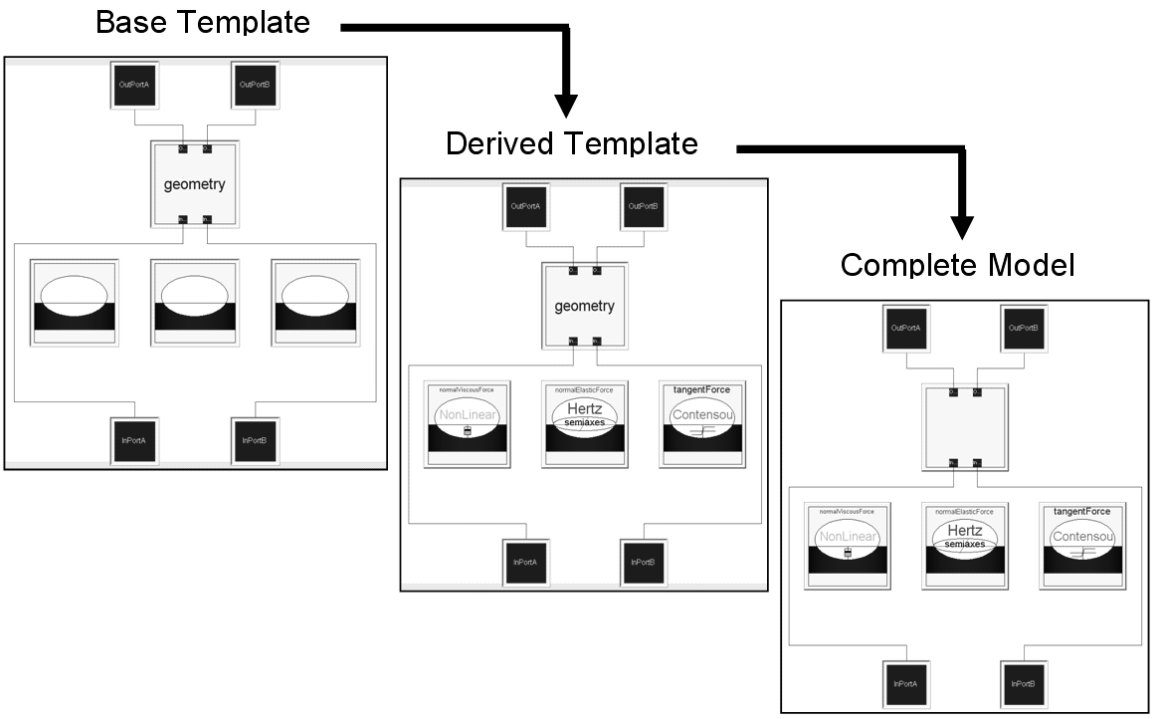

Figure 3: Stages for building up the contact model using templates

One can note the following main conclusions of the paper:

1. Physically-oriented approach for the multibody system dynamics simulation becomes quite easy and efficient, especially if we are going to build up the so-called virtual prototype.

2. An acausal modeling may be efficient and save a lot of time for the system development.

3. It turns out there exists a transparent correspondence between multiport, as a communication network, representation of the multibody dynamics model and its multibond graph representation.

4. Computational experience shows that the differential formulation, if applied properly, of contact tracking algorithm is more preferable than the traditional algebraic or even transcendental formulations. Its differential version becomes more reliable.

5. It turns out that evaluation of the complete elliptic integrals using subsystem of ODEs also has proved to be useful for the Hertz contact model: the computational models have become more reliable and fast.

6. The volumetric algorithm is more reliable and suitable for wide range of the contact area eccentricities, and on the other hand it provides the accuracy of 0.5% compared to the Hertz point algorithm.

7. The Tippe-Top “on head” revolution effect is caused by the dry friction force being distributed over the contact non-zero patch area.

8. For the isotropic case (circular contact area) the average values of the tangent forces for the Coulomb and Contensou–Erismann models are almost identical. But in the anisotropic case the first model becomes inadequate while the second one continues to be correct for the contacting process simulation. This property is important, for example, for a ball bearing simulation where the contact areas are essentially elliptic.

7 ACKNOWLEDGEMENT

The investigation was performed in MAI under financial support provided by RSF, project 14-21-00068.

REFERENCES

[1] Schiehlen, W. and Eberhard, P. *Applied dynamics*. Springer (2014).
[2] Wittenburg, J. *Dynamics of multibody systems: Dynamics of systems of rigid bodies*. Springer (2008).
[3] von Schwerin, R. *Multi body system SIMulation. Numerical methods, algorithms, and software. Lecture notes in computational science and engineering, Vol. 7*. Springer (1999).
[4] Mukherjee, A. and Karmakar, R. *Modelling and simulation of engineering systems through bond graphs*. Alpha Science International Ltd. (2000).
[5] Routh, E. J. *A Treatise on the dynamics of a system of rigid bodies*. London: Vol. 1, (1897), Vol. 2, (1905).
[6] Ascher, U. M. and Petzold, L. R. *Computer methods for ordinary differential equations and differential-algebraic equations*. SIAM (1998).
[7] Fritzson, P. *Principles of object-oriented modeling and simulation with Modelica 2.1*. IEEE Press (2004).
[8] *Dymola. Dynamic modeling laboratory. User manual. Volumes 1, 2. Dymola 7.3*. Dynasim AB (2009).
[9] Booch, G. Maksimchuk, R. A. Engle, M. W. Young, B. J. Conallen, J. and Houston, K. A. *Object-oriented analysis and design with applications (3rd Edition)*. Addison–Wesley (2007).
[10] Cellier, F. E. Elmqvist, H. and Otter, M. Modeling from physical principles. In: Levine W. S. (Ed.), *The control handbook*, CRC Press (1996) 99–107.
[11] Kosenko, I. I. Physically oriented approach to construct multibody system dynamics models using Modelica language, *Proceedings of Multibody 2007, Multibody Dynamics 2007. An ECCOMAS Thematic Conference*, Politecnico di Milano (2007) 20 pp.
[12] Vil'ke, V. G. Kosenko, I. I. and Aleksandrov, E. B., On computer implementation of the Hertz elastic contact model and its simplifications. *Regular and Chaotic Dynamics*. (2009) **14**:693–714.
[13] Flores, P. and Lankarani, H. M. *Contact force models for multibody dynamics*. Springer (2016).
[14] Contensou, P. Couplage entre frottement de glissement et frottement de pivotement dans la théorie de la toupie. *Kreiselprobleme Gyrodynamics: IUTAM Symposium Celerina* (1963) 201–216.
[15] Erismann, Th. Theorie und Anwendungen des echten Kugelgetriebes. *Z. angew. Math. Phys*. (1954) **5**:355–388.

VII International Conference on Computational Methods for Coupled Problems in Science and Engineering
COUPLED PROBLEMS 2017
M. Papadrakakis, E. Oñate and B. Schrefler (Eds)

MOTION OF A CYLINDER RIGID BODY INTERACTING WITH POINT VORTICES

Sokolov S. V.*

*Institute of Machines Science named after A.A.Blagonravov of the Russian Academy of Sciences (IMASH RAN) 4 Maly Kharitonyevsky Pereulok, Moscow 101990, RUSSIA
e-mail: sokolovsv72@mail.ru, web page: http://www.imash.ru/

Key words: point vortices, Hamiltonian systems, stability of equilibrium

Abstract. The dynamical behavior of a heavy circular cylinder and N point vortices in an ideal liquid is considered. The governing equations are presented in Hamiltonian form. Integrals of motion are found. Allowable types of trajectories are discussed. The stability of finding equilibrium solutions is investigated and some remarkable types of partial solutions of the system are presented. The system demonstrate chaotic behavior of dynamics.

1 INTRODUCTION

The problem of falling motion of a body in fluid has a long history and was considered in a series of the classical [7, 15] and modern papers [5, 10, 11, 12, 9, 8]. Some of the effects described in the papers, such as periodic rotation (tumbling), can be encountered only in viscous fluids.

The fluid's viscosity imposes resistive forces on the body. These forces manifest themselves not only through the skin friction but they also serve a source of vortex generation. To evaluate a model which is a more or less realistic and at the same time amenable to analytical treatment it is customary to assume the liquid to be ideal and add the vorticity *ad hoc* meaning that we postulate the existence of, say, circulation, point vortices or vortex sheets etc.

In previous works [14, 13] the problem of motion of the heavy cylinder under the action of gravity and a single point vortex was investigated with non-zero circulation.

In this paper we study the influence of the vorticity on the falling body in a trivial setting: a body (circular cylinder) subject to gravity is interacting dynamically with N point vortices. The circulation around the cylinder is not necessarily zero. So the model we consider here is exact and, at the same time, not so despairingly complex as most of the existing models are.

2 SETTING UP OF THE PROBLEM

Consider a circular cylinder subject to gravity moving in an unbounded volume of ideal liquid at rest at infinity. The cylinders element is orthogonal to the flow; thus the problem is essentially two-dimensional. There are N vortex filaments (point vortices) of strength Γ_i parallel to the cylinders element, here $i = \overline{1, N}$. The circulation Γ of the flow around the cylinder is, generally, different from zero (Fig. 1). Our goal is to detect and investigate the main features of the system.

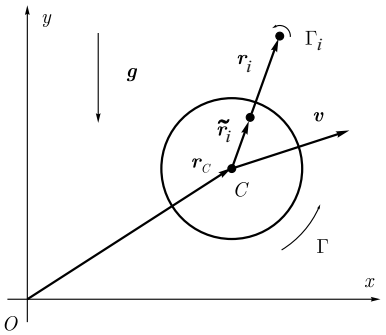

Figure 1: Circular cylinder and point vortices in the gravity field.

3 GOVERNING EQUATIONS

According to [13], the equations of motion for a cylinder and point vortices in the presence of gravity can be written as

$$\begin{aligned}
\dot{\boldsymbol{r}}_i &= -\boldsymbol{v} + \bigtriangledown \widetilde{\varphi}_i(\boldsymbol{r})|_{\boldsymbol{r}=\boldsymbol{r}_i}, \\
\dot{\boldsymbol{r}}_c &= \boldsymbol{v}, \\
a\dot{v}_1 &= \lambda v_2 - \sum_{i=1}^{N} \lambda_i(\dot{\widetilde{y}}_i - \dot{y}_i), \\
a\dot{v}_2 &= -\lambda v_1 + \sum_{i=1}^{N} \lambda_i(\dot{\widetilde{x}}_i - \dot{x}_i) - ag,
\end{aligned} \tag{1}$$

Here $\boldsymbol{r}_c = (x_c,\, y_c)$ is the radius-vector from the origin of a laboratory frame of reference Oxy to the cylinders center, $\boldsymbol{v} = (v_1,\, v_2)$ is the velocity of the cylinder, the radius-vector $\boldsymbol{r}_i = (x_i,\, y_i)$ is from the center of the cylinder to the i-th vortex, and $\widetilde{\boldsymbol{r}}_i = (\widetilde{x}_i,\, \widetilde{y}_i) = \frac{R^2 \boldsymbol{r}_i}{r_i^2}$ is the radius-vector from the center of the cylinder to the image of the i-th vortex (Fig. 1), R — the radius of the cylinder, the constant a is the mass plus the added mass of the cylinder, the constant ag is a gravity force applied to the cylinder, the constants λ and λ_i are related to the circulation and vortexs strength $\lambda = \frac{\Gamma}{2\pi}$, $\lambda_i = \frac{\Gamma_i}{2\pi}$. The density of the

fluid is assumed to be 2π. The function $\widetilde{\varphi}_i(\boldsymbol{r})$ represents that portion of the velocity potential $\varphi(\boldsymbol{r})$ which does not have a singularity at the point $\boldsymbol{r} = \boldsymbol{r}_i$:

$$\varphi(\boldsymbol{r}) = -\frac{R^2}{r^2}(\boldsymbol{r},\, \boldsymbol{v}) - \lambda \arctan\frac{y}{x} + \sum_{i=1}^{N} \lambda_i \left(\arctan\left(\frac{y-\widetilde{y}_i}{x-\widetilde{x}_i}\right) - \arctan\left(\frac{y-y_i}{x-x_i}\right)\right). \quad (2)$$

The equations (1) are similar to those from [13].

As in [13], one can note that the finite-dimensional system (1), which governs the motion of a cylinder and vortices in the gravity field, preserves the standard measure and can be represented in the Hamiltonian form.

Theorem 1. *The equations of motion* (1) *can be represented as follows:*

$$\dot{\zeta}_i = \{\zeta_i,\, H\} = \sum_k \{\zeta_i,\, \zeta_k\} \frac{\partial H}{\partial \zeta_k}, \quad (3)$$

where ζ_i *is the phase vector of the system* (1)*, that is,*

$$\zeta = \{x_1,\, y_1,\, \ldots,\, x_N,\, y_N,\, v_1,\, v_2,\, x_c,\, y_c\},$$

H is the Hamiltonian function, and the components of the skew-symmetric tensor of the Poisson structure $J_{ij}(\zeta) = \{\zeta_i,\, \zeta_j\}$ satisfy the Jacobi identity:

$$\sum_l \left(J_{il}\frac{\partial J_{jk}}{\partial \zeta_l} + J_{kl}\frac{\partial J_{ij}}{\partial \zeta_l} + J_{jl}\frac{\partial J_{ki}}{\partial \zeta_l}\right) = 0, \quad \forall i,\, j,\, k.$$

Proof. It is straightforward to check that the system (1) has a constant of motion which can be interpreted as the energy integral

$$H = \frac{1}{2}av^2 + \frac{1}{2}\sum_{i=1}^{N}\left(\lambda_i^2 \ln(r_i^2 - R^2) - \lambda_i\lambda \ln r_i^2\right) + \frac{1}{2}\sum_{i<j}\lambda_i\lambda_j \ln\frac{R^4 - 2R^2(\boldsymbol{r}_i,\, \boldsymbol{r}_j) + r_i^2 r_j^2}{|\boldsymbol{r}_i - \boldsymbol{r}_j|^2} + agy_c. \quad (4)$$

Assuming H be the Hamiltonian of our system, we now choose the components J_{ij} for the equations of motion (3) to be identical with the equations (1). The non-zero tensor components (as in [13]) read

$$\begin{gathered}
\{v_1,\, x_i\} = \frac{1}{a}\frac{r_i^4 - R^2(x_i^2 - y_i^2)}{r_i^4}, \quad \{v_1,\, y_i\} = -\frac{1}{a}\frac{2R^2 x_i y_i}{r_i^4}, \\
\{v_2,\, x_i\} = -\frac{1}{a}\frac{2R^2 x_i y_i}{r_i^4}, \quad \{v_2,\, y_i\} = \frac{1}{a}\frac{r_i^4 + R^2(x_i^2 - y_i^2)}{r_i^4}, \\
\{v_1,\, v_2\} = \frac{\lambda}{a^2} - \sum_{i=1}^{N}\frac{\lambda_i}{a^2}\frac{r_i^4 - R^4}{r_i^4}, \quad \{x_i,\, y_i\} = -\frac{1}{\lambda_i}, \\
\{x_c,\, v_1\} = \{y_c,\, v_2\} = \frac{1}{a}.
\end{gathered} \quad (5)$$

The check of the validity of the Jacoby identity for the components of (5) is a matter of straightforward computation. □

Thus, the fact that the equations (1) are Hamiltonian allows application of standard tools (e.g. for the stability analysis) from the extensively developed theory of Hamiltonian systems.

4 FIRST INTEGRALS AND REDUCTION

The presence of gravity breaks the rotational symmetry of the system, which implies the absence of an additional integral of motion which existed in the case $g = 0$. However, the system has two integrals of motion due to the translational symmetry: an autonomous integral P — projection of the systems linear momentum on the horizontal axis and a non-autonomous Q — projection of the systems linear momentum on the vertical axis:

$$\begin{aligned} Q &= a(v_2 + gt) + \lambda x_c - \sum_{i=1}^{N} \lambda_i(\widetilde{x}_i - x_i), \\ P &= av_1 - \lambda y_c + \sum_{i=1}^{N} \lambda_i(\widetilde{y}_i - y_i). \end{aligned} \tag{6}$$

Now we reduce the order of our system in the case $N = 1$. The system does not seem to have any additional constants of motion which is confirmed by chaotic behavior of solutions on the Poincaré section surface (Fig. 6, 7). A rigorous proof of non-itegrability of the system consisting of a body (with unequal added masses) with non-zero circulation around it falling in an ideal fluid is given in [2].

Using the autonomous integral P, one can reduce the original three-degree of freedom system to a system with two degrees of freedom.

To do this, put $P = 0$. It is clear that for $\lambda \neq 0$ (the case of $\lambda = 0$ will be addressed elsewhere) this can be always achieved by shifting the origin of the laboratory reference frame. Solving for y_c from the equation $P = 0$, substituting the result into the Hamiltonian (4) and excluding from (1) the equation in $\boldsymbol{r}_c$, we obtain the reduced system:

$$\begin{gathered} \dot{x}_1 = -v_1 + \left.\frac{\partial\widetilde{\varphi}}{\partial x}\right|_{\boldsymbol{r}=\overline{\boldsymbol{r}}_1}, \quad \dot{y}_1 = -v_2 + \left.\frac{\partial\widetilde{\varphi}}{\partial y}\right|_{\boldsymbol{r}=\overline{\boldsymbol{r}}_1}, \\ a\dot{v}_1 = \lambda v_2 - \lambda_1(\dot{\widetilde{y}}_1 - \dot{y}_1), \quad a\dot{v}_2 = -\lambda v_1 + \lambda_1(\dot{\widetilde{x}}_1 - \dot{x}_1) - ag \end{gathered} \tag{7}$$

which remains Hamiltonian with the Hamiltonian function

$$H_c = \frac{1}{2}av^2 + \frac{1}{2}\lambda_1^2 \ln(r_1^2 - R^2) - \frac{1}{2}\lambda_1\lambda \ln r_1^2 + \frac{ag}{\lambda}(av_1 + \lambda_1(\widetilde{y}_1 - y_1))$$

and the bracket structure obtained from (5) by eliminating the rows and columns corresponding to x_c and y_c.

5 CLASSIFICATION OF MOTIONS

Though our system is (comparatively) trivial, very few results concerned with the classification of the possible types of the cylinder and vortex trajectories can be obtained analytically. Numerical evidence show that there exist three types of motion (Fig. 2):

1) the cylinder and vortex are moving close to each other in a horizontal strip of finite width (Fig. 2a);
2) the cylinder "abandons" the vortex and then moves as in the previous case (Fig. 2b);
3) the cylinder "abandons" the vortex and travels down without bound ($y_c \to -\infty$) (Fig. 2c).

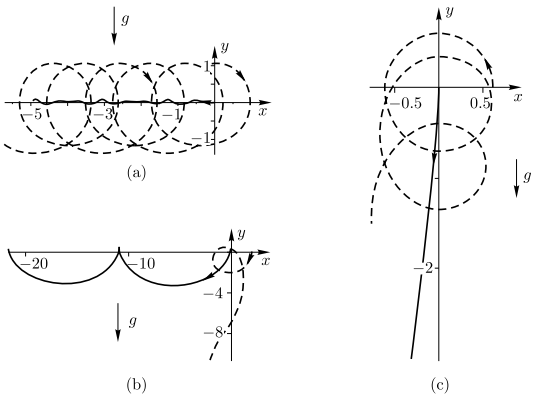

Figure 2: Motion of the cylinder (solid line) and the vortex (dashed line) in the field of gravity: (a) the cylinder and the vortex are moving in a bounded horizontal strip, the vortex is captured by the cylinder; (b) the cylinder moves in a bounded horizontal strip, the vortex is left behind; (c) the cylinder abandons the vortex and falls down without bound ($\lambda = \lambda_1$).

Thus, we have the capture of the vortex by the cylinder as in [4] and motion in a horizontal strip as described in [6].

So we hypothesize (but cannot prove it) that in the course of motion the cylinder is *always confined to a horizontal strip*, except, maybe, for the case $\lambda = \lambda_1$. If the cylinder falls down without bound (the function $y_c(t)$) tends to $-\infty$) the vortex cannot be captured with the cylinder.

6 RELATIVE EQUILIBRIA AND THEIR STABILITY

The stationary solutions of the reduced system (7) are the relative equilibria for the original system (1).

To find the equilibria we equate the right-hand sides of (7) to zero and thereby immediately obtain $v_2 = 0$, $v_1 = -\frac{ag}{\lambda}$. From hydrodynamical considerations it is clear that x_1 is necessarily zero meaning that the vortex and the cylinders center lie on the same vertical

line. (There are two other equilibria lying on the cylinders surface for which $x_1 \neq 0$; but this case is of little interest as the vortex merely annihilates with its image, so we will not consider it). Substituting the found x_1, v_1, and v_2 into the right-hand side of the first equation (7) yields

$$\overline{y}_1^4 + (\widetilde{\lambda}^2 - \widetilde{\lambda}\widetilde{\lambda}_1)\overline{y}_1^3 - \widetilde{\lambda}^2\overline{y}_1 - 1 = 0. \tag{8}$$

Here the following notation is used $\overline{y}_1 = \frac{y_1}{R}$, $\widetilde{\lambda} = \frac{\lambda}{\sqrt{agR}}$, $\widetilde{\lambda}_1 = \frac{\lambda_1}{\sqrt{agR}}$. It is interesting to note that a similar polynomial equation was obtained in [4] where advection of a point vortex in the field generated by an oscillating cylinder was studied.

Thus, the stationary solution of (7) is given by $(x_1,\, y_1,\, v_1,\, v_2) = \big(0,\, y_1,\, -\frac{ag}{\lambda},\, 0\big)$, where $y_1 = \overline{y}_1 R$ and $\overline{y}_1$ is a root of (8). For these solutions the cylinder and vortex are moving horizontally along parallel lines at a constant rate. For a hydrodynamically asymmetric body (the added masses are different) the stability of such rectilinear horizontal motions was investigated in [6].

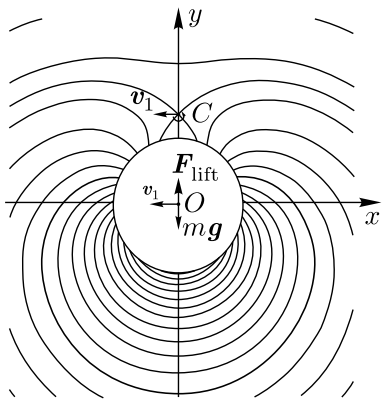

Figure 3: Cylinder and vortex in the state of relative equilibrium.

Physically, it is clear that for a cylinder to move with a constant speed the external forces applied to it must sum up to zero: the gravity must be compensated with the lift, which is due to the circulation. The vortex placed at the stagnation point C (Fig. 3) (at this point the velocity of the fluid particle relative to the cylinder is zero) does not move relative to the cylinder and therefore neither does its image. In this case the vortex exerts no force on the cylinder and therefore cannot prevent the cylinder from moving rectilinearly. The stream lines for this equilibrium case are depicted in Fig. 3.

It follows from (8) that the ordinate of the vortex relative equilibrium depends on the two parameters $\widetilde{\lambda}$ and $\widetilde{\lambda}_1$ (normalized circulation and vortex strength). For some value of $(\widetilde{\lambda},\, \widetilde{\lambda}_1)$ there are up to 4 equilibria (Fig. 4). Here an important restriction $|y_1| > R$ must be obeyed for the vortex to be outside the cylinder. Without loss of generality we assume $\widetilde{\lambda} > 0$. A schematic of the many-leaved surface (8) is given in Fig. 4. Consider the main features of the surface.

1. In the second quadrant of the plane $(\widetilde{\lambda}_1, \widetilde{\lambda})$, where $\widetilde{\lambda}_1 < 0$, $\widetilde{\lambda} > 0$, there is only one equilibrium below the cylinder (the lower leaf of the surface (8)).

2. In the first quadrant $(\widetilde{\lambda}_1 > 0, \widetilde{\lambda} > 0)$ there is an equilibrium above the cylinder (the upper leaf of the surface (8)). The lower leaf has a fold singularity, therefore, as indicted in Fig. 5, there may occur three equilibria: two below and one above the cylinder.

3. The upper leaf of (8) is truncated along the axis $\widetilde{\lambda}_1 = 0$ by the condition $y_1 > R$, meaning that the equilibria positions tend to the cylinders surface from above.

4. As in the previous case, the lower leaf and the fold stitched to it are truncated with the condition $y_1 < -R$ meaning that below the cylinder the equilibria exist in any small neighborhood of its surface.

5. Since (8) is unaltered under the transformation $\widetilde{\lambda}_1 \to -\widetilde{\lambda}_1$, $\widetilde{\lambda} \to -\widetilde{\lambda}$, it is clear that in the third and fourth quadrants the surface (8) can be constructed via rotation by 180° about the $\overline{y}_1$-axis of the surface from Fig. 4.

6. In Fig. 4 the stable equilibria defined by (8) dwell only on the intermediate leaf and are shown with dark-grey shading. The unstable equilibria form the entire upper and lower leaves (light-grey shading); the unstable equilibria on the intermediate leaf form the hatched region.

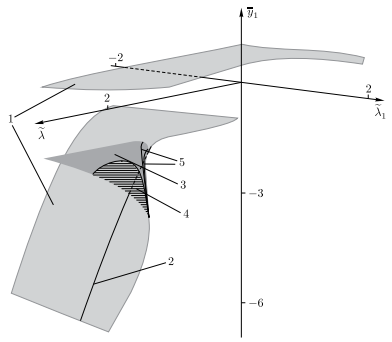

Figure 4: Equilibrium position $\overline{y}_1$ of the vortex depending on the parameters $\widetilde{\lambda}$, $\widetilde{\lambda}_1$: 1 — unstable equilibria ($ind = 1$), 2 — unstable equilibria (the form d^2H_c is degenerate, the instability can be deduced from the linearized equations), 3 — stable equilibria of the center-center type ($ind = 2$), 4 — unstable equilibria of the focus-focus type ($ind = 2$), 5 — resonance curves.

For the stability analysis of the equilibria found we will use the methods and approaches developed in [1]. It is well known that to investigate the stability of an equilibrium solution of a Hamiltonian system the two invariant characteristics of such a solution must be obtained:

1. the index of the quadratic form d^2H_c $\left(\text{i.e. the index of the symmetric } (4\times4)\text{-matrix } \left\|\frac{\partial^2 H_c}{\partial\zeta_k\,\partial\zeta_j}\right\|\right)$, which can vary from 0 to 4;
2. the type of the equilibrium solution depending on the eigenvalues of the linearized vector field $\left(\text{i. e. the eigenvalues of the symplectic } (4\times4)\text{-matrix } \left\|\sum_k J_{ik}\frac{\partial^2 H_c}{\partial\zeta_k\,\partial\zeta_j}\right\|\right)$. This type can be one of the following: center–center, saddle–center, saddle–saddle, focus–focus.

Like in [1], we mark off the eigenvalues of the linearized vector field, which are the roots of the characteristic polynomial

$$\chi(\mu) = \det\left(\sum_k J_{ik}\frac{\partial^2 H_c}{\partial\zeta_k\,\partial\zeta_j} - \mu E\right) = \mu^4 + a\mu^2 + b, \tag{9}$$

on the plane $(a,\ b)$ of the polynomial coefficients. In Fig. 5a from [1], one can see stable and unstable regions, the index of the form d^2H_c, and the types of the equilibrium solutions.

In Fig. 4, the upper and lower leaves are comprised of unstable solutions of the saddle–center type because here the index of d^2H_c is 1. These solutions correspond to the region $b<0$ in Fig. 5a. The points on the intermediate leaf (except for the resonance curves) are either unstable of the focus–focus type or stable of the center–center type; on this leaf the index of d^2H_c is 2.

Consider in greater detail the region in the first quadrant of the plane $(\widetilde{\lambda}_1,\ \widetilde{\lambda})$ where there are three equilibria. A close up of this part of the surface (8) is given in Fig. 5b. As in Fig. 4, the lower and upper leaves of the surface (8) represent unstable solutions with of the saddle–center type with $ind = 1$; the leaves correspond to the region $b<0$ in Fig. 5a. The intermediate leaf contains two types of points: stable (center-center) and unstable (focus–focus); everywhere on this leaf $ind = 2$. The stable solutions correspond to the region $\left(a>0,\ 0<b<\frac{a^2}{4}\right)$ in Fig. 5a. The unstable points form the region $b>\frac{a^2}{4}$. In Fig. 5a and Fig. 5b the third- and fourth-order resonances, defined by the equations $b=\frac{4a^2}{25}$ and $b=\frac{9a^2}{100}$, are shown. The resonances lie within the stable area. The analysis of the stability of the solutions on the boundaries $b=0$, $b=\frac{a^2}{4}$ and the resonance curves is not performed here as it entails a great amount of computation.

Finally, consider the equilibria corresponding to $\widetilde{\lambda}_1 = 2.1$ and $\widetilde{\lambda} = 4$. The Hill domains in the vicinity of these equilibria are depicted in Fig. 5c. The upper and lower equilibria are seen to be unstable and the intermediate one is stable.

Suppose that the circulation around the cylinder increases and the strength of the vortex is fixed. This can be imagined as if a vertical line moves along the $\widetilde{\lambda}$-axis in Fig. 5b. When this line crosses the boundary that corresponds to the parabola $b=\frac{a^2}{4}$ the type of the solution switches from center-center to focus-focus. The Hill domains in the vicinity

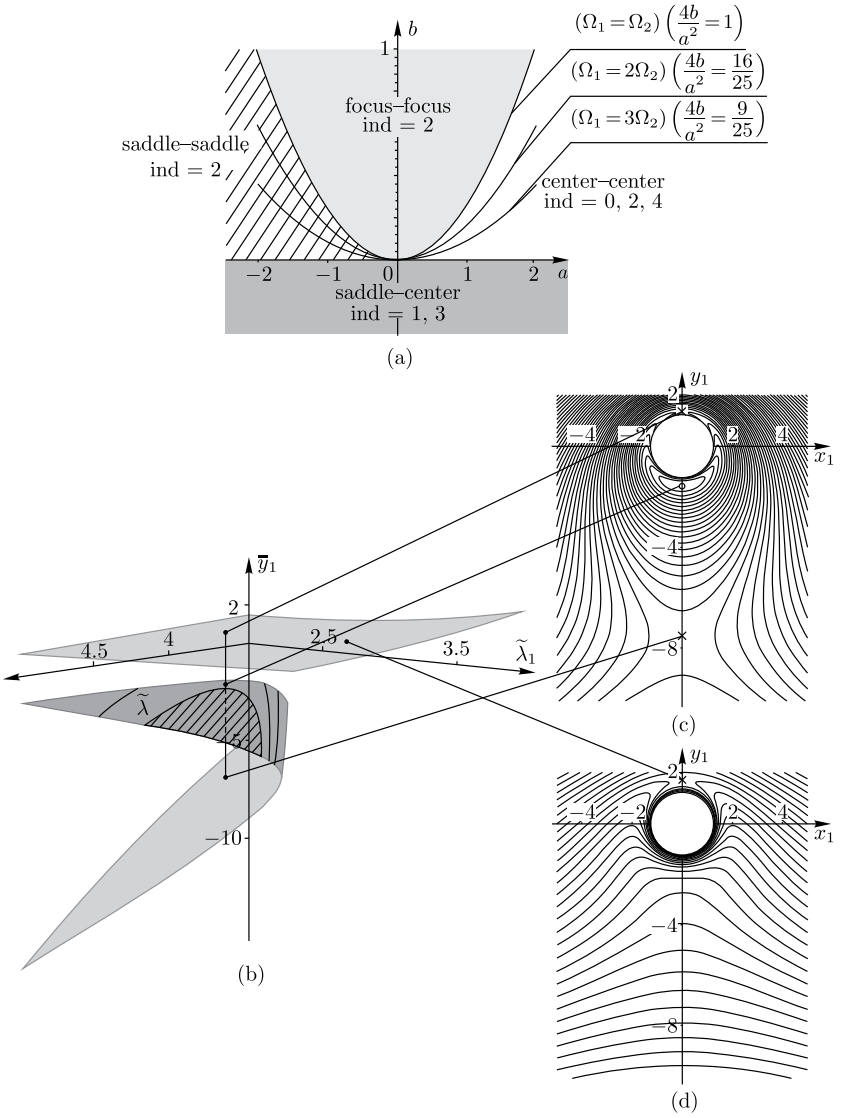

Figure 5: Equilibrium solutions and their stability. (a) Stable and unstable regions in the (a, b) plane of the characteristic polynomial coefficients. The third- and fourth-order resonance curves are shown. (b) The relative equilibrium position of the vortex versus the parameters $\widetilde{\lambda}$, $\widetilde{\lambda}_1$. Depending on the value of $\widetilde{\lambda}$, $\widetilde{\lambda}_1$ there can be a single equilibrium or even three equilibria. (c) The Hill domain for the three-equilibrium case. (d) The Hill domain for the single equilibrium case. In (c) and (d) the unstable equilibria are marked with crosses and the stable equilibria with circles.

of these solutions are analogous to those depicted in Fig. 5c. The intermediate solution becomes unstable.

Now let the circulation be fixed and the vortex strength grow. The imaginary vertical line moves along the $\widetilde{\lambda}_1$-axis. The stable center–center solution approaches the unstable focus–focus solution and they finally merge on the curve that corresponds to $b = 0$. As the vortex strength increases further there remains only one equilibrium (which is unstable) of the saddle–center type and located on the upper leaf (above the cylinder). The schematic of the Hill domain is given in Fig. 5d.

It should be noted that the boundaries that separate the stable solutions with $ind = 2$ from the unstable solutions with $ind = 2$ are very sensitive to the choice of the mass and radius of the cylinder a and R. At the same time, the surface (8) is independent of a and R. The type of the equilibria in Figs. 4 and 5 was determined for $a = 1,\ R = 1$.

7 POINCARÉ SECTION AND CHAOTIC BEHAVIOR OF THE DYNAMICAL SYSTEM

It is known that a system with insufficient number of conserved quantities (first integrals) is usually characterized with chaotic behavior of its trajectories. A strict proof of the property of non-integrability usually involves highly non-trivial mathematical argumentation. On the other hand, the chaotic dynamics of the system's solutions (that can be easily revealed via simulations) indicates the lack of first integrals.

Let us apply this line of reasoning to the system of equations (7), which is a Hamiltonian system with two degrees of freedom. To better understand its dynamics we plot a few Poincaré sections.

The phase vector of the system reads

$$\zeta = \{x_1,\, y_1,\, v_1,\, v_2,\}.$$

We fix $y_1 = 0.9$ thus picking a section plane in a neighborhood of the vortex's relative equilibrium. For $H_c = -17$ the Poincaré section is shown in Fig. 6. The other parameter's values $a = 1$, $R = 0.5$, $g = 10$, $\Gamma = 10$, $\Gamma_1 = 8.4375$.

In Fig. 6 points of the phase plane x_1v_1 which lie outside the region of allowable motion are shown with grey shading. We can see areas of regular dynamics which appear as intersection of the energy level surface and invariant tori. A stochastic layer is presented in the area surrounding second order tori. The appearance of this layer is a striking illustration of chaotic behavior of our system.

We can also build a Poincaré section on the energy level, which permits a spacial separation of points whose projections onto the plane x_1v_1 coincide. Section is depicted in Fig. 7.

In Fig. 7 we can also see regular and chaotic dynamics of the system for the given parameter values. The chaos is evidence of the absence of an additional integral of motion and confirm the hypothesis about non-integrability of our system. It seems to be curious to further explore the dynamics' evolution and possible scenarios of transition to

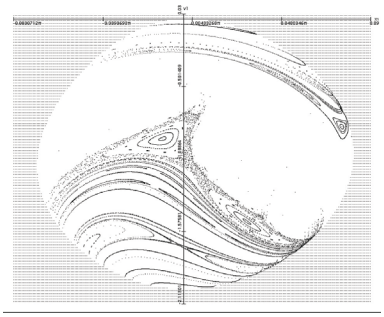

Figure 6: Poincaré section of the reduced cylinder-vortex system for $Hc = -17$; the system exhibits chaotic behavior.

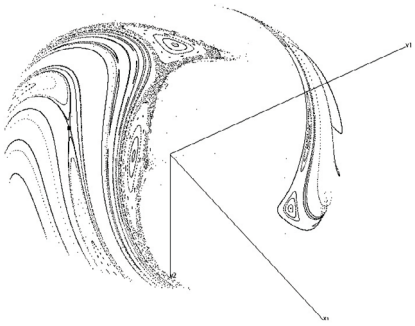

Figure 7: Poincaré section on the energy level $Hc = -17$ of the reduced cylinder-vortex system (the other parameter values are as those in Fig. 6). The small square marker indicates the position of the hyperbolic fixed point.

chaos. Poincaré sections of the reduced cylinder-vortex system are presented. The system exhibits chaotic behavior, which confirms the hypothesis [14, 13] about non-integrability of the system.

8 ACKNOWLEDGMENTS

This work is partially supported by the grants of RFBR No. 160100170, 160100809.

REFERENCES

[1] Bolsinov, A. V., Borisov, A. V., and Mamaev, I. S., The Bifurcation Analysis and the Conley Index in Mechanics, *Regul. Chaotic Dyn.*, 2012, vol. 17, no. 5, pp. 457–478.

[2] Borisov, A. V. and Mamaev, I. S., On the Motion of a Heavy Rigid Body in an Ideal Fluid with Circulation, *Chaos,* 2006, vol. 16, no. 1, 013118, 7 pp.

[3] Borisov, A. V., Ryabov, P. E., and Sokolov, S. V., Bifurcation analysis of the motion of a cylinder and a point vortex in an ideal fluid, *Mathematical Notes,* 2016, vol. 99, no. 5, pp 834–839

[4] Kadtke, J. B. and Novikov, E. A., Chaotic Capture of Vortices by a Moving Body: 1. The Single Point Vortex Case, *Chaos,* 1993, vol. 3, no. 4, pp. 543–553.

[5] Kozlov, V. V., On the Problem of Fall of a Rigid Body in a Resisting Medium, *Mosc. Univ. Mech. Bull.,* 1990, vol. 45, no. 1, pp. 30–36.

[6] Kozlov, V. V., On a Heavy Cylindrical Body Falling in a Fluid, *Izv. Ross. Akad. Nauk Mekh. Tverd. Tela,* 1993, no. 4, pp. 113–117 (Russian).

[7] Maxwell, J. K., On a Particular Case of Descent of a Heavy Body in a Resisting Medium, *Cambridge and Dublin Math. Journ.,* 1854, vol. 9, pp. 145–148.

[8] Sokolov S. V., Falling Motion of a Circular Cylinder Interacting Dynamically with N Point Vortices, *Rus. J. Nonlin. Dyn.,* 2014, vol. 10, no 1, pp. 59–72.

[9] Sokolov, S. V., Falling Motion of a Circular Cylinder Interacting Dynamically with a Vortex Pair in a Perfect Fluid, *Vestn. Udmurtsk. Univ. Mat. Mekh. Komp. Nauki,* 2014, no. 2, 86–99

[10] Sokolov, S. V., On the Problem of Falling Motion of a Circular Cylinder and a Vortex Pair in a Perfect Fluid, *Doklady Mathematics,* 2016, vol. 94, no. 2, pp. 594–597.

[11] Sokolov S. V., Koltsov I. S., Scattering of the Point Vortex by a Falling Circular Cylinder, *Doklady Physics,* 2015, vol. 60. no 11, pp. 511–514.

[12] Sokolov S. V., Koltsov I. S., Chaotic Scattering of the Point Vortex by Falling Circular Cylinder, *Vestn. Udmurtsk. Univ. Mat. Mekh. Komp. Nauki,* 2015, vol. 25, no 2, pp. 184–196.

[13] Sokolov S. V., Ramodanov S. M. Falling Motion of a Circular Cylinder Interacting Dynamically with a Point Vortex, *Reg. & Chaot. Dyn.,* 2013, vol. 18, no 1-2, p. 184–193.

[14] Sokolov S. V., Ramodanov S. M. Falling Motion of a Circular Cylinder Interacting Dynamically with a Point Vortex, *Rus. J. Nonlin. Dyn.,* 2012, vol. 8, no 3, pp. 617–628.

[15] Zhukovskii, N. E., On the Falling in the Air of Light Oblong Bodies Rotating About Their Longitudinal Axis, Paper I, *Collected Papers: Vol. 5,* Moscow–Leningrad: Gostekhizdat, 1937, pp. 72–80.

VII International Conference on Computational Methods for Coupled Problems in Science and Engineering
COUPLED PROBLEMS 2017
M. Papadrakakis, E. Oñate and B. Schrefler (Eds)

ON THE EFFECT OF THE ANISOTROPIC DRY FRICTION AND THE DEFORMED STATE OF TIRES ON THE SHIMMY INITIATION

SERGEY I. ZHAVORONOK[*], ALEXEY A. KIREENKOV[†◊]

[*] Institute of Applied Mechanics of Russian Academy of Sciences,
Leningradskiy Prospekt 7, 125040 Moscow, Russia
e-mail: Zhavoronok@iam.ras.ru

[†] Institute for Problems in Mechanics of Russian Academy of Sciences,
Prospekt Vernadskogo 101, korp.1, 119526 Moscow, Russia
[◊] Moscow Institute of Physics and Technology (State University),
Institutskiy per. 9, Dolgoprudny, Moscow Region, 141701, Russia
e-mail: kireenk@ipmnet.ru, kireenk@mail.ru

Key words: shimmy; anisotropic dry friction; combined kinematics; contact pressure.

Abstract. The shimmy theories based on the Keldysh assumption can be easily implemented analytically and are still quite efficient for the preliminary analysis of the stability of steady state rolling regimes with no slip and spin of tires. On the other hand, such a shimmy theory uses the non-holonomic rolling model, therefore it is inconsistent with unsteady rolling regimes characterized by the non-vanishing sliding and spin. The qualitatively different model accounting the dry friction effect on the stability of motion is constructed on the groundwork of the coupled dry friction theory. This model has shown its' applicability to some practical problems of engineering design even if a wheel is assumed to be rigid. Here the improved model accounting for the tire deforming, the complex contact pressure distribution, and the anisotropy of the dry friction coefficient in case of the combined kinematics is presented.

1 INTRODUCTION

The phenomenon of the shimmy of wheels of aircraft landing gears and automotive vehicles is well-known but not completely studied. Indeed, the traditionally used model of a shimmy proposed by M. V. Keldysh [1] is based on the following assumptions: (a) the sliding in each point of the road-wheel contact area vanishes and (b) the motion instability is induced essentially by the elastic forces appearing in deformed tires. Such an approach result the very simple model with reduced number of degrees of freedom, does not require complex numerical methods and remains still useful in the engineering practice [2]. In the same time the instable motion of various wheels is observed at the stages of non-steady rolling with

significant longitudinal sliding in the contact spot; moreover the spinning can appear in case of the disturbed motion [3]. It is clear that the Keldysh assumptions are inconsistent with such a regime, and the dry friction effects on the motion stability cannot be studied using the traditional shimmy theory [2]. On the other hand the combined kinematics of relative motion in the contact area requires the qualitative improvement of dry friction theories as it was shown by P. Constnsou [4] and Th. Erissmann [5]; the classical Coulomb dry friction law is unable to describe a wide range of phenomena due to the coupling of sliding and spinning.

The rigid wheel shimmy is one of such phenomena; it is induced only by the coupling of the dry friction forces and torque [6, 7]. This effect was found using the new dry friction model so-called "poly-component" or "multi-component" [8, 9] and being the essential improvement of previous theories of Contensou [4] and Erismann [5]. The multi-component theory uses the local formulation of the Coulomb law for each small element of the contact spot where the corresponding summary sliding velocity is resulted by the longitudinal slip and the spinning. Therefore the resultant dry friction force vector and moment are obtained as a result of integration over the contact area; both are depending as well on the slip velocity as on the angular spin velocity. The exact integral formulation for the resultant force vector and couple were obtained in [8] assuming the contact area be small and consequently circular and the contact pressure distribution be Hertzian. These formulae are too complex to use them in the engineering analysis of dynamics of systems with the dry friction; it was shown nevertheless that their linear-fractional approximation is quite sufficient in most dynamical problems [9]. The Pade approximations were later replaced by the new type of the approximate formulae [10]. Such a results were obtained for some others particular cases of the contact pressure distributions [11].

The quasi-rigid wheel theory [9, 10] was applied to investigate the shimmy of landing gears [3, 12-14]. It seems to be a good first approximation, nevertheless this simplest approximate model has almost nothing to do with the real objects of the engineering analysis. Indeed, the Hertzian contact pressure distribution is consistent only with very small deformations of a typical pneumatic tire [15], the contact area is not circular, moreover the dry friction is not isotropic due to the tire tread effect. Thus, the shimmy models [3, 6, 7, 12-14] require some significant improvements as well as the combined dry friction theory [8-11].

The elliptic contact area was considered in [16] under the assumption of the generalized Hertzian contact pressure distribution. In the recently published paper [17] the polynomial approximation of the complex contact pressure distribution in the pneumatic tire obtained from the finite element simulation [15] was introduced into the model assuming the contact spot be circular. On the other hand the dry friction anisotropy was introduced as a generalized Coulomb law by many authors (e. g. see [18-22]), the tensor coefficient of the dry friction was introduced, and the effect of the anisotropy on the dynamics of the material point on the plane was investigated in details [20]. It has to be noted nevertheless that all the mentioned models generalize the classical Coulomb law in case of the simple motion and have nothing to do with the combined kinematics. Here the basics of the improved theory of coupled dry friction are presented, the dry friction anisotropy is introduced, and the formulae for the resultant vector and couple of the dry friction are constructed. Such a model seems to be a good second approximation for a wheel under combined rolling, sliding, and spin and can be applied to study the shimmy initiation conditions.

2 MODEL OF THE COMBINED ROLLING, SLIDING, AND SPIN OF THE RIGID BODY BASED ON THE COUPLED DRY FRICTION THEORY

2.1 On the anisotropic dry friction

In case of the frictional anisotropy induced by the structure of interacting bodies and/or texture of the contacted surface the Amonton-Coulomb dry friction law can be written in the following formulation [18-21]:

$$\mathbf{F} = -\left|N\right|\frac{\mathbf{f}\cdot\mathbf{v}}{\left|\mathbf{v}\right|} \quad (\mathbf{v}\neq 0). \tag{1}$$

Here the second rank tensor $\mathbf{f} = f_{\alpha\beta}\mathbf{e}^{\alpha}\mathbf{e}^{\beta}$ is the dry friction coefficient; $\mathbf{e}^{\alpha}, \alpha = 1,2$ are base vectors of some frame Ox^1x^2 on the plane of interaction of the contacting bodies, $\mathbf{v} = v^{\alpha}\mathbf{e}_{\alpha}$ is the vector of the relative sliding velocity, and the symbol «●» denotes the scalar product. In general $f_{\alpha\beta} \neq f_{\beta\alpha}$ (e. g. see [18, 22]).

Let us consider the dry friction tensor $\mathbf{f}$ be positively defined:

$$\mathbf{v}_1^{\mathrm{T}}\cdot\mathbf{f}_S\cdot\mathbf{v}_1 > 0 \quad \forall\mathbf{v}_1(\mathbf{q}):\ \mathbf{q}\in\Omega\subset R^n, \quad \mathbf{f}_S = \tfrac{1}{2}\left(\mathbf{f}+\mathbf{f}^{\mathrm{T}}\right), \tag{2}$$

where Ω is the configuration space of the considered mechanical system, and $\mathbf{q}$ is the vector of generalized coordinates. Thus, the linear mapping of the set of unit vectors $\mathbf{v}_1$ into the set of dry friction force vectors $\mathbf{F}$ (1) is defined by the linear operator $\mathbf{f}$ (2). As usually, the unit vector $\mathbf{v}_1 = \mathbf{v}/\left|\mathbf{v}\right|$ is the relative sliding director.

The general cohesion condition can be represented in the formulation [20]:

$$I_2(\mathbf{f})\neq 0: \quad I_2^{-2}(\mathbf{f})\left\{I_1^2(\mathbf{f})\left|\mathbf{F}\right|^2 + \left[I_1(\mathbf{f})\mathbf{f}_S + \mathbf{f}^{\mathrm{T}}\cdot\mathbf{f}\right]:\mathbf{F}\otimes\mathbf{F}\right\} = \left|N\right|^2, \tag{3}$$

where $I_1(\mathbf{f})$ and $I_2(\mathbf{f})$ are invariants of dry friction tensor $\mathbf{f}$, and the symbol «⊗» denotes the tensor product. The physical components $f^*_{\alpha\beta}$ of the tensor $\mathbf{f}$ can be defined experimentally on the groundwork of specific tests. For instance the concept proposed by A. Zmitrowiecz [20] can be used; the dry friction forces are measured directly for two non-collinear sliding directions. In general these ones has not to coincide with the base vectors $\mathbf{e}_{\alpha}$ of the main frame Ox^1x^2.

2.2 The local model of the anisotropic dry friction. Differential formulation

In general, the plane-parallel relative motion, i. e. the simultaneous sliding and spinning, of the rigid bodies with the finite contact spot S requires the qualitative improvement of the Amonton-Coulomb dry friction law [5-11]. The first generalized formulation accounting for the spin in the formulae for the dry friction force was proposed by Th. Erissmann [5] and P. Contensou [4]; it was shown that the resultant vector of dry friction forces depends significantly on the spin. V. Zhuravlev [7-9] and A. Kireenkov [9-11] have proposed the further improvement of this concept; finally, the multi-component dry friction theory was

formulated for a general case of combined slip, spin, and rolling [7]. The aim of this theory consists in the differential formulation of the Coulomb law as a local model of the friction interaction in each point of the contact area S:

$$\forall M \in S \quad \boldsymbol{\tau} = -\left|\sigma_{\nu}\right| \frac{\mathbf{f} \cdot \mathbf{v}_{\Sigma}}{\left|\mathbf{v}_{\Sigma}\right|} \quad \left(\mathbf{v}_{\Sigma} \neq 0\right), \tag{4}$$

$$\mathbf{v}_{\Sigma} = \mathbf{v}_0 - R\boldsymbol{\omega}_{\tau} \times \mathbf{e}_3 + \boldsymbol{\omega}_{\nu} \times \mathbf{r}_{\tau}. \tag{5}$$

Here $\mathbf{v}_{\Sigma}$ denotes the summary velocity of the relative slip in the arbitrary point $M \in S$, $\mathbf{v}_0(\mathbf{q})$ is the longitudinal absolute velocity, $\boldsymbol{\omega}_{\tau}(\mathbf{q})$ is the angular velocity of rolling, , $\boldsymbol{\omega}_{\nu}(\mathbf{q})$ is the angular velocity of spinning, $R(M)$ is the curvature radius of the rolling body calculated in the point M, $\mathbf{r}_{\tau}(M)$ is the vector radius of the point $M \in S$ in the plane of contact, $\mathbf{e}_3$ denotes the normal unit vector of the contact plane, $\boldsymbol{\tau}$ is the frictional tangential stress in the contact area S, and σ_{ν} denotes the normal contact pressure. Thus, the cohesion condition (3) can be formulated locally in the point $M \in S$ as follows:

$$I_2^{-2}(\mathbf{f})\left\{I_1^2(\mathbf{f})\left|\boldsymbol{\tau}\right|^2 + \left[I_1(\mathbf{f})\mathbf{f}_S + \mathbf{f}^{\mathrm{T}} \cdot \mathbf{f}\right] : \boldsymbol{\tau} \otimes \boldsymbol{\tau}\right\} = \left|\sigma_{\nu}\right|^2. \tag{6}$$

Let us consider the combined kinematics, i. e. the simultaneous slip, spin, and rolling (5). Therefore, taking into account the dry friction anisotropy, we obtain the following formula for the tangential stress (4):

$$\boldsymbol{\tau}_1 = -\left|\sigma_{\nu}\right|\left|\mathbf{v}_0 + \boldsymbol{\omega}_{\nu} \times \mathbf{r}_{\tau}\right|^{-1} \mathbf{f} \cdot \left(\mathbf{v}_0 - R\boldsymbol{\omega}_{\tau} \times \mathbf{e}_3 + \boldsymbol{\omega}_{\nu} \times \mathbf{r}_{\tau}\right), \tag{7}$$

where the normal pressure accounting for the rolling effect is represented by the linear approximation [23]:

$$\sigma_{\nu} = \sigma_0\left[1 + \left(\mathbf{r}_{\tau} \times \mathbf{h} \cdot \boldsymbol{\omega}_{\tau} / \left|\boldsymbol{\omega}_{\tau}\right|\right) \cdot \mathbf{e}_3\right]. \tag{8}$$

Here $\sigma_0 = \sigma_{\nu}\left(\boldsymbol{\omega}_{\tau} = 0\right)$, and $\mathbf{h} = h_{\alpha\beta}\mathbf{e}^{\alpha}\mathbf{e}^{\beta}$ is the "rolling friction tensor" for the anisotropic elastic body; we assume it being homogeneous and positively defined:

$$\mathbf{h} \neq \mathbf{h}(M); \quad \forall \boldsymbol{\omega}_{\tau} = \boldsymbol{\omega}_{\tau}(\mathbf{q}) \quad \boldsymbol{\omega}_{\tau}^{\mathrm{T}} \cdot \mathbf{h} \cdot \boldsymbol{\omega}_{\tau} > 0. \tag{9}$$

The static normal contact stress σ_0 is determined by the solution of the appropriate contact problem of elasticity theory in quasi-static statement. Thus, the model (7)-(9) allows one to use the static solution as a first approximation to model the coupled rolling and sliding friction, and the complex modeling of the dynamics of contact interaction is not required.

Now, accounting the rolling effect on the contact pressure on the basis of the formula (8) and using the formula (7) for the tangential contact stress that accounts by-turn both sliding (this term is denoted as $\boldsymbol{\tau}_1$) and spinning (this one is denoted as $\boldsymbol{\tau}_2$), we obtain finally the local model of the anisotropic dry friction in case of the combined kinematics:

$$\boldsymbol{\tau} = \boldsymbol{\tau}_1 + \boldsymbol{\tau}_2;$$

$$\boldsymbol{\tau}_1 = -\left|\sigma_0\right|\left[1+\left(\mathbf{r}_\tau \times \frac{\mathbf{h}\cdot\boldsymbol{\omega}_\tau}{\left|\boldsymbol{\omega}_\tau\right|}\right)\cdot\mathbf{e}_3\right]\frac{\mathbf{f}\cdot\left(\mathbf{v}_0 - R\boldsymbol{\omega}_\tau\times\mathbf{e}_3\right)}{\left|\mathbf{v}_0 - R\boldsymbol{\omega}_\tau\times\mathbf{e}_3 + \boldsymbol{\omega}_\nu\times\mathbf{r}_\tau\right|};$$
$$\boldsymbol{\tau}_2 = -\left|\sigma_0\right|\left[1+\left(\mathbf{r}_\tau \times \frac{\mathbf{h}\cdot\boldsymbol{\omega}_\tau}{\left|\boldsymbol{\omega}_\tau\right|}\right)\cdot\mathbf{e}_3\right]\frac{\mathbf{f}\cdot\left(\boldsymbol{\omega}_\tau\times\mathbf{r}_\tau\right)}{\left|\mathbf{v}_0 - R\boldsymbol{\omega}_\tau\times\mathbf{e}_3 + \boldsymbol{\omega}_\nu\times\mathbf{r}_\tau\right|}. \quad (10)$$

2.2 The global model of the anisotropic dry friction under combined kinematics

The dynamic interaction of the slightly deformed rigid body with the rough support plane is defined by the normal reaction $\mathbf{N}$, the resultant vector of tangent forces $\mathbf{T}$, the anti-rolling couple $\mathbf{M}_\tau$, and the dry friction torque $\mathbf{M}_\nu$. These quantities are obtained by integration of the normal contact stress (8) as well as the summary tangential stress (10) over the contact area S. Taking into account the dry friction anisotropy, we can represent the appropriate integral relationships formulated in [16] as follows:

$$\mathbf{N} = \int_S \sigma_\nu \mathbf{e}_3 dS = \int_S \sigma_0 \left[\mathbf{e}_3 + \frac{\mathbf{r}_\tau\times\left(\mathbf{h}\cdot\boldsymbol{\omega}_\tau\right)}{\left|\boldsymbol{\omega}_\tau\right|}\right]dS; \quad (11)$$

$$\mathbf{M}_\tau = \int_S \sigma_\nu \mathbf{r}_\tau\times\mathbf{e}_3 dS = \int_S \sigma_0 \mathbf{r}_\tau\times\left[\mathbf{e}_3 + \frac{\mathbf{r}_\tau\times\left(\mathbf{h}\cdot\boldsymbol{\omega}_\tau\right)}{\left|\boldsymbol{\omega}_\tau\right|}\right]dS; \quad (12)$$

$$\mathbf{T} = -\int_S \boldsymbol{\tau} dS = -\int_S \sigma_0 \left[1 + \frac{\mathbf{r}_\tau\times\left(\mathbf{h}\cdot\boldsymbol{\omega}_\tau\right)}{\left|\boldsymbol{\omega}_\tau\right|}\cdot\mathbf{e}_3\right]\frac{\mathbf{f}\cdot\left(\mathbf{v}_0 - R\boldsymbol{\omega}_\tau\times\mathbf{e}_3 + \boldsymbol{\omega}_\nu\times\mathbf{r}_\tau\right)}{\left|\mathbf{v}_0 + \boldsymbol{\omega}_\nu\times\mathbf{r}_\tau\right|}dS; \quad (13)$$

$$\mathbf{M}_\nu = -\int_S \mathbf{r}_\tau\times\boldsymbol{\tau} dS = -\int_S \sigma_0 \left[1 + \frac{\mathbf{r}_\tau\times\left(\mathbf{h}\cdot\boldsymbol{\omega}_\tau\right)}{\left|\boldsymbol{\omega}_\tau\right|}\cdot\mathbf{e}_3\right]\frac{\mathbf{r}_\tau\times\left[\mathbf{f}\cdot\left(\mathbf{v}_0 - R\boldsymbol{\omega}_\tau\times\mathbf{e}_3 + \boldsymbol{\omega}_\nu\times\mathbf{r}_\tau\right)\right]}{\left|\mathbf{v}_0 + \boldsymbol{\omega}_\nu\times\mathbf{r}_\tau\right|}dS. \quad (14)$$

In the formula (11), the resultant force $\mathbf{N}_0$ of the static contact pressure σ_0 and it's variation $\mathbf{N}_1$ induced by the rolling effect can be written as follows:

$$\mathbf{N}_0 = N_0\mathbf{e}_3, \quad N_0 = \int_S \sigma_0 dS; \quad (15)$$

$$\mathbf{N}_1 = \int_S \sigma_0 \frac{\mathbf{r}_\tau\times\left(\mathbf{h}\cdot\boldsymbol{\omega}_\tau\right)}{\left|\boldsymbol{\omega}_\tau\right|}dS = N_1\mathbf{e}_3, \quad N_1 = -\mathbf{S}_\sigma\cdot\mathbf{h}\cdot\frac{\boldsymbol{\omega}_\tau}{\left|\boldsymbol{\omega}_\tau\right|} \quad (16)$$

We have the similar formulae for the anti-rolling couple where the “static” anti-rolling couple (that vanishes not in case of the rolling asymmetry of the body) and the “dynamic” one are defined by the formulae (17) and (18) respectively:

$$\mathbf{M}_\tau^0 = \int_S \sigma_0 \mathbf{r}_\tau\times\mathbf{e}_3 dS = \mathbf{S}_\sigma; \quad (17)$$

$$\mathbf{M}_\tau^1 = \int_S \sigma_0 \mathbf{r}_\tau\times\frac{\mathbf{r}_\tau\times\left(\mathbf{h}\cdot\boldsymbol{\omega}_\tau\right)}{\left|\boldsymbol{\omega}_\tau\right|}dS = -\mathbf{J}_\sigma\cdot\mathbf{h}\cdot\frac{\boldsymbol{\omega}_\tau}{\left|\boldsymbol{\omega}_\tau\right|}. \quad (18)$$

Here the first moment vector $\mathbf{S}_\sigma$ and the inertia moment tensor $\mathbf{J}_\sigma$ of the plane area of contact S with the static contact pressure distribution σ_0 are introduced:

$$\mathbf{S}_\sigma = \int\limits_S \sigma_0 \mathbf{r}_\tau \times \mathbf{e}_3 dS = \int\limits_S \sigma_0 \epsilon_{\alpha\beta} \xi^\beta \mathbf{e}^\alpha dS; \tag{19}$$

$$\mathbf{J}_\sigma = \int\limits_S \left(\wedge \mathbf{r}_\tau \right) \otimes \left(\mathbf{r}_\tau \wedge \right) dS = \int\limits_S \epsilon_{\alpha\beta} \xi^\beta \epsilon_{\gamma\delta} \xi^\delta \mathbf{e}^\alpha \otimes \mathbf{e}^\beta dS, \tag{20}$$

$$\epsilon_{\alpha\beta} \equiv \epsilon_{\alpha\beta 3} = \left(\mathbf{r}_\alpha \times \mathbf{r}_\beta \right) \cdot \mathbf{e}_3, \quad \alpha, \beta, \gamma, \delta = 1, 2.$$

The homogeneity of the tensor (9) and the formulae (15) - (20) lead to the vanishing as well normal reaction $\mathbf{N}_1$ as the rolling initiation moment $\mathbf{M}_\tau^0$ in the frame $O\xi^1\xi^2$ attached to the center of the figure S, therefore we have the following formulae for the normal reaction and anti-rolling couple:

$$\mathbf{N} = N_0 \mathbf{e}_3; \quad \mathbf{M}_\tau = -\mathbf{J}_\sigma \cdot \mathbf{h} \cdot \left(\boldsymbol{\omega}_\tau / \left| \boldsymbol{\omega}_\tau \right| \right). \tag{21}$$

The resultant vector of the anisotropic dry friction (13) under combined kinematics can be now expressed through the following terms:

$$\mathbf{T} = \sum_{k=1}^{4} \mathbf{T}_k,$$

$$\mathbf{T}_1 = -\int\limits_S \sigma_0 \frac{\mathbf{f} \cdot \mathbf{v}_S}{\left| \mathbf{v}_S + \boldsymbol{\omega}_\nu \times \mathbf{r}_\tau \right|} dS; \tag{22}$$

$$\mathbf{T}_2 = -\int\limits_S \sigma_0 \left[\frac{\mathbf{r}_\tau \times \left(\mathbf{h} \cdot \boldsymbol{\omega}_\tau \right)}{\left| \boldsymbol{\omega}_\tau \right|} \cdot \mathbf{e}_3 \right] \frac{\mathbf{f} \cdot \mathbf{v}_S}{\left| \mathbf{v}_S + \boldsymbol{\omega}_\nu \times \mathbf{r}_\tau \right|} dS; \tag{23}$$

$$\mathbf{T}_3 = -\int\limits_S \sigma_0 \frac{\mathbf{f} \cdot \left(\boldsymbol{\omega}_\nu \times \mathbf{r}_\tau \right)}{\left| \mathbf{v}_S + \boldsymbol{\omega}_\nu \times \mathbf{r}_\tau \right|} dS; \tag{24}$$

$$\mathbf{T}_4 = -\int\limits_S \sigma_0 \left[\frac{\mathbf{r}_\tau \times \left(\mathbf{h} \cdot \boldsymbol{\omega}_\tau \right)}{\left| \boldsymbol{\omega}_\tau \right|} \cdot \mathbf{e}_3 \right] \frac{\mathbf{f} \cdot \left(\boldsymbol{\omega}_\nu \times \mathbf{r}_\tau \right)}{\left| \mathbf{v}_S + \boldsymbol{\omega}_\nu \times \mathbf{r}_\tau \right|} dS, \tag{25}$$

Here (22) is the static dry friction force, (23) is the supplementary quasi-static dry friction force resulted by the rolling effect, (24) is the supplementary dry friction force due to the spin. and the term (25) denotes the variation of the dry friction force due to the coupling of the rolling and spinning of the body.

The torque of the anisotropic dry friction under combined kinematics (14) is also represented as a sum of four terms:

$$\mathbf{M}_\nu = \sum_{k=1}^{4} \mathbf{M}_k,$$

$$\mathbf{M}_1 = -\int_S \sigma_0 \frac{\mathbf{r}_\tau \times (\mathbf{f} \cdot \mathbf{v}_S)}{|\mathbf{v}_S + \boldsymbol{\omega}_\nu \times \mathbf{r}_\tau|} dS; \tag{26}$$

$$\mathbf{M}_2 = -\int_S \sigma_0 \left[\frac{\mathbf{r}_\tau \times (\mathbf{h} \cdot \boldsymbol{\omega}_\tau)}{|\boldsymbol{\omega}_\tau|} \cdot \mathbf{e}_3 \right] \frac{\mathbf{r}_\tau \times (\mathbf{f} \cdot \mathbf{v}_S)}{|\mathbf{v}_S + \boldsymbol{\omega}_\nu \times \mathbf{r}_\tau|} dS; \tag{27}$$

$$\mathbf{M}_3 = -\int_S \sigma_0 \frac{\mathbf{r}_\tau \times [\mathbf{f} \cdot (\boldsymbol{\omega}_\nu \times \mathbf{r}_\tau)]}{|\mathbf{v}_S + \boldsymbol{\omega}_\nu \times \mathbf{r}_\tau|} dS; \tag{28}$$

$$\mathbf{M}_4 = -\int_S \sigma_0 \left[\frac{\mathbf{r}_\tau \times (\mathbf{h} \cdot \boldsymbol{\omega}_\tau)}{|\boldsymbol{\omega}_\tau|} \cdot \mathbf{e}_3 \right] \frac{\mathbf{r}_\tau \times [\mathbf{f} \cdot (\boldsymbol{\omega}_\nu \times \mathbf{r}_\tau)]}{|\mathbf{v}_S + \boldsymbol{\omega}_\nu \times \mathbf{r}_\tau|} dS, \tag{29}$$

Here (26) is the dry friction torque under the pure sliding that is resulted by the coupling of the slip and spin, the formula (27) defines the supplementary quasi-static dry friction torque resulted by the rolling effect on the slip, the "proper static" dry friction torque is defined by the formula (28) and it's variation due to the coupling of the rolling and spinning is given by the term (29). The vector $\mathbf{v}_S$ denotes the summary velocity in the point $M \in S$:

$$\mathbf{v}_S = \mathbf{v}_0 - R\boldsymbol{\omega}_\tau \times \mathbf{e}_3; \quad |\mathbf{v}_\Sigma|^2 = v_S^2 + 2\mathbf{v}_S \cdot (\boldsymbol{\omega}_\nu \times \mathbf{r}_\tau) + (\boldsymbol{\omega}_\nu \times \mathbf{r}_\tau) \cdot (\boldsymbol{\omega}_\nu \times \mathbf{r}_\tau). \tag{30}$$

Thus, the invariant formulation for the coupled dry friction theory is obtained. The constructed model describes the coupling effects under combined sliding, spinning, and rolling of the deformed rigid body with the finite area of contact with the support plane. The invariant relationships (11)-(14) can be rewritten in the coordinate form by the appropriate choice of the main frame.

3 APPROXIMATE MODEL OF THE ROLLING WHEEL

Let us consider the orthotropic dry friction given by the tensor

$$\mathbf{f} = f \begin{pmatrix} 1 & 0 \\ 0 & \kappa \end{pmatrix}, \quad f \neq 0, \quad \kappa \neq 0. \tag{31}$$

Here f and κf are the principal components of the tensor $\mathbf{f}$. Let us introduce the frame Ox^1x^2 attached to the centroid of the contact spot S; the corresponding base vectors $\mathbf{e}_1$ and $\mathbf{e}_2$ are collinear to the principal directions of the tensor $\mathbf{f}$. The static contact pressure symmetry, $\sigma_0(x^1, x^2) = \sigma_0(\pm x^1, \pm x^2)$, as well as the rolling friction isotropy are assumed.

Let us consider the motion defined by the longitudinal velocity $\mathbf{v}_0 = V_0 \mathbf{e}_1'$ along the axis OX^1 of the global rest frame (for more details, see [16]), the rolling angular velocity $\boldsymbol{\omega}_\tau = -\omega_\tau \mathbf{e}_2$, and the spinning velocity ω_ν. Such a situation corresponds to the rolling of the wheel with the thread characterized by the friction factors f along the tread and κf across it. Let us also consider here only circular area of contact with the radius R.

The quantities (22)-(29) can now be simplified as it was implemented in [10, 11, 16, 17].

However the integral relationships are too complex to apply them to the analysis of dynamics of real systems while their linear-fractional approximations are adequately accurate and simple in the same time [7, 9-11, 16]. Let us sketch below only the main results; for more details concerning the construction of the approximate formulae, see [16, 17].

The resultant force vector can be represented as $\mathbf{T} = T_{\|}\mathbf{e}_1 + T_{\perp}\mathbf{e}_2$, so that $T_{\|}$ is the longitudinal and $T_{\perp}$ is the lateral friction force. It was shown [7-11, 16] that the last one is due to the coupling effects. As a result, we have the following formulae:

$$T_{\|} = F_0 \frac{v_s}{\sqrt{v_s^2 + au^2}}; \tag{32}$$

$$T_{\perp} = h\kappa F_0 \frac{uv_s}{\sqrt{\left(u^2 + bv_s^2\right)\left(v_s^2 + au^2\right)}}; \tag{33}$$

$$M_{\nu} = M_0 \frac{u}{\sqrt{u^2 + mv_s^2}}. \tag{34}$$

Here $u = \omega_{\nu} R$, $F_0 = fN_0$ is the longitudinal resting friction force, the resting friction torque can be computed as follows:

$$M_0 = \pi\left(1 + \kappa\right) f \int_0^1 \sigma_0\left(r\right) r^2 dr. \tag{35}$$

Here the dimensionless radial coordinate is introcuced. For the factors a, b, m we have following formulae analogous to these published in [17].

4 ACCOUNTING FOR THE CONTACT PRESSURE DISTRIBUTION

The contact pressure distribution close to the real one as well as the contact spot diameter can be obtained on the basis of the finite element model of a tire; several levels of accuracy of the model can be considered. The first and simplest one consists in the numerical simulation of the quasi-static nonlinear deforming of a tire using the plane elasticity problem statement for the tire cross-section [15]. The contact pressure distribution computed for several levels of the vertical load or the radial deformation of the tire are then interpolated analytically.

The polynomial interpolation of the finite element solution σ_{0i} is constructed as follows:

$$\sigma_0\left(r\right) \approx \sigma_0^k p_k\left(r\right), \quad r \in \left[-1,1\right], \quad k = 0,2\ldots N \in \mathbb{N}, \tag{36}$$

where r is the dimensionless coordinate in the contact spot and $p_k\left(r\right)$ are Legendre polynomials. The contact pressure distribution is assumed to be symmetric, $\sigma_0(r) = \sigma_0(-r)$. The factors $\sigma_0^k \in \mathbb{R}$ are obtained from the solution of the quadratic programming problem:

$$G_{km}\sigma_0^k\sigma_0^m \to \min, \quad G_{km} = 2\delta_{km}/\left(2k+1\right) \tag{37}$$

with the following restrictions:

$$\sigma_0^k p_k\left(r_i\right) \le \sigma_{0i}, \quad \sigma_0^k p_k\left(1\right) = 0, \quad \sigma_0^k \int_{-1}^{1} p_k\left(r\right) dr = \sum_{i=2}^{n} \left(\sigma_{0i} + \sigma_{0i-1}\right)\left(r_i + r_{i-1}\right), \tag{38}$$

where the first one corresponds to the lower approximation of the FEM solution, the second one corresponds to the condition $\sigma_0\big|_{\partial S} = 0$, and the third one guarantees the equivalence of the normal reaction following from the interpolation and the load applied to the FE model. The typical contact pressure and its approximation ($N = 10$) is shown on the Figure 1.

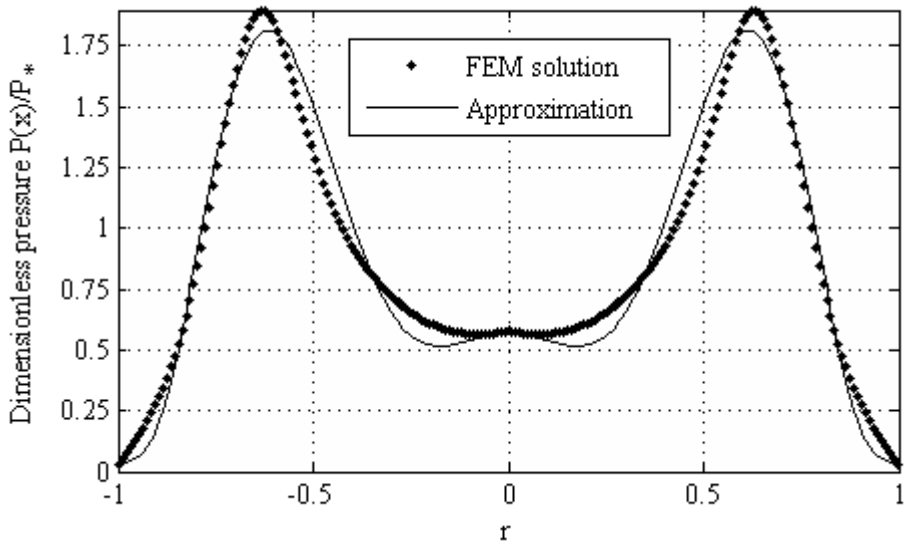

Figure 1: Contact pressure distributions for a typical tire [17]

The high level of vertical loads results the O-shaped area of contact where the contact pressure vanishes near the center of a spot [15]. In such a situation, the higher-order approximation may be required. On the other hand, the strongly deformed state of a tire leads to the accounting for the tangential deformation and the elastic forces in the pneumatics, therefore this model become combined with the Keldysh concept.

CONCLUSIONS

The theory of the coupled dry friction under combined kinematics is improved by accounting for the anisotropy of the dry friction coefficient represented in a form of the second-rank tensor. The general invariant formulation for the resultant vector of dry friction forces as well as for the dry friction couple and the rolling friction torque are obtained in case of the simultaneous sliding, spinning, and rolling of the rigid body. The contact pressure for a tire can be obtained from the numerical simulation on the groundwork of the finite element modeling, thus, the polynomial interpolation of such a solution is introduced, and the coefficients of the approximate model of the dry friction arte obtained. The constructed model being applied to the rolling wheel can be interpreted as the second approximation improving the model of the shimmy of quasi-rigid wheel.

ACKNOWLEDGEMENTS

This research was financially supported by the Russian Foundation for Basic Researches under grant No. 16-01-00809-a.

REFERENCES

[1] Keldysh. M.V. *Selected Works, Mechanics*, Nauka, Moscow (1985).

[2] Zagordan, A.A. Current state of the wheel shimmy theory (in russian), *Journal "Trudy MAI". Moscow Aviation Institute* (2011) **47**:11 pp.

[3] Zagordan, A.A. and Zhavoronok, S.I. Main landing gear shimmy investigation using dry friction multicomponent model (in russian), *Nelineiny Mir* (2011) **10**:646–656.

[4] Contensou, P. Couplage entre frottement de glissement et frottement de pivotement dans la th´eorie de la touplie, in: *Kreisel probleme Gyrodynamics: IUTAM Symp. Celerina,* 1962, Springer, Berlin (1963), 201–216.

[5] Erissmann, Th. Theorie und Anwendungen des echten Kugelgetriebes. *ZAMP* (1954) **5**:355–388.

[6] Zhuravlev V.Ph., Klimov, D.M. Theory of the shimmy phenomenon, *Mech. Solids* (2010) **45**(3):324–330.

[7] Andronov, V.V. and Zhuravlev, V.Ph. *Dry Friction in Problems of Mechanics (in Russian)*, NITs Reg. Khaot. Dinam., Moscow-Izhevsk (2010).

[8] Zhuravlev, V.Ph. On the model of dry friction in the problem of rolling of rigid bodies, *J. Appl. Math. Mech.* (1998) **62**(5):762–767.

[9] Zhuravlev, V.Ph. and Kireenkov, A.A. Padé expansions in the two-dimensional model of Coulomb friction, *Mech. Solids* (2005) **40**(2):1–10.

[10] Kireenkov, A.A. Coupled models of sliding and rolling friction, *Doklady Akademii Nauk* (2008) **419**(6):759–762

[11] Kireenkov, A.A. Coupled model of sliding and spinning friction, *Doklady Akademii Nauk* (2011) **441**(6):750–755.

[12] Bernikova, N.S., Zagordan, A.A., and Zhavoronok, S.I. Main landing gears shimmy models based on poly-component dry friction, in: R. W. Ogden, G. A. Holzapfel (Eds.), *Proc. of the 8th European Solid Mechanics Conf. (ESMC-2012),* Graz, Austria (2012).

[13] Bernikova, N.S., Zagordan, A.A., and Zhavoronok, S.I. Landing gears shimmy models based on the combined anisotropic dry friction theory, in: *Proc. 8th European Nonlinear Dynamics Conf. (ENOC-2014),* Vienna, Austria (2014).

[14] Bernikova, N.S., Stepanov, E.V., Zagordan, A.A., and Zhavoronok, S.I. Modelling of main landing gears shimmy and shimmy-like vibrations on the basis of the multi-component anisotropic dry friction theory, in: Z. Dimitrovova, J. de Almeida, R. Gonalves (Eds.), *Proc. 11th Int. Conf. on Vibration Probl. (ICOVP-2013)*, AMPTAC, Lisbon, Portugal (2013), p. 290.

[15] Bogoslovskii, S.E. and Kurdyumov, N.N. Numerical solution a problem of contact pneumatic truck tire with road surface, *Proceedings of the TSU. Technical Sciences* (2015) **8**(2):138–147.

[16] Kireenkov, A.A. Three-dimensional model of combined dry friction and its application in non-holonomic mechanics. *Proc. 5th European Nonlinear Dynamics Conf. ENOC-2005*, Eindhoven, Netherlands (2005).

[17] Kireenkov, A.A. and Zhavoronok, S.I. Coupled Dry Friction Models in Problems of Aviation Pneumatics' Dynamics, *Int. J. Mech. Sci.* (2017) DOI 10.1016/j.ijmecsci. 2017.02.004.
[18] Kozlov, V. V. Lagrangian mechanics and dry friction (in Russian). *Nonlinear Dynamics* (2010) **6**(4):855–868.
[19] Vil'ke, V. G. Anisotropic dry friction and unilateral non-holonomic constraints, *Mech. Solids* (2008) **72**:3-8.
[20] Zmitrowiecz, A. Mathematical descriptions of anisotropic friction. *Int. J. Sol. Struct.* (1989) **25**(8):837-862.
[21] Dmitriev, N. and Silantyeva, O., Terminal motion of a thin elliptical plate over a horizontal plane with orthotropic friction, *Vestnik St. Petersburg University. Mathematics* (2016) **46**(1):92–98.
[22] Silantyeva, O. and Dmitriev, N., Dynamics of bodies under symmetric and asymmetric orthotropic friction forces, CRC Press (2016) 511–515.
[23] Kireenkov, A.A. Further development of the theory of multicomponent dry friction. *COUPLED PROBLEMS 2015 - Proceedings of the 6th International Conference on Coupled Problems in Science and Engineering*, Venice, ITALY (2015), pp. 203-209.

VII International Conference on Computational Methods for Coupled Problems in Science and Engineering
COUPLED PROBLEMS 2017
M. Papadrakakis, E. Oñate and B. Schrefler (Eds)

DAMPED FREE MOTION OF ROCKING SPECIMENS IN NON-LINEAR TIME HISTORY RESPONSE ANALYSIS

MIZUO INUKAI * **AND TATSUYA AZUHATA**†

* International Institute of Seismology and Earthquake Engineering (IISEE),
Building Research Institute (BRI)
Tsukuba, Ibaraki, 305-0802, Japan
e-mail: inkm@kenken.go.jp, Web page: http://iisee.kenken.go.jp

†IISEE, BRI
Tsukuba, Ibaraki, 305-0802, Japan
e-mail: azuhata@kenken.go.jp

Key words: Rocking Specimen, Non-Linear, Time History Response Analysis.

Abstract. In dynamic soil-structure interaction (SSI), the structure such as a building, the sway of the foundation and the rocking on ground, during an earthquake, are usually analyzed without coupled system. In this paper, assuming a restoring force - displacement characteristics for rocking, while the structure and the sway on the assumption are rigid body, non - linear time history response analysis of rocking in the damped free motion of are carried out, with the comparison of the experimental values.

1 INTRODUCTION

In dynamic soil-structure interaction (SSI), the structure such as a building, the sway of the foundation and the rocking on ground, during an earthquake, are usually analysed without coupled system. But coupled system analyses are possible [1]. In the analysis of the SSI, the three relationships of the restoring force - displacement characteristics are required respectively. Therefore, in this paper, assuming a restoring force - displacement characteristics for rocking, while the structure and the sway on the assumption are rigid body, non - linear time history response analysis of rocking in the damped free motion are carried out, with the comparison of the experimental values.

Restoring force – displacement characteristics of rocking are already analysed when the stiffness is negative and these complementary functions are known without the external forces. However, probably because the period on the ground is not taken into account, the time history response analysis are not so much made. Therefore, in this analysis, assuming a period on the ground in 0.16 seconds, etc. and the moment - rotation angle relationship as the bilinear model, non - linear time history response analysis are executed.

2 NON-LINEAR TIME HISTORY RESPONSE ANALYSIS FOR ROCKING

Generally, the equation of damped free motion of rocking in Figure 1 is described in equation (1). In Figure 1, m is the mass, $B(=2b)$ is the width of the rigid body, H $(=2h)$ is the height and

g is the gravity acceleration. In equation (1), I is the moment of inertia at the ground surface, c_I is the damping coefficient, k_I is the rocking stiffness, $\ddot{\theta}$ is the response acceleration of angle, $\dot{\theta}$ is the response velocity of angle, h_I is the length of the moment arm by external forces and θ is the angle. M ($=k_I\theta$) is the internal moment of the rigid body, the relationship between M and θ is shown in Figure 1 (b) [2]. When k_I is assumed to be too large at $\theta=0$ and M is assumed to be 0, mgb or $-mgb$, the mathematical solutions for each θ are very difficult.

$$I\ddot{\theta} + c_I\dot{\theta} + k_I\theta = -m\ddot{y}h_I \tag{1}$$

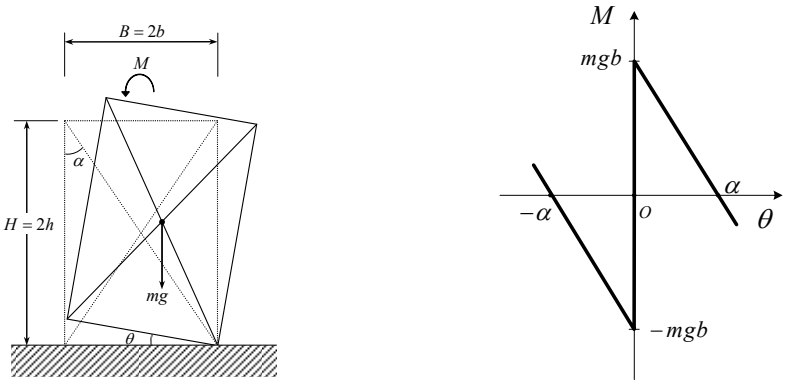

(a) Rigid Body in Motion (b) Relationship of M and θ

The ground is rigid. α is the angle of the width to the height (b/h).

Figure 1: Rigid Body in Motion and the Relationship between the internal moment M of the centre of the gravity and the rotation angle of rocking θ when the ground is rigid

In order to make analysis for rocking, a stiffness at θ (= 0) is needed and the relationship of $M - \theta$ is more difficult than the relationship between the horizontal restoring force F and the horizontal displacement x to understand the rocking motion. If the start of analysis has some horizontal displacement without velocity, and during the motion there are no external forces, the analysis should be simple.

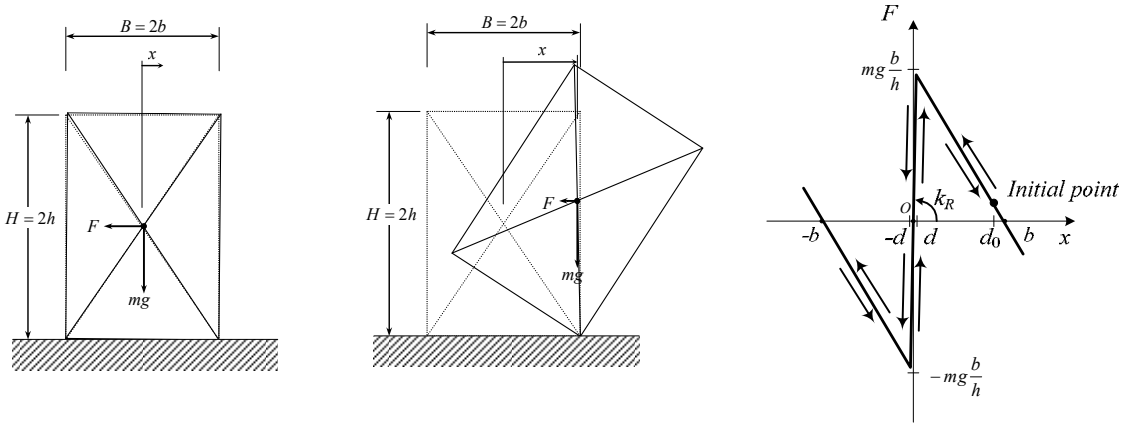

(a) F is almost $mg(b/h)$ (b) x is almost b (c) Relationship of F and x

k_R is the rocking stiffness of the ground based on F and x.

Figure 2: Rigid Body in Motion and the Relationship between the horizontal force F and the horizontal displacement x of the centre of gravity to the ground when the rocking stiffness of the ground is k_R

Therefore, in Figure 2, in this non-linear time history response analysis for rocking, the relationship of $F - x$ is assumed, the rocking stiffness of the ground k_R (>0) is also assumed when x is around zero from $-d$ to d and F is decreased to be zero after F is almost $mg(b/h)$ until x is almost b. The initial point is when x is some value and the velocity is zero.

The relationship of $F - x$ and the equation of damped free motion of rocking are as follows;

$$d < x \quad : \quad F = mg\,\frac{b-x}{h} \tag{2}$$

$$-d \le x \le d \; : \quad F = k_R\, x \tag{3}$$

$$x < -d \; : \quad F = -mg\,\frac{b+x}{h} \tag{4}$$

$$m\ddot{x} + c\dot{x} + F = 0 \tag{5}$$

These complementary functions at time t are known. The undetermined coefficients, A_1, B_1 and others, are calculated by the initial values and the stiffness respectively as follows [3];

$$d < x \quad : \quad x = b + \mathrm{e}^{-h_1 \omega_1 t}(A_1 \cosh \omega_{n1} t + B_1 \sinh \omega_{n1} t) \tag{6}$$

$$-d \le x \le d \; : \quad x = \mathrm{e}^{-h_0 \omega_0 t}(A_0 \cos \omega_{n0}\, t + B_0 \sin \omega_{n0}\, t) \tag{7}$$

$$x < -d \; : \quad x = -b + \mathrm{e}^{-h_2 \omega_2 t}(A_2 \cosh \omega_{n2} t + B_2 \sinh \omega_{n2} t) \tag{8}$$

The functions of velocity are defined as the differential equations at time t of the above functions of displacement.

In equation (6) and (8), because the stiffness (F/x) is negative to be ($-mg/h$), the complementary functions includes the hyperbolic functions (sinh, cosh) and constant b. The parameters, damping factor h_1, circular frequency ω_1, constant A_1, circular frequency ω_{n1}, constant B_1 and others are defined by the initial values $x = d_0$ and the velocity is zero. Some of the parameters, h_1 or ω_1, are defined by imaginary number i ($= \sqrt{-1}$) because the stiffness is negative. For example, according to equation (2) and (5), the stiffness k_1 ($= -mg/h$) is negative and the circular frequency ω_1 should be square root of (k_1/m) ($\omega_1 = \sqrt{k_1/m} = \sqrt{-(g/h)} = i\sqrt{g/h}$) which is defined by i. Not only ω_1 or ω_3 but also h_1 or h_3 are defined by i because the damping coefficient c in equation (5) is a constant real number ($h_1\ \omega_1 = c/(2m) = h_0\ \omega_0 = h_2\ \omega_2$), even if the stiffness was changed. But the product of h_1 and ω_1 canceled i .

By the way, ω_{n0}, ω_{n1} and ω_{n2} are real numbers because the complementary functions are solved by the characteristic equation using p of equation (5), $p^2 + 2h_1\omega_1 p - \omega_1^2 = 0$, $p^2 + 2h_0\omega_0 \times p + \omega_0^2 = 0$ or others, where the coefficient in the square of constant is negative or positive, when all parameters, h_0, h_1, ω_0, ω_1, ω_{n0}, ω_{n1} and others, are real numbers.

Finally the results of equation (6), (7) and (8) give the real numbers.

When x is close to d, after the initial point, the interval time in the analysis was 0.0005 (sec) (=2,000Hz) in equation (6). After the time, when x was d, was defined, the initial values of x and the velocity $\dot{x}$ in equation (7) were defined to continue the analysis.

These analyses were executed to be compared with the test results of the following section.

3 ROCKING SPECIMEN

In recent years, the experiment project of free standing concrete column specimens by placing some situations of ground was produced, when the damped free motion given an initial value of the horizontal displacement was performed by the several corporations [4]. Specimens, height 3.7m, width 1.1m, the thickness 1.5m and the weight 104.9 kN in the free end. The height of the centre of mass (◒) is 1.743m. The specimens were placed on the ground, were inclined to the top displacement horizontally 0.375m and so on.

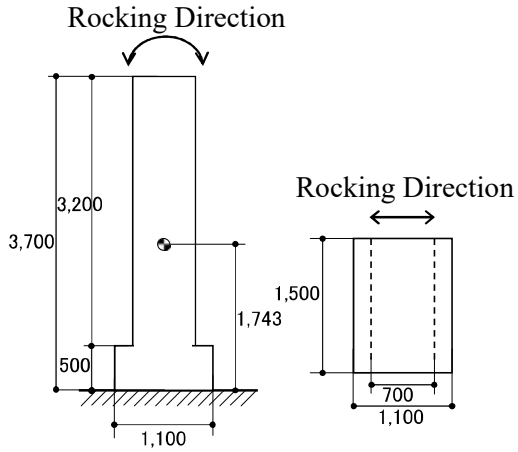

(a) Elevation (b) Plan

Figure 3: Rocking Specimen (Reinforced concrete column on concrete slab)

(a) Rocking Specimen under loading (b) Photo of Rocking Specimen under loading

Figure 4: Rocking Specimen under loading (Reinforced concrete column on concrete slab)

After the horizontal tension force was released, the rocking damped free motions were conducted (Figure 3 and Figure 4). The release points for one loading were at the top

displacement horizontally 0.125m for 2 times, 0.250m for 2 times, 0.375m for 2 times and 0.125m for 1 time. The total number of loadings was 7 times. In the experiment, the acceleration and the displacement of some parts were measured, when these data were compared to this analysis for the horizontal force and the horizontal displacement of the centre of mass.

4 ANALYSIS AND RESULTS

In the analysis, while the damping ratio was a parameter, the response horizontal force F and the response horizontal displacement x of the centre of mass were calculated and compared with the experimental values. In Figure 5, Idealized F/mg and x shows the typical points which are the angle of the width to the height (b/h)(=550/1,743=0.316) in y-axis and the width b (=55cm) in x-axis. Experimental F/mg and x shows the proposed points which are the Uplift point (F/mg, x)=(0.273-, 0.09cm) and the Initial point (0.202-, 19.7cm).

These points are exchanged to the relationship $M - \theta$. In Idealized relationship, $M=mgb$= 57.7kN·m is in y-axis and θ=0.316rad. is in x-axis. In experimental relationship, the Uplift point (M,θ)=(50kN·m, 0.0005rad.) and the Initial point (37kN·m, 0.113rad.) were proposed. The Initial point is located under the line of the Idealized relationship.

According to the elastic stiffness, k_R in equation (3) or ω_0 in equation (7), the period of the contact of the specimen to the ground was calculated to be 0.11 second. Outside of the elastic, the response functions include the hyperbolic functions (sinh, cosh) without trigonometric functions in equation (6) and (8) and don't have any period.

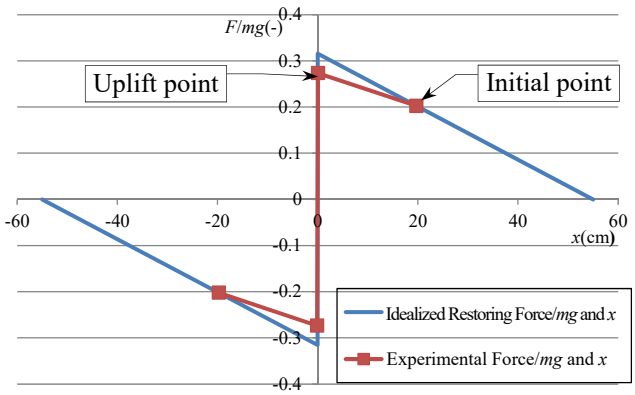

Figure 5: Relationship of F and x of the centre of mass

As the results, Figure 6 shows the non-linear time history response analysis results of the damped free motion of the Rocking Specimen. In Figure 6, δe_G is the horizontal displacement of the centre of gravity to the ground and started at 19.7cm when the top displacement horizontally was 0.375 m in the first time among the 2 times loadings. Until 10 (sec), δe_G has some amplitude and after 10 (sec), it has some residual displacement.

According to the relationship of Figure 5 and equations (2) – (8), the analysis results of x are also shown in Figure 6. They are 2 results when h_0 is 0.3% and h_1 is 0.1/i or h_0 is 0.7% and h_1 is 0.2/i .When h_0 is 0.3%, the amplitude of x are close to the experiment data until 10 (sec). When h_0 is 0.7%, the amplitudes of x are close to the experiment data after 10 (sec). Figure 6

(b) shows the same results of until 5 (sec) of 20 (sec) in Figure (6) (a), while the interval times between the peaks are not similar in the experimental data and the 2 results. In the analysis, the grounding times of the specimen were calculated to be about 0.002 (sec) or more.

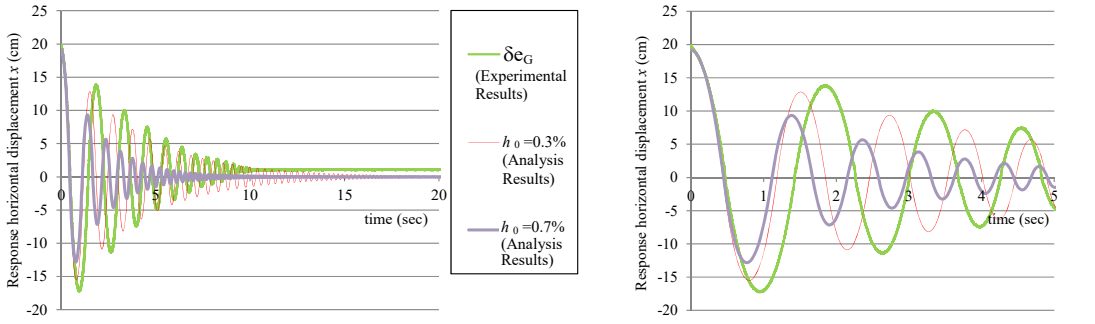

(a) Until 20 (sec)

Notes are same as the Notes of Figure 6 (a)

(b) Until 5 (sec)

Figure 6: Comparison of Experimental Result (δe_G) and Analysis Results (h_0=0.3% and h_0=0.7%)

5 CONCLUSIONS

In this paper, the damped free motions of rocking specimens were analyzed in non-linear time history response analysis. A comparison between these analysis and the experimental results were executed when the initial points were some horizontal displacement and the stiffness during the contact of the specimen to the ground were considered.

The main points of these results are as follows;

(1) When the stiffness is negative, the response horizontal force and the response horizontal displacement were calculated by the hyperbolic functions.
(2) The period by the stiffness during the contact of the specimen to the ground in this analysis was 0.11 (sec).
(3) The similar response displacements to the experimental results were when the damping factors at the displacement zero were 0.3% or 0.7%.
(4) The grounding times of the specimen in this analysis were calculated to be about 0.002 second or more.
(5) The comparison between the analysis and the experimental results were not so much similar, therefore, the coupled system like Soil-Structure Interaction should be necessary.

REFERENCES

[1] Inukai, M. Kashima, T. and Azuhata, T. Predominant Periods of Multi-Degree-of-Freedom-System Analysis and Dynamic Soil-Structure Interaction for Building Structures. *Proceedings of the VI International Conference on Coupled Problems in Science and Engineering*, International Center for Numerical Methods in Engineering (CIMNE), Ebook, pp.278-289, (2015), Venice, Italy.

[2] Ishiyama, Y. Review and Discussion on Overturning of Bodies by Earthquake Motions. *BRI Research Paper No. 85*, Building Research Institute, Ministry of Construction, June

(1980), Tsukuba, Japan.
[3] Muto, K. Umemura, H. and Sonobe, Y. Study of the Overturning Vibration of Slender Structures. *Proceeding of the Second World Conference on Earthquake Engineering*, Science Council of Japan and the Committee for the Second World Conference on Earthquake Engineering, vol.2, pp.1239-1261, (1960), Association for Science Documents Information, Tokyo, Japan.
[4] Takenaka Corporation and Taisei Corporation. Study of Structural Design Methods of Buildings Considering Uplift Behavior. *Summary of Report for 2013 Review and Promotion Project of Building Codes*, Housing Bureau, Ministry of Land, Infrastructure, Transport and Tourism, (2013), Tokyo, Japan.
http://www.mlit.go.jp/common/001037167.pdf (in Japanese)

VII International Conference on Computational Methods for Coupled Problems in Science and Engineering
COUPLED PROBLEMS 2017
M. Papadrakakis, E. Oñate and B. Schrefler (Eds)

NUMERICAL MODELLING OF COUPLED THERMO-HYDRAULIC PROBLEMS FOR LONG-TERM GEOTHERMAL RESERVOIR PRODUCTIVITY

Hua-Peng Chen[1*] and Musa D. Aliyu[1]

[1]Department of Engineering Science, University of Greenwich, Medway Campus, Kent, UK
*Corresponding author: H.Chen@greenwich.ac.uk
M.D.Aliyu@greenwich.ac.uk

Key words: Geothermal energy extraction, coupled thermo-hydraulic, finite element method, multiple phase, productivity simulations.

ABSTRACT

The advent of geothermal energy has opened a new chapter in global energy demand, for clean, renewable, and sustainable sources. This energy form is harnessed by creating a reservoir in a formation that serves as a heat exchanger. Modelling provides a means of representing concepts and approaches in reservoir simulation. Several methods are proposed to simulate geothermal reservoir behaviour under long-term performance, but it is very hard to specify the most powerful and realistic approach in forecasting reservoir lifespan. The aim of this work is to evaluate two different approaches: equivalent porous media (EPM) and dual porosity-permeability (DPP) model, for simulating geothermal reservoir long-term performance and to assess the adequacy of these approaches. The finite element method is employed to develop and simulate the numerical models based on the two different approaches in forecasting the productivities of the reservoirs during exploitation period of 30 years. The parameters investigated are the temperature, density, and viscosity distribution under the influence of coupled thermal and hydraulic processes. The simulation results are analysed and compared with the different approaches using those parameters. The analysis indicates that both the approaches can efficiently estimate the long-term performance of a reservoir to some extent, but further investigations are required regarding the effect of other coupling terms.

1. INTRODUCTION

The transport of fluid and heat through naturally fractured reservoirs is a method that holds importance for many fields of geosciences, ranging from geothermal mining to oil and gas. Studies on fluid and heat transport in naturally fractured reservoirs have a history that spans nearly six decades[1]. Numerous conceptual models have been developed for representing fluid and heat flow in naturally fractured reservoirs, and each model can be differentiated from the other by transport capabilities and storage of the fracture and the porous medium. Thus, the transport characteristics are associated with permeability, and the storage characteristics are related to porosity [2]. It is imperative to consider the various modelling approaches available for simulating heat and fluid flow in naturally fractured reservoirs and understanding the advantages and limitations of each approach.

Since the 1960's, the numerical modelling of naturally fractured reservoirs using dual porosity-permeability models has been the subject of many studies. The modelling approach has been accepted and implemented in different fields of reservoir engineering. For instance, several authors [3]–[8] have developed simulation code applying different techniques using the dual porosity model. On the other hand, the equivalent porous media model is also widely employed in modelling naturally fractured reservoirs, but this is not as common as the former model. Numerous researchers [9]–[13] have used the equivalent porous media approach for modelling different categories of reservoirs. Despite the dissimilarities in modelling assumptions, it appears that no studies have tried to compare the outcomes of those models and determine if they are acceptable. It is evident that additional study is required to better quantify these modelling approaches with the help of valid comparisons.

The objectives of this investigation are to compare two different approaches for fluid and heat transport in a naturally fractured geothermal reservoir; in this case, the dual porosity-permeability (DPP) model and the equivalent porous media (EPM) model. The two models are based on the conservation of mass for flow and the conservation of energy for heat transport in order to evaluate the ability of both models to simulate heat and fluid flow in a naturally fractured geothermal reservoir and assess the advantages and limitations of each model.

2. MODELLING FLUID AND HEAT TRANSPORT IN A FRACTURED RESERVOIR

In this study, the heat and fluid transport analyses in a naturally fractured reservoir are modelled using two alternative approaches: the DPP model and the EPM model. The two approaches are briefly described in this section.

2.1 Equivalent porous media (EPM) model

In the EPM model for naturally fractured systems, the initial assumption is that fracture behaviour is equivalent to porous media for both heat and fluid transport. The modelling approach assumes that an equivalent porous medium can represent the matrix block including fractures with equivalent conductivity in a particular area. It approximates the overall local conductivity of the fractures as well as the matrix with an improved equivalent conductivity [9]. Thus, the continuity equation expressing the conservation of mass in a fully saturated porous medium can be expressed as

$$\phi \frac{\partial \rho_L}{\partial t} + \nabla \cdot (\rho_L v) = 0 \tag{1}$$

where ϕ is the porosity, ρ_L is the fluid density, and v is the Darcy's velocity. The momentum conservation is expressed by Darcy's law

$$v = -\frac{\kappa}{\mu}(\nabla P - \rho_L g \nabla z) \tag{2}$$

in which κ is the hydraulic permeability, μ is the fluid dynamic viscosity, P is the hydraulic pressure, g is the acceleration due to gravity, and z is the vertical depth.

$$(\rho C_P)\frac{\partial T}{\partial t}+\nabla\cdot(\rho_L C_{P,L} vT)-\nabla\cdot(\lambda\nabla T)=0 \tag{3}$$

where T is the temperature, $C_{P,L}$ is the fluid heat capacity, ρC_P is the effective densities and heat capacities of the saturated porous medium, and λ is the effective thermal conductivities. The last two terms are expressed as

$$\rho C_P=(1-\phi)\rho_S C_{P,S}+\phi\rho_L C_{P,L} \tag{4}$$

$$\lambda=(1-\phi)\lambda_S+\phi\lambda_L \tag{5}$$

in which ρ_S is the solid density, $C_{P,S}$ is the solid heat capacity, λ_S and λ_L are the solid and fluid thermal conductivities, respectively. In this case, both expressions are used to represent the porous matrix and the fracture.

2.2 Dual porosity-permeability (DPP) model

In this model, the matrix and fracture system are modelled as separate but connected systems. Fluid mass transfer between the matrix block and fractures occur at the fracture-matrix interface. The approach is based on the concept that unfractured rock accounts for much of the porosity (storage) of the medium but little permeability (flow). On the other hand, fractures may have high permeability with negligible storage.

In this case, the matrix equation for both the fluid and heat transport is the same as equations (1) to (5) represented in the EPM model; therefore, it will not be repeated here. The fluid flow in fracture within a porous matrix is expressed as

$$\phi_f\frac{\partial\rho_L}{\partial t}+\nabla\cdot\rho_L v_f+Q_f+Q_m=0 \tag{6}$$

where ϕ_f is the fracture porosity, Q_m and Q_f are the fluid mass sources/sinks for the fracture and matrix, respectively. The variable v_f is the Darcy's velocity for the fracture expressed as

$$v_f=-\frac{b^2}{12\mu}(\nabla P_f-\rho_L g\nabla z) \tag{7}$$

in which b is the fracture aperture, and P_f is the fluid pressure within the fracture. For the heat transfer in fracture within a porous matrix is given as

$$\rho C_p\frac{\partial T}{\partial t}+\rho_L C_{P,L} v_f T-\nabla(\lambda\nabla T)+Q_{f,E}+Q_{m,E}=0 \tag{8}$$

where $Q_{f,E}$ is the energy sources/sinks for the fracture, and $Q_{m,E}$ is the energy sources/sinks for the porous matrix.

2.3 Coupling heat and fluid flow

The macroscopic equations presented above for both models contain the non-linear coupling between the fluid and heat transport. Heat transport depends on flow via heat convection (i.e., velocity field), as expressed in equation (5). Fluid flow depends on heat transport via the temperature dependence of the fluid density, viscosity, specific heat capacity, and thermal conductivity, as presented below from equations (9) to (12) [14].

$$\rho_L(T)=996.9\left(1-3.17\times10^{-4}(T-298.15)-2.56\times10^{-6}(T-298.15)^2\right) \tag{9}$$

$$\mu(T)=2.414\times10^{-5}\times10^{\frac{247.8}{(T+133)}} \tag{10}$$

$$\lambda_L(T)=-922.47+2839.5\left(\frac{T}{T_0}\right)-1800.7\left(\frac{T}{T_0}\right)^2+525.77\left(\frac{T}{T_0}\right)^3-73.44\left(\frac{T}{T_0}\right)^4 \tag{11}$$

$$C_{P,L}(T)=3.3774-1.12665\times10^{-2}T+1.34687\times10^{-5}T^2 \tag{12}$$

3. MODEL SET-UP AND CONFIGURATION FOR THE BASE CASE

The geothermal reservoir for the base case is assumed to consist of two wellbores (i.e., injection and production) that intersect a fracture within the reservoir domain. Figure 1 shows the geometry of the base case. It represents a three-dimensional (3-D) deep geothermal reservoir with the dimensions 500 m x 500 m x -5050 m, with a thickness of 500 m, and located at about -4550 m below the ground level. The wellbores constitute a doublet, 11 m apart at the ground level, and 400 m apart laterally at the fracture intersection level.

In this study, the fracture is modelled in two different forms. For the EPM model, the fracture is considered as a 3-D domain. In the case of the DPP model, the fracture is represented as a plane surface with thickness.

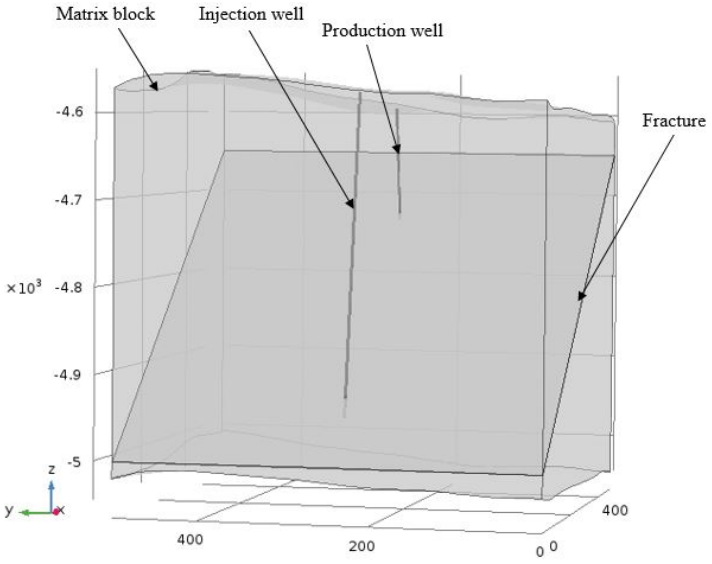

Figure 1: Reservoir geometry

3.1 Initial and boundary conditions

Initially, at t=0, the pressure is hydrostatic, and the temperature is assumed to be

$$T_0 = 12°C - 38°C(K/m)(-z) \tag{13}$$

where T_0 is the initial reservoir temperature. For hydraulic boundary conditions (B.C) a constant injection pressure of 10 MPa is applied. In the case of the thermal B.C an injection temperature of 40°C is employed at the injection wellbore. All other boundaries remain thermally insulated and no flow for the conditions for both the heat and fluid models, respectively. Table 1 presents the material properties employed in the numerical modelling.

Table 1: Physical properties attributed to base case reservoir [8]

Parameter	Value	Symbol
Matrix		
Porosity (%)	0.6	ϕ
Permeability (mD)	0.01	κ
Thermal conductivity (W/m/K)	3.5	λ_s
Heat capacity (J/kg/K)	900	$C_{\rho,S}$
Density (kg/m^3)	2400	ρ_s
Fracture		
Porosity (%)	0.1	ϕ_f
Permeability (mD)	10	κ_f
Thermal conductivity (W/m/K)	2.5	λ_f
Heat capacity (J/kg/K)	750	$C_{\rho,f}$
Density (kg/m^3)	1200	ρ_f

3.2 Computational cost and performance

In order to compare the computational cost and performance for the EPM and DPP models, a backwards difference formula (BDF) is used in the finite element solver to run the long-term simulation for 30 years. For the EPM model, it took 50-time steps with a simulation period of 29,278 seconds to simulate the 30-year numerical experimentation. The physical memory utilised is 14.98 GB, and the virtual memory is 17.26 GB. However, in the case of DPP model, it only took 33 time steps with a solution period of 307 seconds to solve for the entire process. Concerning the physical memory and virtual memory, 2.26 GB and 2.39 GB were applied, respectively.

Thus, the percentage deviation between the two models is 195.85% in terms of simulation time, 147.58% with respect to physical memory, and 151.35% in regards to virtual memory. It is also worth noting that to solve for one model using EPM is equivalent to solving 95 models in DPP.

4. RESULTS AND DISCUSSIONS

Figure 2 shows the temperature breakthrough curves obtained with both the EPM and DPP models for the same base case. Comparison of the two models, EPM and DPP, for the base case shows that very similar breakthrough curves are produced during the first seven years of the simulation. After approximately 7.2 years, the results concerning reservoir productivity, obtained with the EPM model, are slightly better than the one obtained with the DPP model. However, the calculated equivalent porosity and permeability models for the EPM model are extremely high and not realistic, if compared to the simulation domain dimensions. Table 2 presents the percentage deviation between the EPM and DPP models. As can be seen, there is more fitting for both models in the first seven years of production. For the later production period, a drastic drawdown is observed with the DPP model and a maximum deviation of 2.2% is reached between the two models in 30 years.

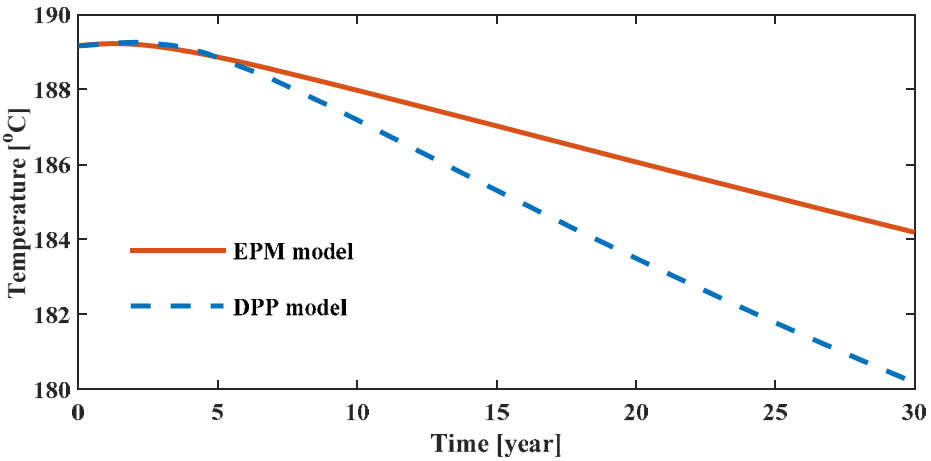

Figure 2: Temperature at the production wellbore for both EPM and DPP models

Table 2: Percentage deviation for the production temperature between the EPM and DPP models

Time (year)	EPM model production temperature (°C)	DPP model production temperature (°C)	Percentage deviation (%)
1	189.22	189.22	0
5	188.86	188.85	0.005
10	187.98	187.19	0.421
15	187.03	185.31	0.924
20	186.07	183.50	1.391
25	185.12	181.78	1.821
30	184.19	180.18	2.201

The density at the production wellbore for both the EPM and DPP models was shown in Figure 3 during a long-term simulation period of 30 years. As demonstrated in Figure 3, the production temperature remains unchanged as seen from the first five years of the simulation for both models. However, if the production temperature decreases, the density rises rapidly due

specifically to its dependence on temperature. In this scenario, the density of the DPP model is higher on the producer than that of the EPM because the EPM model has a higher production temperature. Similarly, Figure 4 presents the viscosity variation with time at the production wellbore for both the models. As can be seen, the case is exactly the same as the density since both properties are temperature-dependant parameters.

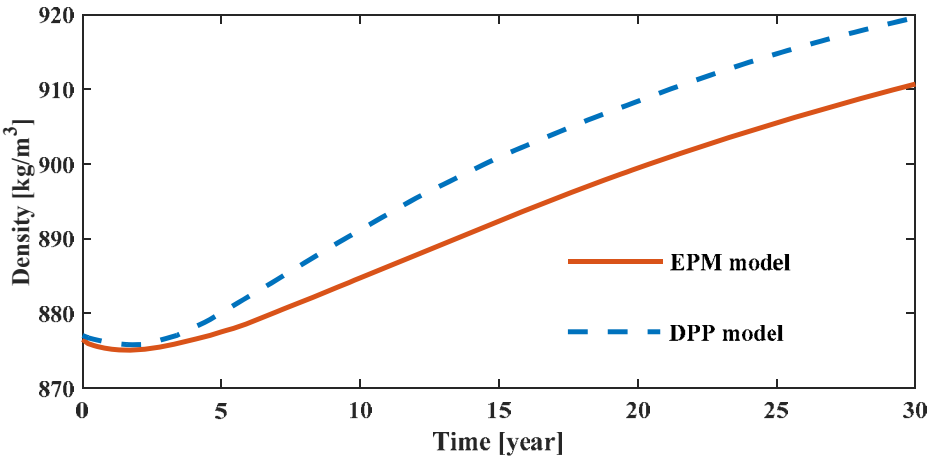

Figure 3: Density at the production wellbore for both EPM and DPP models

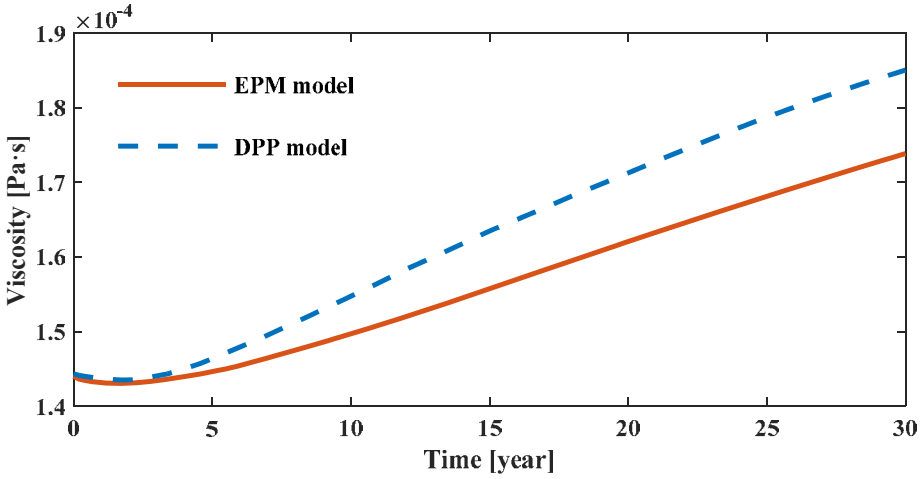

Figure 4: Density at the production wellbore for both EPM and DPP models

Figures 5a-d shows the evolution of the cold water front in the fracture surface at some simulation stages for both the EPM and DPP models. The low-temperature areas are highlighted using the legends with lower and higher threshold values 40°C and 200°C, respectively, indicating the inability of the surface to produce effective temperatures further. Since the exploitation began, the cold water front region in the fracture surface grew gradually from the injection wellbore in an annular shape for both models as shown in Figures 5a-d. As can be seen, the cold water front propagation trends are similar in both the EPM and DPP models, despite the differences in their modelling approaches.

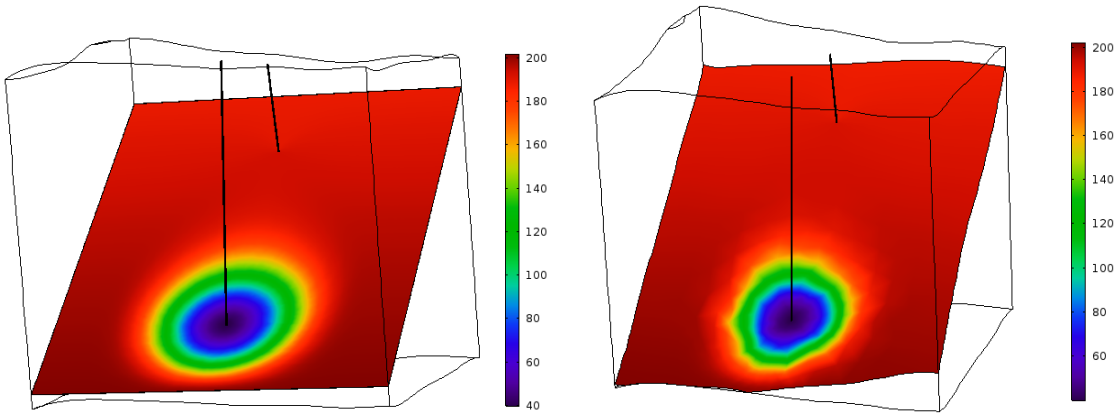

Figure 5a: EPM model at 1-year simulation (left); and DPP model at 1-year simulation (right) [°C]

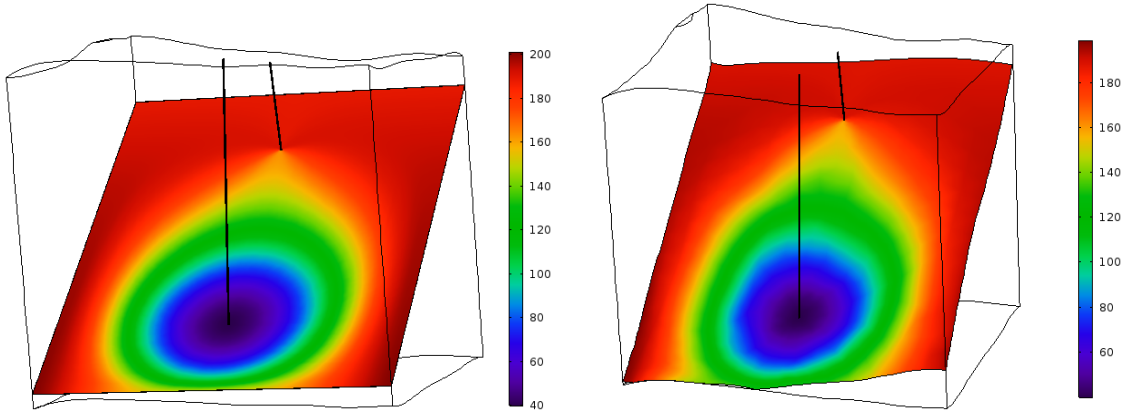

Figure 5b: EPM model at 10-years simulation (left); and DPP model at 10-years simulation (right) [°C]

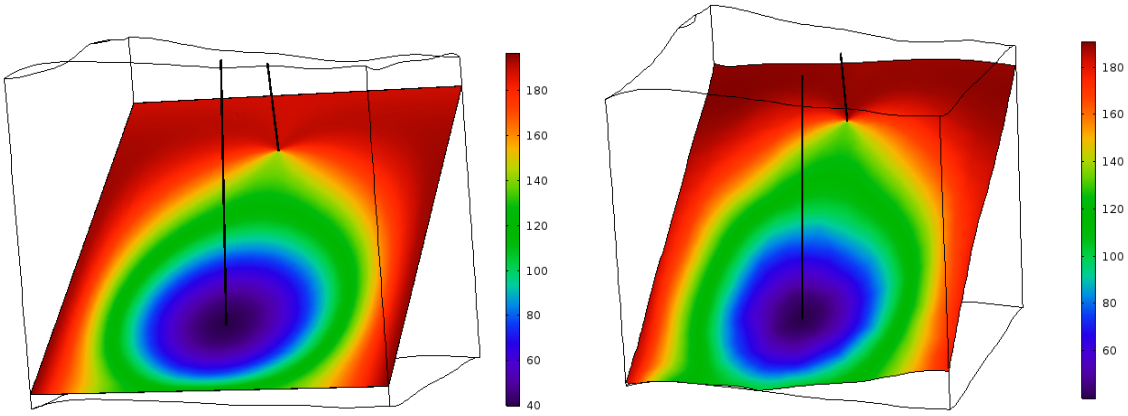

Figure 5c: EPM model at 20-years simulation (left); and DPP model at 20-years simulation (right) [°C]

Figure 5: EPM (left), and DPP (right) models cold water front at fracture surface at various simulation stages [°C]

5. CONCLUSION

This paper compared two modelling approaches, EPM and DPP conceptual models, of a naturally fractured geothermal reservoir using the finite element method to predict the long-term performance of coupled transient processes of heat and fluid transport. Two deep 3-D numerical models of doublet geothermal reservoirs are developed with the same material properties as a base case for the two models to carry a comparative study. The production temperature, density, and viscosity are examined and compared to both the EPM and DPP models during a long-term simulation period of 30 years. Besides, the cold water front evolution has been evaluated at several simulation stages for the models. The simulations show that the two models could be equally well-modelled heat and fluid flow in a naturally fractured geothermal reservoir with negligible errors. Based on the results obtained, the current work suggests that EPM and DPP models can be used for predictions, which are needed for decision making for several subsurface related issues, such as hydrocarbon reservoirs, waste disposal reservoirs, and carbon dioxide (CO_2) sequestration reservoirs.

REFERENCE

[1] M. J. O'Sullivan, K. Pruess, and M. J. Lippmann, "State of the art of geothermal reservoir simulation," *Geothermics*, vol. 30, no. 4, pp. 395–429, Aug. 2001.

[2] J. Willis-Richards and T. Wallroth, "Approaches to the modelling of hdr reservoirs: A review," *Geothermics*, vol. 24, no. 3, pp. 307–332, Jun. 1995.

[3] O. Kolditz, "Modelling flow and heat transfer in fractured rocks: dimensional effect of matrix heat diffusion," *Geothermics*, vol. 24, no. 3, pp. 421–437, Jun. 1995.

[4] T. Kohl and R. J. Hopkirk, "'FRACure' — A simulation code for forced fluid flow and transport in fractured, porous rock," *Geothermics*, vol. 24, no. 3, pp. 333–343, Jun. 1995.

[5] O. Kolditz and C. Clauser, "Numerical simulation of flow and heat transfer in fractured crystalline rocks: Application to the Hot Dry Rock site in Rosemanowes (U.K.)," *Geothermics*, vol. 27, no. 1, pp. 1–23, Feb. 1998.

[6] M. D. Aliyu and H. Chen, "Numerical Modelling of Coupled Hydro-Thermal Processes of the Soultz Heterogeneous Geothermal System," in *ECCOMAS Congress 2016 VII European Congress on Computational Methods in Applied Sciences and Engineering M. Papadrakakis, V. Papadopoulos, G. Stefanou, V. Plevris (eds.) Crete Island, Greece, 5–10 June 2016*, 2016, no. June, pp. 1–13.

[7] M. D. Aliyu, H. Chen, and O. Harireche, "Finite element modelling for productivity of geothermal reservoirs via extraction well," in *Proceedings of the 24th UK Conference of the Association for Computational Mechanics in Engineering 31 March– 01 April 2016, Cardiff University, Cardiff*, 2016, no. April, pp. 331–334.

[8] O. Kolditz, R. Ratke, H.-J. G. Diersch, and W. Zielke, "Coupled groundwater flow and

transport: 1. Verification of variable density flow and transport models," *Adv. Water Resour.*, vol. 21, no. 1, pp. 27–46, Feb. 1998.

[9] R. Ghasemizadeh, X. Yu, C. Butscher, F. Hellweger, I. Padilla, A. Alshawabkeh, and B. Y. Cao, "Equivalent porous media (EPM) simulation of groundwater hydraulics and contaminant transport in Karst aquifers," *PLoS One*, vol. 10, no. 9, pp. 1–12, 2015.

[10] A. Ebigbo, J. Niederau, G. Marquart, I. Dini, M. Thorwart, W. Rabbel, R. Pechnig, R. Bertani, and C. Clauser, "Influence of depth, temperature, and structure of a crustal heat source on the geothermal reservoirs of Tuscany: numerical modelling and sensitivity study," *Geotherm. Energy*, vol. 4, no. 1, p. 5, 2016.

[11] T. Chen, C. Clauser, G. Marquart, K. Willbrand, and H. B??sing, "Modeling anisotropic flow and heat transport by using mimetic finite differences," *Adv. Water Resour.*, vol. 94, pp. 441–456, 2016.

[12] J. Niederau, A. Ebigbo, G. Marquart, J. Arnold, and C. Clauser, "On the impact of spatially heterogenous permeability on free convection in the Perth Basin, Australia," *Geothermics*, vol. 66, no. April, pp. 119–133, Mar. 2017.

[13] D. Blessent, P. R. Jørgensen, and R. Therrien, "Comparing Discrete Fracture and Continuum Models to Predict Contaminant Transport in Fractured Porous Media.," *Groundwater*, vol. 52, no. 1, pp. 84–95, 2013.

[14] E. O. Holzbecher, *Modeling Density-Driven Flow in Porous Media*. Berlin, Heidelberg: Springer Berlin Heidelberg, 1998.

VII International Conference on Computational Methods for Coupled Problems in Science and Engineering
COUPLED PROBLEMS 2017
M. Papadrakakis, E. Oñate and B. Schrefler (Eds)

BOUNDARY ELEMENT ANALYSIS OF STEADY INCOMPRESSIBLE VISCOUS FLOW WITH ISOGEOMETRIC AND ISOPARAMETRIC DISCRETISATION

C. Duenser* and G. Beer*

* Institute for Structural Analysis
Graz University of Technology
Lessingstrasse 25/II, 8010 Graz, Austria
e-mail: duenser@tugraz.at
e-mail: gernot.beer@tugraz.at
web page: http://www.ifb.tugraz.at

Key words: BEM, isogeometric analysis, flow, incompressible

Abstract. In this work the boundary element method (BEM) is applied to steady incompressible viscous flow of Newtonian fluids. The boundary integral equation is derived from the continuity and momentum equation and the primary variables involved are velocity and traction. Due to the non-linearity of the governing differencial equation a volume integral arise in the formulation of the final equation system. Thus, iterative techniques, either a full or modified Newton-Raphson algorithm, are applied in the solution procedure.

The numerical discretisation is done in two different ways, firstly with the use of classical isoparametric continuous elements of linear and quadratic order. Using this type of elements geometry- and mesh-generation is a significant portion of the overall computation effort. In contrast to this, in a second implementation, the discretisation is done with the isogeometric analysis (IGA). With the IGA geometry data can be taken directly from Computer Aided Design (CAD) programs, potentially eliminating the need for mesh generation. The arising surface and volume integrals of the BEM are evaluated with both techniques, the isoparametric application and with the IGA.

Computational results are shown for the two different numerical implementations based on a 2D benchmark example. The accuracy of the results of both methods are compared as well as the computational effort, such as numbers of degrees of freedom and internal point calculations.

1 INTRODUCTION

For the solution of viscous flow problems in many publications domain methods such as the Finite Difference, Finite Elements or Finite Volumes are used. A widely used benchmark example is the forced flow in a cavity and very accurate results are available with a solution of a very fine finite difference discretisation by [1].

In this work we use the Boundary Element Method (BEM). The discretisation is done with the classical isoparametric analysis and with the isogeometric analysis (IGA) [2]. With IGA geometry data can be taken directly from Computer Aided Design (CAD) programs [3], potentially eliminating the need for mesh generation. With the BEM for linear problems unknowns only exist at the domain boundary and the solution inside the domain satisfies the governing differential equation. For the present non-linear problem volume integrals arise.

2 THE BOUNDARY ELEMENT METHOD - BASIC FORMULATION

The laws of conservation of mass and momentum are the basis for the differential equations for steady incompressible flow which are written in the form:

$$\frac{\partial u_j}{\partial x_j} = 0 \qquad \mu \frac{\partial^2 u_i}{\partial x_j \partial x_j} - \frac{\partial p}{\partial x_i} - \rho u_j \frac{\partial u_i}{\partial x_j} = 0 \tag{1}$$

where x_i is the Eulerian coordinate, u_i is the velocity vector, p is the pressure, ρ the mass density and μ the viscosity. The non-linear Equation (1) is considered by the BEM by treating the non-linear terms as body forces. Thus, Equation (1) is reformulated as:

$$\frac{\partial u_j}{\partial x_j} = 0 \qquad \mu \frac{\partial^2 u_i}{\partial x_j \partial x_j} - \frac{\partial p}{\partial x_i} + f_i = 0 \tag{2}$$

with

$$f_i = -\rho u_j \frac{\partial u_i}{\partial x_j} \tag{3}$$

We define fluid stresses as:

$$\sigma_{ij} = \mu \left(\frac{\partial u_i}{\partial x_j} + \frac{\partial u_j}{\partial x_i} \right) \tag{4}$$

and the resulting tractions on boundary S:

$$t_i = \sigma_{ij}\, n_j - p\, n_i \tag{5}$$

where n_i is the unit vector normal to the boundary. Using the reciprocal theorem, the following integral equation is obtained (for a full derivation we refer to [4]):

$$c_{ij}(y)\, \dot{u}_j(y) = \int_S \left[U_{ij}(y,x)\, t_j(x) - T_{ij}(y,x)\, \dot{u}_j(x) \right] dS(x) + \int_{V_0} U_{ij}(y,\bar{x})\, f_j(\bar{x}) dV_0(\bar{x}) \tag{6}$$

where $c_{ij}(y)$ is an integral free term, depending on the shape of the boundary and $\dot{u}_i$ is the velocity perturbation, i.e. the total velocity can be written as:

$$u_i(x) = \dot{u}_i(x) + u_i^0(x) \tag{7}$$

where u_i^0 is the free stream velocity and $U_{ij}(y,x)$ and $T_{ij}(y,x)$ are fundamental solutions for the velocity and traction at point x due to a source at point y.

In Equation (6) f_j appears involving derivatives of velocities. As has been shown in [5] these derivatives can be computed by using finite differences or by taking derivatives of an approximation of the velocity field. In both cases additional computational work needs to be done and errors are introduced.

Alternatively, the requirement of computing derivatives can be eliminated by applying the divergence theorem to the volume integral in Equation (6) resulting in:

$$\begin{aligned} c_{ij}(y)\,\dot{u}_j(y) = &\int_S \left[U_{ij}(y,x)\,t_j(x) - T_{ij}(y,x)\,\dot{u}_j(x)\right] dS \\ &- \int_{S_0} U_{ij}(y,x)\,t_j^0(x) dS_0 + \int_{V_0} U_{ij,k}(y,\bar{x})\,b_{jk}^0(\bar{x}) dV_0 \end{aligned} \tag{8}$$

where $U_{ij,k}(y,x)$ is a derived fundamental solution and:

$$\begin{aligned} b_{ik}^0(\bar{x}) &= \rho\,u_k(\bar{x})\,\dot{u}_i(\bar{x}) \\ t_i^0(x) &= b_{ik}^0(x)\,n_k(x) \end{aligned} \tag{9}$$

3 ISOPARAMETRIC DISCRETISATION

As in the work of [4] for the surface discretisation Lagrangian elements of linear or parabolic order are used to approximate the geometry and the boundary unknowns u and t. For the volume integral in Equation (8) cells are used to evaluate the integral.

3.1 Discretisation - Equation system

We use the collocation method, i.e. we write the integral equations for a finite number (N) of source points at locations $\mathbf{y}_n$. Changing to matrix notation, the integral equations are re-written as:

$$\begin{aligned} \mathbf{c}\left(\mathbf{y}_n\right)\,\dot{\mathbf{u}}\left(\mathbf{y}_n\right) = &\int_S \mathbf{U}\left(\mathbf{y}_n,\mathbf{x}\right)\mathbf{t}\left(\mathbf{x}\right)\mathrm{d}\,S - \int_S \mathbf{T}\left(\mathbf{y}_n,\mathbf{x}\right)\dot{\mathbf{u}}\left(\mathbf{x}\right)\mathrm{d}\,S \\ &- \int_{S_0} \mathbf{U}\left(\mathbf{y}_n,\mathbf{x}\right)\mathbf{t}_0\left(\mathbf{x}\right)\mathrm{d}\,S_0 + \int_{V_0} \mathbf{U}'\left(\mathbf{y}_n,\bar{\mathbf{x}}\right)\mathbf{b}_0\left(\bar{\mathbf{x}}\right)\mathrm{d}\,V_0 \end{aligned} \tag{10}$$

with $n = \{1,\ldots,N\}$. In the above $\mathbf{c}\left(\mathbf{y}_n\right)$ is a matrix containing integral free terms, $\dot{\mathbf{u}}(\mathbf{x})$ and $\mathbf{t}(\mathbf{x})$ are vectors containing perturbation velocities and tractions at point $\mathbf{x}$

on the boundary. $\mathbf{U}(\mathbf{y}_n, \mathbf{x})$ and $\mathbf{T}(\mathbf{y}_n, \mathbf{x})$ are matrices containing fundamental solutions described in [4]. $\mathbf{b}_0(\bar{\mathbf{x}})$ is a body force vector at a point $\bar{\mathbf{x}}$ inside V_0.

For the discretisation of the surface integrals over S the boundary is divided into elements and we apply the isoparametric concept where the same basis functions are used for the approximation of the geometry and the field values.

$$\mathbf{x}^e = \sum_{k=1}^{K} N_k(\xi)\, \mathbf{x}_k^e \qquad \dot{\mathbf{u}}^e = \sum_{k=1}^{K} N_k(\xi)\, \dot{\mathbf{u}}_k^e \qquad \mathbf{t}^e = \sum_{k=1}^{K} N_k(\xi)\, \mathbf{t}_k^e \tag{11}$$

In the above equations the superscript e refers to the number of the element, N_k are element basis functions with respect to the local coordinate ξ for the geometry, velocities and tractions respectively. $\mathbf{x}_k^e$ specify the location of the element nodes and $\dot{\mathbf{u}}_k^e$ and $\mathbf{t}_k^e$ are the parameters for velocities and tractions associated to the node k. K are the number of parameters depending on the order of basis functions (linear or quadratic) for each element.

Inserting the approximations into the integral equations the following discretised integral equations are obtained:

$$\sum_{e=1}^{E}\sum_{k=1}^{K} \triangle\mathbf{U}_{nk}^e \mathbf{t}_k^e = \sum_{e=1}^{E}\sum_{k=1}^{K} \triangle\mathbf{T}_{nk}^e \dot{\mathbf{u}}_k^e + \sum_{e=1}^{E}\sum_{k=1}^{K} \triangle\mathbf{U}_{nk}^e \mathbf{t}_{0k}^e - \sum_{c=1}^{C}\sum_{k=1}^{K} \triangle\mathbf{U'}_{nk}^c \mathbf{b}_{0k}^c \tag{12}$$

Furthermore

$$\triangle\mathbf{U}_{nk}^e = \int_{-1}^{1} \mathbf{U}\left(\mathbf{y}_n, \mathbf{x}^e(\xi)\right) N_k(\xi)\, J\, \mathrm{d}\,\xi \tag{13}$$

$$\triangle\mathbf{T}_{nk}^e = \int_{-1}^{1} \mathbf{T}\left(\mathbf{y}_n, \mathbf{x}^e(\xi)\right) \cdot N_k(\xi)\, J\, \mathrm{d}\,\xi$$

$$\triangle\mathbf{U'}_{nk}^c = \int_{-1}^{1}\int_{-1}^{1} \mathbf{U'}\left(\mathbf{y}_n, \mathbf{x}^e(\xi,\eta)\right) N_k(\xi,\eta)\, J\, \mathrm{d}\,\xi\, \mathrm{d}\,\eta$$

In the above J is the Jacobian of the transformation from local ξ to global (x, y) coordinate systems. The integral free term together with the strongly singular integral term of Equation (10) is evaluated using the rigid body motion shown in [6]. After assembly the following system of equations

$$[\mathbf{U}]\{\mathbf{t}\} = [\mathbf{T}]\{\dot{\mathbf{u}}\} + \{\mathbf{F}\}_0 \tag{14}$$

is obtained, where $[\mathbf{U}]$, $[\mathbf{T}]$ are matrices assembled from element contributions (Equation (13)) and $\{\mathbf{t}\}$, $\{\dot{\mathbf{u}}\}$ are vectors that collect all traction and velocity components on

points $\mathbf{y}_n$. $\{\mathbf{F}\}_0$ relates to the integrals involving body forces. Either $\mathbf{t}$ or $\dot{\mathbf{u}}$ must be known on the boundary, so for a mixed boundary value problem we have

$$[\mathbf{L}]\{\mathbf{a}\} = \{\mathbf{F}\} + \{\mathbf{F}\}_0 \tag{15}$$

where $[\mathbf{L}]$ contains a mixture of $[\mathbf{U}]$,$[\mathbf{T}]$ coefficients and $\{\mathbf{a}\}$ contains a mixture of unknown tractions and velocities. $\{\mathbf{F}\}_0$ is a vector computed with known boundary values.

3.2 Results in the domain

The solution algorithm requires the evaluation of the perturbation velocities inside the domain V_0. The velocity vector $\mathbf{v}$[1] at any internal point $\mathbf{y}_i$ can be computed by

$$\mathbf{v}(\mathbf{y}_i) = \int_S \mathbf{U}(\mathbf{y}_i, \mathbf{x})\,\mathbf{t}(\mathbf{x})\,\mathrm{d}S - \int_S \mathbf{T}(\mathbf{y}_i, \mathbf{x})\,\dot{\mathbf{u}}(\mathbf{x})\,\mathrm{d}S \tag{16}$$
$$- \int_{S_0} \mathbf{U}(\mathbf{y}_i, \bar{\mathbf{x}})\,\mathbf{b}_0(\mathbf{x})\,\mathbf{n}(\mathbf{x})\,\mathrm{d}S_0 + \int_{V_0} \mathbf{U}'(\mathbf{y}_i, \bar{\mathbf{x}})\,\mathbf{b}_0(\bar{\mathbf{x}})\,\mathrm{d}V_0$$

After inserting the approximations for $\dot{\mathbf{u}}$, $\mathbf{t}$ and $\mathbf{b}_0$ the equation above can be written in matrix notation as:

$$\{\mathbf{v}\} = [\mathbf{A}]\,\{\mathbf{t}\} - [\mathbf{C}]\,\{\dot{\mathbf{u}}\} + [\mathbf{D}]\,\{\mathbf{b}_0\} \tag{17}$$

where matrices $[\mathbf{A}]$ and $[\mathbf{C}]$ are assembled from element contributions of Kernel basis function products and $[\mathbf{D}] = \left([\mathbf{D}]^V - [\mathbf{D}]^S\right)$.

3.3 Iterative procedure - Modified Newton-Raphson

There are two possibilities for the iterative procedure: modified Newton-Raphson or full Newton-Raphson. In the former the left hand side of the system of equations is not changed and only a new right hand side is computed at each iteration, whereas in the latter the left hand side is changed at every iteration. The test examples is a pure Dirichlet problem, i.e. $\{\mathbf{a}\} = \{\mathbf{t}\}$ in Equation (15) and therefore the unknown are boundary tractions $\{\mathbf{t}\}$ and the known values are perturbation velocities $\{\dot{\mathbf{u}}\}$ at the boundary. Without loss of generality, the algorithms are detailed for this special case as the extension to mixed boundary conditions is trivial. The iterative procedure for modified Newton-Raphson is essentially the same as used in [5] and described in more detail in [6]. For the first iteration the unknowns are computed by

$$[\mathbf{U}]\{\mathbf{t}\}^0 = \{\mathbf{F}\} \tag{18}$$

For the subsequent iteration we have

$$[\mathbf{U}]\{\mathbf{t}\}^k = \{\mathbf{F}\} + \{\mathbf{F}\}_0^{k-1} \tag{19}$$

[1] The velocities at internal points are referred to as $\mathbf{v}$ to distinguish them from the boundary velocities $\dot{\mathbf{u}}$.

where k is an iteration counter. The velocities at internal points are computed by:

$$\{\mathbf{v}\}^0 = [\mathbf{A}]\ \{\mathbf{t}\}^0 - [\mathbf{C}]\ \{\dot{\mathbf{u}}\} \tag{20}$$

for the first iteration and

$$\{\mathbf{v}\}^k = [\mathbf{A}]\ \{\mathbf{t}\} - [\mathbf{C}]\ \{\dot{\mathbf{u}}\} + [\mathbf{D}]\ \{\mathbf{b}_0\} \tag{21}$$

for the subsequent iterations. To ensure convergence for higher Reynolds numbers we apply a relaxation scheme, i.e. the tractions and velocities are computed by a combination of new and previous values, where β is a relaxation coefficient ($0 < \beta < 1$):

$$\begin{aligned} \{\mathbf{t}\} &= \beta\,\{\mathbf{t}\}^k + (1-\beta)\,\{\mathbf{t}\}^{k-1} \\ \{\mathbf{v}\} &= \beta\,\{\mathbf{v}\}^k + (1-\beta)\,\{\mathbf{v}\}^{k-1} \end{aligned} \tag{22}$$

3.4 Numerical results - Isoparametric discretisation

The implementation of the theory is tested here on the standard problem of a driven cavity. The results are compared with an available fine grained solution of [1] in order to ascertain that good quality of results can be obtained. An incompressible fluid of uniform viscosity ($\mu = 1$) is confined within a square region of dimension $H = 1 \times 1$. The fluid velocities on the bottom, left and right are fixed at zero, while a uniform velocity $u_x = 1$ is specified at the top, which is tapered off to zero very near the corners. The Reynolds number is defined as $Re = \rho\, U\, H/\mu$. The example is tested for different Reynolds numbers by changing the value of ρ.

3.4.1 Definition of geometry

The boundary of the problem is defined by either linear or quadratic boundary elements. The element lengths are graded towards the edges of the cavity. As shown in Figure 1 three mesh densities are considered with 10, 20 and 30 elements along each edge of the cavity. The volume of the domain is discretised with cells with basis functions of

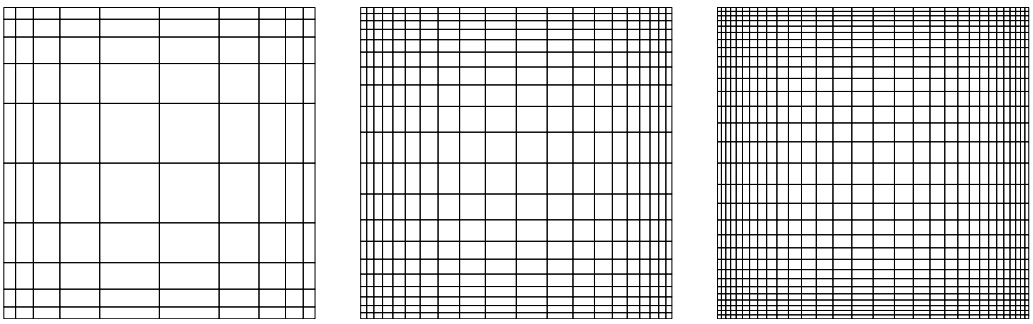

Figure 1: Definition of Geometry with 10, 20 and 30 boundary elements at each edge of the cavity

either linear or quadratic order, describing the geometry and the velocity in the interior. In Table 1 the number of degrees of freedom associated to the nodes at the boundary and the number of internal points are shown for the three meshes and the reference solution of [1].

Table 1: Mesh statistics

Mesh	Degrees of freedom	No. of internal points
10 linear	80	81
10 quadratic	160	261
20 linear	160	361
20 quadratic	320	1121
30 linear	240	841
30 quadratic	480	2581
Reference [1]	-	16641

3.4.2 Results and comparison

Results were computed for the three meshes with linear and quadratic elements for Reynolds numbers 100, 200 and 300 with a modified Newton-Raphson method with relaxation. Figure 2 shows the velocity vectors for Reynolds numbers 0 and 300. A shift in the vortex centre can be clearly seen. Figures 3, 4 and 5 show a comparison of the results obtained for the different meshes. For Reynolds number 100 the variation of x-velocities along a vertical line through the middle for all meshes agree well with the extremely accurate published solution. For the results with Reynolds number 200 and 300 no reference solutions were available. But, as shown in Figure 4 for Reynolds number 200 the results of the different meshes agree well, even for the course meshes. The results for Reynolds number 300 (Figure 5) deviate from each other. With the modified Newton-Raphson iterativie algorithm with relaxation a solution was difficult to achieve and for higher Reynolds numbers no converged results could be obtained.

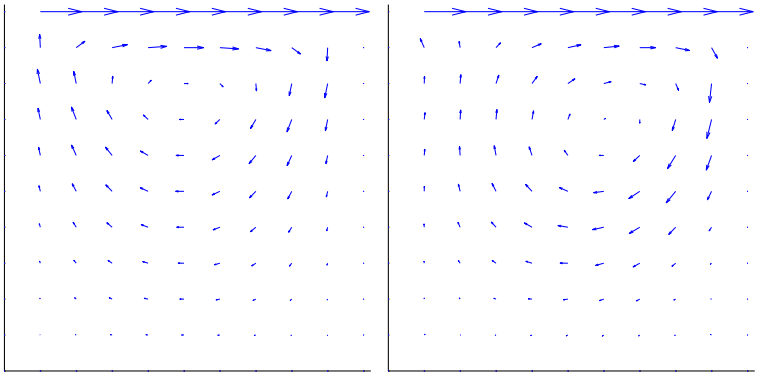

Figure 2: Forced cavity flow: Resulting velocity vectors for Re=0 and Re=300

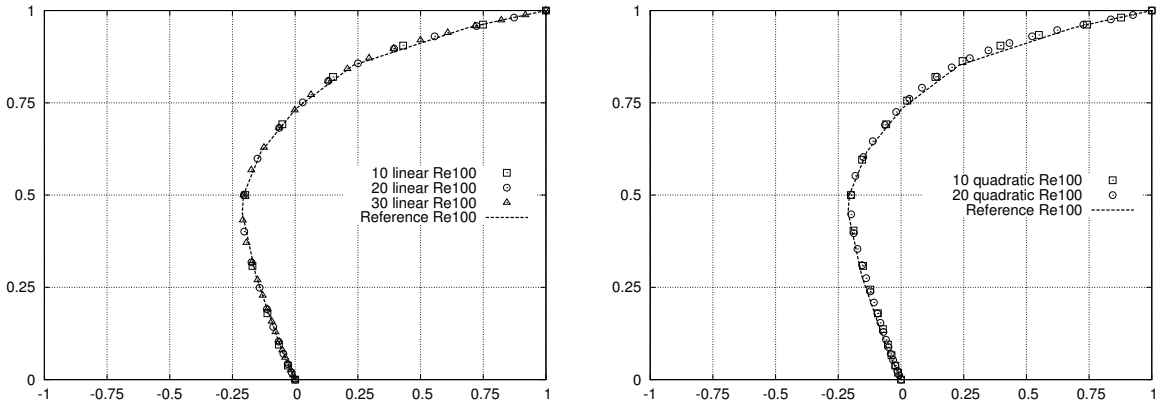

Figure 3: Comparison of velocity in x-direction along a vertical line through centre for Re=100 for linear (left) and quadratic elements (right) together with the reference solution

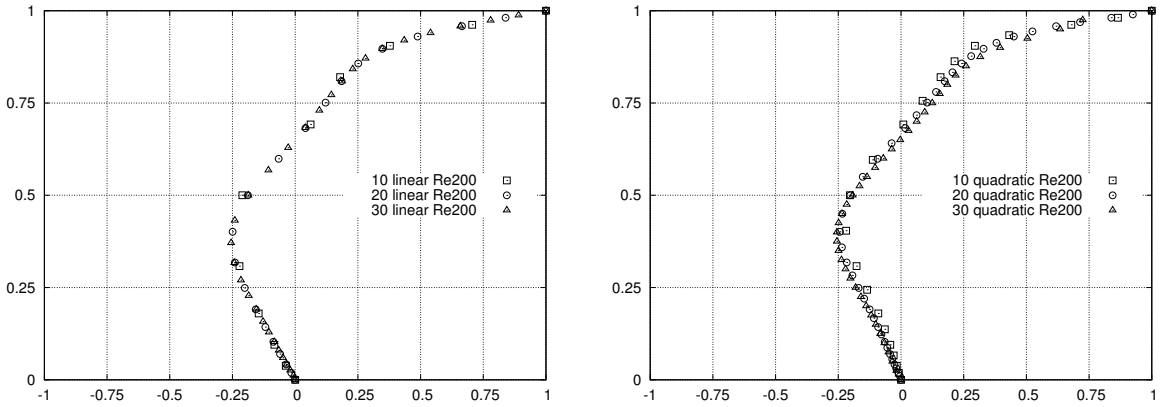

Figure 4: Comparison of velocity in x-direction along a vertical line through centre for Re=200 for linear (left) and quadratic elements (right)

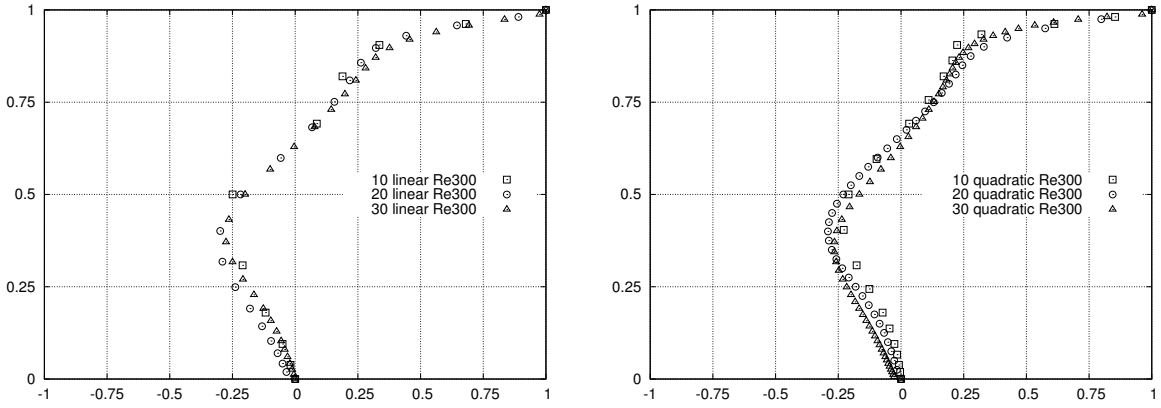

Figure 5: Comparison of velocity in x-direction along a vertical line through centre for Re=300 for linear (left) and quadratic elements (right)

4 ISOGEOMETRIC DISCRETISATION

For the discretisation of the surface integrals over the boundary S of Equation (10) and Equation (12) the boundary is divided into patches and a geometry independent field approximation approach is adopted for each patch, i.e. different basis functions for the description of the geometry and for the field values are used.

$$\mathbf{x}^e = \sum_{k=1}^{K} R_k(s)\,\mathbf{x}_k^e \qquad \dot{\mathbf{u}}^e = \sum_{k=1}^{K^u} R_k^u(s)\,\dot{\mathbf{u}}_k^e \qquad \mathbf{t}^e = \sum_{k=1}^{K^t} R_k^t(s)\,\mathbf{t}_k^e \tag{23}$$

In the above equations the superscript e refers to the number of the patch, R_k, R_k^u and R_k^t are NURBS basis functions with respect to the local coordinate s for the geometry, velocities and tractions respectively. $\mathbf{x}_k^e$ specify the location of control points and $\dot{\mathbf{u}}_k^e$ and $\mathbf{t}_k^e$ are the parameters for velocities and tractions. K, K^u, K^t are the number of parameters for each patch. The advantage of using NURBS is that they are much better suited than Lagrange polynomials for describing smooth boundaries and that superior refinement strategies such as order elevation, knot insertion and k-refinement, can be used. By manipulating the knot vector one can easily influence the continuity of the basis functions for the approximation of unknown values. Inserting the approximations into the integral equations the same final equation system arise as shown in Equation (15). For the evaluation of the domain integral the domain V_0 is described by a mapping method introduced recently for 2D in [7] and extended to 3D in [8]. In this approach the domain is defined by two NURBS curves and a linear interpolation between them as shown in the Figure 6. A detailed description of the evaluation of the volume integral has been recently submitted by Beer et al. [6].

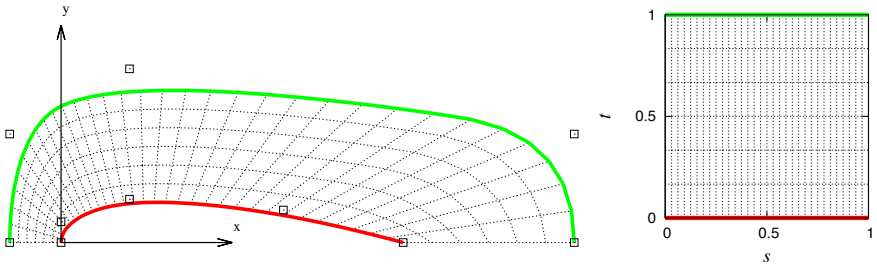

Figure 6: Example of definition of volume V_0 surrounding half of an airfoil in (left) global x,y and (right) local s,t coordinate system. The red curve defines the boundary of the airfoil as well as the bottom boundary of the domain V_0. The green curve defines its top boundary. The associated control points are depicted by hollow squares. Note that only 5 control points are required to accurately define the shape of the airfoil and 5 more control points the surrounding domain.

4.1 Iterative procedure

Additionally to the the modified Newton-Raphson with a relaxation scheme described in section 3.3 a full Newton-Raphson is implemented in the NURBS based code. With this the left hand side of Equation (15) is modified at each iteration. The theory and implementation is described in [6].

4.2 Numerical results - Isogeometric discretisation

For the described driven cavity problem of section 3.4 the boundary is defined by 4 linear NURBS patches. The approximation of the boundary unknown was achieved by inserting knots and by order elevating the basis functions for describing the geometry (from linear to quadratic). Three different refinements were investigated and the resulting locations of collocation points computed using Greville abscissa [9] are shown in Figure 7.

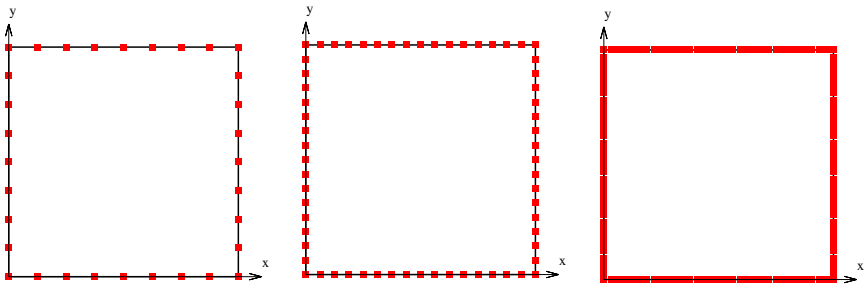

Figure 7: Refinement of solution: Location of collocation points for 3, 7 and 15 knot insertions for each patch

The domain for the volume integration was defined by 2 NURBS curves. The refinement of the boundary values was accompanied by an increased number of internal points as shown in Figure 8. Quadratic interpolation between the points was assumed.

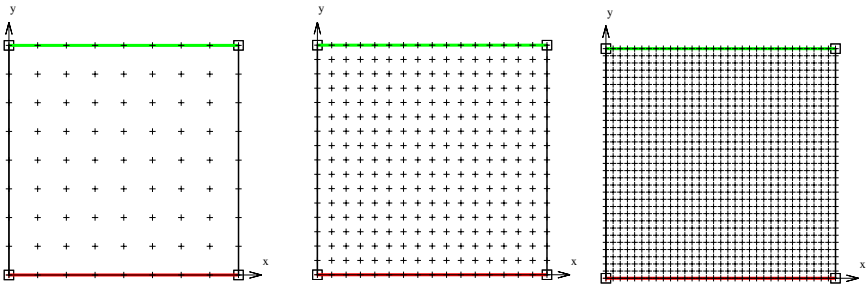

Figure 8: Definition of domain for volume integration with two NURBS curves marked red and green and location of the internal points for the three refinement stages

The number of degrees of freedom and the number of internal points for the different meshes is shown in Table 2.

Table 2: Mesh statistics

Mesh	Degrees of freedom	No. of internal points
mesh1	64	81
mesh2	128	289
mesh3	256	1089
Reference [1]	-	16641

Compared to the isoparametric results with the isogeometric approach a solution for Reynolds number Re=400 with the modified Newton-Raphson as well as with the full Newton-Raphson iteration is possible. There is very little difference between the results obtained with modified and full Newton-Raphson as shown in Figure 9. However, as shown in Table 3 there is a large difference with respect to the number of iterations required to achieve convergence to a tolerance of 10^{-4} with the modified Newton-Raphson requiring a significant higher number of iterations.

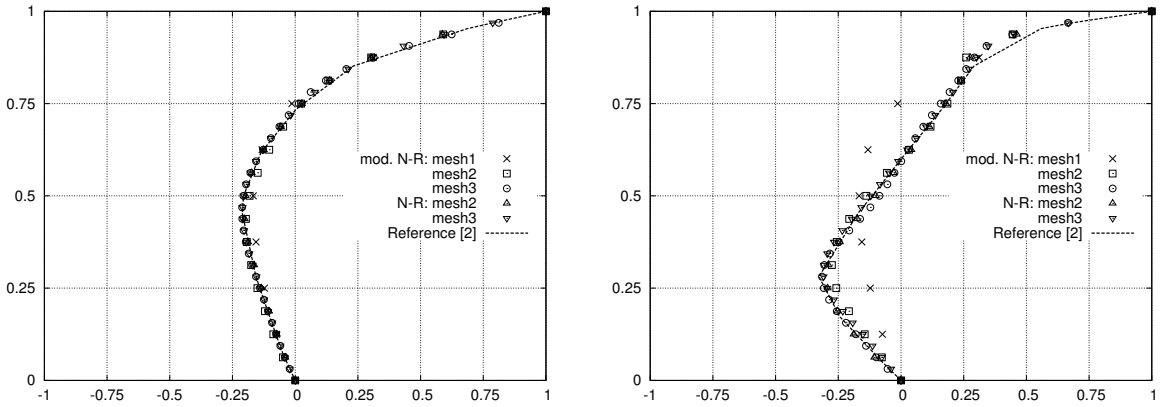

Figure 9: Comparison of velocity in x-direction along a vertical line through centre for Re=100 (left) and Re=400 (right) together with the reference solution

Table 3: Number of iterations required for convergence

		mesh 1	mesh 2	mesh3
Re=100	modified Newton-Raphson	15	19	18
	full Newton-Raphson	3	3	3
Re=400	modified Newton-Raphson	24	39	100
	full Newton-Raphson	-	5	5

5 Conclusion

A comparison of isoparametric and isogeometric BEM discretisation is shown for the benchmark example of the driven cavity problem in 2D. Excellent results for moderate Reynolds numbers could be obtained for both discretisation methods even for coarse meshes. For increasing Reynolds numbers it seems that isogeometric discretisation leads to a better convergence behaviour then isoparametric discretisation. With respect to iterative techniques a full Newton-Raphson method is necessary to achieve results for higher Reynolds numbers with a moderate number of iterations.

REFERENCES

[1] U. Ghia, K. N. Ghia, C. T. Shin, High-Re Solutions for incompressible flow using the Navier-Stokes equations and Multigrid Method, Journal of computational physics 48 (1982) 387–411.

[2] G. Beer, Advanced numerical simulation methods - From CAD Data directly to simulation results, CRC Press/Balkema, 2015.

[3] T. Hughes, J. Cottrell, Y. Bazilevs, Isogeometric analysis: CAD, finite elements, NURBS, exact geometry and mesh refinement, Computer Methods in Applied Mechanics and Engineering 194 (39–41) (2005) 4135–4195.

[4] G. Dargush, P. Banerjee, Boundary Element Methods in Nonlinear Fluid Dynamics, Vol. 6 of Developments in boundary element methods, Elsevier, 1990, Ch. Advanced boundary element methods for steady incompressible thermoviscous flow.

[5] M. Aydin, R. T. Fenner, Boundary element analysis of driven cavity flow for low and moderate Reynolds numbers, International Journal for Numerical Methods in Fluids 37 (2000) 45–64.

[6] G. Beer, V. Mallardo, E. Ruocco, C. Duenser, Isogeometric boundary element analysis of steady incompressible viscous flow, part 1: plane problems, Computer Methods in Applied Mechanics and Engineering submitted February 2017.

[7] G. Beer, B. Marussig, J. Zechner, C. Duenser, T.-P. Fries, Isogeometric boundary element analysis with elasto-plastic inclusions. part 1: plane problems, Computer Methods in Applied Mechanics and Engineering 308 (2016) 552–570.

[8] G. Beer, V. Mallardo, E. Ruocco, B. Marussig, J. Zechner, C. Duenser, T. P. Fries, Isogeometric boundary element analysis with elasto-plastic inclusions. part 2: 3-d problems, Computer Methods in Applied Mechanics and Engineering 315 (2017) 418–433.

[9] R. W. Johnson, Higher order B-spline collocation at the Greville abscissae, Applied Numerical Mathematics 52 (1) (2005) 63 – 75.

VII International Conference on Computational Methods for Coupled Problems in Science and Engineering
COUPLED PROBLEMS 2017
M. Papadrakakis, E. Oñate and B. Schrefler (Eds)

COUPLING FREE-SURFACE FLOW AND MESH DEFORMATION IN AN ISOGEOMETRIC SETTING

STEFANIE ELGETI*, FLORIAN ZWICKE* AND SEBASTIAN EUSTERHOLZ*

*Chair for Computational Analysis of Technical Systems (CATS)
CCES, Schinkelstr. 2, 52062 Aachen, Germany
e-mail: elgeti@cats.rwth-aachen.de, web page: http://www.cats.rwth-aachen.de/

Key words: Isogeometric Analysis, Interface Tracking, Free Surface Flow

Abstract. The simulation of certain flow problems requires a means for modeling a free fluid surface; examples being viscoelastic die swell or fluid sloshing in tanks. In a finite-element context, this type of problem can, among many other options, be dealt with using an interface-tracking approach with the Deforming-Spatial-Domain/Stabilized-Space-Time (DSD/SST) formulation [1]. A difficult issue that is connected with this type of approach is the determination of a suitable coupling mechanism between the fluid velocity at the boundary and the displacement of the boundary mesh nodes. In order to avoid large mesh distortions, one goal is to keep the nodal movements as small as possible; but of course still compliant with the no-penetration boundary condition. One common choice of displacement that fulfills both requirements is the displacement with the normal component of the fluid velocity. However, when using finite-element basis functions of Lagrange type for the spatial discretization, the normal vector is not uniquely defined at the mesh nodes. This can create problems for the coupling, e.g., making it difficult to ensure mass conservation. In contrast, NURBS basis functions of quadratic or higher order are not subject to this limitation. These types of basis functions have already been used in the context of free-surface boundaries, in connection with the NURBS-enhanced finite-element method (NEFEM) [2]. However, this method presents some difficulties due to the fact that it does not adhere to the isoparametric concept. As an alternative, we investigate the suitability of using the method of isogeometric analysis for the spatial discretization. If NURBS basis functions of sufficient order are used for both the geometry and the solution, both a well-defined normal vector as well as the velocity are available on the entire boundary. This circumstance allows the weak imposition of the no-penetration boundary condition. We compare this option with a number of alternatives. Furthermore, we examine several coupling methods between the fluid equations, boundary conditions, and equations for the adjustment of interior control point positions.

1 INTRODUCTION

This paper can be placed in the field of free boundary problems. More specifically, it considers fluid flow problems where the computational domain is part of the solution — for example a computational domain that contains a free surface. Examples are sloshing tanks — under a seismic load, the liquid stored in a tank begins to slosh — and rising bubbles — a liquid bubble enclosed in a second fluid rises or falls due to the buoyancy force.

2 GOVERNING EQUATIONS FOR THE FREE-BOUNDARY VALUE PROBLEM OF FREE-SURFACE FLOW

For free-surface flow, three types of equations are relevant: (1) the Navier-Stokes equations in combination with an appropriate constitutive equation govern the fluid flow, (2) the displacement of the free surface, which is governed by the no-penetration boundary condition, and (3) the equations governing the possible displacement of interior parts of the domain in order to maintain validity of the mesh. This section will discuss the relevant aspects of these equations.

2.1 Governing equations for fluid flow: The Navier-Stokes equations

In the generic incompressible and isothermal fluid flow problem the unkowns are the velocity, $\mathbf{u}(\mathbf{x},t)$, and the pressure, $p(\mathbf{x},t)$. The computational domain at each instant in time, denoted by Ω_t, is a subset of $\mathbb{R}^{nsd}$, where nsd is the number of space dimensions. Then, at each point in time $t \in [0,T]$, the flow problem is governed by the Navier-Stokes equations, which in our notation read:

$$\rho\left(\frac{\partial \mathbf{u}}{\partial t} + \mathbf{u}\cdot\nabla\mathbf{u} - \mathbf{f}\right) - \nabla\cdot\boldsymbol{\sigma} = \mathbf{0} \quad \text{on} \quad \Omega_t \;\forall\; t \in [0,T]\,, \tag{1}$$

$$\nabla\cdot\mathbf{u} = 0 \quad \text{on} \quad \Omega_t \;\forall t \in [0,T]\,, \tag{2}$$

with ρ as the density of the fluid. We consider only Newtonian fluids, meaning that the stress tensor σ is defined as

$$\boldsymbol{\sigma}(\mathbf{u},p) = -p\mathbf{I} + 2\mu\boldsymbol{\varepsilon}(\mathbf{u}) \quad \text{on} \quad \Omega_t\,, \tag{3}$$

with

$$\boldsymbol{\varepsilon}(\mathbf{u}) = \frac{1}{2}(\nabla\mathbf{u} + (\nabla\mathbf{u})^T)\,, \tag{4}$$

where μ denotes the dynamic viscosity. $\mathbf{f}$ includes all external body forces with respect to the unit mass of fluid. Note that the spatial domain is time-dependent, which is indicated by subscript t.

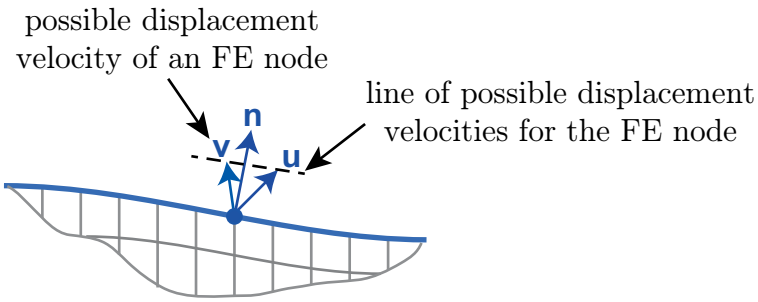

Figure 1: The figure shows an excerpt of a finite element mesh with the free surface indicated in blue. For each FE node, the fluid velocity $\mathbf{u}$ is given. Together with the normal vector $\mathbf{n}$, it serves as a basis for the displacement velocity $\mathbf{v}$.

2.2 Displacement of the free surface: The no-penetration boundary condition

We consider test cases in which the position of the full boundary Γ, or a portion thereof, is not known in advance, but part of the flow solution. The boundary is then defined as a free surface Γ_{free}. In principle, there are two general methods to determine the exact position of the free surface: interface capturing and interface tracking [1]. Interface capturing means that in addition to the finite element mesh for the flow solution, a separate indicator — e.g., a level-set function or particles — is employed to indicate the position of the free surface. In interface tracking — as it is used here —, the computational domain will adapt to the displacement of the free surface. This displacement in turn is governed by the kinematic boundary condition

$$\mathbf{v}(\mathbf{x}) \cdot \mathbf{n}(\mathbf{x}) = \mathbf{u}(\mathbf{x}) \cdot \mathbf{n}(\mathbf{x}) \,. \tag{5}$$

It contains the fluid velocity $\mathbf{u}$ and the displacement velocity $\mathbf{v}$ of the free surface. Notice that several choices for $\mathbf{v}$ are valid (cf. Figure 1); the straightforward one being

$$\mathbf{v}(\mathbf{x}) = \mathbf{u}(\mathbf{x}) \,. \tag{6}$$

However, there exist other choices that still comply with Equation (5), but suppress certain components of the full velocity for the benefit of a higher mesh quality. Behr [11] details two common alternatives: displacement with the normal velocity component with $\mathbf{v} = (\mathbf{u} \cdot \mathbf{n})\mathbf{n}$ and displacement only in a specific coordinate direction $\mathbf{d}$ (e.g., y-direction), i.e., $\mathbf{v} = \frac{(\mathbf{u} \cdot \mathbf{n})\mathbf{d}}{\mathbf{n} \cdot \mathbf{d}}$.

2.3 Retaining mesh quality: Mesh update for inner nodes

As the boundary Γ_{free} is modified, usually the discretization of the interior of the domain needs to be adapted as well. For this purpose, we employ the Elastic Mesh

Update Method (EMUM) [12]. In this method, the computational mesh is treated as an elastic body reacting to the boundary deformation applied to it. The linear elasticity equation is solved for the mesh displacement $\boldsymbol{v}$, which relates to the mesh velocity $\mathbf{v}$ as $\boldsymbol{v} = \mathbf{v}\Delta t$:

$$\nabla \cdot \boldsymbol{\sigma}_{\text{mesh}} = 0\,, \tag{7}$$

$$\boldsymbol{\sigma}_{\text{mesh}}(\boldsymbol{v}) = \lambda_{mesh}\left(\operatorname{tr}\boldsymbol{\varepsilon}_{\text{mesh}}(\boldsymbol{v})\right)\mathbf{I} + 2\mu_{mesh}\boldsymbol{\varepsilon}_{\text{mesh}}(\boldsymbol{v}), \tag{8}$$

$$\boldsymbol{\varepsilon}_{\text{mesh}}(\boldsymbol{v}) = \frac{1}{2}\left(\nabla\boldsymbol{v} + (\nabla\boldsymbol{v})^T\right). \tag{9}$$

λ_{mesh} and μ_{mesh} — in structural mechanics the Lamé-parameters — have no physical meaning within the mesh deformation. They can be chosen freely for each element in order to control its respective stiffness.

3 ISOGEOMETRIC ANALYSIS

Initiated by Hughes at al. [3], a recent trend in the finite element analysis is the use of isogeometric methods. The key idea is to use Non-Uniform Rational B-splines (NURBS) as finite element shape functions. Compared with classic Lagrange polynomial shape functions, this concept has distinct advantages — ranging from higher geometrical accuracy to higher stability of the numerical solution. Details of Isogeometric Analysis can be found in a vast number of sources, e.g., [4]. It has been applied to a variety of applications, e.g., in the context of the phase field method for the Cahn-Hillard equations [5], brittle fracture [6], and topology optimization [7]. In connection with level-set, IGA has been utilized to compute the dam break problem [8, 16] or as a boundary indicator within the finite cell method [9]. Another free-surface-related application is the computation of wave resistance on a ship hull using the isogeometric boundary element method [17]. To the knowledge of the authors, IGA has not been utilized in conjunction with interface tracking of free surfaces.

To achieve an application to interface tracking, one difference between IGA and the standard finite element method becomes crucial: In IGA, the unkown velocities are not stored at points, which lie on the free surface. Instead, the unknown values — termed control variables — can be associated with the control points of the spline.

4 DISPLACEMENT OF THE FREE SURFACE

In Section 2.2 we discussed the importance of displacement conditions that do not involve the full velocity vector, but only a portion of it, pointing in a certain direction. The section named displacement in normal and in vertical direction as examples. Bear in mind that both the vertical and the normal direction vector — but also any other directional vector one could imagine — are all associated with a specific point on the surface. As indicated in the previous section, however, IGA stores the unknowns — in

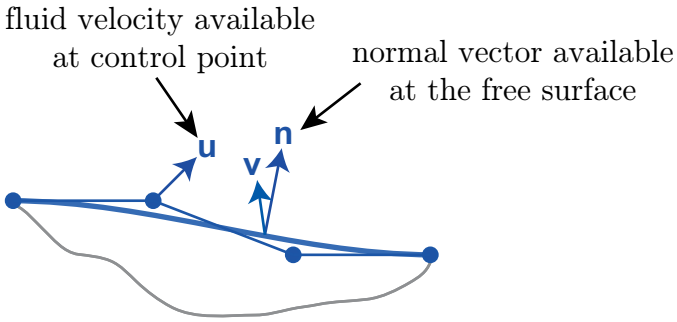

Figure 2: The figure shows a free surface represented by a NURBS curve. The fluid velocity is stored as a control variable, whereas the normal vector is computed on the free surface.

our case velocity information — at the control points. This entails that the kinematic boundary condition, Equation (5), now contains two components — the velocity unknowns and the directional vector — which are evaluated at different locations. It can no longer be directly evaluated and much less directly fulfilled (cf. Figure 2). As a remedy, we propose two displacement methods for the free surface; one based on strong imposition and one on weak imposition of the kinematic boundary condition. The first option entails moving the control points with normal vectors that are computed at the Greville abscissae. The second option considers the weak fulfillment of the no-penetration boundary condition — meaning that an additional equation system will need to be solved.

4.1 Displacement based on the normal vector at the Greville abscissae

As detailed before, there is no notion of a normal vector at a control point. One point on the spline, whose normal vector might come close to a vector that might be considered a normal vector at a specific control point, is the normal vector at the corresponding Greville abscissa. The Greville abscissa is the point on the surface the control point converges to in case of refinement. The Greville abscissa can be computed as the average of the knot values relevant for a control point, excluding the first and last value [18]. Typically, this is also close to the point where the associated basis function is maximal (this is exactly fulfilled for uniform knot vectors). The normal vector of, e.g., a NURBS curve, at any parametric coordinate θ can then be computed as [19]:

$$\boldsymbol{n}(\theta) = \begin{pmatrix} -t_y \\ t_x \end{pmatrix}, \qquad \text{with } \boldsymbol{t}(\theta) = \begin{pmatrix} t_x \\ t_y \end{pmatrix} = \frac{\boldsymbol{C}'(\theta)}{|\boldsymbol{C}'(\theta)|}. \tag{10}$$

The formula requires $\boldsymbol{C}'(\theta)$, the first derivative of the curve with respect to the local parameter θ, for the definition of which we refer to [13].

Based on the fluid velocity at any given control point $\mathbf{P}_i$, we define its displacement (or control point coordinate increment) $\Delta\mathbf{P}_i$ as:

$$\Delta\mathbf{P}_i = (\bar{\mathbf{u}}_i \cdot \mathbf{n})\, \mathbf{n} \cdot \Delta t\,, \tag{11}$$

with $\bar{\mathbf{u}}_i$ the fluid velocity connected to control point i averaged over the time step and $\mathbf{n}$ the time-averaged normal vector evaluated at the i^{th} Greville abscissa.

4.2 Displacement based on a weak formulation of the kinematic boundary condition

In a finite element context, the kinematic boundary condition can also be imposed weakly. The respective formulation reads:

$$\int_{\Gamma_{free}} \mathbf{w}\,\mathbf{F}\left(\mathbf{v},\mathbf{u}\right)\,d\mathbf{x} = 0 \quad \forall \mathbf{w} \in \mathcal{V}, \tag{12}$$

with Γ_{free} as the spatial free surface boundary, the test functions $\mathbf{w}$ in a suitable test space $\mathcal{V}$, surface displacement velocity $\mathbf{v}(\theta)$ and the fluid velocity $\mathbf{u}(\theta)$ both at a given surface point . After discretization, this yields a system of equations that can be solved for new control point coordinates $\mathbf{P}_i$. The fulfillment of the kinematic boundary condition, and thus mass conservation, now depends on how closely the correct boundary $\mathbf{x}(\theta)$ can be interpolated by the spline basis functions. In addition, the exact choice of $\mathbf{F}$ influences mass conservation when using discrete basis functions. $\mathbf{F}\left(\mathbf{v},\mathbf{u}\right)$ can contain any expression that fulfills the kinematic boundary condition.

5 ACKNOWLEDGEMENTS

The authors gratefully acknowledge the support of DFG under the collaborative research projects CoE 128 “Integrative Production Technology for High-Wage Countries” and SFB 1120 (subproject B2). Computing resources were provided by the AICES graduate school, RWTH Aachen University Center for Computing and Communication and by the Forschungszentrum Jülich.

REFERENCES

[1] S. Elgeti, H. Sauerland, Deforming Fluid Domains Within the Finite Element Method: Five Mesh-Based Tracking Methods in Comparison, Archives of Computational Methods in Engineering 23 (2) (2015) 323–361.

[2] T. E. Tezduyar, M. Behr, J. Liou, A new strategy for finite element computations involving moving boundaries and interfaces–the deforming-spatial-domain/space-time procedure: I. the concept and the preliminary numerical tests 94 (3) (1992) 339 – 351.

[3] T. J. R. Hughes, J. A. Cottrell, Y. Bazilevs, Isogeometric analysis: CAD, finite elements, NURBS, exact geometry and mesh refinement 194 (2005) 4135–4195.

[4] J. A. Cottrell, T. J. R. Hughes, Y. Bazilevs, Isogeometric Analysis: Toward Integration of CAD and FEA, John Wiley & Sons, Ltd, 2009.

[5] H. Gómez, V. Calo, Y. Bazilevs, T. Hughes, Isogeometric analysis of the Cahn–Hilliard phase-field model 197 (49) (2008) 4333–4352.

[6] M. Borden, J. Michael, C. Verhoosel, M. Scott, T. J. Hughes, C. Landis, A phase-field description of dynamic brittle fracture, Computer Methods in Applied Mechanics and Engineering 217 (2012) 77–95.

[7] L. Dedè, M. Borden, T. Hughes, Isogeometric Analysis for Topology Optimization with a Phase Field Model 19 (2012) 427–465.

[8] I. Akkerman, Y. Bazilevs, C. E. Kees, M. W. Farthing, Isogeometric analysis of free-surface flow, Journal of Computational Physics 11 (2011) 4137–4152.

[9] E. Rank, M. Ruess, S. Kollmannsberger, D. Schillinger, A. Düster, Geometric modeling, isogeometric analysis and the finite cell method, Computer Methods in Applied Mechanics and Engineering 249 (2012) 104–115.

[10] J. Ferziger, M. Perić, Computational Methods for Fluid Dynamics, Springer, 1999.

[11] M. Behr, Stabilized Finite Element Methods for Incompressible Flows with Emphasis on Moving Boundaries and Interfaces, Ph.D. thesis, University of Minnesota, Department of Aerospace Engineering and Mechanics (1992).

[12] A. Johnson, T. Tezduyar, Mesh update strategies in parallel finite element computations of flow problems with moving boundaries and interfaces 119 (1994) 73 – 94.

[13] L. Piegel, W. Tiller, The NURBS Book, Springer, Berlin, Germany, 1997.

[14] D. Rogers, An Introduction to NURBS with Historical Perspective, Morgan Kaufmann Publishers, 2001.

[15] Y. Bazilevs, V. Calo, J. Cottrell, J. Evans, T. Hughes, S. Lipton, M. Scott, T. Sederberg, Isogeometric analysis using T-splines 199 (2010) 229–263.

[16] R. Amini, R. Maghsoodi, N. Z. Moghaddamog, Simulating free surface problem using isogeometric analysis, Journal of the Brazilian Society of Mechanical Sciences and Engineering 38 (2) (2016) 413–421.

[17] A. Ginnisa, K. Kostasb, C. Politisb, P. Kaklisa, K. Belibassakisa, T. Gerostathisb, M. Scott, T. Hughes, Isogeometric Boundary-Element Analysis for the Wave-Resistance Problem using T-splines, Computer Methods in Applied Mechanics and Engineering 279 (2014) 425–439.

[18] G. Farin, Curves and Surfaces for Computer-Aided Geometric Design: A Practical Guide, Elsevier, 2014.

[19] A. Gray, Modern differential geometry of curves and surfaces with Mathematica, 2nd Edition, CRC Press, Boca Raton, 1998.

VII International Conference on Computational Methods for Coupled Problems in Science and Engineering
COUPLED PROBLEMS 2017
C. Ghnatios, A. Barasinski, I. Fernandez Villegas, G. Palardy and F. Chinesta

COMPUTATIONAL VAMEDECUM OF THE COUPLED MECHANICAL/THERMAL BEHAVIOR OF COMPOSITE MATERIALS DURING ULTRASONIC WELDING

CHADY GHNATIOS[1], ANAIS BARASINSKI[2], IRENE FERNANDEZ VILLEGAS[3], GENEVIEVE PALARDY[3] AND FRANCISCO CHINESTA[4]

[1] Notre Dame University-Louaize
Zouk mosbeh PO box 72, Lebanon
e-mail: cghnatios@ndu.edu.lb, web page: http://www.ndu.edu.lb/

[2]Institut de recherche en génie civil et mécanique - GeM
Ecole Centrale Nantes
1 rue de la Noe 44300, Nantes, France
e-mail: anais.barasinski@ec-nantes.fr - Web page: http://www.ec-nantes.fr

[3] Delft University of Technology, Aerospace Structures and Materials Department
Kluyverweg 1, 2629 HS Delft, Netherlands
e-mail: I.FernandezVillegas@tudelft.nl ; G.Palardy@tudelft.nl - Web page: http://www.tudelft.nl/

[4]Intensive calculation institute - ICI
Ecole Centrale Nantes
1 rue de la Noe 44300, Nantes, France
e-mail: francisco.chinesta@ec-nantes.fr - Web page: http://www.ec-nantes.fr/

Key words: Proper Generalized Decomposition, Ultrasonic welding, Kelvin Voigt, composite materials

Abstract. Aiming faster and more reliable end products, the composite material industry is nowadays an active research topic. Innovative composite forming processes are actively designed and tested. For example, ultrasonic welding of composite thermoplastic materials is being investigated, since it shows many advantages over classical methods. In fact, energy directors allow a preferential heating of the manufactured part through the propagation of mechanical waves in a composite laminate, without including any foreign material in the welded region. However, ultrasonic welding of composite materials is not mastered yet because of the coupled and complex behavior of such materials. Thus, simulation of ultrasonic heating becomes compulsory for understanding the complex multi-physics coupled problem.

In this work, we propose to model the ultrasonic welding process using a dynamic viscoelastic model in the frequency domain. Later on, this model is coupled to the transient

heat equation, giving the temperature field as well as the heat flux in the simulated part. However, the result depends on the chosen experimental and material parameters such as the thickness of the part, its viscosity, its modulus of elasticity, the imposed frequency and displacement... Which makes the optimization of the process a tricky issue requiring a new set of solutions of the problem for each choice of the process parameters.

Using the proper generalized decomposition (PGD), along with a coupled viscoelastic/thermal model, where all the parameters mentioned above are included as extra coordinates of the problem, appears to be a suitable solution for the optimization problem. Moreover, the PGD multidimensional solution considering all the process parameters as extra coordinates is obtained within a realistic timeframe. In fact, by using the PGD, we alleviate the curse of dimensionality since the PGD performs a separation of variables which reduces the problem dimensionality [1]. The result is therefore a computational vademecum that can be used to explore in real time the solution of the problem for any choice of the process parameters, speeding up its optimization [2].

1 INTRODUCTION

Ultrasonic welding is a promising technique for joining composite thermoplastic parts, using mechanical vibration transversally applied to the material. In fact, ultrasonic welding is nowadays one of the most popular methods for joining unreinforced thermoplastic materials in a wide range of industries including automotive, biomedical, electronics [3, 4]... In fact ultrasonic welding features many benefits like high speed welding performed within a fraction of a second to few seconds, and without using any foreign materials in the welded region. However, ultrasonic welding of fiber reinforced thermoplastic composite materials is not popular or industrially applied yet [3], despite the promising results published in previous research works [5, 6, 7]. This can be explained by the lack of understanding of the physics occurring in the process like mechanical strain propagation and heating [3].

Therefore, the simulation of ultrasonic welding of composite thermoplastics becomes compulsory to help the industry understands the coupled multi-physics occurring in the welded part, which may validate the currently used techniques. However, many process and material parameters affect the quality of the weld. Several authors investigated the process parameters independently on a given material [8, 9]. In this work, we choose to include the relevant process and material parameters into the governing equation of the problem as extra coordinates of the problem. For instance, the thickness of the part, its viscosity, the modulus of elasticity, the imposed frequency and displacement amplitude are included as extra coordinates of the problem. This leads to a "complete" solution covering all the possible combinations of parameters, a "computational vademecum". Afterwards, the user may optimize the process using any classical optimization algorithm

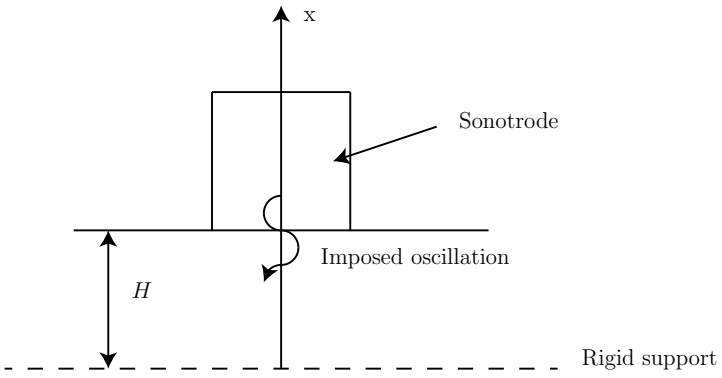

Figure 1: Simulated model

like Newton of Levenberg-Marquardt algorithms since the gradient with respect to the parameters are readily available [10, 11].

However, adding extra coordinates to the problem increases its dimensionality and therefore leads to unrealistic calculation time while using classical simulation techniques. Using the PGD, we can alleviate the curse of dimensionality by decomposition the high dimensionality problem into a sequence of lower dimensionality problems. For instance, one may solve a 3D problem as a sequence of 1D problems or 2D, 1D problems [1]. In this work, we compute a coupled mechanical/thermal vademecum adding five extra coordinates to the space-time dimensions.

In section 2, we review the used Kelvin-Voigt mechanical model to simulate the process, with the PGD construction of the mechanical solution. Later on, section 3 shows the thermal simulation model and its construction using the PGD. In section 4, we compare the obtained vademecum to the solutions obtained using classical algorithms and discuss the result. Finally we draw some conclusions in section 5.

2 MODELING THE STRAIN FIELD IN ULTRASONIC WELDING

In this section we model the ultrasonic welding of thermoplastic materials. The chosen model is illustrated in figure 1. We choose a part of thickness H, where a mechanical vibration is imposed by the sonotrode on the top of the domain. As a mechanical model, we choose the Kelvin-Voigt viscoelastic model which can be represented by a pure elastic spring connected in parallel to a pure viscous damper, thus the stress tensor in the material σ is written as:

$$\sigma = \sigma_{elastic} + \sigma_{viscous} = E \cdot \epsilon + \eta \dot{\epsilon} \tag{1}$$

where E is the modulus of elasticity of the used material, η is its viscosity, ϵ the strain tensor and $\dot{\epsilon}$ the rate of strain tensor. Working in the frequency domain, one may write

the strain as:

$$\epsilon = \epsilon_0 \cdot e^{iwt} \tag{2}$$

w being the angular frequency in rad/s, i the imaginary number and t the time. Replacing ϵ in Eq. (1) leads to:

$$\sigma = \sigma_0 \cdot e^{iwt - i\theta} \tag{3}$$

with $\sigma_0 \cdot e^{-i\theta}$ given by:

$$\sigma_0 \cdot e^{-i\theta} = (E + iw\eta)\,\epsilon_0 \tag{4}$$

Considering the dynamics equation:

$$\rho \ddot{\mathrm{u}} = \nabla \cdot \sigma \tag{5}$$

ρ being the density and ü the displacements, and replacing (3) into (5), rearranging leads to the problem governing equation. For the sake of simplicity and without any loss of generality, we choose to simulate the process in a unidirectional physical domain $x \in [0, H]$ representing the thickness of the welded part. Therefore the governing equation is written by:

$$\begin{cases} -\rho U w^2 = G^* \cdot \frac{\partial^2 U}{\partial x^2} \\ U = U_r + i \cdot U_i \\ G^* = G' + i \cdot G'' = E + i \cdot w \cdot \eta \end{cases} \tag{6}$$

U being the amplitude of the displacement. The boundary conditions of the problem are:

$$\begin{cases} U(x = 0) = 0 \\ U(x = H) = U_0 \end{cases} \tag{7}$$

Eq. (6) is defined in the complex domain, where U and G both have real and imaginary components. The displacement U is solved considering the thickness of the part H, its viscosity η, the modulus of elasticity E, the imposed frequency w and displacement amplitude U_0 as extra coordinates of the problem. Therefore, we will introduce these parameters into the differential equation of the problem written in Eq.(6).

One may note that η, E and w appears naturally in the differential equation, while U_0 appears in the boundary conditions. These parameters can be easily introduced as coordinates of the problem as thoroughly discussed in previous publications [1, 12, 2]. However, introducing the geometrical parameter H as extra coordinate of the problem is slightly more elaborated [13, 14]. First we define the mapping between the real domain of length H and a domain $s \in [0; 1]$ written by:

$$x = H \cdot s \tag{8}$$

Then replacing Eq. (8) into Eq. (6), one may find the integral form of the problem to solve defined in the s domain by:

$$\int_\Omega U^* \cdot \left(\rho U w^2 - G^* \cdot \frac{\partial^2 U}{\partial s^2} \cdot \frac{1}{H^2} \right) H \cdot ds \cdot dE \cdot dH \cdot d\eta \cdot dw \cdot dU_0 = 0 \tag{9}$$

The boundary conditions are now written by:

$$\begin{cases} U(s=0) = 0 \\ U(s=1) = U_0 \end{cases} \tag{10}$$

The problem defined in Eq. (9) can be solved using the PGD with a fixed point, rank one update greedy algorithm as detailed in different publications [1, 10]. The solution is given in a separated form as:

$$U = \sum_{j=1}^{j=N} S_j(s) \cdot \mathcal{H}_j(H) \cdot N_j(\eta) \cdot \mathcal{E}_j(E) \cdot W_j(w) \cdot \mathcal{U}_j(U_0) \tag{11}$$

For this problem, the PGD algorithm converges within less than a minute, at a number of product of functions $N = 25$. Once $U(x, H, \eta, E, w, U_0)$ is computed, one may compute the strain ϵ in a separated form by:

$$\epsilon = \sum_{j=1}^{j=N} \frac{\partial S_j(s)}{\partial s} \cdot \frac{\partial s}{\partial x} \cdot \mathcal{H}_j(H) \cdot N_j(\eta) \cdot \mathcal{E}_j(E) \cdot W_j(w) \cdot \mathcal{U}_j(U_0) \tag{12}$$

where $\frac{\partial s}{\partial x} = \frac{1}{H}$ as per Eq. (8). As one may notice, all the derivatives with respect to all the chosen parameters are now readily available using Eq. (11).

3 MODELING THE THERMAL PROBLEM USING THE PGD

Once $U(x, H, \eta, E, w, U_0)$ and $\epsilon(x, H, \eta, E, w, U_0)$ are available, one may compute the dissipated power through the studied part, defined as:

$$Q = w \eta \epsilon^2 \tag{13}$$

Which lead us to a heat source Q written in a separated form by:

$$Q = w \cdot \eta \cdot \left[\sum_{j=1}^{j=N} \frac{\partial S_j(s)}{\partial s} \cdot \frac{1}{H} \cdot \mathcal{H}_j(H) \cdot N_j(\eta) \cdot \mathcal{E}_j(E) \cdot W_j(w) \cdot \mathcal{U}_j(U_0) \right]^2 \tag{14}$$

$E \in [2,5]\, GPa$
$\eta \in [4000, 8000]\, Pa.s$
$H \in [10^{-4}, 5 \times 10^{-4}]\, m$
$w \in 2\pi \times [20000, 50000]\, rad/s$
$U_0 \in [1,10]\, mm$

Table 1: Chosen intervals of variation of the parameters

Later on, we solve the transient heat equation written by:

$$\rho \cdot C \cdot \frac{\partial T}{\partial t} - K \frac{\partial^2 T}{\partial x^2} = Q \tag{15}$$

where C is the heat capacity of the studied composite material, K its conductivity and T the temperature. Writing the integral form of Eq. (15) in the parametric domain after applying the geometrical transformation written in Eq. (8) gives:

$$\int_\Omega T^* \left(\rho \cdot C \frac{\partial T}{\partial t} - K \frac{\partial^2 T}{\partial s^2} \cdot \frac{1}{H^2} - Q \right) H \cdot ds \cdot dE \cdot dH \cdot d\eta \cdot dw \cdot dU_0 = 0 \tag{16}$$

One may wish to add the conductivity K and the heat capacity C as extra coordinates of the problem. For the sake of simplicity, these 2 parameters are kept as constants in the numerical example shown in section 4. The boundary conditions for the heat problem are given by:

$$\begin{cases} -k \frac{\partial T}{\partial x} = 0 \text{ at } x = 0 \\ \\ -k \frac{\partial T}{\partial x} = h(T - T_{out}) \text{ at } x = H \end{cases} \tag{17}$$

We are therefore imposing convective boundary conditions on the top surface of the domain $x = H$ and an adiabatic boundary condition at the bottom surface at $x = 0$. T_{out} is the outside temperature set to be 293K for the illustrative example shown in section 4 and $h = 25\ W/m^2.K$.

4 NUMERICAL EXAMPLE, VERIFICATION AND DISCUSSION

In the following section, we illustrate a numerical example of ultrasonic welding of a composite material having a density $\rho = 1300\ kg/m^3$, the domains of variation of the parameters are given in table 1.

In figure 2 we illustrate the variation of the displacement amplitude as a function of the position x for the following combination of parameters: E=2 GPa, η=4000 Pa.s, H=0.1 mm, w=2π×20000 rad/s and $U_0 = 1$ mm. We notice that the displacement amplitude is linear function of x since the height of the domain is small with respect to the oscillation period, which is about 15 mm considering the speed of the mechanical wave about 300

m/s and the chosen frequency is 20 000 Hz. Figure 3 illustrates a finite difference solution for the same combination of the parameters. The relative error between the two solutions doesn't exceed 0.4%.

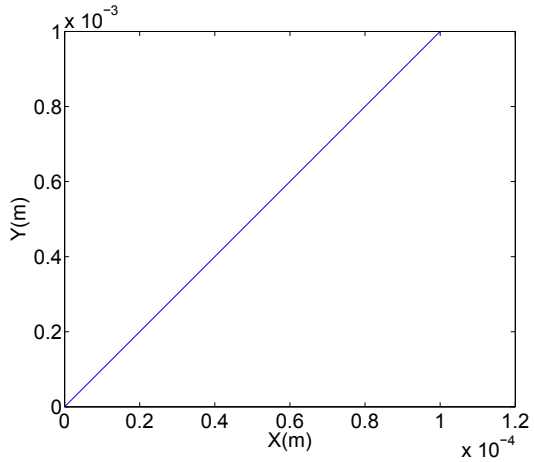

Figure 2: Displacement amplitude as a function of the position x obtained from the computed PGD vademecum

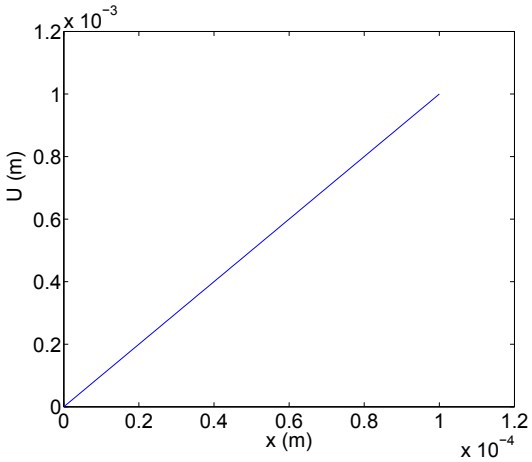

Figure 3: Displacement amplitude as a function of the position x obtained by the finite difference method

Since the displacement amplitude is linear as a function of the thickness of the part, the strain and therefore the heat source Q are nearly constant for the chosen value of H.

In figure 4, we are illustrating the displacement amplitude $||\vec{U}||$ in the middle of the domain at $x = H/2$, as a function of three chosen parameter, E, w and η. In figure 5, we are illustrating the heat source Q as a function of these parameters at the same position. One may notice that the heat source is sensitive to the variation of w and η, but is less sensitive to the changes of the modulus of elasticity of the material E for example. A similar study for H and U_0 shows that the heat source Q changes function of the variations of H, U_0, w and η but less sensitive to the variation of E.

Once the heat source is computed, we solve the transient heat equation for a convective boundary condition on the top of the domain considering $h = 25\ W/m^2.K$, the heat capacity $C = 1450\ J/kg.K$ and a conductivity $K = 0.24\ W/m.K$. Figure 6 illustrates the temperature field in the part as a function of the position x and the time t for E=2 GPa, η=4000 Pa.s, H=0.1 mm, w=$2\pi\times$20000 rad/s and $U_0 = 1$ mm.

Figure 7 illustrates the temperature field for the chosen parameters at $t = 10$ s, while figure 8 illustrates the temperature fields for the same combination of parameters obtained by the finite differences method at $t = 10$ s. The relative error between the two fields is shown in figure 9. We note that the relative error does not exceed 1.5%. This error

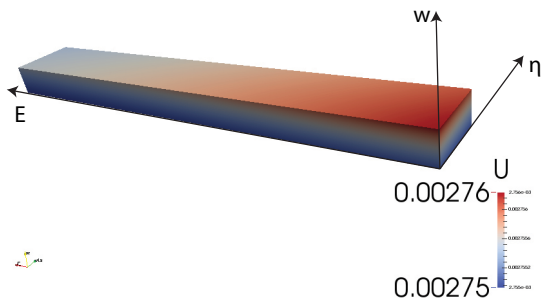

Figure 4: Displacement amplitude as a function of the parameters E, w and η at $x = H/2$

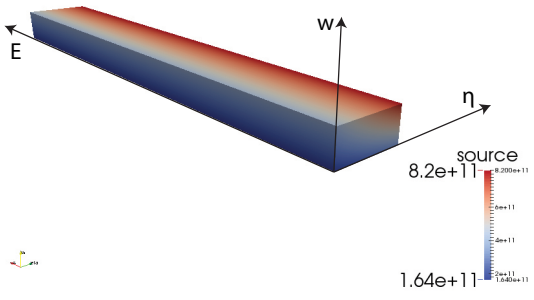

Figure 5: Heat source Q as a function of the parameters E, w and η at $x = H/2$

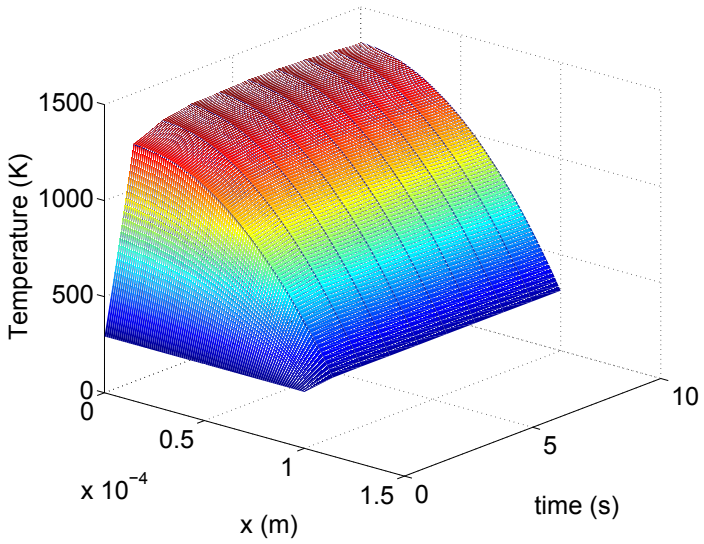

Figure 6: Temperature field in the studied part for the chosen combination of parameters

is larger than the one obtained for the displacement amplitude since the strains are the derivatives of the displacements and therefore the heat source error is generated by the derivatives of U, which is normally larger than the error on U. This error can be reduced by pushing further the PGD convergence for U by increase the value of N beyond 25.

5 CONCLUSIONS

In this work, we illustrate an approach to simulate the temperature fields during ultrasonic welding of composite materials by considering the process and material parameters as extra-coordinates of the problem within realistic time frame. First, we illustrate the coupled viscoelastic mechanical and thermal problems. In our model, we use the Kelvin-Voigt viscoelasticity coupled to the heat equation. The result is a computational vademecum that can be used to optimize the process on the fly, in real time [11].The

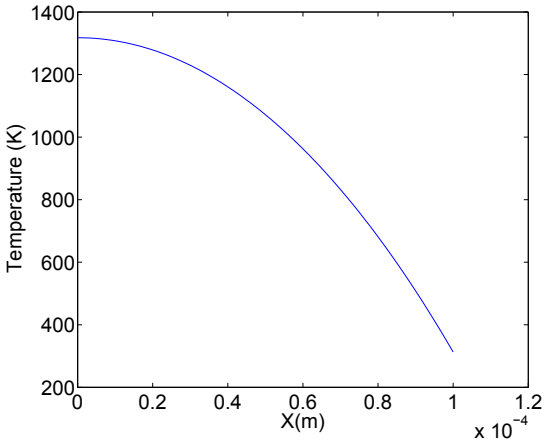

Figure 7: Temperature fields at t=10 s obtained from the PGD solution

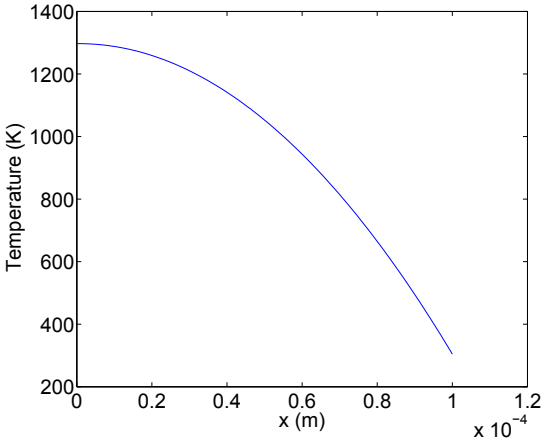

Figure 8: Temperature fields at t=10 s obtained from the finite differences solution at the same combination of parameters

obtained results are verified by comparison to the ones computed by classical algorithms and the resulting relative error is acceptable. The obtained vademecum can also be used to compare to experimental results and identify materials parameters or optimize the process.

REFERENCES

[1] F. Chinesta, A. Ammar, E. Cueto. Recent Advances And New Challenges In the Use Of The Proper Generalized Decomposition For Solving Multidimensional Models. *Archives of Computational Methods in Engineering*, (2009) **17**, 327-350.

[2] J.V. Aguado, J. Borzacciello, C. Ghnatios, F. Lebel, R. Upadhyay, C. Binetruy, F. chinesta. A model reduction based Simulation App for composite Outlet Guide Vanes manufacturing optimization. *Advanced Modeling and Simulation in Engineering Sciences*, (2017) **4**(1), 1-26.

[3] Irene F. Villegas. In situ monitoring of ultrasonic welding of thermoplastic composites through power and displacement data. *Journal of Thermoplastic Composite Materials*, (2015) **28**(1), 66-85.

[4] D. Grewel, A. Benartar, J. Park, Plastics and composite welding handbook. *Hansen Gardner Publications*, Munich, Germany, 2003.

[5] A. Benatar, T. G. Gutowski. Ultrasonic welding of PEEK-Graphite APC2 composites. *Polymer Engineering Science*, (1989) **29**(23), 1705-1721.

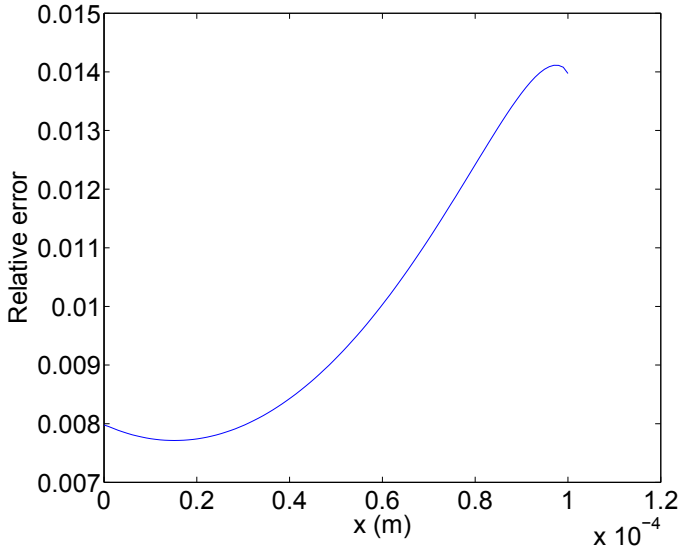

Figure 9: Relative error between the PGD and finite difference solutions illustrated in figure 7 and 8

[6] Z. Zhang, X. Wang, Y. Lu. A study on heating process of ultrasonic welding of thermoplastics. *Journal of Thermoplastic Composite Materials*, (2010) **23**(5), 647-664.

[7] W.X. Chan, S.H. Ng, K.H. Li, W.-T. Park, Y.-J. Yoon. Miro-ultrasonic welding using thermoplastic-elastomericcomposite film. *Journal of Materials Processing technology* (2016), **236**, 183-188.

[8] S.J. Liu, I.T. Chang. Factors affecting the joint strength of ultrasonically welded polypropylene composites. *Polymer composites* (2001), **22**(1), 132-141.

[9] S.J. Liu, I.T. Chang. Optimizing the weld strength of ultrasonically welded nylon composites. *Journal of Composites Materials* (2002), **35**(5), 611-624.

[10] C. Ghnatios. Simulation avancée des procédés thermiques rencontrés lors de la mise en forme des composites. *Ecole Centrale Nantes*, 2012.

[11] C. Ghnatios, C.H. Mathis, F. Chinesta. Poroelastic properties identification through micro indentation modeled by using the Proper Generalized Decomposition.*Proceedings of the 3rd International Conference on Advances in Computational Tools for Engineering Applications (ACTEA)*, (2016), 141-145.

[12] C. Ghnatios, F. Chinesta, E. Cueto, A. Leygue, A. Poitou, P. Breitkopf, P. Villion. Methodological approach to efficient modeling and optimization of thermal processes taking place in a die: application to pultrusion. *Composites Part A: Applied Science and Manufacturing* (2011), **42**(9), 1169-1178.

[13] C. Ghnatios, G. Xu, A. Leygue, M. Visonneau, F. Chinesta, A. Cimetiere. On the space separated representation when addressing the solution of PDE in complex domains. *Discrete and Continuous Dynamical Systems-Series S* (2016), **9**, 475-500.

[14] C Ghnatios, A Ammar, A Cimetiere, A Hamdouni, A Leygue, F Chinesta. First steps in the space separated representation of models defined in complex domains. *ASME 2012 11th Biennial Conference on Engineering Systems Design and Analysis* (2012), 37-42.

VII International Conference on Computational Methods for Coupled Problems in Science and Engineering
COUPLED PROBLEMS 2017
M. Papadrakakis, E. Oñate and B. Schrefler (Eds)

A NEW MATERIAL DESCRIPTION FOR PLANT TISSUES UNDER FROST EXPOSURE

Lukas Eurich*, Arndt Wagner* and Wolfgang Ehlers*

*Institute of Applied Mechanics
University of Stuttgart
Pfaffenwaldring 7, D-70569 Stuttgart, Germany
e-mail: Lukas.Eurich@mechbau.uni-stuttgart.de, www.mechbau.uni-stuttgart.de/ls2

Key words: Plant freezing, thermoelasticity, strain energy, compaction point, Theory of Porous Media

Abstract. Plant tissues exhibit a cellular structure, where the tissue cells compose a solid skeleton, and the intercellular space is filled with gaseous air and/or liquid water. Under frost exposure, the pore water may freeze and turn into solid ice. As a multiphasic material, plant tissues can be meaningfully described by the Theory of Porous Media (TPM). In the proposed TPM approach, the solid constituents, i. e. the solid skeleton and the ice, are kinematically coupled and described within the framework of thermoelasticity. Generally, porous media with assumed materially incompressible solid constituents are described as a compressible material, since a volumetric deformation can be realised by a volume change of the pore space. However, freezing of the pore water leads to an increase of the solidity even until a vanishing of the pore space. Therefore, the so-called point of compaction (compression until the pore space is cleared) needs to be considered in the material description of the solids. The present contribution aims to introduce a quarternary modelling approach applied to frost-resistant plant tissues with an emphasis on the description of coupled thermoelastic effects. In particular, the impact of pore-water freezing on the derivation of a strain-energy function for plant tissues is discussed leading to a new thermodynamically consistent material formulation.

1 INTRODUCTION

Frost-resistant plants have developed several strategies to cope with subzero temperatures. For example, plants have developed strategies to hinder freezing, e. g. by deep supercooling [1], which is a phenomenon describing a significant lowering of the ice nucleation temperature, way below $0°C$. But they have also developed strategies when ice formation cannot be prevented. In that case, the porous structure of plants plays a crucial role. The porous structure is originated by the arrangements of single cells [2]. Therefore,

the tissue cells are considered as the solid skeleton, while the intercellular space is filled with gaseous air and liquid water. The crucial mechanism, when freezing cannot be prevented, is the dehydration of the cell body [2], since freezing within the cells represents a critical process threatening the ability of a plant to survive [3]. This mechanism, where the water is with decreasing temperature no longer trapped within the cell body, leads to a change in solidity. Therefore, the water loss of the cell body represents one type of mass transfer. Another type of mass transfer occurs within the pore space, i. e. the phase change of the water from a liquid state of aggregation to a solid one. This also leads to a change in solidity. Due to the assumed material incompressibility of the solid components, one has to consider the compaction point when the overall behaviour changes its characteristic from compressible to incompressible as the pore space vanishes. This was described by Ehlers & Eipper [4] for materials under isothermal conditions by introducing an additive split of the strain-energy function of a *Simo-Pister*-type material description, where the necessary condition of the compaction point was included. Bluhm [5] extended this approach to non-isothermal conditions, however, with the assumption of constant effective densities and no inclusion of mass transfer. Based on these works, a material description is needed for plant tissues, which can be modelled as thermoelastic porous materials, characterised by two solid (materially incompressible) components including mass transfer and the existence of the compaction point.

2 MODELLING FROST-RESISTANT PLANT TISSUES

2.1 Quarternary modelling approach

Since plants are porous materials, a sound multicomponent and multiphasic model is realised within the TPM. Its current understanding is outlined in the fundamental works of de Boer [6] and Ehlers [7, 8] and citations therein. Relevant approaches with regard to phase transition processes within the TPM are given in Ehlers & Häberle [9] and Bluhm et al. [10].

Applying the TPM to frost-resistant plant tissues, the basic model consists of four constituents φ^α, cf. to Eurich et al. [11], namely tissue cells ($\alpha = S$), which contain initially trapped water, a pore gas ($\alpha = G$) and pore water ($\alpha = L$), which may turn into ice ($\alpha = I$), such that

$$\varphi = \bigcup_\alpha \varphi^\alpha = \varphi^S + \varphi^G + \varphi^L + \varphi^I. \tag{1}$$

As a basic prerequisite of the TPM, these constituents are volumetrically averaged over a representative elementary volume (REV). This results in a homogenised continuum-mechanical model with superimposed and mutually interacting constituents, as shown in Figure 1. The local amount of each constituent φ^α can be addressed by the volume fraction

$$n^\alpha = \frac{\mathrm{d}v^\alpha}{\mathrm{d}v}. \tag{2}$$

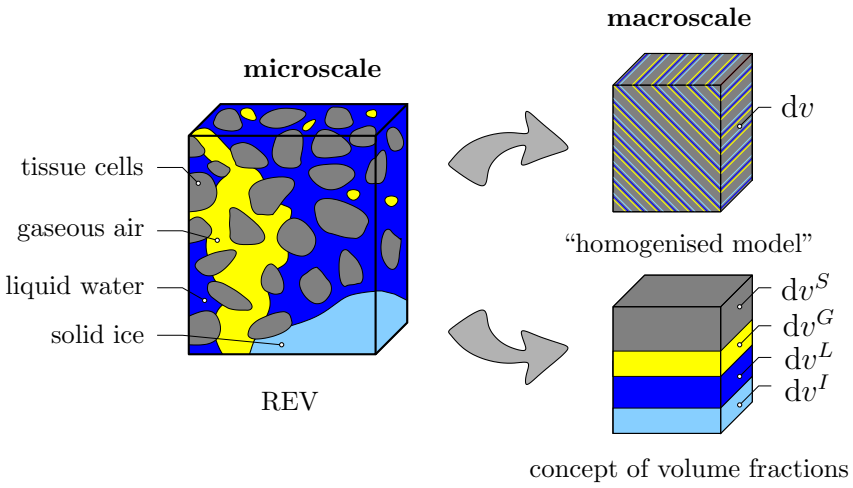

Figure 1: Representative elementary volume (REV) with schematically displayed microstructure of frost-resistant plant tissues and macroscopic multiphasic and multicomponent modelling approach.

Since there is no empty space in the domain, the volumetric constraint

$$\sum_{\alpha} n^{\alpha} = n^{S} + n^{G} + n^{L} + n^{I} = 1 \tag{3}$$

holds. Having the definition of the local volume fraction in mind, two densities can be introduced, the effective (realistic) density $\rho^{\alpha R} = \mathrm{d}m^{\alpha}/\mathrm{d}v^{\alpha}$ as the ratio between the mass element $\mathrm{d}m^{\alpha}$ of a constituent φ^{α} and its volume element $\mathrm{d}v^{\alpha}$ and the partial density $\rho^{\alpha} = \mathrm{d}m^{\alpha}/\mathrm{d}v$ as the ratio between the mass element $\mathrm{d}m^{\alpha}$ and the volume element $\mathrm{d}v$ of the overall aggregate. These two measures are connected by the volume fraction via $\rho^{\alpha} = n^{\alpha}\rho^{\alpha R}$. For materially incompressible constituents (such as in the present model the solid skeleton, the ice and the water), the realistic density depends only on temperature. Instead, the realistic density of materially compressible materials (such as air) is a function of temperature and pressure.

2.2 Kinematics

2.2.1 State of motion and kinematic coupling of the solid constituents

Within the framework of the TPM, each constituent φ^{α} can, in general, have an independent state of motion. In order to guarantee independent motion functions, one has to introduce formally individual motion functions and velocities for each constituent, viz.:

$$\mathbf{x} = \boldsymbol{\chi}_{\alpha}(\mathbf{X}_{\alpha}, t), \quad \overset{\prime}{\mathbf{x}}_{\alpha} = \frac{\partial}{\partial t}\boldsymbol{\chi}_{\alpha}(\mathbf{X}_{\alpha}, t). \tag{4}$$

Therein, the motions and velocities depend on the reference configuration $\mathbf{X}_\alpha$ of the respective constituents. The deformation of the solid skeleton is described by the material deformation gradient

$$\mathbf{F}_S = \frac{\partial \boldsymbol{\chi}_S(\mathbf{X}_S, t)}{\partial \mathbf{X}_S}. \tag{5}$$

For the motion of the ice, a kinematic coupling is introduced as sketched in Figure 2. Therefore, the ice is assumed to be attached to the solid skeleton when the pore water is freezing [10]. This implies that drifting ice particles in the pore space are not considered.

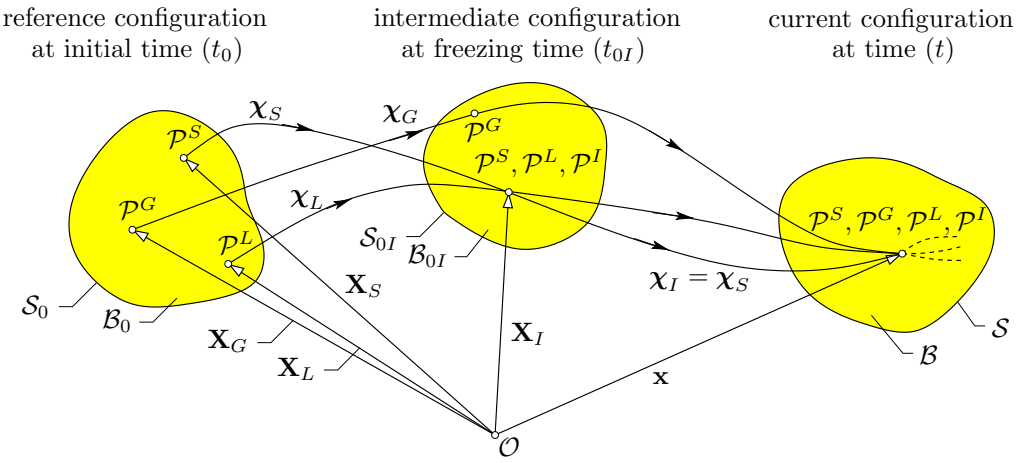

Figure 2: State of motion and kinematic coupling of the quarternary TPM model.

With this kinematic coupling, the motion of the solid skeleton and the ice is divided into a state before the ice formation is initiated, i. e. the pore water is liquid, and a state thereafter. Before freezing, the liquid pore water can be mobile within the pore space. The intermediate configuration represents the reference configuration $\mathbf{X}_I$ where the liquid water turns into solid ice and is attached to the solid skeleton. Therefore, the motion of the solid skeleton and the ice for subsequent configurations is kinematically coupled, indicating an identical state of motion and identical velocities via

$$\boldsymbol{\chi}_I(\mathbf{X}_I, t) = \boldsymbol{\chi}_S(\mathbf{X}_S, t), \quad \Rightarrow \quad \overset{\prime}{\mathbf{x}}_I = \overset{\prime}{\mathbf{x}}_S. \tag{6}$$

In order to define the deformation gradient of the ice, we proceed from the respective derivatives

$$\frac{\partial \boldsymbol{\chi}_S(\mathbf{X}_S, t)}{\partial \mathbf{X}_S} = \frac{\partial \boldsymbol{\chi}_I(\mathbf{X}_I, t)}{\partial \mathbf{X}_S} = \frac{\partial \boldsymbol{\chi}_I(\mathbf{X}_I, t)}{\partial \mathbf{X}_I} \frac{\partial \mathbf{X}_I}{\partial \mathbf{X}_S}. \tag{7}$$

With the definition of the material deformation gradient for the solid skeleton (5), the expression above can be used to formulate the material deformation gradient of the ice according to (7), viz.

$$\mathbf{F}_S \;=\; \mathbf{F}_I \mathbf{F}_{S0} \quad \Rightarrow \quad \mathbf{F}_I \;=\; \mathbf{F}_S \mathbf{F}_{S0}^{-1}. \tag{8}$$

This implies that the deformation gradient of the solid skeleton can be split multiplicatively into the deformation $\mathbf{F}_{S0}$ before the onset of the phase transition and a deformation $\mathbf{F}_I$ after the onset. The volumetric deformation of the solid skeleton and the ice can be derived based on the determinants of $\mathbf{F}_S$ and $\mathbf{F}_I$, via

$$\begin{aligned} J_S \;&=\; \det \mathbf{F}_S \\ J_I \;&=\; \det \mathbf{F}_I \;=\; \det \left(\mathbf{F}_S \, \mathbf{F}_{S0}^{-1}\right) \;=\; \det \mathbf{F}_S \det \mathbf{F}_{S0}^{-1} \;=\; J_S / J_{S0}. \end{aligned} \tag{9}$$

2.2.2 Decomposition of the thermoelastic deformation

The inclusion of thermal effects into the coupled description of deformation for thermoelastic materials can be achieved by a multiplicative split of the deformation gradient $\mathbf{F}_\delta$ for the solid constituents $\delta = \{S, I\}$, cf. [12]. Here, the approach of Lu & Pister [13] is used

$$\mathbf{F}_\delta \;=\; \frac{\partial \boldsymbol{\chi}_\delta(\mathbf{X}_\delta, t)}{\partial \mathbf{X}_\delta} \;=\; \mathbf{F}_{\delta M} \mathbf{F}_{\delta\theta}, \tag{10}$$

where $\mathbf{F}_{\delta M}$ represents the purely mechanical part of the deformation and $\mathbf{F}_{\delta\theta}$ the purely thermal part, which is defined by a fictive mechanical unloading.

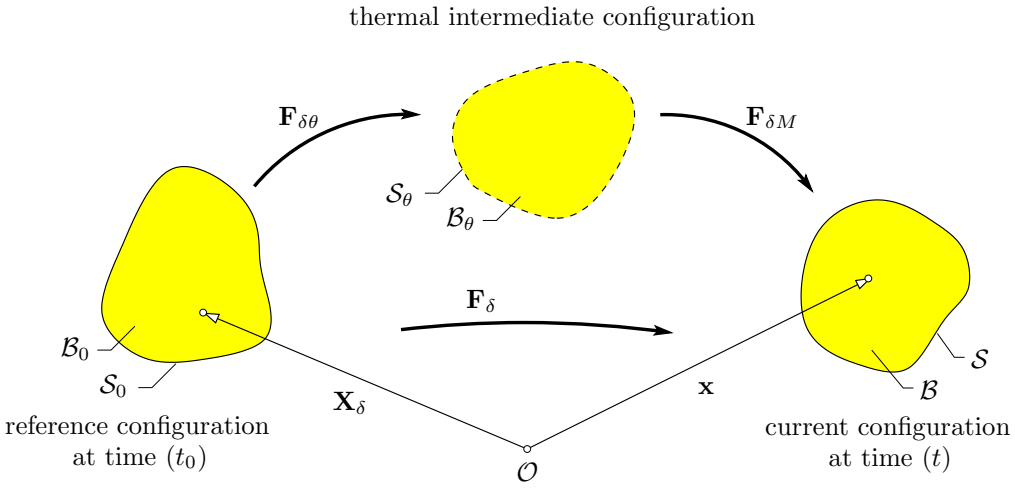

Figure 3: Multiplicative decomposition of the thermoelastic deformation.

Since isotropic thermally induced volume changes are assumed, the thermal deformation is, according to [13], given via

$$\mathbf{F}_{\delta\theta} = (\det \mathbf{F}_{\delta\theta})^{1/3}\,\mathbf{I}, \quad \det \mathbf{F}_{\delta\theta} = \exp\left[3\alpha^{\delta}(\theta - \theta^{\delta}_{0\delta})\right]. \tag{11}$$

2.3 Volume fractions

An energetic inclusion of the compaction point into the material description requires the specification of the volume fractions of the respective solid constituents. These can be derived by evaluating mass balances of the constituents

$$(\rho^{\alpha})'_{\alpha} + \rho^{\alpha}\operatorname{div}\overset{\prime}{\mathbf{x}}_{\alpha} = \hat{\rho}^{\alpha}, \tag{12}$$

where $(\rho^{\alpha})'_{\alpha}$ denotes the material time derivative of the partial density with respect to the motion of φ^{α} and $\hat{\rho}^{\alpha}$ is the mass exchange (in the present case the cell dehydration and the freezing of the pore water). As the material density of the solid skeleton and the ice are due to the material incompressibility solely a function of temperature and given via

$$\rho^{\delta R} = \rho^{\delta R}_{0\delta}(\det \mathbf{F}_{\delta\theta})^{-1} = \rho^{\delta R}_{0\delta} e^{-3\alpha^{\delta}(\theta-\theta^{\delta}_{0\delta})}, \tag{13}$$

the volume fraction can be derived by a formal integration of the mass balances and considering the temperature-dependent density $\rho^{\delta R}$ which results in

$$n^{\delta} = \frac{n^{\delta}_{0\delta}}{\det \mathbf{F}_{\delta M}} \exp\Big(\int_{t_0}^{t} \frac{\hat{\rho}^{\delta}}{\rho^{\delta}}\,\mathrm{d}\tau\Big). \tag{14}$$

This indicates that the volume fraction of the solid skeleton can be decomposed into a growth-dependent part and a part that depends on the mechanical deformation.

3 STRAIN-ENERGY FORMULATION

3.1 Introduction of the compaction point for a thermoelastic solid with mass transfer

For the development of an appropriate material description for the solid skeleton, the material incompressibility needs to be considered. However, due to the porous structure also large volumetric deformations can occur when the porosity changes, which indicates in general $J_S = \det \mathbf{F}_S \neq 1$. Therefore, according to Ehlers & Eipper [4] and Bluhm [5] a compressible material law has to be considered as long as the pore space can be compressed. However, in the present case when ice formation occurs, the pore space vanishes ($n^F = 0$). In accordance, this indicates an incompressible characteristic and, hence, the existence of the compaction point.

As the volume fractions are essential for the development of the strain-energy function, their amount is specified for the respective solid constituents by

$$n^S = \frac{n^S_{0S}\, J_{S\theta}}{J_S} \exp\Big(\int_{t_0}^{t} \frac{\hat{\rho}^S}{\rho^S}\,\mathrm{d}\tau\Big), \quad n^I = \frac{n^I_{0I}\, J_{I\theta}}{J_I} \exp\Big(\int_{t_0}^{t} \frac{\hat{\rho}^I}{\rho^I}\,\mathrm{d}\tau\Big), \tag{15}$$

where $J_{SM} = \det \mathbf{F}_{SM}$, $J_{S\theta} = \det \mathbf{F}_{S\theta}$, $J_{S0} = \det \mathbf{F}_{S0}$, $J_{IM} = \det \mathbf{F}_{IM}$ and $J_{I\theta} = \det \mathbf{F}_{I\theta}$ determine the volumetric deformations. Since the motion of the ice and the solid skeleton is coupled, there exists a relation between the corresponding volumetric deformations according to equation $(9)_2$, which results in

$$\frac{J_{SM}\, J_{S\theta}}{J_{S0}} \;=\; J_{IM}\, J_{I\theta}. \tag{16}$$

At the compaction point, the pore space vanishes indicated by $n^S + n^I = 1$. Considering the integrated volume balances, the volumetric deformation of the solid skeleton is constrained by the compaction point

$$\tilde{J}_S \;=\; n^S_{0S}\, J_{S\theta} \exp\Big(\int_{t_0}^{t} \frac{\hat{\rho}^S}{\rho^S}\, \mathrm{d}\tau\Big) + n^I_{0I} J_{S0}\, J_{I\theta} \exp\Big(\int_{t_0}^{t} \frac{\hat{\rho}^I}{\rho^I}\, \mathrm{d}\tau\Big). \tag{17}$$

Therefore, the constraint for the volumetric deformation of the solid skeleton reads

$$0 < \tilde{J}_S < J_S < \infty. \tag{18}$$

3.2 Additive split of the strain-energy function for the solid skeleton

The basis for the considerations concerning the development of the strain-energy function W^S is a *Simo-Pister*-type material law [14], which was originally proposed for a compressible material under isothermal conditions in the form

$$W^S(I_S, J_S) \;=\; \overline{U^S}(J_S) + w^S(I_S) \;=\; U^S(J_S) - \mu^S \ln J_S + \frac{\mu^S}{2}(I_S - 3), \tag{19}$$

where $I_S = \mathbf{C}_S \cdot \mathbf{I}$ is the first invariant of the right *Cauchy-Green* deformation tensor $\mathbf{C}_S = \mathbf{F}_S^T\, \mathbf{F}_S$. For the specification of $U^S(J_S)$ several approaches, depending on the application, are on the market. Their characteristics are reviewed in Hartmann [15]. For a porous medium under isothermal conditions describing the compaction point, the approach by Ehlers & Eipper [4] is emphasised.

For a thermoelastic material, the above mentioned form of equation (19) can be extended to account for thermal effects [5]

$$\begin{aligned} W^S(\theta, I_S, J_S) \;=& U^S(J_S) - \mu^S \ln J_S + \frac{\mu^S}{2}(I_S - 3) - 3\alpha^S k^S \ln J_S (\theta - \theta^S_{0S}) - \\ & - \rho^S_{0S} c^S \Big(\theta \ln \frac{\theta}{\theta^S_{0S}} - \theta + \theta^S_{0S}\Big), \end{aligned} \tag{20}$$

where μ^S is the second *Lamé* constant, α^S the thermal expansion coefficient, k^S the bulk modulus and c^S the specific heat. The temperature is denoted by θ, whereas θ^S_{0S} is the initial temperature.

3.3 Constraints and a new strain-energy function

Within the framework of the TPM, hyperelastic material descriptions, where the extra stresses can be derived from an energy potential [7], require for the consideration of the compaction point the following conditions to be fulfilled [4].

Undeformed configuration: In the undeformed configuration, i. e. $J_S = 1$, the strain energy as well as the hydrostatic *Cauchy* stress vanishes, viz.:

$$U^S(J_S = 1) = 0 \quad \text{and} \quad \frac{\partial U^S}{\partial J_S}(J_S = 1) = 0. \tag{21}$$

Compaction point: In the case that the deformation reaches the compaction point, the necessary energy and the hydrostatic compressive stress have to be infinite

$$U^S(J_S \to \tilde{J}_S) \to +\infty \quad \text{and} \quad \frac{\partial U^S}{\partial J_S}(J_S \to \tilde{J}_S) \to -\infty. \tag{22}$$

This condition replaces the condition for non-porous, compressible materials, where the singularity is reached when $J \to 0$. Here, the transition from the compressible to an incompressible material law represents a singularity.

Growth condition: When the local porosity approaches unity, the necessary energy and the necessary (tensile) stress have to be infinite

$$U^S(J_S \to +\infty) \to +\infty \quad \text{and} \quad \frac{\partial U^S}{\partial J_S}(J_S \to +\infty) \to +\infty. \tag{23}$$

Convexity condition: In order to ensure local material stability, polyconvexity of the overall strain energy W^S has to be fulfilled [16]. Under the assumption that the volumetric extension U^S is twice differentiable, this conditions requires the second derivative with respect to the Jacobian J_S to be positive semi-definite

$$\frac{\partial^2 U^S}{\partial J_S^2} \geq 0, \quad \forall J_S > \tilde{J}_S > 0. \tag{24}$$

Compatibility assumption: As the linearised material law is supposed to result in *Hooke*'s law, the first *Lamé* constant Λ^S is determined via

$$\Lambda^S := \frac{\partial^2 U^S}{\partial J_S^2}(J_S = 1). \tag{25}$$

A new polyconvex strain energy: An analogous procedure as presented by Ehlers & Eipper [4] leads to a material description in a comparable form that meats the requirement of the present case:

$$\begin{aligned} U^S(J_S) = \frac{\Lambda^S}{\gamma_0^S(\gamma_0^S - 1) + \frac{2}{(\tilde{J}_S - 1)^2}} \Big[J_S^{\gamma_0^S} - \Big(\gamma_0^S + \frac{2}{\tilde{J}_S - 1}\Big) J_S + \\ + \gamma_0^S + \frac{2}{\tilde{J}_S - 1} - 1 + \ln\Big(\frac{(\tilde{J}_S - 1)^2}{(\tilde{J}_S - J_S)^2}\Big) \Big]. \end{aligned} \tag{26}$$

Therein, $\gamma_0^S \geq 1$ is a material parameter controlling the volumetric behaviour, cf. [17].

3.4 Discussion of the volumetric extension to the strain-energy function

Within the framework of hyperelasticity, the mechanical extra stress in terms of *Cauchy* stress can be derived based on thermodynamical considerations via

$$\mathbf{T}^S_{E\,mech} = 2\frac{\rho^S}{\rho^S_{0S}}\mathbf{F}_S\frac{\partial W^S}{\partial \mathbf{C}_S}\mathbf{F}_S^T. \tag{27}$$

For a study concerning the compaction point, only the stress originating from the volumetric extension $U^S(J_S)$ under isothermal conditions is considered, viz.

$$\frac{\partial U^S}{\partial J_S} = \frac{\Lambda^S}{\gamma_0^S(\gamma_0^S-1)+\frac{2}{(\tilde{J}_S-1)^2}}\left(\gamma_0^S J_S^{\gamma_0^S-1} - \gamma_0^S - \frac{2}{\tilde{J}_S-1} + \frac{2}{\tilde{J}_S - J_S}\right). \tag{28}$$

Note that for each configuration the limiting value $\tilde{J}_S$ for the Jacobian J_S may change, particularly due to mass transfer. For further discussions $\gamma_0^S = 2$ was chosen. This yields the form for compressible solid constituents under isothermal conditions according to Simo & Taylor [18], as shown in [15], when there is no compaction point, i. e. $\tilde{J}_S = 0$. This exemplary situation is compared to the case with compaction point, where the limiting value $\tilde{J}_S = 0.5$ of the Jacobian was chosen. Figure 4 shows that a deformation state under compression is penalised when getting too close to the point of compaction.

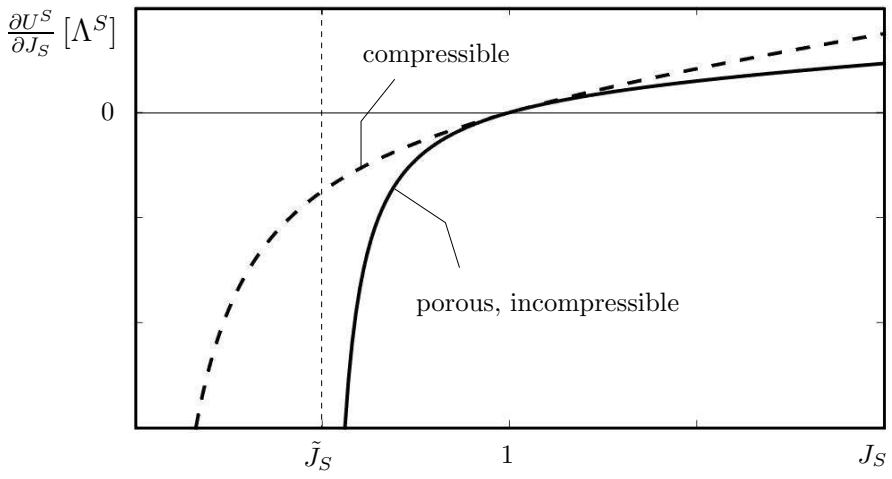

Figure 4: Characterisation of compressible materials and porous, materially incompressible materials with compaction point $\tilde{J}_S$.

Furthermore, the material description has been investigated by a virtual tension-compression test indicating a uniaxial state of stress. Note in passing that stability issues

under compression are not addressed. The deformation is given via

$$\mathbf{F}_S = \begin{bmatrix} \lambda & 0 & 0 \\ 0 & \lambda_L & 0 \\ 0 & 0 & \lambda_L \end{bmatrix} \mathbf{e}_i \otimes \mathbf{e}_j, \quad J_S = \lambda \lambda_L^2, \tag{29}$$

where $\lambda = L/L_0$ is the axial stretch and λ_L the unknown lateral stretch. When isothermal conditions are assumed, the lateral stress according to (27) in the directions $\mathbf{e}_2$ and $\mathbf{e}_3$ vanishes

$$0 = \frac{\nu(\tilde{J}_S - 1)^2}{(1-2\nu)(\tilde{J}_S^2 - 2\tilde{J}_S + 2)} \left[2\lambda\lambda_L^2 - \frac{2\tilde{J}_S}{\tilde{J}_S - 1} + \frac{2}{\tilde{J}_S - (\lambda\lambda_L^2)} \right] + \frac{1}{\lambda}\left(1 - \frac{1}{\lambda_L^2}\right), \tag{30}$$

resulting in an implicit equation in λ_L, which has been solved numerically. For other temperature configurations, a similar derivation can be performed. For a numerical case study, the *Poisson* ratio $\nu = 0.25$ was chosen, which is a commonly applied value for plant tissues. For a given stretch λ, the corresponding lateral stretch λ_L according to (30) is displayed in Figure 5.

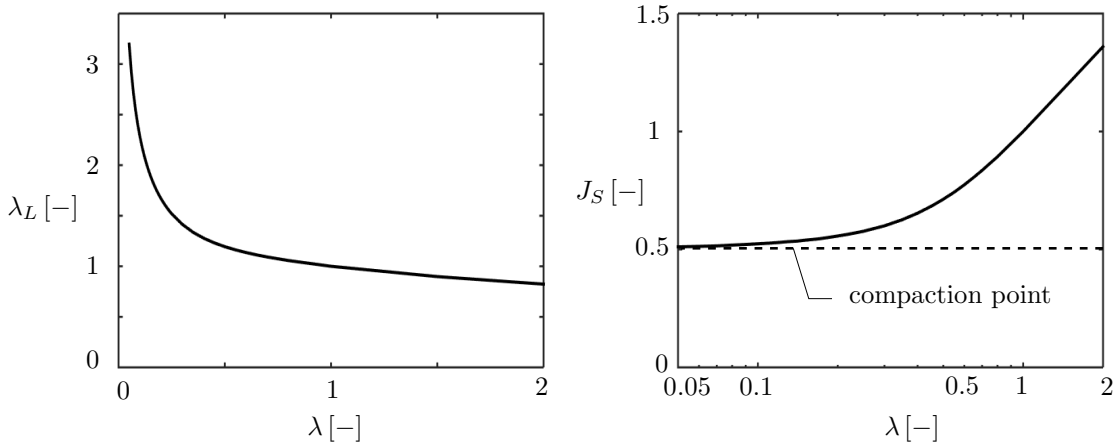

Figure 5: (Left): Lateral stretch - axial stretch for an uniaxial tension-compression test. (Right): Jacobian J_S - axial stretch for an uniaxial tension-compression test. Note that the axis of abscissa is scaled logarithmically. The compaction point is indicated for the compression state.

The sketches in Figure 5 show the lateral stretch λ and the Jacobian J_S as a function of the applied axial stretch, yielding a physically reasonable response. In particular, in the compression regime the volumetric deformation is constraint by the limiting value $\tilde{J}_S$ indicating the point of compaction.

4 CONCLUSION

Within this contribution, the derivation of a material description for frost-resistant plant tissues is addressed. Therefore, a number of basic definitions and considerations are necessary. First, the modelling approach based on the TPM needs to be introduced. Furthermore, the deformation is described in detail under the assumption of thermoelasticity and a kinematic coupling of the ice to the solid skeleton. These notions are crucial for the derivation of the volume fractions of the solids, which essentially determine the compaction point. The compaction point was included in the material description, which has been shown to describe the phenomenon of the compaction point properly.

Acknowledgements. This work has been funded by the German Research Foundation (DFG) as part of the Transregional Collaborative Research Centre (SFB/Transregio) 141 'Biological Design and Integrative Structures'/A01.

REFERENCES

[1] Neuner, G., Xu, B., Hacker, J. Velocity and pattern of ice propagation and deep supercooling in woody stems of *Castanea sativa*, *Morus nigra* and *Querus robur* measured by IDTA. *Tree Physiology* (2010) **30**:1037–1045.

[2] Eurich, L., Schott, R., Wagner, A., Roth-Nebelsick, A., Ehlers, W. Fundamentals of Heat and Mass Transport in Frost-Resistant Plant Tissues. *In Knippers, J. et al. (eds.) Biomimetic Research for Architecture and Building Construction*, Biologically-Inspired Systems, Vol. 9, Springer-Verlag, Cham (2016):97–108.

[3] Pearce, R.S. Plant Freezing and Damage. *Annals of Botany* (2001) **87**:417–424.

[4] Ehlers, W. and Eipper, G. Finite Elastic Deformations in Liquid-Saturated and Empty Porous Solids. *Transport in Porous Media* (1999) **34**:179–191.

[5] Bluhm, J. Constitutive relations for thermo-elastic porous solids. *Zeitschrift für Angewandte Mathematik und Mechanik* (2000) **80**:125–128.

[6] de Boer, R. *Trends in Continuum Mechanics of Porous Media.* Theory and Applications of Transport in Porous Media, Vol. 18, Springer-Verlag, Dordrecht (2005).

[7] Ehlers, W. Foundations of multiphasic and porous materials. *In Ehlers, W. and Bluhm, J. (eds.) Porous Media: Theory, Experiments and Numerical Applications*, Springer-Verlag, Berlin (2002):3–86.

[8] Ehlers, W. Challenges in porous media models in geo- and biomechanical engineering including electro-chemically active polymers and gels. *International Journal of Advances in Engineering Sciences and Applied Mathematics* (2009) **1**:1–24.

[9] Ehlers, W. and Häberle, K. Interfacial Mass Transfer During Gas-Liquid Phase Change in Deformable Porous Media with Heat Transfer. *Transport in Porous Media* (2016) **114**:525–556.

[10] Bluhm, J., Ricken, T., Bloßfeld, M. Ice Formation in Porous Media. *In Markert, B. (ed.) Advances in Extended & Multifield Theories for Continua*, Springer-Verlag, Berlin (2011):153–174.

[11] Eurich, L., Schott, R., Wagner, A., Roth-Nebelsick, A., Ehlers, W. From functional properties of frost-resistant plant tissues towards customised construction materials - A continuum-mechanical approach. *Proceedings in Applied Mathematics and Mechanics* (2016) **16**:81–82.

[12] Hartmann, S. Comparison of the multiplicative decompositions $F = F_\theta F_M$ and $F = F_M F_\theta$ in finite strain thermo-elasticity. *Technical Report Series TU Clausthal* (2012):Fac3-12-01.

[13] Lu, S.C.H. and Pister, K.S. Decomposition of deformation and representation of the free energy function for isotropic thermoelastic solids. *International Journal of Solids and Structures* (1975) **11**:927–934.

[14] Simo, J.C. and Pister, K.S. Remarks on rate constitutive equations for finite deformation problems: computational implications. *Computer Methods in Applied Mechanics and Engineering* (1984) **46**:201–215.

[15] Hartmann, S. The Class of Simo & Pister-type Hyperelasticity Relations. *Technical Report Series TU Clausthal* (2010):Fac3-10-02.

[16] Markert, B. Porous Media Viscoelasticity with Application to Polymeric Foams. *Dissertation Universität Stuttgart, Report No.: II-12* (2005).

[17] Ogden, R.W. Large Deformation Isotropic Elasticity - On the correlation of Theory and Experiment for Compressible Rubberlike Solids. *Proceedings of the Royal Society of London, Series A* (1972) **328**:567–583.

[18] Simo, J.C. and Taylor, R.L. Quasi-incompressible finite elasticity in principal stretches. Continuum basis and numerical algorithms. *Computer Methods in Applied Mechanics and Engineering* (1991) **85**:273–310.

VII International Conference on Computational Methods for Coupled Problems in Science and Engineering
COUPLED PROBLEMS 2017
M. Papadrakakis, E. Oñate and B. Schrefler (Eds)

OPTIMIZATION OF A STRUCTURE UNDER INTENSE THERMAL RADIATION AND ITS SELF-WEIGHT

Nicolau José Moreno Velez*, Miguel António Lopes de Matos Neves† and Hugo Filipe Diniz Policarpo*†

*Instituto de Plasmas e Fusão Nuclear (IPFN)
Instituto Superior Técnico, Universidade de Lisboa
1049-001 Lisboa, Portugal
e-mails: hpolicarpo@ipfn.ist.utl.pt, nicolau.velez@ipfn.ist.utl.pt, web page:
http://www.ipfn.tecnico.ulisboa.pt

†LAETA, IDMEC
Instituto Superior Técnico, Universidade de Lisboa
1049-001 Lisboa, Portugal
e-mail: miguel.matos.neves@tecnico.ulisboa.pt - Web page:
https://www.idmec.ist.utl.pt/laeta/

Key words: Plasma Position Reflectometry (PPR), PPR Antenna, International Thermonuclear Experimental Reactor (ITER), Optimization, Radiation, Temperature Minimization, Displacement Minimization

Abstract. This proceeding presents work being developed to the optimization of thermoelastic structures under thermal radiation and its self-weight, involving thermal conductivity but not convection. For the analysis, it is used a thermal-structural finite element module of a commercial FE program where the radiation is modelled through view factors between elemental surfaces. The thermostructural problem under the assumption of small deformations is then treated as weak coupling problem. Limitations of the available tools are briefly discussed. For the optimization, a SIMP topology optimization (TO) is used to find optimized material distributions along a given spatial domain. The objective is to achieve both lower maximum temperature along the structure as well as lower maximum displacement. Some examples of results are presented for the long hollow truncated rectangle metallic pyramid analysed. The known effect that TO tends to remove most of the material in the design areas is firstly analysed. It is also presented a study of adding uniform coverage in thickness to reduce the maximum temperature and displacement, which resulted in an optimized solution with a small step near the end of the pyramid directly exposed to the radiation source. This somehow unexpected result is discussed.

1 INTRODUCTION

In the past few decades, the search for better structural performance has originated excellent results in the structural optimization field, namely optimization by material distribution. By optimizing the material distribution, a given structure will benefit from a relieve of unnecessary weight and an increase of its global stiffness.

The structure here studied is part of the PPR Diagnostics System [1] belonging to the ITER Tokamak. The PPR components presented are inside a vacuum chamber and therefore immersed in a quasi-vacuum environment. Furthermore, the components are exposed to a plasma radiative source that induces: i) direct heat loads, which will be radiate to the surrounding environment and transferred by conduction to other components in contact and, ii) indirect heat loads, arising from neutronics radiation, that are considered as internal heat generation in the structure.

The main concerns here are both the displacement and the high temperatures achieved as a result of the thermal expansion and the gravity acting on the bodies. Besides the attrition that the antenna will be subjected to, these issues can lead to oscillations/displacements of the structure that can originate clashes between components of the PPR, as well as material phase changes and consequently potential loss of the antennas functionality.

Optimizing a structure in order to minimize its temperatures can have multiple advantages. An example of temperature optimization by material distribution can be described by the components of Earth orbiting satellites, once these structures are also subjected to high amounts of energy coming from the nuclear fusion processes occurring in the Sun. By optimizing these satellites material distribution, besides decreasing maximum temperatures achieved, also the weight of the components may decrease, which would save a considerable amount of fuel spent during operations.

In the field of material distribution optimization, one of the most efficient existing methods is TO. This method, which finds optimized material distribution through element density redistribution, has been studied intensively and many work use the method Solid Isotropic Material with Penalization (SIMP). The initial work is due to Bendsøe and Kikuchi [2] and substantial information can be seen in Sigmund [3] and, in a more embracing way in [4] by Sigmund and Bendsøe. These authors were responsible for introducing this kind of structural optimization, giving way for the creation of new and improved methods. Still, there are not many works in thermoelastic structures with TO as far as their authors knowledge, but just to refer some works as Rodrigues and Fernandes [5], Bruns [6], Deaton [7] and Ricardo et al [8].

This proceeding presents methods being studied to perform material distribution optimization of the ITER PPR Antenna, aiming to decrease both its maximum temperature achieved during the thermal process and the resulting displacements. For that purpose, two main paths are followed. One consists in parametric studies using Finite Element Analysis (FEA) and Adaptive Single Objective (ASO) or Adaptive Multiple Objective

(AMO), implemented in the commercial code used here [9]. The other path consists in using a modified SIMP optimization method, which, besides the displacement optimization, also allows for optimization with temperature objectives.

The techniques applied in the parametric optimization resulted in curious and may be promising outcomes, where both minimized temperature and displacement were achieved.

2 METHODOLOGY

2.1 Thermoelastic problem

The thermoelastic structural analysis is performed as a weakly coupled problem, where first a thermal analysis is conducted with the resulting temperatures being imported to a static analysis (in a unidirectional path). This two-step procedure is suited as temperature influences displacement but the opposite is considered negligible.

Regarding the thermal process, the Hooke's law is applied as:

$$\{\sigma^t\} = [E]\{\varepsilon^t\}, \tag{1}$$

where $\{\sigma^t\}$ is the thermal stresses vector, $[E]$ is the elasticity matrix and $\{\varepsilon^t\}$ is the thermal strain vector.

2.2 Heat transfer problem

The conduction process is solved according to the Fourier's Law:

$$q = -\frac{\Delta T}{R_{cond}}, \tag{2}$$

where ΔT is the temperature difference between two surfaces and R_{cond} the thermal resistance in conduction.

Regarding the radiation process, the amount of energy that reaches a given surface (area) j will be conditioned by the way this surface is disposed towards the emitter one i. This value can be measured by the view factor F_{ij} and its calculation by computational methods can be done through the Nusselt's hemicube method [10] as seen in the hemicube schematic in Fig.1 (where ϕ represents the angle and the hemicube sides are subdivided into N grid cells, named pixels). Following this, the view factor are achieved as:

$$F_{ji} = \sum_{j=1}^{N} \frac{cos(\phi_i)cos(\phi_j)}{\pi R_{ij}^2} \Delta A_j, \tag{3}$$

with N being the number of pixels created, ΔF_n the view factor between the reference surface and each of the target pixels, ϕ_i and ϕ_j the angles between the surfaces and R_{ij} the direct length between the centroid points of the two surfaces.

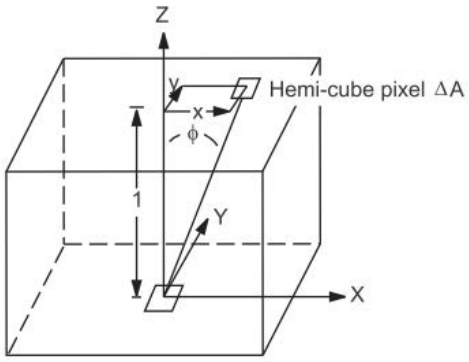

Figure 1: Schematic representation of the hemicube method present in [10].

2.3 Finite element analysis via weak coupling

Regarding the heat transfer, the FEA solves the following equation:

$$\begin{aligned} &[\mathrm{C}]\{\dot{\mathrm{T}}\} + [\mathrm{K}_T]\{\mathrm{T}\} = \{\mathrm{R}_T\} \\ &[\mathrm{K}_T] = [\mathrm{K}_k] + [\mathrm{H}_{conv}] + [\mathrm{H}_{rad}] \\ &\{\mathrm{R}_T\} = \{\mathrm{R}_B\} + \{\mathrm{R}_{hconv}\} + \{\mathrm{R}_{h_{rad}}\} + \{\mathrm{R}_Q\} \end{aligned} \tag{4}$$

where [C] and $[\mathrm{K}_T]$ are the general global specific heat and conductivity matrices, and $\{\mathrm{R}_T\}$, $\{\mathrm{T}\}$ and $\{\dot{\mathrm{T}}\}$ are the general global thermal load, temperature, and the first derivative of the temperature vectors, respectively. Furthermore, $[\mathrm{K}_k]$, $[\mathrm{H}_{conv}]$ and $[\mathrm{H}_{rad}]$ are the global conductivity, convection and radiation matrices, and $\{\mathrm{R}_B\}$, $\{\mathrm{R}_h\}$ and $\{\mathrm{R}_{h_{rad}}\}$ are the global heat flux, convection, radiation and heat generation vectors, respectively. The FEA is established as a nonlinear transient thermal analysis (as radiation is considered and the properties of the materials are temperature dependent) that considers conduction and radiation effects (convection is not considered as the medium is vacuum, which means that $[\mathrm{H}_{conv}] = \{\mathrm{R}_{hconv}\} = 0$) to estimate the temperature distribution along the antenna.

A Steady-State Thermal analysis is performed and followed by a structural elastostatic/steady state analysis:

$$[\mathrm{K}]\{U\} = \{F\} + \{F^{th}\} \tag{5}$$

where, [K] is the global stiffness matrix, $\{F\}$ is the global mechanical load vector, $\{F^{th}\}$ is the global thermal load vector and $\{U\}$ is the global displacement vector.

2.4 Thermostructural analysis

A CAD model of the antenna, is illustrated in Fig. 2 with the respective dimensions: w-width, h-height, t-thickness (uniform) and L-length, presented in Table 1.

In Fig.3 a), the complete model used in both thermal and static analyses is illustrated, where the antenna is located between two blankets and directly faced towards a plasma surface. In this model, a constant temperature of 300 °C [11] is applied to the rear side of

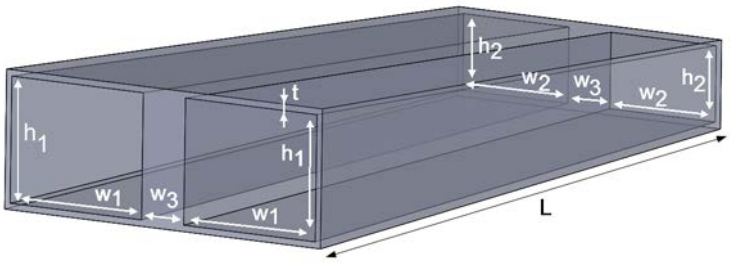

Figure 2: CAD model of ITER PPR antenna (index 1-front, 2-rear).

Table 1: Dimensions (in mm) of the ITER PPR antenna.

w_1	w_2	w_3	h_1	h_2	t	L
25	20	8	20	12	1	115.4

the antenna, where it is structurally fixed, and to the inner surface of the blanket surfaces. An earth gravity acceleration of 9,8066 m/s^2 is considered, acting on a direction parallel ($-z$ axis in Fig.3 b)) to the rear face of the antenna.

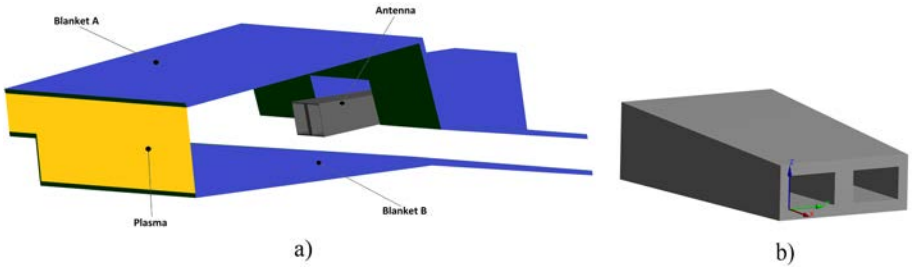

Figure 3: Radiation enclosure model in a) and antenna coordinate system in b).

An initial Steady State Thermal analysis was performed on the model, using the Ansys Workbench software, considering this as the worst case scenario, i.e., when the maximum temperatures will be higher.

From the original antenna FE model, a new model is created (as seen in Fig.4) to perform design optimization and parametric studies.

In the model presented in Fig.4 the illustrated parameters L_c and t_c are respectively the length and thickness of the antenna coverage. This FE model features 3D 20-node structural-thermal FEs with a four degree-of-freedom at each node and 3D radiosity surface FEs for radiosity, overlaid on the exposed face of the 3D thermal FEs.

2.5 Optimization

The structure was subjected to two kinds of optimization: Topology Optimization and Parametric Optimization.

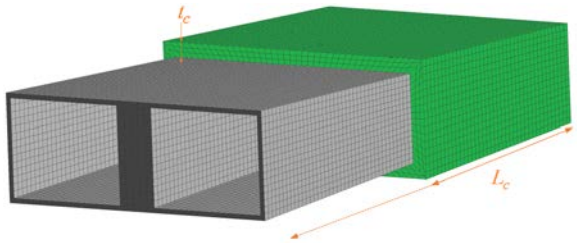

Figure 4: Parameterized CAD model: (w width; h - height, t - thickness (uniform) and L - length).

In the first case, a modified approach of the SIMP is applied to the antenna using:

$$E_i = E_{min} + \rho_i^p (E_0 - E_{min}),\ \rho \in]0, 1] \tag{6}$$

with E_0 being the elastic properties of the solid material, ρ the element relative density, E_i the element elastic properties and E_{min} the elastic property of the "void" material. This allows for the maximization of the material stiffness, which is obtained by searching the best material distribution through compliance or elastic strain energy $\mathbf{C}$ minimization:

$$\begin{aligned} & find\{\boldsymbol{\rho}\} = (\rho_1, .., \rho_i, .., \rho_{n_d}), 0 < \rho_i \leq 1, i = 1, .., n_d \\ & min[\mathbf{C}] = \frac{1}{2}(\{\mathbf{f}\} + \{\mathbf{G}\})^T \{\mathbf{u}\} \\ & s.t. \\ & \{\mathbf{f}\} + \{\mathbf{G}\} = [\mathbf{K}]\{\mathbf{u}\} \\ & V \leq V_{(U)} \end{aligned} \tag{7}$$

where ρ_i is the pseudo-density variables, n_d is the number of densities variables, $\mathbf{f}$ is the thermal load vector, $\mathbf{G}$ the self-weight load vector, $\mathbf{u}$ is the nodal displacement vector and $\mathbf{K}$ is the structural global stiffness matrix. Furthermore, V is the total volume of the material used for the structure and $V_{(U)}$ is the prescribed upper limit.

In the second case, a parametric optimization is performed using available algorithms in the commercial code used. The process is managed by the necessity of having one or more objectives, which will translate in ASO or AMO algorithms, respectively [12].

Since the primal objective of this study is to decrease the maximum temperatures achieved in the antenna while subjected to the operating conditions, the first step is to perform a single objective optimization, i.e., ASO.

On the other hand, even if having minor impact on the project, also the structure displacement is of great importance, which leads to the multiobjective optimization AMO. Here both temperature and displacements are minimized, demanding weights to be attributed to both objectives

3 RESULTS AND DISCUSSION

3.1 A brief verification

To check the procedure used with the TO technique, the curiously named Shape Optimization BETA tool from ANSYS Workbench is used. So, before using the TO commercial tool in the antenna problem, first a verification test was made relatively to the results in [13], where a simple temperature variation is imposed on a clamped-clamped 2D structure subjected to a vertical centered force and a volume constraint of 40%, as illustrated in Fig.5.

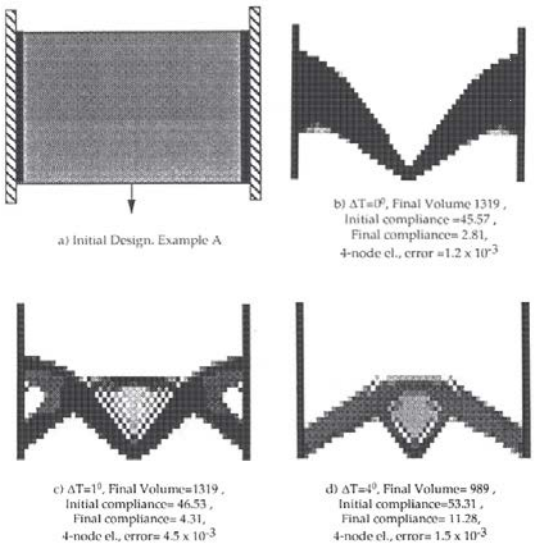

Figure 5: Topology Optimization in thermally loaded structure in [13] for $\Delta T=0°$, $\Delta T=1°$ and $\Delta T=4°$.

Using the already mentioned TO ANSYS tool, the obtained results with the exact same constraints as in [13] are the following (Fig.6).

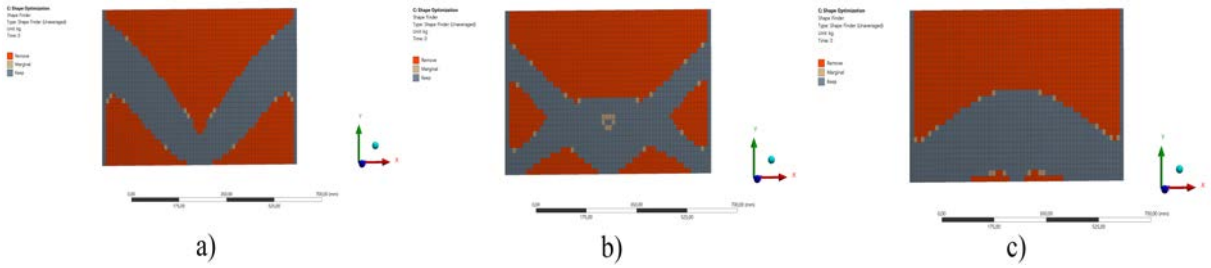

Figure 6: TO results obtained with TO ANSYS tool for a)-$\Delta T=0°$, b)-$\Delta T=1°$ and c)-$\Delta T=4°$.

By observing Fig.6, it is possible to state that all three outcomes based on each ΔT are similar to the ones presented in the mentioned work.

3.2 Application of optimization to the antenna

With this being said, the results obtained when applying this method to the antenna model result in two different solutions, both with a volume constraint of 50%, as follows in Fig.7.

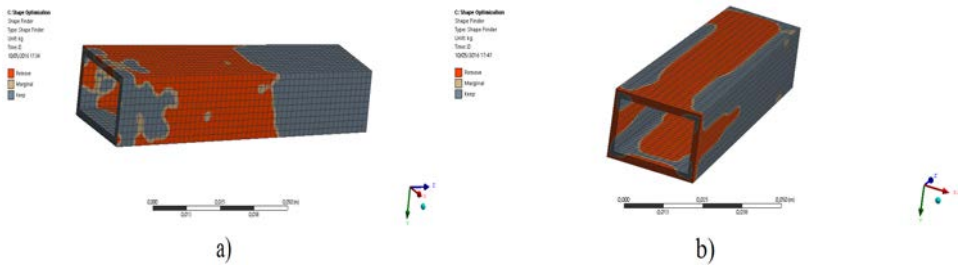

Figure 7: Examples of TO application to the antenna.

Looking at Fig.7, one can see that both results obtained are unwanted. This happens once material from the internal faces is removed, which eliminates the antenna's purpose, given the fact that these internal faces are crucial for the signal propagation.

Therefore, at this step, this TO software reveals itself as inappropriate for the work here being developed.

Regarding the thermostructural analysis, both the results are illustrated in Fig. 8. In Fig. 8 a), the maximum temperatures (T_{max}) along the antenna are portrayed, where one can see that they reach its peak in the frontal face of the antenna, as expected.

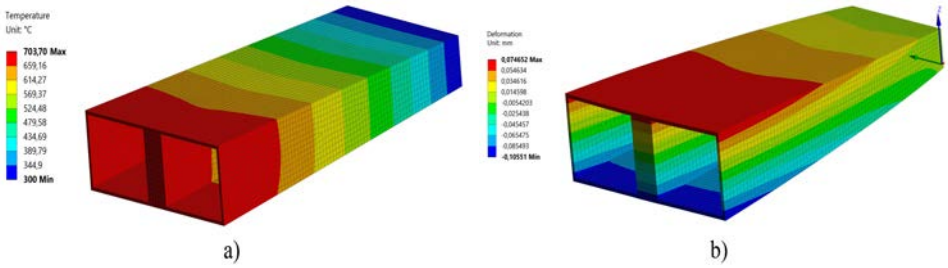

Figure 8: Results for thermostructural analyses: a) Temperature distribution and b) Displacement distribution

Respecting Fig. 8 b), the results for maximum displacement (D_{max}) along the antenna are displayed, where it can be seen that the maximum value also occurs in the frontal part of the antenna, which, given the problem constraints (Fig.3), is what should be expected. This is the first region, of the PPR in-vessel system, facing the plasma, hence the first to be in contact with the plasma loads, reaching a of $\sim 704°C$, a mean temperature of $\sim 557°C$ and a (thermal expansion and displacements due to its dead weight) of $\sim 0,106mm$.

Following this, in Fig.9 are presented the results for the parametric studies, with respect to T_{max} and D_{max}, showing the evolution of these values with the increase of the antenna coverage.

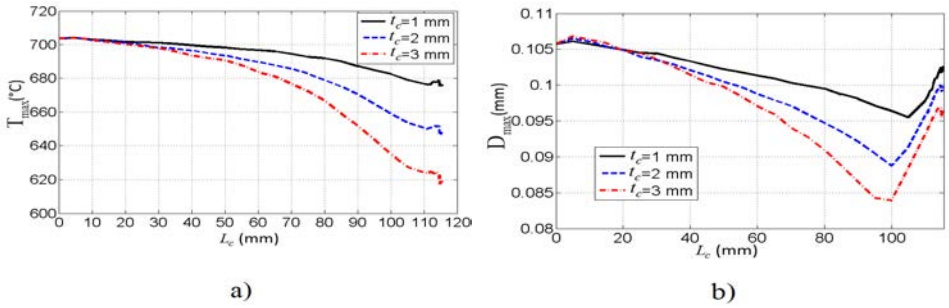

Figure 9: Results for parametric studies: a) temperature and b) displacement.

Looking at both results in Fig.9, it is possible to infer that T_{max} and D_{max} decrease with the coverage increase, until a given point near the full coverage condition. In Fig.9 a), T_{max} decreases until a minimum point located somewhere between $114 \leq L_c \leq 115.4$mm and for maximum thickness (t_c=3mm). In fig.9 b), D_{max} is located somewhere between $95 \leq L_c \leq 110$, also for a maximum value of thickness. With the results of these studies, the optimization action zones are established. Given the importance of T_{max}, a interval of $114 \leq L_c \leq 115.4$mm and maximum thickness for the ASO feature and a combined interval of $95 \leq L_c \leq 115.4$mm and $t_c = 3$mm for the AMO giving T_{max} and D_{max} the same objective weight. The results for the ASO are illustrated in Fig.10, where the minimum T_{max} of 617.3 °C is obtained for $L_c = 114.7$mm, corresponding to 0.7mm from the front edge, originating the CAD model in Fig.11 a).

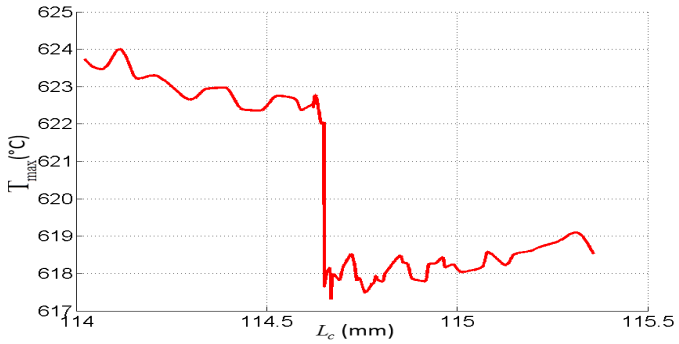

Figure 10: Plot of parametric study of T_{max} in function of L_c

In Fig.12 the results for the AMO are presented, where a Pareto front illustrates the values obtained for an equal weight of 50% for T_{max} and D_{max} as a function of L_c and $t_c = 3$mm. The best value obtained is for $L_c = 102.8$mm, as it is the point where both

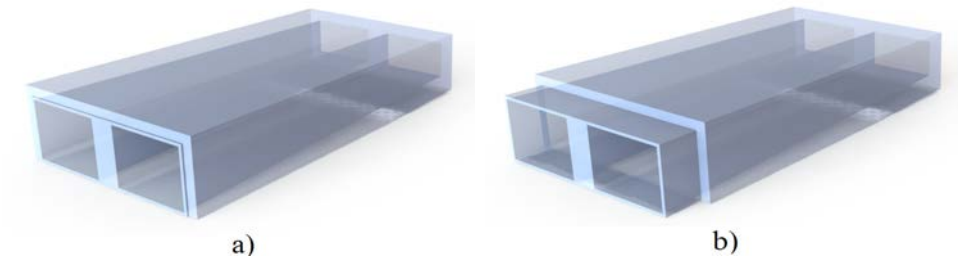

Figure 11: Resulting CAD models from ASO (a)) and AMO (b)) features.

temperature and displacement reveal the best balance of low values. This value presents results of $T_{max} = 631.9°C$ and $D_{max} = 0.087mm$, corresponding to a distance of 12.6 mm from the front edge of the antenna, originating the CAD model illustrated in Fig.11 b).

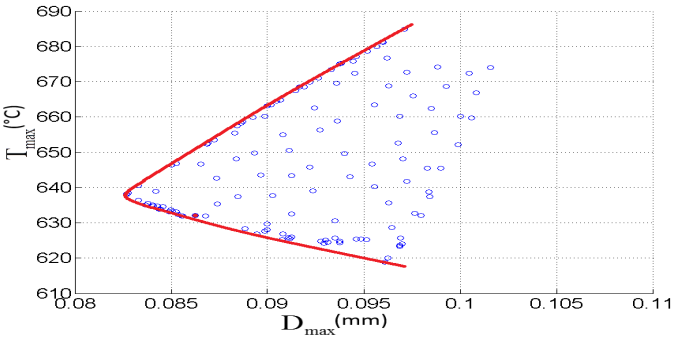

Figure 12: Plot of results from AMO feature.

Both parametric optimization cases reveal improvements in their objectives, which are summarized in Table 2, where results are compared to initial values and is the average temperature of the antenna.

Table 2: Initial and optimized results obtained by ASO and AMO.

	L_c (mm)	t_c (mm)	T_{max} °C	T_{mean} °C	D_{max} (mm)
Initial	0	0	703.7	556.7	0.106
ASO	114.7	3	617.3	500.5	-
AMO	102.8	3	631.9	492.6	0.087

From the data included in Table 2, one can see a decrease in T_{max} and T_{mean} of 86.4°C (12.3%) and 56.2°C (10.1%), respectively in the ASO case. Regarding the AMO case, a decrease in , and of 71.8°C (10.2%), 64.1°C (11.5%) and 0.019 mm (17.9%), respectively is evidenced.

The decreases in temperature are explained by the increase of the heat flux by conduction given the increase in material along the antenna. This phenomenon allied with the structure exposure to the plasma heat radiation leads to the best result at 0,7mm from a full coverage.

In respect to the decrease in D_{max}, it is associated to the gain of structural stiffness by adding material to the rear part of the antenna, restraining its movements.

4 CONCLUSIONS

- This study is at a preliminary step and results need to be better interpreted.
- In this work, several optimization methods, namely TO, ASO and AMO, were used.
- The results obtained for the PPR antenna with the ANSYS TO tool, revealed inappropriate results as one concludes that it does not account for thermal radiation exchanges. This motivated the use of parametric studies ASO and AMO.
- The parametric studies of the antenna indicate that and decrease with the increase of and until the optimum. With ASO one obtains and decrease of 12.3% and 10.1%, respectively and with AMO one obtains a, and of 10.2%, 11.5% and 17.9%.
- With lower values of and, the lifetime of the antenna is extended, less maintainability is required and hence, the availability of the antenna is increased. With lower, the signal attenuation is improved and more accurate estimations for the plasma position are expected.
- Note that this is a preliminary study that needs further improvements regarding the ASO optimum solution. Regarding TO, there are some promising studies in the area that deal with conduction and radiation problems. However, they are still embryonic and not available in commercial codes as far as the knowledge of the authors.

REFERENCES

[1] Varela, P. *55.F3 PPR: System Design Description Document (DDD), ITER_D_SGCQ2S v2.0, July 2016.*

[2] Bendsøe, M.P. and Kikuchi, N. *Generating Optimal Topologies in Structural Design Using a Homogenization Method.* Computer Methods in Applied Mechanics and Engineering 71 (1988).

[3] Sigmund, O. *Design of material structures using topology optimization.* CPh.D. Thesis, Department of Solid Mechanics, Technical University of Denmark, (1994).

[4] Bendsøe, M.P. and Sigmund, O. *Topology Optimization - Theory, Methods, and Applications.* Springer, 2^{nd} edition (2003).

[5] Rodrigues, H. and Fernandes, P. *A material based model for topology optimization of thermoelastic structures*. International Journal for Numerical Methods in Engineering , vol. 38, no. 12, pp. 19511965 (199).

[6] Bruns, T.E. *Topology optimization of convection-dominated, steady-state heat transfer problems*. International Journal of Heat and Mass Transfer, Vol. 50, pp. 2859-2873 (2007).

[7] Deaton, J.D. *Design of Thermal Structures using Topology Optimization*. PhD Thesis, Wright State University, (2009). (Online at http://cecs.wright.edu/cepro/docs/thesis/ Design_of_Thermal_Structures_using_Topology_Optimization_DEATON_2014.pdf).

[8] Ricardo, J. D. R., Coe, G., Carvalho, J. P., Branco, M. B. C., Barroqueiro, B., Abraos, P. and Neves, M. M. *Innovative cork application on a thermal deflector for apogee boost motors*. in the proceedings of the 14th European Conference on Spacecraft Structures, Materials and Environmental Testing (ECSSMET), 27-30 September, Toulouse, France (2016).

[9] *ANSYS Academic Research Help Manual*. Release 17.0 (2016).

[10] *Theory Reference for the Mechanical APDL and Mechanical Applications*. ANSYS, version 12.1, (2009).

[11] Policarpo, H. *F4E-FPA-375-SG04: Plan for the Thermal Analysis of the PPR Invessel Components*. F4E_D_25B8L7 v1.1 (2016).

[12] *Ansys DesignXplorer User's Guide v17,*. (2016).

[13] Rodrigues, H. and Fernandes, P. *Topology optimal design of thermoelastic structures using a homogenization method*. Control and Cybernetics, Vol.23, (1994).

VII International Conference on Computational Methods for Coupled Problems in Science and Engineering
COUPLED PROBLEMS 2017
M. Papadrakakis, E. Oñate and B. Schrefler (Eds)

A FULLY EXPLICIT FLUID-STRUCTURE INTERACTION APPROACH BASED ON THE PFEM

SIMONE MEDURI*, MASSIMILIANO CREMONESI* AND UMBERTO PEREGO*

*Department of Civil and Environmental Engineering
Politecnico di Milano
Piazza Leonardo da Vinci, 32, 20133 Milano, Italy
e-mail: simone.meduri@polimi.it; massimiliano.cremonesi@polimi.it; umberto.perego@polimi.it

Key words: Fluid-Structure Interaction; PFEM-FEM coupling; domain decomposition; explicit dynamics.

Abstract. The efficient numerical simulation of Fluid-Structure Interaction (FSI) problems is of growing interest in many engineering fields. Staggered approaches are particularly interesting because they allow for the reuse of existing softwares. In this work we propose a staggered scheme based on the weakly compressible PFEM for the fluid domain and SIMULIA Abaqus/Explicit for the solid domain. The coupling is treated with a domain decomposition approach based on the Gravouil-Combescure algorithm. The main goal is to show the possibility of a fully explicit coupling with different time step size on the two phases (fluid and solid) and incompatible mesh at the interfaces. 2D test-cases will be presented to validate the proposed coupling technique. The explicit time integration scheme for both the fluid and solid subdomains, together with the explicit treatment of the coupling, makes this method appealing for applications in a variety of engineering problems with fast dynamics and/or a high degree of non-linearity.

1 INTRODUCTION

In the present work, a staggered approach for the solution of the FSI problem is proposed. The fluid domain is discretized with a Particle Finite Element Method (PFEM) [1], while the solid domain with a standard Finite Element Method. The weakly compressible formulation of the fluid flow, originally proposed in [2] for an explicit PFEM, is here used for the fluid domain. The PFEM has shown its capability in simulation of free surface flows in many applications (e.g. [3, 4, 5, 6]). Thanks to the Lagrangian formulation, the free surface is directly defined by the current position of the particles, while the governing equations are imposed like in standard FEM. When the mesh becomes too distorted, a fast remeshing algorithm is used to redefine the connectivities. SIMULIA Abaqus/Explicit has

been used for the solution of the structural domain. This allows to perform simulations with a complete and advanced description on the structural domain, including advanced structural material models and contact. The GC Domain Decomposition method [7] is here used for the coupling: the problem is solved independently on each subdomain and then linked at the interface using a Lagrange multiplier technique. The proposed method allows for different time-steps in the two subdomains and for non-conforming meshes at the interfaces between the solid and fluid domains. Moreover, this approach guarantees an explicit coupling at the interfaces.

2 GOVERNING EQUATIONS

The fluid domain Ω_f^t has been modeled through the weakly compressible Navier-Stokes equations:

$$\frac{d\rho_f}{dt} + \rho_f(\nabla_{\mathbf{x}} \cdot \mathbf{v}_f) = 0 \quad \text{in } \Omega_f^t \times [0,T] \tag{1}$$

$$\rho_f \frac{d\mathbf{v}_f}{dt} = \nabla_{\mathbf{x}} \cdot \boldsymbol{\sigma}_f + \rho_f \mathbf{b_f} \quad \text{in } \Omega_f^t \times [0,T] \tag{2}$$

where $\mathbf{x}$ are the coordinates in the current configuration, ρ_f is the fluid density, $\mathbf{v}_f$ the fluid velocity and $\mathbf{b_f}$ the external forces. The Cauchy stress tensor $\boldsymbol{\sigma}_f$ can be decomposed in its deviatoric and isotropic parts: $\boldsymbol{\sigma}_f = -p_f\mathbf{I} + \boldsymbol{\tau}_f$. In the weakly compressible framework, the pressure field p_f can be directly related to the density ρ_f through the Tait equation:

$$p_f(\rho_f) = p_{0,f} + K_f \left[\left(\frac{\rho_f}{\rho_{0,f}} \right)^{\gamma} - 1 \right] \tag{3}$$

where $p_{0,f}$ is the reference pressure, $\rho_{0,f}$ the reference density, $\gamma = 7$ the specific heat ratio and K_f the bulk modulus.

The solid domain Ω_s^t is governed by the momentum conservation equation:

$$\rho_s \frac{d\mathbf{v}_s}{dt} = \nabla_{\mathbf{x}} \cdot \boldsymbol{\sigma}_s + \rho_s \mathbf{b}_s \quad \text{in } \Omega_s^t \times [0,T] \tag{4}$$

where ρ_s is the solid density, $\mathbf{v}_s$ the solid velocity, $\mathbf{b_s}$ the external forces on the solid domain and $\boldsymbol{\sigma}_s$ represents the stress tensor on Ω_s^t. Standard Dirichlet and Neumann boundary conditions are applied on both the domains.

3 SPACE AND TIME DISCRETIZATION

Following a standard Galerkin finite element approach the semidiscretized equations of motion appear:

$$\mathbf{M}_f \frac{d\mathbf{V}_f}{dt} = \mathbf{F}_{ext,f} - \mathbf{F}_{int,f} = \mathbf{F}_f \quad \text{in } \Omega_f^t \times [0,T] \tag{5}$$

$$\mathbf{M}_s \frac{d\mathbf{V}_s}{dt} = \mathbf{F}_{ext,s} - \mathbf{F}_{int,s} = \mathbf{F}_s \quad \text{in } \Omega_s^t \times [0,T] \tag{6}$$

where $\mathbf{M}$ are the mass matrices, $\mathbf{V}$ the vector of nodal velocities and $\mathbf{F}_{int}$ and $\mathbf{F}_{ext}$ the vectors of internal and external nodal forces, respectively.

The discretized form of fluid mass conservation (2) can be obtained starting from the Lagrangian strong form, leading to:

$$\mathbf{M}_\rho \mathbf{R}_f = \mathbf{R}_0 \tag{7}$$

where $\mathbf{R}_f$ contains the nodal values of the density field (details can be found in [2]).

Equations (5-6) are integrated in time by means of the Central Difference Scheme [8]. It is important to recall that performing a mass lumping in the mass matrices, a fully decoupled system of equations can be obtained and fluid and solid velocities can be computed explicitly node by node.

4 THE COUPLING SOLUTION SCHEME

A staggered approach is here proposed for the solution of the coupled fluid-solid problem. The fluid sub-problem is solved numerically through the weakly compressible PFEM (see [2]). The solid sub-problem is analyzed using the commercial software Abaqus/Explicit [9].

To couple the fluid and the solid domains the so-called GC method (Gravouil-Combescure) [7] has been selected. This algorithm, originally conceived for non-overlapping structural domains, has been recently extended to FSI problems [10]. The proposed approach splits the kinematic solution of each subdomain into two terms: *free* and *link*. The free solution is related to the free motion of each subdomain without considering the interaction with each other; the link solutions introduce a correction to account for the coupling. The correction terms are computed applying boundary tractions at the fluid-solid interface that play the role of Lagrange multipliers for the imposition of a kinematic constraint. The GC coupling algorithm allows for different time steps in the two sub-domains. Moreover, it allows for the use of incompatible meshes at the fluid-solid interface. This algorithm guarantees a stable strong coupling for the staggered solution of the FSI problem. In the present case of explicit fluid and structural solvers, the correction step consists in a small system of decoupled equations, resulting in a fully explicit coupled solver. A detailed description of the proposed approach can be found in [11].

5 NUMERICAL EXAMPLES

5.1 1D Fluid Structure Interaction

A first validation of the present method is obtained considering the 1D example presented in [12]. An elastic column, clamped at its bottom edge, is loaded by a column of water, as shown in Figure 1a. Due to the weight of the water, at the beginning of the analysis the system starts to oscillate vertically, as the horizontal displacement is constrained. The material parameters used for the water subdomain are:

- reference density $\rho_{0,f} = 1000\ kg/m^3$,

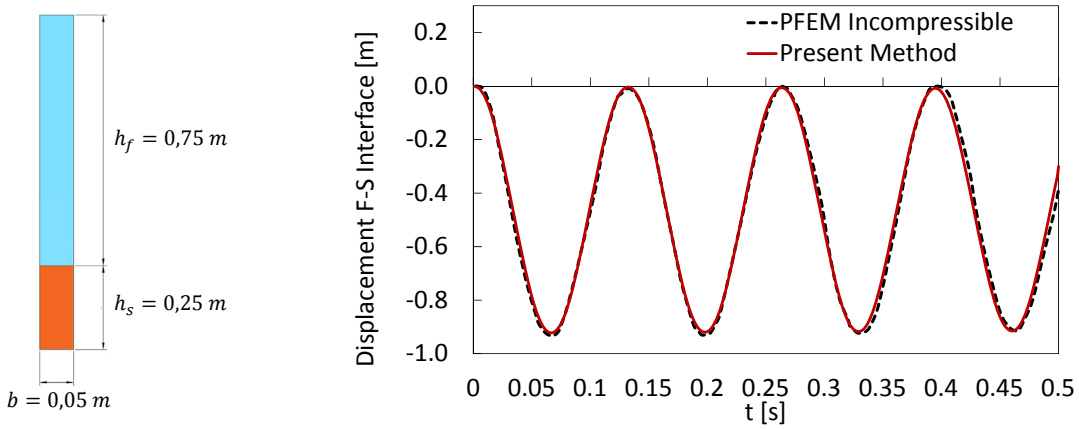

(a) (b)

Figure 1: 1D Fluid Structure Interaction. (a) Geometry of the problem. (b) Vertical Displacement of the fluid-structure interface: comparison with numerical results presented in [12]

- viscosity $\mu_f = 0\ Pa \cdot s$,
- bulk modulus $K_f = 2.2 \cdot 10^9\ Pa$;

while for the structural subdomain, the material parameters are:

- reference density $\rho_s = 1500\ kg/m^3$,
- Young Modulus $E_s = 2.3 \cdot 10^5\ Pa$,
- Poisson ratio $\nu_s = 0.4$.

Figure 1 shows the evolution in time of the vertical displacement at the fluid-structure interface. The results obtained with the present approach are compared with the ones presented in [12], showing a good agreement, both in terms of maximum displacement and frequency of the oscillations. It is worth noting that the structural parameters correspond to a very soft material, with a low Young's Modulus and density close to the fluid one. These conditions are known to be source of numerical difficulties [13, 12]. Consequently, despite its apparent simplicity, this example is a good test for the robustness of a FSI solver.

5.2 Deformable wedge impacting free surface water

In this example, the proposed method is tested on the challenging case of high speed impact of deformable structures against water at rest. The problem setting, presented in [14], is depicted in Figure 2. An aluminum wedge, with an inclination of 10°, is clamped at both its ends, where a vertical velocity of $V_{y,s} = -30\ m/s$ is imposed. The geometrical and mechanical parameters of the analysis are listed in table 1. The impact at high speed

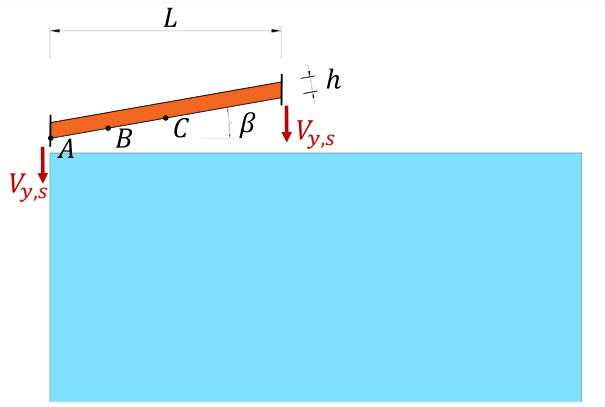

Figure 2: Deformable wedge impacting water free surface. Geometry of the problem

against water causes the deflection of the beam and the creation of lateral water jets. This is qualitatively shown in Figure 3, which collects some snapshots of the simulation. For a quantitative validation, Figure 4 shows the time evolution of the beam deflection at point B, as well as the time evolution of pressure at points A, B, and C, respectively. The results are compared with the numerical ones obtained with the SPH method presented in [14], and the semi-analytical solution presented in [15]. Once again, one can observe a very satisfactory agreement of the comparisons, considering the high level of complexity of the problem at hand.

Data	
L	$0.6\ m$
h	$0.04\ m$
β	$10°$
$V_{y,s}$	$-30\ m/s$
Fluid	
Density	$1000\ kg/m^3$
Viscosity	$0.001\ Pa \cdot s$
Bulk Modulus	$2.2 \cdot 10^9\ Pa$
Alluminium Beam	
Density	$2700\ kg/m^3$
Young Modulus	$67.5\ GPa$
Poisson ratio	0.34

Table 1: Deformable wedge impacting water free surface. Geometry and materials parameters.

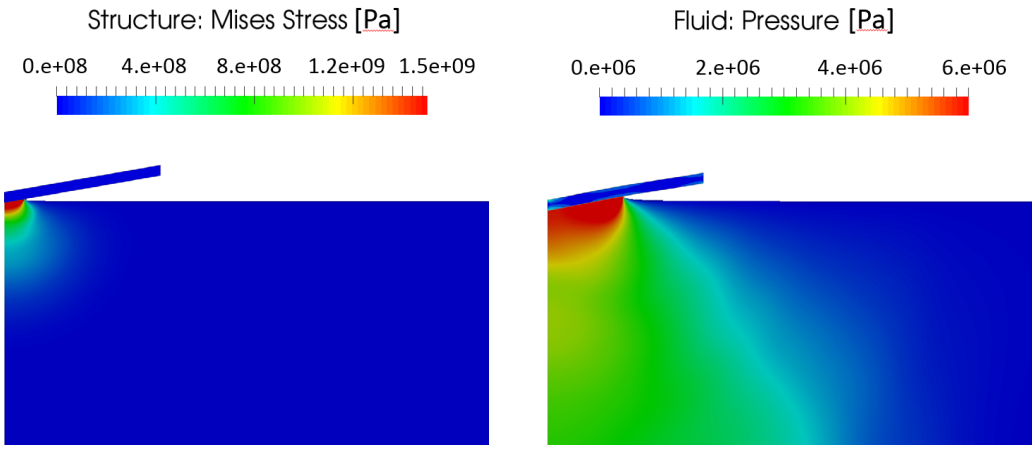

(c) $t = 0.0003\ s$ (d) $t = 0.0013\ s$

(e) $t = 0.0023\ s$ (f) $t = 0.0028\ s$

Figure 3: Deformable wedge impacting water free surface. Snapshots of the simulation at different time instants. Contour plot of the pressure field in the fluid subdomain and Mises stress field in the structural one.

6 CONCLUSIONS

In the present work a fully explicit and fully Lagrangian PFEM-FEM coupling approach has been proposed for the solution of a fluid-structure interaction problem. The employment of a commercial software such as Abaqus/Explicit will allow to exploit all the available features for an advanced modelling of the structural part. The coupling has been performed through the GC domain decomposition method. This method synchronizes the independent solutions of the two subdomains, ensuring the strong coupling and the stability of the staggered approach. A fully explicit approach with different time step sizes and incompatible meshes at the interface has been proposed and validated. Two numerical examples have been used to assess the potential of the proposed numerical scheme.

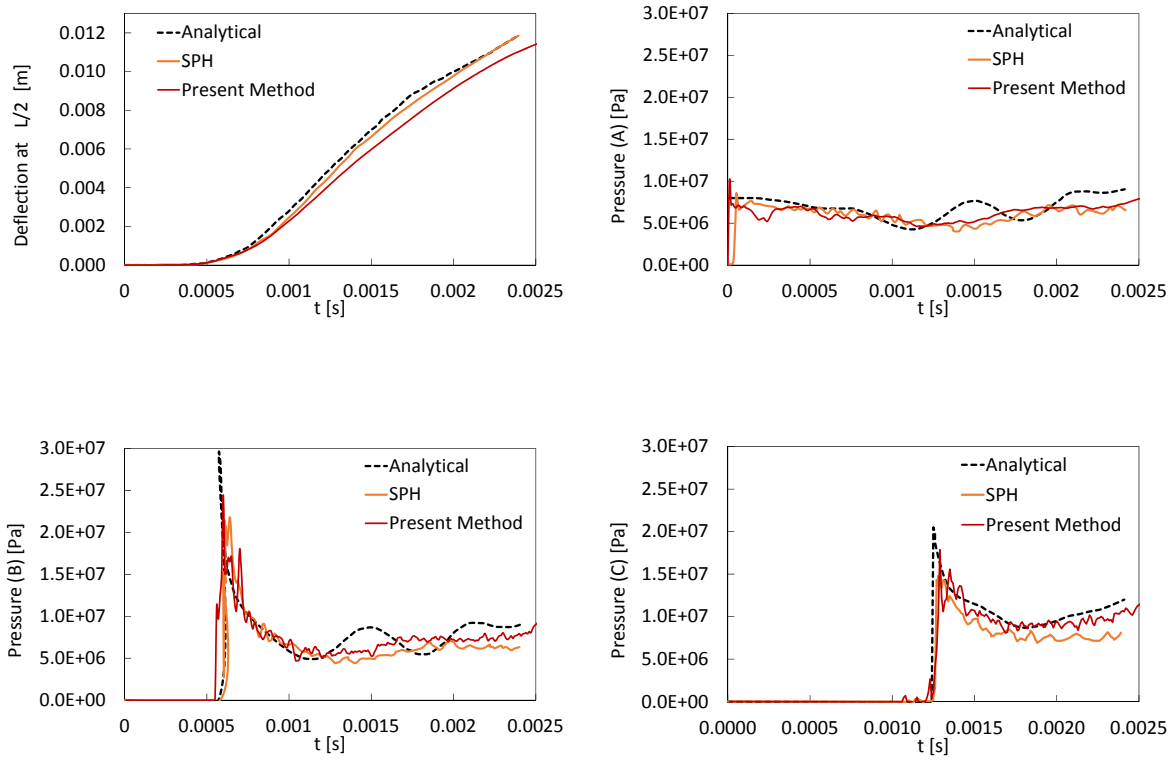

Figure 4: Deformable wedge impacting water free surface. Comparison with the analytical solution presented in [13] and the numerical one presented in [14]. (a): Time evolution of the deflection of the midpoint of the beam. (b)-(c)-(d) Time evolution of pressure at points A, B and C, respectively.

REFERENCES

[1] Oñate, E., Idelsohn, S.R., del Pin, F. and Aubry,R. The Particle Finite Element Method. An Overview. *Int J Computational Method* (2004) **1**:267-307.

[2] Cremonesi, M., Meduri, S., Perego, U. and Frangi, A. An explicit Lagrangian finite element method for free-surface weakly compressible flows. *Comp. Particle Mech.* (2017) DOI: 10.1007/s40571-016-0122-7

[3] Cremonesi, M., Ferri, F. and Perego U. A basal slip model for Lagrangian finite element simulations of 3D landslides. *Int J Numer Anal Met* (2017) **41**:30-53.

[4] Idelsohn, S. R., Mier-Torrecilla, M. and Oñate, E. Multi-fluid flows with the Particle Finite Element Method. *Computer Meth. in Appl. Mech. and Engng.* (2009) **198**:2750-2767.

[5] Idelsohn, S. R., Oñate, E., Del Pin, F. and Calvo, N. Fluid-structure interaction using the Particle Finite Element Method. *Computer Meth. in Appl. Mech. and Engng.* (2006) **195**:2100-2123.

[6] Zhu, M. and Scott, M. H. Direct differentiation of the quasi-incompressible fluid formulation of fluid-structure interaction using the PFEM. *Computer Particle Mech.* (2017) 1-13.

[7] Combescure, A. and Gravouil, A. A time-space multi-scale algorithm for transient structural nonlinear problems. *Mecanique et Industries* (2001) **2**:43-55.

[8] Hughes, T. J. R. The Finite Element Method: Linear Static and Dynamic Finite Element Analysis. Dover Publications. (1987)

[9] Dassault Systèmes SIMULIA. *Abaqus Documentation.* Providence, RI, USA, (2016).

[10] Nunez-Ramirez, J., Marongiu, J. C., Brun, M. and Combescure, A. A partitioned approach for the coupling of SPH and FE methods for transient non-linear FSI problems with incompatible time-steps. *Int. J. Numer. Meth. in Engng.*(2016) 1-46.

[11] Meduri, S., Cremonesi, M., Perego, U., Bettinotti, O., Kurkchubasche, A. and Oancea, V. A staggered fully explicit Lagrangian Finite Element Method for highly nonlinear Fluid-Structure-Interaction problems. *submitted.* (2017)

[12] Idelsohn, S. R., Del Pin, F., Rossi, R. and Oñate, E. Fluid-structure interaction problems with strong added-mass effect. *Int. J. Numer. Meth. Engng.* (2009) **80**:1261-1294.

[13] Causin, P., Gerbeau, J. F. and Nobile F. Added-mass effect in the design of partitioned algorithms for fluid-structure problems. *Computer Meth. in Appl. Mech. and Engng.* (2005) **194**:4506-4527.

[14] Oger, G., Guilcher, P. M., Jacquin, E., Brosset, L., Deu, J. B. and Le Touzé, D. Simulations of hydro-elastic impacts using a parallel SPH model. *Int. J. Offshore and Polar Engng.* (2010) **20**:181-189.

[15] Scolan, Y. M. Hydroelastic behaviour of a conical shell impacting on a quiescent-free surface of an incompressible liquid. *J. of Sound and Vibration* (2004) **277**:163-203.

VII International Conference on Computational Methods for Coupled Problems in Science and Engineering
COUPLED PROBLEMS 2017
M. Papadrakakis, E. Oñate and B. Schrefler (Eds)

COVERING SHOCK WAVES ON MARS INDUCED BY INSIGHT'S HP^3-MOLE - EFFICIENT CO-SIMULATION USING DEM AND MULTI-DOMAIN DYNAMICS

ROY LICHTENHELDT*

* German Aerospace Center (DLR)
Instute of System Dynamics and Control
Münchener Straße 20 82234 Weßling
e-mail: roy.lichtenheldt@dlr.de, web page: http://www.dlr.de/sr/en

Key words: Co-Simulation, Discrete Element Method, soil modeling, Mars

Abstract. NASAs discovery mission InSight (Interior Seismic Investigations, Geodesy and Heat Transport) scheduled for launch in 2018 will investigate the interior of Mars. For the subsurface locomotion, DLR's self-impelling nail nicknamed the "Mole" needs to hammer itself down to 5 m into the martian soil with less than 5 W of input power. A major focus during the Mole's development has been on simulation and analysis using virtual prototypes. As certain aspects of the environmental conditions on Mars cannot be recreated and tested on earth, high-fidelity coupled simulations are required to achieve the accuracy needed. These co-simulations are composed by a multi-body based cross domain model for the hammering device and a discrete element model for the soil. The article focuses on the coupling strategy of both models as well solutions in terms of communication. Furthermore efficiency improvements of the computationally expensive DEM models will be presented. Using these approaches the detailed stroke cycle and shock wave propagation are analyzed. Allowing to evaluate the performance under martian or terrestrial conditions.

1 INTRODUCTION

The question for the formation of our solar system is one major driver of science. Hence NASAs discovery mission InSight (Interior Seismic Investigations, Geodesy and Heat Transport) [1] aims to gather knowledge about Mars' interior structure. Therefore DLR's HP^{3}instrument (Heat Flow and Physical Properties Package) [2] measures the internal martian heat flux in a total depth of 5 m. Thus, its locomotion system, the self-impelling nail nicknamed the "Mole" needs to hammer itself into the martian soil with less than 5 W of input power.
The HP^{3}Mole's development has been supported by simulations since the very beginning,

as certain environmental aspects cannot be covered in terrestrial test setups. The most precise of the models for the HP^{3}Mole is a coupled simulation of a multi-body based cross domain model for the hammering device itself and a discrete element model for the soil. Thereby the first covers the dynamics of the mechanism in several domains within the multi-body framework using a single solver. The surrounding soil is covered by the particle simulation framework DEMETRIA [3] based on Pasimodo [4]. As the effects of the two main domains happen in different timescales, dedicated solvers and communication strategies need to be applied in order to ensure proper data exchange and numerical stability. One further important point is to speed up the computationally expensive DEM model in order to allow for simulations usable in the limited development time frames of low-cost planetary missions.

2 HP^{3}Mole for InSight

DLR's HP^3-Mole is designed as an efficient low-velocity penetrator [2]. An impact driven locomotion has been chosen and the Mole is equipped with an internal hammering mechanism, periodically loaded by a DC-Motor. In order to fullfill its scientific task of measuring thermal properties of the red planet's interior, the Mole is equipped with three scientific payloads: STATIL (Static Tilt Measurement Unit), TEM-A (Thermal Excitation Measurement Active) and TEM-P (Thermal Excitation Measurement Passive), whereby the first two are integrated into the Mole's housing and the latter is included in the science tether dragged behind the Mole. Fig. 1 shows the internals of the Mole, whereas the hammering mechanism is situated in the front part and the payload compartment is seated in the rear section.

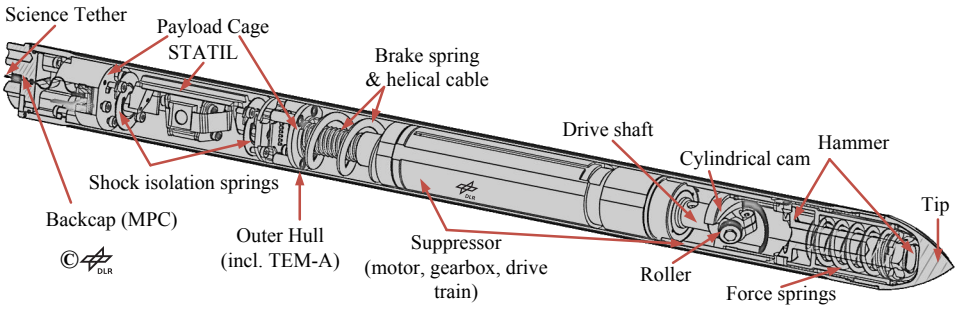

Figure 1: Cut through the flight model generation (PFM/PFE) of the HP^3-Mole , cf.[6]

During the tensioning process, the force spring is periodically loaded due to the drive-shaft roller running up on the cylindrical cam. Once the top of the cam is reached, the hammer is released and the fully loaded force spring it towards the tip. Meanwhile the heavier suppressor mass is accelerated towards the payload compartment. In order to allow the Mole to work as a "mechanical diode", mitigation of the upwards forces takes place by suspending the suppressor on a brake spring. This spring is thereby designed to distribute the suppressor energy over an extended intervall of time, never exceeding the

anisotropic friction forces between the soil and the outer hull surface. During impact of the hammer on the tip, energy is transmitted to the outer hull and the Mole moves into the soil until it is stopped by its resistive forces. Once the suppressor movement reversed due to brake spring and gravity, it moves towards the tip and causes a second major stroke in the same stroke cycle [3, 9, 6]. Due to several subsequent rebounds of hammer and suppressor additional major and minor strokes are carried out. These additional strokes mainly affect the dynamic behaviour of the Mole inside the soil [3, 9, 6].

3 MODELING

Modeling and simulation have been crucial for the development of the HP^{3}Mole. With InSight being a low-cost mission, the number of physical prototypes of the Mole were limited as well as the possibility for risky tests using them. Thus most situations have first been evaluated using virtual prototypes in simulation. Ofttimes the simulation even gave green lights for a risky test in advance. In order to use such simulations as a substitute for real prototypes, high-fidelity models are needed. Therefore high-precision soil models described in [3, 5, 6, 8] have been developed and have also been used to create fast but still precise single point models [11, 3]. Yet precise soil models alone are not sufficient to cover the mutual influences on the dynamics of the mechanism and the soil. Thus an additional cross domain model based on enhanced multi-body dynamics has been developed [3, 6]. The two major models have then been coupled in a co-simulation using the DLR-SR framework DEMETRIA.

3.1 Cross Domain Mechanism Model

To accurately model the behavior of the mechanism several domains must be covered: [9, 11]:

- dynamics and kinematics of mechanisms internal bodies,
- tensioning and release of the force spring including the DC-motors electro-dynamics,
- contact dynamics for the impact driven energy transmission,
- force as well as brake spring including stiffness-contributing parts,
- conditions on Earth and Mars: atmospheric conditions, temperature and gravity,
- critical frictional effects,
- gas flow and pressure distribution in the Mole modeled by dyn. pneumatic networks,
- dynamics and influence of the spring suspended payload STATIL,
- and the modular definition of outer forces (test stands, soil models incl. DEM).

Thereby one key goal is to use as little simulator coupling as possible. Extensive coupling would cause overhead on preprocessing and is prone for numerical problems. Thus all the different physical domains of the mechanism model have been included into the mutli-body system software Simpack. This allows for the use of a single solver and time step size. Validation of the mechanism model is shown in [6, 3].

3.2 Discrete Element Model Soil Modeling

The soil models for the most precise models of the HP^{3}Mole are discrete element models. DEM discretizes the simulation domain by distinct particles, generating a naturally discontinous model of granular matter. Even though computation power heavily increased over the course of the last years, modern computers are still not capable of modeling large scale domains with physical grains sizes. Because of that and due to the focus on workstation computers DEMETRIA uses up-scaling of the particle size according to the tool resolution. Further detail on the calibration-free model parametrization is given in [8].
In DEMETRIA models are divided into three different layers of scale . Regarding overall simulation performance, the macroscopic and mesoscopic layer give the highest potential for speed up, mostly limiting the number of particles included in the model. Thus this article will focus on the macroscopic and mesoscopic layer, whereas the the microscopic layer, covering grain shape, contact models etc., is described in [5, 8, 3].
On mesoscale, boundary and symmetry conditions as well as domain size are most impor-

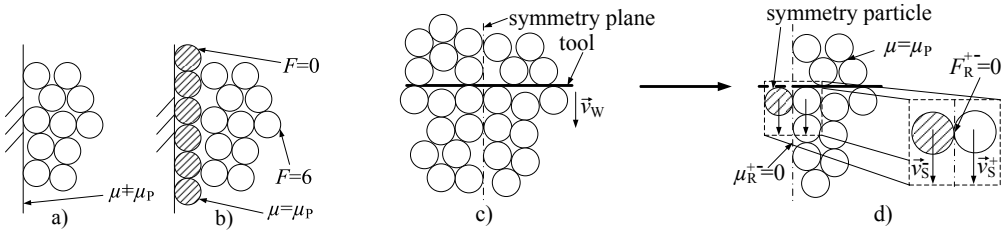

Figure 2: Basic scleronomic boundary conditions: smooth boundary a) and rough boundary b), symmetry condition c), full domain vs. symmetry, d) effects on the symmetry plane, cf. [3]

tant in order to have efficient but yet accurate simulations. The basic boundary conditions are given as scleronomic boundaries. The most simple condition is the smooth boundary mimicking a physical boundary, i.e. a container wall. It is composed by triangulated surfaces possessing the friction parameters of the physical friction pairing. In most cases the simulation domain does not need to have the full extension of the physical container [3]. Once $E_{\mathrm{kin}} \to 0$ is met, the additional particles do not increase accuracy anymore and the simulation domain may be shrunk. In order to cover the correct frictional behaviour including form closure, the rough boundary (Fig. 2) has to be used if the domain size is limited and $E_{\mathrm{kin}} \to 0$ is ensured. It consists of fixed particles possessing interparticle friction, acting as a non moving layer of particles [3]. Symmetry is a special condition, helping to shrink the domain even further. As the symmetry plane always has to cut the domain through the tool, the velocity $\vec{v}_{\mathrm{S}}$ on the left and right hand side of the symmetry plane yields [3]:

$$|\Delta\vec{v}_{\mathrm{S}}| \to 0 \;\forall\; \Delta\vec{v}_{\mathrm{S}} = \vec{v}_{\mathrm{S}}^{+} - \vec{v}_{\mathrm{S}}^{-};\; \wedge\; |\vec{v}_{\mathrm{S}}^{+}| \cong |\vec{v}_{\mathrm{S}}^{-}|; \tag{1}$$

Thus between neighboring particles right at the symmetry plane no frictional forces are present. Hence the following assumption is valid for the frictional interface [3]:

$$|\vec{F}_{\mathrm{R}}^{+-}| = 0 \rightarrow \mu_{\mathrm{R}}^{+-} = 0 \tag{2}$$

Symmetry can either be either plane or rotation symmetric, whereas the extreme cases of these symmetries yield a 2D representation. For the both cases the forces and torques acting on the tool need to be corrected. Details on the correction are given in [3].

In order to increase the performance beyond the usage of symmetry conditions, especially for moving tools, dynamic boundaries may be applied. These boundaries are basically moving the domain together with the tool by constantly loading and deleting particles. The basic principle in 1D and the algorithm to be applied are shown in Fig. 3. Loading of new particles only occurs every n simulation time steps in order to minimize the overhead by memory latency. If particles would be loaded from hard disk rather than main memory n has to increase significantly and loading is only viable for slow movement speeds. Hence only main memory shall be used for loading. As in DEM the particle inventory usually only features values of t and $t-\Delta t$ the older values are stored in a special memory particle [3]. The amount of particles to be loaded is determined by membership functions based

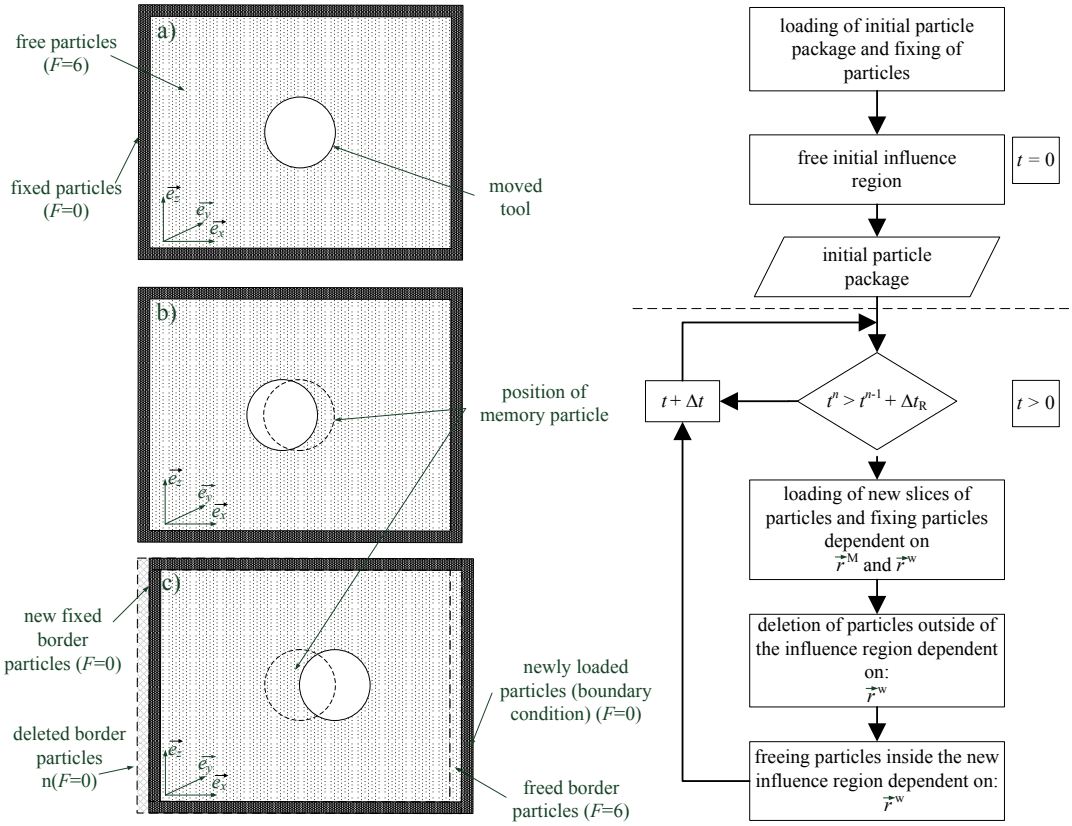

Figure 3: Basic strategy for dynamic boundaries in one dimension, cf. [3]

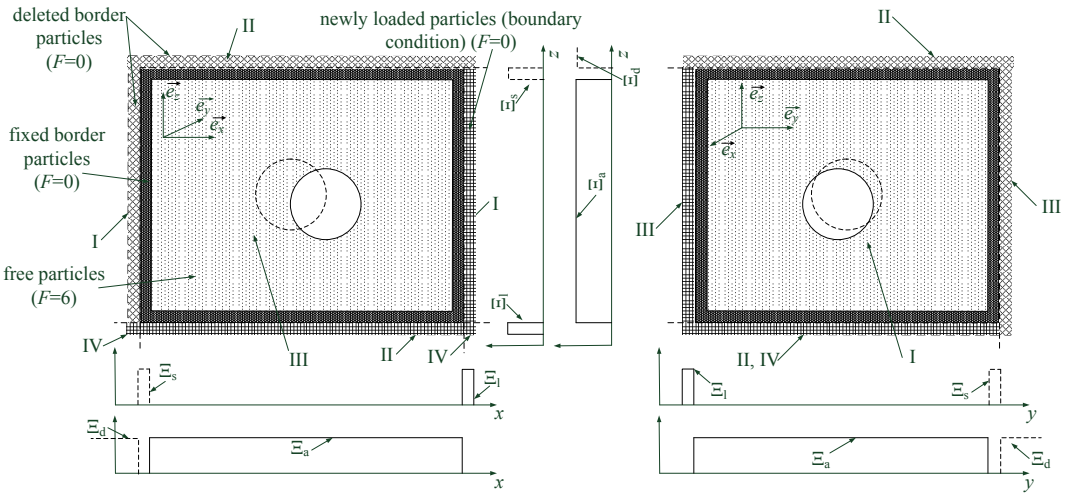

Figure 4: Three dimensional dynamic boundaries with membership functions, cf. [3]

on the influence region of the tool. For full three dimensional the membership functions are visualized in Fig. 4. If the membership function equals 1 then the particle is member of the respective group. The HEAVISIDE membership functions Ξ_{init} (initial package), Ξ_{a} (activating), $\vec{\Xi}_{\text{d}}$ (deletion), Ξ_{s} (fixing) and Ξ_{l} (loading) evaluate to (cf. [3]):

$$\Xi_{\text{init}}(\vec{r}^{\,\text{p}}, \vec{r}^{\,\text{w}}) = \prod_{i=1}^{3}\prod_{h=1}^{2}\Xi_i\Big(\Big(r_i^{\text{p}} - (r_i^{\text{w}} - n_{i,h}^0 r)\Big)\cdot(-1)^{h+1}\Big);\ F_{\text{p}} = 0 \tag{3}$$

$$\Xi_{\text{a}}(\vec{r}^{\,\text{p}}, \vec{r}^{\,\text{w}}) = \prod_{i=1}^{3}\prod_{h=1}^{2}\Xi_i\Big(\Big(r_i^{\text{p}} - (r_i^{\text{w}} - (n_{i,h}^0 - 3)r)\Big)\cdot(-1)^{h+1}\Big);\ F_{\text{p}} \neq 0 \wedge n_f = 3 \tag{4}$$

$$\Xi_{\text{s}}(\vec{r}^{\,\text{p}}, \vec{r}^{\,\text{w}}) = \prod_{i=1}^{3}\prod_{h=1}^{2}\Xi\Big(\Big(r_i^{\text{p}} - (r_i^{\text{w}} - (n_{i,h}^0 - 6)r)\Big)\cdot(-1)^{h+1}\Big);\ F_{\text{p}} = 0 \wedge n_f = 3 \tag{5}$$

$$\vec{\Xi}_{\text{d}}(\vec{r}^{\,\text{p}}, \vec{r}^{\,\text{w}}, \dot{\vec{r}}^{\,\text{w}}) = \prod_{h=1}^{2}\vec{\Xi}\Big(\Big(\vec{r}^{\,\text{p}} - (\vec{r}^{\,\text{M}} - (\vec{n}_h^0 + 5)r)\Big)\cdot(-1)^{h+1}\Big)\vec{\Xi}\Big(\dot{\vec{r}}^{\,\text{w}}\Big) \tag{6}$$

$$\begin{aligned}\Xi_{\text{l}}(\vec{r}^{\,\text{p}}, \vec{r}^{\,\text{w}}, \dot{\vec{r}}^{\,\text{w}}) = \sum_{i=1}^{3}\prod_{h=1}^{2}&\Xi\Big((-1)^{h+1}(r_2^{\text{M}} - r_2^{\text{p}} + n_{2,1}^0 r)\Big)\Xi\Big((-1)^{h+1}(-r_2^{\text{p}} - r_2^{\text{M}} + n_{2,1}^0 r)\Big)\\ &\cdot\Xi_i\Big((-1)^{h+1}(r_i^{\text{p}} - r_i^{\text{M}} + n_{i,1}^0 r)\Big)\Xi_i\Big((-1)^{h+1}(r_i^{\text{w}} - r_i^{\text{p}} + n_{i,1}^0 r)\Big)\\ &\cdot\Xi_i\Big((-1)^{h+1}\dot{r}_i^{\,\text{w}}\Big);\quad |\dot{\vec{r}}^{\,\text{p}}| = 0 \wedge |\vec{\omega}^{\text{p}}| = 0 \wedge F_{\text{P}} = 0\end{aligned} \tag{7}$$

with $\vec{r}^{\,\text{p}}, \vec{r}^{\,\text{w}}$ the position vector of particle and tool, F_{P} the particles DOF and $\underline{n}^0$ the influence region matrix.

The macroscale is containing the description of the interaction of locomotion gear, i.e. the Mole's outer hull and the particles themselves. The hull is modeled as a smooth triangulated mesh featuring the friction parameters of the real hull to the regolith. The mesh is discretized equidistantly in polar coordinates and composed by a parametric description, allowing for automated variation of the outer shape in optimization runs. Due to the simplicity of the equation for the cylindrical part, only the vertex' $\underline{P}_{\mathrm{vT}} = (x_{\mathrm{vT}} \quad y_{\mathrm{vT}} \quad z_{\mathrm{vT}})$ of the Mole tip in cartesian coordinates need to be computed by mathematical bending [3]. The Mole's hull is then composed from the tip $\underline{P}_{\mathrm{vT}}$, hull $\underline{P}_{\mathrm{vZ}}$ and back cap $\underline{P}_{\mathrm{vMPC}}$ vertices [3]:

$$\underline{P}_{\mathrm{vH}} = \left(\underline{P}_{\mathrm{vT}}^{\mathrm{T}} \; \underline{P}_{\mathrm{vZ}}^{\mathrm{T}} \; \underline{P}_{\mathrm{vMPC}}^{\mathrm{T}}\right)^{\mathrm{T}};\; \underline{P}_{\mathrm{vH}} \in \mathbb{R}^{3\times(n+m+l)}, \underline{P}_{\mathrm{vT}} \in \mathbb{R}^{3\times n}, \underline{P}_{\mathrm{vZ}} \in \mathbb{R}^{3\times m}, \underline{P}_{\mathrm{vMPC}} \in \mathbb{R}^{3\times l}$$

In order to model the Mole's dynamics the co-simulation port of Pasimodo [4] is used and the mesh is moved according to the positions received via TCP/IP.

4 CO-SIMULATION

In order to setup the co-simulation pre-existing interface of Pasimodo and Simpack are used. For ease of application Matlab is used as moderator between the two clients [3]. In order to have a fully automated coupling of the tools, all three are wrapped into the DLR-SR Particle simulation framework DEMETRIA. In the following sections the procedure of DEM-MBS coupling in DEMETRIA is explained.

4.1 Coupling of the Tools & Communication

One of the main goals of DEMETRIA is to provide automated simulation setups, ready for variational or optimization runs. Thus DEMETRIA sets up the communication between the different tools, by searching for free ports, blocking them. Once this is done, the clients are started and put into a listening state as shown in Fig. 5. Upon the clients signaling readiness, the server (Matlab) is started, causing the instantaneous start of the coupled simulation [3]. In order to provide stable numerical behaviour, as well as to gain best performance, each client utilizes a specialized integration scheme. The time step size Δt for the particle simulation is thereby chosen as the maximum stable step size for the Newmark-β scheme. As the particle simulation has a much longer per step work load, the step size of the MBS may be chosen below the maximum stable time step, allowing for the observance of higher frequency results. This is especially important for the HP^{3}Mole, as the impact driven energy transmission requires time steps in the range of $[10^{-9}, 10^{-7}]$s. Thus the soil force is held constant for n MBS steps until the next DEM time step is completed. Thus the DEM time step size is also used as communication step size in Matlab utilizing a fixed step discrete scheme. In Fig. 5 the time steps and communication points are visualized. Once a co-simulation job is started and further licenses are available, DEMETRIA's job control allows for additional simulations running in parallel [3].

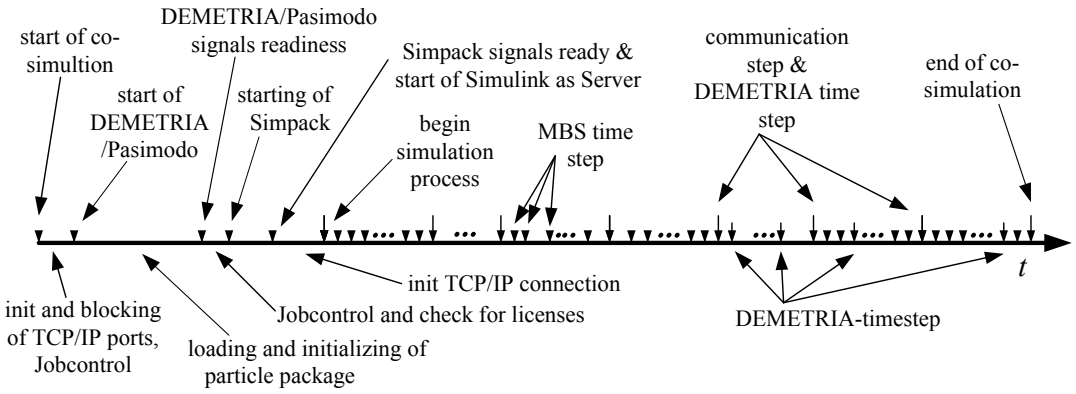

Figure 5: Communication time line for preprocessing and co-simulation, cf. [3]

4.2 Preparation of the Co-Simulation

In order to allow for coupled simulations of the Mole's hammering the particle package needs to be initialized. This is achieved by depositing the particles due to gravity. Once a package has reached equilibrium state, it might be subject to co-simulation or further parameter changes - the latter requiring one more relaxation run. As the Mole is a low velocity penetrator [7], simulating the full depth progress in co-simulation is not feasible in finite time horizons. As shown in Fig. 6 it is valid to drive the Mole's hull rheonomically to the depth of interest. Due to the dynamic boundaries the number of particles is held nearly constant and the layers of locked particles preserve the overburden pressure. Once the hull reached the final depth, the package needs to be relaxed again, as the Mole features one hammering cycle every 3.8 s, only [3]. Thereafter the full co-simulation is carried out for the detailed analysis of a single stroke as shown in Fig. 6. Concluding the full process, one full co-simulation cycle takes one upt to three days of CPU time.

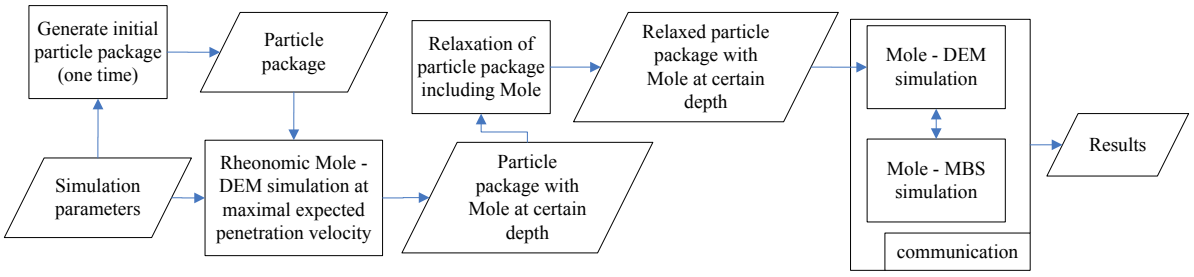

Figure 6: Preparation and procedure of the co-simulation, cf. [3] and [6]

5 ANALYSIS & RESULTS

The co-simulation method developed above has been used intensively to analyze and improve the Mole. The following sections will give a short overview on the results that have been gathered using the simulations. Details on the analysis are given in [6, 9, 3, 11].

5.1 Validation & Verification

The evaluation of the simulations accuracy has been carried out in a three staged process: at first the mechanism model has been validated using different Moles on a health check test stand comparing the Moles transient motion on the teststand, second the soil model has been checked against penetrometer and bevameter measurements comparing stresses and last the full co-simulation has been validated. This full system validation was done with simple and deep penetration tests using flight-like Moles. Thereby the penetration performance, the timing of effects as well as high-speed camera data and x-ray videos have been used. The final evaluation showed less than 16% of error for penetration depth of the complex coupled simulation, whereas low errors in literature range about 30-50%. Details on the validation process can be found in [6, 3].

5.2 Variation of the Outer Shape

Using the HP^{3}Mole co-simulation it is possible to conduct analysis of the mutual influence between soil and mechanism dynamics. Such analysis are not possible using the real prototype and hence the simulation enhances the understanding and development of the mechanism extensively. An example application of the Mole co-simulation is the analysis of the influence of tip geometry on the locomotion performance [9]. As shown in Fig. 7 (left) the shape mainly influences the direction of soil displacement and thus of the propagated wave. Comparisons of the resistive forces of different tips show, that neglecting friction sharper tips gain better performance. Thus a compromise of tip resistance, frictional forces and tip size have to be taken into account for the development. Furthermore the simulations show, that for non-conical tip shapes, quasi static resistance may differ significantly from dynamic resistance during hammering. Thus a final comparison using a full co-simulation is essential. Fig. 7 (right) shows the resultant penetration depths over

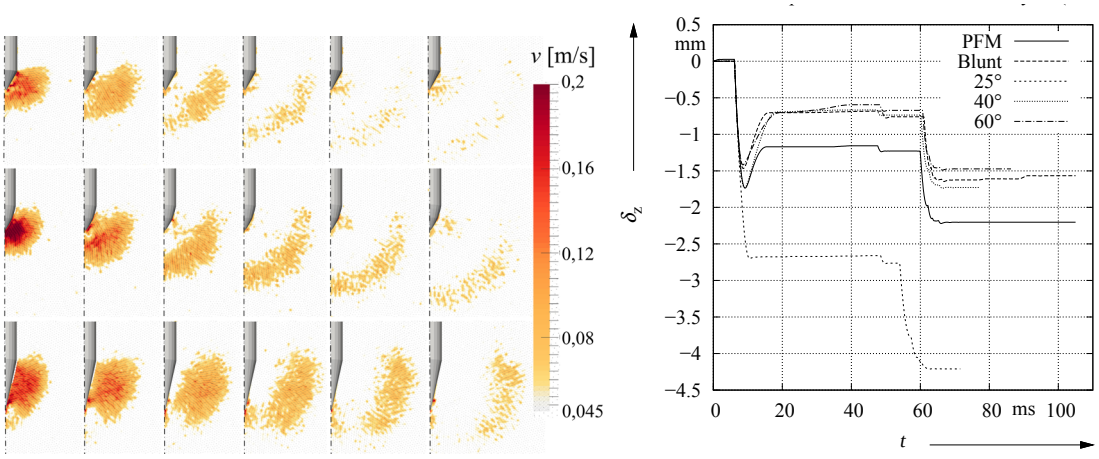

Figure 7: Wave propagation through the soil 2-7 ms for different tip shapes of the HP^{3}Mole (left) and the corresponding penetration depth (right), cf. [3], [9]

one stroke cycle [3]. For conicial tips it is obvious, that the more radial displacement of the soil visible in Fig. 7 (left) allows for higher penetration depth and less elastic rebound due to reflow waves in the soil. Regarding the reflow waves, more radial reflow causes less rebound but higher normal forces on the cylindrical part of the hull and thus higher friction, lowering possible rebound even further.
When non-conical tips are taken into account the actual non-linear shape greatly influences the performance. Comparing the PFM (Protoflight Mole) and Blunt (bullet shape) tip, it is obvious, that the PFM tip outperforms the equally long Blunt tip. They perform similar up to the end of the first stroke, but the Blunt tip then causes higher rebound due to less radial soil displacement. Compared to the conical tips, the PFM tip also outperforms a 40° tip while having the length of a shorter 50° tip. Further analysis for the variation of the outer shape can be found in [9, 3].

5.3 Shock Wave Propagation caused by the Mole - Earth vs. Mars

Shock wave propagation and the shape of the velocity field inside the soil is fairly important for the Mole's locomotion. Propagating waves mostly into vertical direction rather than radially, would cause compaction in front of the Mole's tip and thus the mechanism would increase compaction along the way, impeding its own movement. Regarding the previous sections results, a sharper tip would be most beneficial, keeping in mind the higher drag due to frictional forces. In planetary exploration mass and space budget is limited and thus an experience based trade of between tip length and resistance led to the non-linear shape of the PFM-tip implemented in the flight model. For the Mole development, both martian and terrestrial environment have to be taken into account in simulation in order to extrapolate the terrestrial tests to Mars. Fig. 8 shows the velocity profile of the particles for the Mole with the PFM-tip on Earth and on Mars. Comparing the two different environments, more particles are influenced at higher velocities on Mars, which is especially visible in front of the tip. This difference is caused by the lower gravity of $g = 3.69\,\mathrm{m/s^2}$, as it decreases bulk density with a lower coordination number of the package, which again lead to decreased overburden pressure and thus lower shear strength. The different behaviour at the Mole back cap can also be explained by this effect: Due to lower gravity the particles on top of the Mole experience lower accelerations due to gravity and overburden pressure and thus show lower velocities while closing the cavity towards the Mole. The maximum penetration depth on Mars in 1 m of depth is about 2.8 mm per stroke cycle given the HP^{3}reference simulant. Further results and detailed analysis of the mechanisms stroke cycle can be found in [6, 9, 3, 11].

6 CONCLUSIONS

In this article a method to model the complex behaviour of the HP^{3}Mole using coupled mixed domain models has been proposed. As a special focus methods to improve the performance of the computationally expensive DEM simulations of the soil have been

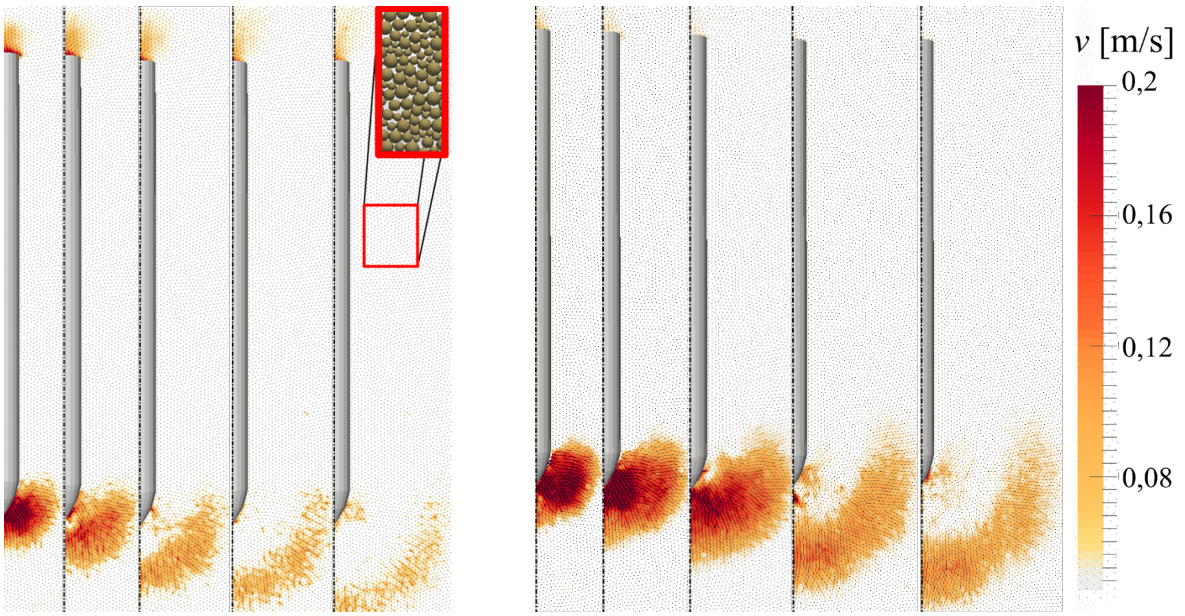

Figure 8: Wave propagation through the soil 2,3,4,6 and 7 ms after the first stroke of the HP^{3}Mole's hammering cycle on Earth, cf. [3], [9] and [6]

given, while maintaining sufficiently high accuracy for critical applications in planetary exploration missions. These improvements were mainly implemented in the mesoscopic layer of the modeling, e.g. by introduction of dynamic boundaries. Furthermore the co-simulation approach using the DLR-SR framework DEMETRIA, focusing on automated simulation cycles has been introduced. Therefore special issues in terms of communication have been discussed. Some of the applications that arose during the development of the HP^{3}Mole's flight hardware have been shown and range from in depth analysis of the stroke cycle and soil wave propagation to optimization and applications in planetary science.
A major limitation of the models is the needed runtime of 1 up to 3 days per stroke cycle and depth. Thus the results and knowledge gathered are used to develop simpler and faster models to allow for mechanism optimization and short term reactions on possible investigations required during the mission after landing on Mars in 2018.
In future work the model will be applied to further research on performance optimization of hammering mechanisms for future missions. The models and their simpler derivatives will be used to analyze the mechanical soil properties of martian regolith in-situ after landing in Elysium Planitia.

REFERENCES

[1] Barnerdt, W.B. et al.: INSIGHT: A discovery mission to explore the interior of Mars. In: 44th Lunar and Planetary Science Conference, Texas, USA, 2013.

[2] Spohn, T. et al.: INSIGHT: Measuring the martian heat flow using the Heatflow and Physical Properties Package (HP3). In: 43th LPSC, Texas, USA, 2012.

[3] Lichtenheldt, R.: Lokomotorische Interaktion Planetarer Explorationssysteme mit weichen Sandböden - Modellbildung und Simulation, ISBN 978-3-8439-2704-8, Munich, 2016

[4] Fleissner, F.: Documentation & Template-Files for "Pasimodo". Inpartik & University of Stuttgart, 2012

[5] Lichtenheldt, R. et al.: Planetary Rover Locomotion on soft granular Soils - Efficient Adaption of the rolling Behaviour of nonspherical Grains for Discrete Element Simulations, Particle-Based Methods III, pp.807-818, ISBN 978-84-941531-8-1, Stuttgart, 2013

[6] Lichtenheldt, R. et al.: Hammering beneath the surface of Mars - Modeling and simulation of the impact-driven locomotion of the HP3-Mole by coupling enhanced multi-body dynamics and discrete element method, 58th IWK, URN (Paper): urn:nbn:de:gbv:ilm1-2014iwk-155:2, Ilmenau, 2014

[7] Seweryn, K. et al.: Low velocity penetrators (LVP) driven by hammering action - definition of the principle of operation based on numerical models and experimental tests. Acta Astronautica, 99, pp.303-317, 2014

[8] Lichtenheldt, R.: A novel systematic method to estimate the contact parameters of particles in discrete element simulations of soil, Particle-based Methods IV, pp 430-441, ISBN:978-84-944244-7-2, Barcelona, 2015

[9] Lichtenheldt, R.: Hammering beneath the Surface of Mars - Analyse des Schlagzyklus und der äußeren Form des HP3-Mole mit Hilfe der Diskrete Elemente Methode, IFToMM D-A-CH, Universität Duisburg-Essen, ISBN 978-3-940402-03-5, 2015

[10] Obermayr, M.: Prediction of Load Data for Construction Equipment using the Discrete Element Method. PhD Thesis, University of Stuttgart, 2013.

[11] Lichtenheldt, R. et al.: Soil Modeling for InSight's HP3-Mole: From Highly Accurate Particle-Based Towards Fast Empirical Models, ASCE Earth and Space, Orlando, 2016

VII International Conference on Computational Methods for Coupled Problems in Science and Engineering
COUPLED PROBLEMS 2017
M. Papadrakakis, E. Oñate and B. Schrefler (Eds)

LARGE-SCALE SIMULATIONS OF VISCOELASTIC DEFORMABLE MULTI-BODY SYSTEMS USING QUADRUPLE DISCRETE ELEMENT METHOD ON SUPERCOMPUTERS

S. TSUZUKI*, D. NISHIURA*, H. SAKAGUCHI*

* Japan Agency for Marine-Earth Science and Technology (JAMSTEC)
3173-25, Showa-machi, Kanazawa-ku, Yokohama-city, Kanagawa, 236-0001, Japan
E-mail : tsuzukis@jamstec.go.jp
Web page : http://str-prtc-gpu-comp.wixsite.com/pm-info-st-personal

Key words: Particle-based Methods, Multi-body Problems, Contact Problems, Viscoelastic Materials, Parallel Computing.

Abstract. Contact problems among viscoelastic materials in the multibody system is one of the challenging topics in science and many engineering applications. We have developed an effective simulation method of combining QDEM (Quadruple Discrete Element Method) for the deformation analysis of structures with the DEM for the collisions among structures. However, it is still difficult to reproduce surface topography of structures because particles only set on four nodes of tetrahedrons in our current method. In this paper, QDEMSM (QDEM with Surface Modeling) is newly developed. Point-polygon collisions and line-line collisions are effectively coupled with QDEM. Our improved method was validated by several simulation results; domino simulations using the 40 pieces of shogi (= Japanese chess) were successfully carried out. It was also found the friction forces acted on the surface critically effected on the propagation speeds of contact forces. In parallel computing, by applying the space-filling curve to decomposition of the computational domain, we make it possible to contain the same number of nodes in each decomposed domain. Our parallel simulation code achieves a good weak scalability on the TSUBAME2.5 supercomputer.

1 INTRODUCTION

It is crucial there to realize large-scale viscoelastic multi-body simulations in many fields (e.g. civil engineering, geoscience, and chemical engineering). Particle-based methods are promising approaches, however, it is still challenging because of the difficulties on several numerical problems; combining the deformation analysis of each structure with the contact analysis among contacting structures is not easy; surface topography of structures should be represented with a sufficiently accurate because friction forces acted on the surfaces are dominant in contact problems; three-dimensional simulations are essential in practical problems; parallel computing on memory-distributed systems is indispensable to realize realistic simulations. For all these reasons, there are few studies on large-scale 3-dimensional viscoelastic multi-body simulations in previous studies.

In this study, we present an effective method of large-scale 3-dimensional viscoelastic multi-body simulations using Quadruple Discrete Element Method (QDEM) [1] on supercomputers. QDEM, which is an explicit particle-based method for viscoelastic deformable materials originally designed to be compatible with the memory-distributed

system, enables easy implementation on supercomputers. The concept of QDEM is straightforward compared with finite-element approaches because QDEM requires only an inter-particle relationship among four particles which consist a quadruple discrete element (for details, see reference [1]). Despite its simplicity, it is known that QDEM has the same numerical accuracy as explicit FEM using primary element [2].

In our previous work, we had developed a simulation method of combining QDEM for deformation analysis of structures with the DEM for collisions among structures for large-scale viscoelastic multi-body problems, which brought a certain level of successful results [3]. However, in our current method, it is difficult to reproduce surface topography of structures because particles only set on four nodes of tetrahedrons. Introduction of an envelope curve by particle-overlapping technique is one approach, but is not compatible with QDEM algorithm. On the contrary, it is reasonable to introduce the collision among triangles (=polygons) of tetrahedrons. However, methodology of it has not been established.

For this purpose, an effective method of QDEMSM (QDEM with Surface Modeling) is newly developed in this paper. We also demonstrate several simulations for practical viscoelastic multi-body problems.

2 A BRIEF OVERVIEW OF QDEM

QDEM is based on a particle concept; a tetrahedron is defined as a representation of the interacting part of four particles (=quadruple discrete element). An inter-particle relationship among neighboring four particles is derived from two rheology models of isotropic elastic solid and viscos fluid. A schematic-view of QDEM and its mathematical formulas are shown at a glance in **Figure.1**. Note that particle motions are updated by the explicit Verlet time integration scheme [4] in this paper. For details, see reference [1, 2].

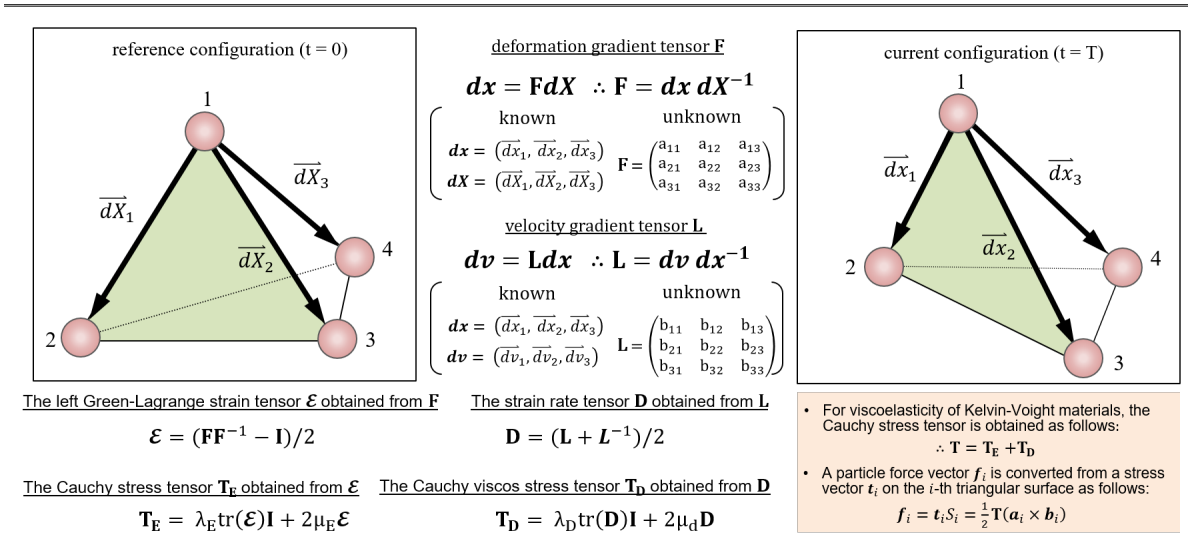

Figure 1 : A schematic-view of QDEM and mathematical formulas in QDEM algorithm.

3 SURFACE MODELING WITH QDEM

There exist the six kinds of possible collisions among the triangles of tetrahedrons. It is idealistic to compute all the six types of collisions. However, it is difficult because of both the high computational costs and lack of methodology. By taking account of real physical

phenomena, (c) and (d) are considered to be dominant in all the possible collisions. Therefore, in this paper, we experimentally introduce calculations of (c) and (d) as the first step toward realistic viscoelastic multi-body simulations.

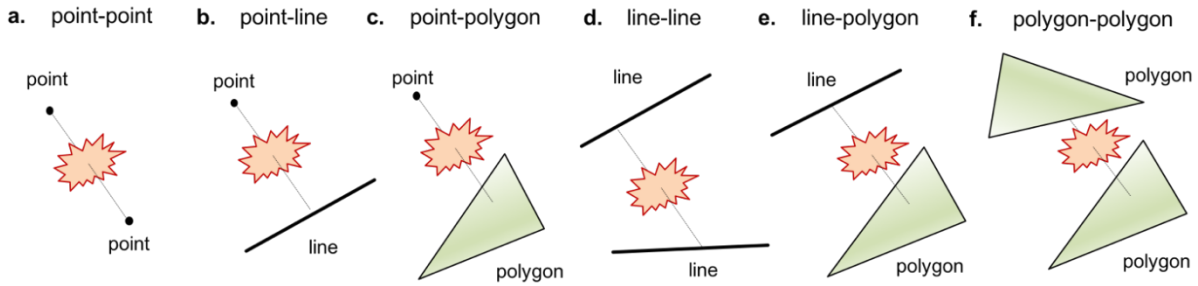

Figure 2 : Six kinds of possible collisions among the triangles(=polygons) of tetrahedrons.

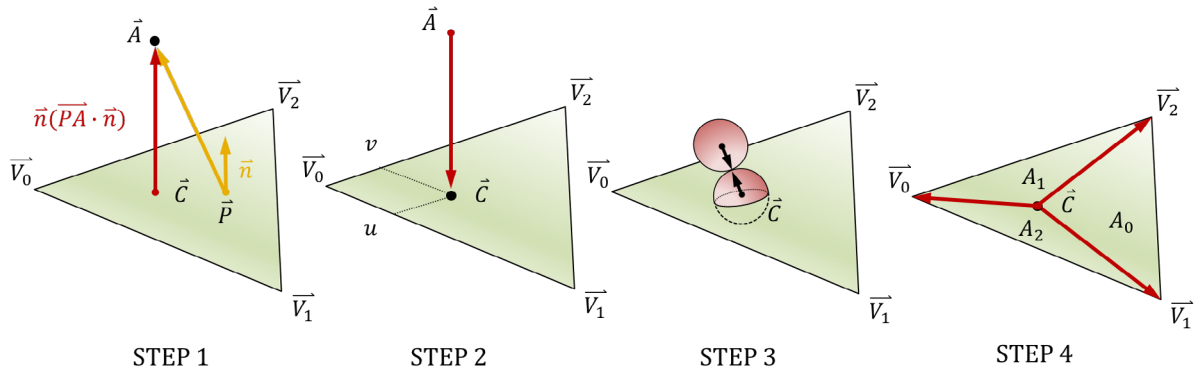

Figure 3 : A four-step procedure to compute point-polygon collisions.

3.1 Point-Polygon Collision

Figure.3 shows a four-step procedure for point-polygon collisions among the triangular surfaces of different tetrahedrons.

First, we calculate the closest point $\vec{C}$ on a triangle from a point $\vec{A}$ as follows:

$$\vec{C} = \vec{A} - \vec{n}(\overrightarrow{PA}\cdot\vec{n}) \tag{1}$$

Here, $\vec{P}$ is an arbitrary point on the triangle, $\vec{n}$ is the normal vector of the triangle, $\vec{A}$ is the center position of a particle, respectively. The geometric relationship is depicted in STEP1.

Second, we judge whether the point $\vec{C}$ is inside the triangle. The point $\vec{C}$ can be represented in two ways as follows:

$$\vec{C} = \overrightarrow{V_0} + u * \overrightarrow{V_0V_1} + v * \overrightarrow{V_0V_2} \tag{2}$$

$$\vec{C} = \vec{A} + t * \overrightarrow{AC} \tag{3}$$

Here, t, u, and v is scalar parameters as shown in STEP2. A 3×3 system of simultaneous equations is obtained by (2) and (3) as follows:

$$u * \overrightarrow{V_0V_1} + v * \overrightarrow{V_0V_2} - t * \overrightarrow{AC} = \vec{A} - \overrightarrow{V_0} \quad (4)$$

The solution of (4) is obtained by using Cramer's Rule. In case of (u, v) fulfills $u \geq 0,\ v \geq 0, u + v \leq 1$, the point $\vec{C}$ is on the triangle. In this case, we assume a virtual particle set on the point $\vec{C}$ and calculate a contact force between two particles by DEM as depicted in STEP3.

Finally, the contact force $\vec{F}$ is divided into each point of the triangle as shown in STEP4. Here, $A_0, A_1,$ and A_2 are the area of $\overrightarrow{CV_1V_2}$, the area of $\overrightarrow{CV_2V_0}$, and the area $\overrightarrow{CV_0V_1}$ respectively. For the simplicity, the divided forces $\overrightarrow{F_0}$, $\overrightarrow{F_1}$, and $\overrightarrow{F_2}$ are simply calculated as follows in this paper.

$$\overrightarrow{F_0} = \frac{A_0}{A}\vec{F}, \overrightarrow{F_1} = \frac{A_1}{A}\vec{F}, \overrightarrow{F_2} = \frac{A_2}{A}\vec{F} \quad (A = A_0 + A_1 + A_2) \quad (5)$$

3.2 Line-Line Collision

The closest points between two lines are obtained by the four-step procedure as shown in **Figure.4**. In case that $d_1 \geq 0\ and\ d_1 \leq \left|\overrightarrow{AB}\right|\ and\ d_2 \geq 0\ and\ d_2 \leq \left|\overrightarrow{CD}\right|$, two lines intersect each other. Thereafter, we compare $\left|\overrightarrow{p_1p_2}\right|$ with the interaction range of DEM calculations. In case the collision is detected, virtual particles are set on the closest points of each line, then the contact forces are calculated by using DEM. For the simplicity, the contact force for normal direction is only considered in case of line-line collisions in this paper.

1. We have four geometric relationships between two lines.

$$\begin{cases} \overrightarrow{n_1} \cdot (\overrightarrow{p_2} - \overrightarrow{p_1}) = 0 & \cdots\cdots (1) \\ \overrightarrow{n_2} \cdot (\overrightarrow{p_2} - \overrightarrow{p_1}) = 0 & \cdots\cdots (2) \end{cases} \qquad \begin{cases} \overrightarrow{p_1} = A + d_1 * \overrightarrow{n_1} & \cdots\cdots (3) \\ \overrightarrow{p_2} = C + d_2 * \overrightarrow{n_2} & \cdots\cdots (4) \end{cases}$$

2. (5) and (6) are obtained by substituting "(4)-(3)" to (1) and (2) respectively.

$$\begin{cases} \overrightarrow{n_1} \cdot \overrightarrow{AC} + d_2 * (\overrightarrow{n_1} \cdot \overrightarrow{n_2}) - d_1 = 0 & \cdots\cdots\cdots\cdots (5) \\ \overrightarrow{n_2} \cdot \overrightarrow{AC} - d_1 * (\overrightarrow{n_1} \cdot \overrightarrow{n_2}) + d_2 = 0 & \cdots\cdots\cdots\cdots (6) \end{cases}$$

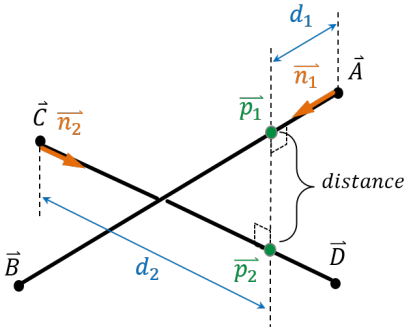

3. d_1, d_2 are obtained by solving the simultaneous linear system of (5) and (6).

$$d_1 = \frac{(\overrightarrow{n_1} \cdot \overrightarrow{AC} - (\overrightarrow{n_1} \cdot \overrightarrow{n_2}) * (\overrightarrow{n_2} \cdot \overrightarrow{AC}))}{(1 - (\overrightarrow{n_1} \cdot \overrightarrow{n_2}) * (\overrightarrow{n_1} \cdot \overrightarrow{n_2}))} \cdots\cdots\cdots\cdots (7) \qquad d_1 = \frac{((\overrightarrow{n_1} \cdot \overrightarrow{n_2}) * (\overrightarrow{n_1} \cdot \overrightarrow{AC}) - \overrightarrow{n_2} \cdot \overrightarrow{AC})}{(1 - (\overrightarrow{n_1} \cdot \overrightarrow{n_2}) * (\overrightarrow{n_1} \cdot \overrightarrow{n_2}))} \cdots\cdots\cdots\cdots (8)$$

4. $\overrightarrow{p_1}$, $\overrightarrow{p_2}$ are obtained by (3), (4), (7), and (8).

Figure 4 : A four-step procedure to compute the closest points between two lines.

4 IMPLEMENTATION

An effective implementation for the computation of QDEM with Surface Modeling on parallel environments is presented by taking account of the locality of QDEM algorithm; QDEM requires only an inter-particle relationship among neighboring four particles (quadruple discrete element) even though structures are represented by groups of particles.

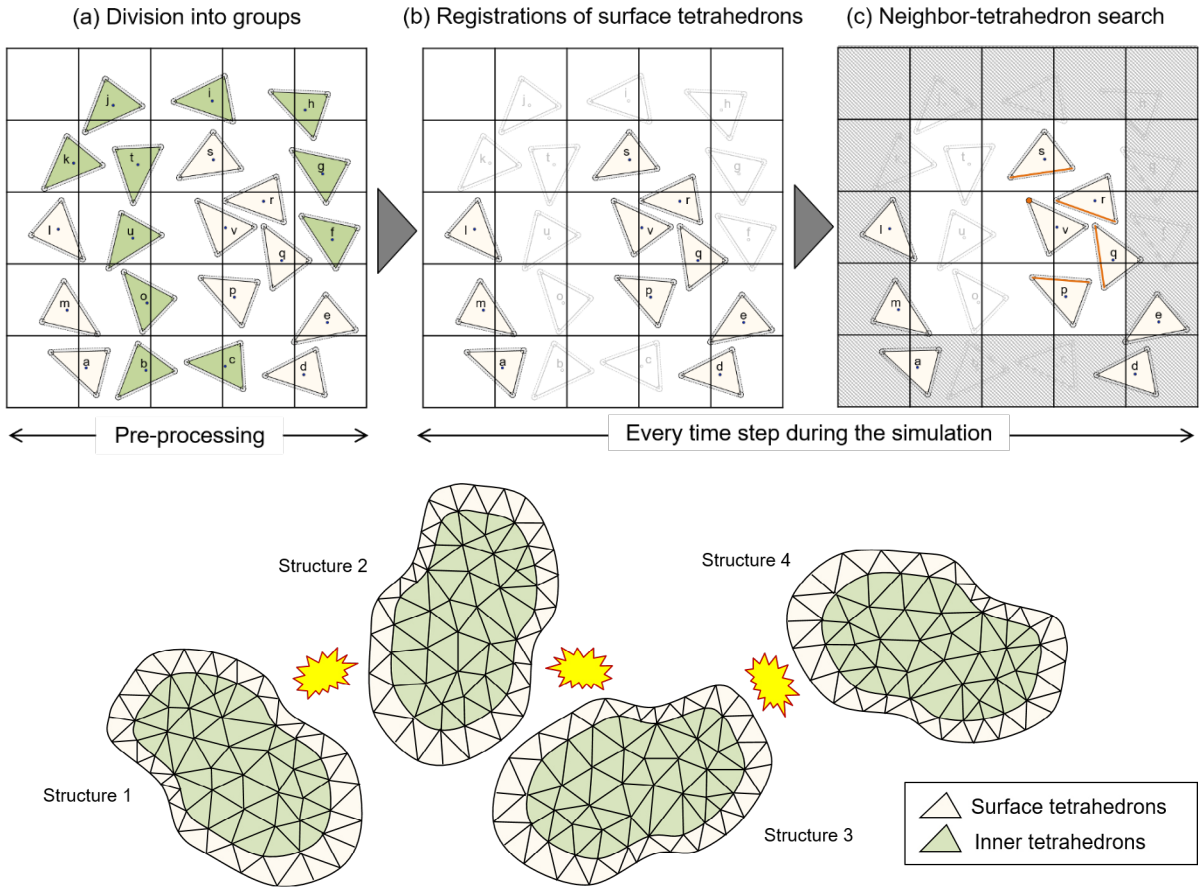

Figure 5 : An schematic view of effective neighbor tetrahedron search (upper) and an illustration of collisions among structures (lower).

4.1 Multithread Computing of QDEM

As well as accelerators, such as GPU or MIC, even scalar-type computers have multiple processing cores on a single chip. Therefore, fine-grain parallelization and multithread programming are required to obtain high performance. In multithread computing of QDEM, the dependent variables of a node (e.g. position, velocity) are defined for each particle. On the other hand, the dependent variables of a quadruple discrete element (e.g. the stress, the four-node connectivity) are defined for each tetrahedron. In the thread assignment for multi-cores, one thread computes one particle in case of point-polygon collision calculations, and likewise one thread computes one tetrahedron in case of line-line collision calculations.

4.2 Neighbor-Tetrahedron List

The (a) in **Figure.5** depicts an imaginary case that all the tetrahedrons (all the triangles in 2D case) are scattered in a computational domain. As with general particle-based simulations, it is inefficient to compute collisions among all the tetrahedrons. Neighbor-tetrahedron lists are used to reduce the computational cost from $O(\mathrm{N}^2)$ to $O(\mathrm{N})$ to find the tetrahedrons in the neighboring cells. A linked-list technique [5] is coupled with neighbor-tetrahedron lists; each

tetrahedron has a memory pointer referring to the next tetrahedron in the same cell. By using chain access of the linked-list, it becomes possible to drastically reduce the memory usage.

In realistic situations, some tetrahedrons are connected to form structures as depicted in the lower column in Figure.5. Even in such cases, the deformation analysis by QDEM is carried out separately in each tetrahedron. Therefore, it is possible to reduce the amount of collision calculations by registering only tetrahedrons which consist the surface of structures. In pre-processing, we divide tetrahedrons into two groups: surface tetrahedrons and inner tetrahedrons. In every time step during the simulation, we register only surface tetrahedrons to the cells as in (b) in Figure.5. Thereafter, we compute point-polygon collisions as shown in (c), followed by line-line collisions.

A constraint is imposed on L_{cell}, the length of a cell of the neighbor-tetrahedron lists, making it larger than the maximum interaction-range of collisions among tetrahedrons; namely:

$$L_{cell} \geq max_{i=0,1,2\ldots N_{tet}}\{D^i_{max}\} + D_{DEM}, \tag{6}$$

Here, N_{tet} is the number of tetrahedrons in the whole computational domain, D_{DEM} is a delimeter of a particle set on the surface. D^i_{max} is the delimeter of a sphere which is large enough to be able to contain i-th tetrahedron.

There exist several ways to determine D^i_{max}; applying the circurmspheres of tetrahedrons is one approach, but it is often too large. In case that tetrahedrons are registered to the cells by their center positions, D^i_{max} can be obtained by:

$$D^i_{max} = 2.0 * \max(d^i_1, d^i_2, d^i_3, d^i_4) \tag{7}$$

Here, d^i_j is a distance between j^{th} vertex and center of i^{th} tetrahedron (j=1,2,3,4,).

4.3 Parallel Computing on the Memory-distributed System

An entire computational domain is decomposed into several sub-domains and the processing unit is assigned to each compute tetrahedrons in the sub-domain. Because of a layer that has the same size as L_{cell} must be copied to the neighboring sub-domains, we pack both the nodes and the tetrahedrons in halo area to a buffer and exchange them by MPI communications [6].

In this paper, we apply the space-filling curve to decomposition of the computational domain because the locality of space-filling curves is compatible with the QDEM algorithm. The computational load of each decomposed domain is dynamically balanced by domain re-decomposition techniques. For details of dynamic domain decomposition using space-filling curves, see reference [7]. Note that our parallel simulation code achieves a weak scalability with 5120 cores on the TSUBAME2.5 supercomputer [8].

4.4 Numerical Experiments

Figure.6 shows a breakdown of the time required for a static analysis including 27 cubes with 33,507 particles and 165,888 tetrahedrons. Each cube has 1,241 nodes (386 for surface nodes) and 6,144 tetrahedrons (2,028 for surface tetrahedrons). The benchmark test was carried out using two sockets of the Intel CPU Xeon X5670 (Uestmere-EP) 2.93 GHz 6-core.

For the sake of simplicity, point-polygon collisions were only introduced. We measured three computational cases: (A) all the tetrahedrons, (B) only surface tetrahedrons, (C) skipping the calculation of non-surface triangles on surface tetrahedrons. The result clearly shows that our method makes it possible to drastically reduce the computational costs.

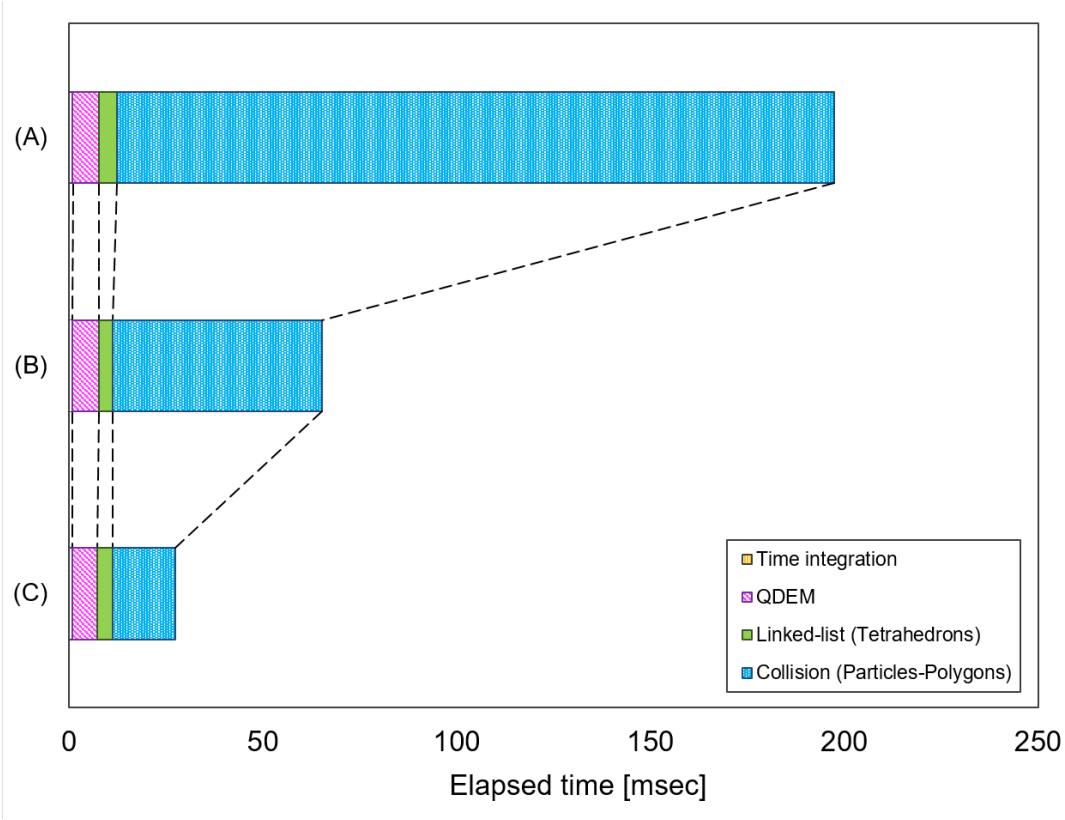

Figure 6 : Breakdown of the time required for a static analysis of 165,888 tetrahedrons.

5 APPLICATION TO A PRACTICAL PROBLEM

We demonstrate domino simulations using shogi pieces (= the pieces of Japanese chess). Unlike the ordinary domino pieces, the shapes of shogi pieces are not rectangular. A single player has 8 kinds of pieces (one king, one rook, one bishop, two gold generals, two silver generals, two knights, two lances, and nine pawns); we have 20 pieces in total for each player. The shapes of these 20 pieces are same, but the scale is different each other. Input physical parameters of our shogi simulations are listed in **Table.1**.

Figure.7 shows snapshots of a shogi simulation of two rooks in case of different kinetic friction coefficients: $\mu = 0.1$ (right), $\mu = 0.5$ (center), and the overlap view of both cases (left). It is cleared that difference of friction forces delayed the propagation speeds of contact forces. **Figure.8** shows snapshots of a shogi simulation of one king and two pawns. It was found that our method could reproduce the effect of eccentric collisions in real problem. **Figure.9** shows snapshots of a shogi simulation of all the forty shogi pieces. A snapshot of stress analysis is shown in the lower-left in Figure.9. **Figure.10.** shows a snapshot of shogi simulations of all the forty pieces in different kinetic friction coefficients: $\mu = 0.1$ (red), $\mu = 0.5$ (yellow). As shown in the two-shogi simulation in Figure.7, it was found that the difference of friction forces delayed the propagation speeds of contact forces.

Table 1 : A numerical condition for domino simulations using shogi pieces.

Initial parameters	Values
Radius of particle [m]	0.04
Density [kg/m^3]	700
Poisson's ratio	0.4
Young's modulus	5.0e+8
Viscosity coefficient	2.5e+5
Kinetic friction coefficient (piece)	0.1
Kinetic friction coefficient (wall)	0.5
Gravity [m/s^2]	9.80665
Number of points / (piece)	797
Number of tetrahedrons / (piece)	2,566
Time step size [s]	6.4e-6

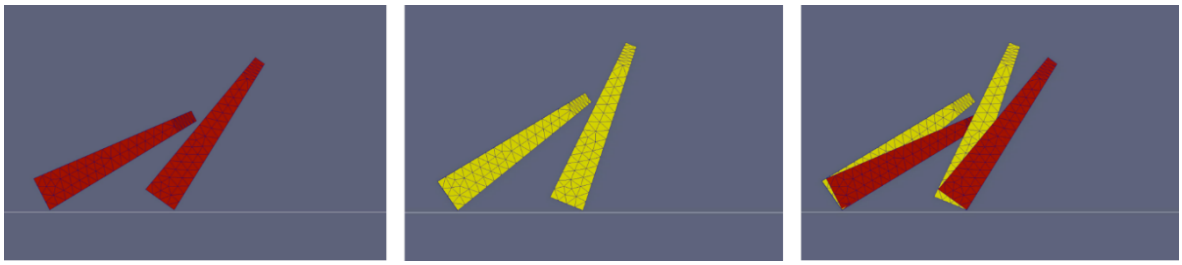

Figure 7 : A domino simulation of two rooks in case of different kinetic friction coefficient.

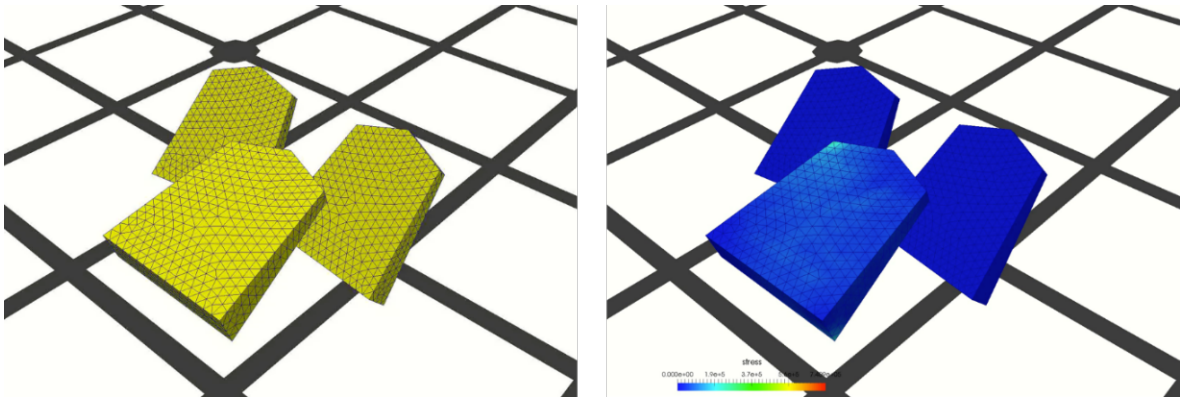

Figure 8 : A domino simulation of one king and two pawns.

6 CONCLUSIONS

An implementation method for effective computations of QDEMSM (QDEM with Surface Modeling) on parallel computing environments is presented.

Our proposal method was validated by several simulation results; domino simulations using the 40 pieces of shogi (= Japanese chess) were successfully carried out. It was also found the friction forces acted on the surface critically effected on the propagation speeds of contact forces.

In parallel computing, by applying the space-filling curve to decomposition of the computational domain, we make it possible to contain the same number of nodes in each decomposed domain. Our parallel simulation code achieves a good weak scalability on the TSUBAME2.5 supercomputer.

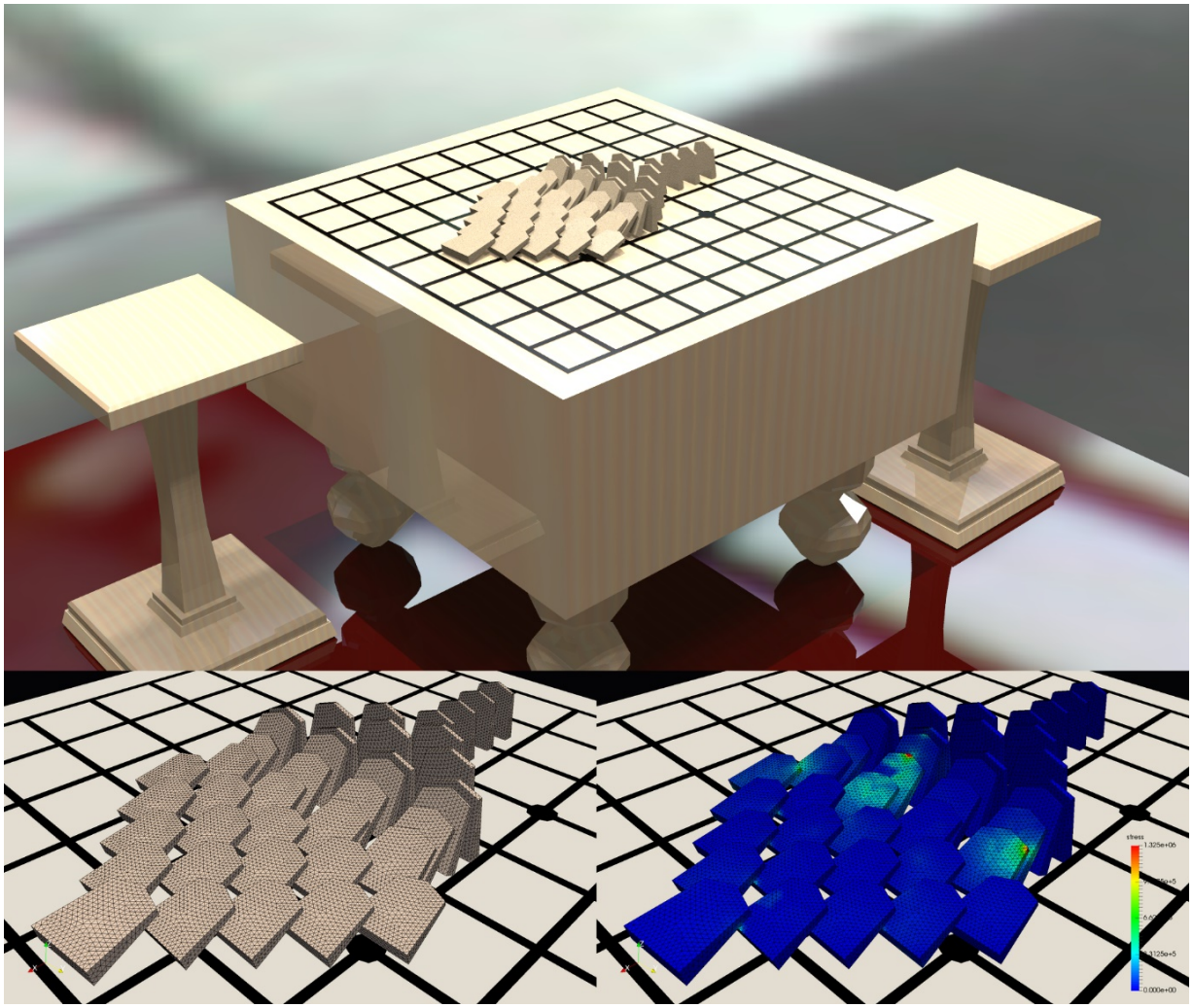

Figure 9 : A domino simulation of all the forty shogi pieces.

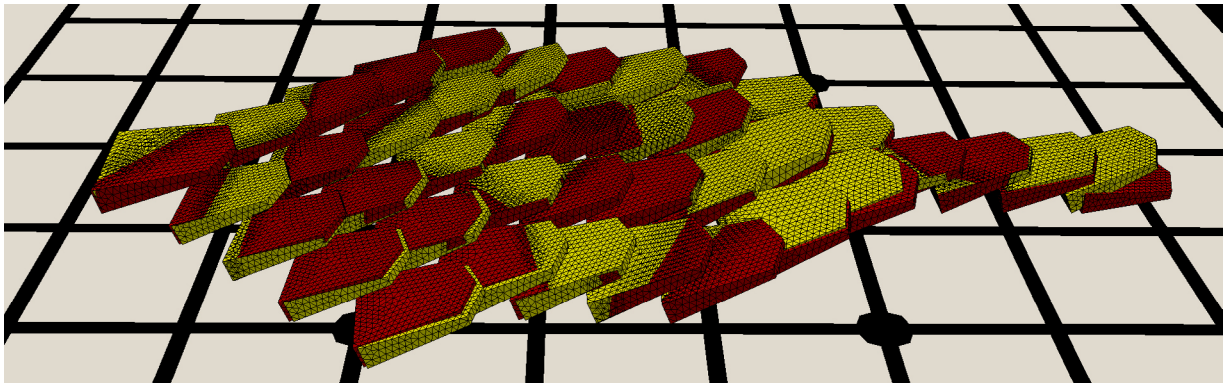

Figure 10 : A snapshot of shogi simulations of all the forty pieces in case of different kinetic friction coefficients: μ = 0.1 (red), μ = 0.5 (yellow).

Acknowledgements

This research was supported by ”Joint Usage/Research Center for Interdisciplinary Large-scale Information Infrastructures (JHPCN)” and ”Grant-in-Aid for JSPS Fellows” in Japan.

REFERENCES

[1] Sakaguchi, H., New computational scheme of discrete element approach for the solid earth multi-materials simulation using three-dimensional four particle interaction. *FRONTIER RESEARCH EARTH EVOLUTION, Vol. II,* (2003).

[2] Nishiura, D., Sakaguchi, H., and Aikawa, A., QDEM: A simple explicit method for deformation analysis of linear viscoelastic materials. *Journal of Computational Physics* (submitting).

[3] Nishiura, D., Sakaguchi, H., Sakai, H., and Aikawa, A., Discrete element modeling of ballasted railway track. *The 3rd International Workshops on Advances in Computational Mechanics* (2015).

[4] Verlet, L., Computer "Experiments" on Classical Fluids. I. Thermodynamical Properties of Lennard-Jones Molecules, *Phys. Rev. 159: 98* (1967)

[5] G. S. Grest, B. D¨unweg, and K. Kremer, Vectorized link cell Fortran code for molecular dynamics simulations for a large number of particles, *Computer Physics Communications,* vol. 55, pp. 269–285 (1989).

[6] MPI Forum, Message Passing Interface (MPI) Forum Home Page, http://www.mpi-forum.org (2009)

[7] S. Tsuzuki, T.Aoki, “Effective Dynamic Load Balance using Space-Filling Curves for Large-scale SPH Simulations on GPU-rich Supercomputers”, *Proceedings of the 6th Workshop on Latest Advances in Scalable Algorithms for Large-Scale Systems. ACM, New York, NY, USA* (2016)

[8] TSUBAME 2.5 hardware software specifications. [Online]. Available: http://www.gsic.titech.ac.jp/sites/default/files/spec25e1.pdf

VII International Conference on Computational Methods for Coupled Problems in Science and Engineering
COUPLED PROBLEMS 2017
M. Papadrakakis, E. Oñate and B. Schrefler (Eds)

PREDICTION OF WOOD PELLETS COMBUSTION BY THE EXTENDED DISCRETE ELEMENT METHOD (XDEM)

Bernhard Peters*, **Mohammad Mohseni***

∗ Université du Luxembourg
6, rue Coudenhove-Kalergi
L-1359 Luxembourg, Luxembourg
e-mail: bernhard.peters@uni.lu, web page: http://www.xdem.de

Key words: Euler-Lagrange-interface, Computational Fuzid Dynamics (CFD), Discrete Elelment Method (DEM), combustion, biomass

Abstract. The objective of this contribution is to predict the combustion of wood pellets in an domestic oven by the Extended Discrete Element Method (XDEM). It poses insofar a challenge as various physical processes such as combustion in conjunction with dynamic motion of pellets all emerged in a gas phase. In order to allow describing the complex interaction between the above-mentioned processes, a coupled Euler-Lagrange approach was chosen. The pellets are treated as discrete cylindrical elements of which the dynamics are tracked with the classical Discrete-Element-Method. It is extended by the thermodynamic state for each pellet to predict both temperature and species distribution inside a pellet during combustion, and thus, allows tracking the reaction progress. Thermal conversion of pellets includes heating, drying, pyrolysis and char combustion. Feeding of particles is taken into account by batches as applied under industry-like operation. The flow of combustion air with its temperature and species distribution is predicted by classical CFD approaches. The pellets interact with the surrounding gas phase via heat, mass and momentum transfer which is taken into account by relevant empirical correlations.

Pellets form a packed bed at the bottom of an cylindrical enclosure through which combustion air is provided. While streaming through the void space between the pellets, intensive heat and mass transfer takes place. Combustion air provide necessary oxygen for combustion while hot pellets transfer heat to the air and thus heating it up. Pellets shrink according to the reaction progress and thus initiate motion of the packed bed. It is also amplified by the batch-wise feeding of pellets matching the given mass flow e.g. combustion rate that introduces significant temporal variations of the entire process. The following figure depicts both surface temperature of pellets and gas velocity.

1 INTRODUCTION

Contrary to continuum models an alternative approach considers the solid phase as discrete, while the flow of liquids or gases is treated as a continuum phase in the void space between the particles, and therefore, is labelled the Combined Continuum and Discrete Model (CCDM) [1, 2, 3, 4]. Due to a discrete description of the solid phase, constitutive relations are omitted, and therefore, leads to a better understanding of the fundamentals. This was also concluded by Zhu et al. [5] and Zhu et al. [6] during a review on particulate flows modelled with the CCDM approach. Based on this approach Sheng et al. [7] investigated into the micro-scale heat transfer of packed beds and micro-fibrous entrapped catalysts and concluded that the thermal resistance of the contact points account for more than 90 % of the total resistance. Similarly, Kon et al. [8] modelled the liquid flow in the lower part of a blast furnace by the MPS method. CCDM has seen a mayor development in last two decades and describes motion of the solid phase by the Discrete Element Method (DEM) on an individual particle scale and the remaining phases are treated by the Navier-Stokes equations.

However, current CCDM approaches should be extended to a truly multi-phase flow behaviour as opposed to the Volume-of-Fluid method and the multi-phase mixture model [9]. Furthermore, particle shapes other than spherical geometries have to be taken into account to meet engineering needs according to Zhu et al. [5] and Zhu et al. [6]. This efforts should ideally be complemented by poly-disperse particle systems as employed by Peters and Dziugys [10]. All these efforts should contribute to a general link between continuum and discrete approaches so that results are quantified for process modelling.

2 NUMERICAL TECHNIQUE

A novel technique referred to as Extended Discrete Element Method (XDEM) [11] has emerged only recently that offers a significant advancement for multi-physics applications. It is based on a coupled discrete and continuous i.e. Lagrange-Euler simulation concept. XDEM treats the solid phase representing the particles and the fluid phase or a structure as two distinguished entities that are coupled through heat, mass and momentum transfer. An outstanding feature of the numerical concept is that each particle in addition to its position and orientation in time and space is described by its thermodynamic state e.g. temperature and reaction progress. The thermodynamic state is described by one-dimensional and transient differential conservation equations for mass, energy and momentum for each individual particle and thus, characterizes the overall behaviour of the reactor as the sum of all particle processes. Predicted results for all individual particles allow a detailed analysis of the reaction process. Through predicting position and orientation of all particles their arrangement in space is known that determines the 3-dimensional distribution of void space between the particles. This essentially represents a porous structure through which the fluid e.g. liquid or gas streams. The fluid is in contact with the surface of the particles and determines heat and mass exchange between

the particles surface and the fluid i.e. temperature and composition in the vicinity of the particle. In order to predict flow through the interstitial space a classical CFD approach is preferred for which the software framework of OpenFoam is employed. Its library offers a large selection of solves for different applications and allows as an open-source software a tailored development of solvers suiting the needs of the above-mentioned applications. Hence, the proposed methodology provides a high degree of resolution ranging from scales within a particle to the continuum phase as global dimensions and offers superior features as compared to traditional and pure continuum mechanics approaches. The latter does not include detailed information on a particulate scale that has to be compensated for by empirical correlations such as distribution of void space in a packed or moving bed. For a more detailed description the reader is referred to Peters et al. [12, 13, 14].

3 RESULT AND DISCUSSION

Fig.1 illustrates the mass fraction of volatile matter during conversion of wood particles in the stove. At the beginning of simulation due to solely drying processes, only water vapour is produced and transferred to the gas phase. This procedure continues until the total amount of water is evaporated which takes around 40 s. Afterwards the thermal devolatilisation of wood commences and gas volatiles of CO_2, CO, CH_4, H_2O and H_2 are delivered and transferred to the gas phase. This process lasts until 120 s. In this moment the pyrolysis is terminated and the gasification as well as combustion processes are started. The gas compositions released by the wood are mixed with the oxygen and combusted above the bed in the chamber. These exothermic reactions generate required energy at the end of pyrolysis leading to char gasification. In addition, the oxygen can go through the pores of particles leading to char combustion at high temperature. However, due to mass transfer of the volatiles and lack of CO_2 and H_2O at the end of pyrolysis, the gasification occurs due to reaction with released CO_2 by char combustion. Since during pyrolysis the produced volatiles prevent the oxygen to enter the particle, the char combustion takes place after pyrolysis. Furthermore, it is shown in fig.2 the behaviour of solid materials during conversion process. At the beginning, wood appears as a sole solid material while drying is taking place. When the pyrolysis commences, the wood is depleted and it is converted partly to the solid char. This procedure continues until around 120 s where the wood is totally consumed and the produced char matter start to be gasified and combusted. Also fig.3 represents the behaviour of liquids during conversion of wood particles in the oven. While the water content of particles are vaporized during drying, and subsequently with onset of pyrolysis, tar is formed by wood devolatilisation. The produced tar is transferred to the gas phase and is combusted with oxygen above the bed leading to generation of carbon monoxide and hydrogen inside the oven. Additionally, fig.4 shows the temperature distribution of particles and gas phase at 250 s. It represents the centre slice inside the chamber showing the gas temperature and the cylinders are solid particles with their surface temperature. The high temperature of particles is due to char combustion leading to generate a vast amount of energy. In the gas phase, the high

temperature region above the bed represents the flame generated due to the combustion of volatiles. which is due to the reactions between the volatiles and injected oxygen through the secondary air inlet.

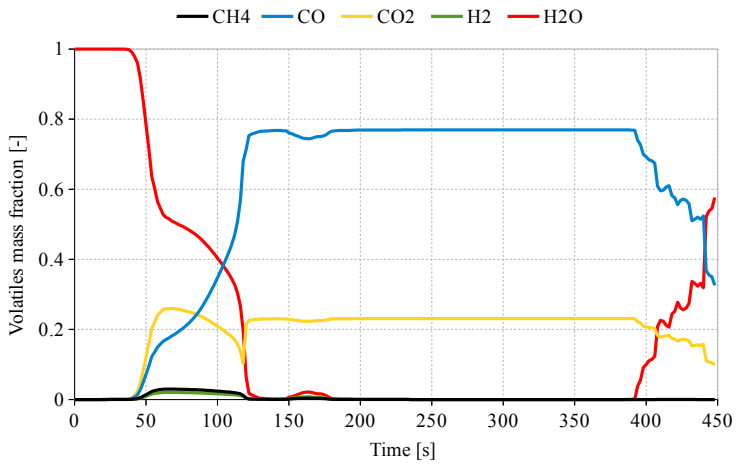

Figure 1: Mass fraction of released gas compositions of the bed

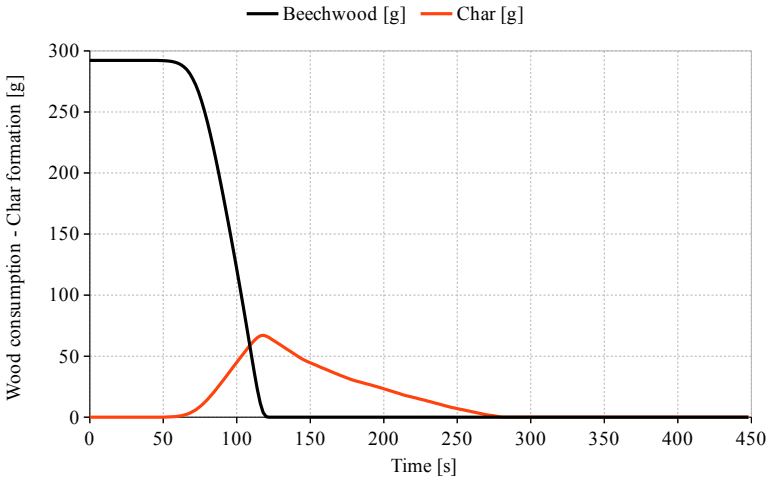

Figure 2: Wood consumption and char formation of the bed

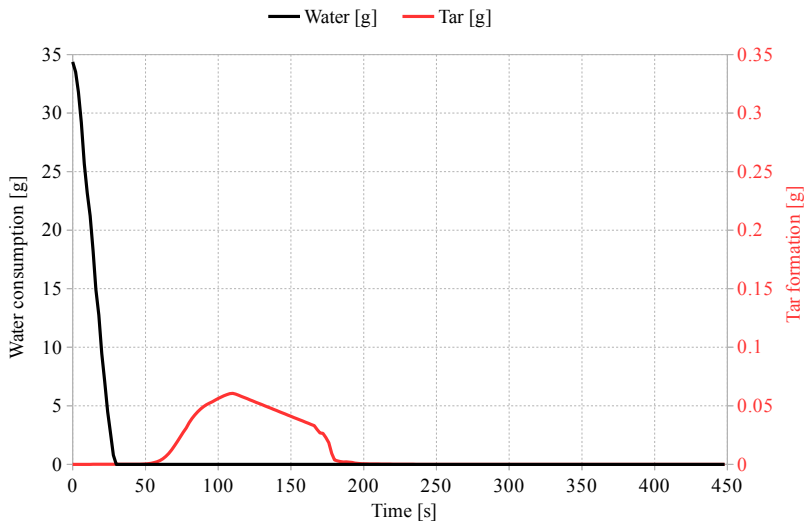

Figure 3: Water content consumption and tar formation of the bed

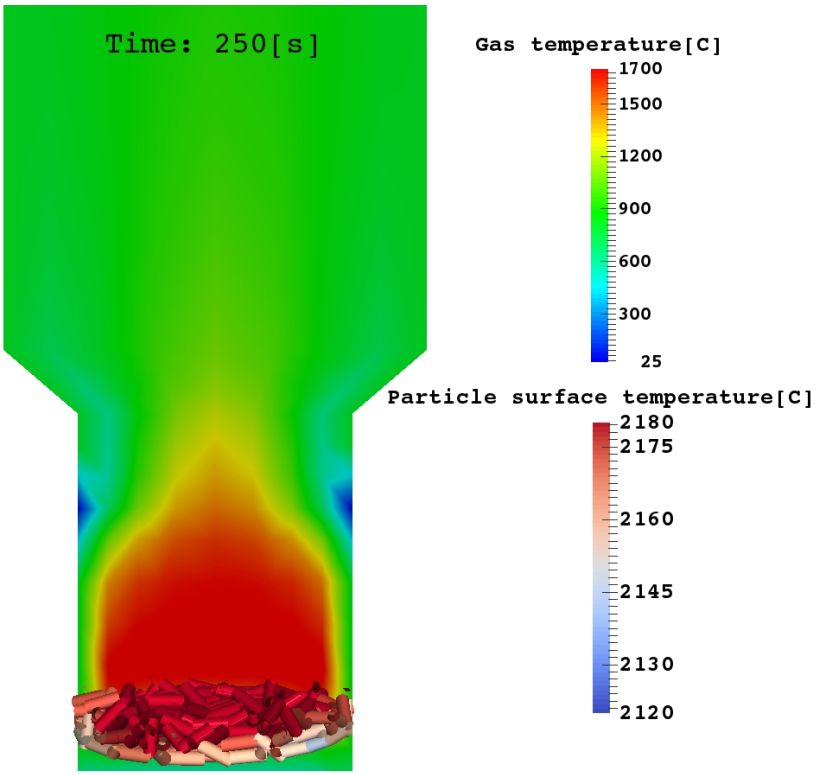

Figure 4: Temperature distribution of particles and gas flow at t=250s

4 CONCLUSIONS

The current contribution describes the Extended Discrete Element Method (XDEM) that is applied to thermal conversion of packed beds as often encountered in process engineering. The methodology relies on a Lagrange-Eulerian approach that couples effectively the particulate phase with a gas streaming through the void space of a packed bed reactor. The particle processes of the packed bed are described by the solution of one-dimensional and transient differential conservation equations for mass and energy. This set of equation is solved individually for each particle of the packed bed by fast and efficient algorithms. Thus, the thermodynamic state of each particle is determined taking into account space and time-dependent boundary conditions prevailing within the reactor such as heat and mass transfer between the particle surface and the surrounding gas phase. The latter is described by solving the conservation equations of classical Computational Fluid Dynamics (CFD). Hence, the numerical concept provide results over a large range of length scales ranging from inner particles processes to the global dimensions of the reactor. The presented approach deals with particle shapes of different sizes and takes heat and mass transfer between the particles surface and the surrounding gas phase into account that distinguishes the presented concept from current approaches. Thus, physics are described to a fine degree that allows an in-depth analysis of obtained results. It unveils the underlying physics of the processes involved and as a computer-aided tool contributes significantly to an improved design and operating conditions.

REFERENCES

[1] Y. Tsuji, T. Kawaguchi, and T. Tanaka. Discrete particle simulation of two-dimensional fluidized bed. *Powder Technol.*, 77(79), 1993.

[2] B. P. B. Hoomans, J. A. M. Kuipers, W. J. Briels, and W. P. M. Van Swaaij. Discrete particle simulation of bubble and slug formation in a two-dimensional gas-fluidized bed: A hard-sphere approach. *Chem. Eng. Sci.*, 51, 1996.

[3] B. H. Xu and A. B. Yu. Numerical simulation of the gas-solid flow in a fluidized bed by combining discrete particle method with computational fluidd dynamics. *Chemical Engineering Science*, 52:2785, 1997.

[4] B. H. Xu and A. B. Yu. Comments on the paper numerical simulation of the gas-solid flow in a fluidized bed by combining discrete particle method with computational fluid dynamics?-reply. *Chemical Engineering Science*, 53:2646–2647, 1998.

[5] H. P. Zhu, Z. Y. Zhou, R. Y. Yang, and A. B. Yu. Discrete particle simulation of particulate systems: Theoretical developments. *Chemical Engineering Science*, 62:3378 – 3396, 2007.

[6] H. P. Zhu, Z. Y. Zhou, R. Y. Yang, and A. B. Yu. Discrete particle simulation of particulate systems: A review of major applications and findings. *Chemical Engineering Science*, 63:5728–5770, 2008.

[7] M. Sheng, C. Gonzalez, W. Yantz, D. Cahela, H. Yang, D. Harris, and B. Tatarchuk. Micro-scale heat transfer comparison between packed beds and micro-fibrous entrained calalysts. *Engineering Applications of Computational Fluid Mechanics*, 7(4):471–485, 2013.

[8] T. Kon, S. Natsui, K. Shin, s. Ueda, R. Inoue, and T. Ariyama. Modelling of liquid flow in the lower part of blast furnace by mps method. In *The 5th International Conference STEELSIM 2013, Sptember 10 - 12, 2013*, 2013.

[9] C. Y. Wang. *Tramsport Phenomena in Porous Media*, chapter Modelling Multiphase Flow and Transport in Porous Media. Oxford Pergamon, 1998.

[10] B. Peters. A discrete approach to model thermal conversion of beds of solid fuels by the discrete particle method (DPM). In *ESCAPE21 - 21st European Symposium on Computer-Aided Process Engineering, Porto Carras Resort, Chalkidiki, Greece, May 29 - June 1, 2011*, 2011.

[11] B. Peters. *Extended discrete element method*, 2017 (accessed January 5, 2017).

[12] Amir Houshang Mahmoudi, Xavier Besseron, Florian Hoffmann, Miladin Markovic, and Bernhard Peters. Modeling of the biomass combustion on a forward acting grate using xdem. *Chemical Engineering Science*, 142:32–41, 2016.

[13] Amir Houshang Mahmoudi, Florian Hoffmann, Miladin Markovic, Bernhard Peters, and Gerrit Brem. Numerical modeling of self-heating and self-ignition in a packed-bed of biomass using xdem. *Combustion and Flame*, 163:358–369, 2016.

[14] B. Peters and F. Hoffmann. Iron ore reduction predicted by a discrete approach. *Chemical Engineering Journal*, 304:692–702, 2016.

VII International Conference on Computational Methods for Coupled Problems in Science and Engineering
COUPLED PROBLEMS 2017
M. Papadrakakis, E. Oñate and B. Schrefler (Eds)

A FINITE ELEMENT ANALYSIS OF THE INFLUENCES OF ULTRASONIC WELDING PARAMETERS ON TEMPERATURE RISE AT INTERFACES OF ALUMINUM STRANDS IN WIRE BONDING PROCESS

Shimaalsadat Mostafavi*, Bernd Markert†

*,† Institute of General Mechanics (IAM)
RWTH Aachen University
Templergraben 64, 52062 Aachen, Germany
e-mails: mostafavi@iam.rwth-aachen.de, markert@iam.rwth-aachen.de
web page: http://www.iam.rwth-aachen.de/

Key words: Ultrasonic Welding, Wire Bonding, Finite Element Analysis, Microsections

Abstract. Wire bonding is an unavoidable step in automotive industry. Multi-strand aluminum cables are used as battery cables integrated in a contact system in automobiles. Ultrasonic welding (USW) of metals is a joining technique as a combination of applying pressure and frictional vibrations within the range of ultrasonic frequencies. In automotive industry, ultrasonic welding is often used for wired connections.
The present work investigates the USW of a bundle of wires and focuses on the influence of some of the ultrasonic welding parameters, such as applied pressure on the wire bundle and vibrational amplitude of the sonotrode, on the temperature rise at the interfaces of each two strands in contact. Microsections obtained during experimental investigations show the softening of aluminum strands at some bonding parts within the wire bundle [1]. This phenomenon can be an interpretation of a local temperature rise close to the melting point of aluminum. The obvious difference in microsections from different weld samples was a motivation for this study to further investigate the thermomechanical aspects of the problem by use of finite element simulations. The represented model is a simplification of the real case and is intended to investigate the temperature rise between strands in connection during ultrasonic welding process.

1 INTRODUCTION

Wire bonding is an unavoidable production step in electronics as well as automotive industry. It is used for the connection of different electronic components and electrical centers in automobiles. Multi-strand aluminum cables are used as battery harnesses inside cars. As an alternative for crimping technology in wire bonding, ultrasonic welding

is applied, which is counted as a rapid manufacturing process in order to create solid state joints between same or different materials at low temperature and low energy consumption compared to other common welding processes, such as oxy-fuel welding and arc welding. In the process of ultrasonic welding extreme thermal loading of mating parts is not applied as in many common welding processes. A combined effect of frictional and plastic heat fluxes and heat dissipations is a source for temperature rise in USW bonding mechanism in general. Based on this combined mechanism and at a specific point, freshly exposed metal surfaces will achieve a metallurgical bonding due to close atomic proximity [2]. De Vries [3] and Elangovan et al. [4], analytically computed the heat generation by friction and plastic deformation separately rather than considering the dynamic thermomechanical process .An ultrasonic welding machine consists of diverse parts, such as a pneumatic cylinder, a piezoelectric converter, a booster and a sonotrode. During ultrasonic welding, pressure is applied on the mating parts via the sonotrode, which also vibrates on top of the parts with an ultrasonic frequency of 20kHz and higher in a subsequent step. The duration of the whole process varies from some milliseconds up to a few seconds depending on the material and the dimension of the mating parts. Despite of the simplicity of the USW process, choosing the right parameters for the process in order to obtain a good quality and long lasting bond is a comlicated task, which has been under investigations for decades. In this study microscopic observations are conducted to investigate the interfacial joining of thin aluminum strands in so-called multi-strand single core cables. Obseravtions of the microsections of different weld samples show softening of aluminum at some bonding parts, which can be an interpretation of a local temperature rise near the melting point of aluminum. This study focuses on the infleuence of two welding parameters, namely sonotrode pressure and amplitude of the sonotrode vibrations, on the temperature distribution between adjoining thin strands during ultrasonic welding by use of finite element (FE) simulations.

2 THERMOMECHANICAL MODEL

A coupled thermomechanical analysis of a FE model is performed in this study. One simplified configuration of the real case is presented, as the numerical simulation of the real model with the real number of strands is extremely elaborative regarding computational time and convergence of the results. The presented model consists of 6 strands as shown in Fig. 1 and is constructed using 3D stress solid elements inside Abaqus as a FE software. Machine parts, such as anvil, sonotrode and side holders, are modeled as rigid bodies and their thermal gradients are not taken into consideration in this study. The sonotrode is a part in every ultrasonic welding assembly, which compresses the parts to be welded mostly from the top and vibrates with frequencies in the ultrasonic range (equal to 20 kHz for the case of this study) in a following step. Three successive steps are defined for the FE model. The first step, which represents the applied pressure of the sonotrode is limited to 10 ms. The following step describes the vibrations of the sonotrode on the top strand and lasts 200 ms. These vibrations are applied through sonotrode along the strands length. A final

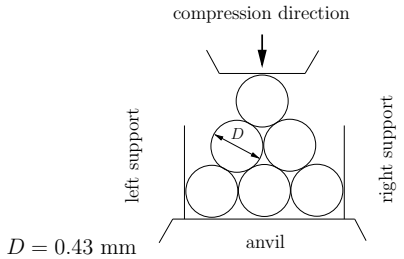

Figure 1: An arrangement of 6 strands

step of cooling down, in which the sonotrode moves upward follows the process and lasts 80 ms. The compression of the mating parts through sonotrode pressure is recalculated in displacement and is applied inside the models for three different pressures, in order to investigate the influence of sonotrode pressure on the temperature rise at the strand interfaces. A downward displacement of 0.46 mm corresponds to a pressure of 1.2 bar as obtained from experiments, which is then calculated for the mentioned number of strands in the FE model. This displacement is applied through a polynomial function on the sonotrode, which is in contact to the top surface of the uppermost strand. Experiments show that the temperature rise happens largely during the second step in USW, where the vibrations are applied on the parts. To investigate this statement, three different vibration amplitudes of the sonotrode are considered, which are implemented through a sinusoidal excitation of the sonotrode with a circular frequency of 125664 cycles/seconds. A summary of the parameter study is given in Table 1. The FE model contains 55554 linear hexahedral elements of type coupled temperature-displacement.

Table 1: Defined parameters for different models

Model	Pressure in bar	Vibration amplitude in μm
Reference model	1.2	6
Model 1	1.5	6
Model 2	1.0	6
Model 3	1.2	7
Model 4	1.2	8

2.1 Theoretical approach

In the mentioned process of ultrasonic wire bonding, heat is generated due to frictional sliding of the sonotrode on the top strand(s) combined with the large plastic deformations of soft thin aluminum strands. In the presented model the generated heat is distributed to the lower strands through thermal conductivity. Transmission of heat through convection and radiation is not considered in this study. If q_f is considered as the heat flux density

generated by frictional vibrations and q_c is the heat flux density due to conduction, then the heat flux densities going out the two sides of the surface in contact, q_1 and q_2 are given as [5]

$$q_1 = q_c - q_f, \quad q_2 = -q_c - q_f, \tag{1}$$

where q_f is calculated as

$$q_f = \eta \ \mu \ \tau \ \dot{s} \ . \tag{2}$$

Herein, η represents the fraction of the dissipated energy caused by friction which is converted to heat and is considered as 1.0 (100 %). The converted heat is distributed equally and instantaneously to the surfaces in contact. μ is the coefficient of friction, τ is the contact stress and $\dot{s}$ is the slip rate between the two surfaces. The contact stress is dependent on the temperatures on either side of the interface as well as the contact pressure p. The conductive heat flux density q_c, across the contact surfaces in eq. (1) is given as

$$q_c = k(h, \bar{\theta}, p) \ (\theta_1 - \theta_2), \tag{3}$$

where k is the heat transfer coefficient and is considered to be a function of the average temperature at the contact point $\bar{\theta}$, the contact pressure p and the overclosure or gap conductance h. θ_1 and θ_2 are the temperatures at the contact surfaces. The portion of the heat generated by plastic straining of the material is calculated, as the material properties of the proposed aluminum alloy are considered to be temperature dependent. To represent the coupled thermomechanical behavior of the model, the Johnson-Cook plasticity model is applied, in which ϵ^p_{eq} is the equivalent plastic strain and $\dot{\epsilon}/\dot{\epsilon}_0$ is the dimensionless term for the effects of strain rate in the constitutive model. The yield stress in this model is obtained as

$$\sigma_y = [A + B(\epsilon^p_{eq})^N][1 + C \ ln\frac{\dot{\epsilon}}{\dot{\epsilon}_0}][1 - (\theta_H)^M] \ . \tag{4}$$

Here, $\dot{\epsilon}_0$ is a reference strain rate and θ_H is given as

$$\theta_H = \frac{\theta - \theta_0}{\theta_M - \theta_0}, \tag{5}$$

in which θ_0 and θ_M represent reference temperature and melting temperature, respectively. The six material constants of the Johnson-Cook model, A, B, C, N, $\dot{\epsilon}_0$ and M are identified based on experimental data collected for the aluminum alloy EN-AW1370 [6]. The volumetric heat generation q_p due to the plastic work is considered using the specific heat of the material [7],

$$q_p = \eta \ \sigma \ \dot{\epsilon}^{pl}, \tag{6}$$

where η is the fraction of dissipated heat due to plastic deformations, which appears as a volumetric heat flux and is set to 0.9. $\dot{\epsilon}^{pl}$ is the plastic strain rate and σ is the effective stress. As the process of USW involves a strong interaction of mechanical and thermal behavior of the mating parts, thermal strains should also be considered through the following equation, which requires the thermal expansion coefficient of the material α and a reference temperature θ_0 for the thermal expansion coefficient

$$\epsilon^{th} = \alpha(\theta)(\theta - \theta_0) \ . \tag{7}$$

The reference temperature in the FE model is set to $20°C$, representing room temperature.

3 MICROSECTION OBSERVATIONS

A deep inspection of the weld zones was done through preparation of microsections of some of weld samples of 27 mm^2 cables. Figs. 2 to 4 show the weld samples with two different sonotrode pressures. Microsections show that welding with a pressure of 2.8 bar results in a good bond between strands, so that the boundary between two strands cannot be recognized (see Fig. 3, position C). Furthermore softening of aluminum at some interface places is observed in Fig. 3. With an increase in the sonotrode pressure, the temperature at strand interfaces increases, but increasing the pressure over a threshold value prevents the wires from having a sliding motion against each other and therefore restricts the temperature rise. High plastic deformation of single strands due to the applied high pressure is observed in experimental results. Figure 4 shows the deformed hexagonal microsection of the wires due to a relative high pressure. This observation is in a good agreement with the work of Ding and Kim [8, 9], who stated that a higher bond force does not result in a higher contact pressure, or higher frictional energy density, suggesting that a high bond force is not directly correlated to better wire bondability. Despite of a high pressure on the strand package, the boundaries are recognizable at almost every interface beween strands (see Fig. 4).

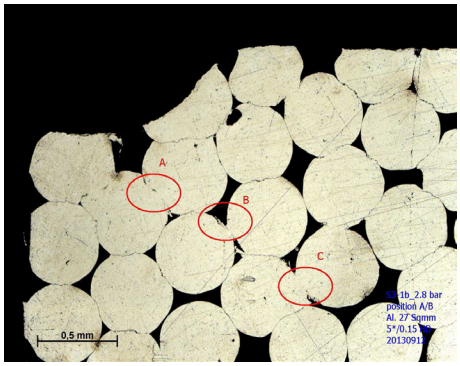

Figure 2: Microsection of weld sample with 2.8 bar

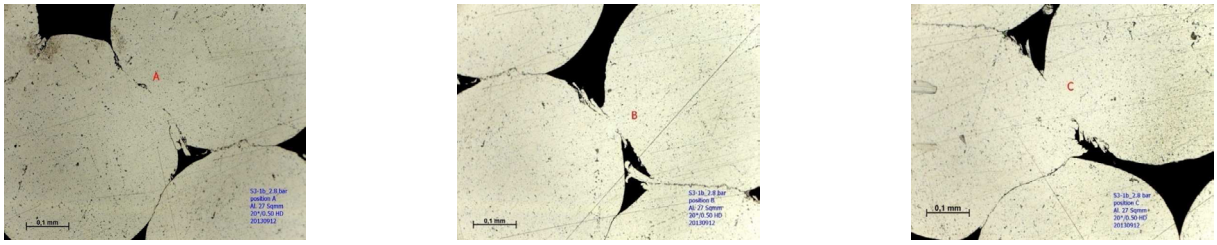

Figure 3: Magnification of positions A, B and C from Fig. 2

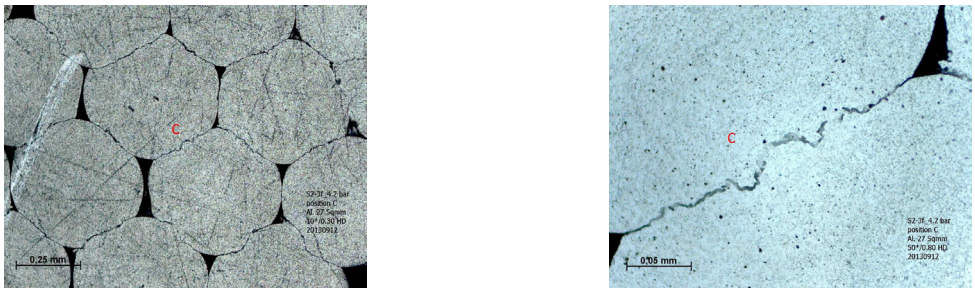

Figure 4: Microsection of weld sample with 4.2 bar (left), magnification of position C (right)

4 NUMERICAL SIMULATIONS OF THE CASE STUDY

For the numerical simulation of the case study, strands with a diameter of 0.43 mm are considered. As mentioned in Section 2, the presented FE model is a simple configuration of 6 strands. Investigation of the microsections shows that each strand during ultrasonic welding is only affected by the adjacent strands and their arrangement is an influencing factor on the final bond quality.
The experimental study of the effect of welding pressure on the bond quality was a motivation for this study to investigate the effect of welding pressure on the temperature rise at strand interfaces. In addition to that, the effect of vibrations amplitude is investigated through FE analysis.

5 RESULTS AND DISCUSSIONS

The presented results in the upcoming sections are captured at the end of the second step in the simulations, where the vibrations of the sonotrode end and before the sonotrode moves upwards.

5.1 Influence of sonotrode pressure on temperature rise at strands interfaces

The simulation results for different sonotrode pressures are shown in Fig. 5, which displays the temperature distribution along a path on the strand surfaces. The highest temperature is observed for the highest pressure, i.e. $P = 1.5$ bar. However, increasing the pressure does not increase the temperature at the surface of the bottommost strand. Furthermore increasing the pressure to 1.5 bar results in a temperature gradient of over

50 degrees at different contact places along the top strand.

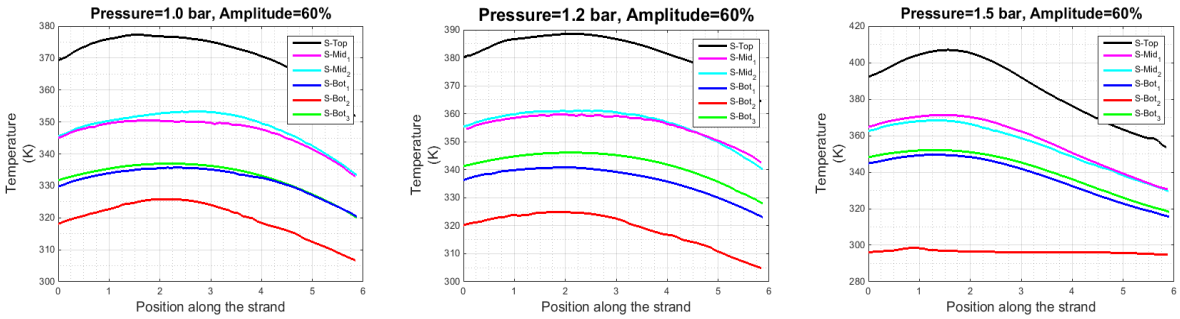

Figure 5: Temperature distribution dependency on pressure along the strand model 2 (left), reference model (middle), model 1 (right)

5.2 Influence of vibrations amplitude on temperature rise at strands interfaces

The simulations are also carried out for three different amplitudes of the vibration. Fig. 6 shows that increasing the amplitude increases the temperature at lower strands about 10 degrees. A sharp temperature drop along the top strand is not observed here and the distribution of temperature has almost the same decreasing slope for all three amplitudes.

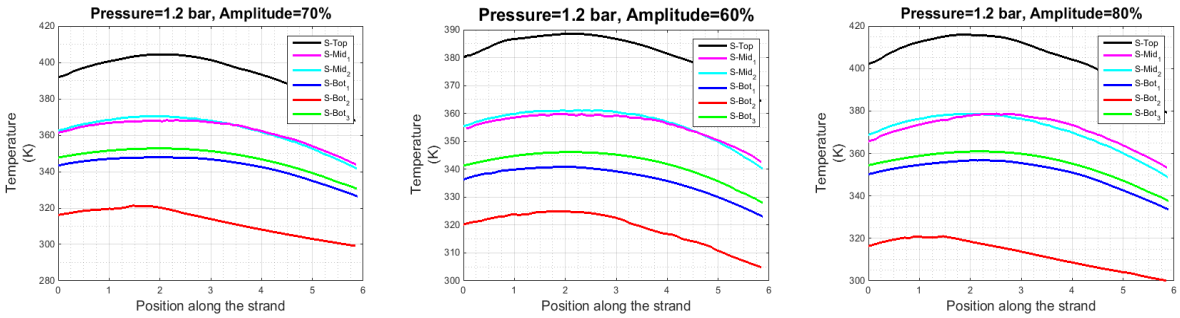

Figure 6: Temperature distribution dependency on vibration amplitude along the strand model 3 (left), reference model (middle), model 4 (right)

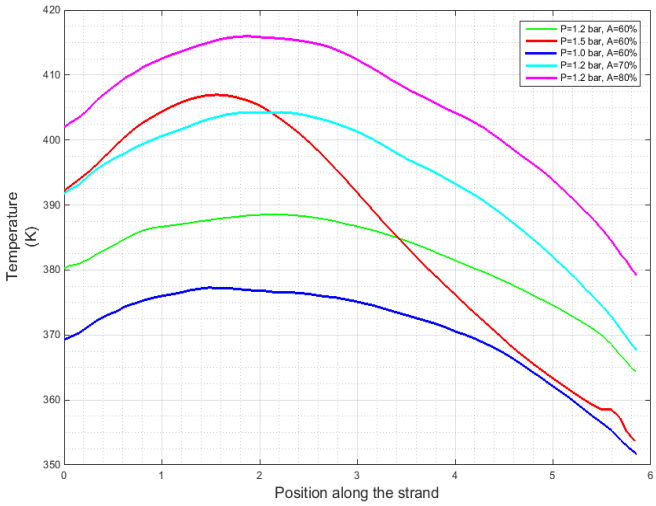

Figure 7: Temperature trend on top strand for different models

6 CONCLUSIONS

Microscopic observations as well as FE analysis of ultrasonic welding of a simple configuration of thin aluminum wires were conducted in this study. The obvious difference in microscopic pictures of weld samples with different welding prressures was a motivation to investigate the influence of pressure as an adjustable welding parameter in the process of USW on the temperature rise on the surface and between strands. Furthermore; the influence of ultrasonic vibration amplitude was also studied. As the microsections show, a higher pressure (or bonding force) results in excessive plastic deformations of the strands. This high pressure prevents the strands to rub against each other, which is the source of frictional energy and consequently generated heat at the strand interfaces. Applying a higher pressure increases the temperature at different places on the strands with a different factor. However, increasing the vibrational amplitude causes the temperature to increase in a similar pattern at almost every place on each strand surface.

7 ACKNOWLEDGEMENT

The authors greatly appreciate the kind cooperation with the ultrasonic welding team at Delphi Deutschland GmbH in Wuppertal, Germany. (They like to acknowledge the computing time grant, which was at their disposal from RWTH Aachen University during this work.)

REFERENCES

[1] Siddiq, A. and Ghassemieh, E. Thermomechanical analyses of ultrasonic welding process using thermal and acoustic softening effects *Mechanics of Materials* (2008) **40**:982-1000.

[2] Zhang, C. and Li, L. A coupled thermal-mechanical analysis of ultrasonic bonding mechanism *Metallurgical and Materials Transactions B* (2009) **40**:196. doi:10.1007/s11663-008-9224-9.

[3] De Vries E. *Mechanics and mechanisms of ultrasonic metal welding*. The Ohio State University, Dissertation (2004).

[4] Elangovan, S., Semeer, S. and Prakasan, K. Temperature and stress distribution in ultrasonic metal welding-An FEA-based study *Materials Processing Technology* (2009) **209**:1143-1150.

[5] *Dassault Systemes*. Abaqus 6.14 Analysis User's Guide, (2014).

[6] Ding, J. and Yuan, H. *Effects of heat treatment on dynamic stress-strain relations of aluminum AW1370 and AW1350*. A thechnical report for Delphi Deutschland GmbH, (2013).

[7] Chen, K., Zhang, Y. and Wang, H. Effect of acoustic softening on the thermal-mechanical process of ultrasonic welding *Ultrasonics* (2017) **5**:9–21, ISSN 0041-624X.

[8] Ding, Y., Kim, J. and Tong, P. Numerical analysis of ultrasonic wire bonding: Effects of bonding parameters on contact pressure and frictional energy *Mechanics of Materials* (2006) **38**:11–24, ISSN ISSN 0167-6636.

[9] Ding, Y. and Kim, J. Numerical analysis of ultrasonic wire bonding: Part 2. Effects of bonding parameters on temperature rise *Microelectronics Reliability* (2008) **48**:149-157.

VII International Conference on Computational Methods for Coupled Problems in Science and Engineering
COUPLED PROBLEMS 2017
M. Papadrakakis, E. Oñate and B. Schrefler (Eds)

COUPLED HYGROTHERMAL, ELECTROCHEMICAL, AND MECHANICAL MODELLING FOR DETERIORATION PREDICTION IN REINFORCED CEMENTITIOUS MATERIALS

A. MICHEL[*], M.R. GEIKER[†], M. LEPECH[††] AND H. STANG[*]

[*] Department of Civil Engineering
Technical University of Denmark (DTU)
2800 Kgs. Lyngby, Denmark
e-mail: almic@byg.dtu.dk, web page: http://www.dtu.dk

[†] Department of Structural Engineering
Norwegian University of Science and Technology (NTNU)
7491 Trondheim, Norway
Email: mette.geiker@ntnu.no, web page: http://www.ntnu.edu

[††] Department of Civil and Environmental Engineering
Stanford University
Stanford, CA 94305, USA
Email: mlepech@stanford.edu, web page: http://www.stanford.edu

Key words: Coupled Problems, Multiphysics Problems, Multiscale Problems, Corrosion, Concrete.

Abstract. In this paper a coupled hygrothermal, electrochemical, and mechanical modelling approach for the deterioration prediction in cementitious materials is briefly outlined. Deterioration prediction is thereby based on coupled modelling of (*i*) chemical processes including among others transport of heat and matter as well as phase assemblage on the nano and micro scale, (*ii*) corrosion of steel including electrochemical processes at the reinforcement surface, and (*iii*) material performance including corrosion- and load-induced damages on the meso and macro scale. The individual FEM models are fully coupled, *i.e.* information, such as such as corrosion current density, damage state of concrete cover, *etc.*, are constantly exchanged between the models.

1 INTRODUCTION

Critical sets of civil infrastructure systems form the foundation for quality of life and enable global development and progress. Consuming vast amounts of material resources and energy, it is essential that global civil infrastructure is designed according to broad, long term design goals for the benefit of our planet and the current and future generations of humans, animals, and plants that will call it home. However, deterioration of civil infrastructure (*e.g.* bridges, tunnels, roads, buildings) together with increasing loads (*e.g.* traffic load, intensity, climate changes, *etc.*) presents a major challenge to achieving these goals in many developed countries [1]. Therefore, the renovation, renewal, and maintenance of existing civil infrastructures is a primary challenge for researchers and practitioners alike. Experience from

the past 20 years has shown that the initial costs of construction are often dwarfed by the costs of repairing, inspecting, and maintaining a civil infrastructure over its useful life [2]. While engineering tools and methods are well developed for the structural design of new structures, tools for assessing current and predicting the future condition of civil infrastructure are less advanced. Existing prediction tools are largely empirical, and thus limited in their ability to predict the performance of new materials, structural, or maintenance solutions. As such, the inability to reliably assess the long-term future ramifications of today's design decisions poses a major obstacle for the design of civil infrastructure. A primary reason for the lack of reliable modelling tools is that deterioration mechanisms are highly complex, involve numerous coupled phenomena that must be evaluated across a range of scales, and often cut across several academic disciplines.

Multi-physics and multi-scale deterioration modelling holds the potential to address these challenges and to enable realistic and reliable long-term performance predictions of civil infrastructure. The basic concept of such a multi-physics and multi-scale modelling framework for reinforced concrete structures is presented in Figure 1. Fundamental, science-based models employed in the modelling framework deal with transport phenomena (moisture, temperature, oxygen, etc.) and phase changes in cementitious materials, electrochemistry (reinforcement corrosion), and fracture mechanics on various length and time scales. These individual science-based models, describing actual physical phenomena, are organized in groups, so-called modules in the modelling framework. To establish a link between the individual modules an interface module is required that allows for passing of information from one module to another, thereby bridging various length and time scales and allowing for concurrent performance simulations of reinforced concrete structures. The interface module may thereby be based on information-passing multi-scale (IPM) methods, thermodynamically constrained internal state variables (ISV), or local enrichment based

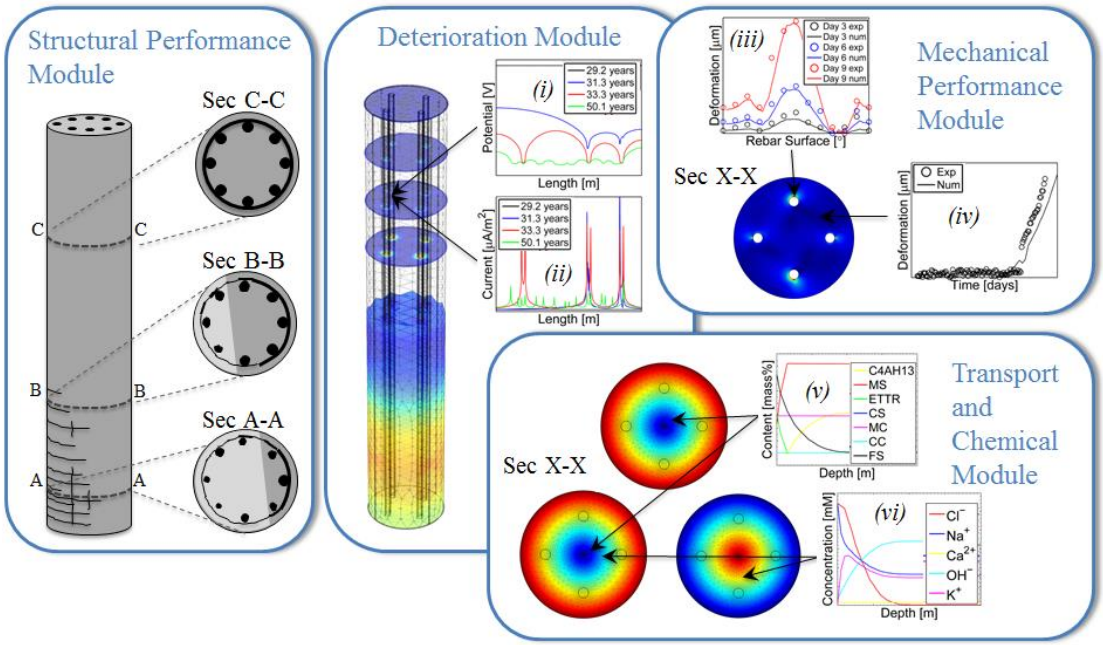

Figure 1: Multi-physical and multi-scale modelling framework for deterioration of reinforced concrete, including physical, chemical, electrochemical, and fracture mechanical processes at the material and meso-scale, which are further coupled with mechanical deterioration processes at the structural/component scale, from [3].

concurrent multi-scale (LECM) methods to bridge time and length scales of the individual models describing actual deterioration phenomena in reinforced concrete.

In the following sections of this paper, the theoretical background of the individual modules for reinforced concrete structures suffering from reinforcement corrosion (the leading deterioration mechanism of civil infrastructure built from reinforced concrete destroying more than 3% of the world's GDP [1]) is outlined. Full coupling of physical and chemical processes, mechanical performance, and electrochemical processes on the material scale of the modelling framework is presented. Although not presented in this paper, results of such coupled transport, chemical, and electrochemical processes may be further used for the evaluation of structural performance as well as sustainability of reinforced concrete structures.

2 MODELLING HEAT, MOISTURE, AND ION TRANSPORT

Within the 'Transport and Chemical Module', coupled transport of heat and moisture, comprising both liquid and water vapour moisture transport, in porous media is modelled using Richard's equation, while multi-ion species transport and the interaction of predominant ions in the cementitious pore solution with solid phases of hydrated Portland cement is modelled by the Nernst-Planck equation and a thermodynamic model, respectively.

2.1 Coupled heat and moisture transport in porous media

Assuming that contributions due to air transfer, gravity, radiation, liquid transport due to temperature gradients, and effects of the gaseous phase on the moisture and heat storage are negligible as well as temperatures remain below the boiling temperature of water [4], coupled heat moisture transport in porous media may be described as follows

$$\begin{aligned} \rho C \frac{\partial T}{\partial t} &= \nabla\left(k_{T,T}\nabla T + k_{T,pC}\nabla pC\right) \\ \frac{\partial \theta_l}{\partial p_c}\frac{\partial p_c}{\partial pC} = C_{pC}\frac{\partial pC}{\partial t} &= \nabla\left(k_{pC,pC}\nabla pC + k_{pC,T}\nabla T\right) \end{aligned} \tag{1}$$

where ρ is the mass density of concrete, C the specific heat capacity of concrete, T the temperature, t the time, pC the logarithm of the capillary pressure, θ_l the moisture content, pc the capillary pressure, C_{pC} the moisture capacity and k transport coefficients for the heat, T, and moisture transfer, pC, respectively. For the solution of the coupled partial differential equations, material specific information on the various transport coefficients (k), capillary pressure curve (θ_{pc}) describing the moisture storage, and boundary conditions are needed. The various transport coefficients of Eq. 1 may be described as follows

$$\begin{aligned} k_{T,T} &= \lambda \\ k_{T,pC} &= -l_{lv}\frac{D_v(\Theta_l)}{R_v T}\frac{p_{v,sat}\varphi}{\rho_l R_v T}\frac{\partial p_c}{\partial pC} \\ k_{pC,pC} &= -K_l(\Theta_l)\frac{\partial p_c}{\partial pC} - \frac{D_v(\Theta_l)}{R_v T}\frac{p_{v,sat}\varphi}{\rho_l R_v T}\frac{\partial p_c}{\partial pC} \end{aligned} \tag{2}$$

$$k_{pC,T} = \frac{D_v(\Theta_l)}{R_v T}\frac{p_{v,sat}\varphi}{\rho_l R_v T}\frac{\partial p_{v,sat}}{\partial T}$$

where λ is the thermal conductivity, l_{lv} the specific latent heat of evaporation, $D_v(\theta_l)$ the moisture dependent vapour diffusion coefficient, R_v the gas constant of water vapour, $p_{v,sat}$ the saturation vapour pressure, ρ_l the density of water, φ the relative humidity and $K_l(\theta_l)$ the liquid conductivity coefficient. The moisture dependent vapour diffusion coefficient, $D_v(\theta_l)$, and the liquid conductivity coefficient, $K_l(\theta_l)$, may be described through a mechanistic modelling approach, see *e.g.*, [5] and [6]. This mechanistic modelling approach considers thereby the microstructure of the porous media. To describe the moisture storage behaviour of porous media, a bimodal function of van Genuchten type may be used, see *e.g.*, [7], which can be given as follows

$$\Theta_{p_c} = \Theta_{cap}\sum_{i=1}^{k}\frac{l_i}{(1+(a_i p_c)^{n_i})^{m_i}} \tag{3}$$

where θ_{cap} is the capillary moisture content, a_i, n_i, and m_i are shape parameters and l_i a weighting factor.

2.2 Multi-ion transport in porous media

The transport of ions in porous media is mainly governed by three different transport phenomena, *i.e.* diffusion, migration, and convection. Nernst-Planck equation allows for the description of multi-ion transport in porous media taking into account these transport phenomena and may be given as follows

$$\frac{\partial c_i}{\partial t} = \nabla\left(D_i\nabla c_i + z_i u_{m,i} F c_i \nabla \mathrm{E} - c_i v\right) \tag{4}$$

where c_i is the ionic concentration, D_i the ionic diffusion coefficient, z_i the charge number of the ionic species, $u_{m,i}$ the ionic mobility, F Faraday's constant, E the electrostatic potential and v the velocity of the solvent. To account for the impact of moisture on the diffusion of ions the relation proposed in [8] may be used

$$D_i(S_l) = D_i^0 S_l^{\xi} \tag{5}$$

where D_i^0 is the free ionic diffusion coefficient in bulk water, S_l the degree of saturation and ξ a model parameter.

2.3 Phase assemblage in hydrated Portland cement

Ions are known to be physically adsorbed and/or chemically bound in porous media, such as concrete, commonly referred to as binding. The bound ions will not participate further in the ingress. With respect to reinforcement corrosion, especially the binding process of chloride ions is of interest as only free chloride ions may initiate reinforcement corrosion. Among others, chloride binding in hydrated Portland cement may be described through thermodynamic modelling for the phase equilibria based on the application of the phase rule as proposed in *e.g.* [9] and [10]. Calculations assume thermodynamically stable or metastable equilibrium at constant temperature and pressure, and therefore strict observance with the phase rule. While the overall reaction scheme for chloride binding in hydrated Portland

cement considering the total content of alkalis can be found [9] and [10], as an example the equations for chloride binding in Portland cement pastes in which Na is still present in the C-S-H and no AFm (alumina, ferric oxide, monosulfate) phases other than monocarbonate are present may be described as follows

$$\begin{aligned} &b \cdot [C_3A \cdot CaCO_3 \cdot 11H_2O]_{(s)} + a \cdot [1.75CaO \cdot SiO_2 \cdot \omega NaOH \cdot 4H_2O]_{(s)} + \\ &\big((\kappa+1) \cdot y \cdot a + b \cdot x\big)CaCl_{2(aq)} + 2 \cdot 0.83 \cdot \kappa \cdot y \cdot aNaOH_{(aq)} \rightarrow \\ &2 \cdot \kappa \cdot y \cdot aNaCl_{(aq)} + a[1.75CaO \cdot SiO_2 \cdot (\omega - 0.34 \cdot \kappa \cdot y)NaOH \cdot yCaCl_2 \cdot 4H_2O]_{(s)} + \\ &\kappa \cdot y \cdot aCa(OH)_{2(s)} + b\left[C_3A \cdot CaCl_{2(x)} \cdot CaCO_{3(1-x)} \cdot 11H_2O\right]_{(s)} + b \cdot x\, CaCO_{3(s)} \end{aligned} \tag{6}$$

where a is the content of C-S-H, b the initial content of monocarbonate, ω the molar ratio of NaOH between chloride-free C-S-H and C-S-H, m the fraction of Friedel's salt in the solid solution phase at the chloride content where all alkalis have been released to the pore solution from the C-S-H, x the fraction of Friedel's salt in the AFm solid solution phase, y the content of $CaCl_2$ in the C-S-H, the relation between y and x may be described as follows

$$\begin{aligned} y &= 0.0601x^2 + 0.0164x \quad \text{for white Portland cement} \\ y &= 0.0376x^2 + 0.0064x \quad \text{for gray Portland cement} \end{aligned} \tag{7}$$

where κ is defined as

$$\kappa = \omega(PS/a)\ 0.2354 \tag{8}$$

where PS is the amount of solution in millilitre.

3 MODELLING REINFORCEMENT CORROSION

Within the 'Deterioration Module' (see Figure 1), electrochemical processes describing corrosion of reinforcement in concrete structures is dealt with. It is thereby assumed that corrosion of reinforcement in concrete can be described by the same electrochemical processes as the corrosion of a metal in an electrolyte [11]. An overview of fundamental electrochemical and physical processes describing the corrosion of steel in concrete is given in Figure 2 as proposed in [12]. Two electrochemical half-cell reactions must take place at the metal surface for corrosion to occur, the anodic (oxidation) and the cathodic (reduction) half-cell reaction. The anodic half-cell reaction is characterised by liberating electrons, which are consumed in the cathodic half-cell reaction. The electrons liberated at the anode are conducted through the metal to the cathode and the electrical circuit is then closed by an ionic exchange current through the concrete. Typical anodic reactions, such as the oxidation of iron are given in Eq. 12, while common cathodic reactions, such as e.g. the reduction of oxygen are presented in Eq. 13, see *e.g.*, [12].

$$\begin{aligned} Fe &\rightarrow Fe^{2+} + 2e^- \\ 2Fe + 3H_2O &\rightarrow Fe_2O_3 + 6H^+ + 6e^- \end{aligned} \tag{9}$$

$$\begin{aligned} O_2 + 4H^+ + 4e^- &\rightarrow 2H_2O \\ O_2 + 2H_2O + 4e^- &\rightarrow 4OH^- \end{aligned} \tag{10}$$

However, depending on the potential and pH at the steel surface, other cathodic reactions, such as the reduction of hydrogen or water, may take place. A detailed overview of thermodynamically feasible anodic and cathodic reactions associated with reinforcement

corrosion can be found in *e.g.* [12]. Thus, for a thorough description of the reinforcement corrosion process, thermodynamics and kinetics must be considered as well as their dependence on other parameters such as *e.g.* temperature, moisture, oxygen, *etc*.

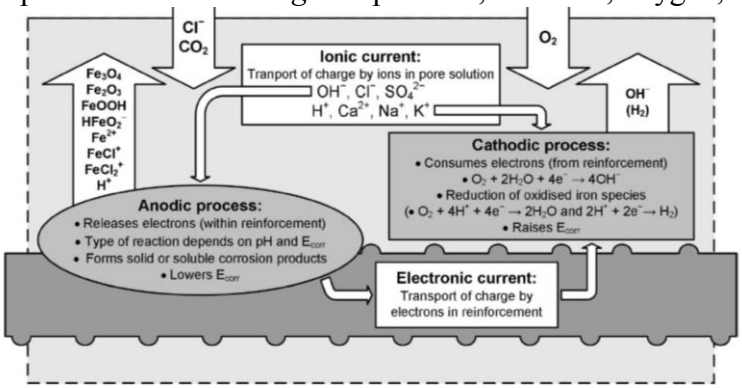

Figure 2: Overview of electrochemical and physical processes describing corrosion in concrete, from [12].

3.1 Corrosion potential and corrosion current density distribution

Two equations may be used to describe the electrochemical processes in the concrete pore solution acting as electrolyte [13]. The first one is Laplace's equation, which describes the potential distribution in an electrolyte assuming electrical charge conservation and isotropic conductivity.

$$\nabla^2 E = 0 \tag{11}$$

The second is Ohm´s law, which may be used to determine the rate of dissolution of iron at any point on the steel surface in concrete if the potential distribution around that point and the resistivity, ρ_{conc}, of the electrolyte is known [14].

$$i_{corr} = -\frac{1}{\rho_{conc}} \frac{\partial E}{\partial n} \tag{12}$$

3.2 Thermodynamics of reinforcement corrosion

Among others, thermodynamics provide the possibility to investigate and assess the likelihood of reactions (in the case of reinforcement corrosion: anodic and cathodic half-cell reactions) to occur under certain conditions. To describe the equilibrium potentials, E_0, of thermodynamically feasible half-cell reactions for the corrosion process, Nernst equation can be used, which may be written as follows (Perez 2004)

$$E_0 = E_0^0 - \frac{RT}{zF} ln\left(\frac{\alpha_{Red/Ox}}{\alpha_{Ox/Red}}\right) \tag{13}$$

where $E_0{}^0$ is the standard equilibrium potential, R the gas constant, and $\alpha_{Red/Ox}$ the chemical activity of the reductant and oxidant, respectively. Nernst equation may be further used to construct pH - potential diagrams, or more frequently called Pourbaix diagrams, providing a graphical overview of thermodynamically favoured reactions (*i.e.* reactions with a negative free enthalpy) as a function of the pH and the half-cell potential. The Pourbaix diagram for iron in chloride ion containing water (commonly used to investigate corrosion reactions of steel in concrete [12]) is illustrated in Figure 3. In combination with the information from the

'Transport and Chemical Module', the pH in the concrete pore solution can be determined. Along with the electric potential, determined from Laplace equation, thermodynamically feasible anodic and cathodic reactions can then be selected when modelling reinforcement corrosion processes.

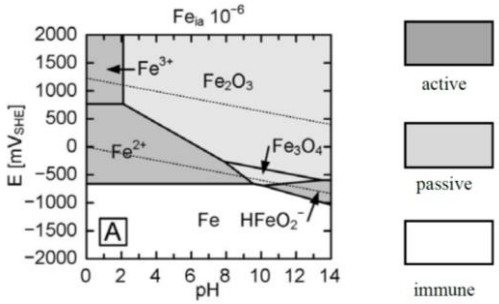

Figure 3: Pourbaix diagram for Fe-Cl-H_2O system at 25°C, with an Fe ion activity of 10^{-6} mol/L and Cl concentration of 0.035 mg/L, after [12].

3.3 Kinetics of reinforcement corrosion

Although thermodynamics provide means to assess the possibility of corrosion reactions to occur under various conditions, no information on the rate of these reactions is obtained. Therefore, the kinetics of electrochemical reactions must be considered to fully assess the corrosion mechanism. Once corrosion is initiated, the potentials of the half-cell reactions on the steel surface are shifted from their equilibrium potentials and a (corrosion) current will start to flow. The shift from the equilibrium potential is known as polarisation and the kinetics of the electrochemical half-cell reactions are governed by the degree of polarisation. A measure for the polarisation is the overpotential, η, which is the difference between the half-cell potential, $E_{c/a}$, and the equilibrium potential, $E_{0a/0c}$. Information on the polarisation of electrodes (anode and cathode) can be summarised in so-called Evan's diagrams relating the half-cell potential to the corrosion current. The Evan's diagram for the anodic and cathodic half-cell reactions assuming the formation of Fe^{2+} at the anode and OH^- at the cathode is given in Figure 4. The corrosion potential (also referred to as mixed potential), E_{corr}, and the corrosion current density, i_{corr}, can be determined from the intersection of the anodic and the cathodic polarisation curve. The relation between the corrosion current and the half-cell potential may be described by the Butler-Volmer equation assuming that the kinetics are governed by activation, concentration, and resistance polarisation and that the electrochemical reactions take place at separate electrodes and the polarisation is high [15].

$$i = i_0 exp(\Psi) \;\; with \;\; \Psi = ln(10)\frac{E - E_0}{b_T} \tag{14}$$

where i is the corrosion current density, i_0 the exchange current density, and b_T the Tafel constant, which is defined as follows

$$b_T = ln(10)\frac{RT}{\alpha zF} \tag{15}$$

where α is the symmetry factor. To include the effects of concentration polarisation on the relation between the half-cell potential and the corrosion current density, Eq. 18 may be extended and written as follows [16]

$$i = i_0 exp\left(\frac{1-\Psi}{1+\mathrm{i_0/i_{lim}}\Psi}\right) \tag{16}$$

where i_{lim} is the limiting corrosion current density, which may be defined as follows [17]

$$i_{lim} = \frac{zFD_{O2}}{\delta} c_{O2} \tag{17}$$

where D_{O2} is the oxygen diffusion coefficient, c_{O2} the oxygen concentration at the electrode surface and δ the diffusion layer thickness. A number of factors influence the shape of the polarisation curve, which in turn governs the kinetics of the corrosion process. Among others, the surface state of the electrode, temperature, moisture content, and geometry are decisive for the overpotential at the anode and cathode [17]. For example, the temperature, moisture content, and geometry are important parameters for diffusion-controlled corrosion. A high moisture content considerably hinders the oxygen transport from the concrete surface to the electrode. This may lead to a depletion of oxygen at the cathode ceasing the cathodic half-cell reaction (assuming reduction of oxygen as governing half-cell reaction) and subsequently the corrosion process itself. Furthermore, several electrochemical parameters, such as the exchange current density or the equilibrium potential are influenced by temperature. This highlights the importance of a fully coupled modelling framework, i.e. coupling between mass and heat transport, phase assemblage, and kinetics and thermodynamics of reinforcement corrosion, for a reliable and realistic assessment as well as long term prediction of the performance of reinforced concrete structures with respect to corrosion.

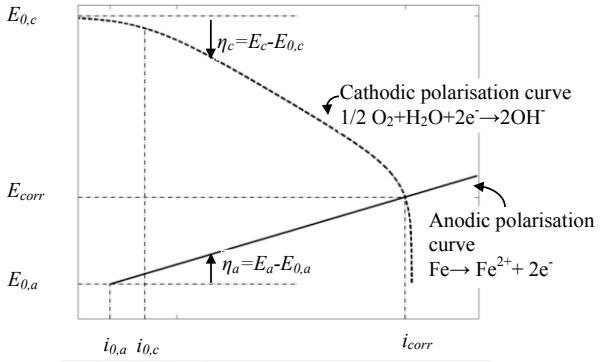

Figure 4: Evan's diagram illustrating the anodic and cathodic polarisation on the steel surface, after [18].

3.4 Initiation of reinforcement corrosion

To link corrosion initiation, *i.e.* the formation of anodic regions at the reinforcement surface, and propagation of reinforcement corrosion a conditional statement may be defined along the reinforcement surface. In case of chloride-induced corrosion, the conditional statement may comprise the definition of a critical chloride threshold for elements along the reinforcement surface, which might be defined as follows

$$BC_{Steel} = \begin{cases} i_a \\ i_c \end{cases} for \begin{matrix} c_{cl} \geq c_{crit} \\ c_{cl} < c_{crit} \end{matrix} \tag{18}$$

where BC_{Steel} is the boundary condition along the steel surface, i_a the anodic polarisation curve, i_c the cathodic polarisation curve, c_{cl} the chloride concentration along the

reinforcement, and c_{crit} the critical chloride threshold defined along the reinforcement. As an approximation c_{cl} may be varied randomly along the reinforcement surface to account for the influence of various parameters and represent a realistic reinforced concrete structure with defects, voids, *etc.* present at the concrete steel interface [19].

4 CORROSION-INDUCED CONRETE DAMAGE

Once corrosion is initiated, electrochemical half-cell reactions are taking place along the reinforcement. The ionic reaction products of these half-cell reactions may further react and form solid corrosion products in the vicinity of the reinforcement. The type of corrosion products formed; depend thereby on the thermodynamic conditions present in the vicinity of the reinforcement [12]. Independent of the type of iron oxides formed as a result of active corrosion, the iron oxides occupy a larger volume than the initial iron that is consumed during the corrosion reaction, see *e.g.*, [20]. The increased volume of corrosion products causes tensile stresses in the surrounding concrete and may lead to concrete cracking, spalling, or delamination if the tensile strength of the concrete is exceeded. This damage process is described in the 'Mechanical Performance Module', which utilizes a thermal analogy to model the expansive nature of solid corrosion products and corrosion-induced damage, see Figure 5. The developed fracture mechanics model, furthermore, accounts for the penetration of solid corrosion products into the available pore space of the surrounding cementitious material, as well as non-uniform distribution of corrosion products around the circumference of the reinforcement, see e.g. [21]. Faraday´s law is used to relate the cross sectional reduction per time unit to the corrosion current density 'Deterioration Module'.

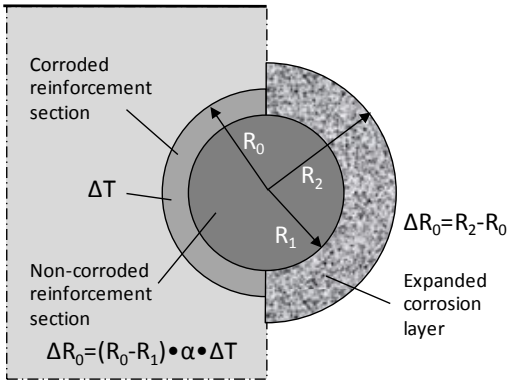

Figure 5: General modelling approach for corrosion-induced damage in concrete including load application and geometrical considerations, from [22].

4.1 Coupled lattice and FEM model

To simulate corrosion-induced damage in concrete, a random, triangular lattice of truss elements is chosen within the present framework. As the formation of cracks is assumed to take place only in the concrete domain, the remaining domains (steel and corrosion layer) are modelled with continuum elements. The random lattice of truss elements in the concrete domain is established by initially creating a regular square lattice in the concrete domain. Within each cell of the regular lattice, a point is selected at random with uniform distribution. Subsequently, Voronoi construction is used to create a random lattice by connecting the three points that are closest to each other. The randomness of the lattice can be varied through the

introduction of a sub-cell in the square lattice, from which the random point is chosen.

Crack formation and growth within the concrete domain is achieved by removing the element with the highest stress to tensile strength ratio and greater than unity. Upon the next loading step the updated system of equations is recomputed and the analysis repeated until the system fails. This step-by-step removal of lattice elements allows for crack evolution in the specimen and for tracking of microcrack propagation and crack pattern in the simulation. To determine the nodal displacements and subsequently the stresses in the elements of the lattice for each analysis step an elastic analysis is performed. 2-D nodal displacements can thereby be obtained as follows for a set of linear equations within a FEM formulation

$$\{F\} = [K]\{U\} \tag{19}$$

where F is the global nodal force vector, K the global stiffness matrix, and U the global nodal displacement vector. The global stiffness matrix is hereby obtained as follows

$$[K] = \int [B^T][D][B]hd\Omega \tag{20}$$

where B is the strain matrix, D the constitutive material matrix, and h the thickness of the domain, Ω. In the present modelling approach, lattice and continuum elements are combined to discretize the various domains of the model, *i.e.* the concrete domain is discretized using truss elements while the corrosion product and reinforcement domain are discretized using bilinear quadrilateral and linear triangular elements, respectively. The thermal analogy to mimic the expansive nature of corrosion products is implemented by equivalent nodal forces, $f_{cp,t}$, for the corrosion product domain, $_{cp}$, which can be determined as follows

$$[f_{cp,t}] = \int_{A_{cp}} [B_{cp}^T][D_{cp}][\varepsilon_{cp,t}]hdA_{cp} \tag{21}$$

in which the thermal strain matrix, $\varepsilon_{cp,t}$, may be given as follows for 2-D

$$[\varepsilon_{cp,t}] = \begin{bmatrix} \alpha\Delta T \\ \alpha\Delta T \\ 0 \end{bmatrix} \tag{22}$$

The modelling approach is formulated in Matlab®, and focus was placed on efficient algorithms to allow for simulations with large numbers of degrees of freedom (DOFs), *i.e.* tens of thousands of elements. To solve the set of linear equations (see Eq. 19) and ensure convergence of the solution, an iterative conjugate gradients squared method solver is used. Finally, it should be noted that the simulation of the corrosion process is time dependent, *i.e.* the corrosion product domain is growing. This requires reassembly of the corrosion product and steel domain for every 'time step'. To account for the corrosion-induced damage from one 'time step' to another, an internal nodal force vector is created for each time step, which assures that corrosion-induced damage is transferred from the previous 'time step'. The internal nodal force vector, f_i, can be calculated as follows

$$[f_i] = \int_A [B^T][\sigma]hdA \tag{23}$$

where σ is the element stress.

5 SUMMARY AND CONCLUSIONS

In this paper, the theoretical background and coupling of chemical, electrochemical, and fracture mechanical processes on different length and time scales in reinforced concrete within a cross disciplinary modelling framework was presented. The presented multi-physics and multi-scale model for corrosion in reinforced concrete structures deals with (*i*) the transport of heat and matter as well as phase assemblage in hydrated Portland cement, (*ii*) corrosion of reinforcement, and (*iii*) material performance including corrosion-induced damages on the meso and macro scale. The modelling framework presented is fully coupled, *i.e.* information, such as phase equilibria, moisture distribution, corrosion rate, damage state of concrete cover, *etc.*, are constantly exchanged between the modules, see Figure 1.

Outcomes of the fully coupled mechanical performance, deterioration, and transport and chemical modules described within this paper may be used for further analysis and coupling within a structural performance module, see Figure 1. In particular, cross sectional reduction of reinforcement due to corrosion and concrete cover damage may be used within such a structural performance module to determine (*i*) structural performance of deteriorated concrete members, (*ii*) change in reinforcement bond strength due to formation of oxidation products, (*iii*) reduction in capacity of corroded reinforcing bars, (*iv*) reduction in ductility of corroded reinforcing bars, *etc.* to assess the structural effects of reinforcement corrosion on concrete structures. Exchange of information between the modules is thereby realized through an 'Interface Module'. Ultimately, such an 'Interface Module' may be built in a standardized manner to allow for future extensions, *e.g.* inclusion of additional deterioration mechanisms such as freeze thaw, alkali silica reaction, of the outlined multi-physics and multi-scale modelling framework. Integration of a standardized 'Interface Module' within the modelling framework will furthermore allow for adaptation of level of detailing relevant for individual cases as well as enable continuously updating based on new knowledge and to identify further research needs.

ACKNOWLEDGEMENTS

The authors gratefully acknowledge financial contributions from the Danish Expert Centre for Infrastructure Constructions, COWIfonden, and the project 'Sustainable Rehabilitation of Civil and Building Structures' funded by Nordic Innovation Centre, Project No. 08190 SR are also greatly appreciated. The authors would also like to thank the United States National Science Foundation for its support of this work, in part, under Grant No. 1453881. Any opinions, findings, and conclusions or recommendations expressed in this material are those of the authors and do not necessarily reflect the views of the US NSF.

REFERENCES

[1] Koch, G.H., Brongers, M.P.H., Thompson, N.G., Virmani Y.P. and Payer, J.H. *Corrosion Cost and Preventive Strategies in the United States*, Report FHWA-RD-01-156, (2002).

[2] Lepech, M.D., Geiker M. and Stang, H. Probabilistic design and management of environmentally sustainable repair and rehabilitation of reinforced concrete. *Cem. Concr. Comp.* (2014) **47**:19-31.

[3] Michel, A, Stang, H., Lepech, M. and Geiker, M.R. Multi-physics and multi-scale deterioration modelling of reinforced concrete, *Key Eng. Mat.* (2016) **665**:13-16.

[4] Janssen, H., Blocken, B. and Carmeliet, J. Conservative modelling of the moisture and heat transfer in building components under atmospheric excitation, *Int. J. Heat. Mass. Transf.* (2007) **50**:1128-1140.
[5] Scheffler, G.A. *Validation of hygrothermal material modelling under consideration of the hysteresis of moisture storage*, Ph.D. thesis, Technical University of Dresden, Dresden, Germany, (2009).
[6] Scheffler, G.A. and Plagge, R. A whole range hygric material model: Modelling liquid and vapour transport properties in porous media, *Int. J. Heat. Mass. Transf.* (2010) **53**:286-296.
[7] Carmeliet, J. and Roels, S. Determination of the moisture capacity of porous building materials, *J. Build. Phys.* (2002) **25**:209-237.
[8] Buchwald, A. Determination of the ion diffusion coefficient in moisture and salt loaded masonry materials by impedance spectroscopy, In: *Proceedings of 3rd International PhD Symposium*, Vienna, (2000).
[9] Nielsen, E.P. *The durability of white Portland cement to chemical attack*, Ph.D. thesis, Technical University of Denmark, Kgs. Lyngby, Denmark, (2004).
[10] Geiker, M., Nielsen, E.P. and Herfort, D. Prediction of chloride ingress and binding in cement paste, *Mater. Struct.* (2007) **40**:405-417.
[11] Schießl, P. (Ed.) *Corrosion of steel in concrete*, Report of the Technical Committee 60 CSC, RILEM, Chapman and Hall, (1988).
[12] Küter, A. *Management of reinforcement corrosion: a thermodynamical approach*, Ph.D. thesis, Technical University of Denmark, Kgs. Lyngby, Denmark, (2015).
[13] Warkus, J., Raupach, M. and Gulikers, J. Numerical modeling of corrosion - Theoretical backgrounds -, *Mater. Corros.* (2006) **57**: 614-617.
[14] Isgor, B.O. & Razaqpur, G.A. Modelling steel corrosion in concrete structures, *Mater. Struct.* (2006) **39**:291-302.
[15] Stern, M. and Geary, A.L. Electrochemical polarization I. A theoretical analysis of the shape of polarization curves, *J. Electrochem. Soc.* (1957) **104**:56-63.
[16] Böhni, H. *Corrosion in reinforced concrete structures*, Woodhead Publishing Ltd., (2005).
[17] Bardal, E. *Corrosion and Protection*, Springer-Verlag, London, UK, (2004).
[18] Martín-Pérez, B. *Service Life Modelling of R.C. Highway Structures Exposed to Chlorides*, Ph.D. thesis, University of Toronto, Toronto, Canada, (1999).
[19] Angst U.M., Geiker, M.R., Michel, A. et al. The steel–concrete interface, *Mater. Struct.* (2017) **50**:143.
[20] Marcotte, T. and Hansson, C. Corrosion products that form on steel within cement paste, *Mater. Struct.* (2007) **40**:325-340.
[21] Thybo, A.E.A., Michel, A. and Stang, H. Smeared crack modelling approach for corrosion-induced concrete damage, *Mater. Struct.* (2017) **50**:146.
[22] Michel, A., Solgaard, A.O.S., Geiker, M., Stang, H. and Olesen, J.F. Modeling Formation of Cracks in Concrete Cover due to Reinforcement Corrosion. *In Oh, B.H., Choi, O.C. and Chung, L. (Eds) Proceedings of FraMCoS-7*, (2010) pp.944-951.

COUPLED MECHANICAL AND ELECTROMAGNETIC MODELING OF EDDY CURRENT SENSORS

NIDHAL JAMIA[1*], MICHAEL I. FRISWELL[1], SAMI EL-BORGI[2] AND PRAKASH RAJENDRAN[2]

[1] College of Engineering, Swansea University
Bay Campus, Swansea SA1 8EN, United Kingdom
e-mail: 842543@swansea.ac.uk, web page: http://www.swansea.ac.uk/

[2] Texas A&M University at Qatar, Mechanical Engineering Program,
Engineering Building, P.O. Box 23874, Education City, Doha, Qatar
e-mail: sami.el_borgi@qatar.tamu.edu, web page: http://www.qatar.tamu.edu/

Key words: Rotating bladed disk, blade tip-timing, eddy current sensors, blade tip clearance, coupled mechanical and electromagnetic problem.

Abstract. To effectively monitor the vibration of blades in a rotating machine, a non-contacting method called blade tip-timing (BTT) has been used. The method is based on the analysis of the differential arrival times of the blades at sensors mounted on the stator to characterize the vibration amplitude and frequency of the blades. These sensors can also provide blade tip clearance measurement. A combination of these data can provide a robust condition monitoring approach for the early detection of blade cracks.
Eddy current sensors (ECS) have shown great potential to assess the health of an engine without any need for direct access to the blade and therefore they are insensitive to the presence of any type of contaminant. Also, both tip timing and tip clearance of each blade could be measured by these sensors in real time and at high resolution.
ECSs measure the magnetic field caused by eddy currents during the blade motion, and hence are a coupled mechanical and electromagnetic problem. An ECS on the casing of a machine has been modeled to fully understand how the dynamic response of the blade is measured by the sensors. Detailed 2-D and 3-D modeling and simulation of a rotating simplified bladed disk passing an ECS is presented.
The effect of the variation of the rotation speed and the gap between the sensor and the blade tip on the accuracy of the measurement is investigated. Such an analysis will enable the reliable monitoring of blade damage during engine operation.

1 INTRODUCTION

In turbomachinery, severe vibratory loads may lead to blade failures and therefore the total failure of the engine. Maintenance of the rotating machine is very important and has a tremendous impact on the life cycle cost of the engine. To obtain the best efficiency, an intelligent assessment is necessary for early damage diagnosis and condition based maintenance activities. Different monitoring techniques have been developed using sensors in the casing

around the rotating part to measure and estimate the time of the arrival (ToA) of the blade tips passing by the sensors. In the 1960s, Fragman et al. [1] developed a contact method where the measurement of rotating blade responses was performed by means of blade mounted strain gauges. This method has several shortcomings such as time and cost, and the low resistance to the harsh environment found inside the machine. As an alternative to this method, many investigators have considered contactless methods to monitor blade vibrations in the rotating machinery due to the non-intrusive and easy installation of sensors which allows prompt detection of potential cracks. One of the well-known contactless method is the Blade Tip Timing (BTT) approach, which estimates the blade vibration that is crucial in the assessment of machine operation and the prediction of blade failure due to fatigue [2]. The concept of this method relies on using a number of probes fixed to a casing of the machine to detect the blade tip as it passes by the probes. Then, the difference between the time of arrival (ToA) of non-vibrating and vibrating blades leads to the estimation of the vibration displacement utilized to identify vibration parameters [3].

During the early 1970s, Zablotsky and Korostelev ([4] and [5]) introduced the first non-contact measurement based on their own device to measure vibration called ELURA. This technique was extended by Heath and Imregun [6] based on an improved formulation to extract the blade arrival times using optical laser probes. Dimitriadis et al. [2] simulated data from traditional BTT tests of rotating blades. They performed a qualitative analysis of different phenomena that can affect the identification of blade vibration parameters such as mistuning or coupling. A modal parameter identification of rotating machine blades was presented by Salhi et al. [7] using a BTT data. Liu and Jiang [8] monitored the blade vibration of a rotating machinery test rig using the BTT method. They proposed a method to improve the accuracy of the measurements in the presence of torsional vibration. Similarly, Madhavan et al. [9] conducted an experiment to monitor the vibration measurement using the BTT technique. Therefore, the focus in the previous researches has been mainly on the experiment work to describe the BTT method.

Several sensing technologies have been proposed to monitor blade positions in turbomachinery relying on capacitance, inductance, optics, microwaves and eddy-currents. The focus in this paper will be mainly on the ECS due to its potential to assess the health of a machine without any need for direct access to the blade (e.g. the possibility to monitor through the casing) and therefore they are insensitive to the presence of any type of contaminant. Also, both tip timing and tip clearance of each blade could be measured by these sensors in real time and at high resolution. Dowell and Sylvester [10] described the physical principles of ECSs and the approach used to develop a health management program for turbomachinery. In addition, Lackner [11] assembled a test rig of three spinning test blades to test the ability of ECSs in a simulated gas turbine environment, he showed that ECSs could mitigate the drawbacks of other types of sensors, such as capacitive sensors. The arrival times of a rotor blade based on ECSs have been measured by Chana and Cardwell [12] in various machine trials to evaluate the ability of these sensors to detect pre-existing damage and to capture dynamic foreign object damage events. More recently, Mandache et al. [13] developed a pulsed eddy current technology to detect the blade and disk damage through the machine casing based on monitoring the blade tip displacement.

The emphasis in the existing literature was on the experimental side more than the modeling side. Therefore, a detailed model of the use of ECS in blade tip timing is required for further development of BTT systems and in order to increase the accuracy of the timing measurement. In this paper, 2-D and 3-D models of a simple rotating bladed disk passing active and passive ECSs are implemented using the COMSOL Multiphysics software to investigate the accuracy of the timing measurement when the blades pass by the sensor. The effect of the rotation speed and the tip clearance between the blade tip and the sensor on the sensor output is investigated.

2 BASIC THEORY OF AN ECS TO ASSESS A MOVING TARGET

2.1 Principe of eddy current sensor

In this section the concept of eddy current monitoring is described. If a conductive target moves through a permanent magnet field or an alternating magnetic field is acting on a moving target, induced eddy currents are generated and detected by the coil system of an ECS. These two cases correspond to a passive eddy current sensor (P-ECS) and active eddy current sensor (A-ECS) that have both been used for BTT measurements. Starting with the case of A-ECS, the operating principles are understood as follows [13]. An alternating current running through a coil of ECS generates a primary time-varying magnetic field formed around the coil. If an electrically conducting target is moving past it, eddy currents are generated and induced in the target due to Faraday's law of induction. A secondary magnetic field is generated by these induced currents and acts against the primary magnetic field as shown in Figure 1. This results in a variation of the coil's impedance which is captured by the sensor. Measuring this discrepancy of coil impedance will reveal particular information, such as the gap between the sensor and the target, or the vibration of the target tip.
A P-ECS follows similar approach to an A-ECS, except that the primary magnetic field is permanent and the induced eddy currents are generated by the motion of the target. Therefore, the sensor picks up the secondary magnetic field generated by these eddy currents. This type of sensor is not considered as a displacement sensor since it measures velocity and hence it does work well for BTT where the blade is always moving past the sensor.

2.2 Modeling the eddy current's effect in a moving target

In this section, the effect of the eddy current in a moving target is modeled using the vector and scalar potential terms. To describe the electro-magnetic field in terms of sources, Maxwell's equations (Eqs. (1)-(4)) along with constitutive equations (Eqs. (5) and (6)) and the magnetic and electric material properties of the moving target are used as [14-15]:

$$\nabla \times H = J + \frac{\partial D}{\partial t} \tag{1}$$

$$\nabla \times E = -\frac{\partial B}{\partial t} \tag{2}$$

$$\nabla \cdot D = \rho \tag{3}$$

$$\nabla \cdot B = 0 \tag{4}$$

$$D = \varepsilon E \tag{5}$$

$$B = \mu H \tag{6}$$

where H is the magnetic field strength, B is the magnetic flux density, E is the electric field, D is the displacement flux density, J is the current density, ρ is the charge density, μ is the magnetic permeability and ε is the electric permittivity of the medium.
In the case of an eddy current sensor monitoring a conductive target, the total electric current generated is given by

$$J = J_t + J_s, \tag{7}$$

where J_t is the electric current density in the conductive target and J_s is the external electric current density induced in the sensor. Following Ohm's law for a moving conductor, along with the presence of the magnetic field, the eddy current generated in the target is defined as

$$J_t = \sigma(E + v \times B) \tag{8}$$

where v is the velocity of the target and σ is the conductivity of the target's medium.
Satisfying two of Maxwell's equations, Eqs. (2) and (4), the magnetic vector potential A and the scalar potential φ are defined as

$$E = -\nabla\varphi - \frac{\partial A}{\partial t} \tag{9}$$

$$B = \nabla \times \mathrm{A} \tag{10}$$

Since the eddy current problem is a magneto-quasi-static problem [16], the displacement current can be ignored, i.e. $\frac{\partial D}{\partial t} \approx 0$. Therefore, substituting Eqs. (6-10) into Eq. (1) yields

$$\nabla \times B = \mu J + \sigma\mu(E + v \times B) \tag{11}$$

By rearranging the terms in Eq. (11) and replacing the electric field and magnetic flux density by their expressions in Eqs. (9) and (10), we obtain, in terms of A and φ, the following magnetic governing equation

$$\nabla \times (\nabla \times \mathrm{A}) - \mu\sigma\left(-\nabla\varphi - \frac{\partial A}{\partial t} + v \times (\nabla \times \mathrm{A})\right) = \mu J_s \tag{12}$$

3 NUMERICAL METHOD FOR TESTING THE BTT USING AN ECS

In this section, a simulation of the distribution of an eddy current by a passive and active ECS in a simple rotating bladed disk is described. This presents a first step towards realistic geometries where it is complicated to change parameters easily. To achieve this task, a commercial FEA software package, COMSOL Multiphysics® [17], was used.

3.1 Geometry of 2-D and 3-D model of a simple bladed disk

A 2-D and 3-D geometry of the model were created using the COMSOL Multiphysics® software. The geometry of the two models is shown in Figure 2 and was generated based on the design parameters given in Table 1. The bladed disk is composed of a disk and 4 simple rectangular blades. A rectangular ECS is fixed at a distance $\boldsymbol{\delta}$ which equals the gap between the blade tip and the sensor. The blades, disk and sensor are assumed to be solid aluminium.

Table 1: Specifications of the bladed disk configuration

Name	Expression	Value	Description
Ω	*2000[1/min]*	*33.333 1/s*	Rotational speed of the rotor
R	*0.1[m]*	*0.1 m*	Radius of the rotor hub
l	*0.1[m]*	*0.1 m*	Blade length
b	*0.005[m]*	*0.005 m*	Blade width
a	*0.003[m]*	*0.003 m*	Overlap of blade into the disk
w_s	*1 [cm]*	*0.002 m*	Sensor width
l_s	*4 [cm]*	*0.005 m*	Sensor Length
δ	*10 [mm]*	*0.005 m*	Gap between Sensor and Blade tip
R_a	$R + l - a + \delta/2$	*0.1995 m*	Radius of Moving surrounding air circle
R_s	$1.25 * R_a$	*0.2495 m*	Radius of Static surrounding air circle
Vcoil	*1e-5[V]*	*1e-5 V*	Coil excitation for P-ECS
f_0	$1000 * \Omega$	*16667 Hz*	Coil excitation frequency for A-ECS

3.2 Modeling the coupled mechanical and electro-magnetic problem using 2-D and 3-D models

3.2.1 Passive ECS model

The 2-D and 3-D domains are discretized by cutting the geometry along the air gap into two parts: one containing the static part of the model (the sensor and surrounding air), and the other containing the moving part (i.e. the disk, the blades and the surrounding air) as shown in Figure 3. The two parts are then meshed separately. Triangular elements were used in the discretization of the 2-D model while in the 3-D model, tetrahedral elements were used. The total number of elements used was 20620 elements in the 2-D model and 48669 elements for the 3-D model as shown in Figure 4. The static part remains stationary while the moving part rotates. These two parts with the corresponding meshes always stay in contact at the cut boundary. The COMSOL software enables the moving mesh for the rotating part and guarantees suitable transformations of the electromagnetic field. In the 2-D model, the COMSOL interface applies Ampere's law to all domains, while in the 3-D model, Ampere's law is applied only for the conductive domains (e.g. bladed disk and sensor). For the free-current domain, such as the surrounding air in the 3-D model, a magnetic flux conservation feature is applied based on the assumption that the magnetic field is curl free in the no-current region and therefore there is an important decrease of computational time.

3.2.2 Active ECS model

This model is based on measuring the change in the coil impedance which is related to the gap between the sensor and the target, and hence the sensor output gives the relative displacement. Therefore, compared to the P-ECS model, the continuous rotation approach is ignored and replaced with a series of blade positions using a sweep of geometry parameter defined as

$$rot_{angle} = t_{para} * \Omega * 2\pi \ \ (rad) \tag{13}$$

where t_{para} is a parametric time and the blade will rotate with respect to this time. Then, the model is solved as a series of frequency domain studies whilst rotating the blades in the geometry via a Parametric Sweep. A frequency domain study defines that an alternative current is used for the coil excitation oscillating at a parameter f_0. This excitation has been set to be 1000 times the spinning blade, to ensure that the quasi-static approximation is valid. A very fine mesh is used for the fan and the coil. The mesh in the blades has been heavily refined to resolve the currents well. Finally, 16235 triangular elements have been used in the 2-D model and 54412 tetrahedral elements for the 3-D model, as shown in Figure 5.

For both models described, a coil feature from the Magnetic Fields interface in COMSOL software was assigned to rectangle 2, as shown in Figure 2, to model the sensor as a conductor subject to an externally applied current or voltage. This feature transforms the applied excitation into local quantities (e.g. electric field and electric current density), and calculates the lumped parameter of interest such as impedance in this case. In addition, due to convergence issues in the 3-D model, the current value in the coil was ramped from a low value using a smoothed step function. Finally, the boundary conditions were fixed by the COMSOL interface, considering continuity of the magnetic potential along the blades and applying the quasi-static approximation where the displacement current density is ignored.

4 SIMULATION RESULTS OF THE ROTATING BLADED DISK USING P-ECS AND A-ECS

All results shown in this section were generated by the COMSOL software for the fixed geometric parameters in Table 1, apart from the parameter that is explicitly varied.

4.1 Validation of results between 2-D and 3-D model

A comparison of the coil output currents corresponding to the 2-D and 3-D models for the P-ECS model, is generated for the same geometric parameters and shown in Figure 6. The same comparison was performed for the A-ECS and is shown in Figure 7. The small difference between the two models is probably due to the effect of the thickness of the disk in the 3-D model. Overall, there is excellent agreement between the two models for P-ECS and A-ECS, giving confidence in the equivalence of the 2-D and 3-D models in this configuration. The 3-D models requires significant computational resources (around 12-16 hours per simulation), and hence the following results are obtained from the 2-D model.

4.2 Simulations for the rotating bladed disk and ECS

In this section, a stationary and time-dependent analyses for an interval of time of 0.36 seconds and at a rotational speed of the rotor equal to 2000 rev/min were performed for the P-ECS model. Regarding the A-ECS model, it is solved for a full period of rotation of the bladed disk $T_0 = 1/\Omega$, for 600 time steps within that time interval.

Figure 8 shows the surface plot of the magnetic flux density's norm for the 2-D model corresponding to the P-ECS and A-ECS cases at the instant when one of the blades passes by the sensor. The magnetic vector potential is also shown by magnetic flux lines induced thorough the plane of the bladed disk. We can notice a variation in the induced magnetic flux lines. This variation is due to the interference between the primary magnetic field generated by the ECS and the secondary magnetic field generated by the moving blades past the sensor. This agrees

with the concept of ECSs described in Section 2.1. Figure 9a shows the corresponding coil voltage captured by the P-ECS when a blade passes by it in the 2-D model. Figure 9b shows the variation of the impedance in the coil due to passing of the blades. As observed for both models, a signal peak is obtained every time a conducting blade enters the field of the sensor which alters the magnetic field through the induced eddy currents in the blades. This describes clearly the behavior of an ECS; based on a reference voltage which will correspond to a known position on the blade, the time of blade passing can be determined. This gives information about the time of arrival of the blade at the sensor probe. In addition, the shape of a single peak corresponding to the P-ECS case, gives a reference to determine when the blade is positioned at the middle of the sensor which gives more detail about the blade positon compared to the shape of signal corresponding to the A-ECS. Figure 10 shows the effect of the variation of the gap (i.e. the distance separating the blade tip and the surface of the sensor during the rotation of the bladed disk) on the sensor output. There is a clear decrease in the signal amplitude with increasing gap between the sensor and blade tip. This shows the sensitivity of the ECS to small distance variations. Finally, Figure 11 shows the effect of the rotational velocity of the bladed disk on the sensor output. The output curves have been shifted so that the blade passes the sensor at the same time. The variation of signal amplitude is more important for the P-ECS than the A-ECS which agree with the fact that the P-ECS is not a displacement sensor and is affected by the target speed while the velocity doesn't affect the A-ECS output. This sensitivity shows that the P-ECS could be more efficient for the BTT measurement.

5 CONCLUSION

This paper has simulated a rotating bladed disk of simple geometry monitored by passive and active eddy current sensors. The aim was to simulate the measurement process used for blade tip timing using eddy current sensors. Eddy current sensors have been considered in this paper due to their robustness in harsh environments. The governing equations modeling the magneto electric field of a moving target have been described for a quasi-static problem. A detailed description of the geometry of the 2-D and 3-D models were described, together with the meshing difficulties encountered due to the rotation, and the physics of the coupled problem of mechanical and electro-magnetic fields. The simulations gave sensor outputs that correspond to those measured and reported in the literature for P-ECS and A-ECS. The parameter studies showed that the eddy current sensor output is sensitive to the air gap and the sensor location, as well as to the rotational speed of the system. This sensitivity can help to understand the errors that could be introduced and the time of blade passing can be estimated more accurately by taking in consideration these effects. Moreover, this modeling approach can be utilized to design and optimize blade tip timing systems with multiple sensors and complex geometries; such studies will be the subject of future research.

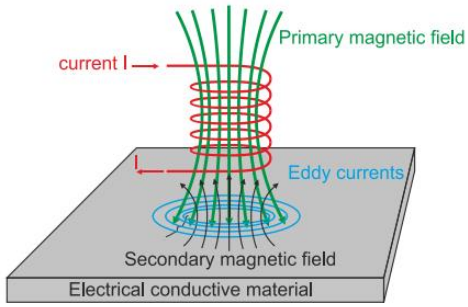

Figure 1: The eddy current sensor concept (adapted from [16]).

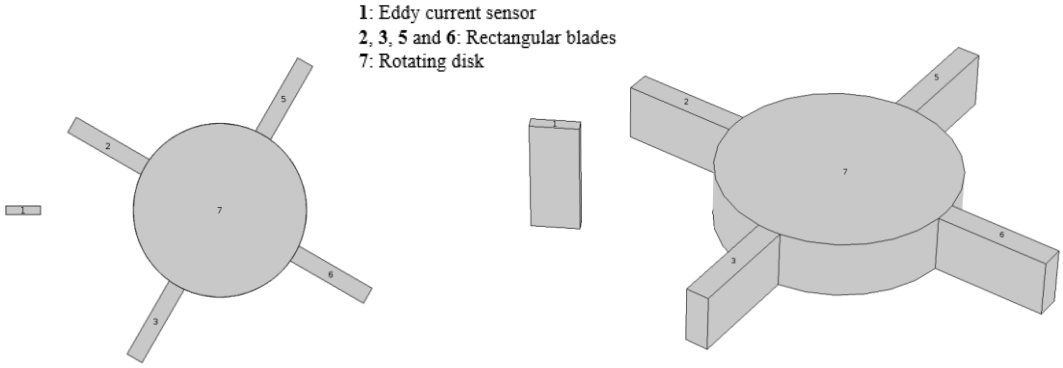

(a) (b)

Figure 2: The geometry of the (a) 2-D model (b) 3-D model

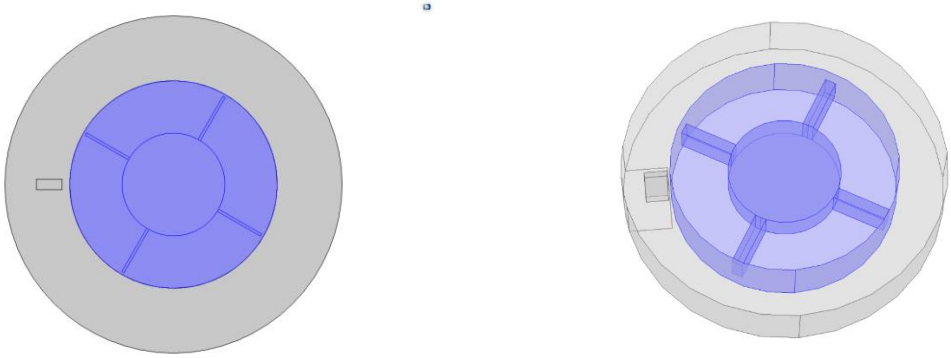

(a) (b)

Figure 3: The static and moving parts of the geometry for the (a) 2-D model (b) 3-D model for P-ECS case

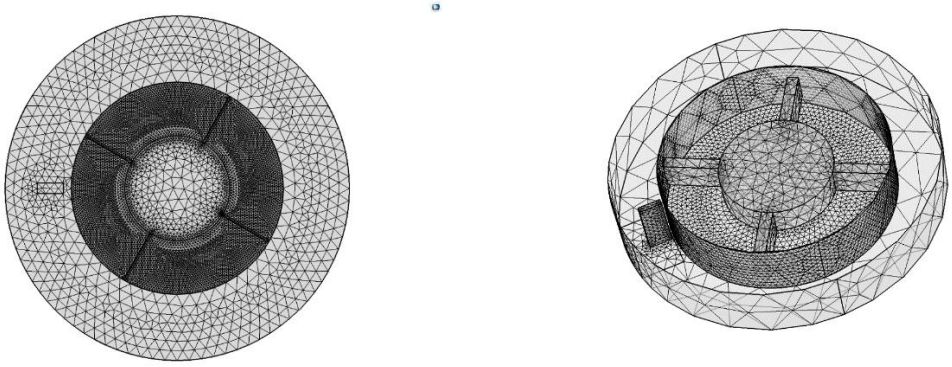

(a) (b)

Figure 4: Meshing details of the (a) 2-D models (b) 3-D model for P-ECS case

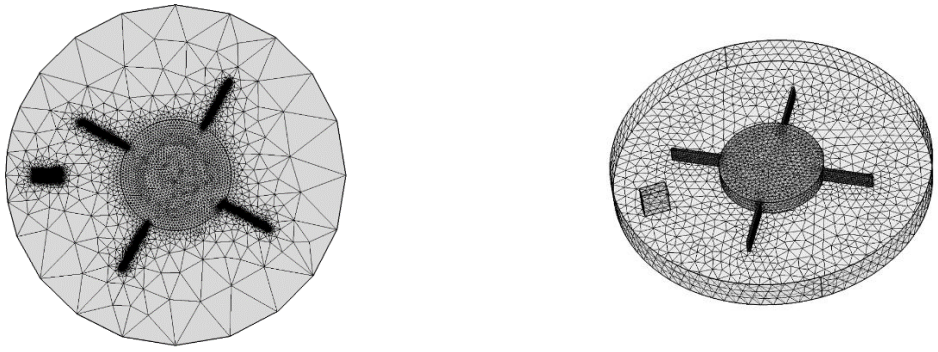

(a) (b)

Figure 5: Meshing details of the (a) 2-D models (b) 3-D model for A-ECS case

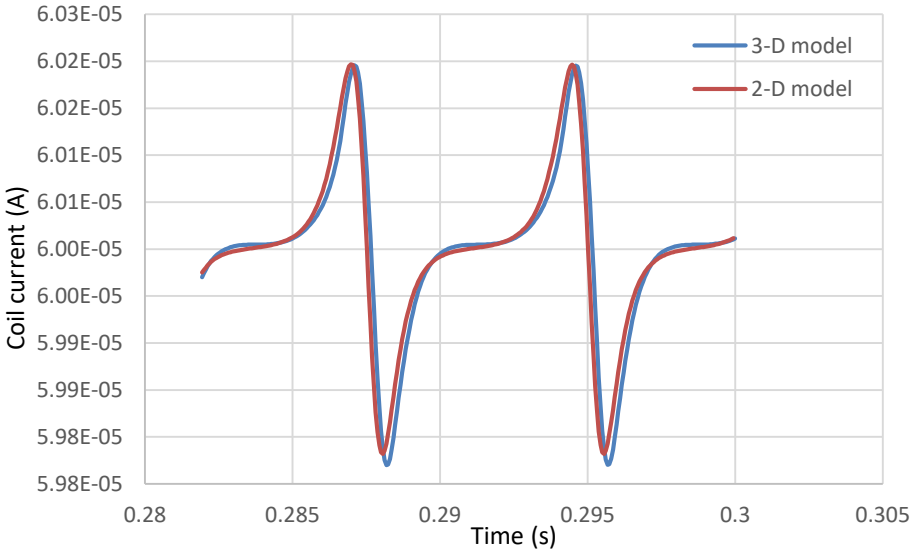

Figure 6: Comparison of the coil current signal of 2-D and 3-D models for the P-ECS case

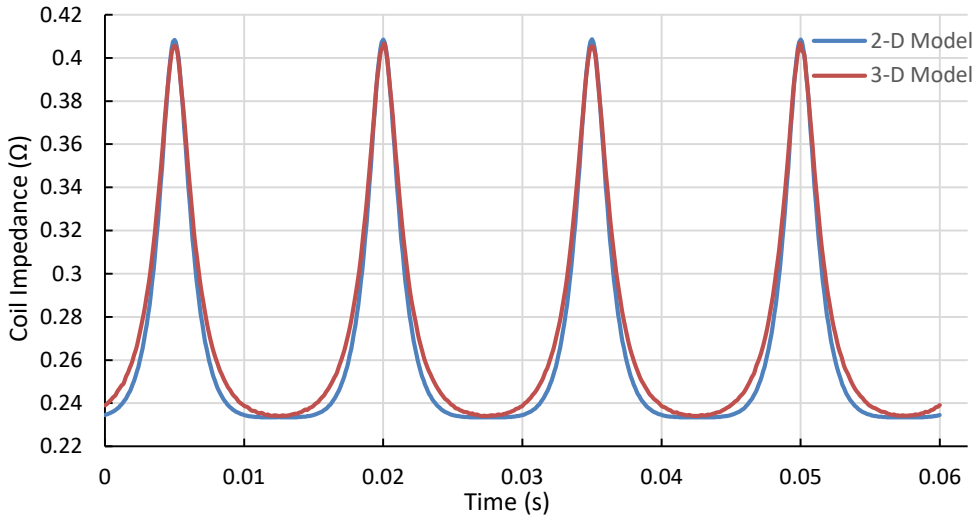

Figure 7: Comparison of the Impedance variation in the coil for the 2-D and 3-D models for the A-ECS case

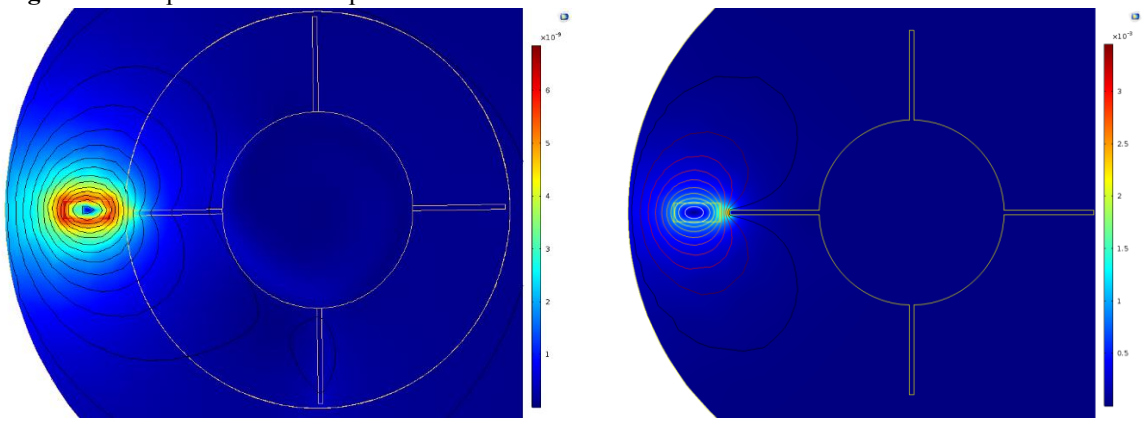

(a) (b)

Figure 8: Magnetic flux density norm (Surface) and Magnetic vector potential Z-component (Contour) for the 2-D model at (a) t = 0.35016s for P-ECS case (b) at t = 0.05s for A-ECS case

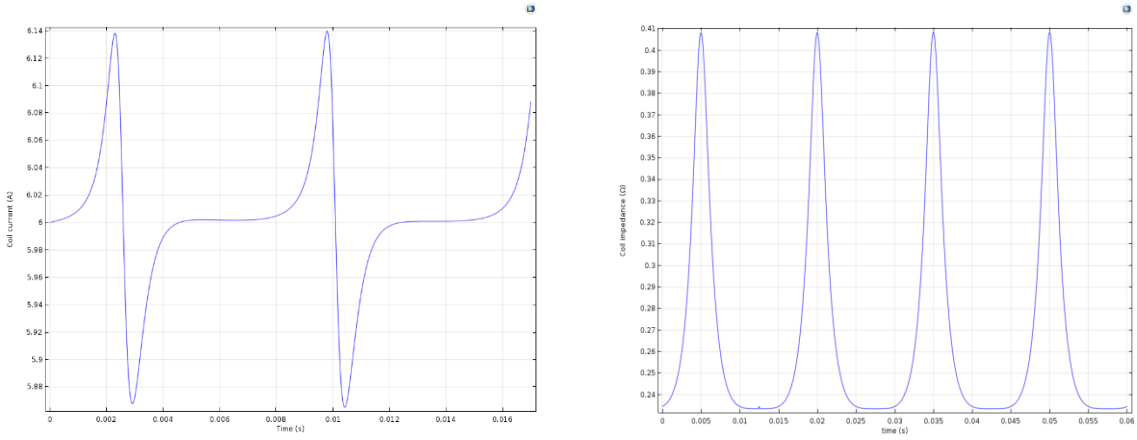

(a) (b)

Figure 9: Output of the ECS corresponding to the 2-D model for the case of (a) P-ECS (b) A-ECS

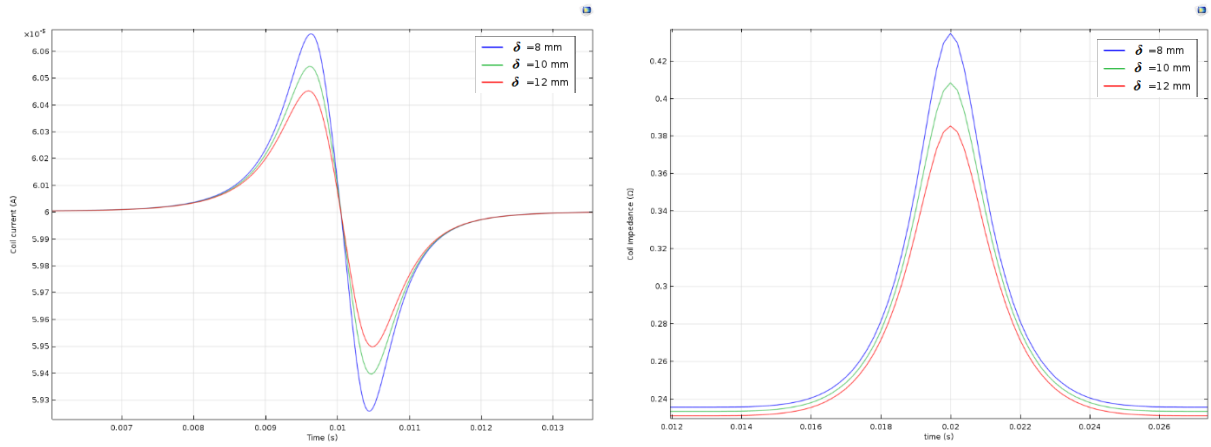

(a) (b)

Figure 10: The induced voltage in the sensor with time for different blade gaps for (a) A-ECS case (b) P-ECS case

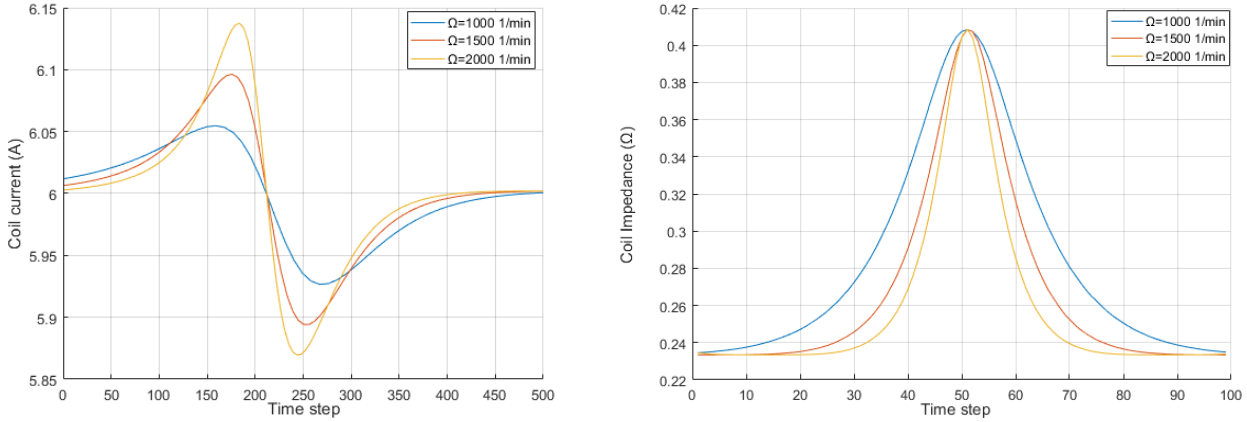

(a) (b)

Figure 11: The induced voltage in the sensor with time for different rotational speeds for (a) A-ECS case (b) P-ECS case (curves shifted to a common point)

ACKNOWLEDGEMENTS

The authors gratefully acknowledge the support of the Qatar National Research Fund through grant number NPRP 7-1153-2-432.

REFERENCES

[1] Fangman, C., Zastrow, V., Bobeck, J. High-speed-turbocharger blade-vibration measurement, Experimental Mechanics, Vol. 7, No. 1, (1967), pp. 19A-21A.

[2] Georgiev, V., Holík, M., Kraus, V., Krutina, A., Kubín, Z., Liška, J., Poupa, M. The Blade Flutter Measurement Based on the Blade Tip Timing Method, Proceedings of the 15th WSEAS International Conference on Systems, Corfu Island, Greece, 2011 July 14–16, pp. 270–275.

[3] Dimitriadis, G., Carrington, I.B., Wright, J.R., Cooper, J.E. Blade-tip timing measurement of synchronous vibrations of rotating bladed assemblies, Mechanical Systems and Signal Processing, Vol. 16, No. 4, (2002), pp. 599-622.

[4] Zablotskiy, I.Y. and Korostelev, Y.A. Measurement of Resonance Vibrations of Turbine Blades with the Elura Device, Energomashinostroneniye, No. 2, (1970), pp. 36-39.
[5] Zablotskiy, I.Y., Korostelev, Y.A, Sviblov, L.B. Contactless Measuring of Vibrations in the Rotor Blades of Turbines, Foreign Technology Division, WP-AFB, Ohio, (1974), 19 pages.
[6] Heath, S. and Imregun, M. An improved single-parameter tip-timing method for turbomachinery blade vibration measurements using optical laser probes, International Journal Mechanical Science, Vol. 38, No. 10, (1996), pp. 1047-1058.
[7] Salhi, B., Lardies, J., Berthillier, M., Voinis, P., Bodel, C. Modal parameter identification of mistuned bladed disks using tip timing data, Journal of Sound and Vibration, Vol. 314, No. (3-5), (2008), 885–906.
[8] Liu, C. and Jiang, D. Improved Blade Tip Timing in Blade Vibration Monitoring with Torsional Vibration of the Rotor, Journal of Physics: Conference Series, Vol. 364, (2012), Conf. (1).
[9] Madhavan, S., Jain, R., Sujatha, C., Sekhar A.S. Vibration based damage detection of rotor blades in a gas turbine engine, Engineering Failure Analysis Vol. 46, (2014), pp. 26–39.
[10] Dowell, M. and Sylvester, G. Turbomachinery Prognostics and Health Management via Eddy Current Sensing: Current Developments, Proceedings of the 1999 IEEE Aerospace Conference, Snowmass at Aspen, CO, 1999 March 6-13, Volume 3 (1999), pp. 1-9.
[11] Lackner, M. Vibration and Crack Detection in Gas Turbine Engine Compressor Blades using Eddy Current Sensors, Master of Science thesis, Massachusetts Institute of technology, Department of Aeronautics and Astronautics, Cambridge (2004).
[12] Chana, K.S. and Cardwell, D.N. The Use of Eddy Current Sensor Based Blade Tip Timing for FOD Detection, Proceedings of the ASME Turbo Expo, Vol. 2, Berlin, Germany, (2008), pp. 169–178.
[13] Mandache, C., Mcelhinney, T., Mrad, N. Aircraft Engine Blade Tip Monitoring Using Pulsed Eddy Current Technology, 4th International Symposium on NDT in Aerospace 2012 - Th.4.A.3.
[14] Karakoc, K., Suleman, A., Park, E-J. Analytical modeling of eddy current brakes with the application of time varying magnetic fields. Applied Mathematical Modeling 40, (2016), pp. 1168-1179.
[15] Rosell, A., Persson, G. Finite element modelling of closed cracks in eddy current testing. International Journal of Fatigue 41, (2012), pp. 30-38.
[16] Pohl, R., Erhard, A., Montag, H-J., Thomas, H-M., Wüstenberg, H. NDT techniques for railroad wheel and gauge corner inspection, NDT & E International, (37), (2004), 89-94.
[17] Weststrate, E., Steinback, M., Rensing, N-M., Tiernan, T. COMSOL Multiphysics Modeling for Design Optimization of Eddy Current Crack Detectors. Excerpt from the Proceedings of the COMSOL Conference 2010 Boston.

VII International Conference on Computational Methods for Coupled Problems in Science and Engineering
COUPLED PROBLEMS 2017
M. Papadrakakis, E. Oñate and B. Schrefler (Eds)

IMPLEMENTATION OF PIEZOELECTRIC COUPLED ELECTRO-MECHANICAL BEHAVIOR FOR DAMAGE DETECTION IN ENGINEERING STRUCTURES

TAMARA NESTOROVIĆ[*] AND NEMANJA MARKOVIĆ[†]

[*] Mechanics of Adaptive Systems, Institute for Computational Engineering
Ruhr-Universität Bochum
Universitätsstr. 150, Building ICFW 03-725, 44801 Bochum, Germany
e-mail: tamara.nestorovic@rub.de

[†] Department for Materials and Structures
Faculty of Civil Engineering and Architecture, University of Niš
Aleksandra Medvedeva 14, 18000 Niš, Serbia
email: nemanja.markovic@gaf.ni.ac.rs

Key words: Damage detection and localization, Piezoelectric coupled problem, Piezoelectric aggregates, Wave propagation, Damage index, Hybrid method.

Abstract. Assessment of the structural condition plays an important role in determining structural reliability. Development of systems which can monitor structural condition should lead to improved structural safety and reliability. Damage detection is a crucial issue in structural health monitoring and represents therefore an important focus of the research interest over the past years. In this work we present the methodology based on implementation of active piezoelectric materials embedded in or attached to engineering structures, which can successfully be implemented for detection of possible damages owing to their coupled electro-mechanical behavior. Here particularly we are focused on piezoelectrically induced wave propagation through concrete structures, with the aim of damage detection. The method presented here is based on determination of damage indices which reflect the energy variations of the output piezoelectric sensor signals. Due to wave energy change in directions between actuators and sensors in the presence of a damage it is possible to locate the damage by overlaying the images of the damage indices in different directions. Implementation of the method is documented by examples.

1 INTRODUCTION

Piezoelectric materials offer a wide range of implementation possibilities owing to the coupled electro-mechanical behaviour which can be manifested in terms of a direct or indirect piezoelectric effect. One important implementation enables structural condition assessment within active structural health monitoring which comprises damage detection, localization and prediction.

In this paper, a novel damage localization method based on the one-dimensional damage index (DI) calculation is proposed. One-dimensional DI based on the wave propagation energy and the wavelet signal decomposition has been widely used for damage detection in reinforced concrete (RC) structures using non destructive techniques, e.g. [1-3]. In this paper, DI is used in an original way as a parameter for 2D damage localization. The wavelet signal decomposition is used as the signal processing tool to analyze the sensor output signals in the

wave propagation. The reasons are the excellent properties and possibilities for the application in relatively narrow frequency band and relatively short time window. The robustness of the approach is based on the multifunctional nature piezoelectric materials owing to the coupled electro-mechanical behaviour, making them suitable for both actuation and sensing. This property is used in the present approach to extend the one-dimensional energy based damage index for 2D damage localization.

2 NUMERICAL MODELING OF THE COUPLED ELECTRO-MECHANICAL BEHVAIOR AND WAVE PROPAGATION

The proposed method for the damage detection and localization based on the damage indices utilizes the electro-mechanical coupling in piezoelectric materials which are used in terms of transducers or smart aggregates (further regarded as PZT SA) integrated on or within a structure under investigation to induce and register the waves propagating through the structure.

2.1 FE modeling of the coupled electro-mechanical behavior of piezoelectric materials

Piezoelectric materials can operate in one of two modes: the converse effect, producing a strain or mechanical deformation in response to an applied electrical field; and the direct effect, producing an electrical charge in response to an applied stress. FE modeling of piezoelectric materials is based on constitutive equations for coupled electro-mechanical behavior. A set of constitutive equations for a piezoelectric linear medium, used for modeling within a standard FE software can be expressed in terms of (1) or (2), with the following notation: σ_{ij}, ε_{ij} mechanical stress and strain tensors, respectively; q_i the electric "displacement" vector, D_{ijkl}^{E} elastic stiffness matrix of the anisotropic material, defined at zero electrical potential gradient; e_{mij}^{φ}, d_{mkl}^{φ} piezoelectric stress and strain coefficient matrices of the anisotropic material, E_i electrical potential gradient vector, $D_{ij}^{\varphi(\varepsilon)}$ dielectric properties strain matrix of the orthotropic material. The electrical behavior is defined by (3).

$$\sigma_{ij} = D_{ijkl}^{E}\varepsilon_{kl} - e_{mij}^{\varphi}E_m \tag{1}$$

$$\sigma_{ij} = D_{ijkl}^{E}\left(\varepsilon_{kl} - d_{mkl}^{\varphi}E_m\right) \tag{2}$$

$$q_i = e_{ijk}^{\varphi}\varepsilon_{jk} + D_{ij}^{\varphi(\varepsilon)}E_j \tag{3}$$

The piezoelectric effect is governed by the coupled mechanical equilibrium (4) and electric flux conservation (5) equations.

$$\int_V \sigma : \delta\varepsilon dV = \int_S t \cdot \delta u dS + \int_V f \cdot \delta u dV \tag{4}$$

$$\int_V q : \delta E dV = \int_S q_S \cdot \delta\varphi dS + \int_V q_V \cdot \delta\varphi dV \tag{5}$$

Here σ is the Cauchy stress tensor, t the traction across a point of the surface of the body, f the body force per unit volume, q the electric flux q_S the electric flux per unit area entering the body at a point on its surface, q_V the electric flux entering the body per unit volume. In modeling of the piezoelectric effect for the characterization of the wave excitation and sensing the coupled piezoelectric behavior is considered in terms of deformation induced by the piezoelectric effect.

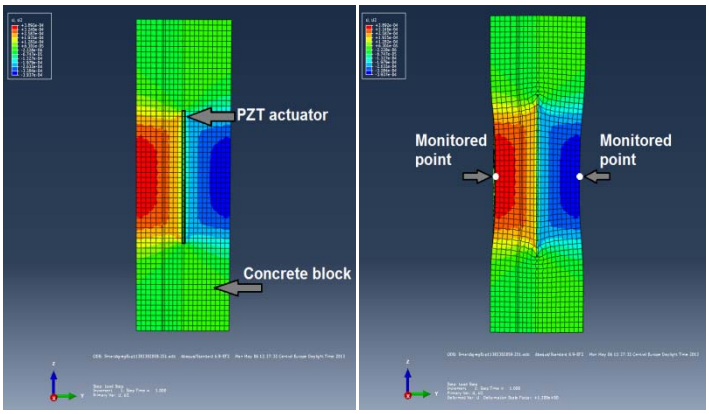

Figure 1: Undeformed (left) and deformed (right) state of the aggregate with bonding between the active piezoelectric material and the surrounding structure

For that purpose application of the voltage to the piezo actuator or embedded aggregate is assumed, which in turn produces appropriate structural deformation. In a particular case of damage detection in concrete structures the model of a piezoelectric material is assumed as orthotropic for the definition of dielectric properties and the concrete structure is modelled with linear elastic material properties assigned from the FE software data bank (here particularly eight-node linear piezoelectric brick element C3D8E in the ABAQUS software). In addition, the proportional Rayleigh damping is assumed. The contact surface between the piezoelectric material and the concrete structure is defined using the tie constraints which assume equal displacement of the corresponding joint nodes. As a result of the quasi-static analysis [4] performed by applying linearly increasing step-wise constant electrical voltage (from 0V to 100V with 10V step) the linear relation between the applied electric voltage and the mechanical displacement at considered contact point is obtained, Fig. 1. Thus, for further numerical consideration the obtained results for the maximal displacement are used as the input parameter for the initiation of the wave propagation modeling using explicit FEM.

2.2 Modeling of the wave propagation using explicit finite element approach

Starting point for modeling of the wave propagation using the Explicit Finite Element Method (EFEM) is the second Newton law written in matrix form [5]:

$$F = M \cdot A \tag{6}$$

with:

$$F_i^m = -\int_\Omega \left(\sigma_{ij}\Phi_{M,j}\right) d\Omega + \int_\Omega f_i \Phi_M d\Omega + \int_{\Gamma_s} g_i \Phi_M d\Omega \tag{7}$$

$$M_{MN} = \int_{\Omega} \left(\rho \Phi_M \Phi_N \right) d\Omega \tag{8}$$

$$A_i^N = \ddot{u}_i^N \left(t \right) \tag{9}$$

Detailed explanation of the terms in (6)–(9) can be found in [5]. The system defined by (6) represents a system of differential equations of second order in time, which in general case can be linear or nonlinear. In order to solve this system, the explicit scheme based on the method of central differences for the approximation of acceleration, velocity and displacement has been used. Assuming that the time range $(0,T)$ is steadily divided into N even sub-domains $[t_n, \ t_{n+1}]$, where $0 = t_0 < t_1 < ... < t_N = T$, $t_{n+1} - t_n = \Delta t = T/N$, the displacement, velocity and acceleration differentiated through time and approximated by the method of central differences, can be expressed in the vector form:

$$\begin{gathered} \partial_t u_{n+1/2}^h = \left(u_{n+1}^h - u_n^h \right) / \Delta t \approx \dot{u}_{n+1/2}^h \\ \partial_{t^2} u_n^h = \left(\partial_t u_{n+1/2}^h - \partial_t u_{n-1/2}^h \right) / \Delta t = \left(u_{n+1}^h - 2u_n^h + u_{n-1}^h \right) / \Delta t^2 \\ \ddot{u}_n^h \approx \left(\dot{u}_{n+1/2}^h - \dot{u}_{n-1/2}^h \right) / \Delta t \end{gathered} \tag{10}$$

$$\begin{gathered} \partial_t u_{n+1/2}^h = \partial_t u_{n-1/2}^h + \partial_{t^2} u_n^h \Delta t \\ u_{n+1}^h = u_n^h + \partial_t u_{n+1/2}^h \Delta t \end{gathered} \tag{11}$$

For the approximation of acceleration by the method of central differences, which is presented by equations (10) and (11), the equation (6) has been defined in the form:

$$\partial_{t^2} u_n^h = M^{-1} \cdot F_n \tag{12}$$

Equation (12) is stable if the time step Δt is less than or equal to the critical time step Δt_{crit}, which for the non-damping systems has been given depending on the biggest frequency in the smallest finite element.

$$\Delta t \le \Delta t_{crit} = \frac{2}{\omega_{\max}} \tag{13}$$

For the modeling of the wave propagation, with the assumption that small deformations can occur, it has been adopted that the critical time step is the time of propagating the waves through the smallest finite element:

$$\Delta t \le \Delta t_{crit} = \frac{\Delta L}{c_L} \tag{14}$$

with: ΔL – the smallest characteristic dimension of the finite element, Δt – the time step and Δt_{crit} – the critical time step.

By the analysis of equation (14) it is easy to come to a conclusion that for the smaller finite elements the smaller time step is required. With this regard the calculation of characteristic values with finer finite element meshes, becomes computationally more demanding.

Furthermore, since it is usual to use at least ten finite elements per wavelength, for modeling of the ultrasound wave propagation even relatively small models are very demanding from the computational point of view.

3 ENERGY BASED DAMAGE LOCALIZATION APPROACH

3.1 One-dimensional damage index

The starting point for the energy based hybrid method is determination of the damage index, which is in the first approach defined as a one-dimensional index calculated based on the time domain measured (output) sensor signal. The output sensor signal can be decomposed into 2^n signal sets (Deubechies wavelet base db9 is used as the mother wavelet) denoted as $\{X_1, X_2, ..., X_{2^n}\}$. Each of the signals X_j can be represented in the following way:

$$X_j = \left[x_{j,1}, x_{j,2}, ..., x_{j,m} \right] \tag{15}$$

where m represents the number of measured data of the time signal, and n is the level of the wavelet signal decomposition (here $n = 3$). The energy of the decomposed output signal S is then defined using the following relation:

$$E_{i,j} = \left\| X_j \right\|_2^2 = x_{j,1}^2 + x_{j,2}^2 + ... + x_{j,m}^2 \tag{16}$$

where i is the time index and j the frequency range, $j = 1, 2, ..., 2^n$. The energy of the decomposed output signal is then defined for an undamaged (health) E_h and damaged state E_o respectively in the following way:

$$E_h = \left[E_{h,1}, E_{h,2}, ..., E_{h,2^n} \right], \quad E_o = \left[E_{o,1}, E_{o,2}, ..., E_{o,2^n} \right]. \tag{17}$$

A one dimensional damage index DI based on the output signal energy variation is formed as a root-mean-square deviation:

$$DI = \sqrt{\frac{\sum_{j=1}^{2^n} \left(E_{o,j} - E_{h,j} \right)^2}{\sum_{j=1}^{2^n} E_{h,j}^2}} \tag{18}$$

Its values may vary from zero for undamaged structures up to the value of one associated with the complete structural collapses. The increase of the damage index is associated with the increase of the damage within a structure and therefore it is possible to monitor condition of the structure by monitoring the variation of the damage index.

3.2 Implementation of the damage indices for 2D damage detection problems

The proposed method is here aimed at damage detection and localization in concrete structures. It is developed for the arbitrary shape of a 2D reinforced concrete element and for the arbitrary configuration and number of the applied PZT SA. The actuator (point i in Fig. 2) at a single time point causes the propagation of a mechanical wave, while all other PZT SA

are used as sensors detecting the transmission wave (points denoted as j, k, …, f in Fig. 2). Successively, the next PZT SA is activated, while all others are used as sensors, etc. In this way the covered area is divided into a finite number of triangles connected along the common edges, which edge points are defined by the PZT SA actuator and the adjacent sensors.

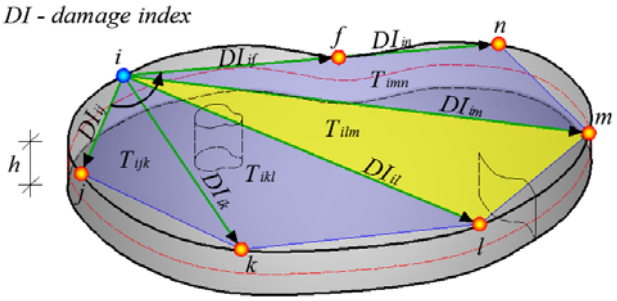

Figure 2: Division of the analyzed area into triangles (T) and damage index values (DI) for actuator-sensor directions

For each actuator-sensor pair, the one dimensional damage index is calculated according to equation (18). It is assumed that the damage index D_{ij} has constant value along the entire actuator-sensor direction. Damage indices for all pairs are stored in the matrix M_{DI}, equation (19). The elements DI_{ij} (i=j) are equal to zero, while other elements are generally non-zero, and for the non-symmetric problem $DI_{ij} \neq DI_{ji}$.

$$M_{DI} = \begin{bmatrix} DI_{11} & DI_{12} & \cdots & DI_{1j} & \cdots & DI_{1n} \\ DI_{21} & DI_{22} & \cdots & DI_{2j} & \cdots & DI_{2n} \\ \vdots & \vdots & \ddots & \vdots & \cdots & \vdots \\ DI_{i1} & DI_{i2} & \cdots & DI_{ij} & \cdots & DI_{in} \\ \vdots & \vdots & \cdots & \vdots & \ddots & \vdots \\ DI_{n1} & DI_{n2} & \cdots & DI_{nj} & \cdots & DI_{nn} \end{bmatrix} \tag{19}$$

The damage indices are interpolated linearly within each of the triangles formed by an actuator and two sensor points. The interpolation procedure is performed within a Matlab code which uses the dimensions of the RC element, coordinates of the PZT SA, connectivity matrix for the triangles defined by the actuator-sensor pairs and DI values for all actuator-sensor pairs as its inputs. The program divides the RC element into the finite element mesh with the mesh density of FL, and calculates the DI for each node n, using the linear interpolation procedure in the following way:

$$DI_n = \frac{\sum_{i=1}^{s} DI_i}{s} \tag{20}$$

where $\sum_{i=1}^{s} DI_i$ is the sum of all damage indices in the current node for all actuator-sensor pairs, while s is the number of summations at current node.

4 IMPLEMENTATION EXAMPLES AND DISCUSSION

Implementation of the DI based method for damage detection and localization is presented by some numerical examples and experimental verification. The wave propagation is employed for detection of crack-type damages as well as for the detection and localization of hole-type damages in RC specimens.

4.1 Detection of inclined and vertical crack using one dimensional DI

Considered structure is an RC element, dimensions 0.6×0.2×0.2 [m] with the reinforcement 4∅20 and with two PZT SA (Fig. 3). The parametric analysis of the damage index variation was performed, depending on the position (L_p), size (H_p) and orientation (α_p) of the crack in the mentioned RC element. The position of the cracks, for models with vertical crack, was varied from the value 0.15m to 0.45m with the increment of 0.05m. The lengths of the cracks 0.05, 0.08, 0.11 and 0.14m were analyzed as well as the crack angles from 60º to 120º, with 10º counterclockwise increments.

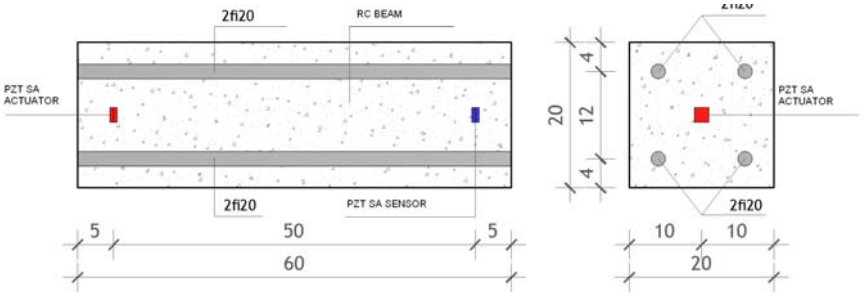

Figure 3: Geometric characteristics of the RC element

Concrete and reinforcement are modeled as linear-elastic materials with following material characteristics: Young's elasticity modulus of concrete is $30 \cdot 10^9$ Pa and of steel $210 \cdot 10^9$ Pa; Poisson's ratio of concrete is 0.2 and of steel 0.3, while the density of concrete is 2400kg/m^3 and of steel 7800kg/m^3.

Displacements obtained from the model of PZT SA were used as an input parameter for modeling of the wave propagation, performed in ABAQUS/EXPLICIT software package. Function of the displacement variation used in the analysis is 3.5-cycle Hanning windowed tone burst signal with duration of $T_{sig}=3.5 \cdot 10^{-5}$ s and central frequency $f_{cen}=100$ kHz.

The contact of the concrete and the reinforcement is defined by *Tie Constraint* surface contact available in ABAQUS/EXPLICIT analysis with the potential for rotational degrees of freedom. The crack was modeled as an opening in the model, having the thickness of a finite element with a length and orientation defined for each individual model separately. The total duration of the simulation was $T_{sim}=0.001$s, and the adopted time increment was $\Delta t=2e^{-7}$s, which satisfies the critical time increment. The applied finite elements were C3D8R eight-node prismatic finite elements with reduced integration and Hourglass control.

Fig. 4 represents the wave propagation through RC element with inclined crack damage. The element is cut through the medium vertical plane in the direction of RC element in order to

better display propagation of the waves inside the RC element. Fig. 4c and 4d show that the waves partly reflect on the crack and return to the actuator, weakening thus the propagating wave and reducing the energy of the output signal. The other part of the wave passes the crack nearby, propagating through the RC element and reaching the PZT SA sensor.

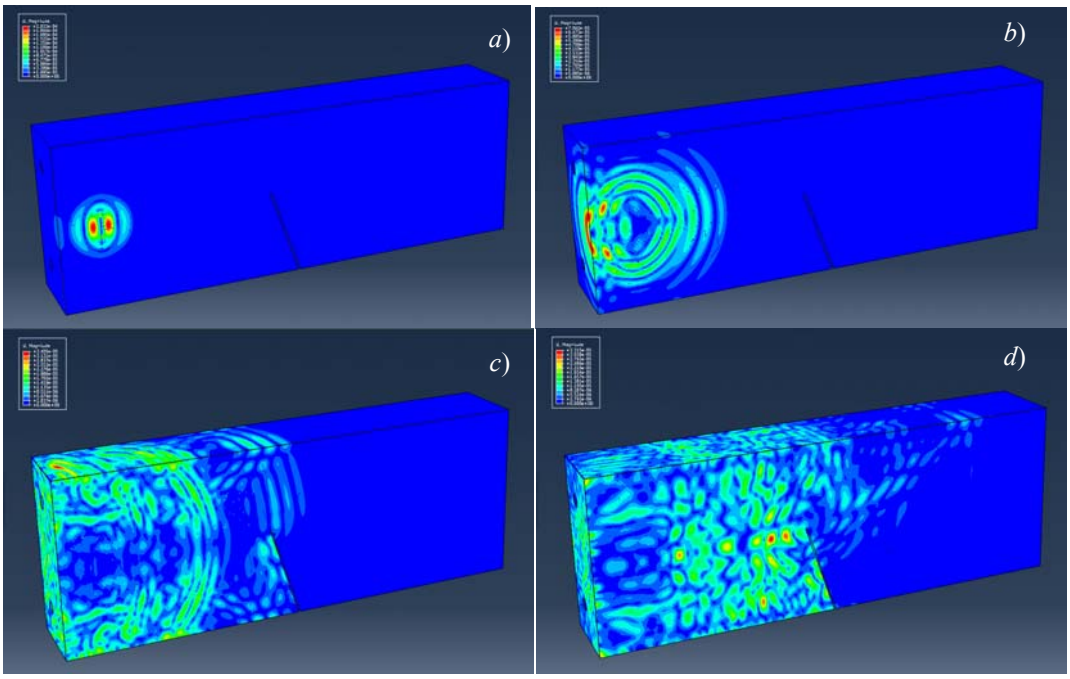

Figure 4: Wave propagation in model with inclined crack caused by PZT PA actuator at different time instants: *a*) $t = 2.0172 \cdot 10^{-5}$ s, *b*) $t = 4.0172 \cdot 10^{-5}$ s, *c*) $t = 8.0172 \cdot 10^{-5}$ s, *d*) $t = 1.4011 \cdot 10^{-4}$ s.

Figures 5 and 6 represent the values of the damage index for different analyzed models depending on the position, length and orientation of the crack. The values are displayed over the geometry of numerical models in order to observe the change of the damage index more easily for the models with vertical (Fig. 5) and with inclined cracks (Fig. 6).

Fig. 5 shows that the change of the damage index value is not drastically depending on the position of the crack and that the values most frequently differ up to several percents. Also, the shape of the damage index variation is convex for the models with crack length of 0.05 m while in case of the models having crack lengths of 0.11 and 0.14 m the shape is concave. The model with the crack length of 0.08 m has approximately same values of the damage index, with the mild convex trend. In case of the model with slant cracks (Fig. 6) the variation of the damage index depending on the gradient of the cracks basically does not exceed 5%. Also the models with vertical cracks mainly do not exceed the mentioned percentage. A small percentage of DI variation depending on the position and orientation of the crack leads to the conclusion that DI is in direct relation with the size of the crack, position of the PZT SA actuator-sensor as well as geometry of RC beam, and does not depend much on the position and orientation of the damage.

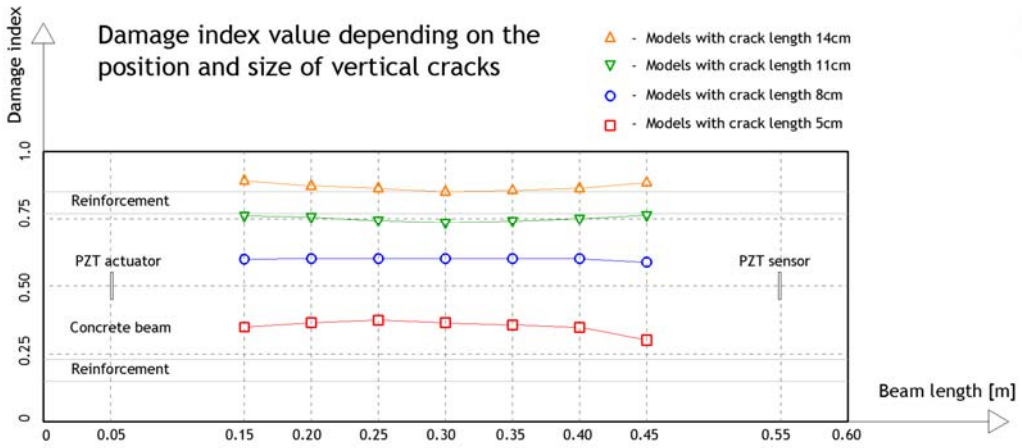

Figure 5: Damage index value depending on the position and size of vertical cracks.

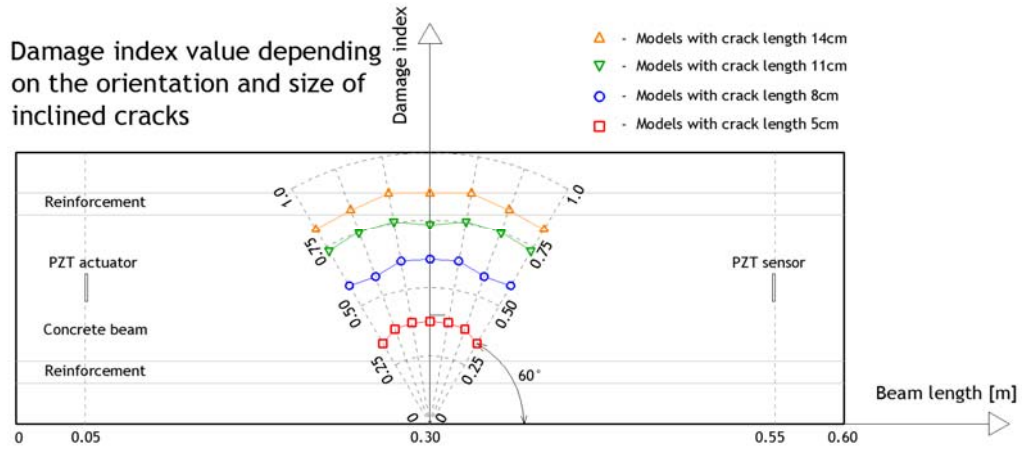

Figure 6: Damage index value depending on the orientation and size of inclined cracks.

4.2 Damage localization using hybrid method

Using the hybrid approach and the methodology explained in section 3.2 damage localization was performed based on several different models of square RC plates with hole-type damages. The analyzed elements have dimensions 40×40 [cm], thickness 4 cm, and are either with a single circular hole of radius 4 cm, or with two holes of the same radii. The behavior of the damaged models has been compared with the intact one. The number of PZT SA has been varied (the models with 12, 16 and 20 actuators/sensors have been adopted). The models with multiple damages have been analyzed in order to check the applicability of the method for the localization of multiple damages in the RC element. Wave propagation modeling was performed under same conditions as in section 4.1. Results of the wave propagation modeling and analyses are presented in the following Fig. 8 and 9.

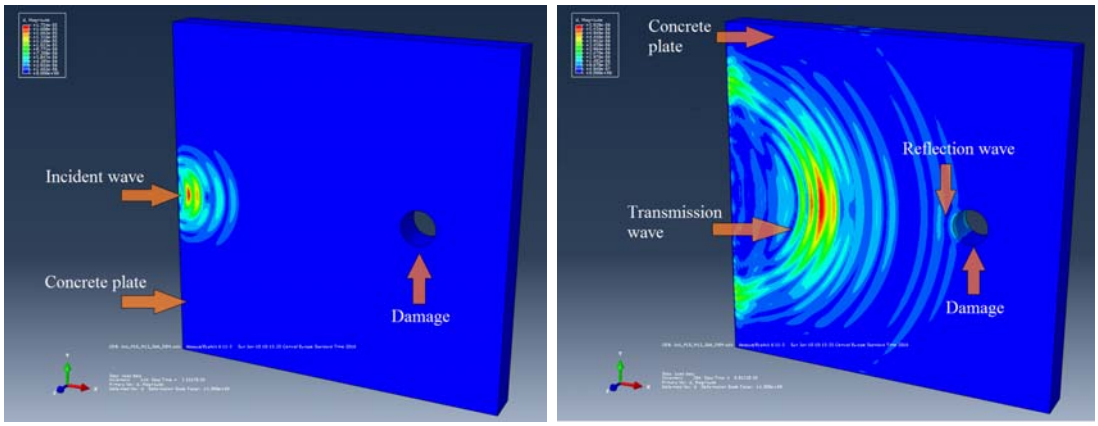

Figure 8: Wave filed: *a*) free wave propagation at t=3.223·10^{-5}s, *b*) wave reflection at t=8.81·10^{-5}s.

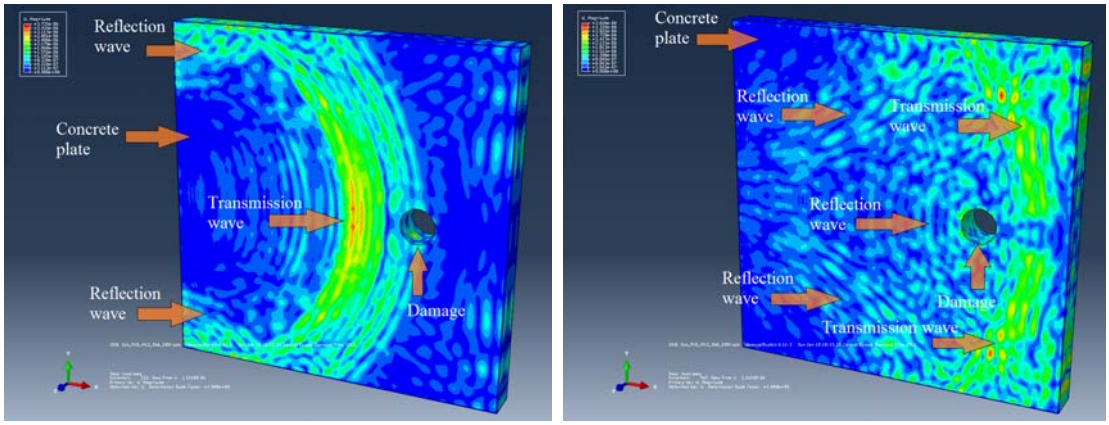

Figure 9: Wave filed: *a*) damage passing at t=1.522·10^{-4}s, *b*) further wave propagation at t=2.240·10^{-4}s.

Fig. 8*a* illustrates the initiation of wave propagation from the actuator through the damaged plate with a single hole. At that moment the wave propagates freely through the RC plate and its propagation is restricted only along the top and bottom plate surface. The first wave reflection from the damage is shown in Fig. 8*b*. The wave reflection from the plate ends, as well as the propagation of the primary part of the wave towards the damage, is clear from Fig. 9*a*. Fig. 9*a* illustrates the propagation of the wave at the moment when the wave passes the damage. It is clear that the entire wave could not pass the damage, and that the part of the wave was reflected in the opposite direction. Further propagation of the reflected waves from the plate ends is shown in Fig. 9*b*.

For different analyzed scenarios, the corresponding models in ABAQUS/EXPLICIT have been generated, and the simulations of the wave propagation for all possible combinations of the PZT SA sensor/actuator have been conducted. For all sensors, the output signals have been read in time domain and the wavelet signal decomposition has been performed. For all decomposed signals, the signal energy has been calculated and the damage indices have been derived. Using the own Matlab code and the previously described procedure of the hybrid

approach the damage localization has been performed. Representative results are presented in Fig. 10 and 11.

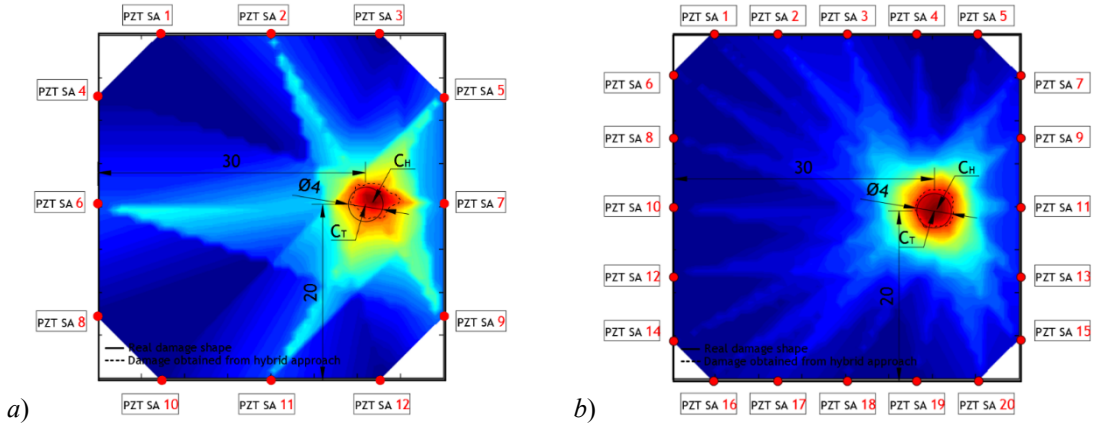

Figure 10: Damage localization for models with different number of sensing points (one hole model) *13 & 15*

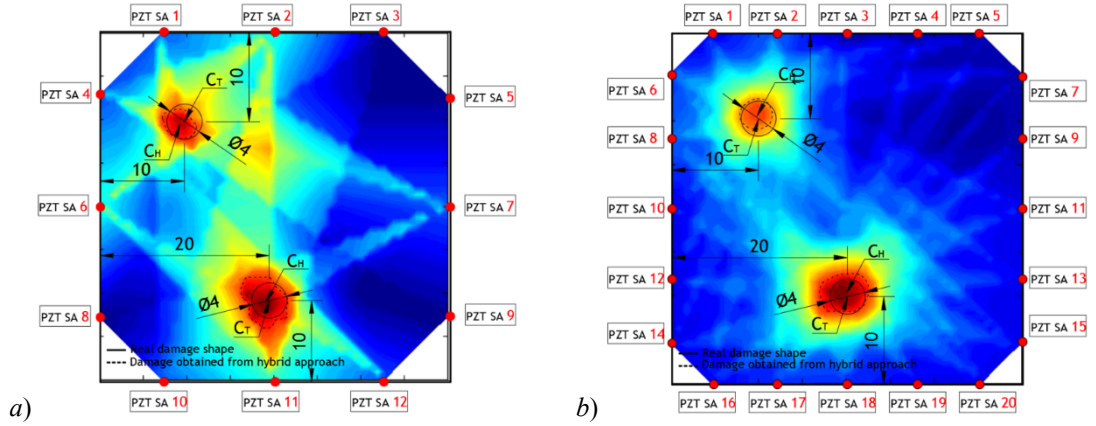

Figure 11: Damage localization for models with different number of sensing points (two hole model) *16 & 18*

The analysis of the obtained results has shown a good agreement between the shape and position of the damage detected by the hybrid approach and its assumed real shape and position. The deviation of the damage centroid position (C_T – "real", C_H – obtained by hybrid approach, Fig. 10 and 11) does not exceed 1 cm for all investigated models, while for most of them it does not exceed the range of several millimeters, which suggests that the proposed approach is very good for the damage localization.

4.3 Experimental verification

Verification of the proposed approach has been performed under laboratory conditions using a laser scanning based system with piezoelectric excitation of the wave propagation. For the excitation the piezoelectric transducer S 24 HB (product of Karl Deutsch) in the frequency range with the central frequency 100Hz was used, and for the response data acquisition – the ultrasonic laser scanning receiver BNT Quartet 500 produced by the Bossa Nova Technologies. Fine resolution positioning of the ultrasonic receiver is enabled by implement-

tation of a positioning system (own development of the Research Group Mechanics of Adaptive Systems, Ruhr University Bochum), installed on the vibration isolating optic table Newport M-RS200-46-8. Results of the damage detection and localization based on the experimentally acquired data with three actuation/sensing points along each side of the RC plates are presented in Fig. 12*a* for the one hole model (compare with Fig. 10*a*) and in Fig. 12*b* for the two hole model (compare with Fig. 11*a*). A very good agreement verifies the proposed approach.

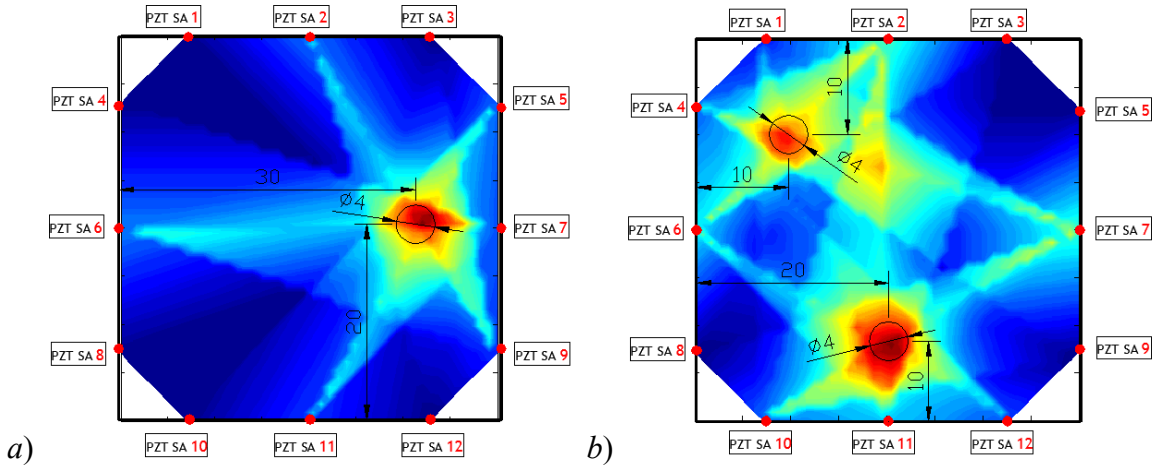

Figure 12: Damage localization based on experimental data.

5 CONCLUSION

The paper presents an efficient hybrid method for damage detection and localization in engineering structures using a damage index approach based on the wave propagation initiated by excitation through piezoelectric materials. The proposed method has been investigated numerically and experimentally and a very good agreement of the obtained results provides a promising basis for further implementation and development.

REFERENCES

[1] Song G., Gu H., Mo Y.L. and Hsu T.T.C. Concrete structural health monitoring using embedded piezoceramic transducers, *Smart Mater. Struct*. (2007) **16**: 959-968.

[2] Hu B., Kundu T., Grill W., Liu B. and Toufing V. Embedded piezoelectric sensors for health monitoring of concrete structures, *ACI Materials Journal* (2013) 149-158.

[3] Liao W. I., Wang J.X., Song G., Gu H., Olmi C., Mo Y.L., Chang K.C. and Loh C.H. Structural Health Monitoring of concrete columns subjected to seismic excitations using piezoceramic-based sensors, *Smart Mater. Struct.* (2011) **20** 125015.

[4] Markovic, N., Nestorovic, T. and Stojic, D.: Numerical modeling of damage detection in concrete beams using piezoelectric patches, *Mech Res Commun* (2015) **64**: 15-22

[5] Shen, R. and Wu, L.G. *Introduction to the Explicit Finite Element Method for nonlinear transient dynamics.* Wiley (2012).

VII International Conference on Computational Methods for Coupled Problems in Science and Engineering
COUPLED PROBLEMS 2017
M. Papadrakakis, E. Oñate and B. Schrefler (Eds)

METHOD OF CALCULATING THE SEPARATION FLOW WITH DUST PARTICLES AT THE ENTRANCE TO ROUND SUCTION PIPE IN CONDITIONS OF THE APPROACH FLOW

A. K. LOGACHEV*, O. A. AVERKOVA*, E. I. TOLMACHEVA*

* Belgorod State Technological University named after V.G. Shukhov
(BSTU named after V.G. Shukhov), 308012 Belgorod, Russia
e-mail: kilogachev@mail.ru, web page: http://www.bstu.ru

Key words: discrete vortex method, separated flows, flows in suction channels, local exhaust ventilation.

Abstract. Modeling the separation flows at the entrance to suction ducts is necessary to determine the efficient intake area, jet contraction coefficient and the velocity fields in their radius of action. The simplest and the most thoroughly researched one is the separation flow at the entrance to the round thin-walled suction pipe, which is a part of many process facilities; simulation of flows in its range of action is considered in many scientific works. For the numerical modeling of such flows the boundary element method [1], the numerical solution of Navier-Stokes equations for viscous incompressible fluid [2] and the discrete vortex method were used. In the paper [3] there was developed a method of mathematical modeling of flow separation at the entrance to suction ducts with the use of stationary discrete vortexes. On the free surface of the flow the free vortexes circulation was set, after which the average velocity in the suction duct and the velocity field were approximately determined. The approach flow should be taken into account only if its velocity is lower than the intake velocity in the pipe. Modernization of this method seems to be of interest, as it would allow calculating the separation flow characteristics for both high-velocity and low-velocity approach flows. This can be obviously achieved if the intake velocity in the pipe is set, and the circulation on the free vortex sheet is determined in the process of the problem solution.
The purpose of this work is developing the method of mathematical modeling of separation flow at the entrance to round thin-walled suction pipe at the presence of an approach flow using stationary discrete vortexes, as well as its verification.
The developed method of mathematical modeling of separation flow at the entrance to suction pipe at the presence of an approach flow allows building the appropriate velocity field of an air flow, the limit trajectories of dust particles and determining the aspiration coefficient.

1 INTRODUCTION

The modeling of separation flows at the entrance to suction ducts is necessary for determining the efficient suction area, the jet constriction coefficient and velocity fields in their range of action. The simplest and the best researched is the separation flow at the entrance to round thin-walled suction pipe, which is a part of many technological facilities; a

lot of scientific research works are devoted to modeling flows in its range of action. For the numerical modeling of such flows the boundary-element method [4], the numerical solution of Navier-Stokes equations for viscous incompressible liquid [2,4] and discrete vortex method [5-7] were used. In this paper [7] there was developed a method of mathematical modeling of flow breakdown at the entrance to suction ducts with the use of stationary discrete vortexes. The free vortexes circulation was set on the free stream surface, after which the average velocity at the suction pipe and the velocity field were calculated approximately. The approach flow is taken into account only if its velocity is lower than the suction velocity in the pipe. Modernization of this method is of great interest, which would allow calculating the properties of separation flow, both for the low-velocity and the high-velocity approach flow. This can be obviously done, if we define the suction velocity in the pipe, and the circulation on the free vortex sheet is determined in the process of numerical calculation.

The purpose of this work is to develop a method of mathematical modeling of the separation flow at the entrance to round thin-walled suction pipe in conditions of the approach flow with the use of stationary discrete vortexes, and its verification.

2 THE MAIN CALCULATION RATIOS AND THE COMPUTING ALGORITHM CONSTRUCTION

The discrete mathematical model (fig.1) is built in the following way. At the flow boundary there are infinitely thin vortex rings (black circles in fig.1) and control points (crosses in fig.1) – the arbitrary points on the circle, embracing the pipe, or on the suction section. Let us point out, that in the suction section on the symmetry axis the zero radius vortex is located, so it's not taken into account. The number of discrete vortex rings is equal to the number of control points. In the control points on the pipe walls the impermeability condition is performed – the velocity along the normal direction amounts to zero. In the suction section the velocity along the outward normal direction is similar and amounts to v_0. The division to discrete vortex rings and control points is uniform, the control points are in the centre among the vortex rings. The distance between two neighbouring vortex rings is equal to discrete pitch size r_h. The free stream surface consists of free vortex rings (hollow circles in fig.1) and is formed on the sharp edge *A* of the pipe. It is determined by iterational method, as further described. Parallely to the pipe axis the flow approaches with the velocity v_∞.

Let us define N – the number of the attached vortex rings; N_s - the number of free vortex rings; x^p - control point, $p = 1,2,\ldots,N$.

The velocity in the arbitrary point *x* along the $\vec{n}$ direction is calculated by the formula:

$$v_n(x) = \sum_{q=1}^{N} \Gamma(\xi^q) G(x,\xi^q) + \gamma \sum_{q=1}^{N_s} G(x,\zeta^q) + n_1 v_\infty , \qquad (1)$$

where ξ^q - the location point of the *q*-th attached vortex ring with circulation $\Gamma(\xi^q)$, $\gamma = \text{const}$ - circulation of a free vortex ring, ζ^q - the location point of the *q*-th free vortex ring.

The function $G(x,\xi)$ expresses the influence on point $x(x_1,x_2)$ of the vortex ring with singular circulation, located in point $\xi(\xi_1,\xi_2)$.

$$G(x,\xi)=\frac{4(A_1b+A_2a)E(t)}{b(a-b)\sqrt{a+b}}-\frac{4A_2F(t)}{b\sqrt{a+b}} \text{ at } b\neq 0,\ G(x,\xi)=\frac{\xi_2^2 n_1}{2a\sqrt{a}} \text{ at } b=0,\ 2x_2\xi_2=b>0,$$

$$a=(x_1-\xi_1)^2+\xi_2{}^2+x_2{}^2>0,\ A_1=\frac{\xi_2{}^2 n_1}{4\pi},\ A_2=\frac{\xi_2}{4\pi}\left[(x_1-\xi_1)n_2-x_2n_1\right],\ F(t)=\int_0^{\pi/2}\frac{d\theta}{\sqrt{1-t^2\sin^2\theta}},\ t=2b/(a+b)$$

$$E(t)=\int_0^{\pi/2}\sqrt{1-t^2\sin^2\theta}\,d\theta;\ F(t)=\sum_{i=0}^{4}c_i(1-t)^i+\sum_{i=0}^{4}d_i(1-t)^i\ln\frac{1}{1-t};\ E(t)=1+\sum_{i=1}^{4}c_i(1-t)^i+\sum_{i=1}^{4}d_i(1-t)^i\ln\frac{1}{1-t};$$

c_i, d_i are taken from tables [8].

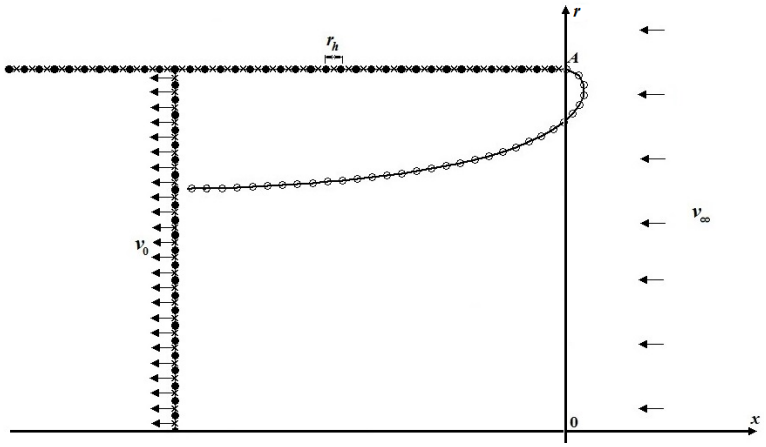

Figure 1: The discrete mathematical model of separation flow at the entrance to round suction duct (pipe) in meridional plane

If the distance from point x to point ξ is smaller than the discrete pitch size r_h, this function is calculated according to formula: $G(x,\xi)=\left((x_1-\xi_1)n_2-(x_2-\xi_2)n_1\right)/(2\pi r_h^2)$. In the case of $x=\xi$ the function is $G(x,\xi)=0$.

The computing algorithm is constructed in the following way. After defining the location points of attached vortexes and the control points a two-dimensional array is formed $G^{pq}=G(x^p,\xi^k);\ p=1,2,\ldots,N;\ q=1,2,\ldots,N$. The initial coefficients at the first unknown vortex circulation on the sharp edge A: $G(x^p,\xi^1)=P(x^p),\quad p=\overline{1,N}$. The vortexes are numbered from this point. Then the iteration procedure starts.

1. A one-dimension array of absolute terms is formed

$$v^p=-n_1v_\infty-\sum_{q=1}^{N}G(x^p,\xi^q),\ p=1,2,\ldots,N.$$

2. The initial coefficients are altered:

$$G(x^p,\xi^1)=P(x^p)+\sum_{k=1}^{N_s}G(x^p,\zeta^k),\quad p=\overline{1,N}.$$

At the first iteration $N_s = 0$ and coefficients $G(x^p,1)$ don't alter.

3. A system of linear algebraic equations in the unknowns $\Gamma(\xi^q)$ is solved:

$$\sum_{q=1}^{N} \Gamma(\xi^q) G(x^p, \xi^q) = v(x^p),\ p = 1,2,3,\ldots N$$

The vortex ring circulation on the sharp edge is memorized: $\gamma = \Gamma^1$.

4. The free stream surface, beginning from the sharp edge *A,* is constructed.

Using the formula (1), at $\vec{n} = \{1,0\}$ the velocity component v_x, is calculated at $\vec{n} = \{0,1\}$ - velocity component v_r. The following point (x',r') is determined from the previous one (x,r) using the formulas: $x' = x + \Delta t v_x / \sqrt{v_x^2 + v_r^2}$, $r' = r + \Delta t v_r / \sqrt{v_x^2 + v_r^2}$, where Δt - is a pitch, which is chosen to be rather small. The free stream surface will consist of free vortex rings, located a discrete pitch size away from each other r_h. So, in the process of calculation, the distance to the previous free vortex ring is checked at each stage. As soon as this distance becomes equal, within the accuracy of insignificant error, to discrete pitch size at a certain point, the next vortex ring is placed into this point. This construction goes on to the exhaust section, after which the iteration procedure begins from 1 and continues, until the absolute difference between the old circulation value γ on the free stream surface and the new one is higher than the given accuracy ε.

3 VERIFICATION OF MATHEMATICAL MODELING METHOD

The calculation was carried out at $\varepsilon = 10^{-8}$, $r_h = 0,000625$ m, the pipe radius R = 0,1m, the suction velocity $v_0 = 1$ m/s; the distance from exhaust section to the pipe entrance 6R; the pipe wall length 11R, the pitch of stream-line construction $5 \cdot 10^{-7}$ m. The calculation results are presented in nondimensional form. The length scale -R, the velocity scale - v_0.

The results of building a stagnation stream-line at the velocity v_∞ of the approach flow of the greater suction velocity are shown v_0 in fig.2. The following notations are introduced here: I – calculations at $\bar{v} = v_\infty / v_0 = 2$; II – at $\bar{v} = 10$; III – at $\bar{v} = 50$; line 1 – calculations by A.K. Gilfanov, Sh.H. Zaripov [4] in a potential model by the boundary-element method, line 2 – calculations by discrete vortex method without accounting the flow breakdown according to the algorithms, designed in this work; line 3 – calculation in the model of viscous incompressible liquid (numerical solution of Navier-Stokes equations) [4]; line 4 - calculations according to the designed method; 5 – free stream surfaces, constructed by the designed algorithms. The comparison of the calculation data demonstrates that the computation of the stagnation stream-line is correct, and the calculations within the framework of this paper are close to calculations with the account of viscosity.

The comparison of the calculated flow patterns at $\bar{v} = 50$ is shown in fig.3. The stagnation stream-line is denoted with a dashed line. The stream-lines are identical except for the separation area. In the model of viscous incompressible medium the separation area size is smaller.

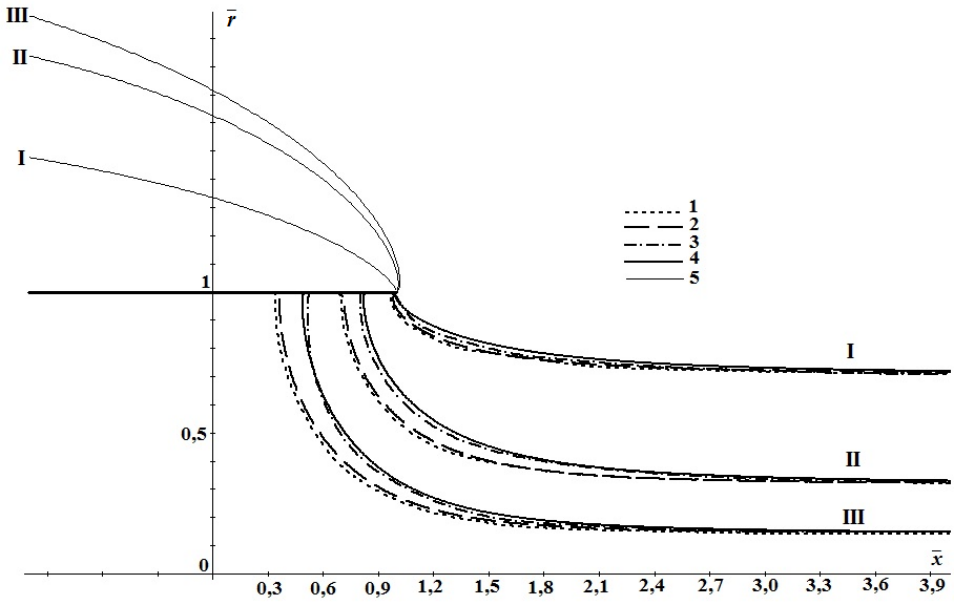

Figure 2: Stagnation and free stream-lines at the entrance to round thin-walled suction duct

The calculations at $\bar{v} = 0,02$ are virtually identical, too (fig.4). A slight deviation is observed at the separation area boundary. In the model of viscous incompressible liquid it shrinks at the removal in the suction duct, unlike the calculations within the framework of this paper.

Fig. 5 shows the flow patterns at the entrance to a slot-like and round suction ducts, constructed within the framework of potential flow model with the use of conformal mapping [9], viscous incompressible liquid with the use of Navier-Stokes equations' numerical solution [9] and the model, presented in this work. The calculations were carried out at various velocities of the approach flow, but not higher than the suction velocity. The stagnation stream-line is shown with a dashed line. Though the flow patterns are similar enough, at the entrance to the a slot-like suction duct the separation area, constructed with conformal mapping method, is narrower than the separation area, constructed with the designed calculation procedure. In the viscous incompressible liquid model the calculated width of separation area is considerably wider, but of the finite length, as compared to calculations within the framework of other models.

Among the aspiration objectives there is studying the dust particle dynamics in the round thin-walled duct's range of action, determining the extreme trajectories of dust particles and the aspiration coefficient.

So, in this work the extreme trajectories of dust particles were constructed, with the use of differential equations system of their movement:

$$\frac{dv_x}{dt} = \frac{u_x - v_x}{\tau}, \frac{dx}{dt} = v_x, \frac{dv_r}{dt} = \frac{u_r - v_r}{\tau}, \frac{dr}{dt} = v_r,$$

where $\tau = 2R \cdot \mathrm{St}/v_\infty$ - relaxation time, St - Stokes number; u_x, u_r - medium velocity components; v_x, v_r - particles velocity components, t – time.

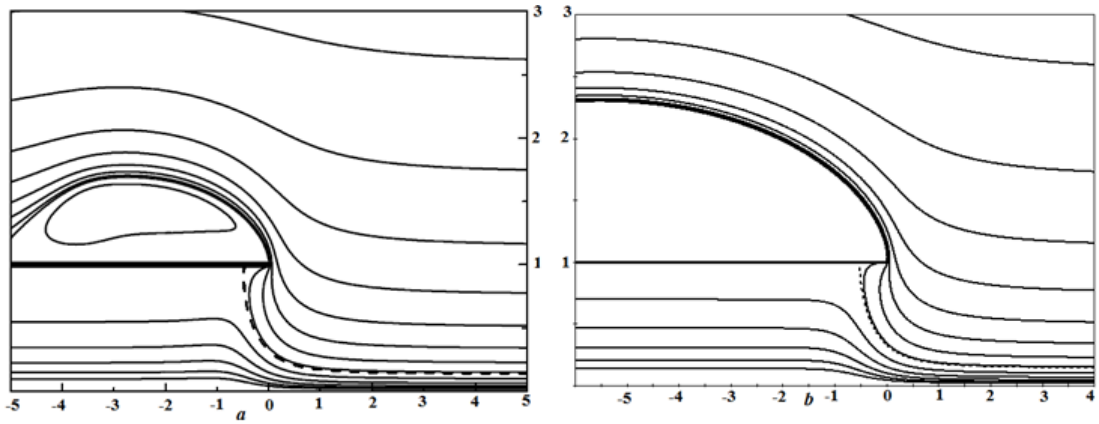

Figure 3: Stream-lines at $\overline{v} = 50$: *a* – calculations in the model of viscous incompressible liquid [4], *b* – calculations according to the designed computational procedure

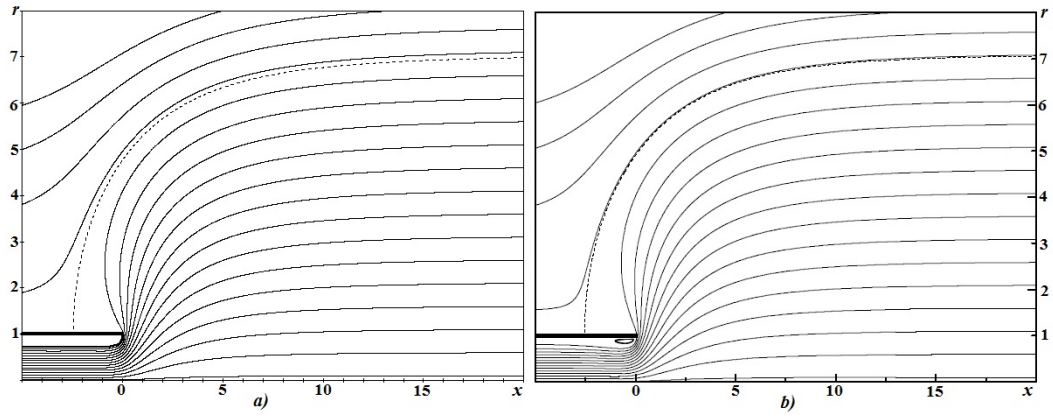

Figure 4: Stream-lines at $\overline{v} = 0.02$: *a* – calculations according to the designed method; *b* – calculations in the model of viscous incompressible liquid [4]

The extreme trajectory was determined by means of bisection method. The Stokes number and the initial position of a dust particle were denoted, the relaxation time was determined. The initial velocities were assumed as equal to the approach flow velocity. To the variable U_l the ordinate of a particle, caught by the pipe, was placed, and in the variable U_p - the ordinate of a deposited particle. In the initial approximation there was set $U_l = R$, $U_p = 40R$. The variable $S_r = (U_p + U_l)/2$. Then a cycle was organized, which performed until the condition $|U_p - U_l| > 0{,}00000001$. In the internal cycle the particles' trajectories were built. At the exit from the internal cycle the particle's getting into the pipe was checked. If yes, then the variable is $U_l = S_r$, otherwise $U_p = S_r$, the particle escape coordinates assumed the value $(100R, Sr)$.

The aspiration coefficient was determined from the formula: $A = (R_c / R)^2 \overline{v}$, where R_c - the initial distance to the symmetry axis of the found extreme trajectory of the dust particle. The withdrawal from the entrance to the suction duct was equal to 100*R*.

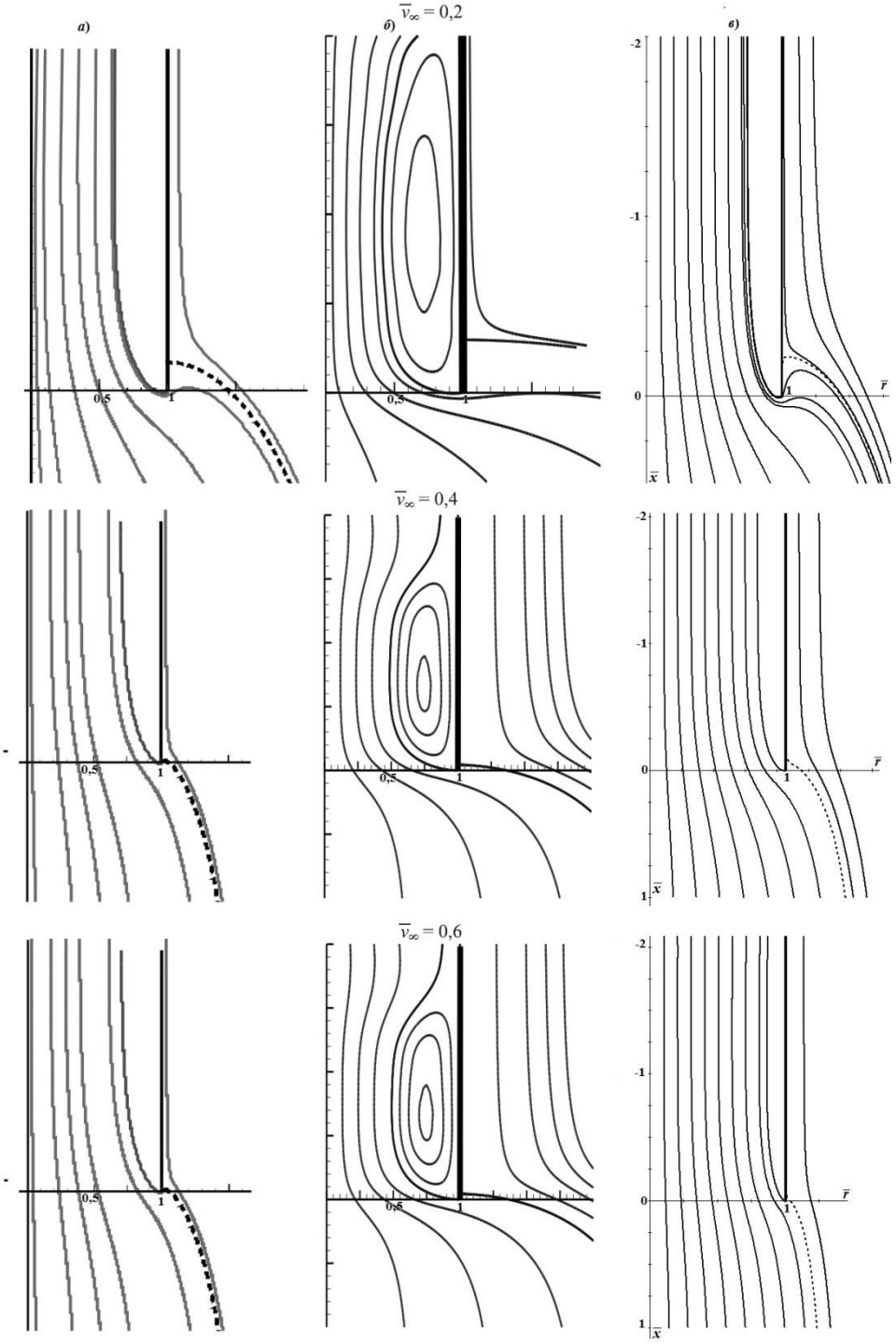

Figure 5: The comparison of stream-lines, constructed: a) for a slot-like suction duct by method of conformal mapping [9]; b) for a slot-like suction duct in the viscous liquid model [9]; в) for a round pipe according to the designed method

The comparison of the aspiration coefficient alteration depending on the dimensionless velocity of the approach flow and various Stokes numbers is presented in Fig.6, where there is a good congruence of calculations with the use of the designed computation procedure and the calculations, performed in [4], in the viscous incompressible liquid model. The maximum difference is observed at St=0,1 and $\overline{v} = 0,02$, but it doesn't exceed 7%.

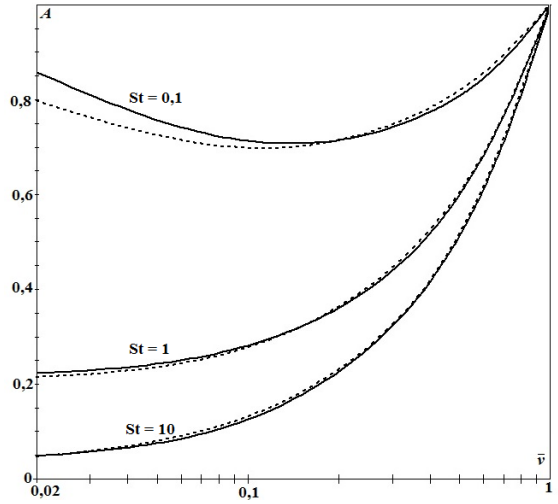

Figure 6: The dependence of aspiration coefficient A on the dimensionless velocity of the approach flow $\overline{v}$

4 THE BELL VENT IN CONDITIONS OF THE APPROACH FLOW

The air flow approaches a bell vent with velocity u_∞ (fig.7 a). In the suction section of the bell there is a parabolic distribution of velocity, which corresponds to the viscous flow in a round duct with the average velocity u_0: $v = 2u_0(1-r^2/R^2)$, where R – is the radius of a suction duct. There should be found the regularities of the aspiration coefficient's alteration depending on the slope angle α, the bell length l and the approach flow velocity u_∞ - $A = (R_c/R)^2\overline{v}$, where R_c - the initial distance to the symmetry axis of the found extreme trajectory of the dust particle, $\overline{v} = u_\infty / u_0$. Let us point out, that the gravitation acceleration is directed oppositely to the velocity in the vent u_0, i.e. the bell vent is located vertically, but for the convenience of presentation it is shown in the horizontal position.

The discrete mathematical model (fig.7b) is built in the following way At the flow boundary there are infinitely thin attached vortex rings (black circles in fig.7b) and control points between them (crosses in fig.7b) - on the circle, embracing the pipe, or on the suction section. Let us point out, that in the suction section on the symmetry axis the zero radius vortex is located, so it's not taken into account. The number of discrete vortex rings is equal to the number of control points. In the control points on the pipe walls the impermeability condition is performed – the velocity along the normal direction amounts to zero. In the suction section the velocity along the outward normal direction is similar and amounts to v_0. The division to discrete vortex rings and control points is uniform, the control points are in

the centre among the vortex rings. The distance between two neighbouring vortex rings is equal to discrete pitch size r_h. The free stream surface consists of free vortex rings hollow circles in fig.7b) and is formed on the sharp edge *A* of the bell. It is determined by iterational method, as further described. Parallely to the pipe axis the flow approaches with the velocity v_∞, which can be directed oppositely to the axis O*x*, or can coincide with it. It must be pointed out, that the free stream surface can also descend into the bell at the low velocities of the approach flow.

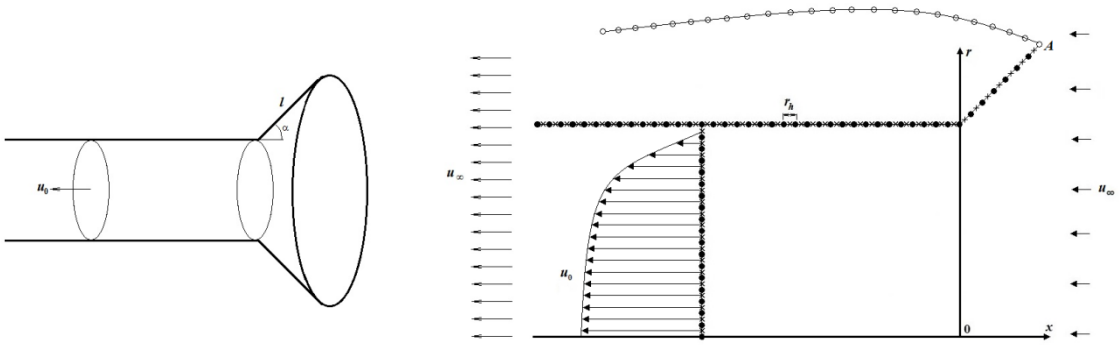

a) b)

Figure 7: The bell vent at the approach flow: a) general flow pattern; b) discrete mathematical model in meridional plane

The dust particles trajectories were built with the use of differential equation of its dynamics:

$$\frac{d\boldsymbol{v}_p}{dt} = \boldsymbol{g} - \frac{\bar{\psi}\chi u_\infty}{2\cdot \mathrm{St}\cdot R}(\boldsymbol{v}_p - \boldsymbol{v}_a), \tag{2}$$

which corresponds to a system of standard differential equations:

$$\frac{dv_{px}}{dt} = -\frac{\bar{\psi}\chi u_\infty}{2\cdot \mathrm{St}\cdot R}\left(v_{px} - v_{ax}\right), \quad \frac{dx}{dt} = v_{px}, \quad \frac{dv_{py}}{dt} = -g - \frac{\bar{\psi}\chi u_\infty}{2\cdot \mathrm{St}\cdot R}\left(v_{pr} - v_{ar}\right), \quad \frac{dy}{dt} = v_{pr}, \tag{3}$$

where $\mathrm{Re} = \rho_a \left|\boldsymbol{v}_p - \boldsymbol{v}_a\right| d_e / \mu$, μ – air dynamic viscosity coefficient, $\mathrm{St} = \rho_p d_e^2 u_\infty / (36\mu R)$, $\boldsymbol{v}_a$ – air velocity; ρ_a – air density; $\boldsymbol{v}_p$ – particle velocity; ρ_p – particle density; d_e – equivalent diameter of a particle; $\boldsymbol{g}$ – free fall acceleration; $S_m = \pi d_e^2 / 4$ – middle section area of a particle; χ – dynamic mode coefficient of a particle;

$$\bar{\psi} = 1, \quad \text{if} \quad \mathrm{Re} < 1; \quad \bar{\psi} = \left(1 + 1/6\cdot \mathrm{Re}^{2/3}\right), \quad \text{if} \quad 1 \le \mathrm{Re} < 10^3; \quad \bar{\psi} = \left(1 + 0{,}065\,\mathrm{Re}^{2/3}\right)^{1.5}, \quad \text{if} \quad \mathrm{Re} \ge 10^3.$$

The equation (2) is not dimensionless, but the Stokes criterion is singled out, on the base of which a number of computational experiments will be carried out.

Here are some results of calculating velocity in the vent $u_0 = 1$ m/s and the approach flow velocity $u_\infty = 0{,}6$ m/s. The following parameters were used in the calculations: discrete pitch size $r_h = 0{,}000625$ m; pipe radius $R = 0{,}1$ m; pipe length 20*R*; the suction opening is located in the centre of the pipe; stream surface construction pitch 0,0000025m; differential equation

integration pitch of dust particle dynamics 0,001 – 0,005; accuracy of free stream surface construction $\varepsilon = 10^{-6}$.

The extreme trajectories of dust particles with numbers $\mathrm{St} = 0,01$ and $\mathrm{St} = 0,001$ almost overlap. The flow breakdown boundary is denoted with a continuous line (fig.8). With the increase of Stokes number St the aspiration area grows. The calculation was carried out at $u_0 = 1$ m/s.

The initial conditions for constructing the dust particles trajectories were set in the following way: $v_{px} = -u_\infty, v_{pr} = 0, x = 30R$. The extreme trajectory was determined with the use of bisection method. The Stokes number and the initial position of a dust particle were denoted, the relaxation time was determined. The initial velocities were assumed as equal to the approach flow velocity. To the variable U_l the ordinate of a particle, caught by the pipe, was placed, and in the variable U_p - the ordinate of a deposited particle. In the initial approximation there was set $U_l = R$, $U_p = 40R$. The variable $S_r = (U_p + U_l)/2$. The initial position of the particle's withdrawal from the axis $r = S_r$. Then a cycle was organized, which performed until the condition $|U_p - U_l| > 0,00000001$. In the internal cycle the particles' trajectories were built. At the exit from the internal cycle the particle's getting into the pipe was checked. If it was caught with a suction opening, then the variable is $U_l = S_r$, otherwise $U_p = S_r$.

In Fig.9 we can see that the extreme trajectories not necessarily finish at the bell boundary. It's explained by the presence of the branch point of dust particles, as shown in Fig.4, where there are presented dust particle's trajectories slightly lower and slightly higher than the extreme trajectory. The extreme trajectories of dust particles constrict to the bell's symmetry axis as compared to Fig.8.

The aspiration coefficient was determined from a formula: $A = (R_c / R)^2 \bar{v}$, where R_c - the initial distance to the symmetry axis of the found extreme trajectory of the dust particle, $\bar{u} = u_\infty / u_0$. The withdrawal from the entrance to the suction duct was equal to $30R$. The dependence of aspiration coefficient on the length of the bell, located 90 degrees to the vent axis is shown in Fig.11. If the Stokes numbers tend to zero, the aspiration coefficient virtually doesn't change and tends to one at any bell length. Indeed, in the supposition of the uniformity of concentrations and velocities of dust particles in the air flow at the considerable distance from the suction duct, the aspiration coefficient is equal to the ratio of the cross-section area of dust particles extreme trajectories to the cross-section area of the aspirated air stream in the same section. If the Stokes number tends to zero, the extreme trajectories of dust particles coincide with stagnation stream-lines. So, the above mentioned areas coincide. To this case the Stokes number St = 0,001 corresponds. Here there is the right line $A \approx 1$. At the growth of the Stokes number, the aspiration coefficient decreases with the increase of the bell length. At the Stokes number St = 0.2 there is a sharp drop of aspiration coefficient in the range of bell length alteration from 0 to 1 calibre. It's interesting, that all the curves intersect in one point, which corresponds to the bell length equal to 0.5 of the caliber (caliber is the pipe radius *R*).

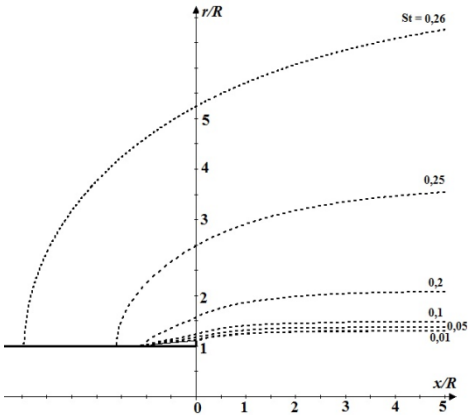

Figure 8: The extreme trajectories of dust particles at: $l/R = 0,1$ $\bar{u} = 0,6$.

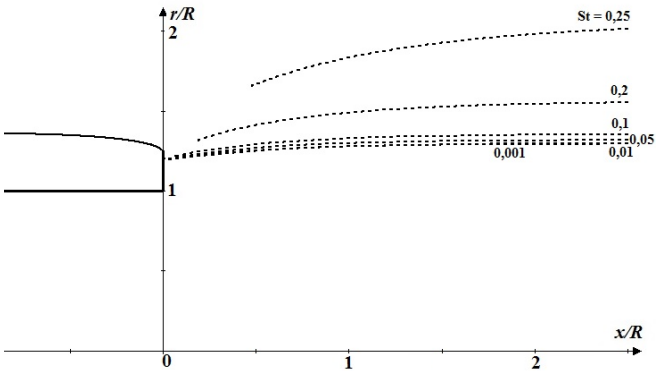

Figure 9: The extreme trajectories of dust particles at $l/R = 0,25$, $\bar{u} = 0,6$

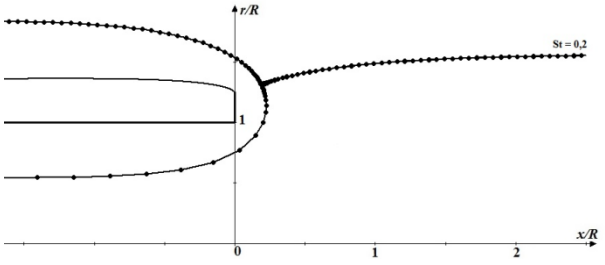

Figure 10: The trajectory of a dust particle at: St = 0.2, $l/R = 0,25$, $\bar{u} = 0,6$

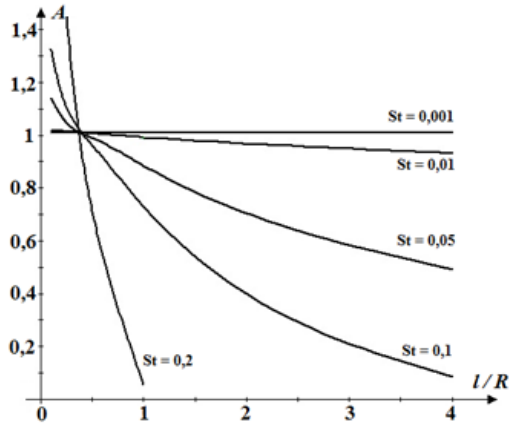

Figure 11: The dependence of aspiration coefficient on the bell length at $\alpha = 90^{\circ}$, $\bar{u} = 0,6$

At the twofold increase of the approach flow velocity the dependence of aspiration coefficient on the dimensionless bell length alters considerably (fig.12). At the Stokes numbers lower than 0.1 the aspiration coefficient tends to one in the whole range of bell length variations. The character of the aspiration coefficient alteration remains the same – it decreases at the bell length increase, but doesn't exceed 1. As the approach flow velocity has increased, it's possible to plot the graphs of the aspiration coefficients alteration at the increase of Stokes numbers to one. In the latter case, it was done in a narrow range of bell lengths alteration.

The determining of regulations in the dependence of aspiration coefficient on the slope angle of the bell to its axis at the fixed bell length is also of interest (fig.13).

As before, at the low Stokes numbers (less than 0.01) the aspiration coefficient tends to one. The graphs of variance are not steady; there is a low at the range of 45-60 degrees.

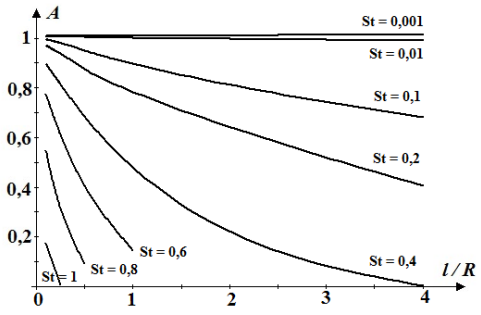

Figure 12: The dependence of aspiration coefficient on the bell length at $\alpha = 90^{\circ}$, $\bar{u} = 1,2$

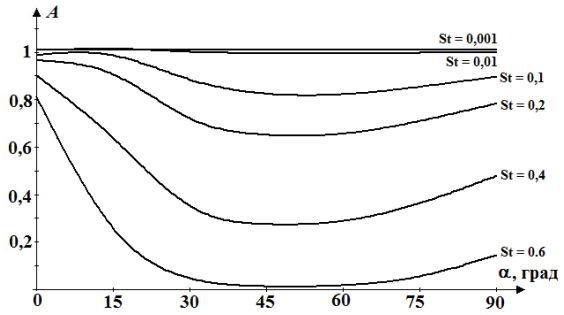

Figure 13: The dependence of aspiration coefficient on the bell length at $l / R = 1$, $\bar{u} = 1,2$ on the slope angle of the bell

CONCLUSIONS

- The developed method of mathematical modeling of the separation flow at the entrance to the suction pipe at the approach flow allows constructing an accurate velocity field of the air flow, extreme trajectories of dust particles and determining the aspiration coefficient.
- The work has been carried out with the financial support of the Grant Council of the President of the Russian Federation (project MD-95.2017.8).

REFERENCES

[1] Logachev, I.N., Logachev, K.I. and Averkova, O.A. *Local Exhaust Ventilation: Aerodynamic Processes and Calculations of Dust Emissions*, CRC Press, (2015).

[2] Gilfanov, A.K., Zaripov, Sh.Kh., and Maklakov, D.V. Calculation of Particle Concentration in the Problem of Aerosol Aspiration into a Thin-Walled Tube. *Fluid Dyn*., (2009) **44 (6)**, 873–881.

[3] O.A. Averkova, I. N. Logachev, K. I. Logachev and A. K. Logachev, The principles of separated flow at the inlet of the protruding duct with screens. *TsAGI Science Journal*, (2013) **44**, 219-243.

[4] Gilfanov, A.K., Zaripov, Sh.Kh. *Mathematical models of aerosols aspiration to thin-walled sample catchers*. Kazan: Kazan University, (2012).

[5] Khodakov, I.V. Modeling of Detached Flow at the Entry Polygonal Suction Hole. *Bulletin of BSTU named after V.G. Shukhov*, (2016) **2**, 11-15.

[6] Khodakov I.V. Numerical and Experimental Research of Detached Flow at the Inlet in the Suction Duct With Mechanical Screens. *Bulletin of BSTU named after V.G. Shukhov*, (2016) **3**, 6-12.

[7] O. A. Averkova, I. N. Logachev, and K. I. Logachev, Modeling of Flow Separation at the Inlet of a Suction Channel in Regions with Cuts, *Vychisl. Metody Programm* (2012) **13**, 298–306

[8] Abramovits, M. And Stigan, I. *Special functions reference book*. M.: Nauka, (1979).

[9] Varsegova, E.N. and Posohin, V.N. A Form of Separated Flow on an Entrance to Suction Slot-Hole Branch Pipe, *News of the Kazan State University of Architecture and Engineering*, (2015) **3**, 98-102.

VII International Conference on Computational Methods for Coupled Problems in Science and Engineering
COUPLED PROBLEMS 2017
M. Papadrakakis, E. Oñate and B. Schrefler (Eds)

Modelling of Industrial Hybrid Bonding Processes considering Fluid-Structure-Interaction

HOLGER FRICKE[*], TILL VALLEE[*] AND BERND MAYER[†]

[*] Fraunhofer Institute for Manufacturing Technology and Advanced Materials (IFAM),
Wiener Straße 12, 28359 Bremen, Germany
e-mail: holger.fricke@ifam.fraunhofer.de
web page: http://www.fertigungstechnik-kleben.de

[†] University of Bremen, Production Technology Department, Polymeric Materials,
Bibliothekstraße 1, 28359 Bremen, Germany

Key words: Adhesive Bonding, Hybrid Bonding, Simulation, Coupled Problems, Applications, Computing Methods.

Abstract. *The subject of the work presented is focused on self-pierce-riveting and clinching in combination with adhesive bonding. In the industrial process chain the rivets and clinch-points are set before the adhesive is cured. A FEA reference model is developed for the elementary mechanical joining processes. The model is then expanded to consider the displacement of the liquid adhesive, including associated internal pressures. Coupled fluid-structure simulations, which include the interaction of the solid matter influenced in the mechanical joining process and the fluid adhesive, are presented. In a last step a surrogate model for the multi-point hybrid joint is developed and applied to industry-relevant structures.*

1 INTRODUCTION

Adhesive joint manufacturing usually starts with the application of the liquid adhesive on one of the adherents to join; thereafter, the second adherent is placed such to achieve an adhesive bonded gap between the parts to be bonded. The last step consists on curing the adhesive until final strength is achieved, a process which in some industrial applications is being accelerated by appropriate means, as heating. In recent years, in the automotive industry, bonding is increasingly being used to achieve lightweight structures with high crash performance. Adhesively bonded joints ensure a much smother load transfer, higher joint capacities, and stiffer connection. In the automotive industry typical connections are, amongst others, bonding complements connections in the car main body (and doors, hoods) that are achieved with traditional mechanical fastening, as for example clinching, hamming and riveting; their main advantage lie in short process times, although with lower total bonding strengths. Specific advantages of adhesively bonded joints and mechanical fastening can be combined in form of hybrid joints, which yield in synergies of manufacturing, strength, crash behavior, and durability performance.

In a specific hybrid bonding process increasingly used in industry, the so called “fixation method”, liquid adhesive is applied between two metal sheets, then mechanical joining is performed while the adhesive is yet uncured, after which the adhesive is cured. Depending on the type of mechanical fastener, e.g. considering hamming or rivets, the hybrid joint can take different designations. The hybrid adhesive-hamming and the hybrid adhesive-clinching process include large plastic deformation of the metal sheets, in presence of the pasty liquid adhesives. The hybrid adhesive-riveting process additionally includes the fracture of the upper metal sheet, influenced by the presence of a pasty fluid. Critical issues in such hybrid joining processes are the formation of adhesive pockets in the region of the mechanical junctions, the potential presence of air bubbles in the adhesive, and the usually large global deformations of the metal sheets between the mechanical joints.

Numerical modelling of aforementioned hybrid joining processes makes it necessary to consider various physics: all effects related to the uncured–thus liquid–adhesive are associated to fluid dynamics, while solid mechanics is needed for the mechanical fasteners, and metal sheets. Since both effects act simultaneously, taking into account the Fluid-Structure-Interaction (FSI) is fundamental. In hybrid bonding processes hydrostatic pressures inside the adhesive pockets can reach very high values, such to lead to plastic deformations of the metal sheets. When transferring high pressures, the exchange process of boundary conditions between the software for the solid metal forming process and the code for simulation of the fluid flow of the liquid adhesive is limited by the stability of the FSI simulation. This requires a careful selection of an adequate code coupling module. On the basis of experimental studies the authors present simulations for the numerical descriptions of hybrid joining processes. Different examples of simulations of hybrid adhesive-clinching, and adhesive-riveting, processes will be presented; from simple–academic–geometries to industry-relevant structures. The elaborated FSI simulations are able to shed additional light on the insights, and on the influence of several key parameters on the process.

2 COUPLING STRATEGY

In hybrid joining processes strong interactions between the two elementary joining steps occur, so that process parameters that have been determined as optimum separately cannot be transferred to the hybrid technology directly. Beside experimental studies, numerical descriptions of hybrid joining processes [1,2,3] are able to shed additional light on the insights on the influence of several key parameters. Because of the strong interactions between the metals and the adhesives, simulation of hybrid joining processes must integrate liquid adhesives flow and mechanical joining processes in parallel.

Literature reports on several experimental studies on hybrid joining applying the fixing method. Correlations between the quality of the mechanical joint, the adhesive and the global deformation were partially investigated using experiments [4,5,6,7]. The main techniques to measure the quality of hybrid bonded specimens are metallographic sectioning of cured compounds and tactile or inductive measuring of deformation while curing. Also the numerical analysis of final cured hybrid joints under mechanical loads is state-of-the-art, see [8,9,10]. The simulation of hybrid bonding processes facing the flow of liquid adhesive including the comparison with experimental data is the topic of one of the authors in [11,12,13].

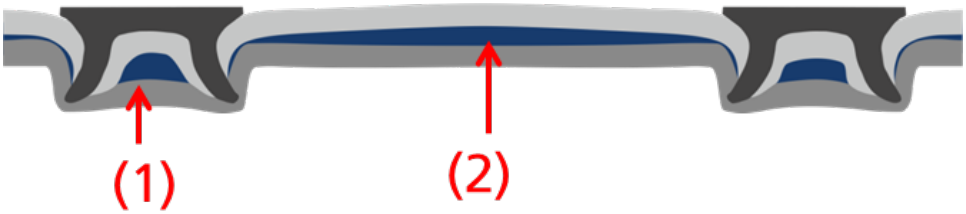

Figure 1: Formation of adhesive bags (1) in hybrid junctions and (2) between hybrid junctions

Stepping in the detail of the simulations, both the elasto-plastic flow processes of the metal parts and the viscous flow of the adhesive must be calculated simultaneously using a fluid-structure-interaction (FSI) simulation. In this case also the strong interactions between the liquid and the solid material must be numerically coupled.

One coupling strategy is to connect a structural with a fluid mechanical code using a special coupling software tool. The transferring software will couple for example a structural domain calculated using structural FEM with a fluid domain calculated using CFD by the exchange of boundary conditions at corresponding time steps. This kind of coupling is implemented in some general purpose simulation packages like Ansys® or Abaqus®. Alternatively a third party software product like MPCCI can be used. But the linking of one software product for the solid metal forming process and another software for simulation of the fluid flow of the liquid adhesive is limited when strong coupling is involved.

Another method is to use advanced material models to handle the liquid flow in a structural numerical code only. Using the Arbitrary Lagrangian Eulerian (ALE), the Coupled Euler Lagrangian method in Abaqus® (CEL), and the fluid-structure coupling analysis using Abaqus® in combination with MPCCI® and Ansys® Fluent® is tested. All methods required high computational effort, even for a single point hybrid joint. The use of surrogate models is able to significantly decrease the complexity of the numerical problem and to describe industrial structures with multiple hybrid joints using a structural numerical code only.

3 SINGLE POINT CLINCH-BONDING AND RIV-BONDING PROCESSES

The basis of the simulation of hybrid bonding processes are stand-alone simulations of mechanical joining processes of clinching and self-pierce-riveting. The models include the experimentally determined strength and yield curve of metal on one hand, and the rheological flow behavior of adhesive. At first a reference model for the elementary clinching and the self-pierce-riveting is qualified for the simulation. In self-pierce-riveting the rivet fractures the metal sheet, which has to be taken into account. Due to the low sensitivity of the failure model on the geometry and force curves a simple ductile model is used. Comparisons between experimental and numerical results (Fig. 1 for the clinch-bonding) indicate that the approach for single point clinch-bonding and riv-bonding processes is validated.

Aforementioned simulations allow understanding the formation of adhesive bags in the mechanical joining zone. Fig. 1 shows the simulation results for hybrid adhesive-clinching of steel-aluminum and steel-steel pairing of sheets after 0.2sec, 0.5sec and 1.0sec. In each time frame the results of the steel/aluminum pairing are shown on the left side and the steel/steel pairing is shown on the right side. The steel sheets are located on the top of the joints and the aluminum sheet on the bottom. The coloring visualizes the von Mises stresses of the metal sheets. The adhesive layer is colored in gray.

The aluminum sheet has a lower stiffness so that it is more deformed under the acting forces. As a result the total amount of the enclosed adhesive at time 0.5sec is higher for the steel/aluminum combination. The punch causes a displacement of the adhesive from the center in radial direction in all material combinations, leading to an accumulation of adhesive in the area of the outer diameter of the punch. At the end of the process the two distinct pockets of glue in the joint zone are bigger for the pairing aluminum/steel. Similar results were obtained for riv-bonding process, which allowed concluding that the simulation method developed here is able to describe the physical processes of single point hybrid bonding correctly.

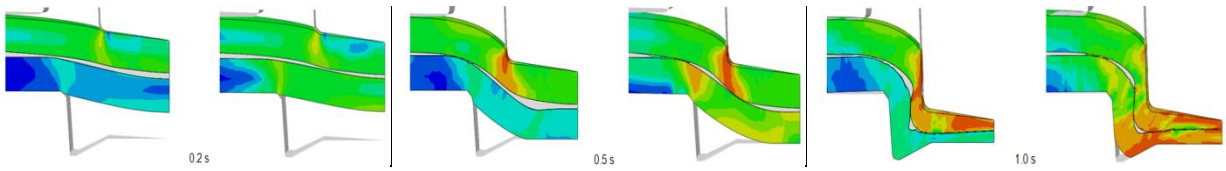

Figure 2: Simulation of the clinch-bonding (after 0.2 sec, 0.5 sec, and 1.0 sec, respectively)

4 MULTI POINT RIV-BONDING PROCESSES

Industrial applications almost always involve multiple joints embedded in 3D geometries, mostly without symmetries to be exploited. To step forward to this applications the methods of simulation need further improvements. For this purpose the individual hybrid joining points of a complex part are modeled using simplified surrogate models. This surrogate model describes the time dependent rate of adhesive flow and the displacement of the metal sheet as boundaries using a geometric cut at a given radius around the respective joining point. The simulation is divided in a local 2½D model and global 3D model with a cylindrical connection region circumvented around the jointing point (see Fig. 3). Here the local model describes the single hybrid joint using FSI and axial symmetric modeling and the global model describes the flow of adhesive through a 3D structure using imported time dependent boundary conditions derived from the local model.

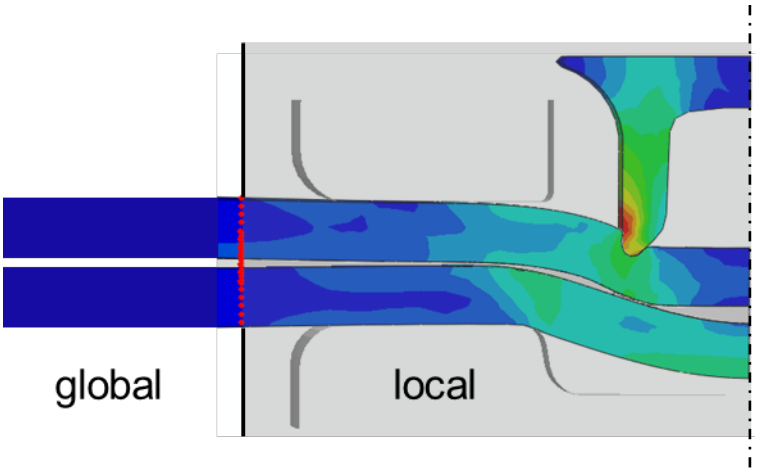

Figure 3: Coupling of local 2½D model and global 3D model with a cylindrical connection region for the riv-bonding process

Using a first python-script, the time dependent results of deformation and adhesive flow occurring in the connection region from the local 2½D FSI simulation are derived and stored in a file. It is possible to set up a database of typically applied hybrid joints by collecting the result files of their local simulation for subsequent use. If required, the extracted flow and deformation data for a special joint type can be transformed into FEM-boundaries acting on each connection region of the global 3D multi-point model. The transformation of data-files to boundaries is automated by a second python-script, which derives the changes in dimension, rotation, translation, time-shift and meshing from the local to the global model. Using the two python-scripts allows to automatically build-up of complex multi-point hybrid joint geometries based upon libraries of materials and adhesive properties, as well as typical hybrid joint elements.

The simulation using a surrogate model enables the modelling of much more complex, industry-related, structures without exceeding the capacity of commercially available computer architectures. The validation of the surrogate model at geometrically simple

samples is the basis to describe more complex structures coming close to components of automotive body-shells.

This is illustrated by the following example of a cap profile with three hybrid junction points in the flange: the adhesive layer in the flange is pressed to its final shape driven by the hydrostatic stresses resulting from the hybrid joining process. The flow of adhesive caused by the mechanical joining process leads to a final deformation of the metal flange of the cap profile. This final deformation is shown for different cut views in Fig. 4.

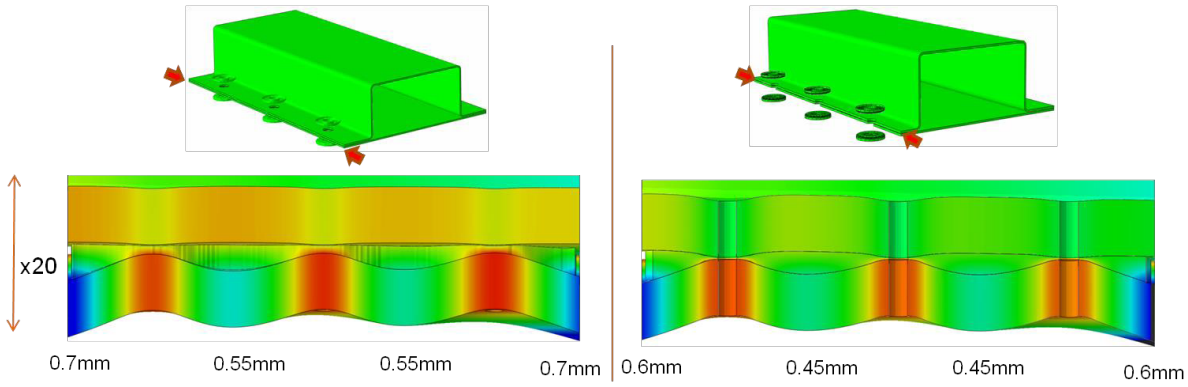

Figure 4: Deformation at the flange of the cup profile at two different cut positions. Colors symbolize the amount of deformation in vertical direction [–0.5mm to +0.05mm]. The vertical axis is scaled with a factor of 20. Numbers denote the height of the final adhesive gaps between the two metal sheets.

5 CONCLUSIONS

The numerical description of the mechanical joining and the adhesive flow helps to understand the hybrid processes and to create solutions for critical joining tasks in industry. Based on the increased process knowledge made possible by the numerical simulations, options for process-optimization of clinch-bonding and riv-bonding processes are derived, leading to a better undercut in the mechanical joint and reduced pockets of adhesive. Process modifications can be used in order to achieve smaller adhesive bags and bigger undercuts in single point joints.

However, the developed simulations for the single point joints are associated with high computational times. Using the developed surrogate model it is possible to study in detail the time-dependent process of adhesive bag formation in multi-point joining processes. The investigations showed that adhesive bags results as a merging of ebbing waves of adhesive. The worked out techniques can be expanded for industrial use to serve as a tool for further optimization of processes. The simulations provide a basis for further numerical investigations of different hybrid joining processes.

6 ACKNOWLEDGEMENT

The presented results are part of research projects of the European Research Association for Sheet Metal Working (EFB) funded by the program for "Industrial Research" (IGF) of the German federal ministry for economic affairs and energy (15725BG and 17534BG).

7 REFERENCES

[1] Fricke, H. and Vallée, T. *Numerical Modeling of Hybrid-bonded Joints*. The Journal of Adhesion (2016) **92**:652-664.

[2] Neugebauer, R. Israel, M. Mayer, B. and Fricke, H. *Numerical and Experimental Studies on the Clinch-bonding and Riv-bonding Process*. Key Engineering Materials (2012) **504-506**:771-776.

[3] Landgrebe, D. Mayer, B. Niese, S. Fricke, H. and Neumann, I. *Adhesive distribution and global deformation between hybrid joints*. Key Engineering Materials (2015) **651-653**:1465-1471.

[4] Voelkner, W. Hahn, O. Liebrecht, F. and Peetz, A. *Untersuchungen zum Fügen von Feinblechen mittels Durchsetzfügen-Kleben und Stanznieten-Kleben* - EFB Forschungsbericht Nr. 102 (1997).

[5] Peschka, M. and Backe, P. *Stanznieten mit Halbhohlniet - Neue Perspektiven beim Fügen hochfester Stahlsorten*. Konstruktion+Engineering 5 (2002).

[6] Hahn, O. Draht, T. Thoms, V. and Liebrecht, F. *Entwicklung der kombinierten Fügetechnik für Hybridbauweisen am Beispiel Stanznieten-Kleben*. Europäische Forschungsgesellschaft für Blechbearbeitung e.V. - Forschungsbericht Nr. 180 (2002).

[7] Hahn, O. and Wibbeke, T.-M. *Optimierung der Fertigungsparameter des Mechanischen Fügens für den Einsatz mit dem Kleben zum Verbinden dünner Bleche*. Europäische Forschungsgesellschaft für Blechbearbeitung e.V. - Forschungsbericht Nr. 216 (2004).

[8] He, X. *A review of finite element analysis of adhesively bonded joints*. International Journal of Adhesion and Adhesives (2011) **31:4**:248-264.

[9] Sadowski, T. Knec, M. and Golewski, P. *Experimental investigations and numerical modelling of steel adhesive joints reinforced by rivets*. International Journal of Adhesion and Adhesives - Special Issue on Joint Design (2010) **30:5**:338-346.

[10] Sadowski, T. Golewski, P. and Zarzeka-Raczkowska, E. *Damage and failure processes of hybrid joints: Adhesive bonded aluminium plates reinforced by rivets*. Computational Materials Science Proceedings of the 19th International Workshop on Computational Mechanics of Materials - IWCMM 19 (2011) **50:4**:1256-1262.

[11] Fricke, H. and Israel, M. *Unterschiedliche Werkstoffe prozesssicher verbinden. Simulation von Hybridfügeprozessen*. Adhäsion Kleben u. Dichten (2011) **55:7/8**:24-29.

[12] Neugebauer, R. Mayer, B. Israel, M. and Fricke, H. *Qualitätssicherung beim Hybridfügen*. Europäische Forschungsgesellschaft für Blechbearbeitung e.V. - Forschungsbericht Nr. 330 (2011).

[13] Fricke, H. and Niese, S. *EFB - Taschenbildung und Klebstoffverdrängung zwischen Hybridfügepunkten*. AIF-IGF 17534 BG/2 [funded by the german federal ministry for economic affairs and energy] (2015).

VII International Conference on Computational Methods for Coupled Problems in Science and Engineering
COUPLED PROBLEMS 2017
M. Papadrakakis, E. Oñate and B. Schrefler (Eds)

MULTIPHYSICS ANALYSES OF THE EFFECT OF PACKAGE ON THE PERFORMANCES OF PMUT TRANSDUCERS

RAFFAELE ARDITO*, LUCA D'ALESSANDRO*, GIANLUCA MASSIMINO*, FRANCESCO PROCOPIO† AND ALBERTO CORIGLIANO*

* Department of Civil and Environmental Engineering
Politecnico di Milano
Piazza Leonardo da Vinci 32, 20133 Milan, Italy
e-mail: raffaele.ardito@polimi.it, www.mems.polimi.it

† Analog, MEMS & Sensors Group
ST Microelectronics
Via Olivetti 2, 20100 Agrate Brianza, Italy
Email: francesco.procopio@st.com, http://www.st.com

Key words: MEMS, Piezoelectric Materials, Vibro-acoustics, Ultrasound Transducers, Finite Element Method.

Abstract. The paper deals with the multiphysics modeling of piezoelectric micromachined ultrasound transducers (PMUT), that can be used in several practical applications. The model accounts for the multiple couplings between the mechanical fields and the electric and acoustic ones. The numerical solution has been sought by means of the finite element method, for the special case of axial symmetry. The model has been validated with reference to experimental data, that have been obtained by the Authors. The numerical procedure has been applied to carry out a parametric analysis of the effect of package, to extract a set of design guidelines.

1 INTRODUCTION

The application of piezoelectric materials in "smart" microdevices is continuously increasing, with different possible uses of both "direct" (conversion of mechanical energy into electric energy) and "indirect" effect. The latter is applied for actuating purposes, e.g. in the case of micropumps [1]; "direct" effect is now widely used for energy harvesting, namely for obtaining an electric power by exploiting some freely available mechanical energy [2,3].

In the case of MEMS, some recent developments in microfabrication techniques allowed for the introduction of layered structures with thin films of piezoelectric materials (namely, PZT or AlN [4]). After a thorough examination of piezoelectric mechanical properties for thin layers, it is possible to provide a comparative table in terms of "Figure Of Merits" (FOM). In that way, one can select the best material for each possible application, with the use of both direct and indirect effects.

The ultrasound transducers (PMUT) are piezoelectric structures which are actuated with the purpose of emitting and receiving ultrasonic waves [5]. Such devices are used in many practical application: acoustic imaging for medical purposes; hydrophones; finger-printing recognition

[6]; range-finders [7]. Further applications are represented by non-destructive testing, velocity sensing and 3D pattern recognition. The complete simulation of the device's behaviour can be obtained by considering multiple coupling between different fields: electro-mechanical coupling for piezoelectric model; acoustic-structural coupling for understanding the efficiency in the emission and in the sensing phase. The model is complicated by the fact that the PMUT devices are usually packaged, so the interaction between the surrounding medium does not involve directly the vibrating diaphragm only but the package as well.

This paper is focussed on the development of a fully-coupled model in order to carry out parametric studies on the effect of package geometry on the PMUT operation. This has been done with reference to axisymmetric models, with the main purpose of reducing the computational burden. This is perfectly suited for the emission of waves from circular diaphragm in circular package; conversely the sensing phase would require a full 3D model. The achieved results have represented a useful guidance in the design of a PMUT prototype, that has been finally subject to experimental tests. The measured data are in good agreement with the numerical predictions.

2 MULTIPHYSICS MODELLING

The finite element model has been developed in COMSOL Multiphysics 5.2. The numerical model includes three physics and their mutual interactions, namely: solid mechanics model of the membrane, piezoelectric effect in the PZT active layer and pressure acoustics model for the fluid far from the membrane. The thermo-viscous acoustics model for the fluid near to the vibrating diaphragm, that has been considered in [8], is here neglected since focus is on the far-field response.

The materials in the layers of the plate are linear elastic and they are characterized by a certain amount of residual stress in the radial direction of the plate. Such a stress field, that is induced by the fabrication processes, plays an important role in the initial deformation and in the geometric stiffness of the structure. In the piezoelectric active layer, the electro-mechanical coupling is enforced through the linearized constitutive relation (see e.g. [1]). The overall structural damping (which is induced by anchor losses, surface effects and the thermo-elastic losses) is modeled by means of an isotropic structural loss factor, that is the inverse of the structural quality factor Q_{struct}.

The acoustic phenomenon far from the emitting source can be considered as an isentropic process, characterized by zero energy dissipation. The computational burden is reduced by considering a spherical pressure acoustic domain with radius equal to 4 λ, where $\lambda = v_s/f_0$ is the typical wavelength, v_s is the sound velocity in air at the reference state (T_{ref} = 293.15 K and P_{ref} = 1 atm), f_0 is the operational frequency of the system, that coincides with the plate fundamental frequency in order to maximize the acoustic efficiency. In this region the lossy Helmholtz equation for the pressure acoustic field is solved, with the Stokes' attenuation factor for the viscous and thermally conductive case [9]. Finally, outside the pressure acoustic domain, the wave radiation into an infinite medium is simulated by means of a Perfectly Matched Layer (PML) of thickness equal to λ.

The electro-thermo-structural-acoustic response is computed by means of a sequence of simulations. First, a non-linear static analysis is performed to compute the pre-deflected configuration induced by the fabrication residual stresses in the plate. An electro-mechanical

static analysis, account taken of the previously computed non-linear deformation, is performed to simulate the effect of the bias voltage that is applied in the actuation phase. Finally, an electro-mechanical-acoustic analysis is performed in the frequency domain to simulate the complete system, under a harmonic voltage perturbation, taking into account the non-linearities introduced before.

3 EXPERIMENTAL VALIDATION

The results of the studies on the single PMUT, without the protecting cap and the package, are shown in the present section along with the comparison with the corresponding experimental data. To compute the pre-deflected configuration of the system, which is characterized by a very high aspect ratio (radius/thickness) of 55, an initial non-linear static analysis is performed, under the residual stresses acting in the radial direction of the plate. The numerically computed profile of the diaphragm along a radius and its comparison with the experimental measured one are presented in Fig. 1.

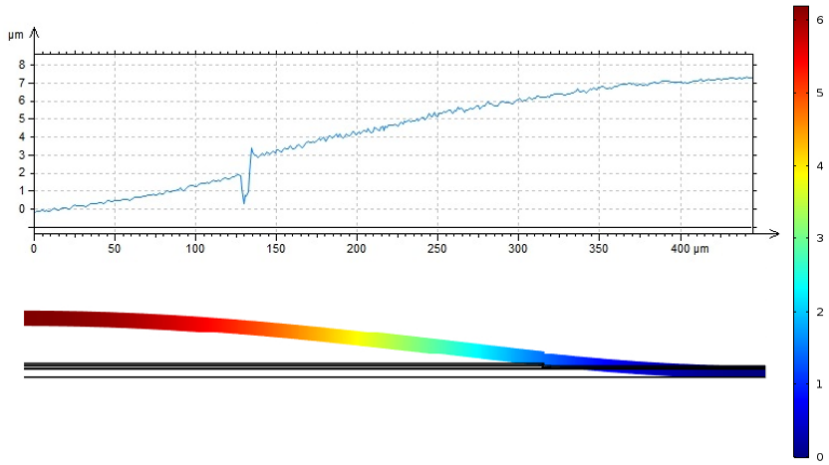

Figure 1: Initial static configuration due to fabrication residual stresses: experimental measured profile by means of MicroXAM-100 3D Surface Profilometer (above), numerically computed [µm] by means of COMSOL Multiphysics 5.2 (below).

The residual stress field determines the initial deformed shape of the layered system characterized by a maximum displacement, which occurs in the center point of the membrane, equal to 7.1 μm for the measured value, while the corresponding numerical value is 6.2 μm. The observed mismatch is attributed to the uncertainty in the experimentally measured residual stresses. The most important effect on the mechanical behavior of the vibrating system, induced by the residual stress state, is the frequency shift for the fundamental eigenfrequency of the membrane, that coincides with the operating one to maximize the acoustic efficiency in the transmission phase. As a matter of fact, the same diaphragm in terms of material and geometry, without the residual stresses, presents a theoretical fundamental eigenfrequency of 111 kHz; taking into account the contribution to the geometric stiffness due to the pre-stress state it decreases to 99.8 kHz in correspondence of an applied static voltage of 0.5 V to the piezoelectric layer of the system. This is correctly captured by the numerical model. To show the shift, a frequency spectrum analysis is performed in the presence of a static voltage of 0.5 V and a harmonic excitation with amplitude of 0.5 V. The numerical electro-mechanical-acoustic

simulation runs in 49 minutes with i7 CPU @3.4 GHz and 16 GB RAM for the complete sweep over the system without the protecting package. The comparison between the non-dimensional experimental spectrum and the numerically computed one for the vertical displacement of the center point of the diaphragm is shown in Fig. 2 together with the extended frequency sweep for the packaged system represented in Fig. 3, which allows one to evaluate the frequency associated with the coupled fluid-structure mode induced by the presence of the cap. The quality factor of the device is $Q = 80$ and it is obtained by means of a free vibration decay test.

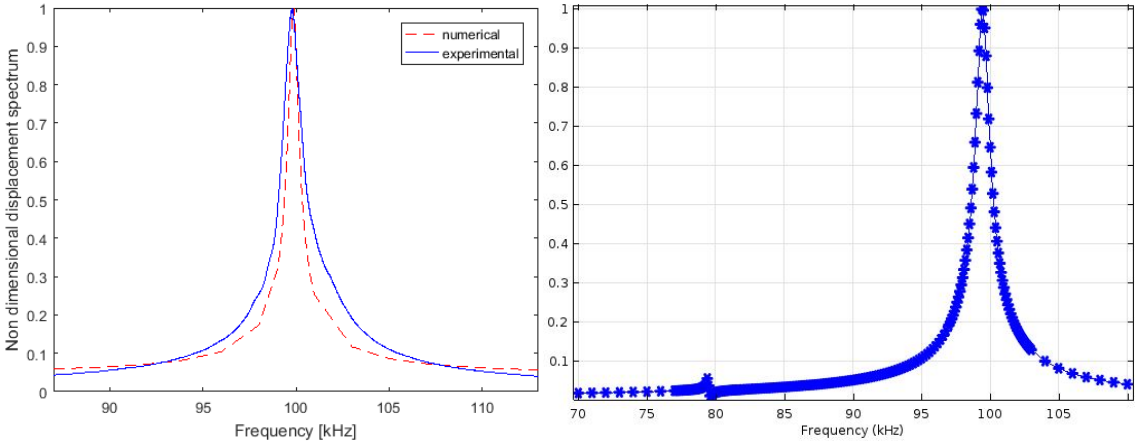

Figure 2: Normalized vertical displacement spectra for the center of the membrane: experimental measurement by means of Polytec MSA-500 Micro System Analyzer and numerical estimation by means of COMSOL Multiphysics 5.2 for the unpackaged PMUT (left), extended frequency sweep for the packaged PMUT (right).

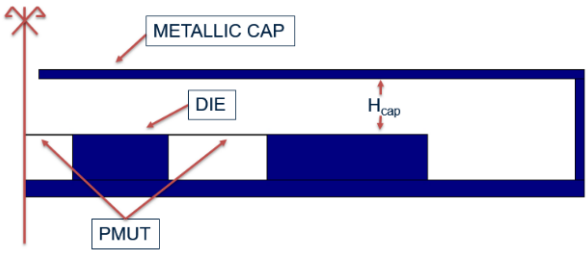

Figure 3: Sketch of the packaged system

4 ANALYSES IN THE PRESENCE OF PACKAGE

4.1 Stand-alone diaphragm vs. packaged device

The acoustic modelling of the surrounding fluid allows to evaluate the acoustic efficiency of the PMUT; the Sound Pressure Level (SPL) can be computed in every point of the fluid domain and outside of it by means of the Helmholtz-Kirchhoff integral technique (*far-field* calculation). The numerically computed SPL frequency response at 15 cm on the vertical axis of symmetry of the diaphragm, for the unpackaged transducer and for the packaged one are presented in Fig. 4. The protecting cap is characterized by a distance from the inner die equal to $H_{cap} = 500\ \mu m$, by a thickness of $t_{cap} = 80\ \mu m$ and by a central hole with radius equal to $R_{hole} = R_{PMUT}/3$ placed over the central vibrating transducer, where R_{PMUT} is the radius of the PMUT (Fig. 3).

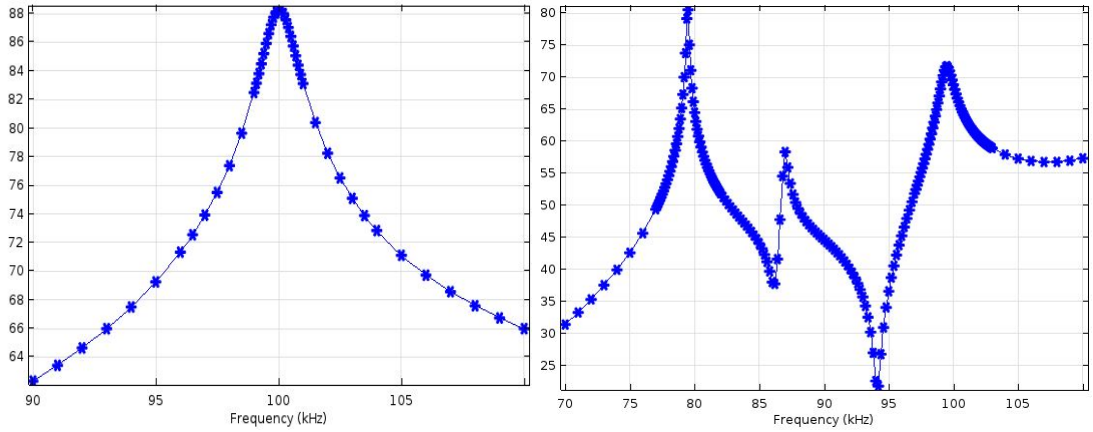

Figure 4: Sound Pressure Level [dB] at 15 cm on the vertical axis of symmetry: unpackaged transducer (left), packaged transducer (right).

It is possible to notice that the maximum value in the SPL at 15 cm occurs, for the system without the protecting cap, in correspondence of the resonance frequency of the membrane (f = 100 kHz), while in the case of the package structure it is 8 dB lower than the previous one and is related to a frequency of 79.5 kHz, which represents the eigenfrequency of the coupled fluid-structure mode associated with the adopted package geometry. Finally, for the device with the protecting cap, it is still possible to notice a local maximum at the corresponding mechanical resonance but it is 16 dB lower than the first one (barrier effect). Both maximum values in the SPL plot are related to a non-directional emitted pressure wave as we can see in Fig. 5 where the polar plot for a distance from the center of the diaphragm equal to 15 cm at the corresponding frequency is shown for the two cases together with the polar plot for the packaged device at the mechanical resonance frequency of the diaphragm.

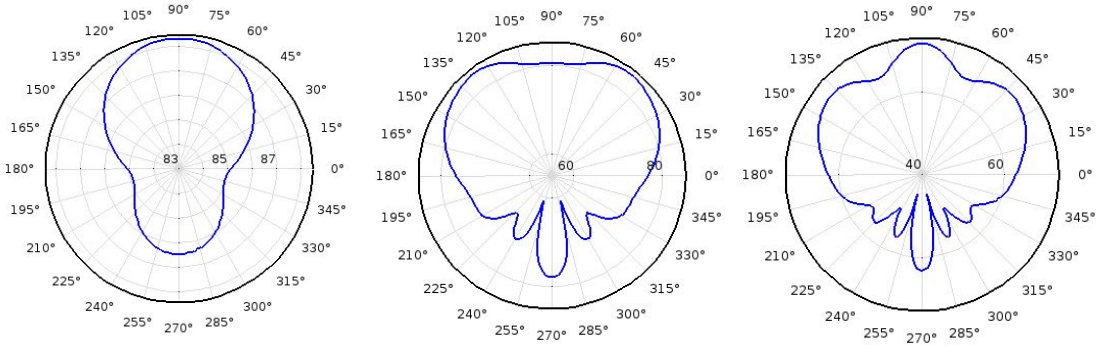

Figure 5: SPL polar plot [dB]: system without package at f = 100 kHz (left), with package at f = 79.5 kHz (central) and 100 kHz (right).

4.2 Simulations for different packages

Going further, several simulations have been performed over devices with PMUTs characterized by a resonance frequency of 63 kHz in the presence of the pre-stress state and a static voltage of 3 V. The numerical procedure has been applied to carry out a parametric analysis over the parameters H_{cap}, R_{PMUT} and t_{cap} to extract a set of design guidelines for the

package structure. The results are shown in the Figures 6-11, for a reduced set of parameters, in terms of vertical displacement frequency response, under a harmonic voltage excitation from 0 to 6 V, for the center point of the membrane belonging to the axis of symmetry, SPL at 15 cm on the axisymmetric axis and polar plot at the corresponding peak value.

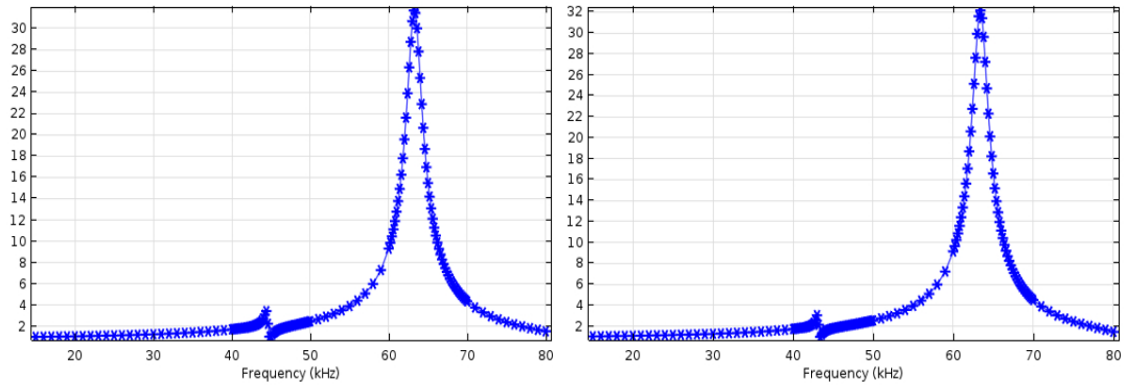

Figure 6: Vertical displacement spectra [µm] for the center point of the membrane belonging to the axis of symmetry by COMSOL Multiphysics 5.2: t_{cap} = 80 µm, R_{hole} = R_{PMUT}/3, H_{cap} = 200 µm (left), 500 µm (right).

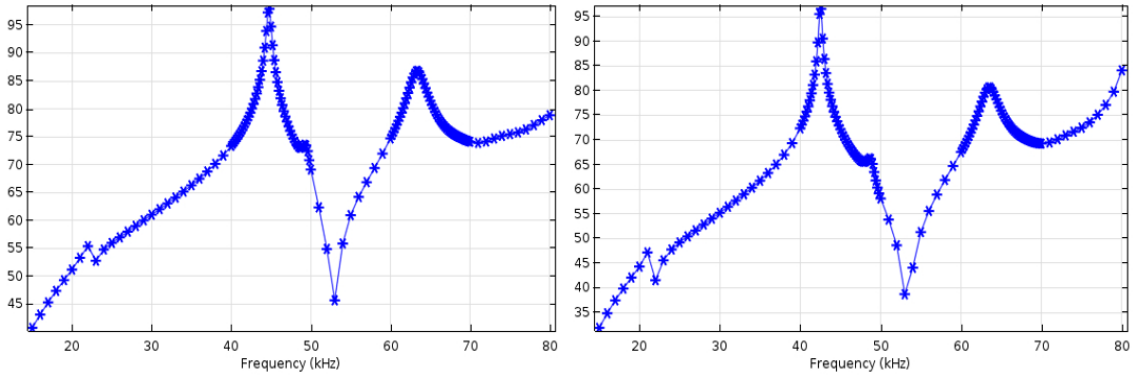

Figure 7: Sound Pressure Level [dB] at 15 cm on the vertical axis of symmetry: t_{cap} = 80 µm, R_{hole} = R_{PMUT}/3, H_{cap} = 200 µm (left), 500 µm (right).

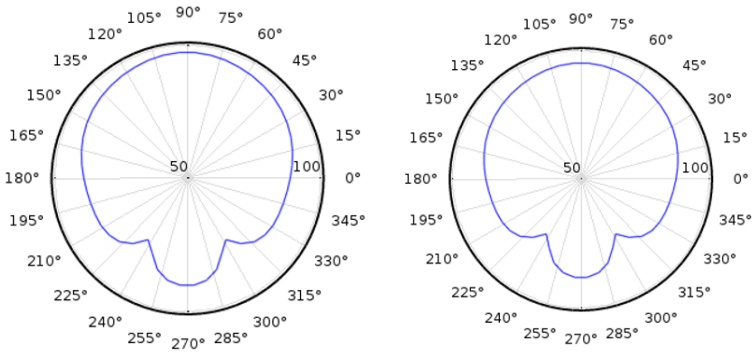

Figure 8: SPL polar plot [dB] at the corresponding peak value in the SPL versus frequency plot: t_{cap} = 80 µm, R_{hole} = R_{PMUT} /3, H_{cap} = 200 µm (left), 500 µm (right).

It is possible to notice that, in all the cases of Figs. 6-8, the peak value in the SPL versus frequency plot appears in correspondence of the frequency of the coupled fluid-structure mode, around 44.5 kHz; moreover, for H_{cap} = 200 μm (Figs. 6-8, left) the maximum in the SPL and the corresponding polar plot is slightly bigger than the case with H_{cap} = 500 μm (Figs. 6-8, right). Generally no great change occurs in the behavior of the system for the adopted package parameters. To emphasize the role of the cap structure, the radius of the hole is increased, keeping H_{cap} = 500 μm and t_{cap} = 80 μm, as it is shown in the Figures 9-11.

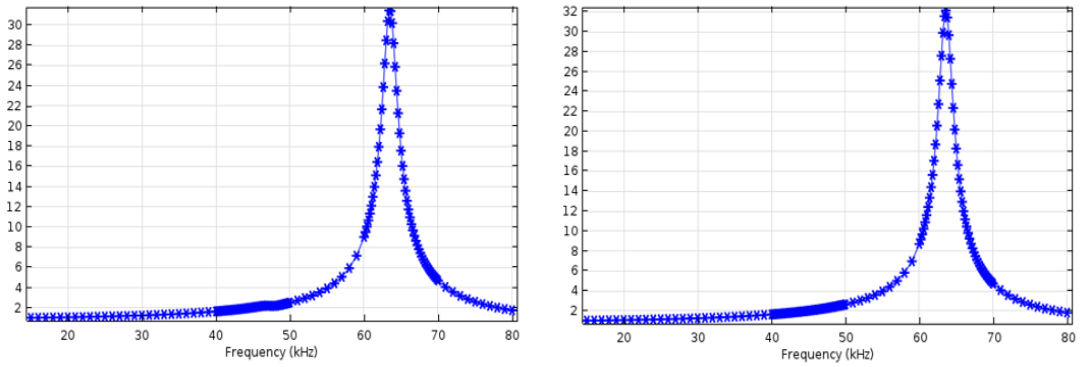

Figure 9: Vertical displacement spectra [μm] for the center point of the membrane belonging to the axis of symmetry by COMSOL Multiphysics 5.2: t_{cap} = 80 μm, H_{cap} = 500 μm, $R_{hole} = R_{PMUT}$ (left), $2R_{PMUT}$ (right).

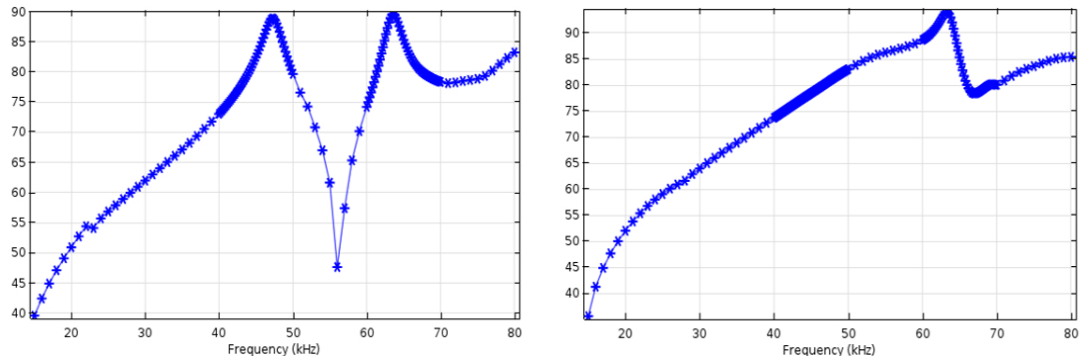

Figure 10: Sound Pressure Level [dB] at 15 cm on the vertical axis of symmetry: t_{cap} = 80 μm, H_{cap} = 500 μm, $R_{hole} = R_{PMUT}$ (left), $2R_{PMUT}$ (right).

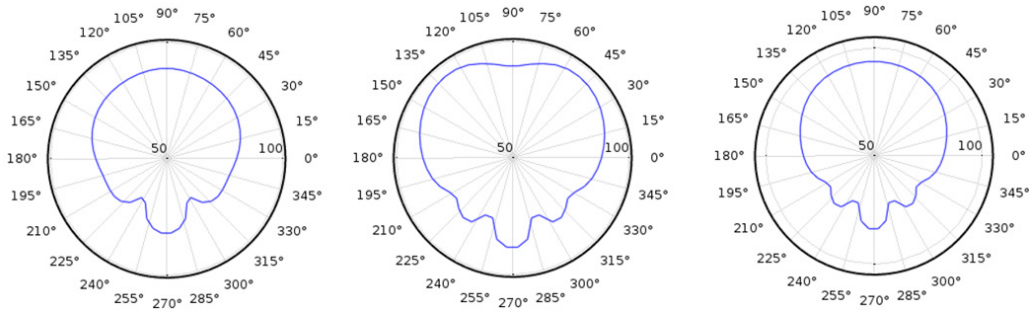

Figure 11: SPL polar plot [dB] at the corresponding peak value in the SPL versus frequency plot: t_{cap} = 80 μm, H_{cap} = 500 μm, $R_{hole} = R_{PMUT}$ at f = 47.5 kHz (left), R_{PMUT} at f = 63 kHz (central), $2R_{PMUT}$ (right).

In this case, it is possible to notice the different behavior of the device for the two values of the hole's radius. For $R_{hole} = R_{PMUT}$ in the SPL versus frequency there are two peaks for the frequency $f_1 = 47.5$ kHz, which is related to the coupled fluid-structure mode, and $f_2 = 63$ kHz, that is the fundamental mechanical frequency of the diaphragm. Furthermore, the peaks are characterized by the same maximum value but they are associated with different SPL polar shape, due to the different fluid response in the wave transmission. Finally, for the case $R_{hole} = 2\ R_{PMUT}$ the package influence over the dynamic behavior of the system is negligible; as a matter of fact, the maximum value in the SPL frequency response appears in correspondence of the mechanical resonance frequency of the membrane, as it occurred for the device without the package structure, and it is the highest registered value due to the lower barriest effect, along the positive vertical direction of the axisymmetric axis, determined by the presence of the cap.

5 CONCLUSIONS

The design of PMUTs should be based on a reliable computational model, that include the complex coupling between different physics, the non-linear behavior and the interaction between different parts of the device. In this paper, we have considered a fully-coupled multiphysics model that encompasses the mechanical, piezoelectric and acoustic fields. The effect of residual stresses has been introduced by a suitable non-linear model. The computational results for the stand-alone diaphragm have been compared to experimental data, showing a satisfactory degree of accuracy. The validated model has been used in order to assess the effect of package on the mechanical and acoustic performance of the PMUT. First, the response of the stand-alone diaphragm has been compared to the case of packaged device, with a hole that is a fraction of the PMUT radius: there is no effect on the mechanical response of the diaphragm itself, but the acoustic emission is strongly influenced by the presence of a coupled acoustic-structure mode. The sound pressure level in the far field is obviously reduced by the presence of the package.

The second step of the analyses has been represented by a parametric study for different geometric features of the package. The distance between the diaphragm and the package seems to play a minor role, since neither the mechanical response nor the sound pressure level is affected by a change of that parameter. Conversely, the variation of the radius of the hole induces a noteworthy modification of the acoustic field. In the case of small radius, the fluid-structure mode is dominant and the maximum sound pressure level can be obtained for a frequency that is far away from the resonance frequency of the diaphragm. When the radius is increased over a certain threshold, the obstructive effect of the package is reduced and the wave emission resembles to that of the stand-alone diaphragm.

REFERENCES

[1] Ardito, R., Bertarelli, E., Corigliano, A. and Gafforelli, G. On the application of piezo-laminated composites to diaphragm micropumps, *Compos. Struct.* (2013) **99**, 231-240.

[2] Roundy, S. and Wright, P.K. A piezoelectric vibration based generator for wireless electronics, *Smart Mat. Struct.* (2004) **13**, 1131–1142.

[3] Ardito, R., Corigliano, A., Gafforelli, G., Valzasina, C., Procopio, F. and Zafalon R. Advanced model for fast assessment of piezoelectric micro energy harvesters. *Front. Mater.* (2016) **3**, 17.1-17.9.

[4] Trolier-McKinstry, S. and Muralt, P. Thin film piezoelectrics for MEMS. *J. Electrocer.* (2004) **12**, 7-17.
[5] Lu, Y. and Horsley, D.A. Modeling, fabrication, and characterization of piezoelectric micromachined ultrasonic transducer arrays based on cavity SOI wafers, *J. MEMS* (2015) **24**, 1142-1149.
[6] Lu, Y., Tang, H., Fung, S., Wang, Q., Tsai, J.M., Daneman, M., Boser, B.E. and Horsley D.A. Ultrasonic fingerprint sensor using a piezoelectric micromachined ultrasonic transducer array integrated with complementary metal oxide semiconductor electronics. *Appl. Phys. Lett.* (2015) **106**, 263503.
[7] Rozen, O., Block, S.T., Mo, X., Bland, W., Hurst, P., Tstai, J.M., Amirtharajah, M.D.R. and Horsley, D.A. Monolithic MEMS-CMOS ultrasonic rangefinder based on dual-electrode PMUTs. *Proc. of IEEE 29th International Conference on Micro Electro Mechanical Systems (MEMS)* (2016) 115-118.
[8] Massimino, G., D'Alessandro, L., Procopio, F., Ardito, R., Ferrera, M. and Corigliano, A. Multiphysics analysis and experimental validation of an air coupled piezoelectric micromachined ultrasonic transducer with residual stresses. *Proc. Engrg.* (2016) **168**, 852-855.
[9] Kinsler, L.E., Frey, A.R., Coppens, A.B. and Sanders, J.V. *Fundamentals of Acoustics*. John Wiley & Sons, (2000).

VII International Conference on Computational Methods for Coupled Problems in Science and Engineering
COUPLED PROBLEMS 2017
M. Papadrakakis, E. Oñate and B. Schrefler (Eds)

NUMERICAL SIMULATION OF DROPLET IMPACT EROSION : DANG VAN FATIGUE APPROACH

G. COUDOUEL[1,2,*], A. COMBESCURE[1] AND J.-C. MARONGIU[2]

[1] Laboratoire de Mécanique des Contacts et des Structures (LaMCoS), UMR CNRS 5259
Institut National des Sciences Appliquées de Lyon (INSA)
20 Avenue Albert Einstein, 69100 Villeurbanne, France
e-mail: {guillaume.coudouel - alain.combescure}@insa-lyon.fr, http://lamcos.insa-lyon.fr/

[2]ANDRITZ Hydro
13 Avenue Albert Einstein, 69100 Villeurbanne, France
e-mail: jean-christophe.marongiu@andritz.com, www.andritz.com/hydro.htm

Key words: Impact, Coupling, Droplet, Erosion, Fatigue, FEM, Fluid SPH, Explicit Dynamics

Abstract. The aim of this work is to understand the erosion mechanism caused by repeated water droplets impingement on a metallic structure, and then perform numerical simulations of the damage. When a high velocity water droplet with small diameter impacts a rigid surface, interaction is driven by inertial effects. Upon impact, the "water-hammer" pressure appears by inertial effect at the center of the contact though the maximum pressure occurs on the envelope of the contact area. Lateral jetting occurs by compression when the wave front travelling inside droplet overtakes the contact area. Concerning the structure, erosion is due to fatigue cracking. First, material grains are weakened during an "incubation" phase. After a large number of impacts, micro-cracks emerge and lead to ejection or fracture of grains, what is called "amplification" phase. Numerical simulation including rigid solid allows to locate the most loaded zones of the area, by observing the pressure and mainly the impulse. A 2-way coupling computation with fluid-structure interaction at macroscopic scale allows to confirm the fatigue-based mechanism by observing the hydrostatic stress. Finally, erosion program developed with Dang Van criterion provides the location of the most eroded zones of the structure during a loading cycle. They locate at the edge of jetting zone, which shows the influence of microjets in the erosion mechanism.

1 INTRODUCTION

This work is part of the PREDHYMA project, which concerns the erosion of Pelton turbines buckets. Hydraulic turbines can undergo severe damaging during operation, because of low quality water or detrimental flow conditions. Damaging induces maintenance costs and power production losses, and can also endanger safety of installations. Hydropower plants operators and turbine manufacturers are interested in extending overhaul periods by reducing damaging intensity and protecting turbine components with surface treatments. Accurate and reliable prediction of damaging is however missing. The present work is related to the erosion arising from repeated impacts of high speed water droplets on specific parts of Pelton turbines. Indeed for high head Pelton units, the jet of water is composed of a liquid core surrounded by droplets. Observations show that regions of impact of these droplets exhibit specific erosion patterns. First, the erosion mechanism is described, which allows to highlight the most important phenomena involved in the generation of damage. Then, numerical simulations are performed. They consist of the impact of a water droplet on a metallic structure, with an erosion post-processing.

2 DROPLET IMPACT EROSION

This part explains the mechanism responsible for the wear of metallic structures by water droplets impingement. Firstly, the mechanisms happening into the droplet in case of impact are presented, like the "water-hammer" pressure and waves propagation. The maximum pressure on the wall appears when side jets emerge from the droplet. Then, the erosion mechanism itself inside the solid is presented. These mechanisms may be split into two groups : the damages acting at macroscopic scale, then the mesosopic ones, such as intergranular cracks propagation leading to grain removal or tilting. This last case produces pits on the surface.

2.1 Liquid-solid impact

2.1.1 Waves propagation

According to Haller and Li [5, 10], when a small diameter and high velocity water droplet impacts a rigid flat target, viscous effects and surface tension can be neglected. Indeed, for a droplet radius $R = 0.1$mm and initial velocity $V = 500\text{m.s}^{-1}$, Reynolds number is Re = 50′000 and Weber number is We = 350′000 [5]. Numerical results from Haller [5] show almost constant temperature, so convective heat transfert is not involved in the fluid motion. Therefore, the fluid behaviour is driven by inertial effects and Euler equations can be considered for numerical simulations. After impact, a shock wave starts moving from the contact zone and propagates along the droplet lateral free surface. This wave follows an unobservable triple point, near the contact edge. Field and Haller [3, 5] build the shock front with the geometric principle of Huygens-Fresnel. The front is the envelope of wavelets created by successive edges of the contact (Figures 1.a and 1.b). The volume defined by the wave front and the contact area is highly compressed (Figure 1.a). Concerning the solid body, the droplet impact induces two main types of waves : spherical waves propagate inside volume and Rayleigh waves on the surface. Spher-

ical waves consist into longitudinal compression waves (P-waves), and transverse shear waves (S-waves). S-waves propagate slower than P-waves for most of metals.

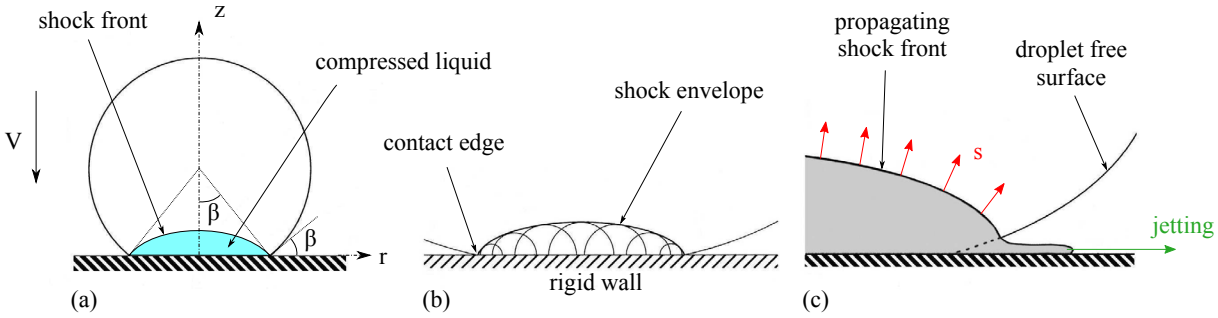

Figure 1: Impact of a spherical droplet on a rigid wall. **(a)** Shock front and highly compressed volume. **(b)** Geometric construction of the waves front. **(c)** Born of lateral micro-jets. (Haller [5]).

2.1.2 Contact pressure and micro-jetting

During the impact of a fluid body on a solid target, the "water-hammer" pressure p_{wh} emerges at the center of the contact area. Field, Heymann, Kennedy and Li [4, 6, 8, 10] give it expression for a rigid solid body in equation (1) :

$$p_{\text{wh}} = \rho_f^0 s V \tag{1}$$

were ρ_f^0 is the initial fluid density, s stands for the compression waves velocity traveling in the droplet (cf. Figure 1.c) and V the normal impact velocity of the droplet. Haller, Heymann and Li [5, 6, 10] approximate s in these conditions and give another expression for p_{wh} with equation (2), where k is a liquid-defendant constant, whose value equals 2 for water, and c_f^0 stands for initial sound velocity in water at room temperature :

$$p_{\text{wh}} = \rho_f^0 c_f^0 V \left(1 + k\frac{V}{c_f^0}\right) \tag{2}$$

Surface tension has no influence on pressure response (cf. 2.1.1) (Haller [5]). Numerical results from Haller [5] and Li [10] show the pressure distribution following the contact area over time. According to Field, Haller, Heymann and Lesser [4, 5, 6, 9], the maximum pressure p_{max} occurs exactly on the edge of the contact area (Figure 2.a). The moment the maximum value acts is not at the start of impingement, but when the shock wave overtakes the contact area. Then, compression with solid leads to jetting by lateral ejection of the fluid (Figures 1.c and 2.b). The maximum pressure locates at the jetting region. These two informations are contained in equation (3) where R_{jet} and t_{jet} are respectively the location and the time of jetting :

$$p_{\text{max}} = p(r = R_{\text{jet}}, t = t_{\text{jet}}) \tag{3}$$

The velocity of the jet can be far higher than the impact velocity V and even the ambient sound velocity c_f^0 (Figure 2.b). Unfortunately analytical expression for maximum pressure does not exist. Numerical results of Haller [5] and Kennedy [8] give respectively $p_{\max} \simeq 2p_{\text{wh}}$ and $p_{\max} \simeq 3p_{\text{wh}}$. However, Haller [5] suggests the time when jets form t_{jet} with the equation (4), where $\hat{s}$ stands for compression waves velocity inside the droplet when jetting :

$$t_{\text{jet}} = \frac{RV}{2\hat{s}^2} \tag{4}$$

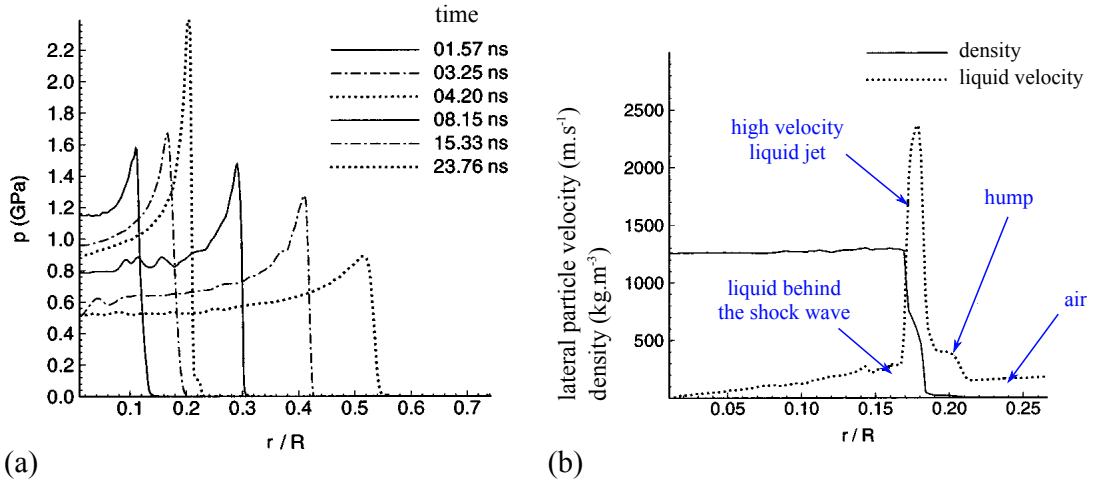

Figure 2: **(a)** Spatial distribution of contact pressure for several times after impact ($R = 0.1$mm, $V = 500$m.s^{-1}). **(b)** Radial velocity and density at the contact zone when jetting. Fluid radial velocity at contact zone (dotted line) shows clearly the jetting initialization at peak location (Haller [5]).

2.2 Erosion mechanism

2.2.1 Macroscopic scale

Claveris [1] worked on droplet impingement erosion of steam turbines blades and splits erosion mechanism into three phases : (i) The first phase is called “incubation period”. During this time no significant loss in mass is observed, but the surface condition changes and becomes more rough. (ii) Then, the loss in mass increases almost linearly until the rate of erosion reach it maximum value and becomes constant. (iii) Finally, erosion rate decreases, possibly again becomes constant, or zero in some cases.

2.2.2 Mesoscopic scale

A mesoscopic description of erosion mechanism is proposed by Kamkar and Luiset [7, 11] as the following steps :

1. The first impacts start to erode grain boundaries and generates pits between grains. Then, microcracks appear at the bottom of these pits.

2. Next, material is removed from surface by two damage modes : a) grain ejection which can produce triple joins, b) grain fracture.

3. After a larger number of impacts, neigbour grains support the same damage mechanism and are ejected or fractured (step 2.). Microckacks are intergranular type, which impair the surface condition, and move in parallel to the surface and propagate in depth. Microvoids born on the surface. The damage zone can be larger than the droplet itself.

4. These defaults are amplified by fatigue.

Finally, erosion is driven by plastic deformation, hardening, intergranular cracks propagation and fatigue mechanism. The cyclic nature of the damage produces a digging by steps (Figure 3).

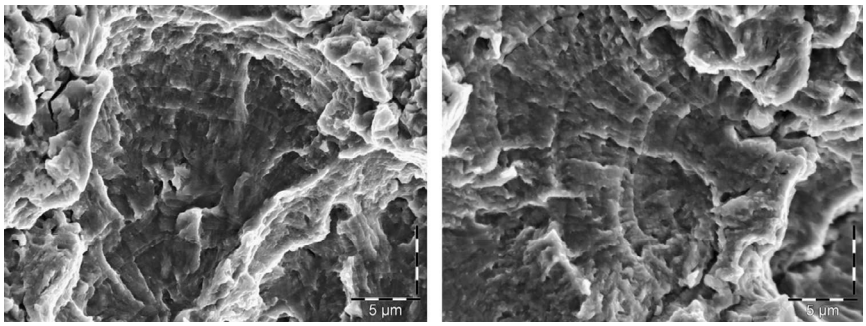

Figure 3: Damage resulting from repeated droplet impacts on stainless steel (Luiset [11]).

3 NUMERICAL SIMULATION OF DROPLET IMPACT EROSION

This section presents the 2D transient simulation of a water droplet impacting on a non-rigid solid body. Then, a fatigue post-processing is performed to estimate the damage over time and therefore the life cycle. The solid dub-domain is computed by the *Finite Elements Method* (FEM) with the explicit dynamics code *EuroPlexus*® [14], which is developed jointly by the french *Commissariat à l'Énergie Atomique et aux Énergies Alternatives* (CEA) and the *European Commission / Joint Research Center* (EC/JRC). This code is suitable for highly non-linear explicit dynamics with erosion. Concerning the fluid sub-domain, *ASPHODEL* code is used. This in-house code developed by *Andritz Hydro* uses the *Smoothed Particle Hydrodynamics* method (SPH) and is efficient to treat free surfaces. The *Fluid-Structure Interaction* (FSI) is performed by the two-way coupling code developed by Nuñez-Ramirez [13], which is energy-conservative at the interface for same time-steps.

3.1 Numerical model features

The solid body consists of a rectangular shaped steel domain. The material considered is homogeneous, isotropic and perfectly bilinear elastoplastic with Young's modulus $E_0 = 200\text{GPa}$, tangent modulus $E_t = 20\text{GPa}$, Poisson's ratio $\nu = 0.228$, yield strength $\sigma_Y = 560\text{MPa}$ and density $\rho_s^0 = 7700\text{kg.m}^{-3}$. The water droplet is a full disc with a radius $R = 0.5\text{mm}$ and moves perpendicularly towards the solid with an impact velocity $V = 100\text{m.s}^{-1}$. The fluid core has a density $\rho_f^0 = 1000\text{kg.m}^{-3}$ and an ambient sound velocity $c_f^0 = 1500\text{m.s}^{-1}$, neither viscosity nor surface tension (see section 2.1.1). Because of the abcense of convective effect (cf. section 2.1.1), the fluid satisfies the Tait equation of state (Macdonald [12]), which is isothermal, where $\gamma_f = 7$ stands for the Grüneisen parameter.

3.2 Droplet impact on a rigid target

Before FSI computation, a fluid computation is performed with the impact of droplet on a rigid wall, in order to understand the nature of loads involved on the solid body. The figure 4.a shows the maximum pressure $p_{\max} \approx 1.7\text{GPa}$, which equals ten times water-hammer pressure calculated with equation (2) and datas from section 3.1, which give $p_{\text{wh}} = 170\text{MPa}$. Maximal pressure locates at $x/R \simeq 0.18$, which corresponds to [5] (see Figure 2). The impulse per unite area, which is calculated by time integration of the pressure, gives a better qualitative idea of load intensity in fast transient dynamics, the load time being responsible for the deformation of surface. The spatial shape of the impulse gives a maximum value at the center of contact and fluctuations are observed at $x/R \simeq 0.18$, because of the instability of signal due to the water ejection. Thus the jetting is located at $R_{\text{jet}} \simeq 0.18 \cdot R = 0.09\text{mm}$.

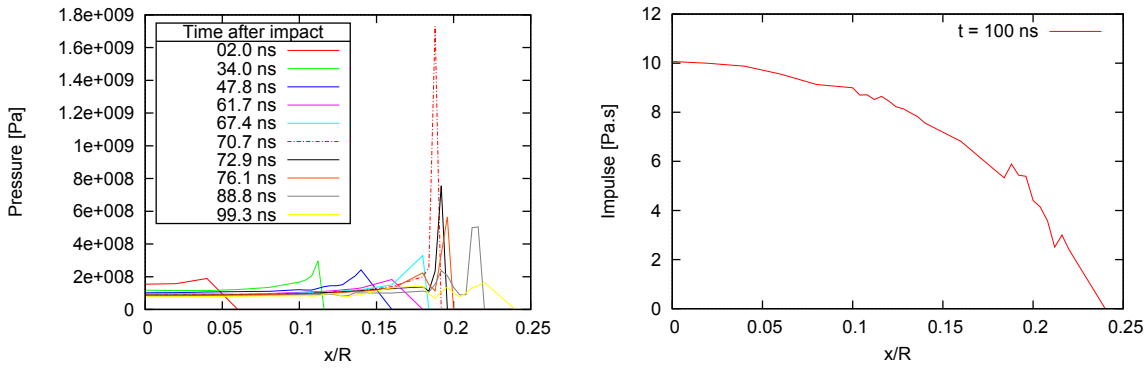

(a) (b)

Figure 4: Load distribution on rigid wall caused by droplet impingement ($R = 0.5\text{mm}$, $V = 100\text{m.s}^{-1}$). Location $x/R = 0$ corresponds to the center of the droplet. **(a)** Pressure distribution on the wall for ten representative times after impact. **(b)** Impulse distribution per unit area on the wall at 100ns after impact.

3.3 FSI computation

3.3.1 Results

Propagation of compression waves is given by observing the evolution and distribution of pressure inside the droplet p_f. A negative pressure corresponds to tension, and positive to compression. Concerning the solid, hydrostatic stress σ_H can be used . Unlike p_f the sign convention of σ_H is the following : $\sigma_H > 0$ in regions subjected to traction and $\sigma_H < 0$ for compression. For solids, shear waves act jointly to compression waves (cf. 2.1.1). They can be observed with the Von Mises stress σ_{VM}. As Von Mises stress stands for the shear intensity and hydrostatic stress gives information about the straction-compression state, these two quantities give general informations about damage by fatigue. Indeed high shear can lead to cracks initiation and a traction state tends to open them (and a compression state to close).

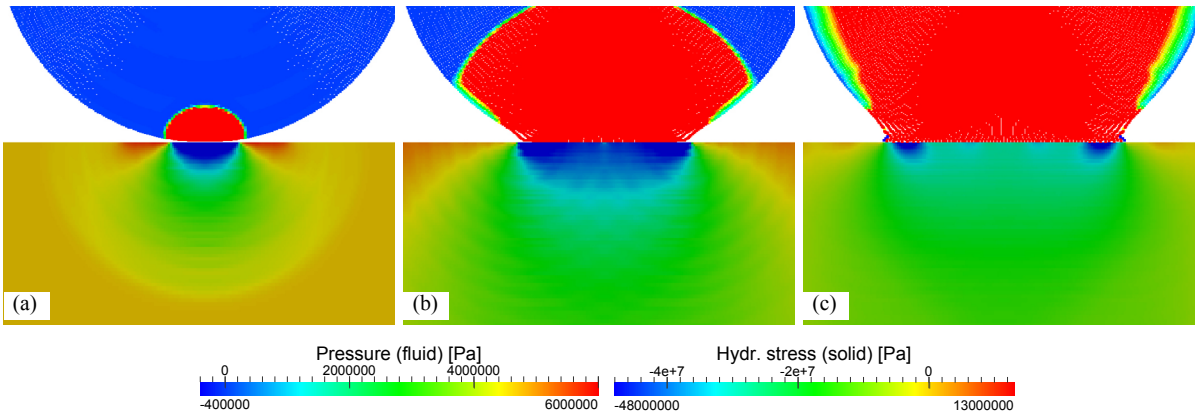

Figure 5: Pressure inside fluid and hydrostatic stress inside solid for several times after impact. **(a)** t = 60ns. **(b)** t = 260ns. **(c)** t = 440ns.

Results show absence of plasticity due to low stress intensity compared to the yield stress (Figures 5 and 6). This assertion is well checked by observing the equivalent plastic strain, which is zero. Analysis of hydrostatic stress allows to globally estimate the type of load inside the solid volume. For a solid region near the surface, the different times of Figure 5 show a change of sign for hydrostatic stress. Indeed, hydrostatic stress in Figure 6.a shows that this region is subject to a traction-compression cycle during the droplet impingement. Figure 6.b shows the shear intensity with the Von Mises stress along time. The value is low compared to yield strength, thus no plasticity occurs in this region.

3.4 Fatigue analysis

3.4.1 Erosion program

The result of simulations allow to define the eroded zones for a given fatigue criteria. After a transient computation, each element of the mesh contains a stress, strains, displacement, etc.

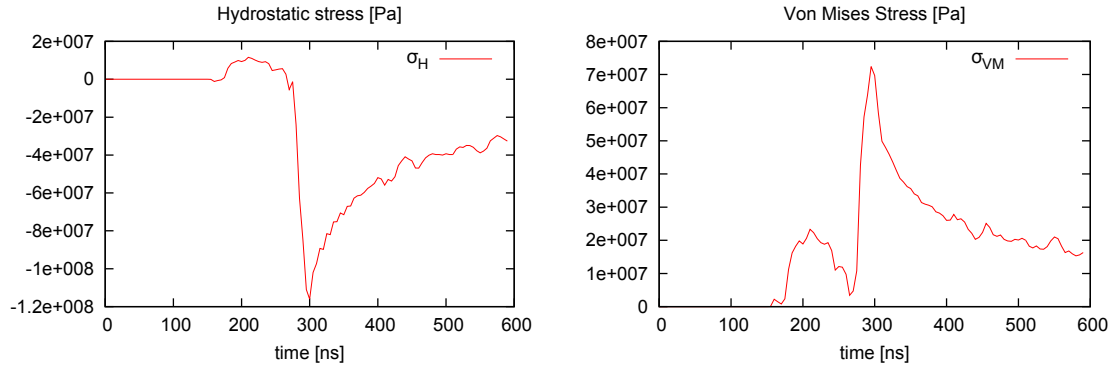

(a) (b)

Figure 6: Stresses at $x = 14.25 * 10^{-5}$m, $z = -2.5 * 10^{-6}$m vs. time. Droplet impacts the solid at $t = 130$ns **(a)** Hydrostatic stress. **(b)** Von Mises stress.

history. These physical quantities are used to define a fatigue criterion, which produces a condition to select which elements of the mesh are eroded and should be removed. This condition is called "fatigue function" and consists into a dimensionless quantity $E \in [0, 1]$. The condition of erosion being $E = 1$, and $E = 0$ corresponding to a virgin element. A fatigue criterion needs a number of load cycles N_{lim} as input, which corresponds to lower limit for non-eroded elements. Fatigue criterion give the opportunity to predict how many identical load cycles N each element can carry before failure. If $N \leq N_{\text{lim}}$, i.e $E = 1$, the element is eroded. This method is a predicting one, and saves a lot of time, because only one load cycle is simulated and not N_{lim}. After removing eroded elements of the mesh, a new FSI interface is computed and another simulation is launched for another number of cycles. The main procedure is detailed on Figure 7. This paper presents only one FSI computation without loop.

3.4.2 Fatigue datas

Generally, resistance to fatigue is checked with a S-N curve such as the Wöhler line (Figure 8), which depends on the material. For a given stress amplitude σ_a, the corresponding number of cycles to failure N is found. If $N \leq N_{\text{lim}}$, fatigue cracking initiates. The fatigue function is then calculated as the ratio between the stress amplitude σ_a and the stress limit σ_{lim}. If E exceeds 1, it value is usually brought back to 1 for more relevance. Indeed, from $E \geq 1$, the element concerned is damaged, regardless of the value of E.

3.4.3 Fatigue criterion

The fatigue damage is evaluated with the second version of Dang Van criterion [2]. The fatigue function E_{DV} is given in equation (5) :

$$E_{\text{DV}} = \sup_t \left\{ \frac{\tau^a(t) + \alpha\sigma_H(t)}{\beta} \right\} \tag{5}$$

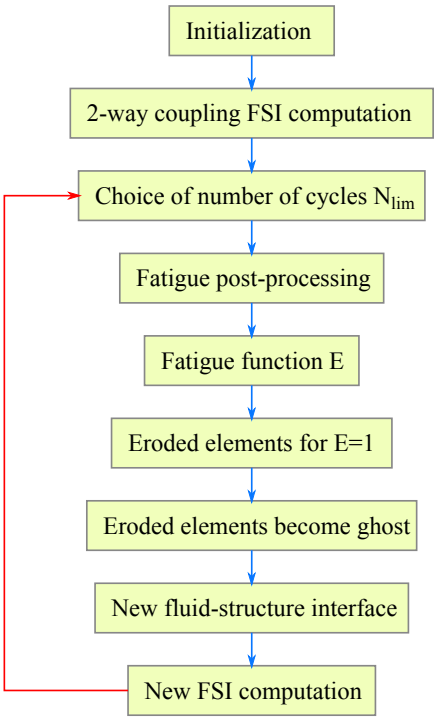

Figure 7: Erosion simulation procedure.

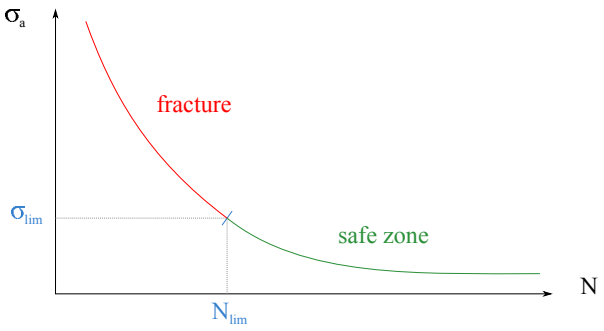

Figure 8: Wöhler line.

Where τ^a stands for shear amplitude and α, β are two coefficients depending on the material given in equation (6) :

$$\alpha = 3\left(\frac{\tau_{-1}}{\sigma_{-1}} - \frac{1}{2}\right) \qquad \beta = \tau_{-1} \tag{6}$$

Where σ_{-1} and τ_{-1} are respectively the endurance limit under symmetrical alternate traction and torsion. As measures for τ_{-1} are difficult to provide, the approximative value $\tau_{-1} = \sigma_{-1}/\sqrt{3}$ is considered. This choice satisfies the validity condition fot the criterion $\tau_{-1}/\sigma_{-1} > 1/2$. It can

be noted that α no longer depends on the material. The shear amplitude τ^a is got by applying the Tresca criterion over the alternate deviatoric stress. Additional informations about shear amplitude are given by Dang [2]. In this study, $\sigma_{-1} = \sigma_{\text{lim}}$. One define commonly the Dang Van equivalent stress σ_{DV} in equation (7) :

$$\sigma_{\text{DV}} = \sup_t \{\tau^a(t) + \alpha\sigma_H(t)\} \tag{7}$$

3.4.4 Results

The results presented in this section concern only one FSI computation and there is no loop described in section 3.4.2. The Dang Van equivalent stress on Figure 9 shows the most loaded zones of the volume, during the load cycle. It maximum value is $\sigma_{\text{DV}} = 30\text{MPa}$. The corresponding number of cycles to failure and damage indicator for $N_{\text{lim}} = 10E6$ are given on Figure 10. It appears that first elements break at 8 millions cycles, i.e. after 8 millions droplets impacts for the following conditions : no change of geometry and the surface is cleaned between each impingement. The eroded zones are enveloping around the jetting area. This results shows the importance of microjets for the erosion mechanism by droplet impact. Thus, the damaged region is crown-shaped. Moreover, erosion acts in depth, because the first elements layer is not eroded. The mesh convergence were checked and there is always a layer of non-eroded elements. But this layer will certainly break after the next impact.

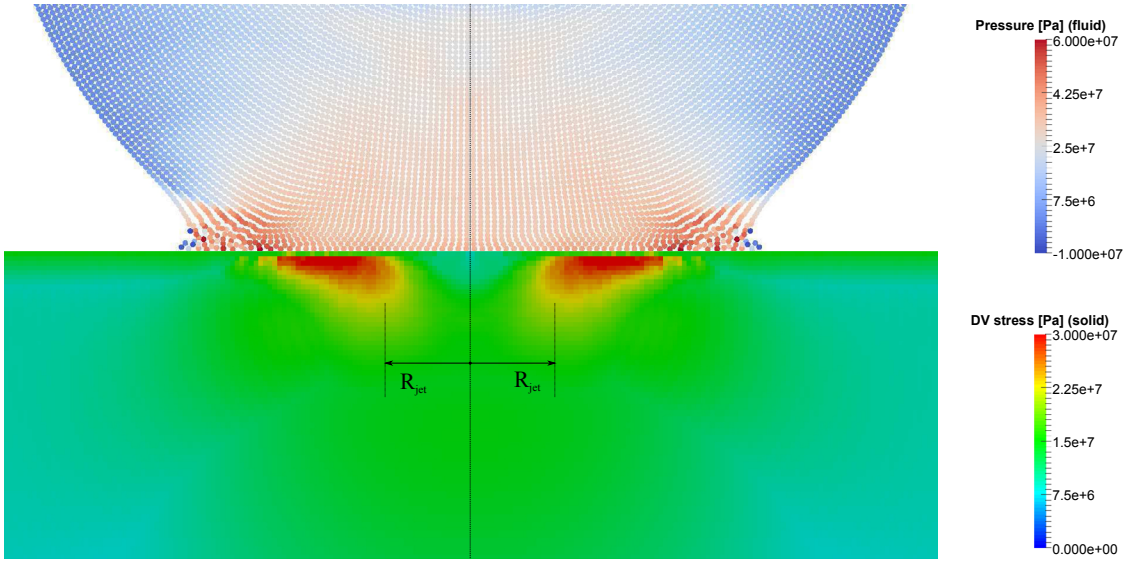

Figure 9: Pressure inside fluid and Dang Van equivalent stress inside solid at $t = 460\text{ns}$ after impact. Mark indicates the position of jetting at $x = R_{\text{jet}}$.

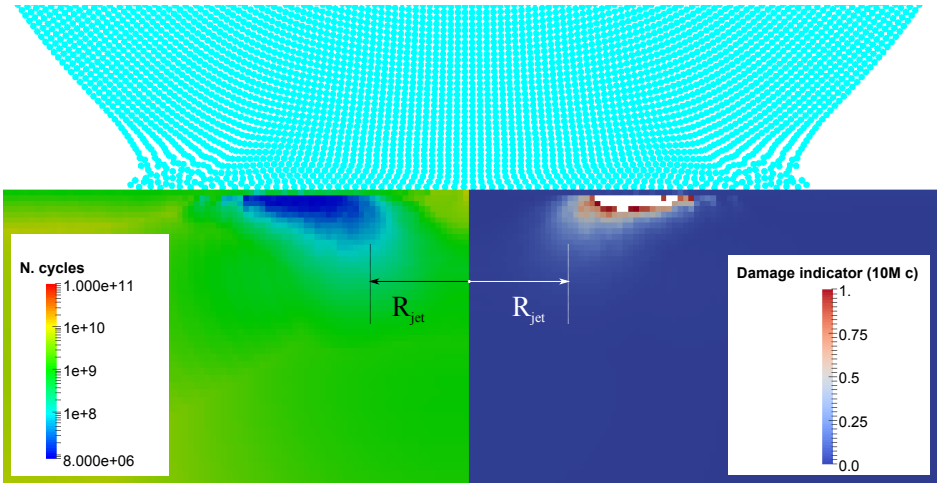

Figure 10: **(Left)** Number of cycles to failure (logarithmic scale) inside solid. **(Right)** damage indicator for $N_{\text{lim}} = 10$M cycles inside solid. Eroded elements are removed from the mesh. Both representations stand for $t = 460$ns after impact. Mark indicates the position of jetting at $x = R_{\text{jet}}$.

4 CONCLUSION

When high velocity droplet with small diameter impacts a rigid target, interaction is driven by inertial effects. Thus, viscous forces and surface tension can be neglected and Euler equations are relevant to represent the fluid behaviour. By inertial effect, water-hammer pressure appears at the center of the contact area, but maximal pressure locates on the contact edge. A compression wave travels inside the droplet, starting from the contact zone. When wave front overtakes contact area, microjets appear near the surface by compression effect. Concerning the structure, erosion is due to fatigue cracking. First, material grains are weakened during an "incubation" phase. After a large number of impacts, micro-cracks emerge and lead to ejection or fracture of grains, what is called "amplification" phase. Numerical simulations are performed subsequently. The droplet impact on a rigid target allows to find the pressure peak and thanks to the impulse, to locate the most loaded zone of the interface. Then, a 2-way coupling FSI computation is build, which gives a general overview of the fatigue mechanism by observing hydrostatic stress. Finally, a fatigue analysis is considered with Dang Van criterion, which supply a forecasting approach by giving informations on structure lifetime. It exposes the erosion shape, which is around jetting zone, showing the influence of microjets on the mechanism of erosion by water impingement. These first results will be a strong basis for a sensitivity analysis on main impact parameters (droplets diameter and velocity). It is also planned to investigate the influence of a thin water layer set on the solid surface to mimic the wet environment, and a multi-layer material to take into account the coated surface of Pelton buckets.

REFERENCES

[1] J. Claverie. *Critère permettant de prévoir le risque dérosion des corps basse pression des turbines à vapeur*, Électricité de France, 1973, ref J/32/062/1.1

[2] Dang Van, K., Griveau, B., Message, O. *On a New Multiaxial Fatigue Limit Criterion: Theory and Application Biaxial and multiaxial fatigue* EGF Publication, 1982, 3, 479-496

[3] J.E. Field. *ELSI Conference: invited lecture: Liquid impact: theory, experiment, applications*, Wear, 1999, 233-235, 1-12

[4] J.E. Field, J.-J. Camus, M. Tinguely, D. Obreschkow, M. Farhat. *Cavitation in impacted drops and jets and the effect on erosion damage thresholds*, Wear, 2012, 290-291, 154-160

[5] K. K. Haller, Y. Ventikos, and D. Poulikakos. *Computational study of high-speed liquid droplet impact*, Journal of applied physics, 2002, 92, 2821-2828

[6] F.J. Heymann. *High-speed impact between a liquid drop and a solid surface*, Journal of Applied Physics, 1969, 40, 5113-5122

[7] N. Kamkar, F. Bridier, P. Jedrzejowski, P. Bocher. *Water droplet impact erosion damage initiation in forged Ti-6Al-4V*, Wear, 2015, 322-323, 192-202

[8] C. F. Kennedy, J. E. Field. *Damage threshold velocities for liquid impact*, Journal of Materials Science 2000, 35, 5331-5339

[9] M.B. Lesser. *Thirty years of liquid impact research: a tutorial review*, Wear, 1995, 186, 28-34

[10] R. Li, H. Ninokata, M. Mori. *A numerical study of impact force caused by liquid droplet impingement onto a rigid wall*, Progress in Nuclear Energy, 2011, 53,7, 881-885

[11] B. Luiset, F. Sanchette, A. Billard, D. Schuster. *Mechanisms of stainless steels erosion by water droplets*, Wear, 2013, 303, 1-2, 459-464

[12] J. R. Macdonald. *Some Simple Isothermal Equations of State*, Rev. Mod. Phys., American Physical Society, 1966, 38, 669-679

[13] J. Nuñez-Ramirez, J.-C. Marongiu, M. Brun, A. Combescure. *A partitioned approach for the coupling of SPH and FE methods for transient nonlinear FSI problems with incompatible timesteps*, International Journal for Numerical Methods in Engineering, 2017, 109, 1391-1417

[14] CEA/DEN/SEMT/DYN *EuroPlexus. A computer program for the finite element simulation of fluid-structure systems under dynamic loading*, Users manual, 2002

Acknowledgement

The research leading to these results has received funding from the European Communitys Seventh Framework Programme (FP7 / 2007-2013) under Grant Agreement 608393 ”PREDHYMA”.

VII International Conference on Computational Methods for Coupled Problems in Science and Engineering
COUPLED PROBLEMS 2017
M. Papadrakakis, E. Oñate and B. Schrefler (Eds)

NUMERICAL SIMULATION OF TUBE-BUNDLE FLOW-INDUCED VIBRATIONS BY USING THE LS-STAG IMMERSED BOUNDARY METHOD

VALERIA V. PUZIKOVA* AND ILIA K. MARCHEVSKY†

*Applied Mathematics dep., Bauman Moscow State Technical University
105005 Moscow, Russia, 2nd Baumanskaya, 5
e-mail: vvp@dms-at.ru

†Applied Mathematics dep., Bauman Moscow State Technical University
105005 Moscow, Russia, 2nd Baumanskaya, 5
e-mail: iliamarchevsky@mail.ru

Key words: Immersed Boundary Method, The LS-STAG Method, Flow-Induced Vibrations, Bundles of Tubes, Airfoil

Abstract. The LS-STAG method is used in the present study for simulation of tube-bundle flow-induced vibrations. Staggered and in-line tube-bundles are considered. Flow regimes at different distances between tubes are investigated. Oscillations amplitudes for tubes from different bundle columns are computed. The LS-STAG method allows to simulate flow-induced vibrations of these tube-bundles on a very coarse mesh.

1 INTRODUCTION

Flow-induced vibrations occur in tubes of heat exchangers and reactor rod systems under the influence of unsteady hydrodynamic forces. These vibrations can cause the destruction of the whole device due to incorrect choice of working flow velocities. Therefore, simulation of tube-bundle flow-induced vibrations is a very important problem.

To simulate these flow-induced vibrations it is necessary to solve coupled hydroelastic problem. Such problems are complicated for numerical solution, since it is necessary to take into account interference between the flow and moving immersed body. In case of sufficiently massive body, coupled hydroelastic problems can be solved using step-by-step numerical algorithm, firstly simulating flow around a body moving with known parameters and then computing the dynamics of the body with known hydrodynamic loads.

Immersed boundary methods [1] are useful for numerical simulation in coupled hydroelastic problems, since they do not require a coincidence of cell edges and boundaries of the computational domain, and allow to solve problems when domain shape is irregular or it

changes in the simulation process due to aeroelastic body motion. The main advantage of these methods is that we don't need mesh reconstruction at each time step.

The LS-STAG cut-cell immersed boundary method [2] for viscous incompressible flows simulation combines the advantages of immersed boundary methods and the level-set method. This method allows to solve problems on the Cartesian grid. In contrast to classical immersed boundary methods, the flow variables are computed in the cut-cells, and not interpolated. Numerical analogues of conservation laws satisfaction in all fluid domain cells is a basis of LS-STAG discretization constructing, which allows to obtain physically realistic numerical solution. For these reasons, the LS-STAG method is used in the present study for simulation of tube-bundle flow-induced vibrations. The immersed boundary is represented with the level-set function [3]. Linear systems resulting from the LS-STAG discretization of the Navier-Stokes or Reynolds-averaged Navier-Stokes equations, are solved using the BiCGStab method [4] with the ILU- and multigrid [5, 6] preconditioning. An original algorithm for the solver cost-coefficient estimation [7] is used for the optimal parameters of the multigrid preconditioner choice.

2 GOVERNING EQUATIONS

The problem is considered for 2D unsteady case when the flow around an airfoil assumed to be viscous and incompressible. The continuity and momentum equations are the following:

$$\nabla \cdot \mathbf{v} = 0, \quad \frac{\partial \mathbf{v}}{\partial t} + (\mathbf{v} \cdot \nabla)\mathbf{v} = -\frac{1}{\rho}\nabla p + \nu \Delta \mathbf{v}. \tag{1}$$

The boundary conditions on external boundaries of computational domain are the following:

$$\mathbf{v}\big|_{\text{inlet}} = \mathbf{v}_\infty, \quad \frac{\partial \mathbf{v}}{\partial \mathbf{n}}\Big|_{\text{outlet}} = 0, \quad \frac{\partial p}{\partial \mathbf{n}}\Big|_{\text{inlet\&outlet}} = 0, \tag{2}$$

and boundary conditions on the camber line of the airfoil are no-slip conditions:

$$\mathbf{v}\big|_{\text{airfoil}} = \mathbf{v}^{\text{ib}}, \quad \frac{\partial p}{\partial \mathbf{n}}\Big|_{\text{airfoil}} = 0. \tag{3}$$

Here $\mathbf{v}^{\text{ib}}$ is the velocity of the immersed boundary. The airfoil assumed to be rigid and it can oscillate with 1, 2 or 3 degrees of freedom. Its motion is described by dynamics equations which in the most common form can be written down as the following:

$$\ddot{\mathbf{q}} = \mathbf{\Phi}(\mathbf{q}, \dot{\mathbf{q}}) + \mathbf{Q}^{\text{flow}} + \mathbf{Q}^{\text{ext}}. \tag{4}$$

Here $\mathbf{q}$ is the airfoil generalized coordinates vector, $\mathbf{\Phi}(\mathbf{q}, \dot{\mathbf{q}})$ is determined by elastic and viscous constraints imposed on the airfoil, $\mathbf{Q}^{\text{flow}}$ is the generalized aerodynamic force, $\mathbf{Q}^{\text{ext}}$ is external mass forces vector.

3 NUMERICAL METHOD

The Cartesian mesh with cells $\Omega_{i,j} = (x_{i-1}, x_i) \times (y_{j-1}, y_j)$ is introduced in the rectangular computational domain. It is denoted that $\Gamma_{i,j}$ is the face of $\Omega_{i,j}$ and $\mathbf{x}^c_{i,j} = (x^c_i, y^c_j)$ is the center of this cell. Unknown components $u_{i,j}$ and $v_{i,j}$ of velocity vector $\mathbf{v}$ are computed in the middle of fluid parts of the cell faces. These points are the centers of control volumes $\Omega^u_{i,j} = (x^c_i, x^c_{i+1}) \times (y_{j-1}, y_j)$ and $\Omega^v_{i,j} = (x_{i-1}, x_i) \times (y^c_j, y^c_{j+1})$ with faces $\Gamma^u_{i,j}$ and $\Gamma^v_{i,j}$, respectively (fig. 1).

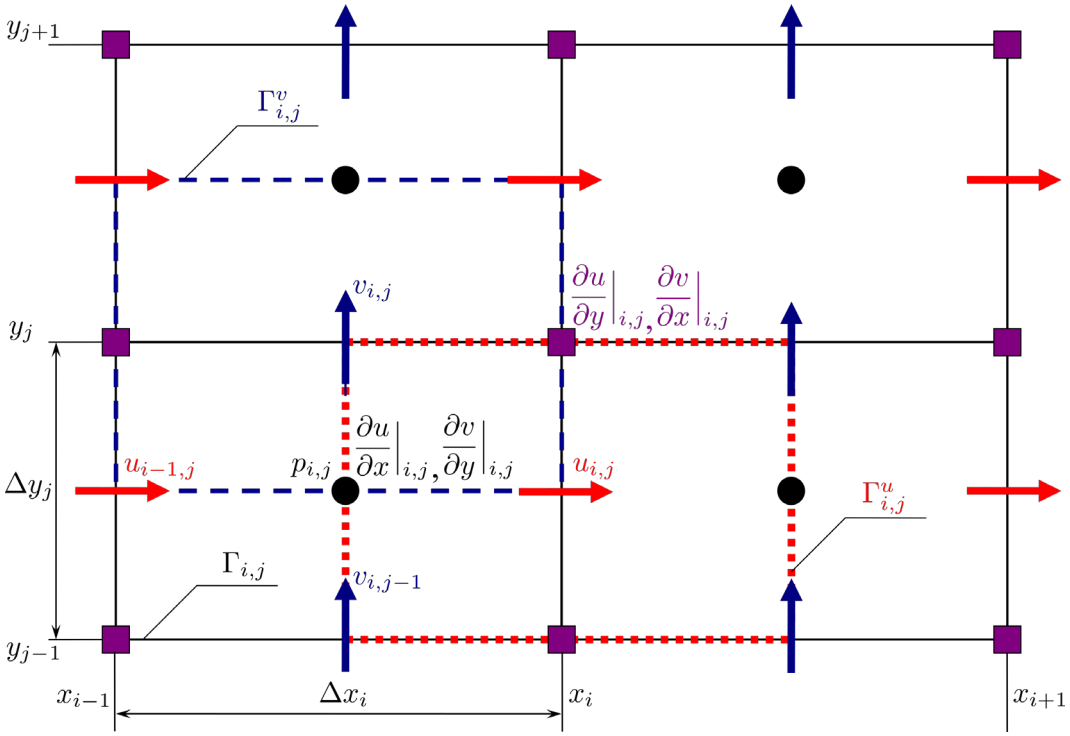

Figure 1: Staggered arrangement of the variables on the LS-STAG mesh

Cells which the immersed boundary intersects are the so-called 'cut-cells' (fig. 2). These cells contain the solid part together with the liquid one. The level-set function φ is used for immersed boundary Γ^{ib} description. The boundary Γ^{ib} is represented by a line segment on the cut-cell $\Omega_{i,j}$. Locations of this segment endpoints are defined by linear interpolation of the variable $\varphi_{i,j} = \varphi(x_i, y_j)$.

The cell-face fraction ratios $\vartheta^u_{i,j}$ and $\vartheta^v_{i,j}$ are introduced. They take values in interval $[0, 1]$ and represent the fluid parts of the east and north faces of $\Gamma_{i,j}$, respectively. One-dimensional linear interpolation of $\varphi(x_i, y)$ on the segment $[y_{j-1}, y_j]$ and $\varphi(x, y_j)$ on the segment $[x_{i-1}, x_i]$ is used for the cell-face fraction ratios computing:

$$\vartheta^u_{i,j} = \frac{\min(\varphi_{i,j-1}, \varphi_{i,j})}{\min(\varphi_{i,j-1}, \varphi_{i,j}) - \max(\varphi_{i,j-1}, \varphi_{i,j})}, \quad \vartheta^v_{i,j} = \frac{\min(\varphi_{i-1,j}, \varphi_{i,j})}{\min(\varphi_{i-1,j}, \varphi_{i,j}) - \max(\varphi_{i-1,j}, \varphi_{i,j})}. \tag{5}$$

According to the concept of the LS-STAG method, normal Reynolds stress components are sampled on the base mesh (similar to pressure discretization) and shear ones are sampled in the upper right corners of the base mesh cells. Thus, for the shear Reynolds stresses an additional mesh (xy-mesh) is introduced. It is denoted that cell $\Omega^{xy}_{i,j} = (x^c_i, x^c_{i+1}) \times (y^c_j, y^c_{j+1})$ is the control volume on the xy-mesh and $\Gamma^{xy}_{i,j}$ represents the faces of this control volume. In case of Reynolds Stress (RSM) RANS models, these meshes are used for transport equation solving for Reynolds stresses. The result then is taken into account in the Helmholtz equation for the velocity. In case of Eddy Viscosity (EVM) RANS models eddy viscosity is sampled on the xy-mesh. It is very suitable that the eddy viscosity at solid boundaries vanishes, so the cut-cells discretization of the eddy viscosity equations and computation of Reynolds stresses becomes simple.

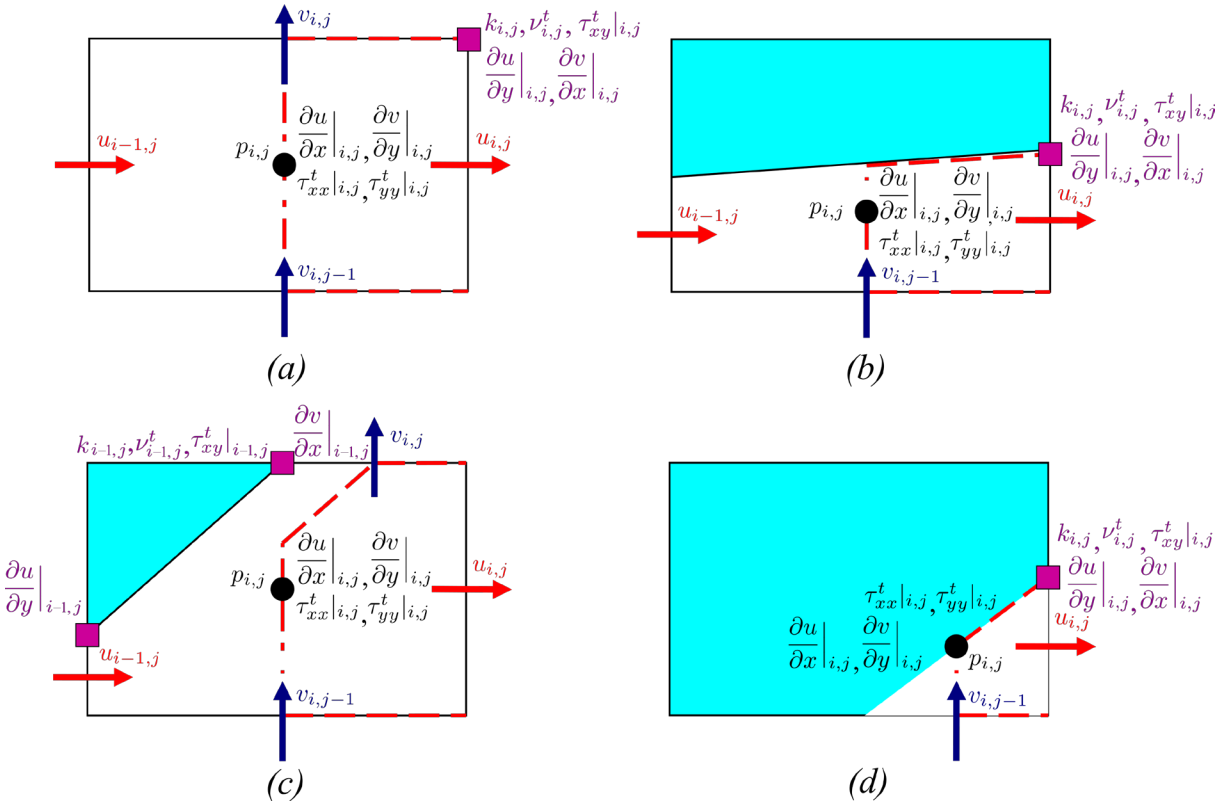

Figure 2: Location of the variables discretization points in the case of generic cells on the LS-STAG mesh: *(a)* Cartesian Fluid Cell; *(b)* North Trapezoidal Cell; *(c)* Northwest Pentagonal Cell; *(d)* Northwest Triangular Cell

Hydrodynamic force can be computed by the following formulae:

$$F_x = \sum_{\text{Cut-cells } \Omega^{ib}_{i,j}} \Big[(\vartheta^u_{i-1,j} - \vartheta^u_{i,j}) \Delta y_j \Big(p_{i,j} - \nu \frac{\partial u}{\partial x}\Big|_{i,j} \Big) - \nu \text{Quad}^{ib}_{i,j} \Big(\frac{\partial u}{\partial y} \mathbf{e}_y \cdot \mathbf{n} \Big) \Big], \tag{6}$$

$$F_y = \sum_{\text{Cut-cells } \Omega^{ib}_{i,j}} \Big[-\nu \text{Quad}^{ib}_{i,j} \Big(\frac{\partial v}{\partial x} \mathbf{e}_x \cdot \mathbf{n} \Big) + (\vartheta^v_{i,j-1} - \vartheta^v_{i,j}) \Delta x_i \Big(p_{i,j} - \nu \frac{\partial v}{\partial y}\Big|_{i,j} \Big) \Big].$$

The quadrature of the shear stresses $\text{Quad}^{ib}_{i,j}$ has to be adapted to each type of cut-cells.

According to the concept of the LS-STAG method, equations (1) should be written in integral form for cell of base mesh, cell of x-mesh and cell of y-mesh respectively:

$$\int\limits_{\Gamma_{i,j}} \mathbf{v} \cdot \mathbf{n} \, dS = 0, \tag{7}$$

$$\frac{d}{dt} \int\limits_{\Omega^u_{i,j}} u \, dV + \int\limits_{\Gamma^u_{i,j}} (\mathbf{v} \cdot \mathbf{n}) u \, dS + \int\limits_{\Gamma^u_{i,j}} p \mathbf{e_x} \cdot \mathbf{n} \, dS - \int\limits_{\Gamma^u_{i,j}} \nu \nabla u \cdot \mathbf{n} \, dS = 0,$$

$$\frac{d}{dt} \int\limits_{\Omega^v_{i,j}} v \, dV + \int\limits_{\Gamma^v_{i,j}} (\mathbf{v} \cdot \mathbf{n}) v \, dS + \int\limits_{\Gamma^v_{i,j}} p \mathbf{e_y} \cdot \mathbf{n} \, dS - \int\limits_{\Gamma^v_{i,j}} \nu \nabla v \cdot \mathbf{n} \, dS = 0.$$

The general form of the LS-STAG discretization for (7) can be written as the following [2]:

$$D^x U_x + D^y U_y + \overline{U}^{ib} = 0, \tag{8}$$

$$\frac{d}{dt}(M^x U_x) + C^x U_x + G^x P - \nu K^x U_x + S^{ib,c}_x - \nu S^{ib,\nu}_x = 0,$$

$$\frac{d}{dt}(M^y U_y) + C^y U_y + G^y P - \nu K^y U_y + S^{ib,c}_y - \nu S^{ib,\nu}_y = 0.$$

Here P is the discrete pressure, U_x and U_y are the discrete components of the velocity vector; $S^{ib,c}_x$, $S^{ib,\nu}_x$, $S^{ib,c}_y$, $S^{ib,\nu}_y$ are source terms; $\overline{U}^{ib}$ is the mass flux; D^x, D^y are the divergence discrete analogues; K^x and K^y represent the discretization of the diffusive terms; C^x and C^y represent the discretization of the convective terms; $G^x = -D^T_x$ and $G^y = -D^T_y$ are the gradient discrete analogues.

The time integration of the differential algebraic system (8) is performed with a semi-implicit Euler scheme. Predictor step leads to discrete analogues of the Helmholtz equation for velocities prediction $\widetilde{U}_x$, $\widetilde{U}_y$ at the time $t_{n+1} = (n+1)\Delta t$:

$$\frac{M^{n+1}_x \widetilde{U}_x - M^n_x U^n_x}{\Delta t} + C^n_x U^n_x + S^{ib,c,n}_x - D^{T,n}_x P^n - \nu K^{n+1}_x \widetilde{U}_x - \nu S^{ib,\nu,n+1}_x = 0, \tag{9}$$

$$\frac{M^{n+1}_y \widetilde{U}_y - M^n_y U^n_y}{\Delta t} + C^n_y U^n_y + S^{ib,c,n}_y - D^{T,n}_y P^n - \nu K^{n+1}_y \widetilde{U}_y - \nu S^{ib,\nu,n+1}_y = 0.$$

Here Δt is a time discretization step. Corrector step leads to the following discrete analogue of Poisson equation for $\Phi = \Delta t(P^{n+1} - P^n)$:

$$A^{n+1}\Phi = D_x^{n+1}\widetilde{U}_x + D_y^{n+1}\widetilde{U}_y + \overline{U}^{ib,n+1}, \tag{10}$$

$A = -D^x(M^x)^{-1}(D^x)^T - D^y(M^y)^{-1}(M^y)^T$. Then flow variables at the time point t_{n+1} are computed by the following formulae:

$$U_x^{n+1} = \widetilde{U}_x + (M_x^{n+1})^{-1}D_x^{T,n+1}\Phi,\ U_y^{n+1} = \widetilde{U}_y + (M_y^{n+1})^{-1}D_y^{T,n+1}\Phi,\ P^{n+1} = \frac{\Phi}{\Delta t} + P^n. \tag{11}$$

4 NUMERICAL EXPERIMENTS

A number of model problems had been considered before simulation of tube-bundle flow-induced vibrations: flow around fixed system of circular airfoils [8], circular airfoil wind resonance and buffeting which are presented below.

4.1 Circular airfoil wind resonance

To simulate wind resonance phenomenon we considered the motion of the circular airfoil with diameter D across the stream (with one degree of freedom). Airfoil constrain is assumed to be linear viscoelastic and its motion (4) is described by the following ordinary differential equation:

$$m\ddot{y}_* + b\dot{y}_* + cy_* = F_y. \tag{12}$$

Here m is the airfoil mass, b is a small damping factor, c is the constraint rigidity, F_y is lift force, y_* is the deviation from the equilibrium. The natural frequency of the system $\omega \approx \sqrt{c/m}$ can be set by varying of the coefficient c.

The deviation from the equilibrium on the n-th step of computation is $y_*^n = Y_C^n - Y_C^0$. Here Y_C^0 is the ordinate of the airfoil center at the initial time and Y_C^n is the ordinate of the airfoil center at the n-th step of computation. Difference analogue of the equation (12) can be written down in the following form:

$$m \cdot \frac{Y_C^{n+1} - 2Y_C^n + Y_C^{n-1}}{(\Delta t)^2} + b \cdot \frac{Y_C^{n+1} - Y_C^{n-1}}{2\Delta t} + c \cdot (Y_C^n - Y_C^0) = F_y|^n. \tag{13}$$

Position of the airfoil center at the next time step can be easily obtained from this equation on every computational step after computing the lift force acting on the airfoil. It allows to reconstruct the level-set function and all matrices required for the computation and to compute the immersed boundary velocity $\mathbf{v}^{ib}$ for recalculation the source terms.

Number of computations have been performed on non-uniform grid 272×292 with time discretization step $\Delta t = 0.0001$ and the following dimensionless parameters:

$$V_\infty = 3.0, \quad \rho = 1.0, \quad \nu = 0.003, \quad D = 1.0, \quad m = 39.75, \quad b = 0.731.$$

These parameters correspond to the Reynolds number Re = 1000. The dimensionless natural frequency of the system is in the following range:

$$\mathrm{St}_\omega = \frac{\omega}{2\pi} \cdot \frac{D}{V_\infty} = 0.150 \ldots 0.280.$$

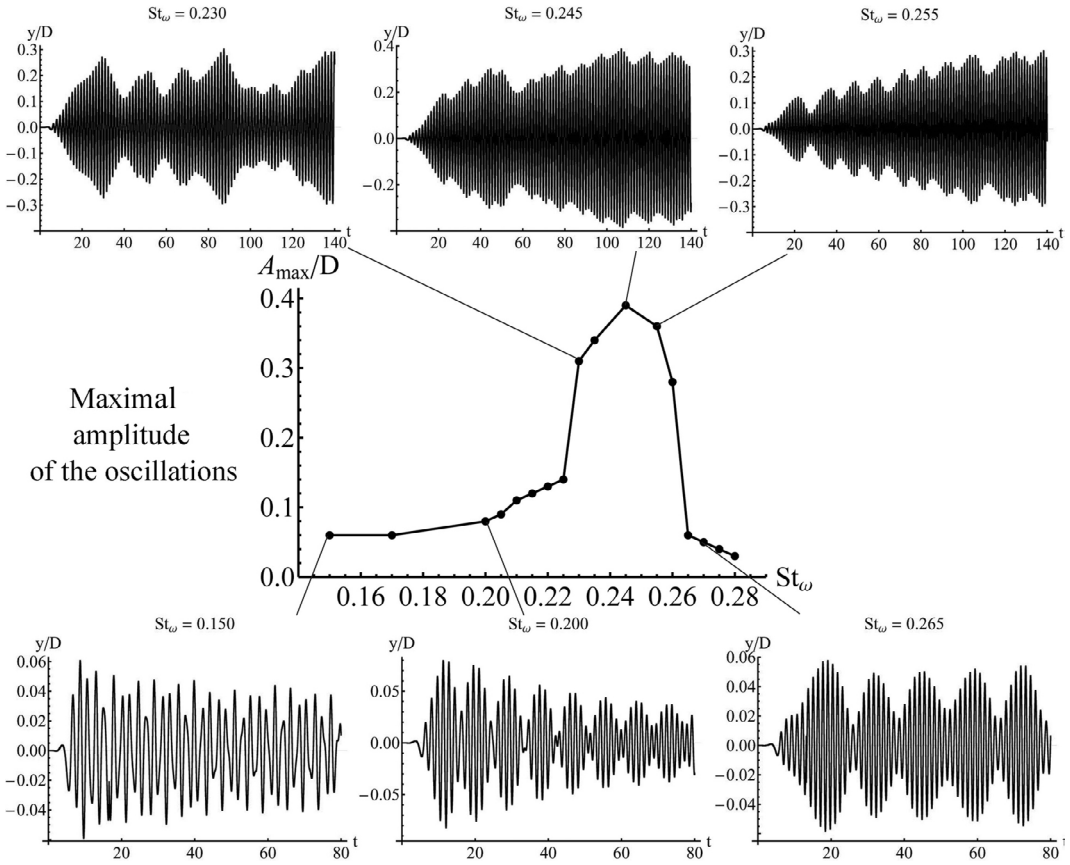

Figure 3: Maximal amplitude of the circular airfoil oscillations at Re = 1000

Computational results are in good agreement with the previous studies [9]. Maximal amplitude (fig. 3) is about $0.4D$ and it occures when the natural frequency of the system St_ω is close to the Strouhal number, calculated for a fixed airfoil $\mathrm{St} \approx 0.24$ [2, 10, 11].

Qualitative differences in airfoil dynamics at Strouhal numbers in investigated region are shown on fig. 3. Slight airfoil vibration is observed when the natural frequency of the system is significantly less than the frequency of vortex shedding. Damped beats appear with increasing natural frequency as you get closer to the Strouhal number. Amplitude of the oscillations increases sharply near the frequency of vortex shedding. Beats disappear and amplitude continues to increase with time. Amplitude of the oscillations decreases sharply and beats are observed again with a further increase of the St_ω.

4.2 Circular airfoil buffeting

To simulate buffeting phenomenon we considered the motion of two equal circular airfoils with diameter $D = 1.0$ across the stream at $V_\infty = 1.0$ (with two degrees of freedom). The distance between airfoils centers is equal to $L = 5.5$ on the horizontal and $T = 0.7$ on the vertical at the initial time. Airfoils constrains are assumed to be linear viscoelastic (fig. 4) and their motion (4) is described by the following equations:

$$m\ddot{x}_{*,i} + b\dot{x}_{*,i} + cx_{*,i} = F_{x,i}, \quad m\ddot{y}_{*,i} + b\dot{y}_{*,i} + cy_{*,i} = F_{y,i}, \quad i = \overline{1,N}. \tag{14}$$

Here $m = 4.7273$ is the airfoil mass, $b = 4\pi m\xi \mathrm{St}_\omega$ is the damping factor, $\xi = 3.3 \cdot 10^{-4}$, $c = m(2\pi \mathrm{St}_\omega)^2$ is the constraints rigidity; $N = 2$ is a number of airfoils, F_x and F_y are drag and lift forces, x_* and y_* are the deviations from the equilibrium on Ox and Oy.

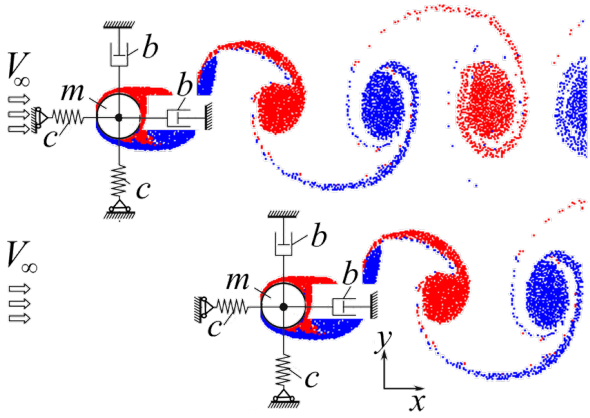

Figure 4: Circular airfoils with Kelvin — Voigt viscoelastic constraints and vortex wake behind them

The deviations from the equilibrium on the n-th step of computation are $x^n_{*,i} = X^n_{C,i} - X^0_{C,i}$, $y^n_{*,i} = Y^n_{C,i} - Y^0_{C,i}$. Here $(X^0_{C,i},\ Y^0_{C,i})$ are coordinates of the airfoil center at the initial time and $(X^n_{C,i},\ Y^n_{C,i})$ are coordinates of the airfoil center at the n-th step of computation. Difference analogues of equations (14) can be written down in the following form:

$$m \cdot \frac{X^{n+1}_{C,i} - 2X^n_{C,i} + X^{n-1}_{C,i}}{(\Delta t)^2} + b \cdot \frac{X^{n+1}_{C,i} - X^{n-1}_{C,i}}{2\Delta t} + c \cdot (X^n_{C,i} - X^0_{C,i}) = F_{xa,i}|^n, \tag{15}$$

$$m \cdot \frac{Y^{n+1}_{C,i} - 2Y^n_{C,i} + Y^{n-1}_{C,i}}{(\Delta t)^2} + b \cdot \frac{Y^{n+1}_{C,i} - Y^{n-1}_{C,i}}{2\Delta t} + c \cdot (Y^n_{C,i} - Y^0_{C,i}) = F_{ya,i}|^n. \tag{16}$$

Computations have been performed on non-uniform grid 666×344 at $\mathrm{Re} = 100$ and $\mathrm{Re} = 1000$. The dimensionless natural frequency of the system was in the range $\mathrm{St}_\omega/\mathrm{St} = 0.50 \ldots 2.00$. Here St is the Strouhal number, calculated for a fixed airfoil at the corresponding Reynolds number. Time discretization step was equal to $\Delta t = 10^{-4}$ ($\Delta t = 5 \cdot 10^{-5}$ at $\mathrm{Re} = 1000$) at $\mathrm{St}_\omega/\mathrm{St} = 0.85 \ldots 1.15$ and $\Delta t = 5 \cdot 10^{-4}$ ($\Delta t = 10^{-4}$ at

$\mathrm{Re} = 1000$) at $\mathrm{St}_\omega/\mathrm{St} = \{0.50, 0.70, 1.40 \ldots 2.00\}$. The uniform mesh block with spatial discretization step $h = D/64$ was used in the proximity of the airfoil.

Since the distance between the airfoils centers along Ox axis is large enough ($> 5D$), upstream airfoil (K_1) behaves like a single airfoil and downstream airfoil (K_2) performs forced oscillations due to periodic vortex-shedding flow past airfoil K_1. Thus, buffeting of airfoil K_2 is observed. Maximal amplitude of the airfoil K_2 oscillations significantly exceeds amplitude of the airfoil K_1 oscillations at $\mathrm{Re} = 100$ (fig. 5). Maximal amplitude of the airfoil K_1 oscillations appear at $\mathrm{St}_\omega \approx \mathrm{St}$ ($\mathrm{St} \approx 0.162$ at $\mathrm{Re} = 100$) as in [12]. This corresponds to the single airfoil behavior in the flow. Maximal amplitude of the airfoil K_2 oscillations along Oy axis appears at $\mathrm{St}_\omega \approx 0.85\mathrm{St}$. Amplitude of airfoil K_2 oscillations along Oy axis is less than amplitude of airfoil K_1 oscillations (fig. 6) at $\mathrm{Re} = 1000$ as in [13]. In this case maximal amplitude of the circular airfoils oscillations appears at $\mathrm{St}_\omega \approx \mathrm{St}$ both along Oy axis and Ox axis.

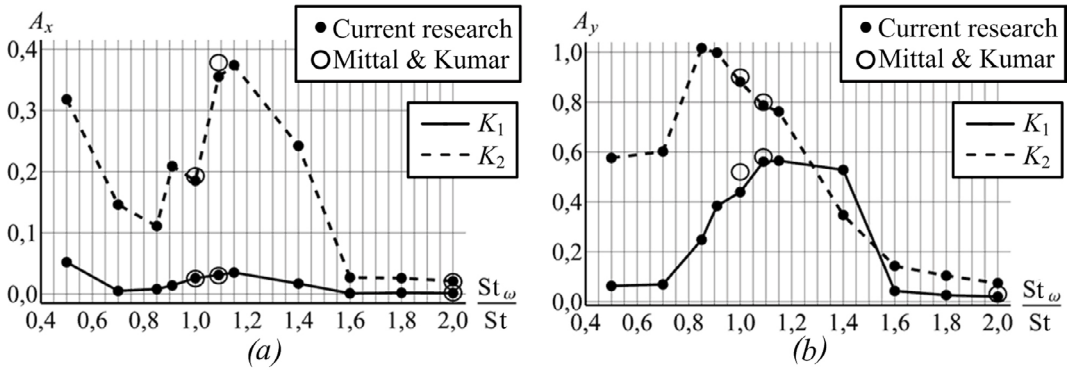

Figure 5: Maximal amplitude of the circular airfoils oscillations at $\mathrm{Re} = 100$: *(a)* along Ox axis; *(b)* along Oy axis

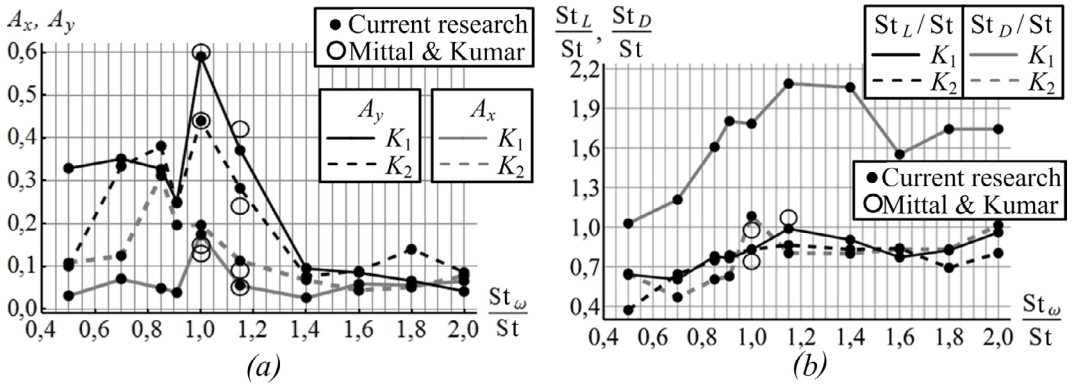

Figure 6: Characteristics of the circular airfoils oscillations at $\mathrm{Re} = 1000$: *(a)* maximal amplitude of the circular airfoils oscillations; *(b)* frequences of lift and drag forces oscillations

4.3 Tube-bundle flow-induced vibrations

We considered the motion of circular airfoils with diameter $D = 1.0$ across the stream at $V_\infty = 1.0$ (with two degree of freedom). Airfoils constrains are assumed to be linear viscoelastic (fig. 4) and their motion (4) is described by the ordinary differential equations (14). Tubes can be destroyed at $\mathrm{St}_\omega \approx \mathrm{St}$ with damping, which corresponds to the damping coefficient $b < 0.1$ [14]. Therefore, simulations were performed at $m = 40$ and $\xi = 3.3 \cdot 10^{-3}$ in this research. These values correspond to the damping coefficient $b = 4\pi m \xi \mathrm{St}_\omega > 0.14$ at $\mathrm{St}_\omega > 0.09$.

Flow pattern depends on the tubes arrangement and tube locations in the bundle [14]. For this reason, we considered flow around six columns of tubes in staggered arrangement and flow around five columns of tubes in in-line arrangements (fig. 7).

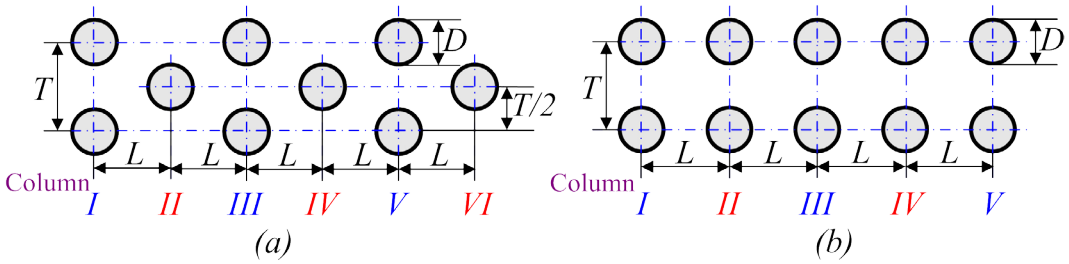

Figure 7: Considered tube arrangements: *(a)* staggered tube arrangement; *(b)* in-line tube arrangement

The distances between airfoils centers are equal to L on the horizontal and T on the vertical at the initial time. When the simulation was performed at $T/D > 4$, vortex streets between the rows do not affect each other, as in [14]. When $L/D > 4$, tubes in the bundle behave as single airfoils.

So, tube-bundle behaves as a single system at lower values of L, T. As an example, here we present computational results at $T/D = 2.0$, $L = T$ in case of in-line tube arrangement and $L = T\sqrt{3}/2$ in case of staggered tube arrangement. Thus, in the first case airfoils in adjacent columns are in the corners of a square, and in the second case they are located at the vertices of an equilateral triangle.

Number of computations have been performed at $\mathrm{Re} = 1000$ on non-uniform grid 846×424 in case of staggered tube arrangement and on non-uniform grid 816×424 in case of in-line tube arrangement. The uniform mesh block with space discretization step $h = D/64$ was used in the vicinity of the airfoil. Time discretization step was equal to $\Delta t = 5 \cdot 10^{-5}$. Computations were performed on a server based on the Intel C610 platform using the Intel Xeon E5-1620 V3 4-core processor (3.5 GHz) with HyperThreading support (8 logical cores). The server is equipped with 16 GB of ECC DDR4-2133 RAM and two hard drives (2 TB), united in a RAID1 disk volume. This server is running Windows Server 2012 R2 operating system. To simulate 50 dimensionless time units it is required about 137 hours.

The natural frequency of the system was in range $\mathrm{St}_\omega/\mathrm{St} = 0.50 \ldots 2.00$. Here St is the Strouhal number, calculated for a fixed tube-bundle at the corresponding Reynolds number. Our simulations showed that $\mathrm{St} \approx 0.205$ in case of in-line tube arrangement. This is in agreement with the fact that for this arrangement in the experiments [14] $\mathrm{St} = \mathrm{St}(T/D) = 0.2 + \exp[-1.2(T/D)^{1.8}]$, i.e. $\mathrm{St}(2.0) \approx 0.215$. In case of staggered arrangement two different frequencies are observed for tubes from even and odd columns (fig. 7) as in [14]. Upper frequency is observed in the tubes from odd columns. This frequency is considered as the vortex shedding frequency. So, we obtain that $\mathrm{St} \approx 0.280$ in case of staggered tube arrangement. This is in agreement with the fact that in the experiments [14] the maximum amplitude of oscillation occurs at a frequency equal to $(0.4 + 2\exp[-0.44(T/D)^{1.8}])/3$, i.e $\mathrm{St} \approx 0.277$ at $T/D = 2.0$. Lower frequency is observed in the tubes from even columns and it is equal St/2. It corresponds to frequency of vortex street interaction.

Computational results (fig. 8) are in qualitative agreement with the experimental data [14]. Tubes from first column behave like a single airfoils. In case of staggered tubes arrangement amplitude of the tubes oscillations along Oy axis significantly decreases with increasing column number.

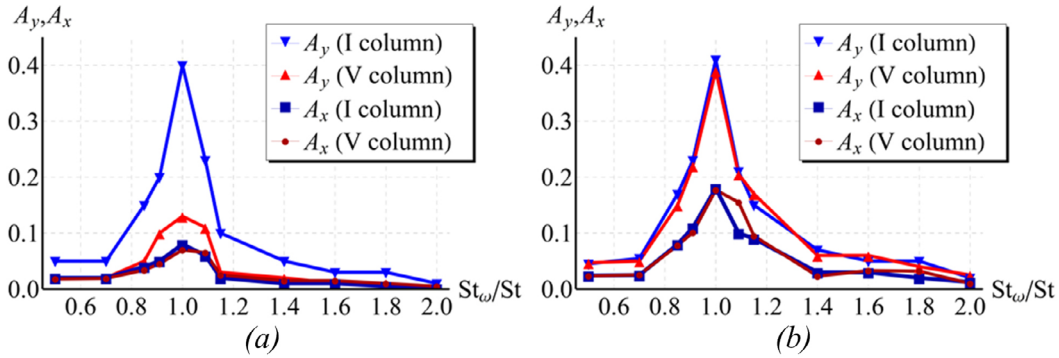

Figure 8: Maximal amplitude of the tubes oscillations at $\mathrm{Re} = 1000$: *(a)* staggered tube arrangement; *(b)* in-line tube arrangement

5 CONCLUSIONS

- A software package is developed for the numerical simulation of the airfoils motion in the viscous incompressible flow by using the LS-STAG method.
- Simulation of a circular airfoil wind resonance and buffeting phenomenons, tube-bundle flow-induced vibrations are considered. The LS-STAG method allows to simulate these phenomenons on a very coarse mesh.
- Computational results are in good qualitative agreement with the experimental data.

6 ACKNOWLEGEMENTS

The work was partially supported by Russian Federation President Grant for young scientists [proj. MK-7431.2016.8].

REFERENCES

[1] Mittal, R. and Iaccarino, G. Immersed boundary methods. *Annu. Rev. Fluid Mech.* (2005) **37**:239–261.

[2] Cheny, Y. and Botella, O. The LS-STAG method: A new immersed boundary/level-set method for the computation of incompressible viscous flows in complex moving geometries with good conservation properties. *J.Comput.Phys.* (2010) **229**:1043–1076.

[3] Osher, S. and Fedkiw, R.P. *Level set methods and dynamic implicit surfaces.* Springer, (2003).

[4] Van der Vorst, H.A. Bi-CGSTAB: a fast and smoothly converging variant of Bi-CG for solution of non-symmetric linear systems. *SIAM J. Sci. Stat. Comp.* (1992). **2**:631–644.

[5] Wesseling, P. *An introduction to multigrid methods.* John Willey & Sons Ltd., (1991).

[6] Van Kan, J., Vuik, C. and Wesseling, P. Fast pressure calculation for 2D and 3D time dependent incompressible flow. *Numer. Lin. Alg. Appl.* (2000) **7**:429–447.

[7] Marchevsky, I.K. and Puzikova, V.V. OpenFOAM iterative methods efficiency analysis for linear systems solving. *Proceedings of the Institute for System Programming of RAS.* (2013) **24**:71–86. [in Russian]

[8] Marchevskii, I.K. and Puzikova, V. V. Numerical simulation of the flow around two fixed circular airfoils positioned in tandem using the LS-STAG method. *J. Mach. Manuf. Reliab.* (2016) **45**:130–136.

[9] Klamo, J.T., Leonard, A. and Roshko, A. On the maximum amplitude for a freely vibrating cylinder in cross flow. *J. of Fluids and Struct.* (2005) **21**:429–434.

[10] He J.W., Glovinski, R., Metcalfe, R., Nordlander, A. and Triaux, J.P. Active control and drag optimization for flow past a circular cylinder. Part I: Oscillatory cylinder rotation. *J. Comput. Phys.* (2000) **163**:87–117.

[11] Henderson, R.D. Nonlinear dynamics and pattern formation in turbulent wake transition. *J. Fluid Mech.* (1997) **352**:65–112.

[12] Mittal, S. and Kumar, V. Flow-induced oscillations of two cylinders in tandem and staggered arrangements. *J. Fluids Struct.* (2001) **15**:717–736.

[13] Mittal S. and Kumar, V. Vortex induced vibrations of a pair of cylinders at Reynolds number 1000. *Int. J. Comput. Fluid Dyn.* (2004) **18**:601–614.

[14] Zukauskas, A., Ulinskas, R. and Katinas, V. *Gidrodinamika i vibratsii obtekayemykh puchkov trub (Fluid Dynamics and Flow-Induced Vibrations of Tube Banks).* Vil'nyus, (1984).

THE METHOD OF LONG-LIFE CALCULATION FOR A FRICTION COUPLE "ROTOR – HYBRID BEARING"

ROMAN N. POLYAKOV*, LEONID A. SAVIN*

*Department "Mechatronics and International Engineering", Orel State University named after I.S. Turgenev, Orel, Naugorskoye Shosse, 29, 302020, Russia
romanpolak@mail.ru, savin@ostu.ru

Key words: Rotor, Rolling-Element Bearing, Fluid-Film Bearing, Hybrid Bearing with Speed Separation, Wear, Long-Life.

Abstract. Reliability of rotating machinery is determined to a considerable degree by the bearing units. For several applications the requirements in rotation speed, bearing load and maximal vibration level are so extreme that neither rolling-element bearings nor fluid-film bearings could provide necessary performance characteristics during all regimes of operation. Hybrid bearings, which are a combination of rolling-element and fluid-film bearings, can improve performance characteristics and reliability of the rotor-bearing systems. The article presents the approach for to formation of the method of resource calculation for hybrid bearing with speed separation. The results show that the resource of the slide bearing increases significantly when it is used in combination with a rolling-element bearing compared to its single setting.

1 INTRODUCTION

When designing rotary machines with multiple start-ups and shutdowns (turbochargers of chemical fuel cell electric vehicles (FCEVs), turbo expanders and different types of pumps for cryogenic engineering and petrochemical industry), the task of ensuring their high reliability is of great importance. It imposes more stringent requirements on the bearings of the rotors of such machines. Most of rotary machines with a rotation rate of 10^5 rpm use a fluide-film bearing (FFB) as a support of the rotor. Fluid-film bearing unlike rolling-element bearings (REB) are not limited in high speed. But at the point of "start-up" and "shutdown" the wear of the FFB is certain to happen because of the dry frictions at these points. When none of the existing types of bearings meets the technical requirements of a rotor machine, the possible solution of the problem is to combine the bearings with different functional principle. It will increase the reliability of a bearing due to the separation and duplication of their functions.

Hybrid bearings are able to eliminate many disadvantages of particular bearing type from the point of view of load capacity, dynamic characteristics, reliability, and life time. The positive effects of hybrid bearings are achieved by separating and/or duplicating bearing functions on different operating regimes. This makes possible to increase demands on operational requirements, thus the efficiency of rotating equipment could be improved.

There are two basic designs of hybrid bearings. Notation suggested in [1, 2, 3] is used in

this work for describing different hybrid bearings. The first design is hybrid bearing with load separation – PL bearing (figure 1a), a shows the scheme of PLEX (Parallel Load, Externally Fed) bearing. In PL bearing REB is less loaded on the main operating mode. Discharge of REB is due to increase in hydrodynamic or hydrostatic reaction in FFB. The second design is hybrid bearings with speed separation – PS bearing. Figure 1b shows the scheme of PSEX (Parallel Speed, Externally Fed) bearing. Well-known squeeze-film dampers are the special case of PSEX bearings. In PS bearing shaft rotates in REB during the start-up and shut-down. As rotating speed increases REB is partially or fully switched off from the operation and shaft starts to rotate in FFB. Switching off of REB is achieved by combining certain geometric and operating parameters, or by using special switching devices. Lubricant supply in FFB can be also provided through the shaft. In this case one can distinguish two more designs – PSIN (Parallel Speed, Internally Fed) bearing, (figure 1c) and PLIN (Parallel Load, Internally Fed). In all concepts the fact that hydrostatic bearing turns on only during the main regime allows to manage without an external pressure supply.

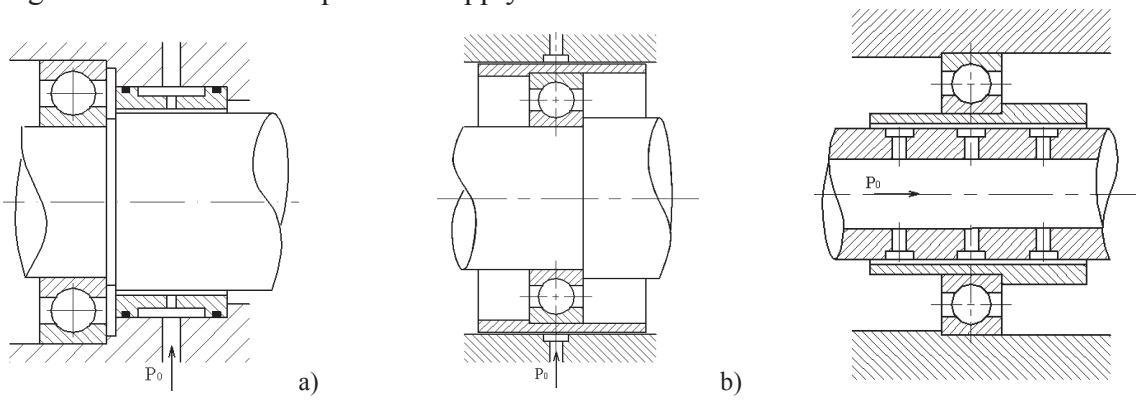

Figure 1: Schemes of the hybrid bearings

The mechanism of the PSEX work assumes the improvement of characteristics of the entire bearing in the following fields [4, 5].

1. *Decreasing of the damaging moments* which affect the sleeve of a rolling element bearing during the transition regimes. It will lead to its long-life improvement. One of the main reasons for losing the efficiency is a sleeve wear during the transition regimes (start-up, shutdown, a contact of a shaft with a sleeve as a result of unstable motion or stressful loads.) The mathematical models of the FFB wear assume that the wear depends on the compressive forces in a contact and speed in relation to the motion of contacting elements. When putting a FFB in the PSEX during the transition regimes, the sleeve of the FFB is affected not by the shaft torque, but the friction torque in the REB, that leads to the speed reduction in a contact, reduction of the distance of friction and thus, to the increase of the FFB and entire PSEX long-life, as the FFB long-life isn't practically limited.

2. *Reducing of the centrifugal loads in a rolling element bearing* due to the speed separation. The mechanism of speed separation assumes the speed reduction of the relative motion of the REB elements and sometimes its complete switching off that leads to its unlimited long-life and opportunity of using at its maximum speed.

3. *Removing from the self-excited oscillation modes* typical for the rotor motion in the fluid film bearings: during the unstable rotor motion, the risk of significant damages (e.g., micro

welding in the FFB sleeve) is practically eliminated due to the possibility of an additional roll in the REB; the mechanism of the development of self-excited oscillations, for example, the unstable part of the fluid film reaction, which causes the turbulence of the rotor in the FFB, is applied to the REB outer ring, which, due to the possibility of an additional roll neutralizes or reduces the negative impact of the reaction of the REB on the rotor.

4**.** *Increasing of the abilities to provide the necessary dynamic characteristics of the bearing* to ensure the transition of the resonant modes with permissible oscillation amplitudes. By choosing appropriate geometrical parameters of REBs and FFBs and taking into consideration the operational ones, we can achieve the required stiffness and damping to provide reasonable amplitude-frequency characteristics of the entire rotor-bearing system.

5. *Improving of the reliability of the bearing* by increasing its efficiency in case of emergency and under the unstable operation due to the duplication of functions of the REB and FFB. In case of emergency in a turbine set (for example, a tearing off of a blade), there can be an abrupt rotor unbalance change and the dynamic loads on the bearings become higher. In case of the FFB failure to transfer the load to the housing and rotor spinning, the REB starts to operate. And for some time it can operate at a rotary speed exceeding its maximum speed and eliminate a significant damage of the entire machine.

2 MATHEMATICAL MODEL

The declared advantage for reducing the damaging moments leads to the necessity to describe this effect, which requires modeling of the coupled problems defining the forces and a friction torque in REBs and FFBs, the dynamics of the rotational motion of the bearing and the FFB sleeve wear.

The defining of the FFB sleeve long-life is based on the solution of the wear equation [6], which can be generally represented as:

$$I = a_0 \left(\frac{p}{HB_{1,2}}\right)^{a_1} \left(\frac{\lambda^*}{h}\right)^{a_2} \left(\frac{E_{1,2}}{\sigma_{0_{1,2}}}\right)^{a_3} (1+\propto K)^{b_1} \left(1+\beta\frac{HB_a}{HB_{1,2}}\right)^{b_2} \left(1+\gamma\frac{Sd_a}{V}\right)^{b_3} \quad (1)$$

where $\frac{p}{HB_{1,2}}$ is a dimensionless group, describing a stress state in a contact (p is a load per unit area, MPa; $HB_{1,2}$ is the hardness of the working surfaces of the shaft and bearing, MPa); $\frac{\lambda^*}{h}$ is a complex, defining the contact mechanism (when there are mechanical impurities in the fluid film $\lambda^* = (R_{a1}^2 + R_{a2}^2)^{1/2}$, here $R_{a1,2}$ is a mean square deviation of the surface roughness mcm; when there are mechanical impurities $\lambda^* = d_a$, here d_a is a given diameter of particles, and under condition $d_a > (R_{a1}^2 + R_{a2}^2)^{1/2}$; $\frac{E_{1,2}}{\sigma_0}$ is a complex regarding plasticity and endurance strength of materials $E_{1,2}$ is a modulus of elasticity, MPa; $\sigma_{0_{1,2}}$ is the endurance strength of materials, MPa; $(1+\propto K)$ is a concentration criterion of the mechanical impurities ($\propto$ is a coefficient, regarding the degree of influence of particles concentration on the wear; K is a concentration 1 kg abrasive in 1 kg fluid); $1+\beta\frac{HB_a}{HB_{1,2}}$ is a criterion of the hardness of impurities ($\pi_т$) (β is a coefficient, regarding the degree of influence of particles concentration on the wear; HB_a is the hardness of mechanical impurities, MPa); $1+\gamma\frac{Sd_a}{V}$ is a criterion of particles shape ($\pi_ф$) (γ is a coefficient, regarding the degree of influence of the

particle geometry on the couple wear, S is a particle surface, V is a particle volume); a_0 is a coefficient, regarding physical-mechanical properties; a_i, b_i are indexes, defined on the basis of the available information on the test of materials.

In the transition regime the fluid film bearing in a hybrid bearing is identical to the friction couple operating in a semi-fluid mode. In relation to the fluid film bearings of the semi-fluid friction, the wear rate of a sleeve made of anti-friction material can be simplified to [7]:

$$I_h = 2{,}29 \cdot 10^6 K \cos^2\varphi_T \psi p_m V_S E_{\text{пр}}, \tag{2}$$

where $V_S = \frac{\pi d n}{60}$ is a sliding speed in a contact; $E_{\text{пр}} = \frac{2}{\frac{1-\varepsilon_1^2}{E_1}+\frac{1-\varepsilon_2^2}{E_2}}$ is a given modulus of elasticity, respectively E_1, E_2 are modulus of elasticity of the material for a shaft and FFB sleeve; $p_m = \frac{F_r}{dl}$ is the medium pressure in a bearing; $\psi = \frac{2h}{d}$ is a relative clearance; K is a coefficient, depending on properties of the materials for a shaft and a sleeve and lubrication conditions; φ_{T} is an angle between a vertical axes and a maximum pressure point on the FFB surface (figure 2).

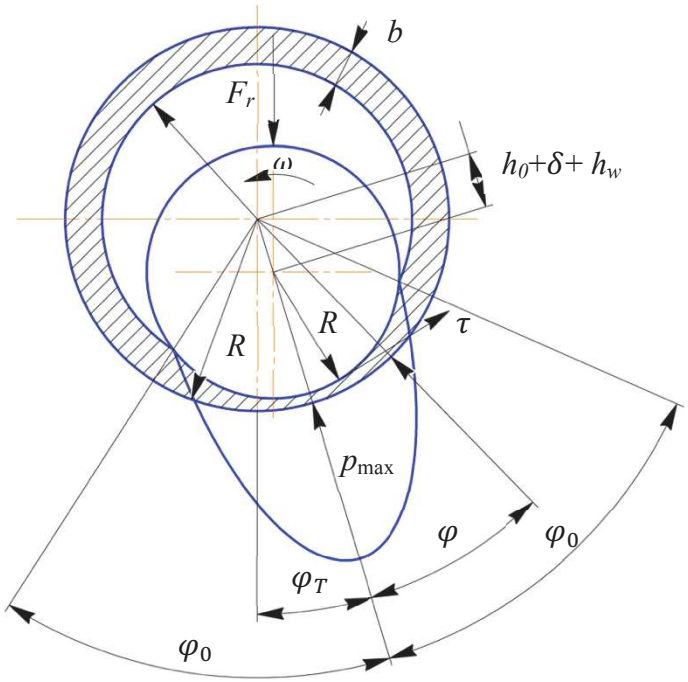

Figure 2: Pressure Distribution in a Fluid Film Bearing

The FFB long-life (hours) and, respectively, of the entire PSEX:

$$L_h \le \frac{[h]}{I} \tag{3}$$

where $[h]$ is a permissible clearance.

The sliding speed in a contact depends on the rotation speed of the REB outer ring, with which a space sleeve is rigidly bound. The space sleeve is a response surface for the FFB. From the point of view of the dynamics, the PSEX can be represented in the form of a dual-

mass six-degree-of-freedom oscillator (figure 3): flat motions and rotor spinning, which has been replaced by a point mass off-centered about the axis of rotation, and flat motions and rotation of the outer ring of the REB. To solve the problem of defining the function of speed separation between the shaft and outer ring of the REB, it is necessary to compose the equation of the rotary motion between the shaft and outer ring of the FFB according to the law of conservation of angular momentum:

$$I\frac{d\omega}{dt} = M_{dr} - M_{fr}^{REB}\ ; \qquad i\frac{d\Omega}{dt} = M_{fr}^{REB} - M_{fr}^{FFB}\ , \tag{4}$$

where I, i are polar moments of inertia of the rotor and outer ring of the REB in combination with a space sleeve; ω, Ω are angular rates of a rotor and outer ring, respectively; M_{dr} is a moment of driving forces; M_{fr}^{REB} is a REB friction torque; M_{rf}^{FFB} is a FFB friction torque.

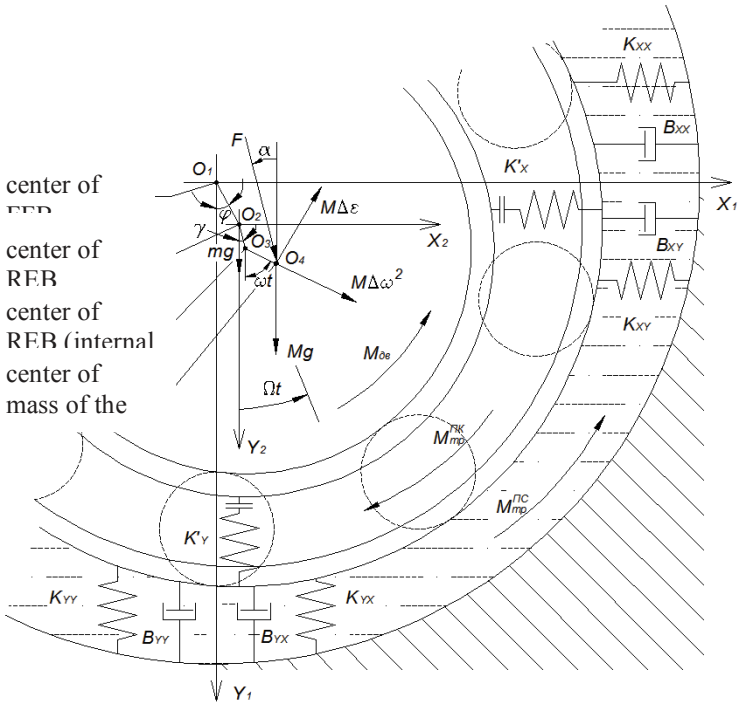

Figure 3: Dynamic Model of the PSEX

The restoring force of the REB depends on the elastic properties of rings and rolling elements, and its defining is based on Hertz's contact deformations theory [8]. The rolling elements are deformed under the influence of an external force F_{Σ} on the value of δ (figure 4). The dependence of the rolling elements reaction on their deformation under the action of external force:

$$R^{REB} = K'\delta^{3/2} \tag{5}$$

where K' is a coefficient of proportionality depending on the material and shape of the contacting surfaces (it can be described as the coefficient of the REB nonlinear stiffness with dimension of $Н/м^{3/2}$) [8].

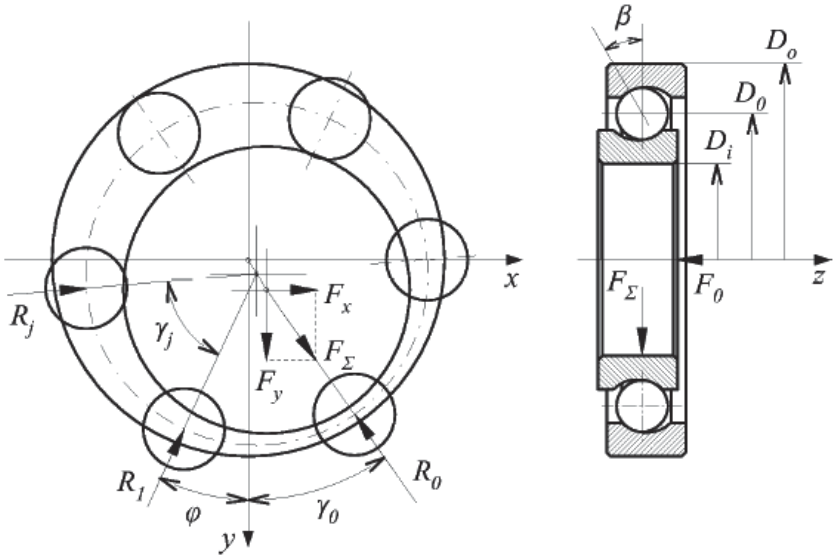

Figure 4: Scheme of the Ball Rolling Element Bearing

The mathematical description of friction forces is based on the semi-empirical method developed and applied at the leading enterprises of the bearing industry [7]:

$$M_{\text{тр}}^{\text{ПК}} = 0.9 \cdot 10^{-6} \left(\frac{F_\Sigma}{C_0}\right)^{0.55} (3F_a - 0.1F_r)D_0 + 2 \cdot 10^{-10}(\nu n)^{2/3} D_0^3) \quad (6)$$

where $F_\Sigma = (XVF_r + YF_a)K_\text{Б}K_\text{Т}$ is an equivalent load on the REB; F_r, F_a are radial and axial loads; X, Y are coefficients recording different damaging action of radial and axial loads. They are defined according to the ratio F_r/C_0, , here C_0 is a static load capacity of the REB; V is a coefficient of rotation; $K_\text{Б}$, $K_\text{Т}$ are safety and temperature coefficients; ν is the kinematic viscosity; n is a frequency of rotation.

The model of a fluid film bearing (figure 5) is based on the equations of hydrodynamic lubrication theory [9,10]. The defining of pressure fields is based on the simultaneous solving of the Reynolds equations for the case of two-dimensional flow of a compressible fluid regarding the effect of turbulence (7), the equations of energy, equations of state, turbulence models, functions of radial clearance and the ratios of speeds on the surface of the shaft.

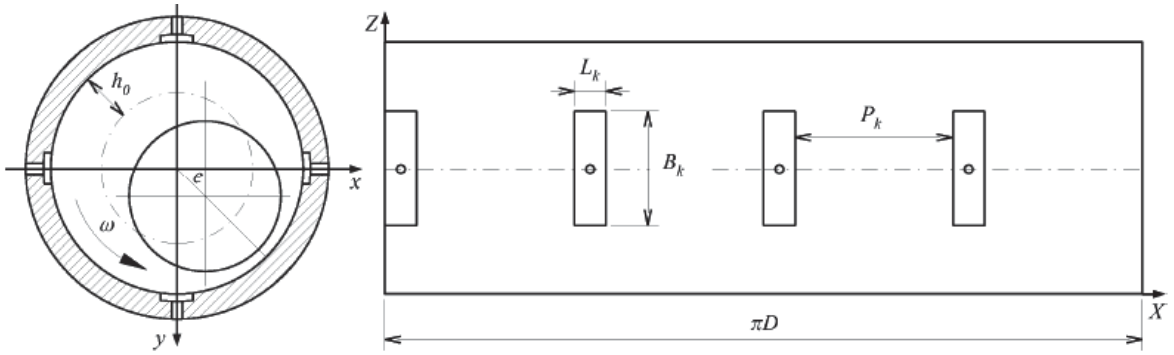

Figure 5: Scheme of the Hydrostatic FFB

The following example is a single line equation:

$$\frac{\partial}{\partial x}\left[\frac{h^3\rho}{\mu K_x}\frac{\partial p}{\partial x}\right]+\frac{\partial}{\partial z}\left[\frac{h^3\rho}{\mu K_z}\frac{\partial p}{\partial z}\right]=6\frac{\partial}{\partial x}(\rho U h)-12\rho V+12h\frac{\partial \rho}{\partial t}. \quad (7)$$

Reaction and friction torque of the fluid film bearing:

$$R_X=-\int_0^L\int_0^{\pi D} p\cos\alpha\, dx\, dz;\ R_Y=-\int_0^L\int_0^{\pi D} p\sin\alpha\, dx\, dz;$$
$$M_{\text{тр}}^{\text{ПС}}=-\frac{D}{2}\int_0^L\int_0^{\pi D}\tau\sin\alpha\, dx\, dz;\ \tau=\frac{h}{2}\frac{\partial p}{\partial x}+\frac{\mu U}{h}. \quad (2)$$

3 RESULTS OF MODELING AND DISCUSSION

The method of the PSEX long-life defining was based on the assumption that since the operation speed of the REB tends to zero and one of the main factors of its destruction – the emergence of large stresses on the outer ring due to centrifugal forces F_{cf} (Figure 6) - is excluded, the main factor that defines the PSEX life is a FFB sleve wear. Thus, the method of the FFB sleeve wear long-life defining has been offered which is based on the assumption of proportionality of wear and torque. The mechanism of PSEX operation assumes that at the start mode the FFB sleeve is affected by the REB friction torque, but not by the machine torque, and also the distance of friction becomes less. The simultaneous solution of the equations of rotary motion and wear dynamics allows to get the dependency of the resource on various working parameters of the PSEX and to compare it with the FFB single setting (Figure 7).

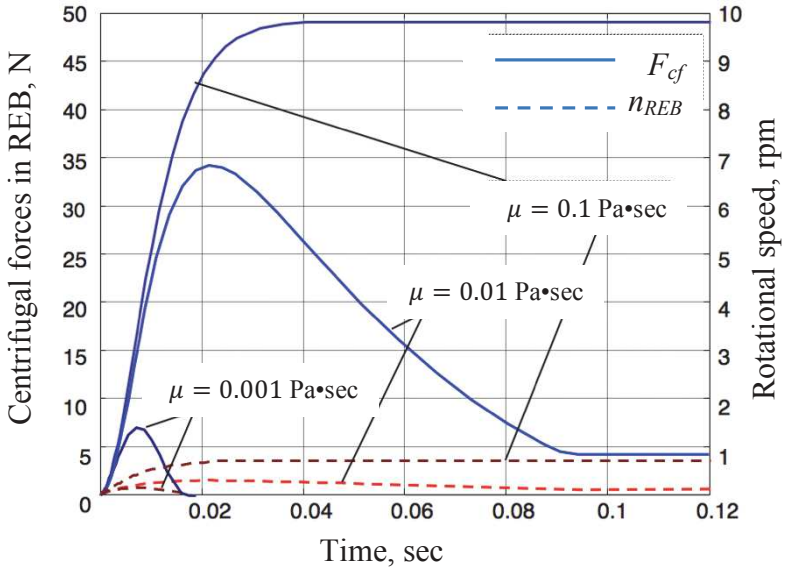

Figure 6: Speed separation in a hybrid bearing

The results show that the FFB long-life improves significantly when it is used in a combination with a rolling-element bearing compared to its single setting. It means that under low loads the resource improvement can be up to 7 times higher compared to a FFB single setting, and under high loads up to 2...3 times.

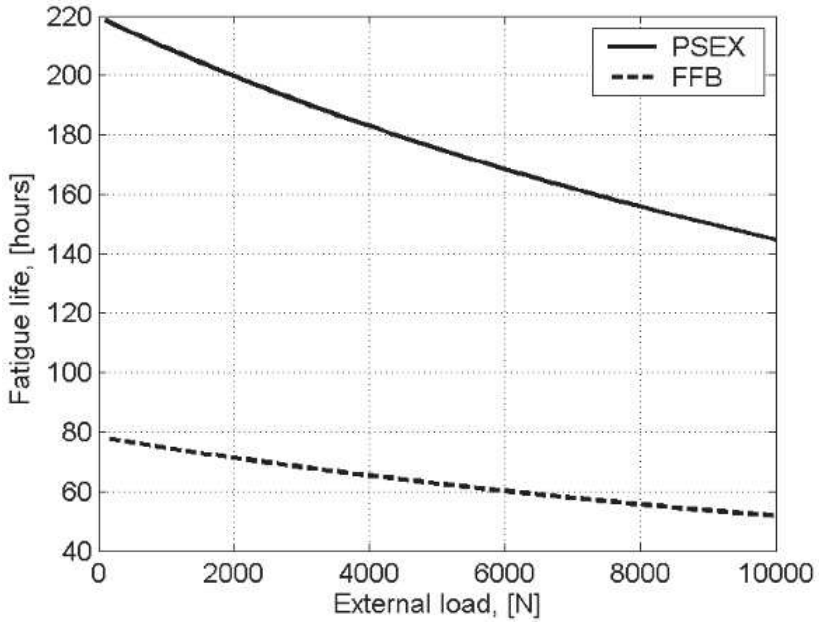

Figure 7: Long-life improvement in a hybrid bearing

ACKNOWLEDGEMENTS

The research was implemented in the framework of the Russian Scientific Foundation project № 16-19-00186.

REFERENCES

[1] Butner M.F., Murphy B.T. *Space shuttle main engine long-life bearings.* NASA CR-179455 (1986).
[2] Parker R.J., Fleming D.P., Anderson W.J., Coe H.H. *Experimental evaluation of the series-hybrid rolling-element bearing.* NASA TN D-7011 (1970).
[3] Anderson W.J., Fleming D.P., Parker R.J. The series hybrid bearing – a new high speed bearing concept. *ASME J. Lubr. Techn.* (1972), 94, 117-124.
[4] Harnoy A. *Bearing Design in Machinery.* N.-Y., 2003. – 628 p.
[5] Polyakov R.N. *Improving dynamics and working life of rotor supports by coupling rolling-element and fluid-film bearings.* LAP Lambert Academic Publishing GmbH & Co. Saarbrucken 2012. − 161 p.
[6] Kragelskii I.V. *Friction and Wear.* Elmsford: Pergamon Press, 1982 (In Russian).
[7] Jilnikov E.P. *Friction and Wear in Aircraft Units*. Samara: SGAU, 2007. – 144 p. (In Russian).
[8] Harris T.A., Kotzalas M.N. *Rolling bearing analysis. Essential concepts of bearing technology.* – 2006. – CRC Press, Boca Raton.
[9] Loycanskyy L.G. *Fluid and Gas Mechanics*. – Nauka Publ. – 1978. (In Russian).
[10] Hori Y. *Hydrodynamic Lubrication.* Springer (2005).

VII International Conference on Computational Methods for Coupled Problems in Science and Engineering
COUPLED PROBLEMS 2017
M. Papadrakakis, E. Oñate and B. Schrefler (Eds)

TIGHTLY COUPLED COMPUTATIONAL FLUID AND CROWD DYNAMICS VIA IMMERSED BOUNDARY METHODS

RAINALD LÖHNER[1], FERNANDO CAMELLI[1] AND EUGENIO OÑATE[2]

[1] Center for Computational Fluid Dynamics
George Mason University, Fairfax, VA 22030, USA
e-mail: rlohner@gmu.edu, fcamelli@gmu.edu, web page: https://cfd.gmu.edu/

[2] International Center for Numerical Methods in Engineering (CIMNE)
Universidad Politécnica de Cataluña
Campus Norte UPC, 08034 Barcelona, Spain
e-mail: onate@cimne.upc.edu, web page: http://www.cimne.com/

Key words: Computational Fluid Dynamics, Computational Crowd Dynamics, Pedestrian Flows, Coupled Problems, Fire and Rescue Operations, Event Planning, Supercomputing

Abstract. A methodology to couple computational fluid and computational crowd dynamics (CFD, CCD) has been developed. Technological advances that made this possible include: a) Mature CFD and CCD codes/solvers; b) Development of immersed boundary methods for moving bodies (CFD); c) Strong scaling to tens of thousands of cores (CFD); and d) Implementation of fast search techniques for information transfer between codes (CFD, CCD).
We consider that tightly coupled simulations such as the ones presented here will lead to more realistic evacuation studies where fire, smoke, visibility and inhalation of toxic materials influence the motion of people, and where a large crowd can block or influence the flow in turn. Cases where this may occur are metro-stations, high-rise buildings and indoor sports arenas, where a crowd can block a considerable portion of the passage area, thereby influencing the flow.

1 INTRODUCTION

Advances in computational fluid and crowd dynamics (CFD, CCD), as well as computer hardware and software, have enabled fast and reliable simulations in both disciplines. A natural next step is the coupling of both disciplines. This would be of high importance for evacuation studies where fire, smoke, visibility and inhalation of toxic materials influence the motion of people, and where a large crowd can block or influence the flow in turn.

Cases where this may occur are metro-stations or high-rise buildings, where a crowd can block a considerable portion of the passage area, thereby influencing the flow. To date, most of the coupling attempts have been uni-directional: in a first step, the flow is precomputed; thereafter, the crowd moves under the influence of this precomputed fire and smoke field. This type of coupling has several justifications: a) In many cases the presence of pedestrians has a negligible influence on the flow; b) Historically, CFD runs were orders of magnitude more expensive than CCD runs; having to run CFD codes to 30-60 mins of simulation time was prohibitive. The present work considers a tight, bi-directional coupling, whereby the flow and the motion of the crowd are computed concurrently and with mutual influences. Enabling technologies that led us to consider this tight coupling as feasible include: a) Development of immersed boundary methods; b) Implementation of fast search techniques for information transfer between codes; and c) Strong scaling to tens of thousands of cores for CFD codes.

2 COUPLING METHODOLOGY

The coupling methodoly used is shown in Figure 1. The CFD code computes the flowfield, providing such information as temperature, smoke and toxic substance concentration, and any other flow quantity that may affect the movement of pedestrians. These variables are then interpolated to the position where the pedestrians are, and are used with all other pertinent information (e.g. will-forces, targets, exits, signs, etc.) to update the position, velocity, inhalation of smoke and/or toxic substances, state of exhaustion or intoxication, and any other relevant quantities that are evaluated for the pedestrians. The position, velocity and temperature of the pedestrians is then transferred to the CFD code and used to modify and update the boundary conditions of the flowfield in the regions where pedestrians are present.

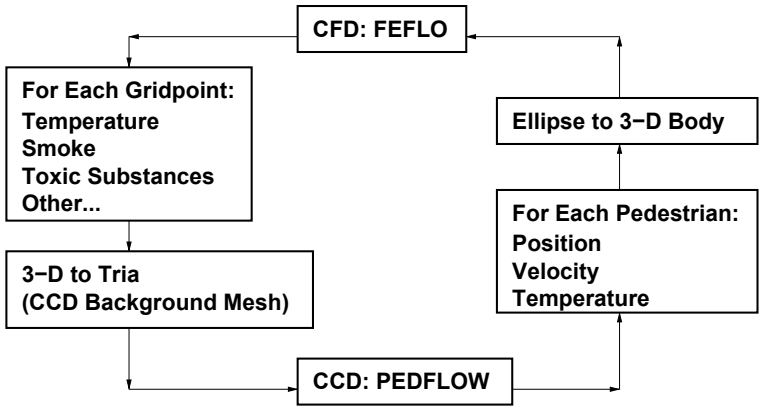

Figure 1 Coupling CFD and CCD Codes

Of the many possible coupling options (see e.g. [1, 13, 2]), we have implemented the simplest one: loose coupling with sequential timestepping ([7, 11]). This is justified, as

the timesteps of both the flow and pedestrian solvers are very small, so that possible coupling errors are negligible.

3 COMPUTATIONAL FLUID DYNAMICS CODE: FEFLO

The FEFLO code has been in development and use for over two decades ([6, 14, 8, 9]). It solves the the incompressible Navier-Stokes and an arbitrary number of transport equations. The code has had a long history of relevant applications involving incompressible flows of various types, from external flow of automobiles to wind engineering and climate control. FEFLO has been ported to vector, shared memory, distributed memory and GPU-based machines.
The information required from CCD codes such as PEDFLOW consists of the pedestrians in the flowfield, i.e. their position, velocity and temperature. As the CCD codes describe the pedestrians as points, circles or ellipses, a way has to be found to transform this data into 3-D objects. Two possibilities have been pursued here:
a) Transform each pedestrian into a set of (overlapping) spheres that approximate the body with maximum fidelity with the minimum amount of spheres;
b) Transform each pedestrian into a set of tetrahedra that approximate the body with maximum fidelity with the minimum amount of tetrahedra.
The reason for choosing spheres or tetrahedra is that one can perform the required interpolation/ information transfer much faster than with other methods.
In order to 'impose' on the flow the presence of a pedestrian the immersed boundary methodology is used. The key idea is to prescribe at every CFD point covered by a pedestrian the velocity and temperature of the pedestrian. For the CFD code, this translates into an extra set of boundary conditions that vary in time and space as the pedestrians move. This is by now a mature technology. Fast search techniques as well as extensions to higher order boundary conditions may be found in [9]. Nevertheless, as the pedestrians potentially change location every timestep, the search for and the imposition of new boundary conditions can add a considerable amount of CPU as compared to 'flow-only' runs.

4 COMPUTATIONAL CROWD DYNAMICS CODE: PEDFLOW

The PEDFLOW code ([10, 12]) has been in development and use for more than a decade. It uses a combination of force-based and agent-based methods. Individuals move according to Newton's laws of motion; they follow (via will forces) 'global movement targets'; at the local movement level, the motion also considers the presence of other individuals or obstacles via avoidance forces (also a type of will force) and, if applicable, contact forces. A complete description of the model, as well as verificaton and validation studies may be found in [10, 3, 4, 15, 5]. Over the last two years the code has been parallelized for both shared (via OpenMP at the loop-level) and distributed (via MPI and domain decomposition) memory architectures. This has allowed real-time micro-

modelling of a million pedestrians ([12]). The geographic information required, such as terrain data (inclination, soil/water, escalators, obstacles, etc.), climate data (temperature, humidity, sun/rain, visibility), signs, the location and accessability of guidance personnel, as well as doors, entrances and emergency exits is stored in a so-called background grid consisting of triangular elements. This background grid is used to define the geometry of the problem. At every instance, a pedestrian will be located in one of the elements of the background grid. Given this 'host element' the geographic data, stored at the nodes of the background grid, is interpolated linearly to the pedestrian. The closest distance to a wall δ_w or exit(s) for any given point of the background grid evaluated via a fast ($O(N \ln(N))$) nearest neighbour/heap list technique ([9, 10]). For cases with visual or smoke impediments, the closest distance to exit(s) is recomputed every few seconds of simulation time.
The information required from CFD codes such as FEFLO consists of the spatial distribution of temperature, smoke, or other toxic or movement impairing substances in space. This information is interpolated to the (topologically 2-D) background mesh at every timestep in order to calculate properly the visibility/ reachability of exits, routing possibilities, smoke and toxic substance inhalation, and any other flowfield variable required by the pedestrians. As the tetrahedral grid used for the CFD code and the triangular background grid of the CCD code do not change in time, the interpolation coefficients need to be computed just once at the beginning of the coupled run. While the transfer of information from CFD to CCD is voluminous, it is very fast, adding an insignificant amount to the total run-times.

5 COUPLING CODE: FEMAP

The transfer of information is guided by the general coupling code FEMAP. FEMAP calls each of the codes as a subroutine, and performs the timestepping as specified by the user. FEMAP is presently linked to several computational structural dynamics (CSD) codes (among them FEEIGEN, DESOL, ASICSD, DYNA3D, SIMPACT, FEAP, NASTRAN), several CFD codes (among them FEFLO and FDFLO), several computational thermodynamics (CTD) codes (among them FEHEAT and NASTRAN) and, as of 2016, also PEDFLOW. FEMAP allows for the use of different levels of parallelism and processors for the different codes, and allows the concurrent use of several CSD, CFD and CTD at the same time.

6 EXAMPLES

1. Metro Center
This example considers an evacuation case due to fire in the Metro Center metro station of Washington, D.C. A fire was assumed in one the the escalators. The flow was computed, together with the production of smoke.

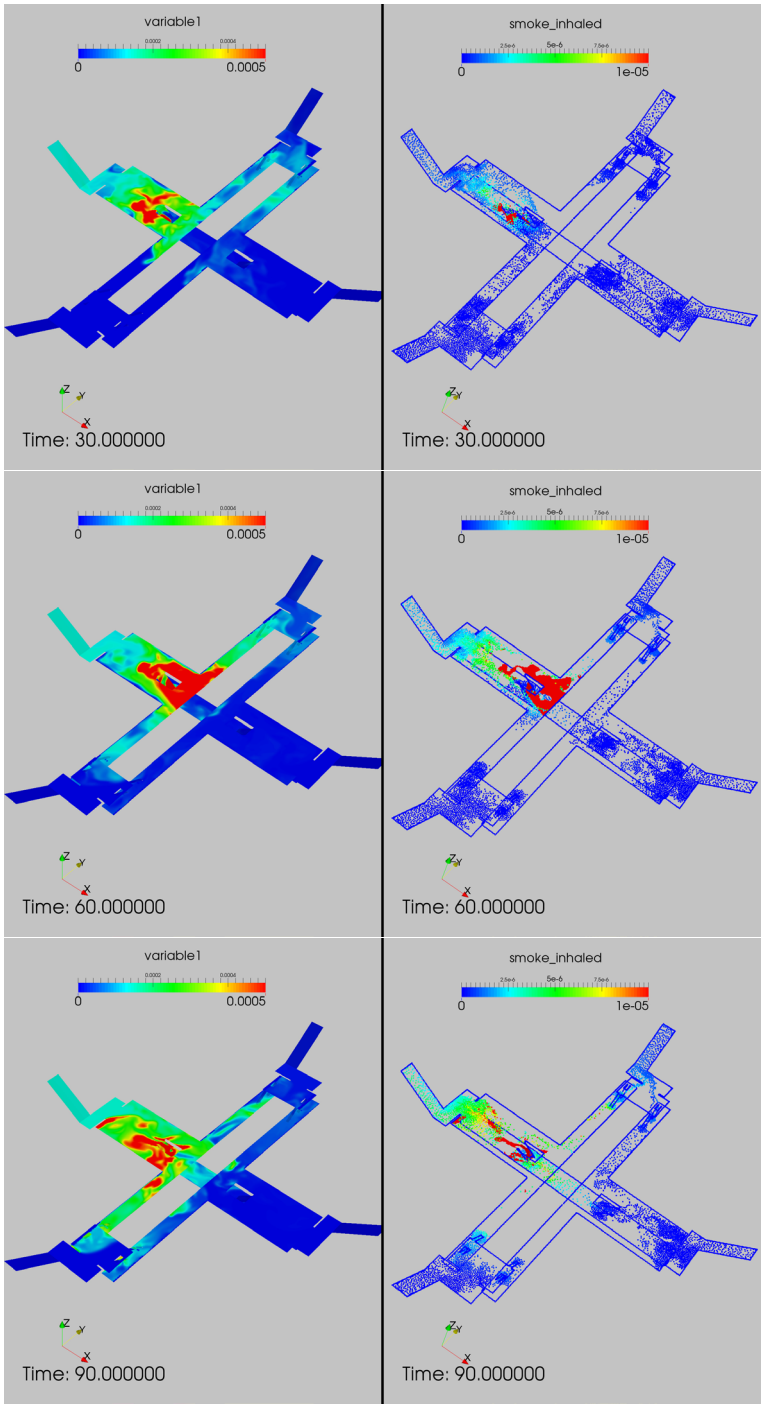

Figures 2.1-2.3: Metro Station Evacuation:
Left: Smoke Density, Right: Pedestrians and Limit of Visibility at Times $T = 30, 60, 90$ *sec*

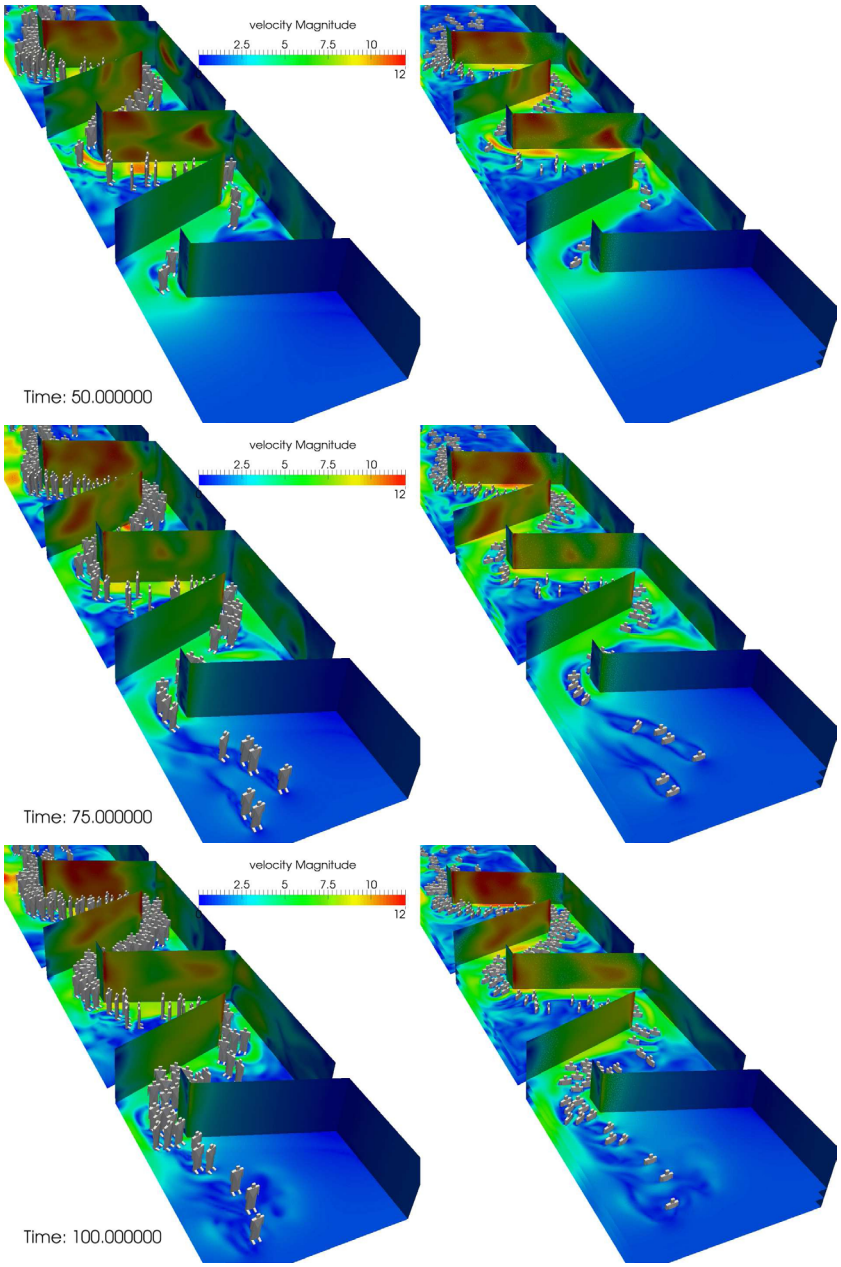

Figures 3.1-3.3: Corridor: Pedestrian and Flowfield at Times $T = 50, 75, 100$ *sec*

The geometry, pedestrians and flowfield may be inferred from Figures 2.1-2.3. The number of pedestrians at the beginning of the run was set to $N_p = 1660$. The perceived distance to closest exit, which is based on visibility, was recomputed every second. Figures 2.1-2.3 show the distribution of smoke (left), as well as the pedestrians colored according to the amount of smoke inhaled (right).

2. Corridor
This example considers the flow inside a narrow, winding corridor in the presence of pedestrians. The geometry, pedestrians and flowfield may be inferred from Figures 3.1-3.3. The pedestrians are entering from the far side (top of figure) at a rate of $f_p = 2\ p/sec.$ The flow is opposite to the movement direction of the pedestrians: it enters from the near side (bottom of figure) with a speed of $v_{in} = 1\ m/sec.$ The CFD mesh had 6.7 Mels. The case was run on an SGI ICEx machine using 48 cores (6 mpi-domains x 8 omp-cores for each domain). Before starting the coupled run, the CFD code was run without pedestrians until a quasi-steady flowfield was established. Note the wake of the pedestrians, as well as the change in the overall flow pattern as a result of the presence of pedestrians in the flowfield.

7 CONCLUSIONS AND OUTLOOK

A methodology to couple computational fluid and computational crowd dynamics (CFD, CCD) has been developed. Enabling technologies that made this possible include:
a) Mature CCD and CFD codes/solvers;
b) Development of immersed boundary methods for moving bodies (CFD);
c) Strong scaling to tens of thousands of cores (CFD); and
d) Implementation of fast search techniques for information transfer between codes (CFD, CCD).
We consider that tightly coupled simulations such as the ones presented here will lead to more realistic evacuation studies where fire, smoke, visibility and inhalation of toxic materials influence the motion of people, and where a large crowd can block or influence the flow in turn. Cases where this may occur are metro-stations, high-rise buildings and indoor sports arenas, where a crowd can block a considerable portion of the passage area, thereby influencing the flow.
Another interesting application area is the study of airborne transmitted diseases, where the detailed modeling of the flow near pedestrians will lead to a higher accuracy in the predictions.

REFERENCES

[1] H.-J. Bungartz and M. Schäfer (eds.) *Fluid-Structure Interaction*, Springer Lecture Notes in Computational Science and Engineering, Springer (2006).

[2] J.R. Cebral and R. Löhner - On the Loose Coupling of Implicit Time-Marching Codes; *AIAA*-05-1093 (2005).

[3] M. Isenhour and R. Löhner - Verification of a Pedestrian Simulation Tool Using the NIST Recommended Test Cases; *The Conference in Pedestrian and Evacuation Dynamics 2014 (PED2014), Transportation Research Procedia* 2, 237-245 (2014).

[4] M. Isenhour and R. Löhner - Verification of a Pedestrian Simulation Tool Using the NIST Stairwell Evacuation Data; *The Conference in Pedestrian and Evacuation Dynamics 2014 (PED2014), Transportation Research Procedia* 2, 739-744 (2014).

[5] M. Isenhour - Simulating Occupant Response to Emergency Situations; *PhD Thesis*, George Mason University, Fairfax, VA (2016).

[6] R. Löhner - A Fast Finite Element Solver for Incompressible Flows; *AIAA*-90-0398 (1990).

[7] R. Löhner, C. Yang, J. Cebral, J.D. Baum, H. Luo, D. Pelessone and C. Charman - Fluid-Structure Interaction Using a Loose Coupling Algorithm and Adaptive Unstructured Grids; *AIAA*-95-2259 [Invited] (1995). -

[8] R. Löhner, Chi Yang, J.R. Cebral, F. Camelli, O. Soto and J. Waltz - Improving the Speed and Accuracy of Projection-Type Incompressible Flow Solvers; *Comp. Meth. Appl. Mech. Eng.* 195, 23-24, 3087-3109 (2006).

[9] R. Löhner - *Applied CFD Techniques, Second Edition*; J. Wiley & Sons (2008).

[10] R. Löhner - On the Modeling of Pedestrian Motion; *Appl. Math. Modelling* 34, 2, 366-382 (2010).

[11] R. Löhner - Coupling Several CFD and CSD Codes in One Application; pp. 1 - 16 in Special Edition *Int. J. of Multiphysics* (2011).

[12] R. Löhner, M. Baqui, E. Haug, B. Muhamad - Real-Time Micro-Modelling of a Million Pedestrians; *Engineering Computations* 33, 1, 217-237 (2016).

[13] M. Schäfer and S. Turek (eds.) - *Proc. Int. Workshop on Fluid-Structure Interaction: Theory, Numerics and Applications*, Herrsching (Munich), Germany, Sept. 29 - Oct 1 (2008).

[14] R. Ramamurti and R. Löhner - A Parallel Implicit Incompressible Flow Solver Using Unstructured Meshes; *Computers and Fluids* 5, 119-132 (1996).

[15] J. Zhang, D. Britto, M. Chraibi, R. Löhner, E. Haug and B. Gawenat - Qualitative Validation of PEDFLOW for Description of Unidirectional Pedestrian Dynamics; *The Conference in Pedestrian and Evacuation Dynamics 2014 (PED2014), Transportation Research Procedia* 2, 733-738 (2014).

VII International Conference on Computational Methods for Coupled Problems in Science and Engineering
COUPLED PROBLEMS 2017
M. Papadrakakis, E. Oñate and B. Schrefler (Eds)

TRANSPOSITION OF A WEIGHTED AH-THROUGHPUT MODEL TO ANOTHER LI-ION TECHNOLOGY: IS THE MODEL STILL VALID? NEW INSIGHTS ON THE MECHANISMS

T. DELETANG [*] N. BARNEL [*] S. FRANGER[†] L. ASSAUD[†]

[*] EDF - R&D – Lab Les Renardières
Département LME / Groupe M2A
Avenue des Renardières - Ecuelles
77818 MORET SUR LOING Cedex FRANCE
e-mail: tiphaine.deletang@edf.fr

[†] Université Paris-Sud – Orsay
Institut de Chimie Moléculaire et des Matériaux d'Orsay
Bâtiment 410/420/430, Université Paris-Sud 11
Rue du Doyen Georges Poitou
91400 ORSAY – FRANCE

Key words: Storage, Lithium-ion cells, Fatigue model, Eyring and Arrhenius kinetics, Butler-Volmer

Abstract: The increasing interest in electric vehicles powered by rechargeable batteries, combined with the wide development of powerful lithium-ion batteries as a renewable energy storage system have raised the need for battery ageing characterization. Several models have been developed for this purpose, including empirical, fatigue and mathematical ones. One of the main issue of these approaches consists of the universality, when extension is required to other chemistries or solicitations. Electrochemical models are supposedly the most extensible. The Weighted Ah-Throughput Model takes into account that certain operating conditions may lead either to an increase or a decrease of the rate of ageing. It modulates the impact of the exchanged Ah by the temperature, the C-rate and the state of charge (SOC), both in calendar and active regime. This influence of the parameters is described here, and compared between two Li-ion chemistries: LFP and NCA. The similitudes enable us to extract the generic hidden mechanisms that, by nature, the fatigue modelling methods do not provide. This innovative method enables us to reach energetic behavior laws. We finally suggest improvements on the tests matrix used to define the model, to better fit the outcome of the study.

1 INTRODUCTION

For lithium-cells to be used in electric vehicles or stationary storage, they have to perform over a long period. However, lithium-cells performances decrease over time, both when they are used (on cycling) and when they are on storage. The ageing is caused mainly by a primary mechanism of a passive layer growing at the negative electrode, corresponding to the so-called solid-electrolyte interphase (SEI), therefore causing the loss of lithium ions cyclability, finally decreasing the total capacity. [1,2,3] This phenomena is mainly responsible for the ageing during active and inactive regimes (pure storage). Another cause of ageing is due to the presence of mechanical defaults in the bulk material at the positive electrode, caused by repeated insertion and deinsertion of lithium ions inside the structure. [4] The lithiation process taking place mainly during the cycling of the battery, it will be neglected during temporal regime. [1]

Current models tend to base the ageing rate of the cell on the solicitation of the batteries. Our approach is different. We consider the ageing to be due to three main parameters, which are temperature, state of charge and rated-current. In this paper, an existing fatigue model for the capacity loss [1] is explored, and is used to analyse our ageing data coming from our cells. Weighting functions distinguishing the impact of temperature, SOC and rated-current are drawn for them. They are compared with the ones already obtained for cells with another chemistry [1]. The two curves will be studied in order to exhibit and discuss the associated mechanisms.

2 EXPERIMENTAL

A 2.4Ah commercial lithium-ion cell based on graphite/iron-phosphate (LiFePO4) called LFP is aged. The battery basic characteristics can be seen in Table 1. The characterization tests were performed using Bitrode platform.

Table 1: LFP cell basic characteristics

Cell	Capacity	Cut-off voltages	Charging Protocol
LFP	2.4Ah	3.65V / 2.45V	CC-CV

The cells were initially virgin before performing the tests. A total of 11 different ageing tests were performed, including 3 different temperatures, 5 different SOC (10%, 50%, 80%, 95%, 100%) and 2 rated-currents. They are either cycled (9 cells) or stored (2 cells). The tests are detailed in the Table 2.

Table 2: Tests matrix

	T (°)	SOC (%)	$I_c(A.Ah^{-1})$	$I_d\ (A.Ah^{-1})$
1	T1	80		
2	T2	80		
3	T1	10	1C	1D
4	T1	50	1C	1D
5	T1	80	1C	1D
6	T1	95	1C	1D
7	T1	100	1C	1D
8	T1	100	C/2	1D
9	T1	100	1C	D/2
10	T2	100	1C	1D
11	T3	100	1C	1D

For each ageing condition, one cell only was used. The cell charging protocol consists on a constant current charge followed by a constant voltage phase (CC-CV). Regularly, every two weeks in average, performance check-ups were performed. The protocol consists in a full CC-CV charge, followed by 30 minutes of rest. Then the capacity is measured counting the discharged ampere-hours at 1D and at the same temperature as the test.

3 MODEL

The rate of each ageing mechanism for a specified chemistry cell is considered in the model to be a function of the mode of operation: cycling or storage. It results in two types of degradation: active degradation, and calendar degradation, the latter appearing both during cycling and storage. The work of Badey [1] integrates this ageing inside an original fatigue model. First, it demonstrates that the irreversible loss of capacity can be calculated by summing these two degradation contributions. Then, according to the author, the decoupling of the two degradations (active and calendar) is ensured by the Weighted Ah-Throughput Model (WTM) which is a modified approach of the Ah-throughput counting method. Both methods consider the ageing as a function of the Ah exchanged and the time. The originality lays in the fact that when the Ah-counting method takes into account only these parameters (Ah exchanged and time), the WTM integrates additionally the strong impact of the operating conditions on the rate of ageing. Therefore it modulates the impact of both modes of degradations by the temperature, the C-rate and the state of charge (SOC), as written in Equation 1.

$$\Delta Q = f(T, I, SOC).Ah + g(T, I, SOC).\sqrt{t} \quad (1)$$

$$\Delta Q = K^{cyc} f_1(T) f_2(I) f_3(SOC).Ah + K^{cal} g_1(T) g_2(I) g_3(SOC).\sqrt{t} \quad (2)$$

(1) The rate is abusively written as I.

Due to the growth of the SEI layer, the calendar life capacity fade typically follows a $\sqrt{t}$-kinetic law. [5] The $f_i(X)$ (resp. $g_i(X)$) function corresponds to the active regime (resp. calendar) ageing contribution attributable to X (T, I or SOC). They are multiplied that way because we consider all the parameters to be intertwined. They have been chosen as dimension-less functions. K^{cyc} and K^{cal} holds the dimensions [%Ah/Ah] and [%Ah.$s^{-0.5}$] respectively.

4 RESULTS

The tests matrix, conceived in order to vary the parameters (T, I or SOC) one by one in each test, is applied on cells based on graphite/iron-phosphate (LiFePO4, LFP. From the cycles' results, we compute the Ah exchanged, and from the check-ups results, we compute the corresponding loss of capacity. Equation 1 can be rewritten as:

$$\frac{\Delta Q}{\sqrt{t}} = K^{cyc} f_1(T) f_2(I) f_3(SOC).\frac{Ah}{\sqrt{t}} + K^{cal} g_1(T) g_2(I) g_3(SOC) \quad (3)$$

A linear regression leads to two proportion coefficients: the multiplicative product of f_i and the multiplicative product of g_i. The first step is to split it apart to determine each element $f_i$and g_i separately. The method used is described in [1]. We can then compute and interpolate the data points obtained for each f_i and g_i.

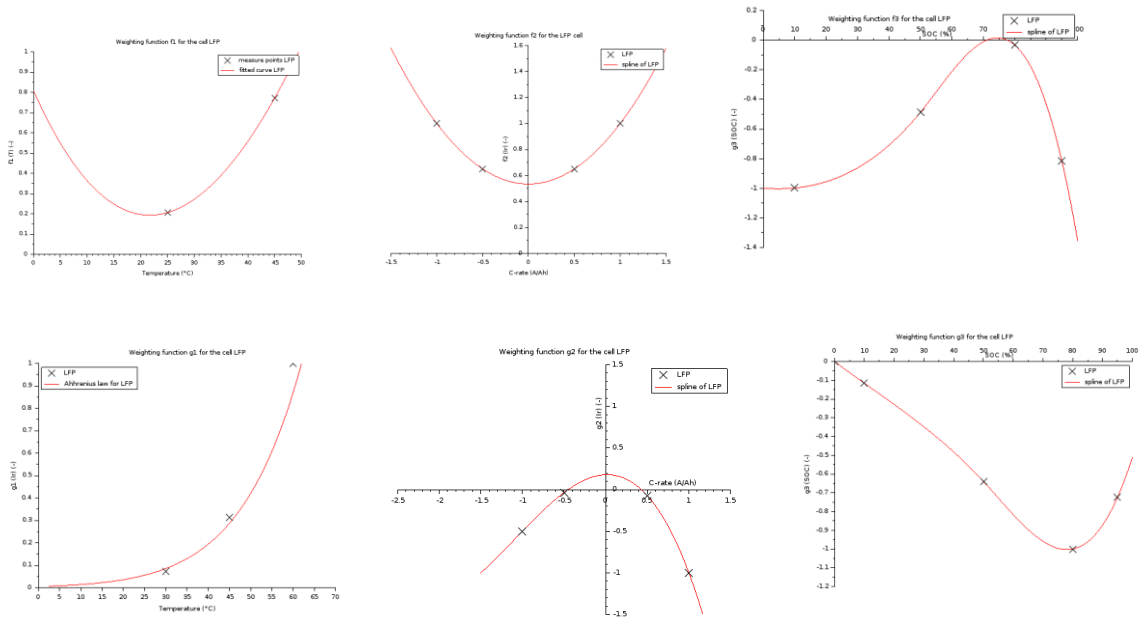

Figure 1: Weighting functions obtained for LFP, obtained for both calendar and cycles ageing. From top to bottom, left to right: f1(T), f2(I), f3(SOC), g1(T), g2(I), g3(SOC).

It has to be noticed that these functions are assumed to be dependent on the Li-ion composition, chemistry, manufacturing, casing, etc. [6,7] Therefore, they have to be computed again for other types of cells models.

Nevertheless, this paper studies the similarities between these functions. Functions coming from the LFP/graphite cells have been compared with the ones coming from literature regarding $LiNi_{0.8}Co_{0.15}Al_{0.05}O_2$/graphite (NCA) cells.

5 DISCUSSION

5.1 Discussion on the g_3 curve

The function g_3 has been chosen negative. Figure 2 shows that the two curves are very similar: a minimum range of values is observed both on NCA and LFP. It corresponds to a maximum impact of the SOC on the calendar ageing. This means that the passivation layer speed is maximum around that average SOC.

Repeating the same modelling, but considering the exchanged watt-hours (and no more the exchanged ampere-hours), we compute the same kind of linear regression:

$$\Delta Q = f^{Wh}(T,I,SOC).Wh + g^{Wh}(T,I,SOC).\sqrt{t} \quad (4)$$

By writing it in an infinitesimal way, we have:

$$\Delta Q = f^{Wh}(T,I,SOC).\delta E + g^{Wh}(T,I,SOC).\sqrt{\delta t} \quad (5)$$

As seen previously (Equation 1), we have:

$$\Delta Q = f^{Ah}(T,I,SOC).dq + g^{Ah}(T,I,SOC).\sqrt{\delta t} \quad (6)$$

On the interval $[50\%;80\%]$ the numerical values show that $g^{Ah}(T,I,50\%) = g^{Wh}(T,I,50\%)$ and therefore, Equation 5 gives $f^{Ah}(T,I,SOC).dq = f^{Wh}(T,I,SOC).\delta E$. We were expecting only one value of extreme SOC, we end up having a range of values.

We can conclude that on this interval, $\delta E = \frac{f^{Ah}(T,I,SOCmin)}{f^{Wh}(T,I,SOCmin)}.dq$, the lost energy during cycling derives from a potential. We find here a behaviour law, independent from the SOC, the latter being not a thermodynamic variable. On this range of SOC, we are independent from the chemistry, this electrical potential accounts for the entire behaviour. This totally confirms our plan to work towards an equivalent circuit model.

Concerning the trial, it shows that it is enough to focus on one SOC (chosen at 50%) to account for the behaviour of the cell at the neighbourhood of 50%.

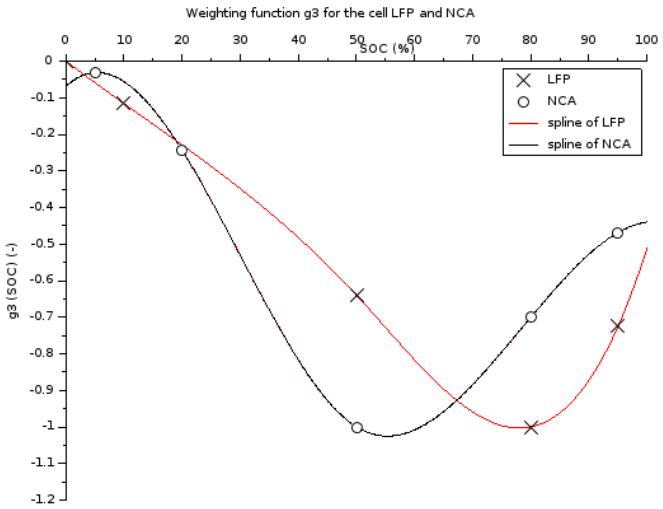

Figure 2: Weighting function g3 for NCA and LFP. Markers represent experimental values.

5.2 Discussion on the f_1 and the g_1 curve

The g_1 function represents the influence of the temperature on the ageing occurring during pure storage.

The g_1 curve, associated with the g_1 function, can be fitted by an Arrhenius law, which represents the speed of the electrochemical reaction depending on the temperature: $g_1(T) = \lambda.e^{\frac{-E_A}{RT}}$. This is coherent with the fact that the calendar ageing is due to the electrolyte

decomposition, and the subsequent SEI formation. [8] The NCA curve has been fitted from experimental values. The difference between both chemistries laws lays in the activation energy value. (Figure 3)

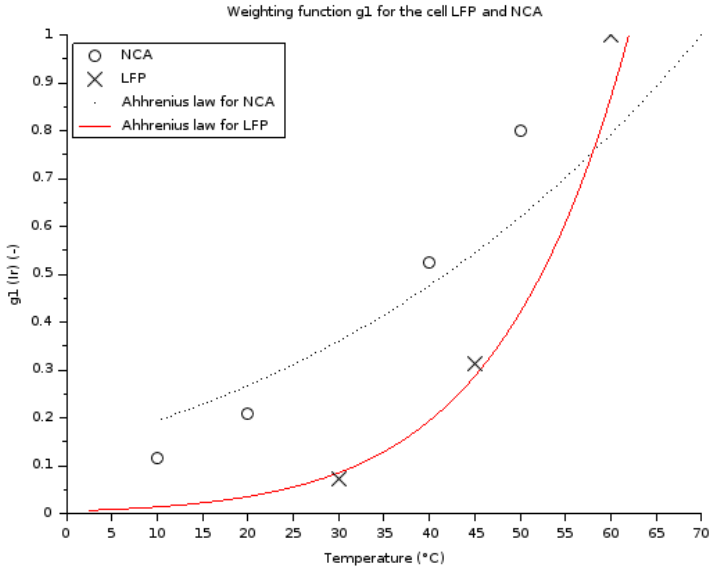

Figure 3: Weighting function g1 for NCA and LFP. Markers represent experimental values.

The f_1 function represents the influence of the temperature on the ageing occurring while battery is cycled. The f_1 curve interpolates the experimental values.

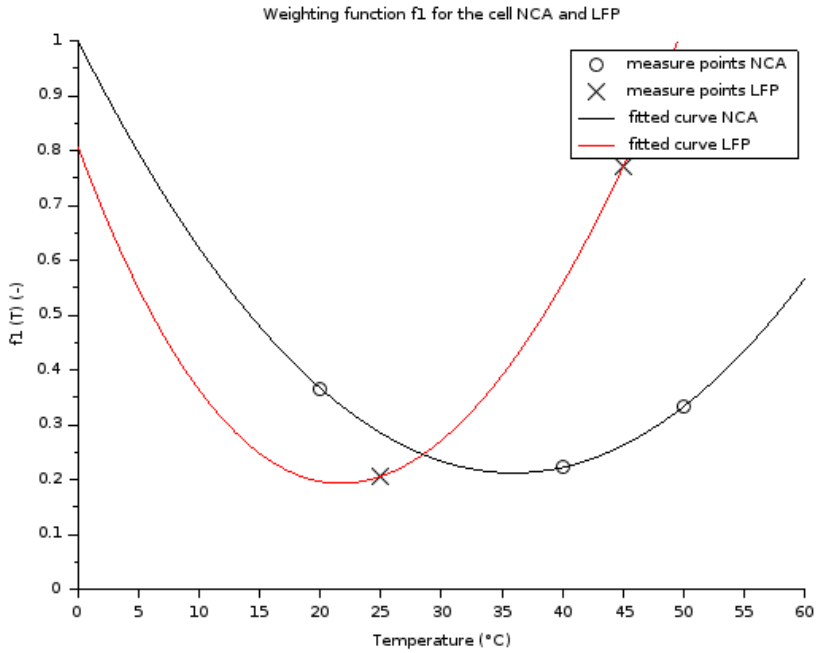

Figure 4: Weighting function f1 for NCA and LFP. Markers represent experimental values.

Again, we can see on Figure 4 that the two curves have the same shape, and shows an extremum of ageing around the same temperature.

Molecular-level understanding of solid-electrolyte interphase (SEI) growth kinetics has been considered as part of a transition state theory, which accounts for the effect of the temperature on the growth rate. This relationship is called the Eyring's law, and is quite similar to the Arrhenius law. We use the so-called Eyring law to point out the speed of the side reaction taking place in the battery cell.

$$k(T) = \alpha.\frac{k_B T}{h}.e^{\frac{-\Delta G_0}{RT}} \tag{7}$$

Where k is the speed constant, related to the degradation rate, h is the Planck constant, R is the gas constant (J.K−1.mol−1). According to the literature, there are reviews providing with some similar models [9]. However these models do not distinguish the SOC from the temperature, simply suggesting a 3D fitting with both parameters taken into account.

The current is linked to the speed constant by the Butler-Volmer law: $i(T) = \lambda.k(T).\left(e^{\frac{-A}{T}} - e^{\frac{B}{T}}\right)$, where λ, A and B are constants.

On the other hand, John Newman explains that the cells generate their own heat. He shows that the energy balance is made of two terms. The first one is associated with the Joules effect, considered as irreversible, and the second one is due to the heat generation at the interface between the electrolyte and the electrode, therefore it is reversible. The irreversible heating source has been described by Hemery [10]:

$$\frac{\partial Q_{irr}}{\partial t} = i(T).[(U - U_{ocv}) + T * \frac{\partial U_{ocv}}{\partial T}] \tag{8}$$

At the first order, $\frac{\partial U_{ocv}}{\partial T}$ is considered to be constant and $U - U_{ocv} = R.i$.
Therefore, Equation (8) becomes:

$$Q_{irr} = i.[R.i + T.\gamma].dt \tag{9}$$

$$Q_{irr} = [R.i + T.\gamma].Ah \tag{10}$$

So, by definition, $f_1(T)$ is proportional to $R.i + T.\gamma$, so, $\frac{f_1(T)}{T} = \mu.\frac{i(T)}{T} + \theta = \varepsilon\left(e^{\frac{-A}{T}} - e^{\frac{B}{T}}\right) + \xi$.
The constant ε has been arbitrarily set equal to 1. From the three points coming from NCA tests, a relationship between A and B can be found: $B = 1.02.A$..Therefore two unknowns are remaining (A and ξ), which is enough to fit the two measurement points obtained for LFP. The fit for NCA and LFP can be seen on Figure 4.

This minimal temperature is thermodynamically justified, the others appear as deviations from ideality.

5.3 Discussion on the f_2 and the g_2 curve

The f_2 function represents the impact of the rated-current on the ageing appearing while cycling.

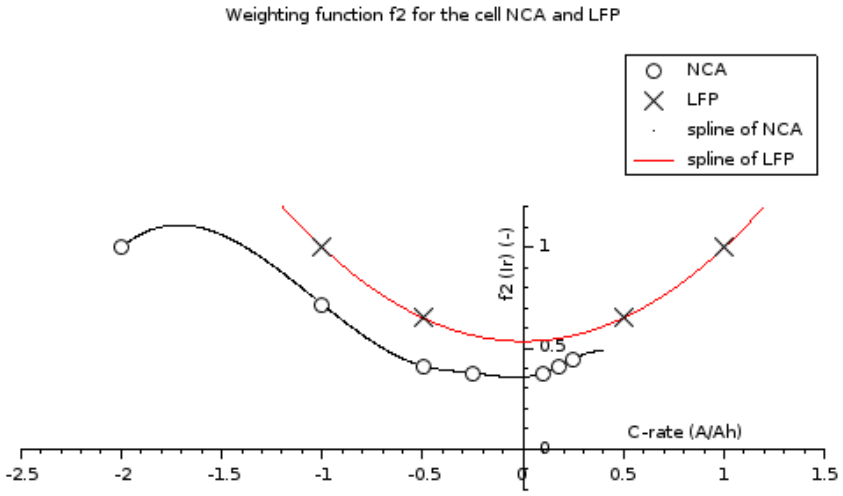

Figure 5: Weighting function f2 for NCA and LFP. Markers represent experimental values.

The LFP curve and the NCA have been fitted with a spline, resulting in polynomial functions. We can see the two curves have a similar shape and are odd around zero.

The g_2 function represents the impact of the rated-current on the ageing appearing during calendar ageing (both in cycling and pure storage).(Figure 6)

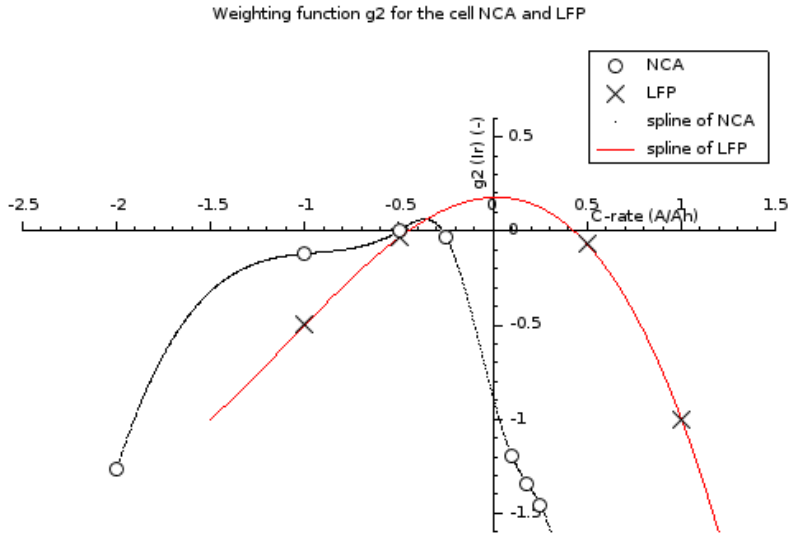

Figure 6: Weighting function g2 for NCA and LFP . Markers represent experimental values. The spline interpolates the data coming from LFP, when the charge and discharge temperature has not been distinguished

The LFP and the NCA curves have been fitted with a spline (Figure 6). However, for the NCA cells, the tests did not feature a constant temperature, due to heating of the internal resistance. Therefore, the charge temperature and the discharge temperature impact had to be differentiated. First both temperatures had to be reconstituted. The method used is detailed in

[1]. This difference is due to a depth of discharge of 100% applied to the cells. However, for the LFP cells, the difference between both temperatures is too small for the method to be relevant.

There seem to exist a relation between the impact of C-rate in charge and the impact in discharge.

Mechanical deformations of the active material are assumed to be responsible for ageing in cycling [11]. Therefore, the f_2 function should explain this phenomena.

We have to keep in mind that lithium-ion cells convert chemical energy to electric energy via redox reaction originating from both lithium-ion motion and electron transfer under a certain applied potential. The ions have the lowest energy when they are intercalated inside the positive electrode (cathode) and highest energy when they are in the negative electrode (anode). Considering cations, this corresponds to low (resp. high) potential accordingly. This electrochemical reaction allows the lithium ions to transfer from the solid phase (the electrode) towards the solution (the electrolyte), via intercalation currents, and vice versa. [12]

The reaction corresponds to the intercalation / deintercalation of lithium ions in the graphitic layers at the anode and in the active material (LFP or NCA) structure at the cathode. [12] The charge transfer is considered to be the limiting factor since the mass transport is insured by a highly ionic concentrated electrolyte. The charge transfer speed decreases with time due to the decay of conductivity in the electrolyte [7] and decrease of the active surface at the electrode.

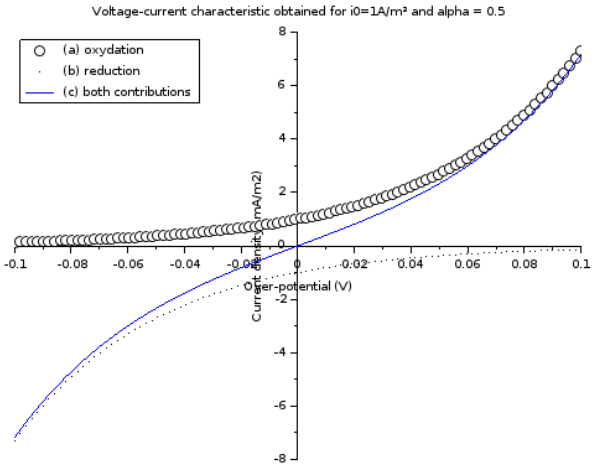

Figure 7 Voltage-current characteristic. (a) oxydation (b) reduction (c) total of both contributions. Markers represent experimental values.

The current-voltage characteristic of this electrode is given by its Butler-Volmer relationship: $i = i_0(e^{\frac{\alpha nF\eta}{RT}} - e^{\frac{-(1-\alpha)nF\eta}{RT}})$, which makes it an odd curve (see Figure 7), where i is the current (A) at the electrode, T the temperature (K), R the molar gas constant (R=8.1345J/(mol.K)), F the Faraday constant (F = 96 485,3329 sC/mol-1), η is the over-potential ($\eta = E - E_{eq}$) and E the electrode potential, i_0 is related to the charge transfer speed constant and the concentration of the Li^+ (in the electrolyte and in the electrode), α

characterizes the symmetrical aspect of the charge transfer. We assume that one electron is involved in the reaction (n=1).

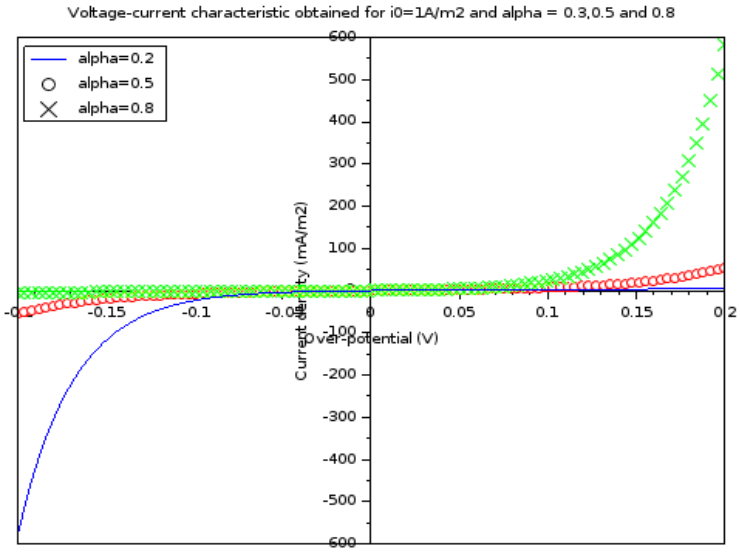

Figure 8 Voltage-current characteristic for different values of alpha coefficient. Markers represent experimental values.

The coefficient of interest is α : when α is close to 0, the over-potential η essentially leads to the reduction of the electrolyte, whereas when it is close to 1, it essentially induces its oxydation. When it is equal to ½ , it means that the over-potential equally affects the activation barrier of oxidation and reduction.(see Figure 8). It accounts for the passive film SEI growth, and whether it is formed rather in charge or in discharge. This provides information on the ability of the insertion and deinsertion of Li^+in the graphitic layers at the anode. The two reactions (growth of the SEI and intercalation of lithium-ion) are correlated. It chemically represents the distance between the activated complex and the final product. For high values of α, the reaction is supposedly easily activated, as the final product is close to the intermediate one.

Approximating the Butler-Volmer equation around the high over-potential regions, ($|\eta| \gg \frac{RT}{F}$ and $\eta > 0$) a limited development of e^x= 1+x of the intensity gives $i = i_0\left(e^{\frac{\alpha F\eta}{RT}}\right)$ and so $\eta = \frac{RT}{\alpha F} ln \frac{i}{i_0}$. Numerically, an over-potential of 100mV at 25°C is enough to decrease the influence of the second term to 2%. This is an anodic over-potential, so if the electrode is an anode, it is home of oxidation during discharge. If < 0 , $i = -i_0\left(e^{\frac{-(1-\alpha)nF\eta}{RT}}\right)$ and so $\eta = -\frac{RT}{(1-\alpha)nF} ln\left(-\frac{i}{i_0}\right)$. This is a cathodic over-potential, during charge.

To get the amount of energy required for the intercalation and deintercalation process, the following integral has to be computed:

Deintercalation process (during the discharge): $\int_0^I i * \eta(i)di = \int_0^I i * \frac{RT}{\alpha nF} \ln \frac{i}{i_0} di$

Intercalation process (during the charge): $\int_{-I}^0 i * \eta(i)di = \int_{-I}^0 -i * \frac{RT}{(1-\alpha)nF} \ln\left(-\frac{i}{i_0}\right) di = \int_0^I i * \frac{RT}{(1-\alpha)nF} \ln \frac{i}{i_0} di$

The impact of charge or discharge is given by $\frac{1}{\alpha} g_2(I_d) = \frac{1}{1-\alpha} g_2(I_c)$.

Therefore, the two processes require equal energy and therefore equally impact the cell if $\frac{1}{\alpha} = \frac{1}{(1-\alpha)}$, so if $\alpha = \frac{1}{2}$. The energy to intercalate lithium ions during charge and deintercalate during discharge at the cathode is the same [1], therefore $\alpha = \frac{1}{2}$, and therefore the f_2 curve is an odd curve. This latter result is confirmed on NCA related curve in Figure9, where the curves obtained for C/2;1D and 1C;D/2 are parallel, and on Figure 5, the acceptable values of C-rate. For very high C-rate, the behavior of the NCA function is sharply different, and is not explained in this paper.

If the two processes require different energy, $\alpha \neq \frac{1}{2}$. The coefficient twists the curve, and reflects the impact of the growing SEI. From the literature review [3,13], the values obtained for $1 - \alpha$ are 0.69 for a temperature of 25°C, and 0.67 at 45°C. However, Delacourt and al [13] obtained a value of 0.95 at the anode that they judge to be too singular.
Nevertheless, considering $1 - \alpha = \frac{2}{3}$ (which is close to 0.69 and 0.67), it results in $g_2(I_d) = \frac{1}{2} g_2(I_c)$.

So when the rate is “high enough” (then the over-potential is “high enough” as well), we have a relationship between the impact of the charge rates and the discharge ones. The discharge affects the ageing two times less than the charge. This result is confirmed by Bashash and al [12], which shows that battery degradation is slower during discharge than during charge. This paper quantifies it. This seems logical as the ions tend to decrease their potential, and are therefore more stable at the cathode, so when the system is rather discharged. Pushing the ions back to the anode (charging the cell) requires more energy to counterbalance and tends to damage the cell more. The result can be observed on Figure 6 where the discharge impact is twice as big as the charge one for LFP.

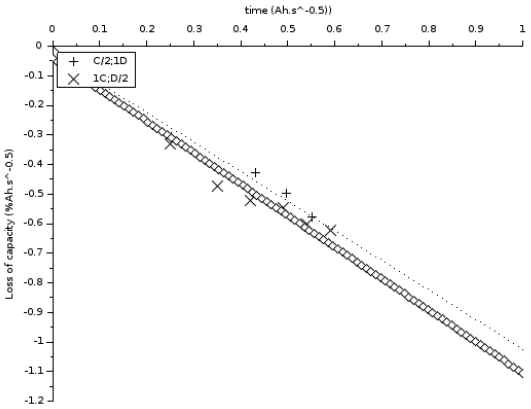

Figure 9 Loss of capacity with respect to CT/√t, for two set of tests : C/2;1D and 1C;D/2. Markers represent experimental values

5.4 Improvements on the tests matrix

It is possible to propose a new test matrix that is more adapted to the needs of the model and to the hardware constraints of the cycling bench and the time constraints. It must be borne in mind that accelerated ageing lasts on average 3 months, and that all cannot be done in parallel, because of the availability of cycling equipment. Better correlation will be obtained by cycling around a SOC point (chosen at 50%) instead of performing 100% DOD cycles (that consists in cycles made of a full discharge and a full charge), because the tests won't heat up.

The "pivot" chosen in the method to obtain the weighting functions has been modified, so that the test does not heat anymore. We obtain the same number of information with less testing. The modified matrix is detailed in Table 3:

Table 3: Tests matrix

	T (°)	SOC (%)	$I_c(A.Ah^{-1})$	$I_d\ (A.Ah^{-1})$
1	T1	80		
2	T2	80		
3	T1	10	1C	1D
4	T1	50	1C	1D
5	T1	80	1C	1D
6	T1	95	1C	1D
7	T1	50	C/2	D/2
8	T2	50	1C	1D
9	T3	50	1C	1D

6 CONCLUSION

This paper compared two Li-ion chemistries in terms of ageing: NCA/graphite and LFP/graphite. The impact of the three ageing parameters has been developed. The similar shapes was explained by similar operating mechanisms, even if the chemistry of the cathode and of the electrolyte were slightly different. The ageing model can be extended to other chemistry, and is coherent with the physical reality of the hidden mechanisms of ageing.

REFERENCES

[1] **Badey, Quentin.** *Étude des mécanismes et modélisation du vieillissement des batteries lithium-ion dans le cadre d'un usage automobile.* s.l. : Thèse de l'Université Paris Sud, 2012.

[2] **I., Bloom et Cole, B.W.** An accelerated calendar and cycle life study – An accelerated calendar and cycle life study of li-ion cells. *Journal of Power Sources.* 2001, pp. A238-A247.

[3] **Aurbach, Doron.** Review of selected electrode–solution interactions which determine the performance of Li and Li ion batteries. *Journal of Power Sources.* 2000, Vol. 89, pp. 206–218.

[4] **Eddahech, Akram.** *Modélisation du vieillissement et détermination de l'état de santé de batteries Li-ion pour application véhicule électrique et hybride.* Bordeaux : s.n., 2013.

[5] **Yoshida, Toshihiro.** Degradation Mechanism and Life Prediction of Lithium-Ion Batteries. *Journl of The Electrochemical Society.* 153, 2006, pp. A576-A582.

[6] **Hemery, Charles-Victor.** *Etude des phénomènes thermiques dans une batterie Li-ion.* Grenoble : s.n., 2013.

[7] **Vetter, J., Novak, P. et Wagner, M.R.** Ageing mechanisms in lithium-ion batteries. *Journal of Power Sources.* 2005, Vol. 147, pp. A269-A281.

[8] **Bashash, Saeid, et al.** Plug-in hybrid electric vehicle charge pattern optimization for energy cost and battery longetivity. *Journal of Power Sources.* 2011, Vol. 196.

[9] *A Model for Predicting Capacity Fade due SEI Formation in a Commercial Graphite/LiFePO4 cell.* **Elkström, Henrik et Lindbergh, Göran.** 162, Stockholm : s.n., 2015.

[10] **Delacourt, C. et Safari, M.** Life Simulation of a Graphite/LiFePO4 Cell under Cycling and Storage. *Journal of the Electrochemical Society.* 2012, Vol. 159, 8.

[11] **Verma, Pallavi, Maire, Pascal et Novak, Pert.** A review of the features and analyses of the solid-electrolyte interphase in Li-ion batteries. *Electrochimica Acta.* 55, 2010, pp. 6332-6341.

[12] **Li, J.** Studies on the cycle life of commercial lithium ion batteries during rapid charge–discharge cycling. *Journal of Power Sources.* 2001, Vol. 102, pp. 294–301.

[13] **Baghdadi, I., et al.** Chemical rate phenomenon approach applied to lithium battery capacity fade estimation. *Microelectronics Reliability.* 2016, Vol. 64, 134-139.

[14] **Chhor, Sarine.** *Etude et modélisation de l'interface graphite/électrolyte dans les batteries Lithium ion.* 2014.

VII International Conference on Computational Methods for Coupled Problems in Science and Engineering
COUPLED PROBLEMS 2017
M. Papadrakakis, E. Oñate and B. Schrefler (Eds)

COUPLED MODELING FOR INVESTIGATION OF BLAST INDUCED TRAUMATIC BRAIN INJURY

X. GARY TAN, ROBERT N. SAUNDERS AND AMIT BAGCHI

U.S. Naval Research Laboratory
Multifunctional Materials Branch
Washington, DC 20375, USA

Key words: Human Biomechanics, Blast, Traumatic Brain Injury (TBI), CSF, ALE, MPM.

Abstract. Modeling of human body biomechanics resulting from blast exposure is very challenging because of the complex geometry and the substantially different materials involved. We have developed anatomy based high-fidelity finite element model (FEM) of the human body and finite volume model (FVM) of air around the human. The FEM model was used to accurately simulate the stress wave propagation in the human body under blast loading. The blast loading was generated by simulating C4 explosions, via a combination of 1-D and 3-D computational fluid dynamics (CFD) formulations. By employing the coupled Eulerian-Lagrangian fluid structure interaction (FSI) approach we obtained the parametric response of the human brain by the blast wave impact. We also developed the methodology to solve the strong interaction between cerebrospinal fluids (CSF) and the surrounding tissue for the closed-head impact. We presented both the arbitrary Lagrangian Eulerian (ALE) method and a new unified approach based on the material point method (MPM) to solve fluid dynamics and solid mechanics simultaneously. The accuracy and efficiency of ALE and MPM solvers for the skull-CSF-brain coupling problem was compared. The presented results suggest that the developed coupled models and techniques could be used to predict human biomechanical responses in blast events, and help design the protection against the blast induced TBI.

1 INTRODUCTION

Blast events accounted for nearly 70% of injuries in wounded service members, and are the main cause of TBI [2]. Compared to impact-related injury, the mechanisms involved in blast injury are much less understood. Primary concussive blast injuries may be caused by the direct transmission of the blast wave across the cranium and the brain, by the impact of blast ejecta on the body (e.g., shrapnel and debris) and by the individual striking an object (e.g., a fall against ground or vehicle). Because of ethical reasons experimental neurotrauma is typically studied using either physical surrogates or animal models [4]. Direct use of animal model results to human is questionable as it is not clear how to reproduce the blast loads on humans in animals. The multi-physics computational models of injury biomechanics complemented with benchmark quality experiments may provide a foundation for better understating of injury mechanisms. Validated models could also be used for the design of improved protective equipment, injury diagnostics, casualty care and forensics [5].

Accurate simulation of blast waves impacting a human body and the resulting human biomechanical response is very challenging as it involves several physical and biomedical

disciplines as well as a range of spatial and temporal scales. A blast wave, interacting with human, transfers energy from the body surface into the interior. The overpressure on the body surface generates two types of waves with the body organs and tissues: pressure waves and shear waves. As the pressure wave traverses an organ such as brain or lung, it creates sharp pressure gradients on sensitive microstructures such as brain neurons. It propagates with specific tissue speed of sound and causes local wave diffractions/reflections on tissue interfaces with impedance differential creating compressive and tension strain responses. Most biological materials are weaker in tension than in compression and thus disruption and therefore damage at the tissue interface may occur. When the pressure wave compresses a gas containing structure such as an alveolus or bowel segment, the subsequent expansion causes damage to the wall of the structure. Shear waves propagate within the body with much slower speed, last much longer and cause larger tissue deformations. The tension and shear waves as well as asynchronous movements of tissues with differing inertia may cause tearing of structures from their attachments and shearing of solid organs. The musculoskeletal system being solid is relatively resistant to the pressure waves while initial shock waves of sufficient intensity may cause long bone fracture [7]. Because of these, the inclusion of whole human body (skin, skeleton, and organs) is important to accurately account for the propagation and spatial distribution of stress waves inside the human body and to predict the complicated dynamic tissue/organ responses to the blast loading.

To simulate the blast-induced human body biomechanics, we developed a whole human body anatomic geometry/mesh model and the FEM biomechanics model. This human body model can be used to simulate the blast wave loading on the body surface, the biomechanical response of the body interior as well as the body biodynamics [10]. A mesh with the maximum element size less than three millimeters was used to resolve the smallest stress wavelength, small geometric features and material interfaces within the human body. The high-fidelity CFD model was used to simulate the interaction between the human body and the blast wave generated by a C4 explosion. Both Eulerian and ALE methods was used and compared for the high explosive burn simulation. The blast pressure loads computed during the CFD analysis are applied to the human body finite element model for biomechanics simulations. Using the human FEM model we investigated the brain biomechanics including the coup-contrecoup phenomena and the injury probability in the brain. The coupled gas dynamics and biomechanics solutions have been validated against the recent shock tube testing data on the physical phantom and animal [11].

For the closed system such as the human head, the interaction between the nearly incompressible CSF and the surrounding tissue is very strong at the fluid-solid interface during the impact [6]. A small change in the fluid volume by the tissue deformation will lead to an excessive flow pressure exerting to the neighboring tissue and thus is very difficult to solve. The Eulerian-Lagrangian coupling approach is computationally expensive in the iterative two-way coupling process and may not converge at all. To be more efficient and numerically stable, we employed both ALE method and MPM method [9] to solve such problem. In ALE, the motion and deformation of all materials are solved in the Lagrangian step, the distorted CSF mesh is then smoothed to preserve the mesh quality, and finally the solutions in the CSF and at the fluid-solid interface are conservatively transferred from the old mesh to the new one. The particle based MPM method has the potential to be another unified approach since both fluid dynamics and solid mechanics are solved simultaneously in the

Lagrangian description. We compared the accuracy and efficiency of both the ALE and the MPM in the skull-CSF-brain coupled problem.

2 METHODS

We describe the computational models and methods for simulating blast wave interaction with a human body and the associated biomechanical response. Several FSI coupling approaches for modeling injury caused by blast wave and impact loads are discussed.

2.1 High-Fidelity Human Model of a Human Body

The human computational models are based on the geometry of a 3D male anatomy model by the Zygote Media Group, Inc. The anatomy model starts with an entire skeleton model based on CT scans, and upon which all the other systems (e.g., skin, organs) fit together.

The generated hexahedral mesh consists of four different materials, i.e. brain with spinal cord, lung, skeleton and tissue for the rest of body. The outer surfaces of different body parts are shown in Figure 1a. The average element size is 2.5mm. The total number of elements is over 4.2 million. The mesh for the CFD simulation of a human standing on the rigid ground was also constructed as shown in Figure 1b, where an octree mesh was used to discretize the air domain between the human body and the outer boundaries. The smaller cell size (2.5mm) near human body is used and total number of cells is about 14 million. The computational meshes generated for these simulations are of good quality and can use relatively large time step sizes without resorting to the artificial time scaling treatment.

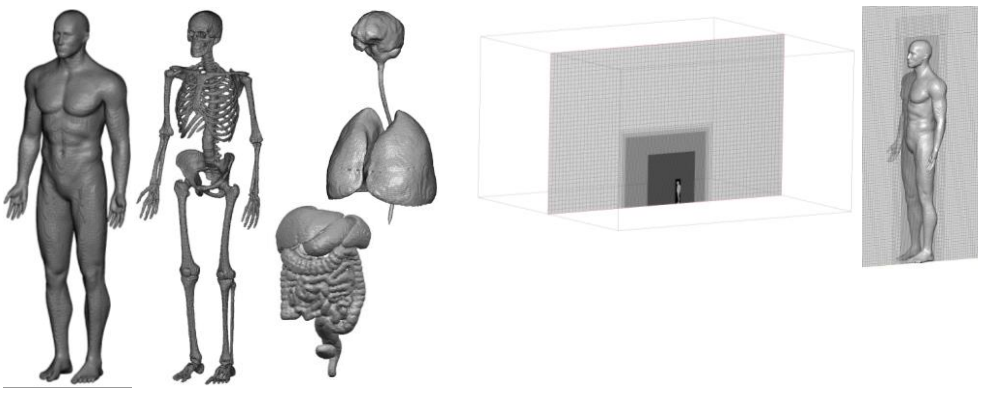

a b

Figure 1. Computational models from Zygote geometry. a) Skin surface, skeleton and lungs, brain, spinal cord and organs underneath skin of FEM mesh, b) CFD mesh for blast interacting with human body and a close-up view of CFD mesh around human body.

Table 1. Mechanical properties used in human FE model [13].

Tissue	Material	Constants	Mass Density Kg/m3
Skeleton	Linear elastic	E=5GPa, ν=0.3	1100
Brain, spinal cord	Viscoelastic	K=2.19GPa, G_0=49KPa, G_1=33KPa, τ=6ms	1000
Lung	Linear elastic	E=50Kpa, ν=0.3	100
Tissue	Linear- elastic	E=80MPa, ν=0.4	1000

We used homogenized material properties for different part of human body as listed in Table 1. The brain and spinal cord was modeled as an isotropic viscoelastic material, without considering the difference between white mater and grey mater. The CSF layer between the skull and the brain was not explicitly modeled but was considered to be part of the brain. The lungs were modeled as separated organs because of the sound speed being much slower in the lung than in other body tissues. All materials other than skeleton, brain and lungs were modeled as soft tissues in which an elastic material was assumed.

2.2 CFD Model of Blast Physics

For accurately capturing the detailed shock wave phenomena around the solid object, we use the CFD method to solve governing equations of the physics laws, i.e., conservation of mass, momentum, and energy. Consider the inviscid compressible Navier-Stokes equations

$$\frac{\partial U}{\partial t} + \nabla \cdot \mathbf{F} = 0 \tag{1}$$

where $U=\{\rho, \rho\mathbf{v}, \rho E\}^T$ and ρ, $\mathbf{v}$, E are the density, the velocity and the total energy and $\mathbf{F}$ is the flux. The equation of state (EOS) and the total energy of ideal gas are as below

$$p = \rho R T, \quad \rho E = \frac{p}{\gamma - 1} + \frac{1}{2}\rho \mathbf{v} \cdot \mathbf{v} \tag{2}$$

where R is the ideal gas constant, T is the temperature, and γ is the adiabatic index.

The high explosive is commonly modeled by the Jones-Wilkins-Lee (JWL) EOS

$$p = A(1 - \frac{\omega\rho}{R_1\rho_0})e^{-R_1\frac{\rho_0}{\rho}} + B(1 - \frac{\omega\rho}{R_2\rho_0})e^{-R_2\frac{\rho_0}{\rho}} + \omega\rho e \tag{3}$$

The material constants are in Table 2. The detonation velocity is used for the calculation of ignition time at the given location of explosive. The intrinsic energy per unit mass e is related to the total energy E by $e = E - (\mathbf{v}\cdot\mathbf{v})/2$. The JWL equation is reduced to the ideal gas law when the density ρ is much smaller than the initial density ρ_0.

Table 2. Mechanical properties in JWL EOS for the explosive charge.

A (GPa)	B (GPa)	R_1	R_2	ω	e_0 (MJ/Kg)	ρ_0 (Kg/m^3)	V_D (m/s)
373.8	3.747	4.15	0.9	0.35	3.68	1630	6930

Both the ALE and the Eulerian methods are employed to solve the above equations. The ALE method involves three-step solution: Lagrangian, remeshing, and advection steps. The equation (1) in the Lagrangian description becomes

$$\rho\frac{D\mathbf{v}}{Dt} + \nabla\cdot(p\mathbf{1}) = 0, \quad \rho\frac{De}{Dt} + p\nabla\cdot\mathbf{v} = 0 \tag{4}$$

which can be readily solved by the explicit FEM solver. Among different remeshing methods to smooth the distorted mesh, we relocate the nodes by solving an elastic solid deformation problem using the implicit FEM solver

$$\nabla\cdot\boldsymbol{\sigma} = 0 \tag{5}$$

along with the prescribed displacement boundary condition and a zero-stress initial condition.

For the advection step, the current solution ϕ such as ρ, $\rho\mathbf{v}$, ρE at each element is transported from the old mesh to the new mesh by the convective velocity **c**

$$\frac{\partial \phi}{\partial t} + \mathbf{c} \cdot \nabla \phi = 0 \tag{6}$$

To maintain the numerical stability and conserve the mass, linear momentum and energy, we use the upwinding process in which the calculation of gradient depends on the direction of the convective velocity **c** and only uses the information from the upstream direction. The nodal velocity was calculated from the new elemental linear momentum using the shape functions. The nodal acceleration was updated from the equilibrium with new state variables.

For the Eulerian approach, the discontinuous Galerkin (DG) method was used to obtain the weighted residual form to (1) for each control volume/cell. The finite volume method is recovered with a constant weighting function in the DG method. We adopted the HLLC solver [14] for the flux calculation. The explicit method was used for the resulting semi-discrete system, of which the first-order forward Euler scheme is particularly efficient and provides a sufficient accuracy for the current applications. For both the Euler method and the advection step of ALE method, the second-order accurate solution was obtained by a piece-wise linear data reconstructions. The limiter function was used to eliminate the spurious oscillations.

2.3 Blast Induced Human Biomechanics

In the blast-human interaction process, the blast duration is very short (a few milliseconds) and during the blast loading the induced human body motion is small (a few centimeters). The one-way (explicit) coupling of flow and biomechanical analyses, in which the blast wave influences the body but the body movement does not influence the blast wave, is sufficient and much more efficient compared to the tightly coupled fluid-structure interaction (FSI) scheme (see, e.g., [1]). In this approach, the blast simulation was first carried out by assuming a rigid stationary human body. The time histories of the flow over-pressures and the corresponding locations are recorded. In the subsequent biomechanical analysis, we apply the overpressure loadings to the closest facet on human body surface for each time step. The force resulting from the flow over-pressure on each face of solid surface is computed by

$$\mathbf{F} = -p\mathbf{n}A \tag{7}$$

in which p is the overpressure, **n** and A are the face normal pointing away from solid and the face area respectively.

For the short-term event such as the blast wave interacting with human body, we choose the explicit finite element solver using the brick element with reduced integration. The hourglass control was used to effectively suppress artificial hourglass modes and meanwhile minimize the nonphysical stiffening of response. The numerical stability was inspected by the total energy balance of kinetic energy, internal energy and external work.

2.4 Head Skull-CSF-Brain Coupling Model

There are two main approaches for simulation of FSI problems: 1) Monolithic approach such as ALE method to solve the flow and the structure simultaneously; 2) partitioned approach to solve the flow and the structure separately. In a typical mesh-based partitioned

approach, the flow problem is solved by the Eulerian CFD solver and the structural problem is solved by Lagrangian FEM solver. The deformation in the fluid mesh due to the motion of fluid-structure interface is solved by the remeshing. With the relaxation of either the deformation to the fluid or the flow pressure to the structure at the interface, the flow and structural interaction is solved successively until the change in the solution is smaller than the convergence criterion. For the closed head with nearly incompressible CSF, the convergence using such approach is very difficult to achieve.

The ALE method is less complicated and more stable than the partitioned method for the closed-head FSI problem. The ALE method solves the CSF flow and the tissue deformation simultaneously. In the Lagrangian step, the Tait EOS is used for the CSF

$$p = \frac{\kappa}{n}[(\frac{\rho}{\rho_0})^n - 1] \tag{8}$$

where κ=2.2GPa, n=7.15. The density and linear momentum in the CSF are advected from the distorted mesh to the new mesh after the remeshing step. The nodal velocity and acceleration in the CSF and at the CSF-tissue interface are then updated for the next Lagrangian step.

A meshless method such as material point method (MPM) is another monolithic FSI method. With the MPM, the Lagrangian material points are used to discretize both fluid and solid. The interaction of the material points is calculated on a fixed background grid on which the momentum equation is solved. Different from other particle based methods, the evaluation of interpolation functions and derivatives relies on the background grid and does not involve the costly neighbor search. Compared to the ALE method, the remeshing and the advection are not needed. Since material points carry the mass and the history-dependent variables, the numerical diffusion associated with the advection is avoided.

3 RESULTS

For the blast and the biomechanics simulations, we used the multi-physics code CoBi, written in C++ and run on both Windows and Linux cluster. The implementations were verified and validated extensively through many related applications [11,12].

3.1 Modeling of Explosive

A spherical TNT charge with radius of 0.05 m is considered at the center of the model and surrounded by the air. A 1.134^o conical model with radius of 0.5m was built in which hexahedral elements with elemental length of 0.001m in the radial direction were used. The detonation starts at the center of charge, and the detonation front is moved with the given velocity of detonation. An element detonates if the detonation front reaches this element. From this time the JWL-equation turns on for this element. The surrounding air uses the same EOS with a different starting density and internal energy.

Both the ALE method and the Eulerian method were used for the high explosive burn simulation for the time duration of 0.1 msec. Both methods conserves the mass (=15.138mg) in the simulations. In terms of energy conservation, the Eulerian method conserves the total energy (=31.676KJ) precisely while the ALE method cannot conserve the energy. Figure 1 show that the mass density ρ, flow velocity $\mathbf{v}$ and flow pressure p propagating along the radial direction at 0.1ms. Compared to the Eulerian method the ALE method is much more diffusive

and thus is less accurate. The solution of $\{\rho, \rho\mathbf{v}, \rho e\}$ along the radius at the end of Eulerian simulation was saved into a file and used as the initial condition in the 3-D simulation of blast loading on the human.

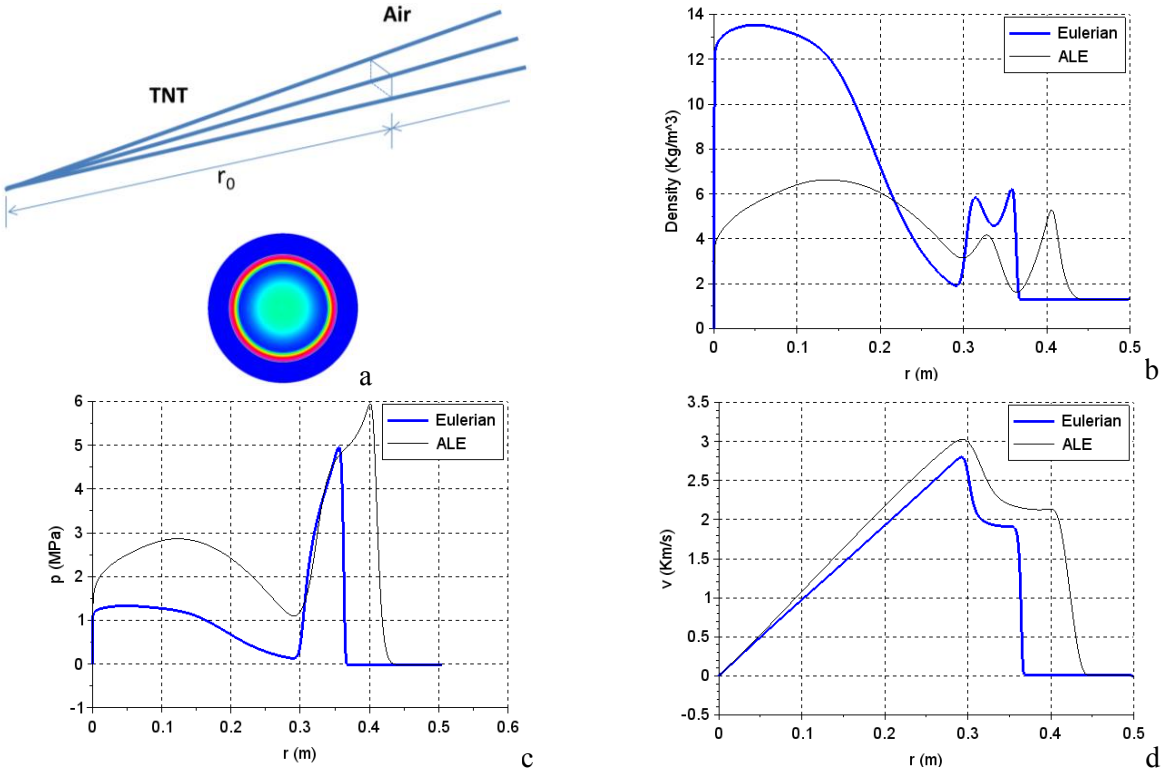

Figure 2. a) Conical model for TNT-air blast simulation with r_0=0.05m and pressure contour at 0.1ms; b) density, c) pressure, d) velocity along radial direction at 0.1ms between ALE and Eulerian methods.

3.2 Blast Loading on Human Body

The explicit flow solver was used to simulate the blast wave induced overpressure field around the human body. The human is facing the explosion. The 5lb C4 explosive is located at 92 inch away from the human body and 50 inch above the ground. The open boundary condition is applied at the outer boundaries. The time step size is about 0.1 micro-sec and the time duration of simulation is 12ms. The developed 1-D and 3-D simulation strategy [13] was used in which the conical model simulated the initial explosion stage before reaching the ground. The 3D simulation was then restarted by using the radial solution as the initial condition.

The results of the blast interaction with the stationary human body surface are shown in Figure 3. The shock front has been captured reasonably well. It takes just a few milliseconds for the blast wave to pass through the human body. After that the pressure field around the human goes back to the ambient and the resultant forces on the human body diminish rapidly. The Mach stem forms and progresses due to the reflection from the presence of ground and the human body. The pressure loading at each time step was saved into a file.

The calculated pressures on the head surface have a sharp rise and experience both positive and negative phases. The reflected pressure peak at forehead is much higher than other

locations. The calculated pressure at the rear portion of head surface is higher than the temple, because of the diffraction of the shock front. The peak pressure at the temple is similar to the incident peak pressure. The ground reflection reaches the forehead at 4.8ms.

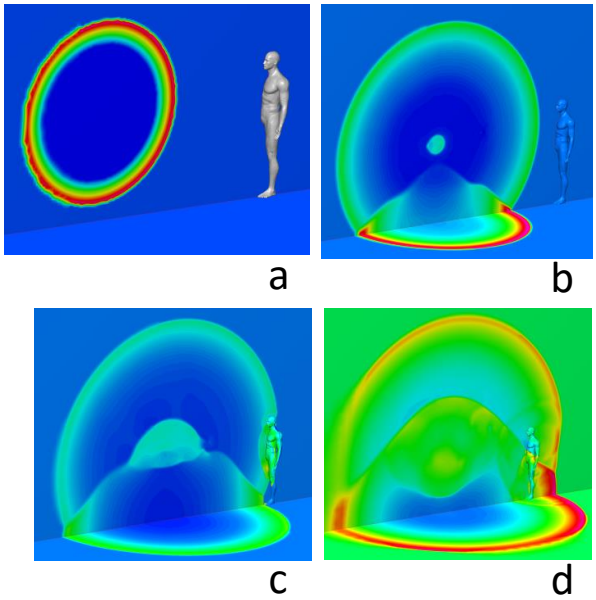

Figure 3. Blast simulation of C4 explosion interacting with human body. a) Initial pressure field from 1D simulation at 0.45msec, b) simulation shows ground reflection at 1.45ms, c) overpressure on human at 2.45ms, d) overpressure on human at 3.95ms.

3.3 Biomechanics Response of Human under Blast Loading

By applying the computed blast loading to the human skin, we simulated the biomechanical response of the human body for 12ms. The time step size is 0.08 micro-sec. In the human body dynamics, the effect of gravity was ignored and no consideration was given to the frictional contact interaction between the human body and the ground.

As shown in Figure 4, in the first few milliseconds the moving shock front diffracts on the human body surface, and reflects around concave regions (eye socket, lower neck, and groin). The blast pressure reaches the face and the chest first since they are closer to the explosive. The high pressure on the lower leg was caused by the ground reflection. The high-amplitude stress wave propagated inside the human body prior to any visible displacement of human body. Figure 4 shows the pressure in two sagittal planes. A stiff material like the skeleton has the higher pressure, while the pressure in a softer material like the lung is much lower. The pressure contours on both surfaces of skeleton and brain at several time instances are shown in Figure 5. Since the explosion occurs in front of the human, the blast wave first reaches the chest and front lobe of the brain. After the blast wind has passed, the human body does not move much and the maximum displacement is a few centimeters, which justifies the one-way coupling strategy for the simulation of blast-human body interaction. The numerical results of brain pressure response are qualitatively similar to the experimental data obtained in [3], in which an elliptical object is subjected to the shock wave loading generated from the shock tube. Several phenomena observed in the testing data during the first 2.5 millisecond were also occurred in the numerical simulation: 1) there was about a 0.1 millisecond time delay of

pressure onset between coup and contrecoup sites, 2) the negative pressure occurred first in the contrecoup site, 3) the positive peak pressure in the contrecoup site was higher than the coup site, 4) at the contrecoup site three positive peaks are gradually weakening, and 5) three negative pressure dips occurred over the cavitation limit of -100kPa.

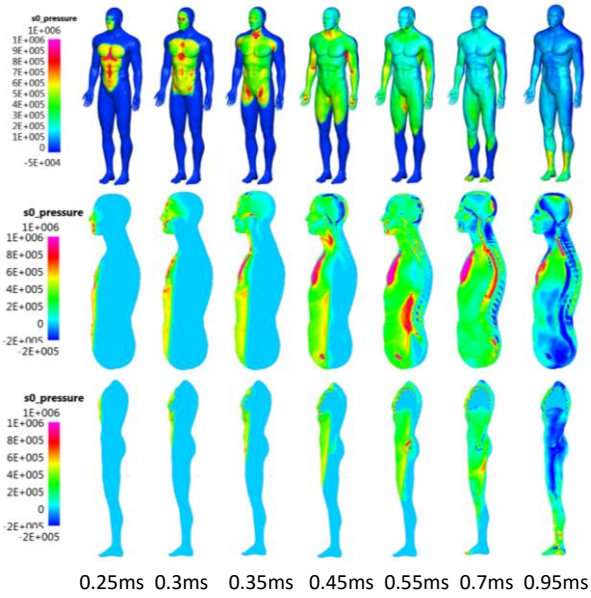

Figure 4. Human biomechanics under blast loading. Blast loading on human skin (top row); Pressure propagation in the middle sagittal plane (middle row); Pressure propagation in the para-sagittal plane (bottom row) at different times. Time offset by 1.8 ms between explosion CFD and FEM simulations.

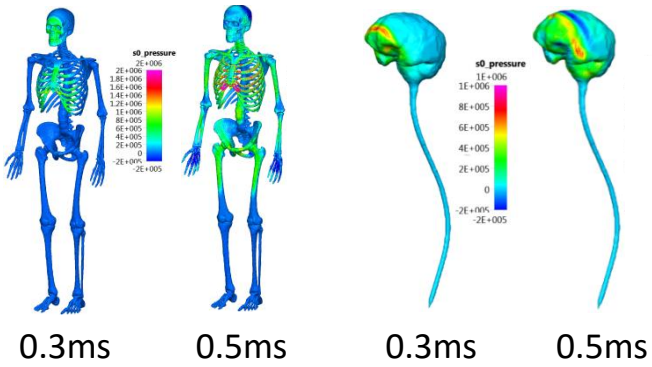

Figure 5. Pressure propagation in skeleton and brain at different times of human body under C4 explosion. Time offset by 1.8 ms between explosion CFD and FEM simulations.

3.4 Modeling of Skull-CSF-Brain Interaction

For the closed-head impact, the interaction between the CSF and the surrounding tissue is strong and difficult to model. We explore both ALE and MPM methods to solve such problem. In Figure 6, the head model with a simplified geometry and high-quality fine mesh was used to simulate the skull-CSF-brain interaction during the impact. Assume the head has been accelerated to the initial velocity of 3m/s after the blast loading and is colliding with a rigid wall. The commonly used partitioned FSI solving approach is unstable for this strong

coupling problem. In the ALE model, the CSF layer was modeled as the ALE fluid and other materials as the Lagrangian solid. In the MPM model, all materials were modeled as Lagrangian particles and a 0.002m uniform background grid was used. The cubic B-spline basis function was used to reduce the grid-crossing errors.

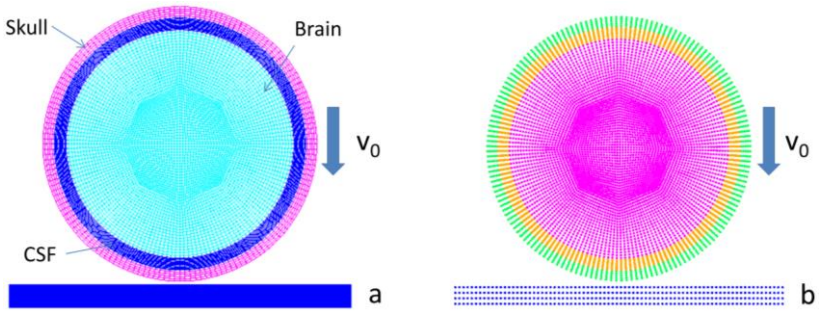

Figure 6. Head model for skull-CSF-brain interaction using ALE method (a) and MPM method (b).

The total simulation time is 5ms and the time interval for remeshing and advection is 20 micro-sec. At 4.36 ms, the head starts to rebound. In Figure 7, the maximum negative pressure in CSF is -236KPa and occurs at 0.92 ms. After 2.18 ms, the pressure in the brain and CSF stays in positive because of the compressed intracranial volume. Compared to the pressure, the shear strains which can cause the injury are developed at the later time (Figure 8). The maximum shear occurs at the CFS-skull and CSF-brain interfaces because the CSF has no shear resistance. Figure 9 shows that the CSF flows around the brain and the flow speed in CSF is in the same level of initial impact speed. At the end of 5ms, the CSF flows upward. With the implemented ALE method we are able to further simulate the CSF-tissue interaction for the closed-head injury during the impact, using an anatomic head model and a robust remeshing technique.

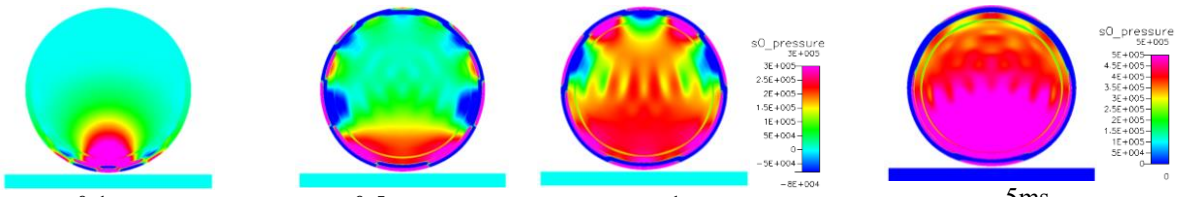

Figure 7. Skull-CSF-brain coupled solution using ALE model. Pressure at t=0.1ms, 0.5ms, 1ms, 5ms.

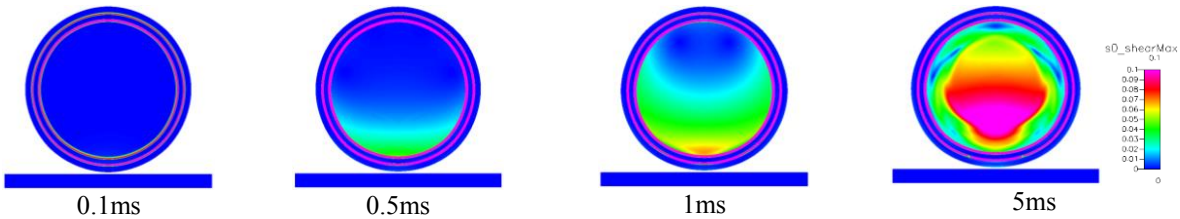

Figure 8. Skull-CSF-brain coupled solution using ALE model. Shear strains at t=0.1ms, 0.5ms, 1ms, 5ms. Maximum shear strains occur at CSF-brain and CSF-skull interfaces.

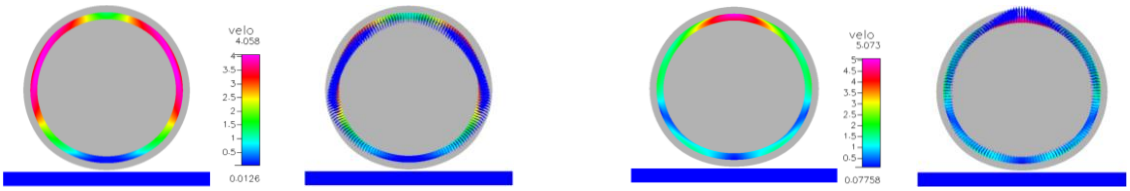

Figure 9. Skull-CSF-brain coupled solution using ALE model. Flow velocity magnitude and direction in CSF at t=1ms, 5ms.

Figure 10 shows the results when solving the same problem using the MPM. The MPM model behaves softer than the ALE model and yields larger contact area between the skull and the wall. Compared to the ALE model, the magnitude of pressure is much higher in the CSF and much lower in the brain. Like in other particle based methods, it is difficult to compute the particle mass density/pressure accurately for the nearly incompressible material under large deformation. To remedy it, the adaptive MPM to resample the particles or treating the evolution of pressure implicitly [8] becomes necessary to obtain the solution with similar accuracy as the ALE method in the skull-CFS-brain interaction problem.

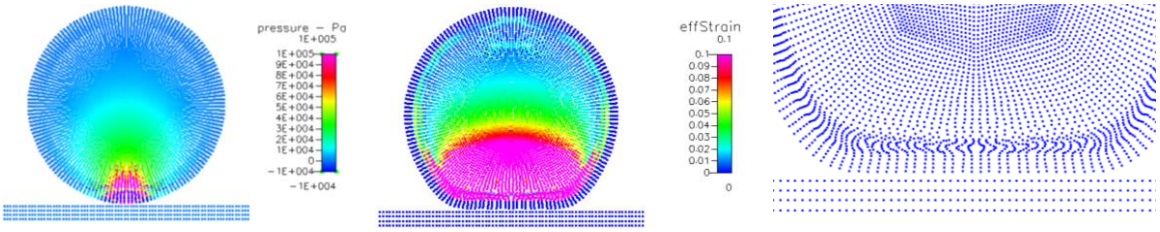

Figure 10. Skull-CSF-brain coupled solution using MPM model. a) pressure at 0.72ms, b) strain at 3ms, c) zoom-in of contact area showing movement of material points in CSF at 3ms.

4 CONCLUSIONS

This paper presented the methods to model the blast-induced human biomechanics and injury. Several coupling approaches were implemented for modeling human body injury caused by IED blast wave and fragmentation/impact loads. The computational methods and simulation results of blast injury mechanisms were described. In modeling the explosive the Euler solver performs much better than the ALE solver since the Eulerian solver conserves the energy precisely. Our computational studies have shown that the disparity of spatial and temporal scales of the problem justifies simplifying assumptions for various phases of blast human injury simulations. The human body can be assumed as rigid for simulations of the blast wave propagation around the body to compute body loading as inputs for biodynamics and biomechanics simulations. For the strong coupling problems of skull-CSF-brain interaction under impact the ALE method solves it with a reasonable response. For the same problem the MPM needs more improvements such as solution adaptation and energy conserving scheme to achieve the similar performance as the ALE method.

The presented coupling framework provides a foundation for a better understanding of blast injury mechanisms, and also for the development of personal protective armor. Several challenges remain, such as better material properties for high strain rate tissue biomechanics, CSF cavitation, accurate models of IED induced penetrating injury, and model validation.

ACKNOWLEDGEMENT

Funding was provided by the Office of Naval Research (ONR) through the Naval Research Laboratory's Basic Research Program. The analysis was supported by the Department of Defense High Performance Computing Modernization Program using the Army and Air Force Research Laboratories and the Engineer Research and Development Center Research Major Shared Resource Centers under project 416, subproject 231.

REFERENCES

[1] Badia, S., Nobile, F., Vergara, C. Fluid-structure partitioned procedures based on robin transmission conditions, *Journal of Computational Physics* (2008) 227:7027-7051.

[2] Eskridge, S.L., Macera, C.A., Galarneau, M.R. et al. Injuries from combat explosions in Iraq: injury type, location, and severity. *Injury* (2012) 43(10):1678–1682.

[3] Goeller, J., Wardlaw, A., Treichler, D., O'Bruba, J., Weiss, G. Investigation of Cavitation as a Possible Traumatic Brain Injury (TBI) Damage Mechanism from Blast, *J. Neurotrauma* (2012) 29(10):1970–1981.

[4] Goldstein, L.E., Fisher, A.M., Tagge, C.A. et al. Chronic traumatic encephalopathy in blast-exposed military veterans and a blast neurotrauma mouse model. *Sci. Trans. Med.* (2012) 4(134):134-160.

[5] Gupta, R.J. and Przekwas, A.J. Mathematical models of blast induced TBI: current status, challenges and prospects, *Frontiers in Neurotrauma* (2013) 4:59.

[6] Halabieh, O., Wan, W.L. Simulating mechanism of brain injury during closed head impact, F. Bello, E. Edwards (Eds.): *ISBMS* (2008), LNCS 5104, 107–118.

[7] Hull, J.B. An investigation into the mechanism of traumatic amputation by explosive blast. Doctor thesis, *University of Birmingham* (1995).

[8] Jiang C. The material point method for the physics-based simulation of solids and fluids, Doctor Thesis, *University of California, Los Angeles* (1995).

[9] Sulsky, D., Chen, Z. and Schreyer, H.L. A particle method for history-dependent materials, *Computer Methods in Applied Mechanics and Engineering* (1994) 5:179–196.

[10] Tan, X.G., Kannan R., Przekwas A.J., Ott K., Harrigan, T., Roberts, J. and Merkle, A. An enhanced articulated human body model under C4 blast loadings, *ASME Int. Mech. Eng. Congress and Exposition* IMECE 2012-89067 (2012).

[11] Tan X.G., Przekwas, A.J., Long, J.B. Validations of virtual animal model for investigation of shock/blast wave TBI, *ASME Int. Mech. Eng. Congress and Exposition* IMECE 2013-64587 (2013).

[12] Tan, X.G. and Przekwas A.J. A computational model for articulated human body dynamics, *Int. J. of Human Factors Modeling and Simulation* (2011) 2:85-110.

[13] Tan, X.G., Kannan R. and Przekwas A.J. A Comparative study of the human body finite element model under blast loadings, *ASME Int. Mech. Eng. Congress and Exposition*, IMECE2012-89072 (2012).

[14] Toro, E.F., Spruce, M. and Speares, M. Restoration of the contact surface in the HLL-Riemann solver, *Shock Waves* (1994) 4:25–34.

VII International Conference on Computational Methods for Coupled Problems in Science and Engineering
COUPLED PROBLEMS 2017
M. Papadrakakis, E. Oñate and B. Schrefler (Eds)

COUPLED NANOSTRUCTURES OF RIBONUCLEIC ACIDS: DEVELOPING DISCRETE-CONTINUUM MODELS FOR LARGE TIME-SCALE SIMULATIONS

Shyam Badu[†] and Roderick Melnik[†]

[†]MS2Discovery Interdisciplinary Research Institute
M2Net Lab, Wilfrid Laurier University
75 University Avenue, Waterloo, ON N3L 3C5, Canada
sbadu@wlu.ca, rmelnik@wlu.ca/

Key words: RNA nanoclusters,Coupled problems in nanotechnology, Biomedicine, Discrete-to-continuum models

Abstract. Continuing progress in the development of theoretical and computational techniques in the field of biomolecular systems involving Ribonucleic acids (RNA) has a very important impact in biomedicine and human health. Many essential biological phenomena in these systems are on the time scale longer then the time it is possible to simulate computationally using existing atomistic models. In this article we describe the development of a continuum model based on atomistic scale parameters. We also present initial results on the mechanical, as well as thermal properties of the RNA nanoclusters obtained by using the finite element methodology. Specifically, using the elastic constants available for the nucleic acid, we report the distributions of the displacement fields due to stress and thermal effects along typical RNA nanotubes that are important for biomedical applications.

1 Introduction

Since the ribonucleic acid (RNA) structures are flexible in nature, it is very easy to create RNA nanoclusters of different sizes and shapes via their self assembly. The motivation for self assembling these RNA nanoclusters is their potential application in the field of human health, biomedicine and bioengineering [1, 2, 3]. For these self assembled RNA nanoclusters it is very important to study their properties in different environments such as physiological solutions [4]. Studies of structural properties of RNA nanoclusters have been performed using molecular dynamics and coarse graining modeling techniques [5, 6, 7]. The building blocks used to model the RNA nanoclusters are the RNA strands such as RNAi/RNAii which are taken from the protein data bank [8]. Up to date the mechanical properties of these ribonucleic acid nanoclusters has not been studied in details.

Thermal stability of these nanoclusters is another issue of great importance. It is shown that the thermal stability of the proteins is increasing in presence of the sugar and polyols in aqueous solution [9]. The importance of such studies also follows from the fact that there can be a change in the molecular structure of the cell, cell membrane and the cell nucleus due to thermal effects. Based on the previous studies, in this paper we develop a discrete-to-continuum model for the analysis of mechanical and thermal properties of RNA nanoclusters. Studies on the mechanical properties have also been reported for soft materials such as collagen fabril protein and polymers [10, 11, 12, 13]. For carbon nanotubes (CNT), that have similar physical structures as RNA nanotubes, the atomistic to continuum modeling has been performed using the finite element method [14, 15] to calculate their elastic properties under stress.

The continuum and particle models of deoxy-ribonucleic acid (DNA) systems have been studied by using discrete base-pair results and approximating the properties for a continuum rod type model to analyze the mechanical properties [16]. The continuum model can also be used to study the protein-protein interaction and protein-nucleic acid interactions to understand the relative stability of A and B forms of deoxy-ribonucleic acids (DNA) [17, 18].

In what follows, we describe the development of a model to study the elastic properties of typical RNA nanoclusters and the effect of thermal change on them.

2 Theoretical Details

We consider the RNA nanotube as a cylindrical shell. This analogy is similar to the continuum approximations used for carbon nanotubes. Therefore, the application of the atomistic parameters of these systems in the development of continuum models can be done in a way similar to the CNT [14, 15]

At the molecular level of consideration, the energy of the entire system is due to the inter-atomic interaction of the atoms where the molecules perform a simple harmonic motion. Under this assumption the energy contribution from bond stretching, bond bending and dihedral angle torsion can be related to the energies of their equivalent continuum elements. From comparison we can relate the atomic parameters to the elastic parameters of the continuum model as follows,

$$V_r = \frac{1}{2}k_r(r - r_0)^2, \tag{1}$$

$$V_\theta = \frac{1}{2}k_\theta(\theta - \theta_0)^2, \tag{2}$$

and

$$V_\phi = \frac{1}{2}k_\phi(\phi - \phi_0)^2, \tag{3}$$

where k_r, k_θ and k_ϕ are the bond stretching, bond bending and the dihedral angle torsional force constant for the molecular system taken into consideration. In equations (1)-(3) r_0,

θ_0 and ϕ_0 are the distance, angle, and dihedral angle at equilibrium. In the continuum model, let us take a small element of the RNA nanotube of length L and diameter d. Suppose that ΔL, $\Delta\theta$, and $\Delta\phi$ are the stretch, bending and the torsional displacement in the cylindrical element of the tube. Now the corresponding types of energies in the continuum model for this cylindrical shell can be expressed based on the following arguments. Firstly, the energy due to the lateral stretching ΔL of the element of length L , with Young's modulus Y and cross-sectional area A, is given by

$$U_A = \frac{1}{2}\frac{YA}{L}(\Delta L)^2. \tag{4}$$

Next, to account for bending phenomena with moment of inertia I and with bending angle α, the expression for the elastic energy is given by

$$U_M = \frac{1}{2}\frac{YI}{L}(2\alpha)^2. \tag{5}$$

Finally, the energy corresponding to the rotational motion of the cylindrical element can be expressed as

$$U_T = \frac{1}{2}\frac{GJ}{L}(\Delta\beta)^2, \tag{6}$$

where $\Delta\beta$ is the twisting angle due to the elastic torsion, of the RNA nanotube, J is the angular momentum, and G is the shear modulus.

The above values for the energy terms, V_r, V_θ and V_ϕ are the bond stretching energy, bond bending energy and the torsional energies corresponding to the atomistic interactions coming from the harmonic motion of the atoms. These quantities are similar to the energy terms U_A, U_M and U_T derived for a finite element representation of the RNA nanotube under the continuum approximation. From comparison of the corresponding energies at these two kind of formulations we find that

$$\frac{YA}{L} = k_r, \qquad \frac{YI}{L} = k_\theta, \qquad \frac{GJ}{L} = k_\phi. \tag{7}$$

Using relations (7), the parameters of the atomistic scale can be used to determine the parameters to be built in into the continuum model. It is possible to calculate the quantities k_r, k_θ, and k_ϕ using the atomistic molecular dynamics simulation technique.

For most of the materials of interest, there is a linear relationship between the strain and stress. The components of the stress tensor in terms of the elastic coefficients and the stress tensor for the linear and isotropic continuum systems can be expressed as [19]

$$\begin{bmatrix}\sigma_{11}\\ \sigma_{22}\\ \sigma_{33}\\ \sigma_{23}\\ \sigma_{13}\\ \sigma_{12}\end{bmatrix} = \frac{Y}{(1+\nu)(1-2\nu)}\begin{bmatrix}1-\nu & \nu & \nu & 0 & 0 & 0\\ \nu & 1-\nu & \nu & 0 & 0 & 0\\ \nu & \nu & 1-\nu & 0 & 0 & 0\\ 0 & 0 & 0 & \frac{1-2\nu}{2} & 0 & 0\\ 0 & 0 & 0 & 0 & \frac{1-2\nu}{2} & 0\\ 0 & 0 & 0 & 0 & 0 & \frac{1-2\nu}{2}\end{bmatrix}\begin{bmatrix}\epsilon_{11}\\ \epsilon_{22}\\ \epsilon_{33}\\ 2\epsilon_{23}\\ 2\epsilon_{13}\\ 2\epsilon_{12}\end{bmatrix} + \frac{Y\alpha\Delta T}{(1-2\nu)}\begin{bmatrix}1\\ 1\\ 1\\ 0\\ 0\\ 0\end{bmatrix} \tag{8}$$

which in tensor form can be written as follows

$$\sigma_{ij} = \frac{Y}{(1+\nu)}\left(\epsilon_{ij} + \frac{\nu}{(1-2\nu)}\epsilon_{kk}\delta_{ij}\right) - \frac{Y\alpha\Delta T}{(1-2\nu)}\delta_{ij} \qquad i,j,k = 1,2,3, \tag{9}$$

where Y is Young's modulus, α is the coefficient of thermal expansion, ΔT is the increase in temperature of the system, and ν is the Poisson ratio, given by the relations

$$\nu = \frac{3K - 2\mu}{(3K + \mu)}. \tag{10}$$

The rate-dependent phenomena can be described for the biosystems such as RNA nanoclusters by introducing viscoelasticity terms. In the constitutive relation described above we can introduce the extra term of the stress that is proportional to the rate of change of the strain as

$$\sigma_{ij}^{v} = \eta\frac{\partial\epsilon_{ij}}{\partial t}, \tag{11}$$

where η is the coefficient of viscosity Therefore the general elastic constitutive equation including rate-dependent term can be expressed as,

$$\sigma_{ij} = \frac{Y}{(1+\nu)}\left(\epsilon_{ij} + \frac{\nu}{(1-2\nu)}\epsilon_{kk}\delta_{ij}\right) - \frac{Y\alpha\Delta T}{(1-2\nu)}\delta_{ij} + \eta\frac{\partial\epsilon_{ij}}{\partial t} \qquad i,j,k = 1,2,3. \tag{12}$$

In (12) the quantities K and μ are the bulk modulus and the shear modulus respectively. Under the underlined assumptions, for the systems like our RNA nanotube the steady state elastic equations can be expressed as

$$\sigma_{ij,j} = 0 \qquad i,j = 1,2,3. \tag{13}$$

with the Cauchy relationship connecting the displacement and strain:

$$u_{ik} = \frac{1}{2}\left(\frac{\partial u_i}{\partial x_k} + \frac{\partial u_k}{\partial x_i}\right) \qquad i,k = 1,2,3. \tag{14}$$

The strain-stress relationships are fully determined once the elastic parameters such as Poisson's ratio and the elastic moduli of the system are available. In our case we use the elastic moduli calculated from the atomistic modeling and the experimental techniques available in literature.

While in the general case (13) is augmented to account for time-dependency, in the current study we calculate the steady-state elastic properties and the thermal effect on them. In order to study the mechanical properties of the RNA nanoclusters in the presence of thermal effect, we have used the finite element method implemented via COMSOL multiphysics. The general partial differential equation representation has been used. We have used the Dirichlet boundary condition at one end of the tube and the Neumann boundary condition at the other end, i.e at z=40nm we set $n \cdot \sigma = 0$.

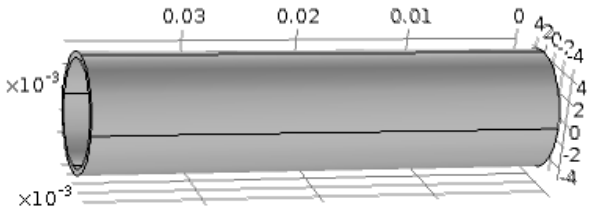

Figure 1: Approximated continuum geometry of the RNA nanotube as a hollow cylinder generated by using COMSOL

3 Results and Discussion

In our current study under the above assumptions, we study the RNA nanotube as a continuous system with the length and the radius equivalent to the size of the RNA nanocluster modeled using the atomistic molecular dynamics simulation. The continuum model of the RNA nanotube of the size 40nm with the 10 rings is presented in Figure 1. Here for calculations of the elastic properties of RNA nanotube, we use the finite element method. For these calculations we use the constitutive relations between strain and stress accounting for the thermal effect in the system. Poisson's ratio and Young's modulus for the nucleic acid system were 0.42 and 300 MPA i.e $3 * 10^8$ PA respectively. They were taken from the literature and obtained by using experimental and atomistic calculations [20]. The results for the displacement field at different positions for the entire volume of the RNA nanotube of size equivalent to 10 rings, i.e 40 nm in length, obtained by using the finite element method at 10 degree and 100 degree K are presented in Figure 2. Corresponding displacements of the points along a line in the direction of the axis of the 10 ring RNA nanotube at these two temperatures are presented in Figure 3. Since the values for the thermal expansion coefficient are not yet available for the bionanosystems like RNA nanoclusters, we have used the average value of the coefficient calculated for the protein system using the molecular dynamics simulation for a wide range of its densities [21]. From our results for the displacement along the RNA nanotube, it is clear that the displacement is increasing as the temperature is increased. During calculation of the displacement field, due to stress and thermal effects in the RNA nanotube, we have fixed one end by Dirichlet boundary condition and on the other end a force via Neumann's boundary condition has been applied. From the obtained results it is clear that there is an increase in the displacement as the temperature is increases.

4 Conclusions and Outlook

We have studied the elastic properties and the effect of thermal changes on them in earlier developed RNA nanotubes by using the finite element method. We have also studied the effect of stress as a function of the temperature change along the entire volume of the RNA nanotube. For calculating these properties of RNA nanoclusters we have used

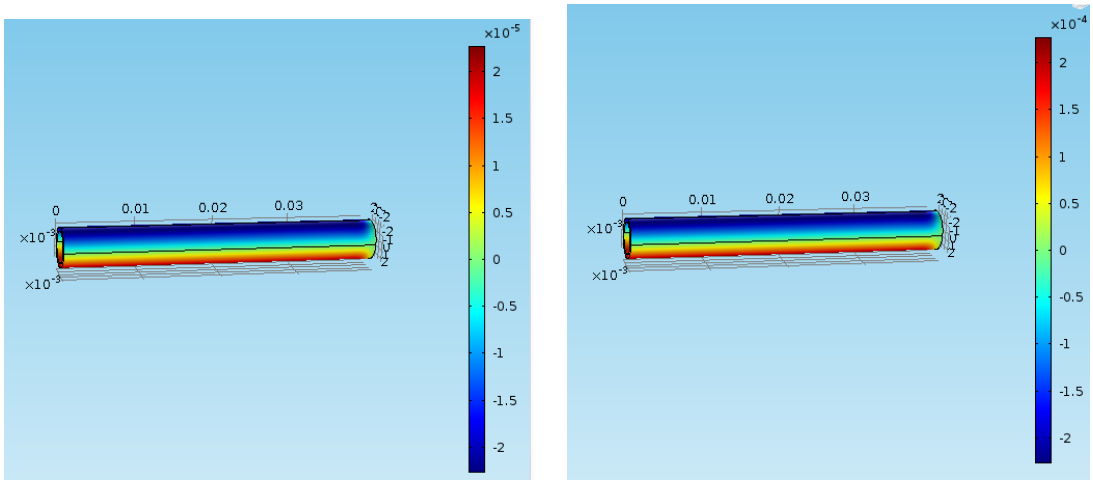

(a) (b)

Figure 2: Distribution of the displacement at different points along 10 ring RNA nanotube at (a) 10 K and (b) 100K using finite element method.

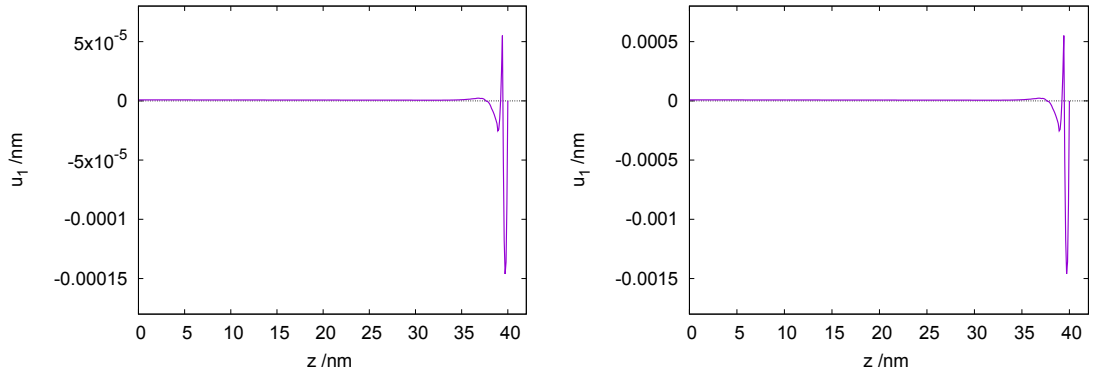

(a) (b)

Figure 3: Displacement along the line in the direction of the axis of the 10 ring RNA nanotube at (a) 10 K and (b) 100K using finite element method.

a cylindrical shell representation of the size equivalent to the size of the RNA nanocluster. The elastic and thermal coefficients have been taken from the literature and calculated for the nucleic acid molecules and the protein systems. The experimental results of such physical quantities are not yet available and we expect that our computational studies will motivate experimentalists to shed new light on underlying problems for RNA nanoclusters.

5 ACKNOWLEDGMENTS

Authors are grateful to the NSERC and CRC Program for their support and Shared Hierarchical Academic Research Computing Network (SHARCNET: www.sharcnet.ca) for providing the computational facilities. Finally, we would like to thank Dr. P. J. Douglas Roberts for helping with technical SHARCNET computational aspects.

REFERENCES

[1] P. Guo, "RNA nanotechnology: Engineering, assembly and applications in detection, gene delivery and therapy," *J. Nanosci. Nanotechnol.*, vol. 5, no. 12, pp. 1964–1982, Dec. 2005.

[2] A. Vaziri and A. Gopinath, "Cell and biomolecular mechanics in silico," *Nature Materials*, vol. 7, no. 1, pp. 15–23, Jan. 2008.

[3] E. Osada, Y. Suzuki, K. Hidaka, H. Ohno, H. Sugiyama, M. Endo, and H. Saito, "Engineering RNAprotein complexes with different shapes for imaging and therapeutic applications," *ACS Nano*, vol. 8, no. 8, pp. 8130–8140, Aug. 2014.

[4] S. Badu, R. Melnik, and S. Prabhakar, "RNA Nanostructures in Physiological Solutions: Multiscale Modeling and Applications," in *Physics of Liquid Matter: Modern Problems*. Springer, Cham, 2015, pp. 337–355.

[5] Y. G. Yingling and B. A. Shapiro, "Computational design of an RNA hexagonal nanoring and an RNA nanotube," *Nano Lett.*, vol. 7, no. 8, pp. 2328–2334, Aug. 2007.

[6] S. R. Badu, R. Melnik, M. Paliy, S. Prabhakar, A. Sebetci, and B. A. Shapiro, "Modeling of RNA nanotubes using molecular dynamics simulation," *Eur Biophys J*, vol. 43, no. 10-11, pp. 555–564, Nov. 2014.

[7] M. Paliy, R. Melnik, and B. A. Shapiro, "Molecular dynamics study of the RNA ring nanostructure: a phenomenon of self-stabilization," *Phys. Biol.*, vol. 6, no. 4, p. 046003, Dec. 2009.

[8] A. J. Lee and D. M. Crothers, "The solution structure of an RNA looploop complex: the ColE1 inverted loop sequence," *Structure*, vol. 6, no. 8, pp. 993–1007, Aug. 1998.

[9] J. K. Kaushik and R. Bhat, "Thermal Stability of Proteins in Aqueous Polyol Solutions: Role of the Surface Tension of Water in the Stabilizing Effect of Polyols," *The Journal of Physical Chemistry B*, vol. 102, no. 36, pp. 7058–7066, Sep. 1998.

[10] M. J. Buehler, "Nanomechanics of collagen fibrils under varying cross-link densities: Atomistic and continuum studies," *Journal of the Mechanical Behavior of Biomedical Materials*, vol. 1, no. 1, pp. 59–67, Jan. 2008.

[11] B. Depalle, Z. Qin, S. J. Shefelbine, and M. J. Buehler, "Influence of cross-link structure, density and mechanical properties in the mesoscale deformation mechanisms of collagen fibrils," *Journal of the Mechanical Behavior of Biomedical Materials*, vol. 52, pp. 1–13, Dec. 2015.

[12] T. Odijk, "Elastic constants of nematic solutions of rod-like and semi-flexible polymers," *Liquid Crystals*, vol. 1, no. 6, pp. 553–559, Nov. 1986.

[13] K. Tashiro, M. Kobayashi, and H. Tadokoro, "Calculation of Three-Dimensional Elastic Constants of Polymer Crystals. 1. Method of Calculation," *Macromolecules*, vol. 11, no. 5, pp. 908–913, Sep. 1978.

[14] H.-C. Cheng, Y.-L. Liu, Y.-C. Hsu, and W.-H. Chen, "Atomistic-continuum modeling for mechanical properties of single-walled carbon nanotubes," *International Journal of Solids and Structures*, vol. 46, no. 78, pp. 1695–1704, Apr. 2009.

[15] K. I. Tserpes and P. Papanikos, "Finite element modeling of single-walled carbon nanotubes," *Composites Part B: Engineering*, vol. 36, no. 5, pp. 468–477, Jul. 2005.

[16] R. S. Manning, J. H. Maddocks, and J. D. Kahn, "A continuum rod model of sequencedependent DNA structure," *The Journal of Chemical Physics*, vol. 105, no. 13, pp. 5626–5646, Oct. 1996.

[17] P. A. Kollman, I. Massova, C. Reyes, B. Kuhn, S. Huo, L. Chong, M. Lee, T. Lee, Y. Duan, W. Wang, O. Donini, P. Cieplak, J. Srinivasan, D. A. Case, and T. E. Cheatham, "Calculating Structures and Free Energies of Complex Molecules: Combining Molecular Mechanics and Continuum Models," *Acc. Chem. Res.*, vol. 33, no. 12, pp. 889–897, Dec. 2000.

[18] J. Srinivasan, T. E. Cheatham, P. Cieplak, P. A. Kollman, and D. A. Case, "Continuum Solvent Studies of the Stability of DNA, RNA, and PhosphoramidateDNA Helices," *J. Am. Chem. Soc.*, vol. 120, no. 37, pp. 9401–9409, Sep. 1998.

[19] A. F. Bower, *Applied Mechanics of Solids*. Boca Raton: CRC Press, 2010.

[20] J. F. Marko and S. Cocco, "The micromechanics of DNA," *Physics World*, vol. 16, no. 3, p. 37, 2003.

[21] M. Hutt, T. Kulschewski, and J. Pleiss, "Molecular modelling of the mass density of single proteins," *Journal of Biomolecular Structure and Dynamics*, vol. 30, no. 3, pp. 318–327, Jul. 2012.

VII International Conference on Computational Methods for Coupled Problems in Science and Engineering
COUPLED PROBLEMS 2017
M. Papadrakakis, E. Oñate and B. Schrefler (Eds)

DESIGN AND DEVELOPMENT OF A MAGNETICALLY-DRIVEN VENTRICULAR ASSIST DEVICE (MVAD): IN VITRO IMPLEMENTATION IN THE FONTAN CIRCULATION

ARKA DAS*, ANTHONY M. KHOURY*, JANSYN K. JOHNSTON*, CHRISTOPHER J. ADAMS*, KRISTIN SVERRISDOTTIR*, FORAM MADIYAR*, EDUARDO DIVO*, ANTHONY NUNEZ§ AND ALAIN KASSAB†

* Department of Mechanical Engineering
Embry-Riddle Aeronautical University
600 S. Clyde Morris Blvd. Daytona Beach, FL 32114, USA
email: divoe@erau.edu, web page: http://daytona.erau.edu

§ Thoracic & Cardiac Surgery
Osceola Regional Medical Center
700 West Oak St. Kissimmee, FL 34741, USA
email: anthony.nunez@cardiovox.net, web page: http://cardiacsurgicalosceola.com/

† Department of Mechanical and Aerospace Engineering
University of Central Florida
4000 Central Florida Blvd. Orlando, FL 32816, USA
e-mail: kassab@ucf.edu, web page: http://www.ucf.edu

Key words: Instructions, Coupled Problems, Multiphysics Problems, Applications, Computing Methods.

Abstract. A rapidly testable novel Magnetically-Driven Ventricular Assist Device (MVAD) with no moving parts that can be used to provide assistance to the cardiovascular circulation while reducing caval pressure in patients who have undergone the Fontan procedure to palliate the Hypoplastic Left Heart Syndrome (HLHS) is proposed and studied. A benchtop Mock Flow Loop (MFL) of the cardiovascular circulation with a Fontan total cavopulmonary connection (TCPC) is configured to validate this hypothesis. The MFL is based on a Lumped-Parameter Model (LPM) comprised of upper and lower systemic circulation as well as left and right pulmonary circulation compartments. Needle valves are used to accurately replicate vascular resistance (R) while compliance chambers are used to mimic vascular compliance (C). The MFL centerpiece is the truncated aortic arch with an implanted MVAD. A ferro-fluid solution is mixed in water to simulate magnetically-charged blood. The pulsating flow is induced by drawing the ferro-fluid from a main reservoir with a Harvard Apparatus Medical pump while the MVAD provides assistive momentum to the TCPC. Flow and pressure sensor data at specific points in the MFL are acquired via a National Instruments multichannel data acquisition board and processed using LabView. Different prototypes of the MVAD are tested to validate the hypothesis.

1 INTRODUCTION

Around 8% of all newborns with a Congenital Heart Defect (CHD) have a single functioning ventricle. This condition is known as the Hypoplastic Left Heart Syndrome (HLHS) where the malformation of the left ventricle renders it minimally or non-functional and therefore the right ventricle is overloaded as it pumps both oxygenated and deoxygenated blood to parallel pulmonary and systemic circulations. As a result, research has been conducted towards the reduction of the load from the single ventricle. This can be achieved by establishing a connection between the systemic and pulmonary circulation resulting in a single univentricular pump powering the entire circuit, [1].

1.1 Palliative Procedure

A surgery is performed in three sequential stages to mitigate the flow pattern of HLHS:

Stage 1: Norwood
Stage 2: Glenn/Hemi-Fontan
Stage 3: Fontan

The Fontan operation has served as the 3rd stage palliation for this anomaly for decades but the surgery entails multiple complications and survival rate is less than 50% by adulthood. In this procedure, the Inferior Vena Cava (IVC) is disconnected from the right atrium and connected directly to the pulmonary arteries for a Total Cavopulmonary Connection (TCPC), [1]. This results in total passive drainage of the caval blood flow to the pulmonary circulation and therefore relieving the single ventricle from pumping blood to the pulmonary circulation.

1.2 Post-Fontan Paradox

The Fontan procedure often leads to multiple complications and survival rate of patients is of less than 50% by adulthood. The circulatory pattern of the patient can fail, even in patients with relatively good ventricular function. Pharmacological therapies have variable success and the probability of successful outcome with heart transplantation is low, [2,3].

1.3 Hypothesis

A novel alternative is proposed by creating a Magnetically-driven Ventricular Assist Device (MVAD) with no moving parts that can be used to provide assistance to the cardiovascular circulation while reducing the caval pressure. A bench top Mock Flow Loop (MFL) of the cardiovascular circulation with a Fontan TCPC coupled with the MVAD is configured to validate this hypothesis.

2 GOVERNING EQUATIONS

A ferro-hydrodynamic (FHD) model, based on the Navier-Stokes equation, to estimate the average ferro-flow velocity is developed. This model considers effective viscosity, magnetic flux density and volumetric concentration of the ferrous particles in the fluid. In this section,

the governing equations to model the coupled problem provided by the fluid and the magnetic domain are discussed.

2.1 Fluid Flow Equations

The velocity field u of the fluid domain is governed by the Navier-Stokes equations such that,

$$\rho\left(\frac{\partial u}{\partial t} + u.\nabla u\right) = -\nabla p + \boldsymbol{F} + \mu(\nabla^2 u) \tag{1}$$

Where $\boldsymbol{F}$ is the Volumetric Body Force exerted on the fluid. In the case of this experiment, the MVAD produces this body force as a result of the magnetic field acting on the ferrous nanoparticles.

2.2 Magnetic Force Equations

The magnetic force can be calculated such that,

$$\boldsymbol{F} = (m \cdot \nabla)\boldsymbol{B} \tag{2}$$

Where **m** is the magnetic dipole moment and **B** is the magnetic flux density provided by the inductance of the electromagnetic coil. The magnetic flux density is directly proportional to magnetic intensity with permeability constant, μ, for a particular medium, where,

$$\boldsymbol{B} = \mu H \tag{3}$$

In this case, the working domain for the electromagnet is air, which has a permeability constant of 1.00000037. The following Maxwell field equations are used to quantify the magnetization effect of the developed electromagnet prototype:

$$\nabla \cdot \boldsymbol{B} = 0 \tag{4}$$

$$\nabla \times \boldsymbol{B} = \mu J + \mu\varepsilon\frac{\partial E}{\partial t} \tag{5}$$

$$\nabla \cdot \boldsymbol{E} = \rho/\varepsilon \tag{6}$$

$$\nabla \times \boldsymbol{B} = -\frac{\partial B}{\partial t} \tag{7}$$

Equations (4) and (5) are known as magnetostatics equations and equations (6) and (7) are known as electrostatics equations. By using the Helmoltz theorem, it is known that **B** is an irrotational vector which can be expressed as,

$$\boldsymbol{B} = -\mu\nabla\varphi \tag{8}$$

Where φ is known as the magnetic scalar potential. The material property of the developed electromagnet depends on the magnetic moment, **m**. The magnetic susceptibility of a material within a magnetic field determines the tendency of the material to form a magnetic dipole. The magnetic susceptibility of iron is $3x10^4$. Hence, the magnetic flux density can be rewritten as,

$$\boldsymbol{B} = \mu(1 + X)\mathrm{H} \tag{9}$$

The magnetization vector **M** which determines the net magnetic dipole of the material can be calculated as,

$$J = \nabla \times \boldsymbol{M} \tag{10}$$

Hence, the magnetization vector can be defined as,

$$M = X\boldsymbol{H} \tag{11}$$

Therefore, by using the above equations, one may obtain the magnetic flux density provided by the electromagnet as,

$$\boldsymbol{B} = \mu\boldsymbol{H} + \boldsymbol{B_{rem}} \tag{12}$$

Where B_{rem} is the remnant flux density.

3 COMPUTATONAL FLUID DYNAMICS

An axisymmetric model of the magnetic inductor used to propel the ferro-fluid within the flow field is developed using COMSOL Multiphysics® Modeling Software. The geometry consists of four different domains with distinctly selected material properties. To represent the accurate mixture of the working fluid which constitutes the water as the main carrier fluid and ferro-fluid as the dispersed phase fluid in the water medium the "Mixture mode" is selected in the software. Through this mode, the volume fraction and velocity of the two fluids of different phases can be controlled by tuning the velocity components *u* and *v,* the pressure *p*, and volume fraction, Φ. This model relies on the following equation to solve for the output.

$$\rho\left(\frac{\partial \boldsymbol{u}}{\partial t}\right) + \rho(\boldsymbol{u}\cdot\nabla)\boldsymbol{u} = -\nabla p - \nabla\cdot\left(\frac{p\Phi_d\rho_d}{\rho\left(1-\frac{\Phi_d\rho_d}{\rho}\right)}\right)\boldsymbol{u}_{slip}\boldsymbol{u}_{slip} + \nabla\cdot(\eta[\nabla\boldsymbol{u} + \nabla\boldsymbol{u}^{\boldsymbol{T}}]) + \rho g + \boldsymbol{F} \tag{13}$$

Where ρ is the mixture density, η is the dynamic viscosity, and *p* is the mixture pressure. In this experiment, the force **F** is coupled with the magnetic force provided by the electromagnets. Hence, this volumetric body force is the resultant of two components that are calculated in the "Magnetostatics" module of the software using the following equations:

$$F_{tx} = \Phi_d\left[\left(M_x\frac{\partial^2 A_z}{\partial x^2} + M_y\frac{\partial^2 A_z}{\partial x\partial y}\right) + \frac{X}{\mu_o}\left(\frac{\partial A_z}{\partial x}\frac{\partial^2 A_z}{\partial x^2} + \frac{\partial A_z}{\partial y}\frac{\partial^2 A_z}{\partial x\partial y}\right)\right] \tag{14}$$

$$F_{ty} = \Phi_d\left[\left(M_x\frac{\partial^2 A_z}{\partial x\partial y} + M_y\frac{\partial^2 A_z}{\partial y^2}\right) + \frac{X}{\mu_o}\left(\frac{\partial A_z}{\partial x}\frac{\partial^2 A_z}{\partial x\partial y} + \frac{\partial A_z}{\partial y}\frac{\partial^2 A_z}{\partial y^2}\right)\right] \tag{15}$$

Where A_z is the magnetic potential.

4 EXPERIMENTAL SETUP

4.1 Benchtop Model

A benchtop Mock Flow Loop (MFL) is designed to resemble the cardiovascular system of the target population for the palliative procedure, using a Lumped-Parameter Model (LPM) of the Fontan circulation anatomy with four branches, or lumps. These lumps represent the upper and lower systemic circulations as well as the left and right pulmonary circulations. Each lump is comprised of an area-reducing needle valve and a flow accumulator to model vascular resistivity and vascular compliance respectively. The MFL is driven by a Harvard Apparatus pulsatile pump.

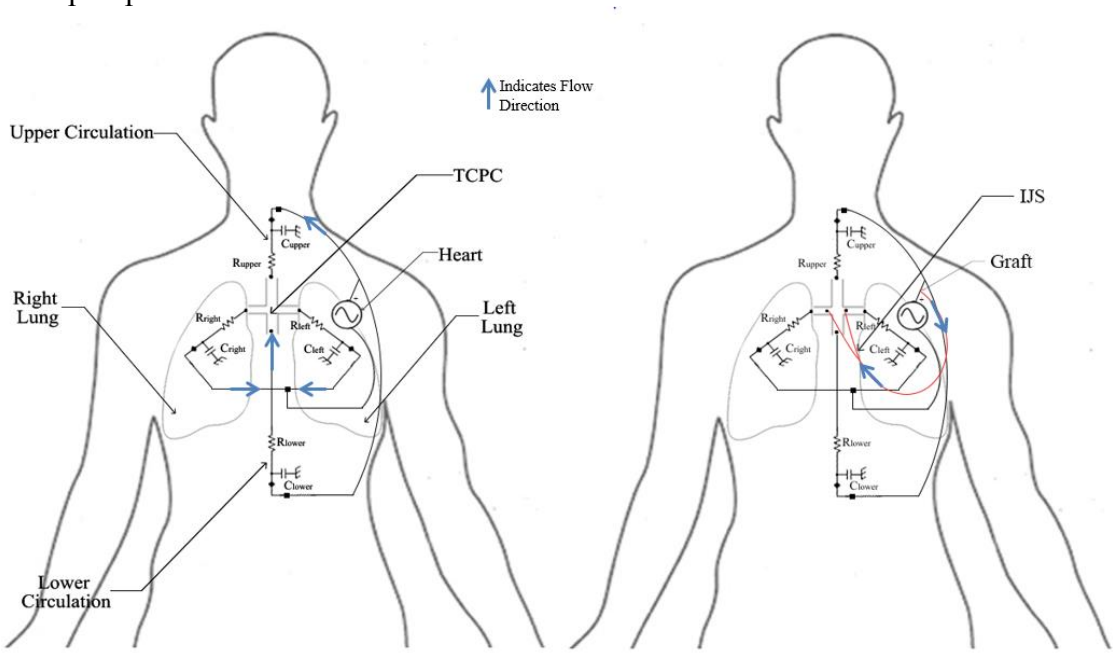

Figure 1: Lumped Parameter Model of the Body

It is important to note that the MFL is not an artificial equivalent of patient anatomy but rather represents an observable analogy of the anatomy, producing flow behavior that is physiologically relevant and accurate.

4.2 Dimensional Analysis

As the MFL will be operated using water instead of blood, it is important to match non-dimensional parameters to ensure physiologically relevant behavior. These non-dimensional parameters include the Womersley number, denoted α, and the Reynolds number, denoted Re. These non-dimensional parameters are matched by adjusting the Harvard Pump settings based on the MFL geometry. This process is described in [3].

4.3 Ferro-fluid

A Ferro-fluid is produced using an appropriate ratio of Ferrous Chloride ($FeCl_2^-$) and Ferric Chloride ($FeCl_3$) solutions mixed together in a base solution of ammonia (NH_3). The solution

is kept at a steady temperature of around 50 degrees Celsius by resting on a hot plate under constant homogenization. Oleic Acid is used as a surfactant to inhibit clumping. The solution is centrifuged to eliminate ammonium hydroxide and to segregate the magnetite particles. The excess liquid is then replaced with Polyethylene Glycol (PEG). The diameter of the ferro-fluid particles is determined by placing a sample of the solution onto a silicon wafer for an examination in a Scanning Electron Microscope (SEM). The ferro-fluid sample is sputter coated with gold particles. For further investigation, the sample was put under a localized Energy-dispersive X-ray spectroscopy (EDX).

4.4 Magnetically-driven Ventricular Assist Device (MVAD)

According to equations (1) and (2), it can be seen that in order to maximize the acceleration of the fluid, one must maximize the magnetic flux density, or gauss (G) affecting the ferro-fluid. Additionally, it is imperative to minimize any obstruction of the flow due to the structure of the MVAD. To do so, the MVAD is essentially constructed by winding magnet wire around a hollow cylinder, which will be seated around the flow field, similar in fashion to an arterial stent. In the experimental development of the MVAD, several designs were considered with respect to core materials and winding configuration and then tested using a Gaussmeter. In all cases, 28 AWG copper wire was used.

5 RESULTS

The results of the prescribed experimentation are summarized as follows.

5.1 Ferro-fluid

The average diameter of the particles is 147 nm (see Fig. 3).

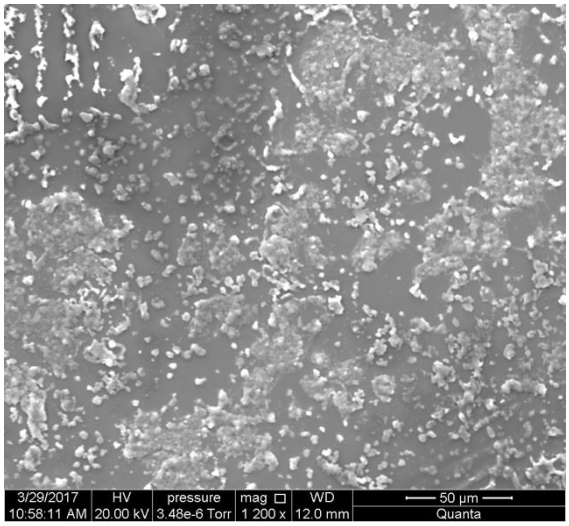

Figure 2: Sample under SEM with Quanta of 50 µm and magnification factor of 1200

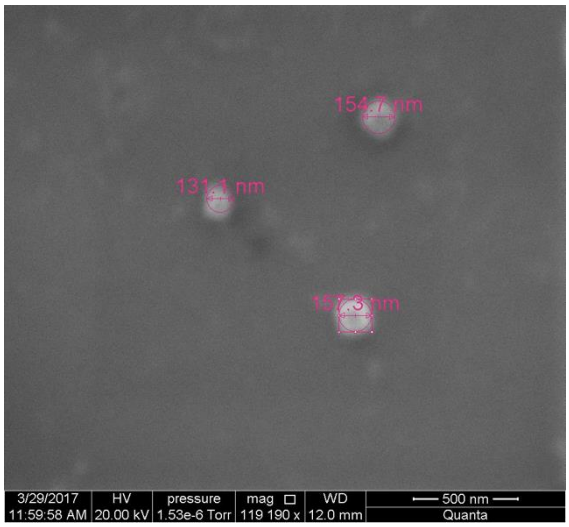

Figure 3: Nanoparticles under SEM with magnification factor of 119190

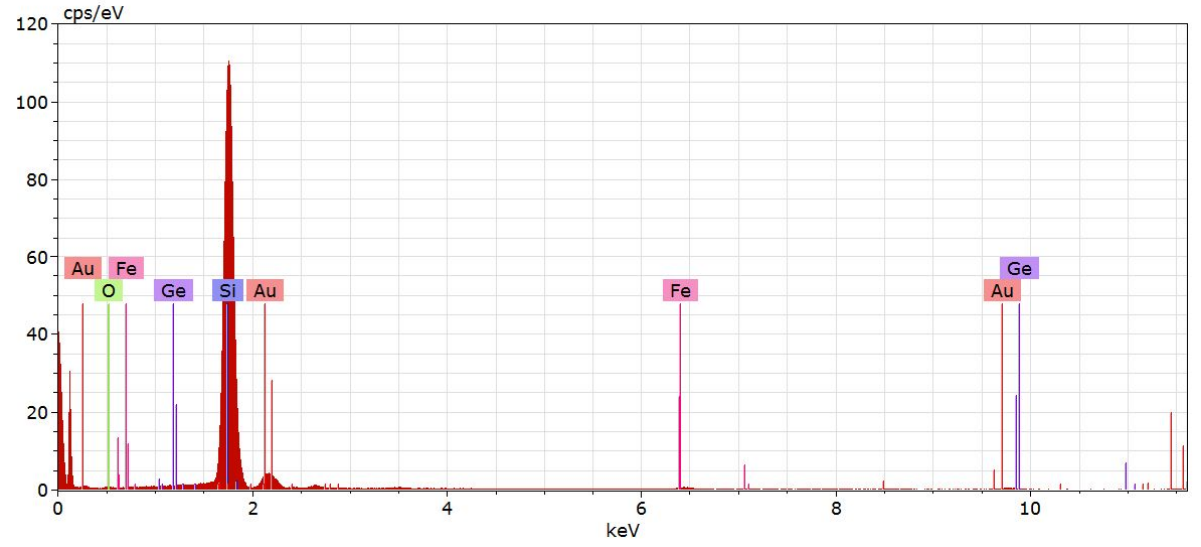

Figure 4: Distribution of elements present in EDX sample along with their energy levels

Table 1: Elements present in EDX sample and respective normalized weights

Element	Atomic Number	Normalized Weight (%)
Silicon	14	82.4
Gold	79	9.6
Oxygen	8	3.3
Germanium	32	2.8
Iron	26	2.0

It can be seen in Fig. 4 that the sample contains iron (Fe) particles at two different energy levels, (K_α and L_α) along with germanium (Ge) and other chemicals in small amounts. The gold (Au) detected in the EDX sample is a result of the sputter coating of the particles. Also, the silicon (Si) results from the silicon wafer on which the specimen is placed.

5.2 Magnetically-driven Ventricular Assist Device (MVAD)

Important observations were made on the subject of electromagnet core materials and winding configuration. Two materials were tested for suitability as the annular base material around which the electromagnet will be wrapped. The first, a steel pipe representative of ferrous based cores. The second, a PVC pipe used to observe non-ferrous core behavior.

Rather counter-intuitively, ferrous based cores proved ill-suited to this application. The ferrous core behaved as a sort of Faraday cage, absorbing the magnetic field generated by the inductive coil. This produced a large magnetic flux density within the bounds of ferrous material itself, but reduced the measureable Gauss present at the center of the annulus, the domain through which the fluid would flow. Due to this, a non-ferrous material is used in the construction of the MVAD core.

It was observed that a singular winding does generate sufficient magnetic flux density to appreciably accelerate the ferro-fluid. Therefore, several variations in wire wrapping, utilizing multiple strands of wire were tested. It was determined that by wrapping several layers of coils, each layer wrapped around the previous layer with wires in parallel circuits to another, one could achieve higher Gauss ratings within the fluid domain at lower power requirements.

Finally, to prevent suspension of the ferrous particles within the magnetic field, several sets of coils are placed along the length of the test section and are sequentially activated to propel the flow.

6 CONCLUSIONS

A Magnetically-Driven Ventricular Assist Device (MVAD) to provide assistance to the cardiovascular circulation while reducing the caval pressure is implemented in computational and benchtop experiments. A benchtop Mock Flow Loop (MFL) of the cardiovascular circulation with a Fontan total cavopulmonary connection (TCPC) is configured. A ferro-fluid solution is mixed in water to simulate magnetically-charged blood. The average ferro-fluid particle diameter produced is approximately 150 nm rendering it suitable for this application as it allows the particles to separate under the presence of an external magnetic field. The pulsating flow is induced by drawing the ferro-fluid from a main reservoir with a Harvard Apparatus Medical pump while the MVAD provides assistive momentum to the TCPC. A functioning MVAD prototype is implemented resulting in observable acceleration of the ferro-fluid. While the MVAD is operable and the non-ferrous core is advantageous to this application, further development must ensue due to the inability of thermoplastics to operate in close proximity to the heat dissipated by the current carrying wire.

REFERENCES

[1] Fontan, F., and E. Baudet. "Surgical repair of tricuspid atresia." *Thorax* 26.3 (1971): 240-248.

[2] Vukicevic M., Chiulli J.A., Conover T., Pennati G., Hsia T.Y., Figliola R.S. "Mock circulatory system of the Fontan circulation to study respiration effects on venous flow behavior." *ASAIO Journal (American Society for Artificial Internal Organs: 1992)* 59.3 (2013): 253

[3] Das A., Khoury A., Tibbets J., Ni M., Divo E., Kassab A., DeCampli W. "Laboratory Development of a Self-Powered FONTAN for Treatment of Congenital Heart Disease." *Proceedings of the 2nd Thermal and Fluid Engineering Conference: (2017)*

VII International Conference on Computational Methods for Coupled Problems in Science and Engineering
COUPLED PROBLEMS 2017
M. Papadrakakis, E. Oñate and B. Schrefler (Eds)

A MONOLITHIC APPROACH FOR THE INCOMPRESSIBLE MAGNETOHYDRODYNAMICS EQUATIONS

KAYHAN ATA AND MEHMET SAHIN[†]

[†] Astronautical Engineering Department, Faculty of Aeronautics and Astronautics
Istanbul Technical University, 34469, Maslak/Isatanbul, TURKEY
e-mail:msahin.ae00@gtalumni.org , web page: http://web.itu.edu.tr/ msahin/

Key words: Incompressible magnetohydrodynamics, semi-staggered finite volume method, monolithic, lid-driven cavity, backward facing step

Abstract. A numerical algorithm has been developed to solve the incompressible magnetohydrodynamics (MHD) equations in a fully coupled form. The numerical approach is based on the side centered finite volume approximation where the velocity and magnetic filed vector components are defined at the center of edges/faces, meanwhile the pressure term is defined at the element centroid. In order to enforce a divergence free magnetic field, a magnetic pressure is introduced to the induction equation. The resulting large-scale algebraic linear equations are solved using a one-level restricted additive Schwarz preconditioner with a block-incomplete factorization within each partitioned sub-domains. The parallel implementation of the present fully coupled unstructured MHD solver is based on the PETSc library for improving the efficiency of the parallel algorithm. The numerical algorithm is validated for 2D lid-driven cavity flows and backward step problems for both conducting and insulating walls.

1 INTRODUCTION

Magnetohydrodynamics (MHD) deals with the interaction between magnetic fields and the fluid flow. The fluid has to be electrically conducting and non-magnetic in order to interact with the magnetic field. The examples of such fluids are liquid metals, hot or cold plasmas and strong electrolytes. The interaction is a result of Ampere's and Faraday's law and also the Lorentz force is involved in the process. First, the relative motion of the fluid and the magnetic field creates an electromotor force (emf) and electrical currents are induced. Then, these currents induce a secondary magnetic field. Finally, the combined magnetic fields interacts with the induced current density and creates the Lorentz force. Magnetohydrodynamics is important for many applications in engineering and scientific phenomenon such as sunspots, solar flares, interaction between solar winds and Earth's magnetosphere, controlled thermofusion, propulsion, electromagnetic pumps, control of liquid metals, etc. [1, 2].

The mathematical description of incompressible MHD flow includes conservation of mass, conservation of momentum, magnetic induction equation and the divergence-free condition of the magnetic field. The coupled system of MHD equations can be solved using two different coupling strategies. The first one is partitioned (staggered) methods which the equations for fluid and magnetic field are solved separately. The other category is the fully coupled (monolithic) methods. In monolithic approaches the equations for both fields are discretized and solved simultaneously. Staggered approaches provide the freedom to choose optimized solvers for each unknown field. But their convergence rate are slow for fixed point (Picard) iterations and they may diverge for strong interactions (i.e Hartman number greater than unity). The advantage of the monolithic approaches is their robustness but this also leads to computational expense because they require the solution of large systems of coupled non-linear equations. The comparison of both methods can be found in [3].

One of the first numerical studies on magnetohydrodynamics is done by Singh and Lal [4] by solving steady MHD flow in a triangular channel with non-conducting walls by finite difference method for different Hartmann numbers. In 1984, they also employed a finite element formulation with triangular elements for unsteady MHD flow in channels with arbitrary wall conductivity and different Hartmann numbers [5]. Gerbeau [6] employed a stabilized finite element method to solve incompressible MHD equations in two dimensions by using Streamline Upwind Petrov Galerkin (SUPG) method for stabilization. Ni and Li [7] developed a consistent conservative scheme for calculation of the current density and the Lorentz force. They apply the consistent projection method to get the velocity and pressure at time level $n+1$ from the known parameters at time level n on a rectangular staggered mesh and for collocated mesh. Badia et al. [8] proposed a finite element formulation with segregating the velocity and magnetic field for incompressible MHD flow. Shadid et al. [9] proposed a scalable implicit and fully coupled solver for incompressible resistive MHD with stabilized unstructured finite element and Newton-Krylov-AMG. Lin et al. [10] investigated the performance of a fully coupled algebraic multilevel preconditioner for Newton-Krylov solution methods and the performance of the preconditioner is demonstrated for several multiphysics problems including MHD. Cyr et al. [11] proposed and investigated the performance of several candidate block preconditioners for MHD system. Using previously developed preconditioners for Navier-Stokes, and an initial Schur-complement approximation for the magnetic and velocity fields, they showed that the splitting the preconditioner is scalable and competitive with other preconditioners, including a fully coupled algebraic multigrid method. Phillips et al. [12] developed a block conditioner for the finite element discretization of exact penalty formulation of steady fully-coupled MHD in two-dimensions. They employed two types of block preconditioners, one is based on the approximation of Schur compliment and the other one is based on the Newton's method. Adler et al. [13] employed a mixed finite-element discretization of a viscoresistive MHD model with a geometric multigrid preconditioner (monolithic approach).

One of the problems in the solution of MHD equations is to satisfy the divergence-free condition of magnetic field. Severeal methods have been proposed to overcome this problem; adding a diffusion term in the magnetic induction equation [14], constraint transport method [15], using magnetic vector potential formulation, projection method that solves a Poisson equation, staggered grid technique, parabolic divergence cleaning method [16].

In the present work, a numerical method based on the side centered finite volume approximation, where the velocity and magnetic filed vector components are defined at the center of edges/faces, meanwhile the pressure term is defined at the element centroid, is developed to solve incompressible MHD equations in a fully-coupled form. In order to solve the overdetermined system, a magnetic pressure is defined at the cell center and the gradient of this pressure is added to the magnetic induction equation with certain boundary conditions as described in [17], that will lead that pressure to be zero all over the domain while satisfying divergence-free condition of magnetic field. The resulting algebraic system is solved using a one-level restricted additive Schwarz preconditioner with a block-incomplete factorization within each partitioned sub-domains.

2 MATHEMATICAL AND NUMERICAL FORMULATION

The conservation forms of the governing equations for incompressible magnetohydrodynamics (MHD) flow are as follows:

$$\rho\frac{\partial \mathbf{u}}{\partial t}+\nabla\cdot\left[\rho\mathbf{u}\otimes\mathbf{u}-\frac{\mathbf{B}\otimes\mathbf{B}}{\mu_m}+\left(p+\frac{B^2}{2\mu_m}\right)\mathbf{I}-\mathbf{T}\right] = 0 \tag{1}$$

$$\frac{\partial \mathbf{B}}{\partial t}-\frac{1}{\mu_m\sigma}\nabla^2\mathbf{B}+\nabla\cdot[-\mathbf{u}\otimes\mathbf{B}+\mathbf{B}\otimes\mathbf{u}] = 0 \tag{2}$$

These equations can be non-dimensionalized as follows using $\mathbf{u}=\mathbf{u}^*U$, $\mathbf{x}=\mathbf{x}^*L$, $t=t^*L/U$, $p=p^*\rho U^2$ and $\mathbf{B}=\mathbf{B}^*B_0$

$$Re\frac{\partial \mathbf{u}}{\partial t}+\nabla\cdot\left[Re\mathbf{u}\otimes\mathbf{u}-SRe\mathbf{B}\otimes\mathbf{B}+\left(p+SRe\frac{B^2}{2}\right)\mathbf{I}-\mathbf{T}\right]=0 \tag{3}$$

$$Re_m\frac{\partial \mathbf{B}}{\partial t}-\nabla^2\mathbf{B}+Re_m\nabla\cdot[-\mathbf{u}\otimes\mathbf{B}+\mathbf{B}\otimes\mathbf{u}]=0 \tag{4}$$

where Re is Reynolds number, Re_m is magnetic Reynolds number and S is the coupling number

$$Re=\frac{\rho UL}{\mu_f},\quad Re_m=\mu_m\sigma UL,\quad S=\frac{B^2}{\rho\mu_m U^2}$$

where $\mathbf{u}$ is the velocity vector, $\mathbf{B}$ is the magnetic field, $\mathbf{T}$ is the fluid stress tensor, $\mathbf{I}$ is identity matrix, ρ is the fluid density, p is the pressure, σ is the electrical conductivity, μ_m is the magnetic permeability and μ_f is the dynamic viscosity of the fluid.

In order to satisfy the solenoidal property of magnetic field, the gradient of a Lagrange multiplier q introduced to the magnetic induction equation as proposed in [17]. q leads to zero over all the domain therefore becomes a dummy variable by applying proper boundary conditions. Therefore the integral form of incompressible MHD equations that govern the viscous fluid flow of a control volume Ω with boundary $\partial\Omega$ can be written in Cartesian coordinate system in dimensionless form as follows:

$$-\oint_{\partial\Omega_e} \mathbf{n}\cdot\mathbf{u}dS = 0 \tag{5}$$

Momentum equation:

$$\begin{aligned} Re\int_{\Omega_d}\frac{\partial\mathbf{u}}{\partial t}dV + Re\oint_{\partial\Omega_d}[\mathbf{n}\cdot\mathbf{u}]\mathbf{u}dS + \oint_{\partial\Omega_d}\mathbf{n}PdS \\ -\oint_{\partial\Omega_d}\mathbf{n}\cdot\nabla\mathbf{u}dS - \frac{SRe}{Re_m}\oint_{\partial\Omega_d}[\mathbf{n}\cdot\mathbf{B}]\mathbf{B}dS = 0 \end{aligned} \tag{6}$$

Magnetic induction equation:

$$\begin{aligned} Re_m\int_{\Omega_d}\frac{\partial\mathbf{B}}{\partial t}dV + Re_m\oint_{\partial\Omega_d}[\mathbf{n}\cdot\mathbf{u}]\mathbf{B}dS + \oint_{\partial\Omega_d}\mathbf{n}qdS \\ -Re_m\oint_{\partial\Omega_d}[\mathbf{n}\cdot\mathbf{B}]\mathbf{u}dS - \oint_{\partial\Omega_d}\mathbf{n}\cdot\nabla\mathbf{B}dS = 0 \end{aligned} \tag{7}$$

Gauss' law of magnetism states that $\mathbf{B}$ is solenoidal:

$$\oint_{\partial\Omega_e}\mathbf{n}\cdot\mathbf{B}dS = 0 \tag{8}$$

In these equations V is the control volume, S is the control volume surface, $\mathbf{n}$ is the outward normal vector and q is Lagrange multiplier.

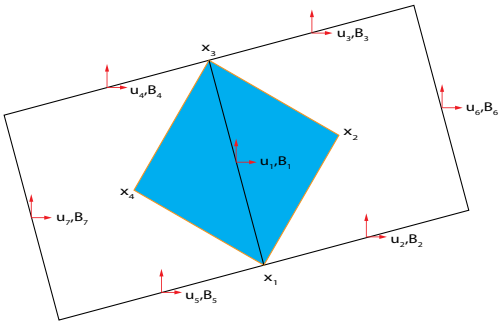

Figure 1: Two-dimensional dual volume

In the present study, semi-staggered Finite Volume Method formulation [18] is applied to the solution of incompressible magnetohydrodynamics equations. The discretization of momentum and magnetic induction equation is done over the dual control volume shown in Figure 1. The local velocity and magnetic field vectors are defined at the center of the each edge. The continuity and divergence of magnetic field equations are integrated over the quadrilateral elements. The pressure and Lagrange multiplier q are defined at the center of elements.The discrezitaziton leads to the following system of algebraic equations

$$\left[\begin{array}{ccc|ccc|c|c} A_{11} & 0 & 0 & A_{14} & 0 & 0 & A_{17} & 0 \\ 0 & A_{22} & 0 & 0 & A_{25} & 0 & A_{27} & 0 \\ 0 & 0 & A_{33} & 0 & 0 & A_{36} & A_{37} & 0 \\ \hline A_{41} & 0 & 0 & A_{44} & 0 & 0 & 0 & A_{48} \\ 0 & A_{52} & 0 & 0 & A_{55} & 0 & 0 & A_{58} \\ 0 & 0 & A_{63} & 0 & 0 & A_{66} & 0 & A_{68} \\ \hline A_{71} & A_{72} & A_{73} & 0 & 0 & 0 & 0 & 0 \\ \hline 0 & 0 & 0 & A_{85} & A_{86} & A_{87} & 0 & 0 \end{array}\right] \left[\begin{array}{c} u \\ v \\ w \\ \hline B_x \\ B_y \\ B_z \\ \hline p \\ \hline q \end{array}\right] = \left[\begin{array}{c} b_1 \\ b_2 \\ b_3 \\ \hline b_4 \\ b_5 \\ b_6 \\ \hline 0 \\ \hline 0 \end{array}\right] \tag{9}$$

where, $A_{11}, A_{22}, A_{33}, A_{44}, A_{55}, A_{66}$ are the convection diffusion operators,$(A_{17}, A_{27}, A_{37}, A_{48}, A_{58}, A_{68})^T$ are the gradient operator and $A_{71}, A_{72}, A_{73} A_{85}, A_{86}, A_{87}$, are the divergence operator. This fully-coupled system will be solved by a monolithic approach. In order to remove the zero block in the original system, an upper triangular right preconditioner is used

$$\left[\begin{array}{cccc} A_{11} & A_{12} & A_{13} & 0 \\ A_{21} & A_{22} & 0 & A_{24} \\ A_{31} & 0 & 0 & 0 \\ 0 & A_{42} & 0 & 0 \end{array}\right] \left[\begin{array}{cccc} I & 0 & A_{13} & 0 \\ 0 & I & 0 & A_{24} \\ 0 & 0 & I & 0 \\ 0 & 0 & 0 & I \end{array}\right] \left[\begin{array}{c} \mathbf{r} \\ \mathbf{s} \\ p \\ q \end{array}\right] = \left[\begin{array}{c} b_1 \\ b_2 \\ 0 \\ 0 \end{array}\right] \tag{10}$$

Then the velocity and magnetic field can be calculates as follows

$$\left[\begin{array}{c} \mathbf{u} \\ \mathbf{B} \\ p \\ q \end{array}\right] = \left[\begin{array}{cccc} I & 0 & A_{13} & 0 \\ 0 & I & 0 & A_{24} \\ 0 & 0 & I & 0 \\ 0 & 0 & 0 & I \end{array}\right] \left[\begin{array}{c} \mathbf{r} \\ \mathbf{s} \\ p \\ q \end{array}\right] \tag{11}$$

In this work, one-level restricted additive Schwarz preconditioner with a block-incomplete factorization is used within each partitioned sub-domains and the implementation is done by PETSc software package developed at Argonne National Laboratories [19]. For domain decomposition METIS library is employed [20].

3 RESULTS

The developed numerical algorithm is applied to lid-driven cavity and backward facing step problems under the effect of external magnetic field and very good agreements are observed with the results available in the literature.

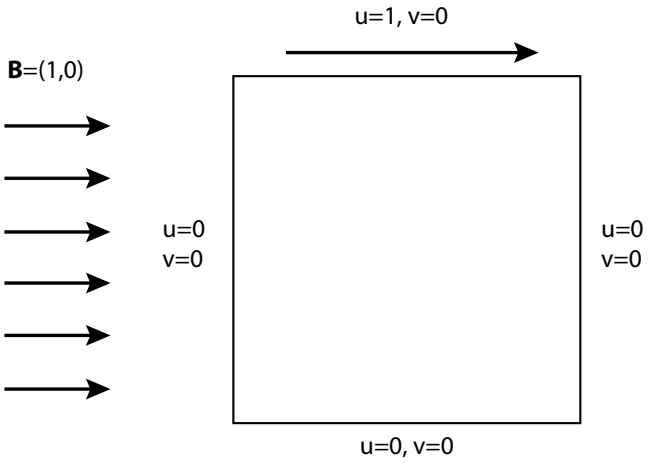

Figure 2: Boundary conditions for cavity problem.

3.1 Lid-Driven Cavity

For this problem, external magnetic field is imposed to classical lid-driven cavity problem. Top wall is moving with velocity $\mathbf{u} = (1,0)$. The walls of the cavity are assumed to be insulating and the magnetic field is in the x-direction, $\mathbf{B} = (1,0)$, see Figure 2.

Different Reynolds numbers and coupling parameters are used for the simulations and compared with the work of Shatrov et al. [21] and Marioni et al. [22]. The streamlines for $Re = 5000$ and $Re_m = 1$ for different coupling parameters are shown in the Figures 3-5. As the coupling number increases, the number of eddies are increased in the cavity. The velocity in the x-direction at the mid-line is shown in the Figure 6 for the upper half o the cavity for $S = 5$ and $S = 30$. Then Reynolds number is increased to 10000 and solved for $S = 0.5$. The velocity streamlines are compared with the reference work [22] in the Figure 7.

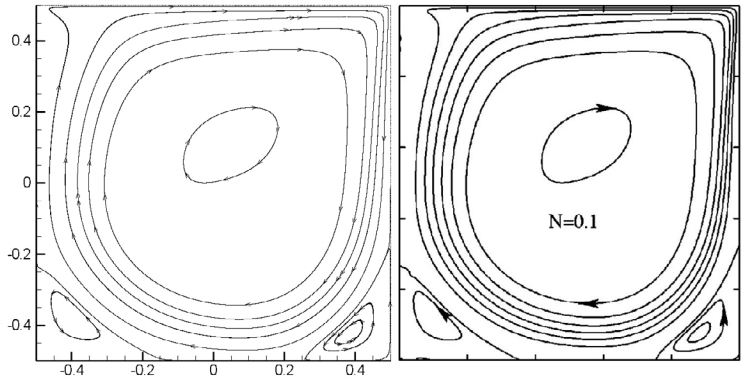

Figure 3: Streamlines at $Re = 5000$, $Re_m = 1$ and $S = 0.1$ for present work (left) and Shatrov et al. (right).

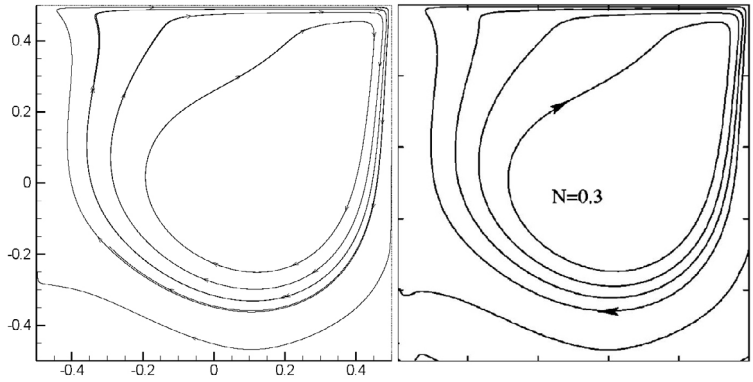

Figure 4: Streamlines at $Re = 5000$, $Re_m = 1$ and $S = 0.3$ for present work (left) and Shatrov et al. (right).

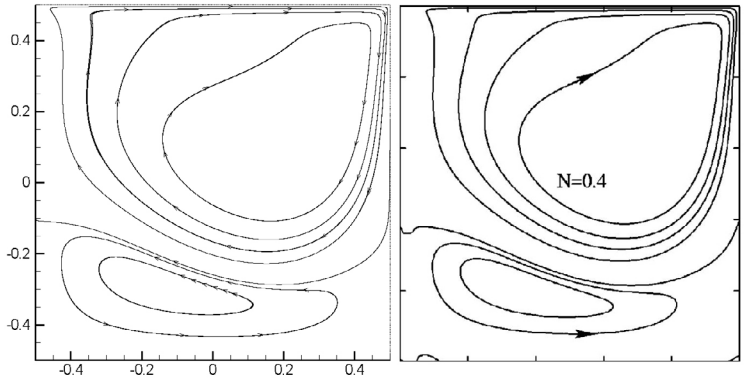

Figure 5: Streamlines at $Re = 5000$, $Re_m = 1$ and $S = 0.4$ for present work (left) and Shatrov et al. (right).

3.2 Backward Facing Step

The first is study on that specific problem is done by Gerbeau [6]. In this problem the walls of the channel are considered to be conducting and transverse magnetic field is applied $\mathbf{B}_0 = (0,1)$. The same geometry and boundary conditions are used for both velocity and magnetic field as described in [23]. The Reynolds number is $Re = 100$ and magnetic Reynolds number is $Re_m = 10^{-5}$. Different coupling parameters are used to observe the effect of magnetic field on the fluid. As it can be seen in Figure 8 and 9, as the coupling number increases the recirculation after the step decreases.

4 CONCLUSIONS

In this study, a semi-staggered unstructured finite volume method is developed for the solution of incompressible magnetohydrodynamics equations. The components of velocity and

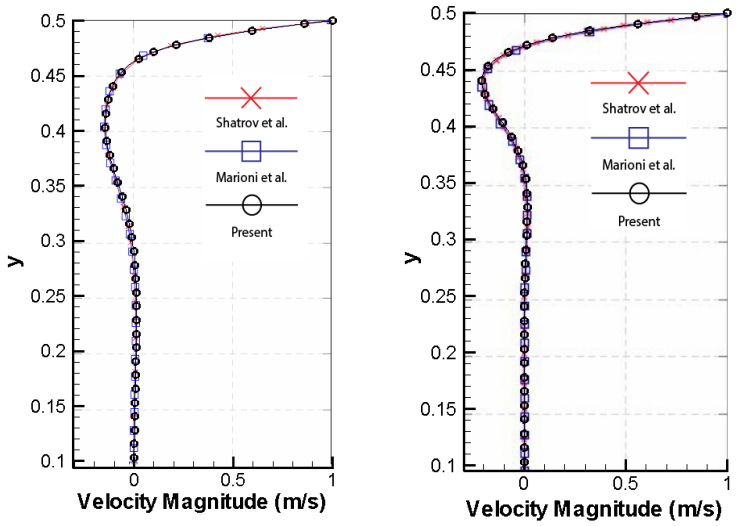

Figure 6: Velocity profile along mid-line for $Re = 5000$, $Re_m = 1$ (a) $S = 5$, (b) $S = 30$

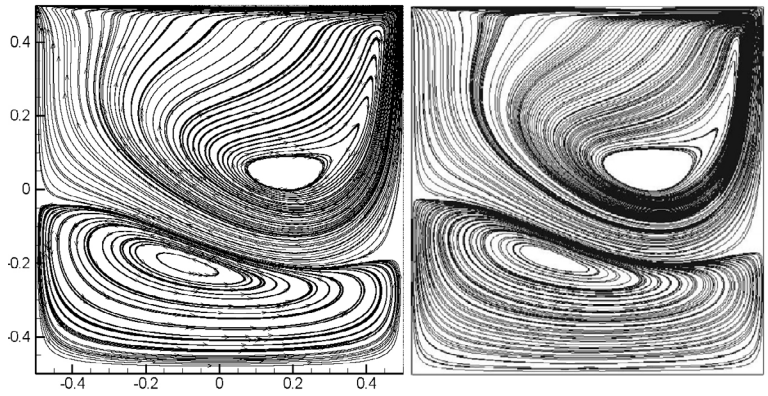

Figure 7: Streamlines at $Re = 10000$, $Re_m = 1$ and $S = 0.5$ for present work (left) and Marioni et al. (right).

magnetic field are defined at the edge centers and pressures are defined at the center of each cell. The resulting system is solved in a fully-coupled approach. The divergence-free condition of the magnetic field is satisfied by introducing the gradient of a scalar multiplier into the magnetic induction equation. One-level restricted additive Schwarz method is used for preconditioning and the implementation of the method is done by using PETSc library. The computational domain is partitioned by METIS libraries. The solver is applied to two-dimensional the lid-driven cavity and backward facing step problems under imposed magnetic field for different Reynolds numbers and coupling parameters.

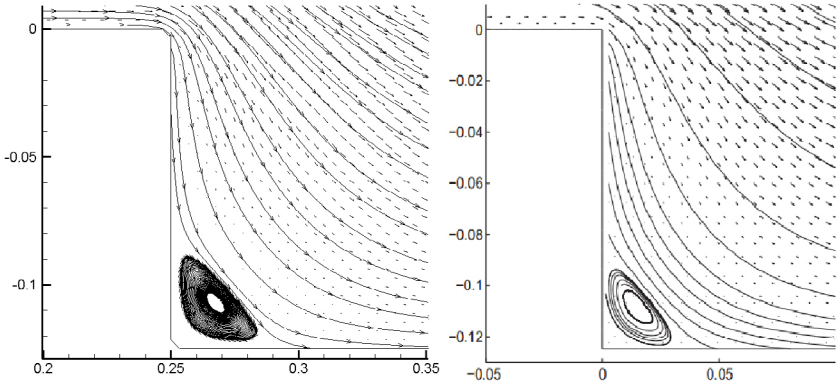

Figure 8: Streamlines for $Re = 100$, $Re_m = 10^{-5}$ and $S = 2.5 \times 10^4$ for present work (left) and Greif et al. (right).

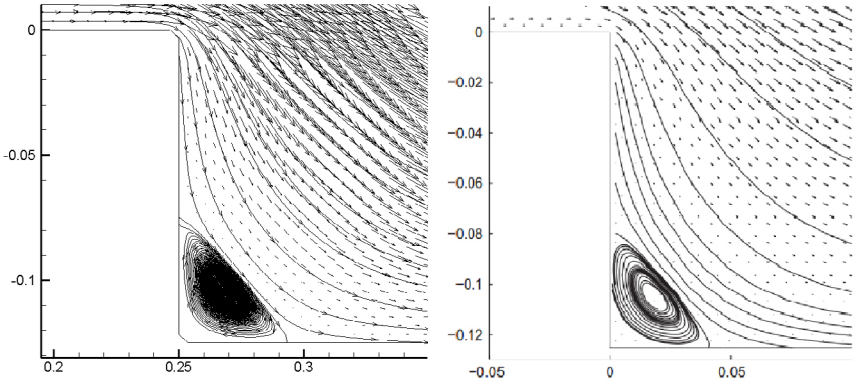

Figure 9: Streamlines for $Re = 100$, $Re_m = 10^{-5}$ and $S = 10^5$ for present work (left) and Greif et al. (right).

REFERENCES

[1] Davidson, P.A. *An introduction to magnetohydrodynamics*. Cambridge University Press, (2001).

[2] Goedbloed, H. and Poedts, S. *Principles of magnetohydrodynamics with applications to Laboratory and astrophysical plasmas*. Cambridge University Press, (2004).

[3] Planas, R., Badia, S. and Codina, R. Approximation of the inductionless MHD problem using a stabilized finite element method. *J. Comput. Phys.* (2011) **230**:52977–2996.

[4] Singh, B. and Lal, J. MHD axial flow in a triangular pipe under transverse magnetic field parallel to a side of the triangle. *Indian J. Technol.* (1979) **17**(5):184–189.

[5] Singh, B. and Lal, J. Finite element method for unsteady MHD flow through pipes with arbitrary wall conductivity. *Int. J. Numer. Meth. Fluids* (1984) **4**:291–302.

[6] Gerbeau, J. F. A stabilized finite element method for the incompressible magnetohydrodynamic equations. *Numer. Math.* (2000) **87**:83–111.

[7] Ni, M. and Li, J. A consistent and conservative scheme for incompressible MHD flows at a low magnetic Reynolds number. Part III: On a staggered mesh. *J. Comput. Phys.* (2012) **231**:281–298.

[8] Badia, S., Planas, R. and Gutierres-Santacreu, J.V. Unconditionally stable operator splitting algorithms for the incompressible magnetohydrodynamics system discretized by a stabilized finite element formulation based on projections. *Int. J. Numer. Meth. Engng.* (2013) **93**:302–328.

[9] Shadid, J. N., Pawlowski, R. P., Cyr, E. C., Tuminaro, R. S., Chacon, L. and Weber, P. D. Scalable implicit incompressible resistive MHD with stabilized FE and fully-coupled Newton-Krylov-AMG. *Comput. Methods Appl. Mech. Engng.* (2016) **304**:1–25.

[10] Lin, P. T., Shadid, J. N., Tuminaro, R. S., Sala, M., Hennigan, G. L. and Pawlowski, R. P. A parallel fully coupled algebraic multilevel preconditioner applied to multiphysics PDE applications: Drift-diffusion, flow/transport/reaction, resistive MHD. *Int. J. Numer. Meth. Fluids* (2010) **64**:1148–1179.

[11] Cyr,E. C., Shadid, J. N., Tuminaro, R. S., Pawlowski, R. P. and Chacon, L. A new approximate block factorization preconditioner for two-dimensional incompressible (reduced) resistive MHD. *SIAM J. Sci. Comput.* (2013) **35**(3):701–730.

[12] Phillips, E. G., Elman, H. C., Cyr,E. C., Shadid, J. N. and Pawlowski, R. P. A block preconditioner for an exact penalty formulation for stationary MHD. *SIAM J. Sci. Comput.* (2013) **36**(6):950–951.

[13] Adler, J. H., Benson, T. R., Cyr,E. C., Maclachlan, S. P. and Tuminaro, R. S. Monolithic multigrid methods for two-dimensional resistive magnetohydrodynamics. *SIAM J. Sci. Comput.* (2016) **38**(1):1–24.

[14] Dedner, A., Kemm, F., Kröner, D., Munz, C.D., Schnitzer, T. and Wesenberg, M. Hyperbolic divergence ckeaning fot he MHD equations. *J. Comput. Phys.* (2002) **175**:645–673.

[15] Lee, D. and Deane, A.E. An unsplit staggered mesh scheme for multidimensional magnetohydrodynamics. *J. Comput. Phys.* (2009) **228**:952–975.

[16] Murawski, K. Numerical solutions of magnetohydrodynamic equations. *Bulletin of the Polish Academy of Sciences. Technical sciences* (2011) **59**:219–226.

[17] Salah, N.B, Soulaiani, A. and Habashi, W.G. A finite element method for magnetohydrodynamics . *Comput. Methods Appl. Mech. Engrg.* (2001). **190**:5867–5892

[18] Sahin, M. A stable unstructured finite volume method for parallel large-scale viscoelastic fluid flow calculations. *J. Non-Newton Fluid* (2011) **166**:779–791.

[19] Balay, S., Abhyankar, S., Adams, M.F., Brown, J., Brune, P., Buschelman, K., Dalcin, L., Eijkhout, V., Gropp, W.D., Kaushik, D., Knepley, M.G., McInnes, L.C., Rupp, K., Smith, B.F., Zampini, S. and Zhang, H. PETSc users manual. *Technical Report ANL-95/11 - Revision 3.7* (2016) Argonne National Laboratory, Argonne, Illinois.

[20] Karypis, G. and Kumar, V. A fast and high quality multilevel scheme for partitioning irregular graphs. *SIAM J. Sci. Comput.* (1998) **20**(1):359–392.

[21] Shatrov, V., Mutschke, G. and Gerbeth, G. Three-dimensional linear stability analysis of lid-driven magnetohydrodynamic cavity flow. *Phys. Fluids* (2003)**15**:2141–2152

[22] Marioni, L., Bay, F. and Hechem, E. Numerical stability analysis and flow simulation of lid-driven cavity subjected to high magnetic field. *Phys. Fluids* (2016) **28**:057102

[23] Greif, C., Li, D., Schotzau, D. and Wei, X.A. A mixed finite element method with exactly divergence-free velocities for incompressible magnetohydrodynamics. *Comput. Methods Appl. Mech. Engrg.* (2010) **199**:2840–2855.

VII International Conference on Computational Methods for Coupled Problems in Science and Engineering
COUPLED PROBLEMS 2017
M. Papadrakakis, E. Oñate and B. Schrefler (Eds)

A STABLE AND EFFICIENT DOMAIN DECOMPOSITION METHOD FOR MAXWELL'S EQUATIONS WITH UNCERTAINTY

ANNA NISSEN*, PER PETTERSSON† AND SVENN TVEIT†

*Department of Mathematics, University of Bergen
P.O.Box 7803, NO-5020 Bergen, Norway
e-mail: anna.nissen@math.uib.no

†Uni Research CIPR
P.O.Box 7800, NO-5020 Bergen, Norway
e-mail: per.pettersson@uni.no, svenn.tveit@uni.no

Key words: Maxwell's Equations, Domain Decomposition, Summation-by-parts Operators, Finite Difference Methods, Generalized Polynomial Chaos

Abstract. Geophysical monitoring of CO_2 sequestration using electromagnetics is prone to large uncertainties. To include uncertainty in Maxwell's equations, we use the polynomial chaos framework and project the equations onto stochastic basis functions. The resulting extended system needs to be solved only once to obtain all statistics of interest. We use high-order finite-difference methods that satisfy a summation-by-parts rule for the spatial discretization of Maxwell's equations. We incorporate spatial adaptivity by decomposing the spatial domain into structured grid blocks, where the discretization of each block is adapted to the local resolution requirement. The spatial discretization is time-stable by a carefully designed numerical coupling between grid blocks of different grid sizes. The combination of spatial adaptivity and high-order finite difference methods on block-structured grids leads to a highly efficient and accurate numerical discretization.

1 INTRODUCTION

Fast and accurate solutions of Maxwell's equations are required to simulate responses in various electromagnetic (EM) applications, e.g., medical and geophysical imaging [1, 2]. In this paper, we are interested in calculating EM responses for time-lapse monitoring of CO_2 sequestration [3] – a geophysical inverse problem.

In geophysical monitoring surveys with EM, signals are transmitted to a subsurface reservoir where they are affected by the subsurface conductivity distribution. The returning signals are measured by surface receivers and converted to a map of the subsurface

conductivity using an inversion method. By incorporating the updated conductivity values from the monitoring survey into a detailed geological description, empirical relations between conductivity and saturation can be used to get updated information on the CO_2 migration path.

To understand and evaluate the risk factors involved in CO_2 storage operations, quantification of uncertainty is very important. In order to solve geophysical monitoring inverse problems, one relies on calculating EM responses using numerical methods. Most often, uncertainty is quantified using Monte Carlo (or sampling-based) algorithms, where the numerical EM simulator is treated as a 'black box' needed to be run many times to achieve sufficiently accurate statistics [4]. Alternatively, uncertainty can be incorporated directly in Maxwell's equations by representing the solution as a spectral expansion in random variables using the generalized polynomial chaos (gPC) framework [5, 6]. Through stochastic Galerkin projection of the problem, repetitive sampling can be completely avoided by solving a single extended system only once.

A large variety of numerical methods exist for solving Maxwell's equations with the finite element (FE), finite difference (FD), and integral equation methods [7, 8]. The most common approaches are FE and FD. In FE methods, discretization of the computational domain is highly flexible using unstructured grids. Hence, complex geometrical features can more easily be captured compared with other methods [9]. However, specialized grid generation software is often required to generate shape regular unstructured grids. Furthermore, special care is needed when solving the resulting FE linear system due to its unstructured nature. On the other hand, FD methods are simple to implement and computationally efficient, due to the resulting linear system being sparse and structured [10]. A challenge of FD methods on structured grids is to handle large computational domains with features on different spatial scales, from sources and receivers on the order of meters to geological features on the order of kilometers. Typically, a fine grid is needed around sources and receivers to obtain highly accurate solutions, while in the far-field, low resolution is sufficient and a coarser grid can be employed.

In this paper, we solve the time-domain, first-order coupled stochastic Galerkin Maxwell's equations using FD methods within the summation-by-parts (SBP) framework, see [11] and references therein. The SBP framework is well suited for designing high-order accurate discretizations that are provably time-stable. In this context, time-stability refers to the property that the growth of numerical errors is bounded, and that a consistent spatial discretization converges to the true solution. In general, proving stability for high-order FD methods is a non-trivial task, in particular for non-uniform grids. A time-stable domain decomposition method based on SBP operators for block-wise spatial adaptivity was developed in [12]. To obtain sufficient resolution for the most important features in the computational domain, we present a numerical discretization that extends the method presented in [12] to the stochastic Galerkin Maxwell's equations. The performance of the method is demonstrated both in the deterministic and the stochastic settings, with geophysical inverse modeling in mind.

2 GENERALIZED POLYNOMIAL CHAOS EXPANSION

In the gPC framework stochastic functions are represented as Fourier series expansions in a set of independent random variables. Assuming a single source of uncertainty the uncertainty of the problem is parameterized by introducing a random variable ξ with known probability measure $\mathcal{P}$. The measure $\mathcal{P}$ could match an estimated empirical distribution of some uncertain input variable, but also be taken as some well-known probability distribution. Next introduce a set of basis functions $\{\psi_i(\xi)\}_{i=1}^{\infty}$ consisting of polynomials that are orthonormal with respect to the measure $\mathcal{P}$, i.e.,

$$\mathbb{E}\left(\psi_i(\xi)\psi_j(\xi)\right) \equiv \int_{-\infty}^{\infty} \psi_i(\xi)\psi_j(\xi)d\mathcal{P}(\xi) = \delta_{ij}.$$

The orthonormal polynomials correspond to classical orthogonal polynomials for some commonly used probability distributions, e.g., Legendre polynomials for uniform distributions and Hermite polynomials for Gaussian distributions. Any function f of finite variance can be approximated by its truncated gPC expansion [6],

$$f \approx \sum_{m=1}^{P} f_m \psi_m(\xi), \tag{1}$$

where the gPC coefficients f_m are defined by the projections

$$f_m = \mathbb{E}(f\psi_m), \quad m = 1, ..., P.$$

The series expansion (1) converges in the L_2 sense as $P \to \infty$. Statistics may be computed directly from the gPC coefficients, e.g., mean and variance are approximated by

$$\mathbb{E}(f) = f_1, \quad \mathrm{Var}(f) = \sum_{m=2}^{P} f_m^2.$$

The extension to multiple independent stochastic dimensions is performed through tensorization of univariate basis functions but not considered in this work.

3 MAXWELL'S EQUATIONS IN TIME DOMAIN

Consider a general spatial domain Ω and temporal domain $t \in [0, T]$. Let $E = (E_x, E_y, E_z)^T$ denote the electric field, $H = (H_x, H_y, H_z)^T$ the magnetic field, ϵ the permittivity, σ the electric conductivity, and μ the magnetic permeability. The three-dimensional Maxwell's equations in the time domain for $(x, y, z) \in \Omega, t \in [0, T]$, are given by

$$\begin{aligned} \epsilon\tfrac{\partial E}{\partial t} - \nabla \times H + \sigma E &= 0, \\ \mu\tfrac{\partial H}{\partial t} + \nabla \times E &= 0, \\ \nabla \cdot E &= 0, \\ \nabla \cdot H &= 0, \end{aligned} \tag{2}$$

with appropriate boundary conditions. Consider a transverse electric wave propagating in the x-y plane. Then (2) simplifies to the two-dimensional hyperbolic system

$$\begin{bmatrix} \epsilon E_x \\ \epsilon E_y \\ \mu H_z \end{bmatrix}_t + \begin{bmatrix} 0 & 0 & 0 \\ 0 & 0 & 1 \\ 0 & 1 & 0 \end{bmatrix} \begin{bmatrix} E_x \\ E_y \\ H_z \end{bmatrix}_x + \begin{bmatrix} 0 & 0 & -1 \\ 0 & 0 & 0 \\ -1 & 0 & 0 \end{bmatrix} \begin{bmatrix} E_x \\ E_y \\ H_z \end{bmatrix}_y + \begin{bmatrix} \sigma & 0 & 0 \\ 0 & \sigma & 0 \\ 0 & 0 & 0 \end{bmatrix} \begin{bmatrix} E_x \\ E_y \\ H_z \end{bmatrix} = 0, \quad (3)$$

where we assume a spatial domain $(x, y) \in \Omega = [0, L_x] \times [0, L_y]$.

3.1 Stochastic Galerkin projection of Maxwell's equations

In geophysical inverse problems, σ is the main source of uncertainty [8], and in the numerical experiments we consider uncertainty in σ only. For completeness we present the problem setup with uncertainty in all material parameters. The field variables E_x, E_y, H_z and any uncertain parameters (ϵ, μ, σ) are expressed as truncated gPC expansions (1) and inserted into the equations (3). A stochastic Galerkin projection onto the basis functions is performed by multiplying the system of equations by each basis function and then integrating with respect to the probability measure $\mathcal{P}$. For projection onto P basis functions, this results in a coupled $3P \times 3P$ system,

$$\underbrace{\begin{bmatrix} \mathbf{A}(\epsilon) & \mathbf{0} & \mathbf{0} \\ \mathbf{0} & \mathbf{A}(\epsilon) & \mathbf{0} \\ \mathbf{0} & \mathbf{0} & \mathbf{A}(\mu) \end{bmatrix}}_{\mathbf{M}} \begin{bmatrix} \mathbf{E}_x \\ \mathbf{E}_y \\ \mathbf{H}_z \end{bmatrix}_t + \underbrace{\begin{bmatrix} \mathbf{0} & \mathbf{0} & \mathbf{0} \\ \mathbf{0} & \mathbf{0} & \mathbf{I} \\ \mathbf{0} & \mathbf{I} & \mathbf{0} \end{bmatrix}}_{\mathbf{B}} \begin{bmatrix} \mathbf{E}_x \\ \mathbf{E}_y \\ \mathbf{H}_z \end{bmatrix}_x + \underbrace{\begin{bmatrix} \mathbf{0} & \mathbf{0} & -\mathbf{I} \\ \mathbf{0} & \mathbf{0} & \mathbf{0} \\ -\mathbf{I} & \mathbf{0} & \mathbf{0} \end{bmatrix}}_{\mathbf{C}} \begin{bmatrix} \mathbf{E}_x \\ \mathbf{E}_y \\ \mathbf{H}_z \end{bmatrix}_y + \underbrace{\begin{bmatrix} \mathbf{A}(\sigma) & \mathbf{0} & \mathbf{0} \\ \mathbf{0} & \mathbf{A}(\sigma) & \mathbf{0} \\ \mathbf{0} & \mathbf{0} & \mathbf{0} \end{bmatrix}}_{\mathbf{D}} \begin{bmatrix} \mathbf{E}_x \\ \mathbf{E}_y \\ \mathbf{H}_z \end{bmatrix} = \mathbf{0}, \quad (4)$$

where we have introduced the matrix $\mathbf{A}(\cdot)$, defined by

$$[\mathbf{A}(r)]_{ij} = \sum_{m=1}^{P} r_m \mathbb{E}(\psi_i \psi_j \psi_m), \quad r = \epsilon, \mu, \sigma.$$

Note that the matrix $\mathbf{A}(\cdot)$ is symmetric, so the matrices $\mathbf{M}, \mathbf{B}, \mathbf{C}$ and $\mathbf{D}$ are also all symmetric. Let $\mathbf{u} = \begin{pmatrix} \mathbf{E}_x & \mathbf{E}_y & \mathbf{H}_z \end{pmatrix}^\mathsf{T}$. We express the system (4) as

$$\mathbf{M}\mathbf{u}_t + \mathbf{B}\mathbf{u}_x + \mathbf{C}\mathbf{u}_y + \mathbf{D}\mathbf{u} = \mathbf{0}. \quad (5)$$

To assign boundary conditions, we use the eigenvalue decompositions of the matrices $\mathbf{B}$ and $\mathbf{C}$,

$$\mathbf{B} = \mathbf{V}_\mathbf{B}^+ \mathbf{\Lambda}_\mathbf{B}^+ \mathbf{V}_\mathbf{B}^{+\mathsf{T}} + \mathbf{V}_\mathbf{B}^- \mathbf{\Lambda}_\mathbf{B}^- \mathbf{V}_\mathbf{B}^{-\mathsf{T}}, \qquad \mathbf{C} = \mathbf{V}_\mathbf{C}^+ \mathbf{\Lambda}_\mathbf{C}^+ \mathbf{V}_\mathbf{C}^{+\mathsf{T}} + \mathbf{V}_\mathbf{C}^- \mathbf{\Lambda}_\mathbf{C}^- \mathbf{V}_\mathbf{C}^{-\mathsf{T}},$$

where superscript $+$ $(-)$ denote the matrices of positive (negative) eigenvalues, $\mathbf{\Lambda}$, and the corresponding eigenvectors, $\mathbf{V}$, respectively. We use the following Dirichlet type boundary conditions

$$\mathbf{V}_\mathbf{B}^{+\mathsf{T}} \mathbf{u} = \mathbf{g}_\mathrm{w}(y,t) \quad \text{at } x = 0, \qquad \mathbf{V}_\mathbf{B}^{-\mathsf{T}} \mathbf{u} = \mathbf{g}_\mathrm{e}(y,t) \quad \text{at } x = L_x,$$
$$\mathbf{V}_\mathbf{C}^{+\mathsf{T}} \mathbf{u} = \mathbf{g}_\mathrm{s}(x,t) \quad \text{at } y = 0, \qquad \mathbf{V}_\mathbf{C}^{-\mathsf{T}} \mathbf{u} = \mathbf{g}_\mathrm{n}(x,t) \quad \text{at } y = L_y,$$

where we use the cardinal directions west (w), east (e), south (s), and north (n) to denote the four boundaries of the computational domain. This choice of boundary conditions leads to a well posed problem (5).

4 NUMERICAL DISCRETIZATION

The stochastic Galerkin Maxwell's equations are discretized with an FD method with an SBP property that allows proof of time-stability for the semi-discrete problem with appropriate boundary conditions [13]. The boundary conditions are enforced to the accuracy order of the scheme through a simultaneous approximation term (SAT) that penalizes the deviation from the exact boundary conditions [14]. By relaxing the condition of exactly satisfying the boundary conditions, we gain flexibility in the formulation that is needed to choose penalty parameters that lead to stability. SBP operators were introduced for the first derivative in [13, 15]. A numerical method based on SBP operators for the deterministic Maxwell's equations with a material discontinuity interface was presented in [16].

In order to be able to resolve point sources and receivers in an extensive computational domain, we decompose the domain into a number of blocks, where the grid sizes can vary between the blocks, see Figures 2(a)-2(c). The SBP-SAT framework is employed to achieve stable and accurate couplings also between the subdomains of different spatial resolution, similar to the treatment of boundary conditions. Due to limited space we have omitted the stability proofs for the discretizations presented in this work.

A fourth-order Runge-Kutta method is used for the temporal integration. The choice of a sufficiently small time-step in combination with high order of accuracy of the time integration leads to a numerical scheme where the error is dominated by the spatial discretization. The spatial error convergence is the focus of this work.

4.1 Spatial discretization of a single domain

We first consider the case of a single domain, i.e., a uniform discretization over the whole domain, and the implementation of boundary conditions. The spatial domain $[0, L_x] \times [0, L_y]$ is discretized at points (x_i, y_j), $i = 1, ..., m_x$, $j = 1, ..., m_y$, and $\Delta x = L_x/(m_x - 1)$, $\Delta y = L_y/(m_y - 1)$. The semi-discrete numerical approximation of $\mathbf{u}(x_i, y_j, t)$ is denoted $\mathbf{v}_{i,j}$ $(= \mathbf{v}_{i,j}(t))$ and assembled in the vector $\mathbf{v} = (\mathbf{v}_{1,1}, ..., \mathbf{v}_{1,m_y}, ..., \mathbf{v}_{m_x,1}, ..., \mathbf{v}_{m_x,m_y})^\intercal$.

In one spatial dimension the first derivative $\mathbf{u}_x$ is approximated by $\mathbf{P}_x^{-1}\mathbf{Q}_x\mathbf{v}$, where $\mathbf{P}_x$ is a positive definite diagonal matrix, scales with Δx, and defines a matrix norm. The matrix $\mathbf{Q}_x$ satisfies

$$\mathbf{Q}_x + \mathbf{Q}_x^\intercal = diag(-1, 0, \ldots, 0, 1) = \mathbf{e}_{m_x}\mathbf{e}_{m_x}^\intercal - \mathbf{e}_1\mathbf{e}_1^\intercal, \tag{6}$$

with $\mathbf{e}_{m_x} = (0, \ldots, 0, 1)^\intercal$ and $\mathbf{e}_1 = (1, 0, \ldots, 0)^\intercal$. The SBP property (6) mimics the semi-discrete (discrete in space, continuous in time) counterpart of integration by parts. This is essential in the derivation of discrete energy estimates to prove time-stability. Operators of accuracy order $2n$, $n \in \mathbb{N}$, in the interior of the domain are combined with boundary stencils of order of accuracy n. In this paper we use fourth-order accurate operators ($n = 2$) from [15].

The Kronecker product notation $\otimes$ is used for extension to more than one spatial dimension and to include the stochastic Galerkin system. The SBP operators can then be handled dimension by dimension. In the following operator subscripts are omitted, as the order of appearance is always (x, y, ξ). Note that size and scaling of $\mathbf{P}$, $\mathbf{Q}$, and $\mathbf{I}$ vary depending on dimension.

In two spatial dimensions, consider the semi-discretization of (5)

$$(\mathbf{I} \otimes \mathbf{I} \otimes \mathbf{M})\mathbf{v}_t + (\mathbf{P}^{-1}\mathbf{Q} \otimes \mathbf{I} \otimes \mathbf{B})\mathbf{v} + (\mathbf{I} \otimes \mathbf{P}^{-1}\mathbf{Q} \otimes \mathbf{C})\mathbf{v} + (\mathbf{I} \otimes \mathbf{I} \otimes \mathbf{D})\mathbf{v} = \text{SAT},$$

where the SAT contributions enforce the boundary conditions and are given by

$$\begin{aligned}\text{SAT} = \tau_{\text{w}}(\mathbf{P}^{-1}\mathbf{e}_1\mathbf{e}_1^\intercal \otimes \mathbf{I} \otimes \mathbf{\Sigma}_{\text{w}}) \left[(\mathbf{I} \otimes \mathbf{I} \otimes \mathbf{V}_{\mathbf{B}}^{+\intercal})\mathbf{v} - \mathbf{g}_{\text{w}})\right] + \tau_{\text{e}}(\mathbf{P}^{-1}\mathbf{e}_{m_x}\mathbf{e}_{m_x}^\intercal \otimes \mathbf{I} \otimes \mathbf{\Sigma}_{\text{e}}) \\ \times \left[(\mathbf{I} \otimes \mathbf{I} \otimes \mathbf{V}_{\mathbf{B}}^{-\intercal})\mathbf{v} - \mathbf{g}_{\text{e}})\right] + \tau_{\text{s}}(\mathbf{I} \otimes \mathbf{P}^{-1}\mathbf{e}_1\mathbf{e}_1^\intercal \otimes \mathbf{\Sigma}_{\text{s}}) \left[(\mathbf{I} \otimes \mathbf{I} \otimes \mathbf{V}_{\mathbf{C}}^{+\intercal})\mathbf{v} - \mathbf{g}_{\text{s}})\right] \\ + \tau_{\text{n}}(\mathbf{I} \otimes \mathbf{P}^{-1}\mathbf{e}_{m_y}\mathbf{e}_{m_y}^\intercal \otimes \mathbf{\Sigma}_{\text{n}}) \left[(\mathbf{I} \otimes \mathbf{I} \otimes \mathbf{V}_{\mathbf{C}}^{-\intercal})\mathbf{v} - \mathbf{g}_{\text{n}})\right].\end{aligned}$$

A stable numerical scheme is obtained by setting the design parameter values to

$$\begin{aligned}&\tau_{\text{w}} = -1, && \tau_{\text{e}} = 1, && \tau_{\text{s}} = -1, && \tau_{\text{n}} = 1, \\ &\mathbf{\Sigma}_{\text{w}} = \mathbf{V}_{\mathbf{B}}^{+}\mathbf{\Lambda}_{\mathbf{B}}^{+}, && \mathbf{\Sigma}_{\text{e}} = \mathbf{V}_{\mathbf{B}}^{-}\mathbf{\Lambda}_{\mathbf{B}}^{-}, && \mathbf{\Sigma}_{\text{s}} = \mathbf{V}_{\mathbf{C}}^{+}\mathbf{\Lambda}_{\mathbf{C}}^{+}, && \mathbf{\Sigma}_{\text{n}} = \mathbf{V}_{\mathbf{C}}^{-}\mathbf{\Lambda}_{\mathbf{C}}^{-}.\end{aligned}$$

4.2 Domain with blocks and T-junction interfaces

In a multi-block setting, single domain discretization operators are used on each block, and the blocks are coupled through numerical interfaces using SAT. Grid block interfaces with different grid sizes are treated with SBP interpolation operators [17] in combination with SAT. When constructing complex block-structured grids so called T-junction interfaces can help to reduce the number of numerical interfaces needed to obtain a stable discretization. This is advantageous because the one-sided FD stencils near interfaces are of lower order of accuracy compared to the interior stencil. A T-junction interface in the vertical direction is shown in Figure 1(a). A grid refinement ratio of $2:1$ is depicted between the left and the right subdomains in Figure 1(b), and this is what we consider in the numerical experiments.

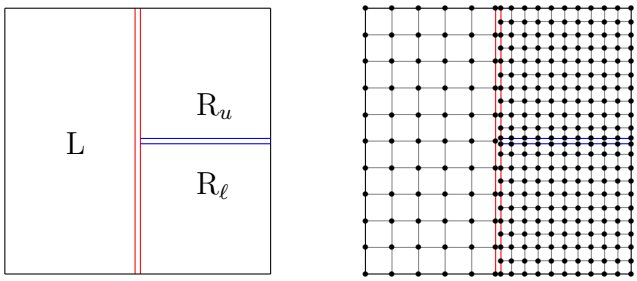

Figure 1: T-junction interface used to obtain a stable discretization on a domain-decomposed grid. The blue lines denote numerical SBP-SAT interfaces between equal grid-size blocks, and red lines interfaces between blocks with different grid sizes. Grid points of two adjacent blocks are co-located at the interface.

Let $\mathbf{v}^{\text{L}}$ be the numerical solution in the left subdomain and $\mathbf{v}^{\text{R}_u}$ and $\mathbf{v}^{\text{R}_\ell}$ denote the numerical solutions in the right upper and lower subdomains, respectively. Further, let $\mathbf{I}_{\text{R}_u\text{R}_\ell}^{\text{L}}$ be an operator that interpolates the solutions on the interface of the right subdomains to the solution on the interface of the left subdomain, and therefore of size $m_y^{\text{L}} \times (m_y^{\text{R}_u} + m_y^{\text{R}_\ell})$. Let $\mathbf{I}_{\text{L}}^{\text{R}_u}$ and $\mathbf{I}_{\text{L}}^{\text{R}_\ell}$ be operators of sizes $m_y^{\text{R}_u} \times m_y^{\text{L}}$ and $m_y^{\text{R}_\ell} \times m_y^{\text{L}}$ that interpolate from the left subdomain to the right upper and lower subdomains. In the case of equal grid sizes, $\mathbf{I}_{\text{R}_u\text{R}_\ell}^{\text{L}}$, $\mathbf{I}_{\text{L}}^{\text{R}_u}$, and $\mathbf{I}_{\text{L}}^{\text{R}_\ell}$ will mainly be identity matrices (with one extra row or column due to duplicate nodes at the T-junction),

except for a few rows and columns around the T-junction. The T-junction operators can be found in [12], and the SBP interpolation operators in [17]. The discretization of (5) for the three blocks in Figure 1 including the coupling of the left domain with the two right domains (double red lines) and the coupling of the two right domains (double blue lines) is given by

$$
\begin{aligned}
&(\mathbf{I}\otimes\mathbf{I}\otimes\mathbf{M})\mathbf{v}_t^{\mathrm{L}} + (\mathbf{P}_{\mathrm{L}}^{-1}\mathbf{Q}_{\mathrm{L}}\otimes\mathbf{I}\otimes\mathbf{B})\mathbf{v}^{\mathrm{L}} + (\mathbf{I}\otimes\mathbf{P}_{\mathrm{L}}^{-1}\mathbf{Q}_{\mathrm{L}}\otimes\mathbf{C})\mathbf{v}^{\mathrm{L}} + (\mathbf{I}\otimes\mathbf{I}\otimes\mathbf{D})\mathbf{v}^{\mathrm{L}} \\
&= \tau_{\mathrm{L}}(\mathbf{P}_{\mathrm{L}}^{-1}\otimes\mathbf{I}\otimes\boldsymbol{\Sigma}_{\mathrm{L}}^{\tau})\left[(\mathbf{e}_{m_x}^{\mathrm{L}}(\mathbf{e}_{m_x}^{\mathrm{L}})^{\intercal}\otimes\mathbf{I}\otimes\mathbf{I})\mathbf{v}^{\mathrm{L}} - (\mathbf{e}_{m_x}^{\mathrm{L}}\otimes\mathbf{I}_{\mathrm{R}_u\mathrm{R}_\ell}^{\mathrm{L}}\otimes\mathbf{I})\begin{bmatrix}((\mathbf{e}_1^{\mathrm{R}_u})^{\intercal}\otimes\mathbf{I}\otimes\mathbf{I})\mathbf{v}^{\mathrm{R}_u}\\((\mathbf{e}_1^{\mathrm{R}_\ell})^{\intercal}\otimes\mathbf{I}\otimes\mathbf{I})\mathbf{v}^{\mathrm{R}_\ell}\end{bmatrix}\right],
\end{aligned}
$$

$$
\begin{aligned}
&(\mathbf{I}\otimes\mathbf{I}\otimes\mathbf{M})\mathbf{v}_t^{\mathrm{R}_u} + (\mathbf{P}_{\mathrm{R}_u}^{-1}\mathbf{Q}_{\mathrm{R}_u}\otimes\mathbf{I}\otimes\mathbf{B})\mathbf{v}^{\mathrm{R}_u} + (\mathbf{I}\otimes\mathbf{P}_{\mathrm{R}_u}^{-1}\mathbf{Q}_{\mathrm{R}_u}\otimes\mathbf{C})\mathbf{v}^{\mathrm{R}_u} + (\mathbf{I}\otimes\mathbf{I}\otimes\mathbf{D})\mathbf{v}^{\mathrm{R}_u} \\
&\quad= \tau_{\mathrm{R}_u}(\mathbf{P}_{\mathrm{R}_u}^{-1}\otimes\mathbf{I}\otimes\boldsymbol{\Sigma}_{\mathrm{R}_u}^{\tau})\left[(\mathbf{e}_1^{\mathrm{R}_u}(\mathbf{e}_1^{\mathrm{R}_u})^{\intercal}\otimes\mathbf{I}\otimes\mathbf{I})\mathbf{v}^{\mathrm{R}_u} - (\mathbf{e}_1^{\mathrm{R}_u}(\mathbf{e}_{m_x}^{\mathrm{L}})^{\intercal}\otimes\mathbf{I}_{\mathrm{L}}^{\mathrm{R}_u}\otimes\mathbf{I})\mathbf{v}^{\mathrm{L}}\right] \\
&\qquad+ \eta_{\mathrm{R}_u}(\mathbf{I}\otimes\mathbf{P}_{\mathrm{R}_u}^{-1}\otimes\boldsymbol{\Sigma}_{\mathrm{R}_u}^{\eta})\left[(\mathbf{I}\otimes\mathbf{e}_1^{\mathrm{R}_u}(\mathbf{e}_1^{\mathrm{R}_u})^{\intercal}\otimes\mathbf{I})\mathbf{v}^{\mathrm{R}_u} - (\mathbf{I}\otimes\mathbf{e}_1^{\mathrm{R}_u}(\mathbf{e}_{m_y}^{\mathrm{R}_\ell})^{\intercal}\otimes\mathbf{I})\mathbf{v}^{\mathrm{R}_\ell}\right],
\end{aligned}
$$

$$
\begin{aligned}
&(\mathbf{I}\otimes\mathbf{I}\otimes\mathbf{M})\mathbf{v}_t^{\mathrm{R}_\ell} + (\mathbf{P}_{\mathrm{R}_\ell}^{-1}\mathbf{Q}_{\mathrm{R}_\ell}\otimes\mathbf{I}\otimes\mathbf{B})\mathbf{v}^{\mathrm{R}_\ell} + (\mathbf{I}\otimes\mathbf{P}_{\mathrm{R}_\ell}^{-1}\mathbf{Q}_{\mathrm{R}_\ell}\otimes\mathbf{C})\mathbf{v}^{\mathrm{R}_\ell} + (\mathbf{I}\otimes\mathbf{I}\otimes\mathbf{D})\mathbf{v}^{\mathrm{R}_\ell} \\
&\quad= \tau_{\mathrm{R}_\ell}(\mathbf{P}_{\mathrm{R}_\ell}^{-1}\otimes\mathbf{I}\otimes\boldsymbol{\Sigma}_{\mathrm{R}_\ell}^{\tau})\left[(\mathbf{e}_1^{\mathrm{R}_\ell}(\mathbf{e}_1^{\mathrm{R}_\ell})^{\intercal}\otimes\mathbf{I}\otimes\mathbf{I})\mathbf{v}^{\mathrm{R}_\ell} - (\mathbf{e}_1^{\mathrm{R}_\ell}(\mathbf{e}_{m_x}^{\mathrm{L}})^{\intercal}\otimes\mathbf{I}_{\mathrm{L}}^{\mathrm{R}_\ell}\otimes\mathbf{I})\mathbf{v}^{\mathrm{L}}\right] \\
&\qquad+ \eta_{\mathrm{R}_\ell}(\mathbf{I}\otimes\mathbf{P}_{\mathrm{R}_\ell}^{-1}\otimes\boldsymbol{\Sigma}_{\mathrm{R}_\ell}^{\eta})\left[(\mathbf{I}\otimes\mathbf{e}_{m_y}^{\mathrm{R}_\ell}(\mathbf{e}_{m_y}^{\mathrm{R}_\ell})^{\intercal}\otimes\mathbf{I})\mathbf{v}^{\mathrm{R}_\ell} - (\mathbf{I}\otimes\mathbf{e}_{m_y}^{\mathrm{R}_\ell}(\mathbf{e}_1^{\mathrm{R}_u})^{\intercal}\otimes\mathbf{I})\mathbf{v}^{\mathrm{R}_u}\right].
\end{aligned}
$$

The coupling terms with τ and η correspond to the couplings at the interfaces with double red lines and double blue lines in Figure 1, respectively. In order to obtain an energy estimate of the semi-discrete numerical scheme (implying time-stability), the parameters are chosen as

$$
\begin{aligned}
&\tau_{\mathrm{L}} = \frac{1}{2}, && \tau_{\mathrm{R}_u} = -\frac{1}{2}, && \tau_{\mathrm{R}_\ell} = -\frac{1}{2}, && \eta_{\mathrm{R}_u} = -\frac{1}{2}, && \eta_{\mathrm{R}_\ell} = \frac{1}{2}, \\
&\boldsymbol{\Sigma}_{\mathrm{L}}^{\tau} = \mathbf{B}, && \boldsymbol{\Sigma}_{\mathrm{R}_u}^{\tau} = \mathbf{B}, && \boldsymbol{\Sigma}_{\mathrm{R}_\ell}^{\tau} = \mathbf{B}, && \boldsymbol{\Sigma}_{\mathrm{R}_u}^{\eta} = \mathbf{C}, && \boldsymbol{\Sigma}_{\mathrm{R}_\ell}^{\eta} = \mathbf{C}.
\end{aligned}
$$

5 NUMERICAL RESULTS

In Sections 5.1 and 5.2 we consider the case $P = 1$, i.e., the deterministic problem, to thoroughly investigate the performance of the presented spatial discretization. Numerical results on the stochastic Galerkin formulation with $P > 1$ is presented in Section 5.3.

5.1 Numerical convergence for the spatial discretization

We carry out a convergence study on the two-level grid in Figures 2(a) and 2(b) using an analytical solution and the method of manufactured solutions to investigate the accuracy of the numerical method [18]. The spatial domain is specified by $L_x = L_y = 300$ m. The analytical solution is given by

$$
E_x(x,y,t) = -E_y(x,y,t) = -376.7H_z(x,y,t) = \cos(\alpha x+\beta)\cdot\cos(\alpha y+\beta)\cdot\cos(\gamma t+\delta), \qquad (7)
$$

with $\alpha = 0.05$, $\beta = 1$, $\gamma = 2\pi/T$, $\delta = -\pi$. The final time is $T = 8\cdot 10^{-4}$ and the parameter values $\epsilon = \mu = 2\cdot 10^{-5}$, $\sigma = 0.1$ are used. The analytical solution (7) solves equation (3) by adding an appropriate right hand side to (3) .

The relative ℓ_2 errors are computed component-wise

$$
\varepsilon_{\ell_2}^{(i)} = \|\mathbf{v}^{(i)} - \mathbf{u}^{(i)}\|_2 / \|\mathbf{u}^{(i)}\|_2, \quad i = E_x, E_y, H_z.
$$

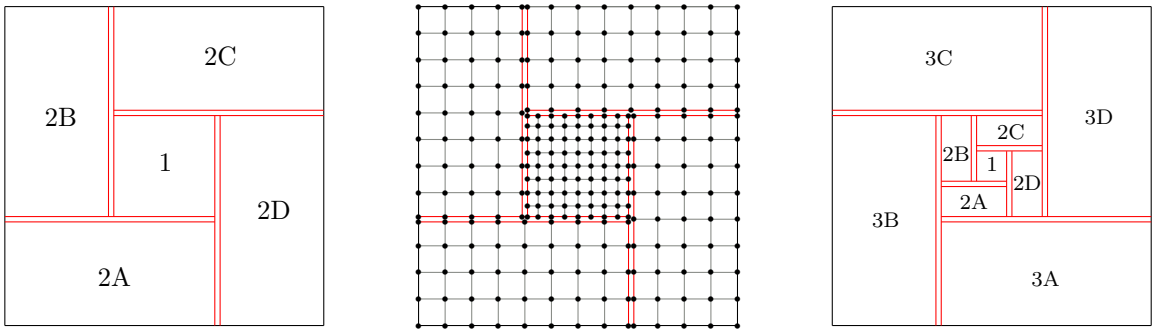

(a) Five grid blocks on two levels of discretization.

(b) Schematic image of grid points for grid in Figure 2(a).

(c) Nine grid blocks on three levels of discretization.

Figure 2: Multi-block grids used in the numerical experiments. All interfaces are of T-junction type.

The discrete ℓ_2 norm over all the spatial blocks is given by

$$\|\mathbf{u}^{(i)}\|_2 = \sqrt{\sum_k \Delta x_k \Delta y_k \sum_{n=1}^{N_k} |\mathbf{u}_{k,n}^{(i)}|^2}, \quad k = 1, 2a, 2b, 2c, 2d,$$

where N_k is the total number of grid points in block k. Let $\mathbf{u}_k^{(i)}$ denote the vector with the exact solution projected on block k and $\mathbf{v}_k^{(i)}$ the vector with the numerical solution on block k, respectively, both for component i. Assuming the same refinement factor c in both dimensions, the numerical convergence rate, $q^{(i)}$, is computed as

$$q^{(i)} = \log(\varepsilon_{\ell_2,c\Delta x}^{(i)} / \varepsilon_{\ell_2,\Delta x}^{(i)}) / \log(c).$$

The ℓ_2 errors and convergence rates are shown in Table 1. Accuracy analysis for the full multi-block discretization is highly non-trivial. The obtained convergence rates of order three are the best one could hope for according to one-dimensional accuracy analysis [19].

$\Delta x, \Delta y$	$\varepsilon_{\ell_2}^{(E_x)}$	$q^{(E_x)}$	$\varepsilon_{\ell_2}^{(E_y)}$	$q^{(E_y)}$	$\varepsilon_{\ell_2}^{(H_z)}$	$q^{(H_z)}$
10	$1.10 \cdot 10^{-3}$		$1.05 \cdot 10^{-3}$		$4.91 \cdot 10^{-1}$	
		3.37		3.34		3.48
5	$1.07 \cdot 10^{-4}$		$1.04 \cdot 10^{-4}$		$4.40 \cdot 10^{-2}$	
		3.25		3.24		3.19
2.5	$1.12 \cdot 10^{-5}$		$1.10 \cdot 10^{-5}$		$4.81 \cdot 10^{-3}$	
		3.00		2.99		3.09
1.25	$1.40 \cdot 10^{-6}$		$1.38 \cdot 10^{-6}$		$5.64 \cdot 10^{-4}$	
		3.22		3.22		3.04
0.625	$1.51 \cdot 10^{-7}$		$1.49 \cdot 10^{-7}$		$6.84 \cdot 10^{-5}$	

Table 1: Numerical convergence for the deterministic problem with two levels, $T = 8 \cdot 10^{-4}$. ℓ_2 error (ε) and order of convergence (q). The grid size refers to the grids on level 2.

5.2 Efficiency of block-decomposed grids

We investigate the efficiency of using the block-decomposed grid depicted in Figure 2(c) compared to uniform grids. The spatial domain is specified by $L_x = L_y = 900$ m, and $\epsilon = \mu =$

$2 \cdot 10^{-5}$, $\sigma = 0.1$. The ratio of grid sizes is 1:2 between levels, and the finest grid is on level 1. We use the initial condition

$$E_x(x, y, t) = -E_y(x, y, t) = -376.7H_z(x, y, t) = e^{-10^{-2}((x-450)^2+(y-450)^2)}.$$

Figure 3 shows the solution at time $T = 0.0048$ computed on the three-level grid depicted in Figure 2(c). Table 2 shows the ℓ_2 errors for the three-level grid and two uniform grids compared to a numerical reference solution computed on a fine uniform grid. Using the three-level grid leads to smaller errors compared to using the uniform grid with equivalent number of degrees of freedom. Errors of the same order of magnitude as for the three-level grid are obtained for a uniform grid with almost twice as many degrees of freedom.

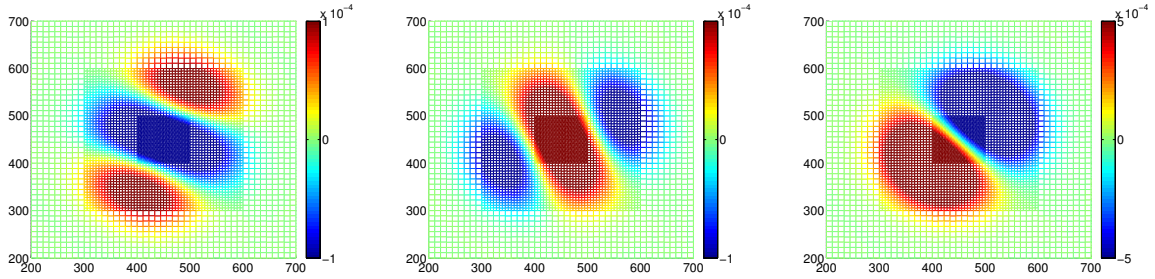

(a) E_x. (b) E_y. (c) H_z.

Figure 3: Solution on three-level grid at time $T = 0.0048$.

total no. of grid points		$\varepsilon_{\ell_2}^{(E_x)}$	$\varepsilon_{\ell_2}^{(E_y)}$	$\varepsilon_{\ell_2}^{(H_z)}$
multi-block grid:	10341	$3.62 \cdot 10^{-3}$	$5.01 \cdot 10^{-3}$	$9.59 \cdot 10^{-4}$
uniform grids:	10404	$1.85 \cdot 10^{-2}$	$1.85 \cdot 10^{-2}$	$1.49 \cdot 10^{-2}$
	19881	$5.93 \cdot 10^{-3}$	$5.93 \cdot 10^{-3}$	$5.75 \cdot 10^{-3}$

Table 2: Numerical convergence for the deterministic problem with three levels, $T = 0.0048$. ℓ_2 errors (ε) for the three-level grid and two uniform grids.

5.3 Convergence of the stochastic Galerkin solution

We now turn to the full stochastic Galerkin system and investigate the performance of different P on the three-level grid in Figure 2(c). We use a lognormal distribution of σ with mean 0.5 and standard deviation 0.2, parameterized with standard Gaussian ξ and Hermite polynomials. The same initial condition as in Section 5.2 is used for the first gPC coefficient and zero for the rest. Mean value and standard deviation of $\mathbf{E}_x$ for $P = 6$ are shown in Figure 4.

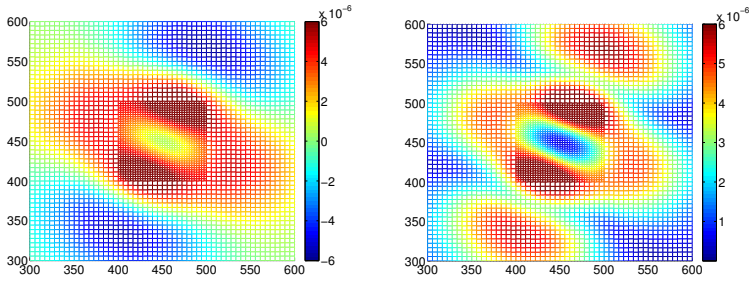

(a) Mean value for $P = 6$. (b) Standard deviation for $P = 6$.

Figure 4: Statistics for $\mathbf{E}_x$ on three-level grid at time $T = 0.012$. Only levels 1 and 2 are shown.

We measure the ℓ_2 norm of the root mean square (RMS) error of the solution

$$\varepsilon_{\ell_2,\mathrm{RMS}} = \frac{\left\| \mathrm{RMS}\left(\mathbf{v}^{(k)} - \mathbf{v}_{\mathrm{ref}}^{(k)}\right)\right\|_2}{\left\| \mathrm{RMS}\left(\mathbf{v}_{\mathrm{ref}}^{(k)}\right)\right\|_2}, \quad \text{where} \quad \mathrm{RMS}(\mathbf{v}_{i,j}^{(k)}) = \sqrt{\mathbb{E}\left[(\mathbf{v}_{i,j}^{(k)})^2\right]} = \sqrt{\sum_{m=1}^{P_{\mathrm{ref}}} \left((\mathbf{v}_{i,j}^{(k)})_m\right)^2}.$$

The ℓ_2 norms of the RMS errors are shown in Table 3. The errors are approximately halved with every increment of P.

P	$\varepsilon_{\ell_2,\mathrm{RMS}}^{(E_x)}$	$\varepsilon_{\ell_2,\mathrm{RMS}}^{(E_y)}$	$\varepsilon_{\ell_2,\mathrm{RMS}}^{(H_z)}$
2	$1.52 \cdot 10^{-1}$	$1.51 \cdot 10^{-1}$	$9.59 \cdot 10^{-2}$
3	$6.77 \cdot 10^{-2}$	$6.74 \cdot 10^{-2}$	$3.64 \cdot 10^{-2}$
4	$3.35 \cdot 10^{-2}$	$3.34 \cdot 10^{-2}$	$1.71 \cdot 10^{-2}$
5	$1.56 \cdot 10^{-2}$	$1.55 \cdot 10^{-2}$	$7.56 \cdot 10^{-3}$
6	$8.32 \cdot 10^{-3}$	$8.27 \cdot 10^{-3}$	$3.79 \cdot 10^{-3}$

Table 3: Discrete ℓ_2 norm in space of RMS errors for different orders P of gPC expansion.

The solution of the stochastic Galerkin Maxwell's equation can be used as a fast surrogate method for sampling in the inverse EM problem. It is essential that the resulting surrogate method represents a probability density function (PDF) that closely resembles the true PDF of the stochastic solution of Maxwell's equations. To quantify this resemblance, we use the Kullback-Leibler divergence, defined for a reference PDF p_{ref} and an estimated PDF p as

$$D_{\mathrm{KL}}(p_{\mathrm{ref}}||p) = \int_{-\infty}^{\infty} \log\left(\frac{p_{\mathrm{ref}}(x)}{p(x)}\right) p_{\mathrm{ref}}(x)\mathrm{d}x. \tag{8}$$

This measure quantifies the amount of information lost when p_{ref} is approximated by p and is equal to zero if the two PDFs are identical. We compute the pointwise in space Kullback-Leibler divergence by first estimating the PDF from the computed gPC coefficients of $\mathbf{v}$ through kernel density estimation methods, assuming a Gaussian kernel. The integral in (8) is then computed

with the trapezoidal rule. Figure 5 depicts the logarithms (base 10) of the Kullback-Leibler divergence for $P = 2, 4, 6$ with respect to a reference PDF generated from the $P = 10$ order gPC expansion. The errors in the PDF estimates are clearly reduced as P increases, but are still quite substantial in some spatial regions. Note that the middle region with the finest grid captures well the PDFs already for $P = 4$. Further investigation is needed to fully evaluate the potential of stochastic Galerkin PDF estimates in geophysical inverse models.

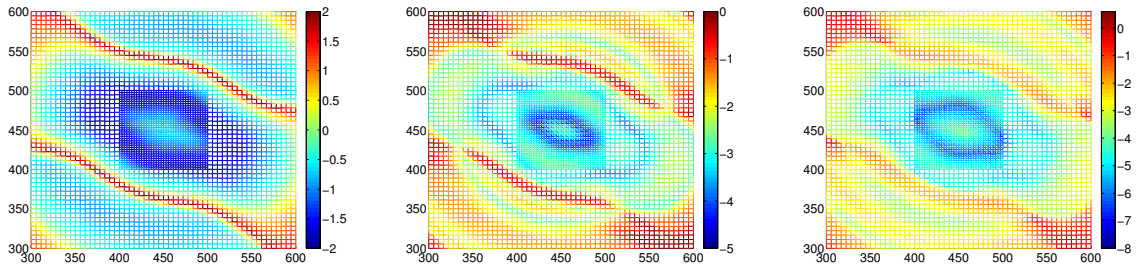

(a) $P = 2$. (b) $P = 4$. (c) $P = 6$.

Figure 5: Logarithm of Kullback-Leibler divergence for $\mathbf{E}_x$ on three-level grid at time $T = 0.012$. Only levels 1 and 2 are shown. Note the different ranges of the color bars.

6 CONCLUSIONS

A time-stable finite difference method for Maxwell's equations has been presented. The proposed method uses the summation-by-parts-operators framework, previously applied to Maxwell's equations on equidistant grids and in this work extended to a stochastic Galerkin formulation and with stable couplings of grid blocks of different grid sizes. This leads to a highly efficient method where regions with high resolution requirements can be sufficiently resolved without the need for excessively fine resolution in the far-field.

We demonstrate third order numerical convergence in space of the method for a deterministic setup on a block-decomposed grids with different grid sizes. In a stochastic setting with lognormal conductivity, the method is evaluated on a block-decomposed grid in terms of convergence with increasing order of gPC expansion. The capabilities of capturing the PDF of the solution is verified by estimating the Kullback-Leibler divergence pointwise in space.

ACKNOWLEDGEMENTS

This work was supported by VISTA (Project 6357) and the SUCCESS Centre for CO_2 storage under grant 193825/S60 from the Research Council of Norway.

REFERENCES

[1] Borcea, L. Electrical impedance tomography. *Inverse Probl.* (2002) **18**(6), R99–R136.

[2] Zhdanov, M. S. Electromagnetic geophysics: Notes from the past and the road ahead. *Geophysics* (2010) **75**(5), 75A49.

[3] Bhuyian, A. H., Landrø, M., and Johansen, S. E. 3D CSEM modeling and time-lapse sensitivity analysis for subsurface CO_2 storage. *Geophysics* (2012) **77**(5), E343.

[4] Gilks, W. R., Richardson, S., and Spiegelhalter, D. J. *Markov Chain Monte Carlo in Practice*. CRC press (1996).

[5] Ghanem, R. and Spanos, P., *Stochastic finite elements: a spectral approach*. Springer, New York (1991).

[6] Xiu, D. and Karniadakis, G. E. The Wiener-Askey polynomial chaos for stochastic differential equations. *SIAM J. Sci. Comput.* (2002) **24**(2):619–644.

[7] Börner, R.-U. Numerical modelling in geo-electromagnetics: advances and challenges. *Surv. Geophys.* (2009) **31**(2), 225–245.

[8] Avdeev, D. B. Three-dimensional electromagnetic modelling and inversion from theory to application. *Surv. Geophys.* (2005) **26**(6), 767–799.

[9] Key, K. and Ovall, J. A parallel goal-oriented adaptive finite element method for 2.5-D electromagnetic modelling. *Geophys. J. Int.* (2011) **186**(1), 137–154.

[10] Commer, M. and Newman, G. A parallel finite-difference approach for 3D transient electromagnetic modeling with galvanic sources. *Geophysics* (2004) **69**(5), 1192–1202.

[11] Svärd, M. and Nordström, J. Review of summation-by-parts schemes for initial-boundary-value problems, *J. Comput. Phys.* (2014) **268**:17–38.

[12] Nissen, A. Kormann, K. Grandin, M and Virta, K. Stable difference methods for block-oriented adaptive grids, *J. Sci. Comput.* (2015) **65**:486–511.

[13] Kreiss, H.-O., and Scherer, G. *Finite element and finite difference methods for hyperbolic partial differential equations*. In Mathematical Aspects of Finite Elements in Partial Differential Equations, pages 179–183. Academic Press, New York (1974).

[14] Carpenter, M. H., Gottlieb, D., and Abarbanel, S. Time-stable boundary conditions for finite-difference schemes solving hyperbolic systems: methodology and application to high-order compact schemes. *J. Comput. Phys.* (1994) **111**(2):220–236.

[15] Strand, B. Summation by parts for finite difference approximations for d/dx. *J. Comput. Phys.* (1994) **110**(1):47–67.

[16] Nordström, J. and Gustafsson, R. High order finite difference approximations of electromagnetic wave propagation close to material discontinuities. *J. Sci. Comput.* (2003) **18**(2), 215–234.

[17] Mattsson, K. and Carpenter, M. H. Stable and accurate interpolation operators for high-order multiblock finite difference methods. *SIAM J. Sci. Comput.* (2010) **32**:2298–2320.

[18] Roache, P.J. Verification of codes and calculations. *AIAA J.* (1988) **36**(5):696–702.

[19] Gustafsson, B., The convergence rate for difference approximations to mixed initial boundary value problems. *Math. Comp.* (1975) **29**:396–406.

VII International Conference on Computational Methods for Coupled Problems in Science and Engineering
COUPLED PROBLEMS 2017
M. Papadrakakis, E. Oñate and B. Schrefler (Eds)

HETEROGENEOUS DEFORMATION DURING ELECTROMAGNETIC RING EXPANSION TEST

K. YANG*, D. CHERNIKOV†, T. SAPANATHAN*,#, R.N. RAOELISON+, V. GLUSCHENKOV†, N. BUIRON* AND M. RACHIK*

*Sorbonne universités, Université de technologie de Compiègne, Laboratoire Roberval CNRS UMR - 7337, Centre de recherche Royallieu, CS 60319, 60203 Compiègne cedex, France
Web page: http://www.utc.fr

† Samara National Research University, 34 Moskovskoye shosse, Samara, 443086, Russia
Web page: http://www.ssau.ru

#Institute of Mechanics, Materials and Civil Engineering, Université catholique de Louvain, B-1348 Louvain-la-Neuve, Belgium
Web page: http://www.uclouvain.be

+ Université de Bourgogne Franche Comté, IRTES-LERMPS, Université de Technologie de Belfort Montbéliard, 90100 Belfort, France
Web page: http://www.utbm.fr

Corresponding author: kang.yang@utc.fr (K. Yang)

Key words: Ring expansion test, Multiphysics Problems, Electromagnetic pulse forming, Finite element method

Abstract. High speed forming methods become attractive in manufacturing and it significantly reduces the cost and energy requirements. Conventional manufacturing processes such as forging, forming, stamping and cutting of metals typically involve a strain rate of $10^2 - 10^4\ s^{-1}$ which includes high energy rate fabrication (HERF) methods [1]. During advanced manufacturing methods such as high speed forming and high speed welding processes, certain local regions (e.g. interfaces) of materials could also experience significantly high strain rate ($> 10^4\ s^{-1}$). In order to understand the physical behaviours of materials and to design/control/optimise, such manufacturing processes that require an appropriate technique to capture the material's viscoplastic property under the high strain rate deformation. Therein, the electromagnetic ring expansion test becomes a promising method to characterize the material behaviours under the high strain rate deformation. The ring expansion is caused by Lorentz force that is generated due to the magnetic induction on the ring. However, the realistic nature of the electromagnetic ring expansion test is quite complex because of the coupling physics between electromagnetic-thermal-mechanical components.

Therefore, in this study we evaluate certain controlling parameters which govern the fundamental behaviour of the electromagnetic ring expansion test. Particularly the rotation and inhomogeneous deformation of the ring are noticeably observed and these phenomena require extra attention.

With the aid of LS-DYNA® package and concurrent experimental verifications, the influencing factors which cause the rotation and inhomogeneous deformation were identified. The analysis shows that the asymmetry of axial compression and radial expansion caused by Lorentz force resulted from the asymmetry of the coil geometry. Following this detailed analysis, this paper proposes the methodologies to reduce the rotation and inhomogeneous deformation of the ring during the electromagnetic ring expansion test.

1 INTRODUCTION

Over the past few decades, electromagnetic ring expansion test has been considered to investigate material properties under high stain rate deformation [2-5]. This technique uses electromagnetic pulse to create Lorentz force that causes the expansion on a metallic ring or tube. During the test, the induced current flow through the ring and the plastic deformation of the material generate heat and thereby it leads to an increase in the temperature of the workpiece. Thus, in order to understand and model the complete physical phenomena, one should consider the multi-physics phenomena of electromagnetic-thermal-mechanical coupled problem.

The workpiece deformation during an electromagnetic ring expansion test occurs at a very high deformation speed (i.e. short duration of time), it requires sophisticated measuring techniques to make some observations and identify the material parameters. Nowadays, thanks to the technological advancements, direct observation using high-speed cameras and photonic Doppler velocimetry (PDV) [6] are widely used in electromagnetic forming research to capture the high speed deformation. However, finite element (FE) simulations provide the alternative solution to understand the realistic behavior and physical phenomena which occur during the test.

In reality, during a ring expansion test, inhomogeneous deformations occur in most of the cases which significantly influence the material parameter identification procedure. In one of our recent work, the suitability of ring expansion test to identify the material parameters was investigated [7]. In that particular study a shield block mechanism was proposed to eliminate the compressive Lorentz force that is one of the reason associated with the inhomogeneous deformation [7] . However, till to date, there exist a lack of research work on the problem of inhomogeneous deformation and its consequences on the material parameter identification. The present work mainly focuses on the causes of the heterogeneous deformation. In this paper, the problem is investigated and the reasons for inhomogeneous deformation are identified with the help of FE simulations. By developing a clear understanding the situation, which can lead to minimize and/or completely eliminate the effect of inhomogeneous deformation during the ring expansion test.

2 METHOD

2.1 Experiment method

The experimental test cases explained in this section were performed in Samara National Research University in Russia. The components of the experimental setup used in this study are shown in Figure 1.

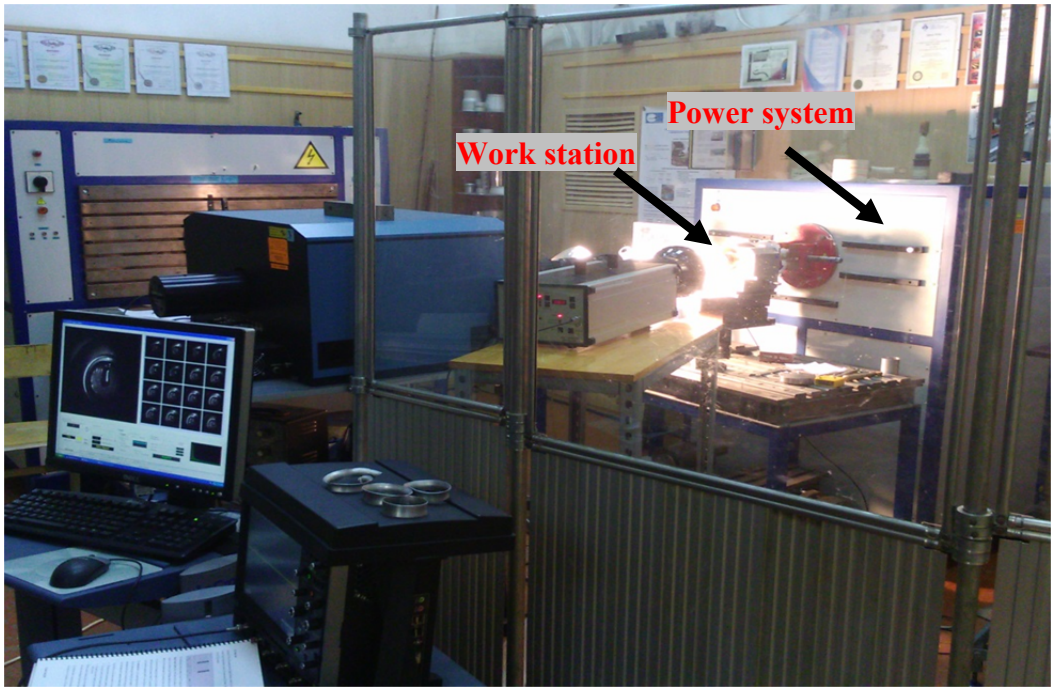

(a)

(b)

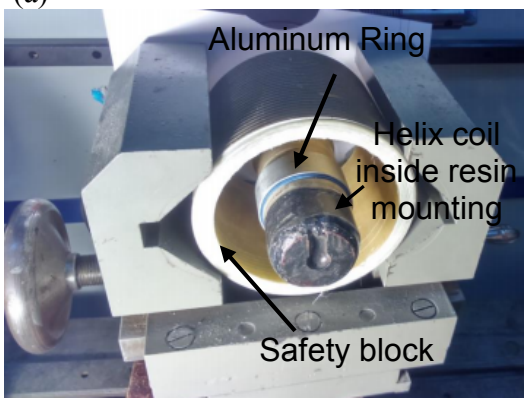

(c)

Figure 1: Images showing the of experimental unit and its components (a) overall view of the apparatus, (b) Rogowski coil used for the electric current measurements (c) helix coil and the ring assembly placed insides a large safety block.

As shown in Figure 1, the major components of the equipment used in these experiments are the pulse generator, and a workstation including a helix coil (reinforced in a fiberglass resin), Rogowski coil and support used to hold the workpiece. The Rogowski coil [8] is used to measure the pulse current flow through the helix coil.

An 8-turn copper helix coil was used here to expand the ring. That has a cross section of *3 mm* × *7 mm* (height × radial direction) and winding pitch is *1 mm*. A shield block is also used for safety reasons to control the ejection of ring pieces at high energy from a fragmentation. Rings were made from an aluminum alloy AA5154 tube. They have an outer diameter of *52 mm*, having either *10 mm* or *5 mm* in height and *1 mm* in thickness. The

maximum energy storage capacity of the power supply is *19.3 kJ*. In order to get a relatively high plastic strain without causing fracture, *1.27 kJ* and *1.83 kJ* energy pulses were respectively used for rings with *5mm* and *10 mm* heights. The frequency of current flow through the coil is *~1.7 kHz*.

2.2 Simulation method

The LS-DYNA® Mechanical and Electromagnetic solvers were enabled to solve this coupled problem [9]. It use a boundary element method coupled with FE method to deal with the electromagnetic calculation [10, 11]. In this paper, LS-DYNA® solver ran on parallel computer network available at University of Technology of Compiègne, using multiple processors (16 Xeon X7542 processors with six-core at *2.67 GHz* (total of 96 cores) and *1 TB* RAM) configured in a Shared Memory Parallel (SMP) computation method.

The meshed models which consist of 8 nodes brick element for both coil and expansion ring were used in the simulation. The element size along the thickness of the ring was set as *0.2 mm*, which sufficiently captures the electromagnetic skin depth effect during the simulation. The element size along the height was set as *1 mm* that was also sufficient to capture the different amount of deformation along the height. The current flow through the helix coil is input to the model, and it was obtained from the experimental measurements using Rogowski coil. Figure 2 shows two different orientations of the meshed model for the case *5 mm* ring height.

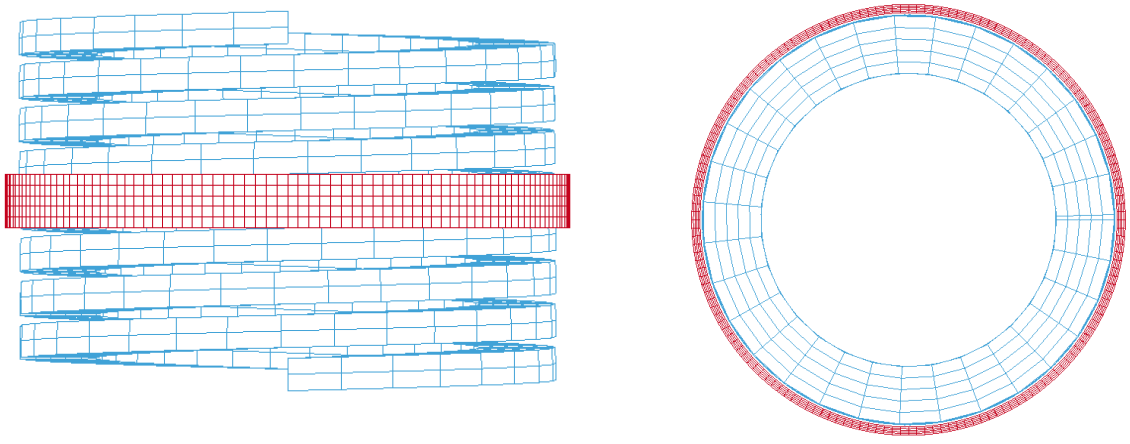

(a) (b)

Figure 2: Meshed model with *5 mm* rings used in LS-DYNA simulations (a) front view and (b) top view.

An appropriate plasticity model and the material properties are required for the simulation to predict an accurate test result. A standard rate dependent plasticity using Cowper-Symonds strain rate dependency model was used here to describe the material behaviors under high strain rate as shown in equation 1.

$$\bar{\sigma} = (\sigma_y + K\bar{\varepsilon}^n)\left[1 + \left(\frac{\dot{\bar{\varepsilon}}}{C}\right)^p\right] \quad (1)$$

where, $\bar{\sigma}$ and $\bar{\varepsilon}$ are the von Mises equivalent stress and strain respectively, $\dot{\bar{\varepsilon}}$ is the strain rate term and σ_y is the yield stress of the material. *K*, *n*, *C* and *p* are material constants given in Table 1. The coil was set as rigid and having fixed boundary condition in this simulation since it has been reinforced using a fiberglass resin mounting.

Table 1: Plasticity model parameters used for the ring material, AA5154

Parameters	*Yield stress (MPa)*	*K(MPa)*	*n*	*C*	*p*
Numerical values for AA5154	*177*	*625*	*1*	*6500*	*0.3333*

3 RESULTS

The final average diameters of *5 mm* and *10 mm* rings after the expansion are *59.4 mm* and *62.6 mm*, respectively. The final shapes of rings after expansion are shown in Figure 3. It is clearly noticeable that each specimen has a certain amount of inhomogeneous deformation.

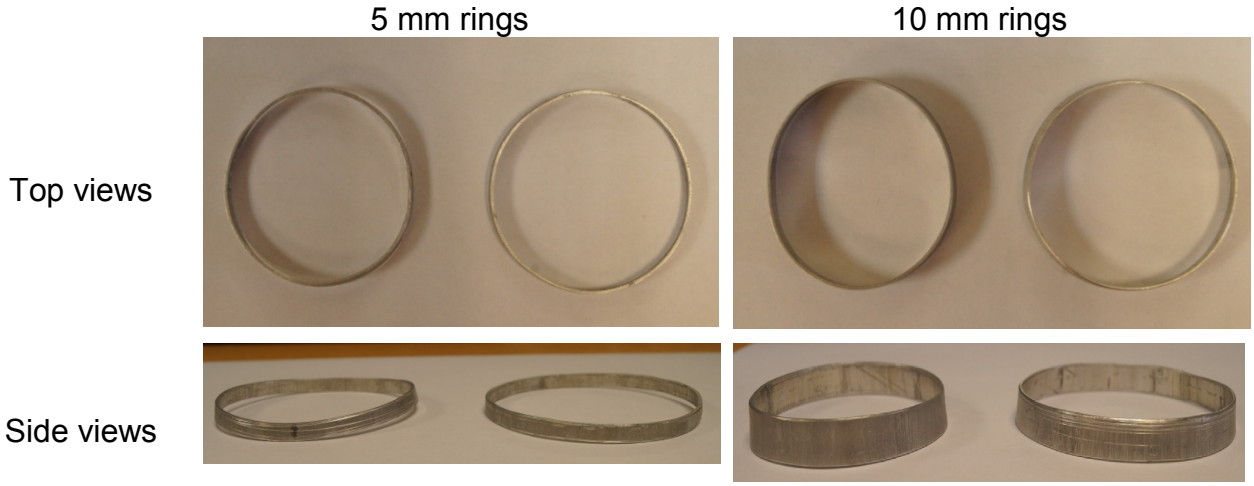

Figure 3: Top views and side views showing the final shape of rings after the expansion test

Although, the *5 mm* rings nearly remain round during the expansion process, they show an out of plane deformation in their side views. On the other hand, the *10 mm* rings have showed in-plane deformation, but the deformations on the top and bottom regions of those rings are clearly different.

Simulation results are also in a good agreement with experimental results as shown in Figure 4. The results have the final average diameters of *60.8 mm* and *63.1 mm* for the rings with *5 mm* and *10 mm* heights, respectively. The numerical simulation also shows some of the inhomogeneous deformation, *e.g.* out of plane deformations of *5 mm* rings. Comparing simulated results to experiments, the reason for inhomogeneous deformations will be discussed in the next section.

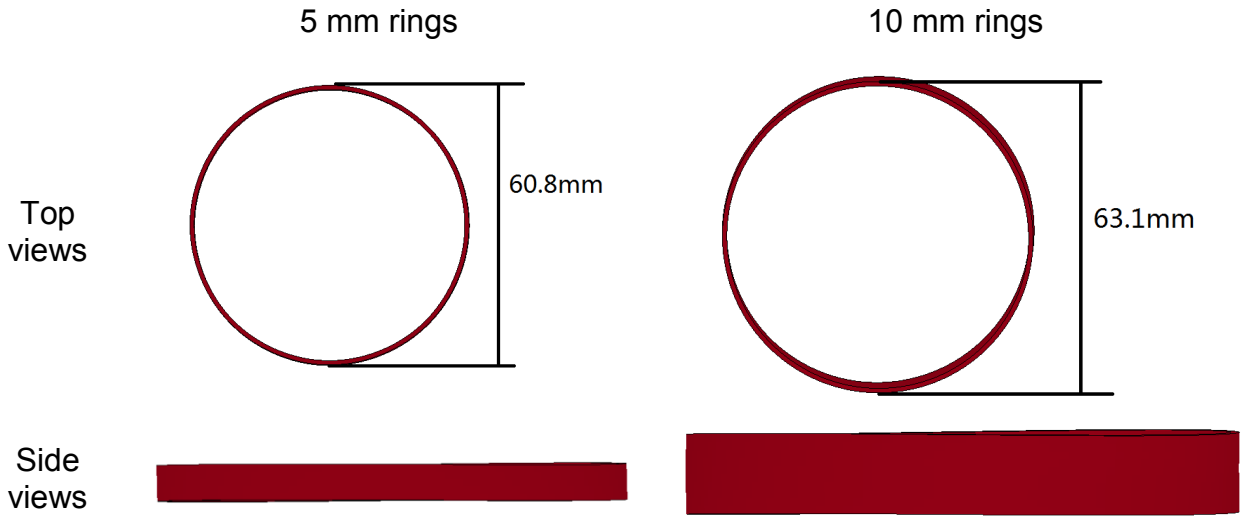

Figure 4: Simulation results showing the final geometry of the rings with *5 mm* and *10 mm* height at the end of the expansion test

4 ANALYSIS OF INHOMOGENEOUS DEFORMATION

4.1 Rigid body rotation

In simulation, the rigid body rotation of rings can be easily observed. Figure 5a shows the simulation result of *5 mm* ring expansion test at the time step of *120 μs* (nearly at the end of input pulse current). During the process, the ring is rotated by an angle of ~5° and thus Lorentz force causes out of plane deformation on the ring.

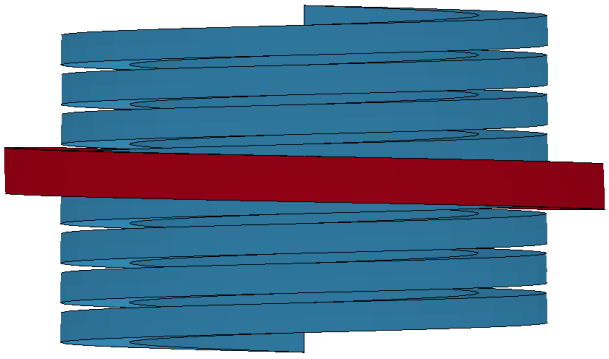

(a)

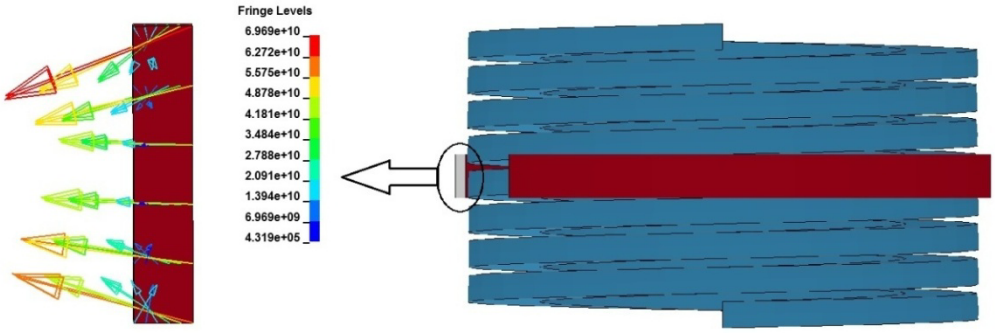

(b)

Figure 5: Simulation result of *5 mm* ring expansion test; (a) Relative location of ring and coil at *120 μs* and (b) Lorentz force vectors on a cross section on the ring (Unit: N/m^3).

Figure 5b shows Lorentz force vectors on a ring cross section at *10 μs*. At this instant, the ring was not rotated. The vectors clearly indicate that there was not only a tensile Lorentz force (in the radial direction) but also a compressive Lorentz force acts on the ring. Besides, the maximum Lorentz force on the top region of the ring ($6.969x10^{10}$ N/m^3) was bigger than that of on the bottom region of the ring (smaller than $6.272\ x10^{10}$ N/m^3). This uneven distribution may be caused by the asymmetry of the coil and the relative longitudinal position of the ring. Vice versa, it also enables a rigid body rotation of the ring during the test.

4.2 Effect of longitudinally non concentric location of the ring

In the previous section the rigid body rotation has been discussed. However, it cannot cause uneven deformations on the top and bottom for *10 mm* rings as shown in Figure 3. Figure 6a shows a schematic illustration with the final dimension of an expanded *10 mm* ring obtained with a case of longitudinally non concentric location of the ring (i.e. Ring center longitudinally has an offset with the centerline of the helix coil).

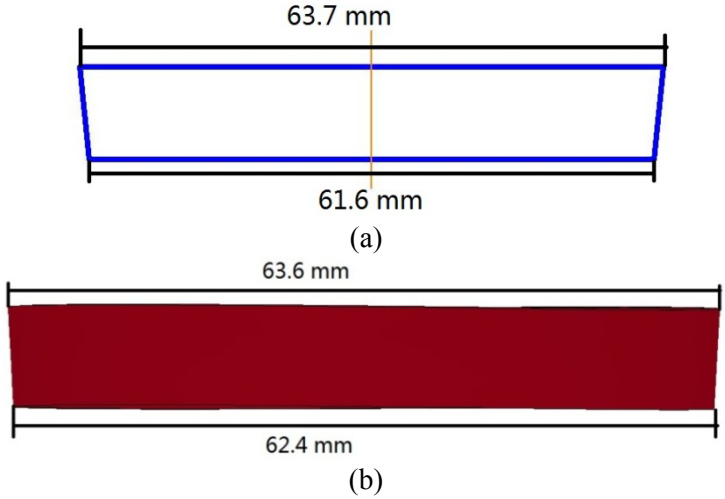

Figure 6: Side view of the *10 mm* ring after the expansion test showing the final dimension (a) schematic illustration showing the results of experiment and (b) a non concentric simulation model.

The experimental results indicate that the top region of the ring has an outer diameter of *63.7 mm* and on the bottom region it has *61.6 mm*. Simulations with the symmetric longitudinal position of the ring with the helix coil (Figure 2, 4 and 5) do not show the uneven deformation, and it is not significantly visible for the *10 mm* ring height. Therefore the uneven deformation must be caused by some other source, and a longitudinally non concentric relative location of ring and coil is investigated here. In this simulation, the ring was positioned 1 mm lower along the longitudinal distance and thus it was no longer concentric to the helix coil. The other conditions were maintained as the same as the *10 mm* ring expansion test case. The simulation result (Figure 6b) clearly shows a good agreement with the experimental result in terms of its final dimensions and its final shape of the ring. The outer diameters on the top and bottom regions of the ring are predicted as *63.6 mm* and *62.4 mm* respectively. The comparison shows that the uneven deformations between the top and bottom are resulted from the relative position of the ring.

5 CONCLUSION

This paper shows an investigation of inhomogeneous deformation that occurs during the electromagnetic ring expansion tests. Experimental test cases clearly show the out of plane deformation for the case of rings with *5 mm* height and uneven deformations for the cases of rings with *10 mm* height. Numerical simulations are used to identify the underlying phenomena of this inhomogeneous deformation during the coupled problem and to completely eliminate or minimize the effect of inhomogeneous deformation that occurs during the ring expansion test. A rigid body rotation was identified as one of the reason for this heterogeneous deformation, and it was caused by the asymmetric distribution of Lorentz force. Relative position of the ring to the helix coil (i.e. non concentric dislocation of ring and coil) is also identified as another reason for these inhomogeneous deformations. However, in order to quantitatively evaluate their individual influences, more tests are required with various ring heights or coil lengths, and with different input energies. Besides, certain techniques such as high speed camera or multi-point PDV can be used to record the deformation and to capture the rigid body movements of rings. Moreover, in order to avoid inhomogeneous deformations, the coil may be fabricated as symmetric part and the ring should be located at the center of the coil to avoid unnecessary expansion behavior of the ring.

REFERENCES

[1] L. Meyer, Material behaviour at high strain rates, in *1st International Conference on High Speed Forming*, Dortmund, (2004), pp. 45-56.

[2] F. I. Niordson, A unit for testing materials at high strain rates, *Experimental Mechanics,* (1965) vol. 5, pp. 29-32.

[3] D. Grady and D. Benson, Fragmentation of metal rings by electromagnetic loading, *Experimental Mechanics,* (1983) vol. 23, pp. 393-400.

[4] M. Altynova, X. Hu, and G. S. Daehn, Increased ductility in high velocity electromagnetic ring expansion, *Metallurgical and Materials Transactions A,* (1996) vol. 27, pp. 1837-1844.

[5] J. Imbert, T. Rahmaan, and M. Worswick, Interrupted pulse electromagnetic expanding ring test for sheet metal, in *EPJ Web of Conferences*, (2015), p. 01048.

[6] J. R. Johnson, G. Taber, A. Vivek, Y. Zhang, S. Golowin, K. Banik*, et al.*, Coupling Experiment and Simulation in Electromagnetic Forming Using Photon Doppler Velocimetry, *Steel Res. Int.,* (2009) vol. 80, pp. 359-365.

[7] K. Yang, G. Taber, T. Sapanathan, A. Vivek, G. Daehn, R. Raoelison, *et al.*, Suitability of the electromagnetic ring expansion test to characterize materials under high strain rate deformation, in *NUMIFORM, 12th international conference on Numerical Methods in Industrial Forming Processes*, Troyes, (2016).
[8] D. A. Ward and J. L. T. Exon, Using Rogowski coils for transient current measurements, *Engineering science and education journal,* (1993) vol. 2, pp. 105-113.
[9] *LS-DYNA Keyword User's Manual R8.0*. Livermore, CA, USA: Livermore Software Technology Corporation (LSTC), (2015).
[10] P.L'Eplattenier, Introduction of an Electromagnetism Module in LS-DYNA, presented at the Ohio State University workshop on Magnetic Metal Forming, Columbus, OH, USA, (2005).
[11] I. Çaldichoury and P. L'Eplattenier. (2012). *EM Theory Manual*.

VII International Conference on Computational Methods for Coupled Problems in Science and Engineering
COUPLED PROBLEMS 2017
M. Papadrakakis, E. Oñate and B. Schrefler (Eds)

NUMERICAL INVESTIGATION OF FLEXIBLE BEAMS FOR ELECTROMAGNETIC ENERGY HARVESTING UNDER THE WAKES FROM UPSTREAM CYLINDER

Samir Chawdhury* **and Guido Morgenthal** †

* † Modelling and Simulation of Structures
Bauhaus University Weimar
Marienstr. 13, 99423 Weimar, Germany
e-mail: samir.chawdhury@uni-weimar.de, web page:
http://www.uni-weimar.de/Bauing/MSK/-en.html

Key words: Electromagnetic energy harvesting, Low wind speed harvesters, Wake flows, Upstream wakes, Vortex Particle Methods, Wireless sensor, Structural health monitoring.

Abstract. The paper investigates the potential of flexible cantilever beams numerically for electromagnetic (EM) energy harvesting under the wakes from upstream cylinder. A two-dimensional fully coupled fluid–structure interaction model has been presented. The flow solver based on the Vortex Particle Method and the structural solver based on corotational finite element formulation are coupled to accurately account for the geometrically nonlinear effects of such very flexible elements. A reference flutter-based harvester is simulated initially for the validation of the solver. The coupled solver is used furthermore to model the power output from the flexible cantilever beam under the wakes from the upstream circular cylinder, particularly, at low wind speeds like 2-4 m/s. Satisfactory results are achieved while the modeled energy outputs of the proposed harvester model are compared with the reference harvester.

1 INTRODUCTION

In recent years, energy harvesting from ambient vibration sources for wireless sensor nodes (WSN) has been extensively investigated, particularly, to replace the conventional use of expensive batteries. With the rapid advancements in wireless technologies and low-power electronics, the power consumption of electronic devices has been reduced to a few milliwatts. Wind energy offers an alternative source of mechanical vibration which can be converted into electrical energy. Structures under wind loading may experience large vibration due to the aerodynamic phenomena like vortex-induced vibration (VIV), galloping, flutter, etc. Akaydin exploited the vibration of the flexible beam under different wind fields in [1] for piezoelectric energy harvesting. The transverse galloping of bluff

sections was utilized in [2] and [3] for piezoelectric induction. On the other hand, the VIV phenomenon was used in [4] for electromagnetic (EM) power generation. The wind-induced vibration of stay cables has been investigated in [5] for EM power generation. The instability phenomena galloping was used by [6] and [7] for EM induction. The susceptibility of the T-shaped cantilever system to rotational flutter was used for EM power generation in [8].

This paper presents a two–dimensional fully coupled fluid–structure interaction (FSI) model for simulating flexible cantilever beams to investigate numerically the potential of electromagnetic (EM) energy harvesting under the wakes from upstream cylinder. The numerical investigations within this study have been carried out using a Computational Fluid Dynamic (CFD) solver VXflow, which is fundamentally based on Vortex Particle Method (VPM). The solver has successfully been used for modeling of flows past complex structural assemblies in [9], [10] as well as for simulation of bridge aerodynamics in [11]. A structural solver based on a corotational finite element formulation is coupled with the mentioned CFD solver to model the large deformation effects.

The energy in the wakes, generated from upstream cylinder under free stream flow, can be used for small-scale energy harvesting [12]. If the resonance frequency of a flexible cantilever system in the downstream become same as the frequency of the upstream vortex shedding, the structure may experience large amplitude vibrations. The potential of conversion of this mechanical vibration into electrical energy using an EM transducer has been studied here numerically. In this study, a T-shaped harvester based on instability phenomenon flutter, which was investigated extensively for EM power generation in [8], has been considered as the reference system and also used for the validation of the proposed coupled solver. Numerical simulations are performed using the validated coupled solver to investigate the efficiency of the proposed harvester model, particularly, under low wind speed in contrast to the reference flutter-based harvester.

2 ELECTROMAGNETIC ENERGY HARVESTING FROM WAKES

2.1 Design of the energy harvester

The vibration of flexible cantilever system under the wakes from upstream circular cylinder has been proposed for electromagnetic (EM) energy harvesting. When the vortex shedding frequency (f_s) of an upstream cylinder comes close to the resonance frequency of the downstream cantilever beam (f_α), large vibration may occur. Using an EM transducer, it is possible to create the required relative movement between magnet and coil for EM power generation. The energy harvesting mechanism from upstream wakes using a prototype flexible cantilever system is presented schematically in Figure 1. For a circular cylinder, the frequency of the vortex shedding can be expressed as [13]:

$$f_s = \frac{StU_\infty}{D} \tag{1}$$

where St is the Strouhal number, U_∞ is the free stream flow, and D is the diameter of the

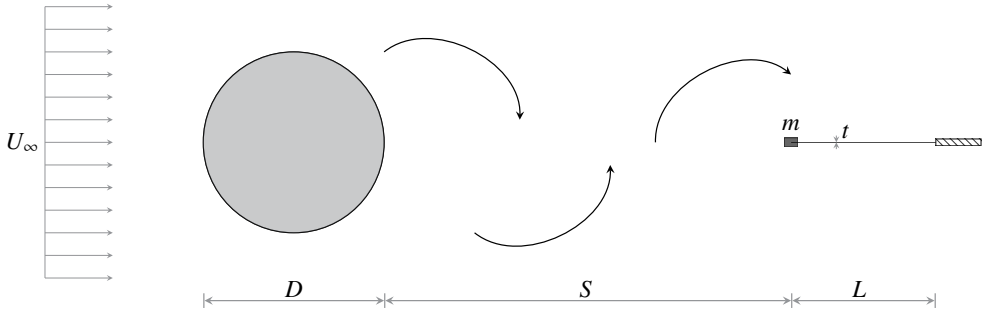

Figure 1: Schematic electromagnetic energy harvesting from wakes from upstream cylinder: an upstream circular cylinder of diameter D generates wakes under the free stream flow U_∞. A downstream flexible cantilever beam, with a magnet of mass m at the cantilever tip, is located at a distance S from the upstream cylinder. Here, t and L are the thickness and the length of the cantilever harvester.

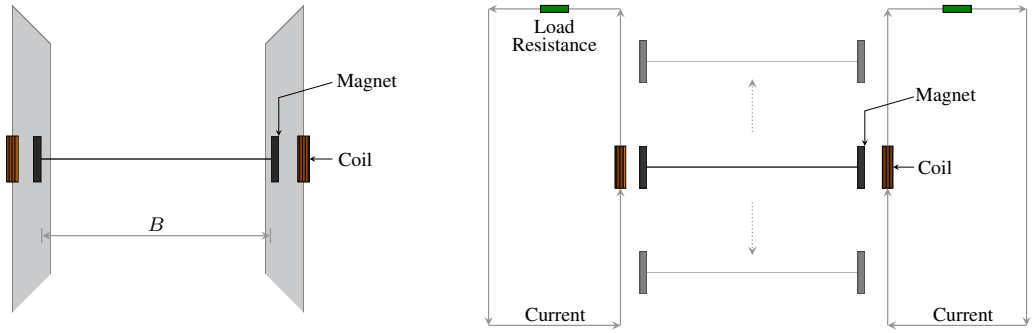

Figure 2: Conversion of mechanical vibration of the flexible cantilever beam in c.f. Figure 1 into electrical power using an electromagnetic transducer: (left) front view and the coils attached to the side walls, (right) the current flow in the circuit due to the relative movement between the magnets and coils.

circular cylinder. For a wide range of high Reynolds number (Re), the strouhal number of circular cylinder is almost constant, which is 0.2 [14]. The Re of a circular cylinder for a free stream flow can be expressed as following:

$$Re = \frac{U_\infty D}{\nu} \tag{2}$$

where ν is the kinematic viscosity of the fluid. Under specific free stream flow, the frequency of vortex shedding depends on the dimension of the circular cylinder. Therefore, to target a specific wind speed for energy harvesting, the options are to change cylinder size and/or to change the system frequency such that f_s and f_α become close to each other. Figure 2 shows the electromagnetic configuration of the proposed harvester. At the resonance state, the vibration of the tip of the cantilever beam causes a relative movement between the magnet and the coil and induces current flow through the circuit. The side walls are provided not only to hold the coils but also to keep the wakes flows less affected along the width of the harvester.

2.2 Concepts of electromagnetism

The fundamental principle of electromagnetism is that the relative movement between magnet and coil results in a varying amount of magnetic flux cutting through the coil. According to Faraday's law of induction, the open-circuit voltage V_{oc} in the loop of the coil can be expressed as follows [15]:

$$V_{oc} = \oint_{l_{coil}} (v \times \beta)\, dl = NlBv, \tag{3}$$

where, B is the magnetic flux density at each coil segment, dl is the vector of each segment of the coil, l_{coil} is the total length of the coil, v is the relative velocity between the center of the coil and the magnet, N is the number of coil turns, and l is the mean circumference of the coil. The Voltage across the load resistance, V_L, can be calculated as follows

$$V_L = V_{oc} \frac{R_L}{R_L + R_C} \tag{4}$$

where R_L and R_C are the load resistance and coil resistance, respectively.

3 FULLY COUPLED CFD SOLVER

3.1 Vortex Particle Method

The Vortex Particle Method (VPM) is fundamentally based on the simplified vorticity description of the fundamental Navier-Stokes (NS) equation. For incompressible unsteady flow of a viscous fluid, the NS equation in terms of the vorticity can be expressed as:

$$\frac{\partial \omega}{\partial t} + (\boldsymbol{u} \cdot \nabla)\, \omega = \nu \nabla^{\mathbf{2}} \omega. \tag{5}$$

For inviscid flow equation (5) can be rewritten in substantial derivative notation such that

$$\frac{\mathrm{D}\omega}{\mathrm{D}t} = 0. \tag{6}$$

Here, equation (6) allows the use of gridless numerical scheme and discretization of particle elements in Lagrangian manner. Further details on the method can be found in [9, 11].

3.2 Structural model

The structural system is modeled as multi-degree of freedom (MDOF) system, in which the system is subdivided into a number 2-D Euler–Bernoulli finite beam elements. The equation of motion for a system with many degrees of freedom can be written as

$$\mathbf{M}\ddot{X} + \mathbf{C}\dot{X} + \mathbf{K}X = F. \tag{7}$$

where $X, \dot{X}, \ddot{X}$ are the vector of nodal displacements, velocities and accelerations respectively; and $\mathbf{M}$, $\mathbf{C}$, $\mathbf{K}$ are the mass, structural damping and stiffness matrix respectively;

and F is the force vector. The damping of the system is approximated based on the assumption of Rayleigh damping approach as follows

$$\mathbf{C} = a_0\mathbf{M} + a_1\mathbf{K} \tag{8}$$

where, a_0 and a_1 are proportionality factor for mass-proportional and stiffness-proportional damping, respectively. As solution algorithm, the commonly used Newton–Raphson algorithm is used. The Newmark-Beta method is employed as the numerical integrator.

3.3 Fluid-structure coupling

At each simulation time step, the calculated pressures on the surface panels from the flow solver are projected into nodal forces for the structural solver. After achieving the solution of the deformed structure, the surface panels and the panel velocities are calculated by projecting the nodal solutions, and supplied to the flow solver. The recalculation of the surface vortices for the updated surface panels are then performed by the flow solver. Finally, the boundary conditions are updated to perform further calculations in loops.

4 MODELING OF ELECTROMAGNETIC ENERGY HARVESTERS

4.1 Introduction

This section presents the utilization of the presented coupled solver for simulating the flexible cantilever beam under the wakes from upstream circular cylinder. The aim is to model the extracted energy outputs from the vibration of the proposed cantilever harvester using an electromagnetic (EM) transducer. However, to understand the efficiency of the proposed harvester model, a flutter-based T-shaped cantilever harvester, which was studied in [8], has been considered as reference harvester. The presented coupled solver is validated initially by comparing the modeled energy outputs with the reference harvester. Furthermore, the validated solver has been shown used to model the proposed EM energy harvesting from upstream wakes. The optimization of the performance of the proposed harvester is also investigated.

4.2 Modeling of T-shaped reference harvester for solver validation

The equation of motion of the prototype harvester considering the influence of electromagnetic transducer can be expressed as follows

$$\mathbf{M}\ddot{X} + (\mathbf{C}_m + \mathbf{C}_e)\dot{X} + \mathbf{K}X = F, \tag{9}$$

where $\mathbf{C}_m + \mathbf{C}_e$ represents the system damping matrix within the framework of the structural solver, c.f. equation (8). The proportional factors, a_0 and a_1, are calculated considering the first two vibration modes of the harvester (ω_1 and ω_2) using equation (10),

$$a_0 = \zeta_t \frac{2\omega_1\omega_2}{\omega_1 + \omega_2}, \; a_1 = \zeta_t \frac{2}{\omega_1 + \omega_2}, \tag{10}$$

where ζ_t is the total system damping ratio. The physical dimensions and the dynamic proerties of the reference T-shaped harvester and also the proposed harvester in Figure 1 are shown together in Table 1. The only difference is that the reference harvester has a vertical plate of height H at the cantilever tip. The damping ratios ($\zeta_t = \zeta_m + \zeta_e(R_L)$) of the reference harvester for different electrical load resistances R_L (100–5000 Ω) were measured experimentally by performing free vibration tests. The corresponding total system damping coefficients ($c_t = c_m + c_e(R_L)$) were calculated using the following equation

$$c_t = c_m + c_e(R_L) = 2m_\alpha(\zeta_m + \zeta_e(R_L))\omega_\alpha, \tag{11}$$

where m_α and ω_α are the rotational mass and frequency of the system. Here, for a cantilever beam with tip mass m, the natural frequency and the rotational stiffness of the system can be calculated using $\omega_\alpha = \sqrt{3EI/mL^3}$ and $K_\alpha = 2EI/L^2$, respectively. The effective rotational mass can be calculated using $m_\alpha = K_\alpha/\omega_\alpha^2$. It is also possible to express the total system damping as follows:

$$c_t = c_m + c_e(R_L) = 2m_\alpha\omega_\alpha\zeta_m + \frac{(NlB)^2}{R_L + R_C}, \tag{12}$$

where the term $R_L + R_C$ in equation (12) indicates the sum of the electrical load resistances and the coil resistances from two sets of closed circuits with magnets and coils. NlB is the electromagnetic transformation factor.

Here, the proposed coupled solver has been used to model the reference T-shaped cantilever harvester. The discretization of the harvester within the framework of the flow and the structural solver has been shown schematically in Figure 3. The non-dimensional size of the boundary element Δ_s for flow solver is chosen such that $\Delta_s/H = 0.05$. The structural solver employs a 2-D finite element formulation to model the prototype harvester. The system is discretized into 62 idealized finite beam elements such that the length of each element is $0.05H$. The two-node elastic beam–column element is used where each node has three degrees of freedoms, which are the translation in horizontal and vertical directions, and in-plane rotation. The mass of the cantilever system is distributed into 63 structural nodes; consequently, the lumped mass at each structural node is assigned 2.39×10^{-5} kg approximately. The mass of the magnet M is assigned at the cantilever tip. The selection of the global time step of the coupled simulation is governed by the time step of the flow solver Δt_f, which is equal to Δ_s/U_∞. On the contrary, the initial time step of the structural solver Δt_s is considered equal to that of the flow solver Δt_f.

Table 1: Physical dimensions and dynamic properties of the prototype harvester.

$B = 0.03$ m, $L = 0.042$ m	H (tip height of T-shape harvester) $= 0.02$ m
t (thickness) $= 1.016 \times 10^{-4}$ m	M (mass of the magnet) $= 0.009$ kg
E (modulus of elasticity) $= 180$ GPa	I (moment of inertia) $= 2.62 \times 10^{-15}$ m^4
ω_α (natural frequency) $= 46.1$ rad/sec	ζ_m (mechanical damping ratio) $= 0.004$

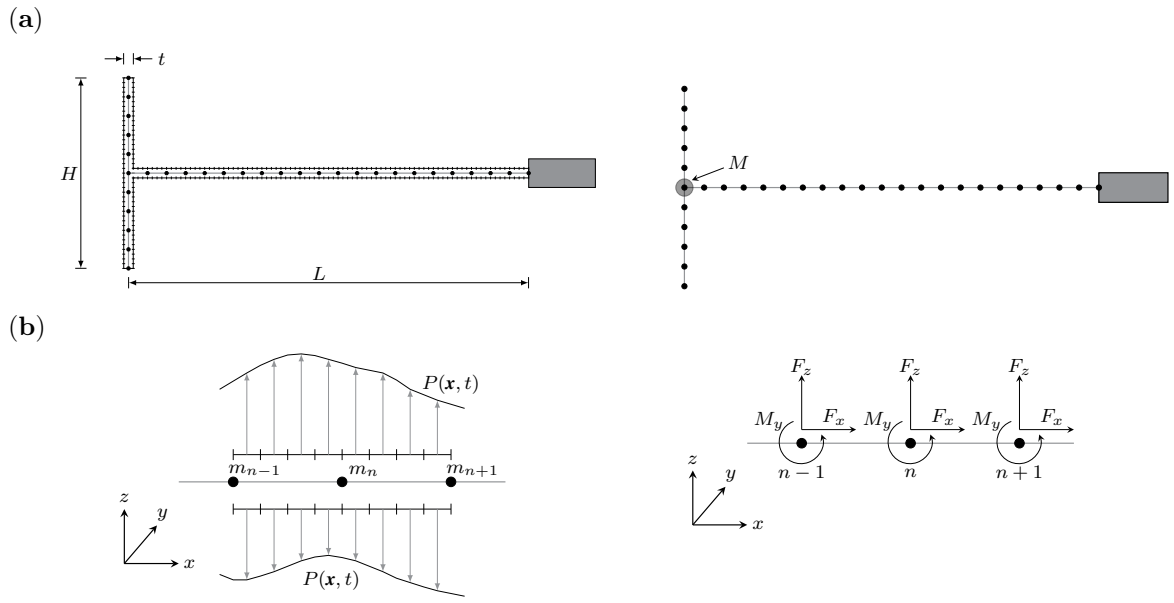

Figure 3: Discretization scheme of the coupled CFD solver in terms of the T-shaped cantilever harvester: (a-left) the discretization of the harvester in flow solver and the structural solver together, (a-right), structural nodes, idealized finite beam elements, lumped masses, and magnet M, (b-left) pressure distribution on surface panels, and (b-right) projected nodal forces for the structural solver.

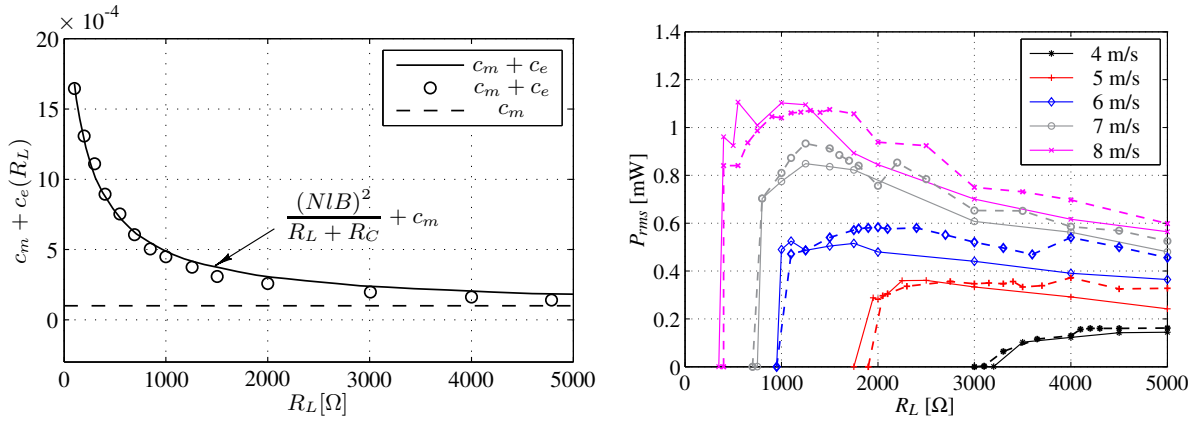

Figure 4: Damping of the reference prototype T-shaped harvester for different electrical load resistances [8]: (left) (○) shows the experimentally measured total damping, while (——) indicates the fitted total system damping. (– – –) represents the mechanical damping only. (right) Comparison of RMS power outputs from CFD simulations (——) with the reference wind tunnel test results (- - -).

A further subdivision into smaller time steps is performed to achieve the convergence of the structural solution. The simulations are performed at different wind speeds (4–8 m/s) under different R_L (100–5000 Ω). The total damping factors measured experimentally in [8] for different R_L are presented in Figure 4 (left). The resistance of the coil R_C was

measured 130 Ω. The average transformation factor NlB is calculated here approximately equal to 1.02 from the fitted damping factors in Figure 4 (left). The voltage across the load resistance, V_L is measured from individual simulation and corresponding root mean square (RMS) power output (P_{rms}) is computed from V_{Lrms} (i.e. V_{Lrms}^2/R_L). Finally, for different wind speeds and R_L, the modeled power outputs are compared in Figure 4 (right) and the results are found satisfactory. More detailed investigations on the reference harvester and and discussions have been presented in [16].

4.3 Modeling of proposed harvester under wakes from upstream cylinders

The validated coupled solver has been employed here to simulate the proposed cantilever harvester under the wakes coming from upstream circular cylinder, c.f. Figure 1. For numerical simulations, the physical dimensions and the mechanical properties of the harvester are considered according to the reference harvester, c.f. Table. 1. In this study, the vertical tip plate of the reference harvester has been removed. Note, it is observed in [8] that at or below the wind speed of 7 m/s for $R_L = 750$ Ω, the T-shaped harvester produced no energy output, c.f. Figure 4 (right). The system damping, which is sum of the mechanical and electrical damping, increases with the reduction in load resistance, c.f. Figure 4 (left). Therefore, for a flutter-based harvester the increment in the system damping necessitates high wind speed for extracting power output. In contrast, the proposed harvester should be able to extract energy at low wind speeds since it exploits the resonance phenomena. Therefore, the interest is to investigate the potential of the proposed harvester considering $R_L = 750$ Ω under wind speed less than 4 m/s. So, the diameter of the upstream circular cylinder D is chosen 0.1 m, which is kept more than twice the length of the harvester, particularly, to reduce the influence of the harvester vibration on upstream wake generation. To induce resonance, it is considered that the vortex shedding frequency f_s is equal to the frequency of the harvester ($f_\alpha = \omega_\alpha/2\pi = 7.34\,Hz$). Then, for chosen circular cylinder with $St = 0.2$ the critical free stream flow U_∞ is calculated 3.67 m/s using equation (1). The corresponding Re according to equation (2) is calculated approximately 25,000 which justifies the consideration of St value of 0.2.

The discretization of the harvester in flow and structural solver has been shown schematically in Figure 3, however, in this case without considering the vertical tip plate. The surface of the harvester and the upstream circular cylinder in the flow solver are discretized into a number of surface panels to solve the N–S equations. The non-dimensional size of these boundary elements for harvester and the cylinder are chosen such that $\Delta_s/D = 0.0097565$. The cantilever beam is discretized into 43 nodal points such that each idealized FE beam length become $0.01D$. The lumped mass approach has been used to approximate the nodal mass of the system. The mass of the cantilever beam is lumped into 43 nodes, in which nodal mass for each node is approximately 2.39e-5 kg. The flexible cantilever harvester is simulated under the wakes coming from upstream circular cylinder at free stream velocity U_∞ of 3.67 m/s. In this study, for $R_L = 750$ Ω the system damping matrix ($\mathbf{C}_m + \mathbf{C}_e$) is calculated using the Rayleigh damping approach according to

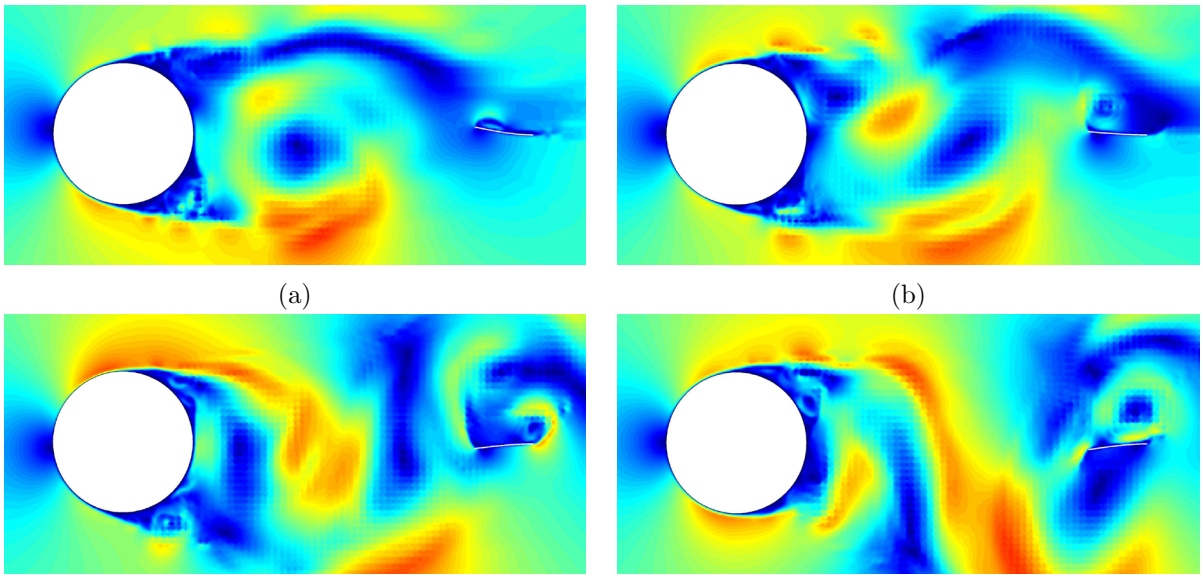

Figure 5: Simulation of proposed harvester under wakes from upstream cylinder at free stream flow of 3.67 m/s. The snapshots of the flow field are shown for case $S = 2D$ and the vibration of the beam at different real times such that (a) $t = 2.6505$ s, (b) $t = 2.6769$ s, (c) $t = 2.7035$ s, and (d) $t = 2.7299$ s.

equation (8). The damping ratio for chosen R_L has been calculated using equation (11) to calculate the Rayleigh damping factors. In four different simulations, the distance between the cylinder and the harvester has been considered $1D, 1.5D, 2D$, and $2.5D$ to investigate their influences on the system vibration. The simulated flow fields and system vibration for case $S = 2D$ are shown in Figure 5 for different simulation steps. For all the simulation cases, the vertical cantilever tip displacements and the corresponding modeled voltages, which is using equation (4), are presented in Figure 6. It is observed that the proposed harvester is producing voltage output for all the cases, and comparatively better for the cases $2D$, and $2.5D$, whereas the reference harvester under the same condition produced no output. The maximum power output P_{max}, which is $V_{L_{max}}^2/R_L$, is observed for case $S = 2D$ approximately 0.15 mW, whereas the root mean square power P_{rms} is observed approximately 0.085 mW for the simulated time.

4.4 Optimization of the performance for proposed harvester

In this section, the performance of the proposed harvester is analyzed by targeting low wind speed like 2–4 m/s since the flutter-based harvesters are generally more efficient at high wind speeds [8]. The wind speed for the proposed harvester can be targeted by modifying the physical configuration of the harvester and/or by modifying the diameter of the upstream cylinder such that the frequency of the vortex shedding and the natural frequency of the harvester corresponds with each other. The two key parameters to target

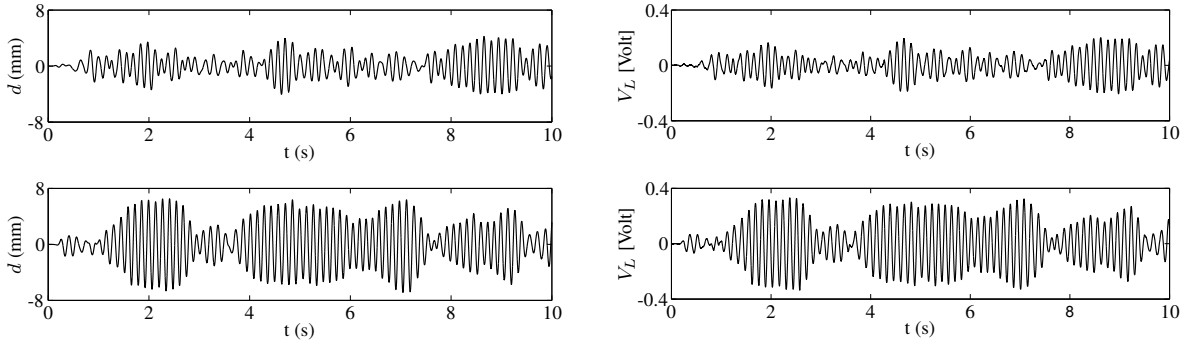

Figure 6: Comparison of vertical tip displacement and voltage output of the harvester under wakes from upstream cylinder ($U_\infty = 3.67$ m/s, $D = 0.10$ m): (top) $S = 1D$ and (bottom) $S = 2D$

a specific wind speed is the diameter of the upstream cylinder and the frequency of the downstream cantilever system.

For a target free stream flow U_∞ using a circular cylinder of diameter D, the frequency of the harvester should be equal to the frequency of vortex shedding such that $f_\alpha = f_s = (U_\infty St)/D$. The length of the harvester L is increased to 0.08 m to allow the cantilever tip to vibrate more for increasing the velocity of vibration (length of the reference harvester was 0.042 m). Accordingly, the diameter D of the upstream cylinder is increased to 0.15 m to reduce the influence of the beam vibration on the wakes generation. The numerical simulations are performed here for wind speed U_∞ of 2, 3, and 4 m. The diameter of the circular cylinder is considered constant for these studied wind speeds. The thickness of the harvester is modified such that the harvester frequency matches with the frequency of vortex shedding under individual wind speed. The vortex shedding frequencies for wind speeds 2, 3, and 4 m/s are calculated 2.66 Hz, 4 Hz, and 6 Hz, respectively. The corresponding thickness of the harvesters are modified to 0.1005 mm, 0.13165 mm, and 0.1725 mm, respectively. Here, the energy harvesters are referred as EH-1, EH-2, and EH-3, respectively. The tip mass of the cantilevers, i.e. the magnet mass, is considered 0.009 Kg according to the reference harvester, c.f. Table 1. The mass of the cantilever beam is lumped into 81 nodes, in which nodal mass for each node is approximately 2.43e-5 kg, 3.1e-5 kg and 4.06e-5 kg respectively for EH-1, EH-2, and EH-3. To maximize the power output, the harvesters are simulated for system damping considering R_L of 100 Ω. Since the studies are performed for low R_L, the resistances of the coil R_C is necessarily should be very low, and hence, is neglected to maximize the voltage. The total system damping ratio ($\zeta_m + \zeta_e(R_L)$) of the harvesters are calculated based on equation (11) using Figure 4 (left) and they are calculated 0.119, 0.081, and 0.055, respectively. The estimated root mean square (RMS) voltage and power outputs are compared for different wind speeds in Figure 7. It is observed that the power output of the harvester EH-3 under wind speed 4 m/s is found approximately 0.84 mW which is almost the harvested power output of the reference harvester at wind speed 7 m/s [8].

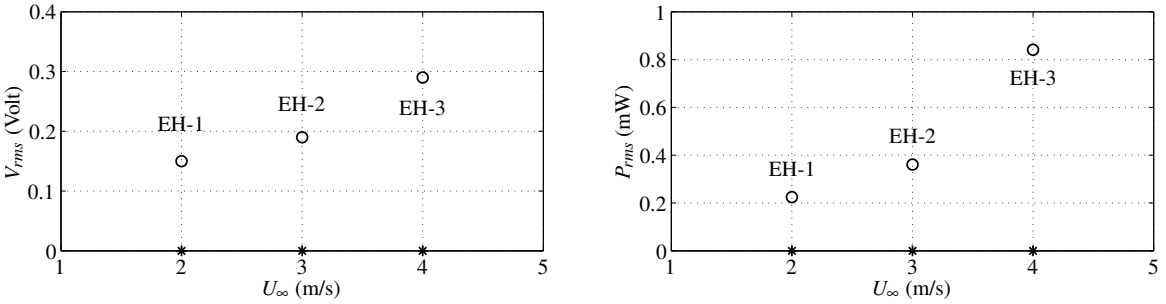

Figure 7: Comparison of modeled energy outputs of modified harvesters with reference harvester at R_L = 100 Ω: (a) RMS voltage (b) RMS power. Here, (∗) indicates the power output of reference harvester.

5 CONCLUSION

The performance of a flexible cantilever beam for electromagnetic (EM) energy harvesting under the wakes from upstream cylinder has been investigated using a proposed two–dimensional fully coupled fluid–structure interaction model. The modeling scheme and validation of the proposed coupled solver have been presented. A flexible cantilever beam can experience large vibration, especially, when the frequency of the vortex shedding from upstream cylinder comes close to the resonance frequency of the system. This fact is exploited in this paper to investigate numerically the potential of a flexible beam for EM energy harvesting under the wakes from upstream circular cylinder. The influential parameters such as the upstream cylinder diameter, the frequency of the downstream harvester and the distance between them have been studied and the results are discussed. The position of the downstream cantilever beam at a distance of twice the diameter of the cylinder diameter has been found more effective for power extraction. It is shown in this study that by changing the harvester frequency or by modifying the cylinder size, it is possible to target a specific wind speed for energy harvesting. However, the focus of the paper is concentrated particularly for harvesting energy from low wind speed like 2–4 m/s. The harvested energy outputs are found satisfactory in comparison with a reference flutter-based EM energy harvester. The ability of the proposed harvester model to extract energy from low wind speed would make it possible to harvest energy for a wide range wind speeds while using the flutter-based harvesters to target the high wind speed.

REFERENCES

[1] Akaydin, H.D., Elvin, N. and Andreopoulos, Y. (2012) The performance of a self-excited fluidic energy harvester. *Smart Materials and Structures* 21(2): 025007.

[2] Abdelkefi, A., Hajj, M.R., and Nayfeh, A.H. (2012) Power harvesting from transverse galloping of square cylinder. *Nonlinear Dynamics*, 70(2), pp.1355-1363.

[3] Ewere, F. and Wang, G. (2013) Performance of galloping piezoelectric energy harvesters. *Journal of Intelligent Material Systems and Structures*, 25(14), pp.1693-1704.

[4] Wang, D.A., Chiu, C.Y., and Pham, H.T. (2012) Electromagnetic energy harvesting from vibrations induced by Kármán vortex street. *Mechatronics* 22.6: 746-756.

[5] Jung, H.J., Kim, I.H. and Jang, S.J. (2011) An energy harvesting system using the wind-induced vibration of a stay cable for powering a wireless sensor node. *Smart Materials and Structures*, 20(7), p.075001.

[6] Dai, H.L., Abdelkefi, A., Javed, U. and Wang, L. (2015) Modeling and performance of electromagnetic energy harvesting from galloping oscillations. *Smart Materials and Structures*, 24(4), p.045012.

[7] Vicente-Ludlam, D., Barrero-Gil, A., and Velazquez, A. (2014) Optimal electromagnetic energy extraction from transverse galloping. *Journal of Fluids and Structures*, 51, pp.281-291.

[8] Park, J., Morgenthal, G., Kim, K., Kwon, S.D. and Law, K.H. (2014) Power evaluation of flutter-based electromagnetic energy harvesters using computational fluid dynamics simulations, *Journal of Intelligent Material Systems and Structures*, 25(14), 1800-1812.

[9] Morgenthal, G. and Walther, J.H. (2007) An immersed interface method for the vortex-in-cell algorithm. *Computers and structures* 85.11: 712-726.

[10] Chawdhury, S. and Morgenthal, G. (2016) Flow reproduction using Vortex Particle Methods for simulating wake buffeting response of bluff structures. *Journal of Wind Engineering and Industrial Aerodynamics*, 151, pp.122-136.

[11] Morgenthal, G. (2002) Aerodynamic analysis of structures using high-resolution vortex particle methods *PhD Thesis, University of Cambridge, Cambridge.*

[12] Akaydin, H.D., Elvin, N., and Andreopoulos, Y. (2010) Energy harvesting from highly unsteady fluid flows using piezoelectric materials. *Journal of Intelligent Material Systems and Structures*, 21(13), pp.1263-1278.

[13] Xu, Y.L. (2013) Wind effects on cable-supported bridges. *John Wiley and Sons.*

[14] Panton, R.L. (2006) Incompressible flow. 2nd edn, *John Wiley & Sons*, Inc., New York.

[15] Priya, S. and Inman, D.J. eds. (2009) Energy harvesting technologies (Vol. 21). New York: Springer.

[16] Chawdhury, S. and Morgenthal, G. (2017) Numerical simulations of aeroelastic instabilities to optimize the performance of flutter-based electromagnetic energy harvesters, *Journal of Intelligent Material Systems and Structures*, under review.

VII International Conference on Computational Methods for Coupled Problems in Science and Engineering
COUPLED PROBLEMS 2017
M. Papadrakakis, E. Oñate and B. Schrefler (Eds)

NUMERICAL STUDIES ON ELECTRO IMPULSE DE-ICING BASED ON COHESIVE CRACK GROWTH AND ADHESIVE DEBONDING

H. Sommerwerk* **and P. Horst†**

* Institute of Aircraft Design and Lightweight Structures, Technische Universität Braunschweig
Hermann-Blenk-Str. 35, 38108 Braunschweig, Germany
e-mail: h.sommerwerk@tu-braunschweig.de, web page: https://www.tu-braunschweig.de/ifl

† Institute of Aircraft Design and Lightweight Structures, Technische Universität Braunschweig
Hermann-Blenk-Str. 35, 38108 Braunschweig, Germany
e-mail: p.horst@tu-braunschweig.de, web page: https://www.tu-braunschweig.de/ifl

Key words: Electro Impulse De-Icing, Cohesive Zone Modeling, Adhesive Ice Debonding, Multiple Radial Cracks.

Abstract. Electro Impulse De-Icing is an alternative de-icing concept which operates based on electro-mechanical impulses. These impulses can be modeled by coupled transient electro-mechanical simulations using the finite element method, whereas the process of ice shedding can be simulated with a simple interfacial shear stress criterion. In this paper, the time-consuming coupled analysis is replaced by a structural simulation where the magnetic forces are approximated by comparison with the coupled results. Although the adhesive de-icing criterion serves to represent the de-icing process very well, it lacks the modeling of a realistic dynamic response of the structure. Therefore, the simulation is extended by a cohesive zone model in order to take into account multiple radially propagating cracks that occur in combination with ice shedding. Numerical studies are performed for an ice-covered aluminium plate and validated by experimental results. The influence of cohesive crack growth and adhesive debonding on the structural response and de-icing behavior is investigated.

1 INTRODUCTION

Electro Impulse De-Icing (EIDI) is an alternative de-icing concept which serves to remove the accreted ice on a structure by electro-mechanical impulses. Induction coils which are placed underneath the structure within a gap of a few millimeters are fed with short and high impulse currents. The resulting time-dependent magnetic fields cause the structure to oscillate, which can shed off the ice.

During Electro Impulse De-Icing cracks inside the ice layer as well as debonding of the ice layer from the structure can be observed. Figure 1 shows these two phenomena after the first electro-mechanical impulse applied to a plate with an ice layer.

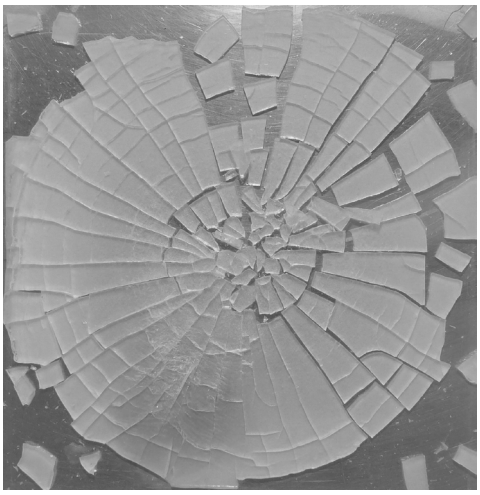

Figure 1: Ice cracking and shedding after Electro Impulse De-Icing of a plate [1]

A common method to predict fracture processes is the cohesive zone model (CZM) which can be used in combination with the finite element method (FEM) [2, 3, 4]. The cohesive crack path is restricted to finite element boundaries, but apart from that, location and path are arbitrary. In addition, no initial crack is necessary in order to predict the onset and propagation of a crack and multiple branching cracks are possible. The implementation is relatively simple and requires only two model parameters [2, 5]. However, it has to be mentioned that the CZM also has some limitations like its mesh dependency [5].

The cohesive zone model has also been applied to ice mechanics, especially the interaction of sea ice and structures is of great interest [5, 6, 7]. However, in the field of aviation, to the authors' knowledge, no approach has been made yet to model aircraft de-icing with CZM. Apart from the fracture-mechanical approaches the de-icing behavior can also be defined by an interfacial shear stress criterion as proposed by Labeas et al. [8]. They modeled the Electro Impulse De-Icing process of an aluminium plate and verified the results by experimental tests. Möhle et al. [1, 9, 10, 11] developed a coupled transient FE model based on a similar adhesive de-icing criterion to successfully predict the Electro Impulse De-Icing process. Like Labeas et al. they also performed simulations with aluminium plates which they validated by experiments with ice-free plates. A similar failure criterion has been used by Strobl et al. [12] who studied the thermal and mechanical de-icing of a hybrid ice protection system.

In this paper, a numerical model is presented to study the Electro Impulse De-Icing of aluminium plates. The cracks inside the ice layer are modeled with cohesive zones,

whereas the debonding of ice from the structure is simulated based on an interfacial shear stress criterion. Different ice debonding criteria are compared and the influence of the two failure criteria, cohesive crack growth and adhesive debonding, on the structural response and the de-icing behavior is studied. Moreover, the numerical results are compared to experimental ones. Finally, the numerical de-icing progress is investigated in detail.

2 FUNDAMENTALS AND METHODS

In the following sections the cohesive zone model and the shear stress criterion used in this paper are presented.

2.1 Cohesive zone model

The cohesive zone model (CZM) is described by a traction-separation law, also known as cohesive law, which defines the bearable loading of a material as a function of its separation. It can be used for both normal (mode I) and tangential (mode II) separation behavior as well as mixed-mode loading cases. The basic idea of the CZM is illustrated in Figure 2a for a mode I loading case. The process zone is replaced by a fictitious crack on which a cohesive stress is acting. This stress prevents the crack from opening and is defined by the cohesive law. Due to the fact that the stress is limited, any unrealistic numerical stress singularity at the crack tip is avoided [2].

The relationship between the cohesive stress σ and the cohesive crack separation δ can be described by different types of cohesive laws. A simple approach is the bilinear law depicted in Figure 2b. At the beginning the crack tip is extended elastically up to a critical cohesive stress, the cohesive strength σ_c, which is reached at a critical cohesive separation δ_c. After this point, failure proceeds irreversibly and the crack separation grows under decreasing cohesive stress until the maximum separation δ_{max} is reached. If the crack is unloaded during this failure process, the current damage state is preserved and the cohesive stress descends linearly to zero as the crack closes. The corresponding

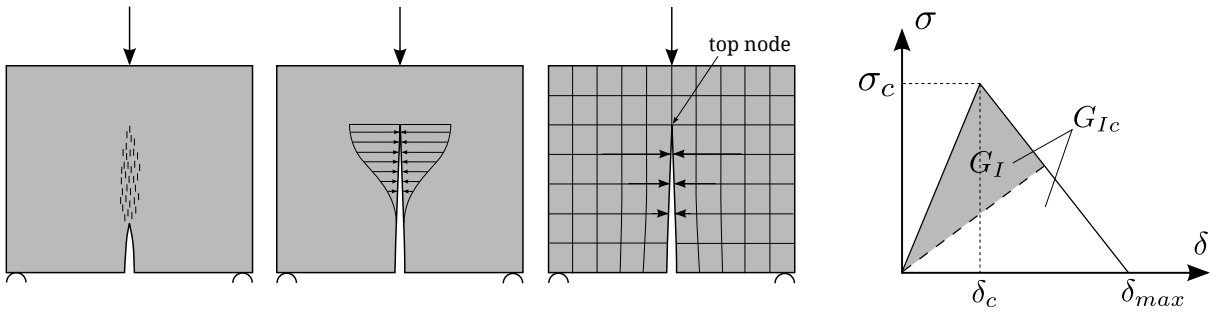

(a) Model and discretization based on [3]

(b) Bilinear cohesive law based on [4]

Figure 2: Cohesive Zone Model (CZM)

area under the graph of the traction-separation law yields the energy release rate G_I, whereas the complete area under the graph denotes to the critical energy release rate $G_{Ic} = \frac{1}{2}\sigma_c\delta_{max}$ for complete failure. The same law can be used for mode II behavior and the parameters are the cohesive shear stress τ_c, the critical tangential cohesive separation γ_c, the maximum tangential cohesive separation γ_{max}, and the critical energy release rate G_{IIc}.

In case of purely brittle materials no separation occurs until the critical cohesive strength is reached ($\delta_c = 0$) which requires the use of a contact algorithm. In order to implement the CZM into a finite element code, the initial slope of the bilinear cohesive law is mostly chosen very high but finite [2].

2.2 De-icing criterion

For modeling the debonding of ice from the structure a de-icing criterion is used which is based on the shear stress in the ice-structure interface. The first criterion used in this paper is the one employed by Möhle et al. [1, 10, 11], in the following called maximum shear stress criterion:

$$\left(\frac{\tau_{xz,mean}}{\tau_{crit}}\right)^2 \geq 1 \quad \text{and} \quad \left(\frac{\tau_{yz,mean}}{\tau_{crit}}\right)^2 \geq 1. \tag{1}$$

In this equation τ_{mean} denotes the average shear stress in the corresponding element and τ_{crit} the critical shear stress in the interface.

Furthermore, a criterion will be used which combines the two failure cases, in the following called quadratic shear stress criterion:

$$\frac{\sqrt{\tau_{xz,mean}^2 + \tau_{yz,mean}^2}}{\tau_{crit}} \geq 1. \tag{2}$$

3 MODEL DESCRIPTION

The model investigated in this paper consists of an aluminium plate with dimensions of 500 mm x 500 mm and a thickness of 3 mm. The plate is partly covered by a 300 mm x 300 mm ice layer of 4 mm thickness as depicted in Figure 3. All four edges of the plate are clamped and a force distribution $F_z(x,y,t)$ depending on location and time is applied to the inner region of the plate in out-of-plane direction. The loading corresponds to the magnetic force impulse which is induced inside the structure by the Electro Impulse De-Icing system. The force function is approximated by comparison with coupled electro-mechanical simulations conducted on the same model by Möhle et al. [9, 10, 11].

Due to symmetry, only a quarter of the plate is implemented in the finite element (FE) model and the required symmetry conditions are applied to the symmetry planes, cf. Figure 3a. Cohesive elements are inserted at all radial element boundaries inside the ice layer, as can be seen in Figure 3b where half of the ice elements are suppressed in order to visualize the cohesive zones. In order to assure that all of the duplicated nodes have a

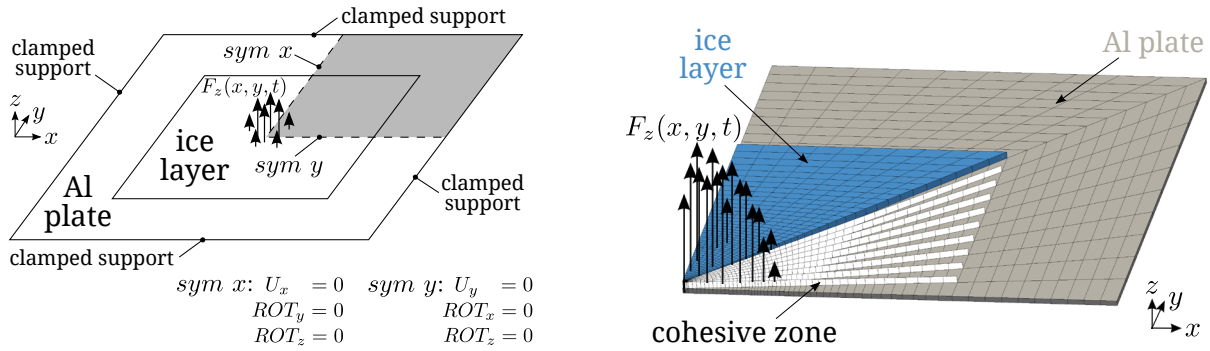

(a) Plate model (b) Quarter FE model

Figure 3: Electro Impulse De-Icing plate model

connectivity to corresponding nodes in the aluminium plate and that at the same time the cohesive elements are able to open up, cohesive zones are also inserted in the aluminium plate in radial direction. In the EIDI experiments additional circumferential cracks arise, cf. Figure 1. However, in a first approach these are neglected in the analysis because they cannot be observed in all experiments but only occur for larger ice thicknesses. In addition, the main goal of this paper is the correct modeling of the structural response of the plate under de-icing. As the results in the next section will show, it is sufficient to model the radial crack paths in order to reproduce the stiffness reduction in the structure.

In order to model ice shedding the interfacial shear stress criteria presented in Section 2 are implemented in the model. For the critical shear stress at the interface a value of 0.45 MPa is used which is determined by Möhle et al. [10, 11] by beam de-icing tests according to Blackburn et al. [13]. In case of failure of an ice-structure interface the material of the corresponding ice element is changed to air to simulate debonding.

Table 1 shows the parameters that are used in the analysis. Isotropic material behavior is assumed for both materials. For mode II behavior the same parameter as for mode I behavior are used ($\tau_c = \sigma_c$, $\gamma_c = \delta_c$, $G_{IIc} = G_{Ic}$). Due to the fact that the plate is clamped at a different temperature than the de-icing experiments are performed, an additional thermal pre-stress due to a temperature change of 2 °C is applied on the initial model. The model is investigated in full transient nonlinear analyses using the FE program *ANSYS*.

Table 1: Material and cohesive parameters [8, 14, 15, 16, 17, 18]

Material	E in GPa	ν	G_{Ic} in J/m^2	σ_c in MPa	δ_c/δ_{max}
Aluminum 2024	73.1	0.33	12×10^3	469	0.3
Glaze ice	9.1	0.30	1.0	0.8	0.1

4 RESULTS

In this section the influence of different ice debonding criteria on the de-icing process is studied. Thereafter, it is evaluated how the cohesive zones and the adhesive debonding criterion affect the structural response of the system. Finally, the de-icing progress over time is investigated in detail.

4.1 Influence of ice debonding criteria on de-icing

In order to quantify the de-icing progress the relative icing I_{rel} is introduced. It can be determined by dividing the remaining ice-covered area after the impulse by the initially ice-covered area before the impulse.

Figure 4 shows the influence of different debonding criteria on the relative icing over time for simulations without and with cohesive zones. In case of the maximum shear stress criterion, approximately 80 % of the ice is removed in the first few milliseconds, irrespective of whether cohesive zones are used or not. When using CZM to model radial cracking, after 7 ms further de-icing can be achieved so that only a relative icing of 6 % remains on the plate. In case of the quadratic shear stress criterion, approximately 95 % is detached from the structure in the first few milliseconds. The influence of the cohesive zones is marginal in this case.

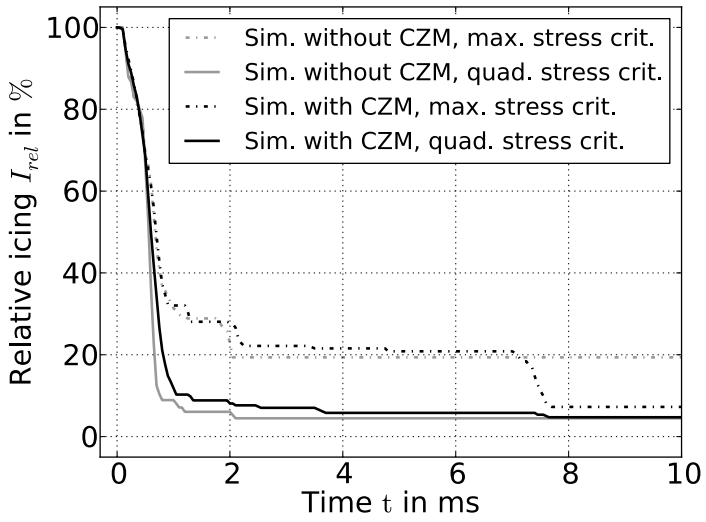

Figure 4: Relative icing over time for different ice debonding criteria without and with CZM

The de-icing results of the different numerical cases are visualized in Figure 5. For the simulation without CZM and use of the maximum shear stress criterion the largest amount of ice remains on the structure, especially in the corner region of the ice layer, cf. Figure 5a. As already concluded from Figure 4, in all other cases more ice can be

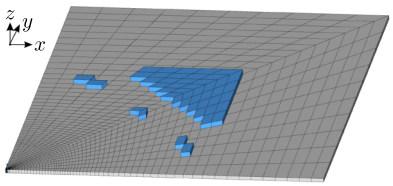

(a) without CZM, maximum shear stress criterion

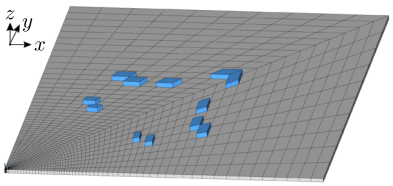

(b) without CZM, quadratic shear stress criterion

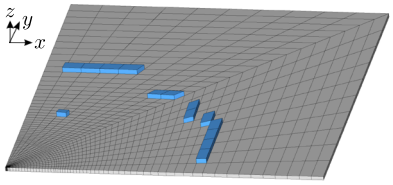

(c) with CZM, maximum shear stress criterion

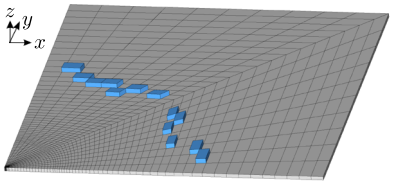

(d) with CZM, quadratic shear criterion

Figure 5: Plate de-icing of the quarter model for different ice debonding criteria without and with CZM after 20 ms

removed. For the simulation without CZM and use of the quadratic shear stress criterion the remaining ice segments are concentrated on the corner as well, cf. Figure 5b. When using cohesive zones, the remaining ice forms a ring, which is in better agreement with the experimental results. This ring shape is approximated best in case of the quadratic debonding criterion, cf. Figure 5d.

The simulations show that the choice of the de-icing criterion strongly influences the amount of ice which is removed from the structure, whereas the cohesive zones affect the region where the ice detaches. It can be concluded that the quadratic shear stress criterion achieves to model the de-icing process more realistically than the maximum shear stress criterion.

4.2 Influence of cohesive zones and ice debonding on structural behavior

In order to compare the structural behavior of the simulations to each other as well as to experimental results, the normal plate deflection at the center of the plate is plotted over time for cases without and with ice. The study presented in this section includes analyses with ice but no failure criterion, with the failure criterion of either modeling of cracking or adhesive debonding of the ice as well as modeling of both failure criteria. In this way the influence of the cohesive zones as well as of the de-icing criterion on the structural response can be investigated separately. Due to the results from the previous section all simulations are performed with the quadratic shear stress criterion.

Figure 6 shows the plate deflection over time of the corresponding experiments and simulations. The curves without ice demonstrate a good agreement between numerical

and experimental results. This confirms the assumption that the electro-magnetic impulse forces can be approximated by an appropriate force distribution.

The curve of the case with ice but no failure criterion (case 'Sim. with ice, no CZM, no de-icing') exhibits a lower amplitude and a higher frequency compared to the case without ice. This results from the fact that the attached ice layer certainly increases the mass of the structure but the stiffness gain predominates. If only ice shedding is included in the model (case 'Sim. with ice, no CZM, with de-icing') a further decrease in amplitude and increase in frequency is noticeable. In case of only crack modeling (case 'Sim. with ice, with CZM, no de-icing'), the amplitude and frequency are similar to the ones with ice. This appears reasonable since the accreted ice increases the mass of the model but due to the cracking barely leads to any stiffness gain. Combination of both failure criteria (case 'Sim. with ice, with CZM, with de-icing') has no impact on the magnitude of amplitude and frequency but serves to reproduce the course of the plate deflection better than without the de-icing criterion.

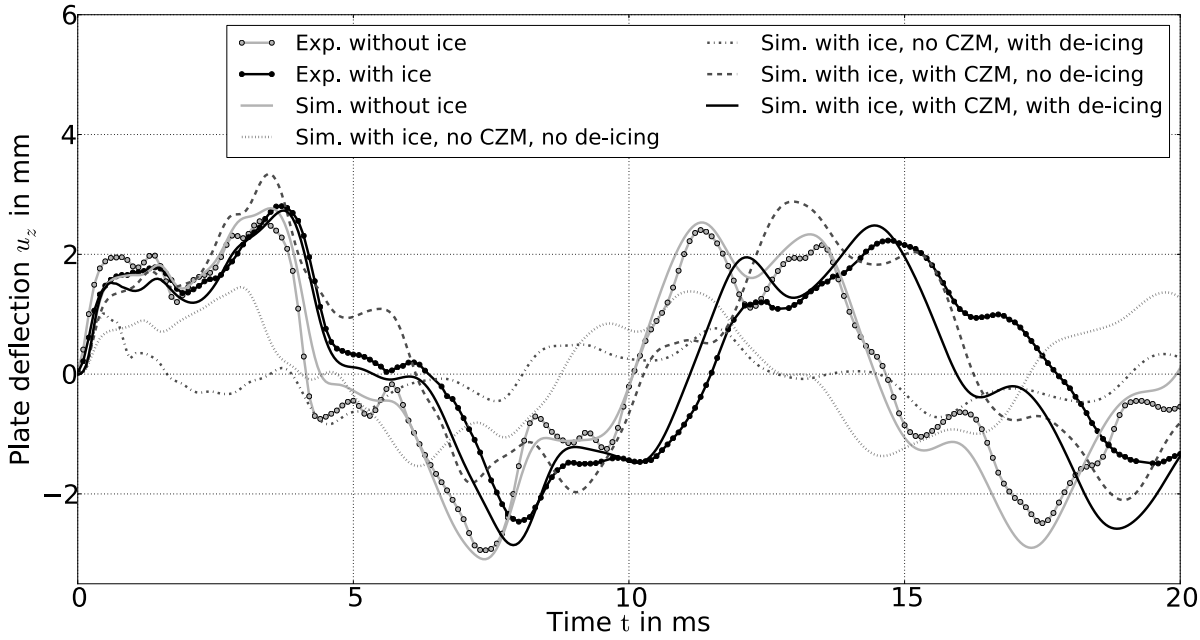

Figure 6: Influence of cohesive zone modeling (CZM) and de-icing on the plate deflection over time at the center of the plate model

4.3 De-icing progress

Figure 7 visualizes the de-icing progress of the plate over the course of the simulation with modeling of cohesive crack growth and adhesive debonding. Ice debonding initiates in the center of the plate where the electro-mechanical impulse is applied. The circular

de-iced region becomes larger and de-icing also occurs in the boundary regions of the ice layer so that after 1.2 ms only a small ring-shaped ice region is left. Most of the ice elements have already detached until this point so that only little further de-icing can be noticed in the following time steps of the simulation.

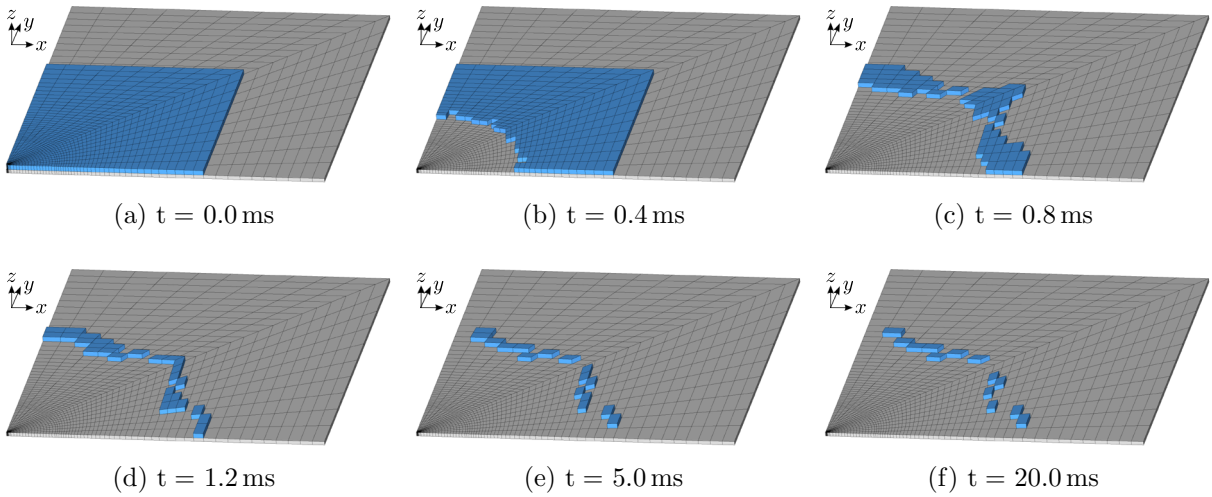

(a) t = 0.0 ms (b) t = 0.4 ms (c) t = 0.8 ms

(d) t = 1.2 ms (e) t = 5.0 ms (f) t = 20.0 ms

Figure 7: Plate de-icing of the quarter model at different time steps

5 CONCLUSIONS

In this paper the Electro Impulse De-Icing of an ice-covered aluminium plate is investigated by numerical simulations, which are validated by experimental results. Cohesive elements are inserted at all radial element boundaries in order to study radial crack onset and propagation, whereas debonding of ice elements is considered by an interfacial shear stress criterion. The influence of the cohesive zones and two different ice debonding criteria on the structural behavior and the de-icing process is studied.

Comparison of the numerical and experimental results shows that the electro-magnetic impulse forces can be approximated adequately. Thus, the model is reduced successfully from a coupled electro-magnetic to a simple structural system. In order to scale the magnetic forces applied to the structural model, only one coupled analysis of the plate without ice is required. The complex simulations with ice, however, are performed based on the presented structural model in order to reduce computing time.

Cohesive zones in the ice layer allow to model the onset and propagation of multiple radial cracks which has great impact on the structural behavior of the system. Thus, in comparison to a model that only takes into account the adhesive debonding of the ice, the structural response of the structure can be improved significantly. However, a combination of both failure criteria yields a plate deflection curve which matches the experimental curves even better.

With regard to aircraft de-icing, the results show that already a few cracks in the ice layer of an ice-covered structure can have a great impact on the structural behavior of the whole structure even though the ice is still attached to it. Thus, it is inevitable for de-icing simulations to model the fracture process of the adhering ice layer.

6 ACKNOWLEDGEMENTS

The authors like to thank the Helmholtz Association for financial support in the project SuLaDI (Supercooled Large Droplets Icing) as well as the Federal Ministry of Economics and Technology for funding under contract 20Y151G.

REFERENCES

[1] Möhle, E., *Simulation und experimentelle Untersuchung eines elektromechanischen Enteisungssystems*. Doctoral thesis, TU Braunschweig, 2014.

[2] Schwalbe, K.-H., Scheider, I. and Cornec, A., *Guidelines for Applying Cohesive Models to the Damage Behaviour of Engineering Materials and Structures*. Springer-Verlag Berlin Heidelberg, 2013.

[3] Petersson, P.-E., *Crack Growth and Development of Fracture Zones in Plain Concrete and Similar Materials*. Doctoral thesis, Lund Institute of Technology, 1981.

[4] Xie, D. and Waas, A. M., Discrete cohesive zone model for mixed-mode fracture using finite element analysis. *Engineering Fracture Mechanics*, **73**, 1783–1796, 2006.

[5] Konuk, I., Gürtner, A. and Yu, S., A Cohesive Element Framework for Dynamic Ice-Structure Interaction ProblemsPart I: Review and Formulation. *28th International Conference on Ocean, Offshore and Arctic Engineering*, Honolulu, Hawaii, May 31 - June 5, 2009.

[6] Gürtner, A., *Experimental and Numerical Investigations of Ice-Structure Interaction*. Doctoral thesis, Norwegian University of Science and Technology, 2009.

[7] Kuutti, J., Kolari, K. and Marjavaara, P., Simulation of ice crushing experiments with cohesive surface methodology. *Cold Regions Science and Technology*, **92**, 17–28, 2013.

[8] Labeas, G. N., Diamantakos, I. D. and Sunaric, M. M., Simulation of the Electroimpulse De-Icing Process of Aircraft Wings. *Journal of Aircraft*, **43**, 6, 1876–1885, 2006.

[9] Möhle, E., Haupt, M. C. and Horst, P., Coupled Numerical Simulation and Experimental Validation of the Electroimpulse De-Icing Process. *Journal of Aircraft*, **50**, 1, 96–102, 2013.

[10] Möhle, E., Haupt, M. C. and Horst, P., Coupled Magnetic and Structural Numerical Simulation and Experimental Validation of the Electro Impulse De-Icing. *54th AIAA/ASME/ASCE/AHS/ASC Structures, Structural Dynamics, and Materials Conference (AIAA 2013-1494)*, Boston, USA, April 8-11, 2013.

[11] Möhle, E. and Horst, P., Simulation and validation of slat-deicing by an electromechanical system. *CEAS Aeronautical Journal*, **6**, 2, 197–206, 2015.

[12] Strobl, T., Storm, S., Thompson, D., Hornung, M. and Thielecke, F., Feasibility Study of a Hybrid Ice Protection System. *Journal of Aircraft*, **52**, 6, 2064–2076, 2015.

[13] Blackburn, C., Laforte, C. and Laforte, J. L., Apparatus for measuring the adhesion force of a thin ice sheet on a substrate. *9th International Workshop of Atmospheric Icing of Structures*, Chester, UK, June 5-8, 2000.

[14] Andrews, E. H. and Lockington, N. A., The cohesive and adhesive strength of ice. *Journal of Materials Science*, **18**, 1455–1465, 1983.

[15] Goodman, D. J. and Tabor, D., Fracture toughness of ice: A preliminary account of some new experiments. *Journal of Glaciology*, **21**, 85, 651–660, 1978.

[16] Barrette, P. and Brassard, C., *Flexural strength of ice from the Rideau Canal: A laboratory investigation*. Technical Report CHC-TR-068, Canadian Hydraulics Centre, September, 2009.

[17] Gow, A. J., Flexural strength of ice on temperate lakes. *Journal of Glaciology*, **19**, 81, 247–256, 1977.

[18] Petrovic, J. J., Review: Mechanical properties of ice and snow. *Journal of Materials Science*, **38**, 1–6, 2003.

VII International Conference on Computational Methods for Coupled Problems in Science and Engineering
COUPLED PROBLEMS 2017
M. Papadrakakis, E. Oñate and B. Schrefler (Eds)

A FLUID-STRUCTURE SOLVER FOR CONFINED MICROCAPSULE FLOWS

B. Sarkis*†, A.-V. Salsac* and J.-M. Fullana†

*Laboratoire BioMécanique et BioIngénierie (UMR CNRS 7338)
Université de Technologie de Compiègne, CNRS, Sorbonne Universités
CS60319, 60203 Compiègne, France
e-mail: a.salsac@utc.fr - web page: http://www.utc.fr/bmbi/

†Institut Jean Le Rond ∂'Alembert (UMR CNRS 7190)
Université Pierre et Marie Curie, CNRS, Sorbonne Universités
4 place Jussieu, 75252 Paris CEDEX, France
e-mail: jose.fullana@upmc.fr - web page: http://www.dalembert.upmc.fr/

Key words: Microcapsules, Fluid-Structure Interaction, Confined Environment, Finite Volumes, Finite Elements, Immersed Boundary Method.

Abstract. We present a fluid-structure coupling method designed to study capsules flowing in a confined environment. The fluid solver is based on the Finite Volume Method and is coupled to a Finite Elements solid solver using the Immersed Boundary Method. We study the relaxation of a spherical capsule, initially deformed into an ellipsoid, and released in a square cross-section channel within a quiescent fluid environment. We perform a convergence study in order to validate the numerical method and consider the effect of the inertial forces on the capsule relaxation.

1 INTRODUCTION

Encapsulation consists in protecting a substance from the surrounding medium with a solid or flexible envelope. One of the main goals of encapsulation is the transport of the substance and the control of its release, whether it is to be prevented or operated at a desired location or rate [1]. Understanding the capsule dynamics provides the possibility to better control the potential release of the inner substance. Flexible capsules find applications in various fields, particularly in biomedical areas (e.g. targeted drug delivery) and food industry. Over the last decades, the flow around flexible capsules and the resulting fluid-structure interactions have been studied experimentally [2, 3, 4], analytically [5, 6] as well as numerically [7, 8]. Small scale experimental setups can provide results in various confined geometries and flow configurations, but the observations are complex due to the scale of the microparticles. Analytical calculations give comprehensive

accurate results but are restricted to simple flow configurations and small deformations of the capsule shape. The advantage of numerical simulations is that they provide a good approximation of quantities that are inacessible through experimental measurement (e.g. membrane tension) and that would be difficult to model analytically (e.g. capsules flowing in complex geometries). They can also simulate a wide range of properties for the flow and capsule, and parameters for the case studied. The fluid-structure interactions of the capsule wall deformation with the internal and surrounding fluid flows can be modeled choosing between two approaches to treat the capsule and the fluids: Lagrangian or Eulerian. The different existing fluid-structure solvers can thus be classified in three groups: fully Lagrangian, fully Eulerian and the mixed Eulerian-Lagrangian. Among the fully Lagrangian approaches, one can mention the Boundary Integral Method [7], which is very precise, computationnaly efficient and robust but only applicable to Stokes flow. On the other hand, fully Eulerian methods comprise the level-set method and Volume Of Fluids (VOF) methods. The latter have the drawback of interface reconstruction, which is hardly compatible with a continuous mapping. The level-set method is a relevant choice: despite the fact that early implementations were neither able to conserve the fluid enclosed mass [9] nor to treat the membrane elastic behaviors, these issues have been solved since then [10]. Finally, the mixed Eulerian-Lagrangian approaches include the Immersed Boundary Method (IBM) [11, 12], which is very popular thanks to its extreme simplicity of implementation. It has the drawback of being typically unstable with stiff membranes but this issue has been recently solved [13]. It is, however, stable in the case of flexible membranes, but capsule flow simulations in complex confined geometries remain challenging [13]. Our aim is to develop a tool able to compute the fluid-structure interactions in confined geometries at potentially non-zero Reynolds numbers. The finite elements solver of Caps3D [7] is coupled with the open-source finite volume solver Basilisk that has been designed to solve multiphase flows [14]. The objective of the present paper is to validate the numerical code by considering the relaxation of a pre-deformed capsule within a confined environment.

2 PROBLEM STATEMENT

We consider an initially spherical capsule of radius a placed in a square cross-section channel of length L and half-width l (Figure 1). Let O be the center of the channel and x the coordinate along the centerline longitudinal axis of the channel, so that it defines the axis O_x. Let y and z be the two other (transversal) coordinates. We respectively call S_i, S_o and S_l the inlet, outlet and (four) lateral sections, the latter being the walls of the channel. The capsule is constituted of a membrane enveloping an internal fluid. The internal and surrounding fluids have the same density ρ and the same viscosity μ. The capsule membrane surface shear modulus is G_s (Figure 1). We neglect the wall thickness and model the capsule wall as a 2D membrane. We thus neglect bending effects. The objective of the fluid-structure solver will be to study the dynamical flow of the capsule flowing in the channel under an average inlet flow velocity $V = 0.05\frac{G_s}{\mu}$. We use as physical

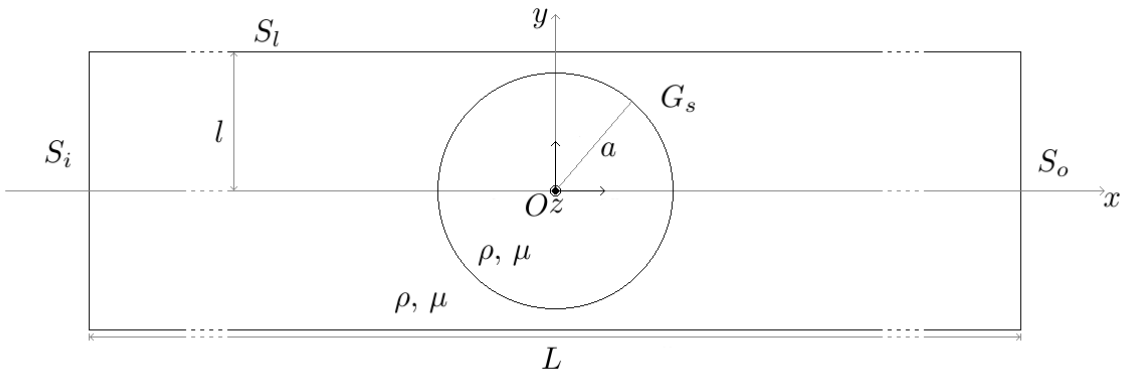

Figure 1: Schematic of the framework. A spherical capsule of radius a and surface shear modulus G_s is placed in a square cross-section chanel of length L and half-width l. The fluid inside and outside the capsule both have a density ρ and a viscosity μ.

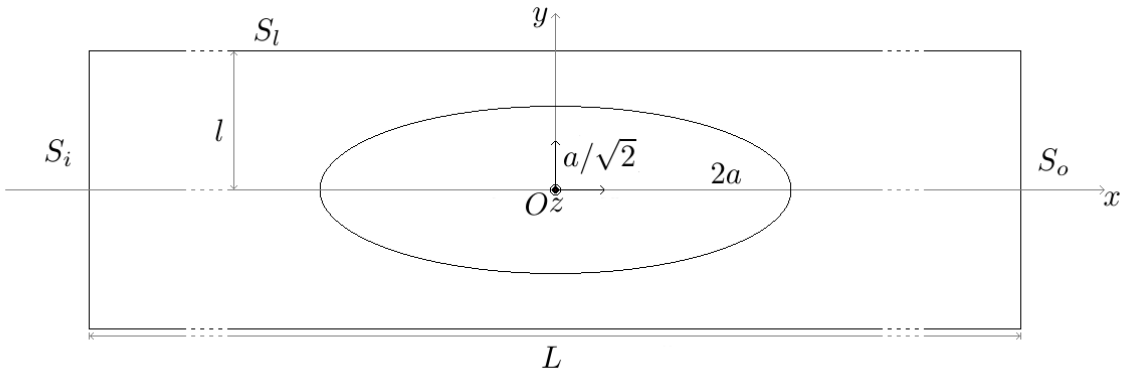

Figure 2: Scheme of the validation case: a spherical capsule of radius a is pre-deformed into an ellipsoid of axes $(2a, a/\sqrt{2}, a/\sqrt{2})$ in a square cross-section channel of length L and half-width l. The half-great axis is along O_x and the half-small axes are in the yOz plane.

kinematic scales l to non-dimensionalize the lengths and $T_V = l/V$ to non-dimensionalize time. The dimensionless coordinates are $x' = x/l$, $y' = y/l$, $z' = z/l$, $t' = t/T_V$. The scale used to non-dimensionalize the forces is $\rho V^2 l^2$. The capsule motion and deformation are governed by the two following dimensionless numbers: the capsule-to-channel size ratio $\frac{a}{l}$ and the Reynolds number $Re = \frac{\rho V l}{\mu}$, which is the ratio of the inertial to viscous forces. For the sake of simplicity, in the following the prime symbols are omitted. To validate the code, we will consider the relaxation of a capsule pre-deformed into an ellipsoid of half-great axis $2a$ along O_x and half-small axes $a/\sqrt{2}$ (Figure 2). In this case, the velocity field is induced by the elastic deformation of the capsule. It is placed at time $t = 0$ at the center of the channel (the capsule center of mass being at O) in a fluid at rest.

3 NUMERICAL METHODS

3.1 Meshing of the capsule and fluid domains

Triangular second-order finite elements are used to mesh the capsule wall. Let $\mathcal{L}$ be the Lagrangian configuration, which is the set of the Lagrangian nodes $\underline{X} = (X_x, X_y, X_z)$ at time t. The meshing $\mathcal{L}$ is built iteratively from an icosahedron [7]. The typical Lagrangian mesh size is h. Two different values of h are considered here: $h = 0.039$ and $h = 0.02$, corresponding respectively to 10 242 and 40 962 Lagrangian nodes ($\text{card}(\mathcal{L}) \in \{10\,242; 40\,962\}$). The mesh size $h = 0.078$ has also been tested but the mesh is found to be too coarse to provide good results. The fluid domain is meshed with a Eulerian regular cartesian grid. Let $\mathcal{E}$ be the set of the Eulerian cubical mesh centers (x, y, z). The non-dimensionalized length of the channel is set to $L = 8$. The Eulerian mesh size is fixed and set to be $\Delta x = 1/32 = 0.03125$. The number of Eulerian meshes is 1 048 576 ($\text{card}(\mathcal{E}) = 1\,048\,576$)). The mesh size $\Delta x = 1/16 = 0.0625$ has also been tested but is not presented here because it is too coarse to provide precise results. Four integration timesteps are considered: $dt = 10^{-3}$, $dt = 5 \times 10^{-4}$, $dt = 2 \times 10^{-4}$ and $dt = 10^{-4}$.

3.2 Membrane equilibrium equations

The membrane solver code, Caps3D, uses the Lagrangian configuration $\mathcal{L}$ to compute the non-dimensionalized Cauchy tension tensor $\underline{\underline{T}}$, which provides the non-dimensionalized tension (lineic force) $\underline{\tau}$ exerted in a direction $\underline{n}$ by $\underline{\tau}(\underline{n}) = \underline{\underline{T}}.\underline{n}$. This tensor is calculated using the strain energy function w_s describing the material constitutive law. In the present study we model the capsule behavior using the Skalak et al. law [15]. For this law, the non-dimensionalized surface energy w_s is given by:

$$w_s = \frac{1}{4}\left(I_1^2 + 2I_1 - 2I_2 + CI_2^2\right), \tag{1}$$

where C is a constant parameter that relates the surface shear modulus G_s and surface area dilatation modulus of the capsule. I_1 and I_2 are the first and second strain invariants of the surface evolution. The Skalak et al. law is particularly adapted to model the strain-hardening behavior of cells, such as red blood cells which have a quasi surface-incompressible membrane (C¿¿1). The surface load $\underline{q}$ exerted by the fluid on the membrane is given by the membrane equilibrium law

$$\underline{\nabla_s}.\underline{\underline{T}} + \underline{q} = \underline{0}. \tag{2}$$

By the action-reaction principle, $-\underline{q}$ is the surface load exerted by the membrane on the fluid. More details may be found in [7, 15].

3.3 Fluid dynamics equations

The fluid equations are solved over the Eulerian grid $\mathcal{E}$ by the open-source code, Basilisk. In order to compute the Eulerian velocity field, Basilisk [14] uses the incom-

pressible ($\underline{\nabla}.\underline{v} = 0$), three-dimensional Navier-Stokes equations

$$\frac{\partial \underline{v}}{\partial t} + (\underline{v}.\underline{\nabla})\underline{v} = -\underline{\nabla} p + \frac{1}{Re}\underline{\Delta u} + \underline{f}, \tag{3}$$

where $\underline{v} = (v_x, v_y, v_z)$ is the fluid velocity, $\rho = \rho(x, y, z, t)$ the fluid density and $\mu = \mu(x, y, z, t)$ the dynamic viscosity. The Navier-Stokes equations are solved using a finite volume approach based on a projection method [16]. For Stokes flows, the non-linear term $(\underline{v}.\underline{\nabla})\underline{v}$ is set to zero. The spatial discretization is done using a octree cubic cell allowing dynamic grid refinement in the lubrication film. The source-term $\underline{f}$ is the volumic force exerted by the capsule on the fluid. Finally, the boundaries are that of a fluid at rest. Basilisk uses Dirichlet and Neumann boundary conditions. For the speed $\underline{v}$ we set a zero Dirichlet boundary condition on the inlet and lateral sections (S_i and S_l) and a zero Neumann boundary condition on the outlet section S_o. Additional optional boundaries are set for the pressure p: a zero Neumann condition on S_i and a zero Dirichlet condition on S_o [16].

3.4 Coupling strategy and method

The coupling strategy is based on the Immersed Boundary Method [11]. At each timestep:

- the forces are transmitted from the capsule membrane to the fluid as source-terms.
- the membrane capsule is advected by the fluid towards a new configuration.

The surface elastic load $\underline{q}$ is converted to fluid source-term volume forces $\underline{f}$ using the following two steps:

- the surface load $-\underline{q}$, defined at each $\underline{X} \in \mathcal{L}$, is first integrated into a ponctual force $\underline{F}(\underline{X})$. This integration is made using a 3 Hammer point scheme. This guarantees the force conservation over each finite element.
- the ponctual force $\underline{F}(\underline{X})$ is then spread into the source-term volumic force $\underline{f}$ by the immersed boundary method. We use the classical cosine immersed boundary filter δ_c [11]:

$$\underline{f}(x, y, z) = \sum_{\underline{X}=(X_x, X_y, X_z)\in\mathcal{L}} \frac{\underline{F}(\underline{X})}{(\Delta x)^3} \delta_c\left(\frac{x - X_x}{\Delta x}\right) \delta_c\left(\frac{y - X_y}{\Delta x}\right) \delta_c\left(\frac{z - X_z}{\Delta x}\right), \tag{4}$$

where

$$\forall s \in \mathbb{R}, \delta_c(s) = \frac{1}{4}\left(1 + \cos\left(\frac{\pi s}{2}\right)\right) \mathbb{I}_{|s|\leq 2}. \tag{5}$$

This filter is theoretically of order 1 [12] but is found to be of an order between 1 and 2 in practice.

The volumic force $\underline{f}$ is injected into equation (3), which is solved to provide the new velocity field $\underline{v}(t+dt)$ and update the position of the capsule nodes:

$$\frac{\underline{X}(t+dt)-\underline{X}(t)}{dt}=\sum_{(x,y,z)\in\mathcal{E}}\frac{\underline{v}(x,y,z,t+dt)}{(\Delta x)^3}\delta_l\left(\frac{x-X_x}{\Delta x}\right)\delta_l\left(\frac{y-X_y}{\Delta x}\right)\delta_l\left(\frac{z-X_z}{\Delta x}\right), \tag{6}$$

where

$$\forall s\in\mathbb{R},\delta_l(s)=(1-|s|)\,\mathbb{I}_{|s|\leq 1}. \tag{7}$$

This filter is of order 2 [12].

3.5 Parameters of the problem

The physical parameters are chosed to model an artificial microcapsule released in the tube:

- Capsule-to-channel size ratio $a/l=0.85$;
- Skalak law with $C=1$.

3.6 Criteria to be observed

3.6.1 Convergence study criteria

The criteria for the convergence at the final time $t=10$ of the simulation are:

- the maximum error norm over $\mathcal{L}$ of the difference of the position $\underline{X}$ for the timestep dt of the considered simulation to that obtained with the smallest integration timestep $dt_{\min}=10^{-4}$:

$$N_\infty=\|\underline{X}_{dt}-\underline{X}_{dt_{\min}}\|_\infty=\max_{\underline{X}\in\mathcal{L}}\|\underline{X}_{dt}-\underline{X}_{dt_{\min}}\| \tag{8}$$

- the maximum norm over $\mathcal{E}$ of the difference of the fluid speed to its theoretical value at $t=+\infty$. In this asymptotical state, the relaxation is over and the fluid is at rest. Thus, the criterion becomes:

$$v_{\max}=\|\underline{v}\|_\infty=\max_{(x,y,z)\in\mathcal{E}}\|\underline{v}(x,y,z)\| \tag{9}$$

- the relative membrane surface difference between the Lagrangian configuration $\mathcal{L}$ and the reference spherical shape $\mathcal{L}_0$: $\frac{d\mathcal{S}_\mathcal{L}}{\mathcal{S}_{\mathcal{L}_0}}=\frac{\mathcal{S}_\mathcal{L}-\mathcal{S}_{\mathcal{L}_0}}{\mathcal{S}_{\mathcal{L}_0}}$, where $\mathcal{S}_{\mathcal{L}_0}=4\pi a^2$
- the relative membrane volume difference between the Lagrangian configuration $\mathcal{L}$ and the reference spherical shape $\mathcal{L}_0$: $\frac{d\mathcal{V}_\mathcal{L}}{\mathcal{V}_{\mathcal{L}_0}}=\frac{V_\mathcal{L}-\mathcal{V}_{\mathcal{L}_0}}{\mathcal{V}_{\mathcal{L}_0}}$, where $\mathcal{V}_{\mathcal{L}_0}=\frac{4}{3}\pi a^3$. This variation is an error, since it should be zero.

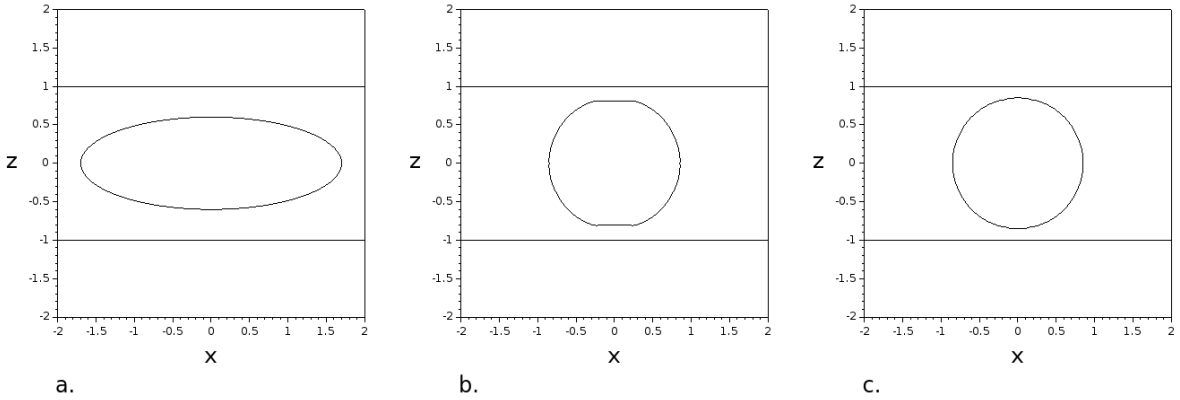

Figure 3: Shape evolution of the capsule relaxing in the channel at $t = 0$ (a), $t = 5$ (b), and $t = 10$ (c) for $h = 0.039$ and $dt = 5 \times 10^{-3}$ in Stokes flow.

3.6.2 Transient state study criteria

During the transient state i.e. $t \in]0, 10[$, the characterization can be done with the parameters of the inertia ellipsoid ϵ of $\mathcal{L}$. The Taylor parametrer is defined by $D_{1,2} = (L_x - L_y)/(L_x + L_y)$, where L_x and L_y are respectively the half-great and half-small axis of ϵ. Under Stokes flow, this approximation is valid: even though the capsule is influenced by the confinement, its shape $\mathcal{L}$ remains roughly ellipsoidal during the transient state (Figure 3). On the contrary, under inertial flow conditions (i.e. solving the full Navier-Stokes equations), the shape is too different from being ellipsoidal. We propose to replace the $D_{1,2}$ parameter with a parameter $\tilde{D}_{1,2} = (\tilde{L}_x - \tilde{L}_y)/(\tilde{L}_x + \tilde{L}_y)$, where $\tilde{L}_x = \max_L(X_x) - \min_L(X_x)$ and $\tilde{L}_y = \max_L(X_y) - \min_L(X_y)$ are the differences of the extremal coordinates of the Lagrangian grid respectively along O_x and O_y. This new definition allows negative values for $\tilde{D}_{1,2}$. For the sake of simplicity, in the following this new parameter is also called "Taylor parameter".

4 RESULTS

4.1 Generalities

The capsule relaxes to its reference spherical geometry. Figure 3 shows the time evolution of the capsule shape for $h = 0.039$ and $dt = 5 \times 10^{-3}$ in Stokes flow. At time $t = 5$ one sees that the capsule shape is influenced by the walls of the channel, the capsule wall becoming parallel to it.

4.2 Final time results

When comparing the capsule shape $\mathcal{L}$ at time t to $\mathcal{L}_0$, we see that the infinite norm $\|\underline{X} - \underline{X_0}\|_\infty$ has an order of magnitude $\sim 1\%$, depending on the Lagrangian mesh size h and time step dt. It is consistent with the evolution of $\mathcal{L}$ towards $\mathcal{L}_0$ over time. Since the final time $t = 10$ is far from the end of the relaxation process which is infinite, the

relaxation is uncomplete and this infinite norm is minorated over $(h, \Delta x, dt) \in (\mathbb{R}^{+,*})^3$ by some constant $K > 0$. Figure 4 presents the values of the 4 criteria defined in subsection 3.6.1. The same orders of magnitude are obtained for the four criteria: they lie between $\sim$0.1% and $\sim$1% for N_∞ (4.a), $v_{\max}$ (4.b), $\frac{d\mathcal{S}_\mathcal{L}}{\mathcal{S}_{\mathcal{L}_0}}$ (4.c) and $\frac{d\mathcal{V}_\mathcal{L}}{\mathcal{V}_{\mathcal{L}_0}}$ (4.d):

- Values of (4.a) prove that the error of convergence has an order of magnitude $\sim 0.1\%$ for the smallest timestep $dt_{\min} = 10^{-4}$;
- Values of (4.b) show that the fluid is almost at rest, but not totally because the final time is $(t = 10)$;
- Values of (4.c) show that the area of $\mathcal{L}$ always differ by less than 1% from that of the reference shape $\mathcal{L}_0$;
- Values of (4.d) show that the volume conservation error is always clearly lower than 1%. They are of the same order or smaller than those obtained by Caroll and Gupta [17]. In the best case, the error is 0.02%, which is indeed much better than [17].

We observe the following effects of the numerical parameters:

- Figure 4.a shows that the errors are larger with $h = 0.020$ than with $h = 0.039$, which appears to be more adapted to $\Delta x = 0.03125$ in this test. We can deduce from this (and from the fact that the above mesh size is too coarse - see subsection 3.1) that $\frac{h}{\Delta x} = \frac{0.039}{0.03125} = 1.248$ is the ideal Lagrangian-to-Eulerian mesh size ratio for our tool and for this test.
- The convergence of N_∞ while varying the timestep dt is of order $\sim$1.5 for $h = 0.039$ (in Figure 4.a, the slope for $h = 0.039$ is $\sim$1.5) and lower for $h = 0.02$. This lower convergence speed confirms the above conclusion about the optimal ratio $\frac{h}{\Delta x} = 1.248$.

4.3 Transient states results

We present in Figure 5a the Taylor parameter as a function of time for the Stokes flow and in Figure 5b for a Navier-Stokes computation with Reynolds number $Re = 10$. We see in Figure 5a a continuous decrease of $D_{1,2}$ under Stokes flow: in Figure 5b the influence of the inertial term appears through damped oscillations around the equilibrium state.

5 CONCLUSION

We have built and tested a tool which couples a finite volume fluid solver with a finite element solid solver using the Immersed Boundary Method. On a simple relaxation case, the coupled solver is shown to give satisfactory numerical precision under Stokes flow,

the timestep convergence being of the order 1.5. When comparing the capsule relaxation under Stokes and Navier-Stokes flow conditions, we find that oscillations in the capsule shape already occur for a flow Reynods Number of 10. The oscillations are due to inertia.

The numerical precision is comparable to that of classical methods, which shows that the immersed boundary method is adapted to solve transient problems. The present approach is also interesting for the advantages of the fluid solver itself. It is massively parallel (OpenMP and MPI) and can thus be used for large spatial simulations. Furthermore, the fluid solver also has an adaptative dynamic meshing that is useful to compute numerical solution near walls. Finally the viscosity and mass density can be changed dynamically, which is interesting to model solid or non-Newtonian cores for capsules flowing in a capillary. The novelty is that the fluid-structure code can resolve the flow of capsules of aspect ratios greater than 1 and non-zero Reynolds numbers, which are required to study capsules in microsystems. The fluid velocity field is also studied by considering the changes in the streamlines when varying the capillary number, which is crucial for the understanding of the fluid dynamics. The numerical model can be a useful complement to experimental measurements, as it provides local field quantities (fluid pressure and velocity, membrane tensions, ...), which cannot easily be evaluated experimentally, as well as information on topographic changes in streamlines. It thus provides useful additional information for the study of capsules in microsystems.

REFERENCES

[1] Johnston, A. P., Cortez, C., Angelatos, A. S. and Caruso, F. Layer-by-layer engineered capsules and their applications. *Curr. Opin. Colloid Interface Sci.* (2006) **11(4)**:203-209.

[2] Chang, K. S. and Olbricht, W. L. Experimental studies of the deformation and breakup of a synthetic capsule in extensional flow. *J. Fluid Mech.* (1993a) **250**:587-608.

[3] Chang, K. S. and Olbricht, W. L. Experimental studies of the deformation and breakup of a synthetic capsule in steady and unsteady simple shear flow. *J. Fluid Mech.* (1993b) **250**:609-633.

[4] Risso, F., Coll-Paillot, F. and Zagzoule, M. Experimental investigation of a bioartificial capsule flowing in a narrow tube. *J. Fluid Mech.* (2006) **547**:149-173.

[5] Barthès-Biesel, D. Motion of a spherical microcapsule freely suspended in a linear shear flow. *J. Fluid Mech.* (1980) **100**:831-853.

[6] Barthès-Biesel, D. and Rallison, J. M. The time-dependent deformation of a capsule freely suspended in a linear shear flow. *J. Fluid Mech.* (1981) **113**:251-267.

[7] Walter, J., Salsac, A.-V., Barthès-Biesel, D. and Le Tallec, P. Coupling of finite element and boundary integral methods for a capsule in a Stokes flow. *Int. J. Numer. Meth. Engng.* (2010) **83**:829-850.

[8] Wang, Z., Sui, Y., Salsac, A.-V. and Barthès-Biesel, D. Motion of a spherical capsule in branched tube flow with finite inertia. *J. Fluid Mech.* (2016) **806**:603-626.

[9] Tryggvason, G., Scardovelli, R. and Zaleski., S. *Direct Numerical Simulations of Gas-Liquid Multiphase Flows*. Cambrige Press University (2011)

[10] de Brauer, A., Iollo, A. and Milcent, T. A cartesian scheme for compressible multi-material models in 3D, *J. Fluid Mech.* (2016) **313**:121-143.

[11] Peskin, C.S. The immersed boundary method. *Acta Numerica* (2002) pp. 1-39.

[12] Beyer, R.P. and Leveque, R.J. Analysis of a One-Dimensional Model for the Immersed Boundary Method. *SIAM J. Numer. Anal.* (1992) **29(2)**:332-364.

[13] Balogh, P. and Bagchi, P. A computational approach to modeling cellular-scale blood flow in complex geometry. *J. Comput. Phys.* (2017) **334**:280-307.

[14] Popinet, S. Basilisk: simple abstractions for octree-adaptive scheme. *SIAM Conf on Para. Proc. for Sc. Comput.* (2016)

[15] Skalak, R., Tozeren, A., Zarda, R. P. and Chien, S. Strain energy function of red blood cell membranes. *Biophys. J.* (1973) **13**:245-264.

[16] Bell, J.B. and Collela, P. A Second-Order Projection Method for the Incompressible Navier-Stokes Equations in Arbitrary Domains. *J. Comput. Physics.* (1989) **85(2)**.

[17] Carroll, R. M. and Gupta, N. R. Inertial effects on the flow of capsules in cylindrical channels. *Int. J. Mult. Flow.* (2016) **87**:114-123.

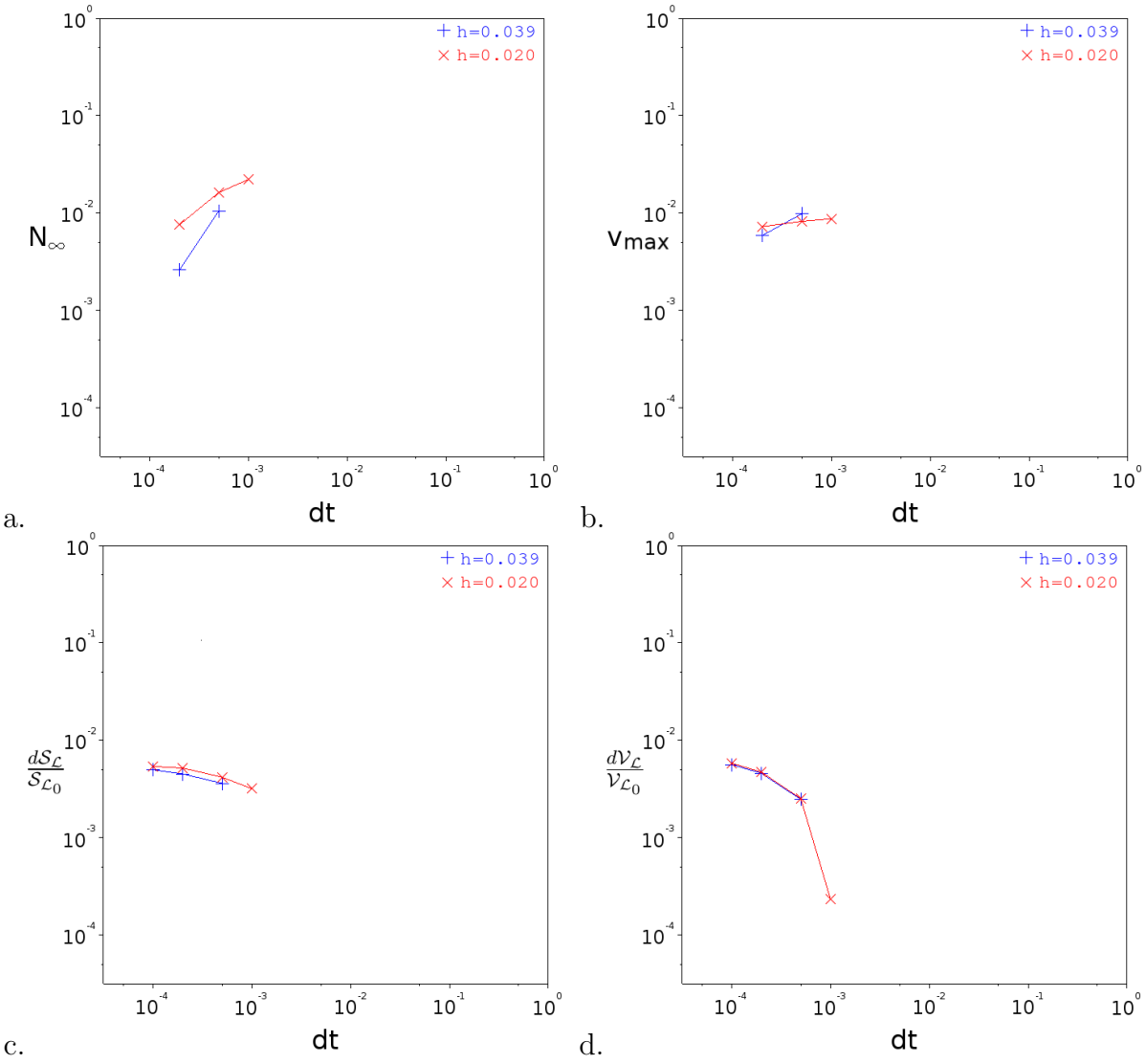

Figure 4: Convergence study: infinite norm error of the Lagrangian nodes positions to the case of the smallest timestep $dt_{\min} = 10^{-4}$ (a); Maximum speed norm in the fluid (b); Surface variation of the Lagrangian configuration compared to the reference spherical shape (c); Volume variation (d) (which is an error since it should be zero). Four different timesteps ($dt = 10^{-3}$, $dt = 5 \times 10^{-4}$, $dt = 2 \times 10^{-4}$, and $dt = 10^{-4}$) and two different Lagrangian meshes ($h = 0.039$ and $h = 0.020$) are tested.

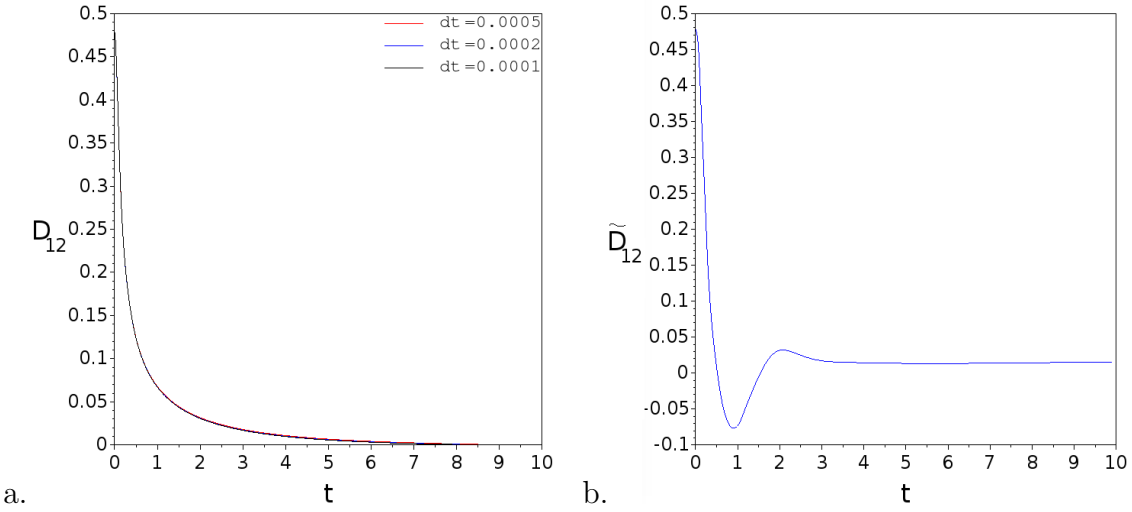

Figure 5: Time evolution of the Taylor parametrer (a) for Stokes flow and for a Navier-Stokes computation with $Re = 10$ (b).

VII International Conference on Computational Methods for Coupled Problems in Science and Engineering
COUPLED PROBLEMS 2017
M. Papadrakakis, E. Oñate and B. Schrefler (Eds)

ACCELERATION OF FLUID-STRUCTURE INTERACTION PROCEDURES BY ANTICIPATORY COUPLING

J.H. Seubers* **and A.E.P. Veldman†**

*†Computational Mechanics and Numerical Mathematics
University of Groningen
Nijenborgh 9, 9747 AG Groningen, The Netherlands
web page: http://www.rug.nl/fmns-research/cmnm
e-mail: *h.seubers@rug.nl, †a.e.p.veldman@rug.nl

Key words: Fluid-solid Interaction, Numerical Method, Strong Coupling, Added Mass

Abstract. Simulating the hydrodynamics of floating structures using a two-way partitioned coupling poses a major challenge when the coupling between the fluid and the structure is strong. The incompressibility of the fluid plays an important role, and leads to strong coupling when the ratio of so-called *added mass* to structural mass is considerate. Existing fluid-structure interaction procedures become less efficient in such cases, and can even become unstable. This paper proposes a coupling method that deals with the added-mass effect by anticipation, and remains stable and efficient at all times.

1 INTRODUCTION

Traditionally, multi-physics problems are classified as 'strongly' or 'weakly' interacting problems. From a physical perspective, the interaction is called *weak* if one subsystem dominates the behaviour of the coupled problem, and it is called *strong* if more than one of the subsystems 'equally contribute to the interaction' [1] or 'have an equal say' [2]. So the physical interaction strength is a scale running from a *one-way* hierarchy between systems to a *two-way* complementary interaction. An example of a hierarchy is the case of a very light particle (e.g. a ping-pong ball) in a large water wave: the motion of the ball follows completely from the motion of the wave. The wave is not affected by the presence of the ball. The exact opposite hierarchy occurs for heavy objects (e.g. a mammoth tanker) in quiet water: the flow of the water is completely determined by the motion of the ship. Of course, many real situations are somewhere in between these asymptotic cases, with *two-way* interaction between the subsystems: some feedback occurs from the water to the ship or from the particles to the water. The more feedback, the stronger the interaction.

In hydrodynamic applications with moving structures, a major factor affecting the interaction strength is the ratio of the *added mass* of fluid to the structural mass. In

the traditional formulation, where the fluid loads are imposed on the structure and the structural motions imposed on the fluid, higher added mass ratios increase the interaction strength. This effect makes simulation by traditional coupling methods of slender structures in large waves computationally expensive. The objective of the proposed method is to reduce the computation time for such applications.

Section 2 provides the motivation and physical background of fluid-structure coupling problems in marine hydrodynamics. The mathematical model of this problem is explained in section 3, which provides the necessary ingredients to analyze the coupling method. The new coupling method is introduced in section 4, where it is compared to existing methods. The properties of the new method are analyzed in section 5, and the results of some numerical experiments are discussed in section 6, leading to the conclusions in section 7.

2 PHYSICAL MODEL

Interactive simulations are important for predicting the behaviour of moored or free-floating ships or platforms in different operating conditions. On deck various operations may be performed that affect the load or inertia distribution of the vessel. The vessel responds not only to incoming waves but to the flow caused by its own motions as well: wave slamming, launching, green water events. The inertia of the water mass involved in these interacting flows is important for predicting the forces on the vessel. In other words, the inertia is an important feedback mechanism that leads to a strong coupling between the flow and the vessel motion.

The ship or platform, which will be referred to as the structure, is modelled as a rigid body with elastic mooring lines. The structure can have an arbitrary shape and can perform large but finite translations and rotations in three dimensions. It cannot deform or change in volume.

The water is modelled as an incompressible, viscous fluid with a free surface. Although the inviscid flow behaviour dominates the coupling, the vorticity and viscosity are included in order to show that the story remains essentially the same. The air flow is not modelled, a vacuum takes its place instead.

The interaction is modelled by conservation of momentum and geometric compatibility between the structure and fluid surface. Note that the topology and position of the fluid-structure interface can change in time.

3 MATHEMATICAL MODEL

Because of its flexibility, the partitioned approach will be adopted in this work. The partitioning cuts the system into two parts, a fluid subsystem (subscript $_f$) and a structure subsystem (subscript $_s$). The two subsystems with appropriate boundary conditions are represented as dynamical systems in a state-space representation, governed by the mass-

spring and Navier-Stokes equations respectively.

$$\mathrm{M}\ddot{\mathbf{x}} + \mathrm{K}\mathbf{x} = \mathrm{B}_s^T \mathbf{f}_s \qquad \rho\Omega\dot{\mathbf{u}} + \mathrm{G}\mathbf{p} + \rho\mathrm{C}(\mathbf{u})\mathbf{u} - \mu\mathrm{L}\mathbf{u} = \mathrm{B}_f^T \mathbf{f}_f \tag{1a}$$

$$\mathbf{y}_s = \mathrm{B}_s \ddot{\mathbf{x}} \qquad \mathbf{y}_f = \mathrm{B}_f \dot{\mathbf{u}} \tag{1b}$$

where $[\mathbf{x}, \mathbf{u}, \mathbf{p}]^T$ are the internal states of the fluid-structure system, $[\mathbf{y}_f, \mathbf{y}_s]^T$ are the motions at the component boundaries, and $[\mathbf{f}_f, \mathbf{f}_s]^T$ are the distributed loads at these boundaries. The domain where these variables live may deform over the time interval $[\mathrm{t}, \mathrm{t} + \Delta\mathrm{t}]$, see fig. 1.

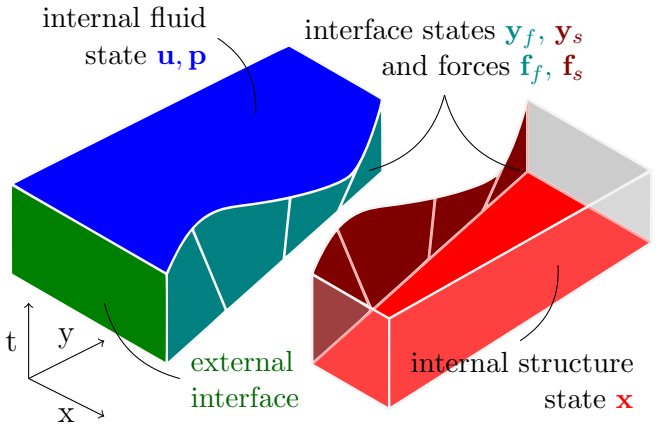

Figure 1: Model interface in space-time.

This mathematical model is not yet complete since the forces are not given. These are determined implicitly by two coupling criteria. The *kinematic* criterion requires that the motions on both sides of the fluid-structure interface are the same,

$$\delta\mathbf{y} := \mathbf{y}_f(t) - \mathbf{y}_s(t) = \mathbf{0}. \tag{2a}$$

The *dynamic* criterion expresses the balance of forces over the fluid-structure interface,

$$\sum \mathbf{f} := \mathbf{f}_f(t) + \mathbf{f}_s(t) = \mathbf{0}. \tag{2b}$$

Since the interaction is concerned with the variables that live on the interface, the internal states $[\mathbf{x}, \mathbf{u}, \mathbf{p}]^T$ are eliminated from the system by linearizing and substituting (1a) into (1b). This will lead to two operators that give the motions $\mathbf{y}$ in terms of the loads $\mathbf{f}$, the so-called Dirichlet-to-Neumann (DtN) operators A_f and A_s.

$$\mathbf{y}_f(t) = \mathbf{y}_f^0(t) + \mathrm{A}_f(t) * \mathbf{f}_f(t), \tag{3a}$$

$$\mathbf{y}_s(t) = \mathbf{y}_s^0(t) + \mathrm{A}_s(t) * \mathbf{f}_s(t). \tag{3b}$$

Together with the unloaded motions $\mathbf{y}^0_{f,s}$, these DtN operators completely describe the response of both subsystems to any load. Therefore, the difficulties of the interaction can be found by studying the properties of the DtN. It is easier to derive the DtN in the Laplace domain, where the time derivatives can be manipulated algebraically. To show how this is done, some simplified models are considered first.

3.1 Response of simplified models

Consider a cylinder on a spring, moving horizontally in a quiescent potential flow (fig. 2). The cylinders response is found by considering the equations of motion in the Laplace domain:

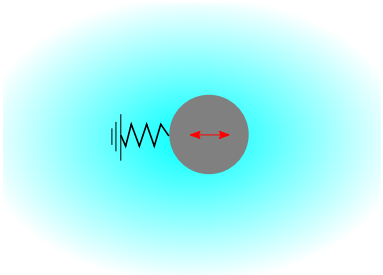

Figure 2: Spring-fixed cylinder moving in infinite potential flow

$$\begin{aligned} s^2\mathrm{m}\hat{x} + \mathrm{k}\hat{x} &= \hat{f}_s + \mathrm{m}(sx_0 + \dot{x}_0), \\ \hat{y}_s &= s^2\hat{x} - (sx_0 + \dot{x}_0). \end{aligned}$$

where m is the cylinder mass and k is the spring stiffness. This yields the response

$$\hat{y}_s = \left(\frac{s^2\mathrm{m}}{s^2\mathrm{m} + \mathrm{k}} - 1\right)(sx_0 + \dot{x}_0) + \left(\frac{s^2}{s^2\mathrm{m} + \mathrm{k}}\right)\hat{f}_s. \tag{4}$$

The DtN operator is recognized as $\hat{A}_s = \frac{s^2}{s^2m+k}$, which represents the acceleration of the cylinder due to an impulsive force at $t = 0$. The acceleration due to any other force can be found by convolution. In particular, the instantaneous acceleration due to a step force f_0 can be found from the initial value theorem,

$$y_s(t{=}0) = f_0 \lim_{s\to\infty} \hat{A}_s(s) = \frac{f_0}{\mathrm{m}}. \tag{5}$$

The fluid response is simply given by the added mass force. In summary, this simple interaction problem is governed by the two DtN operators

$$\hat{A}_s = \frac{s^2}{s^2\mathrm{m} + \mathrm{k}}, \qquad \hat{A}_f = \frac{1}{\mathrm{m}_a}. \tag{6}$$

3.2 Interactive response

Now recall the physical description of the ping-pong ball and the mammoth tanker. Since the feedback from the ping-pong ball on the water is small, we create an asymptotic expansion for the fluid motion $\hat{\mathbf{y}}_f(s)$ starting from the unforced fluid motion $\hat{\mathbf{y}}_f^0(s)$,

$$\hat{\mathbf{y}}_f = \hat{\mathbf{y}}_f^0 + \hat{\mathrm{A}}_f\hat{\mathrm{A}}_s^{-1}\big(\hat{\mathbf{y}}_s^0 - \hat{\mathbf{y}}_f^0\big) + \mathbf{O}(\hat{\epsilon}_f^2). \tag{7}$$

On the other hand, the asymptotic expansion for the mammoth tanker will start with the unforced vessel motion $\hat{\mathbf{y}}_{0s}(s)$, since the feedback from the water is small.

$$\hat{\mathbf{y}}_s = \hat{\mathbf{y}}_s^0 + \hat{\mathrm{A}}_s\hat{\mathrm{A}}_f^{-1}\big(\hat{\mathbf{y}}_f^0 - \hat{\mathbf{y}}_s^0\big) + \mathbf{O}(\hat{\epsilon}_s^2), \tag{8}$$

where the feedback strengths $\hat{\epsilon}_f$, $\hat{\epsilon}_s$ are measured by the disturbance of the motion

$$\hat{\epsilon}_f(s) = \left\|\hat{\mathrm{A}}_f(s)\hat{\mathrm{A}}_s^{-1}(s)\right\|, \qquad \hat{\epsilon}_s(s) = \left\|\hat{\mathrm{A}}_s(s)\hat{\mathrm{A}}_f^{-1}(s)\right\|. \tag{9}$$

At most one of these asymptotic expansions (7) or (8) will converge for a given problem, since $\hat{\epsilon}_f < 1$ implies $\hat{\epsilon}_s > 1$. Supposing that (8) converges, the motion will be given by

$$\hat{\mathbf{y}}_s = \hat{\mathbf{y}}_s^0 + \sum_{i=1}^{\infty}\big(\hat{\mathrm{A}}_s\hat{\mathrm{A}}_f^{-1}\big)^i\delta\hat{\mathbf{y}}^0 = \hat{\mathbf{y}}_s^0 + \big(\mathrm{I} - \hat{\mathrm{A}}_s\hat{\mathrm{A}}_f^{-1}\big)^{-1}\delta\hat{\mathbf{y}}^0 \tag{10}$$

In particular, this provides the interactive motion of the simplified models

$$\hat{y}_s = \hat{y}_s^0 + \sum_{i=1}^{\infty}\left(\frac{s^2\mathrm{m}_a}{s^2\mathrm{m}+\mathrm{k}}\right)^i\delta\hat{y}^0 = \hat{y}_s^0 + \left(\frac{s^2\mathrm{m}+\mathrm{k}}{s^2(\mathrm{m}-\mathrm{m}_a)+\mathrm{k}}\right)\delta\hat{y}^0. \tag{11}$$

Only for $\mathrm{m} > \mathrm{m}_a$, the roots of the denominator are in the left half plane, hence an oscillatory solution bounded by the initial disturbance δy^0 exists. In more complex cases, it could happen that neither expansion converges. In that case, both subsystems contribute equally: the physical interaction is strong. Therefore it makes sense to define the physical interaction strength as a product of the feedback strengths:

Definition 1. The physical *interaction strength* κ of the closed system (eqs. (1a), (1b), (2a) and (2b)) is a number between one and infinity, given by the initial value of the product of the feedback strengths,

$$\kappa = \lim_{s\to\infty}\hat{\epsilon}_f(s)\hat{\epsilon}_s(s)$$

This definition can be seen as the sensitivity of the responses for $t \to 0$. In the simplified scalar model (section 3.1) these sensitivities are the added mass ratio and its reciprocal,

$$\lim_{s\to\infty}\hat{\epsilon}_s = \left(\frac{m_a}{m}\right), \lim_{s\to\infty}\hat{\epsilon}_f = \left(\frac{m}{m_a}\right) \tag{12}$$

Generalizing this to systems, the sensitivities are the maximal and minimal eigenvalues of the matrix $\mathrm{A}_s\mathrm{A}_f^{-1}$. Note that κ is also the condition number of this matrix. Its eigenvalues can be interpreted physically as 'directional' added mass ratios, i.e. depending on the direction of the motion vector. When the interaction strength equals one, the coupled motion is simply a linear combination of the unforced motions $\mathbf{y}_f = (1-\alpha)\mathbf{y}_f^0 + \alpha\mathbf{y}_s^0$. In general however, this rarely occurs and interaction strengths may be higher. For rigid bodies floating in incompressible flow, it will be shown in section 5 that the interaction strength is still a function of mass ratios. But first, the performance of coupling algorithms will be directly related to the interaction strength in section 4.

4 NUMERICAL COUPLING METHODS

The basic coupling methods are related to the asymptotic expansions in eqs. (7) and (8). In marine hydrodynamics, the expansion (8) dominated by the ship motion is most natural, and it converges provided that the added mass is smaller than the ship mass,

$$\left\|\hat{\mathrm{A}}_s(s)\hat{\mathrm{A}}_f^{-1}(s)\right\| < 1 \qquad \text{i.e.} \quad \left|\frac{\mathrm{m}_a s^2}{\mathrm{m}s^2+\mathrm{k}}\right| < 1. \tag{13}$$

This coupling approach works well for weakly coupled problems, provided that the ship is indeed the dominant subsystem. If the ship is less dominant, it may be required to mix the approaches of the mammoth tanker and the ping-pong ball, using combinations of eqs. (7) and (8). Indeed modern domain decomposition approaches like FETI [3] are based on the difference between eqs. (7) and (8), $\delta\mathbf{y} = \mathbf{y}_f - \mathbf{y}_s$. This difference is iteratively reduced by splitting it over the two domains and then enforcing the dynamic criterion eq. (2b),

$$\delta\mathbf{y}_{i+1} = \delta\mathbf{y}_i + \big(\mathrm{A}_f + \mathrm{A}_s\big)\big(\alpha\mathrm{A}_f^{-1} + (1-\alpha)\mathrm{A}_s^{-1}\big)\delta\mathbf{y}_i, \tag{14}$$

where i is the iteration index. An early precursor to this approach is the semi-inverse method by Le Balleur (1978),

$$\delta\mathbf{y}_{i+1} = \delta\mathbf{y}_i - \alpha\big(\mathrm{A}_f + \mathrm{A}_s\big)\delta\mathbf{y}_i. \tag{15}$$

In both methods, a new force is estimated from $\delta\mathbf{y}$ and fed identically (but with opposite sign) to both subsystems to produce the new motions. These forces and motions are notated here as simple vectors, not as functions of time since eqs. (14) and (15) are steady state methods. An extension of the semi-inverse method that operates on time series of forces and motions is known as waveform relaxation [4]. In each iteration, both subsystems are integrated in time based on an estimated force series. The difference in the resulting motion series are multiplied by the relaxation parameter α to produce a new force estimate, exactly as in (15).

FETI, semi-inverse and waveform relaxation methods can all be seen as local preconditioners for the kinematic criterion eq. (2a), see fig. 3. For a suitable range of α, such methods can deal with strongly coupled problems. However, their convergence ($\delta\mathbf{y} \to 0$) slows down as the coupling strength increases.

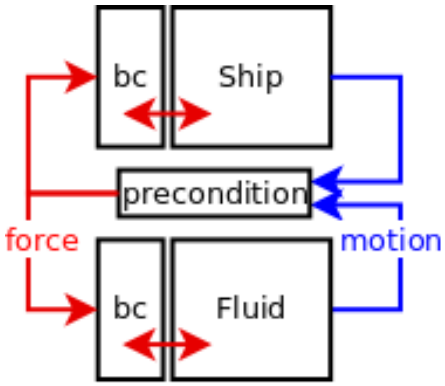

Figure 3: Preconditioning schemes: semi-inverse, FETI, waveform relaxation

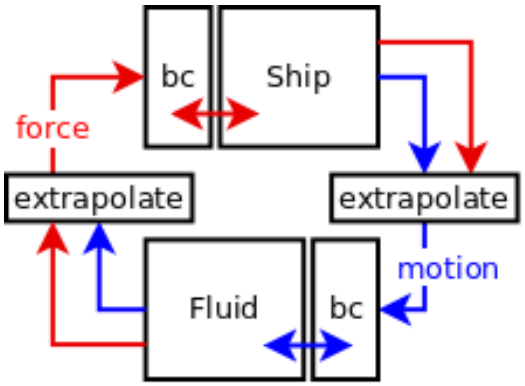

Figure 4: Extrapolation schemes: Gauss-Seidel, IQN, IBQN, manifold mapping

Another family of methods for strongly coupled problems is based on the Gauss-Seidel approach (fig. 4). Instead of applying the coupling criteria (2) directly, the expansion (8) is modified by introducing extrapolation steps. The simplest type of extrapolation is under-relaxation,

$$\mathbf{y}_{i+1} = \mathbf{y}_i + \alpha \mathrm{A}_s \mathrm{A}_f^{-1} \delta \mathbf{y}_i. \tag{16}$$

This method will again converge for suitable α, albeit slower when the interaction becomes stronger. In fact, even for the optimal choice in α, the performance of this method deteriorates linearly with the coupling strength.

4.1 Anticipatory coupling

The quasi-simultaneous method [5] however, avoids the need for extrapolation or relaxation by reformulating the original problem to an equivalent one with reduced coupling strength. This is achieved by replacing the system of coupling conditions (2) by an equivalent system,

$$\mathbf{y}_f + \mathrm{D}_i \mathbf{f}_f = \mathbf{y}_s - \mathrm{D}_i \mathbf{f}_s, \tag{17a}$$

$$\mathbf{f}_f + \mathbf{f}_s = \mathbf{0}. \tag{17b}$$

Note that eq. (17a) is formed by eq. (2a) plus an arbitrary operator D_i times eq. (2b).

Since eq. (2a) was previously used as a boundary condition for the fluid, this simply amounts to a more general boundary condition. A suitable choice of the operator D_i would contain some approximate physics of the structure. In the anticipatory coupling method, we choose D_i as the instantaneous approximation of the structure:

$$D_i = \lim_{s \to \infty} \hat{A}_s. \tag{18}$$

This choice is motivated as follows. The approximation (18) is

- easy to obtain, only the inertia properties such as the mass of the structure are needed.
- exact at $t = 0$, so zero-stability of the subsystems implies zero-stability of the coupling.
- physically consistent, no artificial physics are introduced into the problem.

The difference between D_i and A_s will produce a finite error in the solution at finite timesteps, but this error can be controlled by varying the timestep size, or resorting to any of the above families of coupling methods. The anticipatory algorithm thus takes the following steps:

1. Initialize structural motion $\mathbf{y}_s^{old}$ and loads $\mathbf{f}_s^{old}$ from previous timestep
2. Predict fluid velocities $\tilde{\mathbf{u}}$ due to convection and diffusion
3. Move the geometry based on the structural motion $\mathbf{y}_s^{old}$
4. Compute new fluid force $\mathbf{f}_f^{new}$ in Poisson equation with anticipative condition (17a)
$$\tilde{\mathbf{y}}_f + \mathrm{D}_i \mathbf{f}_f^{new} = \mathbf{y}_s^{old} - \mathrm{D}_i \mathbf{f}_s^{old}$$
5. Compute new structural response $\mathbf{y}_s^{new}$ with dynamic condition (2b)
$$\mathbf{f}_s^{new} = \mathbf{f}_f^{new}$$
6. Enforce the kinematic condition (2a) $\mathbf{y}_f^{new} = \mathbf{y}_s^{new}$ (discarding $\tilde{\mathbf{y}}_f$)
7. Correct fluid velocities $\mathbf{u}$ and update the free-surface position
8. Go to the next timestep

To see the effect of the anticipative condition, it is illustrative to look at the simplified model from section 3.1 again. In this example, the modified Dirichlet-to-Neumann maps become

$$\hat{\mathrm{A}}_f(s) + \mathrm{D}_i = \frac{1}{\mathrm{m}_a} + \mathrm{d}_i, \tag{19a}$$

$$\hat{\mathrm{A}}_s(s) - \mathrm{D}_i = \frac{s^2}{s^2\mathrm{m} + \mathrm{k}} - \mathrm{d}_i. \tag{19b}$$

Although these are only a scalar equation, it is clear that this affects the asymptotic expansion in general as

$$\hat{\mathbf{y}}_s = \hat{\mathbf{y}}_s^0 + (\hat{\mathrm{A}}_s - \mathrm{D}_i)(\hat{\mathrm{A}}_f + \mathrm{D}_i)^{-1}\delta\hat{\mathbf{y}}^0 + \mathbf{O}(\hat{\epsilon}_s^2), \tag{20}$$

hence the feedback strength becomes

$$\hat{\epsilon}_s(s) = \left| \frac{s^2\mathrm{m}_a}{s^2\mathrm{m} + \mathrm{k}} \, \frac{1 - \mathrm{d}_i\mathrm{m}}{1 + \mathrm{d}_i\mathrm{m}_a} + O(s^{-2}) \right|. \tag{21}$$

Therefore any choice $0 < \mathrm{d}_i^{-1} < 2m$ makes $\hat{\epsilon}_s(\infty) < 1$, and then the expansion (8) converges, at least for small enough time intervals.

5 ANALYSIS OF THE METHOD

To extend the convergence result for the simple models to the Navier-Stokes and mass-spring model, we will take the following steps.

- Obtain the DtN operators for the Navier-Stokes and mass-spring models
- Choose D_i based on the instantaneous response from the DtN operators
- Show that the anticipative scheme has a feedback of order $s^{-1} \sim \Delta t$

5.1 Linearized DtN operators

The discrete mass-spring model in (1a) for the structure is transformed into the Laplace domain,

$$(s^2\mathrm{M} + \mathrm{K})\hat{\mathbf{x}} = \mathrm{B}_s^T\hat{\mathbf{f}}_s + \mathrm{M}(s\mathbf{x}_0 + \dot{\mathbf{x}}_0) \tag{22a}$$

$$\hat{\mathbf{y}}_s = s^2\mathrm{B}_s\hat{\mathbf{x}} - \mathrm{B}_s(s\mathbf{x}_0 + \dot{\mathbf{x}}_0). \tag{22b}$$

By eliminating the internal unknown $\hat{\mathbf{x}}$ by the same procedure used in eq. (4) the response of the structure is found

$$\hat{\mathbf{y}}_s = \hat{\mathbf{y}}_s^0 + \mathrm{B}_s\big(\mathrm{M} + s^{-2}\mathrm{K}\big)^{-1}\mathrm{B}_s^T\hat{\mathbf{f}}_s. \tag{23}$$

The treatment of the Navier-Stokes model in (1a) contains an additional step, since both $\hat{\mathbf{p}}$ and $\hat{\mathbf{u}}$ must be eliminated. Starting from the basic equations linearized around $\mathbf{u}_0$ in the Laplace domain

$$-\mathrm{G}^T\hat{\mathbf{u}} = \mathbf{0} \tag{24a}$$

$$(s\rho\Omega + \rho\mathrm{C}(\mathbf{u}_0) - \mu\mathrm{L})\hat{\mathbf{u}} = \mathrm{B}_f^T\hat{\mathbf{f}}_f - \mathrm{G}\hat{\mathbf{p}} + \rho\Omega\mathbf{u}_0 \tag{24b}$$

$$\hat{\mathbf{y}}_f = s\mathrm{B}_f\hat{\mathbf{u}} - \mathrm{B}_f\mathbf{u}_0, \tag{24c}$$

the pressure is eliminated first by using the continuity equation (24a). Denoting the action of convection and diffusion by $\hat{\mathrm{T}}^{-1} = \mathrm{I} + (s\Omega)^{-1}(\mathrm{C}(\mathbf{u}_0) - \nu\mathrm{L})$, an analog for the pressure Poisson equation is found

$$\left(\mathrm{G}^T\hat{\mathrm{T}}\Omega^{-1}\mathrm{G}\right)\hat{\mathbf{p}} = \mathrm{G}^T\hat{\mathrm{T}}\Omega^{-1}\mathrm{B}_f^T\hat{\mathbf{f}}_f + \mathrm{G}^T\hat{\mathrm{T}}\rho\mathbf{u}_0. \tag{25}$$

The momentum (24b) and pressure (25) equations are then used to eliminate $\hat{\mathbf{u}}$ and $\hat{\mathbf{p}}$ from (24c). What remains is the response of the fluid to the imposed loads,

$$\begin{aligned}\hat{\mathbf{y}}_f &= \frac{1}{\rho}\mathrm{B}_f\hat{\mathrm{T}}\Omega^{-1}\left(\mathrm{B}_f^T\hat{\mathbf{f}}_f - \mathrm{G}\hat{\mathbf{p}}\right) + \mathrm{B}_f(\hat{\mathrm{T}}\mathbf{u}_0 - \mathbf{u}_0)\\ &= \frac{1}{\rho}\mathrm{B}_f\left(\mathrm{I} + \hat{\mathrm{T}}\Omega^{-1}\Delta\right)\hat{\mathrm{T}}\Omega^{-1}\mathrm{B}_f^T\hat{\mathbf{f}}_f + \hat{\mathbf{y}}_f^0\end{aligned} \tag{26}$$

where $\Delta = -\mathrm{G}\left(\mathrm{G}^T\mathrm{T}\Omega^{-1}\mathrm{G}\right)^{-1}\mathrm{G}^T$ is the global transport of fluid volume required to satisfy the incompressibility constraint. In summary, the interaction problem eqs. (1a), (1b), (2a) and (2b) is governed by the two DtN operators

$$\hat{\mathrm{A}}_s = \mathrm{B}_s\big(\mathrm{M} + s^{-2}\mathrm{K}\big)^{-1}\mathrm{B}_s^T, \qquad \hat{\mathrm{A}}_f = \frac{1}{\rho}\mathrm{B}_f\left(\mathrm{I} + \hat{\mathrm{T}}\Omega^{-1}\Delta\right)\hat{\mathrm{T}}\Omega^{-1}\mathrm{B}_f^T. \tag{27}$$

5.2 Instantaneous response

The fluid and structure should be aware of each others most immediate response, so they can anticipate what will happen. This is achieved by choosing boundary conditions that approximate the actual response, i.e. that approximate the DtN operators. The approximation here is crucial, since the full nonlinear dynamical DtNs are practically too expensive to use. For coupled simulations with finite time-steps, the instantaneous response would be a good choice of boundary condition. Hereto, we define a splitting of eq. (27) into an instantaneous part $\mathrm{A}_\cdot^0$ and a time dependent part $\hat{\mathrm{A}}_\cdot^+(s)$, such that $\hat{\mathrm{A}}_\cdot(s) = \mathrm{A}_\cdot^0 + \hat{\mathrm{A}}_\cdot^+(s)$.

$$\mathrm{A}_s^0 = \lim_{s\to\infty}\hat{\mathrm{A}}_s = \mathrm{B}_s\mathrm{M}^{-1}\mathrm{B}_s^T, \qquad \mathrm{A}_f^0 = \lim_{s\to\infty}\hat{\mathrm{A}}_f = \frac{1}{\rho}\mathrm{B}_f\left(\mathrm{I} + \Omega^{-1}\Delta\right)\Omega^{-1}\mathrm{B}_f^T. \tag{28}$$

These are the equivalents of the structural mass and added mass from eq. (6). In step 4 of the algorithm, the strong coupling between these masses is ensured by choosing $D_i = \mathrm{A}_s^0 - \hat{\mathrm{A}}_f^+$ in the fluid boundary condition. The fluid system therefore becomes

$$\begin{cases} \hat{\mathbf{y}}_f &= \hat{\mathbf{y}}_f^0 + \hat{\mathrm{A}}_f\hat{\mathbf{f}}_f \\ \hat{\mathbf{y}}_f + \left(\mathrm{A}_s^0 - \hat{\mathrm{A}}_f^+\right)\hat{\mathbf{f}}_f &= \hat{\mathbf{y}}_s - \left(\mathrm{A}_s^0 - \hat{\mathrm{A}}_f^+\right)\hat{\mathbf{f}}_s \end{cases} \tag{29}$$

Note that this is equivalent to

$$\left(\mathrm{A}_s^0 + \mathrm{A}_f^0\right)\hat{\mathbf{f}}_f = \hat{\mathbf{y}}_s^0 - \hat{\mathbf{y}}_f^0 + \left(\hat{\mathrm{A}}_s^+ + \hat{\mathrm{A}}_f^+\right)\hat{\mathbf{f}}_s \tag{30}$$

To solve this set of equations for the fluid force, the structural mass A_s^0 and the added mass A_f^0 must be solved implicitly, while the nonlinear convection-diffusion and spring terms in $\hat{\mathrm{A}}_s^+$ and $\hat{\mathrm{A}}_f^+$ are integrated explicitly. Since both A_f^0 and A_s^0 are symmetric positive (semi)definite, the existing pressure solver can be used to solve this system.

5.3 Consistency and stability

By design, the new fluid system (29) is consistent with the original one. Hence it remains to show that the fluid-structure iteration based on eqs. (17a) and (17b) with this choice of D_i is stable. The expansion obtained by substituting eq. (30) into eq. (3b) is

$$\hat{\mathbf{y}}_s = \hat{\mathbf{y}}_s^0 + (\hat{\mathrm{A}}_s^+ + \hat{\mathrm{A}}_f^+)(\mathrm{A}_f^0 + \mathrm{A}_s^0)^{-1}\delta\hat{\mathbf{y}}^0 + \mathbf{O}(\hat{\epsilon}^2). \tag{31}$$

This iteration is stable if $\left|(\hat{\mathrm{A}}_s^+ + \hat{\mathrm{A}}_f^+)(\mathrm{A}_f^0 + \mathrm{A}_s^0)^{-1}\right| < 1$.

Using a power series expansion of $\hat{\mathrm{A}}_f^+$ and $\hat{\mathrm{A}}_s^+$, it can be shown that these are of order s^{-1} and s^{-2} respectively. Hence any zero-stable time integration scheme can be used with the anticipatory method, resulting in a stable and convergent interaction scheme.

6 RESULTS AND DISCUSSION

Two test cases are presented here to show the performance of the method. The first is a simulation of a lifeboat dropped into a breaking wave. The lifeboat has an average density of $320kg/m^3$, the water a density of $1025kg/m^3$. It is dropped from $37m$ height and hits the water at $t = 2.5s$. The added mass varies greatly over time during the impact, as the boat enters the water and a larger part of the wave has to respond. It is clear that the relaxation-based method (16) is sensitive to this ratio, as the workload increases during the entry phase. The anticipative method (31) however remains efficient regardless of the added-mass ratio, as the boundary condition inside the wave predicts the boat motion. The workload is reduced by a factor around 10 for the complete simulation.

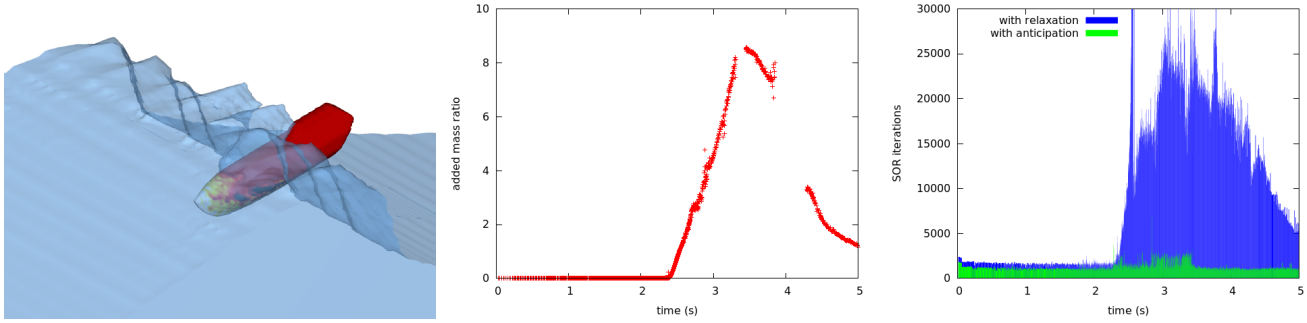

Figure 5: Simulation of a lifeboat dropped into a breaking wave. Left: the situation at $t = 3.0$. Middle: variation of effective added-mass ratio over time. Right: the workload for the simulation corresponds to the area under the curve.

The second test case is a tension-leg platform in a long-crested wave. The wave is a nonlinear 5th-order Stokes wave with a height of $23cm$. Since the variations around the waterline are small compared to the size of the platform, the added-mass ratio is relatively constant. Even for this moderate added-mass ratio however, the anticipative method outperforms the relaxation-based method by a factor 2.5 to 3.0.

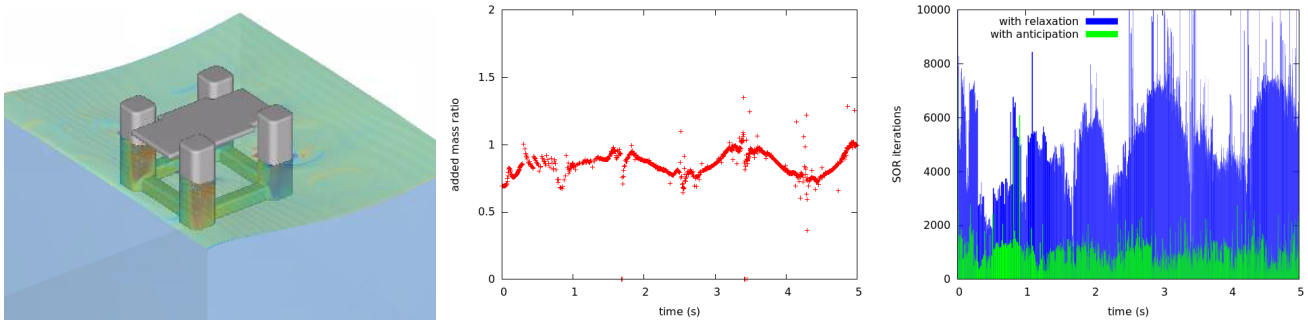

Figure 6: Simulation of tension-leg platform in Stokes-5 wave. Left: platform in wave (tendons not shown). Middle: variation of effective added-mass ratio over time. Right: the workload for the simulation corresponds to the area under the curve.

7 CONCLUSIONS

Analysis of fluid-structure interaction showed that the coupling strength is directly related to the added-mass ratio. This affected the existing partitioned coupling schemes based on the exchange of loads and motions: A stronger coupling with a higher range of added-mass ratios led to loss of performance in these traditional coupling schemes. The anticipatory coupling scheme was shown to be robust and insensitive to the added-mass ratio, using two test cases relevant to marine hydrodynamics. Additionally, theory on the stability and convergence of the method was derived for the general coupling of the Navier-Stokes equations with a mass-spring system.

This work is part of the research programme Maritime2013 with project number 13267, which is (partly) financed by the Netherlands Organisation for Scientific Research (NWO).

REFERENCES

[1] H. Bijl, A. H. van Zuijlen, and S. Bosscher. “Two level algorithms for partitioned fluid-structure interaction computations”. In: *ECCOMAS CFD* (2006).

[2] A. E. P. Veldman. “A simple interaction law for viscous-inviscid interaction”. In: *Journal of engineering mathematics* 65.4 (2009), pp. 367–383. ISSN: 0022-0833.

[3] C. Farhat and F.-X. Roux. “A method of finite element tearing and interconnecting and its parallel solution algorithm”. In: *International journal for numerical methods in engineering* 32.6 (1991), pp. 1205–1227.

[4] E. Lelarasmee, A. E. Ruehli, and A. L. Sangiovanni-Vincentelli. “Waveform relaxation method for time-domain analysis of large scale integrated circuits.” In: *IEEE transactions on computer-aided design of integrated circuits and systems* CAD-1.3 (1983), pp. 131–145.

[5] A. E. P. Veldman. “New, quasi-simultaneous method to calculate interacting boundary layers”. In: *AIAA journal* 19.1 (1981).

VII International Conference on Computational Methods for Coupled Problems in Science and Engineering
COUPLED PROBLEMS 2017
M. Papadrakakis, E. Oñate and B. Schrefler (Eds)

APPLICATION OF THE MODIFIED FINITE PARTICLE METHOD TO THE SIMULATION OF THE CORNEAL AIR PUFF TEST

ANDREA MONTANINO*, MAURIZIO ANGELILLO† AND ANNA PANDOLFI*

*Dipartimento di Ingegneria Civile ed Ambientale (DICA)
Politecnico di Milano
Piazza Leonardo da Vinci, 32, 20133 Milano, Italy
e-mail: {andrea.montanino, anna.pandolfi}@polimi.it

†Dipartimento di Ingegneria Civile (DiCiv)
Universitá degli Studi di Salerno,
Via Giovanni Paolo II, 84084 Fisciano (SA), Italy
e-mail: mangelillo@unisa.it

Key words: Meshless methods, air puff test, Fluid-Structure Interaction

Abstract. We present a numerical procedure for the simulation of the air puff test, a medical procedure used by ophtalmologists for the identification of the Intra Ocular Pressure, and potentially useful for the identification of material properties of the human cornea.

The problem involves the modeling of the cornea, that is a biological tissue, modelled as an hyperelastic material, and the aqueous humor, that is, the fluid filling the anterior chamber of the eye, that is treated as a Newtonian fluid, and modelled using a meshfree formulation, useful for the solution of a Fluid-Structure Interaction problem. Fluid and Structure are coupled using a Dirichlet-Neumann iterative approach, which permits the adoption of a partitioned coupling approach and explicit, fast solvers for the different subproblems.

1 Introduction

The identification of the in-vivo mechanical properties of the external part of the eye is a hot topic in the current literature, since the availability of a patient-specific model of the anterior chamber of eye will open new perspectives in improving the prevalence of positive outcomes of corneal refractive surgery.

In-vivo material properties must be determined necessarily by means of static or dynamic test performed on the external surface of the eye. The most promising tests are

based on the analysis of the dynamic deformation of the cornea induced by a localized time varying pressure. Advanced optical instruments, such as Ocular Response Analyzer (ORA; Reichert, Inc., Buffalo, NY) and Corvis ST (Oculus Optikgerate GmbH, Wetzlar, Germany), use a rapid single air jet which determines the cornea to snap from its original convex shape to a locally concave shape and back, passing through two configurations characterized by a localized flattened zone. The inward deflection is contrasted by the presence of filling fluids (aqueous humor). To provide a correct interpretation of the air puff test and, consequently, to measure from it significant mechanical parameters, it is necessary to develop a numerical model of the eye that accounts for several aspects, i. e.: (i) the exact geometry of the eye [1]; (ii) the use of reliable material models for the tissues [2, 3]; (iii) the fluid-structure interaction [4, 5]; (iv) the presence of surrounding tissues and of optical muscles at the limbus; (iv) the patient-specific fibril organization in the corneal tissue [6].

Recent works [7, 8] pointed out clearly that in order to capture the correct dynamics of the cornea, the air puff test model must include the interaction between the posterior filling fluids and the cornea. It follows that the characterization of the material parameters requires the use of identification algorithms based on advanced stress analysis procedures that can handle solid-fluid interactions.

The numerical approaches presented to date in the literature make use of advanced models of the human cornea, but in general the aqueous humor is not modelled, with some exceptions [9, 10]. A few attempts to account for the presence of the fluid include the use of spring-like elements [11] or added masses [7].

In this study, we aim at modelling explicitly the interaction between aqueous and cornea to elucidate the influence of the fluid on the development of dynamics of the the air puff test. In particular, here we use an analytical structural model (membrane like) for the cornea and a Modified Finite Particle Method (MFPM) [12, 13] for the fluid. We consider an axis symmetric two-dimensional problem, and adopt a simplified Fung's material for the solid. The dynamics of the anterior chamber of the eye undergoing an air puff test is modelled as a fluid-structure interaction (FSI) problem. The solution is based on a partitioned approach, which exploits the advantages of using a structural model for the solid and a meshless discretization for the fluid.

2 Problem formulation

The cornea is modelled as an isotropic hyperelastic membrane, loaded by the physiological pressure of the aqueous humor. We assume a simplified axis-symmetric geometry, where the anterior chamber is modelled as a spherical sector, confined between a deformable anterior membrane of radius R and a rigid posterior support of radius r. The membrane stands for the cornea, while the posterior surface accounts for the iris support backed by the lens. The simplification reduces the analysis of the fluid motion to a two-dimensional problem and the study of the membrane to an one-dimensional problem. The reference configuration of the fluid, under the physiological pressure, is visualized in

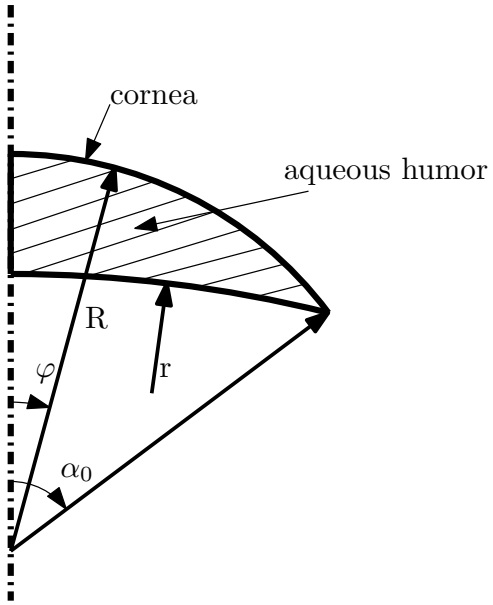

Figure 1: Reference geometry of the simplified model of the anterior chamber of the eye subject to the air puff test. The anterior surface is a deformable, circular membrane of radius R. The posterior surface is a rigid support of radius r.

Fig. 1.

2.1 Corneal membrane

The membrane representing the cornea is described as a circular arc of radius R, length $2\,R\alpha_0$, and thickness h, internally prestressed by the intraocular pressure (IOP) p_0, see Fig. 1. The effect of the air puff test is simulated with a space and time dependent air jet pressure p_a, acting from outside on the anterior surface of the cornea.

The membrane linear momentum balance equation reads

$$h\,\nabla\cdot\mathbf{P} + \mathbf{b}^0 = \rho_c\,h\,\ddot{\mathbf{u}}\,, \tag{1}$$

where ρ_c is the mass density of the cornea, $\mathbf{b}^0$ is the vector of external forces per unit area referred to the reference configuration, and $\mathbf{P}$ is the First Piola-Kirchhoff stress tensor, related to the membrane displacement through the hyperelelastic Fung's constitutive law. We assume that in any location of the cornea the external force is given by the algebraic sum of the fluid pressure p and of the time dependent air jet pressure $p_a = p_a(t)$.

The projection of Equation (1) on the tangential and radial directions gives

$$\frac{h}{R}\left(\frac{\cos\varphi}{\sin\varphi}(P_{11}-P_{22}) + P_{31} + P'_{11}\right) + b^0_1 - \rho_c h\ddot{u} = 0\,,$$
$$\frac{h}{R}\left(\frac{\cos\varphi}{\sin\varphi}P_{31} + P'_{31} - P_{11} - P_{22}\right) + b^0_3 - \rho_c h\ddot{w} = 0\,,$$

where b_1^0 and b_3^0 are the tangential and radial components of the external load, u and w are the membrane displacements along the tangential and radial directions.

2.2 Fluid aqueous humor

In order to facilitate the FSI coupling with the membrane, a Lagrangian approach is taken for the fluid. The aqueous humor is modelled as a Newtonian, weakly compressible fluid. In the present context, the weak compressibility assumption is justified by the possibility of using explicit time stepping algorithms for the integration of the fluid motion.

The governing equations for the fluid in a Lagrangian approach are

$$\rho_f \frac{d\,\mathbf{v}}{dt} = -\nabla p + \mu \nabla \mathbf{v}\,, \tag{2}$$

$$\frac{d\,\rho_f}{dt} = -\rho_f \nabla \cdot \mathbf{v}\,, \tag{3}$$

$$\frac{d\,\mathbf{x}}{dt} = \mathbf{v}\,, \tag{4}$$

where μ is the fluid viscosity, ρ_f the current fluid density, p the current fluid pressure, and $\mathbf{x}$ the fluid particle position. Eq. (2) is the linear momentum balance, Eq. (3) is the mass balance or continuity equation, and Eq. (4) is the definition of the fluid velocity.

Within a Lagrangian meshfree formalism and when explicit time stepping algorithms are adopted, a convenient way to approximate incompressibility is to introduce an equation of state that relates the fluid pressure to the speed of sound c. The set of equations is completed thus with the equation

$$p = p_0 + \frac{\rho_0\, c^2}{\gamma}\left[\left(\frac{\rho}{\rho_0}\right)^{\gamma} - 1\right]\,. \tag{5}$$

where ρ_0 is the reference fluid density and p_0 are the reference fluid pressure. The speed c has to be seen as a numerical parameter rather than a physical parameter, and the chosen value should not be too large, to avoid exceedingly small time steps. For example, in the smoothed particle hydrodynamics (SPH) literature, a fictitious value of $c = 50$ m/s (in contrast to the physical value $c = 340$ m/s) is usually considered adequate for water [14].

3 Solution algorithm

The FSI problem is solved using a partitioned approach, which allows the use of suitable solvers both for the solid subproblem and the fluid subproblem.

The membrane problem is solved using a Finite Difference approximation; in the axis-symmetric approximation, the problem becomes one-dimensional. The circular arc domain $\varphi \in [0, \alpha_0]$ is discretized in N equi-spaced nodes. The spatial partial derivatives are discretized with standard central differences, while the time stepping algorithm is the explicit Verlet's method, belonging to the family of Newmark's methods.

The fluid domain is approximated using the Modified Finite Particle Method (MFPM), a meshless approach particularly suitable for the description of moving boundaries and FSI problems. The method consists in discretizing the differential operators at a discrete number of points of the domain (nodes). The aproximation technique for spatial differential operators of a funtion $f(\mathbf{x})$ at a generic point $\mathbf{x}_i$ is obtained through the projection of the Taylor series expansion of $f(\mathbf{x})$ (centered on $\mathbf{x}_i$ and evaluated at a certain number of neighboor nodes $\mathbf{x}_j$) on some "projection funtions" $W_\alpha(\mathbf{x}-\mathbf{x}_i)$. Further details of the algorithm can be found in the original papers [12, 13].

Time integration is achieved through the following algorithm. Let $\mathbf{x}^n$, $\mathbf{v}^n$, and ρ^n be the arrays containing position, velocity, and density of the nodes at the time step t_n. The algorithm begins by computing the quantities at mid-time step. The node position and density are computed through explicit forward Euler schemes as

$$\mathbf{x}^{n+1/2} = \mathbf{x}^n + \frac{\Delta t}{2}\mathbf{v}^n\,,$$

$$\rho^{n+1/2} = \rho^n - \frac{\Delta t}{2}\rho^n\,\nabla^n\cdot\mathbf{v}^n\,,$$

where $\nabla^n\cdot$ denotes the discrete divergence at t^n, and the mid-time step fluid pressure $p^{n+1/2}$ is evaluated through eq. (5). The velocity at the time t_{n+1} is computed by using the half-step discrete differential operator $\nabla^{n+1/2}$ as

$$\mathbf{v}^{n+1} = \mathbf{v}^n - \frac{\Delta t}{\rho^{n+1/2}}\nabla^{n+1/2}p^{n+1/2} + \mu\,\frac{\Delta t}{\rho^n}\,\nabla^{n2}\mathbf{v}^n\,.$$

The node position and the density are then updated as

$$\mathbf{x}^{n+1} = \mathbf{x}^{n+1/2} + \frac{\Delta t}{2}\mathbf{v}^{n+1}\,,$$

$$\rho^{n+1} = \rho^{n+1/2} - \frac{\Delta t}{2}\rho^{n+1/2}\,\nabla^{n+1}\cdot\mathbf{v}^{n+1}\,,$$

using an explicit advance in time for density using the velocity at the final time step $n+1$. The pressure p^{n+1} is then computed through eq. (5). The algorithm is second-order accurate in the pressures, and first order accurate in the velocities.

The coupling algorithm consists in solving first the solid problem, by imposing, as external loads for the membrane, both the external and the fluid pressure. The membrane velocity is then passed to the fluid solver and imposed as boundary condition for the fluid domain. The fluid pressure at the membrane is then computed, and the procedure is completed if the following condition is respected

$$\frac{\|\mathbf{p}_i^k - \mathbf{p}_i^{k-1}\|}{\|\mathbf{p}_i^{k-1}\|} < \varepsilon \tag{6}$$

where $\mathbf{p}_i^k$ and $\mathbf{p}_i^{k+1}$ are the fluid pressure values at the fluid-solid interface points at time t_i and at two subsequent iterations k and $k+1$, and ε is the desired tolerance. In the present calculations ε is set 10^{-4}.

If Equation (6) is not respected, the new fluid pressure is imposed as external load for the membrane, and the pricedure is repeated untill convergence.

4 Application: the air puff test

The air puff test is a clinical procedure used by ophthalmologists to measure the Intra-Ocular Pressure (IOP). It consists in a rapid air jet pulse that hits the external surface of the cornea, determining the snap of the cornea from its original, convex shape to a temporary, local concave configuration.

The interpretation of the test is made through two instruments: Corvis ST and the Ocular Response Analyzer (ORA) [15]. In particular, Corvis ST, besides the value of IOP, provides kinematic data, such as the displacement u of the apical point of the cornea versus time t. The results are shown in Figure 2(a)

The Ocular Response Analyzer (ORA), instead, returns a number of pressure parameters recorded during the test:

1. P1 and P2 (expressed in mmHg), i.e., the instrument pressures registered at the two times corresponding to the applanation state of the cornea (the first, when the cornea is moving inward switching from convex to concave configuration, and the second, when the cornea is moving outward switching from concave to convex configuration);

2. the Corneal Hysteresis, measured as CH = P1 − P2;

3. the Goldmann equivalent IOP, measured as IOPg = 0.5 (P1 + P2);

4. the Corneal Compensated IOP, measured as IOPcc = P1 − 0.43 P2.

The results of ORA are usually shown in graphs similar to that reported in Figure 2(b), in which the two instant of local applanation are evident.

Though Corvis ST does not provide a pressure profile, the results given by Corvis ST can be reprocessed by using an artificial pressure history of the type

$$p(t) = p_{\max} \exp\left[-b\,(t - t_0)^2/T^2\right]; \tag{7}$$

where $T = 30$ ms is the total duration of the impulse (known), which reaches the peak value $p_{\max}$ at time $t_0 = 15$ ms. For the parameters, we use $b = 25$ [7, 8] and $p_{max} = 10$ kPa. In Figures 3 the pressure profile p is reported together with the apical displacement u versus time t. In Figure 4 the p-u relation is reconstructed. The hysteresis loop that can be seen in Figure 4 is essentially produced by inertial effects [7] and by the fluid viscosity.

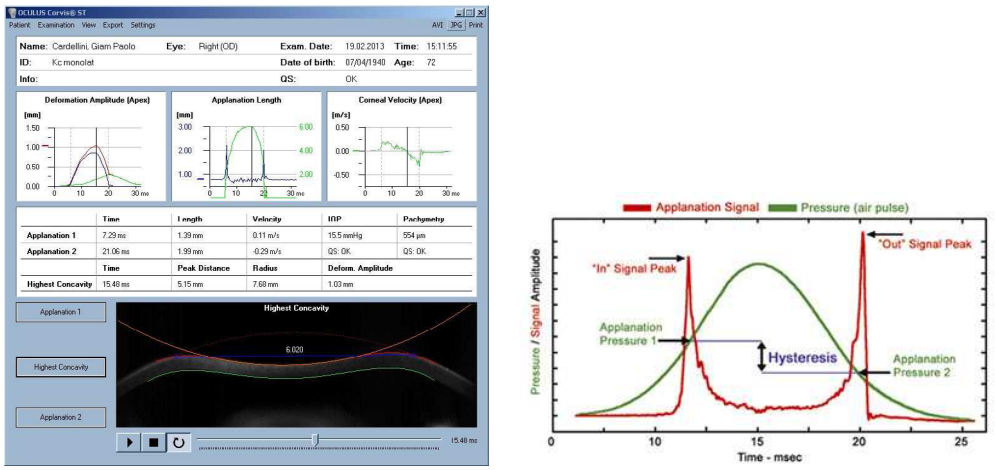

(a) (b)

Figure 2: (a) Example of sheet provided by the Corvis ST. (b) Example of sheet provided by the ORA

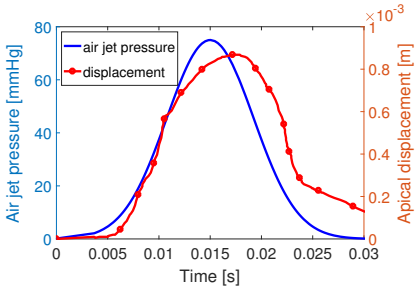

Figure 3: Experimental curves for the apical displacement and external air jet pressure versus time

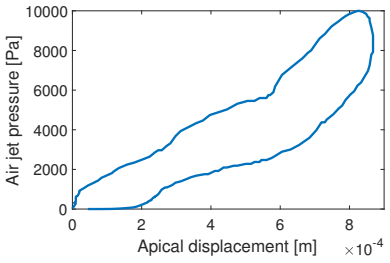

Figure 4: Experimental curve of the air jet pressure versus the apical displacement.

5 Numerical simulations

The model of the cornea is used to simulate the ORA test, using reference parameters. The density of the cornea is similar to the one of the water, $\rho = 1$ kg/m^3. An estimate of the elastic modulus $E_0 = 0.5$ MPa is obtained by fitting with the present material model the numerical results documented in [7], where a sophisticated material model of the cornea has been used to simulate the air puff test. The reference density ρ_0 and pressure p_0 (IOP) of the fluid are assumed to be $\rho_0 = 1$ kg/m^3 and $p_0 = 16$ mmHg (2.14 kPa), a value in the range 12-21 mmHg of the physiological IOP.

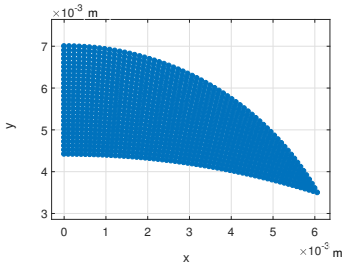

Figure 5: Reference node distribution for the fluid domain

In numerical simulations we consider an ideal geometry of the anterior chamber, characterized by the parameters $R = 7$ mm, $r = 2.04$ mm, $h = 0.5$ mm, and $\alpha_0 = \pi/3$. The posterior surface of the anterior chamber (i.e., the iris) containing the fluid is assumed to be rigid. The fluid is discretized in 1134 nodes, see Fig. 5.

We assume axis-symmetry boundary conditions for both fluid and membrane, by setting on the symmetry axis

$$u = 0\,, \qquad w' = 0 \quad \text{at} \quad x = 0\,, \tag{8}$$

and

$$v_x = 0\,, \qquad \frac{\partial v_y}{\partial x} = 0 \quad \text{at} \quad x = 0\,, \tag{9}$$

being the v_x and v_y the fluid velocity components along the x and y axes.

The point representing the limbus (intersection between anterior and posterior surface) is fixed:

$$u = 0\,, \qquad w = 0 \quad \text{at} \quad \varphi = \frac{\pi}{3}\,. \tag{10}$$

The anterior surface of the cornea is loaded quickly with an impulsive air-jet with pressure history

$$p(t) = p_{\max} \exp\left[-a \, \sin^2 \varphi\right] \exp\left[-b\,(t - t_0)^2/T^2\right]; \tag{11}$$

where $T = 30$ ms is the total duration of the impulse, which reaches the peak value $p_{\max}$ at time $t_0 = 15$ ms. We assume $a = 21.5$, $b = 25$ [7, 8]

The sound speed c appearing in eq. (5) is chosen to enforce the quasi-incompressibility of the fluid and thus it varies with the time step, according to the expression $c = 10 + 20v_{max}$ m/s, where v_{max} is the maximum norm of the value of the fluid velocity magnitude at the previous time step.

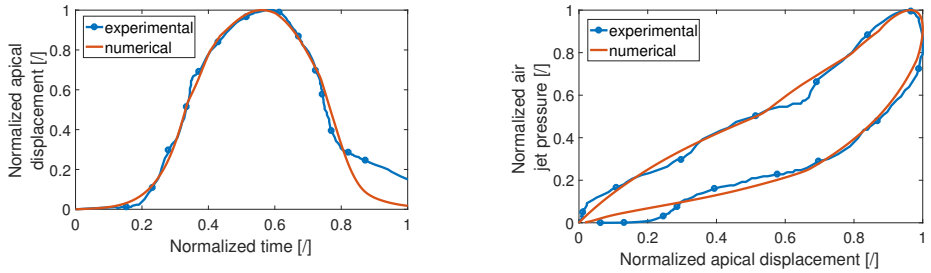

(a) (b)

Figure 6: Comparison with experimental data: (a) Apex displacement versus time. (b) Apex displacement versus air jet pressure.

The output of the analysis are rendered through Figures 6(a) (in terms of normalized displacement and normalized time) and Figures 6(b) (in terms of normalized displacement and normalized pressure), in which also is shown the comparison between the experimental data introduced in Section 4 and the numerical simulation.

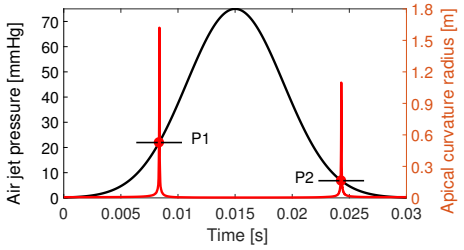

Figure 7: Baseline analysis: corneal applanated states

Fig. 7 visualizes the time history of the air jet pressure and of the corneal curvature at the apex. For the baseline analysis we obtain the following values P1=21.96 mmHg, P2=6.82 mmHg, CH=15.14 mmHg, IOPg=14.39 mmHg, and IOPcc=19.03 mmHg.

The effects of the dynamics of the fluid can be clearly seen in Figure 8, in which we plot the apical displacement and the external air jet pressure versus time. We notice that the maximum apical displacement occurs with some delay with respect to the maximum of the air jet pressure.

We also show, for qualitative comparison, some images taken from the Corvis instrument during an air puff test (Figure 9) with the results of our simulation for the baseline analysis (Figure 10).

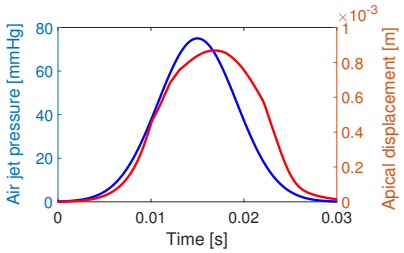

Figure 8: Baseline analysis: external air jet pressure and apical displacement versus time

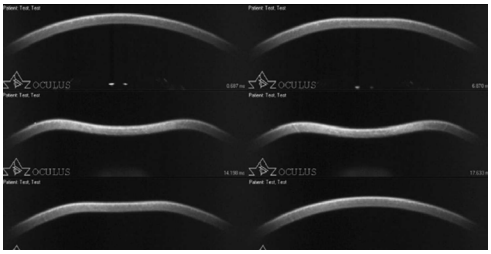

Figure 9: Images recorded by the instrument Corvis ST during an air puff test (from the web)

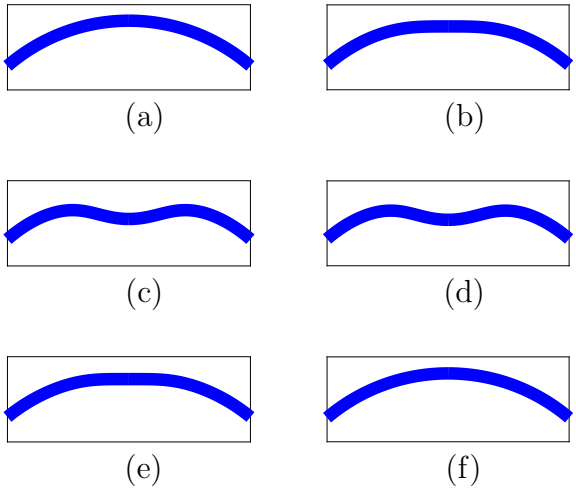

Figure 10: Deformed configurations of the cornea obtained with the baseline analysis: (a) undeformed, physiological configuration; (b) first applanation; (c) deformed configuration during the maximum air jet pressure; (d) deformed configuration at the maximum apical displacement; (e) second applanation; (f) new physiological configuration after the test

6 Conclusion

In the present work we present the simulation of the air puff test using a Fluid Structure Interaction approach. The problem is approached with a partitioned strategy, preserving the efficiency of the different solvers for the solid and fluid part.

The problem is formulated exploiting axial-symmetry: thus, the solid problem becomes one dimensional, and is solved with Finite Differences, and using an explicit Verlet algorithm for the time advance. The fluid problem is solved using a meshfree Modified Finite Particle Method, particularly suitable for the solution of problems with moving boundaries and Fluid Structure Interaction. The coupling algorithm is an iterative Dirichlet-Neumann procedure, which allows the use of suitable solver preserving a strong coupling between the two problems.

W finally observe the evaluability of our numerical simulations, in terms of adherence between the experimental and numerical results, and in terms of efficiency of the numerical approach, thanks to the wide use of explicit algorithms.

References

[1] I. Simonini and A. Pandolfi. Customized finite element modelling of the human cornea. *PLoS ONE*, 10(6):e0130426, 2015. doi: 10.1371/journal.pone.0130426.

[2] A. Pandolfi and F. Manganiello. A material model for the human cornea. *Biomechanics and Modelling in Mechanobiology*, 5:237–246, 2006.

[3] P. Sánchez, K. Moutsouris, and A. Pandolfi. Biomechanical and optical behavior of human corneas before and after photorefractive keratectomy. *Journal of Cataract & Refractive Surgery*, 40(6):905–917, 2014.

[4] M. A. Ariza-Gracia, J. F. Zurita, J. F. Piñero, D. P. ad Rodriguez-Matas, and B. Calvo. Coupled biomechanical response of the cornea assessed by non-contact tonometry. A simulation study. *PLoS ONE*, 10(3):e0121486, 2015.

[5] A. Sinha Roy, M. Kurian, H. Matalia, and R. Shetty. Air-puff associated quantification of non-linear biomechanical properties of the human cornea in vivo. *Journal of the Mechanical Behavior of Medical Biomaterials*, 48(1):173–182, 2015.

[6] A. Pandolfi and M. Vasta. Fiber distributed hyperelastic modeling of biological tissues. *Mechanics of Materials*, 44:151–162, 2012.

[7] Irene Simonini, Maurizio Angelillo, and Anna Pandolfi. Theoretical and numerical analysis of the corneal air puff test. *Journal of the Mechanics and Physics of Solids*, 93:118–134, 2016.

[8] I. Simonini and A. Pandolfi. The influence of intraocular pressure and air jet pressure on corneal contactless tonometry tests. *Journal of the Mechanical Behavior of Medical Biomaterials*, Online First(July):1–15, 2015. doi: http://dx.doi.org/10.1016/j.jmbbm.2015.07.030.

[9] L. Coquart, C. Depeursinge, A. Curnier, and R. Ohayon. A fluid-structure interaction problem in biomechanics: Prestressed vibrations of the eye by the finite element method. *Journal of Biomechanics*, 25(10):1105–1118, 1992. doi: 10.1016/0021-9290(92)90067-B. cited By 26.

[10] S. Salimi, S. Simon Park, and T. Freiheit. Dynamic response of intraocular pressure and biomechanical effects of the eye considering fluid-structure interaction. *Journal of Biomechanical Engineering*, 133(9), 2011. doi: 10.1115/1.4005166. cited By 6.

[11] S. Kling, N. Bekesi, C. Dorronsoro, D. Pascual, and S. Marcos. Corneal viscoelastic properties from finite-element analysis of in vivo air-puff deformation. *PLoS ONE*, 9 (8):e104904, 2014. doi: 10.1371/journal.pone.0104904.

[12] D Asprone, F Auricchio, A Montanino, and A Reali. A modified finite particle method: Multi-dimensional elasto-statics and dynamics. *International Journal for Numerical Methods in Engineering*, 99(1):1–25, 2014.

[13] D Asprone, F Auricchio, A Montanino, and A Reali. Review of the modified finite particle method and application to incompressible solids. *International Journal of Multiphysics*, 9(3), 2015.

[14] Joe J Monaghan. Simulating free surface flows with sph. *Journal of computational physics*, 110(2):399–406, 1994.

[15] D. A. Luce. Tonometer calibration tool, 01 2004. URL `http://www.google.com/patents/US6679842`.

VII International Conference on Computational Methods for Coupled Problems in Science and Engineering
COUPLED PROBLEMS 2017
M. Papadrakakis, E. Oñate and B. Schrefler (Eds)

COMPUTATIONAL STUDY OF FLOW–INDUCED OSCILLATION OF A SIMPLIFIED SOFT PALATE

M. Ehsan Khalili*, Martin Larsson † and Bernhard Müller *

* Department of Energy and Process Engineering
Norwegian University of Science and Technology (NTNU)
Kolbjørn Hejes vei 2, NO-7491 Trondheim, Norway
e-mail: {mohammadtaghi.khalili, bernhard.muller}@ntnu.no

† Sportradar AS
Ferjemannsveien 10, NO-7014 Trondheim, Norway
e-mail: m.larsson@sportradar.com

Key words: Fluid structure interaction; High order finite difference method; Arbitrary Lagrangian–Eulerian formulation

Abstract. Two-dimensional numerical simulations are employed to study fluid structure interaction of a simplified model of the soft palate in the pharynx for uniform inhalation. We take a next step towards a better biomechanical system by modeling the motion of an inextensible flexible plate. The improved structural model discretized by a low order difference method permits us to simulate the two-dimensional motion of the flexible plate. The inspiratory airflow is described by the Navier–Stokes equations for compressible flow solved by a high order difference method. The explicitly coupled fluid structure interaction model is based on the Arbitrary Lagrangian–Eulerian formulation.

1 Introduction

Fluid structure interaction (FSI) refers to the interaction of a flexible structure with fluid flow where the fluid and structure interact over a shared interface. FSI gives rise to a rich variety of physical phenomena with applications in many fields of engineering and biomechanics. One of the prime examples of FSI in biomechanical systems is the dynamics of the upper airways where the interaction between inspiratory and expiratory airflow with soft tissues may lead to flow-induced oscillations and instabilities. Failure to maintain the patency of the upper airway during sleep characterizes obstructive sleep apnea (OSA), a common and disabling disorder wherein the soft palate obstructs the upper airways for prolonged periods of time during sleep. OSA and snoring are closely related to the flow conditions in the upper airways. Snoring is often considered a minor affliction. But when snoring is heavy, it is often associated with the more crippling condition known as OSA.

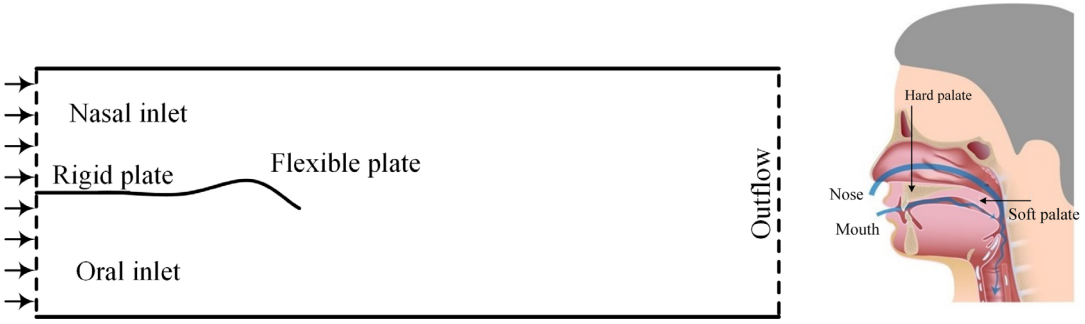

(a) Schematic of the computational model

(b) The anatomy of upper airways.

Figure 1: Computational model and real geometry.

Estimates show that the obstructive sleep apnea syndrome (OSAS) affects 2–4% of the adult population [1] and 10% of snorers are at risk of OSAS [2].

A cantilevered flexible plate immersed in two-dimensional channel flow has previously been shown to capture FSI representative of respiratory airflow and soft-palate dynamics in the upper airway [3, 4, 5, 6]. This is a well-established model wherein a flexible plate representing the soft palate is mounted downstream of a rigid plate representing the hard palate. The rigid plate separates the upper and lower channel flows modeling the flow in the oral and nasal tracts, which interact with the flexible plate motion and then combine into a single channel flow representing the flow in the pharynx, as illustrated in Fig. 1. In these studies, an inviscid flow model was used and viscous effects were implicitly modeled either through the imposition of the Kutta–Joukowski condition [3, 5, 6] or an applied channel resistance [4].

Latterly, researchers have modeled the effects of fluid viscosity explicitly for the laminar regime of Reynolds numbers [7] and investigated constant pressure-drop boundary conditions [8]. In these studies across the low-to-high range of Reynolds numbers, thin plates have been observed to lose their stability at a critical value of flow speed or Reynolds number based on channel height. The destabilization mechanism has been attributed to an irreversible energy transfer from the fluid flow to the plate arising from a phase difference between fluid pressure and plate motion owing to the finite length of the flexible plate [6, 7, 9]. Recently, compressible viscous flow has been employed for this model to characterize the acoustic wave propagation induced by the plate oscillation [10].

In all the studies mentioned above, linear structural mechanics was taken into account by using the one-dimensional Euler–Bernoulli beam equation. Another structural model has been developed by including an inextensibility condition , however, in the interaction with potential flow [11]. Apparently, the soft palate undergoes displacements beyond the linear range, particularly during episodes of obstructed breathing. The soft tissue in the palate is also nearly incompressible and is subjected to fluid friction in a viscous flow field.

Accordingly, the present work accounts for those effects and thereby yields a more faithful biomechanical FSI model. To achieve this, we extend our previous cantilevered plate model [10] to a two-dimensional elastic plate model having an inextensibility condition immersed in compressible viscous flow. This paper presents the development of the improved FSI model and then demonstrates its applicability in simulating flow-induced oscillation of a flexible plate and the characterization of its behaviour in the upper airway.

After outlining the flow and structure models as well as their coupling for FSI, the in-vacuum oscillation of the plate is presented through a verification study of the structural mechanism. Thereafter, the FSI model is used to simulate the flow-induced oscillation of a flexible plate.

2 Model

2.1 Fluid flow

The fluid motion is described by the 2D compressible Navier–Stokes equations in perturbation form. The perturbation formulation is employed to minimize cancellation errors when discretizing the Navier–Stokes equations for compressible low Mach number flow [12, 13, 14]. The conservative form of the 2D compressible Navier–Stokes equations in perturbation formulation can be written as

$$\mathbf{U}'_t + \mathbf{F}^{c'}{}_x + \mathbf{G}^{c'}{}_y = \mathbf{F}^{v'}{}_x + \mathbf{G}^{v'}{}_y \ , \tag{1}$$

where $\mathbf{U}' = \mathbf{U} - \mathbf{U_0}$ is the vector of conservative perturbation variables with $\mathbf{U} = (\rho, \rho u, \rho v, \rho E)^T$ the vector of the conservative variables and $\mathbf{U}_0 = (\rho_0, 0, 0, (\rho E)_0)^T$ the stagnation values. For a complete description of the compressible flow equations, see [10].

2.1.1 Discretization of the compressible Navier–Stokes equations

The high order finite difference method based on summation by parts (SBP) operators [15, 16, 17] is employed for space discretization of the compressible Navier–Stokes equations. We use a globally fourth order SBP operator to discretize the first derivatives and apply them twice to approximate the second derivatives in the viscous terms. The SBP operators correspond to the sixth order central difference operator in the interior, but degrade to third order accuracy near the boundary resulting in fourth order global accuracy [16]. This approach is based on the energy method, which permits us to derive well-posedness for the continuous problem and to guarantee stability for the discrete problem. For the time integration process, the classical fourth order explicit Runge–Kutta method is used. The multi-block structured grid approach is employed to represent the simplified geometry in the upper airways.

Adiabatic no-slip boundary conditions are applied at the walls and the fluid-structure interface. At the inflow, the velocities in the x- and y-directions are imposed using a uniform inlet profile normal to the boundary, $u(x = 0, t) = U_0$ and $v = 0$. In addition,

the inlet temperature is set to $T = T_0 = 310$ K. The outlet pressure is set to atmospheric pressure, i.e., $p' = p - p_0 = p - p_{\text{atm}} = 0$ Pa. The Navier–Stokes characteristic boundary conditions (NSCBC) developed by [18] are employed at the inflow and outflow boundaries to minimize wave reflections. The details of this numerical algorithm and boundary conditions can be found in our previous publication [10].

2.2 The structure model

The plate model is central in order to obtain physical results for simulating the soft palate motion. In the present study, the soft palate is modeled as a two–dimensional, massive, flexible and inextensible plate. This model provides the correlation between the elastic deflection of the plate and the applied force. The flexible plate has its own material density ρ_s, different from the surrounding fluid density ρ_f. The flexibility allows the plate to bend and to react to the force applied by the fluid flow and the flexural force generating a restoring force. Taking into account the inextensibility constraint, the length of the plate remains constant even if an external force is acting on it.

The dynamics of the plate in Lagrangian coordinate s along its undeformed reference configuration can be described by the following equation [19]

$$\rho_s \frac{\partial^2 \mathbf{X}}{\partial t^2} = \frac{\partial}{\partial s}\Big(T\frac{\partial \mathbf{X}}{\partial s}\Big) - \frac{\partial^2}{\partial s^2}\Big(K_B \frac{\partial^2 \mathbf{X}}{\partial s^2}\Big) + \rho_s \mathbf{g} + \mathbf{F}, \tag{2}$$

where s is the arclength, $\mathbf{X} = (x(s,t), y(s,t))^T$ denotes the material position of the plate, T is the tension along the Lagrangian coordinate s, K_B is the flexural rigidity, $\mathbf{g}$ the gravitational acceleration, and $\mathbf{F}$ is the force applied on the plate by the surrounding fluid. Furthermore, ρ_s is the actual line density of the plate defined as the line density difference between the thin plate and the surrounding fluid $\rho_s = \rho - \rho_f A$, where ρ is density of the plate, ρ_f the density of the fluid and A is the cross sectional area of the plate.

The inextensibility constraint of the plate [20, 19], i.e. the local stretching of the plate satisfies $\frac{d}{dt}|\frac{\partial \mathbf{X}}{\partial s}| = 0$, can be expressed as

$$\frac{\partial \mathbf{X}}{\partial s} \cdot \frac{\partial \mathbf{X}}{\partial s} = 1. \tag{3}$$

Following the previous studies [20, 19], the tension T in this model is determined by a Poisson equation derived by inserting the constraint of inextensibility Eq. (3) into the dot product of $\frac{\partial \mathbf{X}}{\partial s}$ and the $s-$derivative of the plate dynamical equation Eq. (2)

$$\frac{\partial \mathbf{X}}{\partial s} \cdot \frac{\partial^2}{\partial s^2}\Big(T\frac{\partial \mathbf{X}}{\partial s}\Big) = \frac{\rho_s}{2}\frac{\partial^2}{\partial t^2}\Big(\frac{\partial \mathbf{X}}{\partial s} \cdot \frac{\partial \mathbf{X}}{\partial s}\Big) - \rho_s \frac{\partial^2 \mathbf{X}}{\partial t \partial s} \cdot \frac{\partial^2 \mathbf{X}}{\partial t \partial s} - \frac{\partial \mathbf{X}}{\partial s} \cdot \frac{\partial}{\partial s}\Big(\mathbf{F}_B + \mathbf{F}\Big) \tag{4}$$

where $\mathbf{F}_B$ is the bending force which by using the Euler–Bernoulli assumption for a thin flexible plate is expressed as

$$\mathbf{F}_B = -\frac{\partial^2}{\partial s^2}\left(K_B \frac{\partial^2 \mathbf{X}}{\partial s^2}\right) \tag{5}$$

The non-dimensional parameters are chosen with respect to the stagnation density ρ_0, stagnation speed of sound c_0 and the length of the flexible plate L, in the same way as for the fluid solver.

The boundary conditions are specified at the free end ($s = L$) and at the fixed end at ($s = 0$) of the plate. The free end boundary condition at the trailing edge is imposed by assuming that the tension, bending moment and shear force are zero

$$T(L,t) = 0, \quad \left.\frac{\partial^2 \mathbf{X}}{\partial s^2}\right|_{s=L} = 0, \quad \left.\frac{\partial^3 \mathbf{X}}{\partial s^3}\right|_{s=L} = 0 \tag{6}$$

The support mechanism at the leading edge is taken into account as

$$\mathbf{X}|_{s=0} = \mathbf{X}_0, \quad \left.\frac{\partial^2 \mathbf{X}}{\partial s^2}\right|_{s=0} = 0 \tag{7}$$

2.2.1 Discretization of the structure model

The discretisation of the governing equation of the plate motion (2) along s is performed on a staggered grid following [19]. The plate is discretized with a finite number of Lagrangian points $\mathbf{X}_i$. The plate tension is defined at the interfaces of the grid cells, and other variables are defined at the primary grid points in the centers of the grid cells, as shown in Fig. 2

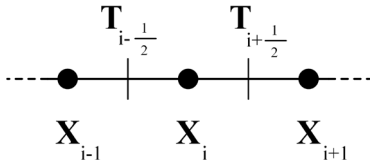

Figure 2: Schematic diagram of staggered grid discretisation on the plate along its Lagrangian coordinate.

Then, the numerical procedure for the non-dimensionalised form of Eqs. (2) and (3) is as follows

$$\mathbf{X}^* = 2\mathbf{X}_i^n - \mathbf{X}_i^{n-1} \tag{8}$$

$$\mathbf{F}_B^* = -D_{ss}(K_B \; D_{ss}\mathbf{X}^*)_i^n \tag{9}$$

$$(D_s\mathbf{X}^*)_{i+\frac{1}{2}} \cdot \Big(D_s(D_s(T^{n+\frac{1}{2}}_{i+\frac{1}{2}} D_s\mathbf{X}^*))\Big) = \rho_s \frac{1 - 2(D_s\mathbf{X} \cdot D_s\mathbf{X})^n_{i+\frac{1}{2}} + (D_s\mathbf{X} \cdot D_s\mathbf{X})^{n-1}_{i+\frac{1}{2}}}{2\Delta t^2} - \rho_s(D_s\mathbf{V} \cdot D_s\mathbf{V})^n_{i+\frac{1}{2}} - (D_s\mathbf{X}^*)^n_{i+\frac{1}{2}} \cdot \Big(D_s(\mathbf{F}^*_B + \mathbf{F}^n)\Big)_{i+\frac{1}{2}} \tag{10}$$

$$\rho_s \frac{\mathbf{X}^{n+1}_i - \mathbf{X}^*_i}{\Delta t^2} = \Big(D_s(T^{n+\frac{1}{2}} D_s\mathbf{X}^{n+1})\Big)_i + (\mathbf{F}_B)^{n+1} + \mathcal{G}\frac{\mathbf{g}}{|g|} + \mathbf{F}^n_i \tag{11}$$

where D_s and D_{ss} are the second order accurate difference operators for the first and second derivatives along s, respectively, and $\mathbf{X}^*$ is the predicted position of the plate. Employing $\mathbf{X}^*$ to calculate the tension helps to reduce the error. The tension is computed at the intermediate step, i.e. $t^{n+\frac{1}{2}}$ and is employed to update the position of the plate, i.e. $\mathbf{X}^{n+1}$. The velocity of the plate is defined as $\mathbf{V}^n_i = (\mathbf{X}^n_i - \mathbf{X}^{n-1}_i)/\Delta t$. $\mathbf{F}^n$ denotes the force exerted by the fluid flow on the structure and is obtained explicitly using the fluid solver at time level n. $\mathcal{G}$ is defined as the non-dimensional gravity $\mathcal{G} = gL/c_0^2$. Equations (10) and (11) constitute diagonally dominant tri- and pentadiagonal linear systems, which are solved by LU decomposition without pivoting, i.e. by the Thomas algorithm and a similar algorithm, respectively. The condition for diagonal dominance of the matrix in Eq. (11) is $K_B \frac{\Delta t^2}{\Delta s^4} \leqslant \frac{1}{4}$.

2.3 Fluid structure interaction

To handle the fluid flow in Eulerian description using moving fluid grids and the plate structure in a Lagrangian formulation using stationary structure grids, the Arbitrary Lagrangian–Eulerian (ALE) formulation is appropriately employed. Considering the velocity of the fluid grids $\dot{x}$ and $\dot{y}$ in the time-dependent coordinate transformation of the fluid flow domain, the grid point velocities are subtracted from the fluid velocity to define the contravariant velocity components $U = \xi_x(u-\dot{x}) + \xi_y(v-\dot{y})$ and $V = \eta_x(u-\dot{x}) + \eta_y(v-\dot{y})$ which yield simple expressions for the transformed inviscid flux vectors $\hat{\mathbf{F}}^c$ and $\hat{\mathbf{G}}^c$ [21]. The mesh update is implemented by remeshing the whole fluid domain in each time step using the positions and velocities of the flexible structure at the boundary and a linear interpolation for interior points in the fluid domain.

Solving fluid flow on a moving mesh, the numerical scheme should satisfy the Geometric Conservation Law (GCL) for mathematical consistency [22], which leads to the 2D Navier-Stokes equations in ALE formulation [23] being expressed as

$$\mathbf{U}'_\tau = \tfrac{1}{J^{-1}}(-\hat{\mathbf{F}}'_\xi - \hat{\mathbf{G}}'_\eta - (J^{-1})_\tau \mathbf{U}'). \tag{12}$$

An explicit, two-way method where forces and deformations are exchanged between the flow and the deformable structure in each time-step is employed to handle the coupling between the fluid and the structure. The fluid and structure interact with each other by applying equal displacement and velocity at the interface, satisfying the no-slip and adiabatic wall boundary conditions. The force exerted by the fluid flow on the plate at

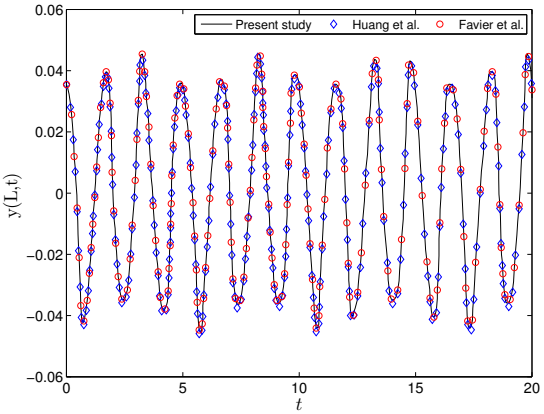

Figure 3: Time history of the y-coordinate position of the trailing edge of the plate subjected to only gravity, without bending force $K_B = 0$. The solid line shows the present model, circles present the results of the study performed by Huang et al. [19] and diamonds represent the results of the study done by Favier et al. [24].

time level n in equations (10) and (11) is given by $\mathbf{F}^n = -(p_U^n - p_L^n)\mathbf{n}$, where p_U and p_L are the pressures on the upper side and lower side of the plate, respectively, and $\mathbf{n}$ is the outer unit vector normal to the plate.

3 Results and discussion

3.1 Verification of structure solver in vacuum

The accuracy of the numerical model of the plate has been first tested and verified by simulating the oscillation and bending of the plate subjected to the gravity force in the absence of surrounding fluid, i.e. a pendulum with gravity acting in the $x-$direction. The plate was initially deformed by using the following initial configuration

$$\mathbf{X}(s,0) = \mathbf{X}_0 + s(\cos\theta, \sin\theta), \quad s \in [0, L], \tag{13}$$

where L is the length of the plate, θ is an angle and $\mathbf{X}_0 = (0,0)$. This particular configuration within the small angle approximation is considered in previous studies [19, 24]. Following them, the test is first performed by setting the initial angle of the plate to $\theta = 0.01\pi$ with a flexural stiffness $K_B = 0$ and non-dimensional gravity equivalent to $\gamma = 10$. The length of the plate is $L = 1$, and it is discretized by $N = 101$ grid points along the Lagrangian coordinate s. The time variation of the y coordinate of the trailing edge is monitored and shown in Fig. 3.

A second verification test is performed for a larger initial deflection angle $\theta = 0.1\pi$ and by including the non-dimensional bending force with $K_B = 0.01$. Fig. 4 illustrates the y-displacement of the trailing edge and the time variation of the plate deformation.

The results obtained in Figures 3 and 4(a) are in good agreement in comparison with

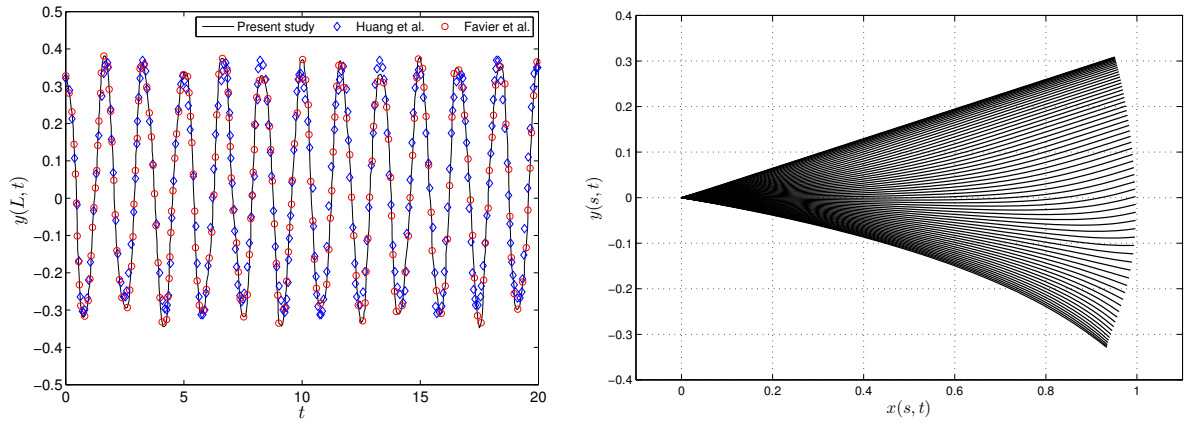

(a) (b)

Figure 4: (a) Time history of the y-coordinate position of the trailing edge of the plate subjected to only gravity $\gamma = 10$, with bending force $K_B = 0.01$. The solid line shows the present model, circles present the results of the study performed by Huang et al. [19] and diamonds represent the results of the study done by Favier et al. [24], (b) The sequence of superposition of the plate from up to down between time $0 - 0.8$.

the available numerical results [19, 24].

3.2 Numercal results of FSI

Having established the credibility of the structural model, we now couple the structure and fluid models to investigate their interaction. The computational domain is a rectangular channel with $0 \leq x \leq 9L$ and $0 \leq y \leq 4L$ where L is the length of the flexible plate. The flexible plate modeling the soft palate is attached to a rigid plate with length L representing the hard palate. The origin of the rigid plate is located in the middle of the height of the channel. Therefore, the leading edge of the flexible plate is placed at $(L, 2L)$. Overall, the computational domain is discretized by 581×281 grid points in longitudinal and transversal directions, respectively. The Reynolds number $\mathrm{Re} = \frac{\rho U L}{\mu} = 378$ and the Mach number $\mathrm{Ma} = \frac{U}{c_0} = 0.1$ are used based on the inlet velocity, density, viscosity, speed of sound and the plate length. The nondimensional line density $\frac{\rho_s}{\rho_0 L}$ is 1, and the nondimensional flexural rigidity $\frac{K_B}{\rho_0 c_0^2 L^3} = 0.0001$ is used. The plate is discretized by $N = 81$ grid points and $\frac{\Delta t c_0}{L} = 0.001$ is chosen. The initial configuration of the flexible plate is a straight line like in the previous section with $\theta = -0.04\pi$. The flexible plate has been fixed to its initial displacement until an approximately steady state flow solution is reached at $\frac{t c_0}{L} = 60$. Then, the flexible plate is released from its initial position and allowed to interact with the flow.

Fig. 5 represents the y-displacement of the trailing edge and the time variation of the plate deformation. The amplitude of the oscillation is decreasing, and the frequency is

about $\frac{fL}{c_0} = 0.6$.

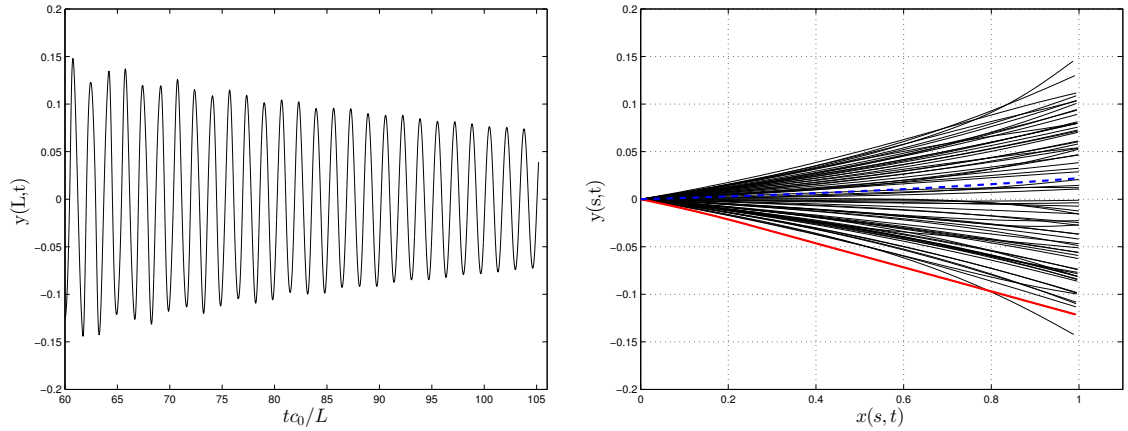

(a) (b)

Figure 5: (a) Time history of the y-coordinate position of the trailing edge of the plate in FSI. (b) Sequence of flexible plate deformation from $tc_0/L = 60$ to $tc_0/L = 105$, the initial and final deformation are marked by the red solid line and the blue dashed line, respectively.

Fig. 6 shows the instantaneous spanwise vorticity contours in the left column and the corresponding pressure field on the right at five time instants. The plate is released to oscillate at nondimensional time $tc_0/L = 60$. The plate oscillation produces a strong acoustic wave near the trailing edge of the plate. The wave hits the top and bottom wall of the channel and the reflected waves propagate into the domain, hitting waves newly produced by oscillating plate and waves reflected the at the inlet. These reflected waves interact and produce a complex interference pattern which leads a very noisy pressure field. The complexity of the reflections and vicinity of the inlet boundary imposing uniform flow to the trailing edge lead to a build-up of vortices near the inlet. Behind the trailing edge of the oscillating plate, a complex vorticity pattern is observed.

4 Conclusions

In the present study, we have implemented a two-dimensional structure model to interact with compressible viscous flow in order to simulate the fluid structure interaction for a simplified model of the soft palate in the pharynx. The soft palate is modeled as a deformable inextensible plate. The FSI algorithm is based on the Arbitrary Lagrangian–Eulerian formulation with an explicit, two-way coupling strategy. The 2D compressible Navier–Stokes equations are computed by highly stable high order summation by parts (SBP) difference operators. The explicit Runge–Kutta method is applied for time integration. The structure model is solved by an implicit second order difference method to determine the flexible plate motion. The accuracy of the structural solver has been as-

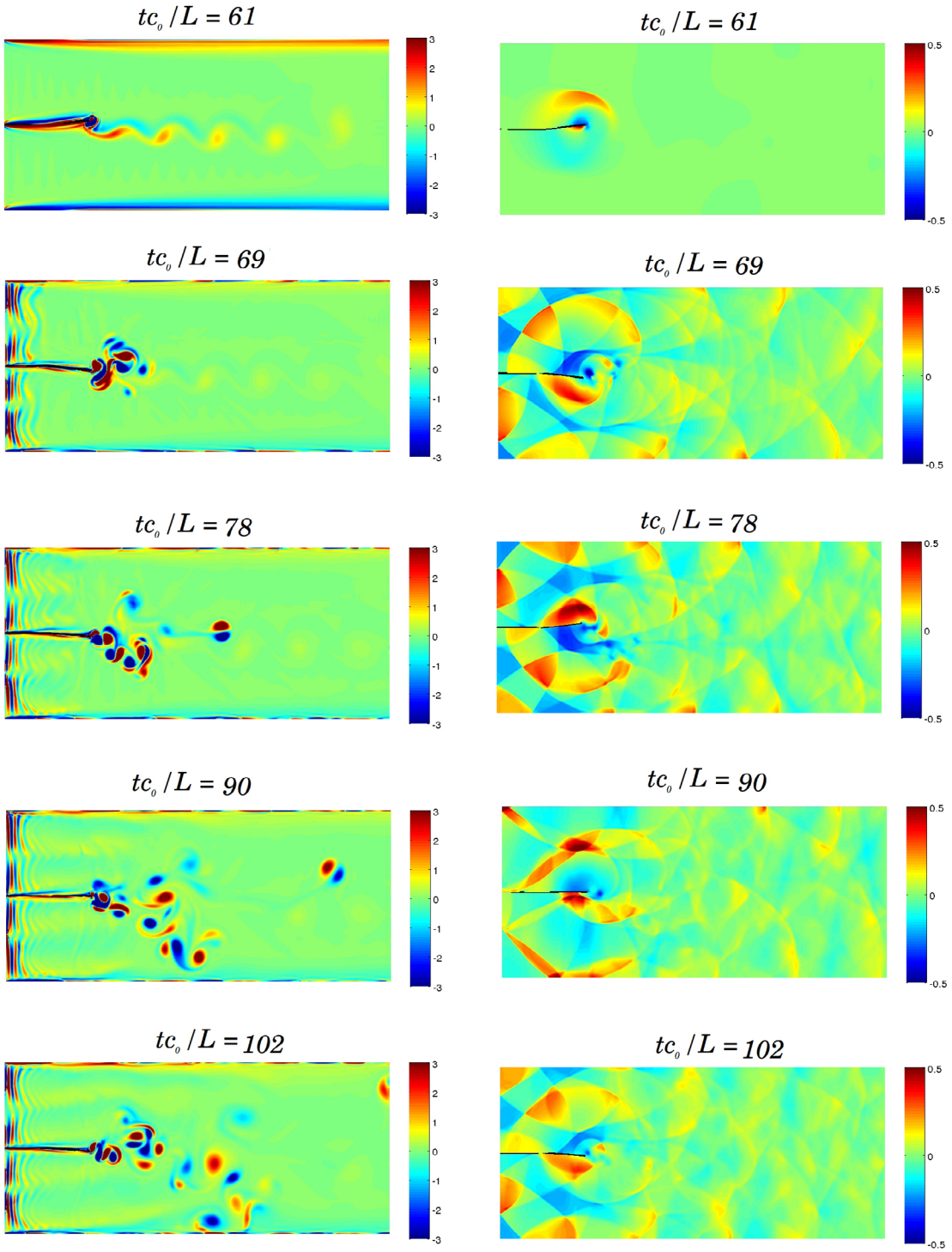

Figure 6: The left column shows the time sequence of vorticity contour plots, $\frac{\omega_z L}{c_0}$, and the right column presents the corresponding acoustic pressure contour plots, $\frac{p'}{\rho_0 c_0}$, at Re = 378 and Ma = 0.1.

sessed through comparisons with previous numerical results. The flow-induced oscillation of the plate is simulated for low Reynolds and Mach numbers. Strong acoustic waves are produced by the oscillating plate. Complex pressure and vorticity patterns are observed.

REFERENCES

[1] T. Young, M. Palta, J. Dempsey, J. Skatrud, S. Weber, and S. Badr, "The occurrence of sleep-disordered breathing among middle-aged adults," *New England Journal of Medicine*, vol. 328, no. 17, pp. 1230–1235, 1993.

[2] C. D. Bertram, "Flow-induced oscillation of collapsed tubes and airway structures," *Respiratory Physiology & Neurobiology*, vol. 163, no. 1, pp. 256–265, 2008.

[3] L. Huang, "Flutter of cantilevered plates in axial flow," *Journal of Fluids and Structures*, vol. 9, no. 2, pp. 127–147, 1995.

[4] Y. Auregan and C. Depollier, "Snoring: Linear stability analysis and in-vitro experiments," *Journal of Sound and Vibration*, vol. 188, no. 1, pp. 39–53, 1995.

[5] C. Guo and M. Païdoussis, "Stability of rectangular plates with free side-edges in two-dimensional inviscid channel flow," *Journal of Applied Mechanics*, vol. 67, no. 1, pp. 171–176, 2000.

[6] R. Howell, A. Lucey, P. Carpenter, and M. Pitman, "Interaction between a cantilevered-free flexible plate and ideal flow," *Journal of Fluids and Structures*, vol. 25, no. 3, pp. 544–566, 2009.

[7] T. Balint and A. Lucey, "Instability of a cantilevered flexible plate in viscous channel flow," *Journal of Fluids and Structures*, vol. 20, no. 7, pp. 893–912, 2005.

[8] G. Tetlow and A. D. Lucey, "Motions of a cantilevered flexible plate in viscous channel flow driven by a constant pressure drop," *Communications in Numerical Methods in Engineering*, vol. 25, no. 5, pp. 463–482, 2009.

[9] L. Tang, M. P. Païdoussis, and J. Jiang, "Cantilevered flexible plates in axial flow: energy transfer and the concept of flutter-mill," *Journal of Sound and Vibration*, vol. 326, no. 1, pp. 263–276, 2009.

[10] M. Khalili, M. Larsson, and B. Müller, "Interaction between a simplified soft palate and compressible viscous flow," *Journal of Fluids and Structures*, vol. 67, pp. 85–105, 2016.

[11] L. Tang and M. P. Païdoussis, "On the instability and the post-critical behaviour of two-dimensional cantilevered flexible plates in axial flow," *Journal of Sound and Vibration*, vol. 305, no. 1, pp. 97–115, 2007.

[12] J. Sesterhenn, B. Müller, and H. Thomann, "On the cancellation problem in calculating compressible low Mach number flows," *Journal of Computational Physics*, vol. 151, no. 2, pp. 597–615, 1999.

[13] B. Müller, "High order numerical simulation of aeolian tones," *Computers & Fluids*, vol. 37, no. 4, pp. 450–462, 2008.

[14] M. Larsson and B. Müller, "Numerical simulation of confined pulsating jets in human phonation," *Computers & Fluids*, vol. 38, no. 7, pp. 1375–1383, 2009.

[15] B. Strand, "Summation by parts for finite difference approximations for d/dx," *Journal of Computational Physics*, vol. 110, no. 1, pp. 47–67, 1994.

[16] B. Gustafsson, *High order difference methods for time dependent PDE*. Berlin: Springer, 2008.

[17] B. Gustafsson, H.-O. Kreiss, and J. Oliger, *Time dependent problems and difference methods*. New York: John Wiley & Sons, 1995.

[18] T. J. Poinsot and S. Lele, "Boundary conditions for direct simulations of compressible viscous flows," *Journal of Computational Physics*, vol. 101, no. 1, pp. 104–129, 1992.

[19] W.-X. Huang, S. J. Shin, and H. J. Sung, "Simulation of flexible filaments in a uniform flow by the immersed boundary method," *Journal of Computational Physics*, vol. 226, no. 2, pp. 2206–2228, 2007.

[20] A.-K. Tornberg and M. J. Shelley, "Simulating the dynamics and interactions of flexible fibers in Stokes flows," *Journal of Computational Physics*, vol. 196, no. 1, pp. 8–40, 2004.

[21] T. H. Pulliam and J. L. Steger, "Implicit finite-difference simulations of three-dimensional compressible flow," *AIAA Journal*, vol. 18, no. 2, pp. 159–167, 1980.

[22] M. R. Visbal and D. V. Gaitonde, "On the use of higher-order finite-difference schemes on curvilinear and deforming meshes," *Journal of Computational Physics*, vol. 181, no. 1, pp. 155–185, 2002.

[23] R. Peyret, H. Viviand, and J. Smolderen, "Computation of viscous compressible flows based on the Navier-Stokes equations," *NASA STI/Recon Technical Report N*, vol. 76, p. 11380, 1975.

[24] J. Favier, A. Revell, and A. Pinelli, "A lattice Boltzmann–immersed boundary method to simulate the fluid interaction with moving and slender flexible objects," *Journal of Computational Physics*, vol. 261, pp. 145–161, 2014.

VII International Conference on Computational Methods for Coupled Problems in Science and Engineering
COUPLED PROBLEMS 2017
M. Papadrakakis, E. Oñate and B. Schrefler (Eds)

DRAG COEFFICIENT OF SPHERICAL PARTICLES IN TURBULENT CHANNEL FLOW

ZDENEK CHARA*, JINDRICH DOLANSKY* AND BOHUS KYSELA*

* Institute of Hydrodynamics CAS, v. v. i.
Pod Patankou 30/5, Prague 166 12, Czech Republic
e-mail: chara@ih.cas.cz, www.ih.cas.cz

Key words: Drag Coefficient, CFD, Lattice Boltzmann Method, Finite Volume Method.

Abstract. *The paper presents results of numerical calculations of drag coefficients of large spherical solid particles. Several hydraulic cases were tested. The first one - the spheres were fixed at different heights above a rough bed of an open channel, the second one - the spheres moved along the channel bed and the third one - the sphere impacted and rebounded from a smooth surface. Finite Volume and Lattice Boltzmann methods were used for the simulations. The Particle Image Velocimetry (2D-PIV) was used to determine the velocity field in the open channel.*

1 INTRODUCTION

The flow of solid particles in a vicinity of a wall is very important for many branches like chemical engineering, civil engineering, environmental problems, hydrotransport. A lot of efforts have been devoted to problems of particles moving in a linear shear flow. The hydrodynamic forces acting on a finite-sized particle moving in a wall-bounded linear shear flow were studied in [1]. The particle Reynolds number varied from 2 to 250. The study showed that the presence of a wall has a significant influence on the drag coefficient. With decreasing a gap size between the particle and the wall the drag coefficient increased. Particle translating and rotating close to a flat wall were studied in [2]. Using DNS simulations a superposition of drag and lift contributions at a modest Reynolds number regime (1-100) was investigated. Measurements of fluctuating forces on a stationary near-bed sediment particle have been performed in [3] for particle Reynolds number range 4000-20000. The results showed that the value of the drag coefficient was about 0.76. Numerical simulations of forces acting on a spherical particle sitting on a bed were performed in [4]. For the calculations the authors used a logarithmic velocity profile as an input. The authors suggested a constant value of the drag coefficient of 0.54 for a range of the Reynolds numbers 1000-10000. They also highlighted an importance of the definition of flow velocity seen by the particle for the calculation of the drag coefficient.

The main objectives of this study are to numerically simulate a flow around large spherical particles in a water channel flow. The ratios of flow depth to particle diameters are 2.5 and 6.8 respectively. In this study we have focused on an initial stage of the particle movement up to $t^* = t\,u/D = 40$.

2 GEOMETRICAL ARRANGEMENT

Schematic view of the geometrical arrangement for the numerical simulations is shown in Fig. 1. The bottom of the channel was covered by a one layer of glass rods of diameter 6 mm. The rods were placed perpendicularly on the flow direction. The spheres of diameters D were fixed in different heights, h, above the bottom. Two smooth spheres of diameter 25.4 and 10 mm were used. The channel flow depth was 65 mm (measured form the center of the bed rods) and the mean velocity was 0.5 m/s. The bulk Reynolds number calculated form the mean velocity and the flow depth was Re = 31000. The gaps between the sphere and the bottom were h=2; 4.3 and 10 mm for the larger particle (D=25.4 mm) and h= 4.3 and 10 mm for the second sphere (D=10 mm). We also tested an influence of the particle rotation on the drag coefficient so the larger sphere placed 4.3 mm above the bottom was allowed to free rotate with an angular velocity ω=60 rad/s at the clock-wise direction about the transverse axis (the flow direction is from the left to the right, see Fig. 1).

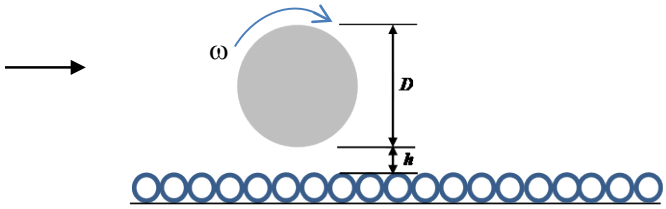

Figure 1: Schematic view

Similar hydraulic conditions were used for the experimental part. The experiments were performed in the horizontal open channel of a cross section 0.25x0.25 m and length 6 m. Both the side walls and the bottom are made from glass plates. As for the numerical simulations the channel bottom was covered by one layer of the glass rods of diameter 6 mm. The rods were placed perpendicularly on the flow direction. The 2D PIV system consisted of a camera NanoSense MK III with 4 GB inner memory and frame rate 1000 fps in full resolution 1280x1024 pixels. The capacity of the camera inner memory enabled to pick up the frames in a total time 3.3 sec. The seeding particles used were hollow glass 10 μm particles (Dantec Inc. DK). As the sources of illumination were used Leica KL2500LCD equipped with lightline with adjustable focusing optics. This light source worked in a continuous mode. The lights were placed above the water level and under the channel bottom. The flow depth in the measuring section was H=64 mm and the flow rate was 8.6 l/s. The bulk flow Reynolds number was Re=33000.

3 NUMERICAL SIMULATIONS

The CFD conducted in this study were large eddy simulations - LES implemented in FVM (Ansys Fluent) and LES implemented in a in-house code of LBM. Size of a computational domain for the channel flow simulated by the FVM was 4.6H x H x 2H where H is the open channel flow depth. Smagorinksy-Lilly approach was used as the sub grid model with C_s=0.14. To achieve a reasonable turbulence level a simulation without the spherical particles was performed. We used periodic flow conditions at the inlet and outlet boundaries and on the side walls a symmetry condition was applied. The water flow surface was modelled as a wall

with zero shear stress. A thickness of the first layer of the boundary layer on the particle surface was 0.05 mm and time steps of the calculations were 0.0005-0.001 sec. The computational mesh consisted of 8.6 million mostly tetrahedron cells.

The channel flow was also modelled using the lattice Boltzmann (LBM) based simulation. The LBM represents a recent numerical approach which excels thanks to its effectiveness and straightforwardness in modeling arbitrary boundaries. The lattice Boltzmann equation

$$f_i\left(\mathbf{x}+\mathbf{c}_i\Delta t, t+\Delta t\right)-f_i\left(\mathbf{x},t\right)=\frac{1}{\tau}\left(f_i^{eq}-f_i\right) \tag{1}$$

represents a discrete analogy to the continuous Boltzmann equation and it is derived by discretization in time and space, and by choice of the discrete velocity space (meaning of individual symbols follows in the text). The LBE describes dynamics of fictive particles propagating along links of an orthogonal lattice, given by the choice of discrete velocities $\mathbf{c}_i$, and interacting in the nodes of the lattice. The fictive particles are represented by distribution functions f_i which give probabilities of finding a fictive particle in a certain time t in a certain node $\mathbf{x}$ with a certain discrete velocity $\mathbf{c}_i$. The LBE can be evaluated in two steps: the stream or propagation step which is described by the left hand side of the LBE, and the collision step which is determined by the term on the right hand side of the LBE. In the first step the values of the distribution functions are shifted to the neighboring nodes along the corresponding directions. In the second step the fictive particles interact in the nodes which is realized through relaxation to the equilibrium distribution functions f_i^{eq} and the rate of the relaxation is given by the relaxation time τ. The total interaction which includes the relaxation is determined by the collision operator. In the examined simulation the LBGK operator, which conserves mass and momentum, with single relaxation time τ was used. From locality of both steps follows possible parallelization of the LBM which leads to its mentioned effectivity.

As the considered flow is characterized by high values of the Reynolds number, the LBM based simulation was enriched by a Smagorinsky subgrid model which modified the value of the relaxation parameter in each node to model influence of unresolved scales on the flow. On the surface of the moving sphere the no-slip boundary condition is imposed which is implemented by the bounce-back algorithm where contribution of momentum transfer from the moving sphere is included. The force, which the flow exerts on the sphere as it moves through the channel, is given by the sum of contributions of incoming and outgoing fictive particles over all boundary nodes

$$\mathbf{F}=-2\sum_{\mathbf{x}_b}\sum_{i}\left(f_i-\frac{w_i}{c_s^2}\rho\left(\mathbf{c}_i\,\mathbf{v}\right)\right)\mathbf{c}_i \tag{2}$$

where w_i represents weights for different lattice directions, c_s is the lattice sound speed, ρ is the flow density and v is the velocity of the sphere. Three different lattice boundary schemes are employed to model boundaries of the channel. The side walls, the inflow and the outflow are connected by the periodical condition, the bed surface is simulated by the bounce-back algorithm and the free surface of the flow is implemented with the help of the modified symmetric condition.

The in-house simulation employed the standard D3Q19 lattice to study the examined process. The computational domain made of 400 × 91 × 91 nodes corresponded to 0.3 × 0.068 × 0.068 m which led to the space step $\Delta x = 7.5 \times 10^{-4}$ m. This resolution determined the number of 34 nodes per the particle diameter D=25.4 mm. Although there is no

straightforward way to choose Δt with respect to Δx within the LBM it was assumed that the order of the time step and the space step were related as $\Delta t / \Delta x = 0.1$.

4 RESULTS AND DISCUSSION

The initial stage of the numerical simulations was focused on the flow around the sphere placed at a stream of a constant velocity without any wall effect. The FVM approach was used. A computational domain of dimensions 0.25 x 0.1 x 0.1 m was built and inside the box we placed the sphere of the diameter D=25.4 mm. The input velocities were 0.15 and 0.47 m/s (Re=3800 and 12000). We also studied a combination of input velocities and streamwise rotation of the angular velocity ω=60 rad/s. The flow was impulsively started from zero to given velocity. The vortex structures behind the sphere are shown in Fig. 2 for the input velocity 0.15 m/s and in Fig. 3 for the input velocity 0.47 m/s. The flow direction is from the left to the right. The vortices are visualized as isosurfaces of the Q-criterion (Q=10 s^{-2}). A relatively stable primary vortex can be seen in the plots (a) and (c) which show the situation without particle rotation for different non-dimensional times $t^* = t\, u/ D$. Due to the rotation the vortical structures are deformed even for low values of the non-dimensional time. Values of the longitudinal force (F) were recorded and finally the drag coefficient was calculated from well-known equation $C_d=F/(0.125\rho u^2 \pi D^2)$. The results are shown in Fig. 4 for the both Reynolds numbers. The drag coefficient of non-rotating sphere of Re=3800 is about C_D=0.43 which corresponds to literature data. For the rotating sphere the drag coefficient significantly fluctuates and its mean value is about C_D=0.51. For Re=12000 the drag coefficient of the non-rotating sphere more or less corresponds to values of lower Re up to t^*=20. In a range $20<t^*<30$ a remarkable increase of the drag coefficient can be observed. In that region the flow behind the sphere becomes fully turbulent. For a region $t^*>30$ the values of the drag coefficient smoothly approach the data of the lower Re. For rotating sphere of Re=12000 the transition to turbulence occurs sooner (t^*=6) and the values of the drag coefficient are higher C_D=0.61.

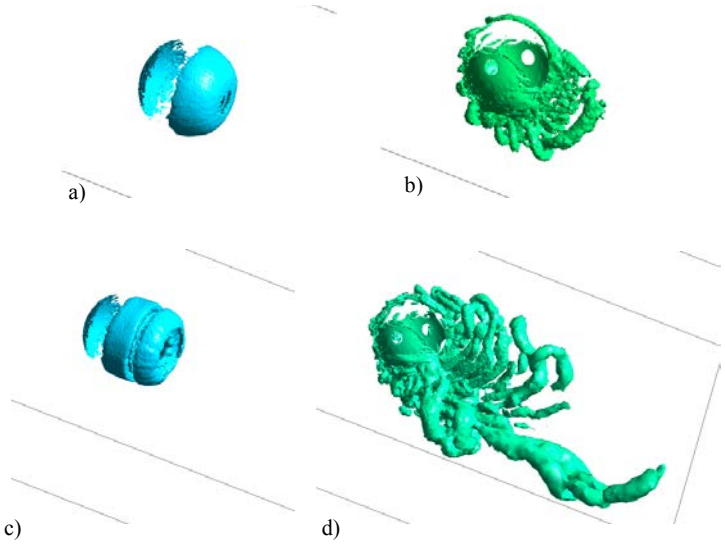

Figure 2: Isosurfaces of the Q-criterion (Q=10 s^{-2}) - a) u=0.15m/s, ω=0, t^*=1.8; b) u=0.15m/s, ω=60, t^*=1.8; c) u=0.15m/s, ω=0, t^*=5.9; d) u=0.15m/s, ω=60, t^*=5.9

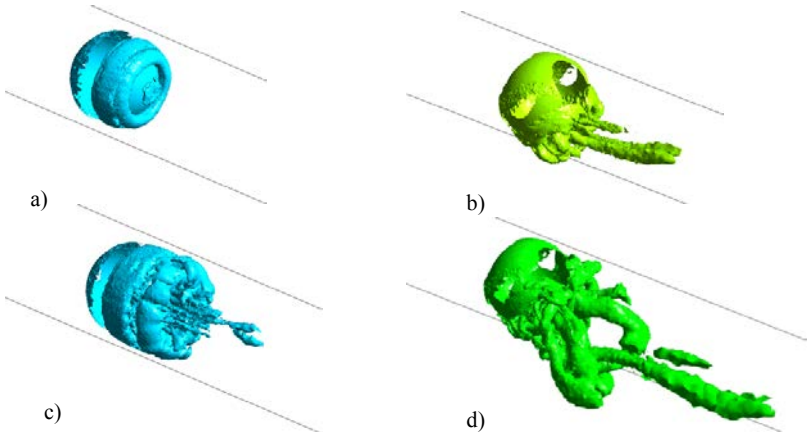

Figure 3: Isosurfaces of the Q-criterion (Q=10 s^{-2}) - a) u=0.47m/s, ω=0, t*=3.7; b) u=0.47m/s, ω=60, t*=3.7; c) u=0.47m/s, ω=0, t*=7.4; d) u=0.47m/s, ω=60, t*=7.4

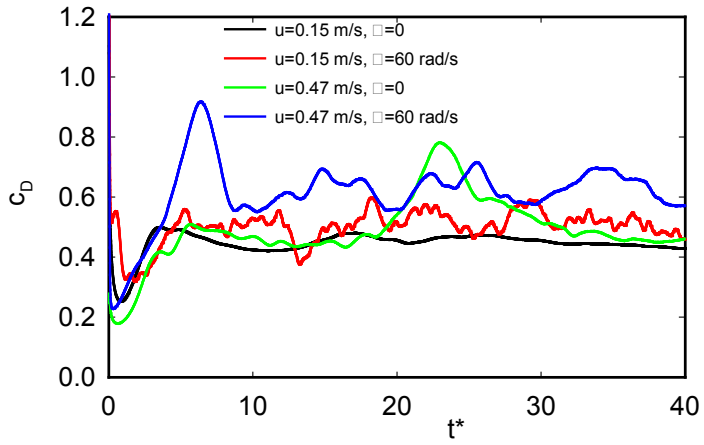

Figure 4: Time histories of the drag coefficients (D=25.4 mm) – constant velocity input

We also simulated an impact of the sphere with smooth wall in the normal direction and a rebound of the sphere from the wall. We used the same computational domain as in the previous case. To avoid difficulties of a grid remeshing close to the sphere surface the sphere was fixed at the initial position above the wall (L/D=4.7) and whole computational box was allowed to move with a constant velocity 0.15 m/s (Re=3800). When the sphere came near the wall the motion was stopped and after a short time (4 ms) the box moved at opposite direction with the same velocity (0.15 m/s). The force on the sphere surface was recorded and the drag coefficient was subsequently calculated. The results are shown in Fig. 5 where t*=0 corresponds to a time of the impact. When the gap between the sphere and the wall is about one sphere diameter the drag coefficient increases up to a value C_D =1.3. But in our case the sphere did not touch the wall (the final gap was 1.5 mm) and the drag coefficient will be probably higher just at the impact. The rebounding phase is characterized by a fluctuation of the drag coefficient.

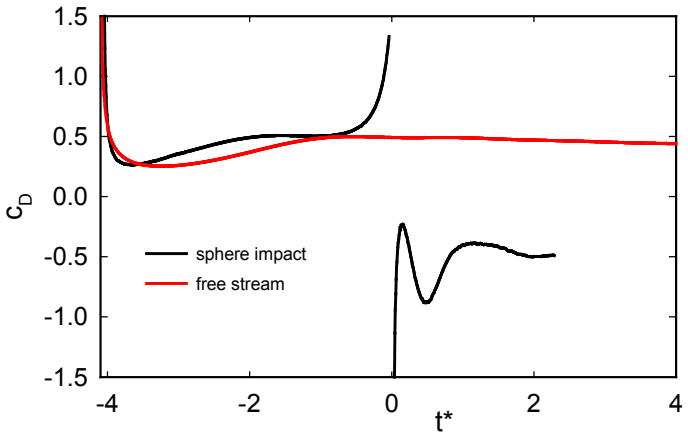

Figure 5: Time history of the drag coefficient during the normal impact with the wall (D=25.4 mm)

The FVM simulation of the channel flow consisted of two steps. The first step was a simulation of the channel flow without any particles. During this phase turbulent flow conditions were achieved. At the second phase the resulted data of velocities and pressure were interpolated onto the computational domain with the particle and the simulation was initialized. It means that the flow around the sphere impulsively started from the time of the initialization. In the case of the LBM-LES simulation a power law equation was used to initialize the velocity profile inside the domain. A comparison of the simulated and measured non-dimensional velocity profiles is shown in Fig. 6. The particle Reynolds numbers were calculated from the mean velocities at positions corresponding to the centers of the particles. The particle Reynolds numbers varied from 4000 (D=10 mm) to 12000 (D=25.4mm).

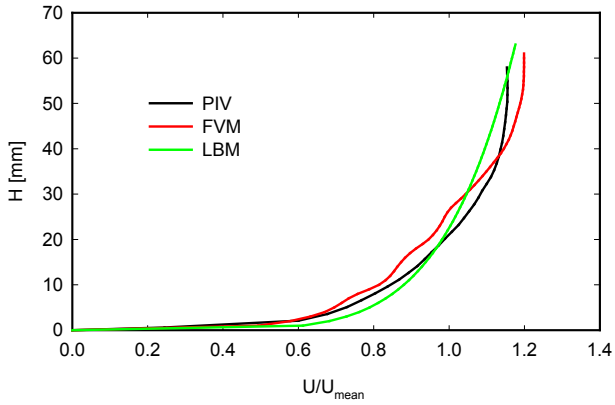

Figure 6: Profiles of the channel mean velocities

The spherical particles were fixed at different positions above the rough bed. For the gap height h=4.3 mm and the particle diameter D= 25.4 mm isosurfaces of the vortex Q parameter are shown in Figs. 7, 8 and 9. Fig. 7 shows the results of the FVM simulations for the non-rotating sphere at different non-dimensional times. Due to the higher velocity at the top of the sphere the primary vortex ring is deformed and it is transported to the central part of the main flow. On the contrary due to the particle rotation (at clockwise direction) the primary

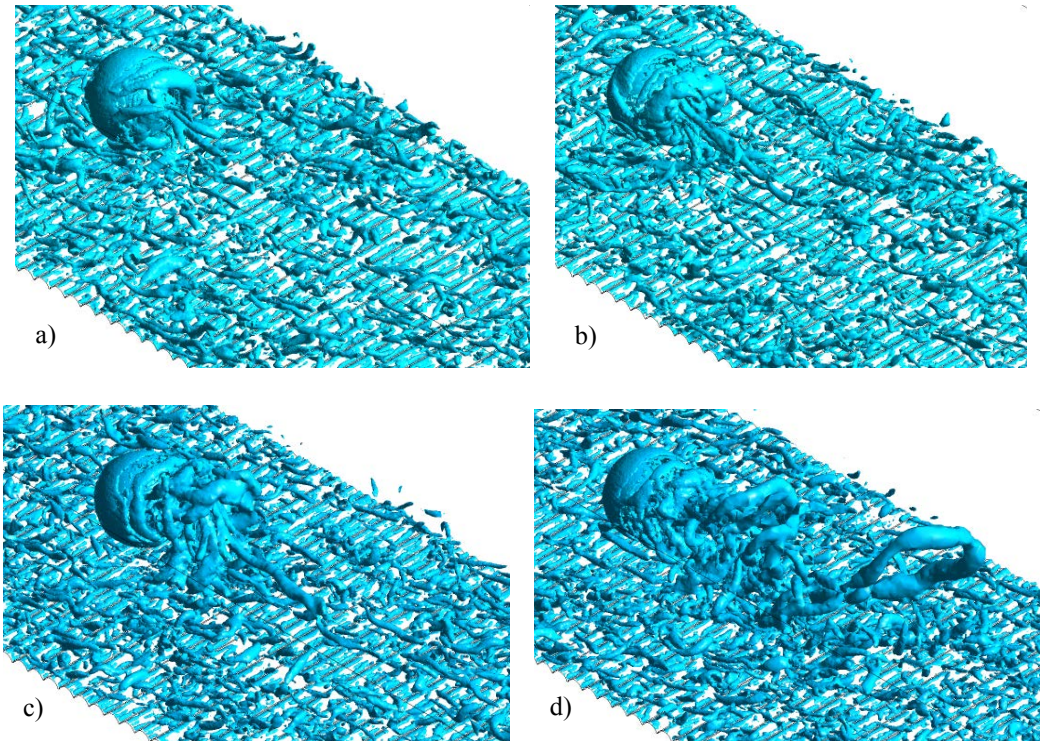

Figure 7: Isosurfaces of the Q-criterion (D=25.4 mm, h=4.3 mm) – a) t^*=1.5, b) t^*=2.2, c) t^*=3.6, d) t^*=7.2

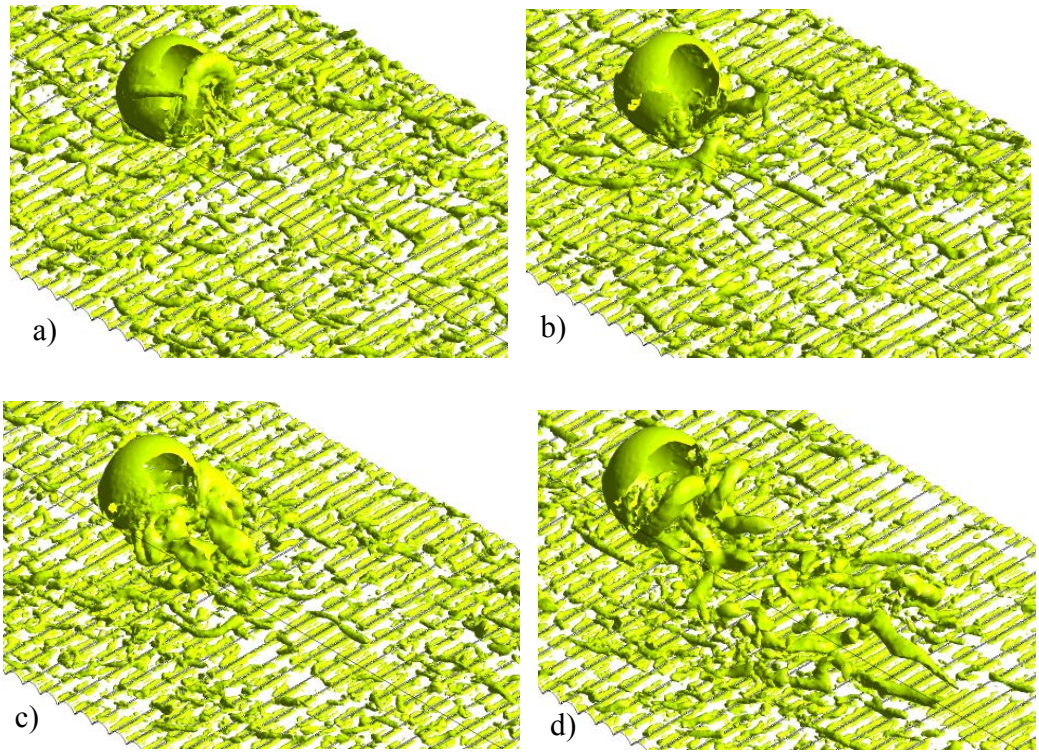

Figure 8: Isosurfaces of the Q-criterion (D=25.4 mm, h=4.3 mm, ω=60 rad/s) – a) t^*=1.5, b) t^*=2.2, c) t^*=3.6, d) t^*=7.2

vortex is not developed, see Fig. 8. Fig. 9 shows the results of the LBM-LES simulations for the non-rotating particle at the same position (h=4.3 mm). The LBM-LES simulation seems to break the main vortical structure into small vortices during a shorter time.

The resulting time histories of the drag coefficients for the larger sphere (D=25.4 mm) are plotted in Fig. 10. For the gap height h = 10 mm the values of the drag coefficients correspond to the values calculated for the free stream input. With decreasing heights of the gap the drag coefficients are increasing. For the gap height h=4.3 mm the value of the drag coefficient is about 0.58, for h = 2 mm the drag coefficient is about 0.63 and for h = 4.3 mm and rotation of ω = 60 rad/s the drag coefficient is about 0.70. The results of the both simulations are in a good agreement. The history of the drag coefficient development for smaller particle (D =10 mm) is shown in Fig. 11. No significant influence of the gap height on the drag coefficient was observed. The drag coefficient in the channel flow is about 10 percent higher compare to the free stream.

The LBM-LES was used to simulate the motion of the spherical particle parallel to the channel bottom. The larger particle (D = 25.4 mm) was initially placed at a position 10 mm above the bottom. The particle moved along the bottom by a constant velocity 0.45 m/s. The channel point velocities were modelled by the power law equation. The developed vortical structures are shown in Fig. 12 as isosurfaces of the Q-criterion. The vortices are relatively stable compare to the flow around fixed particle.

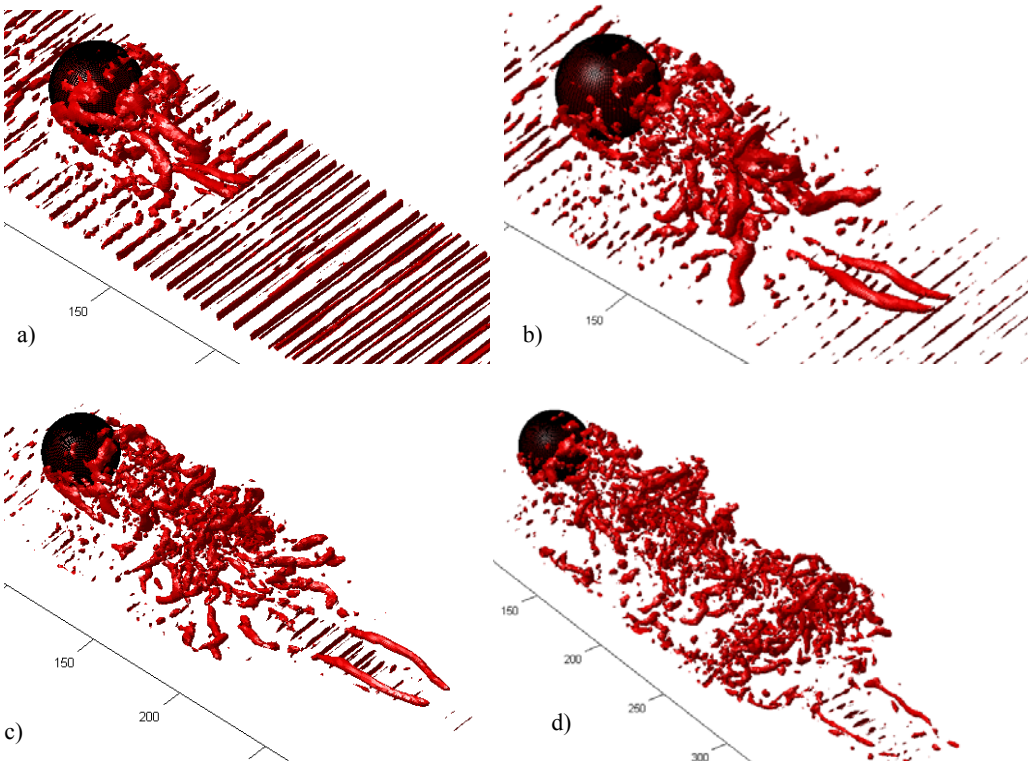

Figure 9: Isosurfaces of the Q-criterion (D=25.4 mm, h=4.3 mm, LBM-LES) – a) t^*=1.8, b) t^*=3.6, c) t^*=5.4, d) t^*=9.1

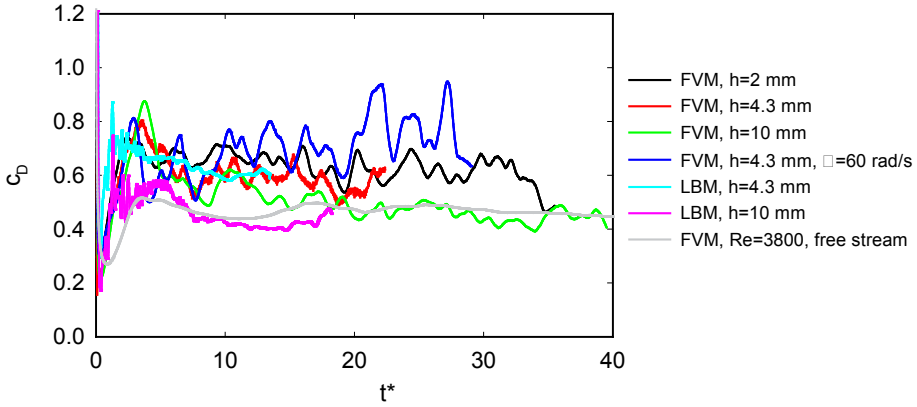

Figure 10: Time histories of the drag coefficients (D=25.4 mm) – channel flow

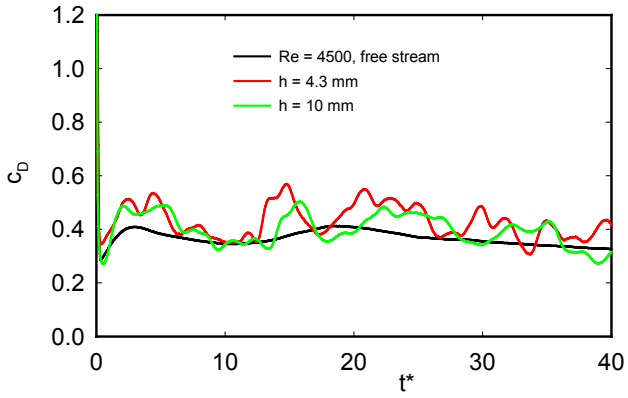

Figure 11: Time histories of the drag coefficients (D=10 mm) – channel flow

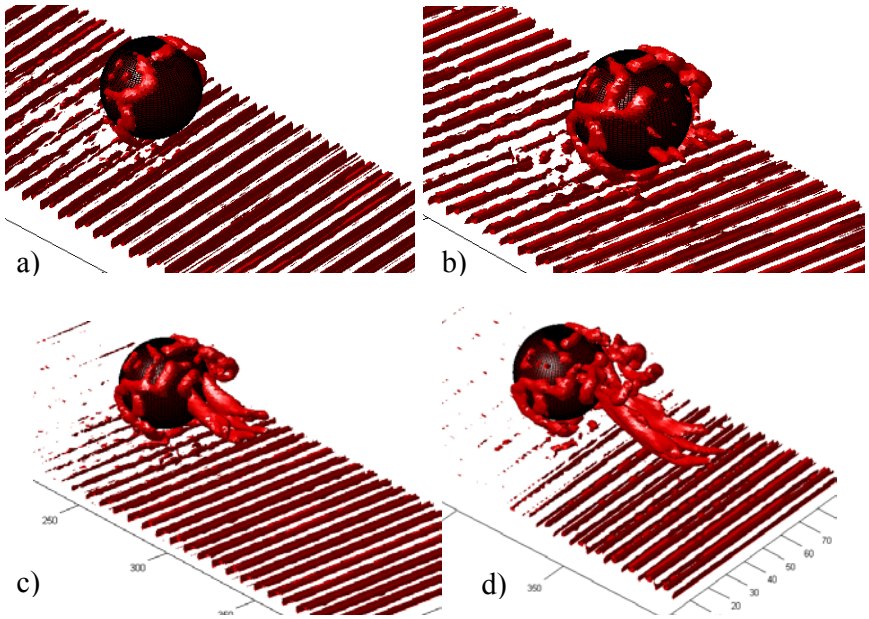

Figure 12: Isosurfaces of the Q-criterion - moving sphere (D=25.4 mm, h=10 mm, LBM-LES) – a) t*=1.8, b) t*=3.6, c) t*=5.4, d) t*=7.1

5 CONCLUSIONS

The paper presents numerical simulations of the flow around large spherical particles. Several geometrical arrangements were studied. The particles were flowed around by a free stream input, the particle impacted and rebounded from a wall, the particles were fixed at different position above rough bed in the channel flow and the particle moved parallelly along the bed. The forces acting on the particle were monitored and the drag coefficients were calculated. It was shown that the drag coefficient is increasing with decreasing the gap height between the particle and the bed.

ACKNOWLEDGEMENT

The supports under project No. 15-18870S of the Grant Agency of the Czech Republic and RVO: 67985874 are gratefully acknowledged.

REFERENCES

[1] Zeng, L., Najjar, F., Balachandar, S. and Fischer,P. Forces on a finite-sized particle located close to a wall in a linear shear flow. *Phys. Fluids* (2006) **21**, 033302.

[2] Lee, H. and Balachandar S. Drag and lift forces on a spherical particle moving on a wall in a shear flow at finite Re. *J. Fluid Mech*. (2010), **657**, 89–125.

[3] Schmeeckle, M. W., Nelson, J.M. and Shreve R.L. Forces on stationary particles in near-bed turbulent flows, *J. Geophys. Res*. (2007) **112**, F02003.

[4] Lee, H. and Balachandar S. (2012), Critical shear stress for incipient motion of a particle on a rough bed, *J. Geophys. Res*., (2012) **117**, F01026.

VII International Conference on Computational Methods for Coupled Problems in Science and Engineering
COUPLED PROBLEMS 2017
M. Papadrakakis, E. Oñate and B. Schrefler (Eds)

EVALUATION OF LINEAR AND QUADRATIC MODAL ANALYSIS FOR A PARTITIONED FSI SOLVER

Alfred E.J. Bogaers*, Oliver F. Oxtoby†, Johan A. Heyns†, Ridhwaan Suliman† and Louw H. van Zyl†

* Advanced Mathematical Modelling, Modelling and Digital Sciences, CSIR, South Africa
email: abogaers@csir.co.za

†Aeronautic Systems, Defence Peace Safety and Security, CSIR, South Africa

Key words: fluid-structure interactions, partitioned, modal analysis, quadratic mode shape components

Abstract. In this paper, linear and quadratic modal approximations of elastodynamic solid deformation in FSI problems are considered. Firstly, the theory of quadratic extension of modal analysis presented in [1] is laid out. The quadratic and linear approximations are then benchmarked against full FEM analysis in various test cases. These are chosen to be representative of flutter considerations in the aerospace field. The quadratic approximation is shown to produce a markedly better prediciton of solid deformation for small to medium deflections.

1 INTRODUCTION

Accurately predicting the onset of flutter is an important consideration when designing and certifying aircraft for an intended flight envelope. It is by now common practice in computational aeroelasticity to approximate the structural deformation using normal linear modal analysis [2, 3]. Linear modal analysis provides an efficient approximation for aeroelastic applications, and has been shown to provide credible flutter predictions [4]. The structural response is described by the system mode shapes and associated natural frequencies, which can either be obtained from experimental ground vibration tests (GVTs) or be approximated numerically using techniques such as the finite element method.

Linear modal dynamic systems are however limited to very small deflections, and are incapable of providing accurate representations for large rotations (for example when performing T-tail flutter analysis [5]). To improve the accuracy of modal analysis for rotating reference frames, Segelman *et al.* [6] introduced the method of quadratic mode shape components.

We aim to demonstrate via examples that these quadratic mode shape components provide an approximation of the geometric non-linearity present within the full elasto-dynamic structural equations, albeit for relatively small deflections. The addition of the quadratic mode shape terms remain a linearised expansion, and therefore retains much of the numerical efficiency offered by normal modal analysis.

Following the work presented in [1], we will outline the procedure for approximating the quadratic mode shape components using a number of static, small strain finite element analyses. The improved accuracy offered by including the quadratic terms will be shown on a number of fluid-structure interactions (FSI) benchmark problems, and compared to high-fidelity FSI simulations.

2 Modal Dynamics

2.1 Linear Modal Dynamics

Using standard FEM analysis software (and to a lesser extent FVM), it is possible to compute the eigenvectors or mode shapes ϕ_i along with the natural frequencies ω_i of a given linear elastic structure. The real space displacement $\boldsymbol{u}$ can then be approximated by the linear expansion of the mode shapes such that

$$\boldsymbol{u} = \sum_{i=1}^{n} q_i \phi_i \tag{1}$$

where q_i are the modal expansion coefficients or modal variables, and n is the number of retained mode shapes. The generalised equation for aeroelastic structural deformation rewritten in terms of the of the modal variables can be expressed as

$$\boldsymbol{M}\ddot{q} + \boldsymbol{C}\dot{q} + \boldsymbol{K}q = Q \tag{2}$$

where $\boldsymbol{M}$, $\boldsymbol{K}$ and $\boldsymbol{C}$ represents the reduced mass, stiffness and damping matrices. Q represents the generalised force vector given by

$$Q_i = \int_{\Omega} d\boldsymbol{F}\phi_i, \tag{3}$$

where $d\boldsymbol{F} = p\boldsymbol{n_f}dA - \boldsymbol{\sigma}\cdot\boldsymbol{n}_f dA$ is the nodal forces along the FSI interface. Here p represents the interface pressure, and $\boldsymbol{\sigma_f}$ the fluid viscous stress tensor and $\boldsymbol{n_f}dA$ the outward pointing surface area normal vector. Typically ϕ_i is interpolated from the structural mesh to the fluid domain interface mesh, where $d\boldsymbol{F}$ then represents the nodal forces acting along the fluid domain's interface. This allows for the generalised forces, Q, and the general elastic equation (2) to be directly computed along the fluid interface.

When computed using the FEM, the mode shapes and elastic equation (2) are typically normalised such that the reduced stiffness and damping matrices become

$$\boldsymbol{M} = \boldsymbol{I} \quad \text{and} \quad \boldsymbol{K} = \text{diag}\left[\omega_n^2\right]. \tag{4}$$

2.2 Quadratic mode shape components

For small displacements, van Zyl *et al.* [1] demonstrated that the linearised expansion in equation (1) can be improved by including coupled quadratic mode shape components ϕ_{ij} such that

$$\boldsymbol{u} = \sum_{i=1}^{n} q_i \phi_i + \sum_{i=1}^{n} \sum_{j=1}^{n} q_i q_j \phi_{ij}. \tag{5}$$

Given the quadratic mode shape components, the generalised force Q_i is now defined as

$$Q_i = \int_{\Omega} d\boldsymbol{F} \cdot \left(\phi_i + \sum_{j=1}^{n} q_j \phi_{ij} \right). \tag{6}$$

The generalised structural equation (2) can be rewritten as

$$M_{ij}\ddot{q}_j + C_{ij}\dot{q}_j + \tilde{K}_{ij} q_j = \tilde{Q}_i, \tag{7}$$

where $\tilde{K}_{ij} = K_{ij} - \int_{\Omega} d\boldsymbol{F} \cdot \phi_{ij}$ and $\tilde{Q}_i = \int_{\Omega} d\boldsymbol{F} \cdot \phi_i$. The linear system (7) is solved at every time step using fourth-order Runge-Kutta integration.

3 APPROXIMATING QUADRATIC MODE SHAPE COMPONENTS FROM FEM

Following the work presented in [1], the quadratic mode shape components can be approximated using a number of static, small strain, linear elastic FEM analyses. This as opposed to [6, 7, 8] which require multiple non-linear static analyses. The method was first proposed using energy arguments derived using truss elements, and later extended to general elastic finite elements.

For the discussion to follow, assume we have available two linear mode shapes, namely ϕ_i and ϕ_j. A linearised approximation for the displacement of node l, of a general elastic element, can then be given as

$$\boldsymbol{u}^l = q_i \phi_i^l + q_j \phi_j^l + \boldsymbol{u}_R \tag{8}$$

where $\boldsymbol{u}_R$ represents an additional rotational displacement term not accounted for by linear modal analysis. The aim of the additional higher order quadratic mode shape components is to counteract the effect of neglecting $\boldsymbol{u}_R$. Given two mode shapes, the additional rotational components can be approximated following [1] as

$$\begin{aligned} \boldsymbol{u}_R &= \boldsymbol{u}_R^{ii} + \boldsymbol{u}_R^{jj} + \boldsymbol{u}_R^{ij}. \\ &= \frac{1}{2} q_i^2 \boldsymbol{R}_i \times \left(\boldsymbol{R}_i \times \boldsymbol{p}^l \right) + \frac{1}{2} q_j^2 \boldsymbol{R}_j \times \left(\boldsymbol{R}_j \times \boldsymbol{p}^l \right) + \frac{1}{4} q_i q_j \left[\boldsymbol{R}_i \times \left(\boldsymbol{R}_j \times \boldsymbol{p}^l \right) + \boldsymbol{R}_j \times \left(\boldsymbol{R}_i \times \boldsymbol{p}^l \right) \right] \end{aligned} \tag{9}$$

Here $\boldsymbol{p}^l$ is a position vector from some point within the element to node l. The exact location of point p is insignificant and can be taken to be element centroid or the average of the nodal co-ordinates. Vectors $\boldsymbol{R}_i$ and $\boldsymbol{R}_j$ are the rigid body rotations associated with mode shapes ϕ_i and ϕ_j respectively for a given element.

In equation (9), the first term, $\frac{1}{2}q_i^2\boldsymbol{R}_i \times \left(\boldsymbol{R}_i \times \boldsymbol{p}^l\right)$, relates to the quadratic component to be cancelled by ϕ_{ii}, the second with ϕ_{jj} and the third with the coupled quadratic mode shape component $\phi_{ij} = \phi_{ji}$. In general, because of the symmetry $\phi_{ij} = \phi_{ji}$, for n linear mode shapes, there will be $(n+3)\,n/2 - n$ quadratic mode shape components to be computed for, i.e.

$$\boldsymbol{\phi}^{ii} = \{\phi_{11}, \phi_{12}, \phi_{1N}, \phi_{22}, \phi_{23}, ...\phi_{2n}, ..., \phi_{nn}\}\,.$$

Computation of the various components of $\boldsymbol{u}_R$ requires isolating the various rigid body rotation vectors, $\boldsymbol{R}_{i,j}$, associated with each of the linear mode shapes $\phi_{i,j}$. Consider Figure 1, where each mode shape is expressed as a displacement vector represented by the summation of rigid body translation and rigid body rotation

$$\{\boldsymbol{\phi}_i\}_{el} = \boldsymbol{T}_{el} + \boldsymbol{R}_{i,el} \times \boldsymbol{p}, \tag{10}$$

where $\boldsymbol{T}_{el} = \{t_x, t_y, t_z\}$ represents the linear translation components and $\boldsymbol{R}_{i,el} = \{r_x, r_y, r_z\}$ the rigid body rotation (angles of rotation) for the given element. The system described by (10) is however over determined, since there are only 6 unknowns to be solved for but $3m$ known components of $\phi_i = \{\phi_{1,x}, \phi_{1,y}, \phi_{1,z}, ..., \phi_{m,z}\}^T$, where m is the number of nodes within the element. The least squares problem to approximate the rigid body rotation vector $\boldsymbol{R}_i$ associated with mode shape ϕ_i for an m noded element can be expressed in matrix form as

$$\begin{bmatrix} \boldsymbol{I} & \boldsymbol{P}_1 \\ \boldsymbol{I} & \boldsymbol{P}_2 \\ \vdots & \vdots \\ \boldsymbol{I} & \boldsymbol{P}_m \end{bmatrix} \begin{Bmatrix} t_x \\ t_y \\ t_z \\ r_x \\ r_y \\ r_z \end{Bmatrix} = \begin{Bmatrix} \phi_{1,x} \\ \phi_{1,y} \\ \phi_{1,z} \\ \vdots \\ \phi_{m,x} \\ \phi_{m,y} \\ \phi_{m,z} \end{Bmatrix}, \tag{11}$$

where $\boldsymbol{P}_l$ is a matrix representative of the cross product between the reference vector associated with node l and the to be computed rotation vector, $\boldsymbol{p}_l^T \times \boldsymbol{R}_i$, i.e.

$$\boldsymbol{P}_l = \begin{bmatrix} 0 & p_{l,z} & -p_{l,y} \\ -p_{l,z} & 0 & p_{l,x} \\ p_{l,y} & -p_{l,x} & 0 \end{bmatrix}, \quad \text{and} \quad \boldsymbol{I} = \begin{bmatrix} 1 & 0 & 0 \\ 0 & 1 & 0 \\ 0 & 0 & 1 \end{bmatrix}. \tag{12}$$

There will be a rotation vector for each element within the structural mesh, for each of the linear mode shapes.

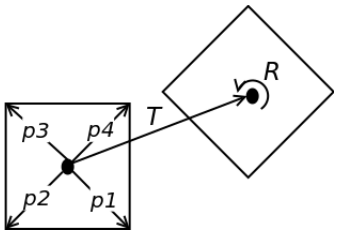

Figure 1: An exaggerated illustration of the translation, $\boldsymbol{T}$, and rotation, $\boldsymbol{R}$, of a two-dimensional 4-noded element.

The quadratic mode shape components $\sum_{i=1}^{N}\sum_{j=1}^{N} q_i q_j \boldsymbol{\phi}_{ij}$ need to cancel out the additional rotational displacement term $\boldsymbol{u}_R$. From a kinetic energy perspective, as explained in [1], in order to minimise spurious contributions to the kinetic energy, the quadratic mode shape components should be orthogonal to the corresponding linear mode shapes. A convenient means is to orthogonalise the linear and quadratic mode shapes with respect to the system stiffness matrix

$$\boldsymbol{\phi}_i^T \left[K\right] \boldsymbol{\phi}_{ii} = 0, \tag{13}$$

where $[K]$ here represents the full FEM, static, small strain stiffness matrix, and not the reduced modal stiffness matrix.

There are therefore two conditions to be satisfied. The quadratic modes shapes need to be orthogonal to the linear mode shapes and need to cancel out the effects of the additional rotational term $\boldsymbol{u}_R$.

The rotational terms are cancelled by computing the reaction forces resulting from the displacement $\boldsymbol{u}_R$, and subsequently computing the equivalent displacement which would cancel out the the reaction forces. Given the rotational displacement $\boldsymbol{u}_R$, the reaction can be computed for a given element as

$$\boldsymbol{f}^i_{\text{el}} = \left[K\right]_{\text{el}} \boldsymbol{u}^i_{R,\text{el}}, \tag{14}$$

where $\left[K\right]_{\text{el}}$ represents the local element stiffness matrix. Using the appropriate global degrees of freedom, the forces should be appropriately summed into the global force vector $\boldsymbol{f}^i_{\text{global}}$. ϕ_{ii} can then be computed by solving the general FEM linear system of

$$\left[K\right] \boldsymbol{\phi}_{ii} = \boldsymbol{f}^i_{\text{global}}. \tag{15}$$

In order to satisfy both the orthogonality constraint (13) along with (15) a Lagrange multiplier system of equations can be constructed and solved for

$$\begin{bmatrix} [K] & [K]\,\boldsymbol{u}^i_R \\ \boldsymbol{u}^{i^T}_R\,[K] & \mathbf{0} \end{bmatrix} \begin{Bmatrix} \boldsymbol{\phi}_{ii} \\ \lambda \end{Bmatrix} = \begin{Bmatrix} \boldsymbol{f}^i \\ 0 \end{Bmatrix}. \tag{16}$$

Similarly, the coupled quadratic modes $\boldsymbol{\phi}^{ij}$ have two orthogonality conditions which have

to be satisfied

$$\begin{bmatrix} [K] & [K]\,\boldsymbol{u}_R^i & [K]\,\boldsymbol{u}_R^j \\ \boldsymbol{u}_R^{iT}\,[K] & 0 & 0 \\ \boldsymbol{u}_R^{jT}\,[K] & 0 & 0 \end{bmatrix} \begin{Bmatrix} \boldsymbol{\phi}_{ij} \\ \lambda_1 \\ \lambda_2 \end{Bmatrix} = \begin{Bmatrix} \boldsymbol{f}^{ij} \\ 0 \\ 0 \end{Bmatrix}. \tag{17}$$

The procedure to approximate the quadratic mode shape components can be summarised as follows:

1. Using a standard FEM package solve for the set of linear mode shapes $\boldsymbol{\phi} = \{\phi_1, ..., \phi_N\}$.
2. For each element compute a reference point p, and compute the corresponding reference vector $\boldsymbol{p}^l$ for each node l.
3. For each of the retained mode shapes $\boldsymbol{\phi}_i$, compute the associated element solid body rotation vector $\boldsymbol{R}^i_{\text{el}}$ by solving the least squares problem (11).
4. Using (9), compute each component of $\boldsymbol{u}^{ij}_{\text{el},R}$.
5. Compute the nodal reaction forces $\boldsymbol{f}^{ij}_{\text{el}} = [K]_{\text{el}}\,\boldsymbol{u}^{ij}_{\text{el},R}$.
6. Sum up $\boldsymbol{f}^{ij}_{\text{el}}$ into the appropriate global force vector $\boldsymbol{f}^i_{\text{global}}$.
7. Solve for the approximate $\boldsymbol{\phi}^{ii}$ and $\boldsymbol{\phi}^{ij}$ components using either (16) or (17) depending on whether there are one or two orthogonality conditions that need to be satisfied.

4 VALIDATING MODAL FSI AGAINST FULL HIGH-FIDELITY FSI

In this section we aim to compare the approximations obtained using linear and quadratic mode shapes and compare these to results obtained using full, high-fidelity FSI simulations. The same spatial and temporal discretisation will be used for both the high-fidelity and modal based ROM. This in turn allows for a direct comparison of the methods, as both sets of simulations will have the same numerical errors.

The normal linear mode shapes and natural frequencies are computed using CalculiX [9]. The fluid flow is computed using OpenFOAM [10], and the fluid and structural domains are implicitly coupled using Aitken's method. The full, high-fidelity FSI simulations are performed using an implicit, partitioned coupling of OpenFOAM and CalculiX [11].

In all test cases, we retain the first 4 linear mode shapes, which corresponds to 10 additional quadratic mode shape components.

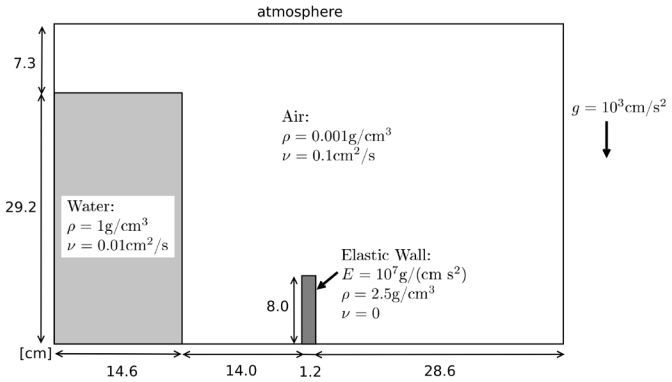

Figure 2: Dam break with elastic structure problem description.

4.1 Dam Break VOF validation

We consider here a simple dam break problem, where a collapsing column of water strikes a flexible elastic structure, which has previously been analysed in [12, 13, 14]. The problem setup is shown in Figure 2, and consists of a 29.2cm column of water which collapses under gravity, striking an 8cm tall, 1.2cm wide, elastic obstacle. The tank is open at the top, and surface tension effects are ignored due to the large length scales.

The problem is solved here using 3672 linear FVM elements and 14 quadratic, full integration solid elements. The time step size is chosen as Δt =0.001s. In Figure 3, the advancing front along with the elastic deformation is shown for various time steps.

A comparison of the tip displacement of the flexible baffle is shown in Figure 4. The improvement in solution accuracy offered by the inclusion of the quadratic mode shape components is directly evident.

4.2 T-Tail

A T-tail like structure is analysed here under fluid cross-flow for 3 different inlet velocities of 1m/s, 3m/s and 5m/s. The problem is selected to illustrate the improved accuracy offered by the quadratic mode shape components when considering larger structural deformations, and problems with rotating reference frames. The geometry along with material properties is outlined in Figure 5. The aim is to provide a preliminary indication of the modal FSI solver using quadratic mode shapes for different deformation magnitudes.

In Figure 6 the T-tail deformations along with pressure contours is shown for the different inlet velocities (computed using the high-fidelity FSI solver) with a comparison of the tip displacements shown in Figure 7. The improvement offered by the inclusion of the additional quadratic mode shape components are once again visible at higher flow rates. The problem clearly highlights, that while the quadratic modes do provide improved accuracy, the applicability remains limited to comparatively small displacements.

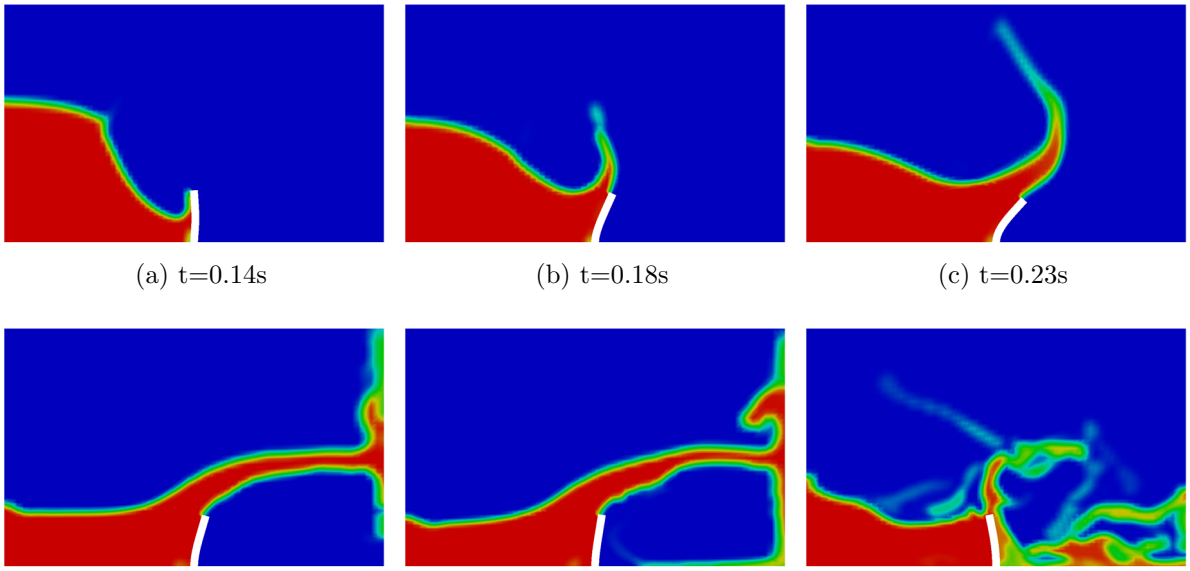

(a) t=0.14s (b) t=0.18s (c) t=0.23s

(d) t=0.38s (e) t=0.46s (f) t=0.8s

Figure 3: Wave interaction with elastic obstruction at various time steps.

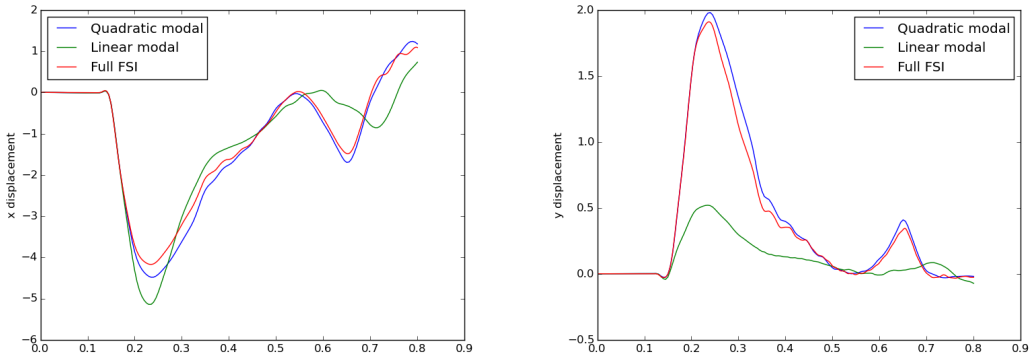

(a) (b)

Figure 4: Comparison of the displacement using linear and quadratic modal dynamics with full high-fidelity FSI. A total of 4 modes are used for the modal dynamics analysis.

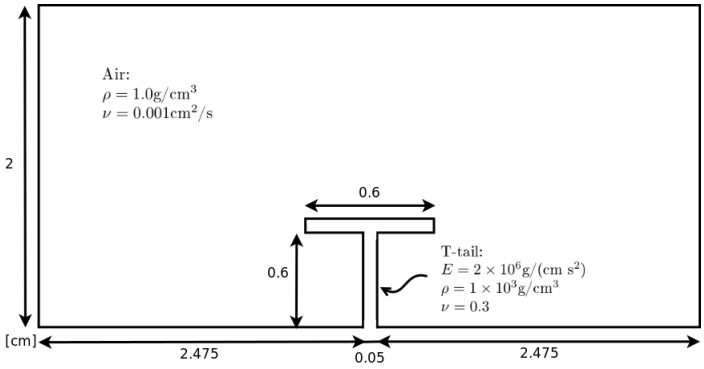

Figure 5: T-Tail material properties and problem description.

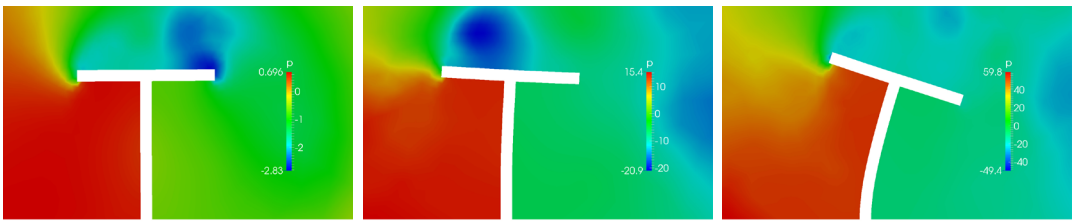

(a) (b) (c)

Figure 6: Pressure contours along with structural deformation at $t = 1.5s$ for inlet velocities of (a) 1m/s, (b) 3m/s and (c) 5m/s.

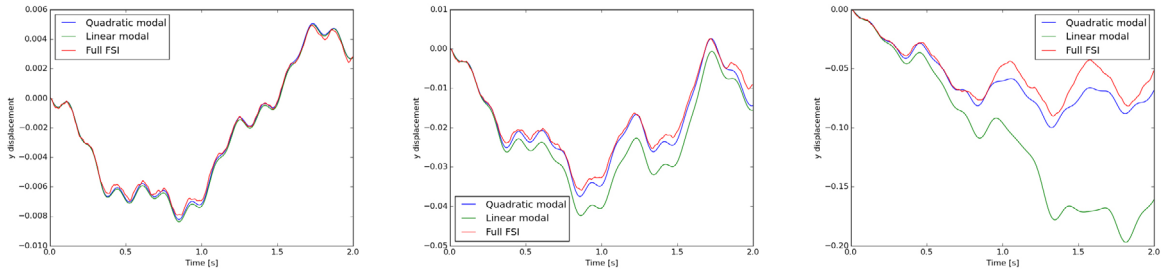

(a) (b) (c)

Figure 7: Comparison of tip y-displacement for inlet velocities of (a) 1m/s, (b) 3m/s and (c) 5m/s. 4 mode shapes are retained for the modal analysis.

Table 1: Comparison of the beam tip frequency of oscillations, compared to the results obtained in [15].

Frequency [Hz]	Linear Modal	Quadratic Modal	Full FSI	Results from [15]
u_x	0.0	3.0	3.72	3.8
u_y	1.85	1.88	1.9	2.0

5 2D flexible beam

In this test problem, flow around a fixed cylinder with an attached flexible beam is analysed. The beam undergoes large deformations induced by oscillating vortices formed by flow around the circular bluff body.

The problem was first proposed by Turek *et al.* [15], and has received substantial numerical verification. The problem layout and material properties are provided in Figure 8(a).

The FSI problem consists of a 0.02m thick, 0.35m long flexible beam, attached to a fixed cylinder with diameter of 0.1m. The cylinder centre is by design constructed to be non-symmetric to remove dependence on numerical errors to induce the onset of deformations. A parabolic inlet boundary condition, with mean flow velocity of $\bar{U} = 1\text{m/s}$ is slowly ramped up for $t < 0.5\text{s}$ via $(1 - \cos(\pi t/2))/2$. The top, bottom and fixed cylinder walls are defined as non-slip boundaries. The problem is solved here using 3800 finite-volume fluid cells, and 72 full integration, bi-quadratic finite elements, with a time step size of $\Delta t = 0.001\text{s}$.

A snapshot of the beam deformation based on the full FSI simulation is shown in Figure 8(b) with a comparison of the beam tip displacements in Figures 8(c) and 8(d). Both the linear and quadratic modal analysis correctly predicts the state of flutter, but are incapable of correctly computing the magnitudes of the oscillating beam. The computed oscillation frequencies is summarised in Table 1. The frequencies computed using both the linear and quadratic mode shapes compare favourably.

6 CONCLUSION

In this study we set out to directly compare linear and quadratic modal analysis on a set of FSI benchmark problems. The procedure to compute the quadratic components using a number of small strain FEM analysis was outlined. Approximating the structural deformation using the quadratic mode shape components adds only a mild additional complexity, retains the numerical efficiency offered by normal linear modal analysis, all the while offering noticeably improved accuracy (albeit still limited to comparatively small structural deformations).

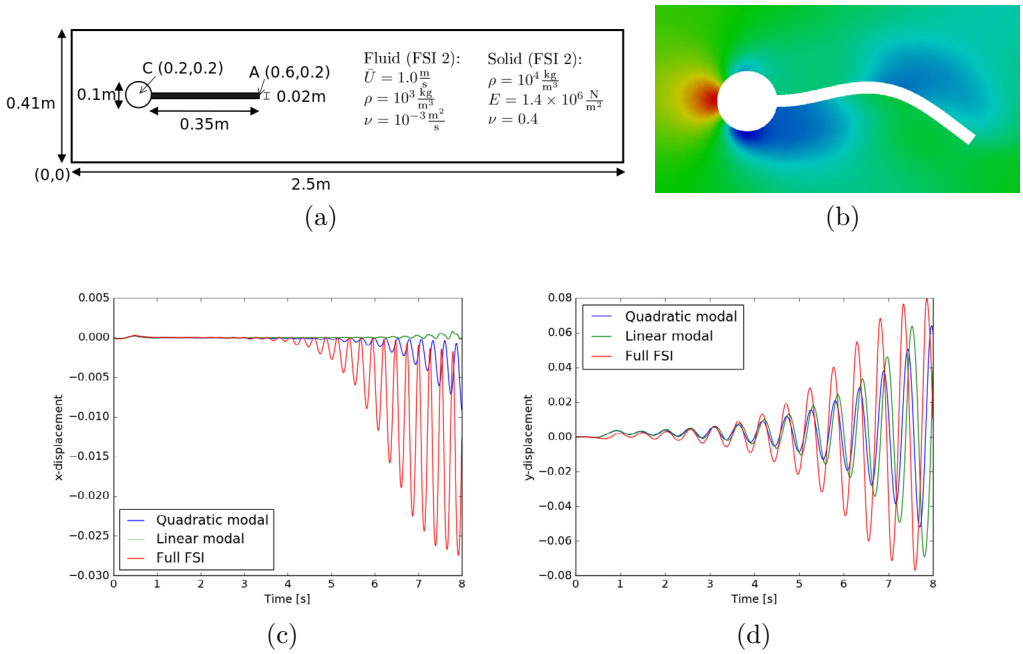

Figure 8: (a) Flexible beam problem description, (b) with a snapshot of the beam displacement and pressure using full, high-fidelity FSI, with a comparison of the beam tip (c) x-displacement and (d) y-displacement.

REFERENCES

[1] Van Zyl, L. & Mathews, E. Quadratic mode shape components from linear finite element analysis. *Journal of Vibration and Acoustics* **134**, 014501 (2012).

[2] Kamakoti, R. & Shyy, W. Fluid–structure interaction for aeroelastic applications. *Progress in Aerospace Sciences* **40**, 535–558 (2004).

[3] Schuster, D. M., Liu, D. D. & Huttsell, L. J. Computational aeroelasticity: success, progress, challenge. *Journal of Aircraft* **40**, 843–856 (2003).

[4] Debrabandere, F., Tartinville, B. & Hirsch, C. A staggered method using a modal approach for fluid-structure interaction computation. In *Proceedings of the 15 th International Forum on Aeroelasticity and Structural Dynamics* (2011).

[5] Van Zyl, L. H. & Mathews, E. H. Aeroelastic analysis of T-tails using an enhanced doublet lattice method. *Journal of Aircraft* **48**, 823–831 (2011).

[6] Segalman, D. & Dohrmann, C. A method for calculating the dynamics of rotating flexible structures, Part 1: Derivation. *Journal of Vibration and Acoustics* **118**, 313–317 (1996).

[7] Dohrmann, C. & Segalman, D. Use of quadratic components for buckling calculations. *Journal of sound and vibration* **208**, 339–344 (1997).

[8] Segalman, D., Dohrmann, C. & Slavin, A. A method for calculating the dynamics of rotating flexible structures, Part 2: Example calculations. *Journal of vibration and acoustics* **118**, 318–322 (1996).

[9] Dhondt, G. Calculix crunchix user's manual version 2.5 (2007).

[10] OpenFOAM: The open source CFD toolbox user guide, version 2.1.0 (2010).

[11] Bogaers, A., Kok, S., Reddy, B. & Franz, T. Quasi-Newton methods for implicit black-box FSI coupling. *Computer Methods in Applied Mechanics and Engineering* **279**, 113–132 (2014).

[12] Kassiotis, C. *Nonlinear fluid-structure interaction: a partitioned approach and its application through component technology.* Ph.D. thesis, Université Paris-Est (2009).

[13] Walhorn, E., Kölke, A., Hübner, B. & Dinkler, D. Fluid–structure coupling within a monolithic model involving free surface flows. *Computers & structures* **83**, 2100–2111 (2005).

[14] Bogaers, A., Kok, S., Reddy, B. & Franz, T. An evaluation of Quasi-Newton methods for application to FSI problems involving free surface flow and solid body contact. *Computers & Structures* **173**, 71–83 (2016).

[15] Turek, S. & Hron, J. *Proposal for numerical benchmarking of fluid-structure interaction between an elastic object and laminar incompressible flow* (Springer, 2006).

VII International Conference on Computational Methods for Coupled Problems in Science and Engineering
COUPLED PROBLEMS 2017
M. Papadrakakis, E. Oñate and B. Schrefler (Eds)

FLUID-STRUCTURE INTERACTION MODELING OF ARTERY ANEURYSMS WITH STEADY-STATE CONFIGURATIONS

Eugenio Aulisa*, Giorgio Bornia† and Sara Calandrini†

* Department of Mathematics and Statistics
Texas Tech University
Lubbock, TX 79409, USA
e-mail: eugenio.aulisa@ttu.edu

† Department of Mathematics and Statistics
Texas Tech University
Lubbock, TX 79409, USA
e-mail: giorgio.bornia@ttu.edu, sara.calandrini@ttu.edu

Key words: Cerebral aneurysms, Incompressible Navier-Stokes equations, Fluid-structure interaction, Intracranial stent.

Abstract. This paper addresses numerical simulations of fluid-structure interaction (FSI) problems involving artery aneurysms, focusing on steady-state configurations. Both the fluid flow and the hyperelastic material are incompressible. A monolithic formulation for the FSI problem is considered, where the deformation of the fluid domain is taken into account according to an Arbitrary Lagrangian Eulerian (ALE) scheme. The numerical algorithm is a Newton-Krylov method combined with geometric multigrid preconditioner and smoothing based on domain decomposition. The system is modeled using a specific equation shuffling that aims at improving the row pivoting. Due to the complexity of the operators, the exact Jacobian matrix is evaluated using automatic differentiation tools. We describe benchmark settings which shall help to test and compare different numerical methods and code implementations for the FSI problem in hemodynamics. The configurations consist of realistic artery aneurysms. A case of endovascular stent implantation on a cerebral aneurysm is also presented. Hybrid meshes are employed in such configurations. We show numerical results for the described aneurysm geometries for steady-state boundary conditions. Parallel implementation is also addressed.

1 INTRODUCTION

Over the last decade numerous advances in the simulation of stented brain aneurysms were proposed, but the majority of them involved only computational fluid dynamics

(CFD). When pure CFD is used for vascular blood flow simulations, it is assumed that the vessel wall remains rigid. The rigid wall assumption does not properly reflect the elastic nature of arterial walls and the behavior of real blood vessels, since vessel walls are deformed by the action of blood flow forces and, in turn, this deformation alters the details of blood flow. For the modeling to be realistic, coupled fluid-structure interaction (FSI) modeling must be employed. In this work, we propose FSI simulations of stenting technology applied to 2D and 3D brain aneurysms geometries. We consider a monolithic coupling between the fluid and the solid, focusing on steady-state formulations. Blood has been considered as an incompressible Newtonian fluid and a hyperelastic solid has been used to represent vessel wall tissue. We describe the solid motion in a Lagrangian way, while the fluid is observed in Eulerian fashion. The deformation of the fluid domain is taken into account according to an Arbitrary Lagrangian Eulerian (ALE) approach, which is one of the most popular techniques in the FSI community ([3], [6], [11]). To solve the FSI system, we propose a monolithic Newton-Krylov solver preconditioned by a geometric multigrid algorithm. Newton linearization is performed as an outer iteration, and the the evaluation of the exact Jacobian matrix associated to the fluid-solid coupled state equations is performed with automatic differentiation tools provided by the Adept software package ([8]). Multigrid F-cycle and V-cycle schemes are considered with a Richardson smoother preconditioned by an additive Schwarz method (ASM). Other works in which multigrid and domain decomposition methods are employed for hemodynamics applications are [10], [9] and [12]. Our solver has been implemented in the open-source *C++ Femus library* (https://github.com/FeMTTU/femus) using the GMRES solver and the geometric multigrid preconditioner interface implemented in the PETSc toolkit [4]. For validation and evaluation of the accuracy and performance of the proposed methodology, we present numerical studies for both 2D and 3D cerebral aneurysm configurations. To simulate the effect of stents, we consider both the meshing of flow diverters and the porous medium (PM) approach ([2]). Advantages of the porous medium method include the reduction of the number of simulation mesh elements, with the resulting reduction of computational time. The paper is organized as it follows. In Section 2 we present the strong formulations of the steady-state incompressible FSI problem under investigation. In section 3 we describe our Monolithic Newton-Krylov solver. Numerical results of benchmark problems are presented in Sections 4 and 5. Finally, we draw our conclusions.

2 FORMULATION OF THE FSI PROBLEM

Let $\Omega = \Omega^f \cup \Omega^s \subset \mathbb{R}^n$ be the current configuration of fluid and solid at time $T = \infty$. Clearly, Ω^f and Ω^s are referred to fluid and solid, respectively. Let $\Gamma^i = \Omega^f \cap \Omega^s$ be the interface between solid and fluid in the current configuration, and let Γ^f and Γ^s be the parts of the boundary adjacent only to the fluid or only to the solid.
We use the *hat* notation to define $\widehat{\Omega}^f := \Omega_0^f$ and $\widehat{\Omega}^s := \Omega_0^s$. Normally, they are referred to as the undeformed or reference configuration. Consequently, we define $\widehat{\Omega} := \Omega_0$ and $\widehat{\Gamma}^i := \Gamma_0^i$. In the following we will use the notations $\widehat{\nabla}$ or ∇ to refer to the gradient

operators and the symbols $\widehat{\mathbf{n}}$ or $\mathbf{n}$ to denote the outward unit normal fields in the reference or in the current configuration, respectively.
The domain $\widehat{\Omega}^s$ is called *Lagrangian domain* and the field $q^s(\widehat{\mathbf{x}})$ defined on it is called *Lagrangian field*. Furthermore, the domain $\widehat{\Omega}^f$ is called *ALE domains* and the field $q^f(\widehat{\mathbf{x}})$ defined on it is called *ALE field*. We remark that $\widehat{\Omega}^s$, $\widehat{\Omega}^f$ were initially occupied only by the solid and fluid, respectively. As a consequence of the solid movement, the domain on which we observe the fluid motion changes, and we need to define a deformation for the fluid domain. The domain Ω^f is occupied only by fluid at time $T = \infty$. The moving domains Ω^f and Ω^s are called *Eulerian domains*, and fields $q(\mathbf{x})$ defined on Eulerian domains are called *Eulerian fields*. Notice that the Eulerian domains dipends on the current configuration at time $T = \infty$. In order to describe the motion of the fluid and solid domains, let us define an invertible and sufficiently smooth mapping $\mathcal{X}$, so that

$$\mathcal{X} : \widehat{\Omega} \to \Omega\,, \quad \mathcal{X}(\widehat{\mathbf{x}}) := \widehat{\mathbf{x}} + \mathbf{d}(\widehat{\mathbf{x}})\,. \tag{1}$$

The field $\mathbf{d}(\widehat{\mathbf{x}})$ is called *displacement field*. The displacement field $\mathbf{d}(\widehat{\mathbf{x}})$ is determined separately in the fluid and solid parts as a solution of two different subproblems. Its restrictions $\mathbf{d}^f(\widehat{\mathbf{x}})$ and $\mathbf{d}^s(\widehat{\mathbf{x}})$ are referred to as *fluid domain displacement* (or *ALE displacement*) and *solid displacement*, respectively. They are required to take on common values at the interface, namely

$$\mathbf{d}^s(\widehat{\mathbf{x}}) = \mathbf{d}^f(\widehat{\mathbf{x}})\,, \quad \widehat{\mathbf{x}} \in \widehat{\Gamma}^i\,. \tag{2}$$

For every $\widehat{\mathbf{x}} \in \widehat{\Omega}$, we also define

$$\mathbf{F}(\mathbf{d}(\widehat{\mathbf{x}})) = \widehat{\nabla}\mathcal{X}(\widehat{\mathbf{x}}) = I + \widehat{\nabla}\mathbf{d}(\widehat{\mathbf{x}})\,, \tag{3}$$

$$J(\mathbf{d}(\widehat{\mathbf{x}})) = \det \mathbf{F}(\mathbf{d}(\widehat{\mathbf{x}}))\,, \tag{4}$$

$$\mathbf{B}(\mathbf{d}(\widehat{\mathbf{x}})) = \mathbf{F}(\mathbf{d}(\widehat{\mathbf{x}}))\mathbf{F}^T(\mathbf{d}(\widehat{\mathbf{x}}))\,. \tag{5}$$

The symbols $\mathbf{F}$ and $\mathbf{B}$ denote the *deformation gradient tensor* and the *left Cauchy-Green deformation tensor*, respectively.

Steady-state solid subproblem. The steady-state solid subproblem consists in finding $(\mathbf{d}^s(\mathbf{x}), p^s(\mathbf{x}))$ such that

$$-\nabla \cdot \boldsymbol{\sigma}^s(\mathbf{d}^s, p^s) - \rho^s \mathbf{f}^s = \mathbf{0}\,, \quad \mathbf{x} \in \Omega^s\,, \tag{6}$$

$$J(\mathbf{d}^s) - 1 = 0\,, \quad \widehat{\mathbf{x}} \in \widehat{\Omega}^s\,, \tag{7}$$

$$\boldsymbol{\sigma}^s(\mathbf{d}^s, p^s) \cdot \mathbf{n}^s - \boldsymbol{\sigma}^f\left(\mathbf{u}^f, p^f\right) \cdot \mathbf{n}^f = 0\,, \quad \mathbf{x} \in \Gamma^i, \tag{8}$$

$$\mathcal{B}^s(\mathbf{d}^s, p^s) = \mathbf{0}\,, \quad \mathbf{x} \in \Gamma^s \tag{9}$$

The first two equations are known as the incompressible elasticity equations. Here, the symbols ρ^s and $\mathbf{f}^s$ denote mass density and body force density for the solid, respectively. In Eq.(9) $\mathcal{B}^s$ denotes an abstract boundary operator for the solid external boundary Γ^s, which may correspond to Dirichlet, Neumann or other types of boundary conditions.

In this solid subproblem the pressure in the solid p^s is an internal variable and it does not have a clear physical meaning. It can be regarded mathematically as the Lagrange multiplier associated to the solid incompressibility constraint. For the solid stress tensor $\boldsymbol{\sigma}^s$ we consider incompressible Mooney-Rivlin, whose Lagrangian description is given for every $(\widehat{\mathbf{x}}, t) \in \widehat{\Omega}^s$ by

$$\boldsymbol{\sigma}^s_{MR}(\mathbf{d}^s, p^s) = -p^s\mathbf{I} + \mathbf{2C_1B(d^s)} - \mathbf{2C_2}(\mathbf{B(d^s)})^{-\mathbf{1}}\,, \tag{10}$$

where the constants C_1 and C_2 depend on the mechanical properties of the material. We remark that the input to this solid subproblem is the stress at the interface coming from the fluid part while the output is the displacement of the solid, namely $\mathbf{d}^s$.

Steady-state fluid subproblem. The steady-state fluid subproblem consists in searching for $(u^f(\mathbf{x}), p^f(\mathbf{x}))$ such that

$$\rho^f\left(\mathbf{u}^f \cdot \nabla \mathbf{u}^f\right) - \nabla \cdot \boldsymbol{\sigma}^f(\mathbf{u}^f, p^f) - \rho^f \mathbf{f}^f = \mathbf{0} \quad \mathbf{x} \in \Omega^f\,, \tag{11}$$

$$\nabla \cdot \mathbf{u}^f = 0\,, \quad \mathbf{x} \in \Omega^f\,, \tag{12}$$

$$\mathcal{B}^f(\mathbf{u}^f(\mathbf{x}), p^f(\mathbf{x})) = \mathbf{0}\,, \quad \mathbf{x} \in \Gamma^f \tag{13}$$

$$\mathbf{u}^f(\mathbf{x}, 0) = 0\,, \quad \mathbf{x} \in \widehat{\Omega}^f\,. \tag{14}$$

The first two equations are referred to as the incompressible Navier-Stokes equations. Here, the symbols ρ^f and $\mathbf{f}^f$ denote mass density and body force density for the fluid. In Eq. (14) $\mathcal{B}^s$ is an abstract boundary operator for the fluid boundary, similarly as before. The fluid stress tensor $\boldsymbol{\sigma}^f$ for incompressible Newtonian fluid flows is given as a Eulerian field for every $(\mathbf{x}, t) \in \Omega^f_t$ by

$$\boldsymbol{\sigma}^f(\mathbf{u}^f, p^f) = -p^f\mathbf{I} + \mu(\nabla \mathbf{u}^f + (\nabla \mathbf{u}^f)^T)\,, \tag{15}$$

where μ is the fluid viscosity. The input to the fluid subproblem is the displacement of the fluid domain and the outputs are both fluid velocity and fluid pressure, which are used to compute the stress at the interface for the solid subproblem.

Steady-state subproblem for the fluid domain displacement. The steady-state subproblem for the fluid domain displacement consists in finding $\mathbf{d}^f(\mathbf{x})$ such that

$$\widehat{\nabla} \cdot \left(k(\widehat{\mathbf{x}})(\widehat{\nabla}\mathbf{d}^f + (\widehat{\nabla}\mathbf{d}^f)^T)\right) = \mathbf{0}\,, \quad \widehat{\mathbf{x}} \in \widehat{\Omega}^f\,, \tag{16}$$

$$\mathbf{d}^f = \mathbf{d}^s\,, \quad \widehat{\mathbf{x}} \in \widehat{\Gamma}^i\,, \tag{17}$$

$$\mathcal{B}^{fd}(\mathbf{d}^f(\widehat{\mathbf{x}})) = \mathbf{0}\,, \quad \widehat{\mathbf{x}} \in \widehat{\Gamma}^f\,. \tag{18}$$

This subproblem is also referred to as the *kinematic equation* or the *pseudo-solid mapping*, as it defines the arbitrary motion of the fluid domain as another elastic solid. In Eq. (18) we denote with $\mathcal{B}^{fd}$ a general boundary operator which can be chosen arbitrarily depending on the problem at hand. The function $k(\widehat{\mathbf{x}})$ may be chosen to be a piecewise-constant

function discontinuous across the element boundary so that smaller elements in the mesh can be made stiffer. We decided to consider

$$k(\widehat{\mathbf{x}}) = \frac{1}{\mathrm{V}_{el(\widehat{\mathbf{x}})}}, \tag{19}$$

where V_{el} is the volume of the mesh element that contains the $\widehat{\mathbf{x}}$ coordinate.
We remark that the input of this subproblem is the displacement of the fluid-solid interface from the solid part, while the output is the displacement of the fluid domain.

If we compare this steady-state formulation with the more general time-dependent one ([3]) we see that the steady-state equations are obtained by setting to zero all partial time derivatives in the three time-dependent subproblems. Notice that, in the steady-state case, we only use the ALE mapping to move from the undeformed to the final deformed configuration of the fluid domain, and we do not have to compute the ALE fluid domain velocity. Moreover, in the time-dependent formulation, there is another input to the fluid system, which is the solid velocity at the boundary, that is now equal to zero.

Intracranial stents as porous media. To model a porous medium stent, we follow the approch given in [2]. We assume a simple homogeneous porous medium which can be modeled by the addition of a momentum source term to the standard fluid flow equations. The pressure gradient can be expressed using the Darcy-Forchheimer equation, which can be averaged as

$$-\frac{\Delta p}{\Delta e} = \Big(\frac{\mu}{\alpha}u + \frac{1}{2}C_2\rho^f u^2\Big), \tag{20}$$

or

$$-\Delta p = bu + au^2\ , \tag{21}$$

to measure the pressure drop between the sides of the stent walls. Here, u is the average velocity, α is the permeability, C_2 is the inertial resistance factor, and Δe is the thickness of the porous medium domain. The coefficients a and b depend on the flow diverter placement in the aneurysm neck. If the aneurysm geometry requires the stent to be placed parallel to the flow, we observe low exchange of blood between the parent artery and the aneurysm cavity. This is because the flow inside the aneurysm dome is created by friction from the parent artery flow. When blood flow points directly into the aneurysm, then the flow diverter is placed perpendicularly to the flow. In this case an intense fluidic exchange between the parent artery and the aneurysm is observed. These two situations are completely different from a fluid mechanics point of view, and Eq. (21) needs to reflect this difference. We use the coefficients a and b provided in [2], which are

$$a = 1452 \ \text{ and } \ b = 4188 \quad \text{for stents placed parallel to flow direction,} \tag{22}$$

$$a = 367.08 \ \text{ and } \ b = 281.35 \ \text{ for stents placed perpendicularly to flow direction.} \tag{23}$$

From (20) and (21), the coefficients of the permeability α and the drag factor C_2 can consequently be obtained as

$$C_2 = \frac{2a}{\rho\Delta e} \quad \text{and} \quad \alpha = \frac{\mu}{b}\Delta e\ . \tag{24}$$

3 MONOLITHIC NEWTON-KRYLOV SOLVER

In a monolithic formulation, we define three unknowns (displacement, velocity and pressure) in a piecewise fashion at each point of the Eulerian domain Ω as

$$\mathbf{d} = \begin{cases} \mathbf{d}^s \text{ in } \Omega^s \\ \mathbf{d}^i \text{ in } \Gamma^i \\ \mathbf{d}^f \text{ in } \Omega^f \end{cases}, \quad \mathbf{u} = \begin{cases} \mathbf{u}^s \text{ in } \Omega^s \\ \mathbf{u}^i \text{ in } \Gamma^i \\ \mathbf{u}^f \text{ in } \Omega^f \end{cases}, \quad \mathbf{p} = \begin{cases} p^s \text{ in } \Omega^s \\ p^f \text{ in } \Omega^f \end{cases},$$

enforcing continuity across the fluid-solid interface only for the displacement and the velocity. The weak formulation of the resulting system is discretized using appropriate finite element spaces and the corresponding Jacobian matrix is obtained by an exact Newton linearization implemented by automatic differentiation ([8]). The solution of the linear systems is performed using a GMRES solver preconditioned by a geometric multigrid algorithm. The smoother is of modified Richardson type, in turn preconditioned by a restricted additive Schwarz method. The coarse grid correction problem is dealt with by a direct solver of the monolithic system.

Structure of the Jacobian. Let $\mathbf{J}^{(k)}$ denote the exact Jacobian at a nonlinear step k. Ordering the variables as

$$\left[\mathbf{d}^s\, \mathbf{d}^i\, \mathbf{d}^f \,\middle|\, \mathbf{u}^s\, \mathbf{u}^i\, \mathbf{u}^f \,\middle|\, p^s\, p^f\, \right]^\intercal \tag{25}$$

we consider the Jacobian to have the following block structure

$$\mathbf{J}^{(k)} = \left[\begin{array}{ccc||ccc||cc} S^{\mathbf{d^s}}_{\mathbf{d^s}} & S^{\mathbf{d^s}}_{\mathbf{d^i}} & 0 & 0 & 0 & 0 & S^{\mathbf{d^s}}_{p^s} & 0 \\ I^{\mathbf{d^i}}_{\mathbf{d^s}} & I^{\mathbf{d^i}}_{\mathbf{d^i}} & I^{\mathbf{d^i}}_{\mathbf{d^f}} & I^{\mathbf{d^i}}_{\mathbf{u^s}} & I^{\mathbf{d^i}}_{\mathbf{u^i}} & I^{\mathbf{d^i}}_{\mathbf{u^f}} & I^{\mathbf{d^i}}_{p^s} & I^{\mathbf{d^i}}_{p^f} \\ 0 & A^{\mathbf{d^f}}_{\mathbf{d^i}} & A^{\mathbf{d^f}}_{\mathbf{d^f}} & 0 & 0 & 0 & 0 & 0 \\ \hline\hline 0 & 0 & 0 & K^{\mathbf{u^s}}_{\mathbf{u^s}} & 0 & 0 & 0 & 0 \\ 0 & 0 & 0 & 0 & K^{\mathbf{u^i}}_{\mathbf{u^i}} & 0 & 0 & 0 \\ 0 & F^{\mathbf{u^f}}_{\mathbf{d^i}} & F^{\mathbf{u^f}}_{\mathbf{d^f}} & 0 & F^{\mathbf{u^f}}_{\mathbf{u^i}} & F^{\mathbf{u^f}}_{\mathbf{u^f}} & 0 & F^{\mathbf{u^f}}_{p^f} \\ \hline\hline V^{p^s}_{\mathbf{d^s}} & V^{p^s}_{\mathbf{d^i}} & 0 & 0 & 0 & 0 & 0 & 0 \\ 0 & W^{p^f}_{\mathbf{d^i}} & W^{p^f}_{\mathbf{d^f}} & 0 & W^{p^f}_{\mathbf{u^i}} & W^{p^f}_{\mathbf{u^f}} & 0 & 0 \end{array}\right] \begin{array}{l} \text{Momentum Solid} \\ \text{Momentum Interface} \\ \text{Kinematic fluid} \\ \\ \text{Kinematic Solid} \\ \text{Kinematic Interface} \\ \text{Momentum Fluid} \\ \\ \text{Continuity Solid} \\ \text{Continuity Fluid} \end{array} \tag{26}$$

Equations and unknowns are ordered following a field-ordering approach as in [7]. It is important to notice that different orderings, though equivalent mathematically, can have a significant effect on the convergence properties and computational time of the solver, especially in the parallel setting.

Geometric Multigrid preconditioner. As a preconditioner to the outer monolithic GMRES iteration, we consider the action of geometric multigrid. Let $\mathbf{\Phi}(\Omega_{h_l})$ and $\mathbf{\Psi}(\Omega_{h_l})$ be the finite element spaces associated to each level of the triangulation $\{\Omega_{h_l}\}_{l=1}^{L}$ with

relative mesh sizes h_l. The *prolongation* I_{l-1}^{l} and *restriction* I_{l}^{l-1} operators

$$I_{l-1}^{l} : \mathbf{\Phi}(\mathbf{\Omega_{h_{l-1}}}) \times \mathbf{\Phi}(\mathbf{\Omega_{h_{l-1}}}) \times \mathbf{\Psi}(\mathbf{\Omega_{h_{l-1}}}) \to \mathbf{\Phi}(\mathbf{\Omega_{h_l}}) \times \mathbf{\Phi}(\mathbf{\Omega_{h_l}}) \times \mathbf{\Psi}(\mathbf{\Omega_{h_l}}) \,, \tag{27}$$

$$I_{l}^{l-1} : \mathbf{\Phi}(\mathbf{\Omega_{h_l}}) \times \mathbf{\Phi}(\mathbf{\Omega_{h_l}}) \times \mathbf{\Psi}(\mathbf{\Omega_{h_l}}) \to \mathbf{\Phi}(\mathbf{\Omega_{h_{l-1}}}) \times \mathbf{\Phi}(\mathbf{\Omega_{h_{l-1}}}) \times \mathbf{\Psi}(\mathbf{\Omega_{h_{l-1}}}) \tag{28}$$

are defined as the natural injection from the coarse to the fine space, and the adjoint of I_{l-1}^{l} with respect to the L^2 inner product, respectively. Clearly, the matrix representations of these operators, $\mathbf{I}_{l-1}^{l}$ and $\mathbf{I}_{l}^{l-1}$, depend on the block row ordering of the Jacobian (Eq. (26)), so that a different Jacobian structure affects the structure of $\mathbf{I}_{l-1}^{l}$ and $\mathbf{I}_{l}^{l-1}$. The block structures of the prolongation and restriction operators are

$$\mathbf{I}_{l}^{l-1} = \left[\begin{array}{ccc||ccc||cc} R_{\mathbf{d^s}}^{\mathbf{d^s}} & 0 & 0 & 0 & 0 & 0 & 0 & 0 \\ R_{\mathbf{d^s}}^{\mathbf{d^i}} & R_{\mathbf{d^i}}^{\mathbf{d^i}} & 0 & 0 & 0 & R_{\mathbf{u^f}}^{\mathbf{d^i}} & 0 & 0 \\ 0 & 0 & R_{\mathbf{d^f}}^{\mathbf{d^f}} & 0 & 0 & 0 & 0 & 0 \\ \hline\hline 0 & 0 & 0 & R_{\mathbf{u^s}}^{\mathbf{u^s}} & 0 & 0 & 0 & 0 \\ 0 & 0 & 0 & R_{\mathbf{u^s}}^{\mathbf{u^i}} & R_{\mathbf{u^i}}^{\mathbf{u^i}} & 0 & 0 & 0 \\ 0 & 0 & 0 & 0 & 0 & R_{\mathbf{u^f}}^{\mathbf{u^f}} & 0 & 0 \\ \hline\hline 0 & 0 & 0 & 0 & 0 & 0 & R_{p^s}^{p^s} & 0 \\ 0 & 0 & 0 & 0 & 0 & 0 & 0 & R_{p^f}^{p^f} \end{array}\right], \quad \mathbf{I}_{l-1}^{l} = \left[\begin{array}{ccc||ccc||cc} P_{\mathbf{d^s}}^{\mathbf{d^s}} & P_{\mathbf{d^s}}^{\mathbf{d^i}} & 0 & 0 & 0 & 0 & 0 & 0 \\ 0 & P_{\mathbf{d^i}}^{\mathbf{d^i}} & 0 & 0 & 0 & 0 & 0 & 0 \\ 0 & P_{\mathbf{d^f}}^{\mathbf{d^i}} & P_{\mathbf{d^f}}^{\mathbf{d^f}} & 0 & 0 & 0 & 0 & 0 \\ \hline\hline 0 & 0 & 0 & P_{\mathbf{u^s}}^{\mathbf{u^s}} & P_{\mathbf{u^s}}^{\mathbf{u^i}} & 0 & 0 & 0 \\ 0 & 0 & 0 & 0 & p_{\mathbf{u^i}}^{\mathbf{u^i}} & 0 & 0 & 0 \\ 0 & 0 & 0 & 0 & 0 & P_{\mathbf{u^f}}^{\mathbf{u^f}} & 0 & 0 \\ \hline\hline 0 & 0 & 0 & 0 & 0 & 0 & P_{p^s}^{p^s} & 0 \\ 0 & 0 & 0 & 0 & 0 & 0 & 0 & P_{p^f}^{p^f} \end{array}\right].$$

Richardson-Schwarz smoother. In the smoothing process, we first partition the whole domain into the fluid and solid subregions, and then we further divide each subregion into smaller non-overlapping blocks $\Omega_k, k = 1, ..., N$. On each subdomain Ω_k we construct a subdomain preconditioner $\mathbf{B_k}$, which is a restriction of the Jacobian matrix $\mathbf{J}$, that is, it contains entries from $\mathbf{J}$ corresponding to the degrees of freedom (DOFs) contained in the corresponding subdomain Ω_k. The exchange of information between blocks is guaranteed by the fact that the support of the test function associated to the displacement and velocity DOFs extends to the neighboring elements. The restricted version of the additive Schwarz (ASM) preconditioner used in the Richardson scheme for the FSI Jacobian system is

$$\mathbf{B}^{-1} = \sum_{k=1}^{N} (\mathbf{R}_k^0)^T \mathbf{B}_k^{-1} (\mathbf{R}_k^\delta) \,. \tag{29}$$

With $\mathbf{R_k}$ we indicate a restriction matrix which maps the global vector of degrees of freedom to those belonging to the subdomain Ω_k. Furthermore, $\mathbf{R_k^0}$ is a restriction matrix that does not include the overlap while $\mathbf{R_k^\delta}$ does.

4 FSI BENCHMARKING: 2D SIMULATIONS

The following 2D simulations of a cerebral aneurysm are based on a 2D hemodynamic model problem from [10]. We start by considering a mesh without stents, and then move to three cases where such devices are included. Figure 1 shows the four configurations.

Stents are flexible, self-expanding porous tubular meshes made of stainless steel or other alloys and are characterized by very thin wires ($30 - 100\mu m$). As a consequence, in 2D flow diverters can be simplified as cutplanes from 3D configurations, so as circular shapes. This is the approach used in the second and third configuration. The difference beetween these two cases is in the number of struts that compose the stent, to be precise five and eleven struts, respectively. In both configurations, the wires have a diameter of approximately $60\mu m$. We conclude our simulations with a case where a stent is modeled as a porous medium. The porous medium strip placed on the neck of the aneurysm has a width of approximately $60\mu m$ ($\Delta e = 60\mu m$). Since the stent is placed parallel to the flow, we know from section 2.4 that the coefficients used to represent the pressure drop are $a = 1452$ and $b = 4188$. In all cases, hybrid meshes are employed. Quads are mainly used to mesh the channel and the arterial wall of the geometry, while triangles are employed in the aneurysm bulge.

Mechanical properties and boundary conditions. Blood is known to be non-Newtonian in general, but, for cerebral aneurysms, treatment of blood as Newtonian does not alter the computational results compared to treating it as non-Newtonian, as Cebral et al. showed in [5]. In this work, we assume blood to be Newtonian. The density and viscosity of the blood were set to 1035 kg/m^3 and $3.5 \times 10^3 Pa \cdot s$, respectively. The following material parameters were used in the simulation: the density of the solid was 1120 kg/m^3, Young's modulus and Poisson's ratio were $1.0MPa$ and 0.5, respectively. In the the porous medium configuration, we considered its width (thickness in 3D) to be $60\mu m$. The boundary conditions we consider are as in [10]. Blood flows from the right to the left part of the channel, and the velocity profile is defined as parabolic inflow

$$v^f(0, y) = 0.05\,(y - 6)(y - 8). \tag{30}$$

Pressure conditions representing the resistance due to the peripheral arterial network are not taken into account in this 2D model, therefore $p = 0$ has been imposed as outflow condition at the lower left part of the artery. The no-slip condition is prescribed for the fluid on the other boundary parts. The boundary displacements at the inlet and outlet of the artery are set to zero.

Numerical results. In all the four simulations we performed, we considered the same physical parameters and boundary conditions. Table 1 shows the changes of pressure, velocity and volume in the aneurysm dome for all four cases. The five struts configuration is the one that allows a greater dicrease in both volume and pressure. We see that doubling the number of struts, the relative difference in volume increases by 28.29% compared to the previous case, while the average pressure increases by 20.75%. This is suggesting that for a given aneurysm geometry, stents with different designs may give different results. Figure 2 shows the pressure distribution for these two configurations. In both cases, the highest pressure point is located on the aneurysm neck, but for the 5 struts geometry this point is at the left of the neck, while for the 11 struts configuration it is at the far right. Pressure values at these points are different as well. We also observe that the behavior

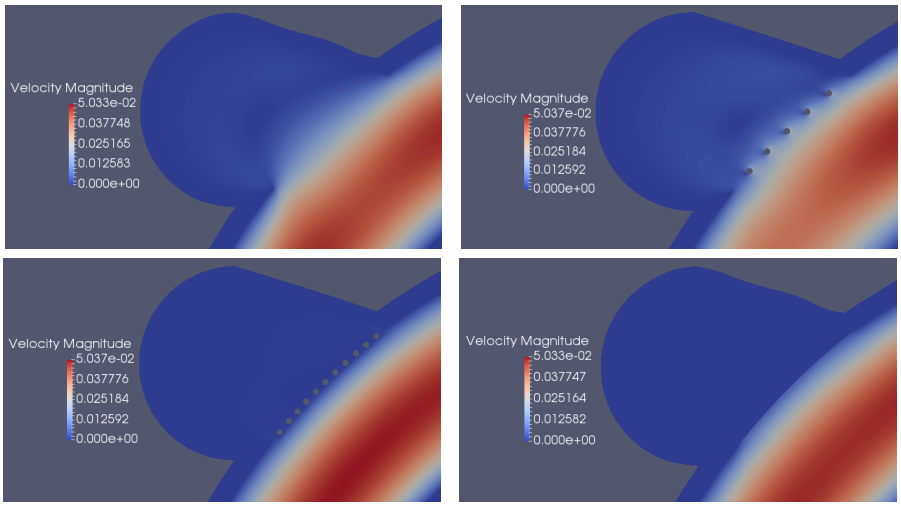

Figure 1: Magnitude Velocity for the four 2D Configurations: no stents (top left), stent with five struts (top right), stent with eleven struts (bottom left), stent modeled as a porous medium (bottom right).

Table 1: volume, pressure and velocity in 2D configurations

	average pressure	average velocity	relative difference in volume
no stents	1.0794	1.4264	0.0166
5 struts	0.7632	1.2029	0.0109
11 struts	0.9630	0.0927	0.0152
porous	0.9955	0.0135	0.0150

of the eleven struts configuration is very similar to the porous medium case in terms of volume and pressure. Average velocities show that these two configurations are the ones that allow a greater decrease of blood velocity inside the aneurysm dome. The similarity beetween the porous medium case and the 11 struts configuration shows the validity of the porous medium approach. Figure 1 shows the velocity magnitude at the aneurysm neck and dome for all four configurations. As we pointed out, the porous medium case resembles the real stent configuration with 11 wires.

5 FSI BENCHMARKING: 3D SIMULATIONS

The cerebral aneurysm considered in this section is a 3D extension of the 2D geometry analyzed above. To make the shape more realistic, changes have been made to the aneurysm dome, based on a real aneurysm view proposed in [10]. We assumed the aneurismal wall to be uniform and equal to $0.25mm$. Two configurations have been considered, one without stents and a second one where such devices are included and modeled as a

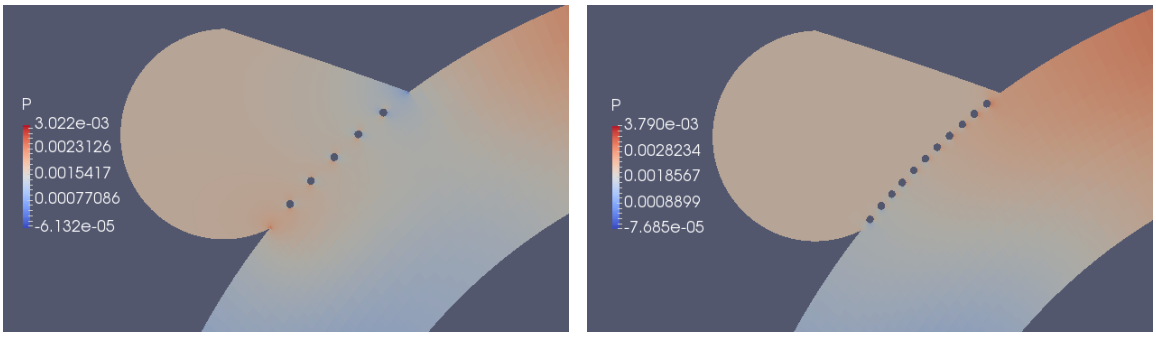

Figure 2: 2D Configurations: pressure distribution for the five struts stent configuration (right), pressure distribution for the eleven struts stents configuration (left).

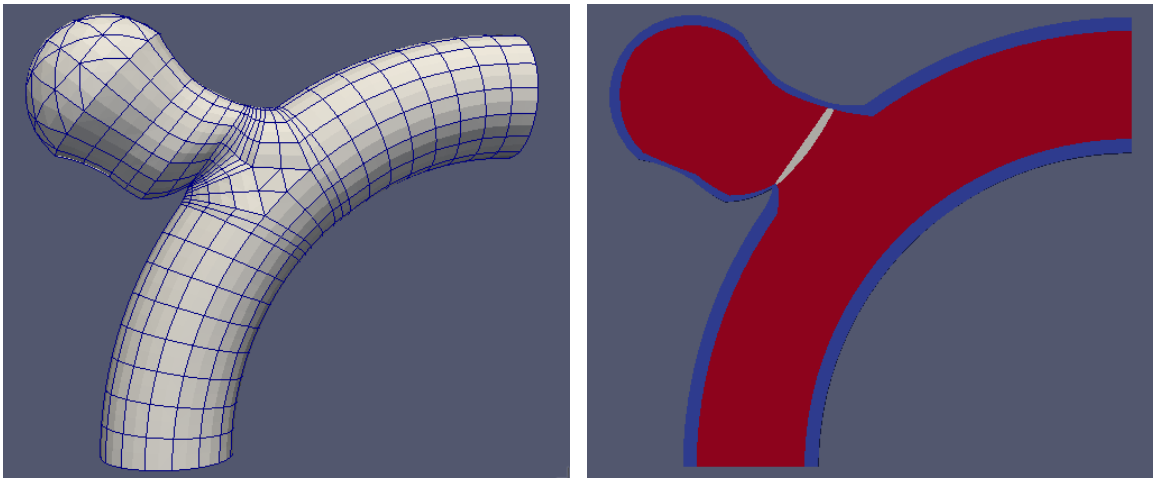

Figure 3: 3D Configurations: geometry with mesh (left), section of the 3D geometry to show the porous medium disk that simulates the intracranial stent.

porous medium disk (Figure 3). Such disk placed on the neck of the aneurysm has a thickness of approximately $112\mu m$. In both our geometries (with and without stents), hybrid meshes are employed. Wedges are needed to mesh the artery lumen, and hexes are used for the arterial wall. Tets are mainly employed in the aneurysm dome.

Mechanical properties and boundary conditions. Except for the Young Modulus value, the physical parameters are the same used in the 2D simulations, both for blood and the elastic artery wall. To clearly see the artery and the aneurysm pulse we considered $0.012MPa$ as our Young modulus value. At the inlet the velocity profile is defined as parabolic inflow and as outflow condition $p = 0$ has been imposed at the lower left part of the artery. The boundary displacements at the inlet and outlet are set to zero.

Numerical results. In both simulations we performed, we considered the same physical parameters and boundary conditions. Table 2 shows the changes of pressure, velocity

and volume in the aneurysm dome for all four cases. The velocity magnitudes at the aneurysm neck and dome are shown in Figure 4. As we observed for the 2D setting, the flow rate changes after the porous medium placement causing a reduction of the velocity magnitude on the aneurysm neck and dome. Therefore the porous medium approach performs well also in a FSI environment.

Table 2: volume, pressure and velocity in 3D configurations

	average pressure	average velocity	relative difference in volume
no stents	322.6082	24.3485	0.0065
porous	323.6605	0.4756	0.0066

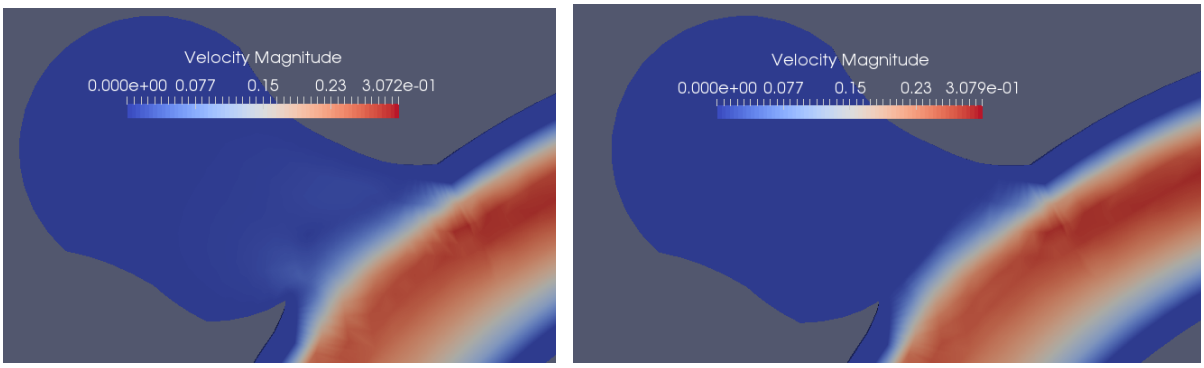

Figure 4: Magnitude Velocity for the 3D Configurations: no stents (left), porous medium (right)

6 CONCLUSION

In this paper we focused on the numerical simulation of FSI problems regarding stented intracranial aneurysms. We presented a monolithic ALE formulation assuming the fluid flow and the hyperelastic material to incompressible. We described the Newton-Krylov solver we employed where we considered the use of geometric multigrid preconditioners. From our simulations, we verified the stability and numerical efficiency of the FSI algorithm and observed that the modelization of a flow diverter as a porous medium is successful in a FSI enviroment. Morover, in the 2D simulations, the different results obtained with the 5 and 11 struts configurations highlight the prominent design dependence on flow diverters performances. Studies about stents optimization techniques can be found in [1] and [13]. In our future work, we will further investigate how to choose the porosity coefficients for any general stent.

REFERENCES

[1] Hitomi Anzai, Makoto Ohta, Jean-Luc Falcone, and Bastien Chopard. Optimization of flow diverters for cerebral aneurysms. *Journal of Computational Science*, 3(1):1–7, 2012.

[2] L Augsburger, P Reymond, DA Rufenacht, and N Stergiopulos. Intracranial stents being modeled as a porous medium: flow simulation in stented cerebral aneurysms. *Annals of biomedical engineering*, 39(2):850–863, 2011.

[3] Eugenio Aulisa, Simone Bnà, and Giorgio Bornia. A monolithic ALE Newton-Krylov solver with Multigrid-Richardson-Schwarz preconditioning for incompressible Fluid Structure Interaction. *Submitted to Siam Journal on Scientific Computing*, 2017.

[4] Satish Balay, J Brown, Kris Buschelman, Victor Eijkhout, W Gropp, D Kaushik, M Knepley, L Curfman McInnes, B Smith, and Hong Zhang. PETSc users manual revision 3.3. *Computer Science Division, Argonne National Laboratory, Argonne, IL*, 2012.

[5] Juan R Cebral, Marcelo Adrián Castro, Sunil Appanaboyina, Christopher M Putman, Daniel Millan, and Alejandro F Frangi. Efficient pipeline for image-based patient-specific analysis of cerebral aneurysm hemodynamics: technique and sensitivity. *IEEE transactions on medical imaging*, 24(4):457–467, 2005.

[6] Jean Donea, S Giuliani, and Jean-Pierre Halleux. An arbitrary Lagrangian-Eulerian finite element method for transient dynamic fluid-structure interactions. *Computer methods in applied mechanics and engineering*, 33(1-3):689–723, 1982.

[7] Miguel Ángel Fernández and Marwan Moubachir. A Newton method using exact Jacobians for solving fluid–structure coupling. *Computers & Structures*, 83(2):127–142, 2005.

[8] Robin J Hogan. ADEPT fast automatic differentiation library for C++: User guide.

[9] Mudassar Razzaq, Hogenrich Damanik, Jaroslav Hron, Abderrahim Ouazzi, and Stefan Turek. FEM multigrid techniques for fluid–structure interaction with application to hemodynamics. *Applied Numerical Mathematics*, 62(9):1156–1170, 2012.

[10] Stefan Turek, J Hron, Martin Madlik, Mudassar Razzaq, Hilmar Wobker, and Jens F Acker. Numerical simulation and benchmarking of a monolithic multigrid solver for fluid-structure interaction problems with application to hemodynamics. In *Fluid Structure Interaction II*, pages 193–220. Springer, 2011.

[11] Thomas Wick. Fluid-structure interactions using different mesh motion techniques. *Computers & Structures*, 89(13):1456–1467, 2011.

[12] Hilmar Wobker and Stefan Turek. Numerical studies of Vanka-type smoothers in computational solid mechanics. *Advances in Applied Mathematics and Mechanics*, 1(1):29–55, 2009.

[13] Y Zhang, W Chong, and Y Qian. Investigation of intracranial aneurysm hemodynamics following flow diverter stent treatment. *Medical engineering & physics*, 35(5):608–615, 2013.

VII International Conference on Computational Methods for Coupled Problems in Science and Engineering
COUPLED PROBLEMS 2017
M. Papadrakakis, E. Oñate and B. Schrefler (Eds)

NUMERICAL AND EXPERIMENTAL INVESTIGATIONS OF THE OSCILLATORY MOTION OF THIN PLATES IN A STILL VISCOUS FLUID

A. NURIEV* AND O. ZAITSEVA†

* Scientific Research Institute of Mechanics
Lobachevsky State University of Nizhni Novgorod
23 Gagarina pr., 603950, Nizhnii Novgorod, Russia
e-mail: nuriev_an@mail.ru

† Higher Institute of Information Technology and Information Systems
Kazan (Volga Region) Federal University
18 Kremlevskaya st., 420008 Kazan, Russia
e-mail: olga_fdpi@mail.ru

Key words: Flat plate, Damped flexural vibrations, Aerodynamic coefficients, Experimental measurements, Numerical simulation

Abstract. The paper is devoted to study of the aerodynamic forces acting on flat plates performing free flexural vibrations in a viscous fluid. The study consists of two parts. In the first part the experimental investigation of the aerodynamic loads based on analysis of damped flexural vibrations of cantilever test samples is conducted. In the second part the aerodynamics of the oscillating plates is investigated using direct numerical simulation.

1 INTRODUCTION

The past few decades have witnessed a rising interest in the study of mechanical vibrations of thin plates in viscous static fluids. The motivations for these studies stem from different practical applications covering diverse fields of knowledge such as atomic microscopy [1], sensors and actuators based on micromechanical oscillators [2], cooling devices [3], marine and offshore equipments [4, 5]. Our interest in this research area is connected with the development of the approach [6, 7] for determination of the damping properties of materials based on the study of the damped flexural vibration of cantilever flat beams.

When studying vibrations in air, it is necessary to accurately determine aerodynamic loads. In the general, the problem of evaluation of aerodynamic forces acting on a cantilever beam is extremely complicated, mainly because of the complexity of three-dimensional gas flows caused by vibrations of the beam. But when the length of the beam considerably exceeds its width and thickness at low structural vibration modes, the length of the vibrational wave is much greater than deviations of the beam, as a result it can be regarded as locally planar. In this case it is possible to use a simplified quasi-two dimensional model of interaction between the beam and a gas, according to which the aerodynamic forces acting on each cross section of the beam are caused by the planar flow around it. These assumptions form a theoretical core that is used for the study of aerodynamics around oscillating plates in the present research.

The study consists of two parts. In the first part the experimental investigation of the aerodynamic loads based on analysis of damped flexural vibrations of cantilever test samples is conducted. In the second part the aerodynamics of the oscillating plates is investigated using direct numerical simulation.

2 THE PROBLEM STATEMENT

Let us consider an elastic plate of length L, width b, and thickness h ($h << b << L$) (Fig. 1). One of its ends is rigidly fixed and the second is free. As soon as the plate is disturbed from the equilibrium, it starts to vibrate harmonically in the surrounding air. The frequency of these vibrations ω weakly varies in the vicinity of the basic natural frequency ω_0 of flexural vibrations of the plate, while the amplitude A weakly decays with time t because of air resistance and internal damping. The problem consists in determining the aerodinamic influence on this process. We will characterize the laws of slow variations of the amplitude and frequency by using the logarithmic decrement of vibrations (LD) $\delta(A)$ and the relative variation of frequency (RVF) $\Omega(A)$ as functions of the current amplitude of flexural vibrations of the plate:

$$\delta = -\frac{2\pi}{A\omega_0}\frac{dA}{dt}, \Omega = \frac{\omega_0 - \omega}{\omega_0}.$$

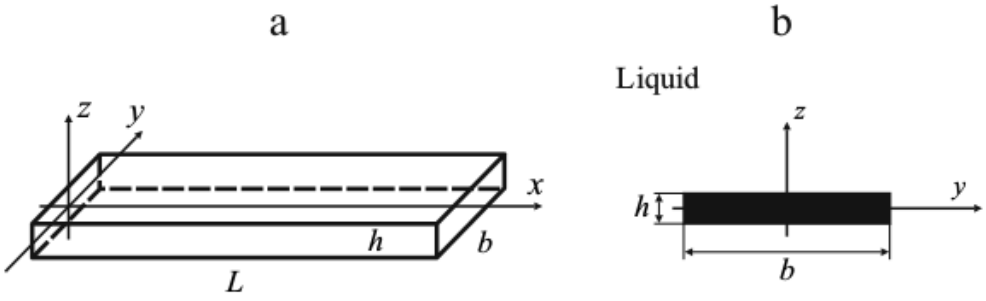

Figure 1: Schemes for the full beam vibration problem (a) and for the associated 2D fluid-structure interaction problem (b).

The equation describing vibrations of a plate according to a cylindrical flexural mode has the form

$$\frac{Ebh^3}{12}w^{IV} + \rho bh\ddot{w} = H + P. \quad (1)$$

Hereinafter, the Roman numerals designate differentiation with respect to spatial coordinate x and dots designate differentiation with respect to time t; w is the displacement of middle line of the plate along the z axis; H and P are the forces of internal friction and aerodynamic resistance; ρ and E are the effective density and Young's modulus of plate material. The boundary conditions correspond to a rigid fixation at $x = 0$ and to a free end at $x = L$.

The drag forces are smaller than the elastic one. Therefore, to a first approximation, we may assume that $H = P = 0$ .In this case, as is known, the basic vibration mode takes the form

$$w = A\cos(\omega_0 t)W(x/L) \quad (2)$$

The constants A and ω_0 represent the amplitude and natural frequency of the basic mode, and the profile W of vibrations ($W(1) = 1$) is described by the formula

$$W(x) = \frac{1}{2}(\cosh kx - \cos kx) - \frac{1}{2}\frac{\cosh kx + \cos kx}{\sinh kx + \sin kx}(\sinh kx - \sin kx).$$

The value of $k = 1.8751$ is the smallest positive root of the characteristic equation $\cos k \cosh k = -1$, and the frequency of natural vibrations is

$$\omega_0 = k^2 \frac{h}{L^2}\sqrt{\frac{E}{12\rho}}.$$

Owing to the presence of small forces (~ ε) in the right-hand side of equation (1), the vibration amplitude A and frequency ω_0 in equation (2) do not remain constant, but slowly vary in time. An analysis of such a variation can be carried out by introducing, along with the fast time t, a slow time $\tau = \varepsilon t$ and performing a two-scale asymptotic expansion. Omitting details of this procedure, we present the final result:

$$\delta = 2\pi F_0^{-1}\frac{\{\sin\omega_0 t\langle(P+H)W\rangle\}}{\langle W^2\rangle}, \Omega = F_0^{-1}\frac{\{\cos\omega_0 t\langle(P+H)W\rangle\}}{\langle W^2\rangle}, F_0 = \rho bhA\omega_0^2. \qquad (3)$$

Hereinafter, the angular brackets designate averaging over the spatial coordinate x, while the braces mean time averaging.

It is obvious that, in view of linearity of the right-hand side parts of equations (3), the different components of forces can be calculated independently from each other. Thus we get the integral relationship between the aerodynamic forces and parameters of beam oscillations (LD and RVF).

3 AN EXPERIMENTAL INVESTIGATION OF AERODYNAMIC FORCES

3.1 Experimental setup

To get a damping parameters of the flexural oscillation of cantilever beam in the surrounded air the experiments for measurement the damped oscillation caused by the initial deflection of the free end of the console from equilibrium was carry out. As experimental samples duralumin beams with the next geometrical parameters are used: thickness h = 1, 2 mm, width b = 20, 30 mm and length L, which varies in the range from 200 to 400 mm with increments of 20 mm. The registration of vibrations is performed by the lightweight MEMS gyroscope mounted on the end of the beams.

As a result of the procedure, approximate relations for the vibration amplitude $A(t)$, frequency $\omega(t) \approx \omega_0$, LD $\delta(t)$ and RVF $\Omega(A)$ as functions of time are determined. From these approximation for each experiment in the range of the realized oscillation amplitudes the dependences $\delta(A)$, $\Omega(A)$ were built.

3.2 Extraction of aerodynamic damping parameters and calculation of force coefficients

In the general case, the parameters of the vibrations of the beam depend on the aerodynamic and mechanical components of damping. To separate of these components from each other in the experiments we use test samples of aluminum alloy. The internal damping of the beams of this material [8, 9] is almost independent of the oscillation amplitude up to very

high strain. The mounting method of samples [9] provides independence of structural damping from oscillation amplitude. Thus, the change of the LD from oscillation amplitude is a consequence of aerodynamic effects.

The influence of the mechanical component of the damping on the RVF of the beam for the parameters of the present experiments is not known. In the subsequent discussion we assume that this influence is extremely small and RVF is completely determined by aerodynamic effects.

Ignoring the three-dimensional effects, consider the impact of aerodynamic flow as a result of quasi-two-dimensional flow around the beam. Also consider that the aerodynamic forces $P(x)$ at each cross section x of the beam can be described by approximation

$$P = -\frac{\pi}{4}\rho_a b^2 C_M \frac{du_0}{dt} - \frac{1}{2}\rho_a b C_D |u_0| u_0 \quad . (4)$$

Here $u_0(x, t) = \partial w/\partial t$ is the velocity of displacement of the current beam cross-section, ρ_a is the air density, C_M and C_D are local coefficients of added masses and drag respectively. Substituting (4) into (3), we get the next equations

$$\delta_P = \frac{\rho_a}{\rho}\frac{4}{3}\frac{A}{h}\frac{\langle C_D W^3\rangle}{\langle W^2\rangle}, \Omega_P = \frac{\pi}{8}\frac{\rho_a}{\rho}\frac{b}{h}\frac{\langle C_M W^2\rangle}{\langle W^2\rangle} \quad (5)$$

which connects the LD and RVF with the drag and added mass coefficients. It should be noted that the added mass force according to (5) affects only on the frequency of beam oscillations, while the drag force affects only on the amplitude of beam oscillations.

For transition from the oscillation parameters to the aerodynamic characteristics the nonlinear integral equations (5) must be solved. For this purpose we used the analytical method proposed in [10]. Thus, each experiment allows finding the dependence of the drag coefficient C_M and the coefficient C_D of added mass from the oscillation amplitude of the beam for the fixed frequency value.

4 NUMERICAL CALCULATION OF AERODYNAMIC FORCES

As an alternative method for determining aerodynamic characteristics numerical simulation is considered. The aerodynamic coefficients C_M and C_D are found during solving the planar fluid flow problem caused by vibrations of an infinitely extended thin rigid plate (Fig. 1b). Such a plate plays the role of a mobile solid boundary for the air surrounding it. In each given cross section x, the velocity of displacement of the boundary is given as

$$u_0(x,t) = -U_0(x)\sin(\omega_0 t),\ U_0(x) = \omega_0 A W(x/L).$$

The fluid flow around the plate generated by its motion is governed by the Navier-Stokes system of equations. Normalizing the spatial coordinates, time and velocity by b, bU_0^{-1}, U_0 respectively, we get the dimensionless formulation of the governing system in the following form:

$$\frac{\partial U}{\partial t} + U\cdot\nabla U = -\nabla p + \frac{1}{\mathrm{Re}}\Delta U,\ \nabla\cdot U = 0 \quad (6)$$

Where $U = (u,v)$ is the dimensionless velocity, p is the dimensionless pressure, $\mathrm{Re} = U_0 R/\nu$ is the Reynolds number.

For solving this problem numerically it is convenient to rewrite governing equations in a

moving (non-inertial) coordinate system associated with the plate. To retain the governing system in the form (6), we determine a new pressure as

$$p = \widetilde{p} + za.$$

Here the first term is the pressure in the fixed coordinate system, the second term is the inertial contribution, a is the acceleration of the moving coordinate system.

On the surface of the plate in the new coordinate system the no-slip conditions are fulfilled:

$$u\,|_{plate} = v\,|_{plate} = 0. \tag{7}$$

At infinity, the variation of velocity is determined by the following harmonic law:

$$u\,|_{\infty} = \sin(\pi t / \mathrm{KC}),\ v\,|_{\infty} = 0. \tag{8}$$

Here KC is the second dimensionless control parameter of the problem - the Keulegan-Carpenter number. A complex of two parameters (Re, KC) completely determines the flow of fluid near the oscillating plate. Sometimes it is also convenient to use their ratio

$$\beta = \frac{\mathrm{Re}}{\mathrm{KC}}$$

which plays the role of the oscillatory Reynolds number and has approximately the same value along the x direction of the flexural oscillating plate.

The forces acting on the plate by a viscous fluid in the dimensionless formulation are calculated as

$$C_P = \int_S pnds - \int_S \overline{\sigma} \cdot nds,$$

where $\overline{\sigma}$ is the viscous stress tensor, S is the surface of the plate and n is the surface normal vector. The force vector C_P can be expanded into a vertical component C_P^y (lift force) and a horizontal component C_P^z, which consists of the drag force and inertia force:

$$C_P^z = \pi(C_M + C_{FK})\frac{du_\infty}{dt} + C_D |u_\infty| u_\infty$$

The inertial force acting on the plate due to the fluid acceleration can be split into two parts: the inertia force of added mass, arising due to the local acceleration near the cylinder, and the Froude-Krylov force (C_{FK}), which is related to the pressure gradient created in the fluid by the flow oscillations (associated with the transition to the moving coordinate system). The C_{FK} force coefficient for the considered case can be calculated as

$$C_{FK} = \frac{1}{\pi}\int_S znds.$$

To determine the quantities C_M and C_D as functions of the parameters β, KC, it is necessary to carry out a numerical solution of problem (6)-(8). The corresponding numerical calculations were performed in the OpenFOAM software package of computational hydrodynamics, based on model presented in [12]. It should also be noted that in the numerical simulations we accurately reproduce the shape of the plates used in the experiments, especially the ratio of width b to thickness h and the form of ends of the samples, which have the rounded corners.

5 RESULTS

As the main results of the study, we present here the dependences of the drag C_D and added mass C_M coefficients of flat plates on the dimensionless vibration amplitude KC.

The functions C_D(KC) are plotted in Fig. 2 for different values of β. Curves 1, 2, 3 represent experimental data obtained for β = 430, 970, 1290 respectively. Solid line with cross-shaped markers corresponds to numerical results for β = 55. As can be seen, present results (both numerical and experimental) are well agreed with the data presented in previous researches [10], [13], [14].

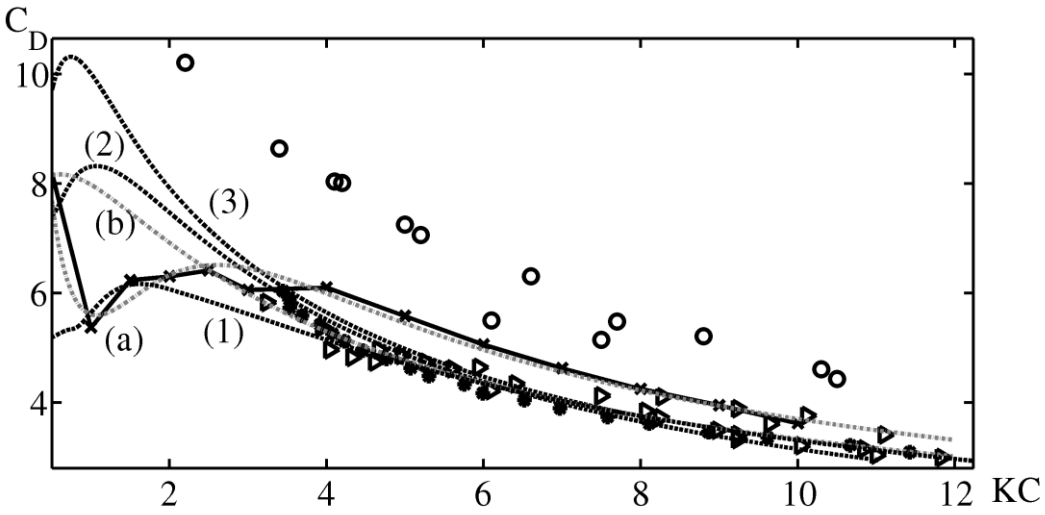

Figure 2: Drag coefficient C_D vs. dimensionless parameter KC. Black doted lines 1, 2, 3 represent experimental results and solid line with cross-shaped markers represent the numerical results of the present study. Gray doted lines a, b illustrate experimental results of [10]. Triangle markers correspond to experimental data of [13], black circles correspond to experimental data of [14] and white circles correspond to experimental data of [15].

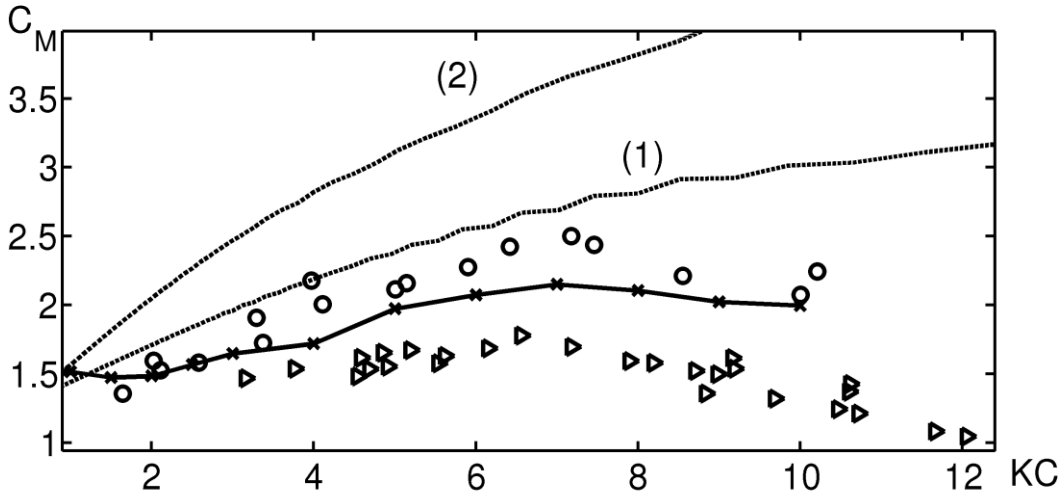

Figure 3: Added mass coefficient C_D vs dimensionless parameter KC. . Black doted lines 1, 2 represent experimental results and solid line with cross-shaped markers represent the numerical results of the present study. Triangle markers correspond to experimental data of [13] and white circles correspond to experimental data of [15].

The functions C_M(KC) for different values of β are plotted in Fig. 3. Curves 1, 2 represent experimental data obtained for β = 430, 970 respectively. As it can be seen, the present experimental results (espesualy for high values of β) lies higher than data from [13], [15] and the data of numerical results (obtained for β = 55). This can be caused by the influence of the non-zero mechanical component of the damping (see section 3.2).

Numerical part of research was supported by RSF (research project No. 15-19-10039), experimental part of research was supported by RFBR (research project No. 15-01-06029).

REFERENCES

[1] Sader, J. E. Frequency response of cantilever beams immersed in viscous fluids with applications to the atomic force microscope. *J. Appl. Phys.* (1998) **84** (1): 64 –76.

[2] Kimber, M., Lonergan, R., Garimella, S.V., Experimental study of aerodynamic damping in arrays of vibrating cantilevers. *Journal of Fluids and Structures*. (2009) **5** (8): 1334–1347.

[3] Bidkar, R.A., Kimber, M., Raman, A., Bajaj, A.K. and Garimella, S.V. Nonlinear aerodynamic damping of sharp-edged flexible beams oscillating at low Keulegan–Carpenter numbers. *Journal of Fluid Mechanics* (2009) **634**: 269–289.

[4] Tao, L. and Thiagarajan, K. Low KC flow regimes of oscillating sharp edges.I Vortex shedding observation. *Applied Ocean Research* (2003) **25** (2): 21–35.

[5] Tao, L. and Thiagarajan, K. Low KC flow regimes of oscillating sharp edges.II Hydrodynamic forces. *Applied Ocean Research* (2003) **25** (2): 53–62.

[6] Paimushin, V.N., Firsov, V.A., Gyunal I. and Egorov, A.G. Theoretical-experimental method for determining the parameters of damping based on the study of damped flexural vibrations of test specimens 1. Expermental base. *Mechanics of Composite Materials* (2014) **50** (2): 127–136.

[7] Egorov, A.G., Kamalutdinov, A.M., Nuriev, A.N. and Paimushin, V.N. Theoretical-experimental method for determining the parameters of damping based on the study of damped flexural vibrations of test specimens 2. Aerodynamic component of damping, *Mechanics of Composite Materials* (2014) **50** (3): 267–278.

[8] Adams, R.D. The damping characteristics of certain steels, cast irons and other metals. *Journal of Sound and Vibration* (1972) **23** (2): 199–216.

[9] Guild, F.J. Property-microstructural relationships in GFRP, Ph.D. thesis, Plymouth Polytechnic (1978).

[10] Kamalutdinov, A.M., Egorov, A.G., Günal, I. and Paimushin, V. Theoretical-experimental method for determining the drag coefficient of thin plate. *Proceedings of the 22nd International Congress on Sound and Vibration Major challenges in Acoustics, Noise and Vibration Research* (2015).

[11] Brumley, D. R., Willcox, M. and Sader, J. E. Oscillation of cylinders of rectangular cross section immersed in fluid. *Phys. Fluids* (2010) 22 (5) 052001.

[12] Nuriev A. N and Zaytseva O. N. Solution to the problem on oscillating motion of a cylinder in a viscous liquid by using the OpenFOAM package. *Vest. Kazan. Tekhnol. Univ*, (2013). **8**: 116-123.

[13] Singh, S. Forces on bodies in oscillatory flow, Ph.D. thesis, University of London (1979).

[14] Bearman, P. W., Graham, J. M. R. and Singh, S. Forces on cylinders in harmonically

oscillating flow. *Proceedings of the Symposium on Mechanics of wave induced forces on cylinders* (1979) 437–449.

[15] Keulegan, G.H. Carpenter, L.H. Forces on cylinders and plates in an oscillating fluid. *Journal of Research of National Bureau of Standards* (1958) **60** (5): 423-440.

VII International Conference on Computational Methods for Coupled Problems in Science and Engineering
COUPLED PROBLEMS 2017
M. Papadrakakis, E. Oñate and B. Schrefler (Eds)

PECULIARITIES OF AIR ENTRAINMENT WITH A LOOSE MATERIAL FLOW AT THE VARIABLE AERODYNAMIC RESISTANCE OF FALLING PARTICLES

O. A. AVERKOVA*, I.N. LOGACHEV* AND K. I. LOGACHEV*

* Belgorod State Technological University named after V.G. Shukhov
(BSTU named after V.G. Shukhov), 308012 Belgorod, Russia
e-mail: kilogachev@mail.ru, web page: http://www.bstu.ru

Key words: aspiration , bulk material transfer, air suction.

Abstract. Gravity flows of loose-matter particles are accompanied with aerodynamic forces that produce ejection of air in the loading and unloading chutes. A flow of loose matter acts like a blower. Head created by this blower (which we choose to call ejection head) comprises a sum total of aerodynamic forces of falling particles divided by cross-sectional area of the flow [1].

Flows of loose material in loading and unloading chutes that arise during operation of high-performance bucket elevators feature elevated volumetric concentrations as high as $\beta_y = 0.01$. Estimates of air ejection caused by such flows should be based upon instantaneous rather than averaged aerodynamic drag coefficient ψ_y.

Within the range of significant volumetric concentrations, varying volumetric concentration of falling particles leads to fluctuations in instantaneous values of the coefficient ψ. These fluctuations cause the ejection head, even in the case of short chutes, to significantly diverge from the head determined using averaged coefficient ψ_y. In order to compute ejection heads inside loading and unloading chutes, it is necessary to introduce an adjustment coefficient K (K is the ratio of the true value of ejection head in an inclined chute to the mean value of this pressure) the value of which will noticeably diverge from one at small initial velocities of particle flow.

It is possible to view flows of particles in chutes at $B < 0.1$ (B is the ratio of the average coefficient of drag encountered by a falling particle to the drag coefficient of an individual particle in the self-similarity area) as blowers with a performance curve determined with formula $p_e(Q) = K_0 z \frac{1}{3}\left[\left|1-\frac{Q}{Sv_k}\right|^3 - \left|n-\frac{Q}{Sv_k}\right|^3\right]$ (Q is the volumetric flow rate of air ejected through the loading chute of the elevator, z is a relative velocity of particles in a pipe, defined as the difference $v-u$, v is the velocity of falling particles, u is the velocity of ejected air, v_n, v_k is the fall velocity of particles at outlet of the chute, $n = v_n / v_k$, S is the cross-sectional area of the chute) in view of the resulting coefficient K_0 (K_0 is the ratio K absent ejection airflow).

For a flow of wheat ($d_e \approx 3$ mm) within the ranges $n > 0.5$ and $\beta_y = 0.001$, increasing drag coefficient along the fall height is only able to produce negligibly small changes in the intensity of ejection head. The adjustment coefficient may be dispensed with ($K = K_0 = 1$), and head value will then be determined using formula $P_{ey} = \frac{\psi_y K_m \varepsilon}{2} \frac{G_m v_k^3}{Sa_\tau} \frac{|1-\varphi|^3 - |n-\varphi|^3}{3}$ (. G_m is mass flow rate of the material, a_τ is the acceleration which, for chutes installed at an angle α to horizontal surface, ε is the ratio of air density to particle density, φ is ejection coefficient).

1 INTRODUCTION

Gravity flows of loose-matter particles are accompanied with aerodynamic forces that produce ejection of air in the loading and unloading chutes. A flow of loose matter acts like a blower. Head created by this blower (which we choose to call ejection head) comprises a sum total of aerodynamic forces of falling particles divided by cross-sectional area of the flow [1]. Aerodynamic force may be expressed using the drag coefficient:

$$R = \psi F_m \frac{|v-u|(v-u)}{2} \rho , \quad (1)$$

where R is the aerodynamic force of a single particle (*N*),
ψ is the drag coefficient,
F_m is the mid-section area of a particle (m^2),
v is the velocity of falling particles (m/s),
u is the velocity of ejected air (m/s),
ρ is the density of air (kg/m^3).

Absolute value of relative velocity $|v-u|$ had to be isolated into a dedicated variable due to the need to vectorize the square of relative velocity for the case involving unidirectional motion of a two-component particle-air medium. This notation means that at $v > u$, R is positive and directed parallel with leading motion of solid particles. At $v < u$ this force is negative i.e. opposite to the falling particles.

The drag coefficient is determined not only by the geometrical shape of particles, but also by their concentration. The greater the volumetric concentration of falling particles, the more pronounced is the effect of aerodynamic shadow on a particle moving toward the “aft” side of a particle ahead of it. The following empirical relationship [53] has been identified for a flow of firm mineral particles sized between 2 and 20 mm falling in inclined chutes:

$$\psi_y = \psi_0 \exp\left(\frac{-1.8\sqrt{\beta_y \cdot 10^3}}{d_e} \right), \quad (2)$$

where ψ_0 is the drag coefficient for a single particle in turbulent surface flow mode (within the self-similarity area),
d_e is equivalent particle diameter (mm),

β_y is volumetric concentration, averaged over the length of the chute and equal to:

$$\beta_y = \frac{2G_m}{S\rho_m\left(v_n + v_k\right)}, \tag{3}$$

G_m is mass flow rate of the material (kg/s),

S is the cross-sectional area of the chute (m^2),

ρ_m is air density (kg/m^3),

v_n, v_k is the fall velocity of particles at inlet/outlet of the chute (m/s).

The majority of crushed mineral particles have a roughly-pointed granular shape and a coefficient $\psi_0 \approx 1.8$. In contrast, cereals are likely to produce oval-shaped fragments when crushed, therefore $\psi_0 \approx 1.0$ can be assumed. If the geometrical shape of these particles were to be evaluated by their dynamic form coefficient, then

$$K_d = \left.\frac{\psi_0}{\psi_b}\right|_{\mathrm{Re}=idem} \approx 2, \tag{4}$$

where ψ_b is the drag coefficient of a sphere within the self-similarity area $\left(\psi_b \approx 0.5\right)$.

Let's determine the ejection head p_e arising within unloading and loading chutes during handling of cereal grain at elevators.

2 VARIATION OF EJECTION HEADS CREATED BY FALLING PARTICLES IN CHUTES WITH VARYING FRONTAL DRAG COEFFICIENTS

By definition, the ejection pressure created in chutes as a result of interaction between components,

$$p_e = \frac{1}{S}\int_0^l R\frac{\beta S dx}{V_p}, \tag{5}$$

where V_p is the volume of a single particle (m^3),

β is the current volumetric concentration of falling particles,

$$\beta = \frac{G_m}{S\rho_m v}; \tag{6}$$

l is chute length (m)

With a small fall height, when the chute length is

$$l < l_y = \frac{1}{\psi_y K_m \varepsilon}, \tag{7}$$

the aerodynamic force is negligibly small compared to gravitational force of a particle and the flow of material can therefore be considered constantly accelerated:

$$\frac{dv}{dt} = \frac{vdv}{dx} = a_\tau, \tag{8}$$

where

$$K_m = \frac{F_m}{V_p} \approx \frac{1.5}{d_e}; \tag{9}$$

$$\varepsilon = \frac{\rho}{\rho_m}; \tag{10}$$

d_e is the equivalent (volumetric) particle diameter (m),

a_τ is the acceleration which, for chutes installed at an angle α to horizontal surface, is equal to

$$a_\tau = g \sin\alpha \left(1 - f_w \mathrm{tg}\alpha\right); \tag{10a}$$

g is gravitational acceleration (m/s^2),

f_w is the friction coefficient for particles rubbing against chute walls (for steel walls, $f_w \approx 0{,}5$).

In this case, the ejection head for prismatic chutes at $S = \text{const}$; $u = \text{const}$; $\psi = \psi_y = \text{const}$ is determined using the equation:

$$P_{ey} = \frac{\psi_y K_m \varepsilon}{2} \frac{G_m}{S a_\tau} \frac{\left|v_k - u\right|^3 - \left|v_n - u\right|^3}{3} \tag{11}$$

or

$$P_{ey} = \frac{\psi_y K_m \varepsilon}{2} \frac{G_m v_k^3}{S a_\tau} \frac{\left|1-\varphi\right|^3 - \left|n-\varphi\right|^3}{3} = \psi_y \frac{G_m v_k}{S} \Phi \frac{\left|1-\varphi\right|^3 - \left|n-\varphi\right|^3}{3}, \tag{12}$$

where φ is the component slip ratio (ejection coefficient)

$$\varphi = \frac{u}{v_k}; \tag{13}$$

$$n = \frac{v_n}{v_k}; \tag{14}$$

$$\Phi = \varepsilon \frac{K_m v_k^2}{2 a_\tau}; \tag{15}$$

Velocity of cereal grains, considering their modest mass together with a large fall height $\left(l > l_y\right)$, is affected by the drag force. Motion equation for particles falling in an inclined chute in this case would appear as:

$$\frac{dv}{dt} = v\frac{dv}{dx} = a_\tau - \frac{R}{V_p \rho_m}. \tag{16}$$

Equations (5) and (16) enable the ejection head p_e to be discovered [52, 24] not only for heavier particles and lower heights $\left(l < l_y\right)$, but for light particles falling from great heights with an observable drag. However, changes in the ψ coefficient over the fall height was not taken into account in this case due to decreasing volumetric concentration of particles owing to (6)

$$\psi = \psi_0 \exp\left(\frac{-1.8\sqrt{\beta \cdot 10^3}}{d_e}\right). \tag{17}$$

Here ψ is a variable quantity that changes over the fall height due to decreasing volumetric concentration β as a result of increasing velocity of particles *v*.
Instantaneous drag coefficient will be expressed by a putative

$$\psi = \psi_0 B^{\sqrt{\frac{v_a}{v}}}, \tag{18}$$

with the following notational simplification:

$$B = e^{\frac{-1.8\sqrt{\beta_y \cdot 10^3}}{d_e}} = \frac{\psi_y}{\psi_0}; \qquad v_a = \frac{v_n + v_k}{2} \quad . \tag{19}$$

Let's now compare this effect for the case of short chutes when

$$a_\tau >> \frac{R}{V_p \rho_m}.$$

In view of (18) and (8), the following relation determines ejection pressure for a constantly accelerated flow of particles in a prismatic inclined chute (at $S = const$):

$$p_{eu} = \psi_0 \frac{G_m v_k}{S} \Phi \int_n^1 B^{\sqrt{\frac{1+n}{2\zeta}}} |\zeta - \varphi| (\zeta - \varphi) d\zeta. \tag{20}$$

This relation also accounts for change in the drag coefficient ψ along the trajectory of falling particles.

In order enable computational comparisons, we'll introduce the value of adjustment coefficient *K* that will determine the ratio of the true ejection head value to its putative value (12):

$$K = \frac{p_{eu}}{p_{ey}}. \tag{21}$$

Let's quantify it. In view of (12), (19) and (20) the expression appears as:

$$K = \frac{3}{(1-\varphi)^3 - |n-\varphi|^3} \frac{1}{B} \int_n^1 B^{\sqrt{\frac{1+n}{2\zeta}}} |\zeta - \varphi| (\zeta - \varphi) d\zeta. \tag{22}$$

Then the ratio of maximum ejection heads would be (at $u = \varphi = 0$)

$$K_0 = \frac{3}{1-n^3}\frac{1}{B}\int_n^1 B^{\sqrt{\frac{1+n}{2\zeta}}}\zeta^2 d\zeta = \frac{6}{1-n^3}\frac{1}{B}\int_1^{\frac{1}{\sqrt{n}}}\frac{e^{pt}}{t^7}dt\,, \tag{23}$$

where

$$p = \sqrt{\frac{1+n}{2}}\ln B\,. \tag{24}$$

Let's resolve the integral by representing the integrand function as a series:

$$\frac{e^{pt}}{t^7} = \sum_{k=0}^{\infty}\frac{p^k}{k!}\zeta^{k-7}\,, \tag{25}$$

which results in:

$$\int_1^{\frac{1}{\sqrt{n}}}\frac{e^{P_t}}{t^7}dt = F(t)\Big|_1^{\frac{1}{\sqrt{n}}} = F\left(\frac{1}{\sqrt{n}}\right) - F(1), \tag{26}$$

where the antiderivative function F is equal to:

$$F(t) = -\frac{1}{6}\frac{1}{t^6} - \frac{p}{5}\frac{1}{t^5} - \frac{p^2}{8}\frac{1}{t^4} - \frac{p^3}{18}\frac{1}{t^3} - \frac{p^4}{48}\frac{1}{t^2} - \frac{p^5}{120}\frac{1}{t} - \frac{p^6}{720}\ln t + \sum_{k\to 7}\frac{p^k}{k!}\frac{1^{k-6}}{k-6}\,, \tag{27}$$

then

$$K_0 = \frac{6}{1-n^3}\frac{1}{B}\left[F\left(\frac{1}{\sqrt{n}}\right) - F(1)\right]. \tag{28}$$

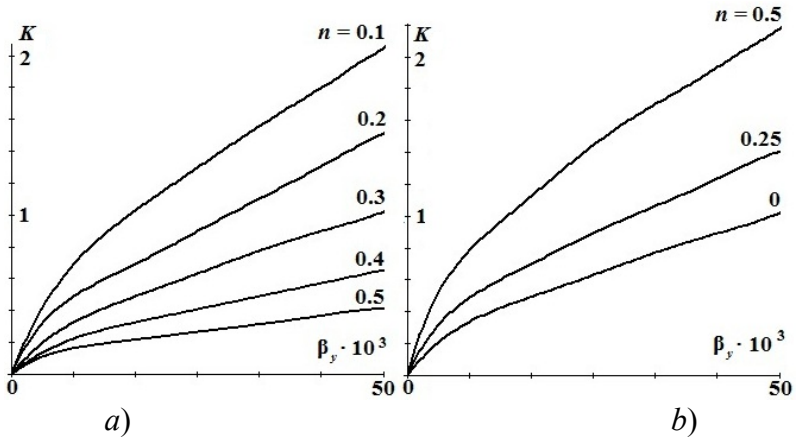

a) *b*)

Figure 1: Variation of the adjustment coefficient as a function of volumetric concentration for a constantly accelerated flow of particles $d_e = 3$ mm (*a* – at $\varphi = 0$; *b* – at $\varphi \neq 0$ and $n = 0.3$)

Tables 1 and 2 summarize the values of the adjustment coefficient K_0 computed using formula (28) and K computed using formula (22). It is apparent from Table 1 that changes in the drag coefficient ψ along a trajectory travelled by a particle only cause a noticeable impact within the area of significant volumetric concentrations, when $B \le 0.3$. For example, for

grains of wheat ($d_e \approx 3$ mm) this corresponds to the averaged volume concentration $\beta_y = 0.004$. The adjustment factor is significantly higher for smaller initial velocities (at $n < 0.5$) of the flow (Fig. 1, a). Its value increases somewhat (Fig. 1, b) when air is flowing inside a chute (at $\varphi \neq 0$). However, considering that the ejection head

$$p_e = K\psi_y \frac{G_m v_k}{S} \Phi \frac{|1-\varphi|^3 - |n-\varphi|^3}{3} \tag{29}$$

diminishes with increasing φ as a result of braking action of the initial section of accelerated flow, the following assumption would be justified for computations

$$K \approx K_0 . \tag{30}$$

Table 1: Adjustment coefficient values for the case of still air in the chute

B	Values of K_0 at n equal to…								
	0.1	0.2	0.3	0.4	0.5	0.6	0.7	0.8	0.9
0.01	2.017	1.717	1.489	1.319	1.198	1.113	1.057	1.023	1.005
0.02	1.786	1.556	1.382	1.251	1.155	1.089	1.045	1.018	1.004
0.03	1.667	1.475	1.326	1.214	1.133	1.076	1.038	1.015	1.003
0.04	1.589	1.420	1.288	1.189	1.118	1.067	1.034	1.014	1.003
0.05	1.531	1.379	1.261	1.171	1.106	1.061	1.031	1.012	1.003
0.06	1.487	1.348	1.239	1.157	1.098	1.056	1.028	1.011	1.003
0.07	1.450	1.322	1.221	1.146	1.090	1.052	1.026	1.010	1.002
0.08	1.420	1.300	1.207	1.136	1.084	1.048	1.024	1.010	1.002
0.09	1.390	1.281	1.194	1.128	1.079	1.045	1.023	1.009	1.002
0.1	1.371	1.265	1.183	1.120	1.075	1.043	1.022	1.009	1.002
0.2	1.234	1.168	1.116	1.076	1.047	1.027	1.014	1.005	1.001
0.3	1.165	1.118	1.081	1.053	1.033	1.020	1.010	1.004	1.001
0.4	1.120	1.086	1.059	1.039	1.024	1.014	1.007	1.003	1.001
0.5	1.088	1.063	1.043	1.028	1.018	1.010	1.005	1.002	1.000
0.6	1.063	1.045	1.031	1.020	1.013	1.007	1.004	1.001	1.000
0.7	1.043	1.030	1.021	1.014	1.009	1.005	1.002	1.001	1.000
0.8	1.026	1.019	1.013	1.008	1.005	1.003	1.002	1.001	1.000
0.9	1.012	1.009	1.006	1.004	1.002	1.001	1.001	1.000	1.000
1.0	1.000	1.000	1.000	1.000	1.000	1.000	1.000	1.000	1.000

Keeping in mind that grain handling facilities in real-world elevator will have a flow velocity at duct inlet of ($0.3 \div 0.5 v_k$) ejection head can thus be determined using formula (12) by introducing an adjustment coefficient exclusively within the area of large volumetric concentrations, at

$$B < 0.1 \text{ and } n < 0.3 . \tag{31}$$

Thus, the flow of loose particulate matter can be considered as a kind of blower with the output described as:

$$p_e(Q) = K_0 z \frac{1}{3}\left[\left|1 - \frac{Q}{Sv_k}\right|^3 - \left|n - \frac{Q}{Sv_k}\right|^3\right], \quad (32)$$

with the following assignment made to simplify the notation:

$$z = \psi_y \frac{G_m v_k}{S} \Phi = \psi_y \frac{G_m v_k}{S} \varepsilon \frac{K_m v_K^2}{2a_\tau}; \quad (33)$$

Q is the volumetric flow rate of air ejected through the loading chute of the elevator (m^3/s).

Table 2: Adjustment coefficient values for the case of moving air in the chute

B	Values of K at n equal to…								
	0.1	0.2	0.3	0.4	0.5	0.6	0.7	0.8	0.9
At $\varphi = 0.25$									
0.02	2.026	1.746	1.526	1.349	1.216	1.122	1.061	1.024	1.005
0.04	1.778	1.571	1.405	1.270	1.167	1.095	1.047	1.019	1.004
0.06	1.650	1.479	1.341	1.227	1.141	1.080	1.040	1.016	1.003
0.08	1.565	1.417	1.298	1.199	1.123	1.070	1.035	1.014	1.003
0.1	1.502	1.371	1.266	1.178	1.110	1.063	1.031	1.012	1.003
0.2	1.326	1.242	1.174	1.116	1.072	1.041	1.020	1.008	1.002
0.4	1.173	1.129	1.093	1.062	1.038	1.022	1.011	1.004	1.001
0.6	1.093	1.069	1.050	1.033	1.021	1.012	1.006	1.002	1.000
0.8	1.039	1.029	1.021	1.014	1.009	1.005	1.002	1.001	1.000
1.0	1.000	1.000	1.000	1.000	1.000	1.000	1.000	1.000	1.000
At $\varphi = 0.5$									
0.02	4.507	2.455	1.822	1.526	1.342	1.198	1.097	1.037	1.008
0.04	3.840	2.152	1.644	1.412	1.270	1.157	1.077	1.030	1.006
0.06	3.482	1.989	1.548	1.351	1.230	1.134	1.066	1.025	1.005
0.08	3.239	1.878	1.483	1.309	1.203	1.119	1.058	1.022	1.005
0.1	3.056	1.794	1.435	1.277	1.183	1.107	1.053	1.020	1.004
0.2	2.499	1.547	1.292	1.185	1.123	1.072	1.035	1.013	1.003
0.4	1.926	1.311	1.161	1.101	1.067	1.039	1.019	1.007	1.002
0.6	1.556	1.173	1.089	1.055	1.037	1.021	1.010	1.004	1.001
0.8	1.261	1.075	1.039	1.023	1.016	1.009	1.005	1.002	1.000
0.9	1.131	1.034	1.019	1.011	1.007	1.004	1.002	1.001	1.000
1.0	1.000	1.000	1.000	1.000	1.000	1.000	1.000	1.000	1.000

CONCLUSIONS

Flows of loose material in loading and unloading chutes that arise during operation of high-performance bucket elevators feature elevated volumetric concentrations as high as $\beta_y = 0.01$. Estimates of air ejection caused by such flows should be based upon instantaneous (relation (18)) rather than averaged aerodynamic drag coefficient ψ_y.

Within the range of significant volumetric concentrations, varying volumetric

concentration of falling particles leads to fluctuations in instantaneous values of the coefficient ψ. These fluctuations cause the ejection head, even in the case of short chutes ($l < l_y$), to significantly diverge from the head p_{ey} determined using averaged coefficient ψ_y. In order to compute ejection heads inside loading and unloading chutes, it is necessary to introduce an adjustment coefficient K the value of which will noticeably diverge from one at small initial velocities of particle flow (at $n < 0.5$, Table 2, Fig. 1).

It is possible to view flows of particles in chutes at $B < 0.1$ as blowers with a performance curve determined with formula (32) in view of the resulting coefficient K_0. For a flow of wheat ($d_e \approx 3$ mm) within the ranges $n > 0.5$ and $\beta_y = 0.001$, increasing drag coefficient along the fall height is only able to produce negligibly small changes in the intensity of ejection head. The adjustment coefficient may be dispensed with ($K = K_0 = 1$), and head value will then be determined using formula (12).

The work has been carried out with the financial support of the Grant Council of the President of the Russian Federation (project MD-95.2017.8).

REFERENCES

[1] Logachev, I.N., Logachev, K.I. and Averkova, O.A. Local Exhaust Ventilation: Aerodynamic Processes and Calculations of Dust Emissions, CRC Press, (2015).

VII International Conference on Computational Methods for Coupled Problems in Science and Engineering
COUPLED PROBLEMS 2017
M. Papadrakakis, E. Oñate and B. Schrefler (Eds)

STAGGERED STRONG COUPLING BETWEEN EXISTING FLUID AND SOLID SOLVERS THROUGH A PYTHON INTERFACE FOR FLUID-STRUCTURE INTERACTION PROBLEMS

David Thomas*, Anil Variyar†, Romain Boman*, Thomas D. Economon†, Juan J. Alonso†, Grigorios Dimitriadis* and Vincent E. Terrapon*

*Department of Aerospace and Mechanical Engineering
University of Liège
Liège, 4000, Belgium
e-mail: {dthomas, r.boman, gdimitriadis, vincent.terrapon}@ulg.ac.be

†Department of Aeronautics and Astronautics
Stanford University
Stanford, CA, 94305, USA
e-mail: {anilvar, economon, jjalonso}@stanford.edu

Key words: Fluid-Structure Interaction, Strong Coupling, Python Wrapper, Computational Aeroelasticity.

Abstract. A Fluid-Structure Interaction (FSI) tool that couples existing independent fluid and solid solvers into a single synchronization and communication framework based on the Python language is presented. Each solver has to be wrapped in a Python layer in order to embed their functionalities (usually written in a compiled language) into a Python object, that is called and used by the coupler. Thus a staggered strong coupling can be achieved for time-dependent FSI problems such as aeroelastic flutter or vortex-induced vibrations (VIV). The synchronization between the solvers is performed with the block-Gauss-Seidel algorithm and a dynamic under-relaxation. The tool allows non-matching meshes between the fluid and structure domains and it is optimised to work in parallel using Message Passive Interface (MPI). These capabilities are demonstrated on typical validation cases. The open-source code SU2 is used to compute the fluid region while the solid region is computed either by a simple rigid body integrator, by an in-house nonlinear Finite Element code (Metafor) or by the structural solver TACS. First, the accuracy of the results is demonstrated and then the modularity of the coupling as well as its ease of use is highlighted.

1 INTRODUCTION

The computation of Fluid-Structure Interaction (FSI) problems is usually based on one of two possible strategies: the monolithic or the partitioned approach [1, 2, 3]. In the monolithic approach, both the structural and fluid problems are solved within one single solver and within the same mathematical framework where the interfacial conditions are implicit to the procedure. On the other hand, the partitioned approach couples two different specialized existing codes. This requires an efficient communication and synchronization framework, but allows the intrinsic features of the individual solvers to be leveraged.

A framework to couple two heterogeneous existing fluid and solid solvers is presented here. It is based on a Python coupling environment designed to interact with the two solvers through their respective Python wrappers. Data exchange and synchronization are thus implemented in a very intuitive and flexible way in Python, whereas the computationally intensive routines within each solver are kept in their native languages (C, C++, ...). Because the coupled solvers are reduced to black-box tools by their wrappers, minimal effort is required to ensure compatibility with the coupler, providing great flexibility regarding the solvers that can be coupled.

The paper is organized as follows. Section 2 is dedicated to describing the governing equations, the computational implementation of the fluid/structural mechanics and the coupling conditions. The implementation of the coupling environment is then presented in Section 3. In Section 4 several FSI test cases are reproduced and results are presented in order to show the accuracy and the flexibility of the coupling tool. Finally, Section 5 summarizes the main concepts and results, and suggests further steps for future work.

2 GOVERNING EQUATIONS OF THE COUPLED PROBLEM

This section summarizes the governing equations and their numerical implementation for both the fluid and solid parts of the coupled problem. The fluid equations in an Arbitrary Lagrangian-Eulerian (ALE) form are solved in a moving domain Ω_f that shares a common boundary Γ with the solid domain Ω_s, in which the solid equations are solved with a Lagrangian formalism. In addition to intrinsic boundary conditions for each of the disciplines, coupling conditions on the displacements, and the loads across the common boundary Γ, are required to achieve a strong coupling scheme.

2.1 Fluid mechanics

The dynamic behavior of a compressible Newtonian fluid is predicted by solving the Navier-Stokes or Euler equations. The conservation of mass, momentum and energy in Ω_f can be written using ALE formalism as [4]

$$\frac{\partial \mathbf{U}}{\partial t} + \nabla \cdot \mathbf{F}^\mathrm{c} - \nabla \cdot (\mathbf{V}_\Omega \mathbf{U}) - \nabla \cdot \mathbf{F}^\mathrm{v} = \mathbf{Q} \qquad \text{in } \Omega_\mathrm{f} \times [0, T] \,, \tag{1}$$

where the conservative variables are given by $\mathbf{U} = [\rho, \rho\mathbf{v}, \rho E]^{\mathrm{T}}$, $\mathbf{F}^{\mathrm{c}}$, $\mathbf{V}_{\Omega}\mathbf{U}$ and $\mathbf{F}^{\mathrm{v}}$ are the advective, ALE and diffusive fluxes, respectively, and $\mathbf{Q}$ is a source term. In these expressions ρ is the fluid density, $\mathbf{v} = [v_1, v_2, v_3]^{\mathrm{T}}$ the velocity field in Cartesian coordinates, E the total energy per unit mass and $\mathbf{V}_{\Omega} = [\mathbf{v}_{\Omega}, \mathbf{v}_{\Omega}, \mathbf{v}_{\Omega}]^{\mathrm{T}}$ the local velocity of the moving domain. The Euler equations are simply recovered by discarding the viscous terms. Note that in the case of a turbulent viscous flow, the Reynolds-Averaged Navier-Stokes (RANS) equations with a turbulence model (e.g., k-ω SST [5], Spalart-Allmaras [6]) could also be solved.

The open-source CFD code SU2 [7, 8] is used to solve the fluid part of the coupled problem. The governing equations are spatially discretized using the Finite Volume Method on a dual-grid using a vertex-based approach. Temporal discretization is achieved through a dual time-stepping [9] strategy, where each physical time step is transformed into a steady problem.

2.2 Solid mechanics

The dynamic behavior of a deformable solid results from the balance between inertial, internal and external forces. The equilibrium equation in Ω_{s} is given by

$$\rho\frac{\partial^2\mathbf{u}}{\partial t^2} - \nabla\cdot\overline{\overline{\sigma}} = \mathbf{f} \qquad \text{in } \Omega_{\mathrm{s}}\times[0,T]\ , \tag{2}$$

where ρ, $\mathbf{u}$, $\overline{\overline{\sigma}}$ and $\mathbf{f}$ are the solid density, the displacement vector, the Cauchy stress tensor and the body forces, respectively. The in-house nonlinear Finite Element code Metafor [10] is used to solve the structural part of the coupled problem. The solver is designed to simulate large structural deformations by expressing the principle of virtual work (PVW) on the deformed configuration. A particular feature of Metafor is also the large range of nonlinear material laws that can be used (elasticity, elasto-plasticity or visco-elasto-plasticity, ...). For each time increment, these nonlinearities are solved with a Newton-Raphson approach. Time discretization typically uses the Generalized-α method but a quasi-static integration is also available when inertia terms are negligible.

Simpler coupled fluid-structure problems involve the motion of non-deformable solids where the dynamics is constrained using stiffness or damping. Such a model is implemented in a in-house rigid body integrator code also based on the Generalized-α method for time integration.

Also, the coupling approach and the Python wrapper/interface developed for the fluid solver SU2 is further tested by coupling it with the Toolkit for Analysis of Composite Structures (TACS) , which is a linear/nonlinear solution capable structural solver developed by Kennedy and Martins [11]. TACS already has a Python interface which makes coupling it with SU2 easy.

2.3 Coupling conditions

The fluid and solid domains are coupled at their common interface Γ through continuity boundary conditions on the displacement $\mathbf{d}^\Gamma$ and the load $\mathbf{t}^\Gamma$,

$$\begin{aligned} \mathbf{d}_\mathrm{f}^\Gamma &= \mathbf{d}_\mathrm{s}^\Gamma \\ \mathbf{t}_\mathrm{f}^\Gamma &= -\mathbf{t}_\mathrm{s}^\Gamma \,, \end{aligned} \tag{3}$$

where the load on the fluid side is given by $\mathbf{t}_\mathrm{f} = -p\mathbf{n}_\mathrm{f} + \overline{\overline{\tau}}\mathbf{n}_\mathrm{f}$, with p the pressure and $\overline{\overline{\tau}}$ the viscous stress, and the load on the solid side by $\mathbf{t}_\mathrm{f} = \overline{\overline{\sigma}}\mathbf{n}_\mathrm{s}$. The normal unit vectors $\mathbf{n}_\mathrm{f}$ and $\mathbf{n}_\mathrm{s}$ are both pointing outwards from their respective domains.

The coupled problem can be solved using a Dirichlet-Neumann approach [12]. Introducing a Dirichlet nonlinear operator $\mathcal{F}$ that computes the fluid load from a given fluid interface displacement,

$$\mathbf{t}_\mathrm{f}^\Gamma = \mathcal{F}(\mathbf{d}_\mathrm{f}^\Gamma) \,, \tag{4}$$

and a Neumann nonlinear operator $\mathcal{S}$ that computes the solid interface displacement as a function of the solid load,

$$\mathbf{d}_\mathrm{s}^\Gamma = \mathcal{S}(\mathbf{t}_\mathrm{s}^\Gamma) \,, \tag{5}$$

Equation (3) can be formulated as a fixed-point problem [13]:

$$\mathbf{d}^\Gamma = \mathcal{S}\left(-\mathcal{F}(\mathbf{d}^\Gamma)\right) \tag{6}$$

where $\mathbf{d}^\Gamma$ is the displacement common to both the solid and fluid interfaces.

Finally, the mesh within the fluid domain must be adapted to accommodate the solid deformation/displacement. The mesh morphing used with the ALE formalism can be expressed as

$$(\mathbf{x}_\mathrm{f}^\Omega, \mathbf{v}_\mathrm{f}^\Omega) = \mathcal{M}(\mathbf{d}_\mathrm{f}^\Gamma) \,, \tag{7}$$

where $\mathbf{x}_\mathrm{f}^\Omega$ and $\mathbf{v}_\mathrm{f}^\Omega$ are the position and velocity of the mesh points, respectively, and $\mathcal{M}$ a mesh deformation operator.

3 IMPLEMENTATION OF THE COUPLING ENVIRONMENT

The coupling environment for solving the FSI problem, represented by Equations (1), (2) and (6), is implemented using a partitioned framework. The coupler is based on a block-Gauss-Seidel (BGS) algorithm, that synchronizes the solvers [13, 14] in a strong coupling scheme. This ensures that the coupling conditions on the FSI-interface at each time step are met by iterating between the fluid ($\mathcal{F}$) and solid ($\mathcal{S}$) computations. These iterations are repeated until a convergence criterion, based on the norm of the difference in the structural displacement between two successive BGS iterations, is met. $\mathcal{F}$ and $\mathcal{S}$ are reduced to abstract black-box calls to the respective solvers. This is achieved through a modular and high-level implementation of the coupling environment using the Python programming language. Modules of the coupled solvers written in C/C++, are wrapped in

a Python layer that behaves as a driving and communicating channel between the coupler and the solver itself. The wrapping is easily performed using the Simplified Wrapper and Interface Generator (SWIG) tool [15]. For data exchange between the solvers and to call required modules, the main coupler (written in pure Python) can directly interact with the solvers through their wrappers as if they were simple Python objects. These communications do not involve any file i/o. The wrapped functionalities of each solver can thus be easily and intuitively managed in Python while the critical and computationally intensive calculations are performed by the native solvers. This wrapping process and the interaction between the solvers and the coupling environment are schematically illustrated in Figure 1.

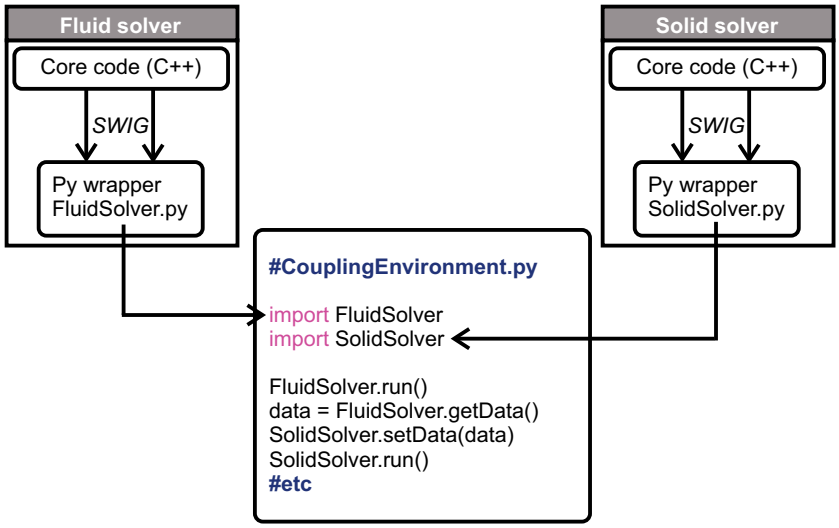

Figure 1: Schematic illustration of the coupling environment and its interaction with the respective fluid and solid Python wrappers.

This generic high-level coupling environment ensures both modularity and flexibility (see Section 4 for examples). In particular, there is no specific restriction on the solvers (fluid or solid) that can be used, except for minimal compatibility requirements between their wrappers and the coupler (e.g. exchanged data must be expressed in a typical array format).

The coupler can also handle parallelized fluid/solid solvers in a very flexible way using the MPI paradigm and its Python bindings mpi4py [16]. The communications between different partitions are performed by the coupler itself (except for intrinsic MPI communications within each solver) before communicating with the solvers. Moreover, the MPI processes can be distributed without any restriction, i.e., one process can instantiate either a fluid or solid partition or even both (since the staggered coupling requires a sequential run of the solvers). Mixing parallel and serial solvers is thus possible. Finally, note that bindings for PETSc (petsc4py) [17] can be interfaced for all parallel linear

algebra operations.

The BGS approach used to couple the solvers is directly implemented in the Python coupler. In order to handle ill-conditioned cases such as those involving strong added-mass effects, dynamic under-relaxation using Aitken's formulation is implemented [13]. A second order predictor [18] is used between time steps to accelerate the convergence of the BGS loop.

Interface interpolations are performed at the coupler level. In a partitioned approach solid and fluid meshes are likely to be created independently of each other for optimality. Consequently, there is no guarantee that the boundary discretization at the fluid-structure interface consist of matching meshes. The data transferred between the two solvers must therefore be interpolated from one grid to the other. This is equivalent to defining a new operator $\mathcal{I}_{\mathrm{s}}^{\mathrm{f}}$ that maps the displacements of the solid interface mesh onto the fluid interface mesh during the communication step of the BGS algorithm,

$$\mathbf{d}_{\mathrm{f}}^{\Gamma} = \mathcal{I}_{\mathrm{s}}^{\mathrm{f}}(\mathbf{d}_{\mathrm{s}}^{\Gamma})\,, \tag{8}$$

or, analogously, an operator $\mathcal{I}_{\mathrm{f}}^{\mathrm{s}}$ that maps the load from the fluid to the solid,

$$\mathbf{t}_{\mathrm{s}}^{\Gamma} = \mathcal{I}_{\mathrm{f}}^{\mathrm{s}}(\mathbf{t}_{\mathrm{f}}^{\Gamma})\,. \tag{9}$$

These operators can be expressed as simple linear algebraic interpolation matrices [19]. Currently the Radial Basis Function (RBF) interpolation technique [20], using either a local $\mathcal{C}^2$ or a global Thin Plate Spline (TPS) function, is implemented in the coupler. The overall coupling algorithm is illustrated in Figure 2.

4 RESULTS

The coupler implementation described in the previous section is now used to solve several FSI test cases in order to demonstrate its accuracy, flexibility and robustness.

4.1 Isogai wing section

The coupling between SU2 and the rigid body integrator is tested using the classical Isogai wing section aeroelastic case (case A) [21, 22]. This test case represents the dynamics of the outboard portion of a swept-back wing in the transonic regime. The airfoil is a symmetric NACA 65a010 profile with a chord $c = 2b$. As shown in Figure 3, the displacement h of the elastic axis is positive downwards and the pitch angle α is positive clockwise. The static unbalance S is defined as the product of the airfoil mass m with the distance $x_{\mathrm{CG}} - x_{\mathrm{f}}$ between the center of gravity and the elastic axis. The structural dynamics is modeled with a spring-dashpot system with stiffnesses K_h and K_α and damping coefficients C_h and C_α for the plunging and pitching mode.

The equations of motion for this aeroelastic system can be written as [23]

$$\begin{aligned} m\ddot{h} + S\ddot{\alpha} + C_h\dot{h} + K_h h &= -L\,, \\ S\ddot{h} + I_{\mathrm{f}}\ddot{\alpha} + C_\alpha\dot{\alpha} + K_\alpha\alpha &= M\,, \end{aligned} \tag{10}$$

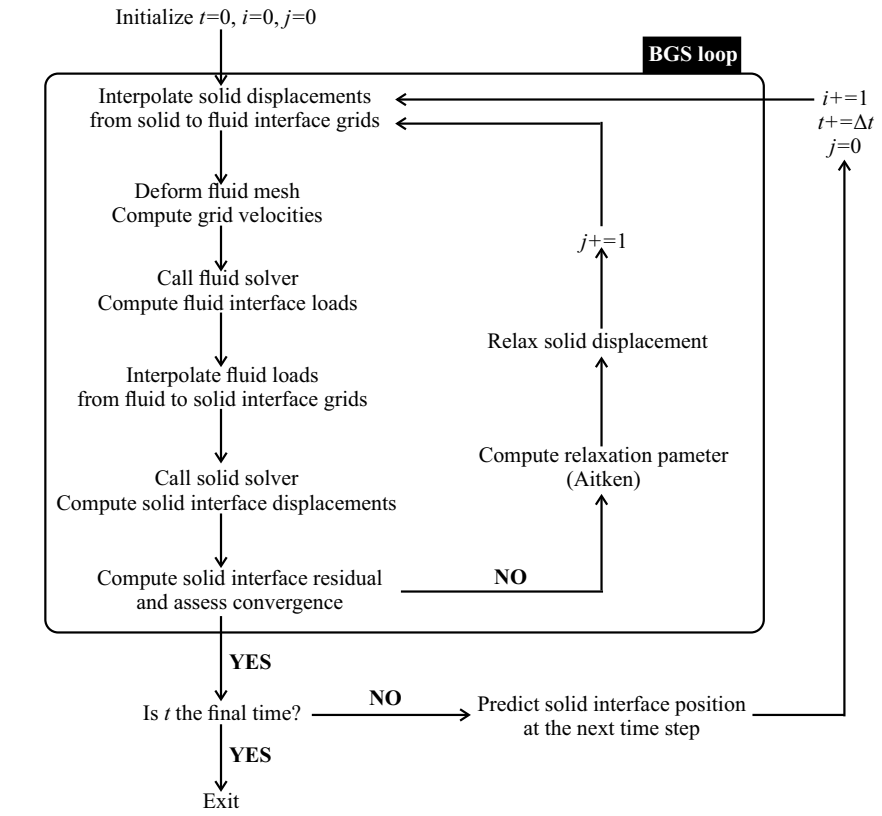

Figure 2: Time-marching coupling algorithm based on a block-Gauss-Seidel scheme (i is the time iterator and j is the FSI iterator).

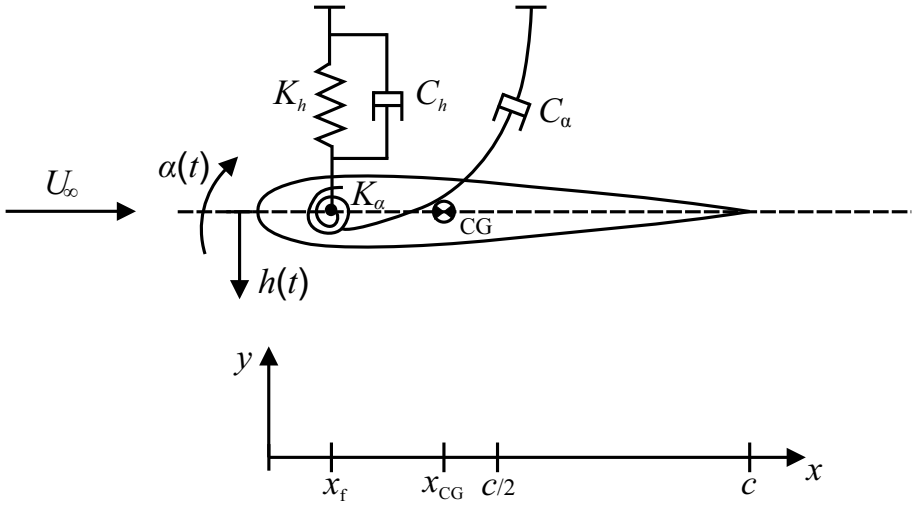

Figure 3: Schematic of a two degrees of freedom pitching-plunging airfoil aeroelastic model.

where I_f is the moment of inertia of the airfoil around the elastic axis, L the aerodynamic lift (positive upwards) and M the aerodynamic moment with respect to the elastic axis (positive clockwise). The overall system is characterized by several non-dimensional parameters, i.e., the normalized static unbalance $\chi = S/mb$ and moment of inertia $r_\alpha^2 = I_\mathrm{f}/mb^2$, the plunging and pitching damping ratios $\eta_h = C_h/2\sqrt{K_h m}$ and $\eta_\alpha = C_\alpha/2\sqrt{K_\alpha I_\mathrm{f}}$, the mass ratio $\mu = m/\pi\rho_\infty b^2$ where ρ_∞ is the free-stream fluid density, and the natural frequency ratio $\overline{\omega} = \omega_h/\omega_\alpha$ where $\omega_h = \sqrt{K_h/m}$ and $\omega_\alpha = \sqrt{K_\alpha/I_\mathrm{f}}$ are the natural frequencies of the uncoupled system. The parameters for the Isogai test case are $\chi = 1.8$, $r_\alpha = 1.865$, $\overline{\omega} = 1$ and $\mu = 60$. There is no structural damping, i.e., $C_h = C_\alpha = 0$. The elastic axis is placed in front of the airfoil at a distance $x_\mathrm{f} = -b$ from the leading edge and the natural pitching frequency is here $\omega_\alpha = 100$ rad/s. The Euler equations are solved in the transonic regime with an initial airfoil pitch angle $\alpha_0 = 0.0174$ rad (1^o). The time step for the simulation is $\Delta t = 0.0016$ s which corresponds to 39 time steps per period of the uncoupled pitch mode. Because of the high mass ratio of the coupled system, low added mass effects are expected, thus no relaxation is used. Three BGS iterations per time step are typically required to achieve a coupling tolerance of 10^{-6} m (10^{-4} times the initial perturbation) on the structural displacement.

Several FSI simulations at different transonic free-stream Mach numbers ($\mathrm{M}_\infty = 0.7 - 0.9$) are performed with variable speed index

$$V^* = \frac{U_\infty}{b\omega_\alpha\sqrt{\mu}} \tag{11}$$

in order to predict the flutter point. Flutter inception is identified as the point for which the damping extracted from the system dynamic response is zero. The computed flutter speed indices are compared with values from the literature [24, 25, 26, 27], as shown in Figure 4. The best approximation curve (spline) is a representation of the limit between the stable and unstable regions. It can be seen that the "transonic dip" and the typical "S-shape" flutter boundary for M_∞ between 0.7 and 0.9 are both well predicted.

4.2 VIV of a flexible cantilever in the wake of a square cylinder

The study of the flexible cantilever attached to the downstream side of a perfectly rigid square cylinder is a classical two-dimensional benchmark test case for FSI [18]. The geometry of the computational domain is described in Figure 5. In this case $H = 0.01$ m. The physical properties of the solid and fluid are summarized in Table 1. The incoming flow velocity is $U_x = 0.513$ m/s, which corresponds to a laminar Reynolds number $\mathrm{Re} = U_x H/\nu_\mathrm{f} = 333$. The top and bottom sides of the channel are modeled as inviscid walls.

The velocity and the Reynolds number are such that an unsteady laminar Von Karman vortex sheet is generated in the wake of the cylinder with a shedding frequency close to the first bending frequency of the flexible cantilever. Therefore, the vortical structure of the wake generates harmonic aerodynamic loads that induce periodic oscillations of the flexible cantilever.

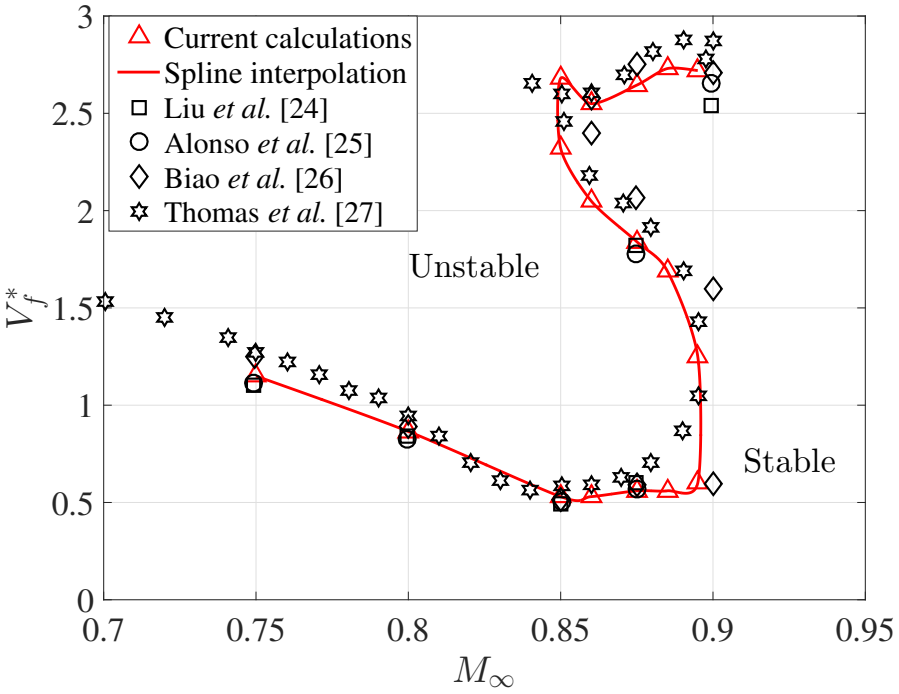

Figure 4: Flutter speed index as a function of the free-stream Mach number. Comparison between current computations and numerical results from the literature.

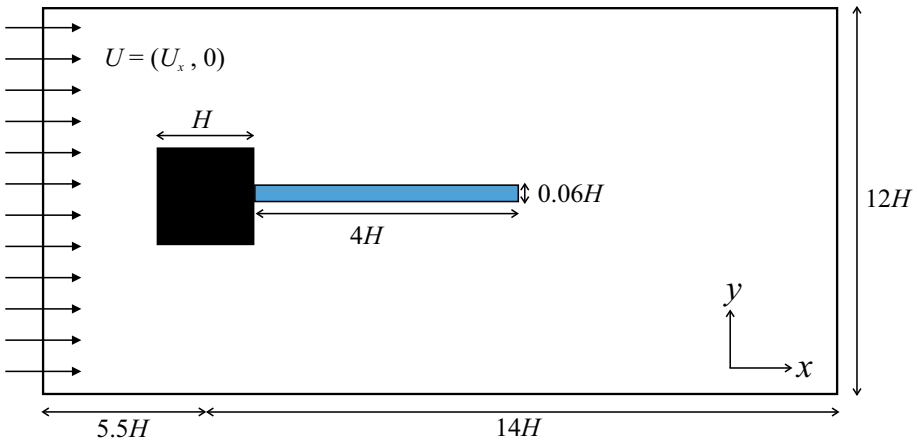

Figure 5: Flexible cantilever attached to a rigid square cylinder. Geometry of the computational domain.

This interaction is numerically reproduced by coupling SU2 and Metafor. A nonlinear formalism is necessary to correctly predict the bending of the cantilever undergoing large displacements. In order to eliminate any interpolation error, the grid discretization is done

Solid		
Density [kg m^{-3}]	ρ_s	100
Young's modulus [Pa]	E	$2.5 \cdot 10^5$
Poisson's ratio [-]	ν_s	0.35
Fluid		
Density [kg m^{-3}]	ρ_f	1.18
Kinematic viscosity [m^2 s^{-1}]	ν_f	$1.54 \cdot 10^{-5}$

Table 1: Solid and fluid physical properties.

so as to have matching meshes at the fluid-structure interface. The mesh is structured in the near-field of the solid bodies (square cylinder and cantilever) and then unstructured throughout the rest of the domain. The time step for the simulation is $\Delta t = 0.0025$ s which corresponds to 122 time steps per period on the first bending mode of the beam. Four BGS iterations with no relaxation are typically required to reach a coupling tolerance of 10^{-6} m (10^{-4} times the expected tip displacement) on the structural displacement.

Habchi *et al.* [18] summarized results from the literature (e.g., [28, 14, 29]). The oscillations frequency typically falls in the range $2.94 - 3.25$ Hz, while the amplitude of the tip displacement is in the range $0.95 - 1.25$ cm. The present computation predicts a maximum tip displacement $d_y = 1.07$ cm and a frequency $f = 3.14$ Hz , which is in very good agreement with results from the literature. The same simulation is repeated using the SU2-TACS framework and a maximum tip displacement $d_y = 1.03$ cm and an average frequency of $f = 2.93$ Hz is observed, matching well with the SU2-Metafor simulation and available data. Figure 6 shows the velocity magnitude contour at several time steps of a period T, where the vortical structures and the large displacement of the cantilever can be observed.

4.3 Static aeroelastic deformation of the AGARD 445.6 wing

The experimental AGARD 445.6 wing test case [30] is a frequently used three-dimensional validation case for transonic flutter simulations. The present computational study is based on the weakened model 3 of the wing. This is a 45° swept-back wing whose geometrical properties are summarized in Table 2. The cross section of the wing is a symmetric NACA 65a004 airfoil. The static aeroelatic case performed by Goura [31] is here reproduced by solving the Euler equations with SU2. The wing is modeled in Metafor with 8-node continuum elements and an orthotropic elastic material whose properties are summarized in Table 3. A modal analysis is first performed and the first four natural frequencies computed are compared with results in the literature in Table 4, showing good agreements with both computational and experimental results. Note that the present results are obtained with volume finite elements, while the results from the literature were based on plate finite elements, which could explain the small discrepancies observed in

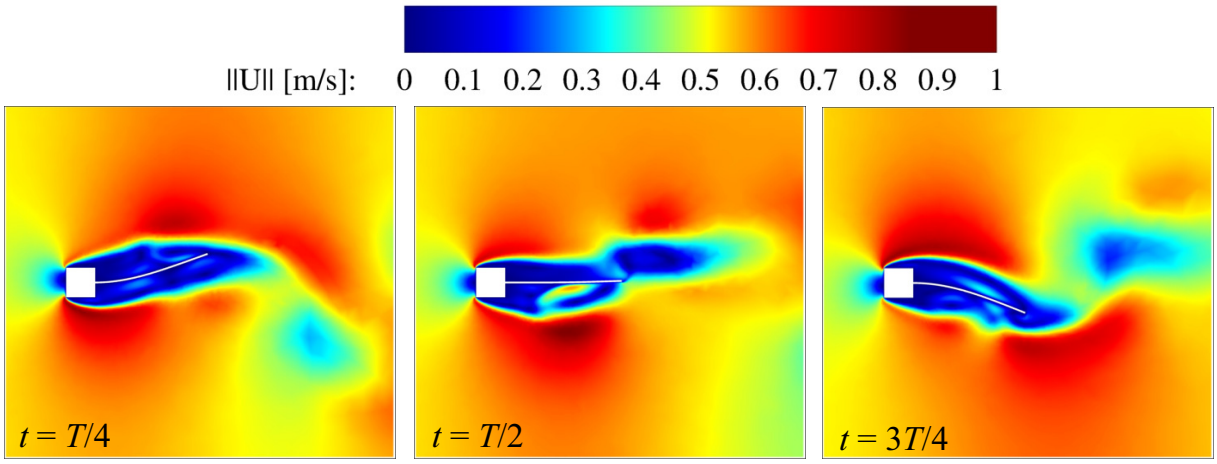

Figure 6: Velocity magnitude contour at three different times of a period. Results from the coupling between SU2 and Metafor.

Root chord [m]	c_r	0.559
Taper ratio [-]	λ	0.658
Tip chord [m]	c_t	0.368
Semi-span [m]	b_s	0.762
Aspect ratio [-]	AR	1.644
Wing surface [m^2]	S	0.353
Mean aerodynamic chord [m]	$\bar{c}$	0.470

Table 2: Geometrical properties of the AGARD 445.6 wing.

Longitudinal Young's modulus [GPa]	E_1	3.151
Transverse Young's moduli [GPa]	E_2, E_3	0.4162
Shear moduli [GPa]	G_{12}, G_{13}, G_{23}	0.4392
Poisson's ratio [-]	$\nu_{12}, \nu_{13}, \nu_{23}$	0.31
Density [kg m^{-3}]	ρ_s	381.98

Table 3: Material properties for the AGARD 445.6 wing.

the natural frequencies.

The coupled simulation is performed in the transonic regime with a free-stream Mach number $M_\infty = 0.8$ at an angle of attack $\alpha = 1°$. The free-stream velocity U_∞ and density ρ_∞ are set to 247.09 m/s and 0.09411 kg/m^3, respectively. A RBF interpolation using the TPS method is used to interpolate data between the solid and fluid meshes at the

	f_1	f_2	f_3	f_4
Present	9.54	40.35	50.22	97.67
Yates* [30]	9.60	38.10	50.70	98.50
Goura [31]	9.67	36.87	50.26	90.00
Beaubien *et al.* [32]	9.46	39.44	49.71	94.39
Zhang*et al.* [33]	9.57	38.17	48.35	91.55

Table 4: First four natural frequencies of the AGARD 445.6 wing from the present calculation and the literature (experimental results are identified by the * symbol). Frequencies are in Hz with f_1 and f_3 corresponding to the first and second bending modes, and f_2 and f_4 to the first and second torsion modes, respectively.

interface. The coupling tolerance is set to 10^{-6} m, which corresponds to 10^{-4} times the expected maximum tip displacement of the wing.

The static aeroelastic deformation at these conditions is illustrated in Figure 7. The values of the vertical displacement of the wing computed at the leading and trailing edges are summarized and compared with other references in Table 5. A discrepancy of 0.4 mm and 0.4-0.9 mm are observed at the leading and trailing edge, respectively, which could be explained by the use here of volume rather than plate finite elements.

	Leading edge	Trailing edge
Present	0.0116	0.0131
Goura [31]	0.0112	0.0127
Melville *et al.* [34]	0.0112	0.0122

Table 5: Vertical displacement of the wing tip at the leading and trailing edges. Values are in m.

5 CONCLUSION

A modular and flexible implementation of a coupling environment for Fluid-Structure Interaction problems was presented. The coupled problem is solved using a partitioned approach in which the fluid and solid solvers communicate through the coupler through a Python layer/interface. This ensures that the high-level management of the two solvers (black-box tools) is very intuitive and flexible and all the intensive calculations remain embedded in their respective core codes.

The results of several test cases were compared to the literature, demonstrating the accuracy of the coupling tool. The high modularity of the framework was demonstrated by using different structural solvers. Moreover, the coupling of other existing solid or

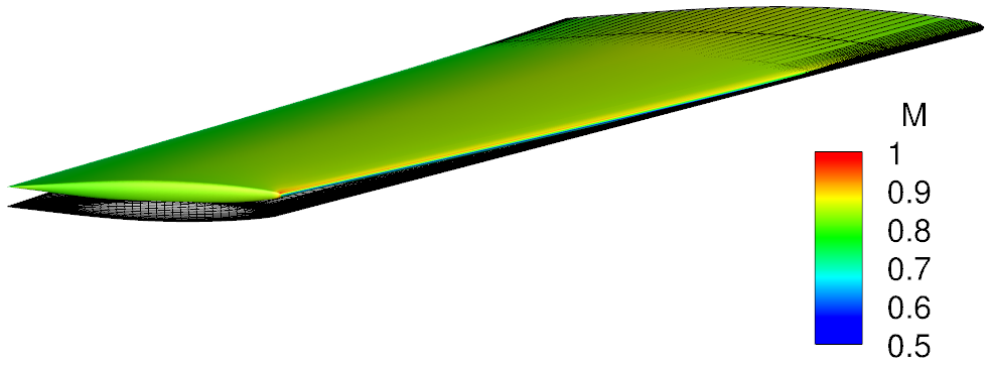

Figure 7: Static aeroelastic deformation of the AGARD 445.6 wing. The initial configuration is in gray. Contours of the Mach number are superposed to the deformed wing.

fluid solvers would be rather straightforward, requiring only minimal adaptations. The framework could also be easily extended to permit the coupling of other physics, such as conjugate heat transfer.

Future work will focus on extending some of the current capabilities of the tool, including the coupling algorithm, and the interpolation methods. Additionally, other multiphysics problems like conjugate heat transfer and coupling with different solvers will also be considered.

REFERENCES

[1] A.Y. Tang and N. Amin. Some numerical approaches to solve fluid structure interaction problems in blood flow. *Abstract and applied analysis*, 2014.

[2] G. Hou, J. Wang, and A. Layton. Numerical methods for fluid-structure interaction - A review. *Communications in Computational Physics*, 12(2):337–377, 2012.

[3] L. Garelli. *Fluid-structure interaction using an arbitrary Lagrangian-Eulerian formulation*. PhD thesis, Universidad Nacional Del Litoral, 2011.

[4] J. Donea, A. Huerta, J.-Ph. Ponthot, and A. Rodriguez-Ferran. *Encyclopedia of Computational Mechanics*, chapter Arbitrary Lagrangian-Eulerian Methods. Wiley, 2004.

[5] F.R. Menter. Zonal two equation $k - \omega$ turbulence model for aerodynamic flows. *AIAA Paper 1993-2906*, 1993.

[6] P.R Spalart and S.R. Allmaras. A one-equation turbulence model for aerodynamic flows. *Recherche aerospatiale*, 1:5–21, 1994.

[7] F. Palacios, M.R. Colonno, A.C. Aranake, A. Campos, S.R. Copeland, T.D. Economon, A.K. Lonkar, T.W. Lukaczyk, T.W.R. Taylor, and J.J. Alonso. Stan-

ford University Unstructured (SU^2): An open-source integrated computational environment for multi-physics simulation and design. In *AIAA 51st Aerospace Sciences Meeting*, Grapevine, TX, 7-10 January, 2013.

[8] R. Sanchez, H.L. Kline, D. Thomas, A. Variyar, M. Righi, T.D. Economon, J.J. Alonso, R. Palacios, G. Dimitriadis, and V. Terrapon. Assessment of the fluid-structure interaction capabilities for aeronautical applications of the open-source solver SU2. In *ECCOMAS Congress, VII European Congress on Computational Methods in Applied Sciences and Engineering*, Crete Island, Greece, June 2016.

[9] A. Jameson and S. Schenectady. An assessment of dual-time stepping, time spectral and artificial compressibility based numerical algorithm for unsteady flow with applications to flapping wings. *AIAA Paper 2009-4273*, 2009.

[10] METAFOR. A nonlinear finite element code. University of Liège, http://metafor.ltas.ulg.ac.be/.

[11] G.J. Kennedy and J.R.R.A Martins. Parallel solution methods for aerostructural analysis and design optimization. *AIAA Paper 2010-9308*, Sept 2010.

[12] J. Degroote, A. Souto-Iglesias, W. Van Paepegem, S. Annerel, P. Bruggeman, and J. Vierendeels. Partitioned simulation of the interaction between an elastic structure and free surface flow. *Computer Methods in Applied Mechanics and Engineering*, 199:2085–2098, 2010.

[13] U. Küttler and W. Wall. Fixed-point fluid-structure interaction solvers with dynamic relaxation. *Computational Mechanics*, 43:61–72, 2008.

[14] C. Wood, A.J. Gil, O. Hassan, and J. Bonet. Partitioned block-Gauss-Seidel coupling for dynamic fluid-structure interaction. *Computers and Structures*, 88:1367–1382, 2010.

[15] D.M. Beazley. SWIG : An easy to use tool for integrating scripting languages with C and C++. In *4th Tcl/Tk Workshop*, Monterey, CA, USA, July 1996.

[16] L. Dalcin, R. Paz, M. Storti, and J. D'Elia. MPI for Python: Performance improvements and MPI-2 extensions. *Journal of Parallel and Distributed Computing*, 68(5):655–662, 2008.

[17] L. Dalcin, R. Paz, P. Kler, and A. Cosimo. Parallel distributed computing using Python. *Advances in Water Resources*, 34(9):1124–1139, 2011.

[18] C. Habchi, S. Russeil, D. Bougeard, J-L. Harion, T. Lemenand, A. Ghanem, D. Della Valle, and H. Peerhossaini. Partitioned solver for strongly coupled fluid-structure interaction. *Computers and Fluids*, 71:306–319, 2013.

[19] A. de Boer, A.H van Zuijlen, and H. Bijl. Review of coupling methods for non-mathcing meshes. *Computational Methods in Applied Mechanics and Engineering*, 196:1515–1525, 2007.

[20] O. Estruch, O. Lehmkuhl, R. Borrel, C.D. Pérez Segarra, and A. Oliva. A parallel radial basis function interpolation for unstructured dynamic meshes. *Computers and Fluids*, 80:44–54, 2013.

[21] K. Isogai. On the transonic-dip mechanism of flutter of a sweptback wing. *AIAA Journal*, 17(7):793–795, 1979.

[22] K. Isogai. Transonic-dip mechanism of flutter of a sweptback wing: Part II. *AIAA Journal*, 19(9):1240–1242, 1981.

[23] R.L. Bisplinghoff, H. Ashley, and R. L. Halfman. *Aeroelasticity*. Dover Publications, 1996.

[24] F. Liu, J. Cai, and Y. Zhu. Calculation of wing flutter by a coupled fluid-structure method. *Journal of Aircraft*, 38(2):334–342, 2001.

[25] J.J. Alonso and A. Jameson. Fully-implicit time marching aeroelastic solution. In *AIAA 32nd Aerospace Sciences Meeting and Exhibit*, 10-13 January, 1994.

[26] Z. Biao, Q. Zhide, and G. Chao. Transonic flutter analysis of an airfoil with approximate boundary method. In *26th international congress of the aeronautical sciences*, 2008.

[27] J.T. Thomas, K.C. Hall, and E.H. Dowell. Reduced-order aeroelastic modeling using proper-orthogonal decomposition. *CEAS/AIAA/ICASE/NASA Langley International Forum on Aeroelasticity and Structural Dynamics*, 1999.

[28] C. Kassiotis, A. Ibrahimbegovic, R. Niekamp, and H. Matthies. Nonlinear fluid-structure interaction problem. Part I : implicit partitioned algorithm, nonlinear stability proof and validation examples. *Computational Mechanics*, 47:305–323, 2011.

[29] M. Olivier, G. Dumas, and J. Morissette. A fluid-structure interaction solver for nano-air-vehicle flapping wings. In *Proceedings of the 19th AIAA computational fluid dynamics conference*, pages 1–15, San Antonio, USA, June 2009.

[30] E.C. Yates. Agard standard aeroelastic configuration for dynamic response I - Wing 445.6. *AGARD Report 765*, 1988.

[31] G.S.L. Goura. *Time marching analysis of flutter using computational fluid dynamics*. PhD thesis, University of Glasgow, 2001.

[32] R. Beaubien, F. Nitzsche, and D. Feszty. Time and frequency domain solutions for the AGARD 445 wing. In *International Forum on Aeroelasticity and Structural Dynamics (IFASD)*, Munich, Germany, 2005.

[33] B. Zhang, W Ding, J. Shengcheng, and J. Zhang. Transonic flutter analysis of an AGARD 445.6 wing in the frequency domain using the Euler method. *Engineering applications of computational fluid mechanics*, 10(1):244–255, 2016.

[34] R.B. Melville, S.A. Morton, and D.P. Rizzetta. Implementation of a fully-implicit, aeroelastic Navier-Stokes solver. In *13th Computational Fluid Dynamics Conference*, Snowmass Village, CO, USA, June-July 1997.

VII International Conference on Computational Methods for Coupled Problems in Science and Engineering
COUPLED PROBLEMS 2017
M. Papadrakakis, E. Oñate and B. Schrefler (Eds)

THE COMPARISON OF DIFFERENT ACOUSTIC APPROACHES IN THE SIMULATION OF HUMAN PHONATION

Jan Valášek*, Manfred Kaltenbacher† and Petr Sváček††

*,†† Department of Technical Mathematics
Faculty of Mechanical Engineering, CTU in Prague
Karlovo nam. 13, 121 35 Praha 2, Czech Republic
e-mail: jan.valasek1@fs.cvut.cz, petr.svacek@fs.cvut.cz

†Institute for Mechanics and Mechatronics
Technical University Vienna
Getreidemarkt 9, 1060 Wien, Austria
e-mail: manfred.kaltenbacher@tuwien.ac.at - Web page: http://www.mec.tuwien.ac.at

Key words: Fluid-Structure Interaction, 2D Navier-Stokes equations, Linear Elasticity, Aeroacoustic Analogies, Perfectly Matched Layer

Abstract. This contribution deals with mathematical modelling and numerical simulation of the human phonation process. This phenomena is described as a coupled problem composed of the three mutually coupled physical fields: the deformation of elastic body, the fluid flow and the acoustics. For the sake of simplicity only a two-dimensional model problems is considered in this paper. The fluid-structure interaction problem is described by the incompressible Navier-Stokes equations, by the linear elasticity theory and by the interface conditions. In order to capture the motion of the fluid domain the arbitrary Lagrangian-Eulerian method is used. The strongly coupled partitioned scheme is used for solution of the coupled fluid-structure problem. For solution of acoustics the acoustic analogies are used. Two analogies are compared - the Lighthill analogy and convected perturbation wave equation. The influence of acoustic field back to fluid as well as to structure is neglected. The numerical approximation of all three physical domains is perforemd with the aid of the finite element method. The numerical results present sound propagation through the model of the vocal tract.

1 INTRODUCTION

The human phonation is very interesting phenomenon and a complex topic of ongoing research, see e.g. [7]. A better understanding of the human phonation process can help physicians and therapists to improve treatment of people with voice disorders, where the

economic losses due to voice malfunction just in USA is estimated up to $160 billion per year, [9]. Recently due to practical inaccessibility of human organs numerical simulations have become to be an important tool used in the research.

The human phonation is a multi-physical problem consisting of three coupled physical fields – the deformation of the vocal folds (elastic body), the fluid flow and the acoustics together with all relevant coupling terms. It is sometimes summarized under fluid-structure-acoustic interaction (FSAI) problem. The mutual coupling between the fluid and the structure is usually strong, i.e. each physical field influences the other one. On the other hand the acoustic field in the considered problem depends on both the fluid and structure fields, but the influence of the acoustic back to the flow field as well as to the elastic body motion can be neglected. Thus it is possible to use only the so-called forward coupling from the fluid flow to the acoustic field, see [11].

There are a lot of papers covering the subject of human phonation ranging from studies of purely flow simulation in 2D or 3D domains like [10] or reports with prescribed motion of vocal folds, see for example [8], up to even 3D simulation of aeroacoustic problem, see e.g. [11]. The critical part for acoustic simulation is reliable solution of fluid flow. In general the maximal velocity lies noticeably under 0.3 Mach number (stated as incompressible limit), the flow passing the glottis is characterized by quite complex turbulent structure. This results in high computation demand namely in 3D, see [10].

This contribution presents the 2D aeroacoustic computation based on fluid-structure interaction (FSI) simulations, where the comparison of results acquired by the Lighthill analogy and the perturbed convective wave equation (PCWE) is shown. Similar hybrid approach has been already adopted in e.g. [11]. Furthermore, to include the effects of time-dependent computational domain for the fluid flow the Arbitrary Lagrangian-Eulerian (ALE) method was used. The linear elasticity theory was used for description of the elastic structure motion. Finally, the acoustics was modelled by Lighthill acoustic analogy and PCWE, [4]. The perfectly matched layer (PML) technique with inverse mapping was applied to solve the open-domain problem, see [5].

The numerical model is based on the finite element method (FEM), which is used for all three physical domains. For stabilization of the fluid flow simulation, the modified Streamline-Upwind/Petrov-Galerkin stabilization is utilized, [3]. In the end the numerical results of flow induced vibration and sound propagation through vocal tract are presented. The pressure spectra obtained by the Lighthill analogy and by PCWE are compared.

2 MATHEMATICAL MODEL

For the sake of simplicity a two-dimensional FSAI problem is considered. The FSI domain, schematically shown in Figure 1, is a subset of a substantially larger domain of sound propagation, see Figure 2. The FSI domain consists of the domain Ω^s_{ref}, representing the elastic structure (the vocal folds), and the domain Ω^f_{ref} occupied by fluid. The deformation of the elastic structure is described in the Lagrange coordinates. The domain Ω^f_{ref} denotes the reference fluid domain, e.g. the domain at the time instant $t = 0$ with

the common interface $\Gamma_{\mathrm{W_{ref}}} = \Gamma_{\mathrm{W_0}}$ between the fluid and the structure domain. The time evolution of the reference domain Ω^f_{ref} to the deformed domain Ω^f_t as well as the reference interface $\Gamma_{\mathrm{W_{ref}}}$ to the interface $\Gamma_{\mathrm{W_t}}$ at any time instant t is described by the ALE method.

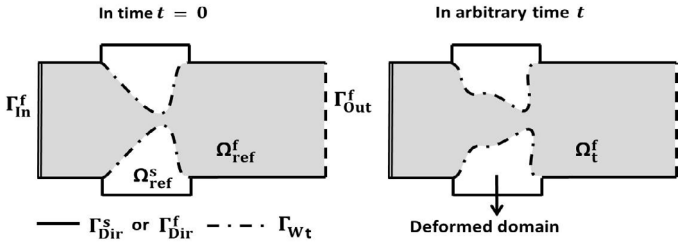

Figure 1: Schematic figure of vocal folds model and fluid domain with boundaries marked before (left) and after (right) a deformation.

2.1 Elastic body

The unknown deformation vector $\mathbf{u}(X,t) = (u_1, u_2)$ of the elastic body Ω^s is sought as a solution of the partial differential equation

$$\rho^s \frac{\partial^2 u_i}{\partial t^2} - \frac{\partial \tau^s_{ij}(\mathbf{u})}{\partial X_j} = f_i{}^s \quad \text{in } \Omega^s \times (0,\mathrm{T}). \tag{1}$$

This equation expresses the dynamic equilibrium between the inertia force and applied volume and surface forces. The structure density is denoted as ρ^s, the tensor τ^s_{ij} is the Cauchy stress tensor, the vector $\mathbf{f}^s = (f^s_1, f^s_2)$ is the volume density of an acting force and $X = (X_1, X_2)$ are the reference coordinates. Under the assumption of the linear relation between the displacement and the stress the generalized Hook law can be used, which for the isotropic case reads

$$\tau^s_{ij} = \lambda^s (\mathrm{div}\ \mathbf{u})\, \delta_{ij} + 2\mu^s e^s_{ij}, \tag{2}$$

where λ^s, μ^s are Lamé coefficients depending on the Young modulus of elasticity E^s and the Poisson ratio σ^s, see e.g. [12]. The tensor $\mathbb{I} = (\delta_{ij})$ is the Kronecker's delta and the tensor $\mathbf{e}^s = (e^s_{jk})$ is the strain tensor. For small displacements it has the form

$$e^s_{jk} = \frac{1}{2}\left(\frac{\partial u_j}{\partial X_k} + \frac{\partial u_k}{\partial X_j}\right). \tag{3}$$

Equation (1) is supplied by the initial and boundary conditions

$$\begin{aligned}
&\text{a)} && \mathbf{u}(X,0) = \mathbf{u}_0(X),\ \frac{\partial \mathbf{u}}{\partial t}(X,0) = \mathbf{u}_1(X) && \text{for } X \in\ \Omega^s,\\
&\text{b)} && \mathbf{u}(X,t) = \mathbf{u}_{\mathrm{Dir}}(X,t) && \text{for } X \in \Gamma^s_{\mathrm{Dir}},\ t \in (0,\mathrm{T}),\\
&\text{c)} && \tau^s_{ij}(X,t)\, n^s_j(X) = q^s_i(X,t), && \text{for } X \in \Gamma^s_{\mathrm{W_t}},\ t \in (0,\mathrm{T}),
\end{aligned} \tag{4}$$

where the $\Gamma_{\mathrm{W_{ref}}}, \Gamma^s_{\mathrm{Dir}}$ are mutually disjoint parts of the boundary $\partial\Omega^s = \Gamma_{\mathrm{W_{ref}}} \cup \Gamma^s_{\mathrm{Dir}}$ (see Figure 1) and $n^s_j(X)$ are components of the unit outer normal to $\Gamma_{\mathrm{W_{ref}}}$.

2.2 ALE method

One of the standard methods, which enable to solve the fluid flow in a time-dependent domain, is the ALE method. The basis of this method is the construction of a diffeomorphism A_t which maps the reference (undistorted) domain $\Omega^f_{\rm ref}$ on to the domain Ω^f_t at any instant time $t \in (0, \mathrm{T})$. The ALE domain velocity $\mathbf{w}_D$ under assumption of continuity of derivatives $\frac{\partial A_t}{\partial t} \in C(\overline{\Omega^f_{\rm ref}})$ is defined as

$$\mathbf{w}_D(A_t(X), t) = \frac{\partial}{\partial t} A_t(X), \quad t \in (0, \mathrm{T}),\ X \in \Omega^f_{\rm ref}. \tag{5}$$

The ALE derivative is then introduced as the time derivative with respect to a fixed point $X \in \Omega^f_{ref}$. It satisfies the following relation

$$\frac{D^A}{Dt} f(x,t) = \frac{\partial f}{\partial t}(x,t) + \mathbf{w}_D(x,t) \cdot \nabla f(x,t). \tag{6}$$

More details and practical construction of ALE mapping is described e.g. in [2] or [14].

2.3 Fluid flow

The motion of the viscous incompressible fluid in time-dependent domain Ω^f_t is described by the fluid velocity $\mathbf{v}(x,t)$ and the kinematic pressure p. This pair of unknowns obey the Navier-Stokes equations in the ALE form, see [2]

$$\frac{D^A \mathbf{v}}{Dt} + ((\mathbf{v} - \mathbf{w}_D) \cdot \nabla)\mathbf{v} - \nu^f \Delta \mathbf{v} + \nabla p = \mathbf{0}, \quad \text{div } \mathbf{v} = 0 \quad \text{in } \Omega^f_t, \tag{7}$$

where ν^f is the kinematic fluid viscosity.

The formulation of Navier-Stokes equations (fluid part of FSI problem) (7) is completed by zero initial and the following boundary conditions

$$\text{a)} \qquad \mathbf{v}(x,t) = \mathbf{w}_D(x,t) \qquad \text{for } x \in \Gamma^f_{\rm Dir} \cup \Gamma_{\rm W_t},\ t \in (0,\mathrm{T}), \tag{8}$$

$$\text{b)} \quad p(x,t)\mathbf{n}^f - \nu^f \frac{\partial \mathbf{v}}{\partial \mathbf{n}^f}(x,t) = -\frac{1}{2}\mathbf{v}(\mathbf{v}\cdot\mathbf{n}^f)^- + p_{\rm ref}\mathbf{n}^f \quad \text{for } x \in \Gamma^f_{\rm In} \cup \Gamma^f_{\rm Out},\ t \in (0,\mathrm{T}),$$

where $\mathbf{n}^f$ is unit outer normal to boundary $\partial\Omega^f_t$ and $p_{\rm ref}$ is a reference pressure (possibly different on the inlet $\Gamma^f_{\rm In}$ and the outlet $\Gamma^f_{\rm Out}$). The condition (8 b) is the modified do-nothing boundary condition, see e.g. [1].

2.4 Aeroacoustics

The acoustic domain Ω^a, where the acoustic problem is solved, is depicted in Figure 2. It is composed of three parts $\Omega^a_{\rm src}, \Omega^a_{\rm air}$ and $\Omega^a_{\rm pml}$, where $\overline{\Omega^a} = \overline{\Omega^a_{\rm src}} \cup \overline{\Omega^a_{\rm air}} \cup \overline{\Omega^a_{\rm pml}}$. The acoustic sources are calculated from the computed flow field in the domain $\Omega^a_{\rm src}$, which is

the same as reference fluid domain, i.e. $\Omega^a_{\text{src}} = \Omega^f_{\text{ref}}$. The change of domain Ω^a_{src} in time is neglected, the sources obtained on Ω^f_t are transformed back to the domain Ω^f_{ref} with the help of the ALE mapping. The domain Ω^a_{air} represents a part of the vocal tract behind the glottis up to mouth including a far field region, i.e. the outer space. The PML domain Ω^a_{pml} closes both the aforementioned domains in order to damp the outgoing sound waves.

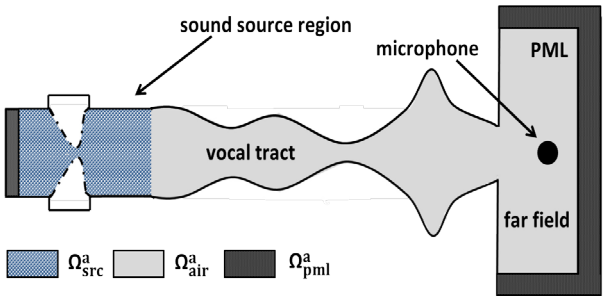

Figure 2: Scheme of acoustic domain. The propagation domain has tree parts – the sound source region, the vocal tract and the far field. Propagation region is enclosed by the PML region.

2.4.1 Lighthill analogy

The Lighthill analogy is inhomogenous wave equation

$$\frac{1}{c_0^2}\frac{\partial^2 p'}{\partial t^2} - \frac{\partial^2 p'}{\partial x_i^2} = \frac{\partial^2 T_{ij}}{\partial x_i \partial x_j}, \tag{9}$$

for unknown pressure fluctuation p' with known values of the Lighthill tensor T_{ij} and a given speed of sound c_0. This equation was derived by Lighthill in 1952 from compressible Navier-Stokes equations under supposition that acoustic waves with origin in a small source region propagate through a voluminous medium in rest state characterized by $\mathbf{v}_0 = \mathbf{0}, p_0$ and rest fluid density ρ^f_0. The formation of sound is here imaginary caused by acting force in the form of Lighthill tensor divergence, see [6]. The components of the Lighthill tensor T_{ij} are given by

$$T_{ij} = \rho^f v_i v_j + ((p - p_0) - c_0^2(\rho^f - \rho^f_0))\delta_{ij} - \tau^f_{ij}, \tag{10}$$

where τ^f_{ij} is the fluid viscous stress tensor. In next the Lighthill tensor is approximated by $T_{ij} \approx \rho^f v_i v_j$, where the viscous stress τ^f_{ij} and the stresses connected with the heat conduction $(p' - c^2\rho')\delta_{ij}$ are neglected, see [6].

2.4.2 Perturbed convective wave equation

Another suitable choice of acoustic analogy is the PCWE. It is based on splitting of physical quantities into mean and fluctuating parts. The fluctuating variables consists of

acoustic parts and non-acoustic components, i.e. incompressible parts

$$p = \overline{p} + p_{ic} + p_a, \qquad \mathbf{v} = \overline{\mathbf{v}} + \mathbf{v}_{ic} + \mathbf{v}_a. \tag{11}$$

With the presumption of incompressible homoentropic flow the splitting leads to the following partial differential equation for $\mathbf{v}^a$ and p^a

$$\frac{\partial p^a}{\partial t} + \overline{\mathbf{v}} \cdot \nabla p^a + \rho_0^f c_0^2 \nabla \cdot \mathbf{v}^a = -\frac{D p_{ic}}{D t}, \qquad \frac{\partial \mathbf{v}^a}{\partial t} + \nabla(\overline{\mathbf{v}} \cdot \mathbf{v}^a) + \frac{1}{\rho_0^f} \nabla p^a = \mathbf{0}, \tag{12}$$

where the substantial derivative $\frac{D}{Dt}$ equals $\frac{D}{Dt} = \frac{\partial}{\partial t} + \overline{\mathbf{v}} \cdot \nabla$. For derivation and discussion see [4]. These equations can be rewritten into one with the help of acoustic potential ψ^a related to the acoustic particle velocity $\mathbf{v}^a = -\nabla \psi^a$ (acoustic velocity field is irrotational)

$$\frac{1}{c_0^2} \frac{D^2 \psi^a}{D t^2} - \Delta \psi^a = -\frac{1}{\rho_0^f c_0^2} \frac{D p_{ic}}{D t}, \tag{13}$$

For further details see [4]. Moreover for low velocities we can disregard convection $\overline{\mathbf{v}} = 0$ and the PCWE formulation (13) simplifies further to

$$\frac{1}{c_0^2} \frac{\partial^2 \psi^a}{\partial t^2} - \Delta \psi^a = -\frac{1}{\rho_0^f c_0^2} \frac{\partial p_{ic}}{\partial t}. \tag{14}$$

Eq. (14) is very similar to Eq. (9), but with a quite big advantage of only first time derivative of right hand source term.

The wave equation (9) or (13), (14) is equipped with the zero initial condition and the boundary of acoustic domain $\partial\Omega^a$ with the outer normal $\mathbf{n}^a$ is considered as sound hard

$$\frac{\partial p'}{\partial \mathbf{n}^a}(x,t) = 0 \quad \text{or} \quad \frac{\partial \psi^a}{\partial \mathbf{n}^a}(x,t) = 0 \qquad \text{for } x \in \partial\Omega^a,\ t \in (0, \mathrm{T}). \tag{15}$$

2.4.3 PML

To tackle the open-boundary problem in bounded domains the PML technique was used. A few additional layers of elements were added along the normal direction of boundaries, which represents interface with open space. Inside these layers the sound waves are effectively damped to zero without any reflection at the interface between propagation region and PML. We further refer to [5].

2.5 Coupling conditions

The FSAI problem is coupled problem of three physical fields. The FSI coupling as well as acoustics-structure has the form of boundary conditions on the common interface, where on the contrary the fluid-acoustics coupling has volumetric character. Only the

forward coupling between FSI and acoustics is used, e.g. the forward acoustic coupling has the form of the flow field postprocessing.

The elastic deformation in FSI problem has prescribed Neumann boundary condition representing the impact of the aerodynamic forces on the elastic body

$$q_i^s(X,t) = -\sum_{j=1}^{2} \sigma_{ij}^f(x)\, n_j^f(x), \quad x = X + \mathbf{u}(X,t),\ X \in \Gamma_{\mathrm{W_{ref}}}, \tag{16}$$

where $\sigma_{ij}^f = \rho^f \left(-p\delta_{ij} + \nu^f(\frac{\partial v_i}{\partial x_j} + \frac{\partial v_j}{\partial x_i})\right)$, $i,j \in \{1,2\}$ are the components of the fluid stress tensor.

The fluid flow problem is completed with the Dirichlet boundary condition postulated by equation (8 a), which represents the continuity between the fluid and the structure velocity across the boundary $\Gamma_{\mathrm{W_t}}$.

Moreover also the location of the interface $\Gamma_{\mathrm{W_t}}$ at time t is also variable and it depends on the solution of FSI problem. Its location corresponding to the force equilibrium between aerodynamic and elastic forces at time instant t and it is implicitly given by structure deformation $\mathbf{u}(t)$ as $\Gamma_{\mathrm{W_t}} = \{x \in \mathbb{R}^2 |\, x = X + \mathbf{u}(X,t),\ X \in \Gamma_{\mathrm{W_{ref}}}\}$.

3 NUMERICAL MODEL

All three subproblems given by partial differential equations (1), (7) and (9) or (14) are solved by the FEM based on the weak formulation in space. Obtained semi-discrete system is subsequently discretized in time by the finite difference scheme with the same constant time step $\Delta t = \frac{T}{N}, N >> 1$.

3.1 Acoustics

Equations (9) are reformulated in the weak sense with the aid of a test function η from the Sobolev space $W^{1,2}(\Omega^a)$, see [4]. The application of the Green theorem together with the definition of boundary condition (15) gives us the final form

$$\int_{\Omega^a} \frac{1}{c_0^2} \frac{\partial^2 p'}{\partial t^2} \eta \,\mathrm{d}x + \int_{\Omega^a} \nabla p' \cdot \nabla \eta \,\mathrm{d}x = -\int_{\Omega^a} (\mathrm{div}\,\mathbf{T}) \cdot \nabla \eta \,\mathrm{d}x. \tag{17}$$

Using the restriction of test functions to a finite element space and seeking the solution as a linear combination of the basis functions η_j with unknown time dependent coefficients $\boldsymbol{\gamma} = \boldsymbol{\gamma}(t)$ leads to

$$\mathbb{M}^a \ddot{\boldsymbol{\gamma}} + \mathbb{K}^a \boldsymbol{\gamma} = \mathbf{b}^a(t), \tag{18}$$

where the components of the vector $\mathbf{b}^a(t) = (b_i^a)$ and of the matrices $\mathbb{M}^a = (m_{ij}^a)$, $\mathbb{K}^a = (k_{ij}^a)$ are given as

$$b_i^a = -\int_{\Omega^a} (\nabla \cdot \mathbf{T}) \cdot \nabla \eta_i \,\mathrm{d}x, \quad m_{ij}^a = \int_{\Omega^a} \frac{1}{c_0^2} \eta_j \eta_i \,\mathrm{d}x, \quad k_{ij}^a = \int_{\Omega^a} \nabla \eta_j \cdot \nabla \eta_i \,\mathrm{d}x. \tag{19}$$

The derivation of the weak formulation of Eq. (13) or (14) is similar. System (18) is numerically discretized in time by the Newmark method.

3.2 Elastic body

The standard finite element discretization of problem (1) leads to the matrix system for the unknown time-dependent vector of coefficients $\boldsymbol{\alpha}(t)$, see e.g. [14], i.e.

$$\mathbb{M}\ddot{\boldsymbol{\alpha}} + \mathbb{C}\dot{\boldsymbol{\alpha}} + \mathbb{K}\boldsymbol{\alpha} = \mathbf{b}(t), \tag{20}$$

where matrices $\mathbb{M} = (m_{ij}), \mathbb{K} = (k_{ij})$ has elements

$$m_{ij} = \int_{\Omega^s} \rho^s \boldsymbol{\phi}_i \cdot \boldsymbol{\phi}_j \, \mathrm{d}X, \qquad k_{ij} = \int_{\Omega^s} \left(\lambda^s (\mathrm{div}\ \boldsymbol{\phi}_i)\, \delta_{rl} + 2\mu^s e^s_{rl}(\boldsymbol{\phi}_i)\right) e^s_{rl}(\boldsymbol{\phi}_j) \, \mathrm{d}X, \tag{21}$$

and the vector $\mathbf{b}(t)$ has components $b_i(t) = \int_{\Omega^s} \mathbf{f}^s \cdot \boldsymbol{\phi}_i \, \mathrm{d}X + \int_{\Gamma^s_{\mathrm{Neu}}} \mathbf{q}^s \cdot \boldsymbol{\phi}_i \, \mathrm{d}S$. The matrix $\mathbb{C} = \epsilon_1 \mathbb{M} + \epsilon_2 \mathbb{K}$ was added as the proportional damping with suitable parameters ϵ_1, ϵ_2. System (21) is numerically discretized in time by the Newmark method, see e.g. [2].

3.3 Fluid flow

The equation (7) is firstly discretized at arbitrary time step $t = t_{n+1}$ in time. The ALE derivative is approximated by the backward difference formula of second order

$$\frac{D^A \mathbf{v}}{Dt}(x, t_{n+1}) \approx \frac{3\mathbf{v}^{n+1}(x_{n+1}) - 4\mathbf{v}^n(x_n) + \mathbf{v}^{n-1}(x_{n-1})}{2\Delta t}, \quad x_i = A_{t_i}(A^{-1}_{t_{n+1}}(x)). \tag{22}$$

For the sake of simplicity in the next section the time index $^{n+1}$ will be omitted. By multiplication of equations (7) by a test function $\boldsymbol{\varphi} \in \mathbf{W}^{1,2}(\Omega^f)$ and $q \in L^2(\Omega^f)$, integration over Ω^f and by using Green theorem the standard weak spatial formulation is obtained, see e.g. [2]. One extra application of Green theorem used partially for the convective term delivers the formulation based on the analysis in [1] or described in [14]. The substitution of test spaces with finite element spaces $\mathbf{X}_h \subset \mathbf{W}^{1,2}(\Omega^f), M_h \subset L^2(\Omega^f)$ let us to write the approximative solution $\mathbf{v}_h, p_h$ as linear combinations

$$\mathbf{v}_h(x,t) = \sum_{j=1}^{2N_h^v} \beta_j^v(t)\, \boldsymbol{\varphi}_j(x), \qquad p_h(x,t) = \sum_{j=1}^{N_h^p} \beta_j^p(t)\, q_j(x), \tag{23}$$

where $\boldsymbol{\varphi}_j, q_j$ are finite element base functions of the spaces $\mathbf{X}_h, M_h$. This approach yields the matrix system

$$\begin{pmatrix} \mathbb{A}(\mathbf{v}_h) & \mathbb{B} \\ \mathbb{B}^T & 0 \end{pmatrix} \begin{pmatrix} \boldsymbol{\beta}^v \\ \boldsymbol{\beta}^p \end{pmatrix} = \begin{pmatrix} \mathbf{g} \\ \mathbf{0} \end{pmatrix}, \tag{24}$$

where $\mathbb{A}(\mathbf{v}_h) = \frac{1}{\Delta t}\mathbb{M} + \mathbb{C}(\mathbf{v}_h) + \mathbb{D}$. The elements of the matrices $\mathbb{M} = (m_{ij}), \mathbb{C} = (c_{ij})$, $\mathbb{D} = (d_{ij}), \mathbb{B} = (b_{ij})$ and the vector components $\mathbf{g} = (g_i)$ are given by

$$m_{ij} = \frac{3}{2}\int_{\Omega^f} \boldsymbol{\varphi}_j \cdot \boldsymbol{\varphi}_i \,\mathrm{d}x, \quad d_{ij} = \int_{\Omega^f} \nu^f \,\nabla\boldsymbol{\varphi}_j \cdot \nabla\boldsymbol{\varphi}_i \,\mathrm{d}x, \quad b_{ij} = \int_{\Omega^f} -q_j \,\mathrm{div}\, \boldsymbol{\varphi}_i \,\mathrm{d}x, \quad (25)$$

$$2 \cdot c_{ij} = \int_{\Omega^f} ((\mathbf{v}_h - 2\mathbf{w}_D^{n+1}) \cdot \nabla)\boldsymbol{\varphi}_j \cdot \boldsymbol{\varphi}_i - (\mathbf{v}_h \cdot \nabla)\boldsymbol{\varphi}_i \cdot \boldsymbol{\varphi}_j \,\mathrm{d}x + \int_{\Gamma^f_{\mathrm{Out}} \cup \Gamma^f_{\mathrm{In}}} (\mathbf{v}_h \cdot \mathbf{n}^f)^+ \boldsymbol{\varphi}_j \cdot \boldsymbol{\varphi}_i \,\mathrm{d}S,$$

$$g_i = \int_{\Omega^f} \frac{4\overline{\mathbf{v}}^n - \overline{\mathbf{v}}^{n-1}}{2\Delta t} \cdot \boldsymbol{\varphi}_i \,\mathrm{d}x - \int_{\Gamma^f_{\mathrm{Out}} \cup \Gamma^f_{\mathrm{In}}} p_{ref}\, \boldsymbol{\varphi}_i \cdot \mathbf{n}^f \,\mathrm{d}S.$$

The system of equations (24) is non-linear. For its solution the linearization $\mathbf{v}_h = \mathbf{v}^n$ is used together with the linear algebra solver from the library UMFPACK. The fluid FEM solver is stabilized by the streamline-upwind/Petrov-Galerkin, the pressure-stabilization/Petrov-Galerkin and 'div-div' stabilization method. It keeps the method stable, consistent and still accurate, see e.g. [3] or for the implementation details [2].

3.4 Algorithm

The advantage of chosen hybrid approach is that sound sources acting on right hand side of acoustic analogies can be computed anytime later from the solution of FSI problem. The partitioned FSI scheme was implemented with the strong coupling, for details see [2].

4 Numerical results

During the whole computation the time step was kept constant $\Delta t = 2.5 \cdot 10^{-5}\,\mathrm{s}$.

4.1 FSI problem

The vocal fold (VF) model shape consisting of four layers and their material parameters were adopted from the article [15] together with initial gap between VFs 2.0 mm. The damping parameters were chosen as $\epsilon_1 = 5\,\mathrm{s}^{-1}, \epsilon_2 = 2.0 \cdot 10^{-5}\,\mathrm{s}$ and the densities $\rho^s = 1000\,\mathrm{kg/m^3}$, $\rho^f = 1.185\,\mathrm{kg/m^3}$ and kinematic viscosity $\nu^f = 1.47 \cdot 10^{-5}\,\mathrm{m/s^2}$ was set.

The FSI problem was solved with the prescribed pressure difference between inlet and outlet with value $p_{\mathrm{ref}} = 2000\,\mathrm{Pa} \cdot \mathrm{m^3/kg}$. The full FSI interaction was enabled at 0.01 s and after a short transition behaviour the typical evolution of the flow induced vibration of VF appeared, see Figure 3. The excitation of first two eigenmodes of VF can be identified with the help of the Fourier transform. These results are in good correspondence with results of paper [15].

4.2 Aeroacoustics

The shape of vocal tract model for vowel \u\ are taken from MRI measurement – [13], where the length is modified due to the smooth connection between the end of the fluid computational domain and the start of sharply narrowing vocal tract domain.

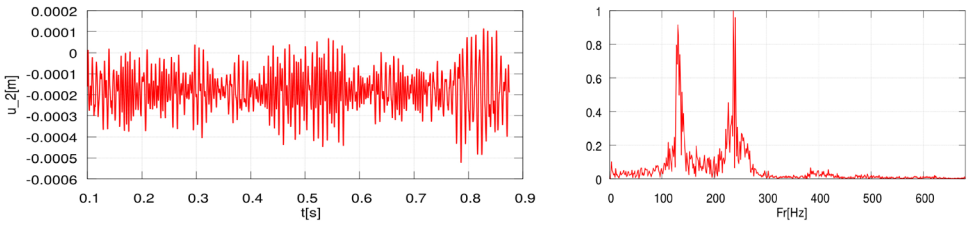

Figure 3: On the left - time behaviour of y-displacement of chosen point from the top of bottom VF. The displacement stored from $t = 0.1\,\mathrm{s}$. On the right - (normalized) Fourier transform of time signal from the left.

Since the acoustic problem does not require so fine grid, the sound source terms of Eq. (9) and (14) were interpolated onto coarser acoustic mesh during their calculation. The computed sound sources were further investigated by Fourier transform. The Figure 4 shows a comparison of the contributions with frequencies 235 and 1371 Hz obtained by different analogies. The sound source density with frequency 235 Hz corresponds to the VF excitation frequency and it is mainly located inside the glottis. The second density with nonharmonic frequency 1371 Hz is distributed in turbulent region behind glottis. It is associated with vorticity of the glottal jet and it has smaller magnitude. Similar character of results was obtained in [11]. The sources of Lighthill analogy is quite sensitive to the high velocity gradients due to the need of second space derivatives, which can lead to numerical artifacts.

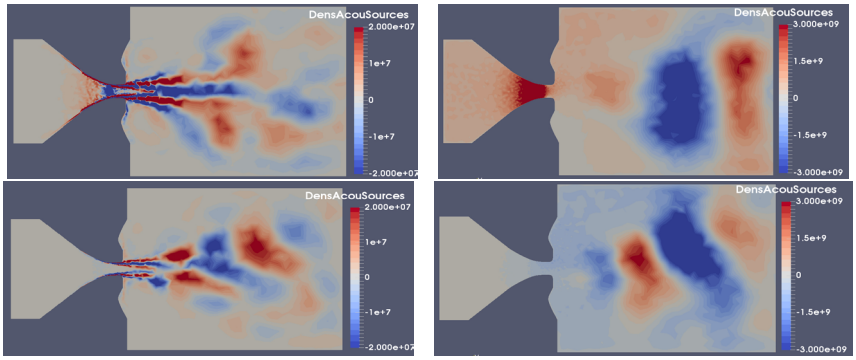

Figure 4: The computed sound source densities for Lighthill analogy on the left and for PCWE on the right for frequencies of 235 (up) and 1371 Hz (down).

Finally, the acoustic simulation was performed in the whole domain Ω^a. The acoustic pressure was monitored outside the mouth at the microphone position ($x = 0.24\,\mathrm{m}, y = 0\,\mathrm{m}$). The Fourier transform of acoustic pressure is depicted in Figure 5. The obtained frequencies for the PCWE case do not coincide with the frequencies of first formants of measured natural pronunciation of vowel \u\ in [13] (black lines in Figure 5). But the frequency peaks quite well answer the peaks of transfer function for vocal tract domain Ω^a_{air} at least for frequencies higher than 1500 Hz, see Figure 5. The differencies can be

caused by the aforementioned prolongation. The frequencies acquired for the Lighthill case do not demostrate agreetment with PCWE results. The effect of vocal tract filtering is clearly visible for higher frequencies.

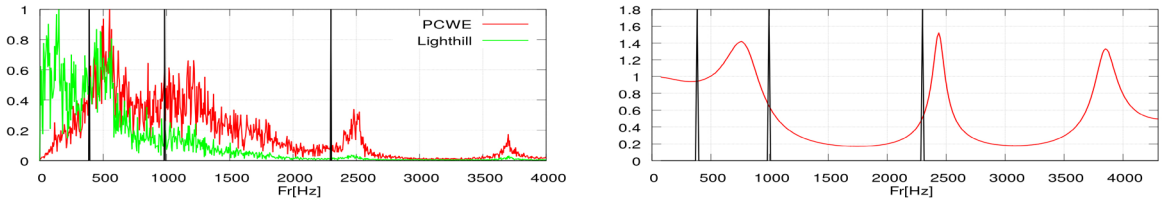

Figure 5: On the left - normalised Fourier transform of acoustic pressure measured at microphone position computed from 0.9 s signal length. The black vertical lines mark the frequencies 389 Hz, 987 Hz and 2299 Hz taken from article [13]. On the right - transfer function of chosen shape of vocal tract.

5 CONCLUSIONS

In this contribution the mathematical description of the FSAI is presented, where the hybrid partitioned approach was applied. The Lighthill acoustic analogy and PCWE approach were utilized for the calculation of the acoustic sources and simulation of their propagation through vocal tract model. The all three physical problems are numerically solved by the FEM. The fluid solver was stabilized by SUPG, PSPG and 'div-div' method. The results of flow induced vibration of vocal folds were computed and postprocessed by in-house developed program to determine the sound sources. They were analysed in frequency domain and then their propagation through vocal tract was simulated by CFS++ solver. The obtained results by PCWE and by Lighthill analogy do not show high correspondence.

Acknowledgment

Authors are grateful for possibility to use *C*FS++ scientific FE library. The financial support for this project was provided by the *Grant No. SGS16/206/OHK2/3T/12* of CTU in Prague.

REFERENCES

[1] M. Braack and P. B. Mucha. Directional do-nothing condition for the Navier-Stokes equations. *Journal of Computational Mathematics*, 32:507–521, 2014.

[2] M. Feistauer, P. Sváček, and J. Horáček. Numerical simulation of fluid-structure interaction problems with applications to flow in vocal folds. In T. Bodnár, G. P. Galdi, and S. Nečasová, editors, *Fluid-structure Interaction and Biomedical Applications*, pages 312–393. Birkhauser, 2014.

[3] Tobias Gelhard, Gert Lube, Maxim A. Olshanskii, and Jan-Hendrik Starcke. Stabilized finite element schemes with LBB-stable elements for incompressible flows. *Journal of Computational and Applied Mathematics*, 177(2):243–267, 2005.

[4] Andreas Hüppe and Manfred Kaltenbacher. Spectral finite elements for computational aeroacoustics using acoustic perturbation equations. *Journal of Computational Acoustics*, 20(02):1240005, 2012.

[5] Barbara Kaltenbacher, Manfred Kaltenbacher, and Imbo Sim. A modified and stable version of a perfectly matched layer technique for the 3-d second order wave equation in time domain with an application to aeroacoustics. *Journal of computational physics*, 235:407–422, 2013.

[6] Michael J Lighthill. On sound generated aerodynamically. i. general theory. In *Proceedings of the Royal Society of London A: Mathematical, Physical and Engineering Sciences*, volume 211, pages 564–587. The Royal Society, 1952.

[7] R. Mittal, B. D. Erath, and M. W. Plesniak. Fluid dynamics of human phonation and speech. *Annual Review of Fluid Mechanics*, 45:437–467, 2013.

[8] Petra Pořízková, Karel Kozel, and Jaromír Horáček. Numerical solution of compressible and incompressible unsteady flows in channel inspired by vocal tract. *Journal of Computational and Applied Mathematics*, 270:323–329, 2014.

[9] Robert J Ruben. Redefining the survival of the fittest: communication disorders in the 21st century. *The Laryngoscope*, 110(2):241–241, 2000.

[10] Rüdiger Schwarze, Willy Mattheus, Jens Klostermann, and Christoph Brücker. Starting jet flows in a three-dimensional channel with larynx-shaped constriction. *Computers & Fluids*, 48(1):68–83, 2011.

[11] P. Šidlof, S. Zörner, and A. Hüppe. A hybrid approach to the computational aeroacoustics of human voice production. *Biomechanics and Modeling in Mechanobiology*, 14(3):473–488, oct 2014.

[12] William S. Slaughter. *Linearized Elasticity Problems*. Springer, 2002.

[13] Brad H Story, Ingo R Titze, and Eric A Hoffman. Vocal tract area functions from magnetic resonance imaging. *The Journal of the Acoustical Society of America*, 100(1):537–554, 1996.

[14] J. Valášek, P. Sváček, and J. Horáček. Numerical solution of fluid-structure interaction represented by human vocal folds in airflow. In Vesely M. and Dancova P., editors, *EFM15 Experimental Fluid Mechanics 2015*, volume 114. EPJ Web of Conferences, March 2016.

[15] S. Zörner, M. Kaltenbacher, and M. Döllinger. Investigation of prescribed movement in fluid-structure interaction simulation for the human phonation process. *Computers & Fluids*, 86:133–140, 2013.

VII International Conference on Computational Methods for Coupled Problems in Science and Engineering
COUPLED PROBLEMS 2017
M. Papadrakakis, E. Oñate and B. Schrefler (Eds)

TRANSIENT MODELLING OF THE ROTOR-TOWER INTERACTION OF WIND TURBINES USING FLUID-STRUCTURE INTERACTION SIMULATIONS

G. SANTO [1]*, M. PEETERS [2], W. VAN PAEPEGEM [2], J. DEGROOTE [1]

[1] Department of Flow, Heat and Combustion Mechanics, Ghent University
Sint-Pietersnieuwstraat 41 – 9000 Ghent, Belgium
{gilberto.santo; joris.degroote}@ugent.be

[2] Department of Materials, Textiles and Chemical Engineering, Ghent University
Technologiepark-Zwijnaarde 907 – 9052 Zwijnaarde, Belgium
{mathijs.peeters; wim.vanpaepegem}@ugent.be

Key words: Fluid-structure interaction, wind energy, composite materials, atmospheric boundary layer.

Abstract. In this work, we focus on the effect of supporting structures on the loads acting on a large horizontal axis wind turbine. The transient fluid-structure interaction (FSI) is simulated by an in-house code which couples two solvers, one for the computational fluid dynamics (CFD) and one for the computational structure mechanics (CSM). Strong coupling is applied as the force and displacement equilibriums are always enforced on the fluid-structure interface.

The flexibility of the three blades of the considered machine is taken into account. The accurate CSM model reproduces in details the composite layups, foam, adhesive and internal stiffeners of the blades. On the other hand, the supporting structures (tower and nacelle) are considered to be rigid.

On the fluid side, a fully hexahedral mesh is generated by a multi-block strategy. The same mesh is continuously deformed and adapted according to the displacement of the fluid-structure interface. The atmospheric boundary layer (ABL) under neutral conditions is included and consistently preserved along the computational domain.

Using the outlined model, the blade deflections with and without supporting structure are compared. The effects of this transient interaction are highlighted throughout the rotation of the rotor, in terms of both wind energy conversion performance of the machine and structural response of each component. The maximal stress in the blade material as a function of time is compared with and without the presence of the tower in the wake of the rotor. Only a few similar works are reported to appear in literature [1, 2], whereas none of them currently includes the ABL or show detailed information about the internal stresses in the composite blades.

1 INTRODUCTION

The actual tendency of increasing the size of the horizontal axis wind turbine's rotor [3] to maximize the captured energy, and the resulting higher slenderness of their blades, have strengthened the necessity to investigate the mutual interaction of wind flow and structural response of the blades. Previous research has shown that the axial deflection of the blade tips can reach peaks of 10-15% of their total span [4, 5]. As a consequence, the deformed shape of the blades influences the wind flow around them, which in turn affects the structural deflection. This results in a fully coupled problem which is important to take into account in several processes such as design and maintenance estimation of modern horizontal axis wind turbines (HAWTs) [6].

Both sides of this problem, namely the fluid and the structural ones, involve a large complexity when it comes to numerical analysis. On the structural side, the blades' inner and outer structures are made of anisotropic composite material and assembled by means of adhesive joints [7]. On the fluid side, the Reynolds number of the flow can go up to 10^8. The consequent high turbulence levels, combined with the rotation of the blades, make the problem even harder to tackle [2, 4, 5]. Additionally, large HAWTs normally are immersed in the atmospheric boundary layer (ABL) which leads to variable velocity and turbulence in altitude [8]. The presence of the supporting structures (tower and nacelle) represents a disturbance for the flow around the blades passing in their region of influence [1]. This effect, addressed as rotor-tower interaction, is here investigated.

The present work aims at simulating the fully coupled fluid-structure interaction (FSI) problem on a full scale 100m diameter HAWT employing accurate flow and structural models, leading to a fully coupled FSI model. The ABL is also taken into account. The effect of the rotor-tower interaction is highlighted by comparison of results obtained simulating only the rotating parts of the considered HAWT ("rotor only") and results obtained including the supporting structures ("full machine"). On the structural side, a complete and accurate model reproducing the complex composite nature of each blade is built and employed. The implicit coupling between the flow and the structural models is guaranteed by the in-house code Tango, resulting in a partitioned approach [12].

2 METHODOLOGY

The details of the computational fluid dynamics (CFD) and computational structural mechanics (CSM) are now discussed.

2.1 The CFD model

The adoption of different reference frames is necessary: a stationary and a rotating domain are created and separated by sliding interfaces. The layout of the complete mesh is displayed in fig. 1, together with the distances (in terms of turbine diameter D) of the boundaries from the rotating domain and the boundary conditions used.

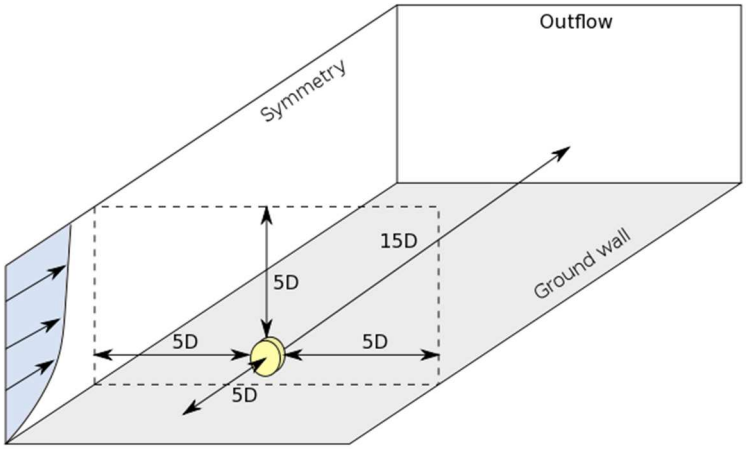

Figure 1: Layout adopted for the HAWT simulations; in yellow, the rotating domain.

Both the "rotor only" (RO) and "full machine" (FM) configurations are displayed in fig. 2. The exact same rotating cylinder is used in both cases while, in the FM case, the stationary domain is adapted to accommodate the supporting structures (tower and nacelle). The tower geometry is chosen to be suitable for the size of the considered HAWT and extracted from [13].

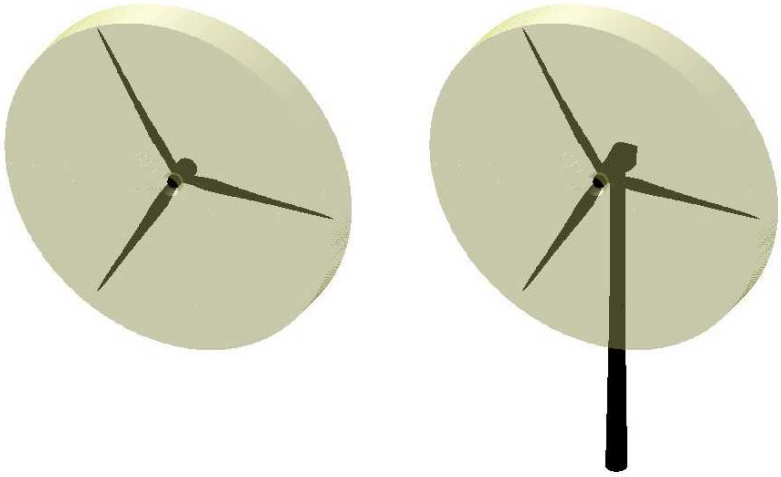

Figure 2: Detail of the rotating domain: (left) RO case and (right) FM case.

Given the low Mach number, the flow is considered incompressible and the turbulence model is chosen to be the $k-\varepsilon$ (unsteady RANS) model, which adds two transport equations.

The ABL inlet conditions first proposed by Richard and Hoxey [8] are employed at the inlet of the stationary domain to replicate the neutral ABL velocity and turbulence stratification. With z the height of the domain (distance from the ground wall), the inlet conditions for velocity u, turbulent kinetic energy k and turbulent dissipation rate ε are

respectively:

$$u(z) = \frac{u_*}{\mathrm{K}} ln\left(\frac{z + z_0}{z_0}\right)$$
$$k = \frac{u_*^2}{\sqrt{C_\mu}}$$
$$\varepsilon(z) = \frac{u_*^3}{\mathrm{K}(z + z_0)}$$

In these equations, u_* represents the friction velocity, an index of the global wind intensity, and z_0 is the aerodynamic roughness length which provides a measure of how rough the ground wall is. In this work, u_* and z_0 are chosen respectively equal to $0.792\ m/s$ and $0.5\ m$, reproducing a rather intense wind over a rough ground. K represents the von Karman constant (0.4187), while C_μ is a constant of the $k-\varepsilon$ model equal to 0.09. In order to guarantee that the imposed inlet profiles are consistently preserved throughout the computational domain, a specific formulation of the wall functions for the ground wall is necessary, according to what was observed by Blocken et al [9] and Parente et al. [10, 11]. Therefore, following what proposed by Parente and Benocci [10], the aerodynamic roughness length is directly included in the ground wall functions, leading to a modified non-dimensional wall distance z^+ and a modified wall function constant E.

$$z^+_{mod} = \frac{(z + z_0)u_*\rho}{\mu}$$
$$E_{mod} = \frac{\mu}{\rho z_0 u_*}$$

On the walls belonging to the wind rotor and the supporting structures, the standard wall functions are employed. The velocity contours are shown in fig. 3, during the FSI simulation with supporting structures. They show clearly the ABL stratification and the recovery of the undisturbed flow conditions beyond the wake of the analyzed machine.

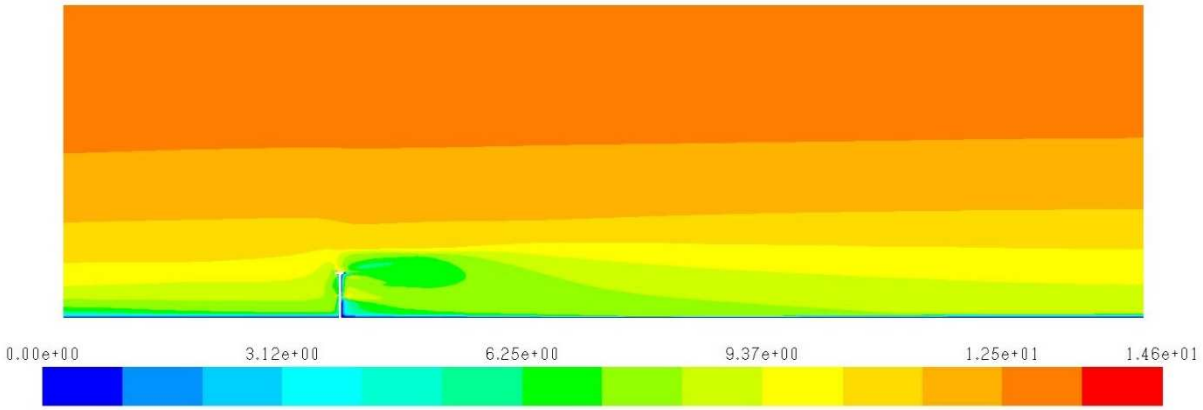

Figure 3: Contours of velocity magnitude (m/s) during FSI-FM simulation.

The mesh is fully hexahedral and built by means of a multi-block strategy. 3 million cells

compose the rotating domain, while the stationary one, is made of 10 million in the RO configuration and 12 million in the FM configuration. Fig. 4 shows two sections of the mesh around a blade, one close to its root and one close to its tip.

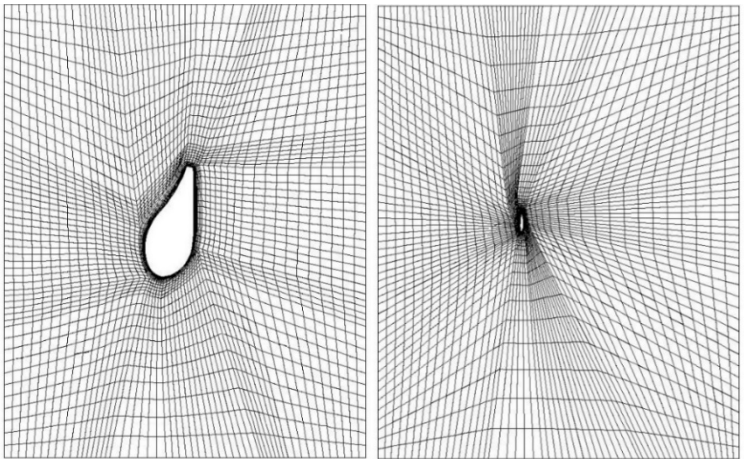

Figure 4: Sections of the mesh around one blade: (left) 20% of the total span and (right) 99% of the total span.

The momentum equations and pressure-based continuity equation are solved together with implicit coupling. 2nd order upwind discretization for momentum is applied and a 2nd order implicit scheme is used for time discretization.

During the FSI simulations, the mesh is adapted only in the rotating domain (fig. 2) in order to allow deformation of the blades as prescribed by the structural solver. The supporting structures are considered to be rigid. A diffusion method based on boundary distance is employed to handle the mesh motion. The need to always preserve the shape of the sliding interfaces translates directly into boundary conditions for the diffusion method.

2.2 The CSM model

The turbine to be analyzed features three $50\,m$ long blades entirely made of composite material. Each blade has a weight exceeding $9\,tons$ and encompasses three shear webs covering a large portion of its span. Shell elements with 3 or 4 nodes and reduced integration are exclusively employed and composite layups are defined to reproduce the composite layering. The elements are positioned on the outer mold layer (OML) with material offset towards the inside, mimicking the blades manufacturing process and maintaining the correct outer blade shape to facilitate the FSI coupling with the CFD model. Different layups are assigned to different regions of the structure, modelling its real composition. A local reference frame is discretely defined in every element in order to fix the global orientation of the layup. In every element, all the layups are then composed of a varying number of plies ranging from 1 to 127. For each ply a material and a thickness are assigned, together with a relative orientation in the form of a rotation angle with respect to the global layup orientation. The shear webs, the shear caps and the adhesive joints are also included. The mesh is created following the process discussed in [14], resulting in a total of 64000 three-dimensional shell elements. The outer structure and the inner shear webs are displayed in fig. 5.

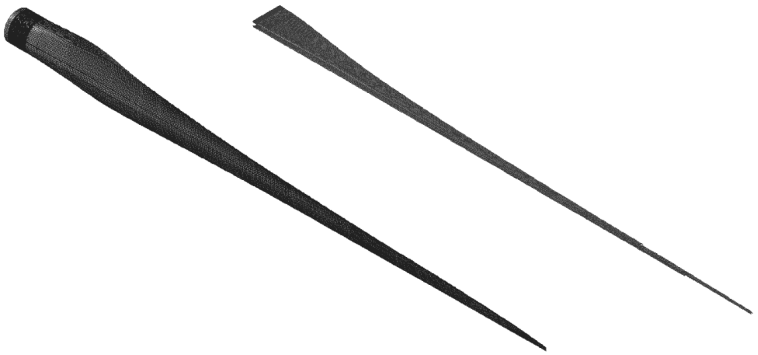

Figure 5: Structural mesh: (left) outer structures and (right) inner shear webs.

During the time span of the simulations, the rotational speed of the machine is fixed at the root of each blade, where all the other degrees of freedom are constrained. The gravity force is also included and accounted for in each simulation.

2.3 FSI coupling

The CFD and the CSM models previously outlined are coupled by means of an in-house code, named Tango [12]. Gauss-Seidel is chosen as coupling algorithm and 3 iterations are performed within every time step, leading to displacement residuals in the order of $3e-2\ m$.

The rotational speed of the turbine is set to $1.3\ rad/s$ which, combined with a wind velocity of $10\ m/s$ at the hub height ($100\ m$) leads to a tip speed ratio λ equal to 6.5. The time step size is chosen to be $0.0403\ s$.

3 RESULTS

In this section the results of various FSI simulations are outlined and compared. Every time-dependent simulation is started from the result of a steady state frozen rotor simulation. In this section, the notation of fig. 6 is used to define the azimuth angle of each blade and the sign of radial and tangential forces and velocities.

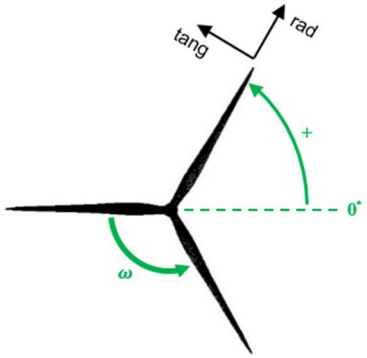

Figure 6: Notation for azimuth angle and components of forces and velocities.

Furthermore the torque (T) and the forces (F) acting on the blades are made non-dimensional by the following formulas:

$$c_T = \frac{T}{\frac{1}{2}\rho v^2 AR}$$
$$c_F = \frac{F}{\frac{1}{2}\rho v^2 A}$$

where $\boldsymbol{\rho}$ is the air density, $\boldsymbol{A}$ the frontal area of the rotor and $\boldsymbol{R}$ its radius; the reference velocity $\boldsymbol{v}$ is chosen to be the free-stream wind velocity at the hub height, namely $\mathbf{10}\ \boldsymbol{m/s}$.

3.1 Rotor only simulations

Starting from a steady state frozen rotor FSI simulation, a first transient FSI simulation is run including only the rotor structures and no supporting structure. The calculation is carried out for two complete revolutions of the rotor. The evolution of the total torque provided by the wind flow to the machine is depicted in fig. 7.

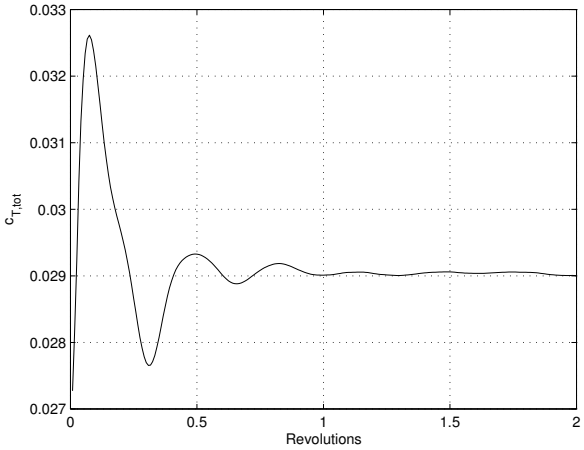

Figure 7: Total torque evolution, RO configuration.

The torque contribution of each blade can be related to its azimuth angle as shown in fig. 8.

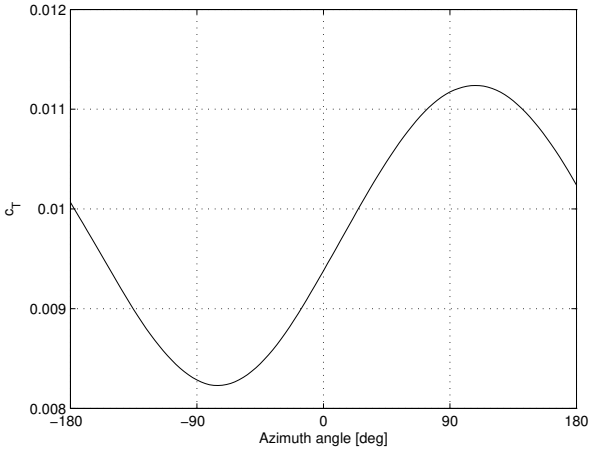

Figure 8: Single blade contribution to the torque, RO configuration.

Fig. 8 clearly shows the effect of the velocity stratification induced by the ABL: for positive azimuth angles, the higher wind velocity induces higher angles of attack on the blade span resulting in higher torque.

In terms of axial force acting on the blade, the same pattern is found. Fig. 9 shows the axial force oscillation during a full revolution, together with the consequent axial displacement of the blade tip.

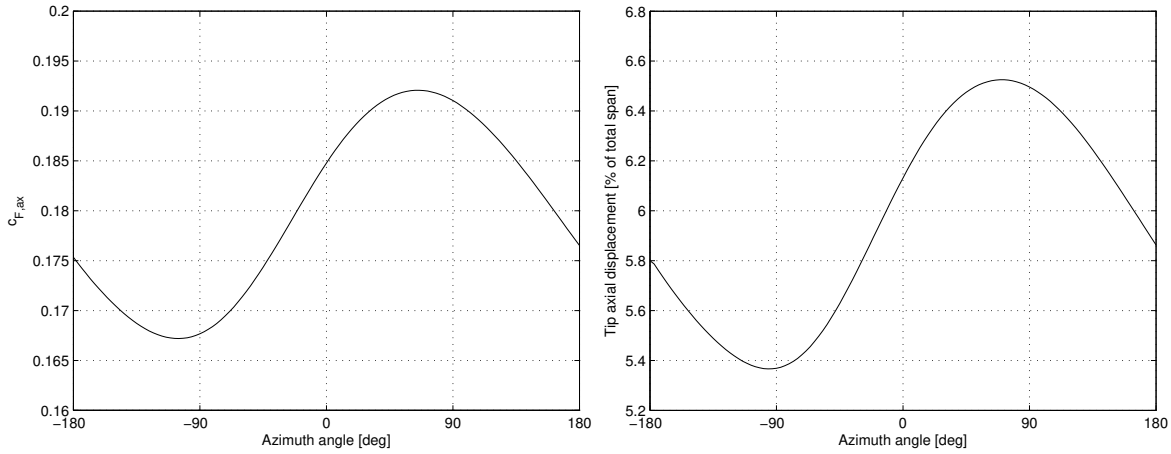

Figure 9: (left) axial force acting on the blade and (right) its axial tip displacement, RO configuration.

It should be noted that the axial force is again higher when the incoming wind velocity is higher, as already observed and commented for the torque. The axial displacement closely follows the oscillation of the axial force and has a mean value of approximately 2.9 m. Fig. 10 shows the deflection of the blade at an azimuth angle of 90 deg.

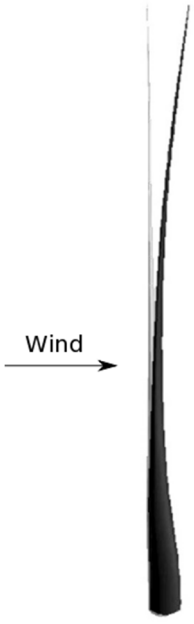

Figure 10: Deformed blade (black) on top of undeformed one (grey), RO configuration.

3.2 Full machine simulations and comparison

The same transient FSI simulation is carried out including the supporting structures and leading to the full machine (FM) configuration. Due to unexpected problems in the mesh motion, only half of a revolution could be simulated. Nevertheless, the passage of the blade in front of the tower was simulated and can be analyzed and compared to the correspondent time span in the RO simulation.

The torque contribution of the blade passing in front of the tower is shown in fig. 11.

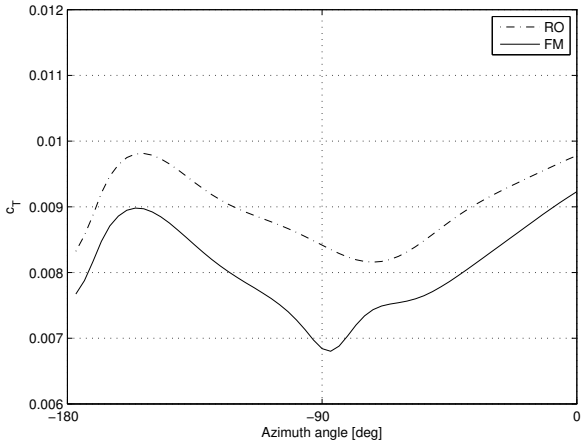

Figure 11: Single blade contribution to the torque, RO vs FM.

It can be seen that the torque provided by the blade is consistently lower (about 5%) in the FM case, compared to the RO configuration. Furthermore, the passage in the front of the tower induces a further drop (5%) which is immediately recovered few degrees later. The tower represents an obstruction and the pressure in the blade-tower clearance is higher than the pressure in the rest of the rotor wake. For this reason, the pressure difference between pressure and suction sides of the blades drops and drags the torque down. This is confirmed by fig. 12 which shows the axial force on the blade as a function of the azimuth angle.

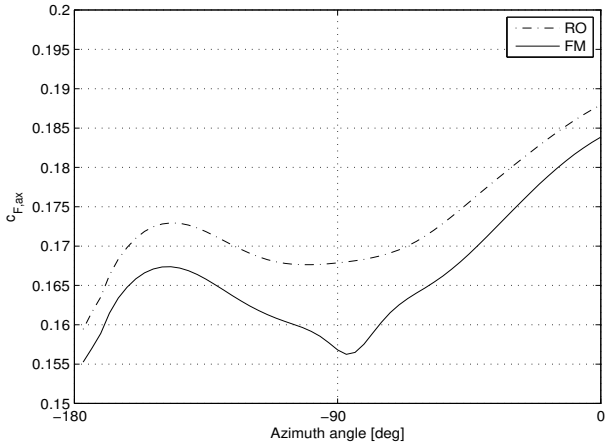

Figure 12: Axial force acting on the blade, RO vs FM.

The torque contribution of each blade can be interpreted as the product of the total tangential force multiplied by the radial position of the center of pressure along the blade span, both shown in fig. 13.

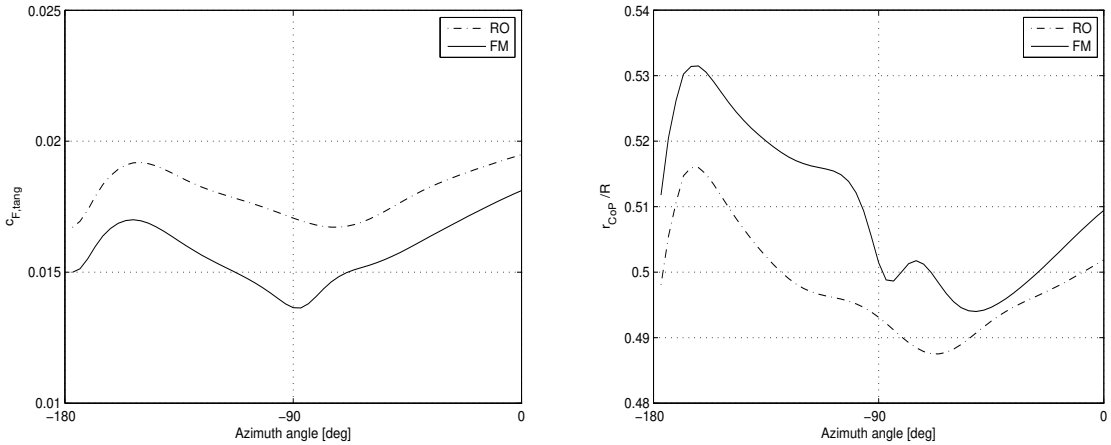

Figure 13: (left) tangential force acting on the blade and (right) relative radial position of the center of pressure, RO vs FM.

The presence of the supporting structures leads to a tangential force consistently lower while the center of pressure is moved towards the tip of the blade due to the presence of the nacelle which reduces the efficiency of the root sections. According to fig. 11, the first effect prevails over the second leading to a lower torque. Splitting the blade into 10 strips, fig. 14 shows the contribution to the torque of each strip at an azimuth angle of $-90\ deg$ for both RO and FM configurations, highlighting how the influence of the tower reduces the torque provided on the entire blade span.

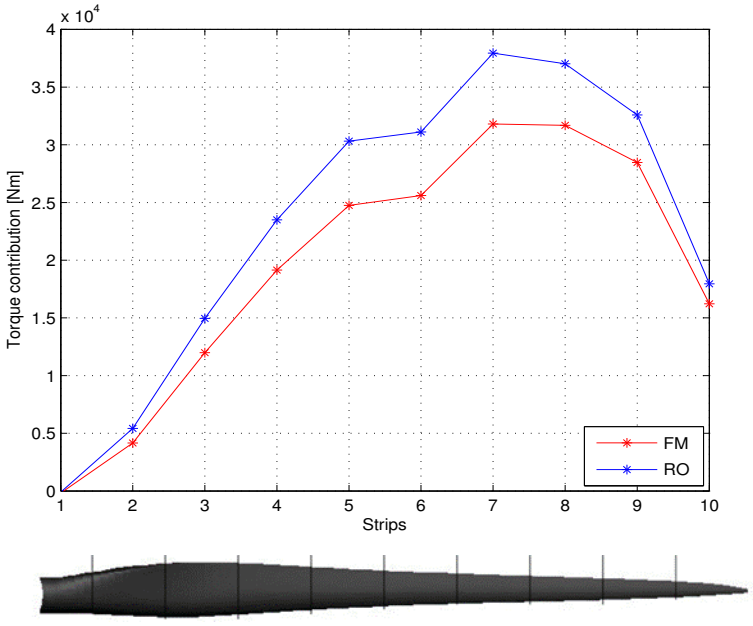

Figure 14: Torque contribution of blade strips, RO vs FM.

4 CONCLUSIONS

The FSI model could be used to investigate the effect of the supporting structures on the performance and loads of a modern HAWT. A drop is observed when the blade passes in front of the tower. The total drop appears to be equally distributed over the entire blade span. At the same time, the axial force transmitted to the blade by the wind is reduced due to the passage in the region of influence of the tower.

Due to unforeseen difficulties in the mesh motion, only half of a complete revolution could be simulated in the full machine configuration. Simulating longer will provide additional insights and details on the investigated phenomenon.

REFERENCES

[1] MC. Hsu, Y. Bazilevs. "Fluid–structure interaction modeling of wind turbines: simulating the full machine". *Computational Mechanics* 2012. DOI: 10.1007/s00466-012-0772-0.

[2] Y. Bazilevs, A. Korobenko, X. Deng, J. Yan, "Novel structural modeling and mesh moving techniques for advanced fluid-structure interaction simulation of wind turbines". *International Journal for Numerical Methods in Engineering* 2015. DOI: 10.1002/nme.4738.

[3] M. Caduff, M.A.J. Huijbregts, H.J. Althaus, A. Koehler, S. Hellweg. "Wind power electricity: the bigger the turbine, the greener the electricity?" *Environmental Science & Technology* 2012. DOI: 10.1021/es204108n

[4] Y. Bazilevs, M.C. Hsu, I. Akkerman, S. Wright, K. Takizawa, B. Henicke, T. Spielman, T.E. Tezduyar. "3D simulation of wind turbine rotors at full scale. Part I: Geometry modeling and Aerodynamics". *International journal for numerical methods in fluids* 2010. DOI: 10.1002/fld.2400

[5] Y. Bazilevs, M.C. Hsu, I. Akkerman, S. Wright, K. Takizawa, B. Henicke, T. Spielman, T.E. Tezduyar. "3D simulation of wind turbine rotors at full scale. Part II: Fluid–structure interaction modeling with composite blades". *International journal for numerical methods in fluids* 2010. DOI: 10.1002/fld.2400

[6] E. Hau. "Wind Turbines: fundamentals, Technologies, Application, Economics" (2nd Edition). *Springer: Berlin*, 2006

[7] YJ Lee, YT Jhan, CH Chung. "Fluid–structure interaction of FRP wind turbine blades under aerodynamic effect". *Composites Part B: Engineering* 2012. ISSN 1359-8368.

[8] P.J. Richards, R.P. Hoxey. "Appropriate boundary conditions for computational wind engineering models using the k-ε turbulence model". *Journal of Wind Engineering and Industrial Aerodynamics* 1993, 46 & 47, 145-153.

[9] Blocken B, Stathopoulos T, Carmeliet J. "CFD simulation of the atmospheric boundary layer: wall function problems". *Atmospheric Environment* 2007. 41:238–252

[10] A. Parente, C. Gorlé, J. van Beeck, C. Benocci. "A Comprehensive Modelling Approach for

the Neutral Atmospheric Boundary Layer: Consistent Inflow Conditions, Wall Function and Turbulence Model". *Boundary Layer Meteorology* 2011. DOI 10.1007/s10546-011-9621-5.

[11] A. Parente, C. Gorlé, J. van Beeck, C. Benocci. "Improved k–e model and wall function formulation for the RANS simulation of ABL flows". *Journal of Wind Engineering and Industrial Aerodynamics* 2011. DOI: 10.1016/j.jweia.2010.12.017.

[12] J. Degroote. "Partitioned simulation of fluid-structure interaction: Coupling black-box solvers with quasi-Newton techniques". *Archives of Computational Methods in Engineering* 2013. DOI: 10.1007/s11831-013-9085-5.

[13] R. Harte, G. Van Zijl. "Structural stability of concrete wind turbines and solar chimney towers exposed to dynamic wind action". *Journal of Wind Engineering* 2007. DOI: 10.1016/j.jweia.2007.01.028.

[14] M. Peeters , W. Van Paepegem. "Development of automated high fidelity finite element models for large wind turbine blades". *16th European Conference on Composite Materials*, Seville, Spain, 22-26 June 2014.

VII International Conference on Computational Methods for Coupled Problems in Science and Engineering
COUPLED PROBLEMS 2017
M. Papadrakakis, E. Oñate and B. Schrefler (Eds)

TRANSMISSION AND REFLECTION OF LONG WAVES OVER STEEP BATHYMETRY VARIATIONS USING LARGE FLOATING STRIPS OF SHALLOW DRAFT

THEODOSIOS K. PAPATHANASIOU*, ANGELIKI KARPERAKI†

* Department of Mechanical, Aerospace and Civil Engineering,
Brunel University London, Uxbridge UB8 3PH, UK
e-mail: theodosios.papathanasiou@brunel.ac.uk

† School of Naval Architecture and Marine Engineering,
National Technical University of Athens, Zografos, 15773, Greece
e-mail: karperaki.ang@gmail.com

Key words: Hydroelasticity, Long Waves, Floating Breakwaters, VLFS, Finite Elements, Wave Reflection.

Abstract. The present study focuses on the determination of reflection and transmission characteristics for the coupled hydroelastic system involving a strip of large extent and shallow draft, floating over steep bathymetric variations and interacting with long waves. A parametric analysis with respect to the floating strip stiffness and the magnitude of the bathymetry variation for specific seabed profiles is conducted. This parametric study is expected to indicate optimum design characteristics, in terms of the strip flexural rigidity, for maximizing long wave reflection or transmission, depending on the specific application.

1 INTRODUCTION

Floating thin plates are commonly employed in the literature to model the response of geophysical formations, such as ice floes [1-2], as well as manmade structures such as floating breakwaters [3-4]. In applications where horizontal dimensions are significantly larger than the thickness of the structure, the hydroelastic effects are of great importance. Under wave excitation, the floating structure is expected to flex, leaving fractions of the incident wave energy to be transmitted, while a part of it is reflected and dissipated due to damping and friction [5]. The study of reflection and transmission characteristics of a coupled hydroelastic system yields valuable information for the optimal design of a floating breakwater structure, aiming in attenuating incoming wave action. Floating breakwaters are effective in sheltering marinas and harbours where the marine environment is of limited fetch [3-4]. The aim of these type of structures is to mitigate the transmitted energy as well as the transmitted, onshore wave amplitude. In the case of geophysical formations, such as ice floes, an estimation of energy transmission through an ice field allows for the prediction of collapse events when quanta of wave energy reach a potentially unstable ice shelf [1].

Regular wave reflection and transmission characteristics of a floating structure, resting on top of an inviscid and irrotational fluid layer is studied by means of linear water wave theory,

where lineariazation of the dynamic and kinematic free surface boundary condition is imposed. Notable are the works of Meylan and Squire [6] and Montiel [7] who consider the wave reflection and transmission for the case of an ice floe of constant depth, the latter catering for the Archimedian draft. The aforementioned works correlated the transmission coefficient of the energy conserving system with the incident wavelength. Additionally, Bennets et al [8] and Smith and Meylan [9] examined the effects of the plate thickness in the transmitted energy.

Typically, due to their small thickness-to-length ratio, hydroelasticity dominated floating structures are modelled under the Kirchhoff thin plate assumptions [1,10,12]. Additionally, as floating breakwaters are commonly positioned nearshore, shallow water assumptions become relevant. Sturova [10] developed an eigenfunction expansion technique for the calculation of the transient hydroelastic response of thin heterogeneous plates, while Praveen et al [11] consider the hydroelastic response of a thick elastic plate under regular long wave action. As nearshore regions are characterised by strongly variable seabed profiles, the effects of variable bathymetry must also be taken into account. In that note, Papathanasiou et al. [12] consider a higher order finite element scheme for the solution of the transient hydroelastic problem posed by a thin, elastic, heterogeneous beam floating over variable shallow bathymetry.

The present study focuses on the determination of reflection and transmission characteristics for the coupled hydroelastic system involving a strip of large extent and shallow draft, floating over steep bathymetry variations and interacting with long waves. The particular problem examined herein is of interest for the analysis and design of novel breakwaters, and the transmission of wave energy in specific areas for harvesting purposes. The treatment of the problem is performed by means of the higher order hydroelastic finite elements developed by Papathanasiou et al [12] for time domain analysis. These elements feature 5th degree Hermite polynomials for the approximation of the floating strip deflection combined with five-node Lagrange interpolation for the water velocity potential.

The Newmark method is employed for the time integration of the resulting discrete system. The reflection and transmission properties of the hydroelastic system are analysed in terms of the transmitted to reflected energy ratio, as calculated after the hydroelastic interactions have seized. A parametric analysis with respect to the floating strip stiffness and the magnitude of the bathymetry variation for specific seabed profiles is conducted. This parametric study is expected to indicate optimum design characteristics, in terms of the strip flexural rigidity, for maximizing long wave reflection or transmission, depending on the specific application. For the efficient operation of breakwaters, reflection is desired to be maximized. Inversely, for wave trapping and harvesting in shallow water regions bounded by shoals, transmission characteristics of the proposed system need to increase.

2 GOVERNING EQUATIONS

In the present section, the governing equations for a coupled hydroelastic problem regarding a thin, floating plate over shallow water bathymetry will be briefly presented. The reader is directed to relevant works in the literature for a more in depth discussion [1,10,12]. The horizontal axis x of a Cartesian coordinate system coincides with the mean water level, the vertical axis z pointed upwards. The plate is assumed to extend indefinitely in the direction vertical to the xz plane. The case of a flexible elastic strip is therefore considered.

The respective 1D domain $\Omega:(-\infty<x<\infty)$ is occupied by a layer of inviscid and irrotational fluid. The floating elastic strip is located at the 1D domain extending from $x=0$ to $x=L$. The thickness distribution of the flexible strip is $\tau(x)$ and its density ρ_p. The density of the fluid (water) is denote by ρ_w. The symbols S_0, S_1, S_2 will be used to denote the three subregions $0<x<L$, $-\infty<x<0$ and $L<0<+\infty$, respectively. The three regions will be termed 'region of hydroelastic interaction', 'region of transmission' and 'region of reflection' respectively. In S_0 the free water surface elevation $\eta(x,t)$ is assumed to coincide with the plate deflection. The velocity potential functions $\varphi_i, i=0,1,2$ will be used for the three abovementioned domains. The bathymetry in the domain of 'hydroelastic interaction' is given by $s(x)-d(x)$, where $s(x)$ is the variable depth of the seabed with respect to the undisturbed free surface and $d(x)=\rho_p\rho_w^{-1}\tau(x)$ is the plate draft (according to Archimedes principle). The semi-infinite, thin strip assumption allows for the modelling of the plate by means of the Euler-Bernoulli beam theory. For the hydrodynamic modeling, the linearized Shallow Water Equations are employed. The following non-dimensional variables are employed for the derivation of the resulting 1-D hydroelastic system

$$\tilde{x}=x/L,\ \tilde{\eta}=\eta/L,\ \tilde{t}=g^{1/2}L^{-1/2}t,\ \tilde{\varphi}_i=g^{-1/2}L^{-3/2}\varphi_i,\ \text{for } i=0,1,2.$$

Hence the non-dimensional initial-boundary value problem is written, after dropping tildes as

$$M\ddot{\eta}+\left(K\eta_{xx}\right)_{xx}+\eta+\dot{\varphi}_0=0,\ x\in S_0, \tag{1}$$

$$\dot{\eta}+(H\varphi_{0x})_x=0,\ x\in S_0, \tag{2}$$

$$\ddot{\varphi}_1-(H\varphi_{1x})_x=0,\ x\in S_1, \tag{3}$$

$$\ddot{\varphi}_2-(H\varphi_{2x})_x=0,\ x\in S_2, \tag{4}$$

with $M(x)=m(x)\rho_w^{-1}L^{-1}$, $K=D\rho_w^{-1}g^{-1}L^{-4}$, $H(x)=\left[s(x)-d(x)\right]/L$ in the 'hydroelastic interaction' region, $H(x)=s(x)/L$ outside the 'hydroelastic interaction' region and g the acceleration of gravity. The flexural rigidity of the plate is $D=E\tau^3(12(1-\nu^2))^{-1}$, where E is the Young's modulus and ν the Poisson's ratio of the plate material. The non-dimensionalised quiescence conditions at infinity are given as

$$\varphi_{1x}=0(x\to-\infty)\ \text{and}\ \varphi_{2x}=0(x\to\infty) \tag{5}$$

At the interfaces between subregions, mass and energy conservation dictated the following matching conditions

$$H(0^-)\varphi_{1x}(0^-,t)=H(0^+)\varphi_{0x}(0^+,t),\ H(1^-)\varphi_{0x}(1^-,t)=H(1^+)\varphi_{2x}(1^+,t)\ \text{and} \tag{6}$$

$$\dot{\varphi}_1(1^-,t)=\dot{\varphi}_0(1^+,t),\ \ \dot{\varphi}_0(1^-,t)=\dot{\varphi}_2(1^+,t) \tag{7}$$

For a freely floating plate, the non-dimensional boundary conditions at the edges of the plate

are

$$K\eta_{xx}\big|_{x=0} = 0\,, \quad K\eta_{xx}\big|_{x=1} = 0 \ \text{ and} \tag{8}$$

$$K\eta_{xxx}\big|_{x=0} = 0\,,\ K\eta_{xxx}\big|_{x=1} = 0\,. \tag{9}$$

The initial- boundary value problem is completed with appropriate initial conditions of the form

$$\eta_0(x,0) = \phi_0(x,0) = 0,\ x \in S_0 \tag{10}$$

$$\phi_1(x,0) = \partial_t \phi_1(x,0) = 0, \tag{11}$$

$$\phi_2(x,0) = 0,\ \partial_t \phi_2(x,0) = -G(x) \tag{12}$$

3 VARIATIONAL FORMULATION

The variational formulation of the initial-boundary value problem is derived in the present section. The procedure presented follows exactly the one adopted in [12]. Equations (13)-(16) are derived by multiplying (1)-(4) with the corresponding weight functions $v \in H^2(S_0)$, $-w_0 \in H^1(S_0)$, $w_1 \in H^1(S_1)$ and $w_2 \in H^1(S_2)$, integrating over the respective sub-regions and performing integration by parts,

$$\int_0^1 Mv\ddot{\eta}dx + \int_0^1 Kv_{xx}\eta_{xx}dx + \int_0^1 v\eta dx + \int_0^1 v\dot{\varphi}_0 dx = 0 \tag{13}$$

$$-\int_0^1 w_0\dot{\eta}dx + \int_0^1 w_{0x}H\varphi_{0x}dx - \left[w_0 H\varphi_{0x}\right]_0^1 = 0 \tag{14}$$

$$\int_{-\infty}^0 w_1\ddot{\varphi}_1 dx + \int_{-\infty}^0 w_{1x}H\varphi_{1x}dx - \left[w_1 H\varphi_{1x}\right]_{-\infty}^0 = 0 \tag{15}$$

$$\int_1^\infty w_2\ddot{\varphi}_2 dx + \int_1^\infty w_{2x}H\varphi_{2x}dx - \left[w_2 H\varphi_{2x}\right]_1^\infty = 0 \tag{16}$$

Adding, Eqs (13)-(16) and employing the farfield and interface conditions the variational problem is reformulated as,

Find $\eta(x,t)$, $\varphi_0(x,t)$, $\varphi_1(x,t)$ *and* $\varphi_2(x,t)$ *such that for every* $v \in H^2(S_0)$, $-w_0 \in H^1(S_0)$, $w_1 \in H^1(S_1)$ *and* $w_2 \in H^1(S_2)$ *it is,*

$$\begin{aligned}\int_0^1 Mv\ddot{\eta}dx + \int_0^1 v\dot{\varphi}_0 dx - \int_0^1 w_0\dot{\eta}dx + \int_{-\infty}^0 w_1\ddot{\varphi}_1 dx + \int_1^\infty w_2\ddot{\varphi}_2 dx \\ + a(\eta,v) + b_0(\varphi_0,w_0) + b_1(\varphi_1,w_1) + b_2(\varphi_2,w_2) = 0\end{aligned} \tag{17}$$

where the bilinear functionals $a(\eta,v) = \int_0^1 \left(Kv_{xx}\eta_{xx} + v\eta\right)dx$, $b_0(\varphi_0,w_0) = \int_0^1 w_{0x}H\varphi_{0x}dx$ $b_1(\varphi_1,w_1) = \int_{-\infty}^0 w_{1x}H\varphi_{1x}dx$, $b_2(\varphi_2,w_2) = \int_1^\infty w_{2x}H\varphi_{2x}dx$ have been introduced.

For the solution of the above variational problem, the finite element scheme proposed by Papathanasiou et al [12] will be adopted. In particular, we are interested for the solution of the initial boundary value problem corresponding to a long wave pulse generated in the 'transmission region', propagating and interacting with the floating plate. A part of this pulse enters the 'reflection region', while another part is reflected and back-propagates towards $+\infty$ The computational spatial domain that will be used is set such that x extends from $-x_A$ to x_B, where these values define a spatial domain large enough so that the pulses do not reach the computational domain boundaries in the examined time interval. Thus the conditions for the velocity potential spatial derivative (velocity) at infinity are also valid at the edges of the computational domain.

4 FINITE ELEMENT FORMULATION

For the free water surface subregions, that is for the 'transmission region' and the 'reflection region', finite elements with fourth order Lagrange polynomial shape function are employed. For the region of the hydroelastic coupling, a special hydroelastic element featuring quantic Hermite polynomials for the plate deflection and fourth order Lagrange shape functions for the approximation of the velocity potential is used. The reader is directed to the work of Papathanasiou *et al* [12] for a more in depth analysis. Hence, the approximate solutions in a given hydroelastic element are defined as,

$$\eta^h = \sum_{i=1}^{6} H_i(x)\eta_i^h(t) \text{ and } \varphi_j^h = \sum_{i=1}^{5} L_i(x)\varphi_{ij}^h(t), j=1,2 \tag{18}$$

Substituting the above into the discretized variation problem defined by Eq. (17) results in a second order system of the form $\mathbf{M}\partial_{tt}u + \mathbf{C}\partial_t u + \mathbf{K}u = 0$, where vector u contains the total nodal unknowns. This ordinary differential equation system has the standard form of the second order equations of structural dynamics. The implication here being each matrix is singular. The stability results in [12] however guarantee a unique solution of this discrete system. That is, an appropriate linear combination of the matrices appearing in this dynamic system must be invertible. This fact enforces the application of an implicit time integration procedure. Subsequently, a Newmark time integration scheme (see [12]) is employed in order to calculate the solution of the ordinary differential equation system. The particular values for the Newmark method $\gamma = 1/2$ and $\beta = 1/4$ have been used in all the numerical results that follow. The number of time steps employed is in all cases sufficient to ensure high accuracy.

5 NUMERICAL RESULTS

The aim of the present study is to examine the reflection and transmission properties of the aforementioned hydroelastic system, under long wave impact. In order to investigate the effect of bathymetric changes, two seabed profiles are examined. The first bathymetric profile (Figure 1) features a single peak, with the depth given by,

$$s(x) = B - b\exp\left(-50(x-x_0)\right)^2 \tag{9}$$

where x_0 is the location of the Gaussian peak. The second profile (Figure 2) features a shoaling region, where the incident wave initially propagates at constant depth B and transmits into the region of shallower constant depth b . The depth function in this case is given as,

$$s(x) = B - \frac{b}{2} + \frac{b}{2}\tanh\left(10(x - x_0)\right) \tag{20}$$

For each bathymetric profile, three different configurations are examined. In the first configuration (Configuration I), the plate is positioned in such a way that $x = 0$ is located exactly above the middle of the varying seabed interval. That is, the incoming pulse begins to interact with the plate before shoaling effects due to bathymetry variations take place. In the second configuration (Configuration II), the plate is positioned with its central point above the middle of the varying seabed region. The third case, Configuration III, involves the plate being positioned with its right hand end being over the middle of the varying topography interval. In this case, the shape of the pulse entering the hydroelastic region is affected by shoaling phenomena (see also Figures 1, 2).

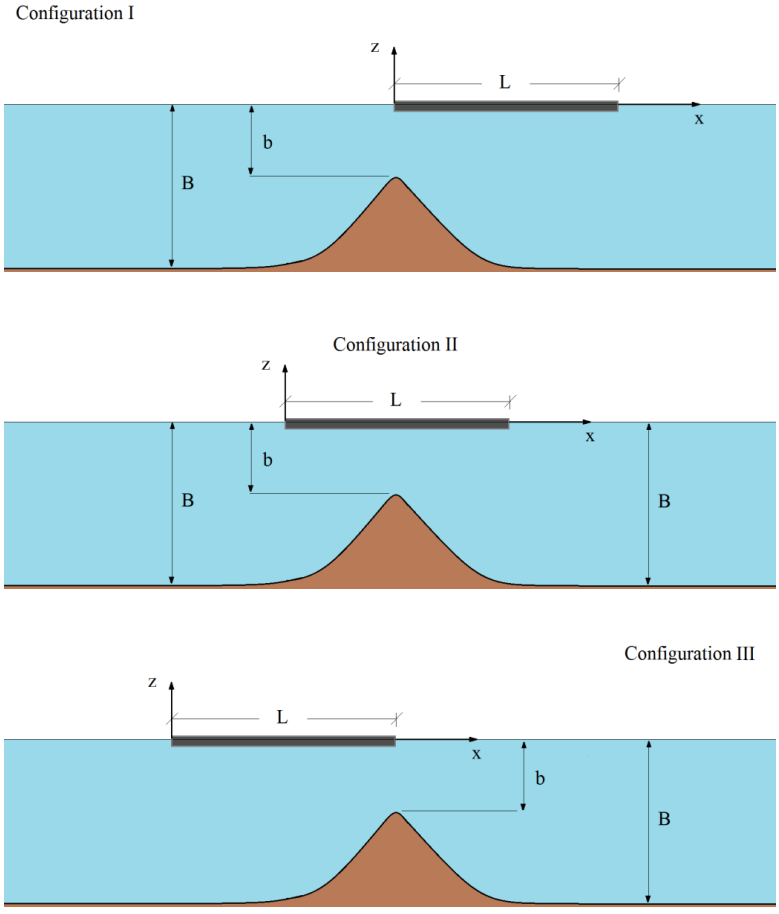

Figure 1: Schematic representations of (top) Configuration I (middle) Cnfiguration II (bottom) Configuration III described by Eq. (19)

Finally, the material constants selected are plate density $\rho_e = 900\ kg/m^3$, water density $\rho_w = 1025\ kg/m^3$, and Poisson's ratio $v = 0.3$, while a set of values for the Young's modulus is employed. The acceleration of gravity is $g = 10\ m/\sec^2$.

An initial elevation pulse of the form $\eta(x) = 2A_0 \exp\left(-\mu\left(x - x_0\right)^2\right)$, where, in the nondimensional setting, $A_0 = 3.3 \cdot 10^{-4}$ is the amplitude, x_0 is the point of origin and μ is a positive parameter controlling the smoothness of the pulse taken as 250, is allowed to propagate from location x_0 in region S_2.

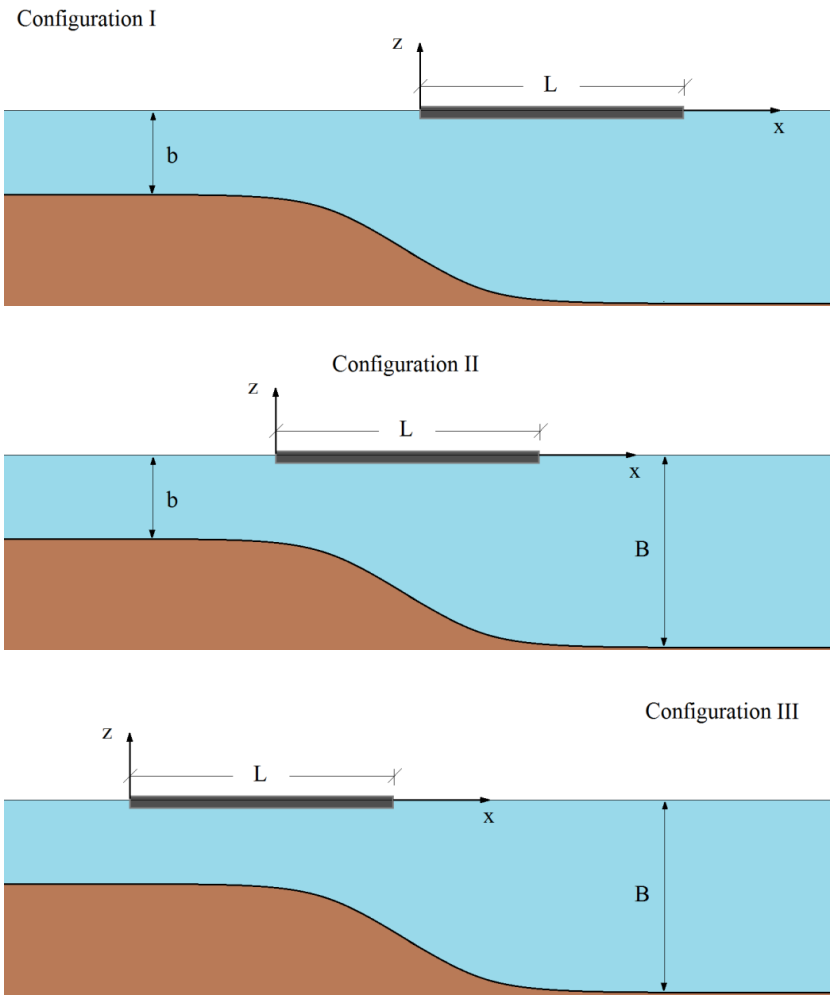

Figure 2: Schematic representations of (top) Configuration I, (middle) Configuration II, (bottom) Configuration III for bathymetric profile described by Eq. (20)

5.1 Bathymetric profile 1

The phenomenon under study involves an initial upper surface elevation disturbance that is split into two propagating waves, travelling in opposite directions, each with amplitude A_0. As the incoming wave impacts the floating plate, the excitation is partially reflected back into S_2. Figure 3 demonstrates the correlation between the ratio of energy in the region of transmission to the total energy and the natural logarithm of the nondimensional stiffness K of the floating plate, after the elastic body has reached a state of rest.

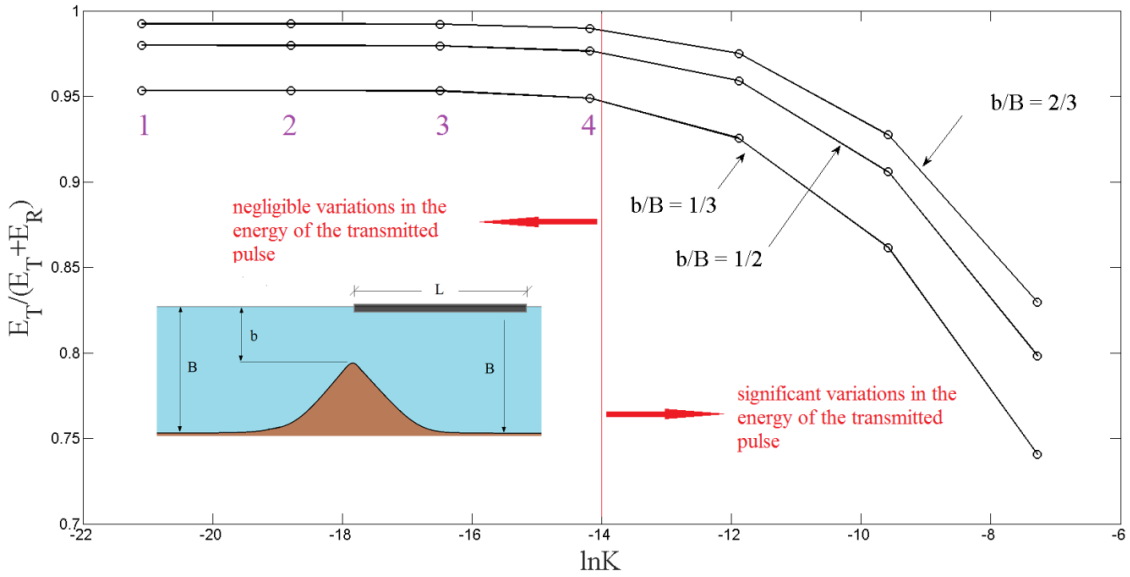

Figure 3: Ratio of the transmitted to total energy of the incoming pulse for Configuration I as a function of the natural logarithm of K. Three values for the ratio b/B have been examined.

Parameter K is derived by considering a set of values $\left(5\cdot10^{6}\sim5\cdot10^{12}\,Pa\right)$ for the Young's Modulus E. It is observed that as the local depth b at the Gaussian peak decreases, larger fractions of wave energy are reflected into S_2, manifested as a drop in the examined transmitted to total energy ratio in Fig. 3. Notably, it is seen that for the first four of the considered values for $\ln K$ (corresponding to $E=5\cdot10^{6}\sim5\cdot10^{9}\,Pa$) the variation of the ratio between the transmitted energy and the total energy is negligible for all examined d/B ratios. Points 1-4 of Fig. 3, suggest that large sums of energy are transmitted into region S_1 for the corresponding stiffness values. Figure 4 depicts the form of the transmitted wave inside region S_1, after the plate has reached a state of rest, corresponding to points 2 (left column) and 4 (right column) for $d/B=1/2$. Despite the fact that large sums of energy are transmitted, as previously shown, the peak amplitude is significantly decreased as the plate becomes stiffer. For a softer plate the incident wave pulse exhibits some hydroelastic dispersion only in the case of Configuration I. This is attributed to the location of the plate with respect to the peak, since hydroelastic interactions take place in deeper water conditions. Increasing plate stiffness successfully reduces the incident wave amplitude, generating a wavetrain in the region of transmission.

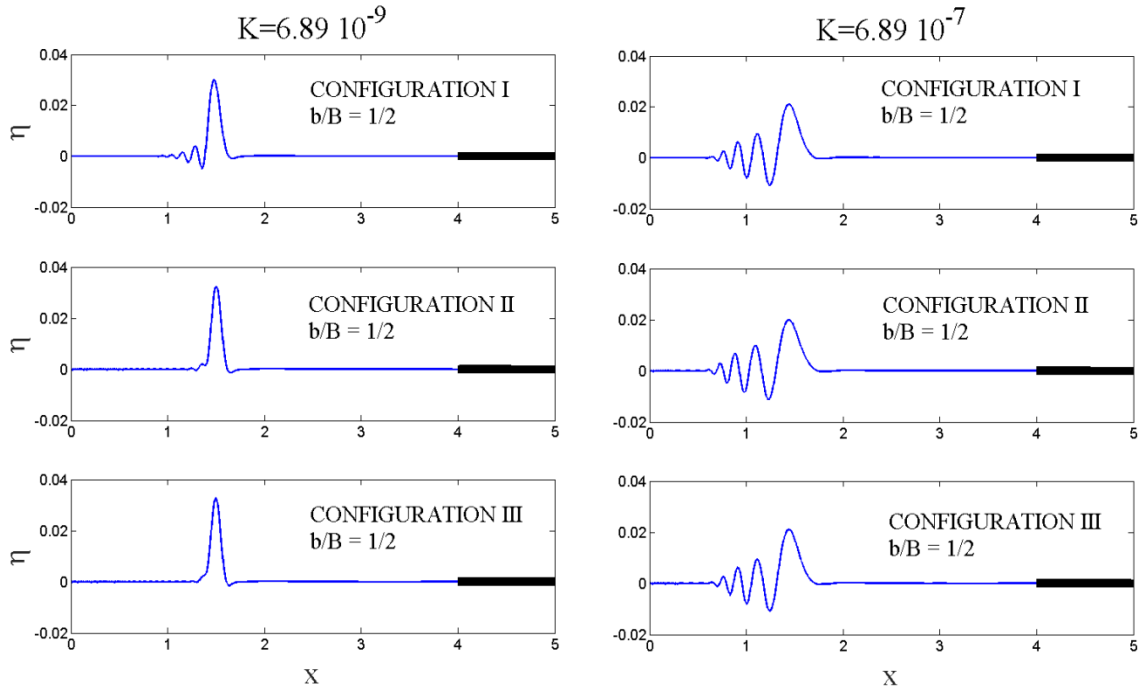

Figure 4: Form of the transmitted pulse for two cases of the plate stiffness and $b/B = 1/2$. The case of a 'soft' plate (left column) and the case of the 'stiff' plate (right hand column) correspond to approximately equal values of the transmitted energy (points 2 and 4 in Figure 3).

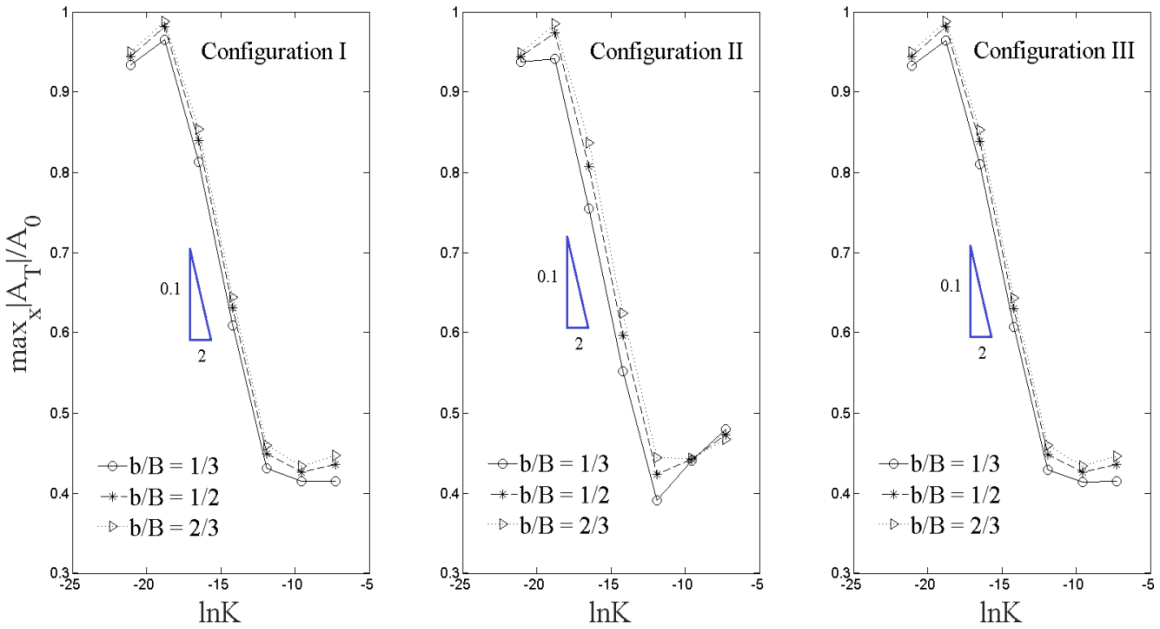

Figure 5: Ratio of the maximum amplitude of the transmitted pulse after hydroelastic interactions occur and the plate is at rest, to the amplitude of the incoming pulse, as a function of the natural logarithm of K. An almost linear decrease of the ratio for intermediate values of the stiffness is observed.

When examining the ratio of the maximum transmitted wave amplitude to the incident amplitude as a function of $\ln K$ for all three configurations and varying b/B ratios an almost linear decrease of the ratio for intermediate values of the stiffness is observed.

5.2 Bathymetric profile 2

The same analysis is applied to the second bathymetric profile featuring a shoaling region. Figure 6 shows the same approximate invariance of the ratio of transmitted to total wave energy for the first four examined values of $\ln K$. As the shallower depth b decreases, the ratio exhibits a drop once again due to larger sums of energy being reflected due to the steeper bathymetric variation.

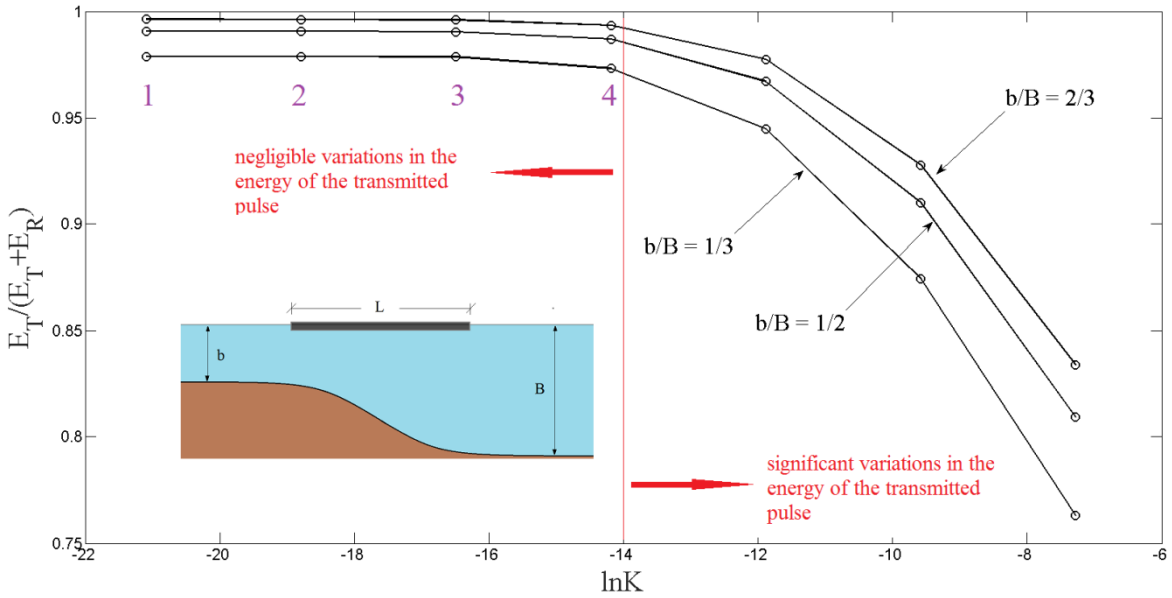

Figure 6: Ratio of the transmitted to total energy of the incoming pulse for Configuration I as a function of the natural logarithm of K. Three values for the ratio b/B have been examined.

In Fig. 7 the transmitted wave forms are again illustrated as in Fig. 4 for the second bathymetric profile. As previously observed, for a softer plate the transmitted wave form is only mildly altered. However, the amplitude of the transmitted wave for a softer plate appears increased for all three configurations. The amplitude is indeed amplified by the decreasing depth, while the stiffness of the plate appears to have minimal impact on wave attenuation. By increasing the plate stiffness the transmitted peak wave amplitude appears reduced. Once again despite the fact that the transmitted energy to total energy ratio shows no dependence upon stiffness for a range of values corresponding to points 1-4 in Fig. 6, the wave amplitude in the region of transmission appears significantly reduced for the values $\ln K$ matching points 2 and 4 (Fig.6). In Fig 8., the ratio of the maximum transmitted wave amplitude to the incident amplitude as a function of $\ln K$ is examined in a similar manner as in Fig. 5. Once again it is observed that the dependence is almost linear. For smaller stiffness values the amplitude increase due to shoaling is observed, with transmitted to incoming wave amplitude ratio increasing for decreasing b/B values.

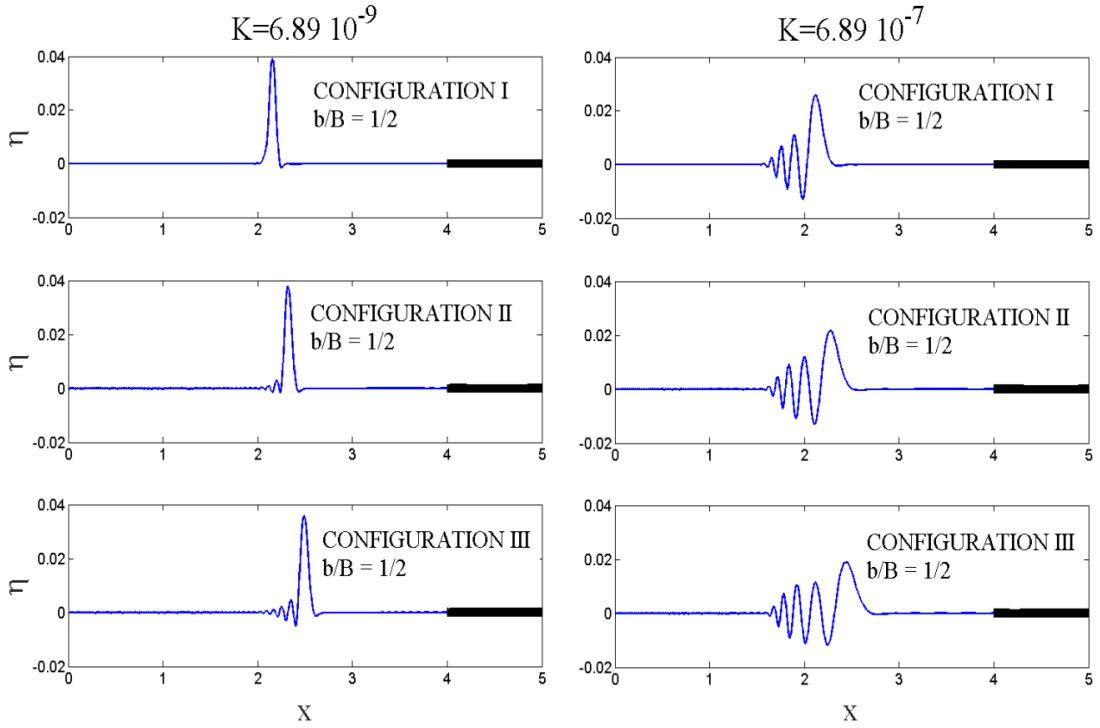

Figure 7: Form of the transmitted pulse for two cases of the plate stiffness and $b/B = 1/2$. The case of a 'soft' plate (left column) and the case of the 'stiff' plate (right hand column) correspond to approximately equal values of the transmitted energy (points 2 and 4 in Figure 6).

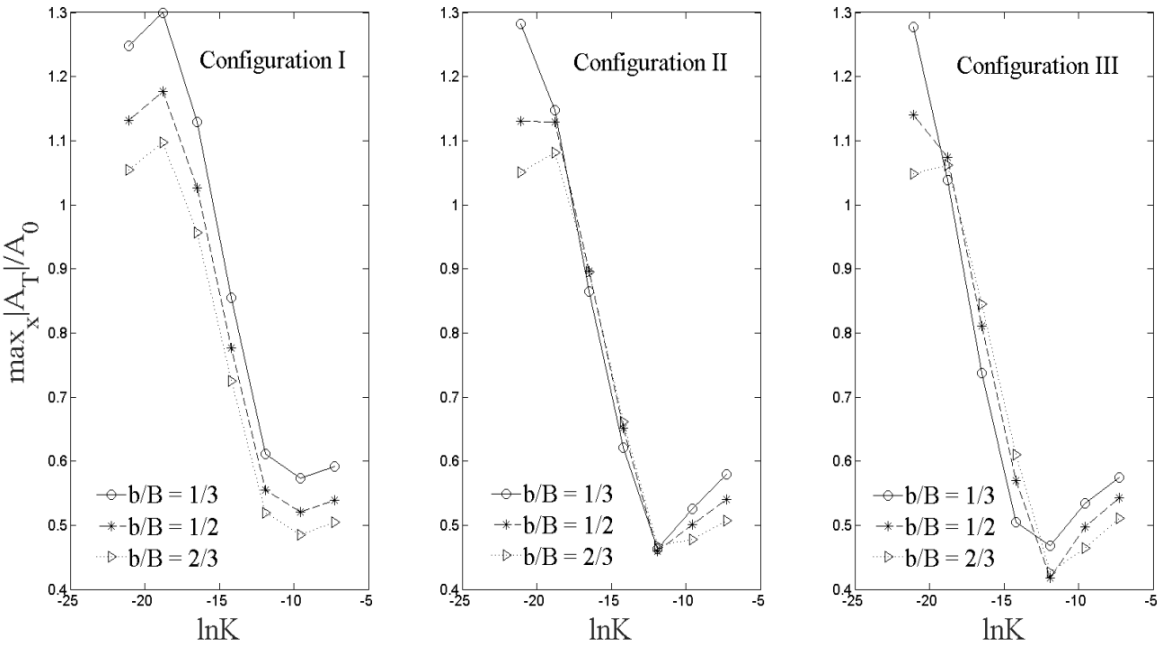

Figure 8: Ratio of the maximum amplitude of the transmitted pulse when the plate is at rest, to the amplitude of the incoming pulse, as a function of the natural logarithm of K. An almost linear decrease of the ratio for intermediate values of the stiffness is observed.

6 CONCLUSIONS

In this contribution the transmission and reflection characteristics of a floating, elastic strip over variable bathymetry, subjected to long wave impact, were examined. A parametric analysis with respect to the floating strip stiffness and seabed variations was conducted with the use of a special hydroelastic element. The ratio of transmitted to total energy, calculated at a moment in time when the plate is at rest, was seen to be independent of plate stiffness up to values reaching $E \sim 10^9 Pa$. However, despite the large calculated values for the transmitted energy, the transmitted wave amplitude was significantly reduced. At the same time, the transmitted pulse features dispersion due to hydroelastic phenomena. This result illustrates the fitness of the examined configurations for wave attenuating applications.

REFERENCES

[1] Papathanasiou, T.K., Karperaki, A.E., Theotokoglou, E.E. and Belibassakis, K.A. Hydroelastic analysis of ice shelves under long wave excitation, *Nat. Hazards Earth Syst. Sci*., (2015), **15**: 1821-1857.

[2] Squire, V.A. Synergies between VLFS Hydroelasticity and Sea Ice Reasearch, *Int. J. offshore polar,* (2008), **18** (3):1-13.

[3] Wang, C.M. and Tay, Z.Y. Very Large Floating Structures: Applications, Research and Development, *Proc. Engineering*, **14**: 62-72

[4] Wang, C.M., Watanabe E. and Utsunomiya, T. *Very large floating structures*, Taylor and Francis, London, (2008).

[5] Koutandos, E., Prinos, P. and Gironella, X. Floating breakwaters under regular and irregular wave forcing: reflection and transmission characteristics, *J. Hydraul. Res.* (2005), Vol 43 **(2)**:174-188.

[6] Meylan, M.H. and Squire, V.A. The response of ice floes to ocean waves, *J. Geopysh Res* (1994) **99** (C1):891-900

[7] Montiel, F., Bennetts L.G. and Squire, V.A. The transient response of floating elastic plates to wavemaker forcing in two dimensions, *J. Fluids Struct.* (2012) **28**: 416–433.

[8] Bennetts, L.G., Biggs, N.R.T. and Porter, D. A multi-mode approximation to wave scattering by ice sheets of varying thickness, *J. Fluid Mech.* (2007) **579**: 413-443.

[9] Smith, M.J.A. and Meylan, M.H. Wave scattering by an ice floe of variable thickness, *Cold Reg. Sci. Technol*. (2011) **67** (1–2): 24–30.

[10] Sturova, I.V. Time-dependent response of a heterogeneous elastic plate floating on shallow water of variable depth. *J. Fluid Mech.* (2009), **637**:305-325.

[11] Praveen, K.M, Karmakar, D. and Nasar, T. Hydroelastic analysis of floating elastic thick plate in shallow water depth, *Perspect. in Sci.* (2016), **8**: 770-772

[12] Papathanasiou, T. K, Karperaki, A., Theotokoglou E.E. and Belibassakis, K.A.. A higher order FEM for time-domain hydroelastic analysis of large floating bodies in an inhomogeneous shallow water environment, *Proc. R. Soc. A*, **471**: 20140643, (2014).

VII International Conference on Computational Methods for Coupled Problems in Science and Engineering
COUPLED PROBLEMS 2017
M. Papadrakakis, E. Oñate and B. Schrefler (Eds)

COMPUTATIONAL METHOD FOR FLUID FLOW PROCESS IN POROUS MEDIA WITH HETEROGENEITY OF PERMEABILITY

ELENA ANDRIYANOVA*, VLADIMIR ASTAFEV*

*Department of Oil and Gas Fields Development
Samara State Technical University
Molodogvardeiscaya str., 244; 443100 Samara, Russia
e-mail: vladimir.astafev@mail.ru, andriyanovaev@inbox.ru

Key words: Flow potential, Darcy flow, boundary conditions, streamlines of fluid flow, waterflooding, hydraulic fracturing.

Abstract. In this paper the solution of coupled problem for fluid flow in the reservoir with hydraulically fractured well will be discussed. The new boundary condition is taken in to account for modeling of different cases of fractured wells location and for the prediction of water tracer lines. The analytical solution for flow potential will help petroleum engineers to predict well productivity and evaluate the most effective well pattern for waterflooding production system with massive hydraulic fracturing.

1 INTRODUCTION

The effective oil and gas field development is a complicated problem, especially in conditions of low oil price and depleted reservoirs. Currently more often we need to produce hard-to-extract oil, which requires application of complicated enhance oil recovery methods and modern geophysical researches. Therefore, for engineers, there is an acute problem of fast evaluation and selection of a suitable production system and a well completion.

One of the most effective enhance oil recovery techniques is hydraulic fracturing (HF) [1]. More than a half of oil reserves are hard to extract or tight reserves, which can be produced only with hydraulic fracturing. The development of tight oil formations is becoming more important today. Many scientists are involved into the modeling of fluid flow to the well with hydraulic fracturing [2]. But generally the highly permeable fracture is considered to cross the well symmetrically. For the selection of the optimal well placement, it is especially important to solve the complex problem, which includes choice of the best production system, well distance and the most suitable completion. The proper way must be based on the economical effectiveness and productivity. Intelligent use of HF allows optimizing the waterflooding especially on the first stage of field development. As modern level of geophysics and technology can study the exact orientation of fractures, we can more accurately predict flow parameters.

Mostly the numerical simulation is used for solutions of complex problems, but commonly these methods are time consuming. The main part of published papers about the waterflooding well placement is dedicated to a one special case. So we need to develop a new more fast and exact semi-analytical technique to estimate the productivity of a well and even

the most suitable well pattern, taking into account fractures.

In addition the in some cases we need to evaluate the fluid flow in the presence of any impermeable fracture. For instance in case we have impermeable tectonic fault or artificial fracture filled with impermeable material, if we need to isolate flow in the reservoir.

2 PROBLEM FORMULATION

Let us consider a plane stationary flow of incompressible fluid to the vertical production well in an isotropic porous medium. This process in the plane *(x,y)* is described by the equation of incompressibility and the Darcy's law of filtration:

$$div\vec{V}(x,y) = 0, \vec{V} = -(k/\mu)grad\ p\,, \tag{1}$$

where $\vec{V}(x,y)$ is the velocity vector of fluid filtration, $p(x,y)$ is the pressure in the liquid, μ is the fluid viscosity and k is the reservoir permeability by the thickness h.

In the works of other authors the high permeable area is usually represented by ellipse [3, 4], while, the different way of problem solution uses the integrals of Cauchy type.

Let us consider, that in the reservoir with the external boundary of radius R_c at the point $M_1(x_1,y_2)$ is placed the production well of radius r_w with a flow rate Q and at the point $M_2(x_1, y_1)$ is placed the injection well of the same radius. Inside the external boundary there is a crack with length $2l$ and thickness 2δ ($\delta << l$) and permeability k_f. Let us consider that the crack is oriented along the axis x, and its center coincides with the origin plane *(x, y)* (Figure 1). In the picture we can see the special case or hydraulic fracturing case, when the fracture crosses the production well. But the solution is suitable for any possible location of wells and fracture.

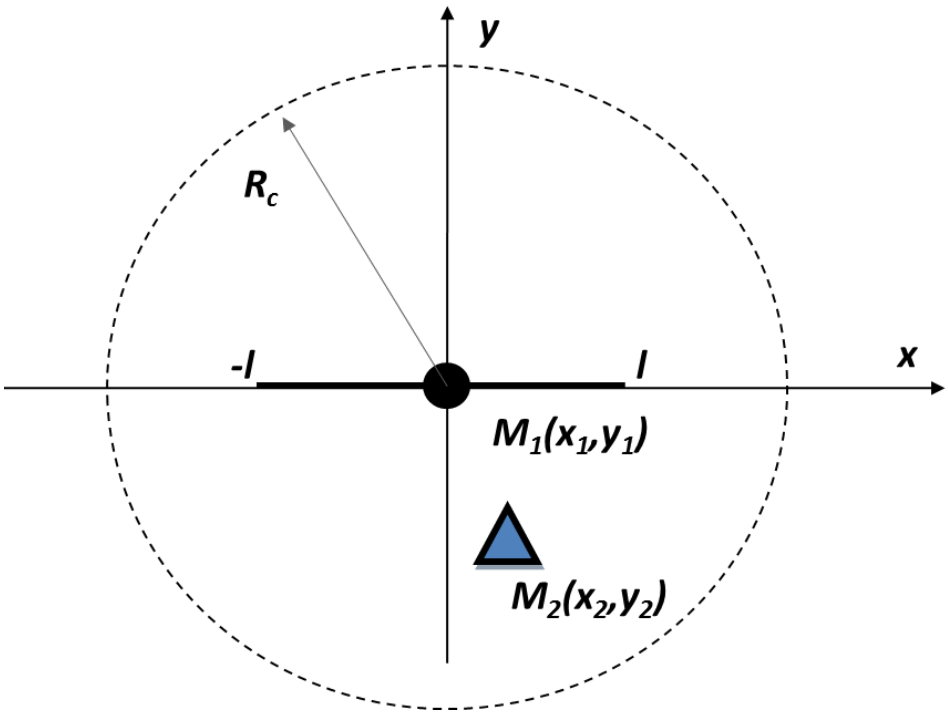

Figure 1: Production and injection wells and fracture places in the plane

3 PROBLEM SOLUTION

Let we define the complex flow potential for an incompressible fluid in the reservoir through $\varphi(z)$ [5]:

$$P(x,y)=Re\ \varphi(z),\ v_n(P) = -\frac{k}{\mu} Im\ \varphi'(x,y).$$

Now let us consider the case when we have a pair of wells, the flow potential can be represented in the form:

$$\varphi(z) = q_1 \ln(z - z_1) + q_2 \ln(z - z_2) + \sum_{n=0}^{\infty} c_n z^{-n}. \tag{2}$$

where $q_{1,2}= \mu Q_{1,2}/(2\pi kh)$ is the modified flow rate, c_n is unknown coefficients in the expansion in Laurent series of the disturbance caused by the presence of reservoir heterogeneity and decaying at infinity.

After the mapping by the Zhukovsky function $z=l(v+v^{-1})/2$, the flow potential (2) takes the next form:

$$\varphi(v) = q_1 \ln(v - v_1) + q_2 .\ln(v - v_2) + \sum_{n=1}^{\infty} a_n v^{-n} + C_0., \tag{3}$$

Further, we consider a case when $q_1=1$ and $q_2=-1$ or injection and production wells. Flow potential in this case can be written as follows:

$$\varphi(v) = \ln \frac{(v - v_1)}{(v - v_2)} + \sum_{n=1}^{\infty} a_n v^{-n} + C_0, \tag{4}$$

where $v_1 = \rho_1 \cdot e^{i\theta_1}, v_2 = \rho_2 \cdot e^{i\theta_2}$ and $a_n = a_n^{(s)} + ia_n^{(\alpha)}$.

$$\varphi(v) = \ln \frac{(v - v_1)}{(v - v_2)} + \sum_{n=1}^{\infty} (a_n^{(s)} + ia_n^{(\alpha)}) v^{-n} = \left\{ \ln \frac{\rho_1}{\rho_2} - \sum_{n=1}^{\infty} \frac{1}{n} \left(\frac{\cos n\theta_1}{\rho_1^{\,n}} - \frac{\cos n\theta_2}{\rho_2^{\,n}} \right) v^n + \sum_{n=1}^{\infty} a_n^{(s)} v^{-n} \right\} +$$

$$+ i \left\{ (\theta_1 - \theta_2) + \sum_{n=1}^{\infty} \frac{1}{n} \left(\frac{\sin n\theta_1}{\rho_1^{\,n}} - \frac{\sin n\theta_2}{\rho_2^{\,n}} \right) v^n + \sum_{n=1}^{\infty} a_n^{(\alpha)} v^{-n} \right\} = \varphi_1 + i\varphi.$$

Many authors, for example Prats [6] and Kanevskaya [3] solved this problem for the hydraulic fracturing or symmetrical case, when the well is located on the fracture line. In that case we need the parameter *Fcd*, dimensionless fracture conductivity, as the fluid just flows into the fracture and then the flow to the well occurs inside the fracture [7]. But if we consider nonsymmetrical case, when the well is located on the some distance from the fracture, or we have a couple of injection and production wells, we need to evaluate the inflow and the outflow from the fracture. Thus we need to take into account the pressure difference above and below the section, and we use more complicated boundary conditions [8-12]:

$$\begin{cases} \alpha_0\sqrt{1-\xi^2}\,\dfrac{d}{d\xi}\mathrm{Re}(\Phi^+ + \Phi^-) = \mathrm{Im}(\Phi^+ - \Phi^-), \\ \beta_0\sqrt{1-\xi^2}\,\dfrac{d}{d\xi}\mathrm{Im}(\Phi^+ + \Phi^-) = -\mathrm{Re}(\Phi^+ - \Phi^-); \end{cases} \tag{5}$$

where Φ^+ and Φ^- is the flow potentials above and below the section, coefficient $a_0=\delta k_f/lk$ is similar to *Fcd* for the hydraulic fractures and $\beta_0=\delta k/lk_f$ is very important for the impermeable case.

Let find $a_n^{(\alpha)}$ and $a_n^{(\beta)}$ from the boundary conditions (5) as:

$$a_n^{(s)} = \frac{n\cdot\alpha_0 - 1}{n\cdot\alpha_0 + 1}\frac{\left(\dfrac{\cos n\theta_1}{\rho_1{}^n} - \dfrac{\cos n\theta_2}{\rho_2{}^n}\right)}{n}; \tag{6}$$

$$a_n^{(\beta)} = -\frac{n\cdot\beta_0 - 1}{n\cdot\beta_0 + 1}\frac{\left(\dfrac{\sin n\theta_1}{\rho_1{}^n} - \dfrac{\sin n\theta_2}{\rho_2{}^n}\right)}{n}. \tag{7}$$

So, if we insert (6)-(7) into (4), flow potential can be expressed by the following form:

$$\varphi(\nu) = \ln\frac{(\nu-\nu_1)}{(\nu-\nu_2)} + \sum_{n=1}^{\infty}\left[\frac{n\cdot\alpha_0 - 1}{n\cdot\alpha_0 + 1}\left(\frac{\cos n\theta_1}{n\rho_1{}^n} - \frac{\cos n\theta_2}{n\rho_2{}^n}\right) - i\frac{n\cdot\beta_0 - 1}{n\cdot\beta_0 + 1}\left(\frac{\sin n\theta_1}{n\rho_1{}^n} - \frac{\sin n\theta_2}{n\rho_2{}^n}\right)\right]\nu^{-n} + C_0. \tag{7}$$

If we consider that wells are located at the y axis, symmetrically from the fracture, or $z_1=iy_0$; $z_2=-iy_0$; $\theta_1 = \dfrac{\pi}{2}; \theta_2 = -\dfrac{\pi}{2}$, then:

$$\nu_1 = \frac{z_1}{l} + \sqrt{\left(\frac{z_1}{l}\right)^2 - 1} = i\left(\frac{y_0}{l} + \sqrt{\left(\frac{y_1}{l}\right)^2 + 1}\right) = i\rho_0,$$

$$\nu_2 = -\nu_1 = -i\rho_0.$$

$$\varphi(\nu) = \ln\frac{(\nu - i\rho_0)}{(\nu + i\rho_0)} + \sum_{n=1}^{\infty}\left[\frac{n\cdot\alpha_0 - 1}{n\cdot\alpha_0 + 1}\left(\frac{\cos n\dfrac{\pi}{2}}{n\rho_0{}^n} - \frac{\cos n\dfrac{\pi}{2}}{n\rho_0{}^n}\right) - i\frac{n\cdot\beta_0 - 1}{n\cdot\beta_0 + 1}\left(\frac{\sin n\dfrac{\pi}{2}}{n\rho_0{}^n} - \frac{\sin n\dfrac{\pi}{2}}{n\rho_0{}^n}\right)\right]\nu^{-n} =$$

$$= \ln\frac{(\nu - i\rho_0)}{(\nu + i\rho_0)} - 2i\sum_{k=0}^{\infty}\frac{(2k+1)\cdot\beta_0 - 1}{(2k+1)\beta_0 + 1}\frac{(-1)^k}{(2k+1)\rho_0{}^{2k+1}}\nu^{-(2k+1)} =$$

$$= \begin{cases} \ln\dfrac{(\nu - i\rho_0)}{(\nu + i\rho_0)} + 2i\sum\limits_{k=0}^{\infty} \dfrac{(-1)^k}{(2k+1)\rho_0^{2k+1}} \nu^{-(2k+1)}; & \beta_0 = 0, \\ \ln\dfrac{(\nu - i\rho_0)}{(\nu + i\rho_0)} - 2i\sum\limits_{k=0}^{\infty} \dfrac{(-1)^k}{(2k+1)\rho_0^{2k+1}} \nu^{-(2k+1)}; & \beta_0 = \infty. \end{cases}$$

The nature of fluid flow, and water trasser lines to the wellbore at different locations of the crack and the well are are shown in Fig. 2-5. All calculations are made for permeable ftacture for the values of $\alpha_0=\infty$; $\beta_0=0$. In the left figeries we can see the water tracer lines, which are showing the water front position, depending on time. This results obtained by the use of the method of calculations, presented by Andrey Kasatkin in 2013 [13]. Different colors in these pictures show the boundaries between the flooding stages, so we can predict the water front at any moment, and water breakthrough time (red zone is the waterflooded area, from the beginning of the process to the half of the process; yellow zone in the pictures is the waterflooded area, from the ½ of the process to the ¾ of the process; blue zone – the waterflooded area, from the ¾ of the process to the water breakthrough time; purple zone or the closest to the production well is the waterflooded area at the breakthrough time). As we can see, the obtained flow potential equation allows us to solve the problem for any wells and fracture location. In this paper we consider particular case, when one well is in the center of the fracture, or the hydraulic fracturing case. By use of boundary conditions (5) we can model fluid flow for different values of fracture permeability or for differernt values of the coefficients α_0 and β_0. If we compare the results, the for same wells locations but for fracture in production or injection well, the breacthrow time is close to equel, but sweep efficiency is greater for the HF in production well. And if we compare different locations of wells, the most efficient case is perpendicular position of fracture line with wells line (Fig. 2).

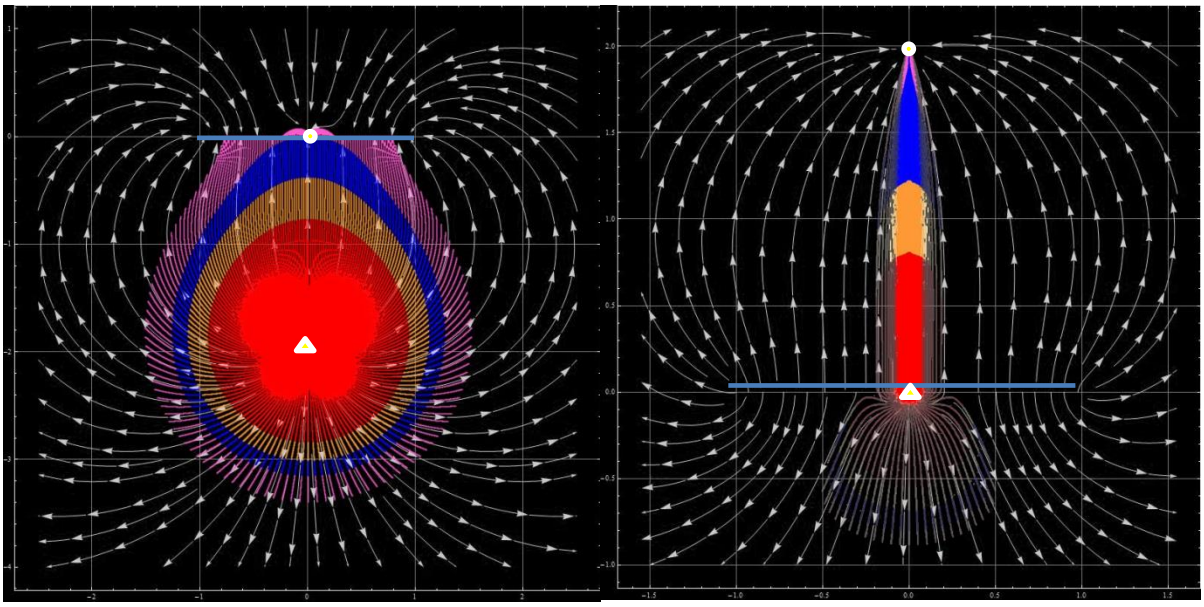

Figure 2: Streamlines and waterflooding process with tracer lines (angle 90).
Left: injection well located at the point (0, -2), the hydraulically fractured production well - at the point (0, 0); right: the hydraulically fractured injection well located at the point (0, 0), the production well - at the point (0, 2).

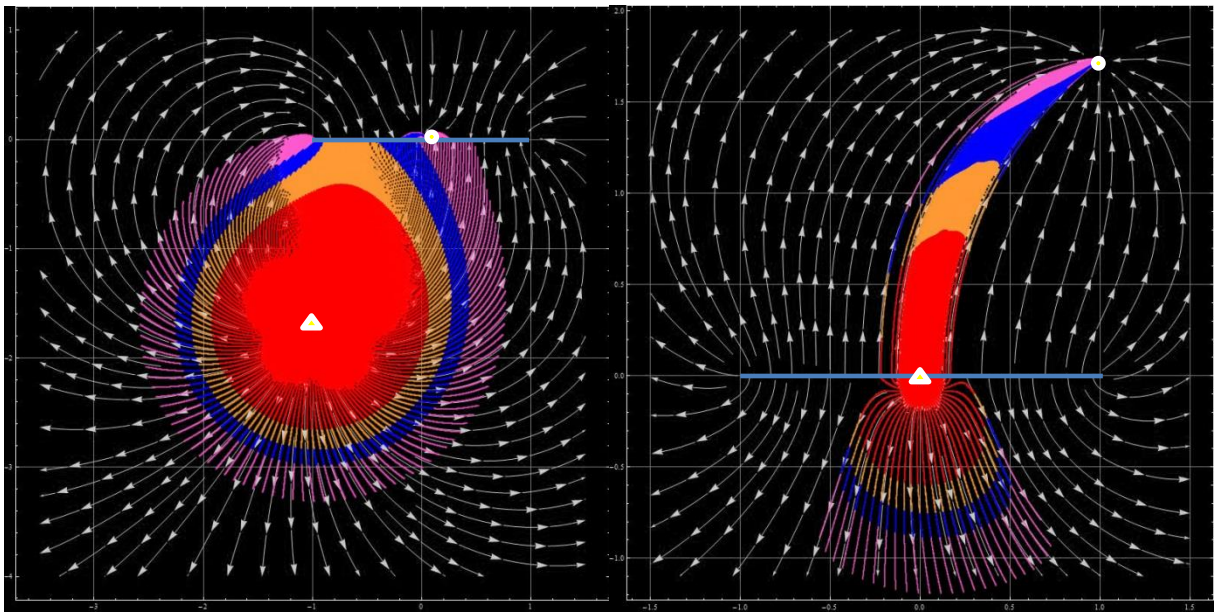

Figure 3: Streamlines and waterflooding process with tracer lines (angle 60).
Left: injection well located at the point (-1, -$\sqrt{3}$), the hydraulically fractured production well - at the point (0, 0); right: the hydraulically fractured injection well - at the point (0, 0), the production well - at the point (1,$\sqrt{3}$).

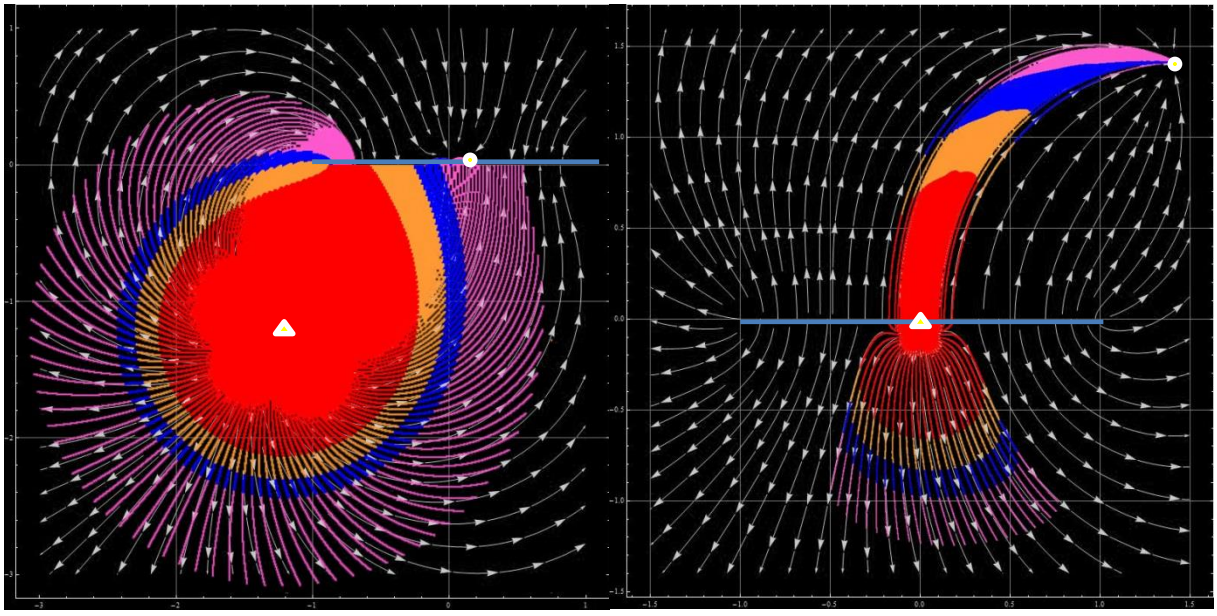

Figure 4: Streamlines waterflooding process with tracer lines (angle 45).
Left: the injection well located at the (-$\sqrt{2}$, $-\sqrt{2}$), the hydraulically fractured production well - at the (0, 0); right, the hydraulically fractured injection well - at the point (0, 0), the production well - at the point ($\sqrt{2}$, $\sqrt{2}$),

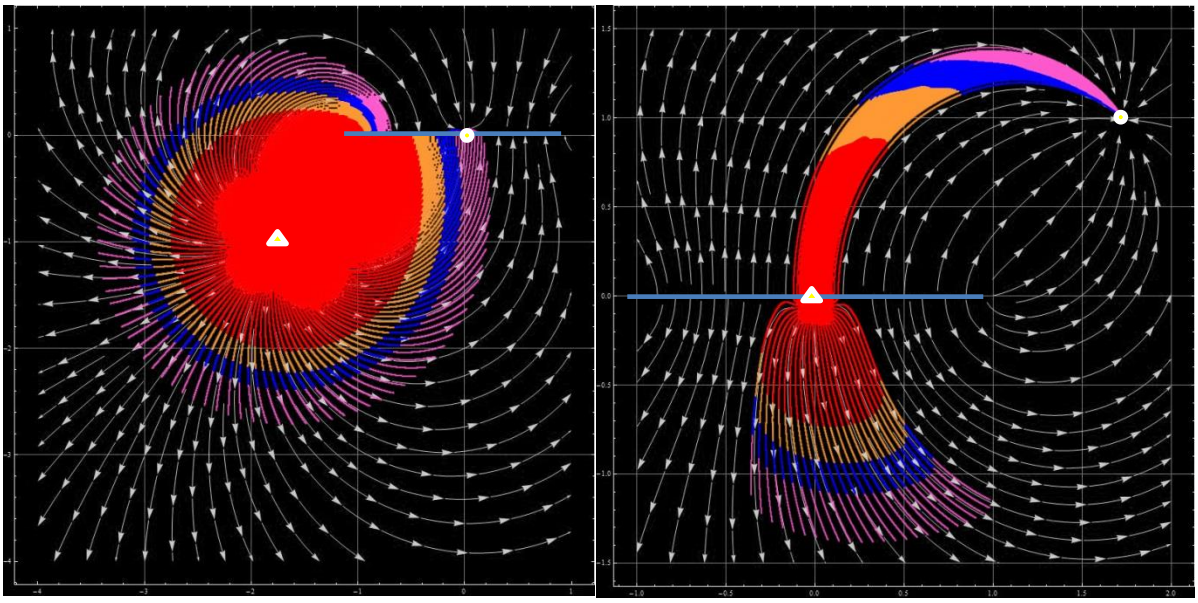

Figure 5: Streamlines waterflooding process with tracer lines (angle 30).
Left: the injection well located at the $(-\sqrt{3}, -1)$, the hydraulically fractured production well at the (0, 0); right, the hydraulically fractured injection well - at the (0, 0), the production well - at the point $(1, \sqrt{3})$.

4 CONCLUSIONS

In this work the formulation and solution of the problem of waterflooding process at the presence of a fracture. The solution obtained by the replacement of ellipse like approximation to the section view of zero thickness but finite conductivity. More general boundary conditions were considered taking into account the pressure difference above and below the section. Thus we obtained more general equation for the flow potential which coincides with previous solutions. This s solution is suitable for any cases of various wells and fracture places and for different values of fracture permeability.

In the final part of the paper the nature of fluid flow and the water trasser lines was analyzed. The tracer lines for waterflooding process were calculated for different case of lacation of hydraulicaly fractured injection and production wells. As the result, we can predict the water front at any time of the process and define the water breakthrow time.

As we can see, the problem has enough interest from the petroleum engineers. Further development of the solutions is to present the flow potential through singular integral equations, which will greatly expand the applications.

ACKNOWLEDGEMENT

This work is performed on the grant of the Russian Science Foundation (Project № 15-17-00019).

The authors express too their gratitude to Andrey Kasatkin for performing calculations in his software package (The certificate on the state registration of the computer program №2015610136).

REFERENCES

[1] Muskat, M. *The Flow of Homogeneous Fluids Through Porous Media*, J. W. Edwards, Inc. Ann Arbor, Michigan (1946).

[2] Fazliev, R.T. *Pattern Water Flooding of Oil Fields,* Izhevsk: IKI (in Russian) (2008).

[3] Kanevskaya, R.D. *Mathematical Modeling of the Development of Oil and Gas using Hydraulic Fracturing.* Moscow, Nedra Publishing (in Russian) (1999).

[4] Kanevskaya, R.D., Andriasov, A.R., Garipova, A.A. Fracturing optimization for multi-well system. *ECMOR IX - Proc. 9th European Conference on the Mathematics of Oil Recovery,* Cannes, France (2004).

[5] Astafiev, V.I., Fedorchenko, G.D. Simulation of fluid flow in the presence of a crack fracture. *Vestnik of SamSTU, Series: Phys.-Math. Sci.,* No. 2 (15), 128-132, (in Russian) (2007)

[6] Prats, M. Effect of vertical fractures on reservoir behaviour – incompressible fluid case. *Society of Petroleum Engineers Journal,* June, 103-118 (1961).

[7] Economides, M., Oligney, R., Valko, P. *Unified Fracture Design. Bridging the Gap Between Theory and Practice.* Alvin, TX, Orsa Press (2002).

[8] V.I.Astafiev, G.D.Fedorchenko, Vestnik of SamSTU, Series: Phys.-Math. Sci., 2 (15), 128-132 (in Russian) (2007).

[9] Andriyanova, E.V. The influence of discontinuities in the reservoir on well productivity. *Proc. 78th EAGE Conference and Exhibition 2016 – Student Programme,* Vienna, Austria (2016) DOI: 10.3997/2214-4609.201601621.

[10] Astafiev, V.I., Andriyanova, E.V. The influence of reservoir permeability heterogeneity on filtration of reservoir fluid to production wells. *Vestnik of SamSTU, Series: Tech. Sci.,* No. 3 (47), 154-161 (in Russian) (2015).

[11] Astafiev, V.I., Andriyanova, E.V. Modeling of the fluid flow to the production well in the presence of discontinuities in the reservoir. *Proc. of the 11th International Conference on Fluid Mechanics, Fluids, Heat and Mass Transfer, Mechanical and Civil Engineering.* Budapest, Hungary, 65-68 (2015).

[12] Astafiev, V.I., Andriyanova, E.V. Influence of reservoir's discontinuities on the process of oil filtration to the production well. *Proc. Fourth International Geoscience Conference, Deep Subsoil and Science Horizons,* Tyumen, Russia (2015) DOI: 10.3997/2214-4609.2014120342015.

[13] Astafiev, V.I., Andriyanova, E.V. The influence of the reservoir discontinuities on fluid filtration to the production well. *WSEAS TRANSACTIONS on FLUID MECHANICS,* **11** (2), 10-17 (2015).

[14] E. V. Andriyanova, V. I. Astafev, A. E. Kasatkin, Modeling of the waterflooding process in the presence of discontinuities in the reservoir. *ECMOR XV - Proc. 15th European Conf. on the Mathematics of Oil Recovery,* Amsterdam, the Netherlands, Volume 2 – pp. 980-992 (2016)

[15] Astafiev, V.I., Kasatkin A.E. Modeling and numerical calculation of piston-like oil displacement for doubly-periodic systems of oil fields development. *Proc. VI International Conference on Coupled Problems in Science and Engineering,* Venice, Italy, 734-743 (2015)

VII International Conference on Computational Methods for Coupled Problems in Science and Engineering
COUPLED PROBLEMS 2017
M. Papadrakakis, E. Oñate and B. Schrefler (Eds)

HYDROMECHANICAL ANALYSIS OF A HYDRAULIC FRACTURING PROBLEM

LETICIA P. MORAIS[*], JORDANA G. S. SABA[†] AND

MANOEL P. CORDÃO-NETO[††]

[*] University of Brasília (UnB) FT/ENC/SG 12
Post-Graduation Program of Geotchnical Engeenering
e-mail: leticia.12.morais@gmail.com web page http://www.geotecnia.unb.br/

[†]University of Brasília (UnB) FT/ENC/SG 12
Post-Graduation Program of Geotchnical Engeenering
e-mail: jordana.quinosan@gmail.com web page http://www.geotecnia.unb.br/

[††]University of Brasília (UnB) FT/ENC/SG 12
Post-Graduation Program of Geotchnical Engeenering
e-mail: mporfirio76@gmail.com web page http://www.geotecnia.unb.br/

Key words: Hydraulic Fracturing, Hydro mechanical, XFEM

Abstract. Hydraulic Fracturing is a well stimulation technique which recently has been widely used for shale gas extraction. Hydraulic fracturing is when a fluid is injected into the wellbore under controlled pressure and flow. The differential pressure generated by the injection of fluid initiates cracks that will propagate into the deep-rock formations, so that it allows the extraction of hydrocarbons trapped into the rock. The technique is used in conventional and unconventional reservoirs of hydrocarbons. In the first case, in conventional reservoirs, the technique is applied in order to increase the production of the well, while in unconventional reservoirs (shale gas) the technique is used to enable the extraction of the gas due to its very low permeability. Furthermore, the process of fracturing the rock at great depths involves the control over the type of fracture created or reactivated, as this will depend on a number of factors. The study of the technique is important to improve the control over the execution of this procedure and also to avoid possible contingencies and accidents. A formulation was implemented in this work capable of representing discontinuities in a continuous mesh using a finite element code. The Extended Finite Element Method (XFEM) was implemented in a hydro-mechanical coupled formulation. Additionally, analyses were performed to identify how the permeability of the rock and the permeability of the fracture influence the hydraulic fracturing. As a result, it was observed that maintaining all of the mechanical properties constant, the hydraulic properties have a great impact on the hydraulic fracturing process. Also, the velocity of propagation of the fracture is affected by the permeability of the rock, and its ratio is inversely proportional.

1 INTRODUCTION

Oil and gas have played a major role in the energy industry for many years and a lot of effort were put into the development of techniques to improve the extraction of oil from non-conventional reservoirs. One of these techniques is the Hydraulic Fracturing, which made possible the extraction of oil from shale reservoir, and increased the production of conventional reservoirs of oil. The technique consists of injecting a high-pressured fluid in the well, which will fracture the rock and will create preferential flow paths for the oil to flow to the well.

The Hydraulic Fracturing is a Hydro-mechanical coupled problem with high complexity because it needs to include the presence of a discontinuity in the medium and consider the intricacy of the flow within the fracture, which even under laminar flow regime is complex. In this work was used a home-made XFEM code to simulate the problem of hydraulic fracture. Darcy' s law was used for the flow within the fracture because of its simplicity and because it is widely use in Geotechnical problems.

2 FORMULATION

2.1 COUPLED HYDROMECHANICAL FORMULATION

The Coupled Hydro mechanical saturated problems are solved using two equations, the first to describe the mechanical behavior of the solid material (static equilibrium) and the last to describe the fluid behavior (continuity). The equilibrium equation for a soil volume is:

$$\frac{\partial \sigma_{ij}}{\partial x_j} + b_i = 0 \tag{1}$$

where σ_{ij} is the total stress tensor, b_i are the body forces and x_j is direction of the Cartesian coordinate system.

In the Equation 1 the tensor σ_{ij} is the sum of the effective stress σ'_{ij} and the pore water pressure u_w. The effective stress in a deformable porous media relates with the strain with a constitutive relation. The media is linear elastic and the problemis consider to be plane strain, where are given stresses in σ_x and σ_y with $\sigma_z \neq 0$. Also, the strain is computed in $\varepsilon_x, \varepsilon_y \, e \, \gamma_{xy}$ and $\varepsilon_z = 0$.

The constitutive relation is given by the D plain strain matrix:

$$D = \frac{E}{(1+\nu)(1-2\nu)} \begin{bmatrix} (1-\nu) & \nu & 0 \\ \nu & (1-\nu) & 0 \\ 0 & 0 & \dfrac{(1-2\nu)}{2} \end{bmatrix} \tag{2}$$

The continuity of the liquid phase is described by the mass conservation equation. Assume that water is incompressible, the equation for the water is given:

$$\frac{\partial(v_i)}{\partial x_i} + \frac{\partial \theta_w}{\partial t} = 0 \tag{3}$$

where $\theta_w = n.S$ is the volumen of water in the soil, n is the porosity, S is the saturation degree and v_i is the water velocity. The velocity can be defined by the Darcy's law as:

$$v_i = -k_{ij}\frac{dh}{dx_j} \tag{4}$$

where k_{ij} is the permeability matrix and $\frac{dh}{dx_j}$ is the hydraulic gradiente vector. If the medium is saturated, homogenous and isotropic, the continuity equation of water can be simplified, assuming that the water volume variation in a porous media is equal to the porous media volumetric variation. Therefore, the Equation (3) is written as:

$$\frac{\partial(v_i)}{\partial x_i} + \frac{\partial \varepsilon_v}{\partial t} = 0 \tag{5}$$

where ε_v is the volumetric variation of a soil element.

2.2 XFEM FORMULATION

XFEM (Extended Finite Element Method) is a numerical method developed to model weak and strong discontinuities within a finite element mesh. In this method, a fracture can be represented in the mesh without explicitly adding it to the finite element mesh.

The Extended Finite Element Method was developed by [1] and [3] to study the propagation of elastic fractures. They used functions to enrich the mesh and describe the presence of a fracture in the displacement field.

According to [2] the approximation of the displacement can be described in a general form as:

$$u(x) = \sum_{i=1}^{n} N_i(x)\bar{u} + enrichement\ terms \tag{6}$$

where n is the set of all nodes and $\boldsymbol{N_i}$ are the shape functions. The enrichment terms uses the Partition of Unity Method, and the shape functions are multiplied by the enrichment functions defined in the nodes of the element located on the discontinuity. The enriched domain is written as

$$u^h(x) = u^{EF} + u^{enr} = \sum_{i=1}^{n} N_i(x)\bar{u} + \sum_{j=1}^{m} N_j(x)\psi(x)\bar{a}_j \tag{7}$$

in which the first term is related to FEM interpolation and the second is the enriched interpolation, m is the set of nodes cut by the discontinuity, $\bar{a}_j$ are the nodal degrees of freedom corresponding to the enrichment function, $\psi(x)$ is the enrichment function.

The type of the function used to enrich the problem will depend on the condition of the problem. In this work it was chosen the Heaviside function and the *crack tip* to simulate the problem of Hydraulic Fractures. The Heaviside function is a step function defined as:

$$H(\xi) = \begin{cases} 1 & \forall \xi > 0 \\ 0 & \forall \xi < 0 \end{cases} \tag{8}$$

The crack tip function is used to approximate the behavior of the tip of the fracture within the element. The asymptotic solution of Williams (1957) for the two-dimensional isotropic media was used to define the four enrichment functions:

$$F(r,\theta) = \sqrt{r}\left\{cos\frac{\theta}{2}, sin\frac{\theta}{2}, sin\frac{\theta}{2}.sin\theta, cos\frac{\theta}{2}.sin\theta\right\} \tag{9}$$

These functions are defined in a local polar coordinate system (r,θ) at the crack tip. Some transformations are made for the Cartesian coordinate.

3. RESULTS

The XFEM code was validated with some problems of fracture known in the literature and it is presented in [4]. After that, some simplified simulations of the Hydraulic fracturing were made. In these simulations, a fluid was injected in a linear, homogenous and elastic media to open and propagate a fracture. It was applied a flow rate in the nodes of the mesh (Figure 1) and it was observed the propagation of the fracture under different conditions. The properties used can be observed on Table 1.

Table 1: Properties used in the simulation

Parameter	Value
Flow rate	2e-5 m^3/s
Poisson	0,3
Elastic Modulus (E)	2Mpa
K_{Ic}	140 $KPa.m^{1/2}$

In the Figure 2 it is illustrated the opening of the fracture with the fluid injection. In the simulation was observed that: the process of fracturing is strongly influenced by the permeability of the media and of the fracture, the influence of the permeability of the media and of the fracture in the relief of porewater pressure inside the fracture and the lost of fracturing fluid to the media (leak-off).

Due to the need of defining the permeability inside the fracture different from the permeability of the surrounding media, it was added in the code a factor to relate the permeability in the porous media with the permeability of the elements cut by the fracture. That was a first approach to deal with this problem. Later it will be used a cubic law to simulate the flow inside the fracture.

Figure 1: Finite Element mesh used in the simulation

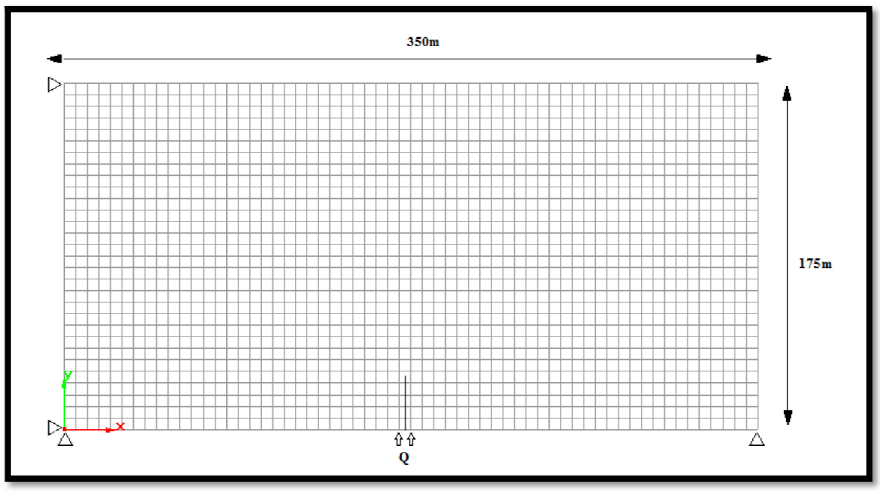

Figure 2: Fracture opening with fluid injection for increasing time

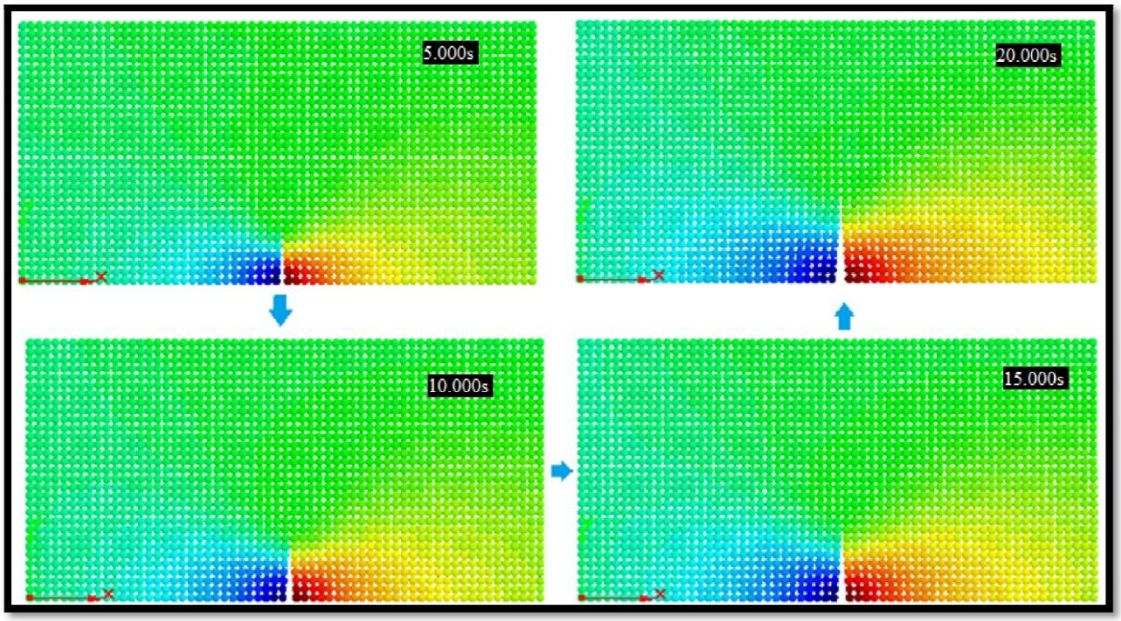

The first study made was a qualitative simulation to observe the relief of pore water pressure. In the Figure 3 it is possible to see the pore water pressure field after injecting the liquid in the media. The values for the permeability of the media and for the permeability of the fracture are on Table 3. In the media with permeability of 1e-5 m/s occurs the relief of the pore water pressure, and due to the boundary conditions and the time of the simulation the pore water pressure field reach a stationary regimen, and the length of the fracture remains constant.

Table 2: Permeability of the simulation

Medium permeability	Fracture permeability
1e-5 m/s	1e-3 m/s
1e-6 m/s	1e-4 m/s
1e-7 m/s	1e-5 m/s
1e-8 m/s	1e-6 m/s

Figure 3: Pore pressure field for different medium permeability (Pore pressure kPa)

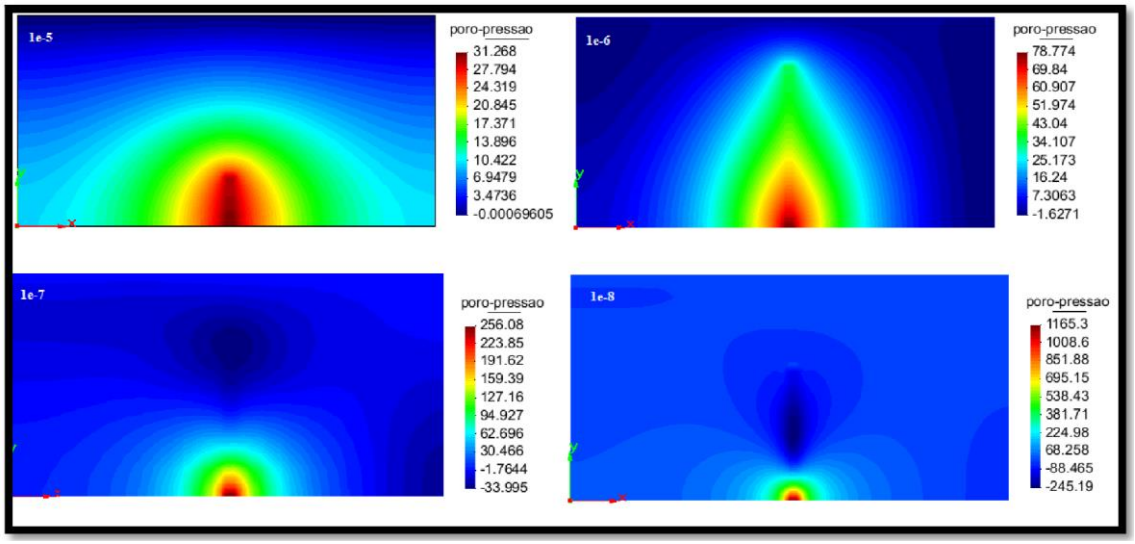

The next simulation was made to observe the relation between the permeability of the media and the loss of fracturing fluid to the media (leak-off). It was injected a fluid with the same rate in medias with different permeabilities, and the permeability of the fracture was constant. The permeability of the media were: 1e-3 m/s, 1e-4 m/s, 1e-5 m/s, 1e-6 m/s, 1e-7 m/s e 1e-8 m/s. The results show that for the media with high permeability (1e-3 m/s and 1e-4 m/s), the injection rate was not sufficient to propagate the fracture because was occurring leak-off with a higher rate than the injection of the fluid and the increase in the pore water pressure (Figure 4).

In the media with lower permeability the process of fracturing was higher because the leak-off process was lower (Figure 5). Despite the large number of variables affecting the process of hydraulic fracturing, when you maintain all other parameters constant and change only the permeability, the result of the fracturing will be different for each permeability value of the media.

Figure 4: Simulation of Hydraulic Fracturing for medias with permeability higher than 1e-5 m/s

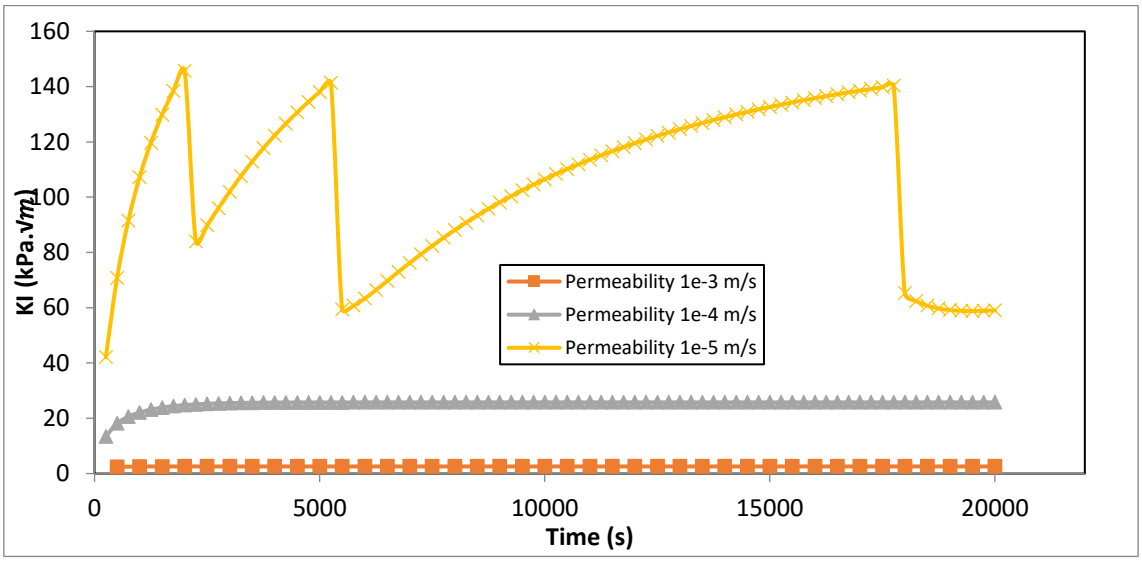

Figure 5: Simulation of Hydraulic Fracturing in medias with permeability lower than 1e-5 m/s

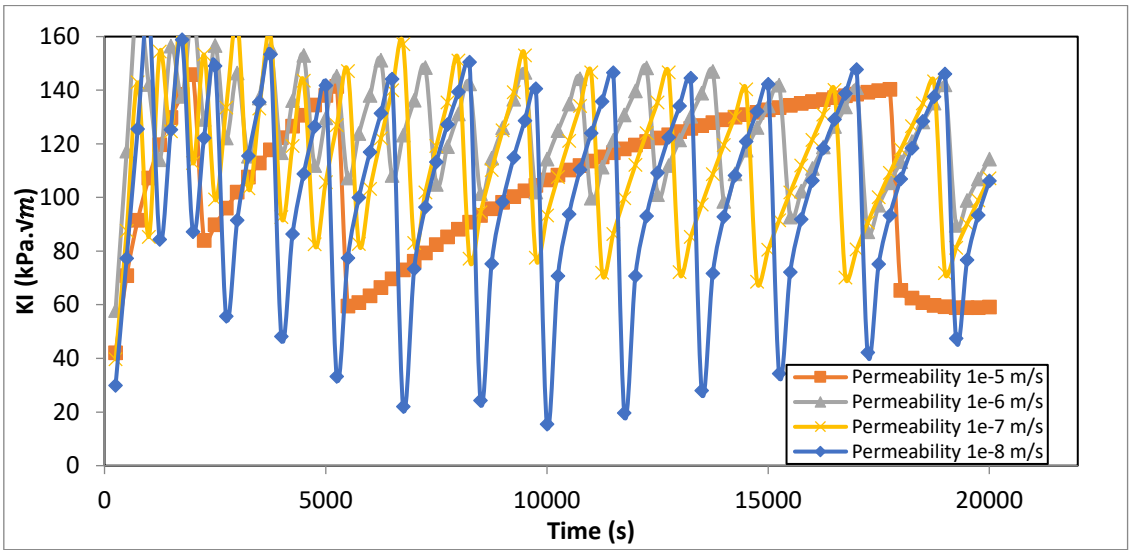

It was observed in the tests that the length of the fracture and the opening of the fracture are directly proportional when the flow rate to open the fracture is constant. In Figure 6 the graphic shows the increase of the length of the fracture with decrease of the permeability of the media, and in Figure 7 the graphic shows the increase of the opening of the fracture with the decrease of the permeability of the media.

The length of the fracture increase with the decrease of the permeability because when the media is very permeable lots of fracturing fluid is lost (leak-off), decreasing the pressure and hence the expansion of the fracture. The same occurs with the opening of the fracture, in the case where the media has high permeability, the leak-off occurs and the pressure of the fluid inside the fracture decreases, with a lower opening of the fracture.

The last test was made varying the permeability inside the fracture and keeping the permeability of the media constant. The permeability of the media adopted was 1e-7 m/s and the permeability inside the fracture was 1e-4 m/s, 1e-5 m/s and 1e-6 m/s. The results are in Figure 8 and 9. This tests showed that when the permeability inside the fracture is very low, the porous pressure is not dissipated and it value is high inside the fracture. Also, due to the low permeability inside the fracture, the pressure is high and the opening of the fracture is high.

Figure 6: Crack grow by Hydraulic Fracturing for medias with permeability lower then 1e-5 m/s

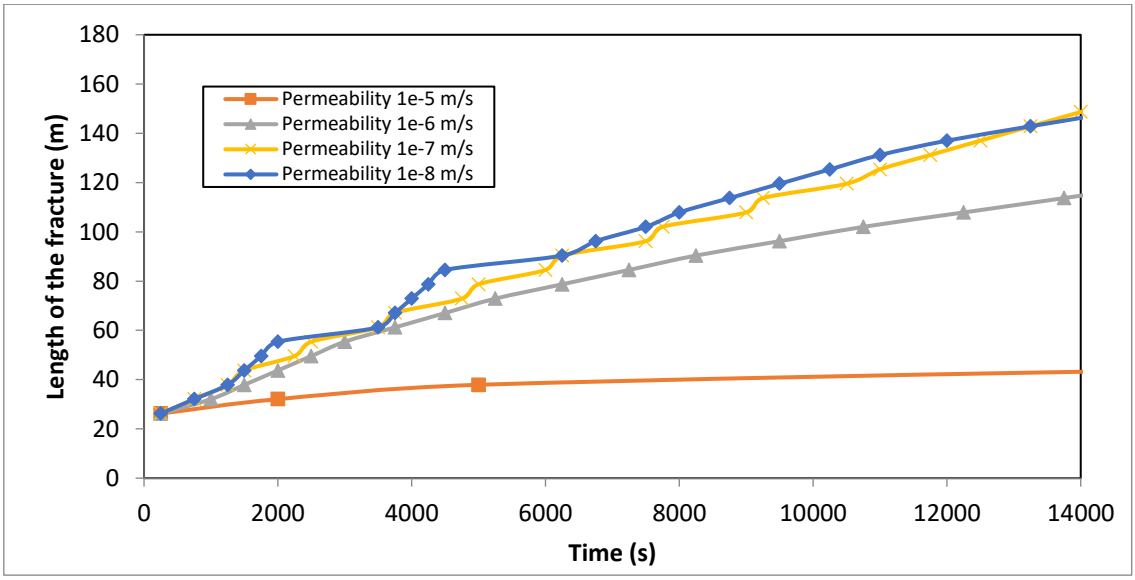

Figure 7: Opening of the fracture by Hydraulic Fracturing for medias with permeability lower then 1e-5 m/s

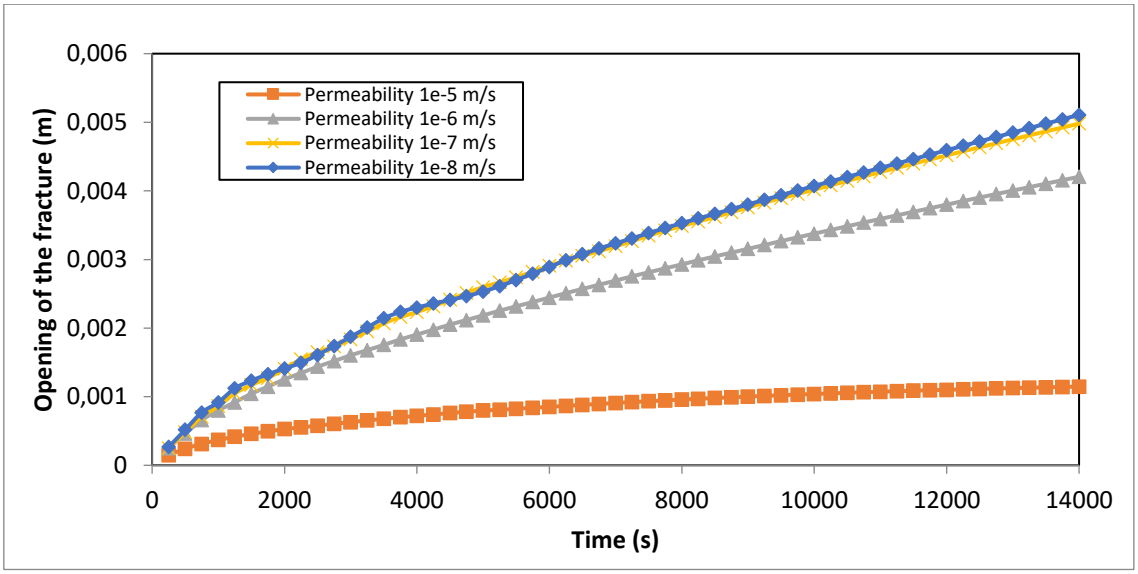

The last test was made varying the permeability inside the fracture and keeping the permeability of the media constant. The permeability of the media adopted was 1e-7 m/s and the permeability inside the fracture was 1e-4 m/s, 1e-5 m/s and 1e-6 m/s. The results are in Figure 8 and 9. This tests showed that when the permeability inside the fracture is very low, the porous pressure is not dissipated and it value is high inside the fracture. Also, due to the low permeability inside the fracture, the pressure is high and the opening of the fracture is high.

Although the simplification of the law to consider the flow inside the fracture, the simulation showed that the permeability has big influence in the hydraulic fracture process. The next step is to implement a more accurate law to describe the flow inside the fracture, for example, the cubic law.

Figure 8: Variation of pore pressure inside the fracture for different permeability inside the fracture

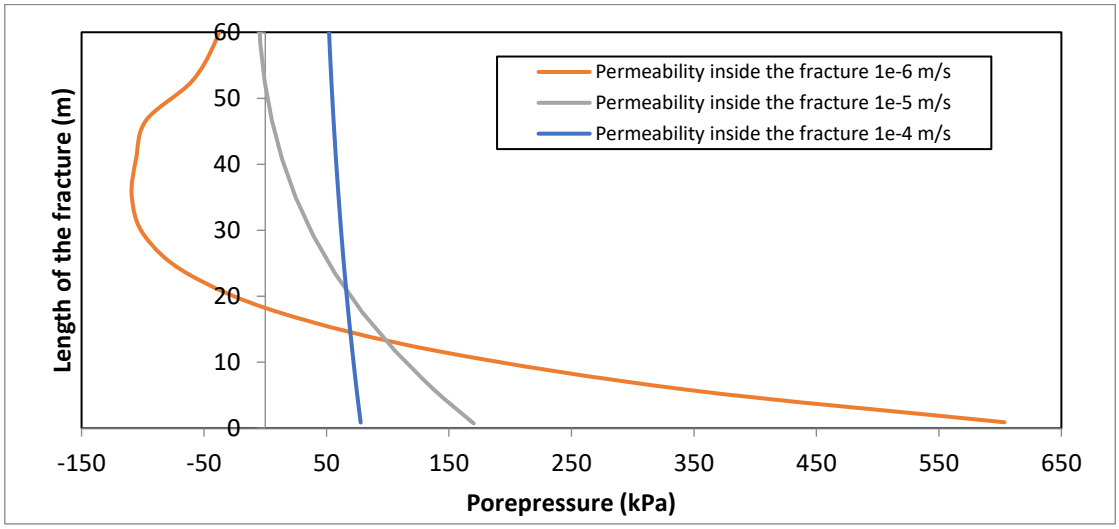

Figure 9: Variation of the opening of the fracture for different permeabilities inside the fracture

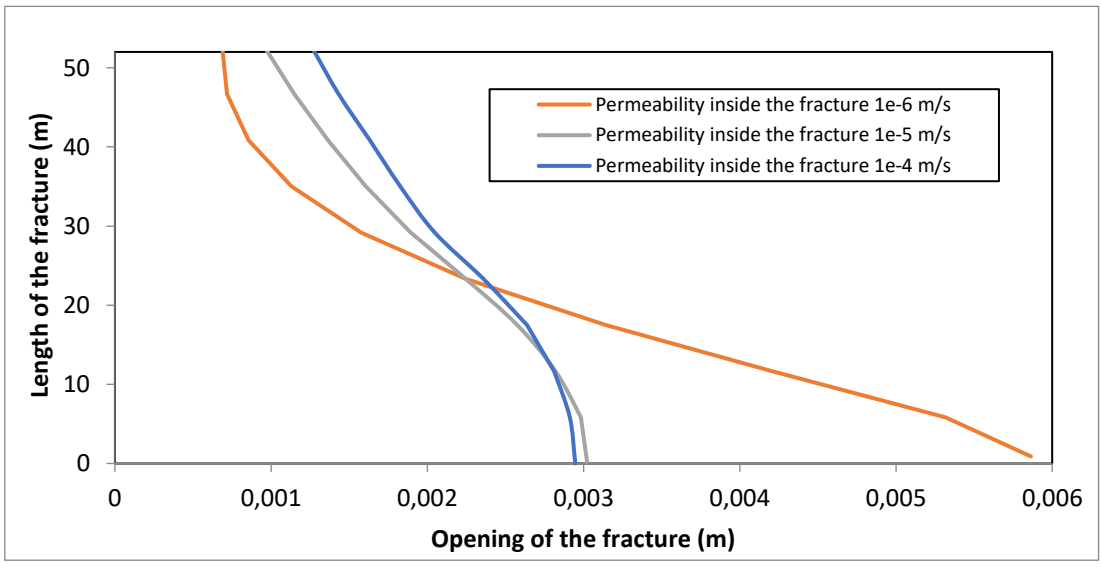

3 CONCLUSIONS

- XFEM method is a good alternative to deal with problems involving Hydraulic Fracturing. The implementation of the XFEM allow the research to use part of existing FEM codes.
- The numerical results show that the permeability of the media and inside the fracture has great influence in the Hydraulic Fracturing process.
- The results of the numerical simulation are in agreement with the results obtained by [5].

REFERENCES

[1] BELYTSCHKO T., BLACK T. (1999). Elastic crack growth in finite elements with minimal remeshing. International Journal for Numerical Methods in Engineering, 45, p. 601–620.

[2]KHOEI, A. R. (2015). Extended Finite Element Method, Theory and Applications, John Wiley, (584 pages) 2015, ISBN: 978-1-118-45768-9

[3]MOËS, N., DOLBOW, J., BELYTSCHKO, T. (1999). A finite element method for crack growth without remeshing. International Journal for Numerical Methods in Engineering, 46, p.131–150.

[4] Morais, L. P. (2016) Análise Hidromecânica do Problema de Fraturamento Hidráulico Dissertação de Mestrado, Publicação G.DM- 267/2016, Departamento de Engenharia Civil, Universidade de Brasília, Brasília, DF, 125p.

[5] Zielonka, M. G., Searles, K. H., Ning, J., Buechler, S. R., "Development and Validation of Fully-Coupled Hydraulic Fracturing Simulation Capabilities", In Proceedings of Simulia Customer Conference. Providence, RI, USA. May 19-22, 2014.

VII International Conference on Computational Methods for Coupled Problems in Science and Engineering
COUPLED PROBLEMS 2017
M. Papadrakakis, E. Oñate and B. Schrefler (Eds)

MULTIPHYSICS NUMERICAL MODEL FOR THE ANALYIS OF CO_2 INJECTION IN CARBONATE ROCKS

VIRGINIA S. A. MONTEIRO [*] AND DEANE ROEHL [†]

[*] Instituto Tecgraf
Pontificia Universidade Catolica do Rio de Janeiro
Marques de São Vicente 225, 22453-900, Rio de Janeiro, Brazil
e-mail: virginiam@tecgraf.puc-rio.br, www.tecgraf.puc-rio.br

[†] Instituto Tecgraf and Department of Civil Engineering
Pontificia Universidade Catolica do Rio de Janeiro
Marques de São Vicente 225, 22453-900, Rio de Janeiro, Brazil
email: deane@tecgraf.puc-rio.br, www.tecgraf.puc-rio.br

Key words: Multiphysics FEM problems, EOR, CCS, Acidification of Carbonate Rocks, Reactive flow, Chemical Reactive Flow, Hydro-Chemical coupling, CO_2 injection.

1 INTRODUCTION

In recent years, it was noticed an increased interest on the development of multi-physics constitutive models to provide reactive chemical analysis of the impacts of CO_2 injection in oil reservoirs. The movement was led by research groups interested in modelling Carbon Capture and Storage (CCS) and Enhanced Oil Recovery (EOR).

Given the rise in global temperature, it was detected that carbon dioxide plays an important role in global warming, contributing to more than 70% of gases of greenhouse effect, with residence time of over 100 years. According to Kyoto protocol, the signatory countries have defined commitments to limit greenhouse emissions. To accomplish the carbon reduction targets, it was created the Clean Development Mechanism (CDM), where developed countries could invest in projects to reduce greenhouse emission in developing countries, being these reductions accounted for carbon credits.

Aiming to fulfil target reductions on carbon emissions, interest grew on the development of solutions for carbon sequestration from the atmosphere. One of the most promisor long-term solutions is the injection of carbon dioxide in underground rocks or carbonate oil reservoirs. The injection of CO_2 in carbonates promotes acidification of underground water making it more prone to react and dissolve the rock porous matrix. With dissolution, the pore structure of the rock changes, modifying the permeability and hydraulic conductivity of the medium.

In order to quantify the long-term impacts of carbon capture by CO_2 injection in reservoirs, it is necessary to understand and quantify the chemical effects of dissolution in porous media, its impacts on rock structure and consequent change in underground flow [1]. In addition, it is necessary to account for the transport of chemical species and its contribution to the reaction. Continuous models were proposed taking into consideration the effect of reaction kinetics [2], diffusive effects [3], and both effects in two scales [4]. The two-scale model proposed by

Panga is similar to the model of heterogeneous catalytic reactors, but considers flow coupling, reaction/dissolution rates, and effects of mass transfer at pore scale. Indeed, the majority of the works on reactive modelling considers the diffusive-convective transport with source/sink term to represent chemical reaction with hydraulic coupling [5].

This work presents a straightforward implementation of a numerical model capable of evaluating the impacts of CO_2 transport in porous media, assessing dissolution and change in porosity in the rock matrix using the FEM.

2 MATERIAL AND METHODS

Chemical interaction between minerals and water originate from the chemical unbalance that persists in the system. Dissolution occurs when fluids are not saturated in respect to some minerals, making the product of ionic activity inferior to the equilibrium constant. In CO_2 injection processes, changes in chemical conditions occur locally given the dissolution of gas in the fluid within the reservoir. Considering the temperature and pressure of the fluid, the increase in CO_2 partial pressure favors the dissolution of carbonate minerals [6].

The porosity change can be computed through the volumetric quantity of minerals dissolved, which corresponds to an approximation to the mass balance. The macro description of dissolution patterns is very complex, being influenced by several factors, such as sample heterogeneity, reaction kinetics, and mass transfer [7].

$$\frac{\partial(\emptyset C_i)}{\partial t} + \nabla.(\boldsymbol{U}C_i) = \nabla.(\emptyset \boldsymbol{D_e}.\nabla C_i) - \ \vartheta_m R_m \ + \Gamma_i \tag{1}$$

A major number of experimental and theoretical studies analyzed the influence of dissolution processes on the physical chemical properties of porous media [8,9]. Mechanisms such as pore coalescence and flow channel formation involve complex effects [10].

To model reactive chemistry, we chose a continuous model approach, describing the phenomena in Darcy scale and an adaptation of the kinetic model from Chou [10], incorporating a term to describe the change on the porous superficial area, as proposed by Noiriel et al. The Finite Element method was chosen for domain discretization and to compute the transport equations and chemical reactions. To evaluate the change in porosity and permeability, the formulation proposed by Hao was implemented [11].

$$R_m = S_0 \left(\frac{\phi_t(1-\phi_t)}{\phi_0(1-\phi_0)}\right)^{\frac{2}{3}} k x_{CO_2} \tag{2}$$

Mineral reaction rate reads Eq. 2. and porosity change is derived directly from the reaction rate of calcite dissolution, as indicated in Eq. 3

$$\frac{\partial \phi}{\partial t} = -\vartheta_m R_m V_m \tag{3}$$

The proposed constitutive model of CO_2 injection in carbonates was implemented in the commercial software COMSOL Multiphysics ("COMSOL") and solved in a fully coupled scheme.

2.1 Coupling strategy

The dissolution of calcite, Eq. 4, solved in COMSOL considers the coupling of three physics: chemical reactions, transport of species and Darcy flow.

$$CaCO_3(s) + CO_2(g) + H_2O \leftrightarrow Ca^{2+}(aq) + 2HCO_3^-(aq) \tag{4}$$

The three physics are linked as described below:

- The transport of dissolved CO_2 in water is computed with transport of species physics. The input velocity field read in the convective term of the convection-diffusion equation Eq. 1 arises from the computed Darcy model;
- Updated species concentration arising from the dissolution reaction are computed in Chemical reaction module taking into consideration the reaction kinetics of the dissolution equation;
- The change in porosity is updated in Darcy model considering the reaction rate of calcite, Eq. 3.

2.2 Solution Method

The problem was solved with the non-linear Newton method, and solver MUMPS considering 723 degrees of freedom and simulation time of 15 hours, time step size 0.5s, solution time 6 min.

3 RESULTS

The proposed constitutive model of CO2 injection in reservoirs implemented in COMSOL was capable of following closely experimental data of carbonate rock dissolution described in the literature [12].

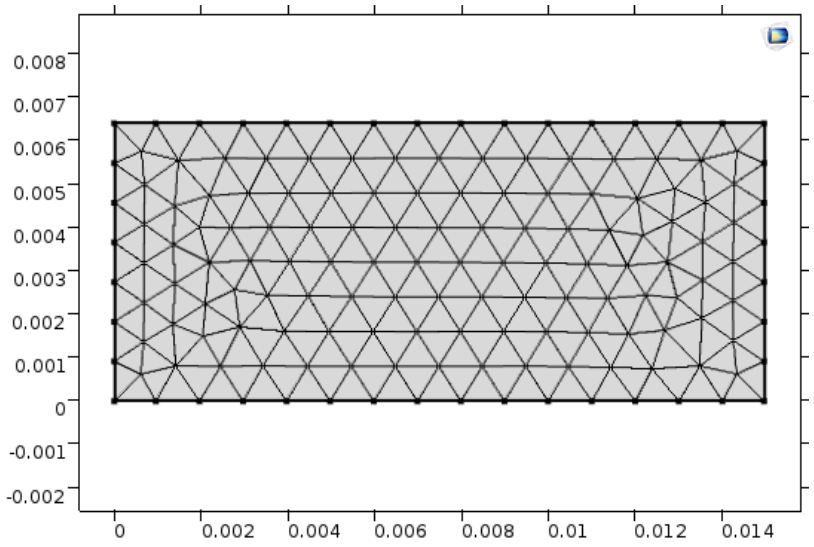

Figure 1: Mesh generated with linear triangular elements

Results from the numerical simulation lead to the identification of uniform porosity change in the porous media, as presented in figure 3.

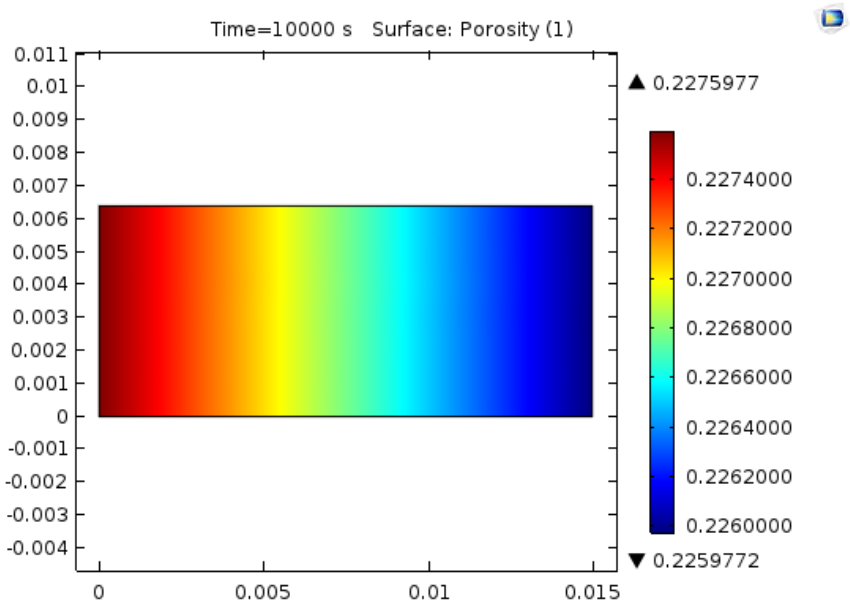

Figure 2: Porosity profile, recovering uniform dissolution, at 10,000s

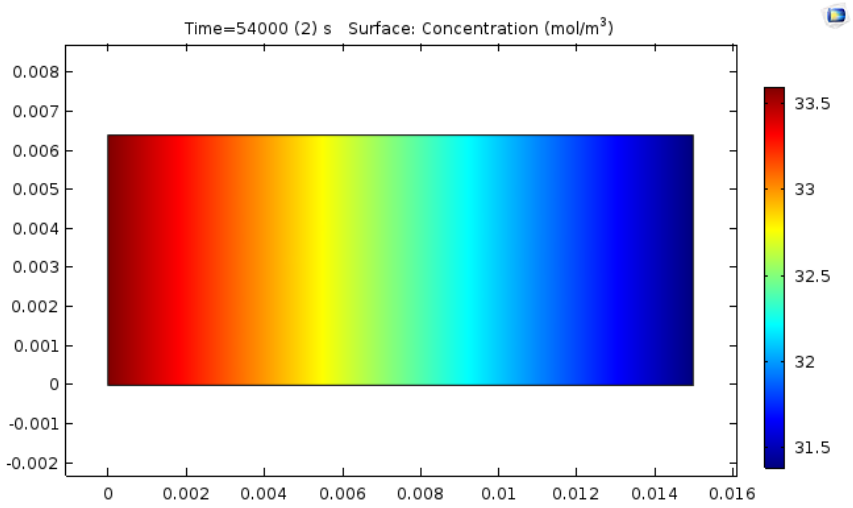

Figure 3: Transient results of CO2 concentration in COMSOL, at 54,000 s

In figure 4 the results from the numerical simulation in COMSOL were compared to experimental data from Noiriel [12](table 1).

Table 1: Noiriel Experimental data

Time (h)	Porosity (%)
0	20.3
9	24.7
15	30.2

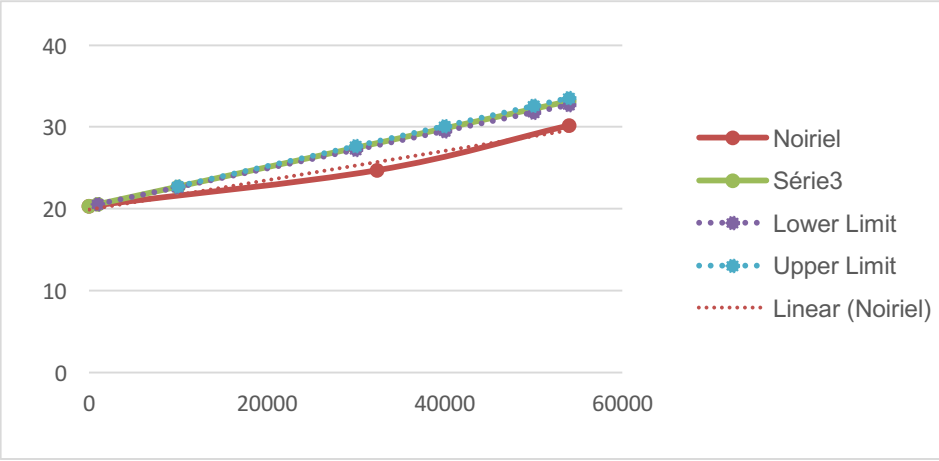

Figure 4: Transient results of porosity change in COMSOL and Noiriel data [12], porosity (%) vs. time (s)

4 CONCLUSIONS

- The continuous model for dissolution was able to recover the porosity changes when compared to the test reactive flow in real rock given initial data on rock porosity obtained with micrography of X-Ray.
- The straightforward approach used for modeling acidification in carbonates is a good alternative for the study and optimization of projects related to CO2 injection in reservoirs in projects of EOR or CCS.
- The fully coupled strategy has significant computational cost; alternative coupling strategies should be tested for larger scales and different dissolution patterns.

The simplified model presented in this paper does not account for precipitation of minerals, and may be extended accordingly [13].

5 ANNEX

Table 2: Variables

C_i	Concentration of species i
$\boldsymbol{D_e}$	Effective diffusivity
ϑ_m	Stoichiometric coefficient
R_m	Mineral reaction rate
$\boldsymbol{U}$	Velocity
Γ_i	Source / Sink term
S_0	Initial superficial area
x_{CO_2}	Molar fraction of CO2
V_m	Molar volume of calcite
k	Chemical kinetic constant
$\emptyset$	Porosity
ϕ_0	Initial porosity
ϕ_t	Current porosity

REFERENCES

[1] Stevens, S.H.; Gale, J.; 2000. *Geologic sequestration may benefit upstream industry*. Oil & Gas (2000), p.40

[2] Liu, X.; Ormond, A.; Bartko, K.; Li, Y.; Ortoleva, P. *A geochemical reaction-transport simulator for matrix acidizing analysis and design*. J. of Pet. Sci. and Eng (1997) 17, 181-196.

[3] Golfier, F.; Zarcone, C.; Bazin, B.; Lenormand, R.; Lasseux, D.; Quintard, M. *On the ability of a Darcy-scale model to capture wormhole formation during the dissolution of a porous medium*. J. Fluid Mech. (2002) 457, 213-254

[4] Panga, M. K. R., Ziauddin, M.; Balakotaiah, V. *Two-scale continuum model for simulation of wormholes in carbonate acidization*, AIChE J. (2005) 51.

[5] Van der Lee, J.; De Windt, L.; Lagneau, V.; Goblet, P. *Module oriented modeling of reactive transport with HYTEC*. Comput. Geosci. (2003), 29, 265-275.

[6] Stumm, W.; Morgan J. *Aquatic Chemistry*, Wiley, New York, (2004) 1024pp.

[7] Steefel, C.; Lasaga, A. *Evolution of dissolution patterns: permeability change due to coupled flow and reaction*. In: Melchior, D. Eds, Chemical modeling of Aqueous Systems II. American chemical society, Washington D.C, (1990) pp. 212-225

[8] Shechter, R.S.; Gidley, J.L.; *The change in pore size distribution from surface reactions in porous media*. AIChE J. (1969) 15, 339-350

[9] Noiriel, C.; Gouze, P.; Bernard, D. *Investigation of porosity and permeability effects from microstructure changes during limestone dissolution*. Geophys. Res. Lett. (2004) 31 (24).

[10] Chou, L.; Garrels, R.M.; Wollast, R. 1989. *Comparative study of the kinetics and mechanisms of dissolution of carbonate minerals.* Chem. Geol., 78, 269-282.

[11] Hao, Y.; Smith, M.; Sholokhova, Y.; Carroll, S. *CO_2-induced dissolution of low permeability carbonates. Part II: Numerical modeling of experiments*, Adv. In Water R. (2013) v. 62C.

[12] Noiriel, C.; Luquot, L., Made, B.; Raimbault, L.; Gouze, P., Lee, J. *Changes in reactive surface area during limestone dissolution: An experimental and modelling study*. Chemical Geology (2009) 265: 160-170

[13] Agada, S.; Chen, F.; Geiger, S.; Toigulova, G.; Agar, S.; Shekhar, R.; Benson, G.; Hehmeyer, O.; Amour, F.; Mutti, M.; Christ, N.; Immenhauser, A. *Numerical Simulation of fluid-flow processes in a 3D high-resolution carbonate reservoir analogue*. Pet. Geo. (2014) 20(1):125.

VII International Conference on Computational Methods for Coupled Problems in Science and Engineering
COUPLED PROBLEMS 2017
M. Papadrakakis, E. Oñate and B. Schrefler (Eds)

PROBABILISTIC ANALYSIS OF A GAS STORAGE CAVITY MINED IN A SPATIALLY RANDOM ROCK SALT MEDIUM

ELHAM MAHMOUDI*†, MARKUS KÖNIG*, TOM SCHANZ†

* Chair of Computing in Engineering
Department of Civil and Environmental Engineering
Ruhr-Universität Bochum
e-mail: elham.mahmoudi@rub.de/ - Web page: http://http://www.inf.bi.ruhr-uni-bochum.de

†Chair of Foundation Engineering, Soil and Rock Mechanics
Department of Civil and Environmental Engineering
Ruhr-Universität Bochum
e-mail: tom.schanz@rub.de/ - Web page: http://http://www.gbf.rub.de

Key words: Stochastic Analysis, Rock Salt Cavern, Finite Element Analysis, Spatial Variability, Random Field

Abstract. In most engineering problems the material parameters spread over spatial extents but this variability is commonly neglected. Analyses mostly assign the mean value of a variable to the entire medium, while in the case of heterogeneous materials as geomaterials, this may lead to an unreliable design. The existing scatter in such materials can be represented in the design procedure using the random field concept.

In this paper, the random field method is used in a probabilistic analysis of a gas storage cavern in rock salt. The rock salt formation, as a porous media with low permeability and particular creep features, has been used for decades as the host rock for the hydrocarbon storage. To achieve a reliable design, a probabilistic model is presented to compute the failure probability of a cavern mined in a spatially varying salt dome. Here, the no-dilatant region around the cavity is regarded as the failure criterion. In this regard, a thermo-mechanical model of a natural gas storage in rock salt, employing BGRa creep law, is developed. Afterwards, the most effective input variable on the model response is identified, using global sensitivity analysis. The Karhunen-Loève expansion is introduced to generate random field. In the following, the subset simulation methodology is utilised to facilitate the execution of Monte-Carlo method. The findings of this study emphasize that considering spatial variability in rock properties significantly affects the reliability of a solution-mined cavity.

1 Introduction

Solution-mined cavities in rock salt represent an adequate opportunity for energy carriers' storage plants. Rock salt is nearly impermeable compared to other geomaterials and excavation in this rock costs relatively low due to the possibility of solution mining. For many decades, abandoned salt mines have been used for underground storage. The first cavern in rock salt for natural gas storage was excavated in Michigan, USA in the 1950s [1]. In the last 30 years, in Germany industry has made large investments in building energy storages in deep underground formations. For instance, the Etzel (IVG) cavern site currently includes 73 existing gas and oil storage caverns with a capacity of approximately 46 million cubic metres [2]. In addition to many caverns around the world storing hydrocarbons, there are also some new trends to provide long-term electrical storage capacities in such cavities in form of compressed air or Hydrogen.

The stability of rock salt caverns is the main concern of the design process of such massive underground structures. Rock salt is categorised as a soft rock and its non-linear time-dependent material behaviour (i.e. creep behaviour) makes rock salt different from other common host rocks. Thereupon, much effort has been paid to provide a consistent knowledge about the behaviour of rock salt enforced by different loading conditions. Moreover, in order to predict and explain the behaviour of the rock salt by mathematical equations, a wide range of constitutive laws have been proposed within different micro and macro observations, e.g., see [3, 4, 5]. Furthermore, numerous studies have been carried on to evaluate the response of the rock salt cavities under storage conditions using numerical simulation methods (e.g., [6, 7, 8, 9]).

However, a clear picture of the rock salt characteristics may only appear by gathering different information sources as laboratory analyses, geotechnical in-situ measurements, and on-site observations. In practice, for such particular structures which are extended vertically downwards more than hundred meters from the ground level, only limited experimental and in-situ data is available. On the other hand, the inherent randomness of natural materials as rocks causes a wide extent of spatial distribution in their physical properties. Considering these facts, the measure of involved uncertainties in the rock salt properties can not be neglected. Hence, a reliable design procedure can not rely merely on deterministic approaches. In order to provide an adequately accurate computational model, stochastic analysis approaches must be utilized, as well. Despite other geotechnical fields of study where the stochastic analyses are well established (e.g. [10, 11]), there are rare studies that investigate the involved uncertainties in the geotechnical design of rock salt cavities. For instance, in [12], the authors performed a probabilistic analysis on a compressed air rock salt cavity, using the subset simulation methodology as a modern Monte-Carlo approach. In that study, the involved input parameters were considered as the random variables, and the defined uncertainty measure applied to the entire medium and the spatial randomness was neglected.

To represent the real spatial variability of a field variable, a significant amount of infor-

mation must be gathered from the field, which is an expensive or even infeasible project. Also, if not enough amount of data is gathered then the parameter identification and design process can be inaccurate. In this regard, a probabilistic analysis concept may be employed to minimise sampling costs while it is still being able to provide informative data. For this, random fields are appropriate as models of the spatially distributed uncertainty and they can be utilised to produce probability measures regarding design criteria [13]. In the random field models, the characteristics of the spatial distribution of mechanical parameters are simulated as functions of spatial location. Various random field generator algorithms are available in the literature, which are shortly reviewed in Sect. 2. Among the others, the series expansion methods can approximate the random field by a finite sum of products of deterministic spatial functions and random variables. In this study, the Karhunen-Loève expansion as a series expansion method, introduced in Sect. 3, is applied to generate random field realisations.

In the following, a typical natural gas rock salt cavern is simulated by finite element method. Within the numerical model, the rock salt behaviour is described by BGRa [3], a well-known creep model. In Sect. 4 the numerical model, boundary and loading conditions are presented. Sect. 5 presents the probabilistic analysis of the considered cavity mined in spatially varying rock salt. The effect of the uncertainties in the input parameters on the system responses is inquired by carrying out a global sensitivity analysis. In the present paper, Sobol's method [14] as a variance-based sensitivity technique is employed. After ranking the importance level of parameters, random field discretization applied on the most governing one. In the following, the failure probability of the system considering dilatant behaviour is evaluated. At the end, a parametric study is conducted to investigate the effect of variations in the assumed autocorrelation lengths. The obtained results are concluded in Sect. 6.

2 Random field discretization

Because of the differences of mineral ingredients, stress history, and other geological factors, constitutive parameters of rocks or soils show spatial differences and correlations as well. The characteristics of the spatial distribution of constitutive parameters can be simulated as a geological parameter field which exhibits spatial variability. In general, a random field is characterised by its mean, variance, and its correlation structure. One of the major features of a random field representation of a material is the concept of statistical dependence between field values at different points, which is known as the correlation structure [15]. The correlation coefficient between two points x_1 and x_2, $\rho(x, x')$ is decreasing gradually as the distance is increasing. On the other hand, when the distance between two realisation points approaches to zero, the material characteristics are identical. It should be stated that higher order moments of random field can also represent its characteristics, but due to difficulties in estimating them, random field models are often represented by information about the three mentioned measures. To accomplish this, firstly a relatively simple joint PDF (e.g., multivariate normal or lognormal distributions)

for the field should be adopted. The correlation structure is often assumed to be a simple function of the distance between points.

A continuous random field $H(x,\theta)$ can be defined as a random function that describes a random quantity at each point $x \in \Omega$ of a continuous domain $\Omega \subset \mathbb{R}^n$. $\theta \in \Theta$ is a coordinate in the sample space Θ. Hence, $H(x_0,\theta)$ denotes the random variable associated with point x_0, and $H(x,\theta_0)$ indicates θ_0 realisation of the field. As mentioned before, a random field can be defined by its mean $\mu(x)$, variance $\sigma^2(x)$ and autocorrelation coefficient function that is

$$\rho(x_1,x_2) = \frac{C_H[H(x_1),H(x_2)]}{\sigma(x_1)\sigma(x_2)}, \tag{1}$$

where $C_H(.,.)$ is the autocovariance function. A random field can be discretised by approximating $H(.)$ by $\hat{H}(.)$, described by means of a finite set of random variables $\{\chi_i$, i = 1,...,n $\}$

$$\hat{H}(x) \xrightarrow{\text{Discretization}} \hat{H}(x) = F[x,\chi]. \tag{2}$$

Sudret & Der Kiureghian [15] classified the most commonly used methods of random field discretization into following main groups

- Point Discretization

  In this group of methods, the random variables χ_i are selected values of $H(.)$ at specific points in a given spatial discretization (e.g., mesh in finite/difference element methods).

- Average Discretization,

  In these methods, the random variable related to a given χ_i is calculated as the weighted integrals of $H(.)$ over a domain Ω_e

  $$\chi_i = \int_{\Omega_e} H(x)\omega(x)d\Omega. \tag{3}$$

  A comparative review on the above mentioned methods was provided in [16].

- Series Expansion methods

  In the series expansion discretization methods, the random field is approximated by an expansion that involves deterministic and stochastic functions. The value of the random field is calculated on the basis of the coordinates of the point in deterministic functions. In these techniques, the field is represented as a series involving random variables and deterministic spatial functions. As examples of this group of methods, one can mention the Expansion Optimal Linear estimation method, proposed by [16]. The Karhunen-Loève expansion method is also a commonly used series expansion method. The Karhunen-Loève is utilised in the present study to discrete the random field and it is briefly described in the following.

3 Karhunen-Loéve expansion

We consider $H(x,\theta)$ as random process, when H denotes the expected value of the random field. The random field can be calculated by the Karhunen-Loéve expansion as follow

$$\hat{H}(x,\theta) = \mu_H + \sum_{i=1}^{\infty} \sqrt{\lambda_i}\phi_i(x)\xi_i(\theta), \tag{4}$$

where λ_i and ϕ_i are the eigenvalues and eigenfunctions of the autocovariance function, and $\xi_i(\theta)$ is a vector of standard uncorrelated random variables. μ_H is the mean function of the field. It should be noticed here that $\xi_i(\theta) : \Theta \to \mathbb{R}$ are the stochastic variables that represent the random nature of the uncertain parameter. For practical purposes, the expansion in Eq. 4 can be truncated to a given number of terms, M as follow:

$$\hat{H}(x,\theta) \approx \mu_H(x) + \sum_{i=1}^{M} \sqrt{\lambda_i}\phi_i(x)\xi_i(\theta), \tag{5}$$

where M is the size of the series expansion, λ_i and ϕ_i are the eigenvalues and eigenfunctions of the covariance function $C(x_1, x_2)$, and $\xi_i(\Theta)$ is a vector of standard uncorrelated random variables. However, the eigenvalues and eigenfunctions λ_i and ϕ_i are the deterministic functions of the Karhunen-Loève expansion. They can be evaluated as the solution of the following Fredholm integral equation:

$$\int_{\Omega} C_H[H(x_1), H(x_2)]\phi_i(x_2)dx_2 = \lambda_i\phi_i(x_1). \tag{6}$$

This integral can be solved analytically only for a few types of the autocovariance functions. Ghanem & Spanos [17] presented the detailed analytical solution of the integral in Eq. 6 for an exponential autocovariance function.

The choice of the number M of terms depends on the required accuracy of the considered problem. Sudret & Der Kiureghian [15] proposed the following error estimate $(err(x))$ after truncating the expansion to M terms,

$$err(x) = \sigma_H^2 - \sum_{i=1}^{M} \lambda_i\phi_i^2(x), \tag{7}$$

where σ_H is the standard deviation of the random field.

4 Deterministic model of a rock salt cavern

Within this study, a gas cavern with the capacity of 368,000 m^3 is simulated by an axisymmetrical numerical model, its casing shoe is assumed to be located in the depth of 400 m. The shape of the cavern after excavation is idealised as a cylinder with the height of 150 m and 60 m diameter. The floor and roof of the cavern are considered as

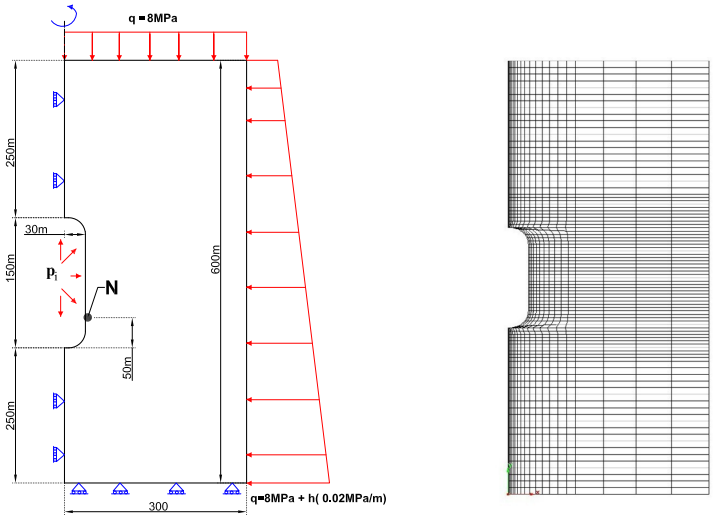

(a) (b)

Figure 1: (a) Representative geometry and boundary conditions of the salt cavern model and (b) Finite element mesh discretization

semi-spheres with 30 m radius. Fig. 1a shows the geometry and boundary conditions of this cavity in detail. The considered mesh discretization is also shown in Fig. 1b. The uniform load at the top of the model substitutes the overburden weight. In order to model the solution mining procedure, the entire excavation phase is simplified by reducing the internal pressure of the cavern to the minimum gas pressure (First discharge phase) in a time interval of 300 days. In this study, the minimum inner pressure of the cavity is assumed to be equal to 4 MPa. In our simulation, the temperature of intact rock salt is assumed to be equal to 50℃. The thermal boundary condition of the wall of the cavity is decreased during the discharge phase to 30℃(for more details about the variation of thermal condition see [8]).

In this study, the creep behaviour of the rock salt is modelled on the basis of the BGRa constitutive model. In this constitutive model, the creep induced strain rate of rock salt is obtained using the following equation:

$$\dot{\varepsilon}_{ij}^{cr} = A \exp(\frac{-Q}{RT})(\frac{\sigma_{ij}}{\sigma_0})^n, \tag{8}$$

where A denotes the value of fluidity at a reference temperature; R is the universal constant of perfect gas (8.314 e3 kJ/(mol.K)) and T is the absolute temperature (For more details see [3]). In the present study, the induced strain rate by the temperature change is also considered as an additional strain tensor in the mechanical model. This quantity is related to the linear thermal expansion coefficient α and the temperature changing rate $\dot{T}$:

$$\dot{\varepsilon}_{ij}^{th} = \alpha \dot{T} \delta_{ij} \tag{9}$$

The mechanical stability of storage cavities is the most important issue which should be assured in an accurate geotechnical design. Therefore, the dilatant zones which can be initiated by a specific stress state in rock salt should be avoided. The dilatancy boundary, which is defined by the beginning of the irreversible volumetric expansion, can be considered as a criterion which divides the stress space into compression and dilatancy regions. A Dilatancy boundary, known as compression/dilation (C/D) boundary can be identified on the basis of experimental data (for more details about different C/D boundaries, the reader is referred to [9]). In the present study, Desai C/D boundary [4] is used as no dilation criterion. In order to determine whether a region in the simulated rock salt cavity encountered dilatancy or not, the following quantity DF is defined.

$$DF = \sqrt{\frac{J_2}{J_2^{dil}(I_1)}}. \tag{10}$$

where $J_2^{dil}(I_1)$ denotes the second stress invariant of C/D boundary corresponding with the value of first invariant (I_1) in each observation point. When $DF < 1$, the stresses are inside the compressibility domain and opening of micro-cracks does not occur and subsequently, damage does not progress. In contrary, when $DF \geq 1$, the cavern may experience long-time failure due to the damage progress.

In the next step, the finite element numerical simulation of the typical cavern is conducted. Although in real cases the designer must assure that no-dilatant region around the entire cavern will take place, in the present study, the considered observation points are limited. The level of one-third of cavern's height from its bottom is generally treated as a benchmark region in measurements and numerical simulations as well. Hence, in this study the DF factor is evaluated in the region of N, illustrated in Fig. 1a.

It is important to note that a stratigraphic unit may consist of several different homogeneous zones. The graphs provided by [18], which are derived from creep tests on two different shafts in Gorleben salt dome (north-east of Germany), indicate the existing of vertical heterogeneity in creep behaviour of this site. The present study considered a one-dimensional (vertical) spatially random field. It should be stated that the method of the Karhunen-Loève can cope with domains of arbitrary geometric mesh, different from the FEM mesh. However, the size of a given element in the deterministic mesh depends on the autocorrelation distances of the rock properties. Der Kiureghian & Ke [19] suggested that the length of the largest element of the deterministic mesh should not be less than half of the autocorrelation distance in that direction. In order to respect this criterion, the geometrical model is vertically divided to 10 m layers, with a specific random value assigned to each layer (with 10 m thickness).

5 Probabilistic analysis

Before generating the random field, the most important input parameter which makes the largest contribution to the variation of model response is identified by conducting

Table 1: Material parameters for rock salt

Elastic Parameters		Creep Parameters			Thermal Properties
E [GPa]	ν [-]	A [s^{-1}]	n [-]	Q [kJ/mol]	α [1/°C]
[19 - 3]	[0.25 - 0.35]	[0.1e-5 - 0.5e-5]	[3 - 5]	[40000 - 70000]	[3e-5 - 5.5e-5]

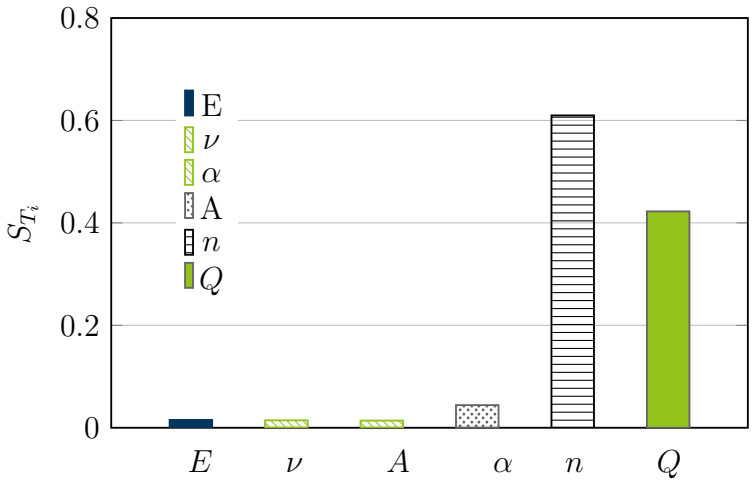

Figure 2: Estimation of total effect sensitivity index S_{Ti}, regarding FS

a global sensitivity analysis. The variance-based technique for evaluating the sensitivity indices of input parameters is proposed by [14]. This methodology was previously introduced to the geotechnical design of solution-mined cavities by the authors [20]. In this paper, Sobol's method (also known as Monte-Carlo based implementation) is utilised to evaluate the sensitivity measures of different constitutive parameters (the reader is referred to [21]). It should be mentioned that the sensitivity analysis is conducted on a random variable homogeneous model. Table. 1 represents the considered range of variation for each input variable. All the input variables follow a lognormal probability distribution function. Fig. 2 depicts the evaluated total-effect sensitivity index (S_{Ti}) for each constitutive parameter. The most influential input parameter on the stress-state of the cavern's wall against dilation is n.

Hence, all parameters but n are fixed to their mean values, and the variable of n is discretized as a random field. The mean value and coefficient of variation of parameter n are respectively $\mu = 4$ and $COV = 10\%$, and follows a lognormal probability density function. Fig. 3 shows a typical random field realisations of the variable n for two different autocorrelation distances. For larger values of autocorrelation distances, the model tends to a homogeneous field, while less autocorrelation lengths limit the correlations in a given simulation to smaller zones. In general, for a specific autocorrelation length, layers which are very close together tend to have similar n values and express a higher correlation.

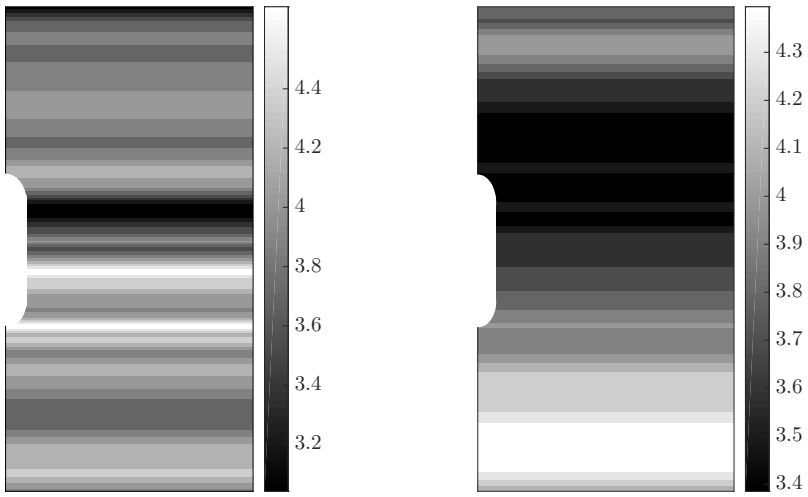

(a) (b)

Figure 3: Random field realisations of the parameter n for autocorrelation distance (a)l_y=30 m (b) l_y=650 m

As mentioned earlier, the size of the Karhunen-Loève expansion M will effect on the accuracy of the approximated random field $\hat{H}$. Fig. 4a depicts the estimated error of random field approximation versus the assumed M value for different autocorrelation lengths. The error estimation converges to less than 5%, if $M \geq 200$. In the present study, M is assumed to be equal to 200 terms to ensure the accuracy level of random field approximation.

The crude Monte-Carlo simulation is a well-established methodology to evaluate the probability of failure which has been used for many decades. As conducting a Monte-Carlo simulation requires thousands of model evaluation and each run of the numerical model in this study takes more than two hours, employing Monte Carlo seems not feasible. In order to address this drawback, the authors applied the subset simulation technique, introduced previously in [22] which decreases the number of required simulation, drastically.

The probability analysis here is conducted for the region N in Fig. 1a and the failure probability for different autocorrelation lengths (l_y) is computed against $DF = 1$. Fig. 4b illustrates the obtained results. In addition to different spatial variability scenarios, we also conduct a homogeneous simulation, where the constitutive parameters are assumed to be random variables. As Fig. 4b clearly shows, with decreasing the autocorrelation length in random field discretization, the probability of encountering a dilatant region at the considered observation point increases. Although in real cases, a local dilatant zone may not mainly endanger the stability of the entire structure, but in our case, we considered the no-dilatant region as the failure criterion, which is conservative.

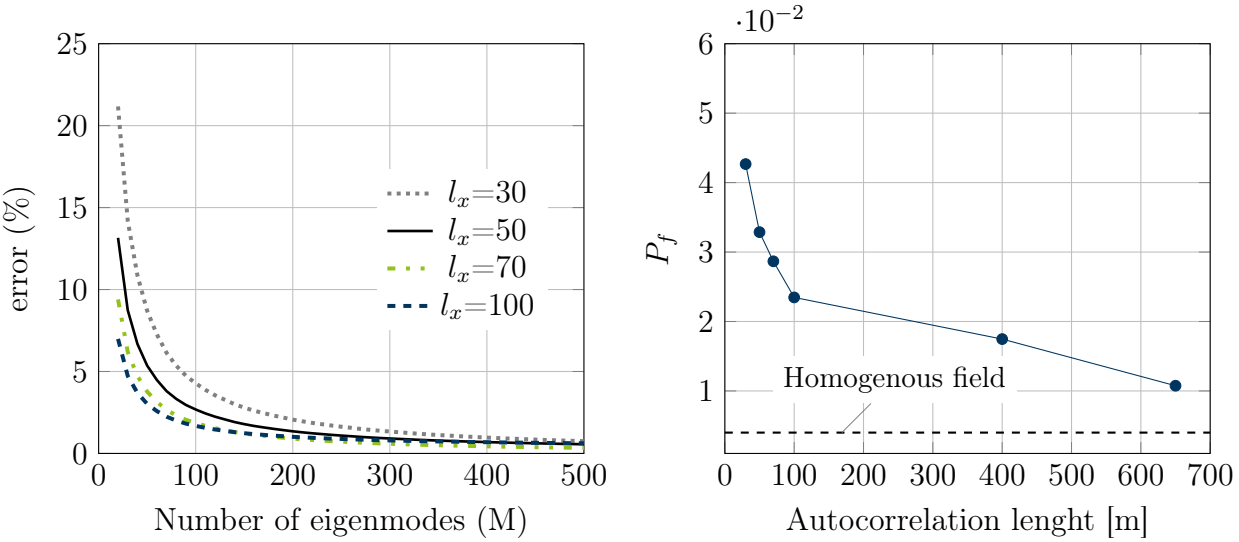

(a) (b)

Figure 4: (a)Error estimation vs. number of eigenmodes for different values of autocorrelation lengths, (b)Probability of failure against dilatancy for different autocorrelation lengths

6 Conclusion

The inherent randomness of natural materials like rocks and soils causes a wide extent of spatial distribution in their physical properties. Thereupon, the spatial variability and consequently the induced uncertainty, have to be considered in the complex geotechnical problems. In this paper, the random field method is applied in a probabilistic analysis of a gas storage cavern in the rock salt. A random field discretization of constitutive parameters of the BGRa creep law using Karhunen-Loéve is conducted. The failure probability of a rock salt cavity against the no-dilatant criterion is calculated for different spatial variability scenarios to present the effect of the autocorrelation lengths on the safety measures of the system against dilation. The obtained failure probabilities are compared with the corresponding results considering homogeneous rock in a random variable analysis. The comparison represents the necessity of considering spatial variability in the material properties.

7 Acknowledgement

The Authors would like to gratefully acknowledge the support of the German Research Foundation (DFG) through the Collaborative Research Center (SFB 837).

REFERENCES

[1] R. Pollak, "History of first u.s. compressed-air energy storage (caes) plant (110mw, 26h), volume 2: construction," final report, Electric Power Research institute, April 1994.

[2] J. Kepplinger, F. Crotogino, S. Donadei, M. Wohlers, and KBB, "Present trends in compressed air energy and hydrogen storage in germany," in *SMRI fall 2011 technical conference*, p. 12, 2011.

[3] U. Hunsche and A. Hampel, "Rock salt- the mechanical properties of the host rock material for radio active waste repository," *Engineering Geology*, vol. 52, pp. 271–291, 1999.

[4] C. Desai and D. Zhang, "Viscoplastic model for geologic material with generalized flow rule," *Int. J. numer. Anal. Met*, vol. 11, pp. 603–627, 1987.

[5] K. Khaledi, E. Mahmoudi, M. Datcheva, and T. Schanz, "Stability and serviceability of underground energy storage caverns in rock salt subjected to mechanical cyclic loading," *International Journal of Rock Mechanics and Mining Sciences*, vol. 86, pp. 115 – 131, 2016.

[6] S. Heusermann, O. Rolfs, and U. Schmidt, "Nonlinear finite element analysis of solution mined storage caverns in rock salt using the lubby2 constitutive model," *Computers and structures journal*, vol. 81, pp. 629–638, 2003.

[7] R.-M. Günther, K. Salzer, T. Popp, and C. Lüdeling, "Steady-state creep of rock salt: Improved approaches for lab determination and modelling," *Rock Mechanics and Rock Engineering*, vol. 48, no. 6, pp. 2603–2613, 2015.

[8] K. Khaledi, E. Mahmoudi, M. Datcheva, and T. Schanz, "Analysis of compressed air storage caverns in rock salt considering thermo-mechanical cyclic loading," *Environmental Earth Sciences*, vol. 75, no. 15, pp. 1–17, 2016.

[9] E. Mahmoudi, K. Khaledi, D. König, and T. Schanz, "Numerical simulation of deep and shallow energy storage systems in rock salt," in *Aktuelle Forschung in der Bodenmechanik 2015* (T. Schanz and A. Hettler, eds.), pp. 69–83, 2015.

[10] K. K. Phoon, *Reliability-Based Design in Geotechnical Engineering: Computations and Applications*. CRC Press, 2008.

[11] G. B. Baecher and J. T. Christian, *Reliability and statistics in geotechnical engineering*. John Wiley & Sons, 2005.

[12] E. Mahmoudi, K. Khaledi, S. Miro, D. König, and T. Schanz, "Probabilistic analysis of a rock salt cavern with application to energy storage systems," *Rock Mechanics and Rock Engineering*, vol. 50, no. 1, pp. 139–157, 2017.

[13] D. V. Griffiths and G. A. Fenton, eds., *Probabilistic Methods in Geotechnical Engineering*. Soringer Wien Newyork, 2007.

[14] I. M. Sobol', "Sensitivity estimates for nonlinear mathematical models," *Mathematical Modelling and Computational Experiment*, vol. 1, pp. 407–414, 1993. English translation of russian original paper Sobol' (1990).

[15] B. Sudret and A. Der Kiureghian, "Stochastic finite element methods and reliability, a state of the art.," Tech. Rep. UCB/SEMM- 2000/08, Dept. of Civil and Environmental Engineering, Univ. of California, Berkeley, 2000.

[16] C. Li and A. D. Kiureghian, "Optimal discretization of random fields," *Journal of Engineering Mechanics*, vol. 119, no. 6, 1993.

[17] R. G. Ghanem and P. D. Spanos, *Stochastic finite elements : a spectral approach*. Mineola, New York: Dover publications 2003, 1991.

[18] V. Bräuer, R. Eickemeier, D. Eisenburger, C. Grissemann, J. Hesser, A. Heusermann, D. Kaiser, and H. K. Nipp, *Geotechnical Exploration of the Gorleben Salt Dome*. Description of the Gorleben site, Bundesanstalt für Geowissenschaften und Rohstoffe, 2011.

[19] A. D. Kiureghian and J.-B. Ke, "The stochastic finite element method in structural reliability," *Probabilistic Engineering Mechanics*, vol. 3, no. 2, pp. 83 – 91, 1988.

[20] E. Mahmoudi, K. Khaledi, , D. König, and T. Schanz, "Sensitivity analyses on the influence of constitutive parameters on the numerical simulation of the behavior of a cavern in rock salt," in *Geomechanics from Micro to Macro*, pp. 933–938, 2015.

[21] K. Khaledi, E. Mahmoudi, M. Datcheva, D. König, and T. Schanz, "Sensitivity analysis and parameter identification of a time dependent constitutive model for rock salt," *Journal of Computational and Applied Mathematics*, vol. 293, pp. 128–138, 2016.

[22] E. Mahmoudi, K. Khaledi, D. König, and T. Schanz, "Probabilistic analysis of a rock salt cavern with application to energy storage systems, using subset simulation methodology," in *Energy Geotechnics* (F. Wuttke, S. Bauer, and M. Sanchez, eds.), pp. 609–615, London: CRC Press, 2016.

VII International Conference on Computational Methods for Coupled Problems in Science and Engineering
COUPLED PROBLEMS 2017
M. Papadrakakis, E. Oñate and B. Schrefler (Eds)

A ONE WAY COUPLED THERMO-MECHANICAL MODEL TO DETERMINE RESIDUAL STRESSES AND DEFORMATIONS IN BUTT WELDING OF TWO ASTM A36 STEEL PLATES

ROSENDO FRANCO*, W. GUILLERMO LOAIZA, PAUL P. LEAN AND HERBERT YÉPEZ

Grupo de Investigación Asistida por Computadora (INACOM/Aula PUCP-CIMNE)
Pontificia Universidad Católica del Perú
Av. Universitaria 1801, Lima 32, Peru
e-mail: rofranco@pucp.edu.pe, http://investigacion.pucp.edu.pe/grupos/inacom/

Key words: Thermo-Mechanical Model, Finite Element Method, Welding Simulation, Residual Stresses

Summary: To simulate the gas metal arc welding (GMAW) process in two ASTM A36 steel plates a finite element numerical model was developed, to obtain the corresponding residual stresses and deformations. The welding process was simulated as a one way coupled thermo-structural problem, considering that the structural field has very little influence in the thermal field, which is widely accepted in the specialized literature. To solve the thermal field, a nonlinear transient problem was created using finite second order elements that have temperature as the only degree of freedom in their nodes. The thermal properties of material were defined as a function of temperature and a combined convection-radiation coefficient was used as boundary condition. The double ellipsoidal model presented by Goldak was used to simulate the heat source and its dimensions were determined from the expressions developed by Christensen. To solve the structural field another nonlinear transient problem was created, considering the same mesh and the same time step of the thermal problem, using finite second order elements that have three displacements as degrees of freedom in their nodes. The mechanical properties of material were defined as a function of temperature, a thermo-elasto-plastic material model was used and the necessary displacement constraints were applied as boundary conditions. The temperature distribution obtained by solving the thermal field at each time step was transferred as a load to the structural problem. In both problems the "birth and death" technique was used to simulate the material deposition, which is implemented in the ANSYS software used in the present study. The activation of "dead" elements of the weld bead in the thermal analysis was performed simultaneously with the passage of the heat source, while in the structural analysis "dead" elements were activated as a function of their temperature. Different activation temperatures of "dead" elements were tested in the structural analysis, obtaining the best results when this temperature takes a value of 80% of material solidification temperature. The model used in this study was validated experimentally, taking as reference the residual displacements in several points of the welded plates. It was verified that there is a good correspondence between numerical and experimental results, with an error of less than 10%.

1 INTRODUCTION

The arc welding process encapsulates several coupled physical phenomena: fluid flow in the weld pool, heat flow in the structure, microstructural evolution of the materials, stress development and distortion of the structure. Theses phenomena have to be modeled as multi-physics problem. The mechanical response of welds is sensitive to the close coupling between thermal energy distribution, microstructure evolution and mechanical behavior. Figure 1 describes the coupling between the different fields in the modeling of welding, where the solid arrows denote strong coupling and the dotted arrows denote weak coupling [1].

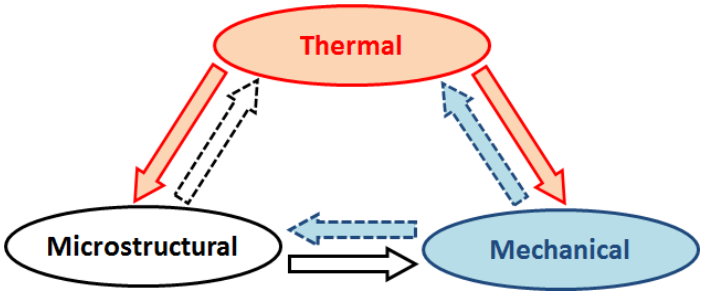

Figure 1: Coupling between different fields in welding analysis [1].

When the purpose of the analysis is to determine residual stresses and deformations of the structure, most authors use the simplest approach, i.e., considers only the one way coupled thermo-mechanical problem. The efforts of investigations are more focused on two main issues: the heat source model used in the thermal problem and the material behavior model used in the mechanical problem. In addition, it is necessary to take into account other important aspects in order to obtain accurate results. Temperature dependent material properties, thermal and mechanical boundary conditions and the material deposition method have significant influence in the simulation results.

In this paper the one way coupled thermo-mechanical approach is used and some important related topics are discussed. Consequently, a finite element numerical model was developed to obtain residual stresses and deformations of welded structure. Finally, the model was applied in the butt welding (GMAW) process of two ASTM A36 steel plates and compared with experimental results.

2 HEAT SOURCE MODEL

It is important to select an appropriate heat source model to obtain the accurate temperature distribution results, which will have a significant impact on the mechanical results, i.e., on the residual stresses and deformations. Especially, the choice of the heat source is sensitive for the results obtained in the fusion zone (FZ) and the heat affected zone (HAZ).

The investigations related to the models of heat sources date from 1935 when Rosenthal started his theoretical studies about arc welding processes. In his works, he has proposed point, linear and plane heat source models [2]. However, measurements of temperatures in the fusion and heat affected zones differ significantly from the values provided by those solutions, since the singularity located at the source origin results in infinite temperature levels [3]. In his book *Thermal Analysis of Welds* Nguyen [4] presents various analytical

solutions for stationary and moving heat sources models, including the Gaussian distributed volumetric heat source. Jeyakumar et al. [5] used this approach to evaluate residual stress in butt welded joint of ASTM A36 steel plates and found good agreement with experimental and others results. Stamenkovic and Vasovic [6] used a simplify method by assuming the welding arc stayed at an element with a constant specific volume heat generation, and then moved to the next element at the end of the load step as the welding was finished.

There is a great variety of models of heat sources documented in the literature but undoubtedly it is the double ellipsoidal model developed by Goldak and Akhlaghi [7] the most used by the researchers in arc welding simulations. Batista et al. [8] used Goldak's model to determine residual stresses in ASTM AH36 steel welded by TIG process. The same model was used by Malik et al. [9] to study circumferentially arc welded thin-walled cylinders to investigate the residual stress fields. The results of simulation in this work show great accuracy for transient temperature distribution and residual stresses in comparison with experimental results they performed. Qureshi et al. [10], Fu et al. [11], Pasternak et al. [12], Wang et al. [13], Chand et al. [14], Nuraini et al. [15], Abit et al. [16], Asserin et al. [17] and many others researchers also used this model in their investigations.

Figure 2 shows the double ellipsoidal model presented by Goldak that has been selected to develop the present work due to its great acceptance.

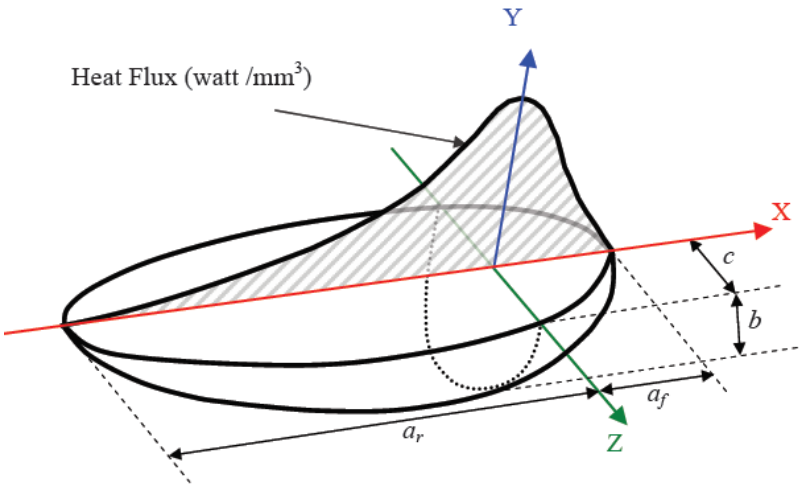

Figure 2: Goldak's double ellipsoidal heat source model [9].

The input heat for the front heat source is:

$$q_f(x,y,z,t) = \frac{6\sqrt{3}\cdot f_f \cdot Q}{\pi\sqrt{\pi}\cdot a_f \cdot b \cdot c} \cdot exp\left(\frac{-3(x-v\cdot t)^2}{a_f^2} + \frac{-3y^2}{b^2} + \frac{-3z^2}{c^2}\right) \quad (1)$$

For the rear heat source is:

$$q_r(x,y,z,t) = \frac{6\sqrt{3}\cdot f_r \cdot Q}{\pi\sqrt{\pi}\cdot a_r \cdot b \cdot c} \cdot exp\left(\frac{-3(x-v\cdot t)^2}{a_r^2} + \frac{-3y^2}{b^2} + \frac{-3z^2}{c^2}\right) \quad (2)$$

Where a_f, a_r, b and c are the ellipsoid dimensions. The parameters f_f and f_r give the

fractions of the heat in the front and rear parts of the source and have to meet the condition $f_f + f_r = 2$. The total heat gained from the welding arc is $Q = \eta \cdot V \cdot I$, η is the efficiency of the arc, V is the welding voltage and I is the welding current. The welding speed is v and t is the time.

The greatest difficulty with the use of the heat source proposed by Goldak is the determination of its geometric and energetic parameters. Some authors recommend to determine the geometric parameters of the ellipsoid (a_f, a_r, b and c) experimentally an calibrate the energetic parameters (f_f and f_r). Batista et al. [8] determined the geometric parameters by metallographic analysis and the energy parameters were obtained with the support of the relationships found in the literature. Asserin et al. [17] adjusted all used parameters by inverse methods from experimental results. To predict the heat source model parameters a neural network was used by Fu et al. [11].

When no experimental data is available, a possible option is to use the procedure developed by Christensen [18]. This procedure proposes empirical expressions and curves based on experimental tests to determine the geometric parameters of the heat source. In order to use the procedure, the parameters of the welding process (Q, v) and some properties of the material are required. Detailed information can be found in [18]. In addition, due to the condition of continuity of the volumetric heat source, the values of q_f and q_r given by equations (1) and (2) must be equal at the $x = 0$ plane. From that condition, another constraint is obtained for energetic parameters as $f_f/a_f = f_r/a_r$. Subsequently, the values for these two coefficients are determined as $f_f = 2 \cdot a_f/(a_f + a_r)$; $f_r = 2 \cdot a_r/(a_f + a_r)$ [19]. The Christensen procedure and the condition of continuity are used in the present paper.

3 MATERIAL BEHAVIOR MODEL

In his paper Lindgren [20] points out that it is important to have a correct description of the material behavior in order to have an accurate model and concludes that the most important mechanical properties are Young's modulus, thermal dilatation, and parameters for the plastic behavior.

The constitutive model of the mechanical analysis can be expressed by the total strain increment $\Delta\varepsilon$ obtained from equation (3) [11,13].

$$\Delta\varepsilon = \Delta\varepsilon^e + \Delta\varepsilon^p + \Delta\varepsilon^T + \Delta\varepsilon^{creep} + \Delta\varepsilon^{tran} \tag{3}$$

Where $\Delta\varepsilon^e$, $\Delta\varepsilon^p$, $\Delta\varepsilon^T$ and $\Delta\varepsilon^{creep}$ are the elastic, plastic, thermal and creep strain increments, respectively. $\Delta\varepsilon^{tran}$ is the strain induced by the phase transformation. Like [11], the phase-transformation related strain increment was neglected in the present work because it has an insignificant contribution to the total strain in low-carbon steel. Considering that welding process is a very short heating process, $\Delta\varepsilon^{creep}$ was also not included in the present study.

Almost all authors that simulate welding processes consider rate-independent plasticity because the material has a high temperature during a relatively short time of the weld thermal cycle, and therefore the accumulated rate-dependent plasticity is neglected [20]. Rate-independent plasticity is characterized by three parameters, they are the yield criterion, the flow rule and the hardening law [20,21].

The model that has been used most widely for rate-independent plasticity is the von Mises

yield criterion given by equation (4), where σ_1, σ_2 and σ_3 are the principal stresses. Malik et al. [9], Qureshi et al. [10], Pasternak et al. [12], Wang et al. [13], Chand et al. [14] and Asserin et al. [17] used von Mises yield criterion in their works. The flow rule states that the plastic flow is orthogonal to the yield surface.

$$\sqrt{\frac{(\sigma_1 - \sigma_2)^2 + (\sigma_2 - \sigma_3)^2 + (\sigma_3 - \sigma_1)^2}{2}} = \sigma_y \tag{4}$$

A hardening law is needed to determine the amount of plastic flow and the evolution of the yield strength of the material [20]. Wang et al. [13] describe and uses four possible hardening laws: (1) perfect plasticity; (2) isotropic hardening; (3) kinematic hardening; (4) combined hardening (isotropic and kinematic). Pasternak et al. [12] used isotropic hardening law. While Malik et al. [9], Qureshi et al. [10], Chand et al. [14] and Asserin et al. [17] used kinematic hardening law.

Taking in to account the literature review a thermo-elasto-plastic material formulation has been chosen for the present research considering the von Mises yield criterion with associated flow rule and the bilinear kinematic hardening model.

4 TEMPERATURE DEPENDENT MATERIAL PROPERTIES

The thermal problem consists in solving the energy conservation equation (5) [10,13,14].

$$\rho c \frac{\partial T}{\partial t}(x, y, z, t) = -\nabla \cdot q(x, y, z, t) + Q(x, y, z, t) \tag{5}$$

Where, ρ is the density of the material, c is specific heat capacity, T is current temperature, q is heat flux vector, Q is internal heat generation rate, t is the time, ∇ represents the spatial gradient operator and x, y, z are the coordinates in the reference plane. The nonlinear isotropic Fourier heat flux constitutive equation is given by (6) [10,14], where k is the temperature dependent thermal conductivity.

$$q = -k \cdot \nabla T \tag{6}$$

As can be seen the thermal properties required to solve the thermal problem are: material density, specific heat and thermal conductivity, all of which are temperature dependent. It would be necessary to know the values of these properties in function of the temperature in order to perform a thorough analysis. Some authors take constant the material density specifically when dealing with steels [9,10].

The mechanical properties required to simulate the mechanical problem are related to the material behavioral model used, which for this study is a thermo-elasto-plastic model with von Mises yield criterion and bilinear kinematic hardening model. Therefore, the modulus of elasticity, the Poisson coefficient, the yield stress, the tangent modulus and the coefficient of thermal expansion are required. All these properties are also temperature dependent.

5 THERMAL AND MECHANICAL BOUNDARY CONDITIONS

The boundary conditions in the thermal problem are referred to the dissipation mechanisms of the heat generated during the welding process, which are the convection and the radiation mechanisms. The current tendency is to use a total temperature dependent heat transfer

coefficient h_{total} to simulate a combined thermal boundary condition, both thermal convection and radiation [10,11,14,17]. Combined heat transfer coefficient can be calculated by equation (7).

$$h_{total} = h + \varepsilon \cdot \sigma \cdot (T + T_{amb}) \cdot (T^2 + T_{amb}^2) \quad (7)$$

Where h is the thermal convection coefficient that is dependent on temperature, ε is the radiation emissivity, σ is Stefan Boltzmann constant (5.67×10^{-8} W m^{-2} K^{-4}), T is the current temperature and T_{amb} is the room temperature. In the present study the combined heat transfer coefficient by (7) is used and applied on all the applicable surfaces including the surface of the weld bead.

The boundary conditions in the mechanical problem were defined following the same approach of [11,13]. The nodal temperatures determined in the thermal analysis were applied as thermal loads in the mechanical analysis. The same finite element meshes associated with the stress element and the thermo-mechanical properties were employed in the mechanical analysis. The mechanical boundary conditions were considered to prevent the rigid body motion of the welded plates.

6 MATERIAL DEPOSITION METHOD

Most authors use the element birth and death technique to simulate the metal deposition on the welding bead [5,6,9,10,15,16,22]. Fanous et al. [23] propose a different method called element movement technique. Other authors do not consider the metal deposition effect or do not refer its consideration [11,13]. Some researchers report difficulties with the birth and death technique. Malik et al. [9] and Qureshi et al. [10] report the possibility of excessive distortion issues in mechanical analysis.

Malik et al. [9], Qureshi et al. [10] and Abit et al. [16] describe the use of the birth and death technique and suggest some recommendations. The whole finite element model is generated in the start. Before first time step all elements representing filler metal are deactivated by assigning them a very low value of conductivity in thermal analysis and very low value of stiffness in mechanical analysis. During the thermal analysis, all the nodes of deactivated elements (except those shared with the base metal) are also fixed at ambient temperature till the birth of the respective element. Deactivated elements are re-activated sequentially when they come under the influence of the heat source. During the mechanical analysis a sequential birth of an element takes place when the element reaches the solidification temperature. In this moment the initial strains in the element are set to zero. Melting and ambient temperatures are set as the temperatures at which thermal strains are zero for thermal expansion coefficients of the filler and base metals. Additional recommendations are reported by Lindgren [24]. For better computational results the heat source is supposed to stay at least once on each element along the welding line, so that the heat input algorithm does not miss elements passed during a time step increment.

The model developed in the present study implements the element birth and death technique and collects all previous recommendations. However, in the present work the effect of the activation temperature of death element is evaluated in the mechanical analysis, including the solidification temperature and lower values. The reason for doing so is due to the researchers' interest in exploring an alternative to calibrate the FE model and perhaps to mitigate the excessive distortion reported by other authors.

7 METHODOLOGY

Considering the information collected and discussed in the previous sections, the flowchart shown in figure 3 was elaborated, establishing the general methodology used in the present investigation.

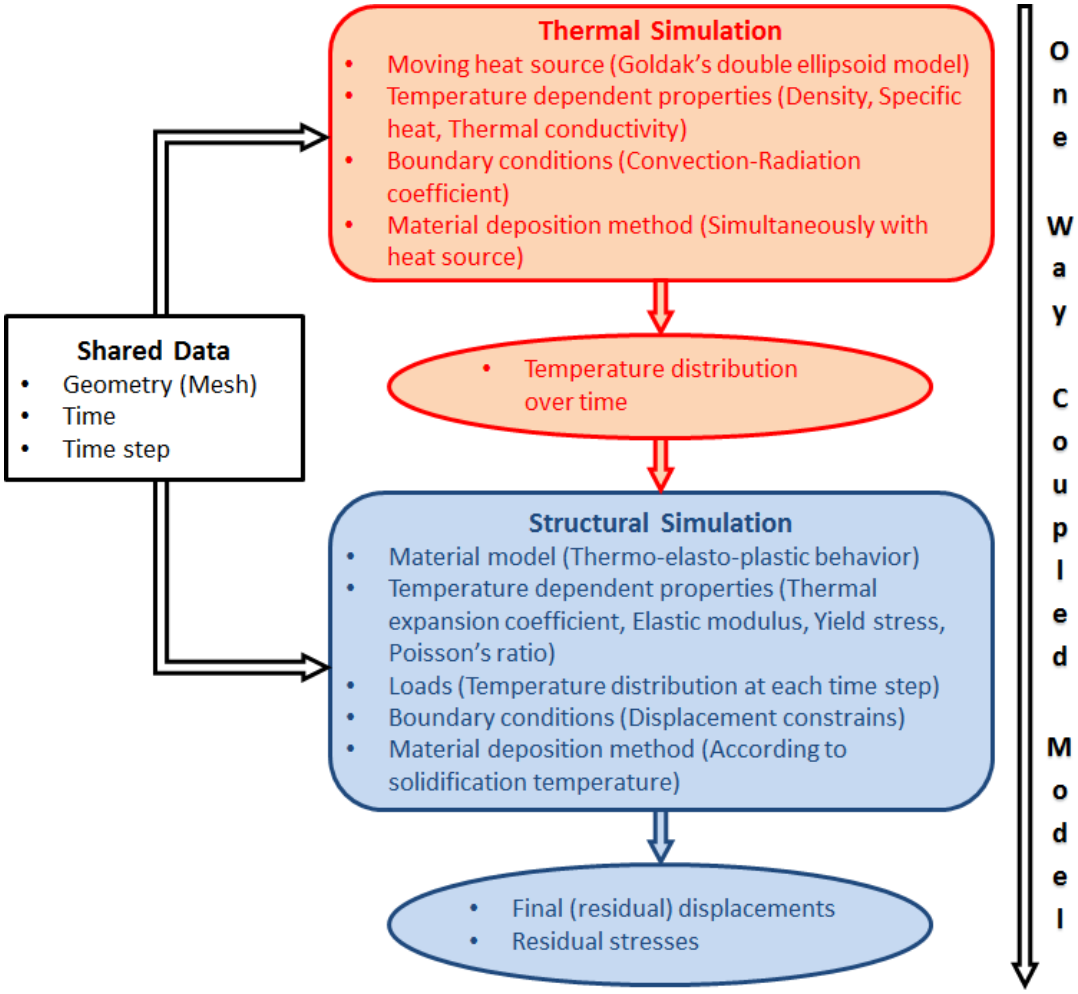

Figure 3: Flowchart of one way coupled model for analysis of residual stresses and deformations.

8 CASE STUDY: BUTT WELDING OF TWO ASTM A36 STEEL PLATES

The finite element numerical model described in the previous sections was used to simulate the gas metal arc welding (GMAW) process in two ASTM A36 steel plates. The objective is to determine the residual stresses and deformations of the welded plates and validate the model with experimental data obtained by the authors. The temperature dependent material properties considered in this study are shown in table 1 [5]. The parameters of the welding process are the same for the numerical analysis as for the experimental tests and are shown in table 2. The Golda's heat source parameters were estimated by using the Christensen procedure and the condition of continuity explained in section 2. The values are shown in table 3.

Table 1: Temperature dependent material properties [5].

Temp (K)	Density (kg/m^3)	Thermal conductivity W/(m·K)	Specific heat (J/(kg·K))	Elastic modulus (GPa)	Poisson's ratio	Thermal expansion coefficient (K^{-1})·10^{-5}	Yield stress (MPa)
298	7880	60	480	210	0.3	1.15	380
373	7880	50	500	200	0.3	1.2	340
473	7800	45	520	200	0.3	1.3	315
673	7760	38	650	170	0.3	1.42	230
873	7600	30	750	80	0.3	1.45	110
1073	7520	25	1000	35	0.3	1.45	30
1273	7390	26	1200	20	0.3	1.45	25
1473	7300	28	1400	15	0.3	1.45	20
1673	7250	37	1600	10	0.3	1.45	18
1773	7180	37	1700	10	0.3	1.45	15

Table 2: Welding process parameters.

Voltage (V)	Current (A)	Velocity (mm/s)	Efficiency (%)
21.1	133	9.5	80

Table 3: Golda's heat source parameters.

Parameter	Value
Length of front ellipsoidal, a_f (mm)	2.02
Length of rear ellipsoidal, a_r (mm)	6.41
Depth of heat source, b (mm)	2.13
Half width of heat source, c (mm)	1.92
Fraction of heat in front ellipsoidal, f_f	0.48
Fraction of heat in rear ellipsoidal, f_r	1.52

8.1 Geometric model and mesh

The geometric model of the welded plates with dimensions is shown in figure 4 a) and consists of a welding coupon 140 mm wide, 3 mm thick and 300 mm long. The discretization of the geometric model was performed with the second order brick elements available in the ANSYS software library used in this work. For the thermal analysis the SOLID279 element was used and for the mechanical analysis the SOLID186 element was used. This way the same mesh can be used for the thermal and mechanical analyzes. Based on maximum reached temperature a mesh sensitivity analysis was performed [9,11]. The final mesh of the model with 132460 elements was chosen for the analysis in order to ensure the mesh independent results. Such a mesh is shown in figure 4 b) with a detail of the weld bead zone.

8.2 Boundary conditions

The combined heat transfer coefficient determined by equation (7) was applied as the thermal boundary condition on all the applicable surfaces including the surface of the weld bead. The emissivity $\varepsilon = 0.51$ and $T_{amb} = 300$ K were considered for the simulation. The temperature dependent thermal convection coefficient h was adopted according to [10].

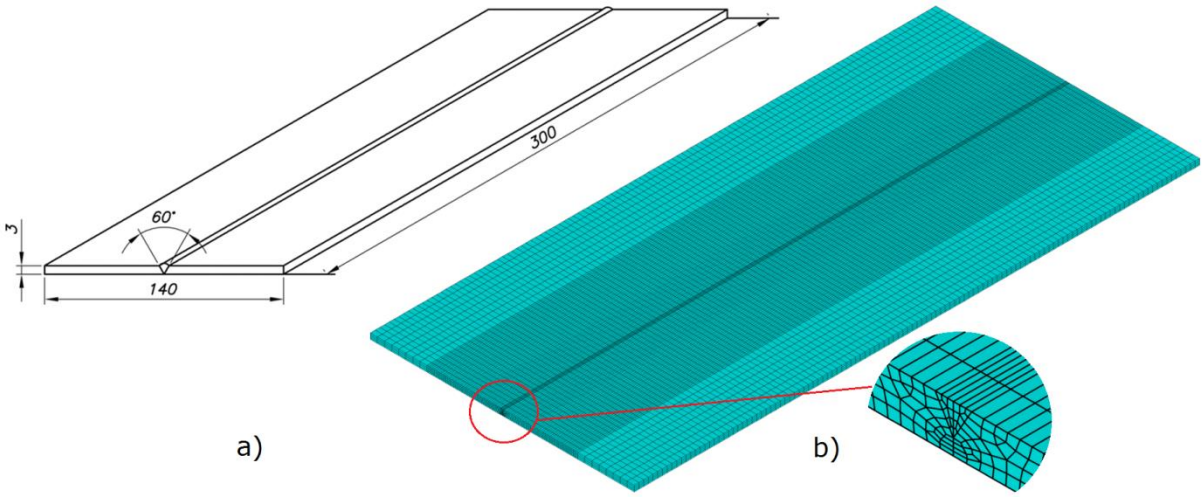

Figure 4: Geometric model. a) Dimensions. b) Mesh and a detail of the weld bead zone.

The nodal temperatures determined in the thermal analysis were applied as thermal loads in the mechanical analysis each time step. The mechanical boundary conditions were considered to prevent the rigid body motion of the welded plates, i.e., normal displacement constrain of the symmetry plane, displacement constrain of two extreme points in vertical (y) direction and displacement constrain of one extreme point in longitudinal (z) direction. The mechanical boundary conditions are shown in the figure 5.

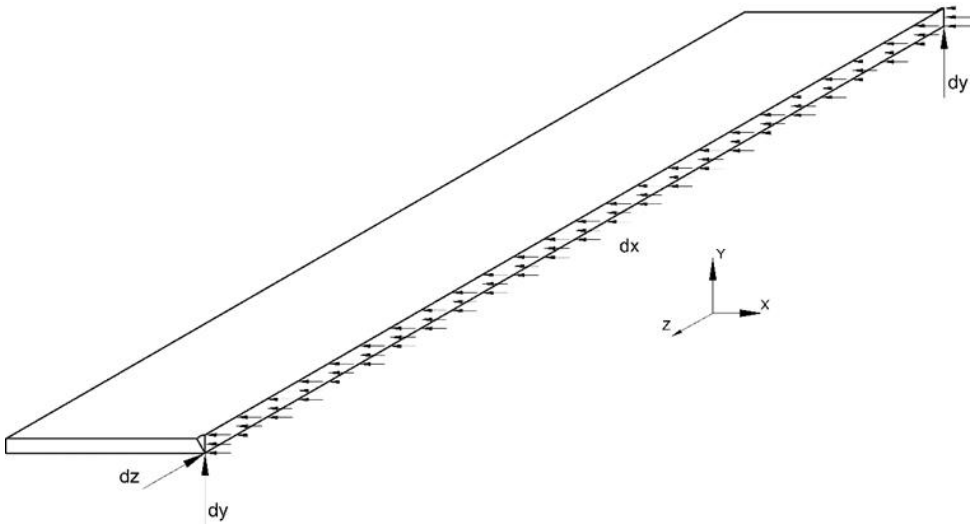

Figure 5: Mechanical boundary conditions.

8.3 Simulation strategy

The methodology described above was implemented in the ANSYS Mechanical APDL environment through macros developed by the authors.

Transient, non–linear thermal and mechanical problems were defined using temperature dependent properties. The welding time was determined considering the welding process

parameters obtaining 31.58 s. An additional time of 2000 s was estimated for the cooling phase. During analyzes the full Newton-Raphson iterative method with a direct sparse matrix solver was used for obtaining the solutions according to [9,10] recommendations..

8.4 Simulation results

Figure 6 a) shows the temperature distribution at the end of the welding time (31.58 s). Figure 6 b) illustrates the temperature profile of five different points up to a time of 100 s. Point 1 is located on the welding line and reaches the highest temperature peak (2240 K).

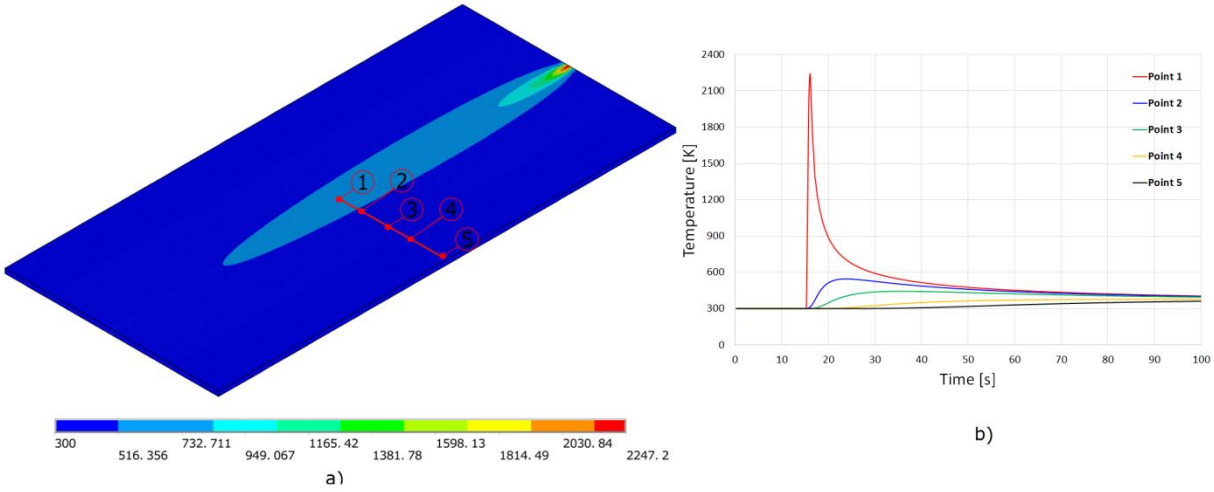

Figure 6: Thermal results. a) Temperature distribution. b) Temperature profile at five different locations.

Figure 7 a) shows that the transverse residual stresses reach a maximum value of 557 MPa. Residual deformations are shown in figure 7 (b). The maximum displacement is reached at the midpoint of the outer edge of the welded plate with a value of 2.76 mm. Simulations of the mechanical problem were performed for three different activation temperatures of death elements (60%, 80% and 100% of material solidification temperature). The results shown in figure 7 correspond to an activation temperature of 80% of the solidification temperature. This setting gives more accurate results.

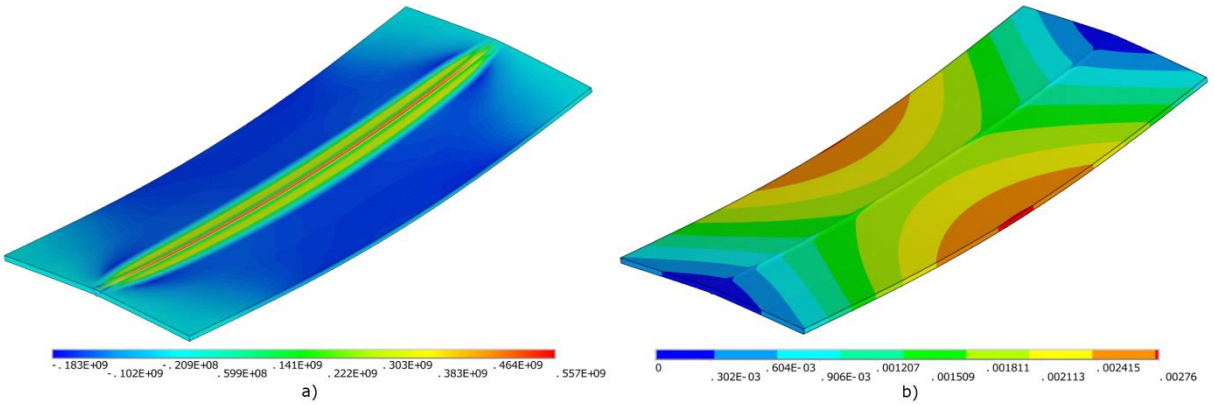

Figure 7: Mechanical results. a) Residual stresses in transversal direction. b) Residual displacements.

8.5 Experimental tests

To validate the developed model, the authors performed experimental tests with the help of a semiautomatic welding machine with GMAW technology. In figure 8 a) the coupons can be seen and in figure 8 b) the arrangement before starting the welding.

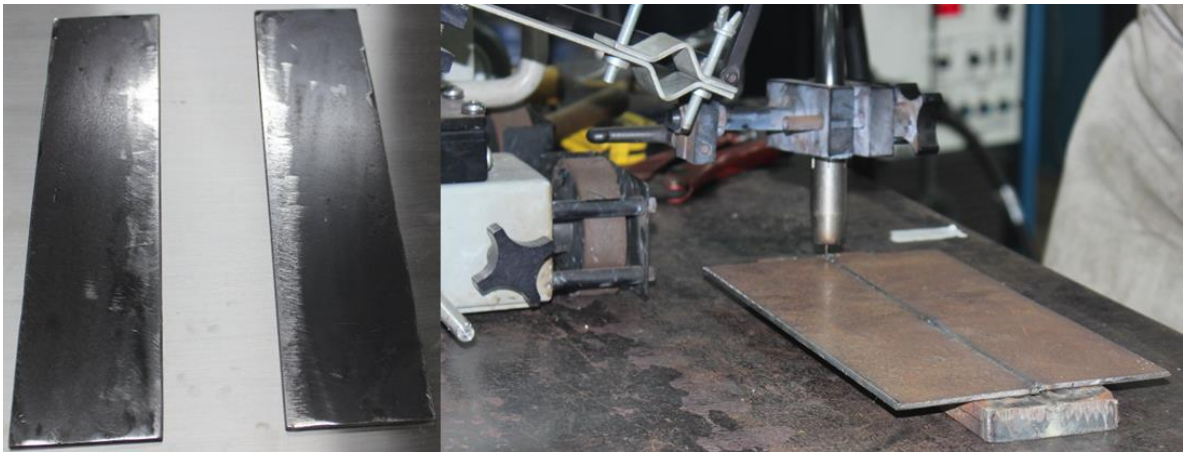

Figure 8: Mechanical results. a) Residual stresses in transversal direction. b) Residual displacements.

After welding and cooling the welded plates, residual displacements at the edges of the plates were measured and an average displacement was obtained. In figure 9 the average experimental result is compared with the numerical results corresponding to the three evaluated activation temperatures. It may be noted that the result for an activation temperature of 60% of the solidification temperature is significantly away from the experimental results. Even though at first glance the results for 80% and 100% appear very similar and better match the experimental result, the results for 80% show a lower standard deviation. In this case the maximum absolute error is about 9.6%.

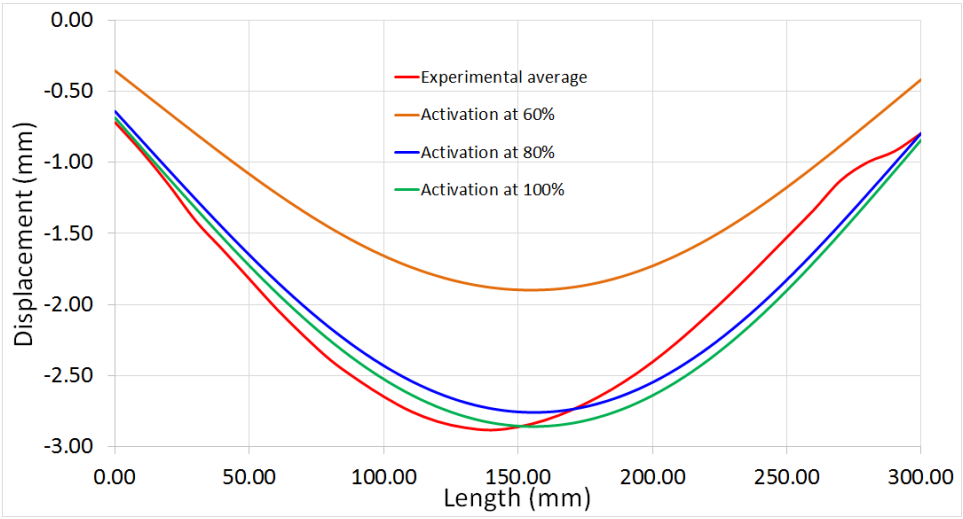

Figure 9: Comparison between numerical and experimental results.

9 CONCLUSIONS

- Based on the best practices reported in the specialized literature, a one way coupled thermo-mechanical model to determine residual stresses and deformations in butt welding of two ASTM A36 steel plates was developed. The model used in this study was validated experimentally by means of measurement of residual displacements in several points of the welded plates. The displacements along the both external sides of the welded plates was averaged and plotted together with numerical results. It was verified that there is a good agreement between numerical and experimental results, with an absolute error of less than 10%.
- Three different activation temperatures of "dead" elements were tested in the structural analysis (60%, 80% and 100% of material solidification temperature). The minimum standard deviation and minimum absolute error were obtained when this temperature takes a value of 80% of material solidification temperature. The evaluation of a greater number of activation temperatures is necessary to reach more conclusive results. It would also be important to analyze the molten zone (FZ) and to evaluate the local behavior when these activation temperatures below the solidification temperature are used.

REFERENCES

[1] Sen, D. *Coupled Field Modeling of Gas Tungsten Arc Welding*. Dissertation for the degree of Doctor of Philosophy in Mechanical Engineering, Virginia Polytechnic Institute and State University, 2012.

[2] Rosenthal, D. Mathematical theory of heat distribution during welding and cutting. *Welding Journal*, vol. 20, n. 5, pp. 220-234, 1941.

[3] Fassani, R.N.S. and Trevisan, O.V. Analytical modeling of multipass welding process with distributed heat source. *Journal of Brazilian Society of Mechanical Sciences and Engineering*, Vol.25, No.3, pp.302-305, 2003.

[4] Nguyen, N.T. *Thermal Analysis of Welds*. WIT Press, Southampton, UK, 2004.

[5] Jeyakumar, M., Christopher, T. and Nageswara Rao, B. Residual Stress Evaluation in Butt Welded Joint of ASTM A36 Steel Plates. *International Journal of Electronics Communication and Computer Engineering*, Vol. 4 (2), pp. 581-587, 2013.

[6] Stamenkovic, D. and Vasovic, I. Finite Element Analysis of Residual Stress in Butt Welding Two Similar Plates. *Scientific Technical Review*, Vol. LIX (1), pp. 57-60, 2009.

[7] Goldak, J. A. and Akhlaghi, M. *Computational Welding Mechanics*. Springer Science+Business Media, Inc., 2005.

[8] Batista, P., Almeida, P., Prasad, Y., Andrade, J., Veras, A., and Sanguinetti, R. Determination of Residual Stresses Numerically Obtained in ASTM AH36 Steel Welded by TIG Process. *Materials Sciences and Applications*, Vol. 4, pp. 268-274, 2013.

[9] Malik, A. M., Qureshi, E. M., Dar, N. U. and Khan, I. Analysis of circumferentially arc welded thin-walled cylinders to investigate the residual stress fields. *Thin-Walled Structures*, ELSEVIER, 2008.

[10] Qureshi, E. M., Malik, A. M. and Dar, N. U. Residual Stress Fields due to Varying Tack Welds Orientation in Circumferentially Welded Thin-Walled Cylinders. *Advances in Mechanical Engineering*, 2009.

[11] Fu, G., Lourenço, M. I., Duan, M. and Estefen, S. F. Influence of the welding sequence on residual stress and distortion of fillet welded structures. *Marine Structures*, ELSEVIER, 2015.
[12] Pasternak, H., Launert, B. and Krausche, T. Welding of girders with thick plates-fabrication, measurement and simulation. *Journal of Constructional Steel Research*, ELSEVIER, 2015.
[13] Wang, Q., Liu, X.S., Wang, P., Xiong, X. and Fang, H.Y. Numerical simulation of residual stress in 10Ni5CrMoV steel weldments. *Journal of Materials Processing Technology*, ELSEVIER, 2016.
[14] Chand, R. R., Kim, I. S., Wu, Q. Q., Kang, B. and Shim, J. Prediction of residual stress and welding deformation in butt-weld joint for different clamped position on the plates. *Int. Journal of Eng. Science and Innovative Tech.* (IJESIT), Volume 3, Issue 5, 2014.
[15] Nuraini, A. A., Zainal, A. S. M. and Azmah Hanim, M.A. The effect of welding process parameter on temperature and residual stress in butt-joint weld of robotic gas metal arc welding. *Australian Journal of Basic and Applied Sciences*, 7(7), pp. 814-820, 2013.
[16] Abid, M., Siddique, M. and Mufti, R. A. Prediction of welding distortions and residual stresses in a pipe–flange joint using the finite element technique. *Modelling Simul. Mater. Sci. Eng.* 13, pp. 455-470, 2005.
[17] Asserin, O., Loredo, A., Petelet, M. and Iooss, B. Global sensitivity analysis in welding simulations - What are the material data you really need? *Finite Elements in Analysis and Design*, 47, pp. 1004-1016, 2011.
[18] Christensen, N., Davies, V. and Gjermundsen, K. Distribution of temperatures in arc welding. *British Welding Journal*, 12(2), pp. 54-75, 1965.
[19] Nguyen, N. T., Ohta, A. and Matsuoka, K. Analytical solutions for transient temperature of semi-infinite body subjected to 3-D moving heat sources. *Welding Journal*, Vol. 78 Issue 8, pp. 265-274, 1999.
[20] Lindgren, L. E. Finite element modeling and simulation of welding. Part 2: Improved material modeling. *Journal of Thermal Stresses*, 24, pp. 195-231, 2001.
[21] Manitaras, T. I. *Elastoplastic Constitutive Models in Finite Element Analysis*. Master Thesis, National Technical University Athens, School of Civil Engineering, Institute of Structural Analysis & Seismic Research, 2012.
[22] Pavani, P., Sivasankar, P., Lokanadham, P. and Uma Mhahesh, P. Finite Element Analysis of Residual Stress in Butt Welding of Two Similar Plates. *International Research Journal of Engineering and Technology*, Vol. 7 (7), pp. 479-486, 2015.
[23] Fanous, I. F. Z., Younan, M. Y. A. and Wifi, A. S. 3-D finite element modeling of the welding process using element birth and element movement techniques. *Journal of Pressure Vessel Technology*, Vol. 125 Issue 2, pp. 144-150, 2003.
[24] Lindgren, L. E. Computational weld mechanics: thermo-mechanical and microstructural simulations. *Woodhead Publishing*, 2007.

VII International Conference on Computational Methods for Coupled Problems in Science and Engineering
COUPLED PROBLEMS 2017
M. Papadrakakis, E. Oñate and B. Schrefler (Eds)

AN ACCURATE SOLUTION OF SINGULAR THERMOPLASTIC PROBLEM OF PRESSURE – DEPENDENT PLASTICITY

SERGEI ALEXANDROV[*] AND WIKTORIA MISZURIS[†]

[*] Institute for Problems in Mechanics
Russian Academy of Sciences
101-1 Prospect Vernadskogo, 119526 Moscow, Russia
e-mail: sergei_alexandrov@spartak.ru, www.ipmnet.ru

[†] Department of Mathematics
Aberystwyth University
Penglais, SY23 3BZ Aberystwyth, UK
email: win@aber.ac.uk

Key words: Friction, Temperature, Pressure – Dependent Plasticity, Singularity.

Abstract. The present paper concerns with a theoretical investigation into heat generation in the continued quasi-static plane strain compression of a thin strip between two rigid, parallel perfectly rough platens. The strip material obeys the double shearing model. The length of the platens is supposed to be much greater than the current strip thickness. The plastic work rate approaches infinity in the vicinity of perfectly rough friction surfaces. Since the plastic work rate is involved in the heat conduction equation, this greatly adds to the difficulties of solutions of this equation. In particular, commercial finite element packages are not capable of solving such boundary value problems. The present approximate solution is given in Lagrangian coordinates. In this case, the original initial/boundary value problem reduces to the standard second initial/boundary value problem for the nonhomogeneous heat conduction equation. Therefore, the Green's function is available in the literature. An example is provided to illustrate the general solution.

1 INTRODUCTION

The temperature of the workpiece rises during plastic deformation because of the heat generated by mechanical work. Under certain conditions, this temperature rise is of considerable importance. From the point of view of phenomenological plasticity theory, the first systematic study on temperature distributions in metal forming processes has been conducted in [1]. A recent review of the literature on this topic has been provided in [2]. Finite element approaches to coupled thermal flow in metal forming processes have been developed in [2 - 4]. Temperature and plastic strain are responsible for the generation of narrow fine grain layers in the vicinity of frictional interfaces [5]. Such layers may have a significant effect on the performance of machine parts [6 – 8]. The gradient in temperature is very high within the fine grain layers [9]. This greatly adds to the difficulties of solutions of corresponding boundary value problems. Moreover, in the case of the maximum friction law

finite element analyses usually fail to converge [10, 11]. Most likely, the reason for that is that exact solutions are singular in the vicinity of maximum friction surfaces for several material models [12 - 15]. In particular, the plastic work rate involved in the heat conduction equation approaches infinity in the vicinity of maximum friction surfaces. The present paper concerns with a theoretical investigation into heat generation in the continued quasi-static plane strain compression of a thin metal strip between two rigid, parallel perfectly rough dies. The maximum friction law is assumed at the die surface. The strip material obeys the double shearing model proposed in [16]. A semi-analytical solution of the aforementioned boundary value problem for the double shearing model without calculating the temperature field has been found in [17]. This solution is used in the present paper. In particular, the solution of the heat conduction equation is facilitated by using Lagrangian coordinates that are readily determined from the solution given in [17]. In these coordinates, the original initial/boundary value problem reduces to the standard second initial/boundary value problem for the nonhomogeneous heat conduction equation. Therefore, the Green's function is available in the literature, for example [18]. A similar method of solution has been used in [19] where the classical model of metal plasticity has been adopted.

2 STATEMENT OF THE PROBLEM

Consider a rigid plastic strip of initial thickness $2h_0$ and initial width $2L_0$. The strip is compressed between two parallel platens. The speed of each platen is U. The current thickness and width of the strip are denoted by $2h$ and $2L$, respectively. The Cartesian coordinate system (x, y) is chosen such that its $x-$ and $y-$ axes coincide with the axes of symmetry of the process (Fig. 1). Therefore, it is sufficient to consider the domain $0 \le x \le L$

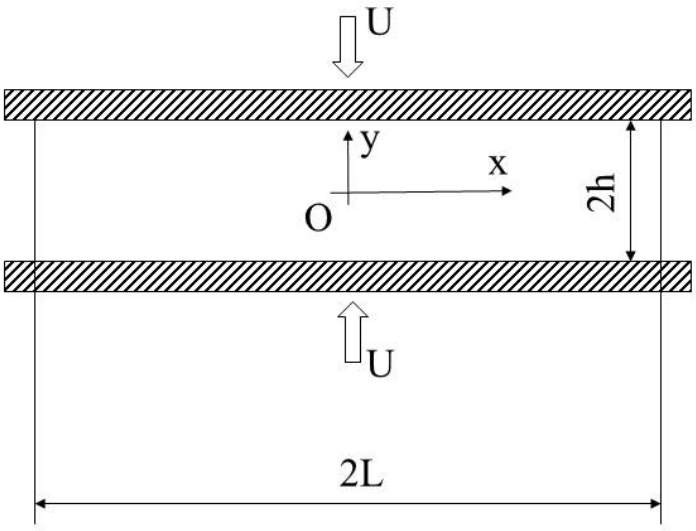

Figure 1: Configuration of the problem and Cartesian coordinte system

and $0 \le y \le h$. It is assumed that the initial temperature of the strip is constant, T_0. The current temperature is denoted by T. Let u_x and u_y be the velocity components referred to the

Cartesian coordinate system. Then, the exact velocity boundary conditions are

$$u_y = 0 \tag{1}$$

for $y = 0$ and

$$u_y = -U \tag{2}$$

for $y = h$. In the case of $h/L << 1$ the exact velocity boundary condition at $x = 0$ is usually replaced with the following approximate condition [17, 20 - 23]

$$\int_0^h u_x dy = 0. \tag{3}$$

It is understood here that the velocity component u_x is calculated at $x = 0$. Let σ_{xx}, σ_{yy} and σ_{xy} be the stress components referred to the Cartesian coordinate system. The exact stress boundary conditions are

$$\sigma_{xy} = 0 \tag{4}$$

for $y = 0$ and the maximum friction law. The representation of the maximum friction law depends on the material model chosen. In the present paper, the double shearing model proposed in [16] is adopted. The system of equations comprising the constitutive equations and equilibrium equations is hyperbolic. Under plane strain conditions the characteristics of the stresses and the velocities coincide. Therefore, there are only two distinct characteristic directions at a point. The maximum friction law demands that a characteristic or an envelope of characteristics coincides with the friction surface. Let ψ be the angle between the direction of the algebraically greatest principal stress and the x – axis measured from the axis anticlockwise. Then, the angles between the characteristic directions and the x – axis are $\psi + \pi/4 + \varphi/2$ and $\psi - \pi/4 - \varphi/2$ [16]. Here φ is the angle of internal friction. The direction of flow dictates that $\sigma_{xy} < 0$ at $y = h$ (Fig. 1). Therefore, $\psi < 0$ at $y = h$ and the maximum friction law can be written as

$$\psi = -\frac{\pi}{4} - \frac{\varphi}{2} \tag{5}$$

for $y = h$. The exact stress boundary conditions at $x = L$ are usually replaced with the following approximate condition [17, 20 - 23]

$$\int_0^h \sigma_{xx} dy = 0. \tag{6}$$

It is understood here that the stress component σ_{xx} is calculated at $x = L$. The magnitude of the shear stress at $y = h$ is denoted by τ_f. Therefore,

$$\tau_f = |\sigma_{xy}|. \tag{7}$$

It is understood here that the stress component σ_{xy} is calculated at $y = h$. The boundary

conditions on the temperature are

$$\frac{\partial T}{\partial y}=0 \tag{8}$$

for $y=0$ and

$$\lambda\frac{\partial T}{\partial y}=\tau_f u_x+q_t \tag{9}$$

for $y=h$. It is understood here that the velocity component u_x is calculated at $y=h$. Also, q_t is the external heat flux through the friction surface from tool into the plastic strip and λ is the coefficient of thermal conductivity. In what follows, c_v and ρ will stand for the specific heat at constant volume and density, respectively. It is assumed that λ, c_v, ρ and q_t are constant. The initial condition is

$$T=T_0 \tag{10}$$

at $h=h_0$.

The Coulomb-Mohr yield criterion can be written as

$$q-p\sin\varphi=c\cos\varphi, \tag{11}$$

where c is the cohesion and

$$p=-\frac{\left(\sigma_{xx}+\sigma_{yy}\right)}{2},\quad q=\frac{1}{2}\sqrt{\left(\sigma_{xx}-\sigma_{yy}\right)^2+4\sigma_{xy}^2}. \tag{12}$$

The flow rule of the double shearing model is [16]

$$\begin{aligned}&\xi_{xy}\cos 2\psi-\frac{1}{2}\left(\xi_{xx}-\xi_{yy}\right)\sin 2\psi+\sin\varphi\left(\omega_{xy}+\frac{d\psi}{dt}\right)=0,\\&\xi_{xx}+\xi_{yy}=0.\end{aligned} \tag{13}$$

Here ξ_{xx}, ξ_{yy} and ξ_{xy} are the strain rate components in the Cartesian coordinates, ω_{xy} is the only non-zero spin component in the Cartesian coordinates and d/dt denotes the convected derivative. The second equation in (13) is the equation of incompressibility. Therefore,

$$h_0L_0=hL. \tag{14}$$

The stress components in the Cartesian coordinates are represented as [16]

$$\sigma_{xx}=-p+q\cos 2\psi,\quad \sigma_{yy}=-p-q\cos 2\psi,\quad \sigma_{xy}=q\sin 2\psi. \tag{15}$$

3 GENERAL SOLUTION

The velocity components are given by [17]

$$\frac{u_x}{U}=\frac{x}{h}-\frac{2}{C}\cos 2\psi+B,\quad \frac{u_y}{U}=-\frac{y}{h}, \tag{16}$$

where B and C are constants of integration. It is evident that the solution (16) satisfies the boundary conditions (1) and (2). The dependence of ψ on y is given in implicit form as

$$\frac{y}{h}=\frac{\sin 2\psi+2\psi\sin\varphi}{C}. \tag{17}$$

It is seen from (15) that this solution satisfies the boundary condition (4). The solution (17) and the boundary condition (5) combine to give

$$C=-\cos\varphi-\left(\frac{\pi}{2}+\varphi\right)\sin\varphi. \tag{18}$$

The solution for q is [17]

$$q=A\exp\left[\frac{\sin\varphi}{\cos^2\varphi}\left(\frac{Cx}{h}-\cos 2\psi\right)\right], \tag{19}$$

where A is a constant of integration. Using this solution p can be found from (11) and, then, the stress components from (15). In particular, the boundary condition (9) can be rewritten as

$$\lambda\frac{\partial T}{\partial y}=UA\exp\left[\frac{\sin\varphi}{\cos^2\varphi}\left(\frac{Cx}{h}+\sin\varphi\right)\right]\left(\frac{x}{h}+\frac{2\sin\varphi}{C}+B\right)\cos\varphi+q_t \tag{20}$$

for $y=h$ or $\psi=-\pi/4-\varphi/2$. The strain rate components are determined from (16) and (17) as

$$\xi_{xx}=\frac{U}{h},\quad \xi_{yy}=-\frac{U}{h},\quad \xi_{xy}=\frac{U\sin 2\psi}{h\left(\cos 2\psi+\sin\varphi\right)}. \tag{21}$$

It is seen from this solution and (5) that $\left|\xi_{xy}\right|\to\infty$ as $y\to h$. Such behavior of the shear strain rate near the maximum friction surface is in agreement with the general theory [13]. The plastic work rate is defined as $W=\sigma_{xx}\xi_{xx}+\sigma_{yy}\xi_{yy}+2\sigma_{xy}\xi_{xy}$. Substituting (15) and (21) into this equation yields

$$W=\frac{2Uq}{h}\frac{\left(1+\cos 2\psi\sin\varphi\right)}{\left(\cos 2\psi+\sin\varphi\right)}. \tag{22}$$

It is known that the variation of temperature in the $x-$ direction is negligible [23]. Therefore, it is usually assumed that T is independent of x. Then, the heat conduction equation can be written as

$$\frac{dT}{dt}=\frac{\lambda}{c_v\rho}\frac{\partial^2 T}{\partial y^2}+\frac{\beta}{c_v\rho}W. \tag{23}$$

Here the factor β determines the portion of plastic work converted into heat. The value of this factor is close to unity. Moreover, the temperature everywhere is directly proportional to β. Therefore, it is assumed that $\beta=1$. It is seen from (5) and (22) that $W\to\infty$ as $y\to h$. Therefore, equation (23) contains a singular term. In general, the assumption that the distribution of temperature is independent of x is not compatible with (20) and (22). Therefore, various approximations are used to get rid of the dependence of the right hand

sides of these equations on x [19, 23]. In what follows, W involved in (23) is replaced with its average value defined as

$$W_a = \frac{1}{L}\int_0^L W dx. \tag{24}$$

Substituting (19) and (22) into this equation and using (14) yields

$$W_a = \frac{2UA}{CL_0}\frac{\cos^2\varphi}{\sin\varphi} w_1(\psi) w_2\left(\frac{h}{h_0}\right), \tag{25}$$
$$w_1(\psi) = \frac{(1+\cos 2\psi \sin\varphi)}{(\cos 2\psi + \sin\varphi)}\exp\left(-\frac{\sin\varphi}{\cos^2\varphi}\cos 2\psi\right), \quad w_2\left(\frac{h}{h_0}\right) = \left[\exp\left(\frac{C\sin\varphi h_0^2 l_0}{\cos^2\varphi h^2}\right) - 1\right]\frac{h}{h_0}$$

where $l_0 = L_0/h_0$. Then, equation (23) becomes

$$\frac{dT}{dt} = \frac{\lambda}{c_v\rho}\frac{\partial^2 T}{\partial y^2} + \frac{2UA}{c_v\rho CL_0}\frac{\cos^2\varphi}{\sin\varphi} w_1(\psi) w_2\left(\frac{h}{h_0}\right). \tag{26}$$

The quantity $\lambda \partial T/\partial y$ at $y = h$ is replaced with

$$\lambda\frac{\partial T}{\partial y} = \lambda\left(\frac{\partial T}{\partial y}\right)_a \equiv \frac{\lambda}{L}\int_0^L \frac{\partial T}{\partial y} dx \tag{27}$$

Substituting the right hand side of (20) into this equation and using (14) yields

$$\lambda\left(\frac{\partial T}{\partial y}\right)_a = q_t + \frac{h^2}{h_0^2}\frac{UA\cos^3\varphi}{l_0 C\sin\varphi}\exp\left(\tan^2\varphi\right)\left\{\begin{array}{l} 1+\left(\frac{l_0 C\sin\varphi}{\cos^2\varphi}\frac{h_0^2}{h^2}-1\right)\exp\left(\frac{l_0 C\sin\varphi}{\cos^2\varphi}\frac{h_0^2}{h^2}\right)+ \\ \left(\frac{2\sin\varphi}{C}+B\right)\left[\exp\left(\frac{l_0 C\sin\varphi}{\cos^2\varphi}\frac{h_0^2}{h^2}\right)-1\right] \end{array}\right\}. \tag{28}$$

Then, the boundary condition (20) becomes

$$\lambda\frac{\partial T}{\partial y} = \lambda\left(\frac{\partial T}{\partial y}\right)_a \tag{29}$$

for $y = h$ or $\psi = -\pi/4 - \varphi/2$. Since $dy/dt = u_y$ and $dh/dt = -U$, it follows from (16) that

$$\frac{dy}{dh} = \frac{y}{h}. \tag{30}$$

It is convenient to introduce a Lagrangian coordinate Y such that $Yh_0 = y$ at $h = h_0$. The solution of equation (30) satisfying this initial condition is

$$y = hY. \tag{31}$$

Using this equation and taking into account that $dh/dt = -U$ equation (26) in the Lagrangian coordinates can be written as

$$\frac{\partial \tau}{\partial p} = a\frac{\partial^2 \tau}{\partial Y^2} + \frac{b}{(p+1)^2} w_1(\psi) w_2\left(\frac{1}{1+p}\right). \tag{32}$$

where

$$a = \frac{\lambda}{c_v \rho h_0 U}, \quad b = \frac{2Ah_0 \cos^2\varphi}{c_v \rho C T_0 l_0 \sin\varphi}, \quad \tau = \frac{T - T_0}{T_0}, \quad p = \frac{h_0}{h} - 1. \tag{33}$$

Using (31) and (33) the boundary condition (8) is transformed to

$$\frac{\partial \tau}{\partial Y} = 0 \tag{34}$$

for $Y = 0$. Analogously, the boundary condition (29) becomes

$$\frac{\partial \tau}{\partial Y} = \frac{h_0 q_t}{\lambda T_0 (p+1)} + \frac{b h_0 \cos\varphi}{2a(p+1)^3} \exp\left(\tan^2\varphi\right) \left\langle \begin{array}{l} 1 + \left[\frac{l_0 C \sin\varphi}{\cos^2\varphi}(p+1)^2 - 1\right] \exp\left[\frac{l_0 C \sin\varphi}{\cos^2\varphi}(p+1)^2\right] + \\ \left(\frac{2\sin\varphi}{C} + B\right)\left\{\exp\left[\frac{l_0 C \sin\varphi}{\cos^2\varphi}(p+1)^2\right] - 1\right\} \end{array} \right\rangle. \tag{35}$$

for $Y = 1$. The initial condition (10) transforms to

$$\tau = 0 \tag{36}$$

at $p = 0$. In order to find B involved in (35), it is necessary to substitute (16) into (3). Using (17) and (18) results in

$$B = \frac{(\pi + 2\varphi + \sin 2\varphi)}{2\left[\cos\varphi + (\pi/2 + \varphi)\sin\varphi\right]^2}. \tag{37}$$

It remains to determine A involved in b. It follows from (11), (14), (15), (19), and (33) that

$$\sigma_{xx} = c\cot\varphi + A\exp\left\{\frac{\sin\varphi}{\cos^2\varphi}\left[Cl_0(p+1)^2 - \cos 2\psi\right]\right\}\left(\cos 2\psi - \frac{1}{\sin\varphi}\right) \tag{38}$$

at $x = L$. Substituting (38) into (6), using (18) and replacing integration with respect to y with integration with respect to ψ by means of (17) and (31) yield

$$A = \frac{c\cos\varphi\left[\cos\varphi + (\pi/2 + \varphi)\sin\varphi\right]}{2} \times \left\langle \int_0^{-\pi/4-\varphi/2} \exp\left\{\frac{\sin\varphi}{\cos^2\varphi}\left[Cl_0(p+1)^2 - \cos 2\psi\right]\right\}(\cos 2\psi \sin\varphi - 1)(\cos 2\psi + \sin\varphi)\, d\psi \right\rangle^{-1}. \tag{39}$$

Equation (32) together with the boundary and initial conditions (34) – (36) comprise the standard second initial/boundary value problem for the nonhomogeneous heat conduction equation [18]. However, a difficulty is that the function $w_1(\psi)$ involved in (32) approaches infinity as $\psi \to -\pi/4 - \varphi/2$ (or $Y \to 1$). In order to overcome this difficulty, it is convenient to introduce the new function u by

$$u = \tau + f(Y)g(p) \tag{40}$$

where $f(Y)$ is a function only Y and $g(p)$ is a function only p. Substituting (40) into (32) yields

$$\frac{\partial u}{\partial p} = a\frac{\partial^2 u}{\partial Y^2} + f(Y)\frac{dg}{dp} - ag(p)\frac{d^2 f}{dY^2} + \frac{b}{(p+1)^2} w_1(\psi) w_2\left(\frac{1}{p+1}\right). \tag{41}$$

Assume that

$$g(p) = \frac{b}{a(p+1)^2} w_2\left(\frac{1}{p+1}\right) \quad \text{and} \quad \frac{d^2 f}{dY^2} = -w_1(\psi). \tag{42}$$

Then, equation (41) becomes

$$\frac{\partial u}{\partial p} = a\frac{\partial^2 u}{\partial Y^2} + f(Y)\frac{dg}{dp}. \tag{43}$$

It follows from (17) and (31) that

$$\frac{d\psi}{dY} = \frac{C}{2(\cos 2\psi + \sin\varphi)}. \tag{44}$$

Using (25), (33) and (44) equation (42) can be rewritten as

$$\begin{aligned} g(p) &= \frac{b}{a(p+1)^3}\left\{\exp\left[\frac{C\sin\varphi l_0}{\cos^2\varphi}(p+1)^2\right] - 1\right\}, \\ \frac{d}{d\psi}\left(\frac{df}{dY}\right) &= -\frac{2(1+\cos 2\psi\sin\varphi)}{C}\exp\left(-\frac{\sin\varphi}{\cos^2\varphi}\cos 2\psi\right). \end{aligned} \tag{45}$$

Differentiating the first equation with respect to p gives

$$\frac{dg}{dp} = \frac{b}{a(p+1)^2}\left\{\frac{3}{(p+1)^2} + \left[\frac{2Cl_0\sin\varphi}{\cos^2\varphi} - \frac{3}{(p+1)^2}\right]\exp\left[\frac{C\sin\varphi l_0}{\cos^2\varphi}(p+1)^2\right]\right\}. \tag{46}$$

The function $f(Y)$ may be chosen such that $df/dY = 0$ at $Y = 0$. Then, the solution of the second equation in (45) can be represented in the form

$$\frac{df}{dY} = -\frac{2}{C}\int_0^{\psi}(1+\cos 2z\sin\varphi)\exp\left(-\frac{\sin\varphi}{\cos^2\varphi}\cos 2z\right)dz. \tag{47}$$

Using (44) this solution can be rewritten as

$$\frac{df}{d\psi} = -\frac{4(\cos 2\psi + \sin\varphi)}{C^2}\int_0^{\psi}(1+\cos 2z\sin\varphi)\exp\left(-\frac{\sin\varphi}{\cos^2\varphi}\cos 2z\right)dz. \tag{48}$$

The function $f(Y)$ may be chosen such that $f = 0$ at $Y = 0$. Then, the solution of equation (48) is

$$f=-\frac{4}{C^2}\int_0^{\psi}\left(\cos 2\chi+\sin\varphi\right)\int_0^{\chi}\left(1+\cos 2z\sin\varphi\right)\exp\left(-\frac{\sin\varphi}{\cos^2\varphi}\cos 2z\right)dzd\chi. \tag{49}$$

Thus equations (17), (31) and (49) supply f as a function of Y in parametric form with ψ being the parameter varying in the range $-\pi/4-\varphi/2\le\psi\le 0$. Substituting this function and (46) into (43) determines the last term of this equation as a function of Y ad p. Using (40) and the functions $f(Y)$ and $g(p)$ found the boundary conditions (34) and (35) are replaced with

$$\frac{\partial u}{\partial Y}=0 \tag{50}$$

for $Y=0$ and

$$\frac{\partial u}{\partial Y}=\frac{h_0 q_t}{\lambda T_0(p+1)}+\frac{bh_0\cos\varphi}{2a(p+1)^3}\exp\left(\tan^2\varphi\right)\left\langle\begin{array}{l}1+\left[\frac{l_0C\sin\varphi}{\cos^2\varphi}(p+1)^2-1\right]\exp\left[\frac{l_0C\sin\varphi}{\cos^2\varphi}(p+1)^2\right]+\\ \left(\frac{2\sin\varphi}{C}+B\right)\left\{\exp\left[\frac{l_0C\sin\varphi}{\cos^2\varphi}(p+1)^2\right]-1\right\}\end{array}\right\rangle \tag{51}$$

$$+\frac{2b}{aC(p+1)^3}\left\{\exp\left[\frac{C\sin\varphi l_0}{\cos^2\varphi}(p+1)^2\right]-1\right\}\int_{-\pi/4-\varphi/2}^{0}\left(1+\cos 2z\sin\varphi\right)\exp\left(-\frac{\sin\varphi}{\cos^2\varphi}\cos 2z\right)dz.$$

.

for $Y=1$. The initial condition (36) becomes

$$u=-\frac{4b}{aC^2}\left[\exp\left(\frac{C\sin\varphi l_0}{\cos^2\varphi}\right)-1\right]\int_0^{\psi}\left(\cos 2\chi+\sin\varphi\right)\int_0^{\chi}\left(1+\cos 2z\sin\varphi\right)\exp\left(-\frac{\sin\varphi}{\cos^2\varphi}\cos 2z\right)dzd\chi. \tag{52}$$

at $p=0$. Here ψ should be eliminated by means of (17) and (31). The constants C, B and A involved in (43), (51) and (52) should be eliminated by means of (18), (37) and (39).

4 ILLUSTRACTIVE EXAMPLE

The numerical solution of equation (43) satisfying the initial condition (52) and the boundary conditions (50) and (51) has been found using the Green's function provided in [18]. It has been assume that $q_t=0$, $\varphi=0.1$, $l_0=5$, $(c_v\rho)=1.8\cdot 10^6\,\mathrm{Nm^{-2}\,deg^{-1}}$, $T_0=1000^0\mathrm{C}$, $h_0=2\mathrm{mm}$, and $c=750\mathrm{MPa}$. The through thickness distribution of the dimensionless temperature determined by means of the numerical solution found and (40) is depicted in Fig. 2 at $a=30$ and several values of h/h_0 and in Fig. 3 at $a=10$ and the same values of h/h_0. In the computations, 15 first terms in the series representing the Green's function have been used. For the set of parameters chosen, the accuracy of the Green's function calculated is higher than the standard MATLAB long format. All computations took a few seconds and provided the accuracy of 10^{-5}. No difference in terms of the computation time and accuracy was observed when the Green's function was evaluated using 11 first terms in its series representation instead of 15 terms. This shows that the integration accuracy rather than the approximation of the Green's function should be improved to obtain a more accurate result.

It is worthy of note that the value of the dimensionless parameter l_0 is rather large and this parameter is involved in the exponential function in (46). This might cause computational difficulties. However, it is seen from (33) and (39) that the product of b and the exponential function in (46) is of the order 1. Therefore, the numerical solution has been found with no difficulty.

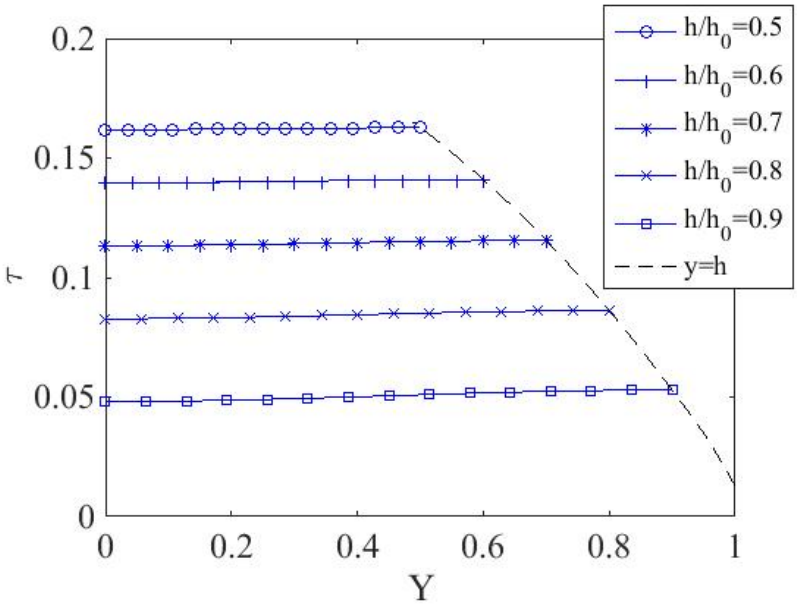

Figure 2: Through thickness distribution of the dimensionless temperature at a = 30 and several values of h/h_0

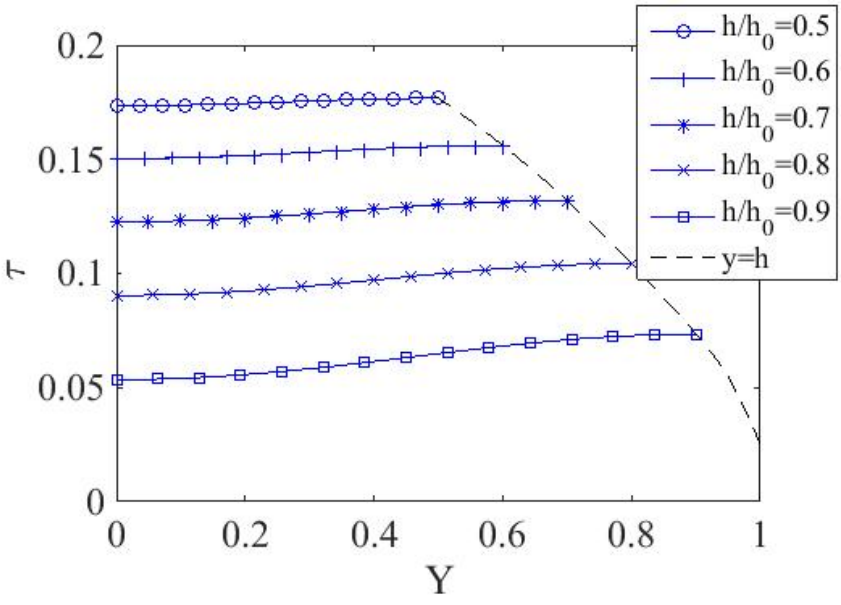

Figure 3: Through thickness distribution of the dimensionless temperature at a = 10 and several values of h/h_0

5 CONCLUSIONS

The distribution of temperature in the continued quasi-static plane strain compression of a thin strip between two rigid, parallel perfectly rough dies has been found. The double shear model has been adopted. Using Largangian coordinates has enabled the original initial/boundary value problem to be reduced to the standard second initial/boundary value problem for the nonhomogeneous heat conduction equation. The Green's function for the latter is known [18].

The heat conduction equation contains a singular term (the plastic work rate appriches infinity near the friction surface). For this reason, commercial finite element packages are not capable of solving such boundary value problems. Probably, the generalized finite element method [24] can be used for this purpose. However, no specific code is currently available. In the present paper, the new unknown u has been introduced in equation (40) to transform the original heat conduction equation to (43). The latter contains no term that approaches infinity near the maximum friction surface.

6 ACKNOWLEDGMENTS

S.A. acknowledges support from the grant RFBR-17-01-00624. W.M. acknowledges FP7 Marie Curie project TAMER: IRSES-GA-2013-610547.

REFERENCES

[1] Tanner, R.I. and Johnson, W. Temperature distributions in some fast metal-working operations. *Int. J. Mech. Sci.* (1960) **1**:28-44.

[2] Hadala, B. Implementation of the heat balance in the finite element solution to the temperature field of the plastically deformed material. *Int. J. Therm. Sci.* (2013) **71**:172-181.

[3] Zienkiewicz, O.C., Jain, P.C. and Onate, E. Flow of solids during forming and extrusion. Some aspects of numerical solutions. *Int. J. Solids Struct.* (1978) **14**:15-38.

[4] Zienkiewicz, O.C., Onate, E. and Heinrich, J.C. A general formulation for coupled thermal flow of metals using finite elements. *Int. J. Numer. Meth. Engng* (1981) **17**:1479-1514.

[5] Griffiths, B.J. Mechanisms of white layer generation with reference to machining and deformation processes. *Trans. ASME J. Trib.* (1987) **109**:525-530.

[6] Griffiths, B.J. and Furze, D.C. Tribological advantages of white layers produced by machining. *Trans. ASME J. Trib.* (1987) **109**:338-342.

[7] Warren, A.W. and Guo, Y.B. Numerical investigation on the effects of machining-induced white layer during rolling contact. *Trib. Trans.* (2005) **48**:436-441.

[8] Choi, Y. Influence of a white layer on the performance of hard machined surfaces in rolling contact. *Proc. IMechE Part B: J. Engng Manufact.* (2010) **224**:1207-1215.

[9] Suliga, M., Szota, P. and Mroz, S. Simulation and measurement of temperature in high speed drawing process of steel wires. *Comp. Meth. Mater. Sci.* (2017) **17**:69-75.

[10] Rebelo, N. and Kobayashi, S. A coupled analysis of viscoplastic deformation and heat transfer-II: Applications. *Int. J. Mech. Sci.* (1980) **22**:708-718.

[11] Chen, J.-C., Pan, C., Rogue, S.M.O.L. and Wang, H.P. A Lagrangian reproducing kernel particle method for metal forming analysis. *Comp. Mech.* (1998) **22**:289-307.

[12] Alexandrov, S. and Richmond, O. Singular plastic flow fields near surfaces of maximum friction stress. *Int. J. Non-Linear Mech.* (2001) **36**:1-11.
[13] Alexandrov, S. and Lyamina, E. Singular solutions for plane plastic flow of pressure-dependent materials. *Dokl. Phys.* (2002) **47**:308-311.
[14] Alexandrov, S. and Mishuris, G. Qualitative behaviour of viscoplastic solutions in the vicinity of maximum-friction surfaces. *J. Engng Math.* (2009) **65**:143-156.
[15] Alexandrov, S. and Jeng, Y.-R. Singular rigid/plastic solutions in anisotropic plasticity under plane strain conditions. *Cont. Mech. Therm.* (2013) **25**:685-689.
[16] Spencer, A.J.M. A theory of the kinematics of ideal soils under plane strain conditions. *J. Mech. Phys. Solids* (1964) **12**: 337-351.
[17] Marshall, E.A. The compression of a slab of ideal soil between rough plates, *Acta Mech*. (1967) **3**:82-92.
[18] Polyanin, A.D. *Handbook of linear partial differential equations for engineers and scientists*. Chapman & Hall CRC Press, (2002).
[19] Alexandrov, S. and Miszuris, W. Heat generation in plane strain compression of a thin rigid plastic layer. *Acta Mech.* (2016) **227**:813-821.
[20] Hill, R. *The mathematical theory of plasticity*. Clarendon Press, (1950).
[21] Collins, I.F. and Meguid, S.A. On the influence of hardening and anisotropy on the plane-strain compression of thin metal strip. *Trans. ASME J. Appl. Mech.* (1977) **44**:271-278.
[22] Adams, M.J., Briscoe, B.J., Corfield, G.M., Lawrence, C.J. and Papathanasiou, T.D. An analysis of the plane-strain compression of viscous materials. *Trans. ASME J. Appl. Mech*. (1997) **64**:420-424.
[23] Nepershin, R.I. Non-isothermal plane plastic flow of a thin layer compressed by flat rigid dies. *Int. J. Mech. Sci*. (1997) **39**:899-912.
[24] Fries, T.-P. and Belytschko, T.: The extended/generalized finite element method: an overview of the method and its applications. *Int. J. Numer. Meth. Eng*. (2010) **84**: 253-304.

VII International Conference on Computational Methods for Coupled Problems in Science and Engineering
COUPLED PROBLEMS 2017
M. Papadrakakis, E. Oñate and B. Schrefler (Eds)

CONVECTIVE STABILITY OF A CHEMICALLY REACTING FLUID IN AN ANNULUS

ILMARS ILTINS*, MARIJA ILTINA* AND ANDREI KOLYSHKIN*

*Department of Engineering Mathematics
Riga Technical University
Riga, Latvia, LV 1007
e-mail: iltins@inbox.lv,

*Department of Engineering Mathematics
Riga Technical University
Riga, Latvia, LV 1007
e-mail: marijai@inbox.lv,

*Department of Engineering Mathematics
Riga Technical University
Riga, Latvia, LV 1007
e-mail: andrejs.koliskins@rtu.lv

Key words: Linear Stability, Convective Flow, Collocation Method

Abstract. Linear stability of a steady convective motion of a viscous incompressible fluid generated by internal heat sources in a tall vertical annulus is investigated. The heat sources are distributed within the fluid in accordance with the Arrhenius law. The problem for the determination of base flow in this case is nonlinear. The base flow velocity and temperature distribution is obtained numerically using Matlab. Linear stability of the base flow is investigated with respect to asymmetric perturbations. The stability boundary depends on the two parameters: the Prandtl number and the Frank-Kamenetskii parameter. It is shown that even for small Prandtl numbers (in contrast with the case of uniformly distributed heat sources) marginal stability curves consist of two separate brances. Calculations show that the base flow is destabilized as both parameters (the Prandtl number and the Frank-Kamenetskii parameter) increase.

1 INTRODUCTION

Analysis of processes of combustion and heat generation is aimed to develop a cleaner and more efficient energy production using different types of biomass. In order to enhance biomass thermo-chemical conversion different technical solutions are proposed [1]. Experimental investigation of the processes of biomass thermo chemical conversion is performed

in [2]. Intensification of combustion processes can be achieved as a result of hydrodynamic instabilities. Linear stability of a steady convective motion between two parallel planes due to heat sources uniformly distributed within viscous incompressible fluid is analyzed in [3], [4]. The case of uniform heat sources distributed in an annulus is considered in [5]. It is shown in [3]–[5] that for small Prandtl numbers instability is associated with the shear mode due to two fluid streams moving in opposite directions while for large Prandtl numbers thermal perturbations are more important and instability occurs in the form of thermal running waves moving along the channel with large wave speed. In addition, calculations in [5] showed that asymmetric mode is the most unstable for large gaps while only axisymmetric perturbations lead to instability for small gaps.

Optimization of the processes of biomass thermo-chemical conversion should be performed under the assumption that internal heat sources are generated in the fluid as a result of exothermic chemical reaction. In the present paper we analyze one of the aspects of the problem - linear stability of a convective motion in a tall vertical annulus. Linear stability problem is solved numerically for different values of the parameters of the problem.

2 FORMULATION OF THE PROBLEM

Consider a tall vertical annulus with the inner and outer radii R_1 and R_2, respectively, filled with a viscous incompressible fluid. The annulus is closed so that the total fluid flux through the cross-section of the annulus is equal to zero. The internal heat sources are distributed within the annulus in accordance with the Arrhenius law [6]:

$$\tilde{Q} = Q_0 k_0 \exp\left[-E/(R\tilde{T}\right], \tag{1}$$

where $\tilde{T}$ is the absolute temperature, R is the universal gas constant, Q_0 and k_0 are given constants and E is the activation energy.The system of the Navier-Stokes equations under the Boussinesq approximation has the form

$$\begin{aligned} \frac{\partial \mathbf{v}}{\partial t} + Gr(\mathbf{v}\nabla)\mathbf{v} &= \nabla p + \Delta \mathbf{v} + T\mathbf{k}, & (2)\\ \frac{\partial T}{\partial t} + Gr\mathbf{v}\nabla T &= \frac{1}{Pr}\Delta T + \frac{F}{Pr}\exp\left[T/(1+bT)\right], & (3)\\ \nabla \mathbf{v} &= 0. & (4) \end{aligned}$$

Here $\mathbf{v}$, T and p are dimensionless velocity vector, temperature and pressure. The following dimensionless quantities are chosen as measures, respectively, of length, R_2, time, R_2^2/ν,velocity, $g\beta R_2^2 RT_0^2/(\nu E)$, temperature,$RT_0^2/E$, and pressure, $\rho g\beta R_2 RT_0^2/E$. Here ρ is the density, β is the coefficient of thermal expansion, and ν is the kinematic viscosity of the fluid. There are four dimensionless parameters characterizing the problem: the Grasshof number $Gr = g\beta RT_0^2 R_2^3/(\nu^2 E)$, the Prandtl number, $Pr = \nu/\chi$, the Frank-Kamenetsky number $F = [Q_0 k_0 E R_2^2/(\kappa RT_0^2)] \exp\left[-E/(RT_0)\right]$, and the parameter $b = RT_0/E$.

Consider a system of cylindrical polar coordinates (r, φ, z) centered at the point O on the axes of the cylinders. The velocity components are denoted as follows: $\mathbf{v} = (v_r, v_\varphi, v_z)$. There exists a steady solution of (2)–(4) of the following form:

$$\mathbf{v} = (0, 0, W_0(r)), \quad T = T_0(r), \quad p = Cz + const. \tag{5}$$

Substituting (5) into (2)–(4) we obtain the nonlinear system of ordinary differential equations

$$\frac{d^2W_0}{dr^2} + \frac{1}{r}\frac{dW_0}{dr} + T_0 + C = 0, \tag{6}$$

$$\frac{d^2T_0}{dr^2} + \frac{1}{r}\frac{dT_0}{dr} + \frac{F}{Pr}\exp\left[T_0/(1+bT_0)\right] = 0. \tag{7}$$

The boundary conditions have the form

$$W_0|_{r=1} = 0, \quad W_0|_{r=R_0} = 0 \quad T_0|_{r=1} = 0, \quad T_0|_{r=R_0} = 0, \tag{8}$$

where $R_0 = R_1/R_2$. Since the annulus is closed, the total fluid flux through the cross-section of the annulus is equal to zero:

$$\int_{R_0}^{1} rW_0(r)\,dr = 0. \tag{9}$$

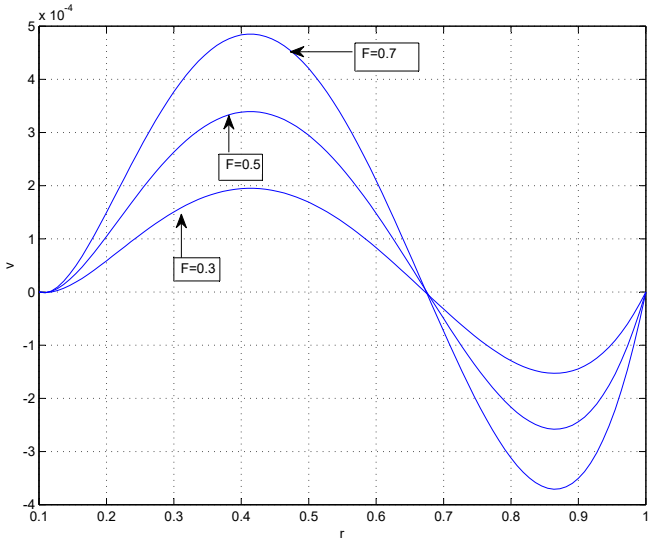

Figure 1: The base flow velocity distribution for three values of the Frank-Kamenetskii parameter F.

3 CALCULATION OF BASE FLOW

Nonlinear problem (6)–(9) is solved numerically using Matlab routune bvp4c. The value of the parameter b for all calculations below is set at 0 since it is very small in applications. First, the temperature distribution can be obtained solving (7) together with the two boundary conditiions (8) for the temperature T_0. Then equation (6) together with the boundary conditions (8) for the function W_0 is solved where the constant C is chosen to satisfy (9). It is shown in [6] that depending on the value of the paramemer b problem (6)-(9) can have several solutions. Only the solution with smallest values of the temperature T_0 is used in our calculations. The ratio of the radii of the cylinders is fixed at $R_0 = 0.1$ for all calculations (stability analysis in [5] showed that asymmetric perturbations are the most unstable for $0 < R_0 < 0.28$). The base flow velocity distribution is shown in Figure

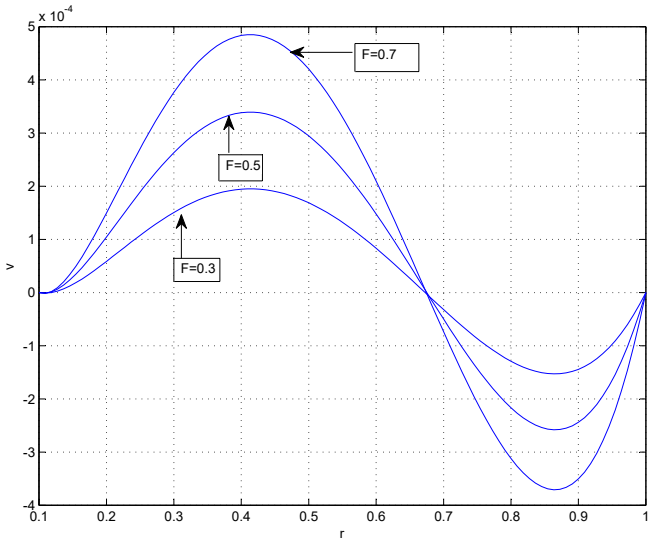

Figure 2: The base flow temperature distribution for three values of the Frank-Kamenetskii parameter F.

1 for three values of the Frank-Kamenetskii parameter F, namely, $F = 0.3$, $F = 0.5$, and $F = 0.7$. Figure 2 plots the distribution of the base temperature T_0 for the same values of the Frank-Kamenetskii parameter.

4 LINEAR STABILITY EQUATIONS

Suppose that $\hat{\mathbf{v}}$, $\hat{T}$ and $\hat{p}$ are small unsteady perturbations of the form

$$\hat{\mathbf{v}}(r,\varphi,z) = \mathbf{u}(r)\exp\left[-\lambda t + i\alpha z + in\varphi\right] \quad (10)$$

$$\hat{T}(r,\varphi,z) = \theta(r)\exp\left[-\lambda t + i\alpha z + in\varphi\right] \quad (11)$$

$$\hat{p}(r,\varphi,z) = q(r)\exp\left[-\lambda t + i\alpha z + in\varphi\right], \quad (12)$$

where $\mathbf{u} = (u(r), v(r), w(r))$, α and n are axial and azimuthal wave numbers, respectively. The perturbed flow is assumed to be of the form $\mathbf{v}_0 + \hat{\mathbf{v}}$, $T_0 + \hat{T}$, $p_0 + \hat{p}$. Substituting the perturbed quantities into (2)–(4) and linearizing the resulting equations in the neighborhood of the base flow we obtain

$$u'' + \frac{u'}{r} - \frac{un^2}{r^2} - \alpha^2 u - \frac{u}{r^2} - \frac{2inv}{r^2} = q' + iGr\alpha u W_0 - \lambda u, \tag{13}$$

$$v'' + \frac{v'}{r} - \frac{vn^2}{r^2} - \alpha^2 v - \frac{v}{r^2} + \frac{2inu}{r^2} = \frac{inq}{r} + iGr\alpha v W_0 - \lambda v, \tag{14}$$

$$w'' + \frac{w'}{r} - \frac{wn^2}{r^2} - \alpha^2 w + \theta = i\alpha q + Gr(uW_0' + i\alpha\theta W_0) - \lambda w, \tag{15}$$

$$\frac{1}{Pr}\left(\theta'' + \frac{\theta'}{r} - \frac{\theta n^2}{r^2} - \alpha^2\theta + F\exp[T_0]\theta\right) = Gr(uT_0' + i\alpha\theta W_0) - \lambda\theta, \tag{16}$$

$$u' + \frac{u}{r} + \frac{inv}{r} + i\alpha w = 0. \tag{17}$$

The perturbed velocity components and temperature are equal to zero at the walls of the

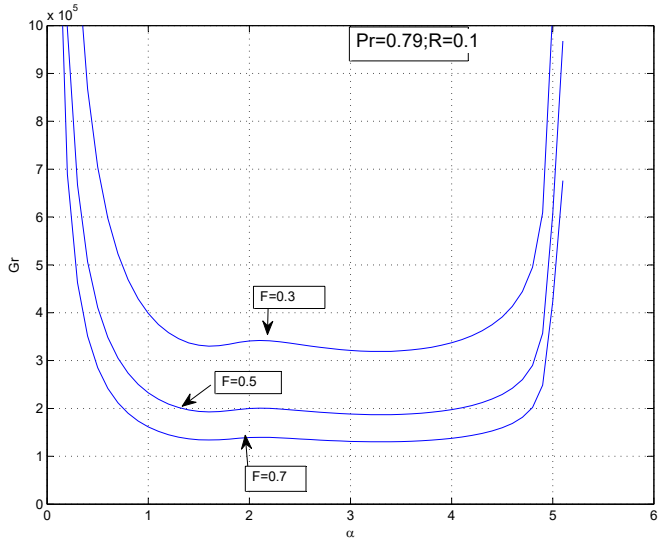

Figure 3: Marginal statbility curves for $0 < \alpha < 5$.

cylinder. In order to reduce the size of the corresponding eigenvalue problem the functions q and w are eliminated from the system. As a result, additional boundary conditions are required to solve the reduced system. These condistions are obtained from the continuity equation (17). Thus, the boundary conditions are

$$u(1) = v(1) = \theta(1) = 0, \quad u(R_0) = v(R_0) = \theta(R_0) = 0, \quad u'(1) = u'(R_0) = 0. \tag{18}$$

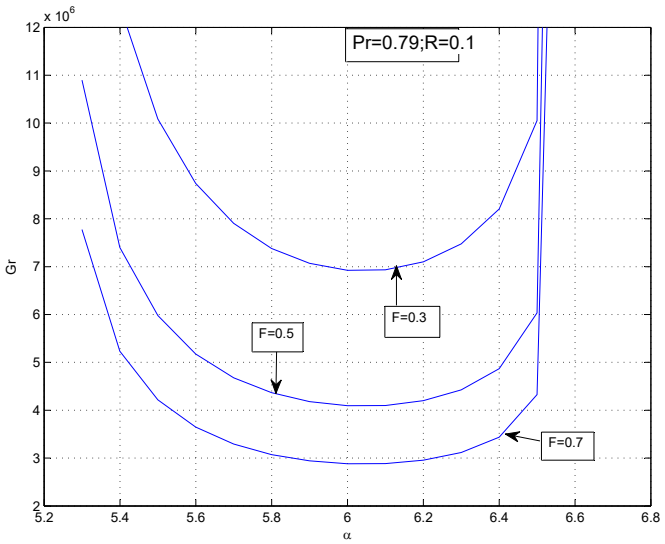

Figure 4: Marginal statbility curves for $\alpha > 5$.

5 NUMERICAL RESULTS

Collocation method based on the Chebyshel polynomials is used to solve the corresponding boundary value problem. The functions $u(r)$, $v(r)$, and $\theta(r)$ are represented in the form

$$u(x) = \sum_{m=0}^{N} a_m(1-x^2)^2 T_m(x), \quad v(x) = \sum_{m=0}^{N} b_m(1-x^2)T_m(x), \quad \theta(x) = \sum_{m=0}^{N} c_m(1-x^2)T_m(x), \tag{19}$$

where $x = 2/(1-R_0)r - (1+R_0)/(1-R_0)$. Here $T_m(x) = cos(marccosx)$ is the Chebyshev polynomial of the first kind of order m and a_m, b_m, and c_m are unknown koefficients. The form of the solution (19) guarantees that all the boundary conditions (18) are automatically satisfied in terms of the transformed variable x. The collocation points are given by

$$x_j = \cos\frac{\pi j}{N}, \quad j = 0, 1, 2, \ldots, N \tag{20}$$

Using (12)–(20) we obtain generalized eigenvalue problem of the form

$$(A - \lambda B)\mathbf{a} = 0, \tag{21}$$

where $\mathbf{a} = (a_0 \ldots a_N b_0 \ldots b_N c_0 \ldots c_N)^T$. Problem (21) is solved numerically using Matlab routine eig. Marginal stability curves for the case $Pr = 0.79$ are shown in Figures 3 and 4 for the three values of the Frank-Kamenetskii parameter. It is seen from the figures that there are two separate brances of the marginal curves: the first branch corresponding to

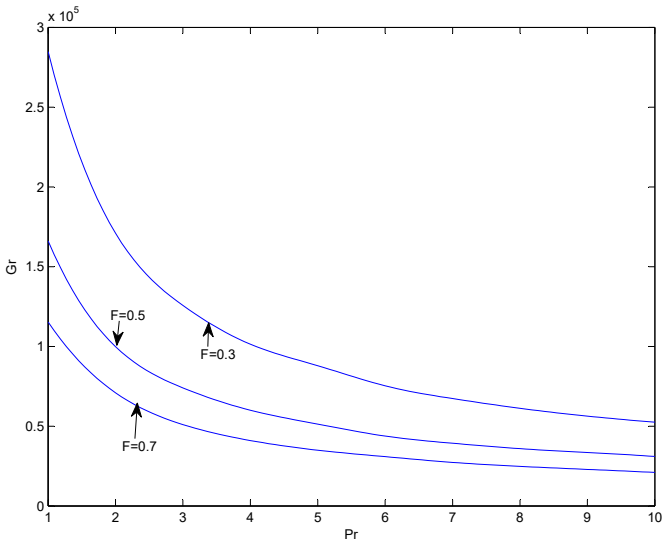

Figure 5: Critical values of the Grasshof number versus Prandtl number.

smaller values of α (and to smaller values of the Grasshof number) in the range $0 < \alpha < 5$ and the second branch corresponding to larger values of α (and to larger values of the Grasshof numbers). Note that two branches of the marginal stability curve are found to exist also in the case of a uniform heat generation, but for considerably larger values of the Prandtl numbers. The region of instability is above the curves.

The critical value of the Grasshof number is defined as the absolute minimum on the marginal curve. Figure 5 plots the critical Grasshof numbers versus the Prandtl number for the three values of the Frank-Kamenetskii parameter. It is seen from the graph that the increase in both parameters has a destabilizing influence of the flow.

6 CONCLUSIONS

Linear stability of a steady convective motion generated by heat sources due to exothermal chemical reaction is analyzed in the paper. Nonlinear problem characterizing base flow is solved numerically using Matlab. Linear stability calculations are performed for the case of asymmetric perturbations. The results show that larger values of the Prandtl number and Frank-Kamenetskii parameter destabilize the flow.

This work was partially supported by the grant 632/2014 by the Latvian Council of Science.

REFERENCES

[1] Nussbaumer, T. Combustion and co-combustion of biomass: fundamentals, technologies, and primary measures for emission reduction. *Energy and Fuels* (2003)

17:1510–1521.

[2] Barmina, I., Purmalis, M., Valdmanis, R. and Zake, M. Electrodynamic control of the combustion characteristics and heat energy production. *Combust. Sci.Technol.* (2016) **188**:190–206.

[3] Gershuni, G.Z., Zhukhovitskii, E.M. and Iakimov, A.A. On the stability of steady convective motion generated by internal heat sources. *J. Appl. Math.Mech.* (1970) **34**:669–674.

[4] Gershuni, G.Z., Zhukhovitskii, E.M. and Iakimov, A.A. Two kinds of instability of stationary convective motion induced by internal heat sources. *J. Appl. Math.Mech.* (1973) **37**:564–568.

[5] Kolyshkin, A.A and Vaillancourt, R. Stability of internally generated thermal convection in a tall vertical annulus. *Can. J.Phys.* (1991) **69**:743–748.

[6] Bebernes, J. and Eberly, D. *Mathematical problems from combustion theory*. Springer, (1989).

VII International Conference on Computational Methods for Coupled Problems in Science and Engineering
COUPLED PROBLEMS 2017
M. Papadrakakis, E. Oñate and B. Schrefler (Eds)

INFLUENCE OF WELDING PARAMETERS ON THE WELDING RESIDUAL STRESSES

S. GKATZOGIANNIS*, P. KNOEDEL AND T. UMMENHOFER

KIT Steel & Lightweight Structures
Research Center for Steel, Timber & Masonry
Otto-Ammann-Platz 1, D-76131 Karlsruhe, Germany
e-mail: stefanos.gkatzogiannis@kit.edu, https://stahl.vaka.kit.edu

Key words: FE simulation, welding , AISI 316L, austenitic steel, residual stresses.

Abstract. FE simulation of welds from austenitic steel was carried out in the current paper. Two different multi-pass welds were modelled. Measurements of welding residual stresses, which were found in literature, were applied for the validation of the results. The validated models were then used as basis for sensitivity analysis. The influence of differentiating the welding speed, the heat input of the weld heat source, intermediate cooling between consecutive weld-passes and welding sequence on the welding residual stresses was investigated.

1 INTRODUCTION

Applications regarding finite element (FE) simulation of welds have expanded rapidly in the last decades due to the increased computational power. The significance of the welding residual stresses (WRS) on the fatigue behaviour of metallic components renders their calculation a significant subject of structural engineering. The WRS and mechanical behaviour of the component in general are strongly coupled with the thermal treatment of the component during welding. The thermal history influences the mechanical behaviour due to the temperature dependency of the material parameters of steel and the microstructural transformations that take place inside a thermal cycle, which also influence the final mechanical behaviour.

This coupling is successfully modelled, when welds are simulated by the use of modern FE Multiphysics Software, provided that a robust modelling of all three following fields has been achieved: the thermal, the mechanical and the microstructural behaviour (wherever necessary) of the investigated component during welding. These three fields interact with each other, although the influence of phase changes and mechanical loading on the thermal behaviour and the microstructural behaviour respectively can be neglected with no significant influence on the calculated WRS [1]. The interactions that necessarily have to be modelled in order to ensure robust results are presented in Figure 1.

The use of the double-ellipsoidal model for the heat-source, which was proposed by Goldak in 1984 [2], is considered today state-of-the-art. In combination with the application of modern three-dimensional FE models, due to the increased computational power, it enables precise FE solutions of the heat transfer problem, which show good agreement with measured temperature profiles [1]. Moreover, available data of mechanical behaviour of steel at elevated temperatures is rapidly increasing in the last years. On this basis, the FE models can be used to predict the

temperature distributions during the welding process and their influence on WRS, if the microstructural transformations have also been robustly modelled. Nevertheless, some difficulties arise regarding the applied welding parameters and material models.

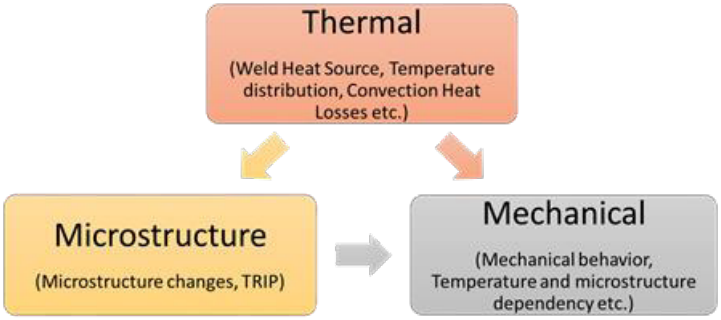

Figure 1: Fields of the weld simulation and interactions taken into consideration

Regarding the welding parameters, the nominal values are usually applied as input during a weld simulation. In practice though, especially in cases where no automated weld-process is applied, welding is carried out under different conditions, especially regarding the welding speed (± 10% deviation is predicted in typical welding procedure specifications (WPS) for the welding parameters). A change of welding parameters, may lead to differentiated WRS profiles. In previous work of the authors for similar components from the same steel grade S355 different WRS profiles were calculated. The resulted longitudinal WRS are presented in Figure 2. Both components were single-pass V grooved welds, with identical weld section geometry and thickness of 5 mm. The first component though, simulated in [1] had length and width of 500 x 200 mm and was supposed to be welded unrestrained with welding speed of 6,7 mm/s (400 cm/min) and effective heat input of 10 kJ/cm. The calculated WRS were compared with profiles from WRS measurements, which were found in [5]. The second one, which is simulated in [4] had length and width of 300 x 300 mm and was restrained during welding. Welding speed and effective heat input in this case were 10 mm/s and 7 kJ/cm respectively. A significant difference between the two calculated profiles is obvious. Reckoning that the boundary conditions have negligible influence on the longitudinal WRS, as it was shown in [6], and the influence of the plate geometry is not expected to cause such a differentiation, as the one presented in Figure 2, the influence of differentiated heat input is obvious. Higher heat input, either through increased heat power of the welding source or lower velocity, is expected to lead to different width of plastic zone and higher strain and stress distributions. Of course, in the case of ferritic or multi-phase steels like S355, the influence of heat input is more complex because it directly effects the cooling behaviour of the component and in extension the microstructure of the fusion zone (FZ) and the heat-affected zone (HAZ). Different microstructure distribution can cause significant differences in the WRS as the mechanical behaviour differs drastically for each steel phase.

On the other hand, uncertainty regarding the applied material parameters, models or applied mechanical restraints is a destabilizing factor in the robustness of results from weld simulations. The temperature dependency of the material parameters, which are applied during a weld modelling, intensifies the influence of heat input. The influence of the temperature-dependent material parameters on the final WRS was studied by Zhu and Chao [8]. Useful simplifications

that retain the preciseness of the results at a required level but also reduce the calculation time or the effort needed for each simulation have been proposed, although a rather primitive 2D model was applied, at least compared to modern 3D possibilities of weld simulation. Teng et al. [7] and Ji et al. [10] applied similar simplified models for investigating the influence of welding sequence in multi-pass butt-welds. In both cases it was successfully proven that selecting appropriate welding sequence during welding, can reduce the tensile WRS confirming textbook knowledge. Nevertheless, reverse welding of selected passes was not investigated.

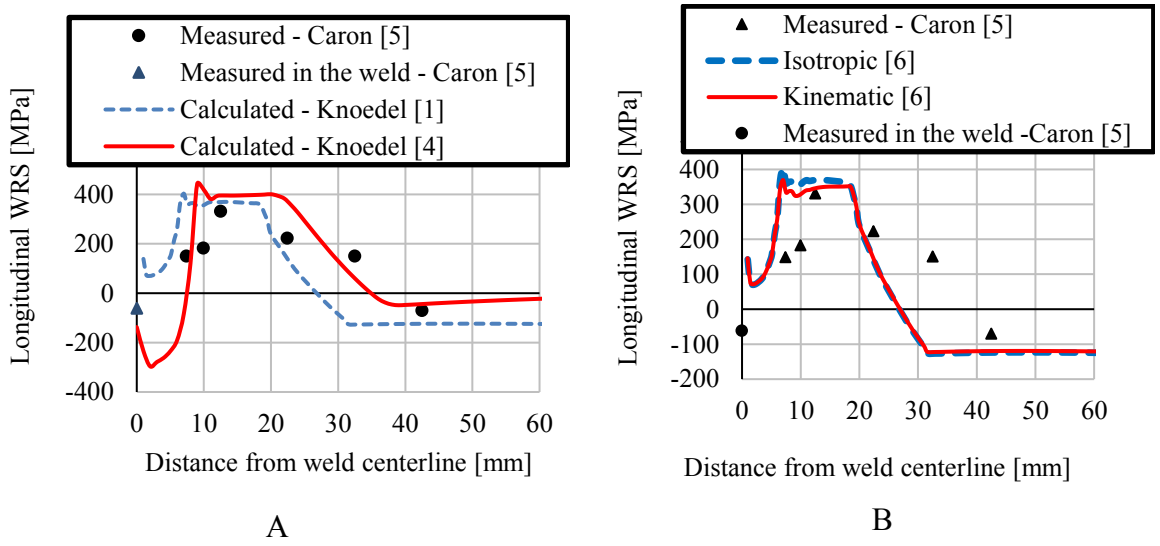

Figure 2: Longitudinal WRS for components from S355 steel – A: Influence of boundary conditions – B: Influence of hardening model

Moreover, more recent studies like those from Gannon et al. [11], Chen et al. [12] and Liu et al. [13] have shown the effectiveness of weld simulation on predicting WRS depending on the welding sequence, by the use of complex modern 3D weld simulation models. These studies focused on the influence of welding sequence on geometries different from a butt-welded plate. The influence of the welding sequence lies on the fact that welding a pass has an effect on the preceding passes, acting for example as thermal stress-relief process. On the other hand, it can result in high cooling rates in the HAZ, producing in this way brittle martensitic microstructures, wherever possible. The effect is therefore more prominent in multi-phase steels. Nevertheless, all the above-mentioned studies investigated austenitic steels, with negligible microstructural changes.

Finally, the influence of the heat input is also significant when the hardening behaviour of steel during reversed plasticity is considered. It was proven in two independent studies from Wohlfart et al. [14] and Mullins and Gunnars [15], that the use of a bilinear isotropic hardening material model during simulation of welding provides WRS with better agreement with measured profiles than kinematic hardening. Both studies were carried out for steels, which in room temperature exhibit the Bauschinger effect and a simulation with a kinematic hardening model would fit better at ambient temperature. It has been proven though by Mataya and Carr [16], that in the case of austenitic stainless steel, when yielding has taken place at elevated temperatures or heat treatment of the material between the consecutive yielding sequences has

taken place, then the Bauschinger effect is eliminated. On the contrary, in a recent study [6] regarding multi-phase single-pass weld from multi-phase S355 steel the kinematic option produced better agreement with measured WRS than the isotropic hardening option (see Figure 3). This could mean that the Bauschinger effect is not temperature-sensitive for carbon steels as in the case of austenitic steels, although the difference between isotropic and kinematic hardening in this case was inside the uncertainty boundaries of weld simulation. More research on this topic is required.

In the current study, a FE model for simulating multi-pass welding of austenitic stainless steel AISI 316L [17] is validated, based on measurements of WRS found in [3]. The model is then applied for a sensitivity analysis in order to define the influence of heat input, deviating from the nominal welding parameters. Moreover, sequence of the welding passes on the calculated WRS of a multi-pass butt-weld is provided. Although numerous papers exist on this subject, they are either applying out-of-date models or investigating different geometries. Finally, applied hardening models and their influence are tested. The phase changes are neglected in all the above cases, which is a standard strategy in the weld simulation of austenitic steels. The investigated material was selected for this reason, so that the influence of the investigated parameters would be directly coupled with the mechanical behaviour of the component, excluding the influence of microstructural changes. The current model will as well act as a stepping-stone, for evolving a model for the simulation of multi-pass welding from multi-phase steel in upcoming studies.

2 THEORETICAL BACKGROUND

During a FE analysis of weld simulation the above mentioned fields, the thermal, the microstructural and the mechanical have to be modelled, so that the WRS can be calculated. Commercial software ANSYS was applied for the present study [17]. The microstructural transformations are neglected in this case and therefore modelling only of the rest two fields is necessary. Temperature dependent material parameters are applied both for thermal and mechanical analyses, ensuring in this way the robust calculation of the WRS.

Modelling of the thermal problem is carried out within a transient thermal analysis. The weld heat source is applied according to the double ellipsoidal model proposed by Goldak [2]. According to Goldak the weld heat source should be modelled as the combination of the halves of two ellipsoids, with same width a and depth b, but different length dimension c. The model is described by the following Equations 1 and 2:

$$q(x,y,z,t) = \frac{6\sqrt{3} f_f Q}{abc\pi\sqrt{\pi}} e^{-3x^2/a^2} e^{-3y^2/b^2} e^{-3[z+v(\tau-t)]^2/c^2} \tag{1}$$

$$q(x,y,z,t) = \frac{6\sqrt{3} f_r Q}{abc\pi\sqrt{\pi}} e^{-3x^2/a^2} e^{-3y^2/b^2} e^{-3[z+v(\tau-t)]^2/c^2} \tag{2}$$

where f_r is the heat fraction deposited in the rear quadrant [J], f_f the heat fraction deposited in the front quadrant [J], Q the energy input rate [J/s], C the characteristic radius of flux distribution [m], v the welding source travel [m/s], t the time [s] and τ a lag factor ("phase shift"). The effective energy input rate is calculated from Equation 5:

$$Q = hVI \tag{3}$$

where V is the voltage around the weld metal arc [V], I the current of the weld metal arc [A] and h the coefficient of the weld heat-source [-]. The heat transfer problem inside the component is governed by the following differential Equation 4:

$$\rho c(\frac{\partial T}{\partial t} + v_x \frac{\partial T}{\partial x} + v_y \frac{\partial T}{\partial y} + v_z \frac{\partial T}{\partial z}) = \dot{Q}_G + \frac{\partial}{\partial x}(Kx \frac{\partial T}{\partial x}) + \frac{\partial}{\partial y}(Ky \frac{\partial T}{\partial y}) + \frac{\partial}{\partial z}(Kz \frac{\partial T}{\partial z}) \tag{4}$$

where ρ is the density [kg/m^3], c the specific heat [J/(kg K)], T the temperature [K], t the time [s], K_{xx}, K_{yy} and K_{zz} the conductivity in the element's x, y, and z directions respectively [W/(m K)], $\dot{Q}$ the heat generation rate per unit volume [W/m^3] and v_x, v_y, v_z the velocity for transport of heat in x, y, and z directions, respectively [m/s]. Finally the boundary conditions of the thermal transient analysis are the surface heat losses through convection and radiation (Equation 5).

$$\frac{q}{A} = h_f (T_s - T_b) \tag{5}$$

Where q / A is the heat flux out of the face [J/s], h_f the heat transfer coefficient [W/(m^2 K)], T_B the bulk temperature of the adjacent fluid [K] and T_S the temperature at the surface of the model [K]. Ansys' 3D solid element "solid70" is applied for the solution of the transient thermal analysis. A "live and death" procedure is followed, in order to simulate the addition of the filler material and the melting and re-solidifying of the FZ. During this procedure the conductivity of the selected elements, i.e. the elements in the weld pass in front of the moving heat source and all elements with temperature above melting, is reduced by 10^{-6}, while the specific heat and the rest thermal properties are set to zero. At each step of the transient thermal solution the temperature of each node and the sequence of alive and dead elements is saved.

Modelling of the mechanical problem is carried out within a quasi-static structural analysis. Coupling with the thermal analysis is achieved through transfer of the nodal temperature history, which was saved during the transient thermal analysis and application of the transferred temperature as body force nodal loads. Thermal strains are calculated from the temperature history based on Equation 6:

$$\varepsilon^{th} = \alpha^{se}(T)(T - T_{ref}) \tag{6}$$

where $\alpha^{se}(T)$ is the temperature-dependent coefficient of thermal expansion. Ansys' 3D solid elements "solid185" is applied for the solution of the quasi-static structural analysis. The same "live and death" sequence from the transient thermal analysis is being followed also in this part, in order to simulate the influence of the solidifying filler material in the FZ. In this type of analysis, the stiffness of the selected elements in each step is reduced by 10^{-6}, and the strains of the deactivated elements is set to zero. The further steps of the solution are based on classical finite element theory for nonlinear materials.

3 INVESTIGATED CASES

Austenitic stainless steel AISI 316L was investigated in all cases of the current work. Temperature dependent material properties of the investigated material, which were found in [19], are presented in Table 1. Temperature dependent values of the yield strength and tangent modulus of the material were found in [3] (see Figure 3). Two different components were investigated.

Component A consisted of a three-pass V-grooved butt-weld, with dimensions 700 x 700 x 8 mm. The component was identical with the welded component found in [3] and with same mechanical restraints and welding parameters (Table 2), so that a validation with the measured WRS provided by Kyriakongonas et al. [3] was made possible. Calibration of the weld heat source was carried out on a smaller, more efficient component with same weld parameters, weld geometry and plate thickness but with a length and width of 350 mm and 300 mm respectively. Thermocouple measurements on an identical component, which were found in [3], were used for the calibration. Component A was then applied for confirming earlier findings regarding appropriate hardening behaviour (isotropic or kinematic) of austenitic steels.

Component B was a five-pass X-grooved weld with dimensions 300 x 300x 10 mm. The component was assumed to be welded unrestrained and symmetry conditions along the welding line were applied. Similar weld parameters with component A were assumed for modelling component B in the investigated case H1. This case was then used as basis for the sensitivity analysis regarding the differentiated welding speed (investigated cases V1 and V2) and heat input (investigated cases Q1 and Q2), as well the influence of welding sequence (investigated cases R1 - R5) and intermediate cooling between consecutive weld-passes (investigated case C1) on the resulting WRS. The investigated components, their respective welding parameters and all the investigated cases are presented in Figure 4, Table 2 and Table 3 respectively.

4 RESULTS AND DISCUSSION

Modelling of component A was carried out, in order to validate the applied method and the provided material properties. During a successful calibration of the weld heat source through trial and error, appropriate cooling intervals and values for the coefficient of the weld heat source were selected and a satisfying agreement with the thermocouples' measurements provided by [3] was met (see Figure 5). The mechanical behaviour of component A was then modelled based on the provided temperature-dependent material parameters and both isotropic and kinematic hardening behaviours have been applied. The calculated longitudinal WRS along with the respective measured profiles are presented in Figure 5. Against initial expectations and previous findings from other authors ([14] and [15]), the option of the kinematic hardening model produced results that clearly fit better to the measured WRS. Both models produced a WRS profile that fits good with measurements away from the weld region (50mm and further) but only kinematic hardening predicted the WRS in the weld area with preciseness. In both cases the current model seem to be overestimate the width of the tensile stress region and therefore between 10 and 50 mm adjacent to the weld the agreement with measured WRS is not satisfying. Nevertheless, the overall performance was considered adequate. By taking into consideration the even better agreement provided by the FE simulation in [3], with same material models and weld parameters, their application for further investigations on component B was considered valid.

Table 1: Material properties of AISI 316L

Temperature [°C]	Conductivity [W / (m K)]	Specific Heat [kJ / (kg K)]	Density [kg / m^3]	Coefficient of Thermal Expansion x 10^6 [-]	Young's Modulus [GPa]	Poisson's Ratio [-]
20	13,3	0,47	7966	15,2	195	0,267
400	19,4	0,55	7814	17,4	172	0,322
1000	27,5	0,676	7535	19,3	100	0,229
1420	31,9	0,765	7320	20,7	10	0,223
1460	320	0,765	7320	20,7	2	0,223
3000	320	0,765	7320	20,7	2	0,223

During the investigations on Component B, both transverse and longitudinal stresses on both, top and bottom, side of the plate were taken into consideration, as the magnitude of the tensile stresses on each of this cases can have significant influence on the fatigue performance of welded joints. Figure 6 presents the results from investigations on the influence of decreased welding speed or increased heat input.

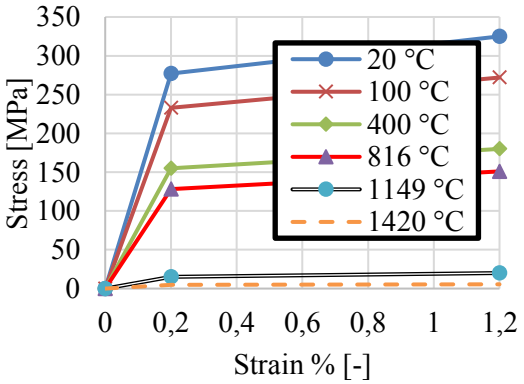

Figure 3: Stress-strain bilinear relationships at different temperature levels for AISI 316L found in [3]

Table 2: Welding parameters for the investigated models

Model	Component A	Component B (investigated case H1)
pass	1-3	1-5
voltage [V]	24	24
current [A]	180	180
welding speed [mm/s - cm/min]	5/30	5/30
welding sequence	A-B-C	A-B-C-D-E
intermediate cooling [s]	800-879-1000	none

The investigated cases are being compared with the investigated case H1. Both the reduction of welding speed and the increase of heat input lead to a beneficial reduction of the longitudinal tensile stresses on the top of the plate, with the reduction of speed at half (V2) producing tensile stresses almost 150 MPa lower than in case H1. The positive effect of the welding speed reduction is obvious also on the transverse WRS profiles on the top of the plate, although it is of a smaller magnitude, around 50 MPa. For cases V1, Q1 and Q2 no significant change is observed in the transverse WRS on the top. On the bottom of the plate (the side of the last weld-pass) all investigated cases provided similar WRS profiles with tensile stresses of the same magnitude and therefore the influence of welding speed and heat input is considered negligible. On the contrary, the application of intermediate cooling between consecutive passes in the investigated case C1 produced WRS profiles with significant increase of tensile stresses in both

longitudinal and transverse directions (see Figure 7). The effect was more profound in the case of transverse WRS on the top of the plate, where an increase of almost 150 MPa was met.

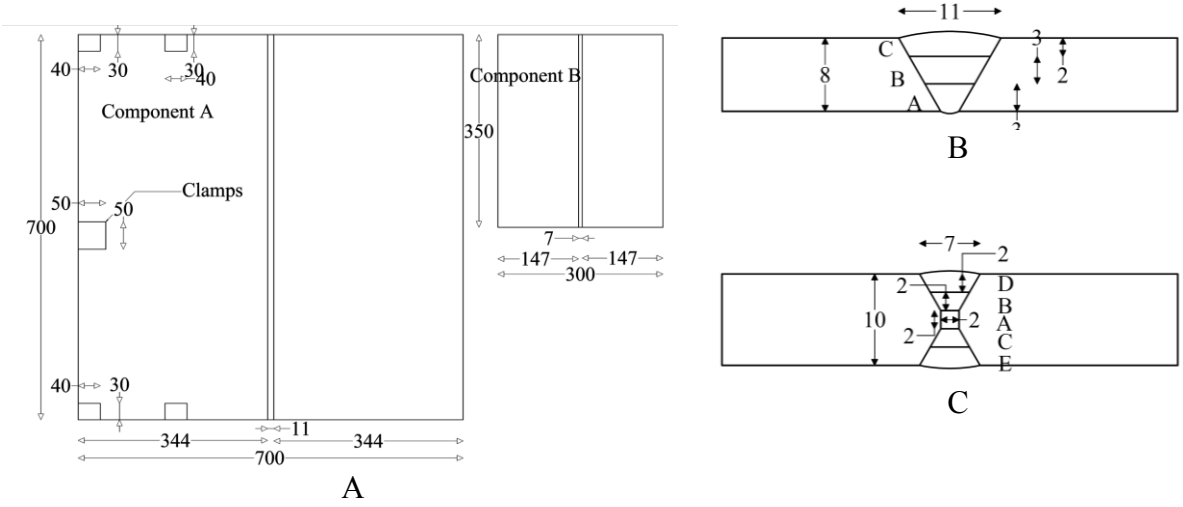

Figure 4: Investigated components – A: Plate dimensions for model A (left) model B (right) B: weld section of component A – C: weld section of component B

Table 3: Investigated cases – Weld passes marked with an apostrophe (B' etc.) are reversely welded

Investigated case	Model	Component	Investigated variable
hardening behaviour	iso	A	isotropic hardening
	kin	A	kinematic hardening
welding parameters	H1	B	welded according Table 2
	V1	B	welding speed – 25% reduced
	V2	B	welding speed – 50% reduced
	Q1	B	heat input - 25% increased
	Q2	B	heat input - 50% increased
	C1	B	intermediate cooling 600s
welding sequence	R1	B	A-B-C-D-E (identical with H1)
	R2	B	A-B'-C-D-E'
	R3	B	A-B-D-C-E
	R4	B	A-B'-D-C'-E
	R5	B	A-B-C-E-D

The results from the investigation of the influence of welding sequence are presented in Figure 8. The current analyses have shown that the anti-symmetric welding sequence A-B-C-E-D, which was modelled in case R5, had a profound effect on the tensile stress in both longitudinal and transverse directions. Maximum calculated tensile stresses on the top of the plate were 450 MPa and 160 MPa in longitudinal and transverse direction respectively, 100 MPa and 30 MPa less than in case R1. Nevertheless, the same sequence produced the highest transverse tensile stresses near the weld area on the bottom of the plate, approximately 25 MPa higher than the rest of the investigated sequences. The influence of this welding sequence on the longitudinal WRS on bottom of the plate is negligible. For the rest of the investigated sequences there was little or no improvement from the symmetric investigated case R1. As a result sequence R5 is considered to be the most advantageous, as the increase of transverse stresses is insignificant,

compared to the decrease of the tensile stresses on top of the plate and the magnitude of the maximum tensile stress is significantly lower than in the rest of the cases.

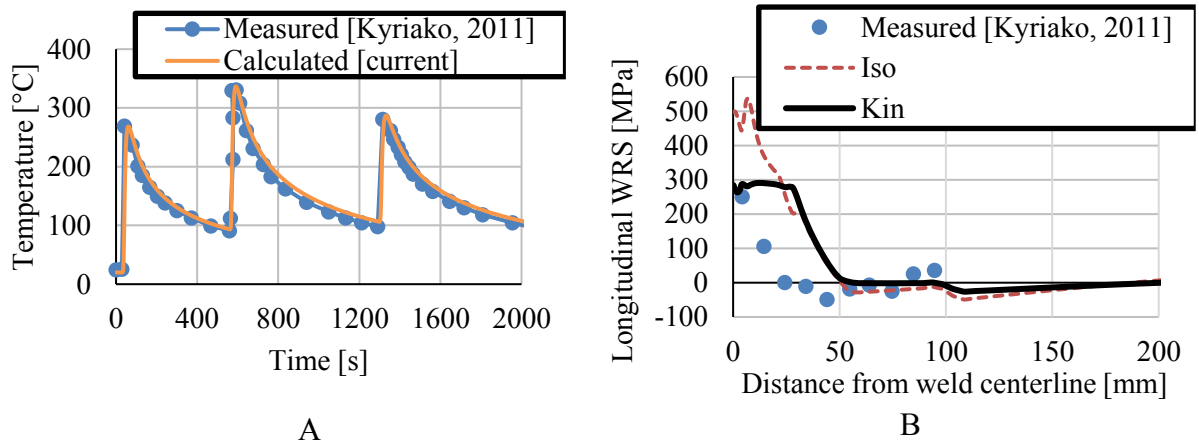

Figure 5: Modelling of component A, measured [3] and calculated profiles – A: Temperature history of node 15 mm adjacent to the weld centreline at the middle on the top of the reduced model – B: Longitudinal WRS on the top of the plate

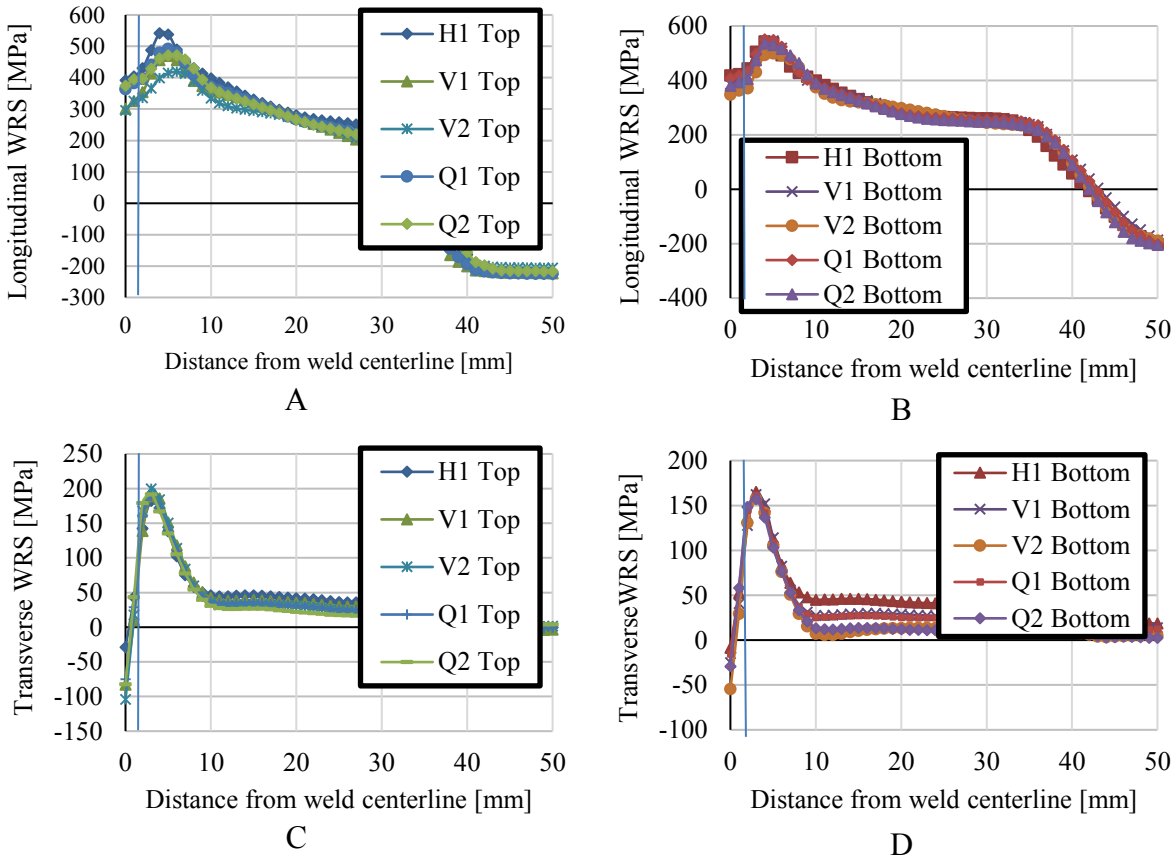

Figure 6: Influence of welding speed and heat input on WRS – A: longitudinal on top of the plate – B: longitudinal on bottom of the plate – C: transverse on top of the plate – D: transverse on bottom of the plate

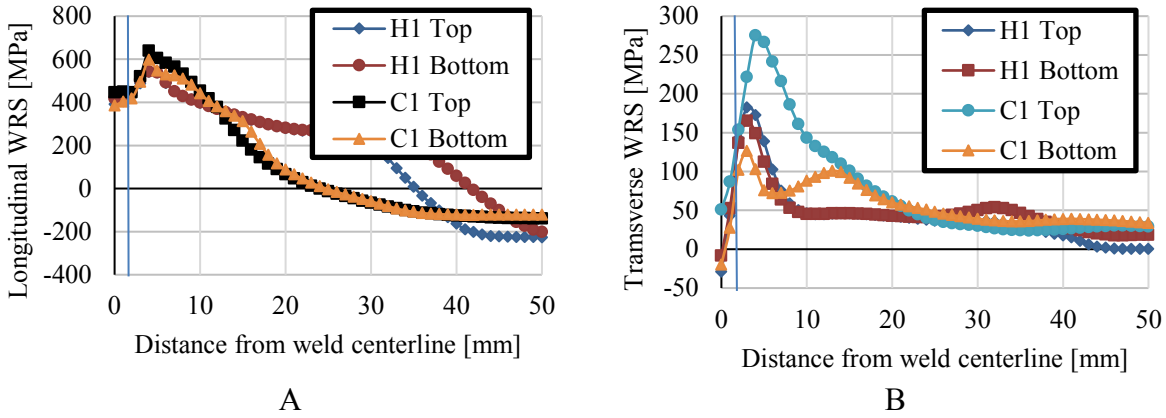

Figure 7: Influence of intermediate cooling – A: on longitudinal WRS – B: on transverse WRS

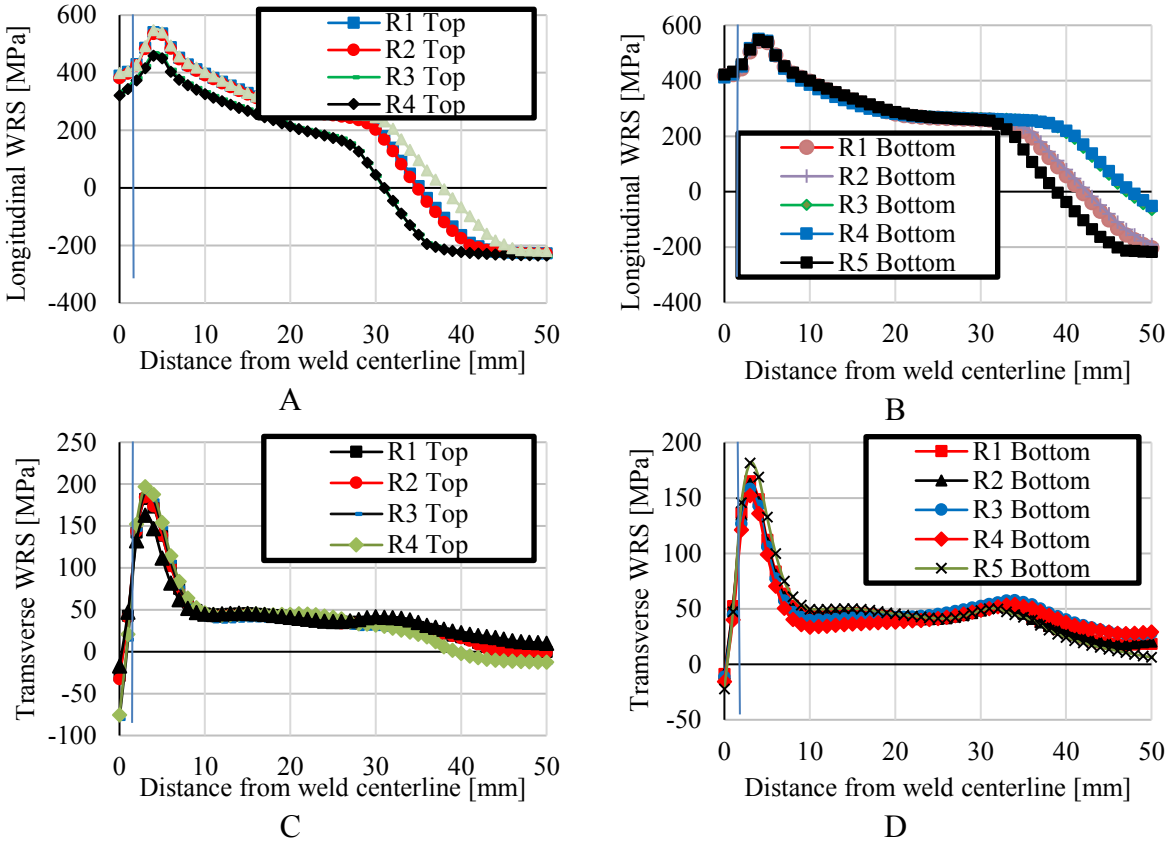

Figure 8: Influence of welding sequence on longitudinal WRS – A: longitudinal on top of the plate – B: longitudinal on bottom of the plate – C: transverse on top of the plate – D: transverse on bottom of the plate

5 CONCLUSIONS AND FUTURE WORK

A series of finite element analyses were carried out in the current paper, so that a sensitivity analysis investigating the influence of various welding parameters could be completed. The applied models were validated based on measurements of WRS found in literature. All the

investigations considered austenitic stainless steel AISI 316L and therefore, no phase transformations were take into consideration. The following safe conclusions could be drawn from the current work:

- Against initial expectations, the option of the kinematic hardening model produced results that clearly fit better to the measured WRS.
- Reduction of welding speed led to reduction of tensile WRS up to 150 MPa and in extension to an optimized predicted fatigue performance of the welded structures. Therefore, reducing welding speed in practice lies on the safe side. Similar, but less profound effect was validated when the heat input of the weld source was increased. Although the heat input rate remains equal in both cases, increase of the heat input and equivalent decrease of welding speed do not produce same WRS profile.
- Intermediate cooling between consecutive weld-passes causes a significant increase of the tensile WRS, even up to 200 MPa. Therefore, it should be avoided in the case of austenitic steels, when the magnitude of tensile stresses is under consideration. On the other hand, prolonged elevated temperatures can cause sigma phase embrittlement. For this reason, it has been "common knowledge" that austenitic steels should be welded as "cold" as possible.
- Antisymmetric welding sequence A-B-C-E-D is proved to be the optimal solution for welding X-grooved 5-pass welds from austenitic steel. A reduction of up to 100 MPa of the longitudinal tensile stresses can be achieved.
- Reverse welding of selected passes seem to have little or no effect on the final WRS, in comparison to the respective forward-only welding sequence.

All the above conclusions can be very useful for the optimization of welding process for austenitic steels. Nevertheless, they cannot be directly adopted for the case multi-phase steels, where microstructural changes can influence profoundly the calculated WRS. The microstructural changes are directly influenced by the investigated variables and further work must be carried out, in order to provide safe conclusions in their case. Finally, reasons for the incompatibility of current and past results regarding the influence of material hardening behaviour on final WRS should be investigated.

ACKNOWLEDGEMENT

The current work was carried out in the framework of the PhD Thesis of the first author [20].

REFERENCES

[1] Knoedel, P., Gkatzogiannis, S. and Ummenhofer, T. Practical aspects of welding residual stress simulation. *Journal of Constructional Steel Research* (2017) **132**:83–96.

[2] Goldak, J.A., Chakravarti, A. and Bibby, M. A new finite element model for welding heat sources. *Metall. Trans. B (1984)* **15**:299–305.

[3] Kyriakongonas, A.P., Papazoglou, V.J. and Pantelis, D.I. Complete investigation of austenitic stainless steel multi-pass welding. *Ships and Offshore Structures* (2011) **6**(1–2):127–144.

[4] Knoedel, P., Gkatzogiannis, S. and Ummenhofer T. FE simulation of residual welding stresses: Aluminium and steel structural components. Selected, peer reviewed papers from the 13th International Aluminium Conference INALCO 2016, September 21-23, 2016,

Naples, Italy. *Key Engineering Materials*, (2016) **710**:268-274, Trans Tech Publications, Pfaffikon, Switzerland.

[5] Caron, J., Heinze, C., Schwenk, C., Rethmeier, M., Babu, S.S. and Lippold J. Effect of continuous cooling transformation variations on numerical calculation of welding-induced residual stresses, *Weld. J.* (2010) 89:151-160.

[6] Gkatzogiannis, S., Knoedel, P. and Ummenhofer, T. FE welding residual stress simulation. Influence of boundary conditions and material models. EUROSTEEL 2017, September 13–15, 2017, Copenhagen, Denmark, (2017), full paper submitted.

[7] Teng, T.L., Chang, P.H. and Tseng, W.C. Effect of welding sequences on residual stresses. *Computers and Structures* (2003) **81**:273–286.

[8] Zhu, X.K. and Chao, Y.J. Effects of temperature-dependent material properties on welding simulation. *Computers and Structures* (2002) **80**:967–976.

[9] Teng, T.L. and Chang, P.H., Tseng, W.C. Effect of welding sequences on residual stresses. *Computers and Structures* (2003) **81**:273–286.

[10] Ji, S.D., Fang, H.Y., Liu, X.S. and Meng, Q.G. Influence of a welding sequence on the welding residual stress of a thick plate. *Modelling Simul. Mater. Sci. Eng.* (2005) **13**:553–565.

[11] Gannon, L., Liu, Y., Pegg, N. and Smith, M. Effect of welding sequence on residual stress and distortion in flat-bar stiffened plates. *Marine Structures* (2010) **23**:385–404.

[12] Chen, Z., Chen, Z. and Shenoi, R.A. Influence of welding sequence on welding deformation and residual stress of a stiffened plate structure. *Ocean Engineering* (2015) **106**:271-280.

[13] Liu, C., Luo, Y., Yang, M. and Fu, Q. Three-dimensional finite element simulation of welding residual stress in RPV with two J-groove welds. *Weld World* (2017) 61:151–160.

[14] Wohlfahrt, H., Nitschke-Pagel, T., Dilger, K., Siegele, D., Brand, M., Sakkiettibutra, J. and Loose, T. Residual stress calculations and measurements – Review and assessment of the IIW round robin results. R*ecommended for publication by commission X: Structural Performances of Welded Joints – Fracture Avoidance*. (2012) Doc. IIW **2224**:120-140.

[15] Mullins, J. and Gunnars J. Influence of hardening model on weld residual stress distribution. Research Report 2009:16, Inspecta Technology AB, Stockholm, Sweden, (2009).

[16] Mataya, M.C. and Carr, M.J. The Bauschinger effect in a nitrogen-strengthened austenitic stainless steel. *Materials Science and Engineering* (1983) **57**:205-222.

[17] ASTM A240/A240M-16a Standard Specification for Chromium and Chromium-Nickel Stainless Steel Plate, Sheet and Strip for Pressure Vessels and for General Applications, ASTM International, West Conshohocken, PA, 2016

[18] ANSYS® Academic Research, Release 17.2, Help System, ANSYS, Inc., (2016).

[19] Dong, P. Residual stress analyses of a multi-pass girth weld: 3-D special shell versus axisymmetric models. *Journal of Pressure Vessel Technology* (2001) **123**:207-213.

[20] Gkatzogiannis, S. PhD Thesis (in progress), KIT, Karlsruhe Institute of Technology, Steel and Lightweight Structures, 2017.

VII International Conference on Computational Methods for Coupled Problems in Science and Engineering
COUPLED PROBLEMS 2017
M. Papadrakakis, E. Oñate and B. Schrefler (Eds)

Reduction of Computation Time by Parallelization and Incorporating Co-Simulation Techniques

Jan Kraft, Bernhard Schweizer

Institute of Applied Dynamics
Technical University of Darmstadt
Otto-Berndt-Straße 2, 64287 Darmstadt, Germany
E-mail: kraft@ad.tu-darmstadt.de – Web page: www.ad.tu-darmstadt.de

Key words: Co-Simulation, Applied-Force Coupling, Dynamical Systems, Parallel Computing.

Abstract. The co-simulation methods considered here are based on the idea of splitting an overall model into different subsystems; the subsystems are then simulated as a coupled problem. Such an approach can be used advantageously for analyzing complex problems, for example the simulation of systems including different physical disciplines so that different specialized solvers have to be coupled in time domain. Another possible application of co-simulation methods, which is discussed here, concerns the parallelization of a monodisciplinary model.

1 INTRODUCTION

Co-simulation or solver coupling methods are used in various fields of applications. Examples can be found in [1] and [2]. The basic idea of co-simulation is to decompose an overall system into coupled subsystems. The formulation of the coupling conditions between the two subsystems depends on the considered problem. In the case of mechanical systems, coupling may be achieved by cutting through joints or by cutting through elements representing a physical force (torque). This leads to a coupling by reaction forces/torques [3][4] (constraint coupling) or to a connection by applied forces/torques (applied-force coupling). Co-simulation methods may further be subdivided into force/force-, force/displacement- and displacement/displacement-coupling approaches [5]. In this contribution, a force/force-decomposition approach is used and the subsystems are connected by nonlinear spring/damper-elements.

The methods presented here are weak coupling approaches, which implies that each subsystem is solved independently from the other subsystems within a macro-time step. Information (i.e. coupling variables) is only exchanged between the subsystems at certain communication-time points. The unknown coupling variables are approximated (extrapolated/interpolated) in the subsystems within a macro-time step. The separate integration of the subsystems is the crucial point for parallelizing the computation.

In this manuscript, two different numerical methods for solving the coupled problem are examined: an explicit co-simulation technique and a semi-implicit integration scheme. The semi-implicit method is based on a predictor/corrector procedure, where the corrector step is carried out only once.

2 CO-SIMULATION METHODS

To investigate the performance of the explicit and the semi-implicit co-simulation approach with regard to computation time, we use a nonlinear, large-scaled test model, which is described in the following subsection.

2.1 Nonlinear test model

One requirement for the test model is that it is straightforward to scale with respect to the number of degrees of freedom and with regard to the number of subsystems. Therefore, a series of n_K masses connected by nonlinear spring/damper-elements is used as test model.

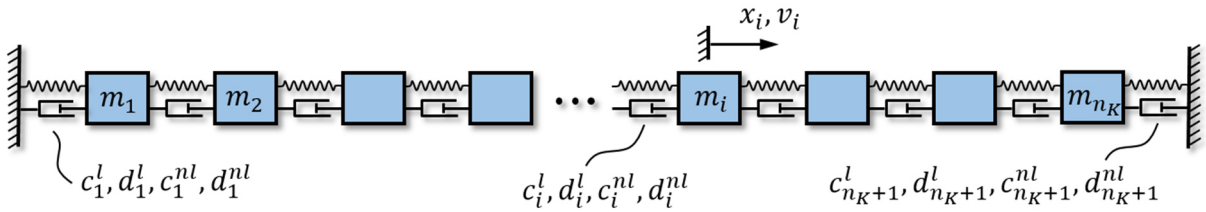

Figure 1: Nonlinear test model

Denoting the displacements of the oscillator-masses by the displacement coordinates x_i and the corresponding velocities by v_i, we obtain a system of $2n_K$ ordinary differential equations of the form

$$\begin{aligned}\dot{x}_i &= v_i \\ \dot{v}_i &= \frac{c_i^l}{m_i}(x_{i-1}-x_i) + \frac{d_i^l}{m_i}(\dot{x}_{i-1}-\dot{x}_i) + \frac{c_{i+1}^l}{m_i}(x_{i+1}-x_i) + \frac{d_{i+1}^l}{m_i}(\dot{x}_{i+1}-\dot{x}_i) \\ &\quad + \frac{c_i^{nl}}{m_i}(x_{i-1}-x_i)^3 + \frac{d_i^{nl}}{m_i}(\dot{x}_{i-1}-\dot{x}_i)^3 + \frac{c_{i+1}^{nl}}{m_i}(x_{i+1}-x_i)^3 + \frac{d_{i+1}^{nl}}{m_i}(\dot{x}_{i+1}-\dot{x}_i)^3\end{aligned} \tag{1}$$

with $i = 1 \ldots n_K$. We assume that the chain is fixed at both ends ($x_0 = \dot{x}_0 = x_{n_K+1} = \dot{x}_{n_K+1} = 0$). The system parameters are the masses m_i, the linear stiffness coefficients c_i^l, the linear damping coefficients d_i^l, the nonlinear stiffness coefficients c_i^{nl} and the nonlinear damping coefficients d_i^{nl}. The values of the parameters used for the simulations are given in Table 1.

Table 1: Model parameters

c_i^l	$1.0e7$
d_i^l	1.0
c_i^{nl}	$1.0e9$
d_i^{nl}	$1.0e$-4
m_i	1.0

2.2 Decomposition of the test model

As mentioned above, the overall system is split into coupled subsystems by a force/force-decomposition approach [5]. This is achieved by cutting through certain nonlinear spring/damper-elements and by using the corresponding forces as coupling variables. The number of subsystems n is arbitrary, but usually it is much smaller than the number n_K of degrees of freedom of the overall system.

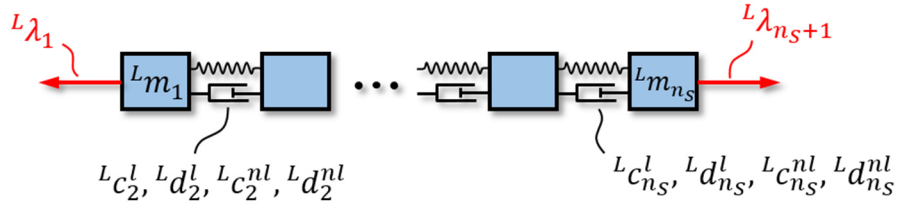

Figure 2: Arbitrary subsystem L

The set of n_S equations of motion for a subsystem reads as

$$
\begin{aligned}
{}^L\dot{x}_j &= {}^Lv_j \\
{}^L\dot{v}_j &= \frac{{}^Lc_j^l}{{}^Lm_j}\left({}^Lx_{j-1} - {}^Lx_j\right) + \frac{{}^Ld_j^l}{{}^Lm_j}\left({}^L\dot{x}_{j-1} - {}^L\dot{x}_j\right) + \frac{{}^Lc_{j+1}^l}{{}^Lm_j}\left({}^Lx_{j+1} - {}^Lx_j\right) \\
&\quad + \frac{{}^Ld_{j+1}^l}{{}^Lm_j}\left({}^L\dot{x}_{j+1} - {}^L\dot{x}_j\right) + \frac{{}^Lc_j^{nl}}{{}^Lm_j}\left({}^Lx_{j-1} - {}^Lx_j\right)^3 + \frac{{}^Ld_j^{nl}}{{}^Lm_j}\left({}^L\dot{x}_{j-1} - {}^L\dot{x}_j\right)^3 \\
&\quad + \frac{{}^Lc_{j+1}^{nl}}{{}^Lm_j}\left({}^Lx_{j+1} - {}^Lx_j\right)^3 + \frac{{}^Ld_{j+1}^{nl}}{{}^Lm_j}\left({}^L\dot{x}_{j+1} - {}^L\dot{x}_j\right)^3 - \frac{{}^L\lambda_j}{{}^Lm_j} + \frac{{}^L\lambda_{j+1}}{{}^Lm_j}
\end{aligned}
\tag{2}
$$

with $j = 1 \ldots n_S$ and ${}^Lc_1^l = {}^Ld_1^l = {}^Lc_1^{nl} = {}^Ld_1^{nl} = {}^Lc_{n_S+1}^l = {}^Ld_{n_S+1}^l = {}^Lc_{n_S+1}^{nl} = {}^Ld_{n_S+1}^{nl} = 0$. The coupling forces are denoted by ${}^L\lambda_j$ and ${}^L\lambda_{j+1}$; they are only required for the coupling bodies ($j = 1$ and $j = n_S$) and are set to zero for the remaining bodies (${}^L\lambda_2 = \cdots = {}^L\lambda_{n_S} = 0$).

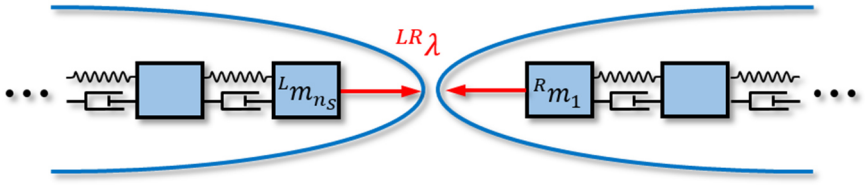

Figure 3: Coupling of two adjacent subsystems L and R

The coupling condition for two adjacent subsystems L and R reads (assuming that body n_S of subsystem L is coupled with body 1 of subsystem R)

$$
\begin{aligned}
{}^{LR}g := {}^{LR}\lambda &- {}^{LR}c_c^l\left({}^Rx_1 - {}^Lx_{n_S}\right) - {}^{LR}d_c^l\left({}^R\dot{x}_1 - {}^L\dot{x}_{n_S}\right) - {}^{LR}c_c^{nl}\left({}^Rx_1 - {}^Lx_{n_S}\right)^3 \\
&- {}^{LR}d_c^{nl}\left({}^R\dot{x}_1 - {}^L\dot{x}_{n_S}\right)^3 = 0
\end{aligned}
\tag{3}
$$

with the coupling force ${}^{LR}\lambda = {}^L\lambda_{n_S+1} = {}^R\lambda_1$, the coupling parameters ${}^{LR}c_c^l$, ${}^{LR}d_c^l$, ${}^{LR}c_c^{nl}$ and ${}^{LR}d_c^{nl}$ and the state variables of the two coupling bodies.

2.3 Explicit co-simulation scheme

To solve the decomposed system as a coupled problem by using an explicit co-simulation method, the time interval is discretized with a macro-time grid. The macro-step size h_{mac} is chosen to be constant. Within an arbitrary macro-step from T_N to $T_{N+1} = T_N + h_{mac}$, each subsystem is integrated using extrapolation (interpolation) polynomials to approximate the coupling forces. After the subsystem integrations, the resulting states of the coupling bodies are substituted into the coupling condition to obtain the coupling force at the new macro-time point T_{N+1} (update of the coupling variables). The explicit co-simulation method has the advantage that a repetition of the macro-step is not necessarily required if a constant macro-step size is used. This may be a crucial point, if commercial subsystem solvers are used which often do not allow solver reintialization.

2.4 Semi-implicit co-simulation scheme

A detailed description of the implemented semi-implicit co-simulation procedure can be found in [6]. The basics of the approach are only briefly explained next.

The macro-time grid is assumed to be equidistant (macro-step size $h_{mac} = const.$). As mentioned above, the presented semi-implicit co-simulation method is based on a predictor/corrector approach with only one corrector step. An arbitrary co-simulation step from T_N to T_{N+1} is explained in the following subsections.

2.4.1 Predictor step

Within the predictor step, each subsystem is integrated twice from T_N to T_{N+1}: firstly with predicted (extrapolated) coupling variables (coupling forces) λ^p (${}^{LR}\lambda^p = {}^{L}\lambda^p_{n_s+1} = {}^{R}\lambda^p_1$) and secondly with perturbed predicted coupling variables λ^Δ (${}^{LR}\lambda^\Delta = {}^{L}\lambda^\Delta_{n_s+1} = {}^{R}\lambda^\Delta_1$). Note that for the reason of a concise representation, the subsystem indeces have been ommitted. The perturbed coupling variables are obtained by adding a small, user-defined perturbation to the predicted coupling variables, i.e. $\lambda^\Delta = \lambda^p + \Delta\lambda$.

With the predicted state variables $\boldsymbol{z}^p$ and the perturbed predicted states $\boldsymbol{z}^\Delta$ at T_{N+1}, the partial derivatives of the states with respect to the coupling variables can be approximated by finite differences

$$\left.\frac{\partial \boldsymbol{z}_c}{\partial \lambda}\right|_{\lambda^p} = \lim_{\Delta\lambda \to 0} \frac{\boldsymbol{z}_c(\lambda^p + \Delta\lambda) - \boldsymbol{z}_c(\lambda^p)}{\Delta\lambda} \approx \frac{\boldsymbol{z}_c^\Delta - \boldsymbol{z}_c^p}{\Delta\lambda}. \tag{4}$$

Note that partial derivatives only have to be calculated for the coupling bodies.

2.4.2 Corrector step

The approximated partial derivatives obtained in the predictor step are utilized to compute improved (corrected) coupling variables. Therefore, the coupling condition (3) is considered as a function of the coupling variable λ at T_{N+1} and expanded in a Taylor series. Choosing λ^p

as expansion point and neglecting higher-order terms $\mathcal{O}(\lambda^2)$, one obtains the linearized coupling condition

$$
\begin{aligned}
g^{lin}(\lambda) &:= g(\lambda^p) + \left.\frac{\partial g}{\partial \lambda}\right|_{\lambda^p} (\lambda - \lambda^p) \\
&= \lambda^p - c_c^l\left({}^R x_1^p - {}^L x_{n_s}^p\right) - d_c^l\left({}^R v_1^p - {}^L v_{n_s}^p\right) - c_c^{nl}\left({}^R x_1^p - {}^L x_{n_s}^p\right)^3 \\
&\quad - d_c^{nl}\left({}^R v_1^p - {}^L v_{n_s}^p\right)^3 \\
&\quad + \left[1 - c_c^l\left(\left.\frac{\partial {}^R x_1^p}{\partial \lambda}\right|_{\lambda^p} - \left.\frac{\partial {}^L x_{n_s}^p}{\partial \lambda}\right|_{\lambda^p}\right) - d_c^l\left(\left.\frac{\partial {}^R v_1^p}{\partial \lambda}\right|_{\lambda^p} - \left.\frac{\partial {}^L v_{n_s}^p}{\partial \lambda}\right|_{\lambda^p}\right)\right. \\
&\quad -3\, c_c^{nl}\left({}^R x_1^p - {}^L x_{n_s}^p\right)^2\left(\left.\frac{\partial {}^R x_1^p}{\partial \lambda}\right|_{\lambda^p} - \left.\frac{\partial {}^L x_{n_s}^p}{\partial \lambda}\right|_{\lambda^p}\right) \\
&\quad \left. -3\, d_c^{nl}\left({}^R v_1^p - {}^L v_{n_s}^p\right)^2\left(\left.\frac{\partial {}^R v_1^p}{\partial \lambda}\right|_{\lambda^p} - \left.\frac{\partial {}^L v_{n_s}^p}{\partial \lambda}\right|_{\lambda^p}\right)\right](\lambda - \lambda^p) = 0 \ .
\end{aligned}
\tag{5}
$$

Solving equation (5) for the coupling variable λ yields the corrected coupling force λ^c. In general, the predicted state variables and the predicted coupling force will not fulfill the coupling condition. The corrected coupling force (together with the corrected state variables), however, fulfills at least the linearized coupling condition (5). The subsystem integration within the corrector step is carried out by interpolating the coupling variables and making use of the corrected coupling forces λ_c.

The corrected state variables together with the corrected coupling force will in general not fulfill the nonlinear coupling conditions. To achieve consistent coupling forces, an update of the coupling forces at T_{N+1} is useful. Therefore, the corrected state variables of the coupling bodies are substituted into the coupling condition (3) in order to calculate updated coupling forces.

2.5 Subsystem solver

The subsystems are solved with the IDA solver from the SUNDIALS (Suite of Nonlinear and Differential/Algebraic Equation Solvers) package [7]. This implicit DAE solver is based on a variable-order variable-coefficient BDF implementation combined with either direct (sparse) or iterative methods for solving the linear system within the Newton iteration. For the present studies, the direct sparse linear solver is used.

2.6 Parallelized computation

Within a macro-step, each subsystem is integrated independently. Exchange of information takes only place before or after the integration processes. Therefore, all subsystems can be solved in parallel. The simulations have been carried out on a cluster so that all subsystem integrations could be fully parallelized.

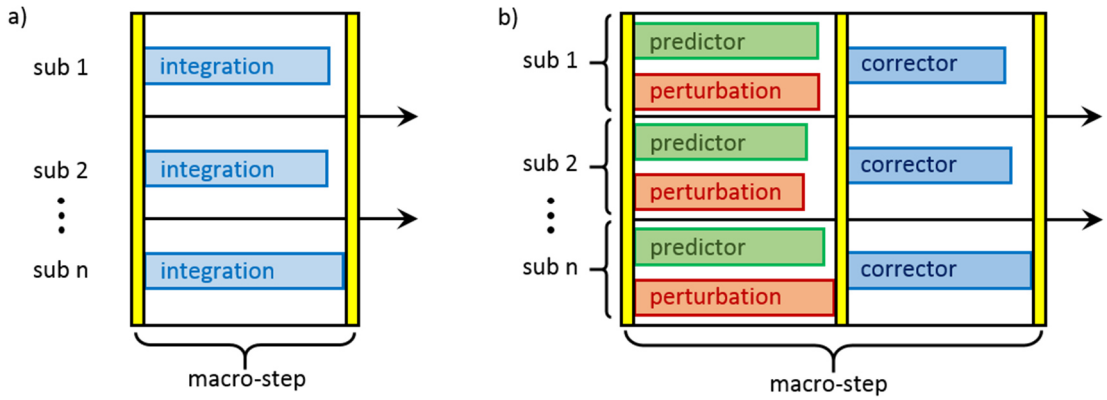

Figure 4: Parallelization scheme: a) explicit co-simulation and b) semi-implicit co-simulation

Applying a parallel implementation, the simulation time is usually strongly reduced. The computation time for the co-simulation can be estimated by

$$T_{cos}^{(expl)} \approx \frac{T_{mon}}{n^P} + C^{(expl)} \quad \text{or} \quad T_{cos}^{(semi)} \approx 2\frac{T_{mon}}{n^P} + C^{(semi)} \,, \tag{6}$$

where T_{mon} denotes the computation time of the monolithic model and n the number of subsystems. P represents the scaling factor of the computation time of the multibody implementation with respect to the number of degrees of freedom. For typical multibody systems, the value of P is between one and three, depending on the formulation of the equations of motion and the solving strategy. The overhead caused by the synchronization of parallel threads and additional calculations due to the co-simulation approach (e.g. solving equations (4) and (5) for the semi-implicit method) is summarized in the parameter C. The formula for T_{cos} implies the assumption that the overall system is split into similar subsystems so that the integration times for the different subsystems are similar.

3 SIMULATION RESULTS

In order to compare the co-simulation results with a reference solution, the normalized root mean square error (NRMSE) is computed for the state variables of the coupling bodies. The reference solution has been obtained by solving the monolithic model with a relative and absolute error tolerance of $1.0e\text{-}12$.

3.1 Convergence Analysis

The convergence behavior of the co-simulation methods is investigated by varying the (constant) macro-step size and by evaluating the local error of the coupling bodies. The test model used for the convergence analysis consists of $n_K = 144$ bodies and it is split into $n = 48$ equally sized subsystems. The model parameters are listed in Table 1. The analyses have been carried out for different approximation orders k of the coupling force. Also, two different error tolerances of the subsystem solver have been analyzed.

Fig. 5 shows the local error of the coupling bodies on position level. Two different subsystem error tolerances have been used, namely $1.0e$-12 (a) and $1.0e$-6 (b). The local

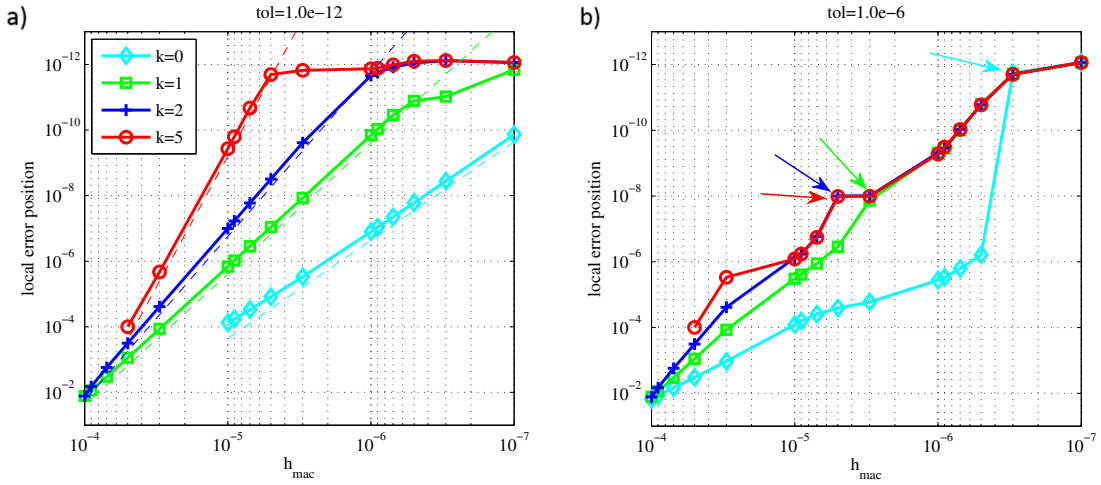

Figure 5: Convergence analysis for the semi-implicit co-simulation with different subsystem error tolerances: a) $1.0e$-12 and b) $1.0e$-6

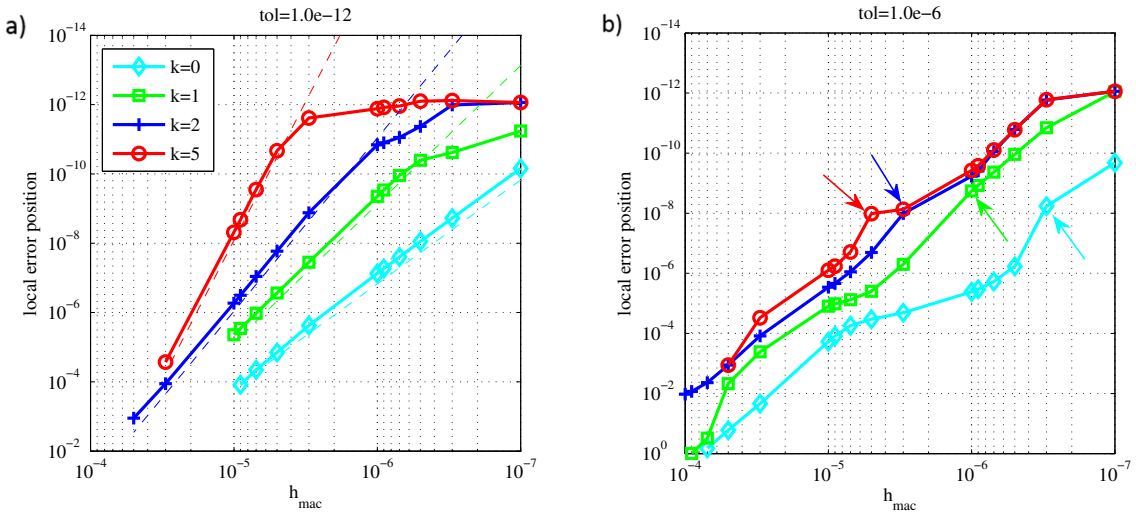

Figure 6: Convergence analysis for the explicit co-simulation with different subsystem error tolerances: a) $1.0e$-12 and b) $1.0e$-6

error of the co-simulation with the subsystem error tolerance $1.0e$-12 shows a convergence order of $\mathcal{O}(h_{mac}^{k+3})$. Errors with a magnitude of less than $1.0e$-12 are not resolved here because of the limited accuracy of the reference solution ($\text{tol}_{ref} = 1.0e$-12). The local error of the velocities (not shown here) converges with $\mathcal{O}(h_{mac}^{k+2})$. The results on the right hand side of Fig. 5 are influenced by inaccuracies of the subsystems solver. For small macro-step sizes, the order of interpolation becomes less relevant, because the subsystem solver takes usually only one integration step within each macro-step. The arrows indicate the point at which the macro-steps are of the same magnitude as the micro-steps (subsystem solver steps). Since the micro-step size is limited by the macro-step size here, the subsystem accuracy increases for small macro-step sizes.

The explicit co-simulation method shows a similar convergence behavior (Fig. 6) as the semi-implicit co-simulation approach.

3.2 Analysis of the computation time

The benefit of a parallel implementation with a co-simulation strategy can clearly be seen in the simulation of large-scaled models. Fig. 7 shows the computation times of models with a varying number of degrees of freedom; the plot has been generated with an explicit co-simulation method. The coupling forces were approximated by polynomials of order two. The co-simulation was carried out using a different number of subsystems. The black dashed line shows the resulting computation time of a monolithic simulation. The macro-step size was set

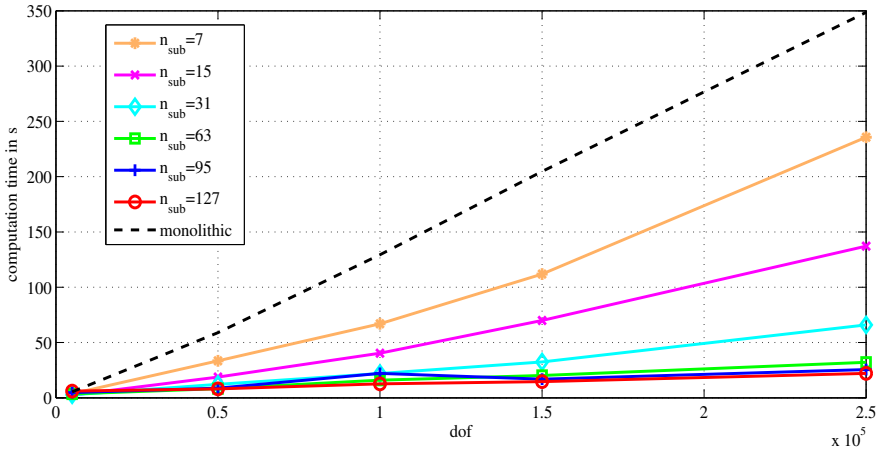

Figure 7: Computation time, explicit co-simulation

to $5.0e$-6 so that the numerical error of the co-simulation is of the same magnitude as the error of the monolithic simulation. Because of the simple structure of the test model, the system matrix is very sparse. Therefore, the computation time scales almost linear with the number of degrees of freedom. The curves in Fig. 7 show that a co-simulation with seven subsystems reduces the computation time by over 33% compared to the monolithic simulation. A co-simulation with 127 subsystems turns out to be 16 times faster than the monolithic simulation. In a further study, not presented here in detail, a model with 2 million degrees of freedom was analyzed. Applying a semi-implicit co-simulation with 287 subsystems reduced the computation time by a factor of 120 compared to the monolithic simulation.

4 CONCLUSIONS

An explicit and a semi-implicit co-simulation approach have been used in order to parallelize a nonlinear dynamical model. The convergence behaviour of the two co-simulation methods has been investigated. It has been shown that the parallel implementation based on a solver coupling approach may significantly reduce the computation time compared to a monolithic model without increasing the numerical error markedly.

REFERENCES

[1] Ambrosio, J.; Pombo, J.; Pereira, M.; Antunes, P.; Mosca, A.: "A computational procedure for the dynamic analysis of the catenary-pantograph interaction in high-speed trains", *Journal of Theoretical and Applied Mechanics*, 50/3, pp. 681-699, Warsaw, 2012.

[2] M. Naya, J. Cuadrado, D. Dopico, U. Lugris. An Efficient Unified Method for the Combined Simulation of Multibody and Hydraulic Dynamics: Comparison with Simplified and Co-Integration Approaches. *Archive of Mechanical Engineering*, Vol. LVIII, pp. 223–243, 2011.

[3] Kübler, R.; Schiehlen, W.: "Two methods of simulator coupling", *Mathematical and Computer Modelling of Dynamical Systems*, Vol. 6, pp. 93-113, 2000.

[4] Arnold, M.: "Stability of sequential modular time integration methods for coupled multibody system models", *Journal of Computational and Nonlinear Dynamics*, Vol. 5, pp. 1-9, 2010.

[5] Schweizer, Bernhard, Pu Li, and Daixing Lu. "Explicit and Implicit Cosimulation Methods: Stability and Convergence Analysis for Different Solver Coupling Approaches." *Journal of Computational and Nonlinear Dynamics* 10.5 (2015): 051007.

[6] Schweizer, B.; Lu, D.: "Semi-implicit co-simulation approach for solver coupling." *Archive of Applied Mechanics* 84.12: 1739-1769, 2014.

[7] Hindmarsh, Alan C and Brown, Peter N and Grant, Keith E and Lee, Steven L and Serban, Radu and Shumaker, Dan E and Woodward, Carol S, and A. Collier: "SUNDIALS: Suite of nonlinear and differential/algebraic equation solvers", *ACM Transactions on Mathematical Software (TOMS)*, Vol. 31, No. 3, 2005.

VII International Conference on Computational Methods for Coupled Problems in Science and Engineering
COUPLED PROBLEMS 2017
M. Papadrakakis, E. Oñate and B. Schrefler (Eds)

SOLVING AN INVERSE COUPLED CONJUGATE HEAT TRANSFER PROBLEM BY AN ADJOINT APPROACH

OLUWADAMILARE R. IMAM-LAWAL*, TOM VERSTRAETE* AND JENS-DOMINIK MÜLLER*

* School of Engineering and Materials Science.
Queen Mary, University of London. Mile End Road, E1 4NS, London, UK.
e-mail: o.r.imam-lawal@qmul.ac.uk, t.verstraete@qmul.ac.uk, j.mueller@qmul.ac.uk

Key words: Conjugate heat transfer, coupled, adjoint methods, inverse problems

Abstract. A framework for obtaining adjoint gradients for coupled conjugate heat transfer problems is presented. The framework is tailored to partitioned approaches in which separate solvers are used for the fluid and solid domains. The exchange of sensitivities between adjoint fluid and solid solvers is necessary in order to obtain gradients and how this is achieved is described. The effectiveness of the procedure is demonstrated by solving a conjugate heat transfer problem using a gradient based approach. The presented method can be extended to sensitivity analysis of multidisciplinary problems where both solvers offer adjoint derivatives.

1 INTRODUCTION

Conjugate Heat Transfer (CHT) describes the process of transferring heat between a fluid and solid and is ubiquitous in engineering applications, e.g the design of modern turbine blades, water cooling of combustion engines, and the heating of vehicles in hypersonic flow [1, 2].

CHT problems may be solved using a monolithic approach in which both fluid and solid equations are solved simultaneously by a single solver. Typically however the segregated or partitioned approach is adopted where separate solvers for the fluid and structure are loosely coupled through boundary conditions. These conditions need to be updated iteratively until the temperature and heat flux are continuous between the two domains [3]. One advantage of the partitioned approach is the flexibility of using different existing solvers for both domains [2, 3].

In this paper, we investigate an inverse heat transfer problem over a flat plate, in which the temperature on the bottom of the flat plate needs to be inferred from the temperature obtained at the interface between the flat plate and the fluid. Several examples of inverse CHT problems exist, however these problems are usually simplified into either inverse

conduction [4, 5] or convection problems [6, 7, 8]. Ahamad and Balaji [9] consider both conduction and convection in their partitioned inverse problem. However, the problem is solved using artificial neural networks. To the authors knowledge, there exist very few inverse problems considering both conduction and convection which are solved with both a partitioned and gradient based approach.

The inverse problem is solved by formulating an optimization problem, which allows the use of classical direct methods to solve the physics involved. Here we use a partitioned method to predict the interface wall temperature starting from a guessed bottom temperature, while a gradient based method is used to reduce the deviation of this interface wall temperature with the desired one. The gradients of the objective w.r.t the control, i.e. the temperature specified on the bottom of the flat plate, are computed using an adjoint approach. Methods for the computation of multidisciplinary gradients have been proposed in [10, 11] and these methods are applied to two loosely coupled solvers leading to a fixed-point formulation of the adjoint system.

This paper is organised as follows: Section 2 first describes the direct problem, relevant equations, and the coupling procedure. The results of the direct problem are then presented and compared to an analytic solution to demonstrate the accuracy of the coupling procedure. Section 3 then describes the inverse problem, the derivation of adjoint gradients for the partitioned approach, and verification of the obtained gradients. The gradients are then used to solve the inverse problem using the steepest descent method. Conclusions are discussed in section 4.

2 DIRECT PROBLEM

The conjugate heat transfer problem to be considered in this work is the laminar flow over a flat plate with finite thickness. The free stream flow temperature is T_∞, while the bottom on the plate is maintained at a temperature T_b. Consequently, there is conjugate heat transfer at the interface between the solid plate and the fluid. The aim of the direct problem is to accurately compute the wall temperature T_w at the interface between the fluid and solid, which is unknown a priori and can only be computed by considering the coupled problem.

The fluid domain is governed by the Navier-Stokes equations for steady, laminar flow:

$$\frac{\partial U}{\partial t} + \frac{\partial F^j}{\partial x_j} = \frac{\partial G^j}{\partial x_j}. \tag{1}$$

where t denotes pseudo time and x_j, $j = 1, 2, 3$ are the cartesian coordinates. The sate vectors U, and the inviscid and viscous flux vectors F^j and G^j are defined as

$$U = \begin{bmatrix} \rho \\ \rho v_i \\ \rho e \end{bmatrix}, F^j = \begin{bmatrix} \rho v_j \\ \rho v_i v_j + p\delta_{ij} \\ (\rho e + p)v_j \end{bmatrix}, G^j = \begin{bmatrix} 0 \\ \tau_{ij} \\ v_j \tau_{ij} - q_j \end{bmatrix}. \tag{2}$$

where, ρ, p and v are the fluid density, pressure and velocity respectively, e the internal

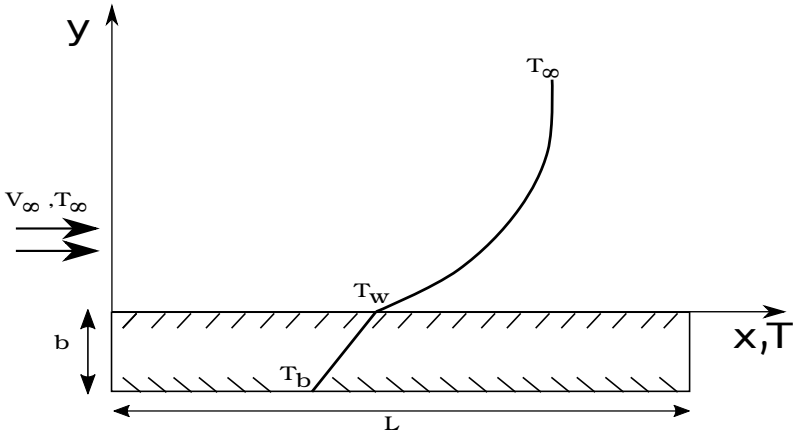

Figure 1: Description of the direct problem.

energy per unit mass, τ_{ij} the viscous stress, and q_j the heat flux. The solid domain is governed by Fourier's law

$$\lambda_s \nabla^2 T = 0, \tag{3}$$

where λ_s is the conductivity of the plate. The values of geometry, boundary conditions, and the Reynolds number of the case are shown in table 1.

Table 1: Table of parameters

Parameter	Value	units
b	0.01	m
L	0.2	m
M_∞	0.1	
P_∞	$1.03 \cdot 10^5$	Pa
T_∞	1000	K
λ_s	0.5555	$\mathrm{W}m^{-1}K^{-1}$
Re_L	$1.132 \cdot 10^5$	

2.1 Coupling method

The problem is solved with a partitioned approach in which separate solvers are used for both domains and where boundary conditions are exchanged at each iteration to achieve continuity of temperature and heat flux across the domains. Different coupling methods exist depending on which boundary conditions are exchanged between both domains. In this work, we use the temperature forward flux back (TFFB) method [12], in which the

wall heat flux distribution, q, is imposed as a boundary condition to the fluid domain, which after invoking the fluid solver $\mathbf{F}$ results in a wall, resulting in a wall temperature distribution, T (see equation 4). This temperature is subsequently imposed as boundary condition on the solid domain and the solid conduction solver, $\mathbf{S}$, then provides an updated heat flux distribution. This loop is continued until there is no change in the boundary conditions exchanged by both solvers.

$$\begin{aligned} T^i &= \mathbf{F}(q^i), \\ q^{i+1} &= \mathbf{S}(T^i). \end{aligned} \tag{4}$$

2.2 Simulation setup

The fluid domain is solved using the STAMPS flow solver, a vertex centered, finite volume solver, which solves the 3-D compressible RANS equation using unstructured grids. A second order accurate spatial discretisation is used with JT-KIRK implicit time stepping and automatic CFL ramping [13]. Two different fluid meshes are used to solve the direct problem in order to carry out a grid independence study. The coarser mesh is shown in Fig. 2 and details on the number of nodes in both meshes are shown in Table 2. The flat plate starts at position x=0 and ends at position x=0.2. The boundary conditions are also indicated in Fig. 2. A small inlet piece is added to the numerical domain in front of the flat plate to avoid inference of the boundary conditions on the results.

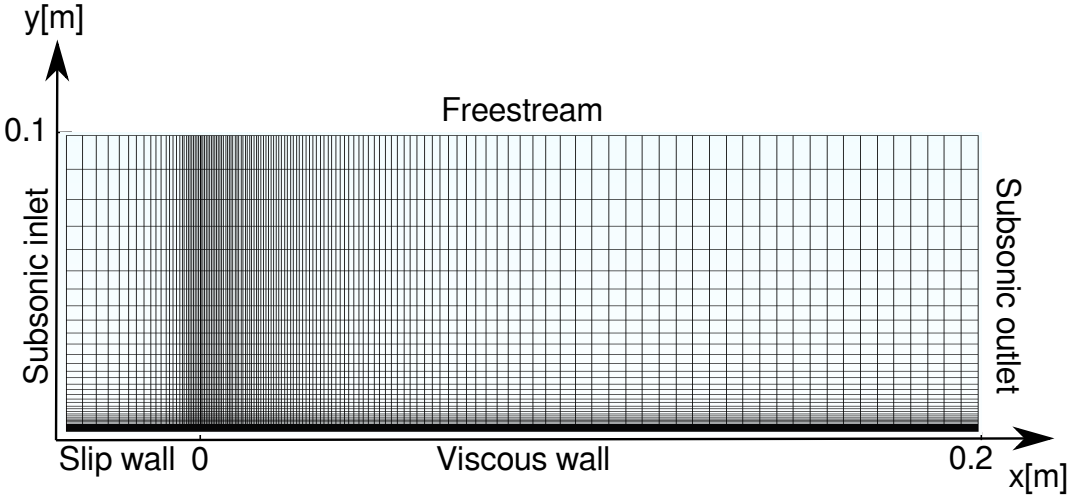

Figure 2: Mesh 1 and fluid simulation set up.

The solid domain is solved using a second order central spatial discretization and explicit time integration is achieved using a first order Euler scheme. A node-centred, structured grid with matching nodes at the interface between the fluid and solid domains is used to avoid interpolation during the exchange of boundary conditions, but in general the coupling procedure would allow for non-matching grids at the interface.

Table 2: Table showing the number of grid points in each part of the mesh

Mesh	Slip wall	Viscous wall	Fluid height
Mesh 1	24	113	97
Mesh 2	48	226	194

2.3 Direct problem results

The coupling procedure is first validated against the Luikov analytic solution for differential heat transfer to ensure the direct CHT problem is solved accurately. A comparison of the obtained streamwise wall temperature and the analytic temperature profile derived by Luikov [14] are shown in Fig. 3a. To check the convergence of the coupling procedure, we define as residual as

$$Res = \sqrt{\sum_{j=1}^{nNodes} (T^{i}_{jNode} - T^{i-1}_{jNode})^2}, \tag{5}$$

where i denotes the coupling iteration. The plot of the residual is shown in Fig. 3b.

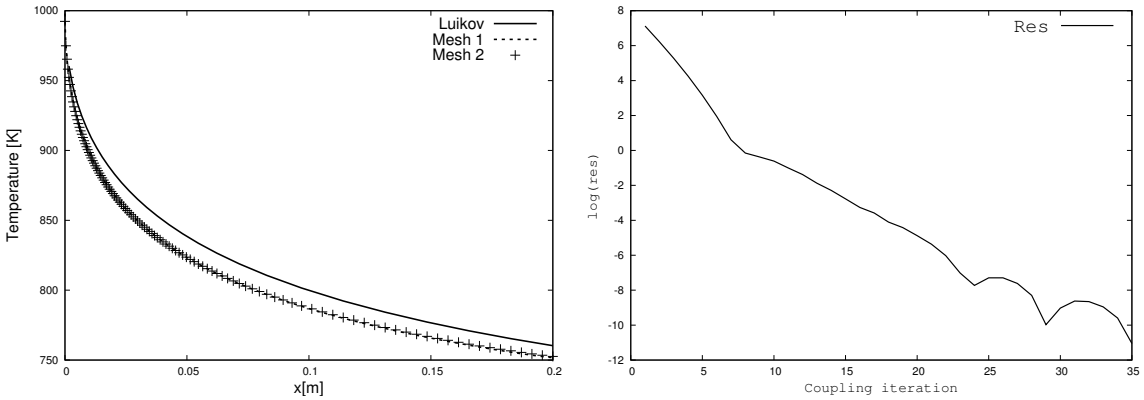

(a) Obtained T_w with $T_b = 600$ K. (b) Convergence of coupling iterations.

Figure 3: Temperature distribution and residual convergence plots of the direct solution.

The obtained temperature distribution shows good agreement with the analytic profile. The discrepancy between the obtained and the analytic temperatures may be because the Luikov solution is only an approximate solution where lateral heat transfer in the solid is not modeled. The results for both meshes also show grid convergence, therefore, in order to reduce the computational cost, Mesh 1 is used to solve the inverse problem.

3 INVERSE PROBLEM

In the inverse problem we seek the bottom temperature T_b which results in the best match for a given the interface wall temperature T_w. We define an objective function (J) as the difference between the given interface temperature (T_{target}) and the obtained interface temperature (T_x) for an estimated bottom temperature ($\tilde{T}_b$).

$$J = \frac{1}{2}\int_0^L (T_{target} - T_x)^2 dx. \tag{6}$$

The objective function depends implicitly on the bottom temperature T_b through the solution of the coupled problem. Each node at the bottom of the plate has an independent value of T_b specified as boundary condition, and is used in this work as a control variable (α) that needs to be changed to drive J to zero. As a result, the control variable α in the discrete problem is an array of size N, being 113 in the present work with Mesh 1.

The objective is hence to minimise equation (6) subject to the constraints of satisfying both the state equations of both domains (equations 1 - 3) and the convergence of the partitioned coupling scheme Eqn. (4) which we can rewrite at steady state in residual form:

$$\begin{aligned} R_f = &\quad T_w^\infty - \mathbf{F}(q_w^\infty) &= 0, \\ R_s = &\quad \mathbf{S}(T_w^\infty) - q_w^\infty &= 0, \end{aligned} \tag{7}$$

where the superscript ∞ denotes the final coupling iteration.

3.1 Minimisation problem

The inverse problem can be solved using a gradient based approach by driving the gradient of the objective w.r.t control variables to zero. Finite differences may be used to obtain the required gradients, however, the accuracy of the method is dependent on the step size, where a too large step size results in truncation errors due to the non-negligible higher order terms, and a too small step size results in numerical imprecision due to round off errors. Furthermore, the coupling algorithm would need to be run as many times we have control variables to obtain the sensitivity with respect to each control parameter.

Alternatively, both the fluid and solid solvers as well as the coupling procedure can be differentiated to obtain the gradients. The gradient of the objective function (sensitivity) w.r.t the control variables, α, is given as

$$\begin{aligned} \frac{dJ}{d\alpha} &= \int_0^L (T_{target} - T_w)\frac{dT_x}{d\alpha}dx, \\ &= -\sum_{j=1}^{N}(T_{target} - T_w)\frac{dT_x}{d\alpha}, \\ &= g^T u, \end{aligned} \tag{8}$$

where

$$\begin{aligned} g_i = &\quad T_{target_i} - T_{x_i} \quad \text{(column vector)}, \\ u_i = &\quad \frac{dT_{x,i}}{d\alpha} \quad \text{(column vector)}. \end{aligned}$$

Equation (9) requires a solve for u for every control variable. A perturbation of the bottom temperature (α) perturbs the heat flux distribution, which in turns perturbs the temperature distribution. This perturbation cascades through the entire coupling procedure and leads to a perturbation in the solution to the coupled problem. Nevertheless, upon convergence of the coupling method, equation (7) must be satisfied. Similarly, the total derivative of the system w.r.t to any control variable must be zero. This leads to the system of equations

$$\begin{aligned} \frac{\partial R_f}{\partial T_w^\infty}\frac{dT_w^\infty}{d\alpha} + \frac{\partial R_f}{\partial q_w^\infty}\frac{dq_w^\infty}{d\alpha} + \frac{dR_f}{d\alpha} &= 0 \\ \frac{\partial R_s}{\partial T_w^\infty}\frac{dT_w^\infty}{d\alpha} + \frac{\partial R_s}{\partial q_w^\infty}\frac{\partial q_w^\infty}{\partial \alpha} + \frac{dR_s}{d\alpha} &= 0, \\ \begin{bmatrix} \frac{\partial R_f}{\partial T_w^\infty} & \frac{\partial R_f}{\partial q_w^\infty} \\ \frac{\partial R_s}{\partial T_w^\infty} & \frac{\partial R_s}{\partial q_w^\infty} \end{bmatrix} \begin{bmatrix} \frac{dT_w^\infty}{d\alpha} \\ \frac{dq_w^\infty}{d\alpha} \end{bmatrix} &= \begin{bmatrix} -\frac{\partial R_f}{\partial \alpha} \\ -\frac{\partial R_s}{\partial \alpha} \end{bmatrix}. \end{aligned} \tag{9}$$

This can be rewritten as

$$\begin{aligned} \mathbf{A}u &= f, \\ u &= \mathbf{A}^{-1}f, \end{aligned} \tag{10}$$

where $\mathbf{A}$ is the extended Jacobian of the system. Solving this linear system once allows to compute the sensitivity by substituting for u in equation (9), which gives

$$\frac{dJ}{d\alpha} = g^T\mathbf{A}^{-1}f. \tag{11}$$

However, since the problem has multiple control variables α, this exercise needs to be repeated for each α, hence requiring N linear system solves (in this work 113). Additionally, the Jacobian matrix in equation (9) is not explicitly computed in the TFFB coupling approach used in the present work.

3.2 Adjoint equations

Regrouping the terms in equation (11) allows to introduce a new variable v as follows:

$$\begin{aligned}\frac{dJ}{d\alpha} &= (g^T\mathbf{A}^{-1})f, \\ &= v^T f, \qquad (12)\\ &= \begin{bmatrix}\bar{T}_w & \bar{q}_w\end{bmatrix}\begin{bmatrix}-\dfrac{\partial R_f}{\partial\alpha} \\ -\dfrac{\partial R_s}{\partial\alpha}\end{bmatrix}, \qquad (13)\end{aligned}$$

where v represents the adjoint values of temperature and heat flux $(\bar{T}_w, \bar{q}_w)$ and is the solutions of the linear system

$$\begin{aligned}\begin{bmatrix}\dfrac{\partial R_f}{\partial T_w}^T & \dfrac{\partial R_s}{\partial T_w}^T \\ \dfrac{\partial R_f}{\partial q_w}^T & \dfrac{\partial R_s}{\partial q_w}^T\end{bmatrix}\begin{bmatrix}\bar{T}_w \\ \bar{q}_w\end{bmatrix} &= \begin{bmatrix}\dfrac{\partial J}{\partial T_w} \\ \dfrac{\partial J}{\partial q_w}\end{bmatrix}, \qquad (14)\\ \mathbf{A}^T v &= g, \\ v^T &= g^T\mathbf{A}^{-1}.\end{aligned}$$

The advantage of computing the sensitivity through equation (12) is that only one solve of the adjoint system (equation (14)) is required to obtain the adjoint variables regardless of the number of control variables.

The adjoint approach can also be obtained using reverse mode automatic differentiation and is the technique which is employed here. It results in an equivalent approach in which the Jacobian is not computed explicitly, rather the full forward run is repeated in reverse as illustrated in Fig. 4. The fluid state at each coupling iteration during the direct solve is stored and used to initialise the adjoint solve in the reverse coupling iteration. The accumulation of $\bar{\mathbf{T}}_\mathbf{b}$ yields the gradient values which are the solution to equation (12).

3.3 Gradient verification

To ensure the adjoint method is implemented correctly, a typical test is executed which compares the results with Finite Differences (FD). Although the accuracy of FD can be a significant issue, it can provide a reasonable indication of whether the adjoint code is implemented correctly. The obtained adjoint and FD gradients are compared in Fig. 5a.

The target temperature is obtained by solving the primal problem with a bottom temperature of 600K and is denoted as $T_{target}|_{T_b=600K}$. $\tilde{T}_b$ is taken as 400K and refers to the estimated bottom temperature that should yield T_{target} .

The adjoint and FD gradients show good agreement to plotting accuracy. Fig. 5b shows the convergence of the coupling procedure for the direct and adjoint solves. For the adjoint convergence, the same residual defined in equation (5) is used with the temperature values replaced by gradient values.

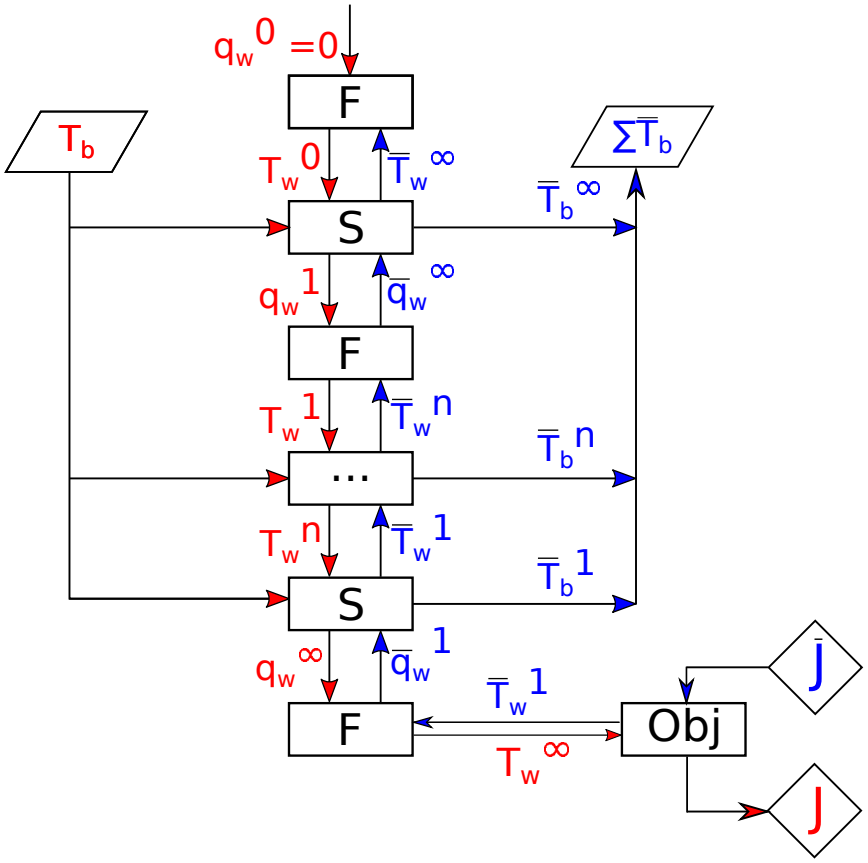

Figure 4: Coupling iterations (Direct = red, Adjoint = blue).

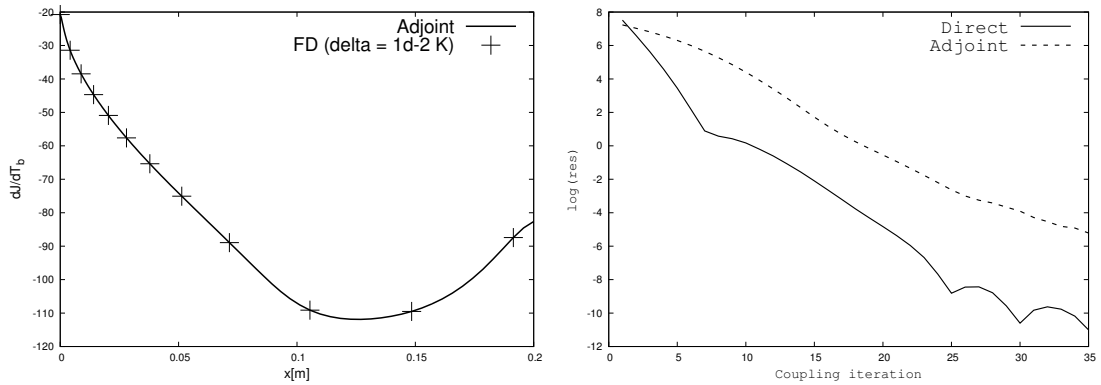

(a) Adjoint vs. FD gradients.

(b) Convergence of coupling iterations.

Figure 5: Gradient comparison and coupling convergence for $\tilde{T}_b = 400$K vs. $T_{target}|_{T_b=600K}$.

3.4 Results

The objective is minimised using the steepest descent algorithm which is run for 15 iterations. We define the difference between the temperatures obtained from the direct

and inverse solution as

$$T_{\text{error}} \quad = \quad T_{\text{Target}} - T_{\text{Inverse}}, \tag{15}$$

The obtained wall temperature distributions and the error for each node are shown in figures 6a and 6b.

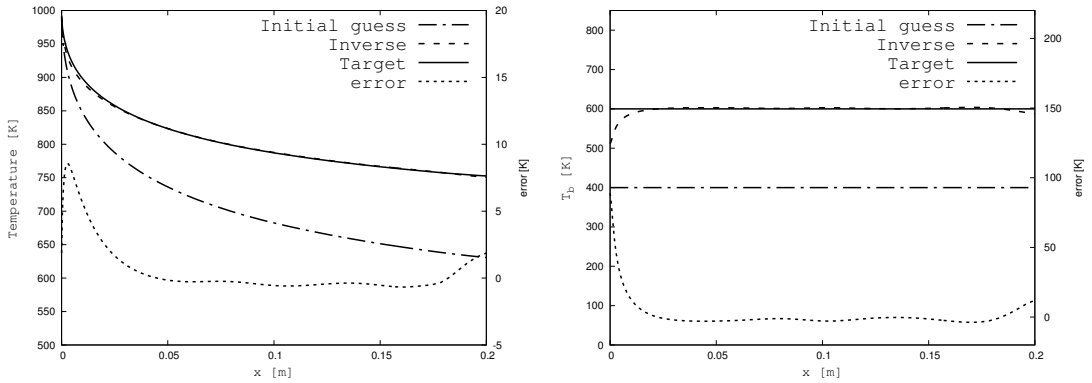

(a) T_w distribution. (b) T_b distribition.

Figure 6: Results of wall and bottom temperature distribution.

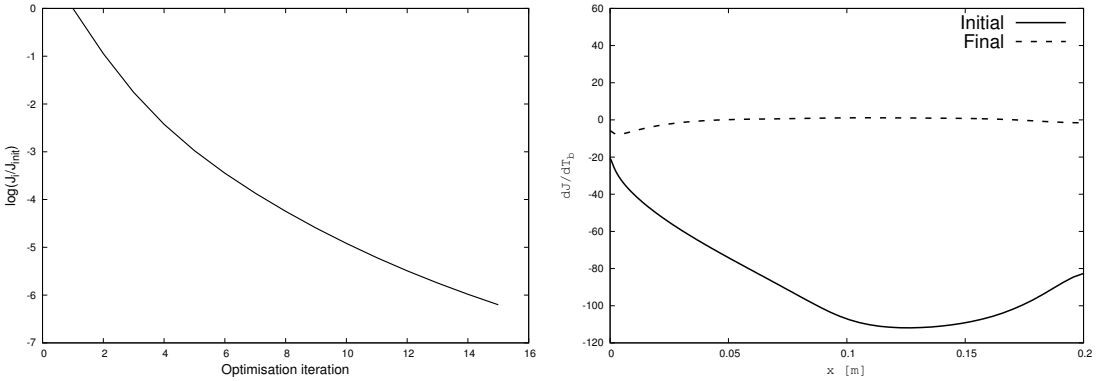

(a) Evolution of the objective function. (b) Gradients of objective w.r.t T_b.

Figure 7: Cost function and gradient plots for $\tilde{T}_b = 400$K vs. $T_{target}|_{T_b=600K}$.

Fig. 6 shows that the inverse solution is significantly closer to the target than the initial values while Fig 7 shows that the values of the objective and sensitivities have been reduced considerably. The results show that the gradient computation procedure described Sec. 3.2 can be successfully utilised by optimisation algorithms. Consequently, the described procedure can be used to obtain sensitivities using any two adjoint solvers which provide the required multidisciplinary gradients.

4 CONCLUSION

This paper discusses the use of a partitioned approach to solve an inverse conjugate heat transfer problem. The partitioned method used is described in section 2 and validated with and analytic solution. In section 3, adjoint methods have been used to solve an inverse problem using a gradient based approach. The derivation of adjoint equations for the partitioned system was presented and the exchange of sensitivity information between the adjoint solvers in order to obtain multidisciplinary gradients was described. The description shows a framework capable of combining any two adjoint solvers in order to compute multidisciplinary gradients. The developed framework was successfully used in an optimisation algorithm to demonstrate its effectiveness. Future work will include the replacement of the simplified heat conduction solver with the reverse-differentiated open-source solver, Calculix. Additionally, the presented framework could be extended to shape optimisation problems involving CHT and multidisciplinary design optimisation.

REFERENCES

[1] Alok Majumdar and S.S. Ravindran. Numerical prediction of conjugate heat transfer in fluid network. *American Institute of Aeronautics and Astronautics*, 2010.

[2] V. Ganine, N.J. Hills, and B.L. Lapworth. Nonlinear acceleration of coupled fluid-structure transient thermal problems by anderson mixing. *International Journal for Numerical Methods in Fluids*, 71:939–959, 2013.

[3] Tom Verstraete and Sebastian Scholl. Stability analysis of partitioned methods for predicting conjugate heat transfer. *International Journal of Heat and Mass Transfer*, 101:852–869, 2016.

[4] Jianhua Zhou, Yuwen Zhang, J.K. Chen, and Z.C. Feng. Inverse estimation of surface heat condition in a three-dimensional object using conjugate gradient method. *International Journal of Heat and Mass Transfer*, 53:2643–2654, 2010.

[5] An inverse heat conduction problem with heat flux measurements. Tahar loulou and elaine p. scott. *International Journal for Numerical Methods in Engineering*, 67:1587–1616, 2006.

[6] Wen-Lih Chen and Yu-Ching Yang. On the inverse heat convection problem of the flow over a cascade of rectangular blades. *International Journal of Heat and Mass Transfer*, 51:4184–4194, 2008.

[7] Chen-Hung Huang and Wei-Chung Chen. A three-dimensional inverse forced convection problem in estimating surface heat flux by conjugate gradient method. *International Journal of Heat and Mass Transfer*, 43:3171–3181, 2000.

[8] Fu-Yun Zhao, Di Liu, Li Tang, Yu-Ling Ding, and Gaung-Fa Tang. Direct and inverse mixed convections in an enclosure with ventilation ports. *International Journal of Heat and Mass Transfer*, 52:4400–4412, 2001.

[9] Shaik Imran Ahamad and C. Balaji. Inverse conjugate mixed convection in a vertical substrate with protruding heat sources: a combined experimental and numerical study. *Heat and Mass Transfer*, 52:1243–1254, 2015.

[10] Antonio Fazzolari, Nicolas R. Gauger, and Joël Brezillon. Efficient aerodynamic shape optimization in mdo context. *Journal of Computational and Applied Mathematics*, 203:548–560, 2005.

[11] Joaquim R. R. A. Martins and John T. Wang. Review and unification of methods for computing derivatives of multidisciplinary computational models. *American Institute of Aeronautics and Astronautics*, 51, 2013.

[12] E. Divo, E. Steinthorsson, F. Rodriguez, A. J. Kassab, and J.S. Kappat. Glenn-ht/bem conjugate heat transfer solver for large-scale turbomachinery models. Technical Report NASA/CR-2003-212195, NASA, 2003.

[13] Shenren Xu, David Radford, Marcus Meyer, and Jens-Dominik Müller. Stabilisation of discrete steady adjoint solvers. *Journal of Computational Physics*, 2015.

[14] A. V. Luikov. Conjugate convective heat transfer problems. *International Journal of Heat and Mass Transfer*, 17:257–265, 1974.

VII International Conference on Computational Methods for Coupled Problems in Science and Engineering
COUPLED PROBLEMS 2017
M. Papadrakakis, E. Oñate and B. Schrefler (Eds)

ADAPTATIVE REDUCED ORDER MODEL TO CONTROL NON LINEAR PARTIAL DIFFERENTIAL EQUATIONS

MOURAD OULGHELOU*, CYRILLE ALLERY†

* †LaSIE, UMR 7356 CNRS, Université de La Rochelle Pôle Science et Technologie
Avenue Michel Crépeau, 17042 La Rochelle Cedex 1, France
* mourad.oulghelou@univ-lr.fr , †cyrille.allery@univ-lr.fr

Key words: Model Order Reduction, POD, PGD, Grassmann manifold, interpolations, sub optimal control

Abstract. In classical adjoint based optimal control of unsteady dynamical systems, requirements of CPU time and storage memory are known to be very important. To overcome this issue, model order reduction techiques operating by the construction of a separated representation of the solution are considered. A spatial basis must be calculated for each variation in control parameters, followed by a Galerkin projection of the equations's residuals on this basis, that results in a low dimentional system of ordinary differential equations. These steps need to be carried out in every iteration of the control algorithm. The most popular reduced order model method is the Proper Orthogonal Decomposition (POD). It is used here for the construction of reduced bases. The interest in this communication is turned to the adaptation of these bases respectivly to control parameter variations. Two adaptation approaches are considered. The first one uses a powerfull interpolation method based on calculus of geodesic paths on the Grassmann manifold. This approach needs a precomputed set of bases associated to a distribution of opetating points, that are calculated using POD method. The second approach uses the Proper Generalized Decomposition (PGD) considered here as a correction method. This method consists in enriching a basis by reducing the error of the approximated solution.

1 Inroduction

In this communication, in order to reduce simulation CPU time of control problems, suboptimal control methodology is considered. It relies on reduced order models techniques allowing to represent the high fidelity solutions as a space time separated form by using for instance the POD [1]. It is expected that only few space basis elements will provide a reasonably good description of the desired dynamic. The projection of governing equations onto this reduced basis results in a set of differential equations with considerably smaller order than the degree of freedom arising from the full equations. In the previous

works established in the topic of sub-optimal control, the POD method was the mostly investigated model reduction approach. For instance Bergmann et al. [2] controlled the time angular velocity of a rotating cylinder to optimize drag of an incompressible viscous flow past a circular cylinder. Ravindran [3] considered the control problem of reducing recirculations behind the step of a flow in a backward facing step channel, where the control was effected either through the movement of a wall portion or through blowing on it. By the parameter variation, the basis was updated using the POD method trough the generation of a new set of snaphots. However this approach still costly, eventhough it is less time consuming compared to the full control. We can cite also the work of Akman [4] who controlled diffusion-convection-reaction equations using POD method to generate reduced bases. In addition, he used subspace angle interpolation method (SAIM) to adapt a basis for new configuration. It consists in adapting two availabale reduced order bases constructed for two different operating points to fit with a new operating point. Tallet et al. [5] controlled in quasi-real time the boundary condition of the anisothermal Navier-Stokes equations in a lid driven cavity. The POD basis considered is generated once for all from multiple configurations, in a manner there is no need to update the spatial basis within the control algorithm, only reduced equations were solved. In the following this approach will be refered to as global basis method (GBM). In this communication, some improvements are proposed to the aformentionned approaches. Using the tools of calculus of geodesic paths on the Grassmann manifold, the notion of subspace angle interpolations appears to be a particular case of to the Grassmann interpolation method (GIM) where more operating points are involved. Consequently, an enhancement of bases adaptation due to this enrichment of samples space is expected. This approach was already used by Amsallem et al. in the context of aeroelasticity to adapt POD reduced order bases to fit with a new physical parameter [6]. The second approach that we propose here for bases adaptation, is the Proper Generalized Decomposition (PGD) [7, 8, 9, 10]. It acts as an enrichment tool of bases within the control loop, and can be seen as a generalization of the POD method.
This communication is organized as follows. Section 2 describes the studied case full control problem. Section 3 introduces the POD reduced order model method used through this communication to construct the set of bases samples required when the control is based on interpolation methods, such as RBF, Lagrange, SAIM, and GIM. The last method is described in Section 4. Section 5 presents the PGD approach used to adapte POD bases bases. in Section 6, the reduced optimal control problem is introduced. Finally, Section 7 presents the numerical results of sub-optimal control, obtained using the aformentioned methods.

2 Optimal control problem formulation

Let $\Omega \subset \mathbb{R}^2$ a bounded domain with boundary $\Gamma \subset \mathcal{C}^2$ and $\mathcal{I} = [0, T]$. Consider the nonstationary nonlinear heat equations with initial condition $u_0 \in L^2(\Omega)$ submitted to a

body force $f_\gamma \in L^2(\mathcal{I}, H^{-1})$ described by the equations

$$\begin{cases} \dfrac{\partial}{\partial t}u - \nu\Delta u + \dfrac{1}{2}u^2 = f_\gamma \quad \text{in } \Omega \times \mathcal{I} \\ u = g \quad \text{on } \Gamma \times \mathcal{I} \\ u(0) = u_0 \quad \text{in } \Omega. \end{cases} \tag{1}$$

We define the cost functional for all $\kappa > 0$

$$\mathcal{J}(u,\gamma) = \frac{1}{2}\int_0^T \int_\Omega |u - \hat{u}|^2 dxdt + \frac{1}{2}\int_\Omega |u_T - \hat{u}_T|^2 dx + \frac{\kappa}{2}|\gamma|^2. \tag{2}$$

where the last term $\frac{\kappa}{2}|\gamma|^2$ serves as a regularization of the constrained minimization problem defined by

$$\min_{\gamma \in U_{ad}} \mathcal{J}(u,\gamma) \tag{3}$$

such that u solves the equations (1) and $U_{ad} = \big\{\gamma \in \mathbb{R}^d \quad s.t. \quad |\gamma| < C\big\}$. In other words, acting on the parameter γ we want to control equations (1) in a way that the seeked parameter is a minimimizer for the cost functional (2). A descent gradient method is used for the numerical search of that minimizer. The adjoint problem is then derived

$$\begin{cases} \dfrac{\partial}{\partial t}\xi + \nu\Delta\xi - u\xi = u - \hat{u} \quad \text{in } \Omega \times \mathcal{I} \\ \xi = 0 \quad \text{on } \Gamma \times \mathcal{I} \\ \xi(T) = \hat{u}(T) - u(T) \quad \text{in } \Omega. \end{cases} \tag{4}$$

and the functional gradient writes

$$\nabla\mathcal{J}(\gamma) = -\int_0^T \int_\Omega \nabla f_\gamma \xi dxdt + \kappa\gamma \tag{5}$$

3 POD reduced order model method

In this section, we seek an approximate separated form of u such as

$$u \approx u_m = \sum_{j=1}^{m} \alpha_j \Phi_j \tag{6}$$

Using the POD method, the optimal separated representation of the solution is achieved in just few basis elements. This basis is extracted from the information contained in a set of realizations called snapshots [1]. Let $(u^1, \ldots, u^M)$ be an ensemble of snapshots of the considered system of evolution respectivly to time instances $(t_1, \ldots, t_M)$. The POD basis is calculated in four steps

(i) build the correlation matrix K from the considered snapshots whose elements are given as $K_{ij} = \frac{1}{M}\int_\Omega u^i u^j dx$ for $1 \leq i, j \leq M$

(ii) compute the eigenvalues $\lambda_1 > \cdots > \lambda_M$ and eigenvectors $y^1, \ldots, y^M$ of K

(iii) set $\Phi_i = \sum_{j=0}^{M} y_j^i u^j$ for $1 \leq i \leq M$

(iv) normalize $\Phi_i = \frac{\Phi_i}{||\Phi_i||}$ for $1 \leq i \leq M$

In order to obtain a low dimentional basis, the modes corresponding to small eigenvalues are neglected. Only the m more energetic first modes are considered ($m << M$). The high fidelity equations are then projected onto this basis, resulting in system of ordinary differential equations of low order (ROM) given by

$$\begin{cases} \sum_{j=1}^{m} M_{ij}\frac{d}{dt}\alpha_j + \nu\sum_{j=1}^{m} R_{ij}\alpha_j + \frac{\nu}{\epsilon}\sum_{j=1}^{m} B_{ij}\alpha_j + \frac{1}{2}\sum_{j,k=1}^{m} N_{ijk}\alpha_j\alpha_k = F_i + \frac{\nu}{\epsilon}G_i \\ \sum_{j=1}^{m} M_{ij}\alpha_j(0) = \langle u_0, \Phi_i\rangle_\Omega \\ \forall i \in 1, \cdots, m \end{cases} \tag{7}$$

$$\begin{aligned} M_{ij} &= \langle \Phi_j, \Phi_i\rangle_\Omega \qquad & N_{ijk} &= \langle \Phi_j\Phi_k, \Phi_i\rangle_\Omega \qquad & F_i &= \langle f, \Phi_i\rangle_\Omega \\ R_{ij} &= \langle \nabla\Phi_j, \nabla\Phi_i\rangle_\Omega \qquad & B_{ij} &= \langle \Phi_j, \Phi_i\rangle_\Gamma \qquad & G_i &= \langle g, \Phi_i\rangle_\Gamma \end{aligned} \tag{8}$$

where $\langle u, v\rangle_\Omega = \int_\Omega uvdx$ and $\langle u, v\rangle_\Gamma = \int_\Gamma uvd\sigma$. The essential boundary condition is enforced in a weak integral form using the penalty method [11]. It consists in writing u in the boundary as

$$u_{/\Gamma} = g - \epsilon\frac{\partial u}{\partial n} \tag{9}$$

where ϵ is a small parameter. So that we can replace the essential boundary condition by the alternative natural boundary condition $\frac{\partial u}{\partial n} = \frac{u_{/\Gamma} - g}{\epsilon}$. This remark explains the presence of the elements B_{ij} and G_i in the ROM equations (7). As $\epsilon \to 0$ the domain boundary will converge to the original boundary condition.

4 ROMs interpolation

An important and practical issue associated with bases produced by the POD method, is their lack of robustness with respect to parameter variations. An attractive idea for adapting them is to use methods of interpolation. Unfortunately, the standard interpolation such as RBF or Lagrange methods of a set of bases does not necessarily produce a basis. However, there exists an appropriate interpolation technique called here the Grassmann interpolation method (GIM) that can always ensure this property.
Let's define first the tangent space at a point of the Grassmann manifold and the concept of Geodesic path between two points on a differential manifold. Consider n_g orthogonal bases of the same dimension generated from the set of configuration parameters $\vartheta = \{\gamma_0, \gamma_1, \ldots, \gamma_{n_g-1}\}$. An important result about the Grassmann manifold $\mathcal{G}(N_b, N_f)$ states that at each of its points $\mathcal{S}$ there exists a tangent space denoted $\mathcal{T}_\mathcal{S}$ [12] of the same dimension, and with an origin the point of tangency. Each point of this tangent space $\mathcal{T}_\mathcal{S}$ can be as well represented by a matrix $\Gamma \in \mathbb{R}^{N_f \times N_b}$. The tangent space is a vector space. Hence, $\mathcal{T}_\mathcal{S}$ is a flat space in which interpolations can be performed as usual.

Let ψ denote an orthogonal matrix whose columns span $\mathcal{S} \in \mathcal{G}(N_b, N_f)$ and χ denote a point of $\mathcal{T}_S$ spanned by the columns of Γ. The exponential mapping Exp maps χ to an N_b dimensional subspace $\mathcal{S}'$ represented by an orthogonal matrix $\psi' \in \mathbb{R}^{N_f \times N_b}$ and based on thin singular value decomposition

$$\begin{cases} \Gamma = U\Sigma V^T \\ \psi' = \psi V \cos(\Sigma) + U \sin(\Sigma) \end{cases} \tag{10}$$

The link between the tangent space $\mathcal{T}_\mathcal{S}$ at a point $\mathcal{S}$ of the Grassmann manifold and the manifold itself is established by the exponential mapping, and explicitly expressed by equations (10). The inverse of this map is defined between a neighborhood of $\mathcal{S}$ and $\mathcal{T}_\mathcal{S}$ by the logarithmic map. This mapping is denoted by $\log_s$ and defined in a neighborhood of $\mathcal{S} \in \mathcal{G}(N_b, N_f)$.
The following result enables the practical computation of the logarithmic map. Let ψ and ψ' denote two orthogonal matrices whose columns span a subspace $\mathcal{S}$ and $\mathcal{S}'$ in the neighborhood of S, respectivly. The image of $\mathcal{S}'$ by the logarithmic map $\log_S$, $\chi = \log_s(\mathcal{S}') \in \mathcal{T}_S$, is represented by the matrix Γ given by

$$(I - \psi\psi^T)\psi'(\psi^T\psi')^{-1} = U\Sigma V^T$$

$$\Gamma = U \tan^{-1}(\Sigma) V^T$$

Let $\{\psi_i \in \mathbb{R}^{N_f \times N_b}\}_{i=0}^{n_g-1}$ denote the representing matrices of $\{\mathcal{S}_i\}_{i=0}^{n_g-1}$ the set of N_b-dimensional subspaces of $\mathbb{R}^{N_f}$ associated with a set $\{\gamma\}_{i=0}^{n_g-1}$ of control parameters. Then the basis adaptation algorithm is resumed in four steps as described in the paper of Amsallem and Farhat [6]

GIM bases interpolation steps:

- **step 0.** Chose a reference point $\mathcal{S}_{i_0}$ to be the origine point of the interpolation.
- **step 1.** using the logarithm map, map each $\mathcal{S}_i$ to a matrix Γ_i representing a point χ_i of $\mathcal{T}_{\mathcal{S}_{i_0}}$

$$(I - \psi_{i_0}\psi_{i_0}^T)\psi_i(\psi_{i_0}^T\psi_i)^{-1} = U_i\Sigma_i V_i^T \qquad \Gamma_i = U_i \tan^{-1}(\Sigma_i)V_i^T \tag{11}$$

- **step 2.** interpolate Γ_{n_b} associated to the target control parameter γ_{n_b}
- **step 3.** using the exponential map $\mathrm{Exp}_{\mathcal{S}_{i_0}}$, map Γ_{n_b} to a subspace $\mathcal{S}_{n_b}$ on $\mathcal{G}(N_b, N_f)$ spanned by a matrix ψ_{n_b}

$$\Gamma_{n_b} = U_{n_b}\Sigma_{n_b}V_{n_b}^T \qquad \psi_{n_b} = \psi_{i_0}V_{n_b}\cos(\Sigma_{n_b}) + U_{n_b}\sin(\Sigma_{n_b}) \tag{12}$$

5 PGD reduced order model method

Consider now a POD basis associated to a parameter $\gamma \in \mathbb{R}^2$ which is insufficient to achieve a good approximation of the solution associated to a neighbor parameter. Assume that a solution u is approximated in this basis like $u_m = \sum_{i=0}^{m}\alpha_i\Phi_i$. The goal is to enrich this expression by a couple $(\alpha_{m+1}, \Phi_{m+1})$ such that $u_{m+1} = u_m + \alpha_{m+1}\Phi_{m+1}$ represents well the solution u.
This can be achieved using the Proper Generalized (PGD) method [7, 8, 9, 10]. Let's start by explaining how to determine the new couple $(\alpha_{m+1}, \Phi_{m+1})$. Suppose that α_{m+1} is known and fixed, $\Phi_{m+1} = \mathcal{S}(\alpha_{m+1})$ is defined in

$$V_{m+1} = \left\{ \Phi_{m+1} \in H^1(\Omega)/\Phi_{m+1_{/\Gamma}} = \frac{1}{\langle \alpha_{m+1}, \alpha_{m+1}\rangle_{\mathcal{I}}} \left(g - \sum_{j=1}^{m} \langle \alpha_j, \alpha_{m+1}\rangle_{\mathcal{I}} \Phi_{j_{/\Gamma}} \right) \right\}$$

for all $\psi \in H_0^1(\Omega)$ by the folowing Galerkin orthogonality criteria

$$\begin{aligned} \sum_{j=1}^{m+1} \left\langle \frac{d}{dt}\alpha_j, \alpha_{m+1} \right\rangle_{\mathcal{I}} \langle \Phi_j, \psi\rangle_\Omega + \nu \sum_{j=1}^{m+1} \langle \alpha_j, \alpha_{m+1}\rangle_{\mathcal{I}} \langle \nabla\Phi_j, \nabla\psi\rangle_\Omega \\ + \frac{1}{2}\sum_{j=1}^{m+1} \langle \alpha_j\alpha_k, \alpha_{m+1}\rangle_{\mathcal{I}} \langle \Phi_j\Phi_k, \psi\rangle_\Omega = \langle \alpha_{m+1} f, \psi\rangle_{\Omega\times\mathcal{I}} \end{aligned} \tag{13}$$

Similarly, if Φ_{m+1} is known and fixed, we define $\alpha_{m+1} = \mathcal{T}(\Phi_{m+1})$ for all $\beta \in L^2(\mathcal{I})$

$$\begin{aligned} \sum_{j=1}^{m+1} \langle \Phi_j, \Phi_{m+1}\rangle_\Omega \left\langle \frac{d}{dt}\alpha_j, \beta \right\rangle_{\mathcal{I}} + \nu \sum_{j=1}^{m+1} \langle \nabla\Phi_j, \nabla\Phi_{m+1}\rangle_\Omega \langle \alpha_j, \beta\rangle_{\mathcal{I}} + \frac{\nu}{\epsilon}\sum_{j=1}^{m+1} \langle \Phi_j, \Phi_{m+1}\rangle_\Gamma \langle \alpha_j, \beta\rangle_{\mathcal{I}} \\ + \frac{1}{2}\sum_{j=1}^{m+1} \langle \Phi_j\Phi_k, \Phi_{m+1}\rangle_\Omega \langle \alpha_j\alpha_k, \beta\rangle_{\mathcal{I}} = \langle \beta f, \Phi_{m+1}\rangle_{\Omega\times\mathcal{I}} + \frac{\nu}{\epsilon}\langle \beta g, \Phi_{m+1}\rangle_{\Gamma\times\mathcal{I}} \end{aligned} \tag{14}$$

Hence, a natural definition of an optimal couple $(\alpha_{m+1}, \Phi_{m+1})$ relies in satisfying simultaniously equation (13) and (14). The problem then reads

$$\text{Find } (\alpha_{m+1}, \Phi_{m+1}) \in \mathcal{I} \times V_{m+1} \text{ such as } \begin{cases} \alpha_{m+1} = \mathcal{T}(\Phi_{m+1}) \\ \Phi_{m+1} = \mathcal{S}(\alpha_{m+1}) \end{cases} \tag{15}$$

The problem can be formulated in terms of α_{m+1} as follow

$$\text{Find } \alpha_{m+1} \in \mathcal{I} \quad \text{such as} \quad \alpha_{m+1} = \mathcal{T} \circ \mathcal{S}(\alpha_{m+1}) \tag{16}$$

This allows to interpret equations (16) as a fixed point problem. Consequently, a classical fixed point algorithm is used to find the new couple $(\alpha_{m+1}, \Phi_{m+1})$

while $m \leq M_{max}$ **do**
  α^0_{m+1} given arbitrary;
  for $k \leftarrow 0$ **to** k_{max} **do**
    solve $\Phi^k_{m+1} = \mathcal{S}(\alpha^k_{m+1})$;
    solve $\alpha^k_{m+1} = \mathcal{T}(\Phi^k_{m+1})$;
    Check convergence $|\sigma^k_m - \sigma^{k-1}_m| < \epsilon_u |\sigma^k_m|$ where $\sigma^k_m = ||\alpha^k_{m+1}||$;
  end
  Enrichement: $\Phi^{m+1} = \text{span}\{\Phi_j\}_{j=0,\cdots,m+1}$
  Update: solve equations (7), $\Lambda^{m+1} = \text{span}\{\alpha_j\}_{j=0,\cdots,m+1}$
  Reduce basis length if necessary.
end

Algorithm 1: PGD Algorithm with update.

The basis length reduction in algorithm (1) consists in performing a POD on the snapshots formed by the reduced basis. In practice we consider only one enrichment, so $M_{max} = 1$.

6 Reduced optimal control problem

Let's now define the control problem in a reduced form, such that the only quantity being manipulated is the temporal basis obtained as a solution of the reduced order model. Let $\hat{u}$ be given in the separated form $\hat{u} = \sum_{j=1}^{\hat{m}} \hat{\alpha_j} \hat{\Phi}_m$. The reduced cost functional writes

$$\mathcal{J}(\alpha, \gamma) = \frac{1}{2} \sum_{k=1}^{m} \left(\int_0^T \alpha_k^2 dt + \alpha_k^2(T) \right) + \frac{1}{2} \sum_{l=1}^{\hat{m}} \left(\int_0^T \hat{\alpha}_l^2 dt + \hat{\alpha}_l^2(T) \right) - \sum_{k=1}^{m} \sum_{l=1}^{\hat{m}} C_{kl} \left(\int_0^T \alpha_k \hat{\alpha}_l dt + \alpha_k(T) \hat{\alpha}_l(T) \right) + \frac{\kappa}{2} |\gamma|^2. \tag{17}$$

where α is now the state variable, $C_{kl} = \left\langle \Phi_k, \hat{\Phi}_l \right\rangle_\Omega$ and $\hat{m}$ is the target solution modes number. The associated adjoint ROM equations follow immediatly from the ROM state equations (7)

$$\begin{cases} \sum_{i=1}^{m} M_{iq} \frac{d}{dt}\beta_i - \nu \sum_{i=1}^{m} R_{iq}\beta_i - \frac{\nu}{\epsilon} \sum_{i=1}^{m} B_{iq}\beta_i - \sum_{i=1}^{m} N_{iqk}\alpha_j\beta_i = \alpha_q - \sum_{i=1}^{\hat{m}} C_{qi}\hat{\alpha}_i \\ \sum_{i=1}^{m} M_{iq}\beta_q(T) = \sum_{i=1}^{\hat{m}} C_{qi}\hat{\alpha}_i(T) - \alpha_q(T) \\ \forall q = 1, \cdots, m \end{cases} \tag{18}$$

Finaly the cost functional gradient writes

$$\nabla \mathcal{J}(\gamma) = -\sum_{j=1}^{m} \int_0^T \beta_j \int_\Omega \nabla f_\gamma \Phi_j dx dt + \kappa\gamma \tag{19}$$

The reduced control algorithm is summerized as follow

γ^0 given arbitrary;
while $\mathcal{J} \leq \epsilon$ **do**
  $\Phi^0 = \Phi(\gamma^k)$ fixed;
  for $l = 0$ **to** k_{max} **do**
    solve ROM state equations (7);
    solve ROM state equations (18);
    Compute the descent direction $d_l = -\nabla \mathcal{J}(\gamma^l)$ using Eq. (19);
    Determine the new control $\gamma_l = \gamma_{l-1} + \sigma_l d_l$ ($\sigma_l > 0$ Armijo line search);
    Evaluate $\mathcal{J}(\gamma^k)$;
  end
  Update Φ^k using one of the methods (PGD, GIM, SAIM ...);
  $k = k + 1$;
end

Algorithm 2: Reduced Optimal Control algorithm

7 Numerical analysis

We consider the non linear heat equations in a 2D square domain $\Omega = [0,1] \times [0,1]$ with a diffusion coefficient $\nu = 10^{-2}$. The optimal control is performed by acting on the parameter $\gamma \in \mathbb{R}^2$ appearing on the source term f_γ. The velocity on the boundary is given by $u_{/\Gamma} = cos(t)(x+y)$ and the source term is defined by $f_\gamma(t,x) = \sum_{k=0}^{1} f_\gamma^{(k)}$. Where $\gamma = (\gamma^{(0)}, \gamma^{(1)}) \in \mathbb{R}^2$ and $f_\gamma^{(k)} = \beta_k(t,\gamma)\chi_{\Omega_k}(x) f_k(x)$, where $k = 0, 1$. χ is the mask

function and :

$$\begin{cases} \beta_0(t,\gamma) = \gamma^{(0)} e^{-t} & f_0(x) = x^2 + y^2 \\ \beta_1(t,\gamma) = \gamma^{(1)} sin(t) & f_1(x) = 1 \end{cases}$$

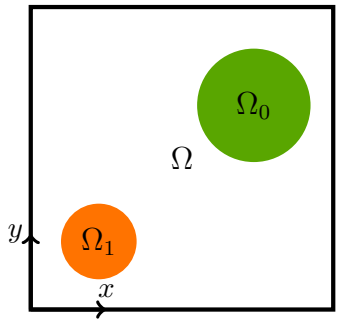

(a) Poistion of subdomains Ω_0 and Ω_1 where external forces $f_\gamma^{(0)}$ (respectively) $f_\gamma^{(1)}$ are applied.

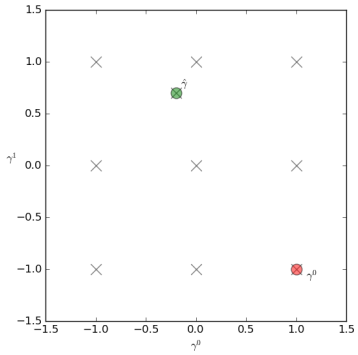

(b) sampling distribution of control parameters, $\hat{\gamma}$ is the target parameter and γ_0 is the first guess.

Figure 1: Space domain Ω and sampling distribution of control parameters.

The high fidelity equations are solved in the time interval $\mathcal{I} = [0, 5]$ using a time step $\delta t = 0.01$ and piecewise second order continuous finite elements on a nonuniform mesh with 17728 triangles. A preconditionned GMRES method is used in the optimization steps. The target solution $\hat{u}$ is the solution associated to $\hat{\gamma} = (-0.2, 0.7)$ and the control starting guess solution is associated to $\gamma_0 = (1, -1)$. These solutions are depicted respectively in figure (2b) and figure (2a) in two time instances $t = T/2$ and $t = T$. These figures show a strongly different dynamic between the initial guess state and the target state.

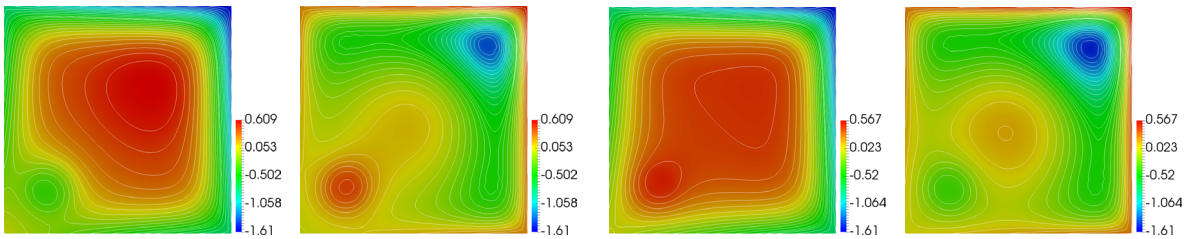

(a) first guess at $t = T/2$(left) and at $t = T$(right)

(b) Target at $t = T/2$(left) and at $t = T$(right)

Figure 2: Isovalues of the control first guess and the target solutions.

In the following, some numerical results illustrating the performance of reduced optimal control using the earlier discussed methods are presented.

The samples bases used for the interpolation methods (SAIM, GIM, RBF, Lagrange) here are genereated using the POD method over the set of operating points $\{\gamma_k\}_{k=1,\cdots,9} \in \mathbb{R}^2$ (see figure (1b)). Each basis is calculated using 500 snapshots and only 5 modes are considered. On the other hand, the snapshots associated to the set of operating points are token altogether to generate the basis used in GBM method.

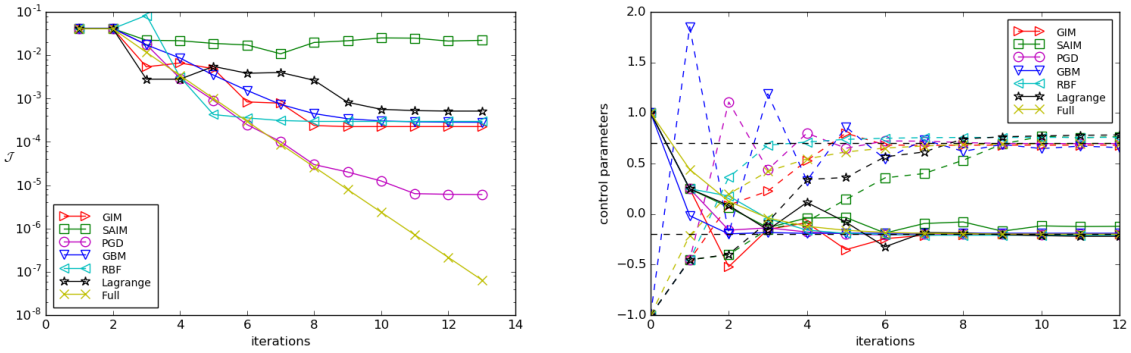

(a) Functional decay

(b) Parameters evolution

Figure 3: Convergence behavior described by the functional decay (left) and the control parameter values respectivly to number of control algorithm iterations (right).

The evolution of the functional $\mathcal{J}$ according to the control algorithm iterations is presented in figure (3a). It is observed that all the methods converge with different order of accuracy. The PGD is the most accurate one with a functional that attained 3×10^{-5} in 8 iterations. Followed by the GIM and GBM methods for which the fonctional attained 2.2×10^{-4} and 2.8×10^{-4} in 9 and 12 iterations respectivly. Then by the classical interpolation methods RBF and Lagrange with a functional that attained 2.9×10^{-4} and 5.1×10^{-4} in 8 and 12 iterations respectivly. And finally the SAIM method where the functional stagnated at 2.1×10^{-2} from the itertation 14 of the control algorithm.

These results are confirmed by figure (3b) where the parameters γ respectivly to control iteration are plotted for each method. The target parameter $\hat{\gamma} = (\hat{\gamma}^{(0)}, \hat{\gamma}^{(1)}) = (-0.2, 0.7)$ corresponds to the horizontal lines plotted in figure (3b). All the methods converge approximatly towards the target parameter $\hat{\gamma}$.

Table (1) illustrates the gains in CPU time and the percenatge of errors between the target solution and the solution achieved using GIM, SAIM, GBM, RBF, Lagrange, and PGD methods within the control algorithm. this error is defined by ε and expressed by

$$\varepsilon = 100 \times \int_0^T \frac{||\hat{u} - u||_{L^2(\Omega)}}{||\hat{u}||_{L^2(\Omega)}} dt$$

The algorithm for each method is stopped when a stagnation of the corresponding functional occurs. τ designate the time needed for the classical adjoint based control algo-

rithm to attain 0.11% of error in 11 iterations. using the interpolation methods GIM, RBF, Lagrange as well as the Global basis method GBM, the reduced optimal control is approximatly about 80 times faster with errors of 1.15%, 8.12%, 11.22% and 6.92% respectivly. the same gain is achieved by the SAIM method, except that the error in this case is of order about 72%. It is worth noting that for the GIM method, further gain in accuracy versus an acceptable loss in CPU time is expected if this method and the PGD method are appropriatly combined.

method	ε	time	γ
Full control	0.11%	τ	$(-0.198, 0.695)$
PGD	1.15%	$\tau/10$	$(-0.206, 0.697)$
GIM	5.88%	$\tau/84$	$(-0.199, 0.681)$
GBM	6.92%	$\tau/80$	$(-0.190, 0.647)$
RBF	8.12%	$\tau/78$	$(-0.209, 0.758)$
Lagrange	11.22%	$\tau/81$	$(-0.212, 0.772)$
SAIM	72.31%	$\tau/88$	$(-0.117, 0.767)$

Table 1: Gains in time obtained using optimal reduced control relativly to the full adjoint based control at iteration 11.

8 Conclusion and Discussion

The aim of this communication was to illustrate the potential gain that can be offered by the use of the GIM and PGD methods in optimal control of non linear partial differential equations. The results of control using PGD method showed a very good accuracy (errors of 1.15%). The most shining property of this method is that it does not need any sampling bases near a parameter to adapt a given basis. The approaches using interpolations such as GIM, RBF and Lagrange as well as the global basis approach GBM give satisfaying results (errors of 5.88%, 8.12%, 11.22% and 6.92% respectivly) with an important speed up in comparison with the full control problem. The main inconvenient of these approaches is that they need a set of precomputed data in different operating points of the full model problem. The generation of a good sampling of these data may need an important offline CPU time of calulations. More particulary, for some problem cases where the control parameter $\gamma \in \mathbb{R}^d$ such that $d > 3$, this approach becomes expensive, and may be considered as limited.

For all these methods, the basis is updated at each iteration of the control algorithm. The CPU time can however be reduced further if the basis update is perfomed only if necessary, which is when the basis runs out of its trust region.

REFERENCES

[1] L. Sirovich, "Turbulence and the dynamics of coherent structures: I, ii and iii," *Quarterly of Applied Mathematics*, pp. 461–590, 1987.

[2] M. B. L. Cordier and J.-P. Brancher, "Optimal rotary control of the cylinder wake using proper orthogonal decomposition reduced-order model," *AIP Physics of Fluids*, 2005.

[3] S. S. Ravindran, "A reduced-order approach for optimal control of fluids using proper orthogonal decomposition," *International Journal for Nnumerical Methods in Fluids*, pp. 425–448, 2000.

[4] T. Akman, "Local improvements to reduced order approximations of optimal control problems governed by diffusion convection reaction equation," *Computers and Mathematics with Applications*, vol. 70, pp. 104–131, 2015.

[5] A. Tallet, C. Allery, and C. Leblond, "Optimal flow control using a pod based reduced-order model," *Numerical Heat Transfer, Part B*, vol. 170, 2016.

[6] D. Amsallem and C. Farhat, "An interpolation method for adapting reduced-order models and application to aeroelasticity," *AIAA Journal*, pp. 1803–1813, 2008.

[7] A. Ammar, B. Mokdad, F. Chinesta, and R. Keunings, "A new family of solvers for some classes of multidimensional partial differential equations encountered in kinetic theory modeling of complex fluids," *Journal of Non-Newtonian Fluid Mechanics*, vol. 139, no. 3, pp. 153 – 176, 2006.

[8] A. Dumon, C. Allery, and A. Ammar, "Proper general decomposition (pgd) for the resolution of navierstokes equations," *Journal of Computational Physics*, vol. 230, pp. 1387 – 1407, 2011.

[9] M. Bergmann and L. Cordier, "generalized spectral decomposition technique to solve a class of linear stochastic partial di erential equations.," *Computer Methods in Applied Mechanics and Engineering, Elsevier*, vol. 196 (45-48), pp. 521–4537, 2007.

[10] P. Ladeveze, *Nonlinear computational structural mechanics: New approaches and non-incremental methods of calculation*. Springer (New York), 1999.

[11] E. Liberge and A. Hamdouni, "Reduced order modelling method via proper orthogonal decomposition (pod) for flow around an oscillating cylinder," *Journal of Fluids and Structures*, vol. 26, no. 2, pp. 292 – 311, 2010.

[12] A. A. M. Sepulchre, "Riemann geometry of grassmann manifolds with a view on algorithmic computation," *Acta Applicandae Mathematicae*, vol. 80, Issue 2, p. 199220, 2004.

VII International Conference on Computational Methods for Coupled Problems in Science and Engineering
COUPLED PROBLEMS 2017
M. Papadrakakis, E. Oñate and B. Schrefler (Eds)

ADDRESSING THE NON-LINEARITY AND SINGULARITY PHENOMENA OF STRESS-BASED OPTIMAL DESIGN OF MATERIAL MICROSTRUCTURES

PEDRO G. COELHO[*], GONÇALO M. GONÇALVES[*], JOSÉ M. GUEDES[†] AND JOÃO B. CARDOSO[*]

[*] UNIDEMI, Dept. of Industrial and Mechanical Engineering, Faculty of Sciences and Technology
Universidade Nova de Lisboa
FCT, 2829-516 Caparica, Portugal
e-mail: pgc@fct.unl.pt, gmgoncalves@campus.fct.unl.pt, jbc@fct.unl.pt

[†] IDMEC, Dept. of Mechanical Engineering, Instituto Superior Técnico
Universidade de Lisboa
Av. Rovisco Pais 1, 1049-001 Lisboa, Portugal
email: jmguedes@tecnico.ulisboa.pt

Key words: Optimization, Topology, Stress, Homogenization, Microstructures.

Abstract. Material design is an active research field since composites have met increasingly interest, for instance, in lightweight construction as it happens in aerospace industry. One assumes in the present work a given macroscopic stress or strain field (one that may occur at a certain point of a macro-structure) and computes through homogenization the micro-stress distribution across the two (weaker and stronger) composite constituents mixed in a unit-cell domain which is representative of a periodic heterogeneous material. Stress gradients depend a lot of design details but typically the stress field is highly non-linear. In the frame of finite element models for material microstructures one pursues here an investigation about mesh convergence. Since stress distribution is strongly design dependent, that motivates one to pursue optimal design of the material microstructure to comply with admissible stress criteria. The inverse homogenization method using density-based topology optimization is applied here for such purpose. This is quite a challenge not only because of the aforementioned non-linearity of the stress field but also due to the singularity phenomena which one overcomes using standard relaxation techniques. Some preliminary results are obtained in order to get some insight into the fine structure of composite materials and the influence of the stresses therein.

1 INTRODUCTION

Material design is an active research field since composites have met increasingly interest, for instance, in lightweight construction as it happens in aerospace industry [1,2]. Fully understanding the overall response of a composite demands greater insight about its microstructure behaviour. Micro-mechanical models detailing the geometry and the interfaces of base constituents of a composite allow fine measure and control of local stresses [3-6]. Homogenization models are often used to transfer data among different design scales. Multiscale analysis coupling macro, meso and micro scales can then be done [7].

For simplicity one assumes in the present work a given macroscopic stress or strain field (one that may occur at a certain point of a macro-structure) and computes through homogenization the micro-stress distribution across the two (weaker and stronger) composite constituents mixed in a unit-cell domain Y, i.e., the representative volume element (RVE) of the material heterogeneous medium Ω.

Stress gradients depend a lot of design details but typically the stress field is highly non-linear. In the frame of finite element models for material microstructures one pursues here an investigation about mesh dependence. By means of ever-increasing mesh refinements and shape functions order one evaluates convergence of micro-stress measures and concludes about mesh quality. Besides investigating the quality of numerical approximation to the stress field, one might also address the quality of the homogenization stress predictions comparing them to the actual composite by repeating an unit-cell a limited number of times and subjecting the resulting numerical model to a battery of load tests for stress assessment. The outcome of this later study is in [8,9] which indicates that it is sufficient to have a few repetitions of unit-cells to replace the non-homogeneous composite Ω by the equivalent homogeneous material with the stress field computed by homogenization.

Since stress distribution is strongly design dependent, that motivates one to pursue optimal design of the material microstructure to comply with admissible stress criteria. Stresses may be either minimized as the objective function or limited by an upper bound in the constraint function. The inverse homogenization method using density-based topology optimization is applied here for such purpose. This is quite a challenge not only because of the aforementioned non-linearity of the stress field but also due to the singularity phenomena which means that stresses tend to finite values as density design variables tend to zero due to degenerated regions of the feasible design domain. To overcome the singularity problem one may use the so-called relaxation approaches, such as the ε-relaxation or *qp*-approach [10,11], which have been applied to the optimal design of structures with success. Bearing this in mind one extends the application of these relaxation techniques to material design in order to obtain some preliminary results and get some insight into the fine structure of composite materials and the influence of the stresses therein.

2 MATERIAL MODEL

The material model considered in the present work is shown in Fig. 1. Assuming solid and void phases mixed one gets a cellular material generated through the repetition of a unit-cell which represents the smallest periodic heterogeneity of the heterogeneous medium Ω. The elastic properties of such medium are computed through homogenization assuming periodic boundary conditions and infinite periodicity of the unit-cell [5]. For optimal material design

purposes one discretizes the unit-cell domain Y in a regular (square-grid) mesh of 20×20 8-node isoparametric hexahedral finite elements. Although three-dimensional elements are used here the focus is on designing optimal 2-D layouts forcing design uniformity in the normal direction. This already easies the natural extension of the problem to 3-D material microstructure designs coming as future work. One assigns a density design variable per each finite element assuming it uniform therein. Solid and void phases correspond to density equal to 1 and 0, respectively. Topology optimization can then be used to search for an unit-cell lay-out improving a measure of structural performance and complying at the same time with specific design requirements. This design method is also known as inverse homogenization and it was originally introduced by Sigmund [12].

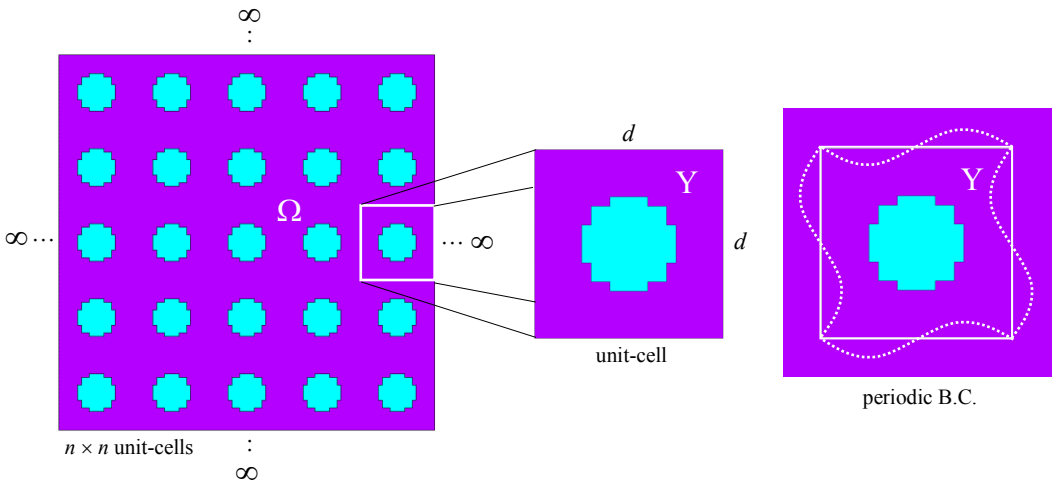

Figure 1: Material model of composite material with periodic unit-cell (array of $n \times n$ unit-cells in domain Ω of size D, in theory $n \to \infty$). Portray of periodic boundary conditions applied to the unit-cell domain Y of size d.

3 OPTIMIZATION PROBLEM FORMULATION

For the sake of demonstration purposes one selects the conventional formulation seen in topology optimization where stiffness is maximized (compliance is minimized) subjected to a volume fraction constraint [13]. While some results are revisited in the present work, using this very well-known formulation, additional results are presented too as an extension of the conventional compliance problem to include stress constraints in order to get not only stiff but also strength oriented optimal designs. In fact, engineering practice demands feasible designs on stresses too. The impact of stress criteria on the final design can be perceived later on as one plots the stress field for the stiff oriented design only where the peak stresses are higher and may exceed an admissible stress threshold.

Eq. (1) shows the optimization problem formulation where the total strain energy is maximized on density based design variables ρ ($\widetilde{\rho}$ is a filtered density as explained afterwards) subjected to a volume fraction constraint $V/V^* \leq 1$ and as many stress constraints as the number of design variables in the problem, n. This way one achieves "pointwise" control over stresses in the full unit-cell domain Y although the problem can rapidly become computationally expensive or even prohibitive. There are aggregation techniques applied to

stress constraints that allow reducing their number in the problem [13]. However, by doing that one lacks local control over stresses jeopardizing the admissible stress requirement. Rather than saving computational effort one meets here the worst case scenario of handling huge number of constraints leaving the matter of getting cheaper computations for future work.

$$\begin{aligned} &\max_{\boldsymbol{\rho}} \frac{1}{2}\int_{Y} \mathbf{E}^{\mathrm{H}}(\tilde{\boldsymbol{\rho}})\bar{\boldsymbol{\varepsilon}}\bar{\boldsymbol{\varepsilon}}\mathrm{d}Y \\ &\text{s.t.:} \\ &\frac{V(\tilde{\boldsymbol{\rho}})}{V^{*}} \le 1 \\ &\frac{\sigma^{e}_{\mathrm{VM}}(\tilde{\boldsymbol{\rho}})}{\tilde{\rho}_{e}^{q}\sigma^{*}} \le 1\,, e = 1,...,n \\ &0 < \rho_{e} \le 1\,, e = 1,...,n \end{aligned} \tag{1}$$

One assumes a solid, isotropic and ductile behavior for the base material used to fabricate the composite. Thus, in terms of the material failure criteria, the stress constraints in Eq. (1) relate the Von-Mises stress with the admissible stress value. This equivalent stress measure depends on the micro-stresses σ_{ij} (at the level of the material microstructure) which are obtained from asymptotic homogenization theory, by considering the displacement test fields χ_k^{rs} as already done in a previous work [6], see Eq. (2).

$$\sigma_{ij} = E_{ijkm}\left(\delta_{kr}\delta_{ms} - \frac{\partial \chi_k^{rs}}{\partial y_m}\right)\varepsilon_{rs}^{0} \tag{2}$$

In Eq. (2), ε_{rs}^{0} is a given macroscopic (average) strain field. The tensor σ_{ij} represent the stress state varying throughout the unit-cell domain Y. Here, the methodology used for obtaining such stresses is based on the software POSTMAT [5,6].

The density term $\tilde{\rho}^{q}$ introduces the *qp*-approach [11] as a relaxation technique to deal with the well-known singularity phenomena in stress-based optimization problems [13]. Exponent q is lower that p in order to relax the constraint and in turn exponent p figures in the SIMP (Solid Isotropic Model with Penalization) model used to interpolate between density and the base material stiffness E^0, i.e., $E=\rho^p E^0$ [14]. The following values are used in the present study, $q = 2.5$ and $p = 3$. In turn, the homogenized stiffness tensor $\mathbf{E}^{\mathrm{H}}$ is computed through the homogenization formulas that can be seen in [5,6].

In problem (1) is used a density filter according to [15,16] to avoid checkerboard problems as well as to smooth enough the density and stress fields such that stress singularities are not prone to occur inside the unit-cell domain while its lay-out changes along the iterations of the optimization process. This filter is given by Eq. (3) where ω is a weighting factor based on a given filter radius $R_{\min}$ and the distance between centers of elements i and e.

Gradient-based algorithms, such as MMA [17], are used to solve problem (1) and thus

sensitivities of constraints and objective functions are required. Deriving analytical sensitivities is quite straightforward as regards compliance and volume functions [13]. Getting this data for stresses is a non-trivial calculus which is beyond the preliminary study presented here. Therefore, as regards stress sensitivity one relays here on the finite difference method that proves to be accurate enough as shown later on. Since one uses here a density filter bear in mind that one has to apply accordingly the chain rule while computing sensitivities, see for details [16].

$$\widetilde{\rho}_e = \frac{\sum_{i \in N_e} \omega(x_i)\rho_i}{\sum_{i \in N_e} \omega(x_i)}, \ \omega(x_i) = \max\left\{0, R_{\min} - \|x_i - x_e\|\right\} \tag{3}$$

4 MESH CONVERGENCE ANALYSIS

Engineers and scientists use finite element analysis to build predictive computational models of real-world scenarios. The accuracy that can be obtained from a finite element model is directly related to the finite element mesh that is used. As the finite elements are made smaller and smaller, as the mesh is refined, the computed solution will approach the true solution. While the same problem is resolved with successively finer and finer meshes one may compare the results between the different meshes. This comparison can be done by analyzing the fields at one or more points in the model or by evaluating the integral of a field over the domain. This leads one to choose an appropriate mesh refinement metric, which can be either local or global.

In the present study one focus on the stress field which can be quite non-linear over the physical domain of the unit-cell and thus the distribution of stress or its peak may easily become mesh dependent. Therefore, here one evaluates how good a stress approximation is by reducing the element size of the mesh successively (*h*-refinement method), dividing in the present study each existing element into four elements (two per edge) without changing the type and shape of the elements (only the size changes). To compare the quality of the different meshes obtained one uses the total Strain Energy *S*, as a global metric, and the Von-Mises stress, as a local metric, evaluated at some predefined nodal points or simply one selects the maximum value in the domain. This convergence analysis is specially relevant as one eventually optimizes the topology of a material microstructure for a given strength criteria and that must relay on a regular grid of FE (see e.g. Fig. 2a) accurate enough to provide reliable stress values which must be kept under an admissible value.

To proceed with the mesh convergence analysis one selects a lay-out simple enough to practice the mesh refinement without compromising any geometric descriptions avoiding that way the "modeling error" and bringing forth as desired the "discretization error" only. Fig. 2b shows such a lay-out where a centered square hole is placed in the unit-cell domain Y matching a volume fraction of 75%. On the top of this lay-out one fits easily regular (square) grid meshes as 8×8, 16×16, 32×32, 64×64 and 128×128. All these meshes preserve the design boundary or contour which is quite reassuring for the success of the proposed mesh convergence study. However, this coincidence is very difficult to achieve in practice when

optimizing topology on the top of square grid meshes which often gives mesh dependent lay-outs. This motivates further mesh convergence analyses beyond the scope of the present study once some feedback is provided by the topology optimization design solution.

The properties of the base material selected are E = 290MPa and ν = 0.3. The void region (hole) has a very small stiffness value to prevent any singular matrixes in the FE model. For each mesh one uses either 8-node or 20-node isoparametric hexahedral finite elements. The material microstructure is subjected to a macroscopic in-plane hydrostatic stress field, i.e., $\sigma_1 = \sigma_2$ = 1MPa. Fig. 2c shows specific node locations, not mesh dependent, where Von-Mises stress values are collected for comparison purposes.

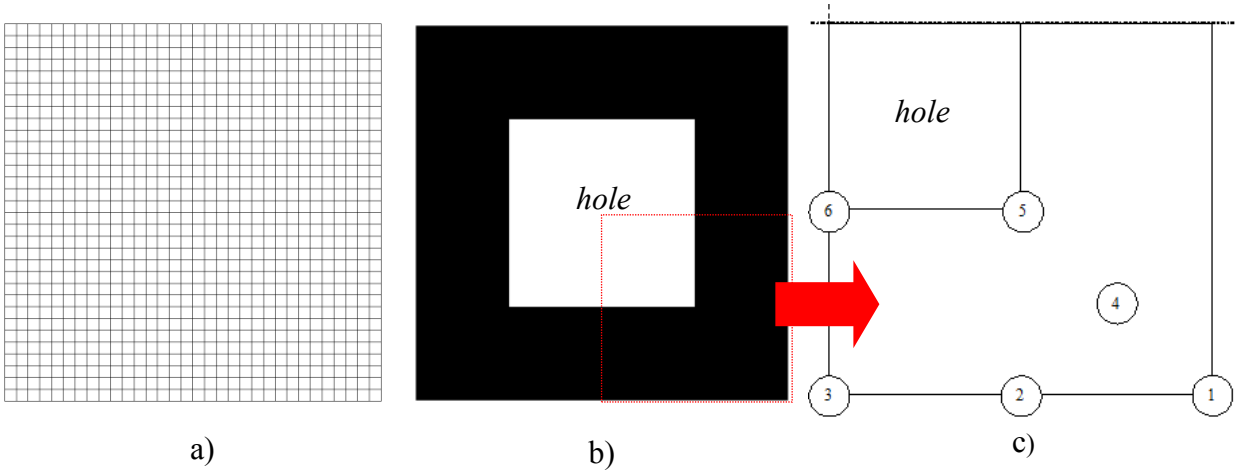

Figure 2: Numerical model for mesh convergence analysis; a) Example of square grid meshes considered (case 32×32 is displayed); b) Lay-out considered: unit-cell with square hole and 75% of volume fraction; c) Location of nodes where Von-Mises stresses are measured (a quarter of the unit-cell is shown).

Fig. 3 plots the element solution of the Von-Mises stress. The element solution is the volume average of the Von-Mises stresses measured at the element gauss points, 2×2×2 and 3×3×3 gauss points for 8-node and 20-node hexahedral elements, respectively.

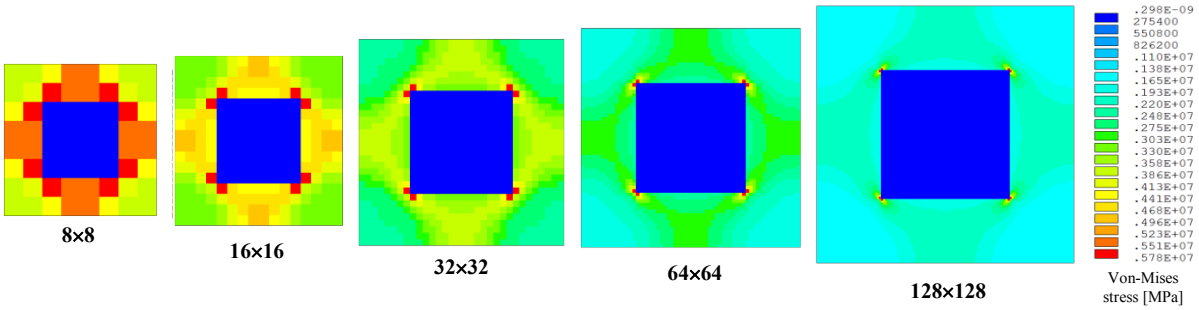

Figure 3: Von-Mises stress plots for meshes of N×N FE with N increasing from 8 to 128. The images get bigger just for the sake of enlarging finer meshes, bear in mind that the unit-cell size is always unitary |Y|=1. Stress scale on the right refers to 128×128 results.

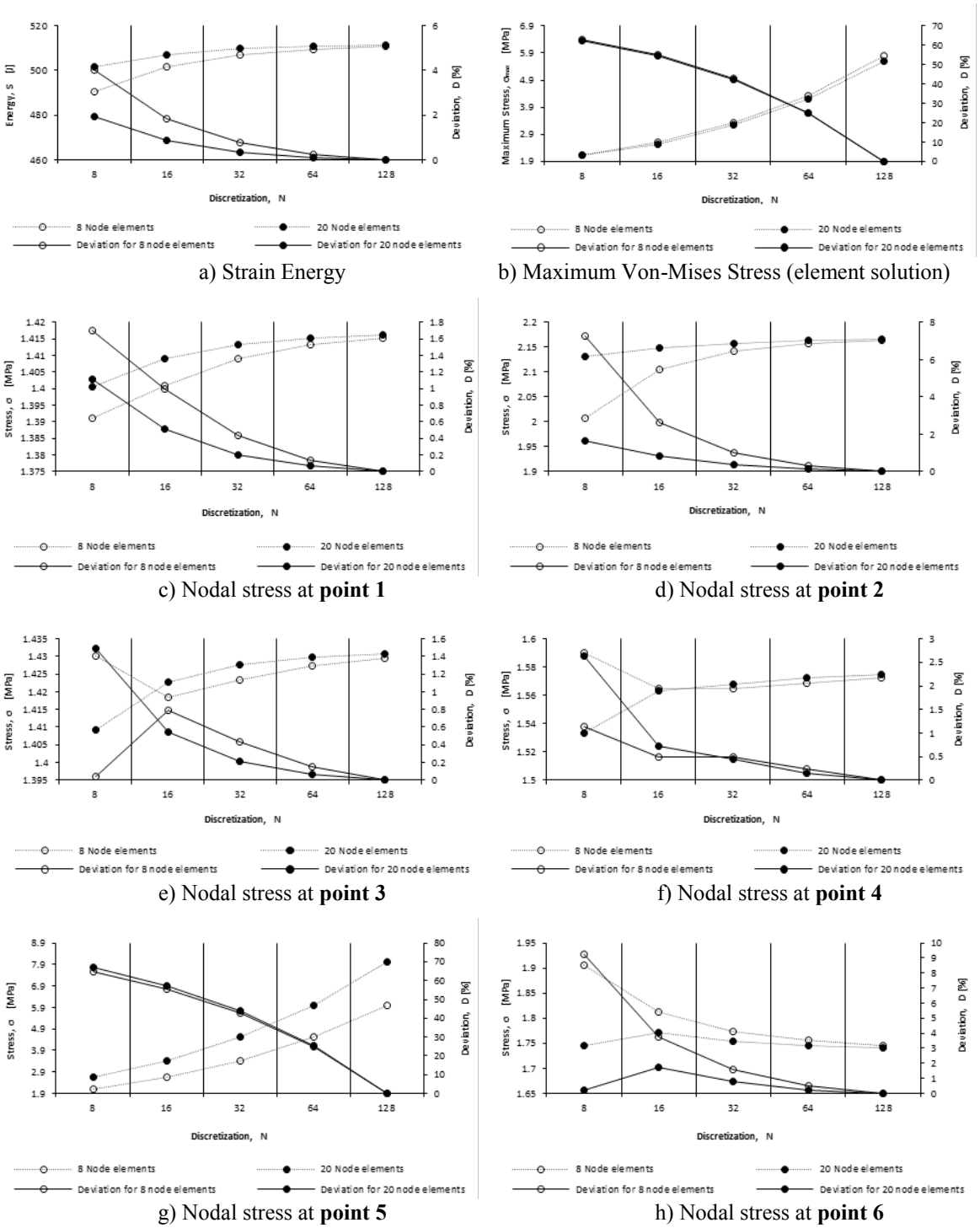

a) Strain Energy

b) Maximum Von-Mises Stress (element solution)

c) Nodal stress at **point 1**

d) Nodal stress at **point 2**

e) Nodal stress at **point 3**

f) Nodal stress at **point 4**

g) Nodal stress at **point 5**

h) Nodal stress at **point 6**

Figure 4: Plots of mesh refinement metrics. Global metric is Strain Energy (S). Local metrics are maximum Von-Mises Stress (σ_{max}) measured in the element and nodal Von-Mises stresses measured at specific locations according to Fig. 2c). Respective deviations in [%] having the finest mesh refinement as the reference.

Fig. 4 shows a set of charts providing the results for the different metrics used as the mesh

is refined. The nodal values plotted should be interpreted with the help of Fig. 2c. Monotonic convergence of the strain energy is obtained as expected from a FE solution (see Fig. 4a).

Analyzing the plotted contours in Fig. 3 one easily perceives a red spot associated to a singularity which could be actually anticipated due to the sharp corner of the hole (see Fig. 4b and 4g). The maximum stress that is actually measured at this corner is non-convergent as the mesh gets finer and finer (theoretically tends to infinite). An experienced analyst may determine that such a red spot (singularity) can be safely ignored once in the real world there are seldom perfectly sharp corners (fillets instead). Thus such high peak stress tend actually to obscure more interesting features in the FE solution (see plots for the remaining nodal points selected: 1,2,3,4 and 6). Anyway, one anticipates here that the singularity existence may become a critical issue when running a stress-based optimization problem where the overall stress level should be kept to a maximum, i.e. under an allowable stress value. A singularity in such optimization problem formulation will lead to solutions that are only optimal in terms of reducing the amplitude of the unphysical peak stress. The procedure of identifying and excluding regions of singularities from the search for a maximum stress will lead to an optimization problem not well posed either. It is preferable that by no means a singularity comes to the fore during the form finding process executed by the optimization algorithm. This motivates further research concerning "red spots" influence while designing material microstructure via topology optimization. As mentioned in the previous section, the use of density filters may play an important role in that regard.

Apart from the singularity noticed, mesh convergence is clearly recognized taking the results obtained with the finest mesh, 128×128, as reference to plot the deviation in %. This also helps to see how rapidly the metrics used converge. Typically, convergent curves show deviations less than 1% above 32×32 meshes which is quite low and results are even better for 20-node brick elements in the mesh.

5 STRESS-BASED OPTIMAL DESIGN

Strength oriented design of material microstructures is the ultimate goal here. To better compare how stress constraints change an optimal design, one solves first the problem (1) simplified, i.e. minimizing compliance subjected to the volume constraint alone. The outcome is a design initially oriented to meet stiffness criteria only.

In the strain formulation used in problem (1) one chooses the macroscopic strain field $\bar{\boldsymbol{\varepsilon}}$ where the longitudinal strains in plane x_1x_2 are equal (hydrostatic case), i.e. $\left(\bar{\varepsilon}_{11},\bar{\varepsilon}_{22},\bar{\varepsilon}_{33},\bar{\varepsilon}_{12},\bar{\varepsilon}_{13},\bar{\varepsilon}_{23}\right)=\left(0.2414,0.2414,-0.2069,0,0,0\right)\times10^{-2}$. In the volume fraction constraint one selects an upper bound of V^*=0.8 (80% of solid phase). The base material properties are E = 290MPa and ν = 0.3. The Method of Moving Asymptotes [17] is chosen as the optimizer to update the density design variables. Although the previous mesh convergence study may provide an indication about what a good mesh is to perform optimization with stress criteria, one decides here to simply come up with some preliminary optimized designs regardless the quality of the mesh. Problem formulation in (1) deals with a rapidly increasing number of constraints as the mesh gets finer and finer. Therefore, for the sake of demonstration purposes only, here one chooses a reasonable number of constraints, 400 = 20×20 mesh, see Fig. 5a. This allow one to get some initial insight about stress criteria influence on the design without getting a too expensive problem to solve. As a future work, finer meshes are recommended

for use as well as techniques to reduce the computational cost.

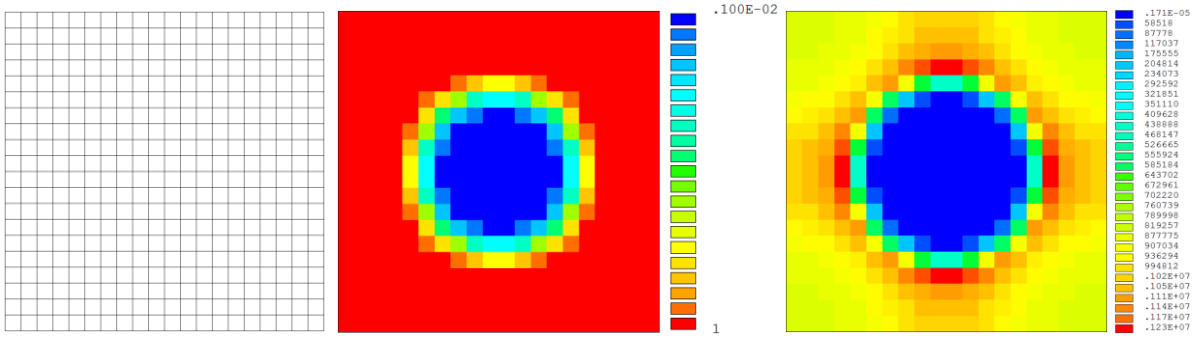

Figure 5: Topology optimization without stress constraints; a) Finite element mesh used 20×20, b) Optimal density distribution, $\rho_{\min}$, c) Equivalent (Von-Mises) stress field, $\sigma_{VM}^{\max} = 1.23MPa$.

Fig. 5b shows the stiffness-oriented optimal design solution, basically a square with a round hole, and Fig. 5c displays the respective equivalent stress distribution where higher stresses are concentrated in the boundary of the hole. Supposing now that the maximum stress value found of 1.23MPa is actually exceeding the admissible stress in 23% i.e., σ_{adm} = 1MPa, one adds a "battery" of constraints as in Eq. (1) to ensure that no point in the design domain violates such stress limit. Imposing the stress constraints, the outcome is a strength-oriented optimal design solution as can be seen in Fig. 6. The history of optimization is shown in terms of the density and stress changes along the algorithm iterations. The regions in "blue" identify density or stress close to zero while "red" regions correspond to full density (=1) or maximum stress (=σ_{adm}). Intermediate colors represent intermediate density and stress values interpreted the same way as in Fig. 5b and 5c. The initial design has two square regions of uniform density such that a material volume fraction of 80% is attained. Furthermore, this design is feasible too regarding stresses as one can easily inspect visually for no red spot is found in the initial stress distribution shown in Fig.6 (left side).

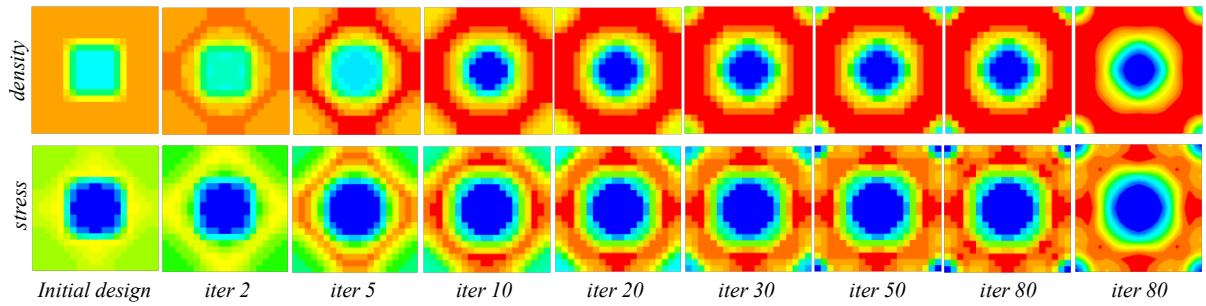

Figure 6: Topology optimization with stress constraints. Changes on the density and stress fields along the algorithm iterations are displayed. Last iteration is repeated here twice to show at last how both fields are smoothed when an image processing technique based on averaging is applied.

Finally, the stiffness and strength oriented optimal designs are compared side by side in Fig. 7. Here one clearly sees the effect of stress constraints on rounding the sharp corners of the initial design of the unit-cell. At these corners, where the stress level is lower, the density is reduced and the region where the hole is located gets more undefined as the gray zone enlarges. This demands for further investigation as regards the size of the mesh used as well as the filter used. Although the optimal microstructure in Fig. 7b is not that much defined as regards its boundary, one has here a preliminary result of stresses constrained (feasible design) which is actually obtained at the expense of getting lower level of stiffness in the objective function value in comparison to Fig. 7a (12% less).

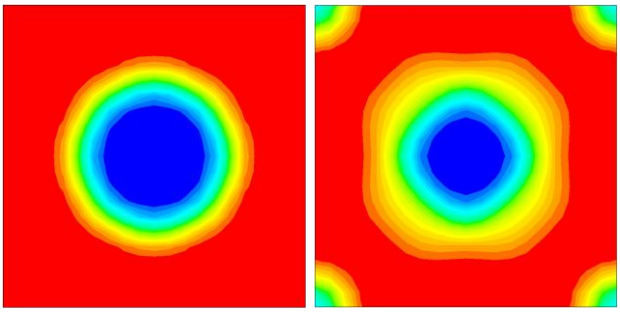

a) b)

Figure 7: Comparison between the non-based and based stress optimization problem; a) without stress constraints; b) with stress constraints.

6 CONCLUSIONS

In this paper periodic composite materials mixing solid and void phases are considered. Homogenization is used to compute equivalent elastic properties as well as to estimate stresses at a local level, i.e. in the unit-cell domain. A mesh convergence analysis is conducted to conclude that metrics such as strain energy and pointwise stresses converge rapidly enough. However, results are shown for a very simple geometry that is a square unit-cell with a square hole which proves to be very convenient because one preserves geometry as the mesh is refined spotting that way discretization errors only. More complex designs should also be taken into account as future work to see also if density filters can smooth the stress field enough to prevent singularities from occurring during the optimization process. Mesh convergence studies in the future should also allow one to conclude what is the best mesh to be used in subsequent microstructure optimization. The optimization process can be quite demanding of computational resources due to the huge number of stress constraints one may face. In order to have a lighter computational load here one used a coarser mesh which motivates further studies with finer meshes. Anyway, results are shown for an optimal design complying with stress requirements considering an in-plane hydrostatic loading case. The unit-cell design differences obtained between stiffness and strength oriented design problems are highlighted. Further developments should include other loading conditions too.

ACKNOWLEDGEMENTS

This work was partially supported by the Portuguese Foundation for Science and Technology, FCT-Portugal, through the projects UID/EMS/00667/2013, PTDC/EMS-PRO/4732/2014 and UID/EMS/50022/2013.

REFERENCES

[1] Jones, R.M. *Mechanics of Composite Materials*. McGraw Hill, (1975).
[2] Mallick, P.K. *Composites Engineering Handbook*. Marcel Dekker, Inc., (1997).
[3] Zohdi T.I. and Wriggers, P. *Introduction to Computational Micromechanics*. Springer-Verlag Berlin Heidelberg, (2005).
[4] Tavares R.P., Melro A.R., Bessa, M.A. and Turon, A. Mechanics of hybrid polymer composites: analytical and computational study. *Comput. Mech.* (2016) **57**:405-421.
[5] Guedes, J.M. and Kikuchi, N. Preprocessing and postprocessing for materials based on the homogenization method with adaptive finite element method. *Comput. Meth. Appl. Mech. Engng* (1990) **83**:143-98.
[6] Ferreira, R.T.L., Rodrigues, H.C., Guedes, J.M. and Hernandes, J.A. Hierarchical optimization of laminated fiber reinforced composites. *Composite Structures* (2014) **107**: 246-259.
[7] Coelho, P.G., Guedes, J.M. and Rodrigues, H.C. Multiscale topology optimization of bi-material laminated composite structures. *Composite Structures* (2015) **132**: 495-505.
[8] Coelho, P.G., Reis R. and Guedes J.M. Convergence analysis of stress fields to homogenization predictions in optimal periodic composite design. *Composite Structures* (2015) **132**: 495-505.
[9] Coelho, P.G., Reis, R. and Guedes, J.M. Convergence analysis of stress fields to homogenization predictions in optimal periodic composite design. *ECCOMAS Congress*. Crete Island, Greece, 5-10 June, (2016).
[10] Duysinx, P. and Bendsøe, M.P. Topology optimization of continuum structures with local stress constraints. *Int. J. for Num. Meth. in Engng* (1998) **43(8)**: 1453-1478.
[11] Bruggi, M. and Venini, P. A mixed FEM approach to stress-constrained topology optimization. *Int. J. for Num. Meth. in Engng* (2008) **73(12)**: 1693-1714.
[12] Sigmund, O. Materials with prescribed constitutive parameters: an inverse homogenization problem. *Int J Solids Struct* (1994) **31(17)**: 2313-29.
[13] Bendsøe, M.P. and Sigmund, O. *Topology optimization: theory, methods, and applications*. Springer, (2003).
[14] Bendsøe, M.P. Optimal shape design as a material distribution problem. *Struct. Optim.* (1989) **1**:193-202.
[15] Bruns T.E. and Tortorelli, D.A. Topology optimization of non-linear elastic structures and compliant mechanisms. *Comput. Meth. Appl. Mech. Eng.* (2001) **190(26-27)**: 3443-3459.
[16] Sigmund, O. Morphology-based black and white filters for topology optimization. *Struct. Multidisc. Optim*. (2007) **33**:401-424.
[17] Svanberg, K. The method of moving asymptotes - a new method for structural optimization. *Int. J. Numerical Meth. Eng.* (1987) **24**: 359-73.

VII International Conference on Computational Methods for Coupled Problems in Science and Engineering
COUPLED PROBLEMS 2017
M. Papadrakakis, E. Oñate and B. Schrefler (Eds)

CONJUGATE HEAT TRANSFER SHAPE OPTIMIZATION BASED ON THE CONTINUOUS ADJOINT METHOD

K.T. GKARAGKOUNIS*, E.M. PAPOUTSIS-KIACHAGIAS† AND K.C. GIANNAKOGLOU††

Lab. of Thermal Turbomachines, Parallel CFD & Optimization Unit
National Technical University of Athens
9, Heroon Polytechniou, NTUA Zografou Campus, 15780, Athens, Greece
e-mails: kogkar@hotmail.com*, vaggelisp@gmail.com† and kgianna@central.ntua.gr††
††web page: http://velos0.ltt.mech.ntua.gr/research/

Key words: Continuous Adjoint Method, Conjugate Heat Transfer, Shape Optimization, Fluid-Solid Interface.

Summary: In this paper, the continuous adjoint method for use in gradient-based optimization methods for coupled problems including heat transfer between bodies (solids) and fluids flowing over or inside them is developed. This kind of problems are usually referred to as Conjugate Heat Transfer (CHT) problems. Emphasis is given to expanding the Enhanced-Surface Integral (E-SI) adjoint formulation recently published by the authors' group for shape optimization problems in fluid mechanics only, to tackle CHT problems. This formulation ensures that the gradient of the objective function is accurately computed, while the computational cost is kept as low as possible.

1 INTRODUCTION

Adjoint methods have widely been used to solve single-discipline optimization problems. However, the advances in computational methods and the capabilities of modern computational platforms have shifted the interest from single-discipline to coupled problems [2]. CHT problems, involving the interaction of fluid flow and heat transfer between fluids and solids, are investigated in this paper, by focusing on the development of the continuous adjoint method for use in the optimization of the shape of solid boundaries/interfaces. To the authors' knowledge, there are a few papers in the literature of continuous adjoint methods which are related to CHT shape optimization problems [3, 9].

The first goal of this paper is to expand a new continuous adjoint formulation, the so-called E-SI one, to CHT problems. This formulation, initially proposed by the authors' group in [7], was originally developed for shape optimization problems in incompressible fluid flows. More convincing applications of the same method, for other objective functions, can be found in [8].

The second goal of this paper is to compare the E-SI formulation as developed for CHT problems with alternative formulations of the continuous adjoint method, according to the literature. As presented in [7, 8], there are two other continuous adjoint formulations, yielding different sensitivity derivative (SD) expressions. The first one is referred to as FI (Field Integral), since the resulting SD expression includes at least one field integral over the solution domain. This method computes accurate SD with computational cost though, that scales with the number of the design (or optimization) variables parameterizing the shape to be designed [4]. The second formulation [1, 5, 10] leads to exactly the same adjoint PDEs and boundary conditions, though to different expressions for the SD, which are now exclusively expressed in terms of surface integrals; this is referred to as the SI (Surface Integral) adjoint formulation. SD computed using the SI adjoint might generally become quite inaccurate; however, the SI formulation is appealing due to its low cost which does not depend on the number of design variables.

In the E-SI adjoint method, apart from the flow PDEs or the heat conduction equation over the solid domain, also the adjoint to the grid displacement equations must be solved. This method computes SD expressed in terms of surface integrals, enhanced with the contributions from the adjoint to the grid displacement PDEs.

The mathematical development includes the formulation of the adjoint to the Fluid-Structure Interface (FSI) conditions. The three continuous adjoint formulations are investigated through applications in 2D problems and the accuracy of the computed SD is validated by comparing them with finite differences (FD).

2 PRIMAL PROBLEM

The overall computational domain Ω comprises the fluid Ω_F and solid Ω_S subdomains, separated by an interface $\overline{S}$. Depending on whether the interface is seen from the fluid or solid point of view, the latter will be denoted by $\overline{S}_F$ or $\overline{S}_S$, respectively. The steady-state Navier-Stokes equations for incompressible fluid flows are given by

$$R^p = -\frac{\partial v_j}{\partial x_j} = 0 \tag{1}$$

$$R_i^v = v_j \frac{\partial v_i}{\partial x_j} - \frac{\partial \tau_{ij}}{\partial x_j} + \frac{\partial p}{\partial x_i} = 0 \tag{2}$$

$$R_F^T = v_j c_p \frac{\partial T^F}{\partial x_j} + \frac{v_j}{2}\frac{\partial v_k^2}{\partial x_j} - \frac{\partial}{\partial x_j}\left(a_{eff} c_p \frac{\partial T^F}{\partial x_j}\right) = 0 \tag{3}$$

where v_i are the velocity components and p stands for the static pressure divided by the fluid density ρ_F. Also, $\tau_{ij} = \nu_{eff}\left(\frac{\partial v_i}{\partial x_j} + \frac{\partial v_j}{\partial x_i}\right)$, where ν_{eff} is the effective viscosity, being either $\nu_{eff} = \nu$ for laminar or $\nu_{eff} = \nu + \nu_t$ for turbulent flows (ν, ν_t stand for the bulk and turbulent viscosities). The same holds for the thermal diffusivity α_{eff}, being either $\alpha_{eff} = \alpha$ or $\alpha_{eff} = \alpha + \alpha_t$ in laminar and turbulent flows respectively, where $\alpha = \nu/Pr$, $\alpha_t = \nu_t/Pr_t$ (Pr, Pr_t are the Prandtl numbers for laminar and turbulent

flows). Moreover, T^F is the fluid temperature and c_p the specific heat transfer coefficient under constant pressure. Repeated indices imply summation.

The boundaries S_F of Ω_F are decomposed as $S_F = S_{F,I} \cup S_{F,O} \cup S_{F,W} \cup \overline{S}_F$, indicating the inlet, outlet, plain and FSI solid walls, respectively. The conditions imposed on the boundaries of Ω_F are summarized in Table 1. The pressure and velocity conditions imposed along $\overline{S}_F$ and $S_{F,W}$ are identical; the temperature conditions are presented later on.

Table 1: Types of boundary conditions imposed along the boundaries of the fluid domain.

Boundary	p	v_i	T
$S_{F,I}$	zero Neumann	Dirichlet	Dirichlet
$S_{F,O}$	Dirichlet	zero Neumann	zero Neumann
$S_{F,W}$	zero Neumann	Dirichlet	zero Neumann

On the other hand, heat conduction in Ω_S is governed by

$$R_S^T = -\frac{\partial}{\partial x_j}\left[k^S \frac{\partial T^S}{\partial x_j}\right] = 0 \tag{4}$$

where k^S stands for the thermal conductivity of the solid region. The solid domain boundaries S_S are decomposed as $S_S = S_{S,o} \cup \overline{S}_S$, where $S_{S,o}$ represents boundaries other than $\overline{S}_S$. For the cases presented herein, T^S is fixed along $S_{S,o}$.

The most critical part of the CHT problem is related to the (physical) conditions imposed along each point at the FSI boundary, which are

$$k^S \frac{\partial T^S}{\partial n}\bigg|_{\overline{S}_S} = -k^F \frac{\partial T^F}{\partial n}\bigg|_{\overline{S}_F} \tag{5}$$

$$T^S = T^F \tag{6}$$

where $k^F = (a + a_t) c_p \rho_F$.

3 CONTINUOUS ADJOINT (E-SI) FORMULATION

Starting point of the continuous adjoint method, according to the E-SI formulation [7], is the augmented objective function

$$L = J + \int_{\Omega_F} q R^p d\Omega + \int_{\Omega_F} u_i R_i^v d\Omega + \sum_{D=F,S} \left\{ \int_{\Omega_D} T_a^D R_D^T d\Omega + \int_{\Omega_D} m_{a,i}^D R_{D,i}^m d\Omega \right\} \tag{7}$$

where $D = F, S$. The objective function J to be minimized, is defined over Ω_S and depends solely on T^S. Also, q, u_i, T_a^D, m_a^D are the adjoint pressure and adjoint velocity

components over Ω_F, the adjoint temperature and the adjoint nodal displacement fields for the $D = F, S$ domains. According to the E-SI adjoint formulation, as proposed in [7, 8], apart from the flow/heat equations, L should also include PDEs governing the Ω_F and Ω_S grid displacement $R^m_{D,i}$. Assuming that, in both domains D, the same Laplacian grid displacement model is valid, $R^m_{D,i}$ can be expressed as

$$R^m_{D,i} = \frac{\partial^2 m^D_i}{\partial x^2_j} = 0,\ D = F, S,\ i = 1, 2, 3 \tag{8}$$

where m^D_i is the nodal (grid) displacement field over domain D.

For the sake of simplicity, during the presentation of the mathematical development of the adjoint CHT equations, we refrain from including the turbulence model and the corresponding adjoint equations. The interested reader should refer to [6, 12].

Development is based on the Leibniz integration rule for domains with varying boundaries, which states that, for any residual R ($R = R_p,\ R_{v_i},\ R_{T_D},\ R_{m_D}$) and adjoint variables Ψ ($\Psi = q,\ u_i,\ T^D_a,\ m^D_a$),

$$\frac{\delta}{\delta b_n}\int_{\Omega_D}\Psi R d\Omega = \int_{\Omega_D}\Psi\frac{\partial R}{\partial b_n}d\Omega + \int_{S_D}\Psi R n_k\frac{\delta x_k}{\delta b_n}dS \tag{9}$$

where n_k are the components of the unit vector normal to the given surface. Eq. 9 is used to develop the integrals on the r.h.s. of eq. 7 and also, the objective function J.

The adjoint equations arise, after eliminating the terms multiplying the variations in $p,\ v_i,\ T^D$ included in the expression of $\delta L/\delta b_n$. After a lengthy development, which is omitted in the interest of space, the field adjoint equations

$$R^q = -\frac{\partial u_j}{\partial x_j} = 0 \tag{10}$$

$$R^u_i = u_j\frac{\partial v_j}{\partial x_i} - v_j\frac{\partial u_i}{\partial x_j} - \frac{\partial \tau^a_{ij}}{\partial x_j} + \frac{\partial q}{\partial x_i} + c_p T^F_a\frac{\partial T^F}{\partial x_i} + T^F_a v_k\frac{\partial v_k}{\partial x_i} - v_i v_k\frac{\partial T^F_a}{\partial x_k} = 0,\ i = 1, 2(, 3) \tag{11}$$

$$R^{T_a}_F = -v_j\frac{\partial T^F_a}{\partial x_j} - \frac{\partial}{\partial x_j}\left(\alpha_{eff}\frac{\partial T^F_a}{\partial x_j}\right) = 0 \tag{12}$$

$$\begin{aligned} R^{m_{a,k}}_F = {} & \frac{\partial^2 m^F_{a,k}}{\partial x^2_j} - \frac{\partial}{\partial x_j}\Bigg[- u_i v_j\frac{\partial v_i}{\partial x_k} - \tau^a_{ij}\frac{\partial v_i}{\partial x_k} + u_i\frac{\partial \tau_{ij}}{\partial x_k} - u_j\frac{\partial p}{\partial x_k} + q\frac{\partial v_j}{\partial x_k} - c_p T^F_a v_j\frac{\partial T}{\partial x_k} \\ & - T^F_a v_j v_i\frac{\partial v_i}{\partial x_k} - \alpha_{eff} c_p\frac{\partial T^F_a}{\partial x_j}\frac{\partial T^F}{\partial x_k} + c_p T^F_a\frac{\partial}{\partial x_k}\left(\alpha_{eff}\frac{\partial T^F}{\partial x_j}\right)\Bigg] = 0 \end{aligned} \tag{13}$$

over Ω_F and

$$R^{T_a}_S = -\frac{\partial}{\partial x_j}\left(k^S\frac{\partial T^S_a}{\partial x_j}\right) + J_S = 0 \tag{14}$$

$$R^{m_{a,k}}_S = \frac{\partial^2 m^S_{a,k}}{\partial x^2_j} - \frac{\partial}{\partial x_j}\left(k_S T^S_a\frac{\partial^2 T^S}{\partial x_j \partial x_k} - k_S\frac{\partial T^S_a}{\partial x_j}\frac{\partial T^S}{\partial x_k}\right) + J_{M,k} = 0 \tag{15}$$

over Ω_S are defined. J_S and $J_{M,k}$ are the contributions from the differentiation of the objective function to the adjoint energy and grid displacement PDEs. The three final terms in eq. 11 are the contribution of the differentiated energy equation to the adjoint momentum equations. In addition, $\tau_{ij}^a = \nu_{eff}\left(\frac{\partial u_i}{\partial x_j} + \frac{\partial u_j}{\partial x_i}\right)$ stands for the adjoint stresses. It should also be noted that, for incompressible flows, the adjoint energy equation is decoupled from the mean flow one, since the first includes the primal velocity and the adjoint temperature. In contrast to the primal system though, the solution of the adjoint energy equations has to precede the solution of the adjoint mean flow equations. Eqs. 12 and 14 are coupled through their boundary conditions along the interface.

The adjoint boundary conditions arise, after eliminating terms in surface integrals multiplying the variations of the field variables w.r.t. b_n. For example, along the inlet, the imposed adjoint boundary conditions are

$$\frac{\partial q}{\partial n} = 0,\ u_i = 0,\ T_a^F = 0,\ m_a^F = 0 \tag{16}$$

Along the other non-FSI boundaries, the boundary conditions are obtained through a development similar to that in [7]. Along the FSI boundaries, the adjoint boundary conditions are similar to the primal ones. The SD expression, including only surface integrals, becomes

$$\begin{aligned}
\left.\frac{\delta J}{\delta b_n}\right|_{E-SI} = & T^J_{surface} - \int_{S_{F,W},\overline{S}_F} \left[\tau_{ij}^a n_j - q n_i\right] \frac{\partial v_i}{\partial x_k}\frac{\delta x_k}{\delta b_n} dS + \int_{S_{F,W}} \alpha_{eff} c_p T_a^F \frac{\partial T^F}{\partial x_j}\frac{\delta n_j}{\delta b_n} dS \\
& + \int_{S_{F,W}} \alpha_{eff} c_p T_a^F \frac{\partial^2 T^F}{\partial x_j \partial x_k} n_j \frac{\delta x_k}{\delta b_n} dS - \int_{S_{S,o}} k^S \frac{\partial T_a^S}{\partial x_j} n_j \frac{\partial T^S}{\partial x_k}\frac{\delta x_k}{\delta b_n} dS \\
& + \int_{\overline{S}_F} \left[T_a^F \left(k^F \frac{\partial^2 T^F}{\partial x_j \partial x_k} - k^S \frac{\partial^2 T^S}{\partial x_j \partial x_k} \right) n_j - k^F \frac{\partial T_a^F}{\partial x_j} n_j \left(\frac{\partial T^F}{\partial x_k} - \frac{\partial T^S}{\partial x_k} \right) \right] \frac{\delta x_k}{\delta b_n} dS \\
& + \int_{\overline{S}_F} T_a^F \left(k^F \frac{\partial T^F}{\partial x_j} - k^S \frac{\partial T^S}{\partial x_j} \right) \frac{\delta n_j}{\delta b_n} dS - \sum_{D=F,S} \left\{ \int_{S_{D,W},\overline{S}_D} \frac{\partial m_{a,i}^D}{\partial x_j} n_j \frac{\delta x_i}{\delta b_n} dS \right\}
\end{aligned} \tag{17}$$

where $T^J_{surface}$ depends on the objective function.

4 Comparing the E-SI with the two alternative adjoint formulations

The E-SI formulation was developed to overcome the disadvantages of the standard formulations (FI and SI) of the continuous adjoint method. Through the E-SI adjoint, it is possible to compute SD as accurate as with the FI adjoint and with the same cost as with the SI adjoint.

The FI gradient arises by further developing the following equation

$$\frac{\delta L}{\delta b_n} = \frac{\delta J}{\delta b_n} + \int_{\Omega_F} q \frac{\delta R^p}{\delta b_n} d\Omega + \int_{\Omega_F} u_i \frac{\delta R_i^v}{\delta b_n} d\Omega + \int_{\Omega_F} T_a^F \frac{\delta R_F^T}{\delta b_n} d\Omega + \int_{\Omega_S} T_a^S \frac{\delta R_S^T}{\delta b_n} d\Omega \tag{18}$$

After a lengthy mathematical development, which is omitted here since it is similar to that presented in [7], the SD expression becomes

$$\begin{aligned}\left.\frac{\delta J}{\delta b_n}\right|_{FI} = \int_{\Omega_F}\Bigg[&- u_i v_j \frac{\partial v_i}{\partial x_k} - \tau_{ij}^a \frac{\partial v_i}{\partial x_k} + u_i \frac{\partial \tau_{ij}}{\partial x_k} - u_j \frac{\partial p}{\partial x_k} + q\frac{\partial v_j}{\partial x_k} - c_p T_a^F v_j \frac{\partial T}{\partial x_k} \\ &- T_a^F v_j v_i \frac{\partial v_i}{\partial x_k} - \alpha_{eff} c_p \frac{\partial T_a^F}{\partial x_j}\frac{\partial T^F}{\partial x_k} + c_p T_a^F \frac{\partial}{\partial x_k}\left(\alpha_{eff}\frac{\partial T^F}{\partial x_j}\right)\Bigg]\frac{\partial}{\partial x_j}\left(\frac{\delta x_k}{\delta b_n}\right)d\Omega \\ &+ \int_{\Omega_S}\Bigg[- k_S \frac{\partial T_a^S}{\partial x_j}\frac{\partial T^S}{\partial x_k} + k_S T_a^S \frac{\partial^2 T^S}{\partial x_j \partial x_k}\Bigg]\frac{\partial}{\partial x_j}\left(\frac{\delta x_k}{\delta b_n}\right)d\Omega + \int_{S_{F,W}} \alpha_{eff} c_p T_a^F \frac{\partial T^F}{\partial x_j}\frac{\delta n_j}{\delta b_n} dS \\ &+ \int_{\overline{S}_F} \alpha_{eff} c_p T_a^F \frac{\partial T^F}{\partial x_j}\frac{\delta n_j}{\delta b_n} dS + \int_{\overline{S}_F} k^S T_a^S \frac{\partial T^S}{\partial x_j}\frac{\delta n_j}{\delta b_n} dS + T^J_{volume} \end{aligned} \tag{19}$$

where T^J_{volume} comes from the differentiation of J. One should notice the presence of the spatial derivatives of the grid sensitivities $\delta x_k/\delta b_n$ for the entire fluid and solid domains. These quantities are computed through FD, by superimposing infinitesimally small pertubations $\pm\epsilon$ on each design variable b_n and adapting the computational grid. From this point of view, the cost of computing the FI–gradient of J scales with the number of b_n and consequently, the use of the FI formulation becomes quite expensive in problems with many design variables. Eq. 19 is complete, without any assumption made and as such, it computes accurate SD.

The development of the SI formulation starts by applying the Leibniz theorem (eq. 9) to eq. 7, in which the integrals concerning the grid displacement equations do not exist. The derivative of L now becomes

$$\begin{aligned}\frac{\delta L}{\delta b_n} = \frac{\delta J}{\delta b_n} &+ \int_{\Omega_F} q\frac{\partial R^p}{\partial b_n} d\Omega + \int_{\Omega_F} u_i \frac{\partial R_i^v}{\partial b_n} d\Omega + \int_{\Omega_F} T_a^F \frac{\partial R_F^T}{\partial b_n} d\Omega + \int_{\Omega_S} T_a^S \frac{\partial R_S^T}{\partial b_n} d\Omega \\ &+ \int_{S_F} \left(qR^p + u_i R_i^v + T_a^F R_F^T\right) n_k \frac{\delta x_k}{\delta b_n} dS + \int_{S_S} T_a^S R_S^T n_k \frac{\delta x_k}{\delta b_n} dS \end{aligned} \tag{20}$$

The last two surface integrals which include the residuals of the PDEs governing the physical problem are dropped out by those developing SI adjoint methods, under the assumption that they are zero on the boundary. This assumption is not valid and as shown in [7], is responsible for the potential loss of accuracy of the SD computed with the SI adjoint formulation (wrong or even wrongly signed SD). After a mathematical

development, the expression of the SD is given by

$$\left.\frac{\delta F_{aug}}{\delta b_n}\right|_{SI} = T^J_{surface} - \int_{S_{F,W},\overline{S}_F} \left[\tau^a_{ij} n_j - q n_i\right] \frac{\partial v_i}{\partial x_k} \frac{\delta x_k}{\delta b_n} dS + \int_{S_{F,W}} \alpha_{eff} c_p T^F_a \frac{\partial T^F}{\partial x_j} \frac{\delta n_j}{\delta b_n} dS$$
$$+ \int_{S_{F,W}} \alpha_{eff} c_p T^F_a \frac{\partial^2 T^F}{\partial x_j \partial x_k} n_j \frac{\delta x_k}{\delta b_n} dS - \int_{S_{S,o}} k^S \frac{\partial T^S_a}{\partial x_j} n_j \frac{\partial T^S}{\partial x_k} \frac{\delta x_k}{\delta b_n} dS$$
$$+ \int_{\overline{S}_F} \left[T^F_a \left(k^F \frac{\partial^2 T^F}{\partial x_j \partial x_k} - k^S \frac{\partial^2 T^S}{\partial x_j \partial x_k} \right) n_j - k^F \frac{\partial T^F_a}{\partial x_j} n_j \left(\frac{\partial T^F}{\partial x_k} - \frac{\partial T^S}{\partial x_k} \right) \right] \frac{\delta x_k}{\delta b_n} dS$$
$$+ \int_{\overline{S}_F} T^F_a \left(k^F \frac{\partial T^F}{\partial x_j} - k^S \frac{\partial T^S}{\partial x_j} \right) \frac{\delta n_j}{\delta b_n} dS \tag{21}$$

The above SD expression consists only of surface integrals without involving the (internal) grid sensitivities. This feature makes this formulation cheaper to evaluate than the FI one and the preferred way of developing the continuous adjoint method by the great majority of researchers.

In both the FI and SI formulations, the same adjoint equations and boundary conditions, as in the E-SI one, arise without involving the adjoint grid displacement equations; the latter is a task with almost negligible cost within each optimization cycle, since it requires the solution of just a single vectorial PDE per solution domain, irrespective of the number of design variables. Note that the adjoint nodal displacement equations can be solved at a post-processing level, after computing the SI derivatives which give just a part of the E-SI ones.

5 APPLICATIONS

The first application aims at comparing the SD computed by the three adjoint formulations (E-SI, FI and SI) using FD as the reference values. The objective function, related to the mean temperature over Ω_S, is

$$J_{T^S} = \frac{\int_{\Omega_S} T_S d\Omega}{\int_{\Omega_S} d\Omega} \tag{22}$$

An S-Bend 2D duct (fluid region Ω_F) in contact with a solid body Ω_S is used. In fig. 1a, the geometry along with the parameterized patches are displayed. In specific, the central part of the FSI boundary is parameterized with 12 NURBS control points, of which the first and last ones are kept fixed. SD are computed w.r.t. the x (first half points in the abscissa) and y (second half) coordinates of these control points.

The flow is laminar; flow conditions and data are shown in Table 2. In fig. 1b, it is shown that the E-SI formulation practically reproduces the FI and FD derivatives. In contrast, this is not the case for the SI derivatives, which substantially deviate from the FD, since at quite a few control points they have different signs, being also an order of magnitude off. In addition, the computation of SD with the E-SI formulation needed

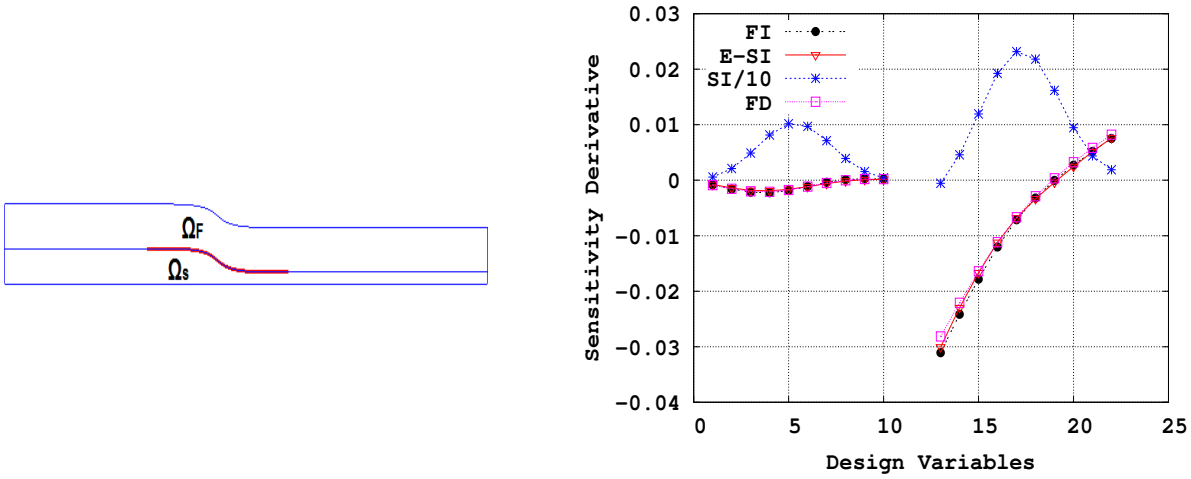

(a) (b)

Figure 1: Laminar flow in an S-Bend 2D duct ($Re = 60$), attached to a solid body. Minimization of J_{TS}. a) The fluid and solid domains along with the parameterized patch (red line). b) Comparison of SD computed with FI, E-SI, SI and FD methods.

$\sim$22 % of the time to compute them with FI, while the SI method needed $\sim$11 %. This difference in computational time between the E-SI and FI formulations increases with the number of design variables. Computations were performed in parallel on 4 Intel(R) Xeon(R) CPU E5-2630 processors at 2.30 GHz.

Table 2: Conditions and data of the two CHT problems.

S–Bend case:		**2D turbine blade case:**	
U_{inlet}	0.1 m/sec	U_{inlet}	25 m/sec
Re	60	Re	$\sim 53k$
c_p	4181 $J/kg/K$	c_p	1068 $J/kg/K$
α	1.45×10^{-6} m^2/sec	α	$\sim 93 \times 10^{-6}$ m^2/sec
Pr	6.62	Pr	0.68
k_S	60 $J/msecK$	Pr_t	1
T^F_{inlet}	291.214 K	k_S	215 $J/msecK$
T^S	300 K	T^F_{inlet}	800 K
		$T_{coolant}$	432 K
		h	2000 J/m^2secK

An optimization problem is solved in the second case. The goal is to minimize the maximum temperature of a 2D blade of a turbine stator. By definition, this is a non-differentiable function and in order to develop the continuous adjoint method for it, the

objective function used is

$$J_{maxT} = \frac{\int_{\Omega_S} \left[1 - \frac{1}{1+e^{k_2(T-T_{crit})+k_1}}\right] d\Omega}{\int_{\Omega_S} d\Omega} \tag{23}$$

where $k_1 = log\left(\frac{1}{1-f_{max}} - 1\right)$, $k_2 = \frac{log\left(\frac{1}{1-f_{max}}-1\right)}{T_{safe}-T_{crit}}$ with $f_{max} = 0.999$ and $f_{min} = 0.001$. In addition, T_{safe} and T_{crit} correspond to two different temperature limits, which are important for the operation of the blade: T_{safe} stands for the temperature below which the turbine blade is supposed to operate safely and T_{crit} for the maximum temperature which the turbine blade withstands. Here, $T_{safe} = 505\ K$ and $T_{crit} = 515\ K$.

In this problem, the flow is turbulent (the Spalart-Allmaras turbulence model [11] was used) and the blade is cooled through coolant fluid which flows through the cooling channels shown in fig. 2. Heat transfer between the coolant flowing through the cooling channels (perpendicular to the 2D mesh) and the blade body is modeled by a 1D heat transfer equation along the holes surface, which reads (h is the heat transfer coefficient)

$$k^S \frac{\partial T^S}{\partial n}\bigg|_{holes} = h\left(T_{coolant} - T^S\right) \tag{24}$$

which is imposed as a boundary condition on the holes surface. The parameterization is made with 62 NURBS control points and the SD are computed with the E-SI continuous adjoint formulation. Flow conditions and data are summarized in Table 2. After only three optimization cycles, the objective function has dropped by 9.1 %. The initial and optimal geometry are presented in figs. 2a and 2b respectively, along with T^S fields. The pressure and suction sides have come closer to the cooling holes, in order for them to lower their temperatures. In addition, the temperature distribution over Ω_S changes, as temperature values between T_{crit} and T_{safe} are observed slightly closer to the TE in the optimized geometry (figs. 2c, 2d). In the optimal geometry, the maximum temperature of the blade has dropped by 2 K (figs. 2a, 2b). In figs. 3a–3f, the primal and adjoint fields over the initial geometry are included. Finally, one should notice that the part of Ω_S with the higher (in magnitude) T_S^a is mostly changed during the optimization procedure.

6 CONCLUSIONS

The continuous adjoint method to support gradient-based optimization in conjugate heat transfer problems between fluid and solid domains has been presented, programmed in OpenFOAM and demonstrated for two objective functions. In the presented test cases, the optimization algorithm controls the shape of (part of) the interface between the fluid and solid domains. The developed continuous adjoint method(s), which can easily be extended to other objective functions, have the advantages of computing accurate gradients while being as fast as possible. To achieve this, the grid displacement equations (i.e. the PDEs which undertake the computational grid adaptation each time the shape of the controlled boundary changes) are considered as extra state equations, next to the fluid flow

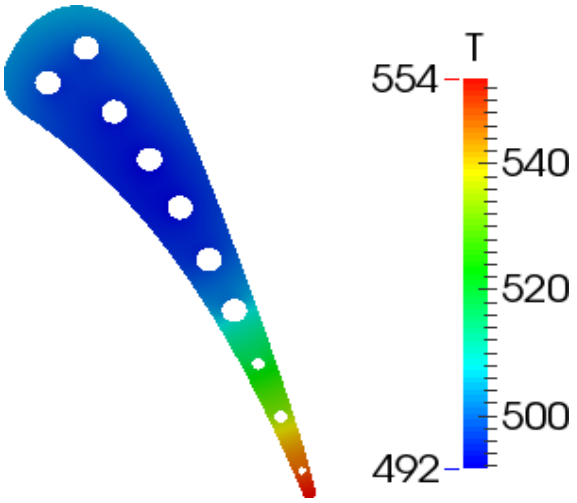

(a) T^S on the initial geometry

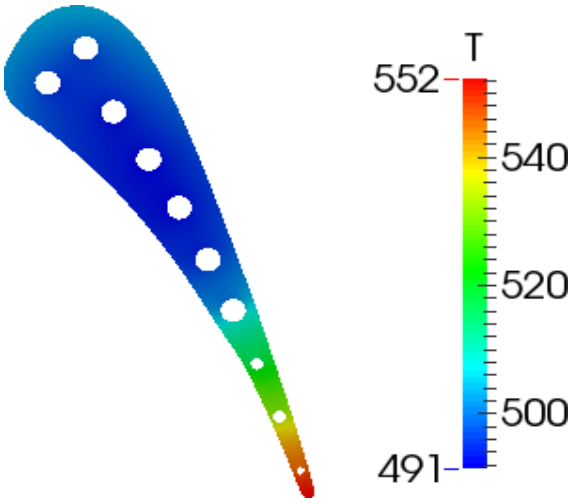

(b) T^S on the optimal geometry

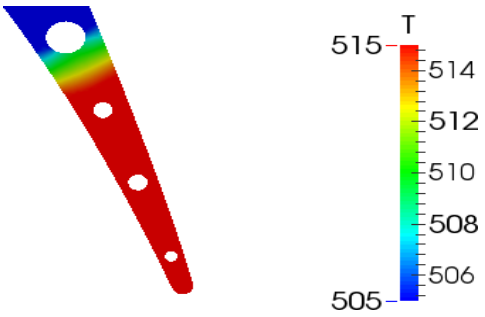

(c) Initial span $T_{crit} - T_{safe}$.

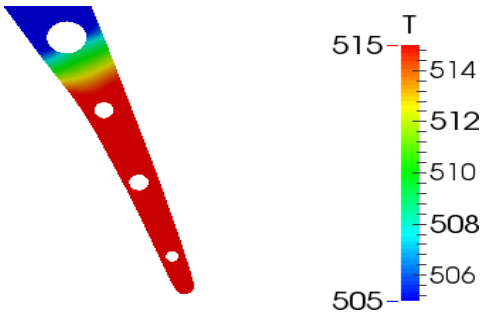

(d) Final span $T_{crit} - T_{safe}$.

Figure 2: Turbulent flow around the 2D blade of a turbine stator. Minimization of J_{maxT}. Temperature over the initial and optimized blade.

PDEs and the PDEs governing heat conduction over the solid domain. By including them into the augmented objective function, an extra set of adjoint grid displacement PDEs results which must be solved, since it contributes to the gradient formula. This method, which is in fact an extension of a similar technique recently proposed by the same group for shape optimization problems in fluid mechanics only, is referred to as the Enhanced-Surface Integral (E-SI) adjoint approach. Among other, we demonstrated that this is as accurate as the more expensive adjoint method which includes field integrals depending on the grid sensitivities and as fast as the most frequently used adjoint formulation with gradients which depend only on surface/boundary integrals; the latter is demonstrated to compute quite wrong derivatives due to the assumptions made during its development.

Acknowledgement:
The early phase of this development was funded by Volkswagen AG (Group Research, K-EFFG/V, Wolfsburg, Germany). The authors would like to thank Dr. C. Othmer for

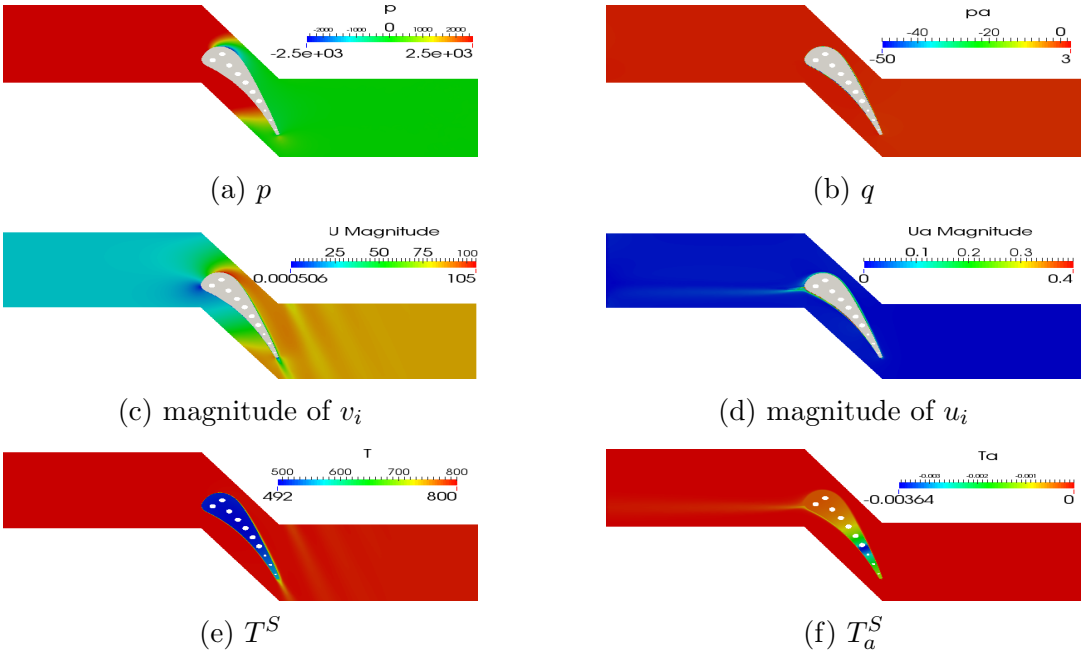

(a) p (b) q

(c) magnitude of v_i (d) magnitude of u_i

(e) T^S (f) T_a^S

Figure 3: Turbulent flow around the 2D blade of a turbine stator. Minimization of J_{maxT}. Primal and adjoint fields over Ω_F and Ω_S for the initial geometry.

his support.

REFERENCES

[1] W.K. Anderson and V. Venkatakrishnan. Aerodynamic design optimization on unstructured grids with a continuous adjoint formulation. *Computers & Fluids*, 28(4-5):443–480, 1999.

[2] B.H. Dennis, I.N. Egorov, G.S. Dulikravich, S. Yoshimura. Optimization of a large number of coolant passages located close to the surface of a turbine blade. In *Proceedings of ASME Turbo Expo 2003 – Power for Land, Sea, and Air*, Atlanta, Georgia, 16 - 19 June 2003.

[3] H. Narten, C. Correia, C. Othmer, R. Radespiel. Adjoint-based cooling efficiency optimization of turbulent ducted flows. In P. Nithiarasu N. Massarotti and B. Sarler, editors, *Third International Conference on Computational Methods for Thermal Problems, THERMACOMP2014*, pages 134–137, Lake Bled, Slovenia, June 2-4 2014.

[4] A. Jameson. Aerodynamic design via control theory. *Journal of Scientific Computing*, 3:233–260, 1988.

[5] A. Jameson and S. Kim. Reduction of the adjoint gradient formula in the continuous limit. In *AIAA Paper 2003-0040, 41th Aerospace Sciences Meeting and Exhibit*, Reno, Nevada, January 2003.

[6] I.S. Kavvadias, E.M. Papoutsis-Kiachagias, G. Dimitrakopoulos, and K.C. Giannakoglou. The continuous adjoint approach to the k–ω SST turbulence model with applications in shape optimization. *Engineering Optimization*, 47(11):1523–1542, 2015.

[7] I.S. Kavvadias, E.M. Papoutsis-Kiachagias, and K.C. Giannakoglou. On the proper treatment of grid sensitivities in continuous adjoint methods for shape optimization. *Journal of Computational Physics*, 301:1–18, 2015.

[8] K.C. Giannakoglou, E.M. Papoutsis-Kiachagias, I.S. Kavvadias, K.T. Gkaragkounis. Continuous Adjoint in Shape & Topology Optimization - Recent Developments & Applications. In *Seminar on Adjoint CFD Methods in Industry and Research*, pages 43–52, Wiesbaden, Germany, 24 - 25 November 2016.

[9] K.C. Kiani M. Zeinalpour, K. Mazaheri. A coupled adjoint formulation for non-cooled and internally cooled turbine blade optimization. *Applied Thermal Engineering*, 105:327–335, 2016.

[10] D.I. Papadimitriou and K.C. Giannakoglou. A continuous adjoint method with objective function derivatives based on boundary integrals for inviscid and viscous flows. *Journal of Computers & Fluids*, 36(2):325–341, 2007.

[11] P. Spalart and S. Allmaras. A one-equation turbulence model for aerodynamic flows. In *AIAA Paper 1992-0439, 30th Aerospace Sciences Meeting and Exhibit*, Reno, Nevada, 6-9 January 1992.

[12] A.S. Zymaris, D.I. Papadimitriou, K.C. Giannakoglou, and C. Othmer. Continuous adjoint approach to the Spalart-Allmaras turbulence model for incompressible flows. *Computers & Fluids*, 38(8):1528–1538, 2009.

VII International Conference on Computational Methods for Coupled Problems in Science and Engineering
COUPLED PROBLEMS 2017
M. Papadrakakis, E. Oñate and B. Schrefler (Eds)

CRASHWORTHINESS OPTIMIZATION OF AN AUTOMOTIVE FRONT BUMPER

S. BORIA*

* School of Science and Technology, Mathematics division
University of Camerino
Madonna delle carceri 9, 62032 Camerino, Italy
e-mail: simonetta.boria@unicam.it, www.simonettaboria.it

Key words: Crashworthiness, Bumper, Optimization, Metamodels, LS-DYNA, LS-OPT.

Abstract. In automotive industry, structural optimization for crashworthiness criteria is of special importance in the early design stage. Crashing performance of structures under dynamic impact can be investigated using finite element codes. By coupling FE simulation tools with nonlinear mathematical programming procedure and statistical techniques, it is possible to optimize the design with reduced number of analytical evaluations. Optimization methods using statistical techniques are widely used in engineering applications to utilize estimated models which are often referred to metamodels. Meta-modeling optimization is performed through construction of objective functions, design of experiment (DOE) and modeling. Various types of meta-modeling techniques were used for crashworthiness optimization.
In this paper the comparative study of Kriging and Radial Basis Function Network (RBFN) was performed in order to improve the crashworthiness effects of a front bumper subsystem subjected to impact. The objective function is the maximization of the specif energy absorption (SEA) and the design variables are geometrical parameters subjected to some design constraints. The optimized solution was achieved interfacing LS-DYNA codes with LS-OPT and using a domain reduction strategy.

1 INTRODUCTION

During the past decades passive safety is treated as an attribute with increased importance in automotive industry. Bumper systems play an important role in the energy management of vehicles during accidents. Structural optimization for crashworthiness criteria is therefore of special importance in the early design stage. Crashing performance of structures under dynamic impact can be investigated using finite element codes. By coupling FE simulation tools with nonlinear mathematical programming procedure and statistical techniques, it is possible to optimize the design with reduced number of analytical evaluations [1]. Optimization methods using statistical techniques are widely used in engineering applications to utilize estimated models which are often referred to metamodels. Meta-modeling optimization is performed through construction of objective functions, design of experiment

(DOE) and modeling. Various types of meta-modeling techniques were used for crashworthiness optimization [2-6].

In this paper the comparative study of Kriging and Radial Basis Function Network (RBFN) was performed in order to improve the crashworthiness effects of a front bumper subsystem subjected to impact. The objective function is the maximization of the specific energy absorption (SEA) and the design variables are geometrical parameters subjected to some design constraints. The optimized solution was achieved interfacing LS-DYNA codes with LS-OPT and using a domain reduction strategy. At first some numerical simulations were conducted in order to find the best solution in terms of section profile and curvature of the beam. Only after, the chosen configuration was implemented in the iterative optimization process. From the obtained results, it is evident how both metamodels are able to improve the crushing performance of the basic system up to 21% in SEA value, giving comparable solutions.

2 METAMODELS

In crashworthiness optimization, direct coupling method may be inefficient and sometimes impossible since iterative non-linear FEA during optimization usually require enormous computational efforts and take the high risk of premature simulation failure prior to a proper convergence. As a result, surrogate models or metamodels are more often used as an alternative for formulating the design criteria in terms of an explicit function of design variables in advance of optimization, which has proven an effective and sometimes a unique approach [7-9].

In this study comparative analysis of Radial Basis Function Network and Kriging metamodels were carried out using Space Filling design of experiment; approximated functions were created using seven simulation points and fifteen iterations with sequential domain reduction strategy [10]. Below a brief description of such models is presented.

2.1 Radial Basis Function Network model

A radial basis function neural network has a distinct 3-layer topology. The input layer is linear. The hidden layer consists of non-linear radial units, each responding to only a local region of input space. The output layer performs a biased weighted sum of these units and creates an approximation of the input-output mapping over the entire space. The most common basis function is Hardy's formula [11], given as:

$$g_h(x_1,...,x_k) = \sqrt{1+\frac{r^2}{\sigma_h^2}} \qquad (1)$$

The activation of the h-th radial basis function is determined by the Euclidean distance $r = \sqrt{\sum_{k=1}^{K}(x_k - W_{hk})^2}$ between the input vector $x = (x_1,...,x_K)$ and RBF center $W_h = (W_{h1},...,W_{hk})$ in K-dimensional space. Parameter σ_h controls the smoothness properties of the RBF unit. For a given input vector x the output of RBF network with K inputs and a hidden layer with H basis function units is given by:

$$Y(x,W) = W_0 + \sum_{h=1}^{H} W_h f(\rho_h) \qquad (2)$$

where W_0 includes the polynomial terms, W_h is the weighted coefficient for the term of the h-th variable, ρ_h is the Euclidean distance and f is the radial basis function.

2.2 Kriging model

In recent years, the Kriging method has found wider application as a spatial prediction method in engineering design. The basic postulate of this formulation, given by Simpson [12], is:

$$y(x) = f(x) + Z(x) \qquad (3)$$

where y(x) is the unknown function of interest, f(x) models the global trend of the function of interest and Z(x) models the correlation between the points by a stochastic process whose mean is zero and variance is σ^2. Z(x) provides local deviations and the covariance between different points is modelled as:

$$Cov(Z(x_i), Z(x_j)) = \sigma^2 \bar{R}([R(x_i, x_j)]) \qquad (4)$$

With L the number of sampling points, $\bar{R}$ is the LxL correlation matrix defined by Gaussian correlation function $R(x_i,x_j)$ as follows:

$$R(x_i, x_j) = \prod_{k=1}^{n} \exp\left[-\theta_k (x_i^k - x_j^k)^2\right] \qquad (5)$$

where n is the number of variables, θ_k is the unknown correlation parameter to determine and x_i^k is the k-th component of sample point x_i.

3 BUMPER SUBSYSTEM OPTIMIZATION STUDY

To apply the methodologies described in the section above, an optimization study on an automotive CAD bumper subsystem for a race car is performed.

3.1 Bumper subsystem

The bumper geometry has been taken from an automotive design practice with a mesh density that is both acceptable for the predictions of interest and also feasible in terms of computational effort. The geometry consists of a cross-section made of a one chamber that represents the transverse bumper and two longitudinal crash boxes (Figure 1). Given the symmetry of the system respect to y-axis, only half structure has been modelled constraining the right degrees of freedom in the reflection plane. Moreover the right end of the longitudinal crash box is rigidly fixed to the frame. The bumper has been realized with an high strength steel.

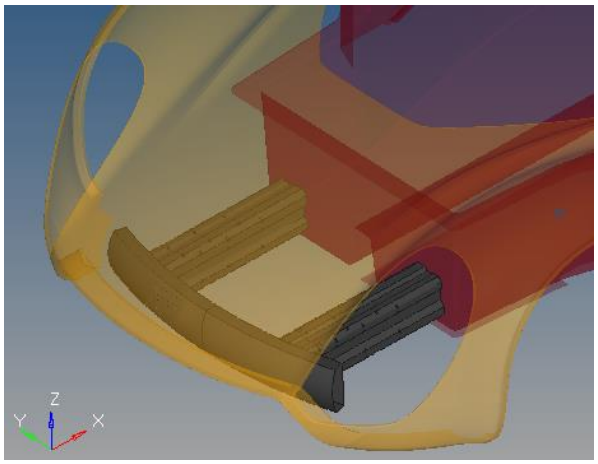

Figure 1: CAD assembly of the bumper subsystem

As regards the initial condition, instead of IIHS low velocity impact [13], Allianz crash repair test and the impact to pole test [14], a full width front impact against a flat rigid barrier at a speed of 56 km/h has been used. In such case, in fact, the bumper subsystem, designed for a race car, must be able to absorb all the kinetic energy during a frontal collision.

3.2 Optimization definition

The optimization process has been conducted through three different approaches. Firstly, an optimized cross section of the transverse beam has been identified. Secondly, a change into the beam curvature has been analyzed and finally, the best configuration has been used for an iterative model in LS-OPT (Figure 2) using two different metamodels, such as Radial Basis Function Network and Kriging.

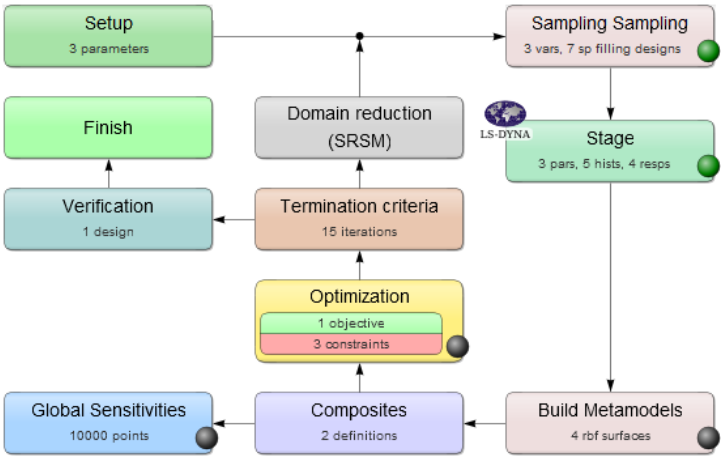

Figure 2: Iterative model in LS-OPT

3.2.1 Section profile optimization

At first, profile optimization was conducted changing the cross section of the transverse

beam. In particular, the work of Belingardi *et al.* [13] showed that the best cross section profile for a bumper, able to guarantee a progressive deformation, was that with a series of internal hinges. Therefore, such configuration was compared with the basic CAD model (Figure 3) in order to identify the best configuration to adopt in terms of section.

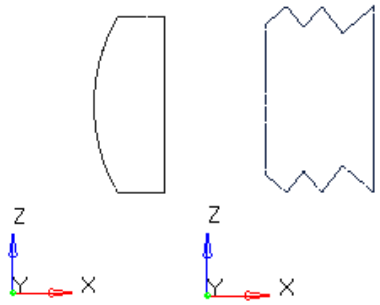

Figure 3: Profile geometries taken into account

The diagram below (Figure 4) shows the force trends vs. displacement for both configurations. Moreover, in table 1 the respective values of maximum and average deceleration, maximum stroke and specific energy absorption (SEA) were compared.

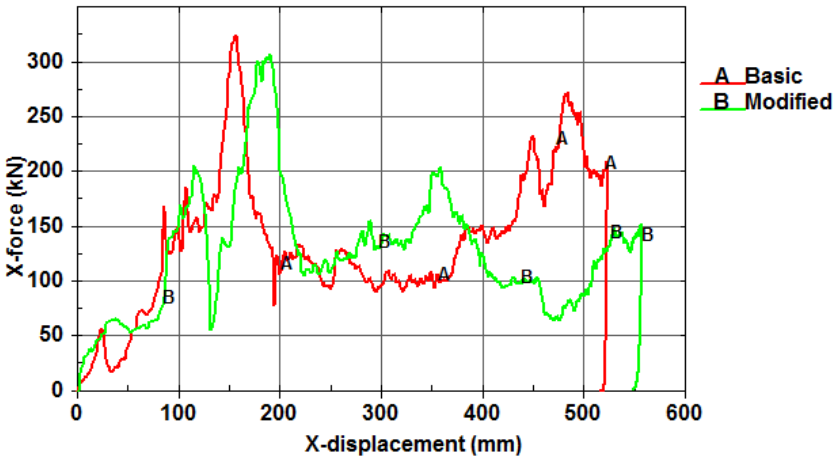

Figure 4: Force vs. Displacement for both section profiles

Table 1: Crash characteristics for both configurations

Configuration	Max deceleration (g)	Average deceleration (g)	Max stroke (mm)	SEA (kJ/kg)
Basic	55.34	25.27	523.28	8.95
Modified	52.36	19.60	557.60	7.77

As mentioned in previous research [13], the modified profile, with a series of hinges, is able to reduce the peak value and guarantee a more stable and progressive deformation, even if it tends to weigh more and absorbs less energy than the basic profile. Therefore the basic

configuration seems to be very attractive from the point of view of future optimization, that will tend to maximize the specific energy absorption.

3.2.2 Beam curvature optimization

Another analyzed change was the beam curvature. In particular the modified profile was tested into three different cases: straight, medium radius and maximum one (Figure 5).

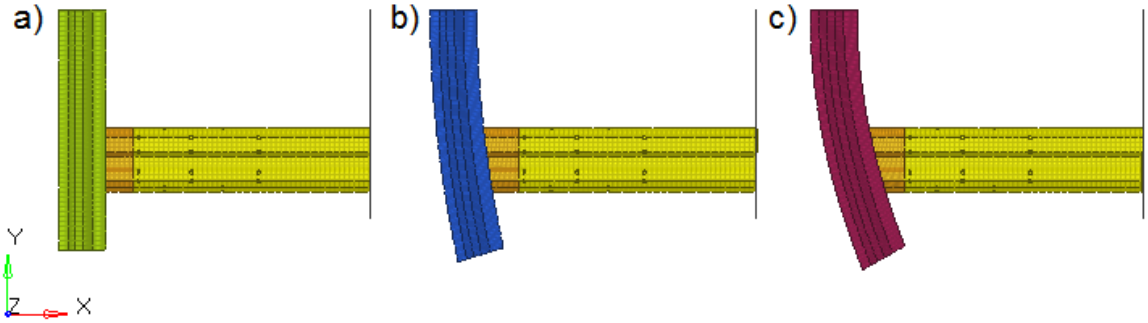

Figure 5: Beam curvature cases: a) straight, b) medium radius, c) maximum radius

The diagram below (Figure 6) shows the force trends vs. displacement for the three configurations. Moreover, in table 2 the respective values of maximum and average deceleration, maximum stroke and SEA were compared.

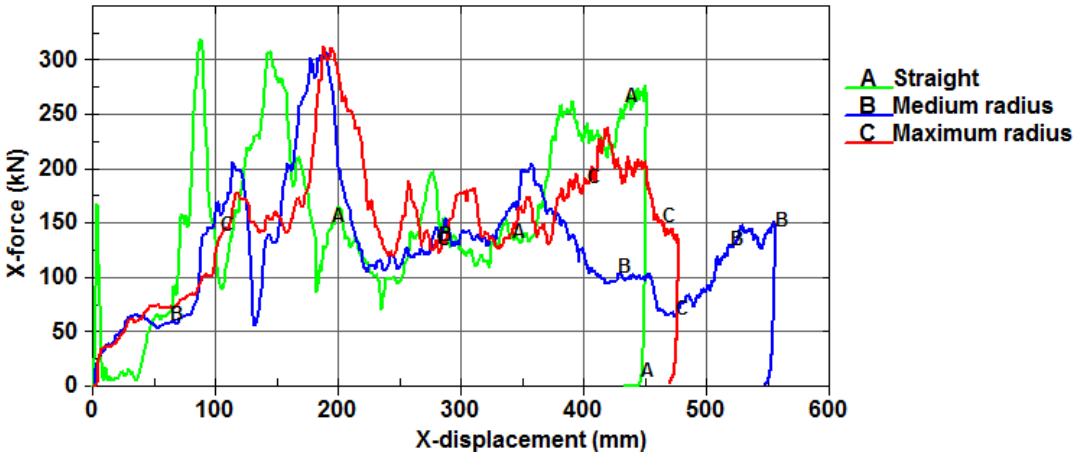

Figure 6: Force vs. Displacement for the three beam curvatures

Table 2: Crash characteristics for the three configurations

Configuration	Max deceleration (g)	Average deceleration (g)	Max stroke (mm)	SEA (kJ/kg)
Straight	54.69	27.85	452.21	7.88
Medium radius	52.36	19.60	557.60	7.77
Maximum radius	53.34	23.84	478.60	7.68

Even if the straight configuration reaches a value of SEA greater than the other, the best behavior seems to be reached by the medium radius. From Figure 6 it is in fact evident how, unlike other cases, the first configuration generates an initial peak load also in the first time instants due to the contact with a larger area since the beginning of impact. Moreover in such case the absorbed energy from the only bumper is very low respect to the presence of a certain level of curvature and the beam tends to slip into high during crush causing a not progressive deformation with a series of peaks (Figure 7). In terms of deformation trend, deceleration values and specific energy absorption the medium radius has the best data and therefore, for the next optimization procedure, the bumper with the basic section profile and a medium curvature will be considered.

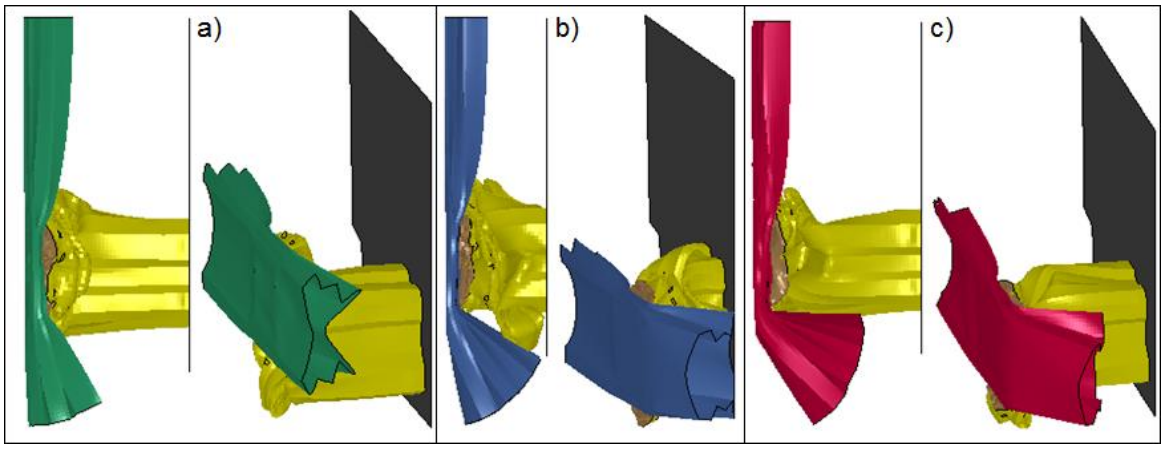

Figure 7: Side and isometric view of the final deformation for each case:
a) straight, b) medium radius and c) maximum radius

3.2.3 Optimization through the iterative models in LS-OPT

Nowadays, with the increasing awareness of the environmental footprint of the vehicle, mass reduction of the different vehicle subcomponents is mandatory. Meanwhile a high level of energy absorption must be guarantee maintaining a deformation level as close as possible to an ideal absorber, without high peaks of deceleration. Therefore, the goal of the optimization process is to obtain an optimized bumper profile in terms of specific energy absorption (SEA), while satisfying a set of design constraints [15].

In order to optimize the bumper, three parameters are considered that correspond to the shell thickness values of the three parts (red, green and blue) in which the bumper subsystem was divided (Figure 8). The parameter ranges and the nominal values are represented in Table 3. From previous numerical simulations, it was noted that the subdivision, in terms of shell thickness, of the longitudinal crash box into two parts is able to guarantee a reduction of the load peak and the introduction of some alternated hole allows to obtain a progressive and controlled deformation during crushing.

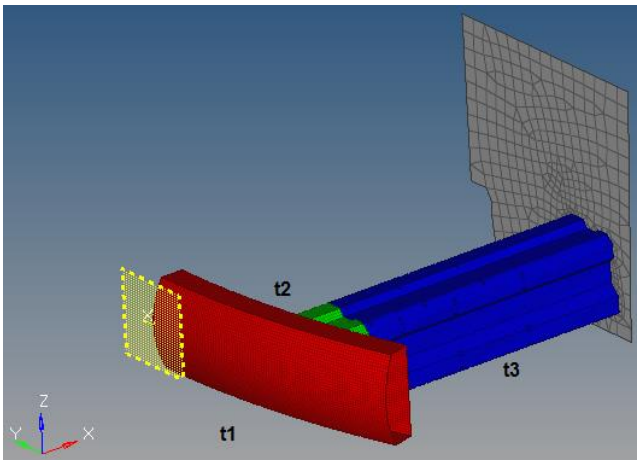

Figure 8: Bumper parameters

Table 3: Design parameters

Parameter	t1	t2	t3
Min (mm)	1	1	1
Max (mm)	3	3	3
Nom (mm)	2	1.5	2

Therefore, the mathematical model for the structural optimization is as follows:

$$\max SEA(t1,t2,t3)$$
$$\text{subject to} \begin{cases} \text{Max\_acceleration}<50\ \text{m/s}^2 \\ \text{Average\_acceleration}<25\ \text{m/s}^2 \\ \text{Max\_stroke}<550\ \text{mm} \end{cases} \quad (6)$$

As mentioned before, such optimization procedure has been implemented in LS-OPT using two different metamodels, such as Radial Basis Function Network and Kriging. At each iteration step, each metamodel evaluates, taking into account also the previous DOE experiments, the best solution to adopt until get to convergence.

4 RESULTS AND DISCUSSION

Table 4 shows the optimal values of thickness for RBFN and Kriging metamodel, respectively. It is evident how different surrogates give feasible and very comparable solutions.

Table 4: Variables optimal values for both surrogates

Metamodel	Design variables		
	t1	t2	t3
RBFN	1.14	1.36	1.99
Kriging	1.21	1.42	1.91

In terms of objective and constraints values it is possible to note how both metamodels are able to improve the basic configuration (Table 5).

Table 5: Optimum results of RBFN and Kriging metamodel

	Basic	RBFN	Kriging
SEA (kJ/kg)	8.94	10.82	10.67
Max_acc (g)	55.02	45.97	46.12
Average_acc (g)	23.39	22.55	21.86
Max_stroke (mm)	521.06	540.21	539.35

Figure 9 shows the optimization history for variables and objective varying iteration step. It is evident how the domain of each thickness tends to reduce in time up to converge to the optimal solution. Moreover also the SEA value tends to stabilize around a value of about 11 kJ/kg.

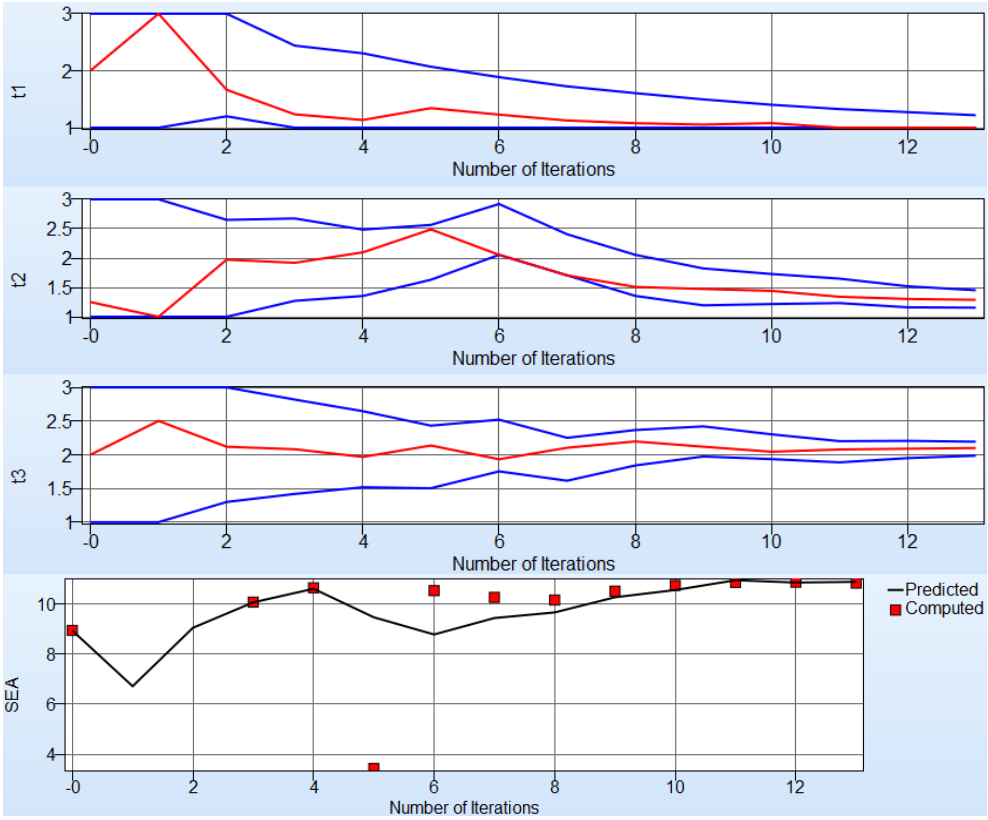

Figure 9: Optimization history for the design variables and objective

Sensitivity analysis allows to determine the significance of the design variables. In LS-OPT two sensitivity measures are implemented: Linear ANOVA and GSA/Sobol. ANOVA depicts positive or negative influence, while Sobol just shows the normalized absolute value and guarantees an easier comprehension (Figure 10). It is evident how the t3 variable, that depicts the thickness of the last zone of the longitudinal crash box, is the most influential parameter for each responses.

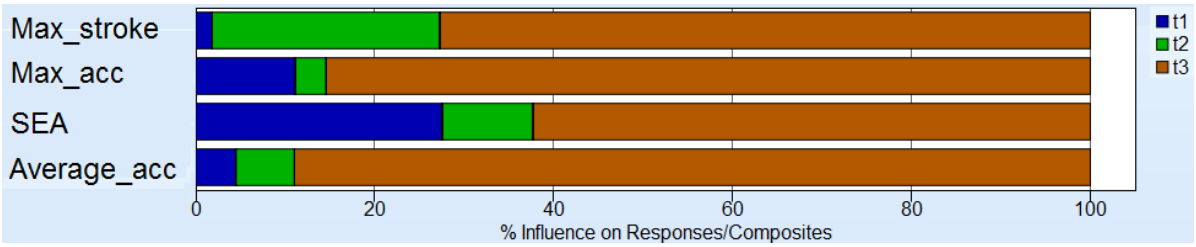

Figure 10: Sobol values for multiple responses

The three dimensional response surfaces obtained from the RBFN and Kriging models and simulation points were plotted for the SEA objective vs. two design variables (Figure 11). It is evident how the Kriging metamodel tends to approximate the DOE experiments (green and red points correspond to feasible and unfeasible solution, respectively) with a more complex surface.

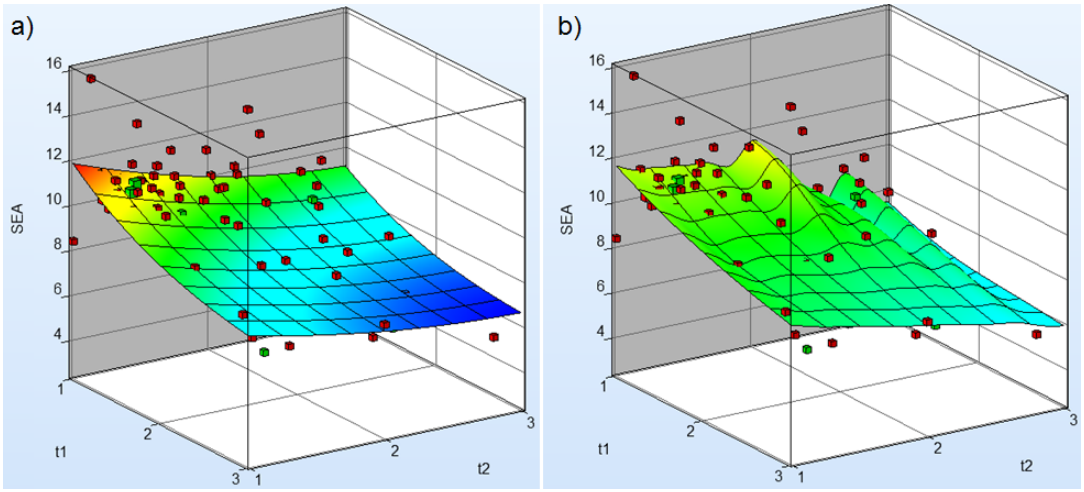

Figure 11: Response surfaces of SEA for RBFN (a) and Kriging (b) metamodels

5 CONCLUSIONS

This paper presents the application of two metamodels, such as Radial Basis Function Network and Kriging, in the context of crashworthiness. In particular the work is dedicated to the development of a front race car bumper subsystem in conventional material with the aim to improve its energy absorption capability. At first the basic configuration has been compared with other solutions, in terms of section profile and beam curvature. Only after, the chosen solution has been analyzed with an optimization process using LS-OPT tool, by considering as design variables the wall thicknesses of the beam and of the longitudinal crash boxes. For this objective, numerical simulations have been conducted through explicit solver LS-DYNA and structural results for the bumper have been compared. The following conclusions can be drawn:

- The adoption of a bumper with internal folds into the profile seems to be best in terms of progressive deformation, even if this implies an higher weigh and a lower SEA

value.

- It is not convenient to realize a bumper using a straight curvature, because it generates initial peaks and lower energy absorption level as well as a not uniform crushing process.
- After the initial deformation, where the only bumper is involved, the energy absorption is guarantee from the longitudinal crash boxes and therefore it seems suitable to divide such structure at least in two zones at different thicknesses and insert some hole to reduce the peaks and guarantee a progressive and controlled deformation.
- Implementation of an optimization process through RBFN and Kriging methods demonstrated that the crushing performance, in term of SEA, of the bumper system can be improved by 21% and 19%, respectively.
- No great differences can be observed from the point of view of the design variables values between the considered surrogates.

REFERENCES

[1] S.S.Esfahlani, H.Shirvani, S.Nwaubani, A.Shirvani, H.Mebrahtu, "Comparative study of honeycomb optimization using Kriging and radial basis function", *Theoretical and Applied Mechanics Letters*, Vol. **3**, (2013).

[2] H.Wang, G.Y.Li, E.Li, Time-based metamodeling technique for vehicle crashworthiness optimization, *Computer Methods in Applied Mechanics and Engineering*, Vol. **199**, N. 37-40, 2497-2509, (2010).

[3] H. Fang, M. Rais-Rohani, Z. Liu, M.F. Horstemeyer, A comparative study of metamodeling methods for multiobjective crashworthiness optimization, *Computers and Structures*, Vol. **83**, pp. 2121-2136, (2005).

[4] M.Avalle, G.Chiandussi, G.Belingardi, Design optimization by response surface methodology: application to crashworthiness design of vehicle structures, *Structural Multidisciplinary Optimization*, Vol. **24**, pp. 325-332, (2002).

[5] G.G.Wang, S.Shan, Review of metamodeling techniques in support of engineering design optimization, *Journal of Mechanical Design*, Vol. **129**, N. 4, pp. 370-380, (2007).

[6] N.Stander, T.Goel, Metamodel sensitivity to sequential adaptive sampling in crashworthiness design, Proceedings of the 12th AIAA/ISSMO Multidisciplinary Analysis and Optimization Conference, Victoria, (2008).

[7] J.Fang, G.Sun, N.Qiu, H.N.Kim, Q.Li, On design optimization for structural crashworthiness and its state of the art, *Structural and Multidisciplinary Optimization*, Vol. **55**, N. 3, pp. 1091-1119, (2016).

[8] F.Duddeck, S.Hunkeler, P.Lozano, E.Wehrle, D.Zeng, Topology optimization for crashworthiness of thin-walled structures under axial impact using hybrid cellular automata, *Structural and Multidisciplinary Optimization*, Vol. **54**, pp. 415-428, (2016).

[9] A.Forrester, A.J.Keane, Recent advanced in surrogate-based optimization, *Progress in Aerospace Sciences*, Vol. **45**, N. 1-3, pp. 50-79, (2009).

[10] N.Stander, K.J.Craig, On the robustness of a simple domain reduction scheme for simulation-based optimization, *Engineering Computations*, Vol. **19**, N. 4, pp. 431-450, (2002).

[11] R.L.Hardy, Multiquadratic equations of topography and other irregular surfaces, *Journal of Geophysical Research*, Vol. **76**, N. 8, pp. 1905-1915, (1971).

[12] T.W.Simpson, *A concept Exploration Method for Product Family Design*, PhD thesis, Georgia Institute of Technology, (1998).

[13] G.Belingardi, A.T.Beyene, E.G.Koricho, Geometrical optimization of bumper beam profile made of pultruded composite by numerical simulation, *Composite Structures*, Vol. **102**, pp. 217-225, (2013).

[14] L.Farkas, S.Donders, D.Schildermans, D.Moens, D.Vandepitte, Optimisation study of a vehicle bumper subsystem with fuzzy parameters, *Proceedings of ISMA2010-USD2010*, pp. 5015-5026, (2010).

[15] S.Boria, J.Obradovic, G.Belingardi, On design optimization of a composite impact attenuator under dynamic axial crushing, FME Transaction, in press.

VII International Conference on Computational Methods for Coupled Problems in Science and Engineering
COUPLED PROBLEMS 2017
M. Papadrakakis, E. Oñate and B. Schrefler (Eds)

DESIGN OF CONTROLLED PIEZOELECTRIC ACTUATORS BY USING TOPOLOGY OPTIMIZATION

Mariana Moretti*, Emílio C. N. Silva†

*†School of Engineering, University of São Paulo. Av. Prof. Mello Moraes, 2231 - São Paulo, SP - Brazil, 05508-030.
*e-mail: mamoretti@usp.br, †e-mail: ecnsilva@usp.br

Key words: Topology Optimization Method, Piezoactuator, Active Control Law, Time-Domain Transient Analysis.

Abstract. Controlled flextensional actuators essentially involve a compliant mechanism assembled in association with piezoceramics featuring sensing and actuation of the structure by the ceramics energy conversion property. For applications that require vibration response attenuation, these devices account with an active feedback control to regulate disturbances that might be introduced to the system. In the field of intelligent structures, the self-monitoring and control assemblage can be largely used in systems such as micro-grippers for sample handling, hard disk reading [1] and atomic force microscopy. One distinct advantage of this kind of structure is their higher accuracy when compared to conventional actively controlled structures because their sensing is distributed instead of being discrete about the response measurement phenomenon. The control law effectiveness in such a controlled system can be enhanced by designing their elastic structure by means of the Topology Optimization Method (TOM), since an optimized material distribution within a fixed domain affects the structure stiffness, vibration modes and response characteristics. Previous works that apply the TOM in controlled piezo-actuators aiming vibration suppression focus on the distribution of piezoceramic material over a host structure either in frequency domain or in time domain [2]. However, the low coupling constants of piezoelectric ceramics may reduce the capability of energy conversion for input displacements or for input voltages in actuating systems. Therefore, in order to avoid an unfeasible or less effective active control targeting vibration suppression, this work focuses on the distribution of the host structure and eliminates the dependence on the magnitude of electro-elastic coupling constants for a satisfactory energy conversion. As stated, the optimized smart devices proposed in this work involve a host structure material distribution which is sensed and actuated by two predefined piezoceramic locations connected through a feedback architecture, while the system is subjected to a transient input load. Approximations to the damping matrix coefficients are considered for both the metallic material and the piezoelectric material, even though the ceramic layers are significantly thinner than the middle layer. The objective function chosen minimizes the

vibration energy of the system subjected to a volume constraint. The dynamic equilibrium equation accounts with an extra damping matrix derived from the current amplification chosen as the feedback control law, or for short, the Active Velocity Feedback (AVF). The material model implemented is the Solid Isotropic Material with Penalization (SIMP) for the 4-node solid finite element with two mechanical degrees-of-freedom (DOFs) per node, and one electrical DOF per node. A density-based filter eliminates the checkerboard pattern, the sensitivity analysis is calculated by the adjoint method, and the Sequential Linear Programming (SLP) algorithm is employed as the optimization procedure. Two-Dimensions (2D) results are presented and the influence of the gain velocity value over the final layouts is analyzed.

1 INTRODUCTION

Refinement on motion precision of actuating systems envision applications in most of the modern electronic devices, which require lighter, less stiff and more vulnerable to transient external loads components [3]. The optical pickup system on hard drive reading, the hard drive base itself and the servovalves in hydraulic control systems are examples of devices that have their work operation based on fast response and vibration suppression actuation. Intelligent structures provide those characteristics given that their self-monitoring feature based on sensors, actuators and an active control law, interfere to the systems dynamics. Among the smart materials employed with sensing and actuation properties to regulate vibrations to the referred systems, the piezoelectric ceramic is the most commonly used of them.

Time-domain formulation for piezoelectric transducers has been studied by Wang (2001) [4], who applied the velocity feedback control and evaluated the system stability according to its piezoceramics placement, by Zhang (2015) [5], who applied LQR and PID control schemes for free vibration and step, harmonic and random excitations to study their influence on the response of flexible structures. For the previously mentioned works, the predefined placement of sensors and actuators associated with an active controller resulted in vibration attenuations of the system. An active vibration control scheme is defined by the extra voltage or electric charge that is supplied to the piezoceramic material [6]. Further improvement to these systems response might require an optimized sensor, actuator and base materials distribution, a structure design conveyed by the Topology Optimization Method (TOM).

With the advancements in processing capability of computers, the TOM have been made possible for the design of systems under dynamical analysis. Jang (2012) [7] showed that, under multiple dynamic loads, the dynamic response topology optimization substantially reduces the strain energy when compared to the static topology optimization. Deng (2014) [8] combined TOM and optimal control method to obtain the optimal match between the material distribution and the control effect applied to heat transfer, steady

flow and structure compliance problems.

Focusing on the dynamic load case scenario and on the TOM for the design of controlled piezoelectric actuators, recent works have optimized the distribution of piezoelectric patches within the structures to enhance the control effects towards a specific operation mode. Wang (2006) [9] applied a genetic algorithm-based topology optimization to the design of sensors and actuators for torsional vibration control of laminated composite plate. In the work of Zhang et al. (2014a) [10], the authors work with an optimized electrode distribution over piezoelectric sensors and actuators attached to a thin-walled shell structure for reducing sound radiation. Yet, in their most recent work, Zhang et al. (2014b) [2] used the same optimized electrode distribution applied to the vibration suppression in time-domain, assuming thin layers of piezoelectric material and therefore rejecting their damping effects.

Besides being more versatile to distribute the piezoceramic material, their low coupling constants may reduce the capability of energy conversion for input voltages in actuating systems, what results in an unfeasible problem when applied to certain active control that depends on the magnitude of electro-elastic coupling constants. In that case, for the active control to be efficient, a large control gain would be needed [11]. Therefore, this work proposes to apply the TOM to the host layer of the structure, given the locations for the sensor and actuator layers, in order to achieve better control performance with lower control gain.

Unlike most part of previous study on topology optimization, this work focuses on a time-domain transient analysis to achieve the goal of vibration suppression on piezoelectric structures. TOM is used to optimize the compliant structure for reduced vibration given two predefined locations for the ceramic layers. The TOM implementation is based on a density material model, the Solid Isotropic Material with Penalization (SIMP) and the velocity feedback control technique is chosen for the regulation. To illustrate the method, bidimensional optimized topologies of flextensional actuators are obtained considering different active control gains. The efficiency of these devices is evaluated for each of the control gains implemented.

2 FEM FOR A TRANSDUCER UNDER AVF CONTROL

In order to develop the closed loop equations of motion for the active controlled piezoelectric transducer, the boundary conditions of the prospective system are presented in figure 1. The solid system $\Omega = \Omega_1 \cup \Omega_2$ is formed by the piezoelectric domain Ω_1 and the elastic domain Ω_2 inside a fixed domain $\bar{\Omega}$ $\left(\Omega \subseteq \bar{\Omega}\right)$ to which constraints and loads are defined. The boundary surface of $\bar{\Omega}$-system, denoted by Γ, is partitioned into prescribed mechanical displacements Γ_u, prescribed traction vector Γ_T, an equipotential electroded region Γ_ϕ and an unelectroded region Γ_D, where it concentrates the free charge density per unit surface area.

The dynamics of deformation here is approximated by a 2D-solid bilinear finite element and the displacement field $\boldsymbol{U} = \begin{bmatrix} \boldsymbol{u} & \boldsymbol{\Phi} \end{bmatrix}^\top$ is given by two mechanical components

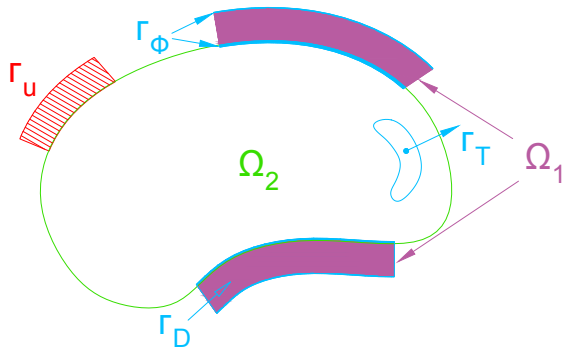

Figure 1: Design domain

$\boldsymbol{u} = [\boldsymbol{u}_x \quad \boldsymbol{u}_y]^\top$ for deformations in directions x and y, respectively. The electric vector component $\boldsymbol{\Phi} = [\boldsymbol{\Phi}_f \quad \boldsymbol{\Phi}_p]$ is subdivided into free voltages, $\boldsymbol{\Phi}_f$, for intermediate nodes in ceramic layers, and prescribed voltages, $\boldsymbol{\Phi}_p$, for electrode nodes. The grounded electrodes are not represented in the equations.

The strain-displacement field is defined by the normal strains S_x and S_y in x and y directions, respectively, and by the in-plane shear strain S_{xy}:

$$\boldsymbol{S} = \begin{bmatrix} S_x & S_y & S_{xy} \end{bmatrix}^\top . \tag{1}$$

Likewise, the stress components are given by the stress vector

$$\boldsymbol{T} = \begin{bmatrix} T_x & T_y & T_{xy} \end{bmatrix}^\top , \tag{2}$$

and along with the electric displacement vector $\boldsymbol{D}$ and the coupling piezoelectric tensor $\boldsymbol{e}$, the piezoelectric constitutive equations are written:

$$\begin{aligned} \boldsymbol{T} &= \boldsymbol{c}^E \boldsymbol{S} - \boldsymbol{e}\boldsymbol{E}, \\ \boldsymbol{D} &= \boldsymbol{e}\boldsymbol{S} + \boldsymbol{\varepsilon}^S \boldsymbol{E}. \end{aligned} \tag{3}$$

In the piezoelectric constitutive equations, $\boldsymbol{c}^E$ is an elastic matrix evaluated under a constant electric field $\boldsymbol{E}$, and $\boldsymbol{\varepsilon}^S$ is a dielectric tensor evaluated under constant strain $\boldsymbol{S}$.

Considering infinitesimal deformation, the linear behaviour of piezoelectric materials and the linear electric and structural fields in plane stress condition result in the material

matrices given by

$$\boldsymbol{c}^E = \begin{bmatrix} c_{11} - \frac{c_{12}^2}{c_{11}} & c_{13} - \frac{c_{12}c_{13}}{c_{11}} & 0 \\ c_{13} - \frac{c_{12}c_{13}}{c_{11}} & c_{33} - \frac{c_{13}^2}{c_{11}} & 0 \\ 0 & 0 & c_{66} \end{bmatrix}, \tag{4}$$

$$\boldsymbol{e} = \begin{bmatrix} 0 & e_{31} - \frac{e_{31}c_{12}}{c_{11}} \\ 0 & e_{33} - \frac{e_{31}c_{13}}{c_{11}} \\ e_{15} & 0 \end{bmatrix}, \tag{5}$$

$$\boldsymbol{\varepsilon}^S = \begin{bmatrix} -\varepsilon_{11} & 0 \\ 0 & -\varepsilon_{33} - \frac{e_{31}^2}{c_{11}} \end{bmatrix}, \tag{6}$$

where $c_{66} = \dfrac{c_{11} - c_{12}}{2}$, [12].

The dynamic equations of motion in matrix form for a bounded piezoelectric body are derived from the Hamilton's principle for a time interval from t_1 to t_2. The interpolation of the displacement field $\{\boldsymbol{u}\}$ and the electric potential $\{\boldsymbol{\Phi}\}$ are done by means of the shape functions $[\boldsymbol{\mathcal{N}}_u]$ and $[\boldsymbol{\mathcal{N}}_\phi]$ for the $Q4$-bilinear finite element. The convenience of applying this technique to solve the piezoelectric equations for the design of optimized transducers, relies on the fact that Topology Optimization procedure is based on systematic analysis of the physical behaviour of the system. Therefore, the FEM is ideal for a design based on computational iterations so the variational formulations of mathematical models can be solved. Combining the equilibrium equations established for all elements, the system of equations in matrix form needs to be solved:

$$\begin{bmatrix} \boldsymbol{M}_{uu} & \mathbf{0} & \mathbf{0} \\ \mathbf{0} & \mathbf{0} & \mathbf{0} \\ \mathbf{0} & \mathbf{0} & \mathbf{0} \end{bmatrix} \begin{Bmatrix} \ddot{\boldsymbol{U}} \\ \ddot{\boldsymbol{\Phi}}_f \\ \ddot{\boldsymbol{\Phi}}_p \end{Bmatrix} + \begin{bmatrix} \boldsymbol{C}_{uu} & \mathbf{0} & \mathbf{0} \\ \mathbf{0} & \mathbf{0} & \mathbf{0} \\ \mathbf{0} & \mathbf{0} & \mathbf{0} \end{bmatrix} \begin{Bmatrix} \dot{\boldsymbol{U}} \\ \dot{\boldsymbol{\Phi}}_f \\ \dot{\boldsymbol{\Phi}}_p \end{Bmatrix} + \begin{bmatrix} \boldsymbol{K}_{uu} & \boldsymbol{K}_{u\phi_f} & \boldsymbol{K}_{u\phi_p} \\ \boldsymbol{K}_{u\phi_f}^\top & -\boldsymbol{K}_{\phi_f\phi_f} & -\boldsymbol{K}_{\phi_f\phi_p} \\ \boldsymbol{K}_{u\phi_p}^\top & -\boldsymbol{K}_{\phi_f\phi_p}^\top & -\boldsymbol{K}_{\phi_p\phi_p} \end{bmatrix} \begin{Bmatrix} \boldsymbol{U} \\ \boldsymbol{\Phi}_f \\ \boldsymbol{\Phi}_p \end{Bmatrix} = \begin{Bmatrix} \boldsymbol{F} \\ \boldsymbol{Q}_f \\ \boldsymbol{Q}_p \end{Bmatrix}, \tag{7}$$

knowing that the global matrices $\boldsymbol{M}$, $\boldsymbol{C}$ and $\boldsymbol{K}$ are defined as below:

$$[\mathcal{M}]_e = \int_{\Omega_e} \rho_e \, [\mathcal{N}_u]_e^\top \, [\mathcal{N}_u]_e \, \mathrm{d}\Omega_e \qquad \boldsymbol{M}_{uu} = \sum_e [\mathcal{M}]_e \tag{8}$$

$$[\mathcal{K}_{uu}]_e = \int_{\Omega_e} [\mathcal{B}_u]_e^\top \left[\boldsymbol{c}^E\right]_e [\mathcal{B}_u]_e \, \mathrm{d}\Omega_e \qquad \boldsymbol{K}_{uu} = \sum_e [\mathcal{K}_{uu}]_e \tag{9}$$

$$[\mathcal{K}_{u\phi}]_e = \int_{\Omega_e} [\mathcal{B}_u]_e^\top \, [\boldsymbol{e}]_e^\top \, [\mathcal{B}_\phi]_e \, \mathrm{d}\Omega_e \qquad \boldsymbol{K}_{u\phi} = \sum_e [\mathcal{K}_{u\phi}]_e \tag{10}$$

$$[\mathcal{K}_{\phi\phi}]_e = \int_{\Omega_e} [\mathcal{B}_\phi]_e^\top \, [\boldsymbol{\varepsilon}]_e \, [\mathcal{B}_\phi]_e \, \mathrm{d}\Omega_e \qquad \boldsymbol{K}_{\phi\phi} = \sum_e [\mathcal{K}_{\phi\phi}]_e \tag{11}$$

$$[\mathcal{C}]_e = \alpha \, [\mathcal{M}]_e + \beta \, [\mathcal{K}_{uu}]_e \qquad \boldsymbol{C}_{uu} = \sum_e [\mathcal{C}]_e \tag{12}$$

where the subscript e stands for a finite element, $[\boldsymbol{\mathcal{B}}_u]$ and $[\boldsymbol{\mathcal{B}}_\phi]$ defines the derivatives of shape functions and α and β are Rayleigh's coefficients for proportional damping. The damping matrix $\boldsymbol{C}_{uu}$ involves the damping effect of the metallic layer and the piezoelectric layers.

For the control problem formulation to be stated, the boundary condition for the electrode on the sensor layer, top ceramic layer identified by s, is that its electrical voltage is null, $\boldsymbol{\Phi}_p^s = 0$, so we can measure its nodal electrical charge $\boldsymbol{Q}_p^s$. Meanwhile, the boundary condition for the actuator layer, bottom ceramic layer identified by a, is that its input voltage is prescribed and identified by $\boldsymbol{\Phi}_p^a$. Additionally, the electric charges at the piezoelectric internal nodes $\boldsymbol{Q}_f$ are null, and the controlled transducer problem to be designed is illustrated in Figure 2

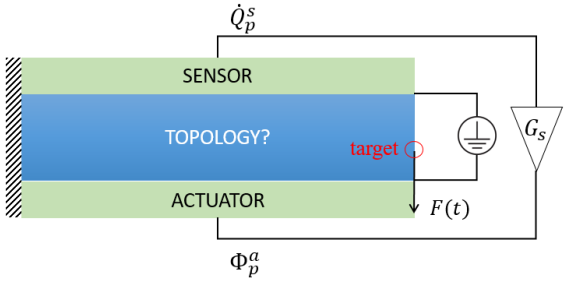

Figure 2: Controlled transducer with metallic layer to be designed by TOM.

Therefore, the system of equations (7) is rewritten so the electrical charges $\boldsymbol{Q}_p^s$ is given as a function of the vector $\boldsymbol{U}$. Given the aforementioned boundary conditions, the electric potential vector on the ceramic internal nodes is defined by

$$\boldsymbol{\Phi}_f = \mathbf{K}_{\phi_f\phi_f}^{-1}\mathbf{K}_{u\phi_f}^{\top}\mathbf{U}. \tag{13}$$

By substituting $\boldsymbol{\Phi}_f$, equation (13), into the two other equations of the system (7), the output forces $\mathbf{F}$ and the measured charges $\mathbf{Q}_p^s$ at the sensor layer are given by the expressions:

$$\mathbf{F} = \mathbf{M}\ddot{\mathbf{U}} + \mathbf{C}\dot{\mathbf{U}} + \underbrace{\left(\mathbf{K}_{uu} + \mathbf{K}_{u\phi_f}\mathbf{K}_{\phi_f\phi_f}^{-1}\mathbf{K}_{u\phi_f}^{\top}\right)}_{\mathbf{H}_{uu}}\mathbf{U}, \tag{14}$$

$$\mathbf{Q}_p^s = \underbrace{\left(\mathbf{K}_{u\phi_p^s}^{\top} - \mathbf{K}_{\phi_f\phi_p^s}^{\top}\mathbf{K}_{\phi_f\phi_f}^{-1}\mathbf{K}_{u\phi_f}^{\top}\right)}_{\mathbf{H}_{u\phi_p^s}^{\top}}\mathbf{U}. \tag{15}$$

Based on the voltage definition for a current amplifier, the sensor output charges $\mathbf{Q}_p^s$ are differentiate in time and multiplied by a constant gain G_s to obtain the sensor voltage output

$$\boldsymbol{\Phi}_p^s = G_s\mathbf{H}_{u\phi_p}^{\top}\dot{\mathbf{U}}. \tag{16}$$

Premultiplying equation (16) by a unit vector $\mathbf{I} = \{1 \quad \dots \quad 1\}$, of the electrode sensor layer nodal size ϕ_p^s, a scalar output voltage φ is obtained. In order to have an equipotential input voltage to the actuator electrode, φ must multiply a unit vector $\boldsymbol{I}^\top$ on the actuator electrode nodal size ϕ_p^a. Therefore,

$$\boldsymbol{\Phi}_p^a = G_s \boldsymbol{I}_{\phi_p^a} \boldsymbol{I}_{\phi_p^s} \boldsymbol{H}_{\phi_p^s u} \dot{\mathrm{U}}. \tag{17}$$

Rewriting the dynamical system (7) in H-matrix form with equation (17) based on previous developments, the equation to be solved by a time integration method is stated:

$$\begin{bmatrix} \boldsymbol{M}_{uu} & \mathbf{0} \\ \mathbf{0} & \mathbf{0} \end{bmatrix} \begin{Bmatrix} \ddot{\boldsymbol{U}} \\ \ddot{\boldsymbol{\Phi}}_f \end{Bmatrix} + \begin{bmatrix} \boldsymbol{C}_{uu} - G_s \boldsymbol{K}_{u\phi_p^a} \boldsymbol{I}_{\phi_p^a} \boldsymbol{I}_{\phi_p^s} \boldsymbol{H}_{\phi_p^s u} & \mathbf{0} \\ G_s \boldsymbol{K}_{\phi_f \phi_p^a} \boldsymbol{I}_{\phi_p^a} \boldsymbol{I}_{\phi_p^s} \boldsymbol{H}_{\phi_p^s u} & \mathbf{0} \end{bmatrix} \begin{Bmatrix} \dot{\boldsymbol{U}} \\ \dot{\boldsymbol{\Phi}}_f \end{Bmatrix} + \begin{bmatrix} \boldsymbol{K}_{uu} & \boldsymbol{K}_{u\phi_f} \\ \boldsymbol{K}_{u\phi_f}^\top & -\boldsymbol{K}_{\phi_f \phi_f} \end{bmatrix} \begin{Bmatrix} \boldsymbol{U} \\ \boldsymbol{\Phi}_f \end{Bmatrix} = \begin{Bmatrix} \boldsymbol{F} \\ \mathbf{0} \end{Bmatrix}. \tag{18}$$

Therefore, equation (18) is the FE system for the transient velocity feedback analysis.

3 THE TOM FOR AN AVF CONTROL LAW

The TOM has been employed to design smart structures based on piezoelectric material such as actuadors [13] and transducers [14] for a static or quasi-static analysis. In the field of intelligent structures, the topology optimization has been first applied in combination with a velocity feedback control by Zhang [2] and [5], who implemented an objective function based on the measurements of the displacement on a target degree of freedom.

In this work, TOM aims to extremize an objective function for a structure under a transient load and a velocity feedback control. It employs a material model concept [15] to distribute void and solid within a design domain aiming to extremise a cost function, and uses the FEM for systematic structure analysis. The SIMP is the material model employed in this work.

For the vibration suppression purpose, the objective function defined in this work considers the minimization of a energy function involving the velocity of a target point, $\dot{u}_{\mathrm{dof}}$. The design variables vector is the pseudodensity ρ of the host layer at each finite element, while a volume constraint $V_{\max}$ limits the material distribution for the design of a lightweight flexible structure with joints optimally located as to condense the ceramics displacements.

Therefore, the objective function defined monitors the vibration response over a given time interval $[0, t_f]$ as follows:

$$f = \int_0^{t_f} g(\dot{\boldsymbol{U}}(t, \boldsymbol{\rho}))\, \mathrm{d}t. \tag{19}$$

The function $g(\dot{\boldsymbol{U}}(t, \boldsymbol{\rho}))$ may be defined to monitor several types of structural behaviour, but here the objective function is to reduce the structure vibration by spanning in time the velocity $\dot{u}_{\mathrm{dof}}$ of a target degree of freedom:

$$g(\dot{\boldsymbol{U}}(t, \boldsymbol{\rho})) = \dot{\boldsymbol{U}}^\top \boldsymbol{B} \dot{\boldsymbol{U}}, \tag{20}$$

where $\boldsymbol{B} = \boldsymbol{B}^\top$ is used to specify the target degree of freedom. It is a null matrix where its diagonal equals 1 only at the target dof.

The optimization problem is stated bellow for the modified damping matrix of the system (18) represented by $\mathbf{C}_{tm}$:

$$\min_{\boldsymbol{\rho}} f(\boldsymbol{\rho}) = \int_0^{t_f} \dot{\boldsymbol{U}}^\top \boldsymbol{B} \dot{\boldsymbol{U}}\, dt$$
$$\text{s.t.} \begin{cases} \mathbf{M}(\boldsymbol{\rho})\ddot{\mathbf{U}} + \mathbf{C}_{tm}(\boldsymbol{\rho})\dot{\mathbf{U}} + \mathbf{K}(\boldsymbol{\rho})\mathbf{U} = \mathbf{F}(t) \\ \dot{\mathbf{U}}|_{t=0} = \dot{\mathbf{U}}_0 \\ \mathbf{U}|_{t=0} = \mathbf{U}_0 \\ \sum_{e=1}^{N_e} \rho_e V_e \leq V_{\max} \\ 0 < \rho_{\min} \leq \rho_e \leq 1 \end{cases} \tag{21}$$

As a solid and void profile is desired, the penalization factor q of the SIMP model accounts with smooth increments along each iteration of the TOM. Denominated the continuation approach, this procedure prevents a premature convergence to a local minima.

Therefore, the element elasticity tensor c^n_{ijkl}, for a basic isotropic metallic material c^E_{ijkl} and void-property material c^0_{ijkl}, is given by

$$\boldsymbol{c}(\rho_n) = \rho_n^q(x_c, y_c)\boldsymbol{c}^E + (1 - \rho_n^q(x_c, y_c))\boldsymbol{c}^0, \tag{22}$$

where (x_c, y_c) is the finite element Cartesian centroid coordinate pair.

4 NUMERICAL IMPLEMENTATION

The steps involved in the topology optimization algorithm are described in the flow chart shown in Figure 3.

The software was implemented in MATLAB with an optimization solver based in the Sequential Linear Programming (SLP), which has proved to be efficient for the kind of problem therein proposed. As a gradient-based mathematical programming algorithm, the SLP needs the sensitivity analysis of the objective function with respect to the design variables, which is calculated through the adjoint function in place of the original objective function as stated below:

$$\mathcal{L}(\dot{\boldsymbol{U}}, \boldsymbol{\lambda}) = \int_0^{t_f} g(\dot{\boldsymbol{U}}(t, \boldsymbol{\rho}))\, \mathrm{d}t + \int_0^{t_f} \boldsymbol{\lambda}^\top(t) \left[\boldsymbol{M}(\boldsymbol{\rho})\ddot{\boldsymbol{U}} + \boldsymbol{C}_{tm}(\boldsymbol{\rho})\dot{\boldsymbol{U}} + \boldsymbol{K}(\boldsymbol{\rho})\boldsymbol{U} - \boldsymbol{F}(t) \right] \mathrm{d}t. \tag{23}$$

Taking the derivative of the Lagrangian (23) with respect to the design variables $\boldsymbol{\rho}$ we

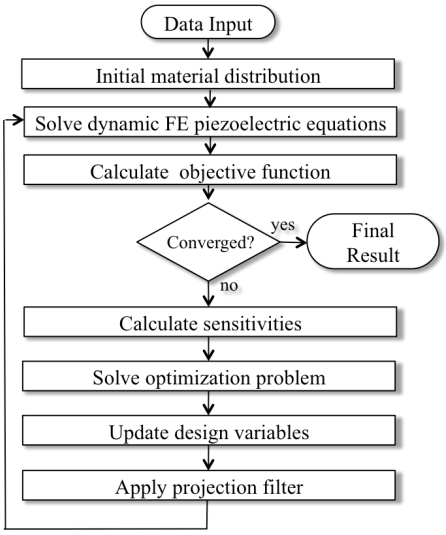

Figure 3: Flowchart of the implemented optimization procedure.

get the final valued adjoit problem

$$\begin{cases} \boldsymbol{M}\ddot{\boldsymbol{\lambda}}^{\top}(t) - \boldsymbol{C}_{tm}\dot{\boldsymbol{\lambda}}^{\top}(t) + \boldsymbol{K}\boldsymbol{\lambda}^{\top}(t) = \frac{\mathrm{d}}{\mathrm{d}t}\left(\frac{\partial g}{\partial \dot{\boldsymbol{U}}}\right)\Big|_{t} \\ \boldsymbol{\lambda}^{\top}(t_f) = \boldsymbol{0} \\ \dot{\boldsymbol{\lambda}}^{\top}(t_f) = \boldsymbol{M}^{-1}\ \frac{\partial g}{\partial \dot{\boldsymbol{U}}}\Big|_{t_f} \end{cases}, \tag{24}$$

and to obtain the initial value primal problem, a change of variable is applied $\tau(t) = t_f - t$:

$$\begin{cases} \boldsymbol{M}\ddot{\boldsymbol{\Lambda}}^{\top}(\tau(t)) + \boldsymbol{C}_{tm}\dot{\boldsymbol{\Lambda}}^{\top}(\tau(t)) + \boldsymbol{K}\boldsymbol{\Lambda}^{\top}(\tau(t)) = 2\boldsymbol{B}\ddot{\boldsymbol{U}}\Big|_{\tau(t)} \\ \boldsymbol{\Lambda}^{\top}(0) = \boldsymbol{0} \\ \dot{\boldsymbol{\Lambda}}^{\top}(0) = -2\boldsymbol{M}^{-1}\ \boldsymbol{B}\dot{\boldsymbol{u}}|_{t_f} \end{cases}. \tag{25}$$

Recalling that $\dot{\boldsymbol{\Lambda}}(\tau(t)) = -\dot{\boldsymbol{\lambda}}(t)$, the sensitivity expression for the transient problem reduces to:

$$\frac{\partial \mathcal{L}(\dot{\boldsymbol{U}}, \boldsymbol{\Lambda})}{\partial \rho_e} = \int_0^{t_f} \boldsymbol{\Lambda}^{\top}(t_f - t)\left[\frac{\partial \boldsymbol{M}(\boldsymbol{\rho})}{\partial \rho_e}\ddot{\boldsymbol{U}} + \frac{\partial \boldsymbol{C}_{tm}(\boldsymbol{\rho})}{\partial \rho_e}\dot{\boldsymbol{U}} + \frac{\partial \boldsymbol{K}(\boldsymbol{\rho})}{\partial \rho_e}\boldsymbol{U} - \frac{\partial \boldsymbol{F}(t)}{\partial \rho_e}\right] \mathrm{d}t. \tag{26}$$

As it is seen by equation (26), the sensitivity analysis of this transient optimization problem involves the solution of two second order linear equations, one in $\boldsymbol{\Lambda}$ and the other one in $\boldsymbol{U}$. Their numerical solutions are obtained by the a-form of Newmark's numerical integration scheme [16].

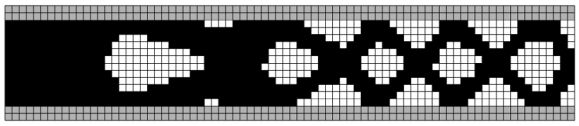

Figure 4: Optimized topology design for $G_s = 0$

5 PRELIMINARY RESULTS

Given a solid initial domain of $2cm \times 0.4cm$, this domain is discretized by a 80×16 finite elements with a pseudodensity vector initially set to $\boldsymbol{\rho} = 1$ at the metallic layer, restricted to $V_{\max} = 0.7$. The optimization problem, equation (21), was evaluated for a null feedback gain and for a feedback gain $G_s = 10000$.

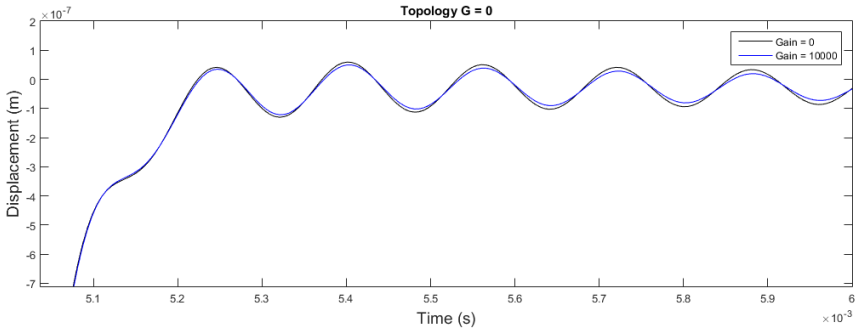

Figure 5: Target displacement for $G_s = 0$ optimized topology

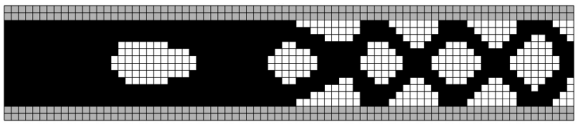

Figure 6: Optimized topology design for $G_s = 10000$

For both simulations, the objective function converged, and from figures 5 and 7 it can be seen that the transient finite element analysis results in a lower vibration amplitude in the presence of a control gain. However, the attenuation obtained for the topology resulted from the optimization that is coupled with a control gain, Figure 6, is increased when compared with the topology resulted from the optimization with null gain, Figure 4, what in terms of objective function values represents an improvement of 1.65%.

6 CONCLUSIONS

The TOM was applied to the design of a vibrational structure controlled by two piezoceramic layers aiming to reduce its displacement in time. The SIMP material model was

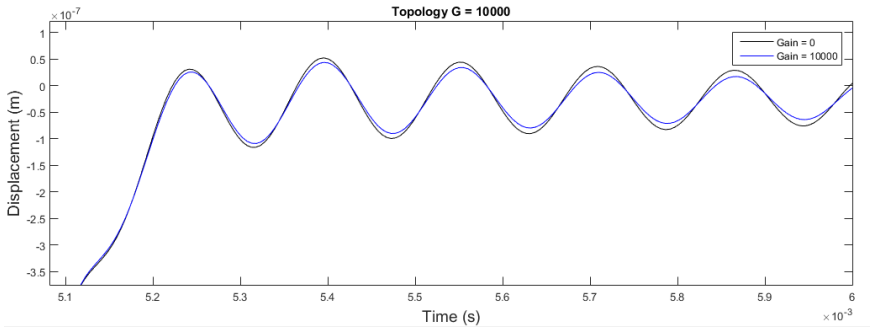

Figure 7: Target displacement for $G_s = 10000$ optimized topology

adopted and the optimization problem was solved with a Sequential Linear Programming (SLP) algorithm. The results show that to the velocity feedback gain chosen the optimization problem converges, and the final topology indicates a better improvement in response attenuation for the gain to which the structure was designed. In future work, formulation will be revised in order to obtain even grater vibration suppression in the presence of an active control feedback.

REFERENCES

[1] Kim, W., Song, Y. H. and Kim, J. E. *Topology optimization of actuator arms in hard disk drives for reducing bending resonance-induced off-tracks*. Structural and Multidisciplinary Optimization, Vol. 46, (2012) **6**:907–912.

[2] Zhang, X. and Kang, Z. *Dynamic topology optimization of piezoelectric structures with active control for reducing transient response*. Computer Methods in Applied Mechanics and Engineering, Vol. 281, (2014) 200-219.

[3] Ou, J. and Kikuchi, N. *Integrated optimal structural and vibration control design*. Structural optimization, Vol. 12, (1996) **4**:209–216.

[4] Wang, S. Y., Quek, S. T. and Ang, K. K. *Vibration control of smart piezoelectric composite plates*. Smart materials and Structures, Vol. 10, (2001) **4**:637–.

[5] Zhang, S., Schmidt, R. and Qin, X. *Active vibration control of piezoelectric bonded smart structures using PID algorithm*. Chinese Journal of Aeronautics, Vol. 28, (2015) **1**:305–313.

[6] Takezawa, A., Makihara, K., Kogiso, N. and Kitamura, M. *Layout optimization methodology of piezoelectric transducers in energy-recycling semi-active vibration control systems*. Journal of Sound and Vibration, Vol. 333, (2014) **2**:327–344.

[7] Jang, H. H., Lee, H. A., Lee, J.Y. and Park, G.J. *Dynamic response topology optimization in the time domain using equivalent static loads*. AIAA journal, Vol. 50, (2012) **1**:226–234.

[8] Deng, Y., Liu, Z., Liu, Y., and Wu, Y. *Combination of topology optimization and optimal control method*. Journal of Computational Physics, Vol. 257, (2014) **-**:374–399.

[9] Wang, S. Y., Tai, K. and Quek, S. T. *Topology optimization of piezoelectric sensors/actuators for torsional vibration control of composite plates*. Smart materials and Structures, Vol. 15, (2016) **2**:253–.

[10] Zhang, X., Kang, Z., and Li, M. *Topology optimization of electrode coverage of piezoelectric thin-walled structures with CGVF control for minimizing sound radiation*. Structural and Multidisciplinary Optimization, Vol. 50, (2014) **5**:799–814.

[11] Ray, M. C., and Reddy, J. N. *Optimal control of thin circular cylindrical laminated composite shells using active constrained layer damping treatment*. Smart Materials and Structures, Vol. 13, (2003) **1**:64–.

[12] Tiersten, H.F. *On the nonlinear equations of thermo-electroelasticity*. International Journal of Engineering Science, Vol. 9, (1971) **7**:587–604.

[13] Kögl, M., and Silva, E. C. N. *Topology optimization of smart structures: design of piezoelectric plate and shell actuators*. Smart materials and Structures, Vol. 14, (2005) **2**:387–.

[14] Silva, E. C. N. and Kikuchi, N. *Design of piezoelectric transducers using topology optimization*. Smart Materials and Structures, Vol. 8, (1999) **3**:350–.

[15] Rozvany, G. I. N. *Aims, scope, methods, history and unified terminology of computer-aided topology optimization in structural mechanics*. Structural and Multidisciplinary Optimization, Vol. 21, (2001) **2**:90–108.

[16] Hilber, H. M., Hughes, T. J. R. and Taylor, R. L. *Improved numerical dissipation for time integration algorithms in structural dynamics*. Earthquake Engineering & Structural Dynamics, Vol. 5, (1977) **3**:283–292.

VII International Conference on Computational Methods for Coupled Problems in Science and Engineering
COUPLED PROBLEMS 2017
M. Papadrakakis, E. Oñate and B. Schrefler (Eds)

DEVELOPMENT OF AN AUTOMATED PROCESS FOR TURBINE BLADE OPTIMISATION

TESSA UROIĆ*, BORNA ŠOJAT* AND HRVOJE JASAK†,*

*Faculty of Mechanical Engineering and Naval Architecture (FSB)
University of Zagreb
Ivana Lučića 5, 10000 Zagreb, Croatia
e-mail: tessa.uroic@fsb.hr, borna.sojat@stud.fsb.hr, hrvoje.jasak@fsb.hr
web page: http://www.fsb.unizg.hr/cfd

†Wikki Ltd.
Unit 459, Southbank House, Black Prince Road, London SE1 7SJ, United Kingdom
e-mail: h.jasak@wikki.co.uk, web page: http://wikki.gridcore.se/wikkiweb/company

Key words: Turbomachinery, Optimisation, Genetic Algorithm, `OpenFOAM`

Abstract. In this paper we present a fully automated procedure for turbine blade optimisation. Optimisation process consists of geometry parametrisation using B-splines, mesh deformation using the dynamic mesh library in `OpenFOAM`, numerical simulation of transonic flow through the blade passage and finding the feasible solutions with the Multi-Objective Genetic Algorithm (MOGA). The process proved to be robust whether starting the optimisation from unfeasible geometry or a conventional blade profile.

1 INTRODUCTION

The motivation for this work comes from industrial demands for faster and more efficient design cycles. Turbomachinery components are regularly found in many energy conversion processes where the work load is predetermined and constant. Thus, it is possible to optimise the components of a machine for a single operating point. The process of turbomachinery optimisation usually consists of several steps: geometry description in a mathematical sense (parametrisation), calculation of objective (fitness) functions, e.g. via computational fluid dynamics (CFD) simulation, and evaluation of the obtained solution(s). There are many optimisation approaches for different applications, from the method of trial-and-error to advanced adjoint optimisation algorithms [1]. The most common is the genetic or evolutionary algorithm which is based on Darwin's theory of natural selection: only the fittest individuals survive and provide their genetic code to the following generation. There are many examples of turbomachinery optimisation using

the genetic algorithm, sometimes combined with surrogate methods to decrease time-to-solution.

Sieverding et al. [2] have developed a two-dimensional optimisation process for industrial axial compressors, where they used a genetic optimisation algorithm and gave special attention to definition of an appropriate fitness function. The separately optimised blade sections are later stacked to create a three-dimensional blade and validated using a commercial CFD code. The parametrisation of the blade section is done using the concept of superposition of camber line and thickness distribution, and both are described by Bezier curves. The optimisation is single objective with a fitness function which takes into account non-dimensional loss coefficients, exit flow angle, etc. The calculation of the function is done by simulating the flow around the blade.

Zheng et al. [3] conducted optimisation of a transonic rotor of an axial compressor. The geometry is parametrised by B-spline and the design parameters were blade sweep and lean angle at four different blade heights. Response surface approximation was used for the objective function, with a polynomial and basis-function response methods. Genetic optimisation algorithms were used for obtaining the optimal solutions for both polynomial and basis-function methods. There were no constraints included, and variation of the blade sections was not considered.

Optimisation of the same transonic rotor was done by Wang et al. [4] also using a surrogate model and genetic algorithm, with an additional uncertainty analysis by probabilistic collocation method. The uncertainty is introduced by varying the outlet static pressure at the design operating point, and the trade-off result is compared to a deterministic single objective optimisation result.

Siddique et al. [5] presented an optimisation process of a centrifugal pump impeller consisting of a CFD simulation and a surrogate-based optimisation method. Inlet and exit angles of the impeller were chosen as the design variables and maximum head and efficiency were the two objective functions.

Ennil et al. [6] used a fully automated CFD simulation coupled with response surface analysis and multi objective genetic algorithm to optimise a small scale axial air driven turbine with respect to energy losses.

Before-mentioned researches do not elaborate the bottleneck of the optimisation process, i.e. the generation of the computational mesh for the CFD simulation.

Page et al. [7] stressed the importance of meshing in the automatic CFD design optimisation processes. They proposed an automatic mesh generation and an adjoint based error analysis to select the optimal mesh configuration for a given geometry and the objective function. The estimation of the error induced by space discretisation was carried out and was used as an indicator to improve mesh quality to obtain a more accurate solution.

However, this approach does not take into account the time needed for generation of a complex mesh and a large number of evaluations which have to be conducted by the genetic algorithm.

Our paper presents a robust, fully automated fast optimisation process for turbomachinery, applied to a single two-dimensional blade pasagge. The process consists of four steps:

1. geometry parametrisation using B-spline curves,
2. deformation of a starting, fully structured computational mesh,
3. CFD simulation of the compressible flow,
4. estimation of the obtained solutions and generation of new geometry by the optimisation algorithm.

Each of these steps will be described in the next section.

2 METHODOLOGY

In this section, each of the four steps of the optimisation loop will be described. The flowchart of the optimisation loop is shown in Fig. 1.

2.1 Geometry parametrisation

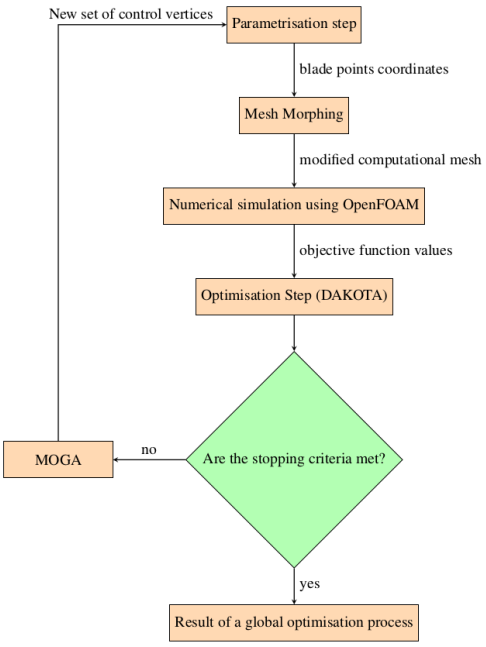

Figure 1: Optimisation loop

To achieve communication between the optimisation algorithm and the CFD simulation, i.e. the mesh deformation utility, it was necessary to describe the blade geometry in a straightforward way. The easiest and most convenient, but maybe not the most practical way for blade profiles, is to represent the geometry with control points. These control points are defined by the optimisation algorithm as the design parameters. However, the following step of the optimisation process, the mesh deformation, requires many more points than the defined number of control points. To *connect* the control points and extract more points in–between which will describe the geometry more precisely, we chose to parametrise the blade using periodic B-spline curves [8]. B-spline approximates the control points and is easily deformed by changing the position of the control points. The result is a smooth and continuous blade surface without any sudden and sharp jumps. Each segment

of the curve between the two control points is of the 5^{th} degree and 40 parametrisation points were extracted from each segment. An example of a parametrised NACA 4421 profile can be seen in Fig. 2.

2.2 Mesh deformation

In [9] an overview of numerical errors resulting from the discretisation procedure (treating convection and temporal terms) and mesh-induced errors is given. Consistent use of discretisation schemes in blade passage simulations can be ensured, but mesh-induced errors are more difficult to measure and control. A large number of geometries are tested by the optimisation algorithm and it is time demanding to create a new computational mesh for each geometry. In order to compare the results for different geometries, similar mesh resolution and quality (orthogonality, skewness) must be ensured for each case. Creating the computational mesh by hand for every single geometry to have more control over the resulting mesh properties is impossible. Automatic meshing algorithms cannot provide the same or even similar mesh configuration for different geometries, no matter how small the shape variation is. This is the reason a mesh morphing procedure was developed for blade geometry optimisation, using the dynamic mesh library implemented in `OpenFOAM` [10].

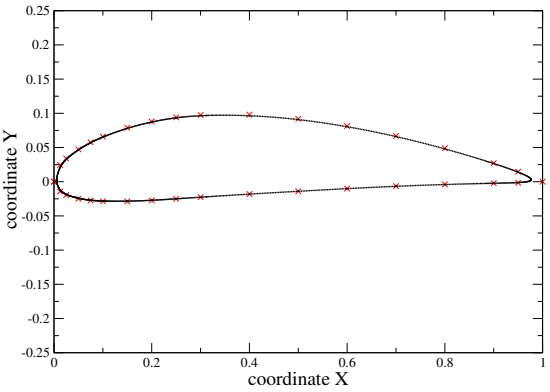

Figure 2: NACA 4421 blade with control points in red and B-spline in black

The morphing procedure is based on the assumption that the computational mesh behaves as an elastic body in a state of equilibrium, as described in [11]. If some force acts on the boundary of the body, it will cause the motion of the boundary which will influence the interior of the body. Influence of boundary motion on interior points of the mesh can be described with a Laplace equation:

$$\nabla \cdot (\gamma \nabla \vec{u}) = 0 \tag{1}$$

where $\vec{u}$ is the displacement vector, and γ is the diffusion coefficient. By applying the Laplace displacement equation with a constant coefficient γ, the largest deformation of the mesh elements occurs near the mesh boundary. It usually leads to extreme mesh distortion and negative cell volumes. This is why a space dependent coefficient of diffusivity is used. Notice that increase of the diffusivity coefficient results in lower deformation of the mesh element. Thus, it is beneficial to define the diffusivity coefficient to be inversely proportional to distance of the mesh element from the mesh boundary. The function can

be linear, quadratic or exponential [11]. In this study, a quadratic function is used:

$$\gamma(l) = l^{-2}, \tag{2}$$

where l is the minimum distance of the mesh element from the mesh boundary.

The Laplace displacement equation (1) is discretised into a linear system of equations:

$$[A] \cdot \vec{u}_k = r_k, \quad k = 1, 3, \tag{3}$$

where $\vec{A}$ is the coefficient matrix, $\vec{u}$ is the unknown vector of displacement and $\vec{r}$ is the right hand side vector. The new geometry configuration is defined with a set of points obtained from the parametrisation which are introduced into the system (3) as a fixed value (Dirichlet) boundary condition.

2.3 Numerical simulation

After obtaining the new mesh from the deformation procedure, simulation of transonic flow through the blade passage is performed using `foam-extend`, a community driven fork of the open source software `OpenFOAM`. The governing equations are the continuty equation (4), momentum equation (5) and energy equation (6).

$$\frac{\partial \rho}{\partial t} + \nabla \cdot (\rho \vec{u}) = 0 \tag{4}$$

$$\frac{\partial \vec{u}}{\partial t} + \nabla \cdot (\rho \vec{u} \otimes \vec{u}) - \nabla \cdot (\nu \nabla \vec{u}) = -\nabla p, \tag{5}$$

$$\frac{\partial \rho e}{\partial t} + \nabla \cdot (\rho e \vec{u}) = \rho \vec{g} \cdot \vec{u} + \nabla \cdot (\sigma \cdot \vec{u}) - \nabla \cdot \vec{q} + \rho Q \tag{6}$$

The energy equation is weakly coupled with the rest of the system because e (specific internal energy), and temperature T influence ρ and convective velocity $\vec{u}$ through the equation of state, written here for the ideal gas (7).

$$\rho = \frac{P}{RT} = \psi P, \tag{7}$$

where ψ is the compressibility,

$$\psi = \frac{1}{RT}. \tag{8}$$

Compressibility effects can be observed at higher fluid velocities, and Mach number is commonly used to determine the critical velocity at which the flow can be considered compressible.

In this study $k - \omega$ SST [12, 13] turbulence model was used.

The results of the numerical simulation were processed, objective function values were calculated from corresponding flow variables and delivered to the optimisation algorithm.

In turbines, stator blades are vital parts of the geometry. They are used to accelerate the fluid flow as much as possible with the smallest possible pressure drop, while directing the fluid flow at optimal attack angle onto rotors. Having this in mind, objective functions were defined as follows. The target was to produce a geometry that would give the largest increase in velocity while keeping the pressure drop as small as possible. Thus, Δu and Δp were defined as:

$$\Delta u = u_{outlet} - u_{inlet} \longrightarrow \text{maximise}, \tag{9}$$

and

$$\Delta p = p_{inlet} - p_{outlet} \longrightarrow \text{minimise}. \tag{10}$$

2.4 Multi-objective optimisation

Within this work genetic optimisation algorithm was used. Genetic algorithm is a derivative free global method. Derivative free methods are usually more robust than the gradient based approaches and they are applied when the problem is non-smooth, multi modal or poorly behaved. On the other hand, this approach is usually more computationally demanding because of its slower convergence rates for finding an optimal solution(s). Multi-objective Genetic Algorithm, MOGA [14], an algorithm specially designed for multi-objective problems was used, since there were two objective functions which are conflicting with each other. This means a unique optimal solution doesn't exist, but the algorithm calculates a set of feasible Pareto solutions. Each solution is a trade-off since the objective functions cannot achieve their optimal values simultaneously.
Settings of the MOGA algorithm were as follows:

- size of a generation: 50
- number of children: 40
- crossover rate: 0.75
- mutation rate: 1
- maximal number of generations: 10

The latter was used as the stopping criterion for the optimisation loop.

To achieve convergence of the optimal solution in a reasonable amount of time, strong geometric constraints were prescribed for the design variables, Fig. 3.

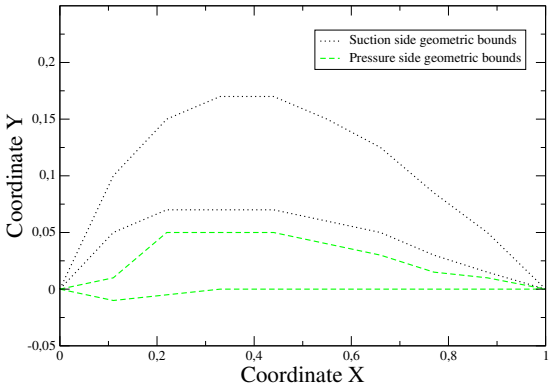

Figure 3: Geometric constraints

3 RESULTS AND DISCUSSION

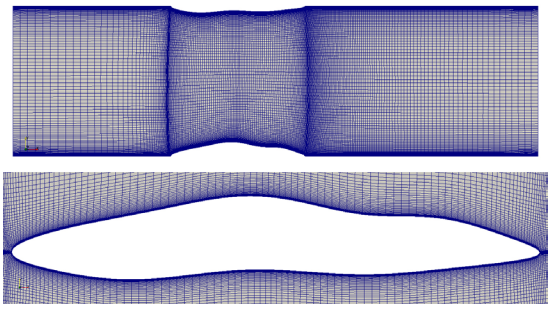

Figure 4: Initial geometry and computational mesh

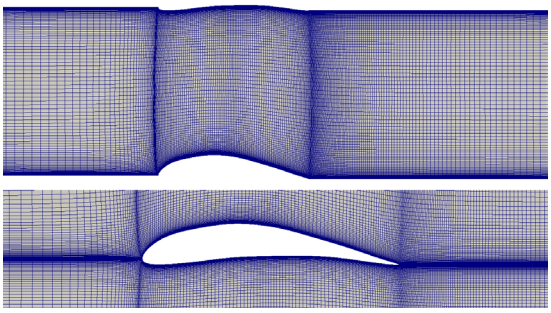

Figure 5: Optimised geometry and computational mesh after second MOGA pass

We decided to start the optimisation process with a *dummy* geometry, a shape which is not a stator blade in any sense, Fig. 4. The reason for such initial geomery is that we wanted to see if the deformation algorithm is able to deform the mesh starting from a distorted and very different shape, while keeping the mesh quality, and to see whether the optimisation process can produce a good result starting from a far from ideal initial geometry configuration. The blade was split into suction and pressure side to form a passage. It is possible to expand the width of the passage in the mesh deformation algorithm to accomodate thicker blades, but this was avoided by prescribing geometric constraints. The computational mesh is fully structured and has approximately 28000 cells. Mesh refinement study was conducted and current mesh density was chosen because it provided satisfactory results while being computationally less expensive than the finest mesh tested. In case of errors appearing in the mesh deformation procedure (negative volume cells, highly skewed or non-orthogonal cells), these cases would be rejected as suboptimal and would not be evaluated, but this happened in none of the cases. The patches parallel to the blade walls were treated as periodic, using General Grid Interface (GGI) [15] for interpolation of flow variables. Value of total pressure was defined at the inlet, and value of static pressure at the outlet. Several attack angles were tested and here the results for attack angle $\alpha = 5°$ are presented.

One iteration of the process, including parametrisation, mesh deformation, numerical simulation and objective function evaluation lasted 13 minutes, on a single Intel i5-4570 (3.2 GHz) CPU core. Numerical simulation took the longest, 12 minutes (92,3%), mesh deformation took less than a minute (7,7%) while geometry parametrisation and objective function evaluation took less than 1 second. In comparison, the same iteration with an automatic meshing algorithm, [16], would take 15 minutes, and it wouldn't be possible to control local mesh quality. The process is easily parallelizable, as multiple evaluations can be done on different processor cores at the same time.

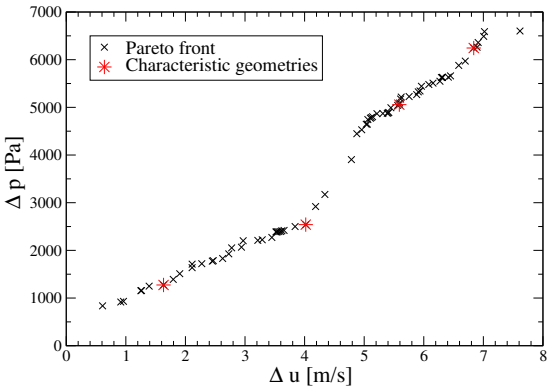

Figure 6: Pareto front

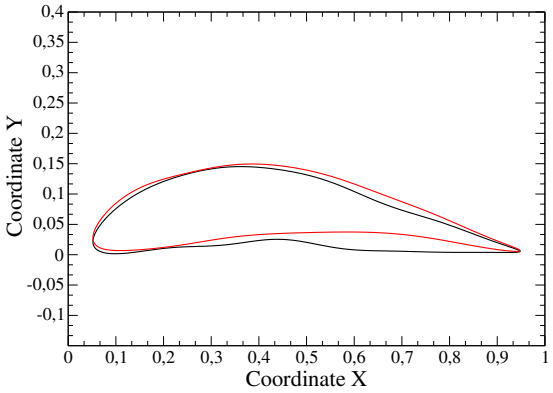

Figure 7: Pareto optimum after second MOGA optimisation (red) compared to the initial optimum (black)

The process ran 887 evaluations before reaching the stopping criterion of 10 generations and the resulting Pareto front is shown in Fig. 6. Red stars represent four chosen characteristic geometries, for which objective functions' values are shown in Tab. 1, as well as the values for the initial geometry. The corresponding geometries are shown in Figs. 8, 9, 10, 11, going from left to right in the Pareto front, Fig. 6.

Table 1: Parameters of four characteristic Pareto front geometries.

Point on the Pareto front	**Objective function values**
Initial geometry	$\Delta u = 2.695$ m/s $\Delta p = 2251.37$ Pa $\Delta p/\Delta u = 835.39$ Pa/ms^{-1}
1	$\Delta u = 1.633$ m/s $\Delta p = 1274.37$ Pa $\Delta p/\Delta u = 780.39$ Pa/ms^{-1}
2	$\Delta u = 4.185$ m/s $\Delta p = 2919.64$ Pa $\Delta p/\Delta u = 697.64$ Pa/ms^{-1}
3	$\Delta u = 5.589$ m/s $\Delta p = 5057.05$ Pa $\Delta p/\Delta u = 904.82$ Pa/ms^{-1}
4	$\Delta u = 6.839$ m/s $\Delta p = 6245.39$ Pa $\Delta p/\Delta u = 913.20$ Pa/ms^{-1}

Solution 2 had the smallest pressure drop for the given velocity increase, and we have

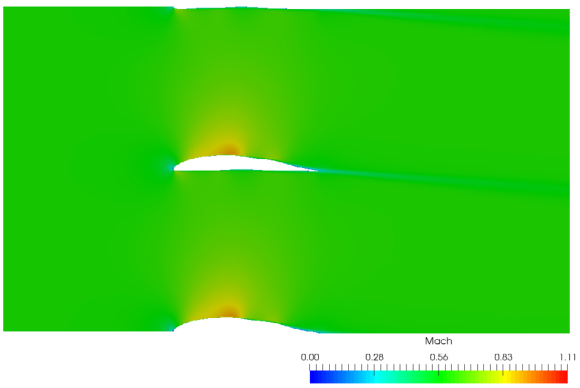

Figure 8: Optimal solution 1

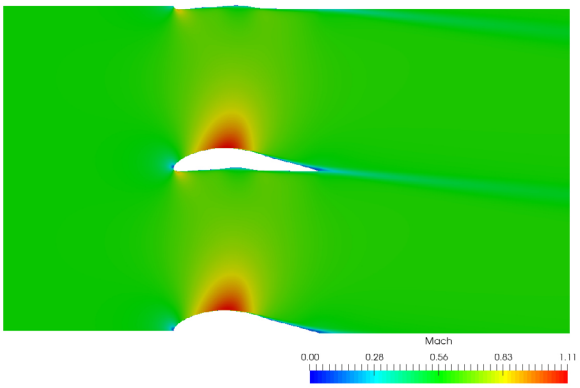

Figure 9: Optimal solution 2

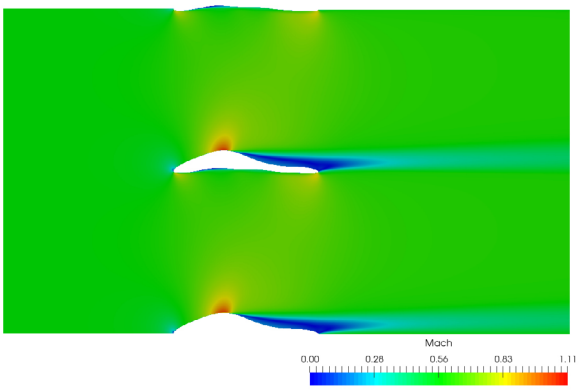

Figure 10: Optimal solution 3

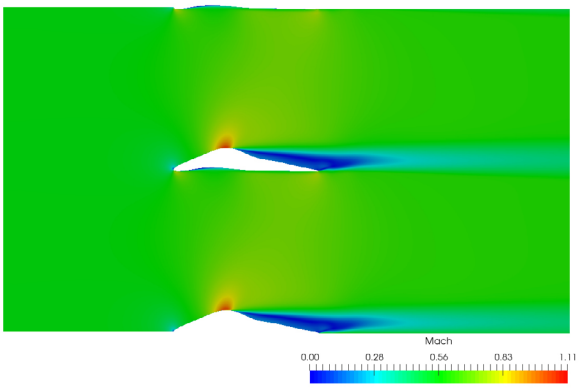

Figure 11: Optimal solution 4

chosen it to conduct further optimisation using MOGA to see whether starting from a feasible solution would produce different results. After 702 evaluations, a final shape of the stator blade was obtained, Figs. 5 and 7. The values of the objective functions for this blade were $\Delta u = 5.576$ m/s and $\Delta p = 3131.40$ Pa, which is 561.59 Pa of pressure drop per 1 m/s velocity increase, while for the first Pareto optimum, this ratio was 697.64 Pa per 1 m/s. Thus, second pass of MOGA, or starting from a feasible initial geometry, produced a better result.

4 CONCLUSIONS

We developed a robust optimisation procedure in which we included a mesh deformation algorithm which enabled us to localise numerical errors induced by the spatial discretisation in the Finite Volume Method. Additionaly, the mesh deformation utility contributed to the efficiency of the overall procedure because it is considerably faster than the automatic meshing algorithm we tested. The procedure could be made even more robust by carefully defining the design variables, e.g. parametrising the camber line with a set of control points and defining a blade thickness distribution. 16 parametrisation control points were chosen as the design parameters. Genetic algorithm which was used has to perform a large number of evaluations to converge to an optimal set of solutions, and strong geometric constraints were prescribed to narrow the design space. Starting the optimisation process from an unfeasible geometry produced a set of feasible solutions without any failures in any of the steps of the process. Starting the optimisation process from *the best* of those solutions yielded an even better solution, according to the objective functions. This optimisation process can be modified for three-dimensional cases and more complex geometries, e.g. for applications in naval architecture, aeronautical engineering, etc.

REFERENCES

[1] Zhang, P., Lu, J., Song, L., Feng, Z. Study on continuous adjoint optimization with turbulence models for aerodynamic performance and heat transfer in turbomachinery cascades *International Journal of Heat and Mass Transfer.* (2017) **104**:1069–1082.

[2] Sieverding, F., Ribi, B., Casey, M., Meyer, M. Design of Induatrial Axial Compressor Blade Sections for Optimal Range and Performance *Journal of Turbomachinery.* (2004) **126**:323–331.

[3] Zheng, R., Xiang, J., Sun, J. Blade geometry optimization for axial flow compressor *Proceedings of ASME Turbo Expo 2010.* (2010)

[4] Wang, X., Hirsch, C., Liu, Z., Kang, S., Lacor, C. Uncertainty-based robust aerodynamic optimization of rotor blades *International Journal for Numerical Methods in Enginnering.* (2013) **94**:111–127.

[5] Siddique, H., Mrinal, K.R., Samad A. Optimization of a Centrifugal Pump Impeller by Controlling Blade Profile Parameters *Proceedings of ASME Turbo Expo 2016.* (2016)

[6] Ennil, A.B., Al-Dadah, R., Mahmoud, S., Rahbar, K., Aljubori, A. Minimization of loss in small scale axial air turbine using CFD modeling and evolutionary algorithm optimization *Applied Thermal Engineering.* (2016) **102**:841–848.

[7] Page, J.H., Watson, R., Ali, Z. Advances of Turbomachinery Design Optimization *Proceedings of 53rd AIAA Aerospace Sciences Meeting.* (2015)

[8] Rogers, D.F. *An introduction to NURBS with historical perspective* The Morgan Kaufmann Series in Computer Graphics (2001)

[9] Jasak, H. *Error analysis and estimation for the Finite Volume Method with applications to fluid flows* PhD thesis, Imperial College of Science, Technology and Medicine, London (1996)

[10] Jasak, H. Open source CFD in research and industry *International Journal of Naval Architecture and Ocean Engineering.* (2009) **1**:89–94.

[11] Tuković, Ž. *Metoda kontolnih volumena na domenama promjenjivog oblika* PhD thesis, Faculty of Mechanical Engineering and Naval Architecture, University of Zagreb (2005)

[12] Menter, F.R. Two-equation eddy-viscosity turbulence models for engineering applications *AIAA Journal.* (1994) **32**:1598–1605.

[13] Menter, F.R., Kuntz, M., Langtry, R. Ten years of industrial experience with the SST turbulence model *Turbulence, Heat and Mass Transfer.* (2003) **4**:625–632.

[14] Adams, B.M. et al. *Dakota, a multilevel parallel object-oriented framework for design optimization, parameter estimation, uncertainty quantification and sensitivity analysis: Version 6.4 User's manual* (2016)

[15] Beaudoin, M., Jasak, H. Development of a General Grid Interface for turbomachinery simulations with OpenFOAM *Proceedings of Open Source CFD International Conference.* (2008)

[16] Retrieved from *http://cfmesh.com/cfmesh/* Last access: 13th March 2018.

VII International Conference on Computational Methods for Coupled Problems in Science and Engineering
COUPLED PROBLEMS 2017
M. Papadrakakis, E. Oñate and B. Schrefler (Eds)

FLUID–STRUCTURE INTERACTION DESIGN OF INSECT–LIKE MICRO FLAPPING WING

D. ISHIHARA[*], N. OHIRA[*], M. TAKAGI[*], S. MURAKAMI[*] AND T. HORIE[*]

[*] Department of Mechanical Systems Engineering
Kyushu Institute of Technology
680-4 Kawazu, Iizuka, Fukuoka 820-8502, Japan
e-mail: ishihara@mse.kyutech.ac.jp, www-solid.mse.kyutech.ac.jp

Key words: Fluid–Structure Interaction, Insect Flapping Flight, Micro–Electro–Mechanical Systems, 2.5–Dimensional Structure, Micro Air Vehicle, Projection Method, Design Window.

Abstract. In this study, a FSI design of an insect–like micro flapping wing is proposed. Similar to actual insects, the proposed design actively uses the FSI to create the passive wing motions. Each design solution has a 2.5–D structure for the MEMS technology. The 3–D unsteady monolithic FSI equation system is solved to find the satisfactory design solutions using a projection method in a parallel computation environment. An area of satisfactory design solutions in a design parameter space or Design Window (DW) is presented. Each design solution in the present DW can generate the thrust sufficient to support the weight of the model insect. Therefore, the insect–like MEMS–based MAVs are possible.

1 INTRODUCTION

In this study, a FSI design of an insect–like micro flapping wing is proposed. Similar to actual insects, the proposed design actively uses the FSI to create the pitching motion of the wing. The proposed design will decrease the mechanical complexity of MAVs. The proposed design requires the accurate and stable analysis for the strong interaction. Furthermore, the speedup of computation is required for the parametric study. Therefore, a projection method using the algebraic splitting [1, 2] is used to solve the 3–D unsteady monolithic FSI equation system in a parallel computation environment.

Each design solution has a 2.5–D structure for the MEMS processing. The initial design parameters are determined based on a model insect. An area of satisfactory design solutions in a design parameter space or Design Window (DW) is presented. DW is convenient for decision-making in MEMS structural design [3]. Each solution in the present DW can generate the thrust sufficient to support the weight of the model insect. These results show the possibility of insect–like MEMS–based MAVs. It follows from the present results that the artificial micro system mimicking the organisms can use the coupled problem to create its function, and the 2.5–D structure can be designed with the aid of recent progress in coupled analysis [4, 5] such that it can be fabricated using the MEMS technology.

2 FLUID–STRUCTURE INTERACTION DESIGN

2.1 Concept

Fig. 1 shows the conceptual view of the insect–like MEMS–based MAV, where the insect flapping flight mechanics and the MEMS technology are combined. Following actual insets, the insect–like MAV can be minimized from 1mm to 1cm in size. At these size scales, the MEMS technology would be most promising. The FSI design is proposed to develop it.

The main design concept is the active use of the FSI to create the function in micro system: Similar to actual insects, an insect–like micro flapping wing actively uses the FSI to create the pitching motion. It will decrease the mechanical complexity of MAVs. Furthermore, the 2.5–D structure is used such that it can be fabricated using the MEMS technology.

2.2 FSI cause of pitching motion

The wing motion consists of the flapping and the pitching as shown in Fig. 2. The interaction between the flapping flexible wing and the surrounding air can create the characteristic pitching motion and the enough lift for the insect to hover [6–9].

2.3 Insect–like micro flapping wing

Fig. 3 shows the schematics of the insect–like micro flapping wing based on the proposed FSI design. As shown in this figure, the 2.5–structure is adopted: The flexible wing is fabricated using the membrane. The beam is used as the leading edge to support the wing membrane. Taking into account micro actuator, the plate spring at the base amplifies the stroke angle using the resonance.

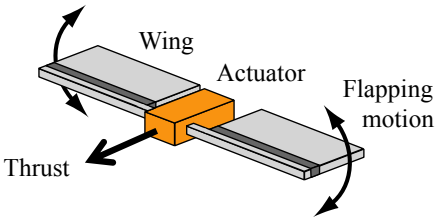

Figure 1: Insect–like MEMS–based MAV.

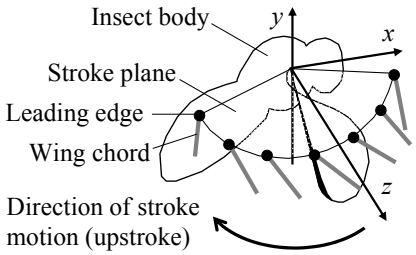

Figure 2: Schematics of insect flapping flight.

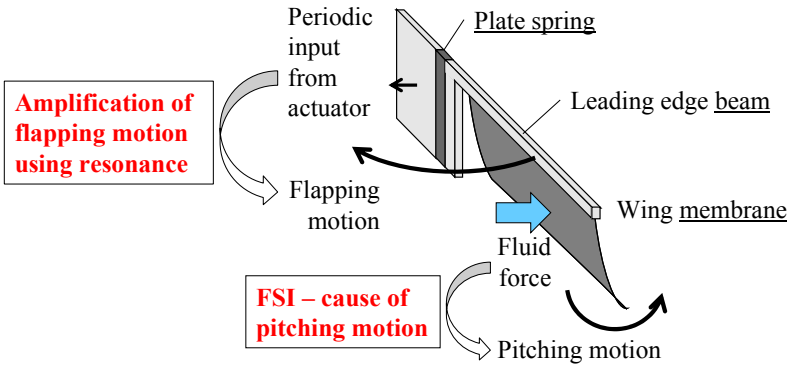

Figure 3: Schematics of the insect–like micro flapping wing based on the proposed FSI design.

3 FLUID–STRUCTURE INTERACTION ANALYSIS

3.1 Governing equations for FSI

The equilibrium equation for the elastic body and the incompressible Navier–Stokes equations are considered to describe the motion of the deformable model wing and the fluid flow surrounding the wing, respectively. The arbitrary Lagrangian–Eulerian method is used to describe the motion of the fluid–structure interface. The interface conditions to describe the interaction between the wing and the surrounding fluid are considered.

3.2 Monolithic equation system for FSI

Applying finite element discretization to the total Lagrangian formulation of the equation of the elastic body, the nonlinear equilibrium equation system can be obtained in matrix form. Similarly, the nonlinear equation system of the incompressible viscous fluid can be obtained in matrix form. Applying the interface conditions to these spatially discretized governing equations, the monolithic equation system can be obtained as

$$ {}_{\mathrm{L}}\mathbf{Ma}+\mathbf{Cv}+\mathbf{N}+\mathbf{q}(\mathbf{u})-\mathbf{Gp}=\mathbf{g}\,,\ {}_{\tau}\mathbf{Gv}=\mathbf{0}\,, \qquad \text{(1a, b)} $$

where **M**, **C,** and **G** are the mass, diffusive, and divergence operator matrices, **N**, **q**, **g**, **a**, **v**, **u**, and **p** are the convective term, elastic internal force, external force, acceleration, velocity, displacement, and pressure vectors, respectively, the subscripts L and τ indicate the lumping of the matrix and the transpose of the matrix, respectively.

Eq. (1) is linearized using the state variable increments to obtain the following equations:

$$ \mathbf{M}^{*}\Delta\mathbf{a}-\mathbf{G}\Delta\mathbf{p}=\Delta\mathbf{g}\,,\ \gamma\Delta t\,{}_{\tau}\mathbf{G}\Delta\mathbf{a}+\mathbf{G}_{\varepsilon}\Delta\mathbf{p}=\Delta\mathbf{h}\,, \qquad \text{(2a, b)} $$

where the pressure and elastic interior force terms are evaluated implicitly, $\mathbf{M}^{*}$ is the generalized mass matrix, Δ denotes the increment, t denotes the current time, Δ**g** and Δ**h** are the residual vectors of Eq. (1), respectively, $\mathbf{G}_{\varepsilon}$ is come from the pressure stabilization [10], and the relations among the state variables are $\Delta\mathbf{u}=\beta\Delta t^{2}\Delta\mathbf{a}$ and $\Delta\mathbf{v}=\gamma\Delta t\Delta\mathbf{a}$ based on Newmark's method. The predictor–multicorrector algorithm is used for the time integration.

3.3 Projection method using algebraic splitting

The monolithic method solves Eq. (2) and satisfies the interface conditions to avoid spurious numerical power on the interface, which yields numerical instability. However, the formulation leads to an ill–conditioned equation system. Therefore, the projection method using the algebraic splitting [2] is used to avoid this difficulty. The present method was first proposed in [1], and modified in [2]. The present method is briefly described as follows:

The state variables is predicted as the intermediate state variables from Eq. (1a) for the known pressure, which is linearized as

$$ \mathbf{M}^{*}\Delta\hat{\mathbf{a}}=\Delta\mathbf{g}\,, \qquad (3) $$

where $\hat{\mathbf{a}}$ is the intermediate acceleration. Subtracting both sides of (3) from (2a) gives,

$$\gamma\Delta t\mathbf{G}\Delta\mathbf{p} = \mathbf{M}^*(\mathbf{v} - \hat{\mathbf{v}}), \tag{4}$$

where $\hat{\mathbf{v}}$ is the intermediate velocity. Left multiplying both sides of (4) by ${}_\tau\mathbf{G}_\mathrm{L}\mathbf{M}^{-1}$,

$$\gamma\Delta t\,{}_\tau\mathbf{G}_\mathrm{L}\mathbf{M}^{-1}\mathbf{G}\Delta\mathbf{p} = {}_\tau\mathbf{G}\mathbf{v} - {}_\tau\mathbf{G}\hat{\mathbf{v}} + {}_\tau\mathbf{G}_\mathrm{L}\mathbf{M}^{-1}\overline{\mathbf{M}}^*(\mathbf{v} - \hat{\mathbf{v}}) \tag{5}$$

is obtained, where $\overline{\mathbf{M}}^*$ equals $\mathbf{M}^* - {}_\mathrm{L}\mathbf{M}$. If the following pressure Poisson equation (PPE)

$$\gamma\Delta t\,{}_\tau\mathbf{G}_\mathrm{L}\mathbf{M}^{-1}\mathbf{G}\Delta\mathbf{p} = -{}_\tau\mathbf{G}\hat{\mathbf{v}} \tag{6}$$

is solved, then Eq. (5) is reduced as

$${}_\tau\mathbf{G}\mathbf{v} + {}_\tau\mathbf{G}_\mathrm{L}\mathbf{M}^{-1}\overline{\mathbf{M}}^*(\mathbf{v} - \hat{\mathbf{v}}) = \mathbf{0}. \tag{7}$$

Since the linear convergence of the state variables is expected for the present definition of $\mathbf{M}^*$, $\hat{\mathbf{v}}$ agrees with $\mathbf{v}$ asymptotically in the nonlinear iterations. Therefore, the second term of (7) will vanish asymptotically, and Eq. (1b) for the unknown fluid velocity is satisfied.

It follows from the above formulation that the monolithic equation system is split into the equilibrium equations (2a) and (3) and the PPE (6), and, different from the other studies using the algebraic splitting, the Schur complement is never produced. The proposed method is summarized as follows: In the nonlinear iterations, Eq. (3) is solved to derive the intermediate velocity, Eq. (6) is solved to determine the current pressure such that the current velocity satisfies the incompressibility constraint, and Eq. (2a) is solved to derive the current velocity.

3.4 Parallel computation

The matrix–vector products provide the most expensive computations in iterative solvers. Therefore, the parallel solution procedure is employed based on the mesh decomposition as follows: The matrix–vector product is computed using a subdomain mesh at each computational node using the element–by–element method, and the nodal data on the domain interface is transferred to complete the corresponding nodal data.

4 NUMERICAL EXAMPLE

4.1 Problem Setup

Mimicking the small fly, the span length L_w and the chord length c_w of the wing are 2.5mm and 0.8mm, respectively. The material properties of air are $\rho = 1.18\times10^{-3}$g/cm^3 and the viscosity $\mu = 1.82\times10^{-4}$g/(cm s). Taking into account the surface micromachining, the following setup is used: The wing membrane is made of the polyimide (the mass density ρ = 1.43g/cm^3, the Young's modulus E = 3GPa, and the Poisson's ratio ν = 0.4), and the thickness t_w is 1–2μm. The leading edge is made of the single crystal silicon (ρ = 2.383g/cm^3, E =

180GPa, and v = 0.3), and the dimension of the cross section is 100μm (width) ×50μm (thickness). The plate spring is made of the same material of the wing membrane, and the length l_s is larger than 50μm for the bending motion.

The amplitude u_0 and the flapping frequency f_φ of the micro actuator is assumed as follows: u_0 is smaller than 100μm based on the actual micro actuator in the MEMS technology, and f_φ is from 100Hz to 1,000Hz based on the actual insects. The design objective is to find the solution that can generate the lift F_L larger than 7μN, which is the weight of the small fly.

4.2 Analysis Setup

The leading edge, the plate spring, and the wing plane are modeled using mixed interpolation of tensorial components shell elements [11] (Fig. 4A, number of nodes: 225, number of elements: 196), while the fluid domain is modeled using stabilized linear equal–order–interpolation velocity–pressure elements [10] (Figs. 4B and C, number of nodes: 46,911, number of elements: 254,352). Δt is set at $1/f_\varphi/5{,}000$. The computational environment is a multiple core processor (10 core Xeon 2.8GHz×2CPU, 32GB memory).

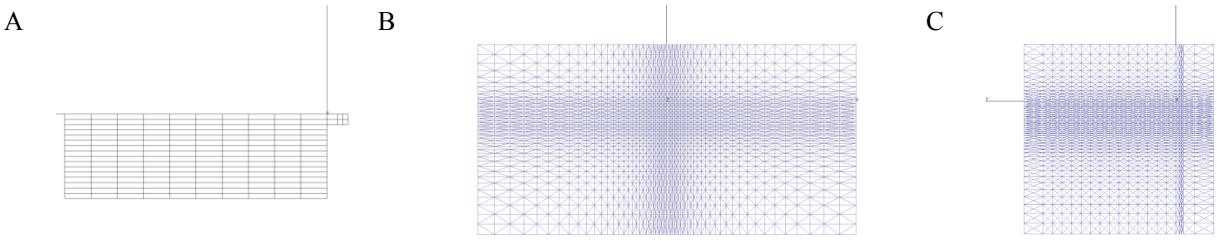

Figure 4: The present finite element meshes. A: *yz*–plane view of the shell mesh. B: *xy*–plane view of the fluid mesh. C: *yz*–plane view of the fluid mesh.

4.3 Results and discussion

In this study, the satisfactory design solutions were found from the parametric study. The dimensional parameters u_0, l_s, and t_w were set at 80μm, 50μm, and 1.6μm, respectively, and f_φ = 428Hz, which is chosen as the design and control parameter, gave the average lift larger than the weight of the small fly (7μN). The time histories of the displacement in this case were given in Fig. 5. As shown in this figure, the wing tip displacement was about 19 times larger than the wing base displacement due to the resonance. The lift variation for flapping frequency is shown in Fig. 6. As shown in this figure, the satisfactory design solutions exist from about 410 to 460Hz (DW).

5 CONCLUDING REMARKS

In this study, the FSI design of the insect–like micro flapping wing was proposed. The concept can be summarized as the FSI–cause of the pitching motion, the 2.5D–structure, and the amplification of the stroke angle using the resonance. The design problem was set taking into account the parameters of the model insect and the constraints from the MEMS technology. The projection method for the monolithic FSI equations was used for the strongly coupled FSI analysis. The existence of the DW shows the possibility of the insect–like MEMS–based MAVs.

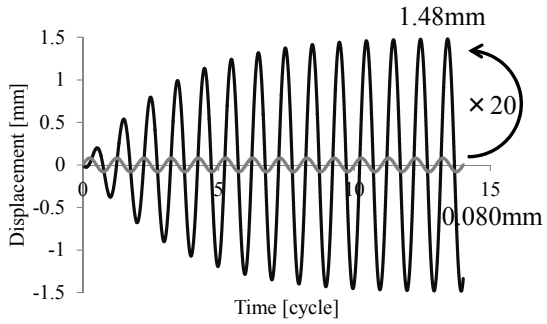

Figure 5: Time histories of the displacement. The black line indicates the wing tip displacement, while the gray line indicates the wing base displacement.

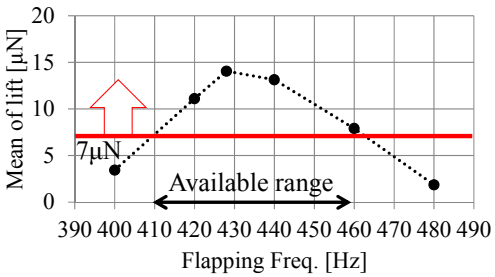

Figure 6: Area of the satisfactory design solutions in the design parameter space or the Design Window (DW).

REFERENCES

[1] Ishihara, D. and Yoshimura, S. A monolithic method for fluid–shell interaction based on consistent pressure Poisson equation. *International Journal for Numerical Methods in Engineering* (2005) **64**:167–203.

[2] Ishihara, D. and Horie, T. A projection method for the interaction of an incompressible fluid and a structure using new algebraic splitting. *Computer Modeling in Engineering & Sciences* (2014) **101**:421–440.

[3] Ishihara, D., Jeong, M.J., Yoshimura, S. and Yagawa, G. Design window search using continuous evolutionary algorithm and clustering –its application to shape optimization of microelectrostatic actuator. *Computers & Structures* (2002) **80**:2469–2481.

[4] Ishihara, D., Horie, T., Niho, T. and Baba, A. Hierarchal decomposition for the structure–fluid–electrostatic interaction in a microelectromechanical system. *Computer Modeling in Engineering & Sciences* (2015) **108**:429–452.

[5] Niho, T., Horie, T., Uefuji, J. and Ishihara, D. Stability analysis and evaluation of staggered coupled analysis methods for electromagnetic and structural coupled finite element analysis. *Computers & Structures* (2017) **178**:129–142.

[6] Ishihara, D., Horie, T. and Denda, M. A two dimensional computational study on fluid–structure interaction cause of wing pitch changes in dipteran flapping flight. *Journal of Experimental Biology* (2009) **212**:1–10.

[7] Ishihara, D., Yamashita, Y., Horie, T., Yoshida, S. and Niho, T. Passive maintenance of high angle of attack and its lift generation during flapping translation in crane fly wing. *Journal of Experimental Biology* (2009) **212**:3882–3891.

[8] Ishihara, D., Horie, T. and Niho, T. An experimental and three–dimensional computational study on the aerodynamic contribution to the passive pitching motion of flapping wings in hovering flies. *Bioinspiration & Biomimetics* (2014) **9**:046009.

[9] Ishihara, D. and Horie, T. Passive mechanism of pitch recoil in flapping insect wings. *Bioinspiration & Biomimetics* (2017) **12**:016008.

[10] Tedzduyar, T.E., Mittal, S., Ray, S.E. and Shih R. Incompressible flow computations with stabilized bilinear and linear equal–order–interpolation velocity–pressure elements. *Computer Methods in Appled Mechanics & Engineering* (1992) **95**:221–242.

[11] Noguchi, H. and Hisada, T. Sensitive analysis in post–buckling problems of shell structures. *Computers & Structures* (1993) **47**: 699–710.

VII International Conference on Computational Methods for Coupled Problems in Science and Engineering
COUPLED PROBLEMS 2017
M. Papadrakakis, E. Oñate and B. Schrefler (Eds)

GLOBAL OPTIMAL DESIGN OF TWO AEROSPACE VEHICLES

A. NASTASE*
* Aerodynamics of Flight, RWTH, Aachen University
Templergraben 55, 52062 Aachen, Germany
e-mail: nastase@lafaero.rwth-aachen.de

Key words: Supersonic Flow, Global Shape Optimization, Solutions for Three-dimensional Hyperbolic PDEs, Meshless, Hybrid Solutions for Navier-Stokes PDEs.

Abstract: A variant of Saenger project is proposed . It is composed of two global optimized and fully- integrated models namely a suborbital small one LEO in form of Catamaran almost blended with two central fuselages almost embeded in the wing thickness and a greater one geostationary one GEO also in form of Catamaran almost blended with two fuselages almost embeded in the wing thickness but located almost parallel to the leading edges, far from the central part of the wing in order to allow the up and go of the LEO in its central part.

1 INTRODUCTION

The new projects of suborbital tourist flight need two global optimized (GO) aerospace vehicles, namely: a greater geostationary (GEO) vehicle and a smaller suborbital one (LEO), which up and go of GEO . Both aerospace vehicles shall be of minimum drag, at two different cruising Mach numbers namely, 2.2 and, respectively, 3. The determination of a global optimized (GO) shape of a flying configuration (FC) (namely the simultaneous optimization of its distributions of camber, twist and thickness and also of the similarity parameters of its planform) leads to an extended variational problem with free boundaries The discontinous surface of an elitary FC is picewise approximed in form of two different superpositions of homogeneous polynoms in two variables, one on the wing and the other on the fuselage. The coefficients of these polynoms, together with the similarity parameters of their planforms, are the free parameters of optimization. An own iterative optimum-optimorum strategy was developed, in order to determine the GO shape of a FC, inside of a class of elitary FCs (optimized with fixed planforms). In the first step of iteration, own developed three-dimensional, hyperbolic potential solutions are used as start sölutions for the optimization A lower limit hypersurface of the inviscid drag functional, as function of the similarity parameters of the planforms of elitary FCs of the class is defined and the elitary FC, which corresponds to the minimum of this hypersurface is, in the same time, the inviscid GO FC of the class. This inviscid GO shape of FC, is used as surrogate model and its friction drag is computed. Up the second step of iteration, the own developed hybrid Navier-Stokes solutions are used as start solutions for the optimization and the new functional is the total drag, including friction. This strategy is applied for the determination of the GO shapes of

both aerospace vehicles, optimized at cruising Mach numbers $M_\infty = 2.2$ and, respectively, $M_\infty = 3$. They fly shock free, without sonic boom interferance and, due to their GO shapes, have high values of L/D (lift to drag), at their cruises..

2 THE START SOLUTIONS FOR THE GLOBAL OPTOMIZATION OF THE SHAPE OF A FLYING CONFIGURATION

Let us firstly introduce the following dimensionless coordinates:

$$\widetilde{x}_1 = \frac{x_1}{h_1} \quad , \qquad \widetilde{x}_2 = \frac{x_2}{\ell_1} \quad , \qquad \widetilde{x}_3 = \frac{x_3}{h_1} \quad , \tag{1}$$

$$\left(\quad \widetilde{y} = \frac{y}{\ell} \quad , \qquad \ell = \frac{\ell_1}{h_1} \quad , \quad c = \frac{c_1}{h_1} \quad , \quad \nu = B\ell \quad , \quad \overline{\nu} = Bc \quad , \qquad B = \sqrt{M_\infty^2 - 1} \quad \right) \quad ,$$

Hereby are ℓ_1 , h_1 , ℓ the half-span, the maximal depth and the dimensionless span of the wing of FC, c_1 and c , the half-span and the dimensionless span of the fuselage, M_∞ the cruising Mach number, $\nu = B\ell$ and $\overline{\nu} = Bc$, the similarity parameters of the planforms of the wing and of the fuselage of FC. The downwashes on the thin and thick-symmetrical components of the wing and of the fuselage of FC are approximed in form of different superpositions of homogeneous polynoms, it is:

$$w \equiv \widetilde{w} = \sum_{m=1}^{N} \widetilde{x}_1^{m-1} \sum_{k=0}^{m-1} \widetilde{w}_{m-k-1,k} \left|\widetilde{y}\right|^k \quad , \qquad w^* \equiv \widetilde{w}^* = \sum_{m=1}^{N} \widetilde{x}_1^{m-1} \sum_{k=0}^{m-1} \widetilde{w}^*_{m-k-1,k} \left|\widetilde{y}\right|^k \tag{2a,b}$$

on the wing and

$$w' \equiv \overline{w} = \sum_{m=1}^{N} \widetilde{x}_1^{m-1} \sum_{k=0}^{m-1} \overline{w}_{m-k-1,k} \left|\widetilde{y}\right|^k \quad , \qquad w^{\bullet'} \equiv \overline{w}^\bullet = \sum_{m=1}^{N} \widetilde{x}_1^{m-1} \sum_{k=0}^{m-1} \overline{w}^\bullet_{m-k-1,k} \left|\widetilde{y}\right|^k \tag{3a,b}$$

on the fuselage of FC. The coefficients of these polynoms, together with the similarity parameters of the planforms of FC, are here considered the free parameters of global optimization. The delta wing fitted with a central fuselage is considered like a discontinous delta wing alone fitted with two artificial ridges located along the jonctions lines wing-fuselage. The corresponding solutions of the boundary value problems concerning the determination of the axial disturbance velocities u and $u^\bullet$ on the thin and thick-symmetrical components of a thick, lifting, integrated wing-fuselage FC with subsonic leading edges are, as in [1]-[4], the following:

$$u \equiv \ell\ \widetilde{u} = \ \ell\ \sum_{n=1}^{N}\ \widetilde{x}_1^{n-1} \left\{ \ \sum_{q=0}^{E\left(\frac{n}{2}\right)} \frac{\widetilde{A}_{n,2q}\widetilde{y}^{2q}}{\sqrt{1-\widetilde{y}^2}} \ + \ \sum_{q=1}^{E\left(\frac{n-1}{2}\right)} \widetilde{C}_{n,2q}\widetilde{y}^{2q}\ \cosh^{-1}\sqrt{\frac{1}{\widetilde{y}^2}}\ \right\} \tag{4a}$$

$$u^* \equiv \ell\ \widetilde{u}^* = \ell\ \sum_{n=1}^{N}\ \widetilde{x}_1^{n-1} \left\{ \ \sum_{q=0}^{n-1} \widetilde{H}^*_{nq}\ \widetilde{y}^q \left(\ \cosh^{-1} M_1 + (-1)^q \cosh^{-1} M_2 \right) \right.$$

$$+ \ \sum_{q=0}^{E\left(\frac{n-2}{2}\right)} \widetilde{D}^*_{n,2q}\ \widetilde{y}^{2q}\ \sqrt{1-\nu^2\widetilde{y}^2} \ + \ \sum_{q=1}^{E\left(\frac{n-1}{2}\right)} \widetilde{C}^*_{n,2q}\ \widetilde{y}^{2q}\ \cosh^{-1}\sqrt{\frac{1}{\nu^2\widetilde{y}^2}}$$

$$\left. + \ \sum_{q=0}^{n-1} \widetilde{G}^*_{nq}\ \widetilde{y}^q \left(\ \cosh^{-1} S_1 + (-1)^q \cosh^{-1} S_2 \right) \right\} \ , \tag{4b}$$

$$M_1 = \sqrt{\frac{(1+\nu)\ (1-\nu\ \widetilde{y})}{2\nu(1-\widetilde{y})}} \quad , \qquad M_2 = \sqrt{\frac{(1+\nu)\ (1+\nu\ \widetilde{y})}{2\nu(1+\widetilde{y})}} \quad ,$$

$$S_1 = \sqrt{\frac{(1+\widetilde{\nu})\ (1-\nu\ \widetilde{y})}{2\ (\ \widetilde{\nu}-\nu\ \widetilde{y})}} \quad , \qquad S_2 = \sqrt{\frac{(1+\widetilde{\nu})\ (1+\nu\ \widetilde{y})}{2\ (\ \widetilde{\nu}+\nu\ \widetilde{y})}}$$

3 THE GLOBAL OPTIMIZED SHAPE OF THE AEROSPACE MODEL LEO

The author has designed a GO shape of a model FADET II, presented in the (Fig.1), which is of minimum drag at cruising Mach number $M_\infty = 3$.

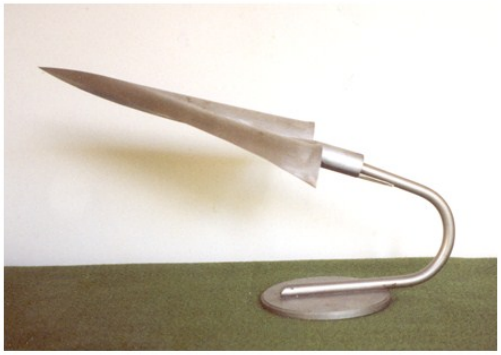

Fig. 1 The global optimized and fully-integrated model FADET II

The constraints used are the following: the lift and the pitchjng moment coefficients are given, the Kutta condition along the sharp leading edges is fulfilled, the relative volumes of the gross wing and of the fuselage are given and the FC is fully-integrated (i.e. its mean surface of FC is continuos and the wing and the fuselage have the same tangent planes along their jonction lines).

The theoretical predicted pressure distribution and the aerodynamic characteristics of this model were checked in the trisonic wind tunnel of DLR Collogne in the frame of research projects of the author, sponsored by the DFG. A very good agreement between the theoretical predicted and the experimental- correlated lift and pitching moment ciefficients are presented in the (Fig.2a,b). A good agreement between the theoretical predicted and the local interpolated values of the measured pressure coefficients on the upper side of the model in its central longitudinal section are presented in the (Fig. 3a-c).

The here proposed aerospace vehicle LEO shall be a Catamaran as presented in the (Fig 4) , which has two short twin central fuselages, only almost embeded in the wing thickness (in order to have windows on both sides!) because it present some advantages in comparison with the aerospace vehicle, which has a longer and greater central fuselage, namely: the Catamaran LEO fly with one characteristic surface instead of a shock surface, has no sonic boom interference, has better structure stiffness, because the fuselages are half so long and has better lateral stability.

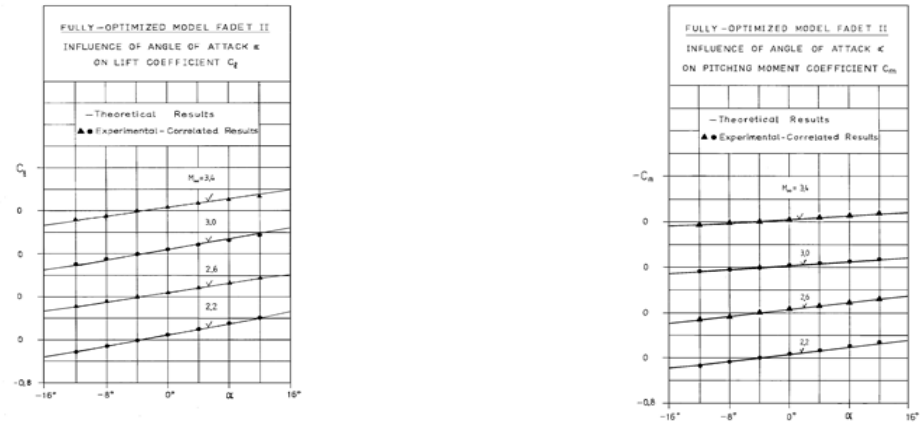

Fig. 2a,b The lift and pitching moment coefficients of global optimized model FADET II

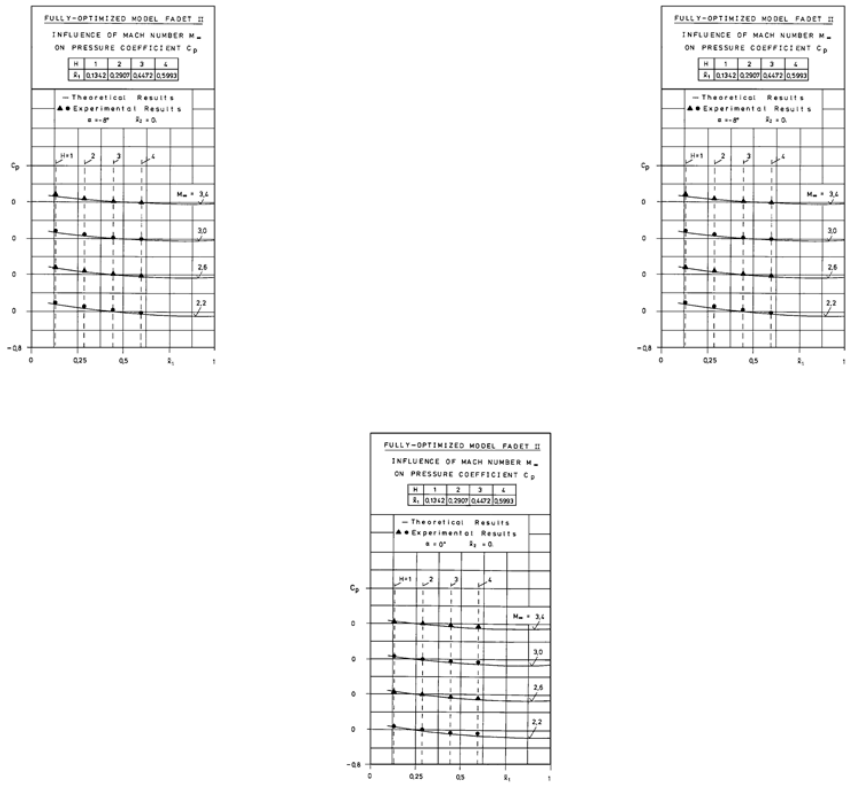

Fig. 3a-c The pressure coefficient on the central upper side section of the global optimized model FADET II for the angles of attack $\alpha = -8^{\circ}, 0^{\circ}, 8^{\circ}$.

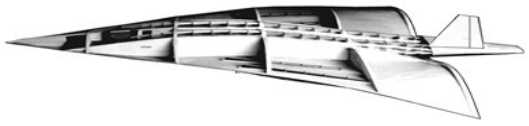

Fig . 4 The global optimized and almost blended Catamaran LEO

4 THE GLOBAL OPTIMIZED SHAPE OF THE AEROSPACE MODEL GEO

The author has designed also the GO shape of the model FADET I ,presented in the (Fig.4), which is of minimum drag at cruising Mach number $M_\infty = 2.2$. The constraintes used are the same as by the model FADET II and the both models have the same area of their planforms.

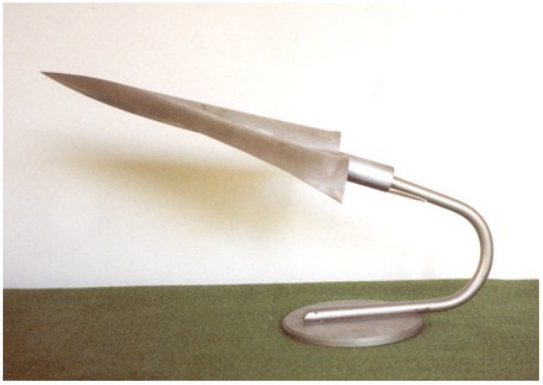

Fig. 4 The global optimized and fully-integrated model FADET I

The theoretical predicted pressure distributions and the aerodynamic characteristics of the GO model Fadet I were checked also in the trisonic wind tunnel of DLR Cologne, in the frame of research projects of the author, sponsored by the DFG. A very good agreements between the theoretical predicted and the experimental correlated values of the measured lift and pitching moment coefficients are presented in the (Fig. 5a,b).

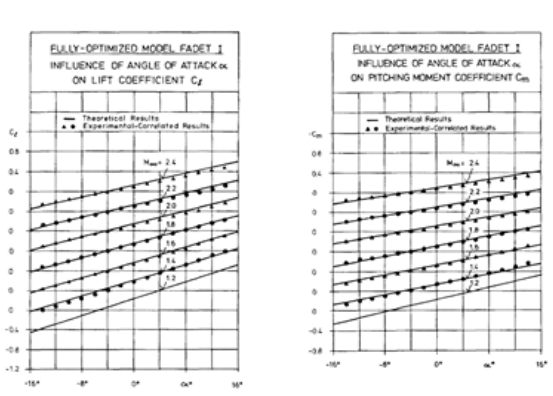

Fig. 5a,b The lift and pitching moment coefficients of the global optimizrd model FADET I

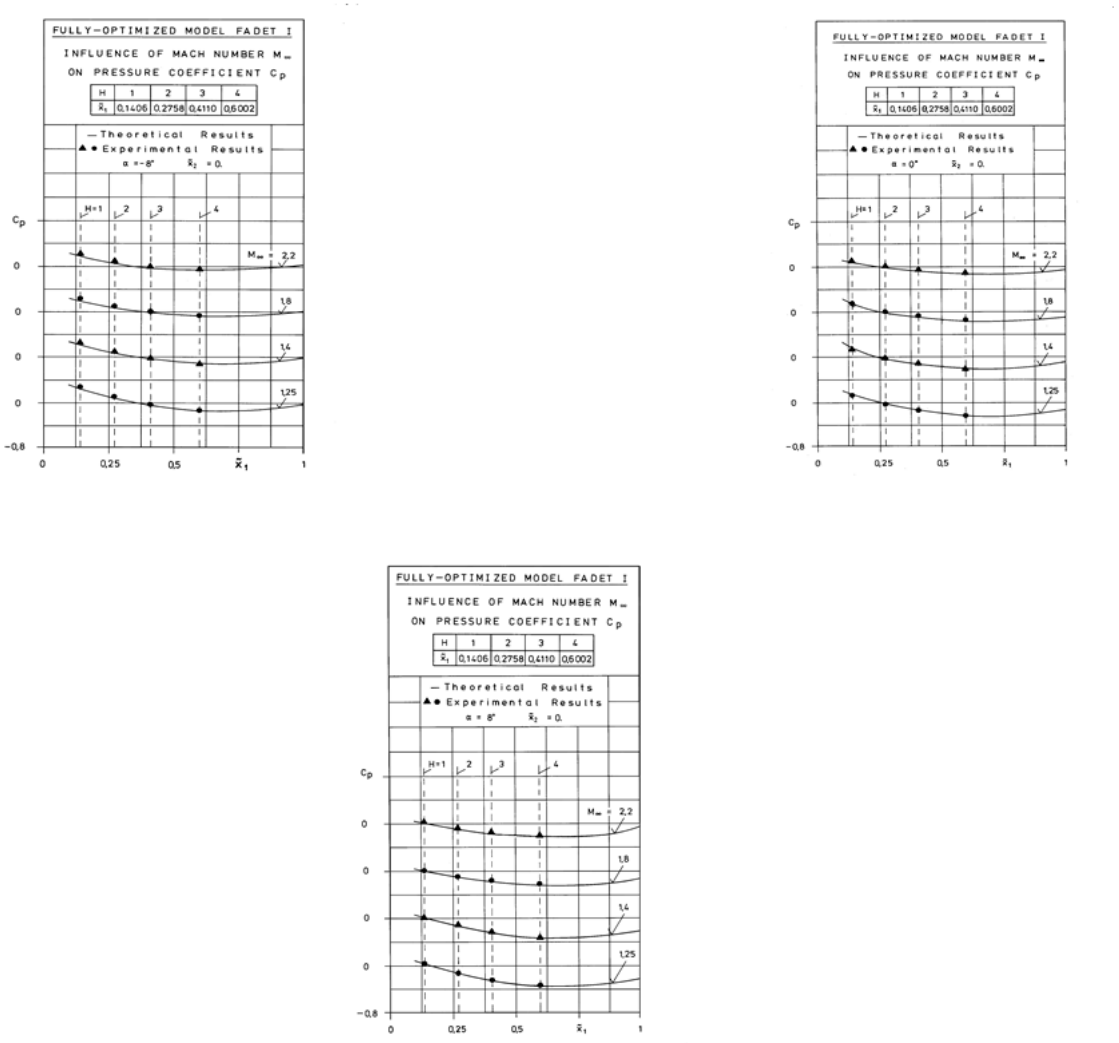

Fig. 6a-c The pressure coefficient on the central upper side section of the global optimized model FADET I for the angles of attack $\alpha = -8^\circ, 0^\circ, 8^\circ$.

A good agreement between the theoretical predicted and the experimental local interpolated values of the measured pressure coefficients on the upper side of the model, along its central longitudinal section are presented in the (Fig. 6a-c).

A comparison of the shapes of global optimized and fully-integrated models FADET I and FADET II is made in the (Fig. 7). An important influence of the cruising Mach number chosen for the optimization, over the GO shapes of the models is observed. The GO shape of the model shall be more slender when the cruising Mach number increases, like is done by gliding birds!

The proposed GO shape of the GEO model shall be similar as the GO shape of the fully-integrated model FADET I but much greater as the GO model LEO in order to can carry the

GO model LEO and the UAVs,, which supply the both aerospace vehicles. The GO model GEO shall be also in form of Catamaran, almost blended with two fuselages almost embeded in the wing thickness but located , as in (Fig. 8), far from the central part of GEO in order to allow the up and go of LEO and of UAVs used for supply.

Fig. 7 The comparison of global optimized and fully-integrated models FADET I and FADET II

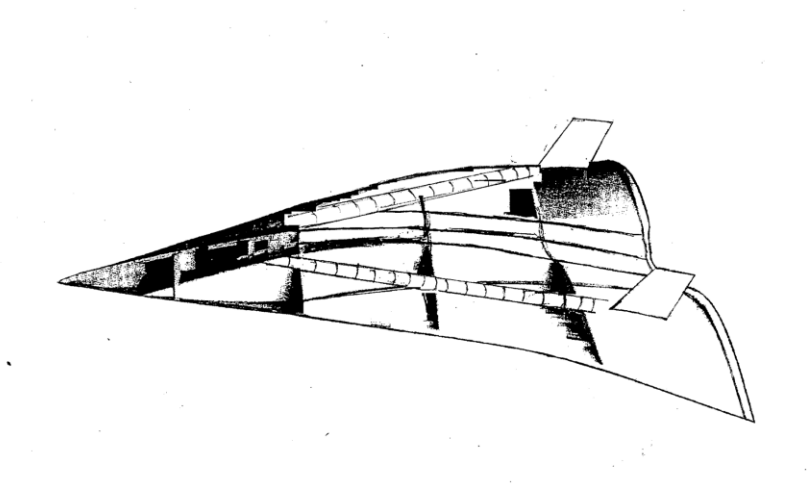

Fig. 8 The global optimized and almost blended catamaran GEO

For the computation of the total drag, hybrid solutions for the Navier-Stokes layer (NSL) are proposed.

5 HYBRID SOLUTIONS FOR THE NAVIER-STOKES LAYER

The new developed, hybrid, meshless solutions for the three-dimensional compressible Navier-Stokes layer (NSL), are presented here in improved form. These NSL's solutions use analytical potential solutions of the flow on the same flying configurations (FCs) twice, namely: at the NSL's edge (instead of parallel flow used by Prandtl in his boundary layer theory) and in the structure of the velocity's components, which are expressed inside the NSL,

as products between the corresponding potential velocity's components with polynomes with arbitrary coefficients, versus a spectral variable. These coefficients are used to satisfy the NSL's partial-differential equations, in an arbitrary chosen number of points.

Let us firstly introduce a spectral coordinate η , it is:

$$\eta = \frac{x_3 - Z(x_1,\ x_2)}{\delta(x_1,\ x_2)} \quad , \qquad (0 \le \eta \le 1) \ . \tag{5}$$

The own proposed discontinuous hybrid solutions for the NSL's PDEs use the potential solutions two times: as outer flow, at the NSL's edge and in the generation of the velocity's components, which are products between the potential solutions (of the same FC) and polynomials with arbitrary coefficients:

$$u_\delta = u_e \sum_{i=1}^{N} u_i\ \eta^i \quad , \qquad v_\delta = v_e \sum_{i=1}^{N} v_i\ \eta^i \quad , \qquad w_\delta = w_e \sum_{i=1}^{N} w_i\ \eta^i \ . \tag{6a-c}$$

The proposed forms for the here introduced logarithmic density function $R = \ln \rho$ and for the absolute temperature T are the following:

$$R = R_w + \left(R_e - R_w \right) \sum_{i=1}^{N} r_i\ \eta^i \quad , \qquad T = T_w + \left(T_e - T_w \right) \sum_{i=1}^{N} t_i\ \eta^i \quad . \tag{7a,b}$$

The pressure p is computed by using the physical equation of perfect gas and, for the viscosity μ , an exponential law is used

$$p = R_g\ \rho\ T = R_g\ e^R\ T \quad , \qquad \mu = \mu_\infty \left(\frac{T}{T_\infty} \right)^{n_1} \tag{8a,b}$$

The coefficients r_i and t_i are determined only as functions of the velocity's coefficients by using the continuity equation and, respectively. the temperature equation, as in [1-4] .

The non-slip boundary condition on the FC's surface is automatically satisfied. The boundary conditions at the NSL's edge lead to the following linear algebraic equations:

$$\sum_{i=1}^{N} u_i = 1 \quad , \qquad \sum_{i=1}^{N} i\ u_i = 0 \quad , \qquad \sum_{i=1}^{N} i\ (i-1)\ u_i = 0 \quad ,$$

$$\sum_{i=1}^{N} v_i = 1 \quad , \qquad \sum_{i=1}^{N} i\ v_i = 0 \quad , \qquad \sum_{i=1}^{N} i\ (i-1)\ v_i = 0 \quad ,$$

$$\sum_{i=1}^{N} w_i = 1 \quad , \qquad \sum_{i=1}^{N} r_i = 1 \quad , \qquad \sum_{i=1}^{N} t_i = 1 \quad . \tag{8a-i}$$

The coefficients of the velocity's components are iteratively determined, by using the impulse equations.

The inviscid drag coefficients of the thin, thick-symmetrical and thick, lifting integrated wing-fuselage FC are:

$$C_d \equiv \ell \widetilde{C}_d = 8\ell \int\limits_{\widetilde{O}\widetilde{A}_1\widetilde{C}} \widetilde{u}\widetilde{w}\widetilde{x}_1 \, d\widetilde{x}_1 \, d\widetilde{y} = \ell \sum_{n=1}^{N} \sum_{m=1}^{N} \sum_{k=0}^{m-1} \sum_{j=0}^{n-1} \widetilde{\Omega}_{nmkj} \widetilde{w}_{m-k-1,k} \widetilde{w}_{n-j-1,j} \tag{9a}$$

$$C_d^* \equiv \ell \widetilde{C}_d^* = 8\ell \left(\int\limits_{\widetilde{O}\widetilde{C}_1\widetilde{A}_1} \widetilde{u}^* \widetilde{w}^* \widetilde{x}_1 \, d\widetilde{x}_1 \, d\widetilde{y} + \int\limits_{\widetilde{O}\widetilde{C}\widetilde{A}_1} \widetilde{u}^* \overline{w}^* \widetilde{x}_1 \, d\widetilde{x}_1 \, d\widetilde{y} \right)$$

$$= \ell \sum_{n=1}^{N} \sum_{m=1}^{N} \sum_{k=0}^{m-1} \sum_{j=0}^{n-1} \left\{ \left[\widetilde{\Omega}_{nmkj}^* \widetilde{w}_{n-j-1,j}^* + \overline{\Omega}_{nmkj}^* \overline{w}_{n-j-1,j}^* \right] \widetilde{w}_{m-k-1,k}^* \right.$$

$$\left. + \left[\widetilde{\Omega}_{nmkj}^{'*} \widetilde{w}_{n-j-1,j}^* + \overline{\Omega}_{nmkj}^{'*} \overline{w}_{n-j-1,j}^* \right] \overline{w}_{m-k-1,k}^* \right\} \tag{9b}$$

$$C_d^{(i)} \equiv \ell \widetilde{C}_d^{(i)} = C_d + C_d^* = \ell \left(\widetilde{C}_d + \widetilde{C}_d^* \right) \quad , \tag{9c}$$

The friction , the friction drag and the total drag coefficients of an integrated wing-fuselage FC are the following:

$$\tau_{x_1}^{(w)} \equiv \tau_{x_1} \Big|_{\eta = 0} = \mu_f \frac{\partial u_\delta}{\partial \eta} \Big|_{\eta = 0} = \mu_f u_1 u_e \quad , \tag{10a}$$

$$C_d^{(f)} = 8 \, \nu_f u_1 \int\limits_{\widetilde{O}\widetilde{A}_1\widetilde{C}} u_e \widetilde{x}_1 \, d\widetilde{x}_1 \, d\widetilde{y} \quad , \qquad C_d^{(t)} = C_d^{(f)} + C_d^{(i)} \tag{10b,c}$$

12 CONCLUSIONS

The Catamaran has some advantages, when it is compared with the STA with one, central, non-integrated fuselage, carrying the same number of passengers, at the same cruising Mach number:

- it flies with a *shock-free surface*;

• it has *no sonic boom interference* because it flies with one *characteristic surface* (the classical STA with one central non-integrated fuselage flies with two shock surfaces, one produced at the frontal part of the fuselage and the other at the roots of the wing and in their intersection zones, the sonic boom interference occurs);
• it has a *better structural stiffness and increased lateral stability*; because instead of one long fuselage there are two twin fuselages embedded in the wing, with half length;
• it needs *less trim* because the weight is better distributed and the pressure center and the center of gravity points are more closely together;
• it has a *higher L/D*, due to global optimization, to full integration, of flattening and due to the fulfilling of the Kutta condition along its subsonic leading edges, which avoids the leading edges conturnements, which cancels the induced drag, destroys the leading edge vortices and increases the lift, not only at cruise but also for large ranges of Mach numbers and angles of attack, etc.

These hybrid solutions are discontinuous numerical solutions with the following important analytical properties, due to the analytical hybridization, namely:

- they have correct last behaviors;
- they have correct jumps along their singular lines (like subsonic leading edges, junction lines wing/fuselage, hinge lines of leading edge flaps, etc.), according to the principle of minimal singularities and the singularities are balanced;
- the solutions are meshless and can be easy and exact derived.

By using of the density function R (instead of the density ρ) all the physical entities can be expressed only as functions of the spectral coefficients of the velocity's components and the NSL's PDEs can be split.

These hybrid solutions do not need interface at the NSL's edge.

REFERENCES

[1] Nastase, A. C*omputation of supersonic flow over flying configurations*. Elsevier, Oxford, UK (2008).
[2] Nastase, A. Hybrid Navier-Stokes solutions for aerodynamical, global optimal shape's design, Proc. of International Conference EngOpt, Paper 750, Rio de Janeiro, Brazil, (2008).
[3] Nastase, A. Use of surrogate models for the global optimization of flying configurations, in supersonic flow, Extended Abs. of EUROGEN 2015, Univ.of Strathclyde, Glasgow, UK, p. 52-57, (2015).
[4] Nastase, A. Evolutionary, iterative optimum-optimorum theory, INCAS Bulletin, Vol. 2, Number 4/ pp. 153-161, (2010).

VII International Conference on Computational Methods for Coupled Problems in Science and Engineering
COUPLED PROBLEMS 2017
M. Papadrakakis, E. Oñate and B. Schrefler (Eds)

HIGH FIDELITY AERO-STRUCTURAL OPTIMIZATION OF A WING USING A STEP-RANGE APPROACH

PAOLO F. SCARAMUZZINO†, ANDREA SICILIANI† AND GIUSEPPE QUARANTA†

†Dipartimento di Scienze e Tecnologie Aerospaziali, Politecnico di Milano
Edifici B12, Campus Bovisa
via La Masa, 34 Milano 20156 Italy
email: giuseppe.quaranta@polimi.it

Key words: Multidisiciplinary Optimization, Wing Design, CFD, FEM, Brequet Range Formula

Abstract. This paper present the effect of using a more detailed model for the computation of the range, when it is used as objective for the multidiciplinary optimization of a transonic wing of a business jet. The new formulation considers the change of angle of attack that the aircraft must follow during cruise.

1 INTRODUCTION

The ever-growing realm of applications and the explosion in computing power is driving optimization research toward new and exciting directions. A considerable amount of research has been conducted on multidisciplinary design optimization (MDO) and its application to aircraft design [1, 2]. In most cases sound coupling and optimization methods were shown to be extremely important because some techniques, such as sequential discipline optimization, were unable to converge to the true optimum of a coupled system. Aerostructural analysis has traditionally been carried out in a cut-and-try basis. Aircraft designers have a preconceived idea of the shape of an optimal load distribution and then tailor the jig shape of the structure so that the deflected wing shape under a 1-g load gives the desired load distribution. Although this approach might suffice for conventional transport aircraft, for which there is considerable accumulated experience, in the case of either new planform concepts or new flight regimes the lack of experience combined with the complexities of aero-structural interactions can lead to designs that are far from optimal. The objective of this work is to develop an MDO framework for high fidelity analysis and optimization of aircraft configurations. The paper presents the current capability of this framework through the aerostructural design of a transonic business-jet wing. This paper focuses on the demonstration of an integrated aero-structural method

for the design of aerospace vehicles. Both aerodynamics and structures are represented using high-fidelity models. The aerodynamic outer-mold line and the structure, with a fixed topology, are parameterized using a large number of design variables. The aerodynamic sensitivities with respect to outer-mold line shape variables are computed using an accurate and efficient adjoint procedure. The structural sensitivities with respect to structural design variables are computed using finite differences. The cross-gradients are evaluated analytically. Kreisselmeier Steinhauser [3] functions are used to reduce the number of structural constraints in the problem. Results of the aerodynamic shape and structural optimization for natural laminar-flow transonic business jet are presented.

The current approach to MDO applied to aircraft design uses the Breguet range equation as objective function [4]. This means that the variation of attitude during cruise, which is related to the loss of weight caused by fuel consumption, is not taken into account. The innovative approach presented in this work is to divide the cruise into several steps; over each step the attitude is considered to be constant, so that the Breguet range formula can be applied. The total range is then evaluated as the sum of the ranges of each step, leading to a sort of multi-objective optimization. The bigger is the number of step considered, the more accurate is the solution obtained. This new approach is called step-range and its results are compared with those obtained through sequential discipline optimization and single objective optimization.

2 NUMERICAL MODELS

In this section the numerical model employed to perform the optimization are presented.

2.1 Aerodynamic model

To investigate the effect of the application of the step-range approach, it has been decided to solve the optimization problem using for aerodynamic forces the inviscid Euler set of equation. This will limit the computational cost with respect to the viscous Navier-Stokes equations. Euler equations neglect fluid viscosity; this simplification fits well for very high Reynolds numbers. So, it could be considered an approximate yet sufficiently accurate model for an initial design through optimization.

The Euler equations are a set of three equations: two scalar and one vectorial:

$$\begin{cases} \frac{\partial \rho}{\partial t} + \boldsymbol{\nabla} \cdot (\rho \mathbf{u}) = 0 \\ \frac{\partial \rho \mathbf{u}}{\partial t} + \boldsymbol{\nabla} \cdot (\rho \mathbf{u} \otimes \mathbf{u} + P\mathbf{I}) = \mathbf{0} \\ \frac{\partial \rho E^t}{\partial t} + \boldsymbol{\nabla} \cdot [\mathbf{u}\,(E^t + P)] = 0 \end{cases} \tag{1}$$

where ρ is the density of the fluid, $\mathbf{u}$ is the velocity vector, P is the pressure, E^t is the total energy ($E^t = \rho e + \frac{1}{2}\rho \mathbf{u}^2$), where e is the specific internal energy) and $\mathbf{I}$ is the identity matrix.

This set of equations must be complemented with two equations of state, e.g.

$$P = P(e, \rho); \quad T = T(e, \rho) \tag{2}$$

As it will be discussed later, the optimization process is gradient based. This means that the gradient of the aerodynamics variables has to be calculated with respect to the design variables. Since the calculation of the gradients at each iteration would take a huge amount of computational time, the Euler equations are solved exploiting an adjoint formulation [5, 6] This leads to a significant reduction of the computational time.

2.1.1 Free Form Deformation

One of the most important points in the definition of a shape parametrization problem is the choice of the parametrization technique. A possible choice is the Free-Form Deformation (FFD) [7, 8]. The basic FFD concept is the deformation of a pre-existing object. This technique deforms a lattice that is built around the object and manipulates the whole space in which the object is embedded. The strong point of the method is that, by deforming the whole volume around the object, the computational grid is also being automatically deformed with the object itself. This feature makes the FFD technique preferable than others which only deform the object. In fact, in this case, the creation of a new computational grid has to be performed. This would lead to the growing of the computational cost. The lattice consists of an ordered mesh of control points and is placed in a way to wrap the object to be deformed. It defines a parametric coordinate system. The control points are used to approximate the curves that describe the object within the box. In particular, it is possible to define three different polynomials for each direction. Bézier curve have been chosen for the parametrization. These curves can be seen as a linear combination of Bernstein basis polynomials [9]. The CFD solver tool for grid deformation through Free-Form Deformation uses the Bzier method to approximate curves. It is possible to extend the Bézier curve into a Bézier box in the three dimension space using a trivariate Bernstein polynomial.

The wing, object of the optimization, has been embedded within a Free-Form Deformation box, as shown in Figure 1. The number of aerodynamic design variables depends on the approximating degree of the Bernstein polynomials. In table 1, the degrees of polynomials chosen in each direction are listed.

Cartesian Direction	**Polynomial Degree**	**No. of Control Points**
i	l = 10	11
j	m = 8	9
k	n = 1	2

Table 1: Description of aerodynamic design variables.

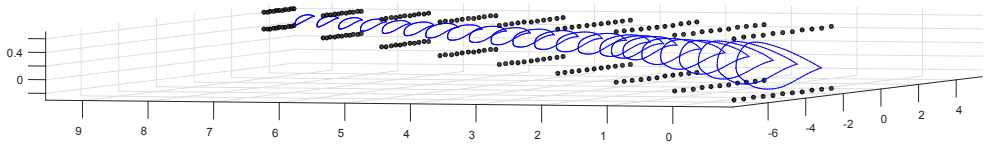

Figure 1: Free-Form Deformation box around the wing.

Hence, the total number of design variables is: $11 \times 9 \times 2 = 198$.

2.2 Structural model

There are several models available to describe the different behavior of a structural element. The choice of one of them depends on the level of accuracy required and on the fulfillment of the hypothesis at the basis of each model. In the preliminary design phase, the wing can be modeled as a beam since it usually has a large aspect ratio.

Knowing the wing layout in terms of number and type of stringers and of panels thickness, its bending and torsional stiffness can be evaluated through a semi-monocoque approach. In order to better reproduce wing torsional stiffness, some structural nodes are allocated spanwise in correspondence of leading and trailing edges and they are rigidly linked to beam axis nodes. In this way, it is possible to keep in consideration the contribute of the ribs.

The typical wing of business jet presents two changes in the sweep angle at trailing edge and so three different parts can be considered: root, center and tip. Each part has been discretized in a certain number of equally-spaced beam elements. Beam elements in CSM solver can be defined as tapered. This implies that the beam properties change along its axis and it can be done by defining different sections at the beginning and at the end of the element.

The beam properties are evaluated through the semi-monocoque approach, so they depend on the number and type of stringers and on panels thickness. If it is supposed that the resulting wing box is symmetric, it is necessary to define three design variables

for each beam section[1]: stringers area, spar webs thickness and skin panels thickness.

It is necessary to impose the continuity of the design variables between two consecutive beam elements, except for those across the sweep angle changes. Tab. 2 lists the number of design variables for each wing block.

Wing Block	**No. Elements**	**No. Design Variables**		
		Stringers Area	**Webs Thickness**	**Panels Thickness**
Root	6	7	7	7
Center	2	3	3	3
Tip	14	15	15	15
Total	22	25	25	25

Table 2: Description of structural design variables

3 WING AERO-STRUCTURAL DESIGN OPTIMIZATION

3.1 Step-range Breguet formulation

The typical multidisciplinary function that takes into account both aerodynamic and structural design aspects is represented by the *range formula*, first derived by Louis Charles Breguet [10].

$$\mathrm{d}R = \frac{V}{c_T}\frac{C_L}{C_D}\frac{1}{W}\,\mathrm{d}W \quad \Rightarrow \quad R = \frac{V}{c_T}\frac{C_L}{C_D}\ln\left(\frac{W_{in}}{W_{fin}}\right) \tag{3}$$

where R is the range, c_T is the specific fuel consumption, C_L is the lift coefficient, C_D is the drag coefficient, W_{in} is the initial weight and W_{fin} is the final weight.

In Eq. (3), V, ${C_T}^2$, C_L and C_D are supposed to be constant. Nevertheless, the aircraft changes its attitude during cruise, if speed and height are constant. For this reason, it is important to focus the attention on the differential formulation of the Eq. (3).

$$C_L = \frac{W}{\frac{1}{2}\,\rho\,V^2 S} \quad \Rightarrow \quad \mathrm{d}R = \frac{V}{c_T}\frac{1}{C_D}\frac{W}{\frac{1}{2}\,\rho\,V^2 S}\frac{1}{W}\,\mathrm{d}W = \frac{2}{c_T\,\rho\,V\,S}\frac{1}{C_D}\mathrm{d}W \tag{4}$$

Integrating Eq. (4) between the initial W_{in} and the final aircraft weight W_{fin}, it becomes:

$$R = \frac{2}{C_T\,\rho\,V\,S}\int_{W_{fin}}^{W_{in}}\frac{1}{C_D}\mathrm{d}W \tag{5}$$

To evaluate the integral in Eq. (5), a relation $C_D = C_D\,(W)$ is needed. Nevertheless this is not linear and not known *a priori* and the aim to find an analytical solution is not effective.

[1]We are supposing that all the stringers are identical for each section. The same hypothesis is applied to spar webs and to skin panels.

[2]In this work C_T is always supposed to be constant.

Eq. (3) can be detailed as follows:

$$R = \frac{V}{c_T}\frac{C_L}{C_D}\ln\left(\frac{W_{stru}+W_{const}+W_{fuel}}{W_{stru}+W_{const}}\right) \tag{6}$$

where W_{stru} is the structural weight, W_{const} is the constant weight and includes: engines, avionics, passengers, fuel for climb and descent, etc., and W_{fuel} is the weight of the fuel can be used for the cruise. Terms affected by the optimization process are C_D and W_{stru}.

Instead of considering a fully constant step range that represents a too strong approximation, let us suppose to divide the fuel consumption into several steps.

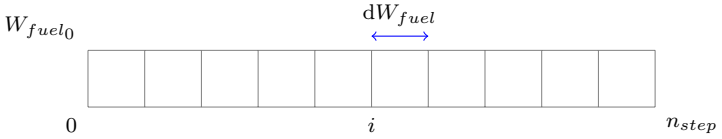

Figure 2: Fuel discretization.

Fig. 2 shows how the fuel for the cruise is divided. Where W_{fuel_0} is the total fuel for the cruise only, n is the step number and $\mathrm{d}W_{fuel} = \frac{W_{fuel_0}}{n}$ is the fuel consumption of each step. Following this approach it is possible to define a *piecewise* constant step range formula, considering a fixed attitude for each single step.

In this case, Eq. (6) can be rearranged in this way:

$$R^{(i+1)} = \frac{V}{c_T}\frac{C_L^{(i)}}{C_D}\ln\left(\frac{W_{stru}+W_{const}+W_{fuel}^{(i)}}{W_{stru}+W_{const}+W_{fuel}^{(i+1)}}\right) \tag{7}$$

with $W_{fuel}^{(i)} = W_{fuel_0} - i\ \mathrm{d}W_{fuel}$ and $i = 0 : n-1$

$$C_L^{(i)} = \frac{W_{stru}+W_{const}+W_{fuel}^{(i)}}{\frac{1}{2}\rho\ V^2 S} \tag{8}$$

Eq. (8) shows that the angle of attack of each step, $\alpha^{(i)}$, is fixed at its beginning. The more the steps are considered, the more accurate the range evaluation is.

3.2 Aerostructural optimization

In general the objective function of a multidisciplinary problem depends not only on the design variables, but also on the physical state variables. So, if the vector of design variables is $\boldsymbol{x}$ and the vector of physical state variables is $\boldsymbol{y}(\boldsymbol{x})$, the objective function $\mathcal{I}$ can be defined as $\mathcal{I} = \mathcal{I}(\boldsymbol{x},\ \boldsymbol{y}(\boldsymbol{x}))$. The objective function, i.e. the range, must be maximized subjected to a set of inequality constraints: $\boldsymbol{g}(\boldsymbol{x},\ \boldsymbol{y}(\boldsymbol{x})) \leq \boldsymbol{0}$. So the optimization problem is summarized as follows:

$$\begin{cases} \min\limits_{\boldsymbol{x}} \mathcal{I}\left(\boldsymbol{x},\ \boldsymbol{y}\left(\boldsymbol{x}\right)\right) \\ \boldsymbol{g}\left(\boldsymbol{x},\ \boldsymbol{y}\left(\boldsymbol{x}\right)\right) \leq \mathbf{0} \end{cases} \tag{9}$$

$$\mathcal{I} = R = R\left(C_D, W\right) = R\left(C_D\left(\boldsymbol{x}, W\left(\boldsymbol{x}\right)\right), W\left(\boldsymbol{x}\right)\right) \tag{10}$$

The derivative of the objective function $\mathcal{I}$ w.r.t the set of design variables $\boldsymbol{x}$ becomes:

$$\frac{\mathrm{d}\mathcal{I}}{\mathrm{d}\boldsymbol{x}} = \frac{\mathrm{d}R}{\mathrm{d}\boldsymbol{x}} = \frac{\partial R}{\partial C_D}\frac{\mathrm{d}C_D}{\mathrm{d}\boldsymbol{x}} + \frac{\partial R}{\partial W}\frac{\mathrm{d}W}{\mathrm{d}\boldsymbol{x}} \tag{11}$$

Since C_D depends on both design variables $\boldsymbol{x}$ and aircraft weight W, while W depends only on design variables, Eq. (11) becomes:

$$\frac{\mathrm{d}R}{\mathrm{d}\boldsymbol{x}} = \underbrace{\frac{\partial R}{\partial C_D}}_{\alpha_{\mathcal{A}}}\frac{\partial C_D}{\partial \boldsymbol{x}} + \underbrace{\left(\frac{\partial R}{\partial C_D}\frac{\partial C_D}{\partial C_L}\frac{\partial C_L}{\partial W} + \frac{\partial R}{\partial W}\right)}_{\alpha_{\mathcal{S}}}\frac{\mathrm{d}W}{\mathrm{d}\boldsymbol{x}}$$

where $\alpha_{\mathcal{A}}$ and $\alpha_{\mathcal{A}}$ can be compiuted analytically.

Applying the penalty method to the problem of Eq. (9) for the constraints, it results: $\mathcal{J}\left(\boldsymbol{x},\ \boldsymbol{y}\left(\boldsymbol{x}\right)\right) = \mathcal{I} + \frac{1}{2}\ \boldsymbol{g}^T\mathbf{P}\boldsymbol{g}$. Splitting the design variables in aerodynamics $\boldsymbol{x}_{\mathcal{A}}$ and structures $\boldsymbol{x}_{\mathcal{S}}$, and considering both aerodynamic $\boldsymbol{g}_{\mathcal{A}}$ and structural $\boldsymbol{g}_{\mathcal{S}}$ constraints, the derivative of $\mathcal{J}$ is:

$$\begin{aligned} \frac{\mathrm{d}\mathcal{J}}{\mathrm{d}\boldsymbol{x}} &= \begin{bmatrix} \frac{\mathrm{d}\mathcal{I}}{\mathrm{d}\boldsymbol{x}_{\mathcal{A}}} & \frac{\mathrm{d}\mathcal{I}}{\mathrm{d}\boldsymbol{x}_{\mathcal{S}}} \end{bmatrix} + \begin{bmatrix} \boldsymbol{g}_{\mathcal{A}}^T & \boldsymbol{g}_{\mathcal{S}}^T \end{bmatrix}\mathbf{P}\begin{bmatrix} \frac{\mathrm{d}\boldsymbol{g}_{\mathcal{A}}}{\mathrm{d}\boldsymbol{x}_{\mathcal{A}}} & \frac{\mathrm{d}\boldsymbol{g}_{\mathcal{A}}}{\mathrm{d}\boldsymbol{x}_{\mathcal{S}}} \\ \frac{\mathrm{d}\boldsymbol{g}_{\mathcal{S}}}{\mathrm{d}\boldsymbol{x}_{\mathcal{A}}} & \frac{\mathrm{d}\boldsymbol{g}_{\mathcal{S}}}{\mathrm{d}\boldsymbol{x}_{\mathcal{S}}} \end{bmatrix} \\ &= \alpha_{\mathcal{A}}\begin{bmatrix} \frac{\mathrm{d}C_D}{\mathrm{d}\boldsymbol{x}_{\mathcal{A}}} & \frac{\mathrm{d}C_D}{\mathrm{d}\boldsymbol{x}_{\mathcal{S}}} \end{bmatrix} + \alpha_{\mathcal{S}}\begin{bmatrix} \frac{\mathrm{d}W}{\mathrm{d}\boldsymbol{x}_{\mathcal{A}}} & \frac{\mathrm{d}W}{\mathrm{d}\boldsymbol{x}_{\mathcal{S}}} \end{bmatrix} + \begin{bmatrix} \boldsymbol{g}_{\mathcal{A}}^T & \boldsymbol{g}_{\mathcal{S}}^T \end{bmatrix}\mathbf{P}\begin{bmatrix} \frac{\mathrm{d}\boldsymbol{g}_{\mathcal{A}}}{\mathrm{d}\boldsymbol{x}_{\mathcal{A}}} & \frac{\mathrm{d}\boldsymbol{g}_{\mathcal{A}}}{\mathrm{d}\boldsymbol{x}_{\mathcal{S}}} \\ \frac{\mathrm{d}\boldsymbol{g}_{\mathcal{S}}}{\mathrm{d}\boldsymbol{x}_{\mathcal{A}}} & \frac{\mathrm{d}\boldsymbol{g}_{\mathcal{S}}}{\mathrm{d}\boldsymbol{x}_{\mathcal{S}}} \end{bmatrix} \end{aligned} \tag{12}$$

The gradient based optimization algorithm starting from an initial guess, looks for a better solution in the design space moving in the opposite direction of the gradient of the function which has to be minimized, i.e.

$$\boldsymbol{x}^{(n+1)} = \boldsymbol{x}^{(n)} - \Gamma\left.\frac{\mathrm{d}\mathcal{J}}{\mathrm{d}\boldsymbol{x}}\right|_n \tag{13}$$

3.3 Problem set up

The first iteration of the optimization process is shown in Fig. 3 and it is performed out of the optimization loop. It consists of three blocks, whose objective is to evaluate the static aeroelastic shape of the wing.

Figure 3: First iteration.

The procedure is a static aeroelastic calculation and can be summarized in the following steps: first, a direct aerodynamics analysis is performed. The aerodynamic loads are then transfered to the structural solver. Once the deformed geometry is known, a new mesh for the aerodynamic computation is produced by the mesh generator. Hence, the static aeroelastic shape of the wing is used as baseline geometry for the optimization problem.

Fig. 4 shows the block diagram that represents the single objective optimization process. It is possible to distinguish four main parts that constitute it: an initial structural analysis, the aerodynamic calculations, the geometric evaluation and a final structural analysis.

The initial structural analysis is performed to obtain the current structural weight of the wing. Thanks to this information, the total lift coefficient is calculated and is then used in the CFD analysis in order to trim the aircraft. The aerodynamic part is composed by several calculations. A direct CFD calculation to have the complete aerodynamic solution is used to perform the adjoint analysis. Other two direct calculations are performed at different lift coefficients to evaluate the aerodynamic performance about of the trim point. Then, a geometric evaluation is executed in order to check if the thickness constraints are satisfied and to provide their sensitivities with respect to the aerodynamic design variables. A second structural analysis evaluates the structural sensitivities. All the sensitivities are collected inside the derivative map, where they are manipulated to obtain the cross derivatives.

The derivative map is used by the optimizer to perform the gradient-driven optimization. A new set of design variables is produced and the optimization loop is repeated until one of the convergence criteria is satisfied.

The extension to multiple objective optimization is straightforward. The multi-objective function is a blend of several single-objective functions. As already discussed, the idea is to divide the entire cruise into a certain number of steps and to maximize the feasible range for each step simultaneously. Hence, the multi-objective function is defined as:

$$R = R_1 + \cdots + R_{n_{step}} = \sum_{i}^{n_{step}} R_i \tag{14}$$

where R_i, with $i = 1 : n_{step}$, represents a portion of the entire cruise range and n_{step} is the number of steps. Consequently, it is necessary to calculate all the parameters for each configuration. A preliminary iteration is needed to evaluate the static aeroelastic shape of the wing for each configuration (Fig. 3).

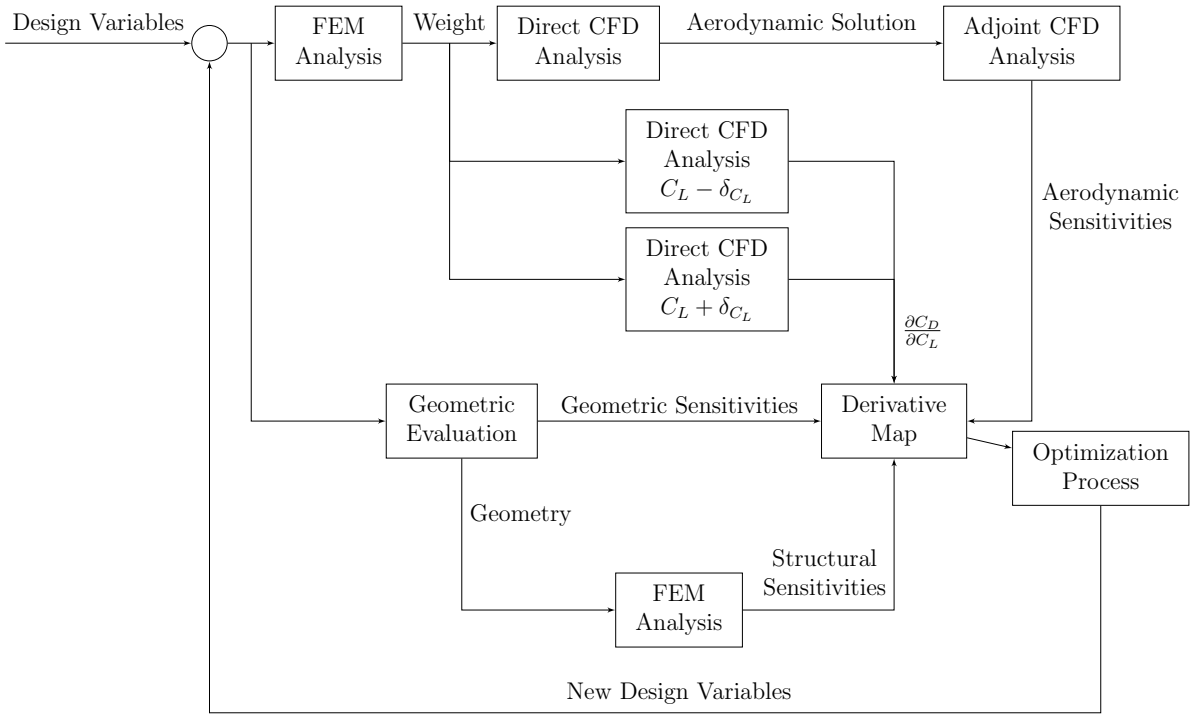

Figure 4: Block diagram for single objective optimization process.

Once all the configurations are evaluated (basically repeating the process resumed in Fig. 4), data are collected and recombined in order to obtain the objective function and the derivative map, which are then sent to the optimization software (Fig. 5). In order to limit the computational cost, if more than three configurations are considered, the recombine block is used to interpolates with respect to all parameters.

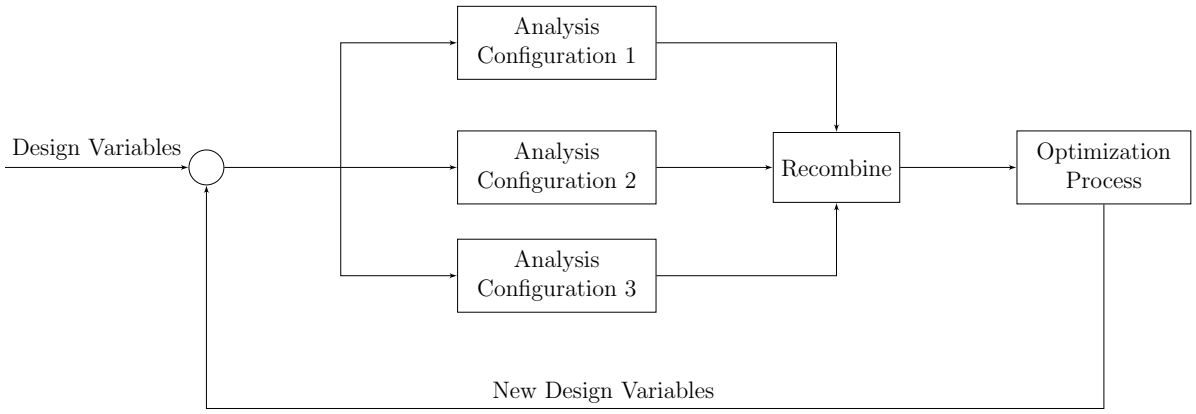

Figure 5: Block diagram for multiple objective optimization process.

4 Management of constraints

Several techniques are available in literature to handle inequality constraints for an optimization problem. In the following we briefly describe the methods that are currently used.

The method used in this optimization process is the penalty method. It consists in adding a penalty term to the objective function, composed by the constraint parameter and a weight term. This indicates how much the constraint can be violated. The aerostructural optimization has been performed imposing the lift coefficient with an equality constraint, while the moment coefficient with an inequality constraint. The thickness has been evaluated at some points along the wing span and chord-wise and controlled with inequality constraints. A

For the structural constraints to limit the computational cost and simplify the management of the problem, it has been decided to adopt the Kreisselmeier-Steinhauser (KS) Method [3]. The KS function uses a "draw-down" factor or aggregation parameter, ρ, which is analogous to the penalty factor in the penalty methods.

The KS function can be used to aggregate the constraints into a single composite function. Suppose that we have the following constraint for each structural finite element:

$$g_m(\boldsymbol{x}) = 1 - \frac{\sigma_m(\boldsymbol{x})}{\sigma_y} \geq 0 \tag{15}$$

where σ_m is the von Mises stress in element m and σ_y is the yield stress of the material. The corresponding KS function is defined as:

$$KS(\mathbf{g}(\boldsymbol{x})) = -\frac{1}{\rho}\ln\left(\sum_m e^{-\rho g_m(\boldsymbol{x})}\right) \geq 0 \tag{16}$$

This function represents a lower bound envelope of all of the constraint inequalities, where ρ is a positive parameter that express how close this bound is to the actual minimum of the constraints. This constraint lumping method is conservative and might not achieve the same results as managing each stress constraints separately. However, the use of KS functions is a viable alternative, being effective in optimization problems with thousands of constraints.

In the problem considered it is necessary to handle a large number of structural constraints so Kreisselmeier-Steinhauser approach with a value of the aggregation parameter equal to $\rho = 200$ has been adopter.

5 RESULTS

5.1 Single-objective optimizations

Fig. 6 compares the contour of the Mach number on the initial and on the optimized wing obtained with the coupled and the uncoupled optimization processes.

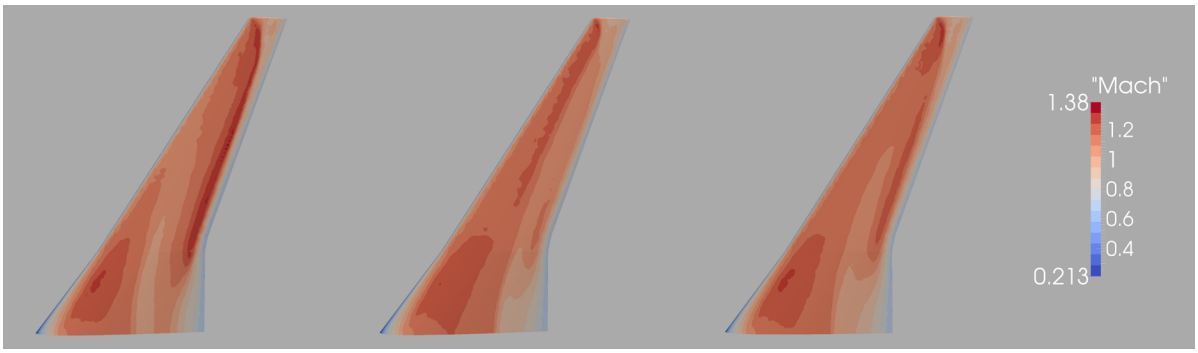

Initial Coupled Uncoupled

Figure 6: Contour of the Mach number on the initial (left) and optimized coupled (center) and uncoupled (right) wing.

The initial wing is characterized by a strong shock located in the aft part of the wing that runs along the 80% of the wing span and a supersonic bubble located in the front part of the wing. The optimized wing obtained from coupled optimization (Fig. 6) shows a weaker shock that moves forward, toward the leading edge. The flow never exceeds Mach 1.2, preventing the buffet onset. There is a small speed up area beyond the shock that affects the aerodynamic performance in a negative way while, the supersonic bubble is flattened down.

The optimized wing obtained from the uncoupled optimization is characterized by a weaker shock than the original wing but it does not move forward, causing a rapid re-compression of the flow near the trailing edge. The flow remains essentially unvaried near the wing tip, possibly causing buffet onset. The supersonic bubble does not change position or intensity.

From the structural point of view, the resistance section of the different structural components has been reduced in order to exploit completely the mechanical properties of the material, leading to an important reduction in the mass of the aircraft (Tab. 3).

Optimization	**Mass (kg)**	**Variation (%)**
Coupled	-187	-16.97
Uncoupled	-183	-16.60

Table 3: Mass variation with respect to the initial wing.

5.2 Multi-objectives optimizations

Two different multi-objective optimizations have been performed. The first one considers three steps in the cruise range, while the second one considers nine steps. In the

second case, to reduce the computational cost only three CFD calculations were performed, interpolating the results for the other steps. The aerodynamic results show an improvement of the performance in both cases. They are summarized in the polar curves (Fig. 7) in the comparison paragraph.

5.3 Comparison

In this section a comparison among all the optimized wings and the initial one is presented.

The comparison of the polar curves is shown in Fig. 7. Both the coupled and the uncoupled wings show a regular and smooth polar curve. The multi-point wings have a particular trend. Starting from the beginning of the cruise, the two curves run in parallel. When they reach $C_L = 0.3$ they distance themselves. Actually, the three-point wing drops at a lower C_D than the nine-point one. After this jump, they almost touch and proceed together. We have to point out that the three-point wing has a better behavior outside the cruise range of points.

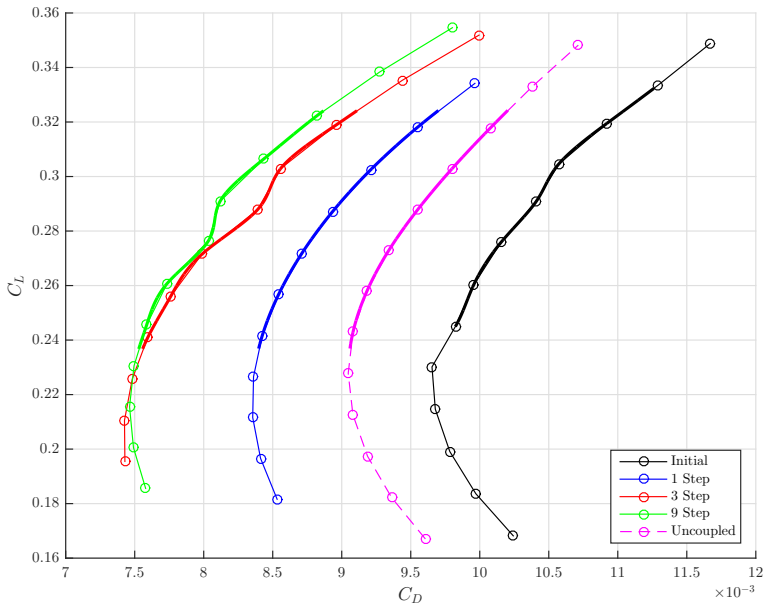

Figure 7: Comparison of the polar curves.

Tab. 4 lists the total range values and the increment with respect to the initial wing.

Wing Geometry	**Total Range** (km)	**Increment** (%)
Initial	5926	
Uncoupled	6482	9.38
Coupled	6924	16.84
Three-Point	7513	26.78
Nine-Point	7647	29.04

Table 4: Total range and percent increment.

6 CONCLUSIONS

The available literature about MDO applied to aircraft design uses the Breguet range equation as objective function. This means that the variation of attitude during cruise, which is related to the loss of weight caused by fuel consumption, is not taken into account. The innovative approach presented in this thesis is to divide the cruise into a certain number of steps; over each step the attitude is considered to be constant, so that the Breguet range formula can be applied. The total range is then evaluated as the sum of the ranges of each step, leading to a sort of multi-objective optimization. The bigger is the number of step considered, the more accurate is the solution obtained. This new approach is called "step-range" and its results are compared with those obtained through sequential discipline optimization and single objective optimization.

Therefore, four different optimization tasks have been performed and the results demonstrate that the method we developed is successful when applied to our specific case. In particular, comparing the results obtained from the single-objective optimizations, we can notice that the coupled technique leads to a larger improvement than the uncoupled one.

Both the three and the nine-point optimizations lead to better results than the single-objective one. As expected, enlarging the number of evaluation along the cruise, the objective function, seen as the sum of sub-functions, increases its value.

The nine-point optimization turns out to be the best procedure in absolute terms, highlighting the effectiveness of the subdivision in different steps of the cruise. Actually, this allows to consider the variation of the aircraft attitude during the cruise. Moreover, we are able to demonstrate that the spline interpolation of the optimization parameters (i.e. objective function, constraints and gradients) leads to a reduction of the computational cost, ensuring, at the same time, accurate results.

The growth of the number of evaluations over the cruise also causes the increase of the number of iterations needed for the optimization process to converge. This could represent a limitation of the number of evaluation points that can be used. Heuristically speaking, the undefined increase of evaluation points would lead to a robust optimization, whose intent is the maximization of the mean value of the objective function, minimizing its standard deviation.

REFERENCES

[1] J. Sobieszczanski-Sobieski and R. T. Haftka. Multidisciplinary aerospace design optimization: survey of recent developments. *Structural optimization*, 14(1):1–23, 1997.

[2] Joaquim RRA Martins and Andrew B Lambe. Multidisciplinary design optimization: a survey of architectures. *AIAA journal*, 51(9):2049–2075, 2013.

[3] G. Kreisselmeier and R. Steinhauser. Systematic control design by optimizing a vector performance index. *International Federation of Active Controls Syposium on Computer-Aided Design of Control Systems, Zurich, Switzerland*, 1979.

[4] Gaetan KW Kenway and Joaquim RRA Martins. Multipoint high-fidelity aerostructural optimization of a transport aircraft configuration. *Journal of Aircraft*, 51(1):144–160, 2014.

[5] Olivier Pironneau. On optimum design in fluid mechanics. *Journal of Fluid Mechanics*, 64(1):97–110, 1974.

[6] Antony Jameson. Aerodynamic design via control theory. *Journal of Scientific Computing*, 3(3):233–260, 1988.

[7] Jamshid Samareh. Aerodynamic shape optimization based on free-form deformation. In *10th AIAA/ISSMO Multidisciplinary Analysis and Optimization Conference*, page 4630, 2004.

[8] Toni Lassila and Gianluigi Rozza. Parametric free-form shape design with pde models and reduced basis method. *Computer Methods in Applied Mechanics and Engineering*, 199(23):1583–1592, 2010.

[9] Jamshid A Samareh. Survey of shape parameterization techniques for high-fidelity multidisciplinary shape optimization. *AIAA journal*, 39(5):877–884, 2001.

[10] John D Anderson. *Introduction to Flight*. Mc Graw-Hill International Editions, Aerospace Science Series, 1989.

VII International Conference on Computational Methods for Coupled Problems in Science and Engineering
COUPLED PROBLEMS 2017
M. Papadrakakis, E. Oñate and B. Schrefler (Eds)

COUPLING MULTIPHYSICS PROBLEMS IN TRANSIENT REGIMES: APPLICATION TO LIQUID RESIN INFUSION PROCESS

RABIH MEZHER*, SIMON BREUMIER, NICOLAS MOULIN, JULIEN BRUCHON, AND SYLVAIN DRAPIER

SMS Division and LGF UMR CNRS 5307
Mines Saint-Etienne - Université de Lyon
158, Cours Fauriel, CS 62362, 42023 Saint-Etienne cedex 2, France
e-mail: *rabih.mezher@emse.fr, simon.breumier@etu.emse.fr, nmoulin@emse.fr, bruchon@emse.fr and drapier@emse.fr

Key words: Resin Infusion, Composite Materials, Fluid-Solid Coupling, Weak Coupling, Message Passing Interface

Abstract. Liquid resin infusion (LRI) process is widely considered in the aeronautics, due to its benefits (low void content and production of large parts), for high performance composite material forming. The main objective of the present work is to simulate numerically the LRI process, in a high performance computing framework, which consists in coupling fluid-solid mechanics. Hence, two fluid flow regimes are coupled with an efficient ASGS stabilized monolithic finite element formulations: the resin flow in both a highly permeable distribution medium (Stokes) and low permeability fibrous orthotropic preforms (Darcy). Moreover, weak coupling algorithms are used along for coupling solid / fluid mechanics, solid / level-set problems and fluid / level-set problems; where the level-set method is used to capture the moving flow front and the Stokes-Darcy interface. To transfer the different physical variables between the above coupled problems, Message Passing Interface (MPI) library is chosen, to ensure the best data transfer performances.

1 INTRODUCTION

In today's aeronautical and automotive industry, composite materials have become the primary choice in the manufacturing processes, due to their light weight, and overall properties (mechanical, thermal, electrical ...). The Liquid Resin Infusion (LRI) processes allow the manufacturing of high performance composites and are among today's competitive techniques, because they can achieve very low void contents, on large pieces and particularly on aircraft parts [1]. In LRI processes, a dry fiber reinforcement is placed (Figure 1) into a mould, and then enclosed in a specific bagging system. Vaccum is then

exerted on the reinforcement, leading to an atmospheric compression of the reinforcement. Hence under this depression, a liquid thermoset resin fills in a stiff distribution medium placed under or over the preform to create a resin-feeding bed. As a result, the resin flows through the layer stacking that swells simultaneously due to the fluid resin pressure effects [2]. When the resin fully impregnates through the reinforcement, the supply of resin is cut off and resin is left for curing, still under vacuum pressure. Even though LRI processes present many advantages, they are difficult to control experimentally. When critical properties are involved in such processes (dimensions of the final pieces, fiber volume fraction, ...), the control becomes even more challenging. Therefore, it is necessary to use numerical simulations in order to control and properly understand the interactions of the fibrous preform non-linear deformations with the resin flow, out of (Stokes flow regime) and in (Darcy flow regime) these orthotropic deformable porous media. The objective of this paper is to present a robust numerical approach, able to couple the different complex problems involved in LRI processes. To assure multiphysic coupling, a suitable coupling method has to be chosen, ensuring the transfers of the different physical variables between the problems. Moreover, an algorithm is later selected to couple the different problems. This paper is structured as follows: first coupled problems are identified and detailed; then the coupling techniques are presented, based on the MPI library [3] for transfering variables between problems; later the algorithm to couple fluid and non-linear solid mechanics is exposed; finally the results of the numerical simulations of the coupled problems featured in resin infusion are shown.

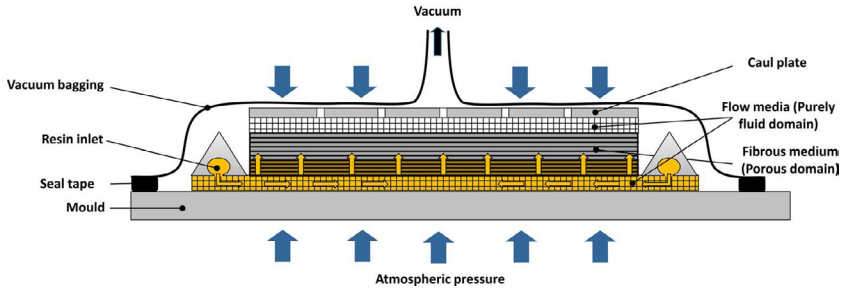

Figure 1: Schematic principle of Liquid Resin Infusion process [2]

2 COUPLED PROBLEMS

Modeling the LRI processes consists in coupling fluid, solid, and porous mechanics in isothermal conditions (Figure 2). First, two fluid flow regimes are coupled, representing the resin flow in both a highly permeable distribution medium (Stokes) and low permeability fibrous orthotropic preforms (Darcy). Darcy system expresses the flow velocity as a function of the pressure gradient and two parameters, the fluid viscosity η and the permeability $\mathbf{K}$ which traduce the ability of the media to be penetrated by the fluid. The

problem is then desribed by finding a velocity field $\mathbf{v}_d$ and a pressure field p_d such that :

$$\begin{aligned} \eta \mathbf{K}^{-1} \mathbf{v}_d + \boldsymbol{\nabla} p_d &= \mathbf{f}_d \\ \boldsymbol{\nabla} \cdot \mathbf{v}_d &= 0 \end{aligned} \tag{1}$$

with $\mathbf{f}_d$ the external forces. Stokes problem expresses the velocity as a function of the pressure gradient and the viscosity; it is written as follows:

$$\begin{aligned} -\boldsymbol{\nabla} \cdot (2\eta \dot{\varepsilon}(\mathbf{v}_s)) + \boldsymbol{\nabla} p_s &= \mathbf{f}_s \\ -\boldsymbol{\nabla} \cdot \mathbf{v}_s &= 0 \end{aligned} \tag{2}$$

with $\mathbf{f}_s$ the external forces; and $\dot{\varepsilon}(\mathbf{v}_s) = \frac{1}{2}\left(\boldsymbol{\nabla}\mathbf{v}_s + \boldsymbol{\nabla}^T \mathbf{v}_s\right)$, is the strain rate. This Stokes-Darcy coupling is numerically achieved with an efficient ASGS stabilized monolithic finite element formulation (for the detailed description the reader can refer to [1]). For the solid problem, the general formulation is written in the framework of an updated Lagrangian formulation [4, 5, 6]:

$$\boldsymbol{\nabla} \cdot \boldsymbol{\sigma} + \mathbf{f} = \mathbf{0} \tag{3}$$

where $\boldsymbol{\sigma}$ is the Cauchy stress tensor and $\mathbf{f}$ are the external forces. Hence, the displacement fields are obtained by solving equation (3). Solid and fluid interact in two ways in the wet preforms, since the resin pressure exerted by the fluid will deform the preforms and lead to a change in their porosity/permeability. In turn this will affect the fluid flow. The preforms exhibit swelling under the effect of the fluid's pressure ; this is modeled by using Terzaghi's equivalent stress. Note that, the dry preforms are compacted, because they are subjected to the external atmospheric pressure; this later results in displacements of the preforms. Last, the level-set approach used to capture the flow front will rely on the physical fluid velocity and on the mesh velocity (i.e. the mesh of the domain is deformed because of mechanical displacements). The level-set function (denoted by ψ) is transported according to the hyperbolic equation:

$$\frac{\partial \psi}{\partial t} + \mathbf{v} \cdot \nabla \psi = 0 \tag{4}$$

where $\mathbf{v}$ is the velocity computed from the Stokes-Darcy problem.

3 COUPLING TECHNIQUES

To perform multiphysical coupling, two approaches can be considered: a monolithic method and a weak coupling based method. The monolithic approach considers the coupled problems as a single block, hence solving simultaneously for two or more problems; this type of approach denotes a strong coupling [2, 9] and is used to couple the Stokes-Darcy problem reported in section 2. The weak coupling based method, consists of seperately solving each problem iteratively, until reaching the global solution. This type

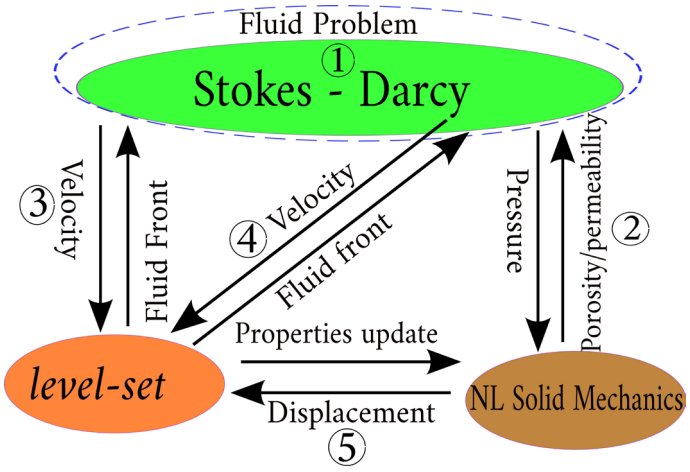

Figure 2: Schematic representation of the coupled problems

of approach is proposed to couple the problems illustrated in Figure 2. Transfering data and variables between the coupled problems, requires the usage of a suitable exchange library. The main objective is to minimise the computation time (and particularly the variable exchange time), when these high performance calculations are done. Within a parallel computing framework, each physical problem can be solved on a processor accessing only to its own memory. In this case, the MPI (Message Passing Interface) library is used for the transfer of the different required data [7].

4 COUPLING ALGORITHM

Non-linear solid mechanics, fluid mechanics and level-set problems are weakly coupled with a sequential algorithm (Algorithm 1). Subsequently, at each time step until the preform is filled, three problems are solved.

Figure 3 details the process of exchanging variables at each time step (Δt being the time step and t denotes the time), showing which variables are sent (respectively received by each code or problem). In what follows, and for the sake of clarity the different problems will be numbered according to Figure 3. Figure 4 shows the global resolution of the problems at each time step. Before the solving process, an initialisation of the Stokes-Darcy interface (denoted by $\Gamma_{s,d}$) and of the initial position of fluid flow front (denoted by Γ_f) is done. Then the fluid problem transfers its velocity ($\vec{v}$) to the level-set problem. After that, the solid problem receives the fluid pressure and the position of the fluid front (i.e. the level-set function value ψ), thus updating the effective stress $\boldsymbol{\sigma}(\boldsymbol{\epsilon})$ according to Terzaghi's law [8]; then the solid problem iterates til convergence. Finally the mesh is updated (this is done at each time step), taking into account the compaction of the preforms ($\vec{u}$ denotes the displacements).

Algorithm 1 Sequential algorithm

Begin of weak coupling: Initialisation of the Stokes-Darcy interface $\Gamma_{s,d}$ and the fluid flow front Γ_f
do:

1. Computation of the preform compaction while considering the fluid pressure with Terzaghi's law (displacements), then update mesh
2. Computation of the Stokes-darcy fluid problem (velolcity and pressure)
3. Computation of the resin flow front motion: resolution of the level-set problem

until the preform is filled $(t + \Delta t)$
End of weak coupling

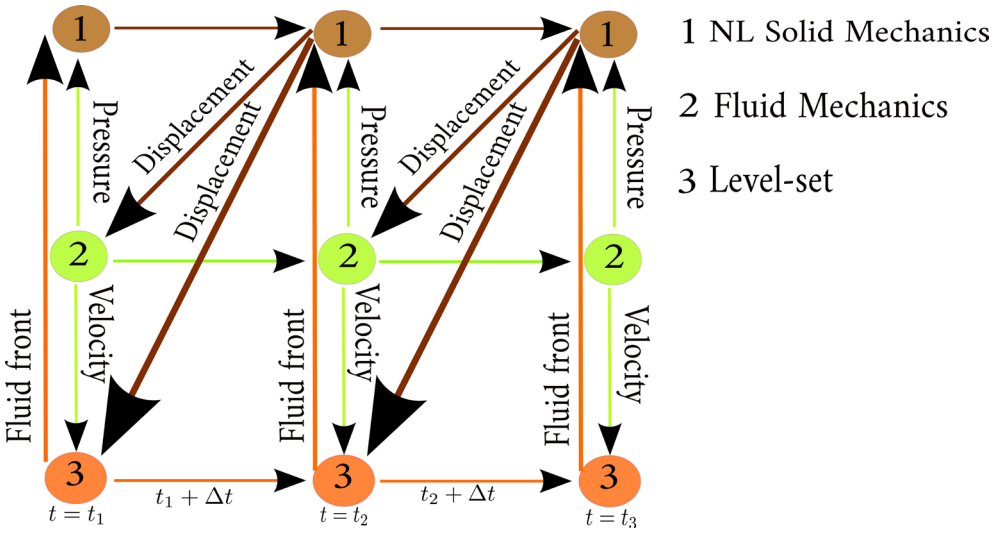

Figure 3: Sequential algorithm with the designated sent and received variables between the three problems (NL is the abbreviation for non-linear)

5 NUMERICAL SIMULATIONS

5.1 Geometry and boundary conditions

The coupling between problems 1, 2, and 3 is simulated on a "T" shaped geometry. This shape represents a part used in aeronautical engineering (stiffened panel). For the Stokes-Darcy problem, one single unstructured mesh is used. Stokes and Darcy subdomains (Figure 5) are subsequently described by using a level-set function. The dimensions of the part are shown in Figure 5, where symmetry conditions are considered. The Stokes-Darcy interface is illustrated by the zero isosurface value coloured in red on Figure 5.

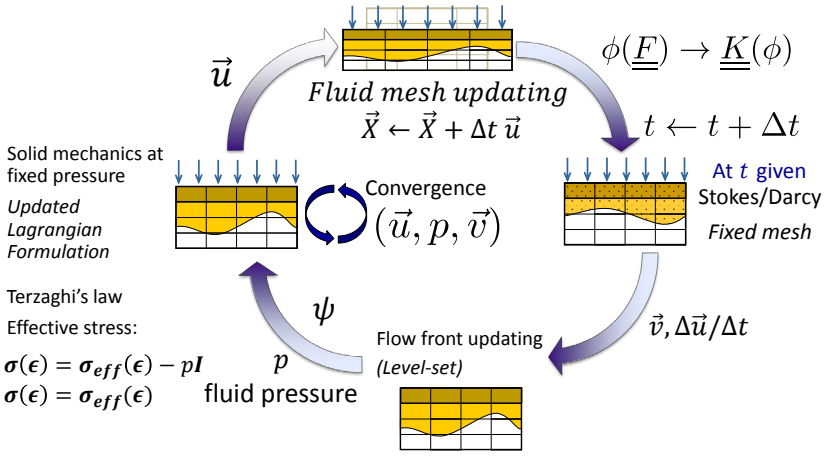

Figure 4: Global time-stepping strategy for solving the coupled problems [2, 5, 9]

A pressure gradient of 10^5 Pa is applied between top and bottom faces of the domain (Figure 5 where σ_n is the normal stress). To represent impervious walls, normal velocities are considered equal to zero (i.e. $\vec{v} \cdot \vec{n} = 0$ on Figure 5, where $\vec{v}$ is the fluid velocity and $\vec{n}$ is the normal vector to the domain boundary), on the remaining boundaries.

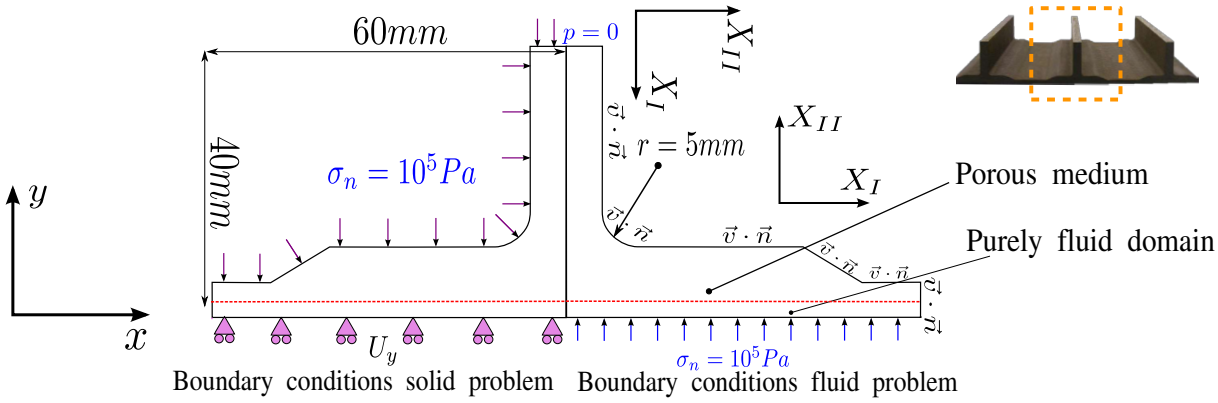

Figure 5: Boundary conditions for both the fluid and solid problem (r is the radius of the curvature) [1]

For the non-linear solid mechanics problem, displacement conditions are inforced as

shown on Figure 5. They represent the contact of the preform with the mould, where U_y denotes the components of the deplacements in the y direction and U_x denotes the deplacements in the x direction ($\vec{U} = U_x.\vec{x} + U_y.\vec{y}$). A pressure of 10^5 Pa is applied on the rest of the boundaries, which is the atmospheric pressure on the vaccum bag.

5.2 Numerical Results

The coupling between the three problems, has been done by using the finite element software Zset [10]. The computations were carried out on one multiprocessor computer; hence, each problem runs on one processor, of the same machine. MPI library was used to handle the exchange in data between codes, in conformity with the scheme presented in Figure 3. Five numerical simulations were executed on five unstructured meshes (denotes by meshes 1, 2, 3, 4 and 5 in Table 1) of linear triangles. The time step used for all simulations was $\Delta t = 0.05\,s$ (sufficiently small in order to reach convergence) for a final physical time of $t = 4\,s$. The mesh size (i.e. number of nodes and elements), as well as the parameters used for the fluid problem (viscosity η, permeabilities K_I and K_{II}; $\mathbf{K} = K_I\ \vec{X}_I \otimes \vec{X}_I + K_{II}\ \vec{X}_{II} \otimes \vec{X}_{II}$) and the solid problem (Young's modulus E, poisson's coefficient ν) are summarized in Tables 1 and 2. In order to emphasize on the performance of the weak coupling using MPI library, we considered only one viscosity on the hole domain (for a more richer description the reader can refer to [1]). Figure

Mesh	Number of nodes	Number of elements
1	1106	2212
2	2060	4120
3	3063	6126
4	12104	23544
5	26726	52462

Table 1: Mesh size parameters

$K_I\ (m^2)$	$K_{II}\ (m^2)$	$\eta\ (Pa.s)$	$E\ (MPa)$	ν
100.10^{-11}	10^{-11}	0.03	210	0.3

Table 2: Parameters for both the fluid and solid problem

6(a) shows the pressure field after the compaction of the preforms under the effect of the atmospheric pressure. Once the preforms are compacted due to the external atmosperic pressure, the mesh geometry is updated. Figure 6(b), shows the velocity field magnitude.

Figure 7(a) shows the displacements U, where the original mesh (coloured in grey) has

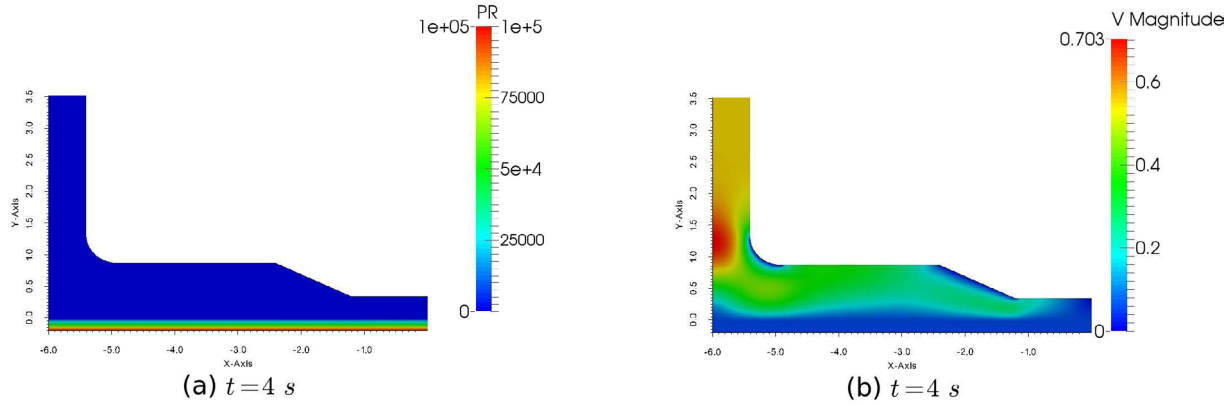

(a) $t = 4\ s$ (b) $t = 4\ s$

Figure 6: Pressure and velocity fields

been superimposed on the deformed mesh, in order to show the preform's compaction. The movement of the fluid flow front (pink line) is also depicted on Figure 7(b). The grey mesh in Figure 8 corresponds to the initial undeformed mesh (before compaction) superimposed on the deformed mesh (i.e. the coloured mesh is the deformed one). It has been represented seperately here from the physical fields, in order to evaluate quantitatively and qualitatively the large deformartions exhibited by the preforms. It is noticebale from Figure 8, that deformations are not homogeneous on the global domain; this is mainly due to the non-homogeneous pressure field owing to Terzaghi's law and anisotropic permeabilities. Two points of interest (points A and B on Figure 8) have been chosen to discuss and emphasize on the thickness variation. The cross section in point A is found to sustain approximately 13% (Table 3, where H_A denotes the height in point A) of thickness variation, while the one in point B undergos 10% (Table 3, where H_B denotes the height in point B) of thickness variation. The numerical values of computation time is shown in Table 4. The computation time (denoted by CT in Table 4) increases with the number of degrees of freedom associated with the sent / received variables. Hence, more time is needed to assure the exchange of much more volumetric data. This evolution is compared with a previous exchange method adopted in [1]. It is clearly shown from Figure 9 (where the computation time of the two methods is shown), that the computation time is much higher with this last technique. Therefore, MPI allowed a significant reduction and optimization in computation time (the percentage of time reduction is shown in Table 4), relative to this classical technique, and especially for high mesh refinements (for 26726 nodes, the computation time is approximately reduced by a factor of 2).

6 CONCLUSION

Starting from previous works done by [1, 2, 4, 9], a robust approach has been proposed in this work to couple monolithic Stokes-Darcy fluid mechanics, non-linear solid mechan-

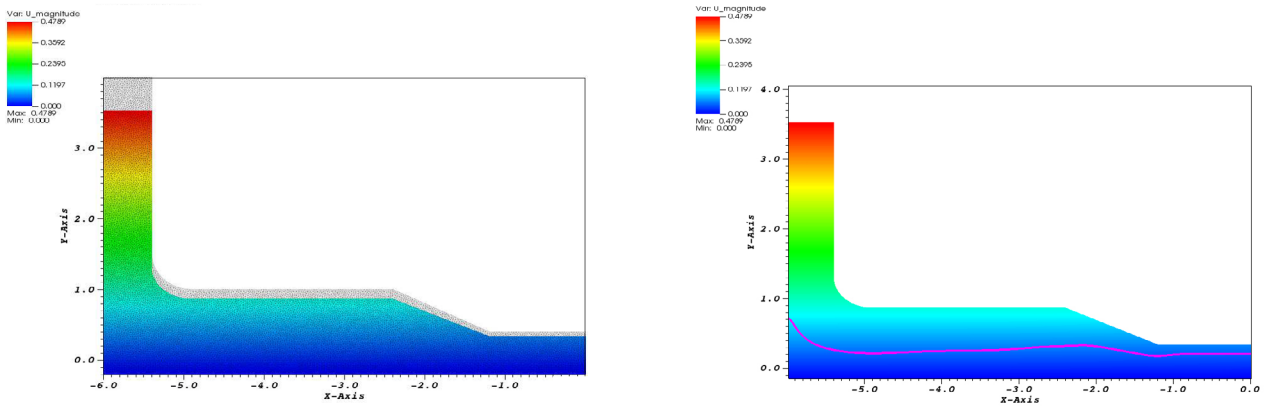

$(a)\, t = 1\, s$ $(b)\, t = 4\, s$

Figure 7: Displacement field magnitude: (a) original non deformed mesh (coloured in grey) superimposed on the deformed geometry and (b) the change in the moving fluid flow front (pink line)

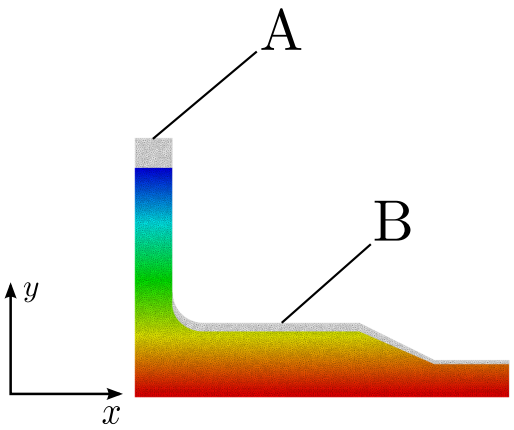

Figure 8: Mesh geometry before and after compaction

Height before compaction	Height after compaction	Percentage of thickness variation
$H_A = 4\,cm$	$H_A = 3.5\,cm$	12.5%
$H_B = 1.1\,cm$	$H_B = 1\,cm$	10%

Table 3: Thickness variations in point A and B in Figure 8

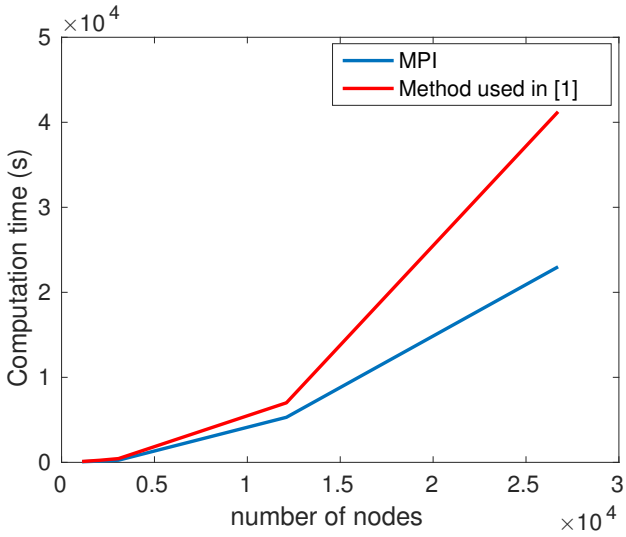

Figure 9: Computation time for both data exchange methods: MPI and method used in [1]

Mesh	Number of nodes	CT (MPI)	CT (method used in [1])	Percentage of time reduction
1	1106	74	104	29%
2	2060	148	245	40%
3	3063	254	442	43%
4	12104	5300	7006	24%
5	26726	23000	41240	44%

Table 4: Numerical values of computation time for both data exchange methods: MPI and method used in [1]

ics and level-set transient problems. The coupling was performed on a complex industrial piece, reported in previous works . It was shown that the coupling of the fluid and solid problems has an effect on the final dimensions of the piece. Moreover, MPI was used to ensure data transfer between distant codes where high performance computation were done on refined meshes. The computation time has been optimized with MPI, in compar-

ison with classic conventional techniques. Future works, should focus on integrating more problems to the couplings, such as temperature and thermo-chemical effects (involved in resin curing). In addition, parallel computations have to be considered for more refined meshes; this is currently a work in progress.

REFERENCES

[1] Blais, M. and Moulin, N. and Liotier, P.J. and Drapier, S. Resin infusion-based processes simulation : coupled Stokes–Darcy flows in orthotropic preforms undergoing finite strain. *Int. J. Mater. Form.* (2017) **10(1)**:43–54.

[2] Abou Orm, L. and Troian, R. and Drapier, S. and Bruchon, J. and Moulin, N. Stokes–Darcy coupling in severe regimes using multiscale stabilisation for mixed finite elements : monolithic approach versus decoupled approach. *European Journal of Computational Mechanics.* (2014) **23**:113–137.

[3] Gropp, W. and Lusk, E. and Skjellum, A. *Using MPI Portable Parallel Programming with the Message Passing Interface*. third edition, scientific and engineering computation series (2014).

[4] Celle, P. and Drapier, S. and Bergheau, J.M. Numerical aspects of fluid infusion inside a compressible porous medium undergoing large strains. *Revue européenne de mécanique numérique. Resin Infusion-Based Processes Simulation.* (2008) **17(5–6–7)**:819–827.

[5] Celle, P. and Drapier, S. and Bergheau, J.M. Numerical modelling of liquid infusion into fibrous media undergoing compaction. *Eur. J. Mech. A. Solids.* (2008) **27(4)**:647–661.

[6] Dereims, A. and Drapier, S. and Bergheau, J.M. and de Luca, P. 3d robust iterative coupling of Stokes, Darcy and solid mechanics for low permeability media undergoing finite strains. *Finite Elem. Anal. Des.* (2015) **94**:1–15.

[7] Garaud, J. D. Développement de méthodes de couplage aéro-thermo-mécanique pour la prédiction d'instabilités dans les structures aérospatiales chaudes. PhD Thesis. (2008)

[8] Terzaghi, K. *Soil mechanics in engineering practice*. John Wiley and Sons, (1996).

[9] Pacquaut, G. and Bruchon, J. and Moulin, N. and Drapier, S. Combining a level-set method and a mixed stabilized P1/P1 formulation for coupling Stokes–Darcy flows. *Int. J. Numer. Meth. Fluids.* (2012) 459–480.

[10] Besson, J. and Foerch, R. Large scale object-oriented finite element code design. *Comput. Methods Appl. Mech. Eng.* (1997) **142(1)**:165–187.

VII International Conference on Computational Methods for Coupled Problems in Science and Engineering
COUPLED PROBLEMS 2017
M. Papadrakakis, E. Oñate and B. Schrefler (Eds)

MIGRATING SOFTWARE TO MOBILE TECHNOLOGY: A MODEL DRIVEN ENGINEERING APPROACH

LILIANA FAVRE[*] AND FEDERICO BRICKER[†]

[*] Universidad Nacional del Centro de la Provincia de Buenos Aires
Comisión de Investigaciones Científicas de la Provincia de Buenos Aires (CICPBA)
Tandil, Argentina
e-mail: liliana.favre@gmail.com

[†] Dokko Group, Tandil, Argentina

Key words: Software Modernization, Reverse Engineering, Model Driven Engineering, Mobile Computing, C++ Language, Haxe Language

1 INTRODUCTION

Nowadays, organizations are facing the problematic of having to modernize or replace their legacy software. This software has involved the investment of money, time and other resources through the ages and there is a high risk in replacing it. The purpose of reengineering is to adapt software in a disciplined way in order to improve its quality in aspects such as operability, functionality or performance. The focus of reengineering is on improving an existing system with a higher return on investment than would be achieved by developing a new system.

In the context of reengineering, the term legacy was associated with software that survived several generations of developers, administrators and users. The entry into the market of new technologies or paradigms is increasingly occurring and, motivates the growing demand for the adaptation of systems developed more recently. Mobile Computing is crucial to harvesting the potential of these new paradigms. Smartphones are the most used computing platform worldwide. They come with a variety of sensors (GPS, accelerometer, digital compass, microphone and camera) enabling a wide range of applications in Pervasive Computing, Cloud Computing and Internet of Things (IoT).

Pervasive Computing, also called Ubiquitous Computing is the idea that almost any device can be embedded with chips to connect the device to a network of other devices. The goal of pervasive computing, which combines current network technologies with wireless computing, voice recognition and Internet capability, is to create an environment where the connectivity of devices is unobtrusive and always available. Cloud Computing is an Internet-based computing for enabling ubiquitous, on-demand network access to a shared pool of configurable computing resources (e.g., networks, servers, storage, applications and services) that can be rapidly supplied with minimal management effort. Cloud computing has long been recognized as a paradigm for Big Data storage and analytics providing computing and data resources in a

dynamic and pay-per use model. Finally, there is no single universal definition for IoT, we could define it as the interconnection via the Internet of computing devices embedded in everyday objects, enabling them to send and receive data. The IoT is becoming so pervasive and several studies predict that will be more than 30 billion IP-connected devices and sensors in the world by 2020.

Pervasive Computing, Cloud Computing and IoT face similar problems related to similar use cases, including smart cities, environmental monitoring, agriculture, home automation, and health. Smartphones have been one of the greatest facilitators of the solution for them.

Frequently, the development of software component and applications aligned to these new paradigms requires adapting existing desktop software to mobile platforms. For instance, there is a need to migrate C/C++ desktop applications developed in different domains of engineering to mobile platforms in order to adapt them to new technologies. On the one hand, most challenges in this kind of software migration are related with the proliferation of mobile platforms that makes mobile development difficult and expensive and, on the other hand with the need to define systematic, reusable processes with a high degree of automation that reduce risks, time and costs.

With respect to the first challenge, the ideal situation is to define multiplatform development. New languages are emerging to integrate the native behaviors of the different platforms targeted in development projects. In this direction, the Haxe language is an open-source high-level cross-platform programming language and compiler that can produce applications and source code for many different platforms from a single code base [7].

With respect to the systematic modernization process, novel technical frameworks for information integration, tool interoperability and reuse have emerged. Specifically, Model Driven Engineering (MDE) has emerged as a new software engineering discipline which emphasizes the use of models and model transformations to raise the abstraction level and the degree of automation in software development. Productivity and some aspects of software quality such as maintainability or interoperability are goals of MDE [4]. A branch of MDE linked to reengineering is Model-Driven Software Modernization (MDSM) [5]

This paper describes an MDE-based modernization framework defined in the context of a software modernization project aimed at migrating non-mobile software to various mobile platforms. An instantiation of the framework for the migration of C/C++ code to different mobile platforms through Haxe is presented. The proposal is validated in Eclipse Modeling Framework (EMF) considering that some of its tools and environments are aligned with MDE [23]. Our approach is supported by metamodels to describe existing systems, discoverers to automatically create models of these systems and, tools to understand and transform complex models.

The structure of the paper is as follows. Section 2 describes background, emphasizing on MDE and multiplatform development. Section 3 presents some relevant work related to our approach. Section 4 describes a MDE framework for software modernization. Section 5 includes a realization of the framework for the migration of C/C++ code to mobile App deployed on different mobile platforms. Finally, Section 6 presents a discussion of our approach and future work.

2 BACKGROUND

This section includes background on Model Driven Engineering (Section 2.1) and multiplatform development in the Haxe language (Section (2.2).

2.1 Model Driven Engineering

Different acronyms are associated with model-driven developments: MBE (Model Based Engineering), MDE (Model Driven Engineering), MDD (Model Driven Development) and MDSM (Model Driven Software Modernization).

MBE is the branch of software engineering in which software models play an important role being the basis of development. However, there is no direct link between models and generated software that is defined through precise transformations.

MDE can be viewed as a subset of MBE. It is the branch of software engineering in which processes are driven by models, i.e. models are the primary artifacts of different software processes. MDE has emerged as a new software engineering discipline that emphasizes the use of models and model transformations to raise the abstraction level and the degree of automation in software development. Productivity and some aspects of the software quality such as maintainability or interoperability are goals of MDE.

Model Driven principles can be summarizes as follows: all artifacts involved in a MDE process can be viewed as models that conform to a particular metamodel, the process itself can be viewed as a sequence of model transformations and all extracted information is represented in an standard way through metamodels. Then, model, metamodel and transformations are crucial in MDE.

Model-Driven Development (MDD) refers to forward engineering processes that use models as primary development artifacts. In an MDD development, everything is a model that conforms to a metamodel and the development itself is seen as a sequence of model-to-model transformations ranging from abstract to concrete levels. A specific realization of MDD is the Model-Driven Architecture (MDA) proposed by the Object Management Group (OMG) [10].

The outstanding ideas behind MDA are separating the specification of the system functionality from its implementation on specific platforms, managing the software evolution from abstract models to implementations. Three concepts are crucial in MDA: model, metamodel and model transformations. Models play a major role in MDA, which distinguishes at least Platform Independent Model (PIM) and Platform Specific Model (PSM) [16]. An MDA process focuses on the automatic transformation of different models that conform to MOF metamodels. The essence of MDA is Meta Object Facility (MOF), an OMG standard for defining metamodels that provides the ability to design and integrate semantically different languages such as general-purpose languages, domain specific languages and modeling languages in a unified way. The modeling concepts of MOF are classes, which model MOF meta-objects; associations, which model binary relations between meta-objects; Data Types, which model other data; and Packages, which modularize the models [17]. Consistency rules are attached to metamodel components by using OCL [18].

Model transformation is another fundamental concept in MDA. A transformation is the process of converting a source model that conforms to a source metamodel, in a target model that conforms to a target metamodel, both metamodels (source and target) conforming to MOF.

The standard proposed by OMG to specify model-to-model transforms is the QVT (Query, View, Transformation) [21]. ATL (Atlas Transformation Language) is the most mature transformation language aligned with MDE that provides ways to produce a set of target models from a set of source models [3].

A particular form of reengineering for the technological and functional evolution of legacy systems begins to be identified in the early 21st century under the designation of Model Driven Software Modernization (MDSM). It is based on model-driven processes of reverse engineering, restructuring and forward engineering [5]. In MDSM, models representing legacy software are discovery semi-automatically through a reverse engineering process and then transformed into models that meet the modernization requirements from which it is possible to forward engineering a new modernized software. The OMG Architecture-Driven Modernization Task Force (ADMTF) is developing a set of specifications and promoting industry consensus on modernization [2].

2.2 Multiplatform Development

The high cost and technical complexity of targeting development to a wide spectrum of mobile platforms has given rise to the cross-platform development. It allows using the same code to deploy an application on multiple platforms such as iOS, Androis or WindowsPhone. In this direction, the Haxe language emerges as an open-source high-level multiplatform programming language and compiler that can produce applications and source code for many different platforms from a single code-base [7].

Reference [6] summarizes the Haxe principles as follows: “support mainstream platforms”, “write once, reuse everywhere”, “always native, no wrapper”, “generated but readable” and “trust the developer”. The Haxe programming language is a high level programming language that mixes features of object oriented languages and functional ones. It is similar (but not pure) to object-oriented languages. The compiler supports novel features such as type inference, enforcing strict *type safety* at compile time. Currently, Haxe supports nine target languages which allow for different use-cases: JavaScript, Neko, PHP, Python, C++, ActionScript3, Flash, Java and C#. Haxe includes a set of common functions that are supported across all platforms, such as numeric data types, text, arrays, binary and some common file formats.

The idea behind Haxe is to allow developers choose the best platform for a specific development. To achieve this, it provides a standardized language, a standard library that works the same on all platforms and platform specific libraries that allow us accessing the full API for a given platform from Haxe.

3 RELATED WORK

Various authors describe challenges of mobile software development, for example, in [8] authors highlight creating user interfaces for different kinds of mobile devices, providing reusable applications across multiple mobile platforms, designing context aware applications and handling their complexity and, specifying requirements uncertainty.

A DSL (Domain Specific Language), named MobDSL, to generate applications for multiple mobile platforms is described in [15]. Authors perform the domain analysis on two cases in the

Android and iPhone platforms. This analysis allows inferring the basic requirements of the language defined by MobDSL.

The proliferation of mobile devices generated the need to adapt desktop applications to mobile platforms. Reference [9] describes a migration process from Java to mobile platforms through the multiplatform language Haxe.

ANDRIU, a reverse engineering tool based on static analysis of source code for transforming user interface tiers from desktop application to Android, is described in [20]. ANDRIU has been developed for migrating traditional systems to Android applications although it was designed to be extended for different migrations to others mobile platforms.

Reference [13] describes six major trends affecting future smartphone design and use: personal computers, internet of things, multimedia delivery, low power operation, wearable computing and context awareness.

Reference [22] reports a practical experience in two transfer of technology projects. Authors analyze the factors that can be taken into account in transfer of technology projects applying metrics to give hints about the potential productivity gains that MDE could bring.

Reference [11] presents a solution for facilitating the migration of applications to the cloud, inferring the most suitable deployment model for the application and automatically deploying it in the Cloud. Reference [14] describes the challenges in mobile computing offloading to cloud through experimentation.

4 A MODERNIZATION FRAMEWORK

We propose a framework for the modernization of desktop software to new technologies. According to the three crucial concepts of MDE, the framework provides sets of models, metamodels and transformations. Figure 1 depicts the main components of the framework.

Three different types of models are distinguished: Platform Independent models (PIM), Platform Specific Model (PSM) and Implementation Specific Model (ISM). A PIM is a model with a high level of abstraction that is independent of an implementation technology. A PSM is a tailored model to specify a system in terms of specific platform such J2EE,.NET, web or mobile. PIM and PSM are expressed in UML and OCL [18]. The subset of UML diagrams that are useful for PSM includes class diagram, object diagram, state diagram, interaction diagram and package diagram. On the other hand, a PIM can be expressed by means of use case diagrams, activity diagrams, interactions diagrams to model system processes and, state diagrams to model lifecycle of the system entities. An ISM is a specification of the implementation (source code) in terms of models.

The framework includes PSMs and ISMs related to the source and target platform. The target PSM and target ISM are related to a cross-platform language that allows writing mobile applications that target all major mobile platforms.

Metamodeling is a powerful technique to specify families of models. A metamodel is a model that defines the language for expressing a model, i.e. “a model of models”. A metamodel is an explicit model of the constructs and rules needed to build specific models. It is a description of all the concepts that can be used in a model. MOF metamodels use an object modeling framework that is essentially a subset of UML 2.5 core. The modeling concepts are

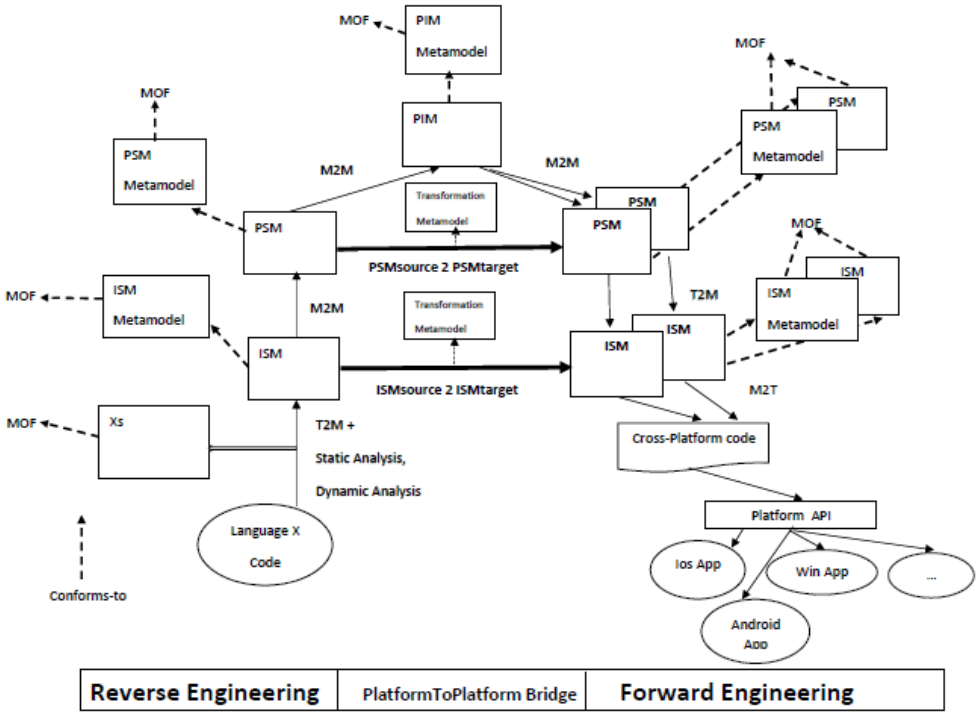

Figure 1. A modernization framework

metaobjects, data types which model other data, and packages which modularize the models. At this level MOF metamodels describe families of ISM, PSM and PIM. Every ISM, PSM and PIM conforms to a MOF metamodel.

The framework includes different kinds of transformations: T2M (Text-to-Model), M2M (Model-to-Model) and M2T (Model-to-Text).

T2M transformations allow representing the source code of the program in terms of a model compatible with MOF. They require to have a metamodel that describes the grammar of the source language. First, a representation of the original code in terms of an Abstract Syntax Tree (AST) is built. The next step in the reverse engineering process involves applying traditional techniques for static and dynamic analysis. The basic representation of the static analysis is an oriented graph that represents all data flow. Static analysis can be complemented with dynamic analysis that analyses traces of execution for different test cases.

Model-to-model (M2M) transformations provide a mechanism for automatically creating target models based on information contained in existing source models.

The framework distinguishes vertical and horizontal model-to-model transformations. Vertical transformations occur when a source model is transformed into a target model at a different abstraction level. They are useful in reverse engineering processes (ISM-to-PSM, PSM-to-PIM transformations) or forward engineering (PIM-to-PSM, PSM-to-ISM). Horizontal

transformations involves transforming a source model into a target model that is at the same abstraction level. They are bridges between different platforms at the same abstraction level (ISM or PSM), for instance *ISMsource2ISMtarget* and *PSMsource2PSMtarget*.

M2T transformations focuses on the generation of textual artifacts from models. In our context, M2T transformations are the processes to extract code from models following the MDE principles.

The framework shows different scenarios of modernization to adapt software to diverse mobile platforms. In the most general form, reverse engineering processes extract PIM models from the code, which are transformed into code through MDD processes for forward engineering. Reverse engineering processes can also recover PSMs that can be restructured at the same level of abstraction through a migration between different platforms. Different instantiations of this framework were analyzed. Next we will describe the instantiation of the framework for the migration of C / C ++ code to the multiplatform Haxe language at ISM level.

5 A FRAMEWORK REALIZATION: FROM C/C++ TO MOBILE PLATFORMS

This section is about an instantiation of the framework. First, we partially show the metamodels that had to be defined in order to realize the objectives of our project: the C/C++ metamodel (Section 5.1) and the Haxe metamodel (Section 5.2). Finally, Section 5.3 describes an instantiation of the framework for migrating (at ISM level) C/C++ code to Haxe that, at the same time, allows generating code on different mobile platforms.

The proposal was validated in the open source application platform Eclipse considering that some of its frameworks and tools are aligned with MDE standards. For example, EMF (Eclipse Modeling Framework) has evolved starting from the experience of the Eclipse community to implement a variety of tools and to date is highly related to MDE. Ecore is the core metamodel at the heart of EMF and can be considered the official implementation of MOF. The subproject M2M supports model transformations that take one or more models as input to produce one or more models as output [12]. ATL is a model transformation language (Atlas Transformation Language) and a toolkit that provides ways to produce a set of target models from a set of source models develop on top of the Eclipse platform [3].

5.1 The C++ Metamodel

The C++ metamodel conforms to Ecore and is partially shown in Figure 2. The root metaclass is *Program* that represents a C++ program, which owns source files, instances of *TranslationUnit*. A translation unit contains declarations such as block declaration, function definitions, template declarations, among others. A *SimpleDeclaration*, instance of *Block-Declaration*, has a *DeclSpecifierSeq* that is a sequence of *DeclSpecifiers* which refers to a declaration specifiers and a type specifier. In addition, a simple declaration has an *InitDeclaratorList* containing a variable declaration list that is a list of specifiers and the name of a variable and its corresponding initialization. A *FunctionDefinition* has a *Declarator* containing the function identifier and the parameter list. *Function* and *CtorOrDestFunction*, instances of *FunctionDefinition*, have a body that contains compound statements such as declarations, iterations, and selections. In addition, a *Function* has a *DeclSpecifierSeq* that is a sequence of *DeclSpecifiers* such as function specifiers and a type specifier. *TypeSpecifier*

subclasses are *SimpleTypeSpecifier*, *ClassSpecifier* and *EnumSpecifier* among others. A *ClassSpecifier* has a *ClassHead* containing the class key (class or struct) and a *MemberSpecification* that contains *MemberDeclarations* such as variables, function declarations, function definitions, constructors, destructor and template members. The full C/C++ metamodel can be found at [10]

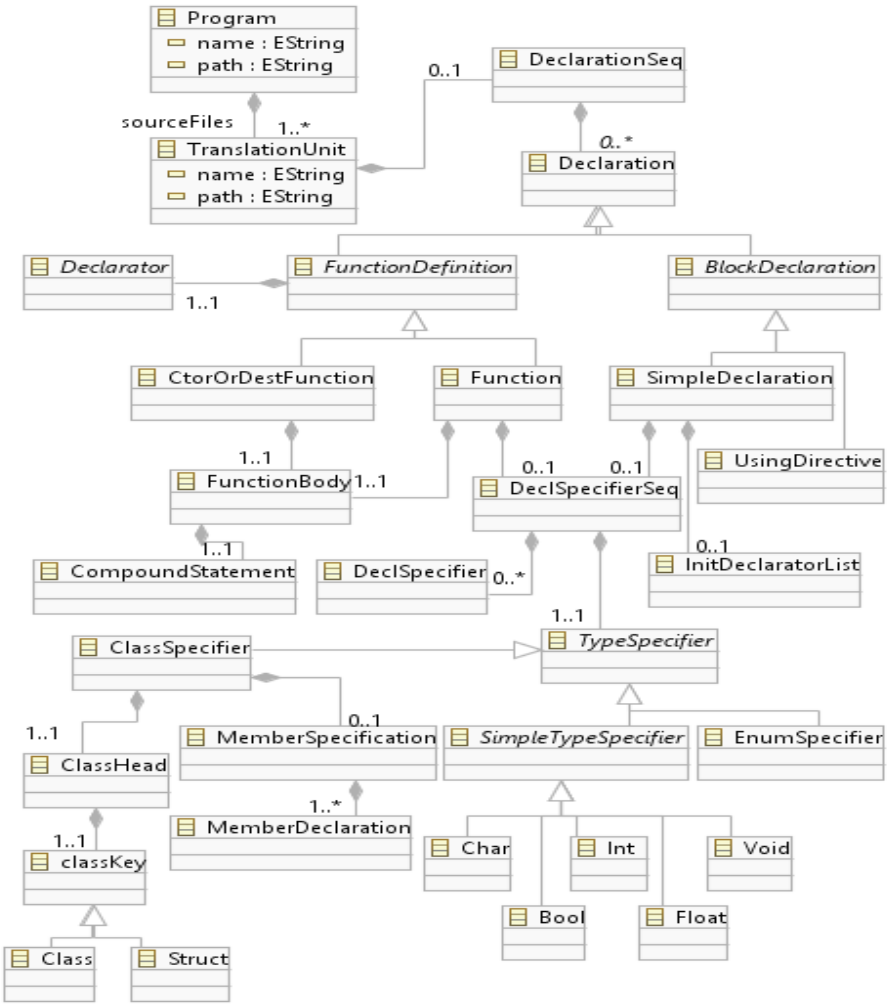

Figure 2. C++ Metamodel

5.2 The Haxe Metamodel

The Haxe metamodel conforms to Ecore metamodel. It is partially shown in Figure 3. The main metaclasses of the HAXE metamodel are those that allow specifying an application using Haxe as language.

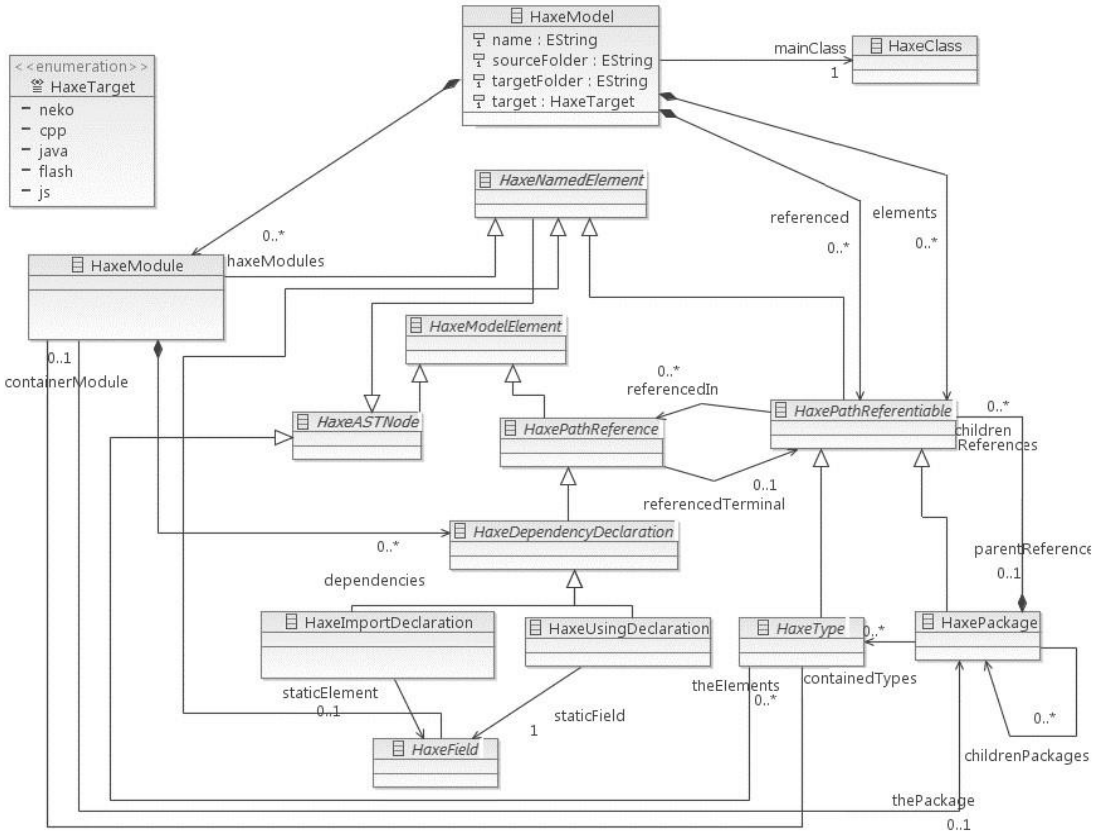

Figure 3. Haxe metamodel

One of the main metaclasses of the metamodel is *HAXEModel*, that serves as element container used to describe an application and store additional information on it, for example, some options of compilation and different metaclasses for modeling such as modules, classes and packages. *HAXEModel* owns *HAXEModule* and *HAXEPathReferentiable*.

Starting from the relations *HaxeModules*, *referenced* and *elements*, the class *HAXEModel* allows storing different information. Relation *HaxeModules* allows accessing the different HAXE modules used in the project. Through relation *elements*, it is possible to access the different elements of the package tree. Relation *referenced* provides access to elements, which are referenced in the project but are not defined completely. In the case of relations and referenced elements, the type used is *HAXEPathReferentiable*, which is the parent type of metaclasses such as *HAXEType* and *HAXEPackage*. The HaxeXE language includes different kind of types such as class (the types class and interface), function, abstract type, enumeration, and anonymous structures.

5.3 The Migration Process

Figure 4 depicts a realization of the framework. The initial transformation T2M obtains a code model that conforms to the C/C++ metamodel. This transformation was based on the generation of a parsing tree with the ANTLR tool through the C ++ grammar. Also a discoverer of a C ++ model that conforms to the C ++ metamodel was built.

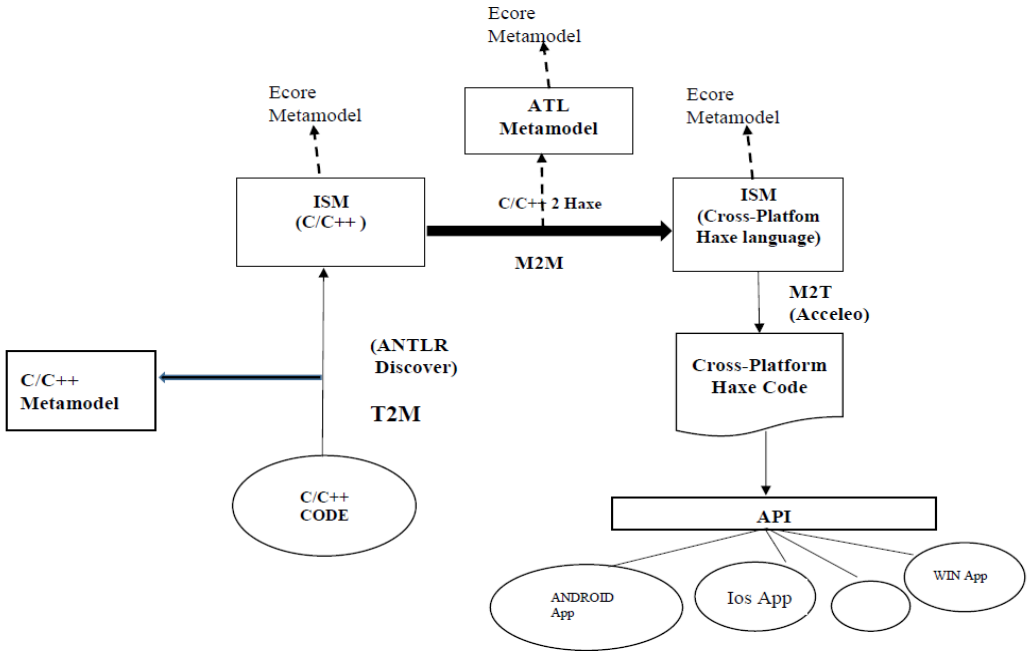

Figure 4. From C/C++ to mobile platforms

The Discover is a Java program whose input is the syntax tree and its output an ISM, the C++ model of the code.

M2M transformations were defined in ATL, the most mature transformation language in the context of MDE. ATL is a model transformation language (Atlas Transformation Language) and toolkit developed on top of the Eclipse platform. The ATL Integrated Development Environment (IDE) provides a number of standard development tools (syntax highlighting, debugger, etc.) that aims to facilitate the development of ATL transformations. ATL is a hybrid language that provides a mix of declarative and imperative constructs.

A model-to-model transformation from C++ to Haxe, called *C/C++ 2 Haxe*, was defined in ATL. It takes as input the model obtained in the reverse engineering phase and release an Haxe model. The transformation specifies families of transformations that produce Haxe models (target) from C++ models (source). Both source and target models must conform to the C++ metamodel and Haxe metamodel respectively.

The *C/C++ 2 Haxe* transformation conforms to the ATL metamodel, that, in the same way conforms to Ecore.

All models obtained in this chain of transformations are saved in the interchange format XMI, an OMG standard that combines XML, MOF and UML. It allows integrating tools, repositories, and applications in distributed heterogeneous environments [24].

Finally, from a model Haxe, it is possible to generate a source code in Haxe by using an M2T transformation defined in Acceleo, that is a code generation system based on MDE. It contains all the tools expected of a quality code generation IDE: simple syntax, efficient and advanced code generation. Its approach, based on prototypes and models, facilitates the creation of text generators based on the source code of existing prototypes [1].

Haxe allows writing mobile applications that target all major mobile platforms in a straightforward way. The generated code is syntactically correct, although, it does not compile on other platforms without doing changes due to the code refers to proprietary technologies of C++. To run on mobile environments, these technologies can be replaced with OpenFL and HAXEUI, that is an open source, multi-platform application-centric user interface framework designed for Haxe and OpenFL [19].

6 CONCLUSIONS

This paper describes migration of desktop applications to new technologies in which smartphones are its great facilitators. A modernization framework based on MDE principles and multiplatform development is presented. A framework realization that allows adapting C/C++ software to different mobile platforms through Haxe is described. Our approach covers a migration method and the presentation of models, metamodels and model transformations. These artifacts could be reused, modified for evolution purposes or, extended for other purposes.

Our approach is supported by metamodels to describe existing systems, discoverers to automatically create models of these systems and, tools to understand and transform complex models. The migration process can be divided in smaller steps focusing in specific activities, and be automated thanks to the chaining of model transformations. Model transformations allow developers to concentrate on the conceptual aspects of the relations between models and delegate the implementation of the transformation. The metamodel approach enables covering different levels of abstraction and satisfying several degrees of detail depending on the needs of the migration. Metamodeling is the key for interoperability of languages and tools.

We believe that our approach provides benefits with respect to processes based only on traditional migration techniques. One of the benefits of applying MDE techniques is to increase productivity in software development due to the automation that is introduced in the generation of artifacts. Besides, the use of MDE in migration projects is more cost-effective when the same process must be repeated frequently as the case of migrations to different platforms.

The advances achieved in MDE infrastructure and training of human resources, could allow us to apply the results in real projects in the scientific and industrial field.

REFERENCES

[1] ACCELEO. Obeo. ACCELEO Generator. http://www.eclipse.org/ACCELEO/ (2017)
[2] ADM. Architecture-driven modernization task force. http://www.adm.org (2017)
[3]ATL. Atlas Transformation Language Documentation. http://www.eclipse.org/atl/documentation/ (2017)
[4] Brambilla, M., Cabot, J. and Wimmer, M. *Model-Driven Software Enginneering in Practice*, Synthesis Lectures on Software Engineering. Morgan & Claypool Publishers (2012)
[5] Bruneliere, N., Cabot, J., Dupé, G. and Madiot, F. MoDisco: A Model Driven Reverse Engineering Framework. *Information and Software Technology*, (2014) 56(8), 1012–1032
[6] Cannasse, N. *HAXE. Too Good to be True?* GameDuell Tech Talk. http://www.techtalk-berlin.de/news/read/nicolas-cannasse-introducing-HAXE/ (2014)

[7] Dasnois, B.. *HAXE 2 Beginner's Guide*. Packt Publishing (2011)
[8] Dehlinger, J. and Dixon, J. Mobile application software engineering: Challenges and research directions. *Proceedings of the Workshop on Mobile Software Engineering*. Berlin, Springer-Verlag (2011) 29-32
[9] Diaz Bilotto, P. and Favre, L. Migrating Java to Mobile Platforms through HAXE: An MDD Approach. Chapter 13. *Modern Software Engineering Methodologies for Mobile and Cloud Environments.* Antonio Miguel Rosado da Cruz, Sara Paiva, eds., IGI GLOBAL (2016) 240-268
[10] Duthey, M. and Spina, C. Migration of C/C++ software to mobile platforms through MDD (Undergraduate Thesis, Thesis Advisor, Favre, L); Computer Science Department, Universidad Nacional del Centro de la Provincia de Buenos Aires, Tandil, Argentina (2016)
[11]Ejarque, J., Micsik, A. and Badia, M. Towards Automatic Application Migration to Clouds, *IEEE 8th Int. Conf. on Cloud Computing* (CLOUD) (2015) pp. 25-32
[12] EMF. Eclipse Modeling Framework (EMF). http://www.eclipse.org/modeling/emf/ (2016)
[13] Islam, N. and Want, R. Smarthphones: Past, present and future. *Pervasive Computing*, (2014) 13(4), 82-92
[14] Joshi, P. Nivangune, A., Kumar, R., Kumar, S., Ramesh, R., Pani, S. and Chesum, A. Understanding the Challenges in Mobile Computation Offloading to Cloud through Experimentation. *2nd ACM Int. Conf. on Mobile Software Engineering and Systems* (P. Joshi MOBILESoft) (2015) 158-159
[15] Kramer, D., Clark, T. and Oussena, S. MobDSL: A domain specific language for multiple mobile platform deployment. *Networked Embedded Systems for Enterprise Applications (NESEA), 2010 IEEE International Conference*, Los Alamitos: IEEE Press. doi:10.1109/NESEA.2010.5678062 (2010) 1-7
[16] MDA. The Model-Driven Architecture. http://www.omg.org/mda/ (2017)
[17] MOF. Meta Object Facility (MOF) Core Specification Version 2.5, OMG Document Number: formal/2015-06-05 http: //www.omg.org/spec/MOF/2.5 (2015)
[18] OCL. OMG Object constraint language (OCL), version 2.4. http://www.omg.org/spec/OCL/2.4 (2014)
[19] OPEN FL, http://www.openfl.org/ (2016)
[20] Pérez Castillo, R., García Rodriguez, I., Gómez Cornejo, R., Fernández Ropero, M. and Piattini, M. ANDRIU. A Technique for Migrating Graphical User Interfaces to Android. *Proceedings of The 25th International Conference on Software Engineering and Knowledge Engineering (SEKE 2013)* Boston: Knowledge Systems Institute (2013) 516-519
[21] QVT. QVT: MOF 2.0 query, view, transformation: Version 1.1. OMG Document Number: formal/2011-01-01. http://www.omg.org/spec/QVT/1.1/SMM (2012)
[22] Sánchez Cuadrado, J., Cánovas, J. and García Molina, J. Applying model driven engineering in small software enterprises. *Science of Computer Programming* (2014) (89)176-198
[23] Steinberg, D., Budinsky, F., Paternostro, M. and Merks, E. *EMF: Eclipse Modeling Framework* (2nd ed.). Addison-Wesley (2009)
[24] XMI. XML Metadata Interchange (XMI) Specification. OMG Document Number: formal/2014-04-04. http://www.omg.org/spec/XMI/2.4.2/PDF/ (2014)

VII International Conference on Computational Methods for Coupled Problems in Science and Engineering
COUPLED PROBLEMS 2017
M. Papadrakakis, E. Oñate and B. Schrefler (Eds)

NOVEL KINETIC CONSISTENT MHD ALGORITHM FOR HIGH PERFORMANCE COMPUTING

B. CHETVERUSHKIN[*], N. D'ASCENZO[†] , A. SAVELIEV[**††] AND V. SAVELIEV[**†]**

[*] Keldysh Institute of Applied Mathematics
Russian Academy of Science (KIAM RAS)
4 Miusskaya sq, 125047 Moscow, Russia
e-mail: chetver@imamod.ru, web page: http://www.kiam.ru

[†]Deutsche Electronen Synchrotron (DESY)
85 Notkestrasse, 22607 Hamburg, Germany
e-mail: ndasc@mail.desy.de - Web page: http://www.desy.de

[††]Hamburg University
85 Notkestrasse, 22607 Hamburg, Germany
e-mail: Andrey.Saveliev@desy.de - Web page: http://www.desy.de

[**] Immanuel Kant Baltic Federal University
14 Alexandr Nevsky str., 236016, Kaliningrad, Russia
e-mail: saveliev@mail.desy.de - Web page http://www.kantiana.ru

Key words: Kinetic algorithms, magnetohydrodynamics, kinetic consistent algorithms, high performance computing

Abstract. The impressive progress of the kinetic schemes in the solution of gas dynamics problems and the development of effective parallel algorithms for modern high performance parallel computing systems led to the development of advanced methods for the solution of the magnetohydrodynamics problem in the important area of plasma physics. The novel feature of the method is the formulation of the complex Boltzmann-like distribution function of kinetic method with the implementation of electromagnetic interaction terms. The numerical method is based on the explicit schemes. Due to logical simplicity and its efficiency, the algorithm is easily adapted to modern high performance parallel computer systems including hybrid computing systems with graphic processors.

1 INTRODUCTION

The tremendous progress in the development of high performance computing systems, especially expecting drastically new exascale computing systems, including the challenges

in architecture, scale, power and reliability, gives new opportunities for the mathematical modeling of important physical phenomena in the present and future. Nevertheless the complexity of the challenges in science and engineering continues to outpace our ability to adequately address them through impressively growing computational power.

A feature of the present is that the development of technologies and computer systems architecture are well ahead of software development. The software problems are primarily associated with the complexity of the algorithms adaptation for the differential equations of mathematical physics to high performance computing systems architecture. In particular they refer to one of the important requirements as the accuracy in combination with the correctness of the initial mathematical models. Another requirement for the methods is their logical simplicity and high efficiency at the same time. The numerical algorithms should be simple and transparent from a logical point of view.

One of the important directions to overcome these problems is the development of a nontraditional approach to initial mathematical models and computational algorithms. In the present study for the solution of the multidimensional gas dynamics and magnetohydrodynamics problems kinetic difference scheme is proposed. It is convenient from the physics point of view to define the gas dynamics and magnetohydrodynamics quantities from close relations between the kinetic and gas dynamics description of physics processes [1, 2, 4, 5, 6, 7].

Another aspect is the study of the explicit finite difference schemes, which seem to be preferable for future high performance parallel computing, especially in terms of their simplicity and well adaptability to parallel program realization, including hybrid high performance parallel computing systems. The weakness of explicit schemes is a strictly limited time step that ensures computational stability. This restriction becomes critical with the growing number of nodes and the reduction in the step of a spatial mesh. The advanced explicit kinetic finite difference schemes have a soft stability condition giving the opportunity to enhance the stability and to use very fine meshes [3].

The mentioned aspects are used for the development of the framework for the study of the dynamics of the conducting gas media in strong magnetic fields at high performance parallel computing systems.

2 THEORETICAL ISSUES

2.1 Gas Dynamics Processes

The kinetic theory describes the gas dynamics by the Boltzmann differential equation through the evolution of the distribution function $f(\mathbf{x}, \boldsymbol{\xi}, t)$ [8]:

$$\frac{\partial f(\mathbf{x}, \boldsymbol{\xi}, t)}{\partial t} + \boldsymbol{\xi} \cdot \nabla f(\mathbf{x}, \boldsymbol{\xi}, t) = C(f) \tag{1}$$

where $C(f)$ is a nonlinear integral operator which describes the collisions between

gas molecules.

This evolution equation follows naturally from the relations between the kinetic and the gas dynamics description of continuous media. The macroscopic observables such as density, momentum, energy flux as a function of $\mathbf{x}$ and t are obtained from the moments of the distribution function with respect to the macroscopic velocity. The evolution equations for these gas dynamics quantities are obtained by integrating Eq. (1) over molecular velocities $\boldsymbol{\xi}$ with summational invariants m,$m\boldsymbol{\xi}$,$\frac{1}{2}m\boldsymbol{\xi}^2$. The computational interest in kinetic formulations of the gas dynamics is high due to the linearity of the differential operator on the left side of Eq. (1). Nonlinearity is confined by the collision term, which is generally local in $\mathbf{x}$ and t.

An important feature is that the collision integral vanishes in the equilibrium state when the local Boltzmann distribution function f is a Maxwellian:

$$f(\mathbf{x},\boldsymbol{\xi},t) = \frac{\rho(\mathbf{x},t)m^{1/2}}{\left(2\pi kT\left(\mathbf{x},t\right)\right)^{3/2}} exp\left\{-\frac{m}{2kT(t,\mathbf{x})}(\boldsymbol{\xi}-\mathbf{u}(t,\mathbf{x}))^2\right\} \tag{2}$$

This leads to the use of this model for numerical methods and possible generalizations in order provide a natural kinetic description of the system of conservation laws. This approximation is sufficient for the gas dynamics processes and is called the kinetic approach [1].

2.2 Electromagnetic Processes

In [9] it was shown that electromagnetic fields do not destroy the validity of the Boltzmann equation and this opened the way for the implementation of the electromagnetic term in the Boltzmann-like distribution function. From the vector nature of the electromagnetic interaction, the distribution function should taking to account the vector behavior and provide correct formulation for the evolution of the magnetic field, i. e. the magnetic field should be generally defined as the momentum of the Boltzmann-like distribution function.

A few useful attempts to formulate the Boltzmann-like statistical distribution function can be found in [11, 12, 13], but physical meaning was not clear defined.

We propose an evaluation of the electromagnetic processes in the context of the distribution function, taking to account the axial nature of the magnetic field.

For the purposes of magnetohydrodynamics, the effect, which a magnetic field exerts on a certain volume, is obtained by integrating the electromagnetic stress tensor over the surface of that volume and the correspondent propagation velocity can be defined as a complex vector of velocity:

$$\mathbf{v}_{em} = \mathbf{u}_{em} + i\mathbf{w}_{em} \tag{3}$$

At first approximation the term defined by electric forces could be considered as drift component in meaning that electric field forces is polar vector nature. The magnetic

field contributions could be defined through the axial vector feature of the magnetic field interaction and define as Alfven velocity:

$$\mathbf{w}_{em} = \frac{\mathbf{B}}{\sqrt{\rho}} \tag{4}$$

2.3 Proposed Distribution Function for MHD

Using the above definitions we define the local complex Boltzmann Maxwellian distribution function of magnetohydrodynamics with drift velocity $\mathbf{u}$ in magnetic field $\mathbf{B}$ at the equilibrium:

$$f_M = \frac{\rho m^{1/2}}{(2\pi kT)^{3/2}} \exp\left\{ -\frac{m}{2kT} \left| (\boldsymbol{\xi} - \mathbf{u}) - i\frac{\mathbf{B}}{\sqrt{\mu_m \rho}} \right|^2 \right\}, \tag{5}$$

The first term on the right-hand side of (5) includes the internal energy and the second term is the magnetic field energy. The hydrodynamics observables are real scalars and vectors. The complex components include the dynamics of the macroscopic observables introduced by the evolution of the magnetic field, keeping their specific pseudo-vectorial nature. The hydrodynamic and electromagnetic observables are obtained respectively as the real and imaginary part of the integral of the distribution function (5) with the summational invariants $\left(m, m\boldsymbol{\xi}, \frac{1}{2}m\boldsymbol{\xi}^2, m\boldsymbol{\xi}^*\right)$ along the line L parallel to the real axis and shifted by $i\mathbf{B}/\sqrt{\mu\rho}$ in the imaginary axis direction.

$$\rho = \int_L m f_M d^3\boldsymbol{\xi} \tag{6}$$

$$\mathbf{u} = \frac{1}{\rho}\int_L m\boldsymbol{\xi} f_M d^3\boldsymbol{\xi} \tag{7}$$

$$E = \int_L \frac{1}{2} m\boldsymbol{\xi}^2 f_M d^3\boldsymbol{\xi} \tag{8}$$

$$\mathbf{B} = -\sqrt{\frac{\mu_m}{\rho}} \int_L m\boldsymbol{\xi}^* f_M d^3\boldsymbol{\xi} \tag{9}$$

For the compressible media, we use the linear approximation of the magnetic permeability:

$$\mu_m = \mu_\rho \rho \tag{10}$$

where μ_ρ is a constant representing the magnetic permeability per unit density. The proposed complex Boltzmann Maxwell like distribution function contains the hydrodynamics terms and the electromagnetic terms. Thus by using this distribution function to calculate the mass, momentum, energy and magnetic field fluxes, most of the electromagnetic contributions are calculated directly, i.e. one does not have to solve the hydrodynamics and magnetic force components separately or differently, as will be shown below.

3 THE IDEAL MAGNETO GAS DYNAMICS EQUATIONS

To provide the first step of the formulation of the MHD conservation laws equation, the equilibrium state is considered with the proposed distribution function. The MHD system of equations is obtained by the integration of (1) with vanishing collision integral with the summational invariants following the definition in (9):

$$\int_L m\frac{\partial f}{\partial t} + \int_L m\boldsymbol{\xi}\cdot\nabla f d^3\boldsymbol{\xi} = 0 \tag{11}$$

$$\int_L m\boldsymbol{\xi}\frac{\partial f}{\partial t} + \int_L m\boldsymbol{\xi}\boldsymbol{\xi}\cdot\nabla f d^3\boldsymbol{\xi} = 0 \tag{12}$$

$$\int_L \frac{1}{2}m\boldsymbol{\xi}^2\frac{\partial f}{\partial t} + \int_L \frac{1}{2}m\boldsymbol{\xi}^2\boldsymbol{\xi}\cdot\nabla f d^3\boldsymbol{\xi} = 0 \tag{13}$$

$$\int_L m\boldsymbol{\xi}^*\frac{\partial f}{\partial t} + \int_L m\boldsymbol{\xi}^*\boldsymbol{\xi}\cdot\nabla f d^3\boldsymbol{\xi} = 0 \tag{14}$$

The result obtained, set of Eq. (14), is the ideal magnetohydrodynamics system of equations:

$$\frac{\partial\rho}{\partial t} + \frac{\partial}{\partial x_i}\rho u_i = 0 \tag{15}$$

$$\frac{\partial}{\partial t}\rho u_i + \frac{\partial}{\partial x_k}\left[\left(p + \frac{B^2}{2\mu_M}\right)\delta_{ik} + \rho u_i u_k - \frac{B_i B_k}{\mu_M}\right] = 0 \tag{16}$$

$$\frac{\partial E}{\partial t} + \frac{\partial}{\partial x_i}\left[u_i\left(E + p + \frac{B^2}{2\mu_M}\right) - \frac{B_i u_k B_k}{\mu_M}\right] = 0 \tag{17}$$

$$\frac{\partial B_i}{\partial t} + \frac{\partial}{\partial x_k}\left[u_k B_i - u_i B_k\right] = 0 \tag{18}$$

In addition an equation for $\nabla\cdot\mathbf{B}$ is obtained as the imaginary part of the integral of the summational invariant (m) respect to the velocities $\boldsymbol{\xi}$:

$$\int_L m\frac{\partial f}{\partial t} + \int_L m\boldsymbol{\xi}\cdot\nabla f d^3\boldsymbol{\xi} = 0 \tag{19}$$

$$\frac{\partial B_i}{\partial x_i} = 0 \tag{20}$$

4 THE QUASI MAGNETO GAS DYNAMICS SYSTEM OF EQUATIONS

The quasy MHD system of equations for the real gases is obtained using the integration technique outlined in section 2 and the balance relation based on the Taylor expancion of the variation of the local distribution function in spatial variables up to third order [**?**]:

$$\frac{f^{j+1} - f^j}{\Delta t} + \xi_i\frac{\partial f^j}{\partial x_i} = \xi_i\xi_k\frac{\partial}{\partial x_i}\frac{\tau}{2}\frac{\partial f^j}{\partial x_k} \tag{21}$$

The evalution equation for the magneto gas dynamic variables (quasi magneto gas dynamic equations) obtained as:

$$\frac{\partial \rho}{\partial t} + \frac{\partial}{\partial x_i}\rho u_i = \frac{\partial}{\partial x_i}\left(\frac{\tau}{2}\frac{\partial}{\partial x_k}\Pi_{ik}\right) \tag{22}$$

$$\frac{\partial \rho u_i}{\partial t} + \frac{\partial}{\partial x_k}\Pi_{ik} = \frac{\partial}{\partial x_k}\Pi^D_{ik} + \frac{\partial}{\partial x_k}\left[\left(\frac{\tau}{2}\frac{\partial}{\partial x_k}\Pi_{ik}\right)u_k\right] \tag{23}$$

$$\frac{\partial E}{\partial t} + \frac{\partial F_i}{\partial x_i} = \frac{\partial Q_i}{\partial x_i} + \frac{\partial}{\partial x_i}\Pi^D_{ik}u_k + \\ + \frac{\partial}{\partial x_i}\left[\left(\frac{E+p}{\rho} + \frac{1}{\mu_m}\frac{B^2}{2\rho}\right)\frac{\tau}{2}\frac{\partial}{\partial x_k}\Pi_{ik}\right] \tag{24}$$

$$\frac{\partial B_i}{\partial t} + \frac{\partial}{\partial x_k}M^B_{ik} = \frac{\partial}{\partial x_k}\Pi^{DB}_{ik} \tag{25}$$

The right-hand of the kinetic magneto gas dynamic Eq. (22-25) contains dissipative terms. In comparison with other methods, the dissipative terms are obtained not by phenomenology with some assumptions about magneto gas dynamics processes but in consistency with the difference scheme of the Boltzmann equation.

Π_{ik} is the momentum flux density tensor for a perfect gas in magnetic field:

$$\Pi_{ik} = \left(p + \frac{B^2}{2\mu_m}\right)\delta_{ik} + \rho u_i u_k - \frac{1}{\mu_m}B_i B_k \tag{26}$$

F_i is the heat transfer flux of a perfect gas in magnetic field:

$$F_i = \left[\left(E + p + \frac{B^2}{2\mu_m}\right)u_i - \frac{1}{\mu_m}B_i u_k B_k\right] \tag{27}$$

M^B_{ik} is the asymmetric product between velocity $\mathbf{u}$ and magnetic field flux $\mathbf{B}$:

$$M^B_{ik} = u_k B_i - u_i B_k \tag{28}$$

The dissipative terms:

$$\begin{aligned}
\Pi_{ik}^{D} =& \frac{\tau}{2}\left(p\frac{\partial u_i}{\partial x_k}+p\frac{\partial u_k}{\partial x_i}-\frac{2}{3}p\frac{\partial u_l}{\partial x_l}\delta_{ik}\right)\\
&+\frac{\tau}{2}\left[\left(\frac{1}{\mu_m}\frac{B^2}{2}\delta_{lk}-\frac{1}{\mu_m}B_lB_k\right)\frac{\partial u_i}{\partial x_l}+\left(\frac{1}{\mu_m}\frac{B^2}{2}\delta_{il}-\frac{1}{\mu_m}B_iB_l\right)\frac{\partial u_k}{\partial x_l}\right.\\
&\left.-\left(\frac{1}{\mu_m}\frac{B^2}{2}\delta_{ik}-\frac{1}{\mu_m}B_iB_k\right)\frac{\partial u_l}{\partial x_l}\right]\\
&+\frac{\tau}{2}\left[\frac{1}{\mu_m}B_l\left(-B_k\frac{\partial u_i}{\partial x_l}-B_i\frac{\partial u_k}{\partial x_l}+B_n\frac{\partial u_n}{\partial x_l}\delta_{ik}\right)\right]\\
&+\frac{\tau}{2}\left[\rho u_iu_l\frac{\partial u_k}{\partial x_l}+u_i\frac{\partial p}{\partial x_k}+u_i\frac{\partial}{\partial x_k}\frac{1}{\mu_m}\frac{B^2}{2}-u_i\frac{\partial}{\partial x_l}\frac{1}{\mu_m}B_lB_k\right]\\
&+\frac{\tau}{2}\left[u_l\frac{\partial p}{\partial x_l}+\gamma p\frac{\partial u_l}{\partial x_l}\right]\delta_{ik}+\frac{\tau}{2}\left[\frac{1}{\mu_m}B_n^2\frac{\partial u_l}{\partial x_l}-\frac{B_nB_l}{\mu_m}\frac{\partial u_n}{\partial x_l}\right.\\
&\left.+\frac{1}{\mu_m}B_nu_l\frac{\partial B_n}{\partial x_l}\right]\delta_{ik}+\frac{\tau}{2}\left[-\frac{B_iB_k}{\mu_m}\frac{\partial u_l}{\partial x_l}+\frac{B_iB_l}{\mu_m}\frac{\partial u_k}{\partial x_l}-\frac{B_i}{\mu_m}u_l\frac{\partial B_k}{\partial x_l}\right]\\
&+\frac{\tau}{2}\left[-\frac{B_kB_i}{\mu_m}\frac{\partial u_l}{\partial x_l}+\frac{B_kB_l}{\mu_m}\frac{\partial u_i}{\partial x_l}-\frac{B_k}{\mu_m}u_l\frac{\partial B_i}{\partial x_l}\right]
\end{aligned}\tag{29}$$

$$\begin{aligned}
Q_i^{D} =& \frac{\tau}{2}\left(\frac{5}{2}p\frac{\partial}{\partial x_i}\frac{p}{\rho}\right)\\
&+\frac{\tau}{2}\left[\frac{5}{2}\left(\frac{B^2}{2\mu_m}\delta_{ik}-\frac{B_iB_k}{\mu_m}\right)\frac{\partial}{\partial x_k}\frac{p}{\rho}\right]\\
&+\frac{\tau}{2}\left[\frac{3}{2}\left(p\delta_{ik}+\frac{B^2}{2\mu_m}\delta_{ik}-\frac{B_iB_k}{\mu_m}\right)\frac{\partial}{\partial x_k}\frac{B^2}{2\mu_m\rho}-\left(p+\frac{B^2}{2\mu_m}\right)\frac{\partial}{\partial x_k}\frac{B_iB_k}{\mu_m\rho}\right.\\
&\left.-\frac{B_iB_k}{\mu_m\rho}\frac{\partial}{\partial x_k}\frac{B^2}{2\mu_m}\right]+\frac{\tau}{2}\left[\rho u_iu_k\frac{\partial}{\partial x_k}\frac{3}{2}\frac{p}{\rho}\right]\\
&+\frac{\tau}{2}\left[\rho u_iu_k\left(p+\frac{B^2}{\mu_m}\right)\frac{\partial}{\partial x_k}\frac{1}{\rho}-u_i\frac{B^2}{\mu_m}\frac{\partial u_k}{\partial x_k}\right]\\
&+\frac{\tau}{2}\left[u_i\frac{B_l}{\mu_m}\left(B_l\frac{\partial u_k}{\partial x_k}-B_k\frac{\partial u_l}{\partial x_k}+u_k\frac{\partial B_l}{\partial x_k}\right)\right]\\
&+\frac{\tau}{2}\left[\frac{1}{2}\rho u_iu_k\left(\frac{B^2}{2\mu_m}\frac{\partial}{\partial x_k}\frac{1}{\rho}-\frac{1}{\rho}\frac{\partial}{\partial x_k}\frac{B^2}{2\mu_m}\right)\right]\\
&+\frac{\tau}{2}\left[B_iB_l\left(-u_k\frac{\partial u_l}{\partial x_k}-\frac{1}{\rho}\frac{\partial p}{\partial x_l}-\frac{1}{\rho}\frac{\partial}{\partial x_l}\frac{B^2}{2\mu_m}+\frac{1}{\rho}\frac{\partial}{\partial x_k}\frac{B_lB_k}{\mu_m}\right)\right]
\end{aligned}\tag{30}$$

$$
\begin{aligned}
\Pi_{ik}^{DB} =& \frac{\tau_l}{2}\left[\frac{1}{\rho}\left(p+\frac{B^2}{2\mu_m}\right)\left(\frac{\partial B_i}{\partial x_k}-\frac{\partial B_k}{\partial x_i}\right)\right] \\
&+\frac{\tau}{2}\left[\left(p+\frac{B^2}{2\mu_m}\right)\left(B_i\frac{\partial}{\partial x_k}\frac{1}{\rho}-B_k\frac{\partial}{\partial x_i}\frac{1}{\rho}\right)\right] \\
&+\frac{\tau}{2}\left[u_k B_l\frac{\partial u_i}{\partial x_l}-u_i B_l\frac{\partial u_k}{\partial x_l}\right]+\frac{\tau}{2}\left[\frac{1}{\rho}\frac{B_i B_l}{\mu_m}\frac{\partial B_k}{\partial x_l}-\frac{1}{\rho}\frac{B_k B_l}{\mu_m}\frac{\partial B_i}{\partial x_l}\right] \\
&+\frac{\tau}{2}\left[u_k B_i\frac{\partial u_l}{\partial x_l}-u_k B_l\frac{\partial u_i}{\partial x_l}+u_k u_l\frac{\partial B_i}{\partial x_l}\right] \\
&+\frac{\tau}{2}\left[B_i u_l\frac{\partial u_k}{\partial x_l}+\frac{B_i}{\rho}\frac{\partial p}{\partial x_k}+\frac{B_i}{\rho}\frac{\partial}{\partial x_k}\frac{B^2}{2\mu_m}-\frac{B_i}{\rho}\frac{\partial}{\partial x_l}\frac{B_k B_l}{\mu_m}\right] \\
&+\frac{\tau}{2}\left[-u_i B_k\frac{\partial u_l}{\partial x_l}+u_i B_l\frac{\partial u_k}{\partial x_l}-u_i u_l\frac{\partial B_k}{\partial x_l}\right] \\
&+\frac{\tau}{2}\left[-B_k u_l\frac{\partial u_i}{\partial x_l}-\frac{B_k}{\rho}\frac{\partial p}{\partial x_i}-\frac{B_k}{\rho}\frac{\partial}{\partial x_i}\frac{B^2}{2\mu_m}+\frac{B_k}{\rho}\frac{\partial}{\partial x_l}\frac{B_i B_l}{\mu_m}\right]
\end{aligned}
\tag{31}
$$

It was shown in [2] that the dissipative terms of the gas dynamics system of equations are small in comparison with the convective terms. The corresponding dissipative terms are associated with the real physics processes and an important remark is that in this case the gas dynamics parameters such as viscosity and heat conductivity are obtained from the kinetic theory.

The Navier-Stokes viscosity is identified as the first term of Eq. (29):

$$
\Pi_{ik}^{NS}=\frac{\tau}{2}\left(p\frac{\partial u_i}{\partial x_k}+p\frac{\partial u_k}{\partial x_i}-\frac{2}{3}p\frac{\partial u_l}{\partial x_l}\delta_{ik}\right)=\mu\left(\frac{\partial u_i}{\partial x_k}+\frac{\partial u_k}{\partial x_i}-\frac{2}{3}\frac{\partial u_l}{\partial x_l}\delta_{ik}\right) \tag{32}
$$

where the bulk viscosity component is neglected and the shear viscosity μ is related to the gas pressure p and the characteristic time τ as $\mu=\frac{\tau}{2}p$.

The Navier-Stokes thermal flux vector is identified as the first term of Eq. (30):

$$
Q_i^{NS}=\frac{\tau}{2}\left(\frac{5}{2}p\frac{\partial}{\partial x_i}\frac{p}{\rho}\right)=k\frac{\partial T}{\partial x_i} \tag{33}
$$

with T gas temperature and k thermal coefficient expressed as $k=\frac{1}{Pr}\frac{5}{2}R\frac{\tau}{2}p$, with Pr Prandtl number.

A similar analysis of the dissipative terms of the electromagnetic processes gives the estimation of their smallness. The correct magnetic viscosity is represent as part of dissepative term. The gas resistivity is identified as the first term of Eq. (31) and also appears as a result of the kinetic formulation:

$$
\Pi_{ik}^{B}=\frac{\tau_m}{2}\left[\left(p+\frac{B^2}{2}\right)\left(\frac{\partial B_i}{\partial x_k}-\frac{\partial B_k}{\partial x_i}\right)\right]=\eta\left(\frac{\partial B_i}{\partial x_k}-\frac{\partial B_k}{\partial x_i}\right) \tag{34}
$$

Where the $\eta=\frac{\tau_m}{2}\left(p+\frac{B^2}{2}\right)$ represents the resistivity.

5 The COMPUTATIONAL ALGORITHM

The computational task consists of the solution of the kinetic consistent MHD system of equations **??**.

The computational algorithm used in this paper is build upon the Finite Volume method applied to the gas dynamic equations and on the Contrained Transport method applied to the magnetic induction equation [14, 15].

In the finite volume method the conserved gas dynamics variables, density, gas momentum and energy, are averaged above the volume of the computational cell. The contrained transport method treatment is based on the area-averaging of the magnetic field through the surfaces of the grid cells.

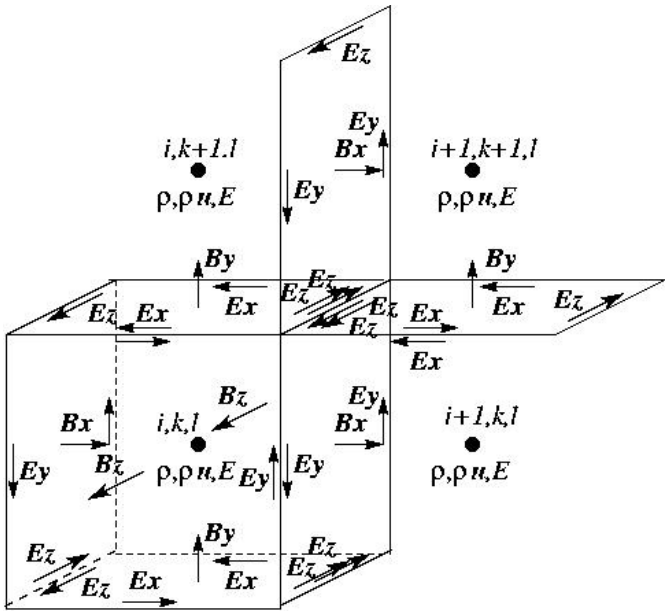

Figure 1: 3D Computational Domain

Fig. 1 shows the four neighbour to the cell (i, k, l) used in evaluations of the hydrodynamics and electromagnetic variables.

The gas dynamics observables - mass density, momentum and energy density are defined at the cell center. The components of the magnetic field are defined at the face centers of the cells. A duality is established between the electric field and the fluxes. This duality is utilized to obtain the electric field at the edges of the computational cell through a reconstruction process that is applied directly to the properly upwinded fluxes. The electric field is then utilized to make an update of the magnetic fields that preserves the solenoidal nature of the magnetic field and ensures that the magnetic field in a magnetohydrodynamics model remains strictly solenoidal up to discretization errors.

The explicit finite volume computational algorithm for the magneto gas gas dynamics

are used. This method has the convinient stability conditions and very important for adaptation on the massive parallel computing systems.

6 RESULTS OF NUMERICAL MODELLING

The parallel implementation of the numerical algorithm is obtained through the doman composition in ditributed memory approach. The communication between processors is performed via MPI protocol. The computational method needs only one layer of ghost cells at the boundary and along the edges of each subdomain which is exchanged between the domains with MPI calls. The algorithm is well suited to distributed memory clusters as it is time explicit and requires only one MPI call per time step, reducing significantly the processor communication time contribution to the total computational time.

The demostration of the method is performed on the basis of the solution of the spherical expansion problem of ionised gas and the solution of the expansion of an ionised gas in strong magnetic field. The initial conditions are the same as proposed in [16] and are expressed in normalized units in order to provide a direct comparison. They consist of a sphere with radius 0.1 placed in the center of the physical region with pressure of 100 in comparison to the overall represented area with pressure 1. The density is uniform and equal to 1 in the full computational domain. For the study of ionized gas in a strong magnetic field the uniform magnetic field $B_z = 5/\sqrt{\pi}$ aligned with the z coordinate is added to the initial conditions. The adiabatic coefficient of the gas is chosen as $\gamma = 5/3$. Reflective border conditions are used throughout the simulation.

The simulations are performed for a Cartesian rectangular mesh $100 \times 100 \times 100$ in the physics domain [0,1].

Fig. 2 present the state of the 3D simulation of the processes for relative time 0.03. On the 3D pictures the arrows represent the velocities of the ionised gas and the color represents the density of gas. 3D figures clearly show the confinement of the ionized gas in the cylindrical area along z due to the magnetic field.

Fig. 3,4 represent the $2D$ projections of the density, pressure and kinetic energy of the gas expansion without magnetic field and the $1D$ density profile for these condition at time $t = 0.03$.

Fig. 5,6 represents the $2D$ projections of the density, pressure, magnetic pressure and kinetic energy for the gas expansion problem of the ionized gas with initial magnetic field and Fig. 7 shows the $1D$ profile of the density for these conditions at time $t = 0.03$.

This test demostrates the ability of the computational algorithm in preserving perfect simmetry. The comparison of the results in [16] shows a reasonable agreement and will be analysed further.

Another significant numerical test is the implosion. It consists of a 3-dimensional generalization of the Sod shocktube problem [17]. The initial condition corresponds to hydrogen gas presenting a discontinuity perpendicular to the diagonal of the computational domain. The left state has initial density $\rho_l = 0.719$ Kg/m^3 and pressure $P_r = 722680$ Pa. The right state has initial density $\rho_r = 0.125 \times \rho_l$ and pressure $P_r = 0.14 \times P_l$. The initial

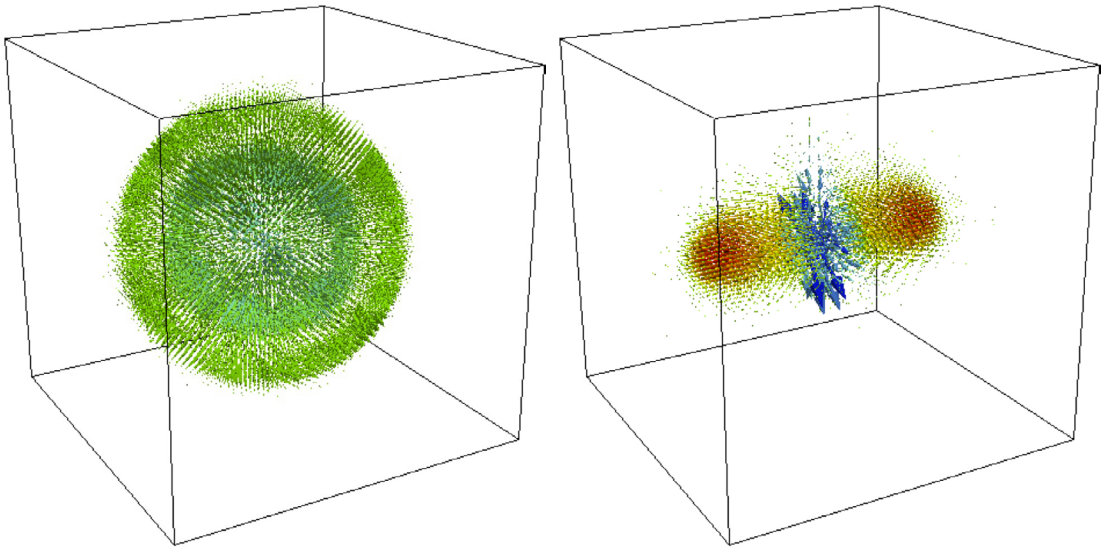

Figure 2: $3D$ view of the conductive gas expancion in strong magnetic field

magnetic field of 0.1 T is aligned with the y-axis. Reflective boundary conditions are used.

The simulations are performed for a Cartesian rectangular mesh $2000 \times 2000 \times 2000$ in the physics domain [0,10] μm.

Fig. 8 represents the $2D$ projections of the density at time $t = 1.76 \times 10^{-8}$ for the two cases with and without magnetic field.

The reflection of the shock generated by the initial contact discontinuity drives consequent vortices and instabilities. The result is characterized by complex shock reflections and rarefactions. In absence of magnetic field the simmetry along the diagonal is preserved. The presence of the magnetic field changes dramatically the picture. The deflection of the charged media flow in the direction of the magnetic field is clearly visible. Another observed effect is the strong smoothing of the instabilities of the gas dynamics, which corresponds to a physical experimental evidence. The possibility of such observation is the basis of the importance of the very detailed space discretization, which is available with the proposed method.

7 CONCLUSIONS

A new 3D kinetic algorithm has been developed for the solution of the magnetohydrodynamics problems. The novel feature of the method is that the local complex Boltzmann-like distribution function incorporated most of the electromagnetic processes terms. The fluxes of mass, momentum and energy across the cell interface as well as the magnetic field are calculated by integrating a local complex Boltzmann-like distribution function over the velocity space. Thus by using this distribution function to calculate the mass, momentum and energy fluxes, most of the electromagnetic contributions are calculated di-

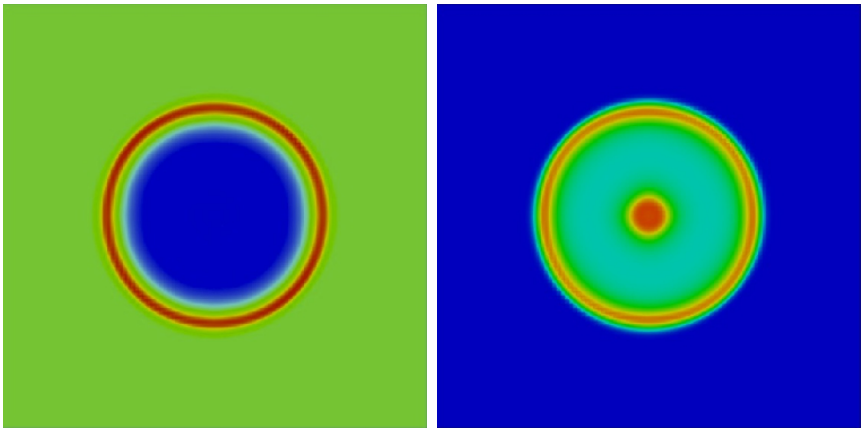

Figure 3: $2D$ gas density and 2D gas pressure projections

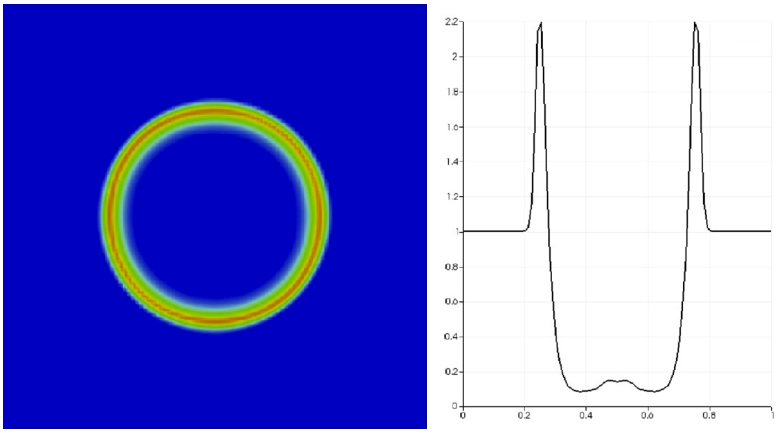

Figure 4: $2D$ kinetic energy and 1D density profile

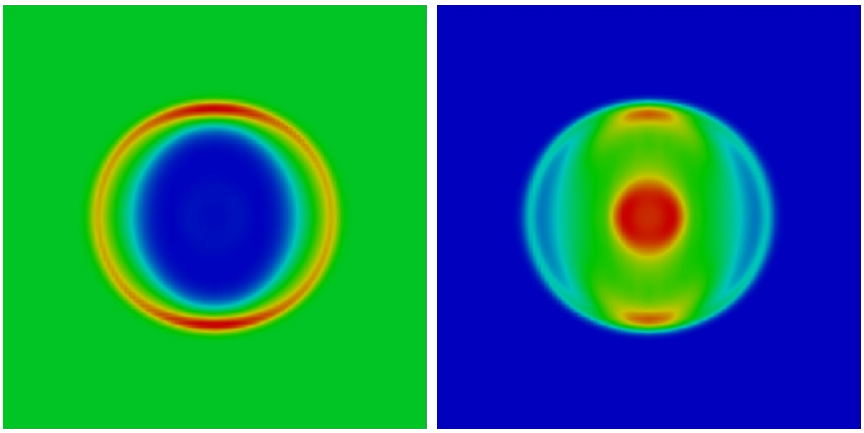

Figure 5: $2D$ gas density and $2D$ gas pressure projections in the magnetic field $5/\sqrt{\pi}$

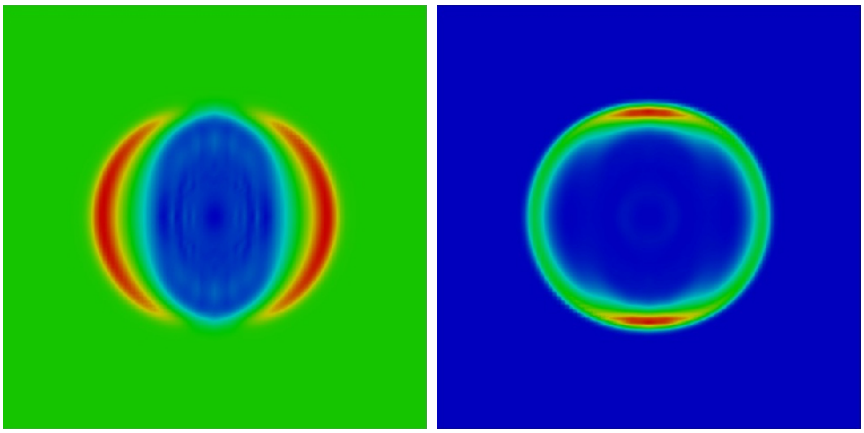

Figure 6: $2D$ magnetic pressure and $2D$ kinetic energy in the magnetic field $5/\sqrt{\pi}$

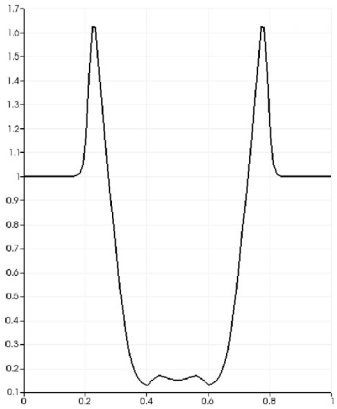

Figure 7: $1D$ density profile in the magnetic field $5/\sqrt{\pi}$

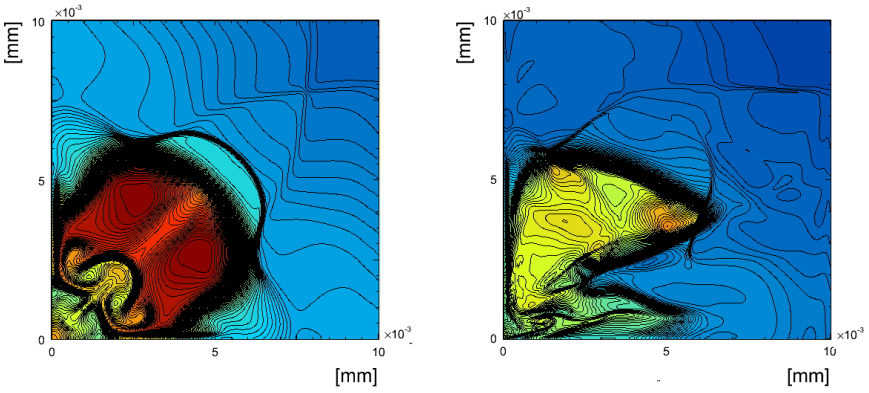

Figure 8: Sod shocktube problem: 2D gas density projections at time 1.76×10^{-8} s without (a) and with (b) magnetic field.

rectly, i.e. one does not have to solve the hydrodynamics and magnetic force components separately or differently.

A staggered, divergence free mesh configuration is used for the evaluation of the electromagnetic behaviour.

Numerical examples demonstrate that the proposed method can achieve high numerical accuracy and resolve strong shock waves of the magnetohydrodynamics problems.

The explicit method is choosen with respect to optimal adaptation on the large scale parallel computing systems. The improvement of the stability conditions wich is one of the limited factor for the explicid method will be study by the imlementation of the hyperbolic type of the magneto gas dynamic equations.

ACNOWLEDGEMENT

This study was supported by Russian Science Foundation grant 14-11-00170

REFERENCES

[1] B.Chetverushin, A.Pavlov, M.Volchinskaya, An Integration Scheme for Gas Dynamic Equations, Keldysh Institute of Applied Mathematics, RAS Preprint 113 (1983).

[2] B.Chetverushin, Kinetic Schemes and Quasi-Gasdynamic System of Equation, CIMNE, 2008.

[3] B.Chetverushkin, Resolution limits of continuous media models and their mathematical formulations, Matem. Mod. 24 (2012) 33-52.

[4] B.N. Chetverushkin, N. D'Ascenzo, V.I. Saveliev, Kinetically Consistent Magnetogasdynamics Equations and Their Use in Supercomputer Computations, Dokl. Math. 90 (2014) 495-498.

[5] B.N. Chetverushkin, N. D'Ascenzo, V.I. Saveliev, Hyperbolic type explicit kinetic scheme of magneto gas dynamics for high performance computing systems, Russ. J. Num. Anal. Math. Model. 30 (2015) 27-36.

[6] B.N. Chetverushkin, N. D'Ascenzo, V.I. Saveliev, Three Level Scheme for Solving Parabolic and Elliptic Equations, Dokl. Math. 91 (2015) 341-343.

[7] B.N. Chetverushkin, N. D'Ascenzo, V.I. Saveliev, On an Algorithm for solving parabolic and elliptic equations, Comput. Math. Math. Phys. 55 (2015) 1290-1297.

[8] L.Boltzmann, Lectures on Gas Theory, Dover, 1964.

[9] L. Tonks, Plasma Electron Drift in a Magnetic Field with a Velocity Distribution Function, Phys.Rev. 52 (1937) 710-713.

[10] L.Landau, E.Lifshitz, The Classical Theory of Fields. Vol. 2., Nauka, 1988.

[11] J.-P.Croisille, R.Khanfir, G.Chanteur, Numerical Simulation of the MHD Equations by a Kinetic-Type Method, J.Sci.Comput. 10 (1995) 81-92.

[12] J.D.Huba, J.G.Lyon, A new 3D MHD algorithm: the distribution function method, J. Plasma Phys. 61 (1999) 391-405.

[13] P.-J.Dellar, Lattice Kinetic Schemes for Magnetohydrodynamics, J. Comput. Phys. 179 (2002) 95-126.

[14] D.Balsara, D.Spicer, A Staggered Mesh Algorithm Using High Order Godunov Fluxes to Ensure Solenoidal Msgnetic Fields in Magnetohydrodynamics Simulation, J. Comput. Physics 149 (1999) 270-292.

[15] D.Balsara, Divergence-Free Adaptive Mesh Refinement for Magnetohydrodynamics, J. Comput. Phys. 174 (2001) 614-648.

[16] H.Tang, K.Xu and C.Cai, Gas-Kinetic BGK Scheme for Three Dimentional Magnetohydros, Numer. Math. Theor. Meth. Appl. 3 (2010) 387-404.

[17] Sod, G. A., A Survey of Several Finite Difference Methods for Systems of Nonlinear Hyperbolic Conservation Laws., J. Comput. Phys., (1978)

VII International Conference on Computational Methods for Coupled Problems in Science and Engineering
COUPLED PROBLEMS 2017
M. Papadrakakis, E. Oñate and B. Schrefler (Eds)

STATISTICAL DISTRIBUTION FUNCTION OF CHARGED PARTICLES IN MAGNETIC FIELD

B. CHETVERUSHKIN[*], N. D'ASCENZO[†] , A.SAVELIEV[**††] AND V. SAVELIEV[**†]**

[*] Keldysh Institute of Applied Mathematics
Russian Academy of Science (KIAM RAS)
4 Miusskaya sq, 125047 Moscow, Russia
e-mail: chetver@imamod.ru, web page: http://www.kiam.ru

[†]Deutsche Electronen Synchrotron (DESY)
85 Notkestrasse, 22607 Hamburg, Germany
e-mail: ndasc@mail.desy.de - Web page: http://www.desy.de

[††]Hamburg University
85 Notkestrasse, 22607 Hamburg, Germany
e-mail: Andrey.Saveliev@desy.de - Web page: http://www.desy.de

[**] Immanuel Kant Baltic Federal University
14 Alexandr Nevsky str., 236016, Kaliningrad, Russia
e-mail: saveliev@mail.desy.de - Web page http://www.kantiana.ru

Key words: MGD pump, numerical methods, kinetic consistent algorithms

Abstract. The statistical distribution function introduced by Boltzmann and his kinetic equation are the fundamental basis of the kinetic theory of gases and of the basic methods of solution of problems in the gas dynamics. At present time one of the areas of high interest in modern physics is the plasma in fusion processes and astrophysics which requires an extension of the kinetic processes to charged particles, in particular regarding the electromagnetic interactions. We propose a unified distribution function which includes the electromagnetic interactions for charged particles and is suitable for the solution of problems of charged particle dynamics with Boltzmann type equations and kinetic consistent magneto gas dynamic equations.

1 INTRODUCTION

The Boltzmann equation is the fundamental basis of the kinetic theory of gases [1]. The distribution function and the kinetic equations were introduced by Boltzmann for the

accurate description of the microscopic properties and the dynamics of gases. The macroscopic properties of gases can be extracted as the moments of the distribution function. Despite the known difficulties in the solution of the Boltzmann equation modern developments are going to explore its solution on powerful high performance computing systems by numerical methods. Two modern examples are Lattice Boltzmann Schemes (LBS) , which use the evolution of the distribution function and calculate the macroscopic gas dynamic parameters as moments of the distribution function [2] and Kinetically Consistent Difference Schemes (KCDS), which derive the gas dynamic equation from the Boltzmann equation by integrating the velocity space with the summational invariants [3]. The resulting equations gives a more reach physical models of the dynamics of gases in comparison to the gas dynamic equations, as the Navie-Stokes equations, which are formulated phenomenologically [4].

Many modern important problems require not only to study the dynamics of neutral particles, as a gas, but also to deal with the dynamics of charged particles, as clouds of electrons, or charged interstellar matter in astrophysics or ionized gas in strong electromagnetic fields as in plasma physics processes. In order to solve these problems one has to take into account the electromagnetic interactions of the charged particles or charged media.

The study of the relations between the statistical gas dynamics and the electromagnetic laws goes in the direction of trying to combine directly the kinetic equations of the charged particles with the electromagnetic equations. One approach was done by Vlasov, who introduced the electromagnetic forces in the kinetic equation - Boltzmann - Vlasov equations. In this approach electromagnetic interactions are introduced phenomenologically as an external Lorentz force [5] in the momentum equation. Few later attempts to implement the electromagnetic terms directly in the distribution function faced the difficulty with the axial vector behavior of the magnetic interactions [6, 7, 8].

We propose a new approach to define an unified distribution function, which includes the electromagnetic terms in the distribution function for the solution of the magneto gas dynamic problem by BLS or KCDS for charged particles in an electromagnetic field.

The main goal of this paper is to formulate the statistical distribution function with included electromagnetic terms and prove at the first step the validity of the proposed distribution function by the reconstruction of the kinetic consistent magneto gas dynamic equations including the equation of the evolution of the magnetic field in the ideal case for charged particles.

2 THEORETICAL ISSUES

The goal of the present study is the definition of the united distribution function describing the dynamics of the charged particles (electron cloud, ionized gas), including conditions with the external electromagnetic field.

2.1 Distribution Function of Gas Dynamic Processes

The kinetic theory describes the gas dynamics by the Boltzmann differential equation through the evolution of the distribution function $f(\mathbf{x}, \boldsymbol{\xi}, t)$ [1]:

$$\frac{\partial f(\mathbf{x}, \boldsymbol{\xi}, t)}{\partial t} + \boldsymbol{\xi} \cdot \nabla f(\mathbf{x}, \boldsymbol{\xi}, t) = C(f), \tag{1}$$

where: $C(f)$ is a nonlinear integral operator which describes the collisions of particles.

The computational interest in the kinetic formulations of gas dynamics is high due to the linearity of the differential operator on the left side of Eq. (1). The nonlinearity is confined by the collision term, which is generally local in $\mathbf{x}$ and t.

Another important feature for numerical methods is that the collision integral vanishes in the equilibrium state when the local Boltzmann distribution function is Maxwellian:

$$f_M = \frac{\rho m^{1/2}}{(2\pi kT)^{3/2}} exp\left\{-\frac{m}{2kT}(\boldsymbol{\xi} - \mathbf{u})^2\right\} \tag{2}$$

The dynamic of the gas could be defined as the time evolution of the Maxwellian distribution function with the conditions that the collision processes is occurred during a characteristic time at the end of which the distribution function became Maxwellian [9]. The macroscopic observables such as density, momentum, energy flux as a function of $\mathbf{x}$ and t are defined from the moments of the distribution function with respect to the particle velocity.

Earlier investigations [11] show that the electromagnetic fields do not destroy the validity of the distribution function and Boltzmann equation and open the way to the implementation of the electromagnetic processes terms in the distribution function.

2.2 Electromagnetic Interactions

From the kinetic relations, in addition to the gas kinetic motions, the motions of the charged particles is defined through nature of the electric and magnetic fields and the forces acting on the charged particles.

The electric field has the polar vector behavior and the corresponding velocity of charged particles follows the direction of the electric field and can be considered as simple drift of the charged particles in the direction of the electric field.

The magnetic field has the axial vector behaviour and acts in a different way respect to other fields. As well known the motions of the charged particles in magnetic field affects only the direction of the velocity and the motion of the charged particle has a circular trajectory in the plane perpendicular to the magnetic field. The theory of complex variables is ideally suited to solve problems involving two dimensional circulation and in

many ways complex variable theory is simpler than real variable theory and much more powerful [12].

As an example let's consider the motions of the charged particle in the uniform magnetic field [13]. The magnetic filed is directed along the z - axis. The equation of the motions is:

$$\frac{d}{dt}\mathbf{p} = \frac{e}{c}\mathbf{v} \times \mathbf{B} \tag{3}$$

can be rewritten in term of momentum:

$$\mathbf{p} = \frac{E\mathbf{v}}{c^2} \tag{4}$$

where E is the energy of particle, which in the magnetic field is constant.

$$\frac{E}{c^2}\frac{d\mathbf{v}}{dt} = \frac{e}{c}\mathbf{v} \times \mathbf{B} \tag{5}$$

Or in the velocity components:

$$\frac{d}{dt}v_x = \omega v_y, \frac{d}{dt}v_y = -\omega_x, \frac{d}{dt}v_z = 0 \tag{6}$$

where: $\omega = \frac{ec\mathbf{B}}{E}$

Multiplying first eq. of 6 on i and summing with second eq. of 6

$$\frac{d}{dt}(v_x + iv_y) = -i\omega(v_x + v_y) \tag{7}$$

from which:

$$v_x + iv_y = v_{0t}e^{i(\omega t+\alpha)} \tag{8}$$

where v_{0t} and α are real.

Select real and imaginary parts:

$$v_x = v_{0t}cos(\omega t + \alpha), \quad v_y = -v_{0t}sin(\omega t + \alpha) \tag{9}$$

where the $v_{0t} = \sqrt{v_x^2 + v_y^2}$ and α defined by the initial conditions.

This relation means that v_{0t} is the velocity of the charged particle in plane xy, constant during the motions in the magnetic field.

2.3 Proposed Distribution Function

Following the above considerations the velocity as result of the electromagnetic interaction can be defined as a complex velocity involving the electric and magnetic terms:

$$\mathbf{v}_{em} \propto \alpha_1 \mathbf{E} + i\alpha_2 \mathbf{B} \tag{10}$$

The important results of this considerations are that the electric field term of the velocity could be consider as contribution to the drift velocity and the magnetic term in the conditions when the Larmor radius is smaller in comparison to the total volume is part of the statistical velocity term.

In order to evaluate the distribution function at the equilibrium state, we refer to the Boltzmann H-theorem [14].

We consider the charged particles as spherical particles. The charged particles gas state is uniform and the velocity distribution function f is independent of x, y, z. The Boltzmann equation reduces to:

$$\frac{\partial f}{\partial t} = \int\int \left(f f^1 - f' f^{1'} \right) v_{rel} d\sigma d\mathbf{p}^1 \tag{11}$$

where:
$v_{rel} = |\mathbf{v} - \mathbf{v}^1|$ is the relative initial velocity
between the two colliding particles,
$d\sigma$ is the differential collision cross section,
$d\mathbf{p}^1$ is the momentum of the second particle.
The $'$ symbol indicates the final states after the collision.

According to the Boltzmann H-theorem the distribution function at the equilibrium should minimize the integral quantity H:

$$H = \int f \log f d\mathbf{c} \tag{12}$$

Combining Eq. 11 and 12 we obtain:

$$\frac{\partial H}{\partial t} = \int \frac{\partial}{\partial t} \left(f \log f \right) d\mathbf{c} = \int \left(1 + \log f \right) \frac{\partial f}{\partial t} d\mathbf{c} \tag{13}$$

from which:

$$\frac{\partial H}{\partial t} = \frac{1}{4} \int\int\int \log(\frac{f f^1}{f' f^{1'}}) \left(f f^1 - f' f^{1'} \right) v_{rel} d\sigma d\mathbf{p}_1 d\mathbf{c} \tag{14}$$

At the equilibrium, according to the H-theorem:

$$\frac{\partial H}{\partial t} = 0 \tag{15}$$

from which the relation is obtained:

$$\log f_0 + \log f_0^1 = \log f_0' + \log f_0^{1'} \tag{16}$$

This relation shows that $\log f$ is an invariant of the collision and can be expressed as the sum of the kinetic invariants:

$$\log f_0 = \beta_1 + \beta_2 \cdot m\boldsymbol{\xi} + \beta_B \cdot m\boldsymbol{\xi} - \beta_3 \frac{m}{2}\xi^2 \tag{17}$$

where:
β_1 is a real number, scalar related to the mass,
$\beta_{\mathbf{2}}$ is a real vector, related to the total momentum including magnetic terms,
$\beta_{\mathbf{B}}$ is a complex vector, related to the magnetic field,
β_3 is a real number, scalar related to the energy

It is convenient to recast the equation 17 in the form:

$$\log f_0 = \log \beta_0 - \frac{m}{2}\beta_3 \left(\boldsymbol{\xi} - \frac{\boldsymbol{\beta}_2}{\beta_3} - \frac{\boldsymbol{\beta}_B}{\beta_3}\right)^2 \tag{18}$$

with β_0 real number, scalar recasting β_1 and β_3.

We require that the distribution function takes only real values in order to preserve its meaning as distribution:

$$\begin{aligned}
&\Im \log f_0 = 0 \\
&\Re\left(\boldsymbol{\xi} - \frac{\boldsymbol{\beta_2}}{\beta_3} - \frac{\boldsymbol{\beta_B}}{\beta_3}\right) \cdot \Im\left(\boldsymbol{\xi} - \frac{\boldsymbol{\beta_2}}{\beta_3} - \frac{\boldsymbol{\beta_B}}{\beta_3}\right) = 0 \\
&\Re\boldsymbol{\xi} \cdot \Im\boldsymbol{\xi} - \frac{\boldsymbol{\beta}_2}{\beta_3} \cdot \Im\boldsymbol{\xi} - \Re\boldsymbol{\xi} \cdot \frac{\boldsymbol{\beta}_B}{\beta_3} + \frac{\boldsymbol{\beta}_2}{\beta_3} \cdot \frac{\boldsymbol{\beta}_B}{\beta_3} = 0 \\
&\Im\boldsymbol{\xi} \equiv \frac{\boldsymbol{\beta}_B}{\beta_3}
\end{aligned} \tag{19}$$

Under this condition the distribution function can be expressed as:

$$\log f_0 = \log \beta_0 - \frac{m}{2}\beta_3 \left|\boldsymbol{\xi} - \frac{\boldsymbol{\beta_2}}{\beta_3} - \frac{\boldsymbol{\beta_B}}{\beta_3}\right|^2 \tag{20}$$

$$f_0 = \beta_0 e^{-\frac{m}{2}\beta_3 \left|\boldsymbol{\xi} - \frac{\boldsymbol{\beta}_2}{\beta_3} - i\Im\frac{\boldsymbol{\beta}_B}{\beta_3}\right|^2} \tag{21}$$

where the module sign indicates explicitly that the complex distribution function f is real-valued and the $\Im$ symbol in the exponential makes explicit the complex nature of the vector $\boldsymbol{\beta}_B$.

The relations 19 and 21 define the distribution function at the equilibrium. The parameters β_0,β_3,$\boldsymbol{\beta}_2$ can be obtained from the moments of the distribution function 21 respect to the kinematic invariants with the integrals respecting the prescription 19. The relation 19 defines the integral in the complex plane along a line L parallel to the real axis and shifted in the direction of the imaginary axis of the quantity $\Im\boldsymbol{\xi} \equiv \left(\frac{\boldsymbol{\beta}_B}{\beta_3}\right)$.

The real and imaginary parts of the moment of the distribution function respect to the mass m:

$$\begin{aligned} \Re &: \int_L m f_0 d^3\boldsymbol{\xi} = \rho \\ \Im &: \int_L m f_0 d^3\boldsymbol{\xi} = 0 \end{aligned} \tag{22}$$

From the first of the equations 22 the relation is obtained:

$$\begin{aligned} &\int_L m\beta_0 e^{-\frac{m}{2}\beta_3\left|\boldsymbol{\xi}-\frac{\boldsymbol{\beta}_2}{\beta_3}\right|^2} d^3\boldsymbol{\xi} \\ &= \int_{-\infty}^{+\infty} m\beta_0 e^{-\frac{m}{2}\beta_3|c|^2} d^3c = m\beta_0\left(\frac{2\pi}{m\beta_3}\right)^{3/2} \\ &m\beta_0\left(\frac{2\pi}{m\beta_3}\right)^{3/2} = \rho \end{aligned} \tag{23}$$

The second of the equations 22 shows that the distribution function is real-valued.

The real and imaginary parts of the moment of the distribution function respect to the momentum $m\boldsymbol{\xi}$:

$$\begin{aligned} \Re &: \int_L m\boldsymbol{\xi} f_0 d^3\boldsymbol{\xi} = \rho\mathbf{u} \\ \Im &: \int_L m\boldsymbol{\xi} f_0 d^3\boldsymbol{\xi} = \frac{\mathbf{B}}{\sqrt{\mu_\rho}} \end{aligned} \tag{24}$$

where:

μ_ρ is a constant with dimensions m^4/C^2 needed for dimensional congruence of the equation.

From the first of the equations 24:

$$\begin{aligned} &\Re\int_L m\boldsymbol{\xi}\beta_0 e^{-\frac{m}{2}\beta_3\left|\boldsymbol{\xi}-\frac{\boldsymbol{\beta}_2}{\beta_3}-i\Im\frac{\boldsymbol{\beta}_B}{\beta_3}\right|^2} d^3\boldsymbol{\xi} \\ &= \Re\int_{-\infty}^{+\infty} m\left(\mathbf{c} + \ Ree\left(\frac{\boldsymbol{\beta}_2}{\beta_3}\right) + i\Im\left(\frac{\boldsymbol{\beta}_B}{\beta_3}\right)\right)\beta_0 e^{-\frac{m}{2}\beta_3|c|^2} d^3c \qquad (25) \\ &= \rho\Re\left(\frac{\boldsymbol{\beta}_2}{\beta_3}\right) \\ &\rho\Re\left(\frac{\boldsymbol{\beta}_2}{\beta_3}\right) = \rho\mathbf{u} \qquad (26) \end{aligned}$$

From the second of the equations 24:

$$\begin{aligned}
&\Im \int_L m\boldsymbol{\xi}\beta_0 e^{-\frac{m}{2}\beta_3\left|\boldsymbol{\xi}-\frac{\boldsymbol{\beta}_2}{\beta_3}-i\Im-\frac{\boldsymbol{\beta}_B}{\beta_3}\right|^2} d^3\boldsymbol{\xi} \\
&= \Im \int_{-\infty}^{+\infty} m\left(\mathbf{c}+\Re\left(\frac{\beta_2}{\beta_3}\right)+i\ m\left(\frac{\beta_B}{\beta_3}\right)\right)\beta_0 e^{-\frac{m}{2}\beta_3|c|^2} d^3c \qquad (27)\\
&= \rho\ Im\left(\frac{\boldsymbol{\beta}_B}{\beta_3}\right) \\
&\rho\Im\left(\frac{\boldsymbol{\beta}_B}{\beta_3}\right) = \frac{\mathbf{B}}{\sqrt{\mu_\rho}} \qquad (28)
\end{aligned}$$

Finally the real and imaginary parts of the moment of the distribution function respect to the thermal kinetic energy:

$$\begin{aligned}
&\Re : \int_L \frac{m}{2}c^2 f_0 d^3\boldsymbol{\xi} = \frac{3}{2}\frac{\rho kT}{m} \\
&\Im : \int_L \frac{m}{2}c^2 f_0 d^3\boldsymbol{\xi} = 0 \qquad (29)
\end{aligned}$$

From the first of the equations 29:

$$\begin{aligned}
&\Re \int_L \frac{m}{2}c^2\beta_0 e^{-\frac{m}{2}\beta_3\left|\boldsymbol{\xi}-\frac{\boldsymbol{\beta}_2}{\beta_3}-i\Im\frac{\boldsymbol{\beta}_B}{\beta_3}\right|^2} d^3\boldsymbol{\xi} \\
&= \Re \int_{-\infty}^{+\infty} \frac{m}{2}c^2\beta_0 e^{-\frac{m}{2}\beta_3|c|^2} d^3c \qquad (30)\\
&= \frac{3}{2}\frac{\rho}{m\beta_3} \\
&\frac{3}{2}\frac{\rho}{m\beta_3} = \frac{3}{2}\frac{\rho kT}{m} \qquad (31)
\end{aligned}$$

The relations 23, 26, 28, 31 define the coefficients β_0, $\boldsymbol{\beta}_2$,$\boldsymbol{\beta}_B$,β_3:

$$\beta_0 = \rho\frac{m^{1/2}}{(2\pi kT)^{3/2}} \qquad (32)$$

$$\boldsymbol{\beta}_2 = \mathbf{u} \qquad (33)$$

$$\boldsymbol{\beta}_B = i\frac{\mathbf{B}}{\sqrt{\rho\mu}} \qquad (34)$$

$$\beta_3 = \frac{1}{kT} \qquad (35)$$

Using the above definitions we obtain the local complex Boltzmann Maxwellian distribution function of charged particles with drift velocity $\mathbf{u}$ including the electric field contribution and statistical term including the ψ as thermal velocity and statistical term as a

function of **B**, taking in to account the axial behavior of magnetic field.

$$f_M = \frac{\rho m^{1/2}}{(2\pi kT)^{3/2}} \exp\left\{ -\frac{m}{2kT} \left| (\xi - \mathbf{u}) - i\frac{\mathbf{B}}{\sqrt{\mu\rho}} \right|^2 \right\}, \tag{36}$$

where:
ρ is the density,
$\boldsymbol{\xi}$ is the particle velocity
u is the drift velocity,
T includes also the electromagnetic contribution,
μ is the magnetic permeability, in general is a function of ρ.

2.4 The Macroscopic Magneto Gas Dynamic Parameters

The macroscopic hydrodynamic and electromagnetic observables are obtained respectively as the real and imaginary part of the integral along the line L parallel to the real axis and shifted by $i\mathbf{B}/\sqrt{\mu\rho}$ in the imaginary axis direction.

$$\rho = \int_L m f_M d^3\boldsymbol{\xi} \tag{37}$$

$$\mathbf{u} = \frac{1}{\rho} \int_L m\boldsymbol{\xi} f_M d^3\boldsymbol{\xi} \tag{38}$$

$$E = \int_L \frac{1}{2} m\boldsymbol{\xi}^2 f_M d^3\boldsymbol{\xi} \tag{39}$$

$$\mathbf{B} = -\frac{1}{\sqrt{\mu\rho}} \int_L m\boldsymbol{\xi}^* f_M d^3\boldsymbol{\xi} \tag{40}$$

Thus, by using this distribution function to calculate the mass, momentum and energy fluxes most of the electromagnetic contribution is calculated directly, i.e. one does not have to solve the hydrodynamic and magnetic force components separately or differently, as it will be shown below.

3 RECONSTRUCTION OF THE IDEAL MAGNETO GAS DYNAMICS SYSTEM OF EQUATIONS

In order to provide the validity of the proposed statistical complex distribution function, we show that the equilibrium condition reproduces correctly the ideal magneto gas dynamics system of equations.

The magneto gas dynamics system of equations is obtained by the integration of Eq. (1) with vanishing collision integral along the line L with respect to the particle velocity $\boldsymbol{\xi}$. The summational invariants $\phi(\xi) = \left(m, m\boldsymbol{\xi}, \frac{1}{2}m\boldsymbol{\xi}^2\right)$ and $\phi(\xi) = m\boldsymbol{\xi}^*$ are used, respectively, for the gas dynamics observables and the magnetic induction:

$$\int_L \phi\left(\boldsymbol{\xi}\right) \frac{\partial}{\partial t} f_M(\mathbf{x}, \boldsymbol{\xi}, t) d\boldsymbol{\xi} + \int_L \phi\left(\boldsymbol{\xi}\right) div(\boldsymbol{\xi} f_M(\mathbf{x}, \boldsymbol{\xi}, t)) d\boldsymbol{\xi} = 0 \tag{41}$$

The continuity equation for the density is obtained from the real part of Eq. (41) with the summational invariant $\phi\left(\boldsymbol{\xi}\right) = m$:

$$\Re : \int_L m \frac{\partial}{\partial t} f_M(\mathbf{x}, \boldsymbol{\xi}, t) d\boldsymbol{\xi} + \int_L m \frac{\partial}{\partial x_i} (\xi_i f_M(\mathbf{x}, \boldsymbol{\xi}, t)) d\boldsymbol{\xi} = 0; \tag{42}$$

After substituting the integration variable and inserting the proposed distribution function, we obtain:

$$\frac{\partial}{\partial t} \int_{-\infty}^{+\infty} m \frac{\rho m^{1/2}}{(2\pi kT)^{3/2}} \exp\left\{-\frac{m}{2kT} \left|\boldsymbol{\xi}'\right|^2\right\} d\boldsymbol{\xi}' + \frac{\partial}{\partial x_i} \int_{-\infty}^{+\infty} m \left(\xi_i' + u_i\right) \frac{\rho m^{1/2}}{(2\pi kT)^{3/2}} \exp\left\{-\frac{m}{2kT} \left|\boldsymbol{\xi}'\right|^2\right\} d\boldsymbol{\xi}' = 0 \tag{43}$$

Finally from the evaluation of the integrals in Eq. (43) we obtain:

$$\frac{\partial \rho}{\partial t} + \frac{\partial \rho u_i}{\partial x_i} = 0. \tag{44}$$

Similarly, using the summational invariants $\phi\left(\boldsymbol{\xi}\right) = (m\boldsymbol{\xi}, \frac{1}{2}m\xi^2)$ respectively, we obtain from (41) the conservation laws for the momentum and energy, including the magnetic field contribution:

$$\frac{\partial}{\partial t}\rho u_i + \frac{\partial}{\partial x_k}\left[\left(p + \frac{B^2}{2\mu}\right)\delta_{ik} + \rho u_i u_k - \frac{B_i B_k}{\mu}\right] = 0 \tag{45}$$

$$\frac{\partial}{\partial t}E + \frac{\partial}{\partial x_i}\left[u_i\left(E + p + \frac{B^2}{2\mu}\right) - \frac{B_i}{\mu}\sum_k u_k B_k\right] = 0 \tag{46}$$

The total energy density includes thermal, kinetic and magnetic energies:

$$E = \frac{3}{2}p + \frac{1}{2}\rho u^2 + \frac{B^2}{2\mu} \tag{47}$$

The magnetic induction evolution equation is obtained from the imaginary part of Eq. (41) with the summation invariant $\phi(\boldsymbol{\xi}) = (m\boldsymbol{\xi}^*)$:

$$\begin{aligned} \Im : \int_L m\xi_i^* \frac{\partial}{\partial t} f_M(\mathbf{x}, \boldsymbol{\xi}, t) d\boldsymbol{\xi} + \int_L m\xi_i^* \frac{\partial}{\partial x_k}(\xi_k f_M(\mathbf{x}, \boldsymbol{\xi}, t)) d\boldsymbol{\xi} \\ = 0; \end{aligned} \tag{48}$$

After substituting the integration variable and inserting the distribution function, we get the equation for the imaginary part as:

$$\begin{aligned} &- \frac{\partial}{\partial t} \int_{-\infty}^{+\infty} m \frac{B_i}{\sqrt{\mu\rho}} \frac{\rho m^{1/2}}{(2\pi kT)^{3/2}} \exp\left\{-\frac{m}{2kT}\left|\boldsymbol{\xi}'\right|^2\right\} d\boldsymbol{\xi}' \\ &- \frac{\partial}{\partial x_k} \int_{-\infty}^{+\infty} \left(m \frac{1}{\sqrt{\mu\rho}} \left(\xi_k' B_i - \xi_i' B_k + u_k B_i - u_i B_k\right) \right. \\ &\left. \frac{\rho m^{1/2}}{(2\pi kT)^{3/2}} \exp\left\{-\frac{m}{2kT}\left|\boldsymbol{\xi}'\right|^2\right\} \right) d\boldsymbol{\xi}' = 0 \end{aligned} \tag{49}$$

The evaluation of the Eq. 49 gives:

$$\frac{\partial}{\partial t} B_i + \frac{\partial}{\partial x_k}\left(u_k B_i - u_i B_k\right) = 0 \tag{50}$$

For the compressible media, we use the linear approximation of the magnetic permeability:

$$\mu = \frac{\mu_v}{\rho} \tag{51}$$

where μ_v is a constant representing the magnetic permeability per volume.

4 CONCLUSIONS

We propose the novel complex Boltzmann Maxwellian distribution function which includes electromagnetic interactions in a natural way and gives the possibility to reconstruct the macroscopic observables and magneto gas dynamic equations through moments of the distribution function.

This approach gives the possibility to use the proposed distribution function for the solution of the magneto gas dynamic problems by kinetic consistent methods and lattice Boltzmann methods, which are now considered as the most perspective ones for the calculation on modern parallel computing systems [15] .

The computational kinetic schemes with the use of the proposed complex distribution function provide a methods derive the full magneto gas dynamic equations for the charged particles in a more physical way.

ACNOWLEDGEMENT

This study was supported by Russian Science Foundation grant 14-11-00170

REFERENCES

[1] Boltzmann L.,Vorlesungen uber Gastheorie, part I, 1896, part II, 1898, "Lectures on Gas Theory" (translation), University Of California press, 1964.

[2] Succi S., The Lattice Boltzmann Equation, Claredon Press, Oxford press, 2001.

[3] Chetverushkin B., Elizarova T., USSR Comput. Math.Phys, 25 (1985) 164.

[4] Batchelor G., An Introduction to Fluid Dynamics, Cambridge University Press,1967.

[5] Vlasov A., J. Experimental and Theoretical Physics 8 (1938) 291.

[6] Croisille J.-P., Khnfir R. and Chanteur G., J. Sci. Comput.10 (1995) 81.

[7] Huba J.D. and Lyon J.G., J. Sci. Comput. 61 (1999) 391.

[8] Dellar P.J., J. Comput. Phys.179 (2002) 391.

[9] Chetverushkin B., Russ. J. Numer. Anal. Math. Modelling, 20 (2005) 337.

[10] Chetverushkin B., Kinetic Schemes and Quasi-Gas Dynamic System of Equations, CIMNE, 2008.

[11] Tones L. and Allis W.P., Phys. Rev. 52 (1937) 117.

[12] Graebel W.P., Advanced Fluid Mechanics, Academic Press, Elsevier (2007).

[13] L.Landau L. and Lifshitz L., The Classical Teory of Fields, Volume 2 of a Course of Theoretical Physics, Pergamon Press, 1971.

[14] L.Landau L. and Lifshitz L., The Physics Kinetic , Volume 10 of a Course of Theoretical Physics, Pergamon Press, 1971.

[15] Ahern S. et al., ORNL/TM-2007/238 (2007).

VII International Conference on Computational Methods for Coupled Problems in Science and Engineering
COUPLED PROBLEMS 2017
M. Papadrakakis, E. Oñate and B. Schrefler (Eds)

FORMAL VERIFICATION OF COUPLING PROPERTIES FOR AN AUTOMOTIVE SOFTWARE INTEGRATION ACROSS XIL

NATARAJAN NAGARAJAN*, EVREN ERMIS*, ANDREAS THUY* AND BERND-HOLGER SCHLINGLOFF†

*ETAS GmbH, Borsigstraße 14, 70469 Stuttgart, Germany
e-mail: firstname.secondname@etas.com, Web page: http://www.etas.com/

†Humboldt Universität zu Berlin
Rudower Chaussee 25, Johann von Neumann Haus, 12489 Berlin, Germany
e-mail: hs@informatik.hu-berlin.de, Web page: https://www.informatik.hu-berlin.de

Key words: Coupling Properties, Coupled Problems, Formal Verification, Applications, XiL

Abstract. Virtualization and desktop testing of an integrated system without inclusion of a physical hardware is a well-established concept due to today's abundant computing power availability. However, only few aspects of reality are introduced in steps into these virtual environments. The aspects of reality like hard-real time deadlines, timing events, coupling frequency and data synchronization between two subsystems in a system offer complexity without fair estimation of its consequence on the system behavior. In this paper, we describe the abovementioned complexity as the coupling properties detailed for a combustion engine example along with its controller. We formally verify the timing, safety, liveness and deadlock properties of the coupling by modeling them as timed transition systems. The example is verified for the idle speed control, smooth mode switching and for injection cutoff control where the interaction between the subsystems is very critical. The paper highlights a very important perspective of strong and weak subsystem coupling while transiting from Model-in-the-loop (MiL) to Software-in-the-Loop (SiL) and finally to Hardware-in-the-Loop (HiL). In conclusion, the input-output behavior of the coupled subsystems is also presented for a realistic observation of the control loop.

1 INTRODUCTION

Virtualization of hardware refers to the process of creating a virtual replica of its physically existing components. In the automotive embedded software environment, virtualization of Electronic Control Unit (ECU) hardware is an established approach for early

software validation [1], [2]. The ECUs in a modern car contain several hundreds of control function modules. Hence, early validation requirements of ECUs drive the activities on virtualization of ECUs.

In the V-Cycle for model-based automotive software development [3], the process steps such as Model-in-the-Loop (MiL), Software-in-the-Loop (SiL) and Hardware-in-the-Loop (HiL) emphasize the early validation of embedded control software. Figure 1 describes the system composition of an engine plant model and its corresponding controller variants in MiL, SiL and HiL process steps. As shown in figure 1, in MiL , SiL and HiL, the control function, the embedded control software and the ECU respectively, are validated by simulating them with the plant model. While validating the controller variants, model coupling plays an important role in the overall system behavior. A controller model/ an embedded control software/ an ECU is said to be coupled with a plant model when there exists an exchange of control signals and data between them. During the validation of embedded control software, the coupling between the controller and plant models varies significantly. While progressing from MiL to HiL, virtual artifacts like virtual buses are replaced by real hardware artifacts such as CAN or analog/ digital hardware. This inclusion of hardware and software artifacts introduce constraints in ensuring a correct coupling between the controller variants and the plant model.

In this paper, we address the constraints introduced by hardware and software artifacts; we categorize the nature of coupling at each of the abovementioned process steps; we derive formal specifications from closed loop engine controller requirements for a correct coupling between controller variants and the plant model. We denote these formal specifications as the coupling properties that must be satisfied at each of the abovementioned process steps.

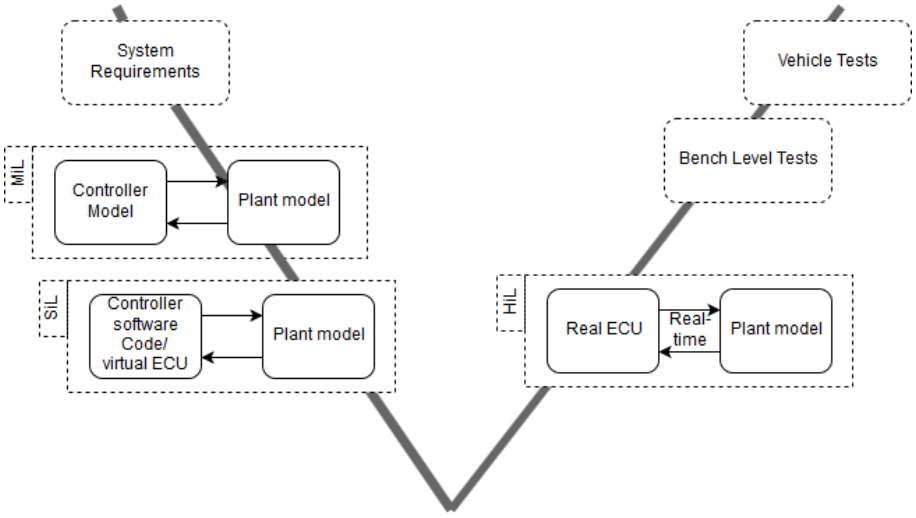

Figure 1: Automotive software development V-Cycle depicting an example system composition of an engine controller and an engine plant model in MiL, SiL and HiL process steps.

2 FORMAL VERIFICATION METHODOLOGY

In the field of engineering, the simulation of physical systems is important in validating the system behavior. However, unexpected system behavior may occur in reality due to incomplete test coverage of the system. Innumerous examples [4] exist in history where safety-critical systems encountered permanent failure after rigorous testing and validation. Formal verification [5] provides a solution by identifying such failures in advance and correcting the system behavior. In order to perform a formal verification, a formal description of the specification is a prerequisite.

In this paper, we describe some of the highly sensitive signals in the engine control loop such as fuel injection quantity, ignition angle, torque generation and throttle actuation. These signals influence the coupling between the controller variants and the plant model. The coupling properties are formally specified using Signal Temporal Logic [6] (STL). In STL, we specify real-valued signals in dense time; we test them on simulation traces generated out of the simulation runs. We prefer STL as it suits our application requirements and visualization of the results is straightforward.

2.1 Signal Temporal Logic (STL)

We provide an introduction to STL and its semantics [6], [7] before illustrating its application in the validation of control problems. Let $x_i[t]$ be a set of signals such that $i \in \mathbb{N}$ and t be a time instant, φ and ψ be STL Formulas, μ an atomic predicate given by $\mu = f(x_1[t], x_2[t], ..., x_n[t]) > 0$ where f is a real-valued function.

An STL formula is recursively defined as follows :

$$\varphi := \mu \mid \neg\varphi \mid \varphi \vee \psi \mid \varphi \, \mathcal{U}_{[\mathrm{a,b}]} \, \psi \tag{1}$$

The expression $(x_i, t) \models \varphi$ denotes that the STL formula φ satisfies the model of signals x_i at time t. The semantics of STL are given by the following clauses:

$$\begin{aligned}
(x_i, t) \models \mu &\iff f(x_1[t], x_2[t], ..., x_n[t]) > 0 \\
(x_i, t) \models \neg\varphi &\iff \neg((x_i, t) \models \varphi) \\
(x_i, t) \models \varphi \vee \psi &\iff (x_i, t) \models \varphi \text{ or } (x_i, t) \models \psi \\
(x_i, t) \models \varphi \, \mathcal{U}_{[a,b]} \, \psi &\iff \exists t' \in [t+a, t+b] \text{ such that } (x_i, t') \models \psi \\
&\qquad \text{and } \forall t'' \in [t, t'] \text{ holds } (x_i, t'') \models \varphi
\end{aligned} \tag{2}$$

In STL, the time references a and b ($a, b \in \mathbb{R}_{\geq 0}$) are added to temporal operators. We define two important temporal operators *eventually* and *always* as follows:

$$\begin{aligned}
&\textit{Eventually} : F_{[a,b]} \, \varphi = \top \, \mathcal{U}_{[a,b]} \, \varphi \\
&(x_i, t) \models F_{[a,b]} \, \varphi \iff \exists t' \in [t+a, t+b] \text{ such that } (x_i, t') \models \varphi \\
&\textit{Always} : G_{[a,b]} \, \varphi = \neg(F_{[a,b]} \, \neg\varphi) \\
&(x_i, t) \models G_{[a,b]} \, \varphi \iff \forall t' \in [t+a, t+b] \text{ holds } (x_i, t') \models \varphi
\end{aligned} \tag{3}$$

Informally, $\varphi \, \mathcal{U}_{[a,b]} \, \psi$ implies that for some time-step in simulation between the time references a and b the STL formula ψ holds true and for every time-step before ψ, the STL formula φ holds true. The temporal operators presented in this section are used to describe the properties of coupling.

3 X-in-the-Loop (XiL) and Coupling

In a V-Cycle for automotive software development, validating a system from MiL to HiL [8] and even further is strongly adhered to. The controller model development ends after its translation into an ECU in the HiL. Beyond the HiL, only the controller variables inside the ECU are adapted for the ECU network and vehicle validation. X-in-the-Loop (XiL) in the controller development process steps abbreviates MiL, SiL and HiL process steps. The X in the XiL represents a controller model in the MiL process step, embedded controller software in the SiL process step and an ECU in the HiL process step.

3.1 Coupling nature across XiL

Figure 2 shows a pictorial representation of our system composition in detail, explaining the coupling nature in the MiL, SiL and the HiL process steps. In the MiL process step, the simulation of an abstract physical plant model with corresponding control function is carried out. Here, we observe the physics involved and gain confidence on the developed control function. In this step, we validate the functional properties of the system. The simulation in MiL process step has a single numeric solver and therefore we denote the interaction between the participating models as *strongly-coupled* [9].

In the SiL process step, the controller model translates into a controller software with virtual software drivers and an operating system. The operating system is responsible for monitoring and triggering the internal events in the controller software. Therefore, the controller software can be concurrently simulated along with the plant model. The SiL process step can be executed both in virtual time and in real-time. In our case study, the SiL process step is performed in real-time. The interaction between the controller software and the plant model is handled by a single global clock. We categorize our SiL process step under *weakly coupled* [9] since the execution time of the control software and plant model can be chosen independently.

In the HiL process step, an ECU is in closed loop with the plant model. The ECU is a separate hardware entity with its own local clock and interacts with the plant model executed on another hardware platform. In the HiL process step, the simulation is real-time. We categorize the interaction of the ECU and the plant model in the HiL process step as *weakly coupled* as the ECU and the plant model have their own local time-scales.

In this paper, we derive closed loop engine control requirements and formalize them. These requirements characterize the closed loop system behavior. We therefore, refer to these requirements as coupling properties and further categorize them as timing, safety, deadlock and liveness properties.

We state the following: A model of a system (controller variants and the plant model) satisfies coupling properties in a XiL when every interpretation of the system model in MiL, SiL and HiL satisfy the respective coupling properties.

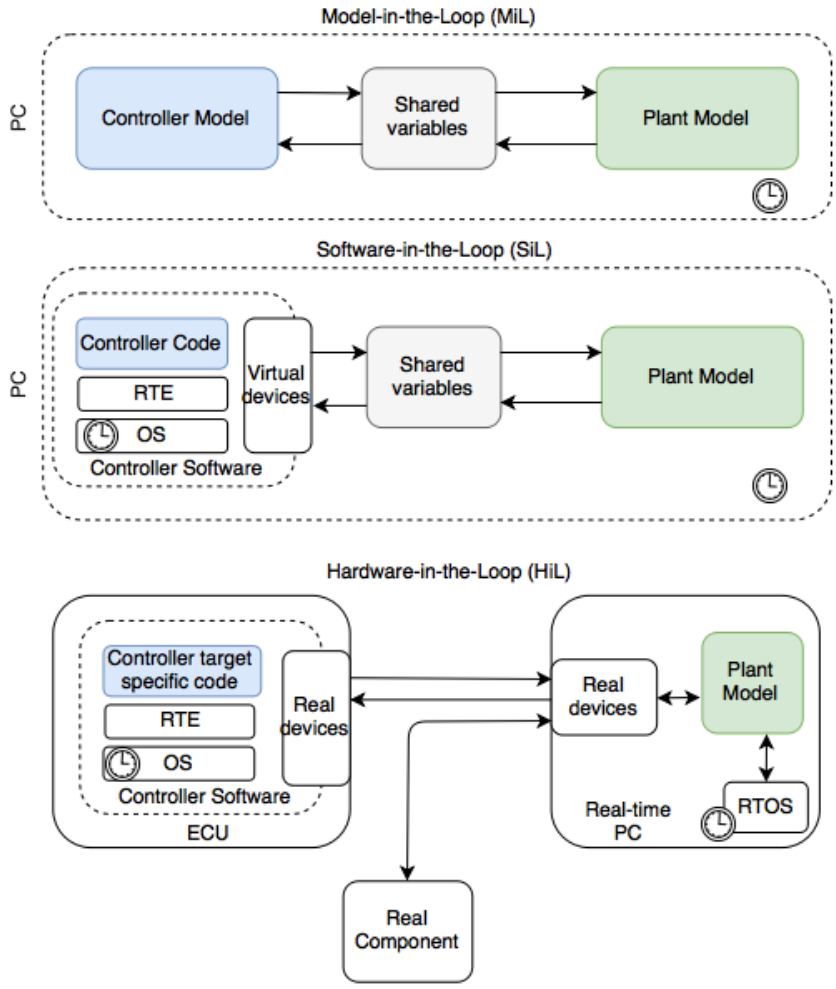

Figure 2: The picture showing the controller development and its coupling with the plant model in the MiL, SiL and HiL process steps.

4 CONTROL PROBLEMS AND COUPLING PROPERTIES

4.1 Control Problems

We have selected three highly critical engine control problems [10] to formally verify our coupling properties. The coupling properties have been formulated from the closed loop engine controller requirements. In this section, we describe each of the control problems and their significance.

Idle speed control [11] is an elementary example for validating a combustion engine closed loop control. During the idling of an engine, the engine speed must be maintained at an optimal desired value. The computations of engine speed in the ECU and in the engine model must be synchronous; any delay in fuel injection quantity estimation and ignition angle estimation will lead to abrupt variation in torque, causing the engine to stall. This demands strict timing and safety requirements in the coupling of the plant and the controller variants.

Smooth switching control is developed in order to avoid erroneous injection, ignition and throttle actuation while transiting to and from idle speed mode. During sudden acceleration demand of the driver, the ECU must linearly actuate the throttle to avoid a bad driving experience. In the above case, the ECU should eventually actuate the throttle by detecting the driver's intention to accelerate. Additionally, the ECU must not actuate the throttle for a duration longer than desired. It is important to witness how the deadlock and safety requirements of the coupling are being satisfied.

In injection cut-off control [12], the objective is to ensure that the passenger has minimal discomfort during release of the accelerator pedal. Upon quick release of the pedal, the torque demand is minimized. This is characterized by undesirable oscillations. In order to minimize the resulting oscillations, the engine controller must have a correct event detection mechanism. The injection cut-off control demands the injection and ignition timing events to be very precise. We translate them into timing requirements of the coupling.

4.2 Coupling Properties

The coupling properties are a set of formal specification of closed loop engine control requirements. These properties must be satisfied in order to ensure a correct coupling between the engine controller variants and the engine model. We consider that the plant and controller models are developed as per required specification and focus on coupling the two participating subsystems. An initial set of 12 properties have been formally verified on the case study. In this paper, we present the STL formalism of three timing properties namely φ_1, φ_2 and φ_3 and one safety property φ_4.

4.2.1 Timing Properties

We formally describe the critical event detection and timing interactions of the coupling between engine controller and engine plant subsystems. Some of the formalism have been generalized for verifying similar constructs. Table 1 describes the list of variables used in the formal description of the timing properties.

Table 1: List of variables used in the formalization of coupling properties.

Variable	Description	Range	Unit
D_{des}	Desired driver actuation	[0,1]	factor of 100 (%)
ω_{Lref}	Lower engine speed threshold	[0,6000]	RPM
ω_{Uref}	Upper engine speed threshold	[0,6000]	RPM
ω_{eng}	Current engine speed	[0,6000]	RPM
ω_{neng}	Calculated engine speed	[0,6000]	RPM
tol_v	Tolerance value	[0,6000]	RPM
t_i	Simulation start time	[0,∞]	seconds (s)
t_f	Simulation end time	[0,∞]	seconds (s)
KW	Current crank angle	[0,720]	degrees (^{0}CA)
CA_{Lx}	Lower crank angle threshold	[-720,720]	degrees (^{0}CA)
CA_{Ux}	Upper crank angle threshold	[-720,720]	degrees (^{0}CA)
E_{fqty}	Fuel injection request event	[0/1]	-
E_{ign}	Ignition angle request event	[0/1]	-
S_{fqty}	Fuel Injection duration	[0,5000]	milli seconds (ms)
S_{ign}	Ignition end angle	[-720,720]	degrees (^{0}CA)
$D_{throttle}$	Desired throttle angle	[0,90]	degrees

1. *In the idle speed control mode, no driver actuation is observed and the engine speed must be maintained within a specified upper and lower engine speed thresholds.*
We translate this specification in STL as follows:

$$\varphi_1 := G_{[t_i,t_f]} \left((\mid \omega_{eng}[t] \mid \leq \omega_{Uref}) \wedge (\mid \omega_{eng}[t] \mid > \omega_{Lref}) \wedge (D_{des} = 0) \right) \tag{4}$$

Explanation of the formulation:
The condition $D_{des} = 0$ implies that there is no driver actuation of accelerator pedal. The idle speed control should be robust enough to detect disturbance and counter-balance the effects. Therefore, it is important to check the engine speed for the complete time duration the controller is in idle control state i.e. in our case, ω_{Uref} is set to 800 RPM. To ensure that the engine does not stall while idling i.e. engine speed is zero, we must also check for a lower bound value ω_{Lref} . In precise formalism given by φ_1 , we use temporal operator *always* to describe a stronger notion on engine speed stability during idle control mode.

2. *A fuel injection request must be triggered within a specified upper threshold value in the crank angle scale.*
   We now translate this specification in STL as follows:

$$\varphi_2 := F_{[t_i,t_f]} \left((\mathrm{KW[t]} > \mathrm{CA_{Lx}}) \wedge \ (\mathrm{KW[t]} \leq \mathrm{CA_{Ux}}) \ \wedge (\mathrm{E_{fqty}} > 0.5) \right) \tag{5}$$

   Explanation of the formulation:
   The engine control functions are normally modeled in crank-angle scale. Therefore, each fuel injection request is a discrete event that is triggered to perform fuel injection estimation. One must ensure that right fuel quantity is updated per combustion cycle to enable desired engine operation.
   We define a measurement window having upper and lower threshold values in crank-angle scale such that we identify the request associated with particular cylinder in this region. i.e. we define the upper and lower threshold values for every cylinder of the engine.

3. *An ignition angle update request must be triggered within a specified upper threshold value in the crank angle scale.*
   We now translate this specification in STL as follows:

$$\varphi_3 := F_{[t_i,t_f]} \left((\mathrm{KW[t]} > \mathrm{CA_{Lx}}) \wedge \ (\mathrm{KW[t]} \leq \mathrm{CA_{Ux}}) \ \wedge (\mathrm{E_{ign}} > 0.5) \right) \tag{6}$$

4.2.2 Safety Property

We formally describe the safety requirements of the coupling between engine controller and engine plant subsystems. The STL formula φ_4 has been provided as an example.

1. *Always the difference between current engine speed in the engine model and computed engine speed in the ECU must be within tolerance limits.*
   We now translate this specification in STL as follows:

$$\varphi_4 := \mathrm{G} \left(|\omega_{\mathrm{eng}}[\mathrm{t}] - \omega_{\mathrm{neng}}[\mathrm{t}]| < \mathrm{tol_v} \right) \tag{7}$$

5 CASE STUDY

5.1 System Description

A three cylinder combustion engine model is coupled to its engine controller as shown in figure 3. An accelerator pedal model is provided to stimulate the driver's input for testing. The engine model [11] consists of analytical parts that involve differential equations and experimental parts that involve data from real measurements. The engine and controller models have processes which are time-dependent and crank-angle dependent. The engine processes related to combustion (the air system, throttle control, fuel injection and ignition) are computed with respect to crank-angle scale. The air flow, manifold

pressure, torque, crankshaft model and ECU event detection are computed with respect to the global simulation time.

Figure 3 shows the system composition with signal flow information between the subsystems. The engine speed is a very critical variable for effective synchronization between engine and controller models.

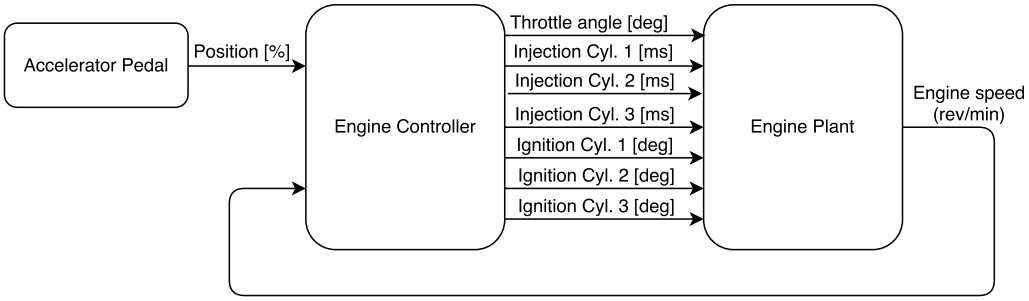

Figure 3: Model of engine controller and engine plant in closed loop

5.2 Results

We used the Breach [6] toolbox to analyze the STL formulations over the combustion engine example.

Figure 4 shows the simulation of engine speed and the satisfaction of STL formula φ_1 under idle speed control mode. The Breach toolbox categorizes the STL satisfaction problem into boolean and quantitative satisfaction. The boolean satisfaction indicates whether the property φ_1 has been satisfied within the specified simulation start and end time. The quantitative satisfaction provides a value for the variables describing the deviation occurring in the engine speeds from the thresholds. Figure 4 shows the boolean satisfaction (the red line) of each sub-formula and quantitative satisfaction (blue line) indicates the deviation. In formula φ_1, we set x as 6 seconds and run the simulation for 30 seconds. We witness that the idle speed is oscillating between 800 RPM and 850 RPM in the interval between 5 and 5.5 seconds. Hence, the boolean satisfaction is pulsating during this time period. We observe that the property is satisfied after 6 seconds.

Figure 5 shows the response curves of sensitive signals (engine speed, air-fuel ratio factor and desired throttle demands) for a step input with varying amplitudes of driver actuation. We performed a partial coverage test on the example by varying the driver actuation signal from (0-100)%. A random set of 15 driver actuation signals were simulated and satisfaction of the coupling properties were verified. At lower engine speeds, the driver demand causes the engine speed to go as low as 500 RPM. On higher engine speeds, the engine compensates the driver demand and achieves a higher engine speed. From this behavior, we inferred that the engine could be susceptible to stalling with lower sudden driver actuation. To confirm our inference, we analyzed the example by randomly

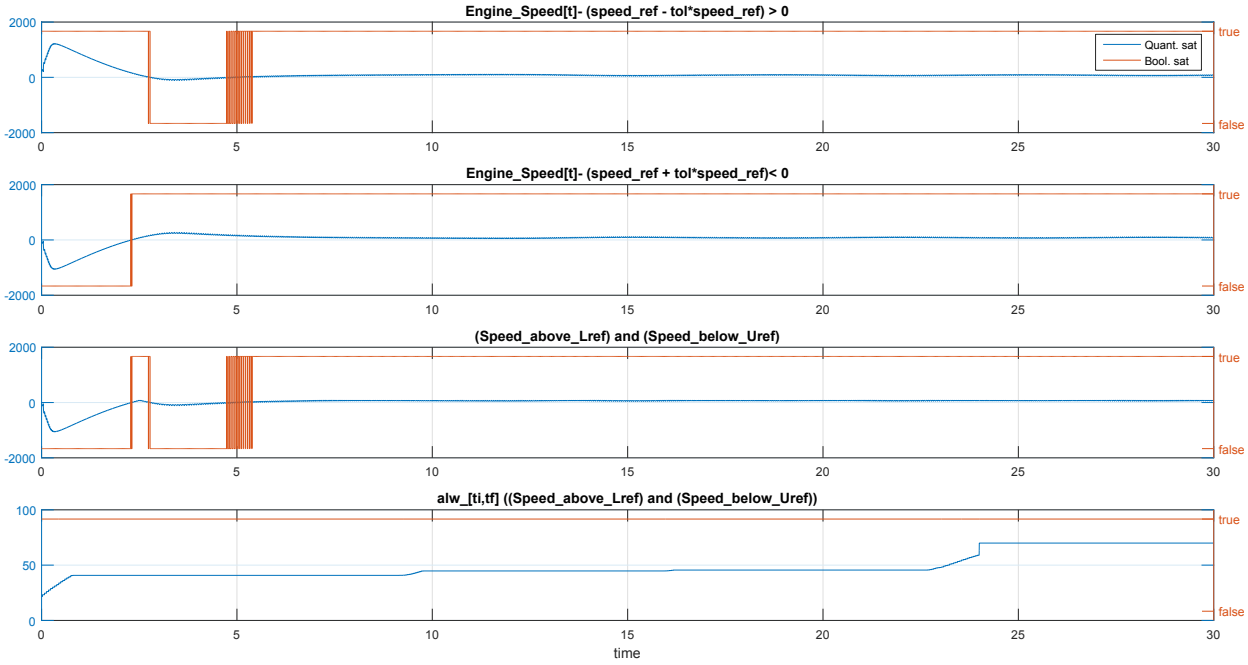

Figure 4: Formal verification of the idle speed control mode. The simulation results show that the engine is stable and the STL formula φ_1 has been satisfied.

generating 50 lower amplitude driver actuation inputs. The STL formulas φ_1, φ_2 and other timing properties could not be guaranteed anymore. These experiments were performed on MiL and SiL process steps by deriving requirements from the HiL process step since the HiL involves the most coupling constraint among the three process steps.

6 CONCLUSIONS & FUTURE WORKS

In this paper, we addressed the coupling constraints introduced in the HiL process steps and translated real-time requirements onto the MiL and the SiL process steps using our combustion engine example; we categorized the nature of coupling in each of the process steps in XiL; we formalized the coupling properties as STL formulas and illustrated its formal verification using the Breach toolbox. We illustrated how XiL can address coupled problems and explained the need to validate MiL and SiL process steps including crucial aspects of reality. We identified the scope of improvements in our modeling and simulation through formal verification of developed coupling properties.

In this paper, we presented coupling properties which address critical aspects of real-time deadline fulfillment, event detection and synchronization. As our next task, we wish to extend our set of coupling properties and address complex timing properties on cylinder pressure and co-simulation of the engine controller variants and the plant model.

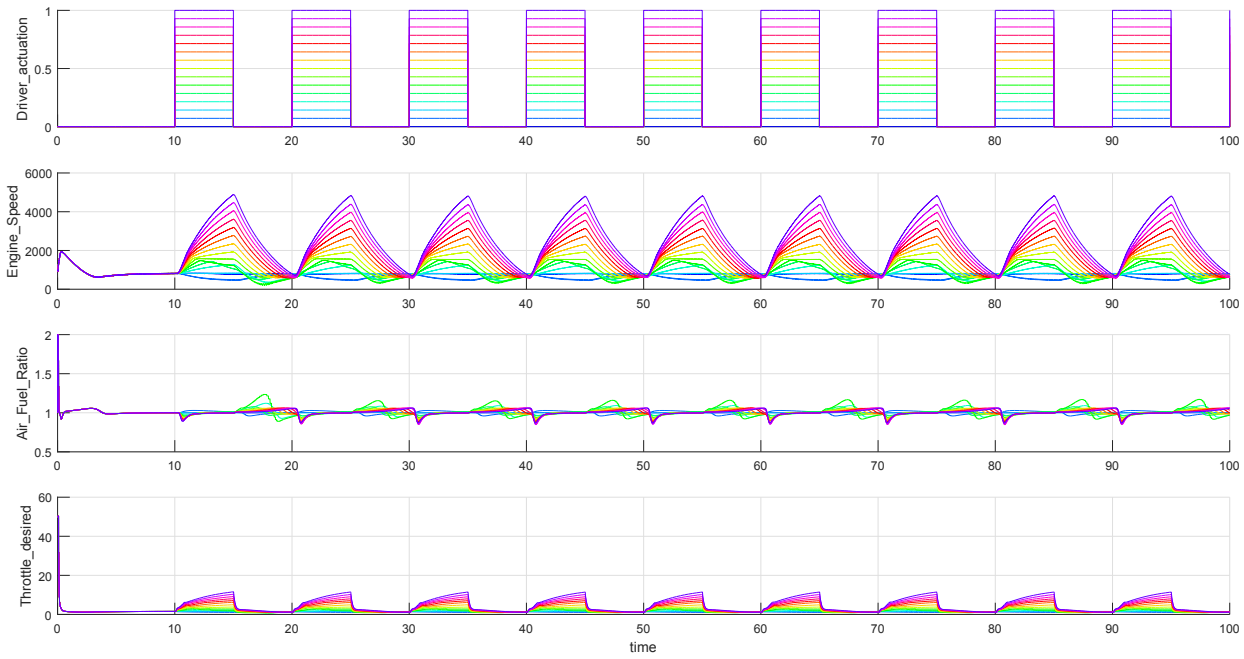

Figure 5: Simulation of random driver actuation inputs between 0% and 100% using Breach toolbox. The simulation results show that the engine is stable under these random input conditions.

REFERENCES

[1] Katyal, R. and S, S., *Virtualization for ECU Platform Software Testing in Automotive Embedded*, SAE Technical Paper 2011-01-1265, 2011, doi:10.4271/2011-01-1265

[2] ETAS GmbH, *Virtualization Is the Key to Greater Efficiency*, ETAS RealTimes Magazine, 2014, `https://www.etas.com/data/RealTimes_2014/rt_2014_1_52_en.pdf`

[3] Schäuffele, Jörg and Zurawka, Thomas, *Automotive Software Engineering - Grundlagen, Prozesse, Methoden und Werkzeuge effizient einsetzen*. ISBN 978-3-8348-03 64-1, Wiesbaden 2010.

[4] Tan, Gang, *A Collection of Well-Known Software Failures*. `http://www.cse.psu.edu/~gxt29/bug/softwarebug.html`, Penn State University, 2016.

[5] Alur, Rajeev, *Formal Verification of Hybrid Systems*. 978-1-4503-0714-7/11/10, EMSOFT 2011, Taipei, Taiwan, October 9-14, 2011.

[6] Donzé, Alexandre, *On Signal Temporal Logic*. EECS294-98, University of California, Berkeley, Spring 2014.

[7] Raman, Vasumathi et. al., *Model Predictive Control with Signal Temporal Logic Specifications*. 53rd IEEE Conference on Decision and Control, December 15-17, 2014, Los Angeles, California, USA

[8] Störmer, Christoph et. al., *ETAS LABCAR-XiL: Bridging the gap between development phases by harmonizing concepts and tools*. 15. Internationales Stuttgarter Symposium, Proceedings, DOI 10.1007/978-3-658-08844-6_30, Springer Fachmedien Wiesbaden 2015.

[9] Valasek, Michael, *Modeling, simulation and control of mechatronical systems*. Simulation techniques for Applied Dynamics, CISM Courses and Lectures, Vol. 507, ISBN 978-3-211-89547-4, Springer Wien, NewYork 2008.

[10] Ras, Jim and Cheng, Albert M.K., *On Formal Verification of Toyota's Electronic Throttle Controller*. 978-1-4244-9493-4/11, IEEE International Systems Conference 2011.

[11] Guzzella, Lino and Onder, C. H., *Introduction to Modeling and Control of Internal Combustion Engine Systems*. ISBN 978-3-642-10774-0, DOI 10.1007/978-3-642-10775-7, Springer-Verlag Berlin Heidelberg 2010.

[12] Villa, T. et. al., *Formal verification of an Automotive Engine Controller in Cutoff Mode*. 0-7803-4394-8/98, Proceedings of the 37th IEEE Conference on Decision & Control, Tampa, Florida, USA, December 1998.

VII International Conference on Computational Methods for Coupled Problems in Science and Engineering
COUPLED PROBLEMS 2017
M. Papadrakakis, E. Oñate and B. Schrefler (Eds)

THE PERTURBATION METHOD IN THE PROBLEM ON A NEARLY CIRCULAR INCLUSION IN AN ELASTIC BODY

MIKHAIL A. GREKOV*, ALEKSANDRA B. VAKAEVA*

*St. Petersburg State University (SPbU)
7/9, Universitetskaya nab., 199034, St. Petersburg, Russia
e-mail: m.grekov@spbu.ru, a.vakaeva@spbu.ru, web page: http://spbu.ru

Key words: Nearly Circular Inclusion, 2-D Problem, Perturbation Method, Complex Potentials, Stress Concentration

Abstract. The two-dimensional boundary value problem on a nearly circular inclusion in an infinity elastic solid is solved. It is supposed that the uniform stress state takes place at infinity. Contact of the inclusion with the matrix satisfies to the ideal conditions of cohesion. To solve this problem, Muskhelishvili's method of complex potentials is used. Following the boundary perturbation method, this potentials are sought in terms of power series in a small parameter. In each-order approximation, the problem is reduced to the solving two independent Riemann – Hilbert's boundary problems. It is constructed an algorithm for funding any-order approximation in terms of elementary functions. Based on the first-order approximation numerical results for hoop stresses at the interface are presented under uniaxial tension at infinity.

1 INTRODUCTION

Stress concentration caused by different defects (such as holes and inclusions) existing in materials and structures is one of the reasons of devices failure. Apparently, it is not possible to obtain an exact analytical solution of an elastic boundary value problem for an arbitrary defect in an infinite plane. The real hole or inclusion has a shape which can't be usually described by a conformal image using, for example, for elliptic holes [1, 2]. So-called circular defects have practically relief surface slightly deviated from a circle and a circular shape of them is nothing but idealization. In the works [3, 4] the perturbation method was used to solve the problem of an elastic infinity plane with a nearly circular hole at the macro- and nanolevel. The results obtained in [3] for the nearly circular holes, by means of the boundary perturbation technique allow us to solve a more complex problem of determining the stress-strain state inside and outside of an elastic inclusion having a different shape.

In the present work, the approach developed in [3] for the analysis of the infinity elastic body with a nearly circular hole is used to study stress-strain state of an elastic plane with a nearly circular inclusion. We consider the 2-D problem on an inclusion in an elastic solid under remote tension. To solve the problem, we use Goursat – Kolosov complex potentials, Muskhelishvili representations and universal boundary perturbation technique applied recently to some problems of elasticity (see, for example [3]–[8]). First, based on Muskhelishvili's technique [9], we seek complex potentials in terms of power series in a small parameter. Then, in each-order approximation, the problem is reduced to the solving two independent Riemann – Hilbert's boundary problems. In contrast to the work [10], where only the first-order approximation has been derived, we construct an algorithm for finding any-order approximation expressed in elementary functions. For the periodic shape of the inclusions determined by the cosine function, the first-order formulas of approximation are derived in a closed form. At the end of the work, we give the most essential numerical results and their analysis for some shapes of the inclusion.

2 STATEMENT OF THE PROBLEM

We consider an infinite elastic body with an inclusion the shape of which is weakly deviated from a circle. Under arbitrary remote loading, the body is in plane strain. So, it leads to the 2-D boundary value problem for the elastic plane of complex variable $z = x_1 + ix_2$ (i is the imaginary unit) with a nearly circular inclusion. Suppose that the matrix corresponds to the domain Ω_1 and the inclusion — to the domain Ω_2, and the interface between the matrix and inclusion Γ is determined by the relation

$$z \equiv \zeta = \rho e^{i\theta} = (1 + \varepsilon f(s))\, s. \tag{1}$$

Here $s = e^{i\theta}$, $f(s)$ is the continuous differentiable function satisfying $|f| \le 1$, ε is the small parameter which is equal to the maximum deviation of the inclusion boundary from the circular one, $\varepsilon > 0$, $\varepsilon \ll 1$. The elastic properties of each domain Ω_k ($k = 1, 2$) are determined by the Poisson coefficient ν_k and the shear modulus μ_k.

It is suppose that contact of the inclusion with the matrix satisfies the ideal conditions of cohesion

$$\Delta\sigma_n(\zeta) = \sigma_n^+ - \sigma_n^- = 0, \quad \Delta u(\zeta) = u^+ - u^- = 0, \tag{2}$$

and stresses σ_{ij} ($i, j = 1, 2$) and the rotation angle ω are specified at infinity as

$$\lim_{z\to\infty} \sigma_{ij} = \sigma_{ij}^{\infty}, \quad \lim_{z\to\infty} \omega = 0. \tag{3}$$

Here, $\sigma_n(\zeta) = \sigma_{nn} + i\sigma_{nt}$, $u = u_1 + iu_2$; σ_{nn}, σ_{nt} are the normal and tangential stress tensor components at the interface, correspondently; u_1, u_2 — components of the displacement vector in the Cartesian coordinates x_1, x_2. In equation (2), $\sigma_n^{\pm} = \lim\limits_{z\to\zeta\in\Gamma} \sigma_n(z)$, $u^{\pm} = \lim\limits_{z\to\zeta\in\Gamma} u(z)$. The superscript "–" corresponds to $z \in \Omega_1$ and "+", to $z \in \Omega_2$.

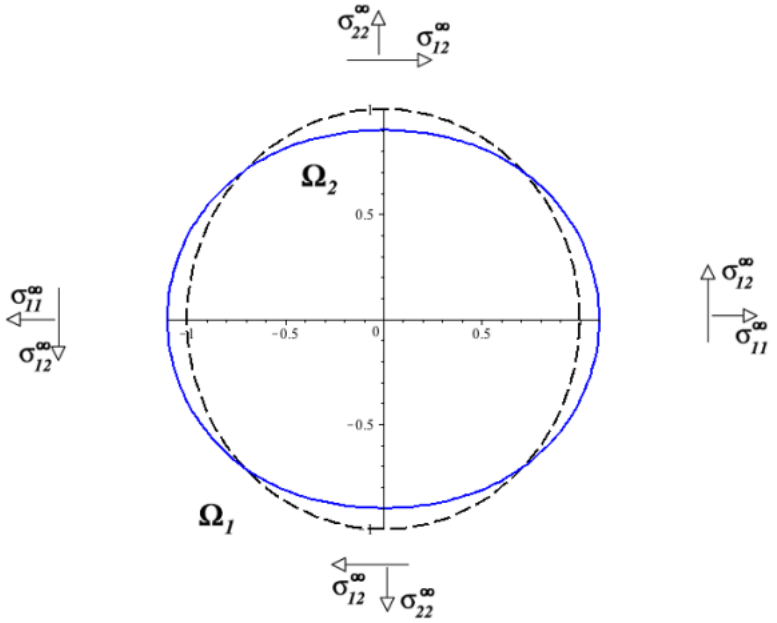

Figure 1: A nearly circular inclusion (firm line) in an infinite elastic plane under arbitrary remote loading ($\varepsilon = 0, 1$).

The boundary of the inclusion determined by equation (1) is shown in Fig. 1 for the function $f(\theta) = \cos 2\theta$ when parameter $\varepsilon = 0, 1$. This function is used in the work to get numerical results.

3 BASIC RELATIONS

According to [5], the stresses and the displacement in each domain Ω_k ($k = 1, 2$) are expresses in terms of two holomorphic functions $\Phi_k(z)$ and $\Psi_k(z)$

$$G(z, \eta_k) = \eta_k \Phi_k(z) + \overline{\Phi_k(z)} + \left[z\overline{\Phi_k'(z)} + \overline{\Psi_k(z)} \right] e^{-2i\alpha}, \quad z \in \Omega_k.$$

Here

$$G(z, \eta_k) = \begin{cases} \sigma_n, & \eta_k = 1, \\ -2\mu_k \dfrac{du}{dz}, & \eta_k = -\varkappa_k, \end{cases}$$

where $\varkappa_k = (3 - \nu_k)/(1 + \nu_k)$ for a plane stress state and $\varkappa_k = 3 - 4\nu_k$ for a plane deformation, σ_n is the traction at the area with the normal $\mathbf{n}$, α is the angle between the direction $\mathbf{t}$ of the area and the x_1 axis.

Following [9], introduce new functions $\Upsilon_k(z)$ holomorphic in the domain $\widetilde{\Omega}_k = \{z : \bar{z}^{-1} \in \Omega_k\}$ with the boundary $\widetilde{\Gamma}$ which is symmetrical to the interface Γ relative to the

unit circle,

$$\Upsilon(z) = -\overline{\Phi(\bar{z}^{-1})} + z^{-1}\overline{\Phi'(\bar{z}^{-1})} + z^{-2}\overline{\Psi(\bar{z}^{-1})}, \quad \bar{z}^{-1} \in \Omega_k. \tag{4}$$

We determine the unknown functions $\Phi_k(z)$ and $\Upsilon_k(z)$ from the boundary conditions (2). Passing to the limit for $z \to \zeta \in \Gamma, z \in \Omega_k$ [5] and taking into account the relation (4), the following boundary equations for complex potentials Φ_k and Υ_k can be written as

$$G(\zeta, \eta_k) = \eta_k \Phi_k(\zeta) + \overline{\Phi_k(\zeta)} + \frac{\rho' - i\rho}{\rho' + i\rho}\left[\frac{1}{\overline{\zeta}^2}\left(\overline{\Phi_k(\zeta)} + \Upsilon_k\left(\frac{1}{\overline{\zeta}}\right)\right) + \left(\zeta - \frac{1}{\overline{\zeta}}\right)\overline{\Phi_k'(\zeta)}\right]\bar{s}^2, \tag{5}$$

where $\Phi_k(\zeta) = \lim\limits_{z\to\zeta} \Phi_k(z)$ when $z \in \Omega_k$ and $\Upsilon_k(\zeta) = \lim\limits_{z\to\zeta} \Upsilon_k(z)$ when $z \in \widetilde{\Omega}_k$.

4 BOUNDARY PERTURBATION TECHNIQUE

In equation (5) $\zeta \in \Gamma$, but $\overline{\zeta}^{-1} \in \widetilde{\Gamma}$. If $\varepsilon = 0$, then $\Gamma = \widetilde{\Gamma}$ that corresponds to the appropriate boundary value problem for the circular inclusion. In the general case for $0 < \varepsilon \ll 1$, the curves Γ and $\widetilde{\Gamma}$ represent small perturbations of the unit circle. Consequently, to find unknown functions $\Phi_k(z)$, $\Upsilon_k(z)$ and the solution of the problem, we can use boundary perturbation procedure. Following [3], [4], [11]–[13], we represent functions Φ_k and Υ_k as power series in the small parameter ε

$$\Phi_k(z) = \sum_{n=0}^{\infty} \frac{\varepsilon^n}{n!}\Phi_{kn}(z), \quad \Upsilon_k(z) = \sum_{n=0}^{\infty} \frac{\varepsilon^n}{n!}\Upsilon_{kn}(z). \tag{6}$$

Expand the boundary values of functions Φ_{kn}, Υ_{kn} at Γ and $\widetilde{\Gamma}$ into Taylor series in the vicinity of unit circle ($|z| = 1$)

$$\Phi_{kn}(\zeta) = \sum_{m=0}^{\infty} \frac{(\varepsilon f(s)s)^m}{m!}\Phi_{kn}^{(m)}(s), \quad \Upsilon_{kn}\left(\frac{1}{\overline{\zeta}}\right) = \sum_{m=0}^{\infty} \frac{(\varepsilon f(\bar{s})\bar{s})^m}{m!}\frac{d^m}{d\bar{s}^m}\Upsilon_{kn}\left(\frac{1}{\bar{s}}\right). \tag{7}$$

We also derive the expressions for all functions in (5) as power series in the small parameter ε [3].

Taking into account the definition of the function G (5), the equations (2) can be transformed into the following

$$m_1 G^+(\zeta, \eta_2) - m_2 G^-(\zeta, \eta_1) = 0, \tag{8}$$

where $m_k = 1, k = 1, 2$ for $\eta_1 = \eta_2 = 1$ and $m_k = \mu_k$ for $\eta_k = -\varkappa_k$.

Substituting (5) into equation (8) and taking into account series (6), (7), we equate the sum of coefficients of the same power ε^n $(n = 0, 1, \ldots)$ to zero. Then we arrive at the

Rimann — Gilbert boundary value problems on the jump of holomorphic functions $\Sigma_n(z)$ and $V_n(z)$ for n-order approximation

$$\begin{array}{l} \Sigma_n^+(s) - \Sigma_n^-(s) = q_n(s), \quad |s| = 1, \\ V_n^+(s) - V_n^-(s) = r_n(s), \quad |s| = 1. \end{array} \tag{9}$$

Here $\Sigma_n^{\pm} = \lim\limits_{|z|\to 1\mp 0} \Sigma_n(z)$, $V_n^{\pm} = \lim\limits_{|z|\to 1\mp 0} V_n(z)$; q_n, r_n – are the known functions depending on all previous approximations and the conditions at infinity (3). The piecewise holomorphic functions $\Sigma_n(z)$, $V_n(z)$ are defined as

$$\Sigma_n(z) = \left\{ \begin{array}{ll} \Upsilon_{1n}(z) + \Phi_{2n}(z), & |z| < 1, \\ \Upsilon_{2n}(z) + \Phi_{1n}(z), & |z| > 1, \end{array} \right. \tag{10}$$

$$V_n(z) = \left\{ \begin{array}{ll} \mu_2 \Upsilon_{1n}(z) - \mu_1 \varkappa_2 \Phi_{2n}(z), & |z| < 1, \\ \mu_1 \Upsilon_{2n}(z) - \mu_2 \varkappa_1 \Phi_{1n}(z), & |z| > 1. \end{array} \right. \tag{11}$$

According to [5], solutions of the problems (9) can be written in terms of Cauchy type integrals

$$\begin{array}{c} \Sigma_n(z) = I_1(z) + b_0 + S_n(z) + D_1, \quad z \in \Omega_1 \cup \Omega_2, \\ V_n(z) = I_2(z) + \mu_1 b_0 - \mu_2 \varkappa_1 D_1 + \mu_2 S_n(z), \quad z \in \Omega_1 \cup \Omega_2, \end{array}$$

where

$$I_1(z) = \frac{1}{2\pi i} \int\limits_{\Gamma} \frac{q_n(\zeta)}{\zeta - z} d\zeta, \quad I_2(z) = \frac{1}{2\pi i} \int\limits_{\Gamma} \frac{r_n(\zeta)}{\zeta - z} d\zeta,$$

and $S_0 = \overline{D}_2 z^{-2}$, $S_n = 0$ $(n = 1, 2, \dots)$, $4D_1 = \sigma_{11}^{\infty} + \sigma_{22}^{\infty} + i8\mu_1\omega^{\infty}/(\varkappa_1 + 1)$, $2D_2 = \sigma_{22}^{\infty} - \sigma_{11}^{\infty} + 2i\sigma_{12}^{\infty}$.

The constant b_0 is found from equation [5]

$$(\mu_1 - \mu_2) b_0 - (\mu_2 + \mu_1 \varkappa_2) \overline{b_0} = \mu_2 (1 + \varkappa_1) D_1.$$

The expressions for the complex potentials of n-order approximations are derived from (10), (11)

$$\Phi_{kn}(z) = \frac{\mu_k \Sigma_n(z) - V_n(z)}{\mu_k + \mu_l \varkappa_k}, \quad \Upsilon_{kn}(\bar{z}^{-1}) = \frac{\mu_k \varkappa_l \Sigma_n(\bar{z}^{-1}) - V_n(\bar{z}^{-1})}{\mu_l + \mu_k \varkappa_l}, \tag{12}$$

where $z \in \Omega_k$, $l = 3 - k$, $k = 1, 2$.

5 FIRST-ORDER APPROXIMATION

The complex potentials in the zero-order approximation which correspond to the solution of the appropriate boundary value problem for the circular inclusion, are determined [5] as

$$\Upsilon_{10}\left(\frac{1}{\bar{z}}\right) = \frac{\mu_1(\varkappa_2+1)b_0 + (\mu_1\varkappa_2 - \mu_2\varkappa_1)D_1}{\mu_2+\mu_1\varkappa_2} + \overline{D_2}\bar{z}^2,$$

$$\Phi_{10} = D_1 + \frac{\mu_1-\mu_2}{\mu_1+\mu_2\varkappa_1}\frac{\overline{D_2}}{z^2}, \quad |z|>1,$$

$$\Upsilon_{20}\left(\frac{1}{\bar{z}}\right) = \frac{\mu_2(\varkappa_1+1)\overline{D_2}\bar{z}^2}{\mu_1+\mu_2\varkappa_1} + b_0,$$

$$\Phi_{20}(z) = \frac{(\mu_2-\mu_1)b_0 + \mu_2(\varkappa_1+1)D_1}{\mu_2+\mu_1\varkappa_2}, \quad |z|<1.$$

By solving corresponding Riemann – Hilbert's boundary problems and taking into account (12), we obtain the complex potentials of the first-order approximation for the nearly circular inclusion the shape of which is determined by the function $f(s) = (s^2+s^{-2})/2 = \cos 2\theta$:

$$\Phi_{11}(z) = \frac{1}{1+M\varkappa_1}(z^{-2}(D_1(1-\beta)+\overline{D_1}+b_0\gamma - M(D_1(2-\beta)+\gamma b_0)) + z^{-4}(\overline{D_2}(\xi+2) - M\overline{D_2}(2+\varkappa_1\xi))), \quad z\in\Omega_1, \tag{13}$$

$$\Upsilon_{11} = \frac{1}{M+\varkappa_2}(\varkappa_2\xi(\overline{D_2}+D_2) + M(\xi D_2 + 2\overline{D_2}) - 2\overline{D_2}(1-\xi) - M\varkappa_1\xi\overline{D_2}) - 3z^2(\varkappa_2(2(1-\gamma)b_0 + (D_1+\overline{D_1})(\beta-1)) + b_0(2-\gamma) + \beta\overline{D_1} - M(D_1(2-\beta)+\gamma b_0)) + 5\xi D_2 z^4(\varkappa_2+M)), \quad z\in\widetilde{\Omega}_1, \tag{14}$$

$$\Phi_{21} = \frac{1}{M+\varkappa_2}(z^{-2}(b_0(2-\gamma)+\beta\overline{D_1} - M(D_1+\overline{D_1}(\beta-1)+b_0(2-\gamma))) + \overline{D_2}z^{-4}(3\xi M - 2M + 2(1-\xi) - \varkappa_1\xi M)), \quad z\in\Omega_2,$$

$$\Upsilon_{21} = \frac{1}{1+M\varkappa_1}(M(\varkappa_1\xi D_2 + \xi D_2 + 2\overline{D_2}) - 2\overline{D_2}(1-\xi) - 3z^2(M\varkappa_1(2(1-\gamma)b_0 + (D_1+\overline{D_1})(\beta-1)) + b_0(2-\gamma) + \beta\overline{D_1} - M(D_1(2-\beta)+\gamma b_0)) + 5M\xi D_2 z^4(\varkappa_1+1)), \quad z\in\widetilde{\Omega}_2.$$

Here, we introduce the following notations

$$M = \frac{\mu_2}{\mu_1}, \quad \xi = \frac{\mu_1 - \mu_2}{\mu_1 + \mu_2 \varkappa_1}, \quad \beta = \frac{\mu_2(\varkappa_1 + 1)}{\mu_2 + \mu_1 \varkappa_2}, \quad \gamma = \frac{\mu_1(\varkappa_2 + 1)}{\mu_2 + \mu_1 \varkappa_2}.$$

For the boundary value problem on an elastic plane with a nearly circular hole, we assume $\mu_2 = 0$ in equations (13), (14) . Then for the case $\omega^\infty = 0$, complex potentials are written in the form:

$$\Phi_{11} = 3\overline{D_2} z^{-4} + 2D_1 z^{-2}, \quad \Upsilon_{11} = \overline{D_2} + D_2 + 6D_1 z^2 + 5D_2 z^4.$$

This solution coincides with the solution obtained in [3]. In this case $\Phi_{21}(z) = 0$, $\Upsilon_{21}(z) = 0$.

In the zero-order approximation, we obtain the expressions for the hoop stresses σ_{tt} at the circular interface for $k = 1, 2$ in the form

$$\sigma_{tt}^{k0}(s) = \Re\left[\Phi_{k0}(s) + 2\overline{\Phi_{k0}}(s) + \Upsilon_{k0}\left(\bar{s}^{-1}\right)\right].$$

In the first-order approximation

$$\sigma_{tt}^{k}(s) = \sigma_{tt}^{k0}(s) + \varepsilon \sigma_{tt}^{k1}(s),$$

where $\sigma_{tt}^{k1}(s) = \Re[F_1]$,

$$F_1 = \left(\Phi_{k1}(s) + 2\overline{\Phi_{k1}(s)} + \Upsilon_{k1}\left(\bar{s}^{-1}\right) + sf(s)\Phi_{k0}'(s) + \bar{s}f(\bar{s})\left(2\overline{\Phi_{k0}'(s)} + \frac{d\Upsilon_{k0}\left(\bar{s}^{-1}\right)}{d\bar{s}}\right)\right) +$$
$$+2\left(\left(if_\theta'(s) - f(s)\right)\left(\overline{\Phi_{k0}(s)} + \Upsilon_{k0}\left(\bar{s}^{-1}\right)\right) + \bar{s}f(s)\overline{\Phi_{k0}'(s)}\right).$$

6 NUMERICAL RESULTS AND DISCUSSION

Selected numerical results obtained for the hoop stress σ_{tt} at the interface are shown in Fig. 2 in the case of the uniaxial tension σ_{22}^∞ along axis x_2, i. e., for $\sigma_{11}^\infty = \sigma_{12}^\infty = 0$, $\sigma_{22}^\infty > 0$ when $\varepsilon = 0$ and $\varepsilon = 0, 1$. The graphs are plotted for two values of the bimaterial parameter $M = \mu_2/\mu_1$.

Analyzing the dependences shown in Fig. 2, we come to the following conclusion:

- For a softer nearly circular inclusion (when $M < 1$) stress concentration in the inclusion and in the matrix is greater than in the case of circular inclusion corresponding to the zero-order approximation. At the same time, stress concentration in the matrix is greater than in the inclusion (Fig. 2a). It is worth noting that in the case of $M < 1$, the zone of compression in the matrix is wider for the nearly circular inclusion than for the ideal circular one.

- If the inclusion more rigid than the matrix ($M > 1$), the results are opposite (Fig. 2b).

- Comparison with similar results obtained for the nearly circular hole ($\mu_2 = 0$) in [3] shows that, for any value of parameter M, the presence of the inclusion reduces the stress concentration in the matrix.

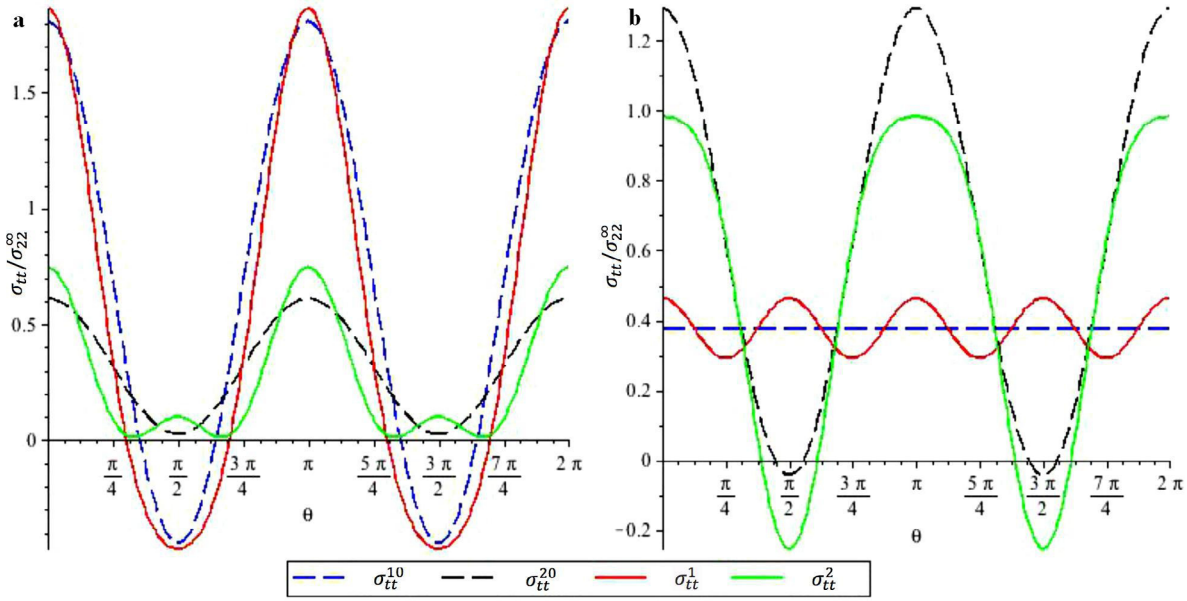

Figure 2: Dependence of hoop stresses σ_{tt} at the boundary of the inclusion, given by the function $f(\theta) = \cos 2\theta$, upon the polar angle θ under uniaxial tension for $\varepsilon = 0, 1$ and $M = 1/3; 10/3$ (a, b).

REFERENCES

[1] Grekov, M.A. and Yazovskaya, A.A. Effect of surface elasticity and residual surface stress in an elastic body weakened by an elliptic hole of a nanometer size. *J. Appl. Math. Mech.* (2014) **78**: 172–180.

[2] Pronina, Y. An analytical solution for the mechanochemical growth of an elliptical hole in an elastic plane under a uniform remote load. *Europ. J. Mech. – A/Solids.* (2017) **61**: 357–363.

[3] Bashkankova, E.A., Vakaeva, A.B. and Grekov, M.A. Perturbation method in the problem on a nearly circular hole in an elastic plane. *Mech. Solids.* (2015) **50**: 198–207.

[4] Grekov, M.A. and Vakaeva, A.B. Effect of nanosized asperities at the surface of a nanohole. *Proceedings of the VII European Congress on Computational Methods in Applied Sciences and Engineering.* (2016) **IV**: 7875–7885.

[5] Grekov, M.A. Joint deformation of a circular inclusion and a matrix. *Vestnik St. Petersburg University: Math.* (2010) **43**: 114–121.

[6] Vikulina, Yu.I., Grekov, M.A. and Kostyrko, S.A. Model of film coating with weakly curved surface. *Mech. Solids.* (2010) **45**: 778–788.

[7] Grekov, M.A. and Kostyrko, M.A. A film coating on a rough surface of an elastic body. *J. Appl. Math. Mech.* (2013) **77**: 79–90.

[8] Vakaeva, A.B. and Grekov, M.A. Effect of surface stresses in an elastic body with a curvilinear nanohole. *Proceedings of The 2015 International Conference "Stability and Control Processes" in Memory of V.I. Zubov (SCP).* (2015) 440–443.

[9] Muskhelishvili, N.I. *Some Basic Problems of the Mathematical Theory of Elasticity.* Groningen: Noordhoff, (1963).

[10] Gao, H. A boundary perturbation analysis for elastic inclusions and interfaces. *Int. J. Solids Struct.* (1991) **28**: 703–725.

[11] Grekov, M.A. and Kostyrko, S.A. Surface defect formation in nanosized film coating due to diffusion processes. *Proceedings of The 2015 International Conference on Mechanics – Seventh Polyakhov's Reading.* (2015) 1–4.

[12] Kostyrko, S.A. and Shuvalov, G.M. Morphological stability of multilayer film surface during diffusion processes. *Proceedings of The 2015 International Conference "Stability and Control Processes" in Memory of V.I. Zubov (SCP).* (2015) 392–395.

[13] Grekov, M.A. The perturbation approach for a two-component composite with a slightly curved interface. *Vestnik St. Petersburg University: Math.* (2004) **37**: 81–88.

VII International Conference on Computational Methods for Coupled Problems in Science and Engineering
COUPLED PROBLEMS 2017
M. Papadrakakis, E. Oñate and B. Schrefler (Eds)

TIME-REVERSAL METHODS FOR ACOUSTO-ELASTIC EQUATIONS AND APPLICATIONS

Franck Assous* **and Moshe Lin***

* Department of Mathematics
Ariel University,
Ariel, 40700, Israel.
e-mail: franckassous55@gmail.com
e-mail: moshelin1@walla.co.il

Key words: Time Reverse, Elastodynamics, Wave propagation, Finite Element, Inverse problems

Abstract. Time reversal (TR) is a subject of very active research. The principle is to take advantage of the reversibility of wave propagation phenomena, for example in acoustics, elastic or electromagnetism in an unknown medium, to back-propagate signals to the sources that emitted them. In a previous paper [1], we introduced a time-reversed method for acoustic equation. In this paper, our aim is to extend this approach to elastodynamics equations. As the application we have in mind are concerned with ultrasound-based elasticity imaging methods, we consider both elastic and acousto-elastic systems of equations. We stress that our method does not rely on any a priori knowledge of the physical properties of the inclusion.

1 INTRODUCTION

Time reversal (TR) is a subject of very active research. The principle is to take advantage of the reversibility of wave propagation phenomena, for example in acoustics,

elastic or electromagnetism in an unknown medium, to back-propagate signals to the sources that emitted them. The initial experiment [2], was to refocus, very precisely, a recorded signal after passing through a barrier consisting of randomly distributed metal rods. Since then, numerous applications of this physical principle have been designed, for instance [3] and references therein. The first mathematical analysis can be found in [4] for a homogeneous medium and in [5], [6] for a random medium.

In a previous paper [1], we introduced a time-reversed method named TRAC (Time-Reversed Absorbing Conditions) for acoustic equation. This method enables one to recreate the past without knowing the location and the properties of the inclusion which diffracted the signals that are back-propagated. This was made possible by removing a small region surrounding the scattering inclusion.

In this paper, our aim is to extend our approach to elastodynamics equations. As the application we have in mind are concerned with ultrasound-based elasticity imaging methods, we also consider a coupled acousto-elastic system of equations, the elastodynamics case being a particular case of the acousto-elastic one. For the sake of simplicity, fluid-solid media that we choose to be "layered". Remark that the method does not require *a priori* knowledge of the physical properties of the inclusion: hard, soft and penetrable inclusions can be treated in the same way.

2 FORWARD PROBLEM

We first formulate the mathematical forward model we consider. As we are concerned with the elastic wave or acousto-elastic wave equation, we will present here the more complete one, that is the second one. The elastic governing equations can be easily derived by removing the fluid part (and related equations) from the model described below.

We consider a two-dimensional fluid-elastic domain Ω made of two parts, an acoustic one Ω_f and and elastic one Ω_s. For simplicity, we will assume that Ω is a rectangle. The acoustic part of the domain Ω_f corresponds to a fluid homogeneous part, characterized

by its density ρ_f and its Lame parameter λ_f. We denote by $\partial\Omega_f$ the boundary of Ω_f and $\mathbf{n}$ is the outward unit normal to the boundary. Introduce the pressure $p(\mathbf{x},t)$ on a time t, $\mathbf{x} = (x_1, x_2) \in \Omega_f$, and $f(\mathbf{x},t)$ is a given source, for instance a Ricker function, the acoustic wave equation in Ω_f is written

$$\frac{1}{\lambda_f}\frac{\partial^2 p}{\partial t^2} - \operatorname{div}\left(\frac{1}{\rho_f}\nabla p\right) = f\,, \tag{1}$$

together with homogeneous initial conditions at the initial time $t = 0$

$$p(t=0) = 0, \quad \frac{\partial p}{\partial t}(t=0) = 0\,. \tag{2}$$

We assume that the boundary $\partial\Omega_f$ can be split in $\partial\Omega_f = \Gamma_f \cup \Gamma_I$, where Γ_I denotes the interface between the fluid and elastic part, assumed, for simplicity reasons, to be horizontal. We supplement the system with absorbing boundary conditions [7] on $\partial\Omega_f$. Denoting by $V_p = \sqrt{\frac{\lambda}{\rho}}$ the wave velocity in the fluid, we get

$$\frac{\partial p}{\partial t} = -V_p\,\nabla p \cdot \mathbf{n} \quad \text{ on } \Gamma_f\,. \tag{3}$$

On the part Γ_I, we add an interface condition for the pressure $p(\mathbf{x},t)$, that will be presented below, see (9).

We then introduce the governing equations of linear elastodynamics for the elastic part of the domain Ω_s, characterized by the density ρ_s, and the Lamé parameter λ_s and μ_s. We assume that the boundary $\partial\Omega_s$ can be split in $\partial\Omega_s = \Gamma_s \cup \Gamma_I$. Denoting by $\mathbf{u}(\mathbf{x},t) = (u_1(x_1,x_2,t), u_2(x_1,x_2,t))$ the velocity on a time t, at a point $\mathbf{x} = (x_1,x_2) \in \Omega_s$, we have

$$\rho_s\frac{\partial^2 u_1}{\partial t^2} - \frac{\partial}{\partial x_1}((\lambda_s+2\mu_s)\frac{\partial u_1}{\partial x_1} + \lambda_s\frac{\partial u_2}{\partial x_2}) - \frac{\partial}{\partial x_2}(\mu_s\frac{\partial u_1}{\partial x_2} + \mu_s\frac{\partial u_2}{\partial x_1}) = 0\,, \tag{4}$$

$$\rho_s\frac{\partial^2 u_2}{\partial t^2} - \frac{\partial}{\partial x_1}(\mu_s\frac{\partial u_1}{\partial x_2} + \mu_s\frac{\partial u_2}{\partial x_1}) - \frac{\partial}{\partial x_2}((\lambda_s+2\mu_s)\frac{\partial u_2}{\partial x_2} + \lambda_s\frac{\partial u_1}{\partial x_1}) = 0\,. \tag{5}$$

The above equations can be written also in the following compact form

$$\rho_s \frac{\partial^2 \mathbf{u}}{\partial t^2} - \nabla \cdot (\mu_s \nabla \mathbf{u}) - \nabla((\lambda_s + \mu_s)\nabla \cdot \mathbf{u}) = 0\,, \tag{6}$$

together with homogeneous initial conditions:

$$\mathbf{u}(t=0) = 0, \quad \frac{\partial \mathbf{u}}{\partial t}(t=0) = 0\,. \tag{7}$$

These equations are also supplemented with the absorbing boundary conditions on Γ_s, as proposed in [8]. Introduce the following matrix A:

- $A = \begin{pmatrix} -\sqrt{\rho_s(\lambda_s + 2\mu_s)} & 0 \\ 0 & -\sqrt{\rho_s \mu_s} \end{pmatrix}$ for vertical boundary edges,
- $A = \begin{pmatrix} -\sqrt{\rho_s \mu_s} & 0 \\ 0 & -\sqrt{\rho_s(\lambda_s + 2\mu_s)} \end{pmatrix}$ for horizontal boundary edges,

and the (2×2) matrix $T := (\tau_{ij})_{1 \le i,j \le 2}$ defined by

- $\tau_{11} = \lambda_s(\frac{\partial u_1}{\partial x_1} + \frac{\partial u_2}{\partial x_2}) + 2\mu_s \frac{\partial u_1}{\partial x_1}$
- $\tau_{12} = \tau_{21} = \mu_s(\frac{\partial u_1}{\partial x_2} + \frac{\partial u_2}{\partial x_1})$
- $\tau_{22} = \lambda_s(\frac{\partial u_1}{\partial x_1} + \frac{\partial u_2}{\partial x_2}) + 2\mu_s \frac{\partial u_2}{\partial x_2}$

$$A \frac{\partial}{\partial t} \begin{pmatrix} u_1 \\ u_2 \end{pmatrix} = \tau_{ij} \cdot \mathbf{n} \tag{8}$$

Finally, we introduce the transmission conditions at the interface Γ_I between the fluid and the solid parts, the pressure-velocity formulation allowing us to express them easily. We set

$$\frac{1}{\rho_f} \frac{\partial p}{\partial x_2} = -\frac{\partial u_2}{\partial t} \tag{9}$$

$$\frac{\partial u_1}{\partial x_2} + \frac{\partial u_2}{\partial x_1} = 0, \qquad \frac{\partial p}{\partial t} = \lambda_s \frac{\partial u_1}{\partial x_1} + (\lambda_s + 2\mu_s)\frac{\partial u_2}{\partial x_2} \tag{10}$$

In particular, these conditions will appear naturally in the variational formulation, that will be basis of the finite element method.

3 TIME REVERSE PROBLEMS

In a second step, we will use time reverse methods to solve time reversed acousto-elastic and elastodynamics problems. Recall that the main idea of time reverse is to take advantage of the reversibility of wave propagation phenomena in a non dissipative unknown medium to back-propagate signals to the sources that emitted them [9]. Examples for time reverse technique (numerical or experimental) are presented in [2, 9, 10, 11].

We first introduce the time-reversed wave equations for the acoustic part of the domain Ω_f. We denoted by $p^R(\mathbf{x}, t')$ the time-reversed pressure, defined by $p^R(\mathbf{x}, t') = p(\mathbf{x}, T - t)$, $\mathbf{x} \in \Omega_f$, where T denotes the final time. Since the wave equation involves only second order time derivatives, this definition ensures that the reverse field $p^R(\mathbf{x}, t')$ is a solution to the wave equation

$$\frac{1}{\lambda_f}\frac{\partial^2 p^R}{\partial t'^2} - \operatorname{div}\left(\frac{1}{\rho_f}\nabla p^R\right) = 0\,, \tag{11}$$

together with initial conditions:

$$p^R(t' = 0) = p(t = T), \qquad \frac{\partial p^R}{\partial t'}(t' = 0) = \frac{\partial p}{\partial t}(t = T)\,, \tag{12}$$

with the TR absorbing boundary conditions on Γ_f, analogous to (3).

Similarly, we also introduce the elastic time-reversed problem associated to equations (4-8). We denote by $\mathbf{u}^R(\mathbf{x}, t') = (u_1^R(x_1, x_2, t'), u_2^R(x_1, x_2, t'))$ the time-reversed velocity solution to linear elastodynamics, that solves

$$\rho_s\frac{\partial^2 u_1^R}{\partial t'^2} - \frac{\partial}{\partial x_1}((\lambda_s + 2\mu_s)\frac{\partial u_1^R}{\partial x_1} + \lambda_s\frac{\partial u_2^R}{\partial x_2}) - \frac{\partial}{\partial x_2}(\mu_s\frac{\partial u_1^R}{\partial x_2} + \mu_s\frac{\partial u_2^R}{\partial x_1}) = 0\,, \tag{13}$$

$$\rho_s\frac{\partial^2 u_2^R}{\partial t'^2} - \frac{\partial}{\partial x_1}(\mu_s\frac{\partial u_1^R}{\partial x_2} + \mu_s\frac{\partial u_2^R}{\partial x_1}) - \frac{\partial}{\partial x_2}((\lambda_s + 2\mu_s)\frac{\partial u_2^R}{\partial x_2} + \lambda_s\frac{\partial u_1^R}{\partial x_1}) = 0\,, \tag{14}$$

together with initial conditions

$$\mathbf{u}^R(t' = 0) = \mathbf{u}(t = T), \qquad \frac{\partial \mathbf{u}^R}{\partial t'}(t' = 0) = \frac{\partial \mathbf{u}}{\partial t}(t = T)\,. \tag{15}$$

The absorbing boundary conditions on Γ_s have the same expression as in (8) simply by replacing $\mathbf{u}$ by $\mathbf{u}^R$.

Finally, we derive the time-reversed continuity transmission conditions at the interface Γ_I that can be written

$$\frac{1}{\rho_f}\frac{\partial p^R}{\partial x_2} = -\frac{\partial u_2^R}{\partial t'} \tag{16}$$

$$\frac{\partial u_1^R}{\partial x_2} + \frac{\partial u_2^R}{\partial x_1} = 0, \qquad \frac{\partial p^R}{\partial t'} = \lambda_s \frac{\partial u_1^R}{\partial x_1} + (\lambda_s + 2\mu_s)\frac{\partial u_2^R}{\partial x_2} \tag{17}$$

In order to create synthetic data, the forward and reverse formulations are approximated by the FreeFem++ package [14] which implements a finite element method in space. In this study we use a standard P^2 finite element method. The advancement in time is given by a second order central finite difference scheme so that it is time reversible also on the numerical level.

4 NUMERICAL RESULTS

In this section, we describe numerical results obtained for a scatter identification problem, in the case of layered acousto-elastic medium. The principle of the method can be described as follows: let us consider an incident wave impinging on an inclusion D characterized by different physical properties from the surrounding medium. This incident wave is generated by a point source such that after a time T_f the total field is negligible. We introduce a boundary - modeling source-receivers array (SRA) - where the forward signal is recorded.

Then, we perform numerically a time-reversed computation, by back propagating the recorded data from the SRA. However, we do not assume we know the physical properties of the inclusion or its location. Hence, the recorded data are back propagated in the medium without the inclusion D. Finally, we intend to image the unknown scatterer in the medium - responsible of the diffraction of the incident wave - by using correlation method between the forward and the reversed wave, in the same spirit as those involved

for instance in time reverse migration [12].

To illustrate our purpose, we consider a two layered medium, made of fluid part (top) and of a elastic one (bottom). The source $f(\mathbf{x}, t)$ and the SRA are located in the homogeneous fluid part of the medium, whereas the inclusion D is located in the elastic part, assumed to be an homogeneous and isotropic medium with propagation velocities V_p and V_s. Hence, the scatterer D is illuminated by an incident acoustic field, that is first transmitted to the elastic medium through the interface Γ_I, and then scattered by the inclusion D, before to be recorded by the SRA. The SRA being located in the fluid part, they are able to record only a scalar quantity (the pressure $p(\mathbf{x}, t)$), and not a vector velocities $\mathbf{u}(\mathbf{x}, t)$.

However, as shown on Figure 1, where the correlation image between the forward and the reversed wave is depicted (only in the elastic layer), one is able to determine the existence and location of the inclusion D. Note also that one can detect the presence of the interface fluid-solid Γ_I.

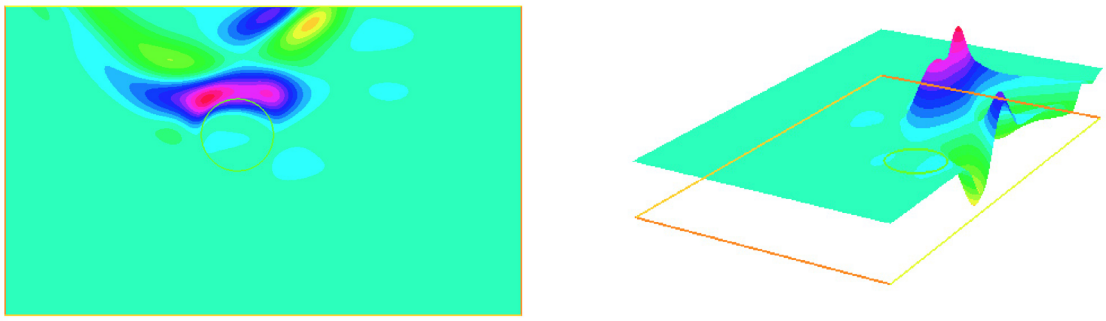

(a) two-dimensional representation (b) three-dimensional representation

Figure 1: correlation between the forward and the reversed wave (representation of the elastic layer)

5 CONCLUSION

In this paper, we proposed a numerical time-reversed approach for elastic or acousto-elastic equations. We have derived a finite element method for both models, implemented

with the Freefem++ software. Preliminary results have been presented to illustrate the feasibility of the algorithm. In particular, the method does not rely on any *a priori* knowledge of the physical properties of the inclusion. In a future paper, other important aspects will also be investigated: more general configurations that mimics a soft tissue, that would lead to (try to) apply our method in the framework of breast tumors detection. In particular, one will consider to use only partial information, or to try to image the scatterer in case of "noisy" (partially unknown) medium. One will also evaluate the quality of the material elasticity parameters obtained by introducing a well adapted cost function, in the same spirit as what is derived for inverse problems. As usual in this context, optimization based algorithm will be necessary to achieve this part.

REFERENCES

[1] Assous, F., Kray, M. and Nataf, F. Time-reversed absorbing conditions in the partial aperture case. *Wave Motion* (2012), **49**: 617–631.

[2] Fink, M., Wu, F., Cassereau, D. and Mallart, R. Imaging through inhomogeneous media using time reversal mirrors. *Ultrasonic Imaging* (1991), **13-2**: 179–199.

[3] Larmat, C., Montagner, J.-P. , Fink, M., Capdeville, Y., Tourin, A. and Clévédé, E. Time-reversal imaging of seismic sources and application to the great sumatra earthquake. *Geophys. Res. Lett.* (2006), **33**: 1–4.

[4] Bardos, C. and Fink, M. Mathematical foundations of the time reversal mirror. *Asymptot. Anal.* (2002), **29**:157–182.

[5] Clouet , J.-F. and Fouque, J.-P. A time-reversal method for an acoustical pulse propagating in randomly layered media. *Wave Motion* (1997), **25**: 361–368.

[6] Blomgren, P., Papanicolaou, G. and Zhao, H. Super-resolution in time-reversal acoustics. *J. Acoust. Soc. Am.* (2002), **111**: 230–248.

[7] Clayton,R. and Engquist, B. Absorbing boundary conditions for acoustic and elastic wave equations. *bull. Seismol. Soc. Amer.* (1977), **67**: 1529–1540.

[8] Halpern, L. Etudes des conditions aux limites absorbantes pour des schémas numériques relatifs a des équations hyperboliques linéaires. *Ph.D Thesis* (1980), Paris VI University.

[9] Assous, F., Kray, M., Nataf, F. and Turkel, E. Time reversed absorbing condition: Application to inverse problems. *Inverse Problems* (2011) ,**27 (6**): 065003.

[10] Givoli, D. and Turkel, E. Time reversal with partial information for wave refocusing and scatterer identification. *Computer methods in applied mechanics and engineering* (2012), **213-216**: 223–242.

[11] Kosmas, P. and Rappaport, C. M. Time reversal with the fdtd method for microwave breast cancer detection. *IEEE Transactions on Microwave Theory and Techniques* (2005), **53 (7)**: 2317–2323.

[12] Claerbout, J.F. *Imaging the Earths interior*. Blackwell, 1985.

[13] Carin, L. , Liu, H., Yoder, T. , Couchman, L., Houston, B. and Bucaro, J. Wideband time-reversal imaging for classification of an elastic target in an acoustic waveguide. *J. Acoust. Soc. Am.* (2004), **115**: 259–68.

[14] Hecht, F. New development in FreeFem++. *J. Numer. Math.* (2012), **20 (3-4)**: 251–265.

VII International Conference on Computational Methods for Coupled Problems in Science and Engineering
COUPLED PROBLEMS 2017
M. Papadrakakis, E. Oñate and B. Schrefler (Eds)

A COMPARATIVE STUDY OF INTERFACE CAPTURING METHODS WITH AMR FOR INCOMPRESSIBLE TWO-PHASE FLOWS

OSCAR ANTEPARA[*†], NESTOR BALCAZAR[*] AND ASSENSI OLIVA[†]

[*]Termo Fluids S.L.
Avda Jacquard 97 1-E, 08222 Terrassa (Barcelona), Spain
e-mail: termofluids@termofluids.com, web page: http://www.termofluids.com/

[†]Heat and Mass Transfer Technological Center (CTTC)
Universitat Politécnica de Catalunya-BarcelonaTech (UPC)
ETSEIAAT, Colom 11, 08222 Terrassa, Barcelona, Spain
e-mail: cttc@upc.edu, web page: http://www.cttc.upc.edu

Key words: Adaptive Mesh Refinement, interface capturing methods, two phase flows

Abstract. This paper presents a comparative study of interface capturing methods with adaptive mesh refinement for Direct Numerical Simulation (DNS) of incompressible two-phase flows. The numerical algorithms for fluid motion and interface capturing methods have been previously introduced in the context of the finite-volume approach for both mass conservative level-set methodology and coupled volume-of-fluid/level-set method for unstructured/structured fixed meshes. The Adaptive Mesh Refinement (AMR) method introduced in consist on a cell-based refinement technique to minimize the number of computational cells and provide the spatial resolution required for the interface capturing methods. The present AMR framework adapts the mesh according to a physics-based refinement criteria defined by the movement of the interface between the fluid-phases. Numerical experiments are presented to evaluate the methods described in this work. This includes a study of the hydrodynamics of single bubbles rising in a quiescent viscous liquid, including its shape, terminal velocity, and wake patterns. These results are validated against experimental and numerical data well established in the scientific literature, as well as a comparison of the different approaches used.

1 INTRODUCTION

Rising bubble in quiescent viscous liquid has become recently in one of the major active research topics in multiphase science. Some computational studies have used detailed simulations of the bubble rising physics in two and three dimensions to explore the fluid effects and its dynamic behavior. In this context, the buoyancy-driven motion of a single

bubble can be used as a well-studied phenomenon to compare and evaluate different interface capturing methods and the use of adaptive mesh refinement algorithm to run dynamic simulations and give a new insight into the utilization of this tool for hexahedral and tetrahedral meshes.

In standard level-set (SLS) methods the interface is defined implicitly by the zero contour of a signed distance function [1]. An advection equation governs the evolution of this function in space and time, combined with a unique re-distancing algorithm. It is established the advantages of this method lies on the accurate computation of interface curvatures and normals, besides the drawback of the appearance of numerical errors that leads to loss or gain of mass. This problem is handled with a conservative level-set (CLS) [11, 6]. A review of the Volume of Fluid(VOF) method can be found in [3, 4]. In this approach, the interface is represented implicitly by a color function, determined to be the fraction of volume in each cell of one of the fluids. The interface needs to be reconstructed using a geometric technique to advect the VOF function[12]. An advantage of VOF method is the fact that certain algorithms can be used to advect the interface so that the mass can be conserved, while still maintaining a sharp representation of the interface. However, a disadvantage of the VOF method is the fact that it is hard to compute correct curvatures from the color function because it presents a step discontinuity at the interface. VOF/LS methods described by many authors [2, 5, 9] results as a combination of both approaches described before, bringing a whole approach for the interface capturing methods. In this way, the interface properties are obtained through a level-set method while mass conservation problems are avoided by using the VOF method.

In this work, the primary motivation is to discuss the simulation of rising bubbles to assess and compare the accuracy of interface capturing methods (CLS and VOF/LS) introduced in our previous works[6, 7, 8, 9, 10]. When using those numerical approaches to solving 2D and 3D multiphase problems, one of the disadvantages is the use of extensive computational resources to address the interfaces of the flows involved entirely. An efficient way to reduce the computational resources, computation time and still be able to have the spatial resolution required is using an adaptive mesh refinement (AMR) method introduced in previous work [13]. Some authors started to use AMR on multiphysics, and multiscale problems to get robust and accurate numerical results for problems, wherein without the use of AMR were much difficult to reach. On the literature, AMR with a Front-Tracking (FT) method was applied to series of rising bubble simulations in the wobbling regime [17]. Also, AMR with a hybrid LS/FT were useful to solve 2D two-phase flows in the presence of surface tension [18].

The outline of the paper is as follows: A summary of the governing equations is given in Section 2. Here, the coupling of the NavierStokes equations for two-phase flow is introduced through the inter-phase conditions, which incorporate surface tension. Moreover, a description of the AMR implementation is shown. The code validation and numerical results are displayed in Section 3. The conclusions are presented in Section 4.

2 MATHEMATICAL MODEL AND NUMERICAL METHODS

2.1 Incompressible two-phase flow

The momentum and mass conservation of two immiscible incompressible and Newtonian fluids are described by the Navier-Stokes equations defined a single fluid in Ω, with a singular source term for the surface tension force at the interface Γ [6, 10, 19, 20, 22]:

$$\frac{\partial}{\partial t}(\rho \mathbf{v}) + \nabla \cdot (\rho \mathbf{v}\mathbf{v}) = -\nabla p + \nabla \cdot \mu \left(\nabla \mathbf{v} + (\nabla \mathbf{v})^T\right) + \rho \mathbf{g} + \sigma \kappa \mathbf{n} \delta_\Gamma \tag{1}$$

$$\nabla \cdot \mathbf{v} = 0 \tag{2}$$

where ρ and μ are the density and dynamic viscosity of the fluids, $\mathbf{g}$ is the gravity acceleration, p is the pressure, $\mathbf{v}$ is the velocity field, the super-index T represents the transpose operator, δ_Γ is a Dirac delta function at the interface Γ, σ is the surface tension coefficient, κ is the curvature of the interface and $\mathbf{n}$ denotes the unit normal vector on the interface. Physical parameters change discontinuously across the interface:

$$\rho = \rho_1 H_1 + \rho_2 (1 - H_1) \qquad \mu = \mu_1 H_1 + \mu_2 (1 - H_1) \tag{3}$$

with ρ_1, ρ_2 and μ_1, μ_2 being the densities and viscosities of the first and second fluids, respectively, whereas H_1 is the Heaviside step function that is one at fluid 1 and zero elsewhere[6, 10].

2.2 Conservative level set equations

In the context of conservative level set (CLS) method[11, 6, 10], a regularized indicator function, ϕ, is employed as follows $\phi(\mathbf{x}, t) = 0.5\,(tanh\,(d(\mathbf{x}, t)/2\varepsilon) + 1)$, where d is a signed distance funtion, $\varepsilon = 0.5h^{0.9}$ is a tunable parameter that sets the thickness of the profile, h is the grid size[6, 10]. With this profile the interface Γ is defined by the location of the $\phi = 0.5$ iso-surface[6, 11], $\Gamma = \{\mathbf{x} \mid \phi(\mathbf{x}, t) = 0.5\}$. Since the level set function is avected by an incompressible velocity field, the following interface transport equation can be written in conservative form:

$$\frac{\partial \phi}{\partial t} + \nabla \cdot \phi \mathbf{v} = 0 \tag{4}$$

The level set function must be reinitialized to keep the profile and thickness of the interface constant following the next equation[6, 11]

$$\frac{\partial \phi}{\partial \tau} + \nabla \cdot \phi(1 - \phi)\mathbf{n} = \nabla \cdot \varepsilon \nabla \phi \tag{5}$$

The reader is referred to [6] for further details on the CLS method on unstructured meshes applied to this work.

2.3 Coupled volume-of-fluid/level-set method

In the volume-of-fluid method[3], an indicator function f is used to track the interface,

$$f(\mathbf{x},t) = \begin{cases} 1 & \text{if } \mathbf{x} \in \Omega_1 \\ 0 & \text{if } \mathbf{x} \in \Omega_2 \end{cases} \tag{6}$$

with Ω_1 and Ω_2 the sub-domains occupied by the fluid 1 and 2 respectively. Discretely, the information stored at the cell Ω_P is the volume-averaged indicator function, namely the volume fraction $f_P = \int_{\Omega_P} f(\mathbf{x},t)dV / \int_{\Omega_P} dV$, where V is the volume of the cell Ω_P. The advection equation for f is given by:

$$\frac{\partial f}{\partial t} + \mathbf{v} \cdot \nabla f = 0 \tag{7}$$

where $\mathbf{v}$ is the fluid velocity. The reader is referred to [12] for further details of the VOF-PLIC method used in the present work. The main idea in the coupled VOF/LS methods [2, 5] is to take the advantages of both approaches (VOF and LS). In the present formulation, the mass losses are reduced through the application of a VOF-PLIC method, while a fine representation of the interface curvature is preserved by utilizing the level set method. From the geometrical data of the interface given by the VOF-PLIC method, a signed distance function is reconstructed following a geometric algorithm[9]. Then, the signed distance function is used to compute surface tension forces. The reader is referred to [9] for further details on the VOF/LS method utilized in the present work.

2.4 Adaptive mesh refinement

Our computational approach uses an adaptive mesh refinement algorithm(AMR) based on a quad/octree for 2D and 3D grids. The reader is referred to [13, 14, 15] for details of the model and the numerical implementation for the use of this methodology to the simulation of turbulent flow around bluff bodies, and [16] for the application of AMR of [13] to the CLS method developed by [6]. The algorithm generates a new mesh according to a physical criterion. The implementation of the AMR algorithm follows the next steps:

Physics-based criterion computation. It is based on the indicator function used to track the interface. On this paper, the cells marked to refinement are the ones with an interface value between 0 and 1. Next, a group of neighbor cells is flagged as well, to ensure a refinement thickness surrounding the interface on both fluids direction. On the moment of one cell of the group does not match the conditions then the subinterval of time is stopped to continue to the next steps. Fig. 1 is an example of the bubble interface and the cells surrounding it to a maximum level.

Creation of the newly adapted meshes. For each AMR time interval, the current mesh, a list of global identifiers of cells, its corresponding level of refinement and, a tree data structure that keeps track of the cells decomposition are processed to create and return the newly mesh.

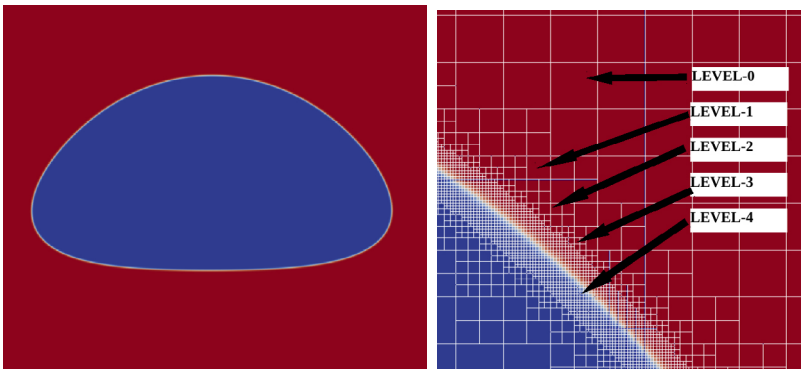

Figure 1: Illustration of refinement process for a two-dimensional rising bubble, where four levels of refinement has been applied.

Solution exchange. The intermediate solutions are transferred from one mesh to the newly. For now, we use a hierarchical cell evaluation mechanism: given any cell in the domain, it provides the value at this point and its hierarchical position on the quad/octree. Then, an average process is performed for the coarsening, and a pass value is done for the refinement process in the computational space.

2.5 Numerical methods

The governing equations have been discretized using a finite-volume(FV) approach on a collocated unstructured grid arrangement according to [6], which automatically adapts to the AMR framework. Convective terms are discretized using TVD Superbee flux limiter scheme [6, 10], unless otherwise stated. Moreover, central difference scheme (CD) is also available for discretization. Diffusive terms are discretized employing CD scheme[6]. Surface tension force is taken into account using a continuos surface model[20], formulated for unstructured meshes by [6, 10]. A fractional step projection method is used for solving the pressure-velocity coupling [21, 10]:

$$\frac{\rho\mathbf{v}^* - \rho^n\mathbf{v}^n}{\Delta t} = \mathbf{C}^n + \mathbf{D}^n + \rho\mathbf{g} + \sigma\kappa\nabla_h(\phi) \qquad \mathbf{v}^{n+1} = \mathbf{v}^* - \frac{\Delta t}{\rho}\nabla_h(p^{n+1}) \tag{8}$$

where, $\mathbf{C} = -\nabla_h \cdot (\rho\mathbf{v}\mathbf{v})$, $\mathbf{D} = \nabla_h \cdot (\mu(\nabla_h\mathbf{v}) + (\nabla_h\mathbf{v})^T)$, $(\nabla_h\mathbf{v})^T$ is calculated by the least-squares method[6]. Combining the incompressible constraint with corrector step in Eq. 8, a Poisson equation for the pressure field is obtained, which is solved by means of a preconditioned conjugated gradient method:

$$\nabla_h \cdot \left(\frac{1}{\rho}\nabla_h(p^{n+1})\right) = \frac{1}{\Delta t}\nabla_h \cdot (\mathbf{v}^*) \tag{9}$$

Further technical details, verifications and validations of the numerical code in the framework of both CLS and VOF/LS methods have been reported in [6, 7, 8, 9, 10]. The

numerical algorithms explained in this work are implemented in a parallel C++/MPI code called TermoFluids.

3 NUMERICAL EXPERIMENTS

Test cases are presented to validate the present numerical methods in the context of single buoyancy driven motion bubbles. In the next sections, the verification and validation of the proposed AMR algorithm with CLS and VOF/LS are shown, in the context of 2D and 3D single bubbles. The dimensionless numbers controlling the rising of a quiescent bubble flows are the Eötvös number (Eo), Reynolds number (Re), Morton number (M) and the ratios of physical properties (density ratio η_ρ and viscosity ratio η_μ) defined as following

$$Eo = \frac{gd^2\Delta\rho}{\sigma} \quad M = \frac{g\mu_1^4\Delta\rho}{\rho_1^2\sigma^3} \quad Re = \frac{\rho_1 U_T d}{\mu_1} \quad \eta_\rho = \frac{\rho_1}{\rho_2} \quad \eta_\mu = \frac{\mu_1}{\mu_2} \tag{10}$$

where the subindex 1 refers to the continuous fluid phase, the subindex 2 refers to the lighter fluid in the bubble, the subindex d refers to the dispersed phase.

$U_T = \int_{\Omega_2} v_y \phi dV / \int_{\Omega_2} dV$ is the terminal velocity of the bubble, $\Delta\rho = \rho_1 - \rho_2$ specifies the density difference between the fluid phases. Furthermore, in order to get a quantitative measure of bubble shape, the sphericity is defined as $\zeta = \pi d^2 / \int_\Omega ||\nabla f|| dV$.

3.1 Two-dimensional rising bubble

Solutions are obtained on a computational domain of [-d_b,d_b];[0,4d_b], where the initial cylindrical bubble of diameter $d_b = 5.0$ is located at x=0, y=d_b (See Fig. 2). The boundary conditions at the top and bottom are non-slip conditions, and on the vertical walls, a free-slip boundary condition is applied. The fluid parameters are: $Eo = 10$, $Re = 35$, $\rho_1/\rho_2 = 10$, $\mu_1/\mu_2 = 10$, where the subscript 1 is used for the continuous fluid phase, Ω_1, while the subscript 2 is assigned to the lighter fluid in the bubble, Ω_2.

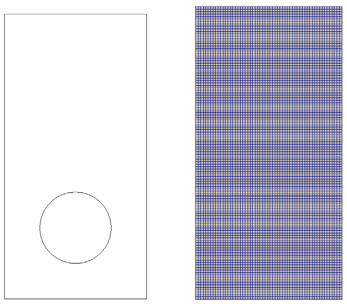

Figure 2: Illustration of the computational domain (left)Bubble initial position (right)computational base grid-number of control volumes 7k.

Present simulations are performed using AMR to ensure grid resolution on the interface

between fluids. Following the numerical studies carried out by [6], a minimum grid size was fixed on the interface with three levels of refinement for VOF/LS($h_{min} = d_b/240$) and three/four levels of refinement for CLS($h_{min} = d_b/240$ and $h_{min} = d_b/480$), to maximize the resolution of the bubble and reduce the overall number of control volumes for this case(total number of control volumes for three levels of refinement 9.3k aprox. and for four levels of refinement 37k aprox.). More refinement was achieved for CLS method because the interface is more wide compared to VOF/LS that has an interface thickness of one cell. The predicted bubble shapes on different times, defined as $t^* = tg^{1/2}d^{-1/2}$, with its AMR mesh are shown in Fig. 3.

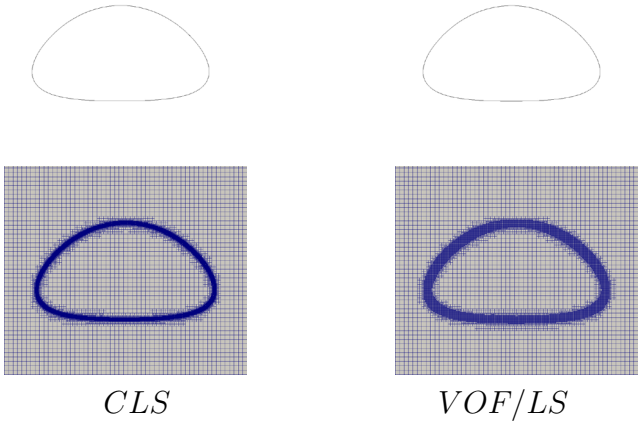

Figure 3: Example of a two dimensional rising bubble with CLS and VOF/LS at $t^* = 4.20$. Bubble shape with its computational grid.

For the sake of comparison, the benchmark quantities are defined as follows:

$$v_c = \frac{\int_{\Omega_2} \mathbf{v} \cdot \mathbf{e}_y dV}{\int_{\Omega_2} dV}, \qquad y_c = \frac{\int_{\Omega_2} \mathbf{x} \cdot \mathbf{e}_y dV}{\int_{\Omega_2} dV}, \qquad \zeta = \frac{\pi d_b^2}{\int_{\Omega} ||\nabla f(\mathbf{x}, t)|| dV}. \tag{11}$$

where v_c is the rise velocity, $\mathbf{e}_y$ is a unit vector parallel to the $y - axis$, y_c is the bubble centroid, ζ is the bubble circularity which takes the value 1 for a perfect circular bubble and values less than unity as the bubble is deformed.

Fig. 4 shows the position of the bubble, terminal Reynolds number, and circularity as a function of time. Our results compare well with the data published by [23, 24]. Both approaches show a correct representation of the dimple ellipsoidal bubble. Where the bubble being initially circular has a horizontal change, then the interfacial curvature gets smaller and, finally, tends to a certain limit value. This bubble deformation develops a slight dimple at the bottom but, at later times, eventually reaches a more stable ellipsoidal shape.

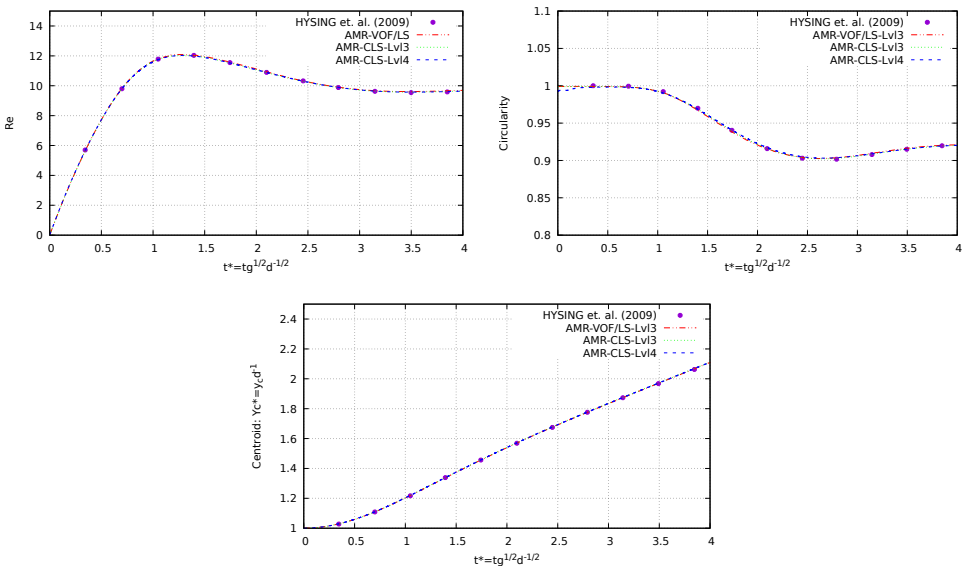

Figure 4: Two dimensional rising bubble results compared against[23]. (left top)Rise velocity (right top)Circularity (bottom)Bubble centroid

3.2 Three-dimensional buoyant bubbles

While the dynamics of a 2D single bubble is important for understanding the physical process of a rising bubble according to the dimensionless numbers, yet more useful information can be extracted from the analysis of a fully 3D single bubble. Experimental studies and correlations are usually invoked for the estimation of some macroscopic characteristics of the rising bubble. Rising bubble in ellipsoidal shape regime in an initially quiescent liquid is explored. The computational domain are $[0,8d_b];[0,16d_b];[0,8d_b]$, where the initial bubble of diameter $d_b = 2.5$ is located at x=0, y=$3d_b$ as it is shown in Fig. 5.

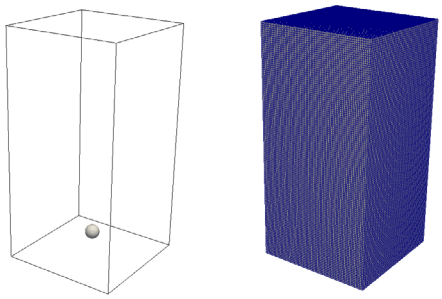

Figure 5: Illustration of the computational domain (left)Bubble initial position (right)computational base grid-number of control volumes 524k.

The fluid parameters are: $Eo = 116$, $Mo = 41.1$, $\rho_1/\rho_2 = 100$, $\mu_1/\mu_2 = 100$, No-

	[25]	[8]	[9]	Present AMR-CLS	Present AMR-VOF/LS
Number of cells		2.30E6	2.92E6	8.25E5	7.75E5
Re	7.16	6.94	7.02	6.79	6.76

Table 1: Present Re computations compared against experimental results from [25] and numerical results from [8, 9].

slip boundary condition is used at the top/bottom boundaries, and free-slip boundary condition is used at the lateral side of the domain. The mesh configurations follow an AMR strategy for 3D hexahedral elements. Following the numerical studies presented by [9], a minimum grid size was fixed on the interface ($h_{min} = d_b/64$), to maximize the resolution of the bubble and reduce the overall number of control volumes for this case (total number of control volumes 825k aprox.).

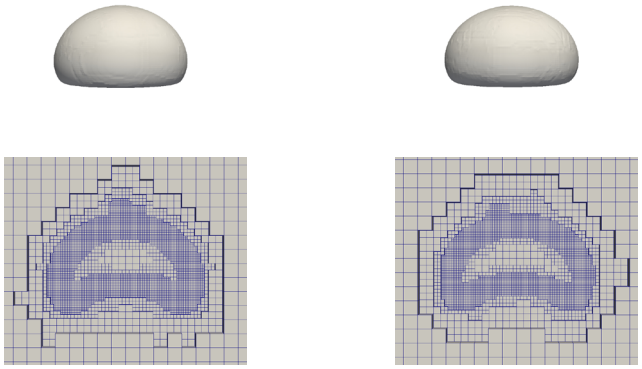

Figure 6: Example of a three dimensional rising bubble with CLS and VOF/LS at $t^* = 6.2$. Bubble shape with its computational grid.

A sequence of shapes for different times is presented in Fig. 6. Bubble start to rise due to buoyancy and starts to stretch tending to form a dimple at the bottom. This is produced due to the bubble tries to achieve a skirted shape but, finally reaches a dimple ellipsoidal shape, where it remains. The numerical prediction for terminal Reynolds number is compared with the numerical results reported by [8, 9] (See Table 1). A close agreement between CLS and VOF/LS results are obtained. Furthermore, CLS shows better mass conservation compared to VOF/LS (See Fig. 7). Here, the instantaneous mass is evaluated and compared with the initial mass, then the mass conservation error is calculated by $Mr = [M(t) - M(0)]/M(0)$ with $M(t) = \int_\Omega f dV$.

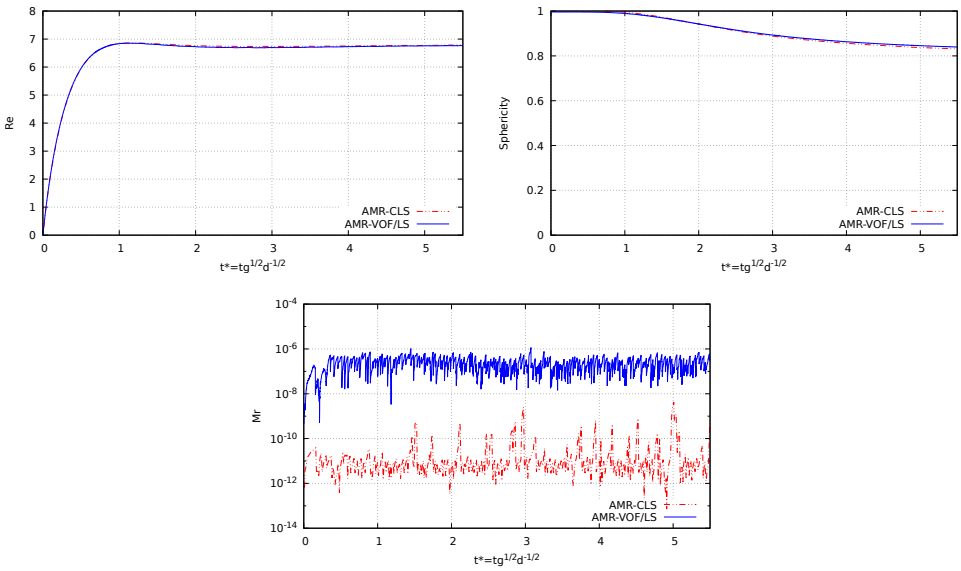

Figure 7: Three dimensional rising bubble results. (left top)Rise velocity (right top)Sphericity (bottom)Mass conservation error

4 CONCLUSIONS

- In this work, a comparative of CLS and VOF/LS for the simulation of incompressible two-phase flows using AMR technique was presented. Both methods were coupled with the Navier-Stokes equations discretized in a finite-volume scheme.

- The combination of the interface capturing methods and AMR technique results in an efficient algorithm that allows simulating complex two-phase flows with a reduction of computational resources in comparison with those used for fixed meshes.

- Present results are in good agreement with numerical and experimental results from the literature. As future work, this methodology will be extended to AMR for tetrahedral meshes, as well as, interfacial flows with heat and mass trasfer, phase change and variable surface tension[10].

5 ACKNOWLEDGMENTS

This work has been financially supported by the *Ministerio de Economía y Competitividad, Secretaría de Estado de Investigación, Desarrollo e Innovación (MINECO)*, Spain (ENE2015-70672-P), and by Termo Fluids S.L. Oscar Antepara acknowledges cofinancial support in form of a doctoral scholarship DI-14-06886 of the *MINECO* and 2015DI-68 of the *Secretaria d' Universitats i Recerca del Departament d'Economia i Coneixement de la Generalitat de Catalunya*, Spain. Néstor Balcázar acknowledges financial support of the *Programa Torres Quevedo, MINECO* (PTQ-14-07186), Spain.

REFERENCES

[1] Sussman, M., Smereka, P., Osher, S., A Level Set Approach for Computing Solutions to Incompressible Two-Phase Flow. *J. Comput. Phys* (1994) **144**:146–159.

[2] Sussman, M., Puckett, E.G., A Coupled Level Set and Volume-of-Fluid Method for Computing 3D and Axisymmetric Incompressible Two-Phase Flows. *J. Comput. Phys* (2000) **162**:301–337.

[3] Hirt, C., Nichols, B., Volume of fluid (VOF) method for the dynamics of free boundary. *J. Comput. Phys* (1981) **39**:201–225.

[4] Gueyffier, D., Li, J., Nadim, A., Scardovelli, R., Zaleski, S., Volume-of-fluid interface tracking with smoothed surface stress methods for three-dimensional flows. *J. Comput. Phys* (1999) **152**:423–456.

[5] Sun, D.L., Tao, J., W.Q., A coupled volume-of-fluid and level-set (VOSET) method for computing incompressible two-phase flows. *International Journal of Heat and Mass Transfer* (2010) **53**:645–655.

[6] Balcázar, N., Jofre, L., Lehmkhul, O., Castro, J., Rigola, J., A finite-volume/level-set method for simulating two-phase flows on unstructured grids. *International Journal of Multiphase Flow* (2014) **64**:55–72.

[7] Balcázar, N., Lemhkuhl, O., Rigola, J., Oliva, A., A multiple marker level-set method for simulation of deformable fluid particles. *International Journal of Multiphase Flow* (2015) **74**:125–142.

[8] Balcázar, N., Lemhkuhl, O., Jofre, L., Oliva, A., Level-set simulations of buoyancy-driven motion of single and multiple bubbles. *International Journal of Heat and Fluid Flow* (2015) **56**:91–107.

[9] Balcázar, N., Lemhkuhl, O., Jofre, L., Rigola, J., Oliva, A., A coupled volume-of-fluid/level-set method for simulation of two-phase flows on unstructured meshes. *Computers and Fluids* (2016) **124**:12–29.

[10] Balcázar, N., Rigola, J., Castro, J., Oliva, A., A level-set model for thermocapillary motion of deformable fluid particles. *International Journal of Heat and Fluid Flow* (2016), Part B,**62**:324–343.

[11] Olsson, E., Kreiss, G., A conservative level set method for two phase flow. *J. Comput. Phys.* (2005) **210**:225–246.

[12] Jofre, L., Lehmkuhl, O., Castro, J., Oliva, A., A 3-D Volume-of-Fluid advection method based on cell-vertex velocities. *Computers and Fluids* (2014) **94**:14–29.

[13] Antepara, O., Lehmkhul, O., Borrell, R., Chiva, J., Oliva, A., Parallel adaptive mesh refinement for large-eddy simulations of turbulent flows. *Computers and Fluids* (2015) **110**:48–61.

[14] Antepara, O., Borrell, R., Lehmkuhl, O., Rodrguez, I., Oliva, A., Parallel adaptive mesh refinement of turbulent flow around simplified car model using an immerse boundary method. *WCCM 2014, ECCM 2014 and ECFD 2014* (2014) 2603–2611.

[15] Antepara, O., Lehmkhul, O., Chiva, J., Borrell, R., Parallel adaptive mesh refinement simulation of the flow around a square cylinder at Re = 22000. *Procedia Engineering* (2013) **61**:246–250.

[16] Schillaci, E., Antepara, O., Lehmkuhl, O., Balcázar, N., Oliva, A., Effectiveness of adaptive mesh refinement strategies in the dns of multiphase flows. *Proceedings of International Symposium Turbulent Heat and Mass Transfer VIII* (2015).

[17] Pivello, M.R., Villar, M.M., Serfaty, R., Roma, A.M., Siveira-Neto, A., A fully adaptive front tracking method for the simulation of two phase flows. *International Journal of Multiphase Flow* (2014) **58**:72–82.

[18] Ceniceros, H.D., Nos, R.L., Roma, A.M., Three-dimensional, fully adaptive simulations of phase-field fluid models. *J. Comput. Phys.* (2010) **229**:6135–6155.

[19] Peskin, C.S., Numerical analysis of blood flow in the heart. *J. Comput. Phys.* (1977) **25**:220–252.

[20] Brackbill, J.U., Kothe, D.B., Zemach, C., A Continuum Method for Modeling Surface Tension. *J. Comput. Phys.* (1992) **100**:335–354.

[21] Chorin, A.J. Numerical solution of the Navier-Stokes equations. *Math. Comput.* (1968) **22**:745–762.

[22] Chang, Y.C., Hou, T.Y., Merriman, B., Osher, S., A level-set formulation of Eulerian interface capturing methods for incompressible two-phase flows. *J. Comput. Phys.* (1996) **124**:462–488.

[23] Hysing, S., Turet, S., Kuzmin, D., Parolini, N., Burman, E., Ganesan, S., Tobiska, L., Quantitative benchmark computations of two-dimensional bubble dynamics. *International Journal for Numerical Methods in Fluids* (2009) **60**:1259–1288.

[24] Hysing, S., Mixed element FEM level set method for numerical simulation of immiscible fluids. *J. Comput. Phys.* (2012) **231**:2449–2465.

[25] Bhaga, D., Weber, M.E., Bubbles in viscous liquids: shapes, wakes and velocities. *J. Fluid Mech.* (1981) **105**:61–85.

VII International Conference on Computational Methods for Coupled Problems in Science and Engineering
COUPLED PROBLEMS 2017
M. Papadrakakis, E. Oñate and B. Schrefler (Eds)

A COUPLED MULTIPHASE-FIELD AND CARBON DIFFUSION MODEL FOR LOWER BAINITIC TRANSFORMATION

MARTIN DÜSING* AND ROLF MAHNKEN*

*Chair of Engineering Mechanics (LTM)
Paderborn University
Warburger Straße 100, 33098 Paderborn, Germany
e-mail: duesing@ltm.upb.de

Key words: Phase-field, Diffusion, Lower Bainite, Cahn-Hilliard, Finite Element Method, Carbide Precipitation

Abstract. A multiphase-field method coupled to a Cahn-Hilliard diffusion model is presented in this paper. The underlying thermodynamic framework is based on the concept of generalized stresses. A prototype model is developed to simulate the lower bainitic transformation, including phase transitions, the separation of carbon within the supersaturated phase and the precipitation of carbides. The system of partial differential equations is solved with the finite element method. Numerical results of the model showing the qualitative mechanism are discussed.

1 INTRODUCTION

In this work the phase-field method is utilized to simulate the lower bainitic transformation, which is one of the most complex transformations in steel. The growth of the bainitic ferrite is assumed to be displacive [1] in contrast to the perlitic transformation which is highly dependent on the carbon diffusion and therefore is ranked as a diffusive transformation. The diffusion of carbon is a major mechanism of the bainitic transformation, too, since the precipitation of carbides from within the supersaturated bainitic ferrite is strongly dependent on the local carbon concentration. The displacive transformation from austenite to bainitic ferrite leads to a supersaturated phase. Within the bainitic ferrite the carbon separates and builds accumulations which precipitate as carbides [1].

To model this material behaviour a system of partial differential equations is developed, based on a thermodynamic framework of generalized stresses as introduced by Gurtin and Fried [2, 3] for a two phase Ginzburg-Landau system and a Cahn-Hilliard equation. We extend this framework for a viscous Cahn-Hilliard equation coupled to multiphase-field models [4] as it is needed for the lower bainitic transformation. The key aspects of the

thermodynamic framework are generalized stresses and microforces which perform work in conjunction with derivatives of the phase-field variables and the carbon concentration. The framework distinguishes between basic balance laws which are universal and constitutive equations which depend on the specific material. The Clausius-Duhem inequality is used to impose restrictions to the constitutive equations. The numerical examples show the qualitative mechanism of the lower bainitic transformation as discussed above.

2 THERMODYNAMIC FRAMEWORK

The thermodynamic framework is based on the microforce balance as introduced by Gurtin and Fried [2, 3] and generalized by Ammar et al. [5]. Thereby, an extended version as described in [4] and [6] is used to combine a multiphase Ginzburg-Landau equation for the phase-field problem coupled with a Cahn-Hilliard diffusion equation. The carbon concentration is identified by c and the phase order parameters are labelled ϕ_i.

For N_p phases we start by defining N_p *vector phase stresses* $\vec{\xi}_i$, *internal scalar phase forces* π_i and *external scalar phase forces* γ_i over the volume B. The power performed on the atomic configurations within a region V of B for each phase i reads

$$\int_V -\vec{\xi}_i \cdot \nabla\dot{\phi}_i \, dV, \quad \int_V \pi_i\dot{\phi}_i \, dV, \quad \int_V \gamma_i\dot{\phi}_i \, dV, \qquad i = 1, ..., N_p. \tag{1}$$

A similar definition is needed for the Cahn-Hilliard equation where ω is introduced as a *scalar internal diffusion force* and $\vec{\lambda}$ as a *vector diffusion stress*. The powers are

$$\int_V -\vec{\lambda} \cdot \nabla\dot{c} \, dV, \quad \int_V \omega\dot{c} \, dV. \tag{2}$$

The system of microforces and microstresses in equations (1) and (2) shall be consistent with the microforce balance for each control volume V

$$\sum_{i=1}^{N_p} \left(-\int_V \vec{\xi}_i \cdot \nabla\dot{\phi}_i \, dV + \int_V \pi_i\dot{\phi}_i \, dV + \int_V \gamma_i\dot{\phi}_i \, dV \right) - \int_V \vec{\lambda} \cdot \nabla\dot{c} \, dV + \int_V \omega\dot{c} \, dV = 0 \tag{3}$$

which leads to the *local microforce balances*

$$\nabla \cdot \vec{\xi}_i + \pi_i + \gamma_i = 0 \quad \text{in} \quad V \qquad \text{for} \quad i = 1, ..., N_p, \tag{4}$$

$$\nabla \cdot \vec{\lambda} + \omega = 0 \quad \text{in} \quad V, \tag{5}$$

$$\vec{\xi}_i \cdot \vec{n} = 0 \quad \text{on} \quad \partial V \qquad \text{for} \quad i = 1, ..., N_p, \tag{6}$$

$$\vec{\lambda} \cdot \vec{n} = 0 \quad \text{on} \quad \partial V. \tag{7}$$

In the isothermal case, which is analyzed here, the *local dissipation inequality*

$$-\dot{\psi} + \vec{\lambda} \cdot \nabla\dot{c} - \omega\dot{c} + \mu\dot{c} - \vec{J} \cdot \nabla\mu + \sum_{i=1}^{N_p} \left(\vec{\xi}_i \cdot \nabla\dot{\phi}_i - \pi_i\dot{\phi}_i \right) \geq 0. \tag{8}$$

can be formulated using mass conservation, the first and the second law of thermodynamics [4], where ψ is the Helmholtz energy, μ the chemical potential and $\vec{J}$ the flux.

In a next step restrictions to constitutive equations can be formulated with the help of the local dissipation inequality (8). After some transformation (for details see [4]) the dissipation inequality reads

$$\mathcal{D} = \nabla\mu \cdot \boldsymbol{A}\nabla\mu + \tau\dot{c}^2 + \sum_{i=1}^{N_p} \beta_i \dot{\phi_i}^2 \geq 0, \tag{9}$$

where $\boldsymbol{A}$ is a mobility tensor and τ and β_i are constitutive moduli. It turns out that the inequality (9) holds for any choice of $\nabla\mu, \dot{c}$ and $\dot{\phi}_i$ if and only if

$$\tau \geq 0, \quad \beta_i \geq 0, \quad \vec{s} \cdot \boldsymbol{A}\vec{s} \geq 0 \quad \forall \vec{s}. \tag{10}$$

3 PROTOTYPE MODEL FOR LOWER BAINITE

3.1 Evolution equations

In this prototype model for lower bainite the evolution of 3 phases, namely bainitic ferrite (ϕ_1), austenite (ϕ_2) and carbide (ϕ_3) is described in parallel with the diffusion of carbon which is strongly coupled to the phase growth. Choosing constitutive equations for the Helmholtz energy ψ, the constitutive moduli τ and β_i and the mobility tensor $\boldsymbol{A}$ to describe the growth kinetics of lower bainite under consideration of the restrictions (10), we finally end up with an evolution equation for the diffusion

$$\dot{c} = \phi_1\kappa\Delta\left(\frac{\partial f(c)}{\partial c} - \rho\Delta c + \tau\dot{c}\right) + \nabla\phi_1\kappa\nabla\left(\frac{\partial f(c)}{\partial c} - \rho\Delta c + \tau\dot{c}\right), \tag{11}$$

where κ is the diffusion coefficient, ρ the balance factor and f the carbon potential function.

Changing parameters as described in [7] and [8] leads to an evolution equation for the multiphase-field with the physical material parameters, interface mobilities ζ_{ij}, interface energies σ_{ij}, interface thicknesses η_{ij} and Gibbs energy ΔG_{ij}

$$\dot{\phi}_i = \sum_{j=1, j\neq i}^{N_p} \zeta_{ij}\left[\sigma_{ij}\left((\phi_j\Delta\phi_i - \phi_i\Delta\phi_j) - \frac{36}{\eta_{ij}^2}\phi_i\phi_j(\phi_j - \phi_i)\right) - \frac{6\cdot\Delta G_{ij}}{\eta_{ij}}\phi_i\phi_j\right]$$
$$\text{for} \quad i = 1, ..., N_p. \tag{12}$$

3.2 Carbide precipitation

A main mechanism of the lower bainitic transformation is the precipitation of carbides, because the small carbides influence the macroscopic material behavior significantly. The simulation of the precipitation process yields several challenges. The phase-field method

(12) is not able to simulate the growth of a phase ϕ_i whose value is zero over the whole domain. Therefore, small nuclei of carbides are defined as initial conditions. However in this special case the nuclei nearly vanish while the austenite transforms into ferrite and cannot grow any more. An elegant way to solve this problem and model the physical precipitation of carbides is to define the thermodynamic driving force as a constitutive equation as follows:

$$\Delta G_{ij}(\vec{z}) = \Delta G^0_{ij}\ v(\phi_i, \phi_j, c) \tag{13}$$

where

$$v(\phi_i, \phi_j, c) = \begin{cases} \dfrac{w(c)}{\phi_3^2} & \text{for } i = 3 \vee j = 3 \\ 1 & \text{otherwise} \end{cases} \tag{14}$$

and ΔG^0_{ij} is a constant material parameter. The function $w(c)$ is a smooth unit step function

$$w(c) = \begin{cases} 0 & \text{for } c < c_{\text{carb}} - \varepsilon \\ 1 & \text{for } c > c_{\text{carb}} \\ \frac{1}{2} + \frac{1}{2} \cdot \sin(\frac{\pi}{\varepsilon} \cdot c + \frac{\pi}{2} - \frac{\pi}{\varepsilon} \cdot c_{\text{carb}}) & \text{otherwise,} \end{cases} \tag{15}$$

where the parameter ε governs the width of the transition zone and c_{carb} specifies the maximum carbon concentration.

The Gibbs energy formulation (13) - (15) does not change the transformation kinetics between austenite (ϕ_2) and bainitic ferrite (ϕ_1). Only in case of high carbon concentration at a certain place the carbide phase (ϕ_3) will grow due to equations (14) and (15). The function v ensures that the carbide phase can grow even if the nuclei have become very small in time.

4 IMPLEMENTATION AND NUMERICAL EXAMPLE

Numerical solutions for the coupled evolution equations (11) and (12) are obtained with the finite element method in two dimensions. Here the partial differential equations are discretized over an domain of 3μm $\times$ 3μm with quadrilateral elements and linear shape functions. The fine mesh has about 16384 elements. For the time discretization an implicit Euler scheme is implemented. Here we used a time step of 0.05s and compute solutions until 30s.

Figure 1 shows representative results of the numerical example. In the first row (a) the austenite phase is shown, in the second the row (b) one can see the bainitic ferrite phase. In Figure 1.c) the carbides are shown. All three phases vary between 0 and 1, where 0 means that the phase is not present at that local point and 1 means that only this phase is present here. The sum of all three phases is one at every local point. The columns in

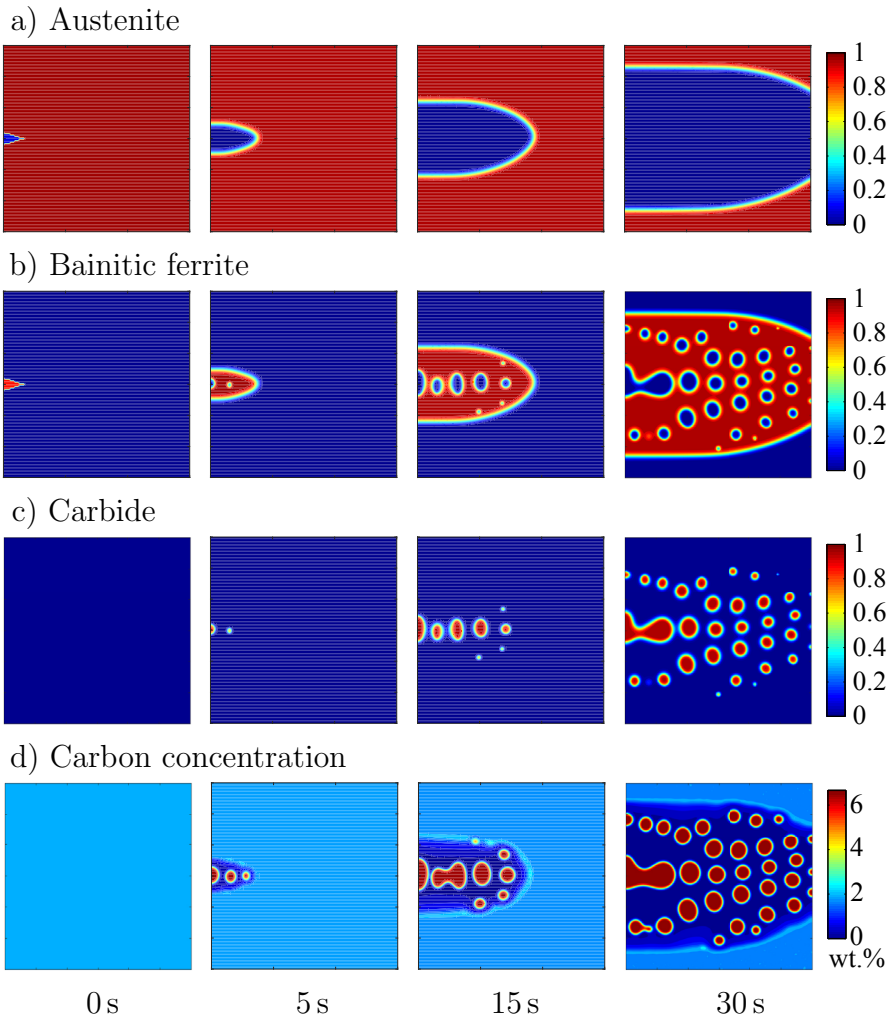

Figure 1: Lower bainitic transformation after 0 s, 5 s, 15 s and 30 s.

Figure 1 represent the results of the four fields after 0s, 5s, 15s and 30s. The first column shows the initial conditions. There is a small nucleus of bainitic ferrite at the right border of the domain. There are no carbides at the beginning and the carbon concentration is uniformly distributed over the whole domain. In fact there are small perturbations of carbon and small initial nuclei of carbides randomly distributed. After 5s the bainitic ferrite sheaf has grown and as shown in Figure 1.d) the carbon within the supersaturated bainitic ferrite starts to separate and build accumulations of carbon. At points where the local carbon concentration reaches the maximum concentration c_{carb} carbides precipitate. In the next two time steps shown here, one can see the growing bainitic ferrite sheaf and the results of the Cahn-Hilliard diffusion equation. Several accumulations of carbon rise up and therefore carbides grow at this places.

5 CONCLUSIONS

A thermodynamic framework and a prototype model for lower bainite are presented in this work. The framework can be used for any kind of Cahn-Hilliard diffusion models coupled to multiphase-field methods. It is based on universal laws, such as mass conservation, energy conservation, the balance of microforces and the second law of thermodynamics, which are strictly separated from constitutive equations. The lower bainite model shows the described growth mechanisms, like the displacive transformation from austenite to bainitic ferrite, the separation of carbon within the supersaturated bainitic ferrite and the precipitation of carbides at carbon accumulations.

REFERENCES

[1] Bhadeshia, H. K. D. H. *Bainite in steels*, The Institute of Materials, Cambridge, Second Edition (2001).

[2] Fried, E. and Gurtin, M. E. Continuum theory of thermally induced phase transitions based on an order parameter. *Physica D: Nonlinear Phenomena* (1993) **68**:326–343.

[3] Gurtin, M. E. Generalized Ginzburg-Landau and Cahn-Hilliard equations based on a microforce balance. *Physica D: Nonlinear Phenomena* (1996) **92**:178–192.

[4] Düsing, M. and Mahnken, R. A thermodynamic framework for coupled multiphase Ginzburg-Landau/Cahn-Hilliard systems for simulation of lower bainitic transformation *Arch. Appl. Mech.* (2016) **86**:1947–1964.

[5] Ammar, K., Appolaire, B., Cailletaud, G., Feyel, F., Forest, S. Finite element formulation of a phase field model based on the concept of generalized stresses. *Comp. Mater. Sci.* (2009) **45(3)**:800–805

[6] Mahnken, R., Cheng, C., Düsing, M., Ehlenbrker, U. and Leismann, T. The concept of generalized stresses for computational manufacturing and beyond. *GAMM-Mitteilungen* (2016), **39**:229–265.

[7] Düsing, M. and Mahnken, R. Simulation of lower bainitic transformation with the phase-field method considering carbide formation. *Comp. Mater. Sci.* (2016) **111**:91–100.

[8] Mecozzi, M., Sietsma, J., van der Zwaag, S., Apel, M., Schaffnit, P. and Steinbach, I. Analysis of the $\gamma \rightarrow \alpha$ Transformation in a C-Mn Steel by Phase-Field Modeling. *Metallurgical and Materials Transactions A* (2005) **36**:2327–2340.

VII International Conference on Computational Methods for Coupled Problems in Science and Engineering
COUPLED PROBLEMS 2017
M. Papadrakakis, E. Oñate and B. Schrefler (Eds)

A FINITE ELEMENT APPROACH FOR A COUPLED NUMERICAL SIMULATION OF FLUID-STRUCTURE-ELECTRIC INTERACTION IN MEMS

Prakasha Chigahalli Ramegowda*, Daisuke Ishihara†, Tomoya Niho† and Tomoyoshi Horie†

*†Department of Mechanical Information Science and Technology
Kyushu Institute of Technology
680-4 Kawazu, Iizuka, Fukuoka, Japan
e-mail: * prakasha@solid.mse.kyutech.ac.jp

Key words: Micro Electro Mechanical System (MEMS), Multiphysics Problems, Fluid-structure-electric interaction, Piezoelectricity, Partitioned iterative coupling, Projection method

Abstract. In this analyze, a novel finite element coupled algorithm using numerical methods to analyze the interaction between fluid-structure-electric fileds has been presented for piezoelectric actuators. Piezoelectricity is fundamentally an interaction between structure and electric fields. In this paper, at first we analyze the piezoelectric interaction using 3D solid elements and MITC4 shell elements. Solid elements are used for electric analysis and MITC4 shell elements are used for geometric nonlinear structural analysis. The induced electric forces and moment of forces are translated from 3D solid elements to MITC4 shell elements using a novel translation method, and displacements from MITC4 shell elements are translated to 3D solid elements using shell element displacement interpolation functions. A projection method is employed in order to solve the interaction between MITC4 shell structure and fluid field.

1 Introduction

Micro Electro Mechanical System (MEMS) based piezoelectric actuators can be used to actuate the thin and flexible wings of micro air vehicles (MAVs). The actuator produces large deformation at its resonance, which is located at the root of the wing, so that the flexible wing can flap and produce enough lift force to support the MAV weight during flight. In the mean time, MAV is surrounded by air and has a significant influence from it on the vibration characteristics of the flapping motion of the wing and hence its response. Therefore, the analysis of fluid-structure-electric interaction must be carefully taken into account during the MAV design process. The analytical solution to the model equations

are limited in the scope. From this view point, a novel finite element method for fluid-structure-electric interaction is imperative.
Block Gauss-Seidel (BGS) partitioned iterative coupling with Newton-Rapson equilibrium iteration is used to analyze the structure-electric interaction using 3D solid elements and MITC4 shell elements. A projection method for FSI [1] is employed to analyze the interaction between MITC4 shell structure and fluid field interaction. This paper treats the interaction between electric field using 3D solid elements and structural fields using MITC4 shell elements. MEMS structures consists of thin layers and undergoes large deformation at resonance, shell elements are more suitable to capture the nonlinear effect than 3D solid elements. That is the reason we employed MITC4 shell elements to perform geometric nonlinear structural analysis. A novel translation method is introduced to exchange the electrical and mechanical variable between solid elements and MITC4 shell elements. It follows from the comparison between the numerical and analytical results that our translation method accurately translates the induced nodal electric forces from 3D solids to MITC4 shell elements and displacements from any material point in shell elements are translated to corresponding nodes in 3D solid elements.

2 Methodology : Fluid-structure-electric interaction analysis

The proposed method to analyze fluid-structure-electric field interaction is schematically given in Figure 1 and Figure 2. At first we analyze the piezoelectric interaction, which is fundamentally an interaction between electrical and structural fields. Partitioned iterative coupling algorithm is used to analyze the structure-electric interaction. Using 3D solid elements, we obtain an induced electric forces due to the inverse piezoelectric effect causing the piezoelectric bimorph actuator to bend. Secondly, a novel translation method is implemented to translate the induced nodal electrical forces from 3D solid elements to the equivalent nodal forces and moments acting on MITC4 shell elements for the purpose to take into account the thin structure of the MEMS based piezoelectric actuators. Block Gauss-Seidel partitioned iterative method is employed to couple electric and mechanical variables [6]. Acceleration based Newmark's time β time integration scheme is employed to analyze structure-electric interaction. The full Newton-Rapson iteration is used for the nonlinear structural analysis in MITC4 shell elements.

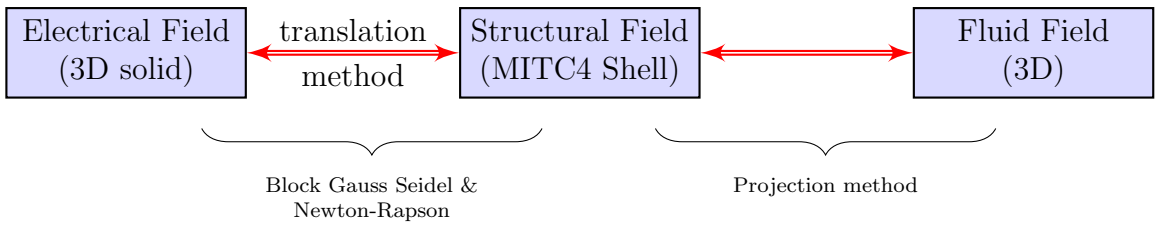

Figure 1: Schematic of fluid-structure-electric field interaction

And finally, a projection method for FSI [1] is employed in order to solve the interaction between MITC4 shell structure and fluid field interaction including the fluid incompressibilty, where the hierarchical decomposition approach [2] is used to couple the structure-electric and fluid-structure interaction analyses. Here structure-fluid interaction is split into the structure-fluid velocity field and pressure field using a kind of algebraic splitting as shown in Figure 2, which avoids larger DOF's of equations in comparison with monolithic coupling and uses the intermediate state variables. The incompressibity constrain is solved using pressure poisson equation (PPE). The predictor-multi corrector algorithm given by Newmark's β method is used for the time integration for the fluid-structure interaction analysis.

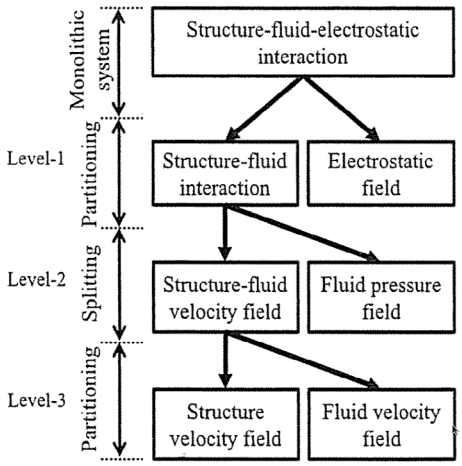

Figure 2: Schematic of hierarchical decomposition of fluid-structure-electric fields [2]

.

We discuses about the interaction between solid and shell elements to analyze piezoelectric effect in detail in the following sections.

2.1 Translation method for interaction analysis between 3D solid and shell elements to analyze piezoelectric effect

The standard finite element equations of piezoelectricity is given as [3]

$$\mathbf{M}\ddot{\mathbf{u}} + \mathbf{K}_{uu}\mathbf{u} + \mathbf{K}_{u\phi}\boldsymbol{\phi} = \mathbf{F}, \tag{1}$$

$$\mathbf{K}_{u\phi}^{T}\mathbf{u} + \mathbf{K}_{\phi\phi}\boldsymbol{\phi} = \mathbf{q}, \tag{2}$$

where $\mathbf{M}$ is the mass matrix, $\mathbf{K}_{uu}$ is the mechanical stiffness matrix, $\mathbf{K}_{u\phi}$ is the piezoelectric stiffness matrix, $\mathbf{K}_{\phi\phi}$ is the dielectric stiffness matrix, $\mathbf{F}$ is the external force vector, superscript T stands for transpose matrix and $\mathbf{q}$ is the surface density charge vector. The term $\mathbf{K}_{u\phi}\boldsymbol{\phi}$ in Eq.(1) is a 3D nodal vector of electrical forces in solid elements. These forces are translated to the equivalent force and moment in shell elements. The transformation

equation to translate the electrical forces from solid to shell is described as

$$ {}^{e}\mathbf{F}^{\text{shell}} = \mathbf{A}\,{}^{e}\mathbf{F}^{\text{solid}}, \tag{3} $$

where $\mathbf{A}$ is the transformation matrix, which connects electric forces from solid to shell. The components of this matrix are obtained from the equilibrium equations of the electric forces and their moment. After translating the electrical nodal forces and moments from solid to shell elements using the relation given in equation (3), displacements are obtained, and they transformed from shell to solid at any material point using the finite element interpolation as

$$ {}^{\mathrm{t}}\mathbf{u}_i = \mathbf{h}_k\,{}^{\mathrm{t}}\mathbf{u}_i^k + \frac{r_3}{2}\mathrm{a}_k\mathbf{h}_k({}^{\mathrm{t}}\mathbf{V}_{ni}^k - {}^{0}\mathbf{V}_{ni}^k), \tag{4} $$

where ${}^{\mathrm{t}}\mathbf{u}_i$ is the displacements of any material point with natural coordinates (r_1, r_2, r_3) of the shell element in the stationary Cartesian directions (x_1, x_2, x_3) at time t, ${}^{\mathrm{t}}\mathbf{u}_i^k$ is the nodal displacements of shell elements into the Cartesian directions (x_1, x_2, x_3) at time t, $\mathbf{h}_k$ is the two dimensional shape functions corresponding to (r_1, r_2) at nodal point k, and a_k is shell thickness at node k along director vector $\mathbf{V}_n^k$. The displacements from any material point ${}^{\mathrm{t}}\mathbf{u}_i$ with isoparametric coordinates (r_1, r_2, r_3) in shell elements are translated to the corresponding nodes in 3D shell elements using,

$$ \mathbf{u}^{\text{solid}} = \mathbf{B}\mathbf{u}^{\text{shell}}. \tag{5} $$

The components of $\mathbf{B}$ matrix are obtained from ${}^{\mathrm{t}}\mathbf{u}_i$.

2.2 Piezoelectric nonlinear dynamic analysis

The nonlinear piezoelectric dynamic analysis is carried out using the block Gauss-Seidel (BGS) partitioned iterative coupling scheme to exchange the mechanical and electrical variables and the full Newton-Rapson (NR) equilibrium iterations to perform nonlinear structural analysis. The total Lagrangian formulation is used to take into account the structural large deformation. Newmark's time integration is employed for the time marching. The linearized coupled equations for the nonlinear piezoelectricity is given as [5],

$$ {}^{\mathrm{t}+\Delta\mathrm{t}}_{0}\mathbf{K}_{\phi\phi}\;{}^{\mathrm{t}+\Delta\mathrm{t}}\boldsymbol{\phi}^{(\mathrm{i})} = {}^{\mathrm{t}+\Delta\mathrm{t}}_{0}\mathbf{q} - {}^{\mathrm{t}+\Delta\mathrm{t}}_{0}\mathbf{K}_{\mathrm{u}\phi}^{\mathrm{T}}\;{}^{\mathrm{t}+\Delta\mathrm{t}}\mathbf{u}^{(\mathrm{i}-1)}, \tag{6} $$

$$ {}^{\mathrm{t}+\Delta\mathrm{t}}_{0}\hat{\mathbf{K}}_{\mathrm{uu}}^{(\mathrm{k}-1)}\boldsymbol{\Delta}\mathbf{u}^{(\mathrm{k}),(\mathrm{i})} = {}^{\mathrm{t}+\Delta\mathrm{t}}\tilde{\mathbf{R}}^{(\mathrm{k}-1)} - {}^{\mathrm{t}+\Delta\mathrm{t}}_{0}\mathbf{F}^{(\mathrm{k}-1)} - {}^{\mathrm{t}+\Delta\mathrm{t}}_{0}\mathbf{K}_{\mathrm{u}\phi}\,{}^{\mathrm{t}+\Delta\mathrm{t}}\boldsymbol{\phi}^{(\mathrm{i})}, \tag{7} $$

$$ {}^{\mathrm{t}+\Delta\mathrm{t}}_{0}\hat{\mathbf{K}}_{\mathrm{uu}}^{(\mathrm{k}-1)} = \mathbf{M}\frac{1}{\beta\Delta\mathrm{t}^2} + {}^{\mathrm{t}+\Delta\mathrm{t}}_{0}\mathbf{K}_{\mathrm{uu}}^{(\mathrm{k}-1)}, \tag{8} $$

where ${}^{\mathrm{t}+\Delta\mathrm{t}}_{0}\mathbf{K}_{\mathrm{uu}}^{(\mathrm{k}-1)}$ is the tangent stiffness matrix in Newton-Rapson iteration $(\mathrm{k}-1)$, ${}^{\mathrm{t}+\Delta\mathrm{t}}_{0}\mathbf{K}_{\phi\phi}$, ${}^{\mathrm{t}+\Delta\mathrm{t}}_{0}\mathbf{K}_{\mathrm{u}\phi}$ and ${}^{\mathrm{t}+\Delta\mathrm{t}}_{0}\mathbf{q}$ are dielectric stiffness matrix, piezoelectric stiffness matrix

and vector of electric charge, respectively. ${}^{t+\Delta t}\boldsymbol{\phi}^{(i)}$ is the electrical potential evaluated from the previous BGS iteration displacement solution ${}^{t+\Delta t}\mathbf{u}^{(i-1)}$. And, $\boldsymbol{\Delta}\mathbf{u}^{(k),(i)}$ is calculated using the updated solution of electric potential in Eq.(7). Then, the displacement is updated using

$$ {}^{t+\Delta t}\mathbf{u}^{(k),(i)} = {}^{t+\Delta t}\mathbf{u}^{(k-1),(i)} + \boldsymbol{\Delta}\mathbf{u}^{(k),(i)}. \tag{9} $$

Here, we propose two approach for the full Newton-Rapson iteration and BGS iteration as follows :

1. Approach 1: For each BGS iteration, only one Newton-Rapson iteration is performed as shown in Figure 3.

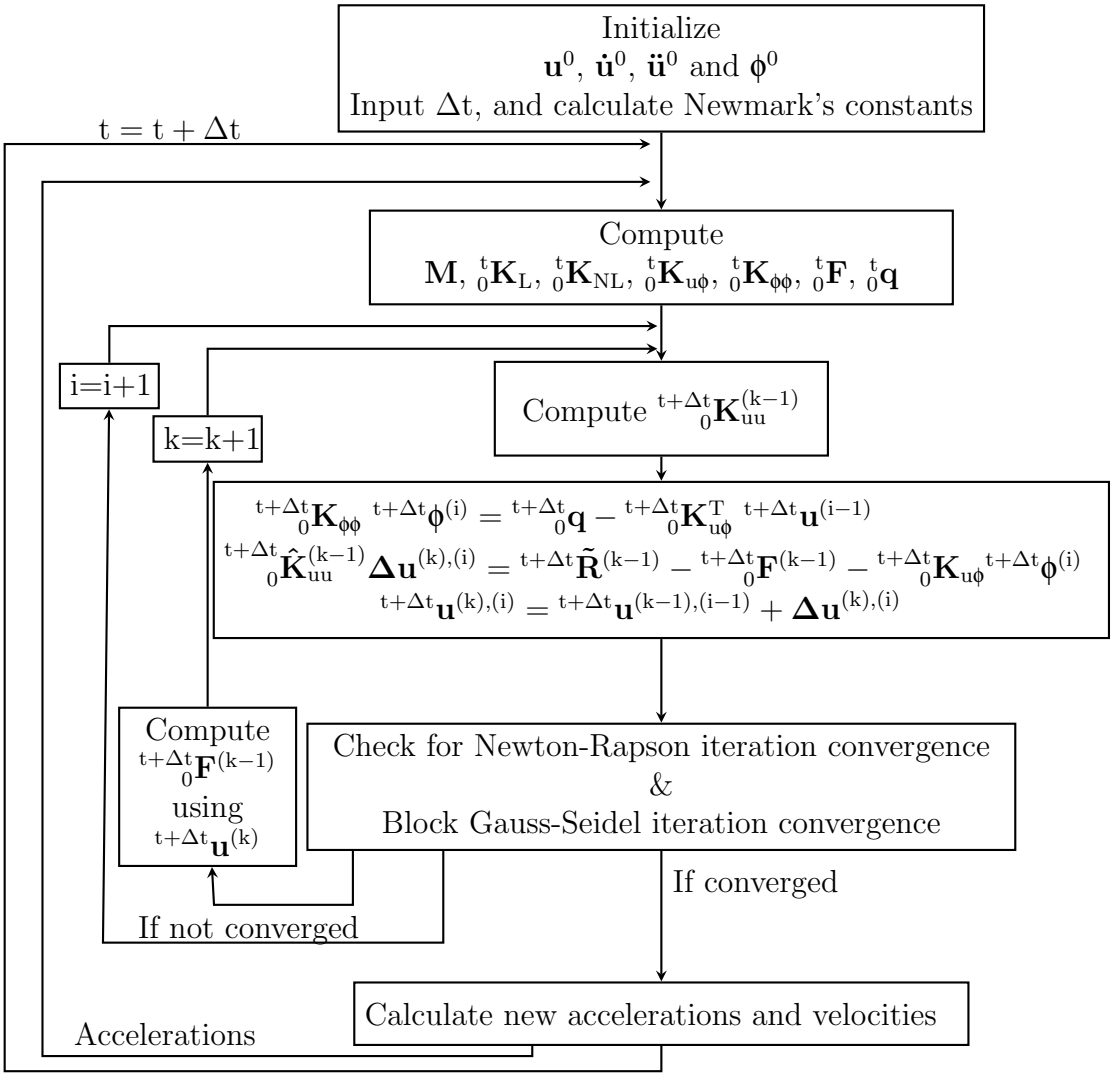

Figure 3: Nonlinear dynamic piezoelectric analysis: Approach (1)-Unified algorithm

2. Approach 2: In this approach, for each BGS iterations, the full Newton-Rapson equilibrium is evaluated until the energy tolerance is satisfied. There are several NR iterations for each BGS iterations in a time step depending on deformation. This approach may be computationally expensive, but the solution accuracy is much better than Approach 1.

3 Numerical problem : Piezoelectric bimorph actuator connected in series

Piezoelectric bimorph actuators are widely used to MEMS. Bimorph actuators consist of a double layer of piezoelectric ceramics as shown in Fig.4. The electrostatic forces across the ceramic layers causes one top layer to contract and bottom layer to expand. The bimorph actuator is connected in series type has dimensions length L=100 mm, width w=1mm and thickness t_p=0.5mm. The mesh for electric analysis consists of 1343 nodes and 160 hexahedron 20 nodes elements and the mesh for structural analysis consists of 82 nodes and 40 MITC4 shell elements. The theoretical solution for deflection in thickness direction along length for this numerical problem is given as [7],

$$\mathrm{u_3(x_1)} = \frac{3\mathrm{x_1^2}}{4t_p} d_{31} E_3, \tag{10}$$

where d_{31} is piezoelectric constant, E_3 is an applied electric field and t_p is the thickness of each piezoelectric layers. The tip deflection is given as,

$$\delta = \frac{3L^2}{4t_p} d_{31} E_3. \tag{11}$$

The material properties used in the analysis are given in Table.1.

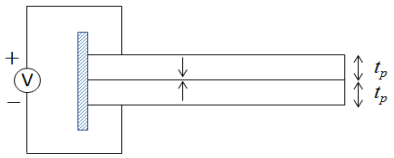

Figure 4: Piezoelectric bimorph actuator connected in series type, ↑ is polarization direction

Table 1: Material properties used for calculation

materials	e_{31} (C/m^2)	d_{31} (C/N)	Young's modulus (N/m^2 $\times 10^9$)	Density (kg/m^3)	ν
PVDF	0.046	2.30×10^{-11}	2.0	1800	0.29

Substituting the actuator dimensions and material properties into Eq. 11 for an applied voltage 1 V, we get tip deflection in thickness direction analytically,

$$\delta = 0.3450 \mu m$$

4 Results and Discussion

The numerical problem described in Figure 4 is examined here using both Approach 1 and Approach 2 described in Section 2.2 to analyze the static and dynamic behaviors.

4.1 Static analysis of bimorph actuator connected in series type

At first, the convergence properties and the solution accuracy of the unified algorithm (Approach 1) is presented. In the Figure 5(a) it shows that 6 BGS iterations and 6 NR iterations are necessary to satisfy the convergence tolerance. The energy tolerance value is set as 1.0×10^{-12}. Figure 5(b) shows the transverse deflection of the bimorph actuator at the interface between two PVDF layers compared with the theoretical solution from Eq. 10. The transverse static deflection using Approach 1 along the length of the bimorph actuator coincides with the theoretical solution. The numerical solution for the deflection at the tip of the actuator is $0.3451\mu m$, and theoretical solution for the same using Eq. 11 is $0.3450\mu m$. The % error between numerical and theoretical solution is less than 0.02%.

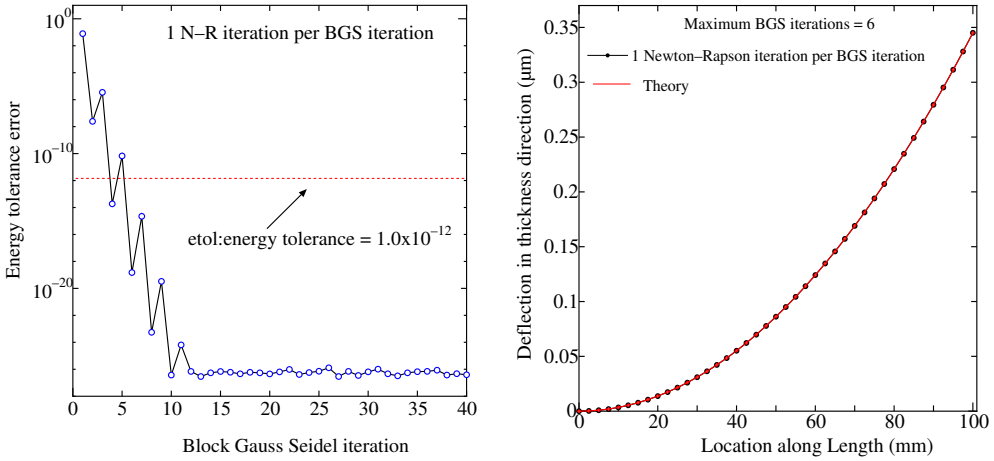

(a) Iteration convergence analyze (b) Static deflection: Accuracy

Figure 5: Numerical analyses using unified algorithm : static deflection

In Approach 2, two NR equilibrium iterations for the first BGS iteration and one NR iteration for successive BGS iterations is sufficient. Approach 2 also has a same level accuracy of solution with Approach 1.

4.2 Dynamic analysis of bimorph actuator: Step response

Here, the vibration characteristics of the numerical problem in Figure 4 are presented for Approach 2. The actuator is driven by a step voltage of 1 V for undamped and numerically damped conditions. Δt is chosen as 1.0×10^{-4} sec for Approach 2, based on the previous convergence, the number of BGS iterations per time step is set as 4. The purpose to analyze the numerical damped case is to find the steady state deflection and to compare the static deflection in order to check the accuracy of the solution. The

Newmark's parameters β and and γ for damped condition are chosen as $\gamma = 0.6$ and $\beta = 0.25 \times (\gamma + 0.5)^2 = 0.3025$. As can be seen in Figure 6(b), the deflection at steady state is close to that of the static theoretical tip deflection.

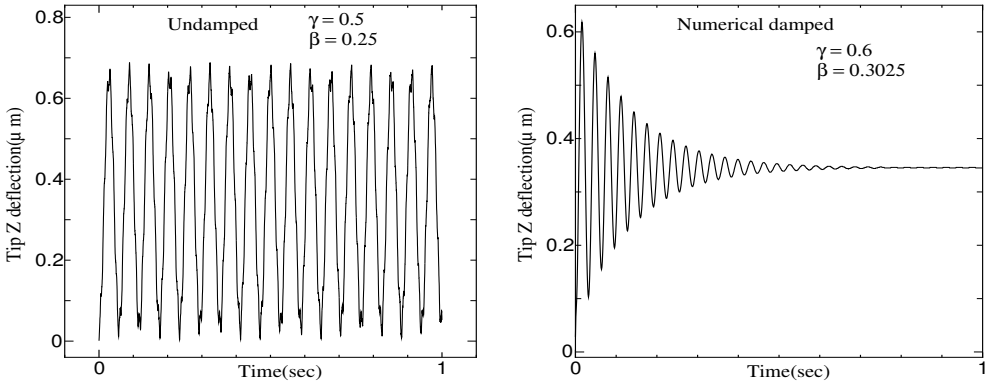

(a) Numerically undamped condition (b) Numerically damped condition

Figure 6: Step response of bimorph actuator

4.3 Dynamic analysis of bimorph actuator: AC response

The piezoelectric bimorph actuator described in Figure bimorph is examined here. The actuator is excited with input voltage $Vsinw$t, where V is the amplitude and w is the angular frequency of the charge q. Although Newmark's time integration is unconditionally stable, the accuracy of the solution of a coupled problem is dependent on the choice of the time increment Δt [8]. The Newmark's parameters β and and γ for AC analysis are chosen as $\gamma = 0.5$ and $\beta = 0.25$. A bias voltage V=1V is applied to both PVDF layers.

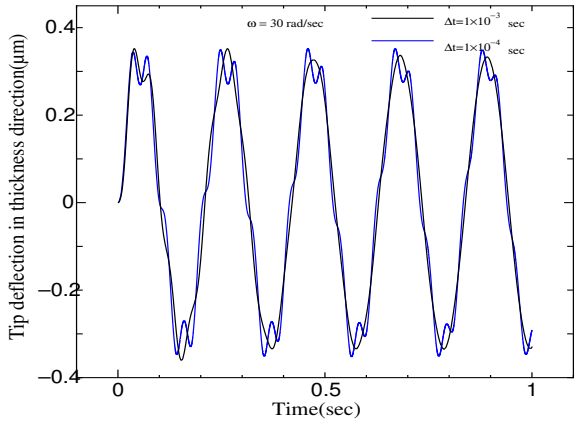

Figure 7: AC response for input frequency ω=30 rad/sec Approach 2

The Figure 7 shows the vibration characteristics of piezoelectric bimorph actuator excited with a bias voltage V=1V at a frequency ω = 30rad/sec using Approach 2. There are 4 BGS iterations per time steps are employed and NR iterations at each BGS iterations varies depending on the energy tolerance and deformation. The actual structural

resonance frequency of the numerical problem is ω_r=107 rad/sec [6]. The input voltage frequency used in this study is far away from the resonance, therefore the maximum deflection is around the steady state. For input voltage frequency of ω_r=107 rad/sec, resonance can be obtained using a very fine time increment for this proposed methods.

5 CONCLUSIONS

The proposed coupled algorithms to analyze the interaction between electric field by employing 3D solid elements and structural field by using MITC4 shell elements accurately take into account the piezoelectric interaction. The translation of nodal electrical forces in solid elements to the equivalent force and moment in MITC4 shell elements, and translation of displacements from shell to solid is accurately done using our translation method. Both Approach 1 and Approach 2 posses a same level accuracy of the solution. As a future work, shell structure and fluid field interaction will be performed using projection method.

REFERENCES

[1] Ishihara, D and Horie, T. A Projection Method For The Monolithic Interaction System Of An Incompressible Fluid And A Structure Using A New Algebraic Splitting, *Computer modeling in Engineering and Science*. (2014) **101**:421-440.

[2] Ishihara, D. Horie, T. Niho, T. and Baba, A. Hierarchal Decomposition For the Structure-Fluid- Electrostatic Interaction in a Micromechanical System, *Computer modeling in Engineering and Science*. (2015) **108**:429-452

[3] Henno Allik and Hughes,J.R. Finite Element Method for Piezoelectric Vibrations, *Int J Numer Meth Eng*. (1970) **2**:151-157.

[4] Dvorkin,E.N and Bathe,K.J. A Continuum Mechanics Based Four-Node Shell Element for General Nonlinear Analysis, *Eng Computation*.(1984) **1**:77-88

[5] Prakasha, C.R, Ishihara, D. Niho,T and Horie,T. A novel coupled algorithm for shell structure-electric field interaction analysis in MEMS piezoelectric actuator, *Proceedings of The 35th JSST Annual Conference International Conference on Simulation Technology*.(2016) : 332-339

[6] Prakasha, C.R. Ishihara, D. Niho, T. and Horie, T. Performance Evaluation Of Finite Element Coupled Algorithms For Structure-Electric Interaction Analysis of MEMS Actuator, *12th World Congress on Computational Mechanics*.(2016):1137-1150.

[7] Smits, G and Ballato, A. Dynamic Admittance Matrix of Piezoelectric Cantilever Bimorphs, *Journal of Microelectromechanical Systems*..(1994) **3**: 105–112.

[8] Niho, T. Horie, T. Uefhji, J. and Ishihara, D. Stability Analysis And Evaluation Of Staggered Coupled Analysis Methods For Electromagnetic And Structural Coupled Finite Element Analysis. *Computers and Structures*, (2017) **178** : 129142.

VII International Conference on Computational Methods for Coupled Problems in Science and Engineering
COUPLED PROBLEMS 2017
M. Papadrakakis, E. Oñate and B. Schrefler (Eds)

A THERMO-HYDRO-MECHANICAL FINITE ELEMENT MODEL OF FREEZING IN POROUS MEDIA—THERMO-MECHANICALLY CONSISTENT FORMULATION AND APPLICATION TO GROUND SOURCE HEAT PUMPS

Tianyuan Zheng[*†], Xing-Yuan Miao[*†], Dmitri Naumov[*†], Haibing Shao[*#], Olaf Kolditz[*†] and Thomas Nagel[*‡]

[*]Department of Environmental Informatics, Helmholtz Centre for Environmental Research – UFZ
Permoserstr. 15, 04318 Leipzig, Germany
e-mail: tianyuan.zheng@ufz.de, web page: http://www.ufz.com/

[†]Applied Environmental Systems Analysis, Technische Universität Dresden
01069 Dresden, Germany
web page: http://tu-dresden.de/

#Faculty of Geoscience, Geoengineering and Mining, Freiberg University of Mining and Technology
Akademiestraße 6, 09599 Freiberg
web page: http://tu-freiberg.de/

[‡]Department of Mechanical and Manuf. Engineering, School of Engineering, Trinity College Dublin
College Green, Dublin 2, Ireland
web page: http://www.tcd.ie/

Key words: freezing and thawing, phase change, Theory of Porous Media, geothermal energy, borehole heat exchanger, OpenGeoSys

Abstract. Freezing phenomena in porous media have attracted great attention in geotechnics, construction engineering and geothermal energy. For shallow geothermal applications where heat pumps are connected to borehole heat exchangers (BHEs), soil freezing around the BHEs is a potential problem due to persistent heat extraction or inappropriate design which can significantly influence the temperature distribution as well as groundwater flow patterns in the subsurface, and even lead to frost heave. A fully coupled thermo-hydro-mechanical freezing model is required for advanced system design and scenario analyses. In the framework of the Theory of Porous Media, a triphasic freezing model is derived and solved with the finite element method. Ice formation in the porous medium results from a coupled heat and mass transfer problem with phase change and is accompanied by volume expansion. The model is able to capture various coupled physical phenomena during freezing, e.g., the latent heat effect, groundwater flow with porosity change and mechanical deformation. The current paper is focused primarily on the theoretical derivation of the conceptual model. Its numerical imple-

mentation is verified against analytical solutions of selected phenomena including pure phase change and thermo-hydro-mechanical process couplings.

1 Introduction

Among different coupled processes, the thermal-hydro-mechanical behaviour of solid-liquid phase change in general and freezing in fluid-saturated porous media in particular is of great interest in soil construction [1], geotechnics [2], energy storage [3] and geothermal applications [4, 5]. Considering shallow geothermal energy, ground source heat pump systems (GSHPS) are increasingly employed as an efficient technology for the heating and cooling of buildings. The general proposition of a GSHPS is to extract heat from the shallow subsurface (50 m – 200 m below the surface) by circulating a heat-transfer fluid through single or multiple borehole heat exchangers (BHE). The energy carried by the circulating fluid is then lifted by heat pumps to temperature levels suitable for domestic applications. In cold regions, the undisturbed soil temperature is already below 10 °C [6]. When its temperature drops below 0 °C due to continuous heat extraction or inappropriate BHE/GSHPS design, freezing of the groundwater surrounding the BHEs will occur [7]. This will not only strongly affect the soil temperature distribution, hydraulic properties and the heat pump efficiency but may also cause mechanical damage to the BHEs and the surrounding facilities [4, 8]. For a discussion of implications on the design length of BHEs and economic aspects, cf. Zheng et al. [5].

In order to quantitatively analyze these coupled multi-physical phenomena on an engineering scale, a reliable macroscopic, fully coupled thermo-hydro-mechanical model is required which captures the relevant phenomena. The macroscopic Theory of Porous Media (TPM) [9, 10, 11] has been selected here as an ideal framework for this task.

A fundamental mathematical model based on mixture theory and thermodynamical principles was established for saturated porous media by [12]. Another macroscopic ternary model [13] incorporating liquid, ice and solid was constructed based on the theory of poromechanics by Coussy. As an extension of this model [13], Zhou & Meschke [2] developed a ternary model in view of a detailed physical description of ice crystallization. In recent years, the Theory of Porous Media was employed and Bluhm et al. [10, 14] presented a ternary model derived from thermodynamical considerations. Later Lai et al. [18] proposed a theoretical model of thermo-hydro-mechanical interactions during freezing and validated it with experiments. For the unsaturated cases, Li et al. [15, 16] demonstrated the heat-moisture-deformation coupling based on a theoretical framework with and without explicit consideration of the gas phase. Differing from considering gas as an extra phase, Liu & Yu [17] directly employed Richard's equation to capture the fluid flow in the unsaturated zone.

In the present paper, a fully coupled thermo-mechanically consistent THM freezing model for liquid-saturated porous materials is derived based on the Theory of Porous Media by exploiting the entropy inequality. In contrast to some of the previous models, Truesdell's metaphysical principles [19] are strictly adhered to for the mixture balance relations. The description of the

mechanical behaviour of the ice and solid phases accounts for their differing natural configurations.

The fundamental kinematics and balance relations are listed in Section 2. The assumptions made and constitutive relations derived from the Clausius-Duhem inequality are presented in Section 3. With the balance relations and constitutive laws, the governing equations are given in Section 4. The verification of the numerical model is performed in Section 5. The paper closes with an illustrative numerical example in Section 6.

2 General definitions

2.1 Kinematics

Consider a medium composed of different phases or constituents α, each represented by a substitute continuum defined on the entire control space. The motion of a constituent α is described by its motion function $\boldsymbol{\chi}_\alpha$ that maps the position $\mathbf{X}_\alpha$ of a material point (particle) in the reference configuration to its spatial location $\mathbf{x}$ in the current configuration:

$$\mathbf{x} = \boldsymbol{\chi}_\alpha(\mathbf{X}_\alpha, t) \tag{1}$$

Each phase can then be assigned a deformation gradient as well as its inverse

$$\mathbf{F}_\alpha = \mathrm{Grad}_\alpha\, \mathbf{x} \quad \text{and} \quad \mathbf{F}_\alpha^{-1} = \mathrm{grad}\, \mathbf{X}_\alpha \tag{2}$$

and the material time derivative following the motion of a phase α defines the phase velocities

$$\mathbf{v}_\alpha = \mathbf{x}'_\alpha = \frac{\partial \boldsymbol{\chi}_\alpha(\mathbf{X}_\alpha, t)}{\partial t} \tag{3}$$

Based on these fundamental kinematic definitions, the entire spectrum of continuum mechanical kinematic quantities becomes available, e.g. the material and spatial velocity gradients:

$$(\mathbf{F}_\alpha)'_\alpha = \mathrm{Grad}_\alpha\, \mathbf{x}'_\alpha \quad \text{and} \quad \mathbf{l}_\alpha = \mathrm{grad}\, \mathbf{x}'_\alpha = (\mathbf{F}_\alpha)'_\alpha\, \mathbf{F}_\alpha^{-1} \tag{4}$$

Following the above relations, the right Cauchy-Green deformation tensor and Green-Lagrangean strain tensor read:

$$\mathbf{C}_\alpha = \mathbf{F}_\alpha^T \mathbf{F}_\alpha \quad \text{and} \quad \mathbf{E}_\alpha = \frac{1}{2}(\mathbf{C}_\alpha - \mathbf{I}) \tag{5}$$

When small-strain conditions are assumed, the finite deformation approach can be reduced to a geometrically linear one via $\mathrm{lin}\, \mathbf{E}_\alpha = \boldsymbol{\epsilon}_\alpha$ and the distinction between reference configuration and current configuration is no longer necessary in the spatial operators. For further definitions, see standard texts on continuum mechanics [19].

Based on Truesdell's metaphysical principles [19], the motion of the mixture is governed by the same equations as the motion of a single body. Hence, summation of the balance equations of the individual phases listed in the subsequent section must yield the balance equations known from continuum mechanics of single phase materials. This condition imposes restrictions on the production terms. For details, the reader is referred to, e.g., [9] and references therein.

3 Balance equations and constitutive relations

3.1 Specific assumptions

To maintain a certain level of generality in the conceptual modelling section, a finite strain setting will be maintained throughout the derivation of the model. A first implementation of the governing equations will then rest on the assumption of linear kinematics.

Before specifying the balance equations, some basic assumptions of the model shall be clarified.

1. A three-phase mixture consisting of solid (S), ice (I) and the aqueous pore fluid (L) is considered: $\alpha = \{\mathrm{S}, \mathrm{I}, \mathrm{L}\}$.
2. For all phases we assume incompressibility in the sense $\varrho_{\alpha\mathrm{R}} = \varrho_{\alpha\mathrm{R}}(T)$.
3. Deformation and flow occur in a quasi-static fashion such that inertial effects can be neglected in the final governing equations: $\mathbf{a}_\alpha = \mathbf{0}$.
4. The local temperatures of all constituents are equal (local thermal equilibrium): $T_\alpha = T$.
5. Mass transfer is limited to the water and ice phases, i.e. $\hat{\varrho}_\mathrm{S} = 0$, $\hat{\varrho}_\mathrm{L} = -\hat{\varrho}_\mathrm{I}$.
6. The constituents solid and ice are kinematically constrained once the ice is formed at time t_F, i.e. $\mathbf{v}_\mathrm{S} = \mathbf{v}_\mathrm{I}$. At that stage, the solid may have undergone a motion already, i.e. the reference coordinates of an ice particle are given by $\widehat{\mathbf{X}}_\mathrm{I} = \chi_\mathrm{S}(\mathbf{X}_\mathrm{S}, t_\mathrm{F})$. The current placement of corresponding solid and ice particles is then given by the motion function of ice and solid via $\mathbf{x} = \chi_\mathrm{S}(\mathbf{X}_\mathrm{S}, t) = \chi_\mathrm{I}(\widehat{\mathbf{X}}_\mathrm{I}, t) = \chi_\mathrm{I}\left(\chi_\mathrm{S}(\mathbf{X}_\mathrm{S}, t_\mathrm{F}), t\right)$.

Assumption 6 will be captured by a multiplicative decomposition of the deformation gradient of the solid into a part before freezing (S0) and a part after freezing (I) following [10]

$$\mathbf{F}_\mathrm{S} = \widehat{\mathbf{F}}_\mathrm{I}\mathbf{F}_\mathrm{S0} \tag{6}$$

It will be assumed that stresses in the ice are only determined by that part of the motion accrued after freezing has occurred, i.e. by $\widehat{\mathbf{F}}_\mathrm{I}$, while the stress response of the solid is characterised by $\mathbf{F}_\mathrm{S}$ itself. Under the small-strain assumption, the decomposition of the motion simplifies to:

$$\boldsymbol{\epsilon}_\mathrm{S} = \boldsymbol{\epsilon}_\mathrm{I} + \boldsymbol{\epsilon}_\mathrm{S0} \tag{7}$$

Based on the general mass balance in the form

$$\phi_\alpha(\varrho_{\alpha\mathrm{R}})'_\alpha + (\phi_\alpha)'_\alpha\varrho_{\alpha\mathrm{R}} + \varrho_{\alpha\mathrm{R}}\phi_\alpha \operatorname{div}\mathbf{v}_\alpha = \hat{\varrho}_\alpha \tag{8}$$

as well Assumptions 5 and 6, the derivatives of the individual volume fractions are obtained from the above mass balances in the following form

$$(\phi_{\mathrm{S}})'_{\mathrm{S}} = -\phi_{\mathrm{S}}\mathrm{div}\mathbf{v}_{\mathrm{S}} - \phi_{\mathrm{S}}\frac{(\varrho_{\mathrm{SR}})'_{\mathrm{S}}}{\varrho_{\mathrm{SR}}} \tag{9}$$

$$(\phi_{\mathrm{I}})'_{\mathrm{S}} = \frac{\hat{\varrho}_{\mathrm{I}}}{\varrho_{\mathrm{IR}}} - \phi_{\mathrm{I}}\mathrm{div}\mathbf{v}_{\mathrm{S}} - \phi_{\mathrm{I}}\frac{(\varrho_{\mathrm{IR}})'_{\mathrm{S}}}{\varrho_{\mathrm{IR}}} \tag{10}$$

$$(\phi_{\mathrm{L}})'_{\mathrm{S}} = -\frac{\hat{\varrho}_{\mathrm{I}}}{\varrho_{\mathrm{LR}}} - \phi_{\mathrm{L}}\mathrm{div}\mathbf{v}_{\mathrm{L}} - \phi_{\mathrm{L}}\frac{(\varrho_{\mathrm{LR}})'_{\mathrm{L}}}{\varrho_{\mathrm{LR}}} - \mathrm{grad}\phi_{\mathrm{L}} \cdot \mathbf{w}_{\mathrm{LS}} \tag{11}$$

Based on Assumption 2, the time derivative of the material density can be expressed via the temperature rate and the volumetric thermal expansion coefficient $\beta_{T\alpha}$

$$(\varrho_{\alpha\mathrm{R}})'_{\alpha} = \frac{\partial \varrho_{\alpha\mathrm{R}}}{\partial T}T'_{\alpha} = -\varrho_{\alpha\mathrm{R}}\beta_{T\alpha}T'_{\alpha} \quad \text{with} \quad \beta_{T\alpha} = -\frac{1}{\varrho_{\alpha\mathrm{R}}}\frac{\partial \varrho_{\alpha\mathrm{R}}}{\partial T} \tag{12}$$

3.2 Saturation condition

The saturation condition for this ternary mixture can be written in absolute and in rate form (following the trajectory of the solid) as

$$\sum_{\alpha}\phi_{\alpha} = 1 \quad \text{and} \quad \sum_{\alpha}(\phi_{\alpha})'_{\mathrm{S}} = 0 \tag{13}$$

Substitution of Eqs. (9)–(11) yields the model-specific form of the mixture volume balance:

$$0 = \mathrm{div}\left[\mathbf{v}_{\mathrm{S}} + \phi_{\mathrm{L}}\mathbf{w}_{\mathrm{LS}}\right] + \hat{\varrho}_{\mathrm{I}}\left(\varrho_{\mathrm{LR}}^{-1} - \varrho_{\mathrm{IR}}^{-1}\right) + \frac{\phi_{\mathrm{S}}(\varrho_{\mathrm{SR}})'_{\mathrm{S}}}{\varrho_{\mathrm{SR}}} + \frac{\phi_{\mathrm{I}}(\varrho_{\mathrm{IR}})'_{\mathrm{S}}}{\varrho_{\mathrm{IR}}} + \frac{\phi_{\mathrm{L}}(\varrho_{\mathrm{LR}})'_{\mathrm{L}}}{\varrho_{\mathrm{LR}}} \tag{14}$$

3.3 Evaluation of the entropy inequality

The entropy inequality will be exploited following the Coleman-Noll procedure. Invoking the assumption of local thermal equilibrium, the production-term constraint in the energy balance, and adding the saturation condition as a constraint to the entropy inequality yields

$$\begin{aligned} 0 \leq \sum_{\alpha=1}^{\kappa}\Bigg\{ & -\varrho_{\alpha}[(\psi_{\alpha})'_{\alpha} + T'_{\alpha}\eta_{\alpha}] - \hat{\varrho}_{\alpha}\left(\psi_{\alpha} - \frac{1}{2}\mathbf{v}_{\alpha}\cdot\mathbf{v}_{\alpha}\right) + \\ & \boldsymbol{\sigma}_{\alpha} : \mathbf{l}_{\alpha} - \hat{\mathbf{p}}_{\alpha}\cdot\mathbf{v}_{\alpha} - \frac{1}{T}\mathbf{q}_{\alpha}\cdot\mathrm{grad}\,T - \lambda(\phi_{\alpha})'_{\mathrm{S}}\Bigg\} \end{aligned} \tag{15}$$

The Lagrange multiplier λ can be understood as a pressure-type reaction force enforcing the saturation constraint.

Employing the principle of phase-separation [9], the free energy of the solid phase is assumed to depend on solid deformation and temperature, the liquid phase free energy only on temperature, and the free energy of the ice phase on the ice volume fraction, temperature and that part of the deformation characterizing ice deformation, cf. Eq. 6. Hence, the following *Ansatz* is made for the specific Helmholtz free energies:

$$\psi_{\mathrm{S}} = \psi_{\mathrm{S}}(\mathbf{C}_{\mathrm{S}}, T) \qquad \psi_{\mathrm{I}} = \psi_{\mathrm{I}}(\widehat{\mathbf{C}}_{\mathrm{I}}, T, \phi_{\mathrm{I}}) \qquad \psi_{\mathrm{L}} = \psi_{\mathrm{L}}(T) \tag{16}$$

where the right Cauchy-Green tensors $\mathbf{C}_{\mathrm{S}} = \mathbf{F}_{\mathrm{S}}^{\mathrm{T}}\mathbf{F}_{\mathrm{S}}$ and $\widehat{\mathbf{C}}_{\mathrm{I}} = \widehat{\mathbf{F}}_{\mathrm{I}}^{\mathrm{T}}\widehat{\mathbf{F}}_{\mathrm{I}}$ have been used.

Neglecting terms associated with the kinetic energy of mass transfer, and using the transformed mass balance equations (9)–(11), inequality (15) can be expanded to

$$\begin{aligned} 0 \leq\ & -\varrho_{\mathrm{S}}(\psi_{\mathrm{S}})'_{\mathrm{S}} + T'_{\mathrm{S}}\left(-\varrho_{\mathrm{S}}\eta_{\mathrm{S}} + \lambda\frac{\phi_{\mathrm{S}}}{\varrho_{\mathrm{SR}}}\frac{\partial\varrho_{\mathrm{SR}}}{\partial T}\right) - \varrho_{\mathrm{I}}(\psi_{\mathrm{I}})'_{\mathrm{S}} + T'_{\mathrm{S}}\left(-\varrho_{\mathrm{I}}\eta_{\mathrm{I}} + \lambda\frac{\phi_{\mathrm{I}}}{\varrho_{\mathrm{IR}}}\frac{\partial\varrho_{\mathrm{IR}}}{\partial T}\right) - \\ & - \varrho_{\mathrm{L}}(\psi_{\mathrm{L}})'_{\mathrm{L}} + T'_{\mathrm{L}}\left(-\varrho_{\mathrm{L}}\eta_{\mathrm{L}} + \lambda\frac{\phi_{\mathrm{L}}}{\varrho_{\mathrm{LR}}}\frac{\partial\varrho_{\mathrm{LR}}}{\partial T}\right) - \hat{\varrho}_{\mathrm{I}}\left(\psi_{\mathrm{I}} + \frac{\lambda}{\varrho_{\mathrm{IR}}} - \psi_{\mathrm{L}} - \frac{\lambda}{\varrho_{\mathrm{LR}}}\right) + \\ & + (\boldsymbol{\sigma}_{\mathrm{S}} + \lambda\phi_{\mathrm{S}}\mathbf{I}) : \mathbf{d}_{\mathrm{S}} + (\boldsymbol{\sigma}_{\mathrm{I}} + \lambda\phi_{\mathrm{I}}\mathbf{I}) : \mathbf{d}_{\mathrm{S}} + (\boldsymbol{\sigma}_{\mathrm{L}} + \lambda\phi_{\mathrm{L}}\mathbf{I}) : \mathbf{d}_{\mathrm{L}} - \\ & - \sum_{\alpha}\hat{\mathbf{p}}_{\alpha}\cdot\mathbf{v}_{\alpha} + \lambda\,\mathrm{grad}\,\phi_{\mathrm{L}}\cdot\mathbf{w}_{\mathrm{LS}} - \frac{1}{T}\mathbf{q}_{\mathrm{SIL}}\cdot\mathrm{grad}\,T \quad \text{with} \quad \mathbf{q}_{\mathrm{SIL}} = \sum_{\alpha}\mathbf{q}_{\alpha} \end{aligned} \tag{17}$$

Now, the terms $\boldsymbol{\sigma}_{\alpha}^{\mathrm{E}} = \boldsymbol{\sigma}_{\alpha} + \lambda\phi_{\alpha}\mathbf{I}$ defining the so-called extra stresses can be introduced. Based on dimensional analyses, it is common practice to neglect fluid extra stresses. Hence, we find a hydrostatic stress state in the fluid and identify the Lagrange multiplier λ with the pore pressure p_{LR}:

$$\boldsymbol{\sigma}_{\mathrm{L}} = -p_{\mathrm{LR}}\phi_{\mathrm{L}}\mathbf{I} \quad \text{with} \quad \lambda = p_{\mathrm{LR}} \tag{18}$$

The constraint on the momentum production terms yields the relation

$$-(\hat{\mathbf{p}}_{\mathrm{S}} + \hat{\mathbf{p}}_{\mathrm{I}}) = \hat{\mathbf{p}}_{\mathrm{L}} + \hat{\varrho}_{\mathrm{I}}\mathbf{w}_{\mathrm{LS}} \tag{19}$$

Similarly to the stresses, the extra momentum production is the constitutively determined term in addition to effects contributed by the Lagrange multiplier—i.e. the liquid pressure—and is defined as

$$\hat{\mathbf{p}}_{\mathrm{L}}^{\mathrm{E}} = \hat{\mathbf{p}}_{\mathrm{L}} - \lambda\,\mathrm{grad}\,\phi_{\mathrm{L}} \tag{20}$$

With Eq. (16) and $(\mathbf{C}_{\alpha})'_{\alpha} = 2\mathbf{F}_{\alpha}^{\mathrm{T}}\mathbf{d}_{\alpha}\mathbf{F}_{\alpha}$ we can now write

$$\begin{aligned} 0 \leq\ & \left(\boldsymbol{\sigma}_{\mathrm{S}}^{\mathrm{E}} - 2\varrho_{\mathrm{S}}\mathbf{F}_{\mathrm{S}}\frac{\partial\psi_{\mathrm{S}}}{\partial\mathbf{C}_{\mathrm{S}}}\mathbf{F}_{\mathrm{S}}^{\mathrm{T}}\right) : \mathbf{d}_{\mathrm{S}} + \left(\boldsymbol{\sigma}_{\mathrm{I}}^{\mathrm{E}} - 2\varrho_{\mathrm{I}}\hat{\mathbf{F}}_{\mathrm{I}}\frac{\partial\psi_{\mathrm{I}}}{\partial\hat{\mathbf{C}}_{\mathrm{I}}}\hat{\mathbf{F}}_{\mathrm{I}}^{\mathrm{T}} + \varrho_{\mathrm{I}}\phi_{\mathrm{I}}\frac{\partial\psi_{\mathrm{I}}}{\partial\phi_{\mathrm{I}}}\mathbf{I}\right) : \mathbf{d}_{\mathrm{S}} - \\ & - \sum_{\alpha}\varrho_{\alpha}\left(\eta_{\alpha} - \lambda\frac{1}{(\varrho_{\alpha\mathrm{R}})^2}\frac{\partial\varrho_{\alpha\mathrm{R}}}{\partial T} + \frac{\partial\psi_{\alpha}}{\partial T}\right)T'_{\alpha} - \hat{\varrho}_{\mathrm{I}}\left[\psi_{\mathrm{I}} + \frac{1}{\varrho_{\mathrm{IR}}}\left(\lambda + \phi_{\mathrm{I}}\frac{\partial\psi_{\mathrm{I}}}{\partial\phi_{\mathrm{I}}}\right) - \psi_{\mathrm{L}} - \frac{\lambda}{\varrho_{\mathrm{LR}}}\right] - \\ & - \varrho_{\mathrm{I}}\phi_{\mathrm{I}}\beta_{T\mathrm{I}}\frac{\partial\psi_{\mathrm{I}}}{\partial\phi_{\mathrm{I}}}T'_{\mathrm{S}} - \hat{\mathbf{p}}_{\mathrm{L}}^{\mathrm{E}}\cdot\mathbf{w}_{\mathrm{LS}} - \frac{1}{T}\mathbf{q}_{\mathrm{SIL}}\cdot\mathrm{grad}\,T \end{aligned} \tag{21}$$

This form motivates the introduction of the extra entropy terms $\eta_{\alpha}^{\mathrm{E}}$ such that

$$\eta_\alpha = \eta_\alpha^{\mathrm{E}} + \lambda \frac{1}{(\varrho_{\alpha\mathrm{R}})^2} \frac{\partial \varrho_{\alpha\mathrm{R}}}{\partial T} = \eta_\alpha^{\mathrm{E}} - \frac{\beta_{T\alpha}}{\varrho_{\alpha\mathrm{R}}} p_{\mathrm{LR}} \tag{22}$$

Based on the *Ansatz* defined in Eq. (16), the following restrictions can be derived:

$$\eta_\alpha^{\mathrm{E}} = -\frac{\partial \psi_\alpha}{\partial T} \quad \text{and} \quad \eta_\alpha = \eta_\alpha^{\mathrm{E}} - \frac{\beta_{T\alpha}}{\varrho_{\alpha\mathrm{R}}} p_{\mathrm{LR}} \quad \text{for } \alpha = \mathrm{S} \text{ and } \mathrm{L} \tag{23}$$

$$\eta_{\mathrm{I}}^{\mathrm{E,F}} = -\frac{\partial \psi_{\mathrm{I}}}{\partial T} \quad \text{and} \quad \eta_{\mathrm{I}} = \eta_{\mathrm{I}}^{\mathrm{E,F}} - \frac{\beta_{T\mathrm{I}}}{\varrho_{\mathrm{IR}}} \underbrace{\left(p_{\mathrm{LR}} + \varrho_{\mathrm{I}} \frac{\partial \psi_{\mathrm{I}}}{\partial \phi_{\mathrm{I}}} \right)}_{p_{\mathrm{red}}} \quad \text{with} \quad \eta_{\mathrm{I}}^{\mathrm{E,F}} = \eta_{\mathrm{I}}^{\mathrm{E}} + \frac{\beta_{T\mathrm{I}}}{\varrho_{\mathrm{IR}}} \varrho_{\mathrm{I}} \frac{\partial \psi_{\mathrm{I}}}{\partial \phi_{\mathrm{I}}} \tag{24}$$

$$\boldsymbol{\sigma}_{\mathrm{S}} = -p_{\mathrm{LR}} \phi_{\mathrm{S}} \mathbf{I} + 2 \varrho_{\mathrm{S}} \mathbf{F}_{\mathrm{S}} \frac{\partial \psi_{\mathrm{S}}}{\partial \mathbf{C}_{\mathrm{S}}} \mathbf{F}_{\mathrm{S}}^{\mathrm{T}} \tag{25}$$

$$\boldsymbol{\sigma}_{\mathrm{I}} = -\phi_{\mathrm{I}} \underbrace{\left(p_{\mathrm{LR}} + \varrho_{\mathrm{I}} \frac{\partial \psi_{\mathrm{I}}}{\partial \phi_{\mathrm{I}}} \right)}_{P\mathrm{red}} \mathbf{I} + 2 \varrho_{\mathrm{I}} \hat{\mathbf{F}}_{\mathrm{I}} \frac{\partial \psi_{\mathrm{I}}}{\partial \hat{\mathbf{C}}_{\mathrm{I}}} \hat{\mathbf{F}}_{\mathrm{I}}^{\mathrm{T}} \tag{26}$$

Introducing the chemical potential-type quantities

$$\Psi_{\mathrm{I}} = \psi_{\mathrm{I}} + \frac{p_{\mathrm{red}}}{\varrho_{\mathrm{IR}}} \quad \text{and} \quad \Psi_{\mathrm{L}} = \psi_{\mathrm{L}} + \frac{p_{\mathrm{LR}}}{\varrho_{\mathrm{LR}}} \tag{27}$$

allows the formulation of the remaining dissipation inequality as

$$\mathcal{D} = -\hat{\mathbf{p}}_{\mathrm{L}}^{\mathrm{E}} \cdot \mathbf{w}_{\mathrm{LS}} - \frac{1}{T} \mathbf{q}_{\mathrm{SIL}} \cdot \operatorname{grad} T - \hat{\varrho}_{\mathrm{I}} (\Psi_{\mathrm{I}} - \Psi_{\mathrm{L}}) \geq 0 \tag{28}$$

Treating physically distinct terms independently, the heat flux vector can be found from the linear relation

$$0 \leq -\mathbf{q}_{\mathrm{SIL}} \cdot \operatorname{grad} T \quad \rightarrow \quad \mathbf{q}_{\mathrm{SIL}} = -\boldsymbol{\lambda}_{\mathrm{SIL}} \operatorname{grad} T \quad \text{with} \quad \mathbf{a} \cdot \boldsymbol{\lambda}_{\mathrm{SIL}} \mathbf{a} \geq 0 \; \forall \; \mathbf{a} \neq \mathbf{0} \tag{29}$$

where $\boldsymbol{\lambda}_{\mathrm{SIL}}$ is the effective heat conductivity tensor of the saturated porous medium.
Similarly, the flow-law can be derived from a linear relationship as

$$0 \leq -\hat{\mathbf{p}}_{\mathrm{L}}^{\mathrm{E}} \cdot \mathbf{w}_{\mathrm{LS}} \quad \rightarrow \quad \hat{\mathbf{p}}_{\mathrm{L}}^{\mathrm{E}} = -\mathbf{S}\mathbf{w}_{\mathrm{LS}} \quad \text{with} \quad \mathbf{a} \cdot \mathbf{S}\mathbf{a} \geq 0 \; \forall \; \mathbf{a} \neq \mathbf{0} \tag{30}$$

Substituting the fluid stress tensor from Eq. (18) and the flow law from relation (30) into the fluid momentum balance and choosing $\mathbf{S}^{-1} = \mathbf{K}/(\mu_{\mathrm{LR}} \phi_{\mathrm{L}}^2)$ recovers a Darcy-like law:

$$\phi_{\mathrm{L}} \mathbf{w}_{\mathrm{LS}} = -\frac{\mathbf{K}}{\mu_{\mathrm{LR}}} \left(\operatorname{grad} p_{\mathrm{LR}} - \varrho_{\mathrm{LR}} \mathbf{b}_{\mathrm{L}} \right) \tag{31}$$

In which K is the permeability and varies with the ice formation which occupies the porosity. Finally, a kinetic law for the phase transition can be defined based on the difference in the chemical potentials of the liquid and ice phases:

$$0 \leq -\hat{\varrho}_{\mathrm{I}} (\Psi_{\mathrm{I}} - \Psi_{\mathrm{L}}) \quad \rightarrow \quad \hat{\varrho}_{\mathrm{I}} = c_{\mathrm{F}} (\Psi_{\mathrm{L}} - \Psi_{\mathrm{I}}) \quad \text{with} \quad c_{\mathrm{F}} \geq 0 \tag{32}$$

For an extended discussion of phase change in this context, see [20].

4 Governing Equations and Numerical Implementation

Free energy formulations for the finite-strain setting can be found in [14, 10, 20] and others. Based on the general constitutive setting outlined above, considerations are now limited to the small strain setting using the decomposition in Eq. (7). For an initial implementation with the purpose of algorithmic testing, some of the physical terms occurring as a consequence of the above derivations and the chosen energy functionals have been neglected. They will be added subject to their relevance indicated by an order-of-magnitude analysis. The following set of governing equations has been implemented into OpenGeoSys [21] for initial testing.

Mixture volume balance

$$0 = \operatorname{div}\left[(\mathbf{u}_\mathrm{S})'_\mathrm{S} + \phi_\mathrm{L}\mathbf{w}_\mathrm{LS}\right] + \hat{\varrho}_\mathrm{I}\left(\varrho_\mathrm{LR}^{-1} - \varrho_\mathrm{IR}^{-1}\right) - \beta_T T'_\mathrm{S} \quad \text{with} \quad \beta_T = \sum_\alpha \phi_\alpha \beta_{T\alpha} \tag{33}$$

Mixture momentum balance

$$\begin{aligned}\operatorname{div}\,(-p_\mathrm{LR}\mathbf{I} + \lambda_\mathrm{S}\mathrm{tr}(\boldsymbol{\epsilon}_\mathrm{S})\mathbf{I} + 2\mu_\mathrm{S}\boldsymbol{\epsilon}_\mathrm{S} - 3\alpha_{T\mathrm{S}}k_\mathrm{S}(T - T_{\mathrm{S}0})\mathbf{I} + \lambda_\mathrm{I}\mathrm{tr}(\boldsymbol{\epsilon}_\mathrm{I})\mathbf{I} + 2\mu_\mathrm{I}\boldsymbol{\epsilon}_\mathrm{I} - \\ 3\alpha_{T\mathrm{I}}k_\mathrm{I}(T - T_{\mathrm{I}0})\mathbf{I} - 3\alpha_{\mathrm{FI}}k_\mathrm{I}(\phi_\mathrm{I} - \phi_{\mathrm{I}0})\mathbf{I}) + \varrho\mathbf{b} = \mathbf{0}\end{aligned} \tag{34}$$

Mixture energy balance

$$(\varrho c_p)^{\mathrm{eff}} T'_\mathrm{S} - \Delta H_\mathrm{I}\hat{\varrho}_\mathrm{I} - \operatorname{div}(\lambda_{\mathrm{SIL}}\operatorname{grad} T) + \varrho_{\mathrm{LR}} c_{p\mathrm{L}}\phi_\mathrm{L}\mathbf{w}_{\mathrm{LS}}\cdot\operatorname{grad} T = 0 \tag{35}$$

The corresponding weak forms are linearized using a Newton-Raphson scheme. The discretized primary variable field $\mathbf{u}_\mathrm{S}$ is interpolated with shape functions an order higher than those used for the remaining primary variables p_LR and T.

5 Verification

Due to the complexity of the fully coupled thermo-hydro-mechanical freezing process and the associated lack of analytical solutions, the initial verification is here separated into a pure thermo-hydro-mechanical part and a pure phase change part, both using analytical solutions.

5.1 Verification of the THM model

In this benchmark, phase change is neglected and a completely sealed specimen is heated up homogeneously. The difference of the thermal expansion coefficients of fluid and solid phase results in a pore pressure which can be determined analytically in the case of an elastic solid skeleton [22]:

$$p_\mathrm{LR} = -K_\mathrm{S}\phi_\mathrm{F}(\beta_{T\mathrm{F}} - \beta_{T\mathrm{S}})\Delta T \tag{36}$$

where K_S is the bulk modulus of the solid matrix, ϕ_F is the porosity and $\beta_{T\mathrm{S}}$= 2.1e-5 and $\beta_{T\mathrm{F}}$ =2.07e-4 are the volumetric thermal expansion coefficients of solid and fluid. Under a homogeneous temperature increment of 80 K, a fluid pressure of 0.1042 MPa develops in the

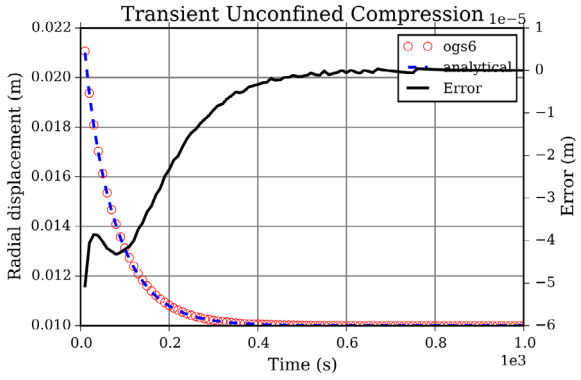

(a) Radial displacement during unconfined compression.

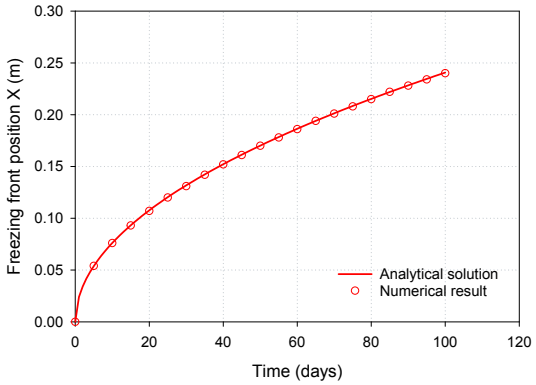

(b) The propagation of the freezing front X over time.

externally load-free specimen under undrained conditions. This value is recovered by the numerical model with a relative error below 10^{-6}. Numerically, the direct linear solver SparseLU (`http://eigen.tuxfamily.org`) and nonlinear tolerances 10^{-8} (absolute error) have been used.

Other tests performed for verification of the THM coupling included transient confined and unconfined compression tests (Fig. 1a) as well as flow under thermal gradients; further details can be found in `https://dev.opengeosys.org/docs/benchmarks/`.

5.2 Phase change verification

In this benchmark, only the thermal problem including phase change is considered and the propagation of the freezing front is calculated by the Neumann analytical solution [23]. A 1 m long water column (achieved by setting the porosity to unity) was connected to a freezing wall of -3 °C. The initial temperature was given as 2 °C in the entire domain. All parameters used in the simulation can be found in [5]. The location of the phase change front $X(t)$ is compared to the analytical solution in Fig. 1b.

6 Numerical Example

In this section, an academic example of the thermo-hydro-mechanical freezing model uses an axisymmetric setup of a cylinder with a radius and height of side 1.0 cm. The domain is divided into 100 elements and the simulation time of 1000 s is split into time steps of 50 s. The externally load-free specimen has an initial temperature of 5 °C. At the bottom, a constant temperature of -5 °C is set as boundary condition. In Fig. 1, the evolving ice saturation with the associated expansion of the specimen is depicted.

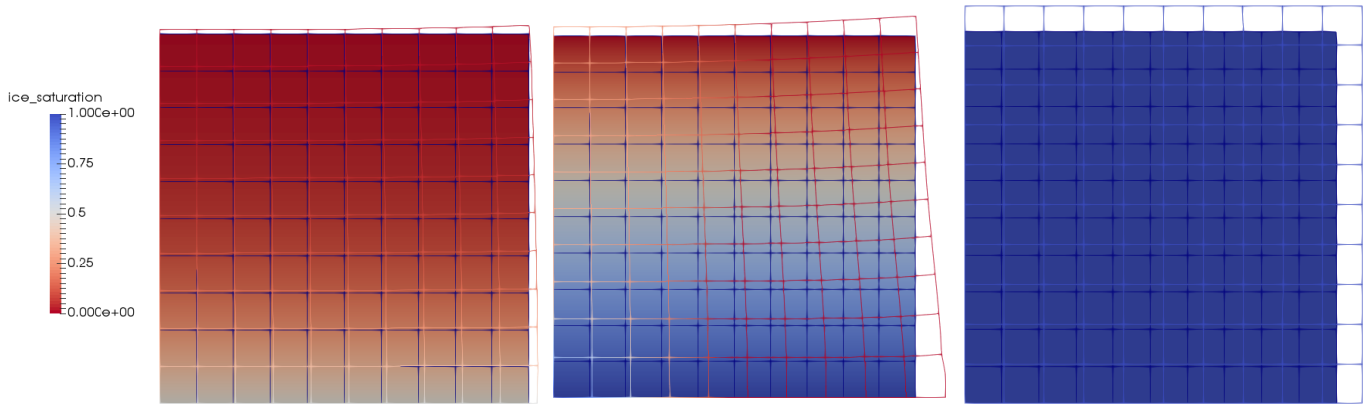

(a) 50 s (b) 150 s (c) 1000 s

Figure 1: Freezing front evolution (colors) and displacement field (overlay grid) during freezing propagation.

7 Conclusion

In this paper, a macroscopic fully coupled thermo-hydro-mechanical model under the framework of the Theory of Porous Media is presented for the simulation of liquid-solid phase change considering effects like the ice volume expansion, hydraulic pressure changes, and the latent effect. It is verified separately with different transient analytical solutions and will be further used to predict the frost evolution around bore-hole heat exchangers.

References

[1] Q. Jilin, Z. Jianming, Z. Yuanlin, Influence of freezing-thawing on soil structure and its soil mechanics significance, Chinese Journal of Rock Mechanics and Engineering 22 (2) (2003) 690–2.

[2] M. Zhou, G. Meschke, A three-phase thermo-hydro-mechanical finite element model for freezing soils, International Journal for Numerical and Analytical Methods in Geomechanics 37 (18) (2013) 3173–3193.

[3] A. Kabuth, A. Dahmke, C. Beyer, L. Bilke, F. Dethlefsen, P. Dietrich, R. Duttmann, M. Ebert, V. Feeser, U.-J. Görke, R. Köber, W. Rabbel, T. Schanz, D. Schäfer, H. Würdemann, S. Bauer, Energy storage in the geological subsurface: dimensioning, risk analysis and spatial planning: the angus+ project, Environmental Earth Sciences 76 (1) (2016) 23. doi:10.1007/s12665-016-6319-5.

[4] S. Erol, B. François, Freeze damage of grouting materials for borehole heat exchanger: Experimental and analytical evaluations, Geomechanics for Energy and the Environment 5 (2016) 29–41.

[5] T. Zheng, H. Shao, S. Schelenz, P. Hein, T. Vienken, Z. Pang, O. Kolditz, T. Nagel, Efficiency and economic analysis of utilizing latent heat from groundwater freezing in the context of borehole heat exchanger coupled ground source heat pump systems, Applied Thermal Engineering 105 (2016) 314–326.

[6] H. Esen, M. Inalli, Y. Esen, Temperature distributions in boreholes of a vertical ground-coupled heat pump system, Renewable Energy 34 (12) (2009) 2672–2679.

[7] W. Yang, L. Kong, Y. Chen, Numerical evaluation on the effects of soil freezing on underground temperature variations of soil around ground heat exchangers, Applied Thermal Engineering 75 (2015) 259–269.

[8] Y. Wang, Q. Gao, X. Zhu, M. Yu, X. Zhao, Experimental study on interaction between soil and ground heat exchange pipe at low temperature, Applied Thermal Engineering 60 (1) (2013) 137–144.

[9] W. Ehlers, Foundations of multiphasic and porous materials, in: W. Ehlers, J. Bluhm (Eds.), Porous Media: Theory, Experiments and Numerical Applications, Springer, Berlin, 2002, pp. 4–86.

[10] J. Bluhm, T. Ricken, M. Bloßfeld, Ice Formation in Porous Media, in: B. Markert (Ed.), Advances in Extended and Multifield Theories for Continua, Vol. 59 of Lecture Notes in Applied and Computational Mechanics, Springer Berlin Heidelberg, 2011, pp. 153–174. doi:10.1007/978-3-642-22738-7_8.

[11] R. de Boer, Thermodynamics of Phase Transitions in Porous Media, Applied Mechanics Reviews 48 (10) (1995) 613–622. doi:10.1115/1.3005042.

[12] M. Mikkola, J. Hartikainen, Mathematical model of soil freezing and its numerical implementation, International Journal for Numerical Methods in Engineering 52 (5-6) (2001) 543–557.

[13] O. Coussy, Poromechanics of freezing materials, Journal of the Mechanics and Physics of Solids 53 (8) (2005) 1689–1718.

[14] J. Bluhm, T. Ricken, W. M. Bloßfeld, Energetische aspekte zum gefrierverhalten von wasser in porösen strukturen, PAMM 8 (1) (2008) 10483–10484. doi:10.1002/pamm.200810483.

[15] N. Li, F. Chen, B. Xu, G. Swoboda, Theoretical modeling framework for an unsaturated freezing soil, Cold Regions Science and Technology 54 (1) (2008) 19–35.

[16] N. Li, F. Chen, B. Su, G. Cheng, Theoretical frame of the saturated freezing soil, Cold Regions Science and Technology 35 (2) (2002) 73–80.

[17] Z. Liu, X. Yu, Coupled thermo-hydro-mechanical model for porous materials under frost action: theory and implementation, Acta Geotechnica 6 (2) (2011) 51–65.

[18] Y. Lai, W. Pei, M. Zhang, J. Zhou, Study on theory model of hydro-thermal–mechanical interaction process in saturated freezing silty soil, International Journal of Heat and Mass Transfer 78 (2014) 805–819.

[19] C. Truesdell, W. Noll, The Non-Linear Field Theories of Mechanics, in: S. Antman (Ed.), The Non-Linear Field Theories of Mechanics, Springer Berlin Heidelberg, 2004, pp. 1–579. doi:10.1007/978-3-662-10388-3_1.

[20] W. Ehlers, K. Häberle, Interfacial mass transfer during gas–liquid phase change in deformable porous media with heat transfer, Transport in Porous Media 114 (2) (2016) 525–556.

[21] O. Kolditz, S. Bauer, L. Bilke, N. Böttcher, J. O. Delfs, T. Fischer, U. J. Görke, T. Kalbacher, G. Kosakowski, C. I. McDermott, C. H. Park, F. Radu, K. Rink, H. Shao, H. B. Shao, F. Sun, Y. Y. Sun, A. K. Singh, J. Taron, M. Walther, W. Wang, N. Watanabe, Y. Wu, M. Xie, W. Xu, B. Zehner, Opengeosys: an open-source initiative for numerical simulation of thermo-hydro-mechanical/chemical (thm/c) processes in porous media, Environmental Earth Sciences 67 (2) (2012) 589. doi:10.1007/s12665-012-1546-x.

[22] X.-Y. Miao, C. Beyer, U.-J. Görke, O. Kolditz, H. Hailemariam, T. Nagel, Thermo-hydro-mechanical analysis of cement-based sensible heat stores for domestic applications, Environmental Earth Sciences 75 (18) (2016) 1293.

[23] J. M. McKenzie, C. I. Voss, D. I. Siegel, Groundwater flow with energy transport and water–ice phase change: numerical simulations, benchmarks, and application to freezing in peat bogs, Advances in water resources 30 (4) (2007) 966–983.

VII International Conference on Computational Methods for Coupled Problems in Science and Engineering
COUPLED PROBLEMS 2017
M. Papadrakakis, E. Oñate and B. Schrefler (Eds)

COMPLEX MODELING OF VVER-1000 USING MCU-ATHLET-FLOWVISION

BAHDANOVICH R.B., BOGDANOVA E.V., GAMTSEMLIDZE I.D., NIKONOV S.P. AND TIKHOMIROV G.V

Department of theoretical and experimental physics of nuclear reactors
National Research Nuclear University MEPhI (Moscow Engineering Physics Institute)
Kashirskoe shosse 31, Moscow, Russia
e-mail: Rynatb@gmail.com, web page: https://mephi.ru/

Key words: Monte-Carlo, Coupled Problems, Multiphysics Problems, Engineering Computer Modeling, Iteration scheme, Power oscillations

Abstract. Nowadays modelling of physical processes is very spread in all fields of physics. It is possible because of high capacity of computing powers and capability of parallel computing. We can observe a trend to more detailed description of simulated systems and growth of calculation schemes complexity. Scientists understand that the feedback of related physical processes occurring simultaneously could have significant impact on the results of modelling and should be solved in the scope of multiphysics. That kind of problems exists in reactor physics. It is vital to perform complex modelling of processes occurring in a fuel core of a nuclear reactor, especially during the design of the next generation nuclear power plants. It is not possible to justify safety of the power reactor without complex calculations. In this paper, we proposed a test case for precise coupled neutronics-thermal hydraulics calculation of VVER-1000 reactor using MCU, ATHLET and FLOWVISION codes. MCU is a general-purpose stochastic neutron-physical code based on the Monte-Carlo method and characterized by large time of calculation, as well as CFD codes. Because of that system code ATHLET was used as a fast thermal hydraulic solver in the iterative scheme. In the end of the calculation we propose to use CFD code FLOWVISION in order to enhance the precision and verify CFD model for the further complication of the geometry. The obtained results showed oscillations of power and fuel temperature profiles. Detailed discussion is given in the article. It is assumed that the test case will be used for simulation of VVER-1000 reactor in accident–related regimes and for codes cross–verification. The obtained experience and developed coupling program (PERL script) will be used to create coupled schemes for complex modelling of generation IV nuclear reactors involving different computer codes.

1 INTRODUCTION

It is currently impossible to imagine modern engineering and construction of nuclear power installation without preliminary mathematical modeling. Analysis and research of various processes and phenomena occurring in the reactors is substantially simplified. Until recently, the process of nuclear installations modeling was limited to simple mathematical models, but with the rapid development of computer technology, it became possible to describe the simulated systems more accurately and complicate the calculation schemes.

Nuclear reactor in operation is a complex system of interacting processes. It is a very difficult issue to compile complex mathematical model describing a nuclear reactor as an integral object. In addition, often, the contribution of different processes is disregarded to some extent, so only one subject area is covered in the research, such as strength analysis, neutron-physical or thermal-hydraulic calculations. However, this is not always correct, because the feedback of related physical processes occurring simultaneously could be significant. There are a number of issues, which could be solved only in the scope of complex modeling. Coupled calculations could be done either on the basis of one calculation program, using simple physical models (BIPR, DYN3D, NESTLE, COMSOL, LOGOS), or by coupling the codes intended to simulate the processes described in different areas of physics (MCU, ATHLET, ANSYS, FlowVision). Such kind of coupling was performed before for different types of reactors [1, 2, 3].

This work is the first step in the validation of the computation scheme to simulate the steady state of the fuel rod of the reactor VVER-1000 with the neutron-physical code MCU [4] and the system code ATHLET [5]. As a simulated model was fuel assembly type TVS–2M No. 111 of the second unit of Rostov NPP.

At present, there are many software packages using various neutron codes and the system code ATHLET for modeling transient processes and emergency operation modes in reactor installations, but they all have a rather complex internal connection structure, which requires not only the creation of additional communication units, but also refinements in the control program, inside the ATHLET. To solve the stationary problem it was decided to build a relationship between the codes in order to be practically limited to using only the external communication between the codes through the input data to them, without making any changes to the internal structure of the codes. This scheme for detailed analysis of fuel assembly parameters using MCU and CFD code FlowVision [6].

At this stage, the neutron and thermal-hydraulic models of the TVS–2M of the reactor VVER–1000 were developed and the issue with the external module for coupling MCU and ATHLET was solved.

2 CODES FEATURES

MCU (Monte Carlo Universal) is a neutron code based on the Monte Carlo method, which allows to simulate the transport of neutrons, gamma rays and electrons of different energies. The code takes into account the effects of the continuous changes in the particle energy, as well as continuous or step–energy dependence of the cross-sections. The accuracy is determined primarily by used libraries of evaluated nuclear data. MCU allows to calculate the real geometry and material composition of the complex media at various temperatures. It contains cross–sections conversion modules in the thermal and resolved resonance region, depending on the temperature of the material (using the Breit-Wigner or Adler-Adler formalisms). It can be used for multi-processor calculations (MPI technology) [7]. MCU is certified in Russia for calculations of various types of reactors including VVER-1000.

To accelerate the calculation, the library for water was prepared in advance with cross-sections in the thermal region, taking into account molecular effects, the temperature range is 559 K-610 K with 0.5 K step.

It is also important to use a model of a monatomic gas in materials containing hydrogen and oxygen that do not form a water molecule. In our model hydrogen and oxygen are present in the cladding material. Otherwise, the MCU program will prepare cross-sections for water in the thermal region despite the fact that it is not there. The average time for calculation of one state (64 cores) was 55 minutes. The maximum statistical error in the local power value does not exceed 4.6% (taking into account three standard deviations in the value of the statistical error of the fission reaction rate).

Thermal hydraulic system code ATHLET (Analysis of Thermal-Hydraulics of LEaks and Transients) developed in Gesellschaft fr Anlagen-und Reaktorsicherheit (GRS mbH) was originally intended for the analysis of the entire spectrum of crash conditions cases and transients in reactor installations, mainly with a water coolant, in conjunction with various three-dimensional neutron-physical programs to calculate the spatial distri- bution of energy release and also, with varying levels of approximation, the spatial distribution of the parameters of the coolant in the core of the reactor (right up to the assemblies). It is widely used in various types of calculations.

ATHLET consists of several modules that allow to describe the various phenomena in the behavior of light water reactors: thermal hydraulic module (TFD), heat transfer and heat conduction unit (HECU), neutron-kinetic unit (NEUKIN) to describe the point and the one-dimensional kinetics, module for operation of the equipment (GCSM) and a module for the numerical integration (FEBE), implements a fully implicit scheme.

Features of hydrodynamic code ATHLET for improved assessment, developed in GRS (Germany) and aimed at the analysis of transient and accidental conditions in reactor facilities, mostly water-cooled ones, in conjunction with a variety of three-dimensional neutron physics program (to calculate the spatial power density field distribution and spatial distribution of the coolant parameters in the reactor core up to pin-by-pin), are

widely used in different types of calculations.

Coupling the ATHLET with a neutron physics program DIN3D [8] was a pilot project. Recently during analysis of the international standard problem Kalinin-3 [9] the following complexes have been applied: ATHLET/BIPR-VVER [10], equipped with a neutron kinetic code developed by the NRC Kurchatov Institute, the coupled complex ATHLET-KIKO3D [11], developed in cooperation with Central Research Institute of Physics (Hungary). We must also mention the calculations concerning the software ATHLET-PARCS [12], applying the neutron-physics code, developed by the USA.

It is necessary to note that all the above coupled codes possess complex internal structure of links, demanding additional blocks of connection but also the further development and completion of the software ATHLET.

Taking into consideration the coupling of ATHLET with MCU code, it is possible

1) to calculate only the steady-state and

2) try to build the interconnection between the codes through entry data without changing the internal structure of the codes.

If we consider the coupling of the MCU code and CFD code (FLOWVISION) designed for three-dimension thermo-hydraulic calculations, the issues are becoming even more complex even in the steady-state with application of only external codes connection.

This is determined mostly by the time consumption of codes operation and the necessity of the iteration procedure caused by the coolant parameters feedback, influencing the distribution of the neutron flux in the model under study.

The research considers the algorithm of reducing the number of iterations for the external connection of the MCU code and CFD code.

The goal is to determine the stationary distribution of the neutron flux in the system with the fixed power of coolant (flow, pressure, temperature) as the entry condition.

The essence of the algorithm is as follows. In the first stage our project, there is only information exchange in the entry data between coupled codes ATHLET and MCU. The calculation of the parameters (of the coolant and the fuel) in the ATHLET was conducted for the averaged through the cross-section geometry of the examined structure. For example, during pin-by-pin analysis of the distribution within assembly there were used averaged control volumes through the cross-section of the assembly.

The data retrieved from ATHLET are converted via a certain software into the necessary set of data for the MCU code, which corrects the distribution of the power density in averaged volumes, and then using a special software, converts this distribution into the entry data for the ATHLET.

It is needed to note that the beginning of the iteration process can be on the conditions of a zero power, and every other iteration can lead to increasing of the power to the required value.

The whole algorithm can be constructed in such a way that ATHLET solves nonstationary problem to obtain stationary parameters at every iteration and further transfers all the necessary data to MCU, capable of solving the stationary problem.

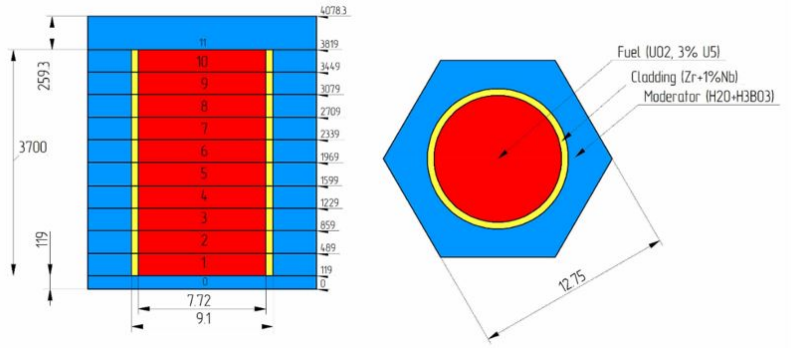

Figure 1: Fuel rod nodalization of VVER-1000 (mm)

On the conditions of a required power level there will be a shift to the detailed distribution of the parameters with the application of the coupled MCU and CFD codes, using averaged values (derived in the coupled ATHLET and MCU) as the initial parameters.

The transition from the coupled ATHLET–MCU to the coupled MCU–CFD using as an intermediate coupled MCU–sub channel code [13] will possibly provide a better approximation for the final result of the coupled MCU–CFD.

3 DESCRIPTION OF THE CALCULATION SCHEME

A detailed description of the calculation scheme is presented in work [14], initial conditions have been specified in accordance with [15].

The primary intent of this paper was to analyze the convergence of the calculation scheme, used for modeling the stationary state of the fuel assembly of the reactor VVER–1000 and create an external module for data exchange between the MCU and ATHLET. The scheme of coupled calculation was developed in such a way to maximally correspond to the state of TVS–2M No.111 of the second unit of Rostov NPP on the date 31.05.2010. The selected state is the most similar to the state of the test case. The following criteria were used to select the state:

1. The coincidence of dimensions.
2. The coincidence of material compositions (low enrichment and burnup, absence of burnable absorbers).
3. The coincidence of initial conditions (maintenance of stationary state operation of the reactor for several days).

The neutron model is an elemental cell of the reactor, consisting of the fuel part of rod and water moderator. During the calculation, the model is divided into 12 axial layers (see Fig. 1).

Simplified fuel assembly using the real geometry, represents a channel with a fuel structure is a thermo–hydraulic model. The nodalization is similar to the neutron model.

The external module is used to connect the calculation codes, written in cross–platform

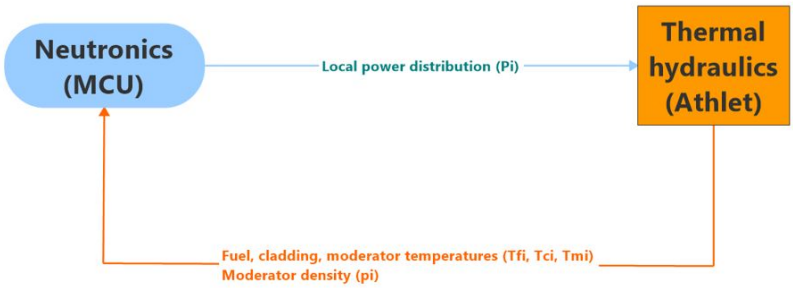

Figure 2: Coupling scheme

script language PERL. The most important features of PERL are the ability to quickly process data arrays, short code length, simplicity of implementation.

The calculation was made as follows (see Fig. 2). At the fuel assembly input, coolant parameters were maintained constant: flow rate, temperature, pressure, boric acid concentration. The first axial distribution of the coolant and fuel parameters was obtained with the zero power level using the ATHLET.

On the basis of the obtained data, the initial power distribution was constructed by MCU.

Further, it was two possible ways to solve the problem.

The initial power distribution received by the MCU was transferred to the ATHLET and was used immediately to calculate parameters at nominal power. In that case, the solution to the problem of obtaining a stationary axial distribution of the coolant and fuel elements was carried out through a nonstationary solution with ATHLET (from the previous state with zero power level), as a fact it was used the relaxation method. After receiving a new steady-state distribution of coolant and fuel rod parameters they were passed to the MCU, where it was taken into account during the calculation of the new power density distribution. The next iteration (data in ATHLET) was carried if there is no compliance of the convergence parameters, where as a parameter to monitor the convergence was selected:

$$dX_i = \frac{X_i - X_{i-1}}{X_i} \tag{1}$$

Where Xi is the local characteristic at the i-th iteration, Xi-1 is the local characteristic at the (i-1) iteration. The exit from the iterative scheme is carried out at the values dXi, presented in Table 1.

Axial distributions of the main thermo–hydraulic parameters obtained from the calculation of TVS–2M steady–state are at the Fig. 3–7.

The convergence parameters of the obtained results at the nominal power level dont correspond to the criterion exit from the iterative scheme. The power and temperature profile oscillations begin. They could be caused by a set of effects that take place in the nuclear reactor:

Table 1: The value of exit parameters of iterative process

Parameter	dXi
Keff	<0.1 %
Pi	<1.0 %
TFi	<0.5 %
TCi	<0.5 %
TMi	<0.5 %
pi	<0.5 %

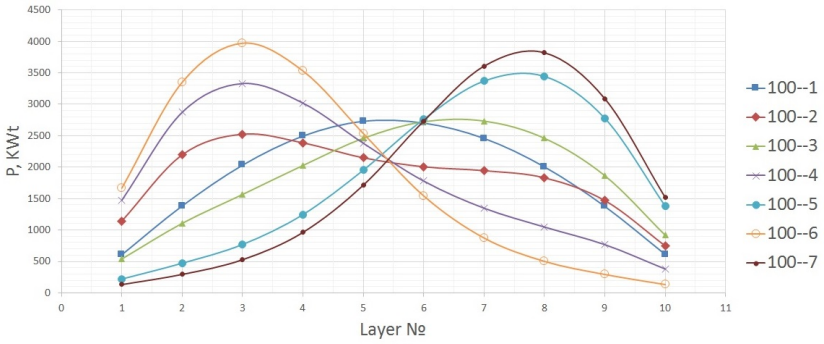

Figure 3: Power distribution (In Power-Iteration format)

- displacement of the power profile maximum to the core bottom, due to the presence of the moderator density profile and the negativity of the reactivity coefficient for the coolant temperature (appears at iteration 100-2);
- fuel temperature feedback (Doppler effect), which causes a decrease in the local power with the increase of temperature and vice versa (appears at the iteration of 100-3);
- displacement of the maximum rate of the fission reaction (and hence the power profile) to the center of the fuel rod due to the effects of leakage at the rod sides.

Also, the presence of a statistical error in calculation of the fission reaction rates may lead to the occurrence of oscillations.

Based on the obtained data, it was decided to gradually increase the power level from 0 to 100% in steps of 10% to improve the convergence of scheme. Preliminary calculations show that this approach allows to find a stable solution up to 40% of the power from the nominal level, however, with a further power jump to 100%, oscillations still arise.

Thus, according to the results, a new problem was state: to find the optimal step of the power level changing for the solution to a coupled problem (no oscillations arise, or they quickly decay) and optimizing the iterative scheme.

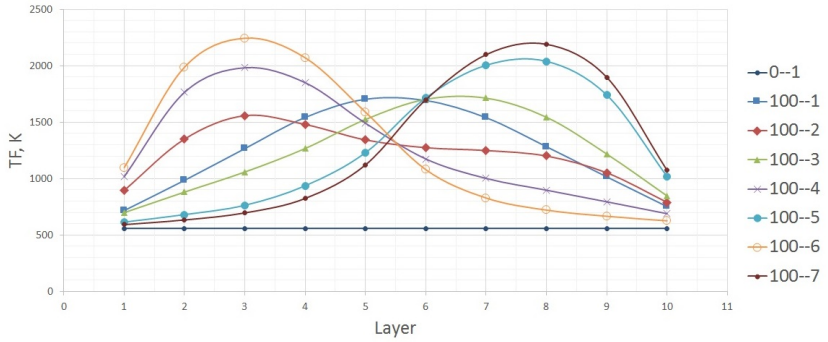

Figure 4: Fuel temperature distribution

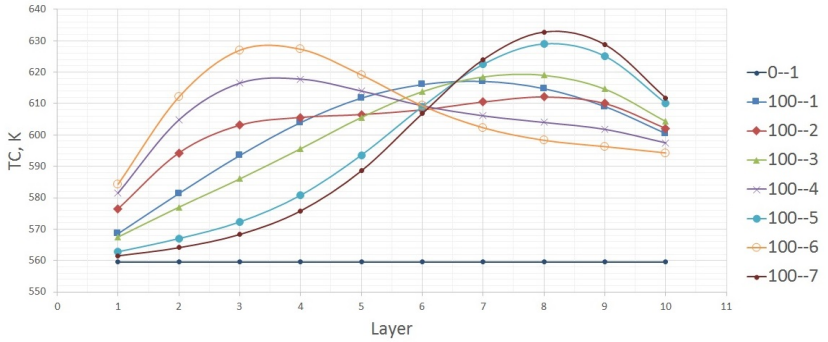

Figure 5: Cladding temperature distribution

4 CONCLUSIONS

This article presents results of the first step of the validation of the computation scheme to simulate the steady–state of the fuel rod of the reactor VVER–1000 with the neutron–physical code MCU, system code ATHLET and code FLOWVISION. As a result, the axial distributions of the main thermo–hydraulic parameters of the reactor VVER–1000 were obtained.

According to the results, it can be concluded that the solution of this problem with instantaneous setting of the nominal power level does not converge to a definite value (undamped oscillations appear). Preliminary calculation shows that a gradual increase in the power level by 10% gives a stable solution (at 40% of nominal power).

Consequently, it is necessary to determine the best step of the power increase value for the quick solution of the coupled simulation problem at nominal power.

5 ACKNOWLEDGEMENT

This work was supported by the MEPhI Academic Excellence Project (agreement with the Ministry of Education and Science of the Russian Federation of August 27, 2013, project no. 02.a03.21.0005).

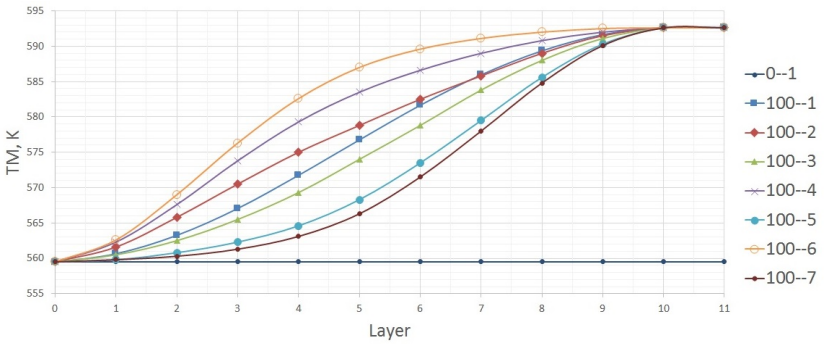

Figure 6: Coolant temperature distribution

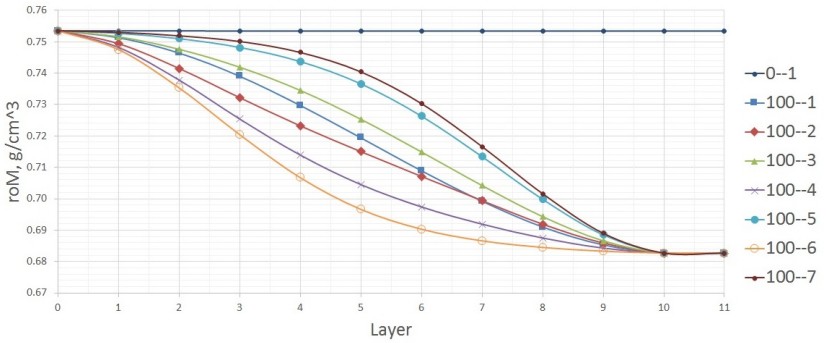

Figure 7: Coolant density distribution

REFERENCES

[1] Sanchez, V. and Al-Hamry, A. Development of a coupling scheme between MCNP and COBRA-TF for the predictor of the pin power of a PWR fuel assembly. *Conf. on Math., Comp. Meth. & React. Phys. (M&C 2009)*, American Nuclear Society, Saratoga Springs, New York, (2009).

[2] Ivanov, A., Sanchez, V and Imke, U. Development of a coupling scheme between MCNP5 and SUBCHANFLOW for the pin- and fuel assembly with simulation of LWR and Innovative Reactors. *Intern. Conf. on Math. and Comp. Meth. Applied to Nucl. Scienc. and Eng. (M&C 2011)*, American Nuclear Society, Rio de Janeiro, Brazil, (2011), ISBN 978–85–63688–00–2.

[3] Waata, C.L., Shulenberg, T., Cheng, X., Starflinger, J. and Bernnat, W. Results of a coupled neutronics and thermal-hydraulics analysis of a HPLWR fuel assembly.*Proceedings of the American Nuclear Society.* International Congress on Advances in Nuclear Power Plants ICAPP05, (2005) **1**:300–306.

[4] Alekseev, N.I., Bolshagin, S.N., Homin, E.A and etc. Status MCU-5. *Questions of Atomic Science and Technology. Ser. Physics of nuclear reactors.* (2011) **14**:4–23.

[5] Lerchl, G. and Austregesilo, H. ATHLET Mod2.2 Cycle A. *Users Manual*, GRS, (2009).

[6] FlowVision Tutorial: Examples of typical tasks. Version 3.09.04. CAPVIDIA, Leuven, Belgium, (2014), p. 404.

[7] Gurevich, M.I., and Shkarovsky, D.A.*Neutron transport calculation by the Monte-Carlo method on the MCU code.* Study guide NRNU MEPHI, (2012).

[8] Grundmann, U., Lucas, D. and Rohde, U. Coupling of the thermohydraulic code ATHLET with the neutron kinetic core model DYN3D.*In: Proc. of Int. Conf. on Mathematics and Computations, Physics and Environmental Analysis*, Portland (USA), Vol. 1., (1995), pp. 257–263.

[9] Tereshonok, V.A., Nikonov, S.P., Lizorkin, M.P., Velkov, K., Pautz, A. and Ivanov, K.*Kalinin -3 Coolant Transient Benchmark Switching-off of One of the Four Operating Main Circulation Pumps at Nominal Reactor Power*, OECD/NEA-DEC, (2008).

[10] Nikonov, S., Pautz, A. and Velkov, K. Detailed modeling of KALININ-3 NPP VVER-1000 reactor pressure vessel by the coupled system code ATHLET/BIPR-VVER,*International Conference on Mathematics and Computational Methods Applied to Nuclear Science and Engineering (M&C 2011)*, ISBN 978–85–63688–00–2, Rio de Janeiro, Brazil, May 8–12, (2011).

[11] Panka, I., Hegyi, Gy., Marczy, Cs. and Keresztri, A. Uncertainties of the KIKO3D–ATHLET calculations using the KALININ-3 benchmark (phase II) data, *25th Symposium of AER on VVER Reactor Physics and Reactor Safety*, Hungary, Balatongyrk, Oct.13-16, (2015).

[12] Pasichnyk, I., Nikonov, S., Zwermann, W. and Velkov, K. Coupled code analysis of uncertainty and sensitivity of Kalinin-3 benchmark, *25th Symposium of AER on VVER Reactor Physics and Reactor Safety*, Hungary, Balatongyrk, Oct.13-16, (2015).

[13] Faghihi, F., Mirvakili, S.M., Safaei, S. and Bagheri, S. Neutronics and sub-channel thermal-hydraulics analysis of the Iranian VVER-1000 fuel bundle. *Progress in Nuclear Energy.* (2016) **87**:39–46.

[14] Bahdanovich, R.B., Bogdanova, E.V., Gamtsemlidze, I.D., Nikonov, S.P. and Tikhomirov, G.V. Test case for VVER-1000 complex modeling using MCU and ATHLET. *IOP Conf. Series: Journal of Physics: Conf. Series.* (2017), 781.

[15] Tereshonok, V.A., Ivchenkov, S.P., Nikonov, S.P., Pitilim, V.A., Sizov, R.A. and Shabunin, A.B. Offers of JSC VNIIAES according to the standard international problem for the reactor plant VVER-1000. All-Russian Scientific Research Institute for the Operation of Nuclear Power Plants (JSC VNIIAES), In. No17.1/33605 from 27.08.2015.

VII International Conference on Computational Methods for Coupled Problems in Science and Engineering
COUPLED PROBLEMS 2017
M. Papadrakakis, E. Oñate and B. Schrefler (Eds)

COMPUTATION METHODS AND TECHNIQUES FOR SOLUTION OF COUPLED MULTIPHYSICS PROBLEMS IN PRECISION CALCULATIONS OF VVER TYPE REACTORS

IVAN SALDIKOV[1]*, GEORGY TIKHOMIROV[1], MIKHAIL TERNOVYKH[1], AND ALEXANDER GERASIMOV[2]

[1]National Research Nuclear University MEPhI (Moscow Engineering Physics Institute),
Department of Theoretical and Experimental Physics of Nuclear Reactors,
31, Kashirskoye shosse, 115409, Moscow, Russia
e-mail: ISSaldikov@mephi.ru

[2]Institute for Theoretical and Experimental Physics,
Department of safe nuclear reactors
25, Bolshaya Cheremushkinskaya ul., 117218, Moscow, Russia

Key words: Coupled Approach, Nuclear Reactors, Temperatire Distribution, Isotopic Composition, Calculations, Computer Codes.

Abstract. Precise simulation of the isotopic composition of nuclear fuel and temperatures during reactor operation requires solution of two coupled tasks from two different fields of physics: neutron-physical calculation and thermal physics calculation. Simple way is based on models using averaged temperature, thermal conductivity factors, and heat power density. In practical situations, changing of isotopic composition and changing of temperature distribution over fuel assembly influence each other. In this paper, coupled approach is presented, based on modern algorithms, methods and codes to solve consistent tasks of thermal conductivity, neutron transport, and nuclide transformation kinetics. It allows to perform neutron-physical and thermal-physical calculation of the reactor with detailed temperature distribution, with account of temperature-depending thermal conductivity and other characteristics. It was applied to studies of fuel cell of the VVER-1000 reactor.

1 INTRODUCTION

Coupled problems are typical in calculations for nuclear power engineering. Nuclear power is one of important sources of energy along with thermal power stations and water power stations. Due to the high level of technology and high safety requirements, nuclear power plants require precision calculation techniques for all stages of development, design, construction, and operation. Nuclear power plants are the field of engineering, in which problems relating to different fields of physics and technology such as nuclear physics, neutron physics, heat engineering, radiochemistry should be solved consistently because the processes from different fields of physics and chemistry influence to each other. In this paper, one such problem is discussed, combining neutron-physical and heat engineering problems

arising in simulation of the isotopic composition of nuclear fuel during operation of nuclear reactors.

Simplified models of calculation are often used in traditional approach to modeling neutron-physical characteristics of fuel rods and isotopic composition in process of nuclear fuel burning. For instance, in many cases neutron-physical characteristics of fuel depending on temperature are determined by use of average temperature of fuel rod, while the existing dependencies of the neutron cross sections on temperature are neglected. In thermal-physical calculations of the radial distribution of fuel temperature, constant average value of thermal conductivity factor is often used. However this factor depends really both on the temperature and on fuel burnup, which change with radius of fuel rod.

In this paper, mathematical models of consistent neutron-physical and thermal-physical calculation are presented. They are realized in codes designed in MEPhI and "Kurchatov Institute". This approach was applied to calculation investigation of fuel element of the power reactor of VVER-1000 type. Short description of benchmarks for verification of obtained results is given. It is demonstrated how the account of dependence of the thermal conductivity factor on temperature affects on the value of temperature in the center of fuel rod for the VVER type reactor.

2 ALGORITHMS AND METHODS

In order to obtain the dependence of temperature on radius of cylindrical fuel rod it is necessary to solve the equation of thermal conductivity with specified boundary conditions. If density of energy release and thermal conductivity factor are constant independent on radius of fuel rod, this problem has an analytical solution. However, thermal conductivity factor of oxide nuclear fuel depends on temperature and on fuel burnup. Energy release density and fuel burnup vary non-uniformly with radius of fuel rod in process of fuel burnup. Swelling of fuel pellet under deep burnup results in reduction of the gap between fuel pellet and cladding.

To value the contribution of each of these effects in change of maximum temperature of fuel rod, it is necessary to be able to calculate fuel burnup and change of isotopic composition, as well as distribution of energy release density on radius of fuel rod. For that it is necessary to solve multigroup equation of transport or diffusion of neutrons and system of equations of isotope kinetics. Remember that usually these equations are solved one after another. Firstly transport equation is solved with macroscopic constants calculated on the base of the known isotopic composition. Then one-group cross sections of all isotopes belonging to equations of isotope kinetics are defined. Hereon the system of the equations of isotope kinetics is solved and new isotopic composition for the given moment of time is calculated. After that, we should solve once again transport equation since change of isotopic composition can result in change of macroscopic constants and of neutron spectrum.

Let’s consider mathematical settings of the above described tasks.

2.1 Neutron diffusion equation

To obtain the one-grup cross sections and neutron fluxes, it is necessary to simulate neutron spectrum and hence to solve the neutron transport equation or diffusion equation. Usually multigroup approach is used for this purpose, in which one must solve a system of

multigroup equations like (1). All symbols are traditional, g is the number of the group while *G* is a full number of groups.

$$\nabla D(\vec{r})\nabla\Phi^{g}(\vec{r})+\Sigma_{t}^{g}(\vec{r})\cdot\Phi^{g}(\vec{r})=\sum_{g'=1}^{G}\Sigma_{s}^{g'\to g}(\vec{r})\cdot\Phi^{g'}(\vec{r})+\frac{\chi^{g}}{4\pi}\frac{1}{K_{eff}}\sum_{g'=1}^{G}\nu_{f}^{g'}\cdot\Sigma_{s}^{g'}(\vec{r})\cdot\Phi^{g'}(\vec{r}) \qquad (1)$$

The solution of these equations in particular geometry with specified boundary conditions allows to determine the neutron spectrum that can be used to obtain the one-group constants. To determine one-group neutron fluxes it is necassaru to calculate additionaly the spatial distribution of energy release density and know the full energy release in a simulated system.

We should keep in mind that diffusion coefficients $D(\vec{r})$ and macroscopic cross-sections $\Sigma^{g}(\vec{r})$ depend not only on the spatial variable, but also on the temperature in the spatial domain. In order to make correct system of multigroup equations with a purpose to prepare prepare one-group cross sections and fluxes, one need to set or be able to calculate the temperature in spatial areas.

2.2 Equation of isotope kinetics

System of equations of isotope kinetics is formulated for vector of isotope concentrations of nuclides $\vec{\rho}^{i}(t)$. Isotope concentrations in each spatial zone with number *i* are assumed to be the same in all points of spatial sone.

$$\frac{d\rho_{l}^{i}(t)}{dt}=\sum_{k}\lambda_{k\to l}\cdot\rho_{l}^{i}(t)-\lambda_{l}\cdot\rho_{l}^{i}(t)+\sum_{m}\rho_{m}^{i}(t)\cdot\sigma_{m\to l}^{i}\cdot\phi^{i}-\rho_{l}^{i}(t)\cdot\sigma_{l}^{i}\cdot\phi^{i} \qquad (2)$$

Each equation of the system of equations of isotope kinetics include the following values in addition to concentrations.

σ_{l}^{i} - one-group cross section of incineration of isotope with number *l* in spatial zone with number *i* due to nuclear reactions on *l*-th isotipe.

$\sigma_{m\to l}^{i}$ - one-group cross section of appearance of isotope with number *l* in spatial zone with number *i* due to nuclear reactions on *m*-th isotipe.

ϕ^{i} - one-group neutron flux in *i*-th spatial zone.

λ_{l} - decay constant of *l*-th isotope

$\lambda_{k\to l}$ - decay constant of *k*-th isotope resulting in appearance of *l*-th isotope.

Vector of concentrations changes in process of burning of nuclear fuel. Concentrations of isotopes may vary in different spatial locations of the fuel core. For example, area with modified microstructure, so-called rim-zone appeares in the outer layer of the fuel rod of thermal-neutron reactors. Its formation is associated with high concentration of fission products [1-3]. Therefore, application of constant concentrations over the whole fuel rod can lead to distortion of the simulation results. Along with isotope concentrations, other properties of fuel composition can vary with radius within fuel rod in the process of burnup and can influence on space distribution of the temperature. These variation of temperature don't take into account in the "classic" approach, and the process of formation of rim-zone can't be calculated.

In order to solve a system of equations (2), one must firstly calculate one-group fluxes ϕ^i and the cross section of the reactions σ_l^i and $\sigma_{m\to l}^i$ from the equation (1). It is also necessary to know the decay constants λ_l and $\lambda_{k\to l}$ for each nuclide and initial concentrations of isotopes ρ_l^i. After the solution of the equation system (2), the new value of the concentration vector $\overline{\rho}^i(t)$ is obtained, which corresponds to a certain moment of time.

2.3 Equation of thermal conductivity

In "classic" approach, the factor of thermal conductivity is considered to be independant on the radius within fuel rod, that allows to obtain an analytical decision, if radial distribution of the energy release density $q_v(r)$ is known.

However, really thermal conductivity factor of oxide nuclear fuel depends on the temperature T of this fuel and fuel burnup B [4] (Fig. 1).

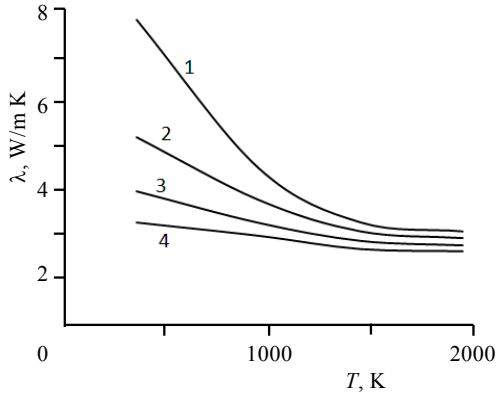

Figure 1. Thermal conductivity factor of oxide fuel depending on temperature at burnup B = 0 (*1*), 30 (*2*), 60 (*3*), 90 (*4*) MW·d/kg U

Thus, equation of thermal conductivity is nonlinear one. In cylindrical geometry:

$$\frac{1}{r}\frac{\partial}{\partial r}\lambda(T(r), B)\cdot r\cdot\frac{\partial}{\partial r}T(r)+q_V(r)=0 \qquad (3)$$

where $\lambda(T(r),B)$ is thermal conductivity factor of fuel matherial depending on temperature and burnup, $q_V(r)$ is energy release density.

Several methods can be used to solve equation (3). One of them consists in dividing the fuel rod into annular zones. Factors of thermal conductivity remain constant within each zone : $\lambda(T(\mathrm{r})) = \{\lambda(T_i)\} = \{\lambda_i\}$.

Then the thermal conductivity equation becomes linear within each zone. However, in this case we need to use iterative procedure. Each iteration specifies the value of thermal conductivity factor in each layer. This allows to consider the dependence of thermal conductivity factor on temperature. Similarly, we can proceed with the dependence of thermal conductivity factor on fuel burnup : in each step of burnup to take from the table the new value of the factor of thermal conductivity and insert it into the equation to find the temperature.

3 COMPLEX MODEL OF NEUTRON-PHYSICS CALCULATION OF FUEL CELL

All of the above described relations and methods of their descriptions can be represented in a model of consistent thermal physical and neutron-physical calculations. In Fig. 2 the following designations are used: Eq.1 – transport equation, Eq.2 – equation of isotope kinetics, Eq.3 – equation of thermal conductivity. DB1 (data base) – dependence of microscopic cross sections from neutron energy, account of shielding, account of the temperature dependence of microscopic cross sections, DB2 – library of decay constant. Σ, σ are macroscopic and microscopic cross sections of interaction of neutrons with nuclei of the medium. Φ – absolute neutron flux (matched with the power and one-group cross sections), φ – multi-group neutron flux (the result of solving the transport equation). ρ is the vector of the nuclide concentration (the result of solving the system of equations of isotopic kinetics). q_v – energy release density. B – fuel burnup. T – temperature (the solution to the thermal conductivity equation). A1, A2, A3, A4, A5 – the algorithms that implement the ratio between the required values based on the model and experimental data :

A1. $\Sigma_{tot}(\vec{r}, E, \overline{\rho}(t), \overline{\sigma}_{tot}(T,t)) = \overline{\sigma}_{tot}(T,t) \cdot \overline{\rho}(t)$

A2. $\Phi = C \cdot \varphi$, Φ – neutron flux, C – constant, φ – eigenvalues.

$\Sigma_{tot}(\vec{r}, E, \overline{\rho}(t), \overline{\sigma}_{tot}(T,t))$ total macroscopic cross section of interaction of neutrons with energy E with nuclei in spatial point $\vec{r}$, which for each time moment t depends also on nuclei density $\overline{\rho}(t)$ and on microscopic cross sections of isotopes $\overline{\sigma}_{tot}(t)$.

A3. $q_v = \Sigma_f E_f \Phi + \Sigma_c \cdot E_c \cdot \Phi$ - energy release density.

A4. $B = \int q(t)dt$ - equation of burnup.

A5. Account of dependence of thermal conductivity on temperature and fuel burnup: $\lambda = \lambda(T, B)$.

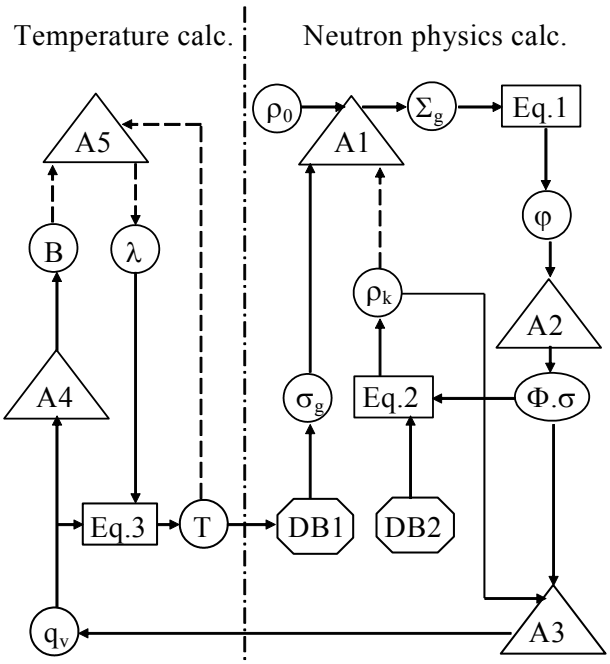

Figure 2. Diagram of consistent thermal physical and neutron-physical calculations

Below we propose 4-steps sequence of calculations of neutron-physical characteristics of fuel rods based on diagram Fig. 2. It allows to simulate physical and neutron-physical characteristic of fuel more correctly and increases accuracy of the results.

1. We assign initial value of energy release density (q_v) and thermal conductivity factor λ. Then iterative procedure is made. Firstly, thermal conductivity equation (Eq.3) is solved. The result is temperature value in the cell. In case the cell is divided into zones, we obtain values of the temperature in each zone of the cell. Secondly we calculate new value of the thermal conductivity factor λ, corresponding to new value of the temperature. These two steps can be repeated many times to obtain required accuracy of the temperature. Simultaneously we get more accurate λ value.

2. This temperature value is used as input parameter for database (DB1) of the temperature dependencies of the microscopic cross sections σ. Using these data of σ together with initial values of nuclide concentrations (ρ_0), we obtain value of macroscopic cross section (Σ_g) by means of algorithm (A1).

3. With this macroscopic cross section we solve the transport equation (Eq.1). As a result, due to algorithm A2, we obtain group neutron fluxes in zones (Φ_g), that is to say spatial dependency of group neutron fluxes. At the same time, we save new values of the microscopic cross sections (Φ σ). We use the group neutron fluxes to calculate new value of energy release. We repeat the steps 1-3 as iterations over the energy release density (algorithm A3). Herewith we make more accurate the temperature distribution and take into account the temperature dependency of the thermal conductivity factor.

4. Using group neutron fluxes along with decay constants (DB2) and new values of the microscopic cross sections, we solve the equation of isotope kinetics (Eq.2). As a result we obtain isotope concentrations on the next step of burnup (ρ_k). With these new values of isotope concentrations and values of microscopic cross sections we obtain new value of macroscopic cross sections (algorithm A1). The steps 3-4 can be repeated several times as iterations.

We can perform iterations over the steps 1-4 to achieve required accuracy. Herewith we shall take into account the dependency of λ on fuel burnup.

Thereby, new complex approach allows to take into account:

– spatial distribution of energy release to determine neutron flux;

– dependence of the diffusion factor and macroscopic cross section not only on spatial value, but also on the temperature in given spatial area;

– presence of spatial-nonuniform structure in fuel rod (rim-zone);

– dependence of thermal conductivity factor of oxide fuel on the temperature of fuel;

– reduction of thermal conductivity factor of fuel in process of burnup.

In order to appreciate efficiency of the presented approach to calculation of temperature distribution over the radius of fuel rod, it is necessary to answer the following questions:

1. How do estimations of the maximum temperature of fuel change when turning from previous approaches to new approaches?

2. Is it necessary to change traditional schemes of calculation of isotopic composition in process of fuel burnup by including in them block of calculation of the temperature distribution?

3. How should we calculate fuel temperature if thermal conductivity factor depends on the temperature and fuel burnup?

4 ALGORITHMS AND CODES USED FOR CALCULATIONS

Thermal-physical calculations in this paper were made using codes HEATING7, UNK_teplo, TempR_5.

HEATING7 is multipurpose code for solution of thermal conductivity tasks [5,6]. It is included into code complex SCALE [7]. However it is not integrated code of the SCALE because it doesn't have standard format of input data and doesn't use in functional sequences of the SCALE.

Heatinh7 can solve stationary and nonstationary thermal conductivity tasks in one-, two- or three-dimensional square, cylindrical or spherical coordinates. Calculating model can include different materials. Thermal conductivity, density and energy release of each material can depend on time and temperature. Energy release can depend on time, temperature, space. Thermal conductivity can be anisotropic. Phase change can be taken into account. Thermal properties of materials can be included by user or can be taken from the own library of material thermal properties.

The energy release may depend on time, temperature, position, and boundary temperatures, which in turn may depend on time and coordinates. The boundary conditions may be assigned on the outer surface of the model or on the surface between parts of the model. They can be specified by temperatures or by any combination of heat flux, forced convection, natural convection and radiation. The parameters of the boundary conditions can depend on time and temperature. The spatial lattice for calculations can be arbitrary for any variable. HEATING uses the scheme of memory distribution during runtime, which allows to avoid the need of re-calculations and to meet the memory requirements for any tasks.The code UNK_teplo can solve the stationary thermal conductivity tasks in one-dimensional cylindrical coordinates with different materials. Density and thermal conductivity materials should be assigned for each layer. Numerical methods are used for calculation of temperature in each layer.

The code TempR_5 allows to calculate temperatures in cylindrical fuel element with piecewise constant thermal conductivity factor. Temperature distribution in each layer is obtained from analytical decision of thermal conductivity equation with assigned constant values of radius, thermal conductivity factor, and temperature. The results of calculation are average values of temperature over the layer, temperatures in points between layers and in the center of fuel element.

UNK_teplo is code for solution of thermal conductivity tasks. Code is included into program complex UNK [5, 8]

UNK_teplo can solve the stationary thermal conductivity tasks in one-dimensional cylindrical coordinates. Calculation model may include various materials. Thermal conductivity and density of each material is specified separately for each layer. Thermal properties of materials can be entered by the user.

Numerical methods are used to obtain the temperature values in each layer. The system of equations compiled according to the finite-difference scheme, then the equations are solved by sweep method.

The calculation of temperatures in the UNK complex is made in coordination with calculation of fuel burnup. Firstly, macro constants are prepared and the temperatures are calculated in different zones of the given geometry. After that, standard module of UNK starts to operate. It calculates the value of K_{eff} , the new macro constants, energy release in each zone. Then temperatures in zones are recalculated.

The code TempR_5 allows to calculate temperatures in cylindrical fuel element with piecewise constant thermal conductivity factor. Temperature distribution in each layer is obtained from analytical decision of thermal conductivity equation with assigned constant values of radius, thermal conductivity factor, and temperature. The results of calculation are average values of temperature over the layer, temperatures in points between layers and in the center of fuel element.

5 RESULTS OF TEST TASKS CALCULATIONS

Application of the proposed approach is illustrated by calculations of the temperature distribution along the radius of the fuel rod of the VVER-1000 reactor. These calculations can be considered as test tasks (benchmarks) to verify the developed algorithms. Test tasks will help to answer the above questions and to indicate the expediency of the complexity of the model for calculation of the fuel rod. We present below several results illustrating the capabilities of the algorithms. The tasks were solved in one-dimensional cylindrical geometry.

Model of the elementary cell of the VVER-1000 is taken as base model. The diameter of the central hole of the fuel pellet was taken as 1.5 mm, the external diameter of the pellet 7.55 mm; internal and external diameters of the cladding 7.72 and 9.17 mm; the pitch of the triangular lattice of rods 12.75 mm, temperature of coolant 575.7 K. For calculations, fuel rod was divided on 11 radial layers.

The temperature of the outer surface of the cladding was the same for all calculations. It was equal to the temperature of the coolant 575,7 K. The thermal conductivity factor was taken as 0.35 W/mK for the center hole and the gas gap between the fuel rod and cladding, and as 20.42 W/mK for cladding. These values were the same for all calculations.

First of all it is necessary to illustrate the advantage of the developed technique, which allows to take into account the dependence of thermal conductivity factor on temperature and on fuel burnup. Fig. 3 shows the results of calculations of the temperature inside the fuel element for four cases. The case 1 (curve *1*) corresponds to the traditional approach, in which λ was taken to be constant throughout the fuel rod. The λ value was calculated for the average temperature over the rod as 1000 K. The case 2 (curve *2*) corresponds to the application of the developed technique, however only dependence λ (T) for burnup B = 0 was considered. In cases 3 and 4, the dependence $\lambda(T, B)$ was takes into account. Calculations were performed for B = 60 (curve *3*) and 120 MW·day/kgU (curve *4*). For all four cases, it was assumed that no gas gap was there between fuel rod and cladding, and energy release density q_{v} = 388 W/cm^3 was constant over the fuel rod.

The results presented in Fig.3 can be easily interpreted using data on $\lambda(T, B)$ from Fig.1. In case 1 for λ = const, we obtain curve *1* in Fig.3. The temperature decreases from the center to the periphery of the fuel rod. Peripheral temperature is determined by the coolant temperature of 575 K.

In case 2 when we consider $\lambda(T)$ at $B = 0$ (the upper curve *1* in Fig.1), the λ increases sharply due to temperature decrease in going from the center of the fuel rod to its periphery. Since the peripheral temperature is specified, the temperature at the center is lower than in case 1. The curve *2* lies below the curve *1*.

In case 3 (the dependence $\lambda(T, B)$ corresponds to the curve *3* in Fig.1) the λ values are much less than in cases 1 and 2. The increase of the λ in going from the center to the periphery of fuel rod is slower than in cases 1 and 2. Since the energy release density is the same in all cases and peripheral temperature is specified, the temperature in the center of the rod is higher than in case 1. The curve *3* in Fig.3 lies above the curve *1*.

In case 4 (curve λ (T, B) is more flatter than curve *4* in Fig.1) similar arguments show that the temperature in the center of the rod is higher than in case 3. The curve *4* in Fig.3 lies above the curve *3*.

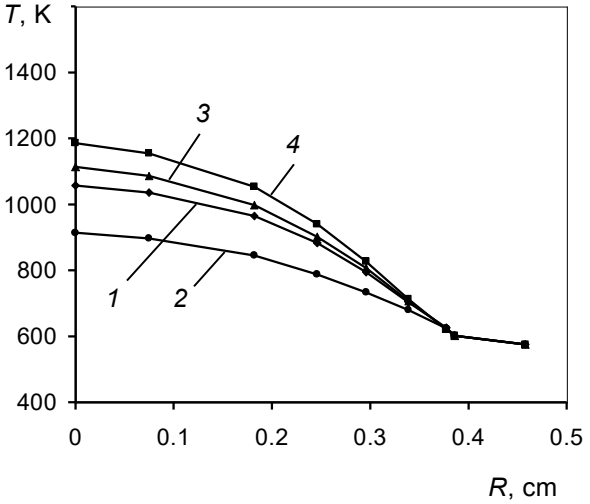

Figure 3. λ = const (*1*), $\lambda(T)$ is considered (*2*), $\lambda(T, B)$ for B = 60 MWd/kg is considered (*3*), $\lambda(T, B)$ for B = 120 MWd/kg is considered (*4*)

These data demonstrate the efficiensy of the developed methods of calculation of the temperature in the fuel element of the VVER reactor. Corrections to the value of the maximum temperature can reach 10-15%.

Let's now to turn to the results showing the capabilities of the algorithms.

In tasks 1 and 2 (Fig. 4, *a*, *b*), the uniform energy release density of 388 W/cm^3 was taken over the whole fuel rod. Thermal conductivity factor of the fuel rod λ was also taken constant. We considered three values of λ = 1.7 (curves *1*), 2.1 (curves *2*) and 3.0 W/mK (curves *3*). The difference between the results shown in Figs.4 and 5 was that Fig.4 corresponded to fresh fuel with the gap between fuel rod and cladding, while Fig.5 corresponded to the "swollen" fuel. There was no gap in this case, and fuel was in thermal contact with cladding.

Results presented in Fig.4 *a*, *b* demonstrate apparent dependence of the temperature curves for different values of λ. The lower λ, the higher is the curve $T(R)$. All three curves converge on the outer surface of the fuel rod. Fig.4 *a* clearly demonstrates sudden change in temperature in the gap between the outer surface of the fuel rod and cladding.

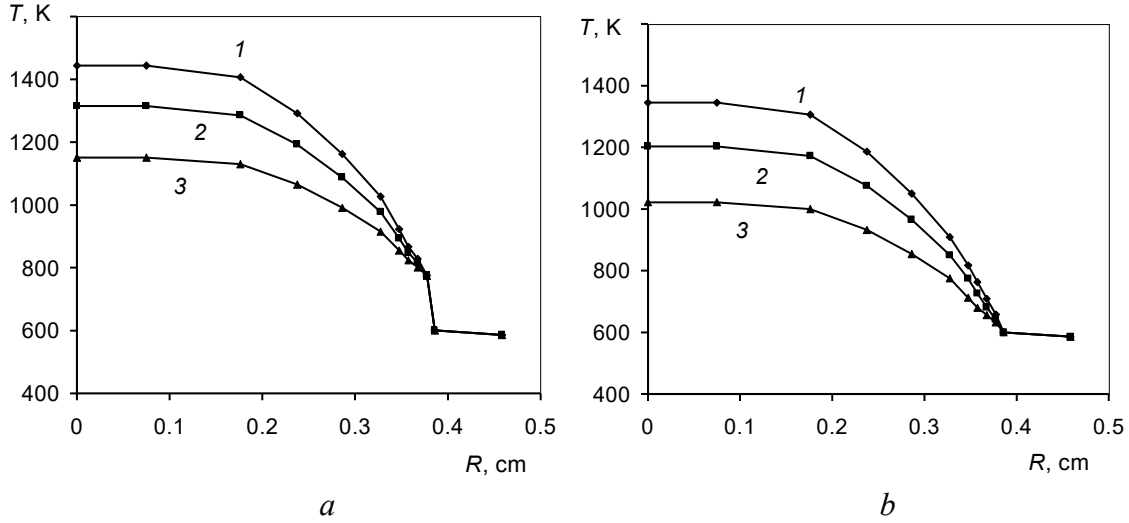

Figure 4. Gap between fuel rod and cladding (*a*) and no gap (*b*). Flat λ and power release

Fig.5 allows to compare the curves *1* of Figs.4 *a* and *b*.

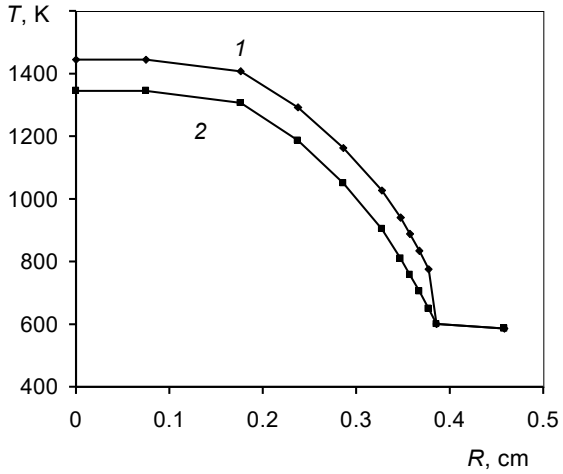

Figure 5. Comparison of curves *1* from Figs. 3 and 4

In task 3 (Fig.6), thermal conductivity factor of fuel λ depended on the radius within the fuel rod. This dependence was the same for curves *1* and *2*. The λ value increased smoothly from 2.1 W/mK in the central layer to 6.5 W/mK in the outer layer of fuel rod. The energy release density was taken to be constant over the volume of the rod and was equal to 388 W/m^3 for curve *1* and 370 W/m^3 for curve *2*. Curve *1* corresponded to the presence of the gap between fuel rod and cladding, while curve 2 corresponded to the absence of the gap, and fuel was in thermal contact with cladding. The result is similar to the curves of Fig. 5, however in Fig. 6, the curves are more flat due to the increase of λ from the center to the periphery.

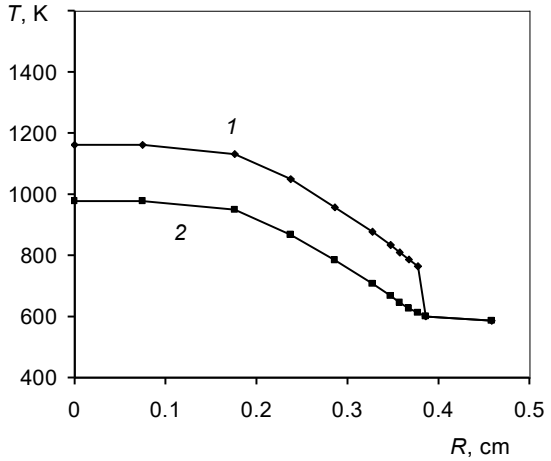

Figure 6. λ increase with radius. Gap between fuel rod and cladding (*1*), no gap (*2*)

6 CONCLUSIONS

Thus, we present a coupled approach to consistent calculation of nuclear fuel for VVER reactors. It is based on modern software and allows to obtain detailed distribution of power density and temperatures in the fuel rod. The proposed approach can serve further for development of verification base for testing of calculations of the fuel rods of VVER reactors.

ACKNOWLEDGEMENT

This work was supported by the MEPhI Academic Excellence Project (agreement with the Ministry of Education and Science of the Russian Federation of August 27, 2013, project no. 02.a03.21.0005).

REFERENCES

[1] Piron, J., Bordin, B., Geoffroy, G. et al., *Proc. of Int. Topical Meeting on Light Water Reactor Fuel Performance.* USA, April 17-21, 321-327 (1994).
[2] Shcheglov, A., Sidorenko, V., Proselkov, V., and Boi'shagin, S. Atomic Energy (1996), **80**, 222-224.
[3] Baranov, V., Ternovykh, M., Tikhomirov, G., Khlunov, A., Tenishev, A., and Kurina, I. *Proc. of the 9-th Int.Conf.on WWER Fuel Performance, Modelling and Experimental Support.* 17-24 September, Helena Resort, Bulgaria, 390-395 (2011).
[4] Kurina, I., Popov, V., and Rumyantsev, V. Atomic Energy (2006), **101,** 802-808.
[5] De Lillo, F., Cecconi, F., Lacorata, G., and Vulpiani, A. EPL, **84** (2008); Davidenko, V., and Tsibulsky, V. *Proc. of the Int. Conf. on the Physics of Nuclear Science and Technology,* Oct. 5–8, Long Island, New York, 1755-1760 (1998).
[6] Childs, K. *HEATING 7.0 User's Manual*, K/CSD/INF/90-32 (Martin Marietta Energy Systems, Inc., July 1990).
[7] SCALE: *A Modular Code System for Performing Standardized Computer Analyses for Licensing Evaluation*, Version 5, ORNL/TM-2005/39, **I-III**, ORNL (2005).
[8] Belousov, I., Davidenko, V., and Tsibulsky, V. Preprint IAE-6083/4, Moscow (1998).

VII International Conference on Computational Methods for Coupled Problems in Science and Engineering
COUPLED PROBLEMS 2017
M. Papadrakakis, E. Oñate and B. Schrefler(Eds)

COMPUTER MODELING OF COUPLED ELECTROMAGNETIC, TEMPERATURE AND MAGNETOHYDRODYNAMIC FIELDS IN THE INDUCTION HEATING AND MELTING DEVICES

VICTOR B. DEMIDOVICH*, IRINA I. RASTVOROVA, VICTOR N. TIMOFEEV†, MAXIM YU. KHATSAYUK†, ALEKSIY A. MAKSIMOV†**

* St.Petersburg Electrotechnical University (LETI), prof. Popov 5, St.Petersburg, Russia
e-mail: vbdemidovich@mail.ru, web page: http://www.eltech.ru

** Saint-Petersburg Mining University, 21 Line, 2, St.Petersburg, Russia,
e-mail: rastvorova@mail.ru web page: http://www.spmi.ru

† Siberian Federal Universities, Academika Kirenskogo str. 26a-302, Krasnoyrask, Russia
e-mail: maxhac@ya.ru, web page: http://www.sfu-kras.ru

Key words: Coupled Electromagnetic, Temperature and Magnetohydrodynamic Fields, Multiphysics Problems, Induction heating and melting, Electromagnetic processing of metals.

Abstract. Computer modeling is necessary part of design new induction heating and melting devices [1]. One of the complicated technologies when it is necessary to simulate coupled electromagnetic, temperature and magnetohydrodynamic fields is heating and melting of titanium alloys in the alternating electromagnetic field. Thermal processing of titanium alloys in the inductor has some features that it is necessary to take into account on the designing of the advanced technology and equipment. Low thermal conductivity and high temperature losses at the surface result in maximum temperature inside of the billet that could under appropriate conditions exceed melting point. In this way it is possible to obtain liquid phase of titanium alloy inside of the billet and protect it from the contact with surrounding atmosphere. To get this it is necessary to choose the right regime of processing, frequency of current, power and thermal conditions. At the same time precise heating with very strong execution of the temperature profile during the heating time are essential for thermal processing of titanium alloys in this technology [2]. Mathematical model comprising computation of electromagnetic, temperature, MHD fields after getting melt zone and dynamic of its growth was developed. The calculation of the melting process has been carried out by the method "enthalpy-porosity" with application of models of turbulent currents k-ω SST in a non-static setting. Electromagnetic forces and heat sources have been defined by solving a harmonic task by the method of finite elements on a vector magnetic potential in the system "inductor – load" for each iteration of the hydrodynamic task. Experiments confirmed need in simulation of MHD fields to receive good coincidence. Using of the developed models for simulation of electromagnetic processing billets make it easy to develop and implement optimal heat processing systems for the crucibleless induction melting of titanium alloys.The calculations on the basis of the model and the analysis of physical processes with non-crucible melting of titanium alloys have also been carried out.

1 INTRODUCTION

For the solution of electromagnetic and thermo-hydrodynamic problems, including peculiarities of the MHD flow processes various software solutions for interfacing software products were developed and implemented. In this coupled model the interpolation algorithm and data exchange between software products ANSYS Mechanical APDL to solve the electromagnetic part and Fluent for solution of thermo-hydrodynamic part was modified and adapted. Parametric model of non-crucible melting the cylindrical titanium billet was developed on the basis of these products [3], including the solution of harmonic electromagnetic problem and thermo-hydrodynamic problem taking into account the turbulent flow and the melting process. The main feature of the model is the transfer of the phase boundary in the electromagnetic part of the problem to rebuild the calculated domain. The resulting model is universal and can be applied for the calculation of a similar system with any geometric, physical and energy parameters.

2 MATHEMATICAL MODEL

The initial stage of mathematical modeling of metal melting process in an electromagnetic field is the implementation of the electromagnetic calculation. A sketch of the system "inductor – billet" is shown in figure 1 and consists of inductor 1 and the billet 2. Such systems are usually had low values of magnetic Reynolds number, that allows to solve the electromagnetic problem, excluding the effect of velocities in the metal on the electromagnetic field. Thus, to solve electromagnetic problem the following assumptions: the electromagnetic field in the calculated domain varies harmonically; the influence of the metal movement in the magnetic field is neglected.

System of equations, which describes electromagnetic field, consists of equations on vector and scalar potential, and continuity equations. Not considering bias currents, and also using Coulomb gauge and considering the absence of free electric charges in the region of computation and the assumptions accepted above we can write down the system of equations as follows:

$$\nabla^2 \dot{\mathbf{A}} = -\mu_a \dot{\boldsymbol{\delta}}; \tag{1}$$

$$\nabla \dot{\boldsymbol{\delta}} = 0 \tag{2}$$

$$\dot{\boldsymbol{\delta}} = -\gamma j \omega \dot{\mathbf{A}} \tag{3}$$

where $\mathbf{A}$ – vector potential; $\boldsymbol{\delta}$ – current density vector; μ_a – absolute magnetic permittivity; γ – electric conductivity; $\omega = 2\pi f$ – electromagnetic field cyclic frequency.

In order to determine electromagnetic field in the region of computation explicitly, equations system shall be finalized with (1 – 3) boundary conditions for tangential and normal component of vector potential:

$$\frac{\partial \dot{\mathbf{A}}_\tau}{\partial n} = 0; \ \dot{\mathbf{A}}_n = 0 \tag{4}$$

where n – normal line to the surface of region of computation

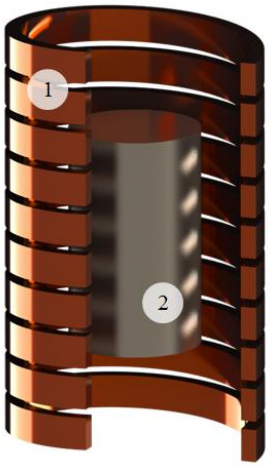

Figure 1. Sketch of the system "inductor-billet"

The next stage of mathematical modelling is the solution of thermo-hydrodynamics problems basing on the results, obtained after electromagnetic calculations. System of equations, which define thermo-hydrodynamic processes, consists of equations of conservation of mass, conservation of motion and conservation of energy. Due to the fact that the appearance of free convective motions and turbulence of flows can be expected, it is necessary to introduce gravitational forces considering density differences and utilization of turbulence model. To allow for free convective motions the Oberbeck–Boussinesq approximation is used. This approximation shows how the dependence of density on temperature linearizes and is taken into account only when there are mass forces. Thus, the fluid can be considered as incompressible. To consider the influence of processes, which happen during melting and solidification stage, thermo-hydrodynamic model is included with melting and solidification model, based on «enthalpy – porosity» method. The influence of electromagnetic field is considered by the introduction of appropriate source elements (which were obtained by electromagnetic calculations) to the equations of motion and energy.

As per the results of analyses of thermo-hydrodynamic calculations correctness, by the example of induction crucible furnace, turbulence model, based on Reynold's averaging of Navier-Stokes equations (RANS), gives temperature distribution results which are not always accurate. Results that are more accurate, in this case, can be obtained by direct numerical simulation of turbulence (DNS – Direct Numerical Simulation). Since turbulence is exceptionally spatial phenomena, the utilization of these models is possible only after the solution of transitional problem in the 3D formulation. The use of complete DNS model for engineering calculations is irrational, because it does not require the discharging of even the smallest vortices. In such cases, they use direct numerical simulation with the usage of large eddy simulation of micro-scale turbulence. (LES – Large Eddy Simulation). Thus, at carrying out the initial calculation for definition of character the system behavior was used LES turbulence method. Taking into account of solidification influence on the character of turbulent flows is implemented by the introduction of additional source elements into the motion quotation, transfer of kinetic energy of turbulent fluctuation and dissipation specific speed.

In this fashion, system of equations, which describe thermos-hydrodynamic process in electromagnetic field, considering solidification process, is as follows:

$$\nabla \mathbf{v} = 0 \tag{5}$$

$$\frac{\partial \rho_0 \mathbf{v}}{\partial t} + \nabla(\rho_0 \mathbf{v}\,\mathbf{v}) = -\nabla p + \nabla \boldsymbol{\tau} + \rho(T)\mathbf{g} + \frac{(1-\beta)^2}{(\beta^3+\xi)} A|\mathbf{v}| + \mathbf{f}_{\text{эм}} \tag{6}$$

$$\frac{\partial \rho_0 H}{\partial t} + \nabla(\rho_0 \mathbf{v} H) = \nabla(\lambda \nabla T) + q_{\text{эм}} \tag{7}$$

where $\mathbf{v}$ – velocity vector; ρ_0 – fluid density at the temperature T_0; t – time; p – pressure; $\boldsymbol{\tau}$ – viscous stress tensor; T – temperature; $\mathbf{g}$ – free fall acceleration vector; β – liquid phase proportion; $\xi = 0.001$ – the figure, preventing division by 0; A – the constant of two phase area, which represents the rapidity of speed reduction to zero during solidification; $H=h+\beta L$ – enthalpy; L – material latent heat; λ – heat conductivity.

Walls heat exchange with the environment happens in accordance with Newton-Richmann law Stefan-Boltzman law:

$$q = -\alpha(T_w - T_0) - \varepsilon\sigma\left({T_w}^4 - {T_0}^4\right) \tag{8}$$

where α – heat exchange coefficient, T_w, T_0 – wall temperature and ambient temperature, ε – emissivity, σ – Stefan-Boltzman constant.

3 THE CALCULATION ALGORITHM

Nowadays there are plenty of ways to solve the multiphase MHD problem and ways of their realization [4, 5]. One of such ways based on combination of ANSYS–Fluent and ANSYS–CFX is method, which is represented in papers [6] for the determination of free surface shape of the melt levitating inside the electromagnetic field. The feature of such an approach is that the coordinates of interphase boundary are included in the solution of electromagnetic problem at $\beta = 0.5$. Basing on these coordinates the realignment of geometry and electromagnetic problem region of computation happens, whereas hydrodynamics problem is solved by fixed VOF method. This approach allows getting the most accurate results in some cases, especially when there are big gradients of electromagnetic values at interphase boundary. However, the consumption of time resources to realign the geometry at each iteration of hydrodynamics problem can significantly slow down the process of calculation.

That's why, the alternate algorithm of solution of such problems was suggested. It is based on ANSYS and Fluent software [7]. The main feature of it is the transfer of complete distribution of the required value in the region of computation of thermo-hydrodynamics part of the problem. Such an approach can be used for the wide range of MHD problems including various phases distribution, interphase boundaries of which are situated in the area of concentration of electromagnetic field and lead to response distortion.

Numerical solution of thermo-hydrodynamic part of the problem considering phase transition and turbulent phenomena is implemented via Fluent, electromagnetic part of the problem was made via ANSYS Classic. To implement the transfer of source elements of equations of motion and energy, which were obtained by the results of solution of electromagnetic part of the problem, from ANSYS into Fluent the data exchange algorithm

was developed. To realize thus algorithm Scheme applicative language, C structural language with User–defined function (UDF) on the bases of integrated Fluent compiler and special Ansys parametric design language (APDL). The algorithm can be separated by two parts: preparatory (Figure 2) and computational (Figure 3).

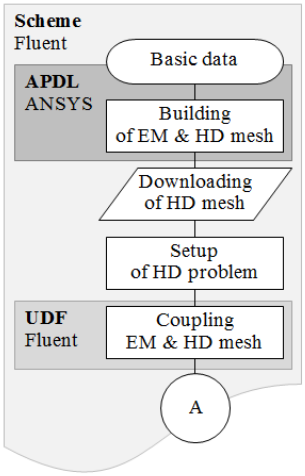

Figure 2. Preparatory part of the algorithm

At the preparatory stage, the following happens: compilation of UDF part of the software; initial data input; construction and uploading of the array of electromagnetic and hydrodynamics problem and their interfacing; adjusting of initial and boundary conditions; materials input; formation of arrays structure for data exchange.

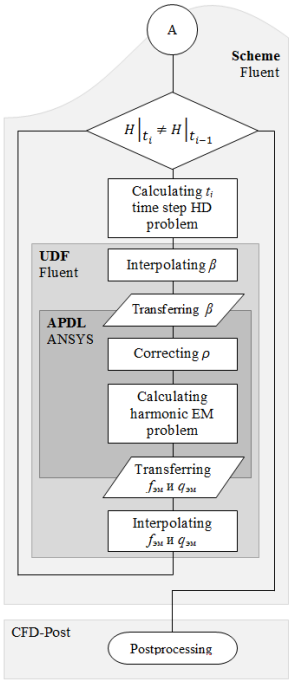

Figure 3. Computational part of the algorithm

After finishing of the preparatory part algorithm goes to implementation of cyclic solution of nonsteady hydrodynamic problem. The first step of cycle is the calculation of "*i*" iteration of hydrodynamic problem. After results, have been finished β liquid phase distribution is automatically extracted and its interpolation on electromagnetic array, and transfer to ANSYS. Basing on β distribution the correction of ingot electrophysical properties happens. Then harmonic electromagnetic problem is solved in the «inductor – ingot» system. Obtained specific electromagnetic forces and power are transferred as motion and energy source into Fluent. The condition of solution cycle completion is the absence of any changes in the system enthalpy. After cycle completes, all the results are sent to CFD-Post postprocessor for automated and manual processing.

4 ANALYSIS OF THE RESULTS

Basing on the obtained mathematical model there was made the numerical experiment for the liquid phase formation inside of cylindrical ingot made from titanium alloy 6Al-4V in electromagnetic field of 10-turns inductor with the current of 2500 A at the frequency of 4 kHz. Then physical experiment was carried out. The basic geometrical dimensions of the system are shown in Figure 4.

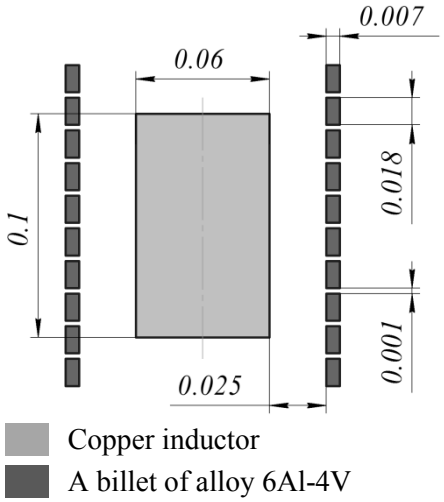

Figure 4. Geometry of induction system

For the imitation of surface constant temperature maintenance the algorithm of supplied power control was used in the model. When the surface gets heated for more than 1407 °C the gradual decrease of the supplied power by 30% happens, up to the temperature of 1644 °C. Function which implements power control is as follows:

$$P(T) = P_0\left(1 - \frac{k_{fall}}{2}\left(1 + \tanh\left(\frac{e}{T_S - T_F}\left(2 \cdot T_{surf\ max} - T_S - T_F\right)\right)\right)\right), \quad (9)$$

where P_0 – basic power; $k_{fall} = 0.3$ – power reduction coefficent; $T_{serf\ max}$ – maximum temperature on the surface; T_S, T_F – temperature of the starting and finishing of power decreasing.

The resulting solution of the problem of liquid phase concentration distribution and temperature field in the volume of billet at different times is presented in Figure 5.

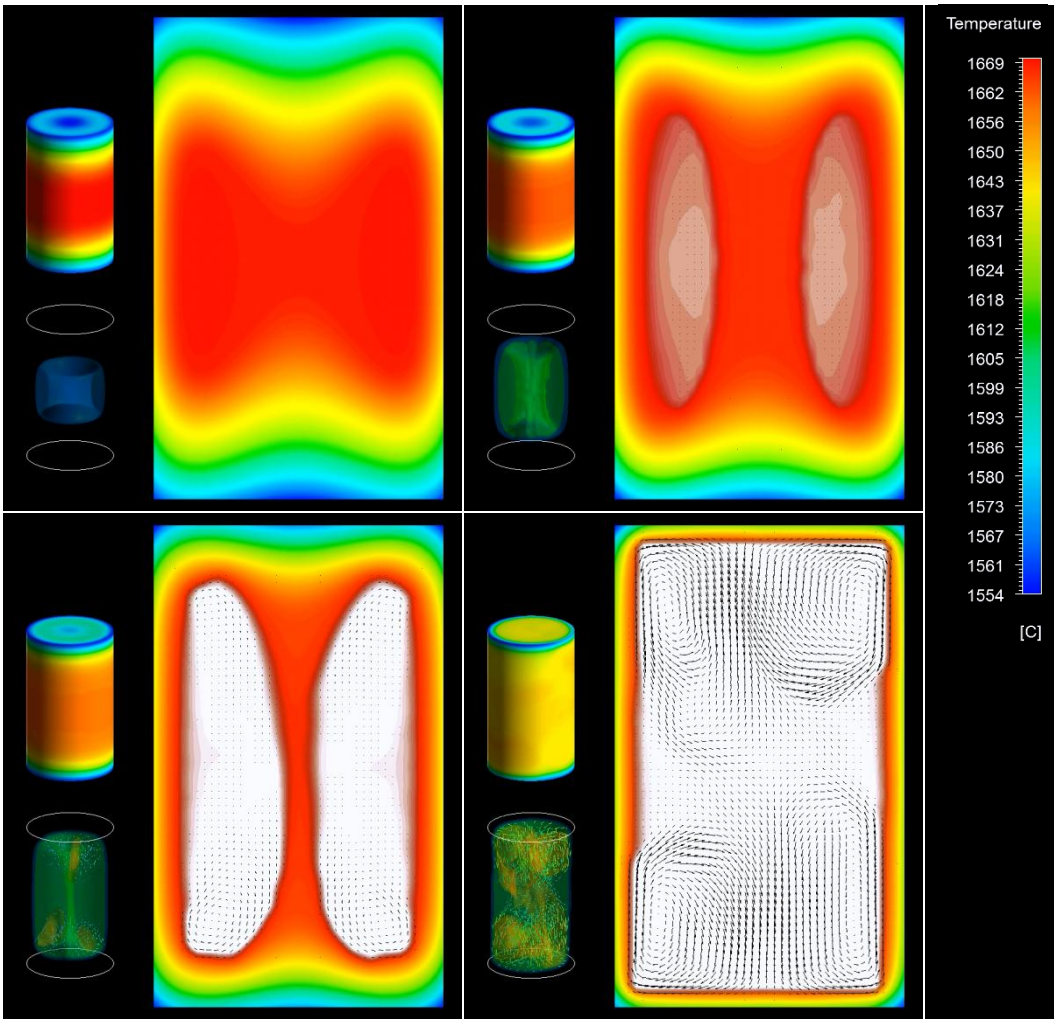

Figure 5. The distribution of the thermal field in the cross section and surface of the billet

The nature of the liquid phase process formation inside of the billet is determined by the distribution of temperature field in cross section of the billet at the moment of reaching the onset temperature of melting. Equalizes of the temperature field to the onset of melting occurs only by conduction in view of heat loss from the surface of the billet and depending on the intensity and distribution of electromagnetic heat sources. In turn, the intensity and distribution of the sources depends on the inductor feeding current (power supplied to the system) and its frequency, respectively. At the same time, a necessary condition is the onset of melting power supply (ΔP) sufficient to raise the temperature to the required value.

5 CONCLUSIONS

There was developed the combined numerical model of the process of 6Al-4V titanium alloy non-vacuum melting considering MHD phenomena and phase transfer processes with the correction of electromagnetic part of the problem. The results of the numerical model

solutions similar to the results of physical experiments that shows the correct operation of the coupled model, given minimal assumptions. This model can be used to identify the key parameters and patterns of energy transduction in the system with different geometric parameters and loading materials. At the same time, one should emphasize the importance of solving the problem of stress strain state in a solid phase billet at the steady state of liquid phase formation taking into account volume distribution of the electromagnetic forces in the surface layers of the workpiece and the hydrostatic pressure on the inner surface of the skull. The solution of this problem will determine the permissible wall thickness of billet and take into consideration the effect of electromagnetic forces in the various energy options on its destruction.

REFERENCES

[1] V. Demidovich, F. Chmilenko, V. Andrushkevich and I. Rastvorova "3D-Simulation of Electromagnetic and Temperature Fields in the Continuous Induction Heaters" *VI International Conference on Computational Methods for Coupled Problems in Science and Engineering COUPLED PROBLEMS 2015*, pp. 976-984 (2015).

[2] V. Demidovich, V. Olenin and E.Grigoriev, "Electromagnetic processing of titanium alloys before plastic deformation", *Proceedings 6th International Conference on ELECTROMAGNETIC PROCESSING of MATERIALS EPM2009*, 2009, Dresden, Germany, pp. 181-184, (2009).

[3] Analysis of transient heat and mass transfer processes in the melt of induction channel furnaces using LES / E. Baake, M. Langejuergen, M. Kirpo, A. Jakovics // Magnetohydrodynamics. № 3. pp. 385-392. (2009)

[4] The Multicell Volume of Fluid (MC-VOF) Method for the Free Surface Simulation of MFD Flows. Part II: Experimental Verifications and Results / O. Pesteanu, E. Baake // *ISIJ International.* №5. pp. 714–721. (2011).

[5] Magnetic levitation of large liquid volume / V. Bojarevics, A. Roy, K. Pericleous // Magnetohydrodynamics. – 2010. – № 4. pp. 317–329.

[6] Numerical modelling of free surface dynamics of conductive melt in the induction crucible furnace / S. Spitans, A. Jakovics, E. Baake, B. Nacke // Magnetohydrodynamics. – 2010. – № 4. – pp. 425–436.

[7] Mathematical modeling of casting processes in electromagnetic field / M. Khatsayuk, A. Minakov, V. Demidovich, M. Pervukhin // Magnetohydrodynamics. – 2015. – № 1. pp. 57–65.

VII International Conference on Computational Methods for Coupled Problems in Science and Engineering
COUPLED PROBLEMS 2017
M. Papadrakakis, E. Oñate and B. Schrefler (Eds)

COUPLED NUMERICAL SIMULATION OF ANTI-ICING PROBLEMS

Emiliano Iuliano* **and Michele Ferraiuolo†**

*Italian Aerospace Research Center (CIRA)
Fluid Mechanics Department
Via Maiorise, 81043 Capua, Italy
e-mail: e.iuliano@cira.it, web page:
http://www.cira.it/it/corporate/chi-siamo/persone/dettaglio-persona?email=e.iuliano@cira.it

†Italian Aerospace Research Center (CIRA)
Thermo-structural Design Department
Via Maiorise, 81043 Capua, Italy
e-mail: m.ferraiuolo@cira.it - Web page: http://www.cira.it/it/corporate/chi-siamo/persone/dettaglio-persona?email=m.ferraiuolo@cira.it

Key words: In-flight icing, coupled approach, FEM, CFD, ice protection system

Abstract.
The paper proposes a coupled methodology able to simulate and optimize the performance of an electrothermal anti-icing system in an integrated fashion: in fact, the classical tool chain of icing simulation (aerodynamics, water catch and impact, mass and energy surface balance) is coupled to the thermal analysis through the surface substrate and the ice thickness. In general, the substrate consists of a multi-layered composite with different properties for each layer and embedded heaters (resistors) at interfaces between layers. The current practice is to size the anti-icing system by evaluating the most critical icing conditions through ice accretion simulation, verifying that no ice is formed on the surface and, finally, estimating the required heating power. In the present approach, the ice protection simulation is not decoupled from the ice accretion simulation, but a single computational work–flow is considered. Validation results obtained on benchmark test cases, drawn from NASA database, will be detailed as well as comparison with numerical results from other authors.

1 Introduction

The formation of ice on aircraft components is a severe issue for in-flight safety. Liquid water droplets may exist in supercooled conditions up to $-40°$, remaining in an unstable state until they undergo an external disturbance, e.g. the impact with an aircraft surface. Depending on the environment and surface substrate conditions, the supercooled droplets may freeze immediately upon contact, partially stick and partially being ejected off the body (splashing, rebounding), deposit and flow along the surface (runback). In case of severe ice accretion, the aerodynamics of the aircraft surface can be severely deteriorated, leading to a decrease in lift and controllability and an increase in drag. Ice protection systems (IPS) are usually designed to prevent ice accretion (anti-icing systems) or to restore clean conditions (de-icing systems). The design of reliable ice protection systems (IPS) is critical and the effectiveness of such devices are required to be thoroughly demonstrated by strict regulations (14 CFR 25.1419 by the FAA or under CS

25.1419 by EASA). Anti-icing systems act to increase the surface temperature above the freezing point, allowing the caught water mass to flow downstream (running-wet anti-icing) or to evaporate (evaporative anti-icing). De-icing systems are activated once a limited amount of ice has already accreted on the aircraft surface, decrease the adhesion forces by de-bonding the inner ice layers and let the aerodynamic forces clean up the surface by removing the detached ice fragments. The heat required by the anti-icing systems is usually provided by electrical heaters embedded within the surface metal skin (electro-thermal anti-icing) or by hot air coming from the engine bleed system and impinging on the internal surface of the metal skin (hot-air anti-icing). De-icing systems may be of different kind: mechanical (pneumatic boots), electro-thermal or electro-mechanical. In case of an anti-icing system, the region to be protected is usually larger than the water droplets impingement area in order to decrease the probability of ice formation due to runback flow.

Numerical simulation represents a crucial step towards the design process of anti-icing systems and the reduction of the experimental testing burden. In the following, a coupled approach is presented which integrates two different physics: the aero-thermodynamics on the airfoil surface, where different phenomena may occur (impingement, water film formation, freezing, evaporation, heat transfer), and the heat conduction through the airfoil skin where heater elements are properly allocated. The coupled procedure is structured in a parametric way in order to be proficiently used within an optimization process to improve the performance of the anti-icing system. The paper is structured as follows: the mathematical models are presented in the next section, then some information about the numerical method are provided and the coupling strategy is presented. The obtained results are shown and discussed in the final section.

2 Mathematical Model

2.1 Heat conduction model

The steady state heat conduction problem with heat generation inside a solid body is governed by the differential equation [15]:

$$\nabla^2 T = \frac{\partial^2 T}{\partial s^2} + \frac{\partial^2 T}{\partial n^2} = -\frac{g}{k} \tag{1}$$

where s and t are the tangential and normal to surface directions, g represents the heat generation of the electrothermal pad elements and k is the thermal conductivity. Convective boundary condition on the skin external surface are applied (see also figure 1):

$$-k_w \frac{\partial T}{\partial n} = h_{eff}(T_s - T_\infty) \tag{2}$$

where k_w is the thermal conductivity of the first layer of the skin, h_{eff} is the effective heat transfer coefficient (see also section 4), T_s is the surface temperature of the skin and T_∞ is the ambient air temperature.

Since the skin is made of several layers characterized by different thermal conductivities, temperature and heat flux continuity conditions are applied at the interface between layers i and $i+1$:

$$k_i \frac{\partial T_i}{\partial n_i} = k_{i+1} \frac{\partial T_{i+1}}{\partial n_{i+1}}$$
$$T_i = T_{i+1}$$

2.2 Messinger model for ice accretion

The pioneering work by Messinger [13] provided a simple model to describe the heat and mass balance onto a surface covered by a thin, continuous water film. In its original form, the model represents a

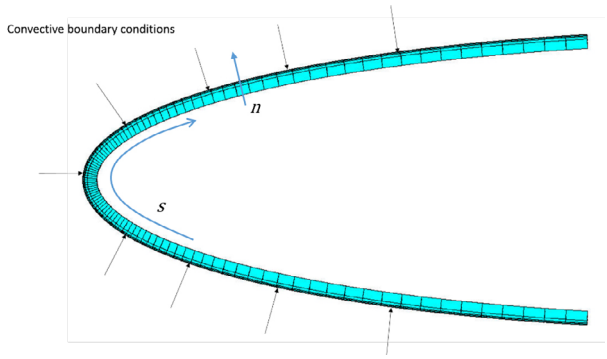

Figure 1: Curvilinear reference system and convective boundary conditions on the skin profile

one-dimensional, equilibrium energy balance to evaluate the equilibrium temperature onto an unheated, insulated surface exposed to icing. In practice, it is evaluated at discrete positions around the leading edge of the body under investigation by using a control volume approach. The calculation normally starts at the air flow stagnation point. The unknowns are the surface temperature and a parameter known as the freezing fraction, f. The latter represents the ratio of the water which freezes at a specified location with respect to the incoming water. Any unfrozen water is assumed to flow back, termed runback water, along the surface and is included in the analysis of the next downstream control volume. From the freezing fraction, the rate of ice growth may be estimated and, consequently, the ice profile can be predicted once fixed the icing time. Otherwise, the simulation of an anti-icing system is carried out by adding heat source terms.

Since the original formulation, several enhancements contributed to the improvement of the model, such as the inclusion of compressibility heating [4], the addition of an energy source from the substrate to simulate anti-icing systems [12], the simulation of conduction through the ice layer [10] an of the resulting phase change due to the heat flow [14].

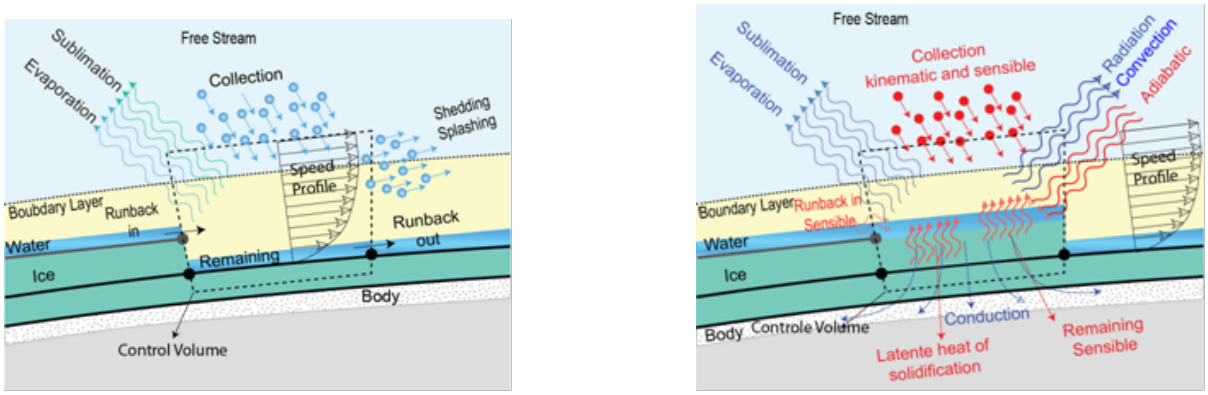

(a) Mass balance

(b) Energy balance

Figure 2: Control volume terms in Messinger model

The Messinger model is based on two main equations: the mass and energy balance on the icing surface. With reference to figure 2, the mass balance states that the water mass incoming into each

control volume cell must be equated by the outgoing water:

$$m_{in} = m_{imp} + m_{rbin} \equiv m_{out} = m_{ice} + m_{evs} + m_{rbo} \tag{3}$$

where $m_{imp} = \beta V_\infty LWC_\infty \Delta S \Delta t$ (β is the droplet collection efficiency, V_∞ is the free-stream droplet velocity and LWC_∞ is the free-stream liquid water content in Kg/m^3, ΔS is the area of the surface element of the control volume and Δt is the icing exposure time) is the impinging water mass, m_{rbin} is the runback water from the upstream cell, $m_{ice} = f m_{in}$ is the freezing water mass, m_{evs} is the mass which undergo evaporation or sublimation and m_{rbo} is the runback water flowing in the next downstream cell. The freezing fraction f can assume values between 0 and 1: a freezing fraction of 1 means that the entire amount of incoming liquid water freezes; a freezing fraction less than 1 means that there will be evaporation and/or liquid runback.

The evaporation/sublimation mass can be estimated by using the Fick's law:

$$m_{evs} = \bar{\rho} h_m (Y_{v,s} - Y_{v,e}) \Delta S \Delta t \tag{4}$$

where $\bar{\rho}$ is the density of the water/vapour mixture, h_m is the diffusive mass transfer coefficient, $Y_{v,s}$ and $Y_{v,e}$ are the water vapor mass fraction evaluated respectively on the surface and outside the boundary layer. By rearranging and exploiting the heat-mass transfer analogy, the evaporation mass can be written as [5]:

$$m_{evs} = \Big(\frac{Pr}{Sc}\Big)^{2/3} \Big(\frac{h}{C_{p,air}}\Big) \frac{M_w}{M_{air}} \Big[\frac{P_{v,s}(T_s) - P_{v,e}}{P_{air} - P_{v,s}(T_s)}\Big] \Delta S \Delta t \tag{5}$$

The water vapor mass fraction (Y_v) are related to the local saturated vapor pressure ($P_{v,s}$) and depends on the local surface temperature T_s. As a consequence, the mass balance equation has three unknowns: the freezing fraction, the surface equilibrium temperature and the outgoing runback mass. The outgoing running back water is computed once the fraction of freezing water f is known. To solve the problem, the heat balance on the surface is considered as sketched in figure 1. Several heat transer mechanisms can be identified, some of them act as heat sinks, some other as heat sources. The general form of the heat balance is epressed with the enthalpy formulation as follows:

$$Q_c + Q_{evs} + Q_f + Q_{sh} + Q_{kin} + Q_{ai} = 0 \tag{6}$$

where the single heat contributions are:

- $Q_c = h_c(T_{rec} - T_s)\Delta S \Delta t$ is the convective cooling heat due to air, h_c is the wall to boundary layer heat transfer coefficient, T_{rec} and T_s are the adiabatic recovery temperature and the surface temperature (unknown);
- $Q_{evs} = -m_{evs}[f L_s + (1-f) L_v] \Delta S \Delta t$ is the heat sink due to evaporation/sublimation, L_v and L_s are the latent heat of evaporation and sublimation;
- $Q_f = f m_{in} L_f \Delta S \Delta t$ is the heat source due to the release of latent heat of fusion (L_f) during the solidification process;
- $Q_{sh} = Q_{sh1} + Q_{sh2}$ is the sensible heat associated to the change of temperature in the control volume. In the most general case, this process can be divided in two thermodynamic sub-processes: first, the system has to be brought from the initial temperature to the freezing point; second, it has

to change its temperature from the freezing point to the equilibrium temperature. The two terms can be written as:

$$Q_{sh1} = m_{imp} C_{p,w} (T_{imp} - T_f) \Delta S \Delta t + m_{rbin} C_{p,w} (T_{rbin} - T_f) \Delta S \Delta t$$
$$Q_{sh2} = m_{in} (1 - f) C_{p,w} (T_f - T_s) \Delta S \Delta t + m_{in} f C_{p,i} (T_f - T_s) \Delta S \Delta t$$

with $C_{p,w}$ and $C_{p,i}$ the specific heat capacity of water and ice.

- $Q_{kin} = \frac{1}{2} m_{imp} U_d^2$ is the kinetic heat source due to incoming droplets;
- Q_{ai} is the heat provided by an anti-icing system. In case of an electrothermal system, it may be expressed in terms of the heat condution flux at the surface:

$$Q_{ai} = -k_w \frac{\partial T}{\partial n} \Delta S \Delta t \tag{7}$$

with k_w the thermal conductivity of the surface layer and $\frac{\partial T}{\partial n}$ the local temperature gradient in the direction normal to the surface.

The two equations are solved by identifying three domains in the (T_s, f, m_{rbo}) solution space (running wet, rime icing and glaze icing) and by iteratively checking the so-called compatibility relations associated to each of them: for instance, the runnig wet regime holds only if $T_s > T_f$, hence if at the end of the computation the value of the surface temperature is not compatible with this hypothesis, the solution is not valid and another regime must be considered. The heat balance equation is solved by using a classical Newton-Raphson method and evaluating at each iteration both the function value and its derivative with respect to the unknown variable (T_s or f, depending on the solution domain).

3 Numerical method

3.1 Heat conduction model

The finite element adopted for thermal analyses is a solid one with 8 nodes on the corners and temperature as the only degree of freedom [11]. This thermal element is linear since it is characterized by no mid-side nodes. The element size in the direction of the curvilinear abscissa of the profile has been set equal to the thickness of the outermost layer of the skin, while a an adequate spacing ratio has been chosen in order to take into account the presence of the electrothermal pad thickness which is much lower than the layer ones. The number of nodes in the layer thickness is such that the element length is the fourth part of the outermost layer thickness. Finally, the sparse matrix direct solver has been employed for the solution.

A parametric model has been designed in Ansys Parametric Design Language (APDL) able to analyze any kind of aerodynamic profile, skin layers layout and electro-thermal pad arrangement. The model has been conceived to be adopted in an optimization process where the capability to vary the location of the pads and their corresponding electric power is required. More specifically, two APDL batch files have been prepared: the first one (geometry/mesh file) needs geometric inputs such as the aerodynamic profile, the number and thickness of the skin layers, the ice profile in case of de-icing simulations and provides as main output the computational mesh; the second one (load/analysis file) contains the pads layout and the load conditions. In a parametric or optimization study, the geometry/mesh file is run only at the beginning of the process and a database file is created by the Finite element commercial code; on the other hand, the load/analysis file is run every time a thermal analysis is invoked and is fed with the surface distribution of the heat transfer coefficient: the design variables can be the location of the pads, the power-up switching sequence or their electric power.

In what follows a detailed description of the geometry/mesh file is given. As above mentioned, the inputs for this file are only geometric. The output is a database file containing the finite element model.

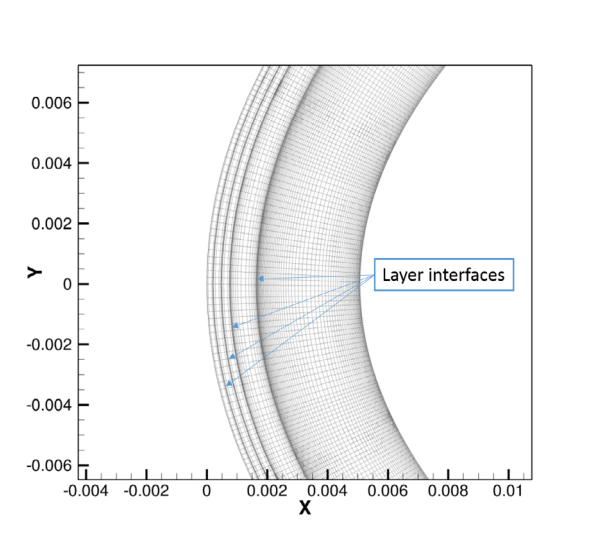

Figure 3: Example mesh in the airfoil skin with layer interfaces

The file is completely parametric and can be adopted for any kind of profile shape. Concerning the mesh generation, a specific procedure has been prepared in order to appropriately mesh the electrothermal pads whose information are given only in the second file. An example of the finite element mesh is provided in figure 3. Indeed, since the pads are supposed to be inserted between two layers and their thickness is typically very small (about 0.05 mm) if compared with the skin layers, the mesh elements are not uniformly spaced throughout the skin thickness but highly stretched in the normal to surface direction in order to have very small elements near the layer interfaces and capture the geometry of the pad elements. This is done for every layer interface as, at the time of the mesh generation, the actual location of the pads is not known yet. Such an approach gives generality to the computational process as it prevents from generating a new mesh for each thermal computation and it allows for an easy and parametric allocation of the pad elements.

In the load/analysis file, heat transfer coefficient distribution, pads power, location and activation sequence are provided. According to these data, the mesh elements which are enclosed in the specified pad region are selected and the corresponding heat power density is assigned to them. The heat transfer coefficient is included here because it represents the total (or effective) surface heat loss and in steady analyses, when a direct coupling between the finite element conduction model and the ice accretion model is realized, it may vary depending on the external conditions; in fact, as it will be described in section 4, multiple steady thermal analyses are conducted by exchanging the total heat transfer coefficient until convergence is reached.

3.2 Messinger model

The main inputs of the Messinger model are the impinging mass m_{imp} and the convective heat transfer coefficient h_c. The first is related to the collection efficiency β which, in turn, depends on the air flow and water droplet field solutions. The second depends on boundary layer characteristics. Both parameters may be computed by using various methods and approaches. Here, the air flow field is obtained by solving the Reynolds-averaged Navier-Stokes equations: to this aim, the in-house multi-block structured flow solver ZEN is used [3]. As a viscous flow solver is available, the heat transfer coefficient can be computed easily from the air flow solution as follows:

- on solid surfaces, no-slip and isothermal boundary conditions are imposed for momentum and energy

equations respectively;

- two computations are launched: the first by imposing the wall temperature $T_{w,1} = T_\infty$, the second by imposing $T_{w,2} = T_\infty - \Delta T_w$ (here $\Delta T_w = 0.5$ Kelvin). As a result, two distributions of the surface heat flux are obtained from the solutions: $\dot{q}_{w,1} = h_c(T_{w,1} - T_{rec})$ and $\dot{q}_{w,2} = h_c(T_{w,2} - T_{rec})$, where T_{rec} is the adiabatic recovery temperature. Having set the difference in wall temperature ΔT_w very small, the dependence of the convective heat transfer on the temperature can be safely neglected. Finally, having two equations with the unknowns (T_{rec}, h_c), it is possible to calculate both the recovery temperature and the heat transfer coefficient at every point of the solid surface.

As regards the collection efficiency, the in-house Eulerian solver Imp2D is employed to compute the water droplet flow field by solving PDE equations for water particles concentration $\rho_d \alpha_d$, momentum $\rho_d \alpha_d \vec{U}_d$ and energy $\rho_d \alpha_d T_d$ balance [7, 8, 6], where subscript d refers to the droplet phase. In the momentum equation, aerodynamic drag and gravity forces are introduced as source terms. The collection efficiency is computed on any solid surface as:

$$\beta = \frac{\rho_d \alpha_d (\vec{U}_d \cdot \vec{n})}{LWC_\infty U_{d,\infty}}$$

where LWC_∞ is the liquid water content of the cloud in Kg/m^3, $U_{d,\infty}$ is the free-stream droplet velocity and $\vec{n}$ is the surface normal unit vector.

Once known h_c and β distribution at any point on the solid surface, equations 3 and 6 can be solved. Given a control volume discretization of the solid surface, the procedure starts from the stagnation point, where no incoming runback mass m_{rbin} is supposed to enter and the outgoing runback mass m_{rbo} is assumed to be poured in equal parts into the adjacent control volumes; then, it proceeds downstream first on the suction side, then on the pressure side separately. For each control volume, up to three icing regimes are sequentially assumed (running wet, rime icing and glaze icing) and the related simplified equations are solved if the compatibility conditions of the former are not satisfied, as described in section 2.2.

4 Coupling approach

Equations 1,3 and 6 represent a mathematical model which has to be solved simultaneously in order to guarantee a physical solution. Moreover, a multi-zonal approach has to be employed with appropriate interface conditions: indeed, equation 1 is valid through the solid skin while equations 3 and 6 describe the physics of the external flow. The set is coupled by the surface temperature field which is an unknown in both cases. The coupling procedure is conceived to balance the total heat lost due to the external flow phenomena (evaporation, convective cooling, impingement, freezing) and the heat flux provided by the anti-icing system. The convergence metric is the effective heat transfer coefficient which is exchanged between the zonal solutions.

Here, an iterative approach is followed aiming at achieving the convergence of surface field data on both models. In other words, the heat conduction solver is iteratively fed with the Messinger model solution to realize the same heat transfer and temperature field according to some norm. The coupling procedure can be summarized as follows:

1. Initialization step: the anti-icing heat source is initialized to null and the effective heat transfer is assumed as purely convective: $Q_{ai,m} = 0$,$h_{eff,m} = h_c$;

2. Messinger model solution: equations 3 and 6 are solved and the surface temperature distribution $T_{s,m}$ is calculated;

3. Exchange parameter evaluation: the effective heat transfer coefficient is estimated by considering the total heat lost on the surface as:

$$h_{eff,hc} = \frac{1}{\Delta S \Delta t} \frac{Q_c(T_{s,m}) + Q_{evs}(T_{s,m}) + Q_f + Q_{sh}(T_{s,m}) + Q_{kin}}{T_{s,m} - T_\infty} \tag{8}$$

4. Heat conduction solution: the surface distribution of $h_{eff,hc}$ is transferred to the heat conduction solver, the temperature field T_{hc} in the solid skin is obtained by solving equation 1 with the boundary condition:

$$\dot{q}_{w,hc} = h_{eff,hc}(T_{s,hc} - T_\infty) = -k_w \frac{\partial T_{hc}}{\partial n} \tag{9}$$

where $T_{s,hc}$ is the new value of the surface temperature;

5. Convergence check: if $\|h_{eff,hc} - h_{eff,m}\|_p < \epsilon$, convergence is assumed and the solution of the coupled problem is found. Otherwise, $h_{eff,m} = h_{eff,hc}$, $Q_{ai,m} = \dot{q}_{w,hc} \Delta S \Delta t$ and one more iterative step is performed going back to point 2. Here, both $p = 2$ and $p = \infty$ are used.

The effective film coefficient h_{eff} is used for estimating the convergence of the coupled problem while a natural choice could have led to use the surface temperature T_s: however, as ice–water phase change may occur in some regions and this could keep the temperature predicted by the Messinger model fixed at the freezing point, a bias would be introduced in those regions between the heat conduction model (which does not include such physics) and the ice accretion model. Consequently, the convergence may not be assured.

5 Results and discussion

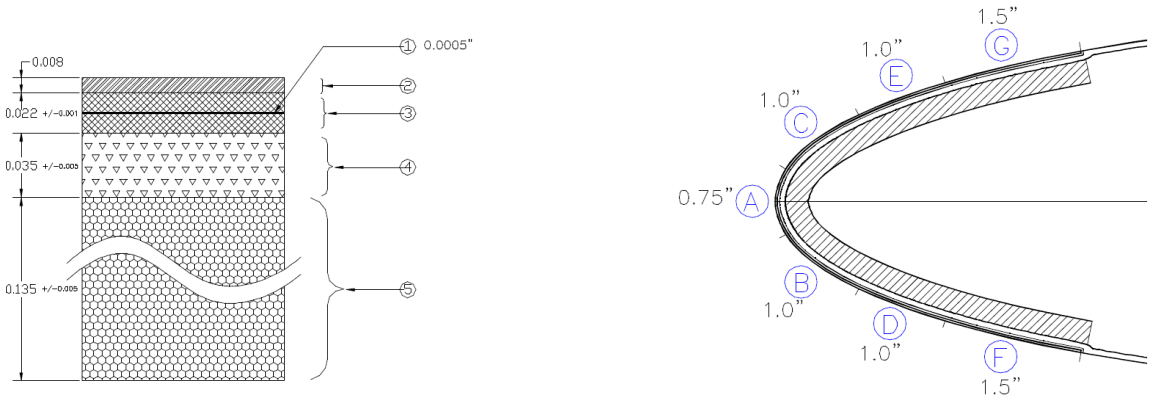

(a) Skin layers

(b) Pads layout

Figure 4: NACA 0012 skin structure (from ref. [1])

Test cases are selected from the paper published by Al-Khalil et al.[1]: both experimental and numerical results are reported for a NACA 0012 airfoil having a span length of 1.828 meters and a chord value of 0.9144 meters. Where available, results are also compared to the numerical analyses carried out by da Silva et al. [16] and by Bu et al. [2].

Both authors performed numerical studies of anti-icing systems using integral and differential boundary layer methods. As sketched in figure 4, the airfoil skin is composed of five material layers and is

Item	Material	Thermal conductivity K		Density, ρ		Specific heat, C_p		Thickness	
		btu/hr.ft.°F	W/m.°C	lbm/ft³	kg/m³	Btu/lbm.°F	J/kg.°C	inches	mm
1	Heating Element (alloy 90)	23.7	41.02	556	8906	0.092	385.2	0.0005	0.0127
2	Erosion Shield (SS 301 H)	9.4	16.27	501	8025	0.12	502.4	0.008	0.2032
3	Elastomer (Cox 4300)	0.148	0.26	86.4	1384	0.3 +/- 0.03	1256 +/- 125.6	0.022 +/- 0.001	0.559 +/- 0.0254
4	Fiberglass/Epoxy Composite	0.17	0.29	112	1794	0.375	1570.1	0.035 +/- 0.005	0.889 +/- 0.127
5	Silicone Foam Insulation	0.07	0.12	40.5	649	0.27 +/- 0.03	1130.4 +/- 125.6	0.135 +/- 0.005	3.429 +/- 0.127

Figure 5: Layer material properties

Table 1: Heaters setup

	Non-dimensional streawise distance s/c		*Anti-icing heat flux* [kW/m^2]			
Heater ID	*Start*	*End*	*22A*	*22B*	*67A*	*67B*
F	0.9178	0.9588	9.92	2.63	20.15	8.37
D	0.9588	0.9868	10.23	2.94	21.70	11.94
B	0.9868	1.0148	32.55	4.03	32.55	10.85
A	1.0148	1.0358	46.50	4.80	46.40	15.19
C	1.0358	1.0628	18.60	2.94	26.35	9.92
E	1.0628	1.0908	6.98	3.41	18.60	12.87
G	1.0908	1.1328	10.23	2.32	18.60	8.68

equipped with seven heating pads (from A to G), all located between the second and third layer starting from the external surface. Figure 5 summarizes the material properties of each layer.

The air flow and the collection efficiency have been computed with in-house solvers (respectively ZEN and Imp2D) on a three-level C-type structured mesh, having 98,000 quadrilateral cells in the finest level. The $y+$ on the airfoil surface ranges from 0.5 to 4. The $k-\omega$ TNT turbulence model by Kok et al. [9] is used.

The icing conditions are shown in table 2. Figure 6 compares the obtained collection efficiency with numerical results by Al-Khalil and Bu papers. The comparison with results by Bu is noticeable in both cases, while the ANTICE predictions result in a more smeared shape, as the impingement peak is slightly lower and the limits are larger. Obviously, the collection efficiency depends only on the icing

Table 2: Test cases icing conditions

Parameter	*Case 22*	*Case 67*
AOA [°]	0	00
V_∞ [m/s]	44.7	89.4
T_∞ [K]	265.5	251.4
LWC_∞ [Kg/m^3]	0.00078	0.00055
MVD_∞ [μm]	20	20

conditions and not on the heaters pad setup, hence evaporative and running wet cases will have the same β distribution if they have been conducted in the same icing conditions.

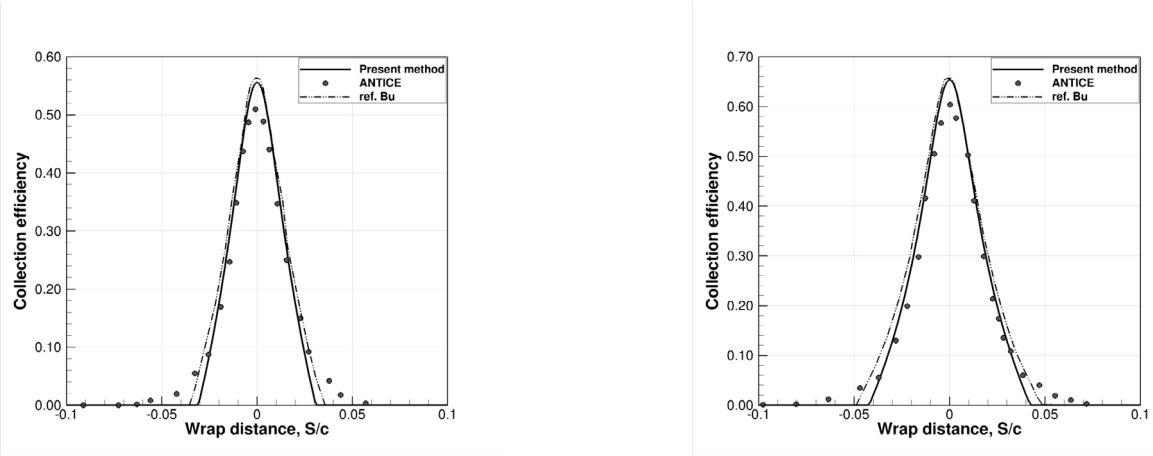

(a) Case 22

(b) Case 67

Figure 6: Collection efficiency compared with literature numerical results

Detailed information about the location and the power densities of the heaters are reported in table 1, where A and B refers to evaporative and running wet cases, respectively. Here s/c represents the non-dimensional wrap distance measured from the airfoil trailing edge in clockwise order. The wrap distance is the same as s/c but re-centered in the airfoil leading edge point. In the following, four cases will be presented, two in running-wet conditions (22B and 67B), two in evaporative mode (22A and 67A). For each condition, four types of output are proposed: the equilibrium surface temperature, the effective (or total) heat transfer coefficient, the runback mass flow rate (per unit span distance) and the mass balance contributions (mass flow rate per unit span distance). Following Al-Khalil observations, the laminar to turbulent transition has been numerically tripped at $s/c = 0.05$ in wrap distance along the airfoil surface in order to match the film coefficient distribution as observed from experimental data.

5.1 Running-wet cases

The running wet cases are referred to as 22B and 67B. For the former, only experimental and ANTICE code data by Al-Khalil [1] are available, for the latter numerical data by da Silva [16] and Bu [2] will be used in addition. Results and comparison plots are summarized in figure 7 and 8. In both cases, the agreement with surface temperature experimental data is quite satisfactory, especially around stagnation and in the outer regions, while some overshoots in the numerical prediction are observed in the middle. However, it can be noticed that such a feature is shared with both ANTICE code and reference data by da Silva and Bu, especially for case 67B. The temperature range is between the freezing point at 273.15 K and 282 K for case 22B and up to 300 K for case 67B.

The effective film coefficient h_{eff} is slightly underestimated by the present method, as observable from figures 7(b) and 8(b). In figure 7(b) it is also reported a comparison of the air-wall (dry conditions) heat transfer coefficient h_c computed with the present method and the ANTICE laminar prediction: the data are in good agreement, at least prior to the transition that has been artificially tripped in the CFD computation. This probably means that the underestimation in the total heat transfer coefficient is due to the presence of the surface water film. A possible answer is given in figures 7(c) and 8(c) where an overestimation of the runback mass flow rate is evident with respect to ANTICE predictions: indeed, for a given impingement mass flow rate, having more water flowing on the surface implies that less water has evaporated, which in turn implies a higher value of the local surface temperature (evaporative cooling is lower) and a lower effective heat transfer coefficient. The impingement, evaporative and freezing mass

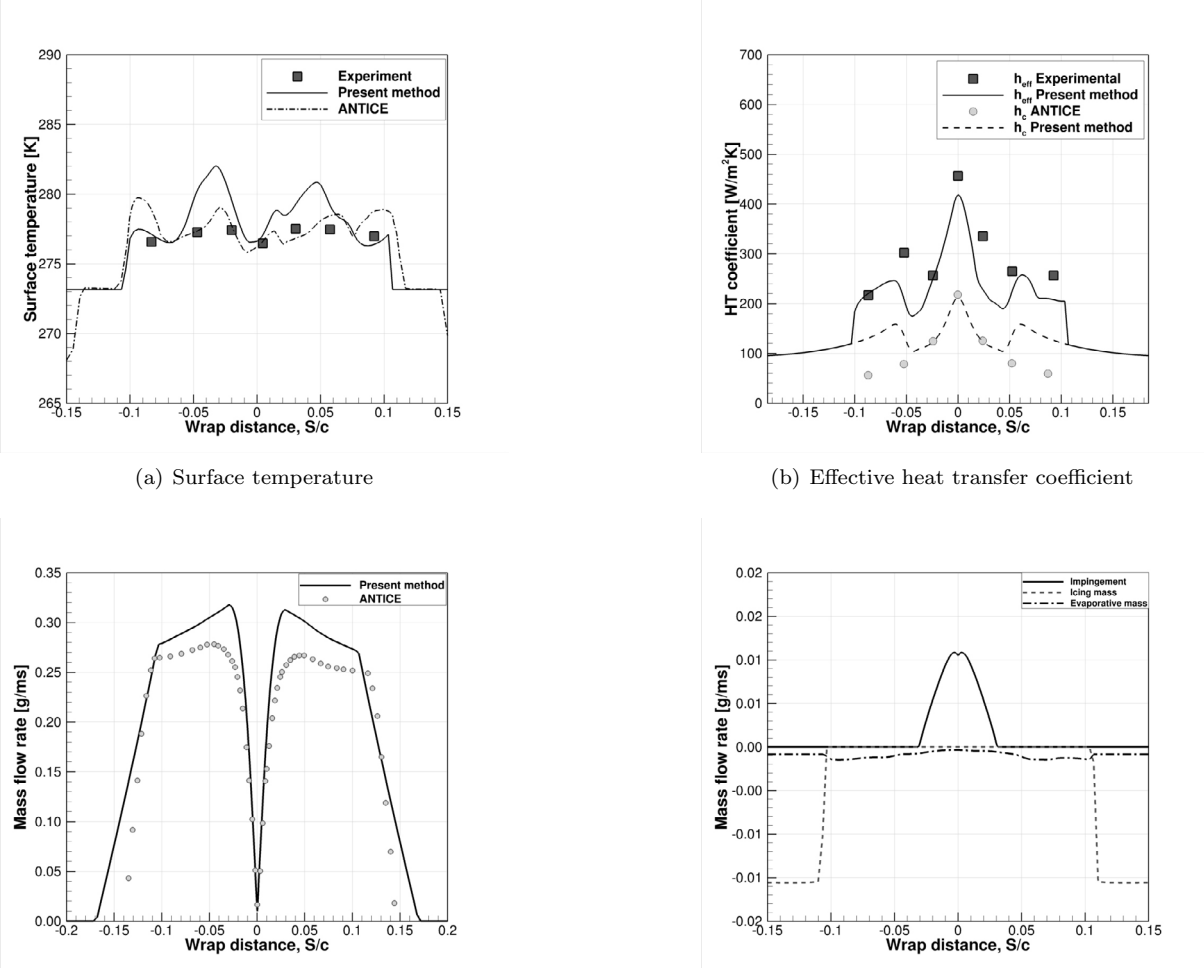

(a) Surface temperature

(b) Effective heat transfer coefficient

(c) Runback mass flux (Kg/ms)

(d) Mass balance contributions

Figure 7: Case 22B (running wet)

flow rates are plot in figures 7(d) and 8(d), where negative values indicate that mass is outgoing from the control volume. The evaporating mass is just a limited portion of the incoming mass due to relatively low surface temperature values; even a small runback ice formation is observed near the impingement limits, as also highlighted experimentally by Al-Khalil.

Figure 9 shows the skin temperature contour map as computed in the last coupled iteration together with the water droplet limiting trajectories and the runback ice formation. For the sake of clarity, the temperature contour levels below 273.15 K have been cut, so that it is easy to identify the freezing point. It can be observed that there are two peak regions in the temperature field close to the impingement limits and that the ice formation starts to grow near the location where the freezing point is met. The ice thickness for case 67B is bigger and less spread than case 22B despite of the noticeably higher heating power: this is explained by two main effects, first the larger impinging mass for case 67B, second, due to lower temperatures, the larger area (even beyond the protected region) covered by water runback for case 22B.

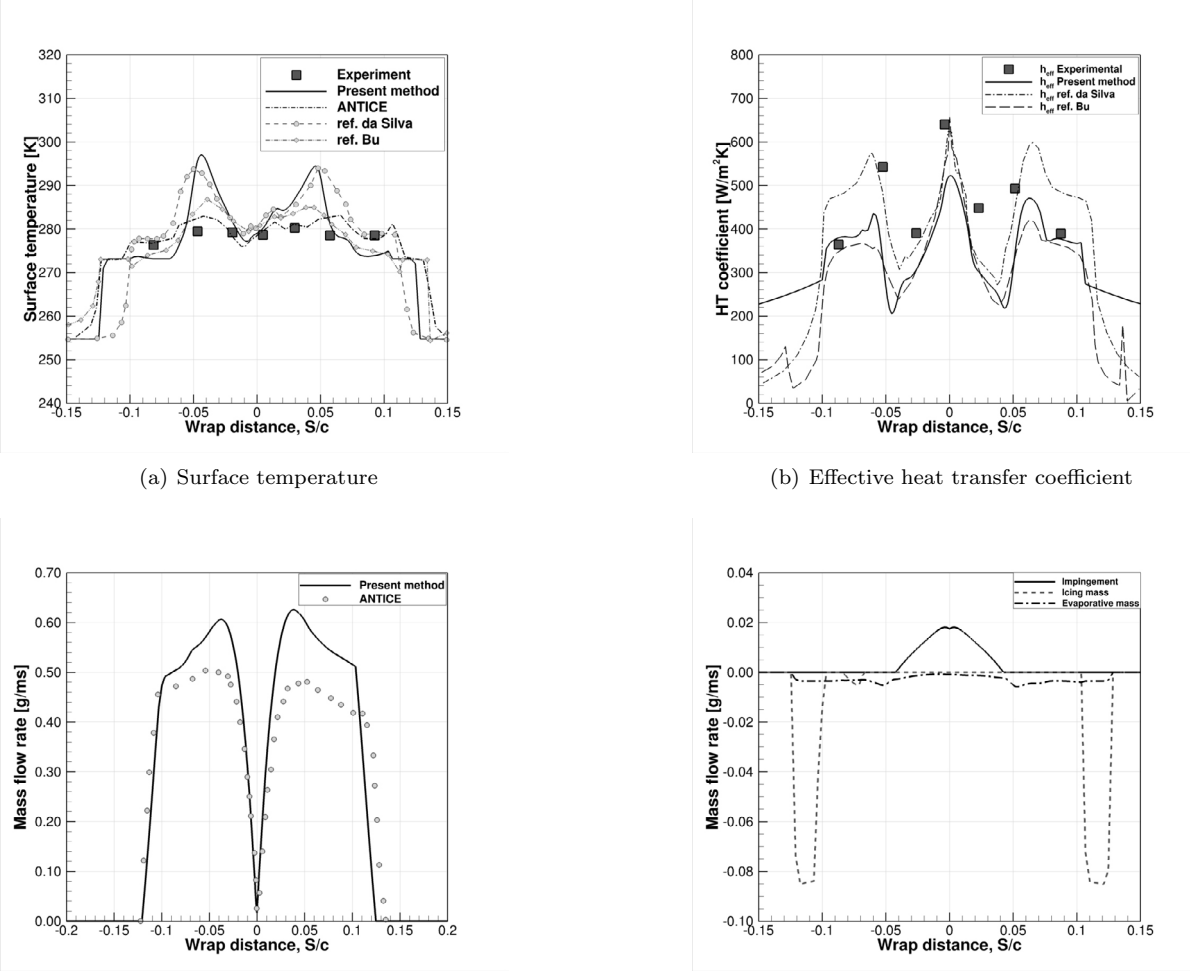

(a) Surface temperature

(b) Effective heat transfer coefficient

(c) Runback mass flux (Kg/ms)

(d) Mass balance contributions

Figure 8: Case 67B (running wet)

5.2 Evaporative cases

The evaporative cases are referred to as 22A and 67A. For both cases, reference data by Al-Khakil, da Silva and Bu are available. Results and comparison plots are summarized in figure 10 and 11. For case 22A, the predicted surface temperature shows a good agreement with the experiment throughout the whole heated region. The effective film coefficient is still underestimated as figure 10(b) indicates, however the trend in the laminar-turbulent transitional area is well captured. Due to high heater power values in combination with low impinging mass, this case is very close to be considered an actual fully evaporative case, as the runback mass in the impinging area is very limited (figure 10(c)) and the most of the impinging water evaporates in the wetted area (figure 10(d)).

Case 67A presents some discrepancies in the surface temperature profile past the impingement limits, where the value of the experiment thermocouple is significantly underestimated by both the present method and Bu's data. The effective film coefficient h_{eff} is still slightly underestimated, as reported in figure 11(b), but the discrepancy is here confined in a narrow region near the stagnation point, while the overall agreement is acceptable. Figures 11(c) provide a confirmation that the runback mass flow rate is

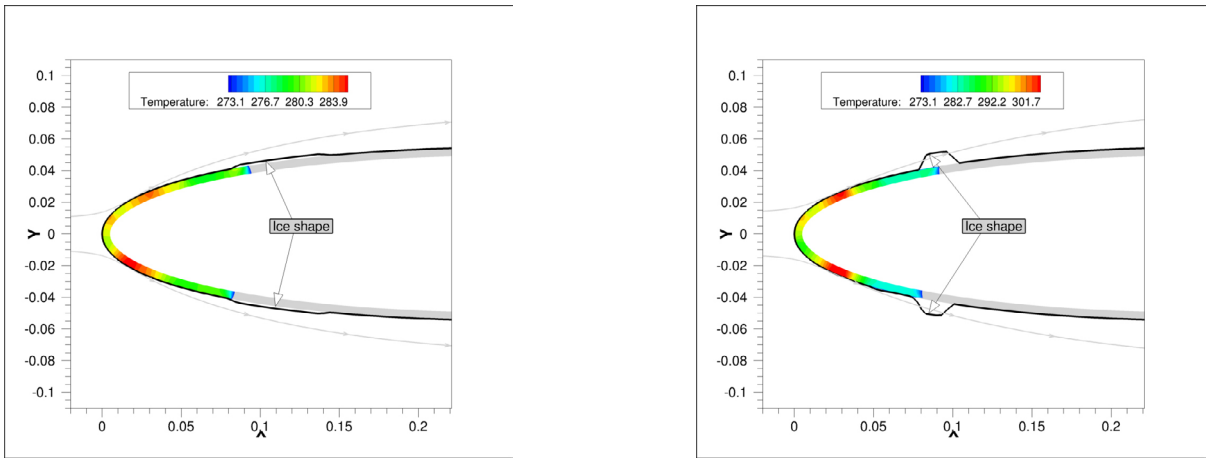

(a) Case 22B

(b) Case 67B

Figure 9: Skin temperature field with water droplet limiting trajectories and runback ice shape

overestimated with respect to Al-Khalil numerical predictions.

Unlike the previous case, the evaporating process does not manage to balance the larger incoming water mass (figure 11(d)), thus being of the same order of magnitude of case 22A. As a consequence, similar features to running-wet cases are observed, i.e. large amount of runback water and small ice formations at the extremes of the protected area. Indeed, figure 12 shows the skin temperature contour map as computed in the last coupled iteration together with the water droplet limiting trajectories and the runback ice formation. For case 22A, as already mentioned, no runback ice is present as the temperature is kept above the freezing point throughout the whole wet area and all the incoming mass is lost by evaporation. On the other hand, a very small triangle–shaped ice accretion is predicted by the present method as a result of some residual water mass flowing downstream and freezing immediately behind the protected area.

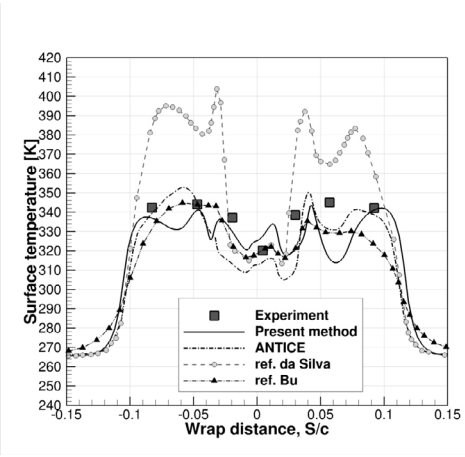

(a) Surface temperature

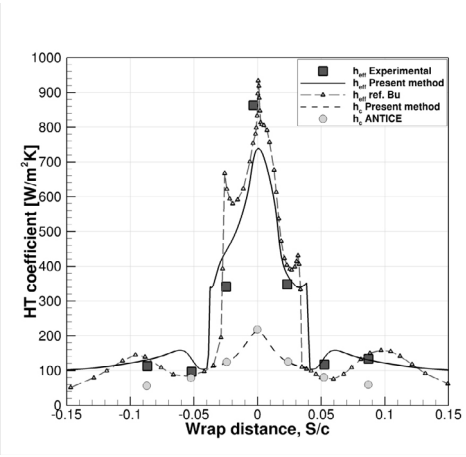

(b) Effective heat transfer coefficient

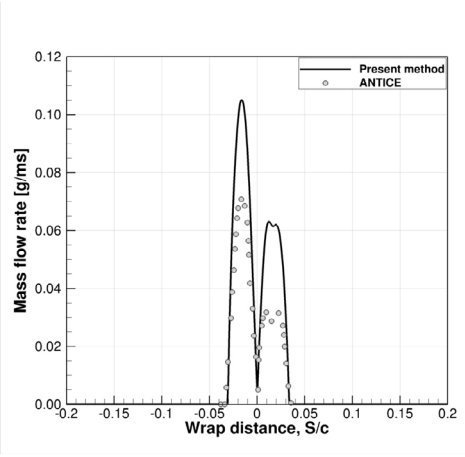

(c) Runback mass flux (Kg/ms)

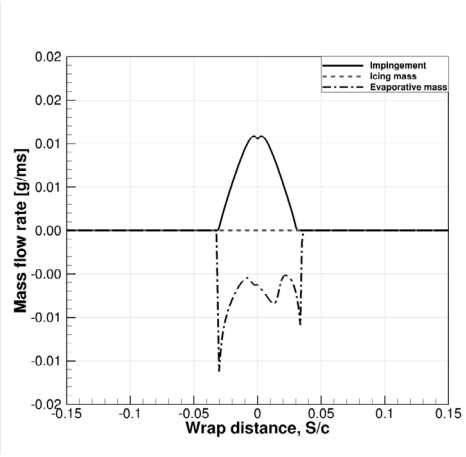

(d) Mass balance contributions

Figure 10: Case 22A (evaporative)

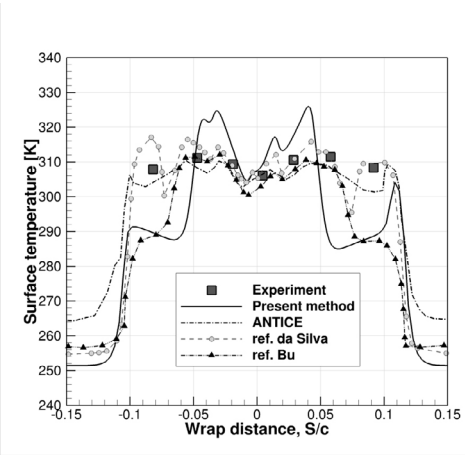

(a) Surface temperature

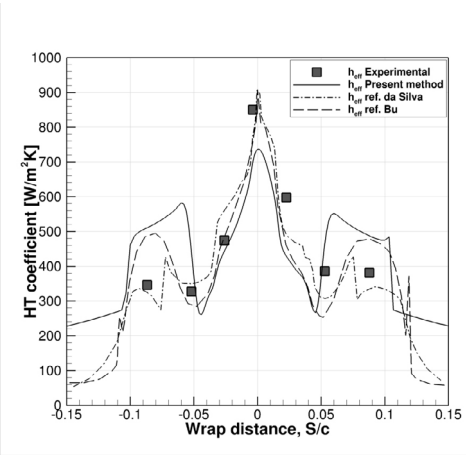

(b) Effective heat transfer coefficient

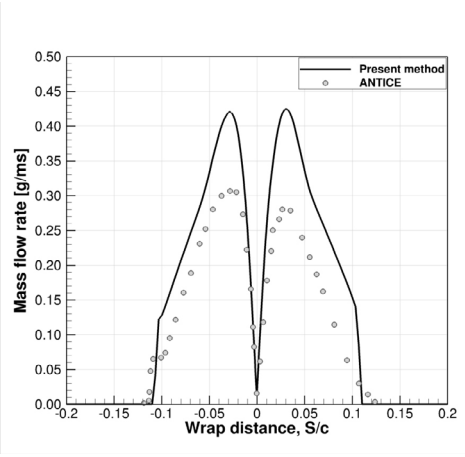

(c) Runback mass flux (Kg/ms)

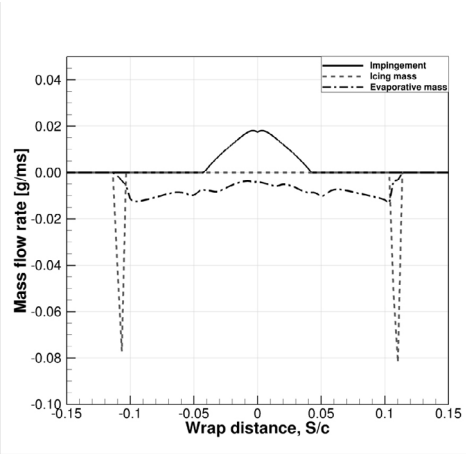

(d) Mass balance contributions

Figure 11: Case 67A (evaporative)

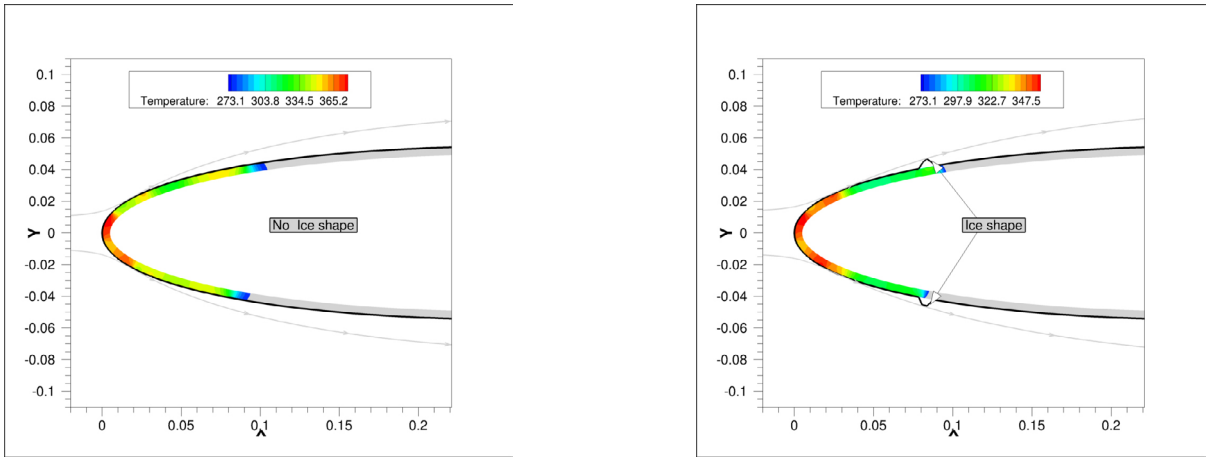

(a) Case 22A

(b) Case 67A

Figure 12: Skin temperature field with water droplet limiting trajectories and runback ice shape

Conclusions

A coupled approach has been presented and tested to numerically simulate anti-icing problems on airfoil shapes. It combines a classical Messinger-based ice accretion simulation with a FEM analysis for solving the heat conduction problem through the airfoil skin. The air flow and the local collection efficiency are evaluated by means of the finite volume method implemented within in-house solvers. In particular, the water droplet flow field is computed in every location of the solution domain by means of a Eulerian approach.

The coupling between the surface mass and energy equations and the heat conduction problem has been realized iteratively by searching for the convergence of the effective film coefficient distribution. Typically, three to five iterations are required to reach the convergence on the L_2 or L_∞ norm.

Results show that a satisfactory agreement has been reached with experimental data and numerical results has been reached, especially in evaporative conditions, while some overshoots are still observed in running wet conditions. A consistent trend has been observed in underestimating the total heat transfer coefficient and overestimating the runback mass flux with respect to ANTICE code by NASA: this can be probably due to the differences outlined in the impinging mass flux more than in the estimation of the evaporative rate. Further investigations will be devoted to extend the coupled code validation and to make comparative studies about the evaporative cooling law as applied to aircraft icing, as also recommended by Al-Khalil.

Electrothermal de-icing cases will be also considered even if no coupling with the external solution is needed.

Finally, the coupled approach has been designed and implemented in a fully parametric mode where the location, extension and power of the heaters can be easily changed. This is of fundamental importance towards the design of electro-thermal anti-icing systems, e.g. by numerical optimization aimed at minimizing the overall power required by the anti-icing system while keeping the surface clear of ice.

REFERENCES

[1] Kamel Al-Khalil, Charles Horvath, Dean Miller, William Wright, Kamel Al-Khalil, Charles Horvath, Dean Miller, and William Wright. Validation of NASA thermal ice protection computer codes. III - the validation of ANTICE. In *35th Aerospace Sciences Meeting and Exhibit*, number AIAA 97-0051. AIAA, American Institute of Aeronautics and Astronautics (AIAA), jan 1997.

[2] Xueqin Bu, Guiping Lin, Jia Yu, Shenghua Yang, and Xin Song. Numerical simulation of an airfoil electrothermal anti-icing system. *Proceedings of the Institution of Mechanical Engineers, Part G: Journal of Aerospace Engineering*, 227(10):1608–1622, 2013.

[3] Pietro Catalano and Marcello Amato. An evaluation of rans turbulence modelling for aerodynamic applications. *Aerospace Science and Technology*, 7:493–509, 2003.

[4] RW Gent, NP Dart, and JT Cansdale. Aircraft icing. *Philosophical Transactions of the Royal Society of London A: Mathematical, Physical and Engineering Sciences*, 358(1776):2873–2911, 2000.

[5] Frank P Incropera and David P De Witt. Fundamentals of heat and mass transfer. 1985.

[6] E Iuliano, G Mingione, F Petrosino, and F Hervy. Eulerian modeling of large droplet physics toward realistic aircraft icing simulation. *Journal of Aircraft*, 48(5):1621–1632, 2011.

[7] Emiliano Iuliano, Vincenzo Brandi, Giuseppe Mingione, Carlo de Nicola, and Renato Tognaccini. Water impingement prediction on multi-element airfoils by means of eulerian and lagrangian approach with viscous and inviscid air flow. In *44th AIAA Aerospace Sciences Meeting and Exhibit*, page 1270, 2006.

[8] Emiliano Iuliano, Giuseppe Mingione, Francesco De Domenico, and Carlo de Nicola. An eulerian approach to three-dimensional droplet impingement simulation in icing environment. In *AIAA Atmospheric and Space Environments Conference*, page 7677, 2010.

[9] Johan C Kok. Resolving the dependence on freestream values for the k-Ω turbulence model. *AIAA Journal*, 38(7):1292–1295, July 2000.

[10] Chao Ma, Yi Hua Cao, and Xin Xing Chu. Ice shape prediction based on an improved thermodynamic model. In *Applied Mechanics and Materials*, volume 192, pages 63–67. Trans Tech Publ, 2012.

[11] Erdogan Madenci and Ibrahim Guven. *The Finite Element Method and Applications in Engineering Using ANSYS®*. Springer-Verlag New York, Inc., Secaucus, NJ, USA, 2007.

[12] Konstanty C. Masiulaniec and William B. Wright. User's manual for the nasa lewis ice accretion/heat transfer prediction code with electrothermal deicer input. Technical Report NASA-CR-4530, NASA, 1994.

[13] Bernard L Messinger. Equilibrium temperature of an unheated icing surface as a function of air speed. *Journal of the Aeronautical Sciences*, 1953.

[14] T.G. Myers and D.W. Hammond. Ice and water film growth from incoming supercooled droplets. *International Journal of Heat and Mass Transfer*, 42(12):2233 – 2242, 1999.

[15] M. Necati OzisiK. *Heat conduction*. John Wiley and sons, second edition edition, 1993.

[16] Guilherme Silva, Otavio Silvares, Euryale Zerbini, Hamid Hefazi, Hsun-Hu Chen, and Kalle Kaups. Differential boundary-layer analysis and runback water flow model applied to flow around airfoils with thermal anti-ice. In *1st AIAA Atmospheric and Space Environments Conference*. American Institute of Aeronautics and Astronautics (AIAA), jun 2009.

VII International Conference on Computational Methods for Coupled Problems in Science and Engineering
COUPLED PROBLEMS 2017
M. Papadrakakis, E. Oñate and B. Schrefler (Eds)

DYNAMIC RECRYSTALLIZATION OF TI-BASED MATERIALS AT CRACK SURFACES AT ELEVATED TEMPERATURES – HYBRID CELLULAR AUTOMATA SIMULATION

DMITRY D. MOISEENKO*, PAVEL V. MAKSIMOV[1], SERGEY V. PANIN[2,†], VIKTOR E. PANIN[3,†], DMITRY S. BABICH[4,††] AND SIEGFRIED SCHMAUDER[5,†††]

*,1,2,3,4 Institute of Strength Physics and Materials Science,
Russian Academy of Sciences (ISPMS SB RAS)
634055, Akademichesky 2/4, Tomsk, Russia
e-mail: moisey@rocketmail.com*, mpv@ispms.tsc.ru[1], svp@ispms.tsc.ru[2], paninve@ispms.tsc.ru[3], dmitriy18197@gmail.com[4], www.ispms.ru

†National Research Tomsk Polytechnic University,
634050, Tomsk, Lenina pr., 30, Russia
www.tpu.ru

††-Tomsk State University,
634050, Tomsk, Lenin Avenue 36, Russia
www.tsu.ru

†††Institute for Materials Testing, Materials Science and Strength of Materials (IMWF)
IMWF Universität Stuttgart, Pfaffenwaldring 32, 70569 Stuttgart, Germany
e-mail: siegfried.schmauder@imwf.uni-stuttgart.de[5], www.imwf.uni-stuttgart.de

Key words: Multiphysics Problems, Recrystallization, Thermal Shock, Computing Methods.

Abstract. In the study a Hybrid discrete-continuum Cellular Automata approach (HCA) based on coupling classical thermomechanics and logics of CA-switching to simulate new phase generation and grain growth is proposed. On the basis of the HCA the numerical experiments on thermal-activated recrystallization of pure titanium in the vicinity of crack edges were conducted. In doing so the 3D cellular automaton simulates the behavior of the V-notched specimen region that imitates the crack tip vicinity. Numerical experiments are aimed at calculating heat expansion in the material under study through taking into account thermal stresses accumulation and microrotation initiation. The latter gives rise to generation of new defects and increasing the local entropy

1 INTRODUCTION

Over the last 50 years, the rapid development of aircraft and space technology as well as ever-increasing demands for equipment in the steel industry emerge new problems for the design of materials and structures operating under extreme conditions. Among them are materials employed for manufacturing nozzles for jet engines, tuyeres and crystallizers of

blast furnaces, etc. High temperature gradients and drops, powerful thermal impacts at engine start or filling melt into the crystallizer, etc., with the regard of cyclic repetition of the processes result in catastrophic degradation of the materials used. The material structure degradation is of very complex nature and is associated with various interdependent and simultaneously developing processes. The latter are accompanied by rearrangement of the internal structure of the substrate material, cracking and spallation of the protective coating, necleation of the brittle thermal-grown oxide layer, etc.

It is well known that experimental studies of materials under extreme condition and subsequent full-scale tests of semi-ready structures are very laborious and expensive. In this regard, theoretical predictions based on computer experiments are very relevant. Hard requirements for new materials call for the necessity to design and develop new advanced methods of computer simulation of the heterogeneous media behavior under extreme loading conditions.

The above said is of particular importance at the design of steam turbine blades. Steam turbines are used in various steam power plants (coal, nuclear, oil), combined cycle power plants as well as combined heat and power plants. Titanium alloys are popular as the blade materials in steam turbines, particularly in low pressure steam turbines that are considered to most significantly affect the power output, size and efficiency of steam turbines. The most promising ways of further increasing the efficiency of steam turbines is by extending the lengths of low pressure steam turbine blades and by increasing the steam reheat temperature. However, this results in substantial centrifugal stresses on blades and rotors and creep effects. As a consequence, advanced titanium alloys and manufacturing processes are needed to design the blades with sufficient reserve strength. Moreover, one of the most significant tasks is the coupled problem of cracking and the simultaneous recrystallization process under heat loading.

Recrystallization processes being applied to materials for steam turbines have been recently very successfully simulated [1, 2]. However, due to the intricate and complexity of the theoretical research of these processes, the development of new simulation methods seems to be very relevant.

In the current research the authors propose a Hybrid discrete-continuum Cellular Automata approach (HCA) based on coupling the classical thermomechanics and logics of CA-switching to simulate new phase generation and grain growth [3]. On the basis of the HCA the numerical experiments on thermal-activated recrystallization of pure titanium in the vicinity of crack edges were conducted. In doing so, the 3D cellular automaton simulates the behavior of the V-notched specimen region that imitates the crack tip vicinity. Numerical experiments are aimed at calculating heat expansion in the material under study through taking into account thermal stresses accumulation and microrotation initiation. The latter gives rise to generation of new defects and increasing the local entropy. Every “newly-nucleated” grain has zero dislocation density, so the gradient of the latter gives rise to additional driving force for the growth of new grains (along with thermal gradient).

The current study is aimed at continuation of our previous investigations already reported at the ECCOMAS-2016 congress. In the paper we concentrated on developing a new advanced and improved modeling algorithm. The latter ensures carrying out detailed studies of the processes related to rearrangement of the internal structure at the crack tip under intensive thermal loading. It should noticed that, the next stage of this study will be related to

finding out the model parameters being correspondent to physical characteristics of the specific material and comparison of the simulation results with experimental ones.

2 SIMULATION TECHNIQUE FOR RECRYSTALLIZATION AND GENERATION OF NEW PHASE ON THE BASIS OF CELLULAR AUTOMATA

This paper is devoted to development of the new algorithm for the grain structure recrystallization with taking into account the possibility of a twin-like growth of new phase crystallites. The discrete-continuum method of heat transfer was designed by the authors earlier [4, 5]. The transfer of mechanical energy within the framework of the hybrid approach of cellular automata was reported in [6-10]. The ideas of the modeling were inspired by the results reported in the book [11] as well as papers [12, 13]. Within the framework of the HCA method, the space occupied by the simulated specimen is represented as a cellular automaton, i.e. as a set of ordered active elements. In doing so, every element imitates an immovable region of space related to particular material being characterized by the following numerical parameters: heat capacity, thermal conductivity, density, etc. Additional material parameters used in model will be described below at explanation of the algorithm details. Note that the active element of the cellular automaton itself is stationary; however mass and energy flows to take place in it gives rise to changing of its properties in time.

In order to determine the temperature of the elements, a discrete model of heat transfer in a heterogeneous medium should be introduced [4, 5]. The values of the temperature, deformation, thermal conductivity, heat capacity and coefficient of linear thermal expansion of each element are specified as initial conditions. Then, for each n-th time step, a new value of the element's temperature is calculated taking into account the heat fluxes affecting from each neighboring element:

$$T_i^n = T_i^{n-1} + \frac{1}{c_i \rho_i V} \sum_{k=1}^{N} Q_{ik}^n , \tag{1}$$

where T_i^{n-1}, T_i^n – temperatures of i-th element at n-1-th и n-th time steps, c_i – heat capacity of i-th element, ρ_i – density of i-th element, V – element volume, Q_{ik}^n – the flow of thermal energy from a neighboring element with an index k into the element under consideration with index i at n-th time step, N – the number of neighbors. Hereinafter, all upper letter indices mean the step numbering in time, unless otherwise is specified. The change in thermal energy Q_{ik}^n is calculated on the basis of the Fourier law:

$$Q_{ik}^n = \frac{\lambda_{ik} \Omega}{l} \left(T_k^{n-1} - T_i^{n-1} \right) \Delta\tau . \tag{2}$$

Here λ_{ik} – coefficient of cross heat conduction, l – distance between the centers of the elements under consideration, Ω – area of adjacent face, $\Delta\tau$ – value of the time step.

As a result of inhomogeneous thermal expansion, internal thermal stresses are accumulated in various structural elements, which in turn are transformed into flows of mechanical energy being redistributed over the mesh of the cellular automaton. Within the framework of the method, grain boundaries were explicitly taken into account including with regard of their

curvature and misorientation angles of the crystal lattice. The developed algorithms have made possible to calculate the magnitude of the local force moments, the vorticity tensor and dissipation of torsion energy through forming new defect structures. There is no detailed consideration of the algorithm subtleties for modeling of the elastic energy transportation in this paper since it was widely described earlier in [6-10].

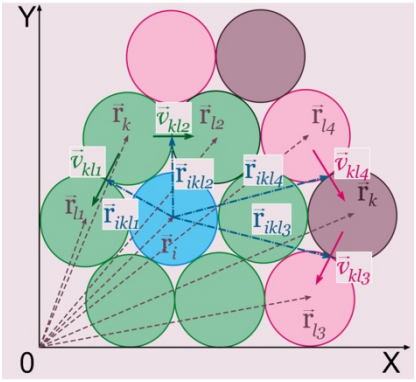

Figure1: A schematic for calculating the angular rate of material torsion for a cell automaton element

The angular velocity of the *i*-th element under the action of the matter flow through the boundary of the *k*-th and *l*-th elements (each *k*-th element is located at the 1st coordination sphere of the *i*-th, while each *l*-th – at the intersection of the 1-st coordination spheres of the *i*-th and the corresponding *k*-th elements) is calculated as follows (see Fig. 1):

$$\vec{\omega}_{ikl} = \frac{\vec{r}_{ikl} \times \vec{v}_{kl}}{\left|\vec{r}_{ikl}\right|^2}. \tag{3}$$

The matter flow velocity at the boundary of the *k*-th and *l*-th elements is calculated using the Thornbull relation:

$$\vec{v}_{kl} = m_{kl}(p_l - p_k)\vec{n}_{kl}, \tag{4}$$

where p_l, p_k – values of pressure (hydrostatic stress) in the *k*-th and *l*-th elements, $\vec{n}_{kl}$ - the vector of the normal to the boundary of the *k*-th and *l*-th elements, m_{kl} - the mobility of the boundary between the *k*-th and *l*-th elements.

The total angular velocity of the *i*-th element is defined as the following sum:

$$\vec{\omega}_i = \sum_{k=1}^{K}\sum_{l=1}^{L}\vec{\omega}_{ikl}. \tag{5}$$

Here K – the number of elements at the 1st coordination sphere of the *i*-th element, L – the number of elements at the intersection of the 1st coordination spheres of the *i*-th element and each *k*-th neighbor.

The three-dimensional rotation angle of the *i*-th element over the time $\tau(\Delta\vec{\gamma}_i)$ is proportional to the total angular velocity:

$$\Delta\vec{\gamma}_i = \vec{\omega}_i\tau. \tag{6}$$

The variation of the force moment of the *i*-th element over the time τ ($\Delta\vec{M}_i$) is calculated as follows:

$$\Delta\vec{M}_i = \frac{G\pi r_c^3 \Delta\vec{\gamma}_i}{2} = \frac{G\pi r_c^3 \vec{\omega}_i \tau}{2}. \tag{7}$$

Here G – the shear modulus of the material being contained in the *i*-th element, r_c – the radius of the element. The term being responsible for the accumulation of latent energy of defects is written as follows:

$$\left[\Delta\vec{A}_d\right]_i^n = \frac{k_{tors} G_i \left|\Delta\vec{\gamma}_i^n\right| \pi r_c^3}{2} \Delta\vec{\gamma}_i^n. \tag{8}$$

Here $\boldsymbol{k_{tors}}$ – defect accumulation rate (can be measured experimentally).

Note that the expression (8) possesses very general nature and, depending on the constructed switching rules of the cellular automaton can bring the meaning of the energy necessary to run a reversible structural-phase transformation. Then the coefficient $\boldsymbol{k_{tors}}$ can be calculated on the basis of the atomic configurations of the initial and final states.

At the first stage of the recrystallization simulation a specimen is modeled by a cellular automaton network of L active elements. The network is divided in M clusters, which are representing single grains of the material. Each *i*-th element has initial values of the temperature T_i^0, thermal energy Q_i^0, elastic energy E_i^0 and dislocation energy Θ_i^0. Each *I*-th grain is also characterized by Euler orientation angles ψ_I, φ_I, η_I. The following algorithm is proposed for the simulation of the generation and growth of new phase nuclei under thermal loading. For each element with index *i* the probability of a new grain nucleus generation inside the *I*-th grain of initial phase ($(p_{sw})_i^n$) is based on the temperature of the element T_i^n which is calculated at every time loop of the algorithm. When the temperature of certain elements reaches the critical value T_{sw1}, its probability takes a non-zero value according to the equation:

$$(p_{sw})_i^n = \begin{cases} 0, & T_i^n < T_{sw1}; \\ 2(p_{sw})_{\max} \dfrac{T_i^n - T_{sw1}}{T_{sw2} - T_{sw1}}, & T_{sw1} \le T_i^n < (T_{sw1} + T_{sw2})/2; \\ 2(p_{sw})_{\max} \dfrac{T_{sw2} - T_i^n}{T_{sw2} - T_{sw1}}, & (T_{sw1} + T_{sw2})/2 \le T_i^n < T_{sw2}; \\ 0, & T_{sw2} \le T_i^n. \end{cases} \tag{9}$$

In this case, T_{sw2} is the temperature threshold at which the probability of nucleating a new phase grain becomes equal to zero. If the element under consideration becomes a nucleation center of a new grain then all adjacent elements located at the first coordination sphere automatically join it. Thus, the grain nucleus of the new phase represents a group of elements.

The nucleation of a new grain entails a reduction of the defects density down to a minimum value for all the elements that have joined it. If this takes place the variable L being responsible for the total number of grains in the specimen is increased by 1, while the index of the new grain becomes equal to L. When all the elements of the cellular automaton have been

analyzed the growth of new grains is realized within the framework of the recrystallization algorithm being introduced by the action of the defect density gradients, thermal and elastic energy. The following calculations are performed at each *n*-th time step of the algorithm. The K_i^n parameter that is equal to the number of neighbors belonging to grains with orientation angles different from θ_I (orientation angle of the *I*-th grain containing the *i*-th element) by less than θ_{HAGB} is calculated for each *i*-th element. The probabilities of transition of *i*-th element from the current *l*-th grain in each of the grains (with the index *K*) is computed:

$$P_{ik}^n = P_{ik}^n (E_K^{n-1} - E_I^{n-1}),\ 1 \le k \le K_i^n. \tag{10}$$

First of all, the specific energy g_{IK} of the boundary between grains *I* and *K* is calculated by the following relation [11]:

$$\gamma_{IK} = \gamma_{HAGB} \frac{\theta_{IK}}{\theta_{HAGB}} \left(1 - \ln \frac{\theta_{IK}}{\theta_{HAGB}}\right), \tag{11}$$

where $\theta_{IK} = |\psi_I - \psi_K|$ - grain misorientation angle of *I*-th and *K*-th grains.

Further, according to the Turnbull equation, the grain boundary velocity is calculated:

$$v_{ik}^n = (m_{ik}^n p_{ik}^n + \hat{m}_{ik}^n \hat{p}_{ik}^n + \tilde{m}_{ik}^n \tilde{p}_{ik}^n) e^{-\frac{2\Omega\gamma_{IK}}{k_B (T_i^{n-1} + T_k^{n-1})}}, \tag{12}$$

where

$$p_{ik}^n = \frac{Q_i^{n-1} - Q_k^{n-1}}{V}, \tag{12a}$$

$$\hat{p}_{ik}^n = \frac{E_i^{n-1} - E_k^{n-1}}{V}, \tag{12b}$$

$$\tilde{p}_{ik}^n = \frac{\Theta_i^{n-1} - \Theta_k^{n-1}}{V}. \tag{12c}$$

These are the driving forces, initiated by the gradients of thermal energy, elastic energy and defect energy, correspondingly. Here m_{ik}^n - grain boundary mobility in thermal recrystallization process, $\hat{m}_{ik}^n$ - grain boundary mobility in mechanical ("cold") recrystallization process, $\tilde{m}_{ik}^n$ - grain boundary mobility in recrystallization process initiated by dislocation density gradient, Ω – area of adjacent active elements, k_B – Boltzmann's coefficient , V – the volume of single active element.

The energy of defects in *i*-th element Θ_i^n at *n*-th time loop is calculated by the following relation:

$$\Theta_i^n = -d_i \rho_i^n G_i b_i^2, \tag{13}$$

where d_i is the coefficient depending on the spatial distribution of the defects, ρ_i^n is the density of defects, G_i is shear modulus, b_i is the Burgers' vector.

When calculating the probability of the grain growth the anisotropy should be taken into account in order to allow for the specific features of the simulated processes. The former is related to the translational symmetry of the crystal which is determined by the crystalline lattice type and orientation, i.e. by directions and relative lengths of its basis vectors $\vec{a},\vec{b},\vec{c}$. The maximum relative length of the basis vector is equal to unit.

Thus, the value of the grain boundary velocity v_{ik}^n must be corrected through taking into account the relative location of the expected grain growth vector ($\vec{u}$) as well as $\vec{a},\vec{b},\vec{c}$ ones.

i) The cosine moduli of the angles between the vector $\vec{u}$ and each of the $\vec{a},\vec{b},\vec{c}$ ones are computed:

$$\begin{aligned} \alpha &= |\cos(\vec{u},\vec{a})|, \\ \beta &= |\cos(\vec{u},\vec{b})|, \\ \gamma &= |\cos(\vec{u},\vec{c})|. \end{aligned} \tag{14}$$

ii) Among the vectors $\vec{a},\vec{b},\vec{c}$, the one is chosen whose cosine with the vector $\vec{u}$ has the maximal modulus:

$$\delta = \max(\alpha,\beta,\gamma) = |\cos(\vec{u},\vec{d})|. \tag{15}$$

iii) By taking into account the anisotropy effect coefficient *k*, the value v_{ik}^n is redefined:

$$\widetilde{v}_{ik}^n = |\vec{d}\,|\, v_{ik}^n\, e^{k\cdot(\delta-1)}, \tag{16}$$

here $k >= 0$ (if $k = 0$, then the lattice anisotropy is absent). It should be stressed, that when the lattice anisotropy s absent, as well as when the vector $\vec{u}$ is co-directed with one of the lattice vectors, the grain boundary movement rate reaches its maximum value.

The switching probability P_{ik}^n of the active element is calculated by the following formula:

$$P_{ik}^n = \frac{\max(0,-v_{ik}^n)\cdot\tau}{l}, \tag{17}$$

where τ is the value of the time step. According to these probabilities, the switches of active elements occur.

When some *i*-th active element reached the necessary "level of switching", the index of state (grain index) should be found, which will become a new state of the element. Here the "level of switching" depends on the variation between the probability P_{ik}^n and random number that generated each time loop for each element.

Along with the grain that will "catch" the element, the index of neighboring active element belonging to the "catching" grain should be calculated. For this purpose one can construct some kind of membership function, which accounts for all switching probabilities P_{ik}^n:

$$f_i^n(\eta,k)=\frac{1}{2}-\frac{\left(\eta-\sum_{j=1}^{k-1}P_{ij}^n\right)\left(\eta-\sum_{j=1}^{k}P_{ij}^n\right)}{2\left|\eta-\sum_{j=1}^{k-1}P_{ij}^n\right|\left|\eta-\sum_{j=1}^{k}P_{ij}^n\right|}. \tag{18}$$

This function is equal to 1 when the random number η belongs to the interval

$$\left(\sum_{j=0}^{k-1}P_{ij}^n;\sum_{j=0}^{k}P_{ij}^n\right), \tag{18a}$$

and it is equal to zero when η is beyond the interval (10a). Moreover, when the element stays in the old grain,

$$k=K_i^n+1 \tag{18b}$$

and

$$P_{i,K_i^n+1}^n=1-\sum_{j=1}^{K_i^n}P_{ij}^n\cdot \tag{18c}$$

Summing up the aforesaid reasoning, the new state (grain index) of *i*-th element at the next time loop will be as follows:

$$Z^{n+1}=\sum_{k=1}^{K_i^n+1}k\cdot f_i^n(\eta,k)\cdot \tag{19}$$

The relation (8) makes it possible to calculate the part of the microflows energy of the material in the cell automaton element, which comes to the formation of deformation defects. From the thermodynamics point of view this means a local variation of the entropy and temperature:

$$\left[\Delta E_d\right]_i^n=T_i^{n-1}\Delta S_i^n+S_i^{n-1}\Delta T_i^n. \tag{20}$$

These relationships will be further used for the criteria of twin structures nucleation as well as subsequent failure of the material.

3 NUMERICAL EXPERIMENTS ON RECRYSTALLIZATION

On the basis of the Hybrid Cellular Automata approach numerical experiments for thermal-activated recrystallization of pure titanium near the crack edges were conducted. The 3D cellular automaton simulates the V-notched specimen region which imitates the vicinity of the crack. In this numerical experiment heat expansion in the material was taken into account along with thermal stresses accumulation and microrotation initiation. The latter gives rise to new defects generation and local entropy increase. As was mentioned above, every "newly-nucleated" grain has zero dislocation density. In doing so the dislocation density gradient initiates additional driving force of new grains growth (along with thermal gradient).

The specimen was simulated by the cellular automata with FCC (Face Centered Cubic) type packing of elements with characteristic size of 1 μm. The specimen dimensions were

$80 \times 120 \times 10$ μm^3. The initial temperature of each element was set at 300 K, the initial values of strains and stresses were equal to zero. The time step was set at 1 ns. For numerical calculation the material constants were taken being typical for pure Ti. In all the numerical experiments the inner surface of the notch was heated at temperature of 1800 K. The scheme of the numerical experiment is depicted in Fig. 2.

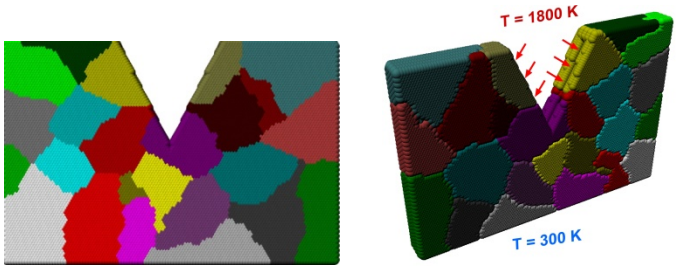

a) b)

Figure 2: Initial structure of the specimen simulated (a) and the loading scheme (b)

The figures below depict the evolution of the spatial distribution of the temperature, grain structure, elastic energy, local force moments and defect accumulation rate.

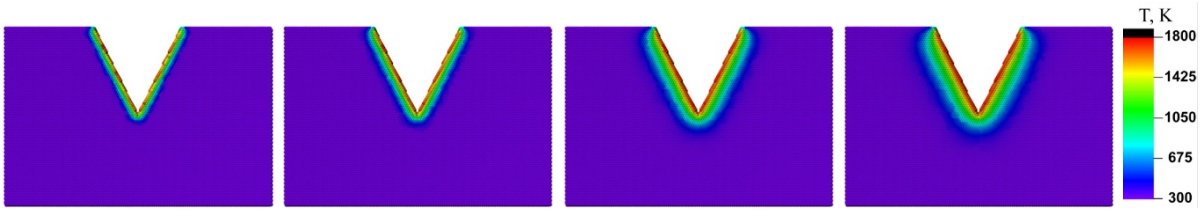

Figure 3: Evolution of the temperature field during heat loading in the vicinity of the notch tip

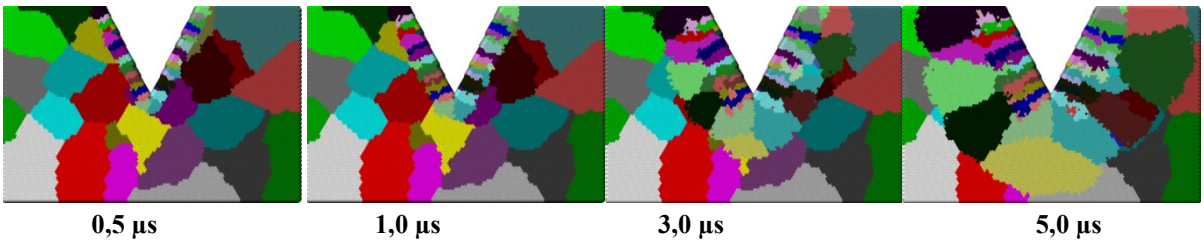

Figure 4: The patterns of grain structure at various time steps

As one can see from all the grain structure distribution patterns, a high temperature gradient gives rise to a characteristic columnar-like growth of the grain structure. The latter is directed from the region with elevated temperatures towards the cooler bulk material. Along with the nucleation and the columnar-like growth of new grains within the bulk material the growth of old ones takes place. In the framework of the current approach, the thermal expansion of the material that initiates the occurrence of thermal stresses is simulated. The inhomogeneous field of thermal stresses generates the appearance of local force moments that are the source of the crystal lattice curvature. Further, the lattice curvature is relaxed at

microrotations giving rise to the increasing defect density in the material. A detailed algorithm and simulation results of these processes are presented in [4]. Since this study is not focused on the analysis of mechanical field effect, the below described results are rather illustrative and mostly give the ideas of further development of the algorithm. It should be particularly noticed that the value of thermal stresses is estimated through the ratio of the elastic energy over the volume of the local structural element. Figure 5 illustrates the thermal stress development in the surface layer.

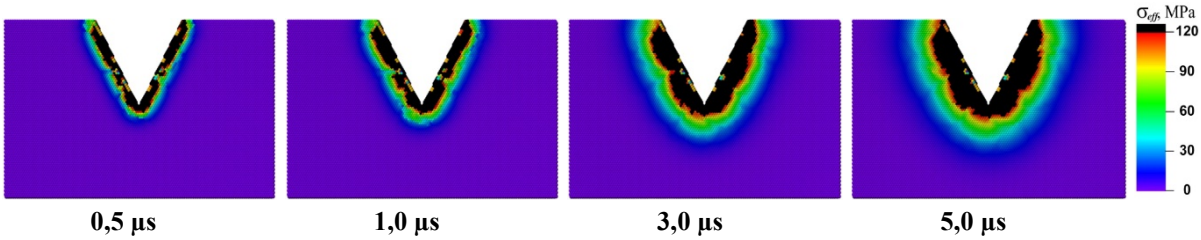

Figure 5: The evolution of the specific elastic energy at the specimen surface at various time steps

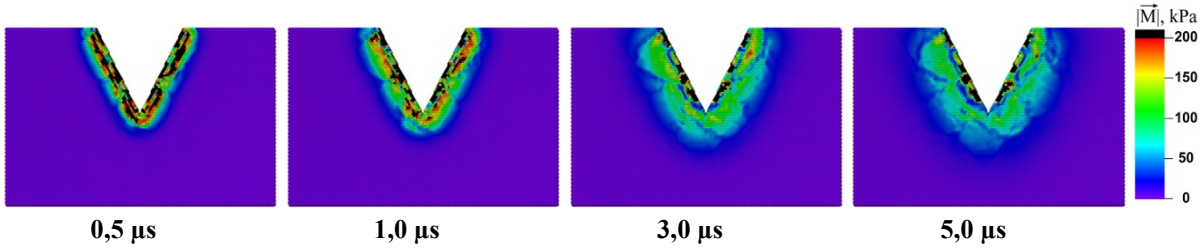

Figure 6: The spatial distribution of the specific force moments at the specimen surface

In this regard, the pattern of spatial distribution of the local force moments in the bulk specimen (Fig. 7) and its surface layer (Fig. 6) are of particular informativeness. The figures illustrate the distribution of the specific values of the local force moment being expressed in Pascals. Despite the fact that these values are three orders of magnitude lower than the level of effective stresses, it is quite enough to generate a substantial curvature of the crystalline lattice and disrupt its translational symmetry.

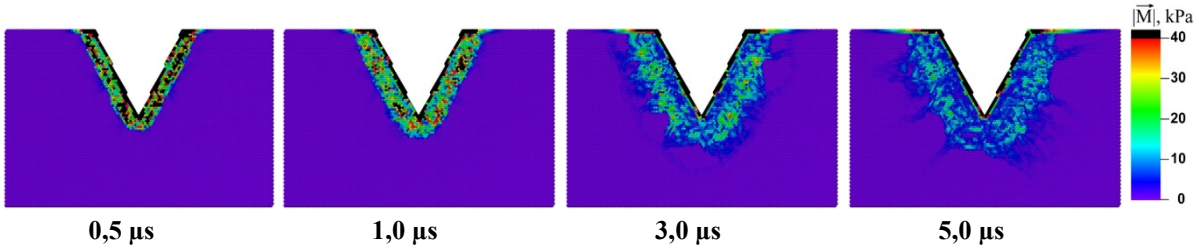

Figure 7: The spatial distribution of the specific force moments in the bulk specimen at various time steps

The spatial distribution of the ratio of the torsion energy increment over the elastic energy influx per the computational algorithm step is presented in Fig. 8. This parameter is directly related to the rate of new defective structures generation in the material.

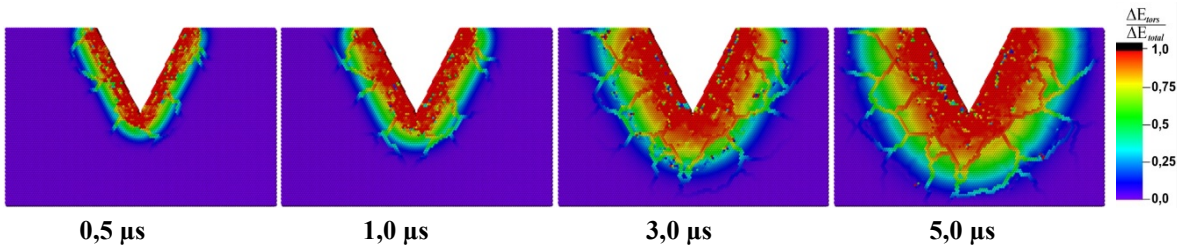

Figure 8: The evolution of the defect accumulation rate in the specimen surface layer

4 CONCLUSIONS

- The new approach of Cellular Automata for the grain structure recrystallization simulation was developed with taking into account the possibility of a twin-like growth of new phase crystallites. The method combines CA-switching mechanisms for structure transformation simulation, classical thermal transfer and such mechanical effects, as thermal expansion and defect generation.
- It was shown that the material adjacent to the crack sides undergoes the changing of its crystal structure. The new grains are generated at the crack sides and grow to form column-like patterns to replace the initial grain structure. This fact results in significant local variation of all mechanical properties of the material. This study is a starting point for developing the algorithms to simulate deformation behavior of turbine blades containing fatigue cracks.
- It is shown that in the mostly heated regions of the specimen not only the nucleation of the new crystalline structure occurs, but the fraction of the elastic torsion energy increase is also very high. Under such conditions, the probability of twin structure nucleation is very high due to the deformation development by the torsion mechanism. The development twinning models will be the matter of the studies in the series of upcoming works.

ACKNOWLEDGEMENTS

The study was conducted under partial support of the project DFG Schm/746-191-1 by the Deutsche Forschungsgemeinschaft and fundamental Research Program of Russian State Academies of Sciences for 2013-2020.

REFERENCES

[1] Ren, F., Chen F., and Chen, J. Investigation on Dynamic Recrystallization Behavior of Martensitic Stainless Steel. *Advances in Materials Science and Engineering* (2014) **2014**: ID 986928.

[2] Wang, Y., Shao, W. Z., Zhen, L., Lin, L. and Cui, Y.X. Investigation on Dynamic Recrystallization Behavior in Hot Deformed Superalloy Inconel 718. *Materials Science Forum* (2007) **546-549**:1297-1300.

[3] Panin, V.E., Egorushkin, V.E., Moiseenko, D.D., Maksimov, P.V., Kulkov, S.N. and Panin, S.V. Functional role of polycrystal grain boundaries and interfaces in micromechanics of metal ceramic composites under loading. *Comput. Mater. Sci*. (2016) **116:**74–81.

[4] Moiseenko, D.D., Maksimov, P.V., Panin, S.V. and Panin, V.E. Defect Accumulation in Nanoporous Wear-Resistant Coatings Under Collective Recrystallization. Simulation by Hybrid Cellular Automaton Method. *Proceedings of VII European Congress on Computational Methods in Applied Sciences and Engineering, Crete Island, Greece, 5–10 June 2016 (Eds.: M. Papadrakakis, V. Papadopoulos, G. Stefanou, V. Plevris)*, **1**:2080 – 2098.

[5] Moiseenko, D.D., Panin, S.V., Maksimov, P.V., Panin, V.E. and Berto, F. Behavior of nanoporous thermal barrier coatings under cyclic thermal loading. Computer-aided simulation. *AIP Conference Proceedings* (2015) **1683**:020152.

[6] Moiseenko, D.D., Panin, V.E. and Elsukova, T.F. Role of local curvature in grain boundary sliding in a deformed polycrystal. *Phys. Mesomech.* (2013) **16:**335-347

[7] Moiseenko, D.D., Pochivalov, Yu.I., Maksimov, P.V. and Panin V.E. Rotational Deformation Modes in Near-Boundary Regions of Grain Structure in a Loaded Polycrystal. *Phys. Mesomech.* (2013) **16:**248-258

[8] Panin, S.V., Vinogradov, A., Moiseenko, D.D., Maksimov, P.V., Berto, F., Byakov, A.V., Eremin, A.V. and Narkevich N.A. Numerical and experimental study of strain localization in notched specimens of a ductile steel on meso- and macroscales. *Advanced Engineering Materials* (2016) **18:**2095-2106.

[9] Moiseenko, D.D., Panin, V.E., Maksimov, P.V., Panin, S.V. and Berto, F. Material fragmentation as dissipative process of micro rotation sequence formation: hybrid model of excitable cellular automata. *AIP Conference Proceedings* (2014) **1623**:427-430.

[10] Moiseenko, D.D., Panin, S.V., Maksimov, P.V., Panin, V.E., Babich, D.S. and Berto, F. Computer simulation of material behavior at the notch tip: Effect of microrotations on elastic energy release. *AIP Conference Proceedings* (2016) **1783:**020157

[11] Humphreys, F.J., Hatherly, M. Recrystallization and Related Annealing Phenomena., Pergamon New York (1995)

[12] Kroc, J. Application of cellular automata simulations to modelling of dynamic recrystallization. *Lecture Notes in Computer Science* (2002) **2329**:773-782.

[13] Godara, A. and Raabe, D. Mesoscale simulation of the kinetics and topology of spherulite growth during crystallization of isotactic polypropylen (iPP) by using a cellular automaton. *Modelling Simulation Materials Science Engineering* (2005) **13**:733-751.

VII International Conference on Computational Methods for Coupled Problems in Science and Engineering
COUPLED PROBLEMS 2017
M. Papadrakakis, E. Oñate and B. Schrefler (Eds)

HOMOGENIZATION OF THE FLUID-SATURATED PIEZOELECTRIC POROUS METAMATERIALS

Eduard Rohan*, Vladimír Lukeš* and Robert Cimrman†

* European Centre of Excellence, NTIS – New Technologies for Information Society Faculty of Applied Sciences, University of West Bohemia, Univerzitní 8, 30614 Pilsen, Czech Republic
rohan@kme.zcu.cz

† New Technologies Research Centre, University of West Bohemia, Univerzitní 8, 30614 Pilsen, Czech Republic cimrman3@ntc.zcu.cz

Key words: Multiscale modelling, Piezoelectric material, Porous media, Homogenization, Sensitivity analysis, Nonlinear problems

Abstract. The paper is devoted to the homogenization approach in modelling of periodic porous media constituted by piezoelectric porous skeleton with pores saturated by viscous fluid. The representative volume element contains the piezoelectric solid part (the matrix) and the fluid saturated pores (the channels). Both the matrix and the channels form connected subdomains. The mathematical model describing the material behaviour at the microscopic scale involves the quasi-static equilibrium equation governing the solid piezoelectric skeleton, the Stokes model of the viscous fluid flow in the channels and the coupling interface conditions on the transmission interface. The macroscopic model is derived using the unfolding method of homogenization. The effective material coefficients are computed using characteristic responses of the porous microstructure. The constitutive law for the upscaled piezo-poroelastic material involves a coefficient coupling the electric field and the pore pressure. A numerical example illustrates different responses of the porous medium subject to the drained and undrained loadings

1 INTRODUCTION

The piezoelectric effects which couple the mechanical deformation and the electrical field have been extensively used in the design of transducers and sensors. The piezoelectric materials have found wast applications in electronics, mechatronics, and micro-system technology. Smart structures based on these materials allow for intelligent self-monitoring and self-control capabilities. Nowadays the piezoelectric sensor-actuator systems can be distributed continuously, being attached to the surface of other structural parts. Such an arrangement can be used *e.g.* in the aerospace industry to control vibrations, or acoustic radiation of thin flexible structures. In the context of porous piezoelectric materials, the

acoustic wave propagation has been subject of several works [10]. In [4] we suggested to exploit the piezoelectric effect in the design of a new type of bio-materials which should assist in bone healing and regeneration. Such possible application for piezoelectric materials in biomedical engineering is motivated by the electrochemical processes in biological tissues, being coupled tightly with periodic mechanical loading. In [7], the shape sensitivity formulae were derived for a class of 2D microstructures comprising one piezoelectric and one arbitrary elastic material, whereby the shape of the interface between the two materials was parameterized. The numerical tests have shown how a suitable geometry of the interface can amplify some of the homogenized coefficients. Sensitivity of the effective medium properties to the microsrtucture properties were also reported in [9].

This paper is focused on the derivation of the effective material coefficients of the fluid-saturated porous media with the piezoelectric skeleton. Although this topic was treated recently in [3], where a special type of piezoelectric anisotropic composite materials was studied using numerical and analytical methods and the porosity influence was examined, we pursue another homogenization approach which was reported in [6]. Assuming a quasistatic loading, such that inertia effects can be neglected, by a decomposed homogenization of the fluid-structure interaction problem we obtain a macroscopic model of the upscaled medium. Here we present only the resulting equations governing the local problems for computing the characteristic responses which are used to evaluate all the homogenized coefficients involved in the constitutive law. A numerical example is included to demonstrate the influence of the pore fluid on the overall response of the upscaled porous piezoelectric medium.

Notations We employ standard bold-face notations for tensors and vectors, alternatively the Einstein summation convention is used. The Lebesgue spaces of 2nd-power integrable functions on a domain D is denoted by $L^2(D)$, the Sobolev space $\boldsymbol{W}^{1,2}(D)$ of the square integrable vector-valued functions on D including the 1st order generalized derivative, is abbreviated by $\mathbf{H}^1(D)$. Further, $H^1_\#(Y_m)$ and $\mathbf{H}^1_\#(Y_m)$ are the Sobolev spaces of scalar and vector-valued Y-periodic functions (the subscript #), respectively, with vanishing mean in Y_m.

2 HOMOGENIZED MODEL OF POROUS PIEZOELECTRIC MATERIAL

The poroelastic medium occupies an open bounded domain $\Omega \subset \mathbb{R}^3$ whereby the following decomposition of Ω into the matrix and channel parts is considered: $\Omega = \Omega^\varepsilon_m \cup \Omega^\varepsilon_c \cup \Gamma^\varepsilon$, $\Omega^\varepsilon_m \cap \Omega^\varepsilon_c = \emptyset$, where $\Gamma^\varepsilon = \overline{\Omega^\varepsilon_m} \cap \overline{\Omega^\varepsilon_c}$ is the interface. By $\partial_{\rm ext}\Omega^\varepsilon_m = \partial\Omega^\varepsilon_m \setminus \Gamma^\varepsilon$ and $\partial_{\rm ext}\Omega^\varepsilon_c = \partial\Omega^\varepsilon_c \setminus \Gamma^\varepsilon$ we denote the exterior boundaries of Ω^ε_m and Ω^ε_c, respectively. Both Ω^ε_m and Ω^ε_c are connected domains generated by the representative periodic cell $Y = \Pi_{i=1}^3]0, \bar{y}_i[\subset \mathbb{R}^3$ which splits into the solid part occupying domain Y_m and the complementary channel part Y_c, thus

$$Y = Y_m \cup Y_c \cup \Gamma_Y \,, \quad Y_c = Y \setminus Y_m \,, \quad \Gamma_Y = \overline{Y_m} \cap \overline{Y_c} \,. \tag{1}$$

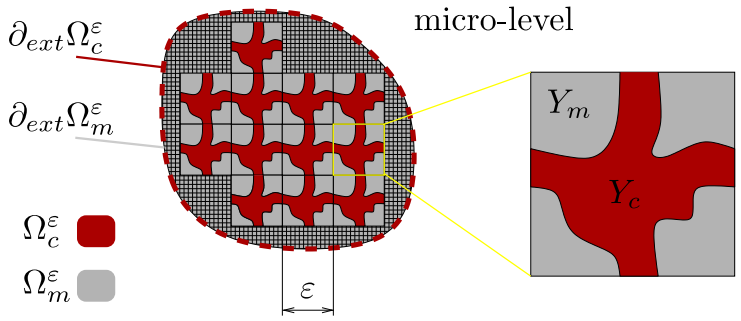

Figure 1: Porous periodic structure in domain Ω is generated using the reference cell Y.

For a given scale, $\ell_i = \varepsilon \bar{y}_i$ is the characteristic size (associated with the i-th coordinate direction, whereby also $\varepsilon \approx \ell_i/L$ for a given macroscopic characteristic length. Below we describe two separate problems which can be upscaled independently, if the inertia effects are neglected:

- steady states of the porous piezoelectric solid saturated by static fluid,
- the Stokes flow in the pores of the undeformed configuration.

2.1 Porous piezoelectric solid saturated by static fluid

We consider the static problem of a deformed piezo-elastic porous structure saturated by a fluid under a constant pressure, whereby the pores are assumed to be connected. In the piezoelectric solid, the Cauchy stress tensor $\boldsymbol{\sigma}^\varepsilon$ and the electric displacement $\vec{D}^\varepsilon$ depend on the strain tensor $\boldsymbol{e}(\boldsymbol{u}^\varepsilon) = (\nabla \boldsymbol{u}^\varepsilon + (\nabla \boldsymbol{u}^\varepsilon)^T)/2$ defined in terms of displacement field $\boldsymbol{u}^\varepsilon = (u_i^\varepsilon)$, and the electric field $\boldsymbol{E}(\varphi^\varepsilon) = \nabla \varphi^\varepsilon$ defined in terms of the electric potential φ^ε, where we adhere to the sign convention employed in [4],

$$\begin{aligned} \sigma_{ij}^\varepsilon(\boldsymbol{u}^\varepsilon, \varphi^\varepsilon) &= A_{ijkl}^\varepsilon e_{kl}^\varepsilon(\boldsymbol{u}^\varepsilon) - g_{kij}^\varepsilon \partial_k \varphi^\varepsilon \ , \\ D_k^\varepsilon(\boldsymbol{u}^\varepsilon, \varphi^\varepsilon) &= g_{kij}^\varepsilon e_{ij}^\varepsilon(\boldsymbol{u}^\varepsilon) + d_{kl}^\varepsilon \partial_l \varphi^\varepsilon \ . \end{aligned} \tag{2}$$

Above, $\mathbb{A}^\varepsilon = (A_{ijkl}^\varepsilon)$ is the elasticity fourth-order symmetric positive definite tensor of the solid, *i.e.* $A_{ijkl} = A_{klij} = A_{jilk}$, the deformation is coupled with the electric field through the 3rd order tensor $\boldsymbol{g}^\varepsilon = (g_{kij}^\varepsilon)$, $g_{kij}^\varepsilon = g_{kji}^\varepsilon$ and $\boldsymbol{d} = (d_{kl})$ is the permitivity tensor.

The state of the solid skeleton is governed by the following boundary value problem involving $\boldsymbol{u}^\varepsilon, \varphi^\varepsilon$ and the static fluid pressure p^ε:

- equilibrium of the stress and electric displacements,

$$\begin{aligned} -\nabla \cdot \boldsymbol{\sigma}^\varepsilon(\boldsymbol{u}^\varepsilon, \varphi^\varepsilon) &= \boldsymbol{f}^\varepsilon \ , \quad \text{in } \Omega_m^\varepsilon \ , \\ -\nabla \cdot \vec{D}^\varepsilon(\boldsymbol{u}^\varepsilon, \varphi^\varepsilon) &= q_E^\varepsilon \ , \quad \text{in } \Omega_m^\varepsilon \ , \end{aligned} \tag{3}$$

  where $\boldsymbol{f}^\varepsilon$ is the volume-force and q_E^ε is the volume electric charge;

- mass conservation (change of fluid and solid volume due to fluid injection $-J^\varepsilon$)

$$\int_{\partial\Omega_c^\varepsilon} \boldsymbol{u}^\varepsilon \cdot \boldsymbol{n}^{[c]} \,\mathrm{dS}_x + \gamma p^\varepsilon |\Omega_c^\varepsilon| = -J^\varepsilon \,, \tag{4}$$

  where γ is the fluid compressibility;

- boundary and interface conditions,

$$\begin{aligned} \boldsymbol{n}^{[m]} \cdot \boldsymbol{\sigma}^\varepsilon(\boldsymbol{u}^\varepsilon, \varphi^\varepsilon) &= \boldsymbol{h}^\varepsilon \,, \quad \text{on } \partial_{\mathrm{ext}}\Omega_m^\varepsilon \,, \\ \boldsymbol{n}^{[m]} \cdot \boldsymbol{\sigma}^\varepsilon(\boldsymbol{u}^\varepsilon, \varphi^\varepsilon) &= -p^\varepsilon \boldsymbol{n}^{[m]} \,, \quad \text{on } \Gamma^\varepsilon \,, \\ \boldsymbol{n}^{[m]} \cdot \vec{D}^\varepsilon(\boldsymbol{u}^\varepsilon, \varphi^\varepsilon) &= \varrho_E^\varepsilon \,, \quad \text{on } \partial_{\mathrm{ext}}\Omega_m^\varepsilon \,, \\ \boldsymbol{n}^{[m]} \cdot \vec{D}^\varepsilon(\boldsymbol{u}^\varepsilon, \varphi^\varepsilon) &= 0 \,, \quad \text{on } \Gamma^\varepsilon \,, \end{aligned} \tag{5}$$

  where $\boldsymbol{n}^{[m]}$ is the outer unit normal vector of the boundary Ω_m^ε, $\boldsymbol{h}^\varepsilon$ and ϱ_E^ε are the applied surface-forces and the surface electric charge, respectively. Obviously, for these conditions $\boldsymbol{u}^\varepsilon$ is determined up to a rigid body motion from the space $\mathrm{RBM}(\Omega_m^\varepsilon)$, and φ^ε up to a constant, provided solvability conditions are satisfied.

To obtain the effective material coefficients describing the piezo-poroelastic material in the limit for $\varepsilon \to 0$, the homogenization method is applied to the weak formulation of the problem (2)-(5) which reads, as follows: Find $(\boldsymbol{u}^\varepsilon, \varphi^\varepsilon, \bar{p}^\varepsilon) \in \mathbf{H}^1(\Omega_m^\varepsilon)/\mathrm{RBM}(\Omega_m^\varepsilon) \times H^1(\Omega_m^\varepsilon) \times \mathbb{R}$ such that:

$$\begin{aligned} &\int_{\Omega_m^\varepsilon} [\mathbb{A}^\varepsilon \boldsymbol{e}(\boldsymbol{u}^\varepsilon) - (\boldsymbol{g}^\varepsilon)^T \cdot \nabla\varphi^\varepsilon] : \boldsymbol{e}(\boldsymbol{v}) \,\mathrm{dV} + \bar{p}^\varepsilon \int_{\Gamma^\varepsilon} \boldsymbol{n}^{[m]} \cdot \boldsymbol{v} \,\mathrm{dS}_x = \int_{\partial_{\mathrm{ext}}\Omega_m^\varepsilon} \boldsymbol{h}^\varepsilon \cdot \boldsymbol{v} \,\mathrm{dS}_x + \int_{\Omega_m^\varepsilon} \boldsymbol{f}^\varepsilon \cdot \boldsymbol{v} \,\mathrm{dV} \,, \\ &\int_{\Omega_m^\varepsilon} [\boldsymbol{g}^\varepsilon : \boldsymbol{e}(\boldsymbol{u}^\varepsilon) + \boldsymbol{d}^\varepsilon \cdot \nabla\varphi^\varepsilon] \cdot \nabla\psi = \int_{\Omega_m^\varepsilon} q_E^\varepsilon \psi \,\mathrm{dV} + \int_{\partial_{\mathrm{ext}}\Omega_m^\varepsilon} \varrho_E^\varepsilon \psi \,\mathrm{dS}_x \,, \\ &\int_{\partial\Omega_c^\varepsilon} \widetilde{\boldsymbol{u}^\varepsilon} \cdot \boldsymbol{n}^{[c]} \,\mathrm{dS}_x + \gamma^\alpha \bar{p}^\varepsilon |\Omega_c^\varepsilon| = -J^\varepsilon \,, \end{aligned} \tag{6}$$

for all $(\boldsymbol{v}, \psi) \in \mathbf{H}^1(\Omega_m^\varepsilon) \times H^1(\Omega_m^\varepsilon)$.

2.2 Stokes flow through rigid porous structure

As pointed out above, the quasistatic viscous flow in the pores can be upscaled separately of the deformation problem. The steady flow problem through the channel network constituting domain Ω_c^ε is defined in terms of the flow velocity $\boldsymbol{w}^\varepsilon$ and pressure p^ε which satisfy the following equations:

$$\begin{aligned} -\eta^\varepsilon \nabla^2 \boldsymbol{w}^\varepsilon + \nabla p^\varepsilon &= \boldsymbol{f}^\varepsilon \,, \quad \text{in } \Omega_c^\varepsilon \,, \\ \nabla \cdot \boldsymbol{w}^\varepsilon &= 0 \,, \quad \text{in } \Omega_c^\varepsilon \,, \\ \boldsymbol{w}^\varepsilon &= 0 \,, \quad \text{on } \Gamma^\varepsilon \,, \\ -p^\varepsilon \boldsymbol{n}^{[c]} + \eta^\varepsilon \boldsymbol{n}^{[c]} \cdot \nabla \boldsymbol{w}^\varepsilon &= \boldsymbol{g}^\varepsilon \,, \quad \text{on } \partial_{\mathrm{ext}}\Omega_c^\varepsilon \,, \end{aligned} \tag{7}$$

where $\boldsymbol{g}^\varepsilon$ is given on the exterior boundary of the channels. It is worth to remark that $\boldsymbol{w}^\varepsilon$ describes the relative velocity of the fluid w.r.t. the solid phase.

By virtue of the small viscosity ansatz [1] we define $\eta^\varepsilon = \varepsilon^2\bar{\eta}$ which decreases with the scale. As discussed *e.g.* in [2], this viscosity scaling applies when the pores are small, so that an internal length scale characterizing the velocity profile in the pores is preserved in the limit $\varepsilon \to 0$.

3 The homogenized poroelastic model

The homogenization methods based on the two scale convergence or the unfolding operator techniques can be applied to describe the limit models arising from asymptotic analyses of the problems (6) and (7) for $\varepsilon \to 0$, cf. [8]. A consistent result has been obtained e.g. in [5].

In this short paper, we merely present the local problems for the so-called characteristic responses describing local fluctuations of the involved fields; the detail derivation of the upscaled model will be published in a forthcoming paper.

3.1 Local problems

We shall use the following bilinear forms:

$$\begin{aligned} a_Y^m(\boldsymbol{u},\,\boldsymbol{v}) &= |Y|^{-1}\int_{Y_m}[\mathbb{A}\boldsymbol{e}_y(\boldsymbol{u})] : \boldsymbol{e}_y(\boldsymbol{v})\;, \\ g_Y^m(\boldsymbol{u},\,\psi) &= |Y|^{-1}\int_{Y_m} g_{kij}e_{ij}^y(\boldsymbol{u})\partial_k^y\psi\;, \\ d_Y^m(\varphi,\,\psi) &= |Y|^{-1}\int_{Y_m}[\boldsymbol{d}\nabla_y\varphi]\cdot\nabla_y\psi\;. \end{aligned} \tag{8}$$

By $\fint_D = |Y|^{-1}\int_D$ with $D \subset \overline{Y}$ we denote the local average. We employ $\boldsymbol{\Pi}^{ij} = (\Pi_k^{ij})$, $i,j,k = 1,2,3$ with components $\Pi_k^{ij} = y_j\delta_{ik}$.

The local microstructural response is obtained by solving the following decoupled problems for the characteristic responses $(\boldsymbol{\omega},\vartheta)$ associated with the macroscopic variables: strain, electric field and the pore pressure.

- Find the strain correctors $(\boldsymbol{\omega}^{ij},\vartheta^{ij}) \in \mathbf{H}^1_\#(Y_m)\times H^1_\#(Y_m)$ for any $i,j = 1,2,3$ satisfying

$$\begin{aligned} a_Y^m\left(\boldsymbol{\omega}^{ij}+\boldsymbol{\Pi}^{ij},\,\boldsymbol{v}\right) - g_Y^m\left(\boldsymbol{v},\,\vartheta^{ij}\right) &= 0\;, \quad \forall\boldsymbol{v}\in\mathbf{H}^1_\#(Y_m)\;, \\ g_Y^m\left(\boldsymbol{\omega}^{ij}+\boldsymbol{\Pi}^{ij},\,\psi\right) + d_Y^m\left(\vartheta^{ij},\,\psi\right) &= 0\;, \quad \forall\psi\in H^1_\#(Y_m)\;, \end{aligned} \tag{9}$$

- Find the electric field correctors $(\boldsymbol{\omega}^k,\vartheta^k) \in \mathbf{H}^1_\#(Y_m)\times H^1_\#(Y_m)$ for any $k = 1,2,3$ satisfying

$$\begin{aligned} a_Y^m\left(\boldsymbol{\omega}^k,\,\boldsymbol{v}\right) - g_Y^m\left(\boldsymbol{v},\,\vartheta^k+y_k\right) &= 0\;, \quad \forall\boldsymbol{v}\in\mathbf{H}^1_\#(Y_m)\;, \\ g_Y^m\left(\boldsymbol{\omega}^k,\,\psi\right) + d_Y^m\left(\vartheta^k+y_k,\,\psi\right) &= 0\;, \quad \forall\psi\in H^1_\#(Y_m)\;, \end{aligned} \tag{10}$$

- Find pore fluid pressure correctors $(\boldsymbol{\omega}^P, \vartheta^P) \in \mathbf{H}^1_{\#}(Y_m) \times H^1_{\#}(Y_m)$ satisfying

$$\begin{aligned} a_Y^m\left(\boldsymbol{\omega}^P,\, \boldsymbol{v}\right) - g_Y^m\left(\boldsymbol{v},\, \vartheta^P\right) &= \fint_{\Gamma_Y} \boldsymbol{v}\cdot\boldsymbol{n}^{[m]}\,\mathrm{dS}_y\;, \quad \forall \boldsymbol{v}\in\mathbf{H}^1_{\#}(Y_m)\;,\\ g_Y^m\left(\boldsymbol{\omega}^P,\, \psi\right) + d_Y^m\left(\vartheta^P,\, \psi\right) &= 0\;, \quad \forall \psi\in H^1_{\#}(Y_m)\;, \end{aligned} \tag{11}$$

3.2 Macroscopic model of the static piezo-poroelastic medium

Using the characteristic responses (9)–(11) obtained at the microscopic scale, the homogenized coefficients describing the effective properties of the deformable porous medium are given by the following expressions:

$$\begin{aligned} A^H_{klij} &= a_Y^m\left(\boldsymbol{\omega}^{ij}+\boldsymbol{\Pi}^{ij},\, \boldsymbol{\omega}^{kl}+\boldsymbol{\Pi}^{kl}\right) + d_Y^m\left(\vartheta^{kl},\, \vartheta^{ij}\right)\;,\\ B^H_{ij} &= a_Y^m\left(\boldsymbol{\omega}^P,\, \boldsymbol{\Pi}^{ij}\right) - g_Y^m\left(\boldsymbol{\Pi}^{ij},\, \vartheta^P\right) = -\fint_{Y_m} \mathrm{div}_y\boldsymbol{\omega}^{ij}\;,\\ M^H &= a_Y^m\left(\boldsymbol{\omega}^P,\, \boldsymbol{\omega}^P\right) + d_Y^m\left(\vartheta^P,\, \vartheta^P\right)\;,\\ D^H_{kl} &= d_Y^m\left(\vartheta^l + y_l,\, \vartheta^k + y_k\right) + a_Y^m\left(\boldsymbol{\omega}^k,\, \boldsymbol{\omega}^l\right)\;,\\ G^H_{kij} &= g_Y^m\left(\boldsymbol{\Pi}^{ij},\, \vartheta^k + y_k\right) - a_Y^m\left(\boldsymbol{\omega}^k,\, \boldsymbol{\Pi}^{ij}\right) = g_Y^m\left(\boldsymbol{\omega}^{kl}+\boldsymbol{\Pi}^{kl},\, y_k\right) + d_Y^m\left(\vartheta^{ij},\, y_k\right)\;,\\ F_i &= \fint_{\Gamma_Y} \boldsymbol{\omega}^i\cdot\boldsymbol{n}^{[m]}\,\mathrm{dS}_y = g_Y^m\left(\boldsymbol{\omega}^P,\, y_i\right) + d_Y^m\left(\vartheta^P,\, y_i\right)\;. \end{aligned} \tag{12}$$

Further we define:

$$\hat{B}_{ij} = B^H_{ij} + \phi\delta_{ij}\;, \qquad \hat{M} = M^H + \gamma\phi\;. \tag{13}$$

The macroscopic problem reads, as follows: Find $(\boldsymbol{u}^0, \varphi^0) \in \mathbf{H}^1(\Omega)/\mathrm{RBM}(\Omega)\times H^1(\Omega)/\mathbb{R}$ and $\bar{p}\in\mathbb{R}$, such that

$$\begin{aligned} &\int_\Omega [\mathbb{A}^H\boldsymbol{e}(\boldsymbol{u}^0) - (\underline{\boldsymbol{G}}^H)^T\nabla\varphi^0 - \bar{p}\hat{\boldsymbol{B}}] : \boldsymbol{e}(\boldsymbol{v}^0)\,\mathrm{dV} = \int_\Omega \hat{\boldsymbol{f}}\cdot\boldsymbol{v}^0\;\mathrm{dV} + \int_{\partial\Omega}\overline{\boldsymbol{h}}(\bar{p})\cdot\boldsymbol{v}^0\,\mathrm{dS}_x\;,\\ &\int_\Omega [\underline{\boldsymbol{G}}^H\boldsymbol{e}(\boldsymbol{u}^0) + \boldsymbol{D}^H\nabla\varphi^0 - \underline{F}\bar{p}]\cdot\nabla\psi^0\,\mathrm{dV} = \int_\Omega \hat{q}_E\psi^0\,\mathrm{dV} + \int_{\partial\Omega}\overline{\varrho_E}\psi^0\,\mathrm{dS}_x\;,\\ &\int_\Omega \left(\hat{\boldsymbol{B}} : \boldsymbol{e}(\boldsymbol{u}^0) - \underline{F}\cdot\nabla\varphi^0 + \hat{M}\bar{p}\right)\,\mathrm{dV} = -J\;, \end{aligned} \tag{14}$$

for all $(\boldsymbol{v}^0, \psi^0) \in \mathbf{H}^1(\Omega)\times H^1(\Omega)$.

To conclude this section, we write the effective constitutive equations for the upscaled porous piezoelectric material:

$$\begin{aligned} \boldsymbol{\sigma}^H &= \mathbb{A}^H\boldsymbol{e}(\boldsymbol{u}) - (\underline{\boldsymbol{G}}^H)^T\nabla\varphi - p\hat{\boldsymbol{B}}\;,\\ \vec{D} &= \underline{\boldsymbol{G}}^H\boldsymbol{e}(\boldsymbol{u}) + \boldsymbol{D}^H\nabla\varphi - \underline{F}p\;,\\ -p &= \frac{1}{\hat{M}}\left(\hat{\boldsymbol{B}} : \boldsymbol{e}(\boldsymbol{u}) - \underline{F}\cdot\nabla\varphi + j\right)\;, \end{aligned} \tag{15}$$

where j is the local fluid volume production in the porous material; in fact $j = \nabla\cdot\boldsymbol{w}$, where $\boldsymbol{w}$ is the seepage velocity. As the consequence of (15), the pressure can be eliminated from $(15)_{1,2}$, so that

$$\begin{aligned} \boldsymbol{\sigma}^H &= \hat{\mathbb{A}}^H \boldsymbol{e}(\boldsymbol{u}) - (\hat{\underline{\boldsymbol{G}}}^H)^T \nabla\varphi + \hat{M}^{-1}\hat{\boldsymbol{B}} j \ , \\ \vec{D} &= \hat{\underline{\boldsymbol{G}}}^H \boldsymbol{e}(\boldsymbol{u}) + \hat{\boldsymbol{D}}^H \nabla\varphi + \hat{M}^{-1}\underline{F} j \ , \end{aligned} \tag{16}$$

where

$$\begin{aligned} \hat{\mathbb{A}}^H &= \mathbb{A}^H + \hat{M}^{-1}\hat{\boldsymbol{B}}\otimes\hat{\boldsymbol{B}} \quad \text{undrained elasticity} \ , \\ \hat{\boldsymbol{D}}^H &= \boldsymbol{D}^H - \hat{M}^{-1}\underline{F}\otimes\underline{F} \quad \text{undrained dielectricity} \ , \\ \hat{\underline{\boldsymbol{G}}}^H &= \underline{\boldsymbol{G}}^H + \hat{M}^{-1}\underline{F}\hat{\boldsymbol{B}} \quad \text{undrained piezoelectric coupling} \ . \end{aligned} \tag{17}$$

The upscaled piezoelectric effect incorporates the electric field induced by increasing the fluid pressure, or fluid contents in the pores. Let us consider injection of a fluid under the pressure $\bar{p}$ into the porous structure such that the macroscopic deformation is disabled. If $\vec{D} = \vec{0}$ (insulated boundary and no volume charge), then the following electric field is established (the fluid content increased by j, see (16))

$$\nabla\varphi = (\boldsymbol{D}^H)^{-1}\underline{F}\bar{p} \ , \ \text{or} \ \nabla\varphi = -(\hat{M}\hat{\boldsymbol{D}}^H)^{-1}\underline{F} j \ . \tag{18}$$

4 Flow in the homogenized fluid-saturated piezo-poroelastic medium

As mentioned earlier, if the inertia effects are neglected, the upscaling result can be obtained in two independent steps. From (14), we obtain the mathematical model describing the static response of the medium, thus no flow occurs. Then, the effective flow of an electrically neutral fluid in the porous material governed by the Darcy law involving the intrinsic hydraulic permeability $\boldsymbol{K}^H$ and the fluid viscosity $\bar{\eta}$. In (14), the last equality can be interpreted locally. Let $p(t,x)$ be the local pressure and $\boldsymbol{w}(t,x)$ the effective flow seepage velocity describing the relative effective fluid velocity w.r.t. the solid skeleton, *i.e.* $\boldsymbol{w} = \phi(\boldsymbol{v}^f - \dot{\boldsymbol{u}})$, where $\boldsymbol{v}^f$ is the mean fluid velocity. Then from $(14)_3$, dropping the superscripts ^{0}, we can derive the following equation:

$$\hat{\boldsymbol{B}} : \boldsymbol{e}(\dot{\boldsymbol{u}}) - \underline{F}\cdot\nabla\dot{\varphi} + \hat{M}\dot{p} + \nabla\cdot\boldsymbol{w} = 0 \ , \ \text{where} \quad \boldsymbol{w} = -\bar{\eta}^{-1}\boldsymbol{K}^H\nabla p \ . \tag{19}$$

The Darcy flow model is the classical result, obtained upon homogenizing the Stokes problem (7), see *e.g.* [1, 2].

Below we present the problem describing the viscous flow in the piezo-poroelastic medium characterized by the effective model parameters (12) and (13). To introduce boundary conditions for the coupled problem, we need the following 3 decompositions of $\partial\Omega$ into disjoint parts:

$$\begin{aligned} \partial\Omega &= \partial_\sigma\Omega \cup \partial_u\Omega \ , \quad \partial_\sigma\Omega \cap \partial_u\Omega = \emptyset \ , \\ \partial\Omega &= \partial_w\Omega \cup \partial_p\Omega \ , \quad \partial_w\Omega \cap \partial_p\Omega = \emptyset \ , \\ \partial\Omega &= \partial_E\Omega \cup \partial_\varphi\Omega \ , \quad \partial_E\Omega \cap \partial_\varphi\Omega = \emptyset \ . \end{aligned} \tag{20}$$

For the displacement, the electric potential and the pressure we may consider the following boundary conditions, where p_∂, w_n and $\boldsymbol{g}^s$ are given:

$$\begin{aligned} \boldsymbol{u} = \boldsymbol{0}\ , \quad & \text{on } \partial_u\Omega\ , \qquad \boldsymbol{n}\cdot\boldsymbol{\sigma} = \boldsymbol{g}^s\ , \quad \text{on } \partial_\sigma\Omega\ , \\ p = p_\partial\ , \quad & \text{on } \partial_p\Omega\ , \qquad \boldsymbol{n}\cdot\boldsymbol{w} = w_n\ , \quad \text{on } \partial_w\Omega\ , \\ \varphi = 0\ , \quad & \text{on } \partial_\varphi\Omega\ , \qquad \boldsymbol{n}\cdot\vec{D} = D_n\ , \quad \text{on } \partial_E\Omega\ . \end{aligned} \tag{21}$$

Therefore, the following spaces and admissibility sets are involved in the weak formulation:

$$\begin{aligned} \boldsymbol{U}(\Omega) &= \{\boldsymbol{u}\in\mathbf{H}^1(\Omega)|\ \boldsymbol{u}=\boldsymbol{0} \text{ on } \partial_u\Omega\}\ , \\ P(\Omega) &= \{p\in H^1(\Omega)|\ p=p_\partial \text{ on } \partial_p\Omega\}\ , \\ \Phi(\Omega) &= \{\varphi\in H^1(\Omega)|\ \varphi=0 \text{ on } \partial_\varphi\Omega\}\ . \end{aligned} \tag{22}$$

The space of test pressure functions $P_0(\Omega)$ is defined according to $(22)_2$ with $p_\partial \equiv 0$ while test displacements belong to $\boldsymbol{U}_0(\Omega)$ which is identified with $\boldsymbol{U}(\Omega)$ due to (21). In analogy, $\Phi_0(\Omega) = \Phi(\Omega)$ is considered as the space of the test electric potentials.

We are now in a position to introduce the weak formulation of the macroscopic problem for the piezo-poroelastic medium. The zero initial conditions are considered for simplicity, i.e. $\boldsymbol{u}(\cdot, t=0) = 0$, $p(\cdot, t=0) = 0$, and $\varphi(\cdot, t=0) = 0$. For any time $t > 0$, the following system is to be satisfied by $(\boldsymbol{u}, \varphi, p) \in \boldsymbol{U}(\Omega)\times\Phi(\Omega)\times P(\Omega)$

$$\begin{aligned} &\int_\Omega [\mathbb{A}^H\boldsymbol{e}(\boldsymbol{u}) - (\underline{\boldsymbol{G}}^H)^T\nabla\varphi - p\hat{\boldsymbol{B}}] : \boldsymbol{e}(\boldsymbol{v})\,\mathrm{dV} = \int_\Omega \hat{\boldsymbol{f}}\cdot\boldsymbol{v}\ \mathrm{dV} + \int_{\partial_\sigma\Omega}\boldsymbol{g}^s\cdot\boldsymbol{v}\,\mathrm{dS}_x\ , \\ &\int_\Omega [\underline{\boldsymbol{G}}^H\boldsymbol{e}(\boldsymbol{u}) + \boldsymbol{D}^H\nabla\varphi - \underline{F}p]\cdot\nabla\psi\,\mathrm{dV} = \int_\Omega \hat{q}_E\psi\,\mathrm{dV} + \int_{\partial_E\Omega} D_n\psi\,\mathrm{dS}_x\ , \\ &\int_\Omega \zeta\left(\hat{\boldsymbol{B}} : \boldsymbol{e}(\dot{\boldsymbol{u}}) - \underline{F}\cdot\nabla\dot{\varphi} + \hat{M}\dot{p}\right)\ \mathrm{dV} + \int_\Omega \nabla\zeta\cdot\bar{\eta}^{-1}\boldsymbol{K}^H(\nabla p - \boldsymbol{f}^f)\ \mathrm{dV} = \int_{\partial_w\Omega} w_n\zeta\,\mathrm{dS}_x\ , \end{aligned} \tag{23}$$

for all $(\boldsymbol{v}, \psi, \zeta) \in \boldsymbol{U}_0(\Omega)\times\Phi_0(\Omega)\times P_0(\Omega)$.

5 NUMERICAL EXAMPLES

We shall illustrate features of the homogenized piezo-poroelastic material using a numerical simulation of a compaction test. To compute numerical solutions of the local problems (9)-(11) at the micro-level and those of the macroscopic problem (23), we use the standard FE method using piecewise linear (conforming) approximation for the macroscopic fields $\boldsymbol{u}$, p, and φ, and the corrector fields $(\boldsymbol{\omega}, \vartheta)$. The macroscopic specimen with dimensions $2h\times 2h\times h$, with $h = 1$ cm, and the representative periodic cell Y generating the porous structure are depicted in Fig. 2. In Tab. 1, the homogenized coefficients are compared with those of the piezoelectric material $BaTiO_3$ constituting the skeleton Y_m. The other homogenized coefficients of the upscaled porous medium are listed in Tab. 2.

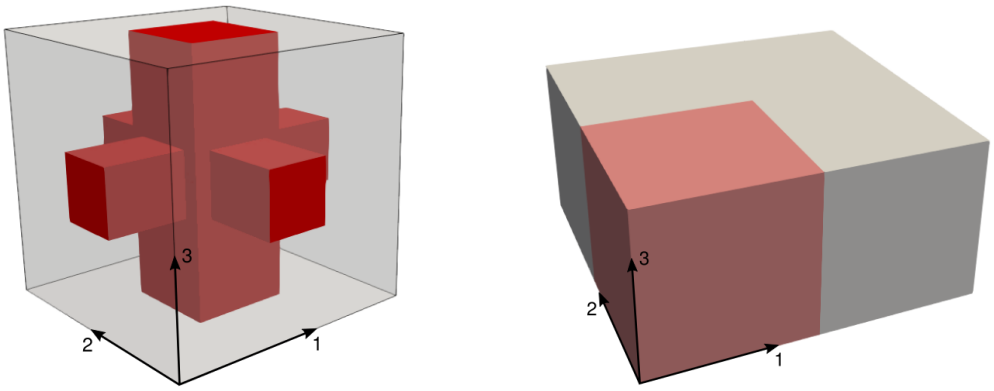

Figure 2: Left: periodic cell Y representing piezoelectric porous microstructure; gray part: solid matrix, red part: fluid channel. Right: Macroscopic domain Ω, only one quarter (as emphasized by the red colour) is used to solve the macroscopic problem due to its symmetry.

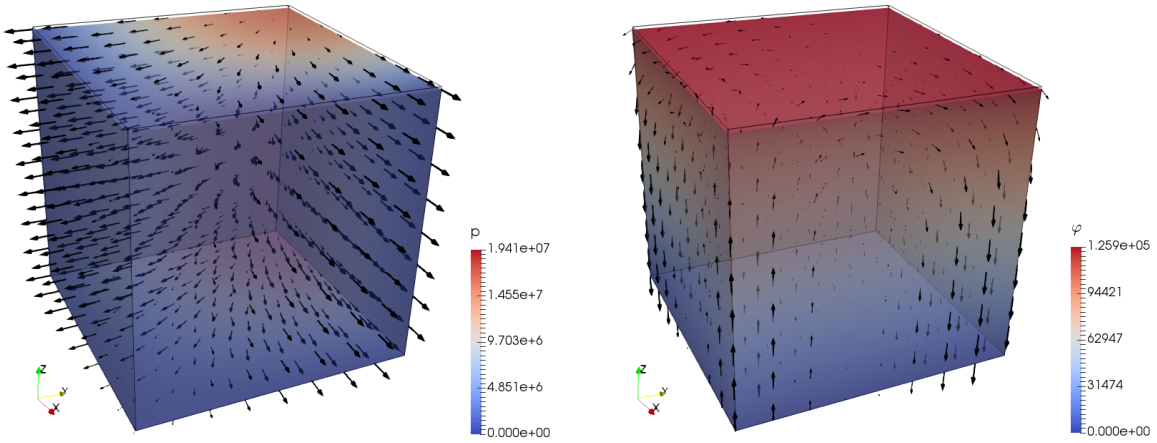

Figure 3: Deformed state of the drained macroscopic specimen at time $t = 0.8\,\mathrm{ms}$ Left: macroscopic pressure p and seepage velocity $\boldsymbol{w}$ (depicted by arrows, max. magnitude $= 7.126 \cdot 10^{-3}$ m/s); Right: electric potential φ and electric displacement $\vec{D}$ (depicted by arrows, max. magnitude $= 3.016 \cdot 10^{-5}$ C/m^2).

elasticity: (in 10× GPa)	A_{1111}	A_{3333}	A_{1122}	A_{2233}	A_{1313}	A_{1212}
skeleton:	15.040	14.550	6.560	6.590	4.240	4.390
homog. porous:	7.816	8.614	2.343	2.724	2.419	1.838

piezo-coupling: (in C/m^2)	G_{311}	G_{322}	G_{333}	G_{223}
skeleton:	-4.322	-4.322	17.360	11.404
homog. porous:	-1.483	-1.483	12.663	6.046

dielectricity: (in 10^{-9} C/Vm)	D_{11}	D_{33}
skeleton:	8.456	10.651
homog. porous:	1.284	1.505

Table 1: Piezoelectric properties of the skeleton and of the homogenized porous material. The transverse isotropy yields the following symmetries: $A_{2233} = A_{1133}$, $A_{1313} = A_{2323}$, $G_{311} = G_{322}$, $G_{223} = G_{113}$, $D_{11} = D_{22}$. Other components are zero.

$\hat{B}_{11}$	$\hat{B}_{33}$	$\hat{M}$	F_3	K_{11}	K_{33}
-	-	10^{-2}/GPa	10^{-11}×m/V	$^{-11}\times$ m^2	$^{-11}\times$ m^2
0.548	0.464	5.352	-1.274	2.474	7.741

Table 2: Homogenized coefficients. Note the symmetries $\hat{B}_{11} = \hat{B}_{22}$, $K_{11} = K_{22}$, other components are zero. Note that the physical permeability is ε_0^2 times smaller, thus, $K_{11}/\bar{\eta} = 2.604 \times 10^{-12}$ m / Pa·s.

Although the homogenized coefficients computed using (12) and (13) are independent of the microstructure size, the hydraulic permeability depends on $\varepsilon_0 > 0$ by virtue of the permeability scaling; we used $\varepsilon_0 = 10^{-4}$, thus the microstructure size is $\ell = 0.1$ mm. Therefore, $\bar{\eta} = \eta/\varepsilon_0^2 = 0.950 \times 10^{-8}$ Pa·s for glycerin considered as the pore fluid with its compressibility $\gamma = 2.30 \times 10^{-10}\,\mathrm{Pa}^{-1}$.

We considered the drained (case I) and undrained (case II) compaction of the macroscopic specimen. In both the cases, the following conditions were prescribed; bottom side: $\boldsymbol{u} \cdot \boldsymbol{n} = 0$, $w_n = 0$, $\varphi = 0$, top side: prescribed $\bar{u} = \boldsymbol{u} \cdot \boldsymbol{n} = -10^{-3} s(t)$ m, $w_n = 0$, $D_n = 0$. The loading function $s(t)$ describes the ramp-and-hold test (the plato for $t > 0.5$ ms). On lateral faces of the specimen, $p = 0$ in case I (drained), while $w_n = 0$ in case II (undrained). No volume forces are considered, thus, $\boldsymbol{f}^f = \hat{\boldsymbol{f}} = \boldsymbol{0}$ in (23).

For case I, in Fig. 3 the pressure, the seepage velocity, and the electric fields are depicted for the deformed state at $t = 0.8$ ms. The spatial pressure variation leads to a nonvanishing field $\vec{D}(x)$; obviously, $\vec{D}$ vanishes in the case II due to the homogeneous distribution of $\boldsymbol{e}(\boldsymbol{u})$, p and $\nabla\varphi$. In Fig. 4 time variation $p(x^A, t)$, $\varphi(x^A, t)$, and $e_{23}(x^A, t)$ is displayed at a point A situated in the middle of the computational domain, $x^A = [0.5h, 0.5h, 0.5h]$ cm, see Fig. 2. While all quantities are constant for the case II in the plato, $t > 0.5$ ms, they change in the case I.

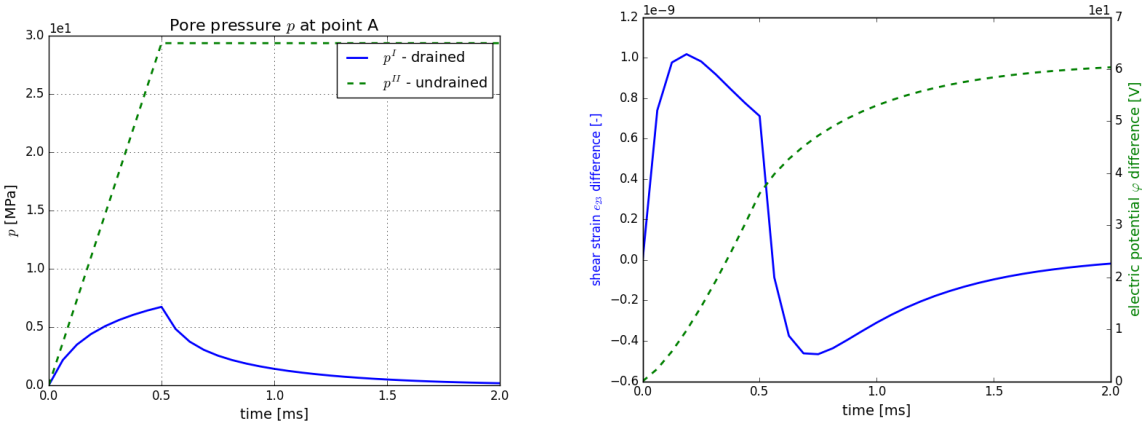

Figure 4: Left: Comparison of time evolution of pressures p^I, p^{II} at macroscopic point A. Right: Difference of the strain component $e^{II}_{23} - e^I_{23}$ (blue solid line) and of the electric potential $\varphi^{II} - \varphi^I$ (green dashed line) at macroscopic point A.

6 CONCLUSIONS

In the present paper we studied the piezoelectric properties of the periodic porous media saturated by viscous fluids under quasistatic loadings. Using the periodic homogenization method, the effective medium coefficients were derived. The porous materials enable to generate the electric field without any macroscopic deformation, just due to an injected volume of fluid in the pores. In the upscaled model, this is respected by the new vector coefficient $\underline{F}$ which is associated with the polarization of the piezomatrial constituting the skeleton. We have shown, how the piezoelectric properties influence the Biot stress coupling coefficients and the Biot compressibility. It is worth noting that the model describes flow of a neutral fluid, whereby electric insulation was considered on the pore surface.

Although the derived model describes the linear response of the homogenized medium, it can be adapted to capture some nonlinear effects, namely those associated with the fluid flow in the pores. Assuming the linear kinematics framework, in [6], we proposed a weakly nonlinear model of the Biot continuum, where the nonlinearity in the homogenized continuum is introduced in terms of the deformation-dependent material coefficients which are approximated as linear functions of the macroscopic response. These functions are obtained by the sensitivity analysis of the homogenized coefficients computed for a given geometry of the porous structure which transforms due to the local deformation. The deformation-dependent material coefficients approximated in this way do not require any solving of local microscopic problems for updated configurations. To deal with the piezo-poroelastic material, we adhere the same approach of [6] and employ the sensitivity analysis developed for the piezoelectric composites in [7].

Acknowledgment This research is supported by project GACR 16-03823S and in part by project LO 1506 of the Czech Ministry of Education, Youth and Sports.

REFERENCES

[1] Hornung, U. *Homogenization and porous media*, Interdisciplinary Applied Mathematics, Springer, Vol. 6 (1997).

[2] Iliev, O., Mikelic, A. and Popov, P. On upscaling certain flows in deformable porous media. *SIAM, Multiscale Model. Simul.* (2008) **7**:93–123.

[3] Iyer, S. and Venkatesh, T.A. Electromechanical response of (3-0, 3-1) particulate, fibrous, and porous piezoelectric composites with anisotropic constituents: A model based on the homogenization method. *International Journal of Solids and Structures* (2014) **51**:1221–1234.

[4] Miara, B., Rohan, E., Zidi, M. and Labat, B. Piezomaterials for bone regeneration design - homogenization approach. *Jour. of the Mech. and Phys. of Solids* (2005) **53**:2529–2556.

[5] Mikelic, A. and Wheeler, M. On the interface law between a deformable porous medium containing a viscous fluid and an elastic body. *Math. Models Meth. Appl. Sci.* (2012) **22**:1–32.

[6] Rohan, E. and Lukeš, V. On modelling nonlinear phenomena in deforming heterogeneous media using homogenization and sensitivity analysis concepts. *Applied Mathematics and Computation* (2015) **267**:583–595.

[7] Rohan, E. and Miara, B. Homogenization and shape sensitivity of microstructures for design of piezoelectric bio-materials. *Mechanics of Advanced Materials and Structures* (2006) **13**:473–485.

[8] Rohan, E., Naili, S. and Lemaire, T. Double porosity in fluid-saturated elastic media: deriving effective parameters by hierarchical homogenization of static problem. *Continuum Mech. Thermodyn.* (2016) **28**:1263–1293.

[9] Koutsawa, Y., Belouettar, S., Makradi, A. and Nasser, H. Sensitivities of effective properties computed using micromechanics differential schemes and high-order Taylor series: Application to piezo-polymer composites. *Mechanics Research Communications* (2010) **37**:489–494.

[10] Vashishth, A.K., and Gupta, V. Wave propagation in transversely isotropic porous piezoelectric materials *International Journal of Solids and Structures* (2009) **46**:3620–3632.

VII International Conference on Computational Methods for Coupled Problems in Science and Engineering
COUPLED PROBLEMS 2017
M. Papadrakakis, E. Oñate and B. Schrefler (Eds)

INVESTIGATION OF ADVANCED TURBULENCE MODELING APPROACHES FOR AEROACOUSTIC PROBLEMS

X. Huang[1,2], M. Schäfer[1,2]

[1]Graduate School Computational Engineering,
Technische Universität Darmstadt, Germany
{huang, schaefer}@gsc.tu-darmstadt.de

[2]Institute of Numerical Methods in Mechanical Engineering,
Technische Universität Darmstadt, Germany
{huang, schaefer}@fnb.tu-darmstadt.de

Key words: Aeroacoustics, Turbulence Model, Synthetic Reconstruction.

Abstract. The influence of a synthetic method for high frequency turbulence on aeroacoustic simulations with turbulence models is investigated. The sound pressure level (SPL) of a detached eddy simulation with and without the synthetic method are compared for a benchmark test case, The results show that the synthetic method is able to increase the simulation accuracy of the high frequency spectrum.

1 INTRODUCTION

Aeroacoustic studies have drawn increasingly more attention in the past years. One of the main tasks is to accurately simulate the acoustic field with a reasonable computational cost. An efficient approach to simulate the acoustic field generated by low Mach number flows is the expansion about incompressible flow (EIF). This approach decomposes the compressible field into an incompressible field and acoustic fluctuations [4, 8]. Based on this decomposition, the acoustic field is governed by the linearized Euler equations (LEE) with an acoustic source term, which can be obtained by solving the incompressible Navier-Stokes equations [6]. The simulation accuracy of the acoustic field strongly depends on that of the flow field. For the simulation of turbulent flow in engineering problems, direct numerical simulation (DNS) cannot be applied due to its unaffordable computational cost. A turbulence model is usually adopted to characterize the unresolved turbulence scales, leading to a significant reduction in computational cost. In Large Eddy Simulation (LES), about 10% of the turbulence is modeled while about 90% is resolved [10]. Delayed Detached Eddy Simulation (DDES) is a hybrid RANS/LES method, wich switches between LES and Reynolds Averaged Navier-Stokes (RANS) modes according

to the grid resolution [11, 12]. However, its main drawback is the loss of high-frequency components in the flow. Consequently, the high-frequency acoustic quantities can not be calculated accurately.

In this work, we study the influence of different turbulence models on the simulation accuracy of acoustic quantities. Considering an aeroacoustic benchmark test case, we compare the accuracy loss of acoustic quantities for different turbulence models including LES and DDES. To compensate the accuracy loss of acoustic quantities in the high-frequency region, the high frequency fluctuation is rebuilt using a synthetic reconstruction model. We adopt this model for the DDES simulation and investigate the performance change. A clear improvement of the high-frequency spectrum can be observed.

2 GOVERNING EQUATIONS

2.1 Linearized Euler equations for aeroacoustic simulation

The Expansion about Incompressible Flow method (EIF) assumes that the compressible flow field at low Mach number can be decomposed into an incompressible flow field and an acoustic field [8, 9]

$$u_i = u_i^{\mathrm{inc}} + u_i^{\mathrm{ac}}, \tag{1}$$

$$p = p^{\mathrm{inc}} + p^{\mathrm{ac}}, \tag{2}$$

$$\rho = \rho^{\mathrm{inc}} + \rho^{\mathrm{ac}}, \tag{3}$$

where u_i, p and ρ are the velocity, pressure and density of compressible flow and superscripts inc and ac represent the components of incompressible flow and acoustic field respectively [6].

The unsteady incompressible flow is governed by the incompressible Navier-Stokes equations

$$\frac{\partial u_i^{\mathrm{inc}}}{\partial x_i} = 0, \tag{4}$$

$$\rho^{\mathrm{inc}} \frac{\partial \left(u_i^{\mathrm{inc}}\right)}{\partial t} + \rho^{\mathrm{inc}} \frac{\partial \left(u_i^{\mathrm{inc}} u_j^{\mathrm{inc}}\right)}{\partial x_j} = \frac{\partial \tau_i^{\mathrm{inc}}}{\partial x_j} - \frac{\partial p^{\mathrm{inc}}}{\partial x_i} + \rho^{\mathrm{inc}} f_i, \tag{5}$$

with time t, external body force f_i and shear stress τ_i^{inc}. For newtonian fluid, the shear stress is given by

$$\tau_i^{\mathrm{inc}} = \mu \left(\frac{\partial u_i^{\mathrm{inc}}}{\partial x_j} + \frac{\partial u_j^{\mathrm{inc}}}{\partial x_i} \right) \tag{6}$$

The governing equations for the acoustic quantities, which is called the linearized Euler

equations (LEE), are given as

$$\frac{\partial \rho^{\mathrm{ac}}}{\partial t} + \rho^{\mathrm{inc}} \frac{\partial u_i^{\mathrm{ac}}}{\partial x_i} + u_i^{\mathrm{inc}} \frac{\partial \rho^{\mathrm{ac}}}{\partial x_i} = 0, \tag{7}$$

$$\rho^{\mathrm{inc}} \frac{\partial u_i^{\mathrm{ac}}}{\partial t} + \rho^{\mathrm{inc}} u_j^{\mathrm{inc}} \frac{\partial u_i^{\mathrm{ac}}}{\partial x_j} + \frac{\partial p^{\mathrm{ac}}}{\partial x_i} = 0, \tag{8}$$

$$\frac{\partial p^{\mathrm{ac}}}{\partial t} + c^2 \rho^{\mathrm{inc}} \frac{\partial u_i^{\mathrm{ac}}}{\partial x_i} + c^2 u_i^{\mathrm{inc}} \frac{\partial \rho^{\mathrm{ac}}}{\partial x_i} = -\frac{\partial p^*}{\partial t}, \tag{9}$$

where p^* is the sum of the incompressible pressure and the synthetic pressure fluctuation. More details will be found in Chap. 5.

2.2 Detached Eddy Simulation model

The $\zeta - f$ model is used as background RANS model for the DDES model. The equations are given as [3]

$$\frac{\partial k}{\partial t} + \overline{u_j^{\mathrm{inc}}} \frac{\partial k}{\partial x_j} = P_k + \frac{\partial}{\partial x_j} \left[\left(\nu + \frac{\nu_t}{\sigma_k} \right) \frac{\partial k}{\partial x_j} \right] - \varepsilon, \tag{10}$$

$$\frac{\partial \varepsilon}{\partial t} + \overline{u_j^{\mathrm{inc}}} \frac{\partial \varepsilon}{\partial x_j} = \frac{C_{\varepsilon 1} P_k - C_{\varepsilon 2} \varepsilon}{\tau} + \frac{\partial}{\partial x_j} \left[\left(\nu + \frac{\nu_t}{\sigma_k} \right) \frac{\partial \varepsilon}{\partial x_j} \right], \tag{11}$$

$$\frac{\partial \zeta}{\partial t} + \overline{u_j^{\mathrm{inc}}} \frac{\partial \zeta}{\partial x_j} = f - \frac{\zeta}{k} P_k + \frac{\partial}{\partial x_j} \left[\left(\nu + \frac{\nu_t}{\sigma_k} \right) \frac{\partial \zeta}{\partial x_j} \right], \tag{12}$$

$$L^2 \nabla f - f = \frac{1}{\tau} \left(C_1 + C_2' \frac{P_k}{\varepsilon} \right) \left(\zeta - \frac{2}{3} \right), \tag{13}$$

where ε is the dissipation, f is the elliptic relaxation term, L is the length scale and τ is the time scale of turbulence.

The DDES model is a hybrid LES/RANS model, which switches between URANS and LES according to the numerical resolution [12]. The dissipation term ε in the k equation is modified to

$$\varepsilon = \frac{k^{3/2}}{l_{\mathrm{turb}}}, \tag{14}$$

where l_{turb} is the length scale of DDES

$$l_{\mathrm{turb}} = l_{\mathrm{RANS}} - f_d \max(0, d - C_{\mathrm{DES}} \Delta\phi). \tag{15}$$

3 IMPLEMENTATION OF SYNTHETIC METHOD

3.1 Synthetic reconstruction of high frequency turbulence

The synthetic method reconstructs the turbulent velocity fluctuations from a given dissipation rate and set of second moments [1]. The velocity fluctuations are given as

$$u_i^{\mathrm{syn}}(x_j, t) = a_{ik} \sqrt{\frac{2}{N}} \sum_{n=1}^{N} \left[p_k^n \cos\left(\hat{d}_j^n \hat{x}_j^n + \omega^n \hat{t} \right) + q_k^n \sin\left(\hat{d}_j^n \hat{x}_j^n + \omega^n \hat{t} \right) \right] \tag{16}$$

$$\hat{x}_j = 2\pi x_j/L, \quad \hat{t} = 2\pi t/\tau, \quad \hat{d}_j^n = d_j^n \frac{V}{c^n}, \quad V = L/\tau, \tag{17}$$

$$c^n = \sqrt{\frac{3}{2}\overline{u_l' u_m'} d_l^n d_k^n / d_k^n d_k^n}, \quad p_i^n = \epsilon_{ijk}\eta_j^n d_k^n, \quad q_i^n = \epsilon_{ijk}\xi_j^n d_k^n, \tag{18}$$

$$\eta_i^n, \xi_i^n = N(0,1), \quad \omega^n = N(1,1), \quad d_i^n = N(0, \frac{1}{2}). \tag{19}$$

where a_{ij} is the Cholesky decomposition of $\overline{u_i' u_j'}$, L and τ are local length and time scales, and N is set to 100. η_i^n, ξ_i^n, ω^n and d_i^n are random numbers with given mean and variance. After the velocity fluctuations are calculated, the pressure fluctuations are obtained using a pressure correction method, which is the standard method in the flow solver FASTEST which is used to solve the incompressible Navier-Stokes equations [7].

3.2 Numerical realization of flow solver and acoustic solver

The work flow of the aeroacoustic simulation after new implementation is shown in Fig.1.

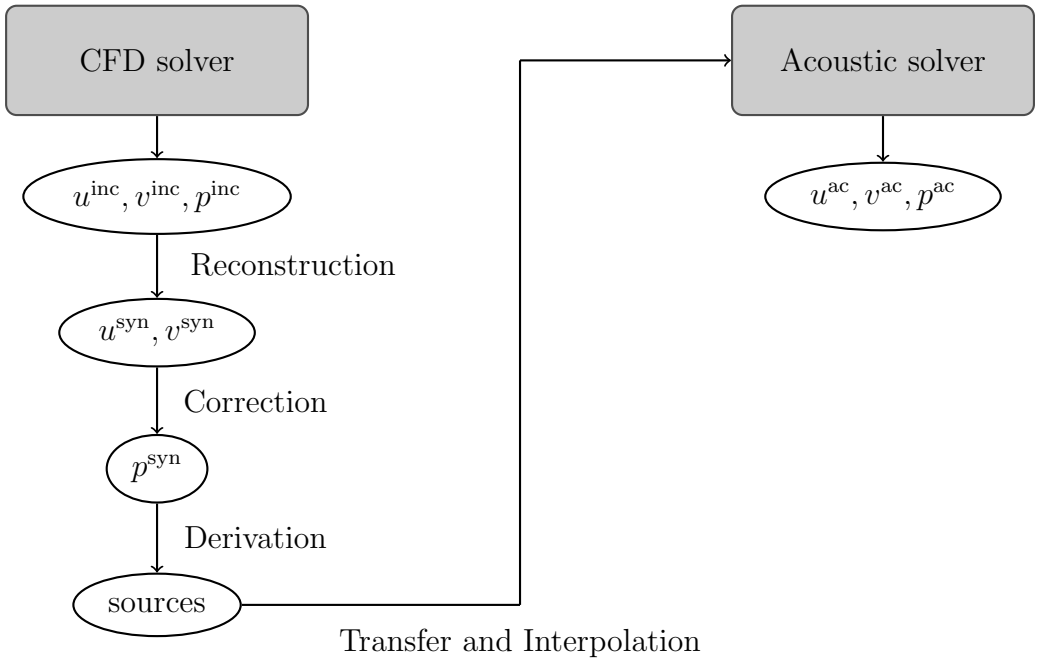

Figure 1: Numerical realization of flow solver and acoustic solver.

First, we solve for the incompressible flow quantities on a flow grid. Second, we reconstruct the high frequency turbulence using the synthetic method. Then we calculate the synthetic pressure using the pressure-correction method. Thereafter, the acoustic source term is calculated by differentiating the pressure with respect to time. Then, we transfer

and interpolate the acoustic sources onto an acoustic grid, which has a larger range and a coarse resolution. For the coupling of these two grids, a trilinear interpolation is utilized. Finally, we solve the LEE to calculate the acoustic quantities.

4 SIMULATION

The acoustic quantities generated by the turbulent flow around a circular cylinder is measured by Etkin et al [2], which is used as reference data in this work. The Mach number is 0.2 and the Reynolds number is approximately 60000. A sketch of the flow domain is given in Fig.2, where D is 0.0125m. The z-direction has a length of $4D$, which is sufficient to capture the three dimensional turbulent features. The experimental data are collected at a point, which is above the cylinder and at a distance of 48D from the cylinder's center.

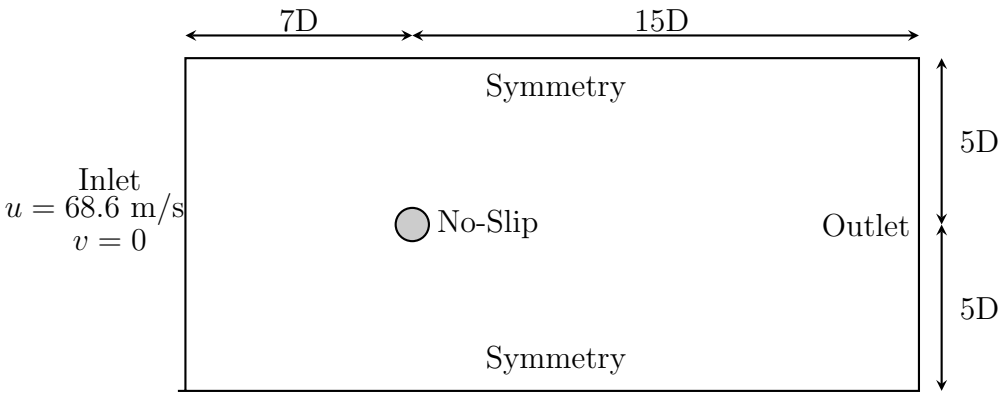

Figure 2: Sketch and boundary conditions of flow domain.

30000 time steps are observed, which is sufficient to acquire a fully developed von Kármán vortex street and a stable propagation process of acoustics. For the LES a flow grid with about 2.5 million cells is used, resulting in a simulation time of approximately 4 days. The grid for the DDES model is created according to the grid resolution requirements from [13]. The DDES model needs 2.5 days to finish the simulation. For all cases, the time step of the flow is set to 3×10^{-6}s, which ensures that the sampling frequency of different simulations are the same.

5 RESULTS AND DISCUSSION

The SPL of different turbulence models without synthetic method are compared with the experimental data in Fig.3. With less computational cost, the DDES method gives a comparable simulation result to that of LES. With regard of the high frequency spectrum, both DDES and LES simulations deviate from the experimental data. The reason is that the high frequency turbulence is filtered or averaged in the turbulence models, so that the acoustic solver can not calculate the high frequency spectrum correctly [5].

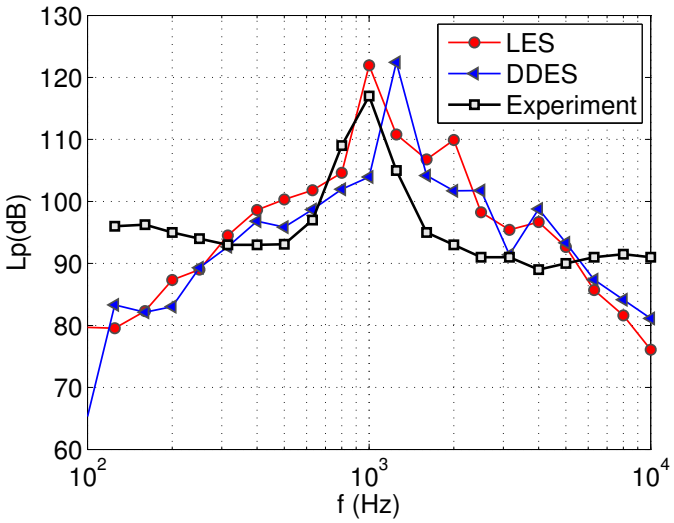

Figure 3: Comparison of SPL of different turbulence models with experimental data [5]

With the help of the synthetic method, the high frequency turbulence is reconstructed. In order to avoid stability problems, a coefficient is used in the pressure. The pressure is given as

$$p^* = \alpha(p^{\text{syn}} + p^{\text{inc}}) + (1 - \alpha)p^{\text{inc}}, \tag{20}$$

where α is the coefficient, which can control the amount of synthetic pressure that is actually used in the simulation, p^{syn} is the synthetic pressure and p^{inc} is the incompressible pressure.

Figure 4 illustrates the simulation results with the synthetic method. The DDES results with the synthetic method shows an obvious improvement of the high frequency spectrum in comparison to that without the synthetic method. The coefficient α also has an influence on the simulation result. Specifically, when $\alpha = 0.1$, the simulation result reaches the best agreement with the experimental data. When α increases further, the simulation result deviates from the experimental data. It is shown that the DDES simulation with the synthetic method achieves even more accurate results than the LES simulation in terms of the high frequency spectrum, even though the DDES simulation requires less cells and less computational cost.

6 CONCLUSION

The synthetic method has been implemented and investigated in the context of aeroacoustic simulations. It has been shown that the synthetic method is able to improve the DDES simulation results in terms of the high frequency spectrum. The coefficient α for pressure is calibrated to 0.1. The DDES simulation provides more accurate results than the LES simulation, which makes the DDES method a very promising technique, since it requires less computational cost.

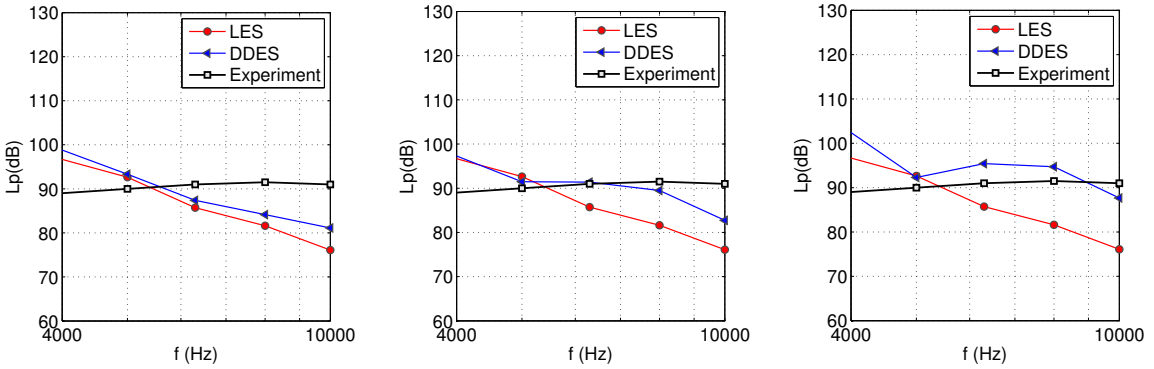

(a) SPL of turubulence models without synthetic method

(b) SPL of turubulence models with synthetic method, $\alpha = 0.1$

(c) SPL of turubulence models with synthetic method, $\alpha = 0.2$

Figure 4: Comparison of SPL of different turbulence models with and without synthetic method

7 ACKNOWLEDGMENT

This work is supported by the 'Excellence Initiative' of the German Federal and State Governments within the Graduate School of Computational Engineering at Technische Universität Darmstadt.

REFERENCES

[1] P. Batten, U. Goldberg and S. Chakravarthy, Interfacing statistical turbulence closures with large eddy simulation. *AIAA Journal*. 42(3):485-492, 2004.

[2] B. Etkin, G.K. Korbacher, R.T. Keefe, Acoustic Radiation from a Stationary Cylinder in a Fluid Stream (Aeolian Tones). *Journal of the Acoustical Society of America*. 2930-36, 1957.

[3] K. Hanjalić, M. Popovac, M. Hadžiabdić, A robust near-wall elliptic-relaxation eddy-viscosity turbulence model for CFD. *International Journal of Heat and Fluid Flow*, 25(6):1047-1051, 2004.

[4] J.C. Hardin, D.S. Pope, An acoustic/viscous splitting technique for computational aeroacoustics. *Theoretical and Computational Fluid Dynamics*. 6(5):323-340, 1994.

[5] X. Huang, M. Schäfer, On the simulation of aerodynamic noise with different turbulence models. *ECCOMAS Congress*. Crete, 2016.

[6] M. Kornhaas, M. Schäfer, D.C. Sternel. Efficient numerical simulation of aeroacoustics for low Mach number flows interacting with structures. *Computational Mechanics*, 55:1143-1154, 2015.

[7] M. Schäfer, *Computational Engineering - Introduction to Numerical Methods*. Springer, 2006.

[8] W.Z. Shen, J.N. Sørensen, Aeroacoustic Modelling of Low-Speed Flows *Theoretical and Computational Fluid Dynamics*. Volume 13, Issue 4, pp. 271-289, 1999.

[9] W.Z. Shen, J.N. Sørensen, Comment on the aeroacoustic formulation of Hardin and Pope. *AIAA Journal*. 37(1):141-143, 1999.

[10] J. Smagorinsky, General circulation experiments with the primitive equations I: The basic experiment *Monthly weather review*, 91(3):99-163, 1963.

[11] P.R. Spalart. Detached-eddy simulation. *Annual Review of Fluid Mechanics*, 41(1):181-202, 2009.

[12] P.R. Spalart, S. Deck, M.L. Shur, K.D. Squires, M.Kh Strelets, A. Travin. A new version of detached-eddy simulation, resistant to ambiguous grid densities. *Theoretical and Computational Fluid Dynamics*, 20(3):181-195, 2006.

[13] P.G. Tucker, Unsteady Computational Fluid Dynamics in Aeronautics, *Fluid Mechanics and Its Applications*, Volume 104, 2014.

VII International Conference on Computational Methods for Coupled Problems in Science and Engineering
COUPLED PROBLEMS 2017
M. Papadrakakis, E. Oñate and B. Schrefler (Eds)

MODELING OF AN ELECTRICALLY DRIVEN DROPLET GENERATOR

YUN OUEDRAOGO*, ERION GJONAJ*, THOMAS WEILAND*, HERBERT DE GERSEM*, CHRISTOPH STEINHAUSEN†, GRAZIA LAMANNA†, BERNHARD WEIGAND†, ANDREAS PREUSCHE‡ AND ANDREAS DREIZLER‡

*Institut für Theorie Elektromagnetischer Felder
Technische Universität Darmstadt
Schloßgartenstr. 8, 64289 Darmstadt, Germany
email: {ouedraogo,gjonaj,thomas.weiland,degersem}@temf.tu-darmstadt.de

†Institut für Thermodynamik der Luft- und Raumfahrt
Universität Stuttgart
Pfaffenwaldring 31, 70569 Stuttgart, Germany
email: {christoph.steinhausen,grazia.lamanna,bernhard.weigand}@itlr.uni-stuttgart.de

‡Fachgebiet für Reaktive Strömungen und Messtechnik
Technische Universität Darmstadt
Jovanka-Bontschits-Str. 2, 64287 Darmstadt
email: {preusche,dreizler}@rsm.tu-darmstadt.de

Key words: Electrohydrodynamics, On-demand droplet, Multiphase flow, VOF

Abstract. An electrohydrodynamic model for the simulation of droplet formation, motion and detachment in an electrically driven droplet generator is introduced. The numerical approch is based on the coupled solution of the multiphase flow problem with the charge continuity equation. A conduction-convection model, taking into account conductive, capacitive and convective currents in the fluid, describes the charge relaxation phenomena in the moving liquid. The charge received by the droplets during acceleration by an external electric pulse is an important parameter influencing dynamics of droplets in the pressure chamber. The model is illustrated with simulations of detachment of high conductivity acetone droplets and low conductivity n-pentane droplets.

1 INTRODUCTION

The application of strong electric fields on liquids is used in many engineering applications to induce liquid atomization in a controlled manner. In electrosprays [1, 2], the droplet size and the opening angle of the spray cone can be affected by charging the liquid

prior to its atomization. In electrically driven on-demand droplet generators, millimetric droplets pending from a capillary can be detached on a controlled manner by applying strong electrical pulses. The method provides reliable injection of liquid samples in the experimental chamber, at a broad range of atmospheric conditions [3].

Deformations of the phase boundary induced by electric fields result in changes in the electric field and force distribution. The mechanical and electric problems are thus strongly coupled. Additionally, due to the presence of intrinsic ionic species and dissolved impurities, liquids exhibit some electrical conductivity associated with charge migration. Dynamic charging effects in liquid droplets and convection of free charge can strongly alter liquid motion. Moreover, the accumulation of free charge in droplets can result in the generation of charged droplets from initially uncharged liquid. This behavior requires an electroquasistatic field representation, taking into account both conduction and displacement electric currents in the liquid.

We discuss a conduction-convection model for the simulation of droplet dynamics under the influence of electric fields. The liquid interface is captured using the Volume of Fluid method , allowing for an efficient representation of topology changes in the phase boundaries. The electric problem is solved using the resulting diffuse interface, and the resulting electric force is introduced as a source term for the hydrodynamic problem. Wetting is taken into account by using a dynamic contact angle model.

The numerical study of liquid droplets generation in an on-demand droplet generator [3] is considered in this work. Detachment dynamics of acetone and n-pentane droplets, exhibiting respectively high and low conductivity, are reproduced numerically, and illustrate the effect of conductivity on electrically induced droplet motion.

2 GOVERNING EQUATIONS

2.1 The Fluid Flow Problem

In this paper, we focus on the application of an external electric pulse to drive droplet detachment. As a result, we restrict the study of the generator to the lower range of temperatures, where droplet injection does not involve phase transitions. Under these atmospheric conditions, the fluid flow problem is governed by the incompressible Navier-Stokes equations:

$$\frac{\partial \rho \vec{u}}{\partial t} + \nabla \cdot \rho \vec{u}\vec{u} = -\nabla p + \nabla \cdot \left(\mu \left[\nabla \vec{u} + \nabla \vec{u}^{\mathrm{T}}\right]\right) + \rho \vec{g} + \vec{f_{\mathrm{s}}} + \vec{f_{\mathrm{e}}}\,, \tag{1}$$

$$\nabla \cdot \vec{u} = 0\,, \tag{2}$$

where $\vec{u}$ denotes fluid velocity, ρ is the density, μ the dynamic viscosity and p the pressure. The driving terms $\vec{f_{\mathrm{s}}}$ and $\vec{f_{\mathrm{e}}}$ are, respectively, the surface tension force density acting at the interface between the two fluid phases, and the electric force density. The former is related to the phase boundary properties according to Young-Laplace equation,

$$\vec{f_s} = 2\gamma H \vec{n}\,, \tag{3}$$

where γ is the surface tension characterizing the fluid-fluid interface, H is the mean curvature and $\vec{n}$ the interface normal.

This surface tension contribution needs also to be considered at contact lines, where the fluid-fluid interface meets solid walls. This is particularly important in the case of this droplet generator, since wetting of the surface of the capillary by test fluids strongly affects the detachment process [4]. The contact line problem is described in terms of a local apparent contact angle, θ. For static contact lines, this angle is limited by a minimal advancing and maximal receding values, θ_{adv} and θ_{rec}, respectively [5]. Those values can be determined experimentally. In dynamic cases, the apparent contact angle value depends on the local contact line velocity, u_{cl}, additionally. In this work, the dynamic contact angle is calculated from the Kistler correlation [6]:

$$\theta = f_{\mathrm{H}}\left(C_a + f_{\mathrm{H}}^{-1}\left(\theta_{\mathrm{adv/rec}}\right)\right)\,, \tag{4}$$

$$\text{with} \quad f_{\mathrm{H}}\left(x\right) = \arccos\left(1 - 2\tanh\left[5.16(\frac{x}{1+1.31x^{0.99}})^{0.706}\right]\right)\,. \tag{5}$$

In (4), the capillary number $\mathrm{Ca} = \frac{\mu_{\mathrm{liquid}}\cdot u_{\mathrm{cl}}}{\gamma}$ is a signed quantity, taken positive for an advancing contact line, negative otherwise.

2.2 The Electric Field Problem

In electrically conductive fluids, the current density, $\vec{J}$, is composed of a conductive and a conductive components:

$$\vec{J} = \rho_e\vec{u} + \kappa\vec{E}\,, \tag{6}$$

where κ is the ohmic conductivity of the fluid and ρ_e the charge density associated with the free charge carriers in the fluid. Using the free charge continuity equation,

$$\frac{\partial\rho_e}{\partial t} + \nabla\cdot\vec{J} = 0\,, \tag{7}$$

and introducing an electric potential so that $\vec{E} = -\nabla\Phi$ yields the equations describing the electric problem:

$$\nabla\cdot\varepsilon\nabla\Phi = -\rho_e\,, \tag{8}$$

$$\frac{\partial\rho_e}{\partial t} + \nabla\cdot(\rho_e\vec{u}) = \nabla\cdot\kappa\nabla\Phi\,, \tag{9}$$

where ε is the permittivity of the media.

The electric force density applied on the fluid can be obtained from the electric field distribution using the Maxwell stress tensor:

$$\vec{f_{\mathrm{e}}} = \nabla\cdot\left(\varepsilon\vec{E}\otimes\vec{E} - \frac{1}{2}\varepsilon E^2\vec{\vec{I}}\right)\,. \tag{10}$$

3 NUMERICAL APPROACH

The electrohydrodynamic problem involves two different fluids, for which a description of the interface is required. We use the Volume of Fluid (VoF) method [7], a diffuse interface approach, to describe the topology of the fluid-fluid interface. The solution to Eq. (1)-(5) and (8)-(10), modeling the coupled problem is implemented, along with the VoF method, using the OpenFOAM [8] framework, as described in detail below.

3.1 Solution of the Fluid Flow Problem

In the Volume of Fluid method, the fluid material properties are represented using the volume fraction, α, of one of the fluids in each cell of the computational grid. The Navier-Stokes equations are solved assuming a single phase whose local material properties are calculated from the volume fraction. The interface is advanced in time by transporting the volume fraction:

$$\frac{\partial \alpha}{\partial t} + \nabla \cdot (\alpha \vec{u}^*) = 0\,, \tag{11}$$

with $\alpha \in [0,1]$. In Eq. (11), $\vec{u}^*$ is a modified velocity field, including an optional numerical compression velocity pointing normal to the interface [9]. The effective fluid properties at the interface between fluid 1 and fluid 2 are determined by weighted averaging as

$$\rho = \alpha \cdot \rho_1 + (1-\alpha) \cdot \rho_2\,, \tag{12}$$

$$\mu = \alpha \cdot \mu_1 + (1-\alpha) \cdot \mu_2\,. \tag{13}$$

The evolution of the volume fraction does not require interface reconstruction, so that topology changes of the phase boundary are implicitly taken into account.

The surface tension force applied on the diffuse interface can be described using the volume fraction, as a body force [10]:

$$\vec{f}_\mathrm{s} = -\gamma \nabla \cdot \left(\frac{\nabla \alpha}{||\nabla \alpha||} \right) \nabla \alpha\,. \tag{14}$$

The contact angle model (4) provides the necessary boundary condition for the computation of the contribution of the surface tension at the contact line. The velocity of the contact line is evaluated, according to the scheme proposed in [5], as

$$u_\mathrm{cl} = \frac{\vec{u}_\mathrm{w} \cdot \vec{n}_\mathrm{i}}{\sqrt{1 - (\vec{n}_\mathrm{w} \cdot \vec{n}_\mathrm{i})^2}}\,, \tag{15}$$

where $\vec{u}_\mathrm{w}$ is the fluid velocity near the solid wall, $\vec{n}_\mathrm{w}$ is the normal vector to the wall and $\vec{n}_\mathrm{i} = \nabla\alpha / ||\nabla\alpha||$ is the normal to the phase boundary interface.

The pressure-velocity equations (1), (2) are solved numerically using the PISO algorithm as implemented, e.g., in the INTERFOAM solver (see [11]). As the electric force density driving fluid motion depends on the fluid velocity through the convection term of the charge conservation equation (9), we apply a fixed-point iteration between the electric field solver and the fluid flow solver at every time step of the simulation.

3.2 Solution of the Electric Field Problem

Sharp interface representations for the material boundaries are usually used in pure electric field computations. Methods based on interface tracking using a moving mesh can be readily applied for droplet simulations [12], as long as topology changes are not involved. The motion of liquids in this work involves strong stretching as well as splitting of the fluid-fluid interface. Sharp interface tracking via a moving mesh would therefore require explicit treatment of interface topology changes, as in e.g. [13]. As droplet detachment from a capillary involves multiple topology changes from the liquid thread and secondary droplets [14], such a treatment would need to be applied frequently. We therefore adopt a VoF-like method for the solution of the electric field equations (9), (10).

The electric field problem is solved on the same computational grid as the fluid problem using averaged electric properties, defined similarly to Eq. (12) and (13):

$$\frac{1}{\varepsilon} = \frac{\alpha}{\varepsilon_1} + \frac{1-\alpha}{\varepsilon_2}\,, \tag{16}$$

$$\frac{1}{\kappa} = \frac{\alpha}{\kappa_1} + \frac{1-\alpha}{\kappa_2}\,. \tag{17}$$

Note that in (16) and (17), harmonic averaging of the material properties is used rather than arithmetic averaging. This relates to the particular form of the expected field solution, where the electric field is essentially normal to the phase boundary for conductive liquids. In that case, harmonic averaging leads to more accurate results than arithmetic averaging [15, 16].

Equations (9), (10) are updated by a time staggering scheme as

$$\nabla \cdot \varepsilon^{n+1/2} \nabla \Phi^{n+1/2} = -\rho_{\mathrm{e}}^{n+1/2}\,, \tag{18}$$

$$\frac{\rho_{\mathrm{e}}^{n+1} - \rho_{\mathrm{e}}^{n}}{\Delta t} + \nabla \cdot (\rho_{\mathrm{e}}^{n+1/2} \vec{u}^{n+1/2}) = \nabla \cdot \kappa^{n+1/2} \nabla \Phi^{n+1/2}\,. \tag{19}$$

The charge density, $\rho_{\mathrm{e}}^{n+1/2}$ in (18), is initially unknown. Thus, an inner fixed-point iteration is applied for the solution of (18), (19) in addition to the outer iteration loop which is applied in every time step of the simulation.

4 Validation Example

In order to validate the numerical approach, a simple one-dimensional example is considered, see Fig. 1. A planar liquid layer of thickness L_l is transported passively with a constant velocity u in a surrounding gaseous environment. The two fluids are characterized by the permittivities, ε_l and ε_g, and electric conductivities, κ_l and κ_g, respectively. At time $t_0 = 0$, an electric voltage U is applied between the two boundaries of the computational domain. When the external voltage is switched on, electric charges start accumulating at the front and back interfaces of the liquid layer. The induced charge moves together with the phase boundaries and keeps increasing until a steady state is

reached. The analytic solutions for the transient electric field and surface charge densities are given by

$$E_{\{l,g\}} = \frac{U}{L} \cdot \left[\frac{\kappa_{\{g,l\}}}{\kappa_*} \cdot \left(1 - \exp^{-\frac{\kappa_*}{\varepsilon_*} t}\right) + \frac{\varepsilon_{\{g,l\}}}{\varepsilon_*} \cdot \exp^{-\frac{\kappa_*}{\varepsilon_*} t} \right], \tag{20}$$

$$\sigma_{\pm} = \pm \frac{U}{L} \cdot \frac{\varepsilon_g \kappa_l - \varepsilon_l \kappa_g}{\kappa_*} \cdot \left(1 - \exp^{-\frac{\kappa_*}{\varepsilon_*} t}\right) \tag{21}$$

where E_l and E_g are the electric field strengths in the liquid and gas layers, respectively, $\sigma_{\pm}$ are the two interface charge densities, $\varepsilon_* = (L_g \varepsilon_l + L_l \varepsilon_g)/L$, $\kappa_* = (L_g \kappa_l + L_l \kappa_g)/L$ and $L = L_l + L_g$ is the total length of the computational domain. Note that this solution does not depend on fluid velocity.

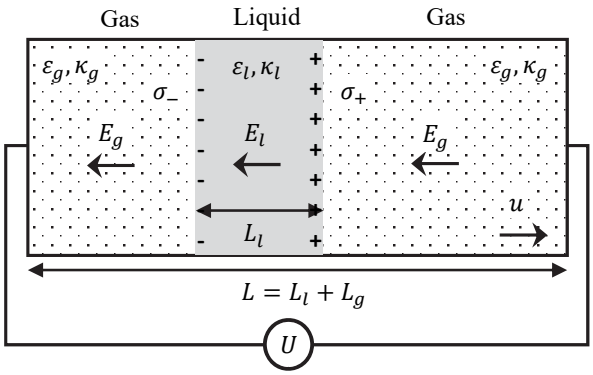

Figure 1: Schematic representation of the moving layer problem.

Figure 2 shows the results of the numerical simulation compared to the analytic solution. The parameters of the problem are chosen as: $u = 1\,\mathrm{m\,s^{-1}}$, $\varepsilon_l = 4 \cdot \varepsilon_0$, $\varepsilon_g = 1 \cdot \varepsilon_0$, $\kappa_l = 1.5 \times 10^{-8}\,\mathrm{S\,m^{-1}}$ and $\kappa_g = 1 \times 10^{-12}\,\mathrm{S\,m^{-1}}$. As seen in the figure, a good agreement between the analytic and numerical results is obtained even for the coarse grid used here. Similarly to the numerical solution for the fluid density, the electric field distribution at the phase boundaries is subject to numerical diffusion. However, the computed total interface charge agrees nearly perfectly with the analytic solution.

5 Droplet Generator Simulations

The model described in the previous section is applied in the simulation of an electrically driven droplet generator [3]. The generator setup is shown in Fig. 3. A metallic capillary tube, kept at ground potential, introduces liquid in the pressure chamber. Two electrodes on each sides of the capillary are connected to a high-voltage source. In order to prevent electric breakdown in the test chamber, the electrodes are embedded in two insulator blocks. The chamber is capable of sustaining a high-pressure and high-temperature environment. The liquid introduced from the capillary can be heated separately. In the

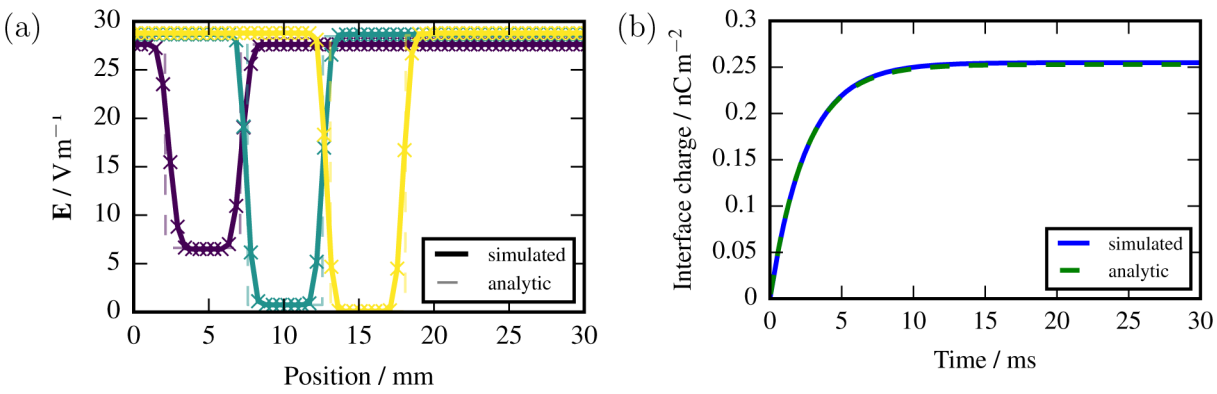

Figure 2: Comparison between analytic and numerical results for the moving liquid layer. (a) Electric field distribution at three different time instants after the external voltage is switched on. (b) Magnitude of the total charge at either fluid interface as a function of time.

simulations and experiments detailed below, the liquid is introduced at the same temperature as the surrounding gaseous environment.

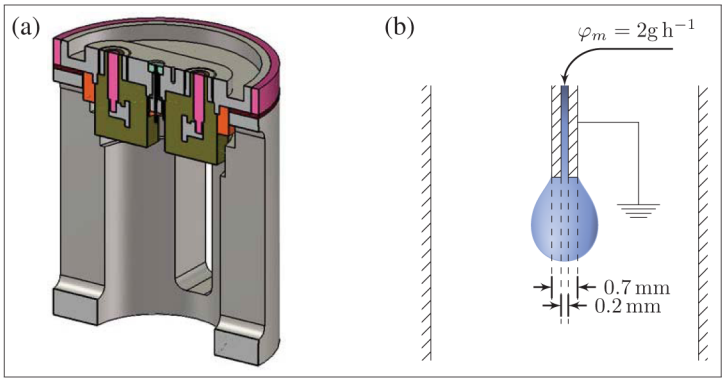

Figure 3: (a) Full model of the droplet generator including capillary, electrodes and test chamber (cf. [3]). (b) Schematic view and main parameters of the simulation model.

Liquid is introduced into the capillary at a constant mass flow rate of $2\,\mathrm{g\,h^{-1}}$, in the absence of electric fields, until a pendant droplet forms at its end.Typical filling times for a single droplet are in the range of 2 s to 6 s, yielding droplet volumes in the range 2 µL to 5 µL, depending on the atmospheric conditions in the chamber and initial liquid temperature. Due to the wettability of the capillary, the droplet wets the sides of the capillary and is held in place by surface tension. As the droplet size increases, the equilibrium between the weight of the droplet and its surface tension leads to slow dewetting of the sides of the capillary. An optical setup monitoring droplet presence then triggers the detachment process. The mass flow is interrupted to prevent from generating additional droplets, while the electric voltage is switched on. Typical electric pulses apply a peak voltage of 1 kV to 5 kV over a duration of 10 ms to 40 ms. The electric forces applied

on the droplet accelerate the droplet for the duration of the pulse, eventually leading to droplet detachment.

Experimental observations show that the dynamics of the flow induced by the electric field strongly depend on the electrical properties of the test liquid. The two cases are analyzed separately in the following sections, in order to emphasize the different charging and fluid flow dynamics.

Although the geometry of the droplet is not axisymmetric, the electric field distribution is nearly so in the vicinity of the capillary. In order to reduce the computational cost of simulations, a 2D axisymmetric approach is therefore used in what follows.

Simulations are performed with a grid resolution of $\frac{1}{\delta x} = 2.5 \times 10^{-5}\,\mathrm{m}^{-1}$, corresponding to approximately 35 cells per primary droplet radius. This resolution is chosen as further refinement of the grid does not influence the dynamics of primary droplets, while still capturing the qualitative behavior of the liquid thread and secondary droplets. The time step size is chosen as $\Delta t = 2\,\mu\mathrm{s}$ for this grid size, according to the stability limit for surface tension driven flow [17].

In order to save computational effort, the initial filling regime is simulated on a reduced domain centered on the capillary. The computational domain is extended vertically for simulating droplet detachment events. The two domains have, respectively, 20960 and 50200 cells for the chosen resolution. The typical time required to simulate the droplet filling is 24 h; the typical time required for simulating droplet detachment is 8 h.

5.1 Acetone Droplet Generation

At 1 bar, 293 K, the electrical conductivity of acetone is $\kappa = 20\,\mu\mathrm{S}$ and its relative permittivity $\varepsilon_\mathrm{r} = 21$. The resulting free charge relaxation time is therefore of the order of 10 µs, orders of magnitude smaller than the voltage pulse duration, $\tau_p \approx 10\,\mathrm{ms}$ and the time scale of fluid motion. Acetone can be therefore considered as highly conductive for the considered experimental conditions. The result of the simulation is shown in Fig. 4. The voltage profile assumed for the simulation, peaks at 2 kV, over a duration of 11.5 ms.

The droplet is initially pulled downwards during the short electric pulse. After the end of the pulse, the droplet continues stretching under its own inertia, eventually leading to detachment. A comparison of the dynamics of the droplet detachment, Fig. 4, at different time instants before and after detachment, shows a close agreement between simulated and experimental dynamics. A slight discrepancy is visible in the form of a secondary droplet, originating from the liquid thread at the time of detachment, that follows the primary droplet in the experiment.

A detailed investigation of the dynamics of detachment is shown in Fig. 5. The volume of the detached primary droplet, illustrated in Fig. 5b is weakly dependent on the applied voltage, varying less 3% in the investigated range of voltages, 2-5kV. The detachment time, illustrated in Fig. 5a, is however strongly dependent on the generator voltage. At lower voltages, a fast variation of the detachment time is observed, while at higher voltages, the detachment time decreases nearly linearly with increasing applied voltage.

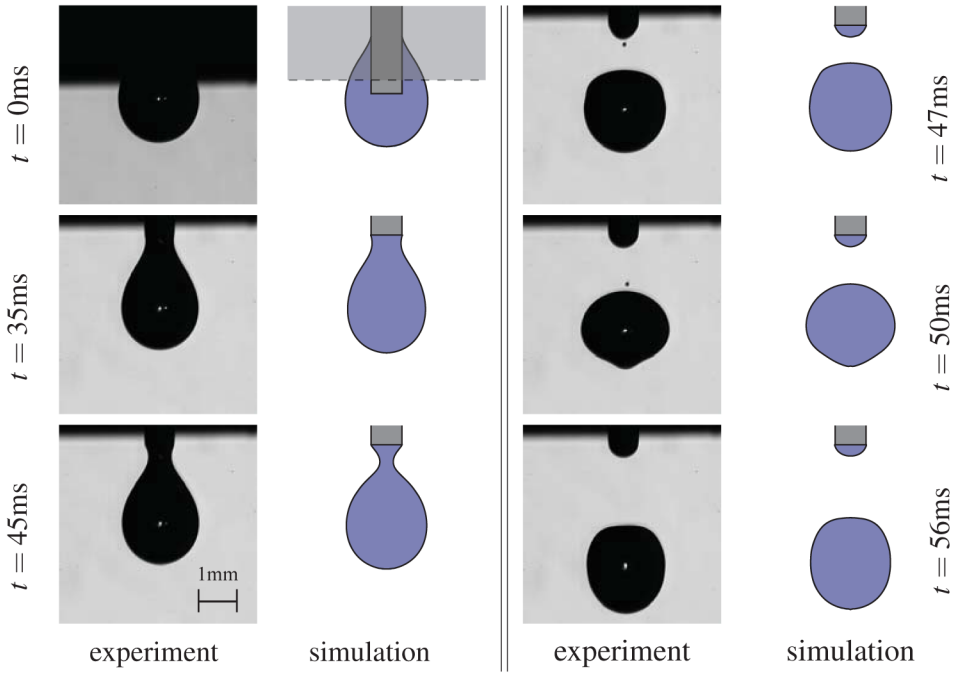

Figure 4: Acetone droplet dynamics: comparison between simulation and experiment for the droplet shape in the generator at different time instants during the detachment process. The experimental images were obtained using a high speed shadowgraphy imaging technique as described in [3].

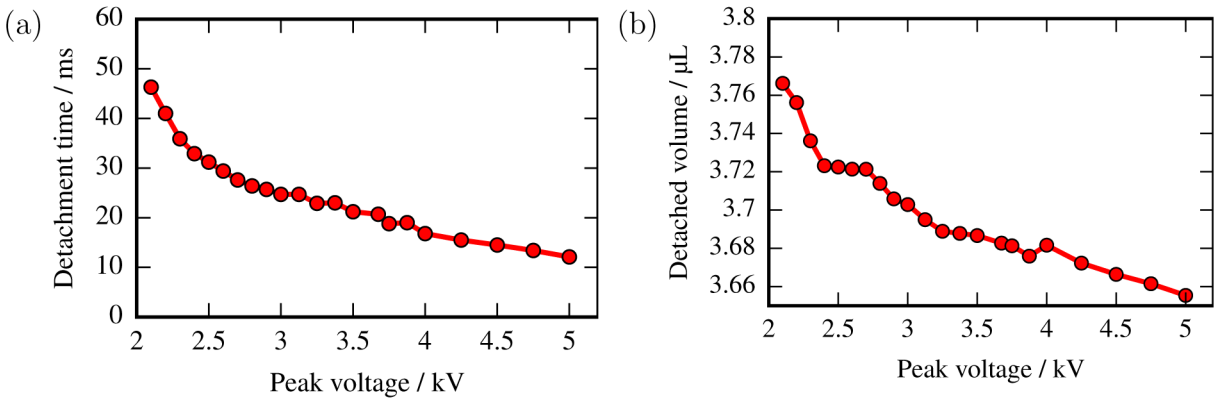

Figure 5: Detachment characteristics vs. applied voltage for acetone droplets. (a) Detachment time and (b) droplet volume vs. generator voltage.

5.2 n-Pentane Droplet Generation

At 1 bar, 293 K, the relative permittivity of n-pentane is $\varepsilon_r = 1.84$. In the absence of impurities, its electrical conductivity is in the range of $\kappa = 20\,\mathrm{pS\,m^{-1}}$. The resulting free charge relaxation time is therefore of the order of 1 s, which is much longer than the applied voltage pulse duration. As a result, the amount of dynamic charging resulting

from the external electric pulse is low, so that electric fields penetrate the droplet. The effective polarization forces initial push the droplet upwards, causing it to ascend on the capillary. The weight of the droplet, unbalanced after the end of the electric pulse, results in the droplet accelerating downwards, eventually leading to detachment.

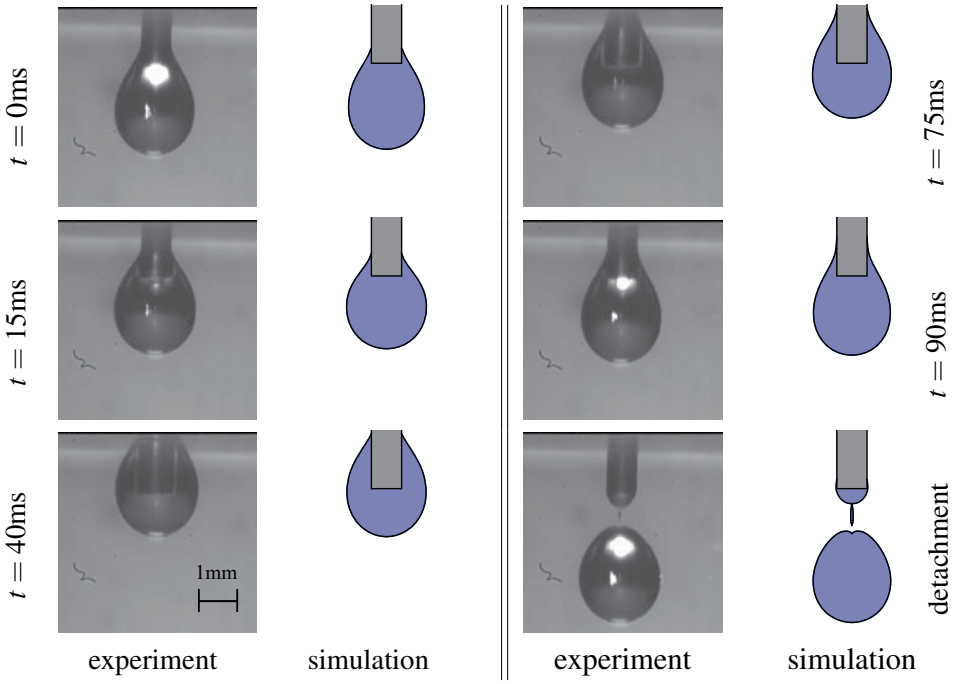

Figure 6: n-pentane droplet dynamics: comparison between simulation and experiment for the droplet shape in the generator at different time instants during the detachment process.

Unlike the case of acetone droplet generation, in the absence of shielding of the capillary by charged conductive liquid, the electric field distribution strongly depends on the location of the droplet on the capillary. The dependency of the detachment time on the applied voltage is thus much lower than in the case of conductive droplets, see Fig. 7a. A small charge is carried by the droplet, after detachment, due to the long relaxation time in n-pentane, as seen in Fig 7b.

6 Conclusion

The proposed electrohydrodynamic simulation approach allows for accurate modeling of droplet dynamics under the influence of strong electric fields. In particular, it takes into account conductive, capacitive as well as convective electrical currents in the fluid. These contributions determine the induced electric charge in the droplet before and after detachment and, therefore, are crucial for the droplet dynamics. Simulation results are shown for an electrically driven droplet generator using highly conductive acetone droplets and low conductivity n-pentane droplets, respectively. In both cases, excellent

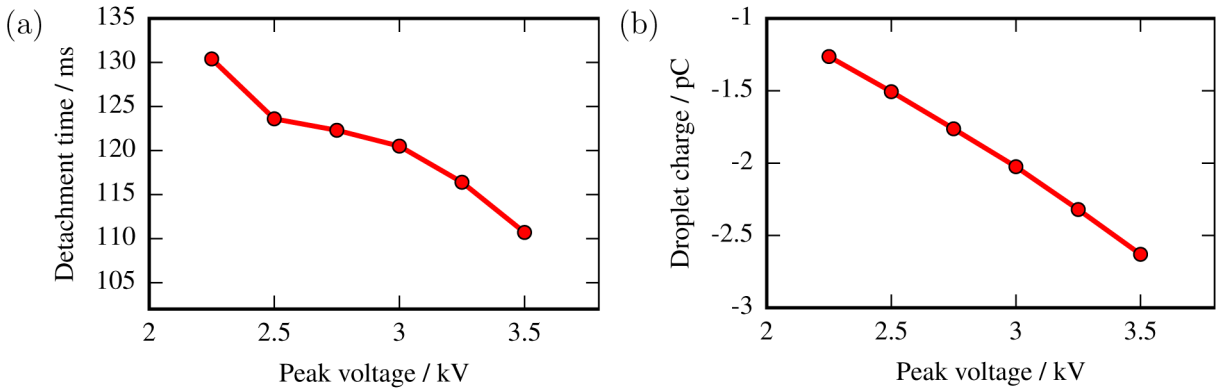

Figure 7: n-pentane droplet characteristics vs. generator voltage. (a) Detachment time and (b) droplet charge after detachment.

agreement with the measurements is found. The droplet charging effect is demonstrated for n-pentane droplets as well as for acetone droplets under long voltage pulses. This investigation shows that due to the very different relaxation times, the charging behavior of the two liquids is very different. This behavior is, furthermore, closely related to the droplet dynamics in the generator. In particular, we demonstrate that due to their electric properties, the detachment mechanisms for acetone and n-pentane droplets are completely different. For low conductivity (n-pentane) droplets, the detachment is primarily due to the uncompensated droplet weight, which dominates droplet dynamics only after the generator voltage is switched off.

ACKNOWLEDGEMENT

This work was funded by the German Research Foundation (DFG) within the Collaborative Research Centre SFB-TRR 75 "Droplet Dynamics Under Extreme Ambient Conditions".

References

[1] M. Cloupeau and B. Prunet-Foch. Electrohydrodynamic spraying functioning modes: a critical review. *J. Aerosol Sci.*, 25(6):1021 – 1036, 1994.

[2] A. Jaworek and A. Krupa. Classification of the modes of ehd spraying. *J. Aerosol Sci.*, 30(7):873 – 893, 1999.

[3] F. Weckenmann, B. Bork, E. Oldenhof, G. Lamanna, B. Weigand, B. Boehm, and A. Dreizler. Single acetone droplets at supercritical pressure: Droplet generation and characterization of PLIFP. *Z. Phys. Chem.*, 225:1417–1431, 2011.

[4] B. Chang, G. Nave, and S. Jung. Drop formation from a wettable nozzle. *Commun. Nonlinear Sci.*, 17(5):2045 – 2051, 2012.

[5] I. V. Roisman, L. Opfer, C. Tropea, M. Raessi, J. Mostaghimi, and S. Chandra. Drop impact onto a dry surface: Role of the dynamic contact angle. *Colloids and Surfaces A: Physicochemical and Engineering Aspects*, 322(13):183 – 191, 2008.

[6] S. F. Kistler. Hydrodynamics of wetting. *Wettability*, 6:311–430, 1993.

[7] C. W. Hirt and B. D. Nichols. Volume of fluid (VOF) method for the dynamics of free boundaries. *J. Comput. Phys.*, 39(1):201 – 225, 1981.

[8] Openfoam. openfoam.org.

[9] H. G. Weller. A new approach to VOF-based interface capturing methods for incompressible and compressible flow. *OpenCFD Ltd., Report TR/HGW/04*, 2008.

[10] J. U. Brackbill, D. B. Kothe, and C. Zemach. A continuum method for modeling surface tension. *J. Computat. Phys.*, 100(2):335 – 354, 1992.

[11] H. Rusche. *Computational fluid dynamics of dispersed two-phase flows at high phase fractions*. PhD thesis, Imperial College London, 2003.

[12] H. Songoro. *Electrohydrodynamic Modeling of Droplet Vibrations under the Influence of Electric Fields*. PhD thesis, Technische Universität, Darmstadt, 2015.

[13] S. Quan and D. P. Schmidt. A moving mesh interface tracking method for 3d incompressible two-phase flows. *J. Comput. Phys.*, 221(2):761 – 780, 2007.

[14] X. Zhang and O. A. Basaran. Dynamics of drop formation from a capillary in the presence of an electric field. *J. Fluid Mech.*, 326:239–263, 11 1996.

[15] G. Tomar, D. Gerlach, G. Biswas, N. Alleborn, A. Sharma, F. Durst, S.W.J. Welch, and A. Delgado. Two-phase electrohydrodynamic simulations using a volume-of-fluid approach. *J. Comput. Phys.*, 227(2):1267 – 1285, 2007.

[16] W. Rohlfs, G. F. Dietze, H. D. Haustein, and R. Kneer. Two-phase electrohydrodynamic simulations using a volume-of-fluid approach: A comment. *J. Comput. Phys.*, 231(12):4454 – 4463, 2012.

[17] C. Galusinski and P. Vigneaux. On stability condition for bifluid flows with surface tension: Application to microfluidics. *J. Comput. Phys.*, 227(12):6140 – 6164, 2008.

VII International Conference on Computational Methods for Coupled Problems in Science and Engineering
COUPLED PROBLEMS 2017
M. Papadrakakis, E. Oñate and B. Schrefler (Eds)

ON THE SIMULATION OF DROPLETIZATION

RAINALD LÖHNER[1], JOSEPH D. BAUM[2], FUMIYA TOGASHI[2], MICHAEL E. GILTRUD[2] AND ORLANDO A. SOTO[2]

[1]Center for Computational Fluid Dynamics
George Mason University, Fairfax, VA 22030, USA
e-mail: rlohner@gmu.edu, web page: https://cfd.gmu.edu/

[2]Applied Simulations, Inc., McLean, VA 22101, USA

Key words: Numerical Algorithms, Computational Fluid Dynamics, Volume of Fluid, Multiphase Flow, Combustion, Fluid-Fluid Coupling

Abstract. Compressible and near-incompressible solvers, together with particle update techniques and chemistry packages are combined in order to compute complex multiphase flows that include dropletization, vaporization and subsquent combustion.

1 INTRODUCTION

Consider the following situation: a high explosive charge is surrounded by a liquid in gas. The explosive is detonated, expanding the liquid, which then breaks up into streaks and blobs. Due to shear, these blobs then break up into droplets. The droplets also vaporize in the surrounding gas. A secondary shock impacting this mass of droplets and vapours may then lead to ignition and combustion. Some of the original liquid mass may remain as a liquid (e.g. on the ground or walls), leading to pool fires once combustion has started.
The simulation of multiphase flows combining gaseous and liquid states has received considerable attention over the last 30 years [15, 34, 36, 33, 25, 35]. Multiphase flow simulations of this type entail a number of complications as compared to single phase flows:

- The equations of state for the liquid phase tend to be complex (e.g. caviation may be present), leading to difficulties with exact or approximate Godunov solvers;
- The speed of sound in the liquid phase is much higher, requiring smaller timesteps and lengthier runs.
- The liquid may break up into droplets that evaporate and mix with the gas phase.

A number of methods have been developed in order to combine gas (compressible) and liquid (near-incompressible) solvers in a single run. The ghost method [9, 8] is a typical method. With the maturity of **single phase** flow codes, a pressing question has been how to combine gas and liquid flow models in a single run. The approach taken here was to use different flow models (and CFD codes), and to couple both via the immersed body method. In the gas region the velocities of the liquid are imposed wherever liquid is present. For the liquid region the pressures of the gas region are imposed wherever gas is present. If the liquid region can no longer be discretized via a continuum method such as the volume of fluid (VOF) or level set (LS) methods, the fluid region is converted to particles, which are incorporated into the gas region.

2 IMMERSED BODY METHOD

Consider the possibility of running concurrently solvers for gases and liquids on the same mesh. As the fluid moves through the domain, the elements and points of the grid where each one of these models is valid changes continuously. For the gas flow/ solver/ region, the **velocities** of the liquid are imposed wherever liquid exists. For the liquid flow/ solver/ region, the **pressures** of the gas are imposed wherever gas is present. In principle, both flow codes could be running concurrently on different grids. Conceptually (and implementationally) this is not different than traditional immersed body methods. Instead of having a rigidly moving body immersed in a compressible flow field, the 'body' happens to be an near-incompressible liquid.
The regions covered by the 'other fluid' for each of the fluids may be treated in a variety of ways. We have experimented with two of these, and at this point use both in production runs.
The first method uses the classic immersed body approach [11, 14, 28, 2, 7, 13, 31, 6, 30, 10, 27, 5, 20] and is sketched in Figure 1. The velocity of the gas is simply set to the velocity of the liquid wherever liquid is present. Instead of having a rigidly moving body immersed in a compressible flow field [5, 20], the 'body' happens to be the liquid. While this works well, one observes that shocks that originate in the gas phase and hit the liquid phase tend to be damped. This is to be expected, as the density and energy are still updated in the gas phase, while the velocity is artificially damped by imposing the (slow) velocity of the liquid. Another disadvantage of this approach is that unnecessary CPU is expended in the gas region covered by liquid.

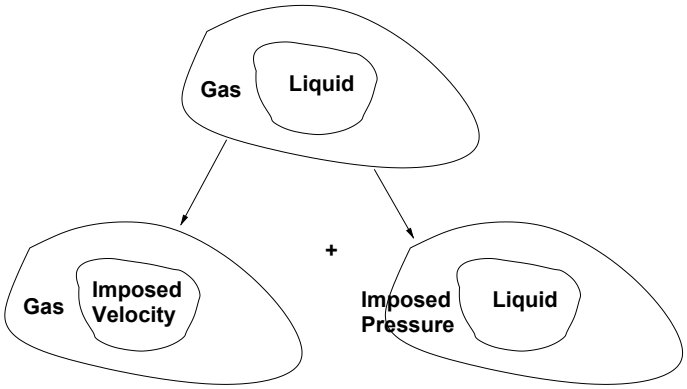

Figure 1 Immersed Body Method

The second option is to deactivate the points and edges in the gas phase covered by liquid. This leads to considerable savings in CPU, but requires the imposition of values for the end-points of edges crossing phases. At every timestep, the edges crossing phases are identified, and the values from the gas phase are extrapolated with imposed mirroring conditions to the points covered by liquids (see Figure 2). This approach is closer to the embedded surface approach [26, 12, 29, 1, 16, 22]. Instead of having a rigidly moving body surface embedded in a compressible flow field [1, 16, 21, 22], the 'body' happens to be an near-incompressible liquid.

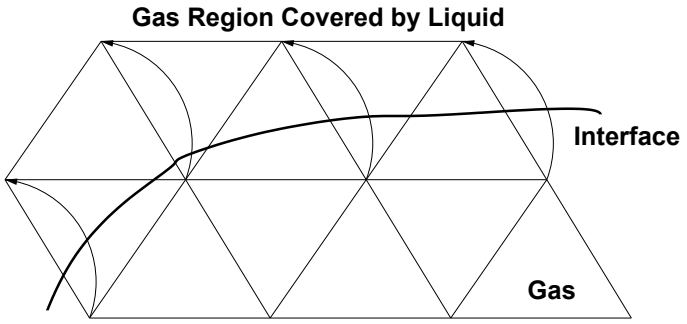

Figure 2 Extrapolation of Unknowns

3 DROPLETIZATION

The transition from liquid to blobs or large droplets uses an approach similar to large-eddy simulation: once the near-incompressible VOF flow solver can no longer discretize accurately the free surface, the badly resolved regions are transformed to blobs and transmitted to the compressible flow solvers. There, they are allowed to break up further into droplets. Several options are possible for this step. We have implemented the widely used Reitz model [32].

The question then becomes how to identify the regions that have become too 'thin' to

accurately describe the liquid via VOF or LS methods. The approach taken here is shown in Figure 3. In a first pass over the edges, the points that are fully inside, on the border of the interface or fully outside the liquid region are marked. In a second (or subsequent) pass(es), a layer is added to the points that are completely inside the liquid region. In this way, the points on the interfaces that are in the liquid but are in 'thin' regions are exposed (see Figure 3). The liquid mass at these points is subsequently transformed into droplets and passed to the code handling the gas phase, where the droplets are treated as Lagrangian particles that can exchange mass, momentum and energy with the gas.

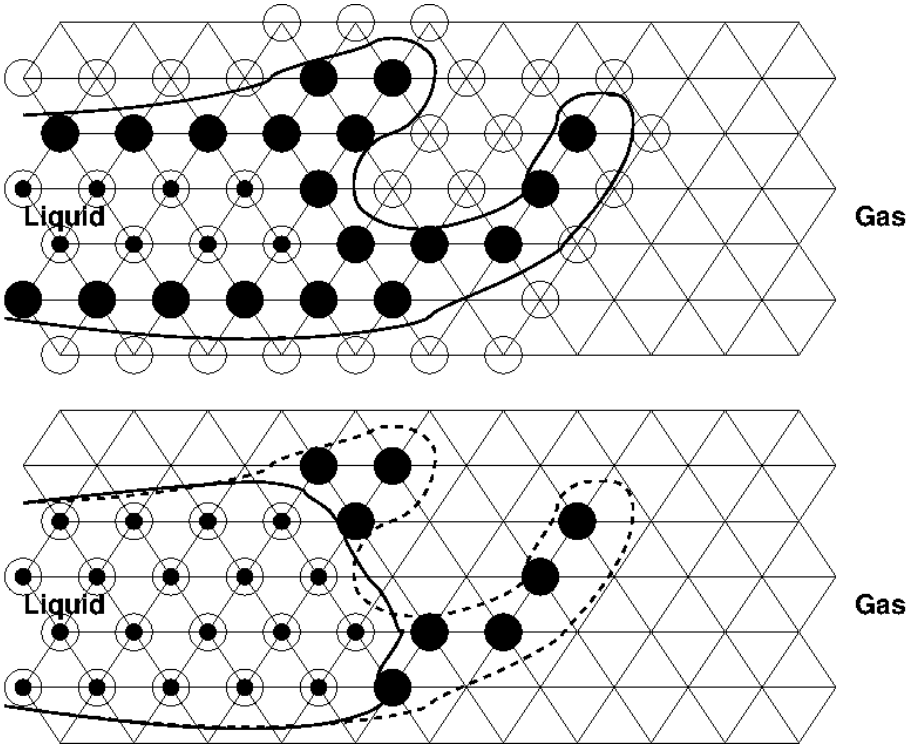

Figure 3 Dropletization of 'Thin' Regions (VOF to Particles)

4 SOFTWARE REALIZATION

The software realization of the procedure outlined above is shown in Figure 4. A master code calls the gas (compressible) and liquid (near-incompressible (+VOF)) codes, as well as the CSD code, as subroutines. The only arguments passed in and out are the (volume) unknowns to be exchanged by the flow codes, as well as the (surface) unknowns to be exchanged by the CSD code and the flow codes. The code computing the gas receives the velocities and VOF mass fraction from the code computing the liquid, updates the variables in time, and outputs the pressures. The code computing the liquid in turn receives the pressures from the code computing the gas, updates the variables in time, and outputs the velocities and VOF mass fraction. In principle, both codes could be

different. In the present case, the original flow code could be run as either compressible or near-incompressible (+VOF). Therefore, it is called twice with an 'instantiation' indicator to differentiate the input and output files required and/or generated for each domain.

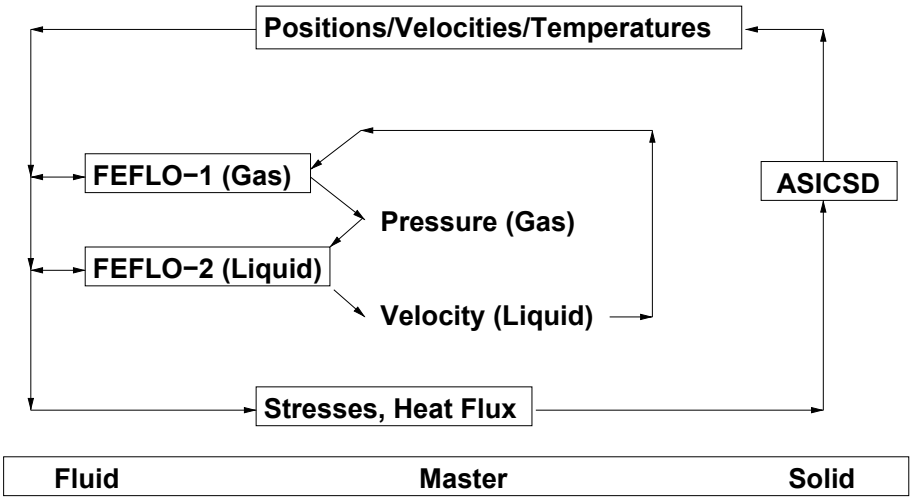

S

Figure 4 Concurrent Run of Same Code Via Multiple Instantiations

A coupling of codes of this kind opens the possibility of taking different timesteps in either code. Indeed, this was pursued here, after it was realized that the solver employed to advance the liquid could run with timesteps up to two orders of magnitude larger than the solver for the gas. For the examples shown below, the timestep taken for the liquid was limited to 2 times the size of the timestep taken by the gas. This implies that, as a whole, the coupling of two codes as proposed here implies a very limited extra amount of CPU (< 3) and memory (< 2) as compared to an optimal multiphase solver.
As stated before, several solvers were combined in order to model these complex multi-physics phenomena. All of the solvers are based on unstructured grids, and use standard edge-based data structures for speed [23]. The different solvers comprise:

- For the gas part: an explicit TVD or FCT solver for chemically reacting, compressible flow [3];
- For the liquid part: a semi-explicit TVD solver for the advective-diffusive terms and a Poisson solver for the pressure terms of the near-incompressible flow [3];
- A volume of fluid approach for the free surface of the liquid [17, 18, 19, 21];
- The Chemkin [4] package for chemistry; and

- A particle update technique that allows for droplet breakup and vaporization [24].

5 RESULTS

Figure 5 shows the result of current runs. A spherical charge of TNT is detonated inside a cylinder of liquid. In order to save CPU resources without compromising the results a section of 30 degrees is considered. The mesh size is approximately 120 Mels. The evolution of the blast waves and the free surface, as well as the droplets and free surface at a late time are shown in Figure 5.

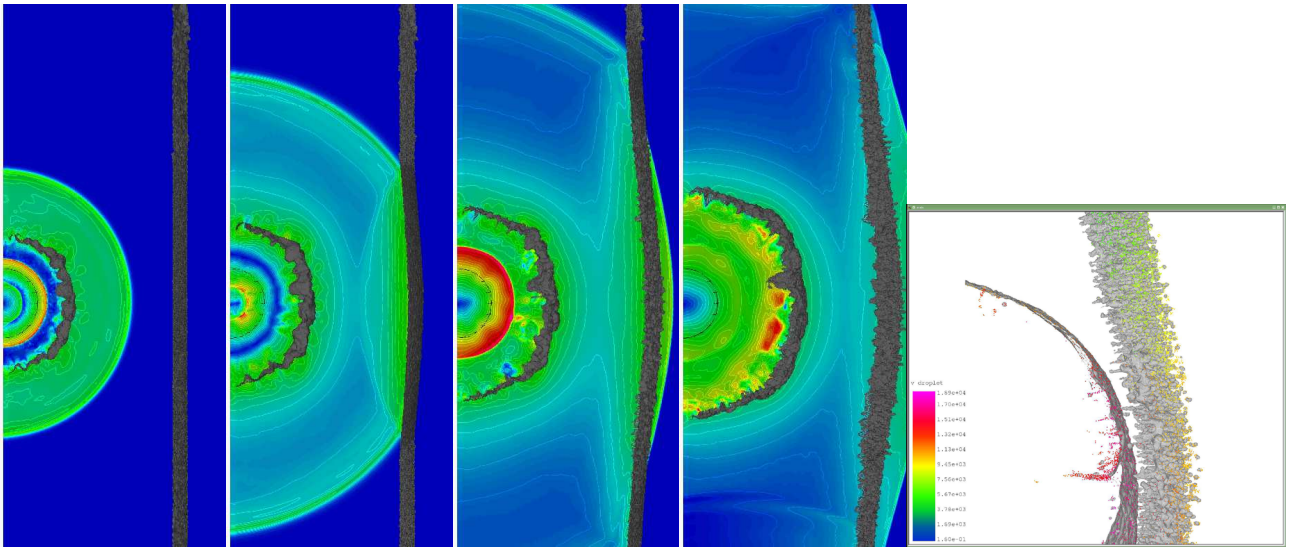

Figure 5 Evolution of Blast Wave (Velocities) And Gas/Liquid Interface

6 CONCLUSIONS AND FUTURE WORK

An approach to compute complex liquid-gas interface evolution problems has been developed. The transition from liquid to blobs uses an approach similar to large-eddy simulation: once the near-incompressible VOF flow solver can no longer discretize accurately the free surface, the badly resolved regions are transformed to blobs and transmitted to the compressible flow solvers as particles. There, they are allowed to break up further into droplets.
Future work includes extensive verification and validation, as well as porting the combination of physics modules used to massively parallel machines.

REFERENCES

[1] M.J. Aftosmis, M.J. Berger and G. Adomavicius - A Parallel Multilevel Method for Adaptively Refined Cartesian Grids with Embedded Boundaries; *AIAA*-00-0808 (2000).

[2] P. Angot, C.-H. Bruneau and P. Fabrie - A Penalization Method to Take Into Account

Obstacles in Incompressible Viscous Flows; *Numerische Mathematik* 81, 497-520 (1999).

[3] J.D. Baum, O.A. Soto, F. Togashi and R. Löhner - Numerical Modeling of Multiphase, Multimaterial Blast/Structure Interactions; *AIAA*-11-3722 (2011).

[4] R.J. Kee, F.M. Rupley and J.A. Miller - Chemkin-II: A Fortran Chemical Kinetics Package for the Analysis of Gas-Phase Chemical Kinetics; *Sandia Nat. Lab. Report SAND-89-8009, ON: DE90000917* (1989).

[5] Y. Cho, S. Boluriaan and P.J. Morris - Immersed Boundary Method for Viscous Flow Around Moving Bodies; *AIAA*-06-1089 (2006).

[6] A. Dadone and B. Grossman - An Immersed Boundary Methodology for Inviscid Flows on Cartesian Grids; *AIAA*-02-1059 (2002).

[7] E.A. Fadlun, R. Verzicco, P. Orlando and J. Moud-Yusof - Combined Immersed-Boundary Finite-Difference Methods for Three-Dimensional Complex Flow Simulations; *J. Comp. Phys.* 161, 33-60 (2000).

[8] Ch. Farhat, A. Rallu and S. Shankaran - A Higher-Order Generalized Ghost Fluid Method for the Poor for the Three-Dimensional Two-Phase Flow Computation of Underwater Implosions; *J. Comp. Phys.* 227, 76747700 (2008).

[9] R. Fedkiw, T. Aslam, B. Merriman and S. Osher - A Non-Oscillatory Eulerian Approach to Interfaces in Multimaterial Flows (The Ghost Fluid Method); *J. Comp. Phys.* 152, 457-492 (1999).

[10] A. Gilmanov and F. Sotiropoulos - A Hybrid Cartesian/Immersed Boundary Method for Simulating Flows with 3-D, Geometrically Complex Moving Bodies; *J. Comp. Phys.* 207, 2, 457-492 (2005).

[11] D. Goldstein, R. Handler and L. Sirovich - Modeling a No-Slip Flow Boundary with an External Force Field; *J. Comp. Phys.* 105, 354366 (1993).

[12] S.L. Karman - SPLITFLOW: A 3-D Unstructured Cartesian/ Prismatic Grid CFD Code for Complex Geometries; *AIAA*-95-0343 (1995).

[13] J. Kim, D. Kim and H. Choi - An Immersed-Boundary Finite-Volume Method for Simulation of Flow in Complex Geometries; *J. Comp. Phys.* 171, 132-150 (2001).

[14] A.M. Landsberg and J.P. Boris - The Virtual Cell Embedding Method: A Simple Approach for Gridding Complex Geometries; *AIAA*-97-1982 (1997).

[15] R.J. LeVeque and K.M. Shyue - Two-Dimensional Front Tracking Based on High Resolution Wave Propagation Methods; *J. Comp. Phys.* 123, 354368. ((1996).

[16] Löhner, R., J.D. Baum, E. Mestreau, D. Sharov, C. Charman and D. Pelessone - Adaptive Embedded Unstructured Grid Methods; *Int. J. Num. Meth. Eng.* 60, 641-660 (2004).

[17] R. Löhner, Chi Yang, J.R. Cebral, F. Camelli, O. Soto and J. Waltz - Improving the Speed and Accuracy of Projection-Type Incompressible Flow Solvers; *Comp. Meth. Appl. Mech. Eng.* 195, 23-24, 3087-3109 (2006).

[18] R. Löhner, Chi Yang and E. Oñate - On the Simulation of Flows with Violent Free Surface Motion; *Comp. Meth. Appl. Mech. Eng.* 195, 5597-5620 (2006).

[19] R. Löhner, Chi Yang and E. Oñate - Simulation of Flows With Violent Free Surface Motion and Moving Objects Using Unstructured Grids; *Int. J. Num. Meth. Fluids* 53, 1315-1338 (2007).

[20] R. Löhner, J.D. Baum, E.L. Mestreau and D. Rice - Comparison of Body-Fitted, Embedded and Immersed 3-D Euler Predictions for Blast Loads on Columns; *AIAA*-07-1133 (2007).

[21] R. Löhner, P. Ravier, J. Roger and P. deKermel - Combination of Compressible and Incompressible Flow Codes via Immersed Methods; *AIAA*-08-0528 (2008).

[22] R. Löhner, J.R. Cebral, F.F. Camelli, S. Appanaboyina, J.D. Baum, E.L. Mestreau and O. Soto - Adaptive Embedded and Immersed Unstructured Grid Techniques; *Comp. Meth. Appl. Mech. Eng.* 197, 2173-2197 (2008).

[23] R. Löhner - *Applied CFD Techniques, 2nd Edition*; J. Wiley & Sons (2008).

[24] R. Löhner, F. Camelli, J.D. Baum, F. Togashi and O. Soto - On Mesh-Particle Techniques; *Comp. Part. Mech.* 1, 199-209 (2014).

[25] H. Luo, J.D. Baum and R. Löhner - On the Computation of Multi-Material Flows Using ALE Formulation; *J. Comp. Phys.* 194, 304-328 (2004).

[26] Melton, J.E., M.J. Berger and M.J. Aftosmis - 3-D Applications of a Cartesian Grid Euler Method; *AIAA*-93-0853-CP (1993).

[27] R. Mittal and G. Iaccarino - Immersed Boundary Methods; *Annu. Rev. Fluid Mech.* 37, 239-261 (2005).

[28] J. Mohd-Yusof - Combined Immersed-Boundary/B-Spline Methods for Simulations of Flow in Complex Geometries; *CTR Annual Research Briefs*, NASA Ames Research Center/ Stanford Univ., 317-327 (1997).

[29] R.B. Pember, J.B. Bell, P. Colella, W.Y. Crutchfield and M.L. Welcome - An Adaptive Cartesian Grid Method for Unsteady Compressible Flow in Irregular Regions; *J. Comp. Phys.* 120, 278 (1995).

[30] C.S. Peskin - The Immersed Boundary Method; *Acta Numerica* 11, 479-517 (2002).

[31] S. Del Pino and O. Pironneau - Fictitious Domain Methods and Freefem3d; *Proc. ECCOMAS CFD Conf.* , Swansea, Wales (2001).

[32] R.D. Reitz - Modeling Atomization Processes in High-Pressure Vaporizing Sprays; *Atomization and Spray Technology* 3, 309-337 (1987).

[33] R. Saurel and R. Abgrall - A Multiphase Godunov Method for Compressible Multifluid and Multiphase Flows; *J. Comp. Phys.* 150, 2, 425-467 (1999).

[34] K.M. Shyue - An Efficient Shock-Capturing Algorithm for Compressible Multicomponent Problems; *J. Comp. Phys.* 142, 208242 (1998).

[35] B. Wang and H. Xu - A Method Based in Riemann Problem in Tracking Multi-Material Interface on Unstructured Moving Grids; *Eng. Appl. Comp. Fluid Mech.* 1, 4, 325-336 (2007).

[36] A.B. Wardlaw and H. Mair - Spherical Solutions of an Underwater Explosion Bubble; *Shock and Vibration* 5, 89102 (1998).

VII International Conference on Computational Methods for Coupled Problems in Science and Engineering
COUPLED PROBLEMS 2017
M. Papadrakakis, E. Oñate and B. Schrefler (Eds)

A DIRECT SOLUTION APPROACH FOR MULTI TIMESCALE OPTIMAL CONTROL PROBLEMS

MATTHIAS BITTNER*, BENEDIKT GRÜTER*, JOHANNES DIEPOLDER* AND FLORIAN HOLZAPFEL*

* Institute of Flight System Dynamics (FSD)
Technical University of Munich (TUM)
Boltzmannstraße 15, 85748 Garching, Germany
e-mail: m.bittner@tum.de, benedikt.grueter@tum.de,
johannes.diepolder@tum.de, florian.holzapfel@tum.de
web page: http://www.fsd.mw.tum.de/

Key words: Optimal Control, Direct Discretization, Multiple Timescales, Stiff Dynamics, Aircraft Trajectory Optimization

Abstract. In high fidelity optimal control problems, a commonly appearing problem emerges from different timescales inherent to the model, resulting in stiff differential equations. When solving these problems using direct discretization, the selection of the discretization nodes for all states is driven by the states associated with the fast dynamics, no matter how strong their influence on the solution is. In this paper, a novel discretization scheme is presented that uses direct collocation for the slow states while the fast states of the model are represented based on a direct multiple shooting scheme. This way, different grids may be chosen for the states, resulting in a slight decoupling of the timescales. A high fidelity air race trajectory optimization problem is implemented to demonstrate how the dimensions of the discretized problem can be significantly decreased by the method, resulting in improved computational performance during the solution process.

1 INTRODUCTION

In many applications, the performance of a system needs to be increased without changing its inherent properties. In these cases, methods for the optimization of operation strategies are required, where optimal control is one such method. When applying optimal control theory to high fidelity models, a problem that appears quite often are different timescales inherent to the model, resulting in *stiff differential equations*.

Especially in mechanical systems, fast dynamics can often be recognized as (small scale) *internal dynamics*, while slower dynamics often represent the more visible (large scale) *outer effects* of the motion of a body. If the model may not be simplified by assuming the fast part of the dynamics to be decayed instantaneously, the selection of an appropriate

discretization grid is driven by the fast and small scale dynamics (in order to keep the integration errors low) whose dynamic effects hardly influence the overall results. In many high fidelity optimal control problems, the required fine grid strongly increases the computational effort of the solution process.

Several approaches have been suggested to overcome this issue in the past. These include *Multirate Runge Kutta* methods [1, 2] that may also be used for pure simulation tasks. Furthermore, a multi timescale collocation method has been presented in [3]. BOTTASSO et. al. have published results based on the combination of single and multiple shooting in [4]. In their work, a discretization scheme is proposed that combines the benefits of *Direct Single Shooting* with those of *Direct Multiple Shooting*.

The method proposed here, is to split the state vector, and thus the dynamic system, into a fast and a slow part. The fast dynamics are discretized using *Multiple Shooting* and the slow ones using *Direct Collocation* that is based on the same grid as the multiple shooting *segment nodes*. The number of Multiple Shooting integration grid points in between these segment nodes may be chosen arbitrarily – forming a second, finer grid to coexist with the collocation grid. In order to be able to evaluate the dynamic equations within the multiple shooting segments, an approximation of the slow states is required that can be calculated based on interpolation.

The presented approach is applied to an aircraft trajectory optimization problem, using a nonlinear high fidelity rigid body simulation model of an aerobatic aircraft. The model features very fast rotational dynamics compared to the translational motion. In this example, a time optimal trajectory through an air race course respecting several boundary conditions and path constraints is calculated. The results show a significant reduction in the dimensions of the numerical optimization problem, also leading to a reduced calculation time.

The method and the results published in this paper are part of the dissertation thesis [5] of the first author.

2 OPTIMAL CONTROL PROBLEM

The problems considered here are optimal control problems of the following form: Determine the optimal control histories $\mathbf{u}_{opt}(t) \in \mathbb{R}^{n_u}$ and the optimal state trajectory $\mathbf{x}_{opt}(t) \in \mathbb{R}^{n_x}$ that minimize the BOLZA cost functional

$$J = e(\mathbf{x}(t_f), t_f) + \int_{t_0}^{t_f} L(\mathbf{x}(t), \mathbf{u}(t), t)\, dt \tag{1}$$

subject to the state dynamics

$$\dot{\mathbf{x}} = \mathbf{f}(\mathbf{x}, \mathbf{u}), \tag{2}$$

the initial and final boundary conditions

$$\boldsymbol{\psi}_0(\mathbf{x}(t_0), t_0) = \mathbf{0} \qquad \text{and} \qquad \boldsymbol{\psi}_f(\mathbf{x}(t_f), t_f) = \mathbf{0}, \tag{3}$$

and the equality and inequality path constraints

$$\mathbf{C}_{eq}(\mathbf{x}(t), \mathbf{u}(t), t) = \mathbf{0} \qquad \text{and} \qquad \mathbf{C}_{ineq}(\mathbf{x}(t), \mathbf{u}(t), t) \leq \mathbf{0}. \tag{4}$$

The problem in the example below is formulated as a multi phase problem. [5, 6]

2.1 Discretization Techniques

Two of the classes of methods for solving optimal control problems are: On the one hand, there are indirect approaches that are based on the derivation of optimality conditions for the continuous problem which are then discretized and solved in a second step. On the other hand, in direct schemes the problem is first discretized and afterwards optimized numerically. The process of discretization turns the infinite dimensional optimal control problem into a finite dimensional numerical optimization problem that can be solved using off-the-shelf optimization algorithms like gradient based *Sequential Quadratic Programming (SQP)* or *Interior Point (IP)* methods.

The two direct solution approaches combined here are *Direct Multiple Shooting* and *Direct Collocation*. In shooting, the dynamic constraint (2) is discretized by performing a forward integration using numerical simulation methods for ordinary differential equations, like Runge Kutta methods. If the simulation of the whole time series is performed in one sweep, the methods are called *Single Shooting* methods. Opposite, in *Multiple Shooting* methods the simulation is reset at some predefined nodes, the so-called *Multiple Shooting Defect Nodes*. The state values at these nodes are introduced as optimization variables in the discretized problem. In order to ensure continuous and feasible state trajectories, for each multiple shooting node an additional set of constraints, the so-called *Multiple Shooting Defects*, are introduced:

$$\mathbf{c}_m = \mathbf{x}_0^m(\mathbf{z}) - \mathbf{x}_0^{m+1}(\mathbf{z}) + \int_{t_{\mathbf{x}_0,m}}^{t_{\mathbf{x}_0,m+1}} \dot{\mathbf{x}}(t)\, dt \qquad \forall m = 1, \ldots, M-1 \tag{5}$$

The gradient information required by the numerical optimization algorithms can be calculated by finite differences or automatic differentiation and sensitivity equations. More details on the latter can be found in literature such as [5, 6].

One way of motivating *Direct Collocation* is by resetting the state values in a multiple shooting method after each integration step. Then, every discretized state value is part of the optimization parameter vector in the numerical optimization problem. Moreover, a collocation defect needs to be introduced for every discretization time step:

$$\mathbf{c}_k = \mathbf{x}_k(\mathbf{z}) - \mathbf{x}_{k+1}(\mathbf{z}) + h_k \cdot \Phi(\mathbf{x}_k(\mathbf{z}), \mathbf{x}_{k+1}(\mathbf{z}), \mathbf{u}_k(\mathbf{z}), \mathbf{u}_{k+1}(\mathbf{z}), \mathbf{p}(\mathbf{z})) \tag{6}$$

Here, Φ represents the increment function of the underlying integration scheme. Remarkably, in collocation methods the use of implicit integration schemes is comparably easy

as all state values are part of the optimization vector and available for the calculation of the defects. Consequently, the solution of the implicit integration scheme is performed by the numerical optimization algorithm automatically. More details on direct and indirect solution methods for optimal control problems can also be found in [6, 5].

3 DYNAMIC AIRCRAFT MODEL

A full nonlinear rigid body simulation model of an aerobatic aircraft incorporating nonlinear aerodynamics is used here. Table 1 lists the states of the model, which is controlled by the deflections of the aileron ξ, the elevator η, the rudder ζ and the thrust lever position $\delta_{T,CMD}$. No wind is considered in the example, rendering all aerodynamic and kinematic quantities equal.

The considered flight trajectory is of small spatial extent, the flight times are comparably short, and the velocities are low enough, such that the earth may be considered as flat and non-rotating. In this case, the position equations of motion for the aircraft can be given with respect to a locally fixed coordinate frame. The attitude dynamics are modeled in accordance to the work [7], given with respect to the kinematic flight path of the aircraft. The rotational and the translational dynamics of the rigid body are based on NEWTON's second law using the moments and forces acting on the system as inputs.

The main categories of external forces and moments influencing the motion of an aircraft are aerodynamics, propulsion and gravity. Here, the thrust dynamics are approximated by a first order system in δ_T. More information on modeling the external forces and moments can e. g. be found in [7, 8, 9, 10, 11].

As the flights are partially conducted in the proximity of stall, a model for the lift coefficient that features a linear dependency on the angle of attack is not sufficient. Hence, a nonlinear function $C^*_{L,\alpha}(\alpha_K)$ is used for modeling its dependence on the angle of attack. Moreover, the propulsion force is assumed to act along the longitudinal axis of the aircraft. As the thrust created by the engine cannot follow the commanded thrust instantaneously, a thrust dynamic is incorporated in the model. Due to the small spatial extent of the trajectories a gravitational model assuming constant acceleration is used. [5]

Table 1: States of the aircraft simulation model

POSITION			ATTITUDE		
Symbol	**Description**	**Unit**	**Symbol**	**Description**	**Unit**
$(x)_N$	x-position in N Frame	m	α_K	Angle of attack	rad
$(y)_N$	y-position in N Frame	m	β_K	Angle of sideslip	rad
$(z)_N$	Downward position	m	μ_K	Bank angle	rad
VELOCITY			ANGULAR RATE		
Symbol	**Description**	**Unit**	**Symbol**	**Description**	**Unit**
V_K	Absolute velocity	m/s	p	Roll rate	rad/s
χ_K	Course angle	rad	q	Pitch rate	rad/s
γ_K	Climb angle	rad	r	Yaw rate	rad/s

4 COMBINED DIRECT COLLOCATION AND MULTIPLE SHOOTING

The proposed approach for overcoming the aforementioned issues combines a direct collocation scheme with a direct multiple shooting approach. The basic idea is to separate the state vector of the dynamic system into two parts, one containing the fast and the other containing the slow dynamics. The fast dynamics are discretized using a multiple shooting approach and the slow ones using a collocation scheme that is based on the same grid as the *Multiple Shooting Defect Nodes*. The number of multiple shooting integration grid points in between these nodes may be chosen arbitrarily, forming another, finer grid. In order to be able to evaluate the dynamic equations in between the multiple shooting segments, an approximation of the slow states is required. These values can be calculated using different interpolation algorithms, where a cubic and a linear interpolation scheme is suggested here. The required gradients can be evaluated using slightly modified sensitivity equations.

Figure 1 visualizes the general idea of the discretization scheme. The two grids inherent to the method can be seen on the abscissa with the large markers representing the collocation and *Multiple Shooting Defect Node* grid

$$\mathbb{G}_{\mathbf{x}_s} = \{t_0 < t_1 < t_2 < \ldots < t_N = t_f\} \tag{7}$$

and the small markers representing the *Multiple Shooting Integration Grid*:

$$\mathbb{G}_{\mathbf{x}_f} = \{\bar{\tau}_{0,0}, \bar{\tau}_{0,1}, \ldots, \bar{\tau}_{0,n_0} = \bar{\tau}_{1,0}, \bar{\tau}_{1,1}, \ldots, \bar{\tau}_{1,n_1} = \bar{\tau}_{2,0}, \ldots, \bar{\tau}_{N,n_N}\} \tag{8}$$

In the following, they will be referred to as the *coarse grid* $\mathbb{G}_{\mathbf{x}_s}$ and the *fine grid* $\mathbb{G}_{\mathbf{x}_f}$. The multiple shooting defect between the k-th and the $k+1$-th multiple shooting segment is visualized as $d_{f,k}$.

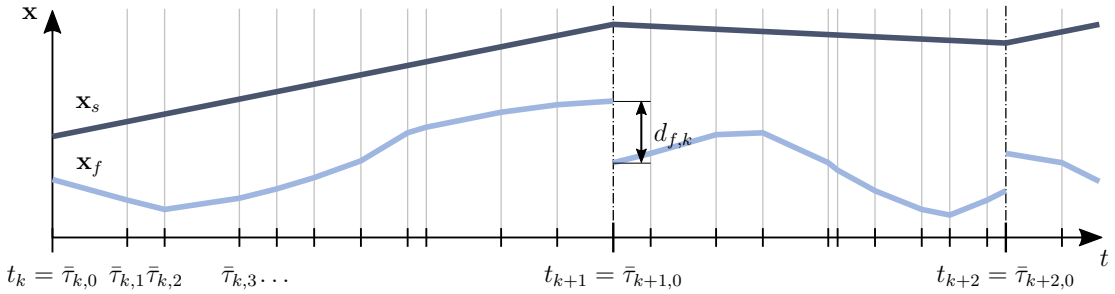

Figure 1: Discretization scheme based on collocation and multiple shooting. [5]

The dynamics of the system are partitioned into a slow part and a fast part by separating the state vector $\mathbf{x}$ into the sub-vector $\mathbf{x}_s$ for the slow states (shown in dark blue in figure 1) and $\mathbf{x}_f$ for the fast states (depicted in light blue in figure 1). Consequently, the state dynamics

$$\dot{\mathbf{x}} = \mathbf{f}(\mathbf{x}, \mathbf{u}, \mathbf{p}) \tag{9}$$

also need to be partitioned into the fast dynamics $\mathbf{f}_f$ and the slow dynamics $\mathbf{f}_s$. Equation (9) can hence be rewritten as:

$$\dot{\mathbf{x}}_s = \mathbf{f}_s(\mathbf{x}_s, \mathbf{x}_f, \mathbf{u}, \mathbf{p}), \qquad \text{and} \qquad \dot{\mathbf{x}}_f = \mathbf{f}_f(\mathbf{x}_s, \mathbf{x}_f, \mathbf{u}, \mathbf{p}) \tag{10}$$

Now, the evaluation of the slow dynamics on the coarse grid is directly possible as all required data is part of the numerical optimization vector in the discretized problem. On the contrary, the slow states are not available on the fine grid. At this point, the aforementioned linear or cubic interpolation schemes are used. For both of them, the normalized time $\bar{\tau}_k \in [0, 1]$ is introduced in each segment $[t_k, t_{k+1}]$ of the coarse grid.

The linear interpolation of the fast states can directly be calculated from the initial and the final state values of each multiple shooting segment (with $\mathbf{x}_s(t_k) = \mathbf{x}_{s,k}$):

$$\mathbf{x}_s(\bar{\tau}_k) = \mathbf{x}_{s,k} + \bar{\tau}_k \cdot (\mathbf{x}_{s,k+1} - \mathbf{x}_{s,k}) \tag{11}$$

When using a cubic interpolation in the segments, the state derivatives at the initial and the final point also need to be considered. They can be calculated from the following state equations:

$$\dot{\mathbf{x}}_{s,k} = \mathbf{f}_s(\mathbf{x}_{s,k}, \mathbf{x}_{f,k}, \mathbf{u}_k, \mathbf{p}) = \mathbf{f}_{s,k} \tag{12}$$

$$\dot{\mathbf{x}}_{s,k+1} = \mathbf{f}_s(\mathbf{x}_{s,k+1}, \mathbf{x}_{f,k+1}, \mathbf{u}_{k+1}, \mathbf{p}) = \mathbf{f}_{s,k+1} \tag{13}$$

Requiring the state values and the state derivatives to match at the initial and the final point of each segment, the following cubic polynomial can be derived:

$$\begin{aligned} \mathbf{x}_s(\bar{\tau}_k) = {} & (2 \cdot \mathbf{x}_{s,k} + \dot{\mathbf{x}}_{s,k} - 2 \cdot \mathbf{x}_{s,k+1} + \dot{\mathbf{x}}_{s,k+1}) \cdot \bar{\tau}_k^3 \\ & + (-3 \cdot \mathbf{x}_{s,k} - 2 \cdot \dot{\mathbf{x}}_{s,k} + 3 \cdot \mathbf{x}_{s,k+1} - \dot{\mathbf{x}}_{s,k+1}) \cdot \bar{\tau}_k^2 + \dot{\mathbf{x}}_{s,k} \cdot \bar{\tau}_k + \mathbf{x}_{s,k} \end{aligned} \tag{14}$$

Similar to all other discretization schemes, the calculation of analytic gradient information can improve the convergence stability and speed of the discretized optimal control problem. As the slow dynamics are solved using a regular collocation scheme, the calculation method of the gradients does not change. The multiple shooting scheme for the fast states is slightly changed as the interpolated slow states have to be added to the equations. Consequently, the respective sensitivity equations need to be adapted accordingly. [5]

The method presented here can be used with a combination of explicit and implicit numerical integration schemes. Therein, explicit algorithms as well as implicit ones can easily be incorporated in the collocation, while for the shooting part the use of implicit methods comes at the cost of a very high computational burden. In this approach, path constraints can easily be calculated from the state histories on the coarse grid, as they are part of the optimization parameter vector. Anyway, it may happen that the states in between two such nodes violate a path constraint which may not be detected. [5]

5 EXAMPLE AND RESULTS

An air race trajectory optimization problem using a high fidelity dynamic model of an aerobatic aircraft is presented and solved here. The race track to be passed by the aircraft in minimum time is built up by seven race gates that are represented by the red crosses in figure 2. As the aircraft has to pass the gates several times, an optimal control problem with 17 point constraints and 16 intermediate phases results.

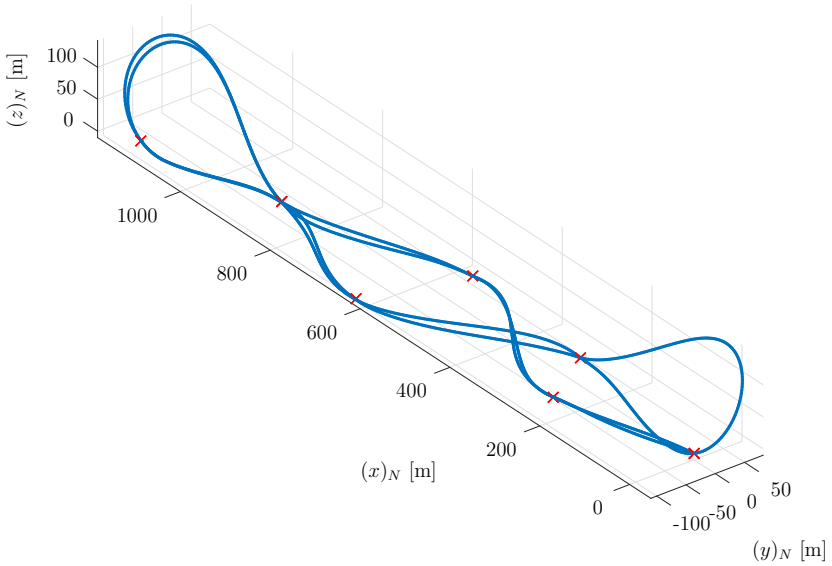

Figure 2: Time optimal spatial trajectory for the combined simulation model. [5]

5.1 Cost function

The cost function to be minimized in the air race example is the overall race time:

$$J = t_f - t_0 \tag{15}$$

which may be formulated as the LAGRANGE part of the cost function (1) as:

$$L(\mathbf{x}(t), \mathbf{u}(t), t) = 1 \tag{16}$$

5.2 Path constraints

Besides the dynamic constraints from the aircraft simulation model presented in section 3, algebraic path constraints have to hold along the trajectory. Table 2 lists these path constraints together with their respective limits. [5]

5.3 Race Gate Constraints

The constraints that apply whenever the aircraft is passing through one of the race gates are listed in table 3. [5]

Table 2: Path constraints applied in the air race example. [5]

Description	Symbol	Unit	Lower Bound	Upper Bound
Altitude limit due to ground clearance (zero-level at center of race gates)	$(h)_N$	m	-10	–
Load factor limits due to regulations	$(n_z)_B$	–	-2	10
Speed limits due to regulations	V_K	m/s	25	102.9
Aerodynamic angle of attack limits	α_A	deg	-10	20
Aerodynamic angle of sideslip limits	β_A	deg	-10	10
Roll rate limits	p_K	deg $/s$	-420	420

Table 3: Constraints applied at the race gates in the air race example. [5]

Description	Symbol	Unit	Tolerance
x-Position at the race gate	$(x)_N$	m	± 0
y-Position at the race gate	$(y)_N$	m	± 0
z-Position at the race gate	$(z)_N$	m	± 0
Orientation at the race gate	χ_K	deg	± 0
Bank angle at the race gate	μ_K	deg	± 10

5.4 Problem Setup

Here, the rotational states are considered to be fast, while the translational ones represent the slow dynamics of the aircraft. Consequently, the fast states in the model from above are

$$\mathbf{x}_f = [\mu_K, \alpha_K, \beta_K, p, q, r]^\intercal \tag{17}$$

while the remaining states are considered to be slow:

$$\mathbf{x}_s = [(x)_N, (y)_N, (z)_N, \chi_K, \gamma_K, V_K, \delta_T]^\intercal \tag{18}$$

In this example, the slow states were discretized on an equidistant grid in normalized time, containing 101 points per phase. For the fast states a subdivision of five grid points was used, resulting in a total of 501 grid points per phase. Overall, in the problem built up from 16 phases, for the slow states 1616 collocation nodes and for the fast states 8016 EULER forward multiple shooting grid points result. For the approximation of the slow states on the grid of the fast states, the linear interpolation from equation (11) has been implemented. The controls are also discretized on the coarse collocation grid and are linearly interpolated to the fine multiple shooting integration grid.

Due to the different lengths in real time of the phases, the distance between two nodes varies for the slow states from $0.024s$ to $0.065s$ and for the fast states from $0.0048s$ to $0.0129s$. *IPOPT* [12] was used to solve the problem to a feasibility tolerance of $tol_C = 10^{-6}$ and an optimality tolerance of $tol_J = 5 \cdot 10^{-6}$. [5]

5.5 Implementation in FALCON.m

The optimal control tool *FALCON.m* (*FSD Optimal Control Tool*) was used here. It has been developed at the Institute of Flight System Dynamics at the Technical University of Munich in order to avoid the need to re-implement discretization code for optimal control problems. After the user implemented all vectors and functions defining the problem, *FALCON.m* automatically calculates a discretized representation of it and uses *IPOPT* [12] to solve it. *FALCON.m* calculates all gradients analytically and determines the sparsity structure of the problem before handing this information to the solver for improved performance. [5]

5.6 Results

The problem was solved on a personal computer equipped with an Intel Core i7-950 CPU with $3.07GHz$ and $20GB$ of RAM and converged in approximately $2144s$ and 1355 iterations. The trajectory that results from the optimization can be seen in figure 2. The minimal race time calculated in the optimization is $60.3512s$. The state histories along the trajectories are depicted in figure 3.

For the sake of comparison, other optimizations have been performed using the simplified point mass simulation model as well as the rigid body simulation model – both in combination with a pure collocation algorithm. Table 4 gives a numeric overview of the different results. It can be seen that the number of optimization variables decreased to 27488 while the number of constraints dropped to 22627 in the discretized problem using the combined discretization scheme as less grid points are required. Even though the number of 764082 structural non-zero elements in the gradient is also comparably low, the sparsity ratio of 99.8772% is not as high as it is with pure collocation – as expected due to the higher interdependence in the shooting scheme and the smaller overall problem size. Additionally, the solution time also decreased, however, not in the same relation as the problem dimensions did, for the same reason as before.

Table 4: Overview of the results using the different simulation models and discretization methods. [5]

	Optim. param.	**Constr.**	**Iter.**	**Solution time**	**Cost func.**
Point mass simulation model (fine grid)	80176	72184	1927	$1730s$	$60.23s$
Combined collocation and shooting	27488	22627	1355	$2144s$	$60.35s$
Rigid body simulation model (fine grid)	136288	112227	883	$2290s$	$60.34s$

The yellow line in figure 4 shows the difference between the mixed collocation and shooting approach and the pure collocation of the rigid body simulation model on the fine grid. The observed difference in the trajectory is within the range of some centimeters. Here, the reason is twofold:

- On the one hand, the discretization of the controls is coarser with the combined solution method, reducing the theoretical "possibilities of the pilot", and

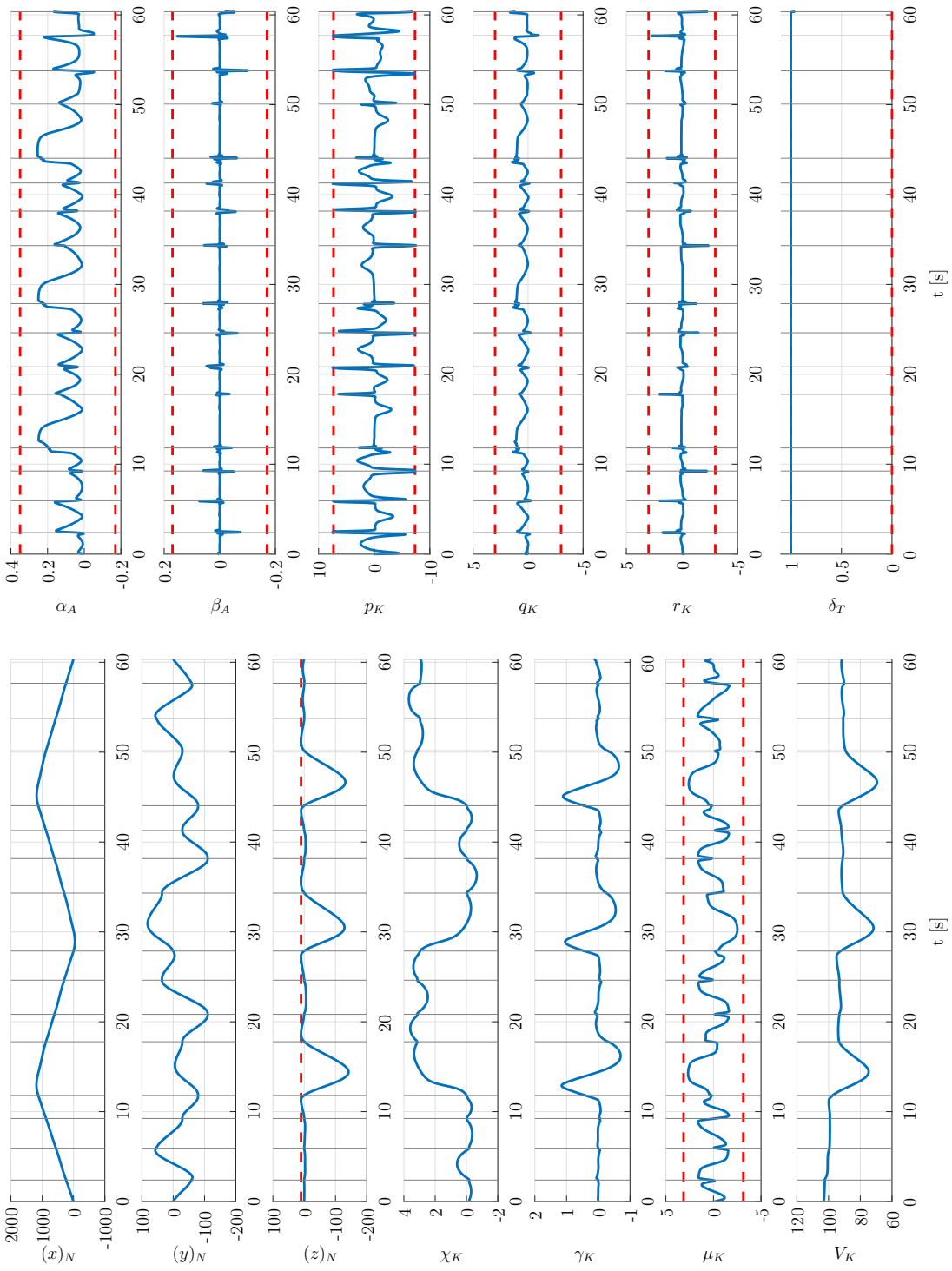

Figure 3: Optimal state histories for the combined simulation model. [5]

- on the other hand, in the two approaches different integration schemes are used for the fast dynamics which influence the numerical solution of the differential equation.

Anyway, the differences in the results achieved are expected to be much lower than any possible errors due to model inaccuracies. [5]

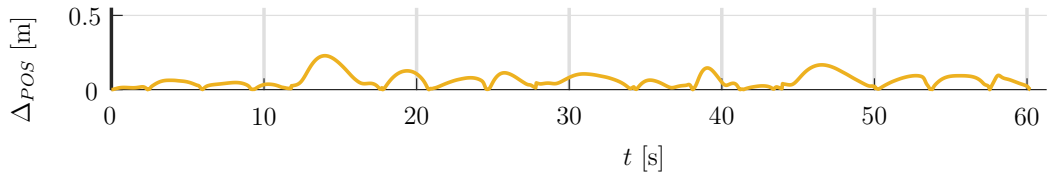

Figure 4: Position difference with respect to the solution for the rigid body simulation model. [5]

6 CONCLUSIONS

In the paper at hand, a novel discretization method for the solution of high fidelity optimal control problems incorporating different timescales is presented. The method splits the dynamic equations of the underlying system into a fast and a slow part. The slow dynamics are solved using a direct collocation scheme based on a relatively coarse grid. Therein, explicit or implicit integration methods may be used, as all state and control values are available in the optimization parameter vector of the discretized problem. The fast states are handled using a multiple shooting approach, with the grid points of the multiple shooting defects in time being equal to the collocation nodes of the slow dynamics. As the multiple shooting method allows for the use of an arbitrary number of integration steps between two defect nodes, the integration grid of the fast states may be chosen finer without increasing the problem dimensions. The multiple shooting approach results in a more dense gradient matrix of the overall problem due to its more nonlinear coupling of the states and controls. The calculation of the slow states between two collocation nodes – that are required to evaluate the fast dynamics – can be done using an arbitrary interpolation method, where in this paper linear and cubic interpolation is suggested. The method is also published as a part of the dissertation thesis of the first author [5].

The application of the method is demonstrated using an exemplary air race trajectory optimization problem incorporating a high fidelity rigid body simulation model with nonlinear aerodynamics. The results show that the problem size can be significantly reduced compared to a full discretization of the high fidelity problem. Similarly, the solution time decreases.

In the examples, a control discretization based on the coarse grid of the method is used, which is not ideal for all the controls as the control surface deflections ξ_{CMD}, η_{CMD} and ζ_{CMD} mainly influence the fast rotational dynamics and consequently also would require faster control inputs. Therefore, a future extension of the algorithm may be the use of a control grid which is similar to the *Multiple Shooting Integration Grid*. Thus, the problem

size will be increased by the additional control parameters without increasing the number of constraints. However, the calculation of the gradient matrix will change in this case, requiring further implementation efforts.

Besides, the combined discretization scheme presented here may be extended in future research by e. g. estimating the integration errors of the simulation in the *Multiple Shooting* segments and using this information for a grid refinement scheme. This way, the number of collocation and shooting nodes may be reduced, further decreasing problem size while increasing solution accuracy and the robustness of the solution process. [5]

REFERENCES

[1] S. Osher and R. Sanders, "Numerical approximations to nonlinear conservation laws with locally varying time and space grids," *Mathematics of Computation*, vol. 41, p. 321, 1983.

[2] M. Günther, A. Kværnø, and P. Rentrop, "Multirate partitioned runge-kutta methods," *BIT Numerical Mathematics*, vol. 41, no. 3, pp. 504–514, 2001.

[3] P. N. Desai and B. A. Conway, "Two-timescale discretization scheme for collocation," *Journal of Guidance, Control, and Dynamics*, vol. 31, no. 5, pp. 1316–1322, 2008.

[4] C. L. Bottasso and G. Maisano, "Efficient rotorcraft trajectory optimization using comprehensive vehicle models by improved shooting methods," in *35th European Rotorcraft Forum Proceedings* (I. Lopez and P. Brandt, eds.), (Red Hook, NY), Curran Associates, 2009.

[5] M. Bittner, *Utilization of Problem and Dynamic Characteristics for Solving Large Scale Optimal Control Problems*. Dissertation, Technische Universität München, München, Submitted 01/18/2017, to be published.

[6] J. T. Betts, *Practical Methods for Optimal Control and Estimation Using Nonlinear Programming*. Advances in Design and Control, Philadelphia: SIAM, Society for Industrial and Applied Mathematics, second edition ed., 2009.

[7] F. Fisch, *Development of a Framework for the Solution of High-Fidelity Trajectory Optimization Problems and Bilevel Optimal Control Problems*. München: Verlag Dr. Hut, 1. aufl. ed., 2011.

[8] L. Höcht, *Advances in Stability Analysis for Model Reference Adaptive Control Systems and Application to Unmanned Aerial Systems*. Dissertation, Technische Universität München, München, 2014.

[9] J. Lenz, *Optimisation of Periodic Flight Trajectories*. PhD thesis, Technische Universität München, München, 2015.

[10] R. Brockhaus, W. Alles, and R. Luckner, *Flugregelung*. Heidelberg, Dordrecht, London, New York: Springer, 3., neu bearb. aufl. ed., 2011.

[11] H. Weirather, *Flugrennsimulation gegen ein zeitoptimiertes Flugzeug*. Bachelor thesis, Technische Universität München, Garching, 2014.

[12] A. Wächter and L. T. Biegler, "On the implementation of a primal-dual interior point filter line search algorithm for large-scale nonlinear programming," *Mathematical Programming*, vol. 106, no. 1, pp. 25–57, 2006.

VII International Conference on Computational Methods for Coupled Problems in Science and Engineering
COUPLED PROBLEMS 2017
M. Papadrakakis, E. Oñate and B. Schrefler (Eds)

ACCURATE AND EFFICIENT, MULTISCALE SIMULATIONS OF NEWTONIAN AND NON-NEWTONIAN FREE-SURFACE FLOWS

JUAN LUIS PRIETO*†, JAIME CARPIO†

† Departamento de Ingeniería Energética
Escuela Técnica Superior de Ingenieros Industriales
Universidad Politécnica de Madrid
c/ José Gutiérrez Abascal, 2, 28006 Madrid, Spain
e-mail: juanluis.prieto@upm.es
ORCID® iD: orcid.org/0000-0001-5085-0482

Key words: Finite Element Method, Free-Surface, Multiscale, Adaptive Mesh Refinement, Non-Newtonian Flows

Abstract. The purpose of this presentation is to outline the main features of a new numerical method under development for the simulation of complex, Newtonian and non-Newtonian free-surface flows. The method makes use of a Particle Level Set (PLS) approach along with Adaptive Mesh Refinement (AMR) techniques to retrieve, accurately and efficiently, the fluid interface at each time step as the zero isocontour of a level set function. The convective terms are dealt with by means of a semi-Lagrangian formulation of the Navier-Stokes equations within a Finite Element framework, leveraging isotropic as well as anisotropic AMR techniques developed via error estimation to produce spatially-adapted "optimal" triangulations. Multiscale simulations of non-Newtonian flows are realized through the kinetic modelling of ensembles of dumbbells scattered over the domain, their internal configurations providing the extra-stress tensor representing the viscoelastic contribution to the Newtonian solvent.

The capabilities of the method are illustrated in a series of 2D simulations of pure-advection and complex free-surface flows, showing surface tension and viscoelastic effects.

1 INTRODUCTION

The development of a general, accurate, robust and efficient method for the solution of multiphase flows is a topic of great interest to the Scientific and Engineering community, due to the large number of applications in which a free-surface is present. Though in recent years significant progress has been made in this field [1, 2, 3] there is still much room for improvement; the purpose of this talk is to present a contribution in this

direction by means of a semi-Lagrangian Particle Level Set method with (An)Isotropic Mesh Refinement capabilities to capture the interface of pure advection and complex Newtonian and non-Newtonian flows, in a robust, accurate and efficient way.

2 METHODOLOGY

We briefly describe next the main features of the method introduced in this talk.

2.1 Time and space discretization

We take advantage of the semi-Lagrangian approach so that for each mesh-point, the departure points $\mathbf{X}$ (or 'feet' of the characteristic curves) are computed according to:

$$\begin{cases} \dfrac{d\mathbf{X}\left(\mathbf{x}, t_n; t\right)}{dt} = \mathbf{u}\left(\mathbf{X}\left(\mathbf{x}, t_n; t\right), t\right), \quad t \in \left(t_{n-1}, t_n\right); \\ \mathbf{X}\left(\mathbf{x}, t_n; t_n\right) = \mathbf{x}. \end{cases} \tag{1}$$

Thus, the Navier-Stokes equations for incompressible, viscous flows can be rewritten in terms of a Stokes-like problem, in which quadratic finite elements are used for velocity, linear discontinuous for the pressure, and linear polynomials are employed for the level set function. Non-Newtonian fluids are considered by means of a multiscale procedure in which kinetic models are coupled with the macroscopic solution of the Navier-Stokes equations. The internal configurations $\mathbf{Q}$ of the polymer particles advected by the flow are ruled by the stochastic differential equation:

$$d\mathbf{Q} = \left[\kappa \cdot \mathbf{Q} - \frac{2}{\zeta}\mathbf{F}\left(\mathbf{Q}\right)\right] dt + \sqrt{\frac{4k_B\Theta}{\zeta}} d\mathbf{W}, \tag{2}$$

with $\mathbf{F}$ the spring-force of the dumbbells, k_B the Boltzmann constant, ζ the friction coefficient, Θ the absolute temperature and $\mathbf{W}$ a three-dimensional Wiener process. These configurations are conveniently integrated by a (weak) second-order scheme, with the polymer stress tensor being computed from their second moments. See [4, 5] for details.

2.2 Interface-capturing technique

The Particle Level Set method captures the interface as the zero isocontour of ϕ (*level set function*) solving at each time step the conservation equation

$$\frac{D\phi}{Dt} = 0, \tag{3}$$

using the semi-Lagrangian approach sketched above. *Marker particles* advected by the flow and placed sufficiently close to the interface enhance shape reconstruction by defining local level set functions. A second-order accurate reinitialization procedure is also used to keep the level set function from developing numerical instabilities as the simulation goes on. For details, see the SLEIPNNIR technique introduced in [6].

2.3 Adaptive Mesh Refinement technique

Isotropic as well as anisotropic mesh refinement is here considered to produce spatially-adapted "optimal" triangulations as presented in [7, 8]. For isotropic mesh refinement one only has to define the size of elements $|K| \propto h_K^d$ with any tolerance criterium: e.g. $min(h_K) = h_{min}$, to produce an equidistribution of the numerical error over all mesh elements. However, for anisotropic mesh refinement not only the size of the element must be provided, but also its shape $S_K = diag\{s_{1,K}, ..., s_{d,K}\}$ and orientation $R_K = \{\mathbf{r}_{1,K}, ..., \mathbf{r}_{d,K}\}$. All this information is wrapped up in the so-called metric tensor, which is evaluated at each element of the spatial triangulation K as folllows:

$$M_K = |K|^{-2/d} R_K S_K^{-1} R_K^T. \tag{4}$$

The optimal size of a given element $|K|$ is computed via a posteriori error estimator of the truncation error incurred in each time subinterval $[t_{n-1},\ t_n]$; then, the optimal shape S_K and orientation R_K are determined using a linear a priori error analysis. 1269+

3 RESULTS

In this section we show some results obtained with our new method for the simulation of free-surface flows: first, we highlight the capabilities in pure advection problems, by means of the Zalesak slotted cylinder; then, we investigate bubble dynamics of Newtonian and non-Newtonian flows.

3.1 Advection problems

The test proposed by Zalesak [9] is carried out using our code with anisotropic mesh refinement active. This benchmark heavily taxes the ability of the free-surface method to accurately represent sharp interfaces, typically resulting in the interface-capturing or interface-tracking techniques rounding corners and eventually producing a degenerated free-surface after just a couple of solid body rotations.

Table 1: Minimum grid size $h_{\min}^{-1}$, number of elements NE, number of mesh-points NP and error in the infinity e_{L^∞}, for the Zalesak slotted cylinder test after 50 revolutions, with anisotropic mesh refinement.

$h_{\min}^{-1}$	NE	NP	Error e_{L^∞}
32	249	510	1.02674×10^{-3}
64	486	983	1.89065×10^{-4}
128	803	1616	6.19143×10^{-5}
256	1053	2118	3.26022×10^{-5}

The results for different minimum grid size $h_{\min}$ with time step size $\Delta t = 10^{-2}$, $N_p = 5 \times 10^4$ marker particles and reinitialization of the level set function are collected in Table 1 after 50 revolutions of the slotted cylinder.

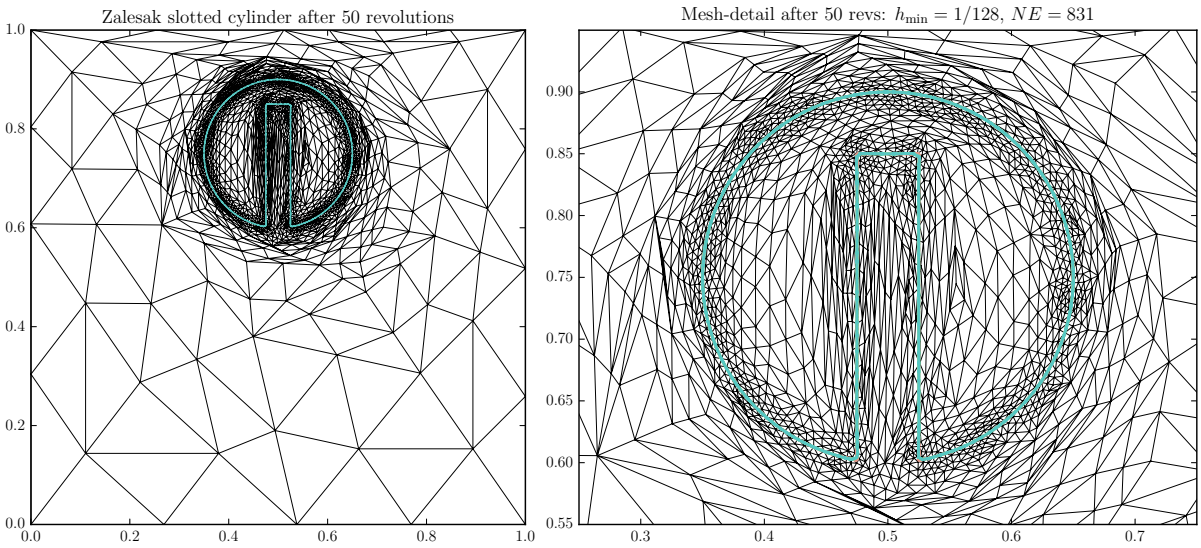

Figure 1: Zalesak slotted cylinder after 50 revolutions. Mesh with minimum grid size $h_{\min} = 1/128$ and $NE = 803$ elements. Time step size $\Delta t = 10^{-2}$; $N_p = 5 \times 10^4$ marker particles. Initial solution also plotted.

We observe very low errors in the infinity norm for a low number of elements NE and of mesh-points NP, along with an almost unchanged interface as plotted in Fig. 1, noticing that the initial interface quite overlaps the final shape when a mesh with as low as 803 elements are used.

3.2 Complex flows

We now move to more demanding problems with non-imposed flows. For this talk we consider the unsteady simulation of a bubble rising by buoyancy effects in a quiescent fluid. The Stokes problem derived from the semi-Lagrangian approach to the Navier-Stokes equations are solved efficiently using the PETSc ('Portable, Extensible Toolkit for Scientific Computation') tool [10], taking advantage of the PCFieldsplit approach based on the Schur-complement, block preconditioning of the Stokes matrix system.

In Fig. 2, we show the final shape of two such simulations along with isovelocity contours of the vertical component of the velocity over a contour-filled plot of that component v_y. The left panel of the Figure shows a Newtonian fluid rising in another Newtonian fluid, with moderate density and viscosity ratios $\rho_2/\rho_1 = 10^{-1} = \mu_2/\mu_1$, using $N_p = 1.5 \times 10^3$ marker particles to improve shape preservation and prevent mass loss; surface tension effects are considered throught the Weber dimensionless number ($We = 35$), whereas the viscous and inertial effects are represented by the Reynolds number ($Re = 35$); the time step size, in this mesh with minimum grid size $h_{\min} = 1/320$, is such that $N_t = 960$ time steps are required to reach the dimensionless time $t = 3$, with an external mass loss of just $1.7645 \times 10^{-5}\,\%$. Under such conditions, the bubble reaches an ellipsoidal-cap

regime, which is in accordance with the findings of [11]. The right panel of Fig. 2 depicts a Newtonian bubble in a viscoelastic fluid represented by means of the FENE kinetic model, with the finite-extension parameter $b_{FENE} = 35$. This simulation scatters 15000 ensembles each of them containing 2500 dumbbells carrying the internal degrees of freedom of the polymer molecules. Compactly-Supported Radial Basis Functions (CSRBFs) are used as explained in [12] to reconstruct the extra-stress tensor that enters as a right-hand side term (body force) in the Navier-Stokes equations; this technique has proved extremely useful in AMR situations, where certain refined regions of the mesh have a low number of ensembles (or are empty of them altogether). The interface of the viscous-elastic ($Re = 35$) bubble develops an incipient tail which due to surface tension effects ($We = 50$) does not attain a cusp-like shape at the final time of the simulation; however, weak 'negative' (downwards) velocities are indeed observed in the wake of the bubble, something of a purely viscoelastic effect [13] which is here attained with a Deborah number $De = 2.5$.

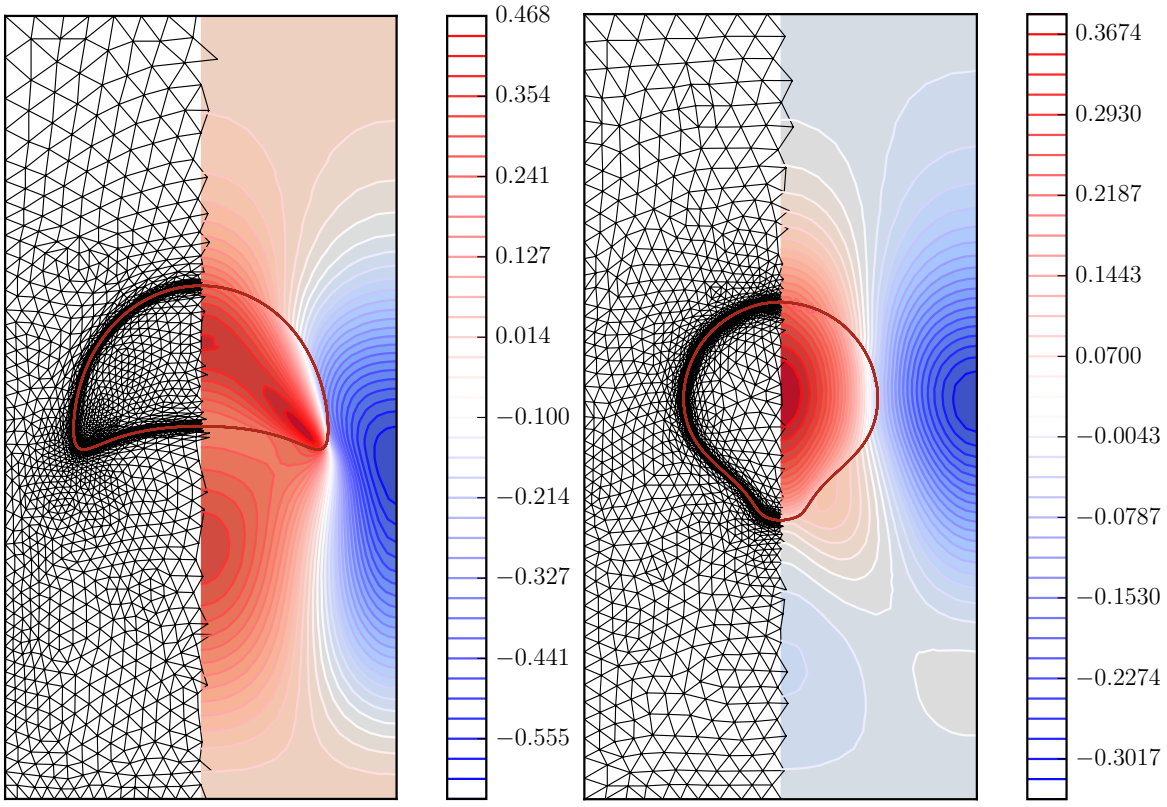

Figure 2: Bubble dynamics simulations at $t = 3$ with isocontours of rise velocity: Newtonian fluid with $Re = 35, We = 35$ (left panel); non-Newtonian fluid with $b_{FENE} = 35, Re = 35, We = 50, c = 4.5, De = 2.5$ (right panel).

4 CONCLUSIONS

Next we collect some of the main points of the method under development presented in this talk:

- We present a new methodology for the simulation of free-surface flows for Newtonian and non-Newtonian flows.
- The method uses a Particle Level Set (PLS) approach along with Adaptive Mesh Refinement (AMR) techniques and the Finite Element Method.
- Pure advection problems are solved accurately even for extremely low number of mesh-points when using anisotropic mesh adaptation.
- Benchmark tests for complex flows both for Newtonian and non-Newtonian fluids show promising results: the simulations are carried out efficiently and accurately with the implementation of the new method.

5 ACKNOWLEDGMENTS

Financial support from project MTM2015-67030-P from Ministerio de Economía y Competitividad is acknowledged.

REFERENCES

[1] Larese, A., Rossi, R. and Oñate, E., Finite Element Modeling of Free Surface Flow in Variable Porosity Media. *Arch Computat Methods Eng.* (2015) **22**(4):637–653.

[2] Cruchaga, M., Battaglia, L., Storti, M. and D'Elía, J., Numerical Modeling and Experimental Validation of Free Surface Flow Problems. *Arch Computat Methods Eng.* (2016) **23**(1):139–169.

[3] Barral, N. and Olivier, G. and Alauzet, F., Time-accurate anisotropic mesh adaptation for three-dimensional time-dependent problems with body-fitted moving geometries. *J. Comput. Phys.* (2017) **331**:157–187.

[4] Öttinger, H.C. *Stochastic Processes in Polymeric Fluids.* Springer, (1996), ISBN: 978-3-642-58290-5.

[5] Prieto, J.L., Stochastic particle level set simulations of buoyancy-driven droplets in non-Newtonian fluids. *J. Non-Newtonian Fluid Mech.* (2015) **226**:16–31.

[6] Prieto, J.L., SLEIPNNIR: A multiscale, particle level set method for Newtonian and non-Newtonian interface flows. *Comput. Methods Appl. Mech. Engrg.* (2016) **307**:164–192.

[7] Carpio, J., Prieto, J.L. and Vera, M., A local anisotropic adaptive algorithm for the solution of low-Mach transient combustion problems. *J. Comput. Phys.* (2016) **306**:19–42.

[8] Carpio, J. and Prieto, J.L., An anisotropic, fully adaptive algorithm for the solution of convection dominated equations with semi-Lagrangian schemes. *Comput. Methods Appl. Mech. Engrg.* (2014) **273**:77–99.

[9] Zalesak, S.T., Fully multidimensional flux-corrected transport algorithms for fluids. *J. Comput. Phys.* (1979) **31**:335–362.

[10] Balay, S., Abhyankar, S., Adams, M.F., Brown, J., Brune, P., Buschelman, K., Dalcin, L., Eijkhout, V., Gropp, W.D., Kaushik, D., Knepley, M.G., McInnes, L.C., Rupp, K., Smith, B.F., Zampini, S., Zhang, H. and Zhang, H. *PETSc Users Manual*. Argonne National Laboratory (2016), ANL-95/11 - Revision 3.7, `http://www.mcs.anl.gov/petsc`.

[11] Clift, R., Grace, J.R. and Weber, M.E. *Bubbles, drops, and particles*. Academic Press, (1978), ISBN: 012176950X.

[12] Prieto, J.L., An RBF-reconstructed, polymer stress tensor for stochastic, particle-based simulations of non-Newtonian, multiphase flows. *J. Non-Newtonian Fluid Mech.* (2016) **227**:90–99.

[13] Chhabra, R. and De Kee, D.. *Transport Processes in Bubbles, Drops & Particles, 2nd Ed.*. Taylor & Francis, (2001).

VII International Conference on Computational Methods for Coupled Problems in Science and Engineering
COUPLED PROBLEMS 2017
M. Papadrakakis, E. Oñate and B. Schrefler (Eds)

FINITE ELEMENT MODELING OF EFFECTIVE PROPERTIES OF NANOPOROUS THERMOELASTIC COMPOSITES WITH SURFACE EFFECTS

ANDREY V. NASEDKIN, ANNA A. NASEDKINA AND ALEXANDR S. KORNIEVSKY

Institute of Mathematics, Mechanics & Computer Science
Southern Federal University
Miltchakova str. 8a, 344090 Rostov on Don, Russia
e-mail: nasedkin@math.sfedu.ru

Key words: Porous Thermoelastic Composite, Nanosized Pore, Stochastic Porosity, Surface Stress, Highly Thermal Conducting Interface, Effective Moduli, Finite Element Method

Abstract. This investigation concerns to the determination of the material properties of nanoscale thermoelastic composites of an arbitrary anisotropy class with stochastically distributed porosity. In order to take into account nanoscale level at the borders between material and pores, the GurtinMurdoch model of surface stresses and the highly conducting model are used. Finite element package ANSYS was used to simulate representative volume and to calculate the effective material properties. This approach is based on the theory of effective moduli of composite mechanics, modeling of representative volumes and the finite element method. Here, the contact boundaries between material and pores were covered by the surface membrane elastic and thermal shell elements in order to take the surface effects into account.

1 INTRODUCTION

As it is well known from experiments, a scale effect can be observed for nanoscale bodies, which results in the change of effective stiffness and other material moduli compared to the corresponding macroscale bodies. Among various approaches that explain this phenomenon, the models of theory of elasticity with surface stresses are widely used now. The idea of surface stresses in solids has been formulated long time ago [27]. However, significant development of this idea was done later in [10, 13, 26]. As it was shown further, the theory of surface stresses can be considered as a particular case of the models with imperfect interface boundaries.

At present the theory of surface stresses, commonly referred to as the model of Gurtin–Murdoch, has been become widely used for describing scale effects at nanolevel, which can

be seen, for example, from overviews given in [3, 28]. In a range of papers this theory was applied for modelling of thermoelastic nanoscale composites. For example, in [1, 2, 16, 17] thermomechanical properties of composites with spherical nanoinclusions (nanopores) and fiber nanocomposites were studied in the frames of the theory of thermal stresses with surface effects. The methodology of finite element approximations for thermoelastic materials with surface effects was demonstrated in [11].

Models of lowly and highly thermal conducting interfaces [18, 19] are well known for modeling of effective thermal conductivity of composites with imperfect interface boundaries. The model of high conductivity with continuous thermal field when passing through the phase interface is similar to the Gurtin-Murdoch model for elastic fields. The model of lowly conducting interface, which includes Kapitsa contact thermal resistance, allows discontinuous temperature field. Generalizations of these models for a more general case of thermoelastic interface boundaries were presented [14], and a related review was given in [12]. The problems on the determination of effective thermal conductivity moduli for composite materials with imperfect boundaries, including micro- and nanoscale, were studied in [6, 15, 18, 19, 20, 30] and others.

This paper considers anisotropic thermoelastic materials with randomly located nanopores. In order to take into account nanoscale level at the borders between material and pores, the Gurtin-Murdoch model of surface stresses and the highly conducting model are used. The paper is organized as follows. Section 2 presents the mathematical statement of a homogenization problem for two-phase composites with special conditions for stresses and heat flux discontinuities at the phase interfaces. Both composite phases are assumed to be anisotropic thermoelastic materials. The boundary value problem statements, their weak formulations and the resulting formulas for determination of the full set of effective constants for a two-phase composite with arbitrary types of phase anisotropy and surface properties are also described. We note that homogenization procedures for porous composites with surface stresses and heat fluxes can be regarded as special cases of the corresponding procedures for two-phase composites with imperfect interface boundaries under negligibly small stiffnesses and thermal stresses for nanoinclusions.

The finite element approximations of the considered homogenization problems are given in Section 3. We note that homogenization problems for the composites under investigation can be solved with the help of known finite element software, using shell finite elements with membrane stresses options and plate thermal elements in order to take into account interphase surface stresses and heat fluxes.

Following [25] Section 4 describes an implementation of the proposed approaches in the finite element software ANSYS. We suggest an algorithm for automatic determination of interphase boundaries and location of shell and plate elements on them, which will work for various sizes of representative volumes built in forms of cubic lattice of hexahedral thermoelastic and thermal finite elements. As an example, in [25] we consider the models of porous material of cubic crystal system for various values of surface moduli, porosity and number of pores. We note the influence of the magnitude of the area of interphase

boundaries on the values of the effective moduli for porous material with nanoscale structure.

2 EFFECTIVE MODULI METHOD FOR HOMOGENIZATION OF THERMOELASTIC MIXED TWO-PHASE NANOCOMPOSITES

Let Ω be a representative volume of thermoelastic two-phase composite body with nanodimensional inclusions; $\Omega = \Omega^{(1)} \cup \Omega^{(2)}$; $\Omega^{(1)}$ is the volume occupied by the main materials of the first phase (matrix); $\Omega^{(2)}$ is the set of the volumes occupied by the materials of the second phase (inclusions); $\Gamma = \partial\Omega$ is the external boundary of the volume Ω; Γ^s is the set of frontier surfaces of materials with different phases ($\Gamma^s = \partial\Omega^{(1)} \cap \partial\Omega^{(2)}$); ν_i are the components of the external unit normal vector $\boldsymbol{\nu}$ to the boundary, outward with respect to the region $\Omega^{(1)}$ occupied by the material of the matrix; $\mathbf{x} = \{x_1, x_2, x_3\}$ is the vector of the spacial coordinates. We assume that the volumes $\Omega^{(1)}$ and $\Omega^{(2)}$ are filled with different anisotropic thermoelastic materials. Then in the framework of linear static theory of thermoelasticity we have the following system of differential equations

$$\sigma_{ij,j} = 0, \quad \sigma_{ij} = c_{ijkl}\varepsilon_{kl} - \beta_{ij}\,\theta, \quad \varepsilon_{ij} = (u_{i,j} + u_{j,i})/2\,, \tag{1}$$

$$q_{j,j} = 0, \quad q_i = -k_{ij}\theta_{,j}\,, \tag{2}$$

where σ_{ij} are the components of the stress tensor $\boldsymbol{\sigma}$; ε_{ij} are the components of the strain tensor $\boldsymbol{\varepsilon}$; u_i are the components of the displacement vector $\mathbf{u}$; θ is the temperature increment from natural state, c_{ijkl} are the components of the forth rank tensor of elastic stiffness moduli; β_{ij} are the thermal stress coefficients; q_i are the components of the heat flux vector $\mathbf{q}$; k_{ij} are the components of the tensor $\mathbf{k}$ of thermal conductivities; $c_{ijkl} = c^{(m)}_{ijkl}$, $\beta_{ij} = \beta^{(m)}_{ij}$, $\sigma_{ij} = \sigma^{(m)}_{ij}$, $\mathbf{x} \in \Omega^{(m)}$, etc.

In accordance with Gurtin–Murdoch model for surface stresses we will assume that on nanosized interphase boundaries Γ^s the following equation is satisfied

$$\nu_i[\sigma_{ij}] = \partial^s_i \sigma^s_{ij}, \quad \mathbf{x} \in \Gamma^s\,, \tag{3}$$

where $[\sigma_{ij}] = \sigma^{(1)}_{ij} - \sigma^{(2)}_{ij}$; $\partial^s_i = \partial_i - \nu_i(\nu_l\partial_l)$ are the components of the surface gradient operator; σ^s_{ij} are the components of the surface stress tensor $\boldsymbol{\sigma}^s$.

We adopt that the surface stresses σ^s_{ij} are related to the surface strains ε^s_{ij} and the temperature θ by the formulas

$$\sigma^s_{ij} = c^s_{ijkl}\varepsilon^s_{kl} - \beta^s_{ij}\,\theta\,, \quad \varepsilon^s_{kl} = (\partial^s_k u_m A_{ml} + A_{km}\partial^s_l u_m)/2, \quad A_{ml} = \delta_{ml} - n_m n_l\,, \tag{4}$$

where c^s_{ijkl} are the components of the forth rank tensor of elastic surface stiffness moduli; β^s_{ij} are the surface thermal stress coefficients; δ_{ml} is the Kronecker delta.

Similarly, for interphase boundaries Γ^s, we accept the equation of highly thermal conducting boundaries

$$n_i[q_i] = \partial^s_i q^s_i, \quad q^s_i = -k^s_{ij}\partial^s_j\theta, \quad \mathbf{x} \in \Gamma^s\,, \tag{5}$$

where k_{ij}^s are the surface thermal conductivities.

Setting the appropriate boundary conditions at $\Gamma = \partial\Omega$, we can find the solutions of the problems (1)–(5) for heterogeneous medium in the representative volume Ω. Then the comparison of the solution characteristics averaged over Ω (such as stresses, heat flux, etc.) with analogous values for homogeneous comparison medium will permit to determine the effective moduli for the composite material. We note that for anisotropic media in order to determine the full set of the effective moduli it is necessary to solve several problems of the considered types for different boundary conditions.

Here the main difficulties consist in the choice of the representative volume and boundary problems for the heterogeneous medium and the comparison medium, as well as the technologies for solving the problems for heterogeneous media. According to the previously developed methods of modeling the thermoelastic composite materials of ordinary sizes [23, 24], we consider analogous approaches for the problems of thermoelasticity with surface effects [25].

For thermoelastic homogeneous comparison medium we adopt that the same equations (1)–(5) are satisfied with constant moduli c_{ijkl}^{eff}, β_{ij}^{eff}, k_{ij}^{eff}, which are to be determined. Note that thermal problem (2), (5) is independent, and so the moduli c_{ijkl}^{eff}, β_{ij}^{eff} and the moduli k_{ij}^{eff} can be found from separate problems.

For determination of the moduli c_{ijkl}^{eff}, β_{ij}^{eff} let us assume that at the boundary Γ the following boundary conditions take place

$$u_l = x_k \varepsilon_{0kl}, \quad \theta = \theta_0, \quad \mathbf{x} \in \Gamma\,, \tag{6}$$

where $\varepsilon_{0kl} = \varepsilon_{0lk}$, θ_0 are some values that do not depend on $\mathbf{x}$. Then $u_l = x_k\varepsilon_{0kl}$, $\varepsilon_{kl} = \varepsilon_{0kl}$, $\theta = \theta_0$, $\sigma_{ij} = \sigma_{0ij} = c_{ijkl}^{\text{eff}}\varepsilon_{0kl} - \beta_{ij}^{\text{eff}}\theta_0$ will give the solution for the problem (1)–(6) in the volume Ω for the homogeneous comparison medium. Note, that for $\theta = \theta_0 = \text{const}$ the equations (2), (5) are satisfied identically, because $q_i = q_{0i} = 0$, $q_i^s = 0$, and this pure thermal problem is not actually used for solution of mechanical problem with thermal stresses (1), (3), (4), (6).

Let us solve now problem (1)–(6) for heterogeneous medium (or (1), (3), (4), (6) because for $\theta = \theta_0$ the equations (2), (5) are satisfied indentically) and assume that for this medium and for the comparison medium the averaged stresses are equal $\langle\sigma_{ij}\rangle = \langle\sigma_{0ij}\rangle$, where hereinafter the angle brackets $\langle(...)\rangle$ denote the averaged by the volume Ω and by the surfaces Γ^s values

$$\langle(...)\rangle = \frac{1}{|\Omega|}\Big(\int_\Omega (...)\,d\Omega + \int_{\Gamma^s} (...)^s\,d\Gamma\Big)\,. \tag{7}$$

Therefore we obtain that for the effective moduli of the composite the equation $\sigma_{ij} = \sigma_{0ij} = c_{ijkl}^{\text{eff}}\varepsilon_{0kl} - \beta_{ij}^{\text{eff}}\theta_0 = \langle\sigma_{ij}\rangle$ is satisfied, where ε_{0kl} and θ_0 are the given values from the boundary conditions (6). Hence, even in the assumption of the anisotropy of the general form for the comparison medium, all the stiffness moduli c_{ijkl}^{eff} and thermal stress coefficients β_{ij}^{eff} can be computed. Indeed, setting in (6) $\varepsilon_{0kl} = \varepsilon_0(\delta_{km}\delta_{ln} + \delta_{lm}\delta_{kn})/2$,

$\varepsilon_0 = \text{const}$, $\theta_0 = 0$, where m, n are some fixed indexes, we get the computation formulas for the elastic moduli c^{eff}_{ijmn}: $c^{\text{eff}}_{ijmn} = \langle\sigma_{ij}\rangle/\varepsilon_0$. If in (6) we set $\varepsilon_{0kl} = 0$, $\theta_0 \neq 0$, than from the boundary problem (1), (3), (4), (6) the thermal stress effective moduli can be obtained: $\beta^{\text{eff}}_{ij} = -\langle\sigma_{ij}\rangle/\theta_0$.

As mentioned above, in order to determine the effective coefficients of the tensor k_{ij} it is sufficient to consider thermal conductivity equation (2) and interface relation (5). For the formulation of the corresponding boundary-value problem we adopt the boundary conditions in the following form

$$\theta = x_j G_{0j}, \quad \mathbf{x} \in \Gamma\,, \tag{8}$$

where G_{0j} are the components of some constant vector that does not depend on $\mathbf{x}$. It is obvious that $\theta = x_j G_{0j}$, $G_j = \partial_j\theta$, $G_j = G_{0j}$, $q_i = q_{0i} = -k^{\text{eff}}_{ij} G_{0j}$ will give the solution of the problem (2), (5), (8) in the volume Ω for the homogeneous comparison medium. Having solved the problem (2), (5), (8) for heterogeneous medium, we can set that for this medium and for the comparison medium the averaged heat fluxes are equal $\langle q_i\rangle = \langle q_{0i}\rangle$. As a result we get the equation for the effective moduli of the composite $k^{\text{eff}}_{ij} G_{0j} = -\langle q_i\rangle$, where G_{0j} are the components of the vector known from the boundary conditions (8). Then for the comparison medium with anisotropy of general form it is not difficult to obtain computation formulas for thermal conductivity moduli k^{eff}_{ij}. Indeed, setting in (8) $G_{0j} = G_0\delta_{jl}$, $G_0 = \text{const}$, where $l = 1, 2, 3$ is some fixed index, we get computation formulas for the moduli k^{eff}_{il}: $k^{\text{eff}}_{il} = -\langle q_i\rangle/G_0$.

The approaches described above are associated with the averaging of the moduli c_{ijkl}, β_{ij}, k_{ij}. Note that the boundary value problems (1), (3), (4), (6) and (2), (5), (8) differ from the usual problems of linear thermoelasticity by the presence of the interface boundary conditions (3)–(5) which are typical for the Gurtin–Murdoch model of surface stresses and the model of highly thermal conducting boundaries for nanosized bodies.

For the numerical solution of the problems (1), (3), (4), (6) and (2), (5), (8) we derive their weak or generalized statements. Previously we introduce the space of the functions θ and the vector functions $\mathbf{u}$, defined on Ω.

On the set of vector functions $\mathbf{u} \in C^1$ which satisfy the first homogeneous boundary condition (6), i.e. $u_l = 0$ on Γ, we introduce the scalar product

$$(\mathbf{v}, \mathbf{u})_{H^1_u} = \int_\Omega \varepsilon_{ij}(\mathbf{v})\varepsilon_{ij}(\mathbf{u})\, d\Omega + \int_{\Gamma^s} \varepsilon^s_{ij}(\mathbf{v})\varepsilon^s_{ij}(\mathbf{u})\, d\Gamma\,.$$

The closure of this set of vector functions $\mathbf{u}$ in the norm generated by the indicated scalar product will be denoted by H^1_u.

For functions $\theta \in C^1$ which satisfy second homogeneous boundary condition (6) or (8), i.e. $\theta = 0$ on Γ, we introduce the scalar product

$$(\eta, \theta)_{H^1_\theta} = \int_\Omega \partial_i\eta\, \partial_i\theta\, d\Omega + \int_{\Gamma^s} \partial^s_i\eta\, \partial^s_i\theta\, d\Gamma\,.$$

The closure of this set of functions φ in the norm generated by the indicated scalar product will be denoted by H^1_θ.

In order to formulate the generalized or weak solution we scalar multiply the first equations (1) by arbitrary components v_i of the vector function $\mathbf{v} \in H^1_u$, and we multiply the first equation (2) by some function $\eta \in H^1_\theta$. By summing over i and by integrating the obtained equations on Ω, and by using the standard technique of the integration by parts with Eqs. (1)–(5), we obtain the following integral relations

$$c(\mathbf{v},\mathbf{u}) - \beta\,(\mathbf{v},\theta) = 0\,, \tag{9}$$

$$k(\eta,\theta) = 0\,, \tag{10}$$

where

$$c(\mathbf{v},\mathbf{u}) = c_\Omega(\mathbf{v},\mathbf{u}) + c_{\Gamma^s}(\mathbf{v},\mathbf{u}), \quad \beta(\mathbf{v},\theta) = \beta_\Omega(\mathbf{v},\theta) + \beta_{\Gamma^s}(\mathbf{v},\theta)\,, \tag{11}$$

$$c_\Omega(\mathbf{v},\mathbf{u}) = \int_\Omega c_{ijkl}\varepsilon_{ij}(\mathbf{v})\,\varepsilon_{kl}(\mathbf{u})\,d\Omega, \quad c_{\Gamma^s}(\mathbf{v},\mathbf{u}) = \int_{\Gamma^s} c^s_{ijkl}\varepsilon^s_{ij}(\mathbf{v})\,\varepsilon^s_{kl}(\mathbf{u})\,d\,\Gamma\,, \tag{12}$$

$$\beta_\Omega(\mathbf{v},\mathbf{u}) = \int_\Omega \varepsilon_{ij}(\mathbf{v})\beta_{ij}\,\theta\,d\Omega, \quad \beta_{\Gamma^s}(\mathbf{v},\mathbf{u}) = \int_{\Gamma^s} \varepsilon^s_{ij}(\mathbf{v})\beta^s_{ij}\,\theta\,d\,\Gamma\,, \tag{13}$$

$$k(\eta,\theta) = k_\Omega(\eta,\theta) + k_{\Gamma^s}(\eta,\theta)\,, \tag{14}$$

$$k_\Omega(\eta,\theta) = \int_\Omega k_{ij}\partial_i\eta\,\partial_j\theta\,d\Omega, \quad k_{\Gamma^s}(\eta,\theta) = \int_{\Gamma^s} k^s_{ij}\partial^s_i\eta\,\partial^s_j\theta\,d\,\Gamma\,. \tag{15}$$

Further, we present the solution $\{\mathbf{u},\,\theta\}$ of the problem (1), (3), (4), (6) in the form

$$u_j = u_{dl} + u_{bl}, \quad \theta = \theta_0\,, \tag{16}$$

where u_{dl} satisfies homogeneous boundary mechanical conditions and ad hoc fitted functions u_{bl} satisfy the inhomogeneous boundary conditions on Γ, i.e.

$$u_{dl} = 0, \quad u_{bl} = x_k\varepsilon_{0kl}, \quad \mathbf{x} \in \Gamma\,, \tag{17}$$

and therefore, $\mathbf{u}_d \in H^1_u$.

By using (16) we can rewrite Eq. (9) in the form

$$c(\mathbf{v},\mathbf{u}_d) = L_u(\mathbf{v}), \quad L_u(\mathbf{v}) = \beta\,(\mathbf{v},\theta_0) - c(\mathbf{v},\mathbf{u}_b)\,. \tag{18}$$

Now we can define the generalized or weak solution of the problem with thermal stresses (1), (3), (4), (6) using introduced functional space. Namely, the functions $\mathbf{u}$, θ in the form (16), (17) are the weak solution of the problem (1), (3), (4), (6), if Eq. (18) with (11)–(13) is satisfied for $\forall\ \mathbf{v} \in H^1_u$.

Analogously, we will find the solution θ of the purely thermal problem (2), (5), (8) in the form

$$\theta = \theta_d + \theta_b\,, \tag{19}$$

where θ_d satisfies homogeneous boundary thermal conditions and θ_b is known function, satisfying the inhomogeneous boundary conditions on Γ, i.e. $\theta_d \in H^1_\theta$

$$\theta_d = 0, \quad \theta_b = x_j G_{0j}, \quad \mathbf{x} \in \Gamma\,. \tag{20}$$

By using (19) we can also rewrite (10) in the form

$$k(\eta, \theta_d) = L_\theta(\eta), \quad L_\theta(\eta) = -k(\eta, \theta_b)\,. \tag{21}$$

Then we can introduce the generalized or weak solution of the thermal problem (2), (5), (8) as the function θ in the form (19), (20), for which Eq. (21) with (14), (15) is satisfied for $\forall\ \eta \in H^1_\theta$.

So far we have been discussing the two-phase composites. However, we can note that the presented models also describe homogenization procedures for porous composites with surface effects, if we put the stiffness and thermal stresses moduli negligible, and set the thermal conductivities equal to the coefficient of thermal conductivity of air.

3 FINITE ELEMENT SOLUTION

For solving problems (18) and (21) for thermoelastic body with surface effects in weak forms we will use classical finite element approximation techniques. Let Ω_h be a region of the corresponding finite element mesh composed of volume elements, $\Omega_h \approx \Omega$, $\Omega_h = \Omega_h^{(1)} \cup \Omega_h^{(2)}$, $\Omega_h^{(j)} \approx \Omega^{(j)}$, $\Omega_h = \cup_k \Omega_{ek}$, where Ω_{ek} is a separate volume finite element with number k. Let also Γ_h^s be a finite element mesh of surface elements conformable with the volume mesh Ω_h, $\Gamma_h^s = \partial\Omega_h^{(1)} \cap \partial\Omega_h^{(2)}$, $\Gamma_h^s \approx \Gamma^s$, $\Gamma_h^s = \cup_m \Gamma_{em}^s$, Γ_{em}^s is a separate surface finite element with number m, and the elements Γ_{em}^s are the faces of the suitable volume elements Ω_{ek} located on the interface boundaries.

We will use the classic Lagrangian or serendipity volume finite elements with nodal degrees of freedom of displacements and temperature. Note that due to the structure of surface mechanical and thermal fields (4), (5), for the elements Γ_{em}^s we can use standard shell or plate elements with elastic membrane stresses options, i. e. only with nodal degrees of freedom of displacements, and the standard thermal shell elements. For these elements we can take a fictitious unit thickness so that the surface moduli from (4), (5) can be determined by the product of specially defined volume moduli and shell thickness.

On these finite element meshes we will find the approximation to the weak solutions $\{\mathbf{u}_h \approx \mathbf{u},\ \theta_h \approx \theta\}$ for static thermoelasic problem in the form

$$\mathbf{u}_h(\mathbf{x}) = \mathbf{N}_u^*(\mathbf{x}) \cdot \mathbf{U}, \quad \theta_h(\mathbf{x}) = \mathbf{N}_\theta^*(\mathbf{x}) \cdot \mathbf{\Theta}\,, \tag{22}$$

where $\mathbf{N}_u^*$ is the matrix of the shape functions for displacements, $\mathbf{N}_\theta^*$ is the row vector of the shape functions for temperature, $\mathbf{U}$, $\mathbf{\Theta}$ are the global vectors of nodal displacements and temperature, respectively. Here, the surface shape functions are the reduction on the boundaries Γ_h^s of the volume shape functions.

According to conventional finite element technique, we approximate the continuous weak formulations of the thermoelasticity problems by the corresponding problems in finite-dimensional spaces. Substituting (22) and similar representations for projection functions into integral relations (9), (10) for Ω_h, we obtain the following finite element system

$$\mathbf{K}_{uu}\cdot\mathbf{U}-\mathbf{K}_{u\theta}\cdot\mathbf{\Theta}=0\,, \tag{23}$$

$$\mathbf{K}_{\theta\theta}\cdot\mathbf{\Theta}=0\,, \tag{24}$$

where

$$\mathbf{K}_{uu}=\mathbf{K}_{uu\Omega}+\mathbf{K}_{uu\Gamma},\quad \mathbf{K}_{u\theta}=\mathbf{K}_{u\theta\,\Omega}+\mathbf{K}_{u\theta\,\Gamma},\quad \mathbf{K}_{\theta\theta}=\mathbf{K}_{\theta\theta\,\Omega}+\mathbf{K}_{\theta\theta\,\Gamma}\,, \tag{25}$$

$$\mathbf{K}_{uu\Omega}=\int_{\Omega_h}\mathbf{B}_u^*\cdot\mathbf{c}\cdot\mathbf{B}_u\,d\Omega,\quad \mathbf{K}_{uu\Gamma}=\int_{\Gamma_h^s}\mathbf{B}_u^{s*}\cdot\mathbf{c}^s\cdot\mathbf{B}_u^s\,d\,\Gamma\,, \tag{26}$$

$$\mathbf{K}_{u\theta\,\Omega}=\int_{\Omega_h}\mathbf{B}_u^*\cdot\boldsymbol{\beta}\,\mathbf{N}_\theta^*\,d\Omega,\quad \mathbf{K}_{u\theta\,\Gamma}=\int_{\Gamma_h^s}\mathbf{B}_u^{s*}\cdot\boldsymbol{\beta}^s\,\mathbf{N}_\theta^*\,d\,\Gamma\,, \tag{27}$$

$$\mathbf{K}_{\theta\theta\,\Omega}=\int_{\Omega_h}\mathbf{B}_\theta^*\cdot\mathbf{k}\cdot\mathbf{B}_\theta\,d\Omega,\quad \mathbf{K}_{\theta\theta\,\Gamma}=\int_{\Gamma_h^s}\mathbf{B}_\theta^{s*}\cdot\mathbf{k}^s\cdot\mathbf{B}_\theta^s\,d\,\Gamma,\,, \tag{28}$$

$$\mathbf{B}_u^{(s)}=\mathbf{L}^{(s)*}(\nabla)\cdot\mathbf{A}\cdot\mathbf{N}_u^*,\quad \mathbf{B}_\theta^{(s)}=\nabla^{(s)}\mathbf{N}_\theta^*\,, \tag{29}$$

$$\mathbf{L}^{(s)*}(\nabla)=\begin{bmatrix}\partial_1^{(s)} & 0 & 0 & 0 & \partial_3^{(s)} & \partial_2^{(s)}\\ 0 & \partial_2^{(s)} & 0 & \partial_3^{(s)} & 0 & \partial_1^{(s)}\\ 0 & 0 & \partial_3^{(s)} & \partial_2^{(s)} & \partial_1^{(s)} & 0\end{bmatrix},\quad \nabla^{(s)}=\begin{Bmatrix}\partial_1^{(s)}\\ \partial_2^{(s)}\\ \partial_3^{(s)}\end{Bmatrix}. \tag{30}$$

In (22)-(30), we use the following vector-matrix notation: $\mathbf{c}$ is the 6×6 matrix of elastic moduli; $c_{\alpha\zeta}=c_{ijkl}$, $\alpha,\zeta=1,...,6$, $i,j,k,l=1,2,3$ with correspondence law $\alpha\leftrightarrow(ij)$, $\beta\leftrightarrow(kl)$, $1\leftrightarrow(11)$, $2\leftrightarrow(22)$, $3\leftrightarrow(33)$, $4\leftrightarrow(23)\sim(32)$, $5\leftrightarrow(13)\sim(31)$, $6\leftrightarrow(12)\sim(21)$; $\boldsymbol{\beta}$=$\{\beta_{11},\,\beta_{22},\,\beta_{33},\,\beta_{23},\,\beta_{13},\,\beta_{12}\}$; $(...)^*$ is the transpose operation; and $(...)\cdot(...)$ is the scalar product operation.

Also, we can represent the finite element solutions in the another variants considering the main boundary conditions: $\mathbf{u}_h=\mathbf{u}_{dh}+\mathbf{u}_{bh}$, $\theta_h=\theta_{dh}+\theta_{bh}$, $\mathbf{u}_{dh}\approx\mathbf{u}_d$, $\mathbf{u}_{dh}=\mathbf{N}_{ud}^*\cdot\mathbf{U}_d$, $\mathbf{u}_{bh}\approx\mathbf{u}_b$, $\mathbf{u}_{bh}=\mathbf{N}_{ub}^*\cdot\mathbf{U}_b$, $\theta_{dh}\approx\theta_d$, $\theta_{dh}=\mathbf{N}_{\theta d}^*\cdot\mathbf{\Theta}_d$, $\theta_{bh}\approx\theta_b$, $\theta_{bh}=\mathbf{N}_{\theta b}^*\cdot\mathbf{\Theta}_b$, $\mathbf{N}_u=\{\mathbf{N}_{ud},\mathbf{N}_{ub}\}$, $\mathbf{N}_\theta=\{\mathbf{N}_{\theta d},\mathbf{N}_{\theta b}\}$,

$$\mathbf{K}_{uu}=\begin{bmatrix}\mathbf{K}_{uu}^{dd} & \mathbf{K}_{uu}^{db}\\ \mathbf{K}_{uu}^{bd} & \mathbf{K}_{uu}^{bb}\end{bmatrix},\quad \mathbf{K}_{u\theta}=\begin{bmatrix}\mathbf{K}_{u\theta}^{dd} & \mathbf{K}_{u\theta}^{db}\\ \mathbf{K}_{u\theta}^{bd} & \mathbf{K}_{u\theta}^{bb}\end{bmatrix},\quad \mathbf{K}_{\theta\theta}=\begin{bmatrix}\mathbf{K}_{\theta\theta}^{dd} & \mathbf{K}_{\theta\theta}^{db}\\ \mathbf{K}_{\theta\theta}^{bd} & \mathbf{K}_{\theta\theta}^{bb}\end{bmatrix},$$

$$\mathbf{U}=\begin{Bmatrix}\mathbf{U}_d\\ \mathbf{U}_b\end{Bmatrix},\quad \mathbf{\Theta}=\begin{Bmatrix}\mathbf{\Theta}_d\\ \mathbf{\Theta}_b\end{Bmatrix},$$

where $\mathbf{U}_b$, $\mathbf{\Theta}_b$ are the vectors, known from the main boundary conditions.

So, after using these expressions we can transform Eq. (23) for the problem with thermal stresses in the form

$$\mathbf{K}_{uu}^{dd} \cdot \mathbf{U}_d = \mathbf{F}_u^d, \quad \mathbf{F}_u^d = \mathbf{K}_{u\theta}^{dd} \cdot \mathbf{\Theta}_d + \mathbf{K}_{u\theta}^{db} \cdot \mathbf{\Theta}_b - \mathbf{K}_{uu}^{db} \cdot \mathbf{U}_b \,, \tag{31}$$

where the vector $\mathbf{\Theta}_d$ is also known, and its component values are equal to θ_0 from (6).

Analogously, for the thermal problem (21) we can rewrite Eq. (24) as the system relative to unknown vector $\mathbf{\Theta}_d$:

$$\mathbf{K}_{\theta\theta}^{dd} \cdot \mathbf{\Theta}_d = \mathbf{F}_\theta^d, \quad \mathbf{F}_\theta^d = -\mathbf{K}_{\theta\theta}^{db} \cdot \mathbf{\Theta}_b \,. \tag{32}$$

Thus, the homogenizing problems for thermoelastic composite with surface stresses and with highly conducting porous boundaries can be solved by finite element approaches. The resulting finite element systems (31), (32) differ from similar systems for the bodies of usual sizes by the matrices $\mathbf{K}_{uu\Gamma}$, $\mathbf{K}_{u\theta\Gamma}$, $\mathbf{K}_{\theta\theta\Gamma}$ in (26)–(28). These matrices arise due to the surface mechanical and thermal effects.

4 DISCUSSION AND CONCLUSION

For automated coating of internal boundaries of pores in the cubic representative volume the following algorithm was used [25]. At the beginning, as a result of the formation of the porous structure, the finite element mesh from octanodal cubic elements was created, some of which had the material properties of thermoelastic material, and the other part of the elements had the material properties of the pores (with negligible elastic stiffness moduli). Further, only the finite elements with thermoelastic material properties were selected. The resulting elements on the outer boundaries were covered by four nodal target contact elements. Then, the contact elements, which were located on the external surfaces of the full representative volume, were removed, and the remaining contact elements were replaced by the four nodal membrane elastic elements. As a result, all the facets of the contact of thermoelastic structural elements with pores were coated by membrane finite elements.

The next step consisted in solving the static problems for obtained representative volume with the main boundary conditions which were conventional for effective moduli method. Further, in the ANSYS postprocessor the averaged stresses were calculated, both on the volume finite elements and on the surface finite elements. Finally, the effective moduli of porous composite with surface effects were calculated from the corresponding formulas of the effective moduli method by using the estimated average characteristics.

In the results of computational experiments, the following features were observed [25]. If we compare two similar bodies, one of which has usual dimensions and the other is a nanoscale body, then for the nanosized body due to the surface stresses the effective stiffness will be greater than for the body with usual sizes. Furthermore, for the porous body of the usual size the effective elastic stiffness decreases with increasing porosity. Meanwhile, the effective stiffness of nanocomposite porous body with the same porosity may either decrease or increase depending on the values of surface moduli, dimensions and

number of pores. This effect is explained by the fact that the sizes of the surface pore with surface stresses depend not only on the overall porosity, but also on the configuration, size and number of pores. We can observe similar effects for the effective thermal conductivity coefficients.

The described methodology could be also applied for mixed anisotropic nanostructured composites with other type of connectivity for different physic-mechanical fields, such as poroelastic, piezoelectric, magnetoelectric (magnetoelectroelastic) and other nanocomposites ([5, 7, 8, 9, 21, 22, 29], etc.) At the element level it allows to take into account local types of inhomogeneities, such as, for example, a rotation of the polarization vectors (element coordinate systems) in the vicinity of the pores for porous piezoceramic materials. For example, for porous piezoelectric nanosized composites the analogous approaches can be applied with taking into account both mechanical and electric surface effects.

5 ACKNOWLEDGMENTS

This work for the first author and for the third author was supported by the Russian Science Foundation (grant number 15-19-10008).

REFERENCES

[1] Chen, T., Dvorak, G.J. and Yu, C.C. Solids containing spherical nano-inclusions with interface stresses: Effective properties and thermal-mechanical connections. *Int. J. Solids Struct.* (2007) **44**:941–955.

[2] Duan, H.L. and Karihaloo, B.L. Thermo-elastic properties of heterogeneous materials with imperfect interfaces: Generalized Levin's formula and Hill's connections. *J. Mech. Phys. Solids* (2007) **55**:1036–1052.

[3] Eremeyev, V.A. On effective properties of materials at the nano- and microscales considering surface effects. *Acta Mech.* (2016) **227**:29–42.

[4] Eremeyev, V. and Morozov, N. The effective stiffness of a nanoporous rod. *Doklady Physics* (2010) **55**(6):279–282.

[5] Eremeev, V.A. and Nasedkin, A.V. Natural vibrations of nanodimensional piezoelectric bodies with contact-type boundary conditions. *Mechanics of Solids.* (2015) **50**(5): 495–507.

[6] Graham, S. and McDowell, D.L. Numerical analysis of the transverse thermal conductivity of composites with imperfect interfaces. *J. Heat Transfer.* (2003) **125**:389–393.

[7] Gu, S.-T., Liu, J.-T. and He. Q.-C. Piezoelectric composites: Imperfect interface models, weak formulations and benchmark problems. *Comp. Mater. Sci.* (2014) **94**:182–190.

[8] Gu, S.-T., Liu, J.-T. and He. Q.-C. The strong and weak forms of a general imperfect interface model for linear coupled multifield phenomena. *Int. J. Eng. Sci.* (2014) **85**:31–46.

[9] Gu, S.-T. and Qin, L. Variational principles and size-dependent bounds for piezoelectric inhomogeneous materials with piezoelectric coherent imperfect interfaces. *Int. J. Eng. Sci.* (2014) **78**:89–102.

[10] Gurtin, M.E. and Murdoch, A.I. A continuum theory of elastic material surfaces. *Arch. Rat. Mech. Analysis.* (1975) **57**:291–323.

[11] Javili, A. and Steinmann, P. A finite element framework for continua with boundary energies. Part III: The thermomechanical case. *Comput. Methods Appl. Mech. Eng.* (2011) **200**:1963–1977.

[12] Javili, A. , McBride, A. and Steinmann, P. Thermomechanics of solids with lower-dimensional energetics: On the importance of surface, interface and curve structures at the nanoscale. A unifying review. *Appl. Mech. Rev.* (2013) **65**:010802.

[13] Hamilton, J.C. and Wolfer, W.G. Theories of surface elasticity for nanoscale objects. *Surface Science.* (2009) **603**:1284–1291.

[14] Kaessmair, S., Javili, A. and Steinmann, P. Thermomechanics of solids with general imperfect coherent interfaces. *Arch. Appl. Mech.* (2014) **84**:1409–1426.

[15] Kushch, V. I., Sevostianov, I. and Chernobai, V. S. Effective conductivity of composite with imperfect contact between elliptic fibers and matrix: Maxwell's homogenization scheme. *Int. J. Eng. Sci.* (2014) **83**:146–161.

[16] Le Quang, H. and He, Q.-C. Size-dependent effective thermoelastic properties of nanocomposites with spherically anisotropic phases. *J. Mech. Phys. Solids.* (2007) **55**:1889–1921.

[17] Le Quang, H. and He, Q.-C. Estimation of the effective thermoelastic moduli of fibrous nanocomposites with cylindrically anisotropic phases. *Arch, Appl. Mech.* (2009) **79**:225–248.

[18] Le Quang, H., Phan, T.-L. and Bonnet, G. Effective thermal conductivity of periodic composites with highly conducting imperfect interfaces. *Int. J. Thermal Sci.* (2011) **50**:1428–1444.

[19] Le Quang, H. , Pham, D. C., Bonnet, G. and He, Q.-C. Estimations of the effective conductivity of anisotropic multiphase composites with imperfect interfaces. *Int. J. Heat Mass Transfer.* (2013) **58**:175–187.

[20] Liu, J.T., Gu, S.T. , Monteiro, E. and He, Q.-C. A versatile interface model for thermal conduction phenomena and its numerical implementation by XFEM. *Comput. Mech.* (2014) **53**:825–843.

[21] Nasedkin, A.V. and Eremeyev, V.A. Harmonic vibrations of nanosized piezoelectric bodies with surface effects. *ZAMM.* (2014) **94**(10):878–892.

[22] Nasedkin, A.V. and Eremeyev, V.A. Some models for nanosized magnetoelectric bodies with surface effects. *Advanced Materials – Manufacturing, Physics, Mechanics and Applications*, Springer Proceedings in Physics, **175**, Eds. I.A. Parinov, S.-H. Chang, V.Y. Topolov. Springer, 373–391 (2016).

[23] Nasedkin, A.V. and Nasedkina, A.A. Finite element modeling and computer design of porous composites. *Poromechanics V. Proc. of the Fifth Biot Conf. on Poromechanics. July 10-12, 2013, Vienna, Austria*. Eds. Hellmich C., Pichler B., Adam D. Publ. ASCE, 608–617 (2013).

[24] Nasedkin, A.V., Nasedkina, A.A. and Remizov V.V. Finite element modeling of porous thermoelastic composites with account for their microstructure. *Computational continuum mechanics* (2014) **7**(1): 100–109. (in Russian)

[25] Nasedkin, A.V., Nasedkina, A.A. and Kornievsky, A.S. Modeling of nanostructured porous thermoelastic composites with surface effects. *AIP Conf. Proc.* (2017) **1798**:020110-1–10.

[26] Povstenko, Y.Z. Theoretical investigation of phenomena caused by heterogeneous surface-tension in solids. *J. Mech. Phys. Solids.* (1993) **41**:1499–1514.

[27] Shuttleworth, R. The surface tension of solid. *Proc. Phys. Soc. A.* (1950) **63**:444–457.

[28] Wang, J., Huang, Z. , Duan, H., Yu, S., Feng, X., Wang, G., Zhang, W. and Wang, T. Surface stress effect in mechanics of nanostructured materials. *Acta Mechanica Solida Sinica.* (2011) **24**:52–82.

[29] Xiao, J.H., Xu, Y.L. and Zhang, F.C. Size-dependent effective electroelastic moduli of piezoelectric nanocomposites with interface effect. *Acta Mechanica.* (2011) **222**(1–2):59–67.

[30] Yvonnet, J., He, Q.-C., Zhu, Q.-Z. and Shao, J.-F. A general and efficient computational procedure for modelling the Kapitza thermal resistance based on XFEM. *Comp. Mater. Sci.* (2011) **50**:1220–1224.

VII International Conference on Computational Methods for Coupled Problems in Science and Engineering
COUPLED PROBLEMS 2017
M. Papadrakakis, E. Oñate and B. Schrefler (Eds)

MICROSCALE ELECTRICAL CONTACT RESISTANCE ANALYSIS FOR RESISTANCE SPOT WELDING

TOMOYA NIHO*, KENJI KUBOTA*, HIROCHIKA ARAMAKI*, HIROYUKI KURAMAE†, DAISUKE ISHIHARA* AND TOMOYOSHI HORIE*

*Department of Mechanical Information Science and Technology
Kyushu Institute of Technology, 680–4 Kawazu, Iizuka, Fukuoka 820–8502, Japan
e-mail: niho@mse.kyutech.ac.jp

†Department of Robotics
Osaka Institute of Technology, 5–16–1 Omiya, Asahi–ku, Osaka 535–8585, Japan
e-mail: kuramae@dim.oit.ac.jp

Key words: Microscale Surface Roughness, Temperature Dependent Material Property, Elasto–Plastic Contact Deformation, Resistance Spot Welding, Statistically Similar Representative Volume Element, Multiscale resistance spot welding analysis

Abstract. Electrical contact resistance is an important parameter for resistance spot welding. In this study, a microscale electrical contact resistance analysis method is proposed for resistance spot welding. The microscale electrical contact resistance analysis method is combination of an elasto–plastic large deformation contact analysis and an electric current analysis. The electric current analysis is performed for deformed shape of asperity. The tendency of the electrical contact resistance on contact pressure and temperature for the electrical contact resistance analysis agrees with that for Babu's electrical contact resistance model.

A multiscale coupled analysis method is also proposed for resistance spot welding. The multiscale analysis consists of macroscale elasto–plastic large deformation contact, electric current and thermal conduction triply coupled analysis and microscale electrical contact resistance analysis. It is confirmed that the resistance spot welding analysis without measurement of electrical contact resistance can be performed by using the microscale electrical contact resistance analysis.

1 INTRODUCTION

Resistance spot welding is widely used for manufacturing industries such as auto motive industry. Since the resistance spot welding is elasto–plastic large deformation contact, electric current and thermal conduction coupled problem, triply coupled analysis is required for examination of welding mechanism and determination of welding conditions.

Many researches have proposed the analysis methods of resistance spot welding[1, 2, 3]. The authors have also proposed the triply coupled analysis model[4], and developed the analysis code which is constructed by commercial code MSC. Marc and in–house electric current–heat conduction coupled analysis code using MPI[5]. Since the numerical instability for coupled analysis[6] may be encountered the analysis of resistance spot welding, evaluation of numerical instability is important for the triply coupled analysis method.

In the analysis of resistance spot welding, electrical contact resistance is an important parameter for nugget formation process. Many theoretical models were presented for electrical contact resistance[7]. Greenwood proposed the electrical contact resistance model for a cluster of spots with various sizes and their distributions[8]. Babu et al. proposed the empirical electrical contact resistance model which is based on Greenwood's model and the measured electrical contact resistance, and is easy to use for resistance spot welding simulation[9].

In this study, a microscale electrical contact resistance analysis method is discussed corresponding to various grade steel plates, surface roughness and zinc plated steel plate. The microscale electrical contact resistance analysis method is combination of an elasto–plastic large deformation analysis and an electric current analysis. Three-dimensional microscale finite element model is constructed based on surface roughness measurement. The tendency of the electrical contact resistance on contact pressure and temperature for the electrical contact resistance analysis is compared to that for electrical contact resistance model. A multiscale coupled analysis method is also proposed for resistance spot welding. The multiscale analysis consists of macroscale elasto–plastic large deformation contact, electric current and thermal conduction triply coupled analysis and microscale electrical contact resistance analysis. The multiscale analysis is executed and is compared with conventional single–scale analysis result using Babu's model.

2 MICROSCALE ANALYSIS METHOD OF ELECTRICAL CONTACT RESISTANCE

The microscale analysis method of electrical contact resistance is shown in Fig. 1. The finite element analysis model is constructed based on microscale measurement of surface roughness. The electrical contact resistance is calculated by elasto–plastic large deformation contact analysis and electric current analysis.

In the elasto–plastic large deformation contact analysis, temperature dependent stress–strain relationship is used. Since the electrical contact resistance is calculated by the microscale analysis, the statistically similar representative volume element (SS–RVE) is used for the analysis, and periodic boundary condition are imposed on the microscale finite element analysis model.

In the electric current analysis, the ϕ method is used to obtain the electric resistance for deformed shape. Boundary condition of $\phi = 0$ and $\phi = \phi_0$ are imposed on bottom surface and contacted node, respectively.

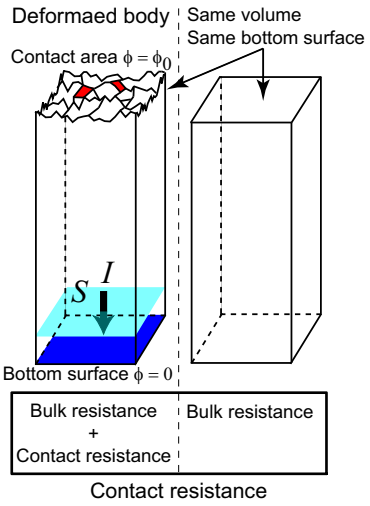

Figure 1: Microscale electrical contact resistance analysis method

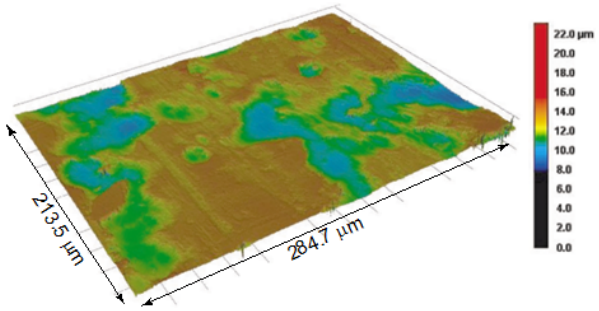

Figure 2: Measured surface roughness of 440 MPa grade steel plate by laser microscope

3 MICROSCALE ANALYSIS OF ELECTRICAL CONTACT RESISTANCE

3.1 Analysis conditions

In order to analyze electrical contact resistance, microscale finite element analysis model is constructed based on laser microscope measurement of surface roughness of 440 MPa grade tensile strength steel plate. The measured surface roughness is shown in Fig. 2. The resolution of in–plane and height directions were 0.139 μm and 0.001 μm, respectively.

The SS-RVEs shown in Fig. 3 are used to discuss the SS-RVE size. Figure 4 shows the finite element analysis model of 100 μm $\times$ 100 μm SS–RVE. The SS–RVE is divided by 20–node solid element. Figure 5 shows time history of contact pressure and temperature to discuss the SS–RVE size.

3.2 Results

Figure 6 shows the contact status for SS–RVEs. The blue area and yellow area are non–contact area and contact area, respectively. The electric current analysis are performed for deformed shape obtained by elasto–plastic large deformation contact analysis.

The time change of electrical contact resistance are shown in Fig. 7. The results for 100 μm $\times$ 100 μm agree well with those for 150 μm $\times$ 150 μm. Therefore, over 100 μm $\times$ 100 μm is required for SS–RVE of the microscale analysis of electrical contact resistance.

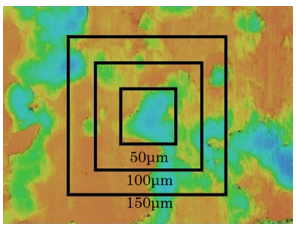

Figure 3: SS–RVEs for measured surface

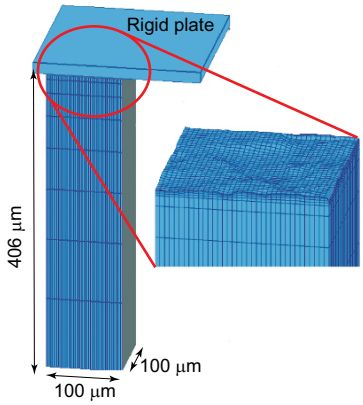

Figure 4: Finite element analysis model of SS–RVE 100 μm $\times$ 100 μm

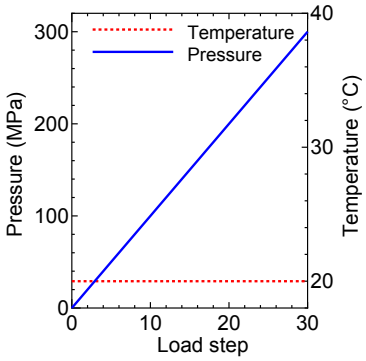

Figure 5: Change of contact pressure and temperature

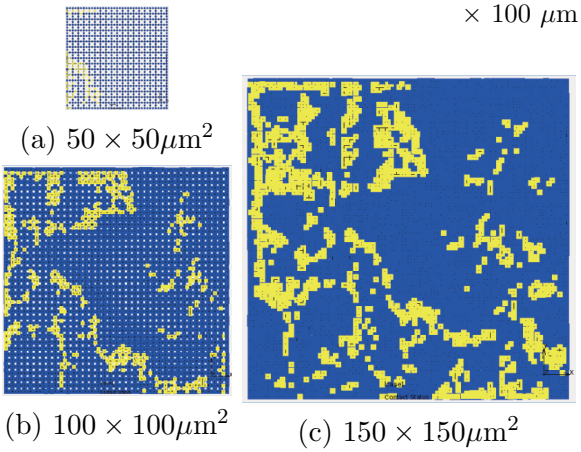

(a) $50 \times 50\mu m^2$

(b) $100 \times 100\mu m^2$

(c) $150 \times 150\mu m^2$

Figure 6: Change of contact status with SS–RVE size (Blue area: Non–contact, Yellow area: Contact)

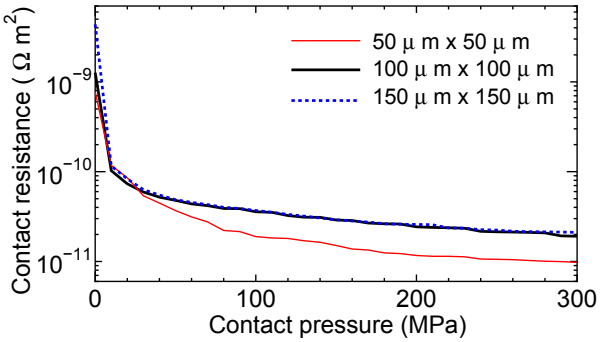

Figure 7: Convergence of electrical contact resistance with SS–RVE size

3.3 Characteristics of electrical contact resistance

Characteristics of electrical contact resistance is discussed for contact pressure and temperature as shown in Fig. 8. The results of microscale analysis are compared to those of Bubu's model[9] expressed as

$$R_{CA} = (\rho_1 + \rho_2)\left(\frac{1}{4}\sqrt{\frac{\pi\sigma_{YS}}{\eta P}} + \frac{3\pi}{16\sqrt{\eta}}\right), \tag{1}$$

where ρ_1 and ρ_2 are electric resistivity, σ_{YS} is yield stress, and η is asperity density.

Figure 9 shows the change of electrical contact resistance for the microscale analysis and Babu's model. The tendency of electrical contact resistance on contact pressure and temperature for the microscale analysis agrees with that for Babu's model.

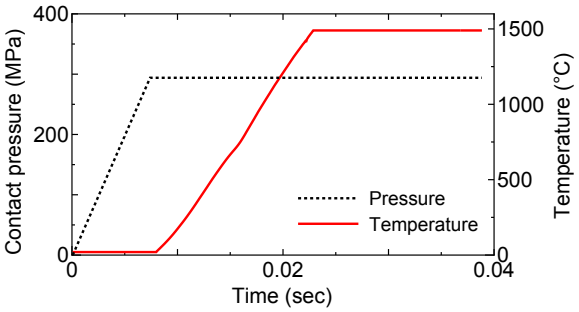

Figure 8: Time change of contact pressure and temperature

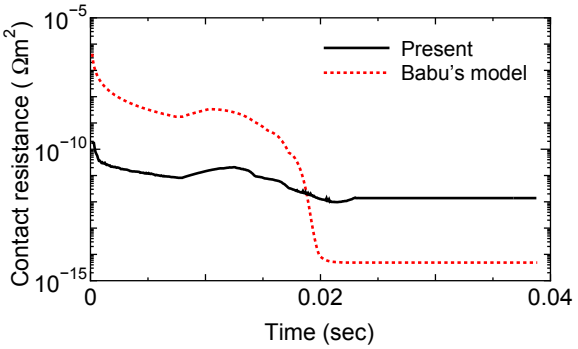

Figure 9: Change of electrical contact resistance with contact pressure and temperature

4 MULTISCALE ANALYSIS OF RESISTANCE SPOT WELDIND

4.1 Method of multiscale analaysis

The multiscale analysis consists of macroscale elasto–plastic large deformation contact, electric current and thermal conduction triply coupled analysis[4] and microscale electrical contact resistance analysis. In macroscale finite element analysis model shown in Fig. 10, there are contact finite elements to evaluate electrical contact resistance on the interface between two steel plates and between the electrode and the steel plate. Microscale analyses are assigned into macroscale contact finite elements to obtain electrical contact resistance. Since microscale finite element analyses are independent each other, the parallel computing technique is employed by the message passing interface (MPI) library.

Figure 11 shows data flow of the multiscale coupled finite element analysis. In the macroscale electric current analysis, the T method is employed to evaluate the Joule heating. The thermal conduction analysis computes temperature distribution by Joule heat with contact dependent thermal conduction paths at the macroscale.

Figure 12 shows macroscale finite element analysis model for resistance spot welding simulation. The macroscale finite element analysis model is divided using axisymmetric 8 node element. Since there are 100 contact finite elements between two steel plates, microscale finite element analyses are assigned into the macroscale contact finite elements to evaluate the electrical contact resistance in every time step.

4.2 Results and discussions

Multiscale resistance spot welding analysis is performed for welding current 9.5 kA and electrode force 1.47 kN. Figure 13 shows the deformation, electric current potential, temperature and nugget for 200 msec. The inside of steel sheets is melted, and nugget is formed on plates interface.

In order to investigate the multiscale analysis results, single–scale analysis is also executed using Babu's model for evaluating the electrical contact resistance. Figure 14 shows comparison of temperature between the multiscale and single–scale analysis results. The

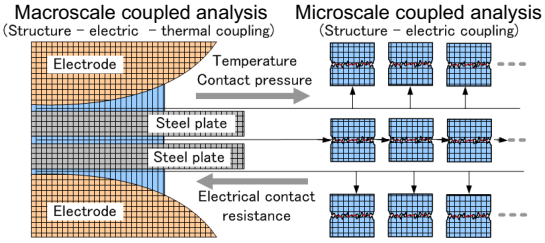

Figure 10: Assignment of microscale finite element analysis into macroscale contact finite elements

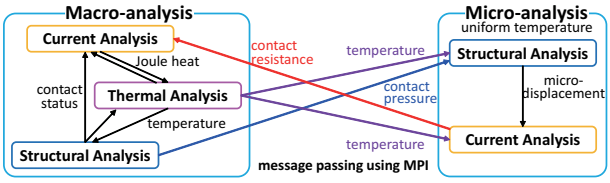

Figure 11: Schematic diagram of multiscale coupled finite element procedure of resistance spot welding

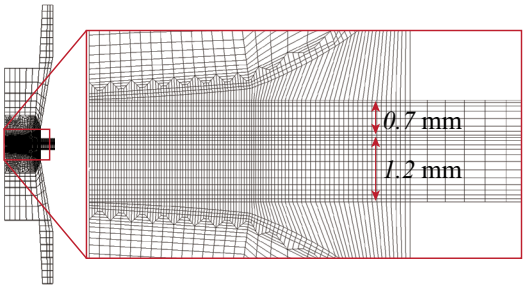

Figure 12: Macroscale finite element analysis model

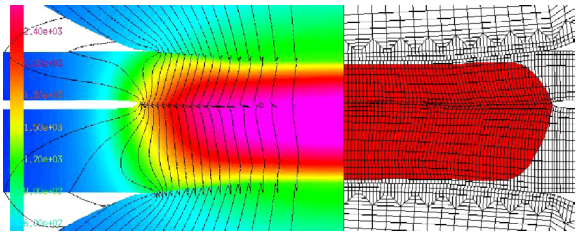

Figure 13: Deformation, electric current potential, temperature and nugget obtained by multiscale resistance spot welding analysis (200 msec)

temperature of single–scale analysis result using Babu's model is higher than that of multiscale one because the electrical contact resistance of Babu's model is higher than that of multiscale analysis. Figure 15 shows comparison of time change of nugget diameter. The nugget growths are different between multiscale and single–scale analyses, however, the final nugget diameters are almost same because the electrical contact resistance is eliminated by high temperature.

5 CONCLUSIONS

The electrical contact resistance analysis method is proposed for resistance spot welding. The method is combination of elasto–plastic large deformation contact analysis and electric current analysis. The microscale finite element analysis model is constructed based on surface roughness measurement. The tendency of the electrical contact resistance on contact pressure and temperature agrees with that of Babu's models.

The multiscale coupled analysis method is also proposed for resistance spot welding. The multiscale analysis consists of macroscale elasto–plastic large deformation contact, electric current and thermal conduction triply coupled analysis and microscale electrical contact resistance analysis. The multiscale resistance spot welding analysis is executed and is compared with conventional single–scale analysis result using Babu's model. It is confirmed that the resistance spot welding analysis without measurement of electrical contact resistance can be performed by using the microscale electrical contact resistance analysis.

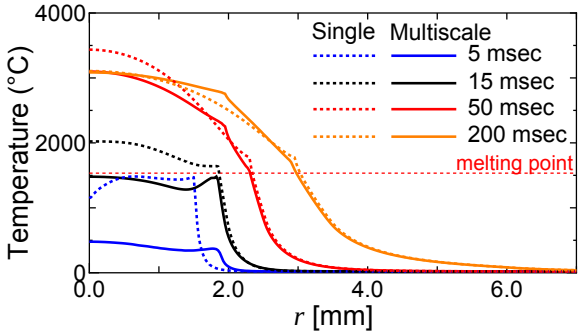

Figure 14: Temperature distribution on steel plates interface for multiscale coupled analysis and singl–scale analysis using Babu's model

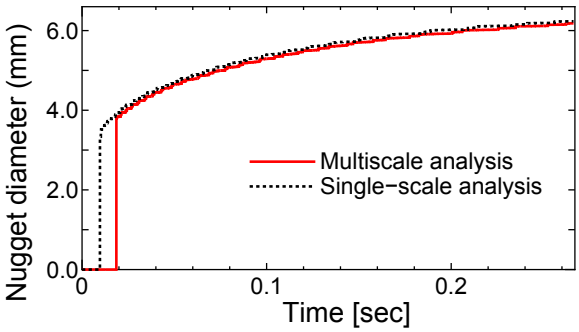

Figure 15: Time change of nugget diameter

REFERENCES

[1] Nied, H.A. The finite element modeling of resistance spot welding process. *Welding Journal*, (1984) **63**–4: 123–132.

[2] Feng, Z., Gould, J.E., Babu, S.S., Santella, M.L. and Riemer, B.W. An incrementally coupled electrical–thermal–mechanical model for resistance spot welding. *Trends in Welding Research: Proceedings of 5th International Conference* (1999): 599–604.

[3] Shen, J., Zhang, Y., Lai, X. and Wang, P.C. Modeling of resistance spot welding of multiple stacks of steel sheets. *Materials and Design* (2011) **32**–2: 550–560.

[4] Niho, T., Horie, T., Morita, Y., Ishihara, D., Yamakawa, D., and Momii, S. Elasto–plastic contact, electric current and thermal conduction triply coupled analysis model for resistance spot welding. *Quarterly Journal of the Japan Welding Society* (2015) **33**–3: 271–282 (in Japanese).

[5] Niho, T., Horie, T. Coupled finite element analysis technique combining in-house code and commercial analysis code. *Transactions of the Japan Society for Computational Engineering and Science* (2015) **2015**: p. 20150015 (in Japanese).

[6] Niho, T., Horie, T., Uefuji, J., and Ishihara, D. Stability analysis and evaluation of staggered coupled analysis methods for electromagnetic and structural coupled finite element analysis. *Computers & Structures* (2017) **178**–1: 129–142.

[7] Hamedi, M. and Atashparva, M. A review of electrical contact resistance modeling in resistance spot welding. *Welding in the World* (2017) **61**–2: 269–290.

[8] Greenwood, J.A. Constriction resistance and the real area of contact. *Brit. J. Appl. Phys.* (1966) **17**: 1621–1632.

[9] Babu, S.S., Santella, M.L., Feng, Z., Riemer, B.W. and Cohron, J.W. Empirical model of effects of pressure and temperature on electrical contact resistance of metals. *Sci. Tech. Welding Joining* (2001) **6**–3: 126–132.

VII International Conference on Computational Methods for Coupled Problems in Science and Engineering
COUPLED PROBLEMS 2017
M. Papadrakakis, E. Oñate and B. Schrefler (Eds)

MONITORING AND LIFETIME PREDICTION OF PVC CABLES: METHODOLOGY BY MULTISCALE AND MULTIDISCIPLINARY APPROACH

J. TIREAU[*], R. MAURIN[*], L. YUE[*], G. MARQUE[*], M. BEN HASSINE[*], I. MKACHER[*], F. DJOUANI[†], X. COLIN[†],

[*] EDF Lab les Renardières
Avenue des Renardières
77818 Moret-sur-Loing, France
e-mail: jonathan.tireau@edf.fr, web page: http://www.edf.fr

[†] Arts et Métiers ParisTech, PIMM
151 Boulevard de l'Hôpital
75013 Paris, France
e-mail : pimm-contact@ensam.eu, web page : http://pimm.paris.ensam.fr

Key words: Poly(vinyl chloride), Cables, Lifetime prediction, Monitoring, Multiscale, Plasticizers loss.

Abstract. Monitoring of the PVC cables as well as the prediction of their residual lifetime are important issues for the maintenance of the French nuclear power plants (NPPs). To date, the unanimously end of life criterion admitted for these cables is a 50% value of elongation at break and, to our knowledge, only destructive tests give access to this parameter. This study reports a relationship between elongation at break of the PVC and their plasticizer content. This correlation opens the door to a monitoring directly on site or by micro sampling since all classic laboratory techniques able to measure this content become ways to judge the condition of the PVC sheaths and insulators. In addition, this study demonstrates the feasibility of prediction of industrial PVC behavior changes. This model, adapted to the case of thin films, involved tools of chemical kinetics and the implementation of a constitutive model.

1 INTRODUCTION

In NPPs, electric cables represent about 1500 km per unit. To date, most of the French power plants currently in operation mainly have qualified electric cables on PVC. All these PVC cables are considered as "sensitive" because of their presence in large number in nuclear units and the high cost that the replacement would represent (cost including heavy maintenance and a long shutdown period).

In this context, EDF R&D manages research projects on PVC cables with the aim to improve the lifetime prediction accuracy of cables, to manage obsolescence and to develop non-

destructive exams to follow their aging on site.

To date, the end-life criterion unanimously adopted for cables is a mechanical one setting on a nominal value of the elongation at break (ε_r = 50%). To our mind, only tensile tests enable the measurement of the elongation at break of a material in a direct way. This technique has the double disadvantage of being destructive and to require sampling on nuclear material which is always a costly and heavy procedure. Thus, it is unbelievable to use this technique for monitoring PVC cables installed all over the French nuclear units.

Previous studies [1-2] conducted on PVC degradation give the demonstration that embrittlement of a plasticized PVC sheath is closely related to its loss of plasticizers. From this observation, EDF R&D decided:

- first, to simulate the physical loss of PVC plasticizers at different temperatures and determine the kinetics parameter of plasticizers evaporation;
- and then to access the elongation at break either by a simple multiscale relation between ε_r and plasticizer content or by the reproduction of the PVC tensile test curve using laws of behaviour.

2 MATERIAL AND AGEING CONDITIONS

2.1 Material and initial characterization

Pure PVC and phthalate plasticizers (DIOP, DEP, DINP, DIDP and DDP) were supplied by Sigma Aldrich. Pellets of industrial formulation were supplied by a cable producer. According to the information provided by this last supplier, this industrial PVC would be plasticized with phthalate. However, the exact formulation and initial plasticizer content were not communicated. Thus, the first stage of this work, carried out within the framework of Ines Mkacher's thesis [3], was to proceed to a shaping of the pellets and to an initial characterization of the industrial PVC films obtained.

The pellets were heat-pressed at 180 ° C for 30 seconds using a platen press. Thin films with a thickness of 130 ± 50 μm were formed. In the same way, thin model films of DIOP, DEP, DINP, DIDP and DDP plasticized PVC were pressed.

Characterization by infrared spectroscopy (IR), thermogravimetric analysis and gel permeation chromatography (GPC) highlight the presence, in the industrial PVC, of $CaCO_3$ fillers (35% by mass) and di-isodecyl phthalate phthalate plasticizers (DIDP, 27% by mass).

2.2 Ageing conditions and aged samples characterization

In order to simulate thermal aging of the PVC, the films were subjected to accelerated aging in a ventilated oven at different temperatures between 95°C and 160°C. Samples were regularly removed from the ovens to be analyzed by IR and tensile tests.

Mechanical characterizations, meaning stress and strain at break determination, were

performed on H2 shouldered test bars, at 23°C and 50% RH conditions, with a 100 N force cell and an elongation speed of 10 mm/min.

Residual content of plasticizers were determined by IR spectroscopy using the Beer Lambert law:

$$C = \frac{AO}{\varepsilon\, e}$$

C is the concentration of chemical species (here an ester of the different phthalates studied), AO is the absorbance also called operational amplitude, ε is the molar absorptivity and e the thickness of the sample crossed by the IR beam. The calibration lines were used to determine the molar absorptivity of the different phthalate. For example, the Figure 1 was used to determine the molar absorptivity of the DIDP plasticizers at 1723 cm^{-1} (ε_{DIDP} = 744 $mol.l^{-1}.cm^{-1}$). The DIDP having two groups of esters per molecule, the molar absorptivity of the ester function is ε_{ester} = 372 $mol.l^{-1}.cm^{-1}$. In the case of model films, infrared analyses were performed in transmission mode and so the e parameter corresponds to the thickness of the film. While in the case of industrial PVC films, the IR analysis were carried out in ATR mode due to the film opacity. The e parameter (e = 2.09 10^{-4} cm) was deduced from the ε_{DIDP} and the AO_{ester} previously obtained on a PVC film with a well-known concentration of DIDP.

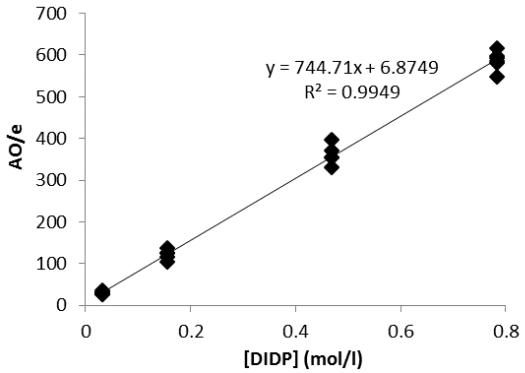

Figure 1: Calibration line obtained with data of ester functions absorbance of DIDP for PVC plasticized with content between 1% and 25% mass.

3 DETERMINATION OF EVAPORATION KINETICS OF PLASTICIZER

To illustrate the results obtained by IR on samples thermally aged, the example of PVC film plasticized with 30% mass of DIDP and exposed in ventilated oven for nearly 50 hours at 140°C can be used. Knowing the molar absorptivity of DIDP plasticizer, the Beer Lambert law enables to calculate the residual concentration of DIDP by simple measurement of absorbance at 1723 cm^{-1}. The concentrations obtained for each sample are summarized in Figure 2. Observations suggest a change occurring in two steps. A first phase, between 0 h and 25 h, during which the loss in plasticizers seems to be nearly linear with exposure time and, then, a second phase during which the losses appear to be zero due to a constant DIDP concentration. The literature showing no reactivity of esters of the DIDP during thermal ageing, observed losses can be correlated in totality to physical losses by evaporation.

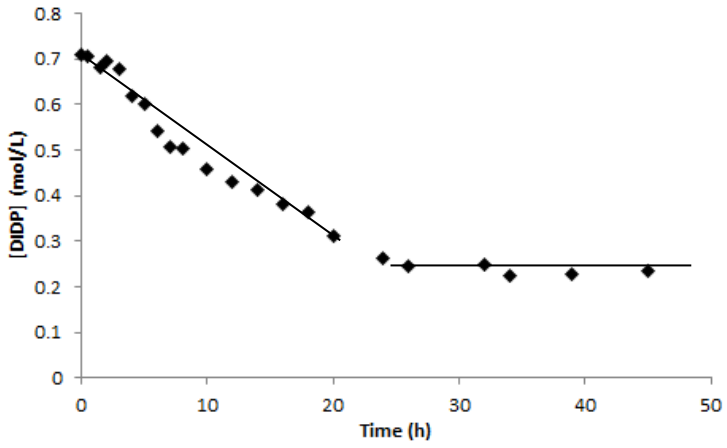

Figure 2: Evolution of DIDP concentration during exposure at 140 ° C of a thin film of a 30% mass plasticized PVC. Data obtained by IR measurements.

A description of the loss of plasticizers by evaporation was proposed by Audouin et al. [4] using the laws of heat transfer and Raoult equation. These authors assume the expression of evaporation rate to be as follow:

$$\frac{dC}{dt} = -\frac{r_{ev}C}{eC_s} = -\beta C \quad (1)$$

Where C is the concentration of adjuvant in the surface layer of the polymer, C_s the concentration at saturation of the adjuvant, e the thickness of the sample, r_{ev} the evaporation rate and β the evaporation kinetics coefficient.

The integration of equation 1 leads to the following relationship:

$$ln\frac{C}{C_0} = -\beta t \quad (2)$$

C_0 corresponds to the initial concentration of plasticizers.

With the aim to determine the kinetics of plasticizers evaporation, the infrared measurements were also performed on model PVC films exposed to different temperatures, such as 95°C, 105°C and 120°C. In the case of DIDP, the kinetics of evaporation obtained for each temperature is presented on the figure 3.

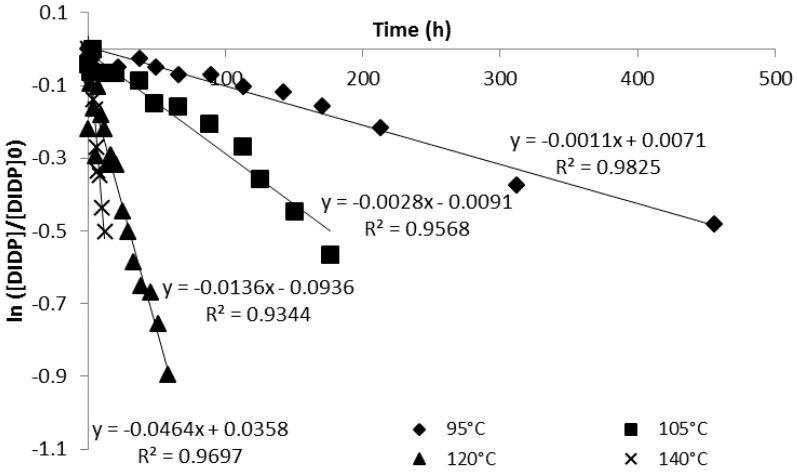

Figure 3: Logarithmic evolution of DIDP concentration in the case of thin film plasticized, initially with 30% mass of DIDP, versus exposure time for temperature between 95°C and 140°C. Data obtained by IR.

Figure 4 presents a logarithmic evolution of the evaporation coefficient (so the slope of the lines illustrated in figure 3) versus the inverse of the temperature. As evaporation is a phenomenon thermally activate, the evaporation coefficient can be expressed with the following equation:

$$\beta_{IR} = \beta_{IR0} exp(-\frac{Ea}{RT}) \quad (3)$$

Where R is the perfect gas constant, so 8.314 $J.mol^{-1}.K^{-1}$
E_a corresponds to an activation energy, here E_a = 13.403 x R, so 111 $kJ.mol^{-1}$
And β_{IR0} corresponds to a pre-exponential factor equal to 1.88 10^9 s^{-1}

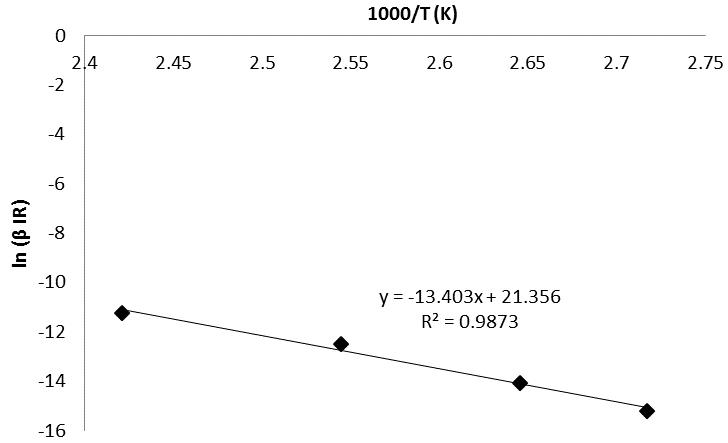

Figure 18: Logarithmic evolution of the DIDP evaporation coefficient versus the inverse of temperature in the case of thin PVC films, initially plasticized with 30% mass, for exposition under air at temperature between 95°C and 140°C. Data obtained by IR.

The same determination was used for DIOP, DEP, DINP and DDP. Table 1 summarizes all the kinetics parameters values obtained. A part of these data were previously published by

Djouani et al. [1].

Table 1: Kinetics parameters obtained for the evaporation of the five plasticizers studied

	DIOP	**DEHP**	**DINP**	**DIDP**	**DDP**
E_a (kJ.mol^{-1})	69	76	93	111	154
β_{IR0} (s^{-1})	8.61 10^5	3.65 10^5	1.28 10^7	1.88 10^9	1.11 10^{14}

3 MODELLING OF PLASTICIZER EVAPORATION

Virtual Polymer is a numerical tool internally developed by EDF which allows to simulate the aging of polymers using the resolution of differential equation (chemical kinetics) and transport (diffusion, evaporation ...).

The equations used for modeling the plasticizers evaporation are the equations 2 and 3:

$$C = C_0 \, exp(-\beta_{IR} t) \tag{2}$$

$$\beta_{IR} = \beta_{IR0} exp(-\frac{Ea}{RT}) \tag{3}$$

Figure 4 shows a comparison, in the case of industrial PVC films, of the evaporation results of plasticizers determined experimentally by IR spectroscopy and by modelling under Virtual Polymer.

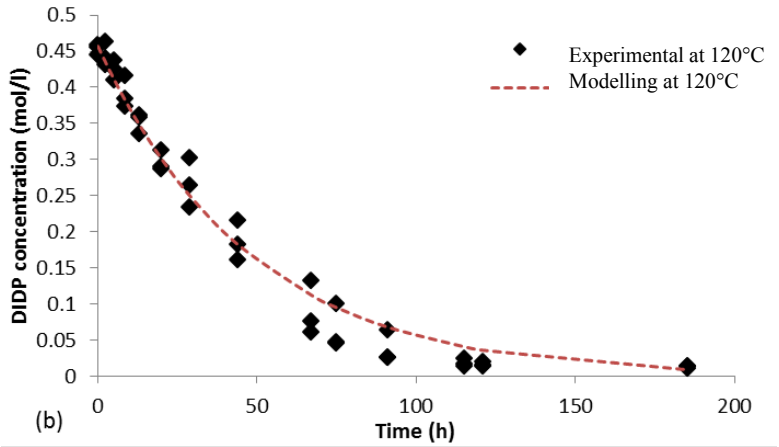

Figure 4: Evolution of the plasticizers concentration in a thin film of industrial PVC exposed to 120°C. Results obtained by modelling (Virtual Polymer) and IR analysis

4 MONITORING AND PREDICTION OF PVC EMBRITTLEMENT

4.1 Monitoring of PVC embrittlement

Linde and Gedde [5] showed, with experimental tests in the case of DIDP and DEHP plasticized PVC samples, that an increase of plasticizers concentration leads to an increase of the elongation at break of the material and to a reduction of its Young modulus. Since the current criterion of end of life of the nuclear cables is a 50% elongation at break value, our attention focus on the possible relation existing between plasticizers content and elongation at break of PVC.

As no relation was found in the literature, we decided to identify an experimental law from data obtained by IR spectroscopy and tensile tests on aged samples of industrial PVC. Figure 5 illustrates the found correlation and gives the empirical law determined.

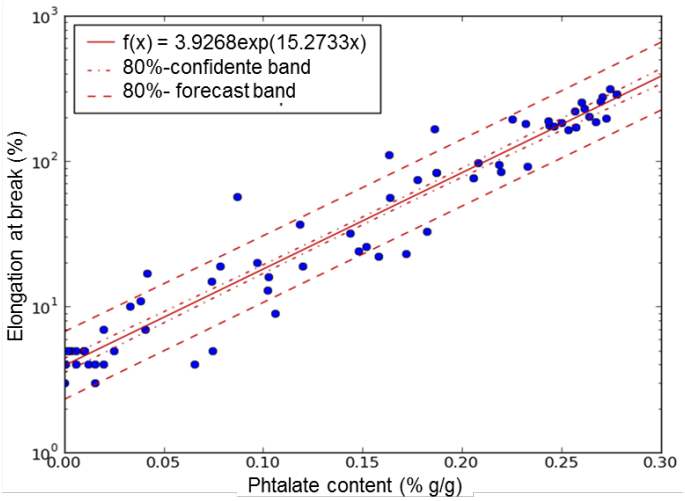

Figure 5: Evolution of the elongation at break (logarithmic scale) versus the concentration of DIDP plasticizers for industrial PVC thin films exposed to thermal ageing between 95°C and 160°C.

On the one hand, this relation opens the door to the estimation of the local mechanical properties of a PVC cable by non-destructive techniques (for example using portable infrared spectroscopy) or by a simple micro-sampling. With only 10 to 20 mg of material, it is possible to determine the plasticizers content (by classical IR spectroscopy, thermogravimetric analysis, gas chromatography, solvent extraction…) and finally to estimate elongation at break of the PVC without performing destructive tensile tests.

On the other hand, this relation indicates that $\varepsilon_r = 50\%$ is reached for a residual content of plasticizers of $17 \pm 3\%$.

4.2 Prediction of PVC embrittlement

Two approaches have been studied to simulate the evolution of mechanical properties of PVC films caused by plasticizers evaporation. One uses the empirical relation of section 3.1 and the other uses the reconstruction of a constitutive law using a phenomenological model

4.2.1 Empirical approach

This empirical relation, described in the §3.1, makes possible the transcription of the chemical data of plasticizers concentration in mechanics data of elongation at break. Thus, all the modelling of plasticizer evaporation can be used to model elongation at break changes. Figure 6 gives examples of comparison of elongation at break data obtained experimentally and by Virtual Polymer.

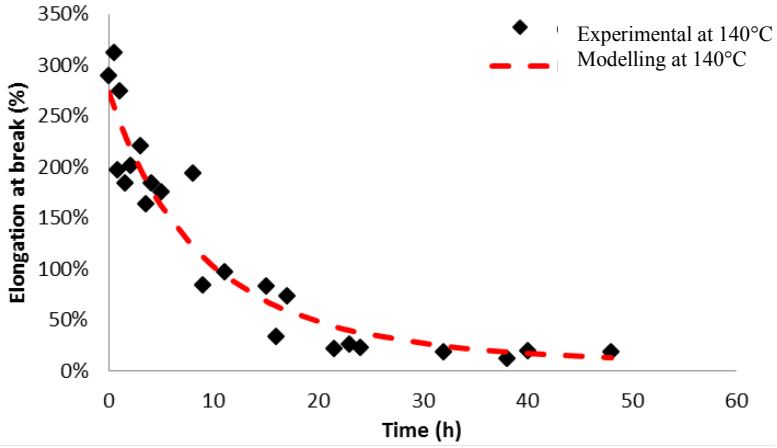

Figure 6: Evolution of the elongation at break of industrial PVC during the thermal ageing in air at 140 ° C. Comparison of numerical simulations to experimental data obtained by uniaxial traction.

The application of this elongation at break modelling at temperatures of 50°C and 70°C, temperatures which can punctually be meet on NPPs, offers the possibility to estimate, for thin film, evolution of the elongation at break in these conditions and to determine the time required to obtain a residual elongation of 50%. As shown in Figure 7, this time t_c is estimated after 3 and 40 years for thermal exposition at 70°C and 50°C respectively in the case of thin film of industrial.

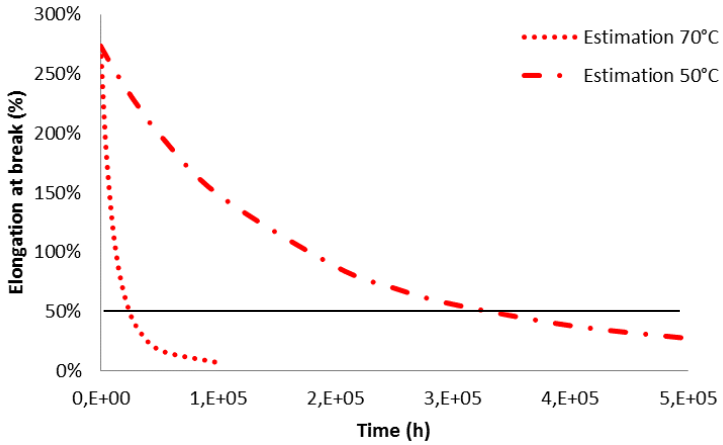

Figure 7: Estimation of the elongation at break of industrial PVC during thermal ageing under air at 50°C and 70 ° C. Data obtained by Virtual Polymer modelling.

4.2.2 Phenomenological approach

Mulliken [2] proposed a predictive model (Boyce-Mulliken model) of the stress-strain behavior of plasticized PVC. As illustrated in Figure 8, this model is composed of: (i) an elastic part (B) corresponding to the entropic hardening element and (ii) an elastic viscoplastic part (A) related to the rotation of macro segments of the main chains of polymer (α) and to the intermolecular resistance (β).

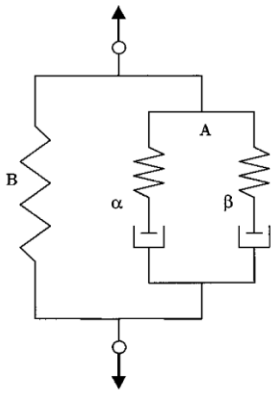

Figure 8: Proposed constitutive model for rate-dependent thermoplastic behaviour [2].

The implementation of the model of Boyce-Mulliken was done using the Mfront tool. Nine parameters of this law have already been identified by Mulliken [2] for DOP plasticized PVC. However, the formulation of our industrial PVC films and the tensile tests mode are different from that of the study of Mulliken [2], so a re-identification of some parameters was necessary.

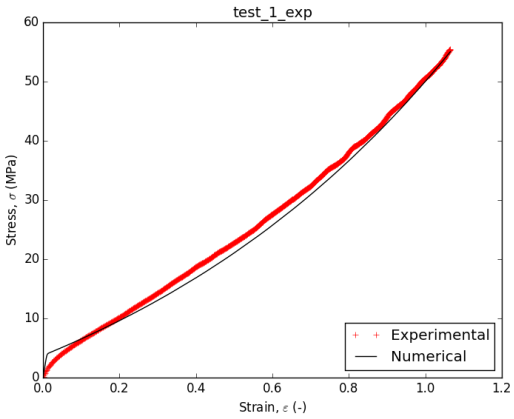

Figure 9: Result of the implementation of the Boyce-Mulliken model for an unaged film of industrial PVC.

As shown in Figure 9, the implementation of this model after re-identification of the parameters properly simulates the stress-strain curves of our industrial material in initial condition. However, for aged samples with a residual content of plasticizers below 17% mass, a discontinuity on one parameter appears. A parameter adjustment appears necessary to compensate this change in mechanical behavior. Figure 10 shows that the re-adjustment of parameter allows to frame all of the curves of traction obtained for the PVC containing 17% mass of plasticizers.

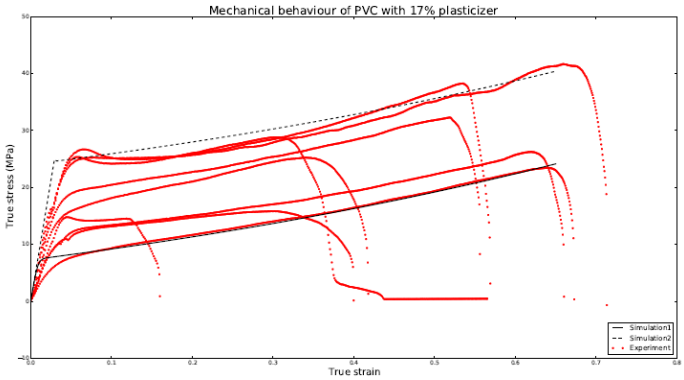

Figure 10: Comparison of the tensile curves obtained experimentally and using the model of Boyce-Mulliken in the case of industrial PVC film containing 17% mass of plasticizers.

The coupling of the kinetic model, used to calculate the plasticizers loss depending on time and temperature, and Boyce-Mulliken model, used to rebuild the tensile curve of a plasticized PVC, enables to simulate the evolution of the mechanical behavior of plasticized PVC films exposed to thermal aging. Figure 11 shows the result on our industrial PVC exposed to 70°C and gives the confirmation of an end of life criterion met after 3 years of exposure.

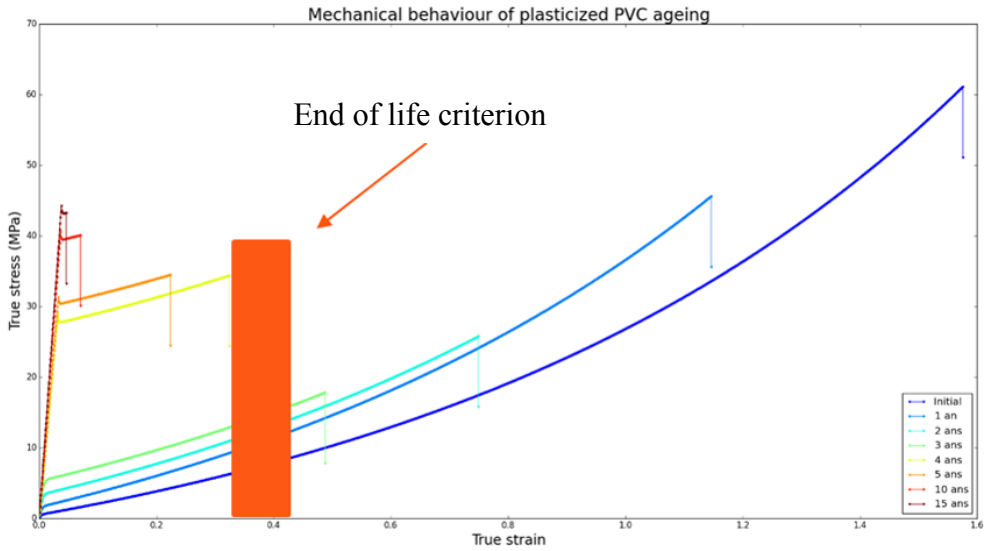

Figure 11: Results of simulation obtained with the coupling of kinetics and Boyce-Mulliken models for industrial PVC films exposed to 70°C

5 CONCLUSIONS

This study reports a relationship between elongation at break of the PVC and their plasticizer content. This correlation opens the door to a monitoring directly on site or by micro sampling since all classic laboratory techniques able to measure this content become ways to judge the condition of the PVC sheaths and insulators. In addition, this study demonstrates the feasibility of prediction of industrial PVC behavior changes. This model, adapted to the case of thin films, involved tools of chemical kinetics and the implementation of a constitutive model.

The next part of this study will be to extend this model to the case of thick PVC in order to simulate the embrittlement of PVC sheaths (thickness of 3-4 mm). Chemical kinetics should take into account the phenomenon of diffusion of plasticizers in the thickness of the PVC sheaths and mechanical modelling should implement simulation in two dimensions.

REFERENCES

[1] Djouani, F. Mkacher, I. Colin, X. Brument Y. and Cristiano-Tassi A. Evaporation kinetics of DIDP plasticizer from PVC, *AIP Conference Proceeding*, (2014) 1599, 1:218-221.

[2] Mulliken, A. Soong, S. Boyce M. and Cohen, R. High-rate thermomechanical behaviour of poly (vinyl chloride) and plasticized poly (vinyl chloride), *J. Phys. IV Proceeding*, (2006) 134: 217-223.

[3] Mkacher, I. Vieillissement thermique des gaines PE et PVC de cables électriques. *Thesis of Arts et Métiers ParisTech* (2012).

[4] Audouin, L. Dalle, B. Metzger, G. Verdu, J. Thermal ageing of plasticized PVC. I. Weight loss kinetics in the PVC – didecylphtalate system. *Journal of Applied Polymer Science* (1992) 45(12):2091-2096.

[5] Linde, E. and Gedde, U.W. Plasticizer migration from PVC cable insulation – The challenge of extrapolation methods, *Polymer Degradation and Stability*, (2014) 101:24-31.

VII International Conference on Computational Methods for Coupled Problems in Science and Engineering
COUPLED PROBLEMS 2017
M. Papadrakakis, E. Oñate and B. Schrefler (Eds)

PHASE-FIELD MODELLING OF TERNARY EUTETIC SOLIDIFICATION IN HOT DIP GALVANIZATION

J.P. MOGERITSCH[1], A. LUDWIG[1], B. BÖTTGER[2], G. ANGELI[3], C.K. RIENER[3], R. EBNER[4]

[1] Chair of Simulation and Modelling of Metallurgical Processes, University of Leoben, Franz-Josef-Str. 18, A-8700 Leoben, Austria
e-mail: johann.mogeritsch@unileoben.ac.at, web page: https://www.unileoben.ac.at/
[2]ACCESS Materials & Processes, Intzestr 5, D- 52072 Aachen, Germany
[3]voestalpine Stahl GmbH, voestalpine-Straße 3, A-4020 Linz, Austria
[4]Material Center Leoben Forschungs GmbH, Roseggerstraße 12, 8700 Leoben

Key words: Phase-field modelling, hot dip galvanization, solidification, Zn-Al-Mg alloys

Abstract. Continuous hot dip galvanizing is one of the commercially most important process techniques used for protecting steel sheets against corrosion. Preheated steel sheets are continuously drawn through a pot with a molten zinc alloy. After passing a gas jet that controls the layer thickness multiple cooling units act to cool down the sheet. During passing these aggregates nucleation, dendritic primary solidification and the formation of a binary and ternary eutectic occurs. In the present paper, the coupled modelling of macroscopic heat flow, multiphase thermodynamics and crystal growth during solidification of a Zn-2.5 wt.% Al-1.5 wt.% Mg alloy is presented. The heat flow problem requires a numerical domain in the order of meters, growth of primary Zn-dendrites in the order of several hundred micrometers, and the interdendritic eutectic in the order of several nanometers. For technical alloys like the ternary system considered here, a thermodynamic database has been online linked to a phase-field model to describe phase transformations including all occurring solid/liquid or solid/solid interfaces. Process simulations have been used for getting appropriate thermal boundary conditions for 3D phase field simulations which were performed at three different length-scales. For modelling primary dendritic Zn-a seed density model was used for predicting the grain structure within the Zn layer. At a smaller length-scale, a small part of a Zn-dendrite surface was taken as starting point for simulating the transition between primary binary eutectic and ternary eutectic coupled growth of Zn-rich, Al-rich, and $MgZn_2$-phases. Finally, the morphology of the ternary eutectic has been evaluated at the smallest length scale. The comparison with real solidification microstructure reveals encouraging agreements.

1 INTRODUCTION

One of the most important material worldwide is steel, used in building, construction and motor vehicle industry. Unfortunately, many steel grades corrode which causes a substantial economic damage especially for the car industry. Demands to reduce this problem and to increase the service life cycle of steel leads to galvanizing, a very effective and low coast solution. Today, the most important production process for these coatings is the continuous hot-dip galvanizing process (or Sendzimir process).

The protection of steel against corrosion takes place at galvanizing plants with an alloy based on the Zn-Al(-Mg)-system [1-3]. Such continuous production plants consist of several different sections connected in series (Fig. 1). In the entry section the steel coils are trailed by welding before the now continuously steel sheet is cleaned and annealed within a furnace. Heating up closely above the zinc pot temperature the sheet is pulled into the galvanizing section through the liquid zinc alloy (~ 450 °C). Here, first a strong boundary layer of Fe-Al is formed on the steel sheet surface. This layer cares for a firmly adhered liquid zinc layer as soon as the sheet moves out of the bath and toward the cooling tower. Immediately after the zinc bath, the desired coating thickness is adjusted by air "knifes". Hereafter, the remaining liquid layer solidifies within the cooling tower and forms the characteristic microstructure for Zn-Al(-Mg) alloys. Finally, the zinc protected steel sheet is again portioned in coils at the exit section and prepared for further processing.

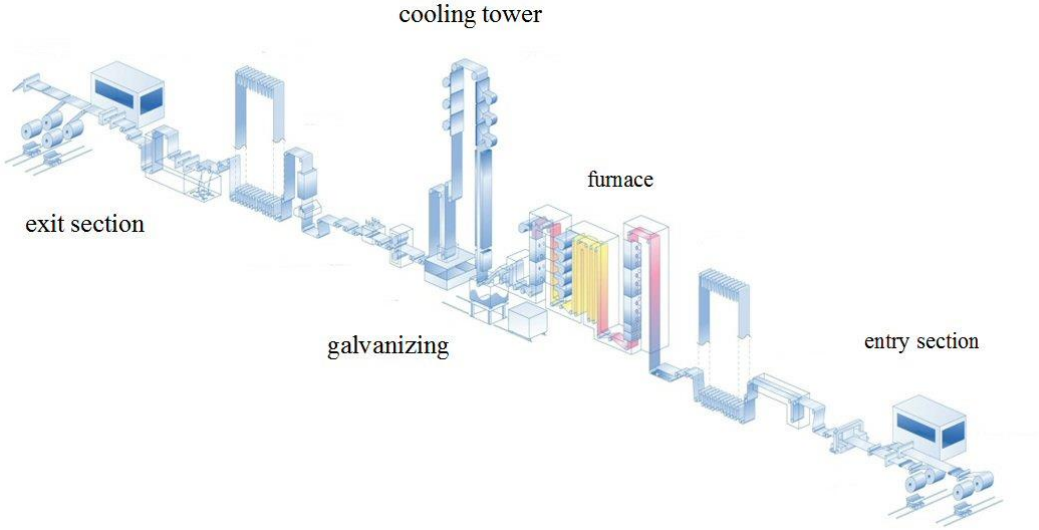

Figure 1: Hot dip galvanizing line at voestalpine Stahl, Linz [4]

The microstructure of the solidified Zn-Al(-Mg) alloy coating consists of primary zinc dendrites and interdendritic binary and ternary eutectics. The binary eutectic consists of the zinc phase combined with either the Laves phase ($MgZn_2$-phase), or the aluminum phase (Al-phase) depending on the bath composition [5]. At room temperature the primary fcc-Al phase decomposed into a secondary fcc-Al phase and a secondary hcp-Zn phase. The ternary eutectic is composed of Zn-, Al- and $MgZn_2$-phase [6-8]. According to [9, 10], in coatings the Mg-

Zn phase in the ternary eutectic is the $MgZn_2$-phase instead of the thermodynamically most stable Mg_2Zn_{11}-phase. In fact, only at cooling rates [11, 12] below or above the typical industry relevant process condition the Mg_2Zn_{11}-phase forms. It has also to be mentioned that the $MgZn_2$-phase forms not only as part of the eutectic, but also as hexagonal precipitates on further cooling to room temperature [6].

Phase-field models have become very popular for the simulation of microstructure evolution during alloy solidification processes. While early approaches rely on idealized descriptions of the phase diagrams [13, 14], more recent models which use thermodynamic databases [15] together with software tools for Gibbs energy minimization [16, 17] and allow for a more realistic description of multicomponent alloy solidification. The software MICRESS[1] is based on the phase-field concept for multiphase systems [16, 18] and allows for direct coupling to thermodynamic databases via the TQ Fortran interface to Thermo-Calc[2]. The software has been applied to a variety of alloy systems including 3D-simulations of Mg-Al dendrites [19] and a ternary eutectic model system [20].

In the present paper, numerical investigations on the formation of typical coating microstructure pattern for Zn-2.5 wt.% Al-1.5 wt.% Mg alloys are presented. The numerical investigations were done in parallel with experimental studies on laboratory prepared coated steel sheet samples.

2 EXPERIMENTAL PROCEDURE

The experimental procedure comprised the instrumented production of coatings with a galvanizing simulation device called GalvaSim [21], the investigation of the zinc coating with a scanning electron microscope (SEM) to obtain the microstructure, and the evaluation of key features to evaluate the numerical investigations.

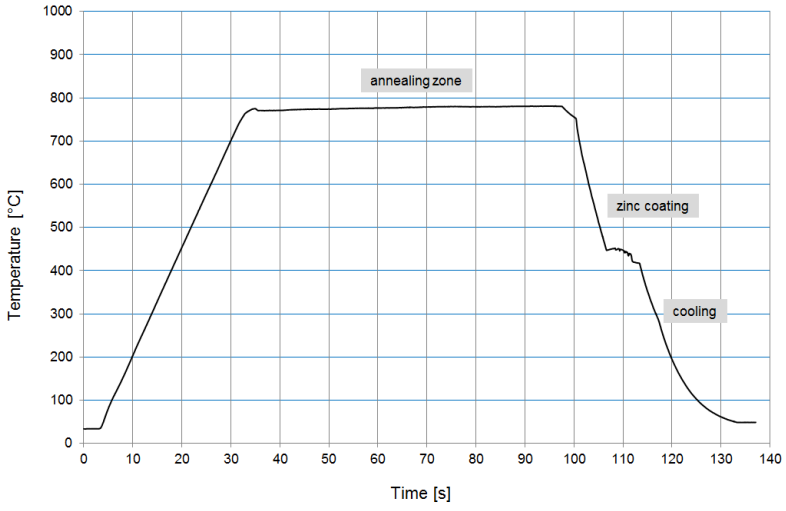

Figure 2: Example of a heat and cooling cycle measured at the galvanizing simulation device GalvaSim.

[1] MICRESS® software: http//:www.micress.de
[2] Thermo-Calc® software: http//:www.thermocalc.se

The voestalpine possesses with GalvaSim a device which allows reproducing the important process steps of a hot-dip-galvanizing process line in an instrumented and controlled way. The simulator consists of an annealing, galvanizing and skin passing section, assembled in vertical arrangement. Samples of different steel grades with various thicknesses and different heating and cooling procedure were coated with numerous Zn-Al(-Mg) alloys. For this work, a 0.75 mm thick DX53 steel sheet was coated with an Zn-2.5 wt.% Al-1.5 wt.% Mg layer of different thicknesses ranging from 10 µm to 100 µm. The applied heating and cooling cycle is shown in Fig. 2.

Small sections of the sample were prepared for SEM investigations. Fig 3 shows corresponding results. The coating surface with the primary dendrites and the surrounding ternary eutectic phase can be seen in Fig. 3a. The primary phase consists of the Zn-phase whereby the ternary eutectic composed of all three phases, Zn, Al and $MgZn_2$. If one compares the differences in length scale it is quite obviously that the size of the eutectic is more than one order of magnitude smaller than the dendritic phase. Also in cross-section the size difference is obvious (Fig. 3b). Additionally, it can be seen that the primary phase is completely surrounded by small Al-phase dots embedded in the $MgZn_2$-phase. It is randomly positioned in the coating layer, so that no clear statement about the actual nucleation positions can be made. The fine eutectic is enlarged shown in Fig. 3c. The structure shows three different phases which identifies the eutectic as being ternary. The eutectic consists of Zn- and $MgZn_2$-lamellae with Al-phase dots located along the $MgZn_2$-lamellae. Note that the Al-phase dot size is approximately equal to the $MgZn_2$-lamellae width. An investigation of the ternary eutectic reveals 44% of the area is covered with Zn-phase (bright), 28.7% with Al-phase (dark), and 27.3% with $MgZn_2$-phase (grey). Beside the ternary eutectic, quite rarely a binary eutectic (not shown here) was detected. This binary eutectic consist of the Zn- and Al-phase.

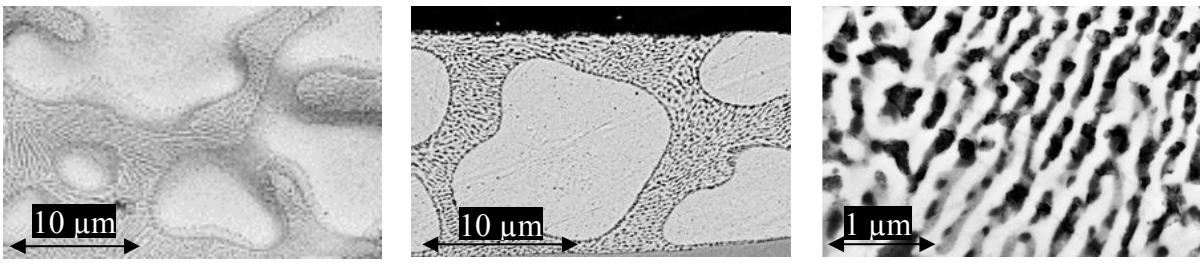

(a) (b) (c)

Figure 3: Microstructure of the investigated Zn-2.5 wt.% Al-1.5 wt.% Mg layer: (a) coating surface, (b) cross section, and (c) ternary eutectic. The Zn-phase appears bright, the $MgZn_2$-phase grey, and the Al-phase dark.

The evaluation of the microstructure revealed some key-features which had to be reproduced by the numerical investigations. This includes the occurrence and amount of the phases, the Al-phase dots surrounding the surface of the dendrites, and the morphological appearance of the ternary eutectic. In addition, the process conditions as measured from the GalvaSim coating device have to matched.

3 NUMERICAL INVESTIGATIONS

Numerical simulations of the solidification process and the microstructure formation were carried out by using Thermo-Calc, MICRESS, ANSYS-FLUENT[3] and Para View[4]. MICRESS was used to calculate the microstructure by a multiphase field method. ParaView visualize 3D results and was used to analyze the formation of the microstructure, with ANSYS-FLUENT we simulated the process conditions and Thermo-Calc provided the thermodynamic information needed (Fig. 4). First a thermodynamic study was performed with Thermo-Calc by using the COST2 [22] data base. This data base provides the thermodynamic data for the ternary phase diagram Zn-Al-Mg [23]. Within the Zn rich corner of the ternary system four phases might exist, the hexagonal close packed (hcp) Zn-phase, the face centered cubic (fcc) Al-phase, the Laves-C14 $MgZn_2$ phase and the intermetallic Mg_2Zn_{11} phase. A ternary eutectic exists at the concentration of 3.9 wt.% Al and 2.4 wt.% Mg [24].

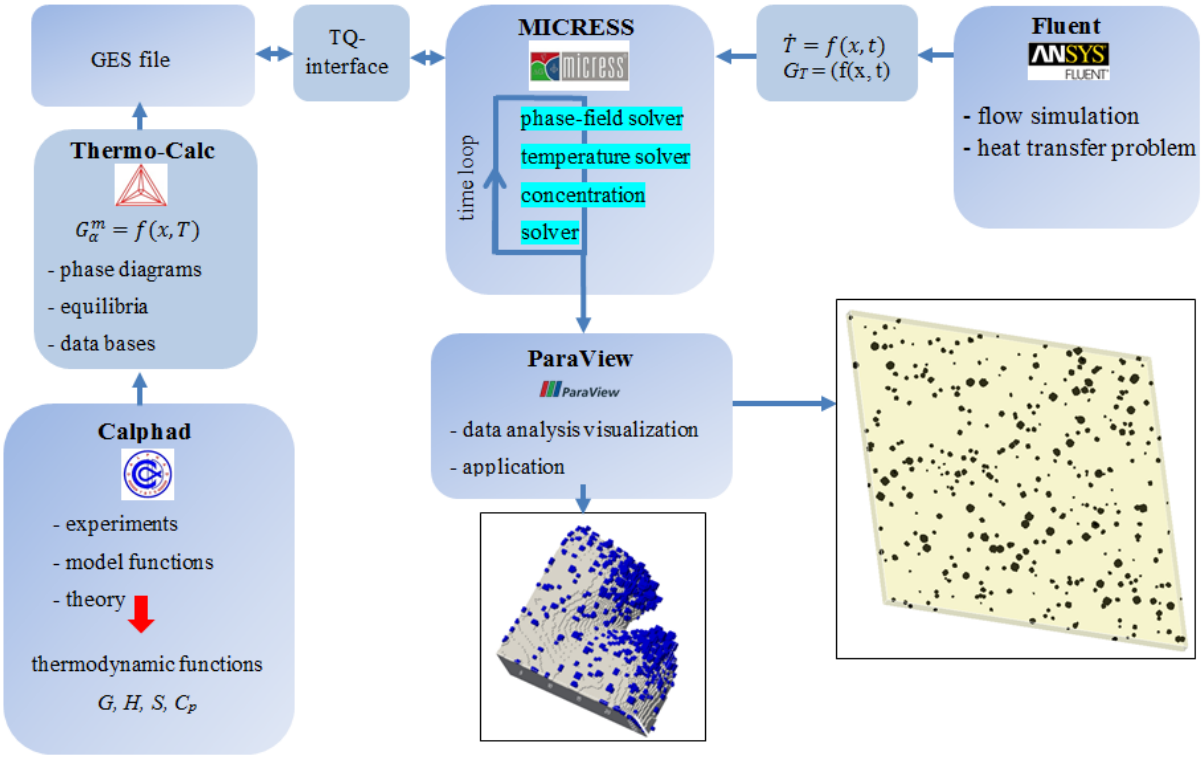

Figure 4: Overview of software being coupled

By using the database COST2 it is possible to calculate the phase equilibria of Zn-Al-Mg alloys as a function of compositions and temperatures. Calculations were made for the ternary phase diagram at different temperature levels, and amounts of phases considering a Scheil-type solidification approach for selected concentrations were estimated. Since the phase Mg_2Zn_{11} occurs only in equilibrium, this phase was erased from the calculations. For Zn-2.5

[3] http://www.ansys.com/Products/Fluids/ANSYS-Fluent
[4] http://www.paraview.org/

wt.% Al- 1.5 wt.% Mg the results of such a ternary solidification simulation is shown in Fig. 5a.

Approximately, 45 wt.% of the total solid is supposed to consist of the primary Zn-phase which starts to solidify at ~373 °C. Only 3 wt.% of a binary eutectic (consisting of Al- and Zn-phase) which starts at 340 °C is predicted. The remaining liquid solidifies at 336 °C as ternary eutectic by adding the $MgZn_2$ phase to the binary eutectic. The corresponding temperature depending amount of phase fractions is shown in Fig. 5b. In solid state the microstructure consists of 82 wt.% Zn-phase, 8.9 wt.% $MgZn_2$-phase, and 9.1 wt.% Al-phase.

In order to estimate the macroscopic temperature field in the coating, the sample within the GalvaSim was cooled down after the coating and the corresponding sheet temperature was recorded. The geometry of the steel sheet and the cooling aggregates were mapped into ANSYS-FLUENT. The unknown radiation heat flux of the sample was adopted in such a way to obtain an equal temperature trend as for the GalvaSim experiments. Additionally, the time-depending temperature gradient within the zinc layer normal to the surface was numerical estimated (Fig. 6). As a result a file was created for further used with MICRESS where corresponding temperatures, cooling rates, and temperature gradients as function of time were listed.

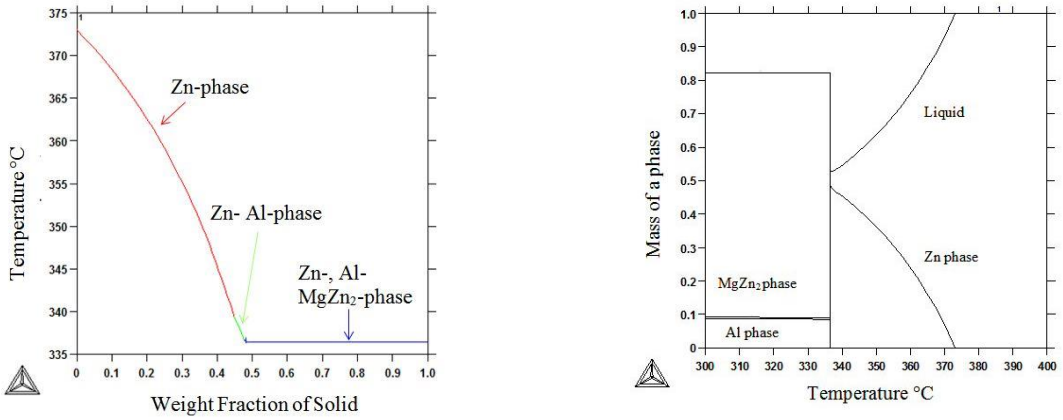

(a) (b)

Figure 5: (a) Increase of solid fraction with temperature based on a ternary Scheil calculation and (b) corresponding evolution of phase fraction as function of temperature for an Zn-2.5 wt.% Al- 1.5 wt.% Mg alloy.

The numerical investigation with MICRESS is divided into three different topics, the nucleation events, the investigations on the binary eutectic and on the lamellae structure of the ternary eutectic. The used physical parameters are given in Table 1.

Table 1: parameters

surfaces energy $\sigma_{s,l}$	$1 \cdot 10^{-2}$	J/m^2
diffusion coefficient in the liquid D_L	$1 \cdot 10^{-9}$	m^2/s
diffusion coefficient in the solid D_s	$1 \cdot 10^{-13}$	m^2/s

The boundary conditions like cooling rate and temperature gradient were read from a file created by ANSYS-FLUENT and based on the experimental data from GalvaSim. The observation of the nucleation of the primary Zn-phase requires a domain which gives a sufficient overview of the coating layer in order to be meaningful. To do so the selected domain is in the order of 280x280x10 μm^3 in size, meshed with around 1.5 million cubic cells with 0.8 µm edge length. As time step we have used $\Delta t = 0.1$ s.

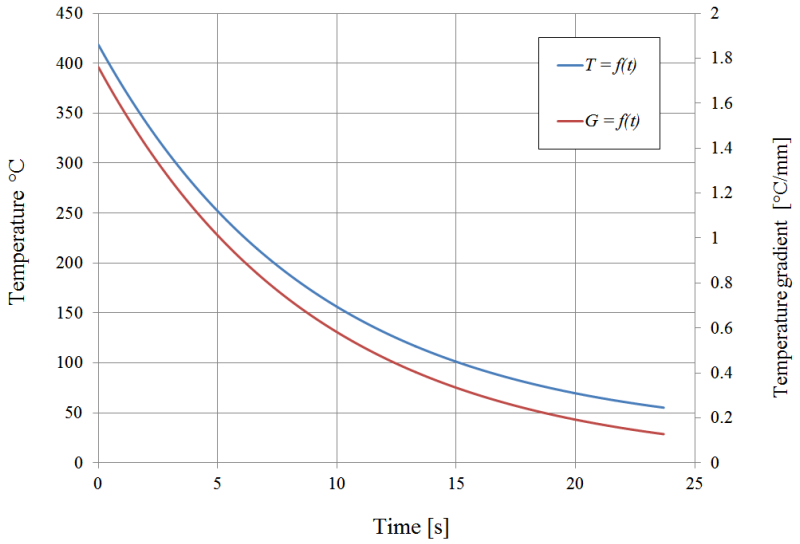

Figure 6: Cooling curve and temperature gradient (normal to surface) calculated by numerical investigation of the macroscopic temperature field in the steel sheet and the coating as to match corresponding GalvaSim results.

As up to now no quantitatively accurate model for describing heterogeneous nucleation of non-inoculated alloys in technical situations exists, MICRESS offers a semi-empirical approach named “seed density model” [17]: A predefined amount number density of possible potential nuclei as seeds are discretely positioned within the domain. They can be divided into different classes with a defined range of effective critical radii and corresponding seed number densities. In this work we have used seven seed classes. Based on the Gibbs-Thomson equation and by knowing the surface energy, σ_{sl}, and the solidification entropy, S_f, the program calculates the undercooling, ΔT_u, necessary to create critical nuclei of the definite size. So, to activate a given size class a certain undercooling is needed. Note that large nuclei need less undercooling and note that the actual undercooling temperature might not be constant within the domain as microsegregation during solidification leads to locally different liquidus temperatures. Since the liquid coating layer is forced to cool and solidify by using cooling aggregates, and the corresponding cooling rates and temperature gradients were calculated macroscopically by ANSYS-FLUENT (Fig. 6), the time-dependent temperature distribution within the domain was known. Fig. 7 gives an example of the corresponding evolution of the nucleation process for the primary Zn-phase. Here, we have applied no-flux boundary conditions at the top and bottom faces and periodic boundary conditions at the side faces.

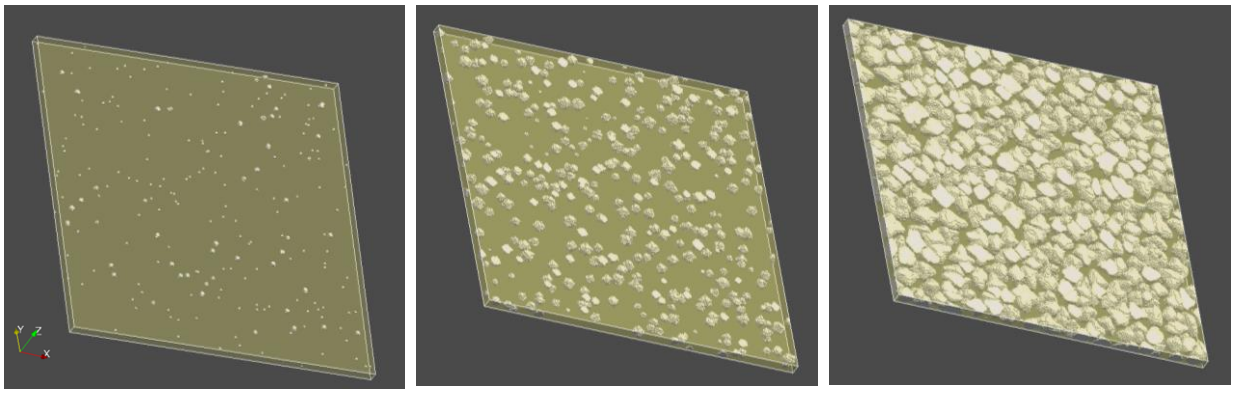

$t = 0.015$ s $t = 0.0335$ s $t = 0.0341$ s

Figure 7: Sequence of nucleation events for the primary Zn-phase in a coating cooled by cooling rates and temperature gradients as given in Fig. 6. The simulated area was 280 µm in width and length with a thickness of 10 µm. 1.5 million numerical volume elements were considered.

While only liquid was present at $t = 0$ s, first nuclei are activated as soon as the local undercooling close to the melt surface exceeds the critical undercooling of the biggest seeding particles as defined by the chosen seeding classes and local temperature. During further cooling these activated nuclei start growing (Fig. 7a). With increasing undercooling, the following seed classes are activated (Fig. 7b). Nucleation is finished as soon as all potential seeds have been activated or have been shielded by neighboring grains as a consequence of segregation or overgrowth (Fig. 7c).

The selected size of the domain allows for a comparison of the final grain structure to experimental observations (Fig. 3a, b) but is insufficient for investigation of the solidification pattern in the eutectic regions. Detailed investigations of the nucleation event for the eutectic required a higher resolution. In order to do so a smaller section of the coating layer from Fig. 7 that contains quarter of a Zn-dendrite as shown in Fig. 8a was selected. Now the domain was 25x25x10 μm^3 in size meshed with around 0.4 million cubic cells with 0.25 µm edge length. For the example shown in Fig. 8, we have used no-flux boundary conditions for the top and bottom faces and symmetry boundary conditions for the side faces with a time step of $\Delta t = 0.05$ s. For the nucleation of the Al- and $MgZn_2$ phase we have applied the "undercooling model" model [28] rather than the "seed density model". The "undercooling model" considers nucleation at a certain undercooling (we have assumed 10 K for the results in this paper) and sets randomly as much nuclei of critical size as possible whereby a predefined minimum distance between the nuclei had to be kept.

The nucleation and growth of the eutectic takes place in three stages. First, nucleation of the Al phase happens mainly on "secondary arms" (Fig. 8b) while the Al-phase continues to growth. Thus, a binary eutectic forms here and there, while the Al-phase continues to nucleate (Fig. 8c). Then, the $MgZn_2$ phase nucleates all over the entire dendritic surface (Fig. 8d) and the competitive growth of all three phases (Fig. 8e) leads to the lamellae growth of the ternary eutectic (Fig. 8f). However, a detailed study of the coupled ternary eutectic growth needs again an even finer grid.

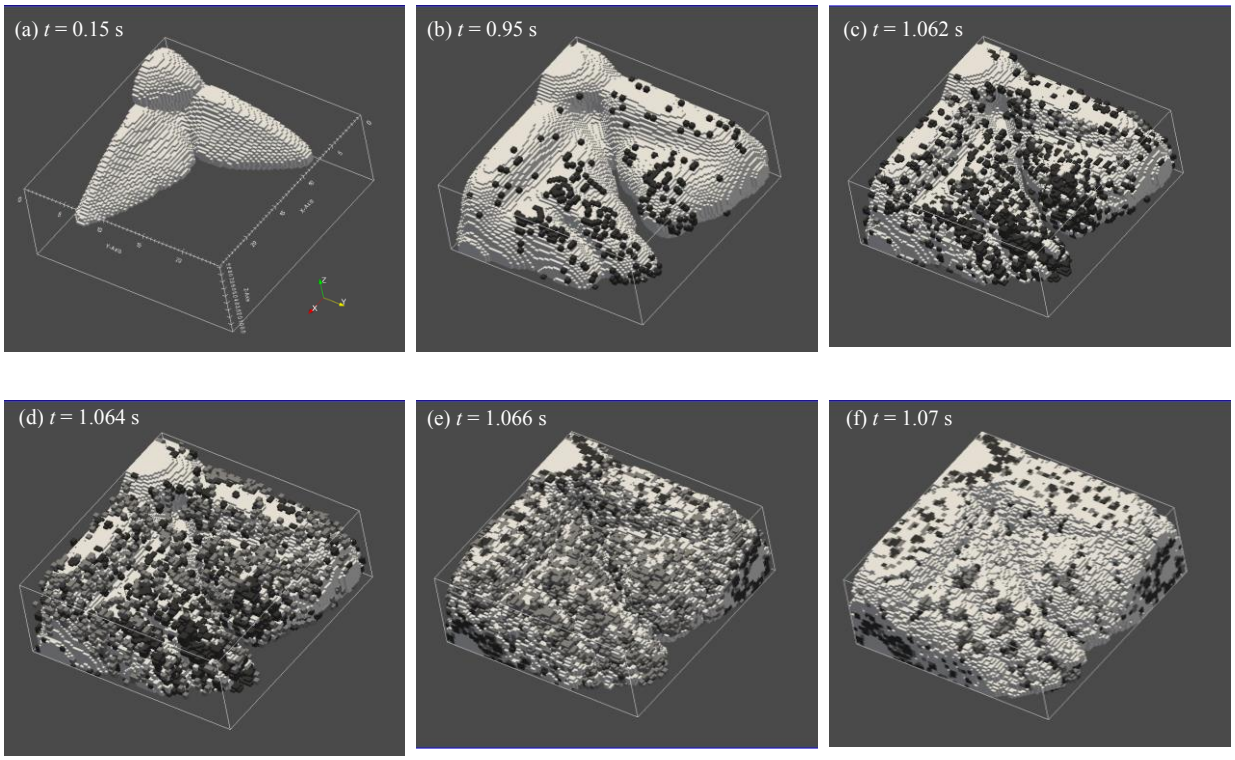

Figure 8: Sequence of nucleation and growth for the binary and ternary eutectic: (a) Segment of a Zn-phase dendrite, (b) and (c) nucleation of the Al-phase (black dots), (d) nucleation of the $MgZn_2$-phase (gray dots), and (e and f) growth of the ternary eutectic.

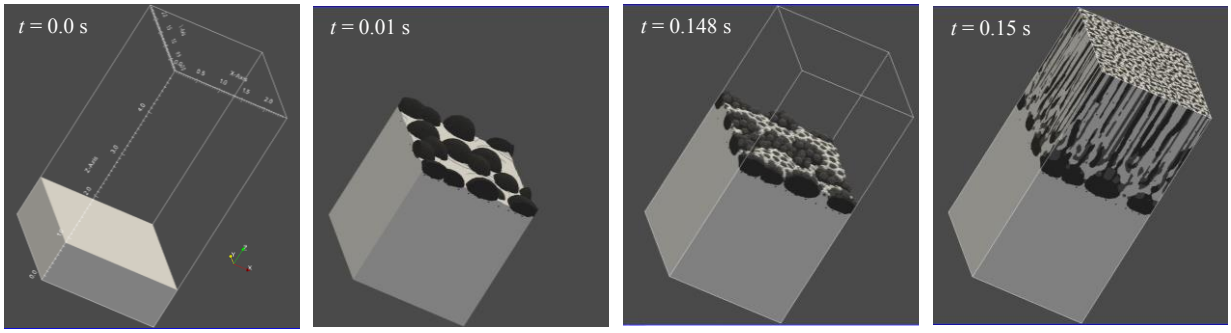

(a) (b) (c) (d)

Figure 9: Formation of the binary and ternary eutectic. (a) surface section of the preexisting zinc phase, (b) nucleation of the Al phase at the zinc surface, (c) nucleation event of the $MgZn_2$ phase, and the solidification pattern of the ternary eutectic.

For a further study of nucleation and growth of binary and ternary eutectic, a domain as small as 2.5x2.5x5 μm^3 was considered. The cubic cells of the numerical grid had an edge length of 12.5 nm, so that the grid consisted of 16 million volume elements. As time step we have used $\Delta t = 0.001$ s. As boundary conditions we applied again no-flux boundary conditions at the top and bottom faces and periodic boundary conditions at the side faces. The starting point of the simulation was now a smaller surface area of a Zn-dendrite represented by a preexisting rectangle grain (Fig. 9a). During cooling the Zn- phase grows until the first Al-phase nuclei occurred at the dendritic surface (Fig. 9b). After a while, the $MgZn_2$ phase nucleated (Fig. 9c)

and the binary eutectic was overgrown by a coupled ternary eutectic (Fig. 9d).

4 DISCUSSIONS

It is theoretically conceivable to simulate the whole sequence of solidification in only one simulation. For that the plate-like domain (280x280x10 μm^3) shown in Fig. 7 would have to be meshed with volume elements as small as 12.5x12.5x12.5 nm^3. That would result in a mesh of 3.2 10^{11} volume elements – 4-5 orders of magnitude larger than what can be processed with modern HPC computers. Therefore, a partitioning in different length scale simulations cannot be avoided.

Ternary Scheil-type solidification simulations (1D without any nucleation) based on Thermo-Calc in combination with the COST2 data base for the Zn-Al-Mg system give already a reasonable idea of the phases that form (as long as the sluggish equilibrium phase Mg_2Zn_{11} is omitted). However, for the exact solidification path (especially when the amount of Al in the ternary alloy is slightly decreased and the binary eutectic changes from fcc-Al/ hcp-Zn/liquid to $MgZn_2$/hcp-Zn/liquid), nucleation and three dimensional morphology development including solute diffusion has to be considered.

A specific experimental feature is the occurrence of the edge of dots of Al- and $MgZn_2$-phase that surround the primary Zn-phase (Fig. 3b). This can be attributed to nucleation of (in the present case first) the Al-phase and (shortly after) of the $MgZn_2$-phase in direct contact with the Zn-phase (Fig. 8d and 9c). Having this configuration, the ternary Zn/Al/ $MgZn_2$-eutectic growth in a coupled and lamellar manner. From the experimental observation (Fig. 3c) it is not clear whether especially the Al-phase forms continuous lamellae or repeatedly nucleates and grows as isolated globular crystals. We have intensively varied the nucleation conditions for the Al-phase ahead of the eutectic front but we could not get ternary eutectic microstructures that resemble the experimental ones. In fact, couple lamellar growth (as the one shown in Fig. 9d) establishes quite automatically and under various conditions. We rather think that the globular appearance of the fcc-Al phase at room temperature may be connect to the afore mentioned solid/solid decomposition. However, the experimental appearance of the ternary eutectic depends quite dramatically on the chosen cross section of the sample. Fig. 10a shows a cross section taken perpendicular to the growth direction and Fig 10b a cross section with same arbitrary inclination.

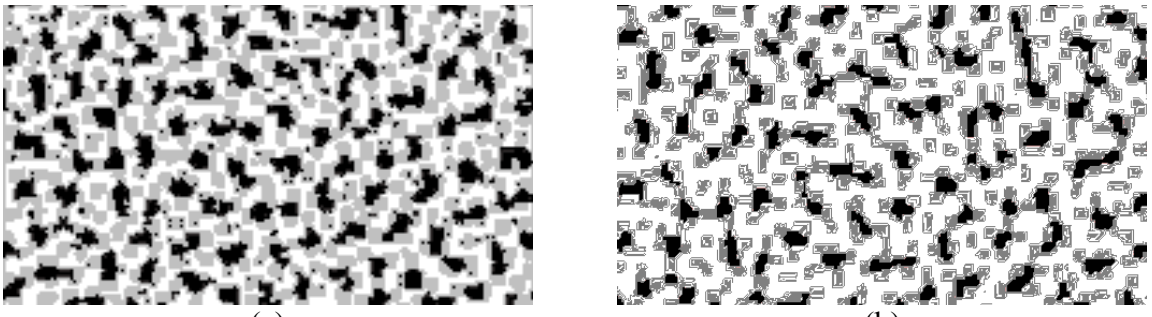

(a) (b)

Figure 10: Cross section through the numerically calculated ternary eutectic taken perpendicular to the growth direction (a) and at some arbitrary inclination (b).

The comparison between experimental observations and numerical predictions for the ternary eutectic is thus done by estimating the phase amount (and length scales) on different cross sections taken at various inclinations (numerical results) and different eutectic grains (experimental results). Table 2 shows the corresponding mean area fractions with standard derivation. Obviously both results match to some extent. In the light of the complexity of the current solidification process the agreement is satisfactory.

Table 2: Amount of phases

	numerical result		experimental result	
phase	area [%]	error bar	area [%]	error bar
Zn	50.9	± 4.6	45.9	± 5.1
Al	18.0	± 5.7	14.6	± 2.4
MgZn2	31.1	± 1.6	39.5	± 7.0

5 CONCLUSIONS

In the present work, we have demonstrated that it is possible to numerically simulate the microstructure formation on solidification of a Zn-2.5 wt.% Al-1.5 wt.% Mg alloy during hot dip galvanization. However, the challenge is that cooling of the coated steel sheets happens on a meter length scale, growth of primary dendrites on a micrometer length scale and nucleation and growth of binary or ternary eutectic on a sub-micrometer length scale. In addition, thermodynamic phase diagram information for the ternary Zn-Al-Mg system must be taken into account on any length scales. Thus, four different process simulations (ANSYS-FLUENT, MICRESS) on different length scales were combined with each other and with a thermodynamic program (Thermo-Calc) that uses information from a specific data base (COST2). In order to match experimental observations, especially the nucleation parameters for three solid phases involved (fcc-Al, hcp-Zn, and $MgZn_2$) were chosen adequately. Although a parameter-free model would be desirable, solidification processes that are govern to a large extend by nucleation (as in the present case) can yet not be described by first principles.

6. ACKNOWLEDGEMENT

Financial support has been provided by the Austrian Federal Government (in particular from Bundesministerium für Verkehr, Innovation und Technologie and Bundesministerium für Wissenschaft, Forschung und Wirtschaft) represented by Österreichische Forschungsförderungsgesellschaft mbH within the framework of the COMET Funding

REFERENCES

[1] Raghavan, V. Al-Mg-Zn (Aluminum-Magnesium-Zinc). *Journal of Phase Equilibria and Diffusion* (2007) **28**: 203-208.

[2] Yu, K., Li, J. Liu, X., Li, J. and Xue, X. Microstructure of Hot-Dip Galvanized Zn-Al-Mg Alloy coating. *J. Shanghai Jiaotong Univ.* (2012) **17**: 663-667.

[3] Marder, A.R. The metallurgy of zinc-coated steel. *Progress in Materials Science* (2000) **45**: 191-271.

[4] https://www.andritz.com/me-hotdipgalvanizinglineno4-brochure_en.pdf.
[5] Tsujimura, T., Komatso, A. and Andoh A. *Influence of Mg content in coating layer and coating structure on corrosion resistance of hot-dip Zn- Al- Mg alloy coated steel sheet.* Galvatech' 01, (2001) 145-152.
[6] De Bruycker, E. *Zn-Al-Mg Alloy Coatings: Thermodynamic analysis and microstructure-related properties.* University Genf, (2006).
[7] Liu, H.Y. and Jones, H. Solidification microstructure selection and characteristics in the zinc-based Zn-Mg System. *Acta Metall. Mater.* (1992) **40:** 229-239.
[8] Akdeniz, M.V. and Wood J.V. Microstructure and phase selection in rapidly solidified Zn-Mg alloys. *J. Mater Sci.* (1996) **31:** 545-550.
[9] Bluni S.T., Marder, A.R. Improvement of Galfan surface appearance for coil coating uses. *4th Int. Zinc Coated Sheet Conf., Paris, France,* (1994) SC6/1. 15.
[10] Lamberights, M. and Leroy, V. ZM-285 Progress Report, ILZRO, (1991) **23**.
[11] Coutsouradis, F.E. Goodwin, J. Pelerin, A.F. Skenazi, A. and Davin XY. Latest developments of Galfan protective coatings. *Stahl und Eisen* (1984) 104: 1073-1080.
[12] Pelerin, J. Bramaud, B. Nouville, J.F. Coutsouradis, D. Herrschaft, D.C. and Radtke, S.F. GALFAN: A new Zninc-Aluminium coating. Part I: Zinc-5% Aluminium-Mischmetall coated sheet. *Proc. 13th Int. Galvanizing Conf., London, UK,* (1982) 49/I.
[13] Tiaden J, Nestler B, Diepers HJ, Steinbach I. Physica D 1998; 115:73.
[14] Boettinger, W.J. Warren, J. Beckermann, C. and Karma A. Phase-field simulation of solidification. *Annu. Rev. Mater. Res*. (2002) **32**: 163-94.
[15] Moelans, N. Blanpain, B. and Wollants P. An introduction to phase-field modeling of microstructure evolution. *Computer Coupling of Phase Diagrams and Thermochemistry* (2008) **32**: 268-294.
[16] Eiken J, Böttger B, Steinbach I. Phys Rev E 2006; 73:066122.
[17] Böttger, B. Eiken, J. and Steinbach, I. Phase field simulation of equiaxed solidification in technical alloys. *Acta Mater.* (2006) **54**: 2697-2704.
[18] Böttger B, Eiken J, and Apel M, Comput. Mater. Sci. 108, 283 (2015).
[19] Eiken, J. Phase-field simulation of microstructure formation in technical magnesium alloys. *Int. J. Mater. Res.* (2010) **101**: 503-509.
[20] M. Apel, B. Böttger, H.-J. Diepers, I. Steinbach: 2D and 3D phase-field simulations of lamellar and fibrous eutectic growth. Journal of Crystal Growth 237-239 (2002) p.154-158.
[21] Tragl, E. Strutzenberger, J. Angeli, G. Pichler, A. Faderl, J. and Haunschmid, H. *Simulators for product- and process development of new steel grades*. Metal (2005). 14th Int. Metall. Mater. Conf., Hradec and Moravici, CZ, 24.-26.5.2005.
[22] European Commission and technical research *Definition of thermochemical and thermophysical properties to provide a database for the development of new light alloys.* COST European cooperation in the field of scientific (1998) **2**: ISBN 92-828-3902-8.
[23] Liang, P. Tarf, T. Robinson, J.A. Wagner, S. Ochin, P. Harmelin, M.G. Seifert, H.J. Lukas, H.L. and Aldinger F. Experimental investigation and thermodynamic calculation of the Al-Mg-Zn system. *Thermochimica Acta* (1998) **314:** 87-110.
[24] De Bruycker, E. Zermout, Z., and De Cooman B.C. Zn-Al-Mg Coating: Thermodynamic analysis and microstructure related properties, *Mater. Sci. Forum* (2007) **539-543**: 1276-1281.

VII International Conference on Computational Methods for Coupled Problems in Science and Engineering
COUPLED PROBLEMS 2017
M. Papadrakakis, E. Oñate and B. Schrefler (Eds)

STRESS CONCENTRATION IN ULTRA-THIN COATING WITH UNDULATED SURFACE PROFILE

SERGEY A. KOSTYRKO*, HOLM ALTENBACH† AND MIKHAIL A. GREKOV*

* Department of Computational Methods in Continuum Mechanics,
St. Petersburg State University,
7/9 Universitetskaya nab., St. Petersburg, 199034, Russia,
e-mail: {s.kostyrko, m.grekov}@spbu.ru, web page: http://www.spbu.ru/

†Institute of Mechanics,
Otto von Guericke University,
Universitätsplatz 2, Magdeburg, 39106, Germany,
e-mail: holm.altenbach@ovgu.de, web page: http://www.ovgu.de

Key words: Surface Stress, Ultra-thin Film, Size Effect, Stress Concentration, Boundary Perturbation, Integral Equations

Abstract. The uniaxial loading of an isotropic film-substrate system with a sinusoidal surface profile and planar interface is considered under plain strain conditions. We formulate the corresponding boundary value problem involving two-dimensional constitutive equations for bulk materials and one-dimensional equations for membrane-type surface and interface with the extra elastic constants as well as the residual surface stresses. The mixed boundary conditions consist of the generalized Young–Laplace equations and relations describing the continuous of displacements across the surface and interphase regions. Using the linear perturbation technique combined with the Goursat–Kolosov complex potentials and the superposition principle, the original boundary value problem is reduced to the analytical solution of the integral equations system.

1 INTRODUCTION

Thin films materials with a layer thickness from hundreds to a few nanometers exhibit unique physical and mechanical properties that can't be observed in bulk materials. Improved material properties are referred to significant modifications in the structure during an atomic growth process and so-called size effect related to surface stresses [1, 2, 3, 4, 5, 6]. At the stage of film deposition and subsequent thermal processing, the film surface evolves into an undulating profile [7]. Misfit stresses enhanced by a curved surface generate severe stress concentrations which may lead to a nucleation of dislocations and microcracks.

Analyzing a regular surface patterns in mono- and multilayer film coatings, we have found that even a slight undulation in surface morphology can result in a substantial increase of hoop stresses near the bottom of cavities [8, 9]. It has been shown that a stress concentration factor depends on the curvature radius and depth of cavities as well as the thickness and stiffness of film layers. However, the effect of surface elasticity on the stress state of thin film was neglected in comparison with the effect of macroscopic bulk elastic behavior. Thus, the aim of the presenting research is to extend the continuum model of coherently strained thin film deposited on a thick substrate [8] to the case of nanoscale film thickness incorporating the coupled effect of surface and interface stresses.

2 PROBLEM FORMULATION

Considering an isotropic ultra-thin film coating with a roughened surface profile and a flat interphase region under plain strain conditions, we arrive at a two-dimensional boundary value problem formulated in the terms of the complex variable $z = x_1 + ix_2$ ($i^2 = -1$ and x_1, $x_2 \in \mathbf{R}^1$ are the global Cartesian coordinates) for a strip Ω_1 of thickness h with an undulated external boundary Γ_1, bonded to a half-plain Ω_2 along a rectilinear interface Γ_2:

$$\Gamma_1 = \{z : z \equiv z_1 = x_1 + i\,[h + \varepsilon a \cos(k_a x_1)]\}\,,\ \Gamma_2 = \{z : z \equiv z_2 = x_2\}\,,\ k_a = \frac{2\pi}{a}, \tag{1}$$

$$\Omega_1 = \{z : 0 < x_2 < \varepsilon a \cos(k_a x_1)\}\,,\ \Omega_2 = \{z : x_2 < 0)\}\,. \tag{2}$$

As follows from the definition of Γ_1, the maximum deviation of the surface from the flat shape $x_2 = h$ is equal to $a\varepsilon$ where a is the wavelength of undulation and ε is a small parameter, i.e. $0 < \varepsilon \ll 1$.

According to the model of surface/interface elasticity proposed by Gurtin and Murdoch [10], the surface and interphase domains are assumed to be a negligibly thin layers adhering to the bulk phases without slipping. Here, we use the simplified constitutive equations taking into account only tangential components of the surface and the interface displacements:

$$\sigma^s_{tt}(z_j) = \gamma^0_j + (\lambda^s_j + 2\mu^s_j)\varepsilon^s_{tt}(z_j),\ z_j \in \Gamma_j,\ j = \{1, 2\}, \tag{3}$$

where ε^s_{tt} and σ^s_{tt} are the nonvanishing components of the surface strain and the Piola–Kirchhoff surface stress tensors, respectively; λ^s_j and μ^s_j are the surface Lamé constants, and γ^0_j is the residual surface stress for surface phase Γ_j.

Hooke's law for the bulk materials in the case of plane strain can be written as:

$$\begin{gathered}\sigma_{nn}(z) = (\lambda_j + 2\mu_j)\varepsilon_{nn}(z) + \lambda_j\varepsilon_{tt}(z),\\ \sigma_{tt}(z) = (\lambda_j + 2\mu_j)\varepsilon_{tt}(z) + \lambda_j\varepsilon_{nn}(z),\ \sigma_{nt}(z) = 2\mu_j\varepsilon_{nt}(z),\ z \in \Omega_j,\ j = \{1, 2\},\end{gathered} \tag{4}$$

where $\sigma_{nn}, \sigma_{tt}, \sigma_{nt}$ and $\varepsilon_{nn}, \varepsilon_{tt}, \varepsilon_{nt}$ are the components of bulk stress and strain tensors, respectively, defined in the local Cartesian coordinate system n, t; λ_j and μ_j are the Lamé constants for the bulk phase Ω_j.

The conditions of mechanical equilibrium on the curved surface Γ_1 and planar interface Γ_2 are described in terms of generalized Young–Laplace equation [1, 11]:

$$\sigma(z_1) = T^s \sigma_s(x_1), \ z_1 \in \Gamma_1,$$
$$\Delta\sigma(z_2) = \sigma^+(z_2) - \sigma^-(z_2) = i\frac{d\tau_s(x_1)}{dx_1}, \ z_2 \in \Gamma_2. \tag{5}$$

Here and below, we use the following notations $\sigma_s(x_1) \equiv \sigma^s_{tt}(z_1)$, $\tau_s(x_1) \equiv \sigma^s_{tt}(z_2)$, $T^s(\cdot) = \kappa(x_1)(\cdot) - i\dfrac{1}{h(x_1)}\dfrac{d(\cdot)}{dx_1}$, $\sigma = \sigma_{nn} + i\sigma_{nt}$, $\sigma^{\pm}(z_2) = \lim\limits_{z \to z_2 \pm i0} \sigma(z)$, κ and h are the local principal curvature and the metric coefficient, accordingly.

Since we assumed that the surface phases and the bulk materials are coherent, the inseparability conditions can be defined as it follows:

$$\varepsilon^s_{tt}(z_1) = \varepsilon_{tt}(z_1), \ \Delta u(z_2) = u^+(z_2) - u^-(z_2) = 0, \ z_1 \in \Gamma_1, \ z_2 \in \Gamma_2, \tag{6}$$

where $u^{\pm}(z_2) = \lim\limits_{z \to z_2 \pm i0} u(z)$, $u = u_1 + iu_2$; u_1 and u_2 are the displacements along the corresponding coordinate axes x_1 and x_2.

At infinity, the stresses σ_{jk} $(j, k = \{1, 2\})$ in coordinates x_1, x_2 and the rotation angle ω are specified as:

$$\lim_{x_2 \to -\infty} (\sigma_{22} - i\sigma_{12}) = \lim_{x_2 \to -\infty} \omega = 0, \ \lim_{x_2 \to -\infty} \sigma_{11} = T_2. \tag{7}$$

A common reason for the appearance of longitudinal stress T_2 is a mismatch between the crystal lattice parameters of a film layer and a substrate.

3 BOUNDARY EQUATIONS

Following the superposition principle [7, 9, 8, 12], the solution of the boundary value problem (1)–(7), specifically the bulk stress vector $\sigma(z) = \sigma_{nn}(z) + i\sigma_{nt}(z)$ and the displacement vector $u(z) = u_1(z) + iu_2(z)$, is presented as a sum of two auxiliary problems. In the first problem, we suppose that the unknown self-balanced load p and surface stress ϑ are applied to the curvilinear boundary Γ_1 of the homogeneous half-plane $D^1_1 = \{z : x_2 < h + \varepsilon a \cos(kx_1)\}$ with the elastic properties of the film. So, the boundary condition in the terms of the stress vector σ^1 related to this problem can be written as:

$$\sigma^1(z_1) = p(z_1) + T^s\vartheta(z_1), \ \int_{-\infty}^{+\infty} p(\zeta)d\zeta = 0, \ z_1 \in \Gamma_1. \tag{8}$$

The stresses σ^1_{jk} $(j,k=\{1,2\})$ and the rotation angle ω^1 at infinity are equal to zero:

$$\lim_{x_2\to-\infty}(\sigma_{22}-i\sigma_{12})=\lim_{x_2\to-\infty}\sigma_{11}=\lim_{x_2\to-\infty}\omega=0. \tag{9}$$

The second problem describes a coupled deformation of two joint half-planes $D^2_1=\{z: x_2>0\}$ and $D^2_2=\{z: x_2<0\}$ with the elastic properties of the film and the substrate, accordingly, caused by the unknown jumps of stresses $\Delta\sigma^2$ and displacements Δu^2 along the rectilinear interface and the longitudinal stresses T_j acting in D^2_j $(j=\{1,2\})$:

$$\Delta\sigma^2(z_2)=\sigma^{2+}(z_2)-\sigma^{2-}(z_2),\ \Delta u^2(z_2)=u^{2+}(z_2)-u^{2-}(z_2),\ z_2\in\Gamma_1, \tag{10}$$

$$\lim_{x_2\to\pm\infty}\left(\sigma^2_{22}-i\sigma^2_{12}\right)=\lim_{x_2\to\pm\infty}\omega^2=0,\ \lim_{x_2\to+\infty}\sigma^2_{11}=T_1,\ \lim_{x_2\to-\infty}\sigma^2_{11}=T_2, \tag{11}$$

where $u^{2\pm}(z_2)=\lim\limits_{z\to z_2\pm i0}u^2(z)$, $\sigma^{2\pm}(z_2)=\lim\limits_{z\to z_2\pm i0}\sigma^2(z)$, $T_1=\dfrac{\mu_1(\varkappa_2+1)}{\mu_2(\varkappa_1+1)}T_2$.

The superposition principle can be expressed as:

$$G(z,\eta_j)=G^1_1(z,\eta_1)\delta_{j1}+G^2_j(z,\eta_j),\ z\in\Omega_j. \tag{12}$$

In Eq. (12), the functions $G(z,\eta_j)$, $G^1_1(z,\eta_1)$, $G^2_j(z,\eta_j)$ are equal, respectively, to $\sigma(z)$, $\sigma^1(z)$, $\sigma^2(z)$ when $\eta_j=1$ and $-2\mu_j v(z)$, $-2\mu_1 v^1(z)$, $-2\mu_j v^2(z)$ when $\eta_j=-\varkappa_j$; $\varkappa_j=3-4\nu_j$ where ν_j is Poisson's ratio of the phase Ω_j; $v(z)=du/dz$, $v^j(z)=du^j/dz$ where the derivative is taken in the direction of the axis t; δ_{j1} is the Kronecker delta and $j=\{1,2\}$.

Taking into account Eq. (12), boundary conditions (5)–(6) and constitutive equations (3)–(4) lead to the system of the boundary equations for the unknown functions p, ϑ, σ_s and τ_s:

$$\sigma^1(z_1)=p(z_1)+T^s\vartheta(z_1), \tag{13}$$

$$\Delta\sigma^2(z_2)=i\tau_s'(z_2)-\sigma^1(z_2),\ \Delta u^2(z_2)=-u^1(z_2), \tag{14}$$

$$\sigma^1(z_1)+\sigma^2(z_1)=T^s\sigma_s(z_1), \tag{15}$$

$$\vartheta(z_1)=\gamma^1_0+(\lambda^s_1+2\mu^s_1)\,\varepsilon^1_{tt}(z_1), \tag{16}$$

$$\sigma_s(z_1)=\gamma^1_0+(\lambda^s_1+2\mu^s_1)\left[\varepsilon^1_{tt}(z_1)+\varepsilon^2_{tt}(z_1)\right], \tag{17}$$

$$\tau_s(z_2)=\gamma^2_0+(\lambda^s_2+2\mu^s_2)\,\varepsilon^2_{tt}(z_2). \tag{18}$$

Thus, the solution of the general boundary value problem (1)–(7) is reduced to the solution of the system (13)–(18). To solve it, the functions σ^k and u^k $(k=\{1,2\})$ are presented in the terms of the Goursat-Kolosov complex potentials and the Muskhelishvili representation [13]. Unfortunately, it's impossible to find the exact solution of the first problem due to the curvature of the external boundary Γ_1. However, we can use the boundary perturbation method as in [1, 5, 9, 8, 12] and obtain the explicit expressions for the first-order approximation.

4 A FIRST-ORDER BOUNDARY PERTURBATION METHOD

The stress σ^k and the displacement u^k vectors are related to the Goursat-Kolosov complex potentials Φ_j^k and Υ_j^k by the following equality:

$$G_j^k(z,\eta_j) = \eta_j \Phi_j^k(w_j) + \overline{\Phi_j^k(w_j)} - \left(\Upsilon_j^k(\overline{w_j}) + \overline{\Phi_j^k(w_j)} - (w_j - \overline{w_j})\,\overline{\Phi_j^{k\prime}}(w_j)\right) e^{-2i\alpha}, \quad (19)$$

where $w_1 = z - ih$ and $w_2 = z$, α is the angle between t-axis of the local coordinates n, t and x_1-axis, the prime denotes differentiation with respect to the argument, the bar over a quantity denotes complex conjugation, Φ_1^1 and Υ_1^1 are the functions holomorphic, respectively, in D_1^1 and $\widetilde{D_1^1} = \{z : x_2 > h - \varepsilon a\cos(k_a x_1)\}$; the functions Φ_j^2 and Υ_j^2 are holomorphic in D_j^2 and D_k^2 $(j,k = \{1,2\},\ j \neq k)$. Assuming $\alpha = 0$ and $\pi/2$ in Eq. (19) and taking the conditions at infinity (9) and (11) into account, one can write:

$$\lim_{x_2\to-\infty} \Phi_1^1(z) = \lim_{x_2\to-\infty} \Upsilon_1^1(z) = 0, \quad \lim_{|x_2|\to\infty} \Phi_2^j(z) = \lim_{|x_2|\to\infty} \Upsilon_2^j(z) = T_j/4. \quad (20)$$

In accordance with the first-order boundary perturbation method [5], we seek the unknown functions Φ_j^k, Υ_j^k, p and ϑ in the following form:

$$\Psi(z) = \Psi_0(z) + \varepsilon\Psi_1(z), \quad (21)$$

where Ψ could be any of the listed functions.

The boundary values of the functions Ψ_n can be presented by the linear Taylor polynomial in the vicinity of the line $x_2 = 0$, treating the real variable x_1 as a parameter:

$$\Psi_n(z_1) = \Psi_n(x_1) + i\varepsilon f(x_1)\Psi_n'(x_1),\ \ f(x_1) = a\cos(k_a x_1). \quad (22)$$

Also, it is possible to write the linearization in the space of the parameter ε for the subsequent functions [1, 5]:

$$e^{-2i\alpha} = 1 - 2i\varepsilon f'(x_1),\ \ \kappa(x_1) = \varepsilon f''(x_1),\ \ h^{-1}(x_1) = 1. \quad (23)$$

Substituting Eqs. (21)–(23) into Eq. (19) when $k = 1$, $z \to z_1$, $\eta_1 = 1$ and $\alpha = \alpha_1$, and equating the coeficients of ε, we obtain the first-order approximation of function $\sigma^1(z_1)$:

$$\sigma^1(z_1) = \sigma_0^1(z_1) + \varepsilon\left[\sigma_1^{1d}(z_1) + \sigma_1^{1u}(z_1)\right], \quad (24)$$

where

$$\sigma_m^1(z_1) = \Phi_{1\,m}^1(\xi_1^1) - \Upsilon_{1\,m}^1(\overline{\xi_1^1}),\ \ m = \{0,1\},\ \ \xi_1^1 = w_1(z_1),$$
$$\sigma_1^{1d}(z_1) = if(x_1)\left[\Phi_{1\,0}^{1\prime}(x_1) + \Upsilon_{1\,0}^{1\prime}(x_1) + \overline{\Phi_{1\,0}^{1\prime\prime}(x_1)}\right] + 2if'(x_1)\left[\Upsilon_0(x_1) + \overline{\Phi_0(x_1)}\right]. \quad (25)$$

Introducing the piecewise function Θ_m holomorphic outside the line $\operatorname{Im} w_1 = 0$

$$\Theta_m(w_1) = \begin{cases} \Upsilon^1_{1\,m}(w_1), & \operatorname{Im} w_1 > 0, \\ \\ \Phi^1_{1\,m}(w_1), & \operatorname{Im} w_1 < 0, \end{cases} \tag{26}$$

we reduce the boundary equation (13) to the sequence of the Riemann–Hilbert problems which solution can be written in the terms of the Cauchy-type integrals [13]:

$$\Theta_m(z) = \frac{1}{2\pi i}\int\limits_{-\infty}^{+\infty} \frac{i\vartheta'_m(\zeta)}{\zeta - z}dt - \frac{1}{2\pi i}\int\limits_{-\infty}^{+\infty} \frac{p_m(\zeta)}{\zeta - z}d\zeta + \frac{1}{2\pi i}\int\limits_{-\infty}^{+\infty} \frac{\sigma^{1d}_m(\zeta)}{\zeta - z}d\zeta. \tag{27}$$

5 SYSTEM OF INTEGRAL EQUATIONS

To solve the second problem, we pass to the limit in Eq. (19) as $z \to z_2$ when $k = 2$, $\alpha = 0$. Taking into account the boundary conditions (14) and the auxiliary functions Σ and V which are holomorphic otside the line $\operatorname{Im} z = 0$

$$\Sigma(z) = \begin{cases} \Upsilon^2_2(z) + \Phi^2_1(z), & \operatorname{Im} z > 0, \\ \\ \Upsilon^2_1(z) + \Phi^2_2(z), & \operatorname{Im} z < 0, \end{cases} \tag{28}$$

$$V(z) = \begin{cases} \mu_1\Upsilon^2_2(z) - \mu_2\varkappa_1\Phi^2_1(z), & \operatorname{Im} z > 0, \\ \\ \mu_2\Upsilon^2_1(z) - \mu_1\varkappa_2\Phi^2_2(z), & \operatorname{Im} z < 0, \end{cases} \tag{29}$$

we arrive to the Riemann–Hilbert problems on the boundary value of functions Σ and V. The solutions of both equations can be written as:

$$\Sigma(z) = \frac{1}{2\pi i}\int\limits_{-\infty}^{+\infty} \frac{i\tau'_s(\zeta)}{\zeta - z}d\zeta - \frac{1}{2\pi i}\int\limits_{-\infty}^{+\infty} \frac{\sigma^1(\zeta)}{\zeta - z}d\zeta,\ V(z) = \frac{\mu_1\mu_2}{\pi i}\int\limits_{-\infty}^{+\infty} \frac{v^1(\zeta)}{\zeta - z}d\zeta. \tag{30}$$

In view of Eqs. (28) and (29), one can obtain the complex potentials Φ^2_j and Υ^2_j as it follows:

$$\begin{cases} \Phi^2_1(z) = -\Phi^2_2(z) + \Sigma(z) + T_1/4, & \operatorname{Im} \mathrm{z} > 0, \\ \\ \Upsilon^2_1(z) = -\Upsilon^2_2(z) + \Sigma(z) + T_1/4, & \operatorname{Im} \mathrm{z} < 0, \end{cases} \tag{31}$$

$$\begin{cases} \Upsilon^2_2(z) = \dfrac{\mu_2\varkappa_1\Sigma(z) + V(z)}{\mu_1 + \mu_2\varkappa_1} + T_2/4, & \operatorname{Im} \mathrm{z} > 0, \\ \\ \Phi^2_2(z) = \dfrac{\mu_2\Sigma(z) - V(z)}{\mu_2 + \mu_1\varkappa_2} + T_2/4, & \operatorname{Im} \mathrm{z} < 0. \end{cases} \tag{32}$$

Using the properties of the Cauchy-type integrals [13], we can rewrite the solution of the second problem in the terms of the complex potentials Φ_1^1 and Υ_1^1 if substitute Eq. (19) when $\alpha = 0$, $\eta_1 = 1$ and $\eta_1 = \kappa_1$ into Eqs. (30) for Σ and V, accordingly:

$$\Sigma(z) = \frac{1}{2\pi i}\int\limits_{-\infty}^{+\infty}\frac{i\tau_s'(\zeta)}{\zeta - z}d\zeta + \begin{cases} \Upsilon_1^1(z+ih) + 2ih\overline{\Phi_1^{1\prime}(z-ih)}, & \operatorname{Im} z > 0, \\ \Phi_1^1(z-ih), & \operatorname{Im} z < 0, \end{cases} \tag{33}$$

$$V(z) = \mu_2 \begin{cases} \Upsilon_1^1(z+ih) + 2ih\overline{\Phi_1^{1\prime}(z-ih)}, & \operatorname{Im} z > 0 \\ -\varkappa_1\Phi_1^1(z-ih), & \operatorname{Im} z < 0, \end{cases} \tag{34}$$

After that, considering Eq. (21) when $k = 2$, $z \to z_1$, $\eta_1 = 1$ and $\alpha = \alpha_1$ and taking into account Eqs. (23)–(25), we derive the first-order approximation for function $\sigma_2(z_1)$:

$$\sigma^2(z_1) = \sigma_0^2(z_1) + \varepsilon\left[\sigma_1^{2d}(z_1) + \sigma_1^{2u}(z_1)\right], \tag{35}$$

where

$$\sigma_m^2(z_1) = \Phi_{1\,m}^2(z_1) - \Upsilon_{1\,m}^2(\overline{z_1}) + 2ih\overline{\Phi_{1\,m}^{2\prime}(z_1)},\ m = \{0,1\},$$

$$\sigma_1^{2d}(z_1) = if(x_1)\left[\Phi_{1\,0}^{2\prime}(x_1) + \Upsilon_{1\,0}^{2\prime}(x_1) + 2\overline{\Phi_{1\,0}^{2\prime}(x_1)} - 2ih\overline{\Phi_{1\,0}^{2\prime\prime}(x_1)}\right] + \tag{36}$$

$$+2if'(x_1)\left[\Upsilon_{1\,0}^2(x_1) - 2ih\overline{\Phi_{1\,0}^{2\prime}(x_1)} + \overline{\Phi_{1\,0}^2(x_1)}\right].$$

Also we can derive the equalities of the first-order approximation for the strains ε_{tt}^k from (4) if we consider the approximation for the stresses σ_{tt}^k and σ_{nn}^k similar to Eq. (21):

$$\varepsilon_{tt\,m}^k(z) = \frac{1}{2(\lambda_j + \mu_j)}\left[(\lambda_j + 2\mu_j)\sigma_{tt\,m}^k - \lambda_j\sigma_{nn\,m}^k\right],\ z \in \Omega_j. \tag{37}$$

To obtain the relations of the stress tensor components $\sigma_{tt\,m}^k$ and $\sigma_{nn\,m}^k$ with the complex potentials $\Phi_{j\,m}^k, \Upsilon_{j\,m}^k$ of the first-order approximation, one can take the angle between t-axis and x_1-axis to be equal first α and then $\alpha + \pi/2$ in Eq. (21), and sum the results:

$$\sigma_{nn\,m}^k + i\sigma_{nt\,m} = \Phi_{j\,m}^k(z) + \overline{\Phi_{j\,m}^k(z)} - \left(\Upsilon_{j\,m}^k(\overline{z}) + \overline{\Phi_{j\,m}^k(z)} - (z-\overline{z})\,\overline{\Phi_{j\,m}^{k\prime}(z)}\right)e^{-2i\alpha}, \tag{38}$$

$$\sigma_{tt\,m}^k + \sigma_{nn\,m}^k = 4\operatorname{Re}\Phi_{j\,m}^k(z),\ z \in \Omega_j.$$

Here, in Eqs. (38) and above in Eq. (37) $j, k = \{1,2\}$, $m = \{0,1\}$.

Finally, we substitute Eqs. (24), (35), (37) and (38) into Eqs. (15)–(18) and take into account Eqs. (25)–(27), (31)–(34) and (36). As a result, the system of the boundary

equations (13)–(18) take the form of the integral equations system in the unknown functions p_m, ϑ'_m, $\sigma'_{s\,m}$ and $\tau'_{s\,m}$ that consists of one singular and three hypersingular equations. The hypersingular equations are obtained similar to [1, 4, 5] as the result of differentiating Eqs. (16)–(18). The kernels of the derived integral equations are the same for each step of approximation. The right-hand sides are the known continuos functions.

In the case of the zero-order approxiamtion, we arrive to the homogeneous integral equations which have only zero solution following from the physical considerations. In accordance with Eqs. (26), (27) and (31)–(34), the complex potentials of the zero-order approximation are equal:

$$\Phi^1_{1\,0}(z) = \Upsilon^1_{1\,0}(z) = 0,\ z \in \Omega_1;\ \Phi^2_{j\,0}(z) = \Upsilon^2_{1\,0}(z) = T_j/4,\ z \in \Omega_j,\ j = \{1, 2\}. \tag{39}$$

As it follows from Eqs. (12), (17)–(19) and (21), they correspond to the piecewise uniform stress state of the film coating with flat surface:

$$\sigma_{11\,0}(z) = T_j,\ z \in \Omega_2;\ \sigma_{s\,0}(z) = \gamma^0_1 + \frac{M_1(1+\varkappa_1)}{4}T_1,\ \tau_{s\,0}(z) = \gamma^0_2 + \frac{M_2(1+\varkappa_1)}{4}T_2, \tag{40}$$

where $M_1 = \dfrac{\lambda^1_s + 2\mu^1_s}{2\mu_1}$, $M_2 = \dfrac{\lambda^2_s + 2\mu^2_s}{2\mu_2}$.

We seek the solution for the first-order approximation in the following form:

$$\begin{gathered} p_1(x_1) = A^1_{-1}e^{-ik_a x_1} + A^1_1 e^{ik_a x_1},\ \vartheta'_1(x_1) = A^2_{-1}e^{-ik_a x_1} + A^2_1 e^{ik_a x_1}, \\ \sigma'_{s\,1}(x_1) = A^3_{-1}e^{-ik_a x_1} + A^3_1 e^{ik_a x_1},\ \tau'_{s\,1}(x_1) = A^4_{-1}e^{-ik_a x_1} + A^4_1 e^{ik_a x_1}, \end{gathered} \tag{41}$$

Based on the properties of the Cauchy-type integrals, the system of the integral equations is reduced to the linear system of algebraic equations for the unknown complex coefficients A^j_k. After finding these coefficients, one can define the complex potentials $\Phi^k_{j\,1}$ and $\Upsilon^k_{j\,1}$ from Eqs. (26), (27), (31)–(34) and, as a consequence, the solution of the original boundary value problem (1)–(7) from Eqs. (12), (19), (21) and (41).

6 RESULTS AND CONCLUSIONS

As a numerical example, we consider the dependence of stress concentration factor $S = \max \sigma^{max}_{tt}/T_2$ on the perurbation wavelength a for $h/a = 0.15$ (Figure 1 (a)), $h/a = 0.3$ (Figure 1 (b)), surface elasticity constants $M_1 = M_2 = 0$ (solid lines), $M_1 = 0.117\,nm$, $M_2 = 0$ (dashed lines), $M_1 = M_2 = 0.117\,nm$ (dot-dashed lines), stiffness ratio $\mu_1/\mu_2 = 10$ (curves 1) and $\mu_1/\mu_2 = 0.1$ (curves 2) in case of $\varepsilon = 0.1$, $\gamma^0_1 = \gamma^0_2 = 0$, $\nu_1 = \nu_2 = 0.3$.

It is seen from the dashed lines on Figure 1 that the surface stress alone reduces the stress concentration factor. Taking into consideration the interface stress (see the dot-dashed lines) decreases the stress concentration factor as well. However, both effects decreases when the size a of the asperities increases, and the solution passes to the classical

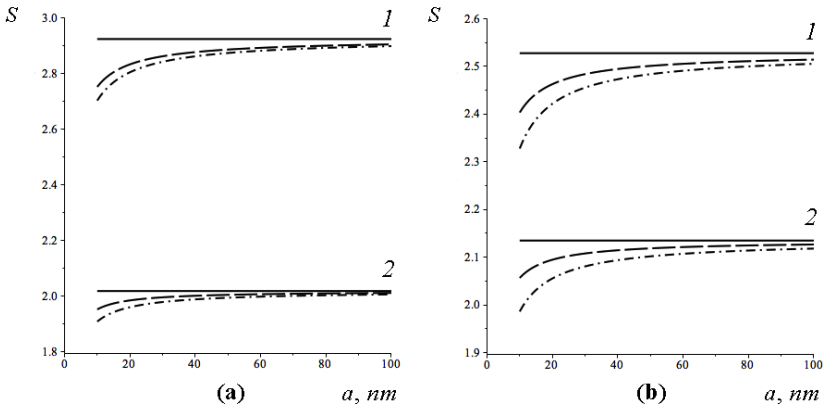

Figure 1: Stress concentration factor $S = \sigma_{tt}^{max}/T_2$ as a function of surface perturbation wavelength a.

one (i.e. to the solid lines). It should be noted that the solid lines correspond to our previous model [8]. The influence of the size of the asperities is greater for the stiffer film when $\mu_1/\mu_2 = 10$ (see the curves 1). As one can see, the stress concentration factor decreases when the stiffnes ratio μ_1/μ_2 decreases. This effect is more sensitive for the films with the smaller thickness (see Figure 1 (a)).

In this paper, we have extended our previous model of thin film with the slightly curved free surface deposited on a thick substrate to the case when the film thickness and the size of surface deffects are in nanometer range. For this purpose, we have used the surface/interface elasticity theory proposed by Gurtin and Murdoch [10], which allowed us to formulate corresponding boundary value problem involving the additional one-dimensional constitutive equations for surface phase and interphase with the extra elastic constants and the residual surface stresses. Based on the linear perturbation technique combined with the Goursat-Kolosov complex potentials and the superposition principle, the original boundary value problem has been reduced to the analytical solution of the system consisting of one singular and three hypersingular integral equations. It has been shown that the coupled effect of surface and interface stresses reduce the stress concentration factor. We have observed that this effect was more sensitive for smaller surface asperities. Finally, it should be noted that the obtained results are in a good agreement with our previous studies [1, 8].

ACKNOWLEDGEMENTS

The work was supported by the Russian Foundation for Basic Research under grant 14-01-00260, German Academic Exchange Service and St. Petersburg State University under joint grant 9.23.1139.2016.

REFERENCES

[1] Grekov, M.A. and Kostyrko, S.A. Surface effects in an elastic solid with nanosized surface asperities. *Int. J. Solids Struct.* (2016) **96**:153–161.

[2] Nazarenko, L., Stolarski, H., Altenbach, H. Effective properties of short-fiber composites with Gurtin-Murdoch model of interphase. *Int. J. Solids Struct.* (2016) **97–98**:75–78.

[3] Altenbach, H., Eremeyev, V.A. and Morozov, N.F. Surface viscoelasticity and effective properties of thin-walled structures at the nanoscale. *Int. J. Eng. Sci.* (2012) **59**:83–89.

[4] Grekov, M.A. and Yazovskaya, A.A. Effect of surface elasticity and residual surface stress in an elastic body weakened by an elliptic hole of a nanometer size. *J. Appl. Math. Mech.* (2014) **78**:172–180.

[5] Grekov, M.A. and Vakaeva, A.B. Effect of nanosized asperities at the surface of a nanohole. *Proceedings of the VII European Congress on Computational Methods in Applied Sciences and Engineering* (2016) **IV**:7875–7885.

[6] Bochkarev, A.O. and Grekov, M.A. The influence of the surface stress on the local buckling of a plate with a circular nanohole. *"Stability and Control Processes" in Memory of V.I. Zubov (SCP), 2015 International Conference* (2015) **IEEE**:367–370.

[7] Grekov, M.A. and Kostyrko, S.A. Morphological evolution in heteroepitaxial thin film structures at the nanoscale. *Def. Diff. Forum* (2015) **364**:112–121.

[8] Vikulina, Yu.I., Grekov, M.A. and Kostyrko, S.A. Model of film coating with weakly curved surface. *Mech. Solids* (2010) **45**:778–788.

[9] Grekov, M.A. and Kostyrko, S.A. A multilayer film coating with slightly curved boundary. *Int. J. Eng. Sci.* (2015) **89**:61–74.

[10] Gurtin, M.E. and Murdoch, A.I. A continuum theory of elastic material surfaces. *Arch. Rat. Mech. Anal.* (1975) **57**:291–323.

[11] Altenbach, H., Eremeyev, V.A. and Lebedev, L.P. On the existence of solution in the linear elasticity with surface stresses. *ZAMM* (2010) **90**:231–240.

[12] Grekov, M.A. and Kostyrko, S.A. A film coating on a rough surface of an elastic body. *J. Appl. Math. Mech.* (2013) **77**:79–90.

[13] Muskhelishvili, N.I. *Some basic problems of the mathematical theory of elasticity.* Leiden, Noordhoff, (1977).

VII International Conference on Computational Methods for Coupled Problems in Science and Engineering
COUPLED PROBLEMS 2017
M. Papadrakakis, E. Oñate and B. Schrefler (Eds)

A COUPLED DISCRETE-ELEMENT MODEL OF FLUID-SATURATED ROCK AND THE RESULTS OF STUDYING OF THE IMPACT OF A FLUID ON THE SHEAR STRENGTH OF A ROCK UNDER COMBINED COMPRESSION AND SHEAR

ANDREY V. DIMAKI, EVGENY V. SHILKO AND SERGEY G. PSAKHIE

Institute of Strength Physics and Materials Science SB RAS (ISPMS SB RAS)
Akademicheskii av. 2/4, 634055 Tomsk, Russia
e-mail: dav@ispms.tsc.ru, web page: http://www.ispms.ru

Key words: Fluid-saturated rock, Strength, Compression, Shear, Porosity, Plasticity, Discrete element method.

Abstract. Within a discrete-element model of a porous permeable elastic-plastic rock, filled with a fluid, we have studied the shear strength of a fractured interface zone (a shear band) between blocks of a geological medium subject to compression and shear. Under these conditions, a fluid pore pressure is controlled by interplay of dilation of the elastic-plastic shear band and fluid transport between the blocks and the interface. We have found that the shear strength is a unique function of a combination of parameters, which includes viscosity of a fluid, permeability of the medium, shear rate and a characteristic size of the system. Based on the simulation results we have constructed the generalized binomial dependence of the shear strength of samples on the obtained combination of parameters.

1 INTRODUCTION

Inelastic deformation and stress relaxation in rocks are conditioned with nucleation and integration of fractures, accompanied with a dilation of a geological medium [1]. Blocks of a geological medium are separated with high-fragmented shear bands, which strength is significantly lower than strength of blocks [2]. In the result, deformation of rocks localizes predominantly within shear bands. Cracks, pores and voids inside a shear band form an interconnected system, which can be filled with a pore fluid in natural conditions. A yield stress and shear strength of a shear band depend on the effective stress $\sigma_{\alpha\beta}^{eff} = \sigma_{\alpha\beta} + \delta_{\alpha\beta}\chi P_{pore}$, where $\sigma_{\alpha\beta}$ is an applied external pressure, P_{pore} – pore fluid pressure, $0 < \chi \le 1$ – a material parameter, $\delta_{\alpha\beta}$ – the Kronecker symbol ($\alpha,\beta = x, y, z$) [3].

Dilation of a shear band under a plastic shearing leads to increasing of the volume of pores and cracks; in the results a fluid pore pressure P_{pore} decreases. A decrease of fluid pore pressure on walls of pores and cracks inhibits the stress relaxation processes, conditioned with a generation of new fractures and an integration of existing ones. This leads to an increasing of a macroscopic strength of a geological material. The mentioned effect has been called as dilatant hardening.

Evidently, in permeable media a value of pore fluid pressure is controlled both by a pore volume change and by a filtration motion of a fluid inside pores and cracks of a material. At that a local filtration rate depends on a permeability, a viscosity of a fluid and a gradient of pore pressure. Relation between a strain rate and a filtration rate determines a regime of deformation of a fluid-saturated material (drained or undrained conditions) [4]. Estimates of strength of a porous fluid-saturated material have been obtained by Biot for limiting cases of drained and undrained conditions [5][6]. The dependencies of a strength of a fluid-saturated materials on a dilation rate, filtration rate and strain rate were studied in detail in further works [7]-[10]. Particularly, it has been shown that the relation between rates of dilation (more precisely, pore volume increase under inelastic deformation) and filtration determines a value of fluid pore pressure in microcracks' tips, thereby controlling a development of faulting [11]-[12].

Despite the successes achieved in studying of mechanical properties of shear bands (including their shear strength), some keystone questions still remain unresolved. For instance, there was no a comprehensive study of strength of shear bands under combined compression and shear in the transition region between undrained and drained conditions (under partially drained conditions). It is clear that features of a shear strength in this region are determined not only by a shear rate and a permeability of a shear band itself, but to a large extent by a compression of a shear band and surrounding blocks of a material, fluid content, saturation and permeability of these blocks, as well as boundary conditions between a fragment of material under consideration and a host massif.

A direct study of deformation and strength of shear bands, appearing in samples under triaxial loading, represents a complicated problem. Therefore, a numerical simulation of a shear band under compression and shear seems to be a prospective approach to obtaining a detailed information about laws which determine strength of a shear band under complex loading conditions [13][14]. The goal of this work is to find a functional form of a dependence of shear band strength on the ratio of shear strain rate to filtration rate under conditions that correspond to rock massifs. The study has been carried out by means of a numerical simulation of a fluid-saturated elastic-plastic permeable medium with the Discrete Element Method (DEM).

2 DESCRIPTION OF A MODEL

During simulation of an elastic-plastic permeable medium, we use a decomposition of the considered problem into two ones: 1) a description of a mechanical behavior of a solid skeleton and 2) a simulation of a mass transfer of a fluid within a filtration volume (which represents a system of interconnected channels, pores, cracks etc.). Following the ideas of Biot [5][6], we assume that stress-strain state of a discrete element is directly connected with a change of volume of pores and pore pressure of a fluid in the "micropores" inside the element.

For simulation of a mechanical response of a material we have implemented the model of rock plasticity with non-associated flow law and von Mises yield criterion (the so-called Nikolaevsky model [15]). This model adequately describes a mechanical response of a wide class of brittle materials (geological materials, ceramics etc.) at different scales with taking into account of influence of lower-scale fractured structure. The Nikolaevsky model

postulates a linear relationship between volume and shear deformation rates of plastic deformation with coefficient Λ named the dilation coefficient. We have adopted the Nikolaevsky model to the DEM with use of so called Wilkins algorithm [16]. In the framework of this algorithm a solution of elastic-plastic problem is reduced to a solution of an elastic problem in increments and following correction of potential forces between particles (discrete elements) in accordance with the requirements of Nikolaevsky model, applied to values of local pressure and stress deviator [16].

In the framework of the proposed approach a solution of an elastic problem represents a calculation of normal and tangential forces acting from discrete element *i* as a result of interaction with a discrete element *j*. The corresponding equations are formulated based on a generalized Hooke's law in hypoelastic form [17]:

$$\begin{cases} \Delta\sigma_{i(j)} = \Delta F_{i(j)}^{centr} \Big/ S_{ij} = 2G_i \Delta\varepsilon_{i(j)} + \left(1 - \dfrac{2G_i}{K_i}\right) \Delta\bar{\sigma}_i^{mean} \\ \Delta\tau_{i(j)} = \Delta F_{i(j)}^{\tan g} \Big/ S_{ij} = 2G_i \Delta\gamma_{i(j)} \end{cases} \tag{1}$$

where symbol Δ indicates an increment of corresponding parameter during a time step Δt of numerical scheme; $\sigma_{i(j)}$ and $\tau_{i(j)}$ – are specific values of pair-wise central $F_{i(j)}^{centr}$ and tangential $F_{i(j)}^{\tan g}$ components of reaction force of *i*-th discrete element to *j*-th neighbour; S_{ij} – a contact square; G_i and K_i – shear and bulk moduli, correspondingly; $\Delta\varepsilon_{i(j)}$ and $\Delta\gamma_{i(j)}$ – increments of normal and shear strain of element *i* in pair *i*-*j*; $\bar{\sigma}_i^{mean}$ – average volume stress in element *i* [17],[18].

A stress state of a porous solid skeleton, containing a system of interconnected pores, channels and cracks depends both on a porosity and geometry of pores and cracks and their spatial distribution [19]. In the absence of a pronounced orientation of cracks in a solid skeleton, the fluid pressure in a pore volume contributes only into a hydrostatic pressure in a solid skeleton (namely, into a hydrostatic tension). In this approximation the influence of a fluid in "micropores" can be taken into consideration by means of including of fluid pore pressure into a relation for a central force:

$$\Delta\sigma_{i(j)} = \Delta F_{i(j)}^{centr} \Big/ S_{ij} = 2G_i \left(\Delta\varepsilon_{i(j)} - \frac{\Delta P_i^{fluid}}{K_i} \right) + \left(1 - \frac{2G_i}{K_i}\right) \Delta\bar{\sigma}_i^{mean} \tag{2}$$

where P_i^{fluid} – contribution of a fluid pore pressure (in "micropores") into a mean stress in a volume of discrete element *i*. Note that the equation (2) is equal to the Hooke's law in a model of linear poroelasticity. The value of P_i^{fluid} is linearly related with average pore pressure P_i^{pore} of a fluid in micropores of discrete element *i*:

$$P_i^{fluid} = a_i P_i^{pore} \tag{3}$$

where $a_i = 1 - K_i / K_{s,i}$. Here $K_{s,i}$ is a bulk modulus of non-porous grains of a solid skeleton of a discrete element *i*. After solution of the elastic problem for an element *i* at current time

step, an achievement of the Mises–Schleicher yield criterion is checked, with explicit taking into account of a fluid pore pressure:

$$\Phi_i = \beta_i \left(\overline{\sigma}_i^{mean} + b_i P_i^{pore} \right) + \overline{\sigma}_i^{eq} \Big/ \sqrt{3} \geq Y_i \tag{4}$$

where Y_i is a shear yield stress of a material of element i, β_i is a coefficient of internal friction, $\overline{\sigma}_i^{eq}$ – von Mises stress, averaged over a volume of a discrete element i, b_i – dimensionless coefficient. A value of the coefficient b_i is determined by geometry of pores, channels and cracks in a solid skeleton. When a configuration of a pore volume allows formation of a uniform distribution of a hydrostatic pressure in a local volume of a solid skeleton, the value of b_i is suggested to be equal to unity [1],[2]. At that, new cracks are assumed to appear from existing micropores or cracks. In the opposite case, when microscopic structure of a solid skeleton provides a more complicated interconnection between a pore pressure and fracture generation, the value of b_i is usually less than unity and depends on a porosity and pore pressure. The lower boundary of b_i usually equals to initial porosity ϕ_0 of non-deformed material [1].

When the yield condition (4) is satisfied, the reduction of components of stress tensor in a volume of discrete element i to a yield surface is performed. In accordance with [17], the mentioned reduction can be performed by means of the following correction of specific normal and tangential forces of interaction between i-th element and j-th neighbor:

$$\begin{cases} \sigma'_{i(j)} = \left(\sigma_{i(j)} - \overline{\sigma}_i^{mean} \right) M_i + \left(\overline{\sigma}_i^{mean} - N_i \right) \\ \tau'_{i(j)} = \tau_{i(j)} M_i \end{cases} \tag{5}$$

where $\left(\sigma'_{i(j)}, \tau'_{i(j)} \right)$ – are reduced values of specific reaction forces; $M_i = 1 - \left(\sqrt{3} / \overline{\sigma}_i^{\text{int}} \right) \left(3G_i \left(\Phi_i - Y_i \right) / \left(K_i \Lambda_i \beta_i + 3G_i \right) \right)$ – coefficient of reduction of stress deviator; $N_i = K_i \Lambda_i \left(\Phi_i - Y_i \right) / \left(K_i \Lambda_i \beta_i + G_i \right)$ – correction to a local mean stress, calculated after solving an elastic problem; Λ_i – dilation coefficient of material of element i.

A volume of a solid skeleton and, correspondingly, a pore volume change under the influence of internal and external stresses. At that, a specific volume of pores ϕ (or so called "microscopic" porosity) can be defined as follows:

$$\phi = \left(V_{pore}^{elast} + V_{pore}^{plast} \right) \Big/ V_{elem} \tag{6}$$

where V_{pore}^{elast} is a part of pore volume, which develops due to elastic deformations of material; and V_{pore}^{plast} is a part of pore volume, that appears as a result of "quasi-plastic" deformation of a material, namely as a result of opening of microscopic pores, cracks and other defects because of dilation of a material. Note that in the framework of the developed model we don't take into account a compaction of pores, which is valid for low-porous materials. Elastic change of pore volume is determined by the relation of bulk moduli of porous solid skeleton K and of non-porous monolithic grains that constitute the solid skeleton K_s:

$$V_{pore}^{elast} = V_{elem}^{init}\left[\phi_0 + 3\sigma_{mean}\left(\frac{1}{K}-\frac{1}{K_s}\right)+3P^{pore}\left(\frac{1}{K}-\frac{1+\phi}{K_s}\right)\right] \tag{7}$$

In turn, "inelastic" change of pore volume due to dilation of a material is given by the following relation:

$$V_{pore}^{plast} = V_{elem}^{init}\Omega_{plast} \tag{8}$$

where Ω_i^{elast} and Ω_i^{plast} represent elastic and inelastic parts of volume deformation of a discrete element, that are formally determined as follows:

$$\begin{cases}\Omega_i^{elast} = 3\left(\bar{\sigma}_i^{mean} + P_i^{fluid}\right)\Big/K_i \\ \Omega_i^{plast} = \left(\varepsilon_i^{xx}+\varepsilon_i^{yy}+\varepsilon_i^{zz}\right)-\Omega_i^{elast}\end{cases} \tag{9}$$

Here $\varepsilon_i^{\alpha\alpha}$ are diagonal components of strain tensor in a volume of a discrete element i [17][18]. We use the modified fracture criterion of Drucker-Prager that takes into account a contribution of a local pore pressure of a fluid in the following way:

$$\sigma_{DP} = 0.5(\lambda+1)\sigma_{eq} + 1.5(\lambda-1)\left(\sigma^{mean} + bP^{pore}\right) = \sigma_c \tag{10}$$

where $\lambda = \sigma_c/\sigma_t$ is the relation between compressive (σ_c) and tensile (σ_t) strengths of a material, the coefficient b is the same as in equation (4).

In the framework of the developed model of a fluid filtration we use the following assumptions: 1) a fluid may occupy a pore volume completely or partially; 2) a fluid is compressible; 3) an adsorption of a fluid on internal walls of pores, capillary effects and the effect of adsorption reduction of strength (Rehbinder effect) are not taken into account; and 4) a statistical distribution of sizes of micropores is not taken into account. In the framework of the latter assumption the pore volume is completely described by the following two parameters: a value of open "microscopic" porosity ϕ and a characteristic diameter of filtration channel d_{ch}, which controls the rate of fluid filtration through a solid porous skeleton. An adequate choice of the value of d_{ch} allows correct description of a mass transfer of a fluid, despite simplicity of the assumptions given above.

A state of a compressible liquid in pores can be described by the following equation [20]:

$$\rho(P) = \rho_0\left(1+\left(P-P_0\right)/K_{fl}\right) \tag{11}$$

where ρ and P are the current values of fluid density and pressure, ρ_0 and P_0 are the values of the density and pressure under atmospheric conditions, K_{fl} – bulk modulus of a fluid. When the fluid occupies a pore volume only partially, we assume the fluid pressure equals to the atmospheric pressure P_0. Neglecting the influence of gravity, the equation of filtration transfer of a fluid can be written in the following form [20]:

$$\phi\frac{\partial\rho}{\partial t} = K_{fl}\nabla\left[\frac{k}{\eta}\nabla\rho\right] \tag{12}$$

where η – fluid viscosity, k – coefficient of permeability of a solid skeleton that can be estimated as follows [20]:

$$k = \phi d_{ch}^2 . \tag{13}$$

Note that, in the framework of the used assumptions, there is no mass transfer between elements with fluid pressure $\rho \leq \rho_0$.

3 SIMULATION OF A SHEAR LOADING IN FLUID-SATURATED MEDIUM

We have considered a shear loading of an infinitely long sample with periodic boundary conditions in lateral direction (see fig. 1a). The sample consists of two linearly elastic blocks separated by an elastic-plastic shear band (interface). Pore volumes of permeable elastic blocks and elastic-plastic interface have been saturated with water under initial atmospheric pressure. The diagrams of uni-axial loading of materials of the blocks and the interface are given in fig. 1b. The considered sample was mounted between thin impermeable layers of material, to which an external loading was applied.

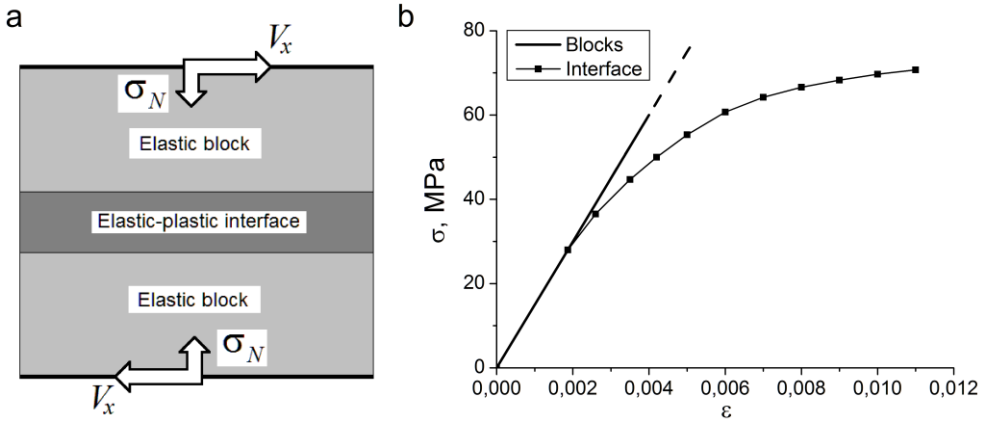

Figure 1: Scheme of loading (a); Diagrams of uni-axial loading of materials of the blocks and the interface (b).

The values of physical-mechanical parameters of the material are given in the table 1. The values of compressible and tensile strengths are given for the elastic-plastic interface, the elastic blocks are considered as indestructible. The total height of the sample was $L = 0.3$ m, the height of the interface was $L_0 = 0.03$ m.

The loading was performed in two stages. At the first stage an initial pre-loading with compression normal force F_N was performed. After that, we fixed the loading until fading of elastic waves in the sample. At the second stage a shear loading in lateral direction with the constant velocity V_x was applied until the sample fractures. At that, top and bottom layers were fixed in vertical direction.

We have found that under relatively small values of the normal pre-loading the fracture of the elastic-plastic interface occurs before a plastic deformation of the interface begins. At certain value of the normal pre-loading, the fracture of the interface goes after a plastic deformation begins and takes place at relatively high values of plastic deformations (see

fig. 2). The latter demonstrates a "brittle-to-ductile" transition which occurs in real materials, in particular, in geological media.

Table 1: Physical-mechanical parameters of the solid skeleton

Parameter name	Value	Parameter name	Value
Open porosity of a skeleton ϕ	0.1	Compressive strength σ_c	70 MPa
Bulk modulus of a porous skeleton K	37.5 MPa	Tensile strength σ_t	23.3 MPa
Bulk modulus of monolithic grains K_s	107.5 MPa	Dilation coefficient Λ	0.36
Density of a porous skeleton	2000 kg/m^3	Internal friction coefficient β	0.57
Poisson ratio of a porous skeleton	0.3	Parameter b	0.1

The results, presented below, have been obtained in the "ductile" regime of fracture, i.e. when fracture occurs significantly after reaching a yield point. At that, the dependence of the shear strength on the normal confining pressure can be approximated with the following equation:

$$\tau_c \approx \tau_{c,0} \left(\sigma_N / \sigma_y \right)^{0.45} \tag{14}$$

where $\tau_{c,0}$ – is a scale factor, having the dimension of stress, and σ_y – is the yield strength.

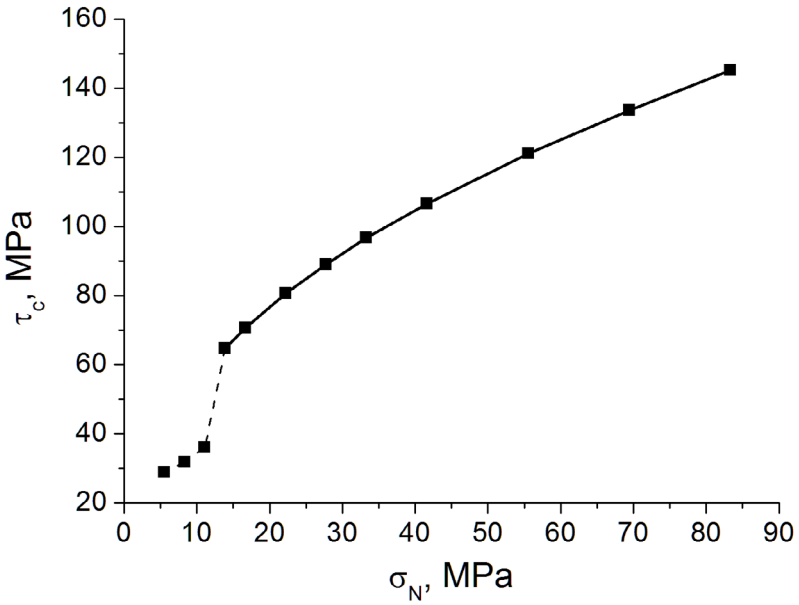

Figure 2: Shear strength of a non-permeable sample vs. different normal loads

The results of a parametric analysis of the problem have allowed us to obtain the governing combination of the parameters, which uniquely determines a value of the shear strength of the interface for a given value of the confining pressure:

$$A_{xy} = \mu \frac{L^2 \phi}{4k} \dot{\varepsilon}_{xy} \ . \tag{15}$$

The combination (15) includes viscosity of a fluid, porosity and permeability of the medium, shear rate and a height of the sample.

The dependency of the shear strength on the permeability of the material demonstrates an exponential decrease and further growth with an increase of the value of the permeability (see fig. 3). The dependencies of shear strength on permeability, obtained for different values of shear rate, viscosity, or height of the interface, can be reduced to a single dependence of shear strength on a unique controlling parameter (15). Note that the increase of the permeability corresponds to the decrease of the value of A_{xy} and vice versa.

The mentioned nonmonotonicity of the dependencies $\tau_c(A_{xy})$ has the following explanation. At relatively small values of permeability a liquid pressure in elastic-plastic interface rapidly decreases down to zero due to increase of the pore volume under dilation of elastic-plastic material. An outflow of the liquid from the regions, surrounding the interface, leads to slight decrease of the degree of constraint of the interface. In the result, the strength of the interface exponentially decreases with the increase of the permeability due to reduction of the mean stress in the interface.

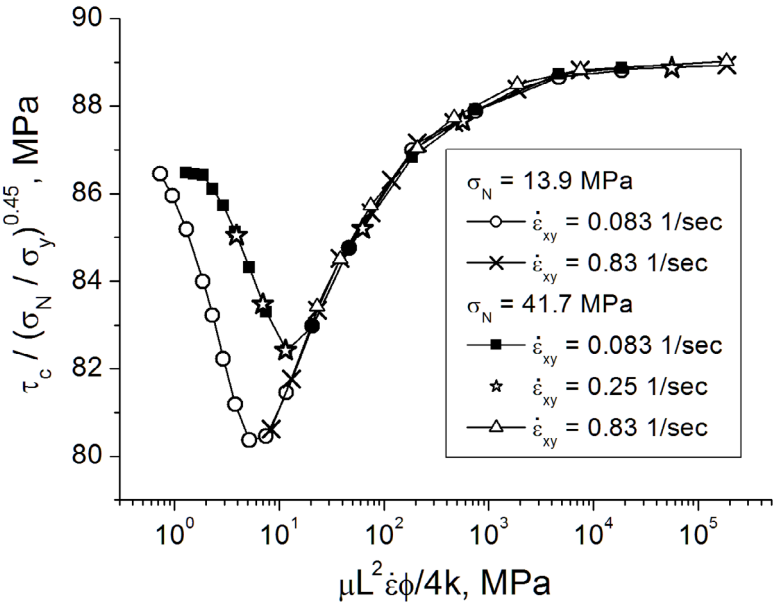

Figure 3: Normalized shear strength of a permeable sample for different shear rates and normal loads

At relatively high values of permeability a fluid pressure in the interface remains non-zero due to a rapid inflow of a fluid from the pore volume of the elastic blocks. The non-zero fluid pressure results in the decrease of the yield criterion in the accordance with the Mises-Schleicher criterion (4), at that, the dilation rate increases. This results in the increase of the degree of constraint and in the corresponding increase of the shear strength of the interface.

A competition of the processes, mentioned above, results in the occurrence of a minimal value of shear strength, where a rate of filtration is still not enough to provide a non-zero fluid pressure in the whole cross-section of elastic-plastic interface and, at the same time, it is enough to significantly decrease a pore pressure in the elastic blocks.

4 DISCUSSION AND CONCLUSIONS

Basing on the results shown above, we can conclude that shear strength of the interface depends on an interplay of the following processes: 1) increase of a mean stress in a medium under shear due to dilation of elastic-plastic shear band after reaching a yield point; 2) mass transfer of a fluid in a pore volume of the interface and the elastic blocks and 3) redistribution of the fluid in the sample due to the pressure gradient.

The observed effects together with the results of numerical simulations allowed us to suggest a generalized dependence of shear strength of an elastic-plastic interface on permeability and shear rate for a given normal load σ_N:

$$\tau_c = \sigma_0 + \sigma_1 \exp\left(-c_1 A_{xy}\right) + \frac{\sigma_2}{1+\left(c_2 A_{xy}\right)^{-p}} \tag{16}$$

where the value $(\sigma_0 + \sigma_1)$ corresponds to the strength of impermeable water-filled sample (under "undrained" conditions) and the value $(\sigma_0 + \sigma_2)$ represents the strength of a "dry" sample. Parameters c_1 and c_2 characterize the rate of change of exponential and sigmoidal branches of the dependence (16) with a change of permeability. Note that the values of σ_0, σ_1 and σ_2 are not constant but depend on a thickness of elastic-plastic interface, physical-mechanical parameters of a material and boundary conditions.

The first term of the dependence (16) describes the exponential decrease of strength of the interface due to the local decrease of the mean stress in the elastic blocks under outflow of a fluid into an excess pore volume in the interface. The second term characterizes the influence of filtration on the decrease of the yield criterion of the interface due to the growth of fluid pressure. This, in turn, leads to the increase of the degree of constraint of the interface.

The parameters of the obtained dependence (16) represent the combinations of the values of loading, width of the interface, physical-mechanical properties of the sample, including permeability, and physical mechanical properties of a fluid. A more detailed analysis of this dependence, including obtaining estimations for its unknown parameters is a subject of further research.

The authors thank the Russian Science Foundation (Project 17-11-01232) for the financial support.

REFERENCES

[1] Paterson, M.S. and Wong, T.F. *Experimental Rock Deformation. The Brittle Field*. Springer-Verlag, Berlin-Heidelberg (2005).

[2] Yamaji, A. *An Introduction to Tectonophysics: Theoretical Aspects of Structural Geology*. TERRAPUB (2007).

[3] Terzaghi, K. Theoretical Soil Mechanics. John Wiley & Sons, New York (1943).
[4] Brace W.F. and Martin R.J. A test of the law of effective stress for crystalline rocks of low porosity. *Int J. Rock Mech. Min. Sci*. (1968) **5**:415-426.
[5] Biot, M.A. General Theory of Three-Dimensional Consolidation. *J. Appl. Phys.* (1941) **12**:155-164.
[6] Biot, M.A. The Elastic Coefficients of the Theory of Consolidation. *J. Appl. Mech*. (1957) **24**:594-601.
[7] Detournay, E., and Cheng, A.H.-D. *Fundamentals of poroelasticity. Chapter 5 in Comprehensive Rock Engineering: Principles, Practice and Projects. Vol. II. Analysis and Design Method*. Pergamon Press (1993).
[8] Lei, X., Tamagawa, T., Tezuka, K. and Takahashi, M. Role of drainage conditions in deformation and fracture of porous rocks under triaxial compression in the laboratory. *Geophys. Res. Lett.* (2011) **38**:124310.
[9] Makhnenko, R.Y. and Labuz, J.F. Dilatant Hardening of Fluid-Saturated Sandstone. *J. Geophys. Res.: Solid Earth* (2015) **120**:909-922.
[10] Heap, M.J. and Wadsworth, F.B. Closing an Open System: Pore pressure changes in permeable edifice rock at high strain rates. *J. Volcanol. Geotherm. Res.* (2016) **315**:40-50.
[11] Rudnicki, J.W. and Chen C.-H. Stabilization of Rapid Frictional Slip on a Weakening Fault by Dilatant Hardening. *J. Geophys. Res.* (1988) **93**:4745-4757.
[12] Atkinson, C. and Cook, J.M. Effect of Loading Rate on Crack Propagation Under Compressive Stress in a Saturated Porous Materials. *J. Geophys. Res.* (1993) **98**:6383-6395.
[13] Garagash D.I. and Rudnicki J.W. Shear heating of a fluid-saturated slip-weakening dilatant fault zone: 1. Limiting regimes. *J. Geophys. Res. Solid Earth* (2003) **108**:2121.
[14] Samuelson, J., Elsworth, D. and Marone, C. Influence of dilatancy on the frictional constitutive behavior of a saturated fault zone under a variety of drainage conditions. *J. Geophys. Res.* (2011) **116**:B10406.
[15] Garagash, I.A. and Nikolaevsky, V.N., Non-associated laws of plastic flow and localization of deformation. *Adv. Mech.* (1989) **12**:131-183.
[16] Wilkins, M.L. *Computer simulation of dynamic phenomena*. Springer-Verlag, Heidelberg (1999).
[17] Psakhie, S.G., Shilko, E.V., Grigoriev, A.S., Astafurov, S.V., Dimaki, A.V. and Smolin, A.Yu. A mathematical model of particle-particle interaction for discrete element based modelling of deformation and fracture of heterogeneous elastic–plastic materials. *Engng. Fracture Mech.* (2014) **130**:96-115.
[18] Psakhie, S.G., Dimaki, A.V., Shilko, E.V. and Astafurov, S.V. A coupled discrete element-finite difference approach for modelling mechanical response of fluid-saturated porous materials. *Int. J. Num. Meth. Engng.* (2016) **106**:623-643.
[19] Kushch, V.I., Shmegera, S.V. and Sevostianov, I. SIF statistics in micro cracked solid: effect of crack density, orientation and clustering. *Int. J. Engng. Sci.* (2015) **47**:192-208.
[20] Basniev, K.S., Dmitriev, N.M., Chilingar, G.V. and Gorfunkle, M. *Mechanics of Fluid Flow*. Hoboken, John Wiley & Sons, Inc. (2012).

VII International Conference on Computational Methods for Coupled Problems in Science and Engineering
COUPLED PROBLEMS 2017
G. Papadrakakis, E. Oñate and B. Schrefler (Eds)

COMPARATIVE ANALYSIS OF A TRANSIENT HEAT FLOW AND THERMAL STRESSES BY ANALYTICAL AND NUMERICAL METHODS

G. ALMEIDA[*], N. COELHO[†] AND N. ALKMIM[*]

[*] Grupo de Dinâmica e Fluido – Estrutura (GDFE)
Universidade de Brasília.
Departamento de Engenharia Civil e Ambiental
Campus Darcy Ribeiro, CEP 70919 – 900, Asa norte, Brasília-DF, Brasil
E-mail: gisele.vilela21@gmail.com
nasser.alkmim@gmail.com

[†] Universidade Federal do Vale do São Francisco - UNIVASF
Avenida Antonio Carlos Magalhães, 510 - Santo Antônio
CEP: 48902-300 - Juazeiro/BA
E-mail: naildea@yahoo.com.br

Key words: Coupled Problems, Finite Differences Method, Finite Elements Method, Heat Transfer, Thermomechanical Applications.

Abstract. The study of heat flow problems is of extreme importance in engineering, there is a need to know the temperatures imposed and generated, when appropriate, in the structural parts to be able to evaluate the stresses that can arise due to the thermal variations. These stresses arise due to imposed constraints, ie bodies can not move freely and consequently undesirable cracks may arise when the stresses are greater than the resistive capacity of the stressed parts. The analysis of these problems can be done in both analytical or numerical way, with the use of calculation methods, such as the Finite Difference Method (FDM) and the Finite Element Method (FEM), with aid of computational programs such as MATLAB, PYTHON and ANSYS, as used in this work. The results presented here show simple cases of transient thermal variation and thermomechanical coupling by two methods of analysis, aiming at the validation of the numerical methods and softwares used. The solutions were satisfactory, the temperatures and stresses were coincident for different methods, making possible to start studying more complex problems with confidence in the implemented code.

1 INTRODUCTION

Heat flow is a common phenomenon in engineering. The temperature variation may be responsible for problems in structural parts due to the appearance of thermal stresses that may exceed the design resistive capacity and, consequently, give rise to fissures.

The study of heat equations is necessary so that it is possible to analyze the behavior of the involved materials in any project. The imposed conditions, initial and boundary conditions have direct influence on the equation results.

One of the main objectives of heat conduction analysis is to know the temperature

distribution, ie, how the temperature varies with the position in the domain. Conductive heat flow at any point in the middle or surface of a body can be determined by the Fourier law, represented by Partial Differential Equations (PDEs) [1].

Among the various mechanisms for solving heat transfer problems, there are the Finite Differences Method (FDM), easy to interpret and manipulate, the Finite Element Method (FEM), widely used in engineering, as well as the Analytical Methods, responsible for Mathematical solutions.

The MDF is a numerical procedure that solves PDEs by discretizing a continuous physical domain into a finite discrete mesh, approaching each partial derivative in the EDP by approximations of finite algebraic differences [2]. The finite difference equation must represent the exact solution of the PDE at each point of the discretized region in which the problem solution is to be obtained [3].

The FEM provides a general and systematic technique for the construction of base functions, which are necessary to model solutions of approximate boundary problems using, for example, the Galerkin method. According to [4], it is possible to construct approximate solutions for differential equations provided with a boundary condition, by dividing the domain of the solution into a finite number of subdomains.

Thermomechanical coupling is an alternative to problem solving using the methods mentioned. First, results of thermal analyzes are obtained. With the thermal distribution associated with the mechanical boundary conditions found, it is possible to find the stresses arising from the heat flux.

Therefore, this work intends to present analysis of heat flow and thermomechanical stresses for simple problems with the objective of accomplishing a preliminary and necessary step for studying the coupled problem in question. Thus, in this work will be presented comparisons between the Finite Element and the Finite Differences Methods for numerical solutions of the General Two-dimensional Heat Conduction Equation in Transient Regime and the coupled case of a plate submitted to a thermal variation.

2 THEORETICAL FUNDAMENTS

Analytical solutions to thermal problems, depending on the geometry and imposed initial and boundary conditions can be very complex or even impossible to determine. Numerical methods allow an easier and faster solution to these problems with the aid of computational tools. Therefore, in this work, the analytical methods, the FDM and the FEM were used, as will be presented in the sequence.

2.1 General Heat Conduction Equation

Heat conduction can be quantified in terms of differential equations. The mathematical model that describes the general heat conduction equation in rectangular coordinates, defined by [1, 2, 3, 4], is given by:

$$k\left(\frac{\partial^2 T}{\partial x^2}+\frac{\partial^2 T}{\partial y^2}+\frac{\partial^2 T}{\partial z^2}\right)+\ \dot{q}\ =\ \rho c\frac{\partial T}{\partial t} \tag{1}$$

In which $\dot{q}$ is the heat generation in respect to time (W/m³), k is the termal conductivity

(W/mºC), c is the specific heat (J/gºC), ρ is specific mass (Kg/m³), $\frac{\partial T}{\partial t}$ is the temperature variation in time, and $\left(\frac{\partial^2 T}{\partial x^2}+\frac{\partial^2 T}{\partial y^2}+\frac{\partial^2 T}{\partial z^2}\right)=\nabla^2 T$ represents the termal gradient.

2.2 General Heat Conduction Equation by Finite Differences Method (FDM):

The FDM allows the temperature calculation at any point in the domain (Figure 1) from its boundary conditions.

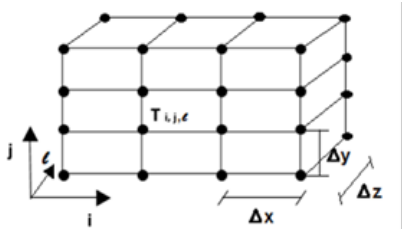

Figura 1: Finite Diferences Mesh Example.
(Coelho,2016)

The method consists in the substitution of differential equations by algebraic equations, making derivative transformations into finite differences. Based on studies carried out by [8,5] the substitutions of First Order Differential Equations and Second Order Differential Equations are shown in table (1) by their respective Finite Differences forms:

Table 1: First and Second order derivatives expressions aproximated through the FDM.

1ª Order of Derivatives:			**2ª Order of Derivatives**	
$\frac{\partial T}{\partial x}$	$\frac{T_{i+1}-T_{i-1}}{x_{i+1}-x_{i-1}}=\frac{T_{i+1}-T_{i-1}}{2\Delta x}$	$\frac{\partial^2 T}{\partial x^2}$	$\frac{T_{i+1,j,l}-2T_{i,j,l}+T_{i-1,j,l}}{(x_{i+1}-x_{i-1})^2}=\frac{T_{i+1,j,l}-2T_{i,j,l}+T_{i-1,j,l}}{\Delta x^2}$
$\frac{\partial T}{\partial y}$	$\frac{T_{j+1}-T_{j-1}}{y_{j+1}-y_{j-1}}=\frac{T_{j+1}-T_{j-1}}{2\Delta y}$	$\frac{\partial^2 T}{\partial y^2}$	$\frac{T_{i,j+1,l}-2T_{i,j,l}+T_{i,j-1,l}}{(y_{j+1}-y_{j-1})^2}=\frac{T_{i,j+1,l}-2T_{i,j,l}+T_{i,j-1,l}}{\Delta y^2}$
$\frac{\partial T}{\partial z}$	$\frac{T_{l+1}-T_{l-1}}{z_{l+1}-z_{l-1}}=\frac{T_{l+1}-T_{l-1}}{2\Delta z}$	$\frac{\partial^2 T}{\partial z^2}$	$\frac{T_{i,j,l+1}-2T_{i,j,l}+T_{i,j,l-1}}{(z_{l+1}-z_{l-1})^2}=\frac{T_{i,j,l+1}-2T_{i,j,l}+T_{i,j,l-1}}{\Delta z^2}$

In the transient case there will be at least one time derivative. According to [5], the term $\frac{\partial T}{\partial t}$, with time increments (κ), is defined as:

$$\frac{\partial T}{\partial t}=\frac{{T_i}^{k+1}-{T_i}^{k}}{\Delta t} \tag{2}$$

By replacing the ODEs with the corresponding differences in Eq. (1), we define the general heat conduction equation in three-dimensional finite differences:

$$\frac{{T^k}_{i+1,j,l}-2{T^k}_i+{T^k}_{i-1},j,l}{\Delta x^2}+\frac{{T^k}_{i,j+1,l}-2{T^k}_i+{T^k}_{i,j-1,l}}{\Delta y^2}+\frac{{T^k}_{i,j,l+1}-2{T^k}_i+{T^k}_{i,j,l-1}}{\Delta z^2}+\frac{q^k}{k}=\frac{1}{D}\frac{{T_i}^{k+1}-{T_i}^{k}}{\Delta t} \tag{3}$$

Beign $D=\frac{k}{\rho c}$, known as termal diffusivity.

Considering $\Delta x^2 = \Delta y^2 = \Delta z^2$, and simplifying Eq. (3), arise the Eq. (4):

$$T_i^{k+1} = F\left(T^k{}_{i+1,j,l} + T^k{}_{i-1},j,l + T^k{}_{i,j+1,l} + T^k{}_{i,j-1,l} + T^k{}_{i,j,l+1} + T^k{}_{i,j,l-1}\right) + (1-6F)T_i^k + G \tag{4}$$

In which,

$$F = \frac{\Delta t.D}{\Delta x^2} \tag{5}$$

$$G = \frac{q^k.\Delta x^2.\Delta t}{\rho c} \tag{6}$$

The expression in FDM allows the calculation of temperature at any point in the domain. The virtual points outside the domain are determined by the boundary conditions. The application of the FDM expression to all points of the domain leads to a system of n equations with n unknowns, of type Ax = B, which is solved by the classical mathematical methods in MatLab. [5].

2.3 General Heat Conduction Equation by Finite Elements Method (FEM):

According to [5], the temperature distribution T (x, y, z, t) inside the solid body is defined as:

$$I = \frac{1}{2}\iiint_V \left[K\left(\left(\frac{\partial \mathrm{T}}{\partial \mathrm{x}}\right)^2 + \left(\frac{\partial \mathrm{T}}{\partial \mathrm{y}}\right)^2 + \left(\frac{\partial \mathrm{T}}{\partial \mathrm{z}}\right)^2\right) - 2\left(\dot{q} - \rho \mathrm{c}\frac{\partial \mathrm{T}}{\partial \mathrm{t}}\right)T\right] dV \tag{7}$$

Using Galerkin's Method as solution to Eq. (7), the following steps were adopted, [19]:

1. Divide the domain V into E finite elements with p nodes;
2. Assume the appropriate variational form of T in finite elements with e elements, expressed by:

$$T^{(e)}(x,y,z,t) = [N(x,y,z)]\vec{T}^{(e)} \tag{8}$$

Where,

$$[\mathrm{N(x,y,z)}] = [\mathrm{N_1(x,y,z)} \quad \mathrm{N_2(x,y,z)} \quad \ldots \quad \mathrm{N_p(x,y,z)}\ ] \tag{9}$$

$$\vec{\mathrm{T}}^{(\mathrm{e})} = \begin{bmatrix} \mathrm{T_1(t)} \\ \vdots \\ \mathrm{T_2(t)} \end{bmatrix} \tag{10}$$

3. The integral of the weighted residue on the element domain is set equal to zero, having the same weights as the interpolation functions N_i. If the solution of the previous equation is not exact, it is replaced by the differential equation, which instead of zero will have a different value called the residual. Thus, the criterion to be satisfied at each instant of time is:

$$\mathrm{I} = \iiint_{\mathrm{Ve}} \left[\mathrm{N_i}\left(\mathrm{k}\left(\frac{\partial}{\partial \mathrm{x}}\left(\frac{\partial \mathrm{T^{(e)}}}{\partial \mathrm{x}}\right) + \frac{\partial}{\partial \mathrm{y}}\left(\frac{\partial \mathrm{T^{(e)}}}{\partial \mathrm{y}}\right) + \frac{\partial}{\partial \mathrm{z}}\left(\frac{\partial \mathrm{T^{(e)}}}{\partial \mathrm{z}}\right)\right)\right) + \dot{\mathrm{q}} - \rho \mathrm{c}\frac{\partial \mathrm{T^{(e)}}}{\partial \mathrm{t}}\right] \mathrm{dV} \tag{11}$$

Rewritng the first termo of the integral:

$$\iiint_{V^e} N_i k \frac{\partial}{\partial x}\left(\frac{\partial T^{(e)}}{\partial x}\right) dV = -\iiint_{V^e} k \frac{\partial N_i}{\partial x}\left(\frac{\partial T^{(e)}}{\partial x}\right) dV + \iiint_{V^e} N_i k \left(\frac{\partial T^{(e)}}{\partial x}\right) l_x dS \tag{12}$$

Being lx the cosine in x-direction. For the complete equation:

$$\begin{aligned} &-\iiint_{V^e} k\left[\frac{\partial N_i}{\partial x}\left(\frac{\partial T^{(e)}}{\partial x}\right) + \frac{\partial N_i}{\partial y}\left(\frac{\partial T^{(e)}}{\partial y}\right) + \frac{\partial N_i}{\partial z}\left(\frac{\partial T^{(e)}}{\partial z}\right)\right] dV + \iiint_{V^e} N_i k\left[\left(\frac{\partial T^{(e)}}{\partial x}\right) l_x + \left(\frac{\partial T^{(e)}}{\partial y}\right) l_y + \right. \\ &\left.\left(\frac{\partial T^{(e)}}{\partial z}\right) l_z\right] dS + \iiint_{V^e} N_i k\left(\dot{q} - \rho c \frac{\partial T^{(e)}}{\partial t}\right) dV \end{aligned} \tag{13}$$

The boundary of element $^{(e)}$ is composed of $S1^{(e)}$, $S2^{(e)}$ and $S3^{(e)}$. The surface integral equals to zero due to $T0$ in $S1^{(e)}$, the derivatives of $T^{(e)}$ in respect to x, y and z are zero too. In $S2^{(e)}$ and $S3^{(e)}$, the boundary conditions satisfies the problem, thus having as surface integral in $S2^{(e)}$ and $S3^{(e)}$:

$$\begin{aligned} &\iint_{S_2{}^{(e)}+S_3{}^{(e)}} N_i k\left[\left(\frac{\partial T^{(e)}}{\partial x}\right) l_x + \left(\frac{\partial T^{(e)}}{\partial y}\right) l_y + \left(\frac{\partial T^{(e)}}{\partial z}\right) l_z\right] dS \\ &= \iint_{S_2{}^{(e)}} N_i q\, dS_2 - \iint_{S_2{}^{(e)}} h\left(T^{(e)} - T_\infty\right) dS_3 \end{aligned} \tag{14}$$

The matricial form of the equation is:

$$\left[K_1{}^{(e)}\right]\vec{T}^{(e)} + \left[K_2{}^{(e)}\right]\vec{T}^{(e)} + \left[K_3{}^{(e)}\right]\dot{\vec{T}}^{(e)} - \vec{P}^{(e)} = \vec{0} \tag{15}$$

In which:

$$\boldsymbol{K_{1ij}}^{(e)} = -\iiint_{V^e} k\left[\frac{\partial N_i}{\partial x}\left(\frac{\partial T N_j}{\partial x}\right) + \frac{\partial N_i}{\partial y}\left(\frac{\partial T N_j}{\partial y}\right) + \frac{\partial N_i}{\partial z}\left(\frac{\partial T N_j}{\partial z}\right)\right] dV \tag{16}$$

$$\boldsymbol{K_{2ij}}^{(e)} = \iint_{S_3{}^{(e)}} h N_i N_j\, dS_3 \tag{17}$$

$$\boldsymbol{K_{3ij}}^{(e)} = \iiint_{V^{(e)}} \rho c N_i N_j\, dV \tag{18}$$

$$\vec{P}^{(e)}{}_i = \iiint_{V^{(e)}} \dot{q} N_i\, dV - \iint_{S_2{}^{(e)}} N_i q\, dS_2 - \iint_{S_2{}^{(e)}} h(T_\infty)\, dS_3 \tag{19}$$

4. The matrix elements can be written in the usual form:

$$[\underline{K_3}]\dot{\underline{\vec{T}^{(e)}}} + [\underline{K}^{(e)}]\underline{\vec{T}}^{(e)} = \underline{\vec{P}} \tag{20}$$

$$[\underline{\boldsymbol{K_3}}] = \sum_{e=1}^{E} [\boldsymbol{K_3}^{(e)}] \tag{21}$$

$$[\underline{\boldsymbol{K}}] = \sum_{e=1}^{E} [\boldsymbol{K_1}^{(e)} + \boldsymbol{K_2}^{(e)}] \tag{22}$$

$$\underline{\vec{P}} = \sum_{e=1}^{E} [\vec{P}^{(e)}] \tag{23}$$

5. The equations must be solved by incorporating the boundary conditions and the initial conditions. The expressions $[\boldsymbol{K_1}^{(e)}]$,$[\boldsymbol{K_2}^{(e)}]$,$[\boldsymbol{K_3}^{(e)}]$ and $\vec{\boldsymbol{P}}^{(e)}$ are written as matrixes with notation:

$$\boldsymbol{K_1}^{(e)} = \iiint_{V^e} [B]^T [D][B] dV \tag{24}$$

$$\boldsymbol{K_2}^{(e)} = \iiint_{S_3{}^e} h[N]^T [N] dS_3 \tag{25}$$

$$\boldsymbol{K_3}^{(e)} = \iiint_{V^e} \rho c[N]^T [N] dV \tag{26}$$

$$\vec{P}^{(e)} = \vec{P}_1{}^{(e)} - \vec{P}_2{}^{(e)} + \vec{P}_3{}^{(e)} \tag{27}$$

Where:

$$\overrightarrow{\boldsymbol{P_1}}^{(e)} = \iiint_{V^e} \dot{q}[N]^T dV \tag{28}$$

$$\overrightarrow{\boldsymbol{P_2}}^{(e)} = \iint_{S_3{}^{(e)}} q[N]^T \, dS_2 \tag{29}$$

$$\overrightarrow{\boldsymbol{P_3}}^{(e)} = \iint_{S_3{}^{(e)}} hT_\infty [N]^T \, dS_3 \tag{30}$$

$$[D] = \begin{bmatrix} k_x & 0 & 0 \\ 0 & k_y & 0 \\ 0 & 0 & k_z \end{bmatrix} \tag{31}$$

$$[B] = \begin{bmatrix} \frac{\partial N_1}{\partial x} & \frac{\partial N_2}{\partial x} & \cdots & \frac{\partial N_p}{\partial x} \\ \frac{\partial N_1}{\partial y} & \frac{\partial N_2}{\partial y} & \cdots & \frac{\partial N_p}{\partial y} \\ \frac{\partial N_1}{\partial z} & \frac{\partial N_2}{\partial z} & \cdots & \frac{\partial N_p}{\partial z} \end{bmatrix} \tag{32}$$

3 RESULTS

The presented results were developed by FDM and FEM in the first problem, with implementation in MATLAB and PHYTON, respectively, showing the transient heat flux for a situation with heat generation. In the second problem, results are displayed for a thermomechanical coupling using the analytical solution compared to the FEM using the ANSYS WORKBENCH software.

3.1 Complete 2D Heat Equation with Internal Heat Generation

The proposed case consists of a concrete plate of unit dimensions, with internal heat generation. The points analyzed were P1, P2 and P3, which are located in the center line of the x-axis, 0.25 m from the upper surface, at the plate central point and 0.25 from the lower surface of the y-axis, respectively. The adopted heat generation is represented by $\dot{q} = q_0.m.e^{(-mt)}$, where q_0= 200 J/m³s.

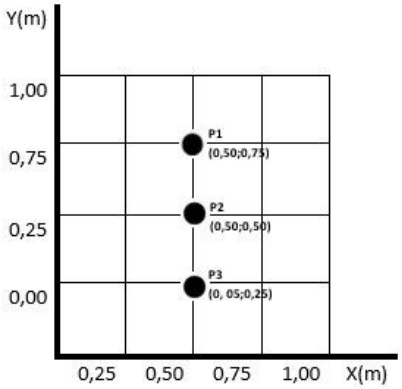

Figure 2: Plate and points analyzed by equaction**.**

The considered thermal and mechanical properties are in Tab. (2):

Table 2: Thermal and mechanical properties

Property	SI	Valor
Thermal Conductivity	k	1,79 (W/m.ºC)
Specific Heat	c	1000(J/g.ºC)
Specific Mass	ρ	2388(Kg/m³)
Thermal Expansion Coefficient	α	$16{,}67.10^{-6}$ (/ ºC)
Elasticity Module	E	210000MPa
Conductive Heat Transfer Coefficient	h	13,95 W/mK

3.1.1 Analysis of Results

The comparison between results was performed by comparing the temperature evolution curves obtained by the numerical solutions of the FDM and FEM at the stipulated time of 17280 s, as a function of the positions shown in Figs (3,4). The first graph, Fig. (03), considered the position variation only around the x-axis by adopting the central position of the plate (0.50 m)

at y. In the abscissa axis the position variations in x (m) were considered and in the ordinates the temperature variation (ºC).

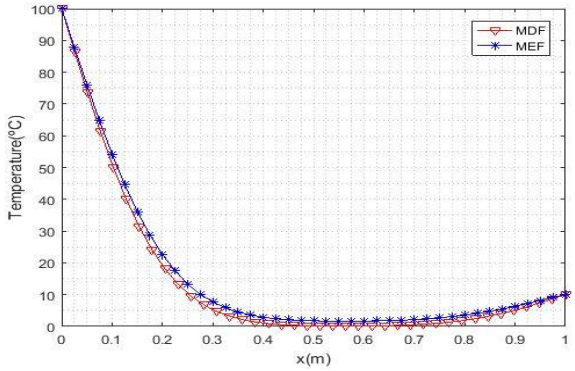

Figure 3: Temperature along the X-axis for the complete 2D equation

Analyzing Fig. (3) it can be seen that in the position x = 0.00 m the temperature corresponds to 100 °C, and for position x = 1.00 m to 10 ° C, which are the initial boundary conditions. In other positions, the results overlap, showing that the results obtained are reliable. The graph in Fig. (4) considered the position variation only around the y-axis and adopted the central position (0.50 m) for x. In the abscissa axis are the position variations in y (m) and in the ordinates the temperature variation (ºC).

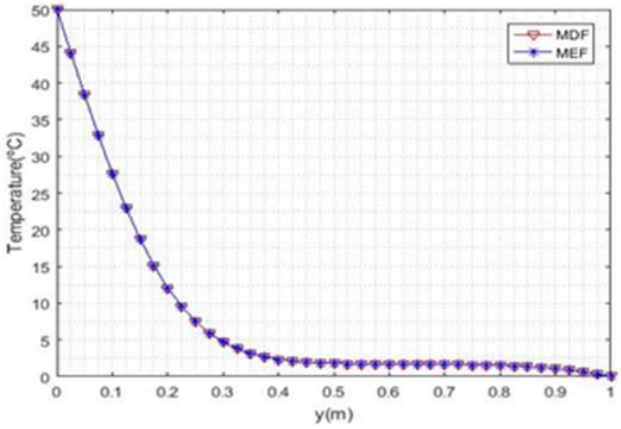

Figure 4: Temperature along the Y-axis for the complete 2D equation

As in the graph of Fig. (3), in Fig. (4), the temperatures dependent on the boundary conditions remained the same, at 50 °C and 0 °C, and the other points presented overlapping results.

Afterwards, the temperature evolution was analyzed as a function of time by the two numerical methods at three points on the plate (P1, P2 and P3). The point P1 is located at the coordinates x = 0.50m and y = 0.25m. P2 at coordinates x = 0.50m and y = 0.50m and point P3 at coordinates x = 0.50m and y = 0.75m. The comparisons can be seen in Figs. (5a), (5b) and

(5c).

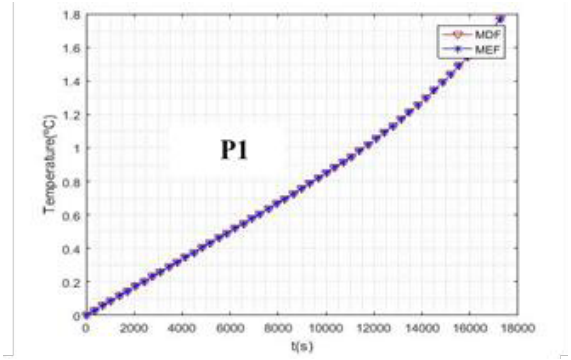

Figure 5.a: Transient temperatura analysis in point P1

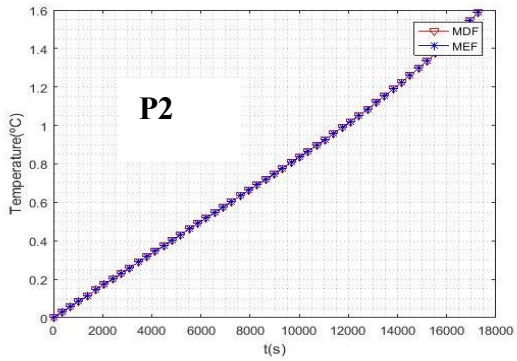

Figure 5.b: Transient temperatura analysis in point P2

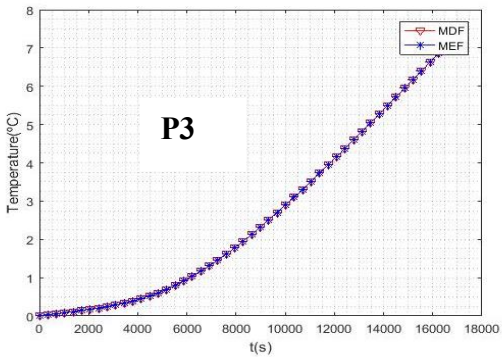

Figure 5.c: Transient temperatura analysis in point P3

In all the graphs of Fig. (5), it can be observed that the results obtained by FDM and FEM are coincident, showing a good treatment of data and that both are efficient in the solution of heat problems.

3.2 Thermomechanical Coupling in a Retangular Plate

In this section, numerical-analytical results will be compared for the case of rectangular plate with fixed boundary conditions subject to a non-uniform heat variation ΔT, according to Fig. (6), as proposed by [20].

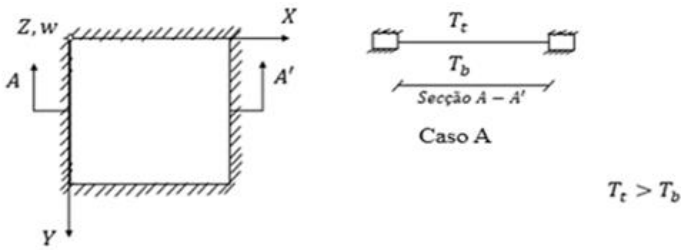

Figure 6: Mechanical results comparison for a bi-crimped beam.

Considering the edges of the plate free to slide, but with restriction to rotation, case A, the moment in the plate is given by Eq. (33).

$$M = -\frac{D\alpha(\Delta T)}{h}(1+\nu) \tag{33}$$

Being M the moment due to the temperature gradient $(\boldsymbol{\Delta T})$, $\boldsymbol{D = \frac{Eh^3}{12(1-\nu^2)}}$ is the flexural stiffness and $\boldsymbol{\nu}$ is the Poisson's coefficient.

The correspondent maximum stress $\sigma_{max,b}$ is given by:

$$\sigma_{max,b} = \pm\frac{6M}{h^2} \tag{34}$$

Was modeled in ANSYS Workbench a solid body of dimensions (x, y, z) = (0.5, 0.5, 0.1), as in Fig. (XX), with temperatures T = 0 °C at z = 0.0 m and T = 100 °C at z = 0.1 m. The results for the temperatures can be visualized in Fig. (XX), presenting a uniform thermal distribution.

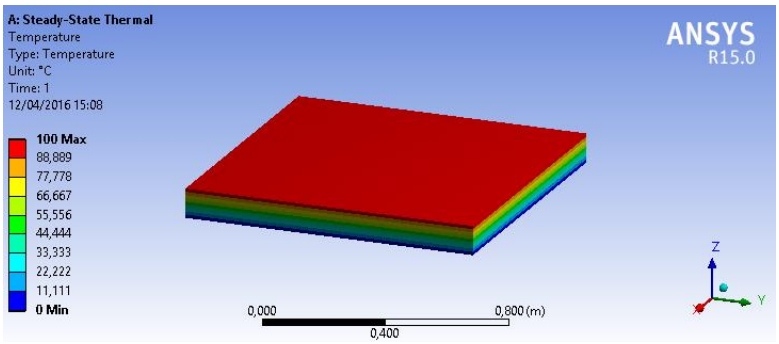

Figura 07: Resultados mecânicos para a viga biengastada

If there is only the displacement restriction at z, the maximum and minimum stresses found at the central points of the body are ± 9.4303E7 Pa. Using Eqs. (33) and (34), the maximum stresses are ±8.57E7 Pa, differing only in 9.0 % from the software result. The graph of Fig. (08) presents the stress distribution in the abscissa axis (Pa), by the thickness in the ordinates axis (m). The 'calculated stress' curve represents the maximum tensions found analytically, 'Stress X' represents the stresses found by the program along the width and 'Stress Z' the stresses in the thickness direction, being free to rotate, the stresses in that axis are zero. However, the maximum stresses by both methods are very close.

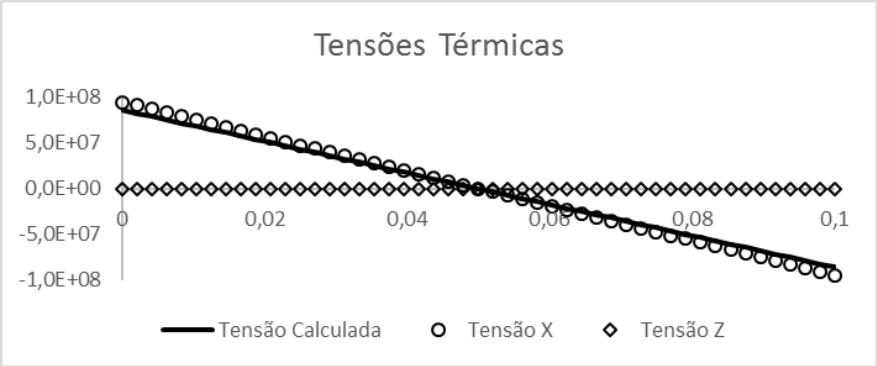

Figure 08: Thermal stresses result comparison for different cases

With this analysis, it can be affirmed that the analytical method and the MEF, applied through the ANSYS, can be used in the resolution of thermomechanical problems in engineering, and can later apply this methodology to more complex situations. Other similar analyzes can be observed in [9].

4 CONCLUSIONS

With the presented results, it is possible to affirm that the thermal and thermomechanical analyzes can be done by means of different methods, like the analytical method, FDM and FEM. The comparisons between the simulations performed with the exposed alternatives were coincident, showing a good treatment of the data and a correct manipulation of the computational tools. It is also noted that the initial conditions and boundary properly applied are essential in order to reach the expected results. Although the cases presented are simple, they are essential if advances are to be achieved, as they are part of a needed preliminary study phase of validation that aims to arrive at solutions, with confidence in numerical simulations, of more complex problems.

5 ACKNOWLEDGMENT

The author thanks UnB, PECC-UnB and FAPDF for their support in the development of this research and my supervisor of scientific initiation Prof. Dr. Lineu José Pedroso, who directed, dedicated time and unconditionally encouraged the accomplishment of this work.

REFERENCES

[1] Incropera, F.P.; Dewitt, D.P. *Fundamentos de Transferência de Calor e de Massa*, 3a Edição, LTC S. A., R. J. 1990.

[2] Hoffman, J. D., 2001. Numerical methods for engineers and scientists, Marcel Dekker, Inc.

[3] Corrêa, L.; Lima, G. A. B.; Ferreira, V. G. Solução Numérica de Equações Diferenciais Parciais via o Método das Diferenças Finitas. II Colóquio de Matemática do Centro Oeste. 2011.

[4] Becker, E., 1981. Finite elements. Englewood Cliffs, N.J: Prentice-Hall

[5] Coelho, N. A.. Métodos Analíticos e Numéricos para o Estudo dos Efeitos Termomecânicos no Concreto Massa Orientados às Barragens de Gravidade. Tese de Doutorado. Universidade de Brasília – UnB. Brasília: 2016.

[6] Almeida, G. V.; Coelho, N. A.; Pedroso, L. J.. Distribuição de temperatura em placas em regime transiente: comparação entre solução analítica e numérica. In:XXXVII Iberian Latin American Congress on Computational Methods in Engineering. Brasília: 2016.

[7] Coelho, N. A.. Um Estudo Numérico do Efeito Térmico em Concreto Massa. Dissertação de Mestrado. Universidade de Brasília – UnB. Brasília: 2012

[8] Coelho, N. A.; Gomes, F. M. P.; Pedroso, L. J.; Silva, D. A.. Um estudo comparativo analítico-numérico de tensões térmicas em casos clássicos de vigas e placas. In: XXXVII Iberian Latin American Congress on Computational Methods in Engineering. Brasília: 2016

[9] Coelho, N. A.; Silva, D. A.; Pedroso, L. J.; Efeito térmico provocado pelo calor de hidratação em barragem de gravidade construída em camadas. In: XXXVII Iberian Latin American Congress on Computational Methods in Engineering. Brasília: 2016b.
[10] Coelho, N. A.; Pedroso, L. J. Estudo da Equação de Calor em Elemento Uni, Bi e Tridimensional. Relatório Técnico – RTP. Universidade de Brasília – UnB. Brasília: 2013.
[11] Gomes, F. M. P.; Coelho, N. A.; Pedroso, L. J.. Uma solução analítico-numérica para a difusividade do calor em um cilindro com e sem geração de calor. In: XXXVII Iberian Latin American Congress on Computational Methods in Engineering. Brasília: 2016.
[12] Gomes, F. M. P.; Concreto nas primeiras idades: propriedades e modelagem termomecânica simplificada. Dissertação de Mestrado. Universidade Federal de Goiás. Goiânia: 2011.
[13] Pedroso, L. J. Manuscritos, esquemas, discussões e notas de seções de orientações, 2013-2016. In: Programa de Pós-Graduação em Estruturas e Construção Civil – PECC, Universidade de Brasília, Brasilia, 2016.
[14] Pedroso, L. J.. Método das Diferenças Finitas em Vigas Esbeltas. Apostilha didática. In: Programa de Pós-Graduação em Estruturas e Construção Civil – PECC, Universidade de Brasília, Brasilia, 2005.
[15] Pedroso, L.J.. Método das Diferenças Finitas. In: Notas de Curso e Apostila Didática, UnB-FT/ENC, Vs.3 - Brasília, DF, 2003.
[16] Pedroso, J. L.. Barragens de Concreto: Aspectos Gerais e Fundamentos do Cálculo de Tensões e da Estabilidade Baseado no Método de Gravidade. Apostila do Curso de Barragens de Concreto. Universidade de Brasília - UnB, Brasília, 2002.
[17] Pedroso,L. J., 2011. Uma Introdução do Método das Diferenças Finitas Centrais em Cavidades Acústicas 2D. Publicação Didática, Universidade de Brasília.
[18] Çengel, Y. A. 2006. Heat and Mass Transfer: A Practical Approach, 3ª Ed., McGraw-Hill, Singapore.
[19] Rao, S. S.; The Finite Element Method in Engineering. 3ª ed. United States of America: Butterworth Heinemann: 1999.
[20] SZILARD, R.. Theory and Analysis of Plates: Classical and Numerical Methods. John Wiley & Sons. New Jersey: 2004.

VII International Conference on Computational Methods for Coupled Problems in Science and Engineering
COUPLED PROBLEMS 2017
M. Papadrakakis, E. Oñate and B. Schrefler (Eds)

MIXED VARIATIONAL FORMULATIONS FOR MULTI-FIELD PROBLEMS

M. DITTMANN* AND C. HESCH*

* Chair of Computational Mechanics
University of Siegen
Paul-Bonatz-Straße 9-11, 57068 Siegen, Germany
e-mail: maik.dittmann@uni-siegen.de, christian.hesch@uni-siegen.de,
web page: https://www.mb.uni-siegen.de/nm/mitglieder/

Key words: Thermomechanical coupled problems, Polyconvex formulations, Hellinger-Reissner type variational principle

Abstract. The present work deals with large strain thermomechanical coupled problems. In particular, a novel polyconvex formulation based on a mixed Hellinger-Reissner type variational principle is introduced along with advanced discretization techniques which reduce the computational effort dramatically. Eventually, the capabilities of the proposed framework are demonstrated within a number of numerical examples.

1 INTRODUCTION

General thermoelastic material models have been investigated over the past decades, see e.g. Reese and Govindjee [1], Holzapfel and Simo [2] and Miehe [3] among many others. In this paper we present a novel computational framework for large strain thermoelasticity. The ideas of a new formulation for polyconvex large strain elasticity originally introduced by Ball [4] and recently resumed by Bonet et al. [5] are extended to non-linear coupled thermoelasticity, see also Dittmann [6]. In particular, the deformation gradient (line map), its co-factor (area map) and its determinant (volume map) along with the absolute temperature are formulated as independent variables to obtain a polyconvex free energy function. Moreover, we introduce work conjugate stresses to the extended kinematic set to define a complementary energy principle of Hellinger-Reissner type, where the introduced conjugate stresses along with the deformed geometry and the absolute temperature constitute the set of primal variables, see also Hesch et al. [7] for the application of a mixed Hu-Washizu type variational principle in the context of coupled phase-field fracture problems. The finite element discretization relies on a quadratic approximation of the deformed geometry and the absolute temperature, whereas discontinuous linear interpolations are used for the conjugate stresses such that the stress unknowns can be

condensed. Eventually, quasi-static as well as transient numerical examples are investigated to demonstrate the capability of the proposed framework.

2 CONFIGURATION AND KINEMATICS

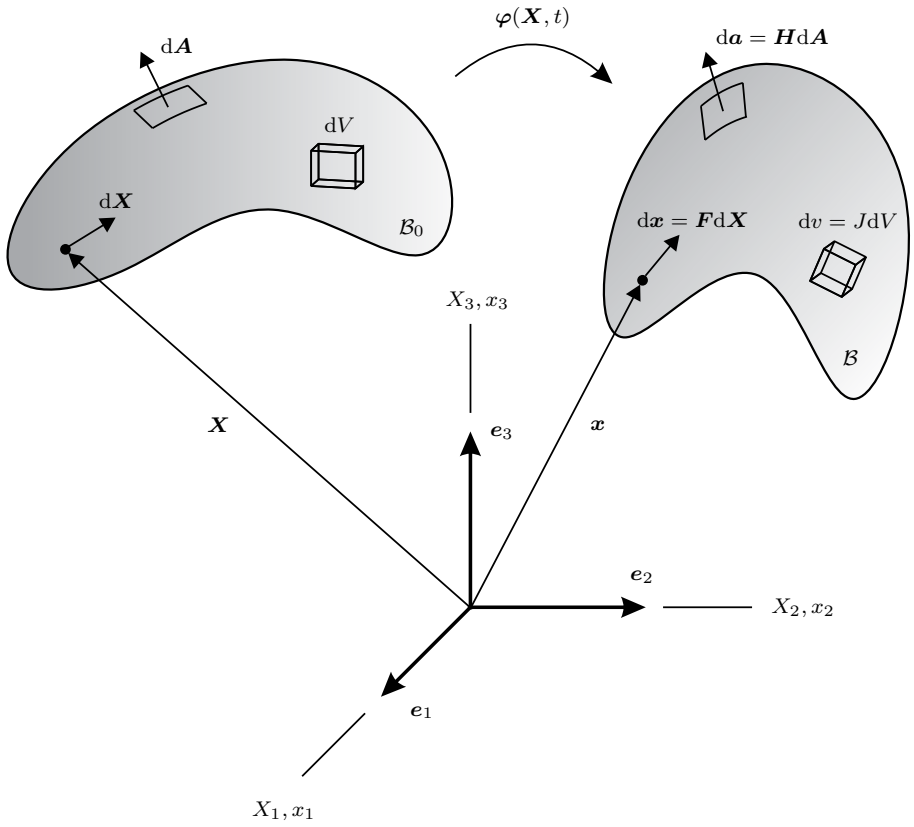

Figure 1: Deformation mapping of a continuum body from a reference configuration $\mathcal{B}_0$ into a current configuration $\mathcal{B}$ and associated strain measures $\boldsymbol{F}, \boldsymbol{H}$ and J

We consider a three dimensional thermoelastic body, i.e. $d = 3$, in its reference configuration occupying a domain $\mathcal{B}_0$ with boundary $\partial\mathcal{B}_0$, see Figure 1. A sufficiently smooth non-linear deformation mapping

$$\boldsymbol{\varphi}(\boldsymbol{X},t) : \mathcal{B}_0 \times \mathcal{T} \to \mathbb{R}^d, \tag{1}$$

is introduced to map a material point $\boldsymbol{X}$ in its reference configuration to its position $\boldsymbol{x} = \boldsymbol{\varphi}(\boldsymbol{X},t)$ in the current configuration $\mathcal{B}$ at time $t \in \mathcal{T} = [0,T]$, where $T \in \mathbb{R}^+$. Furthermore, we introduce the absolute temperature

$$\theta(\boldsymbol{X},t) : \mathcal{B}_0 \times \mathcal{T} \to \mathbb{R}_{\geq 0}, \tag{2}$$

which is assumed to be a sufficiently smooth function. The unknowns $\{\boldsymbol{\varphi}, \theta\}$ represent the non-reducible degrees of freedom to be found for all times of interest.

The deformation gradient tensor $\boldsymbol{F} : \mathcal{B}_0 \times \mathcal{T} \to \mathbb{R}^{d\times d}$ is commonly defined as material gradient of the current configuration

$$\boldsymbol{F} = \nabla(\boldsymbol{\varphi}) = \frac{\partial \boldsymbol{\varphi}}{\partial \boldsymbol{X}}. \tag{3}$$

Moreover, we introduce the determinant $J : \mathcal{B}_0 \times \mathcal{T} \to \mathbb{R}$ as well as the co-factor $\boldsymbol{H} : \mathcal{B}_0 \times \mathcal{T} \to \mathbb{R}^{d\times d}$ of the deformation gradient, usually defined by $J = \det(\boldsymbol{F})$ and $\boldsymbol{H} = J\boldsymbol{F}^{-1}$, respectively. As shown in Figure 1, the three strain measures $\boldsymbol{F}, \boldsymbol{H}$ and J map differential line, area and volume elements between the reference and the current configuration, i.e. $\mathrm{d}\boldsymbol{x} = \boldsymbol{F}\mathrm{d}\boldsymbol{X}$, $\mathrm{d}\boldsymbol{a} = \boldsymbol{H}\mathrm{d}\boldsymbol{A}$ and $\mathrm{d}v = J\mathrm{d}V$. Regarding the latter both mappings, we provide an alternative representation by using the cross product between second order tensors[1]. Thus, the co-factor or area map tensor is given as

$$\boldsymbol{H} = \mathrm{cof}(\boldsymbol{F}) = \frac{1}{2}(\boldsymbol{F} \times \boldsymbol{F}) \tag{4}$$

and the Jacobian determinant or volume map reads

$$J = \det(\boldsymbol{F}) = \frac{1}{6}(\boldsymbol{F} \times \boldsymbol{F}) : \boldsymbol{F}. \tag{5}$$

Note that the tensor cross product operation was originally introduced by de Boer [8] and for the first time applied in the context of solid mechanics in Bonet et al. [5]. The usage of the tensor cross product operation simplifies tremendously the first and second directional derivatives of (4) and (5) with respect to virtual and incremental variations $\delta\boldsymbol{\varphi}$ and $\Delta\boldsymbol{\varphi}$, since differentiation of the inverse of the deformation gradient is not required. For the co-factor follows immediately

$$\mathrm{D}\boldsymbol{H}[\delta\boldsymbol{\varphi}] = \boldsymbol{F} \times \nabla(\delta\boldsymbol{\varphi}), \quad \mathrm{D}^2\boldsymbol{H}[\delta\boldsymbol{\varphi}, \Delta\boldsymbol{\varphi}] = \nabla(\delta\boldsymbol{\varphi}) \times \nabla(\Delta\boldsymbol{\varphi}), \tag{6}$$

whereas the derivatives of the determinant of the deformation gradient read

$$\mathrm{D}J[\delta\boldsymbol{\varphi}] = \boldsymbol{H} : \nabla(\delta\boldsymbol{\varphi}), \quad \mathrm{D}^2J[\delta\boldsymbol{\varphi}, \Delta\boldsymbol{\varphi}] = \boldsymbol{F} : (\nabla(\delta\boldsymbol{\varphi}) \times \nabla(\Delta\boldsymbol{\varphi})). \tag{7}$$

3 POLYCONVEX THERMOELASTICITY

Polyconvexity is accepted as a fundamental mathematical requirement which has to be satisfied by admissible energy density functions to model large strain elastic material behavior.

[1]The definition of the tensor cross product operation is given e.g. in Dittmann [6], Appendix A.

3.1 Free Helmholtz energy

For the consideration of thermomechanical materials, the free Helmholtz energy density can be defined as a polyconvex function[2] of the introduced set of strains and the absolute temperature

$$\Psi(\boldsymbol{F},\theta) := \bar{\Psi}(\bar{\boldsymbol{F}},\bar{\boldsymbol{H}},J,\theta), \tag{8}$$

where the isochoric components of $\boldsymbol{F}$ and $\boldsymbol{H}$ are given as

$$\bar{\boldsymbol{F}} = J^{-1/3}\boldsymbol{F}, \quad \bar{\boldsymbol{H}} = J^{-2/3}\boldsymbol{H}. \tag{9}$$

Thus, a typical thermoelastic compressible Mooney-Rivlin material can be described by the free Helmholtz energy density function

$$\begin{aligned}\bar{\Psi}(\bar{\boldsymbol{F}},\bar{\boldsymbol{H}},J,\theta) = &\underbrace{\alpha(\bar{\boldsymbol{F}}:\bar{\boldsymbol{F}}-d)+\beta((\bar{\boldsymbol{H}}:\bar{\boldsymbol{H}})^{3/2}-d^{3/2})}_{\bar{\Psi}^{\mathrm{iso}}}+\underbrace{\frac{\kappa}{2}(J-1)^2}_{\bar{\Psi}^{\mathrm{vol}}}\\ &+\underbrace{c\left(\theta-\theta_{\mathrm{ref}}-\theta\ln\left(\frac{\theta}{\theta_{\mathrm{ref}}}\right)\right)}_{\bar{\Psi}^{\mathrm{the}}}+\underbrace{(-d\gamma(\theta-\theta_{\mathrm{ref}})\kappa(J-1))}_{\bar{\Psi}^{\mathrm{cpl}}},\end{aligned} \tag{10}$$

where α and β are positive material parameters related to the shear modulus and κ is the positive bulk modulus. Furthermore, the thermal material parameters $c \geq 0$ and γ denote the specific heat capacity and the linear thermal expansion coefficient, respectively. For more details and a proof of polyconvexity see Dittmann [6] and the references therein.

3.2 Conjugate stresses, entropy and Hessian operator

We introduce a set of work conjugate variables to the extended kinematic set and the temperature $\{\boldsymbol{F},\boldsymbol{H},J,\theta\}$ defined as

$$\boldsymbol{\Sigma}_F = \frac{\partial\bar{\Psi}}{\partial\boldsymbol{F}}, \quad \boldsymbol{\Sigma}_H = \frac{\partial\bar{\Psi}}{\partial\boldsymbol{H}}, \quad \Sigma_J = \frac{\partial\bar{\Psi}}{\partial J}, \quad \eta = -\frac{\partial\bar{\Psi}}{\partial\theta}. \tag{11}$$

In addition, work conjugate stresses to the isochoric strain components $\{\bar{\boldsymbol{F}},\bar{\boldsymbol{H}}\}$ can be formulated as

$$\bar{\boldsymbol{\Sigma}}_F = \frac{\partial\bar{\Psi}^{\mathrm{iso}}}{\partial\bar{\boldsymbol{F}}}, \quad \bar{\boldsymbol{\Sigma}}_H = \frac{\partial\bar{\Psi}^{\mathrm{iso}}}{\partial\bar{\boldsymbol{H}}}. \tag{12}$$

Accordingly, the hydrostatic pressure work conjugate to J is given as

$$p = \frac{\partial(\bar{\Psi}^{\mathrm{vol}}+\bar{\Psi}^{\mathrm{cpl}})}{\partial J} \tag{13}$$

and is positive in tension and negative in compression.

[2]Note that polyconvexity is related to the set of strains independent of the temperature field.

Next, we derive the relationship between the first Piola-Kirchhoff stress tensor $\boldsymbol{P}$ and the introduced sets of stresses $\{\boldsymbol{\Sigma}_F, \boldsymbol{\Sigma}_H, \Sigma_J\}$ and $\{\bar{\boldsymbol{\Sigma}}_F \bar{\boldsymbol{\Sigma}}_H, p\}$, respectively. The variation of both energy functions in (8) with respect to the primal variables formally reads

$$\mathrm{D}\Psi[\mathrm{D}\boldsymbol{F}[\delta\boldsymbol{\varphi}], \delta\theta] = \mathrm{D}\bar{\Psi}[\mathrm{D}\boldsymbol{F}[\delta\boldsymbol{\varphi}], \mathrm{D}\boldsymbol{H}[\delta\boldsymbol{\varphi}], \mathrm{D}J[\delta\boldsymbol{\varphi}], \delta\theta]. \tag{14}$$

Recalling (6) and (7) yields

$$\begin{aligned} \boldsymbol{P} : \nabla(\delta\boldsymbol{\varphi}) - \eta\delta\theta &= \boldsymbol{\Sigma}_{\boldsymbol{F}} : \mathrm{D}\boldsymbol{F}[\delta\boldsymbol{\varphi}] + \boldsymbol{\Sigma}_{\boldsymbol{H}} : \mathrm{D}\boldsymbol{H}[\delta\boldsymbol{\varphi}] + \Sigma_J \mathrm{D}J[\delta\boldsymbol{\varphi}] - \eta\delta\theta \\ &= (\boldsymbol{\Sigma}_{\boldsymbol{F}} + \boldsymbol{\Sigma}_{\boldsymbol{H}} \times \boldsymbol{F} + \Sigma_J \boldsymbol{H}) : \nabla(\delta\boldsymbol{\varphi}) - \eta\delta\theta. \end{aligned} \tag{15}$$

Thus, we find that

$$\begin{aligned} \boldsymbol{P} &= \boldsymbol{\Sigma}_F + \boldsymbol{\Sigma}_H \times \boldsymbol{F} + \Sigma_J \boldsymbol{H} \\ &= J^{-1/3}\bar{\boldsymbol{\Sigma}}_F + J^{-2/3}\bar{\boldsymbol{\Sigma}}_H \times \boldsymbol{F} + \left(p - \frac{1}{3} J^{-4/3} \bar{\boldsymbol{\Sigma}}_F : \boldsymbol{F} - \frac{2}{3} J^{-5/3} \bar{\boldsymbol{\Sigma}}_H : \boldsymbol{H} \right) \boldsymbol{H}. \end{aligned} \tag{16}$$

For the Newton-Raphson iteration a linearization is required. Regarding (15), the linearization reads

$$\begin{aligned} \mathrm{D}^2\bar{\Psi}[\delta\boldsymbol{\varphi}, \delta\theta, \Delta\boldsymbol{\varphi}, \Delta\theta] &= \begin{bmatrix} \nabla(\delta\boldsymbol{\varphi}) : & \delta\theta \end{bmatrix} \begin{bmatrix} \mathrm{D}\boldsymbol{P}[\nabla(\Delta\boldsymbol{\varphi}), \Delta\theta] \\ -\mathrm{D}\eta[\nabla(\Delta\boldsymbol{\varphi}), \Delta\theta] \end{bmatrix} \\ &= \begin{bmatrix} \nabla(\delta\boldsymbol{\varphi}) : \\ \nabla(\delta\boldsymbol{\varphi}) \times \boldsymbol{F} : \\ \nabla(\delta\boldsymbol{\varphi}) : \boldsymbol{H} \\ \delta\theta \end{bmatrix}^{\mathrm{T}} [\mathbb{H}_{\bar{\Psi}}] \begin{bmatrix} : \nabla(\Delta\boldsymbol{\varphi}) \\ : \nabla(\Delta\boldsymbol{\varphi}) \times \boldsymbol{F} \\ \nabla(\Delta\boldsymbol{\varphi}) : \boldsymbol{H} \\ \Delta\theta \end{bmatrix} \\ &\quad + (\boldsymbol{\Sigma}_{\boldsymbol{H}} + \Sigma_J \boldsymbol{F}) : (\nabla(\delta\boldsymbol{\varphi}) \times \nabla(\Delta\boldsymbol{\varphi})), \end{aligned} \tag{17}$$

where the Hessian operator is defined as

$$[\mathbb{H}_{\bar{\Psi}}] = \begin{bmatrix} \frac{\partial^2\bar{\Psi}}{\partial\boldsymbol{F}\partial\boldsymbol{F}} & \frac{\partial^2\bar{\Psi}}{\partial\boldsymbol{F}\partial\boldsymbol{H}} & \frac{\partial^2\bar{\Psi}}{\partial\boldsymbol{F}\partial J} & \frac{\partial^2\bar{\Psi}}{\partial\boldsymbol{F}\partial\theta} \\ \frac{\partial^2\bar{\Psi}}{\partial\boldsymbol{H}\partial\boldsymbol{F}} & \frac{\partial^2\bar{\Psi}}{\partial\boldsymbol{H}\partial\boldsymbol{H}} & \frac{\partial^2\bar{\Psi}}{\partial\boldsymbol{H}\partial J} & \frac{\partial^2\bar{\Psi}}{\partial\boldsymbol{H}\partial\theta} \\ \frac{\partial^2\bar{\Psi}}{\partial J\partial\boldsymbol{F}} & \frac{\partial^2\bar{\Psi}}{\partial J\partial\boldsymbol{H}} & \frac{\partial^2\bar{\Psi}}{\partial J\partial J} & \frac{\partial^2\bar{\Psi}}{\partial J\partial\theta} \\ \frac{\partial^2\bar{\Psi}}{\partial\theta\partial\boldsymbol{F}} & \frac{\partial^2\bar{\Psi}}{\partial\theta\partial\boldsymbol{H}} & \frac{\partial^2\bar{\Psi}}{\partial\theta\partial J} & \frac{\partial^2\bar{\Psi}}{\partial\theta\partial\theta} \end{bmatrix}. \tag{18}$$

The first term in $(17)_2$ represents the material part of the linearization, whereas the geometrical part is given via the second term. As shown in Bonet et al. [5], geometrical effects like buckling are solely expressed by the latter term.

3.3 Complementary energy

Assuming that the relationship between the work conjugate variables $\{\bar{\boldsymbol{F}}, \bar{\boldsymbol{H}}, J\}$ and $\{\bar{\boldsymbol{\Sigma}}_{\boldsymbol{F}}, \bar{\boldsymbol{\Sigma}}_{\boldsymbol{H}}, p\}$ is invertible, we define a complementary energy density function by means of the Legendre transformation

$$\bar{\Upsilon}(\bar{\boldsymbol{\Sigma}}_F, \bar{\boldsymbol{\Sigma}}_H, p, \theta) = \sup_{\bar{\boldsymbol{F}}, \bar{\boldsymbol{H}}, J} \{\bar{\boldsymbol{\Sigma}}_F : \bar{\boldsymbol{F}} + \bar{\boldsymbol{\Sigma}}_H : \bar{\boldsymbol{H}} + pJ - \bar{\Psi}(\bar{\boldsymbol{F}}, \bar{\boldsymbol{H}}, J, \theta)\}. \tag{19}$$

Regarding (10), this leads to

$$\begin{aligned}\bar{\Upsilon} &= \bar{\boldsymbol{\Sigma}}_F : \bar{\boldsymbol{F}}(\bar{\boldsymbol{\Sigma}}_F) + \bar{\boldsymbol{\Sigma}}_H : \bar{\boldsymbol{H}}(\bar{\boldsymbol{\Sigma}}_H) + pJ(p,\theta) - \Psi(\bar{\boldsymbol{F}}(\bar{\boldsymbol{\Sigma}}_F), \bar{\boldsymbol{H}}(\bar{\boldsymbol{\Sigma}}_H), J(p,\theta), \theta) \\ &= \frac{1}{4\alpha}\bar{\boldsymbol{\Sigma}}_F : \bar{\boldsymbol{\Sigma}}_F + \alpha d + \frac{2}{3\sqrt{3\beta}}(\bar{\boldsymbol{\Sigma}}_H : \bar{\boldsymbol{\Sigma}}_H)^{3/4} + \beta d^{3/2} + \frac{1}{2\kappa}p^2 + p + d\gamma(\theta - \theta_{\mathrm{ref}})p \\ &\quad - c\left(\theta - \theta_{\mathrm{ref}} - \theta \ln\left(\frac{\theta}{\theta_{\mathrm{ref}}}\right)\right) + \frac{\kappa}{2}(d\gamma(\theta - \theta_{\mathrm{ref}}))^2,\end{aligned} \tag{20}$$

where expressions for $\bar{\boldsymbol{F}}(\bar{\boldsymbol{\Sigma}}_F)$, $\bar{\boldsymbol{H}}(\bar{\boldsymbol{\Sigma}}_H)$ and $J(p,\theta)$ may deduced directly by inverting the relations obtained with (12) and (13).

4 VARIATIONAL FORMULATION

In the sense of a Hellinger-Reissner type variational principle, the original set of unknowns is extended by the stress fields. Accordingly, we define $\{\boldsymbol{\varphi}, \theta, \bar{\boldsymbol{\Sigma}}_F^*, \bar{\boldsymbol{\Sigma}}_H^*, p^*\}$ as extended set of independent variables[3]. Next, we perform two consecutive Legendre transformations

$$\begin{aligned}e(\boldsymbol{F}, \eta) &= \bar{\Psi}(\bar{\boldsymbol{F}}, \bar{\boldsymbol{H}}, J, \theta) + \theta\eta \\ &= -\bar{\Upsilon}(\bar{\boldsymbol{\Sigma}}_F^*, \bar{\boldsymbol{\Sigma}}_H^*, p^*, \theta) + \bar{\boldsymbol{\Sigma}}_F^* : \bar{\boldsymbol{F}} + \bar{\boldsymbol{\Sigma}}_H^* : \bar{\boldsymbol{H}} + p^* J + \theta\eta\end{aligned} \tag{21}$$

and state the global energy balance in terms of the complementary energy density function as follows

$$\begin{aligned}\int_{\mathcal{B}_0} \Bigg(&(\dot{\boldsymbol{\pi}} - \mathrm{Div}(\boldsymbol{P}) - \boldsymbol{B}) \cdot \dot{\boldsymbol{\varphi}} + \left(\bar{\boldsymbol{F}} - \frac{\partial \bar{\Upsilon}}{\partial \bar{\boldsymbol{\Sigma}}_F^*}\right) : \dot{\bar{\boldsymbol{\Sigma}}}_F^* + \left(\bar{\boldsymbol{H}} - \frac{\partial \bar{\Upsilon}}{\partial \bar{\boldsymbol{\Sigma}}_H^*}\right) : \dot{\bar{\boldsymbol{\Sigma}}}_H^* \\ &+ \left(J - \frac{\partial \bar{\Upsilon}}{\partial p^*}\right)\dot{p}^* + \left(\eta - \frac{\partial \bar{\Upsilon}}{\partial \theta}\right)\dot{\theta} + (\theta\dot{\eta} + \mathrm{Div}(\boldsymbol{Q}) - R)\Bigg)\,\mathrm{d}V = 0.\end{aligned} \tag{22}$$

Therein, $\boldsymbol{\pi} = \rho_0 \dot{\boldsymbol{\varphi}}$ denotes the linear momentum and $\boldsymbol{Q} = -\boldsymbol{F}^{-1}\boldsymbol{K}(\theta)\boldsymbol{F}^{-\mathrm{T}}$ is the Piola-Kirchhoff heat flux defined via the Duhamel's law. In what follows, we assume isotropic thermal material behavior and write the positive semi-definite thermal conductivity tensor as $\boldsymbol{K} = K_{\mathrm{ref}}(1 - \omega(\theta - \theta_{\mathrm{ref}}))\boldsymbol{I}$, where ω is a softening parameter. Moreover, $\boldsymbol{B}$ and R are prescribed body forces and heat sources, respectively.

Assuming that the rates of change in (22) can be chosen arbitrary, we apply suitable substitutions, namely $\dot{\boldsymbol{\varphi}} = \delta\boldsymbol{\varphi}$, $\dot{\bar{\boldsymbol{\Sigma}}}_F^* = \delta\bar{\boldsymbol{\Sigma}}_F$, $\dot{\bar{\boldsymbol{\Sigma}}}_H^* = \delta\bar{\boldsymbol{\Sigma}}_H$ and $\dot{p}^* = \delta p$ and obtain

$$\begin{aligned}G_\varphi &= \int_{\mathcal{B}_0} (\delta\boldsymbol{\varphi} \cdot \dot{\boldsymbol{\pi}} + \boldsymbol{P} : \nabla(\delta\boldsymbol{\varphi}))\mathrm{d}V - \int_{\mathcal{B}_0} \delta\boldsymbol{\varphi} \cdot \boldsymbol{B}\mathrm{d}V - \int_{\partial\mathcal{B}_0^T} \delta\boldsymbol{\varphi} \cdot \bar{\boldsymbol{T}}\mathrm{d}A = 0, \\ G_\theta &= \int_{\mathcal{B}_0} (\delta\theta\theta\dot{\eta} - \boldsymbol{Q} \cdot \nabla(\delta\theta))\mathrm{d}V - \int_{\mathcal{B}_0} \delta\theta R\mathrm{d}V - \int_{\partial\mathcal{B}_0^Q} \delta\theta\bar{Q}_{\mathrm{N}}\mathrm{d}A = 0,\end{aligned} \tag{23}$$

[3]In the following the star indicates independent variables.

supplemented by the geometric compatibility conditions

$$
\begin{aligned}
G_{\Sigma_F} &= \int_{\mathcal{B}_0} \left(\bar{\boldsymbol{F}} - \frac{\partial \bar{\Upsilon}}{\partial \bar{\boldsymbol{\Sigma}}_F^*} \right) : \delta \bar{\boldsymbol{\Sigma}}_F \mathrm{d}V = 0, \\
G_{\Sigma_H} &= \int_{\mathcal{B}_0} \left(\bar{\boldsymbol{H}} - \frac{\partial \bar{\Upsilon}}{\partial \bar{\boldsymbol{\Sigma}}_H^*} \right) : \delta \bar{\boldsymbol{\Sigma}}_H \mathrm{d}V = 0, \\
G_p &= \int_{\mathcal{B}_0} \left(J - \frac{\partial \bar{\Upsilon}}{\partial p^*} \right) \delta p \mathrm{d}V = 0.
\end{aligned}
\tag{24}
$$

Note that the thermal compatibility condition $\eta = \partial \bar{\Upsilon} / \partial \theta$ is satisfied locally.

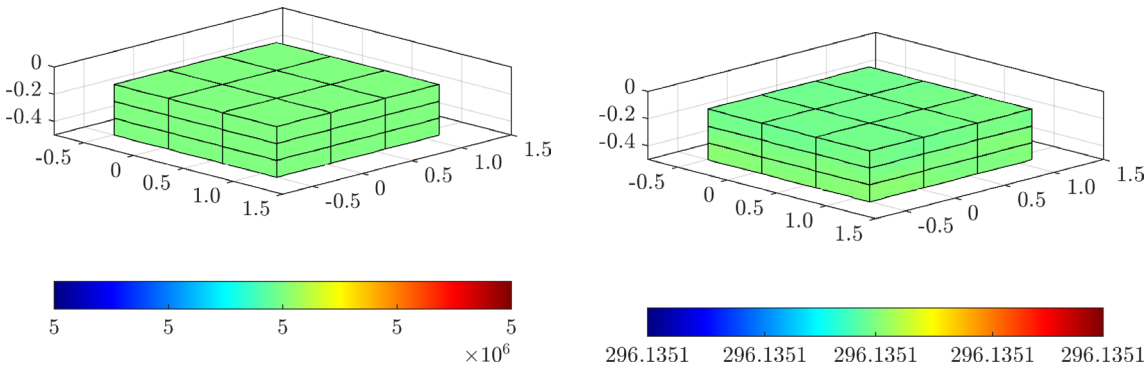

Figure 2: Patch test: Von Mises stress distribution (left) and temperature distribution (right) for the Hellinger-Reissner approach.

5 DISCRETE SETTING AND CONDENSATION

For the spatial discretization we apply a novel scheme which relies on developments suggested in Bonet et al. [5]. In particular, we utilize quadratic finite element based shape functions for the spatial discretization of the geometry and the temperature, whereas element wise linear interpolations are applied to the conjugate stresses such that we can apply a condensation procedure to eliminate this stress unknowns within the global system, see Dittmann [6] for more details. Furthermore, an implicit time integration scheme is applied to the semi-discrete coupled thermoelastic problem to obtain a set of non-linear algebraic equations to be solved via the Newton-Raphson iteration scheme. Eventually, the global system to be solved within each Newton-Raphson iteration reads

$$
\begin{bmatrix}
\boldsymbol{K}_{\varphi\varphi} & \boldsymbol{K}_{\varphi\theta} & \boldsymbol{K}_{\varphi\Sigma} \\
\boldsymbol{K}_{\theta\varphi} & \boldsymbol{K}_{\theta\theta} & \boldsymbol{K}_{\theta\Sigma} \\
\boldsymbol{K}_{\Sigma\varphi} & \boldsymbol{K}_{\Sigma\theta} & \boldsymbol{K}_{\Sigma\Sigma}
\end{bmatrix}
\begin{bmatrix}
\Delta \boldsymbol{q} \\
\Delta \boldsymbol{\Theta} \\
\Delta \boldsymbol{\Sigma}
\end{bmatrix}
=
\begin{bmatrix}
\boldsymbol{R}_{\varphi} \\
\boldsymbol{R}_{\theta} \\
\boldsymbol{R}_{\Sigma}
\end{bmatrix},
\tag{25}
$$

where $\Delta \boldsymbol{q} = [\Delta \boldsymbol{q}_1, \dots, \Delta \boldsymbol{q}_N]$ and $\Delta \boldsymbol{\Theta} = [\Delta \Theta_1, \dots, \Delta \Theta_N]$ represent the incremental variations of the nodal values of the displacement field and the temperature field at the current time step. Moreover, $\Delta \boldsymbol{\Sigma} = [\Delta \bar{\boldsymbol{\Sigma}}_{F,1}, \dots, \Delta \bar{\boldsymbol{\Sigma}}_{F,n}, \Delta \bar{\boldsymbol{\Sigma}}_{H,1}, \dots, \Delta \bar{\boldsymbol{\Sigma}}_{H,n}, \Delta p_1, \dots, \Delta p_n]$ summarizes the incremental variations of the element wise nodal values of the conjugate stress fields.

Solving (25) with respect to $\Delta \boldsymbol{\Sigma}$ yields

$$\Delta \boldsymbol{\Sigma} = \boldsymbol{K}_{\Sigma\Sigma}{}^{-1} (\boldsymbol{R}_\Sigma - \boldsymbol{K}_{\Sigma\varphi} \Delta \boldsymbol{q} - \boldsymbol{K}_{\Sigma\theta} \Delta \boldsymbol{\Theta}) \tag{26}$$

and insertion into (25) gives us the condensed system

$$\begin{bmatrix} \boldsymbol{K}_{\varphi\varphi} - \boldsymbol{K}_{\varphi\Sigma} \boldsymbol{K}_{\Sigma\Sigma}^{-1} \boldsymbol{K}_{\Sigma\varphi} & -\boldsymbol{K}_{\varphi\Sigma} \boldsymbol{K}_{\Sigma\Sigma}^{-1} \boldsymbol{K}_{\Sigma\theta} \\ -\boldsymbol{K}_{\theta\Sigma} \boldsymbol{K}_{\Sigma\Sigma}^{-1} \boldsymbol{K}_{\Sigma\varphi} & \boldsymbol{K}_{\theta\theta} - \boldsymbol{K}_{\theta\Sigma} \boldsymbol{K}_{\Sigma\Sigma}^{-1} \boldsymbol{K}_{\Sigma\theta} \end{bmatrix} \begin{bmatrix} \Delta \boldsymbol{q} \\ \Delta \boldsymbol{\Theta} \end{bmatrix} = \begin{bmatrix} \boldsymbol{R}_\varphi - \boldsymbol{K}_{\varphi\Sigma} \boldsymbol{K}_{\Sigma\Sigma}{}^{-1} \boldsymbol{R}_\Sigma \\ \boldsymbol{R}_\theta - \boldsymbol{K}_{\theta\Sigma} \boldsymbol{K}_{\Sigma\Sigma}{}^{-1} \boldsymbol{R}_\Sigma \end{bmatrix} \tag{27}$$

to be solved with respect to $\Delta \boldsymbol{q}$ and $\Delta \boldsymbol{\Theta}$. In a last step, (26) can be used to obtain the stress update $\Delta \boldsymbol{\Sigma}$.

6 NUMERICAL EXAMPLES

In this section we present quasi-static as well as transient examples to demonstrate the applicability and performance of the Hellinger-Reissner type variational principle for fully coupled non-linear thermoelasticity.

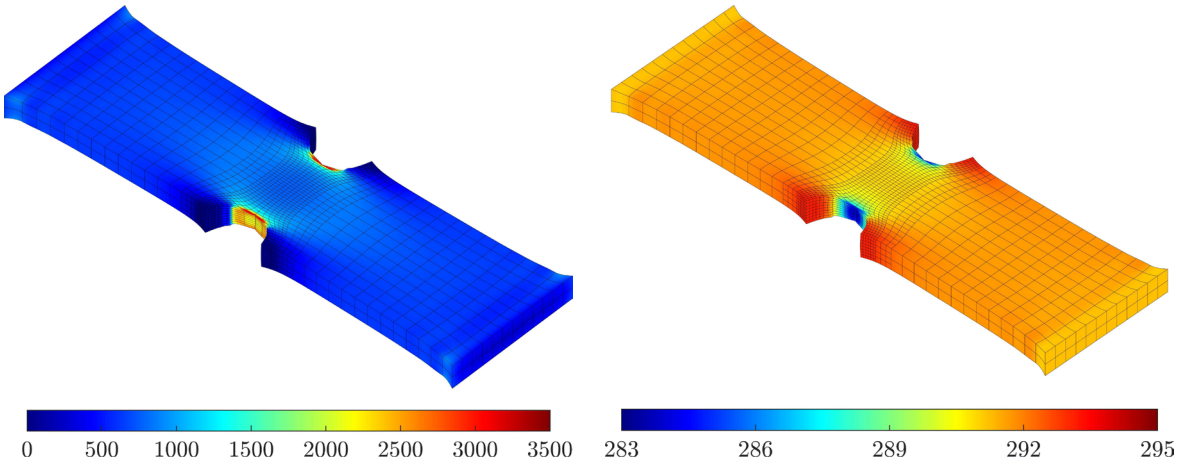

Figure 3: Notched bar: Von Mises stress distribution (left) and temperature distribution (right). Results for a displacement of $u = 3$ using the Hellinger-Reissner approach and the refined mesh are depicted.

6.1 Patch test

We start with a quasi-static patch test example to demonstrate the applicability of the Hellinger-Reissner approach. Here, we consider a block of size $0.5 \times 0.5 \times 0.5$ where

a uniform pressure load of $p = 5 \times 10^6$ is applied. The mechanical parameters for the Mooney-Rivlin material law are given by $\alpha = 15/13 \times 10^5$,$\beta = 10/13 \times 10^5$ and $\kappa = 25/3 \times 10^5$, which correspond to a Young's modulus of $E = 10^6$ and to a Poisson's ratio of $\nu = 0.3$. Moreover, the parameters for the thermal material behavior are specified by $c = 1830$, $\gamma = 0.22333$ and $K = K_{\text{ref}} = 0.55$. The initial temperature is set to 293.15.

Figure 2 shows nearly perfect and uniform results for the von Mises stress distribution and temperature distribution after loading. Therein, the color map for the von Mises stress distribution is in range of $5 \times 10^6 \pm 10^{-5}$, whereas a range wide of $\pm 2 \times 10^{-11}$ is used for the temperature distribution.

6.2 Notched bar

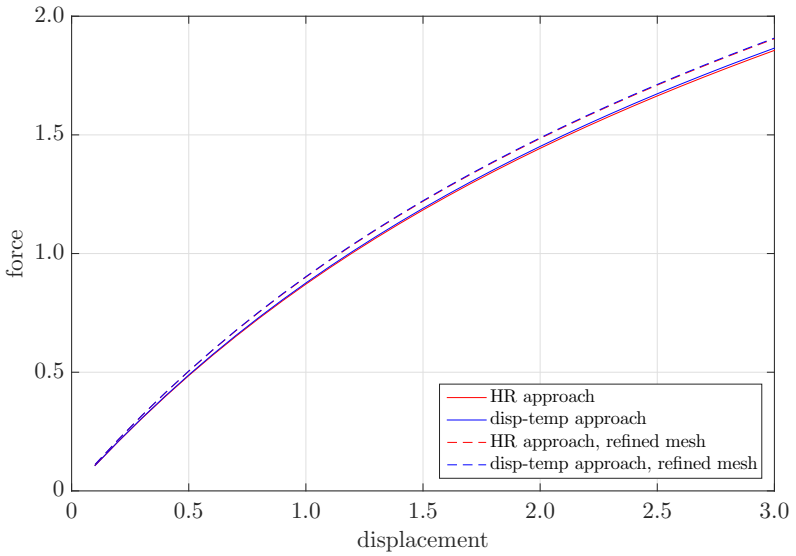

Figure 4: Notched bar: Load-deflection curves for the Hellinger-Reissner and the displacement-temperature based approach using the unrefined as well as the refined mesh.

Next, we consider a further quasi-static example to investigate the convergence of the Hellinger-Reissner approach in comparison to the displacement-temperature based approach. In particular, the ends of a notched rectangular bar of size $10 \times 4.8 \times 1$ are moved apart until an increase of length of approximately 60 percent is achieved, see Hesch & Betsch [9] and Holzapfel and Simo [2] for more details. The Mooney-Rivlin material parameters are given as follows, for the mechanical field the parameters take the values $\alpha = 1500/13$, $\beta = 1000/13$ and $\kappa = 2500/3$, whereas the setting for the thermal field reads $\theta_0 = 293.15$, $c = 1830$, $\gamma = 2.2333 \times 10^{-2}$ and $K = K_{\text{ref}} = 0.55$. The corresponding Young's modulus is given by $E = 1000$ and the Poisson's ratio by $\nu = 0.3$. For the numerical simulations, a mesh consisting of $32 \times 12 \times 2$ elements with 5936 thermal and

mechanical degrees of freedom is used as well as a locally refined mesh consisting of overall 5808 elements with in total 18982 degrees of freedom.

Figure 3 shows the von Mises stress distribution and temperature distribution of the deformed geometry. Eventually, the load-deflection curve is plotted in Figure 4 for the Hellinger-Reissner as well as the displacement-temperature based approach and both meshes. For both approaches nearly identical results are obtained.

6.3 L-shaped block

Eventually, we deal with a transient thermoelastic problem consisting a L-shape block of size $2.4 \times 1.2 \times 3.6$, see also Hesch & Betsch [9]. The L-shape is discretized by 1012 elements with overall 6792 thermal and mechanical degrees of freedom. Additionally, a local refinement is applied to the region where we expect peak stresses due to the notch of the L-shape. The Mooney-Rivlin material parameters are given by $\alpha = 114.9425$, $\beta = 57.4713$ and $\kappa = 3333.3333$, which correspond to a Young's modulus of $E = 1000$ and to a Poisson's ratio of $\nu = 0.45$. The mass density is set to $\rho = 0.5$. Moreover, the thermal material setting reads $\theta_0 = 293.15$, $c = 1830$, $\gamma = 2.2333 \cdot 10^{-4}$ and $K_{\text{ref}} = 0.15$ with $\omega = 0.004$. The body is subjected to a temporal traction load $p(t) = p_{\max} \sin(\pi t)$ during the time interval $t \in [0, 1]$ with a peak load of $p_{\max} = 60$. Afterwards, the body moves freely in space for the time interval $t \in [1, 5]$.

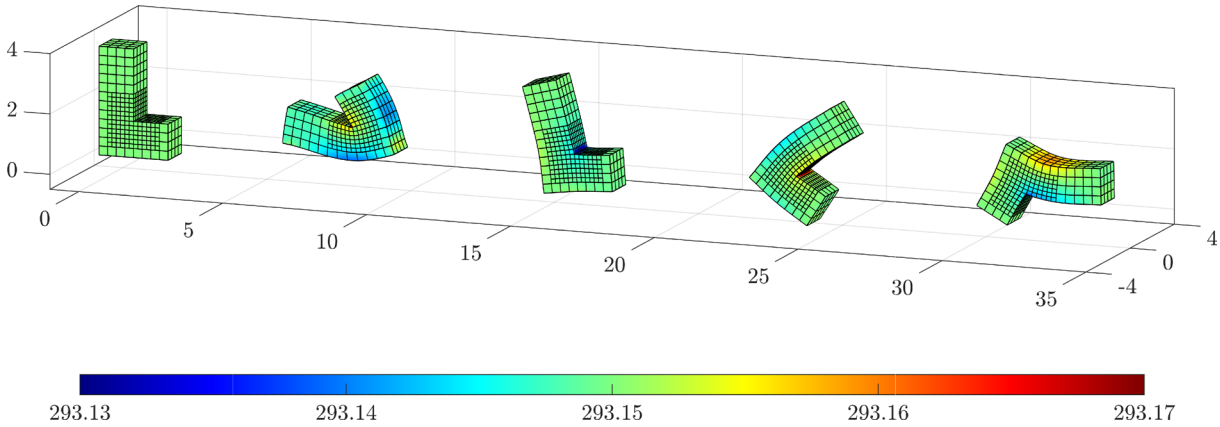

Figure 5: L-shaped block: Snapshots of the deformed configuration at times $t = [0, 0.46, 0.71, 0.96, 1.21]$.

The motion of the body and the associated temperature distribution is illustrated in Figure 5 using a time step size of $\Delta t = 0.01$. For both, the Hellinger-Reissner as well as the displacement-temperature based approach, the applied time step size used in combination with a standard mid-point type time integration scheme is sufficiently small to keep changes in the total energy small enough such that the convergence is not affected, see Figure 6. More advanced energy consistent time integration schemes for

non-linear thermoelasticity can be found in Hesch and Betsch [9] and Dittmann et al. [10]. Additionally, the angular momentum is plotted over time in Figure 6. As expected, the components of angular momentum remain preserved for the considered problem and time integration scheme.

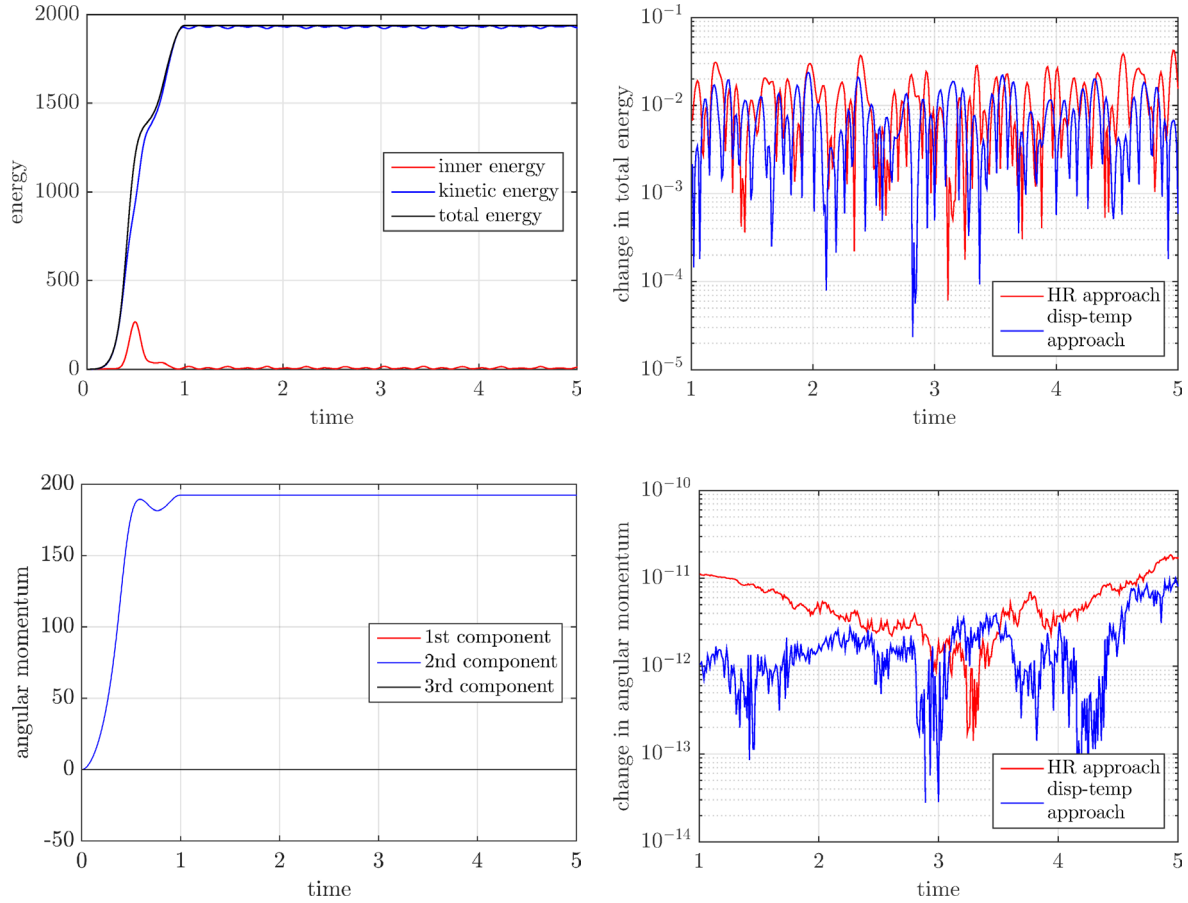

Figure 6: L-shaped block: Energy and angular momentum plotted over time.

7 CONCLUSIONS

In the present work a novel formulation based on a mixed Hellinger-Reissner type variational principle has been applied to large strain thermomechanical coupled problems. A series of computational simulations has demonstrated the applicability and performance of this approach in comparison to standard displacement-temperature based formulations. The numerical results has been shown to be in accordance with the displacement based solution in terms of accuracy and convergence. Thus, the proposed Hellinger-Reissner type variational principle represents a novel and alternative formulation, which provides high

flexibility and simplicity for the modeling of multi-field problems due to the additional primal fields, see also Hesch et al. [7]. Moreover, the construction of the discretization allows for the application of a condensation procedure such that no significant increase of computational effort has been emerged.

REFERENCES

[1] Reese, S. and Govindjee, S. Theoretical and Numerical Aspects in the Thermo-Viscoelastic Material Behaviour of Rubber-Like Polymers. *Mechanics of Time-Dependent Materials* (1997) **1**(4):357–396.

[2] Holzapfel, G.A. and Simo, J.C. Entropy elasticity of isotropic rubber-like solids at finite strains. *Computer Methods in Applied Mechanics and Engineering* (1996) **132**(1):17–44.

[3] Miehe, C. Entropic thermoelasticity at finite strains. Aspects of the formulation and numerical implementation. *Computer Methods in Applied Mechanics and Engineering* (1995) **120**(3–4):243–269.

[4] Ball, J. Convexity conditions and existence theorems in nonlinear elasticity. *Archive for Rational Mechanics and Analysis* (1976) **63**:337–403.

[5] Bonet, J., Gil, A.J. and Ortigosa, R. A computational framework for polyconvex large strain elasticity. *Computer Methods in Applied Mechanics and Engineering.* (2015) **283**:1061–1094.

[6] Dittmann, M. *Isogeometric analysis and hierarchical refinement for multi-field contact problems*. PhD thesis (2017) doi: 10.5445/KSP/1000063914.

[7] Hesch, C. and Gil, A.J. and Ortigosa, R. and Dittmann, M. and Bilgen, C. and Betsch, P. and Franke, M. and Janz, A. and Weinberg, K. A framework for polyconvex large strain phase-field methods to fracture. *Computer Methods in Applied Mechanics and Engineering* (2017) **317**:649–683.

[8] de Boer, R. *Vektor- und Tensorrechnung für Ingenieure*. Springer-Verlag Berlin, Heidelberg, (1982).

[9] Hesch, C. and Betsch, P. Energy-momentum consistent algorithms for dynamic thermomechanical problems—Application to mortar domain decomposition problems. *International Journal for Numerical Methods in Engineering* (2011) **86**(11):1277–1302.

[10] Dittmann, M., Franke, M., Temizer, İ. and Hesch, C. Isogeometric Analysis and thermomechanical Mortar contact problems. *Computer Methods in Applied Mechanics and Engineering* (2014) **274**:192–212.

VII International Conference on Computational Methods for Coupled Problems in Science and Engineering
COUPLED PROBLEMS 2017
M. Papadrakakis, E. Oñate and B. Schrefler (Eds)

NUMERICAL SIMULATION OF SHOCK-TUBE PISTON PROBLEMS WITH ADAPTIVE, ANISOTROPIC MESHES

BARBARA RE*, CÉCILE DOBRZYNSKI† AND ALBERTO GUARDONE*

*Department of Aerospace Science & Technology
Politecnico di Milano, Via La Masa 34, 20146 Milano, Italy
e-mail: alberto.guardone@polimi.it, web page: crealab.polimi.it

†Bordeaux INP, Enseirb-Matmca
Institut de Mathmatiques de Bordeaux
200 av de la vieille Tour, 33405 Talence cedex, France

Key words: Finite-Volume schemes, compressible inviscid flows, shock-tube, anisotropic mesh adaptation

Abstract. Numerical simulations of the flow generated inside a shock-tube by the motion of a magnetically- driven piston are carried out using a novel finite volume adaptive scheme for dynamic meshes. Local modifications of the grid topology, including the addition or deletion of grid nodes are interpreted as a series of fictitious, continuous deformations of the mesh, thus allowing mesh adaptation to be described within the Arbitrary Lagrangian Eulerian (ALE) framework. The local deformations of the mesh elements are taken into account in a conservative fashion by adding additional fictitious fluxes to the ALE formulation of the governing equations for inviscid compressible flows. The solution on the new grid is recovered without any explicit interpolation. Therefore, the method automatically guarantees the solution to be conservative by construction. This peculiar capability is here exploited in preliminary Fluid-Structure Interaction (FSI) computations of compressible shocked flows with rigid, moving bodies. Anisotropic mesh adaptation is used to improve the computational efficiency. The solution compares fairly well with the analytical one-dimensional model.

1 INTRODUCTION

In unsteady numerical simulations, it is often required to deform the grid to comply with the motion experienced by the boundary of the computational domain. In particular, if the interaction between the flow and a deformable structure is investigated as in Fluid-Structure Interaction (FSI) problems, the capability to accurately accomplish this task becomes of primary importance [1, 2, 3].

To solve flow governing equations on a moving or deforming mesh, the formulation of the governing equations has to be modified in some way to account for the relative motion of the grid with respect to the fluid. Arbitrary Lagrangian-Eulerian (ALE) approach is widely used to this aim, since it allows to solve the equations on control volumes that can move and deform independently from the local fluid velocity [4, 5]. A second aspect that should be taken into consideration concerns the movement of the interior mesh points, consequent to the motion prescribed on the boundaries. Small deformations can be easily tackled by means of dynamic grid methods [6] in which the grid connectivity is kept fixed and the grid nodes are simply moved, in order to distribute the boundary deformation among internal grid elements according on their shape and volume. However, the fixed-topology constraint limits the displacement that the mesh is capable to handle without generating entangled or poor-quality elements that may jeopardize the numerical solution of the flow problem.

Mesh adaptation techniques can be exploited along with dynamic grid methods to deal with large boundary displacement [7, 8]. When the mesh quality falls below a certain threshold or null-volume elements appear, the computational grid is modified by local connectivity changes, such as edge swapping, node insertion or deletion [9, 10, 11, 12]. Then, the solution is transfered from the old grid to the adapted one, usually by means of an interpolation step. Unfortunately, this operation may prevent the solution accuracy and undermine the stability and conservativeness of the numerical scheme.

A different approach has been proposed by Guardone and co-workers [13, 14] that exploits mesh adaptation capabilities within the ALE framework, so that it is able to cope with large deformations and at the same time avoids any explicit interpolation step. The volume changes due to mesh adaptation are described as a series of fictitious continuous deformations of the finite volumes that compose the computational domain and they are included into the governing equations as additional ALE fluxes. In this ways, the properties of the fixed-connectivity ALE scheme, such as stability and conservativeness, are preserved also over adaptive grids.

In the present paper, the bi-dimensional version of this scheme is exploited to compute the flow field generated in a shock-tube by a magnetically driven piston. The size, the shape and the orientation of the grid elements is controlled through anisotropic mesh adaptation [15, 16, 17]. Indeed, the mesh is locally modified according to a metric tensor field based on the Hessian of the numerical solution. Due to the one-dimensional character of the flow field, the possibility of prescribing different grid spacing in different direction is crucial and, with respect to isotropic adaptation, it leads to a lower number of grid nodes.

2 NUMERICAL METHOD

The ALE formulation of the Euler equations for a control volume $\mathcal{C}(t)$ moving at velocity $\boldsymbol{v}(\boldsymbol{x}, t)$ reads

$$\frac{d}{dt}\int_{\mathcal{C}(t)} \mathsf{u}\, d\boldsymbol{x} + \oint_{\partial\mathcal{C}(t)} [\mathbf{f}(\mathsf{u}) - \mathsf{u}\boldsymbol{v}] \cdot \boldsymbol{n}\, ds = 0\,, \qquad \text{with} \quad \mathbf{f}(\mathsf{u}) = \begin{bmatrix} \boldsymbol{m} \\ \boldsymbol{m}\otimes\boldsymbol{m}/\rho + P(\mathsf{u})\mathbb{I}^3 \\ \left[E^T + P(\mathsf{u})\right]\boldsymbol{m}/\rho \end{bmatrix} \tag{1}$$

where $\mathsf{u} = [\rho,\, \boldsymbol{m},\, E^T]^{\mathrm{T}}$ is the vector of conservative variables (density, momentum density, and total energy density, respectively), $\mathbf{f}(\mathsf{u})$ is the inviscid flux function, $\boldsymbol{n}(\boldsymbol{x}, t)$ denotes the outward unit vector normal to the cell boundary $\partial\mathcal{C}$, P is the pressure function (which depends on the adopted thermodynamic models) and $\mathbb{I}^2$ is the 2×2 identity matrix. Suitable initial and boundary conditions have be to specified to complement the previous equation [18].

When solving flow equations on a moving computational domain, the evaluation of the geometric quantities connected to the grid movement is crucial. In this regard, it is usually recognized that the fulfillment of the so-called Geometric Conservation Law (GCL) positively affects the stability and the accuracy of the numerical scheme for dynamic grids and allows larger time steps with respect to non-compliant schemes [19, 20, 22, 21]. For the governing equations (1), the GCL can be expressed as

$$\frac{d}{dt}\int_{\mathcal{C}(t)} d\boldsymbol{x} = \oint_{\partial\mathcal{C}(t)} \boldsymbol{v}\cdot\boldsymbol{n}\, ds\,. \tag{2}$$

To spatially discretize Eq. (1), the computational domain Ω is split in N_V non-overlapping finite volumes $\mathcal{C}_i$ and a suitable approximation ϕ is used to integrate the flux that each finite volume exchanges with its neighbors. In the present work, a high-resolution scheme based on the Total Variation Diminishing (TVD) approach [23] is used for the integrated numerical domain fluxes ϕ, by exploiting a flux limiter to control the switch from the centered second-order approximation scheme to the Roe scheme near discontinuities. If node i lies on the boundary, a similar approximation ϕ^∂ is introduced also for the integrated numerical flux across the portion of the cell interface that lies on the boundary, i.e. $\partial\mathcal{C}_{i,\partial} = \partial\mathcal{C}_i \cap \partial\Omega$. The spatially discrete Euler equations read

$$\frac{d}{dt}\left[V_i \mathsf{u}_i\right] = \sum_{k\in\mathcal{K}_{i,\neq}} \phi(\mathsf{u}_i, \mathsf{u}_k, \nu_{ik}, \boldsymbol{\eta}_{ik}) + \phi^\partial(\mathsf{u}_i, \nu_i, \boldsymbol{\xi}_i), \qquad i \in \mathcal{K} \tag{3}$$

where u_i is the average value of u over $\mathcal{C}_i$ and $\mathcal{K}$ is set of the grid nodes. We have defined also the set of the neighboring nodes of the finite volume i as $\mathcal{K}_{i,\neq} = \{k \in \mathcal{K} \mid \partial\mathcal{C}_{ik} \neq \emptyset\}$, where $\partial\mathcal{C}_{ik} = \partial\mathcal{C}_i \cap \partial\mathcal{C}_k$ indicates the portion of the cell interface shared by the volumes i and k. Moreover, we have introduced the integrated normals $\boldsymbol{\eta}_{ik}$, $\boldsymbol{\xi}_i$ and the interface velocities ν_{ik} and ν_i, defined as

$$\boldsymbol{\eta}_{ik} = \int_{\partial\mathcal{C}_{ik}} \boldsymbol{n}_i\,, \qquad \boldsymbol{\xi}_i = \int_{\partial\mathcal{C}_{i,\partial}} \boldsymbol{n}_i\,, \qquad \nu_{ik} = \int_{\partial\mathcal{C}_{ik}} \boldsymbol{v}\cdot\boldsymbol{n}_i\,, \qquad \nu_i = \int_{\partial\mathcal{C}_{i,\partial}} \boldsymbol{v}\cdot\boldsymbol{n}_i\,. \tag{4}$$

Equation (3) is then integrated in time by means of a Backward Euler scheme, namely

$$\frac{V_i^{n+1}\mathsf{u}_i^{n+1} - V_i^n \mathsf{u}_i^n}{\Delta t} = \sum_{k \in \mathcal{K}_{i,\neq}} \phi(\mathsf{u}_i, \mathsf{u}_k, \nu_{ik}, \boldsymbol{\eta}_{ik})^{n+1} + \phi^{\partial}(\mathsf{u}_i, \nu_i, \boldsymbol{\xi}_i)^{n+1} \,. \tag{5}$$

The previous non-linear system is solved through a pseudo-time step technique [24], in which, according to the defect-correction approach [25], a modified Newton method is used to solve the linear system at each pseudo time step.

Similarly, we obtain the Discrete Geometric Conservation Law (DGCL) by applying the same spatial and temporal discretization to Eq. (2):

$$\frac{V_i^{n+1} - V_i^n}{\Delta t} = \sum_{k \in \mathcal{K}_{i,\neq}} \int_{\partial \mathcal{C}_{ik}} \boldsymbol{v} \cdot \boldsymbol{n}_i + \int_{\partial \mathcal{C}_{i,\partial}} \boldsymbol{v} \cdot \boldsymbol{n}_i = \sum_{k \in \mathcal{K}_{i,\neq}} \nu_{ik}(t) + \nu_i(t) \tag{6}$$

The constraint expressed by the previous relation can be enforced by splitting the contributions pertaining to the domain and to the boundary, as

$$\Delta V_{ik}^{n+1} = \Delta t \, \nu_{ik}^{n+1} \qquad \text{and} \qquad \Delta V_{i,\partial}^{n+1} = \Delta t \, \nu_i^{n+1} \,, \tag{7}$$

where ΔV_{ik}^{n+1} and $\Delta V_{i,\partial}^{n+1}$ are the volume swept during the interval from t^n to t^{n+1} by the interface portions $\partial \mathcal{C}_{ik}$ and $\partial \mathcal{C}_{i,\partial}$, respectively. Since we consider known the grid motion, relations (7) allow to easily compute GCL-compliant interface velocities from the positions of the grid nodes at the beginning and at the end of the time step if the finite volumes experience a continuous deformation.

In [13, 14], it has been described how it is possible to compute the swept volumes ΔV_{ik}^{n+1} and $\Delta V_{i,\partial}^{n+1}$ also if the local connectivity changes. A three-steps series of fictitious collapse and expansion operations can be exploited to describe node insertion, node deletion and edge swap as a series of continuous deformations of the finite volumes involved in the connectivity change. In particular, the grid is modified when all involved cell interfaces have a null area, so that this operation does not affect the fulfillment of the DGCL. In this way, we are able to compute the interface velocities through Eqs. (7) also when local grid topology is modified and to include the volume changes due to mesh adaptation into the standard ALE scheme, i.e Eq. (1), without undermining the fixed-connectivity properties and enforcing conservativeness. The main points of this procedure are described in Fig. 1 for the node insertion through edge split. A similar procedure can be applied also to different adaptation techniques [14, 26].

2.1 Anisotropic mesh adaptation

Mesh adaptation is widely used in CFD to cope with large boundary displacements but also to increase solution accuracy, provided that a proper estimation of the solution error is available. Indeed, thanks to a posteriori analysis, the error due to the numerical approximation can be related to the grid spacing and, in particular, an upper-bound of

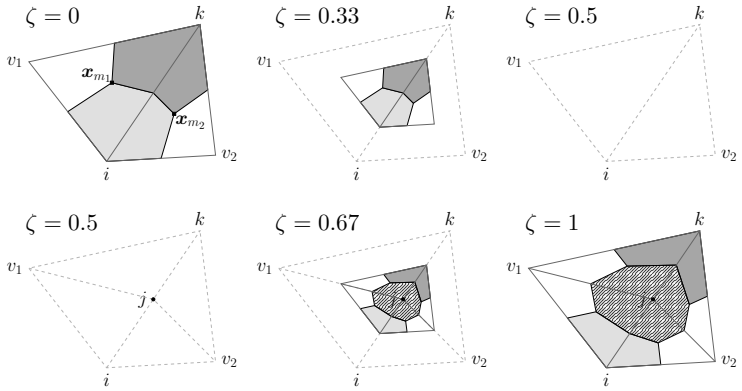

Figure 1: Three-steps procedure applied to the split of edge e_{ik}. The non-dimensional time $0 \leq \zeta \leq 1$ is used to describe the different fictitious steps. The dashed grey lines show the grid connectivity in the original/final configuration ($\zeta = 0/\zeta = 1$), while the portions of the finite volumes associated to i, k and j are shown with light grey □, dark grey ■ and the pattern ▨ , respectively. The label $\boldsymbol{x}_{m_i}$ indicates the barycenter of the element m_i. In the first row the collapse phase $0 < \zeta < 0.5$ is depicted: the quadrilateral i-k-v_1-v_2, composed by the elements that share the edge e_{ik} at $\zeta = 0$, is collapsed over its mid-point. When it reaches a null area, the connectivity is changed ($\zeta = 0.5$): the new point j is inserted, the edge e_{ik} is split into two edges (i-j and k-j) and two new edges are created to connect j to v_1 and v_2. The second row displays the expansion procedure $0.5 < \zeta < 1$: the nodes i, k, v_1, v_2 return to their original positions to reach the final configuration (at $\zeta = 1$).

the interpolation error can be built on the basis of the Hessian matrix $\mathcal{H}_u$ of a certain solution variable u [27, 17].

The target grid spacing can be described through a suitable metric field $\mathcal{M}(\boldsymbol{x})$ that prescribes the size, the shape and the orientation of the mesh elements [28, 29, 30]. For a bi-dimensional domain Ω, the metric field $\mathcal{M}(\boldsymbol{x})$ is a field of symmetric positive matrices of $\mathbb{R}^{2\times 2}$, that defines a Riemannian structure over Ω [31]. The length of a vector $\boldsymbol{w}$ in terms of the anisotropic map $\mathcal{M}$ is given by

$$\|\boldsymbol{w}\|_{\mathcal{M}} = \sqrt{\boldsymbol{w}^{\mathrm{T}} \mathcal{M} \boldsymbol{w}} \, . \tag{8}$$

and, given a point O, the locus of the points P such that $\|P - O\|_{\mathcal{M}} = h$ is represented by an ellipsoid, centered at O. The shape of the element is associated to the lengths of the semi-axes of the ellipse, which are defined by the eigenvalues of $\mathcal{M}$, while the orientation (of the ellipse and of the element) is defined by its eigenvectors.

Following [17], it is possible to control the error over the mesh by defining at each grid point $\boldsymbol{x}_i$ the metric map $\mathcal{M} = R\widetilde{\Lambda}L$ with

$$\widetilde{\Lambda} = \mathsf{diag}\left\{ \min\left(\max\left(\frac{c|\lambda_p|}{\epsilon}, \frac{1}{\ell^2_{\max}} \right), \frac{1}{\ell^2_{\min}} \right) \right\} ,$$

where λ_p, R and L are respectively the p-th eigenvalue, the matrix of the right and of the left eigenvectors of the Hessian matrix $\mathcal{H}_u(\boldsymbol{x}_i)$, ϵ is a given threshold for the maximum

tolerate error, c is a constant that for bi-dimensional problems is 2/9 and $\ell_{\max}/\ell_{\min}$ are the maximum/minimum edge length. Then, mesh adaptation techniques can be used to equi-distribute this error over the mesh by locally modifying the element size [27, 17], since according to the equi-distribution principle, the minimum solution error is achieved over a *unit mesh*, i.e. a mesh that has all edges of unit length according to Relation (8) [28].

3 Computational procedure

In the present work, the external re-mesher library is exploited to efficiently modify the computational grid [32]. Figure 2 outlines the whole computational procedure for the unsteady simulations of the magnetically-induced piston motion. At the beginning of the time step $t^n \leq t \leq t^{n+1}$, the grid and the solution are respectively label as $\mathcal{K}^n$ and $\mathsf{u}(t^n, \mathcal{K}^n)$. Then, the following operations are performed:

1. Mesh deformation: the position of the piston is computed given the flow pressure and the prescribed force $\mathcal{F}_P(t^n)$, the internal grid nodes are displaced to cope with the boundary movement, as described in [26]. The new grid is labeled $\mathcal{K}^{n+}$.
2. Prediction: the solution at next time step, over the grid $\mathcal{K}^{n+}$, is computed. This step prevents a delay between the solution-based mesh adaptation and the actual geometry.
3. Error estimation: the metric map $\mathcal{M}$ is computed on the basis of the new solution $\mathsf{u}^{n+} = \mathsf{u}(t^{n+1}, \mathcal{K}^{n+})$.
4. Mesh adaptation: the grid $\mathcal{K}^{n+}$ and the metric map $\mathcal{M}(\mathsf{u}^{n+})$ are passed as inputs to the library mmg2d, which locally adapt the grid.
5. Mesh update: the flow solver receives from mmg2d all performed local modifications $\Delta\mathcal{K}^{n+}$, that are needed to update the finite volumes discretization and to compute the swept volumes ΔV by means of the three-steps procedure [14].
6. Computation of the solution u^{n+1} on the grid $\mathcal{K}^{n+1}$, using as initial guess u^{n+}.

4 RESULTS

The described method is exploited to simulate the motion of a magnetically-driven piston, controlled by a prescribed force. First of all, we have estimated this force by imposing an harmonic motion to the piston and by evaluating the generated pressure field. Hence, a preliminary simulation is carried out in which we enforce the position of the piston as $x(t) = x_0 + A\cos(2\pi\, f\, t)$, with an amplitude $A = -0.5$ m and a frequency $f = 30$ Hz. The maximum speed reached by the piston during this motion is $V_{P_{\max}} = 94.25$ m/s, which in the case of an impulsively start would generate a shock wave traveling with a Mach number $M_s = 1.18$. In the present simulation, the piston is not started impulsively, so no shock waves are generated at the beginning of the motion.

The length and the height of the piston are $L_P = 0.1$ m and $h_P = 0.05$ m, respectively, and initially it is filled with still air at $T_0 = 288.15$ K and $P_0 = 1$ atm. The aim of this preliminary simulation is to reproduce an infinite-length shock-tube, so the computational domain consists in 20 m-long tube, with open ends at both sides, and the piston is placed

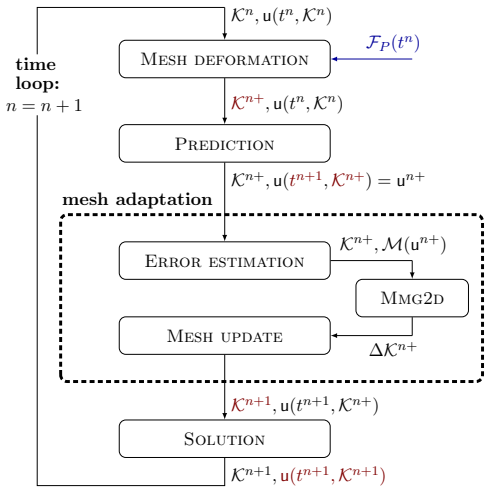

Figure 2: Adaptive computational procedure for unsteady problems. The grid $\mathcal{K}^{n+}$ complies with the boundary displacement at t^{n+1} and, over it, the solution u^{n+} is computed in the *Prediction* step. The metric field $\mathcal{M}(\mathsf{u}^{n+})$ is passed as input to mmg2d which communicates to the flow solver all performed modifications $\Delta\mathcal{K}^{n+}$, so that it can compute the swept volumes ΔV due to mesh adaptation. Finally, the solution at t^{n+1} over the adapted grid $\mathcal{K}^{n+1}$ is computed.

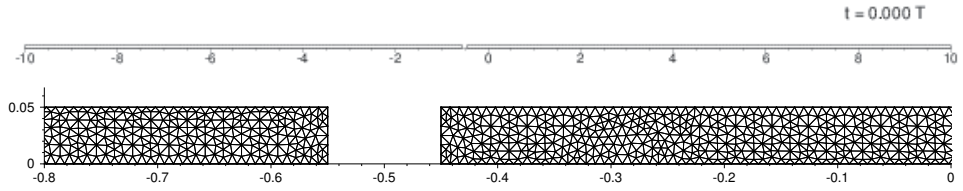

Figure 3: Computational grid for preliminary simulation of the piston subject to an harmonic motion. Top: whole domain; Bottom: detail of the mesh near the piston, with at the beginning of the simulation is centered at $x = -0.5$ m.

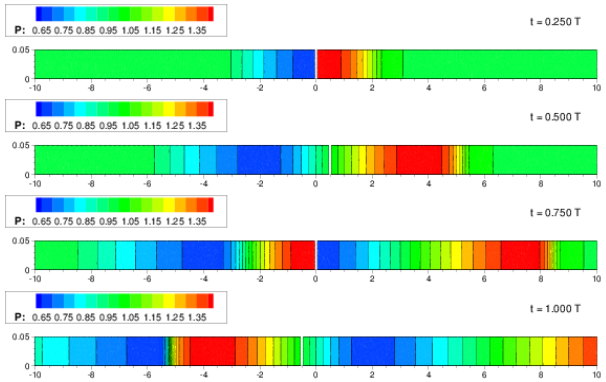

Figure 4: Pressure contour plots of the piston during the first period of the harmonic motion. The pressure is made dimensionless with respect to the initial value P_0. A different aspect ratio on the x and y axis is used to make the results clearer.

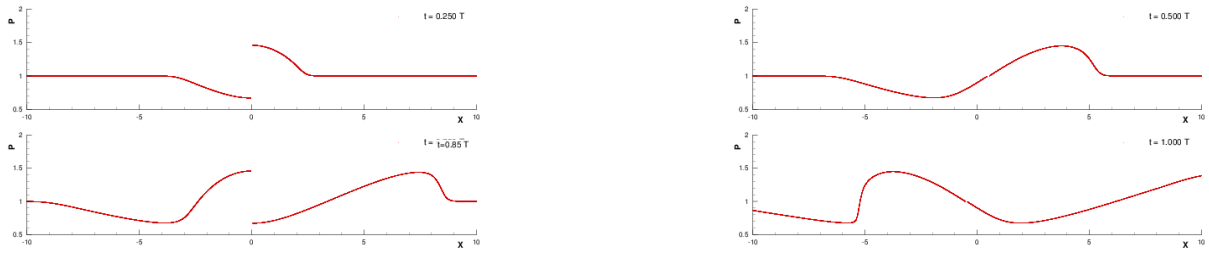

Figure 5: Pressure at all grid points during the first period of the harmonic motion of the piston. The pressure is made dimensionless with respect to the initial value P_0.

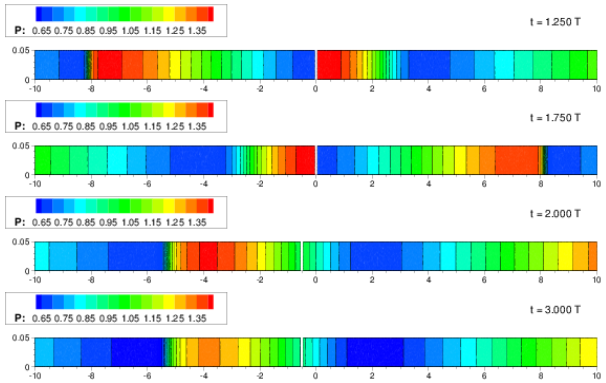

Figure 6: Pressure contour plots of the piston during the second and third period of the harmonic motion. The pressure is made dimensionless with respect to the initial value P_0. A different aspect ratio on the x and y axis is used to make the results clearer.

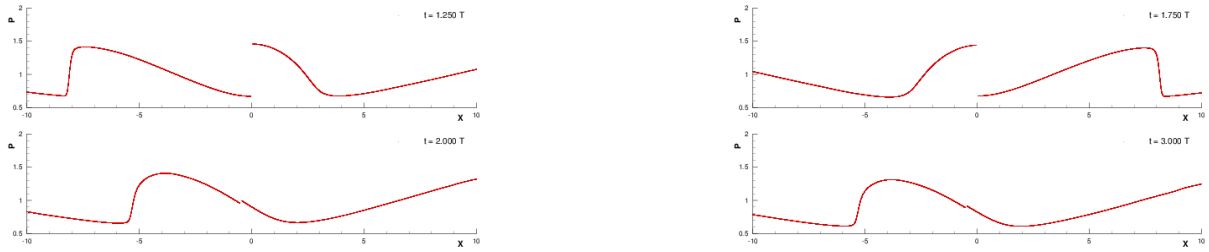

Figure 7: Pressure at all grid points during the second and third period of the harmonic motion of the piston. The pressure is made dimensionless with respect to the initial value P_0.

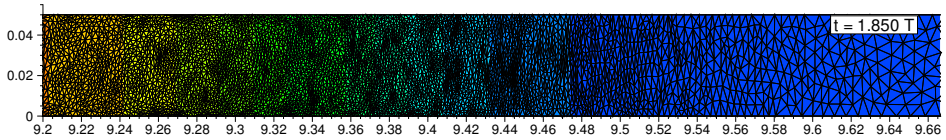

Figure 8: Detail of the adapted mesh during the preliminary simulation of the piston with harmonic motion.

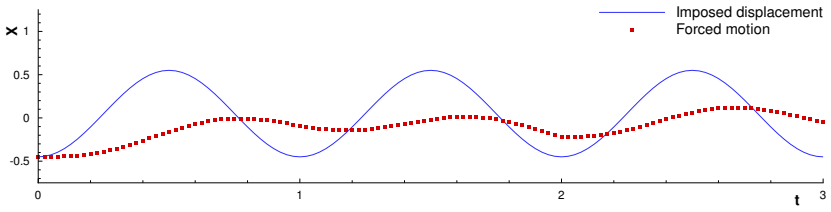

Figure 9: Position of the piston during the harmonic motion (Imposed displacement) and the final simulation in which the force is prescribed (Force motion).

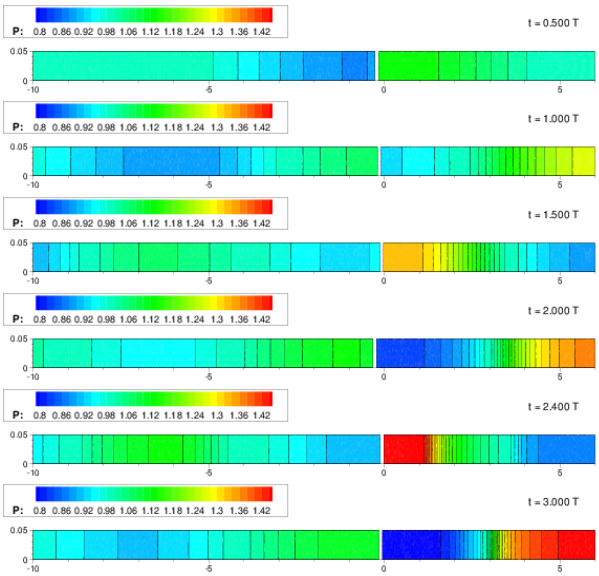

Figure 10: Pressure contour plots of the simulation of the piston with a prescribed force. The pressure is made dimensionless with respect to the initial value P_0. A different aspect ratio on the x and y axis is used to make the results clearer.

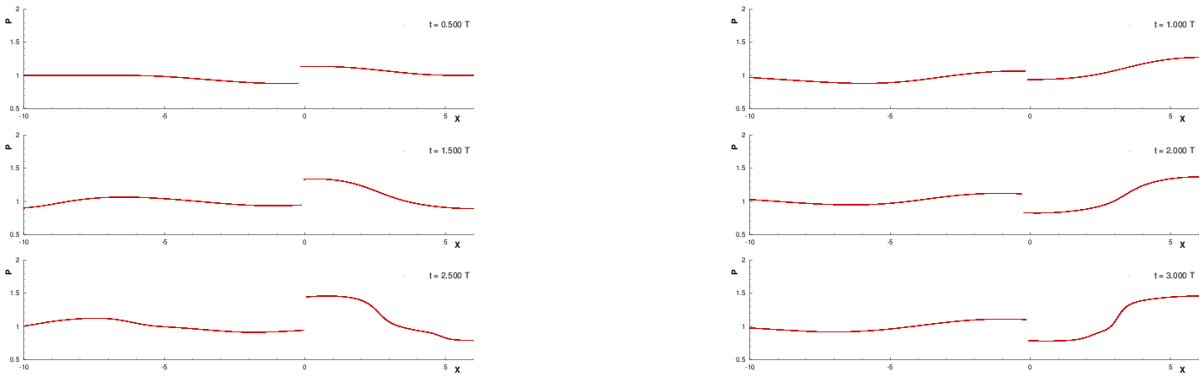

Figure 11: Pressure at all grid points during the simulation of the piston with a prescribed force. The pressure is made dimensionless with respect to the initial value P_0.

in the middle of the tube. The initial grid, shown in Fig. 3, is composed by 20 863 nodes and 36 724 triangles. Each period T is divided in 400 time steps, so that the Courant number is approximately equal to the unity on the initial grid, characterized by a spacing of $\Delta x = 0.008$ m.

When the motion starts, expansive and compressive waves are generated at the opposite sides of the piston and they travel towards the open ends. Initially the fluid on the right side (positive x-direction) is compressed and the compressive waves generated during the time interval $0 < t < 0.25T$ are getting stronger and faster. However, since the piston velocity in this interval is quite small, no shock waves are generated. In the same interval, on the left side of the shock-tube, an expansion fan originates. For time $0.25T < t < 0.5T$, the piston speed is reduced, so that an expansion takes place on the right part and a compression on the left part. These phenomena continue also in the next quarter of period, although the direction of the piston is now towards negative x. At $t = 0.75T$, the velocity of the harmonic motion is maximum in magnitude and it decreases leading to an expansion on the left side and a compression on the right side. The compressive waves generated on the left side of the piston coalesce together generating a shock far from the piston side at about $t > 1.15T$. Figs 4 and 5 show the pressure field during this first period.

In the second period, the flow field is different from the first one, since the fluid in the piston has now a non-null velocity. In particular, a shock wave is generated also on the right side approximately at $t = 1.5T$, when the compressive waves generated at $0.75T < t < T$ coalesce. It should be remarked that, after the shock, the total pressure is lower, even if the shock intensity is quite small. Hence, also the flow field in the third period is slightly different, despite qualitatively the same phenomena take place. Figs 6 and 7 display the pressure field at some times for $T < t < 2T$. At the end of this preliminary simulation, the force due to the pressure acting on the sides of the piston is computed. During this simulation, the Hessian of the pressure is used to increase solution accuracy by means of anisotropic adaptation. Fig. 8 illustrates a detail of the mesh at $t = 1.85T$ near the shock propagating in the right part of the shock-tube.

The force computed in the preliminary simulation is now used to move the piston. In this new simulation, the shock-tube is represented by a wall on the right end and an open-end at left. Assuming a mass $m = 1.0$ kg, at each time step the velocity (in the x direction) of the piston is computed as

$$V_P^{n+1} = V_P^n + \left(\mathcal{F}_P^n + \int_{\partial\Omega_P} P(\mathsf{u}^n)\, \boldsymbol{n}_x \, dS \right) / \left(m\, \Delta t \right) , \tag{9}$$

where $\mathcal{F}_P$ is the force used to move the piston, $P(\mathsf{u})$ is the pressure and $\boldsymbol{n}_x$ is the x-component of the normal to the piston surface, labeled $\partial\Omega_P$.

As expected, the motion prescribed in this second simulation is different, as shown in Fig. 9 because of the different flow fields. Moreover, the compressive waves generated by the piston motion are reflected back from the wall at approximately $t = 0.65T$. The

interaction of the reflected waves with the approaching ones modifies significantly the pressure field, which reaches also a higher maximum value, as shown in Figs. 10 and 11.

5 CONCLUSIONS

A novel adaptive scheme for the finite volume discretization of the Euler equations for unsteady bi-dimensional flow problems is used to exploit anisotropic mesh adaptation within the Arbitrary Lagrangian Eulerian framework, so that also the Geometric Conservation Law is automatically fulfilled and no interpolation of the solution is required between different grids. These features make this technique well suited to tackle Fluid Structure Interaction problems in which the conservativeness of the numerical scheme plays a crucial role.

The described numerical method is used to simulate a magnetically-driven piston in a shock-tube, subject to the prescribed force law that, in an open-ends tube corresponds to an harmonic motion. All significant flow features are correctly captured thanks to mesh adaptation.

REFERENCES

[1] M. Lesoinne, C. Farhat, Geometric conservation laws for flow problems with moving boundaries and deformable meshes, and their impact on aeroelastic computations, *Comput. Methods Appl. Mech. Engrg.* (1996) **134**:71–90.

[2] C. Farhat, M. Lesoinne, P. LeTallec, Load and motion transfer algorithms for fluid/ structure interaction problems with non-matching discrete interfaces: Momentum and energy conservation, optimal discretization and application to aeroelasticity, *Comput. Methods Appl. Mech. Engrg.* (1998) **157**:95–114.

[3] A. Masud, M. Bhanabhagvanwala, R. A. Khurram, An adaptive mesh rezoning scheme for moving boundary flows and fluidstructure interaction, *Comput. Fluids* (2007) **36**:77–91.

[4] C. Hirt, A. A. Amsden, J. Cook, An arbitrary Lagrangian-Eulerian computing method for all flow speeds, *J. Comput. Phys.* (1974) **14** (3):227–253.

[5] J. Donea, S. Giuliani, J. Halleux, An arbitrary lagrangian-eulerian finite element method for transient dynamic fluid-structure interactions, *Comput. Methods Appl. Mech. Engrg.* (1982) **33** (1):689–723.

[6] J. T. Batina, Unsteady Euler airfoil solutions using unstructured dynamic meshes, *AIAA journal* (1990) **28** (8):1381–1388.

[7] T. J. Baker, Mesh Movement and Metamorphosis, *Eng. Comput.* (2002) **18**:188-198.

[8] G. Compère, J. J. Jean-François Remacle, J. Hoffman, A mesh adaptation framework for dealing with large deforming meshes, *Int. J. Numer. Meth. Eng.* (2010) **82**:843–867.

[9] R. Löhner, Mesh Adaptation in fluid Mechanics, *Eng. Fract. Mech.* (1995) **50** (5/6):819–847.

[10] T. J. Baker, Mesh adaptation strategies for problems in fluid dynamics, *Finite Elem. Anal. Des.* (1997) **25** (3-4):243–273.

[11] C. Dobrzynski, P. Frey, Anisotropic Delaunay mesh adaptation for unsteady simulations, in: *Proceedings of the 17th international Meshing Roundtable*. Springer, (2008), pp. 177–194.

[12] C. Dapogny, C. Dobrzynski, P. Frey, Three-dimensional adaptive domain remeshing, implicit domain meshing, and applications to free and moving boundary problems, *J. Comput. Phys.* (2014) **262**:358–378.

[13] A. Guardone, D. Isola, G. Quaranta, Arbitrary Lagrangian Eulerian formulation for two-dimensional flows using dynamic meshes with edge swapping, *J. Comput. Phys.* (2011) **230** (20):7706–7722.

[14] D. Isola, A. Guardone, G. Quaranta, Finite-volume solution of two-dimensional compressible flows over dynamic adaptive grids, *J. Comput. Phys.* (2015) **285**:1–23.

[15] M.J. Castro-Díaz, F. Hecht, B. Mohammadi, O. Pironneau, Anisotropic unstructured mesh adaption for flow simulations, *Int J Numer Meth Fluids* (1997) **25**:475–491.

[16] W. G. Habashi, J. Dompierre, Y. Bourgault, D. Ait-Ali-Yahia, M. Fortin, M.-G. Vallet, Anisotropic mesh adaptation: towards user-independent, mesh-independent and solver-independent CFD. Part I: general principles, *Int. J. Numer. Meth. Fluids* (2000) **32**:725–744.

[17] P.J. Frey, F. Alauzet, Anisotropic mesh adaptation for CFD computations, *Comput. Methods Appl. Mech. Engrg.* (2005) **194**:5068–5082.

[18] R. J. LeVeque, Numerical methods for conservation laws, Birkhäuser, Basel, 1992.

[19] C. Farhat, P. Geuzaine, C. Grandmont, The Discrete Geometric Conservation Law and the Nonlinear Stability of ALE Schemes for the Solution of Flow Problems on Moving Grids, *J. Comput. Phys.* (2001) **174**:669–694.

[20] L. Formaggia, F. Nobile, Stability analysis of second-order time accurate schemes for ALEFEM, *Comput. Methods Appl. Mech. Engrg.* (2004) **193**(39-41):4097–4116.

[21] S. Étienne, A. Garon, D. Pelletier, Perspective on the geometric conservation law and finite element methods for ALE simulations of incompressible flow, *J. Comput. Phys.* (2009) **228** (7):2313–2333.

[22] D. J. Mavriplis, Z. Yang, Construction of the discrete geometric conservation law for high-order time-accurate simulations on dynamic meshes, *J. Comput. Phys.* (2006) **213**:557–573.

[23] A. Harten, High Resolution Schemes for Hyperbolic Conservation Laws, *J. Comput. Phys.* (1997) **135**:260–278.

[24] A. Jameson, Time Dependent Calculations Using Multigrid, with Applications to Unsteady Flows Past Airfoils and Wings, *AIAA paper* (1991) **1596**:1–13.

[25] B. Koren, Defect correction and multigrid for an efficient and accurate computation of airfoil flows, *J. Comput. Phys.* (1988) **77**:183–206.

[26] B. Re, A. Guardone, C. Dobrzynski, An Adaptive Conservative ALE Approach to Deal with Large Boundary Displacements in Three-Dimensional Inviscid Simulations, in: *AIAA SciTech Forum*, Texas, 2017.

[27] V. Dolejší. Anisotropic mesh adaptation for finite volume and finite element methods on triangular meshes, *Computing and Visualization in Science* (1998) **1**(3):165–178.

[28] H. Borouchaki, P.-L. George, F. Hecht, P. Laug, E. Saltel, Delaunay mesh generation governed by metric specifications. Part I. Algorithms. *Finite Elem. Anal. Des.* (1997) **25**:61–83.

[29] S. Del Pino. Metric-based mesh adaptation for 2D Lagrangian compressible flows. *J. Comput. Phys.* (2011) **230**:1793–1821.

[30] T. Coupez. Metric construction by length distribution tensor and edge based error for anisotropic adaptive meshing. *J. Comput. Phys.* (2011) **230**:2391–2405.

[31] P. Frey and P.-L. George. Mesh Generation: Application to Finite Element, Vol. 32, *Wiley* (2010).

[32] C. Dobrzynski, C. Dapogny, P. Frey, A. Froehly, www.mmgtools.org Mmg Platform.

VII International Conference on Computational Methods for Coupled Problems in Science and Engineering
COUPLED PROBLEMS 2017
M. Papadrakakis, E. Oñate and B. Schrefler (Eds)

NUMERICAL SIMULATIONS OF MICRO JETS PRODUCED WITH A DOUBLE FLOW FOCUSING NOZZLE

GREGA BELŠAK[1], SAŠA BAJT[2], KENNETH R. BEYERLEIN[3] AND BOŽIDAR ŠARLER[1,4]

[1] Laboratory for Simulation of Materials and Processes
Institute of Metals and Technology
Lepi pot 11, SI-1000 Ljubljana, Slovenia
email: grega.belsak@imt.si

[2] Photon Science
Deutsches Elektronen-Synchrotron DESY
Notkestraße 85, 22607 Hamburg, Germany
email: sasa.bajt@desy.de

[3] Center for Free-Electron Laser Science
Deutsches Elektronen-Synchrotron DESY
Notkestraße 85, 22607 Hamburg, Germany
email: kenneth.beyerlein@cfel.de

[4] Laboratory for Fluid Dynamics and Thermodynamics
Faculty of Mechanical Engineering
University of Ljubljana
Aškerčeva c. 6, SI-1000 Ljubljana, Slovenia
email: bozidar.sarler@fs.uni-lj.si

Key words: Multiphase Flow, Micro Jet, Double Flow Focusing Nozzle

Abstract. Stable and reliable micro jets are important for many applications. Double flow focused micro jets are a novelty with an important advantage of significantly reduced sample consumption. Numerical simulations of double flow focused micro jets are a highly complex task. They represents a great computational challenge due to the multiphase nature of the problem, strong coupling between the gas and the two liquids and the sub-micron size cells needed. Simulations were performed with the open source computational fluid dynamics toolbox called OpenFOAM. Two multiphase solvers were used, one of which was modified in order to properly describe the interface between the focusing liquid and the gas. In this study two different incompressible physical models were considered and compared. A model with no mixing of the two fluids (multiphaseInterFoam solver) and a model where the diffusion of the two fluids is permitted (modified interMixingFoam solver). The results of simulations for the two different physical models using the same inlet parameters are presented. Additionally, a parametric analysis for the mixing case was performed to study the effects of different parameters on the jet formation. Particularly how the different diffusion values couple with the jet length, diameter and its stability. Results show a match in jet diameter and jet length for both models when the same set of parameters is used.

1 INTRODUCTION

Controlled production of liquid jets by means of a co-flowing immiscible fluid stream can have diverse technical applications. One of these applications is in the field of X-ray serial crystallography. Nozzles that create stable, long and fast jets of just a few micrometres in diameter are needed to deliver protein nanocrystals into the intense X-ray beam. X-rays scattered off these crystals create diffraction patterns that are recorded on a detector. Reconstructed diffraction images provide the atomic resolution protein structure. The main bottleneck in the protein structure determination is the sample preparation, especially for the membrane proteins which do not like to form larger crystals. Serial femtosecond crystallography with x-ray free electron lasers (FEL) opened up the possibly to obtain protein structures also from nanocrystals, which were previously too small for standard X-ray crystallography. Nevertheless, samples are hard to prepare and the amount of the material is very limited. It is critical to develop ways of using the minimum amount of sample material. Delivering such nanocrystals to the X-ray beam in a form of a micro jet proved to have several advantages [1]. Here, we are particularly interested in understanding the nozzle geometry that creates these micro jets. In the past such nozzles were prepared manually, which was time consuming, non-reproducible and limited to simple designs. Ceramic micro-injection moulded nozzles were a step forward ensuring reproducibility and faster assembly [2]. However, because of the high cost of the moulding tools it is desirable to test new designs before investing in a new moulding tool. Recently, a 3D printing technology enabled printing of macroscopic nozzles with a very high precision [3]. These nozzles can be used either for testing a new design or in final application. The development of numerical models presented here, gives an insight in the fluid dynamics of such systems and should help to improve future nozzle designs.

2 DOUBLE FLOW FOCUSING NOZZLE DESIGN

Early experiments were performed using gas dynamic virtual nozzles (GDVN) [4]. This nozzle structure uses two phases to create a stable micro jet:

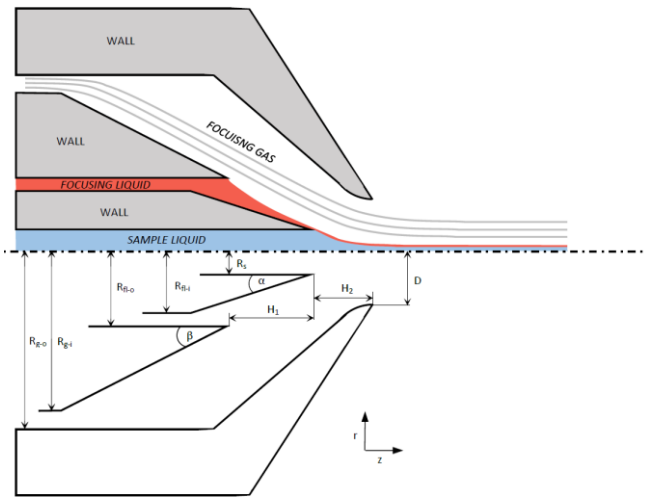

Figure 1: Graphical representation of the double flow focusing nozzle. Typical values are: R_s= 20 µm, $R_{fl\text{-}i}$= 55 µm, $R_{fl\text{-}o}$= 62 µm, $R_{g\text{-}i}$= 175 µm, $R_{g\text{-}o}$= 245 µm, α =17.5°, β= 25°, H_1= 70 µm, H_2= 85 µm, D= 35 µm.

a liquid sample fluid (nanocrystals dispersed in water) and a focusing gas (helium). In such set-up two capillaries are inserted into the nozzle. The central capillary that ends almost at the nozzle orifice is used to deliver sample liquid, while the gas is delivered through the second capillary that ends further upstream of the nozzle tip. The high pressure gas focuses the liquid into a micro jet when flowing through a small nozzle orifice. This approach typically requires sample fluid flow rates of around 20-40 µl/min.

In order to reduce the sample fluid consumption a novel double flow focusing nozzle (DFFN), depicted in figure 1, was developed [5,6]. This approach uses an additional fluid (alcohol) to further focus the sample fluid. The main advantage of using alcohol is its lower surface tension in comparison to water. It acts as a sheath liquid encapsulating the water jet, resulting in extension of the jet length by mitigating its breakup. In this way the sample fluid flow rate can be reduced to around 5 µl/min.

3 GOVERNING EQUATIONS

The multiphase model of isothermal and incompressible flow is governed by the sets of momentum and mass conservation equations for each of the phases *i*:

$$\frac{\partial(\rho_i \alpha_i \vec{u_i})}{\partial t} + \left(\rho_i \alpha_i \vec{u}_i \cdot \nabla\right)\vec{u}_i = -\alpha_i \nabla p + \nabla \cdot \left(\mu_i \alpha_i \nabla \vec{u}_i\right) + \rho_i \alpha_i \vec{g} + \vec{F}_{s,i} \tag{1}$$

$$\frac{\partial \alpha_i}{\partial t} + \vec{u_i} \cdot \nabla \alpha_i = 0 \tag{2}$$

where velocity, phase fraction, density, viscosity and surface tension force for phase *i* are given by $\vec{u}_i$, α_i, ρ_i, μ_i, $\vec{F}_i$, respectively and $\vec{g}$ is gravity. The interface compression method [7] is implemented by adding an additional compression term to the mass conservation equation in order to compress the volume fraction field and maintain a sharp interface between the phases.

$$\frac{\partial \alpha_i}{\partial t} + \vec{u_i} \cdot \nabla \alpha_i + \nabla \cdot \left(\vec{u}_c \alpha_i \left(1 - \alpha_i\right)\right) = 0 \tag{3}$$

Compression velocity $\vec{u}_c$ is applied normally to the interface.

4 NUMERICAL PROCEDURE

Numerical simulation of DFFN micro jets is a highly complex task. Multiphase nature of the problem, strong coupling between the gas and the liquids, the sub-micron size cells needed for high resolution and proper capturing of the flow all represent a great computational challenge. Because of the microscopic nature of the nozzle structure and the physical properties of the fluids used, the Reynolds number is low and therefore the flow is considered laminar. The fluids are considered to be of a Newtonian nature. The chapter is divided into three specific parts, each one describing in details the performed work.

4.1 Pre-processing

The computer model of a DFFN was prepared with FreeCAD, an open-source parametric 3D CAD modeler [8]. Non-axial symmetry of the nozzle structure (circular inner capillary inserted into square middle capillary inserted into circular outer capillary), was treated as axially symmetric (circular inner capillary inserted into circular middle capillary inserted into circular outer capillary) while keeping the cross-sectional area of the channel equal as seen in figure 2 . In this way a three dimensional problem was reduced to a two dimensional one, thus greatly reducing the calculation time and making simulations of micro jets feasible.

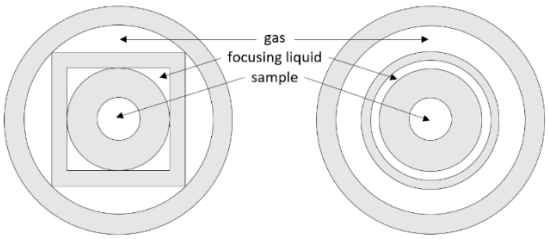

Figure 2: Transformation of the real geometry of the nozzle to axis symmetry.

For the preparation of the high quality mesh the utility called snappyHexMesh was used, which is a part of the open source computational fluid dynamics (CFD) toolbox called OpenFoam [9]. A sample mesh can be seen in figure 3. For the simulations to be run in a reasonable time (up to few days) on a modern computer with approximately 30 cores the number of cells needed to be kept as low as possible. This proved to be a difficult task for two reasons. The first reason is the desired high resolution in the jet region. Experiments show that the typical jet diameter for a DFFN is between 3 and 5 μm. At least 10 cells are needed to properly describe the fluid flow and the four interfaces between the two liquid phases. This constrains the maximal cell size to 0.5 μm. Therefore, a cell size of 0.15 μm was chosen in this study. To keep the computing time reasonable we used the finest mesh only in the area where the jet was expected to form and a coarser mesh elsewhere. The second reason is that the vacuum chamber, the area where the jet leaves the nozzle, needs to be large enough (few millimeters in length). This is because we are setting an artificial condition $(p = 0)$ on the outlet boundary of the vacuum chamber. In order to avoid the numerical errors and to prevent any interference of this artificial boundary condition on the jet formation, the size of the computational domain needs to be few millimeters. Those two constraints led to a mesh with the finest cell size of 0.15 μm with ~ 225 000 cells.

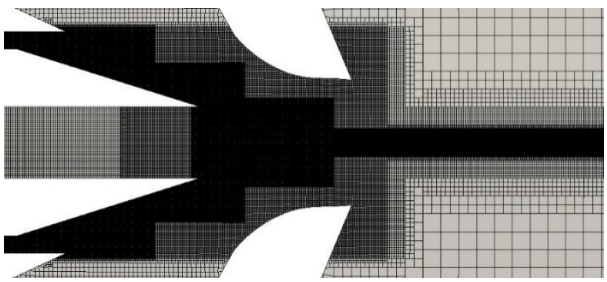

Figure 3: Representation of a mesh used in the simulations

4.2 Processing

Numerical simulations of DFFN were performed with OpenFoam (version 16.10), which has a variety of solvers available to use for many different kinds of fluid flow problems. In this study two different models were considered and hence two different solvers were used. First, a "multiphaseInterFoam" solver was used for a multiphase model where all the fluids are considered incompressible and there is no diffusion between the phases i.e. a non-mixing incompressible model. Second, a modified "InterMixingFoam" solver was used, which describes a set of three incompressible fluids two of which are miscible, i.e. a mixing incompressible model. In the later model diffusion between the sample fluid and the focusing fluid is permitted. As aforementioned the code in this solver had to be slightly modified to properly describe the interface between the focusing fluid and the gas. The inlet parameters and the physical properties of the fluids at room temperature (Table 1) were chosen to resemble the experimental values [6] and were the same in both models.

Table 1: Operating conditions and physical properties used in simulations. Values were obtained from NIST Chemistry Webbook Database

	sample liquid **WATER**	focusing liquid **ALCOHOL**	focusing gas **HELIUM**
Density [kg/m^3]	1000	789	0.33
Dynamic viscosity [kg/ms]	$1.9*10^{-5}$	$1.12*10^{-3}$	10^{-3}
Volumetric flow rate [μL/min]	5	10	/
Mass flow rate [mg/min]	/	/	21.6
Surface tension (water-gas) [N/m]		0.0728	
Surface tension (alcohol-gas) [N/m]		0.0223	
Surface tension (water-alcohol) [N/m]		0.0505	
Diffusion (water-alcohol) [N/m^2]	mixing case	10^{-9}	
	non-mixing case	0	

4.3 Post-processing

Post-processing of the simulations was performed with ParaView [10], an open source, multi-platform data analysis and visualization application. A code was written to automatically extract the jet length, diameter and concentration profile, discussed and presented in the results section. When setting up the simulation case and choosing the velocity inlet boundary conditions for the fluids a uniform axial flow (constant velocity profile) was chosen. There was a concern that this non-physical constant profile would affect the simulations. However, results demonstrated that this is not the case if the capillary is of sufficient length (above 100 μm) and the jet is monitored long enough ($t > 0.3$ ms). Under these conditions the initial constant profile changes to parabolic profile. Full development of this profile along with stabilization of the recirculation zones was used as the benchmark of a steady-state solution.

5 RESULTS

5.1 Mixing model.

The physical model, which permits the mixing between the phases, is explored here. In this three phase system the sample fluid and the focusing fluid were miscible with a diffusion constant of 10^{-9} m^2/s, which is a typical value for water-ethanol system. None of these liquids were allowed to mix with the third, gaseous phase. This model explores how diffusion affects the jet length, the diameter and the concentration profile and allows for a comparison with the experimental data [6]. In the mixing model it is challenging to distinguish between the natural (real) and the numerical (artificial) diffusion. The artificial diffusion arises from the spatial and temporal discretization of a continuous problem and therefore highly depends on the cell size and the time step. The following discretization parameters were chosen in order to keep the numerical diffusion an order of magnitude lower than the natural diffusion (10^{-10} m^2/s) and to prevent it to interfere with the results. In the region of the domain where the diffusion is present, the maximal cell size was set to 0.15 µm. The time step was controlled by setting the Courant number to the value of one, which also ensured stability of the simulation. Results are presented in figure 4.

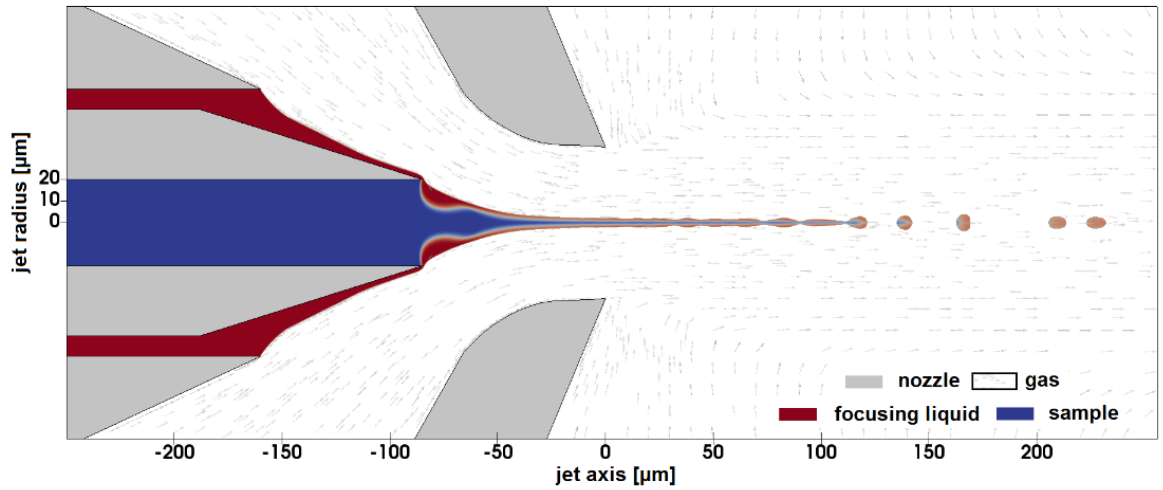

Figure 4: A snapshot of the simulation of the mixing model at time 0.4 ms. The extracted parameters are jet diameter $d_j = 4.5$ µm and average jet length $L_j = 94.2$ µm.

One of the main results of this study is the dependence of the concentration profile, which is measured at the nozzle orifice perpendicularly to the jet axis, to the varying parameters. Figure 5 shows the water concentration profile through the jet for two diffusion values. In the jet only two phases are present: water and alcohol. The total sum of both concentration phases is equal to one. It can be observed that along the jet axis (jet radius zero) the water concentration is at the highest, but still not equal to one, indicating the presence of alcohol along the jet axis. When moving towards the edges of the jet the water concentration decreases, since the alcohol concentration increases. Increasing the diffusion coefficient by an order of magnitude (green line) reduces the concentration of water around the jet axis. This is expected, since higher diffusion coefficient means more alcohol is mixed inside the water.

Results in figure 5 show a noticeable difference in the concentration profile for two diffusion values. This indicates that the observed diffused interface between the water and the alcohol is a result of natural and not numerical diffusion. It is interesting to note that changes of the diffusion coefficient do not affect the jet diameter.

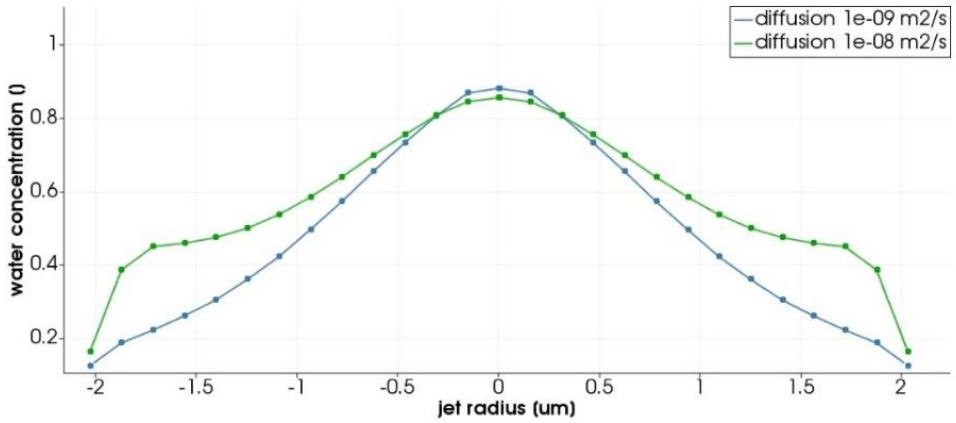

Figure 5: Water concentration profile of a jet measured at the nozzle orifice in the perpendicular direction to jet axis. Two different diffusion values are considered.

5.2 Non-mixing model.

Additionally, a multiphase model consisting of three incompressible fluids and no diffusion between the phases was explored. Results for this immiscible case are presented in figure 6.

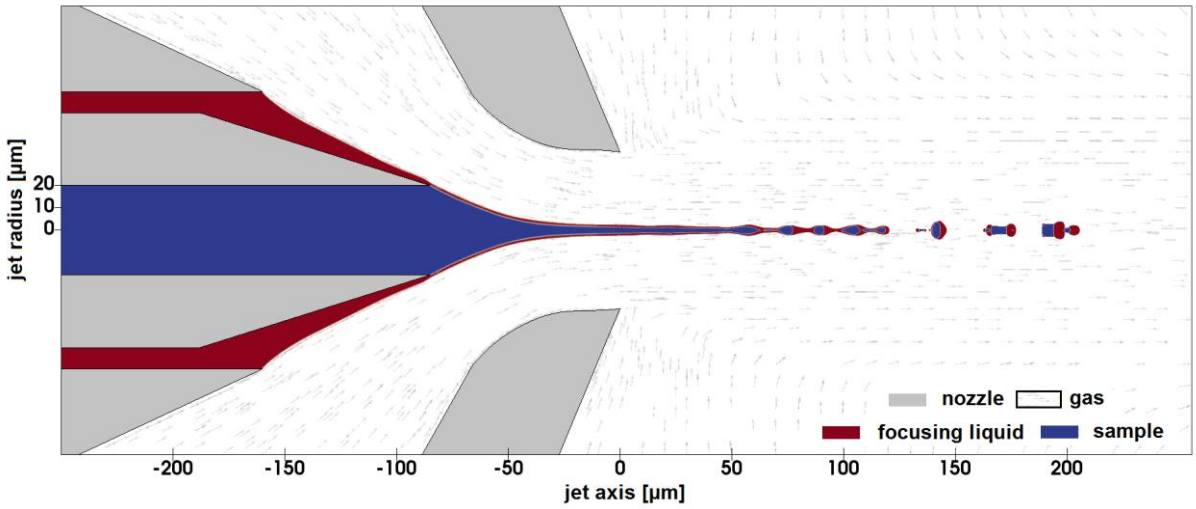

Figure 6: A snapshot of the simulation of the non-mixing model at time 0.4 ms. The extracted parameters are jet diameter $d_j = 4.8$ µm and average jet length $L_j = 97.5$ µm.

5.3 Model comparison

Results of simulations for miscible and immiscible model are presented in table 2. Calculations were performed on the same mesh under identical operating conditions and physical parameters. Findings indicate that diffusion does not affect the jet diameter and only slightly affects the jet length. Interesting thing to note is that in the non-mixing model small water droplets are forming inside the alcohol jet.

Table 2: Comparison of extracted parameters

	average jet **LENGTH** [µm]	jet **DIAMETER** [µm]
Mixing model	94.2 ± 0.3	4.5 ± 0.3
Non-mixing model	97.5 ± 0.3	4.8 ± 0.3

The surprising result is the recirculation zone in the meniscus of the jet. In an immiscible model a stable sample fluid recirculation zone is established. On the other hand in the miscible model there is no sample fluid recirculation, but only a small focusing fluid recirculation in the outermost layers of the jet as shown in figure 7.

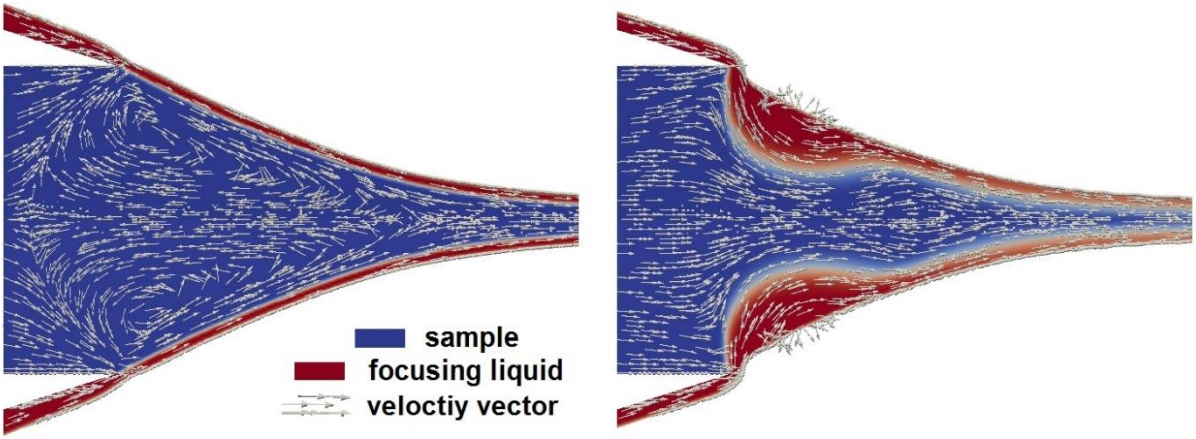

Figure 7: Comparison of recirculation zones. Left panel non-mixing model with recirculation zone. Right panel mixing model where only small recirculation occurs in the outer most layers of the focusing liquid phase.

We believe that with different operating conditions of the gas (higher gas speeds inside the nozzle) the recirculation zone would become even stronger and would also appear in the miscible case.

The numerical results published in [6] differ from the ones obtained here which we attribute to different initial conditions of the gas. In the previous work we assumed lower helium mass flow rate and inserted the gas into the nozzle under higher pressure. As a result the maximal gas velocity developed inside the nozzle orifice was around 65 m/s. Under the present operating conditions, the maximal gas velocity reaches a value of around 350 m/s, resulting in a thinner and shorter jet.

6 CONCLUSIONS

The scope of this work included numerical simulations of DFFNs. All the fluids in these simulations were considered incompressible. Experimental data [6] indicate chocked flow for the gas flowing through such DFFN into a vacuum chamber. Correct description requires a model with incompressible sample and focusing liquid, and compressible focusing gas. It is conceivable that the simulations, where the compressibility is taken into account, would result in different values of the jet diameter and length under the same initial conditions. The length of the jet is expected to change (shorten) when compressibility is added, because we would be able to describe the expansion of the high pressure gas into the low pressure vacuum chamber. This would result in higher gas velocities inside the vacuum chamber. Although not supported with full simulation, we predict that this, along with the changed gas stream shape will affect the jet length and stability. Jet diameter will also be affected by a decrease in pressure and density of gas and increased gas velocity at the nozzle orifice. Future work will include upgraded, more realistic models to address these issues.

7 ACKNOWLEDGEMENTS

We would like to thank Henry N. Chapman (CFEL, Univ. Hamburg, CUI), Dominik Oberthuer (CFEL), Juraj Knoška, and Max O. Wiedorn (CFEL, Univ. Hamburg) for fruitful discussions, and Luigi Adriano (DESY) for technical support. This work was supported by grant of Slovenian Grant Agency (ARRS) J2-7384, Program Group P0-0501-0782 and by Helmholtz Association through project oriented funds.

8 REFERENCES

[1] Chapman, H.N., Fromme, P., Barty, A., White, T.A., Kirian, R.A., Aquila, A., Hunter, M.S., Schulz, J., DePonte, D.P., Weierstall, U., Doak, R.B., Maia, F.R.N.C., Martin, A.V., Schlichting, I., Lomb, L., Coppola, N., Shoeman, R.L., Epp, S.W., Hartmann, R., Rolles, D., Rudenko, A., Foucar, L., Kimmel, N., Weidenspointner, G., Holl, P., Liang, M., Barthelmess, M., Caleman, C., Boutet, S., Bogan, M.J., Krzywinski, J., Bostedt, C., Bajt, S., Gumprecht, L., Rudek, B., Erk, B., Schmidt, C., Hömke, A., Reich, C., Pietschner, D., Strüder, L., Hauser, G., Gorke, H., Ullrich, J., Herrmann, S., Schaller, G., Schopper, F., Soltau, H., Kühnel, K., Messerschmidt, M., Bozek, J.D., Hau-Riege, S.P., Frank, M., Hampton, C.Y., Sierra, R.G., Starodub, D., Williams, G.J., Hajdu, J., Timneanu, N., Seibert, M.M., Andreasson, J., Rocker, A., Jönsson, O., Svenda, M., Stern, S., Nass, K., Andritschke, R., Schröter, C., Krasniqi, F., Bott, M., Schmidt, K.E., Wang, X., Grotjohann, I., Holton, J.M., Barends, T.R.M., Neutze, R., Marchesini, S., Fromme, R., Schorb, S., Rupp, D., Adolph, M., Gorkhover, T., Andersson, I., Hirsemann, H., Potdevin, G., Graafsma, H., B. and Spence, J.C.H. *Femtosecond X-ray protein nanocrystallography.* Nature 470, 73–77, doi: 10.1038/nature09750 (2011).

[2] Beyerlein, K.R., Adriano, L., Heymann, M., Kirian, R., Knoška, J., Wilde, F., Chapman, H.N., and Bajt, S. *Ceramic micro-injection molded nozzles for serial femtosecond crystallography sample delivery.* Review of Scientific Instruments, 86(12), (2015) p.125104. Available at: http://dx.doi.org/10.1063/1.4936843

[3] Nelson, G., Kirian, R.A., Weierstall, U., Zatsepin, N.A., Faragó, T., Baumbach, T., Wilde, F., Niesler, F.B.P., Zimmer, B., Ishigami, I., Hikita, M., Bajt, S., Yeh, S., Rousseau, D.L., Chapman, H.N., Spence, J.C.H., and Heymann, M. *Three-dimensional-printed gas dynamic virtual nozzles for x-ray laser sample delivery*. Opt. Express 24, 11515-11530 (2016)

[4] DePonte, D.P., Weierstall, U., Schmidt, K., Warner, J., Starodub, D., Spence, J.C.H., and Doak, R.B. *Gas dynamic virtual nozzle for generation of microscopic droplet streams*. J. Phys. D 41, 195505 (2008).

[5] Ganán-Calvo, A. M., González-Prieto, R., Riesco-Chueca, P., Herrada, M. A. and Flores-Mosquera, M. *Focusing capillary jets close to the continuum limit.* Nature Physics 3, 737–742, doi: 10.1038/nphys710 (2007).

[6] Oberthuer, D., Knoška J., Wiedorn, M.O., Beyerlein, K.R., Bushnell, D.A., Kovaleva, E.G., Heymann, M., Gumprecht, L., Kirian, R.A., Barty, A., Mariani, V., Tolstikova, A., Adriano, L., Awel, S., Barthelmess, M., Dörner, K., Xavier, P.L., Yefanov, O., James, D.R., Nelson, G., Wang, D., Calvey, G., Chen, Y., Schmidt, A., Szczepek, M., Frielingsdorf, S., Lenz, O., Snell, E., Robinson, P.J., Šarler, B., Belšak, G., Maček, M., Wilde, F., Aquila, A., Boutet, S., Liang, M., Hunter, M.S., Scheerer, P., Lipscomb, J.D., Weierstall, U., Kornberg, R.D., Spence, J.C.H., Pollack, L., Chapman, H.N. and Bajt, S. *Double-flow focused liquid injector for efficient serial femtosecond crystallography.* Sci. Rep. 7, 44628; doi: 10.1038/srep44628 (2017)

[7] Weller, H.G., *A new approach to VOF-based interface capturing methods for incompressible and compressible flow.* Tech.Rep., OpenCFD, 2008.

[8] FreeCAD website: https://www.freecadweb.org/

[9] OpenFoam © 2004-2017 OpenCFD Ltd (ESI Group) website: http://www.openfoam.com/

[10] Ahrens, J., Geveci, B., Law, C. *ParaView: An End-User Tool for Large Data Visualization.* Visualization Handbook, Elsevier, 2005, ISBN-13: 978-0123875822

VII International Conference on Computational Methods for Coupled Problems in Science and Engineering
COUPLED PROBLEMS 2017
M. Papadrakakis, E. Oñate and B. Schrefler (Eds)

NUMERICAL STABILITY OF EXPLICIT AND IMPLICIT CO-SIMULATION METHODS

P. LI*, T. MEYER*, D. LU* AND B. SCHWEIZER*

*Institute of Applied Dynamics
Technical University of Darmstadt
Otto-Berndt-Strasse 2, 64287 Darmstadt, Germany
e-mail: {li, meyer, lu, schweizer}@ad.tu-darmstadt.de, www.ad.tu-darmstadt.de

Key words: Co-Simulation, Numerical Stability, Implicit, Explicit, Applied-Force Coupling

Abstract. Within a co-simulation approach, the subsystems are integrated by specific solvers; data exchange is accomplished only at certain user-defined macro-time points. Due to the approximation of the coupling variables by polynomials and as a result of the data exchange between the subsystems, errors are introduced, which may entail severe stability problems. Hence, the development of stabilized coupling techniques is of special interest. To analyze the stability of co-simulation approaches, we consider two coupled Dahlquist's equations so that the conventional linear stability analysis can be applied. Consequently, the stability of the co-simulation method can be determined by calculating the spectral radius of the governing system of recurrence equations. The numerical stability of classical explicit and implicit co-simulation techniques is investigated here. Also, modified coupling approaches are discussed, which show an improved stability behavior.

1 INTRODUCTION

To couple two or more solvers in time domain, co-simulation methods can be used advantageously in order to analyze multidisciplinary systems, e.g. for investigating flexible multibody systems [1] or for studying Fluid-Structure-Interaction (FSI) problems [2]. Especially for examining vehicle systems, co-simulation has found increasing usage in the last decades [3]. For analyzing monodisciplinary problems, one may also apply co-simulation approaches in order to speed up the simulation by parallelizing the overall dynamical system. For instance, "subcycling algorithms", which are widely applied in the framework of structural dynamics [4], can be regarded as explicit co-simulation methods.

Making use of co-simulation algorithms, subsystems are integrated with individual, specific solvers and coupling data are exchanged at certain discretized time points (macro-time points) only. Usually, the coupling variables are unknown in the integrating process and have therefore to be approximated using polynomials, for instance. As a result, numerical errors are introduced which may result in instability problems.

In this paper, the stability analysis is accomplished with the help of two coupled Dahlquist's equations. A system of two mass-oscillators, connected by a spring-damper element, is used in Section 2 in order to derive the linear system of recurrence equations, which is applied to

analyze the numerical stability of a coupling approach. In Section 3, different explicit and implicit co-simulation algorithms will be considered and corresponding stability plots will be presented in Section 4. A summary of the results is given in Section 5.

2 TEST MODEL FOR STABILITY ANALYSIS OF CO-SIMULATION METHODS

The numerical stability of time integration schemes is defined by Dahlquist's test equation. From the mechanical point of view, this equation can be interpreted as the complex representation of the equations of motion of the autonomous linear mass-spring-damper oscillator. To analyze the numerical stability of co-simulation methods, it is therefore straightforward to use the linear two-mass oscillator as test model, see Figure 1.

Dahlquist's test equation is given by

$$\dot{y}(t) = \Lambda \cdot y(t) \tag{1}$$

where $y(t)$ is a scalar function of time and Λ an arbitrary complex constant. The 2-DOF oscillator can be regarded as two single-mass oscillators (masses m_1/m_2, spring constant c_1/c_2, damping coefficients d_1/d_2), which are coupled by the coupling spring c_c and the coupling damper d_c. Hence, the two-mass oscillator can be considered as two Dahlquist's equations, which are coupled by a linear constitutive equation.

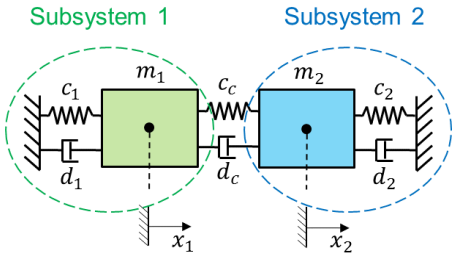

Figure 1: Test model for analyzing the stability of co-simulation methods: linear two-mass oscillator

The equations of motion for the coupled oscillator read as

$$\begin{aligned}
\dot{x}_1 &= v_1 \\
\dot{v}_1 &= -\frac{c_1}{m_1}x_1 - \frac{d_1}{m_1}v_1 + \frac{c_c}{m_1}\cdot(x_2 - x_1) + \frac{d_c}{m_1}\cdot(v_2 - v_1) \\
\dot{x}_2 &= v_2 \\
\dot{v}_2 &= -\frac{c_2}{m_2}x_2 - \frac{d_2}{m_2}v_2 - \frac{c_c}{m_2}\cdot(x_2 - x_1) - \frac{d_c}{m_2}\cdot(v_2 - v_1).
\end{aligned} \tag{2}$$

For the stability analysis of co-simulation methods, it is useful to introduce dimensionless variables. We assume that $\bar{x}_1, \bar{x}_2$ are properly chosen dimensionless position coordinates. The variables $\bar{v}_1 = H \cdot d\bar{x}_1/dt$ and $\bar{v}_2 = H \cdot d\bar{x}_2/dt$ denote dimensionless velocities, where H denotes the macro-step size of the co-simulation approach. The dimensionless time is defined by $\bar{t} = t/H$. Furthermore, it is suitable to define the following 7 parameters:

$$\begin{gathered}
\bar{c}_1 = \frac{c_1 \cdot H^2}{m_1}, \quad \bar{d}_1 = \frac{d_1 \cdot H}{m_1}, \quad \alpha_{m21} = \frac{m_2}{m_1}, \quad \alpha_{c21} = \frac{c_2}{c_1}, \quad \alpha_{d21} = \frac{d_2}{d_1}, \\
\alpha_{cc1} = \frac{c_c}{c_1}, \quad \alpha_{dc1} = \frac{d_c}{d_1}.
\end{gathered} \tag{3}$$

The dimensionless equations of motion for the coupled oscillator can be written as

$$\begin{aligned}
\bar{x}_1' &= \bar{v}_1 \\
\bar{v}_1' &= -\bar{c}_1 \cdot \bar{x}_1 - \bar{d}_1 \cdot \bar{v}_1 + \alpha_{cc1} \cdot \bar{c}_1 \cdot (\bar{x}_2 - \bar{x}_1) + \alpha_{dc1} \cdot \bar{d}_1 \cdot (\bar{v}_2 - \bar{v}_1) \\
\bar{x}_2' &= \bar{v}_2 \\
\bar{v}_2' &= -\frac{\alpha_{c21}}{\alpha_{m21}} \cdot \bar{c}_1 \cdot \bar{x}_2 - \frac{\alpha_{d21}}{\alpha_{m21}} \cdot \bar{d}_1 \cdot \bar{v}_2 - \frac{\alpha_{cc1}}{\alpha_{m21}} \cdot \bar{c}_1 \cdot (\bar{x}_2 - \bar{x}_1) - \frac{\alpha_{dc1}}{\alpha_{m21}} \cdot \bar{d}_1 \cdot (\bar{v}_2 - \bar{v}_1) \ .
\end{aligned} \tag{4}$$

In compact form, the above system of equations can be written as

$$\boldsymbol{z}' = \boldsymbol{A} \cdot \boldsymbol{z} \qquad \text{with } \boldsymbol{z} = (\bar{x}_1 \quad \bar{v}_1 \quad \bar{x}_2 \quad \bar{v}_2)^T \in \mathbb{R}^4 \text{ and}$$

$$\boldsymbol{A} = \begin{pmatrix} 0 & 1 & 0 & 0 \\ -(1+\alpha_{cc1}) \cdot \bar{c}_1 & -(1+\alpha_{dc1}) \cdot \bar{d}_1 & \alpha_{cc1} \cdot \bar{c}_1 & \alpha_{dc1} \cdot \bar{d}_1 \\ 0 & 0 & 0 & 1 \\ \frac{\alpha_{cc1}}{\alpha_{m21}} \cdot \bar{c}_1 & \frac{\alpha_{dc1}}{\alpha_{m21}} \cdot \bar{d}_1 & -\frac{\alpha_{c21}+\alpha_{cc1}}{\alpha_{m21}} \cdot \bar{c}_1 & -\frac{\alpha_{d21}+\alpha_{dc1}}{\alpha_{m21}} \cdot \bar{d}_1 \end{pmatrix} \in \mathbb{R}^{4\times 4} . \tag{5}$$

Obviously, the two-mass oscillator is a mechanically stable system, if $m_1, m_2, c_1, c_2, d_1, d_2 > 0$.

Regarding the two-mass oscillator as two coupled single-mass oscillators, the equations of motion can be formulated in a modular manner according to

$$\begin{aligned}
\boldsymbol{z}' &= \boldsymbol{A} \cdot \boldsymbol{z} + \boldsymbol{B} \cdot \boldsymbol{u} \\
\boldsymbol{g} &= \boldsymbol{C} \cdot \boldsymbol{z} + \boldsymbol{D} \cdot \boldsymbol{u} = \boldsymbol{0} \ .
\end{aligned} \tag{6}$$

The vector $\boldsymbol{z} = (\bar{x}_1 \quad \bar{v}_1 \quad \bar{x}_2 \quad \bar{v}_2)^T \in \mathbb{R}^4$ collects the dimensionless state variables, while the vector $\boldsymbol{u} = (\tilde{\bar{x}}_1 \quad \tilde{\bar{v}}_1 \quad \tilde{\bar{x}}_2 \quad \tilde{\bar{v}}_2 \quad \bar{\lambda}_c)^T \in \mathbb{R}^5$ contains the coupling variables required for the three different test models considered here, namely the force/force-, the force/displacement- and the displacement/displacement-decomposition test model. $\bar{\lambda}_c = \lambda_c \cdot H^2/m_1$ terms the dimensionless coupling force, which is a function of the state variables of the subsystems. $\boldsymbol{A}, \boldsymbol{B}, \boldsymbol{C}$ and $\boldsymbol{D}$ are corresponding coefficient matrices (vectors).

In the framework of a force/force-coupling approach [5], the basic idea is to divide the two-mass oscillator into two single-mass oscillators (two subsystems), which are driven by the coupling force λ_c, see Figure 2.

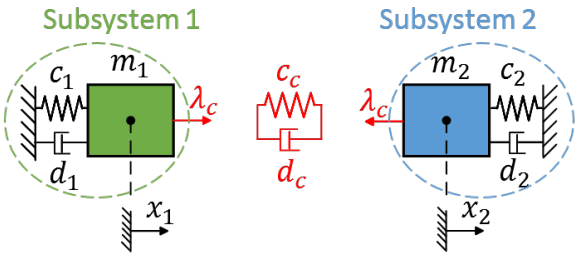

Figure 2: Co-simulation test model for force/force-coupling approach

Regarding the general Eq. (6), it is straightforward to derive the governing system matrices for the force/force-coupling approach, which read as

$$\boldsymbol{A}_{FF} = \begin{pmatrix} 0 & 1 & 0 & 0 \\ -\bar{c}_1 & -\bar{d}_1 & 0 & 0 \\ 0 & 0 & 0 & 1 \\ 0 & 0 & -\frac{\alpha_{c21}}{\alpha_{m21}} \cdot \bar{c}_1 & -\frac{\alpha_{d21}}{\alpha_{m21}} \cdot \bar{d}_1 \end{pmatrix}, \quad \boldsymbol{B}_{FF} = \begin{pmatrix} 0 & 0 & 0 & 0 & 0 \\ 0 & 0 & 0 & 0 & 1 \\ 0 & 0 & 0 & 0 & 0 \\ 0 & 0 & 0 & 0 & -\frac{1}{\alpha_{m21}} \end{pmatrix}, \tag{7}$$

$$\boldsymbol{C}_{FF} = (\alpha_{cc1} \cdot \bar{c}_1 \quad \alpha_{dc1} \cdot \bar{d}_1 \quad -\alpha_{cc1} \cdot \bar{c}_1 \quad -\alpha_{dc1} \cdot \bar{d}_1), \quad \boldsymbol{D}_{FF} = (0 \quad 0 \quad 0 \quad 0 \quad 1).$$

For the case that the co-simulation test model is decomposed by a force/displacement-coupling approach, subsystem 1 will be a force-driven and subsystem 2 a base-point excited single-mass oscillator as illustrated in Figure 3.

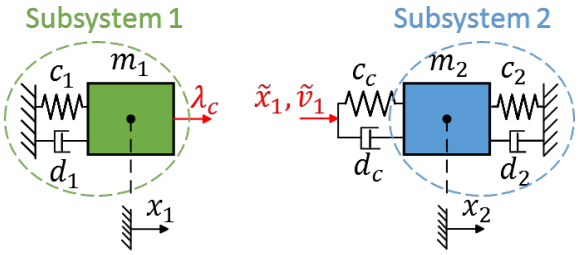

Figure 3: Co-simulation test model for force/displacement-coupling approach

Applying a force/displacement-decomposition, the coupling force λ_c is replaced in subsystem 2 with the help of state variables of subsystem 1, which fulfill the coupling condition $g_c := \lambda_c - c_c \cdot (x_2 - x_1) - d_c \cdot (v_2 - v_1) = 0$. Due to the fact that the state variables x_1 and v_1 are unknown in subsystem 2, they are replaced by two additional coupling variables, which are denoted by $\tilde{x}_1$ and $\tilde{v}_1$.Therefore, the decomposed subsystems can be described by Eq. (6) with the following dimensionless coefficient matrices

$$\boldsymbol{A}_{FD} = \begin{pmatrix} 0 & 1 & 0 & 0 \\ -\bar{c}_1 & -\bar{d}_1 & 0 & 0 \\ 0 & 0 & 0 & 1 \\ 0 & 0 & -\frac{\alpha_{c21} + \alpha_{cc1}}{\alpha_{m21}} \cdot \bar{c}_1 & -\frac{\alpha_{d21} + \alpha_{dc1}}{\alpha_{m21}} \cdot \bar{d}_1 \end{pmatrix},$$

$$\boldsymbol{B}_{FD} = \begin{pmatrix} 0 & 0 & 0 & 0 & 0 \\ 0 & 0 & 0 & 0 & 1 \\ 0 & 0 & 0 & 0 & 0 \\ \frac{\alpha_{cc1}}{\alpha_{m21}} \cdot \bar{c}_1 & \frac{\alpha_{dc1}}{\alpha_{m21}} \cdot \bar{d}_1 & 0 & 0 & 0 \end{pmatrix}, \tag{8}$$

$$\boldsymbol{C}_{FD} = \begin{pmatrix} \alpha_{cc1} \cdot \bar{c}_1 & \alpha_{dc1} \cdot \bar{d}_1 & -\alpha_{cc1} \cdot \bar{c}_1 & -\alpha_{dc1} \cdot \bar{d}_1 \\ -1 & 0 & 0 & 0 \\ 0 & -1 & 0 & 0 \end{pmatrix}, \quad \boldsymbol{D}_{FD} = \begin{pmatrix} 0 & 0 & 0 & 0 & 1 \\ 1 & 0 & 0 & 0 & 0 \\ 0 & 1 & 0 & 0 & 0 \end{pmatrix}.$$

When a displacement/displacement-coupling approach is used to decompose the two-mass oscillator, each subsystem is described by a base-point excited single-mass oscillator, see Figure 4.

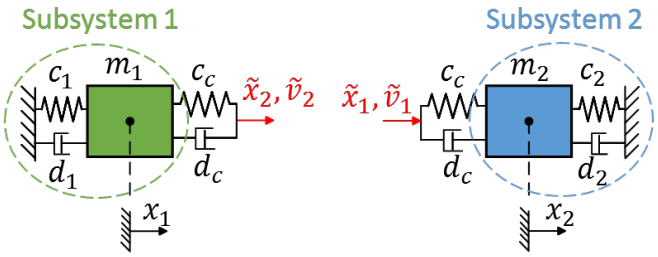

Figure 4: Co-simulation test model for displacement/displacement-coupling approach

For this purpose, the coupling spring/damper system has to be duplicated, i.e. the coupling variable λ_c is replaced in both subsystems by introducing the four coupling variables $\tilde{x}_1, \tilde{x}_2$ and $\tilde{v}_1, \tilde{v}_2$. The corresponding coefficient matrices characterizing the decomposed system are given by

$$\boldsymbol{A}_{DD} = \begin{pmatrix} 0 & 1 & 0 & 0 \\ -(1+\alpha_{cc1})\bar{c}_1 & -(1+\alpha_{dc1})\bar{d}_1 & 0 & 0 \\ 0 & 0 & 0 & 1 \\ 0 & 0 & -\dfrac{\alpha_{c21}+\alpha_{cc1}}{\alpha_{m21}}\bar{c}_1 & -\dfrac{\alpha_{d21}+\alpha_{dc1}}{\alpha_{m21}}\bar{d}_1 \end{pmatrix},$$

$$\boldsymbol{B}_{DD} = \begin{pmatrix} 0 & 0 & 0 & 0 & 0 \\ 0 & 0 & \alpha_{cc1}\cdot\bar{c}_1 & \alpha_{dc1}\cdot\bar{d}_1 & 0 \\ 0 & 0 & 0 & 0 & 0 \\ \dfrac{\alpha_{cc1}}{\alpha_{m21}}\cdot\bar{c}_1 & \dfrac{\alpha_{dc1}}{\alpha_{m21}}\cdot\bar{d}_1 & 0 & 0 & 0 \end{pmatrix}, \tag{9}$$

$$\boldsymbol{C}_{DD} = \begin{pmatrix} -1 & 0 & 0 & 0 \\ 0 & -1 & 0 & 0 \\ 0 & 0 & -1 & 0 \\ 0 & 0 & 0 & -1 \end{pmatrix}, \quad \boldsymbol{D}_{DD} = \begin{pmatrix} 1 & 0 & 0 & 0 & 0 \\ 0 & 1 & 0 & 0 & 0 \\ 0 & 0 & 1 & 0 & 0 \\ 0 & 0 & 0 & 1 & 0 \end{pmatrix}.$$

3 DIRECT AND EXTENDED CO-SIMULATION ALGORITHMS

3.1 Explicit and implicit direct co-simulation algorithm

The direct implicit co-simulation methods investigated here are based on a predictor/corrector approach, which is performed in three steps. To illustrate the integration process, it is convenient to define the vectors $\boldsymbol{z}_{N+1}, \boldsymbol{z}_N$, etc., which collect the state variables of the two subsystems at the macro-time points $\bar{T}_{N+1}, \bar{T}_N$, etc.. The initial conditions for the macro-time step from $\bar{T}_N$ to $\bar{T}_{N+1}$ are given by the state vector $\boldsymbol{z}_N$ at the time point $\bar{T}_N$. The upper indices p and $*$ (e.g. $\boldsymbol{z}_{N+1}^{p}$ and $\boldsymbol{z}_{N+1}^{*}$) term predicted and arbitrary state variables, whereas the corrected variables (e.g. $\boldsymbol{z}_{N+1}$) are defined without an upper index. In the following analysis, only the case of quadratic approximation polynomials ($k = 2$) in combination with force/force-decomposition is discussed in order to derive the governing system of recurrence equations for the decomposed two-mass oscillator system.

Step 1: Predictor step

An analytical integration of subsystem 1 and subsystem 2 with the predicted (extrapolated)

coupling force $\bar{\lambda}_c^p(\bar{t}) = P_{\bar{\lambda}_c}^p\left[\left(\bar{T}_N, \bar{\lambda}_{c,N}\right), \left(\bar{T}_{N-1}, \bar{\lambda}_{c,N-1}\right), \left(\bar{T}_{N-2}, \bar{\lambda}_{c,N-2}\right); \bar{t}\right]$ yields the predicted state variables at the macro-time point $\bar{T}_{N+1}$

$$\boldsymbol{z}_{N+1}^p = \boldsymbol{z}_{N+1}^p\left(\bar{\lambda}_{c,N}, \bar{\lambda}_{c,N-1}, \bar{\lambda}_{c,N-2}, \boldsymbol{z}_N\right). \tag{10}$$

Step 2: Calculation of corrected coupling variables

By analytically integrating both subsystems from $\bar{T}_N$ to $\bar{T}_{N+1}$ with initial conditions $\boldsymbol{z}_N$ and the interpolated coupling force $\bar{\lambda}_c^*(\bar{t}) = P_{\bar{\lambda}_c}^*\left[\left(\bar{T}_{N+1}, \bar{\lambda}_{c,N+1}^*\right), \left(\bar{T}_N, \bar{\lambda}_{c,N}\right), \left(\bar{T}_{N-1}, \bar{\lambda}_{c,N-1}\right); \bar{t}\right]$, we get the following state variables at the macro-time point $\bar{T}_{N+1}$

$$\boldsymbol{z}_{N+1}^* = \boldsymbol{z}_{N+1}^*\left(\bar{\lambda}_{c,N+1}^*, \bar{\lambda}_{c,N}, \bar{\lambda}_{c,N-1}, \boldsymbol{z}_N\right). \tag{11}$$

Note that $\bar{\lambda}_{c,N+1}^*$ represents an arbitrary coupling force at the macro-time point $\bar{T}_{N+1}$.
Rewriting the coupling condition with the arbitrary state variables $\boldsymbol{z}_{N+1}^*$ yields

$$\bar{g}_{c\lambda,N+1} \coloneqq \bar{\lambda}_{c,N+1}^* - \alpha_{cc1} \cdot \bar{c}_1 \cdot \left(\bar{x}_{2,N+1}^* - \bar{x}_{1,N+1}^*\right) - \alpha_{dc1} \cdot \bar{d}_1 \cdot \left(\bar{v}_{2,N+1}^* - \bar{v}_{1,N+1}^*\right). \tag{12}$$

Furthermore, the Jacobian matrix of the coupling equation $\bar{g}_{c\lambda,N+1}$ with respect to the coupling force, i.e. $J_c = \frac{\partial \bar{g}_{c\lambda,N+1}}{\partial \bar{\lambda}_{c,N+1}^*}$, can be calculated. Since only one coupling variable $\bar{\lambda}_{c,N+1}$ is needed for the force/force-coupling method, the Jacobian matrix is represented by a scalar value. As a result, we obtain the linearized coupling equation as

$$\bar{g}_{c\lambda,linear} \coloneqq \bar{g}_{c\lambda,N+1}^p + J_c \cdot \left(\bar{\lambda}_{c,N+1} - \bar{\lambda}_{c,N+1}^p\right) = 0. \tag{13}$$

Solving Eq. (13) gives the corrected coupling force $\bar{\lambda}_{c,N+1}$.

Step 3: Corrector step

Using the corrected (interpolated) polynomial with the corrected coupling force $\bar{\lambda}_{c,N+1}$ from Eq. (13), an analytical integration of subsystem 1 and subsystem 2 gives the corrected states

$$\boldsymbol{z}_{N+1} = \boldsymbol{z}_{N+1}\left(\bar{\lambda}_{c,N+1}, \bar{\lambda}_{c,N}, \bar{\lambda}_{c,N-1}, \boldsymbol{z}_N\right). \tag{14}$$

Substituting the coupling forces at the time points $\bar{T}_{N+1}, \bar{T}_N$ and $\bar{T}_{N-1}$with the help of the coupling equations results in a relationship of the form

$$\boldsymbol{A}_{N+1} \cdot \boldsymbol{z}_{N+1} + \boldsymbol{A}_N \cdot \boldsymbol{z}_N + \boldsymbol{A}_{N-1} \cdot \boldsymbol{z}_{N-1} = \boldsymbol{0}. \tag{15}$$

The real-valued matrices $\boldsymbol{A}_{N+1}, \boldsymbol{A}_N$ and $\boldsymbol{A}_{N-1} \in \mathbb{R}^{4\times4}$ are constant and depend only on the seven parameters of the co-simulation test model defined above. The linear recurrence system (15) can simply be solved by the exponential approach $\boldsymbol{z}_N = \hat{\boldsymbol{z}} \cdot \Lambda^N$, where Λ denotes the eigenvalue and $\hat{\boldsymbol{z}}$ the Eigenvector of the system. Therefore, the corresponding co-simulation method is called numerical stable, if the spectral radius of the recurrence system is smaller than 1.
In the framework of an explicit co-simulation approach, we consider only step 1, i.e. both subsystems are integrated with the help of extrapolation polynomials. Substituting the coupling forces with the help of the coupling conditions, we get a recurrence system of the form

$$\boldsymbol{A}_{N+1} \cdot \boldsymbol{z}_{N+1} + \boldsymbol{A}_N \cdot \boldsymbol{z}_N + \boldsymbol{A}_{N-1} \cdot \boldsymbol{z}_{N-1} + \boldsymbol{A}_{N-2} \cdot \boldsymbol{z}_{N-2} = \boldsymbol{0}. \tag{16}$$

3.2 Extended implicit co-simulation algorithm

The key concept for the extended co-simulation approaches is to extend the coupling equations by derivatives (D-Extension) and integrals (I-Extension) of the original constitutive equations [6]. Therefore, the coupling variables have to be discretized not only at the macro-time points $\bar{T}_{N+1}, \bar{T}_{N+2}$, etc., but also at intermediate time points, e.g. $\bar{T}_{N+1/2}, \bar{T}_{N+3/2}$, etc.. Corresponding polynomials for approximation order $k = 0, 1, 2$ are shown in Figure 5.

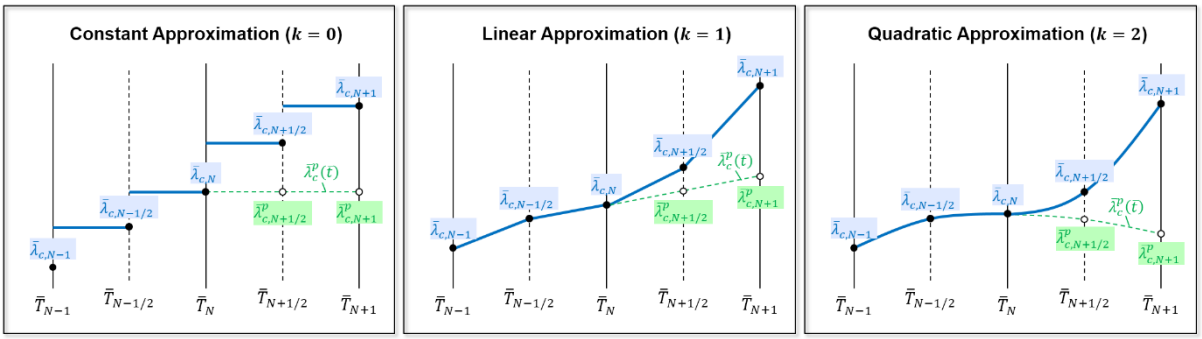

Figure 5: Extended extrapolation and interpolation polynomials for constant, linear and quadratic approximation

Note that the sampling time points between macro steps can be arbitrary and may have an influence on the stability behavior. Here, we consider only the case of equidistantly distributed time points ($\bar{T}_{N+1/2}, \bar{T}_{N+3/2}$, etc.). Based on a predictor-corrector approach, the three integration steps explained above have to be performed with the extended polynomials. In the following, sub-indices D and I (e.g. $\boldsymbol{z}^p_{N+1,D}, \boldsymbol{z}^p_{N+1,I}$) are used to distinguish between D-Extension and I-Extension approaches.

Step 1: Predictor step

An analytical integration of subsystem 1 and subsystem 2 with predicted (extrapolated) coupling forces yields the predicted state variables at the macro-time point $\bar{T}_{N+1}$

$$\begin{aligned} \boldsymbol{z}^p_{N+1} &= \boldsymbol{z}^p_{N+1}(\bar{\lambda}_{c,N}, \bar{\lambda}_{c,N-1/2}, \bar{\lambda}_{c,N-1}, \boldsymbol{z}_N), \\ \boldsymbol{z}^p_{N+1,D} &= (\boldsymbol{z}^p_{N+1})' = \boldsymbol{z}^p_{N+1,D}(\bar{\lambda}_{c,N}, \bar{\lambda}_{c,N-1/2}, \bar{\lambda}_{c,N-1}, \boldsymbol{z}_N), \\ \boldsymbol{z}^p_{N+1,I} &= \int \boldsymbol{z}^p_{N+1}\, d\bar{t} = \boldsymbol{z}^p_{N+1,I}(\bar{\lambda}_{c,N}, \bar{\lambda}_{c,N-1/2}, \bar{\lambda}_{c,N-1}, \boldsymbol{z}_N). \end{aligned} \tag{17}$$

Step 2: Calculation of corrected coupling variables

By analytically integrating both subsystems from $\bar{T}_N$ to $\bar{T}_{N+1}$ and using interpolated coupling forces, we get the following state variables at the macro-time point $\bar{T}_{N+1}$

$$\begin{aligned} \boldsymbol{z}^*_{N+1} &= \boldsymbol{z}^*_{N+1}(\bar{\lambda}^*_{c,N+1}, \bar{\lambda}^*_{c,N+1/2}, \bar{\lambda}_{c,N}, \boldsymbol{z}_N), \\ \boldsymbol{z}^*_{N+1,D} &= (\boldsymbol{z}^*_{N+1})' = \boldsymbol{z}^*_{N+1,D}(\bar{\lambda}^*_{c,N+1}, \bar{\lambda}^*_{c,N+1/2}, \bar{\lambda}_{c,N}, \boldsymbol{z}_N), \\ \boldsymbol{z}^*_{N+1,I} &= \int \boldsymbol{z}^*_{N+1}\, d\bar{t} = \boldsymbol{z}^*_{N+1,I}(\bar{\lambda}^*_{c,N+1}, \bar{\lambda}^*_{c,N+1/2}, \bar{\lambda}_{c,N}, \boldsymbol{z}_N). \end{aligned} \tag{18}$$

Regarding the coupling conditions at the macro-time point $\bar{T}_{N+1}$, we have

$$\begin{aligned}
\bar{g}_{c\lambda} &:= \bar{\lambda}^*_{c,N+1} - \alpha_{cc1} \cdot \bar{c}_1 \cdot \left(\bar{x}^*_{2,N+1} - \bar{x}^*_{1,N+1}\right) - \alpha_{dc1} \cdot \bar{d}_1 \cdot \left(\bar{v}^*_{2,N+1} - \bar{v}^*_{1,N+1}\right), \\
\bar{g}_{c\lambda,D} &:= \bar{\lambda}^{*\prime}_{c,N+1} - \alpha_{cc1} \cdot \bar{c}_1 \cdot \left(\bar{v}^*_{2,N+1} - \bar{v}^*_{1,N+1}\right) - \alpha_{dc1} \cdot \bar{d}_1 \cdot \left(\bar{v}^{*\prime}_{2,N+1} - \bar{v}^{*\prime}_{1,N+1}\right), \\
\bar{g}_{c\lambda,I} &:= \int \left[\bar{\lambda}^*_{c,N+1} - \alpha_{cc1} \cdot \bar{c}_1 \cdot \left(\bar{x}^*_{2,N+1} - \bar{x}^*_{1,N+1}\right) - \alpha_{dc1} \cdot \bar{d}_1 \cdot \left(\bar{v}^*_{2,N+1} - \bar{v}^*_{1,N+1}\right)\right] d\bar{t}.
\end{aligned} \tag{19}$$

Within this step, we have to derive the Jacobian matrix of the coupling equations of (19) with respect to the coupling variables $\boldsymbol{u}^*_c = \left(\bar{\lambda}^*_{c,N+1/2} \quad \bar{\lambda}^*_{c,N+1}\right)^T \in \mathbb{R}^2$, i.e.

$$\boldsymbol{J}_{c\lambda} = \frac{\partial \bar{g}_{c\lambda}}{\partial \boldsymbol{u}^*_c}, \quad \boldsymbol{J}_{c\lambda,D} = \frac{\partial \bar{g}_{c\lambda,D}}{\partial \boldsymbol{u}^*_c}, \quad \boldsymbol{J}_{c\lambda,I} = \frac{\partial \bar{g}_{c\lambda,I}}{\partial \boldsymbol{u}^*_c}. \tag{20}$$

Making use of the partial derivatives, we can calculate the corrected coupling variables so that for D-Extension the coupling conditions $\bar{g}_{c\lambda}$ and $\bar{g}_{c\lambda,D}$ ($\bar{g}_{c\lambda}$ and $\bar{g}_{c\lambda,I}$ for I-Extension) are simultaneously fulfilled at the macro-time point $\bar{T}_{N+1}$. The linearized coupling equations are given by

$$\begin{aligned}
\bar{g}_{c\lambda} &:= \bar{g}^p_{c\lambda} + \boldsymbol{J}_{c\lambda} \cdot \begin{pmatrix} \bar{\lambda}_{c,N+1/2} - \bar{\lambda}^p_{c,N+1/2} \\ \bar{\lambda}_{c,N+1} - \bar{\lambda}^p_{c,N+1} \end{pmatrix} = 0, \\
\bar{g}_{c\lambda,D} &:= \bar{g}^p_{c\lambda,D} + \boldsymbol{J}_{c\lambda,D} \cdot \begin{pmatrix} \bar{\lambda}_{c,N+1/2} - \bar{\lambda}^p_{c,N+1/2} \\ \bar{\lambda}_{c,N+1} - \bar{\lambda}^p_{c,N+1} \end{pmatrix} = 0, \\
\bar{g}_{c\lambda,I} &:= \bar{g}^p_{c\lambda,I} + \boldsymbol{J}_{c\lambda,I} \cdot \begin{pmatrix} \bar{\lambda}_{c,N+1/2} - \bar{\lambda}^p_{c,N+1/2} \\ \bar{\lambda}_{c,N+1} - \bar{\lambda}^p_{c,N+1} \end{pmatrix} = 0.
\end{aligned} \tag{21}$$

Solving the corresponding linearized coupling equations gives the corrected coupling forces $\bar{\lambda}_{c,N+1/2}$ and $\bar{\lambda}_{c,N+1}$ for both the D-Extension and the I-Extension method.

Step 3: Corrector step

Applying an interpolation function with the corrected coupling forces $\bar{\lambda}_{c,N+1/2}$ and $\bar{\lambda}_{c,N+1}$ and substituting the coupling forces with the help of the coupling equations, an analytical integration yields the corrected state variables

$$\boldsymbol{z}_{N+1} = \boldsymbol{z}_{N+1}(\boldsymbol{z}_N, \boldsymbol{z}_{N-1}). \tag{22}$$

This system can symbolically be written as

$$\boldsymbol{A}_{N+1} \cdot \boldsymbol{z}_{N+1} + \boldsymbol{A}_N \cdot \boldsymbol{z}_N + \boldsymbol{A}_{N-1} \cdot \boldsymbol{z}_{N-1} = \boldsymbol{0}. \tag{23}$$

4 STABILITY ANALYSIS OF THE CO-SIMULATION METHODS

The numerical stability of a co-simulation method is defined by the spectral radius of the related system of recurrence equations. The spectral radius is – as outlined in Section 2 – a function of the 7 independent parameters defined in Eq. (3). Instead of using these parameters, it is more convenient to use the subsequent 7 independent parameters for representing the stability behavior

$$
\begin{aligned}
&\overline{\Lambda}_{r1} = -\frac{\bar{d}_1}{2}\,, \overline{\Lambda}_{i1} = \frac{1}{2}\sqrt{4\cdot\bar{c}_1 - \bar{d}_1^2}\,,\\
&\alpha_{m21} = \frac{m_2}{m_1}, \alpha_{\Lambda r21} = \frac{\overline{\Lambda}_{r2}}{\overline{\Lambda}_{r1}} = \frac{\alpha_{d21}}{\alpha_{m21}},\\
&\alpha_{\Lambda i21} = \frac{\overline{\Lambda}_{i2}}{\overline{\Lambda}_{i1}} = \frac{1}{\alpha_{m21}}\frac{\sqrt{4\alpha_{m21}\alpha_{c21}\bar{c}_1 - \alpha_{d21}^2\bar{d}_1^2}}{\sqrt{4\cdot\bar{c}_1 - \bar{d}_1^2}},\\
&\alpha_{\Lambda rc1} = \frac{\alpha_{dc1}}{\alpha_m^*}\,, \alpha_{\Lambda ic1} = \frac{1}{\alpha_m^*}\frac{\sqrt{4\alpha_m^*\alpha_{cc1}\bar{c}_1 - \alpha_{dc1}^2\bar{d}_1^2}}{\sqrt{4\cdot\bar{c}_1 - \bar{d}_1^2}} \quad \text{with} \quad \alpha_m^* = 2\frac{\alpha_{m21}}{1+\alpha_{m21}}.
\end{aligned}
\tag{24}
$$

By fixing 5 parameters, the spectral radius can be plotted as a function of the remaining 2 parameters. In accordance with the 2D stability plots for time integration schemes, where real and imaginary part of the eigenvalue of Dahlquist's test equation are used as axes, we present in the following 2D-stability plots for co-simulation methods, where the spectral radius is depicted as a function of $\overline{\Lambda}_{r1}$ and $\overline{\Lambda}_{i1}$. The five remaining parameters ($\alpha_{m21}, \alpha_{\Lambda r21}, \alpha_{\Lambda i21}, \alpha_{\Lambda rc1}$ and $\alpha_{\Lambda ic1}$) are assumed to be 1 (symmetrical test model) or 10 (unsymmetrical test model). It should be mentioned that the spectral radius has to be computed numerically. The solid circles in the plots indicate stable points, i.e. points for which $\rho < (1 + 10^{-10})$ holds. In order to reduce floating point errors, computation of ρ has been accomplished with 128 digits. Stability plots for the symmetrical and the unsymmetrical test model based on a force/force-decomposition approach can be found in Figure 6 and Figure 7 .

Compared with explicit co-simulation methods, implicit approaches exhibit a significant improvement of the stability behavior. Regarding implicit co-simulation algorithms, D-Extension methods show a better stability behavior than the direct methods. D-Extension in connection with quadratic approximation polynomials ($k = 2$) exhibits the best stability properties for both the symmetrical and the unsymmetrical test model. I-Extension shows for $k = 2$ also an improved stability behavior in comparison with the direct method.

To investigate the influence of the sub-step size on the stability properties, we consider again the I-Extension co-simulation approach for $k = 1$. Not using equidistant sampling points, the numerical stability may be improved. For the analysis, it is useful to define an additional parameter, namely $\alpha_T := (\bar{T}_{N+\alpha} - \bar{T}_N)/(\bar{T}_{N+1} - \bar{T}_N)$ with $\bar{T}_{N+\alpha} \in [\bar{T}_N,\ \bar{T}_{N+1}]$. Stability plots for different values of α_T for $k = 1$ are collected in Figure 8. As can be seen, the numerical stability can be improved for both the symmetrical and unsymmetrical model by modifying α_T.

5 CONCLUSION

Different coupling approaches, where the coupling is realized by constitutive laws, have been discussed within this manuscript. Making use of a linear two-mass oscillator, representing two coupled Dahlquist's equations, a detailed stability analysis has been carried out. Implicit algorithms have been investigated, which are based on a predictor-corrector approach. Also explicit methods have been considered, which only require one single integration step. Also, modified implicit methods have been analyzed, which make use of the derivatives (D-Extension) and integrals (I-Extension) of the constitutive equations. The extended methods

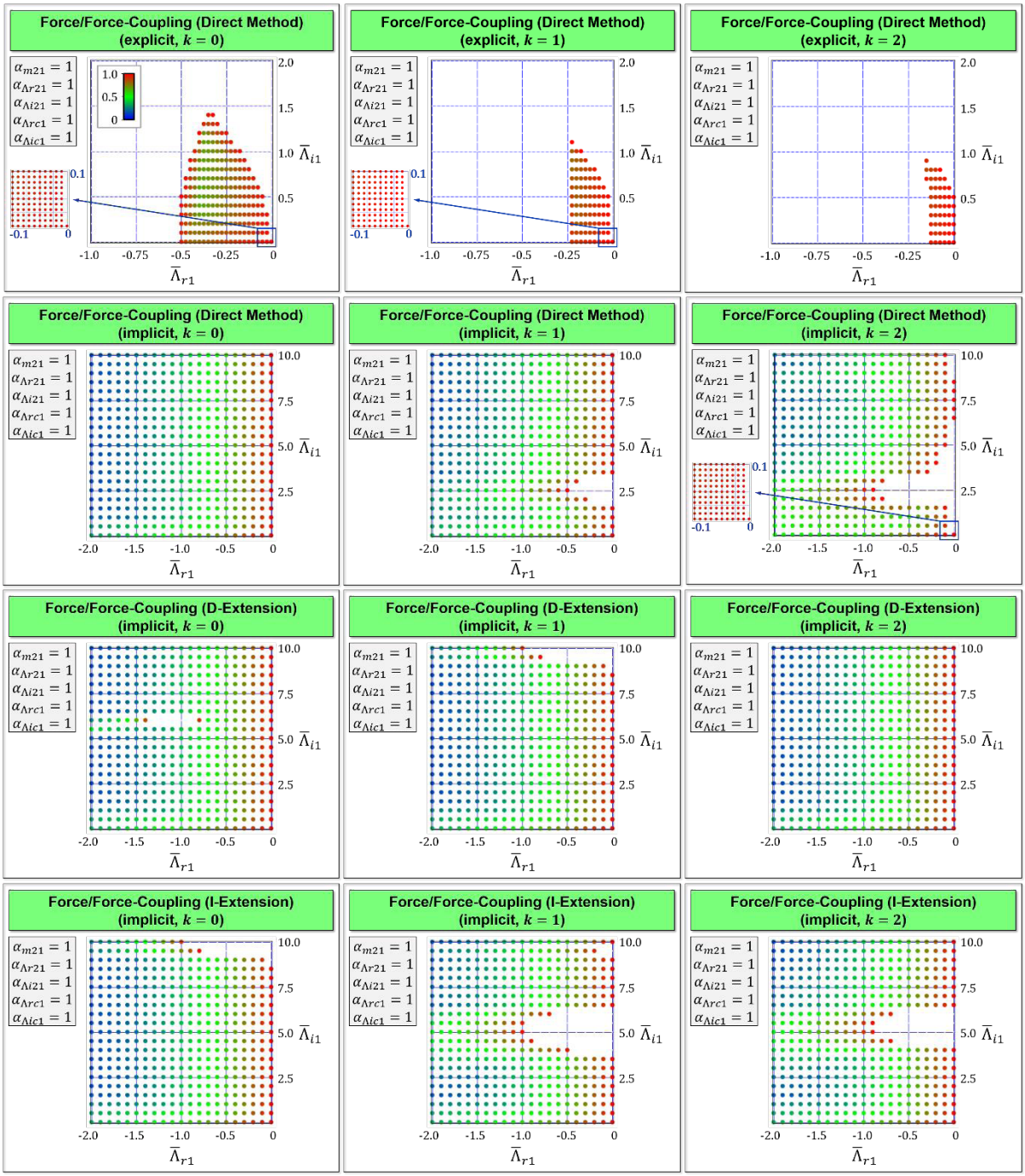

Figure 6: Stability plots for explicit and implicit co-simulation methods using force/force-decomposition with approximation order $k = 0,1,2$ for symmetrical test model

exhibit a better numerical stability behavior, especially in connection with higher-order approximation polynomials.

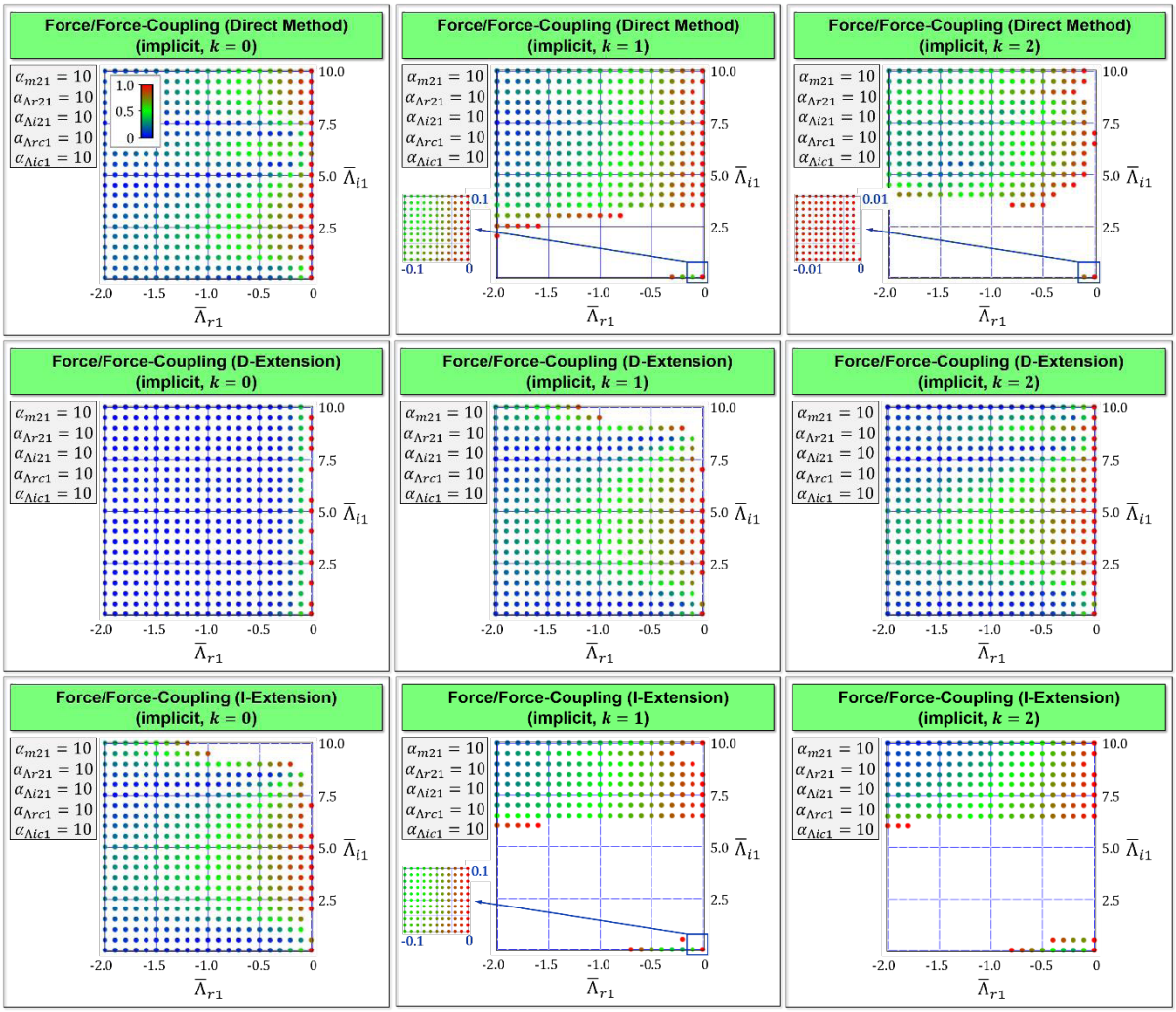

Figure 7: Stability plots for implicit co-simulation methods using force/force-decomposition with approximation order $k = 0,1,2$ for unsymmetrical test model

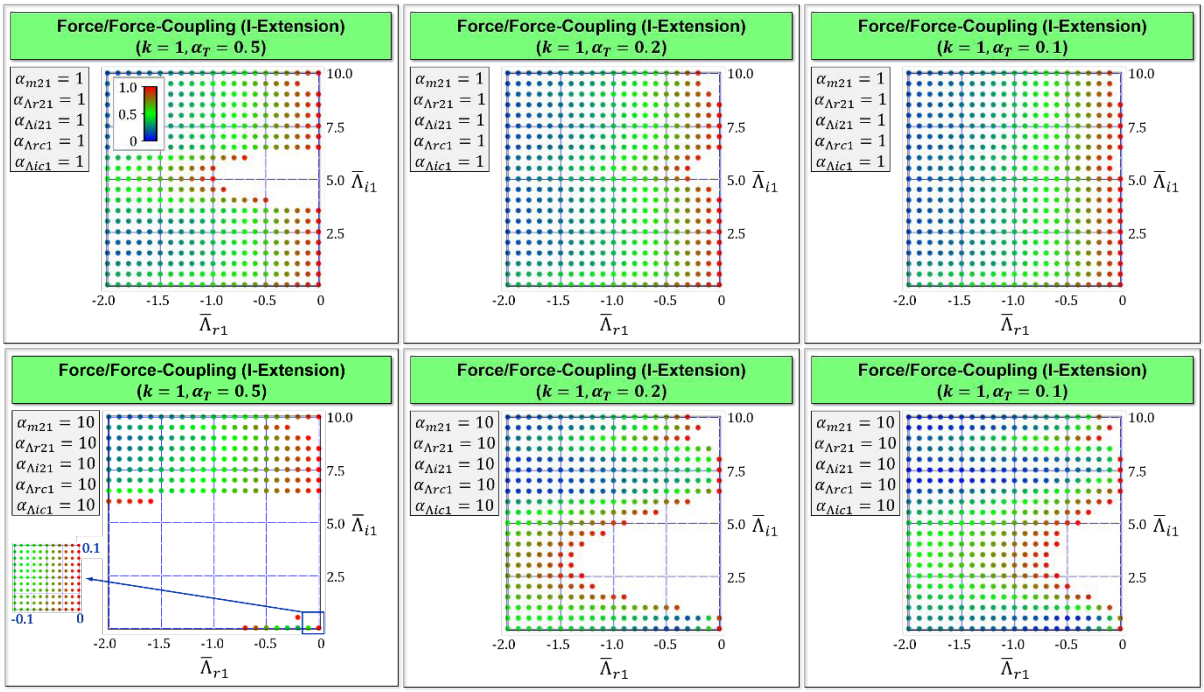

Figure 8: Stability plots for the I-Extension co-simulation method based on a force/force-decomposition approach with approximation order $k = 1$ for different values of α_T

REFERENCES

[1] Ambrósio, J., Pombo, J., Pereira, M., Antunes, P., and Mósca, A., A computational procedure for the dynamic analysis of the catenary-pantograph interaction in high-speed trains, *Journal of Theoretical and Applied Mechanics*, (2012) **50**: 681-699.

[2] Meynen, S., Mayer, J., and Schäfer, M., Coupling algorithms for the numerical simulation of fluid-structure-interaction problems, Proc. *ECCOMAS 2000: European Congress on Computational Methods in Applied Sciences and Engineering, Barcelona, Spain, Sept*, 11-14.

[3] Datar, M., Stanciulescu, I., and Negrut, D., A co-simulation environment for high-fidelity virtual prototyping of vehicle systems, *International Journal of Vehicle Systems Modelling and Testing*, (2012) **7**: 54-72.

[4] Daniel, W. J. T., A study of the stability of subcycling algorithms in structural dynamics, *Computer Methods in Applied Mechanics and Engineering*, (1998) **156**: 1-13.

[5] Schweizer, B., Li, P., and Lu, D., Explicit and Implicit Cosimulation Methods: Stability and Convergence Analysis for Different Solver Coupling Approaches, *Journal of Computational and Nonlinear Dynamics*, (2015) **10**: 051007-051012.

[6] Schweizer, B., Li, P., Lu, D., and Meyer, T., Stabilized implicit co-simulation methods: solver coupling based on constitutive laws, *Archive of Applied Mechanics*, (2015) **85**: 1559-1594.

VII International Conference on Computational Methods for Coupled Problems in Science and Engineering
COUPLED PROBLEMS 2017
M. Papadrakakis, E. Oñate and B. Schrefler (Eds)

NUMERICAL STABILITY OF A FIXED POINT ITERATIVE METHOD TO DETERMINE PATTERNS OF TURBULENT FLOW IN A RECTANGULAR CAVITY WITH DIFFERENT ASPECT RATIOS

B. Bermúdez [*,1], A. Rangel-Huerta[1], D. Alanís[2] and W. Fermín Guerrero S. [3]

[1] Benemérita Universidad Autónoma de Puebla
Facultad de Ciencias de la Computación
Puebla, México
e-mail: bbj@solarium.cs.buap.mx
[2] Universidad Tecnológica de Puebla, Puebla, Mexico
[3] Benemérita Universidad Autónoma de Puebla
Facultad de Ciencias Físico-Matemáticas
Puebla, México

Key words: Navier-Stokes equations, Stream Function-vorticity formulation, Velocity-vorticity formulation, fixed point iterative method

Abstract. 2D isothermal viscous incompressible flows are presented from the Navier-Stokes equations in the Stream function-vorticity formulation and in the velocity-vorticity formulation. The simulation is made using a numerical method based on a fixed point iterative process to solve the nonlinear elliptic system that results after time discretization. The iterative process leads us to the solution of uncoupled, well-conditioned, symmetric linear elliptic problems from which efficient solvers exist regardless of the space discretization. The experiments take place on the lid driven cavity problem for Reynolds numbers up to $Re = 10000$ and different aspect ratios A (A=ratio of the height to the width) $A = 1$ and $A \neq 1$ such as $A = 1/2$, till $A = 3$. It appears that with velocity and vorticity variables is more difficult to solve this kind of flows, at least with a numerical procedure similar to the one applied in stream function and vorticity variables to solve an analogous nonlinear elliptic system. To obtain such flows is not an easy task, especially with the velocity-vorticity formulation. We report here results for moderate Reynolds numbers ($Re \leq 10000$), although with them enough effectiveness is achieved to be able to vary the aspect ratio of the cavity A, which causes the flow to be more unstable. Contribution in this work is to consider rectangular cavities of drag, which can impact on isothermal turbulent flow patterns. Another contribution is to include a wide region of the Reynolds number as well as different aspect ratios where we tested stability of the numerical scheme.

1 INTRODUCTION

In this work, we are dealing with the Navier-Stokes in two different formulations: The Stream Function-vorticity and the Velocity-vorticity formulation. The problem we are going to solve is the well known lid driven cavity problem, with Reynolds numbers $Re \leq 10000$ and different aspect ratios A (A=ratio of the height to the width) of the cavity.

Results, in both formulations, are obtained using a simple numerical scheme based on a fixed point iterative process [1], applied to a nonlinear elliptic system resulting after time discretization. The scheme has shown to be robust enough to handle such Reynolds numbers, ([2] , and [3]) and different aspect ratios of the cavity [5].

Since we are working with Reynolds number up to 10000, as this number increases the mesh has to be refined and a smaller time step has to be used, numerically, by stability matters and physically, to capture the fast dynamics of the flow, as pointed out in ([2], [3]). With the Velocity-vorticity formulation ([6], [7], [4]), a finer mesh and a smaller time step has to be used, and because of this, computing time is in general very large.

2 Mathematical Models

Let $\Omega \subset R^N$ $(N = 2, 3)$ the region of a non-steady, viscous, incompressible flow, and Γ its boundary.

$$\begin{cases} \frac{\partial u}{\partial t} - \nabla^2 \mathbf{u} + \nabla p + (\mathbf{u} \cdot \nabla)\mathbf{u} & = f, \qquad (a) \\ \nabla \cdot \mathbf{u} & = 0 \qquad (b) \end{cases} \tag{1}$$

which are the Navier-Stokes equations in the primitive variables formulation. The system has to be supplemented with appropriate boundary and initial conditions.

2.1 Stream function-vorticity Formulation

First we are going to speak about the Stream function-vorticity formulation.

In this case, we will restrict ourselves to a bidimensional region Ω. Taking the curl in both sides of the equation $(1a)$ and taking into account that

$$\left\{ \; u_1 = \frac{\partial \psi}{\partial y} \, , \quad u_2 = -\frac{\partial \psi}{\partial x} \, , \right. \tag{2}$$

which follows from $(1b)$, with ψ the stream function and u_1, u_2, the two components of the velocity, we get:

$$\begin{cases} \nabla^2 \psi & = -\omega & (a) \\ \frac{\partial \omega}{\partial t} - \frac{1}{Re} \nabla^2 \omega + \mathbf{u} \cdot \nabla \omega = f_\omega & & (b) \end{cases} \tag{3}$$

where ω is the vorticity ($\omega = \frac{\partial u_2}{\partial x} - \frac{\partial u_1}{\partial y}$). These are the Navier-Stokes equations in the Stream function-vorticity formulation. The incompressibility condition $(1b)$, by (2) is

automatically satisfied, and the pressure does not appear any more, which is a great advantage with respect to the primitive variables formulation.

2.2 Velocity-Vorticity Formulation

Taking the curl in

$$\omega = -\nabla \times \boldsymbol{u} \tag{4}$$

and using the identity $\nabla \times \nabla \times \mathbf{a} = -\nabla^2 \mathbf{a} + \nabla(\nabla \cdot \mathbf{a})$ and $(1b)$, a velocity Poisson equation results:

$$\nabla^2 \mathbf{u} = -\nabla \times \boldsymbol{\omega}. \tag{5}$$

Two Poisson equations for the velocity components are obtained, which together with the equation for the vorticity gives us

$$\begin{cases} \frac{\partial u_1}{\partial t} + \nabla^2 u_1 = -\frac{\partial \omega}{\partial y} & (a) \\ \frac{\partial u_2}{\partial t} + \nabla^2 u_2 = \frac{\partial \omega}{\partial x}\,. & (b) \\ \frac{\partial \omega}{\partial t} - \frac{1}{Re}\nabla^2 \omega + \mathbf{u} \cdot \nabla \omega = f_\omega & (c) \end{cases} \tag{6}$$

These are de Navier-Stokes equations in the Velocity-vorticity Formulation.

3 The Numerical Scheme.

Next, we are going to describe the numerical method used for solving the Navier-Stokes equations in both formulations. For the time derivative appearing in the vorticity equation in both schemes, the following second order approximation is used:

$$\frac{\partial f}{\partial t}(\mathbf{x}, (n+1)\Delta t) = \frac{3f^{n+1} - 4f^n + f^{n-1}}{2\Delta t} \tag{7}$$

where $\mathbf{x}\,\epsilon\,\Omega$, $n \geq 1$, Δt denotes the time step, and $f^r \approx f(\mathbf{x}, r\Delta t)$, assuming f is smooth enough.

3.1 Stream function-Vorticity formulation

Speaking about the Stream function-vorticity formulation, it can be observed that the following nonlinear elliptic system has to be solved at each time level:

$$\begin{cases} \nabla^2 \psi = -\omega, \quad \psi|_\Gamma = \psi_{bc}; & (a) \\ \alpha\omega - \nu\nabla^2 \omega + \mathbf{u} \cdot \nabla \omega = f_\omega, \quad \omega|_\Gamma = \omega_{bc}\,, & (b) \end{cases} \tag{8}$$

where $\alpha = \frac{3}{2\Delta t}$, $\nu = \frac{1}{Re}$ and $f_\omega = \frac{4\omega^n - \omega^{n-1}}{2\Delta t}$. To obtain (ψ^1, ω^1), the first subinterval is divided into M subintervals, and a first order scheme, such as Euler, is applied to each of the M subintervals.

Next, we define R_ω by:

$$R_\omega(\omega, \psi) \equiv \alpha\omega - \nu\nabla^2\omega + \mathbf{u} \cdot \nabla\omega - f_\omega \ . \tag{9}$$

System (8) results equivalent to:

$$\left\{ \begin{array}{lll} \nabla^2\psi & = -\omega \ \ in\ \Omega\,, & \psi = \psi_{bc} \quad on\ \ \Gamma \\ R_\omega(\omega, \psi) & = \ \ 0 \ \ in\ \Omega & \omega|_\Gamma = \omega_{bc} \end{array} \right. \tag{10}$$

Now, for solving this system at time level (n+1) the following fixed point iterative process [1] is used:

Given $\omega^{n,0} = \omega^n$, $\psi^{n,0} = \psi^n$ *solve until convergence in* ω *and* ψ

$$\left\{ \begin{array}{l} \nabla^2\psi^{n,m+1} = -\omega^{n,m} \quad in\ \Omega, \\ \psi^{n,m+1} = \psi_{bc}^{n,m+1}\ on\ \Gamma \\ (\alpha I - \nu\nabla^2)\omega^{n,m+1} = (\alpha I - \nu\nabla^2)\omega^{n,m} - \rho_\omega R_\omega(\omega^m, \psi^{n,m+1})\ in\ \Omega, \\ \omega^{n,m+1} = \omega_{bc}^{n,m+1}\ on\ \Gamma,\ \rho_\omega > 0. \end{array} \right. \tag{11}$$

and then, take $(\omega^{n+1}, \psi^{n+1}) = (\omega^{n,m+1}, \psi^{n,m+1})$.

3.2 The Velocity-Vorticity Formulation

In the case of the Velocity-Vorticity formulation, what we do is the following:

For the time derivatives appearing in the vorticity equation (7) is used, and the following semidiscretized system is obtained, in Ω,

$$\left\{ \begin{array}{ll} \frac{\partial u_1}{\partial t} + \nabla^2 u_1 & = -\frac{\partial \omega}{\partial y} \\ \frac{\partial u_2}{\partial t} + \nabla^2 u_2 & = \frac{\partial \omega}{\partial x}, \quad \mathbf{u}^{n+1}|_\Gamma = \mathbf{u}_{bc} \\ R_\omega(\omega, \mathbf{u}) = \mathbf{0}, & \omega|_{\mathbf{\Gamma}} = \omega_{\mathbf{bc}} \end{array} \right. \tag{12}$$

where

$$R_\omega(\omega, \mathbf{u}) \equiv \alpha\omega - \nu\nabla^{\mathbf{2}}\omega + \mathbf{u} \cdot \nabla\omega - \mathbf{f}_\omega \ , \tag{13}$$

Using again the fixed point iterative method described above , we get:

Given $\omega^{n,0} = \omega^n$, $u_1^{n,0} = u_1^n$, $u_2^{n,0} = u_2^n$ *solve until convergence on* ω, u_1 and u_2

$$\begin{cases} \frac{\partial u_1^{n,m+1}}{\partial t} + \nabla^2 u_1^{n,m+1} = -\frac{\partial \omega^{n,m}}{\partial y} \\ \\ \frac{\partial u_2^{n,m+1}}{\partial t} + \nabla^2 u_2^{n,m+1} = \frac{\partial \omega^{n,m}}{\partial x}, \quad \mathbf{u}^{n,m+1}|_\Gamma = \mathbf{u}_{bc}^{n,m+1} \\ \\ (\alpha I - \nu\nabla^2)\omega^{n,m+1} = (\alpha I - \Delta)\omega^m - \rho_\omega R_\omega(\omega^{n,m}, \mathbf{u}^{n,m+1}), \\ \quad \rho_\omega > 0,\ \omega^{n,m+1}|_\Gamma = \omega_{bc}^{n,m}. \end{cases} \tag{14}$$

and then, take $(\omega^{n+1}, u_1^{n+1}, u_2^{n+1}) = (\omega^{n,m+1}, u_1^{n,m+1}, u_2^{n,m+1})$.

4 Numerical experiments

The numerical experiments take place in rectangular domains $\Omega = (a, b) \times (c, d)$, in connection with the lid-driven cavity problem. The boundary condition of $\mathbf{u}$ is given by $\mathbf{u} = (1, 0)$ at the moving boundary $y = d$ and $\mathbf{u} = (0, 0)$ elsewhere.

A translation of the boundary condition in terms of the velocity primitive variable $\mathbf{u}$ to the $\psi - \omega$ variables has to be performed when using the Stream function-vorticity formulation. Following [8], $\psi = 0$ is chosen on Γ, and by Taylor expansion of $(8a)$ on the boundary, with h_x and h_y the space steps, one obtains:

$$\begin{cases} \omega(0, y, t) = -\frac{1}{2h_x^2}[8\psi(h_x, y, t) - \psi(2h_x, y, t)] + O(h_x^2) \\ \omega(a, y, t) = -\frac{1}{2h_x^2}[8\psi(a - h_x, y, t) - \psi(a - 2h_x, y, t)] + O(h_x^2) \\ \omega(x, 0, t) = -\frac{1}{2h_y^2}[8\psi(x, h_y, t) - \psi(x, 2h_y, t)] + O(h_y^2) \\ \omega(x, b, t) = -\frac{1}{2h_y^2}[8\psi(x, b - h_y, t) - \psi(x, b - 2h_y, t)] - \frac{3}{h_y} + O(h_y^2). \end{cases} \tag{15}$$

Now, for the Velocity-vorticity formulation, the boundary conditions are given by:

$$\begin{cases} \mathrm{u}_1 = 0,\ u_2 = 0,\ \omega = \frac{\partial u_2}{\partial x} \text{ on } \Gamma_x = a \\ \mathrm{u}_1 = 0,\ u_2 = 0,\ \omega = \frac{\partial u_2}{\partial x} \text{ on } \Gamma_x = b \\ \mathrm{u}_1 = 0,\ u_2 = 0,\ \omega = -\frac{\partial u_1}{\partial y} \text{ on } \Gamma_y = c \\ \mathrm{u}_1 = 1,\ u_2 = 0,\ \omega = \frac{\partial u_1}{\partial x} \text{ on } \Gamma_y = d \end{cases} \tag{16}$$

In Figure 1 we show results obtained for $Re = 1000$, $A = 1/2$, $Hx = Hy = 1/128$, $dt = .01$ arriving to $T = 100$ (reaching the steady state), and using the Stream Function-vorticity formulation. Left, we show the graphics of the Stream Function, and right the graphics of the isovorticity contours. We did a mesh independence study and results agree

well.

In Figure 2, results are reported for $Re = 1000$ and the same parameters described above, but with aspect ratio $A = 2$.

Now, in the Figure 3, we report results again for $Re = 1000$ and with the same value of the parameters, but now the aspect ratio is $A = 3$.

Next, in Figure 4, results for $Re = 5000$, $A = 2$, $Hx = Hy = 1/512$, $dt = .001$ arriving to $T = 100$.

In Figures 5 and 6, we report results for $Re = 10000$, $Hx = Hy = 1/512$, $dt = .001$ arriving again to $T = 100$. In Figure 5 $A = 2$ and in Figure 6 $A = 3$.

All the above results were obtained using the Stream function-vorticity formulation. And as one can notice, the mesh is not very fine, even for $Re = 10000$ and dt is not so small.

In Figures 7 and 8 we sow results using the Velocity-vorticity formulation. In Figure 7 for $Re = 1000$, $A = 1/2$, $Hx = Hy = 1/256$, $dt = .0001$, $T = 100$. Comparing the results obtained with the Stream Function-vorticity formulation, shown in Figure 1, it can be observed that in Figure 1 more contours appear, and the values of Hx and Hy are the half of the latter and dt ten times higher.

In Figure 8 for $Re = 5000$, $A = 2$, $Hx = Hy = 1/512$ $dt = .0001$, and $T = 100$ also. Figure 4, obtained with the Stream Function-vorticity formulation results much more better, and dt is again is again ten times higher.

Results obtained with the Stream Function-vorticity formulation were obtained in much more less time, using a coarser mesh and more contours appear in the graphics. We could not arrive with the Velocity-vorticity formulation to results for $Re = 10000$ because of the finer mesh needed and also because the dt has to be much more smaller and too much computer time and memory is needed in this last case.

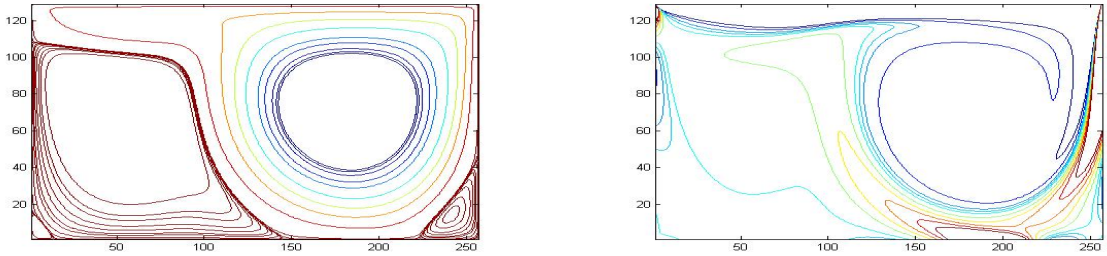

Figure 1: Stream function, left, and isovorticity contours, right, for $Re = 1000$ $A = 1/2$, $dt = .01$, $Hx = Hy = 1/128$, using the Stream function-vorticity formulation.

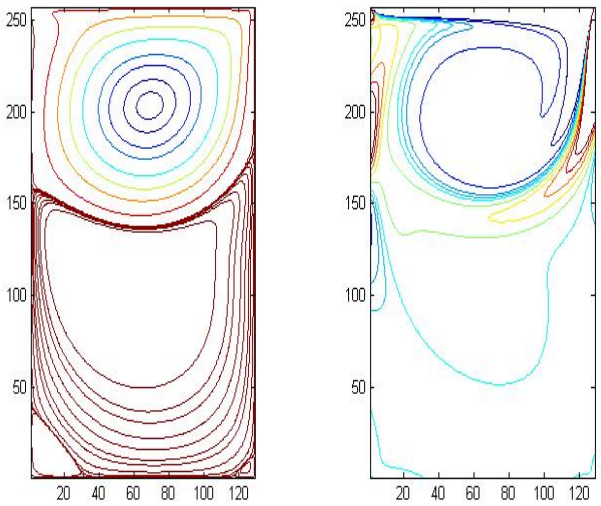

Figure 2: Stream function, left, and isovorticity contours, right, for $Re = 1000$ $A = 2$, $dt = .01$, $Hx = Hy = 1/128$, using the Stream-function-vorticity formulation.

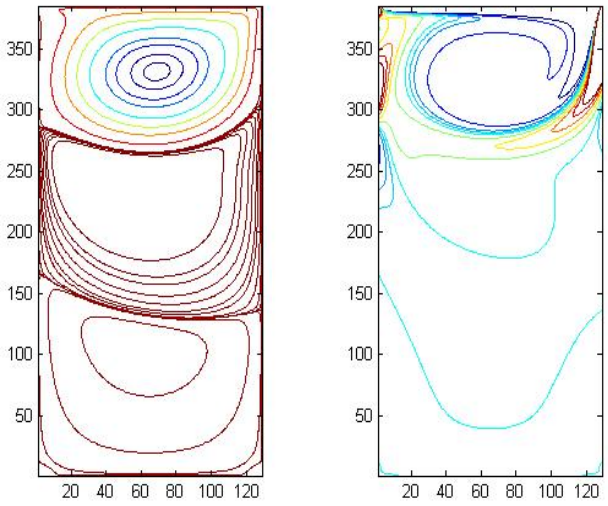

Figure 3: Stream function, left, and isovorticity contours, right, for $Re = 1000$ $A = 3$, $dt = .01$, $Hx = Hy = 1/128$, using the Stream function-vorticity formulation.

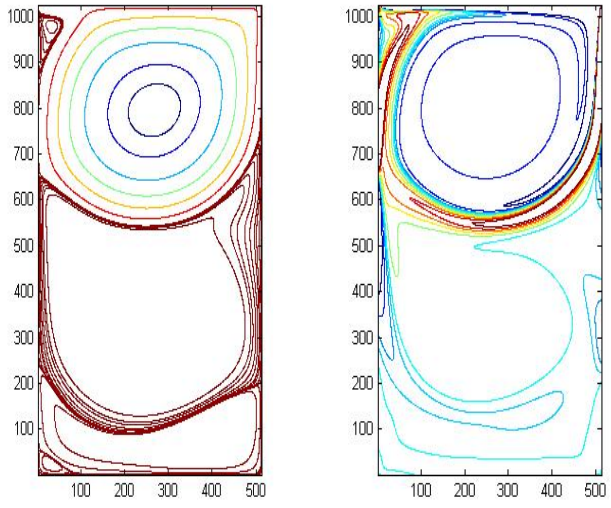

Figure 4: Stream function, left, and isovorticity contours, right, for $Re = 5000$ $A = 2$, $dt = .001$, $Hx = Hy = 1/512$, using the Stream function-vorticity formulation.

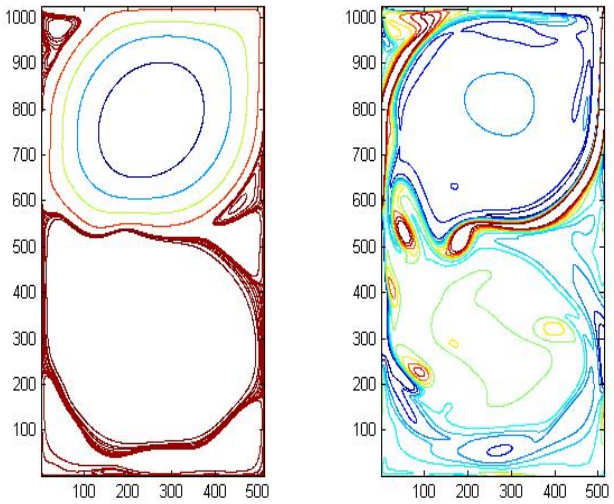

Figure 5: Stream function, left, and isovorticity contours, right, for $Re = 10000$ $A = 2$, $dt = .001$, $Hx = Hy = 1/512$, using the Stream-function-vorticity formulation.

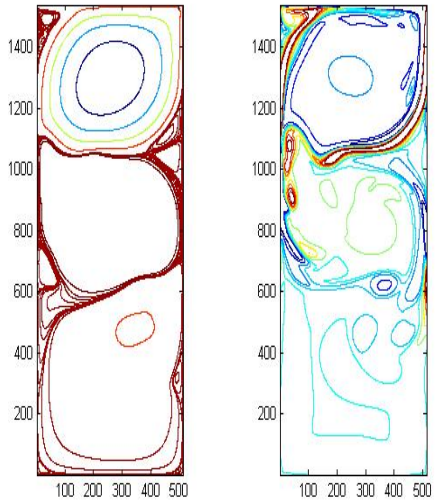

Figure 6: Stream function, left, and isovorticity contours, right, for $Re = 10000$ $A = 3$, $dt = .001$, $Hx = Hy = 1/512$, using the Stream function-vorticity formulation.

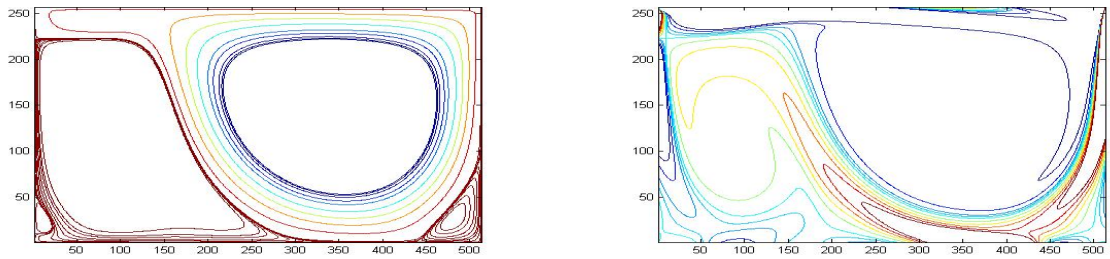

Figure 7: Stream function, left, and isovorticity contours, right, for $Re = 1000$ $A = 1/2$, $dt = .001$, $Hx = Hy = 1/256$, using the Velocity-vorticity formulation.

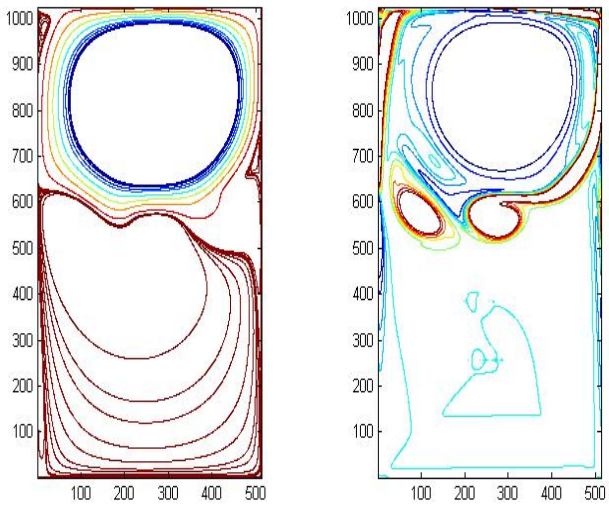

Figure 8: Stream function, left, and isovorticity contours, right, for $Re = 5000$ $A = 2$, $dt = .0001$, $Hx = Hy = 1/512$, using the Velocity-vorticity formulation.

5 Conclusions

We are presenting efficient numerical methods for solving the Navier-Stokes equations in the Stream funtion-vorticity and the Velocity-vorticity formulations. Both formulations provide turbulent flow patterns of the cavity for a wide range of Reynolds numbers. New results of flow profiles in conditions not included in the literature are presented ([7]).

We note that you for this range of numbers, stream flow patterns agree with those reported in the literature ([9]). However, the instrumentation for the Velocity-vorticity formulation is more complicated for effects of maintaining numerical stability. The time step, and the mesh size must be drastically reduced compared with those used in the Stream function-vorticity formulation. This results in a big cost of computing time and memory. In the Velocity-vorticity formulation the cavity flow lines are reproduced (not as well as with the Stream function-vorticity formulation using a coarser mesh size).

The numerical procedure applied to the Stream Function-vorticity formulation is not as good for the Velocity-vorticity formulation, however, the way it behaves, through the discretization parameters, and the order of discretization, gives us another point of view of the behavior of flows under different numerical methods and different formulations. The difficulty of the Velocity-vorticity formulation is reinforced through some works such as [9] who with a very different more sophisticated method reported driven cavity flows for moderate Reynolds numbers, lower than ours.

6 Acknowledgements

The authors would like to acknowledge the support received by the National Laboratory of Supercomputing from of the southeast of Mexico BUAP-INAOE-UDLAP (Laboratorio Nacional de Supercmputo del sureste de México) in running our programs and especially to Dr. Humberto Salazar Ibargüen for his support.

REFERENCES

[1] Nicolás, A. A Finite element approach to the Kuramoto-Sivashinski equation. *Advances in Numerical Methods*, SIAM (1991).

[2] Nicolás A., Bermúdez B., 2D incompressible viscous flows at moderate and high Reynolds numbers, *CMES* (2004) **6(5)** 441–451

[3] Nicolás-Carrizosa A., Bermúdez-Jurez B., Onset of two dimensional turbulence with High Reynolds numbers in the Navier-Stokes equations, *Proceedings IV International Conference on Computational methods for Coupled Problems,* (2011) 1-11.

[4] Blanca Bermúdez y Alfredo Nicolás, Flujos Isotrmicos/Trmicos, Incompresibles y viscosos con Formulacin velocidad-vorticidad, Información Tecnológica, (2010) Vol 21(3), 39-49

[5] Blanca Bermúdez and Alfredo Nicolás, Mixed convection/isothermal viscous incompressible flows with velocity-vorticity variables, Proceedings of the 2nd. International Multiconference on Engineering and Technological Innovation, (2009) 9-14

[6] Nicolás A., Bermúdez B., Viscous incompressible flows by the Velocity-Vorticity Navier-Stokes equations, *CMES* (2007) **20** No. 2, 73–83

[7] Bermúdez B., Nicolás A., The Taylor Vortex and the Driven Cavity Problems by the Velocity-Vorticity Formulation, *Proceedings 7th. International Conference on Heat Transfer and Fluid Mechanics and Thermodynamics* (2010) 629-632

[8] Goyon, O., High Reynolds numbers solutions of Navier-Stokes Equations using incremental unknownks, *Comput. Methods Appl. Math. Engrg.* (1996) 319-335

[9] Grimaldi A., Pascazio G., Napolitano M., A Parallel Multi-block Method for unsteady Vorticity-velocity Equations, texitCMES, (2006) **14(1)** 45–56

VII International Conference on Computational Methods for Coupled Problems in Science and Engineering
COUPLED PROBLEMS 2017
M. Papadrakakis, E. Oñate and B. Schrefler (Eds)

THE INFLUENCE OF THERMAL BARRIERS IN ANISOTROPIC MEDIA APPLIED TO PCB USING MEC

N.C. ANUNCIAÇÃO JR [*], T.S.L. OLIVEIRA[†] AND C.T.M ANFLOR [†]

[*] Grupo de Mecânica Experimental e Computacional (GMEC)
ICESP/Promove
e-mail: engnjunior@gmail.com

[†] Universidade de Brasília (UnB)
Área Especial de Indústria Projeção A, 480, Gama Leste, Brasília – DF, Brasil
email: tatiane.faesb@gmail.com, anflorgoulart@gmail.com

Key words: Thermal Barriers, Optimization, Heat Transfer, Boundary Element Method, Genetic Algorithm, PCB.

Abstract. Many electronical components were developed during the last years and many efforts were devoted to the miniaturization of their components due to the global tendency. The matrix in which the components are mounted are made of composite materials which presented anisotropic behaviour. The main goal of this work relies on determining the influence of the thermal barriers position inside of a PCB. The plate has 168 thermal barriers inside the domain where each one has a 360° of freedom of rotation. A Dirichlet boundary condition was imposed to all corners of the plate to analysis. The heat flux was observed at the A, B, and C corners, as the internal barriers were rotated. A quadratic boundary element was used and The multipoint Genetic Algorithm was employed in order to maximize the objective function at the corner A and minimizing at the corners B and C. Despite the elevated number of variables classified this problem such as non-convex, the final results showed good convergence.

1 INTRODUCTION

Due to the trend of electronics miniaturization, some circuits' settings bring devices with a high power dissipation, which results in serious problems on the behavior of the product. Knowing the limitation for the temperature and the thermal flow inside a printed circuit board (PCB) is crucial to make the right decisions in order to improve a project.

In this sense, several researchers have focused their effort in studying how to improve thermal efficiency of electronic components, which can be done using numerical or experimental techniques [1]. It is common knowledge that experimental techniques are, a few times, extremely expensive due to the need of manufacturing numerous prototypes and considerable cost measuring equipment.

The Finite Element Method (FEM) is widely applied in the numerical techniques. The main characteristic of FEM is the need of an electrical grid to solve the differential equation ruler of the problem.

In cases of optimization, a strict control of the electrical grid is needed to check the

convergence of the solution, which raises the computing cost in a considerable way [7]. On the last few decades, a new method, known as Boundary Element Method (BEM), has been catching the scientific community's attention, because of its characteristic of needing discretization only on its borders. This particularity makes this method be more attractive to optimization problems [2]. This unique characteristic brings an advantage, because during the iterative process of optimization, the geometry of the problem doesn't need rediscretization [3]. Another important factor refers to the matrix system, that, for being smaller than the one generated by the FEM, results in a significant reduction in computing costs for optimization problems. Despites the advantages of BEM, FEM is still the most used method, because the formulation of BEM is more complex. [6] employs FEM and Genetic Algorithm (GA) in the simulation and optimization of a thermal flow in anisotropic materials. In this paper, the thermal flow was controlled by a non-linear programming method, in which each part of the iteration process generated a convex problem of the approach of the solution of the problem. The optimization process employed in this paper was the mathematical method known as "Method of Moving Asymptotes" or MMA, that stabilizes or speeds up the convergence of the process of pursuit for great solution. The author focused his efforts in substantially reducing the maximum temperature of the optimized material and in concentrating the power density in the intended places.

The convergence method that will be employed in this paper is the "Non-dominated Sorting Genetic Algorithm II", mostly known as NSGA II. The algorithm chosen calculates a multi-objective function in which implements the concept of Dominance, in other words, ranks the total population according to the level of importance [9]. The individuals are divided into different levels through this criterion. Using this formulation, the best individuals are stored in the system, as the worst ones are excluded from the system [5]. These results have been assigned to a fundamental reduction in the thermal resistance of the material. Following the same line of investigation, the purpose of this paper is studying the best spatial configuration of the inner fiber of a manufactured PCB with anisotropic behavior to control the thermal flow, employing BEM linked to the GA through the NSGA II process.

2 BEM FOR POTENTIAL PROBLEMS

The heat transfer problem when there is no power supply is controlled by Laplace Equation $\Delta u = 0$. Applying the divergence theorem, Betti's theorem and the weighted residual method makes possible reduce a domain problem into a boundary problem [4]. In the weighted residual method, the function weight used is the fundamental solution of the ruler equation. The problem to be handled is established by a BIE (Boundary Integral Equation), presented as the Eq. (1).

$$\frac{1}{2}u^{i}(x)+\int_{\Gamma}u(x)\,q^{*}(x,x')d\Gamma=\int_{\Gamma}q(x)\,u^{*}(x,x')d\Gamma \tag{1}$$

When it comes to entirely anisotropic devices, the ruler equation is written in Cartesian coordinates [11], the equations can be represented according to the Eq. (2).

$$k_{11}\frac{\partial^2 u}{\partial x_1^2}+2k_{12}\frac{\partial^2 u}{\partial x_1 \partial x_2}+k_{22}\frac{\partial^2 u}{\partial x_2^2}=0 \tag{2}$$

Assuming that the tensile properties of the materials are symmetric, the equations can be written as temperature and flow fundamental solutions according to Eq. (3) and Eq. (4), respectively. The distance value between the point supply and the point field can be acquired according to the Eq. (5).

$$u^* = -\frac{1}{2\pi \mid k_{ij} \mid^{1/2}} ln(r) \tag{3}$$

$$q^* = \left(k_{11}\frac{\partial u^*}{\partial x_1} + k_{12}\frac{\partial u^*}{\partial x_2} \right) n_{x1} + \left(k_{12}\frac{\partial u^*}{\partial x_1} + k_{21}\frac{\partial u^*}{\partial x_2} \right) n_{x2} \tag{4}$$

$$r = \left\{ k_{11}\left(x_1^i - x_i\right)^2 + 2k_{12}\left(x_1^i - x_1\right)\left(x_2^i - x_2\right) + k_{22}\left(x_2^i - x_2\right)^2 \right\}^{1/2} \tag{5}$$

Where $\mid k_{ij} \mid$ is the determinant of the conductivity and s is the inverse of the matrix k, as shown in Eq. (6).

$$\mid k_{ij} \mid = k_{11}k_{22} - k_{12}^2 \quad ; \quad s = k^{-1} = \frac{1}{\mid k_{ij} \mid}\begin{bmatrix} k_{22} & -k_{12} \\ -k_{12} & k_{11} \end{bmatrix} \tag{6}$$

To turn the anisotropic solution into an isotropic solution, it is established that $k_{12} = 0$ e $k_{11} = k_{22}$ to the symmetric properties of the ruler equation of Cartesian coordinates in the Eq. (2). Isoparametric elements are those in which the same functions are used to approach both the geometry and the boundary variable. The values of u and q for any point belonging to the element can, this way, be written in terms of nodal values and interpolation function in accordance with Eq. (7).

$$\begin{aligned} u(\xi) &= N_1u_1 + N_2u_2 + N_3u_3 = \begin{bmatrix} N_1 N_2 N_3 \end{bmatrix}\begin{Bmatrix} u_1 \\ u_2 \\ u_3 \end{Bmatrix} \\ q(\xi) &= N_1q_1 + N_2q_2 + N_3q_3 = \begin{bmatrix} N_1 N_2 N_3 \end{bmatrix}\begin{Bmatrix} q_1 \\ q_2 \\ q_3 \end{Bmatrix} \end{aligned} \tag{7}$$

Where ξ is the isometric coordinates location, determined between [-1,+1] and N_1, N_2 e N_3 are functions of continuous quadratic equations. Considering the discretizations, the integrals of equations can be written according to the Eq.(8) and Eq.(9).

$$\int_{\Gamma j} u^* q \, d\Gamma = \int_{\Gamma j} u^* \left[N_1 \, N_2 \, N_3 \right] q \, d\Gamma = \left[G_1^{ij} \, G_2^{ij} \, G_3^{ij} \right] \begin{Bmatrix} q_1 \\ q_2 \\ q_3 \end{Bmatrix} \tag{8}$$

$$\int_{\Gamma j} q^* u \, d\Gamma = \int_{\Gamma j} q^* \left[N_1 \, N_2 \, N_3 \right] u \, d\Gamma = \left[H_1^{ij} \, H_2^{ij} \, H_3^{ij} \right] \begin{Bmatrix} u_1 \\ u_2 \\ u_3 \end{Bmatrix} \tag{9}$$

The Eq. (8) e (9) are discretized to all the boundary and result as the Eq. (10).

$$c^i u^i + \sum_{j=1}^{N} H^{ij} u^j = \sum_{j=1}^{2N} G^{ij} q^j \tag{10}$$

For reordering of Eq. (10), the unknown variable are placed on the left side {X} and a vector on the right side {F} gotten by multiplying the matrix elements by known values of flow and potential. This procedure results in the system shown in the Eq. (11) that discovers all the boundary unknowns when solved.

$$\left[A \right] \{ X \} = \{ F \} \tag{11}$$

2.1 Continuous Quadratic Elements

In the discretization that uses continuous quadratic elements, the geometry is approached by a quadratic function along each element, therefore, three nodal dots per element are required, according to the Figure 1.

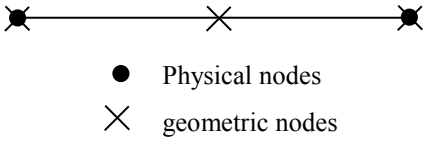

Figure 1: Discretization of the geometry of quadratic elements

The boundary elements Γ_i are considered parabolic, which means they are described by polynomials of 2nd order (parabola equation). This way, 3 points of Γ_i are required so that a parabola can be set. These points are determined by $(x_1, y_1), (x_2, y_2)$ e (x_3, y_3), that correspond, respectively, to the intrinsic coordinates $\xi = -1$, $\xi = 0$ e $\xi = 1$, as illustrated in the Figure 2. Creating a parabolic function to relate x to ξ, there is:

$$x = a\xi^2 + b\xi + c \tag{12}$$

Being:

$$x(\xi = -1) = x_1, \; x(\xi = 0) = x_2 \; e \; x(\xi = +1) = x_3 \tag{13}$$

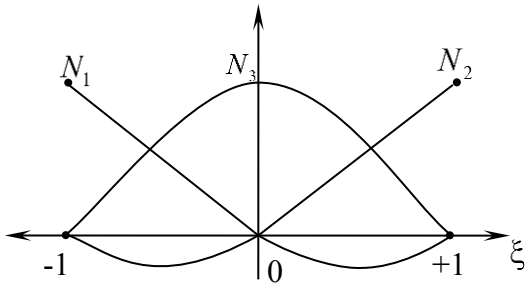

Figure 2: Continuous quadratic Interpolation Functions

The interpolation Functions can be written according to the Eq.(14).

$$x = \underbrace{\frac{\xi}{2}(\xi-1)x_1}_{N_1} + \underbrace{(1-\xi)(1+\xi)x_2}_{N_2} + \underbrace{\frac{\xi}{2}(\xi+1)x_3}_{N_3} \tag{14}$$

Being:

$$x = N_1 x_1 + N_2 x_2 + N_3 x_3 \tag{15}$$

Where $N_1, N_2 \text{ e } N_3$ are the continuous quadratic interpolation Functions determined in accordance with Eq.(16).

$$N_1 = \frac{\xi}{2}(\xi-1),\ N_2 = (1-\xi)(1+\xi) = 1-\xi^2 \ \textit{and}\ N_3 = \frac{\xi}{2}(\xi+1) \tag{16}$$

Likewise, there is:

$$y = N_1 y_1 + N_2 y_2 + N_3 y_3 \tag{17}$$

In the discretization that uses BEM, the geometry is approximated by a quadratic function along each element, and needs three nodal points per element. This way, temperatures and flows are approximated according to the Eq. (18) and (19).

$$u = N_1 u_1 + N_2 u_2 + N_3 u_3 \tag{18}$$

$$q = N_1 q_1 + N_2 q_2 + N_3 q_3 \tag{19}$$

Where u_1 is the temperature in the local node 1, u_2 is the temperature in the local node 2, u_3 is the temperature in the local node 3, q_1 is the flow in the local node 1, q_2 is the flow in the local node 2, q_3 is the flow in the local node 3, N_1 is the Interpolation Function 1, N_2 is the interpolation function 2 and N_3 is the interpolation function 3. The continuous quadratic interpolation functions N_1, N_2 and N_3 are shown by the Figure 2 and the interpolation function

formulation is shown by the Eq. (16). By writing in the matrix form, Eq. (20) and (21) can be found.

$$u = \left[N_1 N_2 N_3\right] \begin{bmatrix} u_1 \\ u_2 \\ u_3 \end{bmatrix} \tag{20}$$

$$q = \left[N_1 N_2 N_3\right] \begin{bmatrix} q_1 \\ q_2 \\ q_3 \end{bmatrix} \tag{21}$$

The integral equation is, then, written according to Eq.(22).

$$c\,u(\mathrm{d}) = \sum_{j=1}^{n_{elem}} \left\{ \left[H_1 H_2 H_3\right]_j \begin{bmatrix} u_1 \\ u_2 \\ u_3 \end{bmatrix}_j - \left[G_1 G_2 G_3\right]_j \begin{bmatrix} q_1 \\ q_2 \\ q_3 \end{bmatrix}_j \right\} \tag{22}$$

3 OPTIMIZATION USING GENETIC ALGORITHM

The optimization via GA is the act of discovering a result or a set of great solutions to some circumstances, in other words, it's the pursuit of a better result to a certain function or a set of functions [10]. The method copies the biological processes based on the evolution of the species, where the procedures are basically: natural selection, pairing and mutation.

A ramdom initial population was created in the numerical implementation, containing enough diversity so that it can combine characteristics in order to produce new populations. The selection operator employed was NSGA II, where an objective function is calculated in order to give the algorithm standards to select the best individuals. The objective function is essential to spread to future generation the best results in each generation. In this case of NSGA II application only the best solutions will keep on existing to the next generations. All the GA procedure can be seen in the Figure **3**.

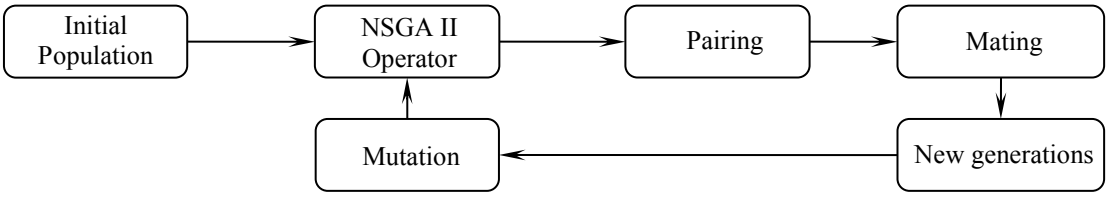

Figure 3: Genetic Algorithm

The pairing operator defines the pairs using the best characteristics from inviduals. The next step is the mating, that consists of creating new topologies (families). In this paper, a pairing based on Charles Darwin's *The Origin of Species*, a *crossover* kind (mating operator), was adopted. This procedure generates two children to each mating, where they will be members

for the next generations. The *crossover* is determined with chromosomal percentages from the parents, where the process can be visualized from the scheme shown in the Figure 4. It is possible to observe that the first son received more chromosomal characteristics from the father, as the second son received more chromosomal characteristics from the mother. The same procedure is repeated, but with individuals carrying different characteristics from the first generation, until the individual who carries the best genetic information is found. The last operator is the mutation, which is responsible for randomly change a small amount of chromosomes. The chromosomes carry genetic information in form of binary numbers. The mutation is illustrated in the Figure 4, that consists in the random change of one of the chromosomes' position from 0 to 1 or vice versa, this simple procedure is one of the biggest GA attractives, because it avoids the algorithm stagnation in a minimum place, increasing the chances of finding the maximum global of the search field.

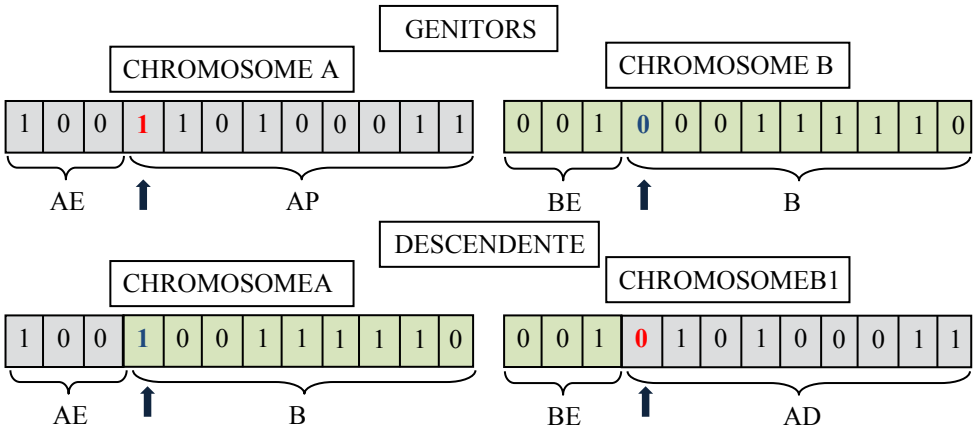

Figure 4: Details of the Pairing, Crossover and Mutation process.

The optimization process described continues until a stop command is reached. The stop command is usually defined as a maximum number of iterations or the maximum/minimum value of the objective function. The Figure 5 shows the algorithm scheme implemented in this paper, where the BEM/GA subroutines are included. In the optimization process the objective function is defined with the specific need of the project. For each individual there is an objective function value, where the best rated are selected and the worst ones are ruled out. In this sense, the population will converge to a best configuration that meets the project specification.

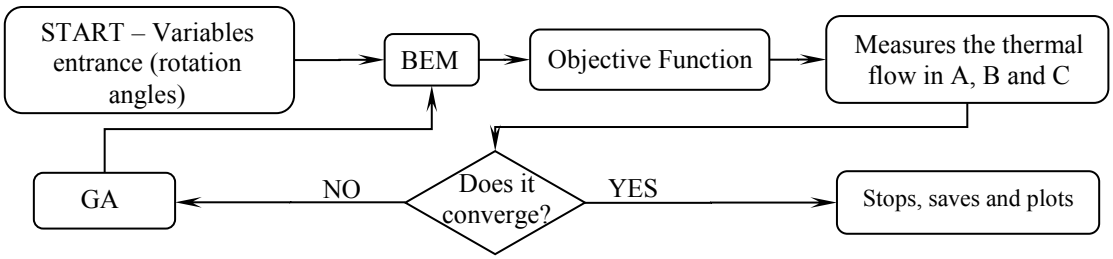

Figure 5: Genetic Algorithm routine associated with BEM

4 NUMERICAL RESULTS

In order to evaluate the methodology proposed to solve a PCB, a rectangular area of 2x1 units is considered, subject to Dirichlet boundary condition in three of its edges (in A, B, C and D) and subject to Neumann boundary condition in others (check Figure 2). All the area was discretized with 1464 boundary continuous quadratic elements. From these 1464 elements, 792 were used discretize the external boundary and the remaining ones were utilized to discretize the holes. Each hole was discretized with 8 elements. In the inner of the domain were inserted 168 holes, which represent the fibers with characteristics of low thermal conductivity materials (insulating). In this sense, was prescribed Neumann condition equals to zero and the numerical integration was accomplished with six Gauss points. To the optimization process for better arrangement of fibers inside the matrix, the GA with theory of evolution was employed. The Table 1 shows the parameters utilized in this process.

Table 1: Optimization Parameters

GA Parameters	
Initial Population	50
Final Population	500
Crossover	5%
Mutation	1%

The initial arrangement of fibers was defined initially as random (iteration 1), and for the optimization process the project variables are the rotation angles of fibers themselves, in which each one of them is able to, idenpendently of each other, rotate 360 degrees. For the optimization process, the objective function aims to maximize the flow at the edge A and minimize it at the edges B and C. Boundary conditions were added to the point D (100º C) and 25º C to the points A, B and C. The purpose consists in measuring the flow fields at the edges displayed as A, B and C in order to meet the multi-objective function, required by the GA.

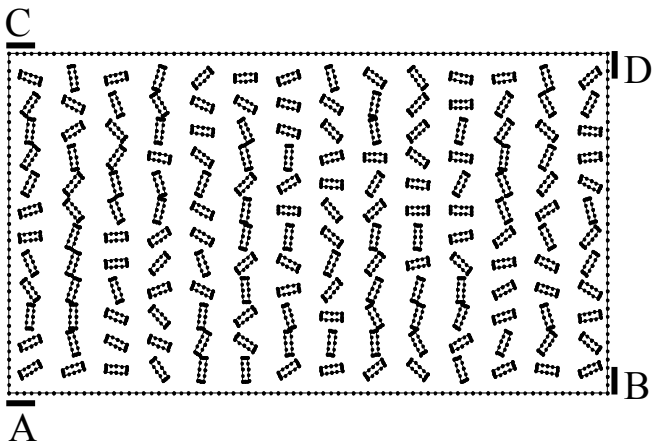

Figure 6: Details of boundary conditions and initial PCB lay-out

In this paper two cases will be analyzed, both isotropic and anisotropic behavior matrix. The

thermal flux behavior, as well as the fibers orientation will be presented and discussed for both cases.

4.1 Isotropic Matrix

In this paper the Eq.(2) is reduced to the isotropic problem when established that $k_{11} = k_{22} = k$ e $k_{12} = 0$ and rewritten according to Eq. (23).

$$k\left(\frac{\partial^2 u}{\partial y_1^2} + \frac{\partial^2 u}{\partial y_2^2}\right) = 0 \tag{23}$$

Where k is the material thermal conductivity for isotropic environments. The isotropic thermal conductivity tensor for the 2D problem studied in this paper is shown in Eq.(24).

$$k = \begin{bmatrix} 1 & 0 \\ 0 & 1 \end{bmatrix} \tag{24}$$

The Figure 7 refers to the iteration 478, which presents the best project configuration after the optimization process reaching the stop command established. The total number of iterations was adjusted in 500, where the population was evaluated until the acquisition of the biggest flow value on the edge A, from the best fiber angles distribution. The Figure 7 makes possible to observe the fibers disposal in the sense of prioritizing the thermal flow from the edge D to the edge A.

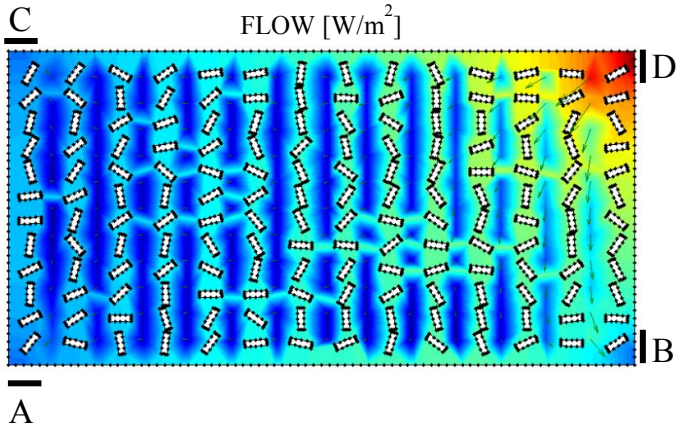

Figure 7: Iteration 478 with better flow distribution

The Figure 8 shows the flow evolution on the edges A, B and C as the iterative process evolves. The disposition of the fibers inside the PCB makes the thermal flows on the three edges oscillate. It happens because the optimization is multi-objective and at the same time that it maximizes on the edge A, it minimizes on the edges B and C. Observing specifically the point A, the iteration 1 was started in 131,29 W/m² and, in the end of the iteration process the flow is maximized to 145,41 W/m². On the edges B and D the thermal flow of the first iteration was measured in 360,54 W/m² and 132,23 W/m², respectively. Considering the last iteration, the

thermal flows values to these edges were minimezed to 132,23 W/m² and 127,54 W/m². By answering the multi-objective function is possible to verify, simultaneously on Figure 7 and Figure 8 that the fibers were rotated in a way to direct the flow field to the edge A.

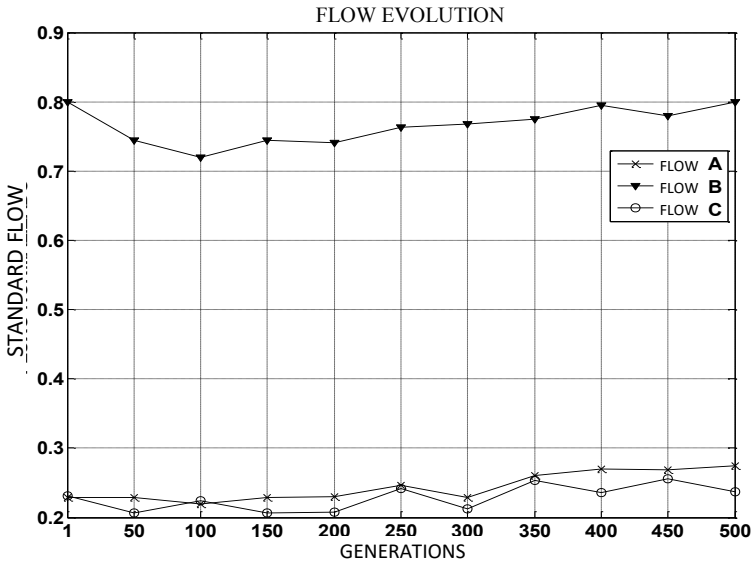

Figure 8: Thermal flow evolution on the edges A, B and C

4.2 Anisotropic Matrix

To materials in a totally anisotropic environment, the ruler equation presented in Eq. (2) is used in its complete form and rewritten again for convenience, as shown in Eq. (25).

$$k_{11}\frac{\partial^2 u}{\partial x_1^2} + 2k_{12}\frac{\partial^2 u}{\partial x_1 \partial x_2} + k_{22}\frac{\partial^2 u}{\partial x_2^2} = 0 \tag{25}$$

Where k_{ij} is the coefficient that represents the property terms of the tensors in directions i e j. In this paper the values of the thermal conductivity tensor to the anisotropic matrix were established in accordance with Eq.(26).

$$k = \begin{bmatrix} 1 & 0,5 \\ 0,5 & 2 \end{bmatrix} \tag{26}$$

The Figure 9 presents the best project configuration, which was reached in the iteration 473 of the optimization process. Despite the anisotropic behavior of the matrix, it is possible to verify the tendency of the fibers in directing their thermal flow to the edge A.

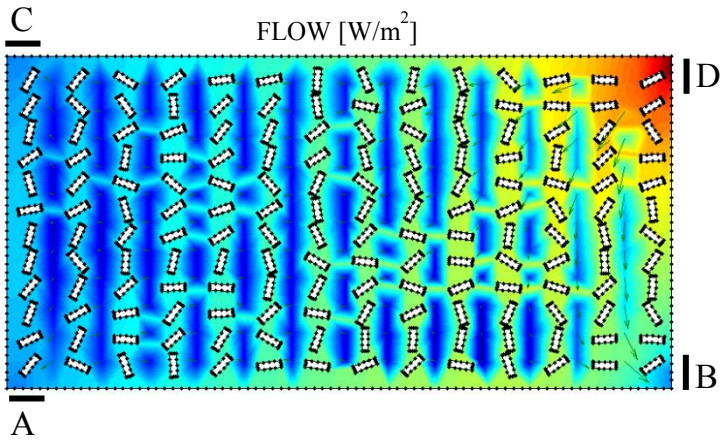

Figure 9: Iteration 473 com better flow distribution

The Figure 10 shows the thermal flow behavior during the evolution of the optimization accomplished by the GA. In the first iteration the thermal flow on the edge A was calculated in 201.67 W/m² being maximized to 217.06 W/m². To the edge B and C the thermal flow in the first iteration was measured in 445.35 W/m² and 135.73 W/m², being minimized at the end of the iterative process to 395.92 W/m² and 122.63 W/m², respectively. Despite not being as evident as in the isotropic case, it is also possible to verify a fiber alignment in the diagonal direction from the edge D to A, with the purpose of prioritizing the thermal flow between these two extremes.

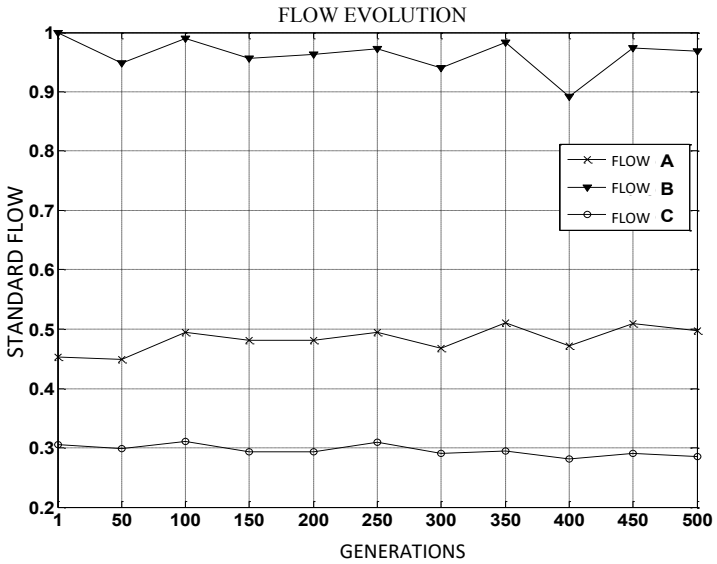

Figure 10: Flow developments on the edges A, B and C

5 CONCLUSIONS

The primary goal of this paper was to control the thermal flow of a Printed Circuit Board (PCB) with anisotropic behavior in three control points, which were defined under the edges A, B, and C. The BEM was used to solve Laplace's equation and, due to its characteristics, proved to be an efficient method to find the solution to the problem studied. Problems of nearly singularity, particular from BEM, were controlled by keeping a minimum distance between inclusions when rotated. The big number of project variables considered in this project rated the optimization problem as nonconvex, which means there is a huge possibility of great solutions. In this sense, as an alternative to the gradient methods, GA was used successfully in pursuing a possible global maximum point. The final results presented coherence with the objective of the multi-objective optimization proposal, which consisted in maximizing the thermal flow on the edge A and minimizing it on the edges B and C. In this meaning, the methodology employed was accepted as viable and can be extended to problems that consider thermal flows inside their domain.

REFERENCES

[1] Andonova, A., kafadarova, N.; *PCB thermal design improvement through thermal vias*. WSEAS, Bulgaria. 2009.

[2] Brebbia, C. A.; Dominguez, J., *Boundary elements: an introductory course*, Computacional Mechanics Publications and McGraw-Hill, Southhampton, 1989.

[3] Brebbia, C.A.; *The Boundary Element Method for engineers*. London: Pentech Press, (1978). 188p.

[4] Brebbia, C.A.; Telles, J.C.F.; Wrobel, L.C. *Boundary Element Techniques: theory and applications in engineering*. London: Springer - Verlag, (1984). 352p.

[5] Castro, R.E.; *Otimização de estruturas com multi-objetivos via Algoritmos Genéticos*. Rio de Janeiro, 2001, 206 p. (COPPE/UFRJ, D.Sc., Engenharia Civil, 2001). Tese – Universidade Federal do Rio de Janeiro, COPPE.

[6] Dede, E.M.; *Simulation and optimization of heat flow via anisotropic material thermal conductivity*, Computational Materials Science, 50 (2), 510-515, (2010).

[7] Guoquan, R; dongwei, LI.; yingqi, J.; *Modal Analysis of the printed circuit board based on Finite Element Method*. International Conference on Computer Science and Eletronic Technology (ICCSET), 150-154, (2014).

[8] Khaji, N.; Hamzehei, S.; *New complex fourier shape functions for the analysis of two-dimensional potential problems using boundary element method*. Computational Materials Science, 37, 260-272, (2013).

[9] Silva, E. R.; *Otimização de estruturas de concreto armado utilizando Algoritmos Genéticos.* São Paulo, 2011. 131p. (Escola Politécnica da Universidade de São Paulo. Departamento de Engenharia de Estruturas e Fundações). Dissertação (Mestrado).

[10] Takahama, T., Sakai, S., Ichimura, T., Isomichi, Y.; *Structural optimization by Genetic Algorithm with degeneration (GAd).* Wiley Periodicals, Inc. Syst Comp Jpn, 35(5):32-43-(2004).

[11] Wrobel, L. C.; *Boundary Element Method - Volume 1*. John Wiley & Sons. Ltd, England, 2002.

VII International Conference on Computational Methods for Coupled Problems in Science and Engineering
COUPLED PROBLEMS 2017
M. Papadrakakis, E. Oñate and B. Schrefler (Eds)

SIMULATION OF MACROSEGREGATION BENCHMARK ON A NON-UNIFORM COMPUTATIONAL NODE ARRANGEMENT WITH A MESHLESS METHOD

VANJA HATIĆ[*] AND BOŽIDAR ŠARLER[*] [†]

[*] Institute of Metals and Technology
Lepi pot 11, 1000 Ljubljana, Slovenia
e-mail: vanja.hatic@imt.si, web page: http://www.imt.si

[†] University Ljubljana, Faculty of Mechanical Engineering
Aškerčeva 6, 1000 Ljubljana, Slovenia
Email: bozidar.sarler@fs.uni-lj.si - Web page: http://www.fs.uni-lj.si

Key words: macrosegregation benchmark, columnar solidification, segregation prediction, meshless method, diffuse approximate method.

Abstract. An application of a meshless numerical method on a macrosegregation benchmark case is developed in the present paper. The test case is solidification in 2D rectangular cavity, filled with liquid metal and chilled from both sides. This is a highly non-linear problem due to a strong coupling of the macroscopic transport equations with the microsegregation model. The main result is the macrosegregation pattern of the solidified metal Al4.5wt%Cu alloy is used for evaluation of the problem. The model uses diffuse approximate meshless method with the second-order polynomial basis for spatial integration and explicit time-stepping. Simulations are performed on uniform and non-uniform computational node arrangements and compared to each other. The results on uniform and non-uniform node arrangements show a very good matching with the finite volume method results and results based on radial basis function collocation method. This shows that diffuse approximate method based on non-uniform node arrangements can be used for solving macrosegregation problems.

1 INTRODUCTION

Macrosegregation is a chemical inhomogeneity of the composition on the macro-scale level [1]. It is an undesired consequence of solidification and one of the major casting defects. Modelling of macrosegregation is therefore highly important for metallurgical and casting industries. Macrosegregation is a consequence of microsegregation, as during the solidification, the solute is pushed out from solid phase to the liquid phase (or vice versa). The solute is then transported from microscopic to macroscopic scale by the relative movement of the liquid and the solid phase in the transition region. There are different mechanisms which are connected with the macroscopic transport of solute. The main mechanisms are the convection-driven macrosegregation, shrinkage-driven macrosegregation, deformation driven macrosegregation, effect of floating grains, and effect of forced flow. Their magnitude and direction can work on different levels and in various directions.

The simulation of macrosegregation patterns is a complex, non-linear problem and involves solution of a coupled heat, mass and species transfer, phase change, and flow phenomena. Furthermore, the transport equations are coupled with the microsegregation model. One of the goals of our research group is to model macrosegregation for direct chill and low-frequency electromagnetic casting with a meshless method [2], [3]. The model for simulation of heat and momentum transfer for this kind of problems has already been developed [4]. The new meshless model for simulation of macrosegregation is in the process of development and is evaluated on a 2D test case, presented in this paper. The numerical benchmark is a 2D ingot solidification of a binary alloy, which has been proposed by Kosec et al. in [5]. In the paper authors presented results obtained with the classical finite volume method (FVM) [6] and meshless local radial basis function collocation method (LRBFCM) [7]. The same problem is solved by the diffuse approximate method (DAM) on a non-uniform node arrangement in the present paper. This is probably the first attempt to solve such kind of problems on non-uniform node arrangement.

2 MODEL FORMULATION

A volume-averaging method is used to model the transport equations. The method assumes that the mushy zone consists of two phases without voids. Each phase is described on the microscopic scale. The conservation equations are therefore derived microscopically and along with the interface boundary conditions make an appropriate description of the solidification process. The averaging of the equations over the representative elementary volume (REV), results in a model that can be used for solving practical problems.

The equations for simulation of the benchmark are simplified to the largest possible degree in order to enable easier comparison of different numerical procedures. The liquid phase is modelled as an incompressible Newtonian fluid. Laminar flow is assumed. Model assumes that the solid and the liquid densities are constant and equal for each phase. The buoyancy effect of density differences is modelled with the Boussinesq approximation. The solid phase is static. The mushy zone is modelled with the Kozeny-Carman relation for the porous flow. The dynamic viscosity of the liquid is assumed to be constant. The diffusion of the species conservation equation on the macroscopic level is neglected for both phases. Local thermal equilibrium is assumed in REV. The thermal conductivity and the specific heat capacity are assumed constant and equal in both phases. The lever rule is used to calculate the liquid volume fraction.

The following macroscopic equations are employed in the model [5]:

$$\nabla \cdot \mathbf{v} = 0, \tag{1}$$

$$\rho \frac{\partial \mathbf{v}}{\partial t} + \frac{\rho}{f_l} \mathbf{v} \cdot \nabla \mathbf{v} = -f_l \nabla p + \nabla \cdot \left(\mu \nabla \mathbf{v} \right) + f_l \mathbf{b} + f_l \frac{\mu}{K} \mathbf{v} ; \tag{2}$$

$$K = K_0 \frac{f_l^3}{\left(1 - f_l\right)^2} ; \; \mathbf{b} = \rho \left(1 - \beta_T \left(T - T_{\text{ref}}\right) - \beta_C \left(C_l - C_{\text{ref}}\right)\right) \mathbf{g} ,$$

$$\rho\frac{\partial h}{\partial t}+\rho\mathbf{v}\cdot\nabla h_l=\nabla\cdot\left(\lambda\nabla T\right), \tag{3}$$

$$\frac{\partial C}{\partial t}+\mathbf{v}\cdot\nabla C_l=0, \tag{4}$$

where t is time, $\mathbf{v}$ is the mixture velocity, ρ is the density, f_l is the liquid volume fraction, p is the pressure, μ is the dynamic viscosity, K_o is the Darcy constant, β_T and β_c are the temperature and concentration volume expansion coefficients, respectively, T is temperature, T_{ref} is the reference temperature, C_l is the liquid concentration, C_{ref} is the reference concentration, $\mathbf{g}$ is the gravity acceleration vector, h is the mixture enthalpy, h_l is the liquid enthalpy, λ is the mixture thermal conductivity, and C is the mixture concentration.

The following microscopic relations are used to calculate the macroscopic values [5]:

$$\mathbf{v}=\mathbf{v}_l f_l, \tag{5}$$

$$h=c_p T+L_f, \tag{6}$$

$$C=\left[f_l+\left(1-f_l\right)k_p\right]C_l, \tag{7}$$

$$T=T_f+m_l C_l. \tag{8}$$

where L_f is the latent heat of fusion, k_p is the partition coefficient, c_p is the specific heat capacity, T_f is the fusion temperature of pure metal, and m_l is the liquidus slope. Note that the equations (3) and (6) are different then in [5] as there was a misprint in the original paper.

3 NUMERICAL BENCHMARK DEFINITION

The geometry of the benchmark case represents a static ingot, with dimensions 2x2 cm, solidifying in a mould. The heat is extracted through the vertical walls. The top and the bottom walls are thermally insulated. The solidifying metal is Al4.5wt%Cu alloy, with the material properties given in Table 1. The duration of the simulation is 50 s.

The initial temperature and concentration are constant and set to 700 °C and4.5 wt%, respectively. The liquid metal is at rest at the beginning of the simulation. The geometry and the boundary conditions are symmetrical along the y axis, therefore only the right half of the ingot solidification is modelled. The symmetry boundary conditions are imposed for all fields on the west boundary. Dirichlet type boundary condition with boundary value equal to 4.5 wt% is imposed for concentration field on the remaining boundaries. The no-slip boundary condition is imposed on the remaining boundaries for the velocity field. The north and south boundaries are thermally insulated and the temperature gradient in the normal direction is equal to zero in these boundary nodes. The east, cooled boundary, is modelled with Fourier type of boundary condition, where the heat transfer coefficient is equal to 500 W/m^2/K and the external temperature is equal to 20 °C.

Table 1: Material properties of the Al4.5wt%Cu alloy used in simulation.

Property	Symbol	Unit	Value
Specific heat capacity	c_p	J/kg/K	$1\ 10^3$
Thermal conductivity	λ	W/m/K	$1.92\ 10^2$
Density	ρ	kg/m^3	$2.45\ 10^3$
Dynamic viscosity	μ	kg/m/s	$1.2\ 10^{-3}$
Gravity acceleration	g	m/s^2	9.80
Darcy constant	K_0	m^2	$5.56\ 10^{-11}$
Latent heat	L_f	J/kg	$4.00\ 10^5$
Fusion temperature	T_f	°C	660.00
Eutectic temperature	T_e	°C	548.00
Eutectic concentration	C_e	wt%	32.60
Liquidus slope	m_l	°C/wt%	-3.43
Partition coefficient	k_p	-	0.173
Thermal expansion coefficient	β_T	1/K	$1.3\ 10^{-4}$
Solutal expansion coefficient	β_C	1/wt%	$-7.3\ 10^{-3}$
Reference temperature	T_{ref}	°C	465.00
Reference concentration	C_{ref}	wt%	4.50

4 MESHLESS NUMERICAL PROCEDURE

A meshless numerical approach is used to perform the spatial discretization. Meshless methods [2], [3] have been in development in the recent decades and have already been applied to a wide range of physical problems [7]–[12]. The main benefit of the meshfree methods is that they do not require generation of elements, which are connected together by nodes in a complex predefined procedure, as it is the case with the classical numerical methods. The computational node arrangement can instead be created with less care. The computational nodes can be unstructured, which enables straightforward coping with irregular and more complicated computational domains [13].

4.1 Diffuse approximate method

Out of many available meshless methods, the diffuse approximate method [4], [8], [9], [13] is used to calculate the presented results. The weighted least squares are used to determine locally smooth and differentiable approximation of discrete data given in the computational nodes. The approximation $\hat{f}^k$ in the chosen node k is evaluated with the following expression:

$$\hat{f}^k(\mathbf{x}) = \mathbf{p}(\mathbf{x}, \mathbf{x}_k)\boldsymbol{\alpha}^k = \sum_{j=1}^{m} p_j(\mathbf{x}, \mathbf{x}_k)\alpha_j{}^k , \tag{9}$$

where $\mathbf{x}_k$ is the position vector of point k, $\mathbf{p}(\mathbf{x},\mathbf{x}_k)$ is the polynomial basis vector of order m and $\boldsymbol{\alpha}^k$ is the vector of coefficients. The quadratic polynomial base is used in the present simulations. The approximation of the solution (9) is obtained with the minimization of the expression:

$$J = \sum_{i=1}^{n} \theta(\mathbf{x}_i,\mathbf{x}) \left[f(\mathbf{x}_i) - \hat{f}(\mathbf{x}_i) \right]^2 , \tag{10}$$

where n is the number of nodes in the computational domain and θ is the Gaussian weighting function, which has a peak value of 1 at the chosen node k and is decreased with the Euclidian distance from this position. The vector of coefficients is obtained with solution of equation:

$$\sum_{i=1}^{n} \sqrt{\theta(\mathbf{x}_i,\mathbf{x}_k)}\mathbf{p}(\mathbf{x}_i,\mathbf{x}_k)\,\boldsymbol{\alpha}^k = \sum_{i=1}^{n} \sqrt{\theta(\mathbf{x}_i,\mathbf{x}_k)} f(\mathbf{x}_i) . \tag{11}$$

4.2 Space and time discretization

An explicit Euler time-stepping scheme is used for time integration. The time-step size is equal to 5 10^{-5} s and is chosen in accordance with the Courant-Friedrichs-Lewy and the Von Neumann stability conditions.

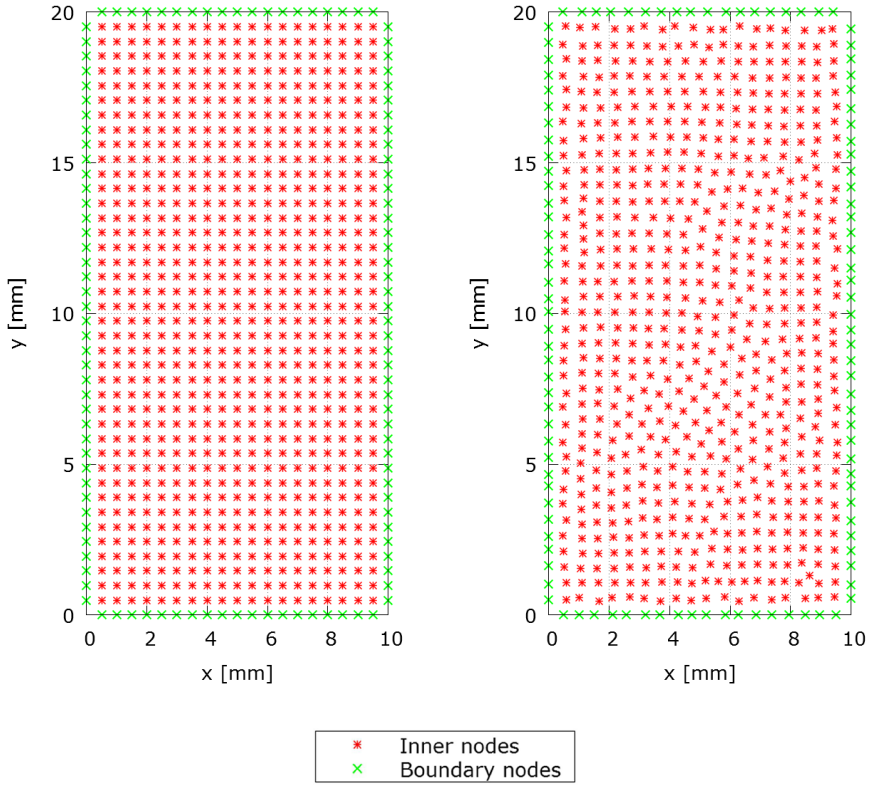

Figure 1: Examples of computational node arrangements used in simulations. Left : Uniform distribution with 878 nodes (21x41). Right : Non-uniform distribution with 754 nodes.

The evaluation of the conservation equations is performed locally. This means that the approximation is evaluated on a small portion of the global domain. Instead of using all the points (n), only a small amount of points (n_{loc}) is used for the approximation. Hence, each computational node of the global domain is assigned with its own local subdomain. The number of nodes in the local neighbourhood has to at least match the size of the basis vector, which is equal to 9 for the case of quadratic polynomial base. The solution (eq. 9) can be unstable for too small subdomains, if the nodes are arranged non-uniformly. Therefore, 13 nodded local neighbourhoods are used.

Two different computational node arrangements are used in simulations. The regular equidistant node arrangement is compared to the non-uniform node distribution. Sample distributions are shown on Figure 1. Simulations are performed on uniform distributions of two different densities 21x41 and 121x241. Non-uniform node distribution densities are chosen in such a way, that they roughly match the uniform ones.

4 RESULTS

The results are tabulated and compared to the finite volume and local radial basis function collocation method solution [5]. The final segregation pattern, after 50 s of simulation time is shown in Figure 2.

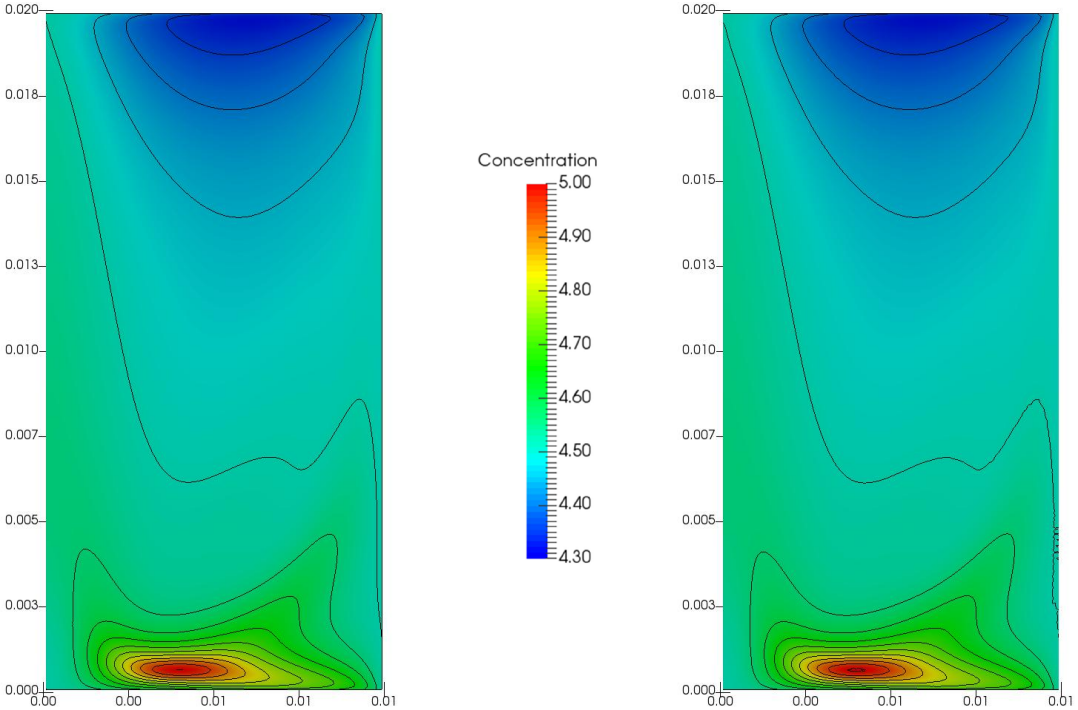

Figure 2: Macrosegregation pattern at the end of solidification for the computational node arrangement 121x241. The figure shows the concentration contour plot after 50 s of solidification. Left: results with the uniform distribution. Right: results with the non-uniform distribution.

The agreement with the reference results is tested in 66 reference points (see [5] for details on their positions) and is very good for both types of node distribution.The root-mean-square deviation, regarding the FVM, is equal to $1.99\ 10^{-3}$ for the uniform and $1.94\ 10^{-3}$ for the non-uniform distribution. The maximum relative difference is equal to $1.27\ 10^{-3}$ and $1.23\ 10^{-3}$ for the uniform and for the non-uniform node distribution, respectively.

As one can see the DAM application of the macrosegregation benchmark on the uniform and the non-uniform node distribution gives the results of the same quality. Furthermore, a comparison with the FVM and LRBFCM results show a very good agreement.

5 CONCLUSIONS

A meshless diffuse approximate method is applied to the 2D columnar solidification of a binary alloy benchmark problem. The simulations are performed on uniform and non-uniform computational node arrangements with different number of computational nodes. The results are compared to the solutions obtained by other methods [5]. DAM is for the first time used to calculate macrosegregation and the described benchmark. The results of the presented method are in a very good agreement with the other models. Furthermore, it is demonstrated that the solution is almost identical for calculations on uniform and non-uniform node distributions. The benchmark test is evaluated in order to confirm the basic model for segregation prediction, which includes only the effects of convection-driven macrosegregation. In the future, the model will be upgraded with the inclusion of the floating-grains effects and used to simulate macrosegregation in direct chill and low-frequency electromagnetic casting of aluminium-alloy billets.

ACKNOWLEDGEMENTS

This work was supported by the Slovenian Research Agency, grant number J2-7384 (BŠ) and the Young Researchers programme (VH).

REFERENCES

[1] Ludwig, A., Wu, M., and Kharicha, A. On Macrosegregation. *Metall. Mater. Trans* (2015) **A 46**:4854–4867.

[2] Liu, G.R. *Mesh Free Methods: Moving Beyond the Finite Element Method* . CRC Press (2009).

[3] Li, H., and Mulay, S.S. *Meshless Methods and Their Numerical Properties*. CRC Press (2013).

[4] Košnik, N., Guštin, A.Z., Mavrič, B., and Šarler, B. A multiphysics and multiscale model for low frequency electromagnetic direct-chill casting. *IOP Conf. Ser. Mater. Sci. Eng.* (2016) **117**:012052.

[5] Kosec, G., Založnik, M., Šarler, B., and Combeau, H. A meshless approach towards solution of macrosegregation phenomena. *Comput. Mater. Contin.* (2011) **22**:169–195.

[6] Založnik, M., and Šarler, B. Modeling of macrosegregation in direct-chill casting of aluminum alloys: Estimating the influence of casting parameters. *Mater. Sci. Eng.* (2005) **A413–414**: 85–91.

[7] Šarler, B., and Vertnik, R. Meshfree explicit local radial basis function collocation method for diffusion problems. *Comput. Math. Appl.* (2006) **51**:1269–1282.

[8] Sadat, H., and Prax, C. Application of the diffuse approximation for solving fluid flow and heat transfer problems. *Int. J. Heat Mass Transf.* (1996) **39**:214–218.
[9] Amaouche, M., Bouda, F.N., and Sadat, H. The onset of thermal instability of a two-dimensional hydromagnetic stagnation point flow. *Int. J. Heat Mass Transf.* (2005) **48**:4435–4445.
[10] Šarler, B. A radial basis function collocation approach in computational fluid dynamics. Cmes-Comput. *Model. Eng. Sci.* (2005) **7**:185–193.
[11] Kosec, G., and Šarler, B. Solution of a low Prandtl number natural convection benchmark by a local meshless method. *Int. J. Numer. Methods Heat Fluid Flow* (2013) **23**:189–204.
[12] Vertnik, R., and Šarler, B. Solution of a continuous casting of steel benchmark test by a meshless method. *Eng. Anal. Bound. Elem.* (2014) **45**:45-61.
[13] Hatić, V., Mavrič, B., and Šarler, B. Simulation of direct chill casting under the influence of low frequency electromagnetic field. *Proceedings of the 25th Anniversary International Conference on Metallurgy and Materials* (2016) p. 62.

VII International Conference on Computational Methods for Coupled Problems in Science and Engineering
COUPLED PROBLEMS 2017
M. Papadrakakis, E. Oñate and B. Schrefler (Eds)

IMPROVED THEORY OF THE COMBINED DRY FRICTION IN PROBLEMS OF AVIATION PNEUMATICS' DYNAMICS

ALEXEY A. KIREENKOV[*†]

[*] Institute for Problems in Mechanics of Russian Academy of Sciences,
Prospekt Vernadskogo 101, korp.1, 119526 Moscow, Russia
[†] Moscow Institute of Physics and Technology (State University),
Institutskiy per. 9, Dolgoprudny, Moscow Region, 141701, Russia
e-mail: kireenk@ipmnet.ru, kireenk@mail.ru

Key words: theory of combined dry friction, shimmy phenomenon

Abstract. It is proposed further development of the theory of multi-component dry friction [1-9] which consists in presenting a more convenient form of the coupled friction models for the problems of the aviation pneumatics dynamics. The constructed dry friction theory allows one not only the analytical solution of model problems but also can be applied in the engineering practice, for instance to predict the shimmy if the sliding and spinning cannot be neglected [4, 9, 10.].

1 INTRODUCTION

The intensive oscillations of main landing gears were observed during operation of many modern aircrafts; sometimes these vibrations have damaged the structure of the landing gears and frames. The well known theories of shimmy are traditionally based on the non-holonomic model of wheels rolling [11]. The qualitatively different models were formulated on the groundwork of the dry friction theory [4, 9, 10.].

The friction force and torque are computed by the integration over the contact area so that the exact dynamically coupled integral model accounting the relationship of all the components of friction is obtained. After that, the exact model is replaced by approximated analytical models [8]. This approach in theories of shimmy was effectively used initially in the work [4] at the simplified suppositions that the distribution of the normal contact stresses inside of contact spot having circle form is obeyed by Herz law. Further development of this approach was presented in work [9]. In this work a new type of the approximate dry friction models for circle areas of contact were used and the real distribution of the contact stresses was taking in the account. Results obtained in work [9] are generalized in this paper for more realistic propositions about contact spots between tire and landing strip which, as supposed, are have axially symmetric convex forms.

The first coupled dry friction models for axially symmetric contact spots were presented in work [2]. These models were built on the assumption of validity of the classical Coulomb's law in differential form for small element of the area inside the contact spot. The exact integral models and their approximate analytical forms based on Pade expansions of the first and second order were constructed. Improvement these models were given in [6-7]. More convenient forms of the exact integral models were proposed by authors of this work. They also are taking into account more realistic presentation about normal pressure inside of contact spot, and approximate models were constructed with aid of a new type of approximations firstly used in [9]. The investigations presented below are based on results works [2, 5, 6, 7, 8, 9].

2 BASIC ASSUMPTIONS

The dry friction models, describing the interaction with the aircraft pneumatics runway are constructed for axially symmetric contact sites under the assumption that the Coulomb law in generalized differential form holds for the small surface element dS in the interior of the contact spot, according to which the differentials of the resultant vector $d\mathbf{F}$ and the moment of friction dM_C with respect to the contact spot center are determined by the formulae [8]:

$$d\mathbf{F} = -f\sigma\frac{\mathbf{V}}{|\mathbf{V}|}\left(1+\mu_1|\mathbf{V}|^3-\mu_2|\mathbf{V}|\right)dS,\ dM_C = -f\sigma\frac{\mathbf{r}\times\mathbf{V}}{|\mathbf{V}|}\left(1+\mu_1|\mathbf{V}|^3-\mu_2|\mathbf{V}|\right)dS, \tag{1}$$

$$\mathbf{V} = (v-\omega\eta,\omega\xi),\ \mathbf{r} = (\xi,\eta),\ \sigma = \sigma(\xi,\eta)$$

where f is the coefficient of friction, $\mathbf{r} = (x, y)$ is the position vector of an elemental area in the interior of the contact spot with respect to its center Fig. 1, ω is the angular velocity of rotation of the contact spot center, $\sigma(x, y)$ - distribution of the normal contact stresses, but μ_1 and μ_2 are the coefficients which can be defined in practice from experiments.

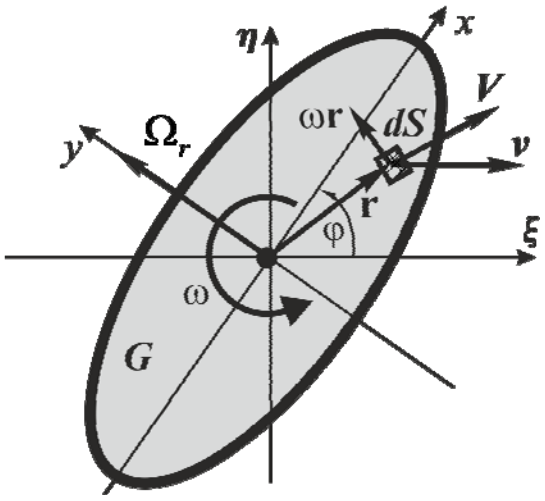

Figure 1: Kinematics inside of contact spot.

Necessity of using of the generalized differential form of the Coulomb law is caused by the numerous experimental investigations which are demonstrate that classic Coulomb law are

not valid even in differential form when contact spot sizes are strong differ from the ‘point contact’.

Formulas (1) demonstrate that two main factor – distributions of velocities and normal contact stresses inside of contact spot are influence on the corresponded force state.

Since the contact spot has axial symmetry, the distribution of normal contact stresses at rest will also have this property and, consequently, will be an even function of its arguments:

$$\sigma_0(-x,-y)=\sigma_0(x,y),\ \sigma_0(-x,y)=\sigma_0(x,y),\ \sigma_0(x,-y)=\sigma_0(x,y) \tag{2}$$

At presence of motion the tangent stresses are appears that lead to distortion in the symmetric diagram of the normal contact stresses distribution. The directions of the relative sliding (axis x) and rolling (axis ξ) are coincide in the case of ideal motion of aviation tyre, but from the shimmy phenomenon they differ on angle φ (Fig. 1).

Since the proposed model are considered as the next approximation of the models developed in [2, 3, 8, 9], then the shifting values of the symmetric diagram of normal contact stresses distribution along the directions of relative slip l and rolling s can be calculated independently (Fig. 2) with aid of results received in works [3, 9].

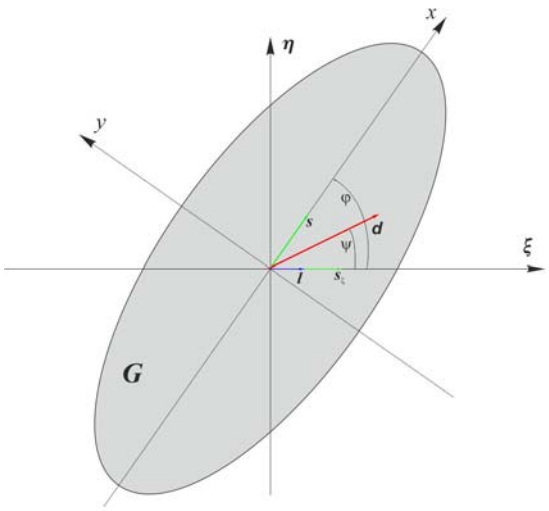

Figure 2: Shift of the center of gravity of the contact spot relatively of geometric center.

The shifting value of the gravity center of the contact spot relatively of the geometric center is described by the vector **d** (Fig.2), module of which is

$$d=\sqrt{s^2+2sl\sin(2\varphi)+l^2} \tag{3}$$

To use these results in the dynamics problems, it is proposed the simple asymptotic representations for the contact stresses distributions based on their general properties

$$\sigma(x,y)=\sigma_0(x,y)(1+d_x x+d_y y) \tag{4}$$

where R is the characteristic size of the area of contact, for instance, the diameter of the corresponded set at the plane $\{x,y\}$, but d_x and d_y are projections of the vector **d** on axes x and y, correspondently.

Since the coefficients μ_1, μ_2 and d_x, d_y are small parameters, their mutual influence is negligibly small in the approximation under consideration, and consequently, the corresponding products can be excluded from the formulas (1). Thus, we have substantial approximation to the real situation in dependence on the general properties of the normal contact stresses distribution and real differential characteristics of the friction law.

3 INTEGRAL DRY FRICTION MODEL

Integration of the corresponded differentials over the contact spot yields the resultant vector $\mathbf{F}$ of the friction force and torque $\mathbf{M_C}$:

$$\mathbf{F} = -f\iint\limits_G \sigma(\xi,\eta)\frac{\mathbf{V}}{|\mathbf{V}|}d\xi d\eta - f\iint\limits_G \sigma_0(\xi,\eta)\mathbf{V}\left(\mu_1\mathbf{V}^2 - \mu_2\right)d\xi d\eta,\ \ \mathbf{F} = (F_{\|}, F_{\perp})$$
$$\mathbf{M_C} = -f\iint\limits_G \sigma(\xi,\eta)\frac{\mathbf{r}\times\mathbf{V}}{|\mathbf{V}|}d\xi d\eta - f\iint\limits_G \sigma_0(\xi,\eta)\mathbf{r}\times\mathbf{V}\left(\mu_1\mathbf{V}^2 - \mu_2\right)d\xi d\eta \tag{5}$$

where $F_{\|}$ and $F_{\perp}$ denote the respective components of the resultant vector directed along the tangent and the normal to the trajectory of motion, but the boundaries of the integration area G are depended on the angle of rotation φ of the coordinate system $\{X,Y\}$ in which the integration area has fixed boundaries with respect to the coordinate system $\{\xi,\eta\}$.

Because modules of the friction torque M_C and normal force component $F_{\perp}$ are smaller then module tangent friction force component $F_{\|}$, as it is shown in previous works [], then influence of the nonlinearity in the differential form of Coulomb law and the distortion in symmetry of normal contact stresses distribution on the their expressions is negligibly small in the approximation under consideration, and consequently, formulas (5) can be rewritten in following form:

$$F_{\|} = F_{\|c} + F_{\|n},\ \ |\mathbf{V}| = \sqrt{v^2 - 2v\omega\eta + \omega^2(\xi^2+\eta^2)}$$
$$F_{\|c} \equiv f\iint\limits_G \sigma(\xi,\eta)\frac{v-\omega\eta}{|\mathbf{V}|}d\xi d\eta,\ \ F_{\|n} \equiv f\iint\limits_G \sigma_0(\xi,\eta)(v-\omega\eta)\left(\mu_1\mathbf{V}^2 - \mu_2\right)d\xi d\eta,$$
$$F_{\perp} = f\iint\limits_G \sigma_0(\xi,\eta)\frac{\omega\xi}{|\mathbf{V}|}d\xi d\eta,\ M_C = f\iint\limits_G \sigma_0(\xi,\eta)\frac{\omega(\xi^2+\eta^2)-v\eta}{|\mathbf{V}|}d\xi d\eta, \tag{6}$$

The orthogonal transformation of rotation on the angle φ:

$$\xi = x\cos\varphi - y\sin\varphi,\ \ \eta = x\sin\varphi + y\cos\varphi \tag{7}$$

enable to transit in formulas (6) to integration over area with fixed boundaries [2, 6, 7]. After this variables changes, expression for $F_{\|n}$ in formulas (7) can be significant simplify with the aid of well known fact that integrals will be zero in the case of a symmetric domain of integration and oddness of the integrand function by one of the arguments and has form:

$$F_{\|n} \equiv f(\mu_1 v^3 - \mu_2 v)\iint\limits_G \sigma_0 dxdy + f\mu_1 v\omega^2\iint\limits_G \sigma_0(2(x^2+y^2) + (y^2-x^2)\cos(2\varphi))dxdy \tag{8}$$

This part of the dry friction force component is polynomial, coefficients of which can be easy calculated if there analytical or numerical dependence of the normal contact stresses distribution $\sigma_0(x,y)$ in rest are known.

The other doubles integrals in formulas (6) can be investigated independently due to linearity of these expressions. In result of the change of variables (7) they have form:

$$F_{\|c} \equiv f\iint\limits_G \frac{\sigma_0(x,y)(1+d_x x+d_y y)(v-\omega(x\sin\varphi+y\cos\varphi))}{\sqrt{v^2-2v\omega(x\sin\varphi+y\cos\varphi)+\omega^2(x^2+y^2)}}dxdy \tag{9}$$

$$M_C = f\iint\limits_G \frac{\sigma_0(x,y)\omega(x^2+y^2)-v(x\sin\varphi+y\cos\varphi)}{\sqrt{v^2-2v\omega(x\sin\varphi+y\cos\varphi)+\omega^2(x^2+y^2)}}dxdy$$

$$F_\perp = f\iint\limits_G \frac{\sigma_0(x,y)\omega(x\cos\varphi-y\sin\varphi)}{\sqrt{v^2-2v\omega(x\sin\varphi+y\cos\varphi)+\omega^2(x^2+y^2)}}dxdy$$

These functions were been investigated in details for Hertz type of the normal contact stresses distributions for elliptic contact spots in [6, 7] and for arbitrary symmetric forms of the contact spots and symmetric distributions of the normal contact stresses in [2].

4 APPROXIMATED DRY FRICTION MODEL

The exact integral models gives a good description of the dry friction effects in the case of combined kinematics, but is inconvenient to be used in problems of dynamics, because it is required to calculate multiple integrals in the right-hand sides of the equations of motion.

Approximated analytical models makes it possible avoid this inconvenience. Procedure of the approximated models construction is based on the analytical properties of the double integrals (9) as functions of the velocities ω and v. One of the main among them are:

Property 1. Exact integral expressions (9) are homogeneous functions of the variables ω and v of zero order of homogeneity: $F_{\|c}(\lambda\omega,\lambda v) = F_{\|c}(\lambda\omega,\lambda v)$, $F_\perp(\lambda\omega,\lambda v) = F_\perp(\lambda\omega,\lambda v)$, $M_C(\lambda\omega,\lambda v) = M_C(\lambda\omega,\lambda v)$. Consequently, their approximations have to be the homogeneous functions of the variables ω and v of zero order of homogeneity. This fact significantly reduces the possible type of approximations, coefficients of which are defined from the behavior these functions as well as the behavior of their first derivatives at zero and at infinity.

Property 2. Expressions (9) have a singularity at the point $(\omega,v)=(0,0)$, because they do not have any limit at this point with respect to both of the variables ω and v. Approximated models have to be the same properties. In other case the physical sense of models will be violated.

In results, approximated model has form:

$$F_{\|c} = \frac{F_0 v}{\sqrt{v^2+a\omega^2}},\ F_\perp = \frac{v\omega^2}{\sqrt{v^6+b\omega^6}},\ M_C = \frac{M_0\omega}{\sqrt{\omega^2+mv^2}} \tag{10}$$

Formulas (10) show that difference of the contact spot form from circle is more strong influent on the dry frictional model than the distortion in the symmetric form of the normal contact stresses distribution.

If the normal contact stresses distribution in the absence of motion is defined by analytical or numerical functions [], then coefficients of the model (10) are calculated by following formulas:

$$F_0 = \iint_G \sigma_0(x,y)dxdy, M_0 = \iint_G \sigma_0(x,y)\sqrt{x^2+y^2}dxdy, \frac{1}{\sqrt{m}} = \frac{1}{M_0}\iint_G \sigma_0(x,y)(x^2\cos^2\varphi + y^2\sin^2\varphi)dxdy \tag{11}$$

$$\frac{1}{\sqrt{a}} = \frac{1}{F_0}\iint_G \frac{\sigma_0(x,y)(x^2\cos^2\varphi + y^2\sin^2\varphi)}{2\sqrt{(x^2+y^2)^3}}dxdy, \quad \frac{1}{\sqrt{b}} = \iint_G \frac{\sigma_0(x,y)(x^2-y^2)\sin 2\varphi}{2\sqrt{(x^2+y^2)^3}}dxdy$$

Thus, a problem of developing of the dry friction models for purpose of investigation of the aviation pneumatics dynamics is reduced to construction, as more realistic as possible, of the normal contact stresses distribution inside of contact spots. The first approximation of this construction is presented in [9].

ACKNOWLEDGEMENTS

This research was financially supported by the Russian Foundation for Basic Researches under grant No. 16-01-00809-a.

REFERENCES

[1] Zhuravlev, V.Ph. and Kireenkov, A.A. Padé expansions in the two-dimensional model of Coulomb friction, *Mech. Solids* (2005) **40**(2):1–10.

[2] Kireenkov, A.A. Three-dimensional model of combined dry friction and its application in non-holonomic mechanics. *Proc. 5th European Nonlinear Dynamics Conf. ENOC-2005*, Eindhoven, Netherlands (2005).

[3] Kireenkov, A.A. Coupled models of sliding and rolling friction, *Doklady Akademii Nauk* (2008) **419**(6):759–762.

[4] Andronov, V.V. and Zhuravlev, V.Ph. *Dry Friction in Problems of Mechanics (in Russian)*, NITs Reg. Khaot. Dinam., Moscow-Izhevsk (2010).

[5] Kireenkov, A.A. Coupled model of sliding and spinning friction, *Doklady Akademii Nauk* (2011) **441**(6):750–755.

[6] G. Kudra, J. Awrejcewicz. Approximate modelling of resulting dry friction forces and rolling resistance for elliptic contact shape, *European Journal of Mechanics - A/Solids* (2013)**, 42**: 358–375.

[7] J. Awrejcewicz, G. Kudra. Mathematical modelling and simulation of the bifurcational wobblestone dynamics, *Discontinuity, Nonlinearity, and Complexity* (2014), **3**(2): 123–132.

[8] Kireenkov, A.A. Further development of the theory of multicomponent dry friction. *COUPLED PROBLEMS 2015 - Proceedings of the 6th International Conference on Coupled Problems in Science and Engineering*, Venice, ITALY (2015), pp. 203-209.

[9] Kireenkov, A.A. and Zhavoronok, S.I. Coupled Dry Friction Models in Problems of Aviation Pneumatics' Dynamics, *Int. J. Mech. Sci.* (2017) DOI 10.1016/j.ijmecsci. 2017.02.004.

[10] Zhuravlev V.Ph., Klimov, D.M. Theory of the shimmy phenomenon, *Mech. Solids* (2010) **45**(3):324–330.

AUTHORS INDEX

This volume contains the full papers accepted for presentation at the VII International Conference on Computational Methods for Coupled Problems in Science and Engineering, COUPLED PROBLEMS 2017
(12 - 14 June 2017, Rhodes Island, Greece).

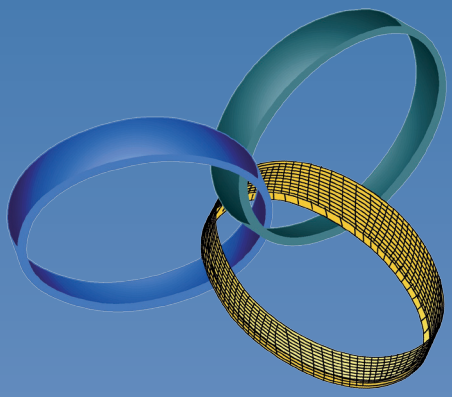

CIMNE
International Center
for Numerical Methods in Engineering

1304